Macromolecules

EDITORIAL

pubs.acs.org/Macromolecules

Editorial

The big event this year, as I am sure you are aware, is the launch of the new online journal *ACS Macro Letters*. Our aim is to provide the most rapid outlet for exciting new developments in all areas of modern polymer science, including highly interdisciplinary topics. As a consequence, *Macromolecules* will no longer be publishing Communications. Although over the past decade we have managed, with your help, to reduce the processing time and increase the rejection rate for Communications, we feel that the new journal can impart more visibility and with even faster turnaround. Submissions to *ACS Macro Letters* are handled by the new Deputy Editor, Dr. Stuart Rowan (Case Western), and two new Associate Editors, Theresa Reineke (University of Minnesota) and Christoph Weder (Fribourg). The community has already responded enthusiastically to the new launch; submissions are running well above the previous rate for Communications to *Macromolecules*. The first issue has just appeared, and I encourage you to visit the Web page for more information about the journal and to read the latest research reports (http://pubs.acs.org/journal/amlccd). Thanks in advance for submitting your best work and for contributing as reviewers to this new venture. The past year was also very successful for *Macromolecules*, with new records for the impact factor (4.838) and total citations (90 314), confirming our preeminent position in both quality and quantity.

Hiroshi Watanabe

In addition to the new editors associated with *ACS Macro Letters*, there have been changes in the editorial team at *Macromolecules*. I am sad to report that, after almost 12 years of distinguished service, Coleen Pugh (University of Akron) has decided to step down to devote her energies to a variety of other projects. We are, however, very pleased to announce that Professor Hiroshi Watanabe, Vice Director of the Institute of Chemical Research, Kyoto University, joined us in March 2011. Hiroshi is well-known for his work in rheology, dynamics, and structures of homopolymers, block copolymers, suspensions, emulsions, gels, and aggregating systems, and he is coauthor of over 250 papers on these topics. After earning his PhD at Osaka University in 1985 under Professor Tadao Kotaka, he was promoted to Assistant Professor in that Department. In 1994, he moved to Kyoto as Associate Professor and was made Full Professor in 2003. He has received many awards and recognitions, including the Japan Research Award from the Society of Rheology, Japan (1994), the Research Award from the Society of Polymer Science, Japan (2008), and Fellowship in the American Physical Society. He has also contributed his talents to the greater community in multiple ways, including as Director, Secretary, and currently Vice President of the Society of Rheology, Japan, and as Member-at-Large of the Executive Committee of the Society of Rheology (USA). I am particularly pleased to emphasize that Hiroshi represents the first Associate Editor for *Macromolecules* to be based in Japan, a country that has long been a strong leader in the field of polymer science.

Timothy P. Lodge
Editor

Published: January 10, 2012

dx.doi.org/10.1021/ma202477f | *Macromolecules* 2012, 45, 1–1

Macromolecules

PERSPECTIVE

pubs.acs.org/Macromolecules

Multicompartment Block Polymer Micelles

Adam O. Moughton,[†] Marc A. Hillmyer,[*,†] and Timothy P. Lodge[*,†,‡]

[†]Department of Chemistry and [‡]Department of Chemical Engineering and Materials Science, University of Minnesota, Minneapolis, Minnesota 55455-0431, United States

ABSTRACT: Multicompartment micelles are an intriguing class of self-assembled aggregates with subdivided solvophobic cores. They have been subject to extensive research in part due to their unique morphological and sequestration properties as a result of multiple distinct chemical environments being in close proximity within one nanostructure. Multicompartment micelles hold potential for use in various applications that include the therapeutic delivery of multiple incompatible drug payloads. The present Perspective reviews recent achievements in strategies for the synthesis, self-assembly, and morphological control of multicompartment micelles and highlights future challenges and potential applications.

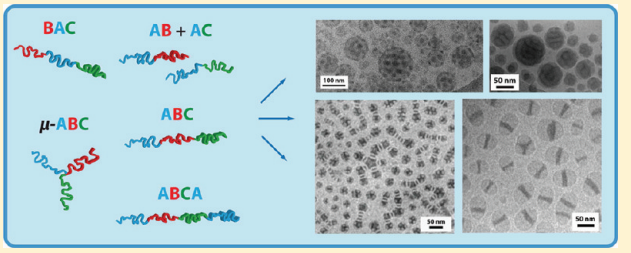

INTRODUCTION

Applications within the burgeoning field of nanotechnology have increasing requirements for new and complex materials with well-defined three-dimensional structure over the 1−1000 nm size range.[1] The self-assembly of synthetic molecules on surfaces or in solution are typical strategies for the production of such materials, and block polymers are a well-studied class of such building blocks due to their nanoscopic dimensions, ease of synthesis, and rich chemical variability.[2−5] In particular, block copolymers readily undergo microphase separation in selective solvents to form micelles, thus affording the opportunity to achieve discrete nanostructures through a spontaneous process.[6] By tuning copolymer properties such as the chemical structure of the monomers, the block molecular weights, and the copolymer architecture, a suite of micellar structures can be achieved. However, in general, an AB diblock copolymer in a selective solvent for the A block will adopt one of only three "classical" morphologies: spheres, cylinders, or bilayers, thereby producing spherical micelles, worm-like micelles, and vesicles, respectively. In each case the solvophobic B block will form a single nanoscale domain. If, on the other hand, a second solvophobic component C is included in the system, for example in an ABC block terpolymer, then it is possible to access many more elaborate structures, with subdivided B and C core domains. Such multicompartment micelles represent a significant step toward hierarchical self-assembly with multiple functions and designed architectural features on several length scales and as such hold great promise for advanced nanotechnological applications.

The concept of multicompartment micelles draws inspiration from naturally occurring blood proteins such as serum albumin, which provide circulatory transport for diverse and often sparingly soluble compounds such as lipids, hormones, vitamins, and metals.[7] Biological systems such as eukaryotic cells also possess subdivided domains, which have various physical and chemical properties and fulfill different cellular functions. These separate compartments often have different environments that are in close proximity and yet facilitate complex chemical and biological processes without mutual interference. A key distinction between eukaryotic and prokaryotic cells is that the former have a distinct nucleus containing their DNA, whereas the genetic material in prokaryotes is not membrane-bound. This is often considered to be one of the most important distinctions between the groups of organisms. The development of multicompartment micelles could therefore be said to advance the scope of current micellar morphologies from a prokaryotic to more of a eukaryotic level of sophistication.

The notion that multicompartment micelles could mimic such biological structures and features was proposed by Helmut Ringsdorf, as part of an overall vision to bridge the research disciplines of materials science and the life sciences.[8−10] As early as 1988, Ringsdorf stated that "polymer science is able to contribute to the simulation of cellular processes".[11] The advancement of multicompartment micelles is undoubtedly an important step toward achieving this goal and affords the prospect of accessing synthetic biological mimics in a facile and tailorable manner, while simultaneously opening up many opportunities within nanotechnology applications.

As the key feature of multicompartment micelles is the microphase separation within the hydrophobic core region of the micelle,[7,12] the discrete subdomains within the core can facilitate the concurrent storage and therapeutic delivery of multiple incompatible hydrophobic payloads in a prescribed stoichiometric ratio. However, crucially these phase-separated core regions must have markedly different solubility characteristics if they are to store cargo with differing chemistries.

Received: August 15, 2011
Revised: November 11, 2011
Published: December 12, 2011

The development and increased understanding of the underlying molecular level principles governing the self-assembly of block terpolymers into multicompartment micelles are of fundamental importance to the control and application of these hierarchical structures.

DESIGN CONSIDERATIONS

The synthesis of well-defined copolymers with fine control over molecular weight, composition, and architecture has become increasingly feasible due to tremendous advances in synthetic polymer chemistry.[5] Thus, the preparation of ABC linear and branched terpolymers, or even more complicated multiblock architectures, utilizing a wide range of monomers can be quite practical. From a design point of view, the most important step is to select B and C components that are sufficiently incompatible that they will segregate into distinct domains. (A will be the used as the solvophilic block and B and C will be used as the two incompatible solvophobic blocks throughout this Perspective).

By analogy with diblock copolymers in the bulk, when the product of the Flory–Huggins interaction parameter, χ_{BC}, and the total solvophobic degree of polymerization ($(N_B + N_C$, relative to a common reference segment volume) exceeds some value of order 10, one can anticipate that such segregation should occur (although other parameters, including architecture, composition, and degree of solvophobicity, will also influence the critical degree of polymerization). Overall, the number and spatial arrangement of the separate B and C domains, and thus the size and structure of the multicompartment micelles themselves, will depend on a variety of factors. Some of these may be also anticipated on the basis of what is already known for diblock systems.[13−21] For example, higher interfacial energy between the core block and the solvated corona favors flatter interfaces and larger core domains. The interfacial energy, in turn, depends on factors that include solvent choice, temperature, and pH. On the other hand, a larger corona block, or a more swollen corona block, favors higher interfacial curvature and smaller core dimensions. The stretching of the core blocks can also play a role, especially when the corona blocks are short (the so-called "crew-cut" micelle regime); core block stretching also favors smaller micelles.[13,14,22] This competition between interfacial energy and chain conformations produces the universal diblock sequence of spherical micelles → cylindrical micelles → vesicles, whether in water,[17,19,20] organic solvents,[23,24] carbon dioxide,[25,26] or ionic liquids.[27−29]

Under certain circumstances, a new regime of behavior can be accessed, the so-called "super strong segregation limit" (SSSL), which was first proposed by Semenov, Khokhlov, and coworkers.[30,31] Within the SSSL, the interfacial energy becomes so large as to overwhelm the entropic penalty to stretch the core blocks, leading to flat interfaces and fully stretched core blocks. One signature of the SSSL is the appearance of disk-like micelles, whereby the finite lateral dimension of such "flat" micelles allows some measure of crowding relief to the corona chains. Although it has been speculated that this regime is likely to be accessed only for charged systems, in fact, disk-like micelles have been found in certain fluorine-containing block polymers.[31,32]

Because of the extreme hydro- and lipophobicity of fluorinated blocks, triblock terpolymers containing both fluorinated and hydrocarbon chains in separate core forming blocks are often used to create multicompartment micelles. This internal segregation between fluorinated and hydrocarbon domains significantly enhances the role of interfacial energy and can push the system into the SSSL. The SSSL is therefore an important factor in dictating the resulting nanostructure for many multicompartment micelles.[31] However, the overall free energy balance is more complicated than for diblock copolymer systems, and no complete theoretical treatment has yet been developed.

If we take A as the solvophilic block, the resulting structure will depend not only on the lengths of the three blocks and the strengths of the two interfacial energies (i.e., between B and C and between B and solvated A) but also on the magnitude of the interfacial energy between C and solvated A. If this latter interfacial energy is too large, C blocks will be sequestered in the micelle interior, but if it is significantly smaller than the B/solvated A interfacial energy, there may be a tendency for B chains to be in the micelle interior, despite the mandatory presence of some B units at the solvated A interface. Thus, ABC and BAC triblocks of equal composition might adopt rather different morphologies. This complication notwithstanding, for linear terpolymers there will be a tendency to form core–shell–corona micelles, i.e., structures with concentric but separate A/B and B/C interfaces. This leads to a restricted class of multicompartment micelles, in that there are only two compartments, and a cargo sequestered within C may only be released through the B block. Nevertheless, experimentally it has been found that even linear block terpolymers can produce a rich variety of structures. The use of the ABC miktoarm star architecture, on the other hand, suppresses the formation of core–shell–corona structures, as the three domains (A, B, and solvated C) must meet along a curve in space. In this case the competition among the three interfacial energies and the relative block lengths can lead to a remarkably rich array of multicompartment micelles for a single polymer system.

Researchers have developed various strategies for the synthesis of multicompartment micelles. Each of these strategies results in different morphologies, depending on the spatial restrictions imparted by the terpolymer chain architecture, as illustrated in Figure 1.

CONCENTRIC CORE/SHELL/CORONA MICELLES FROM LINEAR ABC TRIBLOCK TERPOLYMERS

Micelles produced from linear ABC block terpolymers typically feature a concentric core–shell–corona or "onion-like" arrangement of three different polymer domains. Although this structure might not satisfy a strict definition of multicompartment micelle (since each compartment does not have independent access to the exterior of the micelle), it could certainly prove useful as a delivery vehicle, for example if the payload of the inner C core were delivered on a much longer time scale than that of the B shell. The relative ease with which linear ABC terpolymers may be synthesized might also enhance their potential for commercial exploitation; certainly, a plethora of linear ABC systems have been explored.[33,34]

In 1998, Yu and Eisenberg reported an early example of a linear ABC triblock terpolymer approach. A poly(styrene)-*b*-poly(methyl methacrylate)-*b*-poly(acrylic acid) (PS-*b*-PMMA-*b*-PAA) sample formed spherical, rod-like, and vesicular morphologies in various solvent systems, which included water mixed with organic solvents such as *N*′,*N*′-dimethylformamide or tetrahydrofuran.[35] Research within the scope of linear ABC triblock terpolymers for multicompartment micelle synthesis has included the incorporation of various stimuli responsive blocks

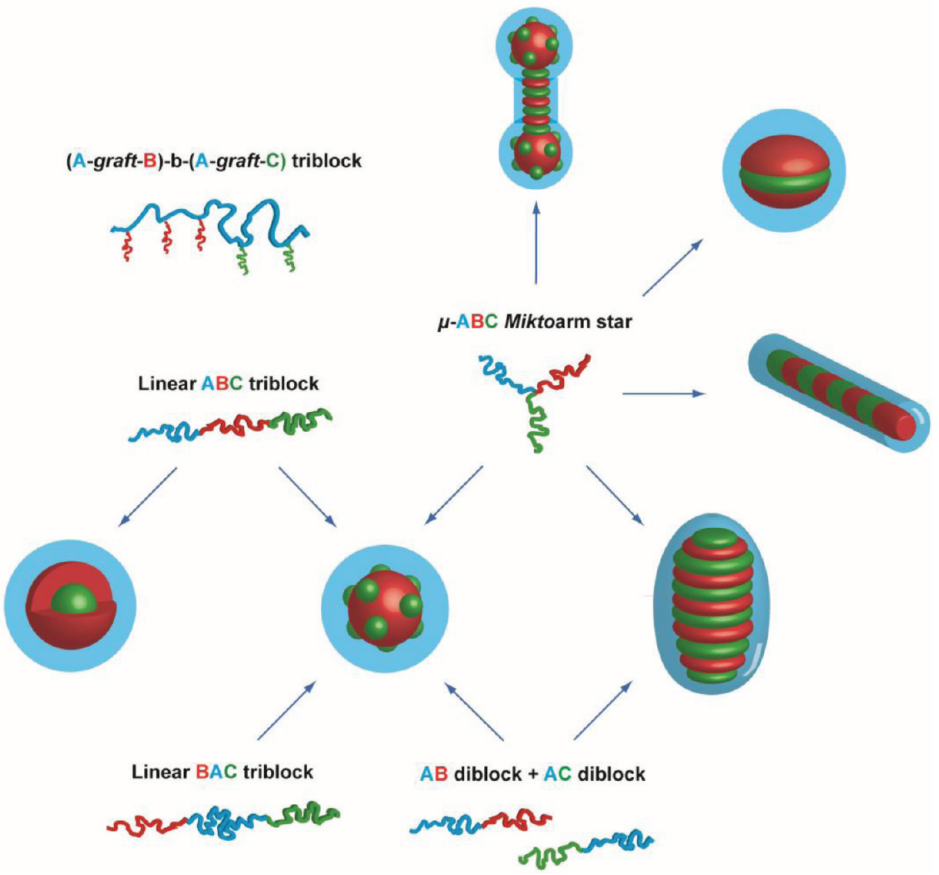

Figure 1. A schematic representation of the five principal strategies adopted for multicompartment micelle production with an illustrative example of the morphology produced.

into the copolymer design and the incorporation of pH-responsive blocks in particular. Jérome and co-workers examined a pH-responsive triblock terpolymer, PS-*b*-poly(2-vinylpyridine)-*b*-poly(ethylene oxide) (PS-*b*-P2VP-*b*-PEO), which self-assembles into core−shell−corona spherical micelles.[36] They showed that the P2VP shell within the three-layer micelle could contract and expand reversibly upon varying the solution pH. This structure may present opportunities to vary the permeability of the shell of onion-like micelles, in an analogous manner to other pH-responsive shell-containing nanostructures.[37]

In a further study, the P2VP shell layer of the aforementioned spherical and cylindrical onion-like micelles was selectively loaded with $AuCl_4^-$ ions.[36,38] These micelles were used as templates for the production of metal nanoshells or nanoparticles, with dimensions readily tuned by the molecular weight of the P2VP shell. They also studied the morphological evolution of PS-*b*-P2VP-*b*-PEO spherical micelles upon varying the solvent[38−40] and similar pH-responsive triblock terpolymer multicompartment micelles utilizing a miktoarm star architecture.[41] In related work, Liu and co-workers have investigated the self-assembly of linear ABC triblock terpolymers into core−shell−corona spherical micelles which displayed stimuli-responsive behavior in response to changes in both pH and temperature. The researchers also investigated the shell-cross-linking of the nanostructures. The cores and coronas of the shell cross-linked micelles also exhibited multiresponsive swelling/shrinking and collapse/aggregation behavior, respectively.[42] This line of research demonstrates the power of employing stimulus-responsive blocks.

Besides concentric spheres from linear ABC terpolymers, research aimed at core/shell/corona cylinders has produced some interesting nanostructures. Recently, the groups of Schubert and Gohy have demonstrated the microwave-assisted synthesis and subsequent self-assembly of linear ABC triblock terpolymers containing three incompatible blocks. Upon studying the morphology of the aggregates by cryo-TEM and DLS, vesicle and aggregated core−shell−corona cylindrical micelles were observed in solution (Figure 2).[43,44] Hu et al. observed twisted cylindrical micelles for a linear ABC triblock terpolymer, poly(glyceryl monomethacrylate)-*b*-poly(2-cinnamoyloxyethyl methacrylate)-*b*-poly(*tert*-butyl acrylate) or PGMA-*b*-PCEMA-*b*-P*t*BA. The researchers studied the morphological evolution from core−shell−corona like cylindrical micelles in water to twisted cylinders with segregated A and C coronal chains in water/methanol mixtures. They attributed the evolution toward the twisted cylinders at high methanol content to the increased space required to accommodate the segregated PGMA coronal chains, which were longer, better solvated, and more crowded than the P*t*BuA coronal chains.[45] The researchers also investigated the self-assembly of the same triblock system in organic solvents, which were selective for the A and C blocks. The triblock formed a rich variety of morphologies with patterns of the A and C chains on the surfaces of the vesicles and nanotubes.[46]

dx.doi.org/10.1021/ma201865s |*Macromolecules* 2012, 45, 2−19

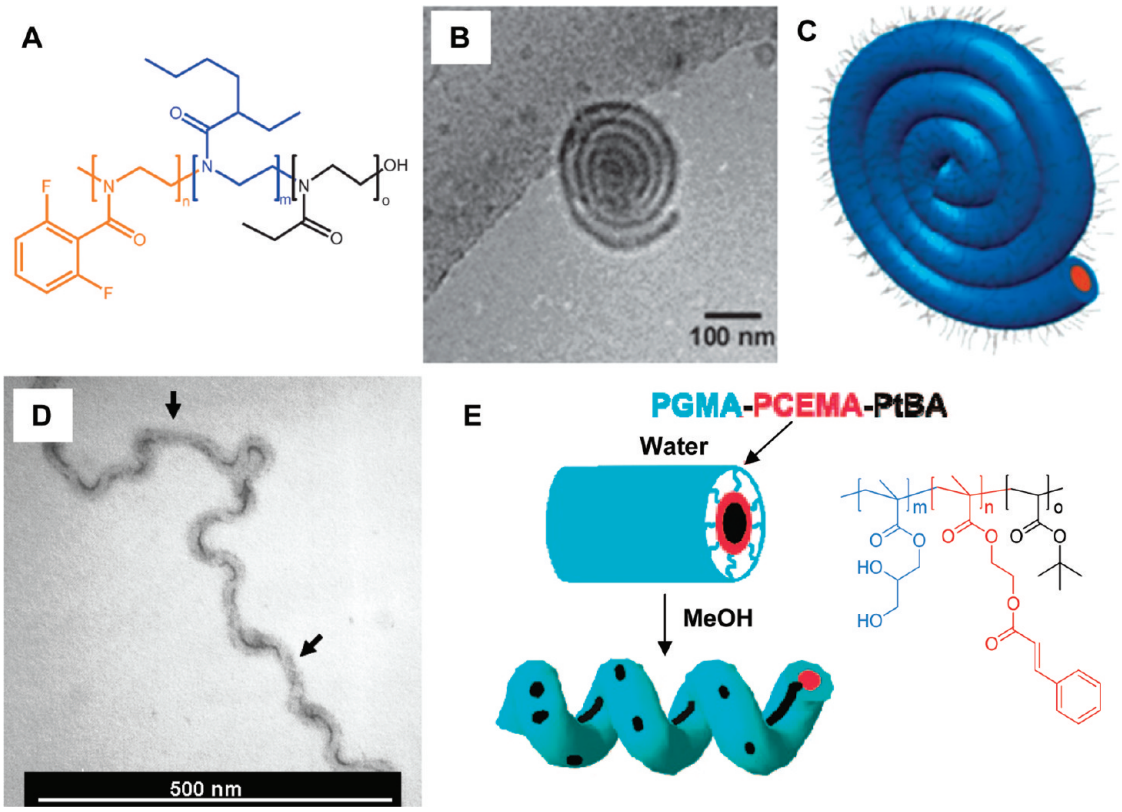

Figure 2. Core−shell corona type cylinders studied by various groups. The ABC triblock terpolymer investigated by Schubert and Gohy and co-workers (A).[44] Cryo-TEM image of spiral-like micellar aggregates made by the ABC triblock terpolymer in water (B) and (C) a schematic representation of the spiral-like aggregates. A cryo-TEM image (D) and schematic of the formation (E) of twisted cylindrical micelles as reported by Hu et al.[45] Reproduced with permission from refs 44 and 45. Copyright 2010 Royal Society of Chemistry and 2008 American Chemical Society.

Müller and co-workers have reported on a polyion complex system utilizing a linear ABC triblock terpolymer. They formed PB-*b*-P2VP-*b*-PMAA core−shell−corona spherical micelles with a PB core, a P2VP shell, and a PMAA corona. However, these concentric spheres evolved into spheres with a patchy shell domain when the middle block, P2VP, was quaternized prior to self-assembly giving a poly(*N*-methyl-2-vinylpyridinium) (P2VPq) shell and thus an ampholytic ABC triblock system. The micelles exhibited a noncontinuous shell due to intermicellar polyion complex formation between negatively charged PMAA coronal blocks and positively charged P2VPq shell blocks.[47] This illustrates a nice example of an evolution from concentric core/shell/corona micelles to more complex micellar nanostructures, with nonconcentric arrangements of their core domains, as will be discussed in detail in the next section.

This group has also studied the assembly behavior of a precursor block to the previous studied PB-*b*-P2VP-*b*-PAA system, a PB-*b*-P2VP-*b*-P*t*BuMA triblock terpolymer.[48] The researchers observed the formation of multicompartment micelles in acetone and studied the subsequent stabilization of the PB compartments with cross-linking of the double bonds. Cross-linking was carried out by "cold vulcanization" with S_2Cl_2 or by UV-photopolymerization in the presence of a tetrafunctional acrylate. The effect of the amount of cross-linking agent, the reaction time, or both on the size and the shape of the generated nanostructures was studied. Such cross-linking within multicompartment micelles represents a useful advance toward their utilization in therapeutic applications.[49]

COMPLEX MULTICOMPARTMENT MICELLES FROM LINEAR TRIBLOCK TERPOLYMERS

As mentioned above, the block sequence in linear triblocks, i.e., ABC, BAC, or ACB, can play a crucial role in dictating the self-assembly behavior and thus the distribution of the solvophobic B and C core domains.[50−53] Nonconcentric nanostructures with disperse and complex arrangements of the core domains have been found for various linear triblocks. Such structures are certainly anticipated for BAC triblocks in an A selective solvent, since the sequence permits the two hydrophobic blocks to form separate core domains surrounded by looping A coronal chains. Yet despite the conformational restrictions imparted by the sequence of linear ABC triblocks and their tendency to favor concentric nanostructures, they have also been shown to form nonconcentric nanostructures.

Laschewsky and co-workers have investigated the sequence of triblock terpolymers on the structure of multicompartment micelles in some detail.[51,54−56] Their first report in this area described the aqueous self-assembly of an ABC triblock terpolymer, poly(4-methyl(4-vinylbenzyl)morpholinium chloride)-*block*-poly(styrene)-*block*-poly(pentafluorophenyl-4-vinyl benzyl ether) (PVBM-*b*-PS-*b*-PVBFP).[54] The polymer consisted of a large volume fraction of a cationically charged block as the hydrophilic (corona forming) A component (PVBM) and two short hydrophobic B and C blocks that were selected for their incompatible nature which favors phase separation within the core: (PS) and a fluorinated block (PVBFP). This was an intriguing study since such a linear ABC terpolymer would be

dx.doi.org/10.1021/ma201865s |*Macromolecules* 2012, 45, 2−19

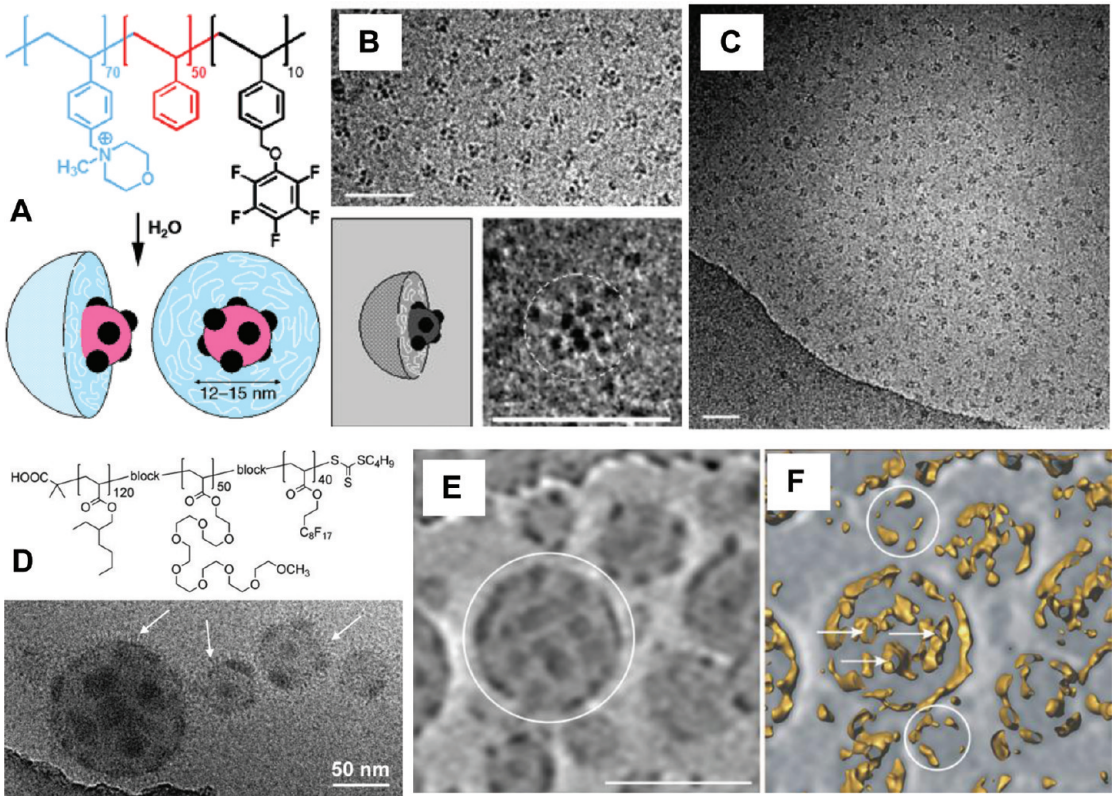

Figure 3. "Raspberry-like" micelles prepared by Laschewsky and co-workers, obtained by the self-assembly of ABC (A−C)[54] and BAC (D−F)[55] triblock terpolymers. (A) A schematic representation of the ABC morphology and (B, C) cryo-TEM images of the ABC nanostructures (scale bars are 50 nm). (D) Chemical structure of the BAC triblock and cryo-TEM images of the "soccer ball"-like micelles. (E) Cryo-TEM image (01-tilt projection) of different sized micelles. The encircled micelle was chosen for the 3D-volume representation in (F) (scale bar is 112 nm). (F) Central cross-sectional slice (5 nm thick) of the micelles' 3D-volume shown together with a surface representation (in gold) highlighting the fluorinated domains. Reproduced with permission from refs 54 and 55. Copyright 2005 Wiley-VCH Verlag GmbH & Co. KGaA and 2009 Royal Society of Chemistry.

expected to form spheres with a core/shell/corona arrangement of the three polymer domains. However, the researchers confirmed that the micelles contained compartmentalized core domains with a "raspberry-like" morphology consisting of small fluorinated PVBFP nodules ($D \approx 3$ nm) within a larger PS core ($D \approx 15$ nm), using cryo-TEM (cryogenic transmission electron microscopy) (Figure 3). The unexpected observation of a raspberry-like morphology was explained by the attachment of the fluorocarbon moieties to the side chain of a PS-like polymer (see Figure 3). Thus, they hypothesized that the fluorinated side chain segregated from the PS-like main chain of the PVBFP block, forming nodules of fluorine rich regions. In particular, the authors noted that this model could account for the core size measured by cryo-TEM, which correlated with the molecular volumes of the polymers.

Multicompartment micelles with a "soccer ball"-like dispersion of core domains were obtained from a linear BAC triblock terpolymer, poly(2-ethylhexyl acrylate)-*b*-poly(oligo-ethyleneglycol monomethyl ether acrylate)-*b*-poly(1*H*,1*H*,2*H*,2*H*-perfluorodecyl acrylate) or PEHA-*b*-POEGA-*b*-PFDA, with a middle hydrophilic (POEGA) A block forming looped coronas and enabling partitioning of the low-T_g B and C blocks. The researchers showed that the fluorinated domains of the PFDA block were dispersed around the hydrocarbon PEHA core.[55] This report is particularly significant since the structure and dispersion of the separate domains within the multicompartment micelles were investigated for the first time by cryo-electron tomography. This technique could be an invaluable tool for the future unambiguous characterization of the internal structure of multicompartment micelles. The use of linear BAC triblock terpolymers appears to be a promising advance for the application of multicompartment micelles, since nonconcentric nanostructures can be achieved using block polymers with a linear architecture. To this end, the self-assembly of a further linear triblock sequence, ACB (i.e., hydrophilic-*b*-fluorophilic-*b*-hydrophobic), into nonconcentric nanostructures has also been investigated recently by Marsat et al.[53]

More recently, the group of Laschewsky have investigated a library-based approach toward various linear ABC and BAC triblock terpolymers synthesized by successive RAFT polymerizations.[56] They studied the self-assembly of each terpolymer in water and proposed that the multicompartment micelles made from the specific block sequence BAC (i.e., lipophilic-*b*-hydrophilic-*b*-fluorophilic) was the most promising for selective solubilization applications. This was based upon the fact that the hydrocarbon (B) and fluorocarbon (C) domains were separate and yet both independently in contact with the corona, thus favoring the independent uptake and release of different incompatible compounds.

Laschewsky and co-workers have also reported linear ABC triblock terpolymers containing a crystalline fluorinated C block. The triblock self-assembled in water to form multicompartment micelles that were investigated with cryo-TEM. Interestingly, they again found extended, nonspherical domains within the

compartmentalized cores, which they ascribed to domains of the fluorinated block.[51] This novel internal structure was attributed to both the phase separation within the core and also the tendency of the fluorinated acrylate monomer to undergo side-chain crystallization. Crystallinity within micelle cores could be another handle for controlling micelle structure and function.[57]

We have observed elliptical domains in linear ABC triblock multicompartment micelles. We initially showed that a linear ABC triblock, poly(ethylene oxide)-*b*-poly(styrene)-*b*-1,2-poly(butadiene) (PEO-*b*-PS-*b*-PB) triblock terpolymer or "OSB", formed core−corona spherical micelles in aqueous solution, where the two hydrophobic blocks PS and PB were mixed homogeneously within the micelle core. However, selective fluorination of the PB block gave a PEO-*b*-PS-*b*-PB:$C_6F_{13}I$ triblock or "OSF" which upon self-assembly resulted in internally segregated micelles with concentric core/shell arrangement of the S and F domains. Furthermore, the strong incompatibility resulting from fluorination resulted in oblate ellipsoids due to the increased interfacial energy between the two internal core-forming blocks. The morphology was confirmed by light, neutron, and X-ray scattering measurements and cryo-TEM imaging.[58]

Several other research groups have investigated the self-assembly of linear ABC and BAC triblocks into more complex multicompartment micelles. Walther et al. studied the extent of *coronal* compartmentalization within micelles formed by a series of bis-hydrophilic ABC terpolymers with two outer water-soluble (A and C) segments, PEO and poly(*N*-isopropylacrylamide) (PNiPAm), and various middle hydrophobic B blocks.[59] The thermally induced collapse of the PNiPAm was exploited to artificially raise the incompatibility of the two coronal blocks and drive phase segregation. After repeated heating cycles, the solution of aggregates consisted of a range of multicompartment architectures, whose coronal phase distribution was derived from cryo-TEM studies of the aggregates obtained at high temperature. This report demonstrates how the relative incompatibility of the blocks within ABC triblocks can be modified according to an applied stimulus.

In early work, Spiess, Nuyken, and co-workers developed a novel strategy for the synthesis of two compartment micellar assemblies based upon the self-assembly of a poly(*N*-acylethyleneimine) that was end-capped with one fluorocarbon and one hydrocarbon chain to give a linear BAC triblock-like architecture. The researchers studied the aggregation behavior of the polymer by pyrene sequestration experiments and dynamic light scattering (DLS) measurements. They also found by ^{19}F NMR spectroscopy that the fluorocarbon chain ends formed pure fluorocarbon phases (indicating the formation of fluorinated subdomains within the cores and hence multicompartment micelles). However, this was only found when the hydrophilic "A" block length was long enough to allow the A chains to loop back on themselves, enabling the two end blocks to form separate B and C core domains.[60] In a related example, ^{19}F NMR spectroscopy analysis was applied to a linear BAB triblock system functionalized at the two A block termini with "B block" perfluoroalkyl units. As previously hypothesized by Spiess and Nuyken, the researchers confirmed that the partitioning of the perfluoroalkyl units into the core to achieve multicompartment domains depends on the length of the midblock chains. They found evidence with ^{19}F NMR spectroscopy that the perfluoroalkyl segments form part of the corona of the micelles in solution when the middle block lengths were too short to permit A chain looping.[61] Kubowicz et al. studied the self-assembly of chain end-capped poly(*N*-acylethyleneimine) homopolymers in more detail and found cylindrical multicompartmentalized micelles that could sequester a fluorinated small molecule in their interior.[62] Zhang et al. subsequently produced novel fluoroalkyl end-capped amphiphilic pH-responsive diblock copolymers that self-assembled into multicompartment micelles in aqueous solutions under basic conditions.[63]

Pochan and Wooley have investigated the formation of various complex morphologies including toroids, disks, and cylinders formed by linear ABC triblock terpolymers, specifically poly(styrene)-*b*-poly(methyl acrylate)-*b*-poly(acrylic acid) or PS-*b*-PMA-*b*-PAA triblocks. They have focused their research efforts on the formation of different morphologies by altering the solvent and terpolymer composition. In particular, they were also able to favor the formation of certain micellar morphologies, including concentric disk-like micelles by coassembly with organic cationic counterions, whereby the multivalency of the counterion was critical for disk formation. The counterion induced morphological evolution due to its interaction with the negatively charged PAA corona block, thereby altering the curvature of the triblock and hence preferred morphology. Using these different approaches, multicompartmentalized PS and PMA domains were observed in each of the identified morphologies.[64−68] Such strategies are particularly powerful given that various multicompartment morphologies may be accessed through the exploitation of different self-assembly conditions and additives for one linear ABC terpolymer system.[21]

Recently, Uchman et al. investigated an interesting ABC triblock terpolymer structure[69] consisting of a poly((sulfamate−carboxylate)isoprene)-*block*-poly(styrene)-*block*-poly(ethylene oxide), PISC-*b*-PS-*b*-PEO. This block was prepared by postpolymerization reaction of the anionically prepared precursor block terpolymer, PI-*b*-PS-*b*-PEO, with chlorosulfonyl isocyanate. The terpolymer formed kinetically trapped multicompartment micelles with the core consisting of PS and PISC domains and PEO in the shell. Upon increasing the pH, the micelles underwent an irreversible transition into spherical micelles, with a PS core and a mixed shell formed by the PEO and PISC blocks as revealed by cryo-TEM (Figure 4). Future work along these lines could be interesting, particularly when studying the morphological evolution of analogous terpolymers, but utilizing a core-forming hydrophobic block with a much lower T_g than PS, thus avoiding kinetically trapped aggregates.

Müller and co-workers utilized a postpolymerization fluorination reaction to selectively modify the side chain of a PB central block within a linear ABC block terpolymer (poly(4-*tert*-butoxystyrene)-*b*-poly(butadiene)-*b*-poly(*tert*-butyl methacrylate) (P*t*BS-*b*-PB-*b*-P*t*BMA).[70] The fluorination of the P*t*BS-*b*-PB-*b*-P*t*BMA block terpolymer altered the solubility of the middle PB block in dioxane. The modified block terpolymers formed spherical micelles with fluorinated PB cores and mixed coronas of P*t*BS and P*t*BMA chains. The mixed corona micelles then underwent microphase separation upon annealing, forming Janus-type corona spherical micelles and also spherical micelles with unequally distributed phase separation within the coronas. As a consequence of this coronal asymmetry, the micelles aggregated to form undulated cylinders when the solvent was changed to ethanol via dialysis. This aggregation minimized unfavorable interactions of the P*t*BS coronas with ethanol, and as such the P*t*BS chains embed within the cores of the newly formed

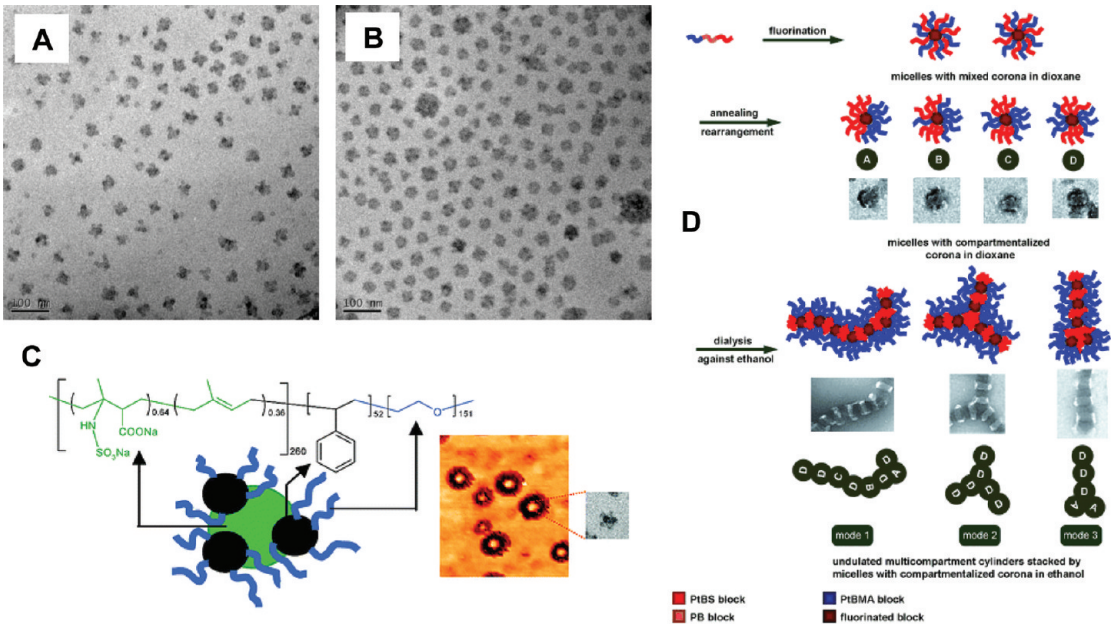

Figure 4. Cryo-TEM images of the PISC-*b*-PS-*b*-PEO micelles deposited from acidic solution (A) and pure water (B) and a schematic showing the relative disposition of each polymer domain with the nanostructures (C).[69] Preparation of undulated multicompartment cylinders by Müller and co-workers (D).[70] Reproduced with permission from refs 69 and 70. Copyright 2009 American Chemical Society and 2009 Wiley-VCH Verlag GmbH & Co. KGaA.

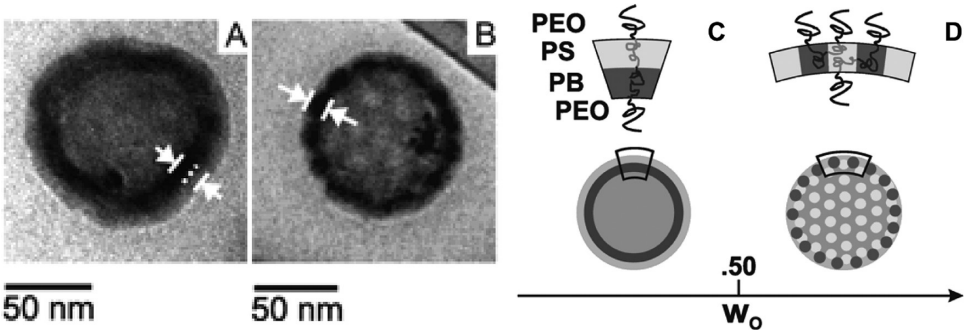

Figure 5. Representative cryo-TEM images of stained vesicles derived from OSBO with 36 wt % O block (A) and 52 wt % O block (B) (arrows indicate the vesicle wall thickness). In (A), the dotted line shows the vesicle wall division into a dark B layer and light S layer. The proposed structural models for the OSBO vesicles with the asymmetric bilayer model (C) and the in-plane ordered bilayer model (D) (dark and light regions correspond to B and S regions, respectively).[75] Reproduced with permission from ref 75. Copyright 2004 American Chemical Society.

cylinders with distinct branching points and end groups dictated by the orientation of the P*t*BS domain within the mixed corona (Figure 4). This development represents an exciting advance in the field of multicompartment micelles since the aggregation of multicompartment micelles appears to be tunable, and this concept may be particularly important for biomimicry, whereby the polydispersity, stability, and aggregation behavior of aggregates become important issues to consider. We note that while this represents an exciting advance, nonaqueous systems may compromise the efficacy of certain proposed applications of multicompartment micelles, and thus more development toward aqueous-based systems with these particular exciting features would be desirable.

Despite the tendency for linear ABC triblocks to form core−shell−corona type micelles, the work described in this section confirms that many researchers have developed various and interesting strategies to create nonconcentric arrangements of B and C core domains, e.g., utilizing a BAC triblock sequence. One strategy that has proved particularly useful is to alter and tune the self-assembly conditions to trap nonconcentric domains and interesting complex structures for ABC terpolymers, and this type of useful approach of modifying the self-assembly conditions has been the subject of a recent Perspective.[21] Such approaches have significantly expanded the morphological scope of multicompartment micelles from linear triblocks.

Many reports on ABC triblocks to date have also included stimuli-responsive A blocks within concentric structures, thus producing responsive coronas. There has also been similar work toward this end for BAC terpolymers, which also include reports of triply responsive structures.[71−74] It would be interesting to study a linear BAC terpolymer containing a charged A block and with neutral hydrophobic B and C blocks which may form quite different structures than a BAC triblock containing a neutral, but hydrophilic, A block. The charge on the A block may alter its

ability to loop back on itself due to repulsive electrostatic interactions on the chain which would prefer a more extended chain conformation, thus possibly influencing the distribution of separate B and C domains or even the morphology.

MULTICOMPARTMENT MICELLES FROM LINEAR MULTIBLOCK TERPOLYMERS

In the first example of a tetrablock strategy, Brannan and Bates prepared ABCA tetrablock terpolymer vesicles from PEO-*b*-PS-*b*-PB-*b*-PEO (or OSBO) terpolymers with varying PEO weight fractions.[75] The vesicles had microphase-segregated hydrophobic PS-*b*-PB cores and hydrophilic PEO coronas. The researchers studied the multidomain features of the PS-*b*-PB vesicle bilayers with classical staining techniques and cryo-TEM as shown in Figure 5. Interpretations of the cryo-TEM results were based on two vesicle structural models, which included vesicles with an in-plane (nonconcentric) bilayer or an asymmetric (concentric) bilayer. The in-plane bilayer was proposed to be either bicontinuously or hexagonally segregated with both PB and PS domains exposed to the inner and outer core/corona interfaces. They went on to propose that this particular bilayer structure is locked in a kinetically trapped state with the PB cylinders stabilized by the surrounding glassy PS domain. The multicompartment in-plane bilayer could be a useful route toward vesicles with a controlled distribution of recognition elements on their outer surface, tunable membrane permeation characteristics, and for the inclusion of incompatible agents within laterally segregated compartments of the membrane. Each PB and PS domain is also exposed to the exterior (as with other nonconcentric multicompartment micelle morphologies) and thus may facilitate the independent uptake and release of incompatible payloads.

Other examples of multiblock terpolymer micelles include the work of Thünemann et al., who synthesized a linear ABCBA pentablock terpolymer consisting of A blocks of PEO, B blocks of poly(γ-benzyl L-glutamate), and a poly(perfluoroether) central block, C. The different components were mutually immiscible and formed two-compartment micelles with a concentric core−shell−corona arrangement of polymer domains and predominantly cylindrical shapes in aqueous solution with cylinder lengths in the range 100−200 nm.[76] Tsitsilianis et al. also used the self-assembly of ABCBA pentablock terpolymers to give pH-tunable multicompartment spherical micelles and hydrogels.[77] This study extended their previous work on three-dimensional network-forming ABC triblock terpolymers.[78] Other research groups along with our own have also reported on multicompartmentalized hydrogels, which significantly expand the scope and utilization of the concept of multicompartmentalization within different nanostructured materials.[79−82]

The groups of Schubert and Gohy investigated the sequential and one-pot synthesis of well-defined triblock and tetrablock ter- and quarterpolymers using the ring-opening polymerization of 2-oxazolines under microwave irradiation, leading to well-defined poly(2-oxazoline) multiblocks.[83] Such an approach holds significant advantages for high throughput synthesis of terpolymers for self-assembly, given the difficulties typically associated with the stepwise synthesis and purification of multiblock terpolymers produced by other polymerization procedures. Upon self-assembly of the terpolymers in water, spherical micelles were found by atomic force microscopy (AFM), TEM, and DLS measurements. Given the incompatible nature of the blocks,

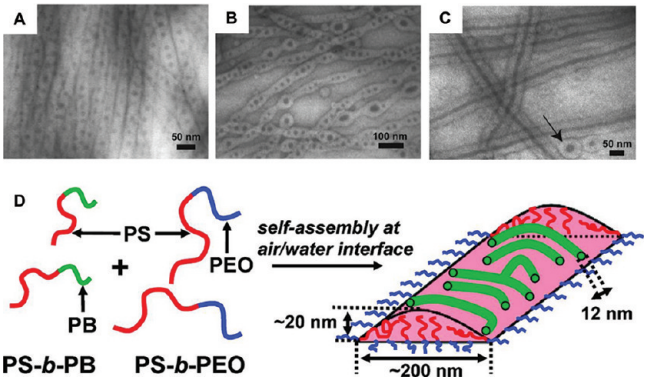

Figure 6. Bright field TEM images showing the evolution of structures of multicompartment wormlike micelles formed from blends of PS−PEO with PS−P2VP in weight ratios of (A) 80:20, (B) 70:30, and (C) 60:40 as reported by Zhu et al.[91] P2VP regions were stained dark by exposure to I_2 vapor. The worm-like micelles showed internal microphase separation into (A, B) spherical and (C) cylindrical P2VP cores surrounded by PS shells. (D) Strategy for the formation of polymeric strands with internal microphase separation utilized by Moffitt and co-workers.[92] Reproduced with permission from refs 91 and 92. Copyright 2008 and 2009 American Chemical Society.

multicompartment micelles were expected, and yet phase separation within the cores of the micelles was not observed. This observation was ascribed to the miscibility of the core-forming blocks due to their low molecular weights.[84]

Schubert and Gohy and co-workers also published two papers on multicompartment micelles from linear multiblock terpolymers (ABC and ABCD) with bis(terpyridine)ruthenium(II) metal−ligand interactions serving as a linkage between the A and B blocks.[85,86] In both studies, the researchers utilized a fluorinated block that displayed upper critical solution temperature (UCST) behavior in isopropanol; the polymer was found to be insoluble in isopropanol below 48 °C. As a result, the ABC triblock displayed interesting thermoreversible behavior in isopropanol, switching from vesicles below the UCST to spherical and cylindrical micelles above the UCST. Future development of this research area could be toward the utilization of the transition metals within the specific interfacial regions of multicompartment nanostructures for catalysis. Such supported catalysts may display unique activity or selectivity due to their location and proximity to different sequestration environments.[87,88]

MULTICOMPARTMENT MICELLES FROM BLOCK COPOLYMER BLENDS

Multiple compartments within a copolymer nanostructure have also been achieved through the blending of AB and BC block copolymers. This approach, while straightforward to carry out, is not generally successful due to the likelihood of macrophase separation. However, the ability to simply mix blocks in varying ratios does represent a powerful, yet straightforward way to systematically tune the resultant micellar structures without having to synthesize more complex multiblock terpolymers. Concentric core−shell corona[89] and nonconcentric nanostructures[90] have been achieved with this approach. A nice example of this strategy was investigated by Zhu et al., who produced worm-like micelles with microphase-separated cores from an (AB) diblock copolymer, PS-*b*-PEO, which was blended with various hydrophobic BC diblocks, including PS-*b*-P4VP, PS-*b*-PI,

dx.doi.org/10.1021/ma201865s |*Macromolecules* 2012, 45, 2−19

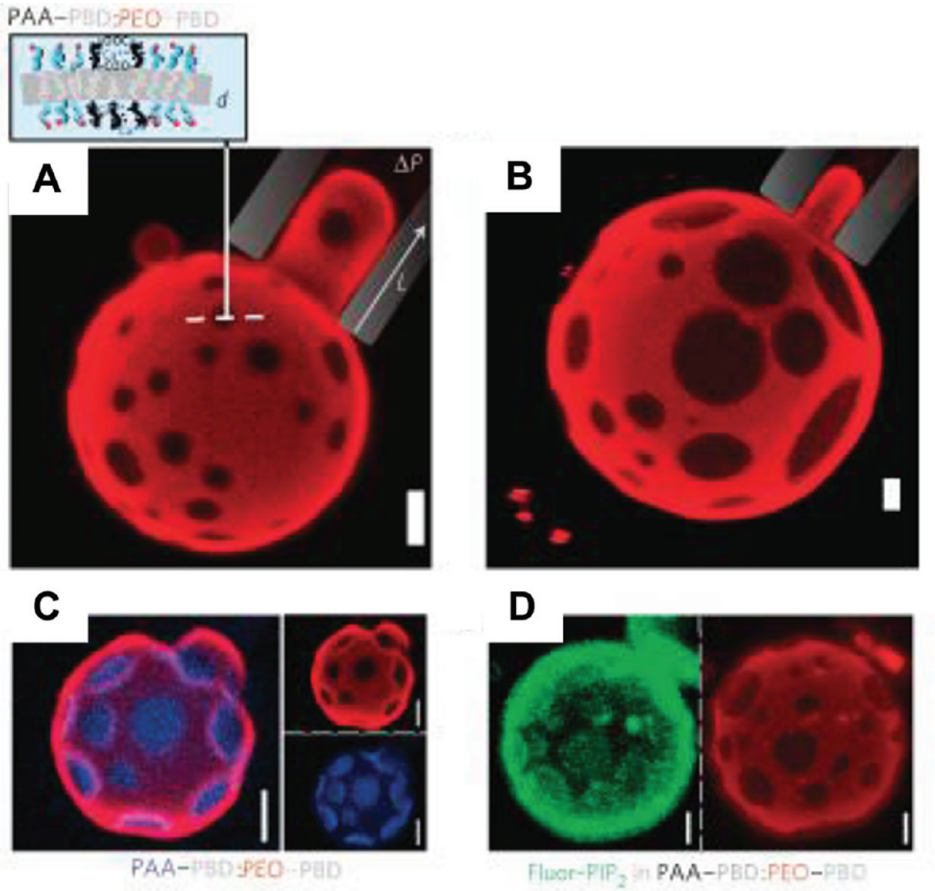

Figure 7. Spotted vesicle structures reported by Christian et al. by mixing two AB and BC diblock copolymers, PAA-*b*-PBD ("AB") and PBD-*b*-PEO ("OB") (A, B), cation-induced, lateral phase segregation of charged AB1 and neutral (fluorescently labeled) OB diblock copolymers at 25% (A) and 50% (B) of the diblock AB. The inset in (A) shows a schematic of a phase-separated membrane. (C) Two-color micrograph of a phase-separated polymersome with individual red (OB18*) and blue (AB1*) channel micrographs to illustrate the extent of demixing. (D) Individual channels for a two-color phase-separated polymersome (50% AB1) with 2% PIP_2—BodipyFL (green) enriched in dark AB1 domains and partially segregated from the OB18*-rich domains (red). Scale bars: 2 μm.[93] Reproduced with permission from ref 93. Copyright 2009 Nature Publishing Group.

and PS-*b*-PB, thus highlighting the versatility of this blending approach (Figure 6A—C).[91] Also, Moffitt and co-workers produced polymeric strands with internally microphase-separated structures produced by the self-assembly of a blend of PS-*b*-PEO and PS-*b*-PB (AB + BC) diblocks, which resulted in the spontaneous generation of aggregates with multicompartmentalized cores consisting of nanoscale cylinders within mesoscale strands (see Figure 6D).[92]

Patterned assemblies such as spotted vesicles and striped cylinders were prepared by Christian et al. by mixing two AB and BC diblock copolymers, PAA-*b*-PBD ("AB") and PBD-*b*-PEO ("OB"), in an aqueous medium.[93] Separate domain formation within the self-assembled aggregates was driven by the selective cross-bridging of the polyanion chains by divalent cations, thereby inducing demixing from the neutral domains, resulting in "ligand-responsive Janus assemblies". The resultant morphologies were remarkable, with spots or rafts within the vesicles and stripes within the cylinders (Figure 7). The lateral segregation within the assemblies was shown to couple weakly to amphiphile curvature and was restricted to narrow regimes of pH and cation concentration that were close to the binding constants for polyacid interactions.

Zheng et al. also utilized a copolymer blending strategy. The researchers prepared polymer spheres bearing hemispherical surface bumps where one type of polymer was concentrated. Their method was used to produce nano- and microspheres with bumpy surfaces with diameters between ca. 30 and ca. 500 nm.[94] The researchers also reported on the coaggregation behavior of a blend of poly(*tert*-butyl acrylate)-*block*-poly(2-cinnamoyloxyethyl methacrylate), P*t*BA-*b*-PCEMA, and polystyrene-*block*-poly(2-cinnamoyloxyethyl methacrylate) PS-*b*-PCEMA, diblock copolymers. This was shown in mixtures of chloroform and hexane, where hexane is a precipitant for PCEMA and PS, but a good solvent for P*t*BA. To ensure their coaggregation, the PCEMA blocks within both diblock copolymers were tagged by the H-bonding DNA base pair thymine and adenine. Coaggregation of the associating diblocks resulted in interesting block copolymer aggregation behavior and morphologies, as studied by DLS and TEM.[95]

A related blending strategy combines AB diblocks with CD diblocks, in which electrostatic attractions between polyanionic B and polycationic C blocks drive the formation of higher-order assemblies. Toward this end, Zhang et al. studied the complexation between PS-*b*-PAA micelles and PEO-*b*-P4VP diblocks to produce three-layered core—shell—corona micellar complexes in ethanol. The micellization of PS-*b*-PAA in ethanol gave rise to spherical core—shell micelles with a PS core and PAA shell. A PEO-*b*-P4VP diblock was then added to form spherical

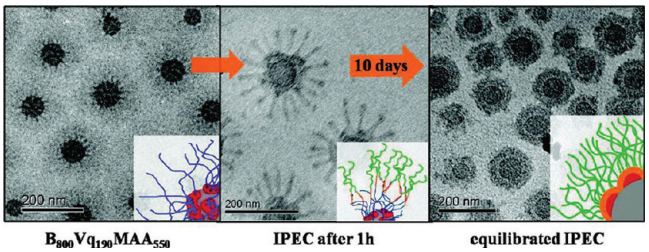

Figure 8. Dynamic multicompartment micelles formed from the interpolyelectrolyte complexation (IPEC) between PB-*b*-P2VPq-*b*-PMAA and P2VP-*b*-PEO block terpolymers.[98] Reproduced with permission from ref 98. Copyright 2009 American Chemical Society.

core−shell−corona micellar complexes, whereby the P4VP block penetrated into the PAA shell of the core−shell micelles.[96] More recently, Lutz et al. investigated a comparable strategy using AB and CD diblock copolymers in aqueous solution.[97] The researchers utilized the electrostatic interaction between a negatively charged sulfonated B block and a positively charged quaternary amine C block to enable self-assembly into large polyion complexes of the A(BC)D-type in aqueous solution via the addition of the CD diblock to spherical micelles of the AB diblock. This two-step self-assembly methodology demonstrates a straightforward method for the preparation of multicompartment nanostructures that could be extended toward the formation of artificial enzymes, given the biomimetic nature of the polyion block copolymers used and the multicompartmentalized cores.

Schacher et al. have recently reported dynamic core−shell−shell−corona micelles formed from two oppositely charged block copolymer systems. The researchers formed cationic PB-*b*-P2VPq-*b*-PMAA micelles with shells made up from a complex with neutral P2VP-*b*-PEO diblocks. The two diblocks were mixed in different molar ratios at high pH, resulting in the formation of multicompartment micelles that exhibited dynamic behavior in solution, as indicated by their structural relaxation over 10 days as observed by DLS, cryo-TEM, and SFM measurements. After short mixing times, striking star-shaped nanostructures were observed, which evolved into spherical core−shell−shell−corona objects after 10 days (Figure 8).[98]

■ MULTICOMPARTMENT MICELLES FROM MIKTOARM STAR-BLOCK TERPOLYMERS

The ABC miktoarm (or μ) (mikto, from the Greek word meaning "mixed")[99] star terpolymer architecture provides a versatile and powerful route toward multicompartment micelles. Most importantly, the miktoarm star architecture effectively suppresses the formation of concentric domains with an "onion-like" arrangement, the default core/shell/corona structure adopted by linear ABC triblock terpolymers. This is due to the mandatory convergence of three blocks at a common point, thereby constraining the resulting A, B, and C nanodomains to meet along a common curve in space. This in turn leads to segregation of all three mutually immiscible polymer chains at their point of contact. Such structural features could enable not only simultaneous storage but also simultaneous or sequential release of internal cargos located within each compartment due to their individual accessibility toward the exterior of the micelle. This feature of multicompartment micelles could therefore be said to satisfy a proposed requirement for the mimicry of biological systems by enabling their compartments to be in close proximity

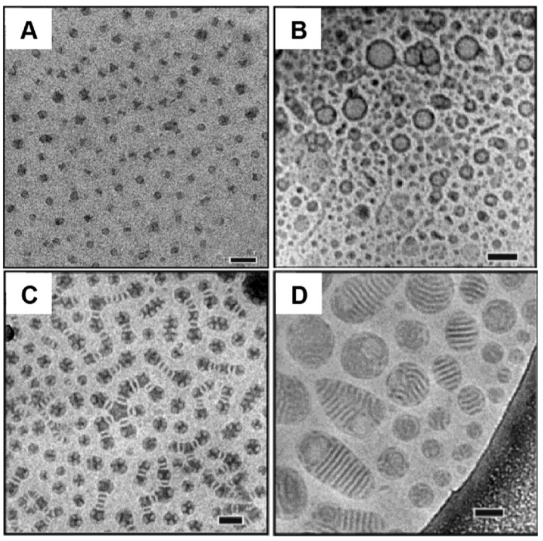

Figure 9. Multicompartment micelles from miktoarm star terpolymers, μ-EOF(*x*-*y*-*z*). Cryo-TEM images of 1 wt % aqueous solutions of (A) μ-EOF(2-13-3.5), (B) μ-EOF(2-4-2.5), (C) μ-EOF(2-9-5), and (D) μ-EOF(2-6-2.5); scale bars indicate 50 nm.[105] Cryo-TEM images adapted from ref 105. Copyright 2006 American Chemical Society.

and yet facilitate complex chemical processes without mutual interference.

Many research groups have developed strategies for the synthesis of miktoarm star terpolymers.[34,100−104] However, few groups have explored the self-assembly of these terpolymers in solution. Our research efforts have focused upon systematically detailing the self-assembly of various miktoarm terpolymers into a rich variety of multicompartment micellar morphologies. Initially, the miktoarm stars contained three mutually immiscible blocks, poly(ethylene oxide) (PEO), poly(ethyl ethylene) (PEE), and poly(perfluoropropylene oxide) (PFPO), and were designated the notation μ-EOF(*x*-*y*-*z*), where *x*, *y*, and *z* represent the "E", "O", and "F" block molecular weights. The first arm, comprised of "O", conferred water dispersibility, colloidal stability, and biocompatibility. The second and third arms were formed from the hydrocarbon block "E" and the fluorinated block "F", thereby installing the necessary 3-fold "philicity" within one architecture. The strong effective pairwise repulsion between E and F ensured their segregation into discrete nanodomains within the hydrophobic cores even at modest molecular weights. These polymers formed approximately spherical micelles with distinct F and E core domains, and segmented worm-like micelles, in which flat nanoscopic disks of E and F were stacked alternately along the cylinder axis, while protected by a common corona of well-solvated O chains. Li et al. were able to show the internal multicompartmentalization of various μ-EOF nanostructures by extensive cryo-TEM measurements in further publications (see Figure 9).[105]

In recent years, several other groups have explored the self-assembly of miktoarm star terpolymers in solution. Walther et al. studied the formation of bridges between multicompartment micelles formed from miktoarm star terpolymers in water.[106] Furthermore, the research group of Liu has investigated the self-assembly of nonlinear chain architectures in double hydrophilic block copolymers, and this research area has been reviewed recently.[107] This work includes several studies on miktoarm star multicompartment micelles in solution and the development of

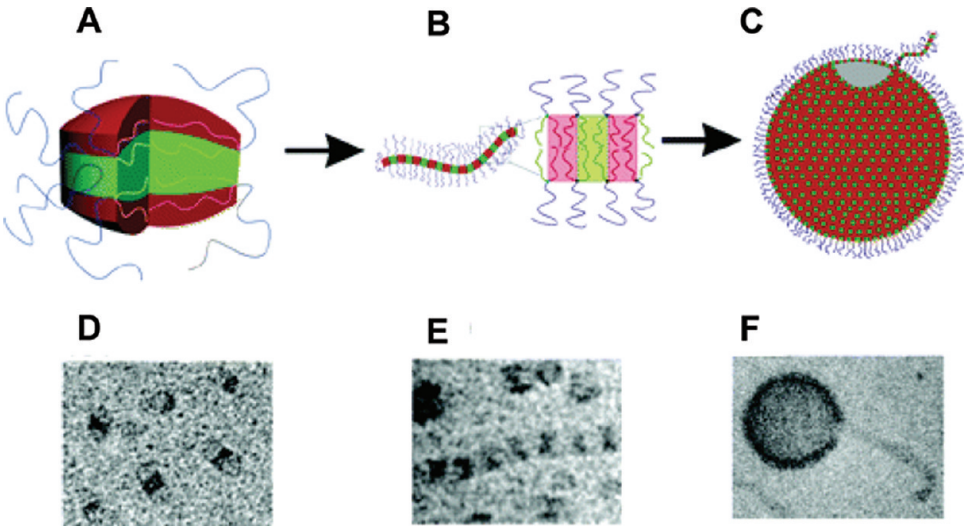

Figure 10. (A−C) Schematic representation of micellar structures self-assembled from μ-EOF star terpolymers: (A) hamburger micelle, (B) segmented worm-like micelle, and (C) nanostructured bilayer vesicle. Representative cryo-TEM images of (D) hamburger micelles, (E) segmented worm-like micelles, and (F) nanostructured vesicles from μ-EOF terpolymers.[105] Reproduced with permission from ref 105. Copyright 2006 American Chemical Society.

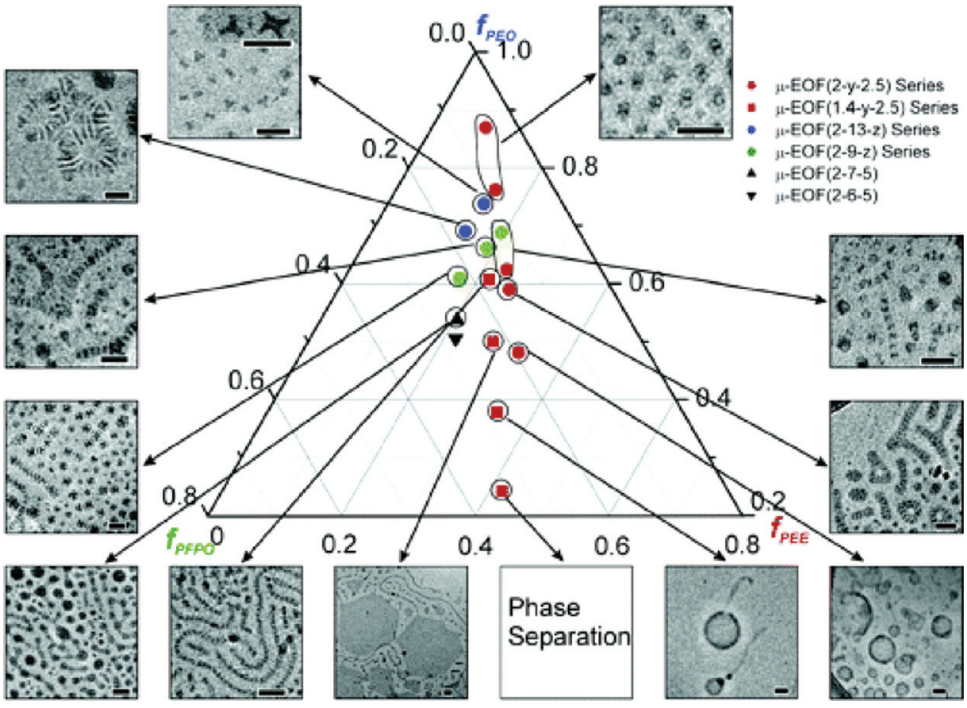

Figure 11. A multicompartment micelle morphology diagram for μ-EOF terpolymers as a function of composition; f_{PEE}, f_{PEO}, and f_{PFPO} are the volume fractions of the PEE, PEO, and PFPO blocks, respectively.[105] Reproduced with permission from ref 105. Copyright 2006 American Chemical Society.

synthetic strategies toward ABC miktoarm stars by various polymerization and click chemistries.[108,109] Multiarmed star copolymers other than miktoarm stars have also received research interest.[110]

As previously mentioned, it is well established that that the micellar morphology of block copolymers in solution can be readily manipulated by altering the copolymer composition. That is, as the solvophobic block to solvophilic block ratio increases, the micelle morphology transforms from spheres to cylinders to vesicles in diblock copolymers. A similar morphological evolution has been found for μ-EOF multicompartment micelles, which change from hamburger micelles to segmented or multicompartment worms, to polygonal bilayers and laterally nanostructured vesicles as the length of the PEO block decreases (Figure 10).[105]

Moreover, increasing the amount of the PFPO block relative to the PEE block drives the micellar structure from hamburger micelles or segmented worms to "raspberry-like" micelles or multicompartment worms.[111] Thus having investigated the morphological evolution of μ-EOF miktoarm star terpolymers in

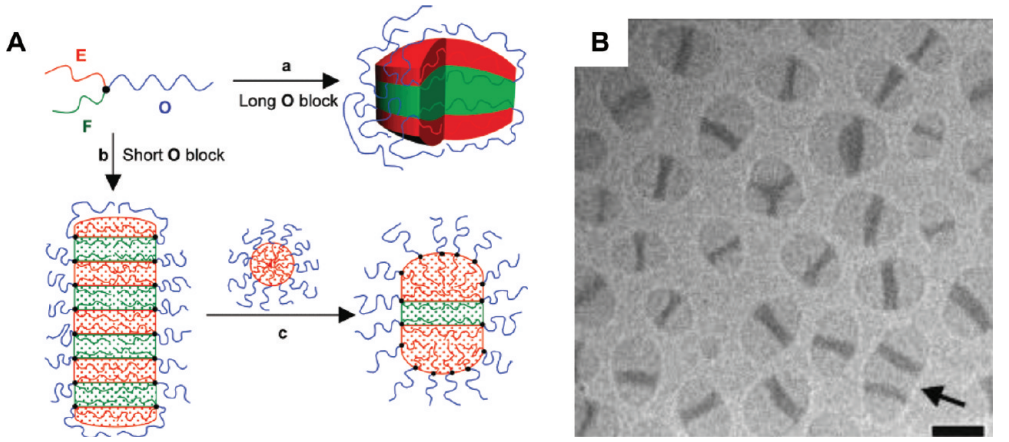

Figure 12. (A) Schematic illustration of multicompartment micelle formation from μ-EOF star terpolymers and binary blends of μ-EOF/EO: (a) hamburger micelle from μ-EOF with a very long O block; (b) segmented worm-like micelle from μ-EOF with a short O block, (c) hamburger micelle from blends of μ-EOF/EO. (B) Representative cryo-TEM image of the "hamburger"-like micelles. Scale bars indicate 50 nm. Reproduced with permission from ref 112. Copyright 2006 American Chemical Society.

detail, Li et al. constructed a multicompartment micelle morphology diagram for μ-EOF miktoarm star terpolymers as a function of composition of the volume fractions of the PEE, PEO, and PFPO blocks based upon extensive cryo-TEM and DLS studies (Figure 11).[105]

Using a μ-ABC/AB blending strategy, relatively narrowly distributed "hamburger" micelles were formed from a binary mixture of spherical micelles, formed from EO diblock copolymers, and segmented worm-like micelles, formed from μ-EOF miktoarm star terpolymers (Figure 12). Cryo-TEM and DLS were used to characterize the evolution of micelle structure and size distribution as a function of annealing time, over the course of several months. The morphological evolution was proposed to occur via a collision/fusion/fission mechanism whereby the long μ-EOF segmented worm-like micelles first fused with EO spherical micelles, followed by fission, giving progressively shorter micelles, which finally evolved into more stable hamburger-like micelles.[112]

Besides the addition of other blocks or manipulating the terpolymer itself, solvent selectivity has also been shown to be an efficient way to achieve various micellar morphologies from a single block copolymer in different selective solvents (or their mixtures).[23,24] This has also been investigated in miktoarm star μ-EOF micellar systems. By incorporating tetrahydrofuran (THF), a good solvent for the E block, into aqueous dispersions of a μ-EOF block, the micellar structure evolved from multicompartment disks to core−shell−corona worms and spheres and finally to mixed corona (E + O) oblate ellipsoidal micelles with increasing THF content (Figure 13).[113] Potentially a molecule sequestered within the E compartment could be released as the E block undergoes the transition from the core to the corona, and thus this type of morphological evolution from multicompartment micelles to mixed corona micelles could be an important step forward in their development for sequential release applications. The THF/water system is not particularly suitable for biomedical applications, and therefore such a morphological evolution in an aqueous solution driven by a stimulus such as pH, temperature, or ionic strength would be particularly desirable.

A stimulus-responsive morphological evolution of multicompartment micelles from miktoarm star terpolymers has recently

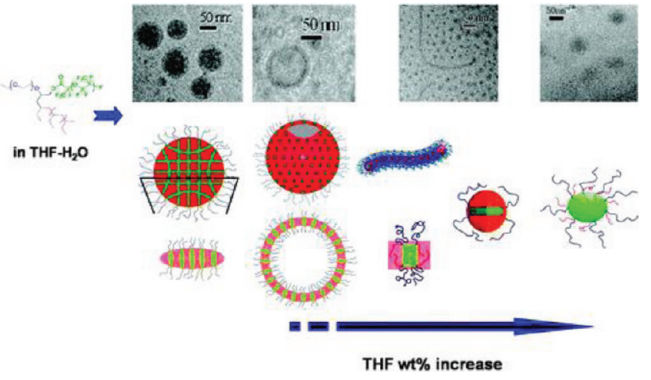

Figure 13. Schematic cartoons and illustrative cryo-TEM and TEM images of the micelle structural evolution μ-EOF micellar systems upon addition of tetrahydrofuran, as previously described.[113] Reproduced with permission from ref 113. Copyright 2008 American Chemical Society.

been realized. Multicompartment micelles were formed from a miktoarm star including a degradable block, which could be selectively etched upon increasing the pH of the solution. Multicompartment micelles with segmented worm-like structures consisting of alternating PEE and poly(γ-methyl-ε-caprolactone) (PMCL) layers were formed upon dispersing a μ-(PEE)-(PEO)-(PMCL) (μ-EOC) miktoarm star block terpolymer in neutral water.[114,115] The hydrolytic degradation of the PMCL chains proceeded by subjecting these micelles to a pH 12 aqueous buffer at 50 °C. After 4 weeks, the majority of the μ-EOC triblocks terpolymers had degraded to give PEE-*b*-PEO (EO) diblocks and PMCL homopolymers. The resulting EO diblocks were expected to assemble into simple cylindrical micelles; however, the "daughter micelle" morphologies were much richer, as observed by cryo-TEM (Figure 14). The initial segmented wormlike micelles evolved into raspberry-like vesicle structures composed of spherical PMCL subdomains embedded in a PEE matrix. This dramatic change in the morphology of the multicompartment micelles was ascribed to a rearrangement of the μ-EOC/EO/PMCL composite micelles to give a nanostructure that minimizes any unfavorable interactions between the

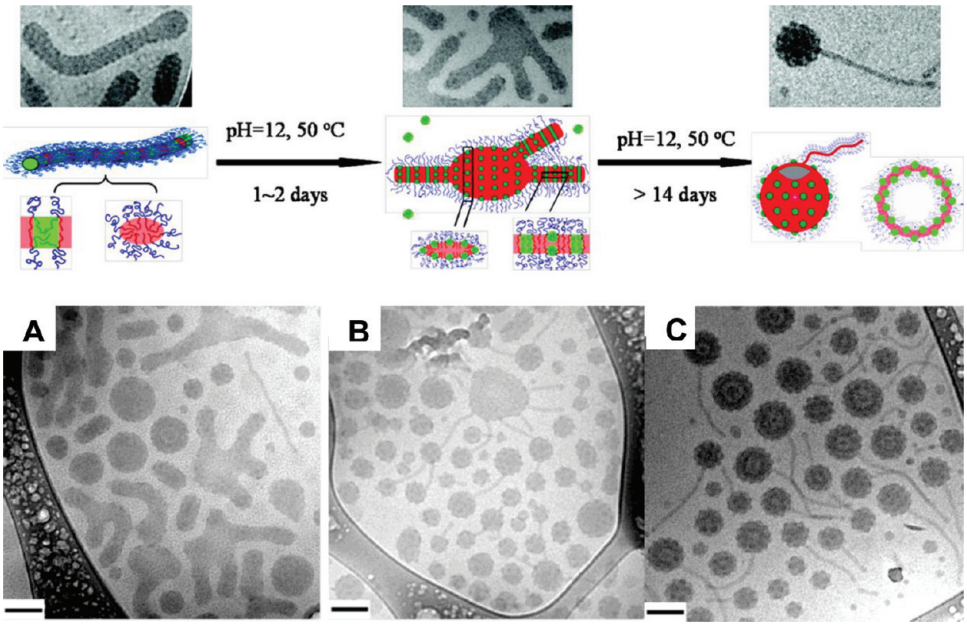

Figure 14. A schematic cartoon and cryo-TEM images following the morphological evolution of μ-EOC miktoarm star block terpolymer multicompartment micelles from segmented wormlike micelles (A) into raspberry-like vesicle structures with PMCL subdomains embedded in a PEE matrix (B, C). Scale bars are 50 nm.[115] Reproduced with permission from ref 115. Copyright 2010 American Chemical Society.

three mutually immiscible polymers. This type of micelle-to-micelle morphological evolution induced by block degradation in a terpolymer system holds great promise for the development of "smart" delivery capabilities, which require a stimulus triggered shape change or release of internally sequestered hydrophobic payloads.

Our group has also reported on a pH-responsive micellar system from a miktoarm star terpolymer, μ-SODA, containing a PS hydrophobic core forming segment and a PEO hydrophilic corona forming block. The third block was a pH-sensitive poly(dimethylaminoethyl acrylate) (PDMAEA) segment that is charged and hydrophilic at low pH, thus partitioning itself within the corona (to give mixed corona spherical micelles with PS cores), and neutrally charged and hydrophobic at high pH to give multicompartment cylindrical micelles with PDMAEA and PS cores. The resulting mixed corona micelle-to-multicompartment micelle transition could be particularly useful for drug delivery applications that require a stimulus triggered release or change in sequestration/shell permeability properties.[116] Liu and co-workers have also reported on the incorporation of stimuli-responsive polymers into miktoarm star architectures. Upon self-assembly, these polymers produced pH-responsive and thermoresponsive multicompartment nanostructures, thus expanding the scope of stimuli-responsive multicompartment micelles for smart delivery applications.[117,118]

MULTICOMPARTMENT MICELLES FROM (A-*GRAFT*-B)-*BLOCK*-(A-*GRAFT*-C) BLOCK TERPOLYMERS

Pioneering work in the area of multicompartment micelles included work on graft copolymers, whereby the incompatible B and C chains were grafted to the side chains of an A block.[119−122] The sizes of the incompatible hydrophobic domains were below the resolution limit of TEM for these systems, and multicompartmentalization was therefore not visualized; however, the nanostructures certainly fulfill a strict criterion of multicompartment micelles in that selective solubilization within them was possible, as demonstrated by dye solubilization studies. These studies could be very interesting to revisit in the future and with current advanced imaging techniques.

THEORETICAL TREATMENTS OF MULTICOMPARTMENT MICELLES

While there has been substantial progress regarding the synthesis and experimental study of multicompartment micelles, analytical theory has been lacking. Few notable exceptions are the work of Zhulina and Borisov, who adapted the established scaling theory of block copolymer micelles to the case of μ-ABC miktoarm stars[123] and the early work of Dormidontova and Khokhlov.[124] On the other hand, extensive computer simulations have been able to reproduce many of the observed morphologies.[125,126] These studies have included investigating the effect of copolymer composition, architecture, the interchain interaction parameters, and blending conditions.[125−144] The primary approaches have been dissipative particle dynamics,[127−135] self-consistent field simulation,[139] and a simulated annealing method.[136,140] Representative examples are shown in Figure 15.

APPLICATIONS OF MULTICOMPARTMENT MICELLES

Research interest in multicompartment micelles is motivated in part by the knowledge that polymer micelles have the ability to selectively store and transport small organic molecules within their hydrophobic interior.[145] The ability to have subdivided cores or several inner compartments becomes particularly attractive for the simultaneous storage and/or release of different stored cargos. Therefore, multicompartment micelles may enable the selective solubilization of a more diverse range of incompatible molecules within their discrete inner compartments, with the possibility of the concurrent transport and subsequent

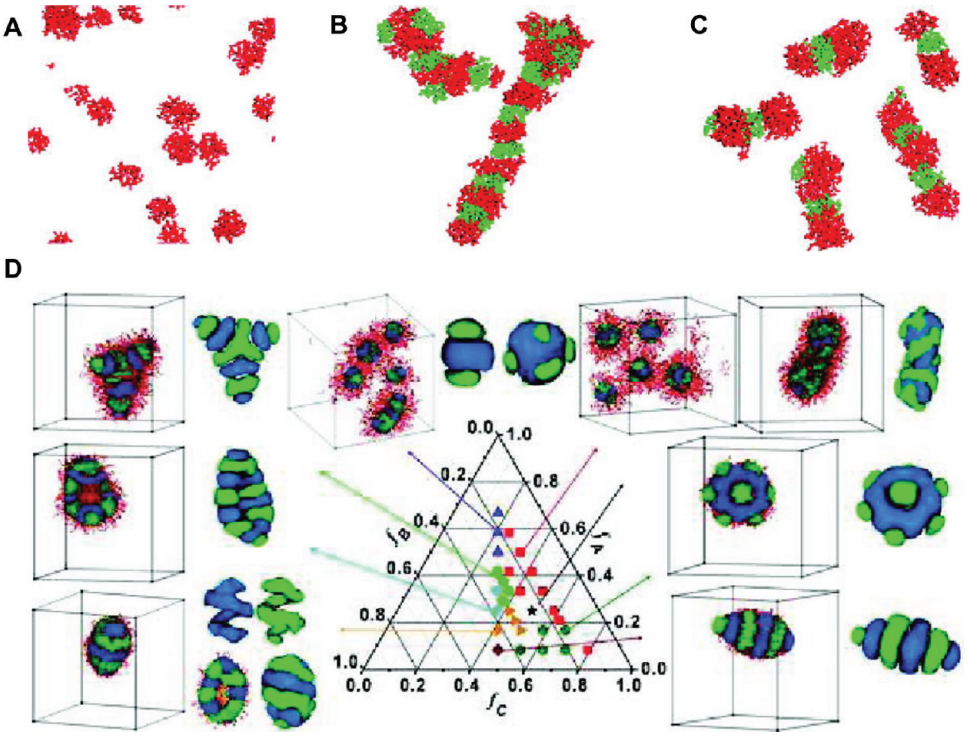

Figure 15. (A−C) Morphologies of micelles obtained by DPD simulations; only the two solvophobic blocks are shown (red and green) for clarity. (A) Spherical micelles formed from diblock copolymers. (B) Worm-like multicompartment micelles formed from star triblock copolymers. (C) "Hamburger" multicompartment micelles formed by blending star triblock and diblock copolymers.[125] (D) Morphologies of micelles from μ-ABC miktoarm stars as a function of composition.[137] Reproduced with permission from refs 125 and 137. Copyright 2007 and 2009 American Chemical Society.

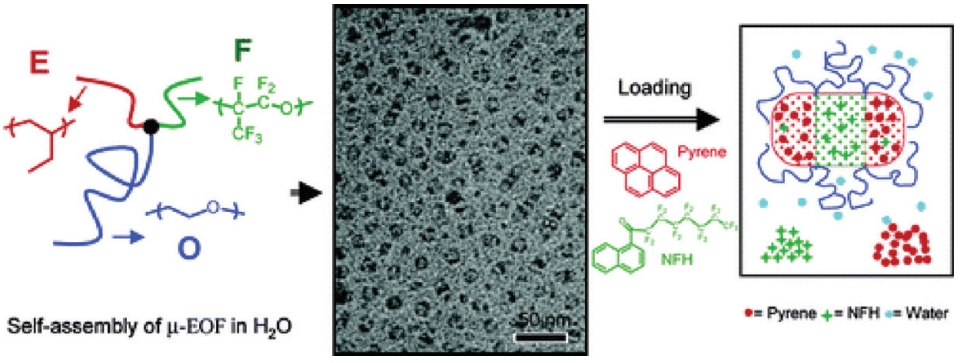

Figure 16. Schematic illustration of the selective storage of dye molecules in μ-EOF multicompartment micelles.[147] Reproduced with permission from ref 147. Copyright 2005 American Chemical Society.

"double delivery" of active agents in a prescribed manner. As such, many applications that exploit this feature may be envisaged, for example, the simultaneous delivery of two incompatible drug or gene therapy payloads. The ability to achieve separate chemical environments within one nanostructure may also afford unique nanocatalysis opportunities. For example, multicomponent asymmetric cascade reactions were recently demonstrated to be catalyzed by two (otherwise incompatible) supported star polymer catalysts in a one-pot combination in water.[146]

To date, the employment of multicompartment micelles for nanotechnology applications that utilize their inherent storage and release benefits remain limited. However, toward this end, some reports have elegantly demonstrated their unique storage capabilities for small dye molecules in water. Early work in the area of multicompartment micelles utilized the uptake of different dye molecules as confirmation for multicompartment micelle formation.[119−121] We demonstrated this for block polymer multicompartment micelles via the simultaneous and segregated storage of two hydrophobic dye molecules within ellipsoidal multicompartment micelles (Figure 16).[147] We demonstrated that it was possible to create multicompartment micelles that can solubilize two distinct molecules within two separate nanosized compartments. Crucially, these findings indicated that there was little relationship between the distinct solubilization efficiencies and therefore that the storage and release of two different hydrophobic payloads simultaneously or sequentially could be realized.

Kakkar and co-workers recently demonstrated the potential of encapsulating small molecules into multicompartment spherical

micelles made from miktoarm star terpolymers. The researchers found an enhancement in the loading capacity of the micelles with an increase in the length of the hydrophobic arm.[104] Laschewsky and co-workers also recently studied the influence of the terpolymer architecture of three linear triblock terpolymers on the selective uptake of two organic small molecules: an aromatic hydrocarbon and an aromatic fluorocarbon.[52,53] Depending on the polymer sequence (i.e., ABC, BAC, or even ACB), various multicompartment micelles were formed that were capable of selective solubilization of the small molecules. Their experiments showed that the terpolymers were capable of simultaneously solubilizing substantial amounts of the hydrocarbon as well as the fluorocarbon molecules. However, the precursor diblock copolymers could not do so, demonstrating the selectivity of the individual hydrocarbon and fluorocarbon blocks and thus underlining the validity of the concept of multicompartment micelles for selective and simultaneous storage of organic molecules.

The 3-fold philicity of existing ABC block terpolymer systems could be exploited to produce multicompartment micelles in "green" solvents such as ionic liquids or supercritical carbon dioxide ($scCO_2$). The self-assembly of diblock copolymers has been shown in both of these solvent systems with a view to enabling the dispersion of otherwise insoluble materials in these media.[25,26,28] Multicompartment micelles could potentially enhance the utility of these solvents even more so than diblock copolymer micelle systems and provide two distinct nanosized domains for transport or reactions of small molecules. Fluorinated polymers are typically utilized as one solvophobic block in ABC block terpolymers for multicompartment micelle formation in water. However, in carbon dioxide, fluorinated polymers are more soluble than most polymers and would act as the solvophilic block, and the hydrophilic and hydrocarbon blocks would then be solvophobic, possibly forming two distinct separate core domains. Multicompartment micelles in carbon dioxide would thus have hydrocarbon and hydrophilic core domains and may then display interesting uptake and transport behavior as a result. For instance, the solubility of inorganic or biological species is very poor in $scCO_2$, and yet these species are increasingly required for catalytic transformations in organic chemistry. Multicompartment micelles could enable the sequestration of distinctly different species (such as metal nanoparticles and enzymes) simultaneously, thus affording the opportunity to perform novel multiphase reactions within one solvent system. The specific placement and utilization of transition metals, nanoparticles, enzymes, or organic catalysts within the interfacial regions of the two domains within multicompartment micelles may also pave the way for many novel and multistep catalytic transformations in $scCO_2$.

The self-assembly of block copolymers has been shown in ionic liquids with various morphologies being explored including spherical micelles and vesicles.[27,28,148] Furthermore, PB-*b*-PEO block copolymer micelles have been shown to shuttle between water and ionic liquids.[149−151] Multicompartment micelles could allow for unique solubility and nanosized environments within ionic liquids; moreover, they may show similar shuttling behavior.

Fluorinated functional groups or fluorine-containing polymers are also interesting for biomedical and pharmaceutical research due to their biological activity imparted by the fluorinated moieties. This has been the subject of some interesting recent research and has been reviewed recently.[152]

The area of multicompartment hydrogels is a particularly intriguing area of research which has shown recent progress.[80−82] This research may afford opportunities to advance hydrogels for biomedical/tissue engineering applications in particular.[153] Such hydrogels typically require a fairly stringent set of physical characteristics which may be imparted by the physical and stimuli-responsive properties of the particular polymers utilized for gel formation. For instance, the gel may be required to be a liquid at room temperature (to enable injection), and yet it must be able to form a gel upon exposure to physiological conditions and potentially be biocompatible and also biodegradable. ABC block terpolymer hydrogels afford the opportunities to tune these different elements into a hydrogel, since both the B and C blocks could be tailored to modify the hydrogel's physical and mechanical properties, and this will no doubt be an interesting topic of ongoing research in coming years.

CONCLUSIONS AND OUTLOOK

Multicompartment micelle research has exploded in recent years with literature reports exploring various new and exciting areas. Some important advances include the ability to synthesize various block terpolymer architectures and compositions with relative ease, thus providing access to a plethora of multicompartmentalized micellar structures in solution and enhancing the ability to systematically study the influence of architecture on their properties. Research progress in this area with linear terpolymers also continues to bear exciting results, particularly upon changing the block sequence to achieve nonconcentric multicompartment micelles. Detailed characterization of the multicompartment micelles has also become more feasible, with cryo-TEM becoming the "gold standard" for the visualization of the aggregates in their native form.[154] ^{19}F NMR spectroscopy and cryo-electron tomography are also powerful tools to elucidate the distribution of the separate domains within multicompartment assemblies in future studies of complex systems.

Particular progress has been made in incorporating stimuli-responsive polymers or moieties within such assemblies, which holds great promise for "smart" delivery applications and may enable for the selective delivery of one payload over another. However, while the separate compartments within multicompartment micelles have been utilized for selective uptake of different organic molecules, a selective release event has yet to be demonstrated and would possibly require a specific trigger for one of the compartments. Therefore, the design of systems which couple a release event of an individual or several hydrophobic payloads in response to a stimulus trigger could be a particularly powerful strategy for simultaneous delivery applications. Furthermore, the ability to change the shape of the assemblies into novel nanostructures in response to a stimulus trigger could also be an advantageous feature, and research has shown particular progress toward this end.

Multicompartment micelles have been proposed to advance the scope of current micellar structures from a prokaryotic to a more eukaryotic level of sophistication. However, current synthetic and assembly methods are not quite in place yet to mimic biological processes; synthetic and self-assembly methods typically produce polydisperse micelle aggregates which can be prone to further aggregation or rearrangement. Biological systems typically do not have this size distribution issue. To fulfill their proposed biomimetic potential, methods to produce monodisperse multicompartment micelles from synthetically accessible block terpolymers are desirable, and these challenges will undoubtedly spur on more research in this exciting area.

AUTHOR INFORMATION

Corresponding Author
*E-mail: lodge@umn.edu (T.P.L.), hillmyer@umn.edu (M.A.H.).

BIOGRAPHIES

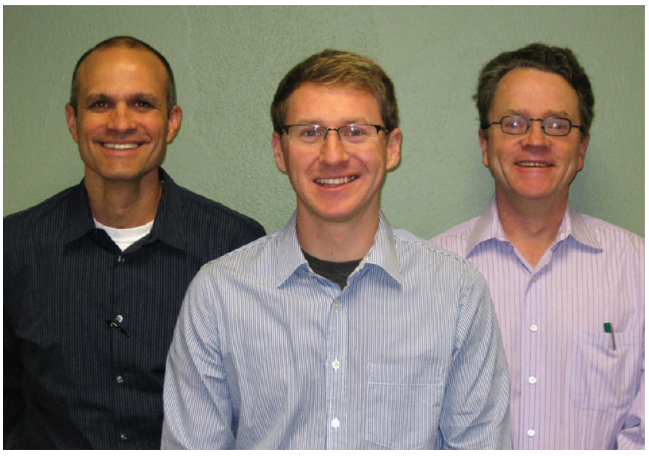

Adam Moughton (middle) received his M.Chem. in Chemistry from the University of Liverpool in 2006 and his Ph.D. in Chemistry from the University of Cambridge in 2010 with Dr. Rachel O'Reilly. He is currently a postdoctoral researcher at the University of Minnesota with Professors Marc A. Hillmyer and Timothy P. Lodge. His postdoctoral research focuses on the synthesis of novel terpolymer architectures and the study of their self-assembly into multicompartment micelles in aqueous solution.

Marc Hillmyer (left) received his B.S. in Chemistry from the University of Florida in 1989 and his Ph.D. in Chemistry from the California Institute of Technology in 1994. After completing a postdoctoral research position in the University of Minnesota's Department of Chemical Engineering and Materials Science, he joined the Chemistry faculty at Minnesota in 1997. He is currently a Distinguished McKnight University Professor of chemistry and leads a research group focused on the synthesis and self-assembly of multifunctional polymers. In addition to his teaching and research responsibilities, Marc also serves as an Associate Editor for the ACS journal *Macromolecules* and is the director of the National Science Foundation funded Center for Sustainable Polymers at the University of Minnesota.

Tim Lodge (right) graduated from Harvard in 1975 with a B.A. cum laude in Applied Mathematics, and in 1980 he earned his Ph.D. in Chemistry at the University of Wisconsin, working with Professor John Schrag. Tim spent 20 months as a National Research Council Postdoctoral Fellow at NIST, collaborating with Dr. Charles Han. Since 1982 he has been on the Chemistry faculty at the University of Minnesota and was promoted to Associate Professor in 1988 and Professor in 1991. In 1995 he also became a Professor of Chemical Engineering & Materials Science. He has authored or coauthored over 300 papers in the field of polymer science and advised or coadvised over 50 Ph.D. students. His research interests center on the structure and dynamics of polymer liquids, including solutions, melts, blends, and copolymers, with particular emphases on rheology, diffusion, scattering, and microscopy techniques.

ACKNOWLEDGMENT

We acknowledge support from the MRSEC Program of the National Science Foundation, through Award DMR-8019885.

REFERENCES

(1) Ober, C. K.; Cheng, S. Z. D.; Hammond, P. T.; Muthukumar, M.; Reichmanis, E.; Wooley, K. L.; Lodge, T. P. *Macromolecules* **2008**, *42* (2), 465–471.
(2) Webber, S. E. *J. Phys. Chem. B* **1998**, *102* (15), 2618–2626.
(3) Riess, G. *Prog. Polym. Sci.* **2003**, *28* (7), 1107–1170.
(4) Lodge, T. P. *Macromol. Chem. Phys.* **2003**, *204* (2), 265–273.
(5) Hawker, C. J.; Wooley, K. L. *Science* **2005**, *309* (5738), 1200–1205.
(6) Cameron, N. S.; Corbierre, M. K.; Eisenberg, A. *Can. J. Chem.* **1999**, *77* (8), 1311–1326.
(7) Laschewsky, A. *Curr. Opin. Colloid Interface Sci.* **2003**, *8* (3), 274–281.
(8) Ringsdorf, H.; Lehmann, P.; Weberskirch, R. Multicompartmentation - a concept for the molecular architecture of life. In *217th ACS National Meeting*, Anaheim, CA, 1999.
(9) Ober, C. K.; Zentel, R. *Macromolecules* **2004**, *37* (23), 8485–8486.
(10) de Gennes, P.-G. *C. R. Acad. Sci., Ser. IIb: Mec., Phys., Astron.* **1999**, *327* (5), 535–538.
(11) Ringsdorf, H.; Schlarb, B.; Venzmer, J. *Angew. Chem., Int. Ed.* **1988**, *27* (1), 113–158.
(12) Lutz, J.-F.; Laschewsky, A. *Macromol. Chem. Phys.* **2005**, *206* (8), 813–817.
(13) Zhang, L.; Eisenberg, A. *Science* **1995**, *268* (5218), 1728–1731.
(14) Zhang, L.; Yu, K.; Eisenberg, A. *Science* **1996**, *272* (5269), 1777–1779.
(15) Chen, L.; Shen, H.; Eisenberg, A. *J. Phys. Chem. B* **1999**, *103* (44), 9488–9497.
(16) Discher, B. M.; Won, Y.-Y.; Ege, D. S.; Lee, J. C. M.; Bates, F. S.; Discher, D. E.; Hammer, D. A. *Science* **1999**, *284* (5417), 1143–1146.
(17) Shen, H.; Eisenberg, A. *J. Phys. Chem. B* **1999**, *103* (44), 9473–9487.
(18) Won, Y.-Y.; Brannan, A. K.; Davis, H. T.; Bates, F. S. *J. Phys. Chem. B* **2002**, *106* (13), 3354–3364.
(19) Jain, S.; Bates, F. S. *Science* **2003**, *300* (5618), 460–464.
(20) Jain, S.; Bates, F. S. *Macromolecules* **2004**, *37* (4), 1511–1523.
(21) Hayward, R. C.; Pochan, D. J. *Macromolecules* **2010**, *43* (8), 3577–3584.
(22) Zhang, L.; Shen, H.; Eisenberg, A. *Macromolecules* **1997**, *30* (4), 1001–1011.
(23) Bang, J.; Jain, S.; Li, Z.; Lodge, T. P.; Pedersen, J. S.; Kesselman, E.; Talmon, Y. *Macromolecules* **2006**, *39* (3), 1199–1208.
(24) Abbas, S.; Li, Z.; Hassan; Lodge, T. P. *Macromolecules* **2007**, *40* (11), 4048–4052.
(25) McClain, J. B.; Betts, D. E.; Canelas, D. A.; Samulski, E. T.; DeSimone, J. M.; Londono, J. D.; Cochran, H. D.; Wignall, G. D.; Chillura-Martino, D.; Triolo, R. *Science* **1996**, *274* (5295), 2049–2052.
(26) Edmonds, W. F.; Hillmyer, M. A.; Lodge, T. P. *Macromolecules* **2007**, *40* (14), 4917–4923.
(27) He, Y.; Li, Z.; Simone, P.; Lodge, T. P. *J. Am. Chem. Soc.* **2006**, *128* (8), 2745–2750.
(28) Simone, P. M.; Lodge, T. P. *Macromol. Chem. Phys.* **2007**, *208* (4), 339–348.
(29) Meli, L.; Lodge, T. P. *Macromolecules* **2009**, *42* (3), 580–583.
(30) Semenov, A. N.; Nyrkova, I. A.; Khokhlov, A. R. *Macromolecules* **1995**, *28* (22), 7491–7500.
(31) Lodge, T. P.; Hillmyer, M. A.; Zhou, Z.; Talmon, Y. *Macromolecules* **2004**, *37* (18), 6680–6682.
(32) Edmonds, W. F.; Li, Z.; Hillmyer, M. A.; Lodge, T. P. *Macromolecules* **2006**, *39* (13), 4526–4530.
(33) Fustin, C. A.; Abetz, V.; Gohy, J. F. *Eur. Phys. J. E* **2005**, *16* (3), 291–302.
(34) Hadjichristidis, N.; Iatrou, H.; Pitsikalis, M.; Pispas, S.; Avgeropoulos, A. *Prog. Polym. Sci.* **2005**, *30* (7), 725–782.
(35) Yu, G.-E.; Eisenberg, A. *Macromolecules* **1998**, *31* (16), 5546–5549.
(36) Gohy, J.-F.; Willet, N.; Varshney, S.; Zhang, J.-X.; Jérôme, R. *Angew. Chem., Int. Ed.* **2001**, *40* (17), 3214–3216.
(37) Rodríguez-Hernández, J.; Chécot, F.; Gnanou, Y.; Lecommandoux, S. *Prog. Polym. Sci.* **2005**, *30* (7), 691–724.

(38) Lei, L.; Gohy, J.-F.; Willet, N.; Zhang, J.-X.; Varshney, S.; Jérôme, R. *Macromolecules* **2003**, *37* (3), 1089–1094.
(39) Lei, L.; Gohy, J.-F.; Willet, N.; Zhang, J.-X.; Varshney, S.; Jérôme, R. *Polymer* **2004**, *45* (13), 4375–4381.
(40) Lei, L.; Gohy, J.-F.; Willet, N.; Zhang, J.-X.; Varshney, S.; Jérôme, R. *Polymer* **2006**, *47* (8), 2723–2727.
(41) Butsele, K. V.; Fustin, C. A.; Gohy, J. F.; Jérôme, R.; Jérôme, C. *Langmuir* **2008**, *25* (1), 107–111.
(42) Jiang, X.; Zhang, G.; Narain, R.; Liu, S. *Langmuir* **2009**, *25* (4), 2046–2054.
(43) Lobert, M.; Thijs, H.; Erdmenger, T.; Eckardt, R.; Ulbricht, C.; Hoogenboom, R.; Schubert, U. S. *Chem.—Eur. J.* **2008**, *14* (33), 10396–10407.
(44) Kempe, K.; Hoogenboom, R.; Hoeppener, S.; Fustin, C.-A.; Gohy, J.-F.; Schubert, U. S. *Chem. Commun.* **2010**, *46* (35), 6455–6457.
(45) Hu, J.; Njikang, G.; Liu, G. *Macromolecules* **2008**, *41* (21), 7993–7999.
(46) Njikang, G.; Han, D.; Wang, J.; Liu, G. *Macromolecules* **2008**, *41* (24), 9727–9735.
(47) Schacher, F.; Walther, A.; Müller, A. H. E. *Langmuir* **2009**, *25* (18), 10962–10969.
(48) Schacher, F.; Walther, A.; Ruppel, M.; Drechsler, M.; Müller, A. H. E. *Macromolecules* **2009**, *42* (10), 3540–3548.
(49) O'Reilly, R. K.; Hawker, C. J.; Wooley, K. L. *Chem. Soc. Rev.* **2006**, *35* (11), 1068–1083.
(50) Patrickios, C. S.; Lowe, A. B.; Armes, S. P.; Billingham, N. C. *J. Polym. Sci., Part A: Polym. Chem.* **1998**, *36* (4), 617–631.
(51) Skrabania, K.; Laschewsky, A.; von Berlepsch, H.; Böttcher, C. *Langmuir* **2009**, *25* (13), 7594–7601.
(52) Laschewsky, A.; Marsat, J. N.; Skrabania, K.; von Berlepsch, H.; Böttcher, C. *Macromol. Chem. Phys.* **2010**, *211* (2), 215–221.
(53) Marsat, J.-N.; Heydenreich, M.; Kleinpeter, E.; von Berlepsch, H.; Böttcher, C.; Laschewsky, A. *Macromolecules* **2011**, *44* (7), 2092–2105.
(54) Kubowicz, S.; Baussard, J.-F.; Lutz, J.-F.; Thünemann, A. F.; von Berlepsch, H.; Laschewsky, A. *Angew. Chem., Int. Ed.* **2005**, *44* (33), 5262–5265.
(55) von Berlepsch, H.; Böttcher, C.; Skrabania, K.; Laschewsky, A. *Chem. Commun.* **2009**, *17*, 2290–2292.
(56) Skrabania, K.; von Berlepsch, H.; Böttcher, C.; Laschewsky, A. *Macromolecules* **2010**, *43* (1), 271–281.
(57) Yin, L.; Hillmyer, M. A. *Macromolecules* **2011**, *44* (8), 3021–3028.
(58) Zhou, Z.; Li, Z.; Ren, Y.; Hillmyer, M. A.; Lodge, T. P. *J. Am. Chem. Soc.* **2003**, *125* (34), 10182–10183.
(59) Walther, A.; Barner-Kowollik, C.; Müller, A. H. E. *Langmuir* **2010**, *26* (14), 12237–12246.
(60) Weberskirch, R.; Preuschen, J.; Spiess, H. W.; Nuyken, O. *Macromol. Chem. Phys.* **2000**, *201* (10), 995–1007.
(61) Kyerematen, S. O.; Henze, T.; Busse, K.; Kressler, J. *Macromolecules* **2010**, *43* (5), 2502–2511.
(62) Kubowicz, S.; Thünemann, A. F.; Weberskirch, R.; Möhwald, H. *Langmuir* **2005**, *21* (16), 7214–7219.
(63) Zhang, H.; Ni, P.; He, J.; Liu, C. *Langmuir* **2008**, *24* (9), 4647–4654.
(64) Pochan, D. J.; Chen, Z.; Cui, H.; Hales, K.; Qi, K.; Wooley, K. L. *Science* **2004**, *306* (5693), 94–97.
(65) Chen, Z.; Cui, H.; Hales, K.; Li, Z.; Qi, K.; Pochan, D. J.; Wooley, K. L. *J. Am. Chem. Soc.* **2005**, *127* (24), 8592–8593.
(66) Li, Z.; Chen, Z.; Cui, H.; Hales, K.; Qi, K.; Wooley, K. L.; Pochan, D. J. *Langmuir* **2005**, *21* (16), 7533–7539.
(67) Cui, H.; Chen, Z.; Wooley, K. L.; Pochan, D. J. *Macromolecules* **2006**, *39* (19), 6599–6607.
(68) Cui, H.; Chen, Z.; Zhong, S.; Wooley, K. L.; Pochan, D. J. *Science* **2007**, *317* (5838), 647–650.
(69) Uchman, M.; Štěpánek, M.; Procházka, K.; Mountrichas, G.; Pispas, S.; Voets, I. K.; Walther, A. *Macromolecules* **2009**, *42* (15), 5605–5613.
(70) Fang, B.; Walther, A.; Wolf, A.; Xu, Y.; Yuan, J.; Müller, A. H. E. *Angew. Chem., Int. Ed.* **2009**, *48* (16), 2877–2880.
(71) Skrabania, K.; Kristen, J.; Laschewsky, A.; Akdemir, Ö.; Hoth, A.; Lutz, J.-F. *Langmuir* **2006**, *23* (1), 84–93.
(72) Cao, Y.; Zhao, N.; Wu, K.; Zhu, X. X. *Langmuir* **2008**, *25* (3), 1699–1704.
(73) Weiss, J.; Laschewsky, A. *Langmuir* **2011**, *27* (8), 4465–4473.
(74) Sugihara, S.; Kanaoka, S.; Aoshima, S. *J. Polym. Sci., Part A: Polym. Chem.* **2004**, *42* (11), 2601–2611.
(75) Brannan, A. K.; Bates, F. S. *Macromolecules* **2004**, *37* (24), 8816–8819.
(76) Thünemann, A. F.; Kubowicz, S.; von Berlepsch, H.; Möhwald, H. *Langmuir* **2006**, *22* (6), 2506–2510.
(77) Tsitsilianis, C.; Stavrouli, N.; Bocharova, V.; Angelopoulos, S.; Kiriy, A.; Katsampas, I.; Stamm, M. *Polymer* **2008**, *49* (13−14), 2996–3006.
(78) Katsampas, I.; Roiter, Y.; Minko, S.; Tsitsilianis, C. *Macromol. Rapid Commun.* **2005**, *26* (17), 1371–1376.
(79) Boschet, F.; Branger, C.; Margaillan, A.; Hogen-Esch, T. E. *Polym. Int.* **2005**, *54* (1), 90–95.
(80) Shunmugam, R.; Smith, C. E.; Tew, G. N. *J. Polym. Sci., Part A: Polym. Chem.* **2007**, *45* (13), 2601–2608.
(81) Taribagil, R. R.; Hillmyer, M. A.; Lodge, T. P. *Macromolecules* **2009**, *42* (6), 1796–1800.
(82) Taribagil, R. R.; Hillmyer, M. A.; Lodge, T. P. *Macromolecules* **2010**, *43* (12), 5396–5404.
(83) Hoogenboom, R.; Wiesbrock, F.; Leenen, M. A. M.; Thijs, H. M. L.; Huang, H.; Fustin, C.-A.; Guillet, P.; Gohy, J.-F.; Schubert, U. S. *Macromolecules* **2007**, *40* (8), 2837–2843.
(84) Hoeppener, S.; Wiesbrock, F.; Hoogenboom, R.; M. L. Thijs, H.; Schubert, U. S. *Macromol. Rapid Commun.* **2006**, *27* (6), 405–411.
(85) Gohy, J.-F.; Ott, C.; Hoeppener, S.; Schubert, U. S. *Chem. Commun.* **2009**, *40*, 6038–6040.
(86) Ott, C.; Hoogenboom, R.; Hoeppener, S.; Wouters, D.; Gohy, J.-F.; Schubert, U. S. *Soft Matter* **2009**, *5* (1), 84–91.
(87) Wurm, F.; Konig, H. M.; Hilf, S.; Kilbinger, A. F. M. *J. Am. Chem. Soc.* **2008**, *130* (18), 5876–5877.
(88) Moughton, A. O.; Stubenrauch, K.; O'Reilly, R. K. *Soft Matter* **2009**, *5* (12), 2361–2370.
(89) Talingting, M. R.; Munk, P.; Webber, S. E.; Tuzar, Z. *Macromolecules* **1999**, *32* (5), 1593–1601.
(90) Gohy, J.-F.; Lefevre, N.; D'Haese, C.; Hoeppener, S.; Schubert, U. S.; Kostov, G.; Ameduri, B. *Polym. Chem.* **2011**, *2* (2), 328–332.
(91) Zhu, J.; Hayward, R. C. *Macromolecules* **2008**, *41* (21), 7794–7797.
(92) Price, E. W.; Guo, Y.; Wang, C. W.; Moffitt, M. G. *Langmuir* **2009**, *25* (11), 6398–6406.
(93) Christian, D. A.; Tian, A.; Ellenbroek, W. G.; Levental, I.; Rajagopal, K.; Janmey, P. A.; Liu, A. J.; Baumgart, T.; Discher, D. E. *Nature Mater.* **2009**, *8* (10), 843–849.
(94) Zheng, R.; Liu, G.; Yan, X. *J. Am. Chem. Soc.* **2005**, *127* (44), 15358–15359.
(95) Yan, X.; Liu, G.; Hu, J.; Willson, C. G. *Macromolecules* **2006**, *39* (5), 1906–1912.
(96) Zhang, W.; Shi, L.; Miao, Z. J.; Wu, K.; An, Y. *Macromol. Chem. Phys.* **2005**, *206* (23), 2354–2361.
(97) Lutz, J.-F.; Geffroy, S.; von Berlepsch, H.; Böttcher, C.; Garnier, S.; Laschewsky, A. *Soft Matter* **2007**, *3* (6), 694–698.
(98) Schacher, F.; Betthausen, E.; Walther, A.; Schmalz, H.; Pergushov, D. V.; Müller, A. H. E. *ACS Nano* **2009**, *3* (8), 2095–2102.
(99) Hadjichristidis, N. *J. Polym. Sci., Part A: Polym. Chem.* **1999**, *37* (7), 857–871.
(100) Fujimoto, T.; Zhang, H.; Kazama, T.; Isono, Y.; Hasegawa, H.; Hashimoto, T. *Polymer* **1992**, *33* (10), 2208–2213.
(101) Li, Z.; Hillmyer, M. A.; Lodge, T. P. *Macromolecules* **2004**, *37* (24), 8933–8940.
(102) Li, C.; Ge, Z.; Liu, H.; Liu, S. *J. Polym. Sci., Part A: Polym. Chem.* **2009**, *47* (16), 4001–4013.
(103) He, T.; Li, D.; Sheng, X.; Zhao, B. *Macromolecules* **2004**, *37* (9), 3128–3135.
(104) Khanna, K.; Varshney, S.; Kakkar, A. *Macromolecules* **2010**, *43* (13), 5688–5698.
(105) Li, Z.; Hillmyer, M. A.; Lodge, T. P. *Langmuir* **2006**, *22* (22), 9409–9417.

(106) Walther, A.; Müller, A. H. E. *Chem. Commun.* **2009**, *9*, 1127–1129.
(107) Ge, Z.; Liu, S. *Macromol. Rapid Commun.* **2009**, *30* (18), 1523–1532.
(108) Rao, J.; Zhang, Y.; Zhang, J.; Liu, S. *Biomacromolecules* **2008**, *9* (10), 2586–2593.
(109) Zhang, Y.; Li, C.; Liu, S. *J. Polym. Sci., Part A: Polym. Chem.* **2009**, *47* (12), 3066–3077.
(110) Mao, J.; Ni, P.; Mai, Y.; Yan, D. *Langmuir* **2007**, *23* (9), 5127–5134.
(111) Li, Z.; Hillmyer, M. A.; Lodge, T. P. *Nano Lett.* **2006**, *6* (6), 1245–1249.
(112) Li, Z.; Hillmyer, M. A.; Lodge, T. P. *Macromolecules* **2006**, *39* (2), 765–771.
(113) Liu, C.; Hillmyer, M. A.; Lodge, T. P. *Langmuir* **2008**, *24* (20), 12001–12009.
(114) Saito, N.; Liu, C.; Lodge, T. P.; Hillmyer, M. A. *Macromolecules* **2008**, *41* (22), 8815–8822.
(115) Saito, N.; Liu, C.; Lodge, T. P.; Hillmyer, M. A. *ACS Nano* **2010**, *4* (4), 1907–1912.
(116) Liu, C.; Hillmyer, M. A.; Lodge, T. P. *Langmuir* **2009**, *25* (24), 13718–13725.
(117) Zhang, Y.; Liu, H.; Hu, J.; Li, C.; Liu, S. *Macromol. Rapid Commun.* **2009**, *30* (11), 941–947.
(118) Zhang, Y.; Liu, H.; Dong, H.; Li, C.; Liu, S. *J. Polym. Sci., Part A: Polym. Chem.* **2009**, *47* (6), 1636–1650.
(119) Kotzev, A.; Laschewsky, A.; Adriaensens, P.; Gelan, J. *Macromolecules* **2002**, *35* (3), 1091–1101.
(120) Szczubiałka, K.; Moczek, Ł.; Goliszek, A.; Nowakowska, M.; Kotzev, A.; Laschewsky, A. *J. Fluorine Chem.* **2005**, *126* (9−10), 1409–1418.
(121) Stähler, K.; Selb, J.; Candau, F. *Langmuir* **1999**, *15* (22), 7565–7576.
(122) Kotzev, A.; Laschewsky, A.; Rakotoaly, R. H. *Macromol. Chem. Phys.* **2001**, *202* (17), 3257–3267.
(123) Zhulina, E. B.; Borisov, O. V. *Macromolecules* **2008**, *41* (15), 5934–5944.
(124) Dormidontova, E. E.; Khokhlov, A. R. *Macromolecules* **1997**, *30* (7), 1980–1991.
(125) Xin, J.; Liu, D.; Zhong, C. *J. Phys. Chem. B* **2007**, *111* (49), 13675–13682.
(126) Cui, J.; Jiang, W. *Langmuir* **2011**, *27* (16), 10141–10147.
(127) Cui, Y.; Zhong, C.; Xia, J. *Macromol. Rapid Commun.* **2006**, *27* (17), 1437–1441.
(128) Xia, J.; Zhong, C. *Macromol. Rapid Commun.* **2006**, *27* (19), 1654–1659.
(129) Xia, J.; Zhong, C. *Macromol. Rapid Commun.* **2006**, *27* (14), 1110–1114.
(130) Zhong, C.; Liu, D. *Macromol. Theory Simul.* **2007**, *16* (2), 141–157.
(131) Xia, J.; Liu, D.; Zhong, C. *Phys. Chem. Chem. Phys.* **2007**, *9* (38), 5267–5273.
(132) Zhao, Y.; Liu, Y.-T.; Lu, Z.-Y.; Sun, C.-C. *Polymer* **2008**, *49* (22), 4899–4909.
(133) Zhao, Y.; You, L.-Y.; Lu, Z.-Y.; Sun, C.-C. *Polymer* **2009**, *50* (22), 5333–5340.
(134) Liu, D.; Zhong, C. *Macromol. Rapid Commun.* **2007**, *28* (3), 292–297.
(135) Xin, J.; Liu, D.; Zhong, C. *J. Phys. Chem. B* **2009**, *113* (28), 9364–9372.
(136) Chou, S.-H.; Tsao, H.-K.; Sheng, Y.-J. *J. Chem. Phys.* **2006**, *125* (19), 194903.
(137) Kong, W.; Li, B.; Jin, Q.; Ding, D.; Shi, A.-C. *J. Am. Chem. Soc.* **2009**, *131* (24), 8503–8512.
(138) Ma, Z.; Yu, H.; Jiang, W. *J. Phys. Chem. B* **2009**, *113* (11), 3333–3338.
(139) Ma, J. W.; Li, X.; Tang, P.; Yang, Y. *J. Phys. Chem. B* **2007**, *111* (7), 1552–1558.
(140) Yin, Y.; Jiang, R.; Li, B.; Jin, Q.; Ding, D.; Shi, A.-C. *J. Chem. Phys.* **2008**, *129* (15), 154903.
(141) Jiang, T.; Wang, L.; Lin, S.; Lin, J.; Li, Y. *Langmuir* **2011**, *27* (10), 6440–6448.
(142) Wang, L.; Lin, J. *Soft Matter* **2011**, *7* (7), 3383–3391.
(143) Huang, C.-I.; Liao, C.-H.; Lodge, T. P. *Soft Matter* **2011**, *7* (12), 5638–5647.
(144) Zhu, Y.; Li, R. K. Y.; Jiang, W. *Chem. Phys.* **2006**, *327* (1), 137–143.
(145) Torchilin, V. P. *Cell. Mol. Life Sci.* **2004**, *61* (19), 2549–2559.
(146) Chi, Y.; Scroggins, S. T.; Fréchet, J. M. J. *J. Am. Chem. Soc.* **2008**, *130* (20), 6322–6323.
(147) Lodge, T. P.; Rasdal, A.; Li, Z.; Hillmyer, M. A. *J. Am. Chem. Soc.* **2005**, *127* (50), 17608–17609.
(148) Bai, Z.; Lodge, T. P. *J. Am. Chem. Soc.* **2010**, *132* (45), 16265–16270.
(149) He, Y.; Lodge, T. P. *J. Am. Chem. Soc.* **2006**, *128* (39), 12666–12667.
(150) Bai, Z.; Lodge, T. P. *Langmuir* **2010**, *26* (11), 8887–8892.
(151) Bai, Z.; Lodge, T. P. *J. Phys. Chem. B* **2009**, *113* (43), 14151–14157.
(152) Amado, E.; Kressler, J. *Soft Matter* **2011**, *7* (16), 7144–7149.
(153) Place, E. S.; George, J. H.; Williams, C. K.; Stevens, M. M. *Chem. Soc. Rev.* **2009**, *38* (4), 1139–1151.
(154) Cui, H.; Hodgdon, T. K.; Kaler, E. W.; Abezgauz, L.; Danino, D.; Lubovsky, M.; Talmon, Y.; Pochan, D. J. *Soft Matter* **2007**, *3* (8), 945–955.

Macromolecules

Article

pubs.acs.org/Macromolecules

2-Isopropenyl-2-oxazoline: A Versatile Monomer for Functionalization of Polymers Obtained via RAFT

Christine Weber,[†,‡,§] Toni Neuwirth,[†] Kristian Kempe,[†,‡] Bengi Ozkahraman,[⊥] Emel Tamahkar,[⊥] Humeyra Mert,[⊥] C. Remzi Becer,*[,†,§,∥] and Ulrich S. Schubert[†,‡,§]

[†]Laboratory of Organic and Macromolecular Chemistry (IOMC), Friedrich-Schiller-University Jena, Humboldtstrasse 10, 07743, Jena, Germany

[‡]Jena Center for Soft Matter (JCSM), Friedrich-Schiller-University Jena, Humboldtstrasse 10, 07743, Jena, Germany

[§]Dutch Polymer Institute (DPI), John F. Kennedylaan 2, 5612 AB Eindhoven, The Netherlands

[⊥]Department of Chemical Engineering, Hitit University, 19030, Corum, Turkey

[∥]Department of Chemistry, University of Warwick, CV4 7AL, Coventry, U.K.

Supporting Information

ABSTRACT: 2-Isopropenyl-2-oxazoline (*i*POx) was polymerized for the first time via a controlled radical polymerization technique. Reversible addition−fragmentation chain transfer (RAFT) polymerization utilizing a dithiobenzoate-based chain transfer agent was employed to form a backbone that is highly reactive toward thiols and acids. Moreover, the statistical copolymerization of *i*POx with methyl methacrylate (MMA) and *N-iso*-propylacrylamide (N*i*PAm) was investigated resulting in two copolymer series with *i*POx content varying from 100% to 13% (PDI = 1.37 to 1.21). The P(*i*POx-*stat*-N*i*PAm) copolymers displayed thermoresponsive behavior in water as well as phosphate buffered saline at higher temperatures in comparison to homopolymers of N*i*PAm due to the hydrophilicity of the introduced *i*POx moieties (T_{cp} = 25 to 75 °C). Futhermore, *i*POx-based (co)polymers were functionalized by polymer analogous addition reactions with thiophenol, benzoic acid and 4-azidobenzoic acid in high conversions (74−100%). The latter adduct represented a suitable building block for the synthesis of a graft copolymer consisting of a PMMA backbone and poly(2-ethyl-2-oxazoline) (PEtOx) side chains via copper-catalyzed azide−alkyne cycloaddition (CuAAC) of PEtOx with alkyne terminus.

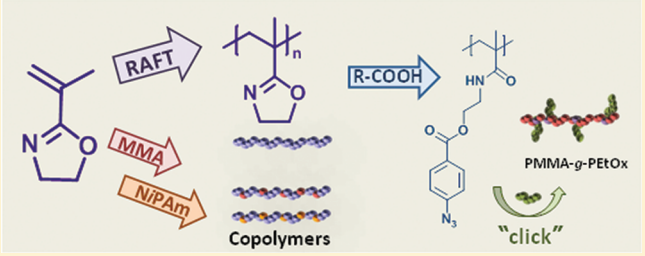

INTRODUCTION

2-Oxazolines are well-known in polymer chemistry for their ability to undergo a living cationic ring-opening polymerization to yield well-defined polymers for use in biomedical applications.[1−8] However, one might be less aware of the fact that the 2-oxazoline ring is also capable of addition reactions with a wide range of nucleophiles, such as carboxylic acids or thiols.[9] These reactions have been exploited for polyaddition reactions of bis-oxazolines and dicarboxylic acids yielding polyesteramides.[10−13] In addition, the 2-oxazoline ring provides a versatile tool for postpolymerization functionalization when it is connected in a pendant fashion to a polymer backbone. Such a structure can be obtained by the polymerization of 2-*iso*-propenyl-2-oxazoline (*i*POx), a commercially available monomer, via its vinylic moiety. This polymerization can be performed under either anionic[14] or free radical[15] polymerization conditions. On the other hand, attempts to polymerize *i*POx cationically via its oxazoline moiety resulted only in ill-defined oligomeric products.[14] It was already demonstrated that the pendant oxazoline ring can be readily used for further modification of the free radically polymerized P*i*POx by attack of acids or thiols, even in aqueous solution.[16] More recently, Jerca et al. reported the functionalization of statistical copolymers of *i*POx and methyl methacrylate (MMA) with a carboxylic acid functionalized azo dye.[17,18] In addition, MMA/*i*POx copolymers are commercially available as water-soluble cross-linking agents for carboxylic acid containing polymers.

Nowadays, controlled radical polymerization (CRP) techniques,[19−21] such as atom transfer polymerization,[22] nitroxide mediated polymerization[23] or reversible addition−fragmentation chain transfer (RAFT) polymerization[24,25] are widely applied for the synthesis of well-defined polymers from a large number of vinylic monomers, such as acrylates, acrylamides, methacrylamides, methacrylates or vinylesters. One major advantage of these polymerization techniques is the utilization of monomers and solvents without extensive purification procedures as well as the good tolerance against other functional moieties, compared to ionic polymerizations. In addition, the utilization of CRP and various click reactions[26−29] enables the engineering of advanced polymer structures, such as

Received: September 21, 2011
Revised: November 25, 2011
Published: December 12, 2011

block or graft copolymers, or the copolymerization with other monomers providing further interesting properties, such as thermoresponsiveness.[30−33] However, to the best of our knowledge, the CRP of *i*POx has not been reported up to now, even though the oxazoline moiety should enable access to a range of interesting polymers via polymer analogous reactions when using a well-defined P*i*POx as a backbone.

In this contribution, we present the homo- and statistical copolymerization of *i*POx utilizing the RAFT polymerization technique (Scheme 1). To the best of our knowledge, this is the first report on a statistical copolymerization of *N-iso*-propylacrylamide (N*i*PAm) and *i*POx. Moreover, we have investigated the thermoresponsive behavior of the obtained polymers. Furthermore, selected polymers were subsequently functionalized with benzoic acid and thiophenol as model compounds to present the versatility of the addition reaction. Last but not least, 4-azidobenzoic acid was reacted as precursor material for the synthesis of graft copolymers via "click" chemistry.

Scheme 1. Schematic Representation of the RAFT Polymerization of 2-Isopropenyl-2-oxazoline

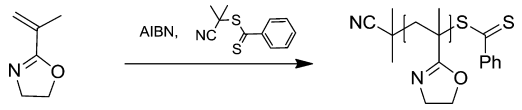

EXPERIMENTAL SECTION

Materials. The monomers *i*POx (99%), methyl methacrylate (MMA, 99%) and *N-iso*-propylacrylamide (N*i*PAm, 97%) were purchased from Aldrich. MMA was destabilized with inhibitor remover (Aldrich) prior to use. 2,2′-Azobis(2-methylpropionitrile) (98%, Acros, AIBN) was recrystallized from hexane and the chain transfer agent 2-cyanopropyl dithiobenzoate (CPDB, 97%) was obtained from Aldrich. Benzoic acid (99.5%) was purchased from Sigma-Aldrich, 4-azidobenzoic acid (98%) from ABCR, and thiophenol (98%), DMF (99.5%) as well as 1,8-diazabicyclo[5.4.0]undec-7-ene (DBU, 99%) from Fluka. Copper(I) iodide (CuI, 99.5%) was purchased from Aldrich. Poly(2-ethyl-2-oxazoline) (PEtOx-TB) was prepared according to a previously published procedure.[34] Preparative size exclusion chromatography was carried out using BioBeads-SX1 from BioRad with THF as eluent. For the cloud point measurements, demineralized water and phosphate buffered saline 10× concentrate (Aldrich) were used. All other chemicals and solvents were obtained from common commercial sources and used without further purification, unless otherwise noted.

Instrumentation. ^{1}H NMR spectra were recorded in $CDCl_3$ or CD_2Cl_2 on a Bruker Avance 300 MHz using the residual solvent resonance as an internal standard. Size exclusion chromatography (SEC) was measured on a Shimadzu system equipped with a SCL-10A system controller, a LC-10AD pump, and a RID-10A refractive index detector using a solvent mixture containing chloroform, triethylamine, and isopropanol (94:4:2) at a flow rate of 1 mL min^{-1} on a PSS-SDV-linear M 5 μm column at 40 °C. The system was calibrated with PMMA (2−88 kDa) standards. For polymers containing secondary amides, a different SEC system was used. This system is equipped with a SCL-10A system controller, a LC-10AD pump, a RID-10A refractive index detector, and both a PSS Gram30 and a PSS Gram1000 column in series, whereby *N,N*-dimethylacetamide with 2.1 g·L^{-1} of LiCl was applied as an eluent at 1 mL min^{-1} flow rate and the column oven was set to 60 °C. GC measurements were performed on a Shimadzu GC-2010 equipped with a Restek Rtx-5 column, a FID detector and a PAL autosampler. IR spectra were recorded on an Affinity-1 Fourier transform infrared spectrophotometer from Shimadzu.

For the measurement of the matrix-assisted laser desorption/ionization (MALDI) mass spectra an Ultraflex III TOF/TOF (Bruker Daltonics, Bremen, Germany) was used. The instrument was equipped with a Nd:YAG laser and a collision cell. All spectra were measured in the positive reflector or linear mode. The instrument was calibrated prior to each measurement with an external PMMA standard from PSS Polymer Standards Services GmbH (Mainz, Germany). Electrospray ionization time-of-flight mass spectrometry (ESI TOF MS) measurements were performed with a micrOTOF (Bruker Daltonics) mass spectrometer equipped with an automatic syringe pump, which is supplied from KD Scientific for sample injection. The mass spectrometer was operating in the positive ion mode. The standard electrospray ion source was used to generate the ions. The ESI TOF MS instrument was calibrated in the m/z range from 50 to 3000 g mol^{-1} using an internal calibration standard (Tunemix solution), which was supplied from Agilent. Data were processed via Bruker Data Analysis software version 4.0. Cloud point temperatures (T_{cp}) were determined using a Crystal 16 from Avantium Technologies being connected to a chiller (Julabo FP 40) at a wavelength of 500 nm and a heating ramp of 1 K min^{-1}. The concentration of the polymer was kept constant at 5 mg mL^{-1}, and T_{cp} values are reported from 50% transmittance in the second heating cycle.

Synthesis. *Kinetic Studies RAFT Polymerization.* *i*POx (1.5 g, 13.5 mmol) was dissolved in 5.2 mL toluene and a solution of 11.1 mg (0.067 mmol) AIBN in toluene as well as a solution of 59.7 mg (0.27 mmol) CPDB in toluene were added. The concentration of the monomer was 2 mol L^{-1} and the ratio of [*i*POx]:[CPDB]:[AIBN] was 50:1:0.25. Subsequently, the mixture was degassed with a gentle flow of nitrogen for 30 min and divided over 7 separate vials that were

Table 1. Characterization Data of Statistical Copolymers of *i*POx with MMA and N*i*PAm

	comonomer type (M)	% *i*POx (feed)	% *i*POx (^{1}H NMR)	DP^c *i*POx:M	M_n [g mol^{-1}]	PDI	conv [%] *i*POx:M
P1	-	100	100	55:0	2700^a	1.37^a	16:0
P2	MMA	90	89	43:5	2840^a	1.34^a	16:19
P3	MMA	75	77	40:12	3350^a	1.34^a	20:19
P4	MMA	50	53	26:23	3820^a	1.31^a	11:16
P5	MMA	25	29	18:44	5360^a	1.23^a	22:22
P6	MMA	10	13	12:84	7370^a	1.21^a	43:39
P7	-	100	100	50:0	2760^b	1.33^b	11:0
P8	N*i*PAm	90	88	31:8	2880^b	1.24^b	32:14
P9	N*i*PAm	75	83	12:2	1960^b	1.36^b	21:5
P10	N*i*PAm	50	62	8:5	2680^b	1.23^b	26:7
P11	N*i*PAm	25	43	5:7	3080^b	1.20^b	29:10
P12	N*i*PAm	10	17	3:13	4000^b	1.22^b	32:12

^{a}Determined via SEC ($CHCl_3$) using PMMA calibration. ^{b}Determined via SEC (DMA) using PMMA calibration. ^{c}Degree of polymerization estimated from the integral ratio of the aromatic signals of the dithiobenzoate end group and signals of both repeating units in the ^{1}H NMR spectra.

dx.doi.org/10.1021/ma2021387 | *Macromolecules* 2012, 45, 20−27

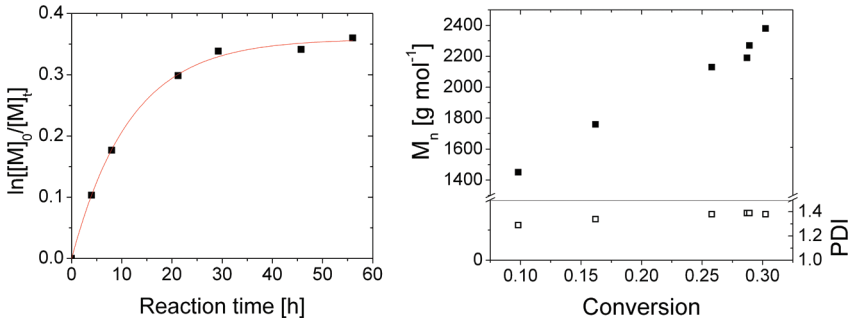

Figure 1. Kinetic plots for the RAFT homopolymerization of *i*POx utilizing CPDB as CTA. SEC traces can be found in ESI (Figure SI-2, Supporting Information).

capped and shortly degassed with nitrogen one more time. All vials were placed simultaneously in an oil bath at 70 °C and taken out after varying reaction times between 4 and 56 h. Subsequent to cooling with tap water, the vials were opened and samples were taken for ^{1}H NMR ($CDCl_3$) and SEC ($CHCl_3$). The conversions were determined by comparison of the integral ratios of the peaks in the ^{1}H NMR spectrum derived from the vinylic protons of *i*POx (5.72 and 5.32 ppm, respectively) and the methylene protons of the oxazoline ring (4.28−3.56 ppm).

RAFT Homo- and Statistical Copolymerization. According to the feed ratios given in Table 1, the appropriate amounts of *i*POx and MMA or *i*POx and N*i*PAm, respectively, were dissolved in toluene and AIBN as well as CPDB were added in a similar fashion as described above. For **P1−6** (MMA copolymers) the ratio of [Monomer]: [CPDB]: [AIBN] was set to 100: 1: 0.25, whereas it was set to 50: 1: 0.25 for **P7−12** (N*i*PAm copolymers). After capping the vials and gently degassing the reaction mixtures with nitrogen, initial samples were taken via syringe and the vials were placed in an oil bath at 70 °C to react for 19 h. Subsequent to cooling with tap water, the vials were opened and final samples were taken for GC ($CHCl_3$) and SEC ($CHCl_3$ for **P1−6** and DMA for **P7−12**) measurements. Monomer conversions were determined via GC using the reaction solvent as an internal standard. The P*i*POx homopolymers and statistical copolymers with MMA were precipitated into cold *tert*-butyl methyl ether and the N*i*PAm copolymers were purified by preparative size exclusion chromatography on a BioBeads-SX1 column with THF as eluent. The resulting pink polymers were dried in a vacuum oven. Yields: **P1**, 48 mg, 5%; **P2**, 115 mg, 11%; **P3**, 205 mg, 16%; **P4**, 397 mg, 21%; **P5**, 574 mg, 31%; **P6**, 812 mg, 45%; **P7**, 209 mg, 21%; **P8**, 144 mg, 13%; **P9**, 180 mg, 14%; **P10**, 311 mg, 16%; **P11**, 278 mg, 14%; **P12**, 322 mg, 16%. ^{1}H NMR (300 MHz, $CDCl_3$): **P1−6** δ/ppm = 4.3−4.1 N−CH_2−, 3.8−3.6 N−CH_2−, 3.9−3.5 O−CH_3, 2.3−1.5 C−CH_2−C, 1.5−0.8 C−CH_3; **P7−12** δ/ppm = 4.3−4.1 N−CH_2−, 4.1−3.8 CH−$(CH_3)_2$, 3.8−3.6 N−CH_2−, 2.3−1.5 C−CH_2−C, 1.5−0.8 C−CH_3.

Addition Reactions with Carboxylic Acids and Thiophenol. In a representative example, P*i*POx (85 mg, corresponding to 0.77 mmol of *i*POx units) and a 2-fold excess of *p*-azidobenzoic acid (106 mg, 1.53 mmol) were dissolved in 2 mL of DMF and stirred for 24 h at 60 °C. The crude product was dissolved in chloroform and extracted with saturated aqueous sodium bicarbonate solution and brine, dried over sodium sulfate and concentrated. Subsequently, the polymer was precipitated into cold diethyl ether and dried in a vacuum oven. Yields: **A1**, 61 mg, 54%; **A2**, 209 mg, 63%; **A3**, 122 mg, 88%; **A4**, 134 mg, 52%. ^{1}H NMR (300 MHz, CD_2Cl_2): **A1** δ/ppm = 7.6−7.0 CH phenyl, 6.7−6.0 NH, 3.6−2.7 S−CH_2−CH_2−NH, 2.3−1.5 C−CH_2−C, 1.5−0.8 C−CH_3; **A2** δ/ppm = 8.2−7.2 CH phenyl, 6.7−6.0 NH, 4.5−4.2 COO−CH_2, 3.8−3.3 CH_2−NH, 2.3−1.5 C−CH_2−C, 1.5−0.8 C−CH_3; **A3** δ/ppm = 8.1−7.6 and 7.1−6.7 CH phenyl, 6.7−6.0 NH, 4.5−4.2 COO−CH_2, 3.8−3.3 CH_2−NH, 2.3−1.5 C−CH_2−C, 1.5−0.8 C−CH_3; **A4** δ/ppm = 8.1−7.6 and 7.1−6.7 CH phenyl, 6.7−6.0 NH, 4.5−4.2 COO−CH_2, 3.8−3.3 CH_2−NH and O−CH_3, 2.3−1.5 C−CH_2−C, 1.5−0.8 C−CH_3.

*Copper-Catalyzed Azide-Alkyne Cycloaddition (CuAAC) of **A4** with Alkyne-Terminated Poly(2-ethyl-2-oxazoline).* The azide-containing copolymer **A4** (21 mg, corresponding to 0.017 mmol azide units), PEtOx-TB (20 mg, 0.02 mmol), and DBU (3.04 mg, 0.02 mmol) were dissolved in 0.25 mL of DMF and degassed for 30 min. Subsequently, CuI (3.8 mg, 0.02 mmol) was added under argon, and the reaction mixture was stirred overnight at ambient temperature. The CuI was removed by flushing the solution over a short aluminum oxide column. The solvent was removed under reduced pressure and the crude product was redissolved in THF in order to purify the polymer by preparative size exclusion chromatography on a BioBeads-SX1 column. Finally, the product (**A5**) was precipitated in ice-cold diethyl ether (yield 30 mg, 83%). ^{1}H NMR (300 MHz, CD_2Cl_2): δ/ppm = 8.4−7.7 (C−H phenyl and C−H triazole), 4.5−4.3 COO−CH_2CH_2, 4.2−4.0 COO−CH_2 PEtOx, 3.9−3.5 O−CH_3 MMA, 3.6−3.3 N−CH_2 PEtOx, 3.1−3.0 N−CH_3 PEtOx, 2.5−2.2 CO−CH_2 PEtOx, 2.1−1.5 CH_2 backbone, 1.5−0.8 CH_3 backbone and CH_3−CH_2 PEtOx.

RESULTS AND DISCUSSION

Homopolymerization of *i*POx. In an initial screening, varying classes of chain transfer agents (CTAs), such as dithiobenzoate, trithiocarbonate, and dithiocarbamate, were applied in order to gain first insights into the RAFT polymerization conditions of *i*POx. All polymerizations were performed in 2 M solution in toluene for 18 h at 70 °C using AIBN as initiator, whereby the ratio of [*i*POx]: [CTA]: [AIBN] was set to 50: 1: 0.25. As depicted in Figure SI-1, Supporting Information, utilization of dithiocarbamate as well as trithiocarbonate-based CTAs resulted in broad molar mass distributions, whereas the RAFT polymerization with the dithiobenzoate-based CTA (CPDB) yielded polymers with a more narrow molar mass distribution (PDI = 1.38). In addition, the lower molar mass of the resulting polymer indicated that the polymerization could be controlled by CPDB to a certain extent. As a result, CPDB was selected for the performance of further experiments, such as kinetic studies and the synthesis of statistical copolymers of *i*POx with other monomers.

The kinetic studies of the RAFT polymerization of *i*POx utilizing CPBD as CTA were performed under similar reaction conditions as described above. The resulting kinetic plots are depicted in Figure 1. Even though the molar mass of the polymer increases in a linear fashion with monomer conversion and the PDI values remain well below 1.4, the semilogarithmic plot reveals that the polymerization slows down significantly at monomer conversions of around 30%. Since the kinetic studies were accomplished in separate vials this fact cannot simply be a result of contamination of the reaction mixture during sampling. Instead, after initiation by AIBN, the intermediate structure during the RAFT process might be too stable to reinitiate the polymerization once it has been formed. This assumption is supported by the fact that CPDB is frequently

dx.doi.org/10.1021/ma2021387 | *Macromolecules* 2012, 45, 20−27

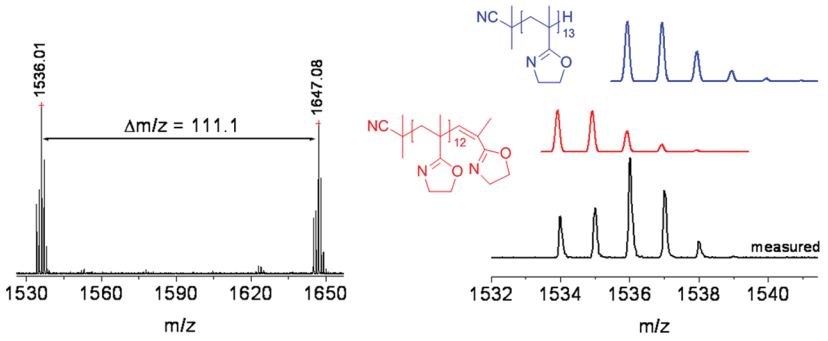

Figure 2. Zoom into the m/z range from 1520 to 1660 of the MALDI TOF mass spectrum of P*i*POx and overlay of measured and calculated isotopic patterns. Both structures are ionized with a sodium cation. The full spectrum is provided in Figure SI-3, Supporting Information.

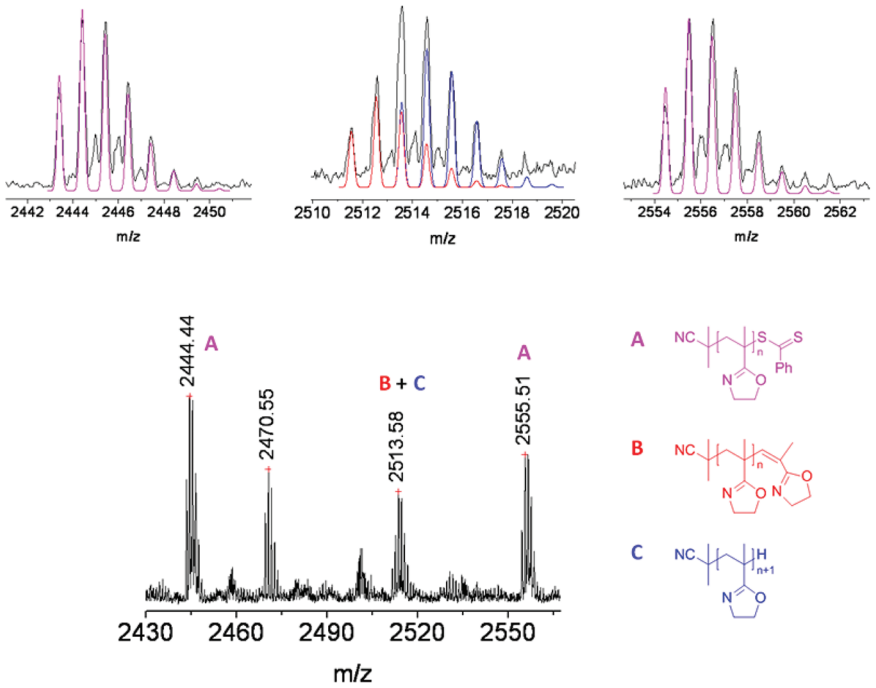

Figure 3. Zoom into the +1 charged region of the ESI TOF mass spectrum of P*i*POx and assignment of the main distributions. All structures are ionized with a proton.

applied for RAFT polymerization of more activated monomers as well as by the observation that free CTA was still present in the reaction solution, even at later stages of the polymerization, as confirmed by preparative SEC on a BioBeads column showing two pink fractions (i.e., P*i*POx and free CPDB) that eluted separately from each other.

Matrix-assisted laser desorption/ionization time-of-flight (MALDI TOF) mass spectrometry analysis of the obtained P*i*POx revealed a single distribution with a m/z difference of 111.1 between two neighboring peaks, which corresponds to the molar mass of the *i*POx repeating unit (Figure 2). Because of the rather harsh ionization during the MALDI process, the dithiobenzoate end group is cleaved and polymer chains with both saturated as well as unsaturated end groups are formed. The m/z difference of 2 between those end groups results in an overlapping of the isotopic patterns of the assigned structures.

In contrast, the softer ionization taking place during electro spray ionization (ESI) partially preserved the dithiobenzoate end group, although also polymer chains with saturated and unsaturated end groups could be assigned. The peak assignment of the resulting ESI mass spectrum of P*i*POx is shown in Figure 3.

Statistical Copolymerization of *i*POx with MMA and NiPAm. Encouraged by the rather successful homopolymerization that delivered P*i*POx with much narrower molar mass distributions compared to the results obtained by free radical polymerization,[15] two series of statistical copolymers of *i*POx with other monomers, i.e., MMA and N*i*PAm, were prepared. In order to evaluate the amount of *i*POx that can be incorporated into a copolymer without suppressing reversible chain transfer, the *i*POx content was varied systematically from 100 to 10% for both series. Except for a ratio of [monomer]:[CTA] of 100:1 for the copolymer series with MMA as reactive monomer, all polymerizations were carried out under similar conditions as described above. The results of the characterization of the obtained copolymers by means of SEC and ^{1}H NMR spectroscopy are summarized in Table 1.

SEC analysis of the statistical copolymers consisting of *i*POx and MMA **P1**−**P6** (Figure 4, top) revealed that, with increasing amount of the more activated MMA in the feed, the molar mass distribution becomes much more narrow with PDI values

dx.doi.org/10.1021/ma2021387 | *Macromolecules* 2012, 45, 20−27

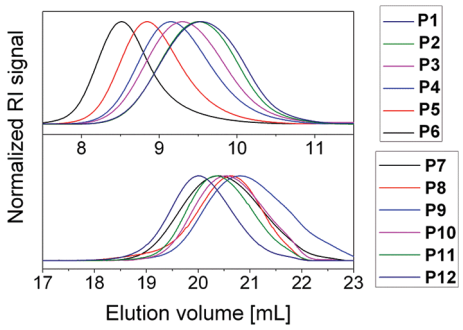

Figure 4. SEC traces of the statistical copolymers of *i*POx with MMA (top, eluent $CHCl_3$) and with N*i*PAm (bottom, eluent DMA).

between 1.37 for the P*i*POx homopolymer and 1.21 for the statistical copolymer containing only 13 mol % *i*POx. In addition, the molar mass of the copolymer increases with the MMA content. In order to evaluate if the latter is simply an effect of a variation in hydrodynamic volume of the polymers with altered composition, the degree of polymerization (DP) of each comonomer was roughly estimated from appropriate signals in the ^{1}H NMR spectra, assuming full end functionalization with the dithiobenzoate moiety. Indeed, keeping in mind the accuracy of the applied method, at least the two copolymers with the largest mole fraction of MMA (**P5** and **P6**) have significantly higher DP values than the copolymers with lower MMA content (see Table 1). In addition, as depicted in Figure 5, the copolymer composition,

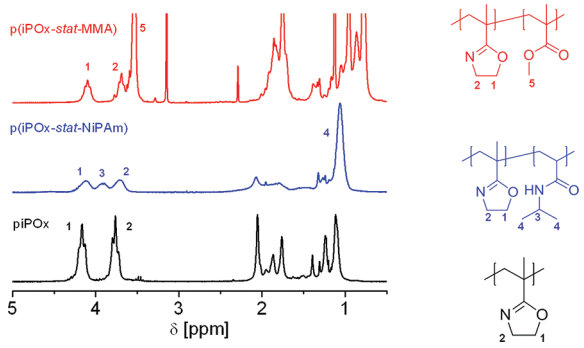

Figure 5. ^{1}H NMR spectra (300 MHz, $CDCl_3$) of a P*i*POx homopolymer (bottom) and statistical copolymers of *i*POx with MMA (top) as well as with N*i*PAm (middle), respectively.

which was calculated from the ratio of the peak integrals of the methylene protons of the 2-oxazoline ring of the *i*POx and the methyl protons of MMA, was found to be close to the feed ratio of both monomers. All these results indicate that the low ability of the intermediate species that is formed during RAFT polymerization of *i*POx to undergo reversible chain transfer can be overcome by utilization of MMA as more activated comonomer.

As next step, *i*POx functionalities were incorporated into a polymer displaying thermo-responsive properties, namely PN*i*PAm. For this second series of statistical copolymers **P7**–**12**, SEC analysis (Figure 4, bottom) revealed a significant increase of the molar mass and a satisfying peak shape only for **P12**, the copolymer with the highest mole fraction of N*i*PAm (83%), even though the PDI values for all copolymers remained well below 1.3, except for **P9**. In addition, the conversion of *i*POx was found to be higher than that of N*i*PAm, which is reflected in an increased mole fraction of *i*POx in the polymers with respect to the feed ratios. However, it was possible to obtain polymers with varying *i*POx content from roughly 17 to 88% (as determined by ^{1}H NMR spectroscopy, Figure 5), that could be used for an investigation of the effect of the *i*POx moieties upon the lower critical solution temperature (LCST) behavior of PN*i*PAm.

Aqueous Solution Behavior of P(*i*POx-*stat*-NiPAm) Copolymers. The thermoresponsive properties of **P7**–**12** in aqueous solution were investigated by means of turbidimetry at a polymer concentration of 5 mg mL^{-1} in water as well as phosphate buffered saline (PBS). In order to determine the reversibility of the coil to globule transition two heating cooling cycles were conducted for each sample with a heating rate of 1 K min^{-1}. Turbidity curves from the second heating run are displayed in Figure 6 (left). The P*i*POx homopolymer **P7** remained water-soluble during the whole investigated temperature range up to 100 °C indicative of its high hydrophilicity. The latter also caused complete solubility of the copolymer with the highest *i*POx content **P8**. Consequently, an increasing mole fraction of *i*POx in the statistical copolymers **P9**–**12** was expected to result in elevated cloud point temperatures (T_{cp}) of the aqueous solutions. Surprisingly, as shown in Figure 6 (right), this holds true only for copolymers with mole fractions of *i*POx above 50%. Below that value, T_{cp} remained rather unaffected by the copolymer composition around 25 to 26 °C in PBS and around 33 to 35 °C in water. As a result of the hydrophilic *i*POx moieties, the latter value is slightly higher than the T_{cp} of a comparable PN*i*PAm solution at 30 °C under similar measurement conditions. In addition, the transition becomes less sharp with increasing *i*POx/N*i*PAm ratio in the copolymer. Possible explanations for this unexpected behavior

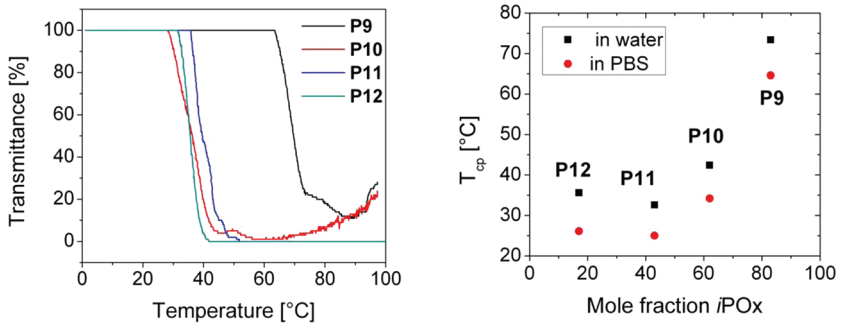

Figure 6. Left: Turbidity curves of aqueous solutions of **P9**–**12** in water (c = 5 mg mL^{-1}, second heating run). Right: Dependence of the cloud point temperature (T_{cp}) of solutions of **P9**–**12** in water and PBS on the copolymer composition (c = 5 mg mL^{-1}, second heating run, 50% transmittance).

dx.doi.org/10.1021/ma2021387 | *Macromolecules* 2012, 45, 20–27

Scheme 2. Schematic Representation of the Addition Reaction of P*i*POx with Thiophenol and Carboxylic Acids

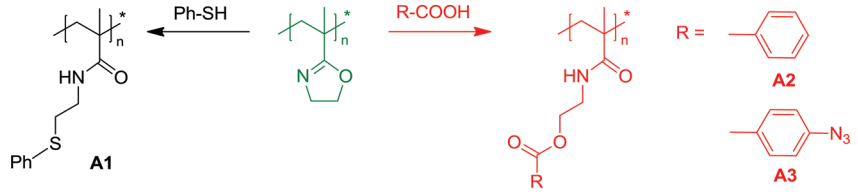

Table 2. Characterization Data of Addition Products Obtained after Reaction of P*i*POx with Thiophenol and Carboxylic Acids

		premodification		postmodification		theoretical	
code	reactant	M_n [a] [g mol^{-1}]	PDI	M_n [a] [g mol^{-1}]	PDI	M_n [b] [g mol^{-1}]	F [c] (%)
A1	thiophenol	2130	1.45	11 200	1.21	11 000	quant.
A2	benzoic acid	2930	1.45	6200	1.35	9500	74
A3	4-azidobenzoic acid	2130	1.45	8070	1.40	12 700	88

[a]Determined via SEC (DMA) using PMMA calibration. [b]Calculated from the DP of the used P*i*POx and the degree of functionalization. [c]Degree of functionalization determined from ^{1}H NMR.

might either be a gradient composition of the copolymers facilitating the solubilization of already collapsed N*i*PAm rich parts by *i*POx rich parts below T_{cp}, or the rather small overall DP of the copolymers **P9**−**12** that exhibit LCST behavior (in the range of 12 to16). Because of the latter small variations of the composition of individual polymer chains directly result in a mixture of thermoresponsive polymers with varying T_{cp}.[35] In this case, polymer chains containing a similar mole fraction of N*i*PAm might be present in both copolymers (**P9** and **P10**) and would collapse prior to chains with smaller N*i*PAm content.

Functionalization of iPOx-Containing Polymers with Carboxylic Acids and Thiols. In order to evaluate the possibility to synthesize functionalized polymers from the *i*POx containing copolymers, polymer analogous addition reactions with benzoic acid and thiophenol as model substances were performed under mild conditions (at 60 °C) using P*i*POx homopolymers as starting material. In addition, 4-azidobenzoic acid was applied as reactant in order to obtain a polymer that is functionalized with multiple azide moieties. The poly(methacrylamide) structure of the resulting addition products **A1**−**3** is depicted in Scheme 2, and analytical data are supplied in Table 2.

Characterization of **A1**−**3** by means of SEC (Figure SI-4, Supporting Information) revealed a significant increase of the hydrodynamic volume of the polymers after the addition reactions and, especially for the addition product with thiophenol **A1**, smaller PDI values when compared to the P*i*POx starting material. It should be noted that the dithiobenzoate end group is cleaved during the reaction process (as indicated by the whitish instead of pink color of **A1**−**3**).

Utilizing ^{1}H NMR spectroscopy the degree of functionalization with the respective acid or thiol could be easily determined by comparison of the peak integrals in the aromatic region with the peak integrals derived from residual oxazoline moieties and the four methylene protons between amide and ester functionalities. As depicted in Figure 7, the reactions with both carboxylic acids reached conversions of 74% for **A1** and 88% for **A2**, respectively. Small residual peaks of the pendant oxazoline rings could be detected in both ^{1}H NMR spectra that were overlapping with the corresponding proton signals of the opened methacrylamide structure. On the other hand, the

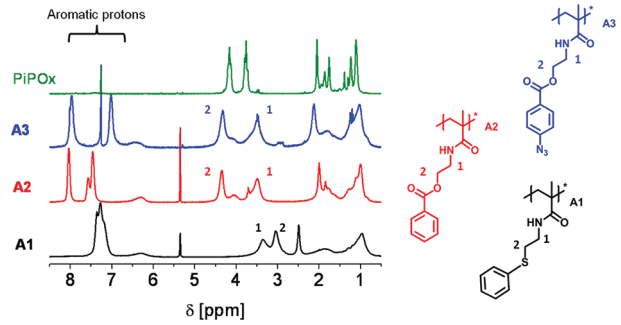

Figure 7. ^{1}H NMR spectra (300 MHz, CD_2Cl_2 or $CDCl_3$) of a P*i*POx homopolymer (top) and of the addition products with thiophenol (**A1**), benzoic acid (**A2**) as well as 4-azidobenzoic acid (**A3**).

addition of thiophenol proceeded quantitatively as demonstrated by the disappearance of the oxazoline derived signals.

The formation of ester functionalities after the polymer analogous reactions with carboxylic acids could be confirmed by means of FT-IR spectroscopy (Figure 8). The IR spectra of

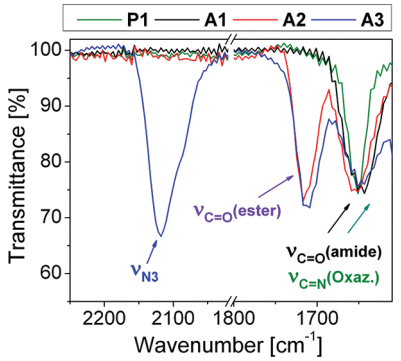

Figure 8. Zoom into the azide and carbonyl vibration region of the FT ATR IR spectra of P*i*POx (**P1**) and addition products with thiophenol, benzoic acid, and 4-azidobenzoic acid, respectively (**A1**−**3**).

both **A2** and **A3** clearly show a characteristic band at 1720 cm^{-1} that can be assigned to the carbonyl stretching vibration of the formed ester. In addition, the IR spectrum of **A3** provides evidence of the presence of azide moieties due to the characteristic ν_{N_3} band at 2120 cm^{-1}. It should be noted that

dx.doi.org/10.1021/ma2021387 | *Macromolecules* 2012, 45, 20−27

Scheme 3. Schematic Representation of the Synthesis Route toward PMMA-*g*-PEtOx

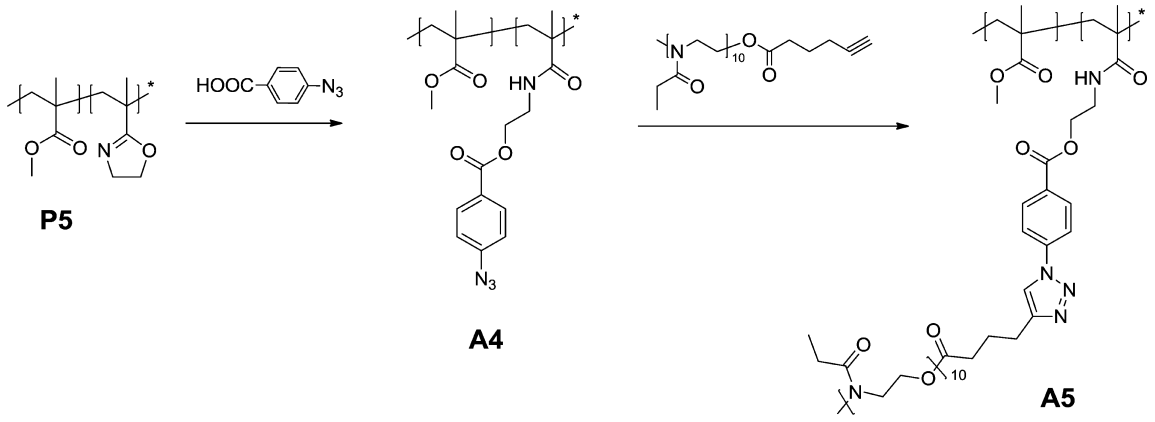

the carbonyl stretching vibration of the amide moiety at 1655 cm^{-1} in the IR spectra of all addition products **A1−3** is overlapping with the −C═N vibration of the oxazoline ring in P*i*POx.

The fact that the copper-catalyzed azide−alkyne cycloaddition (CuAAC) has become a common and versatile method in polymer chemistry led to the availability of a wide range of interesting building blocks for this type of "click" reaction. In this context, addition products of P*i*POx-based copolymers with 4-azidobenzoic acid could serve as starting material for further functionalization, or the synthesis of graft copolymers if the utilized alkyne represents an end functionalized polymer. As depicted in Scheme 3, the latter route was applied in order to obtain a graft copolymer having a PMMA-based backbone and poly(2-ethyl-2-oxazoline) (PEtOx) side chains.

A first hint toward a successful grafting of alkyne-terminated PEtOx onto the azide functionalized PMMA-based copolymer **A4** is provided by SEC analysis of the graft copolymer **A5** (Figure 9). The SEC trace of **A5** is shifted to smaller elution

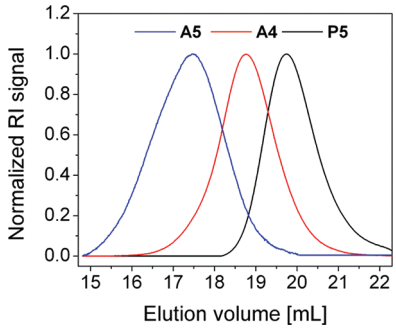

Figure 9. SEC traces (DMA) of **P5** (M_n = 4760 g mol^{-1}, PDI = 1.26), its addition product with 4-azidobenzoic acid **A4** (M_n = 10 220 g mol^{-1}, PDI = 1.29), and the graft copolymer **A5** (M_n = 25 780 g mol^{-1}, PDI = 1.39).

volume when compared to **A4** indicative of its larger hydrodynamic volume due to the grafting process. In addition, the complete removal of the excess of PEtOx after preparative size exclusion chromatography is confirmed by the monomodal peak shape.

With this knowledge it is possible to gain further insights regarding the copolymer composition by interpretation of the ^{1}H NMR spectrum of **A5**. As depicted in Figure SI-5, Supporting Information, the signals of the PEtOx side chains are clearly visible, and the formation of the triazole ring is manifested by a change of the signals in the aromatic region. Most likely due to steric hindrance by already grafted PEtOx, around 20% of the attached azide functionalities underwent no 1,3-dipolar cycloaddition, as could be roughly estimated from the peak integrals of residual 4-azidobenzoate moieties.

CONCLUSION

P*i*POx homopolymers bearing a dithiobenzoate end group could be obtained with PDI values below 1.4 utilizing CPDB as CTA. The irreversible chain transfer taking place during RAFT homopolymerization of *i*POx could be overcome by statistical copolymerization with MMA as well as with N*i*PAm resulting in two copolymer series with varying *i*POx content. The copolymers of N*i*PAm with *i*POx revealed thermoresponsive properties in aqueous media at elevated temperatures compared to PN*i*PAm due to the hydrophilicity of the incorporated *i*POx moieties. In addition, the *i*POx functionalities provided a versatile tool for post polymerization modification of the synthesized homo- and copolymers via addition reactions with nucleophiles, such as carboxylic acids and, in particular, thiophenol. The polymer analogous reaction with 4-azidobenzoic acid supplied polymers carrying multiple azide functionalities that represent suitable building blocks for the subsequent grafting of alkyne-terminated PEtOx onto PMMA by copper-catalyzed 1,3-dipolar cycloaddition. Future work will focus on the full exploitation of the potential to functionalize the well-defined copolymers with biologically active thiols, such as sugars or proteins, and on the development of more challenging copolymer architectures.

ASSOCIATED CONTENT

Supporting Information

SEC traces obtained with varying CTA's and during kinetic studies, full MALDI TOF mass spectrum of P*i*POx, SEC traces of **A1−3**, and ^{1}H NMR spectra of **A4** and **A5**. This material is available free of charge via the Internet at http://pubs.acs.org.

AUTHOR INFORMATION

Corresponding Author

*E-mail: c.r.becer@warwick.ac.uk. Fax: +44 2476 151795.

ACKNOWLEDGMENTS

Anja Baumgaertel and Esra Altuntas are acknowledged for MALDI and ESI MS measurements. This work forms part of

the research program of the Dutch Polymer Institute (DPI), Project Number 612 (technology area HTE) and Project Number 686 (technology area BIO-inspired). The authors thank the Thüringer Ministerium für Wissenschaft, Bildung und Kultur for the financial support of this study (Grant No. B514-09051, NanoConSens). K.K. is grateful to the Landesgraduiertenfoerderung for financial support.

REFERENCES

(1) Aoi, K.; Okada, M. *Prog. Polym. Sci.* **1996**, *21*, 151−208.
(2) Hoogenboom, R. *Angew. Chem., Int. Ed.* **2009**, *48*, 7978−7994.
(3) Schlaad, H.; Diehl, C.; Gress, A.; Meyer, M.; Demirel, A. L.; Nur, Y.; Bertin, A. *Macromol. Rapid Commun.* **2010**, *31*, 511−525.
(4) Makino, A.; Kobayashi, S. *J. Polym. Sci., Part A: Polym. Chem.* **2010**, *48*, 1251−1270.
(5) Kobayashi, S. *Prog. Polym. Sci.* **1990**, *15*, 751−823.
(6) Kobayashi, S.; Uyama, H. *J. Polym. Sci., Part A: Polym. Chem.* **2002**, *40*, 192−209.
(7) Adams, N.; Schubert, U. S. *Adv. Drug Delivery Rev.* **2007**, *59*, 1504−1520.
(8) Weber, C.; Becer, C. R.; Guenther, W.; Hoogenboom, R.; Schubert, U. S. *Macromolecules* **2010**, *43*, 160−167.
(9) Culbertson, B. M. *Prog. Polym. Sci.* **2002**, *27*, 579−626.
(10) Nery, L.; Lefebvre, H.; Fradet, A. *J. Appl. Polym. Sci.* **2009**, *113*, 628−636.
(11) Nery, L.; Lefebvre, H.; Fradet, A. *Macromol. Chem. Phys.* **2004**, *205*, 448−455.
(12) Nery, L.; Lefebvre, H.; Fradet, A. *Macromol. Chem. Phys.* **2003**, *204*, 1755−1764.
(13) Luston, J.; Kronek, J.; Janigova, I. *J. Macromol. Sci. A* **2010**, *47*, 716−724.
(14) Tomalia, D. A.; Thill, B. P.; Fazio, M. J. *Polym. J.* **1980**, *12*, 661−675.
(15) Zhang, N.; Huber, S.; Schulz, A.; Luxenhofer, R.; Jordan, R. *Macromolecules* **2009**, *42*, 2215−2221.
(16) Nishikubo, T.; Kameyama, A.; Tokai, H. *Polym. J.* **1996**, *28*, 134−138.
(17) Jerca, V. V.; Nicolescu, F. A.; Trusca, R.; Vasile, E.; Baran, A.; Anghel, D. F.; Vasilescu, D. S.; Vuluga, D. M. *React. Funct. Polym.* **2011**, *71*, 373−379.
(18) Jerca, V. V.; Nicolescu, F. A.; Baran, A.; Anghel, D. F.; Vasilescu, D. S.; Vuluga, D. M. *React. Funct. Polym.* **2010**, *70*, 827−835.
(19) Braunecker, W. A.; Matyjaszewski, K. *Prog. Polym. Sci.* **2007**, *32*, 93−146.
(20) Rosen, B. M.; Percec, V. *Chem. Rev.* **2009**, *109*, 5069−5119.
(21) Ouchi, M.; Terashima, T.; Sawamoto, M. *Chem. Rev.* **2009**, *109*, 4963−5050.
(22) Coessens, V.; Pintauer, T.; Matyjaszewski, K. *Prog. Polym. Sci.* **2001**, *26*, 337−377.
(23) Grubbs, R. B. *Polym. Rev.* **2011**, *51*, 104−137.
(24) Moad, G.; Rizzardo, E.; Thang, S. H. *Polymer* **2008**, *49*, 1079−1131.
(25) Moad, G.; Rizzardo, E.; Thang, S. H. *Aust. J. Chem.* **2009**, *62*, 1402−1472.
(26) Kempe, K.; Krieg, A.; Becer, C. R.; Schubert, U. S. *Chem. Soc. Rev.* 2012, *41*, 176−191.
(27) Fournier, D.; Hoogenboom, R.; Schubert, U. S. *Chem. Soc. Rev.* **2007**, *36*, 1369−1380.
(28) Mansfeld, U.; Pietsch, C.; Hoogenboom, R.; Becer, C. R.; Schubert, U. S. *Polym. Chem.* **2010**, *1*, 1560−1598.
(29) Becer, C. R.; Hoogenboom, R.; Schubert, U. S. *Angew. Chem., Int. Ed.* **2009**, *48*, 4900−4908.
(30) Rzaev, Z. M. O.; Dincer, S.; Piskin, E. *Prog. Polym. Sci.* **2007**, *32*, 534−595.
(31) Schild, H. G. *Prog. Polym. Sci.* **1992**, *17*, 163−249.
(32) Stuart, M. A. C.; Huck, W. T. S.; Genzer, J.; Muller, M.; Ober, C.; Stamm, M.; Sukhorukov, G. B.; Szleifer, I.; Tsukruk, V. V.; Urban, M.; Winnik, F.; Zauscher, S.; Luzinov, I.; Minko, S. *Nat. Mater.* **2010**, *9*, 101−113.
(33) Soeriyadi, A. H.; Li, G. Z.; Slavin, S.; Jones, M. W.; Amos, C. M.; Becer, C. R.; Whittaker, M. R.; Haddleton, D. M.; Boyer, C.; Davis, T. P. *Polym. Chem.* **2011**, *2*, 815−822.
(34) Weber, C.; Becer, C. R.; Hoogenboom, R.; Schubert, U. S. *Macromolecules* **2009**, *42*, 2965−2971.
(35) Zhao, B.; Li, D. J.; Hua, F. J.; Green, D. R. *Macromolecules* **2005**, *38*, 9509−9517.

Macromolecules

Article

pubs.acs.org/Macromolecules

Kinetics and Modeling of Semi-Batch RAFT Copolymerization with Hyperbranching

Dunming Wang, Xiaohui Li, Wen-Jun Wang,* Xue Gong, and Bo-Geng Li

State Key Laboratory of Chemical Engineering, Institute of Polymerization and Polymer ngineering, Department of Chemical & Biological Engineering, Zhejiang University, Hangzhou, Zhejiang, P.R. China 310027

Shiping Zhu*

Department of Chemical Engineering, McMaster University, Hamilton, Ontario, Canada L8S 4L7

Supporting Information

ABSTRACT: This work reports a kinetic model developed to provide insight into branching mechanisms and control of gelation by semibatch controlled radical copolymerization processes. The semibatch RAFT copolymerization of acrylamide (AM) and *N*,*N*′-methylenebis(acrylamide) (BisAM) in the presence of 3-benzyltrithiocarbonyl propionic acid (BCPA) as chain transfer agent (CTA) was carried out for the model validation. The BisAM was fed to the reactor at a constant rate to yield hyperbranched polyacrylamide (b-PAM) without gelation. Different feeding rates and $[BisAM]_0/[CTA]_0$ ratios were theoretically simulated and experimentally investigated to optimize the instantaneous BisAM concentration in the reactor for branching formations. No gel was formed in the semibatch operation up to 99% total monomer conversion, in contrast to gel occurrence at 70% conversion in its corresponding batch operation. The polymer molecular weight and polydispersity as well as branching density increased slowly throughout the semibatch polymerization. Cyclization reactions were significant and helped to suppress the gelation. The model simulations correlated the experimental data very well.

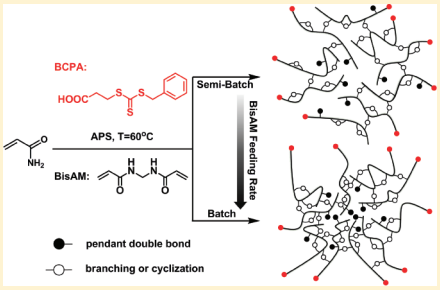

INTRODUCTION

Controlled radical polymerization (CRP) has attracted much attention over the past decade.[1−3] It provides a powerful tool for the synthesis of a large variety of polymers having tailor-made molecular weight (MW) and narrow molecular weight distribution (MWD), as well as well-defined chain architectures such as block, graft, brush, star, and hyperbranched polymers.[4−7] Compared with dendrimers having monodisperse and highly symmetric structure, hyperbranched polymers are polydisperse and possess intrinsic defects in the built-in linear segments.[8] The hyprebranched polymers were normally synthesized by step-growth polymerization of AB_n type monomers.[9−11] Fréchet et al. introduced self-condensing vinyl polymerization (SCVP) for the preparation of hyperbranched polymers in 1995, employing chain-growth mechanism of vinyl inimers through propagation of the double bond and addition of the initiating site to the double bond.[12] This approach was adopted and combined with group transfer polymerization[13,14] and CRPs that included nitroxide-mediated radical polymerization (NMP),[19] atom transfer radical polymerization (ATRP),[16−18] and reversible addition−fragmentation chain transfer (RAFT) polymerization.[19−27] The slow growth in the CRPs gives individual chains sufficient time for chain relaxation and diffusion, which facilitates intermolecular cross-linking and thus makes the CRPs advantageous for the preparation of hyperbranched polymers. Another approach for synthesizing hyperbranched polymers was via copolymerization of a vinyl monomer with a di- or multivinyl comonomer. Sherrington and co-workers[28−32] reported that branched PMMA could be synthesized by the copolymerization of MMA with di- or multivinyl comonomer in the presence of chain transfer agent such as mercaptans. Using RAFT copolymerization, Armes and co-workers[33−35] synthesized branched methacrylic copolymers using disulfide-based dimethacrylate as the branching agent. It was found that the living character of RAFT chemistry was retained under branching conditions, as confirmed by gel permeation chromatography (GPC) analysis of the degraded copolymer chains after selective cleavage of disulfide bonds. Branching in RAFT polymerization of divinylbenzene[36] and copolymerization of methyl methacrylate with ethylene glycol dimethacrylate,[37,38] acrylic acid or acrylamide with *N*,*N*′-methylenebis(acrylamide)[39] was also investigated.

Because of the importance of branched/cross-linked polymers, various theories have been developed for free radical copolymerization with branching/cross-linking. Flory[40] and Stockmayer[41] pioneered the theoretical development with their famous recursive theory of gelation based on a statistical argument, which assumed an equal reactivity for all functional

Received: October 3, 2011
Revised: December 5, 2011
Published: December 22, 2011

groups and free of intramolecular cyclization reactions. While readily satisfied in condensation types of polymerization, these assumptions are clearly violated by chain growth processes and free radical copolymerization of vinyl/divinyl comonomers in particular. The reactivities of various vinyl groups (those on monomer, comonomer and pendant to polymer chain) are usually different. Cyclization reactions are unavoidable and often significant. Since Flory and Stockmayer, there have been many statistical models developed for branching/cross-linking processes with efforts to remove these assumptions. For example, Dusek[42] accounted for nonequal reactivity, Doston[43] included molecular weight drifting of primary chains, Scranton[44] modified cyclization reactions, and so on. However, the branching/cross-linking processes in the free radical polymerization are inherently kinetically controlled. Tobita[45−47] applied a pseudokinetic rate constant method to simplify the kinetic treatment of a multicomponent polymerization to homopolymerization and demonstrated the inhomogeneous nature of polymer networks formed in free-radical polymerization. Zhu[48−50] investigated the radical trapping, the validities of the monoradical assumption, and the stationary-state hypothesis using the method of moments. However, the kinetic approaches are disadvantageous in dealing with the postgelation period, many researchers combined kinetic and statistical approaches in deriving gelation theories, such as Tobita,[51] Ogus,[52] Zhu,[48] and so on.

Compared to slow initiation and fast propagation of the conventional radical polymerization, controlled radical polymerization such as NMP, ATRP, and RAFT is characteristic of fast initiation and slow propagation of polymer chains. The slow propagation gives individual chains sufficient time to relax and diffuse, thus in favor of formation of homogeneous branching or network structures and limiting microgels. Recently, Wang et al.[53] developed a kinetic model for branching and gelation in batch RAFT copolymerization of vinyl/divinyl systems, as an extension of Zhu's previous work on conventional vinyl/divinyl copolymerizaton.[49] Other research groups, such as Matyjaszewski,[54,55] Poly,[56] Armes,[57] Lona,[58] and Perrier[59] also conducted kinetic modeling study on gelation and/or branching in CRP vinyl/divinyl cross-linking copolymerization. However, semibatch models of controlled radical vinyl/divinyl copolymerization have not been developed. Semibatch processes are particularly useful in synthesis of hyperbranched polymers that are free of gels. In our previous work,[60] we prepared hyperbranched polyacrylamide (PAM) via a semibatch RAFT copolymerization by continuous feeding of the branching agent (BA) *N*,*N*′-methylenebis(acrylamide) (BisAM) and the chain transfer agent (CTA) 3-benzyltrithiocarbonyl propionic acid (BCPA). Low CTA levels with the ratios of BCPA/BisAM < 0.05 were used and the systems were free of gels. In contrast, the literatures reported that batch ATRP used initiator/BA ratios >1,[61−67] and batch RAFT polymerization used CTA/BA ratios >0.5[33,34,68−71] in order to minimize gelation. In a semibatch process, the instantaneous BisAM concentration in the reactor was controlled at a relatively low level, resulting in a high instantaneous CTA/BA ratio to effectively suppress cross-linking reactions. In this work, we developed a kinetic model to describe semibatch RAFT copolymerization of vinyl/divinyl systems. The model was experimentally verified and correlated to RAFT AM/BisAM data at various CTA/BA levels. The work provided good insight into the synthesis of gel-free hyperbranched polymers through semibatch CRP processes.

MODEL DEVELOPMENT FOR RAFT BRANCHING PROCESS

Polymerization Scheme and Kinetic Equations. The elementary reactions involved in a batch RAFT copolymerization of vinyl/divinyl monomers are shown in Table 1.

Table 1. Elementary Reactions Involved in the AM/BisAM RAFT Copolymerization

Initiation	$I \xrightarrow{f,k_d} 2P_{0,1,0}$
	$P_{0,1,0} + M_i \xrightarrow{k_{p,i}} P_{1,1,0}$
propagation with comonomer	$P_{n,r,c} + M_i \xrightarrow{k_{p,i}} P_{n+1,r,c}$
transfer to RAFT species	$P_{n,r,c} + P_{m,s,d} \xrightarrow{rdk_{tr}} P_{n,r-1,c+1} + P_{m,s+1,d-1}$
termination by disproportionation	$P_{n,r,c} + P_{m,s,d} \xrightarrow{rsk_{td}} P_{n,r-1,c} + P_{m,s-1,d}$
termination by recombination	$P_{n,r,c} + P_{m,s,d} \xrightarrow{rsk_{tc}} P_{n+m,r+s-2,c+d}$
intermolecular cross-linking	$P_{n,r,c} + P_{m,s,d} \xrightarrow{rmk_{inter}} P_{n+m,r+s,c+d}$
intramolecular cross-linking	$P_{n,r,c} \xrightarrow{rnk_{intra}} P_{n,r,c}$

$P_{n,r,c}$ denotes the macromolecule containing n monomeric units, r radical centers, and c RAFT moieties. I and M_i represent initiator and monomer-i, respectively with M_1 as vinyl monomer AM and M_2 as divinyl monomer BisAM.

The pseudokinetic rate constant method[45] was adopted in this work. The kinetic parameters listed in Table 1 are thus functions of radical fractions ϕ_i, which can be calculated from the instantaneous monomer composition f_i. The pseudorate constants of propagation ($k_{p,i}$), transfer (k_{tr}), termination (k_t), intermolecular cross-linking (k_{inter}), and intramolecular cross-linking (k_{intra}) are expressed as

$$k_{p,i} = \sum_j k_{p,ji}\phi_j \tag{1a}$$

$$k_{tr} = \sum_j k_{tr,j}\phi_j \tag{1b}$$

$$k_t = \sum_i \sum_j k_{t,ij}\phi_i\phi_j \tag{1c}$$

$$k_{inter} = \sum_j k^*_{inter,j}\phi_j(\overline{F_2} - \overline{C} - \overline{D}) \tag{1d}$$

$$k_{intra} = \sum_j k^*_{intra,j}\phi_j(\overline{F_2} - \overline{C} - \overline{D}) \tag{1f}$$

where $\overline{F}_2$ is the cumulative composition of divinyl monomeric units in copolymer chains, $\overline{C}$ is the density of intermolecular cross-linkages, and $\overline{D}$ is the density of intramolecular cross-linkages.

In the simulation, we used the kinetic parameters as summarized in Table 2, assuming polymerization at 60 °C.

dx.doi.org/10.1021/ma202215s | *Macromolecules* 2012, 45, 28−38

The population balance for $P_{n,r,c}$ is

$$\begin{aligned}\frac{dP_{n,r,c}}{dt} &= \sum_i rk_{p,i}M_iP_{n-1,r,c} - \sum_i rk_{p,i}M_iP_{n,r,c} \\ &+ \sum_{m=0}^{\infty}\sum_{s=0}^{\infty}\sum_{d=1}^{\infty}(r+1)dk_{tr}P_{n,r+1,c-1}P_{m,s,d} \\ &- \sum_{m=0}^{\infty}\sum_{s=0}^{\infty}\sum_{d=1}^{\infty}rdk_{tr}P_{n,r,c}P_{m,s,d} \\ &+ \sum_{m=0}^{\infty}\sum_{s=1}^{\infty}\sum_{d=0}^{\infty}s(c+1)k_{tr}P_{n,r-1,c+1}P_{m,s,d} \\ &- \sum_{m=0}^{\infty}\sum_{s=1}^{\infty}\sum_{d=0}^{\infty}sck_{tr}P_{n,r,c}P_{m,s,d} \\ &+ \sum_{m=0}^{\infty}\sum_{s=1}^{\infty}\sum_{d=0}^{\infty}(r+1)sk_{td}P_{n,r+1,c}P_{m,s,d} \\ &- \sum_{m=0}^{\infty}\sum_{s=1}^{\infty}\sum_{d=0}^{\infty}rsk_{td}P_{n,r,c}P_{m,s,d} \\ &+ \frac{1}{2}\sum_{m=0}^{n}\sum_{s=1}^{r+1}\sum_{d=0}^{\infty}(r+2-s)sk_{tc}P_{m,s,d}P_{n-m,r+2-s,c-d} \\ &- \sum_{m=0}^{\infty}\sum_{s=1}^{\infty}\sum_{d=0}^{\infty}rsk_{tc}P_{n,r,c}P_{m,s,d} \\ &+ \sum_{m=0}^{n}\sum_{s=0}^{r}\sum_{d=0}^{c}s(n-m)k_{p,inter}P_{m,s,d}P_{n-m,r-s,c-d} \\ &- \sum_{m=0}^{\infty}\sum_{s=0}^{\infty}\sum_{d=0}^{\infty}rmk_{p,inter}P_{n,r,c}P_{m,s,d} \\ &- \sum_{m=0}^{\infty}\sum_{s=1}^{\infty}\sum_{d=0}^{\infty}snk_{p,inter}P_{n,r,c}P_{m,s,d} \end{aligned} \tag{2}$$

Method of Moments. We define the moments of $P_{n,r,c}$ as

$$Y_{i,j,k} = \sum_{n=0}^{\infty}\sum_{r=0}^{\infty}\sum_{c=0}^{\infty}n^i r^j c^k P_{n,r,c} \tag{3}$$

After some mathematical manipulations, a complete set of moment equations can be derived as summarized in Table 3.

With these moments, we can readily describe the chain properties as listed in Table 4.

Semibatch Reactor Model. A well-mixed isothermal tank reactor is assumed in this work, and only monomer, polymer, and solvent significantly contribute to the volume V and density ρ, because the initiator and chain transfer agent are in trace amounts. The evolution of reaction volume follows

$$\frac{dV}{dt} = V_f - \sum_{i=1}^{n} mw_i R_{p,i}\left(\frac{1}{\rho_i} - \frac{1}{\rho_p}\right)V \tag{4}$$

where V_f is the volumetric feeding rate, mw_i is the molecular weight of monomer i, ρ_i is the density of monomer i, ρ_p is the density of polymer, and $R_{p,i}$ is the reaction rate of monomer i converted to polymer. The evolution of density in the reactor can be obtained through applying a mass balance to all entities:

$$\frac{d(V\rho)}{dt} = V_f\rho_f \tag{5a}$$

Table 2. Kinetic Rate Constants Used in the Simulation of AM/BisAM RAFT Copolymerization

parameter	description	value	reference
k_d (s^{-1})	decomposition rate constant	0.6×10^{-5}	72
k_{p11} ($L{\cdot}mol^{-1}{\cdot}s^{-1}$)	propagation rate constant of AM	4.2×10^3	73
k_{p12} ($L{\cdot}mol^{-1}{\cdot}s^{-1}$)	cross propagation rate constant of BisAM	1.2×10^4	estimated from $r_1 = 0.35$
k_{p22} ($L{\cdot}mol^{-1}{\cdot}s^{-1}$)	propagation rate constant of BisAM	1.2×10^4	$=k_{p12}$
k_{p21} ($L{\cdot}mol^{-1}{\cdot}s^{-1}$)	cross propagation rate constant of AM	6×10^3	estimated from $r_2 = 2$
k_{tc11} ($L{\cdot}mol^{-1}{\cdot}s^{-1}$)	recombination termination rate constant of AM	1×10^6	73
k_{tc22} ($L{\cdot}mol^{-1}{\cdot}s^{-1}$)	recombination termination rate constant of BisAM	1×10^6	$=k_{tc11}$
k_{t12}, k_{t21} ($L{\cdot}mol^{-1}{\cdot}s^{-1}$)	cross termination rate constant	$(k_{t11} \times k_{t22})^1$	74
k_{tr1} ($L{\cdot}mol^{-1}{\cdot}s^{-1}$)	chain transfer rate constant of AM	1×10^7	this work
k_{tr2} ($L{\cdot}mol^{-1}{\cdot}s^{-1}$)	chain transfer rate constant of BisAM	1×10^7	$=k_{tr2}$
$k^*_{p,inter1}$ ($L{\cdot}mol^{-1}{\cdot}s^{-1}$)	intermolecular cross-linkage rate constant of AM	3.2×10^3	this work
$k^*_{p,inter2}$ ($L{\cdot}mol^{-1}{\cdot}s^{-1}$)	intermolecular cross-linkage rate constant of BisAM	3.2×10^3	$=k^*_{p,inter1}$
$k^*_{p,intra1}$ ($L{\cdot}mol^{-1}{\cdot}s^{-1}$)	intramolecular cross-linkage rate constant of AM	70	this work
$k^*_{p,intra2}$ ($L{\cdot}mol^{-1}{\cdot}s^{-1}$)	intramolecular cross-linkage rate constant of BisAM	70	$=k^*_{p,intra1}$

that is

$$\frac{d\rho}{dt} = \frac{V_f\rho_f}{V} - \frac{\rho}{V}\frac{dV}{dt} \tag{5b}$$

where ρ_f is the density of feeding materials. The mass balance equations for species i are

$$\frac{d(VC_i)}{dt} = V_fC_{i,f} + VR_i \tag{6a}$$

that is,

$$\frac{dC_i}{dt} = \frac{1}{V}\left(V_fC_{i,f} - C_i\frac{dV}{dt}\right) + R_i \tag{6b}$$

where C_i and $C_{i,f}$ are the concentrations of species i in the reactor and in the feed, respectively; R_i is the intrinsic reaction rate of species i.

The reactor model, together with the mass balance equations of various species, form a complete set of equations for the semibatch RAFT copolymerization. Three different monomer conversions are defined as follows.

Conversion of AM (X_1):

$$X_1 = \frac{M_{10} - M_{1r}}{M_{10}} \tag{7}$$

Instant conversion of BisAM (X_2):

$$X_2 = \frac{M_{20} - M_{2r} - M_{2t}}{M_{20} - M_{2t}} \tag{8a}$$

Cumulative conversion of BisAM (X_{2cum}):

$$X_{2cum} = \frac{M_{20} - M_{2r} - M_{2t}}{M_{20}} \tag{8b}$$

dx.doi.org/10.1021/ma202215s | Macromolecules 2012, 45, 28−38

Table 3. Moment Equations Developed for RAFT Copolymerization

zeroth-order moments	$\frac{dY_{0,0,0}}{dt} = 2fk_d[I] - \frac{1}{2}k_{tc}Y_{0,1,0}^2 - k_{p,inter}Y_{1,0,0}Y_{0,1,0}$
first-order moments	$\frac{dY_{1,0,0}}{dt} = \sum_i k_{p,i}M_iY_{0,1,0}$
	$\frac{dY_{0,1,0}}{dt} = 2fk_d[I] - k_{td}Y_{0,1,0}^2 - k_{tc}Y_{0,1,0}^2$
	$\frac{dY_{0,0,1}}{dt} = 0$
second-order moments	$\frac{dY_{2,0,0}}{dt} = 2\sum_i k_{p,i}M_iY_{1,1,0} + \sum_i k_{p,i}M_iY_{0,1,0} + k_{tc}Y_{1,1,0}^2 + 2k_{p,inter}Y_{1,1,0}Y_{2,0,0}$
	$\frac{dY_{0,2,0}}{dt} = 2fk_d[I] - 2k_{td}Y_{0,2,0}Y_{0,1,0} + k_{td}Y_{0,1,0}^2 + 2k_{tc}Y_{0,1,0}^2 - 4k_{tc}Y_{0,2,0}Y_{0,1,0} + k_{tc}Y_{0,2,0}^2 - 2k_{tr}Y_{0,2,0}Y_{0,0,1} + 2k_{tr}Y_{0,1,0}Y_{0,0,1} + 2k_{tr}Y_{0,1,1}Y_{0,1,0} + 2k_{p,inter}Y_{0,2,0}Y_{1,1,0}$
	$\frac{dY_{0,0,2}}{dt} = k_{tc}Y_{0,1,1}^2 - 2k_{tr}Y_{0,0,2}Y_{0,1,0} + 2k_{tr}Y_{0,1,1}Y_{0,0,1} + 2k_{tr}Y_{0,1,0}Y_{0,0,1} + 2k_{p,inter}Y_{0,1,1}Y_{1,0,1}$
	$\frac{dY_{1,1,0}}{dt} = \sum_i k_{p,i}M_iY_{0,2,0} - k_{td}Y_{1,1,0}Y_{0,1,0} + k_{tc}Y_{1,1,0}Y_{0,2,0} - 2k_{tc}Y_{1,1,0}Y_{0,1,0} - k_{tr}Y_{1,1,0}Y_{0,0,1} + k_{tr}Y_{1,0,1}Y_{0,1,0} + k_{p,inter}Y_{2,0,0}Y_{0,2,0} + k_{p,inter}Y_{1,1,0}^2$
	$\frac{dY_{1,0,1}}{dt} = \sum_i k_{p,i}M_iY_{0,1,1} + k_{tc}Y_{1,1,0}Y_{0,1,1} + k_{tr}Y_{1,1,0}Y_{0,0,1} - k_{tr}Y_{1,0,1}Y_{0,1,0} + k_{p,inter}Y_{2,0,0}Y_{0,1,1} + k_{p,inter}Y_{1,1,0}Y_{1,0,1}$
	$\frac{dY_{0,1,1}}{dt} = -k_{td}Y_{0,1,1}Y_{0,1,0} + k_{tc}Y_{0,1,1}Y_{0,2,0} - 2k_{tc}Y_{0,1,1}Y_{0,1,0} + k_{tr}Y_{0,2,0}Y_{0,0,1} + k_{tr}Y_{0,0,2}Y_{0,1,0} - k_{tr}Y_{0,1,1}Y_{0,0,1} - k_{tr}Y_{0,1,1}Y_{0,1,0} - 2k_{tr}Y_{0,1,0}Y_{0,0,1} + k_{p,inter}Y_{0,1,1}Y_{1,1,0} + k_{p,inter}Y_{0,2,0}Y_{1,0,1}$
intermolecular	$\frac{d[C]}{dt} = k_{p,inter}Y_{0,1,0}Y_{1,0,0}$
cross-linkage	
intramolecular	$\frac{d[D]}{dt} = k_{p,intra}Y_{1,1,0}$
cross-linkage	
Pendant double bond	$\frac{d[P]}{dt} = k_{p,2}Y_{0,1,0}[M_2] - \frac{d[C]}{dt} - \frac{d[D]}{dt}$
small molecules	initiator: $\frac{d[I]}{dt} = -k_d[I]$
	monomer: $\frac{d[M_i]}{dt} = -k_{p,i}Y_{0,1,0}[M_i]$

Total monomer conversion (X_{total}):

$$X_{total} = \frac{M_{10}X_1 + M_{20}X_{2cum}}{M_{10} + M_{20}} \quad (9)$$

The cumulative copolymer composition ($\overline{F_2}$) is then:

$$\overline{F_2} = \frac{M_{20} - M_{2r} - M_{2t}}{M_{10} - M_{1r} + M_{20} - M_{2r} - M_{2t}} \quad (10)$$

Here M_{i0} is the total mole of monomer i, M_{it} and M_{ir} are the moles of monomer i in the tank and in the reactor, respectively.

Diffusion-Controlled Termination Model. In free-radical polymerization, when the polymerization of branching/cross-linking proceeds to a high conversion, the system becomes viscous. In this work, we consider diffusion-controlled termination reactions, and the termination rate constant is expressed as[75−77]

$$\frac{1}{k_{tii}} = \frac{1}{k_{tii,C}} + \frac{1}{k_{tii,D}} \quad (i = 1, 2) \quad (11)$$

where $k_{tii,C}$ is the chemical termination rate constant, $k_{tii,D}$ is the diffusion-controlled termination rate constant, which can be

dx.doi.org/10.1021/ma202215s | Macromolecules 2012, 45, 28−38

Table 4. Definitions of the Important Chain Structural Properties

chain property	expression
number-average chain length	$r_n = \frac{Y_{1,0,0}}{Y_{0,0,0}}$
weight-average chain length	$r_w = \frac{Y_{2,0,0}}{Y_{1,0,0}}$
polydispersity index	$PDI = \frac{r_w}{r_n}$
weight-average molecular weight	$MW = r_w \times [\bar{F}_2 \times mw_2 + (1 - \bar{F}_2) \times mw_1]$
density of intermolecular cross-links	$\bar{C} = \frac{C}{Y_{1,0,0}}$
density of intramolecular cross-links	$\bar{D} = \frac{D}{Y_{1,0,0}}$

calculated from the following semiempirical free-volume expressions[78]

$$k_{tii,D} = k^0_{tii,D}(r_n)^{-2} \exp(-1/v_f) \tag{12}$$

where $k^0_{tii,D}$ is an adjustable parameter to correlate the experimental data. In our work, $k^0_{t11,D} = 3 \times 10^{16}$ and $k^0_{t22,D} = 1 \times 10^{14}$ are estimated based on the batch monomer conversion data. The free volume fraction v_f is expressed by[79]

$$\begin{aligned} v_f = {} & [0.025 + \alpha_p(T - T_{gp})]\partial_p + \\ & [0.025 + \alpha_{m1}(T - T_{gm1})]\partial_{m1} + \\ & [0.025 + \alpha_{m2}(T - T_{gm2})]\partial_{m2} + \\ & [0.025 + \alpha_s(T - T_{gs})]\partial_s \end{aligned} \tag{13}$$

where α is the thermal expansion coefficient, ∂ is the volume fraction, and T_g is the glass-transition temperature. The subscripts p, mi, and s denote polymer, monomer, and solvent, respectively. The parameters of all physical and transport properties are listed in Table 5.

Primary Cyclization and Secondary Cyclization. Cyclization reactions are important in a free-radical copolymerization with cross-linking and can be divided into two groups: primary and secondary cyclization. Primary cyclization occurs when a radical propagates through pendant double bonds on its own chain; while secondary cyclization occurs when a radical reacts with pendant double bonds on different chains of the same macromolecule.[87−89] Note: a branched macromolecule can contain many primary chains that are connected by cross-linkages. The primary cycles are considered to be ineffective for elastic properties of gel molecules because they are formed by small numbers of monomeric units. However, the secondary cycles are elastically effective since they are formed between primary chains, similar to intermolecular cross-linking.[87] Both intermolecular cross-linking and secondary cycles contribute to the experimental branching density (BD) because the experimental BD is estimated from GPC data.

The primary cyclization reaction rate is assumed to be proportional to the consumption rate of divinyl monomer BisAM, which is expressed as[88]

$$\frac{\mathrm{dCP}}{\mathrm{d}t} = -k_{cp}\frac{\mathrm{d}M_2}{\mathrm{d}t} \tag{14}$$

Table 5. Physical and Transport Properties in the AM/BisAM RAFT Copolymerization

parameter	value	reference
ρ_{m1} (g·cm^{-3})	1100	estimated from ρ_{m1} = 1122 g·cm^{-3} at 30 °C
ρ_{m2} (g·cm^{-3})	1200	estimated from ρ_{m2} = 1240 g·cm^{-3} at 30 °C
ρ_p (g·cm^{-3})	1300	estimated from ρ_1 = 1302 g·cm^{-3} at 23 °C
α_{m1} (K^{-1})	1×10^{-3}	estimated from ref 80
α_{m2} (K^{-1})	1×10^{-3}	$=\alpha_{m1}$
α_{p1} (K^{-1})	4.8×10^{-4}	estimated from ref 80
α_{p2} (K^{-1})	4.8×10^{-4}	$=\alpha_{p1}$
α_p (K^{-1})	$(1 - \bar{F}_2)\alpha_{p1} + \bar{F}_2\alpha_{p2}$	81
α_s (K^{-1})	1.5×10^{-3}	estimated from ref 82
T_{gm1} (K)	250	estimated from refs 80, 83
T_{gm2} (K)	250	$=T_{gm1}$
T_{gp1} (K)	438	84
T_{gp2} (K)	438	$=T_{gp1}$
T_{gp} (K)	$(1 - \bar{F}_2)T_{gp1} + \bar{F}_2T_{gp2}$	85
T_{gs} (K)	153	86

where k_{cp} is a constant and CP is the concentration of pendant double bond to form the primary cycles.

The secondary cyclization reaction rate is assumed to be proportional to the rate of intermolecular cross-linking reaction,[88]

$$\frac{\mathrm{dCS}}{\mathrm{d}t} = k_{cs}\frac{\mathrm{dC}}{\mathrm{d}t} \tag{15}$$

where k_{cs} is the average number of secondary cycles per cross-link, which is considered as a constant, and CS is the concentration of pendant double bond to form the secondary cycles. In this work, k_{cp} = 0.125 and k_{cs} = 4.8 are estimated from the batch experimental branching and cyclization density data. The k_{cp} and k_{cs} values are in the same range as those reported for the copolymerization systems of styrene/divinylbenzene[51,90] and methyl methacrylate/ethylene glycol dimethacrylate.[88]

With these considerations, the fraction of primary cyclization (P) is

$$P = \frac{\mathrm{CP}}{\mathrm{CP} + \mathrm{CS}} \tag{16}$$

The branching density BD is

$$\mathrm{BD} = 2000 \times \frac{C}{Y_{1,0,0}} + (1 - P) \times \mathrm{CD}' \tag{17}$$

dx.doi.org/10.1021/ma202215s | Macromolecules 2012, 45, 28−38

and the cyclization density (CD) is

$$CD = P \times CD' \tag{18}$$

where CD′ is the sum of the densities of primary and secondary cyclizations, which can be expressed by

$$CD' = \frac{D \times V}{2 \times (M_{20} - M_{2t} - M_{2r}) + M_{10} - M_{1r}} \times 1000 \tag{19}$$

The branching frequency (BF) is thus

$$BF = \frac{BD \times MW}{71000} \tag{20}$$

EXPERIMENTAL SECTION

Materials. Acrylamide (AM, ≥98.5%) was purchased from Lingfeng Chemical Reagent Co. Ltd., China. Ammonium persulfate (APS, ≥98%) and *N*,*N*′-methylenebis(acrylamide) (BisAM, ≥98%) were obtained from Sinopharm Chemical Reagent Co. Ltd., China. AM and BisAM were recrystallized in acetone and ethanol, respectively, before use. APS was used as received. 3-Benzyltrithiocarbonyl propionic acid (BCPA) was synthesized according to the literature.[91]

Synthesis of b-PAM by Batch RAFT Polymerization. Batch RAFT copolymerization of AM and BisAM was conducted in sodium acetate/acid acetate buffer solution at pH = 5 with solid content of 4.99 wt % using BCPA as CTA and APS as initiator at 60 °C. Then 0.1 mol of AM and 0.167 mmol of BCPA were added to a 250 mL three-neck flask equipped with a mechanical stirring mixer and contained 100 g buffer solution, and 35.0 mmol BisAM was dissolved in 50 g of deionized water and then transferred into the flask. After deoxygenation with pure nitrogen for about 30 min, 0.083 mmol of APS was injected to initiate the polymerization. The temperature remained at 60 °C. Aliquots were taken at predetermined time intervals. The monomer conversions were determined by gas chromatography.

Synthesis of b-PAM by Semibatch RAFT Polymerization. Semibatch RAFT polymerization was used to synthesize hyperbranched PAM as shown in Scheme 1 in a 1000 mL jacketed reactor equipped with a condenser, a nitrogen inlet, a thermometer, a mechanical stirrer, and a syringe pump. Then 0.7 mol of AM and 1.167 mmol of BCPA were dissolved in 700 g of buffer solution and then charged into the reactor. BisAM (11.7−35.0 mmol) was dissolved in 350 g of deionized water and equipped in constant flow pump. The system was heated to 60 °C by cycling water. Then, 0.583 mmol of APS was injected to initiate the polymerization after deoxygenation by pure nitrogen for at least 30 min. Meanwhile, BisAM was continuously fed into the reaction system at a constant rate of 17.5−7.8 mmol/h over 2 to 4.5 h. Aliquots were taken at predetermined time intervals and quenched by cooling before testing. After complete feeding of BisAM, the polymerization was continued at 60 °C for another 30 min, prior to termination by cooling. The polymer samples were dialyzed for 5 days in a Spectra/Por Dialysis Membrane with molecular weight cutoff of 1000 g/mol.

Scheme 1. Synthesis of Hyperbranched Polyacrylamide (b-PAM) Using Batch or Semibatch Reversible Addition−Fragmentation Chain Transfer (RAFT) Copolymerization of Acrylamide with *N*,*N*′-Methylenebisacrylamide (BisAM)

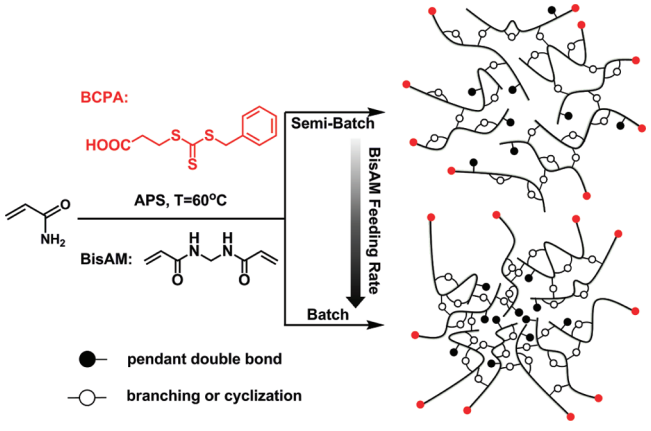

Characterization. Monomer conversions were determined from the residual monomer concentration in the samples and determined using Agilent 6890N gas chromatograph equipped with a capillary column (HP-5, 30 m × 0.32 mm × 0.25 μm). The PAM samples were characterized using Polymer Laboratory PL-GPC 50 gel permeation chromatography (GPC) with differential refractive index (RI), viscometer (IV), and laser light scattering (LS) triple detectors. The detectors were installed in a series of LS, RI, and IV. For LS, the detection angle was 90° and the laser wavelength was 650 nm. A set of three columns of two Ultrahydrogel linear columns (MW ranged from 1 to 7000 kg/mol) and a PL-aquagel-20 column (MW ranged from 100 to 10,000) were equipped in the GPC. Then, 1.0 N $NaNO_3$ aqueous solution was used as eluent at a flow rate 0.8 mL/min and 30 °C. PEO standards (MW_1 = 1190 kg/mol, PDI_1 = 1.21; MW_2 = 885.5 kg/mol, PDI_2 = 1.10; MW_3 = 77.35 kg/mol, PDI_3 = 1.05; as well as a PEO mixed standard having MW from 2 to 162 kg/mol) were used for calibrations. The d*n*/d*c* values for PAM and PEO were 0.170 and 0.133 mL/g, respectively,[73] which were measured using various PAM and PEO samples at different concentrations. The delay volumes between the detectors were determined by PEO standards with 0.163 mL for LS and −0.557 mL for IV. ^{1}H NMR spectra were recorded on a Bruker Advance 400 spectrometer with D_2O as solvent.

RESULTS AND DISCUSSION

Hyperbranched polyacrylamide was synthesized via batch or semibatch RAFT copolymerization of AM and BisAM. The instantaneous content of BisAM in the copolymerization system significantly influenced the branching parameters of b-PAMs. In our work, the instantaneous BisAM content was adjusted by changing the total ratio of $[BisAM]_0/[AM]_0$ and/or feeding rate (r_f). For all experiments, $[AM]_0/[BCPA]_0/[APS]_0$ = 600/1/0.5 and $[AM]_0$ = 0.667 M. Figure 1 shows a typical evolution of the molecular weight of b-PAM samples during the polymerization. As the reaction proceeded, the polymer molecular weight increased and the distribution became broader, indicating branching formation.

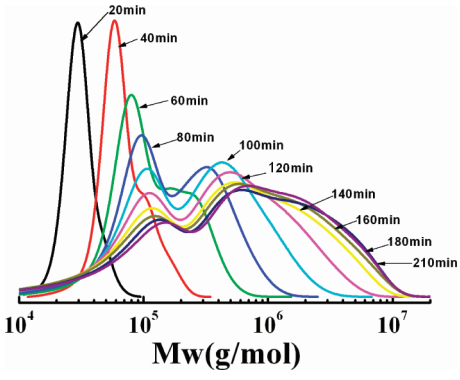

Figure 1. GPC traces of b-PAM samples synthesized by semibatch RAFT polymerization under the condition: $[AM]_0/[BisAM]_0/[BCPA]_0/[APS]_0$ = 600/30/1/0.5 and $[AM]_0$ = 0.667 M in pH = 5 sodium acetate/acid acetate buffer solution at 60 °C and feeding rate of 11.7 mmol/h of BisAM.

dx.doi.org/10.1021/ma202215s | *Macromolecules* 2012, 45, 28−38

The b-PAM samples were also characterized with an NMR spectrometer. In the ^{1}H NMR spectrum (see the Supporting Information), the peaks at 6.8 and 7.5 ppm were the pendant double bonds of BisAM with one vinyl moiety reacted. This suggested that not all the reacted BisAM contributed to branching. The content of the unreacted pendant double bonds (c_p) allowed us to estimate the percentage of pendant double bonds over the total BisAM converted and that of BisAM with both vinyl moieties converted for branching and/or cyclization, following the published procedure.[60]

Branched polymers have a lower root mean-square gyration radius ($(\langle R_g^2\rangle^{1/2})$) and a lower intrinsic viscosity ($[\eta]$).[92] The level of branching density could be described by the contraction factors g and g' as

$$g = \frac{\langle R_g^2\rangle_{br}}{\langle R_g^2\rangle_{lin}} \tag{21}$$

$$g' = \frac{[\eta]_{br}}{[\eta]_{lin}} \tag{22}$$

In our previous work,[60] the relationship of $\langle R_g^2\rangle^{1/2} \sim$ MW and $[\eta] \sim$ MW were determined as $\langle R_g^2\rangle^{1/2} = 1.70 \times 10^{-2} M^{0.583}$ and $[\eta] = 1.12 \times 10^{-4}\ M^{0.769}$. Further, the quantitative relationship between g and g' was also determined as

$$g' = g^{\varepsilon} \tag{23}$$

where the exponential factor ε was 0.74 and it was used for further estimation of branching density from g'. Figure 2 present

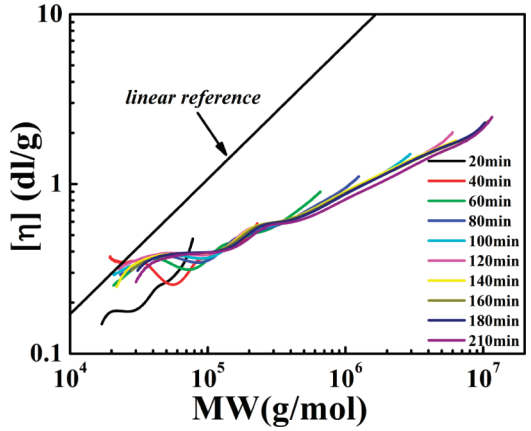

Figure 2. Intrinsic viscosity of b-PAMs at different reaction times as a function of molecular weight under the condition: $[AM]_0/[BisAM]_0/[BCPA]_0/[APS]_0$ = 600/30/1/0.5 and $[AM]_0$ = 0.667 M in pH = 5 sodium acetate/acid acetate buffer solution at 60 °C and feeding rate of 11.7 mmol/h of BisAM.

the $[\eta]$ versus molecular weight correlations for the b-PAM samples, with the linear PAM data included as reference. All the $[\eta]$ values of b-PAMs were substantially lower than their linear counterpart.

Figure 3 plots the contraction factor g', estimated by eq 22, against molecular weight.

For these b-PAMs, the branching units were expected to be distributed randomly along primary chains.[1] The reacted BisAM units served as bridges and connected primary chains forming H-type cross-linkages. The Zimm-Stockmayer equation was applied to estimate the branching frequency BF and branching

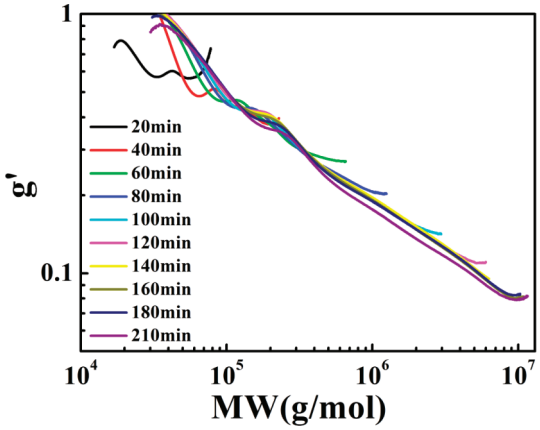

Figure 3. g' of b-PAMs at different reaction times as a function of molecular weight under the condition: $[AM]_0/[BisAM]_0/[BCPA]_0/[APS]_0$ = 600/30/1/0.5 and $[AM]_0$ = 0.667 M in pH = 5 sodium acetate/acid acetate buffer solution at 60 °C and feeding rate of 11.7 mmol/h of BisAM.

density BD:[92]

$$g = \left[\left(\sqrt{1 + \left(\frac{\mathrm{BF}}{6}\right)}\right) + \frac{4 \times \mathrm{BF}}{3\pi}\right]^{-1/2} \tag{24}$$

$$\mathrm{BD} = \frac{35\,500 \times \mathrm{BF}}{M} \times 2 \tag{25}$$

where the g data were obtained through converting g' in Figure 3 using eq 23.

CD could be calculated using eq 26

$$\mathrm{CD} = \frac{m_{BisAM} - m_{BisAM,p}}{2m_{BisAM} + m_{AM}} \times 1000 - \mathrm{BD} \tag{26}$$

where m_{BisAM} and m_{AM} were the moles of BisAM and AM incorporated into the polymer and could be determined by their conversions, respectively. $m_{BisAM,p}$ is the mole of BisAM with one vinyl reacted and the other pendant in the polymer

Effect of Feeding Rate. The feeding period of the same BisAM aqueous solution quantity was varied to adjust the instantaneous BisAM concentration in the copolymerization system from 0 (batch) to 4.5 h to investigate the semibatch effects on MW, PDI, and branching structure. It was found that a shorter feeding period or higher feeding rate increased the instantaneous BisAM concentration and resulted in higher BF and BD.[60] Parts a–c of Figure 4 show good agreement between the experimental data and the theoretical model for the conversion histories of both AM and BisAM, which were insensitive to instantaneous BisAM concentration. A low feeding rate reduced the BisAM amount copolymerized with AM.

Figure 4d shows the MW of the b-PAM samples, determined by triple-detector GPC, plotted as a function of total monomer conversion. In the batch operation, the MW experienced a sudden increase at 70% conversion prior to gelation. However, in the semibatch processes, MW increased slowly up to 90% conversion, followed by sudden increase to about 1.5 × 10^6 g/mol without gelation, as agreed with the model prediction. Figure 4e shows the same trend of PDI as MW. The PDI increased to 4.33 before gelation in the batch, while it reached 6.85–8.15 in the semibatch processes without gelation.

dx.doi.org/10.1021/ma202215s | Macromolecules 2012, 45, 28–38

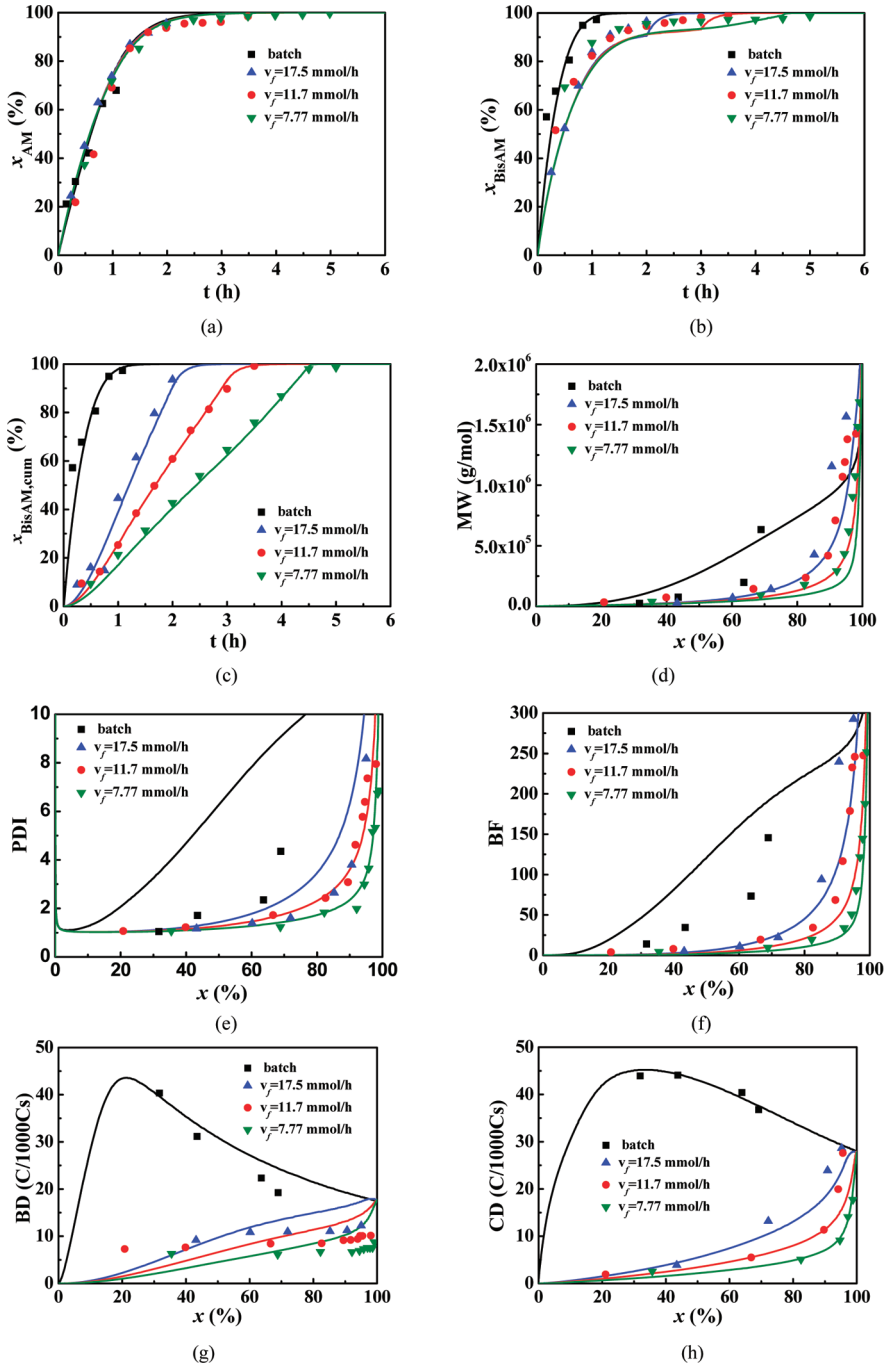

Figure 4. Hyperbranched polyacrylamides synthesized by RAFT copolymerization with different feeding rates of BisAM: (a) AM conversion, (b) instantaneous conversion of BisAM, (c) cumulative conversion of BisAM, (d) MW versus the total monomer conversion, (e) PDI, (f) BF, (g) BD, and (h) CD. Experimental conditions: $[AM]_0/[BisAM]_0/[BCPA]_0/[APS]_0$ = 600/30/1/0.5 and $[AM]_0$ = 0.667 M in pH = 5 sodium acetate/acid acetate buffer solution at 60 °C. The points are experimental data while the lines are theoretical simulations.

The most important parameters of branched polymers are BF and BD, which can be estimated by eqs 24 and 25. The weight-average BF and BD of all the b-PAM samples were calculated from $\sum_i BF_i C_i / \sum_i C_i$ and $\sum_i BD_i C_i / \sum_i C_i$, respectively, where C_i is the polymer concentration at each GPC elution fraction. Parts f and g of Figure 4 show the BF and BD values plotted as a function of the total monomer conversion. Both the experimental data and theoretical model showed that shorter feeding time gave higher BF and BD. The BFs of b-PAMs from batch RAFT copolymerization were much higher than those from semibatch operation. It is clear that the higher instantaneous BisAM concentration in the batch process was advantageous for branching. However, the system could be readily gelled at a low to intermediate conversion. For comparison, in the semibatch processes, the final BFs reached up to 250 to 300 per molecule at high conversions but still free of gels. The BD of b-PAMs from the batch process, unlike BF, MW and PDI, increased in the early stage followed by a decrease to the final value of 19.3 C/1000Cs at gelation. In the semibatch processes, the BDs increased slowly with conversion and reached 8.81−12.3 C/1000Cs at nearly complete conversion without gelation.

dx.doi.org/10.1021/ma202215s | *Macromolecules* 2012, 45, 28−38

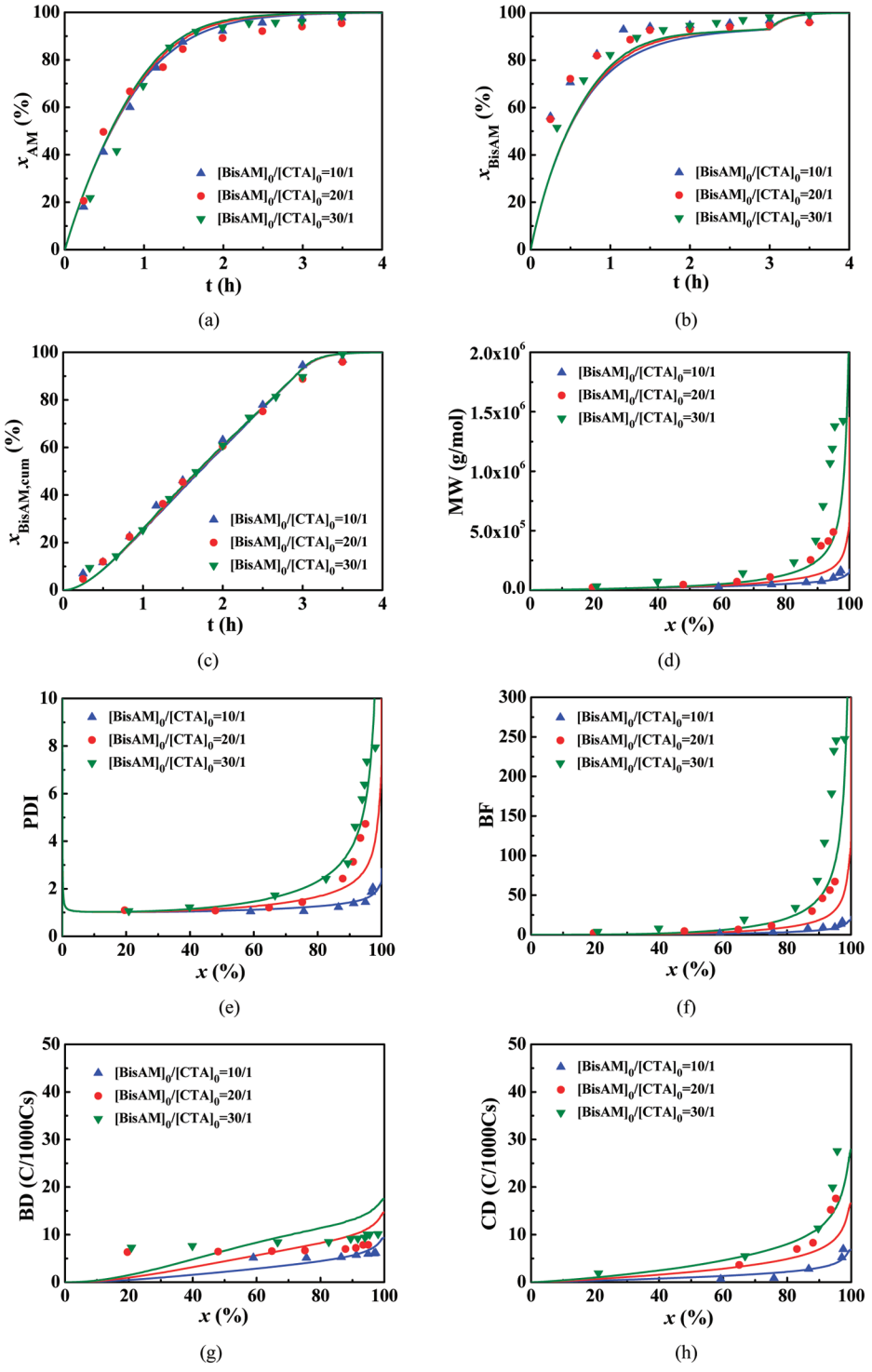

Figure 5. Hyperbranched polyacrylamides synthesized by RAFT copolymerization with different $[BisAM]_0/[CTA]_0$ ratios: (a) AM conversion, (b) instantaneous conversion of BisAM, (c) cumulative conversion of BisAM, (d) MW versus the total monomer conversion, (e) PDI, (f) BF, (g) BD, and (h) CD. Experimental conditions: $[AM]_0/[BCPA]_0/[APS]_0$ = 600/1/0.5 and $[AM]_0$ = 0.667 M in pH = 5 sodium acetate/acid acetate buffer solution at 60 °C. The points are experimental data while the lines are theoretical results.

The experimental BD values were substantially lower than those calculated based on the assumption that all the incorporated BisAM with both vinyl groups reacted contributed to branching through intermolecular reactions. This discrepancy suggested significant intramolecular cyclization reactions occurred. That is, a fraction of the incorporated BisAM formed cyclic structures. Figure 4h shows that, in the batch process, CD increased in the early stage and decreased slowly to 36.7 C/1000Cs just before gelation. However, in the semibatch processes, it increased steadily with conversion to a final value of 17.6−28.5 C/1000Cs. With the feeding rate of 7.8−17.5 mmol/hs, 39.0−60.5% of all double bonds from BisAM were consumed for cyclization and 17.0−26.8% for branching, with the remainder as pendant double bonds. This suggested that cyclization played an important role in postponing gelation.

dx.doi.org/10.1021/ma202215s | *Macromolecules* 2012, 45, 28−38

Effect of BisAM content. Hyperbranched polymers could be prepared by increasing the branching agent BA concentration but at the risk of gelation. Chain transfer agent (CTA) was often added to suppress the network formation. Low BA/CTA levels (<2) were used in the batch process.[28−30,32−34,37,68−71] Employing the semibatch strategy by continuously feeding BisAM reduced the instantaneous BA concentration and facilitated the preparation of b-PAM samples at very high BisAM/CTA ratios (10−30).

Parts a and b of Figure 5 show the AM and BisAM conversions over the reaction time. The cumulative BisAM conversion, given in Figure 5c, was independent of the $[BisAM]_0/[CTA]_0$ ratio, as predicted by the model. However, because the different amounts of BisAM were fed in 3 h or at a constant rate of 11.7 mmol/h, the instantaneous concentrations in the copolymerization systems were different, resulting in the considerable differences in MW and PDI. The MW of b-PAMs prepared at $[BisAM]_0/[CTA]_0$ = 30 was obviously much higher than those of $[BisAM]_0/[CTA]_0$ = 20 and 10. The same observation was made for PDI, as seen in Figure 5, parts d and e.

Figure 5f plots BF as a function of total monomer conversion. With $[BisAM]_0/[CTA]_0$ = 10, the BF was only 16.9 per molecule even when the conversion reached up to 97.5%, while it was 248 per molecule with $[BisAM]_0/[CTA]_0$ = 30. Parts g and h of Figurs 5 show that higher $[BisAM]_0/[CTA]_0$ ratio resulted in higher BD and CD. The final BD and CD of b-PAMs prepared at $[BisAM]_0/[CTA]_0$ = 10/1 to 30/1 were increased from 6.19 to 10.2 C/1000Cs and 6.84 to 27.5 C/1000Cs, respectively. The pendant double bond fractions of the reacted BisAM consumed for branching and cyclization were 38.8−21.8% and 43.1−58.0%, respectively, as the $[BisAM]_0/[CTA]_0$ increased from 10/1 to 30/1.

CONCLUSIONS

The semibatch RAFT copolymerization of acrylamide (AM) and *N*,*N*′-methylenebis(acrylamide) (BisAM) with continuous BisAM feeding in the presence of chain transfer agent (CTA) BCPA was theoretically modeled and experimentally investigated. Guided by the model simulations, hyperbranched polyacrylamide (b-PAM) samples free of gels were successfully prepared. The instantaneous BisAM concentration played a crucial role in suppressing gel formation in the b-PAM synthesis. This parameter could be optimized though modeling by adjusting the BisAM feeding rate and/or the ratio of $[BisAM]_0/[CTA]_0$. Higher instantaneous BisAM concentration gave more branching and cyclization structures in the b-PAMs but at the risk of gelation. The final BD and CD of b-PAMs prepared by batch RAFT copolymerization were 19.3 and 36.7 C/1000Cs, respectively, which were higher than those prepared by the semibatch operations. However, the system gelled at 70% conversion. In comparison, the MW, PDI and BF in the semibatch processes increased gradually with conversion until over 90% without gelation. The experimental data agreed well with the model simulation. The BD of b-PAMs in the semibatch copolymerization also increased slowly with the final value reaching 8.81−12.3 C/1000Cs at the investigated feeding rates and 6.19−10.2 C/1000Cs at the used $[BisAM]_0/[CTA]_0$ ratios, without gelation. It was also found that cyclization consumed almost half of the pendant double bonds of the reacted BisAM. The final CD increased from 17.6 to 28.5 C/1000Cs as the feeding rate increased from 7.8 to 17.5 mmol/h, while it increased from 6.84 to 27.5 C/1000Cs as the $[BisAM]_0/[CTA]_0$ increased from 10/1 to 30/1.

ASSOCIATED CONTENT

Supporting Information

GPC traces, intrinsic viscosities, and g' values of b-PAM samples synthesized by semibatch RAFT copolymerizations, and ^{1}H NMR spectra of b-PAM sample. This material is available free of charge via the Internet at http://pubs.acs.org.

ACKNOWLEDGMENTS

This work is financially supported by National Natural Science Foundation of China (Grant 21074116 and Key Grant 20936006), Zhejiang Ministry of Science and Technology (Strategic Grant 2008C14087), Chinese State Key Laboratory of Chemical Engineering at Zhejiang University (Grants SKL-ChE-08D01 and SKL-ChE-08D02), and the Program for Changjiang Scholars and Innovative Research Team in University in China.

REFERENCES

(1) Goto, A.; Fukuda, T. *Prog. Polym. Sci.* **2004**, *29*, 329−385.
(2) Braunecker, W. A.; Matyjaszewski, K. *Prog. Polym. Sci.* **2007**, *32*, 93−146.
(3) Kamigaito, M.; Ando, T.; Sawamoto, M. *Chem. Rev.* **2001**, *101*, 3689−3745.
(4) Davis, K. A.; Matyjaszewski, K. *Adv. Polym. Sci.* **2002**, *159*, 1−166.
(5) Tsujii, Y.; Ohno, K.; Yamamoto, S.; Goto, A.; Fukuda, T. *Adv. Polym. Sci.* **2006**, *197*, 1−45.
(6) Gao, H. F.; Matyjaszewski, K. *Macromolecules* **2006**, *39*, 3154−3160.
(7) Voit, B. I.; Lederer, A. *Chem. Rev.* **2009**, *109*, 5924−5973.
(8) Hult, A.; Johansson, M.; Malmstrom, E. *Adv. Polym. Sci.* **1999**, *143*, 1−34.
(9) Flory, P. J. *J. Am. Chem. Soc.* **1952**, *74*, 2718−2723.
(10) Mathias, L. J.; Carothers, T. W. *J. Am. Chem. Soc.* **1991**, *113*, 4043−4044.
(11) Miravet, J. F.; Frechet, J. M. J. *Macromolecules* **1998**, *31*, 3461−3468.
(12) Frechet, J. M. J.; Henmi, M.; Gitsov, I.; Aoshima, S.; Leduc, M. R.; Grubbs, R. B. *Science* **1995**, *269*, 1080−1083.
(13) Simon, P. F. W.; Radke, W.; Muller, A. H. E. *Macromol. Rapid Commun.* **1997**, *18*, 865−873.
(14) Sakamoto, K.; Aimiya, T.; Kira, M. *Chem. Lett.* **1997**, 1245−1246.
(15) Hawker, C. J.; Frechet, J. M. J.; Grubbs, R. B.; Dao, J. *J. Am. Chem. Soc.* **1995**, *117*, 10763−10764.
(16) Gaynor, S. G.; Edelman, S.; Matyjaszewski, K. *Macromolecules* **1996**, *29*, 1079−1081.
(17) Matyjaszewski, K.; Gaynor, S. G.; Kulfan, A.; Podwika, M. *Macromolecules* **1997**, *30*, 5192−5194.
(18) Matyjaszewski, K.; Pyun, J.; Gaynor, S. G. *Macromol. Rapid Commun.* **1998**, *19*, 665−670.
(19) Carter, S.; Rimmer, S.; Sturdy, A.; Webb, M. *Macromol. Biosci.* **2005**, *5*, 373−378.
(20) Zhang, C. B.; Zhou, Y. A.; Liu, Q. A.; Li, S. X.; Perrier, S.; Zhao, Y. L. *Macromolecules* **2011**, *44*, 2034−2049.
(21) Wang, Z. M.; He, J. P.; Tao, Y. F.; Yang, L.; Jiang, H. J.; Yang, Y. L. *Macromolecules* **2003**, *36*, 7446−7452.
(22) Heidenreich, A. J.; Puskas, J. E. *J. Polym. Sci., Polym. Chem.* **2008**, *46*, 7621−7627.
(23) Carter, S.; Hunt, B.; Rimmer, S. *Macromolecules* **2005**, *38*, 4595−4603.
(24) Rimmer, S.; Carter, S.; Rutkaite, R.; Haycock, J. W.; Swanson, L. *Soft Matter* **2007**, *3*, 971−973.
(25) Vogt, A. P.; Sumerlin, B. S. *Macromolecules* **2008**, *41*, 7368−7373.
(26) Schmitt, J.; Blanchard, N.; Poly, J. *Polym. Chem.* **2011**, *2*, 2231−2238.
(27) Zhou, X. B.; Zhu, J.; Xing, M. Y.; Zhang, Z. B. A.; Cheng, Z. P.; Zhou, N. A. C.; Zhu, X. L. *Eur. Polym. J.* **2011**, *47*, 1912−1922.

(28) O'Brien, N.; McKee, A.; Sherrington, D. C.; Slark, A. T.; Titterton, A. *Polymer* **2000**, *41*, 6027−6031.
(29) Costello, P. A.; Martin, I. K.; Slark, A. T.; Sherrington, D. C.; Titterton, A. *Polymer* **2002**, *43*, 245−254.
(30) Slark, A. T.; Sherrington, D. C.; Titterton, A.; Martin, I. K. *J. Mater. Chem.* **2003**, *13*, 2711−2720.
(31) Isaure, F.; Cormack, P. A. G.; Sherrington, D. C. *J. Mater. Chem.* **2003**, *13*, 2701−2710.
(32) Isaure, F.; Cormack, P. A. G.; Sherrington, D. C. *Macromolecules* **2004**, *37*, 2096−2105.
(33) Vo, C. D.; Rosselgong, J.; Armes, S. P.; Billingham, N. C. *Macromolecules* **2007**, *40*, 7119−7125.
(34) Rosselgong, J.; Armes, S. P.; Barton, W.; Price, D. *Macromolecules* **2009**, *42*, 5919−5924.
(35) Rosselgong, J.; Armes, S. P.; Barton, W. R. S.; Price, D. *Macromolecules* **2010**, *43*, 2145−2156.
(36) Koh, M. L.; Konkolewicz, D.; Perrier, S. *Macromolecules* **2011**, *44*, 2715−2724.
(37) Liu, B. L.; Kazlauciunas, A.; Guthrie, J. T.; Perrier, S. *Macromolecules* **2005**, *38*, 2131−2136.
(38) Liu, B. L.; Kazlauciunas, A.; Guthrie, J. T.; Perrier, S. *Polymer* **2005**, *46*, 6293−6299.
(39) Taton, D.; Baussard, J. F.; Dupayage, L.; Poly, J.; Gnanou, Y.; Ponsinet, V.; Destarac, M.; Mignaud, C.; Pitois, C. *Chem. Commun.* **2006**, 1953−1955.
(40) Molecular size distribution in three-dimensional polymers. (a) Flory, P. J. 1. Gelation. *J. Am. Chem. Soc.* **1941**, *63*, 3083−3090. (b) Flory, P. J. 2. Trifunctional branching units. *J. Am. Chem. Soc.* **1941**, *63*, 3091−3096. (c) Flory, P. J. 3. Tetrafunctional branching units. *J. Am. Chem. Soc.* **1941**, *63*, 3096−3100.
(41) (a) Stockmayer, W. H. 1. Theory of molecular size distribution and gel formation in branched-chain polymers. *J. Chem. Phys.* **1943**, *11*, 45−55. (b) Stockmayer, W. H. 2. General cross linking. *J. Chem. Phys.* **1944**, *12*, 125−131.
(42) Dusek, K. *Cross-linked Polymers, Chemistry, Properties, and Applications*, Presented at the ACS 193rd Meeting, Polymeric Materials: Science and Engineering, April 5−10, 1987; p 2.
(43) Dotson, N. A.; Diekmann, T.; Macosko, C. W.; Tirrell, M. *Macromolecules* **1992**, *25*, 4490−4500.
(44) Scranton, A. B.; Peppas, N. A. *J. Polym. Sci., Polym. Chem.* **1990**, *28*, 39−57.
(45) Tobita, H.; Hamielec, A. E. *Makromol. Chem. Symp.* **1988**, *20−1*, 501−543.
(46) Tobita, H.; Hamielec, A. E. *Macromolecules* **1989**, *22*, 3098−3105.
(47) Tobita, H.; Hamielec, A. E. *Polymer* **1992**, *33*, 3647−3657.
(48) Zhu, S.; Tian, Y.; Hamielec, A. E.; Eaton, D. R. *Macromolecules* **1990**, *23*, 1144−1150. Zhu, S.; Tian, Y.; Hamielec, A. E.; Eaton, D. R. *Polymer* **1990**, *31*, 154−159. Zhu, S.; Tian, Y.; Hamielec, A. E.; Eaton, D. R. *Polymer* **1990**, *31*, 1726−1734. Yu, Q.; Zeng, F. Q.; Zhu, S. P. *Macromolecules* **2001**, *34*, 1612−1618.
(49) Zhu, S.; Hamielec, A. E. *Macromolecules* **1992**, *25*, 5457−5464. Zhu, S.; Hamielec, A. E. *Macromolecules* **1993**, *26*, 3131−3136.
(50) Zhu, S. *J. Polym. Sci. Polym. Phys.* **1996**, *34*, 505−516.
(51) Tobita, H.; Hamielec, A. E. *Polymer Reaction Engineering*; Springer: Berlin, 1989; p 43.
(52) Okay, O. *Polymer* **1994**, *35*, 796−807.
(53) Wang, R.; Luo, Y. W.; Li, B. G.; Zhu, S. P. *Macromolecules* **2009**, *42*, 85−94.
(54) Gao, H. F.; Polanowski, P.; Matyjaszewski, K. *Macromolecules* **2009**, *42*, 5925−5932.
(55) Polanowski, P.; Jeszka, J. K.; Li, W. W.; Matyjaszewski, K. *Polymer* **2011**, *52*, 5092−5101.
(56) Poly, J.; Wilson, D. J.; Destarac, M.; Taton, D. *J. Polym. Sci., Polym. Chem.* **2009**, *47*, 5313−5327.
(57) Bannister, I.; Billingham, N. C.; Armes, S. P. *Soft Matter* **2009**, *5*, 3495−3504.
(58) Hernandez-Ortiz, J. C.; Vivaldo-Lima, E.; Lona, L. M. F.; McManus, N. T.; Penlidis, A. *Macromol. React. Eng.* **2009**, *3*, 288−311.
(59) Konkolewicz, D.; Gray-Weale, A.; Perrier, S. *Polym. Chem.* **2010**, *1*, 1067−1077.
(60) Wang, W. J.; Wang, D. M.; Li, B. G.; Zhu, S. P. *Macromolecules* **2010**, *43*, 4062−4069.
(61) Wang, A. R.; Zhu, S. P. *Macromolecules* **2002**, *35*, 9926−9933.
(62) Wang, A. R.; Zhu, S. P. *J. Polym. Sci., Polym. Chem.* **2005**, *43*, 5710−5714.
(63) Wang, A. R.; Zhu, S. P. *Polym. Eng. Sci.* **2005**, *45*, 720−727.
(64) Bannister, I.; Billingham, N. C.; Armes, S. P.; Rannard, S. P.; Findlay, P. *Macromolecules* **2006**, *39*, 7483−7492.
(65) Bouhier, M. H.; Cormack, P. A. G.; Graham, S.; Sherrington, D. C. *J. Polym. Sci., Polym. Chem.* **2007**, *45*, 2375−2386.
(66) Yu, Q.; Qin, Z. Q.; Li, J. C.; Zhu, S. P. *Polym. Eng. Sci.* **2008**, *48*, 1254−1260. Yu, Q.; Zhou, M.; Ding, Y. H.; Jiang, B. B.; Zhu, S. P. *Polymer* **2007**, *48*, 7058−7064.
(67) Li, W. W.; Gao, H. F.; Matyjaszewski, K. *Macromolecules* **2009**, *42*, 927−932.
(68) Tao, L.; Liu, J. Q.; Tan, B. H.; Davis, T. P. *Macromolecules* **2009**, *42*, 4960−4962.
(69) Poly, J.; Wilson, D. J.; Destarac, M.; Taton, D. *Macromol. Rapid Commun.* **2008**, *29*, 1965−1972.
(70) Yu, Q.; Xu, S. H.; Zhang, H. W.; Ding, Y. H.; Zhu, S. P. *Polymer* **2009**, *50*, 3488−3494. Yu, Q.; Zhu, Y. S.; Ding, Y. H.; Zhu, S. P. *Macromol. Chem. Phys.* **2008**, *209*, 551−556. Yu, Q.; Zhang, J. Z.; Cheng, M. L.; Zhu, S. P. *Macromol. Chem. Phys.* **2006**, *207*, 287−294.
(71) Li, Y. T.; Armes, S. P. *Macromolecules* **2009**, *42*, 939−945.
(72) Yildiz, U.; Capek, I.; Sarov, Y.; Corobea, M. C.; Polovkova, J. *Polym. Int.* **2009**, *58*, 1411−1421.
(73) Brandrup, J.; Immergut, E. H.; Grulke, E. A.; Abe, A.; Bloth, D. R. *Polymer Handbook*, 4th ed.; Wiley: New York, 1999.
(74) Walling, C. *J. Am. Chem. Soc.* **1949**, *71*, 1930−1935.
(75) Noyes, R. M. *Effect of Diffusion Rates on Chemical Kinetics*. Pergamon: London, 1961.
(76) Zhu, S.; Hamielec, A. E. *Macromolecules* **1989**, *22*, 3093−3098. Zhu, S.; Hamielec, A. E. *J. Polym. Sci. B, Polym. Phys* **1994**, *32*, 929−943. Zhu, S.; Hamielec, A. E.; Pelton, R. H. *Makromol. Chem.—Theory Simul.* **1993**, *2*, 587−604. Wang, A. R.; Zhu, S. P. *Macromol. Theor. Simul.* **2003**, *12*, 196−208.
(77) Delgadillo-Velazquez, O.; Vivaldo-Lima, E.; Quintero-Ortega, I. A.; Zhu, S. P. *AIChE J* **2002**, *48*, 2597−2608.
(78) Marten, F. L.; Hamielec, A. E. *J. Appl. Polym. Sci.* **1982**, *27*, 489−505.
(79) Achilias, D.; Kiparissides, C. *J. Appl. Polym. Sci.* **1988**, *35*, 1303−1323.
(80) Dube, M. A.; Rilling, K.; Penlidis, A. *J. Appl. Polym. Sci.* **1991**, *43*, 2137−2145.
(81) Sun, X. Y.; Luo, Y. W.; Wang, R.; Li, B. G.; Zhu, S. P. *AIChE J.* **2008**, *54*, 1073−1087.
(82) Yao, Y.; Xie, T.; Gao, Y. *Handbook of Chemistry and Physics*; Shanghai Scientific and Technical Publishers: Shanghai, China, 1985.
(83) Jones, K. M.; Bhattacharya, D.; Brash, J. L.; Hamielec, A. E. *Polymer* **1986**, *27*, 602−610.
(84) Schulz, R. C. Acrylamide Polymers. In *Encyclopedia of Polymer Science and Engineering*; Wiley: New York, 1985, p 162.
(85) Suzuki, H.; Mathot, V. B. F. *Macromolecules* **1989**, *22*, 1380−1384.
(86) Fedors, R. F. *J. Polym. Sci. Polym. Lett.* **1979**, *17*, 719−722.
(87) Tobita, H. *Macromolecules* **1992**, *25*, 2671−2678. Zhu, S.; Hamielec, A. E. *Macromolecules* **1992**, *25*, 5457−5464.
(88) Landin, D. T.; Macosko, C. W. *Macromolecules* **1988**, *21*, 846−851.
(89) Elliott, J. E.; Bowman, C. N. *Macromolecules* **1999**, *32*, 8621−8628.
(90) Sajjadi, S.; Keshavarz, S. A. M.; Nekoomanesh, M. *Polymer.* **1996**, *37*, 4141−4148.
(91) Jesberger, M.; Barner, L.; Stenzel, M. H.; Malmstrom, E.; Davis, T. P.; Barner-Kowollik, C. *J. Polym. Sci., Polym. Chem.* **2003**, *41*, 3847−3861.
(92) Zimm, B. H.; Stockmayer, W. H. *J. Chem. Phys.* **1949**, *17*, 1301−1314.

Macromolecules

Article

pubs.acs.org/Macromolecules

Reversible Inter- and Intra-Microgel Cross-Linking Using Disulfides

Jeffrey C. Gaulding,[†] Michael H. Smith,[†] John S. Hyatt,[‡] Alberto Fernandez-Nieves,[‡] and L. Andrew Lyon*,[†]

[†]School of Chemistry & Biochemistry and the Petit Institute for Bioengineering & Bioscience, Georgia Institute of Technology, Atlanta, Georgia 30332, United States

[‡]School of Physics, Georgia Institute of Technology, Atlanta, Georgia 30332, United States

Supporting Information

ABSTRACT: Thermoresponsive hydrogel nanoparticles composed of poly(*N*-isopropylmethacrylamide) (pNIPMAm) and the disulfide-based cross-linker *N*,*N*′-bis(acryloyl)cystamine (BAC) have been prepared using a redox-initiated, aqueous precipitation polymerization approach, leading to improved stability of the disulfide bond compared to traditional thermally initiated methods. The resultant particles demonstrate complete erosion in response to reducing conditions or thiol competition. This stands in contrast to the behavior of thermally initiated particles, which retain a cross-linked network following disulfide cleavage due to uncontrolled chain-branching and self-cross-linking side reactions. The synthetic strategy has also been combined with the nondegradable cross-linker *N*,*N*-methylenebis(acrylamide) (BIS) to generate "co-cross-linked" pNIPMAm-BAC-BIS microgels. These particles are redox-responsive, swell upon BAC cross-link scission and present reactive thiols. This pendant thiol functionality was demonstrated to be useful for conjugation of thiol-reactive probes and in reversible network formation by assembling particles cross-linked by disulfide linkages.

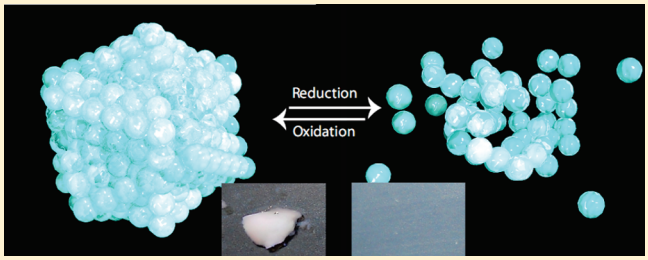

INTRODUCTION

Within the realm of biomaterials, disulfide bonds are of great interest due to their characteristic degradation in response to physiologically relevant reducing conditions.[1,2] Polymeric drug delivery vehicles incorporating disulfide bonds as essential components of vehicular integrity are expected to undergo selective erosion upon entering the intracellular space, providing a means to trigger the delivery of payloads and improve physiologic clearance. Several groups, using a variety of architectures, have exploited this strategy.[2−6] For example, Matyjaszewski et al. have used inverse mini-emulsion atom transfer polymerization to produce nanogels capable of triggered erosion for the delivery of small molecules to cancer cells.[4] Armes and coworkers have included disulfide cross-linking in block copolymer micelles as a method to regulate the release of a payload in the micelle's interior.[5] These examples represent only a small portion of the efforts in this domain.

Our group has worked extensively on the development of drug carriers based on poly(alkylacrylamide) nano- and microparticles (nanogels or microgels).[7−12] However, one limiting characteristic of these vehicles is their nondegradable nature, as the polymer is not erodible and the network is typically cross-linked covalently with noncleavable units. Thus, the use of cross-linkers containing disulfide bonds was envisioned as a potentially useful approach, where disulfide incorporation would enable erosion of drug carriers in a triggered fashion, while also offering introduction of thiol functionalities within microgels for bioconjugation and controlled assembly. Bulk hydrogels that incorporate the reversible disulfide cross-linker *N*,*N*′-bis(acryloyl)cystamine (BAC) have been described in the literature,[13−16] but there are few examples of microgels incorporating this functionality,[4,17−19] and none of these syntheses utilize the aqueous precipitation polymerization method.

Precipitation polymerization has been repeatedly demonstrated to be a useful and versatile means of generating monodisperse micro- and nanoparticles, and is enabling in the synthesis of particles with core/shell topologies.[7,20,21] A notable drawback is that the method utilizes high temperatures (typically >70 °C) to promote the thermal decomposition of a radical source, such as ammonium persulfate (APS). Incorporating a disulfide bond during microgel synthesis by such a process is challenging, as there are numerous side reactions that disrupt the sulfur−sulfur bond. The disulfide bond may be homolytically cleaved at high temperatures, resulting in sulfur radical formation during the synthesis.[22] Additionally, the disulfide bond may enable a chain-transfer reaction, wherein radical attack at the disulfide leads to the formation of a thioether, with a second sulfur radical released as a result (see Supporting Information, Scheme S1).[22] Finally, any conversion of the disulfide to thiols during synthesis would promote a Michael addition between the thiol and the vinyl groups of the monomers, again generating a thioether.[23−26] Thioether formation during synthesis is still an enabling mechanism

Received: October 11, 2011
Revised: December 12, 2011
Published: December 20, 2011

for particle formation; however, the cross-links formed are no longer susceptible to reduction/cleavage.

For bulk hydrogel synthesis, the accelerant *N,N,N′,N′*-tetramethylethylenediamine (TEMED) is commonly used to enable room temperature syntheses. When paired with APS, TEMED acts as a reducing agent, generating much higher levels of sulfate radical in solution than are achieved by thermal dissociation at the same temperature. Recently, we have shown that the use of the APS/TEMED pair is suitable for conducting microgel synthesis using microfluidic devices at lower temperatures,[27] and when utilized in conjunction with precipitation polymerization allows *in situ* encapsulation of proteins and the control of parasitic chain transfer reactions.[28] To attempt to mitigate the effects of the possible side reactions, we focused on the generation of thermoresponsive microgels containing disulfide cross-links by producing the particles at temperatures only slightly above the lower critical solution temperature (LCST) of the thermoresponsive polymer. In this work, we demonstrate the synthesis of thermo-responsive microgels cross-linked with the commercially available disulfide cross-linker BAC, utilizing aqueous precipitation polymerization with a redox initiation pair. These particles are shown to erode in response to reducing conditions, in contrast to comparable particles synthesized using the traditional thermally induced initiation approach. The improved control over disulfide incorporation was used in combination with the nondegradable cross-linker BIS to generate thiol-bearing microgels. These particles are shown to be suitable for iodoacetamide conjugation, and the reversible nature of the disulfide bond is exploited to form and disperse doubly cross-linked bulk gel networks of microgels, illustrating the potential utility of such particles in both bioconjugation and gel assembly.

EXPERIMENTAL SECTION

Materials. All reagents were purchased from Sigma-Aldrich (St Louis, MO) and used as received, unless otherwise noted. The monomer *N*-isopropylmethacrylamide (NIPMAm) was twice recrystallized from hexanes (VWR international, West Chester, PA) and dried in vacuo prior to use. Reagents *N,N′*-bis(acryloyl)cystamine (BAC), *N,N′*-methylenebis(acrylamide) (BIS), sodium dodecyl sulfate (SDS), ammonium persulfate (APS), *N,N,N′,N′*-tetramethylethylenediamine (TEMED), dithiothreitol (DTT), sodium periodate, fluorescein iodoacetamide, methanol, and dimethyl sulfoxide (DMSO) were all used as received. Water used in all reactions, particle purifications, and buffer preparations was purified to a resistance of 18 MΩ (Barnstead E-Pure system), and filtered through a 0.2 μm filter to remove particulate matter.

BAC Cross-Linked Particle Synthesis: Redox. NIPMAm was dissolved in deionized water, to a final total monomer concentration of 140 mM. The solution was filtered, followed by the addition of SDS a final concentration of 6 mM. The solution was heated to 50 °C and purged under nitrogen for 1 h. A solution of 10% (by volume) TEMED in water was added, bringing the TEMED concentration to 2 mM. Polymerization was initiated 10 min later by addition of an aqueous solution of 0.5 M APS (total concentration = 5 mM, an excess relative to TEMED to minimize interaction with BAC), followed immediately by a 172 mM solution of BAC in methanol to achieve a final molar ratio of 5 mol % cross-linker. The solution was allowed to stir at 50 °C for 6 h, then cooled to room temperature and filtered through no. 2 Whatman filter paper. (Anal. Calcd for NIPMAm/BAC/APS: C, 61.53; H, 9.52; N, 10.54; S, 4.04. Found: C, 55.19; H, 9.41; N, 9.78; S, 5.01.)

BAC Cross-Linked Particle Synthesis: Thermal. NIPMAm was dissolved in deionized water, to a final total monomer concentration of 140 mM. The solution was filtered, followed by the addition of SDS a final concentration of 6 mM. The solution was heated to 80 °C and purged under nitrogen for 1 h. Polymerization was initiated by addition of an aqueous solution of 0.1 M APS (total concentration 2 mM), followed immediately by a 172 mM solution of BAC in methanol to achieve a final molar ratio of 5 mol % cross-linker. The solution was allowed to stir at 80 °C overnight, then cooled to room temperature and filtered. (Anal. Calcd for NIPMAm/BAC/APS: C, 63.08; H, 9.76; N, 10.81; S, 3.07. Found: C, 57.20; H, 9.80; N, 9.89; S, 3.04.)

Co-Cross-Linked Particle Synthesis. NIPMAm and BIS (2 mol %) were dissolved in deionized water, to a final total monomer concentration of 140 mM. The solution was filtered, followed by the addition of SDS at a final concentration of 1 mM. The solution was heated to 50 °C and purged under nitrogen for 1 h. A solution of 10% (by volume) TEMED in water was added, bringing the TEMED concentration to 2 mM. Polymerization was initiated 10 min later by addition of an aqueous solution of 0.5 M APS (total concentration 5 mM), followed immediately by a 235 mM solution of BAC in methanol to achieve a final molar ratio of 5 mol % BAC. The solution was allowed to stir at 50 °C overnight, then cooled to room temperature and filtered through a 1.2-μm Acrodisc filter. (Anal. Calcd for NIPMAm/BAC/BIS/APS: C, 61.29; H, 9.44; N, 10.70; S, 4.02. Found: C, 55.95; H, 9.70; N, 9.98; S, 3.45.)

Particle Characterization. The microgels were size analyzed via dynamic light scattering (DLS) using a Dynapro DLS (Wyatt Technology, Santa Barbara, CA) and by asymmetrical flow field-flow fractionation coupled to multiangle light scattering (A4F-MALS) using the Eclipse 1 Separation System (Wyatt) and DAWN-EOS (Wyatt) detector. To characterize their degradation, samples with an identical particle concentration were prepared in pH 8.6 HEPES buffer. To one solution, an excess of DTT was added and allowed to incubate for 90 min. The two samples were analyzed using A4F-MALS using an identical procedure. The eluent was a 10 mM ionic strength (7 mM $NaNO_3$ + 3 mM NaN_3) aqueous buffer, and particle separation was achieved using a variable crossflow method wherein the initial crossflow rate of 1.0 mL/min was reduced over a period of 30 min to 0.1 mL/min. This same protocol was used to distinguish the thermally initiated particles. Particle radii (r_{rms}) values are reported as the average of three separations.

Elemental analysis was performed in duplicate on purified and lyophilized particles by Atlantic Microlabs, Norcross GA.

Fluorescent Labeling. Two 2 mL samples of a 4.5 mg/mL stock solution of co-cross-linked particles were suspended into two centrifuge tubes. The particles were pelleted by centrifugation at 18 000*g* for 10 min. The supernatant was removed from each tube and 1.5 mL of a 10 mM solution of DTT in pH 8.6 HEPES buffer was added to each. After 4 h of reduction, the particles (now presenting reactive thiols) were purified by sequential centrifugation and the supernatant replaced with pH 7.4 HEPES buffer. Each time the particles were pelleted at 18,000*g* for 25 min, and the process was repeated five times. Then, 200 μL of cleaned particle stock was added to 1.1 mg of fluorescein iodoacetamide, along with 1.0 mL of pH 7.4 HEPES buffer +200 μL of DMSO. The microgels were allowed to react at room temperature in the dark overnight. The labeled particles were purified by sequential centrifugation and the supernatant replaced with pH 7.4 HEPES buffer. The particles were stored in the dark while redispersing, and the process was repeated ten times until the fluorescence signal from the supernatant was indistinguishable from that of buffer. Fluorescence was measured using a steady-state fluorescence spectrophotometer (Photon Technology International), equipped with a Model 814 PMT photon-counting detector. Samples were prepared by diluting labeled particles into pH 7.4 HEPES buffer. The excitation wavelength used was 494 nm, and emission spectra were collected from 500 to 600 nm. Unlabeled particles were diluted to a similar concentration and spectra were collected under the same conditions. Additionally, co-cross-linked particles that were not exposed to DTT were also reacted with fluorescein iodoacetamide under the same conditions, similarly purified and spectra collected under the same conditions.

In Situ Erosion. The erosion of pNIPMAm-BAC nanogels was monitored in situ, using a previously reported light scattering method.[29] Using multiangle light scattering (MALS) detection, the

particle weight-average molar mass (M_w) was monitored in real-time during the erosion reaction. Reactants were introduced to the MALS detector using the Calypso syringe pump system (Wyatt Technology Corporation, Santa Barbara, CA). The Calypso hardware consists of a computer-controlled triplet syringe pump and a multichannel degasser, equipped with in-line filters, mixers and valves to allow rapid and automated batch measurements. MALS was performed using the DAWN-EOS (Wyatt Technology Corporation, Santa Barbara, CA) equipped with a temperature-regulated K5 flow cell with a GaAs laser light source (λ = 685 nm). Additional description of MALS analysis is provided in the Supporting Information. Data collection and subsequent analysis was performed using the Astra software Version 5.3.4.14 (Wyatt Technology Corporation, Santa Barbara, CA). Differential refractive index analysis was performed via composition-gradient static light scattering using the Calypso syringe pump and the OptilabrEX systems, equipped with an LED light source (λ = 690 nm).

In a typical erosion reaction, nanogels were prepared via dilution to a concentration of 3.5 × 10^{-2} mg/mL in 0.1 μm-filtered pH 7.0 phosphate buffer (ionic strength = 20 mM). To initiate erosion, the BAC nanogel solution and 20 mM DTT or 40 mM cysteine (prepared in the same buffer) were coadministered to the MALS flow cell via the Calypso syringe pump system. Final concentrations of particles and reducing agent were 1.74 × 10^{-2} mg/mL and 10 mM DTT and 20 mM cysteine, thus yielding 20 mM reactive thiolate in both cases. The particle M_w was monitored at stopped flow using the Astra software with a determined dn/dc value of 0.158 for BAC nanogels. The dn/dc was measured in triplicate using the Calypso syringe pump system coupled with dRI detection using a five-step calibration curve for BAC particles (1.75 × 10^{-1} mg/mL to 3.50 × 10^{-2} mg/mL) suspended in filtered pH 7.0 phosphate buffer (I = 20 mM).

Reversible Gelation. Two large centrifuge tubes were filled with 8 mL of a 4.5 mg/mL stock solution of particles cross-linked with both BIS and BAC. The particles were purified by sequential centrifugation at 15 500g for 25 min followed by redispersion in pH 7.4 HEPES buffer. After cleaning, the supernatant was replaced with 8 mL of 10 mM DTT in pH 8.6 HEPES buffer. The particles were allowed to erode with light agitation overnight. The now thiol-bearing particles were again purified using sequential centrifugation at 15 500g for 60 min, replacing the supernatant with additional 10 mM DTT. After cleaning, the supernatant was replaced with 7 mL of 12 mM $NaIO_4$ in pH 7.4 HEPES. After addition, the solution was centrifuged at 15 500g for 60 min. The resulting pellet was a solid gel, which was scraped from the bottom of the centrifuge tube and provided for rheology measurements.

The reversible nature of the double-network was demonstrated by equilibrating a large piece of the oxidized network in pH 8.6 HEPES buffer. The piece was then split into two approximately equal sized pieces and each piece placed into their own well plate. To one was added 5 mL of a solution of 22 mM DTT in pH 8.6 HEPES, while the other received only an equivalent volume of buffer. The two were allowed to shake for 24 h until complete dissolution of the reduced network in the DTT-containing solution occurred.

Rheology. Oscillatory rheology was carried out using a stress-controlled rheometer (Anton-Parr Physica MCR 501) with cone–plate geometry and a roughened cone with 25 mm diameter and 2° aperture. Before measurement, the instrument was calibrated to account for different sources of instrument error: motor and air bearing noise due to imperfections in motor operation, air bearing surface, turbulence in the air bearing and the effect of the tool's inertia on stress–strain measurements without sample. All measurements were taken above the instrument's minimum torque of 0.1 μNm. Though the rheometer is stress-controlled, strain-controlled measurements can be made because of a feedback loop: stress is applied and the resulting strain is measured, and the loop enables the rheometer to adjust the applied stress to keep strain at the desired value. The time to complete the loop is on the order of milliseconds, so the accessible frequency range has an upper limit of about 100 rad/s. About 0.2 mL of the double network sample was compressed beneath the cone and plate at room temperature. A linearity test was performed at 10 rad/s between 0.1% and 1% strain; for strains below ~0.3%, the system can be safely assumed in the linear regime, as shown in Figure 5a. The frequency measurements were done at constant strain of 0.1% and frequencies on a logarithmic scale decreasing from 100 to 0.01 rad/s with 6 points per decade.

RESULTS AND DISCUSSION

Particle Synthesis and Characterization. In order to minimize interaction between TEMED and BAC, two modifications to conventional precipitation polymerization were necessary: an excess of APS relative to TEMED was utilized, and the BAC was added immediately following initiation by APS. Particle formation was confirmed by DLS, and was successful under the two synthetic protocols described, with the differences limited to the reaction temperature and hence the method of radical generation from APS. Elemental analysis confirms sulfur incorporation for both the thermally and redox-initiated particles with BAC and APS being the two potential sources of sulfur in the monomer feed. For the redox-initiated particles, the reported sulfur values are slightly higher than expected from the feed composition. This may arise from the bifunctional reactivity of the cross-linker, which likely contributes to faster incorporation into the microgels, along with the high sulfate radical yield that is typical for redox initiation. In contrast, the thermally initiated particles were in close agreement with their theoretical composition. This also likely represents efficient incorporation of BAC, with perhaps a lower overall degree of sulfate incorporation.

To more directly probe the cross-link density of the particles, DLS was used to determine the swelling ratio for the particles by determining the hydrodynamic radius above and below pNIPMAm's LCST. The work by Senff and Richtering, Varga et al., and Duracher et al. focused on systematically studying the effect of cross-linking density on the swelling ratio and particle topology (the ratio r_{rms}/r_h) of thermoresponsive microgels.[30−32] The data from the Varga study, which included swelling values in the regime seen for the disulfide cross-linked particles, was used to estimate the BAC particles' cross-link density. By plotting the cross-link density vs swelling ratio for the Varga data and using least-squares regression to determine a model which best fit the data, we were able to use our swelling data to estimate the cross-linking density of the BAC cross-linked particles (see Supporting Information). For the redox-initiated particles, the determined swelling ratio of 1.82 when mapped onto the Varga cross-link model yields an estimated cross-link density of 5.1%, in good agreement with the monomer feed composition. In contrast, the thermally initiated particles exhibited a higher apparent cross-linking (swelling ratio =1.45), corresponding to an estimated cross-link density of 8.4%. The higher apparent cross-linking may be a result of chain-transfer located at the disulfide bond, Michael addition, or any of the other potential cross-link forming side reactions described above.

Particle Erosion. Successful incorporation of BAC within the microgel network should lead to particles that undergo cross-link scission via disulfide reduction. Generally, a reduction in the amount of cross-linking in a particle would cause an increase in particle swelling as the network becomes more flexible. In the extreme case wherein all cross-linking points within the particle are labile, complete dissolution of the microgel should follow reduction. A comparison of the chromatograms shown in Figure 1 highlights the impact the initiation method has on particle erosion following cross-link cleavage. When the thermally initiated particles were exposed to the reductant DTT, a small increase in the A4F retention time and a reduction in the intensity of the scattering signal were observed (Figure 1a).

dx.doi.org/10.1021/ma202282p | Macromolecules 2012, 45, 39−45

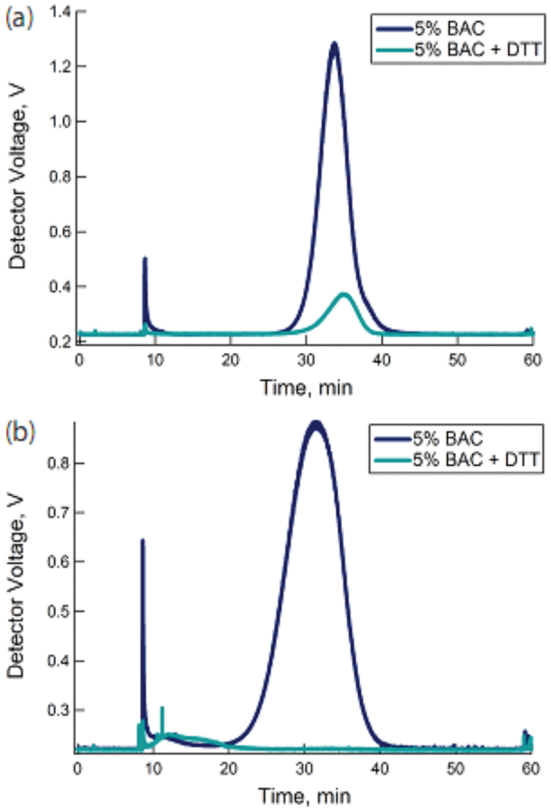

Figure 1. A4F-MALS separation of pNIPMAm-BAC (5%) microgels formed by the (a) thermal and (b) redox initiation methods. Incubating the particles with DTT increased retention of the thermally initiated particles, yet led to degradation of the redox-initiated particles.

The increased retention time in the variable cross-flow separation is indicative of decrease in the particle diffusion coefficient, which we propose occurs due to cross-link scission and the concomitant increase in particle swelling and r_h. The accompanying reduction in scattering intensity is further indicative of particle swelling and thus a reduction in refractive index. The increase in particle r_h suggests a decrease in nanogel density as a result of cross-link scission. Offline analysis of the particles before and after erosion by DLS confirmed the expected changes accompanying cross-link scission, as shown in Table 1. Nanogel erosion resulted in an increase in the swelling ratio from 1.45 to 2.18, which correlates to a remnant cross-link density of 2.4%. A large increase in r_{rms} from 33 to 43 nm also resulted from scission, which was further indicative of network expansion. Interestingly, the particle mass distribution remained consistent throughout erosion reaction for thermally initiated nanogels. The mass distribution may be inferred through the ratio of the r_{rms} (weighted-size by the mass distribution about the center of mass) and the r_h (determined from the diffusion coefficient of the particle). Monitoring changes in mass distribution following erosion is a useful way to characterize the distribution of the labile bonds within the nanogel architecture. For example, changes in mass distribution following erosion would indicate that the labile cross-links were preferentially located in a particular region of the particles. The value of r_{rms}/r_h for the thermally initiated particles (~0.56) is indicative of a radially heterogeneous segment density, with the periphery having a lower density of polymer. This value is frequently observed for nanogels prepared by precipitation polymerization, where dissimilar reactivity between the monomers results in greater polymer segment density toward the interior of spheres.[30] Although erosion caused a shift in the size and molar mass of the particles, there was no measurable change in r_{rms}/r_h. This result suggests that cross-link scission from BAC featuring intact disulfide bonds occurred evenly throughout the structure. As such, the heterogeneous segment density suggests the nonlabile and labile cross-link distributions are similar. However, additional work may be necessary to verify this hypothesis.

In contrast to thermally initiated nanogels, the redox-initiated particles showed complete dissolution after exposure to DTT; as evidenced by the disappearance of the peak associated with the nanogel and the emergence of a peak at very short retention times with diminished scattering signal. The loss of particle retention via A4F is indicative of a drastic increase in the polymer diffusion coefficient, whereas the loss of scattering signal is indicative of a significant reduction in particle density, suggesting potential mass loss from the polymer. Together, those data suggest complete dissolution of the nanogel into low molar mass, oligomeric products (Figure 1b). The differential response seen in the A4F results for the two types of particles is indicative of the difference in network structure between the two. The failure of thermally initiated particles to completely erode into oligomeric chains reveals the presence of non-erodible residual cross-links in the structure, likely thioethers resulting from side reactions. In the redox-initiated case these parasitic reactions are limited, leading to a particle whose network integrity is completely controlled by disulfide cross-links.

In Situ Erosion. In the presence of a strong reducing agent, such as DTT, the nanogels synthesized at lower temperatures via redox initiation completely dissolved into low molar mass components. Thus, we hypothesized that those networks would be similarly sensitive to the presence of cysteine and other thiols in their environment, resulting in thiol−disulfide exchange reactions that would disrupt connectivity in the nanogel network. The time scale of erosion for thiol competition under physiologically relevant reducing conditions, such as those found in the cytoplasm, is of interest in drug delivery applications. Nanogel erosion was monitored in situ via MALS detection, using a similar method as reported previously.[29] Through this approach, changes in the apparent M_w of nanogels were monitored in real-time, enabling a direct comparison of erosion kinetics for particles in response to DTT and cysteine (Figure 2).

Table 1. Size, Swelling, and Topology Characterization for BAC-Cross-Linked Microgels

	r_h, nm (20 °C)[a]	r_h, nm (45 °C)[a]	swelling ratio[b]	r_{rms}, nm[a]	r_{rms}/r_h (20 °C)	est. cross-link density,[c] %
5% BAC (T)	60	41	1.45	32.9 ± 0.1	0.55	8.38
5% BAC (T) + DTT	73	34	2.18	42.4 ± 1.8	0.58	2.43
5% BAC (R)	48	26	1.82	36.9 ± 0.6	0.78	5.12

[a]Sizes reported in pH 8.6 HEPES buffer. [b]Calculated as r_h(20 °C)/ r_h(45 °C). [c]Calculated from swelling ratio using Varga model (see Supporting Information).

dx.doi.org/10.1021/ma202282p | *Macromolecules* 2012, 45, 39−45

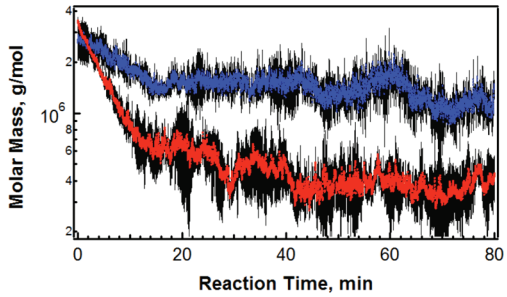

Figure 2. Nanogel erosion via cross-link scission occurs in the presence of DTT (red) or cysteine (blue), monitored in situ via MALS. Error bars (black) represent one standard deviation about the mean of measurements.

In the presence of DTT, the M_w of nanogels decays by an order of magnitude, eventually reaching equilibrium after ~40 min of the reaction (Figure 2). This indicates that swelling is accompanied by mass loss and that both effects give rise to the decrease in light scattering intensity observed via A4F analysis (Figure 1). Erosion also proceeds in the presence of cysteine, but at a much slower rate. The higher reaction rate for DTT may result from differences in the erosion products. Following exchange DTT is released from the thiol by a cyclization reaction, reverting to an internal oxidized disulfide bond and leaving behind a pair of thiols on the microgel. In contrast, cysteine likely disrupts the BAC by participating in a single thiol-disulfide exchange reaction; the resulting product is therefore a mixed-disulfide. This leads to the possibility of reverse reactions and continued thiol-exchange reactions that are not productive toward cross-link scission.

Reactive Thiol Incorporation. The disulfide content imparted by BAC may enable the conjugation of thiolated molecules within the nanogel network by thiol−disulfide exchange reactions, as shown in Figure 2 for cysteine. However, BAC may also be reduced to yield reactive thiols within nanogel networks, which prepares those networks for a variety of other bioconjugation chemistries. For example, reactive thiols within nanogels are of great utility due to their selective reactivity with maleimides, iodoacetamides, and other thiols under mild, aqueous conditions.[33] Yet as depicted in our results, complete reduction of BAC within the colloid results in particle decomposition. We therefore synthesized co-cross-linked particles containing both BAC and a nondegradable cross-linker, BIS. The resultant nanogels underwent a significant size increase in response to the reductant DTT, from an r_h of 183 to 232 nm at 20 °C and a pH of 8.6, accompanied by a large decrease in turbidity due to a decrease in the cross-link density in the network (photographs of these dispersions are available in the Supporting Information). The reduced form of the co-cross-linked particles presented free thiols available for conjugation with an iodoacetamide derivative of fluorescein, yielding fluorescent particles. In contrast, particles containing BAC in the oxidized form showed significantly reduced fluorescence (Figure 3). Epifluorescence microscopy images of the labeled particles are available in Supporting Information.

Reversible Gelation. The reversible nature of the disulfide reduction enables cross-link formation between thiols resulting from BAC reduction. Placing the thiolated particles together at high concentration, such as by centrifugation, enabled the thiols to react under oxidizing conditions and form a double network "gel of microgels", wherein the individual microgels retain their

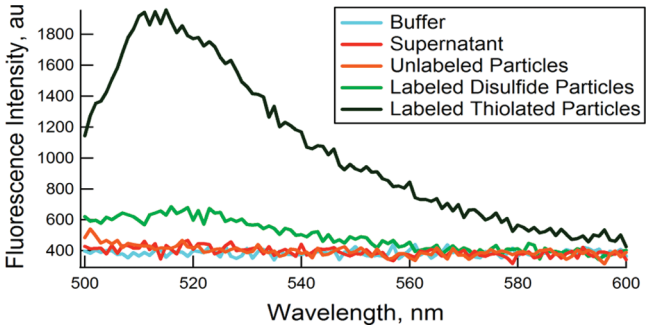

Figure 3. Fluorescence spectra (λ_{ex} = 494 nm) of (dark green) fluorescein-labeled pNIPMAm−BAC−Bis particles, (orange) unlabeled particles, (blue) pH 7.4 HEPES buffer, and (red) the supernatant following purification by centrifugation. Particles that were not reduced and therefore retained their disulfide linkages (light green) had much lower coupling efficiency than that of the reduced particles.

identity through incorporation of the nondegradable BIS cross-linker, yet are tethered to one another by the resulting interparticle disulfide linkages.

Centrifugation of the co-cross-linked particles resulted in a dense pellet (Figure 4, left), whereas nanogels reacted with

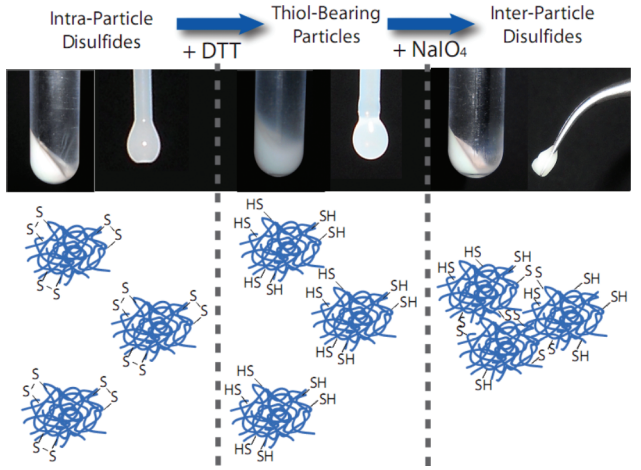

Figure 4. Gelation of pNIPMAm−BAC−BIS particles. Sedimented particles with intraparticle disulfides form a dense pellet, yet retain fluidity (left). Reduction by DTT leads to the production of thiol-bearing particles, a reduction in pellet density, and the retention of particle fluidity (center). Oxidation by $NaIO_4$ restores pellet density, but the resulting solid is a double-network of microgels cross-linked by interparticle disulfides (right).

DTT, due to their decreased density, required a 2−3-fold increase in centrifugation time at the same relative centrifugal force to form a sediment. The resulting pellet of the reduced particles was less turbid in comparison to nondegraded particles (Figure 4, center). Despite those differences, both degraded and nondegraded nanogels were fluid in their highly concentrated, sedimented form, with water-like viscosity rendering them readily capable of being drawn up via pipet for the suspended drop images shown in Figure 4. Exposure of the thiol-bearing particles to the oxidant sodium periodate during centrifugation dramatically increased the viscosity of the particle dispersion as a result of interparticle cross-linking. The volume

dx.doi.org/10.1021/ma202282p | Macromolecules 2012, 45, 39−45

and turbidity of the pellet was similar to the disulfide particles prior to reduction, indicative of the cross-link reformation (Figure 4-right). However, the pellet did not flow when inverted, indicating the formation of a viscoelastic solid capable of being handled with tweezers, as shown in Figure 4.

Through rheological characterization of the resultant solids, we find that the storage modulus of our double-network is ~2000 Pa, while the loss modulus is ~100 Pa, as shown in Figure 5b. As a result, within the experimental frequency range,

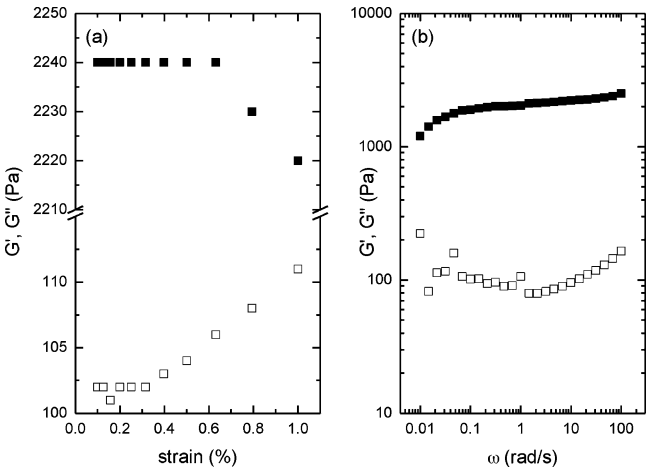

Figure 5. Storage and loss moduli as determined by oscillatory rheology for the pNIPMAm-BAC-BIS oxidized double-network. The linearity test (a) shows G' (closed symbols) and G'' (open symbols) as a function of strain at constant frequency of 10 rad/s and (b) shows both moduli as a function of frequency at constant strain of 0.1%. The storage modulus is an order of magnitude larger than the loss modulus, indicative of the solid-like properties of the microgel double-network.

the complex shear modulus (G^*) is dominated by the contributions from the elastic character of the network. We note that the value of the shear modulus is comparable to that of a variety of disulfide cross-linked hydrogel networks,[34,35] acrylamide-based hydrogels,[36] and densely packed microgel assemblies.[37] The shear modulus is also comparable to similar work by Hu et al.[38] wherein microgels composed of pNIPAm, internally cross-linked with BIS, and bearing *N*-hydroxymethacrylamide form a self-cross-linked "gel of microgels" upon drying that is analogous to the double-network discussed in this work.

The interparticle disulfide bonds that bind the microgels within the double-network can be reduced to restore the constituent thiol-bearing particles. Exposure of the double-network to DTT resulted in network dissolution. As shown in Figure 6, a significant loss in gel turbidity and a clouding of the solution occurred within 2 h. The loss in turbidity likely resulted from a reduction in cross-link density as the interparticle disulfides are cleaved, and the clouding was the result of dispersion of liberated microgels. The double network gel completely decomposed within 24 h. Such a system may be enabling for numerous potential applications, such as creating erodible gels with tunable mechanical properties or acting as a reservoir for delivery of either a drug trapped within the matrix or for the release of microgel delivery vehicles themselves.

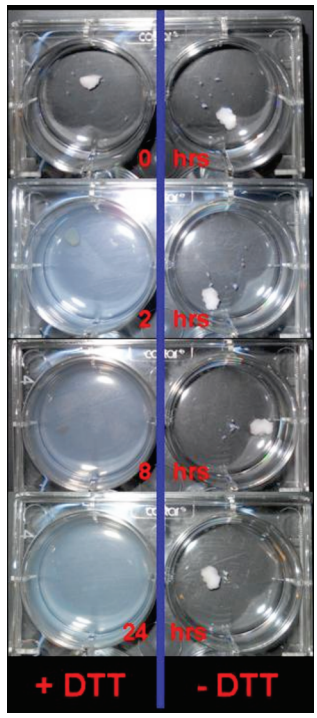

Figure 6. Images depicting the erosion of the pNIPMAm-BAC-BIS double-network. In response to the addition of DTT, the network dissolves leading to the reversion of the particles to their dispersed state in a matter of hours.

CONCLUSIONS

In this work, we have demonstrated the ability to incorporate disulfide cross-links into thermoresponsive microgels using the commercially available cross-linker *N*,*N*′-bis(acryloyl)cystamine while utilizing aqueous precipitation polymerization. Conventional, thermally initiated free radical precipitation polymerization leads to uncontrolled side (self-cross-linking) reactions, leading to significant disruption of the central disulfide bond and generation of a nondegradable network. The use of a redox pair as the radical source during the polymerization leads to a reduction in the temperature needed to conduct the synthesis, while also reducing the rate of parasitic side reactions. Chemical reduction or thiol exchange of the disulfide cross-links leads to fully erodible nanogels, which may be enabling for drug delivery applications. We have demonstrated that these particles erode under mild conditions in the presence of reducing agents or a competing thiol on a time scale of minutes to hours. Furthermore, by incorporating a nondegradable second cross-linking element, intact thiol-bearing microgels can be generated through disulfide reduction, with such particles being amenable to bioconjugation and reversible double-network formation. The ability to incorporate disulfides and thiols into microgels via precipitation polymerization enables these functionalities to be used in parallel with well-characterized techniques to control particle size, topology, and functionality. We envision this additional capability to be enabling for the design of future generations of microgels for numerous applications.

ASSOCIATED CONTENT

Supporting Information

Reaction scheme for thioether formation, model for estimation of cross-linking density, additional discussion of MALS analysis and rheological characterization, vial and microscopy images,

dx.doi.org/10.1021/ma202282p | *Macromolecules* 2012, 45, 39–45

and supplemental DLS data. This material is available free of charge via the Internet at http://pubs.acs.org.

AUTHOR INFORMATION

Corresponding Author

*E-mail: lyon@gatech.edu..

ACKNOWLEDGMENTS

This work was partially supported by the National Institutes of Health (1 R01 GM088291-01). Funding for J.C.G. and M.H.S. was provided by U.S. Department of Education GAANN awards, the Georgia Tech Center for Drug Design, Development and Delivery, and the Georgia Tech TI:GER program. Additional funding for J.C.G. was provided by the National Institutes of Health training grant: G_TBioMAT Graduate Training for Rationally Designed, Integrative Biomaterials (T32 EB 006343). Support for J.S.H. was provided by the NSF through the Georgia Tech MRSEC (DMR-0820382).

REFERENCES

(1) Meng, F. H.; Hennink, W. E.; Zhong, Z. *Biomaterials* **2009**, *30*, 2180−2198.
(2) Saito, G.; Swanson, J. A.; Lee, K. D. *Adv. Drug Delivery. Rev.* **2003**, *55*, 199−215.
(3) Lee, H.; Mok, H.; Lee, S.; Oh, Y. K.; Park, T. G. *J. Controlled Release* **2007**, *119*, 245−252.
(4) Oh, J. K.; Siegwart, D. J.; Lee, H. I.; Sherwood, G.; Peteanu, L.; Hollinger, J. O.; Kataoka, K.; Matyjaszewski, K. *J. Am. Chem. Soc.* **2007**, *129*, 5939−5945.
(5) Li, Y. T.; Lokitz, B. S.; Armes, S. P.; McCormick, C. L. *Macromolecules* **2006**, *39*, 2726−2728.
(6) Lin, C.; Zhong, Z. Y.; Lok, M. C.; Jiang, X. L.; Hennink, W. E.; Feijen, J.; Engbersen, J. F. J. *Bioconjugate Chem* **2007**, *18*, 138−145.
(7) Jones, C. D.; Lyon, L. A. *Macromolecules* **2000**, *33*, 8301−8306.
(8) Nayak, S.; Gan, D. J.; Serpe, M. J.; Lyon, L. A. *Small* **2005**, *1*, 416−421.
(9) Meng, Z. Y.; Hendrickson, G. R.; Lyon, L. A. *Macromolecules* **2009**, *42*, 7664−7669.
(10) Blackburn, W. H.; Dickerson, E. B.; Smith, M. H.; McDonald, J. F.; Lyon, L. A. *Bioconjugate Chem.* **2009**, *20*, 960−968.
(11) Dickerson, E. B.; Blackburn, W. H.; Smith, M. H.; Kapa, L. B.; Lyon, L. A.; McDonald, J. F. *BMC Cancer* **2010**, 10.
(12) Hu, X. B.; Tong, Z.; Lyon, L. A. *J. Am. Chem. Soc.* **2010**, *132*, 11470−11472.
(13) Lee, H.; Park, T. G. *Polym. J.* **1998**, *30*, 976−980.
(14) Hiratani, H.; Alvarez-Lorenzo, C.; Chuang, J.; Guney, O.; Grosberg, A. Y.; Tanaka, T. *Langmuir* **2001**, *17*, 4431−4436.
(15) Aliyar, H. A.; Hamilton, P. D.; Ravi, N. *Biomacromolecules* **2005**, *6*, 204−211.
(16) Pong, F. Y.; Lee, M.; Bell, J. R.; Flynn, N. T. *Langmuir* **2006**, *22*, 3851−3857.
(17) Bajomo, M.; Steinke, J. H. G.; Bismarck, A. *J. Phys. Chem. B* **2007**, *111*, 8655−8662.
(18) Plunkett, K. N.; Kraft, M. L.; Yu, Q.; Moore, J. S. *Macromolecules* **2003**, *36*, 3960−3966.
(19) Oh, J. K.; Tang, C. B.; Gao, H. F.; Tsarevsky, N. V.; Matyjaszewski, K. *J. Am. Chem. Soc.* **2006**, *128*, 5578−5584.
(20) Pelton, R. H.; Chibante, P. *Colloids Surf.* **1986**, *20*, 247−256.
(21) Pelton, R. H. *Adv. Colloid Interface Sci.* **2000**, *85*, 1−33.
(22) Kice, J. L. In *Sulfur in Organic and Inorganic Chemistry*; Senning, A., Ed.; Marcel Dekker: New York, 1971; Vol *1*, pp 153−207.
(23) Mather, B. D.; Viswanathan, K.; Miller, K. M.; Long, T. E. *Prog. Polym. Sci.* **2006**, *31*, 487−531.
(24) Torchinskii, Y. M. In *Sulfhydryl and Disulfide Groups of Proteins*; Consultants Bureau: New York, 1974; pp 46−98.
(25) Cremlyn, R. J. In *An Introduction to Organosulfur Chemistry*; Wiley: New York, 1996; pp 41−61.
(26) Khatik, G. L.; Kumar, R.; Chakraborti, A. K. *Org. Lett.* **2006**, *8*, 2433−2436.
(27) Kim, J. W.; Utada, A. S.; Fernandez-Nieves, A.; Hu, Z. B.; Weitz, D. A. *Angew. Chem., Int. Ed.* **2007**, *46*, 1819−1822.
(28) Hu, X. B.; Tong, Z.; Lyon, L. A. *Langmuir* **2011**, *27*, 4142−4148.
(29) Smith, M. H.; Herman, E. S.; Lyon, L. A. *J. Phys. Chem. B* **2011**, *115*, 3761−3764.
(30) Senff, H.; Richtering, W. *Colloid Polym. Sci.* **2000**, *278*, 830−840.
(31) Varga, I.; Gilanyi, T.; Meszaros, R.; Filipcsei, G.; Zrinyi, M. *J. Phys. Chem. B* **2001**, *105*, 9071−9076.
(32) Duracher, D.; Elaissari, A.; Pichot, C. *J. Polym. Sci., Part A: Polym. Chem.* **1999**, *37*, 1823−1837.
(33) Hermanson, G. T. *Bioconjugate Techniques*; Academic Press: San Diego, CA, 1996; pp 229−286.
(34) Wu, Z. M.; Zhang, X. G.; Zheng, C.; Li, C. X.; Zhang, S. M.; Dong, R. N.; Yu, D. M. *Eur. J. Pharm. Sci.* **2009**, *37*, 198−206.
(35) Van Vlierberghe, S.; Schacht, E.; Dubruel, P. *Eur. Polym. J.* **2011**, *47*, 1039−1047.
(36) Yeung, T.; Georges, P. C.; Flanagan, L. A.; Marg, B.; Ortiz, M.; Funaki, M.; Zahir, N.; Ming, W. Y.; Weaver, V.; Janmey, P. A. *Cell Motil. Cytoskelet.* **2005**, *60*, 24−34.
(37) Senff, H.; Richtering, W. *J. Chem. Phys.* **1999**, *111*, 1705−1711.
(38) Zhou, J.; Wang, G. N.; Marquez, M.; Hu, Z. B. *Soft Matter* **2009**, *5*, 820−826.

Macromolecules

Article

pubs.acs.org/Macromolecules

A Sugar Decorated Macromolecular Bottle Brush by Carbohydrate-Initiated Cationic Ring-Opening Polymerization

Christine Weber,[†,‡,§] Justyna A. Czaplewska,[†,‡] Anja Baumgaertel,[†,‡,§] Esra Altuntas,[†,‡] Michael Gottschaldt,[†,‡] Richard Hoogenboom,[⊥,*] and Ulrich S. Schubert[†,‡,§,*]

[†]Laboratory of Organic and Macromolecular Chemistry (IOMC), Friedrich-Schiller-University Jena, Humboldtstrasse 10, 07743 Jena, Germany

[‡]Jena Center for Soft Matter (JCSM), Friedrich-Schiller-University Jena, Humboldtstrasse 10, 07743 Jena, Germany

[§]Dutch Polymer Institute (DPI), John F. Kennedylaan 2, 5612 AB Eindhoven, The Netherlands

[⊥]Supramolecular Chemistry Group, Department of Organic Chemistry, Ghent University, Krijgslaan 281 S4, 9000 Ghent, Belgium

Supporting Information

ABSTRACT: The capability of a range of protected glucose- (Glc), galactose- (Gal), and fructose- (Fru) based tosylates and triflates to initiate the living cationic ring-opening polymerization of 2-ethyl-2-oxazoline (EtOx) was investigated by detailed kinetic studies utilizing ^{1}H and ^{19}F NMR spectroscopy and SEC as well as MALDI and ESI TOF mass spectrometry. The Glc and Gal tosylates and a sterically hindered Fru triflate revealed slow and incomplete initiation, whereas the Glc and Gal triflates resulted in living polymerizations. Well-defined Glc as well as Gal α-end-functionalized PEtOx was obtained after deprotection. Functionalization of the living oxazolinium chain ends with methacrylate anions resulted in a macromonomer that was applied for RAFT polymerization. Deprotection resulted in a comb polymer that is selectively functionalized with Glc at the ends of all side chains ($DP_{backbone}$ = 13, $DP_{side\ chains}$ = 10, PDI = 1.11).

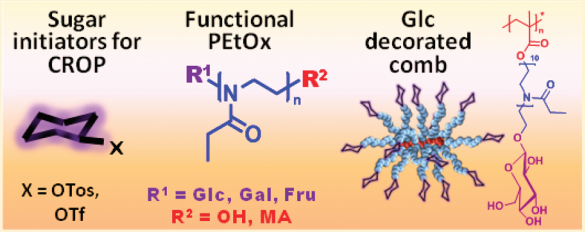

INTRODUCTION

Within the last few years, the biological activity of carbohydrates as cell targeting units stimulated an increasing interest in synthetic glycopolymers that are able to target specific cell types and, therefore, show great potential for applications in intelligent drug delivery systems.[1−4] In particular, branched or dendronized macromolecules have attracted considerable attention since they display an increased capability to block viral adhesion to cells when compared to their linear analogues.[5] Large efforts have been undertaken in the synthesis of dendrimers that bear sugars as targeting units in the outer shell.[6−8] Usually, the conjugation with the carbohydrate is the final step in an extensive synthetic cascade. Recently, hyperbranched polymers that are functionalized with carbohydrates have received special attention because they offer an opportunity to overcome the disadvantageous multi step synthetic procedures for dendrimers.[9−15] However, such structures are less well-defined, which might complicate their structural optimization and approval as pharmaceuticals.[16]

As a consequence, it is highly desirable to establish other macromolecular architectures that are decorated with sugar units in the periphery. In addition, they should be more well-defined than hyperbranched structures while being more readily accessible than dendrimers. Comb polymers that are selectively functionalized with cell targeting sugars at the end of the side chains appear to be ideal candidates for such a task. Utilization of the macromonomer method for the comb synthesis will ensure a dense comb structure since every backbone repeating unit is connected to a side chain. Such macromonomers should, thus, carry the carbohydrate at one chain end as well as a polymerizable end group at the other chain end.

For this challenging synthesis of dual functional macromonomers it is inevitable to apply a living or controlled polymerization technique, such as the living cationic ring-opening polymerization (CROP) of 2-oxazolines (Scheme 1).[17−19] End functionalization of the α chain ends can be achieved by utilization of suitable electrophilic initiators, whereas the living oxazolinium ω chain end provides access to a direct attack of nucleophiles, such as deprotonated carboxylic acids or amines. Next to benzyl halides or carboxylic acid halides, commonly applied functional initiators for the CROP are tosylates and triflates. At the same time, these two substance classes are frequently used intermediates during multi step synthesis of various advanced carbohydrates. It is obvious that hydroxyl functionalities of the carbohydrate itself are not tolerated by an ionic polymerization mechanism, but a range of protecting groups that can be cleaved under varying reaction conditions has been established in carbohydrate chemistry.

Also with respect to potential biomedical applications of the glycosylated comb polymer, poly(2-oxazoline)s (POx) repre-

Received: October 30, 2011
Revised: November 25, 2011
Published: December 9, 2011

Scheme 1. Schematic Representation of the Cationic Ring-Opening Polymerization of 2-Ethyl-2-oxazoline Initiated by Tosylates and Triflates

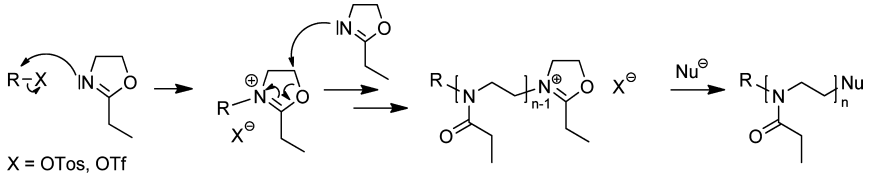

sent a suitable basic polymeric material due to their biocompatibility and stealth effect[17,20] that brought them into discussion as alternatives for the widely applied poly(ethylene glycol) in the field of modern drug delivery.[21,22] In fact, sugar containing linear POx have already been realized, either by post polymerization modifications[23,24] or by copolymerization of carbohydrate-based monomers.[25,26] On the other hand, tosylate and triflate derivatives of other natural compounds, such as steroids[27] or lipids,[27−29] have proven useful as initiators for the CROP of 2-oxazolines, whereas the only carbohydrate-based initiator is an oxazolinium derivative of bicyclic *N*-acetyl-D-glucosamine and, as such, very limited to this specific sugar.[30]

In this contribution we present the initiation of the CROP of 2-ethyl-2-oxazoline (EtOx) with tosylate and triflate derivatives of glucose, galactose as well as the less frequently utilized fructose. The initiation and polymerization kinetics are discussed as well as the end functionalization with methacrylic acid leading toward a sugar-functionalized macromonomer. reversible addition-fragmentation chain transfer (RAFT) polymerization of this macromonomer resulted, to the best of our knowledge, in the first synthesis of a comb polymer that is selectively functionalized with sugars at the ends of the side chains.

EXPERIMENTAL SECTION

Materials. 2-Ethyl-2-oxazoline (99%, Acros, EtOx) was dried over barium oxide and distilled under argon prior to use. Acetonitrile (extra dry) was purchased from Acros and stored under argon. Methacrylic acid (99%, Aldrich, MAA) was used as received. Triethylamine (NEt_3) was dried over potassium hydroxide and distilled under argon. 2,2′-Azobis(2-methylpropionitrile) (98%, Acros, AIBN) was recrystallized from hexane, and the chain transfer agent 2-cyanopropyl dithiobenzoate (CPDB, 97%) was obtained from Aldrich. For the cloud point measurements, demineralized water or phosphate buffered saline 10× concentrate (Aldrich) were used. For the synthesis of the initiators, acetobromo-α-D-Glucose, 97% (AlfaAesar), trifluoromethanesulfonic acid anhydride (Fluka), 2,3:4,5-di-*O*-isopropylidene-β-D-fructopyranose (Carbosynth), 1,2:3,4-di-*O*-isopropylidene-D-galactopyranose (Aldrich), 1,2:3,4-di-*O*-isopropylidene-6-*O*-*p*-toluenesulfonyl-α-D-galactopyranose (Carbosynth) were purchased. 2-Hydroxyethyl 2,3,4,6-tetra-*O*-acetyl-β-D-glucopyranoside was synthesized according to a literature procedure.[2] All other chemicals and solvents were obtained from common commercial sources and used without further purification, unless otherwise noted.

Instrumentation. ^1H and ^{13}C NMR spectra were recorded in $CDCl_3$ or DMSO-d_6 on a Bruker Avance 300 MHz using the residual solvent resonance as an internal standard. ^{19}F NMR spectra were measured on a Bruker Avance 200 MHz spectrometer. Size exclusion chromatography (SEC) for kinetic studies was measured on a Shimadzu system equipped with a SCL-10A system controller, a LC-10AD pump, and a RID-10A refractive index detector using a solvent mixture containing chloroform, triethylamine, and isopropanol (94:4:2) at a flow rate of 1 mL min^{-1} on a PSS-SDV-linear M 5 μm column at 40 °C. The system was calibrated with PS (2000 to 88 000 g mol^{-1}) standards. For **P1−3**, a second Shimadzu system was used, equipped with a SCL-10A system controller, a LC-10AD pump, a RID-10A refractive index detector, and both a PSS Gram30 and a PSS Gram1000 column in series, whereby *N*,*N*-dimethylacetamide with 2.1 g L^{-1} of LiCl was applied as an eluent at 1 mL min^{-1} flow rate and the column oven was set to 60 °C.

For the measurement of the matrix-assisted laser desorption/ionization (MALDI) spectra an Ultraflex III TOF/TOF (Bruker Daltonics, Bremen, Germany) was used. The instrument was equipped with a Nd:YAG laser and a collision cell. All spectra were measured in the positive reflector or linear mode using *trans*-2-[3-(4-*tert*-butylphenyl)-2-methyl-2-propenylidene]malononitrile (DCTB) as matrix and sodium iodide as salt. The instrument was calibrated prior to each measurement with an external PMMA standard from PSS Polymer Standards Services GmbH (Mainz, Germany). ESI TOF MS measurements were performed with a micrOTOF Q-II (Bruker Daltonics) mass spectrometer equipped with an automatic syringe pump from KD Scientific for sample injection. The ESI TOF mass spectrometer was running at 4.5 kV, at a desolvation temperature of 180 °C. The mass spectrometer was operating in the positive ion mode. Nitrogen was used as the nebulizer and drying gas. The concentration of the samples was 10 μg mL^{-1} and all samples were injected using a constant flow rate of 180 μL h^{-1} of the sample solution. The solvent was a chloroform/acetonitrile (10:90) mixture. There was no salt addition prior to analysis, but ionization occurs readily from the sodium content that is naturally present in the glass. The ESI TOF MS instrument was calibrated in the *m*/*z* range from 50 to 3000 using a calibration standard (Tunemix solution) supplied from Agilent. Data were processed via Bruker Data Analysis software version 4.0.

Cloud points were determined on a Crystal 16 from Avantium Technologies being connected to a chiller (Julabo FP 40) using a wavelength of 500 nm and a heating ramp of 1 K min^{-1}. The concentration of the polymer was kept constant at 5 mg mL^{-1}.

Synthesis of Sugar-Based Initiators. 2-*p*-Tolylsulfonyloxyethyl 2,3,4,6-tetra-*O*-acetyl-β-D-glucopyranoside (**I1**),[31] 1,2:3,4-di-*O*-isopropylidene-6-*O*-trifluormethanesulfonyl-α-D-galactopyranose (**I4**),[32] and 2,3:4,5-di-*O*-isopropylidene-1-[trifluoromethylsulfonyl)oxy]-D-fructopyranose (**I5**)[33,34] were synthesized according to previously reported experimental procedures. 2-*p*-Trifluoromethylsulfonyloxyethyl 2,3,4,6-tetra-*O*-acetyl-β-D-glucopyranoside (**I3**) was synthesized from 2-hydroxyethyl-2,3,4,6-tetra-*O*-acetyl-β-D-glucopyranoside[31] as follows: 2-Hydroxyethyl-2,3,4,6-tetra-*O*-acetyl-β-D-glucopyranoside (0.9 g, 2.29 mmol) was dissolved in dry dichloromethane (50 mL) and dry pyridine (2 mL) was added. After cooling to −20 °C the trifluoromethanesulfonic anhydride (2 mL, 11 mmol) was added dropwise. The reaction mixture was stirred for around 2 h at −20 °C. After TLC indicated the disappearance of the starting material, the solution was diluted with dichloromethane, washed with water and saturated sodium bicarbonate solution. After drying over sodium sulfate the solvent was evaporated and the crude product was purified on a short column (silica gel, $CHCl_3$). After evaporation of the chloroform, the purified product was washed with diethyl ether in order to facilitate faster drying under reduced pressure. The product was obtained as a yellow oil (0.75 g, 63%). ^1H NMR (300 MHz, $CDCl_3$): δ/ppm = 5.12 (t, ^3J = 9.5 Hz, H-3, 1H), 5.06−4.93 (dt, ^3J = 9.9 Hz, ^3J = 9.1 Hz, H-4, H-2, 2H), 4.60−4.51 (m, CH_2, H-1, 3H), 4.18 (dd, ^3J = 4.7 Hz, ^2J = 12.6 Hz, H-6, 1H), 4.12−4.01 (m, H-6′, CH_2, 2H), 3.86−3.78 (m, CH_2, 1H), 3.69−3.62 (m, H-5, 1H), 2.02, 1.98, 1.96, 1.94 (4s, CH_3, OAc). ^{13}C NMR ($CDCl_3$): δ/ppm = 170.58, 170.17, 169.35 (CO), 100.58 (C-1), 74.68 (CH_2), 72.55 (C-3), 72.07

dx.doi.org/10.1021/ma202401x | *Macromolecules* 2012, 45, 46−55

Scheme 2. Schematic Representation of Carbohydrate Based Tosylates and Triflates I1-5 Employed as Initiators for the CROP of EtOx

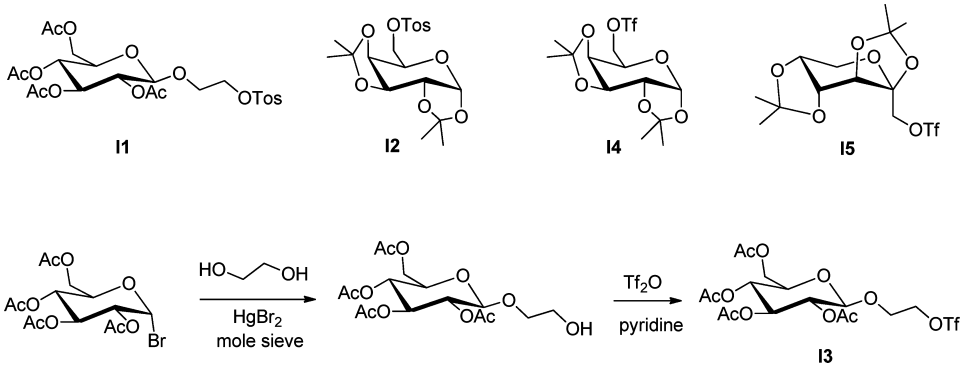

(C-5), 70.74 (C-2), 68.19 (C-4), 66.37 (CH_2), 61.70 (C-6), 20.66, 20.55, 20.45 (CH_3, OAc). ^{19}F NMR (200 MHz, $CDCl_3$): δ/ppm = −75.15. HR ESI MS: calculated for $[C_{17}H_{23}F_3O_{13}S]^{Na+}$, m/z = 547.0688; found, m/z = 547.0704 (error 1.8 ppm). Anal. Calcd for $C_{17}H_{23}O_{13}F_3S{\cdot}0.5\ Et_2O$: C, 40.64; H, 5.03; S, 5.71. Found: C, 40.98; H, 4.73; S, 5.98.

Kinetic Studies. In a representative example for **I1**, a stock solution of EtOx (1.665 g, 16.8 mmol), the initiator **I1** (0.306 g, 0.56 mmol), and acetonitrile (2.53 mL) was prepared under inert conditions and 0.7 mL aliquots were transferred into predried microwave vials that were capped subsequently. The monomer concentration was 4 mol L^{-1}, and the ratio of [monomer] to [intitator] was set to 30. The vials were placed into the autosampler of the microwave, heated to 100 °C for the desired polymerization time and cooled down automatically by a nitrogen flow. A drop of water was added to each vial in order to terminate the polymerization and samples were taken for analysis by means of SEC and ^{1}H and ^{19}F NMR spectroscopy as well as MALDI TOF mass spectrometry. Conversions were determined from ^{1}H NMR spectra in $CDCl_3$ utilizing the peak integrals of the ring protons of EtOx (4.2 and 3.8 ppm, respectively) and the PEtOx backbone signal at 3.4 ppm. For **I1** and **I2**, initiator efficiencies were calculated from peak integrals of the tosylate signals of unreacted initiator and free tosylate counterions in the ^{1}H NMR spectra, whereas the respective peaks in the ^{19}F NMR spectrum were used in case of **I3**−**5**. For characterization of the semitelechelic PEtOx by means of NMR spectroscopy, the crude polymers were purified by precipitation into cold diethyl ether, and dried under reduced pressure.

Deprotection of Glucose-Functionalized PEtOx. A 500 mg sample of acetyl-protected glucose-functionalized PEtOx (DP = 10) was dissolved in 2 mL of dry methanol, and 70 μL of a 0.5 M methanolic solution of sodium methanolate was added. After 1 h, the reaction mixture was diluted with chloroform, washed with saturated aqueous sodium bicarbonate solution and brine, dried over sodium sulfate, and concentrated under reduced pressure. Subsequently, the deprotected glucose-functionalized PEtOx was precipitated into cold diethyl ether and dried under reduced pressure.

Deprotection of Galactose-Functionalized PEtOx. According to a literature procedure,[35,36] 95 mg of isopropylidene-protected galactose-functionalized PEtOx was dissolved in 3 mL of 80% formic acid and stirred for 3 days at room temperature. After neutralization of the reaction mixture with saturated aqueous sodium bicarbonate solution, the crude product was extracted three times with chloroform. The combined extracts were washed with saturated aqueous sodium bicarbonate solution and brine, dried over sodium sulfate, concentrated under reduced pressure, precipitated into cold diethyl ether, and dried under reduced pressure.

Macromonomer Synthesis (P1). **I3** (524 mg, 1 mmol), EtOx (0.991 g, 10 mmol), and acetonitrile (1.49 mL) were transferred to a predried microwave vial and heated to 100 °C for 13.8 min, to reach a $\ln([M]_0/[M]_t)$ of 4 according to the k_p value determined from kinetic studies. After cooling with a nitrogen flow, MAA (127 μL, 1.5 mmol) and NEt_3 (279 μL, 2 mmol) were added via syringe through the septum of the vial and the end functionalization was allowed to complete at 50 °C overnight. The reaction mixture was dissolved in chloroform, washed with saturated aqueous sodium bicarbonate solution and brine, dried over sodium sulfate and concentrated under reduced pressure. Subsequently, the macromonomer **P1** was precipitated into cold diethyl ether, dried under reduced pressure and stored at −20 °C (yield: 1.054 g, 70%). ^{1}H NMR (300 MHz, $CDCl_3$): δ/ppm = 6.01 and 5.54 (=CH_2); 5.19−4.81 (H-2,3,4 Glc); 4.51−3.10 (H-1,5,6 Glc and N−CH_2− PEtOx); 2.53−2.10 (C−CH_2− PEtOx); 2.10−1.81 (CH_3 Glc−OAc and CH_3 MA); 1.19−0.92 (−CH_3 PEtOx). SEC (DMA, RI detection, PS calibration): M_n = 2330 g mol^{-1}, PDI = 1.12.

Comb Polymer Synthesis (P2 and P3). A 1 g sample of **P1** was dissolved in 1.4 mL of ethanol and appropriate amounts of AIBN (0.71 mg, 4.3 μmol) and CPDB (3.82 mg, 17 μmol) were added from stock solutions in ethanol so that the [**P1**]:[CPDB]:[AIBN] ratio was 40:1:0.25 and the monomer concentration 0.5 mol L^{-1}. After degassing of the reaction mixture by gently bubbling with nitrogen, the RAFT polymerization was performed at 70 °C for 16 h (conversion 32%). Subsequent to removal of the solvent under reduced pressure, the crude polymer was dissolved in THF and residual macromonomer was removed via preparative size exclusion chromatography on a BioBeads SX-1 column (eluent THF). After concentration of the desired fractions under reduced pressure, the purified comb polymer **P2** was precipitated into cold diethyl ether (yield: 0.3 g, 30%). ^{1}H NMR (300 MHz, $CDCl_3$): δ/ppm = 5.19−4.81 (H-2,3,4 Glc); 4.51−3.10 (H-1,5,6 Glc and N−CH_2− PEtOx); 2.53−2.10 (C−CH_2− PEtOx); 2.10−1.81 (CH_3 Glc−OAc); 1.41−0.60 (−CH_3 PEtOx, −CH_2− and −CH_3 MA). SEC (DMA, RI detection, PS calibration): M_n = 19 300 g mol^{-1}, PDI = 1.14. The deprotection of **P2** was performed as described above for glucose-functionalized PEtOx yielding the deprotected comb polymer **P3**. ^{1}H NMR (300 MHz, DMSO-d_6): δ/ppm =4.13 (H-1 Glc); 4.02−2.79 (H-2,3,4,5,6 Glc and N−CH_2− PEtOx); 2.41−2.06 (C−CH_2− PEtOx); 1.36−0.57 (−CH_3 PEtOx, −CH_2− and −CH_3 MA). SEC (DMA, RI detection, PS calibration): M_n = 23 600 g mol^{-1}, PDI = 1.11.

RESULTS AND DISCUSSION

Among the large variety of possible carbohydrates, glucose (Glc), galactose (Gal), and fructose (Fru) derivatives were selected to be investigated as initiators for the CROP of EtOx. As depicted in Scheme 2, the leaving group, *i.e.*, tosylate or triflate, was either situated directly at C6 (for Gal-based initiators **I2** and **I4**) or C1 of the sugar (for the Fru-based initiator **I5**), or attached via an ethylene spacer at the anomeric carbon atom (for Glc-based initiators **I1** and **I3**). All initiators were obtained by reaction of the respective alcohols with either tosyl chloride or trifluoromethanesulfonic acid anhydride in the presence of pyridine (Scheme 2).

dx.doi.org/10.1021/ma202401x | *Macromolecules* 2012, 45, 46−55

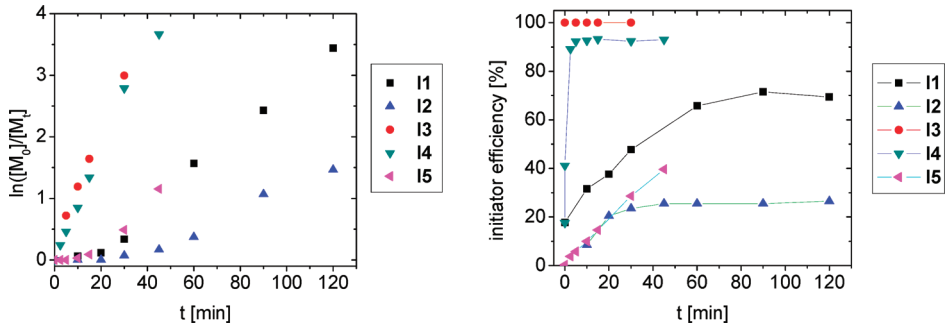

Figure 1. Semi logarithmic kinetic plots (left) and evolution of the initiator efficiency with polymerization time (right) for the CROP of EtOx initiated by **I1**−**5** (T = 100 °C, M/I = 30, [M] = 4 mol L^{-1}). Lines are added to guide the eye. Linear regression of the semilogarithmic kinetic plots for **I3** and **I4** according to $\ln([M]_0/[M]_t) = k_p^{app}\,[I]_0\,t$ resulted in k_p^{app}(**I3**) = 0.0121 L mol^{-1} s^{-1} and k_p^{app}(**I4**) = 0.0105 L mol^{-1} s^{-1}, respectively (k_p(**I3**) = 0.0121 L mol^{-1} s^{-1} and k_p(**I4**) = 0.0124 L mol^{-1} s^{-1}).

Kinetic Studies. Prior to application of the obtained initiators for the synthesis of advanced multifunctional polymers, kinetic studies were performed in order to evaluate the capabilities of **I1**−**5** to initiate the CROP of EtOx. The polymerization temperature was set to 100 °C to avoid potential degradation of the sugar moieties, even though the CROP of 2-oxazolines in general can also be performed at higher temperatures.[37] In order to ensure a sufficiently accurate characterization of the synthesized PEtOx in terms of end group determination, the applied [monomer] to [initiator] ratio was set to 30 in all kinetic studies.

A major requirement for the synthesis of well-defined polymers by an ideal living polymerization mechanism is a fast initiation so that all polymer chains start to grow at the same time. As a result, the chain propagation is the step that determines the polymerization rate, and the polymerization follows pseudo first order kinetics. As can be seen from the semi logarithmic kinetic plot in Figure 1 (left), both tosylate-based initiators **I1** as well as **I2** do not facilitate a sufficiently fast initiation of the CROP of EtOx, as indicated by the initial deviation from linearity due to the slowly increasing number of initiated polymer chains at the beginning of the polymerization. It should be noted that it was not possible to overcome this unfavorable slow initiation of the polymerization by addition of sodium iodide, variation of the polymerization temperature or solvent. Therefore, **I3** and **I4** were investigated under similar polymerization conditions. These initiators are based on the same carbohydrate moieties containing a more reactive triflate as leaving group. Indeed, $\ln([M]_0/[M]_t)$ increases linearly with time during both kinetic studies enabling the calculation of the polymerization rate constants k_p^{app} from the slope of the kinetic plots. Since neither the counterion nor the polymerization conditions differ, both values are very similar (k_p^{app}(**I3**) = 0.0121 L mol^{-1} s^{-1}; k_p^{app}(**I4**) = 0.0105 L mol^{-1} s^{-1}). Despite its theoretically similarly reactive triflate moiety, kinetic studies utilizing the fructose-based initiator **I5** revealed slow initiation. A possible explanation for this unexpected behavior might be a sterical hindrance induced by substituents on the quarternary anomeric carbon atom that is in direct neighborhood of the triflate functionality[38] preventing a nucleophilic attack of the EtOx monomer on C1 of the sugar. A similarly slow initiation due to sterical hindrance and/or electrophilicity because of a larger inductive effect has been reported for the CROP of THF using several triflate initiators[39] as well as for the CROP of EtOx initiated by 3-butynyl tosylate.[40]

In order to gain deeper insights into the kinetics of the initiation step of the polymerization, samples from the reaction solutions of the kinetic studies were analyzed by NMR spectroscopy. As depicted in Figure 2 for **I1**, ^{1}H NMR

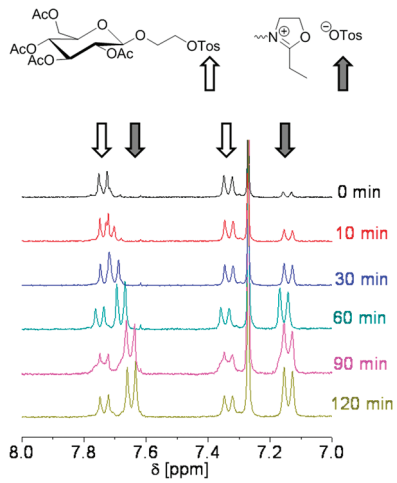

Figure 2. ^{1}H NMR spectra (300 MHz, $CDCl_3$) for the **I1** initiated CROP of EtOx in time for the determination of the initiator efficiency (spectra for **I2** are provided in Figures SI-1, Supporting Information).

spectroscopy can distinguish between the tosylate functionalities that are still connected to the initiator and tosylate moieties that act as counterions of the living oxazolinium species. By integration of the respective peaks in the aromatic region of the ^{1}H NMR spectra, the initiator efficiencies throughout the course of the polymerization can be estimated. For the triflate-based initiators **I3**−**5**, ^{19}F NMR spectroscopy could be applied in a similar fashion since the triflate peak of the initiators at −75 ppm was shifted to −79 ppm for the triflate counterions (Figure 3). As depicted in Figure 1 (right), the tosylate initiators do not reach full initiation efficiency. After an increase at the beginning of the polymerization, the initiator efficiency levels off at 70% for **I1** and at 26% for **I2**, respectively. Comparison of the triflate-based initiators **I3**−**5** reveals a clear trend that is based on the position of the triflate moiety on the sugar ring: **I3**, where the triflate is attached by an ethylene linker, shows full initiation efficiency upon addition of monomer; **I4**, where the triflate is attached at C6 of the galactose is more sterically hindered by the sugar ring and reaches a constant initiator efficiency of 93% after 5 min (explaining the slightly lowered k_p^{app} value due to lowered

dx.doi.org/10.1021/ma202401x | *Macromolecules* 2012, 45, 46−55

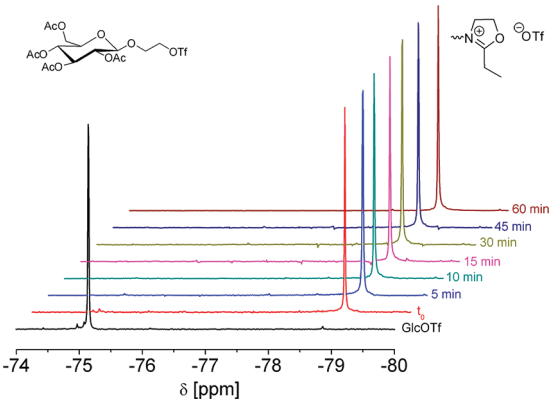

Figure 3. ^{19}F NMR (200 MHz, $CDCl_3$) spectra for the **I3** initiated CROP of EtOx in time for the determination of the initiator efficiency (spectra for **I4** and **I5** are provided in Figures SI-2 and SI-3, Supporting Information, respectively).

[P*]); **I5** reveals a low initiator efficiency that is constantly increasing throughout the polymerization due to the large steric demand of the isopropylidene groups around the quaternary anomeric carbon atom (Figures SI-2 and SI-3, Supporting Information).

The comparison of SEC traces obtained during the kinetic studies utilizing the glucose-based initiators **I1** and **I3** in Figure

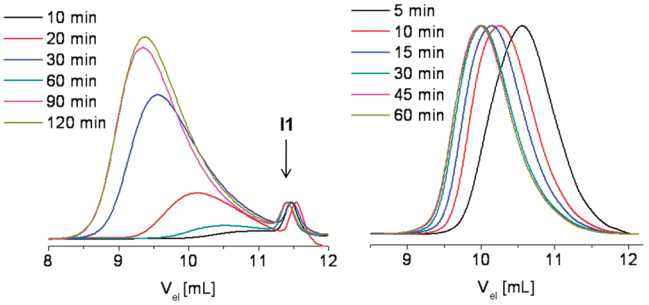

Figure 4. SEC traces ($CHCl_3$, RI detection) from the kinetic studies utilizing the glucose-based initiators **I1** (left) and **I3** (right) for the CROP of EtOx.

4 clearly indicates the higher reactivity of the triflate **I3** with respect to the tosylate **I1**. Whereas throughout the entire polymerization residual **I1** remains visible in the chromatograms and the polymer peaks show low molar mass tailing due to slow initiation, PEtOx that was initiated by **I3** reveals narrow molar mass distributions with PDI values around 1.20 and symmetric peak shapes that are shifted to lower elution volumes with increasing polymerization time. Similar observations for the two galactose-based initiators **I2** and **I4** comply with this initiation behavior (Figure SI-4, Supporting Information), even though in this case also the triflate-based initiator remains slightly visible as small hump in the SEC trace. Utilization of the fructose-based initiator **I5** resulted in SEC traces (Figure SI-5, Supporting Information) that are similar to the rather ill defined PEtOx that was obtained from the tosylate-based initiators **I1** and **I3**, which is in agreement with the slow initiation discussed above.

The results of the SEC characterization for all kinetic studies are summarized in Figure 5. For both **I3** as well as **I4**, the molar mass increases linearly with conversion hinting toward a fast initiation and the absence of chain transfer or termination reactions throughout the polymerization. The slightly higher molar mass of the PEtOx initiated by **I4** with respect to **I3** is a result of traces of unreacted **I4** that slightly increases the actual [M]/[I] ratio. However, the peak maxima (M_p) of the SEC traces derived from the kinetic studies utilizing **I1**, **I2**, and **I5** that revealed incomplete initiation increase more steeply at the beginning of the polymerization than in later stages, reflecting the lower number of polymer chains in the initial stages of the polymerization. In addition, compared to PEtOx initiated by **I3**, the molar masses of PEtOx samples derived from initiators that show incomplete initiation are elevated, because the actual [M]/[I] ratio is larger than 30 since not all initiator molecules initiate a PEtOx chain.

End Group Determination and Deprotection. When a functional initiator is applied for a polymerization, the incorporation as end group of the polymer has to be confirmed. For this purpose, advanced mass spectrometry techniques, such as (tandem) MALDI TOF MS and ESI TOF MS, were applied for the analysis of the synthesized sugar α-end-functionalized polymers. An overlay of MALDI TOF MS spectra of samples from the kinetic studies utilizing **I1** is provided in Figure 6. Next to an increase of the polymer molar mass with reaction time, two m/z distributions can be observed in all spectra, both with an m/z difference of 99 between the corresponding peaks, correlating to the mass of one EtOx repeating unit. Both distributions can be assigned to the desired polymer structure having both the peracetylated glucose (Ac_4Glc) and a hydroxyl group as chain ends, while being ionized with either a proton or a sodium cation. The assignment of the observed peaks was

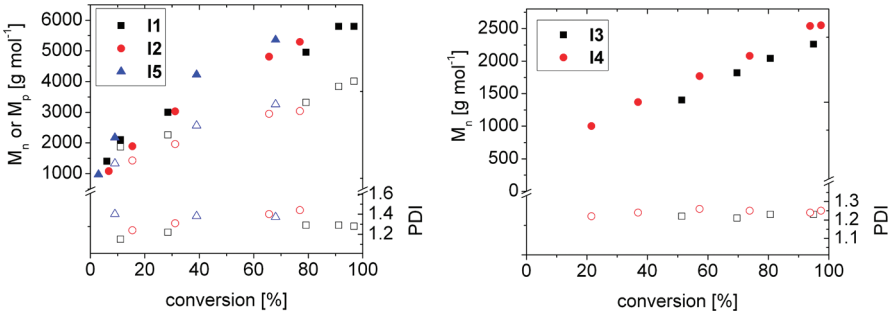

Figure 5. Evolution of the polymer molar mass from SEC analysis (PS calibration) with conversion during kinetic studies of the CROP of EtOx initiated by **I1**–**5** (T = 100 °C, M/I = 30, [M] = 4 mol L^{-1}). Because of partial overlapping of polymer peaks with unreacted initiator, M_n and PDI values have to be considered with care for **I1**, **I2**, and **I5**. Therefore, M_p values are provided additionally (closed symbols, M_p; open symbols, M_n and PDI, respectively).

dx.doi.org/10.1021/ma202401x | *Macromolecules* 2012, 45, 46–55

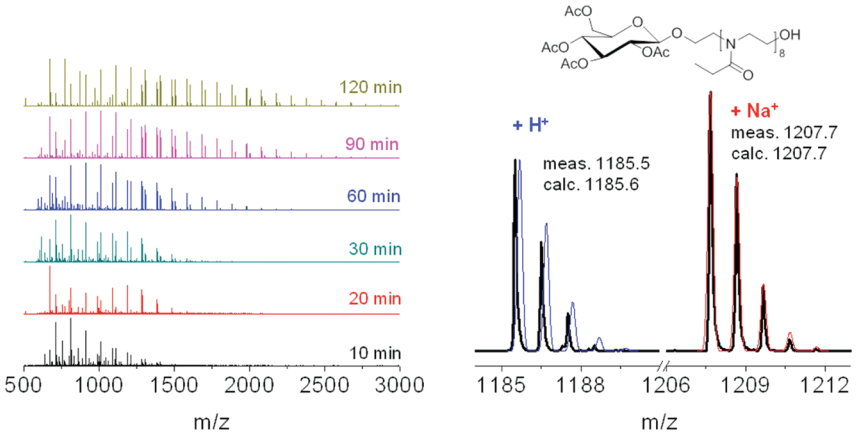

Figure 6. MALDI TOF MS spectra of kinetic samples from the initiation of the CROP of EtOx with **I1** (left) and overlay of isotopic patterns (black, measured; colored, calculated isotopic patterns) for the structural assignment of the observed peaks (right).

further confirmed by application of tandem MS measurements after collision induced dissociation (CID).[41] As depicted in Figure 7, the MS/MS spectra of parent ions from both

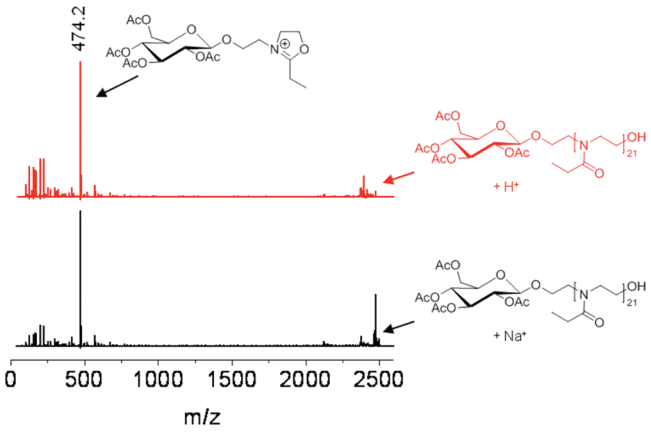

Figure 7. Tandem MS analysis of the mass distributions observed during MALDI TOF MS measurement of the glucose end-functionalized PEtOx initiated by **I1** after 90 min polymerization time (top, parent peak m/z = 2474; bottom, parent peak m/z = 2496).

distributions clearly reveal a highly intense fragment ion at m/z = 474, which can be assigned to Ac_4Glc being connected to one EtOx molecule that is positively charged as oxazolinium species. MALDI TOF MS investigation of the samples from kinetic studies with the triflate-based initiator **I3** resulted in similar spectra with the same m/z distributions as for the tosylate initiator **I1**.

MALDI TOF MS analysis of PEtOx initiated by **I4** reveals three m/z distributions, of which the first can be assigned to the Gal-PEtOx−OH being ionized by a sodium cation. The other two distributions only occur for higher molar mass polymers and cannot be assigned to structures that usually result from chain transfer or coupling reactions during the polymerization (Figure SI-7, Supporting Information). The fact that these m/z distributions are not detected by ESI TOF MS (not shown) suggests a fragmentation of the PEtOx chains during the MALDI process. However, all three distributions reveal a fragment ion at m/z = 342 during MS/MS analysis, which is correlating to the *iso*-propylidene protected galactose oxazolinium species and, thus, confirm the presence of the desired sugar end group. Also MALDI TOF MS of the PEtOx initiated by **I5** clearly shows a main m/z distribution that can be assigned to Fru-PEtOx−OH with a similar fragment ion in tandem MS analysis (Figures SI-9 and SI-10, Supporting Information). However, also the presence of proton initiated PEtOx chains, which result from chain transfer reactions during the polymerization, is revealed by the occurrence of an H-PEtOx−OH + Na^+ species in the MS spectrum.

After confirmation of the synthesis of well-defined glucose and galactose end-functionalized PEtOx, representative samples from the most successful kinetic studies (from **I3** and **I4**) were purified and deprotected, applying well established deprotection methods in carbohydrate chemistry. The acetyl protecting groups of the Glc containing PEtOx (with a DP of 10) were removed via sodium methanolate catalyzed transesterification in methanol.[30] The successful deprotection was confirmed by ^{1}H NMR spectroscopy revealing the disappearance of the signals derived from the acetyl protecting groups as well as a shift of the proton signals of the glucose ring from around 5 ppm in the protected polymer into the region of the PEtOx backbone signal (Figures SI-11 and SI-12, Supporting Information), as confirmed by appearance of the corresponding cross peaks in the HSQC spectrum (Figure SI-13, Supporting Information). Because of the low molar mass of the glucose-functionalized PEtOx, ^{13}C NMR spectroscopy enabled the confirmation of the presence of the deprotected sugar end group. Next to the carbon atoms of the polymer chain, all six carbon atoms of the deprotected glucose moiety could be detected in the expected region from 60 to 110 ppm (Figure SI-11, Supporting Information).

The *iso*-propylidene protecting groups of the galactose end-functionalized PEtOx (with a DP of 20) were removed by acidic hydrolysis in 80% formic acid,[35,36] as confirmed by disappearance of the respective signals in the ^{1}H NMR spectrum (Figure SI-14, Supporting Information). Unfortunately, the higher molar mass of this polymer as well as the coexistence of the various anomers of the deprotected galactose residues prevented the end group analysis by means of ^{13}C NMR spectroscopy. However, the ^{1}H NMR spectrum in DMSO-d_6 shows a multitude of signals between 4 and 5.5 ppm that are most likely derived from the hydroxyl protons of the deprotected galactose moiety because they do not couple in HSQC experiments.

Comb Polymer Synthesis. In addition to the introduction of carbohydrate α end groups to PEtOx, the living character of the CROP initiated by **I3** enabled the attachment of a second

dx.doi.org/10.1021/ma202401x | *Macromolecules* 2012, 45, 46−55

Scheme 3. Schematic Representation of the Synthesis Route toward a Glucose-Functionalized PEtOx-Based Comb Polymer

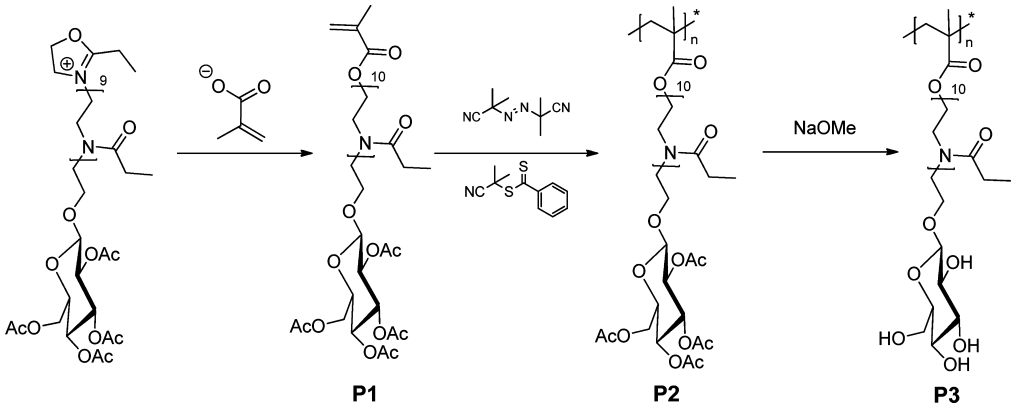

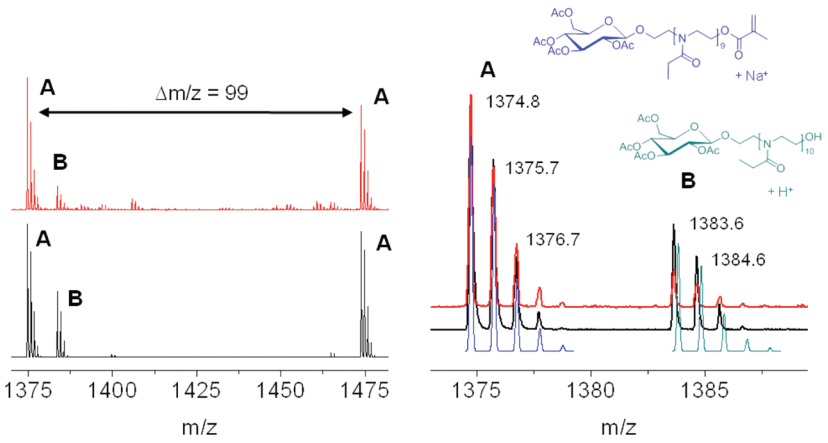

Figure 8. Zoom into the MALDI TOF (bottom, black) and ESI TOF (top, red) mass spectra of the glucose-functionalized Ac_4GlcPEtOxMA macromonomer **P1** (left) and overlay of isotopic patterns (top and middle: measured, bottom: calculated isotopic patterns) for the structural assignment of the observed peaks (right). The minor distributions in the ESI TOF spectrum can be assigned to Ac_4GlcPEtOxMA + H^+ and to Ac_4GlcPEtOxOH + Na^+, respectively.

functional moiety at the ω chain end. Nucleophilic attack of *in situ* deprotonated MAA on the polyoxazolinium chain end resulted in the methacrylate macromonomer **P1** with a DP of 10 that was applied for the synthesis of a comb polymer being selectively functionalized with glucose at the ends of all side chains via RAFT polymerization[42] and subsequent deprotection of the pendant acetyl protected glucose moieties with sodium methanolate (Scheme 3).

Analysis of **P1** by MALDI and ESI TOF MS (Figure 8) revealed two *m*/*z* distributions, of which the major one can be assigned to the desired structure that is ionized with a sodium cation. The second distribution derives from $GlcAc_4$PEtOx chains that are not functionalized with MAA at the ω chain ends but with terminal hydroxyl groups. These peak assignments could be confirmed by tandem MS analysis as described above (data not shown). According to ^{1}H NMR spectroscopy, the degree of functionalization with MAA was found to be 75%, as roughly estimated by comparison of the peak integrals derived from the glucose moieties at the α chain end (~5 ppm, 3H) with those derived from vinylic protons at the ω chain end (5.5 and 6 ppm, respectively, Figure 10). However, small amounts of hydroxyl-functionalized PEtOx will not affect the subsequent polymerization of the methacrylate moiety because they do not interfere with the RAFT polymerization mechanism and can be easily separated from the comb polymer together with residual macromonomer.

The RAFT homopolymerization of **P1** was performed in ethanol using AIBN as initiator and the dithiobenzoate-based chain transfer agent CPDB in an analogous fashion as recently reported for PEtOx-based macromonomers without sugar functionality.[42] Taking into account the macromonomer conversion of 32% and the used [CPDB] to [**P1**] ratio of 1:40, a DP of the methacrylate backbone of **P2** of 13 (corresponding to a theoretical molar mass of 19 000 g mol^{-1}) can be estimated. Characterization of the resulting acetyl protected comb polymer **P2** by SEC revealed a narrow molar mass distribution as well as complete removal of unreacted **P1** after preparative SEC on a BioBeads-SX1 column (Figure 9, Table 1). Because of its increased hydrodynamic volume in DMA the SEC trace of the deprotected comb polymer **P3** is shifted to lower elution volume compared to **P2**, despite of its lower molar mass after loss of the protecting groups. In addition, the unimodal SEC trace of **P3** confirms that the ester functionalities, which connect the side chains with the backbone in the comb structure, were not affected during the deprotection step. Thus, the comb structure remained intact representing the first glyco-comb polymer with a saccharide moiety at each end of the side chains.

Because of a lower mobility of the polymer units in the restricted comb structure, the ^{1}H NMR spectrum of **P2** revealed a slight broadening of the PEtOx derived signals compared to the macromonomer **P1** (Figure 10). In addition,

dx.doi.org/10.1021/ma202401x | *Macromolecules* 2012, 45, 46−55

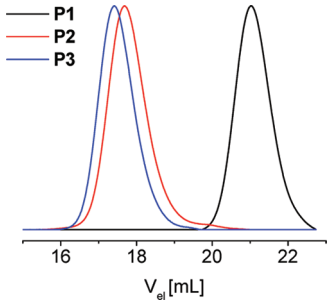

Figure 9. SEC traces (DMA) of the glucose-functionalized macromonomer **P1** as well as the protected and deprotected comb polymers **P2** and **P3**, respectively.

Table 1. SEC characterization results of P1−P3

	M_n(theo) [g mol^{-1}]	M_n(SEC)^a [g mol^{-1}]	PDI (SEC)^a
P1	1450	2330	1.12
P2	19 000	19 300	1.14
P3	16 700	23 600	1.11

^{a}SEC measured in DMA using PS calibration.

the protons of the acetyl protecting groups and of the glucose ring can be clearly detected in both spectra, and the methacrylate backbone of **P2** is reflected in small shoulders next to the CH_3 peak of the PEtOx side chains around 1 ppm in the spectrum. As described above, the successful deprotection of **P2** is demonstrated by the disappearance of the acetyl peaks (around 2 ppm) in the ^{1}H NMR spectrum of **P3**. In addition, the ^{1}H ^{13}C HSQC 2D NMR spectrum (Figure SI-16, Supporting Information) clearly shows the expected cross peaks derived from the deprotected Glc moieties and, thus, confirms that the sugar was not cleaved from the comb polymer during the deprotection reaction.

As reported earlier, comb shaped PEtOx displays lower critical solution (LCST) behavior in aqueous media, which can be investigated, among other methods, by means of turbidimetry.[42] Since **P2** and **P3** are based on the same polymer architecture, they offer the possibility to investigate the influence of the nature of the side chain end groups upon the LCST behavior of the comb polymer. As depicted in Figure 11, the glucose end groups of the side chains point toward the outside of the molecular bottle brush structure and should, thus, dominate its solubility. A similar influence of methyl or ethyl end groups on the solubility properties of polymethacrylates[43,44] and polyvinyl ethers[45] carrying oligomeric ethylene oxide side chains has already been demonstrated by Ishizone and Kobayashi. In fact, the hydrophilicity of the deprotected glucose moieties of **P3** resulted in complete water (and PBS) solubility of the glycopolymer in the investigated temperature range until 100 °C. In contrast, the hydrophobic character of the acetyl protected sugar moieties decreased the cloud point temperature (T_{cp}) of the aqueous solution (c = 5 mg mL^{-1}) in comparison to a comb polymer with methyl end groups at the side chains (T_{cp} = 77.3 °C)[42] by 27.5 to 49.8 °C. As demonstrated by the match of the T_{cp} values from first and second heating cooling cycle, the phase transition occurred sharply and completely reversible with small heating cooling hysteresis of around 2 °C. The well-known salting out effect of chloride ions as chaotropes from the Hofmeister series[46] resulted in a lowered T_{cp} of 46.2 °C when the measurement was performed in PBS.

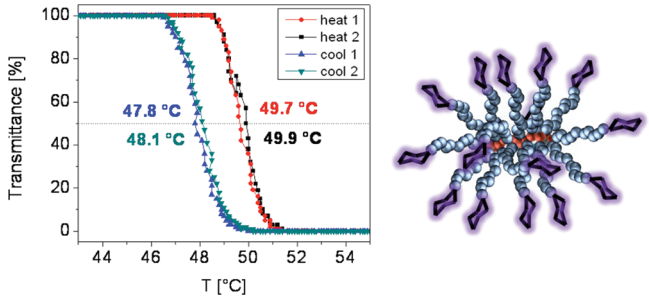

Figure 11. Turbidity curves of an aqueous solution of **P2** (c = 5 mg mL^{-1}) and cloud point temperatures determined at 50% transmittance for two heating cooling cycles (heating rate 1 K min^{-1}) and illustration of the macromolecular bottle brush structure.

The fact that the polymer remains water-soluble at low temperatures reveals the accessibility of carbonyl functionalities

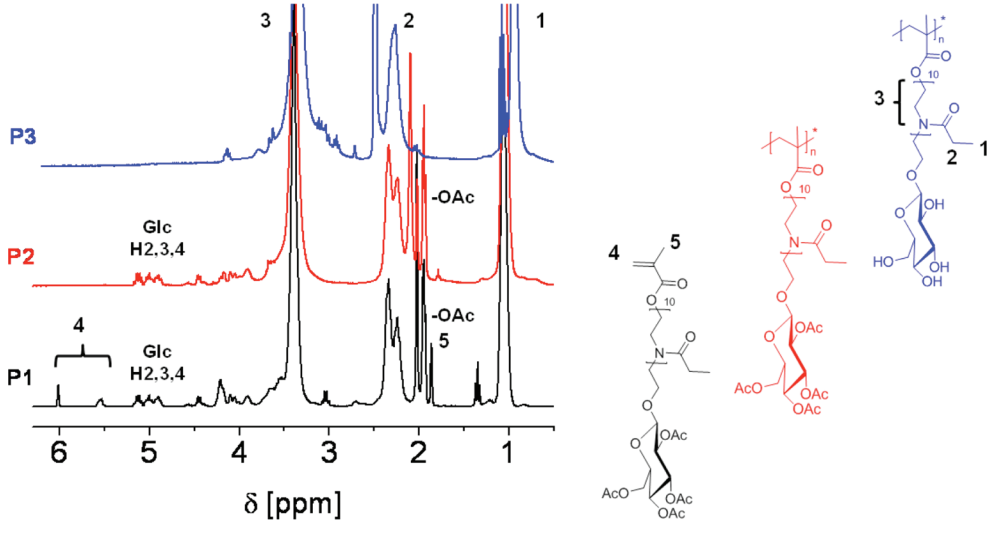

Figure 10. ^{1}H NMR spectra (300 MHz) of the glucose-functionalized macromonomer **P1** as well as the protected and deprotected comb polymers **P2** and **P3**, respectively (solvents: $CDCl_3$ for **P1** and **P2**; DMSO-d_6 for **P3**).

dx.doi.org/10.1021/ma202401x | *Macromolecules* 2012, 45, 46−55

of the PEtOx so that water molecules can penetrate inside the brush structure to build up hydrogen bonds and, thus, solubilize the polymer. Upon increase of temperature, entropic effects decrease the hydrogen bonding strength, the water molecules are expelled from the polymer, and the polymer precipitates due to hydrophobic interaction of the macromolecules with each other. This behavior indicates that **P2** (and consequently also **P3**), do not only display the properties of a glycopolymer, but combines it with the specific properties of PEtOx.

CONCLUSION

Glucose, galactose and fructose end-functionalized PEtOx could be obtained by utilization of the respective sugar triflates as initiators for the CROP of EtOx. Kinetic studies as well as the successful end-capping of the living oxazolinium chain end by *in situ* deprotonated MAA support the characteristics of a living polymerization for the sterically unhindered initiators, enabling the successful synthesis of the first reported comb polymer being decorated selectively with sugar moieties at the end of all side chains. Having established this generally applicable route toward such comb polymers, future work will focus on the investigation of the biological activity of polymers carrying a larger variety of sugar units as well as on the conjugation to other biologically interesting moieties via the living oxazolinium chain end.

ASSOCIATED CONTENT

Supporting Information

Determination of initiator efficiencies for **I2**, **I4** and **I5**, SEC traces from kinetic studies utilizing **I2**, **I4** and **I5**, MALDI TOF (tandem) mass spectra for Gal- and Fru-functionalized PEtOx, ^{1}H and ^{13}C NMR spectra of protected and deprotected Glc and Gal end-functionalized PEtOx, $^{1}H-^{13}C$ NMR HSQC 2D NMR spectra of deprotected Glc end-functionalized PEtOx and **P3**, and full MALDI TOF mass spectrum of **P1**. This material is available free of charge via the Internet at http://pubs.acs.org.

AUTHOR INFORMATION

Corresponding Author

*E-mail: (U.S.S.) ulrich.schubert@uni-jena.de; (R.H.) richard.hoogenboom@ugent.be. Telephone (U.S.S.): +49(0) 3641 9482 00 (Secretary: 01). Fax (U.S.S.): +49(0) 3641 9482 02.

ACKNOWLEDGMENTS

This work forms part of the research program of the Dutch Polymer Institute (DPI, technology area HTE, Project Number 612). The authors thank the Thüringer Ministerium für Wissenschaft, Bildung und Kultur (NanoConSens) for financial support of this study.

REFERENCES

(1) Park, K. H.; Sung, W. J.; Kim, S. W.; Kim, D. H.; Akaike, T.; Chung, H. M. *J. Biosci. Bioeng.* **2005**, *99*, 285−289.
(2) Roy, R. *Trends Glycosci. Glycotechnol.* **1996**, *8*, 79−99.
(3) Rubinstein, A.; David, A.; Kopeckova, P.; Kopecek, J. *Bioconjugate Chem.* **2001**, *12*, 890−899.
(4) Vazquez-Lasa, B.; Donaire, M. L. L.; Parra-Caceres, J.; Garcia-Alvarez, I.; Fernandez-Mayoralas, A.; Lopez-Bravo, A.; Roman, J. S. *Biomaterials* **2009**, *30*, 1613−1626.
(5) Reuter, J. D.; Myc, A.; Hayes, M. M.; Gan, Z. H.; Roy, R.; Qin, D. J.; Yin, R.; Piehler, L. T.; Esfand, R.; Tomalia, D. A.; Baker, J. R. *Bioconjugate Chem.* **1999**, *10*, 271−278.
(6) Matsuoka, K.; Sakamoto, J. I.; Koyama, T.; Miyamoto, D.; Yingsakmongkon, S.; Hidari, K. I. P. J.; Jampangern, W.; Suzuki, T.; Suzuki, Y.; Esumi, Y.; Nakamura, T.; Hatano, K.; Terunuma, D. *Bioorg. Med. Chem.* **2009**, *17*, 5451−5464.
(7) Roy, R.; Meunier, S. J.; Wu, Q. Q.; Wang, S. N. *Can. J. Chem.* **1997**, *75*, 1472−1482.
(8) Klajnert, B.; Appelhans, D.; Komber, H.; Morgner, N.; Schwarz, S.; Richter, S.; Brutschy, B.; Ionov, M.; Tonkikh, A. K.; Bryszewska, M.; Voit, B. *Chem.—Eur. J.* **2008**, *14*, 7030−7041.
(9) Appelhans, D.; Komber, H.; Quadir, M. A.; Richter, S.; Schwarz, S.; van der Vlist, J.; Aigner, A.; Mueller, M.; Loos, K.; Seidel, J.; Arndt, K. F.; Haag, R.; Voit, B. *Biomacromolecules* **2009**, *10*, 1114−1124.
(10) Arce, E.; Nieto, P. M.; Diaz, V.; Castro, R. G.; Bernad, A.; Rojo, J. *Bioconjugate Chem.* **2003**, *14*, 817−823.
(11) Muthukrishnan, S.; Erhard, D. P.; Mori, H.; Mueller, A. H. E. *Macromolecules* **2006**, *39*, 2743−2750.
(12) Papp, I.; Dernedde, J.; Enders, S.; Haag, R. *Chem Commun* **2008**, 5851−5853.
(13) Papp, I.; Dernedde, J.; Enders, S.; Riese, S. B.; Shiao, T. C.; Roy, R.; Haag, R. *Chembiochem* **2011**, *12*, 1075−1083.
(14) Wang, D.; Liu, Y.; Hong, C. Y.; Pan, C. Y. *J. Polym. Sci., Part A: Polym. Chem.* **2005**, *43*, 5127−5137.
(15) Muthukrishnan, S.; Nitschke, M.; Gramm, S.; Ozyurek, Z.; Voit, B.; Werner, C.; Mueller, A. H. E. *Macromol. Biosci.* **2006**, *6*, 658−666.
(16) Voit, B.; Appelhans, D. *Macromol. Chem. Phys.* **2010**, *211*, 727−735.
(17) Hoogenboom, R. *Angew. Chem., Int. Ed.* **2009**, *48*, 7978−7994.
(18) Makino, A.; Kobayashi, S. *J. Polym. Sci., Part A: Polym. Chem.* **2010**, *48*, 1251−1270.
(19) Schlaad, H.; Diehl, C.; Gress, A.; Meyer, M.; Demirel, A. L.; Nur, Y.; Bertin, A. *Macromol. Rapid Commun.* **2010**, *31*, 511−525.
(20) Adams, N.; Schubert, U. S. *Adv. Drug Delivery Rev.* **2007**, *59*, 1504−1520.
(21) Knop, K.; Hoogenboom, R.; Fischer, D.; Schubert, U. S. *Angew. Chem., Int. Ed.* **2010**, *49*, 6288−6308.
(22) Barz, M.; Luxenhofer, R.; Zentel, R.; Vicent, M. J. *Polym. Chem.* **2011**, *2*, 1900−1918.
(23) Diehl, C.; Schlaad, H. *Macromol. Biosci.* **2009**, *9*, 157−161.
(24) Kempe, K.; Neuwirth, T.; Czaplewska, J.; Gottschaldt, M.; Hoogenboom, R.; Schubert, U. S. *Polym. Chem.* **2011**, *2*, 1737−1743.
(25) Kempe, K.; Weber, C.; Babiuch, K.; Gottschaldt, M.; Hoogenboom, R.; Schubert, U. S. *Biomacromolecules* **2011**, *12*, 2591−2600.
(26) Takasu, A.; Kojima, H. *J. Polym. Sci., Part A: Polym. Chem.* **2010**, *48*, 5953−5960.
(27) Einzmann, M.; Binder, W. H. *J. Polym. Sci., Part A: Polym. Chem.* **2001**, *39*, 2821−2831.
(28) Giardi, C.; Lapinte, V.; Charnay, C.; Robin, J. J. *React. Funct. Polym.* **2009**, *69*, 643−649.
(29) Kuhn, P.; Weberskirch, R.; Nuyken, O.; Cevc, G. *Des. Monomers Polym.* **1998**, *1*, 327−346.
(30) Aoi, K.; Suzuki, H.; Okada, M. *Macromolecules* **1992**, *25*, 7073−7075.
(31) Petrig, J.; Schibli, R.; Dumas, C.; Alberto, R.; Schubiger, P. A. *Chem.—Eur. J.* **2001**, *7*, 1868−1873.
(32) Streicher, H.; Busse, H. *Bioorg. Med. Chem.* **2006**, *14*, 1047−1057.
(33) Card, P. J.; Hitz, W. D. *J. Am. Chem. Soc.* **1984**, *106*, 5348−5350.
(34) Maryanoff, B. E.; McComsey, D. F.; Costanzo, M. J.; Hochman, C.; Smith-Swintosky, V.; Shank, R. P. *J. Med. Chem.* **2005**, *48*, 1941−1947.
(35) Ladmiral, V.; Monaghan, L.; Mantovani, G.; Haddleton, D. M. *Polymer* **2005**, *46*, 8536−8545.
(36) Ohno, K.; Izu, Y.; Yamamoto, S.; Miyamoto, T.; Fukuda, T. *Macromol. Chem. Phys.* **1999**, *200*, 1619−1625.
(37) Wiesbrock, F.; Hoogenboom, R.; Leenen, M. A. M.; Meier, M. A. R.; Schubert, U. S. *Macromolecules* **2005**, *38*, 5025−5034.
(38) Baker, S. B. *Can. J. Chem.* **1955**, *33*, 1459−1462.

(39) Dubreuil, M. F.; Farcy, N. G.; Goethals, E. J. *Macromol. Rapid Commun.* **1999**, *20*, 383−386.
(40) Fijten, M. W. M.; Haensch, C.; van Lankvelt, B. M.; Hoogenboom, R.; Schubert, U. S. *Macromol. Chem. Phys.* **2008**, *209*, 1887−1895.
(41) Baumgaertel, A.; Weber, C.; Knop, K.; Crecelius, A.; Schubert, U. S. *Rapid Commun. Mass Spectrom.* **2009**, *23*, 756−762.
(42) Weber, C.; Becer, C. R.; Hoogenboom, R.; Schubert, U. S. *Macromolecules* **2009**, *42*, 2965−2971.
(43) Han, S.; Hagiwara, M.; Ishizone, T. *Macromolecules* **2003**, *36*, 8312−8319.
(44) Ishizone, T.; Seki, A.; Hagiwara, M.; Han, S.; Yokoyama, H.; Oyane, A.; Deffieux, A.; Carlotti, S. *Macromolecules* **2008**, *41*, 2963−2967.
(45) Aoshima, S.; Oda, H.; Kobayashi, E. *J. Polym. Sci., Part A: Polym. Chem.* **1992**, *30*, 2407−2413.
(46) Bloksma, M. M.; Bakker, D. J.; Weber, C.; Hoogenboom, R.; Schubert, U. S. *Macromol. Rapid Commun.* **2010**, *31*, 724−728.

Macromolecules

Article

pubs.acs.org/Macromolecules

Photoinduced Free Radical Promoted Copper(I)-Catalyzed Click Chemistry for Macromolecular Syntheses

Mehmet Atilla Tasdelen,[†,‡] Gorkem Yilmaz,[†] Birol Iskin,[†] and Yusuf Yagci[†,*]

[†]Department of Chemistry, Istanbul Technical University, Maslak, TR-34469, Istanbul, Turkey

[‡]Department of Polymer Engineering, Faculty of Engineering, Yalova University, TR-77100 Yalova, Turkey

Supporting Information

ABSTRACT: Photoinduced copper(I)-catalyzed Huisgen 1,3-dipolar cycloaddition (CuAAC) via photoinduced electron transfer using free radical photoinitiators has been developed as a new platform to serve as orthogonal click system. Photoinitiators acting at near UV and visible range, namely 2, 2-dimethoxy-2-phenyl acetophenone, 2-benzyl-2-dimethylamino-4′-morpholino butyrophenone, 2,4,6-trimethylbenzoyl)-diphenylphosphine oxide, dicyclopentadienyl bis[2,6-difluoro-3-(1-pyrrolyl)phenyl] titanium) and camphorquinone/benzyl alcohol were tested with copper(II) chloride/*N*,*N*,*N*′,*N*″,*N*″-pentamethyldiethylenetriamine complex to catalyze the CuAAC via photoinduced electron transfer reaction. This strategy has been applied in construction of various macromolecular architectures including telechelic polymers and block copolymers. Spectroscopic and chromatographic investigations revealed that successful macromolecular syntheses have been achieved by this technique.

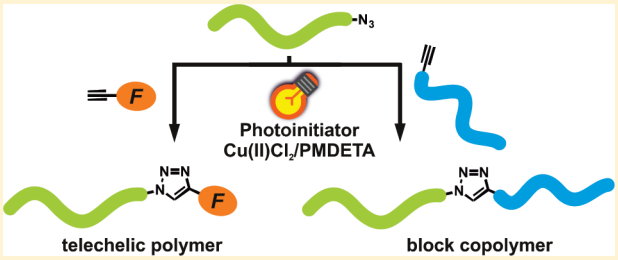

INTRODUCTION

Click chemistry describes a class of chemical reactions that are easy to perform, give rise to their intended products in very high yields with little or no byproducts, work well under many conditions, and are unaffected by the nature of the groups being connected to each other. The most prominent example of click chemistry reaction is based on the well-established copper(I)-catalyzed Huisgen 1,3-dipolar cycloaddition (CuAAC) reaction between azides and terminal alkynes, discovered by the groups of Sharpless[1] and Meldal.[2] The CuAAC click reaction has received considerable attention as powerful modular synthesis approach,[3] which has found numerous applications in organic chemistry, supramolecular chemistry, polymer chemistry, drug discovery, bioconjugation, and materials science.[1,4] However, it has some limitations including the need for a metal catalyst[5] and an inability to control the reaction by external stimulation or to conduct the reaction in the absence of solvent.[6] To further develop this fundamentally important aspect of synthetic chemistry, the discovery of alternative robust, efficient, and orthogonal click reactions or the modification of well-known click reactions is particularly relevant. Light-induced reactions offer the possibility of both spatial and temporal control over the reaction, which are not available in thermal conjugation-reactions.[7] In recent years, photoinduced thiol−ene/thiol−yne coupling,[8] photoinduced 1,3-dipolar cycloaddition reaction of alkenes and nitrile imines,[9] "strain-promoted" cycloaddition reaction of the photochemically generated cycloalkynes and azides[10] photoinduced ester formation reaction of benzodioxinones with alcohols[11] and photoinduced Diels−Alder reactions[12] have been developed. Although thiol−ene/thiol−yne reactions can proceed extremely rapidly yielding products quantitatively under facile conditions (i.e., at ambient temperature and humidity under an air atmosphere), the simultaneous reactions of the photochemically formed primary radicals with enes reduce the click efficiency.[13] In the other methods such as photoinduced acylation reactions using benzodioxinones, the preparation and purification of click reagents cumbersome and result in low product yields.[11a]

Light induced reduction of metal ions such as silver,[14] gold,[15] and copper[16] complexes can be successfully carried out by either direct photolysis or indirect photolysis. In direct photolysis, desired metal ions are generated upon irradiation of its higher oxidation state species at appropriate wavelengths. Typically, the absorption of light by copper ligand promotes the intramolecular electron transfer from the π-system of the ligand to the central ion resulting in the transformation of Cu(II) ion into Cu(I) and the ligand into the radical complex.[17] However, this method involving UV exposure suffers from the need for long irradiation times. For indirect approach, the reduction of the Cu(II) ion is dependent on a photoactivator. Thus, a photoinitiator absorbs light in the UV−visible region, where copper complex is transparent and forms reactive intermediates such as free radicals, which strongly promote the photoreduction of the Cu(II) into Cu(I). The nature of the photochemically generated radicals and the redox properties

Received: November 4, 2011
Revised: December 2, 2011
Published: December 9, 2011

   dx.doi.org/10.1021/ma202438w | *Macromolecules* 2012, 45, 56−61

of the copper complex are quite crucial for the success of the process. Recently, our group has developed a new photochemical protocol to catalyze the CuAAC reaction between azides and alkynes by *in situ* generation of Cu(I) from Cu(II) complex with UV-light.[18] Later on, Bowman and co-workers demonstrated the comprehensive spatial and temporal control of the CuAAC reaction using standard photolithographic techniques by photochemical reduction of Cu(II).[6c]

Herein, we report the wavelength tunability of light-induced CuAAC click reaction using near UV and visible light photoinitiators. In the context of macromolecular engineering, this reaction is very valuable and permitting the preparation of highly defined telechelic polymers and block copolymers. This process gives the spatial control of the click reaction by adjusting the copper concentration of the system and consequently, coupling efficiency by choosing appropriate light intensities.

EXPERIMENTAL PART

Materials. Phenylacetylene (98%, Aldrich), benzyl bromide (98%, Aldrich), sodium azide (99%, Aldrich), dimethyl-d_6 sulfoxide (99.96 atom % D, Aldrich), benzyl alcohol (99%, Aldrich) and copper(II) chloride (98%, Aldrich) were used as received. *N,N,N′,N″,N″*-Pentamethyldiethylenetriamine (99%, Aldrich) was distilled before use. Benzyl azide was synthesized according to literature procedure.[18] ^{1}H NMR (250 MHz, $CDCl_3$): δ (ppm) = 4.4 (Ph−CH_2−N_3), 7.4−7.5 (aromatic protons). 2, 2-Dimethoxy-2-phenyl acetophenone (DMPA, Ciba Specialty Chemicals), 2-benzyl-2-dimethylamino-4′-morpholinobutyrophenone (DBMP, Ciba Specialty Chemicals), 2,4,6-trimethylbenzoyl)diphenylphosphine oxide (TMDPO, Ciba Specialty Chemicals), and dicyclopentadienylbis[2,6-difluoro-3-(1-pyrrolyl)-phenyl] titanium (Titanocene, Ciba Specialty Chemicals) and (camphorquinone (CQ, Ciba Specialty Chemicals) were used as received.

Characterization. UV spectra were recorded on a Shimadzu UV-1601 spectrometer. ^{1}H NMR spectra in DMSO-d_6 with $Si(CH_3)_4$ as an internal standard were recorded at room temperature at 250 MHz using a Bruker DPX 250 spectrometer. FT-IR spectra were recorded on a Perkin-Elmer FT-IR Spectrum One-B spectrometer. Molecular weights were determined by gel permeation chromatography (GPC) instrument, Viscotek GPCmax Autosampler system, consisting of a pump, three ViscoGEL GPC columns ($G2000H_{HR}$, $G3000H_{HR}$ and $G4000H_{HR}$), and a Viscotek differential refractive index (RI) detector with a THF flow rate of 1.0 mL min^{-1} at 30 °C. The RI detector was calibrated with PS standards having narrow molecular weight distribution. Data were analyzed using Viscotek OmniSEC Omni−01 software.

Spectroscopic Investigations of Click Reactions. General experimental procedure for the light-induced copper(I)-catalyzed click reaction: DMSO-d_6 (0.5 mL) and benzyl azide (11 μL, 0.2 mM) were added to an NMR tube containing $Cu(II)Cl_2$ (1.4 mg, 0.02 mM), PMDETA (2.2 μL, 0.02 nM) and a photoinitiator (0.02 mM). After 1−2 min, the phenylacetylene (13 μL, 0.2 mM) was added via syringe. The reaction tube was irradiated by a Ker-Vis blue photoreactor equipped with a circle of 6 lamps (Philips TL-D 18W) emitting light nominally at 400−500 nm. ^{1}H NMR spectra were periodically recorded, with each measurement involving 16 scans. Conversions were determined by integration of the signal from a proton in one of the starting molecules and the corresponding proton in the product (e.g., protons **a** and **d** in Figure S1, Supporting Information).

Synthesis of Polymers with Clickable Functionalities. ω-Azido functional polystyrene[19] (PSt-N_3) ($M_{n,NMR}$: 1910, $M_{n,GPC}$: 2000, M_w/M_n:1.12) and α-alkyne functional poly(ε-caprolactone)[20] (PCL-Alkyne) ($M_{n,NMR}$: 2900, $M_{n,GPC}$: 4400, M_w/M_n:1.12) were synthesized according to literature.

Synthesis of Telechelic Polymers via Click Chemistry. General procedure for the synthesis of telechelic polymers is as follows: polymers bearing clickable functionalities, PSt−N_3 or PCL−Alkyne (1.0 equiv) is dissolved in a glass bottle containing DMSO-d_6 (1 mL). Then $Cu^{II}Cl_2$ (1.5 equiv), PMDETA (1.5 equiv), TMDPO (2.5 equiv), and the corresponding low molar mass acetylene or azido click compounds (1.5 equiv) were added to the solution. After dissolution, the reaction mixture is added to an NMR tube with a syringe. The reaction tube was irradiated by a Ker-Vis blue photoreactor equipped with a circle of six lamps (Philips TL-D 18W) emitting light nominally at 400−500 nm. ^{1}H NMR spectra were periodically recorded, with each measurement involving 16 scans. Conversions were determined by integration of the signal from a proton in one of the starting molecules and the corresponding proton in the product.

Synthesis of Poly(Styrene-*b*-(ε-caprolactone)) (PSt-*b*-PCL) via Click Chemistry. PSt-N_3 (1.0 equiv), PCL-Alkyne (1 equiv), $Cu^{II}Cl_2$ (1.5 equiv), PMDETA (1.5 equiv), and TMDPO (2.5 equiv) were dissolved in DMSO-d_6 (1 mL) in a glass bottle and added into an NMR tube with a syringe. The reaction tube was irradiated by a Ker-Vis blue photoreactor equipped with a circle of six lamps (Philips TL-D 18W) emitting light nominally at 400−500 nm. ^{1}H NMR spectra were periodically recorded, with each measurement involving 16 scans. Conversions were determined by integration of the signal from a proton in one of the starting molecules and the corresponding proton in the product. After complition of the reaction, the reaction solvent is directly transferred into a beaker containing excess methanol/water (10:1, vol/vol) to precipitate the polymer. The obtained polymer is further characterized by FT-IR and GPC measurements.

RESULTS AND DISCUSSION

The use of electron transfer reactions of free radicals in synthetic polymer chemistry dates back to more than 3 decades ago.[21] Photochemically generated electron donor radicals can efficiently be oxidized by appropriate salts to the corresponding cations capable of initiating cationic polymerization of appropriate monomers (Scheme 1).[22]

Scheme 1. Oxidation of Photochemically Formed Radicals by Onium Salts

$$PI \xrightarrow{h\nu} 2R^{\bullet} \xrightarrow{On^+} 2R^+$$

Many UV and visible light free radical photoinitiators were reported to be powerful promoters not only for cationic polymerization but also *in situ* formation of polymer/metal nanocomposites based on both epoxy and (meth)-acrylates.[14,15,23] In order to demonstrate further value of this simple redox process, the CuAAC click reactions between benzyl azide and phenylacetylene as simple model click components were performed in the presence of either type I (2, 2-dimethoxy-2-phenyl acetophenone (DMPA), 2-benzyl-2-dimethylamino-4′-morpholino butyrophenone (DBMP), 2,4,6-trimethylbenzoyl)diphenylphosphine oxide (TMDPO) and dicyclopentadienyl bis[2,6-difluoro-3-(1-pyrrolyl)phenyl] titanium (titanocene)) or type II (camphorquinone (CQ)) visible light photoinitiators with copper(II) chloride/*N,N,N′,N″,N″*-pentamethyldiethylenetriamine complex. The reactions were performed under irradiation at 400−500 nm, where the copper complexes were transparent and the light was absorbed exclusively by the visible light photoinitiators (Figure 1).

First, a control experiment in the absence of a photoinitiator under identical experimental conditions (benzyl azide and phenylacetylene, $Cu^{II}Cl_2$ and *N,N,N′,N″,N″*-pentamethyldiethylenetriamine (PMDETA) ligand) was carried out. In this case, only a little amount of coupled product was formed (Table 1,

dx.doi.org/10.1021/ma202438w | Macromolecules 2012, 45, 56−61

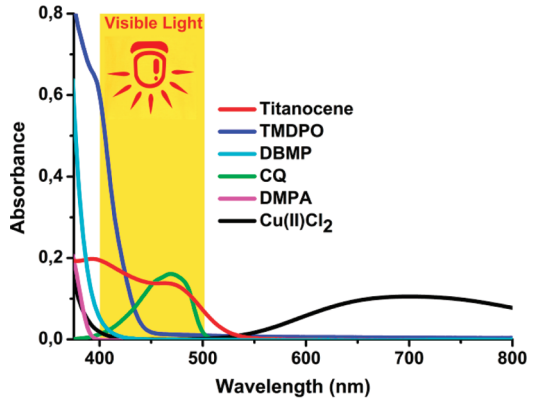

Figure 1. UV−vis spectra of various photoinitiators and $Cu^{II}Cl_2$ in DMSO. Concentration in all cases was 2 mM.

Table 1. Photoinduced Free Radical Promoted CuAAC Click Reaction[a] between Benzyl Azide and Phenylacetylene Using Free Radical Photoinitiators

Entry	Photoinitiator	λ_{max} (nm)	Reducing radical	Φ[b]	Time (min)	Yield[c] (%)
1	-	-	-	-	90	<1
2	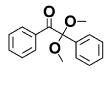 DMPA	340		0.6	90	<5
3	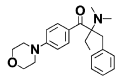 DBMP	330		0.3	60	93
4	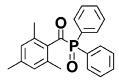 TMDPO	371		0.7	20	94
5	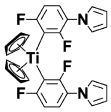 Titanocene	397	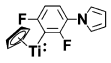	0.7	10	89
6[d]	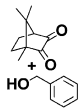 CQ/BzOH	469		0.1	90	83

[a]All reactions were carried out under irradiation at 400−500 nm with a light intensity of 45 mW cm^{-2} at room temperature, in DMSO-d_6. The initial concentrations of azide and alkyne were 0.2 mM and the photoinitiator, $Cu^{II}Cl_2$ and PMDETA were 0.02 mM. [b]Quantum yield.[24] [c]Yield determined by ^{1}H NMR spectroscopy. [d]The ratio of CQ/BzOH = 1/3.

run 1) indicating negligible contribution from self-absorption by the copper complex. The radical photoinitiators including DMPA, DBMP, TMDPO and Titanocene are good sources of electron donor radicals via Norrish type I reaction (Table 1, runs 2−5). However, DMPA was essentially inactive and the click reaction did not proceed even after prolonged irradiation times (90 min) due to its low absorption behavior in the visible light range (Table 1, run 2).

For DBMP, the 2-ethyl-2-benzyl substitution extended its spectral sensitivity to above 400 nm, although the absorption was quite weak at this wavelength. Under visible light irradiation, DBMP generated an inert benzoyl radical[25] and an active aminoalkyl radical, which readily reduced Cu(II) into Cu(I) ion and readily catalyzed the CuAAC click reaction (Scheme 2). After 60 min, the reaction reached up to 93%

Scheme 2. Photochemical Generation of $Cu^{I}Cl$ by Type I Photoinitiator (DBMP)

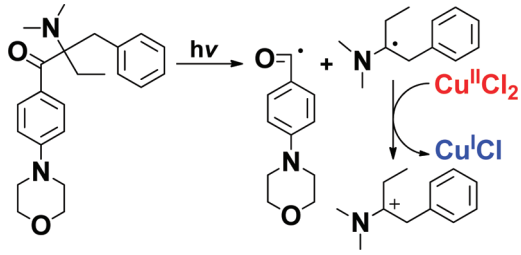

conversion (Table 1, run 3, Figure S1 in the Supporting Information).

Upon photolysis, TMDPO underwent α-scission and produced a benzoyl and phosphinoyl radicals. While both were reactive in typical free radical reactions (addition to olefinic monomers and oxygen, and atom abstractions), the phosphonyl radical displays higher efficiency due to the higher electron density on the phosphorus atom and the more favorable steric conditions arising from its pyramidal structure.[21d,22d,26] However, their participation in electron transfer reactions strongly depended on the substitution with electron donating groups and the reduction potential of the oxidizing salt used. Although unknown, the rate constant for the reaction of phosphinoyl radicals with Cu(II) ($E^{1/2}_{red}$ = 0.16 V (SCE))[27] was expected to be larger than for iodonium salt ($E^{1/2}_{red}$ = −0.2 V (SCE)),[28] which was $k_{et} = 1.6 \times 10^7$ M^{-1} s^{-1}.[22d] Analogous to the reaction with iodonium salts, phosphinoyl radicals readily reduced Cu(II); i.e. quantitative click reaction was attained in 20 min (Table 1, run 4). With the absorption of visible light, titanocene photoinitiator underwent the generation of carbon-centered radicals resulting from a Ti−C bond cleavage. The titanium-centered diradical can readily reduce Cu(II) into Cu(I) as well as promote the CuAAC click reaction. The radical photoinitiator, CQ was also active in the range of visible light and capable of generating radicals via Norrish type II reaction in the presence of hydrogen donor, such as benzyl alcohol. The reducing species involved in Cu(II) ion reduction was frequently benzyl radical, which was well-established as powerful reducing agent (Scheme 3).[17c,29] The Cu(I) ion produced was surely responsible for the initiation of the CuAAC click reaction (Table 1, run 6).

It is clear that both type I and type II visible light photoinitiators were capable of initiating the CuAAC click reaction. The efficiency of the process depends on both the absorbency and quantum yield particular photoinitiator involved (Table 1). As can be seen from Figure 2, where reaction yields were plotted vs time, type I photoinitiators were more efficient in the process. This behavior was due to the fact that, with type II photoinitiators, reactive radicals were produced by a bimolecular reaction with a relatively lower quantum yield. When using type I photoinitiators, the transient

dx.doi.org/10.1021/ma202438w | Macromolecules 2012, 45, 56−61

Scheme 3. Photochemical Generation of $Cu^{I}Cl$ by Type II Photoinitiators (CQ/BzOH)

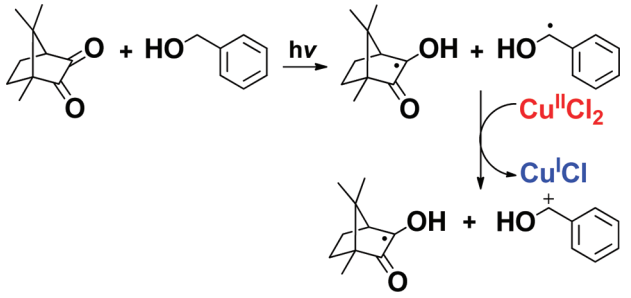

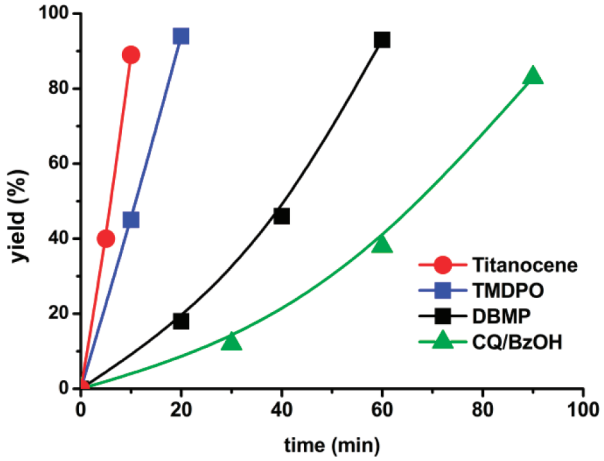

Figure 2. Photoinduced free radical promoted click coupling reaction of benzyl azide and phenylacetylene as a function of time using $Cu^{II}Cl_2$/PMDETA/photoinitiator as the catalyst system. Alkyne/azide ratio: 1. Azide/$Cu^{II}Cl_2$/photoinitiator ratio: 1:0.1:0.1. Yield determined by ^{1}H NMR spectroscopy.

excited states (singlet and triplet) have very short lifetimes, thus preventing any quenching by the metal ions. Notably, titanocene-based photoinitiator was found to be most efficient for the CuAAC click reaction. In all cases, the reaction yields increased with the irradiation time since the oxidizable radicals were continuously produced.

To evaluate the versatility and efficiency of visible light-induced CuAAC process as a new general method in synthetic polymer chemistry, we have conducted selected experiments in polymer functionalization and block copolymer formation. For the telechelic polymer[30] preparation, both azide or alkyne end-functionalized polymers in conjunction with low molecular weight counterparts having various functionalities, namely, propargyl alcohol, 4-pentynoic acid, propargyl pyrene, and benzyl azide were used in the photoinduced click process. In polystyrene functionalization, the successful transformations of azide end groups into functional triazoles were confirmed by the disappearance of the methine proton neighboring the azido group (4.1 ppm) and the appearance of the methine proton neighboring the triazole (5.1 ppm) in the ^{1}H NMR spectra. The additional signal at 8.1 ppm assigned to the proton of the triazole rings was not clearly distinguishable in the NMR spectra as it was partly masked by the broad aromatic regions of polystyrene (Figure S2−4 in the Supporting Information). The integration of aforementioned signals at 4.1 and 5.1 ppm confirmed the successful formation of the triazole chain ends with functional groups. In the poly(ε-caprolactone) case, the signal at 7.9 ppm indicate the formation of triazole (Figure S5 in the Supporting Information). The efficiency of the click reaction, as determined from the ratio of the characteristic peaks of polymers to that of the functional groups are listed in Table 2.

Table 2. Telechelic Polymers via Photoinduced Free Radical Promoted CuAAC click[a] Reaction

Entry	Clickable Polymer	Antagonist molecule	Yield[b] (%)
1	PSt-N_3		93
2	PSt-N_3		88
3	PSt-N_3	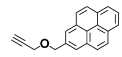	74
4	PCL-Alkyne	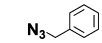	98

[a]All reactions were carried out under irradiation at 400−500 nm with a light intensity of 45 mW cm^{-2} at room temperature, in DMSO-d_6. The initial concentrations of azide and alkyne were 0.5 mM, the photoinitiator was 1.3 mM, and $Cu^{II}Cl_2$ and PMDETA were 0.08 mM; time = 120 min.

To test the suitability of the visible light-induced CuAAC process in the macromolecular synthesis, a block copolymer formation was attempted between an alkyne end-functionalized poly(ε-caprolactone) (PCL−alkyne) (M_n = 4400, polydispersity index (PDI) = 1.12) and an azide end-functionalized polystyrene (PSt−N_3) (M_n = 2000, PDI = 1.12). The reaction was performed under similar experimental conditions as with the small molecular weight precursor. The formation of block copolymer was evidenced by spectral analyses. The ^{1}H NMR spectrum of block copolymer obtained by click reaction indicated characteristic peaks of both precursors (Figure 3).

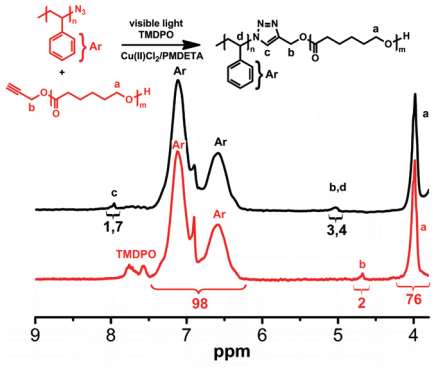

Figure 3. ^{1}H NMR spectra of the mixture of precursor polymers (PSt-N_3 and PCL-Alkyne) and block copolymer (PSt-*b*-PCL) prepared by photoinduced free radical promoted CuAAC click reaction.

While the methylene−oxy protons at 4.6 ppm from the PCL−alkyne completely disappeared, a new signal corresponding to the methyl and methylene protons linked to the triazole ring was observed at around 5.1 ppm (b and d protons in Figure 3). The efficiency of the click reaction for the formation of block copolymer was found to be 86% as determined from integration of the aforementioned signals.

The block copolymer formation was also followed by FT-IR spectroscopy. The IR spectrum associated with block copolymer showed the presence of both components (PSt and PCL) in the structure (Figure S6 in the Supporting

dx.doi.org/10.1021/ma202438w | *Macromolecules* 2012, 45, 56−61

Information). Peaks resonating at 1730, 1360, 1290, 1180, 1100, and 960 cm^{-1} were due to PCL chain whereas transitions from 1595, 1490, and 700 cm^{-1} and overtones between 1945 and 1805 cm^{-1} were specific to the PSt component. As anticipated, the azide and alkyne stretching bands of precursor polymers disappeared completely, confirming that quantitative block copolymer formation by click reaction.

In Figure 4 the normalized GPC curves of the individual precursor polymers as well as of the resulting block copolymer

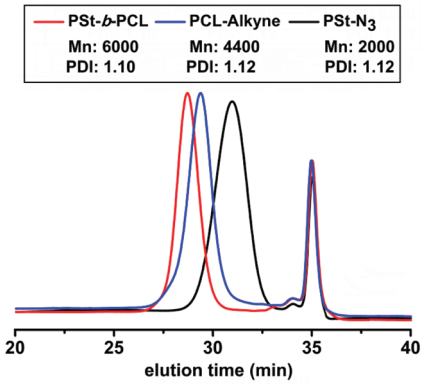

Figure 4. Overlay of GPC traces showing the modular formation of PSt-*b*-PCL from PSt–N_3 and PCL–alkyne.

were shown. In the elution curve of block copolymer, a clear shift toward lower retention times was observed, as well as the disappearance of the chromatographic peak corresponding to precursor polymers. These observations confirm that the described approach is also useful for block copolymer formation.

In summary, a mild and highly versatile visible light-induced CuAAC click reaction via photoinduced electron transfer using free radical photoinitiators has been developed. The applications of this method in the construction of various macromolecular architectures such as the telechelic polymers and block copolymer were also described. The use of visible light to induce the click reaction makes this protocol easy to implement in the biological and material sciences.

■ ASSOCIATED CONTENT

Supporting Information

^{1}H NMR and FT-IR spectra of various products. This material is available free of charge via the Internet at http://pubs.acs.org.

■ AUTHOR INFORMATION

Corresponding Author

*E-mail: yusuf@itu.edu.tr. Fax: +90–212–2856386. Telephone: +90–212–2853241.

■ ACKNOWLEDGMENTS

The authors thank Istanbul Technical University Research Fund.

■ REFERENCES

(1) Kolb, H. C.; Finn, M. G.; Sharpless, K. B. *Angew. Chem., Int. Ed.* **2001**, *40* (11), 2004–2021.
(2) Tornoe, C. W.; Christensen, C.; Meldal, M. *J. Org. Chem.* **2002**, *67* (9), 3057–3064.
(3) Barner-Kowollik, C.; Du Prez, F. E.; Espeel, P.; Hawker, C. J.; Junkers, T.; Schlaad, H.; Van Camp, W. *Angew. Chem., Int. Ed.* **2011**, *50* (1), 60–62.
(4) Lutz, J.-F. *Angew. Chem., Int. Ed.* **2007**, *46* (7), 1018–1025.
(5) Becer, C. R.; Hoogenboom, R.; Schubert, U. S. *Angew. Chem., Int. Ed.* **2009**, *48* (27), 4900–4908.
(6) (a) Diaz, D. D.; Punna, S.; Holzer, P.; McPherson, A. K.; Sharpless, K. B.; Fokin, V. V.; Finn, M. G. *J. Polym. Sci., Part A: Polym. Chem.* **2004**, *42* (17), 4392–4403. (b) Devaraj, N. K.; Dinolfo, P. H.; Chidsey, C. E. D.; Collman, J. P. *J. Am. Chem. Soc.* **2006**, *128* (6), 1794–1795. (c) Adzima, B. J.; Tao, Y.; Kloxin, C. J.; DeForest, C. A.; Anseth, K. S.; Bowman, C. N. *Nature Chem.* **2011**, *3* (3), 256–259.
(7) (a) Yagci, Y.; Jockusch, S.; Turro, N. J. *Macromolecules* **2010**, *43* (15), 6245–6260. (b) Tasdelen, M. A.; Yagci, Y. *Aust. J. Chem.* **2011**, *64* (8), 982–991.
(8) Killops, K. L.; Campos, L. M.; Hawker, C. J. *J. Am. Chem. Soc.* **2008**, *130* (15), 5062–5064.
(9) Wang, Y. Z.; Song, W. J.; Hu, W. J.; Lin, Q. *Angew. Chem., Int. Ed.* **2009**, *48* (29), 5330–5333.
(10) (a) Poloukhtine, A. A.; Mbua, N. E.; Wolfert, M. A.; Boons, G. J.; Popik, V. V. *J. Am. Chem. Soc.* **2009**, *131* (43), 15769–15776. (b) Orski, S. V.; Poloukhtine, A. A.; Arumugam, S.; Mao, L. D.; Popik, V. V.; Locklin, J. *J. Am. Chem. Soc.* **2010**, *132* (32), 11024–11026. (c) Kuzmin, A.; Poloukhtine, A.; Wolfert, M. A.; Popik, V. V. *Bioconjugate Chem.* **2010**, *21* (11), 2076–2085.
(11) (a) Durmaz, Y. Y.; Kumbaraci, V.; Demirel, A. L.; Talinli, N.; Yagci, Y. *Macromolecules* **2009**, *42* (11), 3743–3749. (b) Kumbaraci, V.; Talinli, N.; Yagci, Y. *Macromolecules* **2006**, *39* (18), 6031–6035. (c) Tasdelen, M. A.; Kumbaraci, V.; Talinli, N.; Yagci, Y. *Polymer* **2006**, *47* (22), 7611–7614. (d) Kumbaraci, V.; Talinli, N.; Yagci, Y. *Macromol. Rapid Commun.* **2007**, *28* (1), 72–77. (e) Tasdelen, M. A.; Kumbaraci, V.; Talinli, N.; Yagci, Y. *Macromolecules* **2007**, *40* (13), 4406–4408. (f) Tasdelen, M. A.; Kumbaraci, V.; Jockusch, S.; Turro, N. J.; Talinli, N.; Yagci, Y. *Macromolecules* **2008**, *41* (2), 295–297.
(12) Arumugam, S.; Popik, V. V. *J. Am. Chem. Soc.* **2011**, *133* (14), 5573–5579.
(13) Uygun, M.; Tasdelen, M. A.; Yagci, Y. *Macromol. Chem. Phys.* **2010**, *211* (1), 103–110.
(14) (a) Sangermano, M.; Yagci, Y.; Rizza, G. *Macromolecules* **2007**, *40* (25), 8827–8829. (b) Yagci, Y.; Sangermano, M.; Rizza, G. *Polymer* **2008**, *49* (24), 5195–5198. (c) Maretti, L.; Billone, P. S.; Liu, Y.; Scaiano, J. C. *J. Am. Chem. Soc.* **2009**, *131* (39), 13972–13980. (d) Eksik, O.; Tasdelen, M. A.; Erciyes, A. T.; Yagci, Y. *Compos. Interfaces* **2010**, *17* (4), 357–369.
(15) (a) Yagci, Y.; Sangermano, M.; Rizza, G. *Macromolecules* **2008**, *41* (20), 7268–7270. (b) Yagci, Y.; Sangermano, M.; Rizza, G. *Chem. Commun.* **2008**, No. 24, 2771–2773. (c) McGilvray, K. L.; Decan, M. R.; Wang, D. S.; Scaiano, J. C. *J. Am. Chem. Soc.* **2006**, *128* (50), 15980–15981. (d) Marin, M. L.; McGilvray, K. L.; Scaiano, J. C. *J. Am. Chem. Soc.* **2008**, *130* (49), 16572–16584.
(16) (a) Natarajan, P.; Ferraudi, G. *Inorg. Chem.* **1981**, *20* (11), 3708–3712. (b) David, P. G.; Dasilva, P. A. C. *Bull. Chem. Soc. Jpn.* **1985**, *58* (12), 3566–3569. (c) Pacioni, N. L.; Pardoe, A.; McGilvray, K. L.; Chretien, M. N.; Scaiano, J. C. *Photochem. Photobiol. Sci.* **2010**, *9* (6), 766–774.
(17) (a) Tasdelen, M. A.; Uygun, M.; Yagci, Y. *Macromol. Chem. Phys.* **2010**, *211* (21), 2271–2275. (b) Tasdelen, M. A.; Uygun, M.; Yagci, Y. *Macromol. Rapid Commun.* **2011**, *32* (1), 58–62. (c) Tasdelen, M. A.; Uygun, M.; Yagci, Y. *Macromol. Chem. Phys.* **2011**, *212* (18), 2036–2042.
(18) Tasdelen, M. A.; Yagci, Y. *Tetrahedron Lett.* **2010**, *51* (52), 6945–6947.
(19) Lutz, J. F.; Borner, H. G.; Weichenhan, K. *Macromol. Rapid Commun.* **2005**, *26* (7), 514–518.
(20) Hoogenboom, R.; Moore, B. C.; Schubert, U. S. *Chem. Commun.* **2006**, *38*, 4010–4012.
(21) (a) Yagci, Y.; Ledwith, A. *J. Polym. Sci., Part A: Polym. Chem.* **1988**, *26* (7), 1911–1918. (b) Abdulrasoul, F. A. M.; Ledwith, A.; Yagci, Y. *Polymer* **1978**, *19* (10), 1219–1222. (c) Abdulrasoul, F. A.

M.; Ledwith, A.; Yagci, Y. *Polym. Bull.* **1978**, *1* (1), 1−6. (d) Yagci, Y.; Borbely, J.; Schnabel, W. *Eur. Polym. J.* **1989**, *25* (2), 129−131.
(22) (a) Yilmaz, G.; Beyazit, S.; Yagci, Y. *J. Polym. Sci., Part A: Polym. Chem.* **2011**, *49* (7), 1591−1596. (b) Kahveci, M. U.; Tasdelen, M. A.; Yagci, Y. *Polymer* **2007**, *48* (8), 2199−2202. (c) Durmaz, Y. Y.; Moszner, N.; Yagci, Y. *Macromolecules* **2008**, *41* (18), 6714−6718. (d) Dursun, C.; Degirmenci, M.; Yagci, Y.; Jockusch, S.; Turro, N. J. *Polymer* **2003**, *44* (24), 7389−7396. (e) Yagci, Y.; Schnabel, W. *Makromol. Chem. Macromol. Symp.* **1992**, *60*, 133−143. (f) Yagci, Y.; Onen, A.; Schnabel, W. *Macromolecules* **1991**, *24* (16), 4620−4623. (g) Lalevee, J.; El-Roz, M.; Allonas, X.; Fouassier, J. P. *J. Polym. Sci., Part A: Polym. Chem.* **2008**, *46* (6), 2008−2014. (h) Lalevee, J.; Dirani, A.; El-Roz, M.; Allonas, X.; Fouassier, J. P. *J. Polym. Sci., Part A: Polym. Chem.* **2008**, *46* (9), 3042−3047. (i) Lalevee, J.; El Roz, M.; Tehfe, M. A.; Alaaeddine, M.; Allonas, X.; Fouassier, J. P. *J. Photopolym. Sci. Technol.* **2009**, *22* (5), 587−590. (j) El-Roz, M.; Lalevee, J.; Morlet-Savary, F.; Allonas, X.; Fouassier, J. P. *Macromolecules* **2009**, *42* (13), 4464−4469. (k) Tehfe, M. A.; Lalevee, J.; Allonas, X.; Fouassier, J. P. *Macromolecules* **2009**, *42* (22), 8669−8674. (l) Lalevee, J.; Fouassier, J. P. *Polym. Chem.* **2011**, *2* (5), 1107−1113. (m) Lalevee, J.; Tehfe, M. A.; Morlet-Savary, F.; Graff, B.; Allonas, X.; Fouassier, J. P. *Prog. Org. Coat.* **2011**, *70* (1), 23−31. (n) Lalevee, J.; Blanchard, N.; Tehfe, M. A.; Peter, M.; Morlet-Savary, F.; Gigmes, D.; Fouassier, J. P. *Polym. Chem.* **2011**, *2* (9), 1986−1991.
(23) (a) Sangermano, M.; Roppolo, I.; Camara, V. H. A.; Dizman, C.; Ates, S.; Torun, L.; Yagci, Y. *Macromol. Mater. Eng.* **2011**, *296* (9), 820−825. (b) Yagci, Y.; Sahin, O.; Ozturk, T.; Marchi, S.; Grassini, S.; Sangermano, M. *React. Funct. Polym.* **2011**, *71* (8), 857−862. (c) Amici, J.; Sangermano, M.; Celasco, E.; Yagci, Y. *Eur. Polym. J.* **2011**, *47* (6), 1250−1255.
(24) Gruber, H. F. *Prog. Polym. Sci.* **1992**, *17* (6), 953−1044.
(25) Baumann, H.; Muller, U.; Pfeifer, D.; Timpe, H. J. *J. Prakt. Chem.* **1982**, *324* (2), 217−226.
(26) Yagci, Y.; Schnabel, W. *Makromol. Chem. Rapid Commun.* **1987**, *8* (4), 209−213.
(27) Petrucci, R. H.; Harwood, W. S.; Herring, F. G., *General chemistry: principles and modern applications*, 8th ed.; Prentice-Hall: Upper Saddle River, NJ, 2001; Appendix D.
(28) Bachofner, H. E.; Beringer, F. M.; Meites, L. *J. Am. Chem. Soc.* **1958**, *80* (16), 4269−4274.
(29) (a) Crivello, J. V. *J. Polym. Sci., Part A: Polym. Chem.* **2009**, *47* (3), 866−875. (b) Mayouf, A.; Lemmetyinen, H.; Sychttchikova, I.; Koskikallio, J. *Int. J. Chem. Kinet.* **1992**, *24* (6), 579−585.
(30) Tasdelen, M. A.; Kahveci, M. U.; Yagci, Y. *Prog. Polym. Sci.* **2011**, *36* (4), 455−567.

Macromolecules

ARTICLE

pubs.acs.org/Macromolecules

Well-Defined Poly(lactic acid)s Containing Poly(ethylene glycol) Side Chains

José A. Castillo,[†] Dorothee E. Borchmann,[†] Amy Y. Cheng,[‡] Yufeng Wang,[†] Chunhua Hu,[†] Andrés J. García,[*,‡] and Marcus Weck[*,†]

[†]Molecular Design Institute and Department of Chemistry, New York University, New York, New York 10003, United States

[‡]Woodruff School of Mechanical Engineering and Institute for Bioengineering and Bioscience, Georgia Institute of Technology, Atlanta, Georgia 30332-0400, United States

Supporting Information

ABSTRACT: Poly(ethylene glycol) (PEG) side-chain functionalized lactide analogues have been synthesized in four steps from commercially available L-lactide. The key step in the synthesis is the 1,3-dipolar cycloaddition between PEG-azides and a highly strained spirolactide−heptene monomer, which proceeds in high conversions. The PEG-grafted lactide analogues were polymerized via ring-opening polymerization using triazabicyclodecene as organocatalyst to give well-defined tri- and hepta(ethylene glycol)−poly(lactide)s (PLA) with molecular weights above 10 kDa and polydispersity indices between 1.6 and 2.1. PEG−poly(lactide) (PLA) with PEG chain M_n 2000 was also prepared, but GPC analysis showed a bimodal profile indicating the presence of starting macromonomer. Cell adhesion assays were performed using MC3T3-E1 osteoblast-like cells demonstrating that PEG-containing PLA reduces cell adhesion significantly when compared to unfunctionalized PLA.

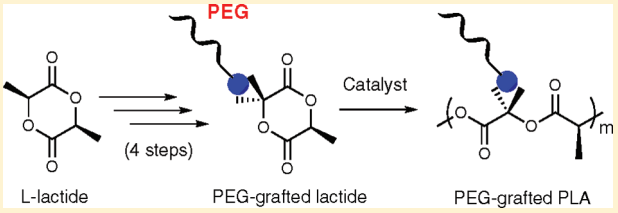

INTRODUCTION

Poly(lactic acid) (PLA), a poly(2-hydroxypropionic acid), is a biodegradable and biocompatible polymer from biorenewable feedstock. Following today's trend of minimizing the impact of chemicals on the environment as well as searching for alternatives to depleting petrochemical resources, PLA is the candidate of choice for polymeric commodities (e.g., packaging materials for food and beverages, plastic bags, and thin film coatings) as well as in the medical field (e.g., for medical devices, sutures, and tissue replacement and as delivery vehicle).[1,2] PLA can be obtained via the polycondensation of lactic acid or the ring-opening polymerization (ROP) of cyclic lactides.[3] One drawback of PLA is its lack of functional side-chain diversity, which limits the possibilities for chemical modification.[2,4] To overcome this limitation, syntheses of modified lactide monomers with functionalized side chains have been reported in the past decade.[2,4−8] We have published the synthesis of cyclic lactides bearing protected alcohols, amines, and carboxylic acid functionalities starting from commercially available amino acids.[9,10] Another versatile synthetic approach has been reported by Yang and co-workers, who have synthesized functional hemilactides through a Passerini-type condensation.[11]

Our ultimate goal is to develop polymeric scaffolds for bone tissue engineering with adequate mechanical properties and controlled architectures that support osteoblast function. Recently, we have reported the synthesis of poly(lactic acid) (PLA)-*block*-poly(norbornene) (PNB) copolymers that bear photo-cross-linkable cinnamate side chains to enhance mechanical strength.[12] In order to improve the properties of these scaffolds further, herein we report the preparation of poly(ethylene glycol) (PEG)-functionalized PLA. We rationalize that this modification should reduce nonspecific protein adsorption, a prerequisite to our scaffold design.[13] It has also been reported that surface PEGylation increases the mechanosensitivity of osteoblasts, i.e., the specific response to mechanical stimulation, and accelerates growth and development of osteoblasts for bone repair and tissue engineering.[14,15]

Several groups have grafted PEG in a random fashion onto PLA. Baker and co-workers reported a postpolymerization modification of propargylglycolide polymers with PEG-azides via Huisgen cycloaddition.[16] Hildgen and co-workers have prepared randomly PEG-grafted PLA to prepare stealth nanoparticles for drug delivery. They initially polymerized D,L-lactide in the presence of allyl glycidyl ether followed by subsequent PEG functionalization.[17] Baker and co-workers have also reported the synthesis of well-defined PEG-grafted PLA based on the condensation of hydroxyacids with PEG side chains. However, this synthetic route consisted of several steps in moderate yields.[18] Despite these elegant approaches, a general approach to prepare well-defined PLA containing PEG side chains still remains a synthetic challenge. In this contribution we report a short and efficient functionalization of L-lactide monomer with PEG side chains and the subsequent

Received: July 17, 2011
Revised: November 14, 2011
Published: December 16, 2011

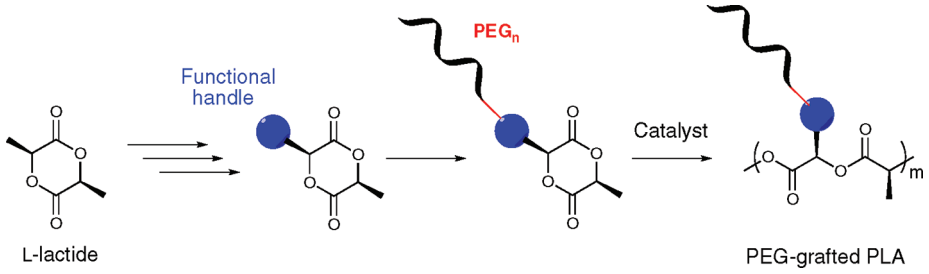

Figure 1. Schematic approach to the preparation of well-defined PEG-grafted PLA from L-lactide.

Scheme 1. General Synthetic Approach To Prepare PEG$_n$-PLA

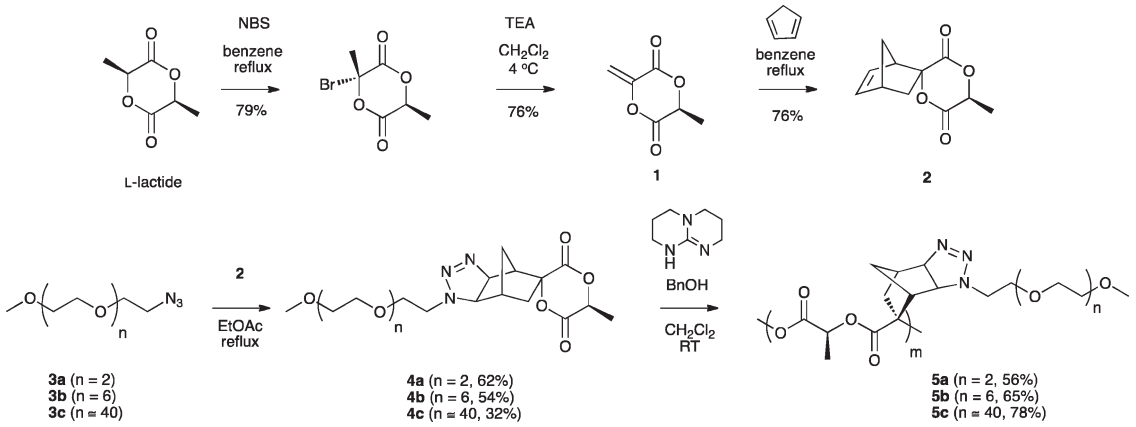

polymerization. Furthermore, since cell adhesion to polymeric surfaces is primarily mediated by adhesive proteins adsorbed from serum such as vitronectin and fibronectin,[19] cell adhesion assays were performed using MC3T3 × 10^{-1} as osteoblast-like cells in order to investigate the reduction of nonspecific protein adsorption caused by the new PEG-grafted polymers.

RESEARCH DESIGN

The main requirement for our research design is that we can functionalize cyclic L-lactide monomers with PEG side chains of different sizes in high yields and in a straightforward fashion in order to prepare well-defined PEG-grafted PLA (Figure 1). Our design is based on some recent work by Jing and Hillmyer, who have reported the synthesis of *exo*-methylene−lactide **1** and spirolactide−heptene **2** (Scheme 1).[20] We rationalized that **2** due to its high ring strain can serve as dipolarophile in cycloaddition reactions. Knowing that azides react readily with strained alkenes such as norbornenes via 1,3-dipolar cycloadditions,[21−23] our hypothesis is that the cycloaddition between PEG-azides and **2** which contains a norbornene moiety might be an easy entranceway toward PEG functionalized cyclic lactides.

EXPERIMENTAL SECTION

Materials. Compounds **1** and **2** were synthesized as described by Jing and Hillmyer.[20] Poly(ethylene glycol) monomethyl ether tosylates **6**, **10**, and **11** were prepared as reported by Ouchi and co-workers.[24] Azido-poly(ethylene glycol) monomethyl ethers **3a**, **3b**, and **3c** were obtained using a methodolgy reported by Saha and Ramakrishnan.[25] Triethylene glycol monomethyl ether (97%), poly(ethylene glycol) methyl ether (M_n ∼ 2000), L-lactide (98%), dicyclopentadiene (97%), 1,5,7-triazabicyclo[4.4.0]dec-5-ene (97%), benzyl alcohol (99.8%), and 1-azidoadamantane (97%) were purchased from Sigma-Aldrich. Tetraethylene glycol (99.5%) was purchased from Acros Organics. Benzene was distilled over sodium and benzophenone under nitrogen before use. Dichloromethane was dried over calcium hydride and distilled under nitrogen prior to use. ^{1}H and ^{13}C NMR spectra were recorded on a Bruker AC 400 spectrometer (400 and 100 MHz for ^{1}H and ^{13}C, respectively). All chemical shifts are reported in parts per million (ppm) with reference to solvent residual peaks. Gel permeation chromatography (GPC) was performed using an HPLC from Agilent Technologies 1200 series and two columns (gel type: AM GPC gel, porosities: 100, 1000, 100 000 Å, linear mixed bed from American Polymer Standards) connected in series with an Optilab rEX refractive index detector from Wyatt Technology. Experiments were performed at room temperature using $CHCl_3$/triethylamine/isopropanol 94:4:2 as eluent, flow rate of 1 mL/min, and molecular weights are reported versus PEG standards (M_n from 1050 to 30 000). Electrospray ionization (ESI) mass spectra were obtained on an Agilent 1100 Series capillary LCMSD trap XCT spectrometer using MeOH/H_2O and ACN/H_2O as eluents. Microwave-assisted reactions were performed using a CEM Discovery microwave reactor. IR spectra were recorded using KBr tablets or poly(ethylene) sample cards on a Nicolet 550 Magna-IR spectrometer. Elemental analysis was performed on a Perkin-Elmer 2400 Series II CHNSO analyzer and by Intertek-QTI. Melting points were determined using a Fisher-Johns apparatus. The MALDI-TOF spectrum of **4c** was recorded on a Bruker UltrafleXtreme using dithranol as matrix and NaCl as doping salt. The sample was prepared following the multiple-layer spotting technique reported by Meier and Schubert.[26] Thermogravimetric analyses were recorded on a Perkin-Elmer Pyris 1TGA from 25 to 550 °C with a heating/cooling rate of 10 °C min^{-1} under N_2. Differential scanning calorimetry (DSC) measurements were acquired

dx.doi.org/10.1021/ma2016387 |*Macromolecules* 2012, 45, 62–69

using a Perkin-Elmer DSC Pyris 1. Samples were run under a nitrogen atmosphere from −10 to 100 °C with a heating/cooling rate of 10 °C min^{-1}. Dialysis membrane Spectra/Por 6, MWCO 1000 and 3500 (38 mm flat width), was purchased from SpectrumLabs and rinsed with water prior to use. About 10 cm of dialysis membrane was used per purification. For **4c** and polymers **5a**−**c**, a dichloromethane solution of product was introduced inside the dialysis bag (MWCO 1000 for macromonomer **4c** and polymers **5a**,**b** and MWCO 3500 for polymer **5c**) that was then introduced to 0.5 L of dichloromethane and gently stirred for about 12 h. Four cycles were performed for each dialysis.

Single Crystal Structure Determination. A colorless block crystal **4d** with the size of 0.12 × 0.22 × 0.30 mm^3 was selected for geometry and intensity data collection with a Bruker SMART APEXII CCD area detector on a D8 goniometer at 100 K. The temperature during the data collection was controlled with an Oxford Cryosystems Series 700 plus instrument. Preliminary lattice parameters and orientation matrices were obtained from three sets of frames. Data were collected using graphite-monochromated and 0.5 mm MonoCap-collimated Mo Kα radiation (λ = 0.710 73 Å) with the ω scan method.[27] Data were processed with the INTEGRATE program of the APEX2 software[27] for reduction and cell refinement. Multiscan absorption corrections were applied by using the SCALE program for area detector. The structure was solved by the direct method and refined on F^2 (SHELXTL).[28] Non-hydrogen atoms were refined with anisotropic displacement parameters, and hydrogen atoms on carbons were placed in idealized positions (C−H = 0.99 or 1.00 Å) and included as riding with U_{iso}(H) = 1.2 or 1.5 U_{eq}(non-H).

Synthesis of Triethylene Glycol Methyl Ether−1,2,3-Δ^2-Triazoline-spiro[6-methyl-1,4-dioxane-2,5-dione-3,2′-bicyclo-[2.2.1]heptane], PEG_3-Spirolactide (4a). Azidotriethylene glycol methyl ether, PEG_3-N_3, **3a** (684 mg, 3.62 mmol), and spiro[6-methyl-1,4-dioxane-2,5-dione-3,2′-bicyclo[2.2.1]hepta-5-ene], **2** (753 mg, 3.62 mmol), were dissolved in EtOAc (20 mL). The reaction was refluxed under nitrogen for 3 days, and the conversion was monitored by ^{1}H NMR spectroscopy. The crude reaction was concentrated under reduced pressure to give a brown oil. This crude product was purified by silica chromatography using EtOAc/hexane 7:3 as eluent to afford the titled triazoline as a yellow oil (897 mg, 62%). ^{1}H NMR ($CDCl_3$, 400 MHz, data shown for major isomer): δ = 5.18 (q, J = 4.9 Hz, 1H, −CH− of LA unit), 4.92 (d, J = 9.8 Hz, 1H, −CH− of triazoline unit), 3.81 (m, 2H), 3.75−3.60 (PEG chain, 12H), 3.57 (m, 3H), 3.37 (s, 3H, CH_3−PEG−), 3.08 (s, 1H), 2.76 (dd, J = 14.3 Hz, J = 5.0 Hz 1H), 2.63 (d, J = 4.9 Hz, 1H), 1.76 (dt, J = 11.7 Hz, J = 1.5 Hz, 1H), 1.69 (d, J = 6.7 Hz, 3H, CH_3− of LA unit), 1.53 (dd, J = 14.1 Hz, J = 3.5 Hz, 1H), 1.28−1.25 (m, 1H). ^{13}C NMR ($CDCl_3$, 100 MHz, data shown for major isomer): δ = 167.9, 167.1, 85.7, 78.7, 73.0, 72.1, 70.8 (×2), 70.7, 70.3, 62.7, 59.2, 49.0, 48.3, 38.3, 31.6, 16.8. ESI-mass: 420.1 (M^++Na^+). MS-ESI $(M + H)^+$ m/z calcd for $C_{18}H_{28}N_3O_7$ 398.42; found 398.1. Elemental analysis: calcd for $C_{18}H_{27}ON_3O_7$: C 54.40, H 6.85, N 10.57; found: C 54.78, H 6.83, N 10.08. IR (KBr) ν (cm^{-1}): 2920.3, 2881.5, 1759.0, 1466.5, 1352.2, 1281.6, 1228.3, 1199.3, 1105.7, 1062.2, 1020.5, 986.9, 851.4, 647.1.

Synthesis of Heptaethylene Glycol Methyl Ether−1,2,3-Δ^2-Triazoline-spiro[6-methyl-1,4-dioxane-2,5-dione-3,2′-bicyclo-[2.2.1]heptane], PEG_7−Spirolactide (4b). Azidoheptaethylen glycol methyl ether, PEG_7-N_3, **3b** (1.30 g, 3.56 mmol), and spiro[6-methyl-1,4-dioxane-2,5-dione-3,2′-bicyclo[2.2.1]hepta-5-ene], **2** (741 mg, 3.56 mmol), were dissolved in EtOAc (20 mL). The reaction was refluxed under nitrogen for 4 days. The conversion after 4 days was measured by ^{1}H NMR spectroscopy to be 78%. The crude reaction was concentrated under reduced pressure to give a brown oil. This solid was purified by silica chromatography using EtOAc/hexane 7:3 as eluent to afford the title triazoline as a yellow oil (1.10 g, 54%). ^{1}H NMR ($CDCl_3$, 400 MHz, data shown for major isomer): δ = 5.18 (q, J = 6.7 Hz, 1H, −CH− of LA unit), 4.90 (d, J = 9.8 Hz, 1H, −CH− of triazoline unit), 3.82 (m, 2H), 3.75−3.61 (PEG chain, 34H), 3.53 (m, 3H), 3.35 (m, 3H, CH_3−PEG−), 3.09 (s, 1H), 2.75 (dd, J = 14.0 Hz, J = 4.9 Hz, 1H), 2.63 (d, J = 4.7 Hz, 1H), 1.78 (m, 1H) (dd, J = 11.6 Hz, J = 1.5 Hz, 1H), 1.69 (d, J = 6.7 Hz, 3H, CH_3− of LA unit), 1.54 (dd, J = 14.1 Hz, J = 3.6 Hz, 1H), 1.26−1.23 (m, 1H). ^{13}C NMR ($CDCl_3$, 100 MHz, data shown for major isomer): δ = 167.9, 167.1, 85.7, 78.7, 73.0, 72.1, 70.8, 70.7 (x2), 70.2, 62.7, 59.2, 48.9, 48.3, 41.0, 38.2. 31.5, 16.7. MS-ESI $(M + H)^+$ m/z calcd for $C_{26}H_{44}N_3O_{11}$ 574.63; found 574.2. Elemental analysis: calcd for $C_{26}H_{43}N_3O_{11}$: C 54.44, H 7.56, N 7.33; found: C 54.85, H 7.76, N 7.12. IR (KBr) ν (cm^{-1}): 2922.3, 2870.3, 2105.6, 1957.5, 1757.7, 1466.3, 1350.9, 1282.0, 1140.8, 1062.6, 986.7, 937.0, 851.7, 743.7, 685.7, 649.0, 571.1.

Synthesis of Poly(ethylene glycol methyl ether)−1,2,3-Δ^2-Triazoline-spiro[6-methyl-1,4-dioxane-2,5-dione-3,2′-bicyclo-[2.2.1]heptane] (M_n ∼ 2200), PEG_{40}−Spirolactide (4c). Azido-poly(ethylene glycol methyl ether) (M_w∼ 2000), PEG_{40}-N_3, **3c** (3.35 g, 1.67 mmol), and spiro[6-methyl-1,4-dioxane-2,5-dione-3,2′-bicyclo[2.2.1]hepta-5-ene], **2** (1.26 mg, 6.0 mmol, 3.6 equiv), were dissolved in EtOAc (40 mL). The reaction was refluxed under nitrogen for 3 days. The crude reaction was concentrated under reduced pressure to afford a dark green solid. The crude product was dissolved in CH_2Cl_2 (∼15 mL), and diethyl ether was added (∼30 mL). The suspension was refluxed for 20 min and cooled down to room temperature, affording a white suspension and a green oil. The layers were separated, and the white suspension was cooled down to 4 °C when a white solid precipitated. This solid was washed with diethyl ether. The crystallyzation was repeated two more times, affording the title compound as a white solid (1.17 g, 32%). The monomer was dialyzed in CH_2Cl_2 using a cellulose membrane (MWCO 1000). Finally, compound **4c** was lyophilized twice from distilled benzene (3 times distilled) prior to polymerization. ^{1}H NMR ($CDCl_3$, 400 MHz, data shown for major isomer): δ = 5.17 (q, J = 6.6 Hz, 1H, −CH− of LA unit), 4.92 (d, J = 9.7 Hz, 1H, −CH− of triazoline unit), 3.73−3.45 (PEG chain), 3.45 (m, 3H), 3.36 (m, 3H, CH_3−PEG−), 3.08 (s, 1H), 2.75 (dd, J = 14.0 Hz, J = 4.9 Hz, 1H), 2.62 (d, J = 4.6 Hz, 1H), 1.87 (dd, J = 11.6 Hz, J = 1.3 Hz, 1H), 1.68 (d, J = 6.7 Hz, 3H, CH_3− of LA unit), 1.53 (dd, J = 14.1 Hz, J = 3.7 Hz, 1H), 1.24 (m, 1H). ^{13}C NMR ($CDCl_3$, 100 MHz, data shown for major isomer): δ = 167.9, 167.0, 88.6, 85.7, 78.7, 77.4, 70.3 (PEG chain), 62.7, 59.2, 56,1, 49.0, 48.3, 44.9, 41.0, 40.0, 39.5, 38.3, 31.6, 27.3, 16.8. Melting point: 45−46 °C. Elemental analysis: calcd for $C_{94}H_{218}N_3O_{45}$: C 53.55, H 10.3, N 2.0; found: C 53.79, H 8.61, N 1.08. IR (KBr) ν (cm^{-1}): 2921.3, 2882.4, 2242.3, 2098.6, 2058.5, 1954.3, 1758.6, 1467.0, 1343.2, 1280.6, 1241.9, 1112.8, 963.0, 843.0, 742.8, 569.8.

Synthesis of Adamantyl-1,2,3-Δ^2-triazoline−Spiro[6-methyl-1,4-dioxane-2,5-dione-3,2′-bicyclo[2.2.1]heptane] (4d). 1-Azidoadamantante (255 mg, 1.44 mmol) and spiro[6-methyl-1,4-dioxane-2,5-dione-3,2′-bicyclo[2.2.1]hepta-5-ene], **2** (300 mg, 1.44 mmol), were dissolved in EtOAc. The reaction was refluxed overnight under nitrogen. The crude reaction was concentrated under reduced pressure to afford an orange solid. The crude product was purified by silica chromatography using EtOAc/hexane 8:2 as eluent to afford the title triazoline as a white solid (290 mg, 52%). ^{1}H NMR ($CDCl_3$, 400 MHz, data shown for major isomer): δ = 5.22 (q, J = 6.7 Hz, 1H, −CH− of LA unit), 4.84 (d, J = 9.9 Hz, 1H, −CH− of triazoline unit), 3.65 (d, J = 9.9 Hz, 1H, −CH′− of triazoline unit), 3.13 (s, 1H), 2.73 (dd, J = 14.1 Hz, J = 4.9 Hz, 1H), 2.42 (d, J = 5.2 Hz, 1H), 2.15−2.08 (m, 7H), 1.86−1.79 (m, 4H), 1.78−1.66 (m, 10H, CH_3− of LA unit and adamantane unit), 1.56 (dd, J = 14.1 Hz, J = 4.6 Hz, 1H), 1.30−1.27 (m, 1H). ^{13}C NMR ($CDCl_3$, 100 MHz, data shown for major isomer): δ = 168.0, 167.2, 86.1, 78.2, 73.0, 58.4, 57.4, 49.1, 43.8, 42.2, 36.4, 31.7, 29.6, 16.8. Melting point: 214−215 °C. MS-ESI $(M + H)^+$ m/z calcd for $C_{21}H_{28}N_3O_4$ 386.46; found 386.2. Elemental analysis: calcd for $C_{21}H_{27}N_3O_4$: C 65.44, H 7.06, N 10.9; found: C 65.53, H 7.00, N 10.9. IR (KBr) ν (cm^{-1}): 3533.7, 3497.0, 2997.3, 2917.6, 2851.5, 2680.6, 2333.5, 1750.1, 1482.3, 1454.8, 1360.3, 1313.2, 1242.6, 1147.6, 1086.6, 1020.0, 987.4, 928.6, 855.7, 826.2, 787.1, 737.5, 693.1, 647.5, 582.3, 485.7.

Scheme 2. 1,3-Dipolar Cycloaddition between 1-Azidoadamantane and Spirolactide 2

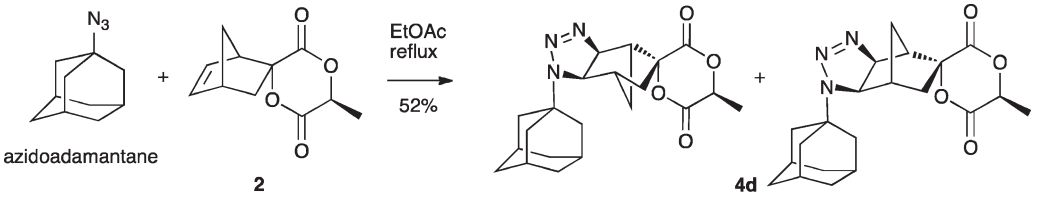

General Procedure for Microwave-Assisted 1,3-Dipolar Cycloaddition. PEG_n-azide (1 equiv) and spirolactide (1 equiv) were mixed in a tube reactor in the absence of solvent. The reaction mixture was irradiated using microwave irradiation at 70 °C for 3 cycles (each 1 h) at 150 W. The conversion was followed by ^{1}H NMR spectroscopy.

Polymerization. All L-lactide analogues were stored under nitrogen in a freezer to ensure stability. Prior to polymerization, monomers **4a,b** were triply recrystallized from EtOAc/hexane while monomer **4c** was triply recrystallized from CH_2Cl_2/diethyl ether. Then, each monomer was frozen in benzene (triply distilled) and lyophilized (3×). The polymerization of **4a** is described as an example. In a nitrogen-filled glovebox, a catalyst/initiator solution was prepared by combining 1,5,7-triazabicyclo-[4.4.0]dec-5-ene (TBD, 18 mg, 0.126 mmol), benzyl alcohol (26 μL, 0.251 mmol), and anhydrous CH_2Cl_2 (25 mL) in a 25 mL volumetric flask. The freshly prepared catalyst/initiator solution (730 μL) was added to the Schlenk flask containing **4a** (290 mg, 0.73 mmol). The initial concentrations were **4a** 1 M (100 equiv), TBD 0.5 equiv, and BnOH 1 equiv. After 24 h, the crude reaction was concentrated under reduced pressure and purified by dialysis (MWCO 1000) from CH_2Cl_2. Polymer **5a** was isolated as a yellow oil (255 mg, 56%). ^{1}H NMR (acetone-d_6, 400 MHz): δ = 5.34−4.70 (m, 2H, −CH- of LA unit and −CH− of triazoline unit), 3.81 (m, 1H), 3.71 (m, 3H), 3.60 (PEG chain, 8H), 3.48 (m, 2H), 3.30 (s, 3H, CH_3−PEG−), 3.23−2.78 (m, 2H), 2.62−2.47 (m, 2H), 1.75 (m, 1H), 1.56 (m, 4H, including CH_3− of LA unit), 1.36 (m, 1H). 1.09 (m, 1H). ^{13}C NMR (acetone-d_6, 100 MHz): δ = 170.8, 170.6, 85.0, 80.7, 72.7, 71.1, 70.5, 63.0, 59.0, 50.0, 48.9, 42.4, 37.8, 29.9, 17.1. Elemental analysis: calcd for $C_{18}H_{27}N_3O_7$: C 54.40, H 6.85, N 10.57; found: C 55.12, H 7.27, N 9.65.

PEG_7-Grafted PLA (5b). Polymer **5b** was prepared as described above and isolated as a yellow oil (454 mg, 65%). ^{1}H NMR (acetone-d_6, 400 MHz): δ = 5.35−4.55 (m, 2H, −CH− of LA unit and −CH− of triazoline unit), 3.85 (m, 1H), 3.72 (m, 4H), 3.59 (PEG chain, 30H), 3.48 (m, 3H), 3.30 (s, 4H, including CH_3−PEG−), 3.24−2.95 (m, 1H), 2.75−2.54 (m, 2H), 1.75 (m, 1H), 1.59 (m, 5H, including CH_3− of LA unit), 1.36 (m, 1H). 1.11 (m, 1H). ^{13}C NMR (acetone-d_6, 100 MHz): δ = 170.9, 170.7, 85.2, 80.6, 70.6, 63.0, 55.1, 48.9, 42.4, 41.9, 29.9, 17.0. Elemental analysis: calcd for $C_{26}H_{43}N_3O_{11}$: C 54.44, H 7.56, N 7.33; found: C 53.57, H 7.72, N 6.90.

PEG_{40}-Grafted PLA (5c). Polymer **5c** was prepared as described above; in this case the initial concentration of monomer **4c** was 0.33 M (100 equiv), TBD 1.5 equiv, and BnOH 3.0 equiv. Polymer **5c** was purified by dialysis (MWCO 3500) from CH_2Cl_2, resulting in a white solid (454 mg, 78%). Melting point: 45−46 °C. ^{1}H NMR (acetone-d_6, 400 MHz): δ = 5.27 (m, 1H, −CH− of LA unit), 3.91−3.51 (PEG chain, 349H), 3.46 (m, 5H), 3.29 (s, 6H, including CH_3−PEG−), 3.10 (m, 2H), 2.81 (m, 11H), 2.63 (m, 2H), 2.50 (m, 1H), 1.65−1.47 (m, 5H, including CH_3− of LA unit), 1.41 (m, 1H), 1.29 (m, 1H). 1.08 (m, 1H). ^{13}C NMR (acetone-d_6, 100 MHz): δ = 162.1, 170.7, 94.8, 86.5, 77.7, 71.4, 69.6, 63.7, 60.6, 58.9, 49.9, 49.0, 39.0, 29.5, 16.7. Elemental analysis: calcd for $C_{94}H_{218}N_3O_{45}$: C 53.55, H 10.3, N 2.0; found: C 54.08, H 9.01, N 1.11.

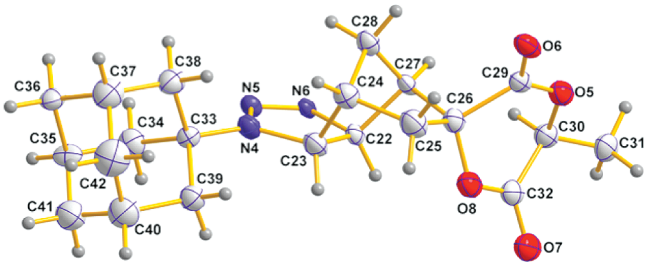

Figure 2. Crystal structure of one isomer of azidomantane−spirolactide **4d**.

Cell Adhesion Assay. Glass slides were spin-coated with polymer solutions (100 mg/5 mL $CHCl_3$) at 500 rpm for 10 s and then at 3000 rpm for 30 s. After air drying, the slides were rinsed with deionized water, 70% ethanol, and Dulbecco's phosphate-buffered saline (DPBS, Invitrogen). MC3T3-E1 osteoblast-like cells (RIKEN Cell Bank) at passage 12 were seeded on coated slides at a cell density of 10 000 cells/cm^2 in serum-containing media (α-MEM supplemented with 10% fetal bovine serum). At 4 h, cells were permeabilized for 3 min in DPBS containing 0.5% Triton X-100 and fixed in 4% paraformaldehyde for 10 min. Slides were blocked in complete DPBS containing 5% goat serum and 0.01% NaN_3 for 1 h and subsequently incubated with antivinculin antibodies (1:400, Upstate Biotechnology V284) and 4′,6-diamidino-2-phenylindole (DAPI, Sigma) in blocking buffer for 1 h. AlexaFluor488-conjugated secondary antibody (Invitrogen) was then incubated for 1 h. Slides were mounted with antifade reagent and viewed with a Nikon E400 fluorescence microscope using 10× and 40× objectives. Images were acquired with SPOT Advanced Software (Diagnostic Instruments, Inc.). To quantify cell adhesion, fluorescence images were analyzed with the ImageJ software (v1.44, NIH) to determine average cell numbers. Cell counts were analyzed using ANOVA with Tukey's test for pairwise comparisons.

RESULTS AND DISCUSSION

Our synthetic strategy to functionalize L-lactide with PEG side chains started with the preparation of spirolactide−heptene **2** according to literature procedures, which was prepared as a mixture of diastereomers (Scheme 1).[20]

We investigated initially whether **2** can react as a dipolarophile in 1,3-dipolar cycloadditions. Since the 1,3-dipolar cycloaddition between 1-azidoadamantane and norbornene has been reported in the literature,[23] we studied, as a proof of concept, the 1,3-dipolar cycloaddition between 1-azidoadamantane and **2** (Scheme 2). The reaction was carried out in EtOAc at reflux. Within 12 h, high conversions of the 1,2,3-Δ^2-triazoline isomers were obtained as characterized by TLC analyses. ^{1}H NMR spectroscopy analysis showed the disappearance of the alkene signals of **2** as well as the formation of two new doublets at 4.84 and 3.65 ppm, which is in good agreement with the chemical shifts of the Δ'-1,2,3-triazoline

dx.doi.org/10.1021/ma2016387 |*Macromolecules* 2012, 45, 62–69

Table 1. Polymer Characterization Data

polymer	M_n $(10^{-3})^a$	PDI[a]	t_R (min)[a]	X_n[b]	M_n $(10^{-3})^c$	conv[d] (%)	yield[e] (%)
PEG_3-PLA **5a**	12	2.1	18.3	30	44	99	60
PEG_7-PLA **5b**	14	1.6	18.3	24	270	82	54
PEG_{40}-PLA **5c**	11	1.4	18.3	5	3200	50	78[f]

[a] GPC in $CHCl_3$/TEA/isopropanol 94:4:2 with PEG standards using refractive index for detection. [b] Degree of polymerization (X_n) calculated from GPC analyses. [c] Number-average molecular weight determined based on ^{1}H NMR end-group analysis. [d] Conversion of polymerization measured by ^{1}H NMR spectroscopy. [e] Isolated yield of polymerization after purification by dialysis in CH_2Cl_2. [f] Polymer **5c** was contaminated with starting macromomoner **4c**.

ring protons reported for the corresponding norbornene adduct with azidoadamantane.[23] The crude reaction was purified by silica gel column chromatography and recrystallized from EtOAc/hexane, affording a mixture of two isomers in a ratio of 1.0:0.4. Single crystal X-ray analysis confirmed the formation of two isomers of **4d** (Scheme 2, Figure 2, and Supporting Information).

After our model reaction afforded the desired cycloaddition product, we investigated the functionalization of **2** with poly(ethylene glycol) moieties. With this aim, we synthesized the three PEG-azides **3a** and **3c** via tosylation and azidation of the corresponding commercially available poly(ethylene glycol) methyl ether using standard conditions (i.e., p-TsCl and NaOH in H_2O/THF and NaN_3/DMF, respectively).[25] In the case of PEG-azide **3b**, we previously synthesized the starting heptaethylene glycol methyl ether (see Scheme S1 in the Supporting Information). The 1,3-dipolar cycloaddition between PEG_3-N_3 **3a** and **2** carried out in EtOAc under reflux for 12 h gave the desired PEG_3-spirolactide **4a**. ^{1}H NMR spectroscopy analyses showed the formation of a new doublet at 4.91 ppm, corresponding to one of the two Δ′-1,2,3-triazoline ring protons, with similar chemical shift and coupling constants to those reported above for the triazoline **4d**. The second doublet overlapped with the PEG chain signal in the ^{1}H NMR spectrum. However, it could be observed easily at 3.65 ppm in the COSY NMR spectrum (Supporting Information). The doublet at 4.91 ppm served as criterion for us to monitor the progress of the reaction by NMR spectroscopy. After 3 days at reflux, the observed conversion was 94%. Based on ^{1}H NMR spectroscopy analyses of the crude reaction mixture, two triazoline isomers were obtained in a ratio of 1.0:0.45. In addition, ^{13}C NMR spectroscopy analysis showed two signals at 168.0 and 167.1 ppm corresponding to the two carbonyl groups on the lactide ring, indicating that the ring was conserved during the cycloaddition and the purification process. The IR spectrum of **4a** does not show a signal corresponding to the starting azide, and the ESI mass spectrum of **4a** showed one signal at 398.1 m/z $(M + H)^+$.

After preparing **4a** successfully (62% yield after silica chromatography), we applied our methodology to azides **3b**, PEG_7-N_3, and **3c**, PEG_{40}-N_3, $M_w \sim 2000$. The 1,3-dipolar cycloadditions between PEG_7-N_3 **3b** and PEG_{40}-N_3 **3c** with **2** in EtOAc at reflux for 3−4 days afforded PEG_7-spirolactide **4b** and PEG_{40}-spirolactide **4c**, respectively, in high conversions (75−80% by ^{1}H NMR spectroscopy). Monomer **4b** was purified by silica chromatography (54% isolated yield), and monomer **4c** was triply recrystallized from a 1:5 mixture of CH_2Cl_2/diethyl ether (32% isolated yield). The MALDI-TOF spectrum for **4c** showed masses from 1713 to 2595 (theoretical $M_n \sim 2200$) (Supporting Information). The 1,3-dipolar cycloaddition was also investigated using microwave irradiation to explore whether microwave irradiation can result in shorter reaction times. The microwave-assisted cycloaddition between **3a** and **2** in an equimolar ratio reached a maximum of 86% conversion after 3 h at 70 °C as observed by ^{1}H NMR spectroscopy. In the case of the cycloaddition between **3c** and **2** in equimolar ratio, the conversion observed was 68% after 3 h at 70 °C. When using the spirolactide **2** in slight excess (**3c**:**2** ratio of 1:1.5 equiv), the reaction proceeded to full conversion.

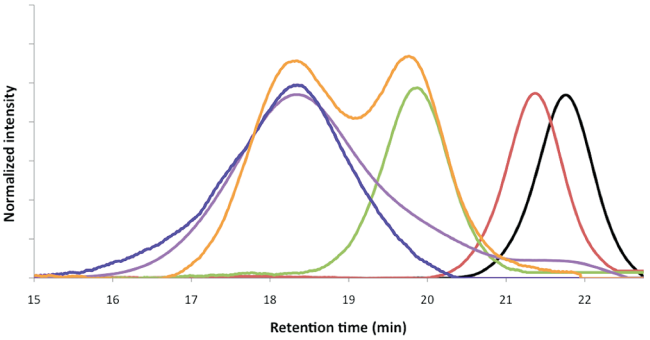

Figure 3. GPC curves of all monomers and polymers in $CHCl_3$/TEA/isopropanol 94:4:2. GPC trace of **4a** (black trace), **4b** (red trace), **4c** (green trace), **5a** (purple trace), **5b** (blue trace), and **5c** (orange trace). All molecular weights are reported versus PEG standards using refractive index for detection.

After the successful synthesis of our three target monomers, we investigated the ring-opening polymerization of **4a**−**c**. The monomers were obtained as a mixture of diastereomers, and we assume that they might possess slightly different reactivities. It is well-known that the ROP of lactides requires high monomer purity,[9,20] and each monomer was purified and dried extensively as can be seen from the Experimental Section. Initially, we investigated the ROP of **4a** using the polymerization conditions reported by us: $SnOct_2$ as catalyst and benzyl alcohol as initiator without solvent under N_2 at 140 °C overnight.[9] Unfortunately, **4a** was not stable under these reactions conditions. Next, we investigated the conditions employed by Hillmyer and co-workers to polymerize **2** (100 equiv) using triazabicyclodecene (TBD, 0.5 equiv) as organocatalyst and benzyl alcohol (1 equiv) as co-initiator.[20] This methodology ensures the preparation of PLA without any metal impurities, which is crucial for the use of our materials in regenerative medicine.[29] The polymerization of **4a** at room temperature after 24 h using the Hillmyer procedure was almost quantitative as measured by ^{1}H NMR spectroscopy. We hypothesize that BnOH attacks the less sterically hindered carbonyl group of the lactide ring, i.e., the carbonyl next to the methyl group.

The kinetics of the polymerization of **4b** was investigated by ^{1}H NMR spectroscopy, showing a maximum of 82% conversion

dx.doi.org/10.1021/ma2016387 |*Macromolecules* 2012, 45, 62–69

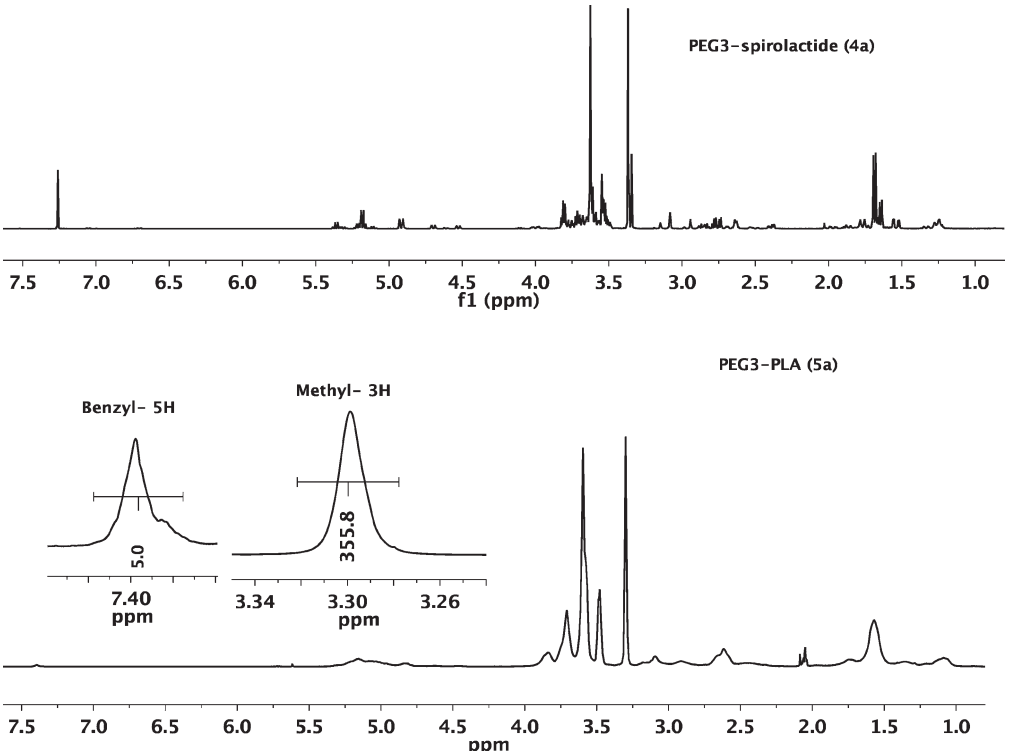

Figure 4. ^{1}H NMR spectrum of PEG$_3$-spirolactide **4a** in $CDCl_3$ (top) and end-group analysis of PEG$_3$-PLA **5a** by the ^{1}H NMR spectrum in acetone-d_6 (bottom).

after 20 h. In the case of monomer **4c**, which is a solid at room temperature and contains a long PEG chain ($M_n \sim 2200$), we decided to dilute the reaction mixture to increase the solubility of the monomer as well as the concentration of the catalyst and co-initiator. The initial concentrations used were **4c** 0.33 M (100 equiv), TBD 1.5 equiv, and BnOH 3 equiv. The polymerization of **4c** was followed by ^{1}H NMR spectroscopy, showing a maximum conversion (~50%) after 36 h. The spectrum of the crude reaction showed two similar and overlapping singlets at 3.29 and 3.30 ppm corresponding to the terminal methyl group of the CH_3-PEG chain (Supporting Information). These two singlets suggest that **4c** and **5c** were present in the crude reaction in similar ratios. We hypothesize that the long PEG chain hinders the polymerization process. Since **4c** is a macromonomer, the long PEG side chain could adopt a random coil conformation that could "internalize" the lactide unit. This conformation would limit catalyst accessibility and thus significantly impede polymerization. Furthermore, the long PEG side chains of the monomers might entangle with the polymer PEG side chains, limiting monomer diffusion.

Isolated yields of all polymers ranged from 54 to 78% (Table 1) after extensive purification by dialysis in CH_2Cl_2 and lyophilization. All polymers were characterized by ^{1}H NMR and ^{13}C NMR spectroscopies, gel-permeation chromatography (GPC), and thermogravimetric analysis (TGA) (Table 1 and Supporting Information). In case of polymer **5c**, after purification by dialysis (MWCO 3500), the ^{1}H NMR spectrum showed again both singlets at 3.3 ppm in similar ratio, indicating that the dialysis process was unsuccessful in removing **4c**.

GPC analyses of the polymers show number-average molecular weights between 11 and 14 kDa and PDI values between 1.4 and 2.1. All values are reported versus PEG standards. We cannot exclude trace contamination of monomers with water due to the hydrophilic PEG side chains despite careful repurifications and lyophilizations using distilled benzene as solvent. The presence of these water molecules might compete with BnOH as co-initiator and would explain the higher than expected PDI values. As expected, GPC analyses of polymers **5a**−**c** show lower retention times (t_R 18.3 min for all three polymers) than monomers **4a**−**c** (Figure 3). The GPC chromatogram of PEG$_{40}$-PLA 5c shows a bimodal profile with a second peak at 19.7 min. This peak overlaps with the signal of the monomer **4c**. Therefore, in the case of polymer **5c**, the PDI value 1.4 was measured in the region of the GPC curve centered at 18 min. That result is in agreement with the NMR spectroscopy data, suggesting that polymer **5c** was still contaminated with the macromonomer **4c** (M_n 2200) after dialysis using a membrane bag MWCO 3500.

Molecular weights of **5a**−**c** were also determined by ^{1}H NMR end-group analysis comparing the integration of the methyl ether group (CH_3-PEG chain) to the benzyl group of the co-initiator (Figure 4). The disagreement between the molecular weights determined by ^{1}H NMR end-group analysis (44 kDa for **5a**, 270 kDa for **5b**, and 3200 kDa for **5c**) and GPC might be due to the high error measuring the small signal in the ^{1}H NMR spectrum corresponding to the co-initiator (benzyl group). Besides, the average molecular weights measured by GPC are not accurate since linear PEG standards were used for calibration while the PEG-grafted polymers **5a**−**c** are brush polymers. The PEG-grafted PLAs have smaller hydrodynamic volumes than linear PEG standards, and consequently, the apparent molecular weight measured by GPC are smaller than that estimated by ^{1}H NMR spectroscopy. Hillmyer and co-workers have recently reported that the polymerization of aliphatic spirolactide derivatives affords polyesters with higher glass transition temperatures than

dx.doi.org/10.1021/ma2016387 |*Macromolecules* 2012, 45, 62–69

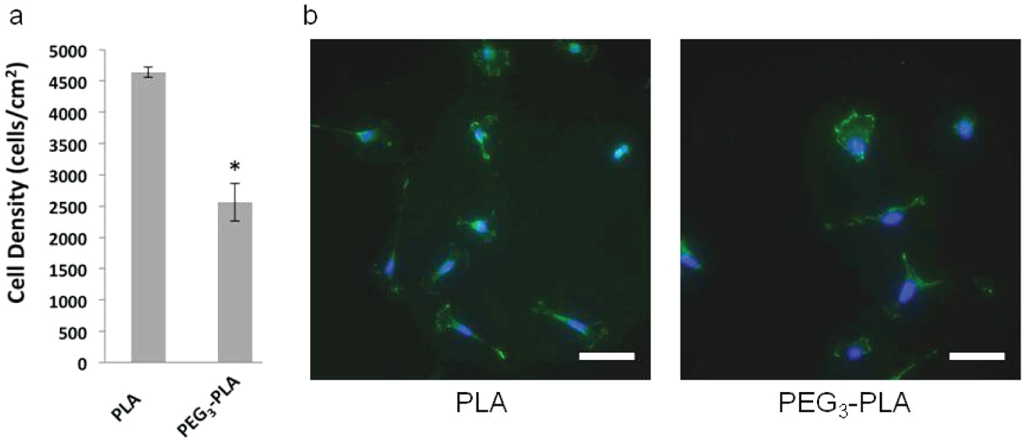

Figure 5. MC3T3-E1 cell adhesion and spreading on spin-coated polymer films. (a) Average density of adherent cells on polymer coatings. Error bars represent standard error of the mean. *P < 0.01compared to PLA. (b) Representative images of adherent cells on polymer films with stained nuclei (DAPI, blue) and focal adhesion protein vinculin (vinc, green). Scale bars are 50 μm.

PLA ($T_g \sim 50$ °C).[30] In contrast, differential scanning calorimetry (DSC) measurements of PEG_3-PLA **5a** and PEG_7-PLA **5b**, which are oils at room temperature, did not show any transition between −10 and 100 °C (Supporting Information). PEG_{40}-PLA **5c** showed a sharp transition around 50 °C, which corresponds to its melting point. Thermogravimetric analysis (TGA) was used to evaluate the thermal stability of polymers **5a**−**c** (Supporting Information). The degradation of **5a** starts at 215 °C, **5b** at 285 °C, and **5c** at 332 °C. Hence, the length of the PEG side chain slightly increases the thermal stability of PEG-grafted polymers.

Cell adhesion studies were performed in order to investigate the capability of the new PEG-grafted PLAs to reduce nonspecific protein adsorption and cell adhesion. Hence, MC3T3 × 10^{-1} cells were seeded in the presence of serum-containing media on PLA (control) and PEG_3-PLA films to examine initial cell adhesion responses. We only examined adhesion to the shorter PEG_3-PLA polymer because the longer PEG chain polymers (PEG_7-PLA and PEG_{40}-PLA) exhibited high water solubility and were rapidly lost from the surface in aqueous solutions. We note that the increased water solubility of the longer PEG chain polymers will be advantageous in future studies dealing with cross-linked scaffolds. The osteoblast-like cells adhered and spread on both PLA and PEG_3-PLA films, but clear differences between PEG-functionalized and control PLA can be seen in cell density and cell morphology. Figure 5a shows that the number of adhered cells was significantly decreased for the PEG-functionalized PLA compared to PLA. Although cells assembled vinculin-containing focal adhesions on both polymer films, differences in morphology were evident (Figure 5b). Cells on PLA were more spread and polarized with focal adhesions localized to the cell tips, whereas cells on PEG_3-PLA showed less spread cells. The differences in cell adhesion and spreading are likely due to differences in protein adsorption between the polymeric films due to the protein adsorption-resistant nature of PEG. The cell adhesion results demonstrate that the addition of PEG chains to PLA modulates biological responses to the base PLA. These results are consistent with previous reports demonstrating changes in cell adhesion following grafting of PEG. Future studies will examine cellular responses within PEG-functionalized PLA scaffolds.

CONCLUSIONS

In this contribution, we have presented a short and general approach to prepare PEG side-chain functionalized L-lactide monomers and their subsequent polymerization. The PEG-spirolactide-based monomers were prepared readily in four steps from commercially available L-lactide in good yields. The key step is the 1,3-dipolar cycloaddition between PEG-azides and the spirolactide−heptene precursor. The monomers were polymerized using TBD as organocatalyst yielding well-defined oligo(ethylene glycol)-functionalized poly(lactic acid) with molecular weights above 10 kDa and polydispersity indices between 1.6 and 2.1. In the case of PEG_{40}-PLA, the measured PDI was 1.4, but the GPC analysis showed a bimodal profile indicating the presence of starting macromonomer despite purification by dialysis. Preliminary biological studies showed that PEG_3-grafted PLA reduces cell adhesion when compared to PLA.

ASSOCIATED CONTENT

Supporting Information. Detailed spectroscopic data and crystallographic data. This material is available free of charge via the Internet at http://pubs.acs.org.

AUTHOR INFORMATION

Corresponding Author

*E-mail: marcus.weck@nyu.edu (M.W.); andres.garcia@me.gatech.edu (A.J.G.).

ACKNOWLEDGMENT

Financial support has been provided by the National Institute of Health (5R01EB008069). The MALDI instrument was purchased with a grant from the National Science Foundation (CHE-0958457).

REFERENCES

(1) Auras, R.; Lim, L.-T.; Selke, S. E. M.; Tsuji, H. *Poly(Lactic Acid): Synthesis, Structures, Properties, Processing, and Applications*; John Wiley & Sons, Inc.: Hoboken, NJ, 2010.

(2) Becker, J. M.; Pounder, R. J.; Dove, A. P. *Macromol. Rapid Commun.* **2010**, *31*, 1923–1937.

(3) Platel, R. H.; Hodgson, L. M.; Williams, C. K. *Polym. Rev.* **2008**, *48*, 11–63.
(4) Pounder, R. J.; Dove, A. P. *Polym. Chem.* **2010**, *1*, 260–271.
(5) Edlund, U.; Kallrot, M.; Albertsson, A.-C. *J. Am. Chem. Soc.* **2005**, *127*, 8865–8871.
(6) Vogeley, N. J.; Baker, G. L.; Smith, M. R., III *Polym. Prepr. (Am. Chem. Soc., Div. Polym. Chem.)* **2005**, *46*, 336.
(7) Leemhuis, M.; van Nostrum, C. F.; Kruijtzer, J. A. W.; Zhong, Z. Y.; ten Breteler, M. R.; Dijkstra, P. J.; Feijen, J.; Hennink, W. E. *Macromolecules* **2006**, *39*, 3500–3508.
(8) Cohen-Arazi, N.; Katzhendler, J.; Kolitz, M.; Domb, A. J. *Macromolecules* **2008**, *41*, 7259–7263.
(9) Gerhardt, W. W.; Noga, D. E.; Hardcastle, K. I.; García, A. J.; Collard, D. M.; Weck, M. *Biomacromolecules* **2006**, *7*, 1735–1742.
(10) Noga, D. E.; Petrie, T. A.; Kumar, A.; Weck, M.; García, A. J.; Collard, D. M. *Biomacromolecules* **2008**, *9*, 2056–2062.
(11) Rubinshtein, M.; James, C. R.; Young, J. L.; Ma, Y. J.; Kobayashi, Y.; Gianneschi, N. C.; Yang, J. *Org. Lett.* **2010**, *12*, 3560–3563.
(12) Wang, Y.; Noga, D. E.; Yoon, K.; Wojtowicz, A. M.; Lin, A. S. P.; García, A. J.; Collard, D. M.; Weck, M. *Adv. Funct. Mater.* **2008**, *18*, 3638–3644.
(13) Heuberger, M.; Drobek, T.; Spencer, N. D. *Biophys. J.* **2005**, *88*, 495–504.
(14) Subramani, K.; Birch, M. A. *Biomed. Mater.* **2006**, *1*, 144–154.
(15) Hamamura, K.; Weng, Y.; Zhao, J.; Yokota, H.; Xie, D. *Biomed. Mater.* **2008**, *3*, 025017–025023.
(16) Jiang, X.; Vogel, E. B.; Smith, M. R.; Baker, G. L. *Macromolecules* **2008**, *41*, 1937–1944.
(17) Sant, S.; Nadeau, V.; Hildgen, P. *J. Controlled Release* **2005**, *107*, 203–214.
(18) Jiang, X.; Milton, R.; Smith; Baker, G. L. *Macromolecules* **2008**, *41*, 318–324.
(19) García, A. J. *Biomaterials* **2005**, *26*, 7525–7529.
(20) Jing, F.; Hillmyer, M. A. *J. Am. Chem. Soc.* **2008**, *130*, 13826–13827.
(21) Dahl, R. S.; Finney, N. S. *J. Am. Chem. Soc.* **2004**, *126*, 8356–8357.
(22) Bräese, S.; Friedrich, A.; Gartner, M.; Schröeder, T. *Top. Heterocycl. Chem.* **2008**, *12*, 45–115.
(23) Sasaki, T.; Eguchi, S.; Yamaguchi, M.; Esaki, T. *J. Org. Chem.* **1981**, *46*, 1800–1804.
(24) Ouchi, M.; Inoue, Y.; Liu, Y.; Nagamune, S.; Nakamura, S.; Wada, K.; Hakushi, T. *Bull. Chem. Soc. Jpn.* **1990**, *63*, 1260–1262.
(25) Saha, A.; Ramakrishnan, S. *Macromolecules* **2009**, *42*, 4956–4959.
(26) Meier, M. A. R.; Schubert, U. S. *Rapid Commun. Mass Spectrom.* **2003**, *17*, 713–716.
(27) APEX2 *(version 2009.11-0). Program for Bruker CCD X-ray Diffractometer Control*; Bruker AXS Inc.: Madison, WI, 2009.
(28) Sheldrick, G. M. *SHELXTL, version 6.14. Program for solution and refinement of crystal structures*; Universität Göttingen: Göttingen, Germany, 2000.
(29) Pratt, R. C.; Lohmeijer, B. G. G.; Long, D. A.; Waymouth, R. M.; Hedrick, J. L. *J. Am. Chem. Soc.* **2006**, *128*, 4556–4557.
(30) Fiore, G. L.; Jing, F.; Young, J. V. G.; Cramer, C. J.; Hillmyer, M. A. *Polym. Chem.* **2010**, *1*, 870–877.
(31) Göpferich, A.; Peter, S. J.; Lucke, A.; Lu, L.; Mikos, A. G. *J. Biomed. Mater. Res.* **1999**, *46*, 390–398.
(32) Iguerb, O.; Poleunis, C.; Mazeas, F.; Compere, C.; Bertrand, P. *Langmuir* **2008**, *24*, 12272–12281.

Macromolecules

ARTICLE

pubs.acs.org/Macromolecules

Facile Synthesis of Flexible, Donor−Acceptor Side-Chain Functionalized Copolymers via Ring-Opening Metathesis Polymerization

Joy Romulus,[†] Sonal Patel,[†] and Marcus Weck*[,†]

[†]Department of Chemistry, Molecular Design Institute, New York University, New York, New York 10003, United States

Supporting Information

ABSTRACT: A series of polymers has been synthesized via ring-opening metathesis polymerization of donor−acceptor side-chain functionalized monomers. The backbones of the polymers are based on poly(norbornene)s and/or poly(cyclooctene)s, while the side-chains consist of electron-rich 1,5-dialkoxynaphthalene and electron-deficient 1,2,4,5-benzenetetracarboxylic dianhydride (pyromellitic dianhydride). The monomers were proven to be living which allowed for the generation of controlled homopolymers and block copolymers. Side-chain functionalized alternating poly(norbornene/cyclooctene)s were generated using a Grubbs-type initiator containing an unsymmetrical N-heterocyclic carbene ligand. Using UV−vis spectroscopy, a charge-transfer band was detected in random and alternating copolymer solutions due to intramolecular interactions.

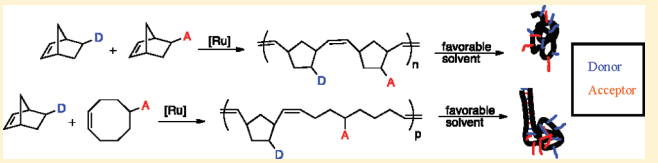

INTRODUCTION

Nature uses a set of noncovalent interactions that drive the folding of biopolymers. When starting from any higher energy configuration, biopolymers assume their native state of minimal conformational energy by specific interactions between the main- and side-chains of the uniquely sequenced biopolymer backbone.[1] From these specific conformations, many functions are carried out such as molecular recognition, information storage, and catalysis.[2] In attempts to mimic this correlation of structure to function, much effort has been dedicated toward applying biological folding principles toward synthetic polymer systems.[3−7] Since polymers allow for the realization of materials[8] with interesting properties,[9−11] well-defined 3D polymeric architectures will be an important stepping-stone to the development of the next generation of functional materials.

Current synthetic 'foldamers'[12] have been employed in a range of applications, such as host−guest systems[13] and optoelectronics.[14,15] Many synthetic polymeric foldamers are driven to secondary structures by taking advantage of the inherent shape arising from rigid polymer backbones[16−18] or by strategically prepositioning recognition units as part of the backbone of the polymer.[14,15,19−24] Increasing the flexibility of the polymeric backbone and exploiting supramolecular interactions between side-chain functional groups possess the possibility to increase the utility of foldameric structures, similar to biomacromolecules. To overcome current limitations in synthetic foldamers and to expand the scope of the existing systems, it is important to develop new methods to fold flexible high molecular weight polymers; that is, polymers without any conformational constraints in the main-chain. In this contribution we report a first step toward this goal by describing a new and versatile set of living, donor−acceptor side-chain functionalized monomers that can generate a variety of random coil homo- and copolymers and study the donor−acceptor interactions between side-chains, a prerequisite to obtain folded structures.

Iverson and co-workers have described synthetic foldamers utilizing donor−acceptor interactions in what they term "aedemers" (aromatic electron donor-acceptor).[25] They have demonstrated the ability of donor−acceptor inter- and intrachain interactions to drive polymers to fold into specific secondary structures, including tweezer-like conformations.[19,25−29] Specifically, they demonstrated the assembly of two side-chain functionalized homopolymers into thread-like arrangements due to side-chain interactions between an electron-rich 1,5-dialkoxynaphthalene (Dan) and an electron-deficient 1,4,5,8-naphthalene tetracarboxylic diimide (Ndi).[26] This was confirmed through atomic-force, optical and scanning-electron microscopies. The polymers used by Iverson and co-workers were functionalized in a postpolymerization fashion. A functional group and living polymerization method, as described here, would allow for a high degree of control during the polymerization as well as complete side-chain functionalization.

This report describes a facile synthesis of controlled, flexible, side-chain functionalized polymers, including homopolymers, random copolymers, block copolymers, and alternating copolymers. The polymer backbone is synthesized via ring-opening metathesis polymerization (ROMP) of norbornenes and cyclooctenes. ROMP is a living polymerization method, allowing for control over the molecular weight of polymers and the synthesis of block and alternating copolymers.[30,31] The driving force designed into the polymers to obtain aggregates and potentially secondary structures arises from donor−acceptor functional groups along the side-chains, electron-rich 1,5-dialkoxy-naphthalene and electron-deficient 1,2,4,5-benzenetetracarboxylic dianhydride (pyromellitic dianhydride).

Received: August 7, 2011
Revised: November 10, 2011
Published: December 12, 2011

dx.doi.org/10.1021/ma201812x | *Macromolecules* 2012, 45, 70−77

This pair allows for directed noncovalent interactions between complementary units. We also report the first highly functionalized alternating copolymerization of two different monomers via ROMP.

EXPERIMENTAL SECTION

General. All reactions were carried out under an inert atmosphere of either nitrogen or argon using standard vacuum and Schlenk techniques or in a glovebox under an atmosphere of N_2. All reagents were purchased either from Acros Organics, Sigma-Aldrich, EMD Chemicals, or Alfa Aesar Chemicals and used without further purification unless otherwise noted. Hexanes, toluene, and tetrahydrofuran (THF) were distilled over Na/benzophenone. Methylene chloride (CH_2Cl_2), acetonitrile, and deuterated chloroform ($CDCl_3$) were distilled over calcium hydride. Grubbs' first-generation initiator was purified by filtration using purified benzene under an atmosphere of argon. ^{1}H NMR spectra were recorded at 25 °C on a Bruker AC 400 (^{1}H: 400.1 MHz) spectrometer. ^{13}C NMR spectra were obtained at 125.0 MHz on a Bruker AC 500 spectrometer. Chemical shifts are reported in parts per million (ppm) with reference to solvent residual nuclei in deuterated solvents. Molecular weights and polydispersity indices were measured using a Shimadzu pump coupled to a Shimadzu UV detector with THF as the eluant and a flow rate of 1 mL/min on American Polymer Standards column set (100, 1000, 100 000 Å, linear mixed bed). All GPCs were calibrated using poly(styrene) standards and carried out at 25 °C. M_w, M_n, and PDI represent the weight-average molecular weight, number-average molecular weight, and polydispersity index, respectively. Bicyclo[2.2.1]hept-5-ene-exo-2-carboxylic acid (norbornene-exoacid) (**4**)[32] was synthesized according to literature procedure.

*2-((5-(Hexyloxy)Naphthalen-1-yl)oxy)ethanol (**3**).* To a solution of 1,5-dihydroxynaphthalene **1** (10.0 g, 49 mmol) in acetonitrile (100 mL) were added K_2CO_3 (15.7 g, 109 mmol), bromohexane (8.1 g, 49 mmol), and KI (cat). The mixture was stirred under refluxed for 18 h and then cooled to room temperature. The solid was filtered off, and the solution was concentrated under reduced pressure. The residue was dissolved in CH_2Cl_2 (10 mL) and washed with dilute hydrochloric acid (10 mL), water (10 mL), and brine (10 mL). After drying over $MgSO_4$, the solvent was removed under reduced pressure, and the resulting residue was subjected to column chromatography (1:3 ethyl acetate (EtOAc): Hexanes) to afford **2** in 33% yield. ^{1}H NMR ($CDCl_3$): δ = 7.88 (d, J = 8.5, 1H), 7.71 (d, J = 8.5, 1H), 7.38 (t, J = 8.1, 1H), 7.29 (t, J = 7.9, 1H), 6.84 (t, J = 6.8, 2H), 4.13 (t, J = 6.4, 2H), 1.92 (dt, J = 14.5, 7.0, 2H), 1.56 (t, J = 7.4, 2H), 1.40−1.36 (m, 4H), 0.92 (t, J = 7.0, 3H); ^{13}C NMR ($CDCl_3$): δ = 155.0, 151.3, 127.3, 125.5, 125.1, 115.0, 113.4, 109.5, 105.4, 68.5, 31.9, 29.5, 26.2, 22.9, 14.3. Elemental analysis calcd % for $C_{16}H_{20}O_2$ (244.15): C 78.65, H 8.25; found: C 78.51, H 8.24.

The same procedure was then repeated using **2** (500.0 mg, 2.05 mmol), chloroethanol (0.98 mL, 1.42 mmol) in acetonitrile (10 mL), K_2CO_3 (507.6 mg, 3.52 mmol), and KI (0.25 g) and subjected to column chromatography (1:4 EtOAc:Hexanes) to afford **3** in 58% yield. ^{1}H NMR ($CDCl_3$): δ = 7.90 (d, J = 8.4 Hz, 1H), 7.82 (d, J = 8.4 Hz, 1H), 7.37 (ddd, J = 7.6, 4.4, 3.6 Hz, 2H), 6.85 (t, J = 8.2 Hz, 2H), 4.26 (t, J = 4.6 Hz, 2H), 4.14−4.08 (m, 4H), 2.12 (t, J = 6.4 Hz, 1H), 1.92 (m, 2H), 1.61−1.53 (m, 3H), 1.42−1.35 (m, 4H), 0.93 (t, J = 7.2 Hz, 3H); ^{13}C NMR ($CDCl_3$): δ = 154.7, 154.2, 126.8, 126.6, 125.3, 124.9, 114.8, 113.8, 105.7, 105.3, 69.7, 68.2, 61.5, 31.7, 29.3, 26.0, 22.6, 14.0 Elemental analysis calcd % for $C_{18}H_{24}O_3$ (288.17): C 74.97, H 8.39; found: C 74.82, 8.41.

*2-(1-(Hexyloxy)naphthalene-5-yloxy)ethyl-norbor-5-ene-2-carboxylate (**5**).* Dialkoxynaphthalene (126.0 mg, 0.44 mmol) **3** and norbornene *exo*-acid **4** (50.3 mg, 0.36 mmol) were dissolved in (30 mL) CH_2Cl_2. A 3 mL solution of dicyclohexylcarbodiimide (DCC) (82.6 mg, 0.30 mmol) was added to the reaction mixture. A catalytic amount of 4-(dimethylamino)pyridine (DMAP) was added, and the solution was stirred at room temperature for 12 h. The mixture was concentrated under reduced pressure. The crude product was purified by column chromatography using 1:4 EtOAc:Hexanes to afford **5**. ^{1}H NMR ($CDCl_3$): δ = 7.88 (d, J = 8.5 Hz, 1H), 7.81 (d, J = 8.5 Hz, 1H), 7.35 (t, J = 8.1 Hz, 2H), 6.83 (d, J = 7.7 Hz, 2H), 6.12 (dd, J = 5.6, 2.9 Hz, 1H), 6.08 (dd, J = 5.6, 3.1 Hz, 1H), 4.58 (m, J = 5.7 Hz, 2H), 4.34 (t, J = 4.8 Hz, 2H), 4.11 (t, J = 6.4 Hz, 2H), 3.06 (s, 1H), 2.90 (s, 1H), 2.29−2.26 (m, 1H), 1.93 (ddt, J = 17.6, 11.6, 5.8 Hz, 4H), 1.58−1.54 (m, 5H), 1.37 (td, J = 8.4, 4.8 Hz, 8H), 0.92 (t, J = 7.1 Hz, 3H). ^{13}C NMR ($CDCl_3$): δ = 176.6, 154.8, 154.2, 138.1, 135.8, 127.0, 126.8, 125.4, 124.9, 115.0, 114.1, 105.8, 105.5, 68.3, 66.6, 62.8, 46.8, 46.5, 43.2, 41.8, 31.7, 30.5, 29.4, 26.1, 22.7, 14.2. Elemental analysis calcd % for $C_{26}H_{32}O_4$ (408.23): C 76.44, H 7.90, O 15.67; found: C 76.04, H 8.01, O 15.95.

*2-Decyl-6-(4-hydroxybutyl)pyrrolo[3,4-f]isoindole-1,3,5,7(2H,6H)-tetraone (**7**).* Pyromellitic dianhydride **6** (6.0 g, 0.028 mol) was dissolved and stirred at 150 °C. To this mixture, decylamine (4.1 mL, 0.021 mol) was added dropwise, and the solution was refluxed for 12 h. 3-Amino-1-propanol (2.1 mL, 0.028 mol) was added, and the mixture was refluxed for an additional 12 h. The solution was cooled to room temperature and concentrated under reduced pressure. The residue was dissolved in dichloromethane (30 mL) and washed with distilled water (3 × 30 mL). The organic layer was dried over $MgSO_4$ and concentrated under reduced pressure. The crude product was purified by column chromatography using 1:3 EtOAc:CH_2Cl_2 to afford **7** in 32% yield. ^{1}H NMR ($CDCl_3$): δ = 8.26 (s, 1H), 3.91 (t, J = 6.5 Hz, 1H), 3.72 (t, J = 7.3 Hz, 1H), 3.65 (q, J = 5.8 Hz, 1H), 2.06 (t, J = 6.2 Hz,), 1.92 (dt, J = 12.4, 6.1 Hz, 1H), 1.68 (t, J = 6.9 Hz, 1H), 1.27 (d, J = 31.5 Hz, 7H), 0.90−0.82 (m, 1H). ^{13}C NMR ($CDCl_3$): δ 171.4, 166.9, 166.5, 137.7, 137.4, 118.5, 60.7, 59.7, 39.1, 35.7, 32.1, 31.4, 29.8, 29.54, 29.40, 28.7, 27.1.

*3-(6-Decyl-1,3,5,7-tetraoxo-6,7-dihydropyrolo[3,4]isoindol-2-yl)-propylnorbor-5-ene-2-carboxylate (**8**).* Norbornene-*exo*-acid **4** (400.0 mg, 2.89 mmol) and **7** (1.0 g, 2.41 mmol) were dissolved in CH_2Cl_2 (20 mL). A 3 mL solution of DCC (547.0 mg, 2.65 mmol) was added to the initial reaction mixture. A catalytic amount of DMAP was added to the solution and stirred at room temperature for 12 h. The CH_2Cl_2 was evaporated under reduced pressure. The crude product was purified by column chromatography using 5% EtOAc/CH_2Cl_2 to afford **8** in 88% yield. ^{1}H NMR ($CDCl_3$): δ = 8.26 (s, 2H), 6.12 (dd, J = 5.6, 3.0, 1H), 6.06 (dd, J = 5.7, 3.1, 1H), 4.14 (t, J = 6.1, 2H), 3.87 (t, J = 6.9, 2H), 3.73 (t, J = 7.4, 2H), 3.03 (dq, J = 2.2, 0.7, 1H), 2.91 (s, 1H), 2.16 (ddd, J = 8.7, 4.5, 1.6, 1H), 2.08 (m, J = 6.5, 2H), 1.91 (dt, J = 11.7, 4.0, 1H), 1.52−1.50 (m, 1H), 1.38−1.28 (m, 18H), 0.87 (t, J = 6.9, 3H).

*4-(6-Decyl-1,3,5,7-tetraoxo-6,7-dihydropyrrolo[3,4-f]isoindol-2-(1H,3H,5H)-yl)butylcyclooct-4-enecarboxylate (**10**).* Cyclooctene-acid **9** (753.0 mg, 2.10 mmol) and **7** (270.0 mg, 1.75 mmol) were dissolved in CH_2Cl_2 (15 mL). A 3 mL solution of DCC (397.2 mg, 1.93 mmol) was added to the initial reaction mixture. A catalytic amount of DMAP was added, and the solution was stirred at room temperature for 12 h. The CH_2Cl_2 was evaporated under reduced pressure. The crude product was purified by column chromatography using 5% EtOAc/CH_2Cl_2 to afford **10** in 83% yield. ^{1}H NMR ($CDCl_3$): δ = 8.26 (s, 1H), 5.67−5.55 (m, 1H), 8.26−0.85 (m, 1H), 4.11−4.09 (m, 1H), 3.85 (t, J = 6.9 Hz, 1H), 3.73 (t, J = 7.3 Hz, 1H), 2.40−2.31 (m, 1H), 2.12 (q, J = 6.5 Hz, 1H), 2.06 (dd, J = 13.0, 6.7 Hz, 1H), 2.00 (t, J = 3.8 Hz, 1H), 1.97 (t, J = 3.8 Hz, 1H), 1.82 (td, J = 14.2, 3.5 Hz, 1H), 1.69 (dt, J = 7.5, 3.6 Hz, 1H), 1.63−1.49 (m, 1H), 1.32−1.24 (m, 1H). ^{13}C NMR ($CDCl_3$): δ = 177.5, 166.3, 137.5, 137.2, 130.6, 129.6, 118.3, 61.6, 43.4, 38.9, 36.0, 32.0, 31.6, 29.64, 29.60, 29.5, 29.4, 29.2, 28.5, 27.9, 27.6, 26.9, 26.0, 24.2, 22.8, 14.2. Elemental analysis calcd % for $C_{26}H_{32}O_4$ (550.69): C 69.79, H 7.69, N 5.09, O 17.43; found: C 69.79, H 7.78, N 5.06, O 18.06.

Scheme 1. Synthesis of Monomers 5, 8, and 10

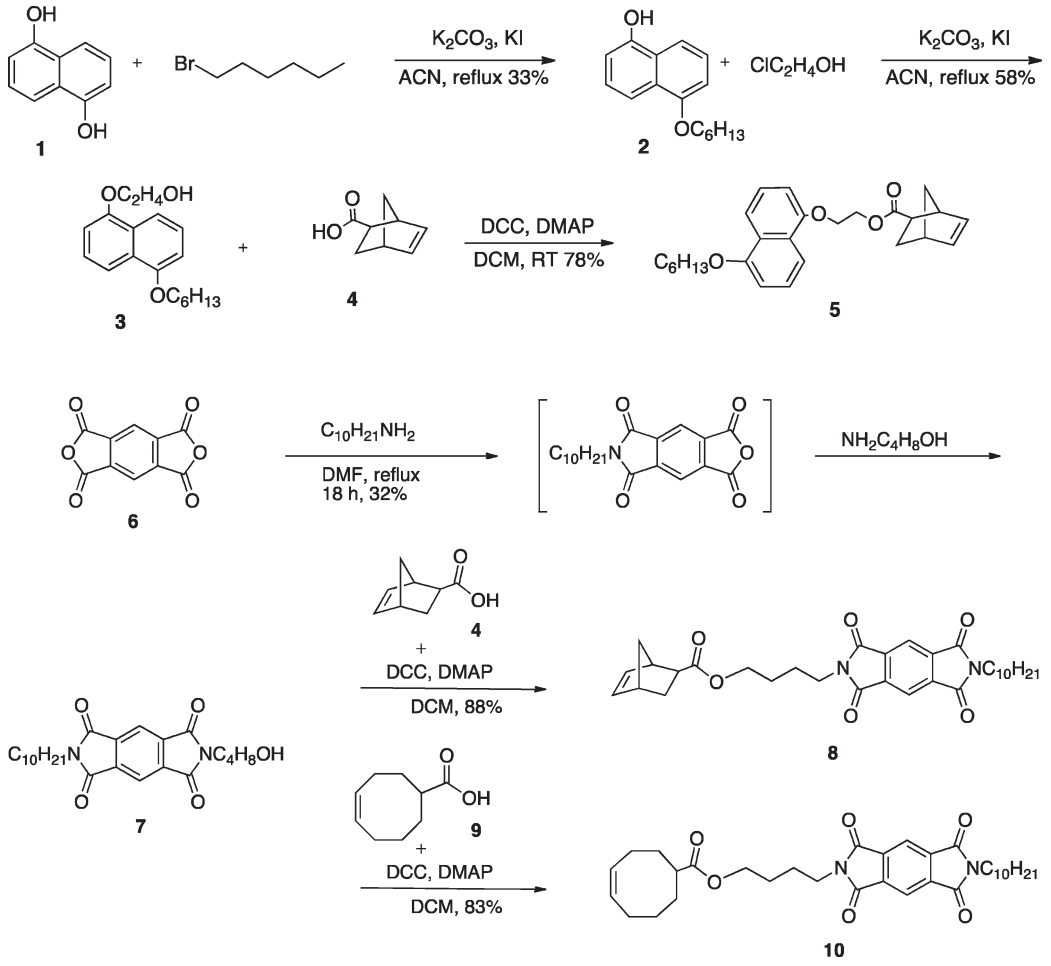

General Polymerization Procedure. The desired quantity of monomer(s) **5** and **8** (for $\mathbf{P_1}$ and $\mathbf{P_2}$) was dissolved in degassed chloroform under an argon atmosphere. A solution of Grubbs' first generation initiator in degassed chloroform was added and stirred at 25 °C. Upon completion of the polymerization, ethyl vinyl ether was added, and the reaction was stirred at 25 °C for 1 h. Each polymer was precipitated into MeOH three times and dried under high vacuum.

$\mathbf{P_3}$. Following the general procedure for $\mathbf{P_1}$, upon complete polymerization of the preceding monomer (as determined by ^{1}H NMR monitoring) the subsequent monomers were added at their appropriate times. After the complete polymerization of the final monomer, ethyl vinyl ether was added, and the reaction was stirred at 25 °C for 1 h.

$\mathbf{P_4}$. To a solution of **5** (10.4 mg, 0.025 mmol) and **10** (700.0 mg, 1.27 mmol) in anhydrous CH_2Cl_2 (2.0 mL) were added **11** (0.39 mg, 5.08 10^{-4} mmol) and (cat.) CuCl. The mixture was stirred at 25 °C for 10 min, and then the polymerization was quenched with addition of ethyl vinyl ether, allowed to stir at 25 °C for 1 h, and then precipitated in MeOH three times. The resulting polymer was further purified via size exclusion chromatography using 1:1 chloroform: methanol eluant.

RESULTS

Monomer Synthesis. Monomers **5**, **8**, and **10** were synthesized as outlined in Scheme 1. *exo*-Norbornene carboxylic acid **4** and cyclooctene carboxylic acid **9** were synthesized according to literature procedures.[32] The norbornene-based donor monomer **5** was synthesized via two Williamson ether syntheses on **1**, followed by standard DCC/DMAP coupling to **4**. The acceptor monomer side-chains were synthesized by a one-pot addition of two different amines to pyromellitic dianhydride **6**, followed by standard DCC/DMAP couplings to either **4** or **9** to complete the norbornene-based and cyclooctene-based acceptor monomers, respectively.

Living Polymerization Studies. For the synthesis of our target copolymers, we evaluated the living character of the ROMP of norbornene monomers **5** and **8**. Each monomer was subjected to ROMP using Grubbs' first-generation initiator at 25 °C in degassed chloroform. Initially, **5** and **8** were polymerized at various monomer to initiator ratios ([M]:[I] = 20:1, 40:1, 60:1, 80:1, 100:1). Gel-permeation chromatograms of each polymer ratio were taken (Figure 1), and the M_n vs [M]:[I] ratios were plotted. For both monomers, a linear relationship was obtained suggesting a high degree of control over the polymerization.

We also monitored the signal of the alkylidene of the ruthenium catalyst during the polymerizations by ^{1}H NMR spectroscopy. A complete shift from 19.9 ppm to 18.7 ppm was observed, and the signal remained constant during the duration of the polymerization. These data strongly indicate that the ruthenium complexes had fully initiated and that the resulting catalysts stayed active throughout the polymerization.

dx.doi.org/10.1021/ma201812x |*Macromolecules* 2012, 45, 70–77

Scheme 2. Illustration of Synthesized Polymers: Homopolymer P_1, Random Copolymer P_2, Block Copolymer P_3, and Alternating Copolymer P_4

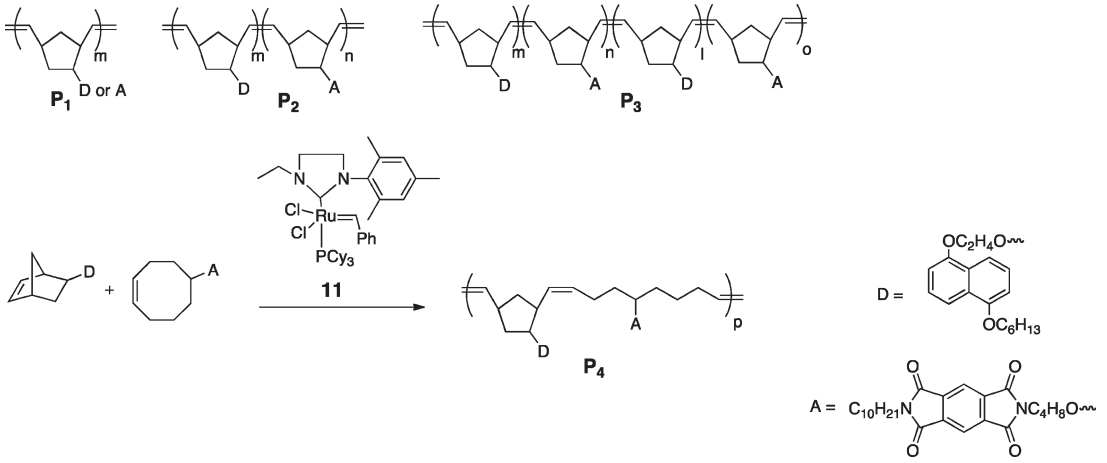

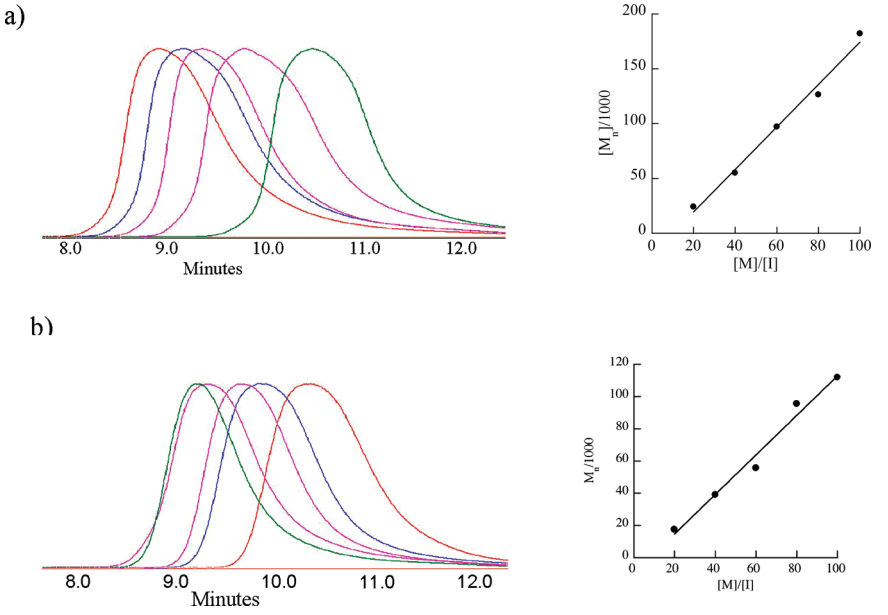

Figure 1. Living polymerization tests of **5** and **8**. a) GPC spectra of **5** using [M]:[I] ratios of 20:1, 40:1, 60:1, 80:1, 100:1; b) GPC spectra of **8** using [M]:[I] ratios of 20:1, 40:1, 60:1, 80:1, 100:1.

Lastly, homoblock copolymerization experiments were conducted on both monomers. Each monomer was first polymerized at a 20:1 [M]:[I] ratio. After complete consumption of the initial batch of monomers, additional monomers were added to the reaction mixtures to obtain 100mers. The gel-permeation chromatography (GPC) data show a complete shift of the lower molecular weight acceptor (M_n = 25 000; PDI = 1.30) and donor (M_n = 15 500; PDI = 1.34) homopolymers (20mers) to higher molecular weight [(M_n = 88 600; PDI = 1.16), (M_n = 144 000; PDI = 1.24); donor, acceptor respectively] homopolymers (100mers), without a trace of the lower molecular weight polymers (**S1c** and **S2c**, respectively). These combined studies prove that both norbornene monomers polymerize in a living fashion.

After demonstrating that monomers **5** and **8** are living, we synthesized a series of random, block, and alternating copolymers. All polymers were characterized using ^{1}H NMR and ^{13}C NMR spectroscopies and GPC. The GPC results are summarized in Table 1.

We initially investigated the random copolymerization of **5** and **8** that provides for the random dispersion of donor and acceptor side-chains along the polymer. The random copolymers were synthesized by combining **5** and **8** in a 1:1 ratio with Grubbs' first generation initiator. GPC data show a unimodal distribution of the random copolymers (M_n = 73 000; PDI = 1.24).

ABAB tetrablock copolymers were synthesized using similar conditions to the block homopolymerization tests in order to see whether or not the polymers would allow for intramolecular donor−acceptor interactions to induce order in the polymer arrangement. Figure 2 shows a kinetic experiment monitoring the ABAB tetrablock polymerization via ^{1}H NMR spectroscopy, in which the olefinic monomer and polymer signals were tracked. The olefin signals for **8** (bottom spectra, Figure 2 left) decrease

dx.doi.org/10.1021/ma201812x |*Macromolecules* 2012, 45, 70–77

over time. Following the complete disappearance of the olefin signal of **8** and an increase of the signals for the polymer backbone double bonds (Figure 2 right), **5** was introduced to the polymerization flask. Again, the signal for the olefinic hydrogens disappeared over time. This procedure was repeated two more times until a tetrablock of **8**:**5**:**8**:**5** was synthesized. After complete polymerization of the final monomer, the polymerization was quenched with ethyl vinyl ether.

Table 1. Gel-Permeation Chromatography and UV-Vis Spectroscopy Characterization of Polymers

	[M]:[I]	$M_n(10^3)$	PDI	CT band λ (nm)
poly-**5**	20	24.0	1.47	-
	40	55.0	1.54	-
	60	97.0	1.53	-
	80	126.5	1.60	-
	100	182.0	1.60	-
poly-**8**	20	17.5	1.59	-
	40	29.0	1.55	-
	60	55.6	1.48	-
	80	95.5	1.60	-
	100	112.0	1.50	-
poly-**8**, **5**, **8**, **5**	30−30−30−30	468.0	1.66	-
random	30−30	73.0	1.24	457[a], 445[b], 437[c]
alternating	10[d]	12.0[e]	1.09[e]	460[a]

[a] $CHCl_3$. [b] THF. [c] Toluene (3 mM). [d] This value reflects the percent of the alternation of the alternating copolymer ($\mathbf{P_4}$) (see Scheme 2) determined by ^{13}C NMR spectroscopy using an inverse-gate ^{1}H decoupling experiment [% alternation = $\int$ ($\mathbf{P_4}$ signals)/$\int$ ($\mathbf{P_4}$ signals + poly-**10** signals)] (see Figure S7 in the Supporting Information). [e] These values reflect the purified polymer sample. It is possible to have a mixture of the alternating copolymer containing a block of pure poly-**10** obtained after the alternation as well as poly-**10** homopolymer. We are not able to distinguish whether the observed signals arise from homopolymer poly-**10** or a block poly-**10** tail end of the alternating copolymer.

We were interested to see whether perfectly alternating copolymers would allow for superior interactions between donor and acceptor side-chains. In contrast to random copolymers where donor and acceptor side-chains are oriented in a random fashion, we rationalized that perfectly alternating copolymers might allow for superior prealignment of side-chains thereby maximizing donor−acceptor interactions.

To date, few investigations on alternating copolymerization via ROMP have been reported.[33,34] In 2006, Blechert and coworkers reported the synthesis of two different unsymmetrical N-heterocyclic amine ligands. These ligands were coordinated to Grubbs' first-generation initiator by replacing one of the phosphine ligands.[35] In 2008, the Blechert group, in collaboration with the Buchmeiser group, applied these complexes toward the alternating copolymerization between norbornene and cyclooctene.[30] They were able to obtain up to 97% alternation according to NMR spectroscopy and thermal gravimetric analysis. However, the polymerization also generated insoluble polymers, which were found to be poly(cyclooctene) homopolymer. The monomers in those investigations were unfunctionalized.

We synthesized the Blechert complex **11** and employed it toward the homopolymerization of **5** and **10**. The homopolymerizations of **5** and **10** using **11** follow comparable rates to the ROMP using Grubbs' first-generation initiator. We then attempted the alternating copolymerization using a ratio of 1:50 between **5** and **10**, following literature procedures.[30] Unfortunately, we were unable to obtain any alternating copolymers. We introduced CuCl as a phosphine scavenger to the reaction in order to enhance the activity of **11**. In the final material using our standard polymerization conditions plus the added phosphine scavenger, we observed two new signals in the ^{13}C NMR spectrum (132 ppm and 127 ppm) as seen in Figure 3, and no signal corresponding to the norbornene homopolymer suggesting that all norbornene monomers must have been incorporated into the polymer in an alternating fashion.

In order to attribute the new signals in the ^{13}C NMR spectra to alternating copolymers and to exclude the possibility of coordination of the copper chloride to the aromatic protons of

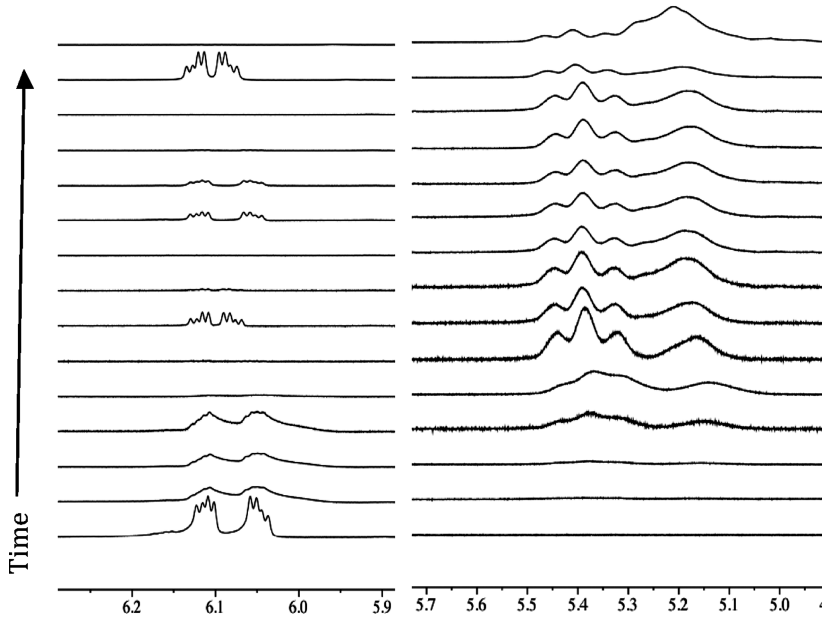

Figure 2. Partial ^{1}H NMR spectra of poly(**8**,**5**,**8**,**5**): Olefin region of the norbornene (left) and polymer (right) during the polymerization progress.

dx.doi.org/10.1021/ma201812x |*Macromolecules* 2012, 45, 70–77

the side-chains, we performed the homopolymerization of both monomers again using **11** with the addition of CuCl. The ^{13}C NMR signals at 132 ppm and 127 ppm were not present in either of the spectra. Next, we performed the alternating copolymerizations using a different phosphine scavenger, $AlCl_3$. Again, the new signals appeared. These data strongly suggest that we have achieved successfully a segment of alternating copolymers of two highly functionalized monomers.

UV−Vis Spectroscopy. After synthesizing random, block and alternating copolymers, we investigated whether or not the donor and acceptor side-chains interact through intrachain charge-transfer. This intrachain charge transfer could align the complementary units and force the polymers into secondary structures. As a control experiment, we prepared mixed monomer and polymer solutions (the following compounds were investigated: monomers **5** and **8**, a 1:1 mixture of **5**/**8**, and a 1:1 mixture of **poly-5**/**poly-8**) at different concentrations to observe whether or not charge-transfer bands were detectable in the UV−vis spectra.[21,22,36,37] All samples were absent of any charge-transfer signals within the reported spectral ranges as seen in Figure 4a, where all of the aforementioned solution traces remained at the baseline of the spectra. The absence of a charge-transfer band within all of the spectra is attributed to the low association constants reported for the Dan-pyromellitic dianhydride complex ($300 \leq K_a \leq 1200\ M^{-1}$ in $CHCl_3$)[37] and the entropic penalty for a stacked arrangement of side-chains from multiple monomers or polymers. Tetrablock copolymer poly-**8**,**5**,**8**,**5** was also tested at various concentrations (70 μM to 5 mM) and did not show any detectable charge-transfer signals.

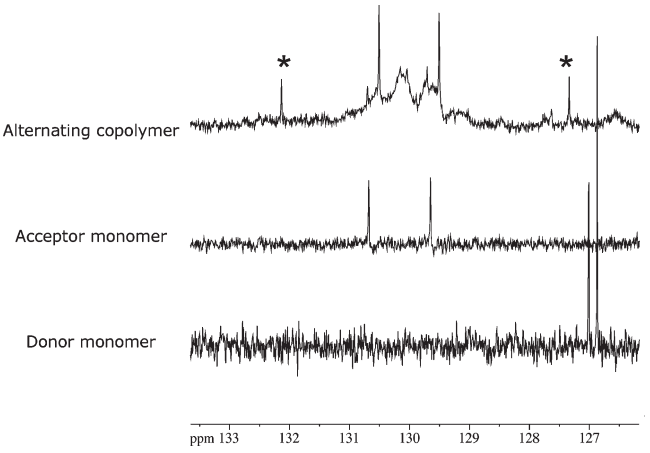

Figure 3. Partial ^{13}C NMR spectrum of **5**, **10**, poly-**5**, poly-**10**, and the alternating copolymer $\mathbf{P_4}$. Signals between 129 ppm and 131.5 ppm correspond to the polymer backbone signals of poly-**10**. The two sharp signals at 129.5 ppm and 131 ppm are from residual monomer **10**, which was not possible to be removed from the polymers despite multiple precipitations and size-exclusion column chromatography. The asterisk denotes the signals for the polymer signals of the alternating copolymer. All other unmarked signals correspond to monomer signals.

Next, we investigated the random copolymer systems by UV−vis spectroscopy. We expected an increase in the probability of complementary donor−acceptor side-chain interactions along the polymer chain due to the close proximity of the side-chains along a single polymer backbone. A new signal was detected at ~450 nm, within the range reported for the charge-transfer interaction of these moieties (Figure 4a).[21,22,36,37] In order to determine whether these interactions resulted from inter- versus intramolecular interactions, a concentration study was carried out varying the concentration from 70 μM to 5 mM. The signal was persistent and follows the expected Beer−Lambert behavior as shown in Figure 4b. This proved that the charge-transfer is occurring intramolecularly.

In order to evaluate whether a change of solvent can be utilized to effect the interactions between the donor−acceptor units in the random copolymer, i.e. whether a solvophobic effect can be detected, we attempted to dissolve it in an array of solvents of varying polarities. The copolymers were only soluble in chloroform, tetrahydrofuran, and toluene. Figure 5 shows the partial UV−vis spectra of the random copolymers in these three solvents.

We observed a shift in the charge-transfer band with the change in solvent polarity.[38] The polymer dissolved in the more polar solvent chloroform (Figure 5), exhibited the most red-shifted charge transfer band at ~460 nm, signifying a more favorable orientation of the aromatic units. The effect from toluene solution, however, is understood by looking at the monomeric region of the UV−vis spectrum (Supporting Information **S4**). There is clearly a significant red-shift of the monomer signals (from 200 to 400 nm). We attribute this result to the

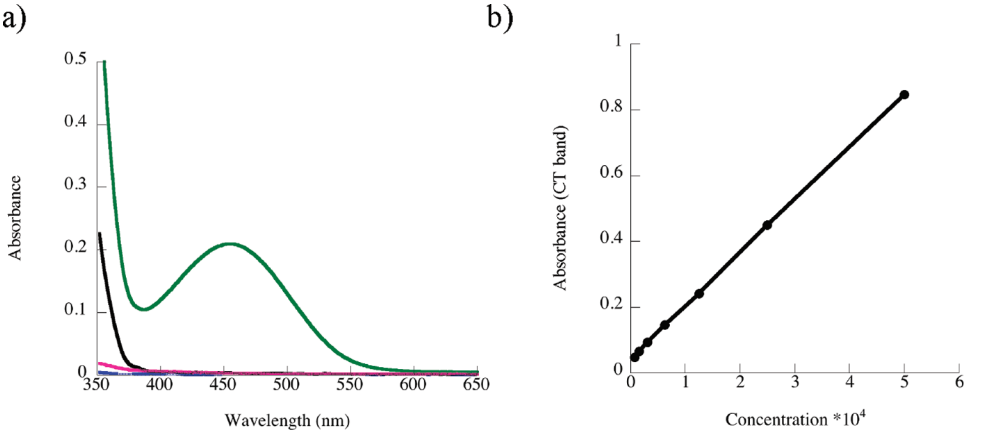

Figure 4. Partial UV−vis spectra of the charge-transfer region in chloroform (3 mM). a) Comparison of monomers, mixed monomers (1:1), mixed homopolymers (40mers; 1:1), random copolymer (40mer), and blocky copolymer (120mer). The green trace is the random copolymer spectrum. All other spectra remain at the baseline. b) Variation of charge-transfer absorbance against concentration of the random copolymer in chloroform.

dx.doi.org/10.1021/ma201812x |*Macromolecules* 2012, 45, 70–77

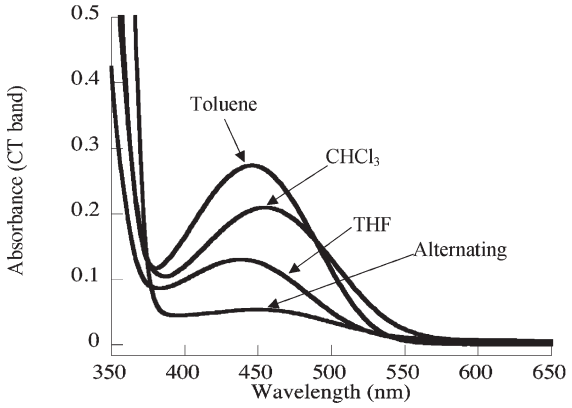

Figure 5. Partial UV−visible spectra of 3 mM random copolymer solutions in toluene, THF, and chloroform as well as a 3 mM solution of the alternating copolymers in $CHCl_3$.

conjugation between the aromatic units of the solvent and the monomer side-chains.[39]

Similar to the random copolymers, the alternating copolymer chloroform solution also shows a charge-transfer absorbance band in the reported spectral range. These results are further discussed in the Discussion section below.

DISCUSSION

Several polymers were synthesized with the desire to study the charge transfer interactions between the side-chain units of the polymers and were characterized by UV−vis spectroscopy. The low association constants reported for the Dan-pyromellitic dianhydride complex resulted in an absence of a charge-transfer band absorption in the UV−vis spectroscopy experiments of the combined 1:1 homopolymer solutions and the blocky copolymer solutions (Figure 4a). The random copolymer and alternating copolymer solutions, however, both exhibited a charge-transfer absorbance signal at ∼460 nm.

While the random copolymers in this study are composed of two norbornene-based monomers, the alternating copolymers were synthesized from the copolymerization of one norbornene-based monomer and one cyclooctene-based monomer. Varying the distance between interacting units of a charge-transfer pair can have a significant effect on the orbital alignment of the donor and acceptor charge-transfer interactions.[40] Looking at the fully norbornene-based polymers versus the norbornene-cyclooctene based alternating copolymer, there is a significant difference in the distance between the donor and acceptor units along the side-chains of the polymers. The side-chains along the poly(norbornene) are spaced between 3 and 4 carbons, whereas in the poly(norbornene-cyclooctene) system the side-chains are spaced apart by 5 to 6 carbons. During the polymerization of the functionalized norbornene monomers, each monomer can add either in a head-to-tail, head-to-head, or a tail-to-tail symmetry resulting in a lack of regiospecificity during the polymerization. This difference in spacing between the poly(norbornene) versus poly(cyclooctene) can significantly effect the alignment of the side-chain units and thus can directly influence the charge-transfer absorbance detectable by UV−vis spectroscopy as seen in Figure 5.[40,41] Furthermore, the 50 fold excess of cyclooctene monomer resulted in the formation of cyclooctene homopolymer and/or long poly(cyclooctene) runs in the copolymers as seen in the ^{13}C NMR spectra. We suggest that these combined structural features resulted in a lower charge transfer absorbance band for the alternating copolymers.

CONCLUSION

In summary, we have introduced a new versatile set of living donor−acceptor side-chain functionalized monomers that were used to generate a variety of homo- and copolymers including block copolymers, random copolymers, and alternating copolymers. Characterization of the polymers by UV−vis spectroscopy shows a charge-transfer absorption band for the random and alternating copolymers. We elucidated that intrachain and not interchain interactions between the donor and acceptor side-chain units are the reason for the charge-transfer band. The described alternating materials are the first to be synthesized from highly functionalized monomers via ROMP. This work is a step forward toward increased control over secondary structure for future functional materials.

ASSOCIATED CONTENT

Supporting Information. ^1H NMR spectra of monomers, monomer living test results, additional UV−vis spectra, and ^1H NMR titration data. This material is available free of charge via the Internet at http://pubs.acs.org.

AUTHOR INFORMATION

Corresponding Author
*E-mail: marcus.weck@nyu.edu.

ACKNOWLEDGMENT

Financial support has been provided by the National Science Foundation (ChE-0911460) and the Kramer Fellowship. This work was supported partially by the MRSEC Program of the National Science Foundation under Award Number DMR-0820341.

REFERENCES

(1) Hill, D. J.; Mio, M. J.; Prince, R. B.; Hughes, T. S.; Moore, J. S. *Chem. Rev.* **2001**, *101*, 3893–4011.
(2) Nelson, D. L.; Cox, M. M. *Principles of Biochemistry;* W. H. Freeman and Company: New York, 2005.
(3) (a) Palmans, A. R. A.; Meijer, E. W. *Angew. Chem., Int. Ed.* **2007**, *46*, 8948–8968. (b) Mes, T.; van der Weegen, R.; Palmans, A. R. A.; Meijer, E. W. *Angew. Chem., Int. Ed.* **2011**, *50*, 5085–5089.
(4) Cornelissen, J. J. L. M.; Rowan, A. E.; Nolte, R. J. M.; Sommerdijk, N. A. J. M. *Chem. Rev.* **2001**, *101*, 4039–4070.
(5) Stone, M. T.; Heemstra, J. M.; Moore, J. S. *Acc. Chem. Res.* **2005**, *39*, 11–20.
(6) Yashima, E.; Maeda, K.; Furusho, Y. *Acc. Chem. Res.* **2008**, *41*, 1166–1180.
(7) Smaldone, R. A.; Moore, J. S. *Chem.—Eur. J.* **2008**, *14*, 2650–2657.
(8) Hu, X.; Tong, Z.; Lyon, L. A. *Macromol. Rapid Commun.* **2011**, 1461–1466.
(9) Capadona, J. R.; Shanmuganathan, K.; Tyler, D. J.; Rowan, S. J.; Weder, C. *Science* **2008**, *319*, 1370–1374.
(10) Huitema, H. E. A.; Gelinck, G. H.; van der Putten, B; Kuijk, K. E.; Hart, M.; Cantatore, E.; Herwig, P. T.; van Breemen, A. J. J. M.; de Leeuw, D. M. *Nature* **2001**, *414*, 599.
(11) Arias, A. C.; MacKenzie, J. D.; McCulloch, I.; Rivnay, J.; Salleo, A. *Chem. Rev.* **2010**, *110*, 3–24.
(12) Gellman, S. H. *Acc. Chem. Res.* **1998**, *31*, 173–180.

(13) Juwarker, H.; Suk, J.-M.; Jeong, K.-S. *Chem. Soc. Rev.* **2009**, *38*, 3316–3325.
(14) Schwab, A. D.; Smith, D. E.; Bond-Watts, B.; Johnston, D. E.; Hone, J.; Johnson, A. T.; de Paula, J. C.; Smith, W. F. *Nano Lett.* **2004**, *4*, 1261–1265.
(15) Yamamoto, Y.; Fukushima, T.; Suna, Y.; Ishii, N.; Saeki, A.; Seki, S.; Tagawa, S.; Taniguchi, M.; Kawai, T.; Aida, T. *Science* **2006**, *314*, 1761–1764.
(16) Smaldone, R. A.; Moore, J. S. *J. Am. Chem. Soc.* **2007**, *129*, 5444–5450.
(17) Sinkeldam, R. W.; van Houtem, M.; Pieterse, K.; Vekemans, J.; Meijer, E. W. *Chem.—Eur. J.* **2006**, *12*, 6129–6137.
(18) Gillies, E. R.; Deiss, F.; Staedel, C.; Schmitter, J. M.; Huc, I. *Angew. Chem., Int. Ed.* **2007**, *46*, 4081–4084.
(19) Lokey, R. S.; Iverson, B. L. *Nature* **1995**, *375*, 303–305.
(20) Maeda, K.; Okada, S.; Yashima, E.; Okamoto, Y. *J. Polym. Sci., Part A: Polym. Chem.* **2001**, *39*, 3180–3189.
(21) Ghosh, S.; Ramakrishnan, S. *Angew. Chem., Int. Ed.* **2005**, *44*, 5441–5447.
(22) Ghosh, S.; Ramakrishnan, S. *Angew. Chem., Int. Ed.* **2004**, *43*, 3264–3268.
(23) (a) Colquhoun, H. M.; Zhu, Z. X. *Angew. Chem., Int. Ed.* **2004**, *43*, 5040–5045. (b) Colquhoun, H. M.; Zhu, Z. X.; Williams, D. J. *Org. Lett.* **2003**, *5*, 4353–4356.
(24) Burattini, S.; Greenland, B. W.; Merino, D. H.; Weng, W.; Seppala, J.; Colquhoun, H. M.; Hayes, W.; MacKay, M. E.; Hamley, I. W.; Rowan, S. J. *J. Am. Chem. Soc.* **2010**, *132*, 12051–12058.
(25) Claridge, T. D. W.; Long, D. D.; Hungerford, N. L.; Aplin, R. T.; Smith, M. D.; Marquess, D. G.; Fleet, G. W. J. *Tetrahedron Lett.* **1999**, *40*, 2199–2202.
(26) Reczek, J. J.; Iverson, B. L. *Macromolecules* **2006**, *39*, 5601–5603.
(27) Nguyen, J. Q.; Iverson, B. L. *J. Am. Chem. Soc.* **1999**, *121*, 2639–2640.
(28) Muller, H. M.; Seebach, D. *Angew. Chem., Int. Ed.* **1993**, *32*, 477–502.
(29) Gennari, C.; Salom, B.; Potenza, D.; Longari, C.; Fioravanzo, E.; Carugo, O.; Sardone, N. *Chem.—Eur. J.* **1996**, *2*, 644–655.
(30) Vehlow, K.; Wang, D.; Buchmeiser, M. R.; Blechert, S. *Angew. Chem., Int. Ed.* **2008**, *47*, 2615–2618.
(31) Lichtenheldt, M.; Wang, D. R.; Vehlow, K.; Reinhardt, I.; Kuhnel, C.; Decker, U.; Blechert, S.; Buchmeiser, M. R. *Chem.—Eur. J.* **2009**, *15*, 9451–9457.
(32) Manning, D. D.; Strong, L. E.; Hu, X.; Beck, P. J.; Kiessling, L. L. *Tetrahedron* **1997**, *53*, 11937–11952.
(33) Nakade, H.; Ilker, M. F.; Jordan, B. J.; Uzun, O.; LaPointe, N. L.; Coughlin, E. B.; Rotello, V. M. *Chem. Commun.* **2005**, 3271–3273.
(34) Bornand, M.; Chen, P. *Angew. Chem., Int. Ed.* **2005**, *44*, 7909–7911.
(35) Vehlow, K.; Maechling, S.; Blechert, S. *Organometallics* **2006**, *25*, 25–28.
(36) De, S.; Ramakrishnan, S. *Macromolecules* **2009**, *42*, 8599–8603.
(37) De, S.; Koley, D.; Ramakrishnan, S. *Macromolecules* **2010**, *43*, 3183–3192.
(38) Cubberley, M. S.; Iverson, B. L. *J. Am. Chem. Soc.* **2001**, *123*, 7560–7563.
(39) Kazakevich, Y.; Lobrutto, R. *HPLC for Pharmaceutical Scientists*; Wiley-Interscience: NJ, 2007; p 429.
(40) Closs, G. L.; Miller, J. R. *Science* **1988**, *240*, 440–447.
(41) Yonemoto, E. H.; Saupe, G. B.; Schmehl, R. H.; Hubig, S. M.; Riley, R. L.; Iverson, B. L.; Mallouk, T. E. *J. Am. Chem. Soc.* **1994**, *116*, 4795.

Macromolecules

Article

pubs.acs.org/Macromolecules

Copper-Mediated CRP of Methyl Acrylate in the Presence of Metallic Copper: Effect of Ligand Structure on Reaction Kinetics

Yaozhong Zhang,[†] Yu Wang,[†] Chi-how Peng,[†] Mingjiang Zhong,[†] Weipu Zhu,[†,‡] Dominik Konkolewicz,[†] and Krzysztof Matyjaszewski*[,†]

[†]Center for Macromolecular Engineering, Department of Chemistry, Carnegie Mellon University, 4400 Fifth Avenue, Pittsburgh, Pennsylvania 15213, United States

[‡]MOE Key Laboratory of Macromolecule Synthesis and Functionalization, Department of Polymer Science and Engineering, Zhejiang University, Hangzhou 310027, China

ABSTRACT: The kinetics of copper-mediated controlled/living radical polymerization (CRP) of methyl acrylate (MA) in the presence of Cu^0 and two different ligands that form active catalyst complexes with copper—TPMA (tris(2-pyridylmethyl)-amine) and Me_6TREN (tris(2-(dimethylamino)ethyl)amine)—are compared. The critical difference between the ligands is that TPMA forms a Cu^I complex that undergoes essentially no disproportionation in a mixture of MA and dimethyl sulfoxide (DMSO), DMSO/MA (v/v = 1/2), while the complex with Me_6TREN undergoes disproportionation to a limited extent. Parameters such as the surface area of Cu^0 wire, the concentration of added $Cu^{II}X_2/L$, and ligand concentration were examined. Both the Me_6TREN- and TPMA-based catalysts efficiently controlled the polymerization of MA. The TPMA-based system showed a power law order of 0.47 for the apparent propagation rate constant with the Cu^0 surface area, very similar to the reported value for the Me_6TREN-based system, which showed a power law of 0.44. These results demonstrate that the polymerization of MA in DMSO in the presence of metallic copper can be explained by a core atom-transfer radical polymerization (ATRP) process in which the Cu^0 acts as a supplemental activator and reducing agent, rather than through the proposed single-electron-transfer living radical polymerization (SET-LRP) mechanism, which requires additional assumptions, such as complete and instantaneous disproportionation of Cu^I/L species.

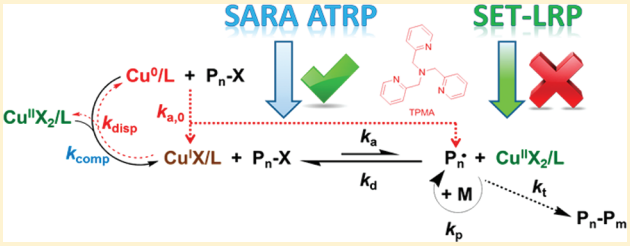

INTRODUCTION

Controlled/living radical polymerization (CRP) methods allow the synthesis of well-defined polymers with narrow distributions, predictable molecular weights, and complex architectures such as block copolymers, stars, and brushes.[1] Atom transfer radical polymerization (ATRP)[2] is one of the most widely used CRP techniques due to the range of architectures that can be synthesized using ATRP and its compatibility with various monomers and reaction conditions.[3] In ATRP radicals are formed by activation of an alkyl halide by a transition metal catalyst in a low oxidation state, typically Cu^I/L, and control is provided via rapid deactivation of the macroradical by the $X-Cu^{II}/L$ complex which is formed by the activation process. This process of activation/deactivation is shown in Scheme 1. In a well-controlled ATRP, the equilibrium is strongly shifted to the dormant alkyl halide by the $X-Cu^{II}/L$ complex or the "persistent radical". One limitation of normal ATRP is that a large amount of the Cu^I activator must be added to sustain an acceptable polymerization rate due to the buildup of Cu^{II} deactivator caused by termination reactions.[2c,4]

Recently, ATRP techniques were developed that reduce the amount of copper catalyst to ppm levels, while still allowing the reaction to occur in a reasonable time frame. A low copper concentration can be used by continuously regenerating the Cu^I/L species by reducing excess $X-Cu^{II}/L$ deactivator complex. This can be achieved by directly applying a reducing potential as is done in electrochemically mediated ATRP (*e*ATRP),[5] using a reducing agent as in activators regenerated by electron transfer (ARGET),[6] or by decomposition of free radical initiators as in initiators for continuous activator regeneration (ICAR) ATRP.[7] These reaction mechanisms are depicted in Scheme 2. Various organic reducing agents such as glucose, ascorbic acid, hydrazine, amines, or excess of ligands,[8] and inorganic reducing agents including tin^{II} 2-ethylhexanoate

Scheme 1. ATRP Equilibrium[a]

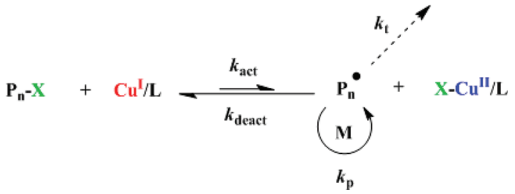

[a] P_n-X is an alkyl halide (macro)initiator, Cu^I/L is the activator complex, $P_n^\bullet$ is a (macro)radical and, $X-Cu^{II}/L$ is the deactivator complex.

Received: August 26, 2011
Revised: November 21, 2011
Published: December 12, 2011

Scheme 2. Mechanistic Description of ARGET ATRP and ICAR ATRP[a]

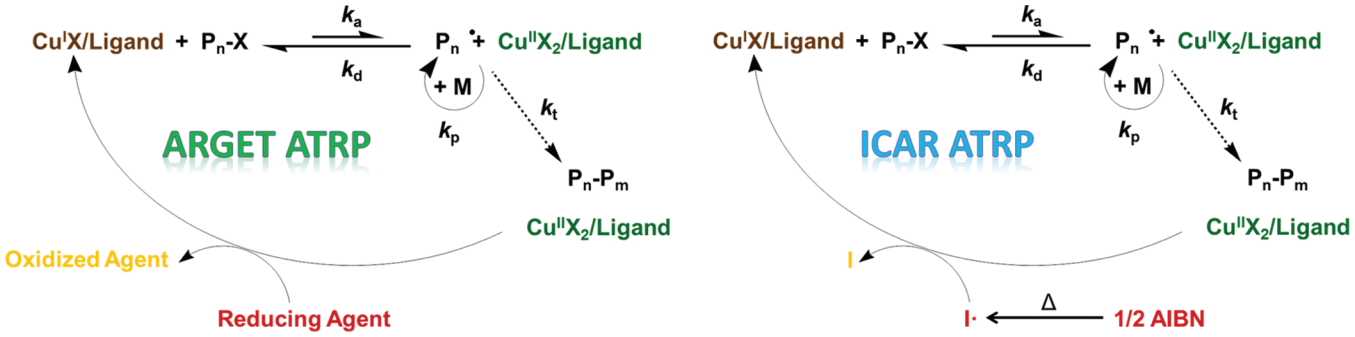

[a]The eATRP mechanism is essentially the same as the ARGET mechanism, except a cathodic current reduces the Cu^{II} species.

Scheme 3. Elementary Reactions for SARA ATRP and SET-LRP Mechanism[a]

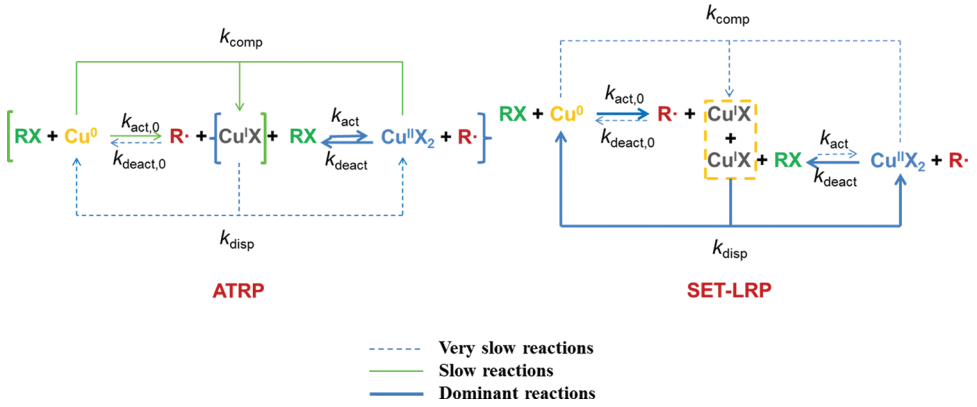

[a]The ligands, propagation, and termination steps are omitted for clarity.

$(Sn(EH)_2)$,[9] have been used in low copper ARGET ATRP systems.

Cu^0, which was first used in an ATRP in 1997,[10] has also been employed as a reducing agent. Initially, Cu^0 was used as the sole source of transition metal, where it acted as a supplemental activator in the presence of ligand to form the major activator, Cu^I/L. Cu^0 was also used to reduce a certain fraction of the added X−Cu^{II}/L complex to form a more active Cu^I/L activator in situ.[11] In this way, Cu^0 plays a dual role of both a supplemental activator and a reducing agent (SARA), leading to the concept of SARA ATRP. Various reaction conditions,[10,12] monomers,[13] and ligands[14] were used in SARA ATRP systems. Furthermore, other zerovalent metals including zinc, magnesium, and iron were used as in the SARA ATRP of methyl acrylate (MA) in dimethyl sulfoxide (DMSO), in addition to Cu^0.[15]

In 2006, Cu^0 was used in conjunction with tris(2-(dimethylamino)ethyl)amine (Me_6TREN) to polymerize MA in DMSO,[12a] leading to a controlled and relatively fast polymerization. Although all components, Cu^0, Me_6TREN, and polar solvents, had been used earlier in ATRP,[16] this particular system was named single-electron-transfer living radical polymerization (SET-LRP). Cu^0 was designated as the only activator in the proposed SET-LRP mechanism and X−Cu^{II}/L as the deactivator, with both the activator and deactivator being constantly regenerated by the instantaneous disproportionation of Cu^I/L. The key reactions in SARA ATRP and SET-LRP are illustrated schematically in Scheme 3.

This paper reports the kinetics of the copper-mediated CRP of MA with Cu^0 and (tris(2-pyridylmethyl)amine) (TPMA) ligand in DMSO and compares the kinetics of this specific polymerization with an equivalent system that uses Me_6TREN as the ligand. This study allows a direct comparison between the kinetics of a CRP conducted with a Me_6TREN-based complex, which can undergo a limited extent of disproportionation, with a catalyst based on TPMA which does not disproportionate to any significant extent.[17] The study will show that the kinetics and mechanism of an ATRP of MA with copper complexes formed with TPMA are essentially the same as those with Me_6TREN ligand. Therefore, the assumptions made in the SET-LRP mechanism, most notably the instantaneous disproportionation of Cu^I/L species, are neither necessary nor sufficient to explain the CRP of MA in DMSO in the presence of Cu^0. A more accurate mechanism for this polymerization is SARA ATRP.

EXPERIMENTAL SECTION

Materials. $CuBr_2$ (99+%, Aldrich) was used as received. Cu^0 (wire, diameter 1.0 mm, 99.9+%, Aldrich) was washed with MeOH/HCl first and then with fresh MeOH before use. Methyl 2-bromopropionate (MBP) (99.5+%, Aldrich), Me_6TREN, and TPMA (99%, ATRP Solutions) were used as received. Methyl acrylate (MA) (99+%, Aldrich) was passed over a basic alumina column to remove antioxidant.

Characterization. All spectroscopic measurements were performed on a Cary 5000 UV/vis/NIR spectrometer (Varian).

Molecular weight and molecular weight distribution were determined by GPC, conducted with a Waters 515 pump and a Waters 2414 differential refractometer using PSS columns (Styrogel 10^5, 10^3, 10^2 Å) in THF as an eluent at 35 °C and at a flow rate of 1 mL/min. Linear PSt standards were used for calibration. Conversions of MA were determined from the area of the DRI response versus those of known concentrations of polymers in THF.

dx.doi.org/10.1021/ma201963c | Macromolecules 2012, 45, 78−86

General Procedures for Comproportionation Experiments. In a typical experiment, a solution of 2.5 mM $Cu^{II}Br_2$ in DMSO with 5.25 mM Me_6TREN was prepared and bubbled with N_2 for 1 h. 4 cm Cu^0 wire was placed in a Schlenk flask with a stirring bar. The flask was closed with a stopper attached to a quartz cuvette (1 cm path length) and was then evacuated and backfilled with nitrogen several times. 4.5 mL of $Cu^{II}Br_2/Me_6$TREN solution was transferred to the Schlenk flask by gastight syringe. The reaction mixture was magnetically stirred in a water bath at 25 °C, and spectra were collected at specific time intervals. The decrease in concentration of $Cu^{II}Br_2/Me_6$TREN was monitored by following the absorption at 950 nm. Since absorption at 950 nm was relatively weak for some solvent/ligand combinations, in those cases, data were measured at the wavelength of their maximum absorbance.

Polymerization of MA in DMSO. In a typical experiment, a solution of MBP in DMSO ($[MBP]_0 = 0.037$ M) and MA was bubbled with N_2 for 1 h; 4 cm Cu^0 wire and 0.017 mmol (4.8 mg) of TPMA were placed in a Schlenk flask, which was then sealed and deoxygenated with N_2. 1.5 mL of the MBP/DMSO solution and 3 mL of MA were added to the Schlenk flask via deoxygenated syringes, and the reaction proceeded at 25 °C.

RESULTS AND DISCUSSION

Comparison of Comproportionation with TPMA and Me_6TREN Ligands. The comproportionation/disproportionation behavior is significantly different for copper complexes based on Me_6TREN and TPMA in DMSO. It would be interesting to study *N,N,N′,N″,N‴,N‴*-hexamethyltriethylenetetraamine (HMTETA), which is a significantly less active ligand, which also undergoes no disproportionation. However, this ligand could not be used for acrylate polymerizations under conditions that are comparable to Me_6TREN.[18] In order to quantify and investigate these differences between the complexes, comproportionation was chosen to avoid issues due to light scattering due to Cu^0 or oxidation of Cu^I.[12b] The comproportionation/disproportionation equilibrium, in the presence of an amount of ligand sufficient to complex all soluble copper species, can be written as

$$Cu^{II}Br_2/L + Cu^0 + L \overset{K^{L_{comp}}}{\rightleftharpoons} 2Cu^{I}Br/L \quad (1)$$

Although this scheme does not consider the detailed speciation of Cu^I and Cu^{II} complexes, it can still be used to compare the extent of comproportionation/disproportionation in the presence of different ligands.

When considering comproportionation or disproportionation of Cu^I, it is important to consider both the solvent and also the ligand(s), since both these factors strongly affect the position of the disproportionation equilibrium. Unfortunately, there are no data in the literature for the comproportionation or disproportionation equilibrium for Cu^I complexes with either Me_6TREN or TPMA in DMSO. However, several trends may be inferred from various literature data for either related complexes in DMSO or these complexes in other solvents. In pure solvent, with no added ligands, the solvent can drastically alter the disproportionation equilibrium constant (K_D) of the Cu^I complexes. For instance, in acetonitrile the log $K_D \approx -21$, while log $K_D \approx 0$ in pure DMSO and log $K_D \approx 6$ in water.[17,19] This however, is for the case where the Cu^I and Cu^{II} are accompanied by noncoordinating anions (BF_4^{2-}, ClO_4^-, etc.) and can only be coordinated by the solvent molecules. One important observation is that in pure DMSO with no added ligand Cu^IBr is quite stable (log $K_D \sim -6$[20] or -9[21]), which is in contrast to log $K_D \sim 0$ for the Cu^I with a noncoordinating anion (0.1 M NH_4ClO_4). This is due to the strong binding of the Br^- anions to Cu^I compared to Cu^{II} (log $K_{CuBr_2} = 4.3$ and log $K_{Cu^IBr_2} = 9.6$, respectively[20]).

Ligands such as Me_6TREN or TPMA have a similar effect on the disproportionation to the halogen anions outlined above. The degree of disproportionation depends on relative stability of Cu^I and Cu^{II} complexes in a manner identical to Br complexation. Although the solvent contributes to the degree of disproportionation, it is also important to consider the nature of the ligand itself. An excellent example of this seen in the comparison of disproportionation equilibrium constants for Cu^I in pure water, where log $K_D \approx 6$, whereas the disproportionation equilibrium constant for Cu^I/TPMA is 6.83×10^{-3} in water.[22] This shows that the equilibrium for the TPMA-based system is strongly shifted toward the comproportionation side, despite the fact the disproportionation is almost complete in the absence of TPMA. This highlights the importance of considering both the nature of the solvent and also the presence of the ligand to properly understand the disproportionation of Cu^I.

When considering the magnitude of the disproportionation equilibrium constant, it has been shown that this equilibrium constant is proportional to the ratio $\beta^{II}/(\beta^I)^2$, where β^I and β^{II} are the complexation constants of Cu^I and Cu^{II}.[17] In water, for TPMA $\beta^I = 7.94 \times 10^{12}$ and $\beta^{II} = 3.89 \times 10^{17}$,[23] while for Me_6TREN $\beta^I = 6.3 \times 10^8$ and $\beta^{II} = 2.69 \times 10^{15}$.[24] Therefore, the $\beta^{II}/(\beta^I)^2$ ratio is 6×10^{-9} for TPMA but a million times larger for Me_6TREN (i.e., 7×10^{-3}). Although there is no such data available for TPMA and Me_6TREN in DMSO, the extent of disproportionation of the TPMA-based complexes in DMSO is expected to be very small. This is due to the significantly lower polarity of DMSO compared to water, combined with the fact that the TPMA-based complexes already undergo only a limited extent of disproportionation in water.[25] The high stability of CuBr species in DMSO further highlights this fact.

In order to quantify the comproportionation/disproportionation beahavior, the evolution of concentration of Cu^{II} species was followed by UV−Vis for systems with TPMA and Me_6TREN ligands in three different solvents: acetonitrile (MeCN), DMSO, and DMSO/MA = 1/2 (v/v). In all cases the initial conditions were $[Cu^{II}Br_2]_0 = 2.5$ mM, $[ligand]_0 = 5.25$ mM, and 4 cm Cu^0 wire ($d = 1$ mm) in 4.5 mL solutions at 25 °C. Essentially complete comproportionation was observed (<1% of Cu^{II} species remained) in each reaction where the ligand TPMA was used and for Me_6TREN in acetonitrile. However, when the ligand Me_6TREN was used, 3% of Cu^{II} remained in DMSO/MA = 1/2 (v/v) solution and 20% of Cu^{II} remained in pure DMSO after 2 days. In pure MeCN, the rates of comproportionation were similar for both TPMA- and Me_6TREN-based complexes. Conversion was greater than 95% after 20 min and reached essentially ~100% within 30 min. In a DMSO/MA = 1/2 (v/v) solution, the comproportionation was faster with TPMA than with Me_6TREN, although both reactions were slower than in MeCN. The slowest reactions were in pure DMSO. When the ligand TPMA was used, the comproportionation reached ~90% in 30 min in DMSO/MA = 1/2 (v/v) and essentially 100% in 60 min, while in pure DMSO, comproportionation with TPMA reached 60% conversion after 30 min and greater than 97% after 60 min, as shown in Figure 1. Since these studies show that comproportionation is slow, the disproportionation must be even slower, rather than instantaneous, since the equilibrium lies strongly toward the comproportionation side.

One other interesting observation in Figure 1 is that the disproportionation is less favored in the DMSO/MA mixed

dx.doi.org/10.1021/ma201963c | *Macromolecules* 2012, 45, 78−86

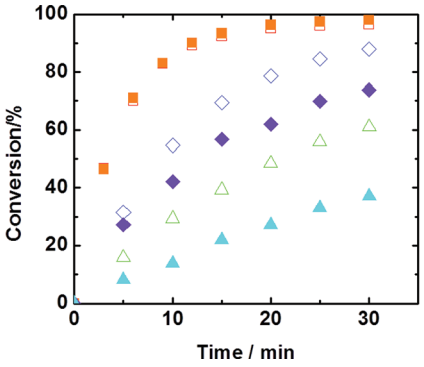

	Time / min	Conv.
TPMA/MeCN	60	~100%
Me_6TREN/MeCN	60	~100%
TPMA/DMSO/MA	60	>97%
Me_6TREN/DMSO/MA	1440	97%
TPMA/DMSO	1140	>97%
Me_6TREN/DMSO	2880	80%

Figure 1. Kinetics of comproportionation in different solvents with different ligands. $[Cu^{II}Br_2]_0$ = 2.5 mM; $[ligand]_0$ = 5.25 mM; 4 cm Cu^0 wire (d = 1 mm); in 4.5 mL solutions at 25 °C. When using DMSO/MA mixture as a solvent, the ratio was DMSO/MA = 1/2 (v/v).

solvent than the pure DMSO. This is because the presence of the monomer decreases the solvent polarity, shifting the equilibrium toward comproportionation. Therefore, the SET-LRP mechanism is less likely to occur under typical polymerization conditions than would be predicted based only the polarity of the solvent. For instance, considering the disproportionation experiments of Cu^I/Me_6TREN, which showed that a maximum of 20% of the Cu^I disproportionated in pure DMSO, the ratio of ligand and copper is above 1.[19] Therefore, in a real polymerization the extent of disproportionation is expected to be even lower due to the addition of monomer.

Comparison of Polymerizations Conducted under Typical Conditions with TPMA and Me_6TREN Ligands. TPMA and Me_6TREN ligands form very active catalyst complexes in ATRP, and there have been many reports of polymerizations carried out with both ligands in the literature.[12a,b,18b,26] One of the most important differences is that the catalyst complexes based on Me_6TREN and TPMA have different stability constants, which causes a difference in their comproportionation/disproportionation,[17] as highlighted earlier. In addition, mechanistic studies revealed that catalysts formed with Me_6TREN have larger values of K_{ATRP} and k_{act} than those formed with TPMA.[18b]

The SET-LRP mechanism was proposed to proceed through the instantaneous and complete disproportionation of Cu^I/Me_6TREN complex in DMSO/MA = 1/2 (v/v) solution, with exclusive activation of alkyl halides by Cu^0.[12a,19] The assumptions in the SET-LRP mechanism can be tested using TPMA-based catalysts, since these complexes essentially only undergo comproportionation and no significant disproportionation in DMSO/MA = 1/2 (v/v), as shown in the literature.[17] In this paper TPMA was used as a ligand in the CRP of MA to determine the effect of a nondisproportionating Cu^I complex on the polymerization kinetics of MA in DMSO solution.

A comparison between the polymerization of MA with catalyst complexes formed with Me_6TREN and TPMA under typical conditions is shown in Table 1. The initial molar ratios of reagents were $[MA]_0/[MBP]_0/[ligand]_0$ = 200/1/0.1, in 33.3% (v/v) DMSO ($[MA]_0$ = 7.4 M), and the reaction was conducted at 25 °C using Cu^0 wire (d = 1 mm, L = 4 cm) as the sole source of transition metal. The polymer conversions reached 89% and 79% after 70 and 90 min in the Me_6TREN and TPMA systems, respectively. The molecular weights of the poly(methyl acrylate) (PMA) agreed with theoretical values, and M_w/M_n values were around 1.3 (Figure 2b).

The Cu complexes with both Me_6TREN and TPMA ligands provided similar control over the polymerization of MA.

Table 1. ATRP of MA with Cu^0 and Either Me_6TREN or TPMA in DMSO[a]

ligand	time (min)	conv (%)	$M_{n,GPC}$	$M_{n,th}$	M_w/M_n
Me_6TREN	70	89	15 500	15 300	1.26
TPMA	90	79	13 700	13 500	1.31

[a] $[MA]_0/[MBP]_0/[ligand]_0$ = 200/1/0.1, in 33.3% (v/v) DMSO ($[MA]_0$ = 7.4 M), at 25 °C, with Cu^0 wire (d = 1 mm, L = 4 cm).

Figure 2a shows that the polymerization rates depend on the ligand used, with the apparent propagation rate constants $k_{p,1}^{app}$ = 0.0332 min^{-1} for the Me_6TREN system and $k_{p,2}^{app}$ = 0.0176 min^{-1} for the TPMA system. In a normal ATRP, the rate of polymerization increases with the ATRP equilibrium constant; therefore, the Me_6TREN catalyst complex with the higher K_{ATRP} should result in a faster polymerization than the TPMA catalyst complex which has a lower K_{ATRP}.[18b] The GPC data in Figure 2b–d for the polymerization of MA with Me_6TREN- and TPMA-based catalysts showed similar behavior. For both polymerizations, the GPC traces show high molecular weight shoulders in the early stage of the reactions, which arises from radical terminations due to the lack of Cu^{II} during the early phase of the reaction.

Influence of Surface of Cu^0 Wire on the Kinetics of Polymerization with TPMA Ligand. Several factors were reported to affect a copper-catalyzed polymerization of MA with Me_6TREN ligand.[27] They include the ligand concentration, addition of Cu^{II} deactivator, and surface area of Cu^0. The effect of the surface area of Cu^0 wire was first examined for the TPMA system to determine the similarities and differences between the polymerizations of MA in DMSO solution with TPMA- and Me_6TREN-based catalysts. The experimental conditions employed in the reactions using TPMA were matched to those used for Me_6TREN-based reactions.[27b]

As seen in Table 2 and Figure 3a, the polymerization of MA with different lengths of Cu^0 wire in the presence of TPMA ligand and DMSO solvent was faster with higher Cu^0 surface area. In all cases the initiation efficiency was high, and the molecular weights agreed well with the theoretical values, as shown in Figure 3b. The polymerizations also gave acceptable levels of control, since all polymers had values of $M_w/M_n \sim 1.3$ at high conversion.

The dependence of the apparent propagation rate constant (slopes in Figure 3a) on the Cu^0 surface area displayed a power-law dependence of 0.47 in the TPMA-based systems, as seen in Figure 3c. This value is very close to the value of 0.44 reported for the Me_6TREN-based systems.[27b] This shows that

dx.doi.org/10.1021/ma201963c | Macromolecules 2012, 45, 78–86

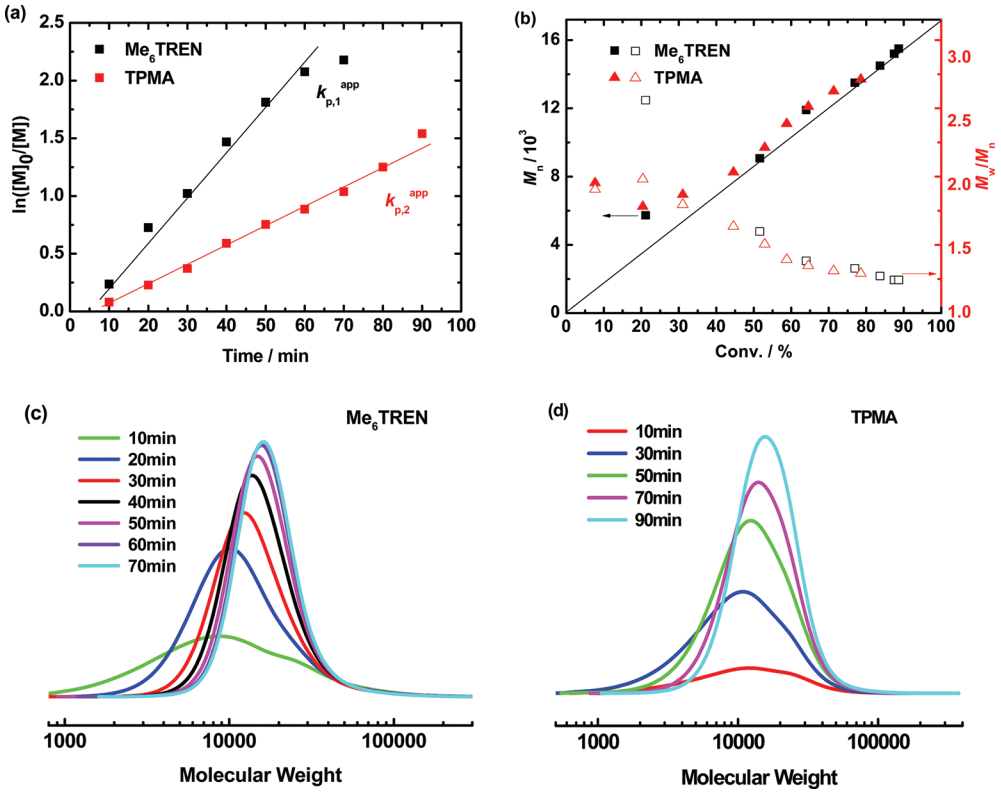

Figure 2. (a) Kinetic plot of $\ln([M]_0/[M])$ vs time. (b) Plot of M_n and M_w/M_n values vs conversion for ATRP of MA with ligand of Me_6TREN and TPMA. (c) GPC traces from ATRP with ligand of Me_6TREN. (d) GPC traces from ATRP with ligand of TPMA. $[MA]_0/[MBP]_0/[ligand]_0$ = 200/1/0.1, in 33.3% (v/v) DMSO ($[MA]_0$ = 7.4 M), at 25 °C, with Cu^0 wire (d = 1 mm, L = 4 cm).

Table 2. ATRP of MA with Different Lengths of Cu^0 wire with TPMA in DMSO[a]

Cu^0 wire length (cm)	surf. area (cm^2)	time (min)	conv (%)	$M_{n,GPC}$	$M_{n,th}$	M_w/M_n	k_p^{app} (min^{-1})
2	0.64	100	70	12 800	12 000	1.34	0.0125
4	1.26	90	79	13 700	13 500	1.31	0.0155
6	1.89	90	82	14 600	14 200	1.24	0.0185
12	3.78	70	85	13 600	14 600	1.35	0.0274
16	5.03	70	89	14 100	15 300	1.20	0.0326

[a] $[MA]_0/[MBP]_0/[TPMA]_0$ = 200/1/0.1, in 33.3% (v/v) DMSO ($[MA]_0$ = 7.4 M), at 25 °C, with Cu^0 wire (d = 1 mm).

the Cu^0 surface area has a similar effect on both TPMA and Me_6TREN catalysts and points toward a similar mechanism. This value, near 0.5 for kinetic plots with both ligands, can be explained in light of the supplemental activator and reducing agent roles of the Cu^0 in SARA ATRP. In SARA ATRP, the activity of the Cu^0 as a reducing agent and supplemental activator is defined by the surface area. In ARGET ATRP shown in Scheme 2, the apparent propagation rate has a square-root dependence on the concentration of the reducing agent.[28] Since the Cu^0 acts as a reducing agent in SARA ATRP, the square-root law in both catalysts can be rationalized in the same way. The other function of Cu^0 in the SARA ATRP system is that of a supplemental activator. There is no kinetic analysis published for a supplemental activator of alkyl halides, but it could be proposed that this slow supplemental activation is similar to the slow generation of radicals by decomposition of a conventional initiator in an ICAR ATRP (shown in Scheme 2).[29] In ICAR ATRP the rate of polymerization follows a 0.5 order with respect to the concentration of conventional initiator, since increased rate of initiator dissociation leads to a higher termination rates,[30] leading to the 0.5 order of reaction rate on conventional initiator concentration. By analogy, a high surface area of Cu^0 leads to a higher rate of generation and termination of radicals by supplemental activation and explains the 0.5 order of the supplemental activator component of SARA ATRP. Since both the supplemental activator and reducing agent roles of Cu^0 in SARA ATRP should follow a square-root dependence in the surface area, the overall dependence should also follow square-root law for both catalysts, as observed experimentally.

Influence of the $Cu^{II}Br_2$/TPMA Concentration on Polymerization Kinetics. The data in Table 3 and Figure 4a show the influence of the concentration of $Cu^{II}Br_2$/TPMA on the rate of polymerization. Varying the initial concentration of $Cu^{II}Br_2$/TPMA results in a small change of the polymerization rate (k_p^{app} values), as reported previously.[14] The degree of control over the polymerization improves with increases in the initial concentration of $Cu^{II}Br_2$/TPMA, since $M_w/M_n \sim 1.1$ value is observed for the systems with high concentrations of $CuBr_2$/L, compared to $M_w/M_n \sim 1.2$ for the systems with lower concentrations of $CuBr_2$/L. The polymers formed using the $Cu^{II}Br_2$/TPMA catalyst or the $Cu^{II}Br_2/Me_6$TREN catalyst are nearly the same, as shown in Table 3.[31] This again suggests that the fundamental polymerization mechanism is the same for both the TPMA- and Me_6TREN-based catalysts, despite the fact that the TPMA system does not undergo significant disproportionation. For both ligands, there is a slight decrease in reaction rate for polymerizations carried out at higher concentrations of Cu^{II}. According to the postulated mechanism for SET-LRP, the polymerization rate should become significantly slower at higher $[Cu^{II}Br_2/L]$, as there should be

dx.doi.org/10.1021/ma201963c | Macromolecules 2012, 45, 78–86

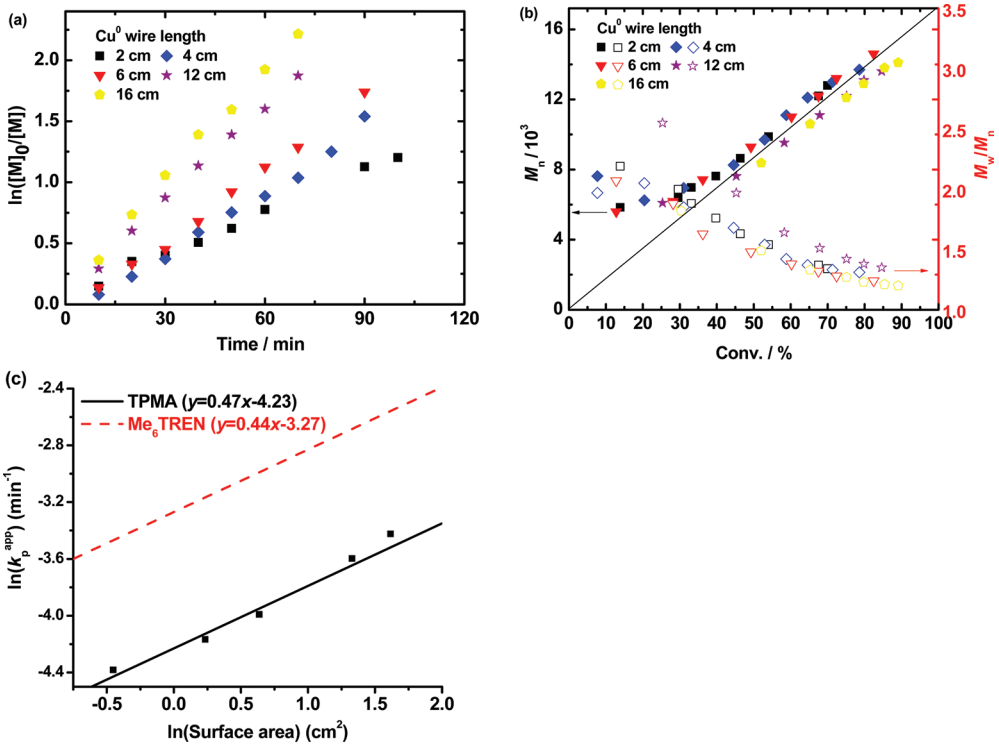

Figure 3. (a) Kinetic plot of $\ln([M]_0/[M])$ vs time. (b) Plot of M_n and M_w/M_n values vs conversion for ATRP of MA with ligand of TPMA. (c) Plot of linear relationship for $\ln(k_p^{app})$ vs ln(surface area) in ATRP with TPMA (black points and solid line) and Me_6TREN (red broken line based on data from Percec et al.[27b] (Reprinted with permission from ref 27b. Copyright 2009 American Chemical Society.) Conditions: $[MA]_0/[MBP]_0/[TPMA]_0$ = 200/1/0.1, in 33.3% (v/v) DMSO ($[MA]_0$ = 7.4 M), at 25 °C, with different lengths of Cu^0 wire (d = 1 mm).

Table 3. CRP of MA with Cu^0 and Different Concentrations of $CuBr_2$/Ligand

ligand	$[MA]_0/[MBP]_0/[Cu^0]_0/[ligand]_0/[CuBr_2]_0$	time (min)	conv (%)	$M_{n,GPC}$	$M_{n,th}$	M_w/M_n	k_p^{app} (min^{-1})
TPMA[a]	200/1/−/0.102/0.002	130	86	17 200	14 700	1.15	0.016
Me_6TREN[b]	222/1/0.1/0.105/0.005	53	89	16 600	15 300	1.21	0.042
TPMA	200/1/−/0.104/0.004	130	87	17 200	14 900	1.14	0.016
Me_6TREN	222/1/0.1/0.11/0.01	57	87	16 400	16 600	1.11	0.037
TPMA	200/1/−/0.12/0.02	130	81	15 300	14 000	1.08	0.014
Me_6TREN	222/1/0.1/0.12/0.02	80	84	16 600	14 500	1.18	0.033
TPMA	200/1/−/0.2/0.1	130	76	14 400	13 000	1.08	0.011

[a]In TPMA system, MA = 3.0 mL, DMSO = 1.5 mL, $[MA]_0$ = 7.4 M, at 25 °C, with Cu^0 wire (d = 1 mm, L = 4 cm). [b]In Me_6TREN system, MA = 1.0 mL, DMSO = 0.5 mL, $[MA]_0$ = 7.4 M, at 25 °C, with Cu^0 < 75 μm (Me_6TREN data was from Percec et al. from ref.[31] Reprinted with permission from Lligadas, G.; Percec, V., *J. Polym. Sci. Pol. Chem.* **2008**, 46, 6880−6895. Copyright 2008 John Wiley and Sons.).

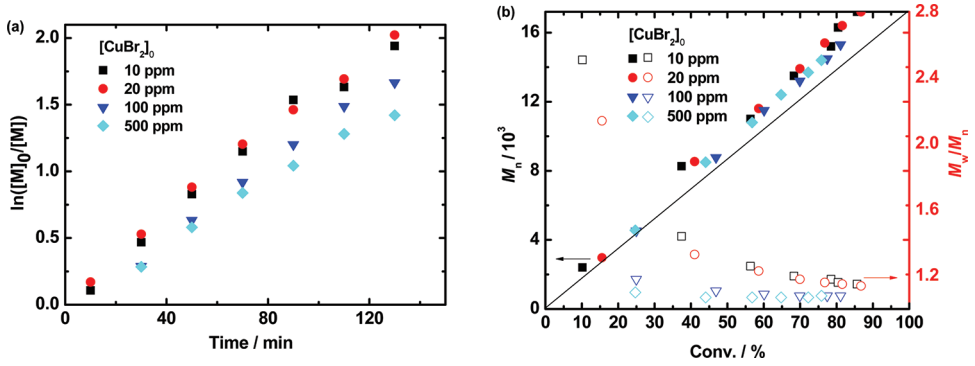

Figure 4. (a) Kinetic plot of $\ln([M]_0/[M])$ vs time and (b) plot of M_n and M_w/M_n values vs conversion for ATRP of MA with ligand of TPMA. $[MA]_0/[MBP]_0$ = 200/1, in 33.3% (v/v) DMSO ($[MA]_0$ = 7.4 M), at 25 °C. Cu^0 wire (d = 1 mm, L = 4 cm).

much more deactivator in the system and concentration of activator does not change. The concept of "internally controlled Cu^{II}" and "externally added Cu^{II}" was proposed to explain the phenomenon in SET-LRP.[27a] However, these concepts are not consistent from a reaction kinetics perspective, since the Cu^{II} species should behave the same way, regardless of whether the

dx.doi.org/10.1021/ma201963c | *Macromolecules* 2012, 45, 78−86

Table 4. CRP with Cu^0 with Different Concentrations of TPMA[a]

$[MA]_0/[MBP]_0/[TPMA]_0$	time (min)	conv (%)	$M_{n,GPC}$	$M_{n,th}$	M_w/M_n	k_p^{app} (min^{-1})
200/1/0.002	300	60	19 400	10 300	1.78	0.0029
200/1/0.005	210	78	13 800	13 500	1.37	0.0072
200/1/0.01	150	83	13 800	14 300	1.38	0.0126
200/1/0.02	110	73	13 800	12 600	1.36	0.0132
200/1/0.05	110	80	15 800	14 200	1.33	0.0143
200/1/0.1	90	79	13 700	13 800	1.33	0.0155
200/1/0.2	110	77	15 600	13 200	1.33	0.0131

[a] $[MA]_0/[MBP]_0$ = 200/1, in 33.3% (v/v) DMSO ($[MA]_0$ = 7.4 M), at 25 °C, with Cu^0 wire (d = 1 mm, L = 4 cm).

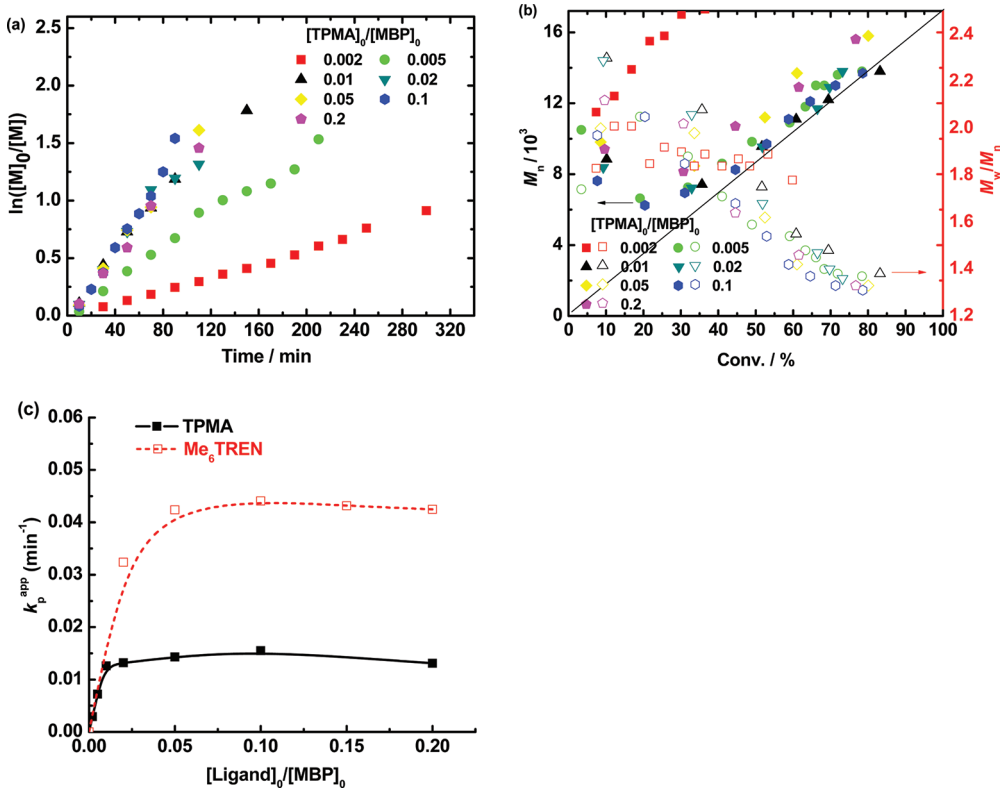

Figure 5. (a) Kinetic plot of $\ln([M]_0/[M])$ vs time. (b) Plot of M_n and M_w/M_n values vs conversion for ATRP of MA with ligand of TPMA. (c) Relationship for $[ligand]_0/[MBP]_0$ vs k_p^{app} for TPMA and Me_6TREN, for TPMA system (black points and solid line) MA = 3.0 mL, DMSO = 1.5 mL, $[MA]_0$ = 7.4 M, at 25 °C, with Cu^0 wire (d = 1 mm, L = 4 cm); for Me_6TREN system MA = 1.0 mL, DMSO = 0.5 mL, $[MA]_0$ = 7.4 M, at 25 °C, with 4.5 cm of 20 Gauge Cu^0 wire (red broken line based on data from Percec et al.[33] (Reprinted with permission from ref 33. Copyright 2009 John Wiley and Sons.)

Cu^{II} was added initially or whether the Cu^{II} was generated as part of the reaction.

SARA ATRP explains the slight decrease in reaction rate by accounting for the dual role of Cu^0 and reactions involving Cu^{II}. Since Cu^{II} is the deactivator complex, its higher concentration should lead to a decrease in reaction rate, through the normal ATRP equilibrium, following a power law of order −1.[2c] A significant decrease in polymerization rate with increasing Cu^{II} concentration would be expected if the only activator would be metallic copper. However, because Cu^0 also acts as a reducing agent, it decreases concentration of Cu^{II} and increases concentration of the major activator Cu^{I}. This resembles ARGET ATRP where the polymerization rate increases with the concentration of added Cu^{II}.[32] Therefore, in SARA ATRP there are two distinct processes that give different dependencies of the polymerization rate on the Cu^{II} concentration. The supplemental activator component is expected to decrease polymerization rate with increasing Cu^{II} concentration, while the reducing agent component is expected to increase polymerization rate with increasing Cu^{II} concentration. The overall reaction rate is a complex function incorporating both roles of Cu^0 and shows only a weak decrease in the polymerization rate with increasing Cu^{II} concentration.

Influence of TPMA Concentration on Polymerization Kinetics. The third parameter examined experimentally in this work was the effect of the concentration of TPMA ligand on polymerization of MA, as shown in Table 4 and Figure 5b. Above a certain minimal concentration of ligand, well-defined polymers with molecular weights agreeing with theoretical values and low M_w/M_n values (~1.3) were obtained. When the concentration of ligand was increased, the polymerization rate increased for low to intermediate ligand concentrations and reached a plateau at higher ligand concentrations, as shown in Figure 5a,c. This phenomenon can be explained by the relative affinities of the ligand to different copper species. The binding constant of amine-based ligands with Cu^{II} is much higher than

dx.doi.org/10.1021/ma201963c | Macromolecules 2012, 45, 78−86

with Cu^{I}.[25] Therefore, Cu^{II} species are preferentially formed when a limited amount of ligand is available, which leads to a slower polymerization rate, due to the deactivating function of Cu^{II}. However, above a certain minimal amount of ligand, there is sufficient ligand to stabilize both Cu^{I} and Cu^{II} species. Any further increase in ligand concentration should have a minimal effect on the $[Cu^{I}]/[Cu^{II}]$ ratio and, consequently, a small effect on the overall reaction rate. This can be seen by in the kinetics of the systems with $[TPMA]_0$:$[MBP]_0$ ratios of 0.05, 0.1, and 0.2, which shows essentially the same slopes in the semilogarithmic plots (Figure 5a). The Me_6TREN-based system requires a slightly higher concentration of ligand to reach the plateau than the TPMA system as shown in Figure 5c. This could be due to the fact that the relative stabilities of the Cu^{I} vs Cu^{II} complexes which are for TPMA ca. 100 times stronger than for the Me_6TREN.[17] Consequently, a smaller amount of ligand is needed to achieve a constant ratio of Cu^{I} activator to Cu^{II} deactivator. This difference is also reflected in the extent of disproportionation, as shown previously.

The kinetics of copper-mediated polymerization of MA with TPMA as ligand provides essentially the same results as those obtained with Me_6TREN. Since TPMA-based complexes do not undergo significant disproportionation, these results indicate that disproportionation of Cu^{I}/Me_6TREN in DMSO/MA does not influence the kinetics of the copper-mediated CRP significantly. These results and recent studies which refute the outer-sphere electron-transfer activation of alkyl halides[26i] suggest that the postulated SET-LRP mechanism is not needed to explain the body of experimental and theoretical data. Instead, these systems are best explained with Cu^{0} having a dual role: acting as a supplemental activator and a reducing agent, leading to the concept of SARA ATRP.

CONCLUSIONS

The kinetics of copper-mediated polymerization of MA, in the presence of Cu^{0} and a polar solvent DMSO, were studied to compare the behavior of complexes based on the ligands TPMA and Me_6TREN. The kinetic studies were used to probe the significance of disproportionation in copper-mediated CRP reactions, since the TPMA-based complexes do not undergo significant disproportionation in DMSO, while Me_6TREN can disproportionate to some extent. In general, the TPMA-based complexes led to good control over the molecular weight and the molecular weight distribution (M_w/M_n = 1.1−1.3) for the polymerization of MA. The kinetics of the polymerization, including the effect of Cu^{0} surface area, concentrations of $Cu^{II}Br_2$/Ligand, and initial ligand concentrations, were explained by the SARA ATRP mechanism in which the added Cu^{0} wire acts as a supplemental activator and a reducing agent. The TPMA-based systems showed similar trends to the polymerizations with Me_6TREN-based complexes which suggests that disproportionation is of minimal kinetic importance in the polymerization of MA, in the presence of Cu^{0} with DMSO as the solvent. These results indicate that SARA ATRP operates in the presence of Cu^{0} with both TPMA and Me_6TREN ligands rather than the postulated SET-LRP mechanism.

AUTHOR INFORMATION

Corresponding Author

*E-mail: km3b@andrew.cmu.edu.

ACKNOWLEDGMENTS

The authors thank Dr. Andrew J. D. Magenau and Dr. Kristin Schröder for helpful discussions and the National Science Foundation (CHE-10-26060) and the members of the CRP Consortium at Carnegie Mellon University for their financial support.

REFERENCES

(1) (a) Braunecker, W. A.; Matyjaszewski, K. *Prog. Polym. Sci.* **2007**, *32*, 93−146. (b) Goto, A.; Fukuda, T. *Prog. Polym. Sci.* **2004**, *29*, 329−385.

(2) (a) Wang, J. S.; Matyjaszewski, K. *J. Am. Chem. Soc.* **1995**, *117*, 5614−5615. (b) Kato, M.; Kamigaito, M.; Sawamoto, M.; Higashimura, T. *Macromolecules* **1995**, *28*, 1721−1723. (c) Matyjaszewski, K.; Xia, J. H. *Chem. Rev.* **2001**, *101*, 2921−2990. (d) Kamigaito, M.; Ando, T.; Sawamoto, M. *Chem. Rev.* **2001**, *101*, 3689−3745. (e) Matyjaszewski, K.; Tsarevsky, N. V. *Nature Chem.* **2009**, *1*, 276−288.

(3) (a) Lee, H.-i.; Pietrasik, J.; Sheiko, S. S.; Matyjaszewski, K. *Prog. Polym. Sci.* **2010**, *35*, 24−44. (b) Sheiko, S. S.; Sumerlin, B. S.; Matyjaszewski, K. *Prog. Polym. Sci.* **2008**, *33*, 759−785. (c) Gao, H.; Matyjaszewski, K. *Prog. Polym. Sci.* **2009**, *34*, 317−350. (d) Davis, K. A.; Matyjaszewski, K. *Adv. Polym. Sci.* **2002**, *159*, 1−166.

(4) Fischer, H. *Chem. Rev.* **2001**, *101*, 3581−3610.

(5) Magenau, A. J. D.; Strandwitz, N. C.; Gennaro, A.; Matyjaszewski, K. *Science* **2011**, *332*, 81−84.

(6) Jakubowski, W.; Matyjaszewski, K. *Angew. Chem., Int. Ed.* **2006**, *45*, 4482−4486.

(7) Matyjaszewski, K.; Jakubowski, W.; Min, K.; Tang, W.; Huang, J. Y.; Braunecker, W. A.; Tsarevsky, N. V. *Proc. Natl. Acad. Sci. U. S. A.* **2006**, *103*, 15309−15314.

(8) Kwak, Y.; Matyjaszewski, K. *Polym. Int.* **2009**, *58*, 242−247.

(9) Jakubowski, W.; Min, K.; Matyjaszewski, K. *Macromolecules* **2006**, *39*, 39−45.

(10) Matyjaszewski, K.; Coca, S.; Gaynor, S. G.; Wei, M. L.; Woodworth, B. E. *Macromolecules* **1997**, *30*, 7348−7350.

(11) Woodworth, B. E.; Metzner, Z.; Matyjaszewski, K. *Macromolecules* **1998**, *31*, 7999−8004.

(12) (a) Percec, V.; Guliashvili, T.; Ladislaw, J. S.; Wistrand, A.; Stjerndahl, A.; Sienkowska, M. J.; Monteiro, M. J.; Sahoo, S. *J. Am. Chem. Soc.* **2006**, *128*, 14156−14165. (b) Matyjaszewski, K.; Tsarevsky, N. V.; Braunecker, W. A.; Dong, H.; Huang, J.; Jakubowski, W.; Kwak, Y.; Nicolay, R.; Tang, W.; Yoon, J. A. *Macromolecules* **2007**, *40*, 7795−7806. (c) Hornby, B. D.; West, A. G.; Tom, J. C.; Waterson, C.; Harrisson, S.; Perrier, S. *Macromol. Rapid Commun.* **2010**, *31*, 1276−1280.

(13) (a) Magenau, A. J. D.; Kwak, Y.; Matyjaszewski, K. *Macromolecules* **2010**, *43*, 9682−9689. (b) Tom, J.; Hornby, B.; West, A.; Harrisson, S.; Perrier, S. *Polym. Chem.* **2010**, *1*, 420−422. (c) Chen, Q. F.; Zhang, Z. B.; Zhou, N. C.; Cheng, Z. P.; Tu, Y. F.; Zhu, X. L. *J. Polym. Sci., Polym. Chem.* **2011**, *49*, 1183−1189. (d) Gao, J.; Zhang, Z.; Zhou, N.; Cheng, Z.; Zhu, J.; Zhu, X. *Macromolecules* **2011**, *44*, 3227−3232.

(14) Kwak, Y.; Magenau, A. J. D.; Matyjaszewski, K. *Macromolecules* **2011**, *44*, 811−819.

(15) (a) Zhang, Y.; Wang, Y.; Matyjaszewski, K. *Macromolecules* **2011**, *44*, 683−685. (b) Mendonça, P. V.; Serra, A. C.; Coelho, J. F. J.; Popov, A. V.; Guliashvili, T. *Eur. Polym. J.* **2011**, *47*, 1460−1466.

(16) (a) Xia, J.; Gaynor, S. G.; Matyjaszewski, K. *Macromolecules* **1998**, *31*, 5958−5959. (b) Matyjaszewski, K.; Nakagawa, Y.; Jasieczek, C. B. *Macromolecules* **1998**, *31*, 1535−1541. (c) Matyjaszewski, K.; Coca, S.; Gaynor, S. G.; Wei, M.; Woodworth, B. E. *Macromolecules* **1997**, *30*, 7348−7350.

(17) Tsarevsky, N. V.; Braunecker, W. A.; Matyjaszewski, K. *J. Organomet. Chem.* **2007**, *692*, 3212−3222.

(18) (a) Bergenudd, H.; Jonsson, M.; Malmström, E. *Macromol. Theory Simul.* **2011**, *20*, 814−825. (b) Tang, W.; Kwak, Y.;

Braunecker, W.; Tsarevsky, N. V.; Coote, M. L.; Matyjaszewski, K. *J. Am. Chem. Soc.* **2008**, *130*, 10702−10713.
(19) Rosen, B. M.; Jiang, X.; Wilson, C. J.; Nguyen, N. H.; Monteiro, M. J.; Percec, V. *J. Polym. Sci., Part A: Polym. Chem.* **2009**, *47*, 5606−5628.
(20) Ahrland, S.; Blauenstein, P.; Tagesson, B.; Tuhtar, D. *Acta Chem. Scand., Ser. A* **1980**, *34*, 265−272.
(21) Foll, A.; Le Démezet, M.; Courtot-Coupez, J. *J. Electroanal. Chem.* **1972**, *35*, 41−54.
(22) Bortolamei, N.; Isse, A. A.; Magenau, A. J. D.; Gennaro, A.; Matyjaszewski, K. *Angew. Chem., Int. Ed.* **2011**, DOI: 10.1002/anie.201105317.
(23) Ambundo, E. A.; Deydier, M.-V.; Grall, A. J.; Aguera-Vega, N.; Dressel, L. T.; Cooper, T. H.; Heeg, M. J.; Ochrymowycz, L. A.; Rorabacher, D. B. *Inorg. Chem.* **1999**, *38*, 4233−4242.
(24) Golub, G.; Lashaz, A.; Cohen, H.; Paoletti, P.; Andrea, B.; Valtancoli, B.; Meyerstein, D. *Inorg. Chim. Acta* **1997**, *255*, 111−115.
(25) Bortolamei, N.; Isse, A. A.; Di Marco, V. B.; Gennaro, A.; Matyjaszewski, K. *Macromolecules* **2010**, *43*, 9257−9267.
(26) (a) Tang, H. D.; Shen, Y. Q.; Li, B. G.; Radosz, M. *Macromol. Rapid Commun.* **2008**, *29*, 1834−1838. (b) De Paoli, P.; Isse, A. A.; Bortolamei, N.; Gennaro, A. *Chem. Commun.* **2011**, *47*, 3580−3582. (c) Pintauer, T.; Matyjaszewski, K. *Coord. Chem. Rev.* **2005**, *249*, 1155−1184. (d) Weitzer, M.; Schindler, S.; Brehm, G.; Schneider, S.; Hormann, E.; Jung, B.; Kaderli, S.; Zuberbuhler, A. D. *Inorg. Chem.* **2003**, *42*, 1800−1806. (e) Eckenhoff, W. T.; Pintauer, T. *Inorg. Chem.* **2010**, *49*, 10617−10626. (f) Cohen, N. A.; Tillman, E. S.; Thakur, S.; Smith, J. R.; Eckenhoff, W. T.; Pintauer, T. *Macromol. Chem. Phys.* **2009**, *210*, 263−268. (g) Yamamura, Y.; Matyjaszewski, K. *J. Polym. Sci., Polym. Chem.* **2008**, *46*, 2015−2024. (h) Lin, C. Y.; Coote, M. L.; Gennaro, A.; Matyjaszewski, K. *J. Am. Chem. Soc.* **2008**, *130*, 12762−12774. (i) Isse, A. A.; Gennaro, A.; Lin, C. Y.; Hodgson, J. L.; Coote, M. L.; Guliashvili, T. *J. Am. Chem. Soc.* **2011**, *133*, 6254−6264.
(27) (a) Nguyen, N. H.; Rosen, B. M.; Percec, V. *J. Polym. Sci., Part A: Polym. Chem.* **2010**, *48*, 1752−1763. (b) Rosen, B. M.; Percec, V. *Chem. Rev.* **2009**, *109*, 5069−5119.
(28) Matyjaszewski, K.; Dong, H.; Jakubowski, W.; Pietrasik, J.; Kusumo, A. *Langmuir* **2007**, *23*, 4528−4531.
(29) West, A. G.; Hornby, B.; Tom, J.; Ladmiral, V.; Harrisson, S.; Perrier, S. *Macromolecules* **2011**, *44*, 8034−8041.
(30) Zhong, M. J.; Matyjaszewski, K. *Macromolecules* **2011**, *44*, 2668−2677.
(31) Lligadas, G.; Percec, V. *J. Polym. Sci., Polym. Chem.* **2008**, *46*, 6880−6895.
(32) Chan, N.; Cunningham, M. F.; Hutchinson, R. A. *Macromol. Chem. Phys.* **2008**, *209*, 1797−1805.
(33) Nguyen, N. H.; Jiang, X.; Fleischmann, S.; Rosen, B. M.; Percec, V. *J. Polym. Sci., Polym. Chem.* **2009**, *47*, 5629−5638.

Macromolecules

Article

pubs.acs.org/Macromolecules

In-Depth LCCC-(GELC)-SEC Characterization of ABA Block Copolymers Generated by a Mechanistic Switch from RAFT to ROP

Christina Schmid,[†] Steffen Weidner,[‡] Jana Falkenhagen,*[,‡] and Christopher Barner-Kowollik*[,†]

[†]Preparative Macromolecular Chemistry, Institut für Technische Chemie und Polymerchemie, Karlsruhe Institute of Technology (KIT), Engesserstr. 18, 76128 Karlsruhe, Germany

[‡]BAM, Federal Institute for Materials Research and Testing, Richard-Willstaetter-Strasse 11, 12489 Berlin, Germany

Supporting Information

ABSTRACT: A recently introduced procedure involving a mechanistic switch from reversible addition−fragmentation chain transfer (RAFT) polymerization to ring-opening polymerization (ROP) to form diblock copolymers is applied to synthesize ABA (star) block copolymers. The synthetic steps include the polymerization of styrene with R-group designed RAFT agents, the transformation of the thiocarbonyl thio end groups into OH functionalities, and their subsequent chain extension by ROP. The obtained linear ABA poly(ε-caprolactone)-*block*-poly(styrene)-*block*-poly(ε-caprolactone) (pCL-*b*-pS-*b*-pCL) (12 500 g mol^{-1} ≤ M_n ≤ 33 000 g mol^{-1}) and the star-shaped poly(styrene)-*block*-poly(ε-caprolactone) (M_n = 36 000 g mol^{-1}) copolymers were analyzed by size exclusion chromatography (SEC), nuclear magnetic resonance (NMR), infrared (IR) spectroscopy, and matrix-assisted laser desorption/ionization (MALDI) mass spectrometry. The focus of the current study is on the detailed characterization of the ABA (star) block polymers via multidimensional chromatographic techniques specifically high performance liquid chromatography coupled to size exclusion chromatography (HPLC-SEC). In particular, we demonstrate the first time separation of poly(ε-caprolactone) (pCL) homopolymer and additionally poly(styrene) (pS) from the ABA poly(ε-caprolactone)-*b*-poly(styrene)-*b*-poly(ε-caprolactone) and star-shaped poly(styrene)-*b*-poly(ε-caprolactone) block copolymer utilizing critical conditions (CC) for pCL with concomitant gradient elution liquid chromatography (GELC).

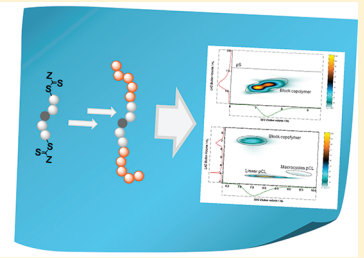

INTRODUCTION

The ability to generate tailor-made macromolecular architectures is of critical importance for the macroscopic properties of polymeric materials.[1] Controlled radical polymerization techniques (CRP) such as atom transfer radical polymerization (ATRP), reversible addition−fragmentation chain transfer (RAFT), or nitroxide-mediated polymerization (NMP) are established methods to prepare well-defined polymer architectures (e.g., topology and end-group functionality).[2] However, because of the specific application areas of block copolymers, e.g., in drug and gene delivery[3] as well as diagnostics,[4] it is advantageous to have the ability to switch from one polymerization technique to another, forming amphiphilic block copolymers synthesized via a RAFT ROP sequence.[5] One method to combine controlled radical polymerization (CRP) with ring-opening polymerization is by utilizing difunctional mediating agents such as the ATRP initiator β-hydroxylethyl α-bromoisobutyrate.[6] An alternative approach to block copolymer formation is via orthogonal modular ligation (click chemistry).[7] For such an approach two homopolymers synthesized via RAFT and ROP are equipped with specific end functionalities, which react via, e.g., [2 + 3] or [2 + 4] cycloadditions to connect the homopolymers, forming a block copolymer.[8] It is also feasible to obtain block copolymers by chain extension of a techelic RAFT generated polymer through the transformation of the thiocarbonyl thio moiety into a thiol by aminolysis.[9]

Previously, our group reported a facile method to alter the end-group functionality of RAFT generated polymers to obtain hydroxyl terminal macromolecules. The method was applied to different polymers and a variety of macroRAFT agents.[10] The advantage of the above strategy is the generation of sulfur-free narrowly dispersed polymers that are equipped with a versatile synthetic handle. The transformation of the trithiocarbonate or the thiocarbonyl thio end group of the polymer chain into a hydroxyl function is achieved by a radical mechanism under ambient conditions involving 2,2′-azobis(isobutyronitrile) (AIBN) in a tetrahydrofuran (THF) solution. We have successfully demonstrated that the OH functional polymer can subsequently be employed as a macroinitiator for ROP.[11] A general reaction scheme for the synthesis of the sulfur-free diblock copolymers via a RAFT ROP sequence is visualized in Scheme 1.

In the current study we follow two aims: First, the above-named end group conversion is applied to obtain more complex and demanding polymer architectures such as ABA block copolymers and star block copolymers. Such an approach is possible by employing multifunctional RAFT agents for the preparation of ω-functional entities, which can be transformed into multifunctional terminal alcohols. For the formation of star

Received: October 6, 2011
Revised: December 6, 2011
Published: December 20, 2011

Scheme 1. General Reaction Scheme of the Modification Technique Enabling a Mechanistic Switch from RAFT Polymerization to ROP

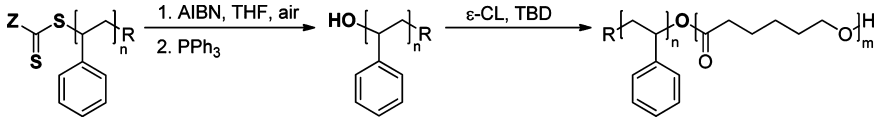

polymers via the RAFT process two approaches can generally be applied, i.e., the Z- and R-approach. For the Z-approach the thiocarbonyl thio groups are connected to the core via the Z-group, while in the R-approach the thio entity is connected to the core via the R-group. Consequently, the thiocarbonyl thio groups of the synthesized polymers are either directly attached to the core (Z-approach) of the star or to the chain end (R-approach) of the polymer chains.[12] Transforming the thiocarbonyl thio groups into hydroxyl functions of star polymers synthesized via the Z-approach would lead to a destruction of the star (and to linear chains) and not to the desired star macroinitiators. For this reason, the R-approach is utilized for the RAFT polymerization in the current study. By transformation of the dithioester groups, multifunctional polymers with OH groups at the chain end are obtained. The ω-hydroxylated star polymers were subsequently employed as macroinitiators for the ring-opening polymerization of ε-caprolactone catalyzed by (1,5,7-triazabicyclo[4.4.0]dec-5-ene (TBD)) (see also Scheme 1).

The resulting copolymers are characterized via spectroscopic, spectrometric, and chromatographic methods. In general, block copolymers and higher architectures are analyzed via SEC, ^{1}H NMR, and—if appropriate—mass spectrometry.[13] Via SEC, the average molecular masses and the polydispersity are determined, but no compositional (chemical) information may be obtained when classical RI detection is employed. NMR spectroscopy yields information on the chemical composition and functional groups; however, topological information on the generated macromolecules is difficult to ascertain. Mass spectrometry is problematic for samples with broad or multiple distributions and high molecular masses.

Thus, the second—and most important goal—of the present study aims at employing hyphenated chromatographic techniques to elucidate the polymer structure, specifically aiming at identifying conditions under which poly(ε-caprolactone) (pCL) can be separated from true (star) block copolymer structures. In the first dimension liquid adsorption chromatography (LAC) is performed. Conventional liquid adsorption chromatography separates samples according to their chemical heterogeneity and molecular mass; however, a special mode can be applied to the system which enables separation of the samples only by chemical heterogeneity irrespective of molecular mass. The special method—liquid chromatography at critical conditions (LCCC) or alternatively named LC at the exclusion adsorption point—was established by Belenky et al.[14] and Entelis et al.[15] Pasch and colleagues have published a detailed description of the theory as well as the experimental approaches of the critical conditions mode.[16] The critical behavior of a polymer depends on a variety of conditions—the mobile phase composition, the temperature, the pressure, and the stationary phase.[17] Commonly, the critical conditions of a polymer are adjusted by varying the composition of a mixture of two solvents. Combining LCCC and SEC to two-dimensional chromatography yields information about the chemical composition in the first dimension and additionally the molecular masses of the separated compounds in the second dimension. One example exemplifying the power of the LCCC method is the ability to separate homopolymers from block copolymers as performed in the current study; yet a wide variety of examples exist.[18]

In our recent publication the critical conditions of poly(styrene) (pS) have been applied on a LAC system to separate poly(styrene) homopolymer from the AB block copolymers of the type poly(styrene)-*b*-poly(ε-caprolactone).[11] The previously reported method will also be used in the current contribution to investigate ABA (star) block copolymers.

Additionally—and most importantly—a new method is introduced to separate (potential) residual poly(ε-caprolactone) (pCL) homopolymer from the generated block copolymer structures. The liquid adsorption chromatography is performed under critical conditions of poly(ε-caprolactone). However, under the critical conditions of pCL the interactions between the stationary phase and the ABA (star) block copolymers are strong and thus the retention is too high, leading to permanent adsorption of the polymers on the column.[19] For this reason, the CC of pCL are combined with a solvent gradient, i.e., leading to an LCCC-gradient elution liquid chromatography (GELC) system. Via such an approach the separation of pCL homopolymer, block copolymers, and even the separation of pS homopolymer is feasible, as will be described below.

It is alternatively possible to hyphenate HPLC with further characterization systems such as, e.g., ESI mass spectrometry.[20] In the current study fractions eluting off an HPLC system are collected and characterized with IR spectroscopy. Additional structural information is provided by MALDI-TOF mass spectrometry. For this purpose a newly designed electrospray deposition interface was used to fractionate and deposit samples onto MALDI targets.

Thus, in summary, we report the extensive characterization of ABA (star) sulfur-free block copolymers synthesized via a recently introduced RAFT/ROP technique, utilizing advanced multidimensional characterization techniques (see Scheme 2).

EXPERIMENTAL SECTION

Materials. Styrene (99% extra pure, stabilized, Acros Organics) was purified by percolating through a column of basic alumina prior to use. The 4-arm (non-rate-retardant) RAFT agent 1,2,4,5-tetrakis(phenylthioacetylthiomethyl)benzene (see Scheme 3, **2**) was synthesized according to a literature procedure[21] with its purity being confirmed by ^{1}H NMR spectroscopy. 2,2′-Azobis(isobutyronitrile) (98%, Sigma-Aldrich) was recrystallized twice from ethanol prior to use. ε-Caprolactone was distilled from CaH_2 and kept over molecular sieves. 1,5,7-Triazabicyclo[4.4.0]dec-5-ene (TBD, Sigma-Aldrich), toluene (extra dry, water <30 ppm, Acros Organics), triphenylphosphine (PPh_3, Merck), glacial acetic acid (Rotipuran, 100% p.a., Roth), benzoic acid (99,5%, Sigma-Aldrich), hydrochloric acid (37%, Roth), *trans,trans*-2,4-hexadien-ol (99%, stabilized Acros Organics), trifluoroacetic acid (HPLC grade, Fisher Scientific), sodium iodide (puriss. p.a., Fluka), tetrahydrofuran (multisolvent, 250 ppm BHT, Scharlau), carbon disulfide (Aldrich), benzyl chloride (Alfa Aesar), α,α'-dibromo-*p*-xylene

dx.doi.org/10.1021/ma2022452 | *Macromolecules* 2012, 45, 87−99

Scheme 2. Synthetic Concept To Obtain ABA (Star) Block Copolymers via RAFT/ROP and a Summary of the Utilized Characterization Techniques[a]

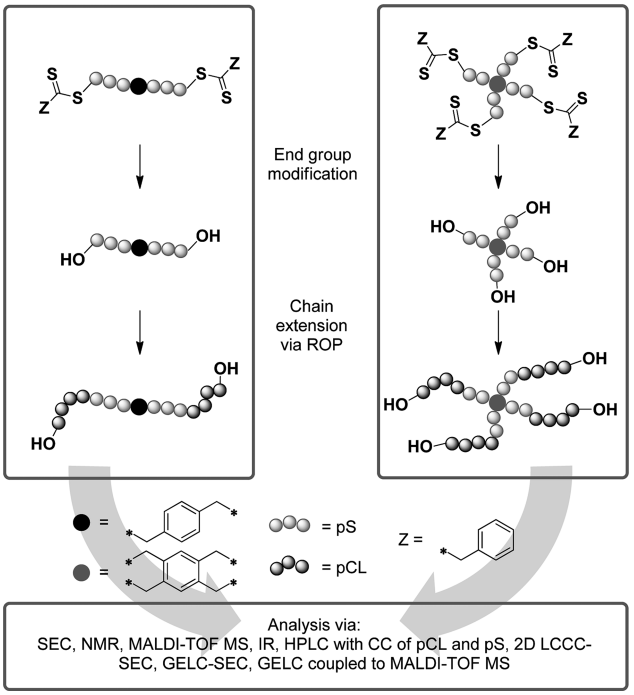

[a]Note that the depicted four-armed star block copolymer represents the target structure only. The experimentally determined number of arms is—for variable reasons—less than four (for details see text).

(Aldrich), 2-butanol (Fluka), and methanol (Chromasolv, Sigma-Aldrich) were used as received.

Synthesis of 1,4-Dis(phenylthioacetylthiomethyl)benzene (2-Armed RAFT Agent), 2. To a Grignard solution of 1.94 g of magnesium metal in 10 mL of diethyl ether, 9.21 mL of benzyl chloride in 30 mL of diethyl ether was added slowly under a nitrogen gas stream. After refluxing the solution for 1 h, the reaction mixture was cooled with ice. The subsequent addition of 4.82 mL of carbon disulfide in 20 mL of diethyl ether was performed at 0 °C, and the reaction mixture was stirred for an additional hour. The mixture was poured into ice-cold water; the aqueous phase was washed two times with diethyl ether and acidified with HCl. The compound was extracted with diethyl ether, and the solvent was removed under reduced pressure. 1.00 g of potassium hydroxide was dissolved in 1 mL of water and mixed with the obtained compound. After drying the mixture under reduced pressure, it was dissolved in 20 mL of dry tetrahydrofuran, and 2.15 g of α,α'-dibromo-*p*-xylene was added. The reaction mixture was refluxed for 1 h. Subsequently, water was added, and the product was extracted twice with toluene. The product 1,4-dis(phenylthioacetylthiomethyl)benzene was obtained after evaporating the solvent and recrystallization from ethanol/chloroform (1/1). ^{1}H NMR (250 MHz, $CDCl_3$): δ [ppm] = 4.25 (s, 4H, CH_2−S), 4.3 (s, 4H, CH_2−CS), 7.15 (s, 4H, Ar−H), 7.15−7.30 (m, 10H, Ar−H).

Preparation of the 2- and 4-Armed Thiocarbonyl Thio Terminal Polystyrenes 3 and 4. A solution of RAFT agent (**1**, **2**) and 2,2′-azobis(isobutyronitrile) in 100 mL of styrene was freed from oxygen by purging with nitrogen for 20 min. The solution was heated to 60 °C for 180 min. The reaction was stopped by cooling with liquid nitrogen, and the polymer was precipitated in cold methanol. The average molecular mass and the polydispersity were determined via SEC, and the corresponding ESI mass spectra combined with the corresponding isotopic pattern simulation can be found in the Supporting Information (Figure S1). The amount of the reacting reagents and the resulting average molecular masses of the poly(styrene) samples are collated in Table 1.

Table 1. Reaction Conditions of the Polymerization with 2-Armed Linear and 4-Armed Star RAFT Agents 1 and 2[a]

structure	RAFT agent	c^0_{RAFT} (mmol L^{-1})	c^0_{AIBN} (mmol L^{-1})	M_n (g mol^{-1})	PDI
3	**1** (2-armed)	10.4	0.06	3400	1.3
4	**2** (4-armed)	5.3	0.15	4200	1.1

[a]c^0_{RAFT} and c^0_{AIBN} are the initial concentrations of the RAFT agent and AIBN, respectively. The molecular structures associated with the listed compounds can be found in Scheme 3.

End-Group Switching (Synthesis of Species 5 and 6).[10] A solution of 2,2′-azobis(isobutyronitrile) (50 mmol L^{-1}) in THF was heated to 60 °C for 120 min under ambient air. 500 mg of RAFT-polymer (**3**, **4**) (10 mmol L^{-1} based on its M_n) was dissolved in the pretreated THF/AIBN solution. The solution was heated subsequently to 60 °C under vigorous stirring. After 40 min, the temperature was reduced to 40 °C, and 3 equiv of triphenylphosphine was added. After 20 min the solution was concentrated under reduced pressure with subsequent precipitation of the polymer in cold

Scheme 3. Overview of the Target Structures Prepared in the Current Contribution: (a) Linear and (b) Star Structures

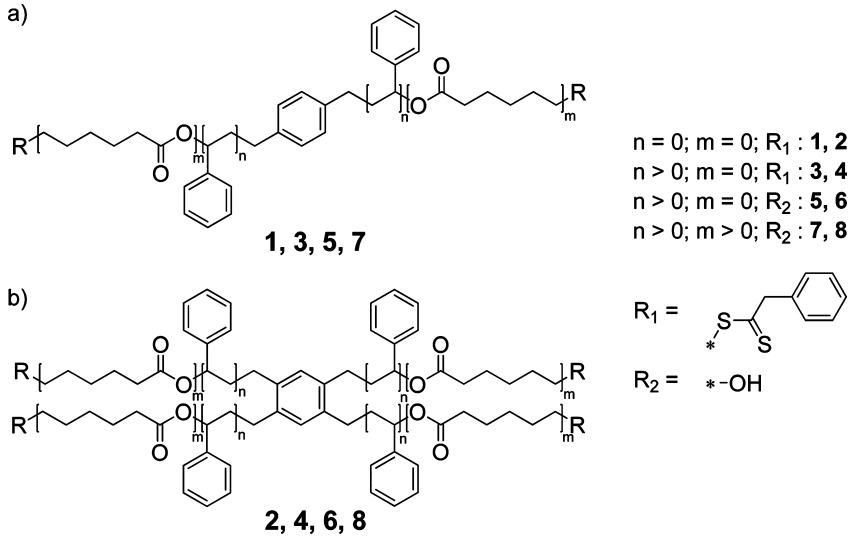

dx.doi.org/10.1021/ma2022452 | *Macromolecules* 2012, 45, 87−99

methanol. The resulting average molecular masses and the PDIs are collated in Table 2. The SEC traces and a typical MALDI-TOF spectrum of **5** can be found in Figure S2 of the Supporting Information.

Table 2. Number-Average Molecular Mass, M_n, and Polydispersity Index, PDI, of the Poly(styrene) Samples after Transformation of the End Group[a]

structure	RAFT polymer	M_n (g mol^{-1})	PDI
5	**3** (2-armed)	3900	1.2
6	**4** (4-armed)	4400	1.1

[a]The molecular structures associated with the listed compounds can be found in Scheme 3.

Ring-Opening Polymerization (Synthesis of Species 7 and 8). The ring-opening polymerization was performed in an inert gas atmosphere (argon) inside a glovebox to rigorously exclude water from the reaction system. ε-CL was added to a solution of TBD and the poly(styrene) macroinitiator in 2 mL of toluene. The solution was stirred for 5 h and subsequently quenched by addition of benzoic acid. The polymer was precipitated in cold methanol. The concentrations of the reacting agents and the resulting average molecular masses of the block copolymer samples are collated in Table 3.

Table 3. Reaction Conditions and Number-Average Molecular Mass, M_n, of the Ring-Opening Polymerizations To Generate ABA (Star) Poly(styrene-*block*-ε-caprolactone) Polymers[a]

structure	$n_{\varepsilon\text{-CL}}$ (mmol)	n_{TBD} (μmol)	n_{pS} (μmol)	M_n (g mol^{-1})	PDI
7a	1.05	5.75	0.77	12 500	1.5
7b	2.63	5.75	1.28	32 000	1.2
7c	1.40	3.59	0.61	33 000	1.3
8	2.63	7.10	1.14	36 000	1.4

[a]The molecular structures associated with the listed compounds can be found in Scheme 3.

Ring-Opening Polymerization (PCL Homopolymer for Determination of CC of pCL). The ring-opening polymerization was performed in an inert gas atmosphere (argon) inside a glovebox to rigorously exclude water from the reaction system. ε-CL was added to a solution of TBD and 2-butanol in 2 mL of toluene. The solution was stirred for 5 h and subsequently quenched via the addition of benzoic acid. The polymer was precipitated in cold hexane:diethyl ether (1:1) mixture. The molecular mass average was determined by SEC after precipitation. The amount of the reacting agent and the resulting molecular mass of the poly(ε-caprolactone) samples are collated in Table 4.

Table 4. Reaction Conditions and Number-Average Molecular Mass, M_n, of the Ring-Opening Polymerizations To Generate Poly(ε-caprolactone) Homopolymer for the Identification of Critical Conditions

$n_{\varepsilon\text{-CL}}$ (mmol)	n_{TBD} (μmol)	$n_{2\text{-butanol}}$ (μmol)	M_n (g mol^{-1})	PDI
2.00	30.0	120	2900	1.4
2.00	15.0	60	6100	1.1
4.00	5.00	20	25000	1.2

Size Exclusion Chromatography (SEC). For the determination of molecular mass distributions (MMD) an SEC system (Polymer Laboratories PL-GPC 50 Plus) comprising an autoinjector, a guard column (PLgel Mixed C, 50 × 7.5 mm) followed by three linear columns (PLgel Mixed C, 300 × 7.5 mm, 5 μm bead size), and a differential refractive index detector was employed. THF was used as the eluent with a flow rate of 1 mL min^{-1}, and the column temperature was set to 40 °C. The SEC system was calibrated using narrow poly(styrene) standards ranging from 160 to 6 × 10^6 g mol^{-1} (Polymer Standard Service GmbH, Mainz). The resulting molecular mass distributions were reassessed by universal calibration using Mark–Houwink parameters for poly(ε-caprolactone) (K = 13.95 × 10^{-5} dL g^{-1} and α = 0.786)[22] and for poly(styrene) (K = 14.1 × 10^{-5} dL g^{-1} and α = 0.70).[23] For the block copolymers the Mark–Houwink parameters for poly(styrene) were employed.

Liquid Chromatography under Critical Conditions (LCCC) Coupled to Size Exclusion Chromatography (SEC). *Liquid Chromatography under Critical Conditions (LCCC) and Concomitant Gradient Elution Liquid Chromatography (GELC).* The measurements were carried out on a Hewlett-Packard (HP1090) HPLC system using a diode array UV detector and an evaporative light scattering detector (PL-ELSD 1000, Sedere, France). The flow rate was 0.5 mL min^{-1}; 25 μL of close to 2 wt % polymer solutions was injected. For the critical conditions of polystyrene a reversed phase system was employed: A YMC-ODSA column (250 × 3 mm inner diameter), 300 Å pore size, 5 μm average particle size. The eluent was a mixture of tetrahydrofuran and water. The critical solvent compositions contain 88.4% (v/v) THF for poly(styrene). Premixing of the mobile phase by weight is necessary for a constant and exact composition. 0.1% acetic acid was added to the system. For the measurements at the critical conditions of poly(ε-caprolactone) an alternative reversed phase system was employed: PLRP-S column (250 × 4.6 mm), 100 Å pore size, 5 μm average particle size. The starting eluent composition contained 30% (v/v) of THF and 70% (v/v) of methanol. The gradient ended in a 80/20% (v/v) mixture of THF and MeOH. The samples were dissolved in 40% THF/60% MeOH.

Size Exclusion Chromatography (SEC). The SEC experiments were performed on a Hewlett-Packard (HP1050) HPLC modular system, including a Mistral column oven (SunChrom). For detection the evaporative light scattering detector (ELSD) and additionally a variable wavelength UV detector (λ = 230 nm) were employed. The flow rate was 3.0 mL min^{-1}. One high-speed column, a SDV-gel column (PSS GmbH Mainz), 5 μm average particle size (20 mm × 50 mm) and THF as mobile phase, was used. 100 μL of a 1 wt % polymer solution was injected. Calibration was performed using poly(styrene) standards (ranging from 760 to 1 × 10^6 g mol^{-1}).

Two-Dimensional Chromatography (LCCC-SEC). The crossover of LCCC fractions to SEC was performed via an 8-port external volume sample injector from Valco Instruments Co. Inc. (VICI). The measurements were evaluated by using the PSS WinGPC (Unity) and PSS 2D Software. The LCCC dimension in 2D mode was operated with a flow rate of 0.02 and 0.1 mL min^{-1}, respectively.

Nuclear Magnetic Resonance (NMR) Spectroscopy. ^{1}H NMR spectroscopy was carried out on a Bruker AM 400 MHz as well as a Bruker AM 250 MHz spectrometer. Sixteen or 32 scans were recorded for each NMR spectrum, respectively. All samples were dissolved in $CDCl_3$. The δ-scale is referenced to tetramethylsilane (δ = 0.00 ppm) as internal standard.

SEC Coupled to Electrospray Ionization Mass Spectrometry (ESI-MS). Spectra were recorded on an LXQ mass spectrometer (ThermoFisher Scientific, San Jose, CA) equipped with an atmospheric pressure ionization source operating in the nebulizer-assisted electrospray mode. The instrument was calibrated in the m/z range 195–1822 using a standard containing caffeine, Met-Arg-Phe-Ala acetate (MRFA), and a mixture of fluorinated phosphazenes (Ultramark 1621) (all from Aldrich). A constant spray voltage of 4.5 kV, a dimensionless sweep gas flow rate of 2, and a dimensionless sheath gas flow rate of 12 were applied. The capillary voltage, the tube lens offset voltage, and the capillary temperature was set to 60 V, 110 V, and 275 °C, respectively. The LXQ was coupled to a Series 1200 HPLC-system (Agilent, Santa Clara, CA) consisting of a solvent degasser (G1322A), a binary pump (G1312A), and a high-performance autosampler (G1367B), followed by a thermostat-controlled column compartment (G1316A). Separation was performed on two mixed bed size exclusion chromatography columns (Polymer Laboratories, Mesopore 250 × 4.6 mm, particle diameter 3 μm)

dx.doi.org/10.1021/ma2022452 | *Macromolecules* 2012, 45, 87–99

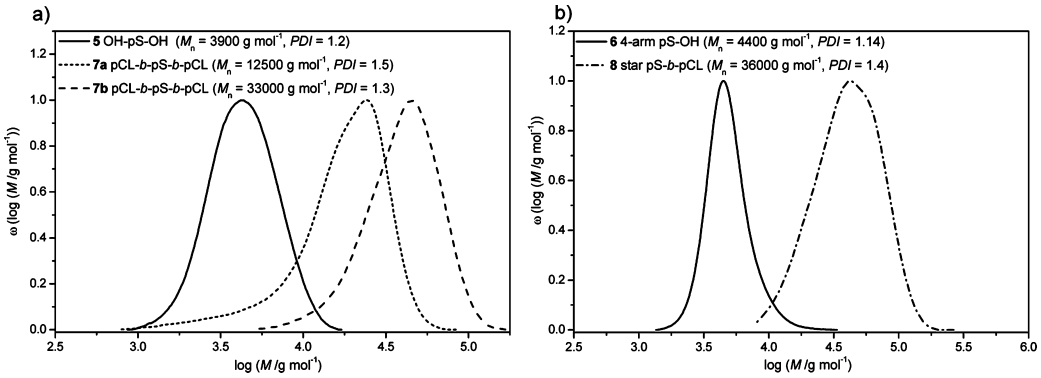

Figure 1. SEC traces of linear ABA block copolymers **7a** and **b** and the star block copolymer **8** synthesized via chain extension with ε-CL employing OH-pS-OH **5** and star pS-OH **6**, respectively, as macroinitiators. The corresponding average molecular masses and the values of the polydispersity are depicted in the graphs.

with precolumn (Mesopore 50 × 4.6 mm) operating at 30 °C. THF at a flow rate of 0.30 mL min^{-1} was used as eluent. The mass spectrometer was coupled to the column in parallel to an RI detector (G1362A with SS420x A/D) in a setup described previously.[24] 0.27 mL min^{-1} of the eluent was directed through the RI detector, and 30 μL min^{-1} infused into the electrospray source after postcolumn addition of a 100 μM solution of sodium iodide in methanol at 20 μL min^{-1} by a microflow HPLC syringe pump (Teledyne ISCO, Model 100DM). 20 μL of a polymer solution with a concentration of ~3 mg mL^{-1} was injected onto the HPLC system. Measurements can also be conducted via direct infusion ESI-MS. However, preseparation via SEC provides an improved ionization due to the absence of low molecular mass impurities and the slice by slice ionization of the investigated polymers. Simulated isotopic pattern distributions were obtained via the built-in simulation tool of the Xcalibur software package.

MALDI-TOF Mass Spectrometry. An Autoflex III MALDI-TOF mass spectrometer (Bruker Daltonics, Germany) was utilized. The system was equipped with a Smartbeam laser (λ = 356 nm). 2000 laser shots were accumulated for one spectrum. Dithranole (THAC) or 2-[(2*E*)-3-(4-*tert*-butylphenyl)-2-methylprop-2-enylidene]malononitrile (DCTB) (10 mg mL^{-1} in THF) was used as matrix. Depending on the polymer structure, 2 μL of a silver trifluoroacetate (AgTFAc) solution (c = 2 mg mL^{-1}) for the ionization of poly(styrene)s or a potassium trifluoroacetate (KTFAc) solution (c = 5 mg mL^{-1}) for poly(ε-caprolactone)s and copolymers was added to the matrix solution. For the sample preparation, a volume of 20 μL of polymer solution was mixed with 50 μL of matrix solution; subsequently, 1 μL was deposited on the MALDI target employing an Eppendorf pipet.

Coupling of HPLC with MALDI-TOF Mass Spectrometry. The electrospray deposition interface consists of a Teflon x–y table, which was adapted to the size of conventional 384 MALDI target plates. A small contact was connected to enable a contacting of the target plate to the ground potential. The spray capillary (stainless steel, 0.1 mm inner diameter) was fixed in a Teflon block. The distance between target plate and capillary could be varied from 0.5 to 3 cm. High voltage (3–5 kV) was generated by a dc power supply (FuG Elektronik GmbH, Rosenheim, Germany) and applied to the capillary. Additionally, heated gas could be applied through a series of concentrically holes around the capillary to enable a better evaporation of solvents. The deposition flow could be varied from 5 to 30 μL min^{-1} by means of an adjustable flow splitter (ASI-QuickSplit, Analytic Scientific Instruments, Richmond, CA). The matrix solution (5–10 μL min^{-1}) was added via a T-piece to the eluent line using a microsyringe pump (Harvard Apparatus, Holliston, MA).

RESULTS AND DISCUSSION

Previously, we reported the synthesis and the advanced characterization of pS-*b*-pCL diblock copolymers based on a mechanistic switch from RAFT to ROP via a modification of the thiocarbonyl thio group to an OH end functionality.[11] In the current contribution—as detailed in the Introduction—we apply such an approach for the generation of ABA linear and star block copolymers (i.e, by using 2-arm and 4-arm thiocarbonyl thio precursors, followed and intertwined with their in depth characterization (see Scheme 3)).

In the initial step, styrene is polymerized utilizing the RAFT agents illustrated in Scheme 3. The thiocarbonyl thio groups are attached to the core via the R group of the chain transfer molecule, and the Z group is located at the periphery, which is necessary for the subsequent end-group modification. The challenge of the reaction is to obtain polymer with a low PDI and high end-group fidelity, which can be hampered by the side reactions occurring in an R-group approach polymerization, i.e., star–star and chain–star coupling. However, side reactions can be reduced by minimizing the radical supply to the system, thus decreasing biradical termination and linear chain contamination.[1,12,21] For the characterization, SEC traces and ESI mass spectra of the linear and 4-arm star RAFT polymers were recorded (refer to Table 1 and Figure S1 in the Supporting Information). The obtained ESI mass spectra were compared with the simulated isotopic patterns confirming the end-group functionality and the purity of the RAFT polymers.

In the following step, the dithioester end groups are converted to OH functionalities as shown in Scheme 2. Depending on the macroRAFT agent used, poly(styrene)s with two or more hydroxyl end groups are obtained. The details for the employed transformation mechanism have previously been reported.[10] The end-group conversion from the thiocarbonyl thio end groups to hydroxyl groups can by assessed via MALDI mass spectra and SEC traces of the converted polymers. A typical MALDI-TOF mass spectrum of a difunctional RAFT polymer is shown in Figure S2, alongside a comparison of the theoretical and experimental isotopic pattern distributions. The four-armed star converted RAFT polymer was unfortunately unable to be imaged with reliable ionization via MALDI-TOF spectrometry. Thus, the number of obtained OH groups can only be indirectly accessed via the ROP process and the subsequent analysis (see below).

The OH converted poly(styrene) materials were employed as macroinitiators for the ROP of ε-caprolactone utilizing 1,5,7-triazabicyclo[4.4.0]dec-5-ene (TBD). Depending on the initial poly(styrene), either linear ABA or star-shaped block copolymers are obtained. The reaction conditions are collated in Table 3. The SEC traces of obtained block copolymers are depicted in Figure 1, and the associated average molecular mass

dx.doi.org/10.1021/ma2022452 | *Macromolecules* 2012, 45, 87–99

and polydispersity indexes (PDIs) are given in Table 5. Inspection of Figure 1a demonstrates that the linear ABA block

Table 5. Collation of the Number Average Molecular Mass, M_n, and the PDI of the Precursor Polymers 5 and 6 as Well as of the ROP-Generated ABA (Star) Block Copolymers 7a,b and 8

structure	polymer	M_n (g mol^{-1})	PDI
5	OH-pS-OH	3900	1.2
6	star pS-OH	4400	1.1
7a	pCL-*b*-pS-*b*-pCL	12500	1.5
7b	pCL-*b*-pS-*b*-pCL	33000	1.3
8	star pS-*b*-pCL	36000	1.4

copolymers **7a** and **7b** exhibit different molecular masses, which is achieved by varying the monomer-to-macroinitiator ratio. Halving the concentrations of **7a** leads to a doubling of the number-average molecular mass. To confirm the obtained results, the procedure leading to **7b** has been repeated (sample **7c**) and the corresponding data are depicted in Figure S3. The shift of the chromatograms toward lower retention volume of the ABA block copolymers compared with the macroinitiator hints at a successful chain extension. The chromatogram of **7b** does not reveal any low molecular mass material, whereas the SEC chromatogram of **7a** exhibits a tailing in the lower molecular mass range as well as a small shoulder. This may be due to incomplete chain extension of the macroinitiator pS or other side reactions such as initiation of ε-caprolactone with water residues or transesterification during the polymerization, which is typically observed at high catalyst content or at high conversion.[25] Clearly, further very detailed investigations are warranted and are provided below. Figure 1b displays the chromatogram of the chain extended star OH poly(styrene) to the possible star block copolymer **8**. Again, visual inspection suggests that nearly no hydroxyl star poly(styrene) initiator remained in the sample.

After determining the molecular masses of the ABA (star) block copolymers, a thorough investigation of the polymer structure is carried out. SEC traces can only provide limited evidence that a chain extension has occurred. For example, the SEC analysis does not indicate which number of OH groups attached to the poly(styrene) have initiated the ring-opening polymerization. With SEC, a block copolymer, an ABA block copolymer, and a 4-arm star block copolymer are not distinguishable. For the further characterization effort ^{1}H NMR spectra were subsequently collected. Figure 2 depicts the ^{1}H NMR spectrum of the ABA block copolymer **7b**. The signals of the NMR spectrum correspond to the expected ^{1}H shifts of poly(styrene) and poly(ε-caprolactone). The signals a–c in Figure 2 can be assigned to the backbone of poly(styrene), and the peaks d–h are associated with the backbone of poly(ε-caprolactone). The end group of the polymer, $-CH_2OH$, is labeled with h′. Assuming that an ABA block copolymer is synthesized and thus two of the $-CH_2OH$ end groups h′ exist—one on each side of the polymer chain—the molecular masses of each block are calculated by integration of the significant signals (c for pS, h for pCL, h′ as end group). For the polymer **7b** a poly(styrene) block of 3900 g mol^{-1} is deduced, and the two poly(ε-caprolactone) blocks together possess an M_n of 22 000 g mol^{-1}. Alternatively, one may assume that only one end group of the poly(styrene) initiated during the ring-opening polymerization, resulting in a simple AB block copolymer. Hence, the block copolymer would feature only one

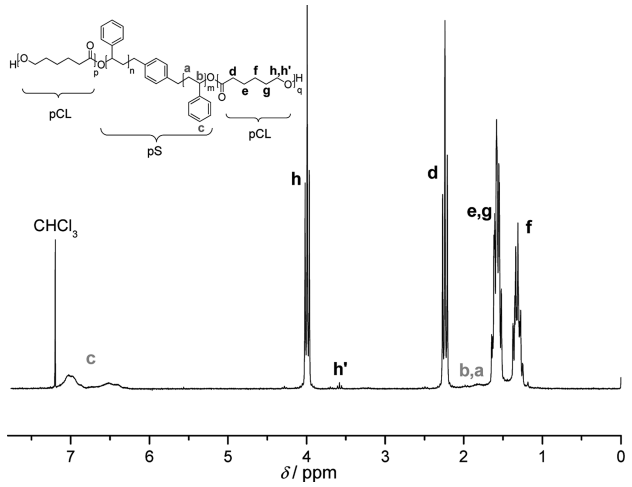

Figure 2. ^{1}H NMR spectrum of the pCL-*b*-pS-*b*-pCL block copolymer **7b**. The signals a–c correspond to the poly(styrene) block and the signals d–h to the poly(ε-caprolactone) block. The two end groups are labeled with h′. The integration of the NMR signals, compared with the SEC analysis, supports the formation of an ABA block copolymer structure (for details see text).

$-CH_2OH$ end group h′. Integrating the significant peaks under the "AB block copolymer" assumption, a poly(styrene) block with a molecular mass of 1900 g mol^{-1} and a poly(ε-caprolactone) block of 11 000 g mol^{-1} are obtained. These results can subsequently be compared with the results of the SEC traces (see Figure 1 and Table 4) where the poly(styrene) block exhibits an average molecular mass of 3900 g mol^{-1} and the chain-extended system with an average molecular mass of 33 000 g mol^{-1} (with pS calibration). The molecular mass of the poly(styrene) block under the hypothetical AB diblock copolymer assumption reads $M_n^{\text{pS-block}}$ = 1900 g mol^{-1} (calculated via NMR signal integration) and does not correspond to the SEC analysis ($M_n^{\text{SEC,pS}}$ = 3900 g mol^{-1}); in contrast, the calculated molecular mass of the poly(styrene) block for the deduced targeted ABA block copolymer ($M_n^{\text{NMR,pS}}$ = 3900 g mol^{-1}) matches perfectly with the SEC analysis. Based on the above calculations, the NMR analysis unambiguously supports an ABA block copolymer structure of polymer **7b**. Concerning the two poly(ε-caprolactone) blocks, it is very likely that the true molecular mass is more realistically reflected by the integration of the NMR signals ($M_n^{\text{NMR,pCL}}$ = 22 000 g mol^{-1}) than by the M_n values derived from the SEC traces, since the obtained data of the SEC are calibrated with linear poly(styrene) standards. The ^{1}H NMR spectra and the associated molecular masses of the ABA (star) block copolymers **7a** and **8** are provided in Figures S4 and S5. The derivation of the number-average molecular mass via the integration of the signals in the NMR spectrum of sample **8** is of particular interest. Here, the integration procedure of the poly(styrene) backbone signal was based on the SEC deduced molecular weight of the poly(styrene) macroinitiator, and subsequently the end-group functionality h′ was evaluated via the integration of the signal h′. The calculations reveal that not all four poly(styrene) chains were extended by ring-opening polymerization, yet the average value is close to 2.6 pCL end groups, which signifies that ~65% of the pS OH end groups were activated as macroinitiators for the chain extension. As a possible reason the steric hindrance of the bulky star macroinitiator can be suggested. Additionally, the potential

dx.doi.org/10.1021/ma2022452 | *Macromolecules* 2012, 45, 87–99

four −OH functions of the poly(styrene) macroinitiator are secondary alcohol termini. As soon as one chain is initiated by ring-opening with pCL, a primary-OH end function is formed. The primary-OH function of the pCL is more reactive to reinitiate the ROP compared to the secondary-OH end group of the poly(styrene) macroinitiator. In addition, it may be possible that not all hydroperoxyl groups have been reduced to hydroxyl moieties. Due to simplicity, sample **8** will still be termed star block copolymer in further performed analysis. The NMR spectral analysis of sample **7a** reveals via an identical calculation that the average value of pCL end groups is 2.1 (**7b**: 2.0). The only possible cause for the higher amount of end groups in the formed ABA block copolymer than were present in the macroinitiator is the presence of a small additional poly(ε-caprolactone), formed during the polymerization process (see below for a detailed discussion).

For block copolymer analysis, ^{1}H NMR spectroscopy and SEC analysis are not sufficient for obtaining information about their exact chemical composition and topology. In addition, evidence regarding the possible existence of homopolymer content in the samples remains circumstantial. Thus, a more in-depth analysis has been performed to obtain additional detailed and accurate information about the ABA (star) block copolymers. Two-dimensional chromatography (2D) is a reliable method to identify the occurrence of side reactions. To obtain a full 2D LCCC-SEC analysis, a range of preanalysis experiments have to be performed. Most importantly, the critical conditions of both block copolymer constituents have to be either known or separately established. The critical conditions for polystyrene are known from a previous study[11] and are thus applied first. A 88.4% (v/v) THF and 11.6% (v/v) H_2O eluent mixture was employed on a reversed phase system (YMC-ODSA column). First, the macroinitiator poly(styrene) samples with two (**5**) and more (**6**) end groups were measured under the critical conditions of poly(styrene) and compared with other poly(styrene) samples (i.e., pS standard, pS RAFT **3**, and pS-OH). The corresponding elugrams are displayed jointly with the elugrams of a poly(styrene) standard, the initial RAFT polymer **3**, and a poly(styrene) with only one hydroxyl function (pS-OH) at the chain end in Figure 3. The pS RAFT polymer **3** contains two dithioacetate end groups. For the synthesis of pS with one OH group the reader is referred to ref 11. The pS standard sample was purchased from PSS Standard Service and synthesized by anionic polymerization. The end groups of the pS standard are consequently ^{t}butyl on one side and H on the other end. Thus, it represents a polymer with hydrophobic end groups. All polymer samples possess average molecular masses in the range between 3000 and 9000 g mol^{-1}.

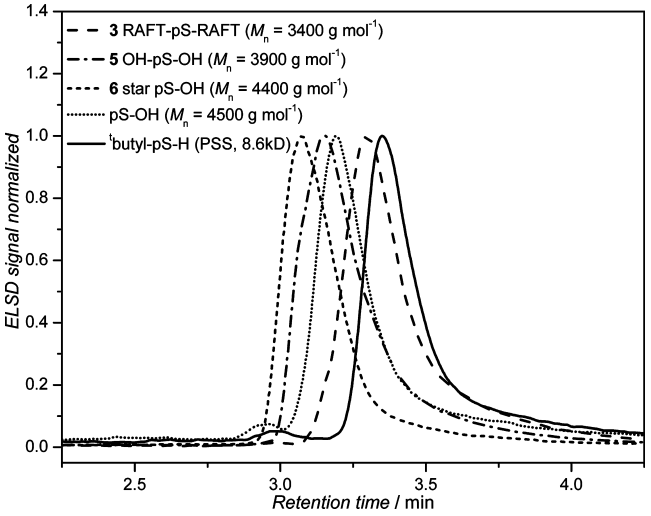

Figure 3. Elugrams of poly(styrene)s with different end groups under critical conditions of poly(styrene) (reversed phase column, 88.4% THF/11.6% H_2O). Depending on the amount of hydrophobic end groups, the elugram is shifted toward higher retention times.

Under critical conditions of pS, pS samples with different molecular masses elute at the same time, yet the elution time depends exclusively on the end group functionality. On a reversed stationary phase the samples elute according to their hydrophobicity.[26] The retention time increases with the amount of hydrophobic functions in the sample. The elugrams in Figure 3 reveal that on such a reversed system the pS samples with the hydrophobic end groups elute later than the poly(styrene)s with hydrophilic end functionalities. Furthermore, it can clearly be observed that the polymer with the most hydrophilic end groups (star pS-OH **6**, i.e., the macroinitiator for the formation of star block copolymers) elutes earlier than the poly(styrene)s with two (OH-pS-OH) **5** or one OH group.

In the next step, the critical conditions of poly(styrene) were applied to ABA (star) block copolymers. Figure 4 depicts the elugrams of the samples compared with the poly(styrene) macroinitiator carrying two hydroxyl end groups. Inspection of the ABA (star) block copolymers reveal that the star block copolymer **8** with an M_n of 36 000 g mol^{-1} elutes first while the ABA block copolymer **7a** with M_n = 12 500 g mol^{-1} elutes last, which indicates that the different block copolymers elute under these conditions on a reversed phase system in the SEC mode. Further inspection of Figure 4 reveals that all elugrams exhibit a slight tailing. It is very likely that the tailing, which can be observed in all elugrams, is due to column interactions. Nevertheless, the tailing could also occur, for example, due to unreacted macroinitiator poly(styrene) homopolymer in the samples, since it is obvious that the tailing of the star **8** and triblock **7** copolymers overlaps with the elugram of the poly(styrene) homopolymer.

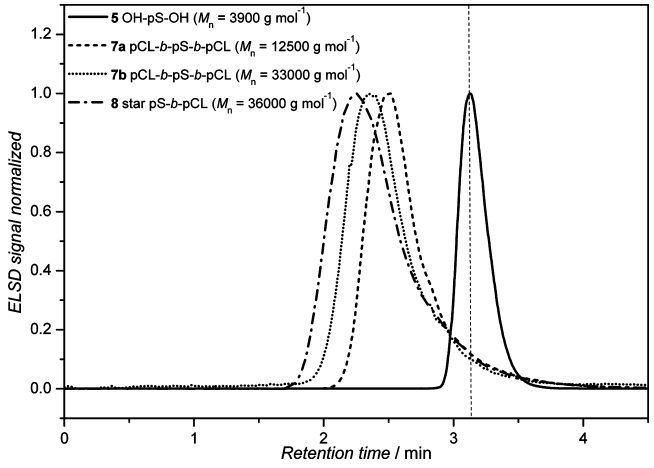

Figure 4. LCCC elugrams of ABA (star) block copolymers under critical conditions of poly(styrene) (88.4% THF, 11.6% H_2O). The elugrams reveal that the ABA (star) block copolymers elute in the SEC mode depending on the size of the pCL blocks in each sample.

Consequently, a method needs to be applied that detects the quantity of potentially remaining homopolymer poly(styrene) within the samples. For that reason two-dimensional LCCC-SEC

dx.doi.org/10.1021/ma2022452 | Macromolecules 2012, 45, 87−99

measurements of the samples **3** and **8** under critical conditions of poly(styrene) were recorded. The corresponding LCCC-SEC chromatogram in combination with one-dimensional elugrams of LCCC and SEC of the sample **7b** is presented in Figure 5, while the LCCC-SEC diagrams of the other samples

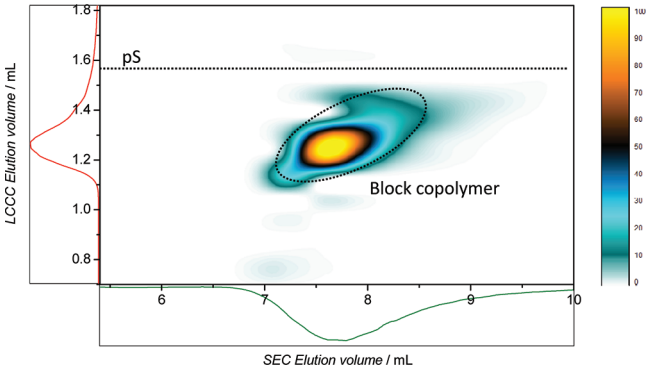

Figure 5. 2D LCCC-SEC plot of the pCL-*b*-pS-*b*-pCL block copolymer **7b**. The LCCC and the SEC traces are attached to the *y*-axis and the *x*-axis, respectively. The *z*-axis is given by the color scheme in percentage.

are collected in Figures S6 and S7. On the *x*-axis the recorded SEC elution volume and on the *y*-axis the LCCC elutions volume is indicated. The evaporative light scattering detector (ELSD) intensity in percentage (*z*-axis) is expressed by different colors. The ABA block copolymer appears diagonal in the 2D plot due to the fact that the sample elutes in the SEC modus. The dotted line in the chromatogram represents the HPLC elution volume of the poly(styrene) macroinitiator under critical conditions of poly(styrene). Within the detection limits of 2D LCCC-SEC chromatography, no residual macroinitiator (poly(styrene) homopolymer) is observed. A similar conclusion can be drawn from the inspection of the LCCC-SEC chromatograms of **7a** and **8**, depicted in Figures S6 and S7.

As described above, the samples are chain extended via ring-opening polymerization. It is commonly known that side reactions can lead to pCL homopolymers in the block copolymer sample.[19] Taking this into account, it is indispensable—besides the identification of residual macroinitiator poly(styrene)—to investigate the (potential) content of poly(ε-caprolactone) homopolymer in the ABA (star) block copolymer samples.

An expedient method to separate pCL homopolymer from the ABA (star) block copolymers is the identification of the critical conditions of poly(ε-caprolactone) on an HPLC system. Critical conditions of pCL for the separation of block copolymers have been applied before.[27] However, these conditions were utilized for the block copolymers poly(*n*-butyl acrylate)-*b*-poly(ε-caprolactone) and poly(ethylene glycol)-*b*-poly(ε-caprolactone) in which the connected block is still less hydrophobic than the poly(styrene) block, and consequently the required separation efficiency for poly(styrene)-*b*-poly(ε-caprolactone) block copolymers is not given. For the establishment of the CC of pCL, the elugrams of poly(ε-caprolactone) homopolymers with different molecular masses were recorded (see Table 4). Employing a reversed phase column (PLRP-S column), the solvent mixture of THF and MeOH was varied until the poly(ε-caprolactone) samples elute at the same retention time. The corresponding elugrams are depicted in Figure 6. A solvent composition of 30% (v/v)

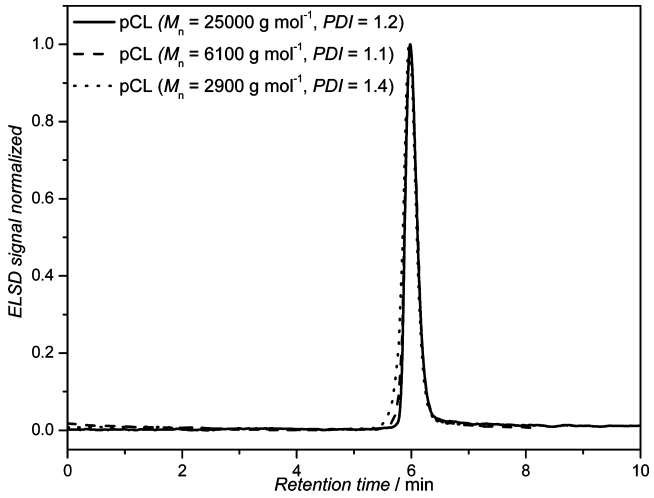

Figure 6. Elugrams of poly(ε-caprolactone) samples with different average molecular masses. The measurement was conducted under critical conditions of pCL. Therefore, a PLRP-S column with an eluent 30/70% (v/v) THF/MeOH was employed.

THF and 70% (v/v) MeOH was finally identified, where the retention times of the variable M_w poly(ε-caprolactone) samples are identical (5.97 min), which indicates the appropriate critical solvent composition is found.

Interestingly, under these conditions the ABA (star) block copolymers are completely adsorbed onto the column. For a preferably complete recovery of the samples, the critical conditions of poly(ε-caprolactone) were combined with a solvent gradient (LCCC × GELC) to ensure that the block copolymers are desorbed completely. To obtain information regarding the effectiveness of the separation, poly(styrene) homopolymer was measured via a LCCC−GELC system. In Figure 7 the elugrams of pCL homopolymer (dotted line,

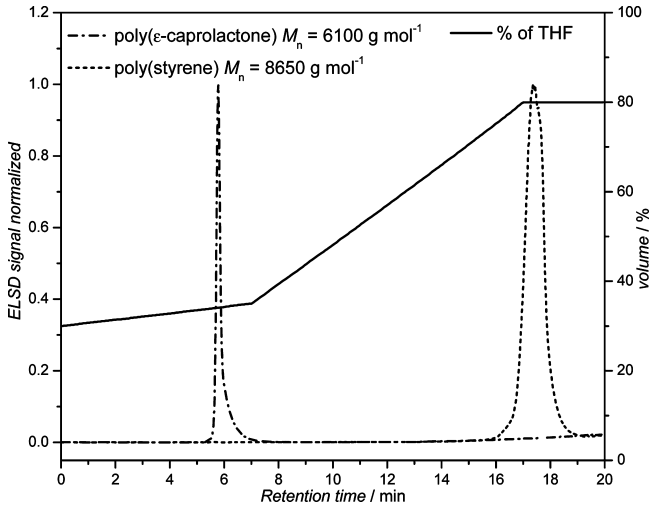

Figure 7. Slight gradient near critical conditions of poly(ε-caprolactone) combined with a gradient as a tool to separate pCL from pS homopolymers.

M_n = 6100 g mol^{-1}, PDI = 1.1) and pS homopolymer (dashed line, M_n = 8650 g mol^{-1}, PDI = 1.03) are displayed. On the left *y*-axis the % (v/v) of THF is indicated. The full line represents the THF content of the solvent mixture at a specific retention time. The measurement commences with a solvent mixture of

dx.doi.org/10.1021/ma2022452 | *Macromolecules* 2012, 45, 87−99

30% THF and 70% MeOH (CC of pCL) and concludes with 80% of THF and 20% of MeOH. The peak retention time of the pCL homopolymer is according to the critical point of pCL at around 6.0 min, whereas the poly(styrene) homopolymer elutes after the solvent gradient at 17.5 min. Via such an approach the two homopolymers pCL and pS are completely separated.

The new hybrid LCCC × GELC method for separating poly(ε-caprolactone) and poly(styrene) was subsequently applied to the ABA (star) block copolymers. Because of the CC of pCL, the possible existence of the pCL homopolymer in the block copolymer can now be detected, and a complete desorption of the sample from the column is provided by the subsequent solvent gradient. Initially, the elugram of the ABA block copolymer **7a** analyzed with the new CC-gradient system is discussed (presented in Figure 8), as the elugram differs

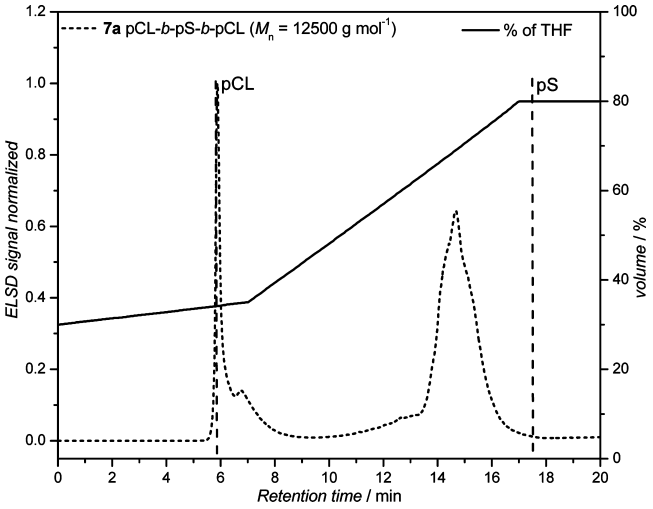

Figure 8. Gradient elution liquid chromatogram of the ABA block copolymer **7a**, conducted under critical conditions of pCL combined with a gradient.

slightly from the samples **7b** and **8**; i.e., **7b** and **8** represent the pure block copolymer structure. Two main signals can be observed. At the elution time of 6 min the first signal is visible. It corresponds to the time at which the pCL homopolymer elutes under critical conditions of poly(ε-caprolactone). The second signal has its peak maximum at 14.7 min retention time. Clearly—compared to Figure 7—the first signal corresponds to the pCL homopolymer in the sample and the second signal corresponds to the block copolymer. Additionally, the pCL signal at 6 min retention time shows a shoulder at higher retention times. This implies that two structures elute between 5.5 and 8 min retention time. Since the HPLC is performed on a reversed phase system, it is very likely that the first part of the signal possesses more hydrophilic end groups than the subsequent shoulder.

In the range of around 17.5 min retention time, at which poly(styrene) homopolymer elutes, no signal is observed. This observation corresponds well with the 2D plot measured under critical conditions of poly(styrene) (see Figure 5) and confirms that the macroinitiator poly(styrene) is completely consumed.

In principle, a separation of a block copolymer AB from the homopolymer B may not be expected in a gradient system when block B is the adsorbing unit. However, since the average molecular mass of the macroinitiator pS is fixed at 3900 g mol^{-1} and thus no smaller average molecular masses of poly(styrene) were expected, the LCCC × GELC system can also be applied for imaging potential residual poly(styrene) homopolymers, as the differences of masses between homo- and copolymer are sufficiently high. The GELC conditions were optimized concerning sample solvent, injection volume, column temperature, and polymer sample concentration, so that a "breakthrough" effect[28] of copolymer and homopolymer poly(styrene) can be excluded, as evidenced by FT-IR and MALDI-TOF-MS measurements (see below). In addition, a GELC chromatogram of an pS-*b*-pCL diblock copolymer is depicted in Figure S8. For the synthesis and the characterization of the diblock copolymer the reader is referred to ref 11. This specific AB block copolymer possesses a small amount of macroinitiator poly(styrene) beside the block copolymer structure. In the chromatogram in Figure S8 a small shoulder is found at 17.5 min retention time besides the intense signal of the block copolymer at 15.2 min retention time. Thus, the chromatogram of the AB block copolymer is an excellent example to prove that polystyrene can be separated block copolymer via the LCCC−GELC system.

One possible option to identify the peaks in Figure 8 is to collect fractions of the sample at specific time intervals and to analyze these fractions via IR spectroscopy. Figure 9a displays

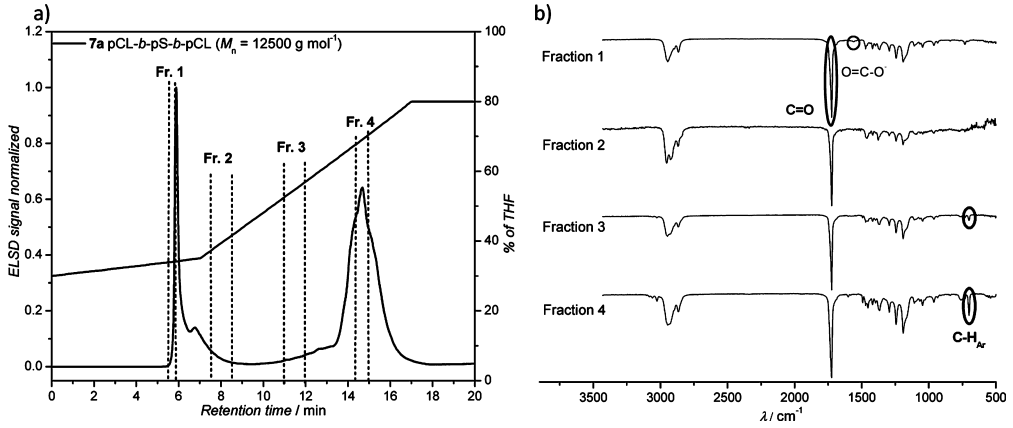

Figure 9. (a) Fractionation of the sample **7a** according to the GELC run for IR spectroscopic measurements; in (b) the IR spectra of each fraction are presented. In the IR spectra of fractions 1 and 2 only the signals associated with the stretching vibration of poly(ε-caprolactone) can be identified, whereas in the spectra of fractions 3 and 4 the characteristic peaks for the stretching from the aromatic ring of poly(styrene) occurs in variable intensities.

dx.doi.org/10.1021/ma2022452 | *Macromolecules* 2012, 45, 87−99

the elugram of the ABA block copolymer **7a** including the division of the elugram in four fractions. Fraction 1 was collected between 5.5 and 5.8 min retention time, fraction 2 between 7.5 and 8.5 min, fraction 3 ranging from 11 to 12 min, and fraction 4 between 14.2 and 15 min. The fractions were selected in such a way that an overlap of two eluted structures is avoided. In Figure 9b, the IR spectrum of each fraction is displayed in the range of 500−3500 cm^{-1}. In all fractions the strong C═O stretching signal at 1724 cm^{-1} appears due to the pCL backbone ester groups.[29] The IR spectra of fractions 3 and 4 additionally feature a signal at 700 cm^{-1}. This signal corresponds to the C−H stretching vibration of aromatic structures and thus signifies the presence of poly(styrene).[30] The presence of both signals in fractions 3 and 4—one corresponding to the backbone pCL and one corresponding to the repeat unit of poly(styrene)—proves the existence of block copolymer in sample **7a**. The signal strength of the $C-H_{Ar}$ stretching is more pronounced in fraction 4; in fraction 3 the signal is rather weak, implying that the block copolymer part with longer pCL block length elutes at lower retentions times whereas the block copolymer with shorter pCL block length elutes at higher retention times. No signal at 700 cm^{-1} is visible in fractions 1 and 2. Consequently, both fractions contain exclusively poly(ε-caprolactone). At first glance both fractions (1 and 2) exhibit the same IR spectrum. A closer survey, however, reveals that in fraction 1 an additional signal at 1558 cm^{-1} appears which cannot be observed in fraction 2. Most likely the signal at 1558 cm^{-1} corresponds to a carboxylate stretching vibration.[31] A possible explanation is that the material in fraction 1 possesses carboxylate end groups, yet fraction 2 does not.

The IR spectra of the fractions confirm that different functional groups (i.e., carbonyl, carboxylate, and aromatic moieties) are present in the different fractions. However, IR spectroscopy cannot identify the exact structure of the polymer, eluting at a specific retention time.

For an unambiguous identification of the possible minor components of sample **7a**, the GELC system was coupled to MALDI-TOF mass spectrometry by means of an electrospray deposition device. A series of MALDI mass spectra recorded at retention times between 5.5 and 8.0 min (see chromatogram, Figure 8) are displayed in Figure 10. The peak-to-peak

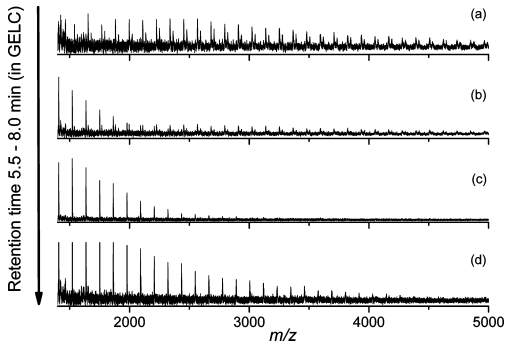

Figure 10. Series of MALDI-TOF mass spectra of sample **7a** recorded between 5.5 and 8.0 min of the GELC chromatogram (see Figure 8).

difference (i.e., mass of repeat unit) of all distributions was m/z 114, which corresponds to pCL. In Figure 10a, a distribution can be identified that is attributed to linear pCL structures. Mass distributions that are characteristic for pCL possessing OH/carboxyl end groups were found, which are formed by water residue initiated ε-CL (see Table S1). As shown in Figure S9, the measured isotope distribution of a linear pCL matches well with the simulated isotopic pattern (in addition see Table S1). A minor distribution is found in the spectra, which correspond to masses where the catalyst TBD is still attached to the linear chains. Figure 10b displays an additional series of peaks shifted by −18 Da from the previous peaks of the main distribution, which can be identified with minor intensity. These peaks correspond to macrocycles (see also overlay of theoretical and measured isotope pattern given in Figure S10). The formation of cyclic structures can occur by backbiting of the hydroxyl end group to an ester group within the chain during the synthetic process.[19] In Figure 10c, these new series can be exclusively found. Its molecular mass distribution increases from Figure 10b to 10d, i.e., with increasing retention times. This correlates well with the assumed adsorption mode where small molecules elute first, whereas higher masses are longer retained on the column.

As shown in the chromatogram of sample **7a** (see Figure 8), a second intensive peak between 10 and 17 min retention time is observed. The MALDI-TOF mass spectra recorded in this range are depicted in Figure 11a. Only relatively noisy spectra with rather low resolution could be obtained due to comparatively high average molecular masses of the copolymers and the block copolymer structure itself. The repeat unit of poly(styrene) is m/z 104, whereas pCL features a repeat unit of m/z 114. As a consequence, mass peaks with distances of m/z 10 were found, as shown in detail in Figure 11b. Figure 11b also reveals a successive shift of −10 Da of the measured peak distributions with increasing retention time (shown by the red lines). Such a shift can be readily explained by molecules having one of the ε-caprolactone units replaced by a styrene unit. Combined with the IR spectroscopy results of fractions 3 and 4 (see Figure 9), the MALDI data confirm our previous assumption that the amount of pCL units in the ABA block copolymer decreases with increasing retention time.

Finally, the 2D GELC-SEC analysis under critical conditions of pCL in combination with a gradient is performed. Figure 12 displays the obtained 2D plot. Because of the studies performed with IR spectroscopy and MALDI-TOF mass spectrometry, the spots in the 2D GELC-SEC plot can now be clearly identified. The narrow spot with the high intensity is associated with linear pCL homopolymer in the sample; the light and slight diagonal spot is identified as macrocyclic pCL in the sample. The broad and most intense spot is the ABA block copolymer. More importantly, the 2D plot reveals the molecular masses of each spot. Following the SEC elution volume, the block copolymer possesses the highest molecular mass and the macrocycles the lowest molecular mass.

As previously indicated, the chromatogram of the ABA block copolymer **7b** and the star block copolymer **8** under CC of pCL combined with the solvent gradient is discussed separately from sample **7a**. Employing the new CC-gradient system, the elugrams of the ABA (star) block copolymers **7b** (dotted line) and **8** (dashed line) are recorded (see Figure 13). The maximum of the elugram is located at 14.0 min retention time for sample **8** and 14.2 min retention time for sample **7b**. Both elugrams possess only a slight increase of the baseline at and after the critical point of pCL, implying that the samples contain only a very small amount of pCL homopolymer. A reason for the high content of pCL homopolymer in sample **7a** compared to the samples **7b** and **8** is most likely associated with a higher ratio of catalyst in the reaction solution compared with the macroinitiator content (see Table 3). Similar to sample

dx.doi.org/10.1021/ma2022452 | *Macromolecules* 2012, 45, 87−99

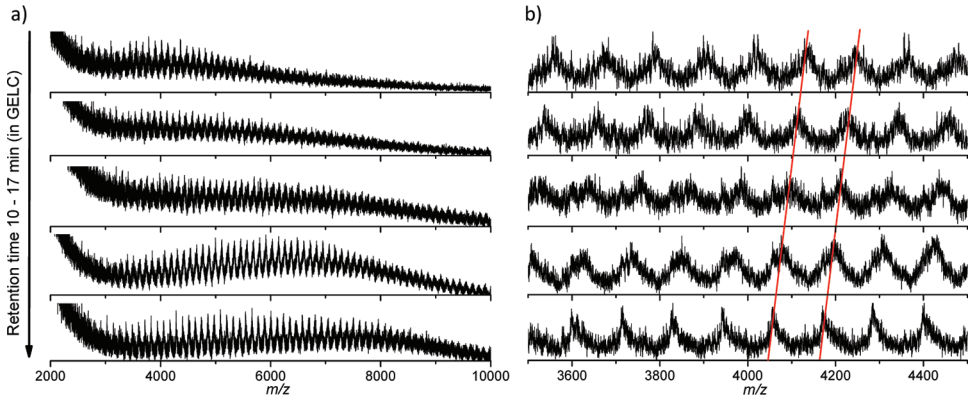

Figure 11. MALDI-TOF spectra of fractions 1, 3, 5, 7, and 9 of sample **7a** in the range of 10−17 min of the GELC elugram; (a) shows the complete detected distribution, whereas (b) is a zoom-in of the spectra in the range of m/z 3500−4500.

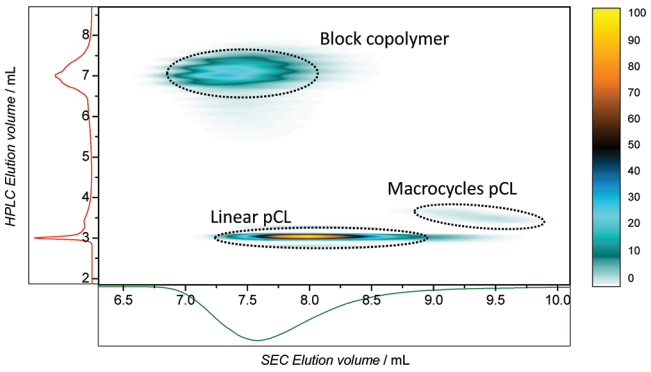

Figure 12. 2D LCCC-GELC-SEC chromatogram of the pCL-*b*-pS-*b*-pCL block copolymer **7a**. The GELC is conducted under CC of pCL combined with a solvent gradient (for details refer to the Experimental Section). The chromatogram reveals the different molecular masses of minor component linear and macrocyclic poly(ε-caprolactone).

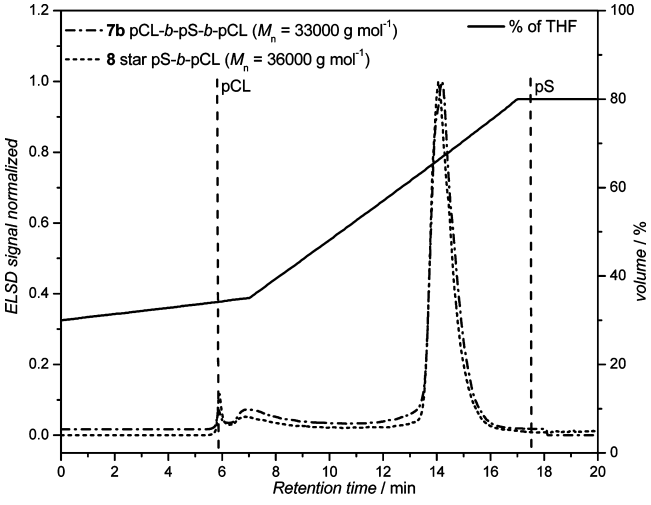

Figure 13. ABA block copolymer **7b** and star block copolymer **8** under the conditions presented in Figure 6. Clearly, the macroinitiator poly(styrene)−OH is completely consumed which conforms to the chromatograms measured under CC of pS. Only a very low amount of pCL homopolymer can be identified analyzing the sample via a LCCC−GELC system starting from the critical conditions of pCL (30/70% (v/v) THF/MeOH) and continuing with a solvent gradient.

7a—in the range around 17.5 min retention time at which poly(styrene) homopolymer elutes—no signals are observed in either one of the elugrams. Thus, samples **7b** and **8** are relatively pure block copolymer structures.

Subsequently, the 2D GELC-SEC analyses of the ABA (star) block copolymers were performed. Figure 14 shows the 2D

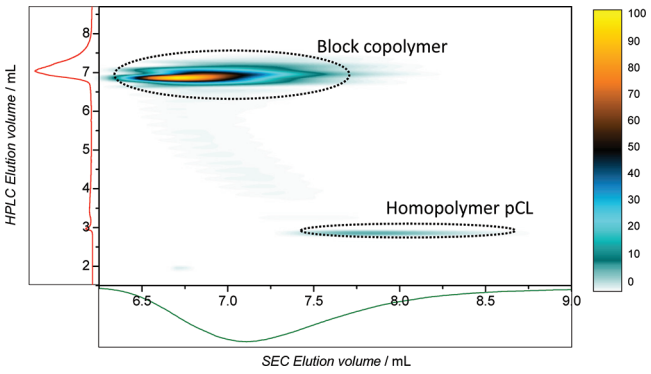

Figure 14. 2D LCCC-GELC-SEC chromatogram of the pS-*b*-pCL star block copolymer **8**. A very small amount of pCL homopolymer is detected.

GELC-SEC plot of the star block copolymer **8**. The 2D plot of **7b** is presented in Figure S11. The LCCC−GELC was carried out under critical conditions of pCL (30/70% (v/v) THF/MeOH) combined with the subsequent solvent gradient up to 80/20% (v/v) THF/MeOH. The GELC and the SEC elugrams which correspond to the 2D plot are plotted along the vertical and horizontal axis. Two spots are visible in the LCCC-SEC chromatogram. The spot that elutes on the GELC at 3 mL retention volume corresponds to the critical point of pCL. Thus, this spot can be assigned to linear pCL homopolymer. In the 2D plots of samples **7b** and **8** no macrocyclic pCL can be observed. The second spot at higher retention volume of the GELC run corresponds to the block copolymer in the sample. Following the SEC retention volume, the first spot of the sample elutes later than the second spot. Thus, the pCL homopolymer possesses a lower molecular mass than the star block copolymer. The content of the pCL homopolymer in the sample **8** cannot be evaluated with full quantitative certainty; however, a semiquantitative statement can be made from the height and the broadness of the spot. According to the z-axis, which is illustrated by a color scheme, the intensity of the pCL homopolymer spot is in the range of 10% height. The spot of the block copolymer reaches 100% and is in comparison to the first spot quite broad.

dx.doi.org/10.1021/ma2022452 | *Macromolecules* 2012, 45, 87−99

Thus, ABA (star) block copolymers with only very low amounts of impurities are synthesized via the newly introduced switch from RAFT to ROP. It is tempting to quantify the chromatographic data for all obtained polymers and to estimate the purities of the generated structures The quantitative data are based on an integration of the ELSD signals and should be treated some care as the correlation between ELSD signals of polymers of different structures is not necessarily strictly linear. For example, the quantitative evaluation of **7b** (by deconvoluting the individual ELSD signals) indicates that it contains 94% of block copolymer, 0.5% of linear pCL, 5.5% of macrocycles pCL, and no homopolymer pS. Thus, it can be clearly seen that the in-depth characterization approach detailed in the current study is excellently applicable toward the characterization of pS-*b*-pCL block copolymers in general. We recommend that the characterization of such block copolymers—regardless via which synthetic process they are produced—should involve at the least the level of detail provided in the current study.

CONCLUSIONS

In the current contribution the procedure of switching from RAFT to ROP was successfully employed to synthesize ABA (star) block copolymers. For this purpose the end groups of 2-arm linear and 4-arm star R-approach RAFT polymers were modified and subsequently utilized as macroinitiators for ring-opening polymerization under organocatalysis. The focus of the present study is on the characterization of the obtained materials by various analytical techniques, including two-dimensional liquid chromatography. The separation of pCL homopolymer from the ABA (star) block copolymers was a particular focus and accomplished by the introduction of a new hybrid LCCC-GELC method—a system which combines the critical conditions of pCL with a solvent gradient—allowing the first time the separation of pCL from pS. The current contribution thus demonstrates a new synthetic approach to ABA (star) block copolymer and—most importantly—a viable and powerful method for their complete characterization.

ASSOCIATED CONTENT

Supporting Information

ESI mass spectra of the star RAFT poly(styrene) samples, SEC and MALDI-TOF mass spectrum of OH-pS-OH **5**, SEC traces of the repeated synthesis, the ^{1}H NMR spectra of samples **7a** and **8**, 2D plots of samples **7b** and **8** under CC of pS, MALDI-TOF mass spectra of the fractions (a) and (c) after coupling to the GELC as well as the 2D LCCC-GELC-SEC plot of sample **7b**. This material is available free of charge via the Internet at http://pubs.acs.org.

AUTHOR INFORMATION

Corresponding Author

*E-mail christopher.barner-kowollik@kit.edu, Tel +49 721 608 45641, Fax +49 721 608 45740 (C.B.-K.); e-mail jana.falkenhagen@bam.de, Tel +49 30 8104 1632, Fax +49 30 8104 1137 (J.F.).

ACKNOWLEDGMENTS

C.B.-K. and J.F. acknowledge funding from the German Research Council (DFG) supporting the current project. In addition, C.B.-K. acknowledges funding from the Karlsruhe Institute of Technology (KIT) in the context of the *Excellence Initiative* for leading German universities as well as the Ministry of Science and Arts of the state of Baden-Württemberg. Additional support from the Federal Institute of Material Testing (BAM) is gratefully acknowledged. We are grateful to Rosemarie Laging (BAM) and Bart Dervaux (Universiteit Gent) for measuring selected MALDI-TOF mass spectra. Bianka Manger (BAM) is acknowledged for assistance with the LCCC-GELC measurements.

REFERENCES

(1) Barner-Kowollik, C. *Handbook of RAFT Polymerization*; Wiley-VCH: Weinheim, Germany, 2008.

(2) (a) Solomon, D. H.; Rizzardo, E.; Cacioli, P. US4581429, 1986 (*Chem. Abstr.* **1985**, *102*, 221335q). (b) Chiefari, J.; Chong, Y. K.; Ercole, F.; Krstina, J.; Jeffery, J.; Le, T. P. T.; Mayadunne, R. T. A.; Meijs, G. F.; Moad, C. L.; Moad, G.; Rizzardo, E.; Thang, S. H. *Macromolecules* **1998**, *31*, 5559−5562. (c) Le, T. P.; Moad, G.; Rizzardo, E.; Thang, S. H. WO9801478, 1998 (*Chem. Abstr.* **1998**, *128*, 115390f). (d) Wang, J.-S.; Matyjaszewski, K. *Macromolecules* **1995**, *28* (23), 7901−7910.

(3) Kataoka, K.; Harada, A.; Nagasaki, Y. *Adv. Drug Delivery Rev* **2001**, *47*, 113.

(4) de Lambert, B.; Charreyre, M.-T.; Chaix, C.; Pichot, C. *Polymer* **2007**, *48*, 437.

(5) (a) Hales, M.; Barner-Kowollik, C.; Davis, T. P.; Stenzel, M. H. *Langmuir* **2004**, *20* (25), 10809−10817. (b) You, Y.; Hong, C.; Wang, W.; Lu, W.; Pan, C. *Macromolecules* **2004**, *37* (26), 9761−9767.

(6) (a) Tao, L.; Luan, B.; Pan, C. *Polymer* **2003**, *44*, 1013−1020. (b) Liu, R.; Shi, Y.; Fu, Z. *Adv. Mater. Res.* **2006**, *11*−*12*, 749−752.

(7) (a) Kolb, H. C.; Finn, M. G.; Sharpless, K. B. *Angew. Chem., Int. Ed.* **2001**, *113*, 2056. (b) Kolb, H. C.; Finn, M. G.; Sharpless, K. B. *Angew. Chem., Int. Ed.* **2001**, *40*, 2004. (c) Barner-Kowollik, C.; Du Prez, F. E.; Espeel, P.; Hawker, C. J.; Junkers, T.; Schlaad, H.; Van Camp, W. *Angew. Chem., Int. Ed.* **2011**, *50*, 60−62.

(8) (a) Gruendling, T.; Oehlenschlaeger, K. K.; Frick, E.; Glassner, M.; Schmid, C.; Barner-Kowollik, C. *Macromol. Rapid Commun.* **2011**, *32*, 807−812. (b) Altintas, O.; Hizal, G.; Tunca, U. *J. Polym. Sci., Polym. Chem.* **2008**, *46*, 1218. (c) Quemener, D.; Davis, T. P.; Barner-Kowollik, C.; Stenzel, M. H. *Chem. Commun.* **2006**, 5051−5053.

(9) Lefay, C.; Glé, D.; Rollet, M.; Mazzolini, J.; Bertin, D.; Viel, S.; Schmid, C.; Boisson, C.; D'Agosto, F.; Gigmes, D.; Barner-Kowollik, C. *J. Polym. Sci., Polym. Chem.* **2011**, *49* (3), 803−813.

(10) (a) Gruendling, T.; Pickford, R.; Guilhaus, M.; Barner-Kowollik, C. *J. Polym. Sci., Polym. Chem.* **2008**, *46* (22), 7447−7461. (b) Gründling, T.; Dietrich, M.; Barner-Kowollik, C. *Aust. J. Chem.* **2009**, *62*, 806−812. (c) Dietrich, M.; Glassner, M.; Gruendling, T.; Schmid, C.; Falkenhagen, J.; Barner-Kowollik, C. *Polym. Chem.* **2010**, *1*, 634−644.

(11) Schmid, C.; Falkenhagen, J.; Barner-Kowollik, C. *J. Polym. Sci., Polym. Chem.* **2011**, *49*, 1−10.

(12) Barner-Kowollik, C.; Davis, T. P.; Stenzel, M. H. C. *Aust. J. Chem.* **2006**, *59* (10), 719−727.

(13) (a) Mishra, A. K.; Patel, V. K.; Vishwakarma, N. K.; Biswas, C. S.; Raula, M.; Misra, A.; Mandal, T. K.; Ray, B. *Macromolecules* **2011**, *44* (8), 2465−2473. (b) Kipping, M.; Krahl, F.; Döring, A.; Adler, H.-J.; Kuckling, D. *Eur. Polym. J.* **2010**, *46*, 313−323. (c) Wolf, F. F.; Friedemann, N.; Frey, H. *Macromolecules* **2009**, *42*, 5622−5628.

(14) Belenky, B. G.; Gankina, E. S.; Tennikov, M. B.; Vilenchik, L. Z. *J. Chromatogr.* **1978**, *147*, 99.

(15) Entelis, S. G.; Evreinov, V. V.; Gorshkov, A. V. *Adv. Polym. Sci.* **1986**, *76*, 129.

(16) Pasch, H.; Trathnigg, B. *HPLC of Polymers*; Springer: Heidelberg, Germany, 1997.

(17) Macko, T.; Hunkeler, D. *Liquid Chromatography under Critical and Limiting Conditions: A Survey of Experimental Systems for Synthetic Polymers*: Springer: Berlin, 2003; Vol. *163*, pp 161−216.

(18) See for example: (a) Falkenhagen, J.; Much, H.; Stauf, W.; Mueller, A. H. E. *Macromolecules* **2000**, *33* (10), 3687−3693. (b) Berek, D. *Anal. Bioanal. Chem.* **2010**, *396*, 421−441. (c) Berek,

D. *Prog. Polym. Sci.* **2000**, *25*, 873−908. (d) Pasch, H.; Gallot, Y.; Trathnigg, B. *Polymer* **1993**, *34*, 4986−4989. (e) Striegel, A. M.; Yau, W. W.; Kirkland, J. J.; Bly, D. D. *Modern Size-Exclusion Liquid Chromatography*, 2nd ed.; Wiley: Hoboken, NJ, 2009. (f) Dugo, P.; Cacciola, F.; Kumm, T.; Dugo, G.; Mondello, L. *J. Chromatogr., A* **2008**, *1184*, 353−368. (g) Gloeckner, G.; Stickler, M.; Wunderlich, W. *Fresenius' Z. Anal. Chem.* **1988**, *330*, 46−49. (h) Gloeckner, G.; Vandenberg, J. H. M. *J. Chromatogr.* **1991**, *550*, 629−638. (i) Kilz, P.; Kruger, R. P.; Much, H.; Schulz, G. *Chromatogr. Charact. Polym.* **1995**, *247*, 223−241. (j) van der Horst, A.; Schoenmakers, P. J. *J. Chromatogr., A* **2003**, *1000*, 693−709. (k) Knecht, D.; Rittig, F.; Lange, R. F. M.; Pasch, H. *J. Chromatogr. A* **2006**, *1130* (1), 43−53.

(19) Ahmed, H.; Trathnigg, B.; Kappe, C. O.; Saf, R. *Eur. Polym. J.* **2009**, *45* (8), 2338−2347.

(20) Falkenhagen, J.; Weidner, S. *Anal. Chem.* **2009**, *81*, 282−287.

(21) Chaffey-Millar, H.; Stenzel, M. H.; Davis, T. P.; Coote, C.; Barner-Kowollik, C. *Macromolecules* **2006**, *39*, 6406.

(22) Schindler, A.; Hibionada, Y. M.; Pitt, C. G. *J. Polym. Sci., Polym. Chem.* **1982**, *20*, 319.

(23) Strazielle, C.; Benoit, H.; Vogl, O. *Eur. Polym. J.* **1978**, *14*, 331−334.

(24) Gruendling, T.; Guilhaus, M.; Barner-Kowollik, C. *Anal. Chem.* **2008**, *80*, 6915−6927.

(25) (a) Lohmeijer, B. G. G.; Pratt, R. C.; Leibfarth, F.; Logan, J. W.; Long, D. A.; Dove, A. P.; Nederberg, F.; Choi, J.; Wade, C.; Waymouth, R. M.; Hedrick, J. L. *Macromolecules* **2006**, *39*, 8574. (b) Pratt, R. C.; Lohmeijer, B. G. G.; Long, D. A.; Waymouth, R. M.; Hedrick, J. L. *J. Am. Chem. Soc.* **2006**, *128*, 4556.

(26) Ahmed, H.; Trathnigg, B.; Kappe, C. O.; Saf, R. *Eur. Polym. J.* **2010**, *46*, 494.

(27) (a) Ahmed, H.; Trathnigg, B. *J. Sep. Sci.* **2009**, *32*, 1390. (b) Chagneux, N.; Trimaille, T.; Rollet, M.; Beaudoin, E.; Gérard, P.; Bertin, D.; Gigmes, D. *Macromolecules* **2009**, *42*, 9435.

(28) Jiang, X.; van der Horst, A.; Schoenmakers, P. J. *J. Chromatogr., A* **2002**, *982*, 55−68.

(29) See for example Zhang, Y.; Liu, H.; Dong, H.; Li, C.; Liu, S. *J. Polym. Sci., Polym. Chem.* **2009**, *47*, 1636.

(30) Liang, C. Y.; Krimm, S. *J. Polym. Sci.* **1958**, *27*, 241.

(31) Hesse, M.; Meier, H.; Zeeh, B. *Spektroskopische Methoden in der organischen Chemie*; Thieme: Stuttgart, 2005.

Macromolecules

Article

pubs.acs.org/Macromolecules

Precise Synthesis of Dendrimer-like Star-Branched Poly(*tert*-butyl methacrylate)s and Their Block Copolymers by a Methodology Combining α-Terminal-Functionalized Living Anionic Polymers with a Specially Designed Linking Reaction in an Iterative Fashion

Hee-Soo Yoo, Takumi Watanabe, Yosuke Matsunaga, and Akira Hirao*

Polymeric and Organic Materials Department, Graduate School of Science and Engineering, Tokyo Institute of Technology, S1-6, 2-12-1, Ohokayama, Meguro-ku, Tokyo 152-8552, Japan

Supporting Information

ABSTRACT: A new stepwise iterative methodology was developed for the synthesis of well-defined high-generation and high-molecular-weight dendrimer-like star-branched poly(*tert*-butyl methacrylate)s (P^{t}BMA)s and block copolymers composed of P^{t}BMA and polystyrene (PS) segments. The methodology involves the following two reaction steps in an iterative process: (1) a linking reaction based on a 1:1 addition reaction of an α-terminal-(3-*tert*-butyldimethylsilyloxymethylphenyl (SMP))$_2$-functionalized living polymer with a core compound or α-terminal-(α-phenyl acrylate (PA))$_2$-functionalized polymers linked to the core and (2) a conversion of the SMP group to the PA function, to be used as the next reaction site. Repetition of the two reaction steps, (1) and (2), allows for the synthesis of high-generation and high-molecular-weight dendrimer-like star-branched polymers. In practice, a series of dendrimer-like star-branched (P^{t}BMA)s up to the fifth generation (5G) were successfully synthesized. The resulting polymers, whose arm segments were four-branched at the core and two-branched at each layer, were all well-defined in branched architecture and precisely controlled in chain length, and the final 5G dendrimer-like star-branched P^{t}BMA possessed a predictable M_n value of 1.07×10^7 g/mol and an extremely narrow molecular weight distribution of 1.03 in M_w/M_n value. The synthetic possibility of similar dendrimer-like star-branched polymers composed of functional polymer segments bearing acid-labile and/or basic groups by the same methodology was also demonstrated. Furthermore, 4G dendritic architectural block copolymers with hierarchic layer structures composed of P^{t}BMA (and poly(methacrylic acid)) and PS segments were synthesized.

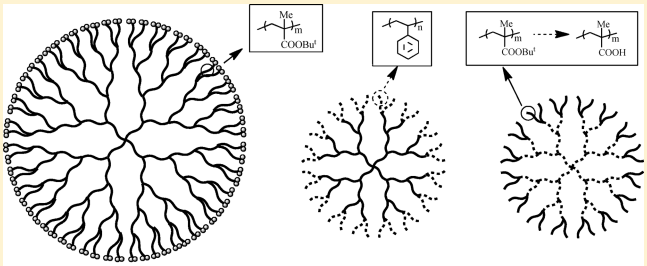

5G Dendrimer-like star-branched P^{t}BMA and 4G block copolymers

INTRODUCTION

For a long time to elucidate how branching architecture influences the properties and behavior of polymers has been a subject from both theoretical and industrial viewpoints. Among various branched polymers so far synthesized, dendrimer-like star-branched polymers have emerged as a new class of hyperbranched polymers synthesized since 1995.[1] They resemble dendrimers in branched architecture but are comprised of dendritically branched high-molecular-weight polymer chains emanating from a central core. Therefore, these polymers are much larger in molecular size and much higher in molecular weight than dendrimers. Dendrimer-like star-branched polymers are known as three-dimensional nanosize globular macromolecules and have manifold unique characteristics, i.e., specific topological hyperbranched and hierarchic layer (or generation) based architectures composed of branched repeating units, disparate branch densities between the core and outermost layer, and many junctions and chain-ends bearing many functional groups.[2−9] Furthermore, it is expected that the polymers behave as independent separate entities in solution as hyperbranched dendrigraft polymers do.[10−12]

Architecturally similar dendrimer-like star-branched block copolymers consisting of different polymer segments introduced at each layer have also been synthesized. As compared to linear block copolymers, they are considered to be unprecedented block copolymers having hierarchic layer-based architectures. Because of their specific and unique architectures, different polymer segments are expected to be phase-separated at the molecular level, followed by self-organizing, to form quite interesting and characteristically shaped domains and supramolecular assemblies ordered in nanoscale, which should be different from those formed by linear block copolymers and even asymmetric star-branched polymers.[13−23] Thus, dendrimer-like star-branched polymers and their block copolymers are promising functional materials with many potential applications in the fields of nanoscience and nanotechnology such as nanoreactors having catalysts and

Received: October 24, 2011
Revised: November 24, 2011
Published: December 9, 2011

enzymes in their layers, multicompartment micelles, carriers of drugs and genetic materials, shape-persistent electronic and photonic nanodevices, etc.

Similar to dendrimer synthesis,[24] a stepwise iterative methodology based on either a divergent or convergent approach has been employed to synthesize dendrimer-like star-branched polymers. However, the synthesis requires one more reaction step for introducing polymer chains between junctions in each layer. As such polymer chains, living polymers are usually used in order to synthesize well-defined dendrimer-like star-branched polymers.

Well-defined dendrimer-like star-branched polymers have so far been synthesized by the following two methodologies: The first methodology is based on a "core-first" divergent approach which initiates growth at a multifunctional core and extends outward by iterating the same or a similar process.[13−20,25−27] The iterative process usually involves two reaction steps: (1) living polymerization of a suitable monomer with a multifunctional initiator in the first iterative process, followed by continuing the same or different living polymerization with a multifunctional initiation site newly prepared at each polymer chain-end in the second or further iterative processes, and (2) a chain-end modification reaction to convert the terminus to two or more initiation sites for the next iteration. The two reaction steps are repeated several times to build up high-generation dendrimer-like star-branched polymers. Indeed, various dendrimer-like star-branched polymers and their block copolymers were synthesized first by Gnanou et al.,[25] and soon after by Hedrick et al.,[26] followed by Percec et al.[27] Given the appropriate choice of living polymerization and chain-end modification, isolation of the polymer synthesized in each iterative process is not necessary, and steric hindrance may be reduced as the iteration proceeds. Therefore, this methodology may be suited for large-scale preparation and high-generation and high-molecular-weight polymer synthesis.

Although defined structures are suggested in most dendrimer-like star-branched polymers so far synthesized by the above methodology, there remains a significant problem in terms of the uniformity of all polymer chains propagated from the multi-initiation sites at each generation. It is actually difficult to know whether the propagation reaction homogeneously proceeds or not at each iterative process. Moreover, it is not possible to determine how many reaction sites work. Therefore, a well-defined structure of polymers synthesized by this methodology is not guaranteed, even by acceptable agreement between the calculated and observed molecular weights in the final product.

As a complementary alternative, a stepwise iterative methodology based on an "arm-first" convergent approach was proposed by Hadjichristidis et al.[28] In this methodology, dendrons used as building units are prepared by repeating a linking reaction between premade living polymers with known molecular weights, followed by connecting them to a multifunctional core to synthesize a dendrimer-like star-branched polymer. Accordingly, this approach offers a distinct advantage in that the resulting polymer structure is readily estimated by comparing the molecular weight of the final product with that of the dendron, and agreement between both values gives a guarantee for the requisite structure if they are within experimental error limits (±3%). In practice, second- and third-generation (2G and 3G) polymers with well-defined structures were synthesized by Hadjichristidis et al.,[28,29] Hutchings et al.,[30] and Monteiro et al.[22,23,31] Since sterically bulky and high-molecular-weight dendrons are always used for the final connecting reaction, this methodology is not appropriate for the synthesis of high-generation and high-molecular-weight polymers.

Recently, we have developed a new stepwise iterative methodology based on an "arm-first" divergent approach having the advantages of the aforementioned two methodologies.[32−38] As illustrated in Scheme 1, the methodology involves the following two reaction steps in the iterative process: (1) a linking reaction of an α-terminal-(3-*tert*-butyldimethylsilyloxymethylphenyl (SMP))$_2$-functionalized living anionic polymer with either

Scheme 1. Synthesis of Dendrimer-like Star-Branched PMMAs up to 7G

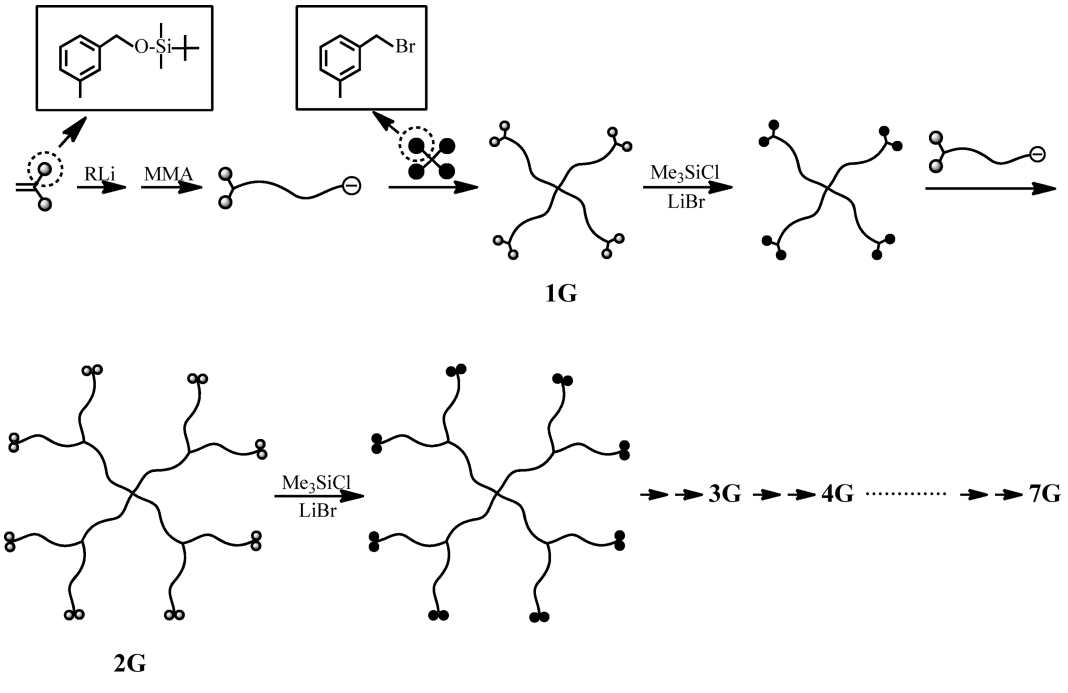

dx.doi.org/10.1021/ma202367e | *Macromolecules* 2012, 45, 100−112

a multifunctional core substituted with benzyl bromide (BnBr) moieties or α-terminal-$(BnBr)_2$-functionalized polymers linked to the core and (2) a transformation reaction of the SMP group to the BnBr function to be used as the next reaction site. By repeating the two reaction steps, dendrimer-like star-branched polymers are progressively synthesized from the core in an outward direction.

Accordingly, steric hindrance may be reduced as the iteration proceeds, and there is no final connection step among sterically bulky and high-molecular-weight dendrons. In order to introduce polymer chains, a termination reaction using premade living anionic polymers of known molecular weights, i.e., the "arm-first" procedure, is employed. Therefore, the possibilities of insufficient initiation and heterogeneous propagation reactions with multifunctional initiation sites often observed in the "core-first" divergent approach are completely avoided. Furthermore, the structure of the resulting polymer is readily estimated by comparing the molecular weight of the final polymer with the total molecular weight of the premade living polymers used in all iterative processes, and the requisite structure is essentially guaranteed by the agreement between both values.

With the use of this methodology, a series of well-defined dendrimer-like star-branched poly(methyl methacrylate)s (PMMA)s up to the seventh generation (or layer) (7G) were successfully synthesized. The final 7G polymer was a huge macromolecule possessing a predictable M_n value of 1.94×10^6 g/mol and a narrow molecular weight distribution of M_w/M_n value of 1.02 and consisting of 508 PMMA with 512 reactive BnBr termini.[33] Furthermore, highly branched dendrimer-like star-branched (PMMA)s were also synthesized by developing the same methodology using an α-terminal-$(SMP)_4$-functionalized living PMMA as a new building block.[35−37] Very recently, well-defined dendrimer-like star-branched polystyrenes (PS)s up to 5G and their block copolymers composed of PMMA and PS segments alternately located in layers have been synthesized by a newly modified methodology.[38]

To the best of our knowledge, the methodology based on the "arm-first" divergent approach may be currently the most reliable system for the synthesis of high-generation and high-molecular-weight dendrimer-like star-branched polymers with well-defined structures. Very unfortunately, however, the number of living polymers usable in the methodology is quite limited because the transformation reaction in step (2) requires highly acidic conditions using $(CH_3)_3SiCl/LiBr$ or $(CH_3)_3SiBr$, under which a variety of polymers bearing either acid-labile and/or basic groups cannot be used. Herein, we propose an alternative and more general and versatile methodology using the α-phenyl acrylate function as a new reaction site in order to overcome such limitations and problems.

EXPERIMENTAL SECTION

Measurements. Size exclusion chromatography (SEC) and right angle laser light scattering (RALLS) were performed on an Ashahi Techneion Viscotek Model 302 TDA with triple detector software. The dn/dc values were automatically measured by this instrument. They were also separately measured with an Ohotsuka Electronics DMR-1020 refractometer operating at 633 nm in order to make sure the values. THF was used as an eluent at a flow rate of 1.0 mL/min at 30 °C. Three polystyrene columns [pore size (bead size): 650 Å (9 μm), 200 Å (5 μm), 75 Å (5 μm)] were used. Calibration curve was made with standard PS samples for determining M_n and M_w/M_n values. ^{1}H (300 MHz) and ^{13}C (75 MHz) NMR spectra were measured on a Bruker DPX300 in $CDCl_3$. Chemical shifts were recorded in ppm downfield relative to $CDCl_3$ (δ 7.26 for ^{1}H NMR and δ 77.1 for ^{13}C NMR). FT-IR spectra were recorded on a JASCO FT/IR-4100 instrument using an attenuated total reflectance (ATR) attachment.

General Procedure. The materials herein used are described in the Supporting Information. In addition, monomer purification under high-vacuum conditions and the synthesis of 1,1-bis(3-(1,3-dioxolan-2-yl) phenyl)ethylene (**3**) and 1,1-bis(3-trimethylsilyloxymethylphenyl)-ethylene (**4**) are also described in the Supporting Information. Except for deprotection and the Mitsunobu reaction, all of polymerization and linking reactions were carried out in sealed handmade glass reactors equipped with break-seals under high-vacuum conditions (10^{-6} Torr). The reactors were sealed off from the high-vacuum line and prewashed with red 1,1-diphenylhexyllithium in heptane prior to the polymerization and linking reactions. All operations were performed according to the usual high-vacuum technique with break-seals.[39]

α-Terminal-(3-*tert*-butyldimethylsilyloxypropyl)-functionalized living PS was prepared by the living anionic polymerization of styrene with 3-*tert*-butyldimethylsilyloxy-1-propyllithium in *tert*-butylbenzene in the presence of a 5-fold excess of TMEDA at 0 °C for 0.5 h and 25 °C for an additional 2 h.[37] α-Terminal-$(SMP)_2$-functionalized living P^{t}BMA was prepared by the living anionic polymerization of ^{t}BMA with the functional initiator from *sec*-BuLi and 1,1-bis(3-*tert*-butyldimethylsilyloxymethylphenyl)ethylene (**1**) in the presence of a 5-fold excess of LiCl at −78 °C for 5 h. Similarly, α-terminal-$(SMP)_2$-functionalized living PMMA, poly(2-(2-methoxyethoxy)ethyl methacrylate), poly((2,2-dimethyl-1,3-dioxolan-4-yl)methyl methacrylate), and poly(ferrocenylmethyl methacrylate) were prepared by the living anionic polymerization of the corresponding methacrylate monomers with the functional initiator from *sec*-BuLi and **1** in the presence of a 5-fold excess of LiCl at −78 °C for 1 h.

The conversion of α-terminal-(3-*tert*-butyldimethylsilyloxypropyl)-functionalized PS to α-terminal-$(SMP)_2$-functionalized PS was carried out according to the procedures previously reported.[38] α-Terminal-$(SMP)_2$-functionalized PS, PMMA, P^{t}BMA, poly(2-(2-methoxyethoxy)ethyl methacrylate), poly((2,2-dimethyl-1,3-dioxolan-4-yl)-methyl methacrylate), and poly(ferrocenylmethyl methacrylate) were treated with $(C_4H_9)_4NF$ (a 10-fold excess for SMP function) in THF at 0 °C for 10 h to deprotect the *tert*-butyldimethylsilyl group. The resulting polymers were purified by reprecipitation twice and freeze-dried from their absolute benzene solutions twice. Two hydroxyl α-termini of each polymer were reacted with a 20-fold excess of α-phenylacrylic acid, Ph_3P, and diisopropyl azodicarboxylate (DIAD) in THF at 25 °C for 15 h to convert to two α-phenyl acrylate (PA) reaction sites. The conversion of the SMP group to the PA reaction site in each polymer was observed by ^{1}H NMR to be quantitative within experimental errors.

In the case of poly(2-*tert*-butyldimethylsilyloxyethyl methacrylate), two trimethylsilyl-protected hydroxyl groups were introduced at the α-chain-end by the polymerization of 2-*tert*-butyldimethylsilyloxyethyl methacrylate with the functional initiator prepared from **4** and *sec*-BuLi in THF at −78 °C for 1 h. The trimethylsilyl group was selectively deprotected to regenerate the hydroxyl group only by pouring the polymer into methanol. Finally, two hydroxyl α-termini were converted to two PA reaction sites by the Mitsunobu reaction in the same manner as that described above.

The linking reaction between a 1.5-fold excess of living PS end-capped with DPE and α-terminal-$(PA)_2$-functionalized polymer was carried out at −78 °C for 15 h. The linking reaction of each of living poly(alkyl methacrylate)s with the corresponding α-terminal-$(PA)_2$-functionalized polymer was performed at −40 °C for 24 h. In the case using living P^{t}BMA, the reaction conditions were those at −25 °C for 24 h. In these reactions except for the use of living PS, a 3-fold (or more) excess of living polymer for the PA reaction site was used. The reactions were all observed to be almost quantitative under such conditions.

Synthesis of 1G and 2G Dendrimer-like Star-Branched (P^{t}BMA)s. A 1G P^{t}BMA was synthesized by the living anionic polymerization of ^{t}BMA with the functionalized initiator prepared from **1** and *sec*-BuLi, followed by reacting with 1,1,4,4-tetrakis(3-bromomethylphenyl)butane (**2**). ^{t}BMA (38.9 mmol) in THF solution

(28.2 mL) was polymerized at −78 °C for 5 h with the functionalized initiator prepared from **1** (0.627 mmol) and *sec*-BuLi (0.509 mmol) in THF (9.80 mL) at −78 °C for 0.5 h, followed by addition of LiCl (2.55 mL) in THF (12.1 mL). Then, **2** (0.0589 mmol, 0.235 mmol for BnBr moiety) in THF (5.50 mL) was added to the resulting living P^{t}BMA solution at −78 °C, and the reaction mixture was allowed to stand in THF at −40 °C for 24 h. After quenching with degassed methanol, the mixture was poured into a mixture of water and methanol (1/4, v/v) to precipitate the polymers. The resulting polymers were characterized by SEC to compare their peak areas. The polymers dissolved in benzene (30 mL) were poured into methanol (150 mL). Then a small amount of water was slowly dropped to the solution at 25 °C until color of the solution was changed to opaque, followed by cooling to 0 °C to precipitate the linked polymer (1.27 g, 85%). The deactivated living P^{t}BMA used in excess in the reaction was readily recovered from the supernatant solution. The linked polymer was purified by reprecipitation twice from THF to a mixture of water and methanol (1/4, v/v) and freeze-dried from its absolute benzene solution twice to afford the 1G polymer, referred to as 1G-P^{t}BMA-SMP$_8$ (2.11 g, 81%). ^{1}H NMR: δ 7.3−6.8 (m, aromatic), 4.69 and 4.64 (d, $-C_6H_4-CH_2-O-$), 2.3−1.6 (m, $-CH_2-C(CH_3)-$), 1.5−0.5 (m, $-CH_2-C(CH_3)-$ and $-O-C(CH_3)_3$), 0.90 and 0.87 (d, $-C(CH_3)_3$), 0.05 and 0.02 (d, $Si(CH_3)_2$).

Under a nitrogen atmosphere, the 1G-P^{t}BMA-SMP$_8$ (1.81 g, 0.290 mmol for SMP group) dissolved in THF (18 mL) was treated with $(C_4H_9)_4NF$ (2.9 mmol) in THF (2.9 mL) at 0 °C for 10 h, and the reaction mixture was poured into a mixture of water and methanol (1/4, v/v) to precipitate the polymer. A 1G-P^{t}BMA-(OH)$_8$ was obtained in 95% yield. The conversion of hydroxyl group to PA reaction site was carried out as follows: Under a nitrogen atmosphere, α-phenylacrylic acid (5.20 mmol), Ph_3P (5.24 mmol), and DIAD (5.21 mmol) were added to the 1G-P^{t}BMA-(OH)$_8$ (1.65 g, 0.264 mmol for hydroxyl group) in THF (40 mL) at 0 °C, and the reaction mixture was allowed to stir at 25 °C for 16 h. After quenching with degassed methanol, reprecipitation twice from THF to a mixture of water and methanol (1/4, v/v) and freeze-drying from its absolute benzene solution twice afford 1G-P^{t}BMA-PA$_8$ in 82% yield. ^{1}H NMR of the deprotected polymer: δ 7.3−6.8 (m, aromatic), 4.61 (s, $-C_6H_4-CH_2-OH$), 2.3−1.6 (m, $-CH_2-C(CH_3)-$), 1.5−0.5 (m, $-CH_2-C(CH_3)-$ and $-O-C(CH_3)_3$), 1G-P^{t}BMA-PA$_8$: δ 7.3−6.8 (m, aromatic), 6.33, 6.27, 5.88, 5.85 (d, $C{=}CH_2$), 5.23 and 5.16 (d, $-C_6H_4-CH_2-O-$), 2.3−1.6 (m, $-CH_2-C(CH_3)-$), 1.5−0.5 (m, $-CH_2-C(CH_3)-$ and $-O-C(CH_3)_3$).

The 2G polymer was synthesized by the reaction of 1G-P^{t}BMA-PA$_8$ with α-terminal-(SMP)$_2$-functionalized living P^{t}BMA in THF at −25 °C for 24 h. The procedure is as follows: ^{t}BMA (15.4 mmol) in THF (11.5 mL) was polymerized with the functional initiator prepared from **1** (0.230 mmol) and *sec*-BuLi (0.205 mmol) in the presence of LiCl (1.05 mmol) in THF (10.5 mL) at −78 °C for 5 h. Then, the 1G-P^{t}BMA-PA$_8$ (0.0621 mmol for PA functionality) in THF (10.0 mL) was added to the above living polymer solution at −78 °C, and the reaction mixture was allowed to stand at −25 °C for 24 h. After quenching with degassed methanol, the reaction mixture was poured into a mixture of water and methanol (1/4, v/v) to precipitate the polymers. The linked polymer was isolated by the fractionation mentioned above; reprecipitation of the resulting polymer twice from THF to a mixture of water and methanol (1/4, v/v) and freeze-drying from its absolute benzene solution twice afford 2G-P^{t}BMA-SMP$_{16}$ in 92% yield. ^{1}H NMR: δ 7.3−6.8 (m, aromatic), 4.69 and 4.64 (d, $-C_6H_4-CH_2-O-$), 2.4−1.6 (m, $-CH_2-C(CH_3)-$), 1.5−0.5 (m, $-CH_2-C(CH_3)-$ and $-O-C(CH_3)_3$), 0.90 and 0.87 (d, $-C(CH_3)_3$), 0.06 and 0.02 (d, $Si(CH_3)_2$).

Synthesis of 3G, 4G, and 5G Dendrimer-like Star-Branched (P^{t}BMA)s. 3G, 4G, and 5G polymers were synthesized by repeating the same reaction sequence under the conditions similar to those mentioned above. A 3.9-, 5.4-, or 6.5-fold excess of α-terminal-(SMP)$_2$-functionalized living P^{t}BMA was used in the reaction with α-terminal-(PA)$_n$-functionalized P^{t}BMA for the synthesis of 3G-P^{t}BMA-SMP$_{32}$, 4G-P^{t}BMA-SMP$_{64}$, or 5G-P^{t}BMA-SMP$_{128}$. The reactions were carried out for longer reaction times of 30, 36, and 48 h. The target polymers were isolated by the fractionation mentioned above and precipitated in a mixture of water and methanol (1/4, v/v). Yields of 3G, 4G, and 5G polymers were around 90%. The ^{1}H NMR spectra of all polymers are as follows: ^{1}H NMR, 2G-P^{t}BMA-PA$_{16}$: δ 7.3−6.8 (m, aromatic), 6.33, 6.27, 5.88, 5.85 (d, $C{=}CH_2$), 5.22 and 5.16 (d, $-C_6H_4-CH_2-O-$), 2.4−1.6 (m, $-CH_2-C(CH_3)-$), 1.5−0.5 (m, $-CH_2-C(CH_3)-$ and $-O-C(CH_3)_3$); 3G-P^{t}BMA-SMP$_{32}$: δ 7.3−6.8 (m, aromatic), 4.69 and 4.64 (d, $-C_6H_4-CH_2-O-$), 2.4−1.6 (m, $-CH_2-C(CH_3)-$), 1.5−0.5 (m, $-CH_2-C(CH_3)-$ and $-O-C(CH_3)_3$), 0.90 and 0.87 (d, $-C(CH_3)_3$), 0.06 and 0.02 (d, $Si(CH_3)_2$); 3G-P^{t}BMA-PA$_{32}$: δ 7.3−6.8 (m, aromatic), 6.33, 6.27, 5.88, 5.86 (d, $C{=}CH_2$), 5.23 and 5.17 (d, $-C_6H_4-CH_2-O-$), 2.4−1.6 (m, $-CH_2-C(CH_3)-$), 1.5−0.5 (m, $-CH_2-C(CH_3)-$ and $-O-C(CH_3)_3$); 4G-P^{t}BMA-SMP$_{64}$: δ 7.3−6.8 (m, aromatic), 4.69 and 4.64 (d, $-C_6H_4-CH_2-O-$), 2.4−1.6 (m, $-CH_2-C(CH_3)-$), 1.5−0.5 (m, $-CH_2-C(CH_3)-$ and $-O-C(CH_3)_3$), 0.91 and 0.88 (d, $-C(CH_3)_3$), 0.06 and 0.02 (d, $Si(CH_3)_2$); 4G-P^{t}BMA-PA$_{64}$: δ 7.3−6.8 (m, aromatic), 6.33, 6.27, 5.88, 5.85 (d, $C{=}CH_2$), 5.22 and 5.16 (d, $-C_6H_4-CH_2-O-$), 2.4−1.6 (m, $-CH_2-C(CH_3)-$), 1.5−0.5 (m, $-CH_2-C(CH_3)-$ and $-O-C(CH_3)_3$); 5G-P^{t}BMA-SMP$_{128}$: δ 7.3−6.8 (m, aromatic), 4.69 and 4.64 (d, $-C_6H_4-CH_2-O-$), 2.4−1.6 (m, $-CH_2-C(CH_3)-$), 1.5−0.5 (m, $-CH_2-C(CH_3)-$ and $-O-C(CH_3)_3$), 0.91 and 0.88 (d, $-C(CH_3)_3$), 0.06 and 0.02 (d, $Si(CH_3)_2$).

Synthesis of 4G Dendrimer-like Star-Branched Block Copolymers, (P^{t}BMA-*b*-(P^{t}BMA)$_2$-*b*-(P^{t}BMA)$_4$-*b*-(PS)$_8$)$_4$ and (PS-*b*-(PS)$_2$-*b*-(PS)$_4$-*b*-(P^{t}BMA$_8$)$_4$. (1) (P^{t}BMA-*b*-(P^{t}BMA)$_2$-*b*-P(P^{t}BMA)$_4$-*b*-(PS)$_8$)$_4$. A 3G-P^{t}BMA-PA$_{32}$ was synthesized by the above-mentioned procedures. Under high-vacuum conditions, styrene (8.64 mmol) in *tert*-butylbenzene solution (4.50 mL) was polymerized with 3-*tert*-butyldimethylsilyloxy-1-propyllithium (0.0940 mmol) in heptane solution (2.90 mL) in the presence of TMEDA (0.486 mmol) at 0 °C for 0.5 h and at 25 °C for an additional 2 h. The living PS solution was cooled to −78 °C, followed by addition of THF (9.70 mL), and DPE (0.142 mmol) in THF solution (5.80 mL) was subsequently added to end-cap the chain-end anion for 1 h. Then, the 3G-P^{t}BMA-PA$_{32}$ (0.500 g, 0.0556 mmol for 32 PA reaction sites) dissolved in THF (8.30 mL) was added to the resulting DPE-end-capped living PS solution ($M_{n,calcd}$ = 9910 g/mol, 0.0940 mmol) at −78 °C, and the reaction mixture was allowed to react at −78 °C for 15 h. The reaction mixture was poured into methanol to precipitate the polymers. The 4G block polymer was isolated by fractional precipitation using a mixture of cyclohexane and hexane at 5 °C, purified by reprecipitation from THF to methanol, and freeze-drying from its absolute benzene solution. The 4G block copolymer was obtained in 81% yield. ^{1}H NMR: δ 7.3−6.2 (m, aromatic), 4.72 and 4.66 (d, $-C_6H_4-CH_2-O-$), 3.4 (s, $-CH_2-O-Si$), 2.8−0.8 (m, $-CH_2-CH-$, $-CH_2-C(CH_3)-$ and $-O-C(CH_3)_3$), 0.84 (s, $-C(CH_3)_3$), 0.06 and 0.03 (d, $Si(CH_3)_2$).

(2) (PS-*b*-(PS)$_2$-*b*-(PS)$_4$-*b*-(P^{t}BMA$_8$))$_4$. A 3G-PS-(3-*tert*-butyldimethylsilyoxypropyl)$_{32}$ was prepared by the procedures similar to those previously reported.[38] The 16 (3-*tert*-butyldimethylsilyoxypropyl) groups were converted to 32 PA reaction sites by the Mitsunobu reaction under the identical conditions as mentioned above. The α-terminal-(SMP)$_2$-functionalized living P^{t}BMA ($M_{n,calcd}$ = 10 200 g/mol, 0.180 mmol) was prepared by the polymerization of ^{t}BMA (12.7 mmol) with the initiator prepared from **1** (0.234 mmol) and *sec*-BuLi (0.180 mmol) in the presence of LiCl (0.918 mmol) in THF at −78 °C for 5 h and reacted with the 3G-PS-PA$_{32}$ (0.0400 mmol for 32 PA reaction sites) in THF at −25 °C for 24 h. The 4G block copolymer was isolated in 90% yield only by precipitation in methanol. ^{1}H NMR: δ 7.3−6.2 (m, aromatic), 4.70 and 4.65 (d, $-C_6H_4-CH_2-O-$), 2.8−0.8 (m, $-CH_2-CH-$, $-CH_2-C(CH_3)-$ and $-O-C(CH_3)_3$), 0.91 and 0.88 (d, $-C(CH_3)_3$), 0.06 and 0.03 (d, $Si(CH_3)_2$).

Synthesis of 4G Dendrimer-like Star-Branched Block Copolymers Composed of Poly(methacrylic acid) (PMAA) and PS Segments, (PMAA-*b*-(PMAA)$_2$-*b*-(PMAA)$_4$-*b*-(PS)$_8$)$_4$ and (PS-*b*-(PS)$_2$-*b*-(PS)$_4$-*b*-(PMAA)$_8$)$_4$. A 4G block copolymer, (PMAA-*b*-(PMAA)$_2$-*b*-(PMAA)$_4$-*b*-(PS)$_8$)$_4$, was prepared as follows: Under a nitrogen atmosphere, the 4G block copolymer, (P^{t}BMA-*b*-(P^{t}BMA)$_2$-*b*-(P^{t}BMA)$_4$-*b*-(PS)$_8$)$_4$ (0.120 g, 0.579 mmol for *tert*-butyl methacrylate monomer unit), and LiBr (0.190 g, 2.19 mmol) were dissolved in a mixed solvent of dry chloroform (10 mL) and dry acetonitrile (10 mL).

dx.doi.org/10.1021/ma202367e | *Macromolecules* 2012, 45, 100−112

Scheme 2. Linking Reaction of α-Terminal-(Formyl)$_2$-Functionalized P^{t}BMA with Living P^{t}BMA

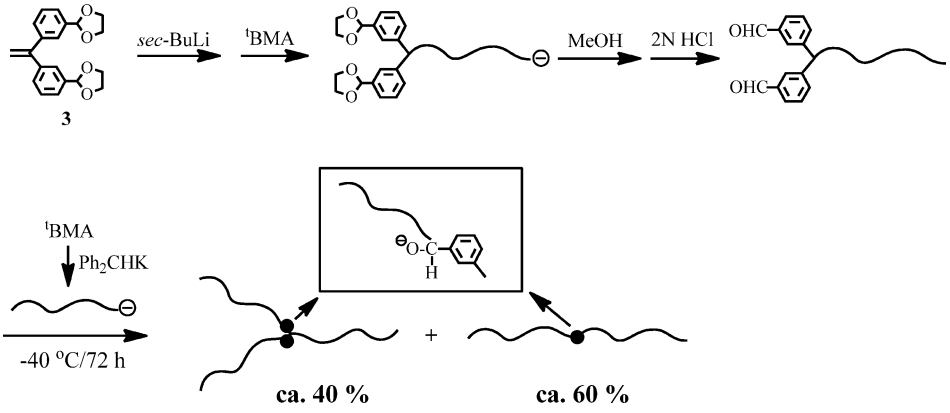

Then, $(CH_3)_3SiCl$ (2.79 mmol) was added to the solution at 25 °C, and the mixture was allowed to react at 40 °C for 24 h. After quenching with methanol, the mixture was poured into methanol to precipitate the polymer. It was carefully washed with methanol and THF and dried in vacuo for 24 h (0.0870 g, 94% yield).

Another block copolymer, (PS-*b*-$(PS)_2$-*b*-$(PS)_4$-*b*-$(PMAA)_8)_4$, was prepared by treatment of the 4G block copolymer, (PS-*b*-$(PS)_2$-*b*-$(PS)_4$-*b*-$(P^tBMA)_8)_4$, with a 1:1 mixture of $(CH_3)_3SiCl$ and LiBr, according to the procedures similar to those mentioned above (92% yield). Both hydrolyzed polymers were observed to be insoluble in most organic solvents and 2 N NaOH aqueous solution.

RESULTS AND DISCUSSION

In order to synthesize high-generation and high-molecular-weight dendrimer-like star-branched polymers with well-defined structures, it is essential that the two reaction steps (1) and (2), as shown in Scheme 1, proceed with almost quantitative efficiencies in each iterative process. In practice, both steps satisfactorily worked at least seven times to result in the successful synthesis of high-generation and high-molecular-weight polymers. Very unfortunately, the number of polymer segments usable in this methodology is quite limited due to the transformation reaction in step (2), which requires highly acidic conditions using Me_3SiCl/LiBr or Me_3SiBr. Under such conditions, PS was stable and usable without difficulty. PMMA was also stable, but only under the conditions using Me_3SiCl/LiBr, and was found to be partly hydrolyzed with Me_3SiBr.[40] On the other hand, polymer segments bearing acid-labile and/or basic groups could not be used. For example, the *tert*-butyl esters of poly(*tert*-butyl methacrylate) (P^{t}BMA) were readily cleaved to result in poly(methacrylic acid). Both the silyl- and acetal-protected functionalities of poly(2-*tert*-butyldimethylsilyloxyethyl methacrylate) and poly((2,2-dimethyl-1,3-dioxolan-4-yl)methyl methacrylate) were completely deprotected. The ferrocene moieties of poly(ferrocenylmethyl methacrylate) were changed to ferrocenium cations. Furthermore, the transformation reaction was observed to insufficiently proceed in the presence of poly(2-vinylpyridine). Thus, the previously reported methodologies, effective for the synthesis of dendrimer-like star-branched PMMA and PS, are not applicable to the synthesis of dendrimer-like star-branched polymers composed of polymer segments bearing acid-labile and/or basic groups.

The SMP group could be transformed into a BnBr reaction site by treatment with CBr_4 and Ph_3P without cleavage of P^{t}BMA. However, the reaction yield was always at around 90% but was not quantitative. Benzyl sulfonates, such as $MeSO_2-O-CH_2C_6H_4-$ and *p*-$Me-C_6H_4-SO_2-O-CH_2C_6H_4-$ functions, are known to readily react with anionic species. They could be quantitatively introduced by deprotection of the SMP group with $(C_4H_9)_4NF$, followed by treatment with either $MeSO_2Cl$ or *p*-$Me-C_6H_4-SO_2Cl$ in pyridine, while P^{t}BMA remained unchanged under such conditions. However, the reaction of either sulfonate with living P^{t}BMA was not quantitative. Thus, the reaction conditions using CBr_4 and Ph_3P and the use of the $MeSO_2-O-C_6H_4-$ or *p*-$Me-C_6H_4-SO_2-O-C_6H_4-$ function instead of the BnBr reaction site are not appropriate for our purpose.

We also considered that a formylphenyl function could be used as a new reaction site because of its high reactivity toward anionic species. As illustrated in Scheme 2, two 3-formylphenyl functions were readily introduced into the α-termini (the initiating chain-end) of P^{t}BMA by using 1,1-bis(3-(1,3-dioxolan-2-yl)phenyl)ethylene, an acetal-protected DPE derivative, **3**, in the polymerization, followed by deprotection under very mild acidic conditions, where P^{t}BMA was stable. Again, unfortunately, the 3-formylphenyl reaction site was reacted with living P^{t}BMA only in a moderate yield which was far from quantitative.[41]

α-Phenyl Acrylate as a New Reaction Site. As the next candidate, the α-phenyl acrylate (PA) function, similar to MMA in structure, was adopted with the expectation that the living polymer of alkyl methacrylate would react with the PA reaction site in a 1:1 addition manner and that further addition of the PA function would be suppressed by a sterically bulky α-phenyl substituent. For the introduction of the PA reaction site, ^{t}BMA was anionically polymerized with the initiator from **1** and *sec*-BuLi, and the resulting polymer was subsequently treated with $(C_4H_9)_4NF$ (deprotection) and then treated with α-phenylacrylic acid, Ph_3P, and DIAD (the so-called Mitsunobu esterification reaction), as shown in Scheme 3. With these treatments, two SMP α-termini were quantitatively converted to two PA reaction sites, while P^{t}BMA remained as it was. Complete conversion was confirmed by the ^{1}H NMR analysis showing that three resonances assigned to benzyl methylene protons ($-C_6H_4-CH_2-O-Si\equiv$) (4.64, 4.69 ppm), *tert*-butyl protons (0.87, 0.90 ppm), and silylmethyl protons (0.02, 0.05 ppm) of the SMP group had completely disappeared, while new resonances corresponding to vinylene protons ($CH_2{=}C(Ph)-$) (5.85, 5.88 and 6.30, 6.33 ppm) and benzyl methylene protons ($-C(=O)-O-CH_2-C_6H_4-$) (5.16, 5.23 ppm) of the PA moiety are observed. The SEC peak of the polymer obtained after the reactions was almost the same in shape and elution count as that of the original P^{t}BMA.

dx.doi.org/10.1021/ma202367e | *Macromolecules* 2012, 45, 100–112

Scheme 3. Linking Reaction of α-Terminal-$(PA)_2$-Functionalized P^{t}BMA with Either Living PMMA or P^{t}BMA

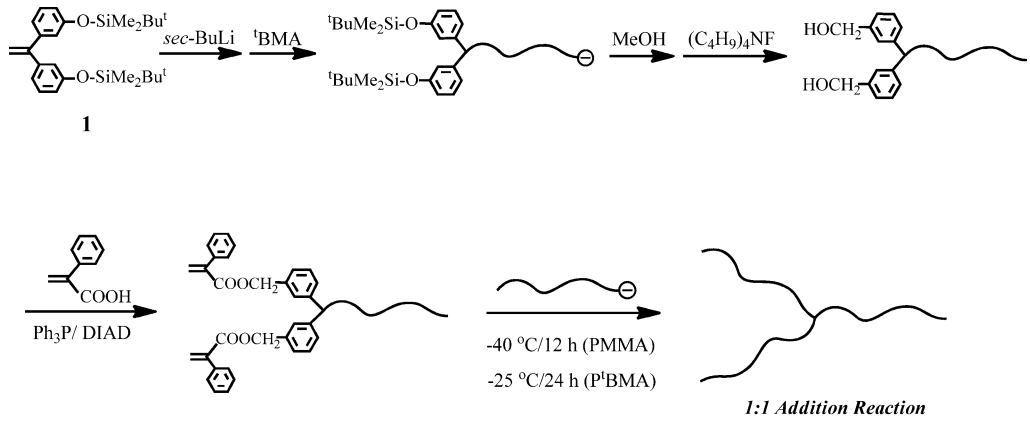

In order to examine the reactivity of the PA reaction sites introduced at the α-termini of P^{t}BMA, the α-terminal-$(PA)_2$-functionalized P^{t}BMA (M_n = ca. 10 kg/mol) was reacted with a 6-fold excess (a 3-fold excess for each PA functionality) of living PMMA (M_n = ca. 10 kg/mol) under the conditions in THF at −40 °C for 24 h. The SEC profile of the reaction mixture, as shown in Figure 1, exhibits only two peaks for the target linked product: a 3-arm star-branched polymer in this case and the deactivated living PMMA used in excess in the reaction. On the basis of the two peak areas, the linking efficiency was estimated to be almost quantitative. The quantitative reaction efficiency was also supported by the observation that no peak for the intermediate polymer was present between the two peaks. Furthermore, higher-molecular-weight polymers were not produced at all, clearly demonstrating that the sterically bulky α-phenyl substituent was effective in suppressing further addition reaction.

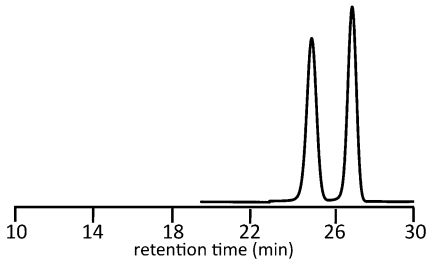

Figure 1. SEC profile of the reaction mixture of the linking reaction between α-terminal-$(PA)_2$-functionalized P^{t}BMA and living PMMA.

The linking reaction was not fast under the conditions at −40 °C. In practice, the intermediate 2-arm linked polymer was mainly formed along with a small amount of 3-armed star (15%) after 3 h. The reaction was observed to be complete after 12 h. A 2-fold excess of living PMMA for the PA reaction site was not enough to complete the reaction, and the reaction yield was around 80% under the same conditions. The linking reaction of the PA reaction site with living P^{t}BMA (M_n = ca. 10 kg/mol) appeared to be somewhat slow and was not complete at −40 °C even after 12 h. However, the reaction was observed to be complete under the conditions at −25 °C for 24 h. Thus, the PA reaction site may be used as the reaction site instead of the BnBr function for our synthetic purpose. We have also recently demonstrated that the PA reaction site is effective to link the polymer chains in the synthesis of multiblock copolymers, triblock terpolymers, and exact graft copolymers.[41−43]

A less hindered α-methyl acrylate (methacrylate) could also be introduced into P^{t}BMA in a similar manner. The resulting α-terminal-(methacrylate)$_2$-functionalized P^{t}BMA was then reacted with living PMMA under the same conditions. In this case, the expected 1:1 addition reaction, followed by an unexpected intramolecular addition reaction, predominantly occurred. Further addition of the methacrylate function was also observed. Thus, the methacrylate function was not suitable as a reaction site.

Synthesis of 1G−5G Dendrimer-like Star-Branched (P^{t}BMA)s. In order to examine the effectiveness of the PA function as a reaction site in the methodology, the synthesis of dendrimer-like star-branched (P^{t}BMA)s, difficult to obtain by our previous methodology, was carried out. A new methodology herein developed is basically similar in procedure to that previously reported.[33] As illustrated in Scheme 4, it involves the following two reaction steps (1)′ and (2)′ corresponding to reaction steps (1) and (2), as illustrated in Scheme 1: (1)′ a linking reaction based on a 1:1 addition reaction of an α-terminal-$(SMP)_2$-functionalized living anionic polymer with either a multifunctional core compound or α-terminal-$(PA)_2$-functionalized polymers linked to the core and (2)′ a conversion of the SMP group to the PA function, to be used as the next reaction site. By repeating the two reaction steps, a series of dendrimer-like star-branched polymers up to 5G could be progressively synthesized from the core in an outward direction.

For the synthesis of a 1G polymer, we used the same core compound substituted with four BnBr functions, as previously used for the synthesis of dendrimer-like star-branched PMMA.[33] At first, an α-terminal-$(SMP)_2$-functionalized living P^{t}BMA was prepared by the anionic polymerization of ^{t}BMA with the functional initiator from **1** and *sec*-BuLi in THF at −78 °C for 5 h and in situ reacted with the core compound at −40 °C for 24 h. A 5-fold excess of LiCl was added for *sec*-BuLi prior to the polymerization of ^{t}BMA in order to narrow the molecular weight distribution. A 2.1-fold excess of living polymer for each BnBr function was used. Throughout this study, living P^{t}BMA was fixed at around 10 kg/mol in molecular weight. The SEC profile of the reaction mixture exhibited only two peaks for the linked product and the deactivated living P^{t}BMA used in excess in the reaction. The linking efficiency was estimated to be almost quantitative by

dx.doi.org/10.1021/ma202367e | *Macromolecules* 2012, 45, 100−112

Scheme 4. Synthesis of Dendrimer-like-Star-Branched P^{t}BMA (2G) by a New Methodology

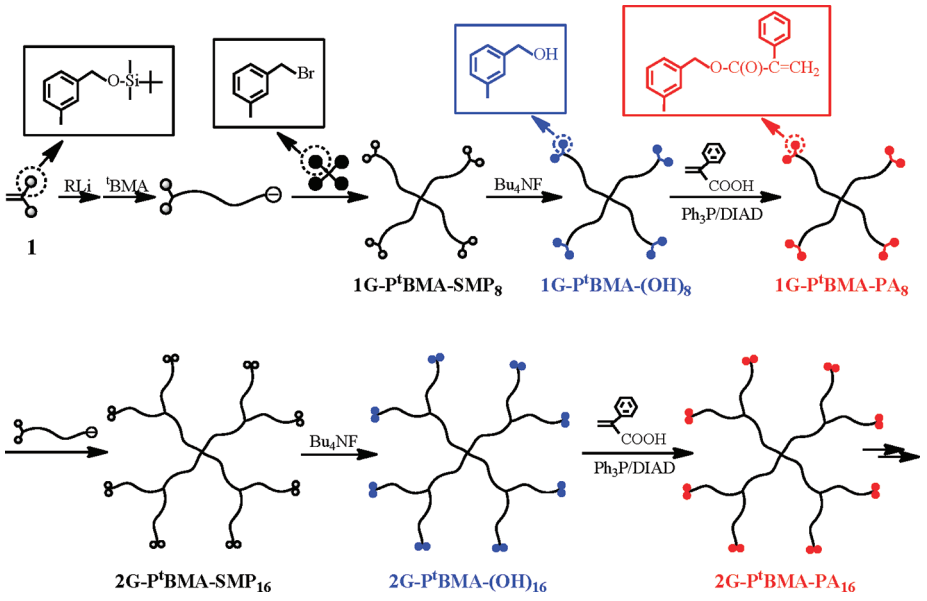

Table 1. Characterization Results of Dendrimer-like Star-Branched P^{t}BMAs

	$M_n \times 10^{-3}$ (g/mol)				$M_w \times 10^{-3}$ (g/mol)		
polymer	calcd	SEC[a]	^{1}H NMR	RALLS[b]	calcd	RALLS[b]	M_w/M_n[a]
1G	52.0	46.5	52.7	50.1	53.0	50.2	1.02
2G	137	101	137	139	140	140	1.02
3G	320	169	324	324	326	327	1.02
4G	573	272	578	582	584	584	1.02
5G	1110	344	1140	1080	1140	1100	1.03

[a]Estimated by SEC using standard PS calibration curve. [b]Determined by SEC-RALLS equipped with a triple detector.

comparing the two peak areas. The linked product was isolated in 85% yield by fractional precipitation (benzene/methanol/water) and characterized by SEC-RALLS. The molecular weight determined by RALLS is in good agreement with that calculated, as listed in Table 1. Thus, the 1G polymer was successfully synthesized. It should be mentioned that the 1G polymer is a four-armed star-branched polymer but not a dendrimer-like star-branched polymer.

The 1G polymer was treated with $(C_4H_9)_4NF$ (deprotection), followed by reacting it with α-phenylacrylic acid, PPh_3, and DIAD to introduce two PA reaction sites at the α-chain-end. The resulting polymer was purified by reprecipitation twice, freeze-dried from its absolute benzene solution, and characterized by SEC and ^{1}H NMR. The SEC peak of the polymer obtained after the two reactions was observed to be almost identical in shape and elution count to that of the polymer before the reactions. Complete conversion to the PA function was confirmed by ^{1}H NMR analysis, showing that the above-mentioned three resonances assigned to the SMP group had completely disappeared, while new resonances corresponding to the protons of the PA termini are observed. Thus, the conversion of two SMP groups to two PA reaction sites at each P^{t}BMA α-chain-end (total, eight PA reaction sites) was quantitative, while P^{t}BMA remained unchanged under such reaction conditions. The polymer thus prepared is abbreviated as 1G-P^{t}BMA-PA$_8$.

With the use of 1G-P^{t}BMA-PA$_8$ as a starting material, a 2G polymer was synthesized by a linking reaction of the 1G-P^{t}BMA-PA$_8$ with α-terminal-(SMP)$_2$-functionalized living P^{t}BMA, prepared in advance. A 3.3-fold excess of the living polymer for each PA function was used, and the reaction was allowed to stand in THF at −25 °C for 24 h. As shown in Figure 2, the SEC profile of the reaction mixture exhibits two distinct sharp monomodal peaks for the linked product and the deactivated living P^{t}BMA used in excess. The reaction efficiency was estimated to be almost quantitative by comparing the two peak areas. The linked polymer was isolated in 92% yield by the fractional precipitation mentioned above.

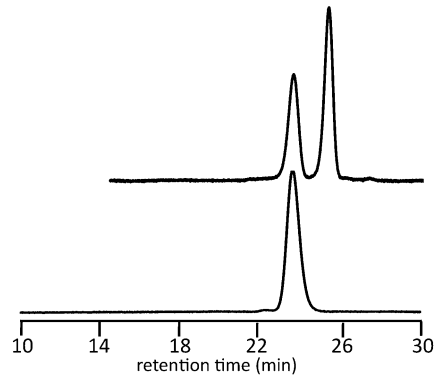

Figure 2. SEC profiles of the reaction mixture (upper) and 2G dendrimer-like star-branched P^{t}BMA (lower).

The isolated polymer possessed a narrow monomodal SEC distribution, the M_w/M_n value being 1.02 (see Figure 2). The M_n value (101 kg/mol) estimated by SEC was relatively

dx.doi.org/10.1021/ma202367e | Macromolecules 2012, 45, 100−112

Scheme 5. Synthesis of Dendrimer-like Star-Branched P^{t}BMAs up to 5G

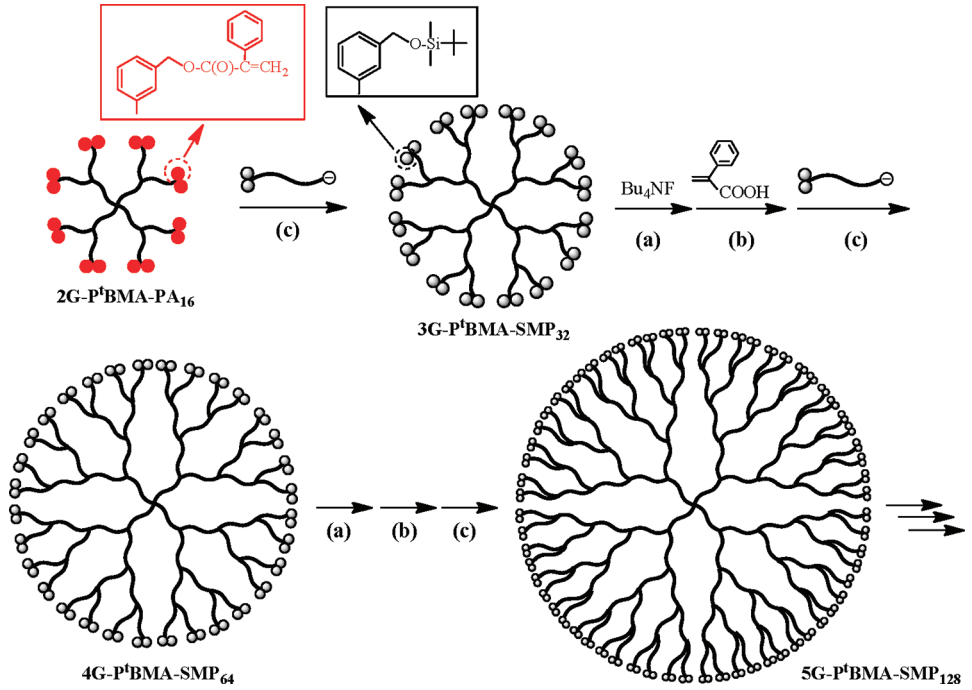

lower than that calculated (137 kg/mol), as expected from its hyperbranched architecture. On the other hand, both of the M_n values (137 and 139 kg/mol) determined by ^{1}H NMR (end-group analysis) and RALLS agree well with the calculated values (also see Table 1). Thus, a well-defined 2G polymer with the expected structures was synthesized. As can be seen in Scheme 4, the 2G polymer possesses a dendrimer-like star-branched architecture, in which four-arm segments are branched at the core and two segments are branched at each branch point in the second layer.

The 2G polymer was treated with $(C_4H_9)_4NF$, followed by reaction with α-phenylacrylic acid under identical conditions. The conversion of 16 SMP α-termini to 16 PA reaction sites was observed by ^{1}H NMR to be quantitative within analytical error limits. The resulting polymer is referred to as 2G-P^{t}BMA-PA$_{16}$. By using this 2G polymer as the starting polymer, the same reaction sequence involving the conversion to the PA reaction site and linking reactions was repeated three more times to synthesize 3G, 4G, and 5G polymers, as illustrated in Scheme 5. A 3.9-fold excess, a 5.4-fold excess, or a 6.5-fold excess of α-terminal-(SMP)$_2$-functionalized living P^{t}BMA for each PA functionality was respectively used in the linking reaction with 2G-P^{t}BMA-PA$_{16}$, 3G-P^{t}BMA-PA$_{32}$, or 4G-P^{t}BMA-PA$_{64}$ for longer reaction times to 48 h. Under such conditions, all linking reactions efficiently proceeded to afford 3G, 4G, and 5G polymers in ca. 100% yield.

All of the polymers were isolated in ca. 90% yields by fractional precipitation and characterized by ^{1}H NMR and SEC-RALLS. As is shown in Table 1, these polymers possess predictable molecular weights in accordance with calculated values and narrow molecular weight distributions. Thus, the iterative process up to the synthetic stage of 5G polymer works very satisfactorily, and therefore, the choice of the two reaction steps (1)′ and (2)′ is appropriate. Figure 3 shows SEC profiles of a series of dendrimer-like star-branched (P^{t}BMA)s from 1G to 5G. In the previous methodology of using the BnBr reaction site, the iterative process also worked effectively and could be

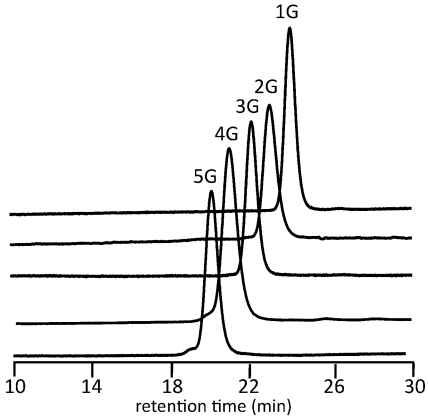

Figure 3. SEC profiles of 1G−5G dendrimer-like star-branched P^{t}BMAs.

done even seven times.[33] However, undesirable coupling dimers (~10%) were often by-produced in the synthetic stages of higher generation (4−7 G) polymers and were extremely difficult to remove from the target polymers, leading to a significant reduction of the isolated polymer yield in each stage. In contrast, the linking reaction, based on a 1:1 addition reaction of living P^{t}BMA with the PA reaction site, proceeded cleanly or along with very small amounts of dimer formation (<3%), even at the synthetic stages of higher-generation polymers (see Figure 3). The superiority of the PA reaction site over the BnBr one in the linking reaction is an additional advantage.

By using the newly proposed methodology using the PA reaction site, a well-defined high-generation (5G) and high-molecular-weight (>10^7 g/mol) dendrimer-like star-branched P^{t}BMA was successfully synthesized for the first time. Since the final 5G polymer still has 128 SMP groups convertible to PA reaction sites if the reaction quantitatively proceeds, 6G and higher-generation polymers can be synthesized by repeating the same reaction sequence. As described later, the resulting

dx.doi.org/10.1021/ma202367e | *Macromolecules* 2012, 45, 100−112

Table 2. Characterization Results of Dendrimer-like Star-Branched PMMAs

	$M_n \times 10^{-3}$ (g/mol)				$M_w \times 10^{-3}$ (g/mol)		
polymer	calcd	SEC[a]	^{1}H NMR	RALLS[b]	calcd	RALLS[b]	M_w/M_n[a]
1G	45.8	43.0	44.7	46.2	47.2	47.6	1.03
2G	128	96.3	126	127	131	130	1.02
3G	281	169	288	282	289	290	1.03
4G	618	229	622	613	637	631	1.03
5G	1200	272	1210	1210	1240	1260	1.04

[a]Estimated by SEC using standard PS calibration curve. [b]Determined by SEC-RALLS equipped with a triple detector.

Scheme 6. Linking Reactions of α-Terminal-$(PA)_2$-Functionalized Poly(alkyl methacrylate with functional groups)s with Their Living Polymers

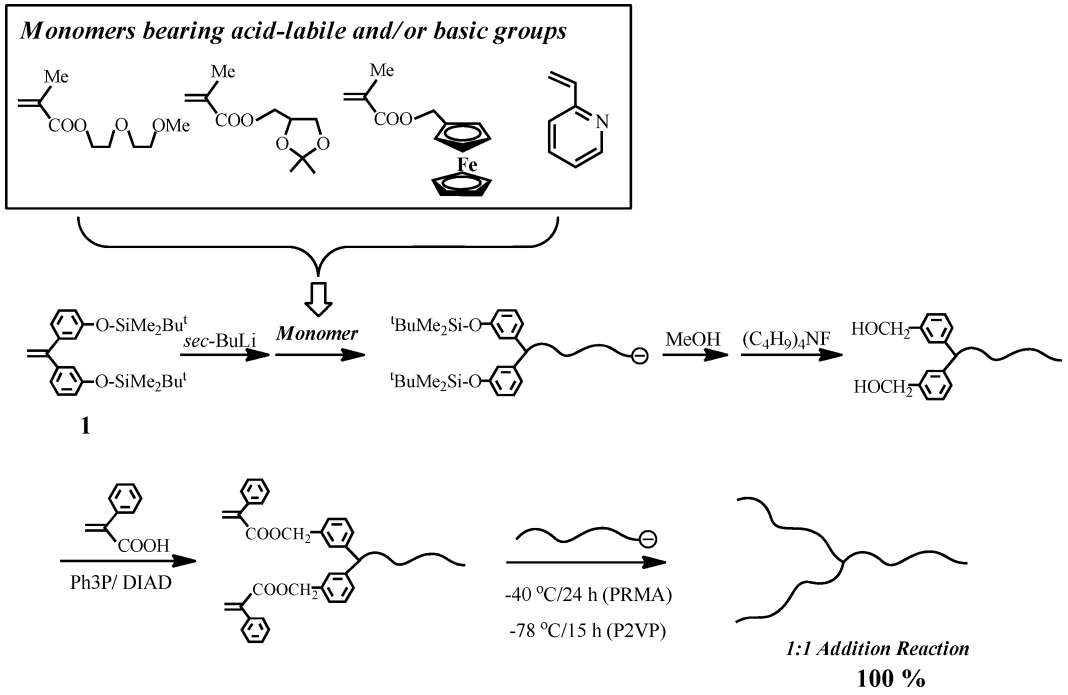

polymer is expected to convert to a new water-soluble well-defined dendrimer-like star-branched polymer composed of poly(methacrylic acid) segments by hydrolyzing P^{t}BMA chains.

Synthesis of 1G–5G Dendrimer-like Star-Branched (PMMA)s. In order to examine the generality of the newly developed methodology using the PA reaction site, the synthesis of a series of dendrimer-like star-branched (PMMA)s up to 5G was carried out under conditions similar to those mentioned above. A 3-fold excess of living PMMA was used in each linking reaction at the synthetic stages of 2G and 3G polymers in THF at −40 °C for 20 h. Different from the linking reaction with living P^{t}BMA, the reaction temperature of −25 °C was not appropriate and the yield was around 70%, possibly due to the instability of living PMMA at −25 °C. For the synthesis of 4 and 5G polymers, a 5.0-fold excess or an 8.0-fold excess of living PMMA was used. Each iterative process was observed to be almost quantitative in yield by comparing the SEC peak areas before and after the reactions. No intermediate polymer between the target polymer and deactivated living PMMA used in excess was produced in any synthetic stage. The target polymers were isolated in ca. 90% yields only by precipitation in methanol.[45] The results are summarized in Table 2. The resulting polymers all possessed narrow molecular weight distributions and molecular weights in agreement with the calculated values within experimental error limits. Thus, the PA reaction site may effectively work in each linking reaction with living PMMA, resulting in the successful synthesis of a series of well-defined dendrimer-like star-branched (PMMA)s up to 5G and probably higher generations.

Synthetic Possibility of Dendrimer-like Star-Branched Polymers Composed of Functional Polymer Segments Bearing Acid-Labile and/or Basic Groups. Similar to the case of P^{t}BMA, the PA reaction site could be introduced into α-chain-ends of various functional polymers bearing acid-labile and/or basic groups in side chains, as shown in Scheme 6. At first, 2-(2-methoxyethoxy)ethyl methacrylate, (2,2-dimethyl-1,3-dioxolan-4-yl)methyl methacrylate, ferrocenylmethyl methacrylate, or 2-vinylpyridine was polymerized with the initiator prepared from **1** and *sec*-BuLi in the presence of a 5-fold excess of LiCl in THF at −78 °C for 1 h. The resulting polymers were all treated with $(C_4H_9)_4NF$ (deprotection) and subsequently with α-phenylacrylic acid under the conditions of the Mitsunobu reaction in the same manner as described above. The conversion of the SMP group to the PA reaction site is always ca. 100% for each polymer, while the ether, acetal, ferrocene, or pyridine moiety in the side chain is stable during the above treatment.

The same procedure cannot be employed for the introduction of the PA function into poly(2-*tert*-butyldimethylsilyloxyethyl methacrylate) because the *tert*-butyldimethylsilyl protecting groups in the polymer side chain are also removed during the

dx.doi.org/10.1021/ma202367e | *Macromolecules* 2012, 45, 100–112

Scheme 7. Preparation of α-Terminal-$(PA)_2$-Functionalized Poly(2-*tert*-butyldimethylsilyloxyethyl methacrylate)

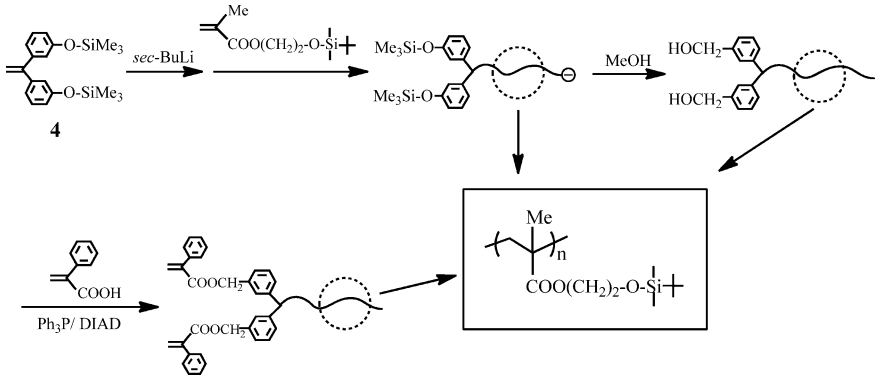

deprotection step of the SMP α-termini. Therefore, trimethylsilyl-protected DPE, **4**, is used instead of **1** in the polymerization, as illustrated in Scheme 7. Two trimethylsilyl groups at the α-chain-end were readily and selectively deprotected by pouring the polymerization mixture in methanol, while the *tert*-butyldimethylsilyl-protected functionality in the side chain remained intact. The PA reaction site could be introduced via the regenerated hydroxyl group by the Mitsunobu reaction with α-phenylacrylic acid. Thus, α-terminal-$(PA)_2$-functionalized poly(2-*tert*-butyldimethylsilyloxyethyl methacrylate) was successfully prepared.

In order to examine the efficiency of the linking reaction, each living polymer was prepared and in situ reacted with the above corresponding α-terminal-$(PA)_2$-functionalized polymer. Both living and chain-end-functionalized polymers were fixed to be around 10 kg/mol in M_n value. A 3-fold excess of each living polymer was in situ used in the reaction at −40 °C for 24 h. Under such conditions, the reaction was always complete. With the use of living poly(2-vinylpyridine), a 1.5-fold excess of living polymer for the PA reaction site was enough to complete the reaction at −78 °C for 15 h.

These results—the quantitative introduction of PA reaction sites and the 1:1 addition reaction to link the polymer chains—strongly indicate that the above functional polymers are usable in the present methodology involving the two reaction steps, (1)′ and (2)′. Accordingly, it may be possible to synthesize new dendrimer-like star-branched polymers composed of the above functional polymers bearing acid-labile and/or basic groups. The synthesis of a variety of such functional dendrimer-like star-branched polymers is now in progress.

Synthesis of 4G Dendrimer-like Star-Branched Block Copolymers Composed of P^{t}BMA and PS Segments. In order to further extend the synthetic possibility of the present methodology herein developed, the synthesis of new block copolymers composed of P^{t}BMA and PS segments was performed by combining the present methodology with the modified methodology effective for the synthesis of dendrimer-like star-branched (PS)s.[37] Two 4G dendrimer-like star-branched block copolymers composed of P^{t}BMA and PS segments were synthesized. The first block copolymer possesses P^{t}BMA segments introduced into the 1G, 2G, and 3G layers and PS segment in the 4G layer, while the other one is a 4G dendrimer-like star-branched block copolymer with an opposite sequence where PS segments are introduced into the 1G, 2G, and 3G layers and P^{t}BMA segments are in the 4G layer. Their structures are shown in Figure 4.

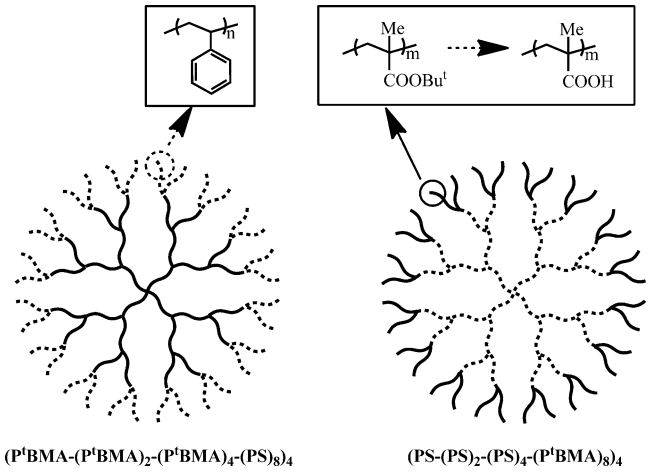

Figure 4. Two 4G Dendrimer-like star-branched block copolymers composed of P^{t}BMA and PS segments.

For the synthesis of the first block copolymer, 3G-P^{t}BMA-PA_{32} was synthesized in the same manner as mentioned above and then reacted with a 1.7-fold excess of α-terminal-(3-*tert*-butyldimethylsilyloxypropyl)-functionalized living PS end-capped with DPE at −78 °C for 15 h. The SEC profile of the reaction mixture showed only two peaks for the linked product and the deactivated living PS used in excess in the reaction. The reaction efficiency was estimated to be ca. 100% by comparing the two peak areas. Thus, the PA reaction site is also capable of undergoing a 1:1 addition reaction to connect the P^{t}BMA chain with two PS chains. The target linked polymer was isolated in 81% yield by fractional precipitation using a mixture of cyclohexane and hexane and characterized by ^{1}H NMR and SEC-RALLS, respectively. The results are summarized in Table 3. The resulting polymer possessed a narrow monomodal SEC distribution and predictable molecular weight and composition, in agreement with the calculated values. The successful synthesis of the expected 4G block copolymer is thus apparent.

For the synthesis of the other block copolymer, a 3G dendrimer-like star-branched PS was prepared by our previous procedure,[38] and the 16 3-*tert*-butyldimethylsilyloxypropyl α-termini were converted to 32 PA reaction sites, as shown in Scheme 8. The 3-*tert*-butyldimethylsilyloxypropyl group was deprotected with $(C_4H_9)_4NF$, followed by treatment with CBr_4 and Ph_3P, and converted to a 3-bromopropyl group. Then, the resulting 3-bromopropyl group was in situ reacted with the functionalized DPE anion prepared from **1** and *sec*-BuLi to

dx.doi.org/10.1021/ma202367e | *Macromolecules* 2012, 45, 100−112

Table 3. Characterization Results of Two 4G Dendrimer-like Star-Branched Block Copolymers Composed of P^{t}BMA and PS Segments

	$M_n \times 10^{-3}$ (g/mol)			$M_w \times 10^{-3}$ (g/mol)		
polymer type	calcd	^{1}H NMR	RALLS[b]	calcd	RALLS[b]	M_w/M_n[a]
$(A\text{-}A_2\text{-}A_4\text{-}B_8)_4$[c]	669	704	692	689	696	1.03
$(B\text{-}B_2\text{-}B_4\text{-}A_8)_4$[d]	818	825	832	851	888	1.04

[a]Estimated by SEC using standard PS calibration curve. [b]Determined by SEC-RALLS equipped with a triple detector. [c](P^{t}BMA-(P^{t}BMA)$_2$-(P^{t}BMA)$_4$-(PS)$_8$)$_4$. [d](PS-(PS)$_2$-(PS)$_4$-(P^{t}BMA)$_8$)$_4$.

Scheme 8. Synthesis of 3G-PS-PA$_{32}$

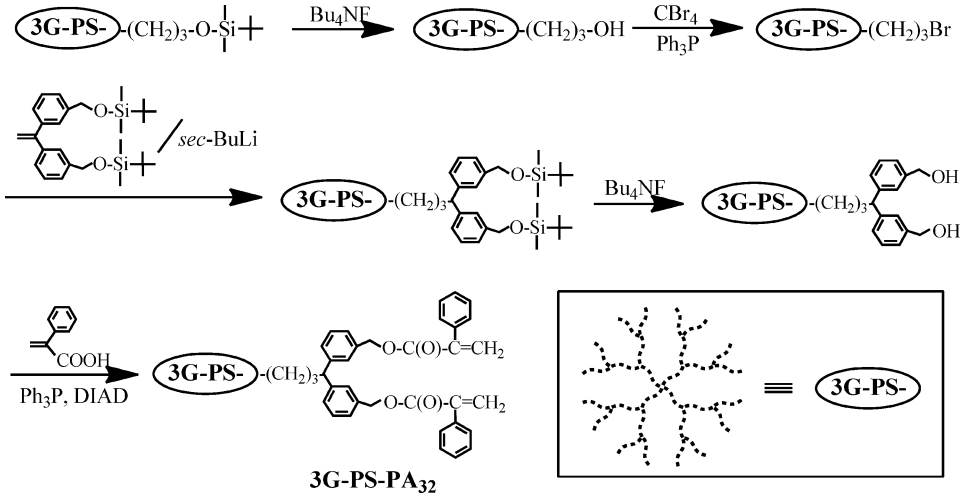

introduce to two SMP groups. Finally, the SMP group was converted to the PA reaction site in the same manner as that described above. The 3G-PS-PA$_{32}$ thus prepared was reacted with a 4.5-fold excess of living P^{t}BMA in THF at −25 °C for 24 h. The successful synthesis of the 4G dendrimer-like star-branched block copolymer having PS (1G, 2G, and 3G) and P^{t}BMA segments (4G) was confirmed by the characterization results of ^{1}H NMR and SEC-RALLS, respectively, as listed in Table 3. The successful synthesis of the two block copolymers clearly indicates that P^{t}BMA as well as PS segments can be introduced into essentially any layer in dendrimer-like star-branched block copolymers composed of P^{t}BMA and PS segments.

Our synthetic interest was also to prepare amphiphilic block copolymers with dendrimer-like star-branched architectures, from which unimolecular micelles, different in inside and outside environments, could be produced. Two block copolymers were synthesized for this purpose. They were treated with $(CH_3)_3SiCl$/LiBr to selectively hydrolyze the P^{t}BMA segments into poly(methacrylic acid) (PMAA) segments without any influence of the PS segments. We monitored the reaction progress by FT-IR and found that selective hydrolysis completely occurred. Prior to the treatment, these two block copolymers were soluble in hexane, benzene, acetone, THF, and chloroform but insoluble in methanol and water. The hydrolyzed block copolymers became insoluble in all of the above organic solvents. The first polymer sample, referred to as (PMAA-*b*-(PMAA)$_2$-*b*-(PMAA)$_4$-*b*-(PS)$_8$)$_4$, composed of PMAA segments at the core and in the 2G and 3G layers and PS segments in the outermost layer, became swollen only in THF, while the second sample of (PS-*b*-(PS)$_2$-*b*-(PS)$_4$-*b*-(PMAA)$_8$)$_4$, composed of PS segments located in the inside layers and PMAA segments in the outermost layer, became swollen only in methanol. Neither sample was soluble nor swollen in a 2 N NaOH solution. Thus, unfortunately, soluble amphiphilic polymers were not obtained. More carefully setting the reaction conditions and post-treatment of hydrolyzed polymers may be needed.

CONCLUSIONS

We have developed a new stepwise iterative methodology using the PA reaction site instead of the BnBr function in order to synthesize well-defined high-generation and high-molecular-weight dendrimer-like star-branched polymers composed of polymer segments bearing acid-labile and/or basic groups. With the use of this methodology, a series of dendrimer-like star-branched (P^{t}BMA)s up to 5G, synthetically difficult to obtain by the previous methodology using the BnBr reaction site, have been successfully synthesized. These polymers, four-branched at the core and two-branched at each layer, were well-defined in architecture and precisely controlled in chain length, and the final 5G polymer was 1.07×10^7 g/mol in M_n value and 1.03 in M_w/M_n.

We have also demonstrated the synthetic possibility of new functional dendrimer-like star-branched polymers composed of water-soluble poly(2-(2-methoxyethoxy)ethyl methacrylate) having an LCST, poly(2-*tert*-butyldimethylsilyloxyethyl methacrylate) convertible to hydrophilic poly(2-hydroxyethyl methacrylate), poly((2,2-dimethyl-1,3-dioxolan-4-yl)methyl methacrylate) convertible to water-soluble poly(2,3-dihydroxypropyl methacrylate), poly(ferrocenylmethyl methacrylate), and poly(2-vinylpyridine) segments. The synthesis of such dendrimer-like star-branched polymers is now in progress.

Finally, two 4G dendrimer-like star-branched block copolymers composed of P^{t}BMA and PS segments were synthesized

dx.doi.org/10.1021/ma202367e | Macromolecules 2012, 45, 100−112

by combining the present methodology with the modified methodology previously reported. These block copolymers could be converted to novel amphiphilic block copolymers by the selective hydrolysis of P^{t}BMA to PMAA. Unfortunately, the resulting hydrolyzed block copolymers were insoluble in most organic solvents and in a 2 N NaOH aqueous solution.

■ ASSOCIATED CONTENT

Ⓢ Supporting Information

Text giving materials, purification of monomers under high vacuum, synthesis of **3** and **4**, synthesis of 1G−5G dendrimer-like star-branched (PMMA)s, synthesis of α-terminal-$(PA)_2$-functionalized poly(2-(2-methoxyethoxy)ethyl methacrylate), poly((2,2-dimethyl-1,3-dioxolan-4-yl)methyl methacrylate), poly(ferrocenylmethyl methacrylate), poly(2-vinylpyridine), and poly(2-*tert*-butyldimethylsilyloxyethyl methacrylate), and linking reaction of α-terminal-$(PA)_2$-functionalized polymer with living anionic polymer. This material is available free of charge via the Internet at http://pubs.acs.org.

■ ACKNOWLEDGMENTS

A.H. gratefully acknowledges partial support by a grant (B: 21350060) from a Grant-in-aid for Scientific Research from the Ministry of Education, Science, Sports, and Culture of Japan. A.H. is also thankful for financial support from Denki Chemical Co. Ltd. in Japan.

■ REFERENCES

(1) Six, J. L.; Gnanou, Y. *Macromol. Symp.* **1995**, *95*, 137−150.
(2) Hirao, A.; Sugiyama, K.; Tsunoda, Y.; Matsuo, A.; Watanabe, T. *J. Polym. Sci., Part A: Polym. Chem.* **2006**, *44*, 6659−6687.
(3) Taton, D.; Gnanou, Y.; Matmour, R.; Angot, S.; Hou, S.; Francis, R.; Lepoittevin, B.; Moinard, D.; Babin, J. *Polym. Int.* **2006**, *55*, 1138−1145.
(4) Taton, D.; Feng, X.; Gnanou, Y. *New J. Chem.* **2007**, *31*, 1097−1110.
(5) Hirao, A.; Sugiyama, K.; Matsuo, A.; Tsunoda, Y.; Watanabe, T. *Polym. Int.* **2008**, *57*, 554−570.
(6) Hutchings, L. R. *Soft Matter* **2008**, *4*, 2150−2159.
(7) Yoo, H.-S.; Hirao, A. Precise Synthesis of Dendrimer-Like Star-Branched Polymers, a New Class of Well-Defined Hyperbranched Polymers. In *Complex Macromolecular Architectures: Synthesis, Characterization, and Self-Assembly*; Hadjichristidis, N., Hirao, A., Tezuka, Y., Du Prez, F., Eds.; John Wiley & Sons (Asia) Pte Ltd.: Singapore, 2011; Chapter 5, pp 133−167.
(8) Hirao, A.; Yoo, H.-S. *Polym. J.* **2011**, *43*, 2−17.
(9) Konkolewicz, D.; Monteiro, M. J.; Perrier, S. *Macromolecules* **2011**, *44*, 7067−7087.
(10) Schappacher, M.; Deffieux, A.; Putaux, J.-L.; Viville, P.; Lazzaroni, R. *Macromolecules* **2003**, *36*, 5776−5783.
(11) Teertsra, S. J.; Gauthier, M. *Prog. Polym. Sci.* **2004**, *29*, 277−327.
(12) Schappacher, M.; Deffieux, A. *Macromolecules* **2005**, *38*, 7209−7213.
(13) Trollsås, M.; Kelly, M. A.; Claesson, H.; Siements, R.; Hedrick, J. L. *Macromolecules* **1999**, *32*, 4917−4924.
(14) Hedrick, J. L.; Magbitang, T.; Cornnor, E. F.; Glauser, T.; Volken, W.; Hawker, C. L. *Chem.—Eur. J.* **2002**, *8*, 3308−3319.
(15) Stancik, C. M.; Pople, J. A.; Trollsås, M.; Lindner, P.; Hedrick, J. L.; Gast, A. P. *Macromolecules* **2003**, *38*, 5765−5775.
(16) Francis, R.; Taton, D.; Logan, J. L.; Masse, P.; Gnanou, Y.; Duran, R. S. *Macromolecules* **2003**, *36*, 8253−8259.
(17) Trollsås, M.; Atthoff, B.; Claesson, H.; Hedrick, J. L. *J. Polym. Sci., Part A: Polym. Chem.* **2004**, *42*, 1174−1188.
(18) Matmour, R.; Lepoittevin, B.; Joncheray, T. J.; El-khouri, R. J.; Tanton, D.; Duran, R. S.; Gnanou, Y. *Macromolecules* **2005**, *38*, 5459−5467.
(19) Feng, X. S.; Taton, D.; Chaikof, E. L.; Borusali, R.; Chaikof, E. L.; Gnanou, Y. *J. Am. Chem. Soc.* **2006**, *128*, 11551−11562.
(20) van Ruymbeke, E.; Orfanou, K.; Kapnistos, M.; Iatrou, H.; Pitsikalis, M.; Hadjichristidis, N.; Lohse, D. J.; Vlassopoulos, D. *Macromolecules* **2007**, *40*, 5941−5952.
(21) van Ruymbeke, E.; Muliawan, E. B.; Hatzikiriakos, S. G.; Watanabe, T.; Hirao, A.; Vlassopoulos, D. *J. Rheol.* **2010**, *54*, 643−662.
(22) Urbani, C. N.; Lonsdale, D. E.; Bell, C. A.; Whittaker, M. R.; Monteiro, M. J. *J. Polym. Sci., Part A: Polym. Chem* **2008**, *46*, 1533−1547.
(23) Urbani, C. N.; Bell, C. A.; Lonsdale, D. E.; Whittaker, M. R.; Monteiro, M. J. *Macromolecules* **2008**, *41*, 76−86.
(24) Grayson, S. M.; Fréchet, J. M. J. *Chem. Rev.* **2001**, *101*, 3819−3868.
(25) (a) Trollsås, M.; Claesson, H.; Atthoff, B.; Hedrick, J. L. *Angew. Chem., Int. Ed.* **1998**, *37*, 3132−3136. (b) Trollsås, M.; Hedrick, J. L. *J. Am. Chem. Soc.* **1998**, *120*, 4644−4651. (c) Hedrick, J. L.; Trollsås, M.; Hawker, C. J.; Atthoff, B.; Claesson, H.; Heise, A.; Miller, R. D.; Mecerreyes, D.; Jérôme, R.; Dubois, P. *Macromolecules* **1998**, *31*, 8691−8705. (d) Trollsås, M.; Claesson, H.; Atthoff, B.; Hedrick, J. L. *Angew. Chem., Int. Ed.* **1998**, *37*, 3132−3136. (e) Trollsås, M.; Atthoff, B.; Würsch, A.; Hedrick, J. L.; Pople, J. A.; Gast, A. P. *Macromolecules* **2000**, *33*, 6423−6438. (f) Würsch, A.; Möller, M.; Glauser, T.; Lim, L. S.; Voytek, S. B.; Hedrick, J. L.; Frank, C. W.; Hilborn, J. G. *Macromolecules* **2001**, *34*, 6601−6615.
(26) (a) Angot, S.; Taton, D.; Gnanou, Y. *Macromolecules* **2000**, *33*, 5418−5426. (b) Gnanou, Y.; Taton, D. *Macromol. Symp.* **2001**, *34*, 333−341. (c) Hou, S.; Chaikof, E. L.; Taton, D.; Gnanou, Y. *Macromolecules* **2003**, *36*, 3874−3881. (d) Rele, S. M.; Cui, W.; Wang, L.; Hou, S.; Barr-Zarse, B.; Taton, D.; Gnanou, Y.; Esko, J. D.; Chaikof, E. L. *J. Am. Chem. Soc.* **2005**, *127*, 10132−10133. (e) Feng, X. S.; Taton, D.; Chaikof, E. L.; Gnanou, Y. *J. Am. Chem. Soc.* **2005**, *127*,
10956−10966. (f) Lepoittevin, B.; Matmour, R.; Francis, R.; Taton, D.; Gnanou, Y. *Macromolecules* **2005**, *38*, 3120−3128. (g) Matmour, R.; Gnanou, Y. *J. Am. Chem. Soc.* **2008**, *130*, 1350−1361. (h) Feng, X.; Taton, D.; Chaikof, E. L.; Gnanou, Y. *Macromolecules* **2009**, *42*, 7292−7298.
(27) (a) Percec, V.; Barboiu, B.; Grigoras, C.; Bera, T. K. *J. Am. Chem. Soc.* **2003**, *125*, 6503−6516. (b) Percec, V.; Grigoras, C.; Kim, H. J. *J. Polym. Sci., Part A: Polym. Chem.* **2004**, *42*, 505−513. (c) Percec, V.; Grigoras, C.; Bera, T. K.; Barboiu, B.; Bissel, P. *J. Polym. Sci., Part A: Polym. Chem.* **2005**, *43*, 4894−4906. (d) Rosen, B. M.; Lligadas, G.; Hahn, C.; Percec, V. *J. Polym. Sci., Part A: Polym. Chem* **2009**, *47*, 3931−3939, and 3940−3948.
(28) Chalari, I.; Hadjichristidis, N. *J. Polym. Sci., Part A: Polym. Chem.* **2002**, *40*, 1519−1526.
(29) Orfanou, K.; Iatrou, H.; Lohse, D. J.; Hadjichristidis, N. *Macromolecules* **2006**, *39*, 4361−4365.
(30) (a) Hutchings, L. R.; Roberts-Bleming, S. J. *Macromolecules* **2006**, *39*, 2144−2152. (b) Kimani, S. M.; Hutchings, L. R. *Macromol. Rapid Commun.* **2008**, *29*, 633−637.
(31) (a) Whittaker, M. R.; Urbani, C. N.; Monteiro, M. J. *J. Am. Chem. Soc.* **2006**, *128*, 11360−11361. (b) Urbani, C. N.; Bell, C. A.; Lonsdale, D. E.; Whittaker, M. R.; Monteiro, M. J. *Macromolecules* **2007**, *40*, 7056−7059. (c) Urbani, C. N.; Bell, C. A.; Whittaker, M. R.; Monteiro, M. J. *Macromolecules* **2008**, *41*, 1057−1060. (d) Urbani, C. N.; Bell, C. A.; Lonsdale, D. E.; Whittaker, M. R.; Monteiro, M. J. *Macromolecules* **2008**, *41*, 76−86. (d) Urbani, C. N.; Lonsdale, D. E.; Bell, C. A.; Whittaker, M. R.; Monteiro, M. J. *J. Polym. Sci., Part A: Polym. Chem.* **2008**, *46*, 1533−1545. (e) Jia, Z.; Bell, C. A.; Monteiro, M. J. *Chem. Commun.* **2011**, *47*, 4165−4167.
(32) Matsuo, A.; Watanabe, T.; Hirao, A. *Macromolecules* **2004**, *37*, 6283−6290.
(33) Hirao, A.; Matsuo, A.; Watanabe, T. *Macromolecules* **2005**, *38*, 8701−8711.
(34) Hirao, A.; Tsunoda, Y.; Matsuo, A.; Sugiyama, K.; Watanabe, T. *Macromol. Res.* **2006**, *14*, 272−286.

(35) Watanabe, T.; Tsunoda, Y.; Matsuo, A.; Sugiyama, K.; Hirao, A. *Macromol. Symp.* **2006**, *240*, 23−30.
(36) Watanabe, T.; Hirao, A. *Macromol. Symp.* **2006**, *245*−*246*, 5−13.
(37) Hirao, A.; Watanabe, T.; Ishizu, K.; Ree, M.; Jin, S.-W.; Jin, K.-S.; Deffieux, A.; Schappacher, M.; Carlotti, S. *Macromolecules* **2009**, *42*, 682−693.
(38) Yoo, H.-S.; Watanabe, T.; Hirao, A. *Macromolecules* **2009**, *42*, 4558−4570.
(39) Hadjichristidis, N.; Iatrou, H.; Pispas, S.; Pitsikalis, M. *J. Polym. Sci., Part A: Polym. Chem.* **2000**, *38*, 3211−3234.
(40) Under the conditions in a mixture of chloroform and acetonitrile (1/1, v/v) at 40 °C for 24 h, ca. 10% of the methyl ester moieties in PMMA were cleaved.
(41) The yield of the linked products in the reaction between the α-terminal-$(formyl)_2$-functionalized P^{t}BMA and a 3-fold excess of living P^{t}BMA was observed to be 65% under the conditions in THF at −40 °C for 72 h.
(42) Sugiyama, K.; Oie, T.; El-Magd, A. A.; Hirao, A. *Macromolecules* **2010**, *43*, 1403−1410.
(43) Hirao, A.; Uematsu, M.; Kurokawa, R.; Ishizone, T.; Sugiyama, K. *Macromolecules* **2011**, *44*, 5638−5649.
(44) Hirao, A.; Matsuo, Y.; Oie, T.; Goseki, R.; Ishizone, T. *Macromolecules* **2011**, *44*, 6345−6355.
(45) PMMAs having M_n values of around 10 000 g/mol were completely soluble in methanol, including a small amount of THF (ca. 5%), while higher molecular weight polymers (M_n > 20 000 g/mol) were precipitated in such a mixed solvent. Accordingly, dendrimer-like star-branched PMMAs (M_n = 46.2−1210 kg/mol) could be isolated only by pouring the reaction mixture into methanol. The deactivated living PMMAs used in excess always remained in the solution (methanol/THF (95/5, v/v)) because of their molecular weights (M_n = 9000−12 000 g/mol).

Macromolecules

Article

pubs.acs.org/Macromolecules

Conjugated Side-Chain Isolated Polythiophene: Synthesis and Photovoltaic Application

Zhi-Guo Zhang, Siyuan Zhang, Jie Min, Chaohua Chui, Jing Zhang, Maojie Zhang, and Yongfang Li*

Beijing National Laboratory for Molecular Sciences, CAS Key Laboratory of Organic Solids, Institute of Chemistry, Chinese Academy of Sciences, Beijing 100190, China

Supporting Information

ABSTRACT: A design concept of "side chain isolation" was proposed for developing new polythiophene derivatives with conjugated side chain (CSC-PTs), and **PT5TPA** with styryl−triphenylamine (TPA) side chain and unsubstituted tetrathienyl spacer was designed and synthesized. Compared to previously reported CSC-PTs, side chain isolated **PT5TPA** showed red-shifted and enhanced $\pi-\pi^*$ transition absorption of the polymer backbone along with the shoulder peak and steep absorption edge, indicating improved planarity of the backbone. In addition, the unsubstituted thiophene spacer along the polymer backbone of the side chain isolated **PT5TPA** results in a lower HOMO energy level of the polymer at −5.1 eV. The polymer solar cell based on **PT5TPA** as donor and indene−C_{60} bisadduct as acceptor displayed a power conversion efficiency of 3.6% with a high open circuit voltage of 0.94 V, under the illumination of AM1.5G, 100 mW/cm^2. The results indicate that the side chain isolated CSC-PTs could open a new way for developing high performance photovoltaic polymers.

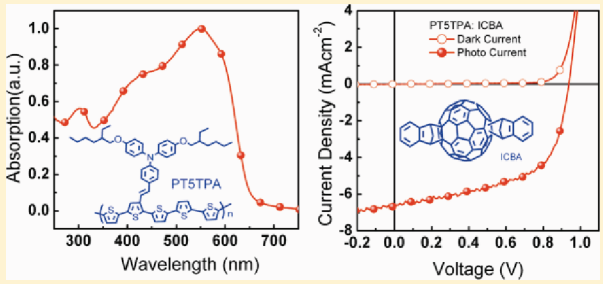

1. INTRODUCTION

Bulk heterojunction (BHJ) polymer solar cells (PSCs) based on *p*-type conjugated polymers as donor[1,2] and *n*-type fullerene[3,4] as acceptor have been intensively studied in recent years for the generation of affordable, clean, and renewable energy.[5] Advantages of the BHJ PSCs include low-cost fabrication of large-area devices, light weight, mechanical flexibility, and easy tunability of chemical properties of the photovoltaic materials.[6]

Poly(thiophene) derivatives (PTs) have been among the most extensively investigated conjugated polymers due to their high charge carrier mobility, strong absorption in visible region and synthetic accessibility.[7−12] Soluble poly(3-alkylthiophene)s, especially regioregular poly(3-hexylthiophene) (P3HT), are the most important semiconducting polymers for the application in PSCs.[9−12] However, the power conversion efficiency (PCE) of the PSCs based on P3HT as donor and PCBM as acceptor is limited at 4−5%,[13,14] because of its larger band gap and its high HOMO (the highest occupied molecular orbital) energy level, which result in limited light absorption and a low open circuit voltage (V_{oc}) of the PSCs. In addition, the high regioregularity-induced crystallization may be an issue of thermal instability of the blend of P3HT and fullerene acceptors.

For broadening the absorption of the PTs, the polythiophene derivatives with conjugated side chain (CSC-PTs, where CSC represents "conjugated side chain") were designed and synthesized in our group.[15−17] The CSC-PTs possess 2-D charge transport properties thanks to the 2-D-conjugated character of the polymer structure, and broad absorptions deriving from both the main chains and conjugated side chains; thus, this family of CSC-PTs demonstrated good device performances in PSCs[15a] and organic field-effect transistors (OFETs).[16] However, due to steric hindrance of the large conjugated side chain with other alkyl side chains on the polymer main chain, the CSC-PTs showed poorer planarity, which is detrimental for the close packing of polymer chains in the solid state, as clearly evidenced for the featureless absorption along with the low absorption intensity of $\pi-\pi^*$ absorption.[15−17] As a result, this structural limitation constrains their application in organic electronics and the highest PCE value of the CSC-PTs reported so far was 3.18%.[15a] To further improve the optical properties, creating the CSC-PTs without scarifying the planarity/conjugation of the thiophene backbone is very desirable. Fulfilling this goal presents serious challenges in chemistry.

To address this issue, here we proposed the "side chain isolation" concept in designing the new CSC-PTs. We selected styryl−triphenylamine (TPA) as the conjugated side chain in considering the high hole mobility and good solubility of the TPA unit, and we used a tetrathiophene unit without side chains as the spacer between the thiophene units with the conjugated side chains for avoiding the steric hindrance of the side chains. In addition, two 2-ethylhexyloxyl groups were directly attached at the terminal of the TPA side chains to

Received: July 25, 2011
Revised: November 23, 2011
Published: December 6, 2011

   dx.doi.org/10.1021/ma201718x | *Macromolecules* 2012, 45, 113−118

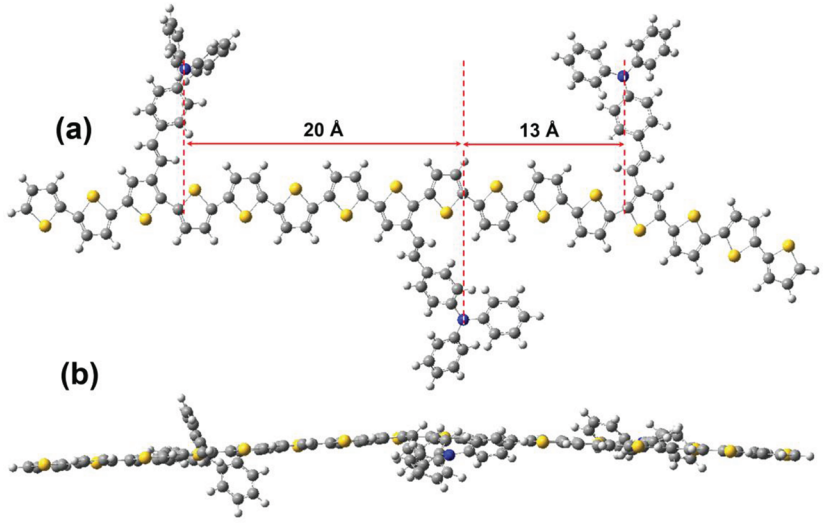

Figure 1. Optimized geometry of PT5TPA: (a) top view and (b) side view.

Scheme 1. Synthesis Route of PT5TPA

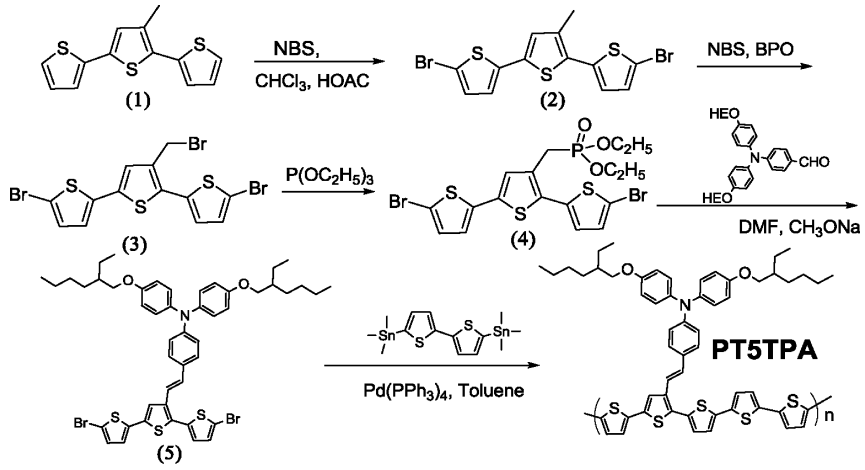

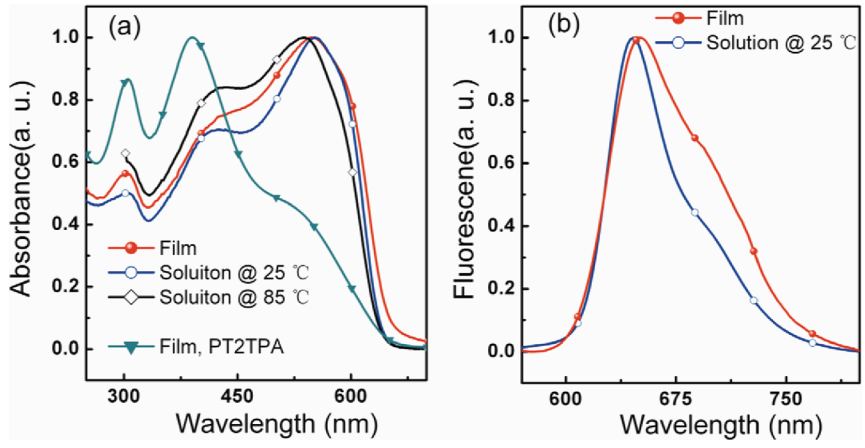

Figure 2. (a) Absorption spectra of PT5TPA in film and in dichlorobenzene solution (at room temperature and high temperature of 85 °C) and the absorption spectrum of PT2TPA film for comparison. (b) PL spectra of PT5TPA in film and dichlorobenzene solution, excited at 430 nm.

ensure good solubility. According to the molecular mechanics simulation (performed with COMPASS force field within the Materials Studio Package[18]) as shown in Figure 1, the side-chains of **PT5TPA** oriented in the tail-to-tail direction are spaced approximately 13 Å apart while those side chains orientated in the head-to-tail fashions are 20 Å apart. Thus, this side chain isolation approach combines the thiophene units bearing conjugated side chain and the unsubstituted tetrathienyl spacers to reduce the steric interactions between the neighbor side chains, which lessens the torsion of the main

dx.doi.org/10.1021/ma201718x | *Macromolecules* 2012, 45, 113–118

chains (see Figure 1b). This CSC-PT of **PT5TPA** demonstrated red-shifted and enhanced $\pi-\pi^*$ transition absorption of the polymer backbone along with the shoulder peak and steep absorption edge, indicating some ordered aggregation of the polymer backbone. In addition, the polymer shows a lower HOMO energy level at −5.1 eV. The PSC based on **PT5TPA** as donor and indene−C_{60} bisadduct ($IC_{60}BA$)[4] as acceptor displayed a PCE of 3.6% with a high open circuit voltage of 0.94 V, under the illumination of AM1.5G, 100 mW/cm^2.

2. RESULTS AND DISCUSSION

Polymer Synthesis and Characterizations. Chemical structure and synthetic route of **PT5TPA** with TPA−vinylene conjugated side chain are depicted in Schemes 1. Bromination of compound **1** with *N*-bromosuccinimide (NBS), performed initially in chloroform at room temperature, and subsequently in anhydrous carbon tetrachloride with benzoyl peroxide (BPO) as catalyst, yielded product **3** with bromomethyl functionality. A Michaelis−Arbuzov reaction[19] was performed between compound **3** with triethyl phosphate afford phosphonate precursor **4**, which was transferred to dibromide monomer **5** via a Horner−Wordsworth−Emmons (HWE) reaction.[20] The polymer was synthesized by palladium(0)-catalyzed Stille polycondensation[21] of an equimolecular mixture of the dibromide and distannyl bithiophene. The polymer is soluble in chlorinated solvents, such as chloroform, chlorobenzene and dichlorobenzene, and exhibited a number-average molecular weight (M_n) of 180.9 K, with a polydispersity index of 3.2. Thermogravimetric analysis (TGA), as shown in Figure S1 in Supporting Information (SI), demonstrated a good thermal stability of the polymer with a 5% weight-loss temperature at 354 °C. DSC was measured in the temperature range of 30−280 °C, but we did not find the glass transition temperature in the temperature range. (see Figure S2 in Supporting Information).

Optical and Electrochemical Properties. Figure 2a shows the absorption spectra of PT5TPA solution in chloroform and film on quartz plate, together with the absorption spectrum of **PT2TPA** film[16a] (**PT2TPA** is a **PT5TPA**-analogue polymer with only one thiophene spacer, named as OTPAV-PT in ref 16a). The solution and film absorption of **PT5TPA** display similar broad absorption band from 300 to 650 nm with three distinct absorption peaks. The two weak absorption peaks around 303 and 413 nm originate respectively from n−π^* transition of TPA group[22] and the absorption of the thiophene units with the conjugated side chain, while the maximum absorption of the copolymer at 555 nm corresponds to the $\pi-\pi^*$ transition of the polymer backbone. Thus, both the main chain and side chain contribute to the broad nature of the absorption spectra of the polymer, which is a common feature for PTs with conjugated side chains.[15,16] Because of an enlarged π-system, the film absorption of **PT5TPA** is red-shifted by ca. 10 nm than that of P3HT. The absorption edge of the polymer film is at 658 nm, corresponding to an optical band gap of 1.88 eV. The similarity of solution absorption to film absorption suggests strong $\pi-\pi$ interactions (aggregation) in solution. As shown in Figure 2a, when the polymer solution was heated to 85 °C, the absorption peaks blue shift, and the shoulder peak at ca. 600 nm weakened, reflecting partial disaggregation of the polymer backbone at high temperature. Also it must mention that the obtained high molecular weight of **PT5TPA** could be overestimated due to the easily formed polymer aggregation state at room temperature.

In comparison with the absorption spectrum of **PT2TPA** film[16a] as also shown in Figure 2a, the $\pi-\pi^*$ absorption of PT5TPA main chains at ca. 500−650 nm is greatly enhanced than that of the CSC-PTs with concentrated side chains.[15−17] Obviously, the side chain isolated **PT5TPA** can minimize the steric interactions between the neighboring side chains, thus preserving backbone planarity, which results in the red-shifted and enhanced $\pi-\pi^*$ transition of the polymer backbone along with the shoulder peak and steep absorption edge. Furthermore, the well-defined spectra of PT5TPA imply an ordered polymer chains and densely packed side chains in the polymer film, which should benefit to higher hole mobility and photovoltaic performance of the polymer. In order to further investigate the ordered structure of the polymer, we measured X-ray diffraction (XRD) of the polymer film on Si substrate. The XRD pattern of the polymer film (see Figure S7 in Supporting Information) indicates that the polymer film is still in amorphous state although the aggregation is enhanced in the polymer. The hole mobility of PT5TPA film was measured to be 1.1 × 10^{-3} cm^2/(V s) by space charge limited current (SCLC) method (see Figure S3 in Supporting Information), confirming the relatively higher hole mobility of the polymer.

Figure 2b shows the photoluminescence (PL) spectra of **PT5TPA** solution in dichlorobenzene and film, excited at 430 nm, which is the maximum absorption wavelength of the conjugated side chains of the polymer. **PT5TPA** shows deep red main chain emission peaked at 670 nm. The results indicate that quick and complete energy transfer occurs from the conjugated side chains to the polymer main chains after the conjugated side chains absorb the photons. This phenomenon ensures that all photons absorbed by the polymer are useful for the photovoltaic conversion.

The electronic energy levels of the conjugated polymers can be measured from the onset oxidation and onset reduction potentials of the cyclic voltammograms (CVs).[23] Figure 3 shows the cyclic voltammogram of **PT5TPA** together with that of P3HT for comparison and that of ferrocene for potential calibration. The redox potential of ferrocene is 0.09 V vs Ag/Ag$^+$. On the basis of 4.8 eV below vacuum for the energy level of Fc/Fc$^+$, the HOMO and LUMO energy levels of PT5TPA were calculated according to the following equations: $E_{HOMO} = -e(E_{ox}^{onset}+4.71)$ (eV) and $E_{LUMO} = -e(E_{red}^{onset}+4.71)$, where

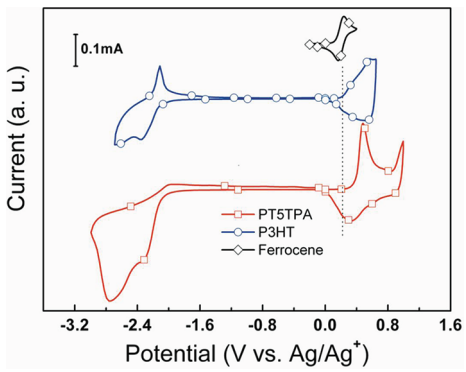

Figure 3. Cyclic voltammograms of PT5TPA and P3HT films on glassy carbon electrode in a 0.1 mol/L *n*-Bu_4NPF_6 acetonitrile solution at a sweep rate of 100 mV/s. The cyclic voltammogram of ferrocene was also put in the figure for the potential calibration.

dx.doi.org/10.1021/ma201718x | *Macromolecules* 2012, 45, 113−118

the unit of E_{ox}^{onset} is V vs. Ag/Ag^+. The onset oxidation potential (E_{ox}^{onset}) and onset reduction potential (E_{red}^{onset}) of **PT5TPA** are 0.39 and −1.63 V vs. Ag/Ag^+ respectively, accordingly, the HOMO and LUMO energy levels of PT5TPA were calculated to be −5.10 and −3.08 eV respectively. Compared to that of P3HT, the onset oxidation potential of **PT5TPA** is positively shifted by ca. 0.2 V and the HOMO energy level of **PT5TPA** is downward shifted by ca. 0.2 eV, which is due to less alkyl substituents of **PT5TPA** than that of P3HT.[12b] The lower HOMO energy level relative to P3HT can provide better air stability in ambient conditions and higher open circuit voltage (V_{oc}) of the PSCs with **PT5TPA** as donor materials because the V_{oc} is usually proportional to the difference between the LUMO level of the acceptor and the HOMO level of the donor.[6]

Photovoltaic Properties. The photovoltaic properties of **PT5TPA** were studied by fabricating the bulk heterojunction PSCs with the device configuration of ITO/PEDOT:PSS/PT5TPA:acceptors/Ca/Al. Here, two different fullerene derivatives $PC_{70}BM$ and $IC_{60}BA$ were used as acceptor in the PSCs. The molecular structures and the electronic energy level diagrams of the donor and acceptor materials were displayed in Figure 4. Figure 5 shows the $J-V$ curves of the PSCs based on

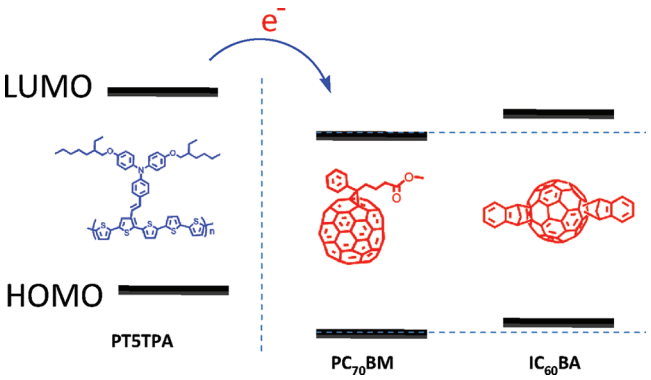

Figure 4. Energy level diagrams for PT5TPA along with acceptors of $PC_{70}BM$ and $IC_{60}BA$.

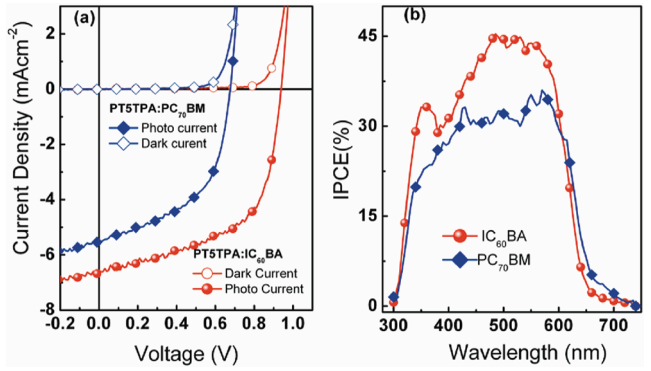

Figure 5. (a) Current density−voltage characteristics of the PSCs based on PT5TPA/fullerene (1:1, w/w) under the illumination of AM1.5G, 100 mW/cm^2. (b) The incident-photon-to-converted-current efficiency (IPCE) spectra of the corresponding devices with different fullerene acceptors.

PT5TPA as donor and $PC_{70}BM$ or $IC_{60}BA$ as acceptor under the illumination of AM 1.5, 100 mW·cm^{-2}. With the widely used $PC_{70}BM$ as acceptor, the PSC showed a PCE of 1.94% along with a V_{oc} of 0.68 V and a FF of 52.2%, while when using $IC_{60}BA$ as acceptor, a higher V_{oc} of 0.94 V was obtained, benefitted from the higher-lying LUMO energy level of $IC_{60}BA$.[4] Together with a J_{sc} of 6.55 mA cm^{-2} and a FF of 58.4%, the PSC based on PT5TPA/$IC_{60}BA$ demonstrated an improved PCE of 3.6%. Although the PCE of 3.6% is lower than that of the PSC based on P3HT/$IC_{60}BA$,[4] it is the highest value reported so far for the CSC-PTs. In the PSCs based on PT5TPA, the FF values (Table 1) are significantly improved in comparison with the CSC-PTs with concentrated side chains,[15,16,17f,24] which could be ascribed to the close aggregation of the polymer main chains in the side chain isolated polymers.

Table 1. Photovoltaic Parameters of PSCs Based on PT5TPA as Donor and $PC_{70}BM$ or $IC_{60}BA$ as Acceptor, under the Illumination of AM1.5G, 100 mW/cm^2

acceptors	weight ratio	V_{oc} (V)	J_{sc} (mAcm^{-2})	FF (%)	PCE (%)	active layer thickness (nm)
$PC_{70}BM$	1:1	0.68	5.46	52.2	1.94	65
$IC_{60}BA$	1:1	0.94	6.55	58.4	3.60	70

3. CONCLUSION

A design concept of "side chain isolation" was proposed for CSC-PTs, and a planar CSC-PT, **PT5TPA**, with styryl−triphenylamine (TPA) side chains and unsubstituted tetrathienyl spacer was designed and synthesized. Compared to previously reported CSC-PTs, side chain isolated **PT5TPA** demonstrated the red-shifted and enhanced $\pi-\pi^*$ transition absorption of the polymer backbone along with the shoulder peak and steep absorption edge. In addition, the unsubstituted thiophene spacer lead the polymer a lower HOMO energy level of −5.1 eV. The PSC based on **PT5TPA** as donor and $IC_{60}BA$ as acceptor displayed a PCE of 3.6% with a high V_{oc} of 0.94 V, under the illumination of AM1.5G, 100 mW/cm^2.

Considering the diversity molecular engineering approach under this side chain isolated polythiophenes, such as changing the nature of side chain and spacer as well as introducing D−A concept, the side chain isolated CSC-PTs could open a new way for developing high performance photovoltaic polymers.

4. EXPERIMENTAL SECTION

4.1. Instrumentation. ^{1}H NMR spectra were measured on a Bruker DMX-400 spectrometer with *d*-chloroform as the solvent and tetramethylsilane as the internal reference. UV−visible absorption spectra were measured on a Hitachi U-3010 UV−vis spectrophotometer. MALDI−TOF spectra were recorded on a Bruker BIFLEXIII. Absorption spectra were taken on a Hitachi U-3010 UV−vis spectrophotometer. Photoluminescence spectra were measured using a Hitachi F-4500 spectrophotometer. Mass spectra were recorded on a Shimadzu spectrometer. Elemental analyses were carried out on a flash EA 1112 elemental analyzer. Thermogravimetric analysis (TGA) was conducted on a Perkin-Elmer TGA-7 thermogravimetric analyzer at a heating rate of 20 °C/min and under a nitrogen flow rate of 100 mL/min. Molecular weight of the polymer was measured by Gel permeation chromatography (GPC), using polystyrene as standard and THF as the eluent. The electrochemical cyclic voltammetry was performed on a Zahner IM6e Electrochemical Workstation, in an acetonitrile solution of 0.1 mol/L tetrabutylammonium hexafluorophosphate (n-Bu_4NPF_6) at a potential scan rate of 100 mV/s with an Ag/Ag^+ reference electrode and a platinum wire counter electrode. Polymer film was formed by drop-casting 1.0 mL of polymer solutions in THF (analytical reagent, 1 mg/mL) onto the glassy carbon working electrode, and then dried in the air.

dx.doi.org/10.1021/ma201718x | *Macromolecules* 2012, 45, 113−118

4.2. Photovoltaic Device Fabrication and Characterization. The PSCs were fabricated with a configuration of ITO/PEDOT:PSS (40 nm)/active layer (65−70 nm)/ Ca(20 nm)/Al(90 nm). A thin layer of PEDOT:PSS (poly(3,4-ethylenedioxythiophene): poly(styrenesulfonate)) was spin-cast on pre-cleaned ITO-coated glass from a PEDOT:PSS aqueous solution (Baytron P VP AI 4083 from H. C. Starck) at 2000 rpm and dried subsequently at 150 °C for 30 min in air, then the device was transferred to a glovebox, where the active layer of the blend of the polymer and fullerene derivative was spin-coated onto the PEDOT:PSS layer. Finally, a Ca/Al metal top electrode was deposited in vacuum onto the active layer at a pressure of ca. 5×10^{-5} Pa. The active area of the device was ca. 4 mm^2.

The thickness of the active layer was determined by an Ambios Tech. XP-2 profilometer. The current density−voltage (J−V) characteristics were measured on a computer-controlled Keithley 236 Source-Measure Unit. A xenon lamp coupled with AM 1.5 solar spectrum filter was used as the light source, and the optical power at the sample was 100 mW/cm^2.

4.3. Materials. 3′-Methyl[2,2′,5′,2″]terthiophene,[25] 5,5′-bis(trimethylstannyl)-2,2′-bithiophene[26] and 4-((4-(2-ethylheptyloxy)phenyl)(4-(2-ethylhexyloxy)phenyl)amino)benzaldehyde[27] were prepared according to the method reported in literatures. Tetrakis(triphenylphosphine)palladium, *N*-Bromosuccinimide and benzoyl peroxide were purchased from Sigma-Aldrich Chemical Co. The synthesis routes for the polymer are shown in Scheme 1.

*5,5″-Dibromo-3′-methyl[2,2′,5′,2″]terthiophene (**2**).* *N*-Bromosuccinimide (NBS, 28.5 g, 160 mmol) was added to a solution of 3′-methyl[2, 2′,5′,2″]terthiophene (20.0 g, 76.3 mmol) in $CHCl_3$ (180 mL) and AcOH (100 mL) at room temperature. After stirring for 3 h, $CHCl_3$ was added and the resulting mixture washed three times with water. The organic layer was dried ($MgSO_4$) and concentrated under reduced pressure. The crude product was purified via silica gel column chromatography afford a green solid with a yield of 27.2 g (85%). GC−MS: m/z = 420. ^{1}H NMR (400 MHz, $CDCl_3$, δ, ppm): 7.02 (d, J = 3.8 Hz, 1 H, Ar−H), 6.96 (d, J = 3.8 Hz, 1 H, Ar−H), 6.88 (m, 3H, Ar−H), 2.33 (s, 3H, CH_3). Anal. Calcd for $C_{13}H_8Br_2S_3$: C, 37.16; H, 1.92; S, 22.89. Found: C, 37.10; H, 1.98; S, 22.75.

*5,5″-Dibromo-3′-bromomethyl[2,2′,5′,2″]terthiophene (**3**).* A mixture of compound **2** (21.0 g, 50 mmol), N-bromosuccinimide (NBS) (8.9 g, 50 mmol), CCl_4 (400 mL), and benzoyl peroxide (BPO) (0.15 g, 0.62 mmol) was refluxed for 3 h. After cooling to the room temperature, the reaction mixture was filtrated. The organic phase was washed with distilled water and dried over anhydrous $MgSO_4$. After removing the solvent, the crude product was purified via silica gel column chromatography to yield a yellow product of compound **3**. ^{1}H NMR (400 MHz, $CDCl_3$, δ, ppm): 7.08−7.07 (m, 2H, Ar−H), 7.05 (d, 1H, J = 3.6 Hz, Ar−H), 6.98 (d, 1H, J = 3.5 Hz, Ar−H), 6.92 (d, 1H, J = 3.6 Hz, Ar−H), 4.53 (S, 2H, $-CH_2-$). Anal. Calcd for $C_{13}H_7Br_3S_3$: C, 31.28; H, 1.41; S, 19.27. Found: C, 31.35; H, 1.38; S, 19.19.

*5,5″-Dibromo-3′-diethoxyphosphorylmethyl[2,2′,5′,2″]-terthiophene (**4**).* A mixture of **3** (15.0 g, 30.0 mmol) and triethyl phosphate (16.6 g, 100.0 mmol) was heated at 160 °C for 3 h. After cooling to room temperature, the triethyl phosphite was distilled off at 120 °C. After removing the solvent, the crude product was purified via silica gel column chromatography to yield a liquid of 15 g (90%). ^{1}H NMR (400 MHz, $CDCl_3$, δ, ppm): 7.13 (s, 1H, ArH), 7.06 (d, J = 4.0 Hz, 1H, ArH), 7.04 (d, J = 4.0 Hz, 1H, ArH), 6.96 (d, J = 3.6 Hz, 1H, ArH), 6.90 (d, J = 3.6 Hz, 1H, ArH), 4.0 (q, 4H, OCH_2), 3.22 (d, J = 20 Hz, 2H, CH_2), 4.0 (t, 6H, CH_3). Anal. Calcd for $C_{17}H_{17}Br_2O_3PS_3$: C, 36.70; H, 3.08; S, 17.29. Found: C, 36.63; H, 3.00; S, 17.32.

*5,5″-Dibromo-3′,3-(4-((4-(2-ethylheptyloxy)phenyl)(4-(2-ethylhexyloxy)phenyl)amino)benzvinyl[2,2′,5′,2″]terthiophene (**5**).* Under an ice−water bath, compound **4** (5.56 g, 10 mmol) and aldehyde (6.50 g, 12 mmol) were dissolved in 30 mL of DMF, and then CH_3ONa (0.6 g, 12 mmol) in 10 mL of DMF was added dropwise to the solution. After reaction for 2 h at room temperature, the solution was poured into water, filtered, and the crude product was purified through silica gel column to yield as a yellow solid of 4.7 g (50%). MALDI-TOF MS: 931.3, calcd for $C_{48}H_{53}Br_2NO_2S_3$: 931.9 ^{1}H NMR (400 MHz, $CDCl_3$, δ, ppm): 7.30 (s, 3H, ArH), 7.05−7.04 (m, 5H, ArH), 6.99 (d, J = 4 Hz, 2H, ArH), 6.94 (d, J = 4 Hz, 2H, ArH), 6.92 (d, J = 4 Hz, 2H, ArH), 6.85−6.83 (m, 5H, ArH), 3.77−3.83 (q, 4H, OCH_2), 1.72 (m, 2H, $CHCH_2$), 1.54−1.32 (m, 16H, CH_2), 0.90−0.96 (m,12H, CH_3). ^{13}C NMR (100 MHz, $CDCl_3$, δ, ppm): 138.327, 135.234,130.903, 130.718, 127.499, 127.063, 126.987, 124.411, 122.688, 120.688, 120.092, 115.472, 113.089, 111.744, 39.635, 30.728, 29.292, 24.060, 23.247, 14.294, 11.334. Anal. Calcd for $C_{47}H_{51}Br_2NO_2S_3$: C, 61.50; H, 5.60; N, 1.53, S, 10.48. Found: C, 61.69; H, 5.55; N, 1.50; S: 10.40.

PT5TPA. Under the protection of argon atmosphere, 0.5 mmol of monomer **5** was put into a two-neck flask. Then 12 mL of degassed toluene and 0.5 mmol of 5,5′-bis(trimethylstannyl)-2,2′-bithiophene were added to the mixture. The solution was flushed with argon for 10 min, and then 25 mg of $Pd(PPh_3)_4$ was added. After another flushing with argon for 20 min, the reactant was heated to reflux for 24 h. Then the reactant was cooled to room temperature and the polymer was precipitated by adding 200 mL of methanol, filtered through a Soxhlet thimble, and then subjected to Soxhlet extraction with methanol, hexane, and chloroform. The polymer was recovered as solid from the chloroform fraction by rotary evaporation. The solid was dried under vacuum for 12 h to get **PT5TPA**.The yield of the polymerization reaction was about 60%. GPC: M_n = 180.9 kg·mol^{-1}, M_w/M_n = 3.2. ^{1}H NMR (400 MHz, $CDCl_3$, δ, ppm): 7.30−6.50 (br, 23H, ArH), 3.86 (br, 4H), 4.87 (s, 2H), 2.26(s, 2H), 1.58−1.02 (m, 40H), 0.89−0.83 (m, 18H). Anal. Calcd for $C_{55}H_{57}NO_2S_5$: C, 71.47; H, 6.21; N, 1.51, S, 17.34. Found: C, 71.38; H, 6.25; N, 1.54; S: 17.41.

■ ASSOCIATED CONTENT

Ⓢ Supporting Information

Figures showing ^{1}H NMR spectra of compound **3, 4**, and **5**, TGA plots, X-ray diffraction pattern, DSC thermogram, and hole mobility measurement of **PT5TPA**. This material is available free of charge via the Internet at http://pubs.acs.org.

■ AUTHOR INFORMATION

Corresponding Author

*E-mail: liyf@iccas.ac.cn.

■ ACKNOWLEDGMENTS

This work was supported by NSFC (Grants No. 20874106, 20821120293, 50933003, 21021091 and 51103164), The Ministry of Science and Technology of China, and the Chinese Academy of Sciences. The authors thank Dr. Hua Geng for the help of the molecular simulation.

■ REFERENCES

(1) Chen, J.; Cao, Y. *Acc. Chem. Res.* **2009**, *42*, 1709.
(2) Cheng, Y.-J.; Yang, S.-H.; Hsu, C.-S. *Chem. Rev.* **2009**, *109*, 5868.
(3) He, Y.; Li, Y. *Phys. Chem. Chem. Phys.* **2011**, *13*, 1970.
(4) (a) He, Y.; Chen, H.-Y.; Hou, J.; Li, Y. *J. Am. Chem. Soc.* **2010**, *132*, 1377. (b) Zhao, G. J.; He, Y. J.; Li, Y. F. *Adv. Mater.* **2010**, *22*, 4355−4358.
(5) Yu, G.; Gao, J.; Hummelen, J. C.; Wudl, F.; Heeger, A. J. *Science* **1995**, *270*, 1789.
(6) Thompson, B. C.; Fréchet, J. M. J. *Angew. Chem., Int. Ed.* **2008**, *47*, 58.
(7) Nagarjuna, G.; Yurt, S.; Jadhav, K. G.; Venkataraman, D. *Macromolecules* **2010**, *43*, 8045.
(8) Grenier, C. R. G.; George, S. J.; Joncheray, T. J.; Meijer, E. W.; Reynolds, J. R. *J. Am. Chem. Soc.* **2007**, *129*, 10694.
(9) Perepichka, I. F.; Perepichka, D. F.; Meng, H.; Wudl, F. *Adv. Mater.* **2005**, *17*, 2281.
(10) (a) Ong, B. S.; Wu, Y.; Liu, P.; Gardner, S. *J. Am. Chem. Soc.* **2004**, *126*, 3378. (b) Ong, B. S.; Wu, Y.; Li, Y.; Liu, P.; Pan, H. *Chem.—Eur. J.* **2008**, *14*, 4766. (c) Li, J.; Tan, H.-S.; Chen, Z.-K.; Goh, W.-P.; Wong, H.-K.; Ong, K.-H.; Liu, W.; Li, C. M.; Ong, B. S.

Macromolecules **2011**, *44*, 690. (d) Li, Y. F.; Zou, Y. P. *Adv. Mater.* **2008**, *20*, 2952.
(11) (a) Sugiyasu, K.; Song, C.; Swager, T. M. *Macromolecules* **2006**, *39*, 5598. (b) Wu, P.-T.; Xin, H.; Kim, F. S.; Ren, G.; Jenekhe, S. A. *Macromolecules* **2009**, *42*, 8817. (c) Miyanishi, S.; Tajima, K.; Hashimoto, K. *Macromolecules* **2009**, *42*, 1610. (d) Li, H.; Sundararaman, A.; Pakkirisamy, T.; Venkatasubbaiah, K.; Schödel, F.; Jäkle, F. *Macromolecules* **2010**, *44*, 95. (e) Rieger, R.; Beckmann, D.; Pisula, W.; Kastler, M.; Müllen, K. *Macromolecules* **2010**, *43*, 6264. Liu, P.; Wu, Y.; Pan, H.; Ong, B. S.; Zhu, S. *Macromolecules* **2010**, *43*, 6368. (f) Liang, Y.; Xiao, S.; Feng, D.; Yu, L. *J. Phys. Chem. C* **2008**, *112*, 7866.
(12) (a) Thompson, B. C.; Kim, B. J.; Kavulak, D. F.; Sivula, K.; Mauldin, C.; Fréchet, J. M. J. *Macromolecules* **2007**, *40*, 7425. (b) Hou, J. H.; Chen, T. L.; Zhang, S. Q.; Huo, L. J.; Sista, S.; Yang, Y. *Macromolecules* **2009**, *42*, 9217.
(13) Ma, W.; Yang, C.; Gong, X.; Lee, K.; Heeger, A. J. *Adv. Funct. Mater.* **2005**, *15*, 1617.
(14) Li, G.; Shrotriya, V.; Huang, J.; Yao, Y.; Moriarty, T.; Emery, K.; Yang, Y. *Nat. Mater.* **2005**, *4*, 864.
(15) (a) Hou, J.; Tan, Z. a.; Yan, Y.; He, Y.; Yang, C.; Li, Y. *J. Am. Chem. Soc.* **2006**, *128*, 4911. (b) Hou, J. H.; Yang, C. H.; He, C.; Li, Y. F. *Chem. Commun* **2006**, 871–873. (c) Hou, J. H.; Huo, L. J.; He, C.; Yang, C. H.; Li, Y. F. *Macromolecules* **2006**, *39*, 594–603. (d) Zhou, E. J.; Tan, Z. A.; Huo, L. J.; He, Y. J.; Yang, C. H.; Li, Y. F. *J. Phys. Chem. B.* **2006**, *110*, 26062–26067.
(16) (a) Zou, Y.; Sang, G.; Wu, W.; Liu, Y.; Li, Y. *Synth. Met.* **2009**, *159*, 182. (b) Wang, Y.; Zhou, E.; Liu, Y.; Xi, H.; Ye, S.; Wu, W.; Guo, Y.; Di, C.-a.; Sun, Y.; Yu, G.; Li, Y. *Chem. Mater.* **2007**, *19*, 3361. (c) Zou, Y.; Wu, W.; Sang, G.; Yang, Y.; Liu, Y.; Li, Y. *Macromolecules* **2007**, *40*, 7231–7237.
(17) (a) Wagner, K.; Crowe, L. L.; Wagner, P.; Gambhir, S.; Partridge, A. C.; Earles, J. C.; Clarke, T. M.; Gordon, K. C.; Officer, D. L. *Macromolecules* **2010**, *43*, 3817. (b) Wang, H.-J.; Chan, L.-H.; Chen, C.-P.; Lin, S.-L.; Lee, R.-H.; Jeng, R.-J. *Polymer* **2011**, *52*, 326. (c) Saini, G.; Jacob, J. *Polym. Int.* **2011**, *60*, 1010. (d) Park, J. W.; Lee, D. H.; Chung, D. S.; Kang, D.-M.; Kim, Y.-H.; Park, C. E.; Kwon, S.-K. *Macromolecules* **2010**, *43*, 2118. (e) Wagner, K.; Crowe, L. L.; Wagner, P.; Gambhir, S.; Partridge, A. C.; Earles, J. C.; Clarke, T. M.; Gordon, K. C.; Officer, D. L. *Macromolecules* **2010**, *43*, 3817. (f) Yu, C.-Y.; Ko, B.-T.; Ting, C.; Chen, C.-P. *Sol. Energy Mater. Sol. Cells* **2009**, *93*, 613.
(18) Sun, H. *J. Phys. Chem. B* **1998**, *102*, 7338.
(19) Bhattacharya, A. K.; Thyagarajan, G. *Chem. Rev.* **1981**, *81*, 415.
(20) Wadsworth, W. S.; Emmons, W. D. *J. Am. Chem. Soc.* **1961**, *83*, 1733.
(21) Carsten, B.; He, F.; Son, H. J.; Xu, T.; Yu, L. *Chem. Rev.* **2011**, *111*, 1493.
(22) (a) Zhang, Z.-G.; Zhang, K.-L.; Liu, G.; Zhu, C.-X.; Neoh, K.-G.; Kang, E.-T. *Macromolecules* **2009**, *42*, 3104. (b) Zhang, Z.-G.; Liu, Y.-L.; Yang, Y.; Hou, K.; Peng, B.; Zhao, G.; Zhang, M.; Guo, X.; Kang, E.-T.; Li, Y. *Macromolecules* **2010**, *43*, 9376.
(23) Sun, Q.; Wang, H.; Yang, C.; Li, Y. *J. Mater. Chem.* **2003**, *13*, 800.
(24) Tsai, J.-H.; Lee, W.-Y.; Chen, W.-C.; Yu, C.-Y.; Hwang, G.-W.; Ting, C. *Chem. Mater.* **2010**, *22*, 3290.
(25) Cunningham, D. D.; Laguren-Davidson, L.; Mark, H. B.; Van Pham, C.; Zimmer, H. *J. Chem. Soc., Chem. Commun* **1987**, 1021.
(26) Kotani, S.; Shiina, K.; Sonogashira, K. *J. Organomet. Chem.* **1992**, *429*, 403.
(27) Tang, R.; Tan, Z. a.; Li, Y.; Xi, F. *Chem. Mater.* **2006**, *18*, 1053.

Macromolecules

Article

pubs.acs.org/Macromolecules

Thioxanthone–Diphenyl Anthracene: Visible Light Photoinitiator

Demet Karaca Balta, Gokhan Temel, Gokce Goksu, Nuket Ocal, and Nergis Arsu*

Department of Chemistry, Yildiz Technical University, Davutpasa Campus, Istanbul 34210, Turkey

ABSTRACT: 7,12-Diphenyl-14*H*-naphto[2,3-*b*]thioxanthen-14-one (TX-DPA) was synthesized and characterized as a potential visible light photoinitiator for radical polymerization. TX-DPA has an excellent absorption character in the visible region and the photophysical properties of TX-DPA were investigated by fluorescence and laser flash photolysis studies and the photopolymerization of methyl methacrylate in air atmosphere helped to understand the initiation mechanism of TX-DPA. Moreover, it is possible that the production of singlet oxygen from the quenching of ^{3}TX-DPA by molecular oxygen resulted in the reaction of singlet oxygen with TX-DPA to form an endoperoxide: decomposition of endoperoxide leads to initiating radicals.

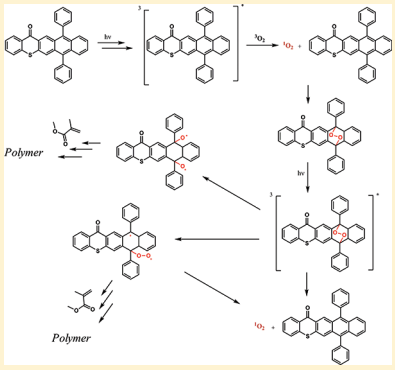

INTRODUCTION

In recent years, many attempts have been made to synthesize photoinitiators that operate in the visible region of the spectrum. The reason for this is that visible light is cheap, safe and possesses high penetration ability in the presence of UV absorbing monomers, pigments and substrates.[1−7]

Thioxanthone (TX) and its derivatives are some of the most widely used type II photoinitiators in various UV curing applications because of their excellent light absorption characteristics.[8] In most cases, the photoinitiating free radicals are generated by hydrogen abstraction of triplet excited states of TX from hydrogen donors such as amines or thiols (see Scheme 1).[9−11]

Scheme 1. Photoinitiated Free Radical Polymerization Using TX as Photoinitiator

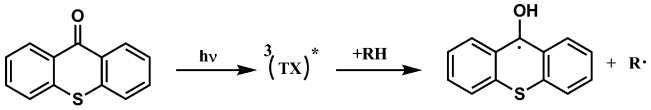

However, low molecular-weight amines, particularly when used at high concentrations, have several intrinsic disadvantages such as odor, toxicity[12] and migration in UV-curing technology and cause a decrease in the pendulum hardness of the cured film.[13] One way to overcome these problems is to chemically incorporate the hydrogen donating sites into TX chromophores.[14−16]

Amine,[17−20] alkyl amino,[21,22] acid,[23−27] or thiol[28] linked photoinitiators are seen in the literature and they may find various applications in the Radiation Curing Industry because of the great advantages of their one-component nature. Because of the one-component structure of the photoinitiator, it can serve as both a triplet photosensitizer and as a hydrogen donor during photopolymerization. Thus, these photoinitiators do not require an additional co-initiator.

An alternative approach concerns the attachment of both chromophoric and hydrogen donating groups into polymer chains.[29−35] This way the odor and toxicity problems perceived with the conventional photoinitiators and amine hydrogen donors have been overcome.

We have also developed a novel thioxanthone based photoinitiator possessing an anthracene group, thioxanthone–anthracene[36] (TX-A, Chart 1), which exhibits completely different photochemical properties compared to conventional TX type photoinitiators.

Chart 1. Structure of TX-A

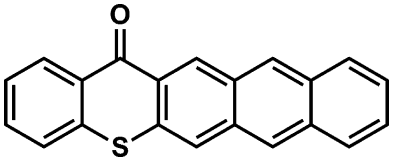

In contrast to TX type photoinitiators, TX-A is an efficient photoinitiator for free radical polymerization of both acrylic and styrenic type monomers in the presence of oxygen without an additional hydrogen donor.[36−38] Moreover, for other TX type photoinitiators oxygen inhibits the polymerization because of the quenching of the excited triplet TX with oxygen. In the case of TX-A, molecular oxygen is essential for the initiation process. The initiation mechanism involves the formation of singlet oxygen by energy transfer from triplet TX-A[39] (Scheme 2).

Received: September 26, 2011
Revised: November 29, 2011
Published: December 16, 2011

Scheme 2. Photoinitiation Mechanism of TX-A in the Presence of Oxygen

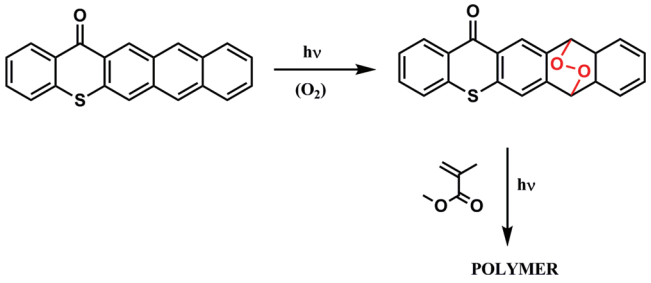

There is another possible application of using an oil soluble initiator in water; complexation of TX-A with β-CD was achieved and photopolymerization of acrylamide with TX-A/β-CD was performed.[40]

Our aim is to synthesize new photoinitiators which have absorption in the visible region and operate in oxygen atmosphere. We achieved the synthesis of 7,12-diphenyl-14*H*-naphto[2,3-*b*]thioxanthen-14-one (TX-DPA). ^{1}H NMR, ^{1}H−^{1}H COSY, elemental analysis, and GC−MS were used for the characterization of TX-DPA. Photophysical properties were determined by the use of UV−vis, fluorescence and laser flash photolysis, and photoinitiated polymerization of methyl methacrylate was performed with TX-DPA by using a xenon lamp as the irradiation source.

RESULTS AND DISCUSSION

Synthesis and Characterization. The synthesis of TX-DPA was achieved by using a similar method to that which was described in our previous publication (see Experimental Section, Chart 2).[36] Since there are more than one ring closure

Chart 2. Synthesis of TX-DPA

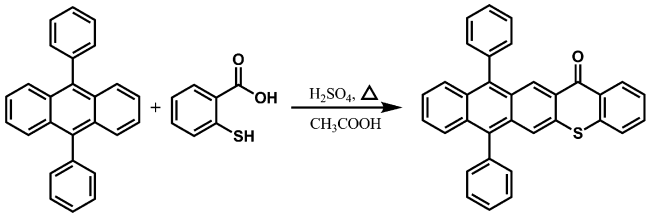

possibilities, due to the aromatic groups on the DPA (see Experimental Section, Chart 3), the COSY NMR method was employed to define the structure of the product in addition to using ^{1}H NMR spectroscopy.

^{1}H−^{1}H COSY was employed to confirm the structure of the compound. Figure 1 shows the ^{1}H−^{1}H COSY spectrum, the peak at 8.03 ppm as doublet is coupled with the H_{15} proton of the phenyl group as expected, while the peak at 7.62 ppm as doublet is coupled with the proton H_{18}. The H_4 proton is determined by ^{1}H−^{1}H COSY as doublet and is clearly coupled with H_3.

Absorption and Fluorescence. TX-DPA has excellent absorption properties in the visible region of the electromagnetic spectrum and the absorption characteristics of TX-DPA were found to be very similar to the parent compounds, both thioxanthone and 9, 10-diphenylanthracene. The molar absorptivities of TX-DPA where the wavelength values were 383 and 450 nm were calculated as 10633 and 4347

Chart 3

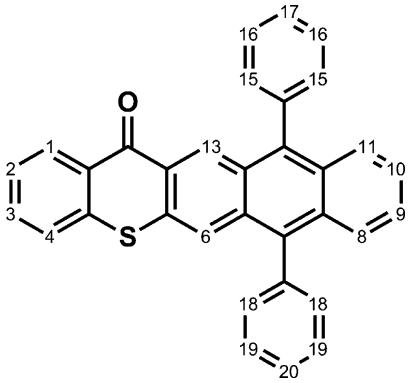

L.mol^{-1}.cm^{-1}, respectively. These high molar absorptivity values would be beneficial for a photoinitiator in the visible region (Figure 2).

A photodecomposition study of TX-DPA was performed in $CHCl_3$ and this solution was exposed to UV light at certain periods of time and the photodecomposition of TX-DPA was followed by detecting UV-spectral changes (Figure 2).

At the end of the irradiation (270 s) while the typical absorption bands of the diphenylanthracene moiety from DPA completely disappeared, the weak absorption of the TX group at 380 nm was still detectable.

Fluorescence measurements were conducted in order to clarify the mechanistic details. As can be seen from Figure 3, the excitation spectrum of TX-DPA is very similar to its absorption spectrum.

The emission spectrum represents the characteristics of the TX moiety rather than DPA. The intersection of the emission and excitation spectra at 464 nm, allowed us to calculate the singlet excited state energy of TX-DPA, as ca. 257.8 kJ/mol.

The fluorescence quantum yield, ϕ_f, was estimated to be 0.45 by using 9,10-diphenylanthracene as the standard. (ϕ_f = 0.95).[41,42] From the calculations, the fluorescence quantum yields ($\phi_{(TX\text{-}DPA)}$ = 0.45) of anthracene chromophore were more dominant than the TX [$\phi_{(TX)}$ = 0.07]. This high fluorescence quantum yield reduced the triplet yield, the state from which initiating radicals are generated.

Fluorescence quenching studies of TX-DPA were performed by adding MDEA at different concentrations and the changes in the fluorescence emissions were recorded for the TX-DPA/ethanol solution. The Stern−Volmer representation (i.e., I_0/I vs [Q]) is shown in Figure 4. It can be observed that the least-squares fit of the experimental results produces a straight line with reasonable point scattering. The linearity of the corresponding plot was always excellent (R^2 > 0.90), and no deviation was detected at high quencher concentrations. The Stern−Volmer quenching constant, K_{sv}, obtained from the slope is 0.86 M^{-1}.

Laser Flash Photolysis. To investigate the properties of the triplet state and its reactivities, laser flash photolysis experiments were performed. Figure 5 shows the transient absorption spectra of TX-DPA directly after irradiation with laser pulses at 355 nm. Three transient absorption maxima were observed at 400, 490, and 590 nm (see Figure 5a) which decayed in a first-order kinetic with a lifetime of 2.6 μs (Figure 5b). The peak at 590 nm was assigned to the triplet−triplet absorption of TX-DPA based on similarities with the triplet−triplet spectra of TX[43] and TX derivatives.[28] Recently we

dx.doi.org/10.1021/ma202168m | *Macromolecules* 2012, 45, 119−125

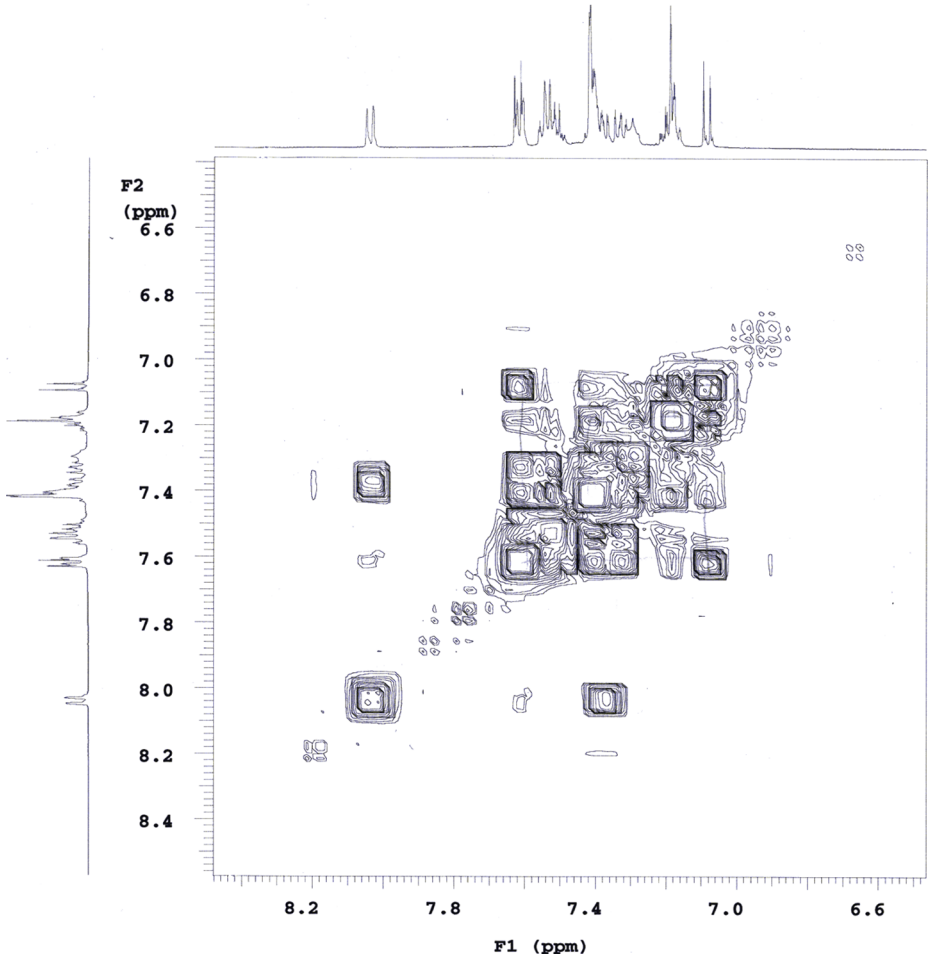

Figure 1. $^{1}H-^{1}H$ COSY spectrum of TX-DPA in $CDCl_3$.

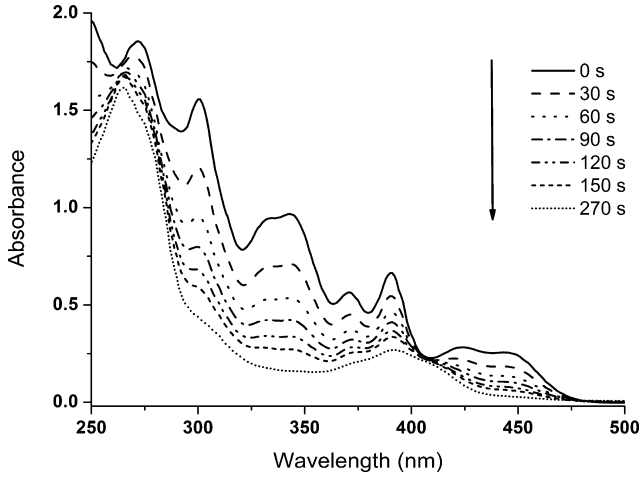

Figure 2. Photobleaching of TX-DPA [4.10×10^{-5} M] in $CHCl_3$ during 0–270 s in air atmosphere with polychromatic light (unfiltered light from a medium pressure mercury lamp).

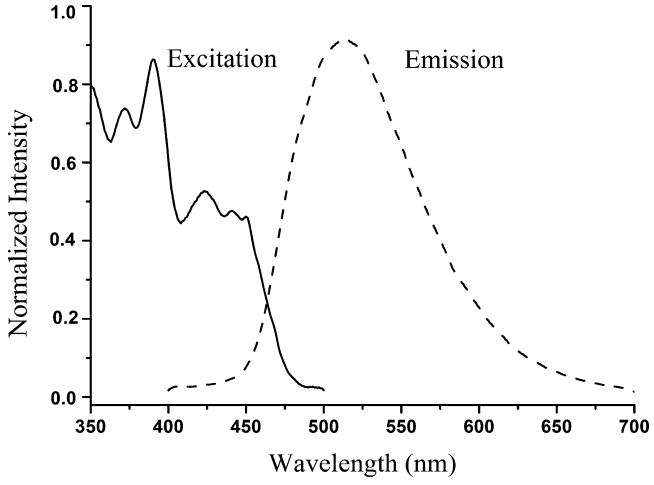

Figure 3. Fluorescence excitation (—) and emission (--) spectra of TX-DPA in ethanol; λ_{exc} = 390 nm.

submitted LFP studies of TX-A, and the triplet lifetime of TX-A was calculated as 28 μs.[39]

Notably, all transients were quenched by oxygen and were tentatively assigned to the triplet state. Quenching experiment of transients with MDEA were also achieved and the rate constant was found as $\sim 2.72 \times 10^{9}$ M^{-1} s^{-1} (see Figure 6).

From the previous studies[36,39] related with anthracene attached thioxanthone (TX-A), polymerization experiments in the presence and absence of oxygen clearly confirmed the crucial role of oxygen for successful polymerization as the efficient initiation of TX-A can be attributed to the formation of endoperoxide by the reaction of TX-A with singlet oxygen.

Photopolymerization. A similar way was followed to determine the initiation mechanism of TX-DPA, and polymer-

dx.doi.org/10.1021/ma202168m | *Macromolecules* 2012, 45, 119–125

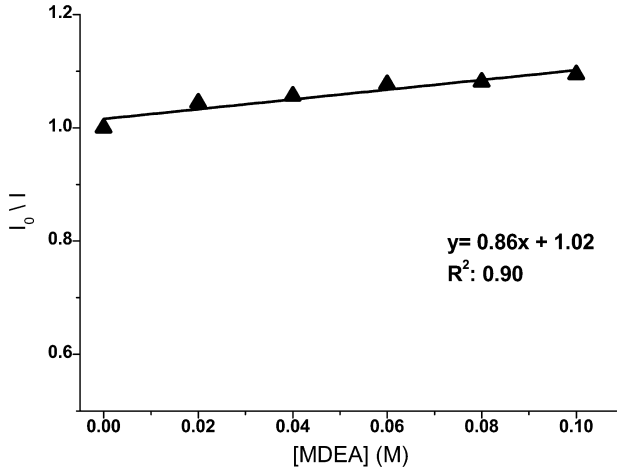

Figure 4. Stern–Volmer plot of the quenching of TX-DPA [1.0×10^{-5} mol L^{-1}] by MDEA in ethanol (λ_{exc} = 390 nm). I_0 = fluorescence intensity of TX-DPA, I = fluorescence intensity in the presence of MDEA.

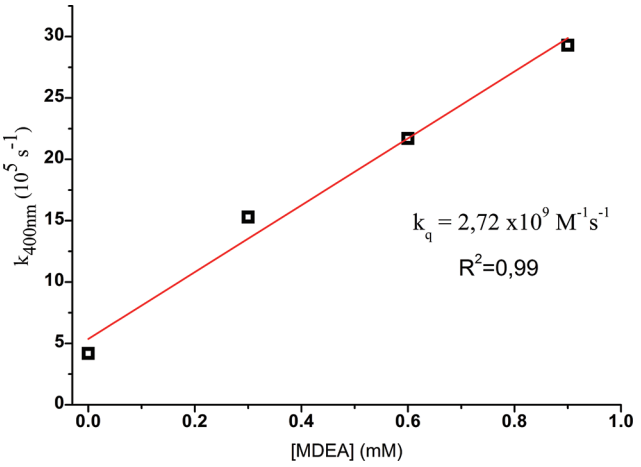

Figure 6. Reaction of MDEA with triplet TX-DPA in acetonitrile solutions 23 °C. Dependence of the pseudo-first-order rate constant of the decay of the optical absorption at 400 nm on the concentration of MDEA after laser excitation (355 nm).

ization experiments of methyl methacrylate with TX-DPA in DMF in the prescence and absence of oxygen atmosphere were performed. Additionally, a tertiary alkyl amine namely *N*-methyldiethanolamine (MDEA) was also added to the same formulation to see the inhibition effect of oxygen beside the synergistic effect of the amine. A xenon lamp source was used as the irradiation source, since TX-DPA has excellent absorption in the visible region.

At the very low initiator concentration level (5×10^{-5} M), polymerization was not observed in air atmosphere, but when MDEA was added to this formulation in air atmosphere, the conversion percentage was found to be 3.50. When the initiator concentration increased to 1×10^{-4} M, some polymer formation was observed but the conversion percentage was still low compared to the formulation containing MDEA. By further increasing the initiator concentration to 5×10^{-4} M, the beneficial effect of oxygen for the formation of endoperoxide appeared and the conversion percentage was 5.3 in air atmosphere, 3.8 in the presence of MDEA, and 2.9 in nitrogen atmosphere. When the obtained results in the prescence of amine and nitrogen atmophere were compared, the beneficial effect of the amine appears to be due to the formation of α-aminoalkyl radicals (see Table 1).

Table 1. Photoinitiated Polymerization of Methyl Methacrylate [4.68 mol L^{-1}] in DMF with TX-DPA in the Absence and Presence of MDEA in/under a Xenon Lamp System

[TX-DPA] (mol L^{-1})	[MDEA] (mol L^{-1})	% convn[a]	$M_n \times 10^{-4}$ (g mol^{-1})	M_w/M_n
5×10^{-5}	-	0.0	-	-
5×10^{-5}	5×10^{-2}	3.5	2.51	1.39
1×10^{-4}	-	0.7	3.50	1.40
1×10^{-4}	5×10^{-2}	4.5	2.30	1.32
5×10^{-4}	-	5.3	4.33	2.09
5×10^{-4}	5×10^{-2}	3.8	2.04	1.25
[b]5×10^{-4}	-	2.9	3.22	1.44
1×10^{-3}	5×10^{-2}	1.2	2.39	1.24
1×10^{-3}	-	1.0	3.65	1.48

[a] t_{irr} = 60 min. [b] Under nitrogen atmosphere $I_{0(UV\text{-}A)}$ = 175 W·m^{-2}

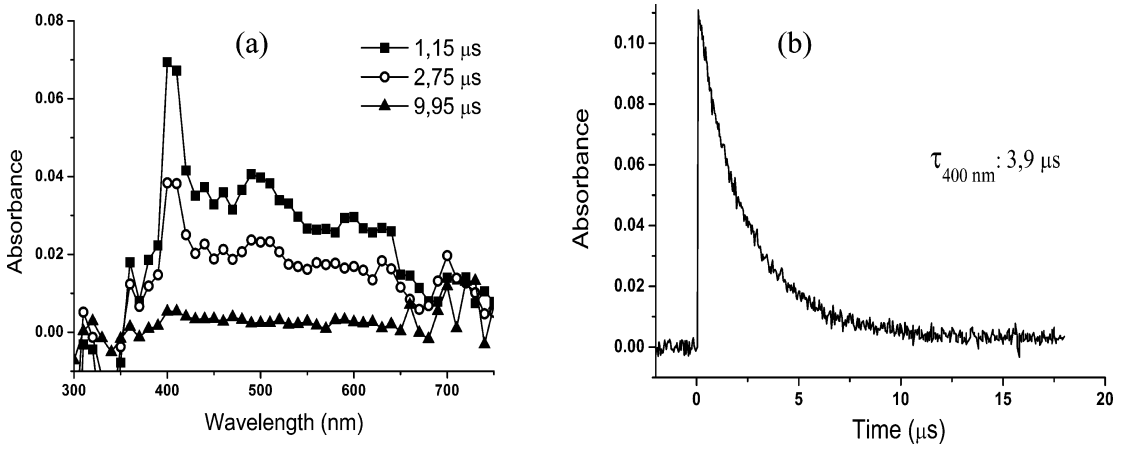

Figure 5. (a) Transient optical absorption spectrum recorded 1.15 μs, 2.27 and 1.4 μs following laser excitation (355 nm, 5 ns) of TX-DPA [2.4×10^{-5} M] in argon saturated acetonitrile solution at 23 °C; .(b) Kinetic traces of the transient optical absorption spectrum at 400 nm recorded 1.15, 2.27, and 1.4 μs following laser excitation (355 nm; 5 ns) of TX-DPA in argon-saturated acetonitrile solution at 23 °C.

dx.doi.org/10.1021/ma202168m | *Macromolecules* 2012, 45, 119–125

For comparison, photopolymerization experiments using either TX or DPA themselves or their combinations in the presence and absence of the hydrogen donor MDEA were performed (Tables 2 and 3).

Table 2. Photoinitiated Polymerization of Methyl Methacrylate [4.68 mol L^{-1}] in DMF with DPA in the Absence and Presence of MDEA in/under a Xenon Lamp System

[DPA] (mol L^{-1})	[MDEA] (mol L^{-1})	% convn[a]
5×10^{-5}	-	0.0
5×10^{-5}	5×10^{-2}	3.8
1×10^{-4}	-	0.0
1×10^{-4}	5×10^{-2}	4.6
5×10^{-4}	-	0.3
5×10^{-4}	5×10^{-2}	6.7
1×10^{-3}	-	0.6
1×10^{-3}	5×10^{-2}	7.9

[a] t_{irr} = 60 min.

Table 3. Photoinitiated Polymerization of Methyl Methacrylate [4.68 mol·L^{-1}] in DMF in the Prescence of 9,10-Diphenylanthracene (DPA) and Thioxanthone (TX) in/under a Xenon Lamp System

[DPA] (mol L^{-1})	[TX] (mol L^{-1})	[MDEA] (mol L^{-1})	% convn[a]
5×10^{-4}	5×10^{-4}	-	0.6
5×10^{-4}	5×10^{-4}	5×10^{-2}	2.3

[a] t_{irr} = 60 min.

Anthracene derivatives are known to form instable endoperoxides upon irradiation.[44] The singlet oxygen ($^1O_2$) addition rate constant was reported in the literature[45,46] as 5.4 × 10^5 M^{-1} s^{-1} for anthracene and 3.0 × 10^6 M^{-1} s^{-1} for diphenylanthracene. The singlet oxygen rate constants and stabilities of the endoperoxides increase as more electron-pushing substituents are added to the anthracene ring. The bimolecular quenching rate constant of singlet oxygen by TX-A was found to be similar to the reported value for anthracene (k_{1O2} = 5.4 × 10^5 M^{-1} s^{-1}).[45] These endoperoxides decompose (thermally and photochemically) through radical intermediates,[47−49] which could initiate the polymerization of the monomers. The endoperoxide of diphenylanthracene-TX is probably formed very easily due to the stability of TX-DPA, and possibly the formation of endoperoxide is not occurring efficiently in room temperature to produce initiating alkoxy and/or peroxy radicals. This could be an explanation of the low polymer yield in the presence of TX-DPA when comparing the results obtained with TX-A as the initiator.[36]

In air atmosphere, the initiating ability of DPA for the MMA polymerization in the presence and absence of TX was seen as proof of the formation of endoperoxide.

For the characterization of the polymer, UV spectroscopy was used. In Figure 7, the absorption spectra of TX-DPA and the poly(methyl methacrylate) obtained from the irradiation with xenon lamp in the absence of MDEA are shown. The UV absorption spectra of purified polymer produced from initiation with a high initiator concentration (5 × 10^{-4} M) showed absorbance at 300 nm, which indicates TX chromophores bound slightly to polymers.

A feasible mechanism for the initiation process involves the formation of an endoperoxide by the reaction of TX-DPA with

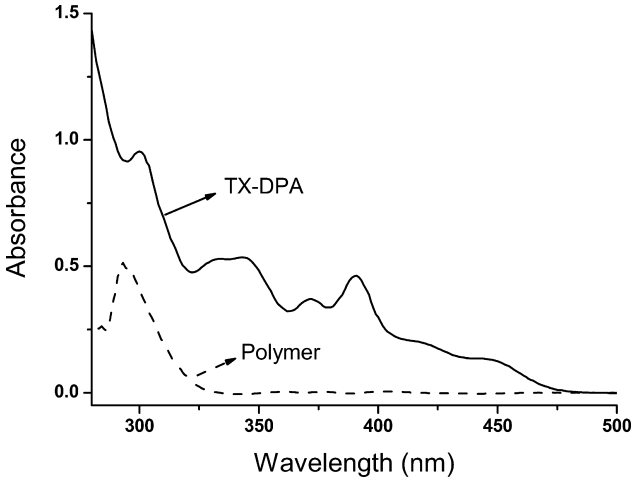

Figure 7. Absorption spectra of TX-DPA (——) and poly(methyl methacrylate) (---) obtained ([PI]: 5 × 10^{-4} M) in THF.

singlet oxygen formed from the triplet excited state in the presence of oxygen as illustrated in Scheme 3. The excitation of this intermediate eventually leads to the formation of peroxy and/or alkoxy radicals capable of initiating free radical polymerization of MMA.

In the presence of MDEA, the possibility of the formation of endoperoxide is getting lower since oxygen in the medium is scavenged by MDEA. Therefore, the TX part plays a more dominant role and so a typical type II initiation mechanism appears (Scheme 4).

■ CONCLUSION

In conclusion, diphenylanthracene (TX-DPA) was successfully synthesized and was found to have excellent optical properties in the visible region of the electromagnetic spectrum. TX-DPA initiated polymerization of methyl methacrylate in the presence and absence of oxygen. The initiation mechanism in the presence of oxygen possibly explains the involvement of the formation of singlet oxygen by energy transfer from triplet TX-DPA and resulted in alkoxy or peroxy radicals after photoexcitation of TX-DPA-O_2 initiated free radical polymerization. High molar absorptivity in the visible region may possibly lead to using this photoinitiator in long wavelength region applications in the presence of oxygen atmosphere.

■ EXPERIMENTAL SECTION

Materials. 9,10-Diphenylanthracene (DPA, 97%, Aldrich) thiosalicylic acid (98.5%, Fluka), glacial acetic acid (Aldrich), *N*-methyldiethanolamine (MDEA, 99%, Aldrich), sulfuric acid (H_2SO_4, 98%, Merck), ethanol (HPLC grade, Aldrich), acetonitrile (HPLC grade, Aldrich), chloroform ($CHCl_3$, ≥99.8%, Fluka), *N*,*N*′-dimethylformamide (DMF, +99%, Aldrich) and thioxanthone (TX, ≥98.5%, Fluka) were used as received. Methyl methacrylate (MMA, ≥99%, Fluka) was washed with 5% aqueous NaOH solution, dried over $CaCl_2$, and distilled over CaH_2 in vacuo. Tetrahydrofuran (99.8%, J.T. Baker) was dried and distilled over $LiAlH_4$.

Synthesis of 7,12-Diphenyl-14*H*-naphto[2,3-*b*]thioxanthen-14-one (TX-DPA). A heated solution of 9,10-diphenylanthracene (2 × 10^{-3} mol) in glacial acetic acid (15 mL) was added slowly to the thiosalycylic acid (2 × 10^{-3} mol) under stirring followed by the addition of 5 mL concentrated sulphuric acid. After the addition, the reaction mixture was refluxed at 120 °C for 5 h after which it was left to stand at room temperature overnight. The resulting mixture was poured carefully under stirring into a 10-fold excess of boiling water. The mixture was stirred under boiling for an additional 5 min. The

dx.doi.org/10.1021/ma202168m | *Macromolecules* 2012, 45, 119−125

Scheme 3. Photoinduced Radical Generation Mechanism of TX-DPA Photoinitiator in the Prescence of Oxygen

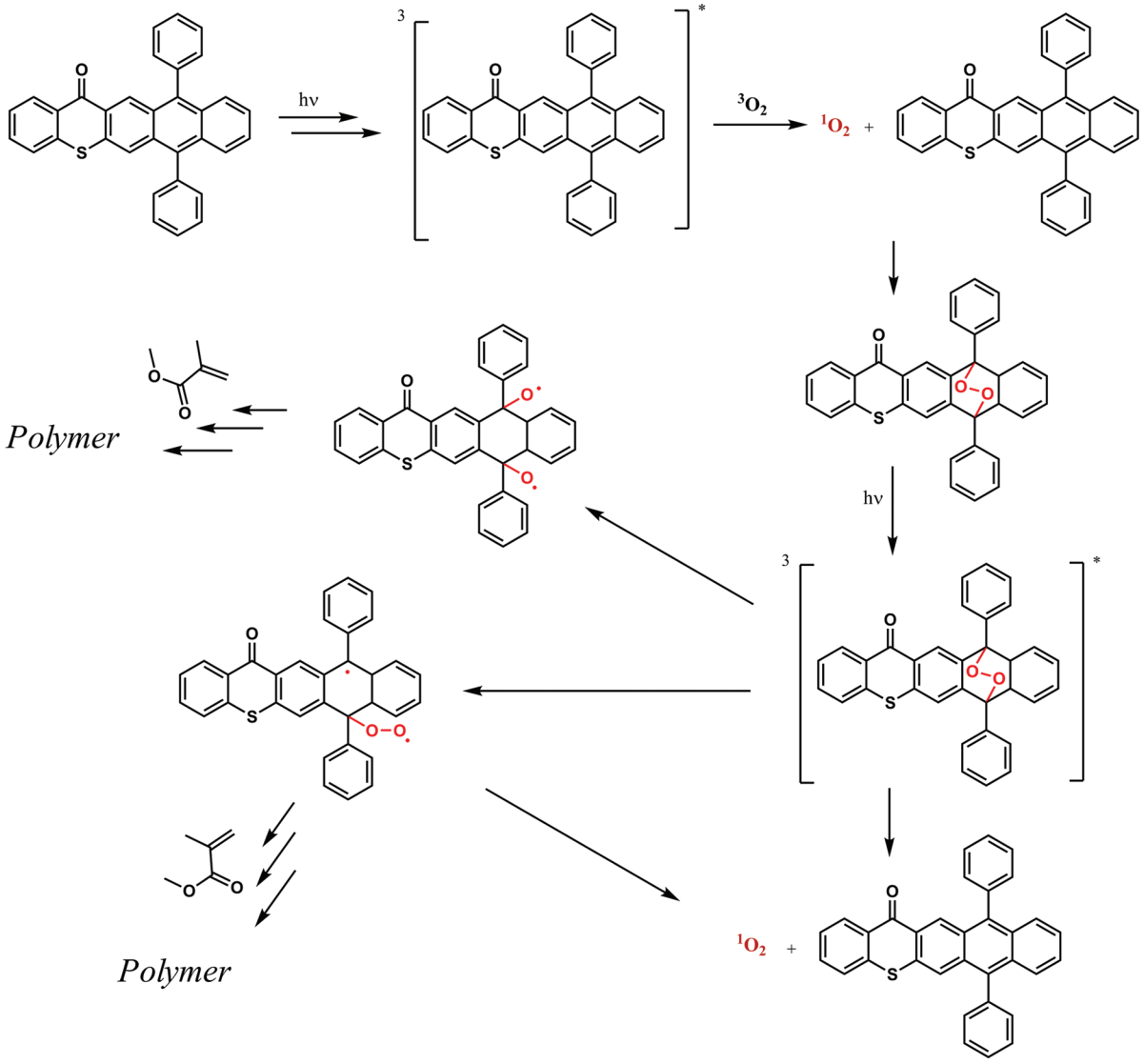

Scheme 4. Photoinduced radical generation mechanism of TX-DPA photoinitiator with *N*-methyldiethanolamine

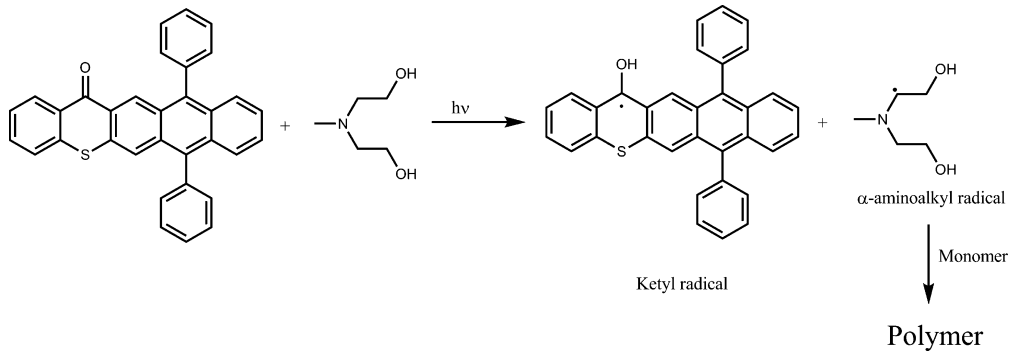

solution was cooled and filtered. The residue product was purified by column chromatography over silica gel eluting with chloroform (Chart 2). M_A ($C_{33}H_{20}OS$): 464 g mol^{-1}; yield: 52%; mp 263–266 °C.

^{1}H NMR (500 MHz) in $CDCl_3$: δ 8.03 (d, J = 8.78 Hz, 1H, H_{13}), 7.62 (d, J = 8.78 Hz, 1H, H_6), 7.61 (dd, J = 8.78 ; Hz, 1H, H_3), 7.55–7.48 (m, 4H, H_1, H_2, H_8, H_{11}), 7.42–7.38 (m, 5H, H_{15}, H_{15}, H_{16},H_{16}, H_{17}), 7.38–7.28 (m, 4H, H_{18}, H_{18}, H_{19}, H_{19}), 7.21–7.15 (m, 3H, H_9, H_{10}, H_{20}), 7.08 (d, J = 8.78 Hz, 1H, H_4) ppm.

IR(KBr): ν (cm^{-1}) aromatic (C–H: 3053), ketone (C═O: 1634), (C═C: 1590).

Anal. Calcd for $C_{33}H_{20}OS$ (464.12 g mol^{-1}): C, 85.31; H, 4.34; S, 6.90. Found, C, 85.29; H, 4.35; S, 6.90.

Photopolymerization. Appropriate solutions of the monomer and TX-DPA in DMF in the absence and presence of *N*-methyldiethanolamine (MDEA) were irradiated in a photoreactor consisting of a 400 W medium pressure mercury lamp with a water cooling system and simultaneously irradiated in a photoreactor

dx.doi.org/10.1021/ma202168m | *Macromolecules* 2012, 45, 119–125

consisting of a 400 W xenon lamp with a water cooling system, in an air atmosphere. Polymers were obtained after precipitation in methanol and drying *in vacuo*. Conversions were calculated for all samples gravimetrically.

Analyses. GPC analyses of the polymer were performed at room temperature with a setup consisting of a pump (Agilent 1100) and three columns (Zorbax PSM); THF was used as the eluent (flow rate 0.3 mL min^{-1}), and detection was carried out with the aid of an Agilent 1100s differential refractometer. The number-average molecular weights were determined using Polymer Laboratories polystyrene standards. UV−vis spectra were taken on an Agilent 8453. IR spectra were recorded on an ATI Unicam Mattson 1000 FT/IR-3 spectrophotometer on a KBr disk. Fluorescence spectra were recorded on a Jobin Yvon−Horiba Fluoromax-P.

AUTHOR INFORMATION

Corresponding Author

*Telephone: + 90 212 383 4186. Fax: +90 212 383 4134. E-mail: narsu@yildiz.edu.tr.

REFERENCES

(1) Fouassier, J. P. *Photoinitiation, Photopolymerization and Photocuring, Fundamentals and Applications*: Hanser Verlag: Munich, Germany, 1995.
(2) Dietliker, K. *Chemistry & Technology of UV & EB Formulation for Coatings, Inks & Paints*; SITA Technology Ltd.: London, 1991.
(3) Davidson, R. S. *Exploring the Science, Technology and Applications of UV and EB Curing*; SITA Technology Ltd.: London, 1999.
(4) Dietliker, K. In *Chemistry & Technology of UV & EB Formulation for Coatings, Inks & Paints*, 2nd ed.; SITA Technology Ltd.: London, 1998; Vol. 3.
(5) Hageman, H. S. *Photopolymerization and Photoimaging Science and Technology*; Elsevier: London, 1989.
(6) Wayne, R. P. *Photochemistry*; University Lectures: London, 1970.
(7) Mishra, M. K.; Yagci, Y. *Handbook of Radical Vinyl Polymerization*; Marcel Dekker Inc.: New York: 1998; Chapter 7.
(8) Davidson, R. S. In *Advances in Physical Chemistry*; Bethel, D., Gold, V., Eds.; Academic Press: London, 1983; p 1.
(9) Encinas, M. V.; Rufs, A. M.; Corrales, T.; Catalina, F.; Peinado, C.; Schmith, K.; Neumann, M. G.; Allen, N. S. *Polymer* **2002**, *43*, 3909−3913.
(10) Corrales, T.; Catalina, F.; Peinado, C.; Allen, N. S.; Rufs, A. M.; Bueno, C.; Encinas, M. V. *Polymer* **2002**, *43*, 4591−4597.
(11) Corrales, T.; Catalina, F.; Allen, N. S.; Peinado, C. *J. Photochem. Photobiol. A: Chem* **2004**, *169*, 95−100.
(12) Vazquez, B.; Levenfeld, B.; Roman, J. *S. Polym. Int.* **1998**, *46*, 241−250.
(13) Paul, S.; *Surface Coating: Science & Technology*; Wiley-Interscience: New York, 1986.
(14) Jiang, X.; Xu, H.; Yin, J. *Polymer* **2004**, *45*, 133−140.
(15) Jiang, X.; Yin, J. *Polymer* **2004**, *45*, 5057−5063.
(16) Pouliquen, L.; Coqueret, X.; Moret-Savary, F.; Fouassier, J. P. *Macromolecules* **1995**, *28*, 8028−8034.
(17) Wen, Y. N.; Jiang, X. S.; Yin, J. *Polym. Eng. Sci.* **2009**, *49*, 1608−1615.
(18) Wen, Y. N.; Jiang, X. S.; Yin, J. *Prog. Org. Coat.* **2009**, *66*, 65−72.
(19) Wei, J.; Liu, F. *Macromolecules* **2009**, *42*, 5486−5491.
(20) Temel, G.; Aydogan, B.; Arsu, N.; Yagci, Y. *Macromolecules* **2009**, *42*, 6098−6106.
(21) Allen, N. S.; Lam, E.; Kotecha, J. L.; Green, W. A.; Timms, A.; Navaratnam, S.; Parsons, B. J. *J. Photochem. Photobiol. A: Chem.* **1990**, *54*, 367−388.
(22) Allen, N. S.; Lam, E.; Howells, E. M.; Green, P. N.; Green, A.; Catalina, F.; Peinado, C. *Eur. Polym. J.* **1990**, *26*, 1345−1353.
(23) Aydin, M.; Arsu, N.; Yagci, Y. *Macromol. Rapid Commun.* **2003**, *24*, 718−723.
(24) Aydin, M.; Arsu, N.; Yagci, Y.; Jockusch, S.; Turro, N. J. *Macromolecules* **2005**, *38*, 4133−4138.
(25) Balta, D. K.; Temel, G.; Aydin, M.; Arsu, N. *Eur. Polym. J.* **2010**, *46*, 1374−1379.
(26) Karaca, N.; Temel, G.; Balta, D. K.; Aydin, M.; Arsu, N. *J. Photochem. Photobiol. A: Chem.* **2010**, *209*, 1−6.
(27) Yilmaz, G.; Aydogan, B.; Temel, G.; Arsu, N.; Moszner, N.; Yagci, Y. *Macromolecules* **2010**, *43*, 4520−4526.
(28) Cokbaglan, L.; Arsu, N.; Yagci, Y.; Jockusch, S.; Turro, N. J. *Macromolecules* **2003**, *36*, 2649−2653.
(29) Temel, G.; Arsu, N. *J. Photochem. Photobiol. A: Chem.* **2009**, *202*, 63−66.
(30) Temel, G.; Karaca, N.; Arsu, N. *Polym. Sci., Polym. Chem. Ed.* **2010**, *48* (23), 5306−5312.
(31) Carlini, C.; Angiolini, L.; Caretti, D.; Corelli, E. *Polym. Adv. Tech.* **1996**, *7*, 379−384.
(32) Jiang, X. S.; Luo, J.; Yin, J. *Polymer* **2009**, *50*, 37−41.
(33) Jiang, X. S.; Luo, X. W.; Yin, J. *J. Photochem. Photobiol. A: Chem.* **2005**, *174*, 165−170.
(34) Balta, D. K.; Cetiner, N.; Temel, G.; Turgut, Z.; Arsu, N. *J. Photochem. Photobiol. A: Chem.* **2008**, *199*, 316−321.
(35) Temel, G.; Arsu, N. *J. Photochem. Photobiol. A: Chem.* **2007**, *191* (2−3), 149−152.
(36) Balta, D. K.; Arsu, N.; Yagci, Y.; Jockusch, S.; Turro, N. J. *Macromolecules* **2007**, *40*, 4138−4141.
(37) Gacal, B.; Akat, H.; Balta, D. K.; Arsu, N.; Yagci, Y. *Macromolecules* **2008**, *41*, 2401−2405.
(38) Akat, H.; Gacal, B.; Balta, D. K.; Arsu, N.; Yagci, Y. *J. Polym. Sci., Polym. Chem. Ed.* **2010**, *48*, 2109−2114.
(39) Balta, D. K.; Arsu, N.; Yagci, Y.; Sundaresan, A. K.; Jockusch, S.; Turro, N. J. *Macromolecules* **2011**, *44* (8), 2531−2535.
(40) Balta, D. K.; Arsu, N. *J. Photochem. Photobiol. A: Chem.* **2008**, *200*, 377−380.
(41) Morris, J. V.; Mahaney, M. A.; Huber, J. R. *J. Phys. Chem.* **1976**, *80*, 969−974.
(42) Dalton, J. C.; Montgomery, F. C. *J. Am. Chem. Soc.* **1974**, *96*, 6230−6232.
(43) Amirzadeh, G.; Schnabel, W. *Macromol. Chem.* **1981**, *182*, 2821−2835.
(44) Stevens, B.; Small, R. D. Jr. *J. Am. Chem. Soc.* **1977**, *81*, 1605−1606.
(45) Monroe, B. M. *J. Phys. Chem.* **1978**, *82*, 15−18.
(46) Olea, A. F.; Wilkinson, F. *J. Phys. Chem.* **1995**, *99*, 4518−4524.
(47) Schmidt, R.; Brauer, H. D. *J. Photochem.* **1986**, *34*, 1−12.
(48) Wilson, T.; Catalani, L. H. *J. Am. Chem. Soc.* **1989**, *111*, 2633−2639.
(49) Jesse, K.; Comes, F. J. *J. Phys. Chem.* **1991**, *95*, 1311−1315.

Macromolecules

Article

pubs.acs.org/Macromolecules

Structure–Property Relationships in Metallosupramolecular Poly(*p*-xylylene)s

Mark Burnworth,[†] Stuart J. Rowan,*[,†] and Christoph Weder*[,†,‡]

[†]Department of Macromolecular Science and Engineering, Case Western Reserve University, 2100 Adelbert Road, Cleveland, Ohio 44106-7202, United States

[‡]Adolphe Merkle Institute and Fribourg Center for Nanomaterials, University of Fribourg, CH-1700 Fribourg, Switzerland

Supporting Information

ABSTRACT: The self-assembly polymerization of ditopic monomers via metal–ligand binding is a facile route for the preparation of metallosupramolecular polymers. Here this approach was used for the synthesis of supramolecular poly(*p*-xylylene)s based on 2,6-bis(1′-methylbenzimidazolyl)pyridine (Mebip) end-capped telechelic oligomers with a *p*-xylylene core and different metal salts. These polymers can be readily processed from solution and merge the ease of processing of supramolecular materials with the good thermal stability of the *p*-xylylene core. The nature of the metal cation (Fe^{2+}, Zn^{2+}, La^{3+}) and counteranion (ClO_4^-, OTf^-, NTf_2^-) was systematically varied, and a tetrafunctional supramolecular cross-linker was used to probe how these modifications influence the materials' properties. Interestingly, and in contrast to other metallosupramolecular polymers, where the nature of the metal salt plays a critical role, only minor property differences were observed for the materials studied. Instead, the properties of the supramolecular poly(*p*-xylylene)s investigated appear to be primarily governed by the crystalline nature of the telechelic oligomer. We note that minor impurities in the latter can exert a significant influence on the metallosupramolecular polymer's properties and report a new protocol for the synthesis and purification of Mebip-end-capped *p*-xylylene telechelic oligomers.

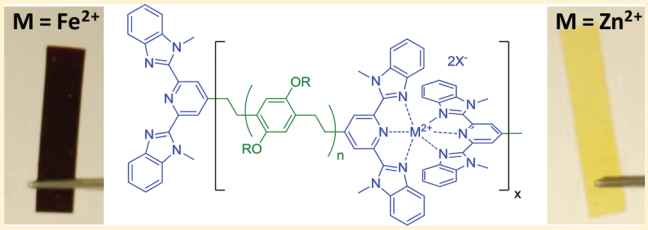

INTRODUCTION

Metallosupramolecular polymers[1] are a class of materials situated at the interface of metal-containing polymers[2] and supramolecular polymers,[3] in which dynamic metal–ligand interactions serve as a reversible supramolecular polymerization motif. Metal coordination allows one to polymerize low-molecular-weight or telechelic cores that carry at least two ligands, typically at the termini (Scheme 1). Popular ligands of choice are multidentate ligands, such as terpyridine (terpy),[4] bipyridine (bpy),[5] and 2,6-bis(1′-methylbenzimidazolyl)-pyridine (Mebip),[6] which can coordinate a range of metal salts (e.g., Co^{2+}, Fe^{2+}, Zn^{2+}, Eu^{3+}). The variation of nature, length, and structure of the core employed to connect the ligands, number, type, and position of the latter, along with the nature of the metal ion, and counterion should allow one to tailor the properties of these polymers. While much work has focused on the synthesis of metallosupramolecular polymers, the elucidation of their properties in solution, and the study of "advanced" properties imparted by the metal (e.g., optical, electrical, magnetic),[2] systematic studies of their solid-state mechanical properties have received comparatively little attention. Therefore, relatively little is known about structure–property relationships of such materials. We have demonstrated that the length of the ditopic core is of great importance; metallosupramolecular polymers only display appreciable mechanical properties if telechelic units or "telechelic oligomers" with molecular weights of a few thousand are employed.[7−14] If ditopic telechelic oligomers with low-glass-transition core (e.g., PEO, poly(THF), poly(ethylene-*co*-butylene)) and terminal Mebip ligands are employed, the metallosupramolecular materials obtained upon addition of 1 equiv of a metal salt can have mechanical properties that lie between those of highly cross-linked elastomers and ultralow-density polyolefins, i.e., a storage modulus of the order of 50 MPa, stress at break of the order of 50 MPa, and a strain at break of around 50%, in some cases after yielding and plastic deformation.[7,12,14] The mechanical properties of these materials are, at least in part, governed by microphase segregation, where the metal–ligand complexes form a "hard phase" that physically cross-links "soft" domains formed by the telechelic cores. The morphology (and therefore the mechanical properties) depends on the polarity of the telechelic oligomer as well as the nature of the metal ion and counterion. With the objective to create arylene alkylene metallopolymers, which combine ease of processing with good high-temperature stability,[15,16] we also investigated the metallosupramolecular polymerization of a crystallizable poly(2,5-dioctyloxy-*p*-xylylene) telechelic oligomer end-capped with Mebip ligands and $Zn(ClO_4)_2$, $Fe(ClO_4)_2$, and mixtures of these salts and $La(ClO_4)_3$. The resulting polymers are readily solution-processable and exhibit a

Received: October 15, 2011
Revised: December 2, 2011
Published: December 9, 2011

Scheme 1. Schematic Representation of the Metallosupramolecular Polymerization of Ditopic Telechelic Oligomers with Either Transition or Lanthanide Metal Ions

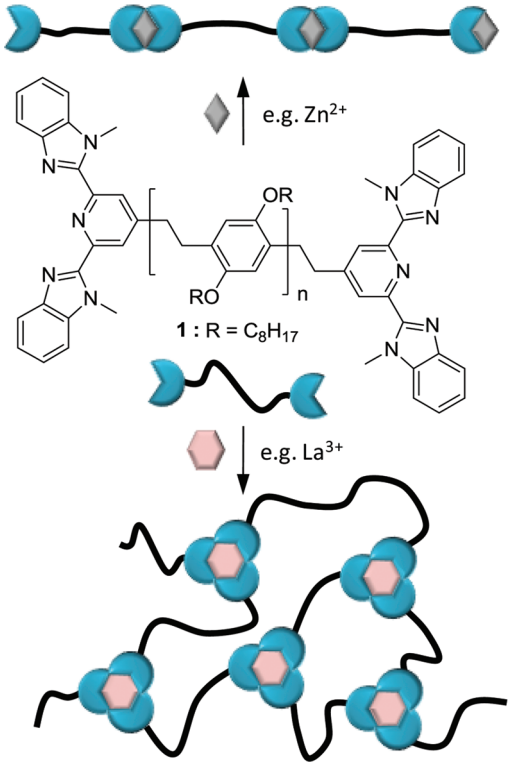

room-temperature storage modulus of ca. 400 MPa, i.e., a much higher stiffness than the aforementioned metallosupramolecular polymers based on a rubbery core. Here, we report an in-depth study of the structure−property relations in such metallosupramolecular poly(*p*-xylylene)s. The nature of the metal cation (Fe^{2+}, Zn^{2+}, La^{3+}) and counteranion (ClO_4^-, OTf^-, NTf_2^-) was systematically varied, and a tetrafunctional supramolecular cross-linker was used to probe how these modifications influence the materials' properties.

EXPERIMENTAL SECTION

General Methods. ^1H and ^{13}C NMR were acquired in $CDCl_3$ using a Varian 600 MHz spectrometer; chemical shifts are expressed in ppm relative to an internal tetramethylsilane standard. Ultraviolet−visible (UV−vis) absorption spectra were obtained on a Perkin-Elmer Lambda 800 spectrometer. Thermogravimetric analyses (TGA) were carried out on a TA Instruments TGA Q500 under N_2 at a heating rate of 10 °C/min. Differential scanning calorimetry (DSC) experiments were carried out on a TA Instruments DSC Q2000 under N_2 at a heating rate of 10 °C/min. Dynamic mechanical thermal analyses (DMTA) were conducted on a TA Instruments Q800 dynamic mechanical analyzer at a heating rate of 3 °C/min under N_2.

Materials. Telechelic oligomer **2** and 2,6-bis(1′-methyl-benzimidazolyl)-4-ethynylpyridine (**3**) were prepared according to the previously reported methods.[8] Zinc bistriflimide[17] and lanthanum bistriflimide[18] were prepared according to literature procedures from the mixture of either zinc dust or lanthanum oxide with bis(trifluoromethane)sulfonimide in water. Unless otherwise stated, all other reagents, solvents, metal salts (triflate and perchlorate), and catalysts were purchased from Aldrich Chemical Co., Fisher Scientific, or Strem Chemicals and were used without further purification. Spectroscopic grade $CHCl_3$ (passed through a plug of basic alumina) and spectroscopic grade CH_3CN were employed for the optical absorption as well as for the metallosupramolecular polymerization reactions. Toluene was distilled from sodium under an inert atmosphere; diisopropylamine and tripropylamine were distilled from calcium hydride under an inert atmosphere.

Synthesis of Telechelic Oligomer 1. Telechelic oligomer **2** (3.05 g, 0.469 mmol), *p*-toluenesulfonyl hydrazide (TSH) (16.01 g, 86.0 mmol), and tripropylamine (TPA) (16.3 mL, 86.0 mmol) were dissolved in xylenes (350 mL), and the solution was heated under reflux at 140 °C. After 3 h, additional portions of TSH (16.01 g, 86.0 mmol) and TPA (16.3 mL, 86.0 mmol) were added, and the reaction mixture was heated under reflux for an additional 2 h. The hot reaction mixture was passed through a plug of basic alumina, and the plug was washed with hot toluene. The combined organic fractions were washed twice with deionized water, and the volume was reduced under vacuum to produce an orange viscous liquid, to which a small amount of $CHCl_3$ was added. The orange solution was then precipitated into well-stirred EtOH (500 mL). After stirring for 2 h, the resulting yellow precipitate was filtered off, dissolved in a minimal amount of $CHCl_3$ and again precipitated into EtOH (500 mL). The yellow precipitate was filtered off and subsequently washed with boiling MeOH, EtOH, CH_3CN, and diethyl ether. Drying overnight under vacuum yielded **1** as a yellow solid (2.52 g, 0.296 mmol, 63%). ^1H NMR (600 MHz, $CDCl_3$): δ = 8.35 (s, 4 H, ArH end group), 7.89 (d, 4 H, J_{H-H} = 8.4 Hz, ArH end group), 7.48 (d, 4 H, J_{H-H} = 7.8 Hz, ArH end group), 7.38 (m, 8 H, ArH end group), 6.73 (s, 4 H, ArH end group), 6.68 (s, 2 H, Ar), 4.26 (s, 12 H N−CH_3 end group), 3.92 (t, 2 H, J_{H-H} = 6 Hz, OCH_2 end group), 3.89 (t, 4 H, J_{H-H} = 6.6 Hz, OCH_2), 3.09 (m, 4H, Ar−CH_2−CH_2−Ar end group), 3.04 (m, 4 H, Ar−CH_2−CH_2−Ar end group), 2.84 (s, 4 H, Ar−CH_2−CH_2−Ar), 1.79 (m, 4 H), 1.50 (m, 4 H), 1.38−1.18 (m, 16 H), 0.87 (t, 6 H, J_{H-H} = 6.6 Hz), 0.79 (t, 6 H, J_{H-H} = 6.6 Hz, CH_3 end group). Degree of polymerization (X_n, determined by NMR) = 28.5; number-average molecular weight (M_n, determined by NMR) = 11 400 g/mol. ^{13}C NMR ($CDCl_3$, 125 MHz): δ = 150.7, 149.5, 142.6, 137.2, 129.3, 125.5, 123.5, 122.8, 120.2, 114.2 109.8, 68.9, 36.3, 31.9, 31.3, 29.8, 29.7, 29.5, 29.4, 26.3, 22.7, 12.4.

Synthesis of 2,7-Diiodo-9,9-di(4-iodobenzyl)fluorene (8).[19] A solution of 2,7-diiodofluorene (**6**, 500 mg, 1.120 mmol) in dimethyl sulfoxide (DMSO, 12 mL) was degassed by sparging with Ar for 30 min, and benzyltrimethylammonium chloride (18 mg, 0.10 mmol) and aqueous NaOH (50 wt %, 0.6 mL) were added. After 10 min, the reaction mixture turned red. 4-Iodobenzyl bromide (**7**, 855 mg, 2.88 mmol) was added, and the reaction mixture was heated to 80 °C for 2 h. The reaction mixture was subsequently cooled to RT, poured into dichloromethane (DCM, 50 mL), and washed 3 times with H_2O. Recrystallization from boiling DCM yielded **8** as a white powder (800 mg, 0.941 mmol, 79%). ^1H NMR (600 MHz, $CDCl_3$): δ = 7.69 (d, 2H, *J* = 1.8 Hz, ArH), 7.54 (dd, 2H, *J* = 8.1, 1.8 Hz, ArH), 7.25 (d, 4H, *J* = 8.4 Hz, ArH), 7.10 (d, 2H, *J* = 8.4 Hz, ArH), 6.33(d, 4H, *J* = 8.4 Hz, ArH), 3.21 (s, 4H, CH_2) ppm. ^{13}C NMR (100 MHz, $CDCl_3$): δ = 149.4, 139.8, 136.8, 136.7, 135.7, 133.7, 132.2, 122.1, 92.3, 92.2, 56.9, 44.8 ppm.

Synthesis of 9. In a nitrogen-filled glovebox, 2,6-bis(1′-methyl-benzimidazolyl)-4-ethynylpyridine (**3**, 600 mg, 1.65 mmol), **8** (335 mg, 0.39 mmol), $Pd(PPh_3)_4$ (22.7 mg, 0.013 mmol), CuI (3.7 mg, 0.019 mmol), and tetrahydrofuran (THF, 35 mL) were introduced into a reaction flask, which was subsequently equipped with a reflux condenser, removed from the glovebox, and connected to a Schlenk line. (iPr)$_2$NH (15.8 mL) was added, and the reaction mixture was stirred for 19 h at 45 °C. The reaction mixture was subsequently poured hot into a saturated aqueous EDTA solution (60 mL), and the mixture was stirred for 1 h. The organic layer was separated off, and the aqueous layer was extracted with $CHCl_3$. The combined organic layers were washed with deionized water and reduced under vacuum to yield a light-brown solid, which was purified by column chromatography ($CHCl_3$, neutral alumina) and subsequent recrystallization (twice) from cold DCM. This afforded **9** as a light yellow solid (310 mg, 0.17 mmol, 44%). ^1H NMR (600 MHz, $CDCl_3$): δ = 8.65 (s, 4H, ArH), 8.38 (s, 4H, ArH), 7.89 (d, 4H, *J* = 7.2 Hz, ArH), 7.83 (s, 2H, ArH), 7.80 (d, 4H, *J* = 7.8 Hz, ArH), 7.52 (dd, 2H, *J* = 7.8, 1.2 Hz, ArH), 7.47−7.41 (m, 10H, ArH), 7.38−7.29 (m, 16H, ArH), 7.17 (d, 4H, *J* = 7.8 Hz, ArH), 6.73 (d, 4H, *J* = 8.4 Hz, ArH), 4.28 (s, 12H, N−

dx.doi.org/10.1021/ma202312x | *Macromolecules* 2012, 45, 126−132

CH_3), 4.19 (s, 12H, N−CH_3), 3.57 (s, 4H, CH_2) ppm. ^{13}C NMR (100 MHz, $CDCl_3$): δ = 150.1, 150.04, 149.98, 149.9, 148.4, 142.9, 142.8, 141.7, 138.0, 137.46, 137.4, 134.2, 134.2, 132.2, 131.5, 130.5, 128.2, 127.2, 127.0, 123.93, 123.86, 123.2, 123.1, 121.1, 120.9, 120.5, 120.1, 110.1, 110.1, 96.7, 96.0, 87.5, 86.4, 57.5, 45.8, 32.8, 32.7 ppm. MALDI MS (matrix: HABA): m/z 1791.347 (required for $C_{119}H_{82}N_{20}$ = 1791.347).

Synthesis of 10. A solution of **9** (75 mg, 0.042 mmol) in *o*-dichlorobenzene (*o*-DCB, 10 mL) was heated under Ar to 130 °C, before diisopropylamine ($(i\text{Pr})_2$NH, 70.4 μL, 0.50 mmol) and *p*-toluenesulfonyl hdrazide (TSH, 62.4 mg, 0.33 mmol) were added. Additional portions of TSH and $(i\text{Pr})_2$NH were added after 4 h (31.2 mg, 0.16 mmol TSH; 35.2 μL, 0.25 mmol $(i\text{Pr})_2$NH), 5.5 h (31.2 mg, 0.16 mmol TSH; 35.2 μL, 0.25 mmol $(i\text{Pr})_2$NH), and 7.5 h (62.4 mg, 0.33 mmol TSH; 70.4 μL, 0.5 mmol $(i\text{Pr})_2$NH), and the reaction mixture was stirred at 130 °C for a total of 26.5 h. The hot reaction mixture was then passed through a plug of basic alumina, and the plug was washed with hot toluene (150 mL). The organic layers were combined, the solvent was evaporated, and the product was dried under vacuum to yield **10** as a yellow solid (60 mg, 0.033 mmol, 78%). ^{1}H NMR (600 MHz, $CDCl_3$): δ = 8.37 (s, 4H, ArH), 8.10 (s, 4H, ArH), 7.82 (d, 8H, J = 7.8 Hz, ArH), 7.42 (d, 4H, J = 7.8 Hz, ArH), 7.37−7.26 (m, 22H, ArH), 7.10 (s, 2H, ArH), 7.07 (d, 2H, J = 7.8 Hz, ArH), 6.74 (d, 4H, J = 7.8 Hz, ArH), 6.54 (d, 4H, J = 8.4 Hz, ArH), 4.19 (s, 12H, N−CH_3), 4.14 (s, 12H, N−CH_3), 3.17 (s, 4H, CH_2), 3.13 (s, 8H, CH_2), 2.86 (m, 4H, CH_2), 2.74 (m, 4H, CH_2) ppm. ^{13}C NMR (100 MHz, $CDCl_3$): δ = 153.5, 153.4, 150.59, 150.57, 149.9, 149.6, 149.0, 142.8, 139.2, 138.6, 138.5, 137.4, 137.3, 135.4, 130.7, 127.4, 127.3, 125.7, 125.5, 125.2, 123.7, 123.7, 123.0, 120.38, 120.37, 119.8, 110.1, 110.0, 56.4, 45.1, 38.3, 37.5, 37.3, 36.2, 32.7 ppm. MALDI MS (matrix: HABA): m/z 1809.274 (required for $C_{119}H_{98}N_{20}$ = 1809.274).

Typical Preparation of Metallosupramolecular Polymer Films. A solution of $Fe(ClO_4)_2$ in CH_3CN (180.4 μL of a 64.8 mM solution) was added to a stirred solution of telechelic oligomer **1** (99.4 mg, 11.7 μmol) in $CHCl_3$ (2 mL, 5.84 mM). The viscosity of the mixture increased noticeably, and the color changed to purple. The solution was transferred to an aluminum solution caster (diameter 3 cm) with a Teflon base. The solvent was evaporated overnight under ambient conditions in a well-ventilated hood, and the resulting films were subsequently dried at room temperature to produce a solid purple film. Yellow films of metallosupramolecular polymers made with different Zn^{2+} salts were prepared by the same method. Yellow films of metallosupramolecular polymers made with $La(NTf_2)_3$ were prepared by the same method, but the telechelic oligomer:metal salt ratio was adjusted to account for 3:1 Mebip:La binding.

General Procedure for UV−vis Titration with Metal Salts. A solution of **1** (50 μM) in a mixture of $CHCl_3/CH_3CN$ (9/1 v/v, 2 mL) was titrated with 25 μL aliquots of a solution of the metal salt (ca. 300 μM) and **1** (50 μM) in the same solvent mixture. The addition was done incrementally; after each addition of an aliquot of the metal salt solution the samples were characterized by UV−vis spectroscopy. The M_n of **1** was calculated from the ion titration experiments with $Fe(ClO_4)_2$: $M_n \approx 8500$ g/mol, $X_n \approx 21$.

RESULTS AND DISCUSSION

Synthesis and Characterization of Telechelic Oligomer 1. The synthetic protocol utilized to prepare the 2,6-bis(1′-methylbenzimidazoyl)pyridine end-capped 2,5-dialkoxy-*p*-xylylene telechelic oligomer (**1**) follows our previously published route[9] and involves the Hahn diimide reduction of the parent conjugated 2,5-dialkoxy-*p*-phenyleneethynylene **2**, which was prepared in greater than 90% yield via the Sonogashira coupling reaction of acetylenes **3**, **5**, and aryl diiodide **4** (Scheme 2). Our original purification of **1** involved precipitating the product into MeOH and washing with boiling MeOH, EtOH, CH_3CN, and room-temperature MeOH.[9] When this procedure was repeated in the context of the present work, close examination of the ^{1}H NMR spectrum showed a peak around 2.32 ppm (Supporting Information, Figure S2), which can also be found in the published spectra of **1**.[9] The signal, along with matching resonances of aromatic protons, is indicative of a small amount (ca. 2% w/w) of residual *p*-toluenesulfinic acid, stemming from the reduction process. In order to probe if this impurity, albeit present only in a small concentration, might impact the properties of the targeted metallosupramolecular polymers, the purification procedure was modified to completely remove this byproduct.

Scheme 2. Synthesis and Structure of the Conjugated Monomer 2, Its Reduction to the Ditopic Telechelic Oligomer 1, and Pictures of the Films Obtained upon Solution-Casting Telechelic Oligomer 1 with Equimolar Amounts of Either $Fe(ClO_4)_2$ or $Zn(ClO_4)_2$[a]

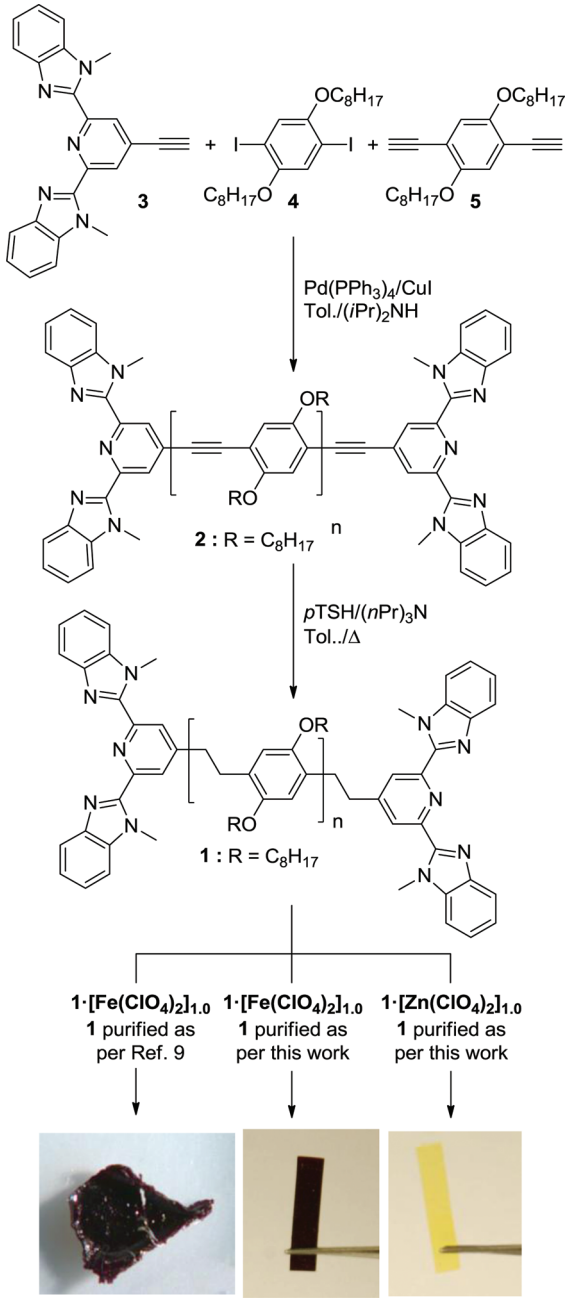

[a]The properties of the resulting films depend on the procedure used to purify **1**.

The new purification method involves repeated precipitation in EtOH and washing with boiling MeOH, EtOH, CH_3CN, and diethyl ether to isolate **1** in 63% yield which was free of the characteristic *p*-toluenesulfinic acid peak at 2.32 ppm (Supporting Information, Figures S1 and S2).

The molecular weight of the metallosupramolecular polymers under investigation can be maximized if telechelic oligomer **1** and Fe^{2+} or Zn^{2+} salts are combined so that the molar ratio of Mebip ligand to metal ion is exactly 2:1 (Scheme 1). In our original study on metallosupramolecular poly(*p*-xylylene)s[9] we employed ^1H NMR spectroscopy-based end-group analysis to establish the molecular weight of **1**. On the basis of our experiences with other ditopic telechelic oligomers, we here conducted UV−vis titration experiments to determine the concentration of the ligands[11] by slowly titrating a solution of **1** (50 μM) with a solution of $Fe(ClO_4)_2$, while maintaining a constant concentration of **1** (Figure 1). As the metal ion was

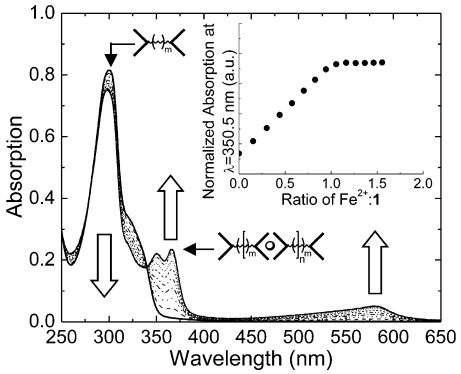

Figure 1. UV−vis absorption spectra acquired upon titration of **1** (50 μM) with $Fe(ClO_4)_2$. Shown are spectra at selected Fe^{2+}:**1** ratios ranging from 0:1 to 1.5:1. The inset shows the normalized absorption at 350.5 nm as a function of Fe^{2+}:**1** ratio.

added to the telechelic oligomer, the absorption spectrum changed from that of the free Mebip ligand with an absorption maximum, λ_{max}, of 300.5 nm to that of the $Mebip_2$:Fe^{2+} complex, which shows additional maxima at 350.5, 366, and 580 nm. The inset of the figure shows that the changes of the absorbance spectrum level off when all Mebip ligands have been complexed with Fe^{2+}. Using the assumption that the telechelic oligomer **1** is fully end-capped with Mebip, the Fe^{2+} concentration at which the optical changes leveled off was used to back-calculate the number-average molecular weight (M_n) and number-average degree of polymerization (X_n) of **1**. The values thus determined (M_n = 8500 g/mol, X_n = 21) are significantly lower than those determined by ^1H NMR end-group analysis (M_n = 11 400 g/mol, X_n = 28.5). The M_n thus determined is consistent with the targeted M_n (8300 g/mol) based on the stoichiometry of the starting materials (**3**, **4**, and **5**). The titration data show that using the M_n determined by NMR end-group analysis would lead to an underestimation of the amount of metal salt required for stoichiometric binding to the ligands that end-cap the telechelic oligomer. Therefore, we used the M_n determined by the UV titration (8500 g/mol) as the molecular weight of **1**.

In order to explore how the above-described changes (new purification method and use of UV titration to achieve stoichiometric ratios) influence the properties of metallosupramolecular polymer based on **1**, a series of thin films were prepared by solution-casting $CH_3CN/CHCl_3$ mixtures of **1** with stoichiometric amounts of either $Fe(ClO_4)_2$, $Zn(ClO_4)_2$, $Zn(OTf)_2$, or $Zn(NTf_2)_2$ (designated as **1**·$[Fe(ClO_4)_2]_{1.0}$, **1**·$[Zn(ClO_4)_2]_{1.0}$, **1**·$[Zn(OTf)_2]_{1.0}$, and **1**·$[Zn(NTf_2)_2]_{1.0}$, respectively). In addition, a film of **1** with 0.66 mol equiv of $La(NTf_2)_3$ (**1**·$[La(NTf_2)_3]_{0.66}$) was prepared, assuming the binding of three Mebip ligands per metal ion (Scheme 1).[9] Our selection of metal salts is rationalized with the objective to cover a range of binding strengths and dynamics (from the dynamic, labile La^{3+} over Zn^{2+} to the kinetically slower Fe^{2+}) and to explore bistriflimide and triflate anions as thermally more stable alternatives to the perchlorate anion. Already a qualitative comparison of the **1**·$[Fe(ClO_4)_2]_{1.0}$ and **1**·$[Zn(ClO_4)_2]_{1.0}$, films made by old and new protocols (Scheme 2), revealed that the new processes results in metallosupramolecular polymer films with much better mechanical properties than the previous materials: the original **1**·$[Fe(ClO_4)_2]_{1.0}$ was very brittle and **1**·$[Zn(ClO_4)_2]_{1.0}$ did not form self-supporting films, very much in contrast to the corresponding materials prepared here. The comparison shows that the protocols reported herein afford metallosupramolecular polymers with significantly improved mechanical properties, presumably on account of a better metal:ligand stoichiometry, which is concomitant with higher self-assembled molecular weight aggregates than previously attainable. The properties of the new materials were hence studied in greater detail.

Characterization of 1 and Its Metallosupramolecular Polymers. The thermal stability of **1** and the metallosupramolecular polymers **1**·$[Fe(ClO_4)_2]_{1.0}$, **1**·$[Zn(ClO_4)_2]_{1.0}$, **1**·$[Zn(OTf)_2]_{1.0}$, **1**·$[Zn(NTf_2)_2]_{1.0}$, and **1**·$[La(NTf_2)_3]_{0.66}$ were investigated by thermogravimetric analysis (TGA) (Figure 2). It was found that the neat telechelic oligomer **1** was stable up to a temperature of ca. 350 °C, above which it degraded with a 90% weight loss at 500 °C. **1**·$[Fe(ClO_4)_2]_{1.0}$ exhibited a 2.5% loss at ca. 190 °C, while **1**·$[Zn(ClO_4)_2]_{1.0}$ displayed a 2.7% weight loss at 285 °C. Consistent with previous studies, these events are attributed to the degradation of the perchlorate counterion.[9] Both perchlorate-based metallosupramolecular polymers display a major weight loss in the range of 350−500 °C, similar to the telechelic oligomer. Expecting a higher thermal stability from this counterion, we also explored series of salts with bistriflimide (NTf_2^-) as the anion. Metallosupramolecular polymers **1**·$[Zn(OTf)_2]_{1.0}$, **1**·$[Zn(NTf_2)_2]_{1.0}$, and **1**·$[La(NTf_2)_3]_{0.66}$ all showed similar trends with an onset of weight loss occurring ca. 350 °C and a single weight loss peak occurring from 350 to 500 °C. Thus, these metallosupramolecular polymers display a higher thermal stability than the corresponding materials comprising perchlorate as the counterion.

Differential scanning calorimetry (DSC) was used to probe thermal transitions of the neat telechelic oligomer **1**, and the metallosupramolecular polymers **1**·$[Zn(ClO_4)_2]_{1.0}$, **1**·$[Zn(OTf)_2]_{1.0}$, **1**·$[Zn(NTf_2)_2]_{1.0}$, and **1**·$[La(NTf_2)_3]_{0.66}$. The neat telechelic oligomer **1** (Figure 3a) displays a glass transition temperature (T_g) of ca. 50 °C and a reversible endothermic transition with a maximum at 164 °C. Likewise, all metallosupramolecular films tested displayed similar thermal transitions with T_g occurring at ca. 50 °C and a reversible endotherm at 164 ± 4 °C (Figure 3b and Supporting Information; no DSC data were acquired for **1**·$[Fe(ClO_4)_2]_{1.0}$ on account of the lower degradation temperature associated with this material). The reversible endotherm displayed by both neat **1** and the resulting metallosupramolecular polymers is ascribed to the melting of the *p*-xylylene core of the telechelic

dx.doi.org/10.1021/ma202312x | *Macromolecules* 2012, 45, 126−132

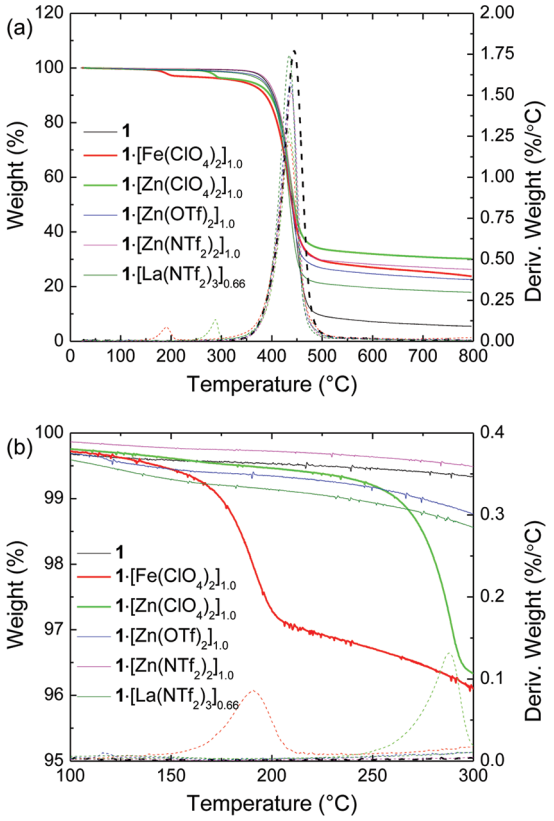

Figure 2. (a, b) Thermogravimetric analysis (TGA) traces of the neat telechelic oligomer **1** (black), **1**·$[Fe(ClO_4)_2]_{1.0}$ (red), **1**·$[Zn(ClO_4)_2]_{1.0}$ (green), **1**·$[Zn(OTf)_2]_{1.0}$ (blue), **1**·$[Zn(NTf_2)_2]_{1.0}$ (magenta), and **1**·$[La(NTf_2)_3]_{0.66}$ (olive). The experiments were conducted at a heating rate of 10 °C/min under N_2.

oligomer.[16b] The crystalline nature of the materials was confirmed by polarized optical microscopy experiments (Supporting Information). Thus, neither the nature of the counterion nor the metal ion exerted a dominant influence on the thermal transitions of the metallosupramolecular polymers studied, which, instead, appear to be largely governed by the crystalline morphology imposed by the crystalline telechelic oligomer.

The mechanical properties of **1**·$[Fe(ClO_4)_2]_{1.0}$, **1**·$[Zn(ClO_4)_2]_{1.0}$, **1**·$[Zn(OTf)_2]_{1.0}$, and **1**·$[Zn(NTf_2)_2]_{1.0}$ were investigated by dynamic mechanical thermal analysis (DMTA). The thin films were heated at a rate of 3 °C/min and tested at a frequency of 1 Hz under N_2. All materials showed very similar mechanical properties with room temperature storage moduli of 440, 390, 420, and 470 MPa, respectively (Figure 4). As in the case of similar systems based on Mebip-terminated telechelic oligomer with a *p*-phenylene ethynylene core,[8,11] a steady decrease of the storage modulus is observed with increasing temperature, consistent with the formation of linear polymers (as opposed to physically cross-linked structures). The **1**·$[La(NTf_2)_3]_{0.66}$ film proved to be more brittle than the samples based on either Fe^{2+} or Zn^{2+} and could not be characterized by DMTA temperature sweeps. The brittle nature of the **1**·$[La(NTf_2)_3]_{0.66}$ could be the result of the weaker, more dynamic nature of the Mebip:La^{3+} bond, which has resulted in weaker materials as has been seen in previous studies,[12−14] but it may also be related to highly cross-linked nature of this material since the La^{3+} ion acts as a cross-linker by binding to three Mebip ligands.

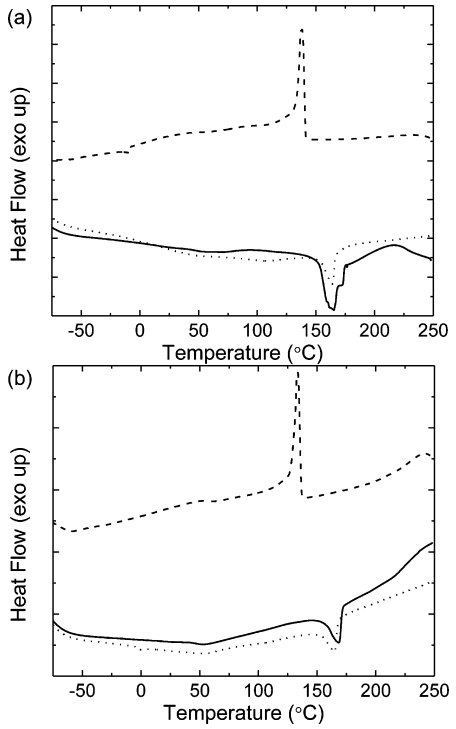

Figure 3. Differential scanning calorimetry (DSC) traces of the neat telechelic oligomer **1** (a) and **1**·$[Zn(NTf_2)_2]_{1.0}$ (b). Traces from first heating (solid), first cooling (dashed), and second heating scans (dot) are shown. The experiments were conducted at a heating rate of 10 °C/min under N_2.

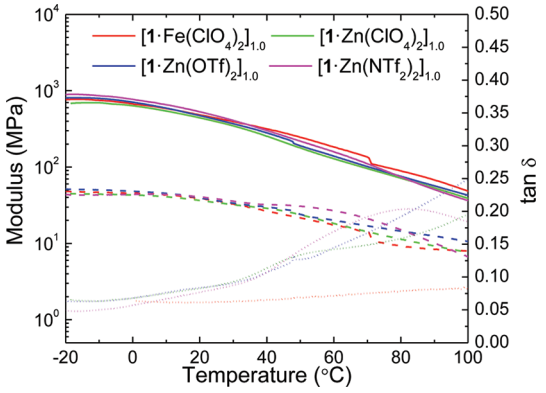

Figure 4. Dynamic mechanical thermal analysis (DMTA) temperature sweeps of **1**·$[Fe(ClO_4)_2]_{1.0}$ (red), **1**·$[Zn(ClO_4)_2]_{1.0}$ (green), **1**·$[Zn(OTf)_2]_{1.0}$ (blue), and **1**·$[Zn(NTf_2)_2]_{1.0}$ (magenta): storage modulus (solid line), loss modulus (dashed line), and tan δ (dotted line). The experiments were conducted at a heating rate of 3 °C/min and a frequency of 1 Hz under N_2.

Synthesis and Characterization of Cross-Linker 10. In order to test the effect of cross-linking without using "trifunctional" lanthanide salts (which, as discussed above, may not afford materials with good mechanical properties on account of weaker binding), a tetrafunctional cross-linker (**10**) carrying four Mebip units was prepared (Schemes 3). It was synthesized via the Sonogashira coupling of the ethynyl-derivatized Mebip (**3**) to a tetraiodofluorene derivative (**8**) followed by diimide reduction of the resulting ethynylene precursor **9**. Initial attempts to carry out the alkyne reduction using literature procedures,[20] namely toluene sulfonyl hydrazide

dx.doi.org/10.1021/ma202312x | *Macromolecules* 2012, 45, 126−132

Scheme 3. Synthesis of Cross-Linker 10

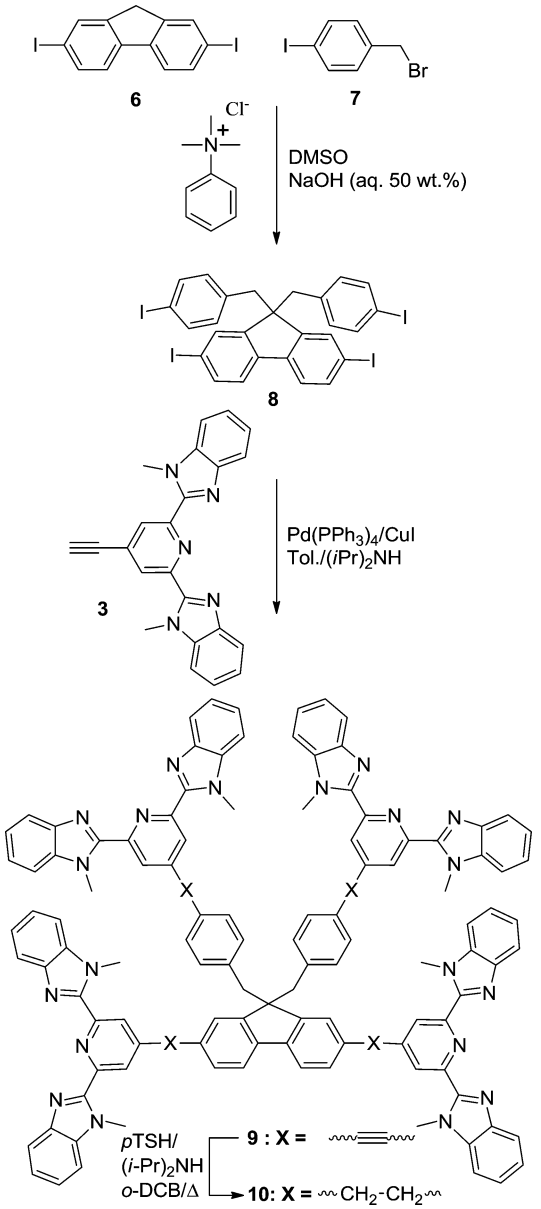

(TSH) and tripropylamine (TPA) in toluene, yielded only mixtures of partially reduced products (Supporting Information). The systematic variation of solvent and amine used allowed us to develop reaction conditions (use of *o*-dichlorobenzene as solvent and diisopropylamine as a less basic amine than TPA; see Experimental Section and Supporting Information) to reduce precursor **9** to cross-linker **10** in good yield. The improvement is presumably the result of a slower decomposition of TSH under the new reaction conditions,[21] which dramatically increases the effectiveness of the reduction.

Dynamic Mechanical Thermal Analysis of Cross-Linked Films. To test the effect that **10** has on the mechanical properties of the metallosupramolecular polymers under investigation, a film composed of 90 mol % of **1** and 10 mol % of **10** was prepared with a stoichiometric amount of $Zn(OTf)_2$ as the metal component ($[\mathbf{1}_{0.9}\mathbf{10}_{0.1}]\cdot[Zn(OTf)_2]_{1.0}$). The mechanical properties of the thin film were tested by DMTA with a heating rate of 3 °C/min and a frequency of 1 Hz under N_2 (Figure 5). Interestingly, it was found that at a content of 10 mol % the cross-linker **10** had little effect on the

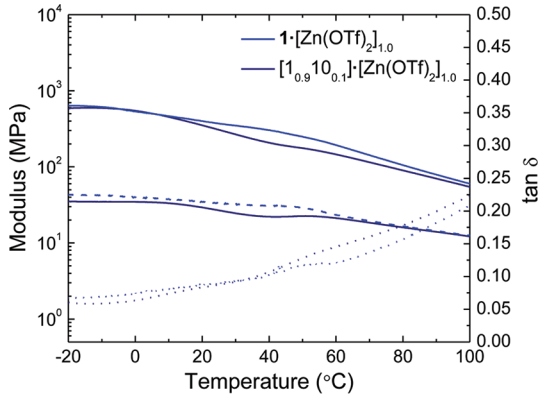

Figure 5. Dynamic mechanical thermal analysis (DMTA) temperature sweeps of $\mathbf{1}\cdot[Zn(OTf)_2]_{1.0}$ (blue), and $[\mathbf{1}_{0.9}\mathbf{10}_{0.1}]\cdot[Zn(OTf)_2]_{1.0}$ (dark blue): storage modulus (solid line), loss modulus (dashed line), and tan δ (dotted line). The experiments were conducted at a heating rate of 3 °C/min and a frequency of 1 Hz under N_2.

materials' mechanical properties. Thus, the result confirms the above conclusion that, unlike other metallosupramolecular polymer systems based on low-T_g telechelic oligomers, the mechanical properties of this film appear to be based primarily on the crystalline polymeric core, with little effect from metal ion, counterion or cross-linking.

■ CONCLUSIONS

Here we have shown that mechanically robust films (storage moduli of ca. 400 MPa) of metallosupramolecular polymers can be created, in which the mechanical properties are primarily governed by the crystalline nature of the telechelic oligomer. As such, the solid-state properties of these materials are much less sensitive to the metal ion salt used in their assembly than comparable metallosupramolecular polymers based on telechelic oligomers with low-T_g cores. Even the introduction of a moderate amount of a tetrafunctional cross-linker did not affect their properties in an appreciable manner. Similarly, the replacement of the perchlorate counterion with either triflate or bistriflimide counterions does not significantly alter the mechanical properties, but the latter materials offer higher thermal stability. We have also shown that the solid-state properties materials are sensitive to certain impurities, which presumably compete with the metal ligand binding and/or an offset of the ideal metal-to-ligand binding stoichiometry, as would be expected for a step-growth-like assembly process. Thus, this highlights important design criteria that need to be taken into account and/or utilized while developing structure/property relationships in metallosupramolecular polymers, especially toward the goal of obtaining systems with enhanced mechanical properties.

■ ASSOCIATED CONTENT

Ⓢ Supporting Information

^1H and ^{13}C NMR spectra of **1**; DSC traces of $\mathbf{1}\cdot[Zn(ClO_4)_2]_{1.0}$, $\mathbf{1}\cdot[Zn(OTf)_2]_{1.0}$, and $\mathbf{1}\cdot[La(NTf_2)_3]_{0.66}$; polarized optical microscopy images of $\mathbf{1}\cdot[Zn(OTf)_2]_{1.0}$. This material is available free of charge via the Internet at http://pubs.acs.org.

dx.doi.org/10.1021/ma202312x | *Macromolecules* 2012, 45, 126–132

AUTHOR INFORMATION

Corresponding Author

*E-mail: stuart.rowan@case.edu (S.J.R.); christoph.weder@unifr.ch (C.W.).

ACKNOWLEDGMENTS

This material is based upon work supported by the U.S. Army Research Office (W911NF-09-1-0288 and W911NF-06-1-0414) and the Swiss National Science Foundation (200021-135405).

REFERENCES

(1) For recent reviews see: (a) Lohmeijer, B. G. G.; Schubert, U. S. *J. Polym. Sci., Part A: Polym. Chem.* **2003**, *41*, 1413. (b) Dobrawa, R.; Würthner, F. *J. Polym. Sci., Part A: Polym. Chem.* **2005**, *43*, 4981. (c) Friese, V. A.; Kurth, D. G. *Coord. Chem. Rev.* **2008**, *252*, 199. (d) McKenzie, B. M.; Rowan, S. J. *The Encyclopedia of Supramolecular Chemistry*; Taylor and Francis: New York, 2007. (e) McKenzie, B. M.; Rowan, S. J. In *Molecular Recognition and Polymers: Control of Polymer Structure and Self-Assembly*; Rotello, V. M., Thayumanavan, S., Hoboken, N. J., Eds.; Wiley: New York, 2008; Chapter 7, p 157.

(2) (a) Whittell, G. R.; Hager, M. D.; Schubert, U. S.; Manners, I. *Nature Mater.* **2011**, *10*, 176. (b) Wang, X. S.; McHale, R. *Macromol. Rapid Commun.* **2010**, *31*, 303. (c) Holliday, B. J.; Swager, T. M. *Chem. Commun.* **2005**, 23.

(3) For some reviews see: (a) Fox, J. D.; Rowan, S. J. *Macromolecules* **2009**, *42*, 6823. (b) Wojtecki, R. J.; Meador, M. A.; Rowan, S. J. *Nature Mater.* **2011**, *10*, 14. (c) Wilson, A. J. *Soft Matter* **2007**, *3*, 409. (d) Serpe, M. J.; Craig, S. L. *Langmuir* **2007**, *23*, 1626. (c) Brunsveld, L.; Folmer, B. J. B.; Meijer, E. W.; Sijbesma, R. P. *Chem. Rev.* **2001**, *101*, 4071.

(4) (a) Kelch, S.; Rehahn, M. *Macromolecules* **1999**, *32*, 5818. (b) Chiper, M.; Hoogenboom, R.; Schubert, U. S. *Macromol. Rapid Commun.* **2009**, *30*, 565. (c) Meier, M. A. R.; Hofmeier, H.; Abeln, C. H.; Tziatzios, C.; Rasa, M.; Schubert, D.; Schubert, U. S. *e-Polym.* **2006**, *16*, 1. (d) El-ghayoury, A.; Hofmeier, H.; de Ruiter, B.; Schubert, U. S. *Macromolecules* **2003**, *36*, 3955. (e) Schwarz, G.; Bodenthin, Y.; Geue, T.; Koetz, J.; Kurth, D. G. *Macromolecules* **2010**, *43*, 494.

(5) (a) Kelch, S.; Rehahn, M. *Macromolecules* **1998**, *31*, 4102. (b) Archar, S.; Puddephatt, R. J. *J. Chem. Soc., Chem. Commun.* **1994**, 1895. (c) Achar, S.; Vittal, J. J.; Puddephatt, R. J. *Organometallics* **1996**, *15*, 43. (d) Kaes, C.; Hosseini, M. W.; Rickard, C. E. F.; Skelton, B. W.; White, A. H. *Angew. Chem.* **1998**, *110*, 970; *Angew Chem., Int. Ed.* **1998**, *37*, 920.

(6) (a) Beck, J. B.; Rowan, S. J. *J. Am. Chem. Soc.* **2003**, *125*, 13922. (b) Zhao, Q. Y.; Beck, J. B.; Rowan, S. J.; Jamieson, A. M. *Macromolecules* **2004**, *37*, 3529. (c) Rowan, S. J.; Beck, J. B. *Faraday Discuss.* **2005**, *128*, 43. (d) Weng, W.; Beck, J. B.; Jamieson, A. M.; Rowan, S. J. *J. Am. Chem. Soc.* **2006**, *128*, 1163. (e) Weng, W.; Li, Z.; Jamieson, A. M.; Rowan, S. J. *Soft Matter* **2009**, *5*, 4647. (f) Kumpfer, J. R.; Wie, J. J.; Swanson, J. P.; Beyer, F. L.; Mackay, M. E.; Rowan, S. J. *Macromolecules* **2011**, DOI: 10.1021/ma201659d.

(7) Beck, J. B.; Ineman, J. M.; Rowan, S. J. *Macromolecules* **2005**, *38*, 5060.

(8) Knapton, D.; Rowan, S. J.; Weder, C. *Macromolecules* **2006**, *39*, 651.

(9) Knapton, D.; Rowan, S. J.; Weder, C. *Macromolecules* **2006**, *39*, 4069.

(10) Burnworth, M.; Knapton, D.; Rowan, S. J.; Weder, C. *J. Inorg. Organomet. Polym. Mater.* **2007**, *17*, 91.

(11) Burnworth, M.; Mendez, J. D.; Schroeter, M.; Rowan, S. J.; Weder, C. *Macromolecules* **2008**, *41*, 2157.

(12) Kumpfer, J. R.; Jin, J. Z.; Rowan, S. J. *J. Mater. Chem.* **2010**, *20*, 145.

(13) Kumpfer, J. R.; Rowan, S. J. *J. Am. Chem. Soc.* **2011**, *133*, 12866−12874.

(14) Burnworth, M.; Tang, L.; M.; Kumpfer, J. R.; Duncan, A. J.; Beyer, F. L.; Fiore, G. L.; Rowan, S. J.; Weder, C. *Nature* **2011**, *472*, 334.

(15) (a) Beach, W. F. Xylylene Polymers. In *Encyclopedia of Polymer Science and Technology*, 3rd ed.; Kroschwitz, J., Ed.; John Wiley & Sons: New York, 2004; Vol. *12*, p 587 ff. (b) Greiner, A.; Mang, S.; Schäfer, O.; Simon, P. *Acta Polym.* **1997**, *48*, 1.

(16) Steiger, D.; Tervoort, T.; Weder, C.; Smith, P. *Macromol. Rapid Commun.* **2000**, *21*, 405.

(17) Earle, M. J.; Mcauley, B. J.; Ramani, A.; Seddon, K. R.; Thomson, J. M. PCT Pub. No. WO02/072260, Sept 19, 2002.

(18) Bhatt, A. I.; May, I.; Volkovich, V. A.; Collison, D.; Helliwell, M.; Polovov, I. B.; Lewin, R. G. *Inorg. Chem.* **2005**, *44*, 4934.

(19) Setayesh, S.; Grimsdale, A. C.; Weil, T.; Enkelmann, V.; Müllen, K.; Meghdadi, F.; List, E. J. W.; Leising, G. *J. Am. Chem. Soc.* **2001**, *123*, 946.

(20) Beck, B. J.; Kokil, A.; Ray, D.; Rowan, S. J.; Weder, C. *Macromolecules* **2002**, *35*, 590.

(21) Nakagawa, T.; Makotot, O. J. *J. Polym. Sci., Part A: Polym. Chem.* **1968**, *6*, 1795.

Macromolecules

Article

pubs.acs.org/Macromolecules

Unusual Temperature-Dependent Photophysics of Oligofluorene-Substituted Tris-Cyclometalated Iridium Complexes

Qifan Yan, Yuanpeng Fan, and Dahui Zhao*

Beijing National Laboratory for Molecular Sciences, Department of Applied Chemistry and the Key Laboratory of Polymer Chemistry and Physics of the Ministry of Education, College of Chemistry, Peking University, Beijing 100871, China

Supporting Information

ABSTRACT: The photophysical properties of a series of tris-cyclometalated Ir(III) complexes bearing oligofluorene-substituted 2-phenylpyridine (ppy) and/or 1-phenylisoquinoline (piq) ligands were studied at both room temperature and 77 K, for delineating the oligomer-substitution effects on the photophysics in such metal-complex-containing conjugated oligomers/polymers. Unique temperature dependence was observed with the triplet excited-state lifetime of the studied oligomers. Molecules having one of the three ppy ligands substituted with an oligofluorenyl group at varied positions exhibited two distinct types of phosphorescing behaviors. When the oligoflurene group was coupled to ppy in a conjugative fashion (i.e., at 5- or 4′- position), the complexes appeared to emit from a ^{3}MLCT-dominated state perturbed by LC transition, as evidenced by the relatively short lifetimes of phosphorescence as well as hypsochromic shift upon lowering the temperature. Surprisingly, even shorter triplet lifetimes were detected at 77 K for such oligomers. When the oligofluorenyl was tethered to the phenyl ring of ppy meta to pyridine, emission properties were consistent with a ^{3}LC-dominated state, mixed with a certain MLCT component. Uniquely, for these oligomers an evident bathochromic shift of emission with a significantly retarded radiative decay rate was observed at 77 K. Furthermore, when a piq ligand was incorporated, red phosphorescence characteristic of Ir-piq-based ^{3}MLCT transition emerged, disregarding the substation position of the oligofluorene. All these different photophysical behaviors, particularly their unique temperature dependence, were explained by considering an energy transfer process between different triplet states, with dominant MLCT and LC characteristics. In complexes having all ppy-derived ligands, these two states were of similar but different energy. While one played a more important role than the other, both were contributing to the phosphorescence emission. The temperature dependence of the photophysics reflected the equilibrium shifting process. When the ^{3}MLCT-dominated state was lower in energy, faster radiative decay and shorter lifetimes were manifested upon lowering the temperature, as a result of more favored ^{3}MLCT-dominated state. Whereas if the ^{3}LC-dominated state was more stable, slower radiative decay emerged at decreased temperature due to further a reduced MLCT contribution. The bathochromic shift was also a result of equilibrium shifting to the state of lower energy. When the piq ligand was engaged, the emission was governed by the ^{3}MLCT state of the Ir-piq moiety, which had much lower energy compared to the triplet states localized in oligofluorenyl ppy. DFT calculations substantiated the above hypothesis by identifying separate molecular orbitals possessing mixed but imbalanced MLCT and LC components.

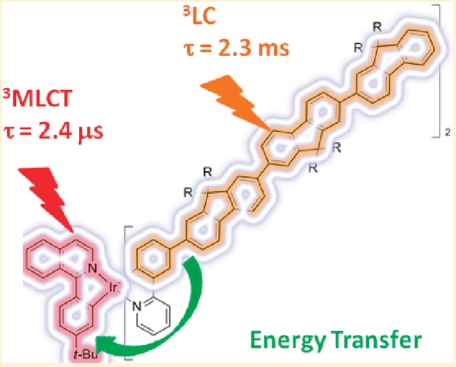

INTRODUCTION

Cyclometalated iridium(III) complexes have been extensively studied mainly for their exceptional phosphorescence properties, exhibited by virtue of the large spin−orbital coupling (SOC) constant and efficient intersystem crossing (ISC) imparted the heavy metal.[1] Incorporation of such metal complex moieties into conjugated polymer scaffolds has proven an effective approach to accessing triplet excited states of polymer materials and inducing enhanced phosphorescence emission.[2] In addition to light-emitting diodes (LEDs),[3] iridium complexes have also found versatile applications in more diverse fields, including sensors,[4] biolabeling,[5] and photovoltaic devices.[6] For attaining optimal performance, various applications actually demand much differed photophysical properties. With the phosphorescent materials harvesting the triplet excitons, the internal efficiency of LEDs can be considerably improved.[7] In addition to pure light color, phosphors in LEDs are generally desired to possess high quantum yields and short lifetimes, i.e., rapid radiative and slow nonradiative decay rates, in order to maximize the brightness while suppressing triplet−triplet annihilation.[8] In contrast, long-lived excitons are advantageous for sensory applications; that is, spontaneous radiative and nonradiative rates should both be slow.[9] Long-lifetime emission is favorable for bioimaging applications, which helps minimizing the interference of background fluorescence.[10] Moreover, the long lifetime of triplet excitons has

Received: October 31, 2011
Revised: November 21, 2011
Published: December 8, 2011

also been shown facilitating charge separation in photovoltaic devices.[11] Apparently, to suit such a wide range of applications, the ability to tailor the materials properties by structure modifications is highly desirable, and a proper understanding of the correlation of photophysical properties with chemical structures is indispensable for rational molecular designs.[2,12]

To this end, along with investigations focused on exploring innovative applications,[13] systematic research was performed to delineate the structure−property relationship in organometallic phosphors.[14−16] The basic principles and common characteristics of triplet emission in small-molecule complexes have generally been established. Specifically for cyclometalated iridium complexes, Thompson and co-workers carefully studied a number of blue-emitting complexes and elucidate the origin of the temperature dependence of their radiative decay process.[16] Tsuboyama and co-workers surveyed a series of homoleptic iridium complexes of red phosphorescence,[15] showing that for typical metal-to-ligand charge transfer (MLCT) excited state the emission underwent hypsochromic shift upon freezing the solvent, resulting from subsided solvent relaxation around the more polar excited state.[17] In contrast, phosphorescence from ligand-centered (LC) triplet state ($^3\pi-\pi^*$) was much less sensitive to temperature, with minimal change in both band shape and emission wavelength.[15a,18] Moreover, a slower radiative decay rate was typically observed with the ^{3}LC state compared to that of ^{3}MLCT state due to a limited participation of heavy metal orbitals in the LC transition.

Moreover, a number of unique systems featuring an intramolecular energy transfer process between different triplet states have been reported. Earlier examples were some Ru complexes covalently linked to pyrene units.[19] More recently, Thompson et al. studied a benzoporphyrin−Pt complex attached with four BODIPY units exhibiting triplet energy transfer.[20] Ceroni and Zhao groups independently investigated Ru complexes coupled with trithiophene oligomer and pyrene units, both of which displayed reversible triplet energy transfer.[21]

In addition to studies on small molecules, Ir complexes have also been incorporated into linear[2,22] and dendritic[23] polymer scaffolds. In these systems, the auxiliary structures not only facilitated photon and carrier collections but also suppressed triplet−triplet annihilation by acting as antenna and/or insulating layers. However, compared to small-molecule systems, the photophysical details of metal-complex-containing conjugated polymers is more obscure and less understood,[18,24,25] but relevant information is useful to avail more precise structure−property prediction and efficient material designs.

Among different iridium complexes, tris-cyclometalated systems are of particular interest because of their extraordinarily high phosphorescing quantum efficiency[16b,26] as well as the noncharged nature and chemical stability. Following a previous investigation,[25] herein we report a more in-depth study on the temperature dependence of the photophysics of a series of tris-cyclometalated Ir(III) complexes having oligofluorenyl 2-phenylpyridine (ppy) and 1-phenylisoquinoline (piq) ligands (Charts 1 and 2). On the basis of the experimental results, we proposed that an energy transfer between different triplet states (MLCT- and LC-dominated, respectively) occurred and was responsible for the observed unique temperature-dependent photophysics exhibited by the studied molecules. On the other hand, the current study also demonstrated effective approaches to tuning the triplet state properties of related materials by modulating the ligand structures.

Chart 1. Chemical Structures of Oligofluorenyl Ir(ppy)$_3$ and Reference Complex Ir(ppy)$_3$

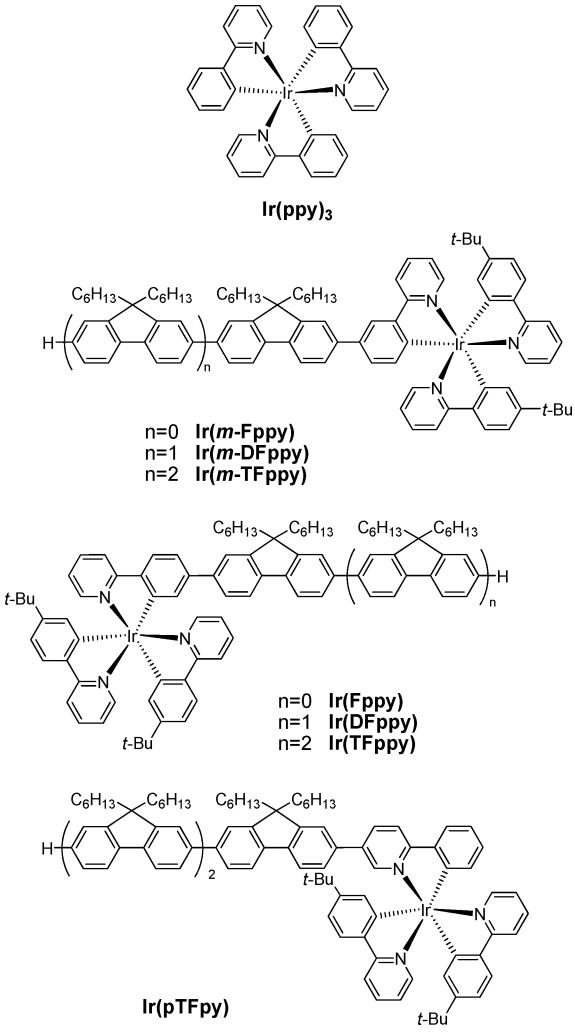

RESULTS AND DISCUSSION

Materials. Reference compounds Ir(ppy)$_3$ and Ir(piq)$_3$ were obtained according to procedures reported in the literature.[8e,15a] Oligofluorene-substituted Ir(ppy)$_3$ complexes (Chart 1) were synthesized using our previously reported methods.[25] Similar protocols were used to obtain oligofluorene-substituted complexes containing piq ligands (Chart 2). Specifically, 1-chloroisoquinoline was reacted with *tert*-butyl or bromine-substituted phenylboronic acids under Suzuki coupling conditions, yielding the corresponding substituted-piq ligands. Various tris-cyclometalated Ir(III) complexes with brominated ppy and piq ligands were subsequently acquired via Nonoyama reactions followed by ligand-exchange reactions. The *tert*-butyl groups on the phenyl rings helped improve the solubility of bromine-substituted complexes and allowed the use of column chromatography for their purification and separation from byproducts generated in ligand-exchange reactions. These intermediate complexes were then subjected to Suzuki coupling conditions to react with oligofluorenylboronic acids of different chain lengths, offering the target oligomeric complexes (synthetic details are described in the

dx.doi.org/10.1021/ma2024123 | *Macromolecules* 2012, 45, 133−141

Chart 2. Chemical Structures of Oligofluorenyl Ir(ppy)(piq)$_2$ and Ir(ppy)$_2$(piq) with Reference Complex Ir(piq)$_3$

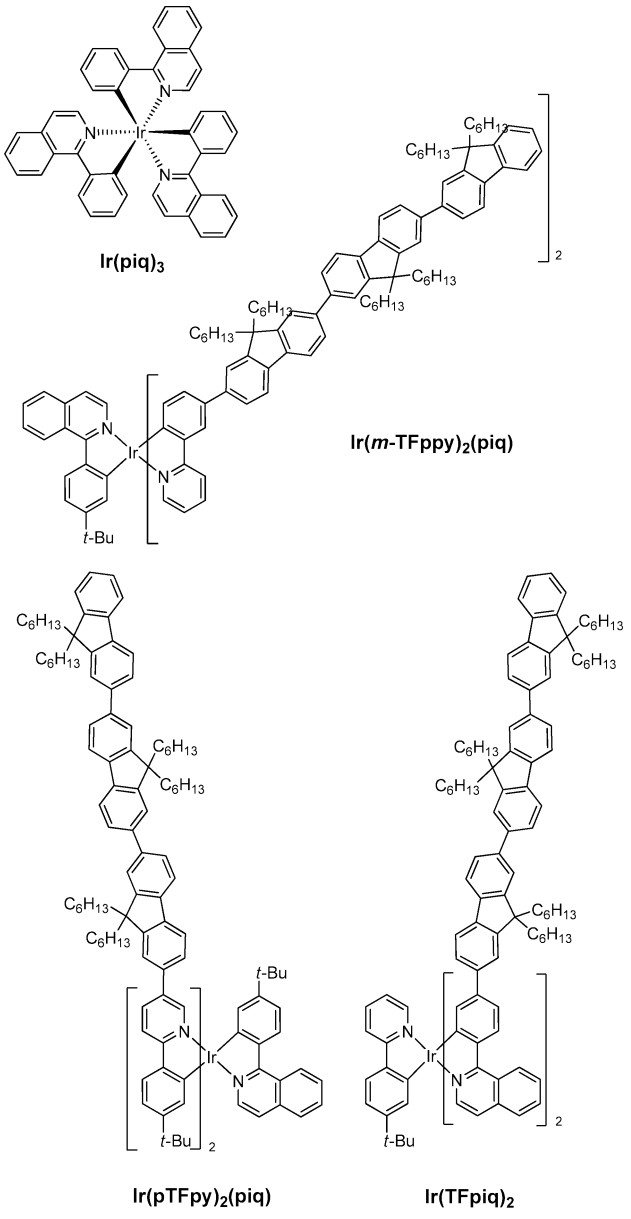

Supporting Information). The structures of all newly synthesized complexes were characterized and confirmed by ^{1}H NMR and mass spectroscopies.

Absorption Spectra. For complex series having an oligofluorene chain attached to the phenyl ring of ppy meta to the pyridine unit, i.e., Ir(*m*-Fppy), Ir(*m*-DFppy), and Ir(*m*-TFppy), both the absorption maxima and absorbability increased with the oligofluorene chain length (Figure 1a). Evidently, the absorption spectra were dominated by the spin-allowed LC $^1\pi-\pi^*$ transition of the oligofluorene moiety. The minor band centered at about 450 nm, showing a lower extinction coefficient, was from MLCT transitions, which remained nearly unchanged with the oligofluorene chain extension. Generally, these absorption features were similar to those of complexes Ir(Fppy), Ir(DFppy), and Ir(TFppy).[25]

The three oligomer complexes having piq ligands and trifluorenyl groups at different positions also exhibited principal

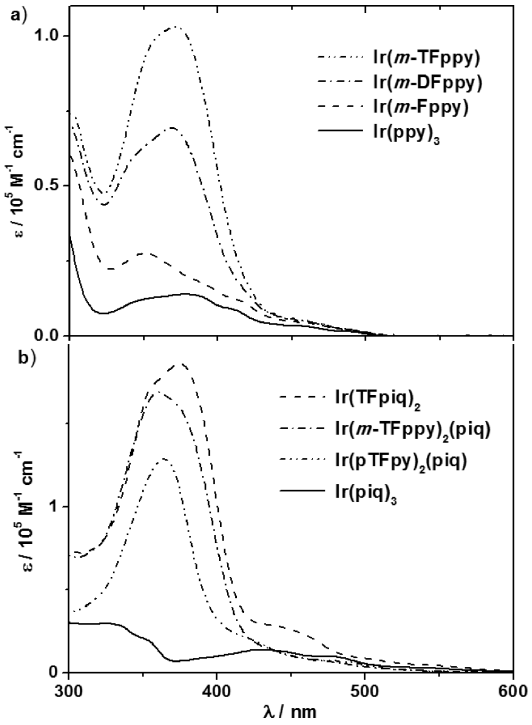

Figure 1. Absorption spectra of some oligofluorene-substituted Ir(III) complexes in comparison with those of Ir(piq)$_3$ and Ir(ppy)$_3$ (spectrum of Ir(*m*-TFppy) was reproduced from ref 25).

absorption peaks at ca. 370 nm (Figure 1b). These optical bands with large extinction coefficients were as well ascribed to the spin-allowed $\pi-\pi^*$ transition of the trifluorene groups. The major absorption band of complex Ir(pTFpy)$_2$(piq) exhibited a nearly identical maximum wavelength with that of Ir(pTFpy), suggesting that the excitation transitions took place relatively independently in each ligand. Complex Ir(TFpiq)$_2$ with a trifluorenyl directly linked to piq manifested a slightly red-shifted absorption maximum relative to those of Ir(pTFpy)$_2$(piq) and Ir(*m*-TFppy)$_2$(piq), imaginably due to electronic coupling between the trifluorenyl group and the piq unit.[15a]

In summary, the absorption spectra of all studied oligomeric Ir(III) complexes corresponded mainly to intraligand electronic transitions. Charge transfer between the iridium center and ligands played a minor role in the excitation process.

Photoluminescence Properties. The photoluminescence properties of all oligomer complexes were investigated at both room temperature and 77 K. The spectra are shown in Figures 2–4 and Figure S1, with relevant data summarized in Table 1 in comparison with those of reference compounds Ir(ppy)$_3$ and Ir(piq)$_3$. The emission spectra were collected by exciting at the absorption maxima of respective oligomer complexes, corresponding to the $^1\pi-\pi^*$ transition of the oligofluorenyl-substituted ligands. The observed properties of sensitivity to oxygen, large Stokes shift, and microsecond-ordered lifetimes all suggested that the emissions originated from triplet excited states. The fact that no significant fluorescence was detected with any of the oligomers confirmed that intersystem crossing occurred very rapidly and efficiently in these oligomeric iridium complexes.

Our study was first focused on the complexes having all ppy-derived ligands. Compared with phosphorescence spectra collected at 298 K,[25] an evident hypsochromic shift was

dx.doi.org/10.1021/ma2024123 | *Macromolecules* 2012, 45, 133–141

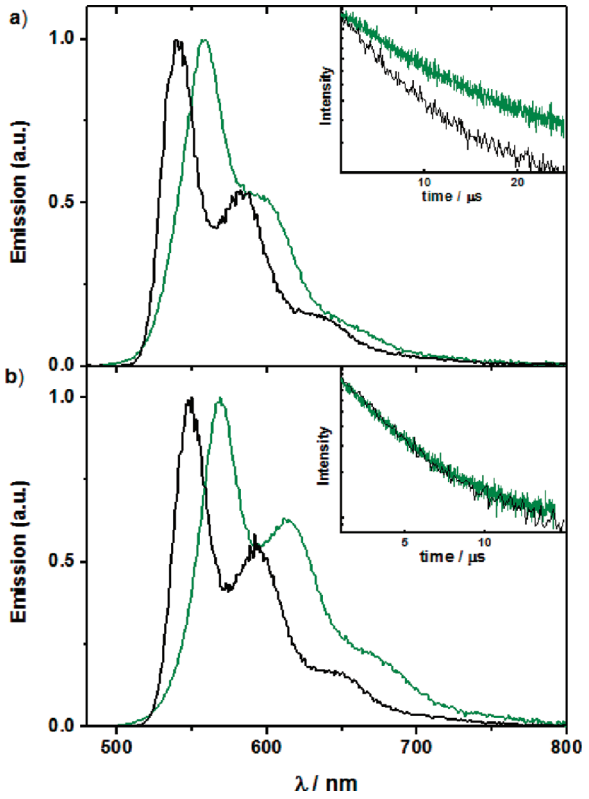

Figure 2. Steady-state photoluminescence spectra and time-resolved emission decay curves (inset) of (a) Ir(TFppy) and (b) Ir(pTFpy) at 77 K (black lines) and 298 K (green lines, the room-temperature data were reproduced from ref 25); reduced lifetimes were observed at the lower temperature (12 and 7.4 μs for Ir(TFppy), 4.2 and 3.6 μs for Ir(TFppy) at 298 and 77 K, respectively).

exhibited by the emissions of both Ir(TFppy) and Ir(pTFpy) at 77 K, with evident vibronic features shown at both high and low temperatures (Figure 2). These optical features clearly revealed the complex nature of the triplet excited state in these oligomers to be the admixture of MLCT and LC states. Namely, the appearance of resolved vibronic structures at room temperature testified the LC characteristic, while the hypsochromic shift upon temperature decrease evidenced the charge transfer feature, which entailed solvent relaxation for stabilizing the more polar excited state at higher temperatures. Such solvent reorganization motions were substantially suppressed upon freezing the solvent.

Surprising results emerged when time-resolved emission data were obtained. Typically, the triplet-state lifetimes of small-molecule metal complexes extend upon lowering the temperature. One of the reasons for longer lifetime is that nonradiative decay rate contains a temperature-dependent component, which decreases with temperature because excitons of reduced thermal energy are less likely to overcome the activation barrier and access the nonradiative decay pathways. Another origin of the temperature-sensitive lifetime for iridium complexes lies in the different radiative decay rates of the three sublevels of the triplet state. The situation is well presented by $Ir(ppy)_3$, which features a very small nonradiative decay rate and a large zero-field splitting, as illustrated by Thompson et al.[16b] Thermal population of the higher triplet substates that are capable of faster radiative decay was proposed to account for the reduced lifetime of $Ir(ppy)_3$ at increased temperatures. However, contrary to these previous observations of common small-molecule

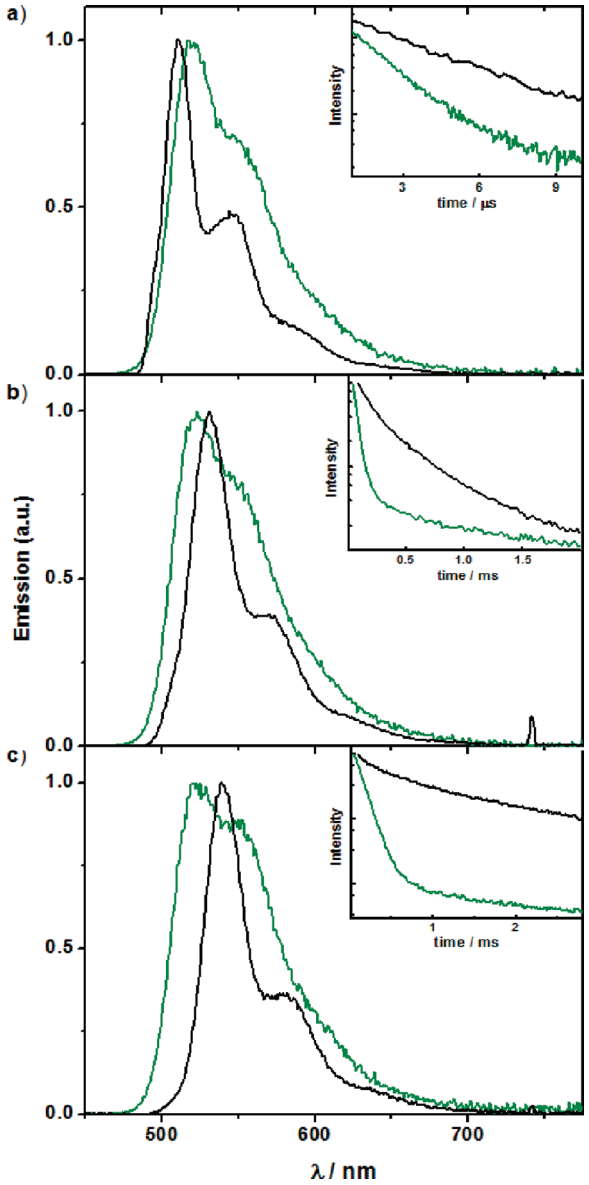

Figure 3. Normalized photoluminescence spectra and time-resolved emission decay curves (inset) of (a) Ir(*m*-Fppy), (b) Ir(*m*-DFppy), and (c) Ir(*m*-TFppy) at 77 K (black line) and 298 K (green lines); extended lifetimes were detected at lowered temperature (1.5 and 3.5 μs for Ir(*m*-Fppy), 45 and 236 μs for Ir(*m*-DFppy), 114 and 645 μs for Ir(*m*-TFppy) at 298 and 77 K, respectively).

iridium complexes, oligomers Ir(TFppy) and Ir(pTFpy) both exhibited substantially reduced lifetimes at the cryogenic temperature (Figure 1 and Table 1).

To seek explanation for this unusual temperature dependence of lifetimes, additional data were collected. First, the chain length effect of the oligofluorenyl on the triplet exciton lifetime was evaluated. All three complexes having oligofluorenyl positioned on the phenyl ring of ppy para to the pyridine unit, Ir(Fppy), Ir(DFppy), and Ir(TFppy), showed hypsochromically shifted phosphorescence spectra upon lowering the temperature (Figure S1). While $Ir(ppy)_3$ showed lifetimes of 1.5 and 3.4 μs at 298 and 77 K, respectively, complex Ir(Fppy) with one fluorene unit attached exhibited nearly unchanged lifetime values of 4.1 and 4.0 μs at the same temperatures (Table 1). When the oligomer chain was further extended,

dx.doi.org/10.1021/ma2024123 | *Macromolecules* 2012, 45, 133–141

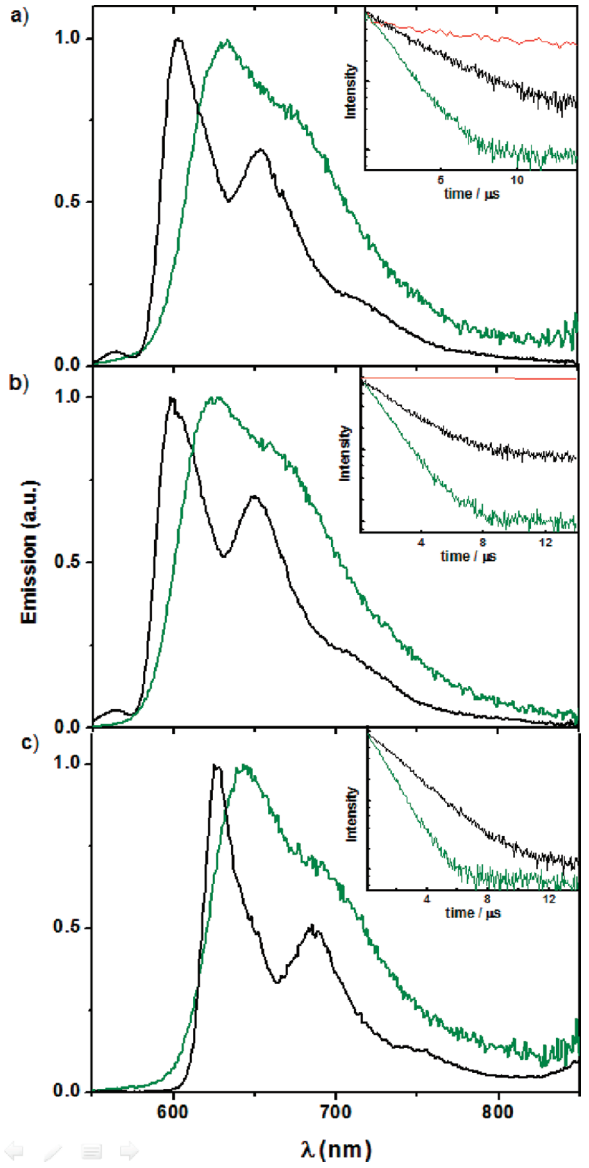

Figure 4. Normalized photoluminescence spectra and time-resolved emission decay curves (inset) of (a) Ir(pTFpy)$_2$(piq), (b) Ir(*m*-TFppy)$_2$(piq), and (c) Ir(TFpiq)$_2$ at 298 (green lines) and 77 K (black lines); the lifetimes of the main emission peaks were determined to be 1.2 and 2.9 μs for Ir(pTFpy)$_2$(piq), 1.4 and 2.4 μs for Ir(*m*-TFppy)$_2$(piq), and 1.2 and 2.0 μs for Ir(TFpiq)$_2$ at 298 and 77 K, respectively; the red decay curves were obtained from the minor emission peak at 563 nm at 77 K, with a lifetime of 7.0 μs and 2.3 ms for Ir(pTFpy)$_2$(piq) and Ir(*m*-TFppy)$_2$(piq), respectively.

i.e., for Ir(DFppy), shorter lifetimes were observed at 77 K, similar to the observation made with Ir(TFppy). In general, for this homologue series, the triplet-state lifetime and its dependence on temperature manifested a tendency to be less similar to that of Ir(ppy)$_3$ as the oligomer chain grew longer.

However, rather distinct results were obtained from another oligomer series, which had the oligofluorenyl group tethered to phenyl ring of ppy meta to pyridine. In this series, with a single fluorenyl group, complex Ir(*m*-Fppy) exhibited very similar properties to those of Ir(ppy)$_3$, i.e., showing very short excited-state lifetime and a near-unity quantum efficiency, reflecting a very rapid radiative decay and a negligible contribution of nonradiative pathways. Also similar to Ir(ppy)$_3$, moderately extended lifetime and hypsochromic shift of emission were observed with Ir(*m*-Fppy) when the temperature was lowered to 77 K (Figure 3a and Table 1). In stark contrast, when more fluorene units were appended, dissimilar photophysical properties were displayed by Ir(*m*-DFppy) and Ir(*m*-TFppy). While the emission quantum yield remained a significant value of 0.82, the excited state lifetime at 298 K became substantially prolonged to 45 μs for Ir(*m*-DFppy). More remarkably, when the temperature was lowered to 77 K, a particularly longer lifetime of over 200 μs was detected. On the basis of the radiative and nonradiative decay rates (k_r and k_{nr}, respectively) calculated using the quantum yield (Φ) and lifetime (τ) values at 298 K, it was evident that a decrease of k_{nr} could not solely be responsible for such a long lifetime at 77 K, considering its relatively small value even at room temperature. In other words, k_r must have dropped significantly with temperature for this molecule. Moreover, the phosphorescence of Ir(*m*-DFppy) exhibited a noticeable bathochromic shift at lowered temperature (Figure 3b). This phenomenon was rather unusual and not commonly observed previously with either ^{3}MLCT- or ^{3}LC-governed emissions.[15] An even more significant bathochromic shift and further extended lifetime (>600 μs) of emission were observed with Ir(*m*-TFppy) at 77 K.

By analyzing the data presented above, the following information was deduced. Consistent with the conclusion drawn earlier,[25] the emission of oligomers Ir(Fppy), Ir(DFppy), and Ir(TFppy) originated from mixed MLCT and LC transitions. As the oligofluorene chain was extended, the contribution of MLCT to the excited state was reduced relative to that of the LC state. This was evidenced by the decreased k_r and k_{nr} with increasing oligofluorenyl chain length. However, the MLCT state remained the more important contributor over the entire series, as evidenced by the hypsochromic shift of phosphorescence observed at lowered temperature. On the other hand, for complexes having oligofluorenyl and pyridyl groups placed at meta positions, the triplet excited state appeared to experience a transition from being MLCT-dominated state, in Ir(*m*-Fppy), to LC-prevailed one, as in Ir(*m*-DFppy) and Ir(*m*-TFppy).[27]

Such disparate photophysical behaviors of the above two series at room temperature were reasonably well explained by the different electronic coupling effect of *m*- vs *p*-phenylene linkage. For Ir(ppy)$_3$, the MLCT process primarily relies on the LUMO of pyridine moiety to accept the negative charge. When the oligofluorene was located at the para position of the pyridine unit, the negative change could be effectively delocalized and thus stabilized by the entire conjugated oligofluorenyl ppy ligand. In contrast, delocalization of the negative change to the oligofluorene chain was not viable for the meta linkage. Consequently, for oligomer series Ir(*m*-Fppy), Ir(*m*-DFppy), and Ir(*m*-TFppy), the energy level of MLCT-dominated state remained relatively constant, whereas the energy level of the LC-dominant state was continuously lowered with extended π-conjugation. When the appended chain was short, as in Ir(*m*-Fppy), the LC-dominated excited state was still higher in energy and the MLCT process prevailed. As the oligomer chain grew longer, the LC-dominated state became lower in energy than the MLCT state. Hence, the lowest triplet state turned from a typical MLCT-dominated state to one mostly dictated by the LC process as more fluorene units were appended.

Nonetheless, the unique temperature-dependent phenomena still awaited explanation, namely the shortened lifetimes of Ir(DFppy), Ir(TFppy), and Ir(pTFpy) but significantly

dx.doi.org/10.1021/ma2024123 | *Macromolecules* 2012, 45, 133–141

Table 1. Photoluminescence Properties of Studied Oligofluorene-Substituted Iridium Complexes[a]

complex	λ_{max} (nm) (298|77 K)	Φ(298 K)	τ (μs)[b] (298|77 K)	$k_r\|k_{nr}$[c] (/10^5 s^{-1})
$Ir(ppy)_3$[d]	510|495	0.97[e]	1.5|3.4	6.5|0.2
Ir(Fppy)[d]	550|527	0.81	4.1|4.0	2.0|0.46
Ir(DFppy)[d]	558|536	0.67	8.0|6.0	0.84|0.41
Ir(TFppy)[d]	559|540	0.67	12|7.4	0.56|0.27
Ir(pTFpy)[d]	568|549	0.82	4.2|3.6	2.0|0.43
Ir(*m*-Fppy)	518|503	>0.99	1.5|3.5	6.6|0.07
Ir(*m*-DFppy)	523|531	0.82	45|236	0.18|0.04
Ir(*m*-TFppy)[d]	524|540	0.50	114|645	0.04|0.04
$Ir(piq)_3$	619|598	0.60[f]	1.1|2.5	5.5|3.6
$Ir(pTFpy)_2(piq)$	628|604	0.69	1.2|2.9 (7.0[g])	5.8|2.6
$Ir(m\text{-}TFppy)_2(piq)$	622|600	0.72	1.4|2.4 (2.3×10^3 [g])	5.1|2.0
$Ir(TFpiq)_2$	641|626	0.44	1.2|2.0	3.7|4.7

[a]Data separated by "|" were obtained at 298 and 77 K, respectively; $Ir(ppy)_3$ and oligofluorenyl $Ir(ppy)_3$ were measured in degassed toluene; $Ir(piq)_3$ and oligofluorenyl $Ir(ppy)_2(piq)$/$Ir(ppy)(piq)_2$ were measured in degassed MeTHF. [b]Lifetimes shorter than 20 μs were measured by the time-correlated single-photon counting method using NanoLED of 339 or 369 nm as the excitation light source; lifetimes longer than 20 μs were measured using a pulsed Xe lamp as the excitation light source. [c]k_r and k_{nr} (radiative and nonradiative decay rates) were calculated at 298 K using $k_r = \Phi_p/\tau$ and $k_{nr} = (1 - \Phi_p)/\tau$, respectively. [d]Data at room temperature were from ref 25. [e]This value from ref 16b was used as the standard for the quantum yield measurement of oligofluorene-substituted $Ir(ppy)_3$ complexes. [f]This value from ref 28 was used as the standard for the quantum yield measurement of oligofluorenyl $Ir(ppy)_2(piq)$ and $Ir(ppy)(piq)_2$ complexes. [g]Data measured at 77 K for the minor emission band with a maximum at 563 nm.

prolonged ones of Ir(*m*-DFppy) and Ir(*m*-TFppy) in companion with different chromic shift of emissions at lowered temperature. These observations led to a hypothesis of an energy-transfer process between two triplet states, with dominant MLCT and LC characteristics in these oligomers.[27] In the above oligomer complexes, because these two states possessed similar energy, a reversible energy transfer might have occurred, and the emission appeared as a single decay process due to rapid equilibration. For the oligomer series featuring para-linked oligofluorenyl and pyridine, both the energy levels of the MLCT- and LC-dominated states were lowered upon elongation of the oligofluorene chain. Although the LC-dominated state was stabilized more effectively than the MLCT state at the same chain length, the latter remained lower in energy and being the major contributor to the emission over the entire series, which was evidenced by the hypsochromic shift of emission with decreased temperature. As the temperature decreased, the MLCT-dominated state of lower energy was favored even more strongly, thus giving rise to faster radiative decay and shortened lifetime. It should be noted that in these oligomers the MLCT-dominated state is probably significantly mixed with LC transition. On the other hand, the LC-dominated state might not possess a very significant radiative decay rate, due to the minimal involvement of the metal atom, but its presence affected the emission lifetime by entailing the energy-transfer process.

For the meta-linked series, as aforementioned, while the LC state gained stabilizing energy from the oligomer chain extension, the MLCT state remained roughly unaffected due to the meta linkage between the pyridine unit and oligofluorene chain. Therefore, in Ir(*m*-Fppy) the MLCT-dominated state was much lower in energy compared to the LC-dominated state, and therefore the molecule exhibited very similar properties to those of $Ir(ppy)_3$. The lifetime dependence on temperature of Ir(*m*-Fppy) likely followed a similar scenario to that of $Ir(ppy)_3$. That is, increased thermal population of higher triplet state sublevels brought about faster radiative decay at increased temperature. However, when the LC-dominated state was stabilized and overrode the MLCT-dominated state, it became the more important contributor to the emission, as in Ir(*m*-DFppy) and Ir(*m*-TFppy), and the temperature dependence of photophysics readily revealed the equilibrium shifting of the energy-transfer process. The higher MLCT state became less populated at lower temperature, resulting in further retarded decay rates and extended lifetimes. Since the LC-dominated state was of lower energy, bathochromic shift of emission emerged as the temperature dropped. It is noteworthy that the LC-dominated state in Ir(*m*-DFppy) and Ir(*m*-TFppy) was likely more emissive than those in Ir(DFppy), Ir(TFppy), and Ir(pTFpy), since the oligofluorene segment was electronically coupled to the metal center via a *p*-phenylene unit, and thus a more direct d-orbital contribution to the LC-dominated transition was viable. This was clearly viewed from the DFT-calculated molecular orbitals (Figure S3).

The triplet energy transfer in previously reported systems typically took place between ^{3}MLCT and LC states localized on separate chromophores,[19−21] and the $^3\pi-\pi^*$ state mostly served as a "dark" energy reservoir, affecting the exciton lifetime. A distinct difference of our current system is that the MLCT- and LC-dominated triplet states might be both emissive. Because of a more integrated coupling of the oligofluorene with the metal center, substantial mixing of the transition metal d-orbital with the LC process occurred, enabling a pronounced radiative decay rate of the LC-dominated state.[27] Furthermore, with a relatively small k_{nr} value typical of Ir complexes, the emission from the LC-dominant state was detectable. On the other hand, likely due to the large size and disorder of the oligomeric ligands, the MLCT- and LC-dominated states were relatively localized and vibrational coupling between them was not particularly efficient. All these factors contributed to the observation of the energy transfer process.

Subsequent investigations were conducted with the three complexes accommodating piq ligands (Figure 4 and Table 1). The reference complex $Ir(piq)_3$ emitted red phosphorescence with a quantum yield of ca. 0.6. At room temperature, a very short excited-state lifetime of 1.1 μs was exhibited, characteristic of a typical ^{3}MLCT state. Its significantly red-shifted emission

compared to that of $Ir(ppy)_3$ was due to the enlargement of the π-system upon fusing a benzo group to the pyridine unit, which substantially enhanced the electron-accepting ability and lowered the MLCT transition energy.

Notably, at both 298 and 77 K the photophysical properties exhibited by $Ir(pTFpy)_2(piq)$ and $Ir(m\text{-}TFppy)_2(piq)$ were akin to that of $Ir(piq)_3$, but distinctly different from those of related oligomers Ir(pTFpy) and Ir(*m*-TFppy). Specifically, both $Ir(pTFpy)_2(piq)$ and $Ir(m\text{-}TFppy)_2(piq)$ emitted red phosphorescence with wavelength maxima at ca. 600 nm. The room-temperature lifetimes were slightly longer than 1 μs. At 77 K, the emission maxima were blue-shifted by >20 nm, exhibiting slightly extended lifetimes of 2−3 μs. All these results suggested that the two oligomer complexes were emitting from a triplet state similar to that of $Ir(piq)_3$, that is, the ^{3}MLCT of Ir-piq moiety.

The property difference between $Ir(pTFpy)_2(piq)$/$Ir(m\text{-}TFppy)_2(piq)$ and Ir(pTFpy)/Ir(*m*-TFppy) was understandable considering the energy levels of relevant triplet states. The emission wavelengths clearly revealed that the ^{3}MLCT state of Ir-piq was considerably lower in energy than both ^{3}MLCT- and ^{3}LC-dominated states conferred by oligofluorenyl ppy.[15a] Notably, since the emissions of these oligomers were recorded by exciting at their absorption maxima (corresponding to $\pi-\pi^*$ transition of trifluorenyl ppy), an interligand energy transfer to the Ir-piq MLCT state presumably happened upon excitation. Imaginably, this energy-transfer process was nearly irreversible considering the large energy difference. Hence, phosphorescence from oligofluorenyl ppy-based MLCT- or LC-dominated states was undetectable at room temperature for $Ir(pTFpy)_2(piq)$ and $Ir(m\text{-}TFppy)_2(piq)$. Nonetheless, at 77 K a trace of emission from these trifluorenyl ppy triplet states was detected, when the emission bands were narrowed and better resolved. A very small emission band was detected at ca. 560 nm, the lifetime of which was ca. 7 μs for $Ir(pTFpy)_2(piq)$ and over 2 ms for $Ir(m\text{-}TFppy)_2(piq)$. These values corresponded in magnitudes to those observed for Ir(pTFpy) and Ir(*m*-TFppy) at the same temperature, suggesting that these minor emission bands were from the MLCT- and LC-dominated triplet states of the oligofluorenyl ppy ligands, respectively.

Upon the attachment of a trifluorenyl group directly to piq unit, complex $Ir(TFpiq)_2$ exhibited a phosphorescence peak at ca. 640 nm, bathochromically shifted by >20 nm relative to that of $Ir(piq)_3$. The quantum efficiency was lowered to 0.44 at room temperature, resulting from both decreased k_r and increased k_{nr} compared to those of $Ir(piq)_3$. The bathochromic shift was apparently due to the π-system extension via conjugative coupling of trifluorenyl with piq. While the increased k_{nr} was a reasonable consequence of the energy gap law, the slightly smaller k_r perhaps implied a slight mixing of the LC state with MLCT transition in trifluorenyl piq.[15]

CONCLUSION

In the current study, the photophysical behaviors of a series of tris-cyclometalated Ir(III) complexes having oligofluorene-substituted ppy and piq ligands were examined at both room temperature and 77 K, in comparison with those of the prototype molecules $Ir(ppy)_3$ and $Ir(piq)_3$. Basically, phosphorescent properties with unique temperature dependence were observed, which were explained by referring to an energy-transfer process between different triplet states in the complexes. The involved states and relevant energy transfer processes in various molecules are schematically depicted in Figure 5. The respective energy levels were estimated based on the emissions of the oligomers at 77 K.[29]

Depending on the ligand structure and anchoring position of the oligomer, complexes displayed three distinct types of photophysical behaviors. In the first case, the two triplet states were of similar energy, but the energy level of the MLCT-dominated state was slightly lower than that of the LC-dominated state. This situation was presented by complexes Ir(DFppy), Ir(TFppy), and Ir(pTFpy). A reversible energy

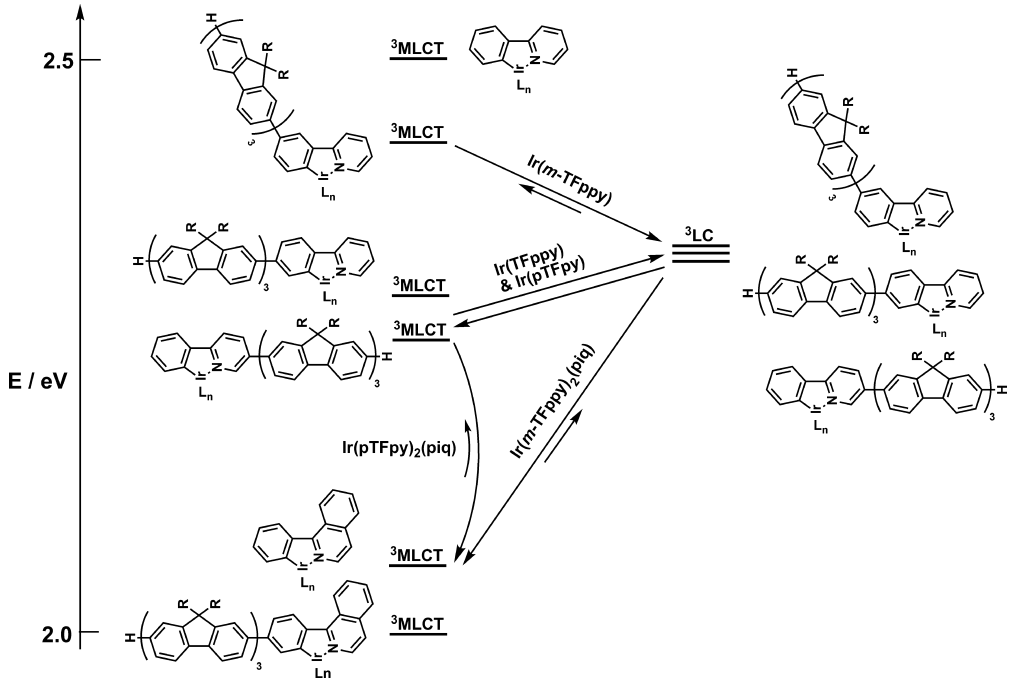

Figure 5. Schematic representation of the energy transfer processes among different triplet states in varied trifluorene-substituted iridium complexes.[29]

dx.doi.org/10.1021/ma2024123 | *Macromolecules* 2012, 45, 133−141

transfer thus took place between the two triplet states with the equilibrium favoring the LC-dominated state. As the temperature decreased, the equilibrium was more strongly biased, giving rise to faster radiative decay and shortened exciton lifetime. The emission wavelength change with temperature confirmed the greater contribution from the MLCT transition in these oligomers. A different energy level arrangement was illustrated by complexes Ir(*m*-DFppy), Ir(*m*-TFppy), in which the LC-dominated state was slightly more stable than MLCT-dominated state. The much longer emission lifetime evidenced the dominant role of the LC transition. At reduced temperature, further prolonged lifetime and bathochromic shift of emission were manifested, resulting from a further shifted equilibrium toward the LC-dominated state. The third scenario emerged when the oligomer complexes incorporated piq as ligand. Since the ^{3}MLCT state of Ir-piq moiety was much lower in energy compared to both MLCT- and LC-dominated states located in oligofluorenyl ppy ligand, the emission naturally originated from the former state. The fact that the photophysical properties of Ir(pTFpy)$_2$(piq) and Ir(*m*-TFppy)$_2$(piq), including the temperature dependence, were comparable to those of Ir(piq)$_3$ served as unambiguous evidence for the similar nature of their lowest triplet states. Additionally, the properties of Ir(pTFpy)$_2$(piq) and Ir(*m*-TFppy)$_2$(piq) also proved that interligand energy transfer occurred efficiently, irrespective of the oligomer substitution position on ppy.

The current investigation demonstrated that, by manipulating the relative energy levels of the ^{3}MLCT and ^{3}LC states through ligand structure modifications, photophysical properties (e.g., lifetime, k_r, etc.) could be tuned in a wide range. By virtue of the rapid intersystem crossing and large spin−orbital coupling constant of the iridium center, optimal quantum yields were achieved in all different cases. Additionally, when large oligomer/polymer chains are covalently tethered to the complex, photophysical properties that are unconventional for small molecule systems may emerge. Our results delineated certain structure−property correlation and provided useful information for rational designs of relevant metal-complex-containing conjugated polymers, while offer the possibility of tailoring the triplet state properties to suit various applications.

EXPERIMENTAL SECTION

General Procedures. UV−vis absorption spectra were recorded on a Hitachi U-4100 spectrophotometer. Photoluminescence spectra were recorded on a Horiba Jobin Yvon FluoroMax-4P spectrofluorometer with a right-angle geometry, using 1 cm quartz cuvettes for solution samples. The emission spectra were corrected for the wavelength dependency of the detector sensitivity and monochromator gratings. For quantum yield measurements, the optical density of the solutions was approximately 0.05−0.1 (at concentrations of ca. 1.0×10^{-6} M) at the excitation wavelength. A quantum yield value of 0.97 for Ir(ppy)$_3$ in toluene[16b] was used as the standard for oligofluorenyl Ir(ppy)$_3$ complex series with an excitation wavelength of 340 nm. A quantum yield of 0.60 for Ir(piq)$_3$ in dichloromethane[28] was used as the standard value for oligofluorenyl Ir(ppy)$_2$(piq) and Ir(ppy)(piq)$_2$ with an excitation wavelength of 350 nm. The solutions used for quantum yield measurements were degassed by bubbling N_2 for 8 min prior to experiments. The precision of quantum yield measurements was ±5% upon repetition. Samples for photoluminescence measurements at 77 K were contained in a quartz tube placed in a Dewar cooled by liquid nitrogen.

Lifetime Measurements. Samples for phosphorescence lifetime measurement were dissolved in MeTHF (distilled from CaH_2) or toluene (purified by Mbraun SPS-800 solvent purification system) at similar concentrations for quantum yield measurements. Samples were degassed by conducting three freeze−pump−thaw cycles before the cuvettes were sealed under vacuum. Lifetimes shorter than 20 μs were measured with time-correlated single-photon counting using a Horiba Jobin Yvon FluoroHub-B instrument and FluoroMax-4P spectrofluorometer and NanoLED of 339 or 369 nm as the excitation source. The full width at half-maximum (fwhm) of the instrument response function (IRF) obtained by an aqueous solution of Ludox colloidal silica was typically ∼1 ns in our system. Phosphorescence lifetimes were fitted with single-exponential decay functions without deconvolution. Single-exponential fits were performed using Horiba Jobin Yvon DAS6 software. Lifetimes longer than 20 μs were measured with FluoroMax-4P spectrofluorometer with program pulsed Xe lamp as the excitation source. fwhm of the Xe lamp pulse was typically ∼3 μs. Phosphorescence lifetime was fitted with single-exponential decay functions without deconvolution. Single-exponential fits were performed using the Origin software.

ASSOCIATED CONTENT

Supporting Information

Synthetic procedures, additional absorption and emission spectra, and DFT calculated molecular orbitals. This material is available free of charge via the Internet at http://pubs.acs.org.

AUTHOR INFORMATION

Corresponding Author

*E-mail: dhzhao@pku.edu.cn.

ACKNOWLEDGMENTS

This work was supported by the National Natural Science Foundation of China (Projects 51073002 and 21174004) and the Fok Ying-Tung Educational Foundation (No. 114008).

REFERENCES

(1) Ulbricht, C.; Beyer, B.; Friebe, C.; Winter, A.; Schubert, U. S. *Adv. Mater.* **2009**, *21*, 4418.

(2) (a) Carlise, J. R.; Wang, X.-Y.; Weck, M. *Macromolecules* **2005**, *38*, 9000. (b) Evans, N. R.; Devi, L. S.; Mak, C. S. K.; Watkins, S. E.; Pascu, S. I.; Köhler, A.; Friend, R. H.; Williams, C. K.; Holmes, A. B. *J. Am. Chem. Soc.* **2006**, *128*, 6647. (c) Liang, B.; Wang, L.; Xu, Y.; Shi, H.; Cao, Y. *Adv. Funct. Mater.* **2007**, *17*, 3580. (d) Haldi, A.; Kimyonok, A.; Domercq, B.; Hayden, L. E.; Jones, S. C.; Marder, S. R.; Weck, M.; Kippelen, B. *Adv. Funct. Mater.* **2008**, *18*, 3056. (e) Powell, A. B.; Bielawski, C. W.; Cowley, A. H. *J. Am. Chem. Soc.* **2010**, *132*, 10184. (f) Ma, Z.; Ding, J.; Zhang, B.; Mei, C.; Cheng, Y.; Xie, Z.; Wang, L.; Jing, X.; Wang, F. *Adv. Funct. Mater.* **2010**, *20*, 138. (g) Lai, W.-Y.; Levell, J. W.; Jackson, A. C.; Lo, S.-C.; Bernhardt, P. V.; Samuel, I. D. W.; Burn, P. L. *Macromolecules* **2010**, *43*, 6986.

(3) (a) Thompson, M. E.; Djurovich, P. I.; Barlow, S.; Marder, S. R. In *Comprehensive Organometallic Chemistry*; O'Hare, D., Ed.; Elsevier: Oxford, 2007; Vol. *12*, pp 101−194. (b) *Highly Efficient OLEDs with Phosphorescent Materials*; Yersin, H., Ed.; Wiley-VCH: Berlin, 2007. (c) Chou, P. T.; Chi, Y. *Chem.—Eur. J.* **2007**, *13*, 380. (d) You, Y.; Park, S. Y. *Dalton Trans.* **2009**, 1267. (e) Wong, W.-Y.; Ho, C.-L. *J. Mater. Chem.* **2009**, *19*, 4457. (f) Kamtekar, K. T.; Monkman, A. P.; Bryce, M. R. *Adv. Mater.* **2010**, *22*, 572.

(4) (a) Sax, S.; Fisslthaler, E.; Kappaun, S.; Konrad, C.; Waich, K.; Mayr, T.; Slugovc, C.; Klimant, I.; List, E. J. W. *Adv. Mater.* **2009**, *21*, 3483. (b) Zhao, Q.; Li, F.; Huang, C. *Chem. Soc. Rev.* **2010**, *39*, 3007. (c) Lo, K. K.-W.; Li, S. P.-Y.; Zhang, K. Y. *New J. Chem.* **2011**, *35*, 265.

(5) (a) Lo, K. K.-W.; Tsang, K. H.-K.; Sze, K.-S.; Chung, C.-K.; Lee, T. K.-M.; Zhang, K. Y.; Hui, W.-K.; Li, C.-K.; Lau, J. S.-Y.; Ng, D. C.-M.; Zhu, N. *Coord. Chem. Rev.* **2007**, *251*, 2292. (b) Fernández-Moreira, V.; Thorp-Greenwood, F. L.; Coogan, M. P. *Chem. Commun.* **2010**, *46*, 186. (c) Zhao, Q.; Huang, C.; Li, F. *Chem. Soc. Rev.* **2011**, *40*, 2508.

(6) Schulz, G. L.; Holdcroft, S. *Chem. Mater.* **2008**, *20*, 5351.

(7) (a) Baldo, M. A.; O'Brien, D. F.; You, Y.; Shoustikov, A.; Sibley, S.; Thompson, M. E.; Forrest, S. R. *Nature* **1998**, *395*, 151. (b) O'Brien, D. F.; Baldo, M. A.; Thompson, M. E.; Forrest, S. R. *Appl. Phys. Lett.* **1999**, *74*, 442. (c) Adachi, C.; Baldo, M. A.; Thompson, M. E.; Forrest, S. R. *J. Appl. Phys.* **2001**, *90*, 5048.

(8) (a) Tamayo, A. B.; Alleyne, B. D.; Djurovich, P. I.; Lamansky, S.; Tsyba, I.; Ho, N. N.; Bau, R.; Thompson, M. E. *J. Am. Chem. Soc.* **2003**, *125*, 7377. (b) Sajoto, T.; Djurovich, P. I.; Tamayo, A.; Yousufuddin, M.; Bau, R.; Thompson, M. E. *Inorg. Chem.* **2005**, *44*, 7992. (c) Zhou, G.; Wong, W.-Y.; Yao, B.; Xie, Z.; Wang, L. *Angew. Chem., Int. Ed.* **2007**, *46*, 1149. (d) Ho, C.-L.; Wong, W.-Y.; Gao, Z.-Q.; Chen, C.-H.; Cheah, K.-W.; Yao, B.; Xie, Z.; Wang, Q.; Ma, D.; Wang, L.; Yu, X.-M.; Kwok, H.-S.; Lin, Z. *Adv. Funct. Mater.* **2008**, *18*, 319. (e) Lee, S. J.; Park, K.-M.; Yang, K.; Kang, Y. *Inorg. Chem.* **2009**, *48*, 1030.

(9) (a) Huynh, L.; Wang, Z.; Yang, J.; Stoeva, V.; Lough, A.; Manners, I.; Winnik, M. A. *Chem. Mater.* **2005**, *17*, 4765. (b) Schmittel, M.; Lin, H. *Inorg. Chem.* **2007**, *46*, 9139. (c) Liu, Z.; Bian, Z.; Bian, J.; Li, Z.; Nie, D.; Huang, C. *Inorg. Chem.* **2008**, *47*, 8025. (d) Mak, C. S. K.; Pentlehner, D.; Stich, M.; Wolfbeis, O. S.; Chan, W. K.; Yersin, H. *Chem. Mater.* **2009**, *21*, 2173. (e) Ji, S.; Wu, W.; Wu, W.; Song, P.; Han, K.; Wang, Z.; Liu, S.; Guo, H.; Zhao, J. *J. Mater. Chem.* **2010**, *20*, 1953.

(10) Lo, K. K.-W.; Hui, W.-K.; Chung, C.-K.; Tsang, K. H.-K.; Ng, D. C.-M.; Zhu, N.; Cheung, K.-K. *Coord. Chem. Rev.* **2005**, *249*, 1434.

(11) (a) Shao, Y.; Yang, Y. *Adv. Mater.* **2005**, *17*, 2841. (b) Wong, W.-Y.; Wang, X.-Z.; He, Z.; Djurišić, A. B.; Yip, C.-T.; Cheung, K.-Y.; Wang, H.; Mak, C. S. K.; Chan, W.-K. *Nature Mater.* **2007**, *6*, 521. (c) Li, Y.; Mastria, R.; Li, K.; Fiore, A.; Wang, Y.; Cingolani, R.; Manna, L.; Gigli, G. *Appl. Phys. Lett.* **2009**, *95*, 043101. (d) Ning, Z.; Zhang, Q.; Wu, W.; Tian, H. *J. Organomet. Chem.* **2009**, *694*, 2705. (e) Clem, T. A.; Kavulak, D. F. J.; Westling, E. J.; Fréchet, J. M. J. *Chem. Mater.* **2010**, *22*, 1977. (f) Wong, W.-Y.; Ho, C.- L. *Acc. Chem. Res.* **2010**, *43*, 1246.

(12) (a) Yersin, H.; Donges, D. *Top. Curr. Chem.* **2001**, *214*, 81. (b) Yam, V. W.-W. *Acc. Chem. Res.* **2002**, *35*, 555. (c) Baranoff, E.; Scopelliti, I. J. R.; Solari, E.; Grätzel, M.; Nazeeruddin, M. K. *Dalton Trans.* **2011**, *40*, 6860.

(13) For recent examples, see: (a) Zhao, Q.; Liu, S.; Li, F.; Yi, T.; Huang, C. *Dalton Trans.* **2008**, 3836. (b) Chiu, Y.-C.; Chi, Y.; Hung, J.-Y.; Cheng, Y.-M.; Yu, Y.-C.; Chung, M.-W.; Lee, G.-H.; Chou, P.-T.; Chen, C.-C.; Wu, C.-C.; Hsieh, H.-Y. *ACS Appl. Mater. Interfaces* **2009**, *1*, 433. (c) Xie, Z.; Ma, L.; deKrafft, K. E.; Jin, A.; Lin, W. *J. Am. Chem. Soc.* **2010**, *132*, 922. (d) Palmer, J. H.; Durrell, A. C.; Gross, Z.; Winkler, J. R.; Gray, H. B. *J. Am. Chem. Soc.* **2010**, *132*, 9230–9231. (e) Chen, Z.-Q.; Bian, Z.-Q.; Huang, C.-H. *Adv. Mater.* **2010**, *22*, 1534. (f) Costa, R. D.; Orti, E.; Bolink, H. J.; Graber, S.; Housecroft, C. E.; Constable, E. C. *J. Am. Chem. Soc.* **2010**, *132*, 5978. (g) Tan, W.; Zhou, J.; Li, F.; Yi, T.; Tian, H. *Chem.—Asian J.* **2011**, *6*, 1263.

(14) Flamigni, L.; Barbieri, A.; Sabatini, C.; Ventura, B.; Barigelletti, F. *Top. Curr. Chem.* **2007**, *281*, 143.

(15) (a) Tsuboyama, A.; Iwawaki, H.; Furugori, M.; Mukaide, T.; Kamatani, J.; Igawa, S.; Moriyama, T.; Miura, S.; Takiguchi, T.; Okada, S.; Hoshino, M.; Ueno, K. *J. Am. Chem. Soc.* **2003**, *125*, 12971. (b) Okada, S.; Okinaka, K.; Iwawaki, H.; Furugori, M.; Hashimoto, M.; Mukaide, T.; Kamatani, J.; Igawa, S.; Tsuboyama, A.; Takiguchi, T.; Ueno, K. *Dalton Trans.* **2005**, 1583.

(16) (a) Lamansky, S.; Djurovich, P. I.; Mruphy, D.; Abdel-Razzaq, F.; Lee, H.-E.; Adachi, C.; Burrows, P. E.; Forrest, S. R.; Thompson, M. E. *J. Am. Chem. Soc.* **2001**, *123*, 4304. (b) Sajoto, T.; Djurovich, P. I.; Tamayo, A. B.; Oxgaard, J.; Goddard, W. A. III; Thompson, M. E. *J. Am. Chem. Soc.* **2009**, *131*, 9813.

(17) King, K. A.; Spellane, P. J.; Watts, R. J. *J. Am. Chem. Soc.* **1985**, *107*, 1431.

(18) (a) Glusac, K. D.; Jiang, S. J.; Schanze, K. S. *Chem Commun.* **2002**, 2504. (b) Cunningham, G. B.; Li, T.; Liu, S.; Schanze, K. S. *J. Phys. Chem. B* **2003**, *107*, 12569.

(19) (a) McClenaghan, N. D.; Leydet, Y.; Maubert, B.; Indelli, M. T.; Campagna, S. *Coord. Chem. Rev.* **2005**, *249*, 1336. (b) Lavie-Cambot, A.; Lincheneau, C.; Cantuel, M.; Leydet, Y.; McClenaghan, N. D. *Chem. Soc. Rev.* **2010**, *39*, 506.

(20) Whited, M. T.; Djurovich, P. I.; Robert, S. T.; Durrell, A. C.; Schlenker, C. W.; Bradforth, S. E.; Thompson, M. E. *J. Am. Chem. Soc.* **2011**, *133*, 88.

(21) (a) Manca, P.; Pilo, M. I.; Sanna, G.; Zucca, A.; Bergamini, G.; Ceroni, P. *Chem. Commun.* **2011**, *47*, 3413. (b) Ceroni, P. *Chem.—Eur. J.* **2011**, *17*, 9560. (c) Ji, S.; Wu, W.; Wu, W.; Guo, H.; Zhao, J. *Angew. Chem., Int. Ed.* **2011**, *50*, 1626.

(22) (a) Sandee, A. J.; Williams, C. K.; Evans, N. R.; Davies, J. E.; Boothby, C. E.; Köhler, A.; Friend, R. H.; Holmes, A. B. *J. Am. Chem. Soc.* **2004**, *126*, 7041. (b) Tavasli, M.; Bettington, S.; Bryce, M. R.; Al Attar, H. A.; Dias, F. B.; King, S.; Monkman, A. P. *J. Mater. Chem.* **2005**, *15*, 4963–4970. (c) Jiang, J. X.; Xu, Y. H.; Yang, W.; Guan, R.; Liu, Z. Q.; Zhen, H. Y.; Cao, Y. *Adv. Mater.* **2006**, *18*, 1769. (d) Schulz, G. L.; Chen, X.; Chen, S.-A.; Holdcroft, S. *Macromolecules* **2006**, *39*, 9157.

(23) (a) Qin, T.; Ding, J.; Wang, L.; Baumgarten, M.; Zhou, G.; Mullen, K. *J. Am. Chem. Soc.* **2009**, *131*, 14329. (b) Chen, L.; Ding, J.; Cheng, Y.; Xie, Z.; Wang, L.; Jing, X.; Wang, F. *Chem.—Asian J.* **2011**, *6*, 1372.

(24) Kozhevnikov, D. N.; Kozhenikov, V. N.; Shafikov, M. Z.; Prokhorov, A. M.; Bruce, D. W.; Williams, J. A. G. *Inorg. Chem.* **2010**, *50*, 3804.

(25) Yan, Q.; Yue, K.; Yu, C.; Zhao, D. *Macromolecules* **2010**, *43*, 8479.

(26) (a) Tanaka, I.; Tabata, Y.; Tokito, S. *Jpn. J. Appl. Phys., Part 2* **2004**, *43*, L1601. (b) Kawamura, Y.; Goushi, K.; Brooks, J.; Brown, J. J.; Sasabe, H.; Adachi, C. *Appl. Phys. Lett.* **2005**, *86*, 071104. (c) Holzer, W.; Penzkofer, A.; Tsuboi, T. *Chem. Phys.* **2005**, *308*, 93. (d) Endo, A.; Suzuki, K.; Yoshihara, T.; Tobita, S.; Yahiro, M.; Adachi, C. *Chem. Phys. Lett.* **2008**, *460*, 155.

(27) It should be noted that in such organometallic complexes it is unlikely that electronic transitions of sheer MLCT or LC properties could exist exclusively. The "MLCT-dominated state" discussed herein refers to the excited state featuring a prevailing MLCT transition, but it usually incorporates certain contribution from the LC $\pi-\pi^*$ transition; similarly, the "LC-dominated state" is used to describe an excited state with a predominant LC $\pi-\pi^*$ transition property, which inevitably contains minor MLCT component. Such a complex nature of electronic transitions comprising imbalanced contributions from two types of processes was supported by DFT-calculated molecular orbitals, which showed simultaneous contributions, with differed composing ratios, from both d-orbital of the transition metal and π-orbital of the oligofluorenyl moiety (see the Supporting Information for calculated molecular orbitals).

(28) Huang, Y.-T.; Chuang, T.-H.; Shu, Y.-L.; Kuo, Y.-C.; Wu, P.-L.; Yang, C.-H.; Sun, I.-W. *Organometallics* **2005**, *24*, 6230.

(29) Estimated energies of oligofluorenyl-ppy based LC states from currently studied complexes were consistent with data of related structures from references: Hertel, D.; Setayesh, S.; Nothofer, H.-G.; Scherf, U.; Müllen, K.; Bässler, H. *Adv. Mater.* **2001**, *13*, 65 , and ref 16b.

Macromolecules

ARTICLE

pubs.acs.org/Macromolecules

Self-Healing Polymer Films Based on Thiol−Disulfide Exchange Reactions and Self-Healing Kinetics Measured Using Atomic Force Microscopy

Jeong Ae Yoon,[†] Jun Kamada,[†,‡] Kaloian Koynov,[§] Jake Mohin,[†] Renaud Nicolaÿ,[†] Yaozhong Zhang,[†] Anna C. Balazs,[⊥] Tomasz Kowalewski,[*,†] and Krzysztof Matyjaszewski[*,†]

[†]Department of Chemistry, Carnegie Mellon University, 4400 Fifth Avenue, Pittsburgh, Pennsylvania 15213, United States

[‡]Material Science Laboratory, Mitsui Chemicals, Inc., 580-32 Nagaura, Sodegaura, Chiba 299-0265, Japan

[§]Max Planck Institutes for Polymer Research, Ackermannweg 10, Mainz 55128, Germany

[⊥]Chemical Engineering Department, University of Pittsburgh, Pittsburgh, Pennsylvania 15213, United States

Supporting Information

ABSTRACT: Self-healing polymeric materials with branched architectures and reversible cross-linking functionalities at the periphery of branches were synthesized by atom transfer radical polymerization (ATRP). Poly(*n*-butyl acrylate) grafted star polymers were prepared by chain extension ATRP from cross-linked cores comprised of poly(ethylene glycol diacrylate). These polymers were further used as macroinitiators for the consecutive chain extension ATRP of bis(2-methacryloyloxyethyl disulfide) (DSDMA), in which way disulfide reversible cross-links (SS) were introduced at the branch peripheries. The SS cross-linked polymers were then cleaved under reducing conditions to form thiol (SH)-functionalized soluble star polymers. The SH-functionalized star polymer solutions were deposited on silicon wafer substrates and converted to insoluble SS re-cross-linked films via oxidation. The self-healing of prepared polymer films was studied by continuous atomic force microscopy (AFM) imaging of cuts micromachined with the AFM tip and by optical microscopy. The re-cross-linked star polymer (X3) showed a rapid spontaneous self-healing behavior, with the extent of healing dependent on the initial film thickness and the width of the cut. The self-healing behavior observed for this sample was attributed to the regeneration of SS bonds via thiol−disulfide exchange reactions. This study demonstrated the suitability of grafted multiarm polymer architectures as building blocks of self-healing polymeric materials and pointed to the importance of low intrinsic viscosity of material and high accessibility of functional groups responsible for healing.

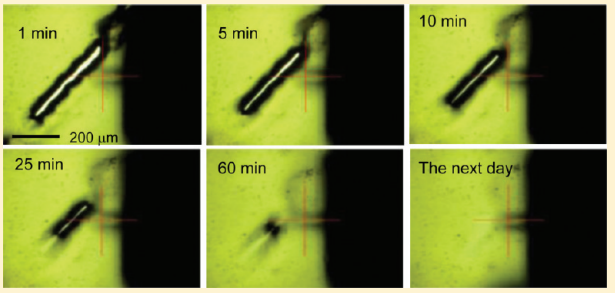

INTRODUCTION

Self-healing polymeric materials[1−9] have attracted attention due to their built-in ability to repair physical damage, effectively preventing catastrophic failure and extending the material lifetime. The physical damage that needs to be healed can include fracture due to mechanical (viscoelastic or elastic) deformation, chemical corrosion, and degradation by irradiation. Studies on self-healing materials focus on the dependence of their ability to heal on the extent of damage at both the micro- and mesoscale. Pre-emptive self-healing processes on such scales can prevent the development of catastrophic damage[10] by suppressing the escalation of chemical bonds dissociation. Such escalation normally leads to the formation of microcracks or microcavities, eventually causing the macroscopic damage, which would require welding or relamination to repair. Hence, many of developed self-healing systems focus on molecular level interactions regardless of whether the study involves covalent or noncovalent bonds. In practice, reversible interactions are of particular interest due to their capability to heal repeated damage at the same position. Examples of reversible interactions include dynamic covalent bonds,[11−14] metal−ligand interactions,[15] multiple hydrogel bonding,[7] ionic interaction,[16] and $\pi-\pi$ interactions.[17,18] However, many of these systems are still limited in practice due to the requirement for external stimuli, e.g., heat,[19,20] UV irradiation,[3,13] or acid/base,[21] to trigger the healing response.

Herein, we present a new approach to self-healing polymeric materials that is based on reversible covalent cross-linking through thiol/disulfide redox dynamic exchange reactions. While the redox reaction can be accelerated by the presence of catalysts,[22−25] in principle, it can proceed under ambient conditions without the need of any external triggers. Furthermore, mechanical breakage of a disulfide (SS) bond generates thiyl

Received: July 3, 2011
Revised: October 6, 2011
Published: December 16, 2011

Scheme 1. Synthesis of SS-Functionalized Star Polymers (SS)

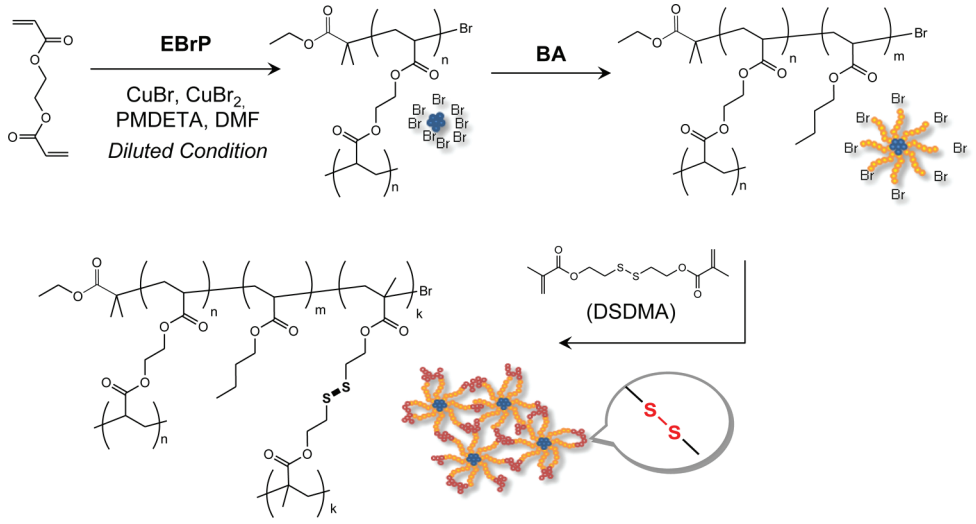

radicals, which rapidly exchange with other SS bonds. Through this process, some fraction of the energy accumulated by the initial elastic deformation can be released, thereby preventing catastrophic fracture.

In addition, we consider which polymeric architecture would be best-suited for self-healing materials. Since bond formation/re-formation essentially needs intimate contact of materials, the flow properties of materials should be seriously considered, so that the surfaces of the damaged materials can readily approach a distance close enough for bond re-formation. Taking these requirements into consideration, polymers with a branched architecture,[26−28] which are characterized by low intrinsic viscosity, should be more suited than a linear counterpart with a similar molecular weight and were selected for this study. The functional groups responsible for healing were introduced into the periphery of a branched polymer, to ensure their accessibility for intermolecular interactions and thus facilitate a rapid self-healing process.

All the mentioned concepts had been computationally demonstrated in our earlier work.[29] In this series of simulations, it was demonstrated that a presence of a fraction of labile bonds, such as disulfide bonds, can improve the mechanical properties of cross-linked polymeric networks. Keeping in mind design principles outlined above, polymer networks studied herein were assembled from multiarm star polymers containing thiol (SH) groups at the arm periphery and prepared by atom transfer radical polymerization (ATRP).[30−33] Such synthesized star polymers were cast from solution to form films in which the peripheral SH groups were cross-linked to SS bonds via oxidation. The self-healing process was then studied by inducing mechanical damage through micromachining with the atomic force microscope (AFM) tip, followed by imaging of the repair process using time-lapse AFM or optical microscopy. AFM has been extensively used in the field of micro/nano fabrication with the precise control of a feature size and position.[34] Examples of techniques developed for this purpose include mechanical scratching (nanoshaving),[35−39] dip-pen lithography,[40−45] nanografting,[46−49] electrochemical AFM nanolithography,[50−52] and thermal AFM nanolithography.[53] Among these methods, the mechanical scratching technique can be easily applied to a simple generation of cuts with dimensions ranging from nanometers to micrometers. This method does not need the use of a special apparatus, such as a conductive tip and a conductive sample stage, and thus can be applied to a wide range of materials, e.g., metals, semiconductors, polymers, etc. In addition, we have assessed the mechanical rigidity of the healed area using HarmoniX tapping mode AFM.[54] The time-resolved tip−sample force measured in this mode along the topography is converted to the corresponding force−distance curve and, in turn, to Young's modulus. The values of Young's modulus measured by AFM were compared with the values obtained with microindentation experiments and with the shear moduli from dynamic mechanical analysis (DMA). Results of these observations and measurements provided the basis for the proposed mechanism of self-healing processes observed in the studied materials.

EXPERIMENTAL SECTION

Experimental details are described in the Supporting Information.

RESULTS AND DISCUSSION

Synthesis of Polymers. SS arm cross-linked, star branched polymers were synthesized by ATRP, as summarized in Scheme 1. The star polymers were synthesized using the core-first approach, and in a subsequent step, the arms were macroscopically cross-linked by chain extension with DSDMA. The detailed descriptions of the synthesis of this star polymer can be found in our recent publication.[55] On average, three SS cross-links were incorporated into each arm of the star, and the number-average number of arms per star (N_{arm}) was equal to 23. The N_{arm} value was calculated based on the equation $N_{arm} = M_{w,star,MALLS}/M_{w,arm,RI}$, where $M_{w,star,MALLS}$ is the absolute molecular weight of the star polymer and $M_{w,arm,RI}$ is the weight-average molecular weight of the linear arm chains. The peripheral SS cross-linkages were subsequently cleaved to form a soluble SH end-functionalized star polymer (SH6, Scheme 2). Notice that after reduction one SS group is converted into two SH groups; i.e., on average six SH groups were positioned at the end of each arm. Solutions of SH6

dx.doi.org/10.1021/ma2015134 |Macromolecules 2012, 45, 142–149

Scheme 2. Reduction and Oxidation of SH/SS-Functionalized Star Polymers and Preparation of Permanently Cross-Linked Star Polymers as a Control

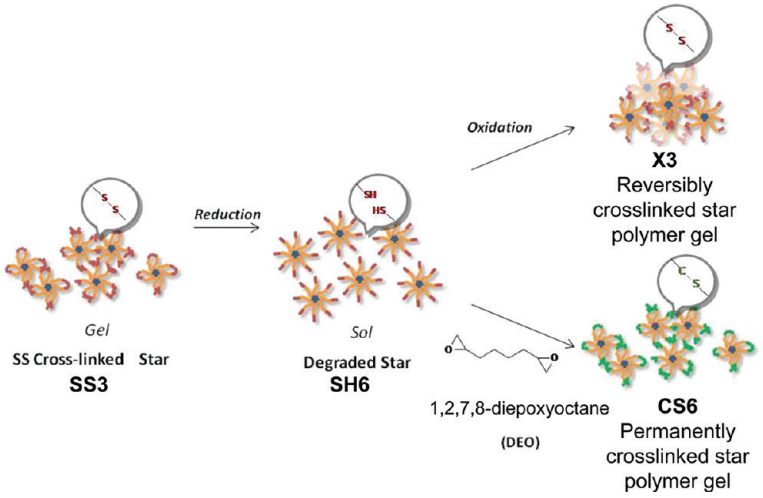

were used to form uniform polymer films by various coating methods.

Cross-Linked Film Formation. Solutions (0.1−10% w/v in THF) of the SH-functionalized polymers (SH6) were prepared and deposited on pieces of silicon wafers to form thin polymer films. In order to prepare a thicker free-standing film, a solution containing a higher concentration of the polymer, ca. 20−50% w/v in $CHCl_3$/THF (8/2), was deposited within a glass vial and dried under vacuum at 40 °C for 2 h. The films were oxidatively cross-linked under the presence of an oxidation catalyst, e.g., I_2 or $FeCl_3$, and became insoluble in solvents such as $CHCl_3$ or THF used for rinsing. The reduction/reoxidation process is schematically illustrated in Scheme 2. The final re-cross-linked polymers are referred to as X3. The re-formation of SS bonds upon reoxidation was confirmed by Raman spectroscopy, which is also discussed in our recent publication.[55] In that study, the restoration of the ν_{C-SS} band at 642 cm^{-1} and ν_{S-S} band at 513 cm^{-1} was evident and was attributed to the reformation of SS bonds in response to the redox conditions.

A permanently cross-linked star polymer with *inert* C−S bonds was prepared as a control sample by the reaction of SH6 and 1,2,7,8-diepoxyoctane under basic conditions. This permanently cross-linked gel is referred to as CS6 in subsequent discussion. Since both X3 and CS6 gels were based on the same precursor SH-functionalized star polymer, SH6, they are expected to have similar gel structures and cross-linking densities. Generally, a swelling ratio is a useful parameter to characterize a gel structure and cross-linking density. The swelling ratio of CS6 in THF was 7.3 while that of X3 was 6.5, indicating that these gels have comparable cross-linking densities.

Self-Healing Behavior of Reversibly Cross-Linked Star Polymers. Studies of the self-healing behavior of the reversibly cross-linked star polymer gel films (X3) were conducted using AFM. AFM is an excellent tool to induce damage on a surface and to observe topographic changes after damage on the nanometer to micrometer scale,[56] which is the focus of self-healing systems. Furthermore, recent development in AFM techniques allows precise characterization of mechanical properties of surfaces, which is helpful in assessing the degree of healing. In our study, surface scratches ranging from nanometers to micrometers in size were made in a controlled way using commercial silicon probes. The damage was induced in two different modes. In the first mode, an interleave tapping mode scanning was used with a given "negative lift height". The interleave scan is a secondary scan following a normal topography scan with the distance from the surface maintained at a given height. In this study, the lift height was set at −50 to −300 nm from the film surface, which forced the probe to tap at a very close proximity to the surface and eventually penetrate through the surface, since the probe free oscillation amplitudes were set at ca. 40 nm. Through this "chiseling" process, cuts with the depths ranging from 5 to 100 nm could be prepared. This method is advantageous in that the damaging process and the subsequent observation by continuous imaging could be done consecutively within the same AFM run without changing the cantilever or imaging mode. However, this method could not be used for making "deep cuts" with depths of the order of few hundred nanometers to micrometers. For those cases, the microscratching method using a contact mode scanning under large tip deflection conditions was used. Using this method, deep cuts with lengths up to several micrometers length were easily prepared. Also, the damage width could be easily controlled in this manner simply by applying different scan aspect ratios. However, this method had a limitation for a detection of very rapid healing process. Since the cantilever used for microscratching was relatively stiff, with a nominal spring constant k = 42 N/m, contact mode imaging operation tended to further damage the sample, and the image quality was low. Therefore, the AFM operation mode had to be changed from contact mode to tapping mode for observation of the self-healing process, which consumed a few minutes after completing the sample damaging scans.

Initially, a cut with 0.4 μm width and 17 nm depth was inflicted on a 50 nm thick X3 film using the negative lift interleave mode scanning. The employed lift height and scan rate were set at −300 nm and 80 μm/s, respectively. After making the cut, evolution of the appearance of the cut region was monitored by continuous tapping mode AFM imaging. Height mode AFM images collected in such a way are shown in Figure 1a,b. The damaged area decreased in size within minutes, and after 12 min the depth of the damage had dramatically decreased to 5−10 nm,

dx.doi.org/10.1021/ma2015134 |*Macromolecules* 2012, 45, 142–149

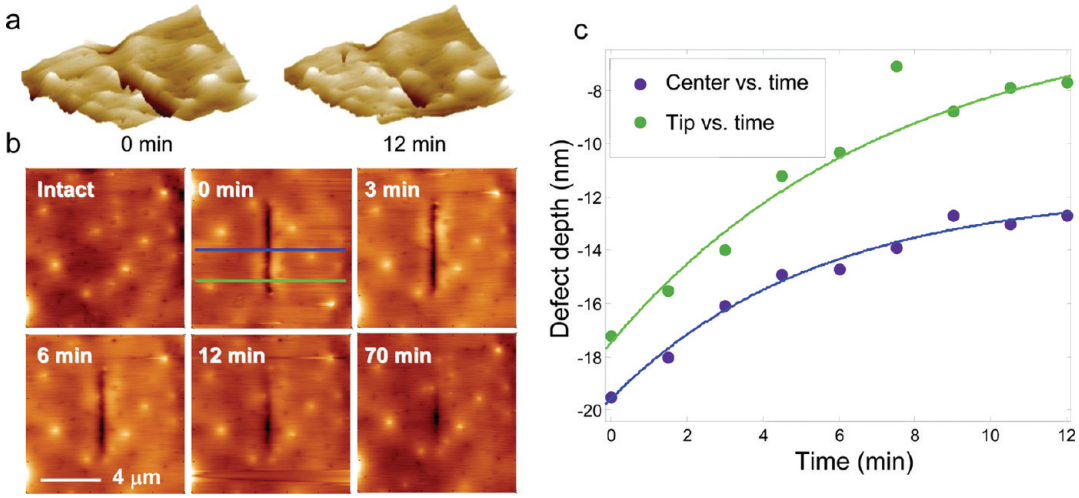

Figure 1. Time-dependent change of height mode AFM image for the cut on the surface of X3 film: (a) 3D images, (b) 2D height mode images, and (c) evolution of damage depth for 12 min measured at two positions. The surface of film is referenced to zero for the *Y*-axis. The "center" position describes the center of the damage and the "tip" position, 2 μm away from the "center".

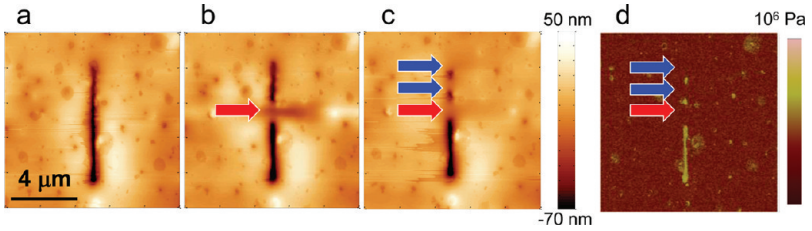

Figure 2. Healing response of X3 film accelerated by AFM tip stroke with contact mode scanning: (a) original cut, (b) after the first series of strokes at the position marked by a red arrow (+0.5 V), (c) after the second series of strokes at two positions marked by of blue arrows (0 V), and (d) HarmoniX mode modulus map in a logarithmic scale. Brighter color represents higher modulus. The brightest regions in the damaged area correspond to high Young's modulus of silicon wafer exposed at the bottom of the deep cut.

depending on position (Figure 1c). This healing response occurred at room temperature, and no external stimulus was required for it to occur. The temporal change of cut depth was measured at two positions: the center of the cut (blue cross-line) and the "tip" (green cross-line), which is defined as a point 2 μm away from the center position. While it is evident that the damage at the center position was not fully healed, the damage at the edge position was totally healed after 70 min (Figure 1b). Detailed analysis of the healing behavior shows that the healing response could be driven by the bond re-formation initiated from the bottom of the cut and at the edge of the cut, where the cut surfaces are accessible to each other. This assumption was validated from the following experiment done with a penetrating cut.

A *penetrating* cut with 0.3 μm width was made in the same 50 nm thick X3 film using the contact mode microscratching method. In contrast to the case with the shallow scratch damage discussed above, the damage remained unrepaired even after 3 h. This indicates that the stiffness of the cross-linked film of X3 was sufficiently high to retain the shape without flowing, thus preventing the intimate contact of two damaged surfaces. It also demonstrates that such contact is essential for the healing process. Subsequently, in order to bring about contact between the cut surfaces, the damaged area was gently stroked by the AFM tip under contact mode scanning in the direction perpendicular to the cut. Parts b and c of Figure 2 show the results obtained after two series of strokes, with deflections respectively equal to +0.5 and 0 V (uncalibrated optical detector signal). The more positive deflection indicates a stronger applied force. Immediately thereafter, it was observed that only the stroked area became as smooth as the original film. In this situation, the motion of AFM tip could make the cut surfaces accessible to each other and enhanced the healing response. The mechanical properties of the resulting film were studied in order to analyze the extent of healing using HarmoniX tapping mode modulus mapping. Results of this measurement are shown as a false color Young's modulus map shown in Figure 2d. As evident from this image, the Young's moduli of damaged areas, indicated by arrows, were indistinguishable from the intact area, providing the proof of the potential usefulness of this material for self-healing surfaces. The Young's modulus measured by the HarmoniX analysis was of the order of kPa. This value is far smaller than the shear modulus (5 MPa at 25 °C) measured by DMA[55] but is comparable to Young's modulus values measured by microindentation experiments (20 kPa). A discussion of the procedures involved in mechanical measurements is provided in the following section.

The relationship between the film thickness and healable cut width is an interesting issue when studying the utility of the healing mechanism. A wider penetrating cut, ca. 30 μm wide and 500 μm long, was made on a >15 μm thick X3 film with a razor blade. The film thickness was estimated by observation of the AFM probe traveling distance from a light landing on the surface to a forced contact to the silicon wafer substrate. The film was

dx.doi.org/10.1021/ma2015134 |*Macromolecules* 2012, 45, 142–149

kept under ambient atmosphere, and the damaged area was monitored by an optical microscope of the AFM system (Figure 3). The healing response was clearly observed within a minute. The cut was repaired autonomously from both ends, where the cut surfaces were closest to each other. After 1 h, the cut had almost completely disappeared, and eventually on the next day, the surface had been totally repaired. A similar behavior can be observed in the movie taken with the same film (Supporting Information). In this movie, it is evident that the healing process starts from the ends of the cut, and once the separate cut edges contact, further smoothening follows. These results suggest that thicker films can heal wider cuts because the droop caused by higher surface tension can provide contact between the damage surfaces, which triggers the healing process.

In order to systematically study the effect of cut width on healing, cuts with different widths, i.e., 1.25, 2.5, 5, 10, and 20 μm, were made on the surface of a 1.5 μm thick X3 coating using AFM contact mode microscratching. Since X3 does not freely flow at room temperature, the healing response of X3 was expected to provide information on the width of a cut that could undergo damage repair for a given film thickness. The healing response was monitored for 2 h (Figure 4). While narrower cuts with 1.25 or 2.5 μm width quickly healed within 20 min, the medium width cut (5 μm) was only partially healed. For wider cuts, with 10 and 20 μm widths, the cut widths decreased to ~5 and ~13 μm within the 2 h and even after prolonged observation for a day, further healing process was negligible (Figure SI2 in Supporting Information). From the images shown in Figure 4, it was evident that the material removed from the scratched areas was piled up in the form of lumps around the cuts. These piles served as reservoirs of material that released it back to the cuts and facilitated the healing process.

After careful consideration of the observed healing behavior, a mechanism for the self-healing process was proposed, as schematically shown in Figure 5. When a cut with the width L is made on a film with the thickness h, the film initially flows back to the center of the cut due to the surface tension driven viscoelastic restoration, which is commonly observed for viscoelastic

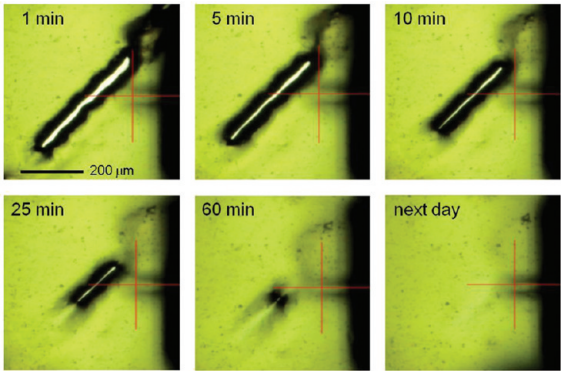

Figure 3. Optical microscope images of the self-healing response of X3 coating for a penetrating cut. The experiment was conducted under ambient condition (film thickness >15 μm).

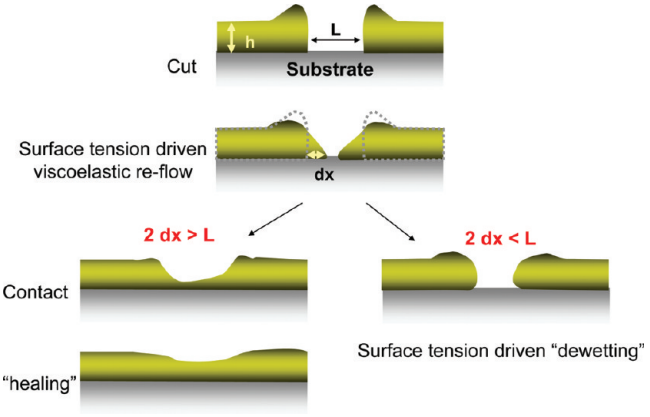

Figure 5. Proposed self-healing process for X3. When 2 dx (the initial flowing-back distance) is larger than L (cut width), self-healing occurs.

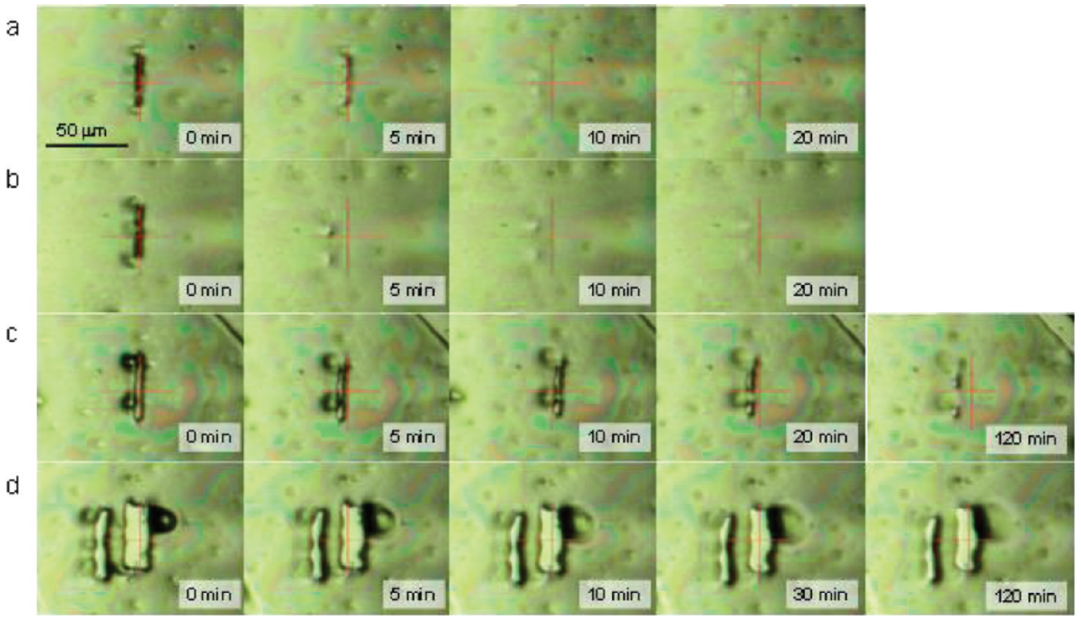

Figure 4. Optical microscope images of the self-healing responses against different width cuts penetrating X3 coating. The initial cut width in parts a, b, c, and d are 1.25, 2, 5, and (10 and 20 μm), respectively. The experiment was conducted under an ambient condition (film thickness: 1.5 μm).

dx.doi.org/10.1021/ma2015134 |*Macromolecules* 2012, 45, 142–149

materials. The travel distance of this reflow is dx for each exposed surface. However, the film cannot flow freely due to its cross-linked nature. When the total travel distance 2 dx is larger than L, the cut surfaces contact each other, and within this state, reactions such as thiol−disulfide exchange reaction, disulfide−disulfide exchange reaction, and reduction of thiols to disulfides can occur. These reactions regenerate chemical bonds between cut edges and eventually heal the damage. Since surface tension is proportional to the exposed surface, i.e., the film thickness, a thicker film can heal a wider cut. This is in fact observed from the rapid healing of a 30 μm wide cut in the thicker film (see Figure 3). In the case where 2 dx is smaller than L, the cut surfaces cannot make contact, and surface tension driven dewetting prevents the healing process from occurring. Figure SI1 shows an example of the case when the two cut surfaces did not make contact after the initial reflow. Re-examination of the cut shown in Figure 2 after 25 days revealed the absence of any healing over this period. It should be stressed that the exchange reactions should be particularly active at two ends of a cut, since these are the regions where the edges remain in contact from the beginning. As a result, it was seen that tip positions healed more quickly, as shown in Figure 1, and the healing proceeded from the tips in a "zip-up" fashion (see Figure 3 and the movie file in the Supporting Information).

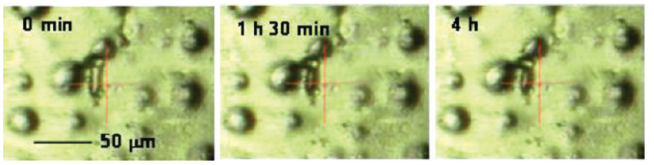

Figure 6. Optical microscope images of the cut imposed on permanently cross-linked control sample CS6 (film thickness ~2 μm).

The role of reversible cross-linking bonds in the self-healing behavior was assessed by comparing damage induced to a control sample containing permanent cross-linking bonds (X3 vs CS6). A cut, with the size of 20 μm × 5 μm ($L \times W$), was made on a 2 μm thick CS6 film by AFM microscratching, and the cut was observed over a period of 4 h, as shown in Figure 6. While a 5 μm width cut on X3 underwent a significant healing over a shorter period, 2 h, the cut made on a film of CS6 only decreased the length from 20 to 17 μm over a period of 4 h. The observed decrease of the cut dimension occurred purely by the viscoelastic restoration. However, unlike the X3, the control sample could not undergo self-healing, i.e., the regeneration of chemical bonds. Therefore, there was no further change during prolonged observation (Figures SI2c and SI3).

Characterization of Mechanical Properties of Star Polymer Based Samples. In an attempt to judge if the inability of permanently cross-linked CS6 material to self-heal in comparison with the reversibly cross-linked X3 could be caused by major differences in mechanical properties of both materials, the samples were characterized using dynamic mechanical analysis (DMA), compression testing, and microindentation. DMA measurements were performed using ARES rheometer (Rheometric Scientific) in parallel plate shear geometry with constant deformation frequency of 10 rad/s and temperature varied at 2 °C/min from −80 to 180 °C. The results are compared with the precursors

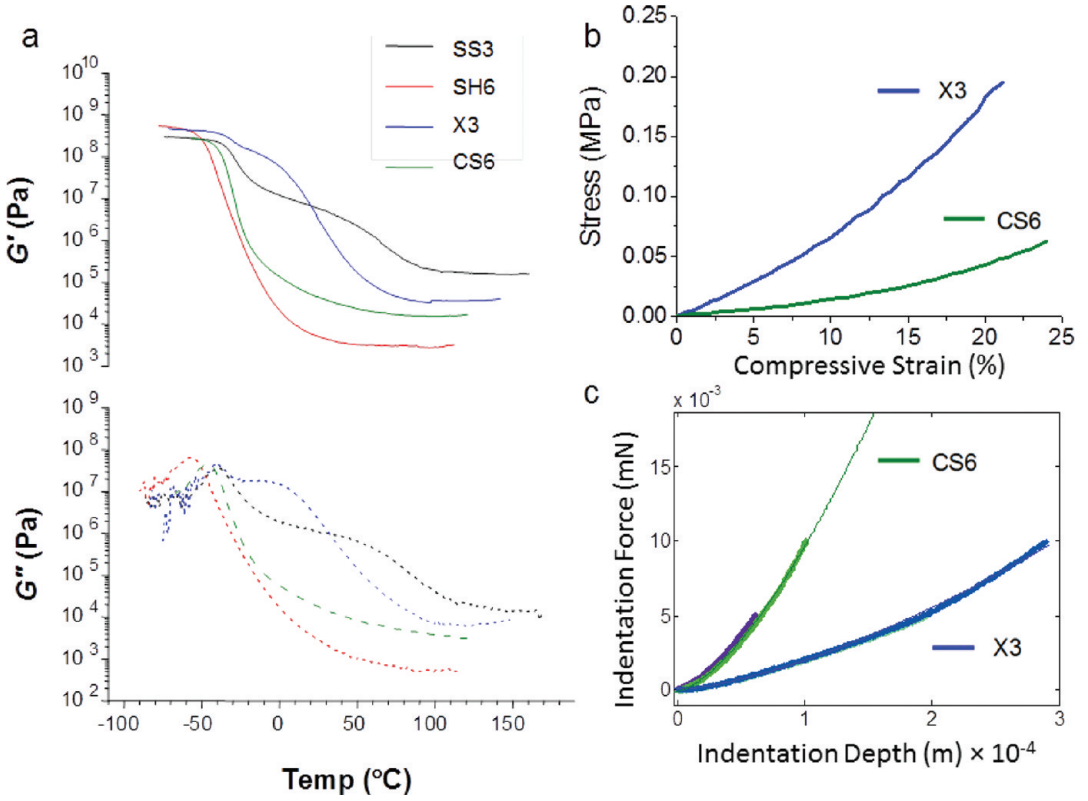

Figure 7. Mechanical measurements. (a) Temperature dependence of the storage modulus (G') and the loss modulus (G'') of SH/SS-functionalized star polymers (SS3, SH6, and X3) compared with the permanently cross-linked star polymer (CS6). (b) Compression measurements of X3 and CS6. (c) Indentation measurements of X3 and CS6 using a glass hemisphere (diameter = 6 mm) indenter. The experimental data were fit to the Hertz model for a spherical indenter, yielding Young's moduli of X3 and CS6 equal to 40 and 190 kPa, respectively.

dx.doi.org/10.1021/ma2015134 |*Macromolecules* 2012, 45, 142–149

SS3 and SH6 in Figure 7 a. The detailed discussion of DMA for SS3, SH6, and X3 can be found in our recent publication, in which the rubbery plateau above 100 °C was attributed to the presence of intermolecular SS cross-linking.[55] Based on this assignment, a higher value of storage modulus G' of X3 (35 kPa) in comparison with CS6 (15 kPa) indicates higher degree of intermolecular cross-linking for X3. Higher stiffness of X3 vs CS6 was even more pronounced at room temperature (5 MPa vs 0.05 MPa). While the 2 orders of magnitude difference of rigidities between X3 and CS6 measured by DMA at room temperature might appear to be quite significant, one should keep in mind that the time scale of DMA measurements (10 rad/s ∼ 60 Hz) implies that this difference pertains to viscoelastic processes occurring within tens of milliseconds. For self-healing processes, such as those observed here, the appropriate time scale is of the order of thousands of seconds, which implies that the difference of rigidity measured at 10 rad/s at higher temperatures within the rubbery plateau (factor of 2−3) is more relevant. Higher stiffness of X3 material was also evident in compression measurements performed with the ARES rheometer on disk-shaped samples (diameter ∼6 mm, thickness ∼1 mm). Confirming the validity of the previous reasoning regarding deformation time scales, inspection of the slopes of the initial linear portions of stress strain curves shows that the ratio of materials' moduli measured in this relatively slow deformation mode did not exceed the factor of 4. Since self-healing experiments performed here all involved healing of surface scratches, samples X3 and CS6 were also studied through microindentation experiments with a glass hemisphere probe (diameter = 6 mm) in order to gain some insight into the mechanical properties of the near-surface regions. Inspection of force−indentation curves from these measurements (Figure 7c) confirmed that the stiffness of both samples was of the same order magnitude; however, this time Young's modulus of sample X3 calculated based on the Hertz contact mechanics model (40 kPa) was lower than the modulus measured for sample CS6 (190 kPa). For the purpose of this discussion, it is important to note only that the measured values were within the same order of magnitude and that they were comparable with the shear moduli measured at with DMA in the rubbery plateau range. The significance of the apparent "reversal" of stiffness of both materials should be weighed against the well-known indentation size effect phenomenon,[57] where the interplay of elastic deformation and plastic flow in indentation measurements often causes material's hardness to appear to increase with the decrease of indentation depth. Altogether, the main conclusion that could be drawn from macroscopic mechanical measurements is that since long-time-scale viscoelastic properties of materials X3 and CS6 were not drastically different, the dramatic difference in their ability to self-heal was indeed rooted in chemistry (the ability of X3 to re-form chemical bonds) rather than in some mechanical differences.

CONCLUSIONS

Disulfide (SS) cross-linked redox responsive star polymer gels (SS3) were successfully synthesized using ATRP. The SS functionalities were introduced into the periphery of star polymers by chain extension using a SS cross-linking agent bis(2-methacryloyloxyethyl) disulfide (DSDMA). The SS cross-linked polymers were cleaved under reducing conditions to form SH-functionalized soluble polymers (SH6). The SH-functionalized polymers were converted to insoluble SS re-cross-linked gels (X3) via oxidation. The self-healing properties of X3 were observed by the combination of the AFM micromachining technique and continuous AFM imaging as well as optical microscopy. X3 showed a rapid self-healing behavior without external triggers. The healing capability was dependent on the initial film thickness and the width of damage. This validated the concept of using SS cross-linked redox responsive polymer as self-healing materials. Through this study, it was shown that the grafted polymer architecture does promise a successful approach to self-healing polymeric materials, thanks to the intrinsic low viscosity and the high accessibility to functionality.

ASSOCIATED CONTENT

Supporting Information. Experimental details. This material is available free of charge via the Internet at http://pubs.acs.org.

ACKNOWLEDGMENT

The authors thank Dr. James Spanswick for helpful discussions. CRP Consortium in Carnegie Mellon University, DoE ER45998, and Mitsui Chemicals, Inc., are acknowledged for the financial support.

REFERENCES

(1) Murphy, E. B.; Wudl, F. *Prog. Polym. Sci.* **2010**, *35*, 223.
(2) Corten, C. C.; Urban, M. W. *Adv. Mater.* **2009**, *21*, 5011.
(3) Ghosh, B.; Urban, M. W. *Science* **2009**, *323*, 1458.
(4) Urban, M. W. *Prog. Polym. Sci.* **2009**, *34*, 679.
(5) Bergman, S. D.; Wudl, F. *J. Mater. Chem.* **2008**, *18*, 41.
(6) Wu, D. Y.; Meure, S.; Solomon, D. *Prog. Polym. Sci.* **2008**, *33*, 479.
(7) Cordier, P.; Tournilhac, F.; Soulié-Ziakovic, C.; Leibler, L. *Nature* **2008**, *451*, 977.
(8) Wool, R. P. *Soft Matter* **2008**, *4*, 400.
(9) Balazs, A. C.; Emrick, T.; Russell, T. P. *Science* **2006**, *314*, 1107.
(10) van der Zwaag, S., Ed. *Self Healing Materials: An Alternative Approach to 20 Centuries of Materials Science*; Springer: Berlin, 2007.
(11) Maeda, T.; Otsuka, H.; Takahara, A. *Prog. Polym. Sci.* **2009**, *34*, 581.
(12) Bilig, T.; Oku, T.; Furusho, Y.; Koyama, Y.; Asai, S.; Takata, T. *Macromolecules* **2008**, *41*, 8496.
(13) Nicolaÿ, R.; Kamada, J.; Van Wassen, A.; Matyjaszewski, K. *Macromolecules* **2010**, *43*, 4355.
(14) Fairbanks, B. D.; Singh, S. P.; Bowman, C. N.; Anseth, K. S. *Macromolecules* **2011**, *44*, 2444.
(15) Kersey, F. R.; Loveless, D. M.; Craig, S. L. *J. R. Soc., Interface* **2007**, *4*, 373.
(16) Wang, Q.; Mynar, J. L.; Yoshida, M.; Lee, E.; Lee, M.; Okuro, K.; Kinbara, K.; Aida, T. *Nature* **2010**, *463*, 339.
(17) Burattini, S.; Colquhoun, H. M.; Fox, J. D.; Friedmann, D.; Greenland, B. W.; Harris, P. J. F.; Hayes, W.; Mackay, M. E.; Rowan, S. J. *Chem. Commun.* **2009**, 6717.
(18) Hansen, M. R.; Graf, R.; Sekharan, S.; Sebastiani, D. *J. Am. Chem. Soc.* **2009**, *131*, 5251.
(19) Chen, X.; Dam, M. A.; Ono, K.; Mal, A.; Shen, H.; Nut, S. R.; Sheran, K.; Wudl, F. *Science* **2002**, *295*, 1698.
(20) Zhang, Y.; Broekhuis, A. A.; Picchioni, F. *Macromolecules* **2009**, *42*, 1906.
(21) Skene, W. G.; Lehn, J. M. P. *Proc. Natl. Acad. Sci. U. S. A.* **2004**, *101*, 8270.
(22) Cleland, W. W. *Biochemistry* **1964**, *3*, 480.
(23) Humphrey, R. E.; Hawkins, J. M. *Anal. Chem.* **1964**, *36*, 1812.
(24) Humphrey, R. E.; Potter, J. L. *Anal. Chem.* **1965**, *37*, 164.

(25) Jocelyn, P. C. *Methods Enzymol.* **1987**, *143*, 246.
(26) Gao, H. F.; Matyjaszewski, K. *Prog. Polym. Sci.* **2009**, *34*, 317.
(27) Barner, L.; Davis, T. P.; Stenzel, M. H.; Barner-Kowollik, C. *Macromol. Rapid Commun.* **2007**, *28*, 539.
(28) Peleshanko, S.; Tsukruk, V. V. *Prog. Polym. Sci.* **2008**, *33*, 523.
(29) Kolmakov, G. V.; Matyjaszewski, K.; Balazs, A. C. *ACS Nano* **2009**, *3*, 885.
(30) Wang, J.-S.; Matyjaszewski, K. *J. Am. Chem. Soc.* **1995**, *117*, 5614.
(31) Kato, M.; Kamigaito, M.; Sawamoto, M.; Higashimura, T. *Macromolecules* **1995**, *28*, 1721.
(32) Matyjaszewski, K.; Xia, J. *Chem. Rev.* **2001**, *101*, 2921.
(33) Kamigaito, M.; Ando, T.; Sawamoto, M. *Chem. Rev.* **2001**, *101*, 3689.
(34) Rosa, L. G.; Liang, J. *J. Phys.: Condens. Matter* **2009**, *21*, 483001.
(35) Xie, Y. L.; Cheong, F. C.; Zhu, Y. W.; Varghese, B.; Tamang, R.; Bettiol, A. A.; Sow, C. H. *J. Phys. Chem. C* **2009**, *114*, 120.
(36) Yan, Y. D.; et al. *J. Micromech. Microeng.* **2008**, *18*, 035002.
(37) Shi, J.; Chen, J.; Cremer, P. S. *J. Am. Chem. Soc.* **2008**, *130*, 2718.
(38) Headrick, J. E.; Armstrong, M.; Cratty, J.; Hammond, S.; Sheriff, B. A.; Berrie, C. L. *Langmuir* **2005**, *21*, 4117.
(39) Liu, G. Y.; Xu, S.; Qian, Y. L. *Acc. Chem. Res.* **2000**, *33*, 457.
(40) Nie, Z. H.; Kumacheva, E. *Nature Mater.* **2008**, *7*, 277.
(41) Huo, F. W.; Zheng, Z. J.; Zheng, G. F.; Giam, L. R.; Zhang, H.; Mirkin, C. A. *Science* **2008**, *321*, 1658.
(42) Onclin, S.; Ravoo, B. J.; Reinhoudt, D. N. *Angew. Chem., Int. Ed.* **2005**, *44*, 6282.
(43) Gates, B. D.; Xu, Q. B.; Stewart, M.; Ryan, D.; Willson, C. G.; Whitesides, G. M. *Chem. Rev.* **2005**, *105*, 1171.
(44) Ginger, D. S.; Zhang, H.; Mirkin, C. A. *Angew. Chem., Int. Ed.* **2004**, *43*, 30.
(45) Piner, R. D.; Zhu, J.; Xu, F.; Hong, S. H.; Mirkin, C. A. *Science* **1999**, *283*, 661.
(46) Liang, J.; Rosa, L. G.; Scoles, G. *J. Phys. Chem. C* **2007**, *111*, 17275.
(47) Tan, Y. H.; Liu, M.; Nolting, B.; Go, J. G.; Gervay-Hague, J.; Liu, G. Y. *ACS Nano* **2008**, *2*, 2374.
(48) Yu, J. H.; Ngunjiri, J. N.; Kelley, A. T.; Gano, J. C. *Langmuir* **2008**, *24*, 11661.
(49) Tang, Q.; Shi, S. Q.; Zhou, L. M. *J. Nanosci. Nanotechnol.* **2004**, *4*, 948.
(50) Seo, K.; Borguet, E. *Langmuir* **2006**, *22*, 1388.
(51) Brower, T. L.; Garno, J. C.; Ulman, A.; Liu, G.-y.; Yan, C.; Gölzhäuser, A.; Grunze, M. *Langmuir* **2002**, *18*, 6207.
(52) Hurley, P. T.; Ribbe, A. E.; Buriak, J. M. *J. Am. Chem. Soc.* **2003**, *125*, 11334.
(53) Vettiger, P.; Cross, G.; Despont, M.; Drechsler, U.; Durig, U.; Gotsmann, B.; Haberle, W.; Lantz, M. A.; Rothuizen, H. E.; Stutz, R.; Binnig, G. K. *IEEE Trans. Nanotechnol.* **2002**, *1*, 39.
(54) Sahin, O.; Magonov, S.; Su, C.; Quate, C. F.; Solgaard, O. *Nature Nanotechnol.* **2007**, *2*, 507.
(55) Kamada, J.; Koynov, K.; Corten, C.; Juhari, A.; Yoon, J. A.; Urban, M. W.; Balazs, A. C.; Matyjaszewski, K. *Macromolecules* **2010**, *43*, 4133.
(56) Yufa, N. A.; Li, J.; Sibener, S. J. *Polymer* **2009**, *50*, 2630.
(57) Nix, W. D.; Gao, H. *J. Mech. Phys. Solids* **1998**, *46*, 411.

Macromolecules

ARTICLE

pubs.acs.org/Macromolecules

Orientation Change of Diblock Copolymer Thin Films by the Addition of Amphiphilic Surfactants: Effect of Film Thickness and Surfactant Concentration

Jeong Gon Son,[†,‡] Huiman Kang,[§] Ki-Yeon Kim,[⊥] Jung-Soo Lee,[⊥] Paul F. Nealey,[§] and Kookheon Char*[,†]

[†]School of Chemical and Biological Engineering The National Creative Research Initiative Center for Intelligent Hybrids The WCU Program of Chemical Convergence for Energy & Environment, Seoul National University, Seoul 151-744, Korea

[‡]Nanohybrids Research Center, Korea Institute of Science and Technology, Seoul 136-791, Korea

[§]Department of Chemical and Biological Engineering, University of Wisconsin—Madison, Madison, Wisconsin 53706, United States

[⊥]HANARO Center, Korea Atomic Energy Research Institute, Daejeon 305-353, Korea

ABSTRACT: We systematically investigated the effect of surfactant addition on the orientational change in polystyrene-*block*-poly(methyl methacrylate) (PS-*b*-PMMA) block copolymer films as a function of film thickness and surfactant (oleic acids (OAs)) concentration using microscopic analysis, neutron reflectivity, and theoretical calculations. The orientation of PS-*b*-PMMA films containing OAs as surfactants was found to be determined by the competitions among the surfactant-assisted neutral field and preferential fields at both top surface and bottom interface. In the case of a BCP film containing a small amount of OAs, the integer film thickness of domain spacing L_0 (long spacing of lamellae-forming BCP) prefers to form the perpendicular orientation of microdomains while the parallel orientation is observed when the film thickness is close to the half-integers of L_0. We also found that the periodic orientation of block domains gradually dies out to the perpendicular orientation as the film thickness as well as the surfactant concentration is increased. Neutron reflectivity analysis of *deuterated* polystyrene-*block*-poly(methyl methacrylate) (*d*PS-*b*-PMMA) block copolymer thin films containing OA surfactants was also performed to gain insights into the orientation of BCP films across film thickness due to the addition of OAs. With the free energy calculations on BCPs mixed with OA surfactants at different film thicknesses, the periodic orientation of block domains is qualitatively confirmed.

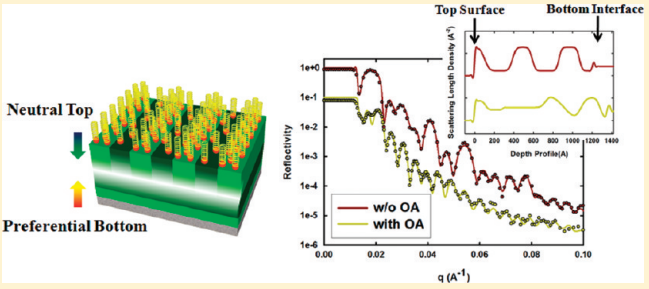

INTRODUCTION

Block copolymer (BCP) thin films have recently received intense attention due to their potential applications as templates for nanolithography,[1−10] separation membranes,[11] and nanoscale object arrays.[12−15] These block copolymer chains, which two or more polymer chains of different chemical structure are covalently bonded together, could self-assemble and microphase-separate to molecular dimensions, thus forming 10−100 nm periodic nanoscale features. Control of block copolymer morphologies and their size is easily achieved by varying the volume fraction of each block and the total molecular weight. In the case of symmetric A−B diblock copolymers, the microphase-separated morphology of the block copolymers is the lamellar structure. In film geometry, there is an additional factor that should be considered: preferential wetting of a given block at both top surface and bottom interface to minimize interfacial as well as surface energies. As a result, parallel orientation of BCP domains typically initiates at both interfaces and then propagates throughout the entire film.[16−19] In addition, the commensurability of film thickness with characteristic block copolymer period (L_0) also mainly influences structures of the film.[20−23] The films with thickness incommensurate with the domain spacing of BCP (L_0) induces quantization of the film thickness in discrete integer values of L_0 and generation of terrace structures (i.e., islands or holes) at the surface in order to maintain the domain spacing across the whole thickness of the film.

In particular, for the practical point of view, the perpendicular orientation of BCP nanostructural domains in the films has the advantage over the parallel orientation. Many research groups thus have managed to obtain this perpendicular morphology by a variety of methods including applying electric field,[24−26] neutral brushes on substrates,[27−30] solvent annealing,[31] and introducing rough substrates.[32] Among them, random copolymer brushes to create enthalpically neutral substrates through minimizing the difference in interfacial tensions between each block and a substrate have been the approach most widely used. The neutral substrates simply cause nonpreferential wetting between BCP

Received: July 6, 2011
Revised: November 12, 2011
Published: December 05, 2011

segments and the substrate and induces the perpendicular orientation of the BCP films from the bottom substrate toward the polymer surface exposed to air. However, this approach has inevitable limitations that the quality of the perpendicular domain orientation is significantly dependent on the film thickness,[33−35] and relatively thick films above several L_0 thickness usually form the mixed orientation where parallel and perpendicular orientations are respectively observed at the top surface as well as at the bottom interface[36,37] because these BCP films are hard to overcome the preferential wetting at the top surface.

Recently, our research group reported a new approach using surfactants to induce the perpendicular orientation from the top BCP surface toward the bottom of a substrate.[38] An inherent feature of amphiphilic surfactants, located at the surface (or interface) to tailor the surface properties of a material and preferably interacting with specific block domains of BCPs, could easily create energetically neutral conditions at the top surface of BCP thin films, as confirmed by thermogravimetric analysis (TGA) and neutron reflectivity (NR) experiments. The simplicity of this technique, which forms nanopatterns at the film surface after short annealing time on any substrates, makes it promising for further development in that field. However, this facile processing method did not show the perpendicular orientation at the bottom interfaces because of the preferential wetting at the bottom substrate. Therefore, orientational competition between surfactant-assisted neutral field and preferential wetting field and should be investigated.

Thus, in this paper, we systematically analyzed the competitions between neutral field and preferential field at the top surface and bottom interface, respectively, of the lamellae-forming symmetric polystyrene-*block*-poly(methyl methacrylate) (PS-*b*-PMMA) block copolymer films containing oleic acids as surfactants through investigating the film thickness and commensurability effect. Neutron reflectivity analysis of *deuterated* polystyrene-*block*-poly(methyl methacrylate) (*d*PS-*b*-PMMA) block copolymer thin films containing surfactant was also investigated for the effect of surfactant addition on the orientation of BCP films across the film thickness. For the theoretical insight of these features, we also performed the free energy calculations on various orientation models of BCP films containing surfactant. Then, the effect of surfactant amount on the top and bottom neutrality influencing the domain orientation of BCP thin films was examined according to film thickness.

EXPERIMENTAL SECTION

Materials. Polystyrene-*block*-poly(methyl methacrylate) (PS-*b*-PMMA) diblock copolymers were purchased from Polymer Source. Molecular weight of a symmetric diblock copolymer was 104 kg/mol (52K−52K, denoted as SML100) with a polydispersity index of 1.09. Fully deuterated polystyrene-*block*-poly(methyl methacrylate) (*d*PS-*b*-PMMA) diblock copolymers were also purchased from Polymer Source, and the molecular weight was 92 kg/mol (40K−52K, denoted as *d*SML100) with a polydispersity index of 1.06. Average domain spacing (L_0) measured by small-angle X-ray scattering (SAXS) experiments were 48 and 46 nm, respectively. Oleic acid (∼99%) was purchased from Sigma-Aldrich. PS-*random*-PMMA brushes (5K, 58:42 fractions) for neutral substrates were synthesized by atomic transfer radical polymerization (ATRP), as reported in the literature.

Thin Film Preparation. For neutral substrates, 1 wt % hydroxyl-terminated PS-*random*-PMMA random copolymer brushes were dissolved in toluene and deposited on piranha cleaned SiO_x/Si wafer substrates by spin-coating at 3000 rpm. The samples were then annealed at 190 °C for 3 days in vacuum to form a covalent bond between the hydroxyl-terminate random copolymer brush and the SiO_x/Si substrate. Unbound polymers were washed three times by sonication for 3 min in warm toluene. 1−7 wt % SML100 or *d*SML100 block copolymer mixed with 1−10 wt % oleic acid dissolved in toluene and was stirred overnight at room temperature. The mixed solutions were spin-coated on piranha cleaned SiO_x/Si substrates for preferential wetting or neutral substrates. All films were then annealed at 170 °C for 3 days under a N_2 atmosphere.

Thin Film Characterization. A variable-angle multiwavelength ellipsometer (Gaertner L2W16C830) was used to measure the thickness of thin films. Surface morphologies of thin films was observed by an atomic force microscope (AFM, Digital Instrument, Nanoscope IIIA) in tapping mode and field emission−scanning electron microscope (FE-SEM, LEO 1550-VP, and JEOL JSM-7401F) operated at 1 kV without metal coating. Quantitative information about the orientation of block copolymer film surface was gathered from an image analysis of at least five FE-SEM images and the AFM phase images. We first divided the PS and PMMA area of 5 μm × 5 μm sized images and calculated area fraction of the PMMA region on the BCP film surface. In the case of FE-SEM images, PMMA domains shrink while PS domains are cross-linked after electron beam irradiation during FE-SEM study of PS-*b*-PMMA thin films. In AFM phase images, AFM can detect phase lag variation of AFM cantilever oscillation from interaction difference between AFM tip and the PS-*b*-PMMA film surface. Samples for neutron reflectivity experiments were prepared on 3 in. diameter and 5 mm thick SiO_x/Si wafer. Neutron reflectivity experiments were carried out with vertical reflectometer at HANARO, Korea Atomic Energy Research Institute. The neutron wavelength (λ) was 2.46 Å with $\Delta\lambda/\lambda$ = 0.03. The scattering length density profiles according to film thickness were obtained from fitting the reflectivity data with the Parratt32 Program.

RESULTS AND DISCUSSION

Commensurability Effect with Neutrality. In general, in the case of asymmetric wetting with PS-*b*-PMMA, which has one block (PS block) preferably wetting the top surface of the film while the other block (PMMA block) located at the bottom of the film in contact with a Si wafer, BCP thin film forms the smooth parallel orientation at the half-integers of L_0 and the bicontinuous terrace (hole−island) structure at the integers of L_0 to relieve the stress originating from the mismatch between film thickness and natural domain spacing despite of the increase in free energy induced from the increase in surface area. Even the case for perpendicular domain orientations on neutral substrates, film thickness is a significant factor for the integrity of microdomain orientation. While block copolymer thin films containing a small amount of surfactants caused the perpendicular domain orientation from the top surface (i.e., polymer and air surface) in our previous results, such orientations would also be affected by the domain commensurability because of the preferential wetting at the bottom substrate.

As a result, we first verify the microdomain orientation of BCP films containing surfactant as a function of film thickness. We prepared BCP films containing 2 wt % oleic acid (surfactant) placed on preferential SiO_x/Si wafer at different film thicknesses and then thermally treated the BCP films at 170 °C in a N_2 atmosphere. At the early stage (∼10 min) of thermal annealing, all the BCP films formed the perpendicular orientation at the top surface due to the saturation of surface with surfactants. However, surprisingly, the initial perpendicular orientation at a certain film thickness (i.e., half-integer thicknesses) becomes smeared as

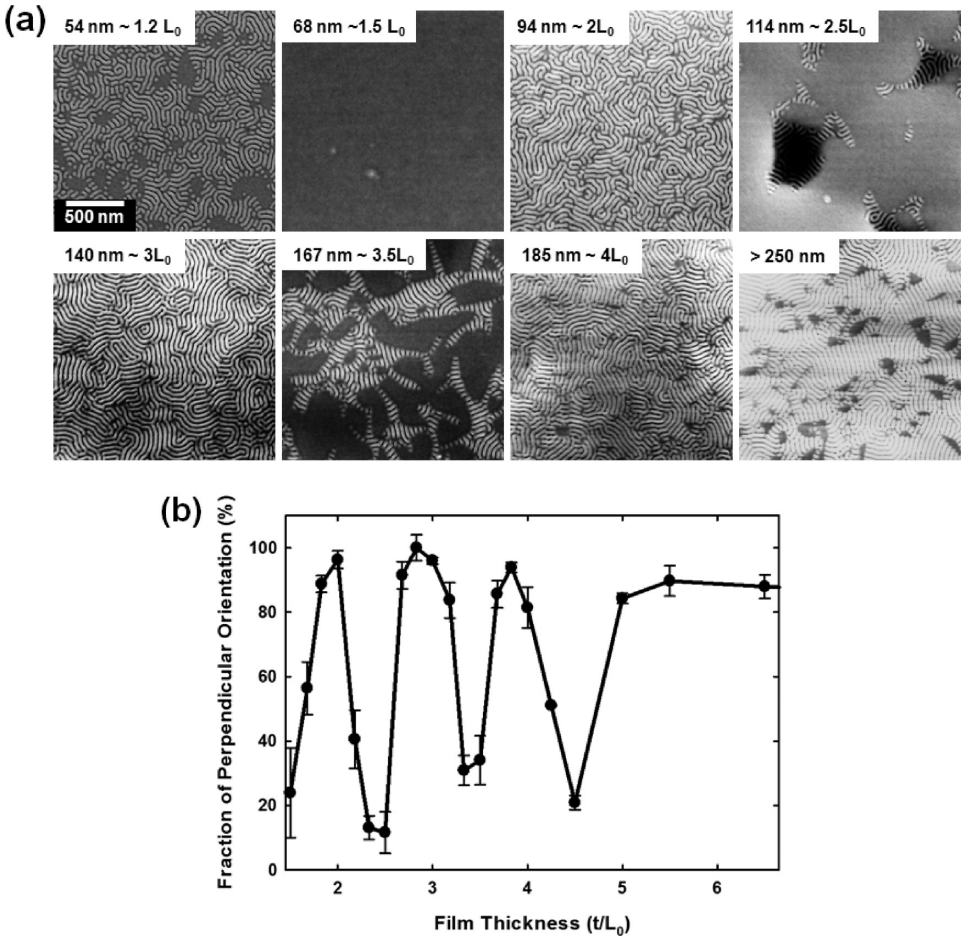

Figure 1. (a) Surfactant-assisted orientation with the addition of 2 wt % oleic acid (OA) of lamellae-forming PS-*b*-PMMA (SML100) films on silicon substrates as a function of film thickness after thermal annealing at 170 °C for 3 days in N_2 atmosphere. (b) Perpendicularly oriented surface area fraction diagram of the SML100 films with surfactant (2 wt % of oleic acid) on silicon wafer as a function of reduced film thickness.

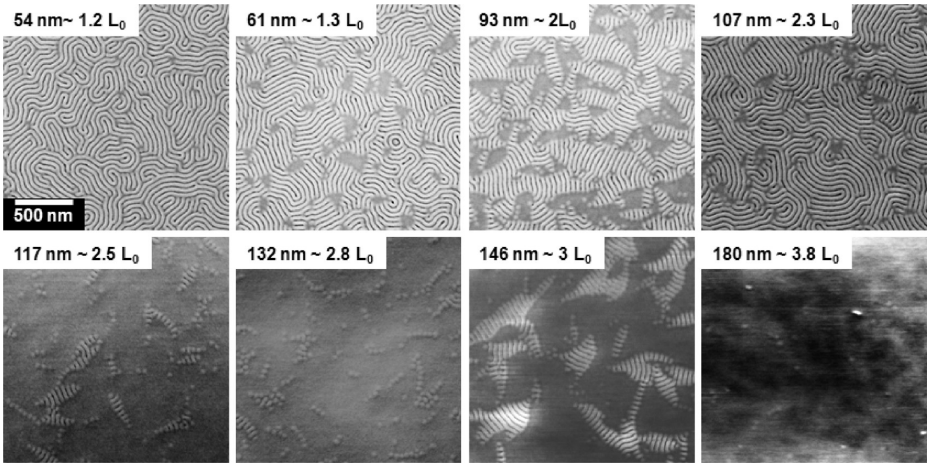

Figure 2. Pristine lamellae-forming PS-*b*-PMMA films (without containing surfactant) on energetically neutral substrates (PS-*random*-PMMA brushes grafted onto Si wafers) as a function of film thickness after thermal annealing at 170 °C for 3 days.

annealing time lapses. Thus, we annealed the BCP films with surfactants for 3 days to observe the equilibrium block copolymer orientation without extensive degradation of block copolymers. Figure 1a illustrates the FE-SEM images of PS-*b*-PMMA block copolymer thin films containing 2 wt % oleic acid at different film thicknesses after 3 days of thermal annealing at 170 °C. These figures reveal that perpendicular and dominant parallel orientations at top surface of the films are alternately varied as the film

dx.doi.org/10.1021/ma201435v |*Macromolecules* 2012, 45, 150–158

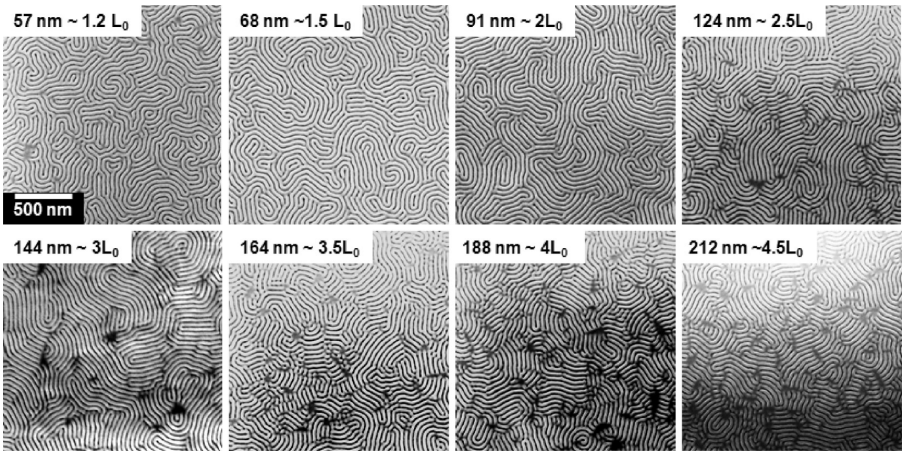

Figure 3. Orientation of PS-*b*-PMMA films containing 2 wt % OA surfactant placed on neutral substrates as a function of film thickness after thermal annealing at 170 °C for 3 days.

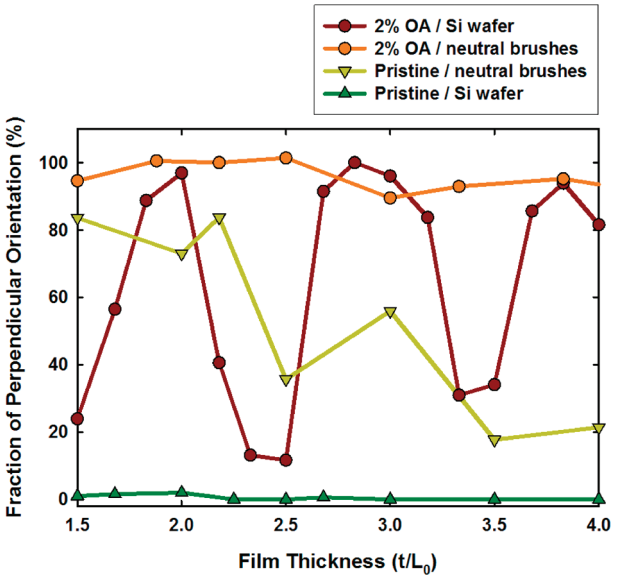

Figure 4. Comparison of the degree of orientation of BCP films at the top surface for SML100 with 2 wt % OA on Si wafers, SML100 containing 2 wt % OA placed on neutral substrates, pristine SML100 (without OA surfactant) placed on neutral brush, and pristine SML100 placed on Si wafers as a function of normalized film thickness after thermal annealing at 170 °C for 3 days in a N_2 atmosphere.

thickness is increased. Figure 1b shows the surface area fraction of perpendicular orientation for BCP films containing surfactants at top surface from the FE-SEM and AFM phase images as a function of film thickness normalized by the domain spacing L_0. As a point of notice, the perpendicular surface morphologies are dominantly observed close to the integer values of L_0 (domain spacing of BCP used) thickness while the parallel dominant morphologies were observed near the half-integers of L_0. When the film thickness is above 250 nm, this periodic change in domain orientation gradually smears out and the perpendicular domain orientation with small cavities is obtained almost independent of film thickness. As demonstrated from the microscopic investigation on the domain orientation at the top surface and its quantification analysis, in the case of competitions between top neutrality due to the addition of surfactants and bottom preference on SiO_x substrate, the interplay between film thickness and the characteristic BCP domain spacing, L_0, could significantly affect the orientation of block copolymer domain. And for BCP films of over 250 nm thick, due to the sufficient distance from both interfaces, the top neutrality and bottom preference are individually active in the orientations at both interfaces, resulting in the formation of perpendicular orientation at top surface regardless of film thickness.

For the reference, we also examined the pristine block copolymer orientation (without surfactant) on the neutral brushes. This approach has been well-known for the perpendicular orientation of only ultrathin ($\sim 1L_0$ or 40 nm) block copolymer film because nonpreferential interface only exists at the bottom of the films.[27,28] Russell and co-workers also demonstrated the mixed orientation of the block copolymer films ($\sim$150 nm, $4-5L_0$) on the neutral substrate because of the preferential wetting on the air surface.[36,37] As can be seen in Figure 2, the BCP film below 100 nm thickness formed perpendicular orientation due to energetically neutral brushes; otherwise, the films over 100 nm thickness lost perpendicular orientation and formed mixed orientation because of preferential wetting at the top surface. This orientation change aspect is different from surfactant containing BCP films. We also investigated the domain orientation of block copolymer film containing surfactant on neutral brush substrates to generate energetic neutrality at both interfaces, as shown in Figure 3. The film with dual neutral interfaces formed fine perpendicular orientation almost independent of film thickness. Note that the perpendicularly oriented lamellae morphology was obtained regardless of the film thickness, which was in large contrast with the case obtained on silicon substrates inducing preferential wetting for PMMA block with substrate.

To generalize orientation change caused by geometry of neutrality for the BCP film, overall surface area fraction of perpendicular orientation of top and/or bottom neutrality was performed, as can be seen in Figure 4. In the case of preferential substrates, pristine BCP films orient in parallel to the substrate forming holes or islands depending on the film thickness (hence, commensurability, images not included in this article.). However, in a PS-*b*-PMMA film placed on a SiO_x/Si wafer, the surface energy difference between PS ($\gamma_{PS} \sim 41.5$ mN/m) and PMMA ($\gamma_{PMMA} \sim 44.5$ mN/m) blocks is much smaller than the interfacial energy difference between PS$-SiO_x$/Si wafer

dx.doi.org/10.1021/ma201435v |*Macromolecules* 2012, 45, 150–158

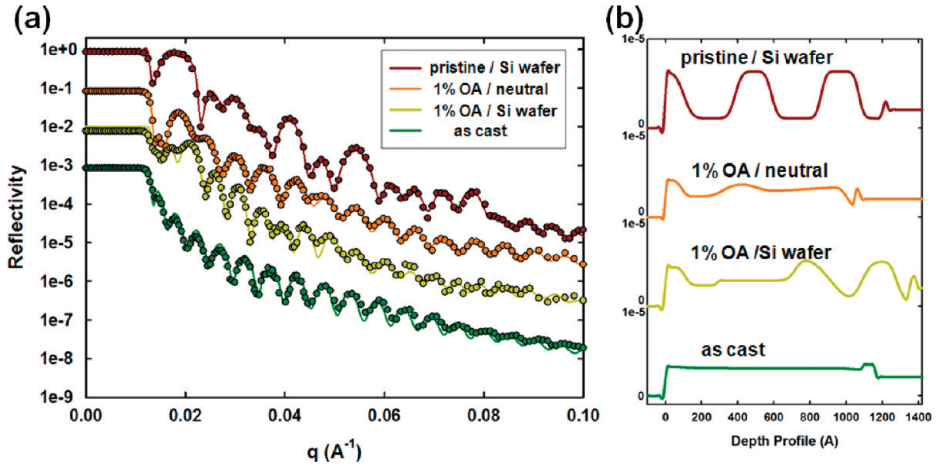

Figure 5. (a) Neutron reflectivity of as-cast pristine *d*PS-*b*-PMMA film (without OA surfactant) placed on a Si wafers and *d*PS-*b*-PMMA films containing 2 wt % OA surfactant placed on neutral brushes and Si wafers after annealing at 170 °C for 3 days. (b) Scattering length density profiles of the films across the film thickness obtained from fitting the reflectivity data of (a).

($\gamma_{PS-SiO_x} \sim 31.3$ mN/m) and PMMA−SiO_x/Si wafer ($\gamma_{PMMA-SiO_x} \sim 13.0$ mN/m). This implies that the propagation of parallel orientation originating from the SiO_x/Si wafer, without neutral brushes, is so intense that the BCP film maintains the parallel orientation at the half-integer ($\sim x0.5L_0$; commensurability condition for the asymmetric wetting) film thickness even in the presence of OA surfactant at the surface. However, perpendicular orientation is preferred in the case where the BCP film thickness is the integer film thickness ($\sim xL_0$; co-continuous morphology with a step height of L_0 without surfactants) in the presence of OA surfactants on the surface. When neutral brushes are used, the interfacial energy difference between PS and PMMA blocks against the substrate is significantly reduced that the commensurability constraint is not so strong, easily leading to the perpendicular orientation at the substrate propagating into the film. However, when the BCP film is very thick (>100 nm), the perpendicular orientation originating from the bottom substrate is overshadowed by the parallel orientation from the top surface due to the surface energy difference between PS and PMMA blocks. Upon addition of OA surfactants, the surface energy difference is further reduced such that the top surface had also the perpendicular orientation, as shown in Figure 3.

To characterize the orientation configuration across the film thickness of block copolymer polymer films in the case of confliction between top neutrality and bottom preference, we performed neutron reflectivity[19,21,39−42] (NR) experiments which is known as one of the best spectroscopic techniques for structural analysis of polymer films. This technique provides excellent spatial resolution down ~1 nm, with penetration depths over hundreds of nanometers, compared with other surface analysis techniques. NR mainly detects the variation in scattering length density (SLD) in a film depth direction. Thus, we performed the NR experiments of oleic acid with fully deuterated-PS-*block*-PMMA (*d*PS-*b*-PMMA) for verifying orientation of block copolymer thin film containing surfactant, as shown in Figure 5a. The SLD value of fully deuterated PS (*d*PS) is $\sim 5.99 \times 10^{-6}$ Å^{-2}, which is much higher than that of PMMA (1.05×10^{-6} Å^{-2}) and OA (7.62×10^{-8} Å^{-2}). Through a fitting process from these reflectivity data, SLD profiles as a function of distance from polymer/air interface for each of samples also could be obtained, as can be seen in Figure 5b. In the case of unannealed film, the reflectivity data showed a critical angle at $q = 0.013$ A^{-1} and Kiessig fringes characteristic of the film thickness without any distinguishable features, and the SLD profile was essentially flat throughout the film because of randomly dispersed polymers by spin-coating. After annealing $2.5L_0$ thickness BCP film without surfactant during 24 h at 170 °C in a N_2 atmosphere, high-order Bragg peaks are particularly evident, indicating the formation of parallel lamellae, as predicted. Their SLD profile showed an oscillation having period of ~46 nm emanating from the polymer/air interface. Regions high in SLD correspond to *d*PS; the low SLD part corresponds to PMMA-rich regions, adjacent to a thin silicon oxide layer (SLD value of SiO_x is around 3.1×10^{-6} Å^{-2}). However, in the case of $3L_0$ thick PS-*b*-PMMA films containing 1 wt % of surfactant for perpendicular domain orientation at surface, the reflectivity illustrated only a first-order Bragg peak, indicating the parallel orientation was partially formed in the films. Its SLD profile showed relatively flat with small fluctuation at the upper part of the film, indicating perpendicularly oriented structures with small defects (as can be seen in surfactant concentration section) and parallel orientation from the bottom to $1.5L_0$ thickness of the film originated from preferential wetting of BCP with substrate. Block copolymer films on neutral brush with surfactant showed a little tiny first-order Bragg peak in reflectivity data and fairly flat SLD profile at the lower part as well as higher part of the film owing to dual neutrality of the films. These neutron reflectivity results clearly illustrated the orientation configuration difference of BCP films with top, bottom, and dual (top and bottom) neutrality.

Free Energy Calculation. This orientation change according to film thickness caused by competition between neutral field and preferential field could be understood through free energy calculation of the BCP films based on the surface and interface energy minimization and commensurability. In the case of asymmetric wetting BCP films, such as PS-*b*-PMMA, parallel orientation at half-integer of L_0 thickness is fairly stable because surface and interfacial energy minimization with commensurability is satisfied (PS which is lower surface energy domain locates on top, while PMMA which is lower interface energy domain with SiO_x substrate locates at the bottom interface of the film without any tensions) in that thickness. However, parallel

Scheme 1. Schematic Illustration of Lamellar Block Copolymer Thin Films with Different Orientations: (a) Perpendicularly Oriented Lamellar Morphology; (b) Parallel Oriented Lamellar Morphology; (c) Mixed Morphology with the Parallel Orientation near Substrate and Perpendicular Orientation at the Upper Part of the Film

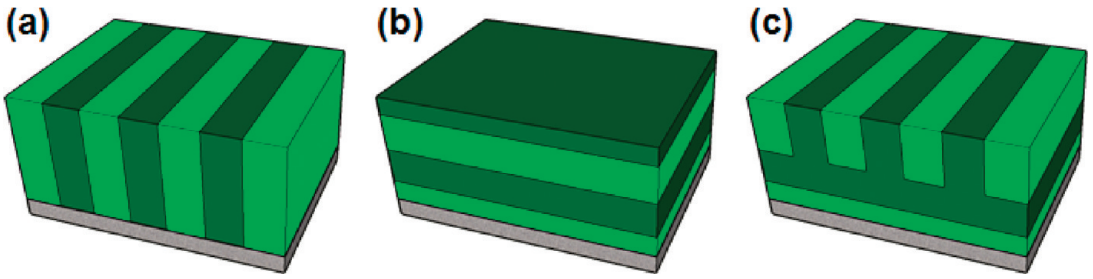

orientation at the integer thicknesses of L_0 is not stable because surface energy minimization from both sides of film surface and interface conflicts with maintaining block copolymer period at this thickness, as also known as incommensurability. In this case, normal BCP films typically form terrace morphology in order to maintain the natural domain spacing with surface energy minimization, which also forms additional surfaces and needs mass transfer. In contrast, BCP films containing OA surfactants result in the perpendicular orientation at the top surface, not a terrace morphology, without any surface energy compensation because the OA surfactants segregated to the top surface of the films (~17.8% at the surface, as confirmed from neutron reflectivity)[37] during the annealing process, leading to the neutral top surface of a BCP film.

On the basis of the Turner model[43−50] which investigated the equilibrium properties of an A−B diblock copolymer in its lamellar phase under confinement between two identical flat plates, we assumed that the copolymer is compositionally symmetric which A and B blocks have an equal number of segments $N/2$ and each of persistence length a. And the BCP films is supported by the flat substrate and exposed to the air surface. Following the Turner approach, we also assumed the strong segregation limit, $\chi N \gg 10$, for the sake of simplicity in free energy calculations, in which A and B microdomains are phase-separated with narrow interfaces because of high molecular weight, and large interfacial energy though PS-*b*-PMMA, used in the present study, has not so high value of χ.

The microphase separation in bulk block copolymer systems are easily explained with free energy calculation that balances the interfacial energy from segregation the A and B blocks (F_{AB}) with the entropic penalty for deforming the chains from their disordered state conformation (F_{el}). In the thin film geometry, surface and interface interaction terms should be taken into account, the expression for the free energy of bulk films is altered to include the air−polymer interactions ($F_{surface}$) and polymer−substrate interactions ($F_{interface}$). We assumed the film forms the asymmetric wetting against film surface and bottom interface. The resulting free energy, F, is given by

$$\frac{F}{kT} = \frac{F_{el} + F_{AB} + F_{surface} + F_{interface}}{kT} = \frac{3p}{8N}\left(\frac{L}{a}\right)^2 + 2pN\left(\frac{a}{L}\right)\gamma_{AB} + pN\left(\frac{a}{L}\right)\frac{1}{n}(\gamma_{surface} + \gamma_{interface}) \quad (1)$$

where p is the number of copolymer chains in the system, L is the lamellar period, γ_{AB} is the interfacial tensions between A and B segments, n is the value of the number of lamellar layers, and $\gamma_{surface}$ and $\gamma_{interface}$ are the surface tension of the BCP films and interfacial tension between substrate and polymer, respectively. We reduced the parameters through the bulk equilibrium lamellar period, L_0, with corresponding bulk equilibrium free energy, F_0, and free energy equation changes to

$$\frac{F}{F_0} = \frac{1}{3}\left[\lambda^2 + \frac{2}{\lambda} + \frac{1}{n\lambda}\frac{\gamma_{surface} + \gamma_{interface}}{\gamma_{AB}}\right] \quad (2)$$

where the normalized period λ is given by $\lambda = L/L_0$.

We considered the models for the calculation of BCP thin films containing surfactants, as can be seen in Scheme 1: (a) perpendicular lamellar, (b) parallel lamellar, and (c) mixed orientation which is perpendicular orientation at upper part of the film and parallel orientation at lower part. In the perpendicular orientation as described in Scheme 1a, imposed thickness constraint performs perpendicularly to the laterally ordered lamellae, and A and B segments are coexisted at the surface and interface, respectively. The free energy of the perpendicular orientation is then expressed as

$$\frac{F_{perp}}{F_0} = \frac{1}{3}\left[3 + \frac{1}{d}\frac{\gamma_{AS} + \gamma_{BS} + \gamma_A + \gamma_B}{2\gamma_{AB}}\right] \quad (3)$$

where γ_{AS} and γ_{BS} are the A block/substrate and B block/substrate interfacial tensions and γ_A and γ_B are the surface tensions of A and B block, respectively. In the case of parallel orientation of the BCP film as described as Scheme 1b, the thickness constraint conflicts against parallel oriented lamellae and results in a lamellar period L, which is perturbed from L_0 when the film thickness $d \neq (n + 1/2)L_0$ in the case of asymmetric wetting BCP film. Owing to preferential wetting at the top and bottom interfaces, lower value of surface and interfacial energy should be chosen, γ_A and γ_{BS}, respectively. The resulting free energy of parallel orientation of BCP film is

$$\frac{F_{para}}{F_0} = \frac{1}{3}\left[\lambda^2 + \frac{2}{\lambda} + \frac{1}{n\lambda}\frac{\gamma_{BS} + \gamma_A}{\gamma_{AB}}\right] \quad (4)$$

BCP film also can form mixed orientation which originate from surfactant-assisted neutral field at film surface and preferential field at substrate, as shown in Scheme 1c. This mixed structure is not necessary to consider thickness constraint with commensurability and high interfacial energy difference between

dx.doi.org/10.1021/ma201435v |*Macromolecules* 2012, 45, 150–158

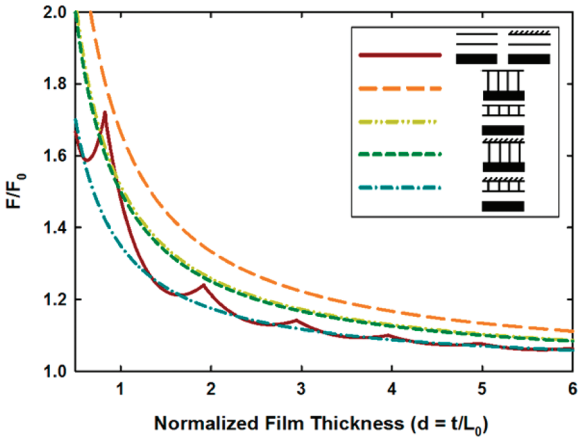

Figure 6. Free energy calculation of parallel, perpendicular, and mixed orientation of lamellae-forming diblock copolymer films placed on non-neutral substrates as a function of normalized film thickness.

A and B with substrate. However, the films should be regarded the additional interface between A block and B block from transitional region. The free energy of mixed oriented BCP film is

$$\frac{F_{mix}}{F_0} = \frac{1}{3}\left[3 + \frac{1}{d}\frac{\gamma_{BS} + \frac{1}{2}(\gamma_A + \gamma_B) + \frac{1}{2}\gamma_{AB}'}{\gamma_{AB}}\right] \quad (5)$$

where γ_{AB}' is the additional interfacial tension between A and B because of the orientation transition in the middle of the film. Figure 6 shows the free energy curves of these BCP film models without and with surfactants that we assumed surface tensions of A and B at film surface had equivalent values. The parameters set up based on the strong segregation limit and references[43−50] as $\Gamma_s = \gamma_{AS}/\gamma_{AB} = 1$, $\Gamma_A = \gamma_A/\gamma_{AB} = 1$, $\delta_S = (\gamma_{BS} - \gamma_{AS})/\gamma_{AB} = -1$, and $\delta_A = (\gamma_B - \gamma_A)/\gamma_{AB} = 1$ when the top surface of the film is not neutral and $\delta_A = (\gamma_B - \gamma_A)/\gamma_{AB} = 0$ when the top surface is neutral for both segments due to the surfactant effect of surfactant addition. In the case of the mixed orientation, an additional interface term, γ_{AB}', is different from γ_{AB} because the free energy penalty from these transition points of the domains does not correspond with the real value of interfacial tension between general BCP segments. As shown in the graph, the free energy curve of parallel orientation shows the fluctuating shape originating from the contraction or stretch of block copolymer chains according to film thickness while that of other orientation monotonically decreased. In the case of preferential wetting with both air surface and bottom substrate without any surfactant, comparing upper three graphs, parallel orientation is dominantly much stable than mixed orientation or perpendicular orientation at any thicknesses. The other case, neutral top surface and preferential bottom interface which originated from the existing of surfactant in the film, mixed and perpendicular orientation can earn free energy advantages from neutral top surface while the free energy of parallel orientation does not changed. Thus, parallel orientation could be most stable in part of half-integers of L_0 in film thickness in which there is no contraction or the extension and at rest of these thicknesses mixed orientation is most stable structure among the models tested, as we experimentally obtained. Through this free energy calculation of the BCP film with surface neutrality, the orientation change of BCP

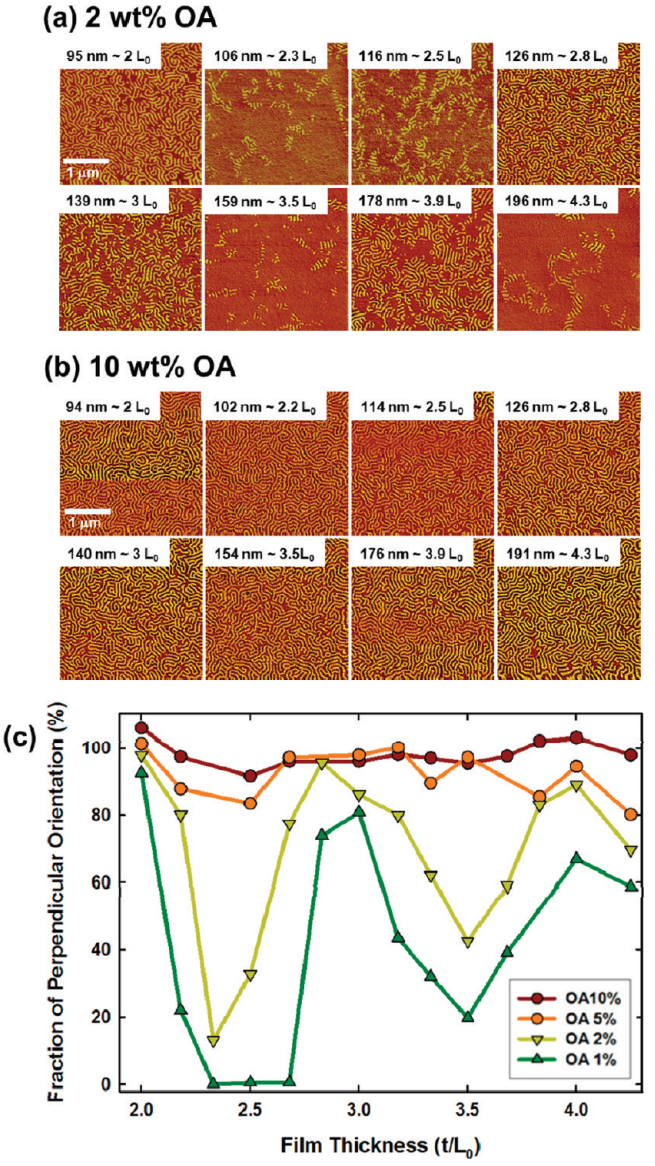

Figure 7. Surfactant-assisted orientation of lamellae-forming *d*PS-*b*-PMMA (*d*SML100 with $L_0 \sim 46$ nm) films placed on silicon substrates as a function of film thickness after thermal annealing at 170 °C for 3 days in a N_2 atmosphere: (a) 2 wt %; (b) 10 wt % oleic acid added to the block copolymers. (c) Fraction of perpendicular orientation of block copolymer films with different amount of surfactants placed on Si wafers as a function of normalized film thickness. Surfactant concentrations are 1, 2, 5, and 10 wt %.

film with surfactant as a function of the film thickness was successfully confirmed.

Surfactant Concentration Effect. We have proven the small amount of surfactants could affect the morphology of the block copolymer films. However, the effect of surfactant amounts in the film on the orientation of BCP film nanostructures was not much investigated. Thus, different surfactant concentration films with a function of film thickness were prepared for surfactant-assisted orientation of lamellae-forming *d*PS-*b*-PMMA films on silicon surfaces to investigate simultaneously with microscopic tools and in-depth NR experiments. Surfactant concentrations were varied from 1 to 10 wt %. Over 10% of OA concentration, the surfactants, more preferably associating with PMMA blocks,

dx.doi.org/10.1021/ma201435v |*Macromolecules* 2012, 45, 150–158

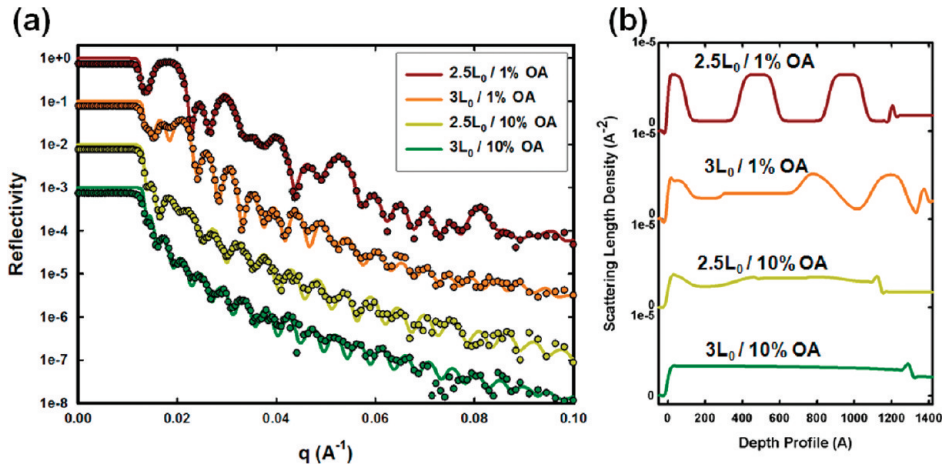

Figure 8. (a) Neutron reflectivity data for *d*SML100 thin films with two different film thicknesses ($2.5L_0$ and $3L_0$) containing two different amounts of surfactants (1 and 10 wt %) placed on Si wafers annealed at 170 °C for 3 days. (b) Scattering length density (SLD) profiles of the BCP films across the film thickness obtained from the fitting of the reflectivity data.

could have deleterious effects on microphase separation of a BCP film itself as well as the persistent length of vertically oriented lamellar domains. Figure 7a,b illustrates the AFM phase images of different surfactant concentration samples as a function of film thickness. Lower concentration (2 wt %) samples showed periodical tendency between parallel and perpendicular orientation as a function of film thickness, as already seen before in the former part. While high concentration of surfactant in the BCP film, such as 10 wt %, dominantly showed perpendicular orientation in all thickness and periodicity between perpendicular and parallel orientation according to film thickness was almost diminished. We also verified this tendency with the perpendicularly oriented surface area fraction of 1, 2, 5, and 10 wt %, as presented in Figure 7c. These surface area fractions more clearly indicate the surfactant concentration effect on the orientation of the block copolymer thin films. As the surfactant concentration increased, perpendicularly oriented regions gradually widened; a fluctuating tendency of orientation according to film thickness was gradually weak. Above a specific amount of surfactant, perpendicularly oriented block copolymer film were constantly observed regardless of film thickness. This result implies the amount of surfactants has a critical role to change the orientation of the BCP film.

The neutron reflectivity experiment for in-depth directional orientation analysis of the surfactant containing block copolymer film was investigated according to film thickness as well as the surfactant concentration effect on the orientation of the films. Figure 8a shows the NR profile for *d*PS-*b*-PMMA film with half-integer thickness with low concentration of surfactant, integer thickness with low concentration, half-integer thickness with high concentration, and integer thickness with high concentration samples. The scattering length density (SLD) profiles obtained from the best fit to the reflectivity profiles are shown in Figure 8b as a function of distance from the Si substrate. In the case of half-integer thickness with low concentration of surfactant (1 wt %), the reflectivity peak showed strong a Bragg peak at $q = 0.018$ Å^{-1} with clear high-order Bragg peaks suggesting from layered structures, and the SLD profile indicated well-developed layer structure which means the parallel orientation of the BCP film microdomains even though the existence of surfactant. At the integer thicknesses of L_0 with low surfactant concentration showed a relatively small main Bragg peak, and its fitted SLD profile indicated layered structure only at bottom part of the films because of the top neutrality from existence of surfactant, which is explained the former part of this paper. In contrast with low surfactant concentration, reflectivity profiles of high concentration of surfactant samples only showed the Kiessig fringes characteristic of the film with no other distinguishable features not only at integer thickness film but also at half-integer thickness film. And the SLD profiles of high surfactant concentration films exhibit fairly flat throughout the film, implying that parallel oriented nanostructures did not exist and perpendicular oriented BCP domains were dominant in whole thickness of these films including top surface and bottom interface while the low amount of solvent containing BCP films formed mixed orientations. These results reveal high concentration of surfactant in the films affect not only the top surface of the film but also the bottom interface which has an additional role of preventing preferential wetting between BCP film and substrates. We think that higher OA concentration films are such that surfactant molecules, more closely associated with the PMMA block, are saturated at both the surface and SiO_x interface, affecting the orientation at the top and bottom interfaces simultaneously, and we assume that residual surfactants might have an effect on the microphase separation of BCPs or the persistence length of lamellae structures, which deserve to be corroborated later (i.e., cross-sectional TEM along with NR with deuterated OAs).

CONCLUSION

We intensively investigated the surfactant approach to induce the orientation change of the BCP film as a function of film thickness and surfactant concentration through microscopical analysis, neutron reflectivity, and theoretical calculation. The film thickness effect on the surfactant-assisted orientation of PS-*b*-PMMA film was effectively demonstrated that perpendicular orientation is preferred when the film thickness is the integers of L_0 while parallel orientation is preferred when the film thickness is near the half-integers of L_0. And these periodical phenomena are gradually smeared, and perpendicular orientation is formed by increasing film thickness and surfactant concentration. Then, through the theoretical free energy calculation of the surfactant-

assisted orientation based on thickness-dependent orientation results, this periodical tendency was successfully proven. This surfactant method presented in this article is simply quite robustly forming neutral surface at the top of the film and applicable to other systems including hierarchical micro-nanopatterned media and inkjet printable BCP nanopatterns. Furthermore, orientation change of BCP film would provide reliable information about commensurability of BCP film with geometry of neutral interfaces.

AUTHOR INFORMATION

Corresponding Author
*E-mail: khchar@plaza.snu.ac.kr.

ACKNOWLEDGMENT

This work was financially supported by the National Research Foundation of Korea (NRF) Grant funded by the Korean Ministry of Education, Science and Technology (MEST) (the National Creative Research Initiative Center for Intelligent Hybrids (No. 2010-0018290), WCU (World Class University) Program (R31-10013), and the BK Program at Seoul National University). This work is also performed by the Collaborative Program of Nanoscale Science and Engineering Center of National Science Foundation (NSF) (DMR-0425880).

REFERENCES

(1) Park, M.; Harrison, C.; Chaikin, P. M.; Register, R. A.; Adamson, D. H. *Science* **1997**, *276*, 1401.
(2) Park, M.; Chaikin, P. M.; Register, R. A.; Adamson, D. H. *Appl. Phys. Lett.* **2001**, *79*, 257.
(3) Black, C. T.; Guarini, K. W.; Milkove, K. R.; Baker, S. M.; Russell, T. P.; Tuominen, M. T. *Appl. Phys. Lett.* **2001**, *79*, 409.
(4) Kim, H. C.; Jia, X. Q.; Stafford, C. M.; Kim, D. H.; McCarthy, T. J.; Tuominen, M.; Hawker, C. J.; Russell, T. P. *Adv. Mater.* **2001**, *13*, 795.
(5) Shin, K.; Leach, K. A.; Goldbach, J. T.; Kim, D. H.; Jho, J. Y.; Tuominen, M.; Hawker, C. J.; Russell, T. P. *Nano Lett.* **2002**, *2*, 933.
(6) Cheng, J. Y.; Ross, C. A.; Chan, V. Z. H.; Thomas, E. L.; Lammertink, R. G. H.; Vancso, G. J. *Adv. Mater.* **2001**, *13*, 1174.
(7) Naito, K.; Hieda, H.; Sakurai, M.; Kamata, Y.; Asakawa, K. *IEEE Trans. Magn.* **2002**, *38*, 1949.
(8) Guarini, K. W.; Black, C. T.; Zhang, Y.; Babich, I. V.; Sikorski, E. M.; Gignac, L. M. *Electron Devices Meeting, IEDM '03 Technical Digest. IEEE International* 2003, 22.2.1.
(9) Chai, J.; Wang, D.; Fan, X.; Buriak, J. M. *Nature Nanotechnol.* **2007**, *2*, 500.
(10) Darling, S. B. *Prog. Polym. Sci.* **2007**, *32*, 1152.
(11) Yang, S. Y.; Ryu, I.; Kim, H. Y.; Kim, J. K.; Jang, S. K.; Russell, T. P. *Adv. Mater.* **2006**, *18*, 709.
(12) Lopes, W. A.; Jaeger, H. M. *Nature* **2001**, *414*, 735.
(13) Darling, S. B.; Yufa, N. A.; Cisse, A. L.; Bader, S. D.; Sibener, S. J. *Adv. Mater.* **2005**, *17*, 2446.
(14) Watanabe, S.; Fujiwara, R.; Hada, M.; Okazaki, Y.; Iyoda, T. *Angew. Chem., Int. Ed.* **2007**, *46*, 1120.
(15) Sohn, B. H.; Seo, B. H. *Chem. Mater.* **2001**, *13*, 1752.
(16) Hasegawa, H.; Hashimoto, T. *Macromolecules* **1985**, *18*, 589.
(17) Fredrickson, G. H. *Macromolecules* **1987**, *20*, 2535.
(18) Henkee, C.; Thomas, E. L.; Fetters, L. J. *J. Mater. Sci.* **1988**, *23*, 1685.
(19) Anastasiadis, S. H.; Russell, T. P.; Satija, S. K.; Majkrzak, C. F. *J. Chem. Phys.* **1990**, *92*, 5677.
(20) Coulon, G.; Deline, V. R.; Russell, T. P.; Green, P. F. *Macromolecules* **1989**, *22*, 2581.
(21) Anastasiadis, S. H.; Russell, T. P.; Satija, S. K.; Majkrzak, C. F. *Phys. Rev. Lett.* **1989**, *62*, 1852.
(22) Lee, S.-H.; Kang, H.; Kim, Y. S.; Char, K. *Macromolecules* **2003**, *36*, 4907.
(23) Lee, S.-H.; Kang, H.; Cho, J.; Kim, Y. S.; Char, K. *Macromolecules* **2001**, *34*, 8405.
(24) Morkved, T. L.; Lu, M.; Urbas, A. M.; Ehrichs, E. E.; Jaeger, H. M.; Mansky, P.; Russell, T. P. *Science* **1996**, *273*, 931.
(25) Thurn-Albrecht, T.; Steiner, R.; DeRouchey, J.; Stafford, C. M.; Huang, E.; Bal, M.; Tuominen, M.; Hawker, C. J.; Russell, T. P. *Adv. Mater.* **2000**, *12*, 1138.
(26) Thurn-Albrecht, T.; Schotter, J.; Kastle, C. A.; Emley, N.; Shibauchi, T.; Krusin-Elbaum, L.; Guarini, K.; Black, C. T.; Tuominen, M. T.; Russell, T. P. *Science* **2000**, *290*, 2126.
(27) Mansky, P.; Liu, Y.; Huang, E.; Russell, T. P.; Hawker, C. *Science* **1997**, *275*, 1458.
(28) Huang, E.; Rockford, L.; Russell, T. P.; Hawker, C. J. *Nature* **1998**, *395*, 757.
(29) Ryu, D. Y.; Shin, K.; Drockenmuller, E.; Hawker, C. J.; Russell, T. P. *Science* **2005**, *308*, 236.
(30) In, I.; La, Y.-H.; Park, S.-M.; Nealey, P. F.; Gopalan, P. *Langmuir* **2006**, *22*, 7855.
(31) Kim, S. H.; Misner, M. J.; Xu, T.; Kimura, M.; Russell, T. P. *Adv. Mater.* **2004**, *16*, 226.
(32) Sivaniah, E.; Hayashi, Y.; Matsubara, S.; Kiyono, S.; Hashimoto, T.; Fukunaga, K.; Kramer, E. J.; Mates, T. *Macromolecules* **2005**, *38*, 1837.
(33) Morkved, T. L.; Jaeger, H. M. *Europhys. Lett.* **1997**, *40*, 643.
(34) Fasolka, M. J.; Banerjee, P.; Mayes, A. M.; Pickett, G.; Balazs, A. C. *Macromolecules* **2000**, *33*, 5702.
(35) Ryu, D. Y.; Wang, J.-Y.; Lavery, K. A.; Frockenmuller, E.; Satija, S. K.; Hawker, C. J.; Russell, T. P. *Macromolecules* **2007**, *40*, 4296.
(36) Huang, E.; Russell, T. P.; Harrison, C.; Chaikin, P. M.; Register, R. A.; Hawker, C. J.; Mays, J. *Macromolecules* **1998**, *31*, 7641.
(37) Huang, E.; Mansky, P.; Russell, T. P.; Harrison, C.; Chaikin, P. M.; Register, R. A.; Hawker, C. J.; Mays, J. *Macromolecules* **2000**, *33*, 80.
(38) Son, J. G.; Bulliard, X.; Kang, H.; Nealey, P. F.; Char, K. *Adv. Mater.* **2008**, *20*, 3643.
(39) Russell, T. P. *Mater. Sci. Rep.* **1990**, *5*, 171.
(40) Mansky, P.; Russell, T. P. *Macromolecules* **1995**, *28*, 8092.
(41) Mansky, P.; Russell, T. P.; Hawker, C. J.; Mays, J.; Cook, D. C.; Satija, S. K. *Phys. Rev. Lett.* **1997**, *79*, 237.
(42) Tokarev, I.; Krenek, R.; Burkov, Y.; Schmeisser, D.; Sidorenko, A.; Minko, S.; Stamm, M. *Macromolecules* **2005**, *38*, 507.
(43) Turner, M. S. *Phys. Rev. Lett.* **1992**, *69*, 1788.
(44) Walton, D. G.; Kellog, G. J.; Mayes, A. M.; Lambooy, P.; Russell, T. P. *Macromolecules* **1994**, *27*, 6225.
(45) Pereira, G. G.; Williams, D. R. M. *Macromolecules* **1999**, *32*, 758.
(46) Pereira, G. G.; Williams, D. R. M. *Macromolecules* **1999**, *32*, 8115.
(47) Ashok, B.; Muthukumar, M.; Russell, T. P. *J. Chem. Phys.* **2001**, *115*, 1559.
(48) Tsori, Y.; Andelman, D. *Macromolecules* **2002**, *35*, 5161.
(49) Potemkin, I. I. *Macromolecules* **2004**, *37*, 3505.
(50) Potemkin, I.; Busch, P.; Smilgies, D.-M.; Posselt, D.; Papadakis, C. M. *Macromol. Rapid Commun.* **2007**, *28*, 579.

Macromolecules

Article

pubs.acs.org/Macromolecules

Degree of Perfection and Pattern Uniformity in the Directed Assembly of Cylinder-Forming Block Copolymer on Chemically Patterned Surfaces

Huiman Kang,[†] Gordon S. W. Craig,[†] Eungnak Han,[‡] Padma Gopalan,[‡] and Paul F. Nealey*[,†]

[†]Department of Chemical and Biological Engineering, University of Wisconsin—Madison, 1415 Engineering Drive, Madison, Wisconsin 53706, United States

[‡]Department of Material Science and Engineering, University of Wisconsin—Madison, 1509 University Avenue, Madison, Wisconsin 53706, United States

ABSTRACT: Thin films of cylinder-forming polystyrene-*b*-poly(methyl methacrylate) block copolymer (PS-*b*-PMMA) were self-assembled on two sets of surfaces homogeneously covered with random copolymer brush composed of PS and PMMA (P(S-*r*-MMA)), having styrene fractions, F_{St}, ranging from 0.57 to 1.0: one set that had been exposed to the lithographic materials and processes without having been patterned and one set that had not. The resulting self-assembled morphologies revealed that the lithographic process shifted the nonpreferential composition of the P(S-*r*-MMA) brush from $F_{St} \sim 0.70$ to $F_{St} \sim 0.79$. PS-*b*-PMMA films were then directed to assemble with density multiplication on chemical patterns made from P(S-*r*-MMA), in which the surface chemistry of the background region of the pattern after lithography ranged from weakly PMMA-preferential (WMP, $F_{St} = 0.70$) to nonpreferential (NP, $F_{St} = 0.79$) to weakly PS-preferential (WSP, $F_{St} = 1.00$). The extent of density multiplication ranged from 1:1 to 16:1. The assemblies were analyzed in terms of defect quantity and cylinder diameter uniformity, as observed by top-down scanning electron microscopy (SEM). In general, many fewer defects were observed for the assemblies on the WSP chemical pattern than on the WMP chemical pattern. The best assemblies occurred on the NP chemical patterns, with no defects apparent in the SEM images of assemblies with up to 4:1 density multiplication and with spot size variation sufficiently low for bit patterned media applications. As the extent of density multiplication was increased (6:1, 9:1, and 16:1), the defect density monotonically increased.

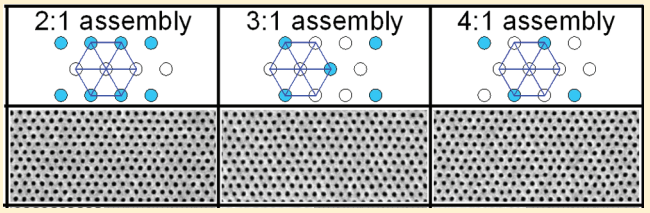

INTRODUCTION

Over the past decade, tremendous advances have been made in directing the assembly of block copolymer films to form templates that enhance and augment the lithographic process.[1−7] The primary motivation for investigating directed assembly on lithographically patterned surfaces is to improve the uniformity in size and shape of patterned features,[6,8] including nonregular structures,[9−11] and to enhance the resolution of the patterning process.[12,13] Resolution enhancements are possible via directed assembly with density multiplication, in which the density of features of the assembled block copolymer film is an integer multiple, known as the density multiplication factor, *n*, of the feature density of the underlying pattern. In the case of directed assembly with density multiplication on a chemical pattern, researchers have shown the ability to direct the assembly of block copolymers on low-density patterns of one chemistry, which is preferentially wet by one block, on a background of a different chemistry. The low-density pattern consists of guiding lines[9,12,14] or spots[13,15−17] for directed assembly of lamellae- and cylinder-forming block copolymers, respectively.

Recent simulations have suggested that the composition of the background and the dimensions of the guiding pattern dictate the quality of the assembly made with density multiplication. For example, Detcheverry et al. showed that vertical lamellae were only achieved in directed assembly with density multiplication when the interaction between one of the blocks of the copolymer and the background was relatively weak.[18] In their work, Detcheverry et al. identified six different stable morphologies that could assemble from a lamellae-forming block copolymer, depending on the width of the guiding lines and the chemistries of the guiding lines and background. Similarly, in the case of density multiplication with cylindrical domains, Ruiz et al. performed simulations in which the best assemblies were formed when the background had a weak affinity for one of the blocks of the copolymer.[13] When the background had a medium or strong affinity for one of the blocks, the cylindrical domains would be truncated near the chemical pattern. For both the cylinder- and lamellae-forming block copolymers, the formation of thermodynamically stable domains that do not have a uniform structure throughout the film has serious technological implications for their use in advanced lithography or as templates. At the same time, understanding the phenomena that generate other nonbulk

Received: October 6, 2011
Revised: November 9, 2011
Published: December 5, 2011

structures could open the door for technological applications that require a bicontinuous, three-dimensional morphology.

The fact that previous experimental work on the assembly of cylinder-forming polystyrene-*block*-poly(methyl methacrylate) block copolymers (PS-*b*-PMMA) used chemical patterns that started with materials that would give very different background interaction strengths, ranging from density multiplication on backgrounds based on PS brush, which would have a strong affinity for the PS block in PS-*b*-PMMA,[13] to interpolation on a nonpreferential brush made from a random copolymer of PS and PMMA (P(S-*r*-MMA)),[19,20] suggests that any understanding of the effect of the background chemistry on directed assembly must also take into account the potential that the pattern formation process could alter the chemistry of the background. In previous directed assembly research, the chemical pattern was often defined by depositing a polymer brush that would serve as the background region and then patterning and oxidizing regions of the brush to create the guiding features.[11,21−23] However, recent work has shown that the patterning process used to pattern a polymer brush could alter its surface chemistry.[24] In order for directed assembly with density multiplication to find the broadest technological implementation, it is necessary to enhance our understanding of how the background chemistry, along with other process inputs such as the density multiplication factor, affects process outputs, such as defect density.

Here we explore the effect of two fundamental process parameters: the composition of the chemical pattern and the density multiplication factor, n, on the number of defects and nonuniformities that form in equilibrated cylindrical domains assembled with density multiplication. We used a well-understood model system, consisting of PMMA-cylinder-forming PS-*b*-PMMA directed to assemble on a lithographically defined, chemically nanopatterned, spotted array, with varying chemical compositions and values of n ranging from 1 to 16. The background of the chemical patterns was composed of a P(S-*r*-MMA) with varying mole fraction of styrene, F_{St}.[23] F_{St} was chosen such that the background region was either weakly PS-preferential (WSP), nonpreferential (NP), or weakly PMMA-preferential (WMP).[25,26] Along with examining the effect of F_{St}, we also examined the effect that the lithographic process could have on the interaction of the PS-*b*-PMMA film with the patterned P(S-*r*-MMA) brush. The assemblies were imaged with top-down scanning electron microscopy (SEM) to quantify the uniformity of the domain diameters, and the SEM micrographs were analyzed with Voronoi diagrams to determine an accurate count of assembly defects.

EXPERIMENTAL SECTION

Materials. Asymmetric PS-*b*-PMMA (50.5 kg/mol PS, 20.9 kg/mol PMMA, and PDI = 1.06, bulk d-spacing ≈37 nm, bulk center-to-center distance between cylinders (L_0) ≈43 nm) was purchased from Polymer Source, Inc., and used as received. Hydroxyl-terminated P(S-*r*-MMA) (M_n = 6.2−6.8 kg/mol, PDI = 1.20−1.25) was synthesized as described before.[26] F_{St} values of the synthesized P(S-*r*-MMA) brushes were 0.57, 0.70, and 0.79. Hydroxyl-terminated polystyrene (PS-OH (F_{St} = 1); M_n = 6.0 kg/mol, PDI = 1.07) was synthesized using anionic polymerization. PMMA photoresist was purchased from MicroChem Corp. and had a M_n of 950 kg/mol.

Preparation of Chemically Patterned Surfaces. A ∼20 nm film of PS-OH or P(S-*r*-MMA)-OH was spin-coated onto a piranha-cleaned silicon wafer from a 1.0 wt % toluene solution and annealed under vacuum at 160 °C for 2 days in order to graft the polymer to the wafer via a dehydration reaction. Ungrafted polymer was then extracted using repeated sonication in warm toluene for no more than 10 min, resulting in a brush-coated wafer, as explained previously.[11,23] The procedure to pattern the grafted PS-OH or P(S-*r*-MMA)-OH brushes was described in earlier work.[11] A 50 nm thick PMMA photoresist film was spin-coated from a chlorobenzene solution on top of a brush-coated substrate. E-beam lithography was performed using a LEO 1550-VP field emission SEM operating with a J. C. Nabity nanoscale pattern generation system. Exposures utilized an accelerating voltage of 20 keV, a beam current of ∼27.5 pA, and line doses in the range of 0.08−0.60 nC/cm. All samples were developed for 30 s in a 1:3 solution of methyl isobutyl ketone:isopropyl alcohol (IPA), followed by IPA rinsing and nitrogen drying. Subsequently, the photoresist pattern was transferred to a chemical pattern in the PS or P(S-*r*-MMA) brushes by oxygen plasma etching, using a PE-200 Benchtop Plasma System (Plasma Etch, Inc.) plasma etch device, operated at 10 mTorr O_2 and a radio-frequency power of 80 W for 10 s. The oxygen-plasma-treated regions of the brushes were preferentially wet by PMMA, and the wetting property of the untreated region depended on the composition of brushes. Both spot location and density were defined during the e-beam patterning, as shown in Figure 1. A basic pattern for directed assembly of cylinder-forming block copolymer was a hexagonal array of spots. For controlling the density multiplication factor, we patterned with a rectangular array of spots for 2× and 6× multiplications, a 90° tilted hexagonal array of spots for 3× multiplication, and a hexagonal array of spots with 2, 3, and 4 times to the original periodicity for 4×, 9× and 16× multiplications, respectively.

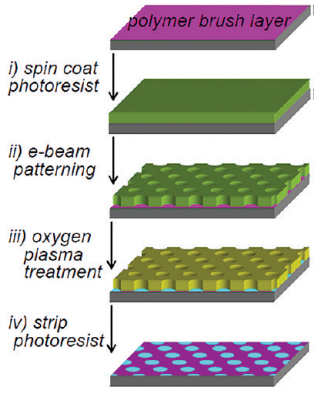

Figure 1. Representative schematic of chemical pattern fabrication with an e-beam lithographic process.

Thin Film Fabrication. PS-*b*-PMMA thin films were spin-coated from 1.3% solutions in toluene onto substrates coated with either unpatterned or chemically patterned surfaces. The resulting block copolymer thin film was 37 nm thick, as measured by ellipsometry (Rudolph Research Auto EL). The film was annealed under vacuum at 230 °C for 2 h, which provided sufficient time to achieve equilibrium morphology on the chemical pattern.

Characterization and Analysis. The patterns and the domain structures of the assembled block copolymer films on the chemical nanopatterns were imaged using a LEO 1550-VP field emission SEM with 1 keV acceleration voltage. To assist in image contrast of the films, the PMMA portions of the film were removed with 0.5 J/cm^2 exposures of 254 nm ultraviolet light followed by a 30 s rinse in glacial acetic acid, subsequent washing with deionized water, and drying by nitrogen gun. The analysis of the behavior of the self-assembled films on the different P(S-*r*-MMA) brushes was repeated three times to verify our observations. The sizes and locations of the hexagonally ordered spots on the various chemical patterns were determined by analyzing top-down SEM images of the postdevelop photoresist layer with ImageJ 1.40 g software, after normalizing the brightness and contrast of the images with Photoshop. Voronoi diagrams were generated through a custom MATLAB program.[27] The data presented

dx.doi.org/10.1021/ma202249n | *Macromolecules* 2012, 45, 159−164

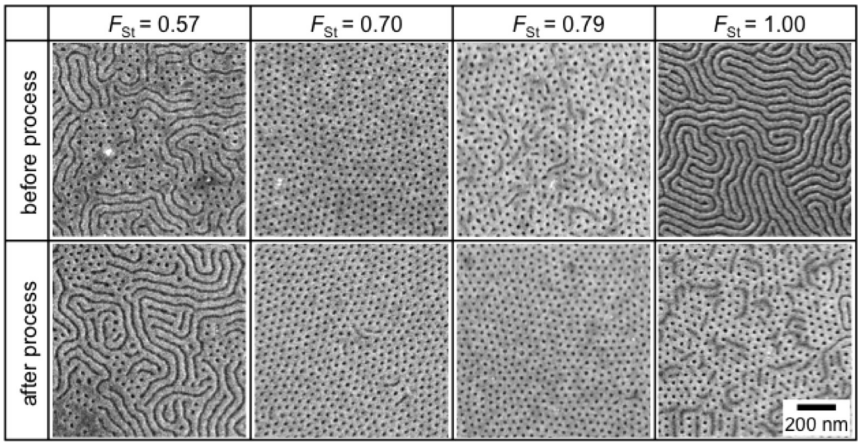

Figure 2. Top-down SEM images of PS-*b*-PMMA thin films on random copolymer brushes with varying styrene content. The random copolymer brushes of bottom row of SEM images were treated with the same lithographic process used to make chemical patterns, except that they did not undergo the e-beam exposure step. The images shown here are representative of the results from three repeats of each experiment.

for each condition were collected from more than 2000 spots per sample.

RESULTS AND DISCUSSION

We investigated the effect of F_{St} and n on the quality and uniformity of the assembled block copolymer film by creating chemical patterns following the scheme shown in Figure 1. Hydroxyl-terminated P(S-*r*-MMA), with specific values of F_{St}, was grafted onto a silicon wafer and used as an imaging layer. The spot pattern was formed with electron-beam lithography, using a 50 nm thick layer of PMMA photoresist. After developing the exposed resist, the resist pattern was transferred to the polymer brush by a brief oxygen plasma treatment. A thin film of PS-*b*-PMMA was subsequently spin-coated onto the chemical pattern, annealed under vacuum, and imaged with a SEM. The oxygen-plasma-treated spots were strongly preferential to the PMMA block of PS-*b*-PMMA, while the interaction of the background with the PS-*b*-PMMA varied with the F_{St} of the P(S-*r*-MMA) used to make the imaging layer. The key aspect of this approach is the ability to change the chemistry of the deposited brushes and hence the wetting properties and interfacial interactions of the blocks of the copolymer with the background region.

Although the wetting behavior of the brush as a function of F_{St} is well-understood for brushes as deposited (prior to processing),[26] it is possible that the chemisty of the background regions will change after patterning of the photoresist and subsequent photoresist stripping. To investigate the effect of lithographic processing on grafted brush layers with varying F_{St}, we examined 37 nm thick films of PS-*b*-PMMA self-assembled on top of unpatterned P(S-*r*-MMA) brushes with F_{St} values of 0.57, 0.70, 0.79, and 1 (PS homopolymer brush), both before and after exposure to the same chemical processing steps used in the lithographic process. The self-assembly behavior of thin films of PS-*b*-PMMA as a function of F_{St}, both before and after the lithographic process steps, is shown in the top-down SEM images in Figure 2. Prior to the lithographic process steps, parallel cylinders formed on the brushes that were either PMMA- or PS-preferential (F_{St} = 0.57 or 1, respectively), while perpendicular cylinders formed on the brushes with F_{St} of 0.70 or 0.79, matching previous reports on the self-assembly of PS-*b*-PMMA on unpatterned P(S-*r*-MMA).[25,28,29] In the case of self-assembly on the unpatterned P(S-*r*-MMA) brushes after exposure to the lithographic process, the range of morphologies that was observed was generally the same as in the self-assembled films on brushes that were not exposed to lithography, and only the range of compositions over which parallel or perpendicular cylinders were observed shifted to higher values of F_{St}. Perpendicular cylinders were predominant in the films on the brushes with F_{St} equal to 0.70, 0.79, and 1. Significantly, the sample with the most perpendicular cylinders, indicative of a nonpreferential (NP) substrate, shifted from F_{St} = 0.70 before processing, in agreement with previous reports,[28] to F_{St} = 0.79 after processing. Similar shifts were seen in the F_{St} values for brushes that were weakly PMMA preferential (WMP, 0.59 before processing to 0.70 after processing) or weakly PS preferential (WSP, 0.79 to 1). A structure similar to that shown in Figure 2 for F_{St} = 1 was also observed by Ruiz et al. in assemblies of cylinder-forming PS-*b*-PMMA on unpatterned regions of PS brush (F_{St} = 1) after the brush had undergone lithographic processing.[13] Our results suggest that the lithographic processing alters the wetting behavior of the brush in such a way as to appear to increase the F_{St} value of the P(S-*r*-MMA) by 0.09−0.11. The presence of residual lithographic process material, which we hypothesize to be traces of entrained PMMA photoresist, is one possible reason for the shift of the NP F_{St} to a larger value after the lithographic process. For the rest of the paper we will refer to the WMP, NP, and WSP substrates *after lithographic processing*, corresponding to the brushes with F_{St} values of 0.70, 0.79, and 1, respectively.

Directed assembly with density multiplication was studied with chemical patterns made on the WMP, NP, and WSP substrates and designed with n ranging from 1 to 16. The effect of the background chemistry and n on the directed assembly of PS-*b*-PMMA is shown in the top-down SEM images and inset Voronoi diagrams in Figure 3A. On the patterns made with the WMP P(S-*r*-MMA) brushes the assembled block copolymer film had defects in the hexagonal arrangement of the cylinders, even on the 1:1 (n = 1) chemical pattern. The defects were especially apparent in the Voronoi diagrams, in which colored spots indicated locations where the nearest neighbors to a cylinder did not form a hexagon, instead forming a pentagon, heptagon, or other polygon. As n increased from 2 to 4, the number of defects monotonically increased. In contrast to the results of directed assembly on the WMP brushes, directed

dx.doi.org/10.1021/ma202249n | *Macromolecules* 2012, 45, 159−164

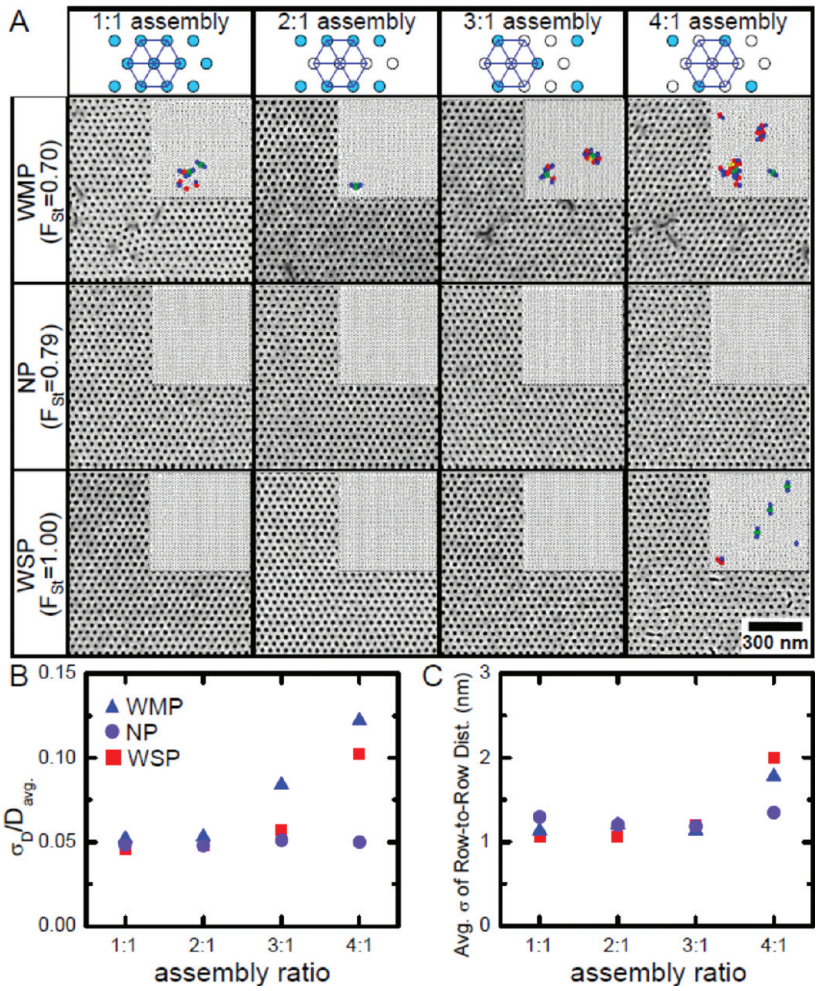

Figure 3. Effect of interfacial interactions and density multiplication assembly ratios on assembled PS-*b*-PMMA thin films on chemical patterns. (A) Top-down SEM images and corresponding Voronoi diagrams, shown as insets. (B) Statistics of spot size variation and (C) spot location variation. Filled and unfilled spots in the schematics on the top row represent patterned and density multiplied spots, respectively. Standard deviation of spot diameter (σ_D) over averaged spot diameter (D_{avg}) and averaged standard deviation of row-to-row distance versus assembly ratio of density multiplication were determined from more than 2000 spots for each system.

assembly on the NP or WSP brushes yielded assemblies for which images at this magnification typically showed few, if any, defects, except for the WSP substrate on the 4:1 (n = 4) chemical pattern. For 4:1 density multiplication on the three substrates in the test, the best assembly was observed on the substrate that exhibited NP behavior after processing in Figure 2. Our results at 4:1 density multiplication were similar to the results of Tada et al., who observed that the fewest defects in an assembly of cylinder-forming PS-*b*-PMMA were observed on a PS brush made with an intermediate M_n value, which corresponded to a moderate contact angle of PS on the brush.[16] Their measured contact angle of 6° suggested that their optimal PS brush was neither strongly PS- nor PMMA-preferential, but instead either NP or WSP.

The effect of n and the surface chemistry of the background on the assembly was also analyzed in terms of the standard deviations of the spot diameter (σ_D) and the spot spacing (σ_S) in the top-down SEMs of the assembled domains, as shown in Figure 3B,C. On the WMP brushes with n > 2, there was more variation in σ_D than there was on the corresponding assemblies on the NP and WSP brushes. On the WSP brushes, σ_D/D_{avg} could be kept at ~0.05 for n values up to 3 (D_{avg} = average spot diameter). On the NP brushes, n could be increased to 4 without causing σ_D/D_{avg} to increase beyond 0.05. It is worth noting that this level of σ_D/D_{avg} is acceptable for some applications, such as bit patterned media application, in which the variation of the bit (spot) size and location must not surpass ~5% to maintain adequate signal-to-noise ratio.[30,31] In terms of σ_S, all three substrates yielded uniform σ_S for n values up to 3. When n equaled 4, the σ_S values increased for all 3 substrates, with the value for the NP substrate increasing the least.

In general, Figure 3 shows that as n increased, the optimal background composition of the three compositions tested shifted from WSP at n = 1 to NP at n = 4, with WSP appearing to be slightly better at n = 2 and NP to be slightly better at n = 3. The effect of n and F_{St} on the quality of the assembly can be understood in terms of their effect on the free energy of the system. When n = 1 (1:1 assembly), only the PS block will be above the background, and therefore the system with the highest F_{St} (the WSP background, in this case) will have the lowest energy of the systems in Figure 3. In the case of directed assembly with density multiplication (n > 1), some PMMA will be above the background. Ruiz et al. used molecular simulations that minimized the free energy of a cylinder-forming block copolymer assembled with density multiplication on a chemical

dx.doi.org/10.1021/ma202249n | *Macromolecules* 2012, 45, 159–164

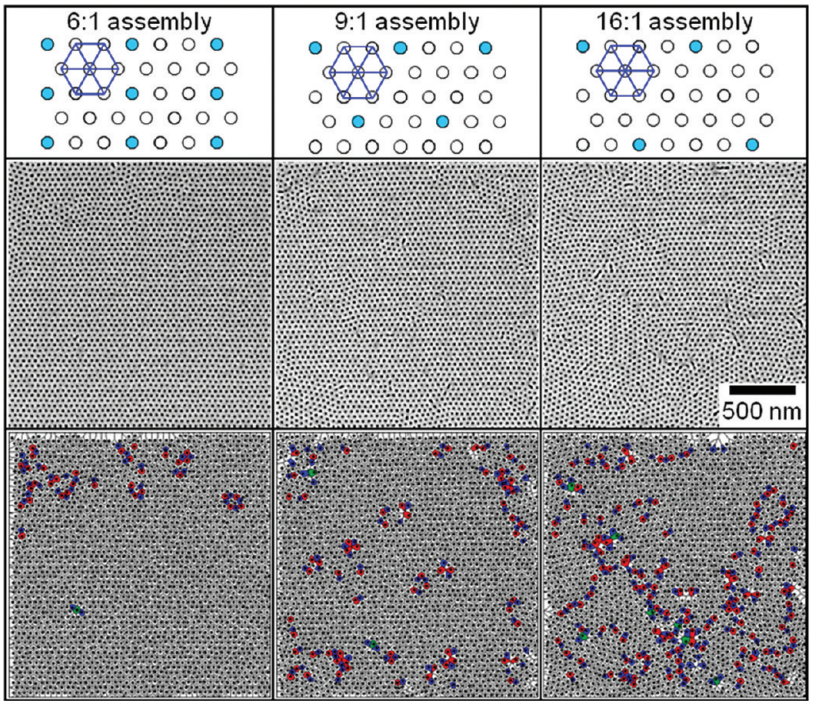

Figure 4. Top-down SEM images of PS-*b*-PMMA thin film on various chemical patterns with NP background and higher density multiplication, and corresponding Voronoi diagrams.

pattern to show that the best three-dimensional structures were obtained with a WSP background.[13] Here we show that the WSP background yielded the assemblies with the most uniform shape and the fewest defects when $n = 2$. As n is further increased to 3 and 4, the amount of PMMA above the background increases. To minimize the free energy of the system provided by the background, the MMA content of the background will increase, F_{St} will correspondingly decrease, and the lowest energy background will transition from WSP to NP.

The asymmetry of the defect density about the NP chemical composition ($F_{St} = 0.79$), with few defects observed in the assemblies on the NP and WSP chemical patterns, but many defects observed on the WMP chemical pattern, is most likely due to the affinity of the background region for PMMA on the WMP substrate. As a result of the PMMA affinity, one potential configuration for the morphology of the blend is to have PMMA cylinders lying flat against the background region of the chemical pattern in addition to wetting the spots of the chemical pattern. Even if the parallel domain structure did not propagate upward through the blend film, the presence of the PMMA cylinders against the substrate would impede the ability of the chemical pattern to guide the assembly.

Following the studies described above, we assembled PS-*b*-PMMA thin films on chemical patterns with NP background regions and n values of 6, 9, and 16. As shown in the top-down SEM images and Voronoi diagrams in Figure 4, as n increased, more defects were present in the hexagonal arrangement of the assembled cylinders, even when the best background composition for assemblies with large n was used. The effect of n can be seen most clearly in the Voronoi diagrams in Figure 4. As n is increased, the number of defect structures monotonically increases. The combined effect of the background surface chemistry and n on the ability of a chemical pattern to direct assembly with density multiplication is analogous to previous results on 1:1 chemical patterns, in which the ability to obtain defect free structures depended on the surface chemistry of the chemical pattern,[32] and the commensurability of the chemical pattern period[23] or layout[33] with the bulk morphology of the block copolymer.

The combination of results shown in Figures 3 and 4 lead us to hypothesize that the number of defects and nonuniformities in directed assembly with density multiplication increase monotonically as the assembly moves away from the ideal condition. The steady increase in the number of defects as n increased, shown in Figure 4, supports this hypothesis. Similarly, Tada et al. observed that the tolerance for incommensurability between the spacing of the chemical pattern and the bulk morphology decreased as n increased.[15] In terms of the surface chemistry, the assemblies for $n = 4$ in Figure 3 show that as the surface chemistry moved away from an optimum, the number of defects increased. While we did not attempt to optimize the surface chemistry in this study, we could conclude that the NP brush must have been the closest to the optimum of the three brushes that we studied. The NP brush also exhibited nonpreferential behavior, indicating that it fell within a range of surface chemistries that exhibit NP behavior for the self-assembly of cylinder-forming block copolymers.[25]

■ CONCLUSION

In summary, we can conclude that to achieve the optimum conditions for directed assembly of cylindrical domains with density multiplication, in terms of minimizing defects and nonuniformities, it is necessary to use a background material in the chemical pattern that is tuned for the overlying material. At low n it will be necessary to have a brush that is more WSP than at high n. This conclusion points to the need to develop a chemical pattern system in which the composition of the background region can be tuned independently of the guiding lines. It is also important to understand the effect that previous

dx.doi.org/10.1021/ma202249n | *Macromolecules* 2012, 45, 159–164

processing can have on the interaction of the chemical pattern with the block copolymer. In our case, the lithographic process used to define the chemical pattern substantially affected the surface chemistry of the brush and therefore its interaction with the block copolymer. The findings in this work should be useful in integrating directed assembly of block copolymers with density multiplication into technologies requiring superior resolution and minimal pattern defects, such as advanced lithography and bit patterned media.

AUTHOR INFORMATION

Corresponding Author

*E-mail: nealey@engr.wisc.edu.

ACKNOWLEDGMENTS

This work was supported by the Semiconductor Research Corporation (2008-OJ-1674.002) and the NSF UW Nanoscale Science and Engineering Center (DMR-0425880).

REFERENCES

(1) Cheng, J. Y.; Ross, C. A.; Smith, H. I.; Thomas, E. L. *Adv. Mater.* **2006**, *18* (19), 2505−2521.

(2) Nealey, P. F.; Edwards, E. W.; Müller, M.; Stoykovich, M. P.; Solak, H. H.; De Pablo, J. J. *IEEE Tech. Dig. IEDM* **2005**, 356−359.

(3) Park, M.; Harrison, C.; Chaikin, P. M.; Register, R. A.; Adamson, D. H. *Science* **1997**, *276*, 1401−1404.

(4) Park, S.; Lee, D. H.; Xu, J.; Kim, B.; Hong, S. W.; Jeong, U.; Xu, T.; Russell, T. P. *Science* **2009**, *323*, 1030−1033.

(5) Ross, C. A.; Cheng, J. Y. *MRS Bull.* **2008**, *33* (9), 838−845.

(6) Stoykovich, M. P.; Nealey, P. F. *Mater. Today* **2006**, *9* (9), 20−29.

(7) Hawker, C. J.; Russell, T. P. *MRS Bull.* **2005**, *30* (12), 952−966.

(8) Stoykovich, M. P.; Daoulas, K. C.; Muller, M.; Kang, H. M.; de Pablo, J. J.; Nealey, P. F. *Macromolecules* **2010**, *43* (5), 2334−2342.

(9) Liu, G.; Thomas, C. S.; Craig, G. S. W.; Nealey, P. F. *Adv. Funct. Mater.* **2010**, *20* (8), 1251−1257.

(10) Stoykovich, M. P.; Kang, H.; Daoulas, K. C.; Liu, G.; Liu, C. C.; de Pablo, J. J.; Mueller, M.; Nealey, P. F. *ACS Nano* **2007**, *1* (3), 168−175.

(11) Stoykovich, M. P.; Muller, M.; Kim, S. O.; Solak, H. H.; Edwards, E. W.; de Pablo, J. J.; Nealey, P. F. *Science* **2005**, *308* (5727), 1442−1446.

(12) Cheng, J. Y.; Rettner, C. T.; Sanders, D. P.; Kim, H. C.; Hinsberg, W. D. *Adv. Mater.* **2008**, *20* (16), 3155−3158.

(13) Ruiz, R.; Kang, H.; Detcheverry, F. A.; Dobisz, E.; Kercher, D. S.; Albrecht, T. R.; de Pablo, J. J.; Nealey, P. F. *Science* **2008**, *321*, 936−939.

(14) Cheng, J. Y.; Sanders, D. P.; Truong, H. D.; Harrer, S.; Friz, A.; Holmes, S.; Colburn, M.; Hinsberg, W. D. *ACS Nano* **2010**, *4* (8), 4815−4823.

(15) Tada, Y.; Akasaka, S.; Takenaka, M.; Yoshida, H.; Ruiz, R.; Dobisz, E.; Hasegawa, H. *Polymer* **2009**, *50* (17), 4250−4256.

(16) Tada, Y.; Akasaka, S.; Yoshida, H.; Hasegawa, H.; Dobisz, E.; Kercher, D.; Takenaka, M. *Macromolecules* **2008**, *41* (23), 9267−9276.

(17) Kang, H. M.; Detcheverry, F.; Stuen, K. O.; Craig, G. S. W.; de Pablo, J. J.; Gopalan, P.; Nealey, P. F. *J. Vac. Sci. Technol., B* **2010**, *28* (6), C6B24−C6B29.

(18) Detcheverry, F. A.; Liu, G. L.; Nealey, P. F.; de Pablo, J. J. *Macromolecules* **2010**, *43* (7), 3446−3454.

(19) Park, S. H.; Shin, D. O.; Kim, B. H.; Yoon, D. K.; Kim, K.; Lee, S. Y.; Oh, S. H.; Choi, S. W.; Jeon, S. C.; Kim, S. O. *Soft Matter* **2010**, *6* (1), 120−125.

(20) Kim, S. O.; Kim, B. H.; Meng, D.; Shin, D. O.; Koo, C. M.; Solak, H. H.; Wang, Q. *Adv. Mater.* **2007**, *19* (20), 3271−3275.

(21) Wilmes, G. M.; Durkee, D. A.; Balsara, N. P.; Liddle, J. A. *Macromolecules* **2006**, *39* (7), 2435−2437.

(22) Bosworth, J. K.; Paik, M. Y.; Ruiz, R.; Schwartz, E. L.; Huang, J. Q.; Ko, A. W.; Smilgies, D. M.; Black, C. T.; Ober, C. K. *ACS Nano* **2008**, *2* (7), 1396−1402.

(23) Edwards, E. W.; Montague, M. F.; Solak, H. H.; Hawker, C. J.; Nealey, P. F. *Adv. Mater.* **2004**, *16* (15), 1315−1319.

(24) Liu, C. C.; Han, E.; Onses, M. S.; Thode, C. J.; Ji, S. X.; Gopalan, P.; Nealey, P. F. *Macromolecules* **2011**, *44* (7), 1876−1885.

(25) Han, E.; Stuen, K. O.; La, Y. H.; Nealey, P. F.; Gopalan, P. *Macromolecules* **2008**, *41* (23), 9090−9097.

(26) Mansky, P.; Liu, Y.; Huang, E.; Russell, T. P.; Hawker, C. *Science* **1997**, *275* (5305), 1458−1460.

(27) Liu, C. C.; Craig, G. S. W.; Kang, H. M.; Ruiz, R.; Nealey, P. F.; Ferrier, N. J. *J. Polym. Sci., Part B: Polym. Phys.* **2010**, *48* (24), 2589−2603.

(28) Han, E.; Stuen, K. O.; Leolukman, M.; Liu, C. C.; Nealey, P. F.; Gopalan, P. *Macromolecules* **2009**, *42* (13), 4896−4901.

(29) Ryu, D. Y.; Ham, S.; Kim, E.; Jeong, U.; Hawker, C. J.; Russell, T. P. *Macromolecules* **2009**, *42* (13), 4902−4906.

(30) Yang, X. M.; Wan, L.; Xiao, S. G.; Xu, Y. A.; Weller, D. K. *ACS Nano* **2009**, *3* (7), 1844−1858.

(31) Richter, H. J.; Dobin, A. Y.; Lynch, R. T.; Weller, D.; Brockie, R. M.; Heinonen, O.; Gao, K. Z.; Xue, J.; van der Veerdonk, R. J. M.; Asselin, P.; Erden, M. F. *Appl. Phys. Lett.* **2006**, *88* (22), 222512.

(32) Craig, G. S. W.; Nealey, P. F. *J. Vac. Sci. Technol., B* **2007**, *25* (6), 1969−1975.

(33) Park, S. M.; Craig, G. S. W.; La, Y. H.; Solak, H. H.; Nealey, P. F. *Macromolecules* **2007**, *40*, 5084−5094.

Macromolecules

Article

pubs.acs.org/Macromolecules

Ultrathin Free-Standing Polymer Films Deposited onto Patterned Ionic Liquids and Silicone Oil

Robert J. Frank-Finney, Patrick D. Haller, and Malancha Gupta*

Mork Family Department of Chemical Engineering and Materials Science, University of Southern California, 925 Bloom Walk, Los Angeles, California 90089, United States

ABSTRACT: We studied the vapor deposition of polymers onto the surfaces of silicone oil and imidazolium-based ionic liquids (ILs). We found that the deposition of poly(2-hydroxyethyl methacrylate) (PHEMA) and poly(*N*-isopropylacrylamide) (PNIPAAm) resulted in polymer particles on silicone oil whereas continuous polymer skins formed on 1-butyl-3-methylimidazolium hexafluorophosphate ([bmim][PF_6]), 1-butyl-3-methylimidazolium tetrafluoroborate ([bmim][BF_4]), and 1-ethyl-3-methylimidazolium tetrafluoroborate ([emim][BF_4]). The silicone oil and ILs were patterned onto a common substrate by exploiting their different wetting properties. Ultrathin free-standing PHEMA and PNIPAAm films of different shapes were produced by confining the shape of the IL within a wax barrier, surrounding it with silicone oil, and then depositing the polymer. The silicone oil prevented the polymer film from connecting to the underlying substrate and maintained the shape of the polymer film during deposition. Our process allows for multidimensional control over the resulting free-standing film: the area of the shape can be controlled by patterning the IL, and the thickness of the film can be controlled by adjusting the duration of polymer deposition. The films are highly pure and do not contain any residual monomer or solvent entrapment which extends their potential applications to include in vivo biomedical research.

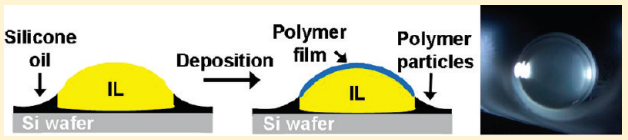

INTRODUCTION

The initiated chemical vapor deposition (iCVD) technique is a one-step, solventless free radical polymerization process that can be used to deposit a wide range of polymer films such as poly(2-hydroxyethyl methacrylate) (PHEMA),[1] poly(4-vinylpyridine) (P4VP),[2] and poly(1*H*,1*H*,2*H*,2*H*-perfluorodecyl acrylate) (PPFDA).[3] The iCVD technique is typically used to deposit polymer coatings onto solid substrates such as silicon wafers,[4] membranes,[5] wires,[6] carbon nanotubes,[7] and fibers.[8] We recently demonstrated the ability to deposit polymer coatings onto ionic liquids (ILs).[9] ILs are salts that are liquids at ambient temperatures, and they have recently attracted significant interest as environmentally friendly alternatives to traditional volatile organic solvents because they are non-volatile, nonflammable, and can be easily recycled.[10,11] Our previous work examined the deposition of PHEMA and PPFDA in the presence of 1-butyl-3-methylimidazolium hexafluorophosphate ([bmim][PF_6]) droplets. We found that polymerization occurred at the vapor−IL interface and/or within the bulk IL depending on the solubility of the monomer within the IL and the reaction conditions such as the duration of deposition and stage temperature.

In this paper, we use iCVD to deposit polymers onto silicone oil for the first time. We observe different polymer morphologies on the silicone oil as compared to the ILs, and we exploit this difference to fabricate ultrathin free-standing polymer films of different shapes by combining the silicone oil and ILs onto a common substrate. The generality of our fabrication method is demonstrated for multiple polymers and a range of imidazolium-based ILs. Our ability to produce free-standing polymer films is useful for a wide variety of applications in optics,[12] sensing,[13,14] and separations.[15] The fabrication of free-standing polymer films typically requires multiple steps such as spin-coating polymers onto sacrificial layers and then removal of the sacrificial layers using several steps of washing with various solvents.[16−20] The fabrication process that we present in this paper is environmentally friendly because no organic solvents are used in any of the steps. The free-standing polymer films produced by our method are highly pure and do not contain any residual monomer or solvent entrapment which will allow biomedical researchers to use these films for in vivo applications such as tissue engineering, surgical applications, and drug delivery.

RESULTS AND DISCUSSION

We studied the deposition of PHEMA onto 5 μL droplets of silicone oil, [bmim][PF_6], 1-butyl-3-methylimidazolium tetrafluoroborate ([bmim][BF_4]), and 1-ethyl-3-methylimidazolium tetrafluoroborate ([emim][BF_4]) placed on a silicon wafer. In the iCVD process, monomer and initiator molecules are flowed continuously into a vacuum chamber where the initiator molecules are broken into free radicals by a heated filament array. Polymerization occurs on the surface of the substrate via a free-radical mechanism.[21] In the case of the imidazolium-based ionic liquids, HEMA monomer molecules can absorb into the ILs and polymerization can occur at both the vapor−IL interface and within the bulk IL. In the case of silicone oil,

Received: October 9, 2011
Revised: December 10, 2011
Published: December 19, 2011

   dx.doi.org/10.1021/ma202268j | *Macromolecules* 2012, 45, 165−170

HEMA molecules do not appreciably absorb into the silicone oil, and therefore polymerization should only occur at the vapor−silicone oil interface. Figure 1 shows the images of the

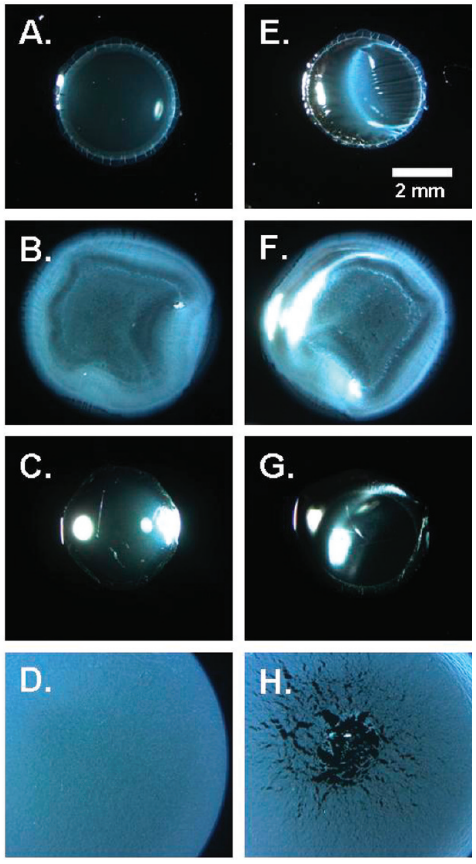

Figure 1. Images of 15 min of deposition of PHEMA onto (A) [bmim][PF_6], (B) [bmim][BF_4], (C) [emim][BF_4], and (D) silicone oil. (E−H) The droplets were subjected to a continuous stream of air to show that a continuous skin of PHEMA formed on the ILs, but only particles of PHEMA formed on the silicone oil.

droplets taken after 15 min of deposition. A continuous polymer skin that completely encapsulates the droplet formed on all three ILs, while unconnected polymer particles formed on the silicone oil. An air stream was applied to the droplets to demonstrate the continuous nature of the polymer skins on the ILs and the granular nature of the polymer on the silicone oil. Fourier transform infrared spectroscopy (FTIR) was used to study the chemical structure of the PHEMA deposited on silicone oil and the ILs. Figure 2 shows that all of the spectra have the expected PHEMA peaks including the broad O−H stretching peak from 3600 to 3100 cm^{-1}, C−H stretching peaks from 3050 to 2800 cm^{-1}, the C═O peak from 1750 to 1685 cm^{-1}, C−H bending from 1520 to 1350 cm^{-1}, and C−O stretching from 1310 to 1210 cm^{-1}.[9] The spectra are nearly identical, demonstrating that the polymer is highly pure and that varying the liquid substrate does not affect the composition of the polymer.

The different polymer morphology on the silicone oil versus the ILs can be exploited to fabricate free-standing films. The skins that are formed on the IL droplet are connected to the underlying silicon wafer and therefore cannot be removed without tearing. For example, Figure 3A shows that PHEMA completely encapsulates [bmim][PF_6] droplets that are placed

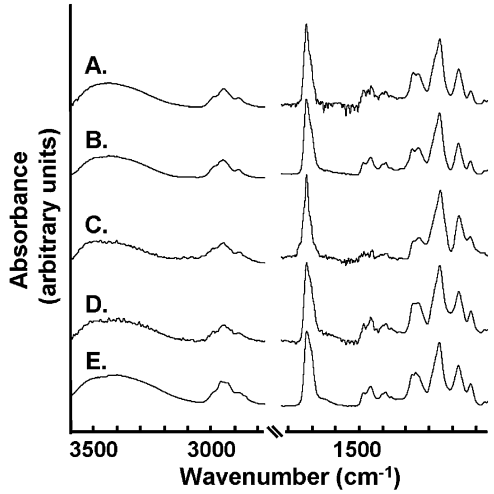

Figure 2. FTIR spectra of (A) a PHEMA film deposited onto a wafer, (B) a PHEMA skin formed on [bmim][PF_6], (C) a PHEMA skin formed on [bmim][BF_4], (D) a PHEMA skin formed on [emim]-[BF_4], and (E) PHEMA particles deposited onto silicone oil.

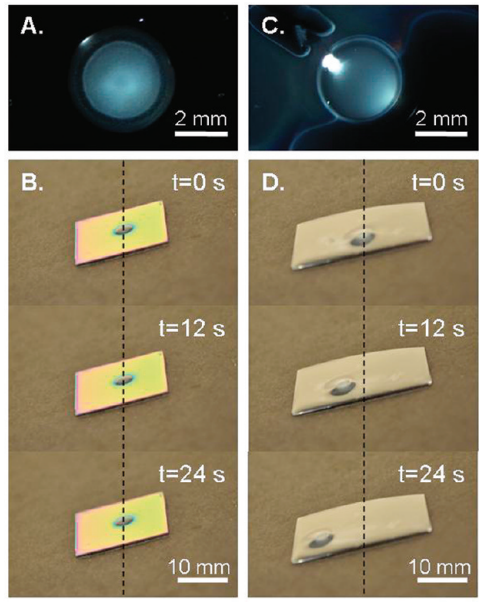

Figure 3. Images of 60 min of deposition of PHEMA onto a [bmim][PF_6] droplet that was placed on (A) a silicon wafer and (C) a silicon wafer covered with a layer of silicone oil. (B, D) The substrate was tilted at a 15° angle after the deposition.

directly onto silicon wafers. These encapsulated droplets do not move when the substrate is tilted at a 15° angle (Figure 3B). In order to make free-standing polymer films, we combined the ILs and silicone oil onto a common substrate. Silicone oil was first dispensed onto silicon wafers and allowed to spread over the wafer surface. The silicone oil completely wets the surface of the silicon wafer, forming a thin layer (~30 μm) onto which IL droplets can then be placed. Figure 3C shows that a continuous PHEMA film forms on the IL droplet, whereas only polymer particles form on the surrounding silicone oil. Figure 3D shows that the droplet slides when the substrate is tilted at a 15° angle. This verifies that the silicone oil acts as a lubricating layer to prevent the polymer that forms on the IL from connecting to the underlying wafer. The contact angles for [bmim][PF_6], [emim][BF_4], and [bmim][BF_4] are 38°, 28°,

dx.doi.org/10.1021/ma202268j | *Macromolecules* 2012, 45, 165−170

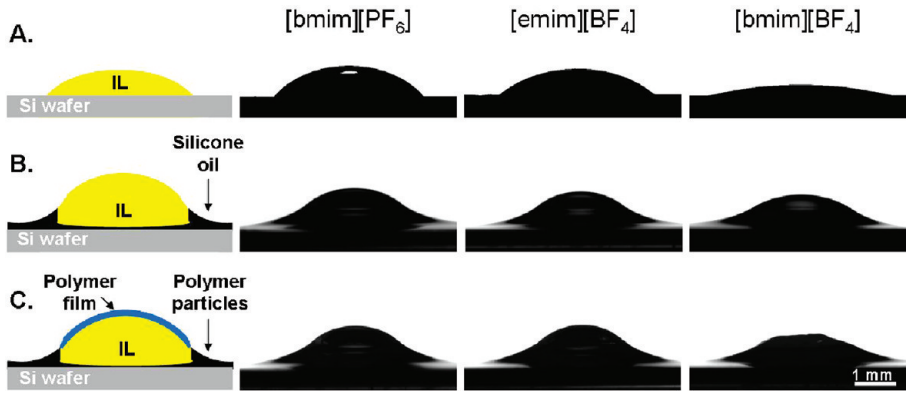

Figure 4. Contact angle goniometer images of (A) IL droplets on silicon wafers, (B) IL droplets on a layer of silicone oil, and (C) the same droplets after 60 min of deposition of PHEMA.

and 19°, respectively, on a silicon wafer (Figure 4A). When the IL is placed on top of the silicone oil, a thin layer of oil remains between the IL and the underlying silicon wafer, and the silicone oil forms a concave meniscus on the side of the IL droplet. This meniscus makes it impossible to measure a contact angle for the IL on the silicone oil; however, Figure 4B shows that the trend in wettability is the same on silicone oil as on a silicon wafer, i.e., that [bmim][BF_4] wets the most and [bmim][PF_6] wets the least. Without the use of silicone oil, the IL droplet spreads on the silicon wafer during PHEMA deposition due to both monomer absorption into the IL and the increased attraction between the IL and the PHEMA film formed on the silicon substrate surrounding the droplet. In contrast, the use of silicone oil prevents the IL droplets from spreading during PHEMA deposition. Comparison of parts B and C of Figure 4 shows no noticeable change in the curvature or diameter of the IL droplets after polymer deposition. We believe that the meniscus acts as a barrier to prevent the spreading of the IL droplet during deposition.

The shape of the free-standing polymer film can be controlled by patterning the IL and silicone oil onto the substrate. Figure 5 shows a schematic of this fabrication method. First, an outline of a shape is drawn onto the substrate using wax. The IL is then dispensed into the outline. The wax barrier contains the IL within the shape because the IL does not wet the wax. In the case of [bmim][BF_4], the wax outline was drawn onto a bare silicon wafer. In the cases of [bmim][PF_6] and [emim][BF_4], the wax outline was drawn onto a silicon wafer that was precoated with PHEMA in order to increase the spreading of the IL into the corners of the shape. Silicone oil was then added in multiple locations around the outside of the wax barrier and allowed to spread over the barrier and encompass the IL. The silicone oil serves two purposes in this fabrication process: it maintains the shape of the original IL droplet during deposition, and it prevents the polymer film from connecting to the underlying substrate. We would like to note that there is no lubricating layer of silicone oil underneath the IL in this fabrication method since the IL is dispensed before the silicone oil. Therefore, the IL will not slide when the substrate is tilted. After deposition of polymer, the free-standing polymer film can be removed from the IL either by inserting a razor underneath the film and lifting it off or by submerging the entire substrate in silicone oil which allows the film to float off the IL.

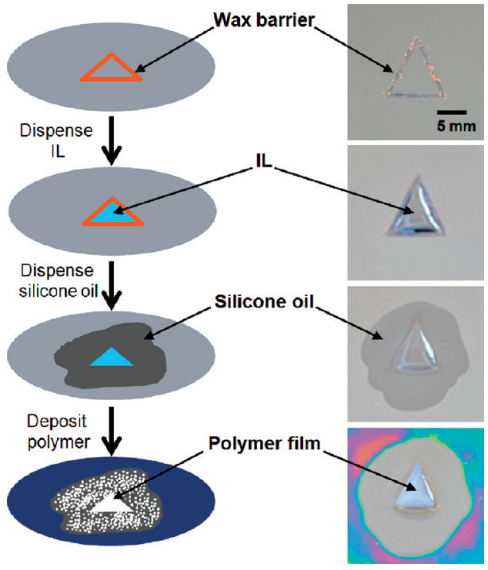

Figure 5. Fabrication method for making shaped polymer films.

Figure 6 shows the generality of our fabrication method for two different ILs and two different polymers. A triangular PHEMA film was formed on [bmim][BF_4] after 30 min of deposition. The FTIR spectrum of the PHEMA film showed no difference from the spectrum of PHEMA deposited on a silicon wafer, indicating the high purity of the film. The free-standing film had an average thickness of 510 ± 64 nm at the edge of the triangle and 663 ± 35 nm at the center. The increased thickness at the center of the film is caused by the integration of polymer chains that form within the bulk IL since polymerization takes place simultaneously at both the vapor−IL interface and within the IL at the conditions used for our study.[9] Similar to PHEMA, the deposition of poly(*N*-isopropylacrylamide) (PNIPAAm) also results in polymer particles on silicone oil and polymer skins on each of the three ILs. Therefore, we can use our fabrication method to form shaped PNIPAAm films. A square PNIPAAm film was formed on [bmim][PF_6] after 135 min of deposition. The film had an average thickness of 445 ± 30 nm at the edge of the square and 469 ± 41 nm at the center. The PNIPAAm film had the expected FTIR peaks: asymmetric $-CH_3$ stretching at 2969 cm^{-1}, asymmetric $-CH_2-$ stretching at 2931 cm^{-1}, symmetric $-CH_3$ stretching at 2880 cm^{-1}, secondary amide C═O stretching at 1652 cm^{-1}, $-CH_3$ and $-CH_2-$ deformation at 1458 cm^{-1}, and $-CH_3$ deformation at 1387 and 1366 cm^{-1}.[22] Compared to the PNIPAAm deposited

dx.doi.org/10.1021/ma202268j | *Macromolecules* 2012, 45, 165−170

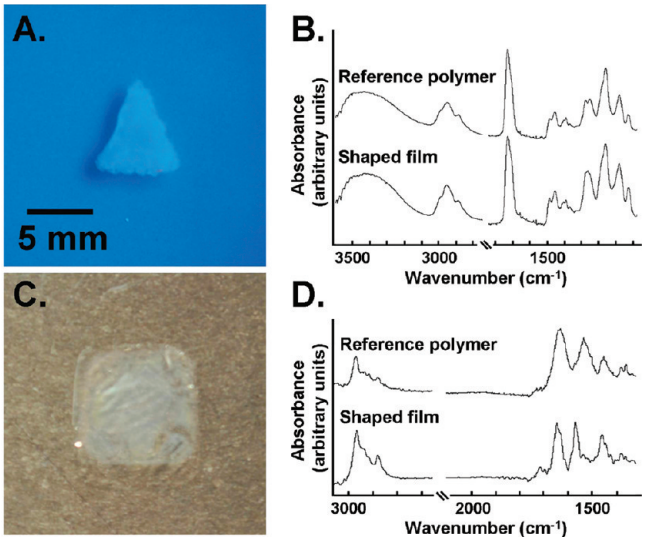

Figure 6. Images and corresponding FTIR spectra of free-standing shaped films of (A, B) PHEMA formed on [bmim][BF_4] and (C, D) PNIPAAm formed on [bmim][PF_6]. The films were removed from the template and placed in a bath of silicone oil for imaging.

onto a wafer, the shaped free-standing PNIPAAm film had a shift in the location of the secondary amide N−H stretching from 1540 to 1575 cm^{-1}. This is likely due to the mobility of the PNIPAAm chains in the free-standing film that allows for hydrogen bonding between the C═O and N−H groups.[23]

In addition to PHEMA and PNIPAAm, we found that the deposition of several other polymers including poly(*o*-nitrobenzyl methacrylate) (P*o*NBMA) and poly(pentafluorophenyl methacrylate) (PPFM) also yields particles on silicone oil and skins on the ILs. The formation of particles on silicone oil has also been examined in the deposition of silver,[24] copper,[25] gold,[26] and C_4F_8[27] precursors. Ye et al. proposed that silver clusters that formed on silicone oil do not merge into a film because an adsorbed layer of oil molecules surrounds the particles and thereby prevents coalescence.[28] Similarly, we believe that a polymer skin does not form on the silicone oil in cases where the silicone oil wets the polymer. For example, the silicone oil wets PHEMA, PNIPAAm, P*o*NBMA, and PPFM (the contact angles of silicone oil on these polymers are 6°, 39°, 7°, and 24°, respectively), and the depositions of these polymers all result in the formation of particles. After long deposition times (e.g., ∼2 h in the case of PHEMA), the concentration of polymer particles becomes great enough to completely cover the oil surface such that additional polymer can no longer interact with the underlying silicone oil, and further deposition results in a continuous film that grows on the layer of particles. In contrast to the above polymers, we have found that the deposition of PPFDA results in continuous polymer films on droplets of both silicone oil and all three imidazolium-based ILs (Figure 7A–D). We believe that the formation of a continuous PPFDA skin on silicone oil is due to the poor wetting between PPFDA and silicone oil, as silicone oil has a high contact angle on PPFDA (70°). When PPFDA was deposited onto IL droplets placed on a layer of silicone oil, a continuous polymer skin formed that encapsulated the two-liquid system and connected to the underlying silicon wafer (Figure 7E). Therefore, the IL droplet did not move when the substrate was tilted at a 15° angle (Figure 7F), which is in contrast to the deposition of PHEMA which resulted in a

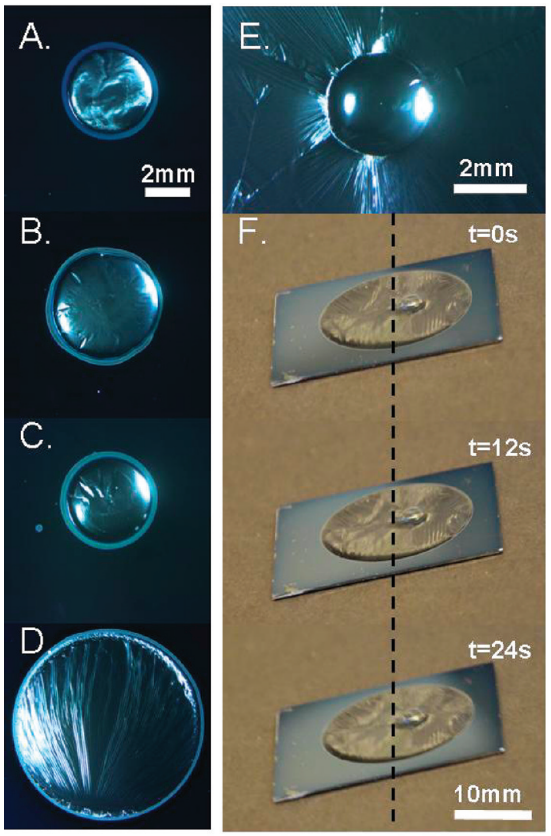

Figure 7. Images of 30 min of deposition of PPFDA onto droplets of (A) [bmim][PF_6], (B) [bmim][BF_4], (C) [emim][BF_4], and (D) silicone oil placed on a silicon wafer. (E) Images of PPFDA deposited onto a droplet of [bmim][PF_6] placed on a silicon wafer covered with a layer of silicone oil and (F) tilted at a 15° angle.

continuous film on only the IL surface (Figure 3C,D). Therefore, while free-standing films could be formed using PHEMA, PNIPAAm, P*o*NBMA, and PPFM, they could not be formed using PPFDA.

■ CONCLUSION

We have demonstrated that the deposition of both PHEMA and PNIPAAm on silicone oil results in the formation of polymer particles, whereas deposition onto imidazolium-based ILs results in polymer skins which completely encapsulate the ILs. We exploited this difference in polymer morphology to fabricate ultrathin free-standing polymer films of different shapes by combining the ILs and silicone oil onto a common substrate. Our study reveals some very interesting surface tension effects: when the IL is placed on top of the silicone oil, a thin layer of oil remains between the IL and the underlying silicon wafer and the silicone oil forms a concave meniscus on the side of the IL droplet. This meniscus helps maintain the shape of the IL and thereby the shape of the resulting polymer. FTIR analysis shows that the free-standing polymer films are highly pure (free of residual monomer, IL, and silicone oil) which will enable their use for biomedical applications. The free-standing PNIPAAm films have many potential uses due to their temperature-responsive hydrophilicity.[29,30]

Our fabrication process is environmentally friendly because no organic solvents are used in any of the steps and ionic liquids are nonvolatile, nonflammable, and can be easily recycled. We demonstrated the generality of our fabrication

dx.doi.org/10.1021/ma202268j | *Macromolecules* 2012, 45, 165–170

method across a range of imidazolium-based ILs ([bmim][PF_6], [bmim][BF_4], and [emim][BF_4]). Our ability to produce free-standing polymer films of controlled shape, size, and thickness is useful for a wide variety of applications in biosensing, biomimicry, and separations. In addition to PHEMA and PNIPAAm, we have found that the depositions of several other polymers including P*o*NBMA and PPFM also yield particles on silicone oil and skins on ILs. This allows us to extend our fabrication method to make light-responsive[31] and click-active polymer films.[32] Furthermore, films with multiple functionalities (e.g., mechanical strength, temperature-responsive swelling, photoresponsive solubility) can be made by sequentially stacking polymers.

EXPERIMENTAL SECTION

1-Butyl-3-methylimidazolium hexafluorophosphate ([bmim][PF_6]) (97%, Aldrich), 1-ethyl-3-methylimidazolium tetrafluoroborate ([emim][BF_4]) (97%, Aldrich), 1-butyl-3-methylimidazolium tetrafluoroborate ([bmim][BF_4]) (97%, Aldrich), poly(dimethylsiloxane) (Xiameter PMX-200 350 cSt, Aldrich), 2-hydroxyethyl methacrylate (HEMA) (98%, Aldrich), *N*-isopropylacrylamide (NIPAAm) (97%, Aldrich), 1*H*,1*H*,2*H*,2*H*-perfluorodecyl acrylate (PFDA) (97%, Aldrich), and *tert*-butyl peroxide (TBPO) (98%, Aldrich) were used without further purification. All depositions were carried out in a custom designed reaction chamber (GVD Corp, 250 mm diameter, 48 mm height). For the deposition of PHEMA, the HEMA monomer was heated to a temperature of 55 °C, the stage temperature was maintained at 35 °C using a recirculating chiller, and the reactor pressure was kept constant at 110 mTorr. For the deposition of PNIPAAm, the NIPAAm monomer was heated to a temperature of 60 °C, the stage temperature was maintained at 55 °C using a recirculating chiller, and the reactor pressure was kept constant at 100 mTorr. For the deposition of PPFDA, the PFDA monomer was heated to a temperature of 50 °C, the stage temperature was maintained at 35 °C using a recirculating chiller, and the reactor pressure was kept constant at 140 mTorr. For all depositions, a nichrome filament array (80% Ni, 20% CR, Omega Engineering) was placed 32 mm above the substrate and was resistively heated to 240 °C. The TBPO initiator was maintained at room temperature and flowed into the reactor at a rate of 0.92 sccm using a mass flow controller (Model 1479A, MKS).

The morphology of the polymer on the poly(dimethylsiloxane) silicone oil and the ILs was tested by first dispensing 5 μL of liquid directly onto a silicon wafer. Contact angles were then measured using a goniometer (ramé-hart Model 290-F1). After deposition, images of the polymer on the droplets were taken using a microscope and a Nikon D3000 camera. The continuity of the skins and particles was tested by subjecting the droplets to a continuous stream of air. In order to make shaped films, outlines of shapes were first drawn onto the substrate with a wax crayon using a ruler, and then IL was dispensed into the interior of the wax outline using a micropipet. For [bmim][BF_4], the shape was drawn onto an unmodified silicon wafer. For [bmim][PF_6] and [emim][BF_4], the shape was drawn onto a silicon wafer which had first been coated with a thin layer of PHEMA to increase the wetting of the IL into the corners of the shapes. Silicone oil was then dispensed (5 μL) at each edge of the shape and allowed to slowly spread over the wax and encircle the IL. After deposition of polymer, the polymer film was removed from the IL either by inserting a razor underneath the film and lifting it off or by submerging the entire substrate in silicone oil which allowed the film to float off the IL. The thickness of the polymer films was determined from JEOL-6610 low-vacuum scanning electron microscopy (SEM) images. For SEM sample preparation, the films were transferred onto a clean silicon wafer and blown flush against the wafer. The wafer underneath the skin was then cracked and mounted in a substrate holder such that the cross section could be visualized. A thin gold coating was sputtered onto the surface of the sample before imaging. Fourier transform infrared spectroscopy (FTIR) (Thermo Nicolet iS10) was used to study the chemical composition of the PHEMA and PNIPAAm films. Films were removed to a clean wafer by placing the wafer surface on top of the polymer film and lifting the film off. The films were rinsed with methanol and hexane before analysis. The FTIR of the PHEMA particles on silicone oil was measured by first separating the PHEMA from the silicone oil through extraction with methanol and then drop-casting the resulting solution onto a clean wafer.

AUTHOR INFORMATION

Corresponding Author

*E-mail: malanchg@usc.edu.

ACKNOWLEDGMENTS

This work was supported by the National Science Foundation under Grant EEC-0310723, the Mork Family Graduate Fellowship (R.F.F.), and the James H. Zumberge Faculty Research and Innovation Fund.

REFERENCES

(1) Chan, K.; Gleason, K. K. *Langmuir* **2005**, *21*, 8930−8939.
(2) Tenhaeff, W. E.; McIntosh, L. D.; Gleason, K. K. *Adv. Funct. Mater.* **2010**, *20*, 1144−1151.
(3) Gupta, M.; Gleason, K. K. *Langmuir* **2006**, *22*, 10047−10052.
(4) Lau, K. K. S.; Gleason, K. K. *Adv. Mater.* **2006**, *18*, 1972−1977.
(5) Gupta, M.; Kapur, V.; Pinkterton, N. M.; Gleason, K. K. *Chem. Mater.* **2008**, *20*, 1646−1651.
(6) O'Shaughnessy, W. S.; Murthy, S. K.; Edell, D. J.; Gleason, K. K. *Biomacromolecules* **2007**, *8*, 2564−2570.
(7) Alf, M. E.; Godfrin, P. D.; Hatton, T. A.; Gleason, K. K. *Macromol. Rapid Commun.* **2010**, *31*, 2166−2172.
(8) Ma, M.; Mao, Y.; Gupta, M.; Gleason, K. K.; Rutledge, G. C. *Macromolecules* **2005**, *38*, 9742−9748.
(9) Haller, P. D.; Frank-Finney, R. J.; Gupta, M. *Macromolecules* **2011**, *44*, 2653−2659.
(10) Holbrey, J. D.; Seddon, K. R. *Clean Prod. Processes* **1999**, *1*, 223−236.
(11) Welton, T. *Chem. Rev.* **1999**, *99*, 2071−2083.
(12) Porel, S.; Singh, S.; Harsha, S. S.; Rao, D. N.; Radhakrishnan, T. P. *Chem. Mater.* **2005**, *17*, 9−12.
(13) Jiang, C.; Markutsya, S.; Pikus, Y.; Tsukruk, V. V. *Nature Mater.* **2004**, *3*, 721−728.
(14) Zhai, L.; Nolte, A. J.; Cohen, R. E.; Rubner, M. F. *Macromolecules* **2004**, *37*, 6113−6123.
(15) Zimnitsky, D.; Shevchenko, V. V.; Tsukruk, V. V. *Langmuir* **2008**, *24*, 5996−6006.
(16) Mamedov, A. A.; Kotov, N. A. *Langmuir* **2000**, *16*, 5530−5533.
(17) Ono, S. S.; Decher, G. *Nano Lett.* **2006**, *6*, 592−598.
(18) Zhuk, A.; Pavlukhina, S.; Sukhishvili, S. A. *Langmuir* **2009**, *25*, 14025−14029.
(19) Lutkenhaus, J. L.; Hrabak, K. D.; McEnnis, K.; Hammond, P. T. *J. Am. Chem. Soc.* **2005**, *127*, 17228−17234.
(20) Stroock, A. D.; Kane, R. S.; Weck, M.; Metallo, S. J.; Whitesides, G. M. *Langmuir* **2003**, *19*, 2466−2472.
(21) Lau, K. K. S.; Gleason, K. K. *Macromolecules* **2006**, *39*, 3695−3703.
(22) Pan, Y. V.; Wesley, R. A.; Luginbuhl, R.; Denton, D. D.; Ratner, B. D. *Biomacromolecules* **2001**, *2*, 32−36.
(23) Katsumoto, Y.; Tanaka, T.; Sato, H.; Ozaki, Y. *J. Phys. Chem. A* **2002**, *106*, 3429−3435.
(24) Michely, T.; Ye, G. X.; Weidenhof, V.; Wuttig, M. *Surf. Sci.* **1999**, *432*, 228−238.
(25) Chen, M. G.; Yu, S. J.; Feng, Y. X.; Jiao, Z. W.; Yu, M. Z.; Yang, B. *Thin Solid Films* **2010**, *518*, 2674−2677.
(26) Xie, J. P.; Yu, W. Y.; Zhang, S. L.; Chen, M. G.; Ye, G. X. *Phys. Lett. A* **2007**, *371*, 160−164.
(27) Deng, Y. H.; Ye, C.; Yuan, Y.; Liu, H. M.; Cui, J. *Chin. Phys. Lett.* **2011**, *28*, 046601.

(28) Ye, G. X.; Michely, T.; Weidenhof, V.; Friedrich, I.; Wuttig, M. *Phys. Rev. Lett.* **1998**, *81*, 622−625.
(29) Akiyama, Y.; Kikuchi, A.; Yamato, M.; Okano, T. *Langmuir* **2004**, *20*, 5506−5511.
(30) Castellanos, A.; DuPont, S. J.; Heim, A. J; Matthews, G.; Stroot, P. G.; Moreno, W.; Toomey, R. G. *Langmuir* **2007**, *23*, 6391−6395.
(31) Haller, P. D.; Flowers, C. A.; Gupta, M. *Soft Matter* **2011**, *7*, 2428−2432.
(32) Francesch, L.; Borros, S.; Knoll, W.; Förch, R. *Langmuir* **2007**, *23*, 3927−3931.

Macromolecules

ARTICLE

pubs.acs.org/Macromolecules

Interface and Interphase Dynamics of Polystyrene Chains near Grafted and Ungrafted Silica Nanoparticles

Tinashe V. M. Ndoro,* Michael C. Böhm, and Florian Müller-Plathe

Eduard-Zintl-Institut für Anorganische und Physikalische Chemie and Center of Smart Interfaces, Technische Universität Darmstadt, Petersenstraße 20, D-64287 Darmstadt, Germany

ABSTRACT: The chain and segmental dynamics of free and grafted 20-monomer atactic polystyrene chains surrounding a silica nanoparticle have been investigated employing atomistic molecular dynamics simulations. The effect of the nanoparticle curvature and grafting density on the mean square displacement of free polystyrene chains and also on the mean relaxation time of various intramolecular vectors was investigated as a function of separation from the surface. Confinement, reduced surface curvature, and densification resulted in a reduction of the mean square displacement and an increase in the mean relaxation time of the $C_\alpha-H$ bond vector and chain end-to-end vector in the vicinity of the surface. Depending on the property investigated, the thickness of the interphase, i.e., the distance beyond which the polymer has bulk behavior, varies between 1 and 3 nm, corresponding to 1−3 radii of gyration of the bulk polymer. Therefore, the presence of a surface has a significant influence on the dynamics of the surrounding polymer chains especially the ones in the interfacial region.

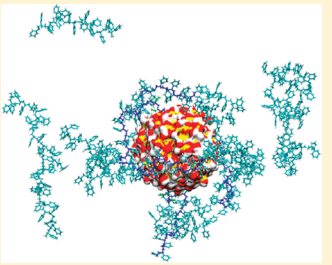

1. INTRODUCTION

The possibility of achieving significant enhancements in material properties (i.e., mechanical, electrical, optical, and thermal) by adding minute amounts of filler particles has spurred research in polymer nanocomposites.[1−24] At the nanometer scale, the size of the filler particles is often of the same order of magnitude as that of the polymer coil resulting in a drastic increase in the nanoparticle−polymer interfacial surface area. Also, at this small scale, the filler particle surface curvature and filler−polymer interactions play significant roles in influencing the structural arrangement, mobility, and overall relaxation of the polymer chains.[17,25,26] In our previous work,[20] we studied the structural properties of free atactic polystyrene (a-PS) melt chains surrounding single silica nanoparticles that were either grafted with a-PS or ungrafted, which revealed enhanced density and tangential orientation of the polymer chains along the particle surface. This current work employs atomistic molecular dynamics (MD) simulations to investigate surface induced changes in the polymer dynamical properties.

The study of polymer dynamics at the polymer−solid interface continues to be the focus of intensive research by both experimental[12,27−33] and computational[10,24,33−42] methods. The understanding of this polymer−solid interface can contribute to many industrial processes of significant importance that involve surface coating, lubrication, wetting, and adhesion.[43] Several polymer−surface parameters including the surface area/curvature[44] and roughness,[45] and repulsion/attraction to the polymer[13,24−26] influence the polymer dynamics which in turn determine the overall material properties. To understand the role of these parameters, many studies have been carried out in systems containing thin polymer films[14,27−29] as well as nanoparticles.[2,14,25,31,46,47] However, there is not a general consensus on whether the polymer chains' mobility is always reduced or enhanced in the polymer−surface interfacial region.

Some of the experimental[25,27,29,30,44,47−49] researchers have reported the existence of an immobilized interfacial polymer layer due to adhesion of the polymer chains on the surface. It has also been shown that this adhesion can be weakened by grafting polymer chains to the surface and enhanced by increasing the interfacial surface area, and the polymer-surface attraction.[29,44] On the contrary, Bogoslovov et al.[33] reported that the local segmental dynamics of poly(vinyl acetate) adjacent to spherical silica particles were similar to the bulk behavior. In addition, faster overall relaxation of free polystyrene chains close to a surface has been reported.[28,32] These experimental results suggest the absence of a universal behavior in describing the local motion of the polymer chains in the vicinity of solid surfaces. Even though Akcora and co-workers[12] have attributed this discrepancy to the chemical specificity of the polymer and surface as the main determining factor in influencing an increase or decrease in the interfacial polymer dynamics, many questions still remain unanswered.

In parallel to experimental investigations, computer modeling and theoretical approaches have also been employed to study the dynamical properties of polymer chains in the vicinity of surfaces. Results from quantum chemistry,[37] mode-coupling theory,[50] coarse-grained (CG),[26,40,41,51] and atomistic[3,4,10,34−37,42,52] simulations have revealed that the presence of a surface alters the dynamical properties of the interfacial polymer chains compared to the bulk melt. For example, the polymer chains close to

Received: September 9, 2011
Revised: October 28, 2011
Published: December 06, 2011

spherical nanoparticles have been reported by Goswami and Sumpter[40] to exhibit Rouse-like motion, an intermediate sub-diffusive regime that was followed by the usual Fickian diffusion. Together with other investigators, they explained that the reduced diffusion of the polymer chains at the surface was a consequence of attractive interactions between the monomers and the nanoparticles.[26,36,41,50] Furthermore, Borodin et al. have shown that attractive interactions between the surface and the polymer chains resulted in an enhanced polymer density close to the surface which in turn further decreased the polymer local mobility. Moreover, Yelash et al.[10] showed that the slowed-down polymer dynamics close to a "flat" surface resulted from the slow monomer desorption kinetics at the surface. However, the extent of the local changes in the polymer dynamics surrounding spherical particles of different grafting densities and surface curvature remains unresolved. Our current work investigates the role of the spherical silica nanoparticle diameter and grafting density (ρ_g, chains/nm^2) in altering the dynamical properties of a-PS chains in the interfacial and interphase region using atomistic MD simulations. This has enabled us to make a connection to our previous[20] work on the silica surface influence on a-PS structural properties. This work will enhance the understanding of experimental findings in which it is more difficult to locally resolve dynamical properties.

2. MODEL AND SIMULATION DETAILS

All-atom molecular dynamics (MD) simulations were carried out on nanocomposite systems consisting of atactic polystyrene (a-PS, $-[C_8H_8]-_n$) in contact with either an ungrafted or an a-PS-grafted spherical silica (SiO_2) nanoparticle as in our previous work.[20] Simulations were generally performed at a temperature, T, of 590 K and pressure, P, of 101.3 kPa. The exception was during the investigations of the influence of T and P on the reorientation of intramolecular vectors where T varied from 490 to 690 K while P was increased from 101.3 to 40520 kPa. Nanoparticles with diameters of 3, 4, and 5 nm have been chosen to vary the surface curvature while grafting densities of 0.0 (bare, ungrafted), 0.5, and 1.0 chains/nm^2 were contrasted. Both free and grafted a-PS polymer chains in our model system have n = 20 monomers, since at present only low molecular weight polymers can be investigated atomistically in reasonable time and length scales. The grafted chains are attached to the silica surface via a linker unit, $(-[CH_2CHC_2H_3]_3(CH_3)_2Si-)$, also employed in experiments.[53] In all studied systems, the minimum number of polymer chains is 202, that is, the sum of both free and grafted chains. For example, a particle of 3 nm diameter has 14 or 28 grafted chains for grafting densities of 0.5 and 1.0 chains/nm^2, and is surrounded by 188 or 174 free chains, respectively. Those which have diameters of 4 and 5 nm have 25 and 40 grafted chains for a grafting density of 0.5 chains/nm^2 while being surrounded by 202 and 162 free chains, respectively. For the higher grafting case of 1.0 chains/nm^2, the 4 nm diameter has 50 grafted and 177 free chains while the 5 nm diameter has 80 grafted and 122 free chains. In all cases, the ungrafted particles are surrounded by 202 free a-PS chains. The cubic simulation box sizes vary between 9.23 and 9.71 nm. The bulk a-PS melt mass density was 910.9 ± 1.5 kg/m^3 at 590 K and 101.3 kPa (experimental[54] density at the same temperature and pressure = 904.0 ± 0.1 kg/m^3) while that of the silica nanoparticle was 2770.6 ± 7.6 kg/m^3 (density of natural quartz[55] = 2635−2660 kg/m^3).

The force field parameters (containing the Lennard-Jones and Coulomb terms) for the polymer and anionic linker molecule are based on the OPLS-AA force field[56] for hydrocarbons and have been designed to describe mixtures of a-PS with benzene[57] and ethylbenzene.[58] On the other hand, the silica Lennard-Jones and Coulomb interaction parameters were obtained from a model that describes bulk crystalline silica.[59] For a complete description of the studied systems and force field parameters, we refer to our previous work,[20] where the same parameters have been employed.

Simulation runs were carried out in the isothermal−isobaric (NPT) ensemble using the molecular dynamics simulation code YASP.[60] During the MD simulations, the Berendsen[61] thermostat and barostat were used to maintain the system at prescribed temperatures T and pressures P. Coupling times of 0.2 ps (T) and 0.5 ps (P) were chosen. The integration has been performed employing the Verlet−leapfrog integration algorithm with a time step of 1 fs. Nonbonded interactions and the Verlet neighbor list (updated every 15 time steps) had cutoff radii of 1.0 and 1.1 nm, respectively. The reaction-field correction for the Coulombic[60] interactions was employed, assuming the average effective dielectric constant of the continuum ε_{RF} to be 3.7 (experimental dielectric constant: 2.4−2.7 for amorphous PS and 4.4−4.6 for amorphous silica at room temperature).[55]

To allow sampling of different configurations, the temperature was elevated from the setup temperature of 490 to 990 K. Later, it was decreased at 100 K/ns for 5 ns and final equilibration runs were performed at 590 K. To investigate the effect of temperature on the reorientational dynamics of intramolecular vectors, a further decrease in temperature steps of 10 K was carried out, simulating for 0.5 ns in the NVT ensemble and then for 1.25 ns in the NPT ensemble at each temperature. Following this, production simulations were performed for a further 4 ns at both 540 and 490 K. Equilibrated systems at 590 K were further simulated at 640 and 690 K also for 4 ns having made a single temperature step increase from the lower (590 K) to the higher temperatures. The influence of pressure was studied by increasing the pressure from 101.3 to 20260 and 40520 kPa at 590 K and simulating the systems for 4 ns. During production, configurations were sampled every 2000 time steps (2 ps). The mean square displacement analysis performed at a temperature of 590 K and pressure of 101.3 kPa was done from a 50 ns production run. At the same temperature and pressure, the reorientation of chain segment vectors has been done by averaging three different trajectory files of length 16 ns.

3. RESULTS AND DISCUSSION

3.1. Mean Square Displacement of Polymer Chains. As a measure of the mobility of free chains, their center of mass (COM) mean square displacement (MSD) was calculated. Shells of equal thickness (either 0.5 or 1.0 nm) surrounding the spherical nanoparticle were constructed to define different spatial regions as a way to investigate how far reaching the silica surface influences the polymer chain dynamics. Note that 1 nm is approximately the unperturbed radius of gyration (R_g) of the considered polymer chain.[20] Representative MSD plots for this motion, $\langle(R_{COM}(t) - R_{COM}(0))^2\rangle$, are shown in Figure 1. $\langle ... \rangle$ denotes the ensemble average in the particular shell or for all polymer chains in the reference bulk a-PS melt (T = 590 K, P = 101.3 kPa). $R_{COM}(t)$ is the position of the chain COM at a given time t. The MSD of every polymer chain was counted for the shell

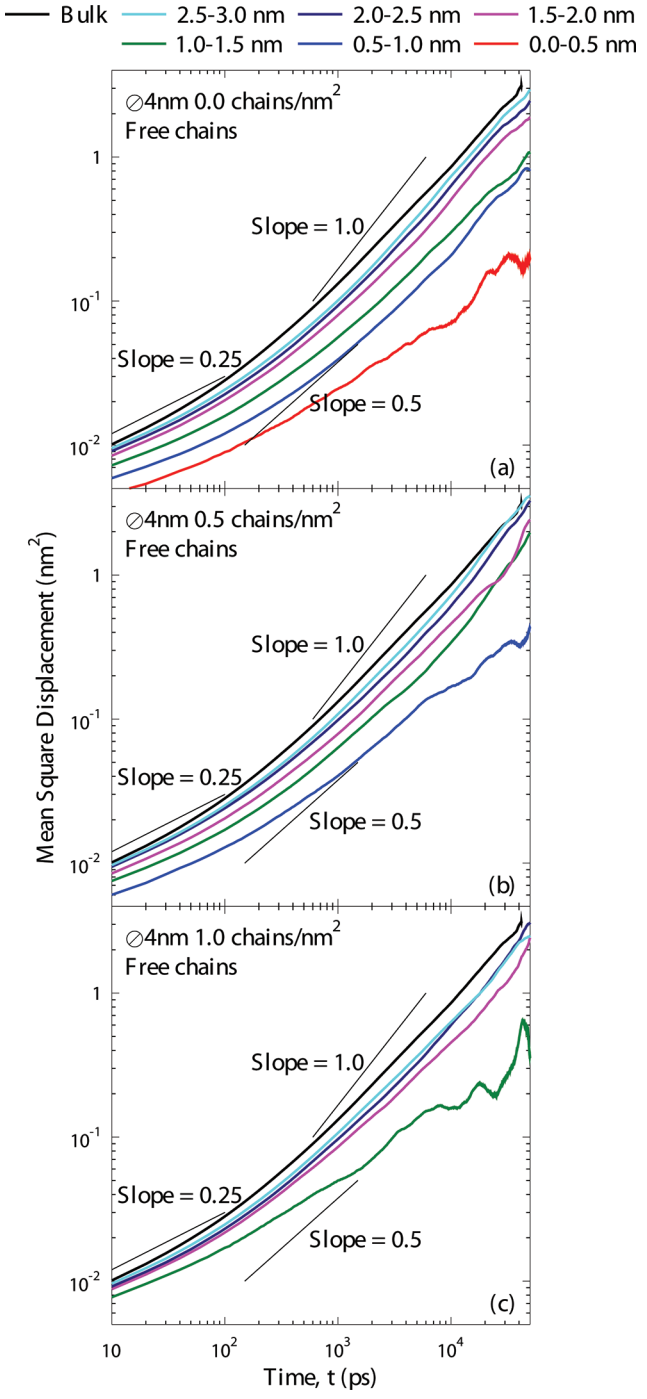

Figure 1. Center of mass mean square displacement of free 20 monomer polystyrene chains which reside the most in one of the six shells surrounding spherical particles of diameter =4 nm and different grafting densities. The simulations have been performed at T = 590 K and P = 101.3 kPa. Each of the shells has a width of 0.5 nm. Shell 1 (0.0−0.5 nm) is missing in panel b while both shells 1 (0.0−0.5 nm) and 2 (0.5−1.0 nm) are not present in panel c because the ability of free polymer chains to penetrate the grafted chains regime reduces with increasing grafting density. The physical meaning of the added slopes (thin black lines) of 0.25, 0.5, and 1.0 has been explained in the text.

in which its COM spent the most residence time during the 50 ns production runs. While the chains COMs resided for at least 50% of the time in a shell of 1 nm thickness, their residence time increased in shells closer to the surface due to confinement. Despite the increasing migration between shells at larger surface separation, chain COMs still spent on average about 75% of the simulation time in a given shell.

For one illustrative example, we use a finer shell width (0.5 nm), namely for the chain MSDs in a system containing the 4 nm diameter particles of different grafting densities (Figure 1). Chain residence times in these narrower shells are shorter; thus their minimum residence time reduces to 40%. Still, the MSDs in the four inner shells are distinctly different. Error bars from a comparison of 3 shorter trajectories of 15 ns each with different average shell populations were negligible as the MSD in each shell remained distinctly different. There is no MSD data for shell 1 and/or 2 for the grafted systems because free chains cannot penetrate the grafted polymer layers at close distance, as we have reported in our previous work[20] on structural properties of the same system. For the free a-PS chains, the following general trend can be extracted from Figure 1: with decreasing separation from the nanoparticle surface, the MSD is reduced, i.e. the chains exhibit attenuated dynamics. In contrast to the polymer chain behavior near the nanoparticle surface, the free chains residing in the outer shells approach bulk-like MSDs. However, even for the bulk 20 monomer a-PS melt, we only observe Rouse diffusion dynamics characterized by an MSD slope of 0.5 compared to the Einstein diffusive limit of 1. This is due to the long time scale of Einstein diffusion, which is not accessible in this type of simulation. (Note: Both slopes have been added to Figure 1.) Consequently, we have not calculated the diffusion coefficient but have found that our bulk MSD data is similar to that of an 18 monomer bulk a-PS melt.[62] While the free polymer chains in shells nearer to the surface have reduced MSDs due to confinement and increased density,[20] those in shells further away from the surface experience a reduced surface influence. At a distance of 2.5−3.0 nm, the chains approach bulk-like movement. In addition, it is observed for all grafting densities that the chains closest to the nanoparticle exhibit a qualitatively different diffusion behavior; their MSD follows a power law with an exponent visibly below 0.5.

We compare the chain mobilities using shells of 1 nm width to investigate the effect of the surface curvature and grafting density (Table 1). As the systems are subdiffusive and diffusion coefficients thus not meaningful, we use the center-of-mass MSD after 40 ns as a comparative measure of the chain mobility. Near the particle surface (<1 nm) it is a factor 2−3 lower than in the outer shell (2−3 nm) for the bare nanoparticles A similar decrease is also observed when comparing MSDs as a function of distance from the surface when the surface is grafted. At the same time, the MSD of free chains in general decreases more in the vicinity of the particle when the particle is larger. This is a consequence of a surface curvature which decreases with particle size. This geometrical change promotes chain and segmental tangential orientation to the surface, denser packing within the interphase region, in addition to simply providing more geometrical hindrance to diffusion.[20] Therefore, the confinement experienced by the free chains not only increases when they are closer to the surface but also when the surface curvature is reduced as the particle surface then approximates more and more the limit of a flat surface. From recent calculations, it follows that the surface-polymer attractions[13,25,26,36] also play an increasing role with an increase in the interfacial surface area. In the employed force-field, the silica nanoparticles as well as the phenyl ring atoms have partial charges. In single nanoparticle simulations, the interfacial surface

dx.doi.org/10.1021/ma2020613 |*Macromolecules* 2012, 45, 171–179

Table 1. Normalized Mean Square Displacements, MSD_{Shell}/MSD_{Bulk}, after 40 ns

free bulk chains MSD = MSD_{Bulk} = 2.97 nm^2			
shell: distance from the nanoparticle surface (nm)	nanoparticle diameter ∅ = 3 nm	nanoparticle diameter ∅ = 4 nm	nanoparticle diameter ∅ = 5 nm
Free Chains, Grafting Density = 0.0 chains/nm^2			
0−1	0.49	0.22	0.18
1−2	0.88	0.41	0.36
2−3	1.03	0.77	0.55
Free Chains, Grafting Density = 0.5 chains/nm^2			
0−1	0.35	0.11	0.13
1−2	0.88	0.52	0.29
2−3	0.86	0.89	0.62
Free Chains, Grafting Density = 1.0 chains/nm^2			
0−1	0.44	–	–
1−2	0.64	0.48	0.25
2−3	0.89	0.74	0.66

The data in the Table 1 is for the normalized chain center of mass mean square displacements (MSD_{Shell}/MSD_{Bulk}) of 20-monomer atactic polystyrene chains at a temperature of 590 K and atmospheric pressure. MSD_{Shell} symbolizes the value derived for the considered shell while MSD_{Bulk} represents the bulk value. For high grafting densities of 1.0 chains/nm^2 for the 4 and 5 nm diameter particles, there are no free chains in the first shell (0−1 nm).

area doubles and almost triples when moving from a particle with a diameter of 3 nm to one of 4 and 5 nm, respectively. Therefore, all these factors have a combined effect of reducing the free chains MSDs in shells that are both closer to the surface and even more so in those surrounding particles of decreasing surface curvature.

Furthermore, the average MSDs of free chains COMs in the first shells around grafted particles are less than in the same shell surrounding bare particles (Table 1). The reason for the further reduced MSDs within the distance of 0−1 nm from the surface is the intermixing of free chains with grafted chains, which in turn have an excluded volume for free chains and a lower mobility, as they are fixed to the silica surface. The grafted chains affect the dynamics of the free chains in other ways (see below). Numbers in Table 1 reflect the combined effect of both the nanoparticle surface and the grafted chains on the mobility of the free chains. Clearly, the surface reduces the mobility of free chains as the mean square displacement in any given system always increases with the shell number away from the surface. Comparison between the MSD in the same shells surrounding grafted particles of the same diameter but different grafting density shows that the mobility of free chains generally decreases even though the change is rather small. For example, making a comparison from the 0.5 to 1.0 chains/nm^2 grafting density systems shows that the MSD changes from 0.88 to 0.64 nm^2, 0.52 to 0.48 nm^2, and 0.29 to 0.25 nm^2 in the second shell surrounding nanoparticles with a diameter of 3.0, 4.0, and 5.0 nm, respectively. Therefore, both the excluded volume of the grafted chains and the surface cooperatively reduce the free chains MSD but clearly the surface has a much more dominant effect.

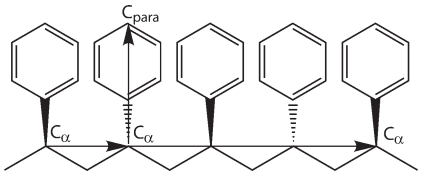

Figure 2. This schematic diagram shows a 5 monomer fragment of a polystyrene chain to show the one monomer ($C_\alpha-C_\alpha$) long, three monomers ($C_\alpha\cdots C_\alpha$) long, and $C_\alpha-C_{para}$ segment vectors. They have been considered in the study of the chain segmental dynamics by calculating the reorientation $P_1(t)$ and $P_2(t)$ time-autocorrelation functions of theses vectors. The hydrogen atoms have been omitted in this figure.

The MSD after 40 ns has also been calculated for the grafted chains (not shown), in full knowledge that they cannot diffuse. It is generally found that their mobility is greatest when their center of mass is predominantly found in the shell separated 1−2 nm from the nanoparticle surface. This is not too surprising, since the closer chains are more squashed against the nanoparticle and in general experience a higher polymer density[20] which restricts their motion. In the other limit, a chain, whose center of mass resides predominantly at large distances from the nanoparticle surface (2−3 nm shell), maintains a stretched conformation and is less mobile for that reason.

3.2. Reorientation of Intramolecular Vectors. The analysis of both the local segmental and chain dynamics is useful to understand the nanoparticle induced changes on the properties of the surrounding polymer chains. To study both the free and grafted chain and local segmental reorientation dynamics in the modeled nanocomposites, we have investigated the relaxation times of various intramolecular vectors which include those shown in the schematic representation in Figure 2.

In addition to the one monomer ($C_\alpha-C_\alpha$), three monomers ($C_\alpha\cdots C_\alpha$), and $C_\alpha-C_{para}$ vectors, the reorientation of the $C_\alpha-H$ and the end-to-end vector was also studied. For the latter, both C atoms are the terminal C_α of free chains, while one of the two terminal C atoms of a-PS bonds to the linker molecule in the case of grafted chains. Since the induced structural orientation of the one monomer and three monomers segments is similar,[20] we have only focused on reorientation results of the three monomers segment in this work. Also, having observed that the reorientation of the $C_\alpha-C_{para}$ and $C_\alpha-H$ vectors is of similar magnitude, focus has been put on the $C_\alpha-H$ bond vector.

The advantage of calculating relaxation correlation times is that—in principle—they can be compared to those obtained experimentally. The vector of interest in dielectric spectroscopy (DS) studies is $C_\alpha-C_{para}$ while the quantity of interest is the first Legendre polynomial:[63] $P_1(t) = \langle\cos(\theta(t))\rangle$. On the other hand, the spin relaxation time in nuclear magnetic resonance (NMR) spectroscopy studies can be directly related to the reorientation of the C−H bond vector in which case the quantity of interest is the second Legendre polynomial:[63] $P_2(t) = 1.5\langle\cos^2(\theta(t))\rangle - 0.5$. In both cases, $\theta(t)$ is the angle by which the vector has rotated in a time t. The relaxation times τ_1 and τ_2 are obtained as time integrals of the corresponding correlation function; see below. A similar investigation of polymer chain segment vector relaxation times has been carried out by Harmandaris et al.[62] to investigate the effect of temperature and pressure on a pure melt of 18 monomer a-PS chains. They reported that the ratio of the mean relaxation time at all temperatures obtained from the $P_1(t)$ and $P_2(t)$ curves, that is, τ_1/τ_2 varied between 2.2 and 2.7, similar

dx.doi.org/10.1021/ma2020613 |*Macromolecules* 2012, 45, 171–179

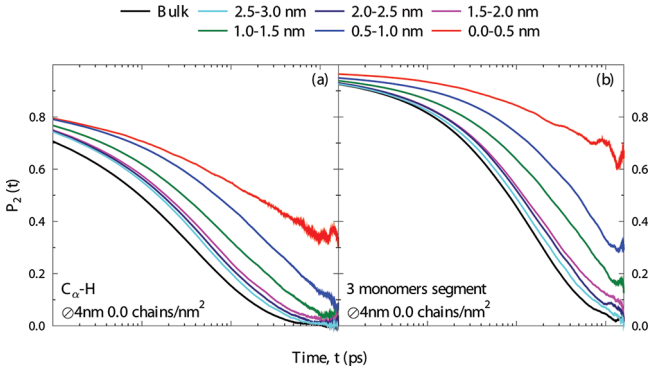

Figure 3. $P_2(t)$ time-autocorrelation function for the C_α-H bond vector (left panel) and the three monomers segment vector (right panel) of free polymer chains surrounding a bare particle of diameter = 4.0 nm during a 16 ns simulation period. Sampling for the respective shells has been explained in the text. The simulations have been performed at T = 590 K and P = 101.3 kPa.

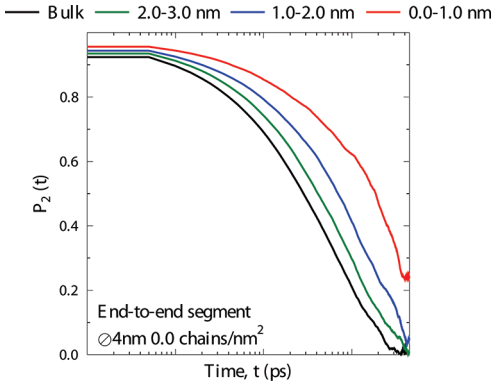

Figure 4. $P_2(t)$ time-autocorrelation function for the end-to-end vector of free chains surrounding a bare silica spherical particle of diameter = 4.0 nm at T = 590 K and P = 101.3 kPa during a 50 ns simulation period. Sampling of the respective shells took into account only those chains whose center of mass resided predominantly in that particular shell.

to our results in which this ratio is 2.7 for the C_α-H segment reorientation. For more details, see below. In addition, earlier work of He et al.[64] correlated NMR experiments with the results of the segmental dynamics of a pure melt of 20 monomer a-PS that had been obtained from MD simulations. They also observed a similar nonexponential decay of the $P_2(t)$ curves as in our melt a-PS system and this validates our model system. Our contribution explains the influence of the surface curvature and grafting density on the dynamics of both free and grafted chains (see below). In a series of simulations, we determined how they deviate from the bulk polymer dynamics.

We have again employed the shell construction in calculating the $P_1(t)$ and $P_2(t)$ time-autocorrelation functions for the various intramolecular vectors. For the present problem, the vectors contribute to the statistics of that shell where their midpoint has the greatest residence time. An exception is the end-to-end vector which contributes to the statistics of that shell where the chain COM resides the most. The logarithmic plots of the $P_2(t)$ time-autocorrelation functions in a period of 16 ns for the C_α-H and three monomer segment vector around a bare nanoparticle are shown in Figure 3, a and b, respectively, as examples of local vectors of free chains. A finer 0.5 nm resolution of the shell thickness has been chosen to have a better local resolution. The other local vectors, $C_\alpha-C_\alpha$ and especially $C_\alpha-C_{para}$ behave similar to the $C_\alpha-H$ vector, and so have not been shown. In all autocorrelations, there is a fast initial decrease in the first 10 ps which corresponds to the so-called primitive relaxation (bond and angle vibrations and librations) followed by the segmental (α-) relaxation at longer times. The results observed by Harmandaris et al.[62] in neat PS agree with this behavior. The trends for the $C_\alpha-H$ and the three monomer segment vector autocorrelation functions are similar to the relaxation of the end-to-end vector (see Figure 4) at the chain level. A comparison between panels a and b of Figure 3 shows the following: (i) The segments close to the nanoparticle (<1 nm) relax significantly slower than bulk chain segments, whereas those in the outer shells quickly approach bulk dynamics. The reasons for the "surface-near" changes are the same as given above for the mean square displacements: adhesion and steric hindrance. (ii) The relaxation of segments close to the nanoparticle becomes slower with increasing particle diameter (i.e., decreasing curvature) while the slow region extends further into the more distant shells (not shown). This is an effect of decreasing surface curvature, as shown for example by the increase in the polymer density surrounding small to larger particles. Again, we refer to Figure 1 of our recent MD study.[20] These two trends are qualitatively the same for the reorientation autocorrelation of all vectors investigated. However, from Figure 3 it is also evident that the strongest slowing down is always found in the layer nearest to the nanoparticle (<1 nm). This coincides with the distance at which static orientational anomalies disappear. Short polymer segments feel an orienting effect of the surface up to 1 nm. Beyond that distance, they are randomly oriented.[20]

As a measure of long-scale relaxation, we also present the autocorrelation functions of the end-to-end vectors of free chains around the bare particle in Figure 4 for a period of 50 ns. The same qualitative trends as already shown in Figure 3 are observable. Note, however, that the overall decay of the autocorrelation functions is slower with increasing vector length. To give an idea of this behavior, we have calculated the relaxation times via the $P_2(t)$ correlation functions according to the procedure outlined below in the bulk at 590 K. The values of these times are 6.4 ns for the end-to-end vector, 2.4 ns for a segment of three monomers, and 0.6 ns for the C_α-H bond vector.

As an example to quantify the vector relaxation as a function of the separation from the surface, the mean reorientational relaxation times, $\langle\tau\rangle$, of the $C_\alpha-H$ bond vector were obtained from the time integral of the $P_2(t)$ curve. For practical reasons, they were least-squares fitted by a Kohlrausch–Williams–Watts (KWW) stretched exponential function whose time integral is analytical.

$$\langle\tau\rangle = \int_0^\infty P_1(t)\,dt \approx \int_0^\infty \exp\left(-\left(\frac{t}{\tau_\kappa}\right)^\beta\right) dt = \frac{\tau_\kappa}{\beta}\Gamma\left(\frac{1}{\beta}\right) \quad (1)$$

In eq 1, the parameter $\langle\tau\rangle$ is the mean relaxation time obtained from the area under the curve $P_2(t)$, t is the time, β the stretching exponent, and $\Gamma(1/\beta)$ the complete gamma function. In the case of an exponential decay with β = 1, the parameter τ_κ would be equal to the mean relaxation time $\langle\tau\rangle$. The KWW function provides a very reasonable fit, as can be seen in the examples shown in the next section (cf. Figure 6). We note here that some of the autocorrelation functions, most notably for the end-to-end vectors and segment vectors in the immediate vicinity of the

dx.doi.org/10.1021/ma2020613 |Macromolecules 2012, 45, 171–179

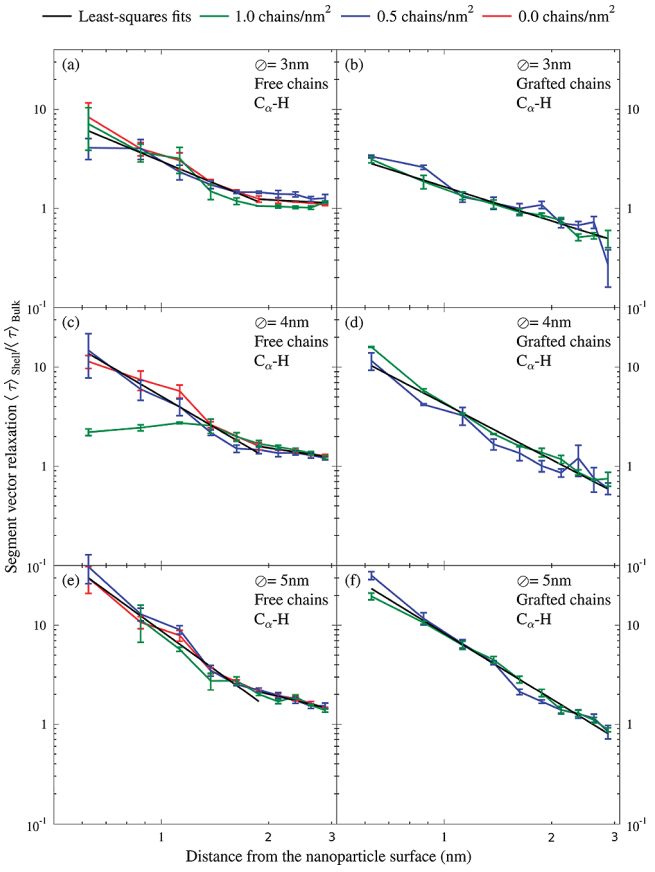

Figure 5. $P_2(t)$ based normalized mean relaxation times relative to the bulk value (τ_{bulk} = 0.6 ns) for the C_α−H bond vector of both free and grafted chains as a function of the distance from the nanoparticle surface which varied in curvature. Sampling for the respective shells of thickness 0.25 nm took into account only those bond vectors whose midpoint resided the most in that particular shell. The simulations have been performed at T = 590 K and P = 101.3 kPa. The error bars are the error of the average value computed in determining the standard deviation. The straight black lines are least-squares fits to all curves simultaneously in the corresponding range (except part c, where the 1.0 chains/nm^2 curve has been omitted from the fit).

surface, did not converge to zero in the accessible simulation time of 50 ns (cf. Figure 4). We have nonetheless followed the above procedure and used the KWW function fitted to the initial decay of the autocorrelation to extrapolate it to long times. We are aware that the resulting reorientation times are, at best, order-of-magnitude estimates and should be taken with care.

Having computed the normalized mean relaxation times in each of the shells relative to a bulk a-PS melt at the same T = 590 K and P = 101.3 kPa, $\langle\tau\rangle_{Shell}/\langle\tau\rangle_{Bulk}$, a comparison which shows the effect of the surface curvature and grafting density is given in Figure 5 for the C_α−H vector. Shells that are 0.25 nm wide were chosen to have a finer resolution as a function of the separation from the surface. In the very first shell (0−0.25 nm) rather large relaxation times (2−3 orders higher than bulk) are found, which are however not included in the figure due to their large scatter. We find that the dynamics of local segments of both free and grafted chains are affected to a different extent in the various shells. There is usually a strong slowing-down in the closest layers (<1 nm), with the reorientational relaxation time increasing by factors between 4 and 30 in comparison to the bulk value taking into account the large error bars. Segment vectors located beyond 2 nm from the surface are only moderately affected; their relaxation times increase by factors between 1.1 and 2.0. The effect on the segments located >2.5 nm away is marginal, with relaxation times only a few percent larger or smaller than in the bulk. The trend of stronger slowing-down with increasing particle diameter appears again for the segment reorientations. For the grafted chains, it can be noted that their segments reorient generally with similar speeds as the free-chain segments in the same shell. However, there is a difference between these local reorientations of free and grafted chains for small particle diameters (3 and 4 nm) and large distances (>2 nm). Whereas the free-chain dynamics approach bulk behavior (Figure 5a,c,e), the outer monomers of the grafted chains actually relax faster than bulk chains (Figure 5b,d). This is noteworthy, as this is the only point where we observe an increase of the polymer dynamics apparently caused by the nanoparticle. This is a chain-end effect which decreases with particle diameter, disappearing altogether for the largest particle (Figure 5f), because the chains attached to a high curvature surface experience a much greater volume increase away from the surface and hence are more mobile.

With the reorientation of the C_α−H vector reflecting very localized dynamics, it is no surprise that the grafting density has only a small effect on them, if any at all. The unusually fast reorientation for a diameter of 4 nm and a grafting density of 1.0 chains/nm^2 (Figure 5c) is probably due to very limited statistics, as few free chains can penetrate the grafted brush. This topic has been discussed several times.

In the chosen double−logarithmic presentation of Figure 5 it becomes clear that the local reorientation times are distance dependent. The slope for the reorientation of the C_α-H vector of *grafted* chains (Figure 5b,d,f) seems to increase with the particle diameter from 1.15 (∅ = 3 nm) via 1.87 (∅ = 4 nm) to 2.21 (∅ = 5 nm). This reflects once more the fact that a flatter surface has a longer-ranged effect on the polymer dynamics, and is thus in line with the findings above. Note, however, that this correlation has been checked only under conditions where a "flatter surface" simultaneously implies a "larger surface area". In contrast to the grafted chains, however, there appears to be two domains for the C_α-H reorientation of the *free* chains with different slopes (Figure 5a,c,e). Close to the surface (<1.625 nm) the slope depends on the particle diameter, increasing from 1.50 to 2.11 and then to 2.61 between the highest and lowest surface curvature. At larger distances (>1.625 nm), the slopes are smaller and increase from 0.19 (∅ = 3 nm) via 0.55 (∅ = 4 nm) to 0.86 (∅ = 5 nm). It therefore appears that the dynamics of free chain segments close to the surface have strong distance dependence, which itself is affected by the surface curvature. At larger separation from the surface, the distance dependence is smaller and less influenced by the surface curvature in the now familiar way: a lower curvature leads to a more far-reaching influence on the dynamics. The distance which separates both regimes is approximately 1.625 nm, close to a value that corresponds to 1.5 times the radius of gyration of the unperturbed chain (∼1 nm), and also to approximately 3 times the monomer diameter. As to why grafted and free chains behave qualitatively different, we can only speculate. A possible reason is that grafted chains have monomers that are close to the surface. Thus, a monomer of a grafted chain far from the surface is necessarily connected to chain parts at closer distances and may feel their influence on its own reorientation dynamics. In contrast, the monomer of a free chain at the same far distance will most likely not belong to a chain which has also

segments close to the surface. Therefore, its behavior will carry less influence from near-surface dynamics.

While the normalized relaxation times of the local vectors are qualitatively similar when comparing the C_α−H vector to C_α−C_{para} for example, the end-to-end vectors have much longer relaxation times (see Figure 4). Also their slowing-down near the nanoparticle with respect to bulk behavior is stronger. In all shells, even the outermost, the end-to-end relaxation is more affected than the local segment relaxation. A particular strong hindrance of reorientation is observed in the first shell (<1 nm). Here, the mean distance of the chain from the surface is less than its unperturbed R_g and an increase of 2−3 orders of magnitude is estimated for the grafting density of 0.5 chains/nm^2. The reason is intermingling of free chains with grafted chains, which due to their attachment to the surface can only sway, but not fully reorient. It is reasonable to expect that this slows the free chains, too. For the grafting density of 1 chain/nm^2, one would expect even slower reorientation. However, at this density and the lower curvatures (4 and 5 nm diameter), the grafted brushes effectively expel free chains from this region: The distance at which there are more free polymers than grafted polymers has been found to be 1.8 and 2 nm for particles of 4 and 5 nm diameter, respectively.[20]

3.3. Temperature and Pressure Influence on the Reorientation of the C_α−H Bond Vector. In practical applications, polymers are exposed to a variety of temperature and sometimes pressure conditions which determine how well they can be processed and thus the resulting material characteristics, e.g., mechanical and electrical properties. Whenever property changes are observed, they indicate modifications of the polymer structure and dynamics at the nanoscale. As such, it is important to understand how dynamic polymer properties are altered by temperature and pressure changes. Therefore, we have investigated the temperature and pressure effect on the reorientation of the C_α−H bond vector which can be measured by NMR spectroscopy. Figure 6 summarizes the influence of either temperature (panels a and b) or pressure (panels c and d) on the $P_2(t)$ time-autocorrelation function of the C_α-H vector. As a representative example, we have chosen the relaxation of the segment vectors of the free chains in three shells of thickness = 1.0 nm surrounding a 4 nm bare particle. In studying the influence of temperature, the pressure was kept constant at 101.3 kPa while the temperature was varied between 490 and 690 K in steps of 50 K. To observe the influence of the pressure, the temperature was kept constant at 590 K while pressure values of 101.3, 20260, and 40520 kPa were chosen.

The density of the simulated bulk a-PS changes from 855.2 ± 3.6 kg/m^3 at 690 K to 883.3 ± 3.2 kg/m^3, 910.9 ± 1.5 kg/m^3, 941.1 ± 2.7 kg/m^3, and 967.9 ± 2.1 kg/m^3 at 640, 590, 540, and 490 K, respectively. This density reduction with decreasing temperature slows down the segmental dynamics by a factor of 4 in the bulk a-PS melt when reducing the temperature from 590 to 490 K. A similar decrease has been observed in the first shell surrounding the nanoparticle, with the slowest $P_2(t)$ curve decay always occurring at the lowest temperature (see Figure 6a). The reorientation times at different temperatures were obtained as outlined in section 3.2 for a three shell resolution. Note: $P_2(t)$ curves corresponding to shells 2 and 3 have not been shown since their trends are similar to that shown in shell 1. Their distribution indicates a Williams−Landel−Ferry temperature dependence at lower temperatures. The high temperature region between 590 and 690 K was subjected to an Arrhenius fit (not shown) in order to estimate very roughly the activation energy for C_α-H reorientation at different distances

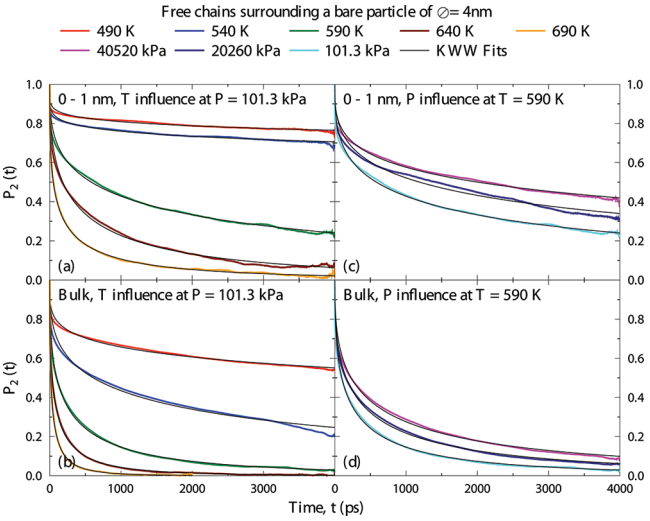

Figure 6. $P_2(t)$ time-autocorrelation function for the C_α-H bond vector of free chains surrounding a 4 nm diameter bare particle as a function of temperature (left panels) and pressure (right panels). The KWW fits are shown in black. Sampling for the shell took into account only those bond vectors whose midpoint resided the most in that particular shell. The simulations have been performed at T = 590 K (right-hand panels) and P = 101.3 kPa (left-hand panels).

from the nanoparticle surface. The activation energy evaluated in the present study converges with increasing distance (0−1 nm, 89 kJ/mol; 1−2 nm, 76 kJ/mol; 2−3 nm, 70 kJ/mol) toward the value for the bulk (66 kJ/mol). Still, it is about 1.4 times higher in the first layer around the nanoparticle than in the bulk.

On the other hand, even though a reduction in the segmental dynamics is also observed when increasing the pressure from 101.3 to 40520 kPa at 590 K, the magnitude is much smaller due to less efficient densification effects within the employed pressure range. The density of the bulk a-PS at 590 K only increases from 910.9 ± 1.5 kg/m^3 at a pressure of 101.3 kPa to 930.1 ± 2.7 kg/m^3, and 945.9 ± 2.4 kg/m^3 at 20260 kPa, and 40520 kPa, respectively. However, distinction can still be clearly made when comparing the dynamics in each of the shells under different pressure conditions. In summary, the general observed trend is that of slower segmental dynamics with decreasing temperature, increasing pressure, and decreasing separation from the silica surface.

4. SUMMARY AND CONCLUSION

The chain and segmental dynamics of 20-mer atactic polystyrene melts in the interfacial and interphase region surrounding spherical silica nanoparticles of diameters 3.0, 4.0, and 5.0 nm have been investigated by atomistic MD simulations. We have determined the average mean square displacement of the center of mass of the polymer chains in different spatial regions (shells) surrounding the nanoparticle. Similarly, the reorientation of intramolecular vectors (C_α−H bond vector, three monomers segment, and the end-to-end vector) as measured by $P_2(t)$ relaxation curves has been investigated.

The global chain dynamics are described by the center-of-mass mean square displacement as well as by the relaxation of the end-to-end vector. Both quantities indicate a strong slowing down of the chain motion near the nanoparticle. Within a distance from the surface corresponding to one R_g (i.e., the radius of gyration of an unperturbed bulk chain) the polymer dynamics are reduced, in

dx.doi.org/10.1021/ma2020613 |Macromolecules 2012, 45, 171–179

some cases by several orders of magnitude. In contrast, the chain dynamics are almost normal and bulk-like if the polymer chain is more than $2R_g$ away from the surface. The dynamic behavior of matrix polymer chains is affected both by the grafting state of the nanoparticle (moderately) and its diameter or curvature (strongly). A lower curvature radius leads to slower polymer dynamics and to an increased thickness of the "slow zone" around the particle. This is due to both increased geometric hindrance and—in the case of grafted particles—increased crowding of the grafted brushes.

The local polymer dynamics have been monitored by the reorientation of various intramolecular vectors; they all show a similar behavior. For example, taking the methine $C_\alpha-H$ bond vector, we can show that the local mobility is considerably slowed in the presence of the nanoparticle. The grafting state of the surface has little influence on the local reorientation, but the surface curvature which in the chosen setup is also coupled to the surface area, has a pronounced effect. The $C_\alpha-H$ reorientation near the surface is slowed by about a factor of 8 compared to the bulk for a particle of 3 nm diameter. This reduction in dynamics is increased to a factor of 30 for the 5 nm diameter particle. The reorientation dynamics have been shown to be distance and surface curvature dependent. The sensitivity of this relationship is greatest close to the particle surface and under lower surface curvature. This indicates that the zone of slowed dynamics expands, as the surface becomes flatter. An interesting feature is found for the free chains, which show two regimes roughly separated by a distance of $\sim 1.5R_g$ from the surface. Below this boundary, the slope is large (1.5−2.6) and curvature dependent; whereas above this limit it is smaller (<1) but still curvature dependent. Additionally, the activation energy for the segment reorientation at a close distance from the surface ($<1R_g$) is markedly different from the rest of the system (~1.4 times the activation energy in the outer shell ($>2R_g$) or in the bulk).

We therefore find that for the dynamical properties, both the chain mobility and the segment mobility are significantly slowed close to the nanoparticle surface. Chain mobility is affected even at a distance of $2-3R_g$ from the surface, whereas segment mobility becomes bulk-like beyond $2R_g$. It is interesting to juxtapose the dynamical interphase thickness with the interphase thickness calculated previously by various structural features[20] for the same system. Density oscillations cease after $2R_g$. The chains' sizes and orientations become bulk-like and random after $\sim 1.5R_g$, whereas the segment orientation becomes random within a distance less than $1R_g$. The emerging picture is therefore that most surface-induced modifications of the polymer properties have a range of about $2R_g$. Segment properties may converge earlier, whereas the whole chain dynamics may extend further. The interphase, defined by whatever property, however, has a thickness of this order of magnitude. Note that these statements are specific to the chosen chain length. The 20-mer system studied here is far from the length where the polymer behavior becomes generic. Moreover, the position dependence of the segmental structure and dynamics may well be governed by the monomer diameter, rather than the chain length R_g, as the dominating length scale. In our short polymers, the two scales just happen to be similar in magnitude.

AUTHOR INFORMATION

Corresponding Author

*E-mail: t.ndoro@theo.chemie.tu-darmstadt.de. Telephone: +31 (0) 46 4761045.

ACKNOWLEDGMENT

Financial support from the European Union through the project "NanoModel" under grant number 211778 is gratefully acknowledged. We would like to acknowledge the DFG Priority Program 1369 for providing the computer resources. Fruitful discussions with Evangelos Voyiatzis, Simon Butler, Frédéric Leroy, Mohammad Rahimi, Azadeh Ghanbari, Enrico Riccardi, and colleagues in the NanoModel project are especially appreciated.

REFERENCES

(1) Vacatello, M. *Macromolecules* **2001**, *34*, 1946–1952.
(2) Starr, F. W.; Schrøder, T. B.; Glotzer, S. C. *Macromolecules* **2002**, *35*, 4481–4492.
(3) Brown, D.; Mélé, P.; Marceau, S.; Albérola, N. D. *Macromolecules* **2003**, *36*, 1395–1406.
(4) Barbier, D.; Brown, D.; Grillet, A.-C.; Neyertz, S. *Macromolecules* **2004**, *37*, 4695–4710.
(5) Everaers, R.; Sukumaran, S. K.; Grest, G. S.; Svaneborg, C.; Sivasubramanian, A.; Kremer, K. *Science* **2004**, *303*, 823–826.
(6) Bansal, A.; Yang, H.; Li, C.; Cho, K.; Benicewicz, B.; Kumar, S. K.; Schadler, L. S. *Nat. Mater.* **2005**, *4*, 693–698.
(7) Sen, S.; Xie, Y.; Kumar, S. K.; Yang, H.; Bansal, A.; Ho, D. L.; Hall, L.; Hooper, J. B.; Schweizer, K. S. *Phys. Rev. Lett.* **2007**, *98*, 128302–128305.
(8) Sen, S.; Xie, Y.; Bansal, A.; Cho, K.; Schadler, L.; Kumar, S. K. *Eur. Phys. J. Spec. Top.* **2007**, *141*, 161–165.
(9) Akcora, P.; Liu, H.; Kumar, S. K.; Moll, J.; Li, Y.; Benicewicz, B. C.; Schadler, L. S.; Acehan, D.; Panagiotopoulos, A. Z.; Pryamitsyn, V.; Ganesan, V.; Ilavsky, J.; Thiyagarajan, P.; Colby, R. H.; Douglas, J. F. *Nat. Mater.* **2009**, *8*, 354–359.
(10) Yelash, L.; Virnau, P.; Binder, K.; Paul, W. *Phys. Rev. E* **2010**, *82*, 50801–50804.
(11) Lo Verso, F.; Egorov, S. A.; Milchev, A.; Binder, K. *J. Chem. Phys.* **2010**, *133*, 184901–184910.
(12) Akcora, P.; Kumar, S. K.; Sakai, V. G.; Li, Y.; Benicewicz, B.; Schadler, L. S. *Macromolecules* **2010**, *43*, 8275–8281.
(13) Jancar, J.; Douglas, J. F.; Starr, F. W.; Kumar, S. K.; Cassagnau, P.; Lesser, A. J.; Sternstein, S. S.; Buehler, M. J. *Polymer* **2010**, *51*, 3321–3343.
(14) Harton, S. E.; Kumar, S. K.; Yang, H.; Koga, T.; Hicks, K.; Lee, H.; Mijovic, J.; Liu, M.; Vallery, R. S.; Gidley, D. W. *Macromolecules* **2010**, *43*, 3415–3421.
(15) Kumar, S. K.; Krishnamoorti, R. *Annu. Rev. Chem. Biomol. Eng.* **2010**, *1*, 37–58.
(16) Dukes, D.; Li, Y.; Lewis, S.; Benicewicz, B. C.; Schadler, L. S.; Kumar, S. K. *Macromolecules* **2010**, *43*, 1564–1570.
(17) Kalb, J.; Dukes, D.; Kumar, S. K.; Hoy, R. S.; Grest, G. S. *Soft Matter* **2010**, *7*, 1418–1425.
(18) Vogiatzis, G.; Voyiatzis, E.; Theodorou, D. N. *Eur. Polym. J.* **2011**, *47*, 699–712.
(19) Chevigny, C.; Jestin, J.; Gigmes, D.; Schweins, R.; Di-Cola, E.; Dalmas, F.; Bertin, D.; Boué, F. *Macromolecules* **2010**, *43*, 4833–4837.
(20) Ndoro, T. V. M.; Voyiatzis, E.; Ghanbari, A.; Theodorou, D. N.; Böhm, M.; Müller-Plathe, F. *Macromolecules* **2011**, No. 44, 2316–2327.
(21) Milano, G.; Santangelo, G.; Ragone, F.; Cavallo, L.; Di Matteo, A. *J. Phys. Chem. C* **2011**, *115*, 15154–15163.
(22) Chevigny, C.; Dalmas, F.; Di Cola, E.; Gigmes, D.; Bertin, D.; Boue, F.; Jestin, J. *Macromolecules* **2011**, *44*, 122–133.
(23) Ghanbari, A.; Ndoro, T.; Leroy, F.; Rahimi, M.; Böhm, M.; Müller-Plathe, F. *Macromolecules* **2011**submitted for publication.
(24) Liu, J.; Wu, Y.; Shen, J.; Gao, Y.; Zhang, L.; Cao, D. *Phys. Chem. Chem. Phys.* **2011**, *13*, 13058–13069.
(25) Mortezaei, M.; Famili, M. H. N.; Kokabi, M. *Compos. Sci. Technol.* **2011**, *71*, 1039–1045.
(26) Binder, K.; Milchev, A.; Baschnagel, J. *Annu. Rev. Mater. Sci.* **1996**, *26*, 107–134.

(27) Rittigstein, P.; Priestly, R. D.; Broadbelt, L. J.; Torkelson, J. M. *Nat. Mater.* **2007**, *6*, 278–282.
(28) Yang, Z.; Fujii, Y.; Lee, F. K.; Lam, C.-H.; Tsui, O. K. C. *Science* **2010**, *328*, 1676–1679.
(29) Priestly, R. D.; Ellison, C. J.; Broadbelt, L. J.; Torkelson, J. M. *Science* **2005**, 309.
(30) Kropka, J. M.; Putz, K. W.; Pryamitsyn, V.; Ganesan, V.; Green, P. F. *Macromolecules* **2007**, *40*, 5424–5432.
(31) Kropka, J. M.; Sakai, V. G.; Green, P. F. *Nano Lett.* **2008**, *8*, 1061–1065.
(32) Oh, H.; Green, P. F. *Nat. Mater.* **2009**, *8*, 139–143.
(33) Bogoslovov, R. B.; Roland, C. M.; Ellis, A. R.; Randall, A. M.; Robertson, C. G. *Macromolecules* **2008**, *41*, 1289–1296.
(34) Vogel, M. *Macromolecules* **2009**, *42*, 9498–9505.
(35) Eslami, H.; Müller-Plathe, F. *J. Phys. Chem. B* **2009**, *113*, 5568–5581.
(36) Borodin, O.; Smith, G. D.; Bandyopadhyaya, R.; Byutner, O. *Macromolecules* **2003**, *36*, 7873–7883.
(37) Smith, J. S.; Borodin, O.; Smith, G. D.; Kober, E. M. *J. Polym. Sci., Part B: Polym. Phys.* **2007**, *45*, 1599–1615.
(38) Dionne, P. J.; Ozisik, R.; Picu, C. R. *Macromolecules* **2005**, *38*, 9351–9358.
(39) Dionne, P. J.; Picu, C. R.; Ozisik, R. *Macromolecules* **2006**, *39*, 3089–3092.
(40) Goswami, M.; Sumpter, B. G. *Phys. Rev. E* **2010**, *81*, 41801–41808.
(41) Torres, J. A.; Nealey, P. F.; de Pablo, J. J. *Phys. Rev. Lett.* **2000**, *85*, 3221–3224.
(42) Harmandaris, V. A.; Daoulas, K. C.; Mavrantzas, V. G. *Macromolecules* **2005**, *38*, 5796–5809.
(43) Jones, R. A. L.; Richards, R. W. *Polymers at surfaces and interfaces*; Cambridge University Press: Cambridge, U.K., 1999.
(44) Mortezaei, M.; Farzi, G.; Kalaee, M. R.; Zabihpoor, M. *J. Appl. Polym. Sci.* **2011**, *119*, 2039–2047.
(45) Scheidler, P.; Kob, W.; Binder, K. *Europhys. Lett.* **2002**, *59*, 701–707.
(46) Chen, L.; Zheng, K.; Tian, X.; Hu, K.; Wang, R.; Liu, C.; Li, Y.; Cui, P. *Macromolecules* **2010**, *43*, 1076–1082.
(47) Whittington, A. P.; Nguyen, S. T.; Kim, J.-H. *Nanoscape* **2009**, *6*, 26–30.
(48) Mortezaei, M.; Famili, M. H. N.; Kalaee, M. R. *J. Reinf. Plast. Comp.* **2011**, *30*, 593–599.
(49) Robertson, C. G.; Rackaitis, M. *Macromolecules* **2011**, *44*, 1177–1181.
(50) Egorov, S. A. *J. Chem. Phys.* **2011**, *134*, 84903–84908.
(51) Eslami, H.; Karimi-Varzaneh, H. A.; Müller-Plathe, F. *Macromolecules* **2011**, *44*, 3117–3128.
(52) Eslami, H.; Müller-Plathe, F. *J. Phys. Chem. B* **2010**, *114*, 387–395.
(53) Hübner, E.; Allgaier, J.; Meyer, M.; Stellbrink, J.; Pyckhout-Hintzen, W.; Richter, D. *Macromolecules* **2010**, *43*, 856–867.
(54) Höcker, H.; Blake, G. J.; Flory, P. J. *Trans. Faraday Soc.* **1971**, *67*, 2251–2257.
(55) Lide, D. R. *CRC Handbook of Chemistry and Physics*, 74th ed.; CRC Press: Boca Raton, FL, 1993.
(56) Jorgensen, W. L.; Maxwell, D. S.; Tirado-Rives, J. *J. Am. Chem. Soc.* **1996**, *118*, 11225–11236.
(57) Müller-Plathe, F. *Macromolecules* **1996**, *29*, 4782–4791.
(58) Qian, H.-J.; Carbone, P.; Chen, X.; Karimi-Varzaneh, H. A.; Liew, C. C.; Müller-Plathe, F. *Macromolecules* **2008**, *41*, 9919–9929.
(59) Lopes, P. E. M.; Murashov, V.; Tazi, M.; Demchuk, E.; MacKerell, J.; Alexander, D. *J. Phys. Chem. B* **2006**, *110*, 2782–2792.
(60) Müller-Plathe, F. *Comput. Phys. Commun.* **1993**, *78*, 77–94.
(61) Berendsen, H. J. C.; Postma, J. P. M.; van Gunsteren, W. F.; DiNola, A.; Haak, J. R. *J. Chem. Phys.* **1984**, *81*, 3684–3690.
(62) Harmandaris, V. A.; Floudas, G.; Kremer, K. *Macromolecules* **2011**, *44*, 393–402.
(63) Abramowitz, M.; Stegun, I. A. *Handbook of Mathematical Functions with Formulas, Graphs, and Mathematical Tables*, 9th ed.; Dover Publications: New York, 1972.
(64) He, Y.; Lutz, T. R.; Ediger, M. D.; Ayyagari, C.; Bedrov, D.; Smith, G. D. *Macromolecules* **2004**, *37*, 5032–5039.

Macromolecules

Article

pubs.acs.org/Macromolecules

Effect of Copolymerization in the Dynamics of Poly(trimethylene terephthalate)

Michelina Soccio,* Aurora Nogales, and Tiberio A. Ezquerra

Instituto de Estructura de la Materia, IEM-CSIC, Serrano 121, Madrid 28006, Spain

Nadia Lotti and Andrea Munari

Dipartimento di Ingegneria Civile, Ambientale e dei Materiali, Universitá di Bologna, Via Terracini 28, Bologna 40131, Italy

ABSTRACT: The structure-dynamics relationships in random copolymers of poly(trimethylene terephthalate) and poly(neopenthyl terephthalate) (PTT−PNT) have been investigated by means of X-ray scattering and dielectric loss spectroscopy experiments. The results show that the incorporation of neopenthyl terephthalate units into PTT chain decreases the ability to crystallize of the resulting copolymers as compared to that of PTT. The subglass dynamics of the copolymers is characterized by the existence of two processes, β_1 and β_2. We propose that the high frequency secondary relaxation β_1 is associated with the most flexible part of the repeat unit, whereas the low frequency mode β_2 has been assigned to the carbon of the ester groups linked to the aromatic ring. On the contrary the poly(neopenthyl terephthalate) (PNT), presents only one subglass process, that we hypothesize to have the same origin of the relaxation of β_2 relaxation in PTT. The segmental dynamics for the amorphous specimens, characterized by the α-process, follows an expected molar ratio behavior. A particular effect characterized by a reduction of the segmental mobility induced by the presence of the counits is observed in the copolymers.

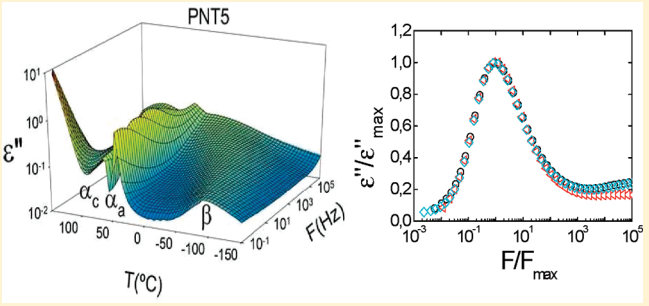

INTRODUCTION

Poly(trimethylene terephthalate) (PTT) is a linear aromatic polymer, belonging to the terephthalic acid containing polyesters, among which poly(ethylene terephthalate) (PET) and poly(butylene terephthalate) (PBT), that combines the outstanding properties of PET and the processing characteristics of PBT. This fact makes PTT highly suitable for uses in fiber, film, and engineering thermoplastic applications. In particular, PTT possesses strong flexibility and more than 90% elastic recovery, relatively large refractive index (1.638), and good transparency from visible lights to near-infrared. These properties make PTT very interesting for, among other applications, photonics and miniaturized photonic devices.[1] PTT has been used recently as a model semirigid chain polymer to study the thermodynamics of polymer crystallization.[2] However, PTT crystallization rate is too fast, and this causes difficulties in the manufacturing processes. Poly(neopenthyl terephthalate) (PNT) shares with PTT the main aspects of the chemical structure of the monomer, differing only in the central carbon group of the aliphatic segment, in which the hydrogen atoms are replaced by methyl groups. This chemical modification inhibits crystallization in PNT. Modification of industrially interesting polymers, by copolymerization, in order to improve a particular property of the original system, is a broadly used practice. The different properties obtained by copolymerization with respect to those of the homopolymer are a direct consequence of the changes in the structural and dynamical behavior of the system, due to the intrinsic heterogeneity imposed by the comonomer along the polymer chain. Well known examples are the decrease of crystallinity in polypropylene (iPP) by introducing randomly along the chains different sequences of polyethylene (PE), which modifies the toughness of the original system,[3] or the decrease in mechanical fragility of the biodegradable polymers of poly(hydroxy butyrate) (PHB) with different comonomers.[3] Random copolyesters are indeed gaining industrial relevance mainly due to the possibility of tailoring the thermal and dynamical behavior, by changing the kind, relative amount, and distribution of the comonomeric units along the polymer chain. In this view, several copolyesters of PTT have been synthesized and their thermal and mechanical properties reported.[4−13] Recently, some of us have synthesized a series of random copolymers of poly(trimethylene terephthalate) and poly(neopenthyl terephthalate) (PTT−PNT) by melt polycondensation. By controlling the molar composition the thermal properties, including crystallization kinetics, have been varied.[14,15] In order to better understand the fundamental origin of the different properties obtained for these PTT-based

Received: October 22, 2011
Revised: December 1, 2011
Published: December 16, 2011

   dx.doi.org/10.1021/ma202361r | *Macromolecules* 2012, 45, 180−188

copolymers and the role of the methyl groups incorporated in the segment, we have carried out an exhaustive dielectric spectroscopy study in the copolymer range from 0 to 40% of PNT. The aim of the present work is to establish, for this copolymeric system, relationships between the relaxation behavior, as characterized by dielectric loss spectroscopy, and the degree of ordering, as revealed by X-ray scattering methods.

EXPERIMENTAL SECTION

Samples. Poly(trimethylene terephthalate) (PTT), poly(neopenthyl terephthalate) (PNT), and poly(trimethylene-*co*-neopenthyl terephthalate) copolymers (PTT−PNT) of various compositions were synthesized according to the well-known two-stage polycondensation procedure described elsewhere.[14] The chemical structure of the counits is presented in Figure 1. The molar composition and the chain structure of the samples were determined by means of ^{1}H NMR spectroscopy.[14] Both thermal and structural characterization data are collected in Table 1. The nomenclature used in this work to identify samples with different content of neopenthyl terephthalate (NT) units is presented in Table 1.

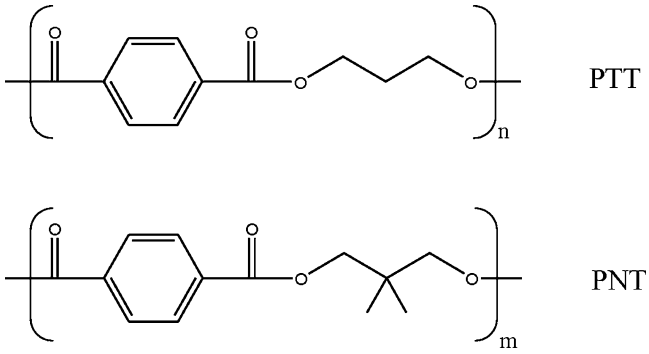

Figure 1. Chemical structure of the homopolymers involved in the PTT−PNT random copolymers investigated: poly(trimethylene terephthalate) (PTT) and poly(neopenthyl terephthalate) (PNT).

The samples in the form of film were prepared as follows. After vacuum drying at 25 °C for 24 h, the powders originated from the synthesis were melt pressed at T_m + 30 °C for 2 min and subsequently quenched to room temperature using iced water. In that way polymer amorphous films of about 250 μm were obtained.

Diferential Scanning Calorimetry. DSC experiments were carried out, before and after the dielectric measurement, using a Perkin-Elmer DSC4 instrument provided with an ethanol cooling bath. The temperature was calibrated by using indium. The samples were encapsulated in aluminum pans, and the typical sample weights used in these experiments were about 6 mg. The heating rate employed was 20 °C/min.

Dielectric Spectroscopy. Complex dielectric permittivity measurements ($\varepsilon^* = \varepsilon' - i\varepsilon''$) were performed over a frequency range of $10^{-1} < F < 10^6$ Hz in a temperature range of −150 °C < T < +150 °C (140 °C for PNT and PNT40). A Novocontrol system integrating an ALPHA dielectric interface was employed. The temperature was controlled by means of a nitrogen gas jet (QUATRO from Novocontrol) with a temperature error of (0.1 during every single sweep in frequency). Films for dielectric spectroscopy were provided with circular gold electrodes (2 cm diameter) by sputtering the metal onto both free surfaces. The dielectric relaxations were empirical described in terms of the Havriliak−Negami (HN) equation:

$$\varepsilon^* = \varepsilon_\infty + \frac{\varepsilon_0 - \varepsilon_\infty}{[1 + (i\omega\tau)^b]^c} \quad (1)$$

Here ε_0 and ε_∞ are the relaxed (ω = 0) and unrelaxed (ω = ∞) dielectric constant values, τ is the central relaxation time of the relaxation time distribution function, and b and c ($0 < b, c < 1$) are shape parameters which describe the symmetric and the asymmetric broadening of the relaxation time distribution function, respectively.[16] An additional contribution of the conductivity process was taken into account by adding a term $-i(\sigma/(\varepsilon_{vac}\omega))^s$ to eq 1. Conductivity is usually associated with generation and transport of polarization-induced charges through the polymer under the action of an electric field. Here σ is related to the direct current electrical conductivity, ε_{vac} is the dielectric constant of vacuum, and the value of the coefficient $0 < s < 1$ depends on the conduction mechanism.[17] More precisely, the experimental data were analyzed using different approaches depending on the studied temperature range. Under the T_g, the relaxation spectrum was interpreted as due to local modes (β processes), in this view we have employed the Cole−Cole (CC) analysis (eq 1 with c = 1). When the α relaxation appears in the experimental frequency window ($T > T_g$), the dielectric loss spectrum is described as a superposition of one CC function (β relaxation) to one HN (α relaxation).

X-ray Scattering. Wide-angle X-ray scattering (WAXS) experiments were conducted, before and after dielectric measurement, at room temperature by means of a Seifert (XRD 3000) symmetrical reflection $\theta/2\theta$ scanning diffractometer with Ni-filtered Cu Kα wavelength. The goniometer geometry was set with the Si(111) Bragg peak. The instrumental resolution was $\Delta s = 8.3 \times 10^{-4}$ Å^{-1}. The instrumental background was subtracted. A crystallinity index, X_c^{WAXS}, was calculated as the ratio between the integrated area below the deconvoluted crystalline peaks to the total experimental scattered integral intensity.[18] The error in the crystallinity index was evaluated as ≈0.1%, which mainly appears from the limitation of the covered angular range. Small angle X-ray scattering (SAXS) characterization was achieved by means of a X-ray scattering device Nanostar from Bruker using the same wavelength as in WAXS experiments.

RESULTS AND DISCUSSION

Dielectric Spectroscopy of the Amorphous PTT−PNT System. The dielectric spectra of this series of copolymers are characterized by a clear low temperature process (β relaxation) and a more intense α relaxation appearing at temperatures above the glass transition temperature T_g. Figure 2 shows, as an

Table 1. Characterization Data for the Crystallizable Copolymers[a]

sample	PNT/PTT molar ratio	M_w	Dc_p^a (J/g °C)	Dc_p (J/g °C)	ΔH_m (J/g)	X_c	L (nm)	l_1 (nm)	l_2 (nm)	w_c (wt %)	w_a (wt %)	w_i (wt %)
PTT	0/100	56 100	0.159	0.059	64	0.35	6.5	2.0	3.5	0.43	0.37	0.20
PNT5	5/95	56 900	0.190	0.082	59	0.35	7.0	2.3	3.6	0.37	0.43	0.20
PNT10	10/90	61 900	0.278	0.127	51	0.34	7.7	2.5	3.7	0.30	0.46	0.24
PNT20	20/80	61 900	0.295	0.168	39	0.26	9.8	2.5	5.4	0.20	0.57	0.23
PNT30	30/70	79 600	0.376	0.241	28	0.13	12.6	2.6	7.5	0.13	0.64	0.23

[a]Molecular weights (M_w). Specific heat increments for amorphous (Dc_p^a) and crystallized (Dc_p) specimens. Heats of fusion (ΔH_m), degree of crystallinity (X_c) calculated by WAXS, and long period (L) were estimated for samples crystallized during dielectric measurement. l_1 (lamellar thickness) and l_2 (interlamellar amorphous thickness) were calculated from the correlation function. Weight fractions of the crystalline phase (w_c), amorphous phase (w_a) and interphase (w_i) were calculated from DSC results as described in the text.

dx.doi.org/10.1021/ma202361r | *Macromolecules* 2012, 45, 180−188

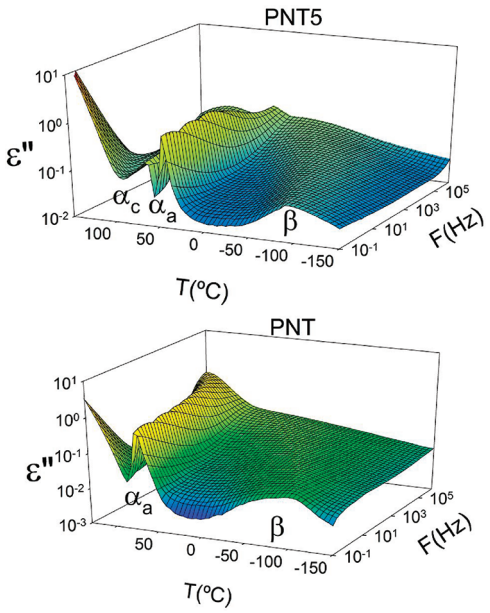

Figure 2. Dielectric loss values as a function of temperature and frequency for two selected amorphous polymers of the series: PNT5 (top) and PNT homopolymer (bottom).

example, the dielectric loss values as a function of temperature and frequency for PNT5 (top) and PNT (bottom), both the samples are initially amorphous. The relaxation processes appear as maxima in ε'' versus frequency and move toward higher temperatures as frequency increases. At temperatures below the glass transition temperature, both systems exhibit a broad maximum of the dielectric loss, labeled as β process. At temperatures above T_g, (see Table 2), a strong increase in ε''

Table 2. T_0 and D Obtained from the Fittings of τ_{max} to Equation 2 and T_g Values from DSC of the Amorphous Samples

samples	D	T_0 (K)	T_g (K)
PTT	5.2	272.1	327
PNT5	5.2	273.4	329
PNT10	5.4	274.0	332
PNT20	5.7	274.6	335
PNT30	6.2	274.7	337
PNT40	6.1	275.7	342
PNT	6.2	290.2	351

values is observed, and it is labeled as α process. For the PNT5 sample, the α-relaxation peak, once over the T_g, undergoes a sudden decrease in ε''. This effect is typical of a sample that crystallizes during the dielectric scan. Therefore, in the crystallizing systems, we can distinguish two α-relaxation regions, the first related to the sample before the crystallization (α_a), the second related to the sample after the crystallization (α_c). PTT and its copolymers with PNT content up to 30%, present an analogous trend. As one can see, the PNT homopolymer (Figure 2, bottom) behaves quite different: the α-relaxation peak preserves the shape and the apparent intensity throughout the whole temperature scan. PNT40 is characterized by the same behavior of the PNT homopolymer.

In order to show more clearly these features, Figure 3 presents dielectric loss values (ε'') as a function of temperature

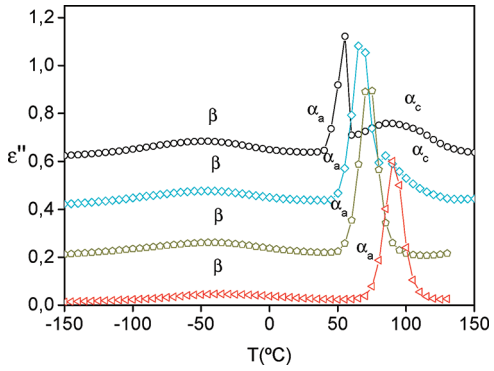

Figure 3. Isochronal ε'' data for PTT, PNT20, PNT40, and PNT (from top to bottom) at 891 Hz. The data have been vertical shifted 0.2 units for better visualization.

at a fixed frequency ($F = 10^3$ Hz) for the two homopolymers and two intermediate copolymers.

At low temperatures, all the curves are quite similar, being characterized by a broad and not very intense maximum, corresponding to the β process. The samples look different in the high temperature range. In the PTT homopolymer and in the copolymers with PNT content up to 30%, above T_g, the α relaxation becomes less intense and wider due to crystallization process.

On the other hand, for PTN40 and PNT samples, a decrease of the α peak intensity at higher temperature is not evidenced. This fact suggests that for these samples no crystallization occurs during the dielectric measurement. In order to confirm this, differential scanning calorimetry (DSC) and wide-angle X-ray scattering (WAXS) experiments were performed before and after the dielectric spectroscopy experiments. DSC experiments of samples before dielectric spectroscopy (Figure 4a) reveal

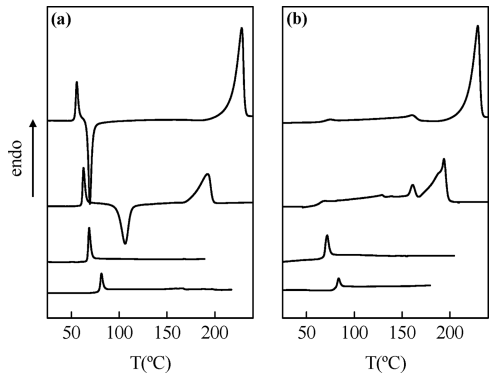

Figure 4. DSC curves of PTT, PNT20, PNT40, and PNT (from top to bottom): amorphous (a) and crystallized (b).

that PTT and PTT–PNT random copolymers containing up to 30 mol % of NT-counits are characterized by a glass transition followed by an exothermal "cold crystallization" peak and a melting endotherm at higher temperature. The glass transition temperature (T_g) of the samples depends on the comonomeric content of PNT. As it has been reported previously,[14] T_g versus composition increases gradually from the value corresponding to the PTT homopolymer toward the one obtained for the PNT homopolymer. This dependence can be well described by the Wood equation.[19] The position of the exothermal crystallization peak that appears above T_g also exhibits a dependence with the comonomeric content. This is due to a

dx.doi.org/10.1021/ma202361r | Macromolecules 2012, 45, 180–188

fraction of amorphous material that, once T_g is exceeded, acquires enough mobility to rearrange and crystallize. As the amount of PNT units increases the crystallization of the initially amorphous samples is less efficient, and therefore, the temperature at which the exothermic cold crystallization peak occurs increases. The "cold crystallization" peak is difficult to observe in the PNT30 sample. In all the samples with PNT content up to 30%, the area of crystallization peak very well compares with the corresponding heat of fusion, indicating that these polymers are completely amorphous at the beginning of the DSC scan. This fact was also corroborated by WAXS (not shown here). On the other hand, in the calorimetric curves of pure PNT and PNT40 copolymer, only an intense endothermal baseline deviation associated with the glass transition is observed. Specific heat increments (Δc_p) and melting enthalpies (ΔH_m) for all the investigated samples are reported in Table 1. Glass transition temperatures (T_g), are reported in Table 2.

β relaxation of the Amorphous Copolymers. The β relaxation process observed below T_g as a broad maximum in Figure 2, moving toward higher frequencies as temperature increases, can be related, in general, to the local chain dynamics.[17,20,21] Figure 5 shows, for a given temperature, the

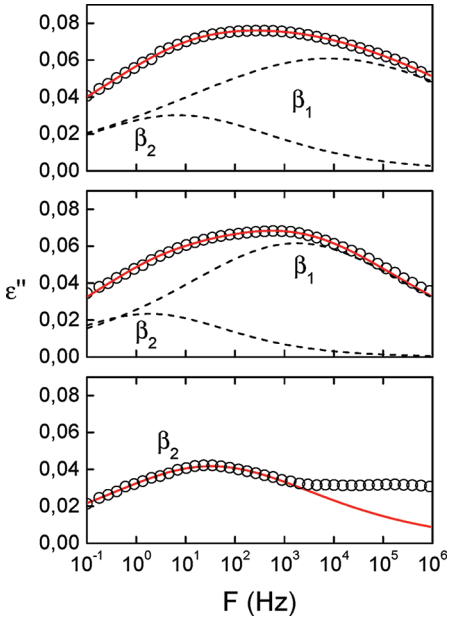

Figure 5. β relaxation of amorphous PTT, PNT20, and PNT (from top to bottom) at $T = -70$ °C. Continuous lines represent best fits according to CC equation, dashed lines show the separated contribution of the different relaxation processes.

β relaxation for the two amorphous homopolymers and a selected copolymer (PNT20) in the amorphous state. Close inspection to the β relaxation (Figure 5) reveals that it is rather broad and, in the case of PTT and PNT20, it is clearly composed of two processes, designated as β_2 and β_1 in order of increasing frequency. However, this bimodal character is not equally obvious for PNT, for which we cannot fit properly with CC-functions the higher frequency zone.

In the PTT homopolymer, the slowest β process (β_2) shows smaller intensity as compare to β_1. Interestingly, this trend is followed by the copolymers, where the intensity of β_1 relaxation appears to be smaller than in the case of the homopolymer PTT. A bimodal shape of the glassy dynamics was already observed in copolymers of poly(ethylene terephthalate) and poly(ethylene 2,6-naphthalene dicarboxylate).[22,23] To estimate the time of maximum loss, τ_{max}, for both contributions, a strategy based on the Coburn and Boyd procedure[24,25] was followed. Figure 6 shows the τ_{max} as a function of the reciprocal

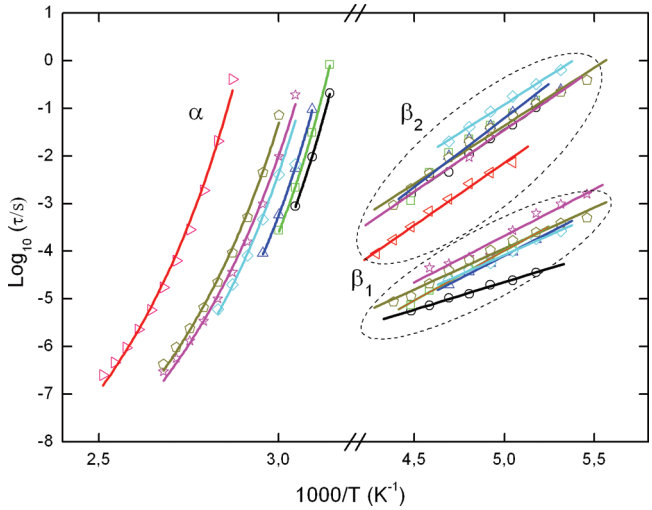

Figure 6. Evolution of the central relaxation time as a function of the reciprocal temperature for the amorphous samples, for the α relaxation and the local processes β_1 and β_2. Key: (○) PTT, (green □) PNT5, (blue △) PNT10, (aqua ◇) PNT20, (pink ★)PNT30, (olive ⬠) PNT40, and (red ◁) PNT. Thick continuous lines correspond to best linear fits for β relaxations and best fits to the VFT equation, with parameters presented in Table 2 for α relaxation. Discontinuous and thinner lines are just a guide to the eyes.

temperature. In such a representation, all β processes follow an Arrhenius behavior. This is characteristic of subglass relaxation processes.[21] From the slope of the τ_β in this representation it is possible to obtain the activation energy (E_a). Concerning the β_1 relaxation, a dependence of the process with molar ratio is observed, being the activation energy 23 kJ mol^{-1} for PTT, and around 37 kJ mol^{-1} for PTT−PNT copolymers. The activation energy calculated for the β_2 process is $E_a \approx 49$ kJ mol^{-1} for all the copolymers and the two homopolymers; in this case no significant molar ratio dependence of E_a is observed. The activation energy values are consistent with the assignment of this process to the subglass relaxation associated with the ester groups placed in the polymeric chain.[21,24,26] Moreover, the position of τ_{max} of the lower frequency β process, β_2, is not significantly affected by the composition for the copolymers investigated in this paper (containing up to 40% of NT units). This behavior is in agreement with that observed in other aromatic copolymeric systems.[27,28] Nevertheless, for PNT homopolymer β_2 process seems to be faster than the same relaxation in the case of PTT and the copolymers. Concerning PTT and its copolymers, the molecular origin of the high frequency mode of the β relaxation (β_1) can be associated with the rotation of the ester oxygen linked to the aliphatic carbon of the diol subunit, as suggested recently.[23] The β_1 relaxation of NT monomeric units is expected to overcome a higher energy barrier as compared to TT ones. In fact the glycolic part of NT unit is characterized by the presence of two methyl groups in β-position with respect to the oxygen atom, instead of two hydrogen atoms as in PTT. The presence of these two methyl

dx.doi.org/10.1021/ma202361r | Macromolecules 2012, 45, 180−188

groups could be the responsible of the hindering of this mode in PNT. This fact supports the idea that the molecular origin of the β_1 relaxation is related to the distinct arrangement of the glycolic group attached to the ester one. As to the low frequency β process, β_2, Figure 6 shows that the slope of $\log_{10}\tau_{max}$ vs reciprocal temperature and consequently the corresponding activation energy E_a, keeps almost a constant value of ≈49 kJ mol^{-1} as the NT unit content is increased. This result indicates that the molecular origin of the β_2 process can be associated with a bond that is present in both repeating units forming the copolymers: the chemical link between the aromatic ring carbon to the ester carbon.

From inspection of Figure 6, one sees that τ_{max} values for the β_2 relaxation of PNT homopolymer and PTT−PNT copolymers, are located within the range of the β_2 relaxation of the PTT homopolymer and present similar activation energies.

α Relaxation of the Amorphous Copolymers. Figure 7 shows the α relaxation for the two amorphous homopolymers

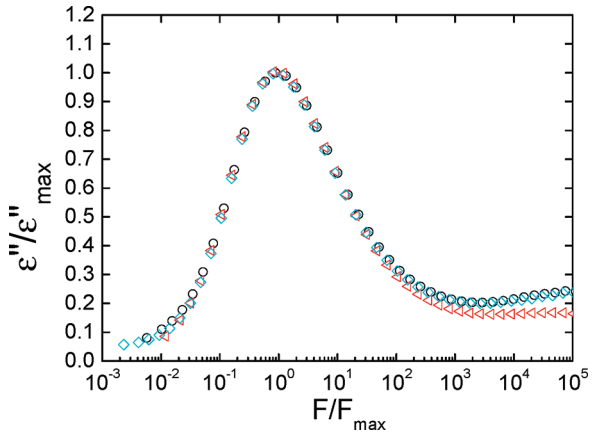

Figure 7. Normalized ε'' values for the two homopolymers PTT at 50 °C(○), PNT at 80 °C (red ◁) and a selected copolymer at 60 °C (PNT20, blue ◇). Both samples are amorphous. The temperatures were chosen to have approximately the same frequency of maximum loss.

and a selected copolymer (PNT20) in the amorphous state. The temperatures have been chosen in order to exhibit similar frequency of maximum loss in the α relaxation region, and the curves have been normalized to compare the relaxation shape of each sample. The α relaxation for the amorphous homopolymers and amorphous copolymer is characterized by a relatively narrow peak in ε'' as a function of frequency. At higher frequencies the less intense contribution of the β relaxation region is also revealed. As observed, the shape of the relaxation for similar dynamic conditions is nearly the same for PTT, PNT and for the copolymer, with the broadening b parameter being around 0.8 and the asymmetry parameter c = 0.4, independently of the comonomeric content.

The main differences appear in the relaxation time temperature dependence. As shown in Figure 6, the α-relaxation τ_{max} values for the amorphous specimens shift, for similar temperature, toward higher values as the neopenthyl terephthalate units content increases. This can be explained on the basis of the progressive decrease in chain flexibility as the amount of NT units increases.[29,30]

In the amorphous state, the frequency of α-relaxation maximum loss exhibits a typical Vogel−Fulcher−Tamann (VFT) dependence:

$$\tau_{max} = \tau_0 \exp\left(\frac{DT_0}{T - T_0}\right) \quad (2)$$

where τ_0 is a characteristic time, T_0 is the Vogel temperature, and D is the fragility strength parameter.[31] This behavior is characteristic of cooperative segmental motions appearing above the glass transition temperature. To obtain accurate fits, and in accordance with Angell's proposal,[32] a value of τ_0 of 10^{-14} s was assumed. Continuous lines in Figure 6 represent the best fits of the experimental τ_{max} values to eq 2, before crystallization occurs. The corresponding parameters are collected in Table 2. In analogy with what happens with the T_g (Table 2), the obtained values for D and T_0 increase with increasing neopenthyl therephthalate content, as expected on the basis of the progressive decreasing of backbone flexibility.

One striking fact that comes out by comparing Figures 5 and 7 is that, apparently, the β relaxation is more affected in its shape by the composition than the α relaxation. This effect may indicate that the local motions, in particular the faster local process (β_1) that becomes less intense in the copolymers to almost disappear in PNT, could be directly involved in the location of the glass transition temperature of the system. It is known that for random copolymers the shape of the relaxation spectrum associated with the segmental dynamics, and therefore the relaxation time distribution function, is mainly affected by the chemical heterogeneity[28] that in the case of PTT and PNT homopolymers is not so high. This could explain why the α relaxation maintains the same shape regardless of the content of neopentyl terephthalate units. Nevertheless the chain rigidity of PNT is higher than PTT one and this leads to a gradual increase of the T_g as the NT-units content goes up.

α Relaxation and Crystallization. As mentioned above, in the PTT homopolymer and in the copolymers with PNT content up to 30%, the initial strong increase of ε'' values as a function of temperature (Figure 3) associated with the α relaxation of the initially amorphous samples is followed by a decrease and a subsequent shoulder for higher temperatures. These are characteristic signatures of a polymer crystallization process as revealed by dielectric spectroscopy[33,34] and it has been reported also for PTT[35] and other semicrystalline polymers.[36−38] Figure 8 shows for PTT−PNT copolymers, the α relaxation curves of the crystallized materials. The values of crystallinity degree (X_c) are collected in Table 1. The temperatures have been chosen to exhibit similar frequency of maximum loss. The differences in the α peak shape of semicrystalline samples, compared with the amorphous ones (Figure 2), are evident. For PNT10, PNT20, and PNT30 copolymers, as crystallization proceeds, a significant broadening in the low frequency side of the α relaxation is detected (see Figure 8). This effect, previously reported[38,39] for PET, can be described by an additional α-process, α', appearing at lower frequency as crystallinity develops and corresponding to the segmental relaxation of a confined amorphous phase coexisting with the initial one. Consequently an additional Havriliak−Negami contribution must be taken into account to consider a second α process.[38] Figure 8 shows the separate contribution of every process as well as the total fittings where the α' relaxation at low frequency has been considered to be symmetric. The rising of this new α' relaxation may indicate a more heterogeneous crystallization for the PTT−PNT copolymers in comparison to the PTT case. The α' process is located at

dx.doi.org/10.1021/ma202361r | Macromolecules 2012, 45, 180−188

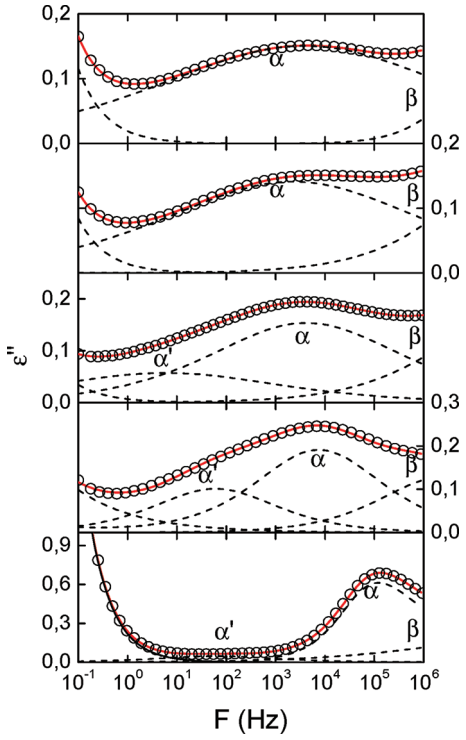

Figure 8. Isothermal ε'' data of semicrystalline PTT−PNT copolymers (PTT, PNT5, PNT10, PNT20 and PNT30 from top to bottom) as a function of frequency for some selected temperatures (100° for PTT and PNT5, 90° for PNT10, 85° for PNT20, and 80 °C for PNT30). Continuous lines represent best fits according to HN equation for the α-region, dashed lines show the separated contribution of the different relaxation processes and conductivity.

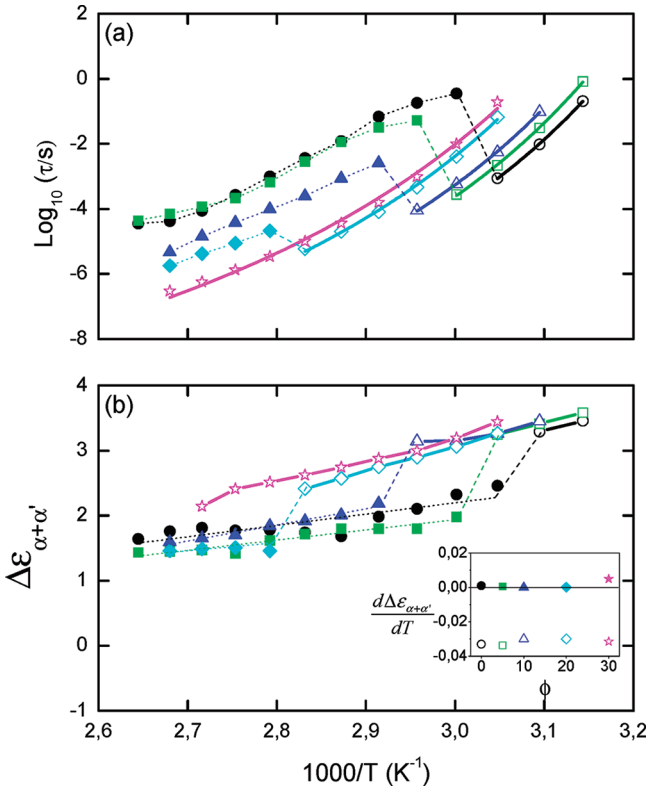

Figure 9. (a) Characteristic time of the α relaxation and (b) total dielectric strength ($\Delta\varepsilon_\alpha+\Delta\varepsilon_{\alpha'}$) as a function of the reciprocal temperature for the initially amorphous samples (open symbols) which crystallize upon heating during the dielectric spectroscopy scan (full symbols). Inset: $\Delta\varepsilon_{\alpha+\alpha'}$/dT vs NT-units content (ϕ) for amorphous and crystallized samples. Key: (○) PTT, (green □) PNT5, (blue △) PNT10, (aqua ◇) PNT20, (pink ★) PNT30, (olive ⬠) PNT40, and (red ◁) PNT.

lower frequencies with respect to the α one and is related to the rigid confined amorphous phase that develops during crystallization process. This effect can be understood as appearing as a consequence of the increasing heterogeneity of amorphous phase with NT content, that for the PNT40 copolymer is so high that completely inhibits crystallization under these conditions. In this case a shift toward lower times of τ_{max} of the α relaxation is not observed. PNT homopolymer is characterized by the same trend of PNT40.

The observed slowing down for the α relaxation of the semicrystalline samples compared to that of the amorphous system also presents particular features depending on the NT content. As mentioned in the previous section, (Figure 6), τ_{max} for the α-process as a function of the reciprocal temperature of all the samples in the first stage (amorphous) of measurement displays a curvature characteristic of a Vogel−Fulcher−Tamman (VFT) dependence. An effect of composition is evident also in this case: as the NT units content increases, the τ_{max} values move toward higher values indicating that the relaxation becomes slower. As we can see en Figure 9a, at a given temperature, a clear change in τ_{max} versus 1/T dependence due to crystallization is evident. This is a consequence of the characteristic slowing down of the amorphous phase segmental dynamics induced by the crystalline phase.[33,39,40] The jump of τ_{max} is less dramatic with increasing NT units, and disappears in PNT40 and PNT homopolymer. These latter samples show a VFT trend for the whole temperature range. This effect is accompanied by a decrease of the dielectric strength $\Delta\varepsilon_{\alpha+\alpha}$ induced by crystallization which turns less intense, as a function of temperature in all the crystallizing samples (Figure 9b). For PTT and the copolymers containing up 30% of counits the strong reduction of the $\Delta\varepsilon_{\alpha+\alpha}$ values is associated with the decrease of the amorphous mobile phase which is transferred to the crystalline phase. From the inset in Figure 9b, one can see that the slope of $\Delta\varepsilon_{\alpha+\alpha}'$ is not affected by the composition, while it seems to depend on the semicrystalline nature of the material. In particular, at temperature closed to the glass transition (before crystallization) the slope is negative as expected for bulk amorphous systems. On the contrary, it becomes positive or almost zero for the crystallized materials. In this case the slope has been taken at temperatures much higher than the T_g. This is due to the restriction of the crystallites or rigid amorphous phase on the amorphous chains.[24]

A different behavior is observed in samples with high amount of NT units. The symmetric broadening b, which is situated around 0.8 for all the samples while still amorphous, goes down to values around 0.3−0.4 for the low NT content copolymers, while remain almost constant for PNT40 and PNT, due to the absence of crystallization. Respect to the asymmetric broadening parameter c, a similar behavior to parameter b was found. For the amorphous state in all cases, c assumes a value of 0.5 but a dramatic and instantaneous increase up to 1, at different temperatures, is observed for the crystallizable samples as a consequence of the crystallization phenomenon. As recently proposed by Sanz et al.,[41] the significant broadening of the

dx.doi.org/10.1021/ma202361r | Macromolecules 2012, 45, 180−188

dielectric segmental relaxation in semicrystalline polymers can be attributed to the averaging effect of measuring a homogeneous relaxation over an inhomogeneous environment providing different characteristic relaxation times. Similarly, Napolitano et al.[42] showed that in the case of polymers adsorbed on a substrate, where the segmental dynamics is restricted as it is in a semicrystalline polymer, the α relaxation also broadens.

In order to better understand the observed dynamical changes during crystallization and to correlate those with structure, several additional experiments were performed. The thermal characterization was carried out also on the all copolymers after dielectric measurement. Figure 4b shows the differential calorimetry scans obtained after the dielectric experiment. In the PTT homopolymers, and the copolymers with PNT content up to 30%, the T_g can be detected as a step in the DSC traces, and no signs of further crystallization are observed. Therefore, the observed melting peak should be associated with the crystals that have been formed during the dielectric experiments. However, for the PNT40 copolymer and the PNT homopolymer the DSC traces before and after the dielectric experiment are nearly identical, indicating that no crystallization has been induced during the dielectric experiment. In order to further characterize the samples after the dielectric experiment, small and wide-angle X-ray scattering (SAXS and WAXS) patterns were obtained from the specimens from the dielectric experiment. Figure 10 illustrates the SAXS

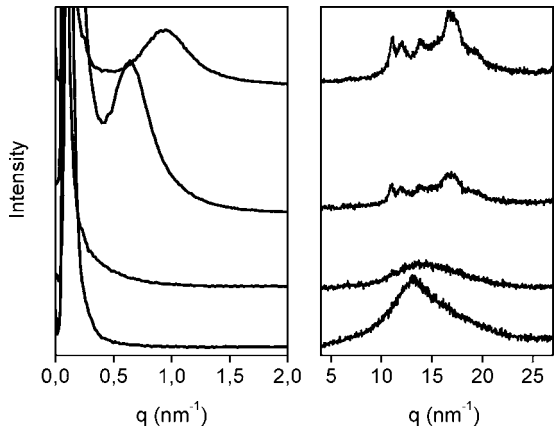

Figure 10. SAXS (left panel) and WAXS (right panel) diffracted intensity as a function of scattering vector q, for PTT, PNT20, PNT40, and PNT (from top to bottom), after the dielectric scan.

and WAXS patterns at room temperature of PTT−PNT samples as a function of the scattering vector q ($q = 4\pi \sin(\theta)/\lambda$, 2θ being the scattering angle), performed after dielectric measurement. Samples with PNT content below 30% exhibit a clear maximum in the small angle scattered intensity, indicating the existence of a lamellar crystal packing with an average periodicity given by the long period values ($L = 2\pi/q_{max}$, where q_{max} is the scattering maximum). As is shown in Table 1, the long period values tend to increase with counits content. This trend correlates well with the melting point dependence on molar ratio which exhibits a minimum for the PNT30,[43,44] suggesting that for a given composition non crystallizable comonomeric units tend to hinder the crystallization of the PTT segments, leading to thinner and more disperse lamellae.[43−45] The SAXS patterns were also analyzed according to the classical one-dimensional electron density correlation formalism by Vonk[46,47] using the methods described by Strobl and Schenider.[48] The electronic density correlation function was calculated from the Fourier transform of the Lorentz-corrected profile.

The lamellar variables obtained from this analysis of the scattering data are long period (L), linear degree of crystallinity (X_{cL}), crystalline lamellar thickness (l_c), and amorphous layer thickness (l_a). The average linear degree of crystallinity in the lamellar stacks can be determined from the following equation:[49]

$$x_1 x_2 = B/L^M{}_c \quad (3)$$

where B is the first intercept of the correlation function with the abscissa, $L^M{}_c$ is the long spacing calculated from the first maximum in the correlation function, and x_1 and x_2 are the volume fractions of the two phases, within the lamellar stacks, respectively ($x_1 + x_2 = 1$). The thickness of the two phases can be calculated as $l_1 = x_1 L^M{}_c$ and $l_2 = x_2 L^M{}_c$. From the correlation function itself it is not possible to associate l_1 or l_2 with the thickness of the crystalline lamellae unless further information is obtained from other methods.

The WAXS patterns (Figure 10) obtained from the samples after the dielectric experiment reveals that they have crystallized, except in PNT40 and PNT. The patterns indicate that the crystal phase is to be related to the lattice of the PTT homopolymer, as supported by the presence of the most intense Bragg peaks, around 2θ = 11.1, 12.0, 13.9, and 16.9, characteristic of PTT.[50,51] As evidenced by the T_g data (Table 2), PTT−PNT random copolymers possess lower flexibility in comparison with original PTT. We can hypothesize that the decrease in chain flexibility of the copolymer decreases the facility of PTT segments to find a crystalline register. Moreover, with increasing NT content, the amount of crystallizable units decreases. As a consequence, the crystallinity of the samples goes down with the increment of NT counits, as can be appreciated in Figure 10, right panel, by the lowering of the area under the peaks (see also the values of crystallinity degree (X_c) collected in Table 1).

Looking at the obtained values for X_c from WAXS, it is possible to infer, that we may assign the thinner value to the lamellar thickness (l_1). Assuming that, our results indicate that for PTT, and for all the copolymers, the lamellae are very homogeneously distributed along the sample. These results are in line with similar observations by Ivanov et al, on PTT crystallized under different conditions.[52,53] The interlamellar amorphous thickness (l_2) increases as the amount of NT units increases. This would imply that the amorphous phase that relax and give rise to the α relaxation is less restricted due to the presence of crystals, since they are further apart. In one hand, this can explain the decrease in the τ_{max} jump observed in the VFT representation (Figure 6a). On the other hand, this remaining amorphous phase is expected to be more enriched with more rigid NT units that can not be incorporated into the crystals. As mentioned above, in the case of PNT10, PNT20 and PNT30, when the sample crystallizes, a new α' process appears. Previous DSC results indicate that, a rigid amorphous phase (RAP) is formed and that this RAP is mainly due to noncrystallizable NT units.[14] To determinate the interphase content in each sample crystallized during the dielectric measurement, the weight fractions of the crystalline phase (w_c), amorphous phase (w_a) and interphase (w_i) were calculated according to the following relationships:

$$w_c = (\Delta H_m w_{PT})/\Delta H^\circ{}_m \quad (4)$$

$$w_a = \Delta c_p/\Delta c_p{}^a \quad (5)$$

$$w_i = 1 - w_c - w_a \quad (6)$$

Here ΔH_m is the melting of fusion of the crystallizable TT units, and $\Delta H^\circ{}_m$ is the equilibrium melting enthalpy of PTT (150 J/g). Δc_p and $\Delta c_p{}^a$ correspond to the experimental specific heat increments of the semycrystalline and fully amorphous copolymer respectively and w_{PT} is the weight fraction of trimethylene terephthalate units. Looking at the results summarized in Table 1, one can see that as NT unit content increases, w_c values decrease, w_a fractions increase, while the weight fractions of interphase (w_i) remains almost constant. This means that even if the overall degree of crystallinity is lower, i.e. there are fewer crystals, each crystal operates a more effective restriction on the amorphous region. Therefore, we may attribute the α' relaxation to the relaxation at higher temperatures of this RAP inferred by DSC. The final situation on the crystallized copolymer sample would be a less restricted "original" α relaxation due to less hindering of crystals distributed further apart but a new α' relaxation that could be attributed to the relaxation of the RAP mainly composed of noncrystallizable NT units and that it probably located at the interphase of the crystals.

CONCLUSIONS

In conclusion, the introduction of rigid neopenthyl terephthalate units into the more flexible PTT chain decreases the ability to crystallize of the resulting copolymer. X-ray scattering experiments indicate that the crystalline phase, that develops during heating, is related to the lattice characteristic of the trimethylene terephthalate units. The subglass dynamics of PTT−PNT copolymers is characterized by the existence of two processes, β_1 and β_2, which have been assigned to the relaxation of the bond between the ester oxygen and the aliphatic carbon of the diol subunit, and to the bond between the aromatic ring carbon to the ester carbon, respectively. The segmental dynamics of the copolymers is characterized by the existence of a α process which follows an expected molar ratio dependence, since it moves to higher temperatures as the counit content is increased, while the shape of the distribution of segmental relaxation times is not affected by the composition, being the same for the neat homopolymers and for the copolymers. Our results indicate that by copolymerization it is possible to obtain crystallizable polymeric systems in which the characteristic dynamical retardation of the amorphous phase upon crystallization could be modulated.

AUTHOR INFORMATION

Corresponding Author

*Telephone: +34915616800 Ext 942412. Fax: +34915645557. E-mail: m.soccio@iem.cfmac.csic.es.

ACKNOWLEDGMENTS

The authors acknowledge financial support from Grants MAT2008-03232 and MAT2009-07789 from MICINN, Spain. M.S. acknowledges the tenure of a JAE-Doc contract.

REFERENCES

(1) Yu, H.; Liao, D.; Johnston, M. B.; Li, B. *ACS Nano* **2011**, *5* (3), 2020−2025.
(2) Ivanov, D. A.; Bar, G.; Dosiere, M.; Koch, M. H. J. *Macromolecules* **2008**, *41* (23), 9224−9233.
(3) Barham, P. J.; Organ, S. J. *J. Mater. Sci.* **1994**, *29* (6), 1676−1679.
(4) Tsai, R.-S.; Lee, Y.-D. *J. Polym. Res.* **1998**, *5* (2), 77−84.
(5) Cheng-Fang, O. *Eur. Polym. J.* **2002**, *38* (12), 2405−2411.
(6) Jeong, Y.; Jo, W.; Lee, S. *Fibers Polym.* **2004**, *5* (3), 245−251.
(7) Wu, T.-M.; Lin, Y.-W. *J. Polym. Sci., Part B: Polym. Phys.* **2004**, *42* (23), 4255−4271.
(8) Shyr, T.-W.; Lo, C.-M.; Ye, S.-R. *Polymer* **2005**, *46* (14), 5284−5298.
(9) Seo, Y. W.; Pang, K.; Kim, Y. H. *Macromol. Mater. Eng.* **2006**, *291* (11), 1327−1337.
(10) Jia, H. B.; Xu, Y.; Ye, S. R.; Qian, J. W. *J. Mater. Sci.* **2006**, *41* (15), 4970−4973.
(11) Zou, H. T.; Jiang, J. M.; Yang, S. L.; Li, G. *J. Macromol. Sci., Part B: Phys.* **2006**, *45* (4), 581−592.
(12) Szymczyk, A. *Eur. Polym. J.* **2009**, *45* (9), 2653−2664.
(13) Szymczyk, A.; Senderek, E.; Nastalczyk, J.; Roslaniec, Z. *Eur. Polym. J.* **2008**, *44* (2), 436−443.
(14) Soccio, M.; Lotti, N.; Finelli, L.; Gazzano, M.; Munari, A. *J. Polym. Sci., Part B: Polym. Phys.* **2008**, *46* (2), 170−181.
(15) Soccio, M.; Lotti, N.; Finelli, L.; Munari, A. *J. Polym. Sci., Part B: Polym. Phys.* **2008**, *46* (8), 818−830.
(16) Havriliak, S.; Negami, S. *Polymer* **1967**, *8* (4), 161-&.
(17) Kremer, F.; Schonhals, A., *Broadband Dielectric Spectroscopy*; Springer Verlag: Heidelberg, Germany, 2002.
(18) Blundell, D. J.; Osborn, B. N. *Polymer* **1983**, *24* (8), 953−958.
(19) Wood, L. A. *J. Polym. Sci.* **1958**, *28* (117), 319−330.
(20) Sanz, A.; Nogales, A.; Ezquerra, T. A.; Lotti, N.; Finelli, L. *Phys. Rev. E* **2004**, *70* (2), 6.
(21) McCrum, N. G.; Read, B. E.; Williams, G., *Anelastic and Dielectric Effects in Polymeric Solids*; John Wiley and Sons: New York, 1967.
(22) Bravard, S. P.; Boyd, R. H. *Macromolecules* **2003**, *36* (3), 741−748.
(23) Nogales, A.; Sanz, A.; Ezquerra, T. A. *J. Non-Cryst. Solids* **2006**, *352* (42−49), 4649−4655.
(24) Coburn, J. C.; Boyd, R. H. *Macromolecules* **1986**, *19* (8), 2238−2245.
(25) Nogales, A.; Sanz, A.; Sics, I.; García-Gutiérrez, M. C.; Ezquerra, T. A. Order and segmental mobility in crystallizing polymers. *Lecture Notes Phys.* **2007**, *714*, 435−456.
(26) Hedvig, P., *Dielectric spectroscopy of polymers*; Wiley: New York, 1977.
(27) Tatsumi, T.; Ito, E.; Hayakawa, R. *J. Polym. Sci., Part B: Polym. Phys.* **1992**, *30* (7), 701−706.
(28) Ezquerra, T. A.; Balta Calleja, F. J.; Zachmann, H. G. *Acta Polym.* **1993**, *44* (1), 18−24.
(29) Couchman, P. R. *Macromolecules* **1987**, *20* (7), 1712−1717.
(30) Ngai, K. L.; Roland, C. M. *Macromolecules* **1993**, *26* (11), 2688−2690.
(31) Richert, R.; Angell, C. A. *J. Chem. Phys.* **1998**, *108* (21), 9016−9026.
(32) Angell, C. A. *Polymer* **1997**, *38* (26), 6261−6266.
(33) Williams, G. Molecular aspects of multiple dielectric relaxation processes in solid polymers. In *Electric Phenomena in Polymer Science*; Springer: Berlin and Heidelberg, Germany: 1979; Vol. *33*, pp 59−92.
(34) Sanz, A.; Nogales, A.; Ezquerra, T. A.; Lotti, N.; Munari, A.; Funari, S. S. *Polymer* **2006**, *47* (4), 1281−1290.
(35) Sanz, A.; Nogales, A.; Ezquerra, T. A.; Soccio, M.; Munari, A.; Lotti, N. *Macromolecules* **2010**, *43* (2), 671−679.
(36) Nogales, A.; Denchev, Z.; Sics, I.; Ezquerra, T. A. *Macromolecules* **2000**, *33* (25), 9367−9375.
(37) Nogales, A.; Ezquerra, T. A.; Denchev, Z.; Sics, I.; Calleja, F. J. B.; Hsiao, B. S. *J. Chem. Phys.* **2001**, *115* (8), 3804−3813.
(38) Alvarez, C.; Sics, I.; Nogales, A.; Denchev, Z.; Funari, S. S.; Ezquerra, T. A. *Polymer* **2004**, *45* (11), 3953−3959.
(39) Fukao, K.; Miyamoto, Y. *Phys. Rev. Lett.* **1997**, *79* (23), 4613.

(40) Ezquerra, T. A.; Majszczyk, J.; Baltá-Calleja, F. J.; Lopez-Cabarcos, E.; Gardner, K. H.; Hsiao, B. S. *Phys. Rev. B* **1994**, *50* (9), 6023.
(41) Sanz, A.; Nogales, A.; Ezquerra, T. A.; Haussler, W.; Soccio, M.; Lotti, N.; Munari, A. *Macromolecules* **2011**, *44* (20), 8124−8128.
(42) Napolitano, S.; Wübbenhorst, M. *Nature Commun.* **2011**, *2*, 160.
(43) Righetti, M. C.; Pizzoli, M.; Munari, A. *Macromol. Chem. Phys.* **1994**, *195* (6), 2039−2047.
(44) Righetti, M. C.; Pizzoli, M.; Lotti, N.; Munari, A. *Macromol. Chem. Phys.* **1998**, *199* (9), 2063−2070.
(45) Munari, A.; Manaresi, P.; Chiorboli, E.; Chiolle, A. *Eur. Polym. J.* **1992**, *28* (1), 101−106.
(46) Kortleve, G.; Vonk, C. G. *Colloid Polym. Sci.* **1968**, *225* (2), 124−131.
(47) Vonk, C. G.; Kortleve, G. *Colloid Polym. Sci.* **1967**, *220* (1), 19−24.
(48) Strobl, G. R.; Schneider, M. *J. Polym. Sci., Part A-2: Polym. Phys.* **1980**, *18* (6), 1343−1359.
(49) Hsiao, B. S.; Verma, R. K. *J. Synchrotron Radiat.* **1998**, *5* (1), 23−29.
(50) Desborough, I. J.; Hall, I. H.; Neisser, J. Z. *Polymer* **1979**, *20* (5), 545−552.
(51) Poulin-Dandurand, S.; Pérez, S.; Revol, J.-F.; Brisse, F. *Polymer* **1979**, *20* (4), 419−426.
(52) Ivanov, D. A.; Bar, G.; Dosière, M.; Koch, M. H. J. *Macromolecules* **2008**, *41* (23), 9224−9233.
(53) Ivanov, D. A.; Hocquet, S.; Dosiére, M.; Koch, M. H. J. *Eur. Phys. J. E: Soft Matter Biol. Phys.* **2004**, *13* (4), 363−378.

Macromolecules

Article

pubs.acs.org/Macromolecules

Temperature-Variable FTIR and Solid-State ^{13}C NMR Investigations on Crystalline Structure and Molecular Dynamics of Polymorphic Poly(L-lactide) and Poly(L-lactide)/Poly(D-lactide) Stereocomplex

Pengju Pan,*[,†] Jinjun Yang,[‡,§] Guorong Shan,[†] Yongzhong Bao,[†] Zhixue Weng,[†] Amin Cao,[⊥] Koji Yazawa,[‡] and Yoshio Inoue[‡]

[†]State Key Laboratory of Chemical Engineering, Department of Chemical and Biological Engineering, Zhejiang University, 38 Zheda Road, Hangzhou 310027, China

[‡]Department of Biomolecular Engineering, Tokyo Institute of Technology, 4259-B-55 Nagatsuta, Midori-ku, Yokohama 226-8501, Japan

[§]School of Environmental Science and Safety Engineering, Tianjin University of Technology, Tianjin 300384, China

[⊥]Laboratory for Polymer Materials, Shanghai Institute of Organic Chemistry, Chinese Academy of Sciences, Shanghai 200032, China

Supporting Information

ABSTRACT: Crystalline structure and molecular dynamics in α and α' crystals of poly(L-lactide) (PLLA) and PLLA/poly(D-lactide) (PDLA) stereocomplex (sc) crystals have been investigated by the temperature-variable FTIR and solid-state ^{13}C CP-MAS NMR spectroscopy. The crystal forms of polylactide (PLA) have different band frequencies, correlation field splittings in FTIR spectra and different line shapes, and resonance splittings in solid-state NMR spectra, which become more distinct with cooling to the cryogenic conditions. The well-resolved splittings in NMR resonances of α crystals, attributable to the crystallographically inequivalent sites within crystal unit cell, are considered to be due to the dipolar interactions related to the carbonyl, methyl, and methine groups. The splittings in FTIR bands and NMR resonances are absent in α' crystals, indicating the disordered conformation and loose molecular lateral packing within their crystal lattices. The significant FTIR frequency shifts of ν(C═O), ν(CH$_3$), and ν(CH) modes during stereocomplex crystallization of PLLA/PDLA blend and the appearance of spectral splittings at cryogenic conditions suggest the coexistence of weak C−H···O═C hydrogen bonds and dipolar interactions between PLLA and PDLA chains in the sc crystals of PLA. Below the glass transition temperature (T_g), the spin−lattice relaxation times of PLA with different crystalline structures increase in the order of amorphous ≈ α' < α < sc.

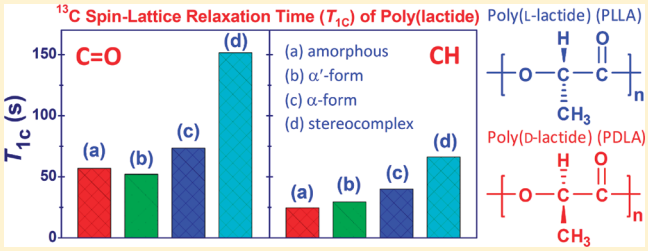

INTRODUCTION

Polylactide or poly(lactic acid) (PLA) has been considered as one of the most promising bio-based thermoplastics because its monomer, lactic acid, can be produced from renewable resources (e.g., starchy materials and sugars). The attributes of biodegradability, biocompatibility, good mechanical properties, and versatile fabrication processes make it a promising material for biomedical applications (e.g., implant materials, surgical suture, and controlled drug delivery systems) and commodity applications in substitution of the conventional oil-based thermoplastics.[1] Since lactic acid is a chiral molecule, the stereoregular PLA exists in two enantiomeric isomers, poly(L-lactide) (PLLA) and poly(D-lactide) (PDLA).

One of the most remarkable issues regarding the solid-state structure of PLA is its crystal polymorphism. The common stereoisomer of PLA, i.e., PLLA, can crystallize in α,[2−6] β,[7,8] and γ[9] polymorphs, depending on the crystallization conditions. The usual polymorph, α form, generally produced from the cold, melt, or solution crystallization, is characterized by an orthorhombic (or pseudo-orthorhombic) unit cell packed by two antiparallel left-handed helical chains in a distorted 10_3 conformation.[2−6] The β form, adopting a 3_1 helical conformation, can be attained via stretching its α counterpart at high temperature to a high drawing ratio.[7,8] Very recently, a metastable α' form has been proposed for the stereoregular PLA melt-crystallized at low crystallization temperature T_c (<100 °C) compared to the normal α crystals produced at high T_c (>120 °C).[10−15]

A wide range of physical properties such as thermal, mechanical, and electrical properties are influenced by the crystal modifications of polymorphic polymers.[16] In addition, crystalline structure is a key factor for the hydrolytic and enzymatic degradations of biodegradable polymers.[17,18] In the case of PLLA, Kanamoto and co-workers have reported that the

Received: August 21, 2011
Revised: December 2, 2011
Published: December 19, 2011

β-form PLLA had a higher tensile strength and modulus than its α counterpart.[19] Cocca et al. have reported that α-form PLLA possessed a higher Young's modulus and a better barrier to water vapor than its α′ counterpart.[20] Therefore, study on the relationships between crystal structure and crystallization condition is of fundamental importance because it allows for tuning the physical performances of polymeric materials by controlling their processing conditions. In the practical melt processing, stereoregular PLA is usually molded at 100−120 °C because of the relatively fast crystallization over this temperature region. The α′ and α mixed crystals are generally produced in this temperature range.[12−15] Therefore, study on the solid-state structure of α′ and α crystals of PLA would be important from the perspective of practical applications.

Previous studies have reported that the α′ and α crystals of PLA have different crystallization kinetics and thermal stability.[12−15,21] From the wide-angle X-ray diffraction (WAXD) and Fourier transform infrared (FTIR) spectroscopy analyses, it has been proposed that the α′ and α crystals have similar chain conformation and orthorhombic unit cell,[10,11] while the lateral dimension of α′ crystal lattice is slightly larger than that of its α counterpart.[12−14] On the basis of the infrared and Raman spectroscopic analyses, Hsu and co-workers[21] have recently found that the α′ crystals have conformational disorder and the disorder in chain packing and conformation results in the different crystalline forms. Because of the very similar WAXD patterns of α′ and α crystals, their structural difference is relatively difficult to elucidate, and many aspects still remain unclear. On the other hand, a notable structural feature of PLLA α crystals is the deviation of crystal system from the normal orthorhombic unit cell and the torsion of helix conformation.[2−6] The WAXD pattern of α-form PLLA displays some extra meridional reflections on the layer lines, indicating some extent of helix distortion from the pure 10_3 conformation.[2−4] The reason for helix distortion is still under debate. Hoogsteen et al. have suggested that the interchain interactions between methyl groups may force this distortion because a 10_3 helix with twisted grooves restricts the translation of neighboring chains with respect to each other by a kind of interlocking of methyl groups.[3] Puiggali et al.[5] as well as Sasaki and Asakura[6] have found the molecular distortion in the α crystals of PLLA, which is resulted by the asymmetric interchain interactions. More well-established experiments are required to elucidate the structural features of α′ and α crystals as well as the structural differences between them.

The PLLA/PDLA stereocomplex (sc) is another crystalline form of PLA. It is generally produced in the crystallization of 1:1 PLLA/PDLA blend from melt or solution.[22] Sc form is characterized by a triclinic unit cell packed by one PLLA and one PDLA chain, both adopting a 3_1 conformation.[22] A characteristic feature of sc form is its high melting point T_m, higher by ∼50 °C than those of the homocrystals. Compared to the homocrystals, sc crystals possess higher thermal stability, mechanical strength, tensile modulus, and hydrolytic and enzymatic degradation resistance.[23] The promising physical properties of sc-form PLA are due in part to the specific molecular packing and interchain interactions (e.g., van der Waals interactions[24] or interchain hydrogen bonds[25,26]) between the left- and right-handed helices of PLLA and PDLA chains. From this viewpoint, study on the crystal structure of sc crystals would shed light on the structure−property relationships of PLA materials.

High-resolution solid-state nuclear magnetic resonance (NMR) spectroscopy has revealed a high sensitivity to the microstructures of polymer chains in solid, and it is a powerful tool to study the molecular dynamics and relaxation.[27] With aid of this technique, the conformation, molecular packing, intrachain, and interchain interactions in the different crystal modifications of isotactic polypropylene (i-PP),[28−30] syndiotactic polypropylene (s-PP),[31,32] and isotactic poly(1-butene) (i-PB)[33] have been successfully investigated; some of this structural information cannot be attained from the diffraction techniques. Although several authors have reported the solid-state ^{13}C NMR spectra of α[34−36] and sc-form[37] PLAs, a systematic analysis and comparison of spectral features and molecular dynamics between the α′, α, and sc-form PLAs have been unexplored.

Experimental studies[38,39] and theoretical calculations[40] have indicated that the polymer crystals undergo a thermal anisotropic expansion or contraction with the temperature changes. This process can lead to the changes of crystal lattice spacing, conformational characteristics, and intrachain or interchain interactions, which in turn result in the alterations of macroscopic properties (e.g., mechanical properties[40]). Accordingly, FTIR[38,41−43] and NMR[30,33] studies with the temperature-variable techniques can provide new insights into the structural features of polymer crystals, particularly for the different crystal modifications of a given polymer. In this work, the solid-state structures of different crystalline forms (α′ and α crystals) of PLLA and sc crystals of PLLA/PDLA blend were investigated and analyzed using the temperature-variable FTIR and solid-state ^{13}C NMR techniques over a wide temperature range (140 to −140 °C). Molecular dynamics of these crystal forms were analyzed by the ^{13}C spin−lattice relaxation measurements. Based on these results, the structural features such as molecular packing, interaction, and mobility of different crystals of PLA were discussed.

EXPERIMENTAL SECTION

Materials. PLLAs with a low and high molecular weights, PLLA-L (M_n = 15.4 kg/mol, M_w/M_n = 1.38) and PLLA-H (M_n = 118 kg/mol, M_w/M_n = 1.49), were kindly supplied by Unitika Co. Ltd. (Kyoto, Japan). The L-isomer content in PLLA was ∼99.5%. PDLA (M_n = 23.0 kg/mol, M_w/M_n = 1.33) was synthesized via the ring-opening polymerization (ROP) of D-lactide (PURAC, The Netherlands). The samples were purified by precipitation into ethanol from the chloroform solution and then were dried under vacuum at 70 °C for 48 h.

Preparation of Various Crystal Forms of PLA. The α′- and α-form PLAs were prepared by the isothermal melt crystallization of PLLA-H at 80 and 140 °C for 6 h after melting at 200 °C for 2 min, respectively. To prepare the sc-form PLA, equivalent amounts of PLLA-L and PDLA were dissolved in chloroform (∼1 g/50 mL). The solution was cast on a Petri dish, and the solvent was allowed to evaporate under ambient conditions. It was then dried in a vacuum oven at 70 °C for 48 h. Sc-form PLA was prepared by isothermal melt crystallization of 1:1 PLLA-L/PDLA blend at 200 °C for 2 h under the protection of dry N_2 after melting at 240 °C for 2 min. Amorphous PLLA-H and 1:1 PLLA-L/PDLA blend samples were prepared by quenching from 200 and 240 °C to ∼25 °C, respectively. Unless otherwise specified, the sample "amorphous PLA" represents amorphous PLLA-H quenched from the melt.

Measurements. Differential Scanning Calorimeter. The measurements of differential scanning calorimeter (DSC) were performed on a Pyris Diamond DSC instrument (Perkin-Elmer Inc., Waltham, MA) equipped with an intracooler cooling accessory. The temperature and heat flow were calibrated by the indium standard at different heating rates. The preweighted sample (∼7 mg) was sealed in

an aluminum pan and then heated from 0 to 200 °C for amorphous, α′-form, and α-form PLAs or 250 °C for sc-form PLA at a heating rate of 10 °C/min to observe the melting behavior.

FTIR Spectroscopy. FTIR measurements were performed on a FTIR-6100 spectrometer (JASCO, Japan) equipped with an IMV-4000 multichannel infrared microscope (JASCO, Japan) and a MCT detector worked in the transmission mode. PLLA-H or 1:1 PLLA-L/PDLA blend sample was sandwiched by two BaF_2 windows and then melt-crystallized at the corresponding temperatures to prepare the α′-, α-, and sc-form PLAs or quenched to ∼25 °C from melt to prepare the amorphous sample, as above mentioned. The sample is thin enough to follow the Beer−Lambert law. The sample was cooled from 140 °C (for α and sc form), 80 °C (for α′ form), or 40 °C (for amorphous sample) to −140 (or −100) °C at a cooling rate of 5 °C/min in a LK-600 hot stage (Linkam Scientific Instrument Ltd., Surrey, UK) equipped with a L600A liquid N_2 cooling unit. FTIR spectra were recorded during the cooling process. The spectra were registered with 64 scans and a resolution of 2 cm^{-1}, and 4 data points were collected within each frequency interval of 2 cm^{-1}.

Solid-State NMR Spectroscopy. Solid-state ^{13}C NMR spectra were acquired on a JEOL JNM-ECA 500 MHz spectrometer operating at 500 MHz for ^1H and 125.8 MHz for ^{13}C using the cross-polarization (CP), magic-angle spinning (MAS), and high-power ^1H decoupling. CP-MAS spectra were measured with a 3.1 μs ^1H π/2 pulse, a 3 ms CP pulse with a 7% ramp on the ^1H channel and an rf field strength of 65 kHz, a MAS speed of ∼5 kHz, and a 5 s recycle delay. Two-pulse phase modulated (TPPM) ^1H decoupling with a 15° phase shift and a rf field strength of 80 kHz was applied during acquisition. ^{13}C chemical shift was referenced externally to the methyl carbon resonance of hexamethylbenzene at 17.4 ppm. The ^{13}C spin−lattice relaxation times (T_{1C}s) were measured at ∼25 °C with a conventional CPT1 pulse sequence reported by Torchia.[44]

RESULTS AND DISCUSSION

DSC Melting Behavior. Figure 1 shows the DSC heating curves of α′-, α-, and sc-form PLAs. The DSC curve of amorphous PLA is included for comparison. The thermal parameters including crystallization temperature (T_c) used for the sample preparation, melting point (T_m), melting enthalpy (ΔH_m), and degree of crystallinity (X_c) of three crystal forms of PLA are summarized in Table 1. X_c was estimated by comparing the ΔH_m value with the value of an infinitely large crystal (ΔH_m^0), which was taken as 93 J/g[45] for the α′ and α homocrystals and 142 J/g[46] for the sc crystals. Sc crystals exhibit a melting point at 232 °C that is more than 50 °C higher than the homocrystals. The DSC curve of α′ crystals shows an exotherm (P_{ex}) prior to the dominant melting peak, corresponding to the α′-to-α crystalline phase transition.[12−15] Because of the α′-to-α transition upon heating, the melting point observed from the DSC curve of α′ crystals corresponds to the α crystals developed in phase transition. ΔH_m values of the prepared crystal forms of PLA increase in the order of α′ < α < sc, exhibiting the same tendency to melting point and thermal stability.

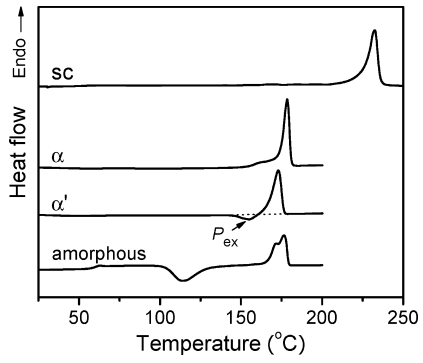

Figure 1. DSC heating curves of amorphous, α′-, α-, and sc-form PLAs recorded at a heating rate of 10 °C/min.

Table 1. Thermal Parameters of α′, α, and sc Crystals of PLA

crystal form	composition	T_c (°C)	T_m (°C)	ΔH_m (J/g)	X_c (%)
α′	PLLA	80	173	41	44
α	PLLA	140	179	62	67
sc	1:1 PLLA/PDLA	200	232	80	56

Temperature-Dependent FTIR Spectra. We first compared the FTIR spectra of amorphous, α′-, α-, and sc-form PLAs, as shown in Figure 2. As expected, the amorphous PLA and 1:1 PLLA/PDLA blend prepared by quenching exhibit the same FTIR spectra, since PLLA and PDLA are identical from a spectroscopic point of view. So, we used the quenched PLLA as a representative amorphous PLA sample to make a comparison to the crystalline ones. FTIR spectra are sensitive to the crystal forms of PLA (Figure 2), which will be discussed in combination with the temperature-dependent spectra in the following sections.

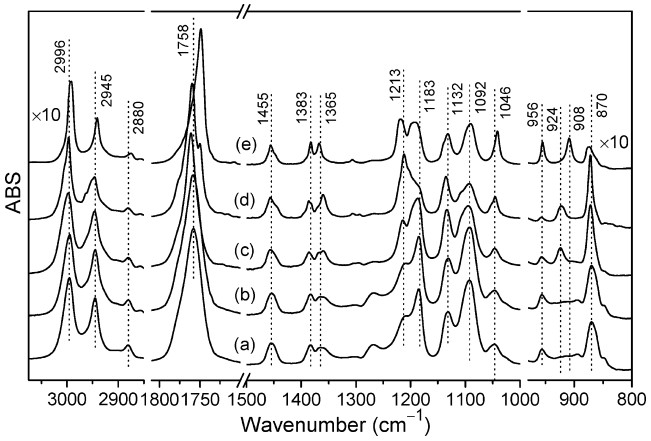

Figure 2. FTIR spectra of (a) amorphous PLLA, (b) amorphous 1:1 PLLA/PDLA blend, (c) α′-, (d) α-, and (e) sc-form PLAs collected at ∼25 °C. Spectral intensities in the wavenumber regions of 3075−2850 and 980−800 cm^{-1} were magnified by 10 times.

The crystalline structures of different PLA crystals were investigated by temperature-variable FTIR spectroscopy over the temperature range of 140 to −140 °C. The temperature-dependent FTIR spectra and their corresponding second derivatives for different crystals of PLA are shown in Figure 3 and Figures S1−S3. Assignments of FTIR bands for amorphous and crystalline PLAs are summarized in Table 2.[47] Considering the band frequency shift with temperature, the wavenumbers shown in Figure 3 and Table 2 were derived from the spectra collected at 20 °C. As seen in Figure 3 and Figure S1, aside from the spectral intensity and band frequency, the line shape of α′ crystals is nearly unaltered with cooling from 80 to −140 °C. This is similar to the amorphous PLA (data not shown). In contrast, the line shape of α crystals varies remarkably with temperature (Figure 3 and Figure S2). Its spectrum splits into quite a few new components with cooling to −140 °C, such as the components at 3006 cm^{-1} of $\nu_{as}(CH_3)$, 2964 cm^{-1} of $\nu_s(CH_3)$, 1777 and 1749 cm^{-1} of $\nu(C{=}O)$, 1468 and 1443

dx.doi.org/10.1021/ma201906a | Macromolecules 2012, 45, 189−197

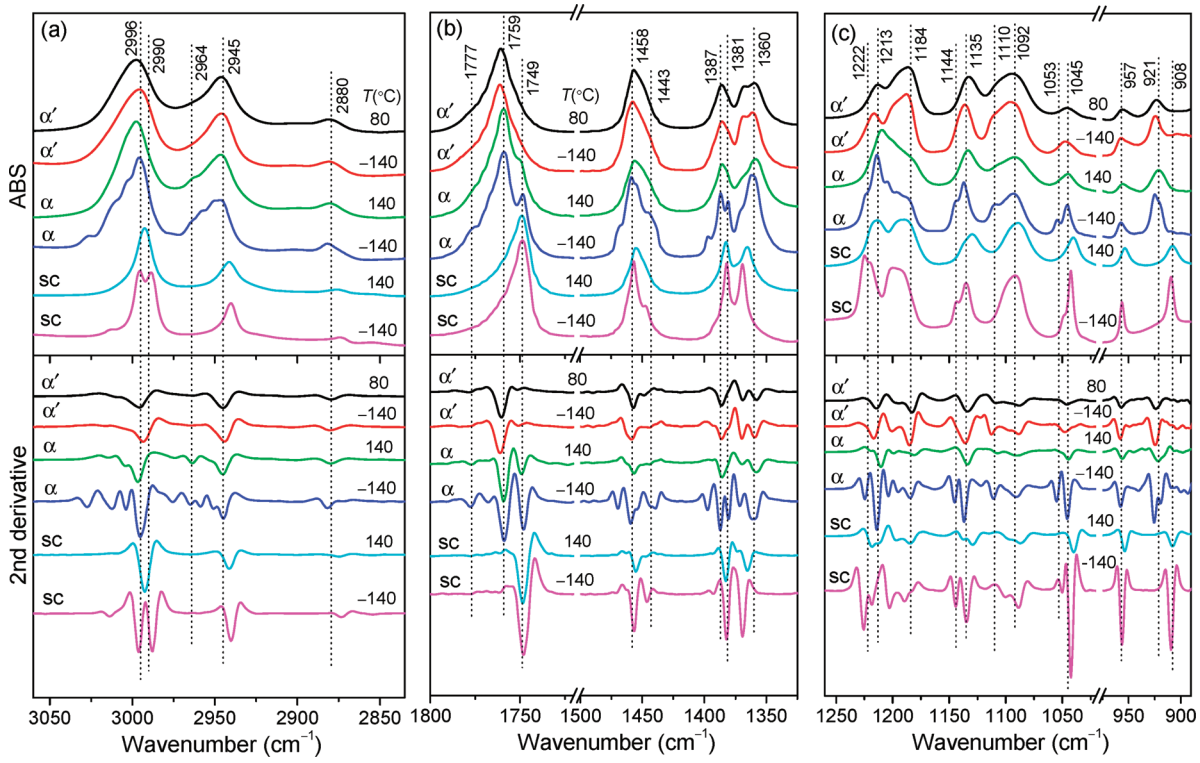

Figure 3. Temperature-dependent FTIR spectra and their second derivatives of α'-, α-, and sc-form PLAs. Intensities of FTIR spectra and their second derivatives in the wavenumber ranges of 1500−1325 and 975−890 cm^{-1} were magnified for clarity.

cm^{-1} of $\delta_{as}(CH_3)$, 1396 and 1381 cm^{-1} of $\delta_s(CH_3)$, 1222 cm^{-1} of $\nu_{as}(COC)$ + $r_{as}(CH_3)$, 1144 cm^{-1} of $r_{as}(CH_3)$, and 1053 cm^{-1} of $\nu(C-CH_3)$ (Table 2). These splitting bands can be identified distinctly from the second derivatives of original FTIR spectra at low temperature (e.g., below −40 °C), as shown in the lower panels of Figure 3 and Figure S2. Most of these splitting components cannot be observed at high temperature (e.g., above 80 °C). The pure crystalline band of α crystals at 924 cm^{-1}, which is absent in the spectrum of amorphous PLA (Figure 2) and associated with the combination of $r(CH_3)$ and $\nu(C-COO)$ modes of molecular chains with the 10_3 helix conformation in crystalline phase of PLA,[10,47] also splits into a doublet (924, 919 cm^{-1}) at low temperature.

A remarkable difference between the temperature-dependent FTIR spectra of α' and α crystals is the spectral splitting. So far, two interpretations, that is, the intrachain coupling and interchain coupling (i.e., correlation field splitting),[48,49] have been proposed to explain the vibrational splitting of $\nu(C{=}O)$ mode in the α-form PLLA. The former is sensitive to chain conformation and the distribution of conformers. The correlation field splitting, also called as factor group splitting or Davydov splitting, occurs due to the lateral interactions between the molecular chains contained in a crystal unit cell.[50] It has been reported that the unit cell dimension of polymer crystals along molecular axis (c-axis) is much less sensitive to temperature than is the transverse axes (a- or b-axis).[39,40] The chain conformation of crystalline PLA, which is sensitive to the length of c-axis and a key factor for intramolecular interactions, would not change markedly upon cooling. Furthermore, the temperature dependence of spectral splitting is a characteristic phenomenon of correlation field splitting.[50] Therefore, it is reasonable to conclude that the spectral splitting in α crystals is originated from the correlation field splitting, rather than the intrachain coupling. The correlation field splitting in α-form PLA is mainly resulted by the interchain dipolar interactions between the dipolar groups (carbonyl, methyl, and methine groups) of adjacent molecular chains packed within the crystal unit cells.[49]

The absence of correlation field splitting in α' crystals suggests the much weakened interchain interactions in its crystal lattice. This is due in part to the larger lattice dimension and interchain distance,[12−14] as evidenced by WAXD analysis. On the other hand, since the correlation field splitting usually takes place in an ordered structure with tightly packed molecular chains, the absence of spectral splitting may suggest the lateral disordered and loose molecular packing of the α' crystals. The molecular packing is considered to be a key factor influencing the polymorphism of PLA, analogous to the cases of i-PP[28,29] and aliphatic polyketones derived from ethene and carbon monoxide (ECO).[50] The α and β crystals of ECO possess the similar all-trans conformation, while due to the interchain dipolar interactions, the α crystals of ECO with tight molecular packing have more evident band splitting in Raman spectra than their β counterparts.[50]

Sc crystals of PLA exhibit different FTIR spectra from the homocrystals. First, one can clearly identify a new band at 908 cm^{-1} (Figures 2 and 3c), which is characteristic of the sc crystals with a 3_1 helical chain conformation.[47] This band has been observed for the β-form PLLA that adopts a similar 3_1 helical conformation.[8] Second, compared to the amorphous, α'-, and α-form PLAs, the band wavenumber of $\nu(C{=}O)$ mode in sc form is ~10 cm^{-1} lower and those of $\nu_{as}(CH_3)$, $\nu_s(CH_3)$, and $\nu(CH)$ modes are 4−6 cm^{-1} lower (Figure 3 and Table 2). The distinct low-frequency shifts of $\nu(C{=}O)$, $\nu(CH_3)$, and $\nu(CH)$ modes in the stereocomplex crystallization suggest the

dx.doi.org/10.1021/ma201906a | Macromolecules 2012, 45, 189−197

Table 2. Assignments of FTIR Bands for Amorphous, α′-, α-, and sc-Form PLAs

vibration modes	amorphous	α′	α	sc
$\nu_{as}(CH_3)$[a]	2996 (m)[b]	2996 (s)	3015 (vw, sb)[c]	2995 (m, sb)
			3006 (vw, sb)	2992 (m)
			2996 (s)	2990 (m, sb)
$\nu_{s}(CH_3)$	2945 (m)	2945 (m)	2964 (vw, sb)	2941 (m)
			2945 (m)	
ν(CH)	2880 (w)	2880 (w)	2880 (w)	2875 (w)
ν(C═O)	1758 (vs)	1761 (vs)	1777 (vw, sb)	1749 (vs)
			1768 (vw, sb)	
			1759 (vs)	
			1749 (m, sb)	
$\delta_{as}(CH_3)$	1455 (m)	1458 (s)	1468 (w, sb)	1456 (m)
			1458 (s)	1447 (vw, sb)
			1443 (w, sb)	
$\delta_{s}(CH_3)$	1383 (m)	1386 (m)	1396 (vw, sb)	1382 (m)
			1387 (m)	
			1381 (m, sb)	
$\delta_{s}(CH_3)$ + δ(CH)	1365 (m)	1369 (m)	1370 (w)	1368 (m)
		1360 (m)	1360 (m)	
$\nu_{as}(COC)$ + $r_{as}(CH_3)$	1213 (m)	1215 (m)	1222 (vw, sb)	1222 (s)
	1183 (s)	1186 (s)	1213 (s)	1216 (s)
			1202 (vw, sb)	1191 (s)
			1184 (m)	
$r_{as}(CH_3)$	1132 (s)	1134 (s)	1144 (vw, sb)	1142 (vw, sb)
			1135 (s)	1132 (s)
$\nu_{s}(COC)$	1092 (s)	1110 (w)	1110 (vw, sb)	1090 (s)
		1092 (s)	1092 (s)	
ν(C−CH_3)	1046 (m)	1046 (m)	1053 (w, sb)	1053 (vw, sb)
			1045 (m)	1042 (s)
$r(CH_3)$ + ν(C−COO)	956 (w)	957 (w)	957 (w)	955 (w)
		924 (w)[d]	924 (w)[d]	908 (w)[d]
			919 (vw, sb)	
ν(C−COO)	870 (m)	872 (m)	872 (m)	874 (w)

[a] ν, δ, and r denote stretching, bending, and rocking, respectively; as and s represent asymmetry and symmetry, respectively. [b] vs, s, m, w, and vw are the abbreviations of very strong, strong, medium, weak, and very weak, respectively. [c] sb denotes the splitting band, whose intensity increases with cooling. [d] Bands at 924 and 908 cm^{-1} are characteristic of the 10_3 helical conformation of homocrystals (α′ and α form) and 3_1 helical conformation of sc crystals, respectively.

existence of weak C−H···O═C hydrogen bonds between the PLLA and PDLA chains in sc crystals.[25,26] Third, the spectral splitting is detected in sc crystals at low temperature, such as the components at 2990 and 2995 cm^{-1} of $\nu_{as}(CH_3)$, 1447 cm^{-1} of $\delta_{as}(CH_3)$, 1153 cm^{-1} of $r(CH_3)$, and 1042 cm^{-1} of ν(C−CH_3) mode. These splitting bands cannot be clearly observed at room temperature and become pronounced with cooling, which is characteristic of the correlation field splitting. Therefore, it is considered that the interchain dipolar interactions related to the carbonyl, methyl, and methine groups exist in the sc crystals (especially at cryogenic conditions), except for the C−H···O═C hydrogen bond interactions. These results imply the tight lateral packing of molecular chains in sc-form PLA.[25,26]

Temperature-Induced Changes in FTIR Intensity and Wavenumber. Temperature-induced changes in the intensity and frequency of various vibrational bands were evaluated based on the FTIR spectra. Intensity changes and frequency shifts of each band were respectively normalized by $[I(T) - I(T_0)]/I(T_0)$ and $WN(T) - WN(T_0)$, where $I(T)$ and $WN(T)$ represented the peak height and wavenumber of a given band at a temperature T, respectively; $I(T_0)$ and $WN(T_0)$ denoted those at an initial temperature T_0, respectively. Here, T_0 was taken as 40 °C for amorphous PLA and 80 °C for the α′-, α-, and sc-form PLAs. Figures 4 and 5 show the normalized intensity changes and frequency shifts of the selected bands for various PLA samples as a function of temperature, respectively. The changes in intensity and wavenumber were found to be reversible upon reheating (data not shown).

As seen in Figures 4 and 5, the intensities gradually increase and most of the bands shift to high wavenumber with cooling, which can be expected since the molecular potential energy drops and the motions of molecular groups become less active with lowering temperature. This phenomenon is analogous to those observed in other polymers,[38,41−43] which has been attributable to the change of interchain forces with temperature.[38] As shown in Figure 4, the temperature-induced intensity changes of amorphous and α′-form PLAs are in the similar ranges (10−20%) with cooling from 40 to −100 °C, which may suggest the weaker interchain interactions in α′ crystals. Obviously, the intensity enhancements of α and sc crystals upon cooling are larger than those of amorphous and α′-form PLAs. Therefore, it is considered that the interchain coupling plays an important role in the temperature-dependent spectral intensity, and the tight packing mode of molecules and more ordered structure increase the sensitivity of spectral intensity to temperature. However, there is not a direct and unambiguous link between the frequency shift and crystal modification for PLA. The values of wavenumber shift in various PLAs are very similar, all of which range 0−4 cm^{-1} with cooling (Figure 5).

Temperature-Dependent Solid-State NMR Spectra. Solid-state structures of different crystals of PLA and amorphous PLA were studied by the solid-state ^{13}C CP-MAS NMR spectroscopy over the temperatures ranging from 80 to −100 °C. Figure 6 shows the temperature-dependent NMR spectra for the carbonyl, methine, and methyl carbons of different crystalline forms of PLA. Each carbon exhibits a single and broad resonance, and no discernible alteration in line shape and chemical shift is detected in the NMR spectra of α′ form with changing temperature (Figure 6 and Figure S4). These findings resemble those observed in amorphous PLA.[51] NMR spectra of α crystals are of much interest (Figure 6 and Figure

dx.doi.org/10.1021/ma201906a | Macromolecules 2012, 45, 189−197

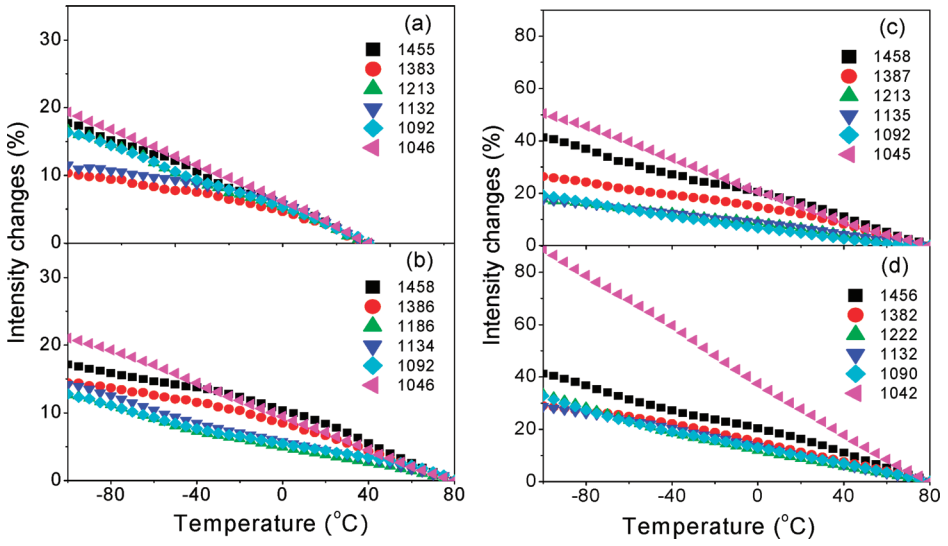

Figure 4. Temperature dependence of normalized intensity changes for FTIR bands of (a) amorphous, (b) α'-, (c) α-, and (d) sc-form PLAs upon cooling.

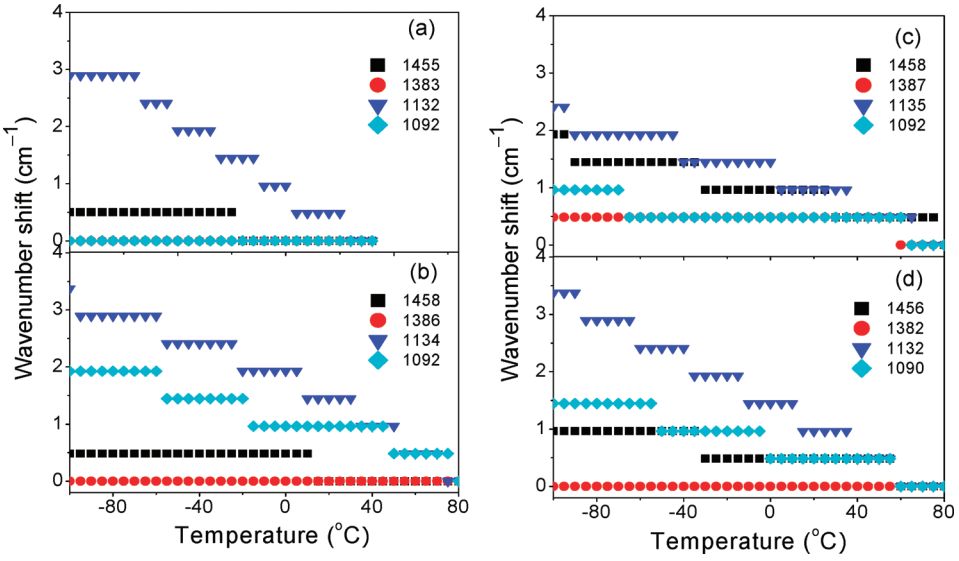

Figure 5. Temperature dependence of wavenumber shifts for FTIR bands of (a) amorphous, (b) α'-, (c) α-, and (d) sc-form PLAs upon cooling.

S5). First, each carbon resonance splits into multiple well-resolved peaks that include four major peaks (P_1–P_4) for carbonyl resonance, three major peaks (P_5–P_7) for methine resonance, and two major peaks (P_8 and P_9) for methyl resonance, where the peaks P_3, P_5, and P_8 are dominant. These results are in agreement with those reported by Thakur et al.[35] and Tsuji et al.[36] Second, chemical shifts of the dominant peaks P_3, P_5, and P_8 are nearly invariable with cooling. However, the splitting peaks gradually shift away from the dominant peaks with lowering temperature. Third, the resonance splitting becomes more marked with cooling, analogous to that observed in the FTIR spectra. The peak shoulders (indicated by arrows in Figure 6 and Figure S5) appear in P_5 and P_8 at low temperature, while they disappear at high temperature.

The difference between NMR spectra of stereoregular PLAs crystallized at low and high temperatures indicates the formation of α' metastable crystals at low T_c (e.g., 80 °C). In the measurements of spin–lattice relaxation, it was found that the splitting peaks for a given carbon of α crystals decayed at a comparable rate, and therefore the splitting peaks could not be assigned individually to amorphous or crystalline component. The resonance splitting can be induced by the intramolecular (e.g., s-PP[31]) or intermolecular (e.g., α-form i-PP[28,29]) interactions in polymer crystals. Because the intrachain interactions that depend on conformation are comparable for α' and α crystals and change little with temperature, the interchain couplings that depend on the lateral molecular packing within crystal lattice may be a predominant contribution to the resonance splittings of α crystals. The splitting peaks in each resonance region represent the crystallographically inequivalent sites in molecular chains. An exact assignment for each split component of α crystals cannot be made from the present results; this needs to be further investigated. It is notable that the resonance splitting in α-form PLA is much more remarkable than that reported in the α-form i-PP[28–30] and i-PB.[33] This is possibly due to the more complicated interchain interactions of α-form PLA, as indicated in the previous studies.[2–6]

dx.doi.org/10.1021/ma201906a | *Macromolecules* 2012, 45, 189–197

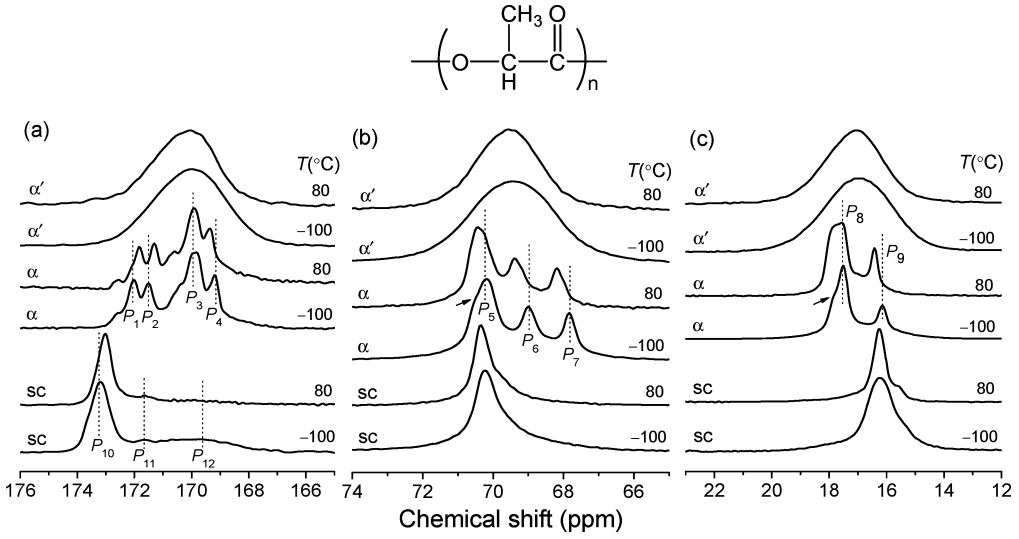

Figure 6. Temperature-dependent ^{13}C CP-MAS NMR spectra for (a) carbonyl, (b) methine, and (c) methyl carbons of different PLA crystals.

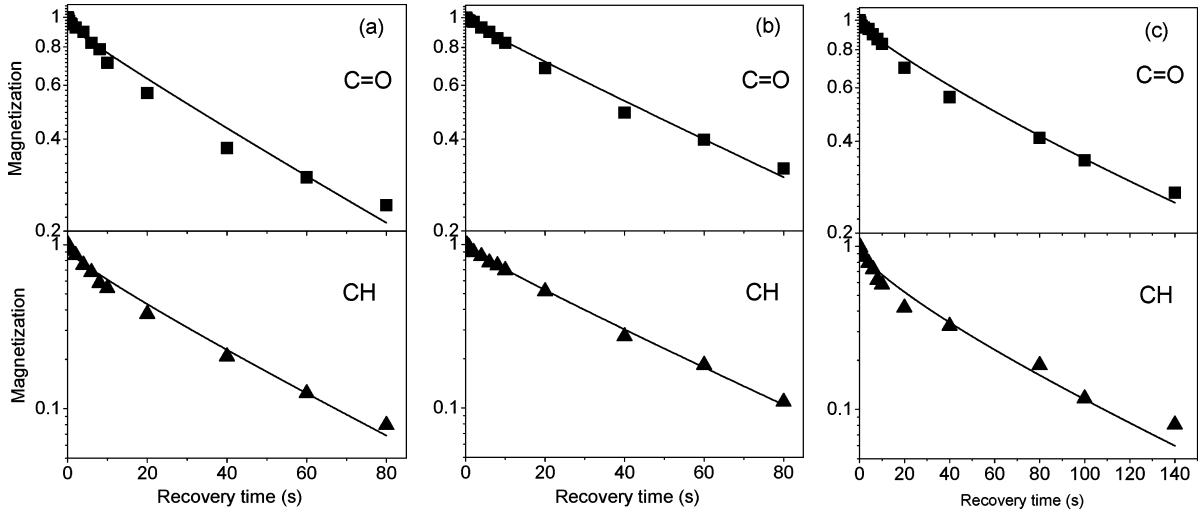

Figure 7. ^{13}C spin−lattice decay curves for carbonyl and methine of (a) α'-, (b) α-, and (c) sc-form PLAs. Solid lines are the fits to the data using eq 1.

The extent of resonance splitting depresses with increasing temperature, similar to those observed in the α crystals of i-PP[30] and i-PB.[33] Upon cooling, the interchain distance decreases accompanied by the strengthening of interchain interactions, accounting for the enhancement in environmental difference between the crystallographically inequivalent sites. At high temperature, more active molecular motion and dipolar exchange between the inequivalent sites can average the line shape and in turn diminish the spectral splitting.[30,33]

The broadening of NMR spectra of α' form is consistent with its FTIR spectra that show broadening compared to the α form. This broadening in NMR spectra resembles the case of β-form i-PP.[28,29] The broadening of ^{13}C CP-MAS NMR spectra can be resulted by many factors such as order/disorder at molecular distances, spherulite shape/size/orientation, etc. However, with combination of the FTIR results that reflect the molecular-level interactions, the NMR spectral broadening and absence of resonance splitting in α' form would suggest its loose and disordered molecular packing. All the carbon atoms in a given group of α' crystals would be in an averaged environment due to the disordered packing mode.

As seen in Figure 6 and Figure S6, sc crystals of PLA exhibit a different ^{13}C solid-state NMR spectrum from the homocrystals, including the line shapes and chemical shifts. As for the sc crystals, three peaks, that is, a sharp peak P_{10}, a weak component P_{11}, and a broad peak P_{12}, are observed in the carbonyl resonance region, while a single sharp peak is basically detected for the methine and methyl resonances. This is consistent with the results reported by Tsuji et al.[37] In the carbonyl resonance region, the peaks P_{10} and P_{11} have been assigned to the crystalline phases of sc and homocrystals, respectively.[37] The broad peak P_{12} is ascribed to the free amorphous phase of PLA, and its chemical shift is very close to the amorphous sample. At temperature above T_g (e.g., 80 °C), the amorphous phase mobility will increase and result in a poor cross-polarization efficiency, leading to the disappearance of P_{12}. Besides, the cold crystallization of free amorphous phase above T_g may also account for the disappearance of P_{12} at 80 °C.

Spin−Lattice Relaxation Time. ^{13}C spin−lattice relaxation measurements were used to assess the molecular dynamics of different crystals of PLA. T_{1C}s of carbonyl and methine

dx.doi.org/10.1021/ma201906a | Macromolecules 2012, 45, 189−197

carbons that had a slower relaxation were only measured. Figure 7 show typical decay curves for the resonances of carbonyl and methine carbons in α′- α-, and sc-form PLAs measured at ∼25 °C. The decay curve of amorphous PLA is shown elsewhere.[51] Because the molecular motions in both amorphous and crystalline phases must be highly restricted below T_g, the relaxation time of amorphous and crystalline phases of semicrystalline PLA will be in a similar order of magnitude (or comparable) at a temperature below T_g (∼60 °C for PLA). As reported in a previous study,[51] the decay curve of spin−lattice relaxation of the fully amorphous PLA can be well fitted by the Kohlraush−Williams−Watts (KWW) function,[52,53] which is generally used to express the magnetization below T_g because the distribution of relaxation rate usually gives rise to a nonexponential recovery.[52] To evaluate the T_{1C} of semicrystalline PLAs, we add an exponential term to the KWW function to reflect the contribution of crystalline phase. The equation used for fitting is expressed as

$$M_z(t) \propto (1 - X_c)\exp\left[\left(\frac{-t}{T_{1C,a}}\right)^{\beta}\right] + X_c \exp\left(\frac{-t}{T_{1C,c}}\right) \quad (1)$$

where the first (KWW function) and second terms denote the contributions of amorphous and crystalline phases, respectively. M_z is the normalized magnetization, and t is the relaxation time that is a variable used in the experiment. X_c is the degree of crystallinity, as shown in Table 1. $T_{1C,c}$ is the T_{1C} of crystalline phase. $T_{1C,a}$ is the T_{1C} of amorphous phase in the semicrystalline or fully amorphous PLA. β is a stretching parameter ($0 < \beta \leq 1$) of the KWW function, representing the deviation of relaxation from the pure exponential nature.[52,53] $T_{1C,a}$ and β are 54.1 s and 0.898 for the carbonyl carbon and 22.8 s and 0.859 for the methine carbon of amorphous PLA, respectively, as determined in our previous report.[51]

T_{1C} of the crystalline phase ($T_{1C,c}$) of α′-, α-, and sc-form PLAs were estimated by fitting the normalized magnetization in spin−lattice relaxation using eq 1. The results of T_{1C} are tabulated in Table 3. The mean T_{1C} of amorphous PLA, $\langle T_{1C,a}\rangle$, is included for comparison. As seen in Table 3, T_{1C} of PLA depends on the crystalline structure remarkably. The relaxation time, usually inversely proportional to relaxation rate and molecular mobility, increases in the order of amorphous ≈ α′ < α < sc for PLA below T_g. For protonated carbons, the fluctuation of C−H dipolar coupling is the predominant relaxation. This can include three contributions, that is, coupling of carbon atom with (i) directly bonded protons, (ii) intrachain, or (iii) interchain nonbonded nearby protons.[27] The strength of dipolar interaction depends on internuclear distance between ^{13}C and ^{1}H. It ranks in the order of (i) directly bonded protons > (ii) intrachain > (iii) interchain nonbonded nearby protons, and the resultant relaxation time should be T_{1C} (i) < T_{1C} (ii) < T_{1C} (iii). On the other hand, tight packing probably inhibits local mobility, resulting in a longer T_{1C}. The carbonyl carbons have slower relaxation rate compared to protonated carbons because of the weak C−H dipolar interaction. The contribution (i) may be the same for different PLA samples because of the identical bond lengths. The contribution (ii), depending on the conformation, is considered to be similar for the α′ and α crystals, while might be larger for sc crystals because of the more contracted conformation. The contribution (iii), which has been reported to be a crucial factor influencing the relaxation time of various polymorphs of poly(3-hydroxypropionate) (PHP),[42] depends on the lateral interchain distance. It is considered that the lateral molecular packing is a key factor for the different molecular dynamics of various PLA crystals. The very similar relaxation rate of the α′ crystals and amorphous PLA further confirms the disordered and looser molecular packing of α′ crystals, which is somewhat analogous to the amorphous sample. Because of the tighter packing and shorter interchain distance, α crystals exhibit a slower relaxation than their α′ counterparts. In the case of sc crystals, two racemic chains with opposite handedness allow the tighter packing and smaller interchain distance within crystal cell, which may account for the slower relaxation.

Table 3. Spin−Lattice Relaxation Times of Amorphous, α′-, α-, and sc-Form PLAs

parameters	carbon	amorphous	α′	α	sc
$\langle T_{1C,a}\rangle^a$ (s)	C=O	57.0			
	CH	24.7			
$T_{1C,c}$ (s)	C=O		52.1	73.5	151.5
	CH		29.4	40.0	66.2

[a]The mean T_{1c} value of amorphous PLA was cited from ref 51.

CONCLUSION

The molecular interaction, packing, and dynamics in various crystal forms of PLA have been investigated by the temperature-variable FTIR and solid-state ^{13}C NMR spectroscopy. The different crystal forms of PLA show distinct spectral features in line shapes and band/resonance splittings upon cooling to the cryogenic conditions. The well-resolved splittings in FTIR bands and NMR resonances of α-form PLA are ascribed to the correlation field splitting and crystallographically inequivalent sites within the crystal lattices, respectively; however, these splitting are absent in PLA α′ crystals. These results indicate the conformational disorder and loose molecular packing in the α′ crystals of stereoregular PLA crystallized at low temperature. As a result of the tight lateral molecular packing, the interchain interactions exist extensively between the two antiparallel packed chains within the lattice of α-form PLA; it is predominantly the dipolar interactions involving carbonyl, methyl, and methine groups. The frequency shifts in stereocomplex crystallization and the correlation field splittings at cryogenic conditions suggest the coexistence of weak C−H···O=C hydrogen bonds and dipolar interactions between the PLLA and PDLA chains packed in sc crystals of PLA. The spin−lattice relaxation times of various PLA crystals rank as amorphous ≈ α′ < α < sc below T_g. In a word, the lateral arrangement and packing of molecular chains in the crystalline phase, which are the origin of the interchain interactions, play an important role in the polymorphism of PLA. This would be an important factor influencing the physical proprieties (e.g., mechanical, barrier properties, and biodegradability) of PLA materials.

ASSOCIATED CONTENT

Supporting Information

Figures showing temperature-dependent FTIR spectra and ^{13}C CP-MAS NMR spectra of PLLA with different crystalline

forms. This material is available free of charge via the Internet at http://pubs.acs.org.

AUTHOR INFORMATION

Corresponding Author

*Tel +86-571-87951334; e-mail panpengju@zju.edu.cn.

ACKNOWLEDGMENTS

We are grateful to Dr. Kazue Ueda (Unitika Co. Ltd.) for kindly supplying PLLA samples, Prof. Minoru Sakurai (Tokyo Institute of Technology) for the use of FTIR instrument, and Dr. Tadashi Shimizu and Dr. Masataka Tansho (National Institute of Material Science) for the use of solid-state NMR instrument. Financial support from State Key Laboratory of Chemical Engineering (SKL-ChE-11D05), Fundamental Research Funds for the Central Universities, and National Natural Science Foundation of China (51103127) is greatly appreciated.

REFERENCES

(1) Auras, R.; Lim, L.-T.; Selke, S. E. M.; Tsuji, H. *Poly(lactic acid): Synthesis, Structures, Properties, Processing, and Applications*; John Wiley & Son: Hoboken, NJ, 2010.
(2) De Santis, P.; Kovacs, A. J. *Biopolymers* **1968**, *6*, 299.
(3) Hoogsteen, W.; Postema, A. R.; Pennings, A. J.; ten Brinke, G.; Zugenmaier, P. *Macromolecules* **1990**, *23*, 634.
(4) Kobayashi, J.; Asahi, T.; Ichiki, M.; Oikawa, A.; Suzuki, H.; Watanabe, T.; Fukada, E.; Shikinami, Y. *J. Appl. Phys.* **1995**, *77*, 2957.
(5) Aleman, C.; Lotz, B.; Puiggali, J. *Macromolecules* **2001**, *34*, 4795.
(6) Sasaki, S.; Asakura, T. *Macromolecules* **2003**, *36*, 8385.
(7) Eling, B.; Gogolewski, S.; Pennings, A. J. *Polymer* **1982**, *23*, 1587.
(8) Sawai, D.; Takahashi, K.; Sasashige, A.; Kanamoto, T.; Hyon, S. H. *Macromolecules* **2003**, *36*, 3601.
(9) Cartier, L.; Okihara, T.; Ikada, Y.; Tsuji, H.; Puiggali, J.; Lotz, B. *Polymer* **2000**, *41*, 8909.
(10) Zhang, J.; Duan, Y.; Sato, H.; Tsuji, H.; Noda, I.; Yan, S.; Ozaki, Y. *Macromolecules* **2005**, *38*, 8012.
(11) Zhang, J.; Tashiro, K.; Domb, A. J.; Tsuji, H. *Macromol. Symp.* **2006**, *242*, 274.
(12) Pan, P.; Kai, W.; Zhu, B.; Dong, T.; Inoue, Y. *Macromolecules* **2007**, *40*, 6898.
(13) Kawai, T.; Rahman, N.; Matsuba, G.; Nishida, K.; Kanaya, T.; Nakano, M.; Okamoto, H.; Kawada, J.; Usuki, A.; Honma, N.; Nakajima, K.; Matsuda, M. *Macromolecules* **2007**, *40*, 9463.
(14) Zhang, J.; Tashiro, K.; Domb, A. J.; Tsuji, H. *Macromolecules* **2008**, *41*, 1352.
(15) Yasuniwa, M.; Sakamo, K.; Ono, Y.; Kawahara, W. *Polymer* **2008**, *49*, 1943.
(16) Pan, P.; Inoue, Y. *Prog. Polym. Sci.* **2009**, *34*, 605.
(17) Furuhashi, Y.; Iwata, T.; Kimura, Y.; Doi, Y. *Macromol. Biosci.* **2003**, *3*, 462.
(18) Gan, Z.; Kuwabara, K.; Abe, H.; Iwata, T.; Doi, Y. *Polym. Degrad. Stab.* **2005**, *87*, 191.
(19) Sawai, D.; Yokoyama, T.; Kanamoto, T.; Sungil, M.; Hyon, S. H.; Myasnikova, L. P. *Macromol. Symp.* **2006**, *242*, 93.
(20) Cocca, M.; Di Lorenzo, M. L.; Malinconico, M.; Frezza, V. *Eur. Polym. J.* **2011**, *47*, 1073.
(21) Kalish, J. P.; Aou, K.; Yang, X. Z.; Hsu, S. L. *Polymer* **2011**, *52*, 814.
(22) Okihara, T.; Tsuji, M.; Kawaguchi, A.; Katayama, K.-I.; Tsuji, H.; Hyon, S.-H.; Ikada, Y. *J. Macromol. Sci., Phys.* **1991**, *B30*, 119.
(23) Tsuji, H. *Macromol. Biosci.* **2005**, *5*, 569.
(24) Brizzolara, D.; Cantow, H. J.; Diederichs, K.; Keller, E.; Domb, A. J. *Macromolecules* **1996**, *29*, 191.
(25) Zhang, J.; Sato, H.; Tsuji, H.; Noda, I.; Ozaki, Y. *Macromolecules* **2005**, *38*, 1822.
(26) Sarasua, J. R.; Rodríguez, N. L.; Arraiza, A. L.; Meaurio, E. *Macromolecules* **2005**, *38*, 8362.
(27) Mirau, P. A. *A Practical Guide to Understanding the NMR of Polymers*; Wiley-Interscience: Hoboken, NJ, 2005.
(28) Bunn, A.; Cudby, M. E. A.; Harris, R. K.; Packer, K. J.; Say, B. J. *Polymer* **1982**, *23*, 694.
(29) Gomez, M. A.; Tanaka, H.; Tonelli, A. E. *Polymer* **1987**, *28*, 2227.
(30) Saito, S.; Moteki, Y.; Nakagawa, M.; Horii, F.; Kitamaru, R. *Macromolecules* **1990**, *23*, 3256.
(31) Bunn, A.; Cudby, M. E. A.; Harris, R. K.; Packer, K. J.; Say, B. J. *J. Chem. Soc., Chem. Commun.* **1981**, 15.
(32) Ohira, Y.; Horii, F.; Nakaoki, T. *Macromolecules* **2001**, *34*, 1655.
(33) Miyoshi, T.; Hayashi, S.; Imashiro, F.; Kaito, A. *Macromolecules* **2002**, *35*, 2624.
(34) Howe, C.; Vasanthan, N.; MacClamrock, C.; Sankar, S.; Shin, I. D.; Simonsen, I. K.; Tonelli, A. E. *Macromolecules* **1994**, *27*, 7433.
(35) Thakur, K.; A., M.; Kean, R. T.; Zupfer, J. M.; Buehler, N. U.; Doscotch, M. A.; Munson, E. J. *Macromolecules* **1996**, *29*, 8844.
(36) Tsuji, H.; Kamo, S.; Horii, F. *Polymer* **2010**, *51*, 2215.
(37) Tsuji, H.; Horii, F.; Nakagawa, M.; Ikada, Y.; Odani, H.; Kitamaru, R. *Macromolecules* **1992**, *25*, 4114.
(38) Takahashi, Y. *Macromolecules* **2001**, *34*, 7836.
(39) Davis, G. T.; Eby, R. K.; Colson, J. P. *J. Appl. Phys.* **1970**, *41*, 4316.
(40) Lacks, D. J.; Rutledge, G. C. *Macromolecules* **1995**, *28*, 1115.
(41) Snyder, R. G.; Maroncelli, M.; Strauss, H. L.; Hallmark, V. M. *J. Phys. Chem.* **1986**, *90*, 5623.
(42) Su, Z.; Zhao, Y.; Kang, N.; Zhang, X.; Xu, Y.; Wu, J.; Wang, D.; Han, C. C.; Xu, D. *Macromol. Rapid Commun.* **2005**, *26*, 895.
(43) Zhu, B.; Kai, W.; Pan, P.; Yazawa, K.; Nishida, H.; Sakurai, M.; Inoue, Y. *J. Phys. Chem. B* **2008**, *112*, 9684.
(44) Torchia, D. A. *J. Magn. Reson.* **1978**, *30*, 613.
(45) Fischer, E. W.; Sterzel, H. J.; Wegner, G. *Kolloid Z. Z. Polym.* **1973**, *251*, 980.
(46) Loomis, G. L.; Murdoch, J. R.; Gardner, K. H. *Polym. Prepr.* **1990**, *31*, 55.
(47) Kister, G.; Cassanas, G.; Vert, M. *Polymer* **1998**, *39*, 267.
(48) Meaurio, E.; Zuza, E.; Lopez-Rodriguez, N.; Sarasua, J. R. *J. Phys. Chem. B* **2006**, *110*, 5790.
(49) Aou, K.; Hsu, S. L. *Macromolecules* **2006**, *39*, 3337.
(50) Lagaron, J. M.; Powell, A. K.; Davidson, N. S. *Macromolecules* **2000**, *33*, 1030.
(51) Pan, P.; Zhu, B.; Dong, T.; Yazawa, K.; Shimizu, T.; Tansho, M.; Inoue, Y. *J. Chem. Phys.* **2008**, *129*, 184902.
(52) Böhmer, R.; Diezemann, G.; Hinze, G.; Rössler, E. *Prog. Nucl. Magn. Reson. Spectrosc.* **2001**, *39*, 191.
(53) Yazawa, K.; Inoue, Y.; Yamamoto, T.; Asakawa, N. *Phys. Rev. B* **2006**, *74*, 094204.

Macromolecules

Article

pubs.acs.org/Macromolecules

Structure–Property Relationships in Biomedical Thermoplastic Polyurethane Nanocomposites

Azlin F. Osman,[†] Grant A. Edwards,[†] Tara L. Schiller,[⊥] Yosephine Andriani,[†] Kevin S. Jack,[†] Isabel C. Morrow,[‡,§] Peter J. Halley,[†] and Darren J. Martin*[,†]

[†]Australian Institute for Bioengineering and Nanotechnology, The University of Queensland, Building 75, Cnr College and Cooper Rds, Brisbane 4072, Australia

[‡]ARC Centre of Excellence for Functional Nanomaterials, The University of Queensland, Australia

[§]Australian Microscopy and Microanalysis Research Facility, The University of Queensland, Australia

[⊥]Department of Materials Engineering, Monash University, Clayton 3800, Australia

ABSTRACT: Polyurethanes are excellent potential materials for the construction of implantable medical components due to their exceptional mechanical properties and biocompatibility. Currently, soft silicone materials are employed as insulation for implantable cochlear electrode arrays. Siloxane-based thermoplastic polyurethane (TPU) nanocomposites containing synthetic layered silicates are being investigated as new insulation materials with superior tensile and tear strength and reduced surface tack, potentially allowing for thinner insulation and more intricate electrode designs. In this work, ElastEon E5-325 (Aortech Pty Ltd.) TPU nanocomposites reinforced with 2 and 4 wt % low aspect ratio organo-hectorite and high aspect ratio organo-fluoromica (Lucentite SWN, Somasif ME100, both modified with octadecyltrimethylammonium (ODTMA)) were prepared by a solvent casting technique. The mechanical properties of the resulting nanocomposites were measured by tensile, tear, stress relaxation, and creep testing and morphologically were characterized by DSC, DMTA, XRD, TEM, and strained *in situ* synchrotron SAXS. We found that the hydrophobic low aspect ratio organohectorite acts as a very potent interfacial compatibilizer. At 2 wt % loading, the resulting nanocomposite displays vastly superior mechanical properties to both soft silicone and ElastEon. In addition to providing 30 nm × 1 nm synthetic nanosilicate reinforcing elements which are readily capable of orientation and reinforcement, these nanosilicates also serve to provide more cohesive hard microdomains and thus creep resistance and dimensional stability. Interestingly, at a higher (4 wt %) loading of organohectorite, gross morphological changes in the TPU microdomain texture are observed, adversely effecting the mechanical properties of the TPU.

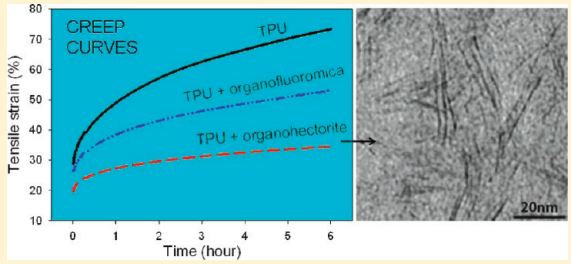

INTRODUCTION

The addition of nanoscale inorganic particles into bulk polymers in order to generate nanocomposites with improved mechanical and chemical properties relative to the parent materials is a rapidly expanding field. The limitless scope for nanofiller materials chemistry and surface chemistry is enabling researchers expanded freedom to bestow further desirable properties on the resulting nanocomposites, thereby enabling the production of novel materials with numerous potential applications. Thermoplastic polyurethane (TPU) is the material of choice for many biomedical applications due to the relative ease of fabrication into devices, flexibility, biocompatibility, biostability, and electrical insulation properties. Polyether-based TPUs have been the materials of choice for certain types of medical implants for many years.[1,2] However, there were some cases where the TPU degraded and led to surface or deep cracking, stiffening, erosion, or the deterioration of mechanical properties such as tensile and flexural strength.[3−7] These inherent deficiencies in the material eventually caused implant malfunction. Poly(dimethylsiloxane) (PDMS)-based TPU were then commercialized and introduced to overcome these problems. The PDMS/poly(hexamethylene oxide) (PHMO)-based TPU based on an optimized formulation (Elast-Eon) from AorTech Biomaterials Pty Ltd. exhibits properties comparable to those of medical grade polyether-based TPU materials such as Pellethane 80A.[8] Elast-Eon TPU are now widely accepted as being the most biostable of all the TPUs and as such are imminently suitable for long-term implantation.[9]

Use of TPU as the nanocomposite matrix presents some interesting challenges to the understanding of the nanoscale and microscale morphology due to the preexisting morphology of the segmented TPU domains (the so-called phase-separated soft and hard segment rich phases). Knowledge in the TPU nanocomposite area has progressed recently, with several research papers discussing the effects of nanofillers on TPU morphology, highlighting the importance of understanding the

Received: September 29, 2011
Revised: December 2, 2011
Published: December 12, 2011

specific hard segment and soft segment interactions with the nanofillers in correlation with the resulting nanocomposite properties. As reported by Mishra et al.,[10,11] Korley et al.,[12] Kim et al.,[13] and Barick et al.,[14] the surface modifier hydrophobicity can affect the degree of interaction between the nanosilicate and the TPU segments, and thus their dispersion in the matrix, and consequently determines the mechanical behavior of the resulting nanocomposites. In more recent work, Smart et al.[15] demonstrated that the degree of TPU hard and soft segments−nanofiller interactions in a TPU-functionalized carbon nanotube system depended on the functional group alkyl tail lengths, and this strongly influenced the nanofiller dispersion in the TPU and tensile properties of the nanocomposite. These findings show that there is a possibility to control the degree of specific segmental interactions with particular nanofiller in the TPU matrices by exploiting the molecular interactions. If we understand and control these molecular interactions, then we have an opportunity to target and improve specific macroscopic properties of the TPU nanocomposites.

In an attempt to produce new biomaterials with improved properties for the insulation of cochlear electrode arrays, we have recently generated ElastEon E5-325 TPU nanocomposites containing high and low aspect ratio organosilicates with a hydrophobic surface modification. Here we describe the complete mechanical and morphological characterization of the E5-325 TPU and associated nanocomposites in attempt to develop an in-depth understanding of structure−property relationships of these materials, most importantly the interplay between TPU nanophase domains with engineered low and high aspect ratio nanofillers. To the best of our knowledge, this is the first time the structure−property relationships of the PDMS-based TPU nanocomposites have been thoroughly studied. The interactions of these organically modified layered silicate nanofillers in concert with a TPU host polymer incorporating such a hydrophobic soft segment has provided us with new and interesting ways to perturb biomedical TPU property profiles.

EXPERIMENTAL SECTION

Materials. Nusil MED 4860 is a medical grade elastomer with two-part silicone system in 1:1 mix ratio (part A:B). Part A consists of 30 wt % amorphous silica, while part B includes an additional 5 wt % dimethyl, methylhydrogen siloxane copolymer. Once these two parts mixed, Nusil MED 4860 undergoes rapid curing at 165 °C for 5 min due to the presence of platinum. This material was supplied by Cochlear Ltd. and is commercially available from Nusil (via EIM distributors in Australia).

ElastEon E5-325 TPU consists of a 1000 g/mol poly(dimethylsiloxane) (PDMS) and 700 g/mol poly(hexamethylene oxide) (PHMO) mixed soft segment in a 98:2 (w/w) ratio and a hard segment composed of alternating 4,4′-methylene diphenyl diisocyanate (MDI) and 1,4-butanediol (BDO) sequences. The hard segment concentrations is 32.5 wt %. This TPU was supplied by AorTech Biomaterials Pty Ltd. Hectorite (Lucentite SWN) is a synthetic trioctahedral smectite and was used as-supplied from the Kobo Products, Inc. It is a white powder with the chemical formula $Na_{0.66}[Si_8(Mg_{5.34}Li_{0.66})O_{20}(OH)_4]^{-0.66}$ and an average particle diameter size of approximately 30−50 nm. Fluoromica (Somasif ME100), which is a synthetic mica (tetrasilicic trioctahedral fluoromica), was supplied by Kobo Products, Inc. It is a white fine powder having an average platelet size of ∼650 nm[16] with the chemical formula $Na_{0.66}Mg_{2.68}(Si_{3.98}Al_{0.02})O_{10.02}F_{1.96}$. This comparison of nanosilicate aspect ratio is an important part of this study. The surface modification of the nanosilicate was performed by exchanging with octadecyltrimethylammonium (bromide) (ODTMA) using a previously published method.[16,17]

Sample Preparation. E5-325 TPU nanocomposites with two different types of ODTMA-modified nanosilicates; ME100 (ME) and Lucentite (Lu) were prepared in 2 and 4 wt % compositions. These organosilicates were prepared as 5 wt % solution in toluene, while the TPU was prepared as 5 wt % solution in dimethylacetamide (DMAc). To ensure dispersion, the organosilicate was placed in a small glass bottle and was then placed in an ultrasonic bath for ∼1 h. The sample was then dispersed further by a high-energy ultrasonic probe for 2 min of exposure and then followed by another hour of dispersion in the ultrasonic bath. These steps were done to ensure a high level of swelling in the nanoclays before homogenizing. The dispersed organosilicate was added to solution of TPU in DMAc. This was done to give a final composition of 2 and 4 wt % of nanofiller loading in the TPU. The combined solution was then mixed vigorously for 1 min in a high-shear homogenizer, followed by stirring overnight at room temperature with a magnetic stirrer. The solution was then poured into a glass mold. The films were dried at 60 °C for ∼72 h under a nitrogen purge. It is important to ensure that the films are free of moisture. If moisture is not carefully excluded during casting, this can result in low-quality cloudy films with inferior properties. The solvent-cast films were then annealed under vacuum at 85 °C for ∼5 h and left to age for at least a week prior to testing. In subsequent discussion, these nanocomposites are referred to as 2MEO, 4MEO, 2LuO, and 4LuO. A number denotes the nanosilicate wt % loading (2 or 4) in the TPU. The first two letters represent type of nanosilicate used (ME = ME100, Lu = lucentite), and the last letter (O) represents the ODMTA modification.

Mechanical Testing. All mechanical tests were carried out at room temperature on an Instron model 5543 universal testing machine with a capacity of 500 N load cell. Five (5) and three (3) replicates of each material were used for tensile and tear tests, respectively. For the tensile tests, dumbbells were punched from an ASTM D-638-M-3 die and a crosshead speed of 50 mm/min was applied. Stress relaxation tests were performed by stretching the specimens to the desired strain (50%) and recording stress vs time data for 10 times the time taken to reach the desired strains. The creep test was conducted according to ISO 899-1:2003, with a stress of 2 MPa and 6 h holding time. Tear strength was measured according to the ISO 34-1:1994 Method B(a), using angle test specimen (type B) without nick, with a crosshead speed of 500 mm/min. For all tests, pneumatic grips were used to prevent specimen slippage.

Transmission Electron Microscopy (TEM). Thin sections of ∼80 nm thickness were cut using a Diatome diamond knife on a Leica Ultracut UC6FCS cryogenic ultramicrotome at temperatures between −80 and −110 °C to ensure the polymers were in a glassy state. Sections were picked up using 2.3 M sucrose and mounted on 200 mesh copper grids (ProSciTech, Australia). Deionized/Milli-Q/tap water was washed over the grids five times. The grids were then allowed to air-dry in self-closing forceps prior to viewing. Samples were examined at low magnification (12000×) on a JEOL 1011 TEM, Japan, at 100 kV, and images were captured on a SIS Morada 4K CCD camera system. Samples examined at higher magnifications (23000×−93000×) were examined on a Technai F30 FEG TEM (FEI Co., Eindhoven, The Netherlands) operating at 300 kV, and images were captured with a Direct Electron LC1100 lens-coupled 4k × 4k CCD camera system.

X-ray Diffraction (XRD). XRD measurements were conducted on a Bruker D8 Advance X-ray diffractometer with a 0.2 mm slit, using Cu Kα radiation generated at 40 kV and 30 mA. Samples were scanned over a range of $2\theta = 0.5°-10°$ using an increment of 0.02 and a scan speed of 1 s. Samples were mounted on a low background holder and fixed with tape to ensure the surface was flat.

Dynamic Mechanical Thermal Analysis (DMTA). Dynamic mechanical measurements were made using a Rheometric Scientific dynamic thermal mechanical analyzer (DMTA IV) equipped with tensile head and reducing force option. Analysis was performed at 0.1% strain in tension mode using a frequency of 2 Hz and a heating

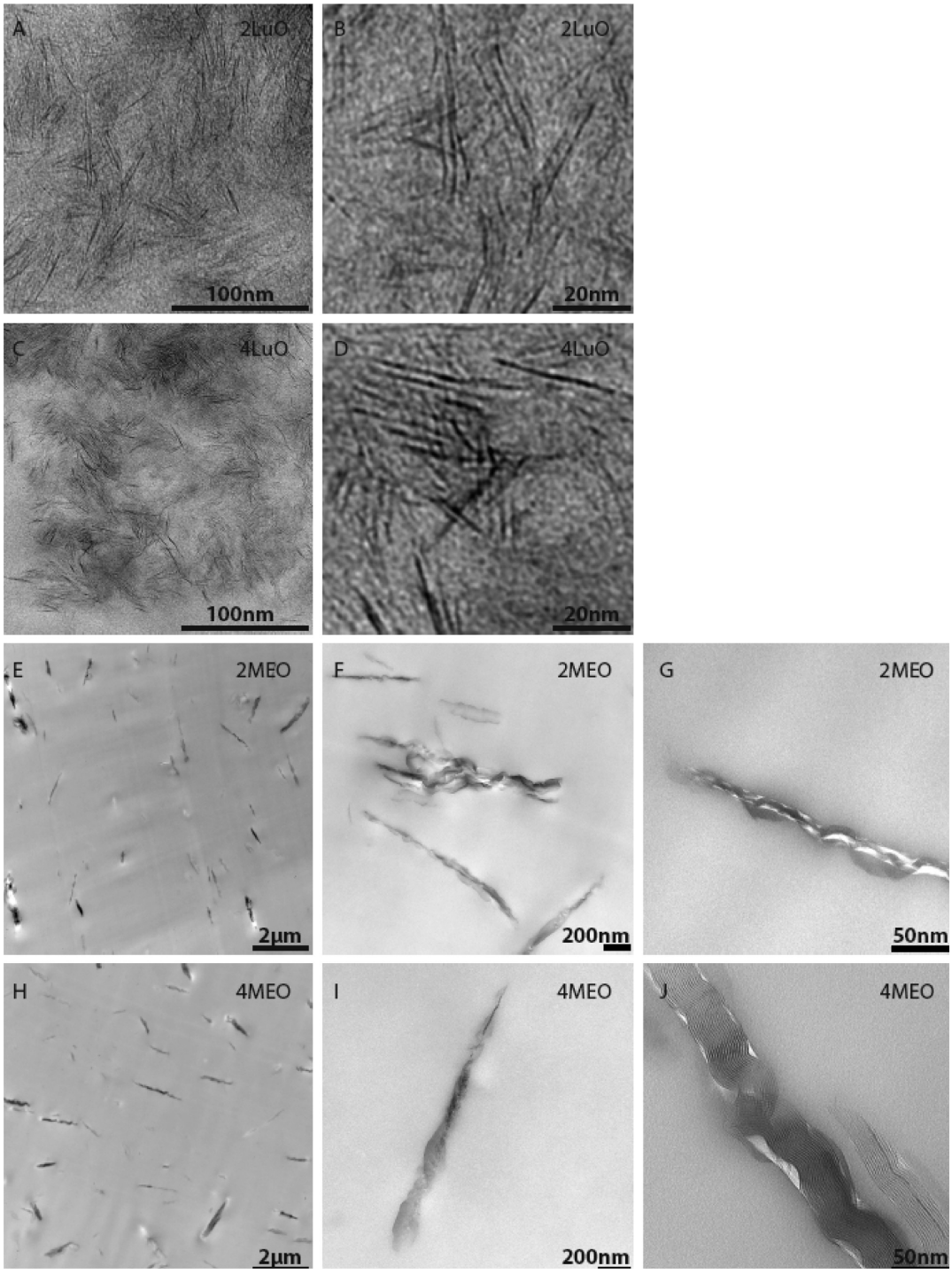

Figure 1. TEM micrographs of 2LuO (A, B), 4LuO (C, D), 2MEO (E–G), and 4MEO (H–J).

rate of 2 °C/min from −100 to 110 °C. We determined that this strain allowed measurements to be taken in the linear viscoelastic regime.

Differential Scanning Calorimetry (DSC). DSC measurements on the TPU and TPU nanocomposites were carried out using the Mettler Toledo DSC 1 Star. The sample weight was ∼6 mg, and the heating rate employed was 10 °C/min. The temperature applied was started from 25 to 250 °C and then cooled to 25 °C at the same ramping rate.

Small-Angle X-ray Scattering (SAXS). *In situ* tensile deformation studies using small-angle scattering (SAXS) technique were carried out on the SAXS/WAXS beamline at the Australian Synchrotron, Melbourne, to obtain morphological information during deformation of TPUs in real time. Two sample-to-detector distances of 0.96 m (short) and 7.2 m (long) were used to measure scattering vector (q) ranges of 0.002–0.06 and 0.015–0.50 Å, respectively. The wavelength of the X-ray beam was 1.240 Å (12 keV). Samples were cut with a dumbbell die with a width of ∼2.5 mm and 15 mm gauge length and strained at a rate of 15 mm/min. Measurements were collected at 0%, 50%, 100%, 200%, 400%, 600%, and 800% strain. For SAXS analysis of the TPU under relaxation, the samples were left to relax after straining for 10 min before collecting a SAXS pattern. The SAXS images were taken immediately after the desired values were reached during either the deformation or the relaxation process. Data acquisition times of 1 and 2 s were used for each measurement at the short and long sample-to-detector distance, respectively.

dx.doi.org/10.1021/ma202189e | *Macromolecules* 2012, 45, 198–210

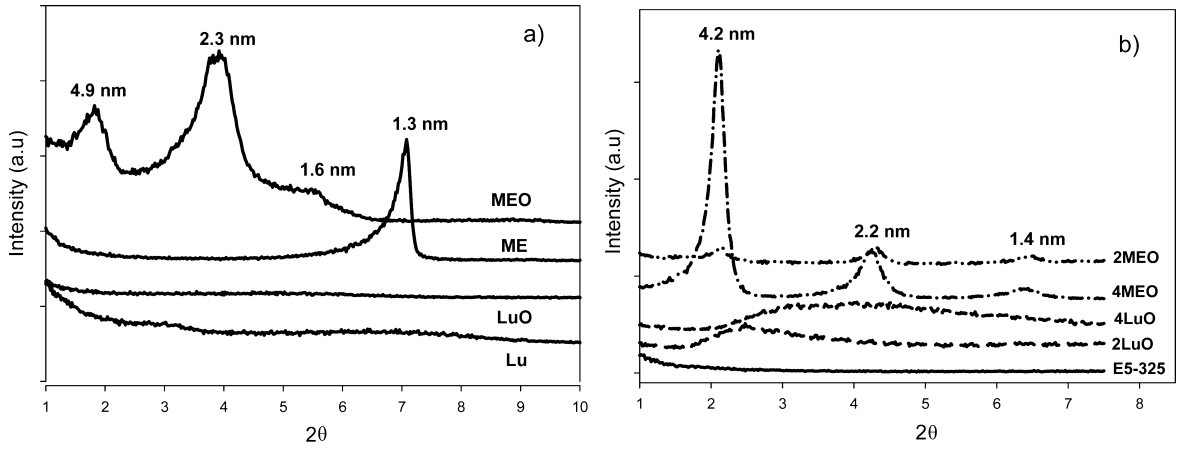

Figure 2. XRD pattern of the (a) pristine ME and Lu nanosilicates and after ODTMA modification (b) the E5-325 TPU containing 2 and 4 wt % MEO and LuO.

Scattering Analysis. Data were analyzed using SAXS15ID version 3299, a program developed at ChemMat CARS as the user interface and control program. The intensity was normalized by the intensity measured at the beamstop to account for changes in transmission due to changes in sample thickness with strain and then further corrected for background scattering. SAXS data averaged over 10° segments in the strain and transverse directions was analyzed using Zernike Prins (ZP) model, which was previously used by Laity et al.[18] and Finnigan et al.[19] to successfully fit SAXS data from TPUs subjected to uniaxial deformation. Based on ZP model, the scattering from two-phase systems can be represented as the product of the form factor, $P(q)$, and the structure factor, $S(q)$:[18−20]

$$I(q) = AP(q)S(q) \tag{1}$$

where q is the scattering vector and A consists of both instrument- and sample-dependent terms and can be treated as a scaling factor. $P(q)$ describes the interference effects between X-rays scattered by different parts of the same scattering body (microdomain) and is dependent upon both the size and shape of the scattering body.[20] The form factor of a sphere of radius (R) is given by

$$P(q) = \left\{3\frac{\sin(qR) - qR\cos(qR)}{(qR)^3}\right\}^2 \tag{2}$$

$S(q)$ represents the interference effects between X-rays scattered by different scattering bodies in the sample and depends on their relative positions and can be described by[18,20]

$$S(q) = \frac{1 - A^2}{1 - 2A\cos(qd) + A^2} \tag{3}$$

where

$$A = \exp\left\{-\frac{q^2\sigma^2}{2}\right\} \tag{4}$$

for the case of a Gaussian distribution of nearest-neighbor distances (d) on the lattice, with standard deviation σ.[18]

The Herman orientation function (f) was used to assess the orientation of both high and low aspect ratio organo-silicates in TPU during tensile deformation and is given by the following equation:[21,22]

$$f = \frac{\langle\cos^2\Phi\rangle - 1}{2} \tag{5}$$

where

$$\langle\cos^2\Phi\rangle = \frac{\int_0^{\pi/2} I(\Phi)\sin\Phi\cos^2\Phi\,d\Phi}{\int_0^{\pi/2} I(\Phi)\sin\Phi\,d\Phi} \tag{6}$$

In this case, f was calculated from the azimuthally averaged data, where $\langle\cos^2\Phi\rangle$ is the average cosine squared weighted by intensity I as a function of the radial angle, Φ. The value of f is equal to 1 and −0.5 when the orientation of the organo-silicate is completely aligned perpendicular and parallel to the direction of strain, respectively, and is zero for random (isotropically) orientated organo-silicates.

RESULTS AND DISCUSSION

Nano-silicate, Organo-silicate, and Nanocomposites Structure. TEM images of the nanocomposites containing ODTMA modified ME (MEO) and ODTMA modified Lu (LuO) are displayed in Figure 1. In general, the low aspect ratio LuO in 2 wt % (2LuO) and 4 wt % (4LuO) dispersed and exfoliated well in the TPU matrix, which is probably due to the hydrophobic ODTMA surfactant providing a favorable thermodynamic driving force for TPU intercalation. The 2LuO system provides 30 nm × 1 nm synthetic clay reinforcing elements which are readily capable of orientation and reinforcement in the TPU. In contrast, 2MEO and 4MEO exhibited an ordered intercalated structure that also contained larger organo-silicate tactoids (in the order of several micrometers) dispersed throughout the TPU matrix. The high aspect ratio MEO with lower mobility and higher spatial restrictions is believed to experience frustrated orientational freedom in the matrix, thus making it more difficult for the intercalated TPU to peel the platelets away from the well-intercalated tactoids.

The XRD signature of any polymer−silicate nanocomposite may be influenced by the average platelet size, degree of nanosilicate interplatelet registration, orientation, and increase in basal spacing (d-spacing) of the nanosilicate due to intercalation by host polymer. The increase in d-spacing depends on the amount of TPU intercalated in the galleries of the silicates,[23−26] and of course, this is a function of nanosilicate loading and also nanocomposite processing history. XRD patterns of the nano-silicates (ME and Lu) and their corresponding organo-silicates, MEO and LuO are shown in Figure 2a, and XRD patterns for their respective nano-composites are shown in Figure 2b. The modification of ME

dx.doi.org/10.1021/ma202189e | Macromolecules 2012, 45, 198−210

Table 1. Mechanical Properties of E5-325 (Neat Host TPU and Nanocomposite) and Nusil MED4860

material	tensile strength (MPa)	Young's modulus (MPa)	elongation at break (%)	toughness (MPa)	tear strength (MPa)
Nusil MED 4860	7.5 ± 0.1	2.7 ± 0.2	595 ± 39	35 ± 4	41 ± 14
E5-325	20 ± 2	10 ± 2	883 ± 63	91 ± 20	53 ± 3
2LuO	23 ± 2	14.4 ± 0.4	1053 ± 60	137 ± 16	70 ± 9
4LuO	10 ± 4	52 ± 12	177 ± 15	15 ± 2	45 ± 1
2MEO	24 ± 1	14.5 ± 0.7	1003 ± 38	131 ± 9	64 ± 1
4MEO	20.2 ± 0.9	11.9 ± 0.3	903 ± 83	105 ± 16	60 ± 5

with ODTMA was observed to substantially increase the (d_{100}) basal spacing from 1.3 to 4.9 nm. However, MEO exhibited several well-defined diffraction peaks as compared to the pristine ME, corresponding to *d*-spacings of approximately 4.9, 2.3, and 1.6 nm, respectively. The additional observed peaks are caused by the interstratified superstructure of the fluoromica, which originates from an inherent heterogeneity.[27,28] This charge heterogeneity may allow different amounts of surfactant chains to intercalate the fluoromica layers, and hence monolayer−bilayer or bilayer−pseudotriple layer arrangements are all possible.[28] The high aspect ratio fluoromica can give rise to long-range order in the resulting organosilicate tactoids (with respect to synthetic hectorites or natural nanosilicates, for example), and this gives rise to strong diffraction peaks. Lu and LuO, in contrast, demonstrate a weak and diffuse diffraction shoulder. One reason for the lack of a strong diffraction peak and the appearance of this diffuse shoulder is that the small aspect ratio of the Lu and LuO may not allow sufficient intensity of the diffraction to be measured due to a reduction in length and ordering of the repetitive layer structure. Existing papers such as those by Finnigan et al.[19] have quantified this effect for TPU systems. This makes interpretation of XRD patterns from LuO-based TPU nanocomposites more difficult, but useful supplementary information can be gleaned. The XRD profile of the neat host TPU shows no significant peak. This is expected, as both soft and hard domains present within a PDMS-based TPU do not show any diffraction peaks between $2\theta = 0.5°$ and 10°,[29,30] and this TPU segmental microphase periodicity can only be detected at lower angles. 2MEO and 4MEO nanocomposites exhibited three well-defined diffraction peaks centered at $2\theta = 2.1°$, $2\theta = 4.2°$, and $2\theta = 6.4°$, corresponding to *d*-spacings of approximately 4.2, 2.2, and 1.4 nm. The small differences in *d*-spacing between the pristine organosilicate and the nanocomposites suggest that there are some large tactoids present where very little, if any, polymer has intercalated into the interlayer spacing. 2LuO, in contrast, demonstrates a weaker and broader peak centered at (d_{001}) of ~2.5°, which corresponds to a *d*-spacing of 3.6 nm. There is also a disruption in the ordering of the organo-silicate platelets when 4LuO is dispersed in the E5-325 TPU matrix. It displays a broad and diffuse diffraction shoulder.

Mechanical Properties. The mechanical properties of solvent cast E5-325 (neat host TPU and nanocomposites) and Nusil MED 4860, a biomaterial that is currently used for insulation in cochlear implants, are summarized in Table 1. The low strain behavior and representative stress−strain curves are shown in Figure 3.

The tensile curve of the neat host E5-325 TPU is similar to that of other TPUs.[26,31,32] E5-325 TPU displays greater tensile properties when compared with Nusil MED4860, showing gains of 167% in tensile strength, 48% in elongation at break, 160% in toughness, and 29% increase in tear strength. Adding 2 wt % of modified organo-silicates further increases the

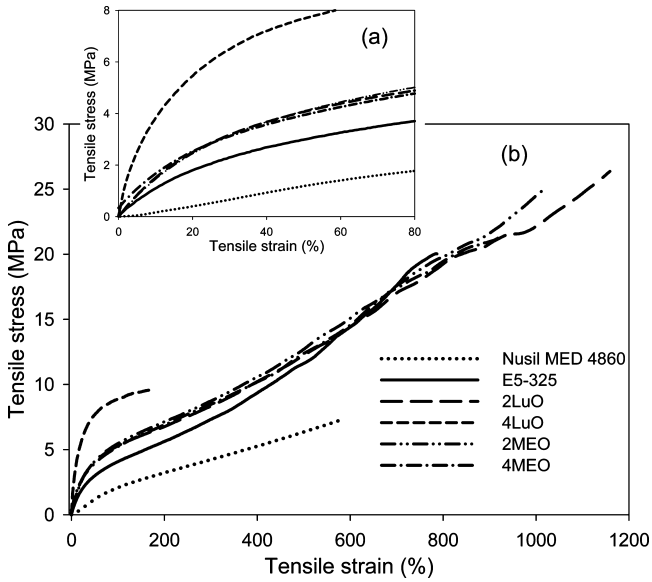

Figure 3. (a) Low strain behavior and (b) stress−strain curves of Nusil MED 4860 and E5-325 (neat host TPU and nanocomposites).

mechanical properties of this PDMS-based TPU. The best mechanical properties were achieved when 2 wt % LuO was added, giving rise to an increase of 15% in tensile strength, 19% in elongation at break, 51% in toughness, and 32% increase in tear strength. We believe that the superior dispersion and delamination of LuO in the TPU matrix (Figure 1) resulted in greater nanofiller−matrix interactions. It has been suggested by Wang and Pinnavaia[33] that the enhancement in tensile strength of elastomeric polyurethane is directly attributed to the reinforcement provided by the dispersed silicate nanolayers. The improvement in extensibility maybe attributed to the plasticizing effect of onium ions, which effects the conformation of the TPU chains at the nanosilicate−matrix interface.[33] These ions would promote relaxation at local stress regions, allowing the material to achieve a higher elongation at the break.[33] However, anomalous behavior was observed when the nanocomposite was prepared at 4 wt % LuO. The addition of this low aspect ratio and hydrophobic organo-silicate resulted in a drastic increase in Young's modulus, and this was accompanied by a large reduction in tensile strength and elongation at break. The Young's modulus was substantially increased by ~420% while the elongation at break was significantly reduced by ~80%. When introduced at 4 wt % loading, the LuO caused a strong perturbation of the TPU morphology. One hypothesis is that the LuO organo-silicate acts as a very potent compatibilizer between the hard segments and soft segments, thereby altering the underlying TPU morphology. The incorporation of 2 wt % modified ME resulted in a slight increase in tensile strength and modulus, with a modest increase in elongation at break as compared to

the neat host TPU. However, increasing the organo-silicate loading from 2 to 4 wt % resulted in the reduction of both tensile strength and elongation at break, which suggests that there was reduced quality of organo-silicate dispersion compared to the 2 wt % counterpart. The TEM image of 4MEO (Figure 1J) indicates that this material contains larger tactoids than that of 2MEO.

We have also performed the stress relaxation and tensile creep analysis of selected samples to measure their time-dependent dimensional stability under tensile deformation. Stress relaxation data obtained at 50% strain are presented in Figure 4. The data were normalized against the stress, $\sigma(t')$, at t

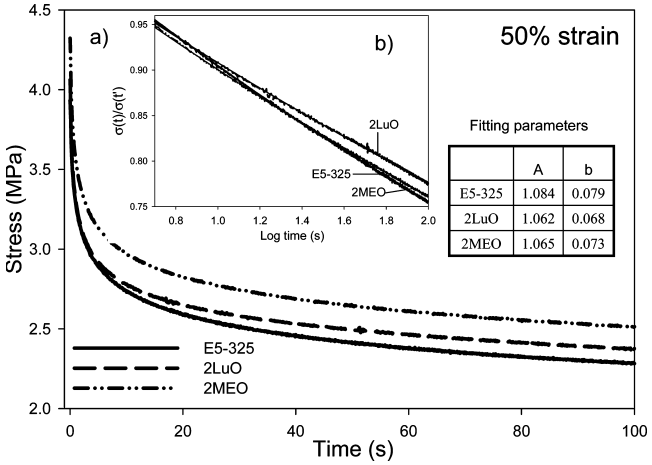

Figure 4. Stress relaxation data obtained at 50% strain.

= 5 s and demonstrated a power-law dependence ($\sigma(t)/\sigma(t') = At^{-b}$), as displayed in Figure 4b. The fitting constants, A and b, from the power law analysis are provided in the inserted table in Figure 4. The slopes of the curves reveal that the stress relaxation rate is reduced with the addition of 2LuO, while the rate is almost unchanged with the 2MEO inclusion. This clearly shows that the low aspect ratio organo-silicate (LuO) was most effective at retarding stress relaxation. According to Sternstein and Zhu,[34] at low strain, the stress relaxation rate in the nanocomposites is considered to be the result of strain-induced disentanglements and slippage of chain segments at the filler surface. Therefore, the low aspect ratio and better dispersed LuO are somehow contributing to reduced strain-induced molecular or segmental slippage and hence a lower stress relaxation rate. The tensile-creep modulus (E_t) (the ratio of applied stress to tensile-creep strain) was used to evaluate the creep resistance of the TPU and the nanocomposites. E_t values for neat E5-325 TPU, 2LuO, and 2MEO measured at a stress of 2 MPa are shown in Table 2, while their representative tensile-

Table 2. Tensile-Creep Modulus (E_t) of the E5-325 (Neat Host TPU and Nanocomposites) Measured at a Stress of 2 MPa

material	tensile creep modulus (MPa)
E5-325	4 ± 1
2LuO	8 ± 1
2MEO	5.3 ± 0.4

creep curves are displayed in Figure 5. The results indicate that the creep resistance of the E5-325 TPU was markedly improved

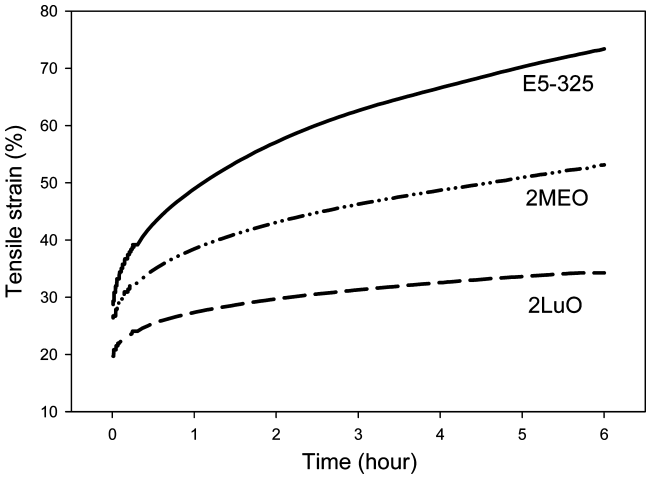

Figure 5. Tensile-creep curves of E5-325, 2LuO, and 2MEO at an applied stress of 2 MPa.

with the addition of 2 wt % LuO and MEO. The highest E_t was achieved by 2LuO with an increase of 100%, while 2MEO resulted in an increase of 26%. This proves that both organosilicates are capable of increasing the creep resistance and dimensional stability of the TPU, in agreement with the stress relaxation study. For an in-depth look into possible reasons for these changes in TPU mechanical behavior with the organo-silicate addition, we performed the DMTA, DSC, and strained synchrotron SAXS analysis to provide information with respect to possible morphological changes and specific TPU–nanofiller molecular interactions.

Dynamic Thermal Mechanical Analysis (DMTA). Tan δ plots in Figure 6a revealed two main peaks for the neat host E5-325, similar to that previously reported by Runt et al.[29,30] on ElastEon TPU with 98% α,ω-PDMS and 2% PHMO and 40% hard segment, where Tα_1 and Tα_2 were observable at −105 and 2 °C, respectively. The first peak corresponds to a low-temperature process (Tα_1), which relates to segmental motion in the PDMS phase.[30] The second peak appears at higher temperature (Tα_2), and this is assigned to the α,ω-PDMS end-group (soft microphase) segmental motion.[29,30]

In our case, Tα_1 is observed in the −84 to −86 °C range, whereas Tα_2 is observed in the 3 to 18 °C range. The Tα_2 of the TPU increased with the addition of the organo-silicates, and this shift was more pronounced in the LuO nanocomposites. The addition of 2 wt % LuO to the E5-325 resulted in an increase of Tα_2 from −3.0 to 7.1 °C while the addition of 4 wt % LuO has significantly increased the Tα_2 from −3.0 to 18.0 °C. In fact, this 4LuO sample exhibits unusual dynamic mechanical properties compared with the neat TPU and its 2 wt % counterpart. It displays a much higher Tα_2 and damping capacity in the rubbery region but lower damping capacity in the glassy region. It is probable that there is phase mixing between the hard and soft segments due to compatibilization of soft and hard segments by this particular organosilicate, so that the Tα_2 of the soft segment is markedly increased. This is supported by Runt et al.,[30] who reported that the position of the Tα_2 can be influenced by the inclusion of single MDI and short MDI-BDO sequences into the soft phase. In agreement with the tensile modulus results, the storage modulus was observed to increase with the addition of 2 and 4 wt % organosilicates, indicating reinforcement has been provided to the TPU matrix. Somewhat incongruous values for the storage

dx.doi.org/10.1021/ma202189e | Macromolecules 2012, 45, 198–210

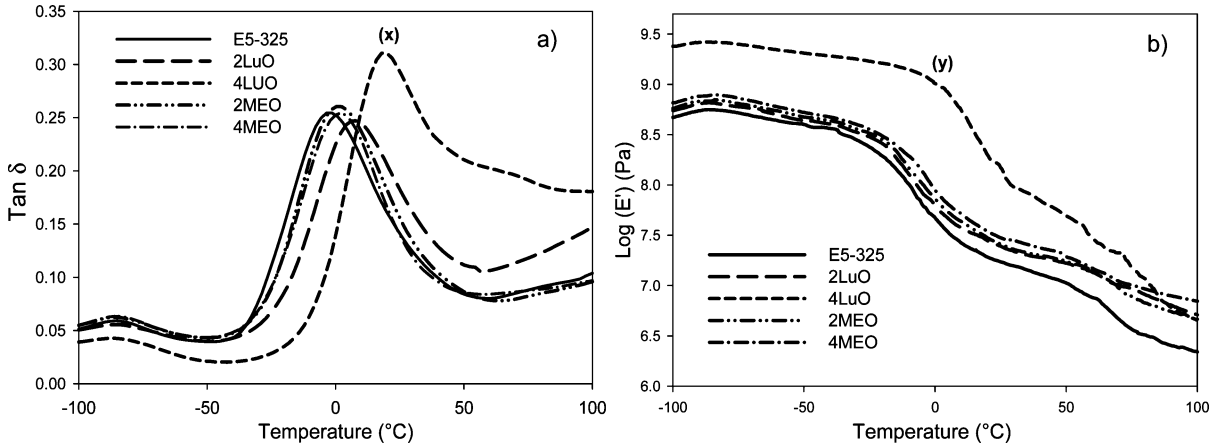

Figure 6. DMTA data as a function of temperature: (a) damping factor (tan δ); (b) storage modulus (E') for E5-325 (host TPU and nanocomposites). Curves (x) and (y) demonstrate that the 4LuO has a much higher soft microphase transition temperature (Tα_2) and storage modulus as compared to the neat host TPU, which indicates pronounced phase mixing.

Table 3. Transition Temperatures (α_1 and α_2) Determined from DMTA Curves

		damping peaks	
matrix	nanofiller	α_1 (°C)	α_2 (°C)
E5-325 TPU		−85.4	−3.0
	2LuO	−85.6	7.1
	4LuO	−86.3	18.0
	2MEO	−86.1	2.1
	4MEO	−84.2	2.0

modulus were observed for the 4 wt % LuO, nanocomposite system (Figure 6b). In agreement with mechanical test results, LuO was most effective in increasing the modulus of E5-325 at room temperature. However, these values are much higher in the glassy region but dropped drastically in the rubbery region (~50 °C). On the basis of this analysis, it was postulated that the addition of 2 wt % LuO in the TPU resulted in a "partial compatibilizing effect" while adding the organosilicate at 4 wt % induced almost full compatibilization between the hard and soft segments. The DSC and *in situ* SAXS data presented in the following section provide further supporting evidence for this phenomenon.

Differential Scanning Calorimetry (DSC). Table 4 summarizes the DSC features of the solvent-cast E5-325 (neat host TPU and nanocomposites) while Figures 7a and 7b present the heating and cooling thermograms, respectively. The enthalpy of fusion of hard segment melting endotherms is labeled as ΔH_m while the enthalpy of crystallization of hard segment is indicated by ΔH_c.

From the heating scan, we observed two to four endotherms in the DSC thermograms, and they have been labeled T1, T2, T3, and T4. Previous DSC analysis by Runt et al.[35] on similar PDMS-based TPU systems with PDMS/PHMO (in a ratio of 80/20) and 32.5% hard segment demonstrated an endotherm at ~50 °C and has been proposed to correspond to the ordering of single ("lone") MDIs.[35,36] A T2 endotherm was observable in the 99−115 °C range and is related to the T_g of the hard domains (T_{gH}) where the T_g of the high-molecular-weight hard segments (MDI-BDO) has been found to be around 110 °C.[37] In the case of 2LuO, a broader and more diffuse T2 peak suggests a more substantial paracrystalline interphase in this particular nanocomposite, compatibilized by the LuO organosilicate. At the same filler concentration, the LuO nanocomposites showed higher ΔH_m values when compared to the MEO nanocomposites. The ΔH_m values are highest for E5-325 containing 4LuO and lowest for E5-325 with 2MEO. In the 2LuO, a sharp hard segment melting endotherm (T3) centered at ~197 °C was observable and could be attributed to the nucleation or "self-assembly" of a higher melting hard microphase. In the case of 4LuO, the high-temperature melting endotherms (T3 and T4) were also appearing at temperatures of 194−207 °C. These high melting endotherms were perhaps due to sluggish, but preferential, organization of the longer hard segment present in this system at elevated temperatures. This is based on the previous DMTA analysis, where we have postulated that the 4LuO had

Table 4. Summary of DSC Heating and Cooling Curves of E5-325 (Neat Host TPU and Nanocomposites)

		heating					cooling	
		endotherm peak					crystallization exotherm	
matrix	nanofiller content	T1 (°C)	T2 (°C)	T3 (°C)	T4 (°C)	hard phase ΔH_m (J/g)[a,b]	peak (°C)	ΔH_c (J/g)[b]
E5-325 TPU		60	102			14.0	86	14.8
	2LuO	59	100	197		13.8	133	c
	4LuO	57	98	194	207	42.0	123	2.5
	2MEO	58	101			11.1	88	13.6
	4MEO	62	107			15.9	87	13.8

[a]Enthalpy of fusion values are the sum of the T1−T4 melting enthalpies. [b]Enthalpies were calculated per gram of hard segment (not per gram of sample). [c]Endotherm was too small to calculate an enthalpy value.

dx.doi.org/10.1021/ma202189e | *Macromolecules* 2012, 45, 198−210

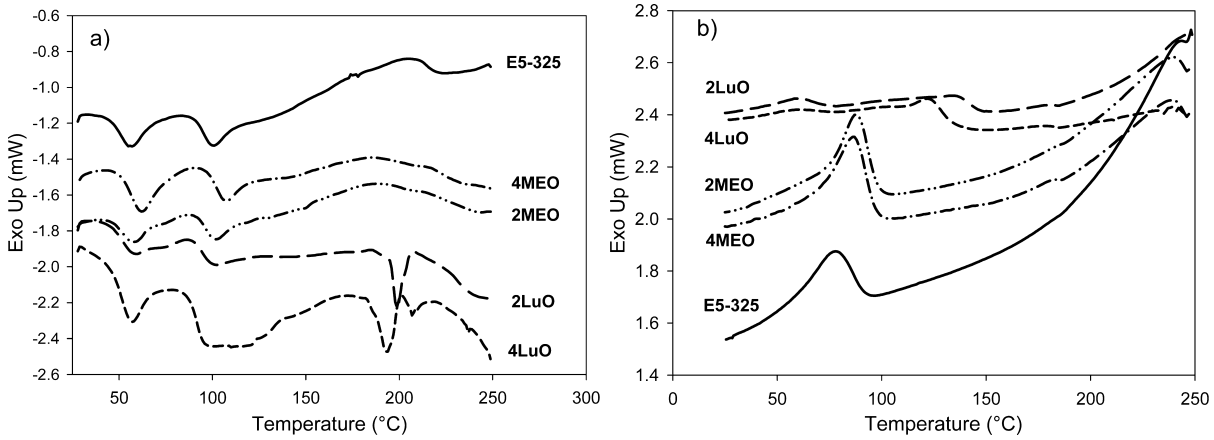

Figure 7. Typical DSC (a) heating curves and (b) cooling curves for the neat host TPU and containing LuO and MEO.

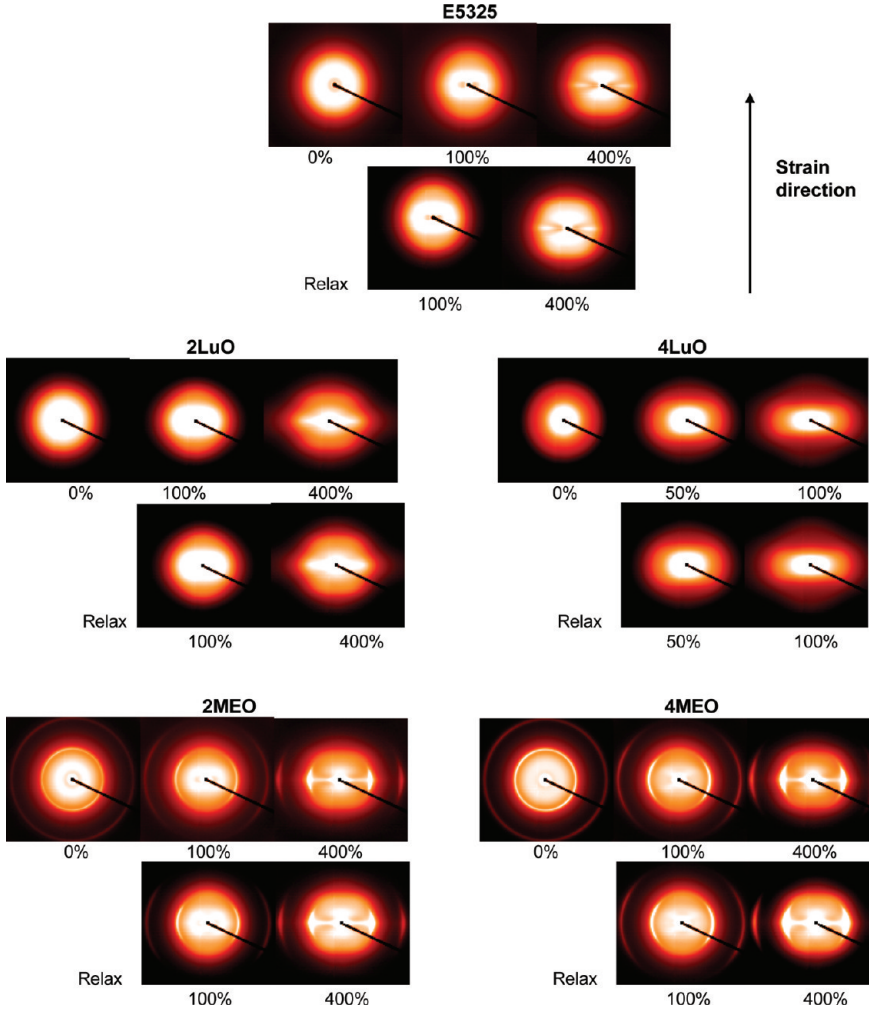

Figure 8. 2D SAXS patterns at selected strains for E5-325 (neat host TPU and nanocomposites) obtained from the short sample-to-detector distance. The relaxed state refers to images taken 10 min after strain measurements were taken.

compatibilized the hard and soft TPU segments. However, the longer hard segments are potentially excluded (insoluble) from the soft segments and interphases due to their thermodynamic incompatibility. Therefore, the high melting endotherms appear to relate to selective crystallization of the longer hard segment fractions that may be unable to dissolve in this phase-mixed system. As discussed previously, the anomalous tensile test and DMTA results obtained from these nanocomposite systems are attributed to these significant TPU morphological changes. Based on the cooling scan, crystallization exotherm peaks at 88 to 87 °C were observable for the E5-325 containing 2MEO and 4MEO, respectively. Meanwhile, for LuO nanocomposites, the crystallization exotherms were seen to occur at higher temperature which suggests that these lower aspect ratio organo-silicates provide a proportion of the TPU hard segments with a higher driving force to crystallize. However,

dx.doi.org/10.1021/ma202189e | *Macromolecules* 2012, 45, 198–210

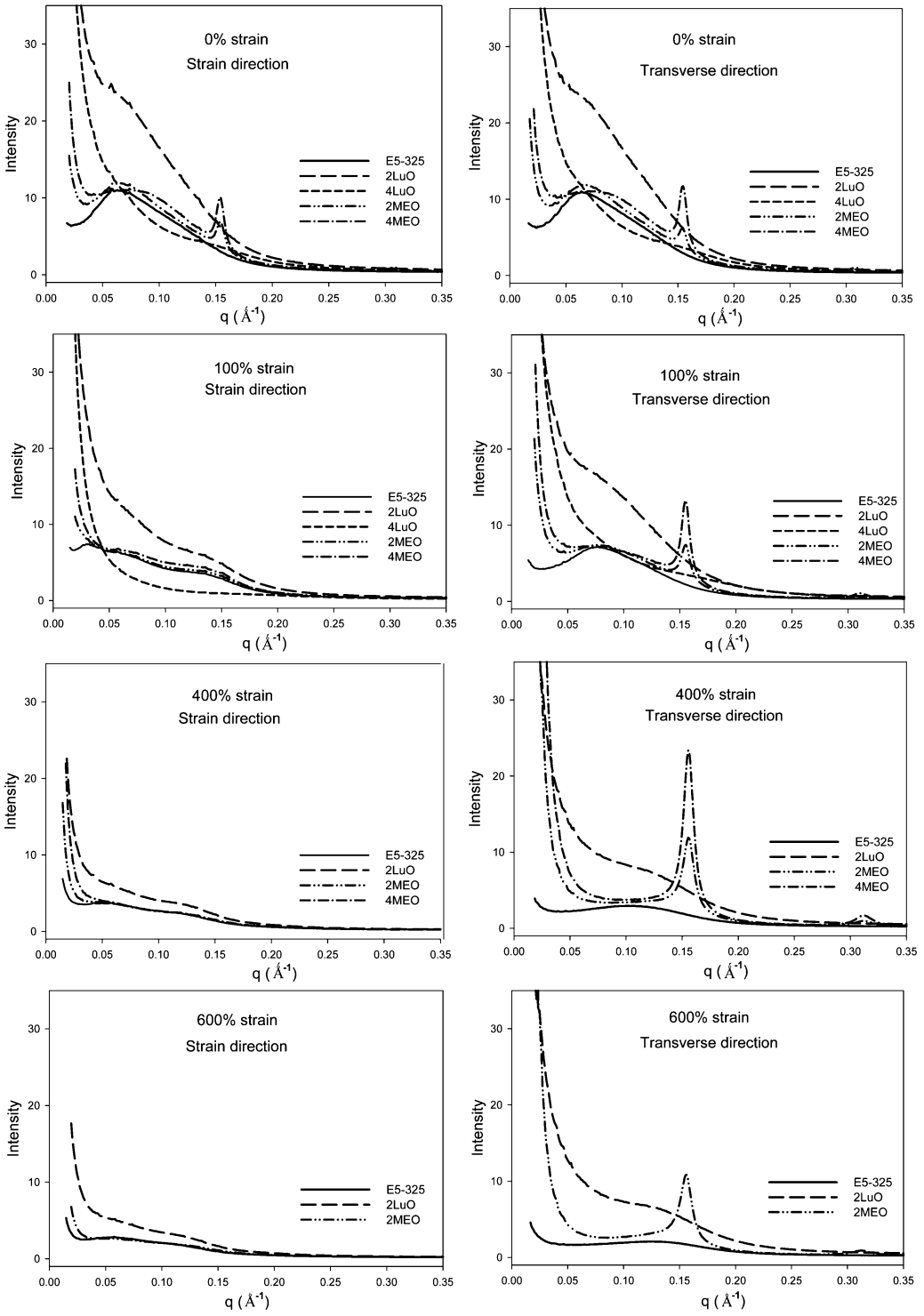

Figure 9. 1D profiles of E5-325, 2LuO, 4LuO, 2MEO, and 4MEO at 0%, 100%, 400%, and 600% strain in the strain and transverse direction, obtained from the short sample-to-detector distance.

they also exhibited lower ΔH_c values with a broader and weaker peak, which indicates that there is a disruption to the reorganization of complete population of hard segments during cooling from melt, perhaps brought about by the hydrophobic LuO simultaneously acting as both a nucleating and a compatibilizing agent.

***In Situ* Strained Small-Angle X-ray Scattering (SAXS).** Complete morphological characterization is vital to develop an in-depth understanding of structure−property relationships of the E5-325 TPU and associated nanocomposites. Static morphology and morphological evolution during stretching are both very important in these systems. *In situ* SAXS analysis of strained films is perhaps one of the most useful ways to probe structural changes.[19,38−40] The response of this microstructure to deformation facilitates an understanding of organosilicate orientation, TPU microdomain deformation, and associated cooperative toughening mechanisms. *In situ* SAXS under tensile deformation was therefore performed for all

dx.doi.org/10.1021/ma202189e | *Macromolecules* 2012, 45, 198−210

Table 5. Zernike Prins (ZP) Fits of SAXS Data of E5-325 (Neat Host TPU and Nanocomposites)

		strain direction			transverse direction		
strain (%)		d, nm (±0.5)[a]	R, nm (±0.5)	σ/d (±0.05)	d, nm (±0.5)	R, nm (±0.5)	σ/d (±0.05)
0	E5-325	9.5	2.7	0.32	9.4	2.7	0.22
	2LuO	9.8	2.7	0.57	9.7	2.7	0.35
	2MEO	8.3	2.7	0.43	8.2	2.7	0.44
	4MEO	6.8	2.6	0.51	6.8	2.6	0.51
50	E5-325	11.4	2.8	0.35	8.7	2.7	0.61
	2LuO	10.1	2.9	0.42	8.7	2.7	0.89
	2MEO	9.0	2.8	0.21	7.9	2.7	0.59
	4MEO	7.6	2.6	0.58	6.7	2.5	0.56
100	E5-325	16.9	2.7	0.62	8.2	2.7	0.60
	2LuO	10.7	3.0	0.37	7.9	2.7	0.50
	2MEO	7.4	2.7	0.23	7.2	2.5	0.77
	4MEO	7.7	2.6	0.38	6.4	2.3	0.90
200	E5-325	7.5	2.7	0.74	7.5	2.6	0.61
	2LuO	9.8	2.9	0.44	6.0	2.7	0.94
	2MEO	7.5	2.7	0.64	6.3	2.2	0.77
	4MEO	7.1	2.6	0.35			
400	E5-325	8.5	2.6	0.50	6.5	2.5	0.60
	2LuO				5.3	2.5	0.85
	2MEO	7.8	2.7	0.81			
	4MEO	10.8	2.6	0.42			
600	E5-325	8.6	2.6	0.91	5.9	2.5	0.53
	2LuO				5.2	2.5	0.74
	2MEO	7.3	2.4	0.93			
	4MEO[b]						

[a]Expected uncertainty due to sample variations and curve fitting. [b]Sample broke.

samples, in an effort to better elucidate the mechanisms responsible for the mechanical behaviors observed. The scattered radiation achieves higher intensity levels when organo-silicates are incorporated into TPU due to their very high electron scattering length density with respect to TPU segments. Therefore, analysis at different q regions was done in order to differentiate between TPU morphology and contributions from the nanofillers. The SAXS data obtained at the short sample-to-detector distance (q range of 0.015−0.50 Å) was used to study changes in TPU microphase morphology, while the data collected at the long sample-to-detector distance (q range of 0.002−0.06 Å) was used to follow the evolution of nanosilicate morphology during uniaxial loading.

TPU Microphase Morphology during Deformation. 2D SAXS images at selected strains for the neat host TPU and nanocomposites collected at the short sample-to-detector distance during deformation are shown in Figure 8, together with the images acquired after relaxing the stretched films for 10 min. Their respective 1D SAXS profiles are shown in Figure 9.

In the initial unstrained state, all samples show isotropic SAXS patterns, indicating that the hard segment domains are randomly oriented, which then transforms to increasingly anisotropic patterns upon stretching. The neat E5-325 exhibits a typical TPU SAXS pattern.[19,32,41,42] At 100% strain, the ring deforms to an ellipsoid with the long axis along the equator. The *in situ* SAXS studies of TPU containing 42 wt % hard segment by Blundell et al.[41] showed that the elliptical SAXS pattern is attributed to an affine deformation of the two-phase structure of TPU, similar to the findings of Desper and co-workers.[42] It is reasonable to assume that the soft segments are mainly involved in the deformation of this material during the first 100% strain, and the TPU hard segments respond to the alignment of the soft segment chains at this stage. The SAXS pattern reveals scattering lobes on the meridian and a streak in the equatorial direction when the strain reaches 400%. This scattering pattern is an indicative of a certain degree of orientation of the hard segments and the existence of oriented soft segment microphases, all of which are aligning in the stretch direction. The equatorial streak appears as a result of reduced electron density contrast between the hard segment nanofibrils and the aligned soft segment chains and/or the decrease in coherent scattering due to the small size of the broken down hard domains. This effect can be observed from the reduction of the average hard domain spacing (Table 5) when the strain reaches and surpasses 200%.

At low elongation (100%), the 2D SAXS pattern of 2LuO is similar to the neat TPU, showing an ellipse scattering. However, upon straining to 400%, the equatorial scattering appears wider with respect to that observed in other materials, suggesting the presence of longer, more fragmented hard segment domains. The SAXS pattern of 4LuO, due to strong phase mixing, exhibits plastic behavior rather than elastomeric deformation as the system was tested about its T_g. The sample broke at 125% strain. Conversely, the SAXS patterns for MEO nanocomposites demonstrate an isotropic outer ring prior to straining, which then progressively transforms into two arcs in the equator upon straining. This outer ring is located in the high q region, relates to the diffraction from registered high aspect ratio fluoromica tactoids, and is understandably more intense in the material containing a higher organo-fluoromica loading (4MEO). At 100% strain, the two arcs observed in the region of q = 0.15−0.17 Å^{-1} represent the oriented nanoparticles, and the respective scattering peak at q = 0.155 Å^{-1} can be observed in the SAXS profile (Figure 9). At 400% strain, the

dx.doi.org/10.1021/ma202189e | *Macromolecules* 2012, 45, 198−210

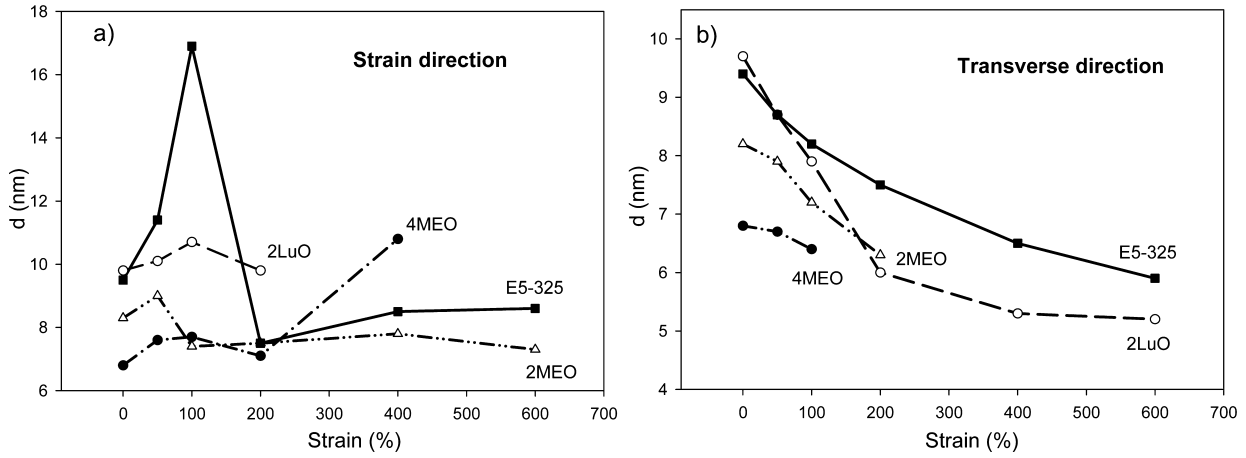

Figure 10. Estimated average hard domain spacing (d) of the neat host TPU and nanocomposites determined from the Zernike−Prins model in the (a) strain and (b) transverse direction.

arcs become broader, which suggests that a higher fraction of nanoparticles become oriented in the strain direction.

For all strained samples, slightly intensified scattering was observable from SAXS patterns during the relaxation process, indicating a slight recovery of phase separation and hard segment ordering. However, the nanocomposite samples show a lesser degree of recovery due to reduced TPU microphase mobility as a result of organosilicate inclusion.

The 1D SAXS profiles presented in Figure 9 of the neat host TPU and nanocomposites reveal prominent peaks in the region of q = 0.06−0.09 Å^{-1}, corresponding to the segmental microphase periodicity in the materials. Further stretching results in the decrease in the scattering intensity, in both strain and transverse directions, which suggests a disruption of the hard segment domain fraction.[43] Another two reflections (q = 0.155 and q = 0.31 Å^{-1}), corresponding to diffraction from the fluoromica tactoids with d-spacing of 4.2 and 2.1 nm, respectively, were observable in the undeformed 2MEO and 4MEO samples. Both scattering peaks appear stronger and shift slightly toward higher q in the transverse direction as the strain increases from 0% to 600%, suggesting greater organosilicate alignment and reduced spacing between the individual platelets. The XRD analysis on the undeformed 2MEO and 4MEO as shown in Figure 2b also confirms the presence of a similar organo-silicate d-spacing.

Based on Figures 8 and 9, there are clear differences in periodicity and in the degree of order between the LuO and MEO nanocomposite systems. Other than a broader peak, 2LuO demonstrates much higher scattering intensity in the q region between 0.02 and 0.15 Å^{-1}, even after silicate subtraction. Although the LuO organosilicate is believed to induce some degree of phase mixing in the system, there is also strong evidence from the DSC thermograms for the nucleation of "self-assembly" of a higher melting (T_m) hard microphase. We believe that a population of longer hard segments and LuO platelets may be cooperating to form a restructured hard domain. The high-intensity scattering observed might be due to the better contrast of this more well-ordered hard segment population. The intensity curves of the 4LuO decrease monotonically without a diffraction maximum. This featureless SAXS pattern implies the strong phase mixing between the hard and soft segments in this TPU nanocomposite system. Similarly, no significant scattering from the organo-silicate was detected in the XRD analysis.

The change in hard domain spacing (d) with deformation for E5-325 TPU and nanocomposites was also studied from the SAXS patterns. The morphological data obtained from the ZP fitting, combined with the direct visualization of the 1D scattering profiles, are tabulated in Table 5 and presented graphically in Figure 10.

For the neat host TPU, the d-spacing is observed to increase sharply in the strain direction at the initial stages of deformation. The randomly oriented hard domains subjected to tensile deformation exhibited an increase of d-spacing from 9.5 to 16.9 nm upon 100% strain. In relation to affine deformation, it is reasonable to assume that the TPU hard blocks respond to the alignment of the soft segment chains at this stage. Subsequent deformation up to 200% strain resulted in a decrease in the d-spacing to 7.5 nm, as the hard segment aggregates are disrupted, broken down to smaller widths, and partially aligned in the direction of stretch. Further stretching gives no significant effect to the d-spacing of the neat TPU. Conversely, straining the TPU nanocomposites up to 200% is associated with only slight shifts of d in the strain direction, most notably seen in the 2LuO system. On the basis of TEM images, 2LuO demonstrates greater organo-silicate dispersion and exfoliation in the TPU compared to the other nanocomposites, showing more individual organo-silicate layers available for molecular interaction with the TPU segments. This should result in higher restriction in mobility of the segment chains. In addition, the DSC, tensile creep, and stress relaxation studies also suggest the presence of additional hard domain connectivity in this system, which could lead to a better retention of hard domain spacing upon deformation. The ZP model was unable to fit the scattering data of high strained 2LuO in strain direction because the scattering peak had diminished. 2 wt % MEO at 100% resulted in the decrease of d, which could be due to rotation, reorganization, and tilting of the hard domains, perhaps induced by their interaction with the high aspect ratio platelets. Further stretching gives no significant effect to the interdomain spacing of this material. For all samples, a decrease in d is observed in the transverse direction with increasing strain. This is expected as the system was subjected to uniaxial deformation. As compared to other systems, 2LuO, which contains more cohesive hard microdomains, presents a significant reduction of d in the transverse direction, possibly due to the deformed hard domain and better preferred orientation of LuO with straining. The ZP model was

dx.doi.org/10.1021/ma202189e | Macromolecules 2012, 45, 198−210

unable to fit the scattering data of high strained MEO nanocomposites in the transverse direction because the scattering peak had diminished. In all cases, the hard segment radius of gyration (R) did not change significantly over the entire strain range. The data fitting was more sensitive to the position of the peak in the scattering profile, and hence the d value, than to the form factor contribution, and hence the R value.

Organo-silicate Orientation during Tensile Deformation. The orientation of the organo-silicate during uniaxial deformation plays an important role in the toughness enhancement of the TPU.[19,44] The scattering profiles obtained from the deformation process provide very useful insights into morphological changes in the nanostructure during strain. Figure 11 displays the selected 2D SAXS patterns of the neat

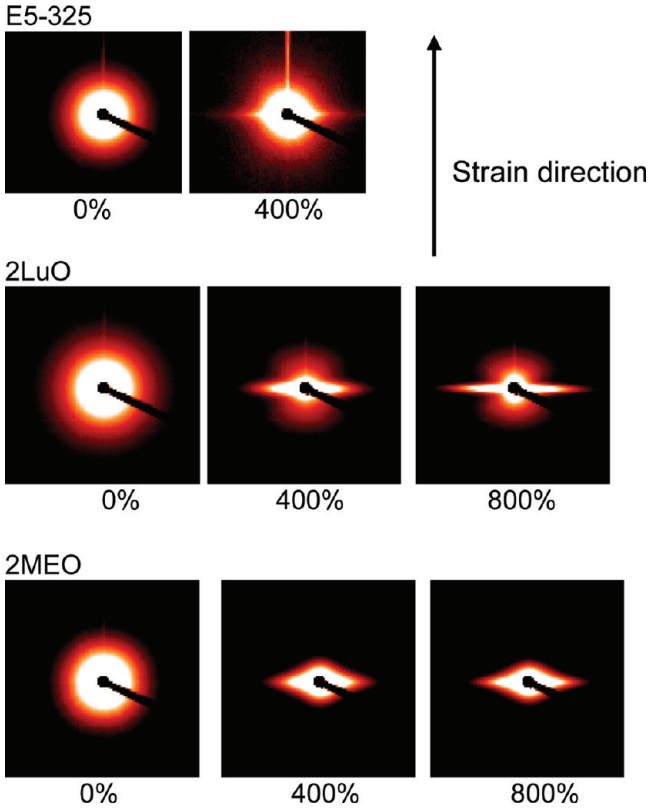

Figure 11. Selected 2D SAXS patterns at various strains for E5-325, 2LuO- and 2MEO, obtained from the long sample-to-detector distance.

host TPU and nanocomposites, obtained from the long sample-to-detector distance.

For the neat TPU, the absence of organo-silicate led to the isotropic SAXS patterns during unstrain and 400% strain. Note that the sample broke before reaching 800% strain. Meanwhile for the nanocomposites, the initially isotropic SAXS patterns were found to become anisotropic as the strain was increased. For 2LuO, the meridian stripe was seen to develop at 400% strain, which then become increasingly sharper toward the transverse direction when the strain reached 800%. This is indicative of significant platelet alignment in the strain direction. In comparison, the MEO nanocomposites demonstrate different scattering geometry. A diamond-shaped pattern suggests that there was alignment of fluoromica tactoids in both the strain and transverse direction, presumably due to delamination of matrix and nanofiller in some instances and effective load transfer and tactoid orientation in others.[19] The Herman orientation function (f) was calculated at q = 0.0031, where the scattering is dominated by the nanosilicates. These values are illustrated in Figure 12.

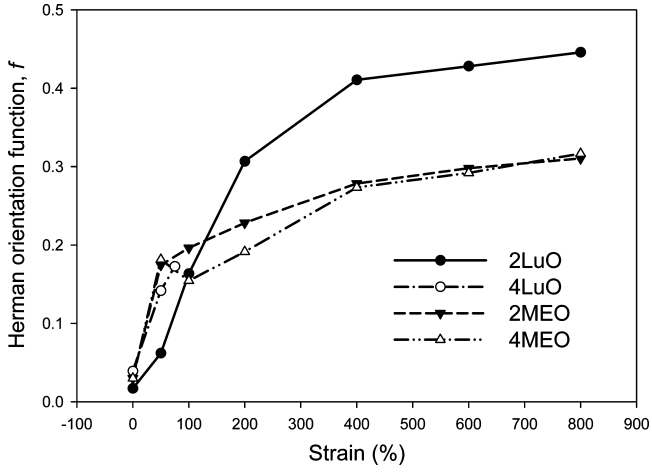

Figure 12. Herman orientation function versus strains for E5-325 TPU nanocomposites.

In the initial stages of deformation, the preferred orientation and alignment of high aspect ratio MEO nanocomposites are due to casting and settling during solvent casting. However, the degree of platelets alignment at high strains (>200%) was significantly greater for 2LuO than for 2MEO and 4MEO nanocomposites. This suggests that the low aspect ratio LuO aligns more preferentially in the strain direction than the high aspect ratio MEO at similar concentration during uniaxial tension of TPU, which is similar to the findings reported by Finnigan et al.[19] Large tactoids present in 2MEO and 4MEO are less mobile and having lower capability to align in the strain direction. Tactoids and unaligned platelets led to the formation of voids due to developed tensile stresses at the interface between the tactoids and the TPU. This can be visualized from the stress whitening effect developed in both 2MEO and 4MEO sample upon straining (figure not shown). This explains why the presence of 2LuO in the TPU leading to greater improvement in toughness compared to the 2MEO. As expected, the lower concentration of MEO (2 wt %) was found to be more aligned than the higher concentration MEO (4 wt %) in the TPU matrix.

■ SUMMARY

In summary, both high and low aspect ratio organosilicates resulted in broadly enhanced mechanical properties of this PDMS-based TPU system when added at 2 wt %. The low aspect ratio organosilicate when added in 2 wt % was seen to disperse and delaminate well in the TPU matrix, providing additional hard domain connectivity and brought about appreciable enhancements in tensile and tear strength and also markedly improved creep resistance. However, in the case of higher filler loadings (4 wt %), the hydrophobic low aspect ratio organosilicates induced profound morphological changes in the TPU microdomain texture, thus adversely effecting the mechanical properties of the E5-325 TPU. This can be seen from a dramatic increase in soft microphase transition temperature and profound stiffening effect. Thus, it is proposed

dx.doi.org/10.1021/ma202189e | Macromolecules 2012, 45, 198–210

that the hydrophobic low aspect ratio organosilicate acts as a very potent interfacial compatibilizer, which can effectively alter the morphological response of the TPU to deformation but needs to be introduced carefully in order to exploit its full utility.

AUTHOR INFORMATION

Corresponding Author

*E-mail: darren.martin@uq.edu.au.

ACKNOWLEDGMENTS

The authors thank Aortech Biomaterials Pty Ltd. and Cochlear Ltd. for research materials and financial support. This work was carried out in part on the SAXS/WAXS beamline at the Australian Synchrotron, Victoria, Australia. We also appreciate the facilities as well as the scientific and technical assistance of the Centre for Microscopy and Microanalysis, University of Queensland, and personally to Dr. Garry Morgan for the expert F30 training he provided. Azlin F. Osman expresses her appreciation to the Ministry of Higher Education Malaysia and University Malaysia Perlis for financial support. Finally, we also thank Prof. James Runt (Penn State University) and Dr. Nigel Kirby (Australian Synchrotron) for much time and effort adapting our tensometer for the Australian Synchrotron.

REFERENCES

(1) Anderson, J.; Hiltner, A.; Wiggins, M.; Schubert, M.; Collier, T.; Kao, W.; Mathur, A. *Polym. Int.* **1999**, *46*, 163−171.

(2) Pinchuk, L. *J. Biomater. Sci., Polym. Ed.* **1995**, *6*, 225−267.

(3) Szycher, M.; McArthur, W. In *Surface Fissuring of Polyurethanes Following in Vivo Exposure*; ASTM International: West Conshohocken, PA, 1985; p 308.

(4) Lelah, M.; Cooper, S. *Polyurethanes in Medicine;* CRC Press, Inc.: Boca Raton, FL, 1986; p 225.

(5) Szycher, M. *J. Biomater. Appl.* **1988**, *3*, 297.

(6) McCarthy, S.; Meijs, G.; Mitchell, N.; Gunatillake, P.; Heath, G.; Brandwood, A.; Schindhelm, K. *Biomaterials* **1997**, *18*, 1387−1409.

(7) Williams, D. F. *Progress in Biomedical Engineering*; Elsevier: Amsterdam, 1987.

(8) Gunatillake, P.; Meijs, G.; Mccarthy, S.; Adhikari, R. *J. Appl. Polym. Sci.* **2000**, *76*, 2026−2040.

(9) http://www.aortech.com/technology/elast-eon.

(10) Mishra, A.; Nando, G.; Chattopadhyay, S. *J. Polym. Sci., Part B: Polym. Phys.* **2008**, *46*, 2341−2354.

(11) Mishra, A.; Chattopadhyay, S.; Nando, G. *J. Appl. Polym. Sci.* **2010**, *115*, 558−569.

(12) Korley, L. S. T. J.; Liff, S. M.; Kumar, N.; McKinley, G. H.; Hammond, P. T. *Macromolecules* **2006**, *39*, 7030−7036.

(13) Kim, W.; Chung, D.; Kim, J. *J. Appl. Polym. Sci.* **2008**, *110*, 3209−3216.

(14) Barick, A. K.; Tripathy, D. K. *J. Appl. Polym. Sci.* **2010**, *117*, 639−654.

(15) Smart, S.; Fania, D.; Milev, A.; Kannangara, G.; Lu, M.; Martin, D. *J. Appl. Polym. Sci.* **2010**, *117*, 24−32.

(16) Campbell, K. T. The Structure of Segmented Polyurethane Nanocomposites. PhD Thesis, University of Queensland, 2005.

(17) Martin, D.; Edwards, G. Polymer Composites Having Particles with Mixed Organic Modifications. 15 April, 2009.

(18) Laity, P. R.; Taylor, J. E.; Wong, S. S.; Khunkamchoo, P.; Norris, K.; Cable, M.; Andrews, G. T.; Johnson, A. F.; Cameron, R. E. *Polymer* **2004**, *45*, 7273−7291.

(19) Finnigan, B.; Jack, K.; Campbell, K.; Halley, P.; Truss, R.; Casey, P.; Cookson, D.; King, S.; Martin, D. *Macromolecules* **2005**, *38*, 7386−7396.

(20) Pethrick, R. A.; Dawkins, J. *Modern Techniques for Polymer Characterisation*; J. Wiley: New York, 1999.

(21) Roe, R. J.; Roe, R. *Methods of X-ray and Neutron Scattering in Polymer Science*; Oxford University Press: New York, 2000.

(22) Malwitz, M. M.; Lin Gibson, S.; Hobbie, E. K.; Butler, P. D.; Schmidt, G. *J. Polym. Sci., Part B: Polym. Phys.* **2003**, *41*, 3237−3248.

(23) Pinnavaia, T.; Lan, T.; Wang, Z.; Shi, H.; Kaviratna, P. In *Clay-Reinforced Epoxy Nanocomposites: Synthesis, Properties, and Mechanism of Formation*; ACS Publications: Washington, DC, 1996; pp 250−261.

(24) Alexandre, M.; Dubois, P. *Mater. Sci. Eng., R* **2000**, *28*, 1−63.

(25) Chen, C.; Mao, C.; Tsai, M.; Yen, F.; Lin, J.; Tseng, C.; Chen, H. *J. Appl. Polym. Sci.* **2008**, *110*, 237−243.

(26) Finnigan, B.; Martin, D.; Halley, P.; Truss, R.; Campbell, K. *J. Appl. Polym. Sci.* **2005**, *97*, 300−309.

(27) Breu, J.; Seidl, W.; Stoll, A.; Lange, K.; Probst, T. *Chem. Mater.* **2001**, *13*, 4213−4220.

(28) Yang, J.; Han, Y.; Choy, J.; Tateyama, H. *J. Mater. Chem.* **2001**, *11*, 1305−1312.

(29) Choi, T.; Weksler, J.; Padsalgikar, A.; Runt, J. *Polymer* **2009**, *50*, 2320−2327.

(30) Hernandez, R.; Weksler, J.; Padsalgikar, A.; Runt, J. *Macromolecules* **2007**, *40*, 5441−5449.

(31) Liff, S.; Kumar, N.; McKinley, G. *Nature Mater.* **2007**, *6*, 76.

(32) Yeh, F.; Hsiao, B.; Sauer, B.; Michel, S.; Siesler, H. *Macromolecules* **2003**, *36*, 1940−1954.

(33) Wang, Z.; Pinnavaia, T. *Chem. Mater.* **1998**, *10*, 3769−3771.

(34) Sternstein, S.; Zhu, A. J. *Macromolecules* **2002**, *35*, 7262−7273.

(35) Hernandez, R.; Weksler, J.; Padsalgikar, A.; Choi, T.; Angelo, E.; Lin, J.; Xu, L.; Siedlecki, C.; Runt, J. *Macromolecules* **2008**, *41*, 9767−9776.

(36) Martin, D.; Meijs, G.; Renwick, G.; Mccarthy, S.; Gunatillake, P. *J. Appl. Polym. Sci.* **1996**, *62*, 1377−1386.

(37) Pongkitwitoon, S.; Hernández, R.; Weksler, J.; Padsalgikar, A.; Choi, T.; Runt, J. *Polymer* **2009**, *50*, 6305−6311.

(38) Yeh, F.; Hsiao, B. S.; Sauer, B. B.; Michel, S.; Siesler, H. W. *Macromolecules* **2003**, *36*, 1940−1954.

(39) Christenson, E. M.; Anderson, J. M.; Hiltner, A.; Baer, E. *Polymer* **2005**, *46*, 11744−11754.

(40) Koerner, H.; Kelley, J. J.; Vaia, R. A. *Macromolecules* **2008**, *41*, 4709−4716.

(41) Blundell, D. J.; Eeckhaut, G.; Fuller, W.; Mahendrasingam, A.; Martin, C. *Polymer* **2002**, *43*, 5197−5207.

(42) Desper, C.; Schneider, N.; Jasinski, J.; Lin, J. *Macromolecules* **1985**, *18*, 2755−2761.

(43) Fu, B.; Hsiao, B.; Pagola, S.; Stephens, P.; White, H.; Rafailovich, M.; Sokolov, J.; Mather, P.; Jeon, H.; Phillips, S. *Polymer* **2001**, *42*, 599−611.

(44) Shah, D.; Maiti, P.; Jiang, D. D.; Batt, C. A.; Giannelis, E. P. *Adv. Mater.* **2005**, *17*, 525−528.

Macromolecules

Article

pubs.acs.org/Macromolecules

New Insights into Structure–Property Relationships in Thermosetting Polymers from Studies of Cocured Polycyanurate Networks

Andrew J. Guenthner,*[,†] Kevin R. Lamison,[‡] Vandana Vij,[‡] Josiah T. Reams,[§] Gregory R. Yandek,[†] and Joseph M. Mabry[†]

[†]Propulsion Directorate, Air Force Research Laboratory, Edwards AFB, California 93524, United States

[‡]ERC Incorporated, Air Force Research Laboratory, Edwards AFB, California 93524, United States

[§]National Research Council, Air Force Research Laboratory, Edwards AFB, California 93524, United States

Supporting Information

ABSTRACT: Studies of the physical properties of the cocured networks formed from three similar dicyanate ester monomers revealed a number of unexpected variations from simple linear mixing rules. These variations shed light on important synergistic effects in cocured thermosetting networks and their possible causes. The monomers utilized were the dicyanate esters of Bisphenol A (BADCy) and Bisphenol E (LECy) and the silicon-containing analogue of Bisphenol A (SiMCy). The most important of the synergistic effects was a decrease of ~25% in moisture uptake seen only in conetworks of LECy and SiMCy. For all other systems, a clear relationship between moisture uptake and the number density of cyanurate rings was observed. This relationship generally applies to many types of cyanate esters and gives an indication of the importance of specific sites (as opposed to free volume alone) in moisture uptake. Numerous additional examples of nonlinear mixing relations were observed in the glass transition temperature, density, and thermochemical stability of fully cured networks. Interestingly, the most widespread deviations from linear behavior were observed for conetworks of SiMCy and LECy, suggesting that factors such as the mismatch in network segment size may be more important than differences in flexibility or symmetry in driving significant physical interactions among conetwork components.

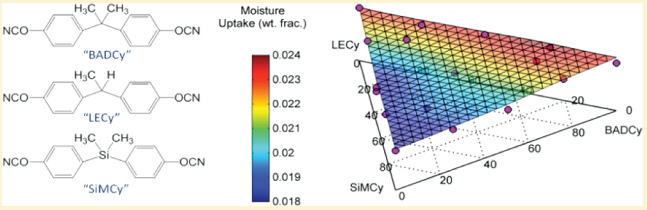

INTRODUCTION

Cyanate ester resins[1−4] have gained increasing prominence as "next generation" thermosetting monomers used as adhesives and composite resins in a wide range of high-performance aerospace,[5] electronics,[6,7] and alternative energy[8] applications. The low toxicity, low shrinkage, and low generation of volatiles during thermal cure of cyanate esters (primarily via cyclotrimerization) to form polycyanurates, along with the ability to be used in fabrication processes as varied as filament winding,[9] resin transfer molding,[10−12] and nanostructure casting,[13] make polycyanurates highly attractive for commercial product development. In addition, the highly selective nature of the cure reaction,[14,15] along with the ease of detection of both the extent of cure and side reactions in the solid state,[1] make cyanate esters especially useful in fundamental studies of macromolecular network formation, structure, and properties. Thus, a well-developed understanding of the relationships among network physical and chemical characteristics, processing, and resultant solid-state properties for cyanate esters is not only highly feasible but also has the potential to significantly improve the design and performance of thermosetting resins used in many technologically important products ranging from microcapacitors[6] to interplanetary space probes.[16]

One of the major challenges associated with developing structure–property relationships for cyanate esters, or for any thermosetting polymer, involves the ability to examine the physical structure of the cured macromolecular network at the molecular level. Though much useful information can be ascertained from examination of the soluble fraction in a partially polymerized system, as described by Kasehagen and Macosko[17] for the dicyanate ester of bisphenol A (hereafter "BADCy"), the structure arising from the later, postvitrification stages of cure is much more difficult to examine. Georjon and Galy,[18] for instance, have shown through positron annihilation studies that a substantial amount of free volume develops during the final stages of cyanate ester cure, with significant impacts on properties such as moisture uptake. While infrared and solid-state NMR spectroscopy can provide useful data on the chemical structures present even after complete conversion, and X-ray data can provide valuable information on local ordering and orientation, much desirable information on physical aspects of the network structure is extremely difficult to obtain directly. As a result, indirect methods such as the study of volumetric changes or examination of primary and secondary thermomechanical transitions[19] must be used to gather evidence of

Received: November 15, 2011
Revised: December 14, 2011
Published: December 23, 2011

these aspects. There exists, therefore, a critical need for innovative approaches to further expand the available repertoire of indirect experimental methods that can be used to probe the molecular level structures and interactions in thermosetting polymer networks. Such innovative techniques will reveal important clues to help understand the nature of the networks and facilitate considerable progress in developing structure−property relationships.

In this paper, we illustrate the use of three-component cocured network studies to probe the molecular level interactions in well-defined thermosetting polymer networks. Most physical properties of interest in these cocured networks are expected to follow simple linear rules of mixing because phase separation is absent and the components are highly similar. Using three-component systems, not only can the presence of nonlinear behavior be detected, but nonlinearities that apply equally to all the components are easily distinguished from those that appear only for certain combinations of components. These component-specific nonlinearities serve as an indication of important interactions. Thus, by mapping the compositional patterns of property variations, and in particular patterns of systematic deviation from expected values, unexpected interactions among the components of cocured networks can be discovered.

Furthermore, by utilizing the synthetic flexibility afforded by cyanate esters to formulate and compare conetworks with well-defined and systematic differences in segment structure, important information may be inferred on the roles played by various structural parameters (such as the rigidity of network segments or the distance between cross-links) in controlling physical properties of interest. Whereas previous two-component cocured cyanate ester network studies[20−24] have provided some tantalizing hints that synergistic and/or unexpected interactions among components may frequently take place, the carefully crafted three-component studies presented herein reveal many synergistic interactions (such as unexpectedly low moisture uptake) that offer significant opportunities for exploitation. Consequently, the techniques and results described herein provide a vivid illustration of how well-designed studies of molecular level interactions in cocured networks enable substantial advances in the development of structure−property relationships and improved performance not only for cyanate esters but for thermosetting polymers in general.

RESULTS AND DISCUSSION

Because of the large number of variables (31 in all) and compositions studied, only the most significant highlights of the results are discussed in detail in this section. A comprehensive description of all of the variables examined, and all of the results for all of the properties of interest, including those not discussed in detail herein such as "wet" T_g values and char yields, are provided in the Supporting Information.

The three monomers utilized for the study of conetworks constituted a set of highly similar dicyanate monomers, two of which (Primaset BADCy and its asymmetric and more flexible counterpart, Primaset LECy) are commonly used commercial products. The third monomer, a silicon-containing analogue of BADCy known as SiMCy, retains the symmetry of BADCy while affording more flexible network segments as in LECy but with a larger segmental volume. The set thus allows a systematic study of the interactions among rigid/flexible, symmetric/asymmetric, and larger/smaller network segments.

It should be noted that, due to the highly similar nature of the monomers, phase separation (at scales of 0.1 μm and above) was avoided both during the mixing of monomers (as evidenced by their transparent and homogeneous appearance when melted), as well as in the cocured networks (which always showed single glass transitions over a range no broader or less well-defined for multiple component networks than for single component networks), and for which sample castings always appeared transparent and homogeneous. Moreover, examination of the cured networks by infrared spectroscopy showed no indications of the formation of significant amounts of side products or other unexpected chemical structures that might give rise to nonlinear rules of mixing in multicomponent networks. The reliable formation of networks with well-defined chemical structures by curing in an inert atmosphere at relatively low temperatures is in accord with the expected chemical behavior of cyanate ester networks.

To study the interactions among components, robust regressions were performed on all sample data, with particular effort given to identifying meaningful deviations from linearity caused by compositional variations specific to two components, which is the signature characteristic of significant molecular level interactions. In addition, the data were also examined for correlations among properties as well as the effect of segment structure on the estimated physical property values for pure components. Table 1 summarizes the key results obtained from the robust regression analyses in terms of the predicted values of the properties for BADCy, LECy, and SiMCy along with the effect of conversion. Note that the conversion for all samples was in the range 0.95−1.00, and in cases where it was found to be a significant factor, variations due to differences in conversion among samples were specifically included in the regression models.

Moisture Uptake. Figure 1 shows both the individually measured moisture uptake values (not adjusted for degree of conversion, as dots) and a grid depicting the smoothed values of moisture uptake (at full conversion). As explained in the Experimental Section, the smoothed values were utilized to identify any systematic deviations from linearity as a function of composition. Robust regression of the data showed that the moisture uptake was predicted with a standard error of just 0.12% (absolute) when the degree of conversion was taken into account. As reported previously,[25] SiMCy exhibits a significantly lower moisture uptake compared to BADCy and LECy. In addition, as first reported for BADCy by Georjon and Galy,[18] the degree of cure had a strong influence on moisture uptake (statistically significant at 94% confidence). Interestingly, Georjon and Galy showed that the free volume in BADCy increased with increasing conversion for the range of conversions investigated (85−100%). The report is consistent with earlier data[26−28] reporting an increase in molar volume at room temperature at conversions above the gel point for many cyanate esters as well as with our own density measurements. The increase in free volume was naturally linked to the increased water uptake. Our results, however, show a clear decrease in water uptake with increasing SiMCy content, even though, as discussed in the section on density, the overall free volume in the system increased with increasing amounts of SiMCy.

The results of the conetwork study, therefore, indicate that moisture uptake in cyanate esters is not simply a matter of free volume, but rather appears to depend on the availability of a specific type of free volume. The free volume that is presumably "frozen in" during the later stages of cure was noted by Georjon and Galy to possess a larger characteristic size, according to

Table 1. Key Properties of Single Component Cyanate Ester Networks Obtained from Robust Regressions of Data for Conetworks

		value (from robust regression, at full cure)			
parameter (data source)	units	BADCy	LECy	SiMCy	effect of cure[c]
T_g (uncured, DSC)	°C	−38 ± 2	−47 ± 2	−46 ± 2	n/a
T_g (fully cured, TMA)[a]	°C	309 ± 7	294 ± 8	266 ± 7	n/a
T_g (fully cured, DSC)[b]	°C	300 ± 5	290 ± 5	267 ± 5	n/a
density (as-cured)[a]	g/cm^3	1.195 ± 0.003	1.220 ± 0.003	1.175 ± 0.003	−0.14 ± 0.06
CTE (as-cured, TMA)[a]	ppm/°C	59 ± 2	64 ± 2	74 ± 2	−30 ± 14
CTE (fully cured, TMA)[b]	ppm/°C	56 ± 3	62 ± 3	69 ± 3	n/a
water uptake (as-cured)[a]	wt %	2.34 ± 0.12	2.36 ± 0.13	1.76 ± 0.11	+4.9 ± 2.3
T-5% loss (TGA, N_2)	°C	418 ± 2	419 ± 2	418 ± 2	n/a
T-5% loss (TGA, air)	°C	417 ± 2	417 ± 2	415 ± 2	n/a
char yield (TGA, N_2)	wt %	49 ± 4	57 ± 3	48 ± 3	n/a
char yield (TGA, air)	wt %	20 ± 6	41 ± 6	51 ± 6	n/a

[a]"As-cured" in the description of the data source means that the reported values were obtained from a regression of conetwork data on samples cured at 210 °C for 24 h, which resulted in conversions of 95−100%, in which the extent of cure was included as a regression variable (the reported values thus represent an extrapolation to full cure). [b]"Fully cured" in the description of the data source means the values were obtained from a regression of conetwork data on samples that had been previously heated to 350 °C to ensure full cure. [c]"Effect of cure" denotes the expected change in value for a hypothetical 100% increase in conversion (note that the data is only valid for conversions of 95−100%, however).

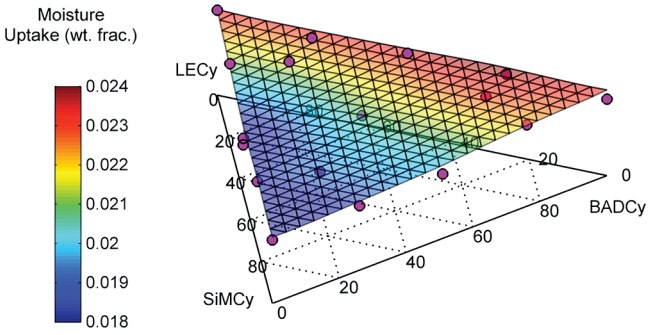

Figure 1. Moisture uptake as a function of composition. The dark circles indicate individual measurements (at varying conversions of 0.95−1), while the grid indicates the calculated values of the smoothed data (extrapolated to full conversion), thereby highlighting the effect of composition.

positron annihilation lifetime data, than the free volume initially present in the system. It is reasonable to expect that such free volume would form at characteristic locations near the triazine rings in the developing cyanate ester network, where, during vitreous cure (the glass transition temperature of the polycyanurate networks is significantly higher than the cure temperature during the late stages of cure), van der Waals volume is reduced by cross-linking, creating free volume that is unable to relax or diffuse away to any significant extent. On the other hand, it is reasonable to expect that the extra free volume in SiMCy as compared to BADCy or LECy would be associated with the longer and more flexible Si−C bonds that discourage tight packing of chain segments and, hence, that such free volume is not likely to be concentrated near cyanurate rings. This concept is illustrated graphically in Figure 2, which depicts a model of a dicyanate ester network segment, with the likely locations of pockets of unoccupied volume pointed out.

Thus, it appears that a specific type of free volume, located near cyanurate rings and formed presumably because vitrification of the network prevents shrinkage, serves as a preferred site for moisture uptake in cyanate esters. If the aforementioned hypothesis is correct, then there should be a positive correlation between the number density of cyanurate rings and moisture

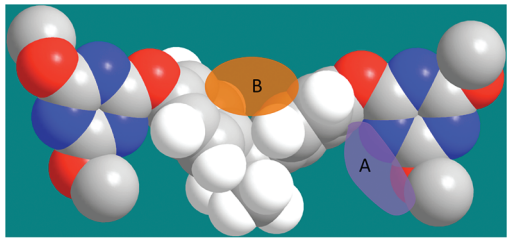

Figure 2. Space-filling model of a cured BADCy network segment (nitrogen = blue, oxygen = red) showing two full cyanurate rings. Regions where unoccupied volume might be expected to form are labeled "A" and "B". The affinity of water molecules for regions "A" and "B" is expected to be quite different.

uptake in cyanate esters. In Figure 3, the moisture uptake data (plotted as the number density of water molecules in the

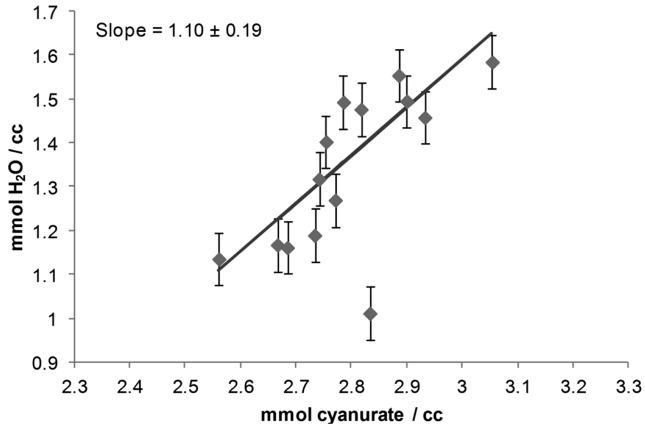

Figure 3. Water uptake as a function of cyanurate ring concentration in cyanate ester conetworks. Note that the ring density specifically takes into account the extent of cure, and the fitted regression line excludes the single outlying data point (50 wt % LECy, 50 wt % SiMCy, outlying value successfully replicated in two additional tests).

saturated system) is plotted as a function of the number density of cyanurate rings, based on the molar volume of the system and the extent of cure determined via the diBenedetto

dx.doi.org/10.1021/ma202513h | Macromolecules 2012, 45, 211−220

equation.[29] A strong positive correlation was indeed observed, as is evident by comparison with a similar plot (Figure 4) showing moisture uptake as a function of total molar free volume. There was, however, a notable outlier: a SiMCy/LECy conetwork with anomalously low moisture uptake behavior that was reproduced in two subsequent, independent tests. As discussed later, such anomalous behavior was a characteristic of the SiMCy/LECy conetworks in particular, but this specific effect was perhaps the most technologically significant among all those that were discovered.

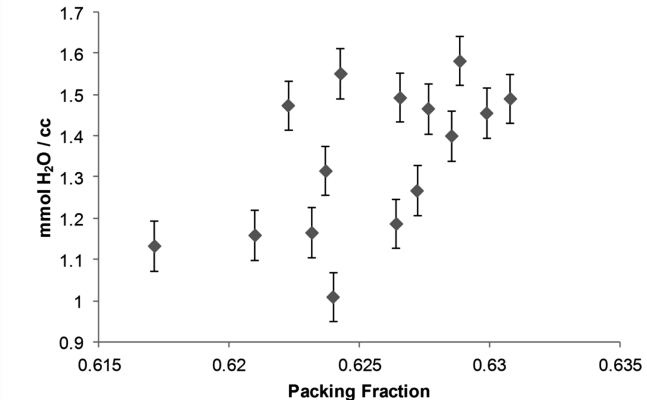

Figure 4. Water uptake as a function of packing fraction at 20 °C in cyanate ester conetworks.

It should be noted that the hypothesis discussed above appears to be at least approximately true for a number of different cyanate esters. Such external validation is important because, considering only the cocured network data, a number of properties may correlate with moisture uptake due to confounding with compositional variation. In systems with a modestly lower cyanurate ring density, such as the trifluoromethyl analogue of BADCy and ortho-methylated BADCy, moderately lower moisture uptake (1.8 and 1.4 wt %, respectively)[1,24] has been observed, while systems with considerably lower cyanurate ring density, such as the dicyclopentadiene-containing dicyanates (1.2 wt %)[1] and the bisphenol M analogue of BADCy (0.6 wt %),[1] have shown considerably lower water uptake. On the other hand, systems with a higher cyanurate ring density, such as the experimental monomers REX371 (3.8 wt %)[1] and ESR255 (2.8 wt %),[24] have exhibited higher water uptake values. (Quantitative comparisons are difficult due to a lack of data on the extent of cure and as-cured density of these previously reported systems.)

Both the three-component conetwork data reported herein and the aforementioned data on similar compounds all indicate a higher sensitivity of moisture uptake to cyanurate ring density than would be expected based on a simple model wherein the density of favorable sites for moisture uptake is simply proportional to the density of cyanurate rings. For instance, a 10% decrease in cyanurate ring density in SiMCy (compared to BADCy) leads to a 25% decrease in moisture uptake, while a 30% decrease in cyanurate ring density in the Bisphenol M analogue leads to a 75% decrease in moisture uptake. The high sensitivity to cyanurate ring density may be due to the need for multiple cyanurate rings in close proximity to create favorable sites for moisture uptake, either because interacting or closely spaced cyanurate groups are needed to create a sufficiently hydrophilic environment, or perhaps because flexible linkages between cyanurate rings lessen the amount of free volume created during the postgel stage of cure. Additional studies of free volume formation and moisture uptake as a function of conversion may provide clarification.

Finally, the idea that free volume formed during vitreous cure of thermosetting polymers may be an especially important determinant of moisture uptake has important implications for the design of thermosetting polymers with both a high glass transition temperature (which is generally aided by high densities of both hydrophilic groups that strongly interact with one another as well as high cross-link densities) and low moisture uptake. In particular, a thermosetting polymer designed to include hydrophilic groups that are shielded and/or located away from cross-linking sites (as in polybenzoxazines) may be well-suited to both high glass transition temperatures and low moisture uptake, as has been observed.[30,31] On the other hand, hydrophobic groups, if placed in rigid groups in positions away from hydrophilic cross-linking sites, may decrease moisture uptake less than expected.

Density and Packing. Figure 5 shows the individually measured density values as well as the smoothed density data at full conversion (grid) as a function of composition. From Table 1 and Figure 5 it can be seen that SiMCy forms the network with the lowest density of all three studied, with LECy exhibiting the highest density. The reported values for the pure components are similar to previously reported values[1,25] when the effects of catalyst and the extent of cure are considered. Regression analysis indicated a statistically significant effect (p = 0.03) of the extent of cure on density, with a decrease in density of about 0.014 g/cm^3 for every 10% increase in the extent of cure, similar to the levels observed by Georjon and Galy for BADCy (at conversions of 0.85−1.00).[18] Thus, the data indicates that even for more flexible network segments, the formation of cyanurate rings at high conversions leads to the creation of additional free volume. The free volume associated with cyanurate ring formation was calculated on a molar basis for the different compositions studied and found to be 34−40 cm^3/mol, with an uncertainty of ~15 cm^3/mol. Based on the slope of the line in Figure 3, roughly one additional mole of water uptake occurs for each additional mole of cyanurate rings formed at high conversion in these systems. Thus, about half of the free volume created by cyanurate ring formation at late stages of cure appeared to be occupied by water under saturated conditions. These data clearly indicate that free volume

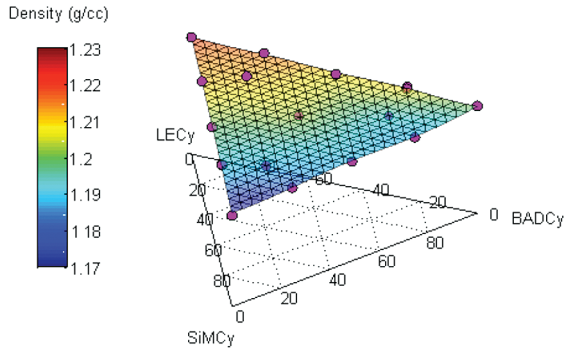

Figure 5. Density at 20 °C as a function of composition. The dark circles indicate individual measurements, while the grid indicates the calculated values of the smoothed data at full cure, thereby highlighting the effect of composition.

dx.doi.org/10.1021/ma202513h | Macromolecules 2012, 45, 211−220

associated with cyanurate ring formation is likely to be a far greater influence on system properties than the comparatively small differences (2−3 cm^3/mol) due to packing of the network segments.

The three monomers studied each exhibited subtle differences in packing fraction. Using the van der Waals volume calculated from the Bicerano correlation,[32] the packing fractions at 20 °C were determined for all blend compositions. Extrapolated values at 0 K and the cure temperature (210 °C) were also calculated, and the results are tabulated in the Supporting Information. LECy exhibited the highest packing fraction in all cases, with the difference being largest (about 0.007) at 0 K. SiMCy, on the other hand, showed the lowest packing fraction at room temperature and above but exhibited an almost identical packing fraction to BADCy when extrapolated to 0 K. Thus, intrinsically better packing was seen in LECy, while the looser packing seen in SiMCy was associated with a greater coefficient of thermal expansion, which is perhaps traceable to the generally lower dissociation energy of silicon−carbon bonds[33] (thereby rendering the bond length more sensitive to thermal fluctuations).

Additional Physical Properties. Figures 6 displays the individual and smoothed linear coefficient of thermal expansion

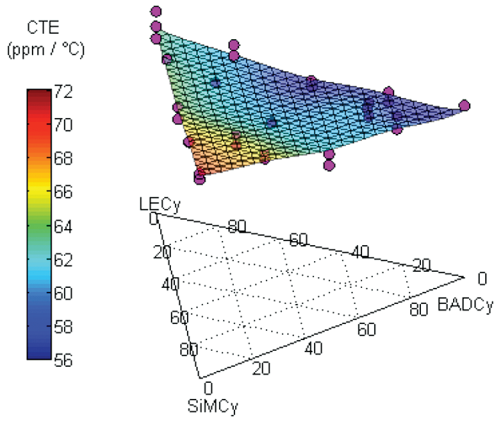

Figure 6. Linear coefficient of thermal expansion (measured on fully cured samples) as a function of composition (note there are two measurements per sample). The dark circles indicate individual measurements, while the grid indicates the calculated values of the smoothed data, thereby highlighting the effect of composition.

data for the fully cured networks obtained by TMA after multiple heating cycles, while Figure 7 illustrates the deviation of the smoothed data from linearity. The coefficient of thermal expansion for SiMCy is quite a bit larger than that of LECy, which is slightly greater than that of BADCy. Measurements of the "as-cured" samples revealed a statistically significant effect due to the extent of cure, with about a 3 ppm/°C decrease for every 10% increase in conversion. Although there did seem to be a reasonable negative correlation between the coefficients of thermal expansion and the glass transition temperatures of the fully cured networks (Figure 8), the differences in thermal expansion were much greater than expected from relationships (such as the one proposed by Seitz[34] for polymers) based on T_g values. The systematic deviations shown in Figure 7 clearly point to a lower than predicted (based on a linear rule of mixtures) coefficient of thermal expansion when network segments of more than one type are cocured. This result is a good example of a nonlinearity that does not indicate component specific interactions and is expected based on a very simple model

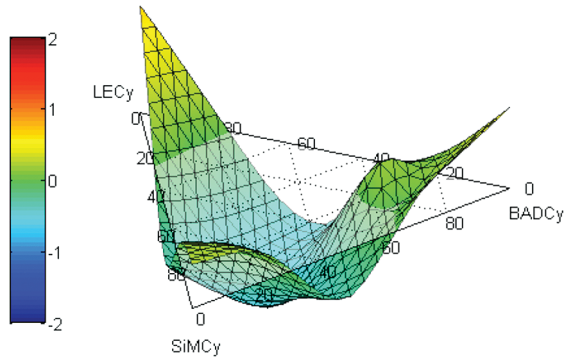

Figure 7. Smoothed deviation from predicted values based on a robust linear regression for the linear coefficient of thermal expansion (in units of Studentized residuals, measured on fully cured samples) as a function of composition. The data treatment is designed to reveal the nonlinear effects of composition and shows systematically low values for all multicomponent samples.

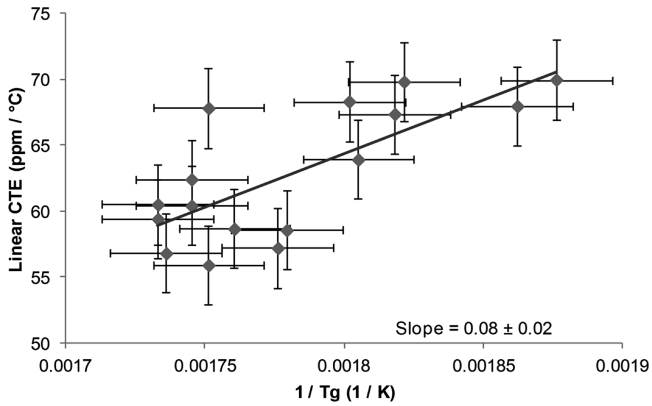

Figure 8. Linear coefficient of thermal expansion of fully cured conetworks as a function of the inverse of the fully cured glass transition temperature.

for thermal expansion that assumes equal displacement of interpenetrating network segments (see Supporting Information), provided there is a difference in the bulk modulus of the component networks segments, and that increased bulk modulus correlates with decreased thermal expansion (as is typical). The formula for a ternary conetwork is

$$\alpha_{eff} = \frac{\alpha_1\varphi_1K_1 + \alpha_2\varphi_2K_2 + \alpha_3\varphi_3K_3}{\varphi_1K_1 + \varphi_2K_2 + \varphi_3K_3} \quad (1)$$

in which α_{eff} is the effective linear coefficient of thermal expansion, and α_i, ϕ_i, and K_i refer to the linear coefficient of thermal expansion, volume fraction, and bulk elastic modulus of the ith component, respectively. Using the data for fully cured samples, it was possible to extract a rough estimate of the bulk modulus ratios involved, with the result that the modulus of LECy segments was 10−40% that of BADCy segments and the modulus of SiMCy segments was 20−40% that of BADCy segments. These ratios, while qualitatively matching expectations based on the molecular structure of the segments, seem quantitatively too small. More sophisticated models that take into account both shear and bulk moduli, which have generated useful predictions for cyanate ester nanocomposites,[35] may thus be needed.

A similar nonspecific interaction among components can be seen in thermochemical stability properties, as shown in

dx.doi.org/10.1021/ma202513h | Macromolecules 2012, 45, 211−220

Figures 9 and 10. In Figure 9, the maximum decomposition rate under nitrogen is plotted (rates under air were quite similar, see

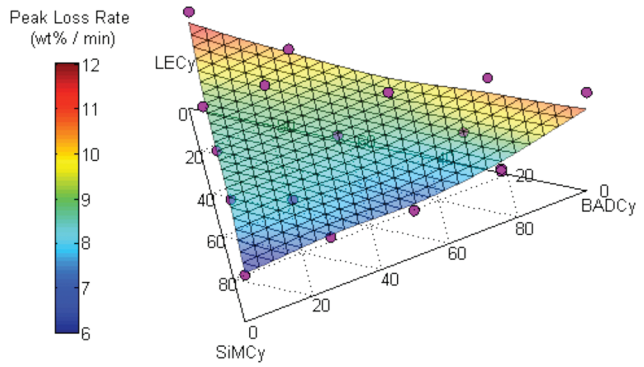

Figure 9. Maximum decomposition rate (under N_2) as a function of composition. The dark circles indicate individual measurements, while the grid indicates the calculated values of the smoothed data, thereby highlighting the effect of composition.

Supporting Information) as individual and smoothed data. Figure 10 illustrates the deviation from a weight fraction-based

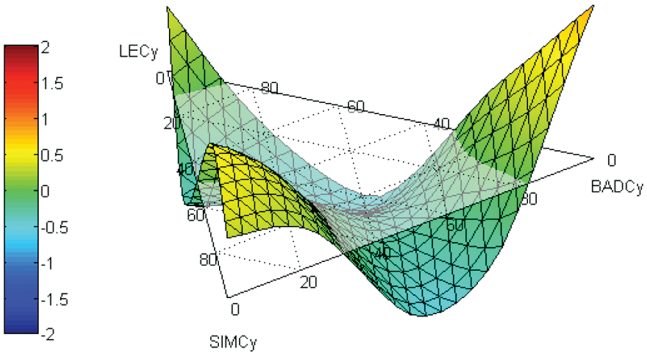

Figure 10. Smoothed deviation from predicted values based on a robust linear regression for the maximum decomposition rate under N_2 (in units of Studentized residuals) as a function of composition. The data treatment is designed to reveal the nonlinear effects of composition and shows systematically low values for multicomponent samples.

linear rule of mixtures. The multicomponent networks all show a fairly marked negative deviation in maximum loss rate, presumably because the chemically more heterogeneous nature of the samples causes the thermal decomposition to unfold at slightly different times in different segments, leading to a broadening of the mass loss rate curve. (A similar effect is seen in the char yield data as well.) This effect is in addition to the differences among the single-component networks, which can be seen in the individual TGA curves (Figure 11). It should be noted that, as previously observed,[25] SiMCy provided greater char yields than BADCy or LECy in air; however, it was also observed (see Supporting Information) that the char yield was greatest in conetworks containing around 25 wt % SiMCy segments and 75 wt % LECy segments.

In addition to analysis of individual variables, a meta-analysis of all of the variables and deviations from linearity was undertaken (see Supporting Information, Tables S2 and S3). The most important result was that in the majority of cases in which

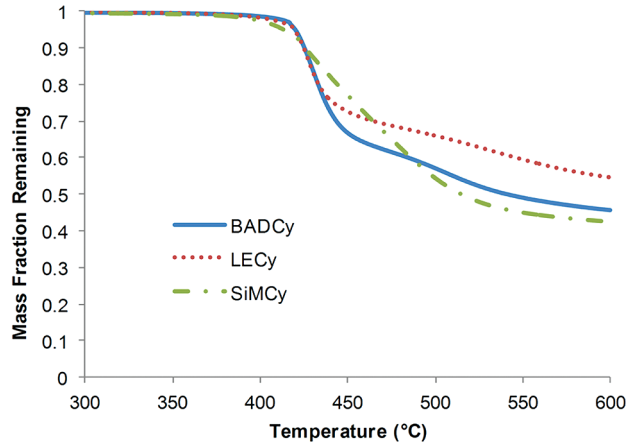

Figure 11. TGA curves of BADCy, LECy, and SiMCy single-component networks under nitrogen.

a significant deviation from linearity in the smoothed data was found based on the interaction of two components, the two components were SiMCy and LECy. Specific deviations for conetworks containing significant amounts of SiMCy and LECy included unusually low moisture uptake, high char yields in nitrogen and air, high decomposition onset temperature in air, low glass transition temperature at full cure, and increased packing fraction at 0 K. An example of data indicating such a component-specific interaction is shown in Figure 12, in which

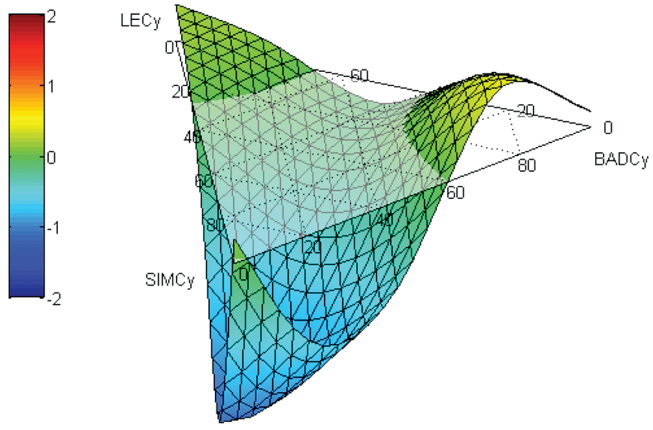

Figure 12. Smoothed deviation from the prediction of the Gordon–Taylor equation for the fully cured DSC glass transition temperature (in units of Studentized residuals) as a function of composition. The data treatment is designed to reveal the effects of interaction among components and shows systematically low values for SiMCy/LECy conetworks.

the deviation from the Gordon–Taylor equation for the fully cured glass transition temperature of the network, found by DSC, is plotted. The same DSC scan detected no anomalies in the cure kinetics, and a separate TMA scan exhibited a similar negative deviation (though less clearly distinguished from random error) in the value of the fully cured T_g.

Thus, the interactions between SiMCy and LECy segments appear to be significantly greater than those between BADCy and LECy segments or BADCy and SiMCy segments. Among the three components, segments made from LECy and SiMCy differed the most in terms of their molar volume or, alternatively,

dx.doi.org/10.1021/ma202513h | *Macromolecules* 2012, 45, 211–220

their average distance between network junctions. The fact that SiMCy/LECy networks were more prone to deviations from simple rules of mixtures in their physical properties therefore suggests that differences in segment size may be more readily exploited for the purpose of creating useful synergistic interactions in thermosetting polymer networks than, for instance, differences in symmetry (most prominent in BADCy/LECy and SiMCy/LECy networks) or in flexibility (most prominent in BADCy/SiMCy networks). Though such a hypothesis is speculative, it represents a good starting point for future investigations of synergistic interactions in highly cross-linked polymer networks. Skillful prediction of such synergism may enable significant technological advances in fields such as aerospace and microelectronics, for which the physical properties of such networks are of great importance.

CONCLUSIONS

Studies of three-component cocured networks formed from similar dicyanate ester monomers have revealed a number of interesting and unexpected deviations from linear rules of mixtures for physical properties, thus confirming the importance of molecular level interactions among network segments. Among the most interesting results was an unexpected 25% reduction in moisture uptake for conetworks of equal amounts of LECy and SiMCy segments. For all other conetworks, a clear relationship between moisture uptake and the number density of cyanurate rings was observed. This relationship appears to hold generally for many types of cyanate esters. When combined with previously reported studies of density changes during cure, it is apparent that the net increase in free volume at room temperature associated with the final stages of cure provides favorable sites for moisture uptake, whereas increased free volume due to less efficient packing of network segments has, comparatively, very little influence on moisture uptake. In addition, a meta-analysis of all of the reproducible deviations from linear rules of mixtures for the physical properties of the cocured networks was performed. The analysis showed that the majority of the deviations from linearity that appeared to be driven by interactions among components occurred in samples containing mixtures of SiMCy and LECy segments, suggesting that interactions between segments that differ substantially in molar volume may be useful for generating synergies in the physical properties of highly cross-linked polymer networks.

EXPERIMENTAL SECTION

Materials. 2,2′-Bis(4-cyanatophenyl)propane (the dicyanate ester of Bisphenol A, or BADCy) and 1,1′-bis(4-cyanatophenyl)ethane (the dicyanate ester of Bisphenol E, or LECy) were purchased from Lonza and used as received. Nonylphenol (technical grade) was purchased from Aldrich, and copper(II) acetylacetonate was purchased from ROC/RIC; both were used as received. Bis(4-cyanatophenyl)-dimethylsilane (SiMCy) was synthesized based on the procedure first reported by Wright[36] and later elaborated by Guenthner et al.[25] A typical synthesis was as follows.

General Synthetic Methods. All manipulations of compounds and solvents were carried out using standard Schlenk line techniques. Tetrahydrofuran (THF), ether, hexane, and toluene were dried by passage through columns of activated alumina under a nitrogen atmosphere and then degassed prior to use. Dichlorodimethylsilane and triethylamine were purchased from Aldrich Chemical Co. and were distilled before use. 4-(Benzyloxy)bromobenzene was obtained from Aldrich and recrystallized from acetone before use. Cyanogen bromide, *n*-butyllithium, and 10% palladium on carbon (wet, Degussa type) were obtained from Aldrich Chemical Co. and used as received. ^{1}H, ^{13}C, and ^{29}Si NMR measurements were performed using a Bruker AC 300 or Bruker 400 MHz instrument. ^{1}H and ^{13}C NMR chemical shifts are reported relative to the deuterated solvent peak (^{1}H, ^{13}C: acetone-d_6, δ 2.05 ppm, δ 29.9 ppm). ^{29}Si NMR chemical shifts are reported relative to external tetramethylsilane at 0 ppm. Hydrogenation was done using a Parr Hydrogenator equipped with pressure safe vessels and Viton seals. Samples were run on a TA Instruments Q2000 differential scanning calorimeter (DSC) under nitrogen flowing at 50 mL/min, with 5 min for equilibration at the maximum and minimum temperatures, to establish the melting point from a consistent thermal condition. Elemental analyses were performed on Perkin-Elmer EA2400 Series II combustion analyzer. Syntheses are modified from the reported literature.

Preparation of Bis(4-benzyloxyphenyl)dimethylsilane (1). A chilled (−78 °C) THF (400 mL) solution of 4-(benzyloxy)bromobenzene (20.00 g, 76.0 mmol) was treated with 2.2 M *n*-BuLi (34.6 mL, 76 mmol) and allowed to react with stirring for 1 h at −78 °C. This mixture, now heterogeneous, was treated with slow addition of dichlorodimethylsilane (4.90 mL, 40 mmol, diluted with THF) and the cooling bath removed. The mixture was allowed to react with stirring for an additional 2 h and then diluted with ether (600 mL) and stirred for 10−15 min. The organic layer was washed with water (2 × 200 mL) and brine (200 mL) and then dried over $MgSO_4$, stirring for 1/2 h. The mixture was filtered, and the solvents were removed under reduced pressure on a rotary evaporator. The crude product was redissolved in a minimum amount of chloroform and precipitated into methanol (400 mL). This was stirred overnight, filtered, and dried under nitrogen to afford **1** as a white solid (14.1 g, 87% yield). ^{1}H NMR (acetone-d_6) δ: 7.48 −7.01 (m, 18), 5.12 (s, 4 H), 0.49 (s, 6 H). ^{13}C NMR (acetone-d_6) δ: 160.75 (C1), 138.39 (C6), 136.43 (C3), 130.40 (C4), 129.34 (C7), 128.67 (C9), 128.67 (C8), 115.36 (C2), 70.21 (C5), −1.88 ($SiCH_3$). ^{29}Si NMR (acetone-d_6) δ: −9.26. Anal. Calcd for $C_{28}H_{28}O_2Si$: C, 79.20; H, 6.65; N, 0.00. Found: C, 78.77; H, 6.75; N, 0.01.

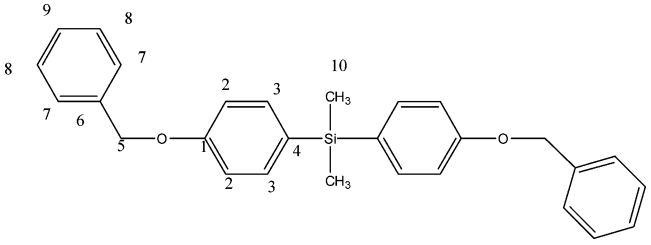

Preparation of Bis(4-hydroxyphenyl)dimethylsilane (2). A THF (200 mL) solution containing **1** (10.00 g, 23.55 mmol) and 10 wt % palladium on carbon (600 mg) was placed in a 1000 mL pressure safe vessel equipped with Viton seals and connected to a hydrogenator. This was placed under an atmosphere of hydrogen (35 psi) and allowed to react with stirring for 24 h. The catalyst was removed by filtration through Celite, and the solvent was removed under reduced pressure to afford 4.80 g (83% yield) of **2** as an off-white solid. For purification, compound **2** was washed twice with dry hexane, dried, then stirred overnight in dry toluene, and filtered. The white product was then dried under dynamic vacuum. ^{1}H NMR (acetone-d_6) δ: 8.40 (s, 2H), 7.38−6.84 (dd, 8 H), 0.46 (s, 6 H). ^{13}C NMR (acetone-d_6) δ: 159.70 (C1), 136.49 (C3), 128.89 (C4), 115.92 (C2), −1.65 ($SiCH_3$). ^{29}Si NMR (acetone-d_6) δ: −9.59. Anal. Calcd for $C_{14}H_{16}O_2Si$: C, 68.81; H, 6.60; N, 0.00. Found: C, 67.67;H, 6.75; N, 0.01.

Preparation of Bis(4-cyanatophenyl)dimethylsilane (3). A chilled (−20 °C) ether (50 mL) solution containing bis(4-hydroxyphenyl)dimethylsilane, **2** (3.75 g, 15.4 mmol), and cyanogen bromide (4.05 g, 38.2 mmol) was treated with triethylamine (3.90 g, 38.5 mmol) in a dropwise manner. This mixture was allowed to react for 2 h with stirring at −20 °C. The mixture was filtered to remove the hydrobromide salt, and the organic layer was washed with (2 × 100 mL) DI water, followed by a brine wash, and then dried over $MgSO_4$. The solvents were removed under reduced pressure, and crude product

dx.doi.org/10.1021/ma202513h | *Macromolecules* 2012, 45, 211−220

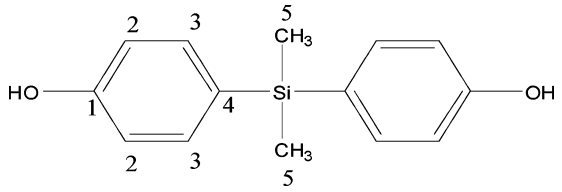

(3.79 g, 84% yield) was recrystallized from ether to afford 2.7 g (60% yield) of **3** as white crystalline solid (mp 60.17 °C). ^{1}H NMR (acetone-d_6) δ: 7.76- 7.40 (dd, 8H), 0.6 (s, 6H). ^{13}C NMR (acetone-d_6) δ: 158.02(C1), 137.87 (C4), 137.59 (C3), 115.73 (C2), 109.52(OCN), −2.47 ($SiCH_3$).). ^{29}Si NMR (acetone-d_6) δ: −7.08. Anal. Calcd for $C_{16}H_{14}N_2O_2Si$: C, 65.28; H, 4.79; N, 9.52. Found: C, 65.17; H, 4.83; N, 9.45.

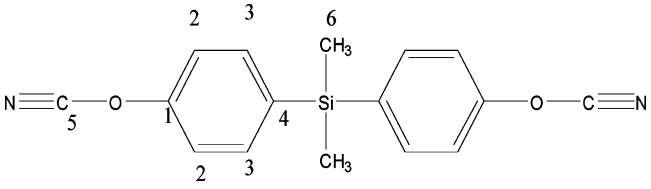

Design of Experiments. Compositions for analysis were chosen based on an experimental design that roughly followed a Simplex lattice for 16 samples with 3 components. The design featured equally spaced binary conetworks with a mass fraction difference of 0.25 (accounting for 12 points), along with four ternary conetworks, three in which each of the three components comprised a substantial majority and one at the compositional centroid (equal mass of all components). This design afforded slightly more data for the ternary conetworks than an equally spaced design would have provided, allowing for distinctions to be drawn between systems for which one component dominates versus the case where no component dominates. The difference of 0.25 in mass fraction for binary conetworks was taken as sufficiently small to reliably capture any systematic trends, while minimizing the number of data points required. At least one additional composition was chosen as a replicate for each type of experiment conducted. In addition, all significant outliers were subjected to replication in order to better understand their anomalous nature.

Sample Fabrication. Batches of catalyst comprised of 30 parts by weight nonylphenol to 1 part by weight copper(II) acetylacetonate were prepared by mixing the ingredients in a vial and heating to 60 °C, while stirring vigorously until complete dissolution took place (typically 1−2 h). These batches were retained for up to 30 days. Because of the low-humidity ambient environment, the only precautions taken when storing the Primaset BADCy and LECy resins were the use of tightly sealed containers and avoidance of exposure to high-humidity environments. However, for the novel material SiMCy, for which the stability data are unknown, the sample was stored at or below 4 °C as an added precaution.

Uncured samples for differential scanning calorimetry (DSC) analysis were prepared by mixing prescribed ratios of the three monomers with 2.0 parts per hundred by weight of catalyst at 95 °C. The mixture was then partially degassed at 95 °C for 30 min under reduced pressure (300 mmHg), and ∼5 mg was transferred to a DSC pan. To prepare cured samples, silicone molds made from R2364A silicone from Silpak Inc. (mixed at 10:1 by weight with R2364B platinum-based curing agent and cured overnight at room temperature, followed by postcure at 150 °C for 1 h) were prepared by degassing for 60 min at 95 °C and 300 mmHg. The uncured cyanate ester mixture was mixed and degassed using the method for preparing DSC samples described above and then poured into the prepared mold (no release agent was used). The open mold and sample were then placed under flowing nitrogen at 95 °C, ramped 5 °C/min to 150 °C and held for 1 h, and then ramped 5 °C/min to 210 °C and held for 24 h to produce void-free disks measuring approximately 11.5−13.5 mm in diameter by 1−3 mm thick and weighing 200−400 mg. Multiple disks were used for oscillatory thermomechanical analysis (TMA), density measurements, and hot water exposure tests. In addition, small chips weighing ∼5 mg were removed from the disks, crushed, and utilized for thermogravimetric analysis (TGA).

Characterization. DSC was performed on a TA Instruments Q2000 calorimeter under 50 mL/min of flowing nitrogen. Uncured samples for heat of cyclotrimerization and cured glass transition temperature analysis were heated to 350 °C, then cooled to 100 °C, and reheated to 350 °C, all at 10 °C/min. Uncured samples used for melting point determination were subjected to a program consisting of alternate heating and cooling steps at 5 °C/min between 0 and 100 °C. For uncured samples used to determine the glass transition temperature prior to onset of cure, alternate heating and cooling ramps at 5 °C/min between −70 and 0 °C were used. Finally, when used to determine extent of cure for partly cured samples (for diBenedetto equation validity checks), uncured samples were heated to 200 °C at 5 °C/min, then cooled to 0 °C, and reheated to 350 °C, at 10 °C/min.

TGA was conducted on a TA Instruments Q5000 thermogravimetric analyzer under both nitrogen and air at a flow rate of 25 mL/min by heating samples at 10 °C/min to 600 °C. Oscillatory TMA was conducted with a TA Instruments Q400 series analyzer under 50 mL/min of nitrogen flow. The disks were held in place via a 0.2 N initial compressive force with the standard 5 mm diameter flat cylindrical probe while the probe force was modulated at 0.05 Hz over an amplitude of 0.1 N (with a mean compressive force of 0.1 N), and the temperature was ramped twice (heating and cooling) between 100 and 200 °C (to determine thermal lag) followed by heating to 350 °C, cooling to 100 °C, and reheating to 350 °C, all at 10 °C/min. For samples previously exposed to hot water, the heating rate was increased to 20 °C/min, and the thermal lag determination was performed after, rather than before, the first heating to 350 °C, in order to minimize drying before determination of the glass transition temperature. Details of the oscillatory TMA technique and the determination of thermal lag have been published elsewhere.[37] The oscillatory TMA experiments provided both coefficient of thermal expansion data as well as glass transition temperatures based on changes in the oscillatory response of the sample.

Densities were determined by placing sample disks in solutions of $CaCl_2$ (as the dihydrate) and deionized water and varying the $CaCl_2$ concentration until neutral buoyancy was observed on bubble-free samples over a period of several minutes at 20 °C. The density of the neutrally buoyant solution was determined by placing 10.00 mL in a volumetric flask (calibrated with deionized water at 20 °C) and weighing and checked against the predicted density of the solution at ambient temperature based on the known concentration of $CaCl_2$. For hot water exposure testing, sample disks were placed in ∼300 mL of deionized water at 85 °C for 96 h, with sample weight measured before and after exposure. The exposed samples were then analyzed via oscillatory TMA to provide "wet" glass transition temperature data.

Analysis of Conetwork Data. From the numerous tests conducted, key response variables were analyzed as a function of several different compositional variables, with mass fraction being the default choice. Density and coefficient of thermal expansion data were analyzed as a function of volume fraction using the measured density values for single components to convert from mass fraction. Although slightly different estimates for the pure component densities were subsequently determined using the analysis methods described below, the effect on the previously calculated volume fractions was well within their experimental uncertainties; thus, an iterative process of correction was judged unnecessary. Moisture uptake and heat of reaction data were analyzed on a mole fraction basis, while glass transition temperature values were analyzed on the adjusted weight fraction basis provided by the Gordon−Taylor equation, with the measured glass transition temperatures (via DSC) of the pure components at full cure used as the basis for conversion. As with the volume fraction, these values differ slightly from subsequent estimates, but the effect was sufficiently small that iteration was judged unnecessary.

For samples heated to 210 °C for 24 h, the degree of conversion was determined using the diBenedetto equation, as follows. First, as part of the normal procedure for oscillatory TMA measurements, two

measurements of the glass transition temperature were performed on the first and second heating to 350 °C. Trials of different heating rates (reported in detail elsewhere)[38] confirmed that the heating rates used were sufficiently rapid to avoid significant in situ cure and to capture the "as-cured" glass transition temperature on the first heating. The glass transition temperature measured on the second heating (after exposure to 350 °C) was then taken as the "fully cured" glass transition temperature. The fully cured glass transition temperature obtained via oscillatory TMA was then compared to the fully cured glass transition temperature obtained via DSC after heating to 350 °C. The oscillatory TMA values were found to be 4 ± 9 °C higher than the DSC values on average.

Since the difference was not statistically significant (it was similar to the value of the random error in the TMA glass transition temperature measurements), the two measurements were considered similar enough that the glass transition temperatures of the uncured resin (obtainable only by DSC) were used without modification in the diBenedetto equation, along with the as-cured and fully cured glass transition temperature values obtained by TMA. Based on measurements of partly cured samples, a value of 0.37 was estimated and subsequently used for the parameter λ in the diBenedetto equation. The uncertainty in λ was relatively large, at about 0.1; however, changes in the value of λ did not affect the significance of conversion as a regression variable, only the value of the regression coefficient. Moreover, the standard errors of these regression coefficients were 25−50% of their respective values; hence, a relative error of 25% in λ produced only a marginal increase in the uncertainty associated with the regression coefficient.

Using the appropriate measure of composition and, where appropriate, the degree of conversion, as independent variables, the key experimental parameters (31 in total) were analyzed via robust regression, using a bisquare weighting function and an iterative weighting algorithm available in MATLAB and described in detail in the references listed in the program.[39−42] For iteration, the default weighting parameter of 4.655 was utilized. Given the large numbers of data points analyzed, the likelihood of encountering apparent outliers due to random variation was quite high. The use of the robust regression, which assigned lower weight to the outliers, but did not ignore them, was considered the most appropriate method for dealing with these outliers. In cases where the degree of cure was not significant at the 90% confidence level, it was excluded as an independent variable for further analysis.

For each regression, the (external) Studentized residuals were analyzed in multiple ways. In addition to visual examination of the normal distribution plot and a plot of residuals versus predicted value, the residuals were analyzed for any systematic deviations as a function of composition. Systematic deviations were identified by smoothing the Studentized residuals using a Gaussian blur (treating the two independent compositional variables as plotted on a triangular ternary diagram) with a characteristic radius of 0.25. The smoothed data was then plotted on a ternary diagram and inspected for discernible patterns. (All plots are provided in the Supporting Information and were generated using the MATLAB routine "ternplot.m" written by Carl Sandrock.) Utilizing a few sets of pseudorandom numbers generated by Microsoft Excel in place of the dependent variable, it was observed that the smoothing procedure resulted in smoothed Studentized residuals with a standard deviation of around 0.3, with absolute values exceeding 0.5 in only about 10% of cases. We thus used an absolute value of 0.5 as a rough cutoff value for assessing the significance of the smoothed residuals. In particular, when such a residual was encountered, the values of neighboring residuals were examined. Since very large single outliers can substantially influence their neighbors in the smoothed data, we also examined the unsmoothed Studentized residuals of neighboring points. These cases, along with a diagram identifying all "neighboring" compositional points, are discussed in detail in the Supporting Information.

The final result of these procedures was a set of identified deviations from linearity, for which a meta-analysis was undertaken. The deviations were classified according to three types: deviations in unsmoothed data (absolute value of $t > 2$), isolated deviations in smoothed data (absolute value of $t > 0.5$), and deviations in smooth data comprising a cluster of neighboring points. The deviations were then tabulated based on their numbers and subtotaled based on the corresponding network compositions (with tables provided in the Supporting Information). It was found that all of the clusters of significant deviation in the smoothed data contained at least 50% of the components SiMCy or LECy, with the majority of these clusters containing conetworks composed primarily of SiMCy and LECy. Similar, but less dramatic, trends were seen for the other categories of deviations, with deviations being most common in SiMCy-rich conetworks and in conetworks with at least 50% SiMCy or LECy.

■ ASSOCIATED CONTENT

Supporting Information

Sections S1.1−S1.31 (results and discussion on a variable-by-variable basis), Tables S1−S3, Figures S1.1−S1.31, S2.1−S2.31, and S3.1−S3.31 (normal probability, residual, and smoothed residual plots for all variables, respectively), and Section S2 (derivation of CTE model). This material is available free of charge via the Internet at http://pubs.acs.org.

■ AUTHOR INFORMATION

Corresponding Author

*E-mail: andrew.guenthner@edwards.af.mil.

■ ACKNOWLEDGMENTS

Support from the Air Force Office of Scientific Research, the Air Force Research Laboratory, and the National Research Council Research Associateship Program (JR) is gratefully acknowledged.

■ REFERENCES

(1) Hamerton, I., Ed. *Chemistry and Technology of Cyanate Ester Resins*; Chapman & Hall: London, 1994.
(2) Nair, C. P. R.; Mathew, D.; Ninan, K. N. Cyanate ester resins, recent developments. In *New Polymerization Techniques and Synthetic Methodologies*; Springer: Berlin, 2001; Vol. *155*, pp 1−99.
(3) Fang, T.; Shimp, D. A. Polycyanate Esters -- Science and Applications. *Prog. Polym. Sci.* **1995**, *20*, 61−118.
(4) Hamerton, I.; Hay, J. N. *High Perform. Polym.* **1998**, *10*, 163−174.
(5) McConnell, V. P. Resins for the Hot Zone Part II: BMIs, CEs, Benzoxazines & Phthalonitriles. *High Perform. Compos.* Sept **2009**, 43−49.
(6) Chao, F.; Bowler, N.; Tan, X. L.; Liang, G. Z.; Kessler, M. R. *Composites, Part A* **2009**, *40*, 1266−1271.
(7) Buckley, L. J.; Snow, A. W. *Abstr. Pap. Am. Chem. Soc.* **1996**, *211*, 37-POLY.
(8) Savary, F.; Bonito-Oliva, A.; Gallix, R.; Knaster, J.; Koizumi, N.; Mitchell, N.; Nakajima, H.; Okuno, K.; Sborchia, C. *IEEE Trans. Appl. Supercond.* **2010**, *20* (3), 381−384.
(9) Esslinger, J. R. Jr.; Fruchtnicht, O. C. *SAMPE J.* **2004**, *40*, 9−15.
(10) Das, S.; Castelli, L. M.; Falchetto, A. In Novel use of cyanate esters: VARTM, filament winding and pultrusion. *SAMPE Conference Proceddings*; Society for the Advancement of Material and Process Engineering: 2004; pp 1895−1904.
(11) He, S. B.; Liang, G. Z.; Yan, H. X.; Wang, J. H.; Yang, L. L. *Polym. Adv. Technol.* **2009**, *20*, 143−146.
(12) Abali, F.; Shivakumar, K.; Hamidi, N.; Sadler, R. *Carbon* **2003**, *41*, 893−901.
(13) Yameen, B.; Duran, H.; Best, A.; Jonas, U.; Steinhart, M.; Knoll, W. *Macromol. Chem. Phys.* **2008**, *209*, 1673−1685.
(14) Fyfe, C. A.; Niu, J.; Rettig, S. J.; Burlinson, N. E.; Reidsema, C. M.; Wang, D. W.; Poliks, M. *Macromolecules* **1992**, *25*, 6289−6301.
(15) Gupta, A. M.; Macosko, C. W. *Macromolecules* **1993**, *26*, 2455−2463.
(16) Wienhold, P. D.; Persons, D. F. *SAMPE J.* **2003**, *39* (6), 6−17.
(17) Kasehagen, L. J.; Macosko, C. W. *Polym. Int.* **1997**, *44*, 237−247.

(18) Georjon, O.; Galy, J. *Polymer* **1998**, *39*, 339−345.
(19) Georjon, O.; Galy, J. *J. Appl. Polym. Sci.* **1997**, *65*, 2471−2479.
(20) Koh, H. C. Y.; Dai, J.; Tan, E. *J. Appl. Polym. Sci.* **2006**, *102*, 4284−4290.
(21) Goertzen, W. K.; Kessler, M. R. *Composites, Part A* **2007**, *38*, 779−784.
(22) Hamerton, I.; Howlin, B. J.; Klewpatinond, P.; Takeda, S. *Macromolecules* **2009**, *42*, 7718−7735.
(23) Hwang, H. J.; Li, C. H.; Wang, C. S. *J. Appl. Polym. Sci.* **2005**, *96*, 2079−2089.
(24) Shimp, D. A.; Ising, S. J.; Christenson, J. R. Cyanate Esters -- A New Family of High Temperature Thermosetting Resins. In *High Temperature Polymers and Their Uses*; Society of Plastics Engineers: Cleveland, OH, 1989; pp 127−140.
(25) Guenthner, A. J.; Yandek, G. R.; Wright, M. E.; Petteys, B. J.; Quintana, R.; Connor, D.; Gilardi, R. D.; Marchant, D. *Macromolecules* **2006**, *39*, 6046−6053.
(26) Shimp, D. A.; Craig, W. M. New Liquid Dicyanate Monomer for Rapid Impregnation of Reinforcing Fibers. In *34th International SAMPE Symposium*; SAMPE International: 1989; pp 1336−1346.
(27) Snow, A. W.; Armistead, J. P. Naval Research Laboratory Memorandum Report 6848, Naval Research Laboratory, Washington, DC, 1991.
(28) Shimp, D. A.; Ising, S. J. In *35th International SAMPE Symposium*; SAMPE International: 1990; p 1045.
(29) Pascault, J. P.; Williams, R. J. J. *J. Polym. Sci., Part B: Polym. Phys.* **1990**, *28*, 85−95.
(30) Ishida, H.; Allen, D. J. *J. Polym. Sci., Part B: Polym. Phys.* **1996**, *34*, 1019−1030.
(31) Shieh, J.-Y.; Lin, C.-Y.; Huang, C.-L.; Wang, C.-S. *J. Appl. Polym. Sci.* **2006**, *101*, 342−347.
(32) Bicerano, J. *Prediction of Polymer Properties*, 3rd ed.; Marcel Dekker: New York, 2002; p 756.
(33) Lide, D. R. *CRC Handbook of Chemistry and Physics*, 82nd ed.; CRC Press: Boca Raton, FL, 2001.
(34) Seitz, J. T. *J. Appl. Polym. Sci.* **1993**, *49*, 1331−1351.
(35) Badrinarayanan, P.; Kessler, M. R. *Compos. Sci. Technol.* **2011**, *71*, 1385−1391.
(36) Wright, M. E. *Polym. Prepr.* **2004**, *45* (2), 294.
(37) Guenthner, A. J.; Yandek, G. R.; Mabry, J. M.; Lamison, K. R.; Vij, V.; Davis, M. C.; Cambrea, L. R. Insights into moisture uptake and processability from new cyanate ester monomer and blend studies. In *SAMPE International Technical Conference*; SAMPE International Business Office: Salt Lake City, UT, 2010; Vol. *55*, pp 42ISTC−119.
(38) Guenthner, A. J.; Lamison, K. R.; Yandek, G. R.; Masurat, K. C.; Reams, J. T.; Cambrea, L. R.; Mabry, J. M. *Polym. Prepr.* **2011**, *52* (2), xxx.
(39) duMouchel, W. H.; O'Brien, F. L. Integrating a Robust Option into a Multiple Regression Computing Environment. In *Computer Science and Statistics: Proceedings of the 21st Symposium on the Interface*; American Statistical Association: Alexandria, VA, 1989.
(40) Holland, P. W.; Welsch, R. E. *Commun. Stat., Part A* **1977**, *6*, 813−827.
(41) Huber, P. J. *Robust Statistics*; John Wiley & Sons: Hoboken, NJ, 1981.
(42) Street, J. O.; Carroll, R. J.; Ruppert, D. *Am. Stat.* **1988**, *42*, 152−154.

Macromolecules

Article

pubs.acs.org/Macromolecules

Preparation of Novel, Nanocomposite Stannoxane-Based Organic–Inorganic Epoxy Polymers containing Ionic bonds

Adam Strachota,*[†] François Ribot,[‡,§] Libor Matějka,[†] Paul Whelan,[†] Larisa Starovoytova,[†] Josef Pleštil,[†] Miloš Steinhart,[†] Miroslav Šlouf,[†] Jiřina Hromádková,[†] Jana Kovářová,[†] Milena Špírková,[†] and Beata Strachota[†]

[†]Institute of Macromolecular Chemistry, Academy of Sciences of the Czech Republic, Heyrovskeho nam. 2, CZ-162 00 Praha, Czech Republic

[‡]UPMC, Chimie de la Matière Condensée de Paris (UMR 7574), Collège de France, 11 place Marcelin Berthelot, 75005 Paris, France

[§]CNRS, Chimie de la Matière Condensée de Paris (UMR 7574), Collège de France, 11 place Marcelin Berthelot, 75005 Paris, France

ABSTRACT: Polymer nanocomposites of epoxies with a novel filler, amino-functional butyltin oxide cage (stannoxane), were prepared and characterized. The nanofiller displays a promising antioxidizing effect, besides mechanical matrix reinforcement. The reinforcement can be assigned to physical interactions among the polymer bonded nanofiller. Moreover, the stannoxane cage undergoes a rearrangement to larger poly amino-functional nano-objects at higher temperatures, which highly reduces its extractability: it is practically not extractable from the nanocomposites in most cases. This, together with the fact that only a few weight percent are needed to achieve an optimal effect, makes it attractive as an antioxidative stabilizer. Epoxy–stannoxane nanocomposite synthesis, stannoxane reactivity and dispersion (morphology via TEM and SAXS), as well as the nanofiller effect on mechanical properties (DMTA) and on thermal stability are discussed. A brief comparison is drawn between the stannoxanes and the previously investigated POSS nanofiller.

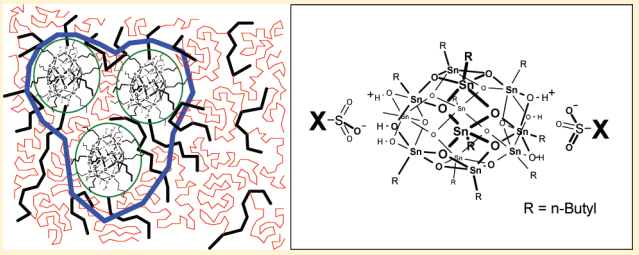

1. INTRODUCTION

Novel nanocomposite polymers were synthesized by the authors via reactive incorporation of butyl tin oxide cages (Scheme 1) into an epoxy matrix in order to achieve simultaneous mechanical reinforcement and antioxidative stabilization of the polymer. A general advantage of nanocomposites in comparison with classical ones consists in the small size of filler, which mostly makes possible the use of the same processing techniques for the nanocomposite, like for the neat polymer matrix[1−4] In case that the filler is sufficiently small in comparison to visible light wavelength, optical transparency is also preserved. Additionally, the intrinsic properties of the selected nanofiller can provide specific chemical,[5−7] optical,[8−10] electrical,[11−13] magnetic,[14−17] or gas barrier[18−21] properties to the final nanocomposite.

In their recent work, the authors investigated epoxy-nanocomposites reinforced by chemically bonded inorganic polyhedral oligomeric silsesquioxane (POSS) cages[22−24] and demonstrated the key importance of POSS–POSS interactions for the mechanical reinforcement in these nanocomposites. The organic substituents attached onto the POSS surface were shown to control the filler–filler interaction.[23] The physical cross-linking and the topological constraint to elastic chain motion caused by hard domains of aggregated (matrix-bonded) POSS nanofiller was demonstrated[24,25] to contribute to mechanical reinforcement as well as to increased thermal stability.

The ellipsoid shaped, 2 nm wide and 4 nm long[26] dodecameric butyl tin oxide ("stannoxane") cages shown in Scheme 1 are of similar size like POSS (with substituents typically 1.5 nm). The stannoxane cages are expected to possess interesting chemical properties, i.e. antioxidative ones, derived from tin chemistry. This attracted the authors' interest to epoxy-nanocomposites with the novel stannoxane filler. Only a few pioneering works were published up to date about polymeric materials containing stannoxane cages: Ribot et al. reported the preparation of carboxylate-based self-assembled organic–inorganic hybrids[27,28] with stannoxane and methacrylate–stannoxane copolymer.[29]

The attachment of two functional (or eventually inert) substituents by ionic bonds in axial positions of the stannoxane cage is a unique feature. The ionic bonding may cause interesting effects in stannoxane copolymers, especially concerning their eventual segmentation and mechanical behavior under stress. Ionic dissociation of the stannoxane end groups, anion exchange as well as supramolecular assembly under specific conditions were reported by Ribot et al.[30,31] It is

Received: May 24, 2011
Revised: November 24, 2011
Published: December 13, 2011

Scheme 1. Butylstannoxane Dodecamer Building Blocks $[(nC_4H_9{-}Sn)_{12}(O)_{14}(OH)_6][O_3S{-}X]_2$: (a) Chemical Structure of "Sn4", an Aromatic Diamine, and of "Sn_0" Non-Functional; (b) Symbolic Representation of Ionic Bonds in the Stannoxane Cages

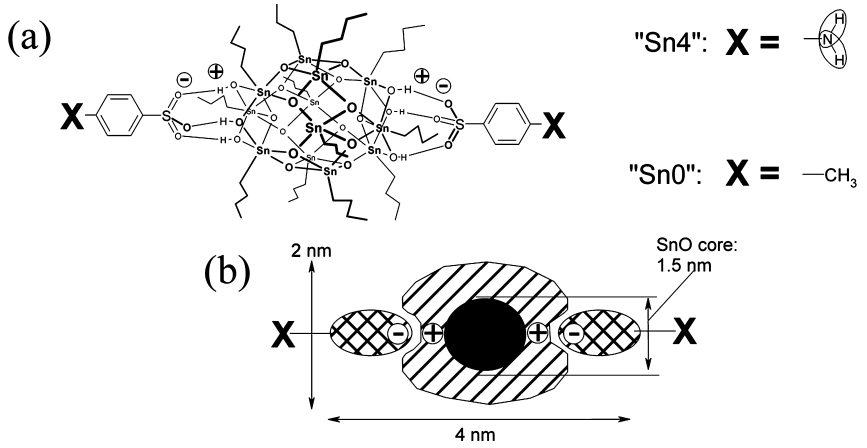

Scheme 2. Synthesis and Derivatization of the *n*-Butylstannoxane Dodecamer

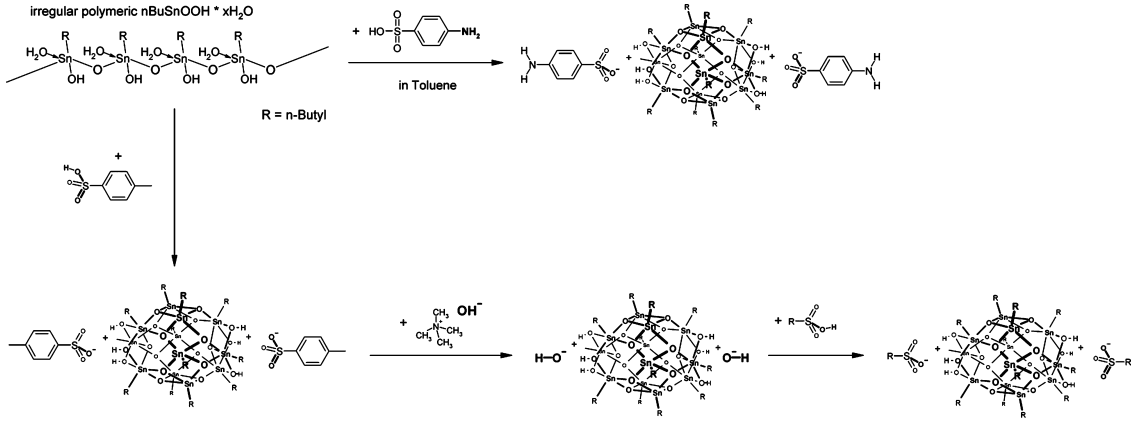

known,[32−35] that copolymers containing nonpolar main repeat units and small amounts of comonomer with an ionic side group (e.g., metal carboxylate or sulfonate), so-called ionomers, display valuable mechanical and melt properties. These result from association of the ionic-pair side groups to so-called multiplets (acting as reversible physical cross-links), small strong associates of up to eight ionic pairs. The ionic multiplets are able to aggregate to larger, looser, ion-rich domains (clusters), which contain also trapped nonpolar polymer segments. The nonpolar domains, ionic multiplets and multiplet clusters dominate the phase behavior of ionomers. In case of the studied stannoxane nano-objects, the effects of ionic bonding are expected to be weaker than in the above-mentioned ionomers, due to the fact that ionic bonding occurs between large neutral segments of the stannoxane, and that the ionic bonds are partly hidden, as illustrated symbolically in Scheme 1**b**, which is a strong difference to, e.g. sodium sulfonate side groups with "naked" metal cations. The ionic character of the bond to axial substituents is also likely moderated by hydrogen bridging, as marked by dotted bonds in Scheme 1a. The axial bifunctionality itself is a very valuable synthetic property of the stannoxane cages in comparison to most known nanofillers of similar size: e.g., POSS is typically obtainable in monofunctional or polyfunctional form. As a result of the bifunctionality, the stannoxanes can be easily incorporated into polymer backbones[27,28] or into other linear structures. In the present contribution, however, they are used as a four-functional reactant, with two two-functional "end-groups" in the axial positions.

Well-defined oligomeric alkylstannoxane cages similar to the one shown in Scheme 1 were first prepared in 1989 by Puff and Reuter,[36] followed by Dakternieks.[37] In some analogy to siloxane chemistry, a large family of stannoxane compounds exists,[38−40] including structures like linear, branched and ladder polymers, networks, drums and cages of different sizes. In 2000, Ribot,[26,41] one of the authors, developed a new, high-yield synthesis route (Scheme 2) to the butyl stannoxane dodecamer (Scheme 1), thus making possible the synthesis of large amounts and thorough product characterization. Ribot et al. also reported the cage's thermal lability[26] at temperatures above 250 °C.

Ribot's route to the stannoxane dodecamer (Scheme 2[26,41]) was used in this work, starting from the inexpensive butyltin oxide hydroxide polymer. The final product can be obtained in one step via reaction with the corresponding sulfonic acid, whose anions will form the axial functional substituents. In case that the acid is too weak, or does not support product crystallization, a longer (three-step) version of the synthesis is chosen (Scheme 2), via stannoxane dodecamer with toluenesulfonyl "end-groups", whose ionic substituents are subsequently exchanged for the strongly basic hydroxy anions. The latter ones are finally neutralized by the sulfonic acid to

dx.doi.org/10.1021/ma201178j | *Macromolecules* 2012, 45, 221−237

Scheme 3. Components and Idealized Structures of the Prepared Polymer Networks: (a) Diglycidyl Ether of Bisphenol A (DGEBA) and Phenyl Glycidyl Ether (PGE); (b) Poly(oxypropylene) α,ω-Diamine Jeffamine D2000, *n* = 33.6; (c) Symbolic Representation of the Stannoxane Nano-Building Blocks "Sn4" and "Sn_0"; (d) Explanation of Symbolic Building Block Representations used in Parts e–g; (e) Reference Network DGEBA–D2000[a]; (f) Network with "Sn4" Nano-Building Block Replacing Part of D2000[a]; (g) Network with Incorporated Non-Functional "Sn_0" Nano-Building Block

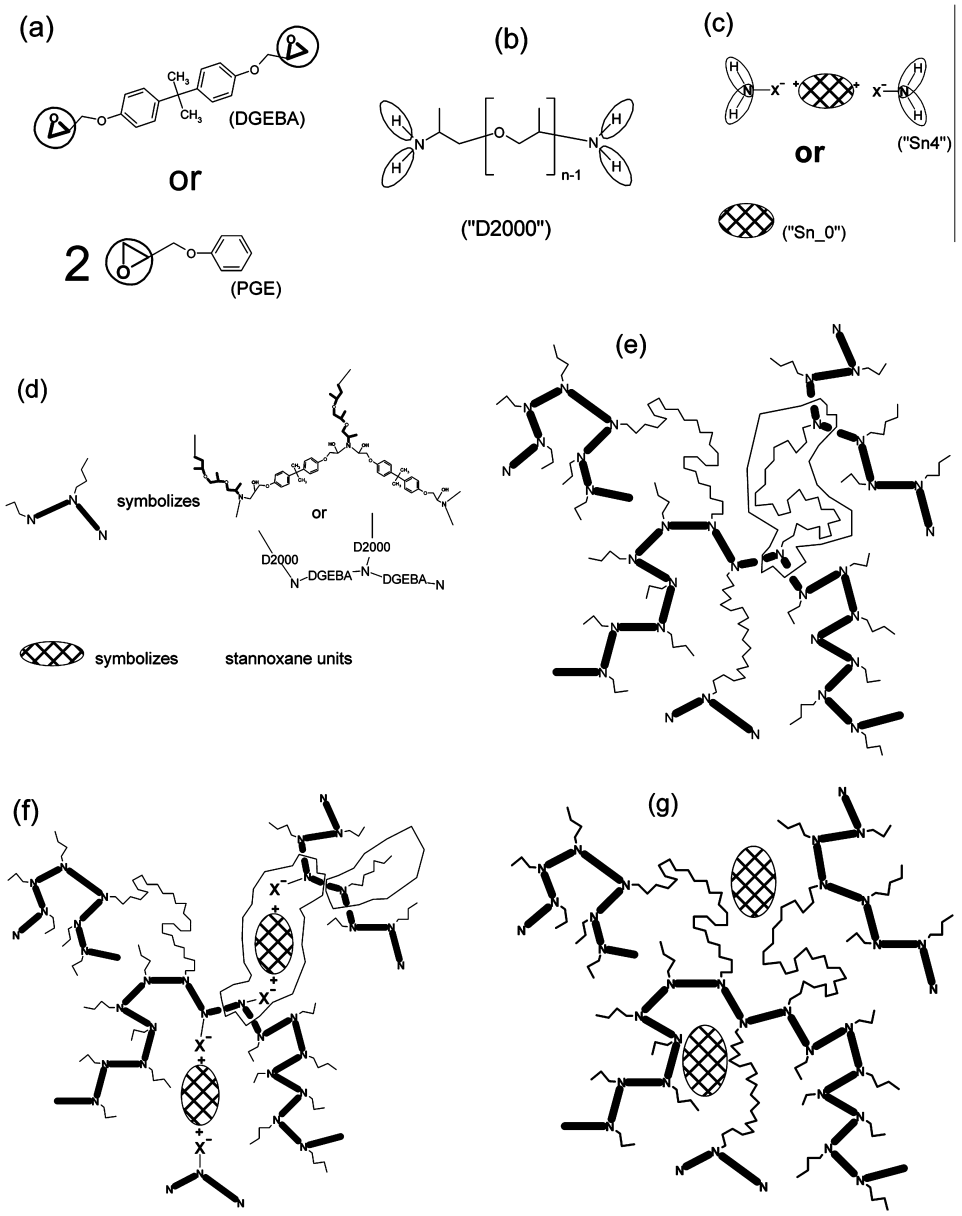

[a]In the images e and f, the components of the low molecular weight network model are encircled.

obtain the product with the desired functionality. The amino-functional stannoxane used in this work was prepared by the longer route, while the inert one in one step. Generally, a number of derivatives with different ionic end-groups can be prepared via the longer synthesis path, by neutralization of butylstannoxane dodecamer dihydroxide, e.g., compounds with carboxylate,[27,28] dialkylphosphinate,[30] or even sulfate[31] or oxalate[31] anions. Some anionic end groups could not be introduced up to date, however: This is especially the case of anions derived from aminoacids (amino-sulfonic, amino-carboxylic, etc.) whose zwitterionic state, as used for the neutralization step in the longer synthesis (Scheme 2), is too weakly acidic. In such cases, no neutralization (no end-group exchange) or only a partial one takes place. Highly "amino-reactive" amino–carboxylates or amino–sulfonates with primary aliphatic amino groups were not yet prepared for this reason. It was still possible to prepare an aminopropylsulfonate with a secondary, cyclohexyl-substituted aliphatic amino group using route of Ribot.[41] The reactivity of the latter product is reduced by sterical hindrance, however.

Previous studies of epoxy–POSS nanocomposites and the unique features of the newly available stannoxane cages inspired the investigation of novel epoxy-stannoxane nanocomposites. In order to achieve high sensitivity to mechanical reinforcement and to oxidative conditions, an elastomeric epoxy matrix was chosen, based on poly(oxypropylene)-α,ω-diamine (D2000)

dx.doi.org/10.1021/ma201178j | *Macromolecules* 2012, 45, 221–237

Table 1. List of the Prepared Polymers and Nanocomposites

sample name	mol % of Sn cage[a]	wt % of Sn cage	type of Sn cage	postcuring	fraction of gel w_g	w_g of filler	w_g of matrix
24-Sn_0	0	24.4	Sn_0	NO	0.89	0.64	0.97
24-Sn_0-pc	0	24.4	Sn_0	180 °C/12 h, under Ar	0.84	0.78	0.86
24-Sn_0-pcO	0	24.4	Sn_0	180 °C/12 h, in air	0.68	0.85	0.63
4-Sn4	4	4.1	Sn4	NO	0.97	0.98	0.97
4-Sn4-pc	4	4.1	Sn4	180 °C/12 h	0.88	0.99	0.88
10-Sn4	10	10.2	Sn4	NO	0.97	0.98	0.97
10-Sn4-pc	10	10.2	Sn4	180 °C/12 h	0.89	0.99	0.88
25-Sn4	25	24.4	Sn4	NO	1.00	1	1
25-Sn4-pc	25	24.4	Sn4	180 °C/12 h, under Ar	0.92	0.99	0.90
25-Sn4-pcO	25	24.4	Sn4	180 °C/12 h, in air	0.78	0.94	0.73
25-Sn4−240-Ar	25	24.4	Sn4	240 °C/30 min, under Ar	0.75	0.93	0.69
25-Sn4−240-O	25	24.4	Sn4	240 °C/30 min, in air	0.84	0.96	0.80
50-Sn4	50	45.5	Sn4	NO	0.97	0.98	0.96
50-Sn4-pc	50	45.5	Sn4	180 °C/12 h, under Ar	0. 93	1	0.87
50-Sn4-pcO	50	45.5	Sn4	180 °C/12 h, in air	0.91	0.98	0.85
100-Sn4[b]	100	80.3	Sn4	NO	x	x	x
DGEBA−D2000	0	0	no	NO	0.96	no	0.96
DGEBA−D2000-pc	0	0	no	180 °C/12 h, under Ar	0.85	no	0.85
DGEBA−D2000-pcO	0	0	no	180 °C/12 h, in air	0 (liquid)	no	0
DGEBA−D2000−240-Ar	0	0	no	240 °C/30 min, under Ar	0.72	no	0.72
DGEBA−D2000−240-O	0	0	no	240 °C/30 min, in air	0.61	no	0.61

[a]mol %("Sn4") = 100% * n(H(−N) stannoxane)/{n(H(−N) D2000) + n(H(−N) stannoxane)} where n is the chemical amount in mol. [b]The sample is too fragile for sol−gel analysis.

and diglycidylether of bisphenol A (DGEBA), see Scheme 3. The butylstannoxane nanofiller was expected to play two functions simultaneously: to reinforce the epoxy matrix mechanically, and at the same time to provide chemical stabilization similarly to tin based antioxidants. The stannoxane cages are covered by butyl groups, which—in analogy to similar POSS compounds—should lead to some solubility in the epoxy matrix, but also to a marked tendency to phase separation at medium and higher weight loads. As consequence, a relatively easy dispersion in the epoxy matrix should be achieved, while still preserving a considerable reinforcing effect by stannoxane-stannoxane interaction and aggregation. Of high interest was the effect of ionic attachment of the stannoxanes' functional substituents on thermomechanical properties, as well as the effect of high-temperature rearrangement of stannoxane cages.

2. EXPERIMENTAL PART

2.1. Materials. The poly(oxypropylene) diamines "Jeffamine D2000" (*molecular weight* = 1968 g/mol) and "Jeffamine D230" (*molecular weight* = 230 g/mol) were donated by Huntsman Inc. Diglycidyl ether of Bisphenol A ("DGEBA", 99.7% pure) was purchased from SYNPO a.s. Pardubice. Phenyl glycidyl ether (PGE) and 4,4′-diamino-diphenylsulfone ("DDS", IUPAC name: 4-[(4-aminophenyl)sulfonyl]phenylamine) were purchased from Sigma-Aldrich.

The amino-functional and the nonfunctional Stannoxane cages were synthesized as described earlier in the literature,[26,41] according to Scheme 2. Butyl tin oxide hydroxide hydrate, $BuSnO(OH).H_2O$, was used as starting material and reacted with toluenesulfonic or with sulfanilic acid to yield salts of the stannoxane cage dication shown in Scheme 2, "Sn_0" and "Sn4". The toluenesulfonate was converted into the dihydroxide in an ion exchange reaction using tetramethylammonium hydroxide. The dihydroxide was subsequently neutralized with sulfanilic acid, thus obtaining an improved yield of "Sn4". All above-mentioned chemicals were purchased from Sigma-Aldrich.

2.2. Nanocomposite Synthesis. The standard preparation method of epoxy-stannoxane nanocomposites was the so-called homogeneous procedure (homogeneous reaction mixture): The molten and supercooled epoxide DGEBA, the liquid Jeffamine D2000, and a 50 wt % stannoxane cage solution in toluene were mixed, the homogeneous clear reaction mixture was heated to 120 °C and stirred in an open vessel until gelation (typically ca. 40 min). Subsequently, the remaining solvent was removed by briefly applying vacuum at 120 °C. The plastic (and also clear, homogeneous) early postgel mixture was pressed into a mold (30 × 10 × 1 mm) and cured at 120 °C for 3 days. No air was entering the mold during the process.

For evaluation of the ability of the stannoxane to disperse via a reaction blending, so-called "heterogeneous" and "fine-heterogeneous" preparation procedures were also tested in addition to the homogeneous one. In the "fine-heterogeneous" synthesis the solvent (toluene) was removed at 25 °C under vacuum, just after mixing (stirring for 5 min) all components at room temperature. This led to microprecipitation of stannoxane (uniform crystals of around 5 μm size, as observed by optical microscopy), the precipitate having approximately a 100 times higher surface area in comparison to powdered "Sn4" stannoxane (grains of average width of 50 μm), hence the designation "fine-heterogeneous". The reaction mixture of milk-like color was poured into a mold (30 × 10 × 1 mm) and cured at 120 °C for 3 days.

In the case of the so-called "heterogeneous" preparation, neat powdered stannoxane (50 μm grains) was simply added to the other reaction components without any compatibilization. After thoroughly stirring the components at room temperature for 10 min, the opaque heterogeneous mixture was poured into a mold (30 × 10 × 1 mm) and cured at 120 °C for 3 days.

Postcuring of the prepared networks was achieved by heating the samples to 180 °C under argon atmosphere for 12 h.

"Oxidative post-curing" of the prepared networks was achieved by heating the samples to 180 °C in circulating air for 12 h.

The most important samples prepared are listed in Table 1. Only stoichiometric formulations were prepared, the stoichiometry being defined by the molar ratio of functional groups r = (amino-H)/(epoxy) = 1. The stannoxane ("Sn4") content in the formulations was quantified by the molar ratio of stannoxane amino-protons to all amino protons. This also corresponds to the molar percent of the organic diamine, "D2000", which was replaced by the equally diamino-functional stannoxane "Sn4" (both are four-functional in epoxy−amine additions). For example the abbreviation "25-Sn4" in Table 1 describes

dx.doi.org/10.1021/ma201178j | *Macromolecules* 2012, 45, 221−237

a polymer, in which 25 mol % of D2000 were replaced by "Sn4". In case of the nonfunctional nanofiller "Sn_0", its amount is given in wt %, e.g. "24-Sn_0". Special curing conditions are also part of the sample names, e.g. "25Sn4-pc" means additional 12-h postcuring at 180 °C under argon for the sample "25-Sn4".

2.3. Determination of the Gel Fraction. The sol−gel analysis of the network samples prepared was carried out as follows: The samples investigated were swollen and extracted with toluene/tetrahydrofuran (1:1). All the samples were extracted for 3 days while the solvent was changed every day for a pure charge. After the extraction, the samples were dried (vacuum, 100 °C) until weight constancy and the fraction of gel (w_g) was determined as

$$w_g = \text{mass (dry, after extraction)}/\text{mass (dry, before extraction)}$$

2.4. Determination of Stannoxane Content as SnO_2 Ash. The remaining stannoxane ("Sn4" or "Sn_0") content in the prepared nanocomposites after sol extraction was determined as SnO_2 ash mass. The analyses were performed as follows: The nanocomposite samples were put into a platinum pot together with the double of their weight of sulfuric acid. This mixture was slowly pyrolyzed in air (heating at around 337 °C, the boiling point of H_2SO_4). The remaining ash was heated to ca. 1000 °C for 15 min. The pyrolysis with the sulfuric acid was repeated once more with the ash. The dry SnO_2 ash was then weighed. From this result, the content on tin and on stannoxane (using the known weight fraction of tin in "Sn4" or "Sn_0") was calculated.

2.5. Dynamic-Mechanical Thermal Analysis (DMTA). Dynamic mechanical properties of the nanocomposite products were tested with rectangular platelet samples, using an ARES LS2 apparatus from Rheometric Scientific (now TA Instruments). An oscillatory shear deformation at the constant frequency of 1 Hz and at the heating rate of 3 °C/min was applied, and the temperature dependences of the storage shear modulus and of the loss factor (G' and $\tan(\delta)$, respectively) were recorded. The temperature range was typically from −100 to +120 °C (or −100 to +100 °C in case of nanocomposites which were not postcured; in some cases the DMTA was recorded up to +150 °C). The geometry of the deformed area of all the tested samples was the same: 30 mm height, 10 mm width, and 1 mm thickness.

2.6. NMR Spectroscopy. Proton-decoupled ^{119}Sn solution NMR experiments were performed on a Bruker (Karlsruhe, Germany) Avance DPX 300 spectrometer at 111.92 MHz. The ^{119}Sn $\{^1H\}$ spectra were obtained with a composite pulse decoupling sequence (CPD). $CDCl_3$ was used as solvent. The ^{119}Sn chemical shifts are quoted relatively to the tetramethyltin standard (δ = 0 ppm), in whose place the nonvolatile tetrabutyltin was used (δ = −7 ppm).

2.7. Small-Angle X-ray Scattering (SAXS). SAXS measurements were performed on a reconstructed Kratky kamera with a 60 μm entrance slit and a 42 cm sample-to-detector distance. Ni-filtered Cu Kα radiation (λ = 0.154 nm) was recorded with a linear position-sensitive detector (Joint Institute for Nuclear Research, Dubna, Russia). The experimental (smeared) SAXS curves are presented as a function of the magnitude of the scattering vector $q = (4\pi/\lambda) \sin \theta$ (2θ is the scattering angle).

2.8. Transmission Electron Microscopy (TEM). The TEM microscopy was performed with the microscope JEM 200CX (JEOL, Japan). TEM microphotographs were taken at the acceleration voltage of 100 kV, recorded on a photographic film, and digitized with a PC-controlled digital camera DXM1200 (Nikon, Japan). Ultrathin sections for TEM, approximately 50 nm thick, were cut with ultramicrotome Leica Ultracut UCT, equipped with cryo attachment.

2.9. Thermal Gravimetric Analysis (TGA). Mass-loss/temperature curves were obtained with a Perkin-Elmer TGA7 device. The samples were measured at a heating rate 10 °C/min. Nitrogen or air was used as a purge gas.

3. RESULTS AND DISCUSSION

The presented investigation of novel epoxy stannoxane nanocomposites is discussed in four chapters, dedicated to four interesting aspects of this work: the nanofiller dispersion in the epoxy matrix, the nanofiller's tendency to oligomerization and its consequences, the antioxidative effect of the nanofiller, and a brief comparison of the stannoxane nanofiller with the highly popular POSS nanofiller.

3.1. Dispersion of the Stannoxane Nanofiller in the Epoxy Matrix. In this chapter, topics related to nanofiller dispersion are discussed: the dispersion technique, the relative reactivity of the amino-functional nanofiller, sol−gel analysis of the prepared nanocomposites (filler extractability), the verification of the dispersion via TEM and the effect of the nanofiller dispersion on the mechanical properties.

The amino-bifunctional butylstannoxane dodecamer "Sn4" (size: 2 × 2 × 4 nm,[26] structure: Scheme 1), was successfully dispersed in the DGEBA−D2000 epoxy matrix, which was proven by transmission electron microscopy (TEM, see below: Figure 2 and section 3.1.3). The cage-like "Sn4" compound is only moderately soluble in the mixture of the matrix components, DGEBA and D2000, even at the cure temperature of 120 °C. The cure temperature and duration were chosen in analogy to previous work on inorganic nanocomposites with the same matrix.[22−24] The study of compatibilization and subsequent reactive incorporation of "Sn4" was of key importance. For this purpose, a homogeneous (solvent present until gelation), a finely heterogeneous (microsuspension; solvent present only during mixing) and a heterogeneous (suspension; without any solvent) preparation procedures were tested for the composition "25-Sn4". The morphology analyses, and even the mechanical properties (DMTA) of the nanocomposites showed, that only the solvent-assisted homogeneous preparation led to a good dispersion of the stannoxane nanobuilding blocks (comparison of Figure 2, parts a and b). This preparation was selected as standard procedure. In case of the heterogeneous and fine heterogeneous preparation, considerable filler incorporation was nevertheless achieved (see DMTA in Figure 4). This suggests, that reaction blending might be successful at small weight loads of "Sn4". However, for reasons of good comparability, all samples, even such with small "Sn4" content were prepared by the homogeneous procedure, using toluene as solvent.

A more advanced, solvent-free synthesis might be of interest for eventual larger-scale production of the nanocomposites, especially of such with low "Sn4" content: the reaction of excess DGEBA with "Sn4" in presence of solvent, followed by solvent removal, and the use of the DGEBA−Sn4(DGEBA)$_4$ mixture as epoxy component, eventually after addition of further DGEBA, in order to achieve the desired "Sn4" content. This synthesis was also tested, namely for the DGEBA/"Sn4" ratio of 8/1 (critical theoretical ratio for gelation would be 6/1). In place of a soluble mixture of epoxides, an insoluble polymer network with relatively good mechanical properties was obtained. The result indicated, that a careful optimalization of this synthesis route would be necessary, especially in order to prevent epoxy group homopolymerization. Consequently, the "DGEBA-capping route" was abandoned in this work, while it is still being further developed, especially for further improvement of antioxidative properties. The most important of the prepared samples are listed in Table 1, including their abbreviations, compositions and cure conditions.

dx.doi.org/10.1021/ma201178j | Macromolecules 2012, 45, 221−237

3.1.1. Relative Reactivity of the "Sn4" Nanofiller. The reactivity of the amino-functional stannoxane cages plays an important role in the morphology formation of the stannoxane−epoxy nanocomposites (Scheme 3). The same reactivity of amino groups of nanofiller ("Sn4") and of the organic amine (D2000) would favor a good dispersion of "Sn4" in the matrix. In contrast, a distinctly higher or lower "Sn4" reactivity would favor its preferential incorporation in early or late stages of the polymer formation, respectively, which in both cases would result in microphase separation and formation of "Sn4"-rich domains.

Using the same experimental technique like in previous work,[24] the relative reactivity of amino groups of "Sn4", of poly(oxypropylene)-α,ω-diamine ("Jeffamine D230", model for D2000) and of 4,4′-diaminodiphenylsulfone ("DDS", model for end-groups of "Sn4") were compared: The amines were reacted with excess phenyl glycidyl ether (PGE) at same stoichiometric ratios, concentrations and temperature, and the consumption of epoxy groups was measured via ^{1}H NMR, using the characteristic signal of the oxirane ring at 2.81 ppm (>CH- proton). The consumption of amino groups was assumed to be equal to the consumption of epoxy groups, thus assuming only negligible homopolymerization of PGE at the rather moderate reaction temperature of 120 °C. The reactivity comparison is shown in Figure 1. The half times of the reaction are as follows:

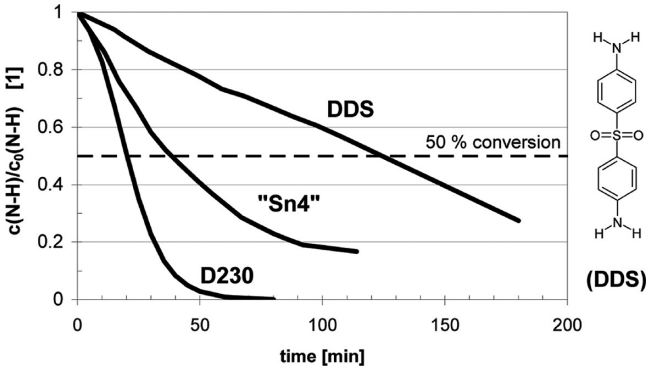

Figure 1. Relative reactivity: kinetic curves of consumption of N−H functionalities of the diamines "Sn4", DDS and of Jeffamine D230, in reaction with excess phenylglycidyl ether, T = 120 °C, in sealed ampule, r(H(−N)/Ep) = 0.25, c_0(Ep) = 3.48 M, c_0(Am) = 0.85 M, in toluene, determined via epoxy group conversion.

125 min for DDS, 39 min for "Sn4" and 20 min for Jeffamine D230. The nanofiller "Sn4" is markedly less reactive than the amino component of the matrix because "Sn4" is an aromatic primary amine, while Jeffamines D are aliphatic primary amines. "Sn4" is hence incorporated preferentially only in the later stages of the polymer synthesis, which together with the limited solubility in the matrix favors its aggregation to "Sn4"-rich domains.

Interesting is the much higher reactivity of the "Sn4" aromatic diamine in comparison with the model compound DDS. This finding suggests a catalytic role of the stannoxane cage, probably of its OH groups. The stannoxane catalytic effect with respect to the epoxy-amine addition was proven by gelation experiments with "Sn4" and also with its nonfunctional counterpart "Sn_0": The time of gelation (reaction samples in sealed ampules, visual observation of solidification with the precision of ±1 min) of the neat DGEBA−D2000 system at 120 °C is 70 min, while the system "25-Sn4" (fine heterogeneous preparation) gels already in 48 min. Similarly, the system DGEBA−D2000−24 wt %Sn_0 ("24-Sn_0") also gels faster: in 51 min, despite the moderate dilution of the system by the nonfunctional "Sn_0" cage. The "Sn4" stannoxane cages hence speed-up the formation of the DGEBA−D2000 network, and in spite of the lower reactivity of their own amino groups they probably also achieve at least an incomplete covalent attachment to the polymer matrix (see Sol−Gel Analysis discussion just below) in late reaction stages, due to the mentioned catalytic effect.

3.1.2. Sol−Gel Analysis: Study of Nanofiller Extraction. The extraction of the eventual unbound stannoxane nanofiller from the epoxy nanocomposites was tested using a 1:1 toluene/tetrahydrofuran mixture, in which both nanofillers "Sn4" and "Sn_0" are highly soluble (up to ca. 65 wt %), and which also easily swells the DGEBA−D2000 matrix. The results are summarized in Table 1. Given the lower reactivity and late incorporation of stannoxane "Sn4" into the epoxy matrix, a microphase separation of some unbound "Sn4" domains would be expected, especially at a high "Sn4" loading, in analogy to similar POSS systems.[24] An increased "Sn4"-rich sol fraction should be the result. However, it was determined that "Sn4"-containing nanocomposites show very small sol fractions, even smaller than the neat epoxy matrix. Moreover, a low sol fraction was found even in the nanocomposites with the inert, nonfunctional "Sn_0" filler, which should be extractable as it does not form bonds to the matrix. In the case of the sample "24-Sn_0" (24 wt % of "Sn_0") the achieved gel fraction was 89%, indicating that more than the half of the chemically unbound "Sn_0" filler was not extracted. This result is explained by the stannoxane cage tendency to rearrange to larger (nonextractable) polymers under the synthesis conditions. The ^{119}Sn NMR analysis (see further below, chapter 3.2) proved that 18% of the stannoxane cages polymerize (more exactly oligomerize) during the standard-applied cure at 120 °C for 3 days under argon. The polymerized stannoxane fraction (larger structures, which only difficultly can disentangle from the epoxy network) is the likely reason for the low extractability of nonfunctional "Sn_0", as well as of eventual unbound "Sn4". Furthermore, the above discussed catalytic effect of the stannoxane on the epoxy-amine reaction leads necessarily to a high conversion of the organic matrix and to a decreased fraction of the sol. This same catalytic effect also increases the likeliness of bonding of the less reactive "Sn4" diamine to the matrix by at least one bond (out of four possible).

Interesting results are obtained if the fractions of gel are determined for matrix alone and for nanofiller alone (in addition to the overall gel fraction, see Table 1). The stannoxane gel fractions are always relatively high, in most cases close to 1, and markedly higher than gel fractions of the cyclopentyl−POSS−DGEBA nanofiller which was investigated in a similar bonding situation in previous work[24] (w_g(POSS) was in the range 0.49−0.66). The partial gel fractions of the matrix in the nanocomposites are also slightly higher or identical like in the case of the neat DGEBA−D2000 matrix (Table 1), as far as the compared samples were cured at 120 °C.

3.1.3. Nanofiller Aggregation Study by TEM. The degree of nanofiller dispersion or eventual aggregation in the epoxy-stannoxane nanocomposites was assessed by means of transmission electron microscopy (TEM). The homogeneously prepared (toluene present until gel point) epoxy-"Sn4"

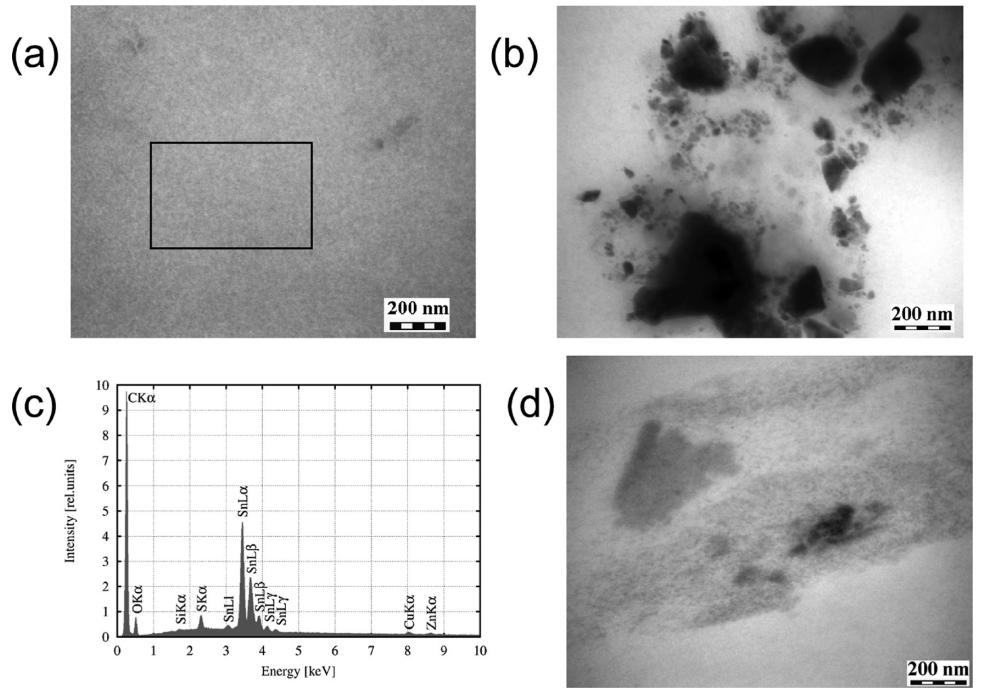

Figure 2. TEM micrographs of nanocomposites: (a) "50-Sn4"; (b) "25-Sn4-fine-heterogeneous preparation"; (c) EDXS analysis of "50-Sn4" (image a) 600 × 400 nm area; (d) "24-Sn_0".

nanocomposites (even with 50 mol % "Sn4") display a very fine nanofiller dispersion (Figure 2a), homogeneous up to the 10 nm scale. Somewhat smaller heterogeneities can be observed in the micrograph. The elemental EDXS analysis (Figure 2c) proves the presence of Sn from stannoxane in the nearly homogeneous nanocomposite the morphology of which is shown in Figure 2a. Fine heterogeneous sample preparation (solvent present only during mixing) leads to imperfect dispersion with numerous large stannoxane domains (dark), sized typically between 50 and 400 nm, as shown in Figure 2b. In contrast to the "Sn4" nanocomposites, the ones with the nonfunctional "Sn_0" nanofiller are always highly heterogeneous (Figure 2d), because the nonfunctional "Sn_0" can not undergo reaction blending and is only moderately soluble (like "Sn4") in the epoxy matrix if no solvent is present. Hence, independently of the preparation technique, "Sn_0" precipitates in later matrix formation stages. "Sn_0" domains of varying size, up to hundreds of nanometers can be seen in Figure 2d. Large "Sn_0" crystallites (sized ca. 2000 × 400 nm) can also be observed (not depicted).

3.1.4. Effect of the Dispersed Nanofiller on Thermomechanical Properties. The incorporation of the "Sn4" nanofiller markedly influences the thermomechanical properties of the DGEBA−D2000 matrix. Figure 3 shows the temperature dependence of the shear storage modulus G' and of the loss factor $\tan(\delta)$ of DGEBA−D2000−Sn4 polymers with 0−100 mol % "Sn4". Until 10 mol % of "Sn4", the nanofiller effect is moderate, but clearly visible, particularly by increasing T_g values (shift of $\tan(\delta)$ maxima). The content of 25 mol % or more of "Sn4" leads to distinctly different DMTA profiles.

Figure 4 illustrates the effect of nanofiller dispersion technique on the thermomechanical properties: A small increase of reinforcement can be seen if comparing the DMTA profiles of samples prepared by the "heterogeneous" and "fine heterogeneous" techniques, respectively. The reinforcing effect of "Sn4" markedly increases, if the sample is prepared by the homogeneous technique, using toluene as solvent.

The somewhat complex glass transition behavior of the DGEBA−D2000−Sn4 nanocomposites can be explained by taking into account the miscibility of phases in this copolymer: The DGEBA−D2000 matrix is a copolymer of two fully miscible phases (see structure in Scheme 3**e**). The more rigid phase consists of DGEBA units connected through nitrogen atoms ("−DGEBA−N−DGEBA−N− chains"; N originates from amino groups which underwent addition to the epoxy end-groups of DGEBA). This rigid phase alone displays a glass transition (T_g) around +70 °C. The second phase of the matrix consists of flexible elastic D2000 chains (poly(propylene oxide), T_g around −70 °C). The D2000 chains interconnect the DGEBA−N−DGEBA−N− chains at every N atom. The described copolymer displays a uniform glass transition near −29 °C, which is a result of the full miscibility of its phases.

The $\tan(\delta) = f(T)$ graphs of the nanocomposites in Figure 3 display profiles typical of copolymers with immiscible phases. It is possible to assign three main thermal transitions: the glass transition of the unhindered DGEBA−D2000 copolymer around −30 °C (predominantly movements of the flexible D2000 chains), the glass transition of DGEBA−D2000 immobilized by the sterical constraint of closely neighboring hard nanofiller domains in the region from −15 to +15 °C, and the glass transition assigned to the stannoxane-rich copolymer domains which shifts from +30 °C to +70 °C. The latter domains contain the DGEBA−Sn4 copolymer and some included D2000 chains. The transition is likely due to the loosening of larger secondary aggregates (see Scheme 4) composed of primary strong ones (composition: DGEBA−Sn4), between which some immobilized matrix (composition DGEBA−D2000) is included. The secondary "Sn4" aggregates are expected to be few and weak (more intercalated) at low "Sn4" contents, but stronger at high contents, with average distances between primary and also between secondary

dx.doi.org/10.1021/ma201178j | *Macromolecules* 2012, 45, 221−237

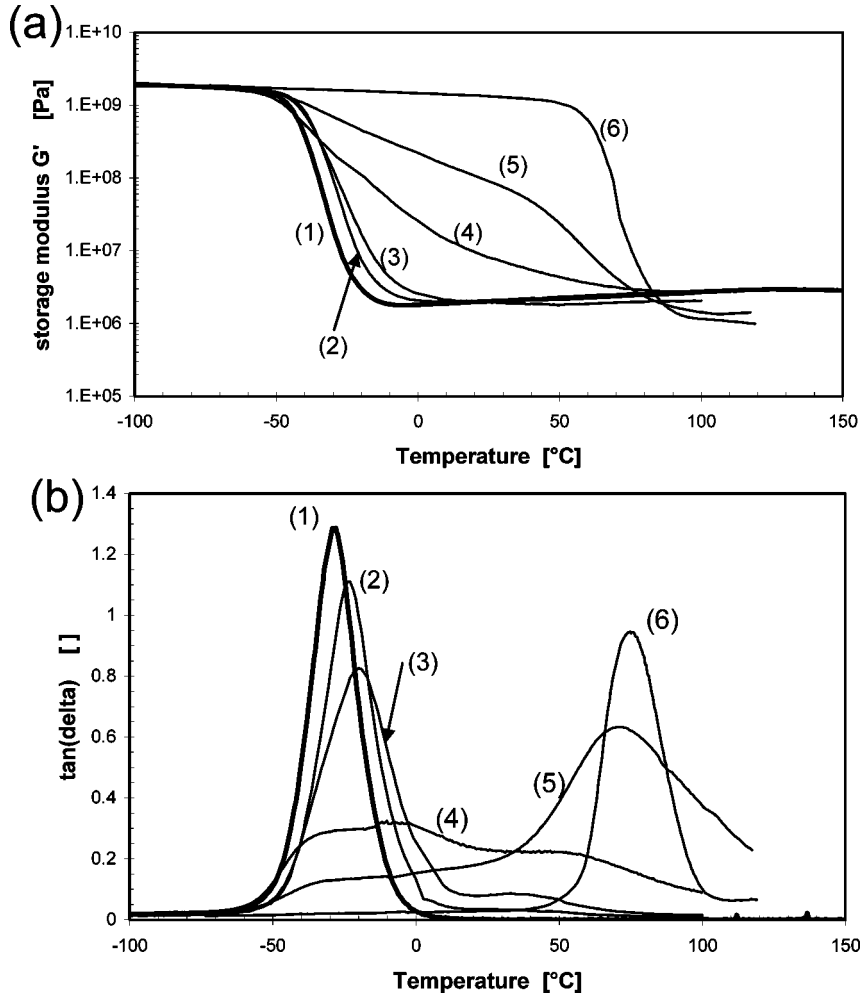

Figure 3. Shear storage modulus G' (a) and loss factor $\tan(\delta)$ (b) as a function of temperature: Effect of increasing content of the stannoxane "Sn4" on the mechanical properties of the epoxy nanocomposites: (1) DGEBA–D2000 reference; (2) 4 mol % D2000 replaced with "Sn4"; (3) 10 mol % "Sn4"; (4) 25 mol % (24 wt %) "Sn4; (5) 50 mol % "Sn4"; (6) 100 mol % "Sn4".

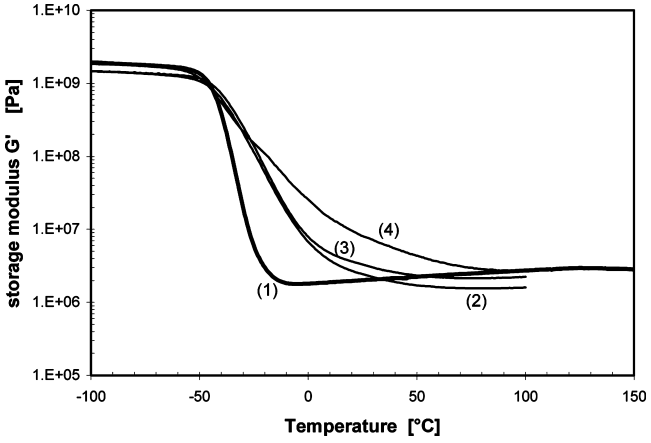

Figure 4. Effect of dispersion technique in samples cured at 120 °C: (1) neat DGEBA–D2000 matrix, (2) heterogeneous preparation of 25 mol % Sn4, (3) "fine heterogeneous", (4) homogeneous.

aggregates becoming short. Finally, at 100 mol % of "Sn4", only one phase, the DGEBA–Sn4 copolymer, is present in the sample, with all "Sn4" units in close contact, which leads to the highest T_g of the "stannoxane-rich phase". For comparison, the melting of neat "Sn4" occurs at a much higher temperature, 253 °C, followed by rapid polymerization. The presented interpretation is supported by the behavior of analogous samples, which underwent the polymerization (more exactly oligomerization) of the "Sn4" cages in the stannoxane domains (see further below, chapter 3.2). The proposed nanofiller arrangement is somewhat similar to the one observed in the so-called ionomer polymers,[32−35] which was mentioned in the introduction.

The contents of the different phases in the nanocomposites are illustrated by the $\tan(\delta) = f(T)$ graphs (Figure 3b): With increasing "Sn4" content, the peak of the free DGEBA–D2000 rapidly decreases and broadens and the peak of the immobilized DGEBA–D2000 adds to the first. The peak of the stannoxane-rich-phase's glass transition grows, shifts to higher temperatures and becomes narrower. For compositions with very small or very high nanofiller content, sharp transitions are observed indicating rather uniform systems. At low "Sn4" contents, especially at 4 mol % the behavior is close to a system with all phases miscible (copolymer effect of rigid "Sn4"), while at higher "Sn4" loadings the behavior of immiscible phases prevails, in parallel to the observed solubility of "Sn4" in the matrix.

The epoxy networks with high "Sn4" content show smaller rubbery moduli than the neat matrix after the relaxation of the

dx.doi.org/10.1021/ma201178j | Macromolecules 2012, 45, 221–237

Scheme 4. Thermal Rearrangement of Aggregated Butylstannoxane Cages to Larger Structures, Which Keep the Ionic-Bonded Functional Substituents[a]

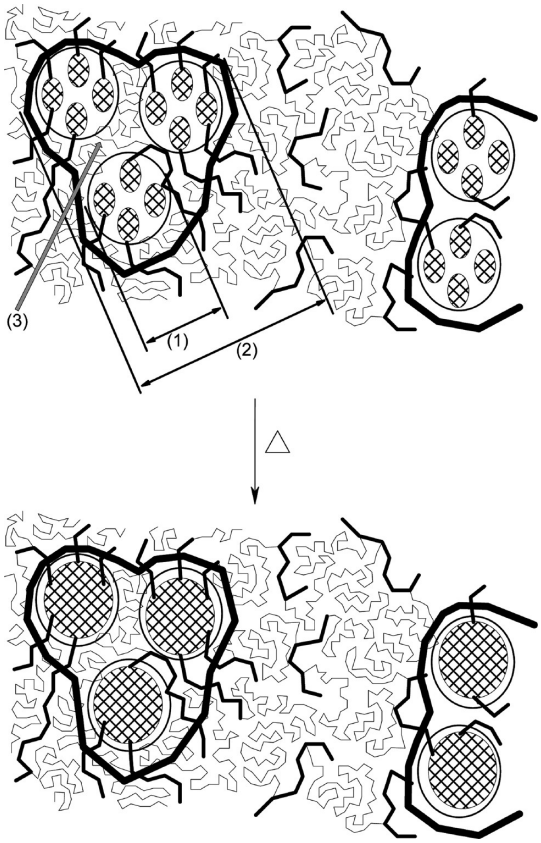

[a] Explanation: (1) = primary "Sn4" aggregates; (2) = secondary "Sn4" aggregates; (3) = matrix chains inclusions in the secondary aggregates.

reinforcing structures at high T, obviously due to incomplete conversion of "Sn4" amino goups and the resulting lower cross-linking density.

3.2. Rearrangement of the Stannoxane Cages to Larger Structures. An interesting property of the "Sn4"-epoxy nanocomposites is the oligomerization of "Sn4" inside of its domains, which was found to occur during the nanocomposites postcure at elevated temperatures. The "Sn4" polymerization and its effects on material properties were studied exemplarily for the nanocomposite with 25 mol % "Sn4" by means of SAXS, TEM, ^{119}Sn−NMR, and DMTA. On the other hand, attempts to easily detect the "Sn4" polymerization by means of differential scanning calorimetry (DSC) failed, probably due to approximate thermo-neutrality of the process. Melting closely followed by rapid polymerization at 253 °C can be observed on a thermostated plate, if a neat "Sn4" sample is put on it near this temperature, and if the heating rate is fast.

Nanocomposite was investigated in order to increase the degree of chemical incorporation of the less reactive aromatic-amino-functional stannoxane into the epoxy polymer. For this purpose, samples were annealed at 180 °C for 12 h, under argon atmosphere (in order to prevent oxidative side-reactions). The temperature program was chosen on the base of previous experience with epoxy-nanocomposite synthesis[22−24] and with reactivity of aromatic amines toward epoxides.[42] At the chosen postcure temperature, however, a partial rearrangement of "Sn4" aggregates to larger structures (Scheme 4) was suspected,[26] as well as some thermal degradation of the matrix (see Table 1, gel fraction of the neat matrix after postcure). The rearrangement of "Sn4" was indeed proven as discussed below, and was found to be a prominent process during the postcure at 180 °C, and even to occur to a small extent at 120 °C. Because of a complex nanocomposite morphology (Scheme 4), only an oligomerization of "Sn4" is possible, and additionally, this process does not affect significantly the thermomechanical properties of the nanocomposites, but may help to reduce the stannoxane extractability. The "Sn4" polymerization to larger cages probably involves a reversible dissociation of the ionic bonds to the functional substituents, as proposed in Scheme 5. This would be in analogy to the known finding,[38,26] that protonation/deprotonation reactions play a key role in the synthesis and reorganization of different stannoxane structures.

3.2.1. Stannoxane Cage Polymerization Studied by SAXS and TEM. The study of "Sn4" cages polymerization via a temperature-dependent SAXS experiment is illustrated in Figure 5a: A specimen of the "25-Sn4" nanocomposite was gradually heated to 240 °C and subsequently cooled to room temperature, while SAXS patterns were recorded, all under argon atmosphere.

The SAXS patterns of the DGEBA−D2000−Sn4 nanocomposites cured at 120 °C can be assigned as follows: The scattering intensities show a distinct interference maximum near q = 0.42 Å^{-1}, which characterizes the size of a single "Sn4" stannoxane cage, more exactly its highly dense inorganic tin−oxo core (1.5 nm). This interference maximum was found not to shift with changing "Sn4" content (from 4 to 100 mol %, see Figure 5b) and hence corresponds to an internal distance inside the "Sn4" cage. A marked increase of scattering intensity followed by a plateau is observed in the region q = 0.1 to 0.05 Å^{-1} and can be fitted using the Guinier function for spherical particles. This pattern can be assigned to X-ray scattering on larger heterogeneities − aggregates of "Sn4" building blocks, sized typically around 11 nm. Such an aggregate size was found for 25 and 50 mol % "Sn4", while with 10 mol % the aggregate size was smaller: 6−7 nm (at 4 mol % "Sn4": too weak scattering from aggregates).

Upon annealing the "25-Sn4" sample (Figure 5a) little change occurs in the SAXS patterns, until the temperature increases above 220 °C. Above this temperature the patterns

Scheme 5. Postulated Mechanism of the Dissociation/Reconnection of the Ionic Bond to the Functional Substituent, via Deprotonation/Protonation of a Bridging Oxygen Atom (Analogy to, e.g., Ammonium and Phosphonium Salts)

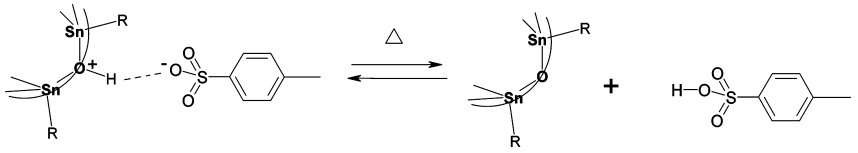

dx.doi.org/10.1021/ma201178j | Macromolecules 2012, 45, 221−237

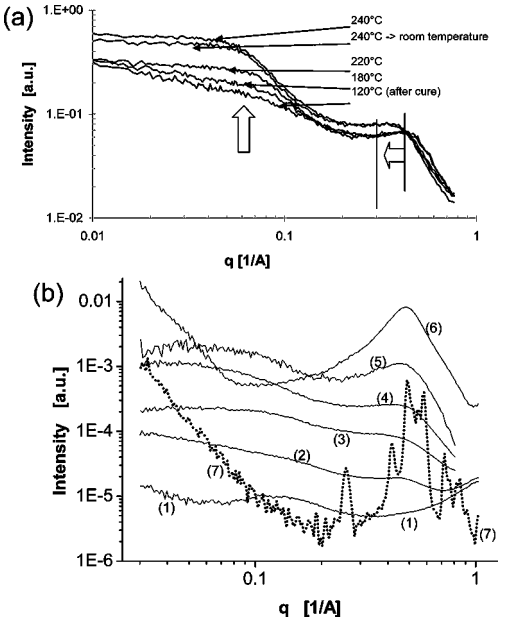

Figure 5. (a) SAXS investigation of stannoxane polymerization in the nanocomposite "25-Sn4": heating from 30 to 240 °C at 5 °C/min, followed by cooling at the same rate. (b) SAXS patterns of the nanocomposites prepared. Effect of Sn4 filler amount: (1) = 0 mol % (neat matrix), (2) = nanocomposite with 4 mol % Sn4, (3) 10 mol % Sn4, (4) 25 mol % Sn4, (5) 50 mol % Sn4, (6) 100 mol % Sn4, and (7) neat Sn4 (dotted).

markedly change, and the profile finally observed at 240 °C does not change any more after the sample is cooled back to room temperature. The annealing causes a shift of the "Sn4-width-interference" maximum to lower q values (Figure 5a), around 0.32 $Å^{-1}$, corresponding to an increased size of the inorganic cage cores (1.9 nm). At the same time, the slope and the plateau intensity in the small-angle region increase. This indicates changes in the stannoxane aggregates: The slope increase suggests their increasing compactness. Furthermore, the Guinier analysis of the small-angles region indicates that the stannoxane domains also decrease in size from 11 to 5 nm. The SAXS observations allow in combination with the above-discussed DMTA results the following interpretation: Before annealing, the (2 nm wide) "Sn4" building blocks form strong and small primary aggregates containing only a few units, sized around 3 nm (interpenetration of the butyl substituents). The primary aggregates are loosely assembled to secondary aggregates (Scheme 4) sized around 11 nm and intercalated with matrix. Upon heating above 220 °C, the "Sn4" units in the primary aggregates quickly polymerize to larger compact blocks which extend over the whole primary aggregates. The original large and loose secondary domains differentiate into several smaller and denser regions in which a few primary domains are more compactly arranged. These smaller aggregates are then separated by wider matrix intercalations and become distinguishable by means of SAXS.

In order to evaluate the changes of stannoxane domain size by an additional independent method, TEM images of an exemplary sample (50 mol % "Sn4") annealed under argon at 180 and at 240 °C were acquired. No visible difference of domain morphology was observed in comparison with the micrograph taken prior to annealing (Figure 2a). This means that in spite of the above observed "fracturing" of the secondary domains to smaller units, the latter ones remain arranged to similar patterns like before the annealing.

3.2.2. Polymerization of the Stannoxane Cage Studied via ^{119}Sn NMR. The polymerization of the stannoxane nanobuilding blocks under standard preparation conditions and at elevated temperatures (postcuring) was studied quantitatively using ^{119}Sn NMR. Solid-state NMR spectra of both neat stannoxane[26] and of the epoxy-stannoxane nanocomposite (not depicted) consist of complex signals and are hence difficult to compare and evaluate unequivocally. On the other hand, the liquid ^{119}Sn NMR spectrum of the stannoxane cage is very simple: 2 singlets corresponding to 2 types of Sn atoms in the structure (see Figure 6a). For this reason, a liquid low-molecular-weight model (see Scheme 3) of the nanocomposite with 25 mol % "Sn4" (DGEBA−D2000−Sn4) was synthesized, possessing also the same reactivity of the components: Monofunctional phenyl glycidyl ether (PGE) was used as the epoxy component in place of bifunctional DGEBA. The soluble PGE−D2000−Sn4 model made it possible to measure liquid ^{119}Sn NMR spectra of the stannoxane after the epoxide-amine addition at 120 °C, and after subsequent heating (postcuring) at elevated temperatures. In this way the stannoxane polymerization at different conditions was determined quantitatively using an internal integration standard (tetrabutyltin added just prior to NMR analysis). The Figure 6 compares the spectra of the low molecular weight model PGE−D2000−Sn4 just after component mixing at room temperature (Figure 6a), after cure at 120 °C for 3 days (Figure 6), after cure at 120 °C and subsequent postcure under Ar at 180 °C for 12 h (Figure 6c), and after cure and subsequent postcure at 240 °C for 30 min under Ar (Figure 6d). The signal of the integration standard (nBu$_4$Sn) can be seen at −7 ppm, while the stannoxane cage signals appear at −273 ppm (five-coordinated Sn atoms in "equatorial region" of the cage) and −453 ppm (six-coordinated Sn atoms in "polar regions"). The rearranged (polymerized) stannoxane does not display (as reported in ref 26) any new Sn NMR signals, probably due to signal broadening given by irregular structures and possibly also due to long relaxation times of the tin atoms in the large polymeric stannoxane structures.[26] The results in Figure 6 show, that the stannoxane building blocks mainly survive (82% unchanged, 18% polymerized) the cure at 120 °C. A relatively large part survives also the postcuring at 180 °C under argon (44%). The tin signals of the surviving cages become broader, probably due to an increased amount of chemical defects in their close surrounding. The short (30 min) heating to 240 °C leads to the complete disappearance of the two stannoxane dodecamer signals, indicating a complete rearrangement of all stannoxane cages to polymer. The results are in good correlation with the temperature dependent SAXS profiles discussed above.

3.2.3. Effect of Stannoxane Polymerization on Thermomechanical Properties. Interestingly, the polymerization of the "Sn4" nanofiller building blocks was found not to cause any marked change in the thermomechanical properties (DMTA profiles in Figure 7) of the standard homogeneously prepared DGEBA−D2000−Sn4 nanocomposites. The DMTA profiles of the nanocomposites postcured under argon at 180 °C for 12 h are nearly the same like DMTA profiles after the standard cure at 120 °C for 3 days, which are shown in the comparison in Figure 7 further below. Only small differences were observed: the tan(δ) values for the postcured samples were always slightly lower, and the tan(δ) peaks assigned to the loosening of the secondary stannoxane aggregates (glass transition of the

dx.doi.org/10.1021/ma201178j | *Macromolecules* 2012, 45, 221−237

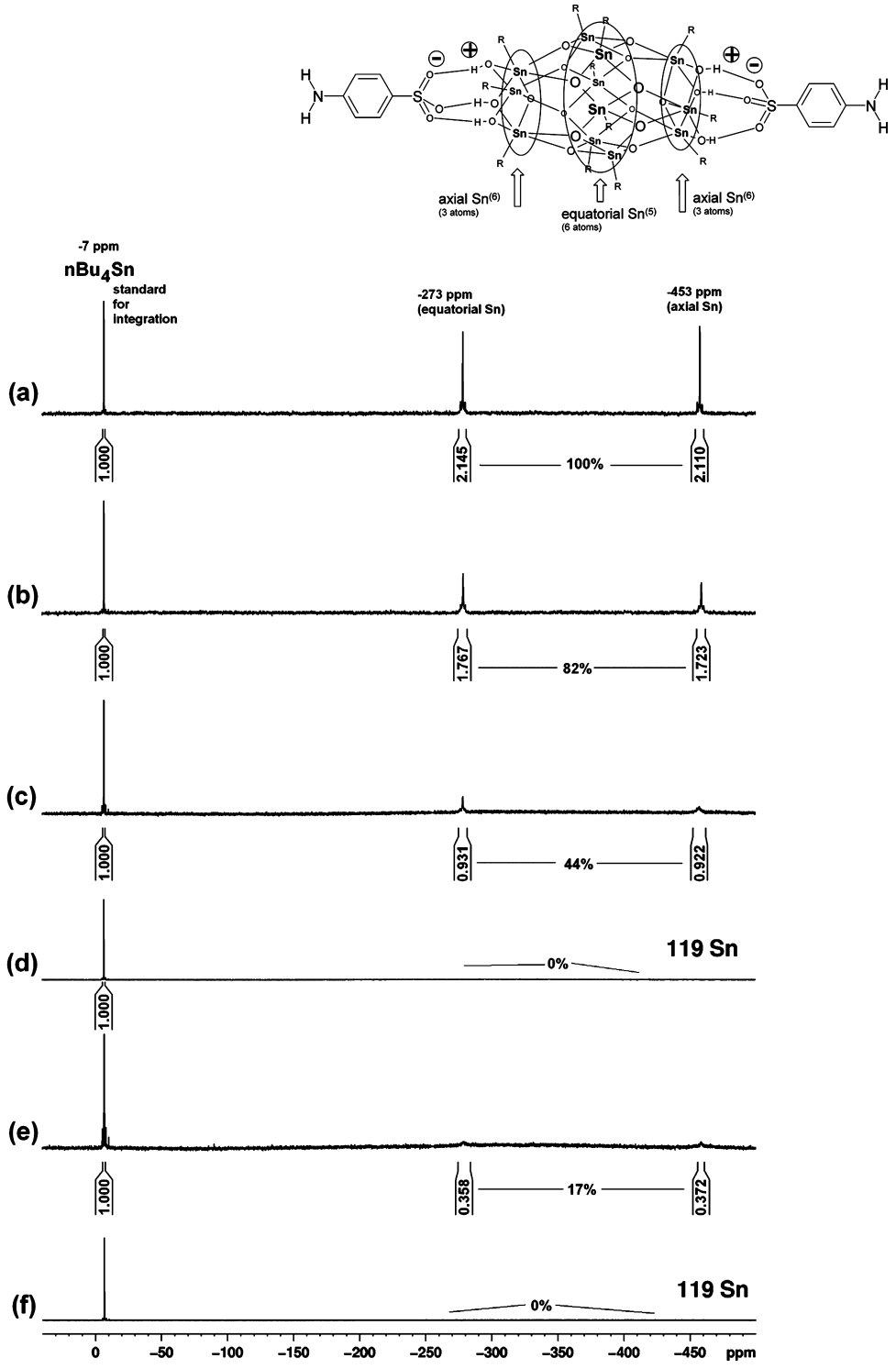

Figure 6. ^{119}Sn NMR spectra: (a) of the PGE−D2000−Sn4 mixture containing 25 mol % of amino groups from "Sn4", after mixing at room temperature (low molecular weight model of the nanocomposite with 25 mol % "Sn4"); (b) low molecular weight model after 3-days-cure at 120 °C under argon; (c) additionally postcured for 12 h at 180 °C under argon; (d) additionally postcured for 30 min at 240 °C under Ar; (e) additionally oxidatively postcured for 12 h at 180 °C under air; (f) additionally postcured for 30 min at 240 °C under air.

stannoxane-rich phase) were shifted to moderately higher temperatures. Both effects could have been caused by the polymerized primary stannoxane domains being more rigid (and more compactly arranged) than the nonpolymerized ones and causing a more efficient immobilization of the epoxy chains.

Brief postcuring at 240 °C (30 min under argon, DMTA not depicted in Figure 7 because of strong overlaps) has a nearly identical effect on the mechanical properties like postcuring at 180 °C, but the rubbery moduli are lower, indicating that the thermal matrix degradation is no longer negligible. The postcure at 240 °C was tested in order to obtain samples

dx.doi.org/10.1021/ma201178j | *Macromolecules* 2012, 45, 221−237

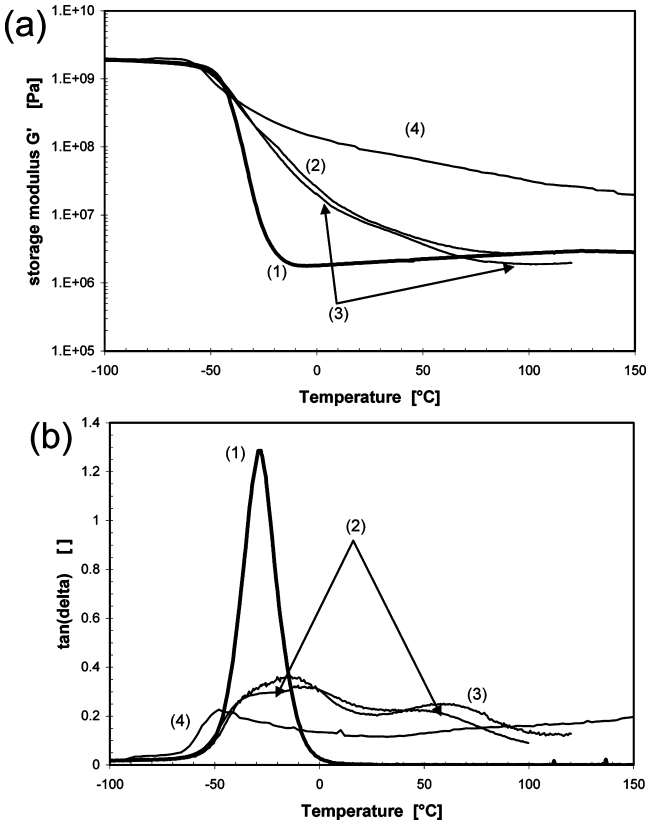

Figure 7. Effect of cure conditions on the thermomechanical properties of the "25-Sn4" nanocomposite, Shear storage modulus G' (a) and loss factor tan(δ) (b) as a function of temperature: (1) neat DGEBA–D2000 matrix cured at 120 °C; (2) "25-Sn4" nanocomposite cured at 120 °C; (3) "25-Sn4" additionally postcured for 12 h under argon; (4) "25-Sn4" additionally postcured for 12 h in air.

with completely polymerized stannoxane nanofiller (postcure at 180 °C/12 h leads only to 56 % of "Sn4" being polymerized).

3.2.4. Sol–Gel Analysis after Stannoxane Polymerization. The samples postcured under argon at 180 °C for 12 h, and especially at 240 °C for 30 min, display higher sol fractions, especially for the matrix component, (Table 1) than the standard (120 °C) cured ones. This is obviously due to the thermal degradation of the DGEBA–D2000 matrix, as observed via DMTA (see above). An analogous degradation can be also observed for the neat matrix.

3.3. Antioxidative Stabilizing Effect of the Stannoxane. A very attractive property of the stannoxane nanofiller consists in its behavior as an antioxidative stabilizing agent in the studied epoxy matrix. The effect was studied via sol–gel and thermogravimetric analysis, and also via DMTA. The mechanism of the stabilization was verified by means of ^{119}Sn NMR, ^{1}H NMR (using liquid low molecular weight analogues), through comparative tests with the "Sn_0" filler and by study of viscosity changes in liquid nanocomposite anologues. The antioxidative effect of the "Sn4" nanofiller manifests itself very strongly in the mechanical properties (DMTA). The tests of oxidative degradation of mechanical properties were performed by exposing the samples to the temperature of 180 °C in circulating air, for 12 h, while the neat matrix DGEBA–D2000 degrades to a brown liquid in half this time (in 6 h) under these conditions. Except for the exposition to air, the oxidative postcure conditions were the same like in case of the nonoxidative postcure under argon. A strong antioxidative effect of-"Sn4" is observed in the sol–gel analysis of oxidized samples, while the TGA results alone did not show any marked effect. "Sn4" hence achieves a strong stabilization, without at the same time preventing small mass losses.

3.3.1. Sol–Gel Analysis. The stannoxane nanobuilding blocks strongly hinder the oxidtaive fragmentation of the epoxy matrix, as can be seen from comparison of gel fraction of "oxidative post-cured" (12 h/180 °C/air) samples (Table 1). The neat matrix degrades quantitatively to a brown liquid mixture (gel fraction falls to 0%). In the "Sn4" nanocomposites the gel fraction falls to values between 80 and 70%, depending on the stannoxane content. While the oxidative degradation is not prevented completely, the stabilization is still fairly successful from the point of view of sol–gel analysis. The brief oxidative postcure at 240 °C leads to a smaller drop in the gel fraction then the prolonged one at 180 °C. It has to be taken into account, that the oxidative postcure at 240 °C for 30 min makes possible a complete oligomerization of "Sn4" (only about 1 min is needed for this process at 240 °C), but the oxidative degradation is a slower process: approximately 2 h would be needed for the degradation of the neat matrix, as determined by visual observation.

3.3.2. Thermogravimetric Analysis (TGA). The results of thermogravimetric stability investigations of epoxy–stannoxane nanocomposites are illustrated in Figure 8. Only TGA traces in air are shown. From the thermogravimetric point of view, the stannoxane "Sn4" in most cases does not stabilize the nanocomposites against mass loss upon oxidative heating. This is in contrast to the observed stabilization of mechanical properties against their oxidative degradation, as discussed below. "Sn4" itself displays a slightly smaller stability in air and in nitrogen than the neat matrix DGEBA–D2000. This means that "Sn4" starts to significantly react with oxygen somewhat earlier than the matrix, which also might explain its tendency to oxidative cross-linking reactions with the matrix, which are discussed just below. Still, some nanocomposites display moderately improved TGA stability in air, e.g., the one with 50 wt % "Sn4". Normally cured, postcured, and oxidatively postcured samples display very similar TGA profiles.

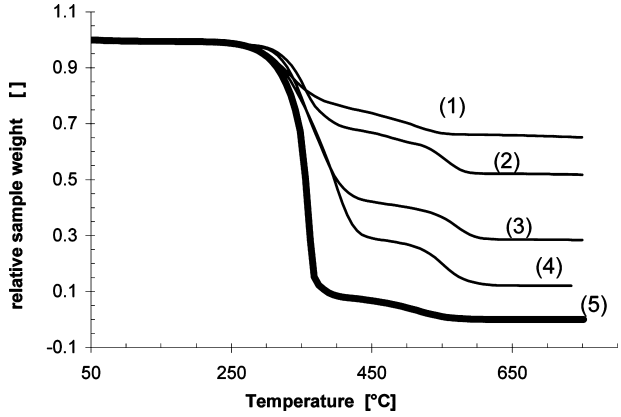

Figure 8. TGA traces in air: relative sample weight in dependence of the temperature (at 10 °C/min): (1) neat "Sn4" stannoxane; (2) epoxy–stannoxane nanocomposite cured at 120 °C containing 100 mol % "Sn4"; (3) 50 mol % "Sn4"; (4) 25 mol % "Sn4"; (5) DGEBA–D2000 reference.

3.3.3. Antioxidative Stabilization Observed via DMTA. Epoxy–"Sn4" nanocomposites postcured in air at 180 °C for 12

dx.doi.org/10.1021/ma201178j | *Macromolecules* 2012, 45, 221–237

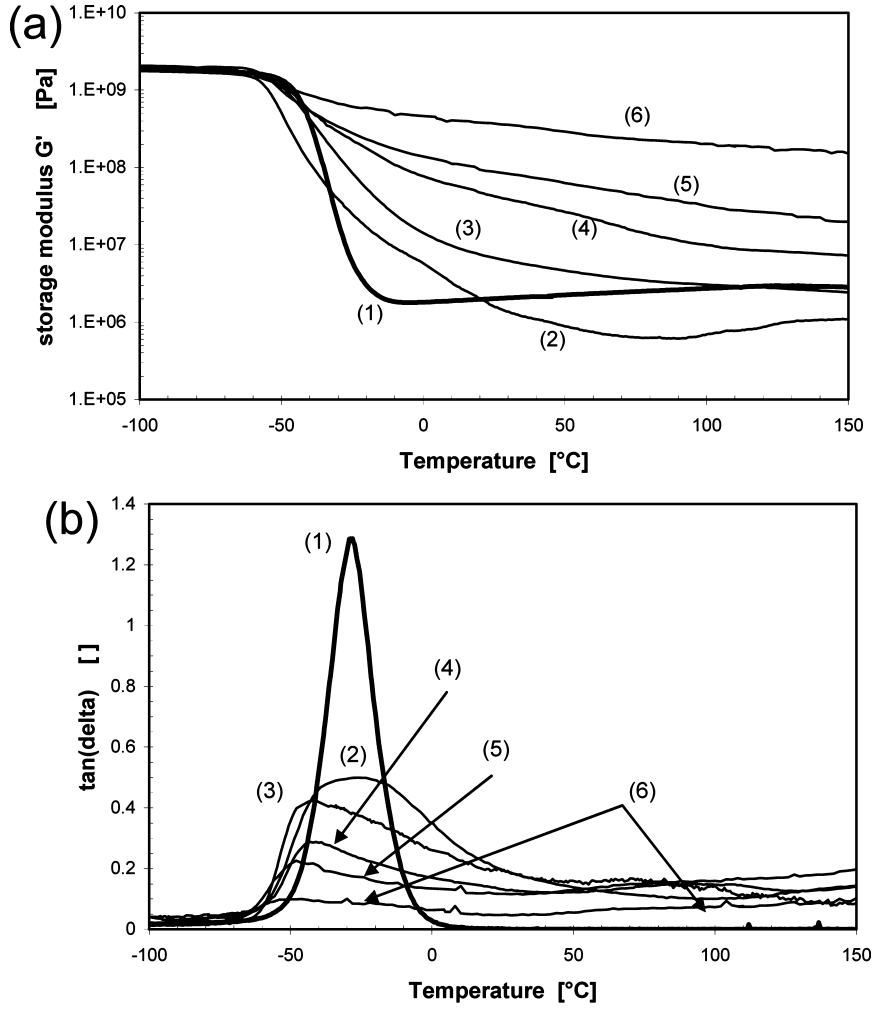

Figure 9. Shear storage modulus G' (a) and loss factor tan(δ) (b) as a function of temperature. Effect of oxidative postcure: (1) reference network DGEBA–D2000 cured at 120 °C; epoxy-"Sn4" nanocomposites after oxidative postcure in air at 180 °C for 12 h; (2) composite with 4 mol % "Sn4", (3) with 7%, (4) with 10%, (5) with 25%, and (6) with 50%.

h, display a dramatically increased rubber modulus after this treatment, especially if the stannoxane content is high, see Figure 9. In contrast to this, the reference sample, DGEBA–D2000, degrades to a brown liquid during this postcure.

The $G' = f(T)$ profiles indicate an increase in cross-link density: Markedly higher equilibrium rubber moduli are observed in comparison to the neat matrix. The effect of mechanical reinforcement via "oxidative post-curing" increases very strongly with increasing "Sn4" content (Figure 9). The amount of 7 mol % (corresponding approximately to 7 wt %) of "Sn4" seems to be optimal to prevent oxidative degradation of mechanical properties under the given treatment (12 h/180 °C/air) and to keep a good material toughness at the same time. Smaller nanofiller amounts are no more sufficient for stabilization, while high stannoxane contents lead not only to strong modulus increase but also to fragility (small deformation at break: only about 1% for "S0-Sn4-pcO") after the oxidative treatment. The tan(δ) = $f(T)$ profiles of the oxidatively postcured samples differ strongly from profiles of analogous samples cured at 120 °C (Ar) or postcured at 180 °C under argon. An increase of T_g and a broadening of the transition region of the stannoxane-rich phase is observed, indicating larger structures with stronger mutual interactions. The transitions of the neat matrix are also broadened, due to some amount of oxidative damage.

3.3.4. Explanation of the Antioxidative Effect. The presumed mechanism of the antioxidative action of "Sn4" is most likely based on radical cross-linking reactions between the stannoxane and the matrix as suggested in Scheme 6. Such reactions are expected to lead to additional covalent matrix-stannoxane and stannoxane-stannoxane bonds, and thus to an increased chemical cross-link density. This effect counteracts and overrides the cross-link density decrease caused by oxidative matrix degradation, and leads to the observed rubber moduli increase and to the preservation of a relatively high fraction of gel, see Table 1. The behavior of the liquid low molecular weight models of the nanocomposites (used for NMR experiments) is a further evidence of the oxidative cross-linking reactions: Upon postcuring in air at 180 °C, the complex viscosity of the liquid model increases strongly (from 5 to 65 Pa·s), while after the 240 °C postcure in air, the liquid model becomes a rubbery gel, and can be only partly dissolved. Analogous postcuring under argon leads to no marked viscosity increase (from 5 to 6 Pa·s).

The effects of oxidative cross-linking were also followed via ^{119}Sn NMR (Figure 6e,f): Only 17% of the original dodecameric stannoxane cages survive after the oxidative

dx.doi.org/10.1021/ma201178j | *Macromolecules* 2012, 45, 221–237

Scheme 6. Possible Oxidative Radical Cross-Linking Reactions Involving: (a) Stannoxane and the Epoxy Matrix; (b) Two Stannoxane Cages

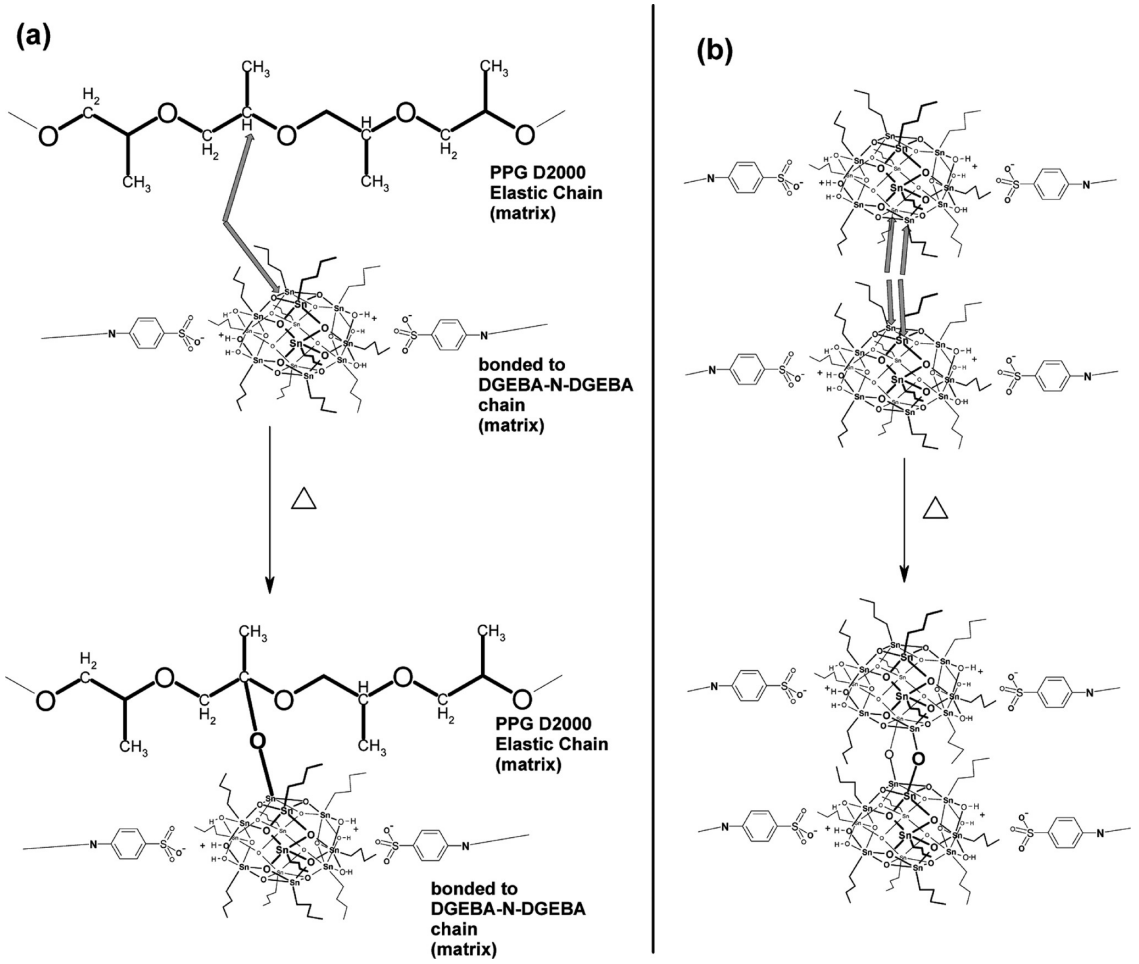

postcure at 180 °C (12 h), while under argon, 44% survived an analogous postcure. The missing 27% are presumedly the stannoxane units which were linked to the D2000 (Scheme 6a) molecules or with each other (Scheme 6b) by radical cross-linking. A further confirmation of the oxidative radical cross-linking was sought via ^{1}H NMR spectroscopy (Figure 10) using also the liquid model: An oxidative radical reaction involving the break of the Sn−C bonds (butyl groups) would lead to the decrease of the butyl groups signals in the spectra of the oxidatively postcured samples. Reactions involving the ionic bonded functional substituents of the stannoxane would lead to the change or disappearance of their aromatic signals. Indeed, a strong decrease of the integrals of stannoxane butyl groups (relative to D2000 "matrix" signals) is observed in Figure 10. The signals of the aromatic functional groups seem also to undergo some change, meaning that these groups do not stay intact, but their intensity is too small for a reliable evaluation.

In search of a more direct proof for stannoxane bonding to the matrix via oxidative cross-linking, the nanocomposite with the nonfunctional stannoxane "Sn_0" (24 wt %) was investigated under postcure and oxidative postcure conditions. "Sn_0" does not reinforce the DGEBA−D2000 matrix; neither does it do so after cure at 120 °C, or after subsequent 180 °C postcuring under argon, as demonstrated by DMTA profiles in Figure 11. However, after oxidative postcuring (12 h/180 °C/air), the DMTA profile changes (Figure 11 curve 4) to a shape similar like in case of the nanocomposite containing 25 mol % of chemically bonded "Sn4" (Figure 3 curve 4), with a typical broad transition region caused by mutual interactions of matrix bonded stannoxanes. This directly proves the chemical attachment of the previously unbonded stannoxane "Sn_0" to the epoxy matrix, as a result of the oxidative postcure. From the application point of view it can be seen, that the "Sn_0" filler is much less an efficient stabilizer then "Sn4" (comparison of the oxidative postcuring of "24-Sn_0" and of "25-Sn4"). This is a result of the strong microphase separation of "Sn_0" in the nanocomposites with DGEBA−D2000, which leads to large "Sn_0" domains (TEM, see above, Figure 2d) with a small specific surface.

3.4. Brief Comparison of Stannoxane vs POSS. In view of the authors' recent research about POSS−epoxy nanocomposites,[22−25] it is interesting to compare the effect of silsesquioxane (POSS) and stannoxane ("Sn4") cage-like nanofillers. If similar amounts of "Sn4" (which replaces D2000) and of the strongly reinforcing cyclopentyl−POSS−DGEBA (which replaces DGEBA) are incorporated into the DGEBA−D2000 matrix, e.g., around 25 wt %, then the mechanical reinforcing effects in the rubber region are of comparable strength for both fillers, while marked differences are also obvious, as illustrated in Figure 12. In case of nanocomposites cured at 120 °C under air exclusion, "Sn4" is rather a weaker reinforcing agent than Cp−POSS−DGEBA:

dx.doi.org/10.1021/ma201178j | *Macromolecules* 2012, 45, 221−237

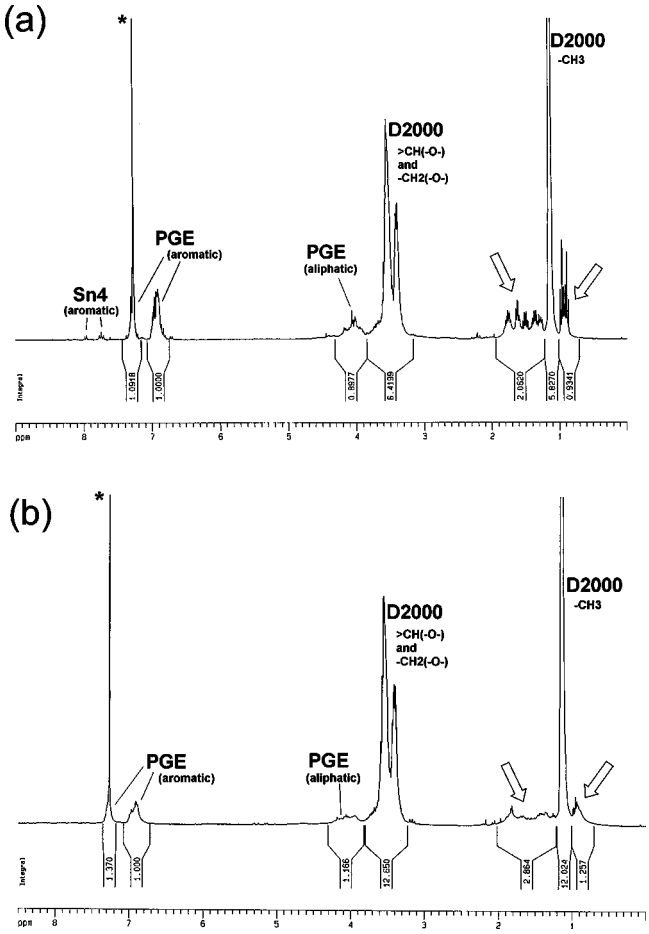

Figure 10. ^{1}H NMR spectra of the low molecular weight model of "25-Sn4" (PGE–D2000–Sn4): (a) after cure at 120 °C for 3 days under argon; (b) after subsequent oxidative postcure at 180 °C in air for 12 h. Signals of butyl substituents of "Sn4" are marked with arrows.

Stronger reinforcement by "Sn4" is only observed between −30 °C and +20 °C, while at higher temperatures Cp–POSS–DGEBA reinforces much stronger. On the other hand, in case of samples treated by oxidative postcure, the stannoxane causes a stronger reinforcement than POSS (cured at 120 °C, postcured or oxidatively postcured) in the complete temperature range.

A typical feature of the stannoxane-filled nanocomposites is the continuous decrease of the reinforcing effect with temperature. On the other hand, reinforcement with POSS leads to a "lifted" plateau of shear modulus in the rubber region, followed by a relatively steep step in modulus around 130 °C, where the most of the reinforcing POSS structures relax. As already discussed above, several thermal transitions are observed in the stannoxane-epoxy nanocomposites, (free matrix, matrix hindered by sterical constraint, and "Sn4"-rich phase), adding together to form a broad transition region. Especially broad is the transition of the "Sn4"-rich phase: the strong primary stannoxane (matrix-bonded "Sn4") aggregates are associated with looser, matrix intercalated secondary ones, which display a wide range of stabilities. In contrast to this, Cp–POSS–DGEBA at 25 wt % reinforces by small primary aggregates (of matrix-bonded POSS), which all possess rather similar stability and disconnect in a narrow temperature range. (Only at very high Cp–POSS–DGEBA loads are effects like matrix immobilization observed.)

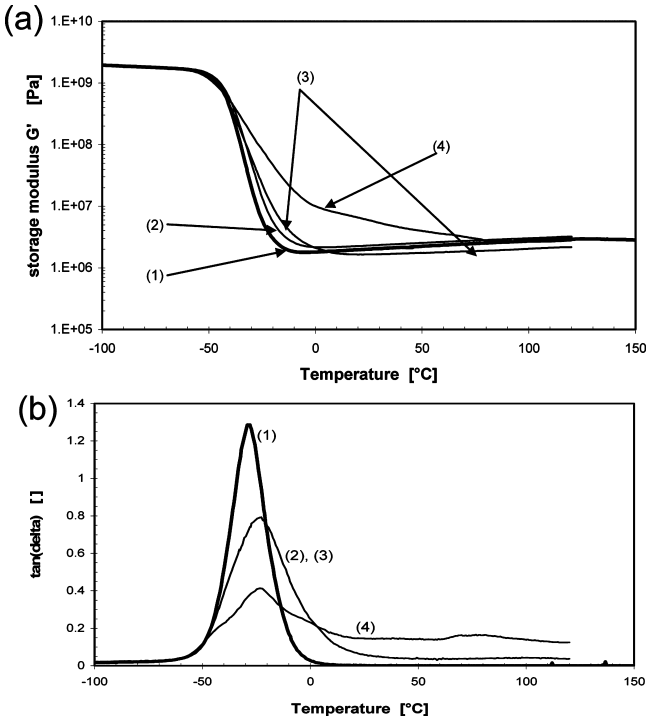

Figure 11. Shear storage modulus G' (a) and loss factor tan(δ) (b) as a function of temperature. Effect of inert nanofiller "Sn_0" on mechanical properties (DMTA profiles) depending on curing and postcuring conditions: (1) DGEBA–D2000 reference (120 °C); (2) network with 24 wt % "Sn_0" cured at 120 °C; (3) "24-Sn_0" postcured (180 °C) under argon; (4) 24 wt % "Sn_0" oxidatively postcured in air (180 °C).

A unique and attractive feature of the stannoxane, which was not yet found for POSS, is its ability of stabilizing epoxies against oxidative degradation of mechanical properties via radical cross-linking reactions. Such behavior was not observed in nanocomposites with POSS. Cp–POSS–DGEBA can still slow down the oxidative degradation (probably by hindering oxygen diffusion) in comparison to the neat matrix as illustrated in Figure 12: while the neat matrix degrades to a liquid after the applied oxidative postcure, the Cp–POSS–DGEBA reinforced nanocomposite displays a decrease of the modulus in the rubber region by one order, but still remains a soft solid. Postcure under argon at 180 °C also leads to a small but significant degradation of the POSS-reinforced sample (Figure 12). However, under more drastic conditions, like treatment with atomic oxygen (low earth orbit conditions)[43,44] or under irradiation with hard UV light[45] (which is able to photochemically fragment the matrix), POSS was observed to protect nanocomposites via formation of a protectiove SiO_2 layer, which is an attractive feature.

4. CONCLUSIONS

Novel hybrid organic–inorganic epoxy networks containing butylstannoxane dodecamer nanobuilding blocks, with two ionic-bonded amino-functional substituents, were successfully prepared. The addition of toluene as solvent was necessary in order to disperse the nanofiller homogeneously.

Nanometer-scaled phase separation nevertheless occurs in the later stages of the nanocomposite syntheses, because the nanofiller solubility in the matrix is only moderate. This

dx.doi.org/10.1021/ma201178j | Macromolecules 2012, 45, 221–237

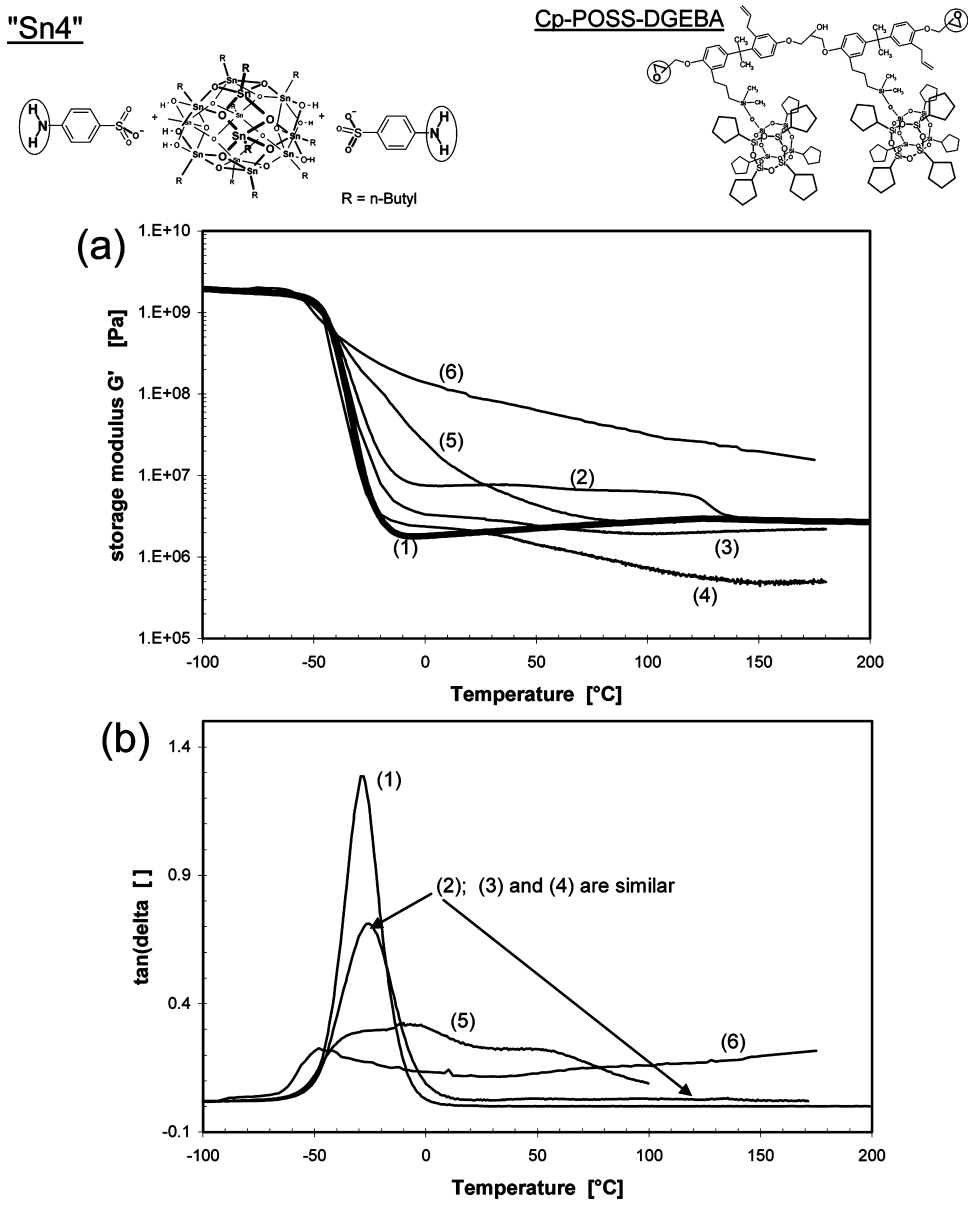

Figure 12. Comparison of stannoxane "Sn4" and of the strongly reinforcing cyclopentyl–POSS–DGEBA nanofillers in their effect on the DGEBA–D2000 thermomechanical properties. DMTA spectra: (1) DGEBA–D2000 reference; (2): 33 epoxy-mol % (25 wt %) cyclopentyl–POSS–DGEBA cured at 120 °C; (3) POSS nanocomposite additionally postcured at 180 °C for 12 h under argon; (4) POSS nanocomposite additionally postcured at 180 °C for 12 h in air; (5) 25 amino-mol % (24 wt %) Sn4 cured at 120 °C; (6) 25 mol % Sn4 additionally postcured at 180 °C under air; (a) $G' = f(T)$; (b) $\tan(\delta) = f(T)$.

nanoaggregation was observed via SAXS and TEM and plays a useful role in the mechanical matrix reinforcement.

The stannoxane dodecamers were shown to partly oligomerize (18%) during the epoxy network cure at 120 °C. At higher temperatures, the nanofiller oligomerization inside its domains becomes prominent. This process does not change the sample's overall morphology, and the thermo-mechanical properties remain practically unchanged. However, the oligomerization most likely contributes to the nanofiller's low extractability, which is a useful effect.

The ability of the stannoxane nanofiller to protect (via oxidative cross-linking) the epoxy matrix against the oxidative degradation of mechanical properties is a very attractive feature. For this purpose, already a few weight percent of stannoxane are sufficient. In this context, the difficult extractability of the stannoxane (stabilizer) is highly advantageous.

AUTHOR INFORMATION

Corresponding Author

*Telepnone: (+420) 296 809 384. E-mail: strachota@imc.cas.cz.

ACKNOWLEDGMENTS

The authors thank Ms. Miroslava Kremličková for carrying out the TGA experiments, Ms. Dana Kaňková for recording a large part of the NMR spectra, Ing. Magdalena Perchacz MSc. for taking part in the final stages of the synthesis work, and Ms. Zuzana Walterová and Ms. Zuzana Kálalová for the determination of the tin content via ash analysis.The authors thank the Grant Agency of the Academy of Sciences of the Czech Republic, Grant Nr. IAA400500701, the European Community's Human Potential Program under Contract

HPRN-CT-2002−00306, and the Czech Science Foundation, Grant Nr. 108/11/2151 for the financial support of this work. The authors thank Huntsman Inc. for the donation of Jeffamine D2000.

REFERENCES

(1) Miri, V.; Elkoun, S.; Peurton, F.; Vanmansart, C.; Lefebvre, J. M.; Krawczak, P.; Seguela, R. *Macromolecules* **2008**, *41*, 9234−9244.
(2) Treece, M. A.; Oberhauser, J. P. *Macromolecules* **2007**, *40*, 571−582.
(3) Lee, Y. H.; Bur, A. J.; Roth, S. C.; Start, P. R. *Macromolecules* **2005**, *38*, 3828−3837.
(4) Durmus, A.; Ercan, N.; Soyubol, G.; Deligoz, H.; Kasgoz, A. *Polym. Compos.* **2010**, *31*, 1056−1066.
(5) Matteucci, S.; Van Wagner, E.; Freeman, B. D.; Swinnea, S.; Sakaguchi, T.; Masuda, T. *Macromolecules* **2007**, *40*, 3337−3347.
(6) Weng, C. J.; Huang, J. Y.; Huang, K. Y.; Jhuo, Y. S.; Tsai, M. H.; Yeh, J. M. *Electrochim. Acta* **2010**, *55*, 8430−8438.
(7) Tunc, S.; Duman, O. *LWT-Food Sci. Technol.* **2010**, *44*, 465−472.
(8) Rao, Y. Q.; Chen, S. *Macromolecules* **2008**, *41*, 4838−4844.
(9) Kuila, B. K.; Park, K.; Dai, L. M. *Macromolecules* **2010**, *43*, 6699−6705.
(10) Antonello, A.; Brusatin, G.; Guglielmi, M.; Martucci, A.; Bello, V.; Mattei, G.; Mazzoldi, P.; Pellegrini, G. *Thin Solid Films* **2010**, *518*, 6781−6786.
(11) Kim, H.; Abdala, A. A.; Macosko, C. W. *Macromolecules* **2010**, *43*, 6515−6530.
(12) Moniruzzaman, M.; Winey, K. I. *Macromolecules* **2006**, *39*, 5194−5205.
(13) Sahoo, S. K.; Kim, D. W.; Kumar, J.; Blumstein, A.; Cholli, A. L. *Macromolecules* **2003**, *36*, 2777−2784.
(14) Hammond, M. R.; Dietsch, H.; Pravaz, O.; Schurtenberger, P. *Macromolecules* **2010**, *43*, 8340−8343.
(15) Robbes, A. S.; Jestin, J.; Meneau, F.; Dalmas, F.; Sandre, O.; Perez, J.; Boue, F.; Cousin, F. *Macromolecules* **2010**, *43*, 5785−5796.
(16) Horak, D.; Trchova, M.; Benes, M. J.; Veverka, M.; Pollert, E. *Polymer* **2010**, *51*, 3116−3122.
(17) Horak, D.; Babic, M.; Jendelova, P.; Herynek, V.; Trchova, M.; Likavcanova, K.; Kapcalova, M.; Hajek, M.; Sykova, E. *J. Magn. Magn. Mater.* **2009**, *321*, 1539−1547.
(18) Priolo, M. A.; Gamboa, D.; Holder, K. M.; Grunlan, J. C. *Nano Lett.* **2010**, *10*, 4970−4974.
(19) Kim, H.; Macosko, C. W. *Macromolecules* **2008**, *41*, 3317−3327.
(20) Russo, G. M.; Simon, G. P.; Incarnato, L. *Macromolecules* **2006**, *39*, 3855−3864.
(21) Dong, W. F.; Liu, Y. Q.; Zhang, X. H.; Gao, J. M.; Huang, F.; Song, Z. H.; Tan, B. H.; Qiao, J. L. *Macromolecules* **2005**, *38*, 4551−4553.
(22) Matějka, L.; Strachota, A.; Pleštil, J.; Whelan, P.; Steinhart, M.; Šlouf, M. *Macromolecules* **2004**, *37*, 9449−9456.
(23) Strachota, A.; Kroutilová, I.; Kovářová, J.; Matějka, L. *Macromolecules* **2004**, *37*, 9457−9464.
(24) Strachota, A.; Whelan, P.; Kříž, J.; Brus, J.; Urbanová, M.; Šlouf, M.; Matějka, L. *Polymer* **2007**, *48*, 3041−3058.
(25) Brus, J.; Urbanova, M.; Strachota, A. *Macromolecules* **2008**, *41*, 372−386.
(26) Eychenne-Baron, C.; Ribot, F.; Steunou, N.; Sanchez, C. *Organometallics* **2000**, *19*, 1940−1949.
(27) Ribot, F.; Banse, F.; Diter, F.; Sanchez, C. *New J. Chem.* **1995**, *19*, 1145−1153.
(28) Ribot, F.; Lafuma, A.; Eychenne-Baron, C.; Sanchez, C. *Adv. Mater.* **2002**, *14*, 1496−1499.
(29) Ribot, F.; Veautier, D.; Guillaudeu, S. J.; Lalot, T. *J. Mater. Chem.* **2005**, *15*, 3973−3978.
(30) Ribot, F.; Escax, V.; Martins, J. C.; Biesemans, M.; Ghys, L.; Verbruggen, I.; Willem, R. *Chem.—Eur. J.* **2004**, *10*, 1747−1751.
(31) Van Lokeren, L.; Willem, R.; van der Beek, D.; Davidson, P.; Morris, G. A.; Ribot, F. *J. Phys. Chem. C* **2010**, *114*, 16087−16091.
(32) Weiss, R. A.; Yu, W. C. *Macromolecules* **2007**, *40*, 3640−3643.
(33) Osborn, S. J.; Hassan, M. K.; Divoux, G. M.; Rhoades, D. W.; Mauritz, K. A.; Moore, R. B. *Macromolecules* **2007**, *40*, 3886−3890.
(34) Shah, R. K.; Paul, D. R. *Macromolecules* **2006**, *39*, 3327−3336.
(35) Xu, L.; Weiss, R. A. *Macromolecules* **2003**, *36*, 9075−9084.
(36) Puff, H.; Reuter, H. *J. Organomet. Chem.* **1989**, *373*, 173−178.
(37) Dakternieks, D.; Zhu, H.; Tiekink, E. R. T.; Colton, R. J. *J. Organomet. Chem.* **1994**, *476*, 33−38.
(38) Chandrasekhar, V.; Gopal, K.; Singh, P.; Narayanan, R. S.; Duthie, A. *Organometallics* **2009**, *28*, 4593−4601.
(39) Holmes, R. R. *Acc. Chem. Res.* **1989**, *22*, 190−194.
(40) Ribot, F. In *Tin Chemistry: Fundamentals, Frontiers, and Applications*; Davies, A. G.. Gielen, M., Pannell, K. H., Tiekink, E. R. T., Eds. ; Wiley, Chichester (UK), 2008; pp 69−92.
(41) Eychenne-Baron, C.; Ribot, F.; Steunou, N.; Sanchez, C. *J. Organomet. Chem.* **1998**, *567*, 137−142.
(42) Matejka, L. *Macromolecules* **1989**, *22*, 2911−2917.
(43) Gilman, J. W.; Schlitzer, D. S.; Lichtenhan, J. D. *J. Appl. Polym. Sci.* **1996**, *60*, 591−596.
(44) Verker, R.; Grossman, E.; Eliaz, N. *Acta Mater.* **2009**, *57*, 1112−1119.
(45) Sarantopoulou, E.; Kollia, Z.; Cefalas, A. C.; Siokou, A. E.; Argitis, P.; Bellas, V.; Kobe, S. *J. Appl. Phys.* **2009**, *105*, 114305.

Macromolecules

ARTICLE

pubs.acs.org/Macromolecules

Impressive Fatigue Life and Fracture Toughness Improvements in Graphene Oxide/Epoxy Composites

Daniel R. Bortz,*[,†] Erika Garcia Heras,[‡] and Ignacio Martin-Gullon[†]

[†]Department of Chemical Engineering, University of Alicante, Alicante, Spain

[‡]Grupo Antolín Ingeniería, Crta Irún 244, Burgos, Spain

ABSTRACT: Epoxy systems have proven popular having important applications in aerospace and wind energy, but fracture and fatigue resistance of this polymer remain less than desired. Graphene oxide, a form of atomically thin carbon, possessing impressive multifunctional properties and an ideal interface for interacting with polymer matrices, has emerged as a viable reinforcement candidate. In this work, we report enhancements of 28−111% in mode I fracture toughness and up to 1580% in uniaxial tensile fatigue life through the addition of small amounts (≤1 wt %) of graphene oxide to an epoxy system. Graphene oxide was uniquely synthesized by unraveling and splaying open helical-ribbon carbon nanofibers. The resulting oxygenated basal planes and edges of the graphene oxide sheets were observed to promote onset of the cross-linking reaction and led to an increase in total heat of reaction effecting slightly higher glass transition temperatures of the cured composites. Measured improvements were also detected in quasi-static tensile and flexural stiffness and strength. The addition of only 0.1 wt % graphene oxide yielded a ∼12% increase in tensile modulus. At 1 wt %, flexural stiffness and strength were 12 and 23% greater than the unmodified epoxy. Sheets were observed to be well-dispersed and at various orientations within the matrix, enabling their large, 2D, and zero bulk dimensions to pin incipient matrix cracks, a toughening mechanism not typically detected in nanocomposites.

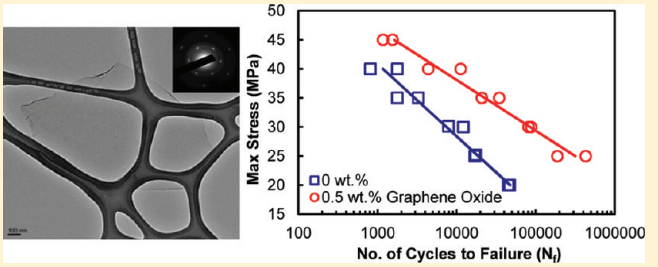

The 2004 report[1] on the isolation of the most basic graphitic building block, atomically thin carbon known as graphene, truly excited science. Since then, enormous electron mobility[2] and thermal conductivity[3] values of these materials have been reported. Mechanically, single-layer graphene, the thinnest known material, has also been shown to possess the highest measured modulus and break strength of any substance to date.[4] The range of potential applications for this material is indeed exciting, and although more discoveries and intrinsic measurements are to be made, translating its properties to the macro-scale has now become a prime scientific focus. The introduction of graphene sheets into polymeric matrices for instance has been proposed as an alternative[5] or supplementation[6] to more traditional carbon nanotube (CNT) reinforcement. Several studies have recently shown improved quasi-static,[7] fatigue,[8] and electrical properties[5] for graphene-based polymer composites. Numerous reviews on the subject have also become available.[9−11] Some debate has arisen over the appropriate graphene structure for use in polymer composites, e.g., graphene oxide (G−O) or a reduced form containing fewer surface and edge oxygen groups. Although promising results have been reported by several groups working with reduced forms of graphene in epoxy matrices, e.g., Rafiee et al.,[8,12,13] it appears that from the most recent literature[14,15] the oxide form may be more advantageous for composite synthesis and future scale-up operations.

The "wrinkled" surface of reduced graphene is often credited as a favorable medium for creating a robust interface able to locally interlock with the matrix. At the same time, the atomically smooth surface has been shown to effect low interfacial strength in strain-dependent Raman spectroscopy measurements.[16] Furthermore, restacking of the sheets following chemical or thermal reduction due to their instability in popular solvents used in polymer processing can hinder performance, similar to the consequences of agglomeration in CNT composites. The latter concern however has been partially alleviated through the use of surfactants[17] or polymer blending prior to reduction.[5] The functional groups (epoxide, hydroxyl, carboxyl, and carbonyl) present on the basal planes and edges of G−O facilitate solubility in water or protic solvents. Moreover, the groups may further improve matrix affinity and allow for additional surface chemistry tailoring if desired. Unfortunately, these compounds also result in G−O being electrically insulating, thus limiting the multifunctionality observed in other graphite-based nanocomposites.

Literature with respect to graphene synthesis is predominantly populated with methods relating to the intercalation of graphite by oxidation and subsequent exfoliation of the planar graphite oxide layers. More recently, fabricating graphene nanoribbons by methods pertaining to the "unzipping" of CNTs have emerged as alternatives with hopes for improving quality and yield. Kosynkin et al.[18] first highlighted the common oxidative method by applying a Hummers and Offeman[19] based treatment to lengthwise unzip and roll open both single and multiwall carbon

Received: July 8, 2011
Revised: November 5, 2011
Published: December 02, 2011

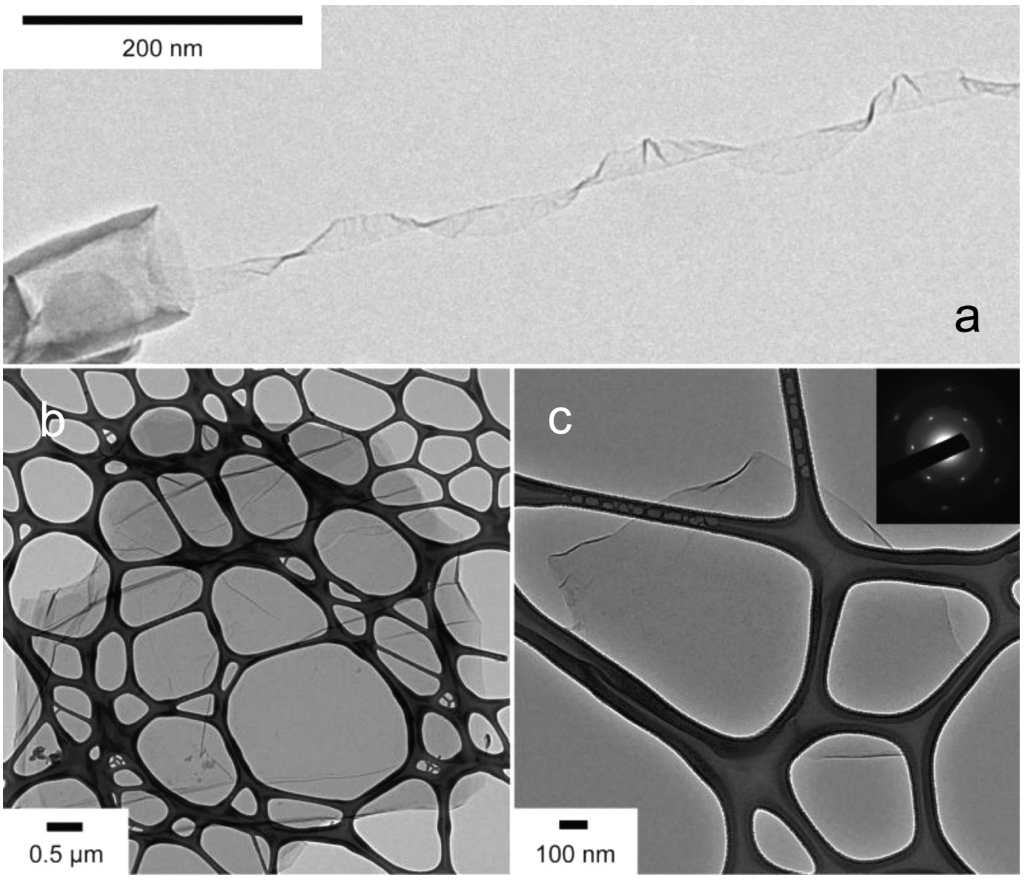

Figure 1. Series of high-resolution TEM images documenting (a) the unraveling of the graphene layers of a helical-ribbon carbon nanofiber (reprinted with permission from ref 21; copyright 2007 Elsevier), (b) a few-layer sheet having ~8 μm lateral dimension, and (c) what appears to be a monolayer graphene oxide sheet with ~2 μm lateral dimension.

nanotubes (SWCNTs and MWCNTs). Herein, we expand on our teams work previously presented by Varela-Rizo et al.[20] in which the technique of Kosynkin and colleagues was modified to successfully unravel and splay open the graphene layers of helical-ribbon carbon nanofibers (CNFs).[21] The result is mostly mono- and few-layer G−O sheets (Figure 1) that are highly soluble in water and polar organic solvents, a key feature for their use in composite systems. Conversion is high but not 100%, meaning some oxidized fiber fragments remain unexfoliated. The unique mechanism responsible for formation of the sheets has yet to be fully explained though is probably similar to the chemical unzipping of CNTs described by Kosynkin et al. The G−O sheets were subsequently introduced in small amounts ($\leq$1% by weight) to a commercially available thermosetting epoxy system. We report the effect on the epoxide cure kinetics by monitoring the cross-linking reaction via differential scanning calorimetry (DSC). Glass transition temperature (T_g) as well as thermo- and quasi-static mechanical properties were subsequently measured. We further demonstrate large improvements in fracture toughness, and up to 1580%, over the full range of applied stress amplitudes in uniaxial tensile fatigue life of the graphene oxide nanocomposites.

EXPERIMENTAL DETAILS

Graphene Oxide Preparation. A detailed description and characterization of graphene oxide synthesis was previously reported.[20] A typical process involved suspending a commercially available helical-ribbon CNF (GANF, Grupo Antolín Ingeniería, Spain) in concentrated sulfuric acid (H_2SO_4, 95−97%, VRW) followed by treatment with potassium permanganate ($KMnO_4$, VRW) at elevated temperature. After oxidation was complete the reaction was terminated by pouring over an ice/hydrogen peroxide (H_2O_2, 30%, VRW) mixture. Multiple water washings and filtrations followed by a final ethanol (VRW) washing and filtration concluded the process. The material collected from the final filtering was dried under vacuum. The oxidized solid was subsequently suspended in acetone at a concentration of 2.5 mg/mL and exfoliated by high-energy sonication to yield graphene oxide. High-resolution transmission electron microscopy confirmed unraveling and isolation of the fiber's graphene planes (Figure 1). Lateral dimensions typically measured 0.5−10 μm.

Graphene Oxide Dispersion in the Epoxy Matrix. A bisphenol A/F diglycidyl ether blend (Resoltech 1800/1805, Eguilles, France) was used as the polymer matrix. The resin was added to the graphene oxide/acetone suspension and heated to 60 °C for 12 h to allow for slow solvent evaporation. An additional 12 h of heating under vacuum conditions ensured complete acetone removal. The resulting dispersion was passed through a three-roll calender mill with gap settings of 5 μm and roller speeds of 30, 60, and 180 rpm. Dilution with neat resin produced final graphene nanocomposites at concentrations of 0.1, 0.25, 0.5, and 1 wt %. The diamine hardener, 1,2-diaminocyclohexane, was added to the dispersions at a weight ratio of 100:17 and mixed with a laboratory mixer at 5000 rpm for 5 min. The resulting mixtures were poured into a silicone mold and degassed at −1 bar for 30 min. The individually cast specimens, having dimensions of 250 × 25 × 2.5 mm

Table 1. Cure Reaction and Thermomechanical Properties of the Various Neat and Reinforced Epoxy Systems[a]

material	T_{on} (°C)	T_p (°C)	H (J/g)	E''_p (°C)	T_g (°C)
neat matrix	60.50 (0.68)	81.99 (0.47)	209.10 (6.65)	100.73 (1.11)	126.30 (0.10)
0.1 wt % graphene oxide	58.96 (0.50)	81.92 (0.86)	207.15 (3.32)	106.18 (2.58)	126.46 (0.47)
0.25 wt % graphene oxide	58.37 (2.51)	82.78 (0.58)	232.15 (11.81)	108.39 (1.85)	126.89 (0.15)
0.5 wt % graphene oxide	57.43 (2.19)	82.78 (0.01)	229.25 (13.79)	117.64 (0.79)	129.33 (0.09)
1 wt % graphene oxide	54.80 (0.10)	83.53 (0.01)	228.35 (5.30)	114.90 (1.52)	128.05 (0.88)

[a] Onset temperature of curing (T_{on}), peak exothermic temperature (T_p), and total heat of cross-link reaction (H) as measured by DSC for neat and nanocomposite materials. Loss modulus peak (E''_p) and glass transition temperature (T_g) as measured by DMA for neat and nanocomposite materials. Standard deviations are in parentheses.

for static tensile and tension−tension fatigue testing, 63.5 × 12.7 × 4 mm for mode I fracture toughness testing, and 60 × 12.7 × 3.2 mm for flexural and dynamic mechanical analysis (DMA), were released from the mold after 12 h at 40 °C. Recommended by the manufacturer, initial curing for 15 h at 60 °C and a postcure of 6 h at 110 °C were carried out in a programmable laboratory furnace. Finally, in order to remove stress concentrating surface defects, specimen surfaces were smoothed with 600-grit silicone carbide paper prior to characterization.

Characterization. X-ray photoelectron spectroscopy (XPS) experiments were carried out on a VG-Microtech Multilab 3000 system. The X-ray microprobe pass energy was fixed at 26.0 eV. DSC scans (TA Instruments Q100) to study the effect of graphene oxide on the cure kinetics of the cross-link reaction were performed by preparing a small dispersion and placing a 4−5 mg sample in an open aluminum pan. Scans were in flowing air (50 mL/min) from 25 to 160 °C at a heating rate of 2 °C/min. Samples were quickly cooled, and secondary scans were then executed to ensure a complete cure was achieved. Glass transition temperatures were taken from the tan δ peak on fully cured samples by single cantilever mode DMA (TA Instruments 2980) from 30 to 180 °C at 2 °C/min and 1 Hz.

Quasi-static tension and tensile fatigue testing were performed on a servo-hydraulically controlled Instron 8516. Displacement rates during static testing of the nanocomposites were the ASTM D 3039 recommended 2 mm/min. Modulus was measured with a clip on type extensometer over a gauge length of 25 mm between 0.001 and 0.003 absolute strains. Fatigue testing was performed at $R = 0.1$ (R is the ratio of minimum to maximum stress in a fatigue cycle) and 5 Hz. Two specimens were tested at each of five stress levels. Flexural properties were measure according to ASTM D 790 at a span-to-thickness ratio of 16 and at a crosshead rate of 1.4 mm/min ($\varepsilon = 0.01\ \text{min}^{-1}$).

Fracture toughness of the nanocomposites was measured following ASTM D 5045 using single edge notched bend (SENB) specimens. A 1 mm wide sharpened notch was machined at the midpoint of each specimen. A precrack was then initiated by tapping a fresh razor blade in the notch. Specimens were loaded to failure at 10 mm/min using an Instron 3344 equipped with a 2 kN load cell. Load−deformation values were recorded, and precrack lengths were measured post mortem by optical microscopy. The critical-stress-intensity parameter (K_{Ic}) was calculated according to the standard; critical strain energy release rate (G_{Ic}) was tabulated by integration of each load−deformation curve.

Sheet resistance was measured on prepared films by painting two rectangular electrodes (25 × 2 mm) parallel to one another and separated by 25 mm. The resistance between the two electrodes was then quantified by using a two-point measurement device operating at 10 V, fulfilling the requirements of ASTM D257. Scanning electron microscopy (SEM) of gold-coated fracture surfaces was performed using a JEOL JSM-840 SEM at 15 kV. Transmission electron microscopy (TEM) of ultramicrotomed G−O nanocomposites (~80 nm thickness) positioned on a standard copper grid was performed at 200 kV using a JEOL 1020 TEM.

RESULTS AND DISCUSSION

Cross-Link Reaction Monitoring, XPS, and Thermomechanical Properties. After the intercalation reaction and exfoliation in acetone, graphene oxide/epoxide resin dispersions were prepared by the controlled and thorough evaporation of acetone followed by three-roll calender milling. Cross-linking was achieved through the stoichiometric addition of a diamine hardener (1,2-diaminocyclohexane). Results from DSC scans on unreacted dispersions and DMA scans on fully cured specimens are given in Table 1. Onset of the cure reaction (T_{on}) was observed to decrease as a function of G−O concentration, up to a maximum of about 6 °C at 1 wt %. Peak heat flow (T_p), i.e., the temperature of maximum exothermic heat flow during the cure reaction, remained largely unaffected. Integrating the area of each exothermic peak also revealed an increase in the total heat of reaction, H, in the nanocomposites. This effect though appeared saturated at 0.25 wt % G−O. The acceleration effect in the early stage of the cure reaction could be explained by an increase in the oxygen-containing functionalities on the surfaces and edges of the sheets.[18] Such an increase in oxygen groups could produce a catalytic effect on epoxide ring opening, resulting in higher initial reaction rates. Comparison of the XPS spectra of the parent CNFs and G−O corroborates the existence of a greater quantity of surface oxygen functionalities in the graphene oxide materials (Figure 2). The O 1s/C 1s peak area ratio increased from 0.05 for the CNFs to 0.68 in the case of G−O. This led to an increase in the relative mass of oxygen from 5% to 40%.

Subsequent DSC scans did not display any further exothermic behavior, confirming a complete cure had been achieved. The second scans however did not allow for an accurate measure of T_g. Thus, glass transition temperatures were taken from the tan δ peak of DMA scans and exhibited increases of 2−3 °C at 0.5 and 1 wt % G−O loadings as compared to the neat sample. A more substantial shift to higher temperatures, up to ~17 °C, was detected in the peak of the loss modulus curve. This behavior suggests a change in molecular mobility relative to the neat epoxy matrix.[22] Horizontal shifting by the loss modulus curve indicates the entire polymer matrix was effectively altered by interactions with the graphene oxide surface. If a region of nonbulk polymer near the surface of the filler (interphase) had been created, the loss modulus curve would have instead exhibited broadening toward higher temperatures; this was not observed. Combined, these results indicate G−O inclusion could impart slightly higher cross-link densities to the network architecture, though the modest T_g increases suggest only minor overall affect. The 2D, zero bulk structure of the G−O planes did not however appear to stimulate the formation of an interphase zone as is common in materials having lower cross-link densities.[23]

dx.doi.org/10.1021/ma201563k |Macromolecules 2012, 45, 238–245

Nanocomposite Mechanical and Electrical Properties. Monotonic material performance of the graphene oxide based nanocomposites is summarized in Figure 3. Tensile modulus was enhanced by 12% at 0.1 wt % G−O. Higher loadings also displayed increased tensile stiffness when compared to the control but more modest than the 0.1 wt % G−O group. Ultimate tensile strength showed a maximum improvement of about 13% in samples with 0.5 wt % G−O compared to the control group. Above this concentration both tensile stiffness and strength decreased. At 1 wt % G−O, tensile modulus was nearly equal to the neat matrix and strength was slightly less than the control. Flexural modulus and strength similarly saw the largest incremental increase at the lowest G−O concentration, 9 and 18%, respectively, at 0.1 wt % G−O. Unlike the tensile results though, gains continued as a function of graphene oxide content across the full range of concentrations. At 1 wt % G−O, flexural modulus and strength were 12 and 23% greater than the control group.

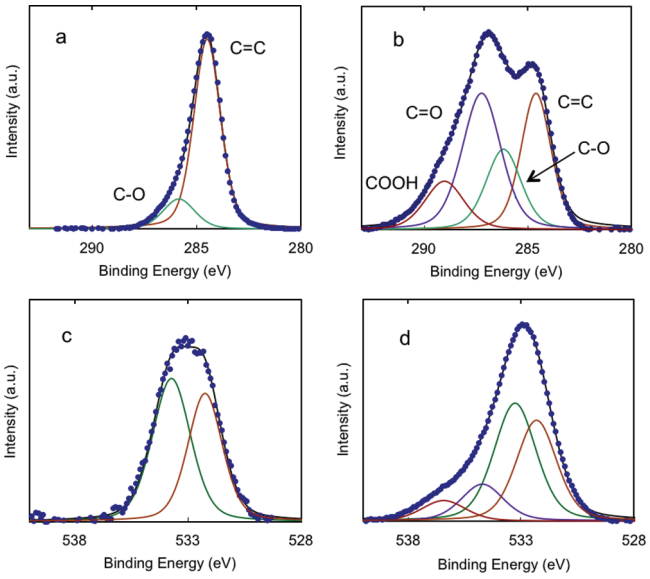

Figure 2. High-resolution XPS C 1s spectra and fitting curves: (a) parent carbon nanofibers and (b) graphene oxide and O 1s spectra and fitting curves; (c) parent carbon nanofibers and (d) graphene oxide.

More significant improvements were observed in fracture toughness. Graphene oxide addition led to enhancements of the critical stress intensity factor (K_{Ic}) of approximately 28−63% with respect to the control. Similarly, improvements of 29−111% were detected in the critical strain energy release rate (G_{Ic}). The rate of improvement was quite impressive up to 0.5 wt % G−O, whereas doubling the graphene oxide concentration to 1 wt % G−O revealed a saturation of the toughening effect, only increasing K_{Ic} by a further ∼1% over the 0.5 wt % G−O loaded composite.

The characteristic brittleness and low fracture toughness of cured epoxy systems are a product of their high cross-link densities, which result in poor absorption of energy during fracture. These factors frequently lead to mirror-like fracture surfaces, e.g., Figure 4a. Evidence of toughening caused by fiber pullout, rupture, crack bridging, and the nucleation of voids surrounding debonded fibers are often visible on CNT reinforced epoxy composite fracture surfaces.[24−26] These mechanisms appeared absent in the current G−O composites. Initial SEM evidence indicated a departure from the smooth fracture surface by the composite materials (Figure 4b). The coarse, multiplane features on the composite fracture surface suggest that the graphene oxide sheets have induced the deflection of propagating crack fronts. This process introduces off-plane loading that generates new fracture surfaces, thus

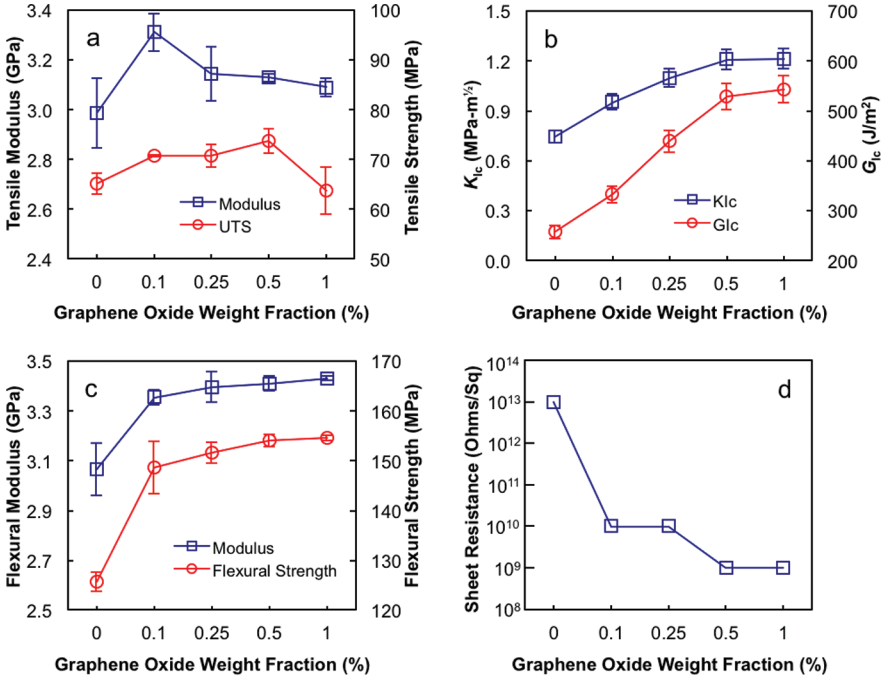

Figure 3. Quasi-static mechanical and electrical properties of both neat epoxy and epoxy composites containing various weight fractions of graphene oxide: (a) Tensile modulus and ultimate tensile strength, (b) flexural modulus and ultimate flexural strength, (c) critical stress intensity factor and critical strain energy release rate, and (d) surface resistivity.

dx.doi.org/10.1021/ma201563k |*Macromolecules* 2012, 45, 238–245

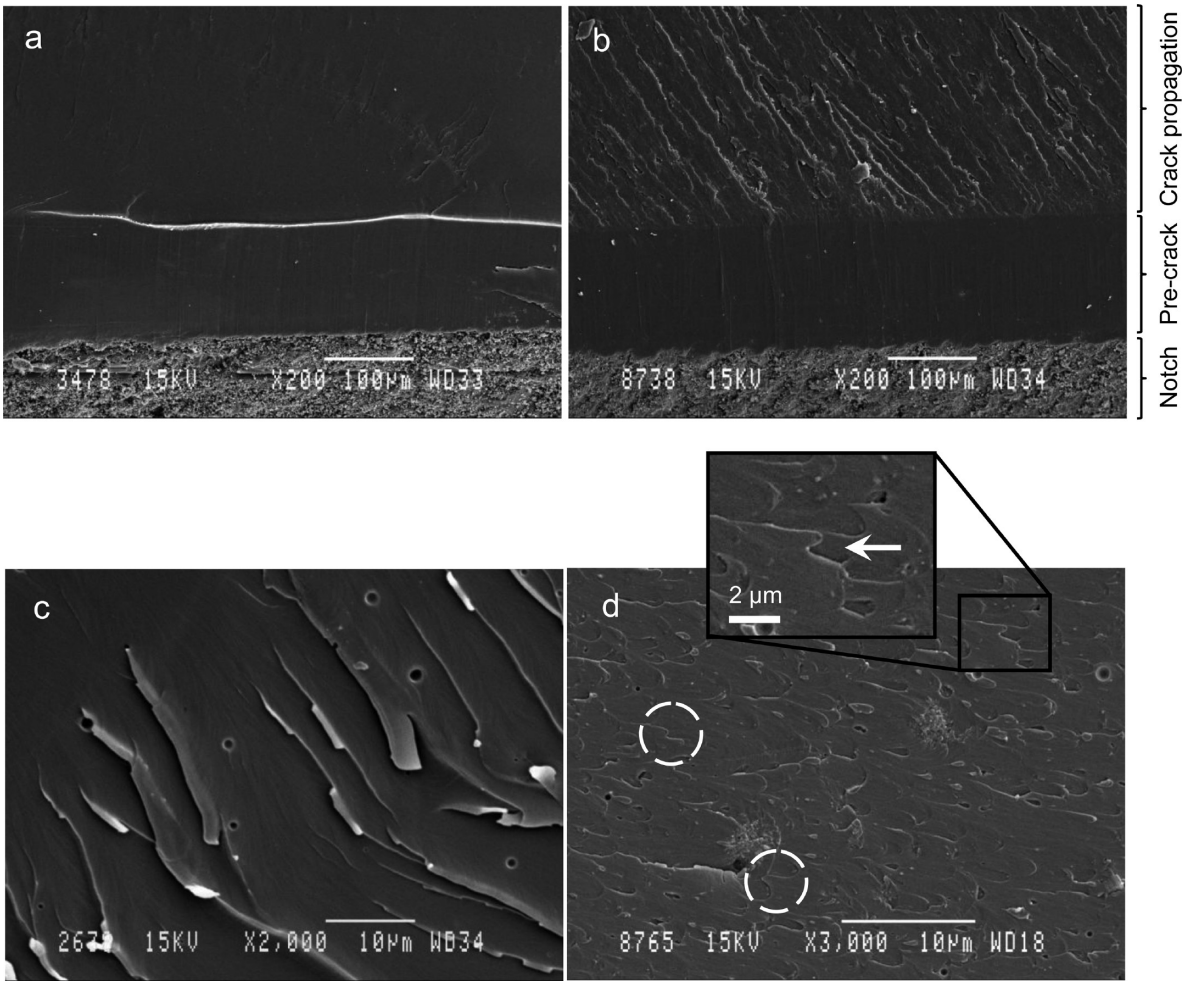

Figure 4. Fracture surfaces indicating the machined notch, precrack, and propagation zone for the neat polymer system (a) and 1 wt % graphene oxide composite (b); crack propagation is from bottom to top in both micrographs. Note the rougher propagation zone of the reinforced specimen. A high-resolution view (c) of the river marks leading back to the crack initiation site in a neat specimen. Evidence of crack pinning (d) was observed by the "bowlines" (white circles and arrow) left behind when the crack front bowed out between graphene oxide sheets. Crack propagation is from right to left.

increasing the required strain energy for the continuation of fracture.[27]

Under higher magnification, evidence of crack pinning was detected (Figure 4b). Crack pinning occurs when a propagating crack encounters a series of impenetrable obstacles, the crack front bows out between particles but remains pinned at the particles. The process is identifiable by the bow-shaped lines left behind on fracture surfaces. Typically, nanometer-sized particles and fibers cannot account for the pinning of cracks because their relative size is much smaller than the crack tip opening displacement (CTOD). The micrometer 2D dimensions of the current G−O sheets though are understood to be large enough to explain the observation of pinning. The CTOD, δ, can be estimated according to[28]

$$\delta = \frac{K_{Ic}{}^2}{E\sigma_y}(1-\nu^2) = \frac{G_{Ic}}{\sigma_y} \quad (1)$$

where E, σ_y, and ν^2 are the Young's modulus, yield stress, and Poisson's ratio of the unmodified matrix. Table 2 gives calculated CTODs on the order of 5−8 μm for the various loadings, similar to the 2D length scale of the G−O sheets observed in Figure 1, corroborating the SEM evidence.

Table 2. Theoretical Values of CTOD (δ) Assuming a Measured Matrix Yield Stress (σ_y) of 65.1 MPa

material	G_{Ic} (J/m^2)	δ (μm)
neat matrix	257	3.9
0.1 wt % graphene oxide	332	5.1
0.25 wt % graphene oxide	439	6.7
0.5 wt % graphene oxide	528	8.1
1 wt % graphene oxide	542	8.3

High conductivities and low percolation thresholds have been reported by chemically reduced graphene-based composite materials.[5] The oxygen functionalities blanketing the surfaces and edges maintain G−O as chiefly insulative, thus limiting conductivity even after network formation is achieved. Nonetheless, surface resistivity was shown to decrease by 4 orders of magnitude by G−O addition. Even moderate reductions in sheet resistance can be significant for applications such as electrostatic painting.

Results from tension dominated ($R = 0.1$) uniaxial fatigue tests conducted at a single graphene oxide concentration of 0.5 wt %

dx.doi.org/10.1021/ma201563k |*Macromolecules* 2012, 45, 238–245

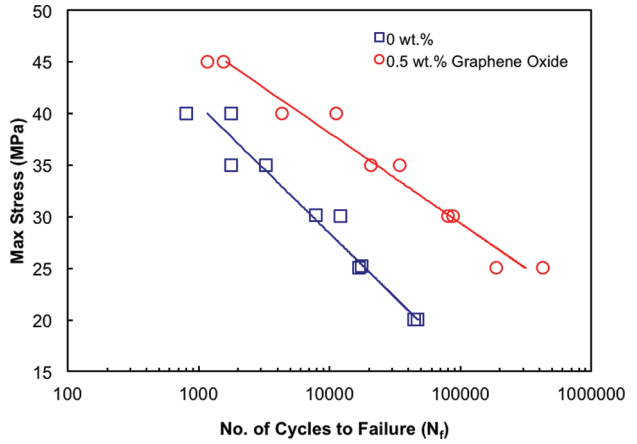

Figure 5. Fatigue performance of both neat epoxy and epoxy composites containing 0.5 wt % graphene oxide. The solid lines represent least-squares fits taking into account the abscissa contains the dependent variable. Neat matrix data reprinted with permission from Elsevier.[30]

are given in Figure 5. Significant improvements in mean fatigue life (taken as the linear fit[29]) were realized over the full range of applied stress amplitudes. Mean life at the highest comparable stress level, 40 MPa, was 420% greater than that of the control. Enhancements at lower stresses were more impressive, 1580% at 25 MPa. Prior results[30] along with other studies[31] have demonstrated improvements in the fatigue life of epoxy systems via CNT/CNF reinforcement. Typically, these gains are observed at low applied stress/strain regimes, where imbedded filaments can more readily interact with the surrounding matrix. Improvements are seldom reported at loads approaching 50% of the ultimate tensile strength. Here, fatigue life is often on par with or even inferior to the virgin material due to what can be described as competition between well-dispersed and nested regions of filaments. That is, high stress intensities due to loading in conjunction with the stress concentrating effects of the agglomerated areas ultimately overcome the beneficial effects of isolated filaments. The data shown in Figure 5 do not follow this trend. Instead, a shift to longer lives and slight "flattening" of the $S-N$ curve (smaller slope) is observed.

Complementary results were recently reported by Rafiee et al.[8] and Yavari et al.[32] In the former communication, the authors reported a significant decrease in the fatigue crack propagation rate of a graphene/epoxy nanocomposite through the addition of 0.125 wt % of what was referred to as partially oxygenated graphene sheets. Although they did not report on fatigue life, the authors described a 25-fold reduction in crack growth rate at $\Delta K = 0.5$ MPa·m$^{1/2}$. In the other letter, a graphene/epoxy composite was used to fabricate a glass fiber laminate to form a three-phase hierarchical composite. These structures were then subjected to fatigue loading in both bending and tensile configurations. Increases in fatigue life were more substantial in bending, up to 2 orders of magnitude greater than the traditional glass fiber composite. In tension, fatigue life was improved by 200–400% over the neat matrix composite. In both reports the authors claimed that the wrinkled texture of the thermally reduced graphene sheets were able to interlock with the epoxy matrix and led to improved interfacial adhesion.

Accordingly, the mechanism(s) responsible for the added longevity in the current graphene oxide composites were further examined. The presence of well-dispersed G–O sheets at various

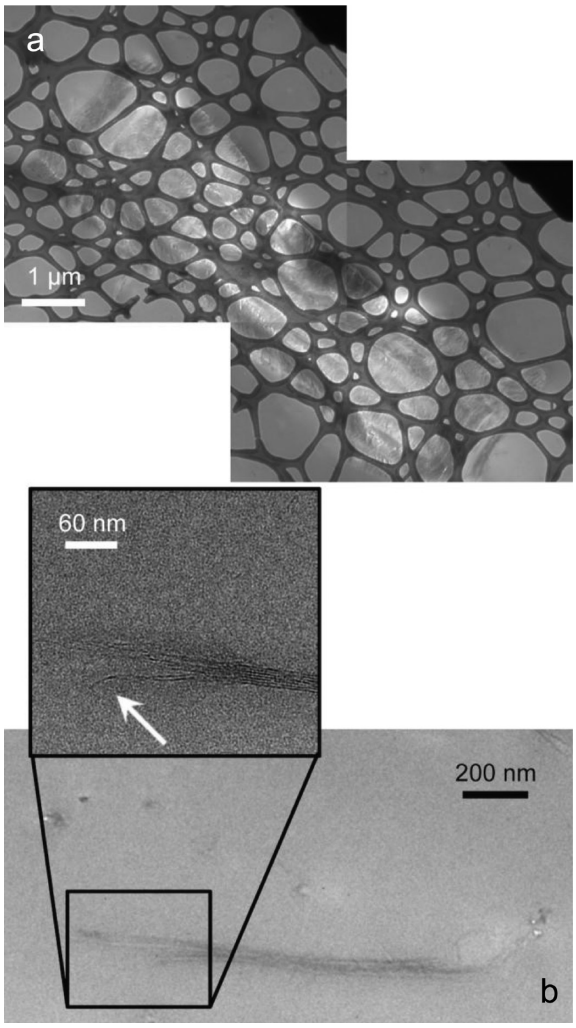

Figure 6. High-resolution TEM observation of two graphene oxide sheets embedded within the epoxy matrix. A large sheet (a) with ~11 μm lateral distance with basal planes orientated perpendicular to the viewing angle and a sheet (b) with basal planes oriented parallel to the viewing angle containing ~7 graphene layers tapering to a single dangling sheet (white arrow).

orientations within the matrix (Figure 6) suggests that some of these sheets would have their basal planes oriented to intercept incipient cracking. The large surface area of the sheets, combined with their anticipated strong interfacial bonding (due to their extremely high specific surface area) and enormous tensile properties, could then act to arrest crack growth. Such an explanation could further account for the earlier observation of crack pinning on fractured surfaces. It is unclear if a subsequent frictional pullout or bridging mechanism, often observed in fibrous nanocomposites, could further explain the improvements in fatigue and toughness. To this regard, Raman spectroscopy based interfacial stress transfer studies of graphene nanocomposites have generated some confusion indicating both low interfacial shear stresses[16] and large debonding strains.[33] Surface chemistry differences in such atomically thin materials may lead to significant inconsistencies in these measurements, particularly since the likely presence of surface groups in the oxide form can lead to a degree of covalent interaction at the graphene/matrix interface.

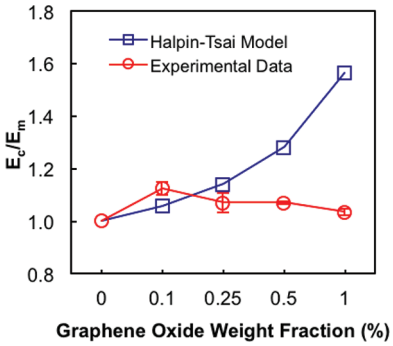

Figure 7. Comparison between measured and modeled (Halpin−Tsai) normalized stiffness's of graphene oxide nanocomposites. Adequate agreement is observed up to 0.25 wt % before divergence from modeled behavior.

Therefore, to gain further insight into the effectiveness of G−O/matrix stress transfer, a modified version[13] of the classic Halpin−Tsai model[34] was evaluated to compare predicted and measured composite stiffness values. The modified method takes the G−O sheets as effective rectangular solid fibers with appropriate length (l), width (w), and thickness (t) values and estimates the ratio of elastic modulus of the nanocomposite (E_c) to the neat matrix (E_m) as

$$\frac{E_c}{E_m} = \frac{3}{8}\frac{1 + ((w + l)/t)\left(\frac{(E_{G-O}/E_m) - 1}{(E_{G-O}/E_m) + ((w + l)/t)}\right)V_{G-O}}{1 - \left(\frac{(E_{G-O}/E_m) - 1}{(E_{G-O}/E_m) + ((w + l)/t)}\right)V_{G-O}} + \frac{5}{8}\frac{1 + 2\left(\frac{(E_{G-O}/E_m) - 1}{(E_{G-O}/E_m) + 2}\right)V_{G-O}}{1 - \left(\frac{(E_{G-O}/E_m) - 1}{(E_{G-O}/E_m) + 2}\right)V_{G-O}} \quad (2)$$

where the G−O elastic modulus (E_{G-O}) is assumed 1 TPa,[4] E_m is 2.99 GPa, and G−O weight fractions were converted to volume fractions based on the standard density of graphite (ρ = 2.25 g/cm^3) and the manufacturer's listed matrix density (ρ = 1.12 g/cm^3). Since the sheets have no genuine length or width and were of various graphene layers, approximations based on observed dimensions from our TEM characterization had to be introduced. Thus, average l, w, and t were assumed equal to 5 μm, 5 μm, and 4 nm, respectively.

Predicted and measured normalized composite tensile moduli are compared in Figure 7. Reasonable correlation between the values is observed up to 0.25 wt % G−O. Higher loadings however trend significantly below the model. This disagreement could be explained by several circumstances. First, as is the case with fibrous nanocomposites, nonuniform dispersion could account for some level of discrepancy between predicted and measured performance. Since G−O was fabricated in a top-down process, unconverted CNF fragments could also contribute to the formation of agglomerated regions within the matrix. Moreover, the unconverted fragments indicate that G−O do not constitute the total reinforcement weight fraction, thereby introducing an additional gap between the model and reality. Finally, more basic questions regarding the adequacy of the theoretical prediction can also be asked. For example, how does the matrix interact with atomic-sized thicknesses, and how should stress-based interlayer interactions in few-layer G−O be described? Forthcoming research will answer these and other fundamental questions and provide more accurate descriptions of the atomic level interactional behavior of these materials.

CONCLUSIONS

In this paper, we have demonstrated significant toughness and fatigue life improvements through the addition of uniquely synthesized and scalable graphene oxide sheets to a thermosetting epoxy system. The fatigue life improvements were observed over the full range of experimental stress levels offering potential performance improvements to numerous applications. We have further shown the effects on the cross-linking reaction and monotonic tensile and flexural properties disseminated by the sheets. The oxygen-containing functionalities present on the basal plane surfaces and edges of the graphene oxide sheets triggered onset of the cure reaction at lower temperatures and resulted in slightly larger exotherms in calorimetric scans. Consequently, moderately higher glass transition temperatures and shifting of the loss modulus were measured in the nanocomposites. Decreases in sheet resistance of 4 orders of magnitude occurred. A larger decrease was not observed due to the insulating nature of graphene oxide. Improvements in stiffness and strength were modest but significant, particularly the increases at low graphene oxide weight fractions. The notable toughening and longevity enhancements were products of the deflection and pinning of small-scale propagating cracks. The latter is not typically observed in nanofilled polymer composites; however, the 2D dimensions of the graphene oxide sheets were similar to the calculated crack tip opening displacements based on measured fracture energies. Thus, the occurrence and consequent microscopic evidence of pinning are considered justified.

AUTHOR INFORMATION

Corresponding Author
*E-mail: bortz.d@gmail.com.

ACKNOWLEDGMENT

This work was supported in part by the Investigación en Nuevos Materiales para su Aplicación en la Industria Aeronáutica (NACAR) project through Grupo Antolín Ingeniería, Burgos, Spain.

REFERENCES

(1) Novoselov, K.; Geim, A.; Morozov, S.; Jiang, D.; Zhang, Y.; Dubonos, S.; Grigorieva, I.; Firsov, A. Electric field effect in atomically thin carbon films. *Science* **2004**, *306* (5696), 666–669.

(2) Heersche, H. B.; Jarillo-Herrero, P.; Oostinga, J. B.; Vandersypen, L. M. K.; Morpurgo, A. F. Bipolar supercurrent in graphene. *Nature* **2007**, *446* (7131), 56–59.

(3) Balandin, A. A.; Ghosh, S.; Bao, W.; Calizo, I.; Teweldebrhan, D.; Miao, F.; Lau, C. N. Superior thermal conductivity of single-layer graphene. *Nano Lett.* **2008**, *8* (3), 902–907.

(4) Lee, C.; Wei, X.; Kysar, J. W.; Hone, J. Measurement of the elastic properties and intrinsic strength of monolayer graphene. *Science* **2008**, *321* (5887), 385–388.

(5) Stankovich, S.; Dikin, D. A.; Dommett, G. H. B.; Kohlhaas, K. M.; Zimney, E. J.; Stach, E. A.; Piner, R. D.; Nguyen, S. B. T.; Ruoff, R. S. Graphene-based composite materials. *Nature* **2006**, *442* (7100), 282–286.

(6) Yang, S. Y.; Lin, W. N.; Huang, Y. L.; Tien, H. W.; Wang, J. Y.; Ma, C. C. M.; Li, S. M.; Wang, Y. S. Synergetic effects of graphene platelets and carbon nanotubes on the mechanical and thermal properties of epoxy composites. *Carbon* **2011**, *49* (3), 793–803.
(7) Qiu, J.; Wang, S. Enhancing polymer performance through graphene sheets. *J. Appl. Polym. Sci.* **2011**, *119* (6), 3670–3674.
(8) Rafiee, M.; Rafiee, J.; Srivastava, I.; Wang, Z.; Song, H.; Yu, Z.; Koratkar, N. Fracture and Fatigue in Graphene Nanocomposites. *Small* **2010**, *6* (2), 179–183.
(9) Potts, J. R.; Dreyer, D. R.; Bielawski, C. W.; Ruoff, R. S. Graphene-based polymer nanocomposites. *Polymer* **2011**, *52* (1), 5–25.
(10) Kim, H.; Abdala, A. A.; Macosko, C. W. Graphene/polymer nanocomposites. *Macromolecules* **2010**, *43* (16), 6515–6530.
(11) Sengupta, R.; Bhattacharya, M.; Bandyopadhyay, S.; Bhowmick, A. K. A review on the mechanical and electrical properties of graphite and modified graphite reinforced polymer composites. *Prog. Polym. Sci.* **2011**, *36* (5), 638–670.
(12) Rafiee, M.; Rafiee, J.; Wang, Z.; Song, H.; Yu, Z.; Koratkar, N. Enhanced mechanical properties of nanocomposites at low graphene content. *ACS Nano* **2009**, *3* (12), 3884–3890.
(13) Rafiee, M. A.; Lu, W.; Thomas, A. V.; Zandiatashbar, A.; Rafiee, J.; Tour, J. M.; Koratkar, N. A. Graphene nanoribbon composites. *ACS Nano* **2010**, *4* (12), 7415–7420.
(14) Kinloch, I. A.; Gong, L.; Raju, A.; Riaz, I.; Jalil, R.; Novoselov, K. S.; Young, R. J. Understanding the potential of graphene within composites: Interfacial stress transfer in ideal graphene composites. In *ImagineNano Graphene2011*, Bilbao, Spain, 2011.
(15) Wang, Y.; Shi, Z.; Fang, J.; Xu, H.; Yin, J. Graphene oxide/polybenzimidazole composites fabricated by a solvent-exchange method. *Carbon* **2011**, *49* (4), 1199–1207.
(16) Gong, L.; Kinloch, I. A.; Young, R. J.; Riaz, I.; Jalil, R.; Novoselov, K. S. Interfacial stress transfer in a graphene monolayer nanocomposite. *Adv. Mater.* **2010**, *22* (24), 2694–2697.
(17) Stankovich, S.; Piner, R. D.; Chen, X.; Wu, N.; Nguyen, S. B. T.; Ruoff, R. S. Stable aqueous dispersions of graphitic nanoplatelets *via* the reduction of exfoliated graphite oxide in the presence of poly (sodium 4-styrenesulfonate). *J. Mater. Chem.* **2005**, *16* (2), 155–158.
(18) Kosynkin, D. V.; Higginbotham, A. L.; Sinitskii, A.; Lomeda, J. R.; Dimiev, A.; Price, B. K.; Tour, J. M. Longitudinal unzipping of carbon nanotubes to form graphene nanoribbons. *Nature* **2009**, *458* (7240), 872–876.
(19) Hummers, W. S., Jr.; Offeman, R. E. Preparation of graphitic oxide. *J. Am. Chem. Soc.* **1958**, *80* (6), 1339–1339.
(20) Varela-Rizo, H.; Rodriguez-Pastor, I.; Merino, C.; Martin-Gullon, I. Highly crystalline graphene oxide nano-platelets produced from helical-ribbon carbon nanofibers. *Carbon* **2010**, *48* (12), 3640–3643.
(21) Vera-Agullo, J.; Varela-Rizo, H.; Conesa, J. A.; Almansa, C.; Merino, C.; Martin-Gullon, I. Evidence for Growth Mechanism and Helix-Spiral Cone Structure of Stacked-Cup Carbon Nanofibers. *Carbon* **2007**, *45* (14), 2751–2758.
(22) Eitan, A.; Fisher, F. T.; Andrews, R.; Brinson, L. C.; Schadler, L. S. Reinforcement Mechanisms in MWCNT-Filled Polycarbonate. *Compos. Sci. Technol.* **2006**, *66* (9), 1162–1173.
(23) Putz, K. W.; Palmeri, M. J.; Cohn, R. B.; Andrews, R.; Brinson, L. C. Effect of Cross-Link Density on Interphase Creation in Polymer Nanocomposites. *Macromolecules* **2008**, *41* (18), 6752–6756.
(24) Fiedler, B.; Gojny, F.; Wichmann, M.; Nolte, M.; Schulte, K. Fundamental Aspects of Nano-Reinforced Composites. *Compos. Sci. Technol.* **2006**, *66* (16), 3115–3125.
(25) Gojny, F. H.; Wichmann, M. H. G.; Fiedler, B.; Schulte, K. Influence of different carbon nanotubes on the mechanical properties of epoxy matrix composites-A comparative study. *Compos. Sci. Technol.* **2005**, *65* (15−16), 2300–2313.
(26) Hwang, G. L.; Shieh, Y. T.; Hwang, K. C. Efficient load transfer to polymer grafted multiwalled carbon nanotubes in polymer composites. *Adv. Funct. Mater.* **2004**, *14* (5), 487–491.
(27) Faber, K.; Evans, A. Crack Deflection Processes-I. Theory. *Acta Metall.* **1983**, *31* (4), 565–576.
(28) Kinloch, A. J.; Young, R. J. *Fracture Behaviour of Polymers*; Applied Science Publishers: London, 1983.
(29) Standard practice for statistical analysis of linear or linearized stress-life (*S-N*) and strain-life (*ε-N*) fatigue data. ASTM E 739-91.
(30) Bortz, D. R.; Merino, C.; Martin-Gullon, I. Carbon nanofibers enhance the fracture toughness and fatigue performance of a structural epoxy system. *Compos. Sci. Technol.* **2011**, *71* (1), 31–38.
(31) Zhang, W.; Picu, R. C.; Koratkar, N. Suppression of Fatigue Crack Growth in Carbon Nanotube Composites. *Appl. Phys. Lett.* **2007**, *91*, 193109.
(32) Yavari, F.; Rafiee, M. A.; Rafiee, J.; Yu, Z. Z.; Koratkar, N. Dramatic Increase in Fatigue Life in Hierarchical Graphene Composites. *ACS Appl. Mater. Interfaces* **2010**, *2* (10), 2738–2743.
(33) Srivastava, I.; Mehta, R. J.; Yu, Z. Z.; Schadler, L.; Koratkar, N. Raman study of interfacial load transfer in graphene nanocomposites. *Appl. Phys. Lett.* **2011**, *98* (6), 3102.
(34) Mallick, P. K. *Fiber-Reinforced Composites: Materials, Manufacturing, and Design*; CRC Press: Boca Raton, FL, 1993.

Macromolecules

ARTICLE

pubs.acs.org/Macromolecules

Small-Angle X-ray Scattering Study of Charged Triblock Copolymers as a Function of Polymer Concentration, Temperature, and Charge Screening

Manja Annette Behrens,[†] Anna-Lena Kjøniksen,[‡,§] Kaizheng Zhu,[‡] Bo Nyström,[‡] and Jan Skov Pedersen[†,*]

[†]Department of Chemistry and iNANO Interdisciplinary Nanoscience Center, Aarhus University, Langelandsgade 140, DK-8000 Aarhus C, Denmark

[‡]Department of Chemistry, University of Oslo, P.O. Box 1033, Blindern, N-0315 Oslo, Norway

[§]Department of Pharmacy, School of Pharmacy, University of Oslo, P.O. Box 1068, Blindern, N-0316, Oslo, Norway

ABSTRACT: In the current study, the influence of electrostatic interaction on micelle formation has been investigated by characterizing a series of charged thermo-responsive triblock copolymers by densitometry and small-angle X-ray scattering in a wide temperature range from 20 to 90 °C and by varying the salt concentration of the solvent. The copolymers, $MPEG_{45}$-*b*-$P(NIPAAM)_n$-*b*-$P(SSS)_{22}$, were composed of methoxypoly(ethylene glycol) (MPEG, hydrophilic), poly(*N*-isopropylacrylamide) (PNIPAAM, temperature sensitive), and poly(4-styrenesulfonic acid sodium) (PSSS, charged). The PNIPAAM block constituted between 20 and 50% of the polymer repeat units. The single polymers were described with a Gaussian chain model, where the repulsive interchain interactions were taken into account in aqueous solution. Above the critical micelle temperature (CMT) the polymer with the medium PNIPAAM block formed spherical micelles, whereas the copolymer with the largest PNIPAAM block formed cylindrical micelles. Addition of salt to the solution affected the formed micelles as well as the CMT of the system.

INTRODUCTION

Amphiphilic block copolymers self-assemble in aqueous solution, forming micellar structures above the critical micelle concentration (CMC), or above the critical micelle temperature (CMT). The size and shape of these structures are governed by many factors, among these copolymer composition, solvent quality and selectivity, and temperature. Diblock copolymers containing poly(ethylene glycol) (PEG), as the hydrophilic block, are together with hydrophobic blocks known to form micelles in aqueous solution. In these systems the hydrophobic block can consist of a range of different polymers.[1,2] PEG forms a hydrated outer corona of the micelles and the hydrophobic block will form a core, which can provide a compartment to hold hydrophobic drugs in aqueous solution. PEG is hydrophilic until the lower critical solution temperature (LCST) is reached, which in water is above 100 °C.[2] To induce self-assembly in a system containing PEG the second block must be hydrophobic or become hydrophobic when an external parameter such as temperature is varied. The temperature responsive polymer poly(*N*-isopropylacrylamide) (PNIPAAM) has been widely studied with the aim of using it in pharmaceutical or biomedical applications. It undergoes a coil-to-globule transition at its LCST at approximately 32 °C in water,[3,4] below which water is a good solvent for the polymer. The phase transition is reversible, thus micelles, where PNIPAAM constitutes the hydrophobic block can be formed and disassembled by simply changing the temperature. A block copolymer consisting of PEG and PNIPAAM can form micelles above the transition temperature of PNIPAAM, where the exact CMT of the system depends on the size of the PEG block. In general, a longer PEG block results in a higher CMT.[5,6]

In the present study a series of triblock copolymers composed of MPEG, PNIPAAM, and poly(4-styrenesulfonic acid sodium) (PSSS) was investigated. The PEG block is denoted MPEG as it is a methoxypoly(ethylene glycol) block. In addition to the two blocks previously described, the PSSS block is charged and soluble in aqueous solution. Introduction of this third component gives a polyelectrolyte character to the triblock copolymer. In 2008, a triblock copolymer of a similar composition, though with a short PSSS block, was investigated and found to form polymeric micelles.[7] The aim of the current study is to investigate micelle formation in a wide temperature range and to describe the influence of electrostatic interactions on the single polymer behavior and on the micelle structure. The chemical structure of the triblock copolymer is shown in Figure 1. The polymers have the following composition $MPEG_{45}$-*b*-$P(NIPAAM)_n$-*b*-$P(SSS)_{22}$. The length of the PNIPAAM block is varied and *n* assumes values of 17, 48, and 66, respectively.

The variation of the size of the PNIPAAM block was introduced to facilitate investigation of the impact of PNIPAAM block size on the CMT and micelle structure formed by the triblock copolymer. The three triblock copolymers were investigated in

Received: July 14, 2011
Revised: November 2, 2011
Published: December 01, 2011

dx.doi.org/10.1021/ma2016216 | *Macromolecules* 2012, 45, 246–255

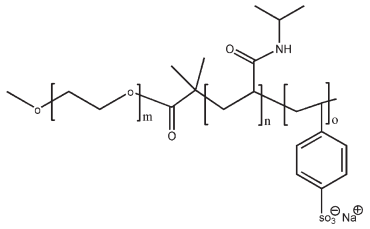

Figure 1. Chemical structure of the charged triblock copolymer. The different copolymers consist of *m* repeat units of MPEG, *n* repeat units of PNIPAAM and *o* repeat units of PSSS. The parameters *m* and *o* are kept constant with values of 45 and 22, respectively, and the index *n* has the values of 17, 48, and 66.

the range of concentrations from 0.5 to 2 wt % in three aqueous solvents: Pure water, 30 mM and 500 mM NaCl. This vast parameter space was studied to investigate the influence of the electrostatic interactions, originating from the PSSS block, on micelle formation. The scattering experiments were carried out in the temperature range from 20 to 90 °C, in steps of 5 °C. The scattering study presented in this paper is an extension of a previous study where the self-assembly behavior of the polymers was investigated at a single concentration of 1 wt % and only in two solvents: Pure water and aqueous 500 mM NaCl.[8] The structural information obtained in the present work is significantly increased by applying more advanced modeling of the SAXS data in addition to investigating the systems for a broader span of external parameters. Describing the scattering data with a more advanced model gives much more detailed structural information, that when evaluated over a board parameter space describes in detail how the single dissolved polymers interact and how they self-assemble above their CMT, in addition to how these self-assembled structures change as a response to changes in the external parameters. In addition to the SAXS experiments, apparent partial specific volumes of the polymers were determined to obtain information on the change with temperature. The partial specific volume is denoted apparent because all changes in the partial specific volume are associated with the dissolved molecule, despite changes to the solvent in the vicinity of the solute also takes place. From modeling the SAXS data, information on the size and shape of the self-assembled structures was obtained. Also detailed information on the single polymer chain structure and interactions was extracted.

MATERIALS AND METHODS

Materials. The charged triblock copolymers were synthesized by atom transfer radical polymerization (ATRP). A description of the synthesis and subsequent characterization of the polymer with respect to polydispersity, composition *et cetera* can be found in Kjøniksen et al.[8] The triblock copolymer with a composition of $MPEG_{45}$-*b*-$P(NIPAAM)_n$-*b*-$P(SSS)_{22}$ was investigated. The length of the middle block was varied yielding values of n = 17, 48, and 66. For each copolymer, aqueous solutions of 0.5, 1, or 2 wt % were prepared without salt and with salinities of 30 and 500 mM NaCl, respectively.

Densitometry. The solution density measurements were performed on a DMA5000 densitometer from Anton Paar. The instrument employs an oscillating tube technique, where the relationship between the period of oscillation and the density is utilized. A U-tube is oscillated and its fundamental frequency is a function of the systems mass, thus the oscillating frequency is a function of the sample density. The relation holds as long as the sample has a relative low viscosity. From the measured density the apparent partial specific volume can be determined. This was done for concentrations of 1 and 2 wt % of the three different triblock copolymers in all solvents in a temperature range from 20 to 90 °C in steps of 5 deg. In the temperature range from 20 to 50 °C the accuracy of the measurement is 0.000020 g/cm^3, and it is 0.000050 g/cm^3 from 55 to 90 °C. Because of the relatively low concentration of polymer, the derived apparent partial specific volumes have an accuracy of about 0.1−0.3%. The apparent partial specific volume was obtained from the density measurements. The measured density of the solution containing the solute is directly related to its apparent specific volume, v_{solute}, by

$$v_{solute} = \left(\frac{1}{c_{solute}}\right)\left(\frac{1}{\rho_{solute}}\right) - \left(\frac{1 - c_{solute}}{c_{solute}}\right)\left(\frac{1}{\rho_{solvent}}\right) \quad (1)$$

where c_{solute} is the weight fraction of the solute, ρ_{solute} and $\rho_{solvent}$ are the measured density of the solution with solute and the pure solvent, respectively.

Small-Angle X-ray Scattering. The SAXS measurements were performed on the laboratory-based facility in the Department of Chemistry at Aarhus University, Denmark. The instrument is a NanoSTAR camera from Bruker AXS optimized for solution scattering.[9] The scattering intensity, $I(q)$, is displayed as a function of the modulus of the scattering vector $q = 4\pi(\sin\theta)/\lambda$. The X-ray wavelength, λ, is 1.54 Å and 2θ is the angle between the incident and scattered X-rays. The three triblock copolymers were investigated in a temperature range from 20 to 90 °C in steps of 5 deg. The data was collected for each polymer at three concentrations, 0.5, 1, and 2 wt %, and in three different solvents, water and aqueous solutions with 30 and 500 mM NaCl, respectively. The samples were kept in homemade reusable quartz capillary sample holders, which were thermostated using a Peltier element (Anton Paar). All scattering data obtained for the polymers had an acquisition time of 1 h and subsequent all necessary buffers (backgrounds) were collected for an hour. Background subtractions and conversion of the data to absolute scale by use of water as primary standard was performed using the SUPERSAXS program package.[30]

Small-Angle X-ray Scattering Models. Modeling of the scattered data was performed using appropriate analytical models and optimized by a weighted least-squares procedure.[10] Small-angle X-ray scattering from a dilute solution of spherical particles can be written as the product of the form factor, $P(q)$, and structure factor, $S(q)$, multiplied by the number density of particles, n, $I(q) = nP(q) \times S(q)$.

For unimeric polymers without interchain interactions the data was described using a Gaussian chain, given by the Debye function[11]

$$P_{chain}(q) = \frac{2[\exp(-x) - 1 + x]}{x^2} \quad (2)$$

where $x = q^2R_g^2$ and R_g is the ensemble average root-mean-square of the radius of gyration. For the longest polymer at the highest salt concentration, excluded volume effects had to be taken into account and the data was fitted using the model developed by Pedersen and Schurtenberger.[12] All the copolymers have a charged block situated at one end, and when the charge interactions are not screened by addition of salt, these interactions must be taken into account. Here, it is assumed that the repulsion arising from interaction between the charged blocks can be approximated by a potential centered at one end of the polymer chain and that the effects can be described by an effective hard-sphere model, while the polymer structure is still described as a Gaussian chain. The repulsion between the polymers is thus described by an effective hard-sphere radius, R_{HS}, and an effective hard-sphere volume fraction, η_{HS}. The center of the hard sphere is placed at one end of the polymer. The scattering intensity then becomes

$$I(q) = P_{chain}(q) + A_{chain}^2(q)[S_{HS}(q, R_{HS}, \eta_{HS}) - 1] \quad (3)$$

where the form factor and form factor amplitude is that of a Gaussian chain[13] $A_{chain} = [1 - \exp(x)]/x$ and the expression for the structure factor of hard spheres is taken from Kinning and Thomas.[14]

dx.doi.org/10.1021/ma2016216 |*Macromolecules* 2012, 45, 246–255

The polymers self-assemble above the CMT, and depending on the polymer composition, either spherical or cylindrical micelles were observed. The form factor for a spherical core−shell micelle with a large number of chains in the corona, N, can be described by[13]

$$P_s(q) = [\Delta\rho_{shell} V_{tot} \Phi(qR_{out}) \exp\left(-\frac{q^2\sigma^2}{2}\right) - (\Delta\rho_{shell} - \Delta\rho_{core}) V_{core} \Phi(qR_{core})]^2 + N(\Delta\rho_{chain} V_{chain})^2 P_{chain}(q) \quad (4)$$

where the excess scattering length density of the core, the shell and the chains are $\Delta\rho_{core}$, $\Delta\rho_{shell}$, and $\Delta\rho_{chain}$, respectively, $V_{out} = 4\pi R_{out}^3/3$ is the volume related to the outer surface R_{out}, $V_{core} = 4\pi R_{core}^3/3$ is the volume of the core with radius R_{core} and σ describes the width of the outer interface between corona and solvent. V_{chain} is the volume of a chain and N the number of chains. $\Phi(qR)$ is the form factor amplitude for a spherical particle given by Rayleigh[15]

$$\Phi(qR) = \frac{3[\sin(qR) - qR(\cos qR)]}{(qR)^3} \quad (5)$$

The last term in eq 4 represents the scattering from the internal structure of the corona.

For long cylinders, $L \gg R$, the expression for the form factor is a product of a term originating from the cross-section and a longitudinal term, $P_{cyl}(q) = P_{cross-section}(q) \times P_{longt}(q)$.[16] The form factor for a micelle with a large aggregation number is given by[16]

$$P_{cyl}(q) = P_{longt}(q) \left[\Delta\rho_{shell}\pi R_{out}^2 L \frac{2J_1(qR_{out})}{qR_{out}} \exp\left(-\frac{q^2\sigma^2}{2}\right) - (\Delta\rho_{shell} - \Delta\rho_{core})\pi R_{core}^2 L \frac{2J_1(qR_{core})}{qR_{core}}\right]^2 + N(\Delta\rho_{chain} V_{chain})^2 P_{chain}(q) \quad (6)$$

where $J_1(x)$ is the first-order Bessel function of the first kind and the longitudinal term of the form factor is that of an infinitely thin rod.[17] The micelles have a core radius, R_{core}, and an outer radius, R_{out}, in addition to a graded outer interface. Further, $\Delta\rho_{shell}$, $\Delta\rho_{core}$ and $\Delta\rho_{chain}$ are again the excess scattering length density of the corona, the core and the chains, respectively. Also V_{chain} is the volume of a chain and N the number chains. The random phase approximation (RPA) was implemented to account for the interparticle interactions of the cylindrical micelles[18]

$$S(q) = \frac{1}{1 + \nu_{RPA} P_{longt}(q)} \quad (7)$$

where ν_{RPA} is proportional to the concentration of the cylinders.[19]

We judged that it would be very difficult to obtain reliable values for the scattering length densities of the individual blocks, thus the data were not fitted on an absolute scale. The specific densities of PNIPAAM and PEG have been determined to be between 1.15 and 1.18 g/cm^3 at 20 °C and would therefore be difficult to distinguish by SAXS.[3,20] Furthermore, it would be difficult to obtain the specific density of the PSSS block, partly because it composes a small part of the copolymer but more importantly because the partial specific volumes obtained for the different blocks are highly influenced by a complicated interplay of hydration and disassociation of counterions, which in turn are influenced by the actual local densities of the various components.[21] This essentially makes it not possible to determine the excess electron densities of the different blocks, as it would be for the blocks in the copolymer. As it turned out that there is no sharp step in the polymer density at the core−corona interface, the core and the corona could not be distinguished, leading to a simplified model where the core and corona was taken as one component. The model used to describe the scattering data from the micelles reduced to a corona with the addition of the polymer term with a radius of gyration and a scale factor as fitting parameters. We also note that the models could fit the data without including polydispersity of radius and length of the micelles, which indicates that the effects of polydispersity are small.

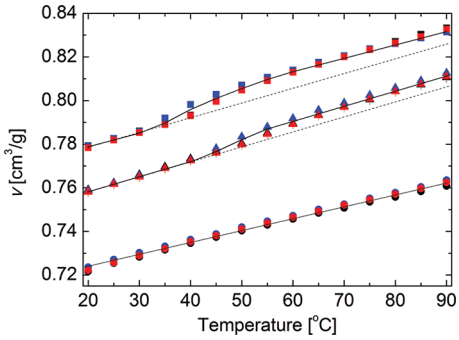

Figure 2. Apparent partial specific volume obtained for the polymers with n = 17 (circle), 48 (triangle), and 66 (square), at different solvent conditions. The symbols for the polymers in solutions without added salt are black, and for 30 mM and 500 mM NaCl they are red and blue, respectively. All lines are trend lines to guide the eye, the black lines show the behavior of the copolymers and the dashed a linear extrapolation of the increase at low temperatures.

To obtain the average radial scattering density distribution, $\Delta\rho_{mic}(r)$, the form factor amplitude for the micelle, $A_{mic}(q) = A_{core}(q) + A_{corona}(q)$, was Fourier transformed

$$\Delta\rho_{mic}(r) = \frac{1}{2\pi^2}\int_o^\infty A_{mic}(q)\frac{\sin(qr)}{qr} q^2 \, dq \quad (8)$$

For the cylindrical micelles the radial profile was calculated as the Hankel transform of the cross-section scattering amplitude

$$\Delta\rho_{cross-sec}(r) = 2\pi\int_0^\infty A_{cross-sec}(q) J_0(qr) \, dq \quad (9)$$

where $A_{cross\text{-}sec}(q)$ is the scattering amplitude for the cylinder cross-section as given by the term in the square brackets in eq 6 and $J_0(x)$ is the zero-order Bessel function of first kind.

The aggregation numbers, N_{agg}, were determined from the forward scattering, $I(q = 0)$, for both the spherical and cylindrical micelles. Values of N_{agg}, were calculated by taking the ratio between the forward scattering for a single polymer chain at 20 °C and that of the aggregated structure at the measured temperatures above the CMT:

$$N_{agg} = \alpha\frac{I^{agg}(q=0)}{I^{polymer}_{20°C}(q=0)} \quad (10)$$

where α is a correction factor introduced to accounting for the variation of contrast with temperature. Values of α were obtained from the apparent partial specific volumes as a function of temperature.

RESULTS

Apparent Partial Specific Volume. The density was measured and converted to apparent partial specific volume, as described in the section Materials and Methods. The measurement were carried out in salt-free solution and with added salt as indicated above and no significant difference was observed at the different conditions. Moreover, the experiments were conducted at concentrations of 1 and 2 wt %, however, only the results for 1 wt % are displayed in Figure 2. For all three copolymers an increase in the apparent partial specific volume is detected with

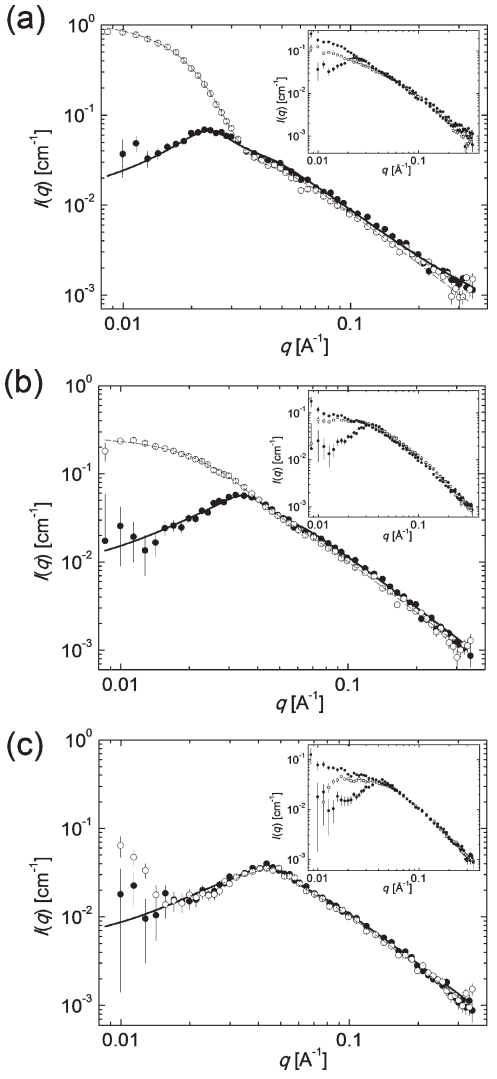

Figure 3. Scattering data for 1 wt % solutions of the copolymers with n = 66 (a), 48 (b), and 17 (c) without added salt at 20 °C (closed symbols) and 75 °C (open symbols). The lines are model fits at 20 (full line) and 75 °C (dashed line). The inserted plots shows scattering data obtained for the polymers at 20 °C in a salt-free aqueous solution (closed black symbols), with 30 mM (open symbols) and 500 mM NaCl (closed gray symbols).

increasing temperature, consistent with increased thermal motion. However, the increase is higher than that of water, which can be associated with a gradual dehydration of the water-soluble polymer blocks with increasing temperature. The copolymer with the shortest PNIPAAM block (n = 17) does not display any abrupt change as was found for pure PNIPAAM at the LCST.[3,4] For a longer PNIPAAM block a more pronounced change is observed though not as abrupt as for pure PNIPAAM. The polymer with the medium length of the PNIPAAM block (n = 48), displays a change around 55 °C in the apparent partial specific volume, whereas for the polymer with the longest PNIPAAM sequence (n = 66) the apparent partial specific volume exhibits a change around 40 °C.

Scattering Data and Fits. A subset of the scattering data obtained for the three polymers is shown in Figure 3. The data for the polymer with n = 66 in salt-free aqueous solution is displayed at 20 and 75 °C. At 20 °C strong interchain interactions are evident as a correlation peak is present at low q. At elevated

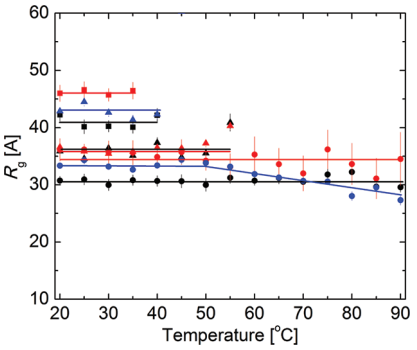

Figure 4. Radius of gyration for the polymers with n = 17 (circle), 48 (triangle) and 66 (square) all at a concentration of 1 wt %. The results are obtained at different conditions: In solution without salt (black symbols), with 30 mM NaCl (red symbols), and with 500 mM NaCl (blue symbols). All lines are guide to the eye, these are black for the aqueous polymer solutions without salt, red for solutions with 30 mM NaCl, and blue for solutions with 500 mM NaCl.

temperatures, the scattering intensity increases at low q, whereby the correlation peak is masked. The increase in intensity can be associated with the self-assembly of the polymer into larger structures. These structures will be examined in a later section of the paper. The inset of Figure 3a shows the scattering data obtained at 20 °C with increasing salt concentration. Higher salinity screens the electrostatic interactions between the polymers, as reflected by the decrease of the correlation peak and subsequent disappearance. At low q there is a difference between the solution containing 30 mM and 500 mM NaCl, indicating that 30 mM NaCl is not sufficient to completely screen the electrostatic interactions. This will be discussed further in the next section. For the polymer with the medium length of the PNIPAAM block (n = 48) (Figure 3b), the behavior is similar. A correlation peak is observed at 20 °C, and at 75 °C self-assembly of the polymer chains is reflected in the scattering intensity at low q, which masks the correlation peak. The scattering data for n = 17 (Figure 3c) display a correlation peak over the entire temperature range, suggesting that self-assembly of the polymer chains does not take place in the temperature range investigated. Screening of the electrostatic interactions between the polymer chains by addition of salt also occur for the polymers n = 48 and n = 17.

Single Polymer Chains and Inter-Chain Interactions. Below the CMT, the triblock copolymers are expected to exist as unimers. The noninteracting polymers are described with a Gaussian chain model for the shorter chains, and an excluded volume chain model for the long chains at high salt concentration. The electrostatic interactions of the polymers are described with a Gaussian chain model modified to take repulsive interchain interactions into account as described in the section "Small-Angle X-ray Scattering models". Since one end block is charged, interchain interactions are present in salt-free aqueous solution regardless the length of the PNIPAAM block and polymer concentration. This is clearly seen as a correlation peak and a decrease in scattering intensity is observed at low q, as previously pointed out. The model gives excellent agreement with the data (Figure 3).

The radius of gyration, R_g, obtained from the model fits for the polymer with n = 17, decreases with increasing polymer concentration (Figure 4). Further, a decrease in R_g is observed above 50 °C in 500 mM NaCl. R_g values are only shown for a polymer concentration of 1 wt % in Figure 4. For the copolymers with

dx.doi.org/10.1021/ma2016216 |Macromolecules 2012, 45, 246–255

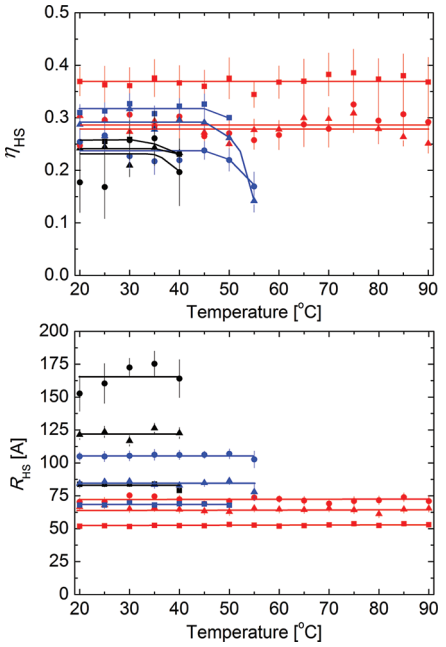

Figure 5. Effective hard-sphere volume fraction, η_{HS} (upper panel) and effective hard-sphere radius (lower panel) for solutions of the polymers without salt at polymer concentrations of 0.5 wt % (circle), 1 wt % (triangle), and 2 wt % (square). The color code for the polymers are n = 17 (red symbols), 48 (blue symbols) and 66 (black symbols). All lines are guide to the eye, these are black for the polymer with n = 66, blue for n = 48, and red for n = 17.

n = 48 and 66, similar concentration dependence of R_g is observed. The R_g of the polymers increases with increasing PNIPAAM block length, which is consistent with the overall increase in polymer size. The effective hard-sphere volume fraction, η_{HS}, is found to increase with increasing concentration (Figure 5), as would be expected due to a closer packing of the polymer chains. For the polymers with n = 48 and 66, a temperature dependence of R_g is observed, whereas no effect of temperature is evident for n = 17. This behavior is in agreement with the presence of CMT; hence the reduction of the solvent quality for the polymers with medium and long PNIPAAM blocks (Table 1).

In aqueous solution in the presence of 30 mM NaCl, the behavior of the polymers is highly dependent on the polymer concentration. The polymers with n = 17 and 48 at a concentration of 2 wt % still display interchain repulsive interactions, whereas at lower concentrations the repulsive interactions are no longer evident and the scattering data can be modeled using a Gaussian chain model. The effective hard-sphere radius is ~32 Å for both polymers in 30 mM NaCl (data not shown); this value is significantly smaller than in salt-free solution. Thus, the electrostatic interactions are partially screened by the addition of salt, however not fully screened as repulsion between the single polymer chains is observed. For the polymer with n = 66, interchain interactions are not observed.

For the copolymers in the presence of 500 mM NaCl interchain interactions are absent, which corresponds to effective screening of the electrostatic interactions of the PSSS block. The scattering data from the polymers with n = 17 and 48 can be described with a Gaussian chain model, whereas for the copolymer with n = 66 excluded volume effects are taken into account. The radius of gyration obtained for n = 66 is large (ca. 75 Å; data not shown) compared to the values observed for the corresponding solutions containing less or no salt. This suggests that the polymer with n = 66 does not exist as unimers under these conditions, however it still displays characteristic polymer behavior. The polymers with the short and medium PNIPAAM block lengths are expected to exist as unimers in the aqueous solution with 500 mM NaCl as their radii of gyration are comparable with the values observed at the other conditions, though slightly larger.

Table 1. Overview of the Critical Micelle Temperatures (CMT) Determined by SAXS

	polymer/solution								
	water			30 mM NaCl			500 mM NaCl		
concentration [wt %]	0.5	1.0	2.0	0.5	1.0	2.0	0.5	1.0	2.0
n = 17	---	---	---	---	---	---	---	---	---
n = 48	60	60	60	60	60	55	50	50	45
n = 66	45	45	45	45	40	40	35	35	35

Micelle Structure. Above the CMT, the triblock copolymers self-assemble into micellar structures. The scattering data in this range are fitted by use of either a spherical or a cylindrical core−shell model. The data for the shortest PNIPAAM block (n = 17) show that self-assembly of the unimers does not take place in the temperature interval investigated for this copolymer, whereas the data for the other copolymers (n = 48 and n = 66) show that self-assembly of single chains occurs above their respective CMT.

Recently, it was shown that the polymer with n = 48 has a hydrodynamic radius ~300 Å above its CMT in both pure water and with 500 mM NaCl.[8] This size is compatible with spherical micelles. Therefore, the structures formed above the CMT by n = 48 are modeled as spherical core−shell particles, where the shell is composed of polymer chains. It turned out that the difference in scattering length density between the core and shell is small, which made it impossible to distinguish between these two components in the structure. Good fits were obtained for the model by formally setting R_{core} to zero (Figure 3).

From the fitting procedure the parameter R_{out} is obtained. The micelle radius is found to be highly dependent on temperature and less on polymer concentration (Figure 6). An increase in micelle radius is also seen with increasing salt concentration. From the radial profiles of 1 wt % samples at all solvent conditions at 70 and 90 °C (Figure 7), an increase in micelle size with temperature and salt concentration is observed. The smallest micelles are observed in the salt-free solution, where polymer concentration had little effect on the micelle structure. In aqueous solution with 30 mM NaCl, the micelles at polymer concentrations of 1 and 2 wt % were similar and approximately 33% larger than the corresponding micelles formed in the salt-free solution. The micelles formed at a polymer concentration of 0.5 wt % had a radius 66% larger than those observed in the salt-free solution.

A difference in micelle size as a function of polymer concentration in aqueous solution with 30 mM NaCl is clearly seen between the micelles formed at 0.5 and 1 wt % in the radial profiles at 70 and 90 °C (Figure 7). At concentrations of 1 and 2 wt %, similar radial profiles are obtained, however, they are only shown for 1 wt %. Moreover, it appears that the micelles formed at 70 °C in 0.5 wt % solutions are similar in size to those observed

dx.doi.org/10.1021/ma2016216 |*Macromolecules* 2012, 45, 246–255

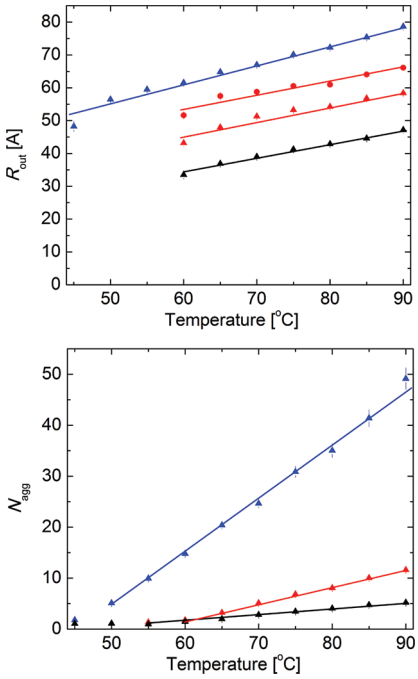

Figure 6. R_{out} (upper panel) for the polymer with n = 48 at different polymer concentrations, 0.5 (circle) and 1 wt % (triangle), shown at the conditions indicated, with water (black symbols), 30 (red symbols) and 500 mM NaCl (blue symbols). Aggregation numbers (lower panel) with the same notation for the symbols as used in the upper part of the figure. The lines are guide to the eye and they are black for polymers in water, red in 30 mM NaCl, and blue in 500 mM NaCl.

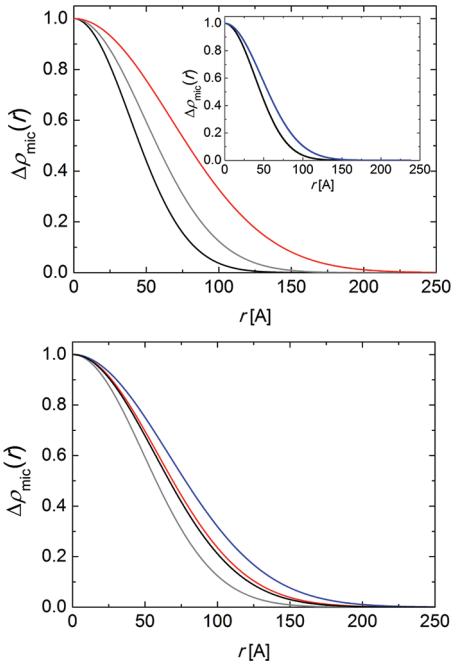

Figure 7. Average density distribution profiles for the polymer with n = 48. Top: Radial profile for the polymer with a concentration of 1 wt % at 70 °C in salt-free solution (black line), with 30 mM NaCl (gray line) and with 500 mM NaCl (red line). The inserted plot shows radial profile for 1 wt % in salt-free solution at 70 (black line) and 90 °C (blue line). Bottom: Radial profiles for the polymer in aqueous solution with 30 mM NaCl at 1 wt % at 70 °C (gray line) and 90 °C (black line) and for 0.5 wt % at 70 (red line) and 90 °C (blue line).

for 1 wt % at 90 °C. This suggests that the electrostatic interactions originating from the PSSS block are only partially screened in the presence of 30 mM NaCl in the solution since the largest micelles are observed at the lowest polymer concentration. Electrostatic repulsion limits the increase of the micelle size. However, for the low polymer concentration, the relative concentration of salt ions to polymer is higher, hereby allowing for a higher degree of screening of the electrostatic interactions and thus a larger micelle.

Increasing the salt concentration to 500 mM gives a 100% increase in the micelle size compared to that observed in aqueous solution without added salt. No significant difference is observed between the concentrations, suggesting that the electrostatic interaction of PSSS block in the triblock copolymers are fully screened at this salt concentration in the polymer concentration range investigated. The growth of the micelles is also reflected in the aggregation numbers found to be ~5 in pure water, ~15 in 30 mM, and ~50 in 500 mM NaCl at the highest temperature (Figure 6).

Self-assembly of unimers is evident for the polymer with n = 66 at all considered conditions, though the shape of the scattering data is significantly different from those of the polymer with n = 48. Dynamic light scattering measurements[8] have shown that the polymer with n = 66 has an apparent hydrodynamic radius of ~1000 Å above the CMT in contrast to the ~300 Å observed at the same conditions for the polymer with n = 48. This observed size for the polymer with n = 66 is not compatible with spherical micelles as the size exceeds the length of the fully stretched molecule. Therefore, the scattering data are fitted using cylindrical core−shell particles. The length of the cylinder could not be resolved with the SAXS setup used and therefore it is fixed at 1000 Å, which is significantly larger than what can be resolved. As for the polymer n = 48, the core and corona could not be distinguished in the model because of similar scattering length densities, as described in the paragraph "Small-Angle X-ray Scattering models". Good agreement between the experimental scattering data and the model fits are obtained (Figure 3).

The cross-section radius of the micelles is dependent on temperature and salt concentration, however, not on polymer concentration for the polymer n = 66 (Figure 8). The trend for the cross-section radius is only displayed for 1 wt % concentration since similar behavior is observed for concentrations of 0.5 and 2 wt %. This is also the case for the aggregation number; thus this quantity is also only displayed for 1 wt %. In aqueous solution, the cross-section radius increased by approximately 33% over the considered temperature interval; this behavior is similar to that observed for the polymer with n = 48 in aqueous solution. From the radial profiles at 50 and 90 °C, one sees that in aqueous solution the micelles increase in size with temperature (Figure 9), as observed from the cross-section radius. Although the cross-section radius is concentration independent, the aggregation number, N_{agg}, exhibits a clear increase with increasing concentration (data not shown). Note that the aggregation number is given per unit length of the micelles.

For the polymer n = 66 in aqueous solution of 30 mM NaCl, the cross-section radius and the aggregation number are both concentration independent. In addition, the cross-section radius is also temperature independent and the micelles have the same size as the corresponding polymer in the salt-free solution at 90 °C. In contrast, N_{agg} displays a clear effect of temperature

dx.doi.org/10.1021/ma2016216 |*Macromolecules* 2012, 45, 246–255

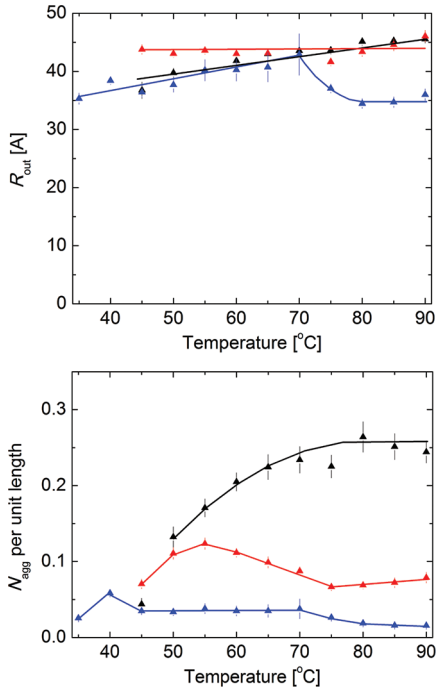

Figure 8. R_{out} (upper panel) and aggregation number per unit length (lower panel) for the polymer with $n = 66$ at a polymer concentration of 1 wt % (triangle), shown for the three different solvent conditions: Water (black symbols), 30 mM NaCl (red symbols), and 500 mM NaCl (blue symbols). The lines are guide to the eye and they are black for polymers in water, red in 30 mM NaCl, and blue in 500 m M NaCl.

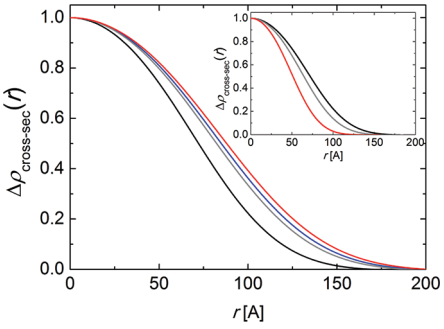

Figure 9. Average density distribution profiles for the cross-section for the polymer with $n = 66$ with a concentration of 1 wt % at 50 °C (black line) and 90 °C (blue line) and in an aqueous solution with 30 mM NaCl at 50 °C (gray line) and 90 °C (red line). The inserted plot shows average density distribution profiles for the cross-section for the polymer with $n = 66$ with a concentration of 1 wt % in a salt-free aqueous solution at 50 °C (black line) and in an aqueous solution of 500 mM NaCl at 50 (gray line) and 90 °C (red line).

(Figure 8), where N_{agg} has a maximum at 55 °C and a minimum at 75 °C.

In aqueous solution with 500 mM NaCl, the cross-section radius follows the trend observed in aqueous solution without salt up until 70 °C, above which a decrease in the cross-section radius occurs. The radial profiles show that at 50 °C the micelles are slightly smaller than those in the salt-free solution, whereas at 90 °C, a significant difference is evident (Figure 9). The aggregation number is low relative to the two other conditions with different levels of salt addition and constant up until 70 °C, above which a further decrease takes place (Figure 8).

DISCUSSION

Investigation of the polymer series PEG_{48}−$PNIPAAM_n$−$PSSS_{22}$ for a range of polymer concentrations and solvent conditions and in a wide temperature interval by SAXS and densitometry has provided detailed information on the structures below and above the CMT in addition to information on interchain interaction. The CMT depends on the size of the PNIPAAM block, the shorter the block length the higher the CMT. This is expected because the polymer will become more hydrophilic in aqueous solution at higher temperatures as the PNIPAAM block length decreases. Thus, as the PNIPAAM block size is decreased the effect of the hydrophilic blocks become more pronounced as they raise the CMT of the copolymer. A similar trend was observed in PEG−PNIPAAM systems, when the ratio of NIPAAM/EO was decreased.[5] Increase of the salt concentration in the solution depresses the CMT as seen by the shift of the onset of micelle formation to lower temperature as addition of salt decrease the solvent quality of water for PEG and for PSSS by screening the interactions between the charged blocks. Additionally, when the electrostatic interactions of the PSSS block are screened this block becomes more hydrophobic due to the presence of the phenyl rings. This behavior has also been observed for systems of PNIPAAM−PSSS, where addition of KCl influenced the LCST by decreasing the transition temperature with increasing salt content.[22]

The apparent partial specific volume increases with increasing length of the PNIPAAM block in the polymer and with raising temperature. This trend is consistent with a relatively large specific volume of the PNIPAAM block and increased thermal motion. At the LCST there is a small additional increase of the partial specific volume, which for increasing PNIPAAM block length moves closer to the LCST of the corresponding homopolymer PNIPAAM for which it is around 32 °C[3]. This increase in apparent partial specific volume was not observed for the polymer with $n = 17$, consistent with absence of self-assembly in the system.

Below the CMT in aqueous solution, R_g of the polymers increase with increasing PNIPAAM block length, which is in agreement with the fact that all blocks in the polymers are at good solvent conditions. This trend of R_g is also evident in aqueous solutions with 30 and 500 mM NaCl. The R_g for the individual polymer chains decreases with increasing concentration in aqueous solution, probably because the volume available for the individual polymer chains decreases with increasing polymer concentration. Moreover, the decrease of R_g with increasing polymer concentration is also observed for the polymers in solutions with 30 and 500 mM NaCl. Additionally, R_g of the polymer with $n = 17$ in 500 mM NaCl is constant until 50 °C, after which it decreases. This effect is evident as the unimers do not self-assemble despite the decrease in solvent quality for the MPEG block and the PSSS block is less soluble in water at this salt concentration. Thus, the polymer contracts above 50 °C.

In aqueous solution the charged PSSS block gives rise to repulsive interchain interactions. The position of the correlation peak in the SAXS data moved to higher scattering vectors with decreasing length of the PNIPAAM block, corresponding to a decrease in the average distance between the polymer chains. The effective hard-sphere radius, R_{HS}, is concentration dependent,

displaying a decrease in radius with increasing concentration. This is associated with the decreasing volume available for the polymers with increasing concentration.

The effective hard-sphere radius is independent of temperature, however, the effective hard-sphere volume fraction, η_{HS}, displays clear temperature dependence, where the onset of the decrease is located at approximately 10 °C below the CMT. The η_{HS} is not observed to decrease over a broad temperature range. This in combination with the fact that R_{HS} is not changing over the considered temperature range suggests a relative drastic change in solvent quality though not as dramatic as found for pure PNIPAAM.[3]

The micelle formation was induced by changing external factors, such as temperature and solvent conditions of the system. Increase of the temperature affects both the solubility of the PNIPAAM and the MPEG block. The first become hydrophobic at elevated temperatures causing micelle formation, because the isopropyl group and the main chain dehydrates above the LCST.[23] Furthermore, it can be estimated from measurements by Dong and Hoffman that PNIPAAM associates approximately 10 water molecules per repeat unit at temperatures below the transition temperature; this number decreases to between two and three above the transition point and also the hydration state of PNIPAAM above its transition temperature does not change significantly.[24,25] PEG becomes less soluble in aqueous solution at elevated temperatures as the solvent quality decreases. PEG associates two to three water molecules per EO monomer, thus rendering PEG water-soluble. At elevated temperatures the structure of the PEG chain changes, disrupting the hydrogen bonds between oxygen in PEG and the water molecules, thereby rendering PEG less soluble in water.[26] The solvent quality for PEG can also be changed by introducing salt to the system, as the salt ions will disrupt the hydrogen bonds between oxygen in PEG and the hydrogen in water. Florin et al.[27] showed that addition of 100 mM NaCl lowers the cloud point of PEG by 3 °C. Thus, addition of 30 mM NaCl would only slightly affect the transition temperature of MPEG and the main effect of the added salt must therefore arise from the screening of the interactions between PSSS blocks. MPEG is expected to follow a similar trend to PEG as the methoxy-group is small compared to the PEG block. Further, it was observed that that addition of 400 and 600 mM lowered the cloud point of PEG with 16 and 20 °C, respectively.[27] Therefore, addition of 500 mM NaCl to the solution will significantly affect the solubility of MPEG in the temperature interval investigated. The addition of salt has another effect on the system, as the charge interactions of the PSSS block will be screened at low salt concentrations, facilitating closer packing of the polymers in the micelle corona. Furthermore, the PSSS block will become less soluble in water, when counterions are associated with the polymer, due to the aromatic character of the block.

The formation of spherical micelles is affected both by the decreased solvent quality for MPEG and the charge screening of PSSS as observed by increase in the size and aggregation number with both increasing temperature and salt concentration. Polymers composed of PEG and PNIPAAM have previously been shown to form spherical micelles in aqueous solution.[28] The difference in micelle radius between 0.5 wt % and the two higher polymer concentrations in 30 mM NaCl is associated with the relative lower electrostatic screening of the PSSS block at the two higher polymer concentrations due to a lower salt-ion to polymer charge ratio. Thus, the micelles formed in solutions of 0.5 wt % can pack the outer chains closer due to screening, and furthermore the decreased solubility of the PSSS block also promotes closer packing of the molecules. The significant increase in the value of the aggregation number upon addition of 500 mM salt, accompanied by only a doubling of the micelle radius relative to that in aqueous salt-free solution is also a consequence of the polymers close packing as a result of the association of counterions to the PSSS block and the following increased hydrophobicity of this block. Raising the temperature in aqueous solution should make the MPEG chains contract as the solvent quality decreases;[29] however, this may not be evident in the micelle structure as the PSSS chains are rigid as a consequence of the phenyl rings and the electrostatic interactions along the PSSS chain.

The cylindrical micelles formed by the polymer with $n = 66$ showed a behavior in aqueous solution, similar to the polymer $n = 48$, as the cross-section radius and aggregation number per unit length increased with temperature. The increase in micelle size and aggregation number can be associated with the decreased solvent quality for MPEG at elevated temperatures favoring less interaction with the solvent, resulting in micelle growth. Considering formation of intermicellar aggregates instead of cylindrical micelles for the polymer $n = 66$ with the longest PNIPAAM block, this seems unlikely as the individual structures should have PNIPAAM exposed to facilitate interaction and formation of interparticle aggregates at and above the CMT. Above the CMT PNIPAAM is hydrophobic and we therefore find it unlikely that these should be exposed in the outer part of the micelles, which is necessary for these to interact. Also at the CMTs observed in the systems, the MPEG block is still soluble in water and at good solvent conditions and should therefore not promote attractive interparticle interactions. The scattering data could not be described as spherical micelles, especially the low q part was poorly described, and as the scattering data could be described as cylindrical micelles we believe this to be the most likely explanation of the larger structures that light scattering shows is present.

Introducing salt in the system changed its behavior. At 30 mM NaCl the cross-section radius was constant and the aggregation number varied. The observed constant cross-section radius can be associated with a balance between the stabilizing effect of the MPEG chains, which decreases with increasing temperature, hereby favoring more polymers in the micelles, and that the chains can pack closer when the interactions between PSSS is partially screened, though PSSS still being water-soluble. Increase of the salt concentration to 500 mM yields behavior different from that observed in 30 mM NaCl. The cross-section radius follows the same trend as observed in aqueous solution without salt up to 70 °C, and the aggregation number is low and constant up to 70 °C. At higher temperatures both the cross-section radius and the aggregation number decreased. At this salt concentration the solvent quality of water for MPEG is significantly decreased and the PSSS block will be more hydrophobic. The PSSS block is significant shorter than the MPEG chains, thus even if the PSSS blocks are still present in the outer part of the micelle it could be somewhat shielded from interactions with water by the MPEG blocks. However, as the MPEG chains contract with increasing temperature this could change. The decrease in cross-section radius at 70 °C can be associated with the contraction of the MPEG chains as the transition temperature is approached.

The behavior of the triblock copolymer systems are summarized in Figure 10. At ambient temperature, the copolymers are present as single dissolved polymer chains and the interactions

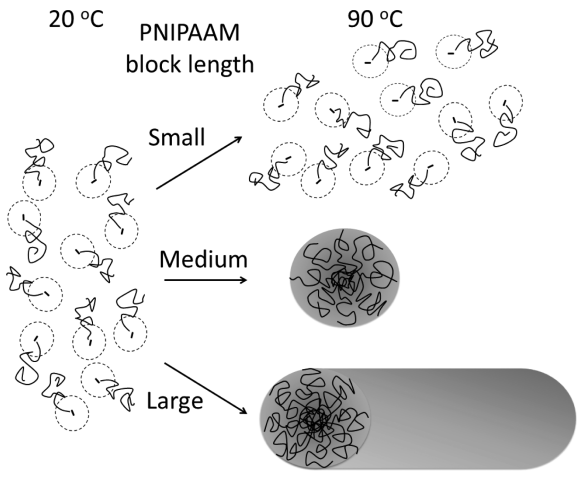

Figure 10. Summary of the temperature induced changes for different PNIPAAM block length. At ambient temperature in aqueous solution the charged triblock copolymers display repulsive interactions between the chains. At elevated temperatures the copolymers with the smallest temperature sensitive block do not self-assemble, whereas the copolymers with the longer temperature sensitive blocks do. The behavior depicted here is in aqueous solution, and a similar trend is observed upon addition of salt to the solution, with the exception that the repulsive interactions between the polymers are screened by the added salt.

arising from the charged block can be described as an effective hard-sphere repulsion in aqueous solution. Increasing the temperature induces micelle formation in the copolymers with the medium and large temperature sensitive block, where, respectively, spherical and cylindrical micelles are formed. No temperature induced self-assembly occurs for the copolymer with the shortest PNIPAAM block length in the entire temperature interval investigated and the copolymer is described as single dissolved polymer chains with repulsive interchain interactions. A similar trend is observed upon addition of salt to the system, with the exception that the repulsive interchain interactions originating from the charged block are screened by the salt ions.

CONCLUSION

The reported SAXS and densitometry data cover a broad temperature range (20−90 °C) and gives a detailed picture of the solution and aggregation behavior of $MPEG_{45}$-*b*-P(NIPAAM)$_n$-*b*-$P(SSS)_{22}$ with varying PNIPAAM block length. Below the CMT, the three polymers displayed repulsive interchain interactions in aqueous solution arising from the charged PSSS block. Raising the salt concentration in the solutions to 30 mM partially screened the electrostatic interactions and the polymers are still observed to exist in the form of unimers, as found in aqueous solution. A further increase of the salt concentration up to 500 mM fully screened the charge interactions and caused the polymer with the longest PNIPAAM block ($n = 66$) to aggregate. The aggregates still displayed polymeric behavior despite that the polymer was no longer observed to exist as unimers.

The micelle formation of the three block copolymer $MPEG_{45}$-*b*-P(NIPAAM)$_n$-*b*-$P(SSS)_{22}$ is affected by the polymer composition, charge interaction screening, and solvent quality for the MPEG block. The onset of micelle formation was highly dependent on the size of the PNIPAAM block. Increasing the PNIPAAM block length advanced the onset of micelle formation. Furthermore, by increasing the salt concentration lowered the CMT with approximately 10 °C. However, increasing the salt content in the solvent could not induce micelle formation in the polymer with the shortest PNIPAAM block size ($n = 17$) in the parameter space investigated. This polymer displayed single polymer behavior at all the studied conditions and at all polymer concentrations and temperatures investigated.

The micelle shape was dependent on PNIPAAM block length, and it was observed that polymers with $n = 48$ and 66 formed spherical and cylindrical micelles, respectively. Addition of salt had a pronounced effect on the size, structure, and aggregation number of the micelles. Micelles formed in solutions of the copolymer with $n = 48$ increased in both size and aggregation number upon addition of salt. This is attributed to decreased solvent quality, whereas micelles formed by $n = 66$ displayed a more complicated behavior. The micelles grow with increasing temperature in aqueous solution as a consequence of poorer solvent quality. However, for solutions of this polymer with 30 mM salt, the micelle cross-section radius was constant. This feature may arise from an intricate interplay between decreased solvent quality and partial screening of the electrostatic interactions. Finally, in the presence of 500 mM salt, the micelles behave as in aqueous solution without salt up to 70 °C, above this temperature and they decreased in cross-section radius, probably due to the contraction on the MPEG chains.

The current study has provided new insight into the aggregation behavior of a complex polymer system with block copolymers consisting of hydrophilic blocks, blocks with temperature-induced hydrophobicity, and polyelectrolyte chains. The complicated nature of the polymer, results in a behavior that depends critically on a broad set of external parameter, namely, polymer composition, polymer concentration, salt concentration, and temperature. The many competing interactions in these systems make it particularly difficult to rationalize the behavior, although several clear trends are observed.

ACKNOWLEDGMENT

M.A.B and J.S.P. gratefully acknowledges support from the Danish Council for Independent Research: Natural Sciences. B.N. gratefully acknowledges the support from the Norwegian Research Council for the PETROMAKS project.

REFERENCES

(1) Neradovic, D.; Soga, O.; Van Nostrum, C. F.; Hennink, W. E. *Biomaterials* **2004**, *25*, 2409.
(2) Sommer, C.; Pedersen, J. S. *Macromolecules* **2004**, *37*, 1682.
(3) Stieger, M.; Richtering, W.; Pedersen, J. S.; Lindner, P. *J. Chem. Phys.* **2004**, *120*, 6197.
(4) Schild, H. G. *Prog. Polym. Sci.* **1992**, *17*, 163.
(5) Virtanen, J.; Holappa, S.; Lemmetyinen, H.; Tenhu, H. *Macromolecules* **2002**, *35*, 4763.
(6) Zhu, K.; Pamies, R.; Kjøniksen, A.-L.; Nyström, B. *Langmuir* **2008**, *24*, 14227.
(7) Kjøniksen, A.-L.; Zhu, K.; Pamies, R.; Nyström, B. *J. Phys. Chem. B* **2008**, *112*, 3294.
(8) Kjøniksen, A.-L.; Zhu, K.; Behrens, M. A.; Pedersen, J. S.; Nyström, B. *J. Phys. Chem. B* **2011**, *115*, 2125.
(9) Pedersen, J. *J. Appl. Crystallogr.* **2004**, *37*, 369.
(10) Pedersen, J. S. *Adv. Colloid Interface Sci.* **1997**, *70*, 171.
(11) Debye, P. *J. Phys. Colloid Chem.* **1947**, *51*, 18.
(12) Pedersen, J. S.; Schurtenberger, P. *Macromolecules* **1996**, *29*, 7602.
(13) Pedersen, J. S.; Gerstenberg, M. C. *Macromolecules* **1996**, *29*, 1363.

(14) Kinning, D. J.; Thomas, E. L. *Macromolecules* **1984**, *17*, 1712.
(15) Rayleigh, L. *Proc. R. Soc. London, Ser. A* **1910**, *84*, 25.
(16) Pedersen, J. *J. Appl. Crystallogr.* **2000**, *33*, 637.
(17) Neugebauer, T. *Ann. Phys.* **1942**, *42*, 509.
(18) Edwards, S. F. *Proc. Phys. Soc.* **1966**, *88*, 265.
(19) Cotter, M. A.; Martire, D. E. *J. Chem. Phys.* **1970**, *52*, 1909.
(20) Sommer, C.; Pedersen, J. S.; Stein, P. C. *J. Phys. Chem. B* **2004**, *108*, 6242.
(21) Tondre, C.; Zana, R. *J. Phys. Chem.* **1972**, *76*, 3451.
(22) Nowakowska, M.; Szczubialka, K.; Grebosz, M. *Colloid Polym. Sci.* **2004**, *283*, 291.
(23) Maeda, Y.; Higuchi, T.; Ikeda, I. *Langmuir* **2000**, *16*, 7503.
(24) Lele, A. K.; Hirve, M. M.; Badiger, M. V.; Mashelkar, R. A. *Macromolecules* **1997**, *30*, 157.
(25) Dong, L. C.; Hoffmann, A. S. *Proc. Int. Symp. Contr. Rel. Bioact. Mater.* **1990**, *17*, 116.
(26) Holmberg, K.; Jönsson, B.; Kronberg, B.; Lindman, B. *Surfactants and Polymers in Aqueous Solution. Chapter 4: Physicochemical Properties of Surfactants and Polymers Containing Oxyethylene Groups*; Wiley: New York, 2002; pp 97−118.
(27) Florin, E.; Kjellander, R.; Eriksson, J. C. *J. Chem. Soc., Faraday Trans. 1: Phys. Chem. Condens. Phases* **1984**, *80*, 2889.
(28) Topp, M. D. C.; Dijkstra, P. J.; Talsma, H.; Feijen, J. *Macromolecules* **1997**, *30*, 8518.
(29) Sommer, C.; Pedersen, J. S.; Garamus, V. M. *Langmuir* **2005**, *21*, 2137.
(30) Oliveira, C. L. P.; Pedersen, J. S. Unpublished results.

Macromolecules

Article

pubs.acs.org/Macromolecules

Ordering of Sphere Forming SISO Tetrablock Terpolymers on a Simple Hexagonal Lattice

Jingwen Zhang,[†] Scott Sides,[‡] and Frank S. Bates*[,†]

[†]Department of Chemical Engineering and Materials Science, University of Minnesota, Minneapolis, Minnesota 55455, United States

[‡]Tech-X Research Corporation, Boulder, Colorado 80303, United States

ABSTRACT: Hexagonally ordered spherical and cylindrical morphologies (P_6/mmm and P_6/mm space group symmetries) have been identified in bulk poly(styrene-*b*-isoprene-*b*-styrene-*b*-ethylene oxide) (SISO) tetrablock terpolymers. These materials were synthesized by adding up to 32% by volume O blocks to a parent hydroxy-terminated SIS triblock copolymer containing 40% S by volume, and the resulting morphologies were characterized by small-angle X-ray scattering, transmission electron microscopy, differential scanning calorimetry and dynamic mechanical spectroscopy. Disordered, spherical and cylindrical phases were documented with increasing O content, where both ordered states exhibit hexagonal symmetry. Theoretical calculations based on a numerical self-consistent field theory for polymers provide crucial insights into the molecular configurations associated with these morphologies. These results offer a new approach to independently control domain shape and packing in block copolymer melts through manipulation of the magnitude and sequencing of the binary segment−segment interactions ($\chi_{SI} \leq \chi_{SO} \ll \chi_{IO}$), which dictate core segregation and the effective interdomain interactions.

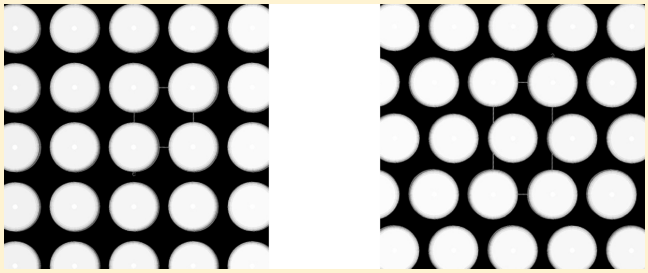

I. INTRODUCTION

Modern synthetic polymerization chemistry affords access to a rapidly expanding portfolio of block and graft copolymer architectures generated from a rich array of monomers. Linking the resulting morphological features and related physical properties with the molecular structures constitutes a central challenge to polymer scientists and engineers. This article describes new and surprising results regarding the ordering of sphere forming ABAC tetrablock terpolymers.

Access to powerful characterization tools, most notably synchrotron small-angle X-ray scattering (SAXS), and the application of sophisticated theoretical techniques have greatly enhanced the pace of discovery in the field of block copolymers. Linear AB diblock copolymers, the simplest case, provide instructive examples of this synergy. Until the mid-1980s, just three diblock morphologies were recognized based primarily on data obtained using transmission electron microscopy (TEM) and laboratory based SAXS instruments: spheres, cylinders and lamellae. The concept of ordered bicontinuous phases, well established in the area of surfactancy,[1] evolved between 1985[2] and 1994,[3] eventually resulting in the identification of the fascinating gyroid phase. (Initial claims of a cubic double diamond phase are now generally attributed to the gyroid.[4,5]) Significantly, experiments and theory both played critical roles in unraveling the molecular factors responsible for formation of the gyroid.[6] Several years ago self-consistent field theory (SCFT) anticipated a fifth phase in diblocks,[7] an orthorhombic network structure dubbed O^{70}. (This remarkable prediction evolved from an investigation of ABC triblocks).[8] Soon after publication of this theoretical work synchrotron SAXS experiments revealed the existence of O^{70} within a narrow slice of parameter space[9] defined by the composition (f) and combination parameter $\chi_{AB}N$, where χ_{AB} is the Flory−Huggins segment−segment interaction parameter and N is the degree of polymerization. Recently we documented the σ-phase in a low molecular weight sphere forming poly(isoprene-*b*-lactide) (IL) diblock copolymer melt using synchrotron SAXS and TEM.[10] This sixth ordered equilibrium structure, which has not been accounted for theoretically, makes contact with several seemingly unrelated fields in materials science.[10−12]

Adding more block types geometrically expands the complexity of microphase formation. Linear ABC triblock terpolymers have produced over 30 well-defined ordered morphologies and more are likely to be discovered. Three chemically distinct block types offer attractive design flexibility (e.g., glassy, rubbery, and semicrystalline domains arranged in tailored microstructures)[13−24] but entail a daunting array of structural choices. Fortunately, SCFT can provide pivotal guidance in relating morphology to the block sequence and the trio of interaction parameters, χ_{AB}, χ_{BC}, χ_{AC}, as evidenced by the successful modeling of entire ABC phase portraits.[8,25,26]

So, why add another block to an already complicated system? We believe that the ABAC tetrablock terpolymer architecture (and the coupled version ABACABA) affords the polymer

Received: September 29, 2011
Revised: November 20, 2011
Published: December 7, 2011

scientist and engineer a rich set of new design options. For example, ABA triblocks make excellent thermoplastic elastomers and tough plastics. Addition of a fourth chemically distinct block can direct this mechanically robust unit into otherwise inaccessible morphologies depending on the relative magnitude of χ_{AB}, χ_{BC} and χ_{AC}. Recently we have exploited this idea with fully saturated CECPCEC multiblocks that are driven to order from the homogeneous melt by poly(ethylene) (E) crystallization.[27] Combining minority amounts of glassy poly(cyclohexylethylene) (C) and E with a majority of rubbery poly(ethylenepropylene) (P) in a heptablock architecture leads to a versatile new class of thermoplastic elastomers with a convenient and invariant (with respect to molecular weight and composition) processing temperature. These characteristics result from the combined effects of the specified block sequence and $\chi_{EP} \ll \chi_{CP} < \chi_{CE}$.[28]

In this article we examine the consequences of inverting the block placement with respect to the interaction parameters in a series of SISO tetrablocks, where $\chi_{SI} \leq \chi_{SO} \ll \chi_{IO}$. This arrangement discourages contact between O and I blocks leading to spherical domains of O, clad in a shell of S and embedded in a matrix of I and S. These tetrablocks have been prepared by adding O blocks of varying length to a common SIS parent triblock (40% S) that is disordered above about 80 °C (i.e., $T > T_g$). We report a new finding that compliments our recent discovery of the σ-phase in a similar material prepared from a compositionally symmetric SIS triblock (50% S): packing of spherical microdomains on a simple hexagonal lattice (P_6/mmm symmetry). SCFT calculations do not account for the experimental packing symmetry but do anticipate a spherical morphology (BCC symmetry) and provide valuable insight into the distribution of blocks within the ordered structure.

These findings lead us to a conjecture that the tetrablock terpolymer molecular architecture offers previously unrecognized potential for controlling the shape and packing symmetry of microphase separated block copolymers through delicate manipulation of the effective interdomain interactions.

II. EXPERIMENTAL SECTION

Synthesis and Chemical Characterization. Figure 1 shows the molecular architecture for the poly(styrene-*b*-isoprene-*b*-styrene-*b*-ethylene oxide) (SISO) tetrablock terpolymers described in this article, which were prepared using a two-step living anionic polymerization procedure that is described in detail in a previous publication.[22] Monomers and solvent were purified as described elsewhere.[29] In the first step, styrene was initiated by *sec*-butyllithium and polymerized at 40 °C in cyclohexane under argon. An aliquot of this product was removed for size-exclusion chromatography (SEC) analysis prior to the addition and complete reaction of isoprene monomer, followed by another carefully metered amount of styrene, equal in mass to the first charge. After completion of this triblock polymerization, a 10-fold molar excess of ethylene oxide, relative to styryllithium, was added to the living polymer solution and allowed to react for 60 min and then the reaction was terminated with excess degassed methanol. The hydroxyl functionalized triblock copolymer product (SIS−OH) was precipitated in methanol, decanted, and dried in a vacuum oven at room temperature. In the second step, the SIS−OH compound was reacted with potassium naphthenalide in tetrahydrofuran at 40 °C followed by the addition of a measured amount of ethylene oxide, then terminated with excess degassed methanol after 48 h. Five SISO tetrablock copolymers were produced in this way, each containing the same SIS core and varying O block lengths. Excess tetrahydrofuran solvent was removed by rotary evaporation then the SISO polymers were redissolved in dicholoromethane and washed once with an aqueous sodium bicarbonate mixture and several times with distilled water to remove residual salts. Finally, the tetrablocks were precipitated in a 3:1 solution of methanol and isopropanol, decanted, filtered, redissolved in benzene and freeze-dried under vacuum. Before freeze-drying, 0.5 wt % (relative to the polymer) of BHT antioxidant was added to the solution to minimize subsequent degradation of the PI blocks. Figure 1 illustrates the molecular structure of the SISO tetrablock terpolymers.

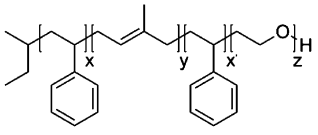

Figure 1. Molecular structure of SISO tetrablock terpolymers.

Chemical Characterization. SISO tetrablock copolymer compositions were determined by ^{1}H nuclear magnetic resonance (NMR) spectroscopy using a 300 MHz Varian instrument operated at room temperature with deuterated chloroform as the solvent. We estimated the mole fractions of styrene, isoprene, and ethylene oxide repeat units based on the integrated area under well-defined resonances, and these values were converted to weight fractions and volume fractions based on the published homopolymer densities at 140 °C (ρ_S = 0.969 g/cm^3, ρ_I = 0.830 g/cm^3, ρ_O = 1.064 g/cm^3).[30]

The absolute number-average molecular weight of the first poly(styrene) block ($M_{n,S}$) and the molecular weight distribution and polydispersity index (PDI) of all the specimens, were obtained using size exclusion chromatography (SEC). A Waters 150-C ALC/GPC configured with Phenomenex Phenogel columns was operated with chloroform as the solvent at room temperature. Polystyrene standards from Polymer Laboratories were used as the basis to calculate the polydispersity, which in all cases was less than 1.1. The overall number-average molecular weight of each tetrablock copolymer, $M_{n,SISO}$, was calculated using the $M_{n,S}$ and the weight fractions determined by ^{1}H NMR. Table 1 lists the chemical characterization data for all the SISO samples.

Small-Angle X-ray Scattering (SAXS). Synchrotron SAXS data were obtained at the DuPont−Northwestern−Dow Synchrotron Research Center at the Advanced Photon Source using sample−detector distances of 5.50 and 6.52 m with radiation wavelength λ = 0.729 Å. Scattering patterns were recorded with a Mar CCD area detector. Two-dimensional data were azimuthally averaged and are represented as intensity vs scattering wave vector, $q = |\mathbf{q}| = 4\pi/\lambda \sin(\theta/2)$, where θ is the scattering angle. SIS and SISO-1 were annealed at 110 °C for 5 min at Argonne before taking measurements. The other tetrablock specimens were annealed at 120 °C under vacuum for 1 day, quenched in liquid nitrogen, reheated to 120 °C at Argonne, and annealed for 5 min before taking measurements. Temperature was controlled to within ±1 °C using a DSC instrument while specimens were maintained under a helium purge.

Transmission Electron Microscopy (TEM). TEM data were obtained using a Tecnai T12 transmission electron microscope operating at 120 kV at the University of Minnesota Characterization Facility. Samples were annealed under vacuum at target temperatures for specified times prior to quenching in liquid nitrogen to preserve the melt morphology. Thin slices (~60 nm) of polymer specimens were prepared by microtoming at −70 °C using a Reichart ultramicrotome fitted with a Microstar diamond knife and collected on copper grids (Ted Pella). Microtomed sections were stained with the vapor from a 4% aqueous osmium tetraoxide solution for 10 min to obtain electron contrast; this reagent reacts preferentially with the PI blocks.

Differential Scanning Calorimetry (DSC). DSC experiments were conducted on a TA Instruments Q1000 DSC. Approximately 5−10 mg of polymer was heated to 150 °C to minimize the effects of prior thermal history before cooling to −100 at 10 °C/min. Data were acquired during a second heating cycle, also at 10 °C/min. The degree of crystallinity of the PEO was determined by integrating the

Table 1. SIS and SISO Characterization Data

sample	M_n/kDa	PDI	f_S[a]	f_I[a]	f_O[a]	phase[b]	d/nm[c,d]	% cryst.[e]	T_{ODT}/°C[f]
SIS	23.3	1.03	0.39	0.61	0.00	DIS	-	0.0	<80
SISO-1	23.6	1.04	0.38	0.60	0.02	DIS	-	36.2	<80
SISO-2	24.4	1.04	0.35	0.56	0.09	HEX	21.8, 18.9	39.8	213 ± 2
SISO-3	25.0	1.08	0.34	0.53	0.12	HEX	25.8, 22.3	55.3	>250
SISO-4	26.1	1.06	0.32	0.50	0.19	HEX	29.7, 25.7	68.3	>250
SISO-5	29.0	1.07	0.27	0.41	0.32	HEX	35.5	70.8	>250

[a]Volume fractions calculated with from densities at 140 °C.[30] [b]HEX-hexagonally packed spheres for SISO-2, -3, -4 and hexagonally packed cylinders for SISO-5. [c]Temperature is 120 °C. [d]Lattice dimensions listed for SISO-2, -3, -4 correspond to a and c and characteristic morphological length scale ($d = 2\pi/q^*$) for SISO-5. [e]Percent crystalline of the PEO domains was determined by differential scanning calorimetry. [f]Order−disorder transition temperatures were determined by dynamic mechanical spectroscopy.

baseline-corrected melting peaks and normalizing this value to the heat of fusion of bulk PEO (213 J/g),[31]

$$X_c = \frac{\Delta H_m}{w_{PEO}\Delta H^o_{m,PEO}} \quad (1)$$

Dynamic Mechanical Spectroscopy (DMS). DMS data were obtained between 80 and 250 °C with a Rheometrics Scientific ARES strain-controlled rheometer fitted with 25 mm diameter parallel plates; these temperatures are above the glass transition and melting temperatures of the PS and PEO blocks ($T_{g,S} \approx 60$ °C, and $T_{m,O} < 60$ °C). Samples were prepared by compression-molding the polymer powder into 25.0 mm ×0.8 mm disks at 140 °C using 2000 psi of pressure for 5 min. All samples were initially heated to 250 or 10 °C above the order−disorder transition temperatures (T_{ODT}), whichever was lower, to minimize the effects of prior thermal history. After cooling, isochronal (ω = 1 rad/s) dynamic elastic (G') and loss (G'') moduli were recorded with a strain amplitude of 1% while heating at 1.5 °C/min. A linear viscoelastic response was verified by running strain sweeps from 0.1 to 10% at representative temperatures. Isothermal frequency sweeps ($100 \leq \omega \leq 0.1$ rad/s) also were conducted at selected temperatures.

III. THEORETICAL CALCULATIONS

Numerical self-consistent field theory (SCFT) for dense polymer melts has been highly successful in describing complex morphologies in block copolymers.[32] Field-theoretic simulations such as these are able to access large length and time scales that are difficult or impossible for particle-based simulations such as molecular dynamics, while still incorporating more realistic polymer models than many macroscopic, continuum simulations. We briefly describe the model and simulation method for a dense melt of AB diblock copolymers in bulk. For the experimental system in this paper the A species will represent monomers of poly(styrene) and the B species will represent monomers of poly(isoprene); extension to SISO follows the methodology outlined for an AB diblock. The chemical specificity of S and I blocks is captured in the model through the value of the Flory parameter χ, which controls the strength of the chain segregation that drives the formation of nanoscale morphologies. The Hamiltonian of a dense melt of n polymer chains containing distinct monomers A and B can be written as:

$$H = \frac{1}{4R_{g0}^2}\sum_{\alpha=1}^{n}\int_0^1 \mathrm{d}s\left(\frac{\mathrm{d}\vec{r}_\alpha}{\mathrm{d}s}\right)^2 + \rho_0^{-1}\int \mathrm{d}\vec{r}\ \chi\hat{\rho}_A(\vec{r})\hat{\rho}_B(\vec{r}) \quad (2)$$

The first term in H gives the free-energy contribution from the so-called "Gaussian thread" model.[33] This model can be derived as the continuous limit of a polymer chain consisting of spherical beads connected by harmonic springs (the radius of gyration of an unperturbed chain in a dense melt of identical chain is R_{g0}). The position r of a bead s contour steps along the αth chain is given by the space curve $r(s)$. The second term in H represents the free-energy contribution from a model in which dissimilar monomers in contact have a higher free-energy than like monomers in contact. The strength of this tendency for chemically dissimilar monomers to segregate is parametrized by the aforementioned χ value and is a function of the specific chemical species A and B as well as temperature. The model given by eq 2 is for a linear AB diblock copolymer. However, the model is easily generalized to a tetrablock copolymer like those described in this study.

The Hamiltonian represented by eq 2 can be used to form the partition function of a dense melt of n copolymer chains. The monomer density operators may be recast as continuous monomer density fields by application of a Hubbard-Stratonovich transformation[34] that introduces chemical potential fields $\omega(r)$ that are conjugate to the monomer density fields. The partition function then takes the form:

$$Z = \int D\rho_A D\rho_B D\omega_A D\omega_B Dp\, e^{-\beta F} \quad (3)$$

where ρ_A and ρ_B are the smeared out density fields and ω_A and ω_B are the conjugate chemical potential fields that are introduced through the field theory transformations. The p field is introduced through the constraint of overall monomer incompressibility. The integrals are over all possible realizations of the fields with F given by:

$$F = \int \mathrm{d}r\ [\rho_0^{-1}\chi\rho_A\rho_B - i\omega_A\rho_A - i\omega_B\rho_B - ip(\rho_0 - \rho_A - \rho_B)] - n\ln Q[i\omega_A, i\omega_B; N] \quad (4)$$

where Q is the single-chain partition function,[32] and is a functional of the chemical potential fields and a function of the chain length N. The integrals in eq 3 are still intractable, so a mean-field approximation is made where the extremum of F is assumed to make the largest contribution to the overall sum. A system of equations is then generated that needs to be solved self-consistently in order to satisfy the mean-field approximation. An iterative algorithm is used to find solutions for the $\rho(r)$ and $\omega(r)$ fields that satisfy the SCFT mean-field equations.[34] For the rest of this discussion, this SCFT algorithm is denoted by R_{sc} . For fields at iteration step n, the fields at iteration n+1 can be obtained by $\omega_{n+1} = R_{sc}[\omega_n]$. However, for large simulation grids this iterative algorithm can lead to field solutions that contain topological defects,[35] analogous to the defects observed in experimental TEM images.

A "spectral filtering"[36] algorithm has been shown to help reduce the presence of topological defects in numerical SCFT calculations of block copolymer structure by removing certain frequency components of the chemical potential fields during the relaxation of these fields toward the lowest free-energy configuration. The spectral filtering function X_{sp} is defined by the following:

$$X_{SP} = \begin{cases} \hat{\omega}(\vec{k}) & \hat{\omega}(\vec{k}) > (f_{cut} \times \max|\hat{\omega}|) \\ 0 & \hat{\omega}(\vec{k}) \leq (f_{cut} \times \max|\hat{\omega}|) \end{cases} \quad (5)$$

where the $\hat{\omega}$ represents a Fourier transformed field and f_{cut} parametrizes the "strength" of the filtering function and takes values between 0 and 1. The SCFT mean-field algorithm R_{sc} is applied for a sufficient number of iterations n_{start} to initiate phase segregation. Then the filtering algorithm R_{filter} is applied

$$R_{filter}[\omega, f_{cut}] = \begin{cases} \hat{\omega}(\vec{k}) = \hat{F}[\omega(\vec{r})] \\ \hat{\omega}(\vec{k})_{SF} = X_{SF}[\hat{\omega}(\vec{k}); f_{cut}] \\ \hat{\omega}(\vec{r}) = \hat{F}^{-1}[\omega(\vec{k})_{SF}] \end{cases} \quad (6)$$

where the strength of the filtering f_{cut} is a free parameter for a particular simulation run. This spectral filtering has been found to assist the relaxation algorithm R_{sc} in finding ordered mesophases. The spectral filtering essentially keeps the largest components of the frequency spectrum of the transformed chemical potential field, which then acts as an effective initial condition for the self-consistent algorithm. The assumption for this procedure is that the topological defects one is trying to remove will tend to have the smallest frequency components. The filtering operation R_{filter} is applied every 1000 field iterations, i.e., applications of R_{sc}. This procedure continues until an ordered mesophase is obtained or the fields reach a steady state configuration. This filtering procedure (also described elsewhere[36]) has been improved upon in this study. The older spectral filtering algorithm (outlined above) uses a single frequency cutoff in the transformed chemical potential fields $\omega(k)$. The newer method used here subdivides frequency space into distinct regions, each with its own frequency cutoff value. This new spectral filtering algorithm is implemented in a parallel framework in the PolySwift++ code. For all SCFT simulations employed in this study the following protocol is used. For each one of the four samples, a series of simulations is run with different filtering strengths for $f_{cut} = f$ 0.6, 0.4, 0.2, and 0.0. Typically, the most well-order structure has the lowest free-energy as well. For samples whose location in phase space is near a boundary between different space groups, it has been observed that the spectral filtering algorithm can bias the sample toward the incorrect morphology. Ultimately, the free-energy of the bulk system for each of the f_{cut} values must be compared and the run with the lowest free-energy value is chosen as the most likely space group that will be obtained in the experiments.

In order to make comparisons with experimental data the energy and length scales must be matched to the SCFT simulation parameters. The length scale enters the theory through the unperturbed radius of gyration:

$$R_{g0}{}^2 = \frac{b^2 N}{6} \quad (7)$$

where N is the chain length (number of independent chain segments) and b is the statistical segment length. The energy scale enters through the temperature dependent Flory–Huggins parameters $\chi(T)$, which have been reported for poly(isoprene), poly(styrene), and poly(ethylene oxide)[37]

$$\chi_{IS}(T) = 26.4T^{-1} - 0.0287$$
$$\chi_{SO}(T) = 29.8T^{-1} - 0.0229$$
$$\chi_{IO}(T) = 90.0T^{-1} - 0.0579 \quad (8)$$

based on a common segment volume of 118 A^3. Segregation strength in the SCF theory is proportional to χN, which has been calculated for each of the six samples under consideration using the molecular weights and block volume fractions (f) listed in Table 1.

IV. RESULTS AND ANALYSIS

Figure 2 shows a three-dimensional phase map for SISO tetrablock terpolymers. This depiction does not include the role

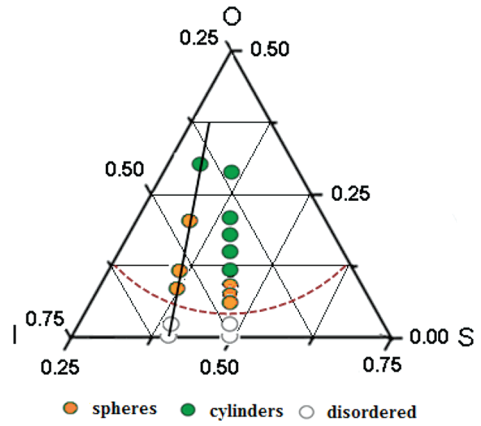

Figure 2. Poly(styrene-*b*-isoprene-*b*-styrene-*b*-ethylene oxide) (SISO) phase portrait in the vicinity of the order–disorder transition, which is indicated by the dashed curve. Filled and open circles indicate ordered and disordered states, respectively, within the experimental temperature range $100 \leq T \leq 250$ °C. Specimens considered in this work were prepared by adding O blocks to a SIS triblock containing 40% S and 60% I as identified by the line. The isopleth with 50 vol % S and 50 vol % I was published elsewhere.[38]

of segregation strength, χN, which forms a fourth axis. Because SISO tetrablocks are prepared from a common (parent) SIS triblock, each set of materials lies on an isopleth with constant f_S and f_I and varying f_O. Also, there is another important symmetry parameter associated with these materials: The ratio of poly(styrene) block molecular weights (proportional to x and x' in Figure 1). In this (and a previous) report we focus on tetrablocks with $x = x'$.

Figure 2 contains two isopleths, one with $f_S = 1 - f_I = 1/2$, which was considered in an earlier publication,[38] and a second for the case presented here, $f_S = 0.39$. These polymers were designed to bridge the order–disorder transition with increasing O content based on the trends reported by Epps et al.[24] for ISO triblocks prepared from a parent IS diblock with $f_S = 0.42$ and $M_n = 12.7$ kg/mol and $0 \leq f_O \leq 0.35$. Thus, the parent SIS compound (Table 1) was designed with 1.8 times the overall molecular weight of the disordered IS diblock,[24] precisely the ratio that theoretically corrects for the architectural difference.[39] In this section, we present and evaluate

dx.doi.org/10.1021/ma202196c | Macromolecules 2012, 45, 256–265

experimental and theoretical results that establish the phase behavior and structure of this set of SISO materials.

Order and Disorder. SAXS results acquired at 120 °C (110 °C for SIS and SISO-1) are presented in Figure 3. These

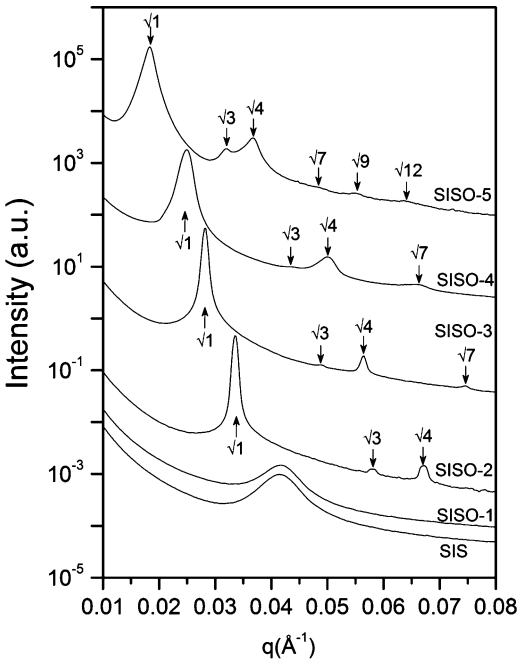

Figure 3. Synchrotron SAXS data for the series of SISO tetrablock copolymers with a fixed ratio S:I of 4:6 and O content ranging from 0 to 32% by volume. Samples were prepared by annealing at 120 °C for 1 day, quenched in liquid nitrogen, reheated, and annealed at 120 °C for 5 min before taking the measurements. The arrows identify relative peak positions associated with hexagonal symmetry. Scattering patterns have been progressively shifted vertically for clarity.

scattering patterns fall into two categories. SIS and SISO-1 each produced a single broad peak consistent with a state of disorder, while SIS-2, -3, -4, and -5 generated three or more well-defined diffraction peaks with relative positions $(q/q^*)^2$ = 1, 3, 4, 7, 9, 12, which we associate with a state of hexagonal order.

Dynamic mechanical spectroscopy data support the conclusions drawn from Figure 3 regarding order and disorder as highlighted in Figure 4. SISO-1 displays terminal viscoelastic

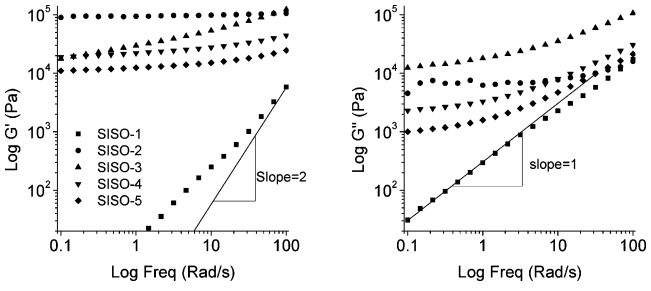

Figure 4. Dynamic elastic (G') and loss (G'') moduli measured at 120 °C (110 °C for SISO-1) as a function of frequency. These results indicate states of order except for SISO-1, which is disordered.

behavior ($G' \sim \omega^2$ and $G'' \sim \omega$) above 80 °C (the lowest feasible measurement temperature beyond the polystyrene glass transition) while the remaining tetrablocks are decidedly nonterminal consistent with a triply periodic ordered morphology between 80 and 160 °C. These trends are anticipated by the corresponding ISO results;[24] i.e., adding an O block to SIS leads to a rapid rise in T_{ODT} with increasing O molecular weight. However, whereas the ISO triblocks were shown to have either tricontinuous cubic (Q^{230}) or lamellar (LAM_3) order, the SISO isopleth contains exclusively hexagonal order.

Representative TEM images obtained from SISO-2, -3, -4, and -5 are presented in Figure 5. Samples were annealed in a

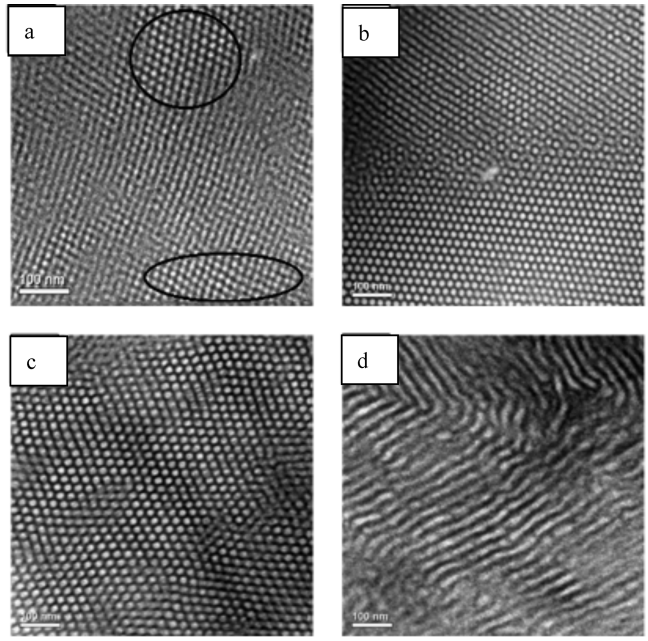

Figure 5. TEM micrographs obtained from OsO_4 stained SISO tetrablock copolymers. Key: (a) SISO-2 (160 °C, 1day), (b) SISO-3 (120 °C, 1day), (c) SISO-4 (120 °C for 1 day), and (d) SISO-5 (160 °C for 3 days), where the temperature and time in the parentheses indicate the annealing conditions prior to microtoming. Panels a–c contain ordered arrays of spherical microdomains while panel d is consistent with a cylindrical morphology. Transition from 6-fold to 4-fold symmetric projections (circled in panel a) that share common planes of spheres is consistent with a simple hexagonal lattice. Panel b contains two large grains separated by an unusual grain boundary structure that is similar to the sigma phase morphology.[10]

vacuum oven for at least 1 day (120 °C for SISO-3 and 160 °C for SISO-2, SISO-4 and SISO-5) prior to quenching into liquid nitrogen to preserve the melt morphology.

These images reveal a surprising result. While SISO-5 (f_O = 0.32) contains a cylindrical morphology, as would be expected based on the hexagonal symmetry identified by SAXS (Figure 2), this is clearly not the case for the three other ordered materials ($0.12 \leq f_O \leq 0.19$). Dozens of TEM images taken from numerous thin sections obtained from these polymers are all consistent with spherical microdomains in sharp contrast with the network structures reported for the analogous ISO compounds.[40] Micrographs taken from SISO-2, -3, and -4 each exhibit regions with distinct 6-fold symmetry defined by well delineated circular white domains distributed on a continuous black matrix. The picture from sample SISO-3 shows two well ordered grains that intersect at a grain boundary. Significantly, the grain at the top of this image is tilted such that planes of spheres are rotated away from the 6-fold axis resulting in a projection that reveals black and

dx.doi.org/10.1021/ma202196c | Macromolecules 2012, 45, 256–265

modulated white layers. This projection confirms that the crystal is not comprised of cylinders; based on the estimated thickness of the microtomed sections (ca. 60 nm) and the sphere diameter (16 nm) we would expect to observe up to three layers of spherical domains. Thus, we conclude that the hexagonal arrangements (6-fold symmetry) derive from vertically aligned stacks of spheres. Also, the grain boundary structure (which resembles the recently reported σ-phase packing symmetry, see below)[10] is not compatible with a cylindrical morphology.

Additional insight into the hexagonal packing geometry can be gleaned from Figure 5a, which contains regions with 6-fold and 4-fold symmetry. The square arrangements are accessed from the hexagonal ones along specific planes of spheres, which identify the axis of rotation required to transform from one projection to the other. We compare two possible packing scenarios corresponding to the space groups P_6/mmm (primary or simple hexagonal) and P_{6_3}/mmc (hexagonal close packed or HCP) in Figure 6 projected along the c (6-fold) axis and rotated

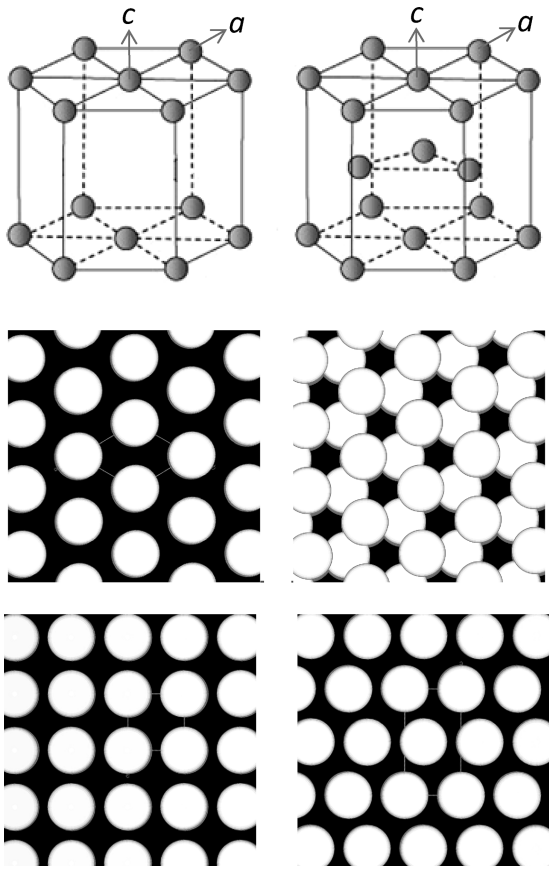

Figure 6. Simulated projections of hexagonal crystal structures formed from spherical (30% by volume) domains: P_6/mmm with $c = a\sqrt{3}/2$ (left) and $P6_3/mmc$ (right). The top images represent projections along the 6-fold (c) axis, while the bottom pictures were obtained by projecting along the a axis, i.e., after rotating the crystal by 90°. Comparison of these images with the TEM results in Figure 5 indicates that the spheres pack on a simple hexagonal lattice.

90° around the normal to the (100) plane. These images have been constructed using a 30% volume fraction of spheres (f_O plus $f_S/2$ for SISO-3, see below). Clearly, HCP packing does not account for the experimental results. Alternating (ABAB...) hexagonal stacking of spheres leads to a projected image of black domains on a white matrix and rotation around the [100] direction fails to produce a 4-fold projection. Simple (primary) hexagonal packing with the placement of one sphere on each lattice point accounts for the 6-fold TEM projections and setting $c = a\sqrt{3}/2$ (see below) generates the square projections as shown in Figure 6.

The choice of c/a impacts the allowed Bragg reflections accessed by the SAXS experiments. Table 2 lists the relative positions of the first nine allowed (hkl) reflections for P_6/mmm with $c = a$, $c = a\sqrt{3}/2$ and $c = (1/2)a$ along with HCP ($P6_3/mmc$ with $c = 1.63a$). All four hexagonal systems anticipate the experimentally documented ($hk0$) reflections evident in Figure 3. However, between one and four additional peaks associated with (hkl) scattering ($l \neq 0$) are permitted over the available q range. We have definitively disqualified HCP on the basis of the TEM results and do not further consider this option. TEM appears to favor the ratio $c = a\sqrt{3}/2$ based on the square projection along the a axis (see Figures 5a and 6). This assignment brings the (001) Bragg powder peak into coincidence with the (100) and the (111) and (002) into alignment with the (200).

However, two additional allowed reflections are absent, (101) and (201) at relative positions $(q/q^*)^2 = 2$ and 5, respectively. The ratio $c/a = 1/2$ results in a different set of coincident reflections and just one absent scattering peak, (111) at $(q/q^*)^2 = 6$. With $c = a$ there are four missing peaks. While the combined SAXS and TEM data establish P_6/mmm symmetry we cannot assign unit cell dimensions with certainty due to the lack of (hkl) diffraction. On the basis of the regions of 4-fold symmetry seen in the TEM images in Figure 5a, we tentatively assign the lattice parameter $c = a\sqrt{3}/2$ to the hexagonally packed sphere phase and make use of this result in the remainder of this report. Nevertheless, we cannot rule out other possibilities without additional diffraction data.

One explanation for the absence of (hkl, $l \neq 0$) diffraction may be a lack of long-range order (i.e., weak correlations) along the 6-fold axis (i.e., the [001] direction) relative to the strong in-plane ($hk0$) order. A complete loss of correlation between stacks (lines) of spheres would result in a columnar structure and eliminate (hkl, $l \neq 0$) scattering. Obviously, there is some degree of correlation as clearly evidenced by Figure 5a, where rotation around the (100) plane leads to patches of 4-fold symmetry. Nevertheless, the 6-fold coordination is generally much more prominent than the 4-fold packing in these images, consistent with the argument of weaker stacking correlations.

Block Segregation. A tetrablock molecular architecture affords additional levels of microphase complexity over those available to triblock terpolymers, including segregation of the O, terminal S and interior S′ blocks from I-rich domains. The actual state of microdomain segregation cannot be simply determined by TEM or SAXS without making assumptions regarding the unit cell dimensions (see previous paragraphs). DSC results shown in Figure 7 reveal endotherms between 20 and 70 °C that can be attributed to the melting of O crystals during heating for all five tetrablocks, with calculated crystallinities ranging from 36 to 71% (Table 1).

These results indicate that the thermodynamically incompatible O blocks microphase separate in the melt state. (SISO-1 is an exception since the melting temperature $T_{m,O}$ deviates from the trend set by the other specimens, i.e., a decreasing $T_{m,O}$ with O molecular weight. We attribute this behavior to crystallization from the homogeneous disordered state.) Segregation of the S blocks is difficult to establish by DSC due to the presence of the melting endotherms. Subtle evidence of an

dx.doi.org/10.1021/ma202196c | Macromolecules 2012, 45, 256–265

Table 2. Allowed Reflections for Different *a* and *c* Relationships

	(100)	(001)	(110)	(101)	(111)	(200)	(002)	(201)	(210)
expt data	$\sqrt{1}$	$\sqrt{1}$	$\sqrt{3}$	-	$\sqrt{4}$	$\sqrt{4}$	$\sqrt{4}$	-	$\sqrt{7}$
$c = a$	$\sqrt{1}$	$\sqrt{1.5}$	$\sqrt{3}$	$\sqrt{3.5}$	$\sqrt{7.5}$	$\sqrt{4}$	$\sqrt{3}$	$\sqrt{9.5}$	$\sqrt{7}$
$c = a\sqrt{3/2}$	$\sqrt{1}$	$\sqrt{1}$	$\sqrt{3}$	$\sqrt{2}$	$\sqrt{4}$	$\sqrt{4}$	$\sqrt{4}$	$\sqrt{5}$	$\sqrt{7}$
$c = a/2$	$\sqrt{1}$	$\sqrt{3}$	$\sqrt{3}$	$\sqrt{4}$	$\sqrt{6}$	$\sqrt{4}$	$\sqrt{3}$	$\sqrt{7}$	$\sqrt{7}$
$c = 1.63a$ (HCP)	$\sqrt{1}$	-	$\sqrt{3}$	$\sqrt{1.28}$	-	$\sqrt{4}$	$\sqrt{1.13}$	$\sqrt{4.28}$	$\sqrt{7}$

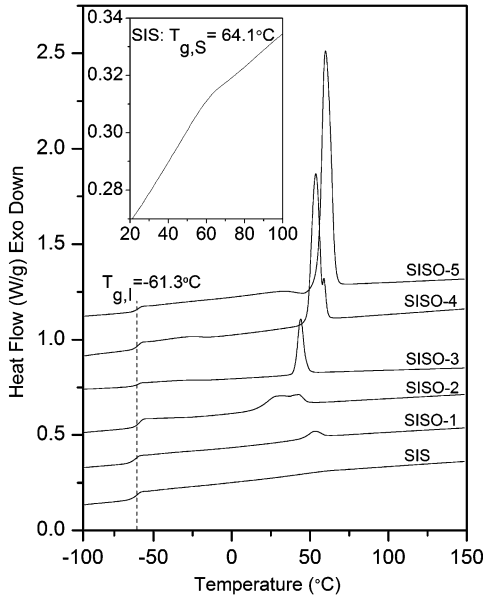

Figure 7. DSC traces obtained from the SIS triblock and SISO tetrablocks. Curves have been shifted vertically for clarity. Endotherms between 20 and 70 °C reflect melting of poly(ethylene oxide) consistent with segregation of the O blocks in a core−shell morphology. The small peak at 55 °C for SISO-1 is attributed to crystals formed from the homogeneous melt. All the specimens display a glass transition at −61 °C, which is associated with poly(isoprene). The inset shows evidence of a poly(styrene) glass transition in SIS, suggestive of composition fluctuations or segregation at $T < 65$ °C for this specimen.

S block glass transition is evident in the thermal trace for the disordered SIS triblock (inset to Figure 7) suggestive of fluctuation effects[41] or possibly microphase separation below 80 °C. Every specimen displays a glass transition at about −60 °C attributable to I-rich domains.

Three distinct limiting states of melt segregation can be postulated for the SISO system as illustrated in Figure 8: (a) a segregated O core immersed in a matrix containing a homogeneous mixture of S, S′ and I; (b) an O core surrounded by a segregated S′ shell distributed in a mixed S and I matrix; (c) an O core surrounded by a shell of segregated S and S′ with a continuous matrix of I. Critical insights into the state of segregation and the transition from a spherical to cylindrical morphology are provided by the SCFT calculations.

Figures 9 and 10 summarize results obtained at $T = 120$ °C for $f_O = 0.12$ (corresponding to SISO-3) and $f_O = 0.32$ (corresponding to SISO-5). The theory correctly anticipates the transition from a spherical (BCC lattice) to cylindrical (hexagonal lattice) morphology with increasing O content. Here we focus on the distribution of block segments across a unit cell, which is difficult to characterize experimentally. Although the theory does not account for the experimentally documented spherical packing symmetry, the composition

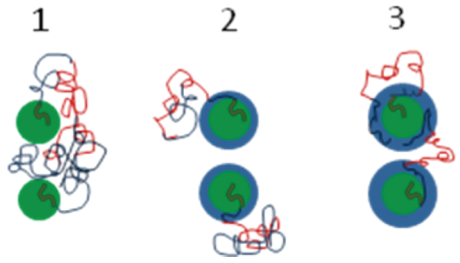

Figure 8. Discrete states of microphase separation for sphere forming SISO tetrablock copolymers. (1) Segregation of O blocks from mixed inner and outer S and I blocks. (2) Segregated core of O surrounded by a shell of inner S blocks embedded in a matrix of mixed I and outer S blocks. (3) Core of O surrounded by a shell of segregated inner and outer S blocks embedded in a matrix of I. Self-consistent field theory calculations indicate that the actual morphology is a hybrid of parts 2 and 3 as shown in Figure 9.

profile around each domain is relatively insensitive to the exact state of order.

Figure 9 illustrates variations in the volume fraction of poly(styrene) segments computed along two directions that each intersect the sphere centers: [111] (direction of closest packing in the BCC lattice, Figure 9a) and [100] (Figure 9b). The theory allows us to separate the location of the inner and outer S segments (S′ and S, respectively) as a function of position. These calculations reveal that the predicted placement of poly(styrene) segments represents a hybrid of models (2) and (3) shown in the Figure 8. Most of the inner S′ segments are located in a shell around a mostly segregated O core while the outer S segments are distributed between the S shell and the I rich matrix. Comparison of the computed composition profiles at different locations in the unit cell demonstrates that the S′ repeat units are dispersed rather uniformly in the radial direction away from the spherical cores; i.e., the concentration midway between the sphere centers at $^1/_2,^1/_2,0$ position (along [100]) and at the $^1/_4,^1/_4,^1/_4$ (along the line of closest packing [111]) are nearly equivalent. We believe that the constraints imposed by optimal placement of the inner S′ and outer S blocks are responsible for the experimentally determined hexagonal lattice as discussed in the following section.

We have estimated the area fraction of white domains in parts a−c of Figure 5 using the best ordered (hexagonal) sections of the micrographs. These have been converted to volume fractions assuming $c = a\sqrt{3/2}$ and the results are listed in Table 3 along with the values expected for models 1−3 (Figure 8). On the basis of this analysis the volume fraction of white spherical domains ranges from 20 to 30%, somewhat less than the sum of the O and S block volume fractions. Comparison of these measurements with the theoretical predictions is complicated by the staining process used to obtain TEM contrast. The osmium tetraoxide reacts selectively with poly(isoprene) creating the dark regions. As shown by the theoretical calculations, we expect a sharp but continuous gradient of

dx.doi.org/10.1021/ma202196c | *Macromolecules* 2012, 45, 256−265

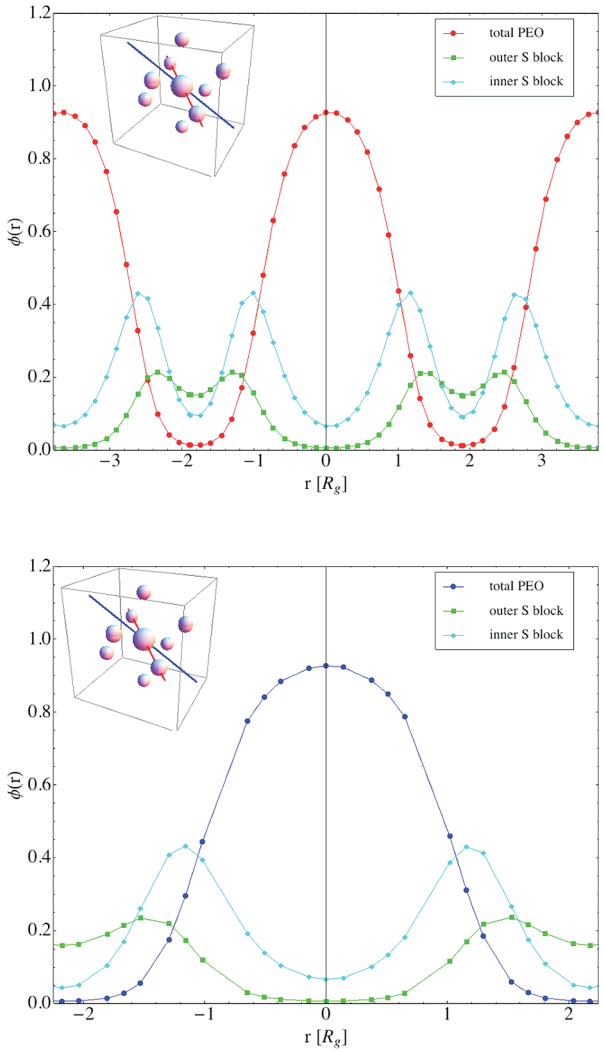

Figure 9. SCFT simulated density profiles of O, terminal S and interior S′ blocks against position variable, *r*, for a model of the SISO-3 tetrablock copolymer. The calculation yields BCC symmetry, contrary to the experimental result, which is attributed to the mean-field nature of the theory. Top panel: [111] unit cell direction denoted by the red line in the inset. Bottom panel: [100] unit cell direction denoted by the blue line in the inset. These results indicate that the SISO tetrablock copolymers segregate with a distribution of blocks that is a hybrid of models 2 and 3 illustrated in Figure 8.

I blocks from the matrix toward to spherical cores, terminating just beyond the O−S interface. Assuming the stain partially penetrates the S and S′ rich shell and reacts with I in the interfacial region, the estimated core volume fractions are roughly consistent with the theoretical values.

Figure 10 shows a representative SCFT calculation for the f_O = 0.32 case, which yielded a hexagonally packed cylindrical morphology formed by an O core, a shell of S and S′, and an I rich matrix. As with the spherical geometry, the inner S′ and outer S blocks are distributed asymmetrically around the O cores, with a significant fraction of the S blocks mixed into the I matrix.

V. DISCUSSION

The results presented in the previous section expose a remarkable finding: Ordering of spherical microdomains on a simple hexagonal (P_6/mmm space group) lattice. We have

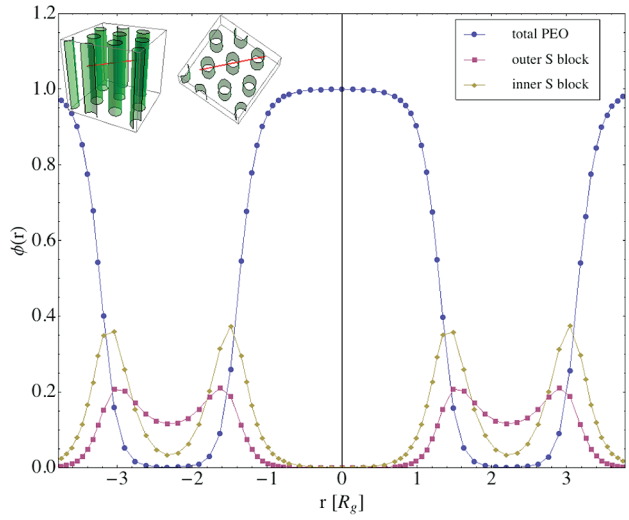

Figure 10. SCFT simulated density profiles of O, terminal S and interior S′ blocks against position variable, *r*, for a model of the SISO-5 tetrablock copolymer with hexagonal (P_6/mm) symmetry. Density profiles were calculated along the [100] unit cell direction as shown in the inset.

Table 3. Comparison between Calculated and Experimental Spherical Volume Ratio

	% theoretical volume[a]			experimental result[e]		
sample	PEO	PEO+1/2 PS	PEO +PS	*a* (nm)[b,c]	*d* (nm)[b,c]	volume (%)[d]
SISO-2	9	27	44	20.0 ± 0.8	13.3 ± 1.0	20 ± 5
SISO-3	12	29	46	22.6 ± 1.2	16.0 ± 1.2	25 ± 7
SISO-4	19	35	51	27.2 ± 0.7	20.6 ± 1.2	30 ± 6

[a]Theoretical spherical volume fractions based on experimental data from Table 1. [b]Lattice dimension and sphere diameter are obtained from TEM images for SISO-2, -3, and -4 respectively. *c* could be calculated using $c = a\sqrt{3}/2$. [c]Temperature is 120 °C. [d]Volume fraction is the volume ratio between the sphere and the hexagonal unit cell. [e]On the basis of the assumption that $c = a\sqrt{3}/2$. The indicated uncertainty does not include the possibility that $c \neq a\sqrt{3}/2$.

become accustomed to BCC packing of single component asymmetric block copolymers as anticipated by Leibler[42] more than 30 years ago based on self-consistent field theory and confirmed experimentally soon thereafter.[43] This behavior can be rationalized on the basis of minimizing the extent of chain stretching and compression driven by the constraint of maintaining a uniform density due to the incompressibility of polymer melts. Simple geometric calculations show that closely packed spheres (FCC and HCP) fill space with a more heterogeneous distribution of matrix space (i.e., wider range of relative spacing between spheres) than a BCC lattice, hence the later is favored with single component block copolymer melts.

Simple hexagonal ordering is rare across all areas of materials science and engineering, as exemplified by the elements in the periodic table. Most elements pack onto three types of lattices: FCC, HCP, and BCC. (Covalently bonded compounds such as Cl_2, O_2, and sulfur tend to crystallize with orthorhombic symmetry, while carbon forms either diamond or graphite.) There are a few exceptions to this trend including the group VB elements As, Sb and Bi, along with Hg, which solidify into rhombohedral crystals, and tetragonal In and Sn. Crystal symmetry is controlled by the detailed nature of the interatomic potential, which depends in a complex way on the electronic

dx.doi.org/10.1021/ma202196c | *Macromolecules* 2012, 45, 256−265

configuration and the underlying orbital symmetries. Subtle effects in certain heavy elements produce the most exotic results. For example, simple cubic packing in polonium has been attributed to relativistic corrections to the effective mass of valence electrons,[44] while uranium and tantalum form a σ-phase with 30 atoms per tetragonal unit cell.[45] We are not aware of any reports that assign the P_6/mmm space group to single component crystalline materials, although certain intermetallic compounds (e.g., $CaCu_5$) order with this symmetry.[46]

Ordered sphere forming block copolymers appear to offer a fascinating counterpart to monatomic crystals. We believe the interparticle potential that controls sphere packing is sensitive to the overall corona block molecular weight and architecture. In a recent publication, we have shown that a low molecular weight poly(isoprene-*b*-lactide) (IL) diblock and a SISO tetrablock copolymer can form the σ-phase, a crystal approximant to dodecagonal quasicrystals.[10] The results reported here represent another variation on this theme, driven by changes in the composition of the multiblock copolymer. The sequence of blocks in SISO enforces a spherical morphology over a wider range of sphere volume fractions (relative to diblocks) as a consequence of the unfavorable segment−segment interactions between I and O blocks. Formation of a shell rich in S (and S′) segments screens these contacts. However, the matrix material contains S, I, and S′ segments distributed anisotropically around the core and shell structure as suggested by the SCFT calculations. Unfortunately, the field theory calculations are not readily transformed into an effective interdomain interaction potential that might be employed to model ordering. Nevertheless, we can draw a loose yet provocative analogy between ordering in sphere forming block copolymers, which is governed by statistical mechanical concepts, and crystallization of the elements, which requires incorporation of sophisticated quantum mechanical principles. (Here we note that the number of blocks per sphere can vary somewhat (as shown for the σ-phase[10]) while the atomic structure of each element is invariant. On the other hand, electrical charge generally is not distributed uniformly throughout the unit cell of an elemental crystal.)

Changing the composition and molecular weight of the corona blocks, which affects the segregation strength, will influence the tendency to order on a particular lattice. To date there are at least three documented examples: $Im\bar{3}m$ (BCC), $P4_2/mnm$ (σ-phase), and P_6/mmm. Fundamental arguments supporting the general occurrence of BCC and icosahedral packing (closely related to the σ-phase) were advanced by Alexander and McTague[47] based on Landau theory and subsequently applied to diblock copolymers by Roan and Shakhnovich using the density-wave mean field theory developed by Leibler.[48,49]

There are a variety of reasons why the present SCFT simulations did not precisely reproduce the observed hexagonal spherical packing morphology. Fluctuation effects are not included in the current mean-field formulation of the SCFT simulations. For dense copolymer melts fluctuation effects are most relevant near phase boundaries between morphologies. Fluctuation effects are known to shift the location of phase boundaries, but have not heretofore been shown to create ordered phases with new space groups. Our conjecture for the source of this discrepancy between experiment and simulation is the Gaussian chain model used in the present SCFT algorithms. Including finite-chain length effects could change the effective domain−domain interactions by introducing anisotropic forces between these spherical domains. This is related to the analogy made above to the novel crystalline order seen in some metals with large atomic number and anisotropic outer shell electronic orbitals. Extending the model to include finite chain length effects, and improving the numerical methods to find these novel phases, will be the focus of future work.

VI. CONCLUSION

We have demonstrated in this work that a SISO tetrablock terpolymer molecular architecture introduces levels of morphological control unavailable to more conventional ISO triblocks. Combined use of synchrotron SAXS and TEM conclusively demonstrate P_6/mmm space group symmetry for specimens containing a fixed ratio, $f_S/f_I = 2/3$, of poly(isoprene) (I) and poly(styrene) block volume fractions (equal length S blocks) and between 9 and 32% poly(ethylene oxide) (O). Unfavorable segment−segment interactions between the I and O blocks drive the formation of spherical microdomains for $f_O = 0.09$, 0.12, and 0.19, while a $f_O = 0.32$ specimen contains a cylindrical morphology. Self-consistent mean-field theory calculations correctly anticipates the core (O) and shell (S) domain geometries but fail to account for simple hexagonal packing of the spheres. Nevertheless, these calculations provide important insight into the distribution of block segments within the ordered structures including the asymmetric placement of interior and terminal S blocks within the core, shell and matrix domains. These results, together with an earlier publication,[38] demonstrate a powerful approach to manipulating block copolymer structure outside the traditional paradigms (AB, ABA, ABC) with respect to composition.

■ ACKNOWLEDGMENTS

This work was supported by the U.S. Department of Energy, Basic Energy Sciences, Division of Materials Science and Engineering, under Contract Number DEAC05-00OR22725 with UT-Battelle LLC at Oak Ridge National Laboratory. Some of the facilities employed derived support from the University of Minnesota Materials Research Science and Engineering Center (MRSEC) (NSF-DMR-0819885). Portions of this work were performed at the DuPont−Northwestern−Dow Collaborative Access Team (DND-CAT) located at Sector 5 of the Advanced Photon Source (APS). DND-CAT is supported by E. I. du Pont de Nemours & Co., the Dow Chemical Company, and the State of Illinois. Use of the APS was supported by the U.S. Department of Energy, Office of Science, Basic Energy Sciences, under Contract No. DE-AC02-06CH11357. Parts of this work were carried out in the University of Minnesota College of Science and Engineering Characterization Facility, which receives partial support from NSF through the NNIN program. We thank Fang Zhou for her assistance in microtoming the TEM sections.

■ REFERENCES

(1) Larson, R. G. *J. Chem. Phys.* **1992**, *96*, 7094−7918.
(2) Robledo, A.; Varea, C.; Martina, E. *J. Phys. Lett.* **1985**, *46*, L967−L972.
(3) Hajduk, D. A.; Harper, P. E.; Gruner, S. M.; Honeker, C. C.; Kim, G.; Thomas, E. L.; Fetters, L. J. *Macromolecules* **1994**, *27*, 4063−4075.
(4) Hajduk, D. A.; Harper, P. E.; Gruner, S. M.; Honeker, C. C.; Kim, G.; Thomas, E. L.; Fetters, L. J. *Macromolecules* **1994**, *27*, 4063−4075.
(5) Schulz, M. F.; Khandpur, A. K.; Bates, F. S.; Almdal, K.; Mortensen, K.; Hajduk, D. A.; Gruner, S. M. *Macromolecules* **1996**, *29*, 2857−2867.
(6) Matsen, M. W.; Schick, M. *Phys. Rev. Lett.* **1994**, *72*, 2660−2663.

(7) Tyler, C. A.; Morse, D. C. *Phys. Rev. Lett.* **2005**, *94*, 208302.
(8) Tyler, C. A.; Qin, J.; Bates, F. S.; Morse, D. C. *Macromolecules* **2007**, *40*, 4654−4668.
(9) Takenaka, M.; Wakada, T.; Akasaka, S.; Nishitsuji, S.; Saijo, K.; Shimizu, H.; Kim, M. I.; Hasegawa, H. *Macromolecules* **2007**, *40*, 4399−4402.
(10) Lee, S.; Bluemle, M. J.; Bates, F. S. *Science* **2010**, *330*, 349−353.
(11) Niemann, S.; Jeitschko, W. *J. Solid State Chem.* **1995**, *114*, 337−341.
(12) Liu, P.; Stigenberg, A. H.; Nilsson, J. O. *Acta Metall. Mater.* **1995**, *43*, 2881−2890.
(13) Mogi, Y.; Kotsuji, H.; Kaneko, Y.; Mori, K.; Matsushita, Y.; Noda, I. *Macromolecules* **1992**, *25*, 5408−5411.
(14) Gido, S. P.; Schwark, D. W.; Thomas, E. L.; do Carmo Goncalves, M. *Macromolecules* **1993**, *26*, 2636−2640.
(15) Mogi, Y.; Nomura, M.; Kotsuji, H.; Ohnishi, K.; Matsushita, Y.; Noda, I. *Macromolecules* **1994**, *27*, 6755−6760.
(16) Stadler, R.; Auschra, C.; Beckmann, J.; Krappe, U.; Voight-Martin, I.; Leibler, L. *Macromolecules* **1995**, *28*, 3080−3097.
(17) Breiner, U.; Krappe, U.; Abetz, V.; Stadler, R. *Macromol. Chem. Phys.* **1997**, *198*, 1051−1083.
(18) Breiner, U.; Krappe, U.; Thomas, E. L.; Stadler, R. *Macromolecules* **1998**, *31*, 135−141.
(19) Brinkmann, S.; Stadler, R.; Thomas, E. L. *Macromolecules* **1998**, *31*, 6566−6572.
(20) Shefelbine, T. A.; Vigild, M. E.; Matsen, M. W.; Hajduk, D. A.; Hillmyer, M. A.; Cussler, E. L.; Bates, F. S. *J. Am. Chem. Soc.* **1999**, *121*, 8457−8465.
(21) Bailey, T. S.; Hardy, C. M.; Epps, T. H. III; Bates, F. S. *Macromolecules* **2002**, *35*, 7007−7017.
(22) Bailey, T. S.; Pham, H. D.; Bates, F. S. *Macromolecules* **2001**, *34*, 6994−7008.
(23) Avgeropoulos, A.; Paraskeva, S.; Hadjichristidis, N.; Thomas, E. L. *Macromolecules* **2002**, *35*, 4030−4035.
(24) Epps, T. H. III; Cochran, E. W.; Bailey, T. S.; Waletzko, R. S.; Hardy, C. M.; Bates, F. S. *Macromolecules* **2004**, *37*, 8325−8341.
(25) Qin, J.; Bates, F. S.; Morse, D. C. *Macromolecules* **2010**, *43*, 5128−5136.
(26) Wang, J. F.; Mueller, M.; Wang, Z. G. *J. Chem. Phys.* **2009**, *130*, 154902.
(27) Alfonzo, C. G.; Fleury, G.; Chaffin, K. A.; Bates, F. S. *Macromolecules* **2010**, *43*, 5295−5305.
(28) Cochran, E. W.; Morse, D. C.; Bates, F. S. *Macromolecules* **2003**, *36*, 782−792.
(29) Ndoni, S.; Papadakis, C. M.; Bates, F. S.; Almdal, K. *Rev. Sci. Instrum.* **1995**, *66*, 1090−1095.
(30) Fetters, L. J.; Lohse, D. J.; Richter, D.; Witten, T. A.; Zirkel, A. *Macromolecules* **1994**, *27*, 4639−4647.
(31) Brandrup, J.; Immergut, E. H. *Polymer Handbook*; Wiley: New York, 1989.
(32) Fredrickson, G. H.; Ganesan, V.; Drolet, F. *Macromolecules* **2002**, *35*, 16−39.
(33) Doi, M.; Edwards, S. *The Theory of Polymer Dynamics*; Clarendon Press: Oxford, 1986.
(34) Sides, S. W.; Fredrickson, G. H. *Polymer* **2003**, *44*, 5859.
(35) Hammond, M. R.; Sides, S. W.; Fredrickson, G. H.; Kramer, E. J. *Macromolecules* **2003**, *36*, 8712−8716.
(36) Bosse, A. W.; Sides, S. W.; Katsov, K.; Garcia-Cervera, C. J.; Fredrickson, G. H. *Poly. Sci. B: Polymer Physics* **2006**, *18*, 2495.
(37) Frielinghaus, H.; Hermsdorf, N.; Almdal, K.; Mortensen, M. L.; Corvazier, L.; Fairclough, J. P. A.; Ryan, A. J. O.; Hamley, I. W. *Europhys. Lett.* **2001**, *53*, 680.
(38) Bluemle, M. J.; Zhang, J.; Lodge, T. P.; Bates, F. S. *Macromolecules* **2010**, *43*, 4449−4452.
(39) Wu, L.; Cochran, E. W.; Lodge, T. P.; Bates, F. S. *Macromolecules* **2004**, *37*, 3360−3368.
(40) Epps, T. H. III; Cochran, E. W.; Hardy, C. M.; Bailey, T. S.; Waletzko, R. S.; Bates, F. S. *Macromolecules* **2004**, *37*, 7085−7088.
(41) Bates, F. S.; Rosedale, J. H.; Fredrickson, G. H.; Glinka, C. J. *Phys. Rev. Lett.* **1988**, *61*, 2229.
(42) Leibler, L. *Macromolecules* **1980**, *13*, 1602−1617.
(43) Bates, F. S.; Cohen, R. E.; Berney, C. V. *Macromolecules* **1982**, *15*, 589−592.
(44) Dominik, L.; Martin, F.; Mojmir, S. *Phys. Rev. Lett.* **2007**, *99*, 106402.
(45) Jiang, A.; Yohannan, A.; Nnolim, N. O.; Tyson, T. A.; Axe, L.; Lee, S. L.; Cote, P. *Thin Solid Flims* **2003**, *437*, 116−122.
(46) Fornasini, M. L.; Manfrinetti, P.; Mazzone, D. *J. Solid State Chem.* **2006**, *179*, 2012−2019.
(47) Alexander, S.; McTague, J. *Phys. Rev. Lett.* **1978**, *41*, 701−705.
(48) Roan, J. R.; Shakhnovich, E. I. *J. Chem. Phys.* **1998**, *109*, 7591−7611.
(49) Brezin, E.; Halperin, B. I.; Leibler, S. *J. Phys.* **1983**, *44*, 775−783.

■ NOTE ADDED AFTER ASAP PUBLICATION

This article posted ASAP on December 7, 2011. Equation 2 has been revised. The correct version posted on December 8, 2011.

Macromolecules

Article

pubs.acs.org/Macromolecules

Microphase Separation and Crystallization of All-Conjugated Phenylene–Thiophene Diblock Copolymers

Xinhong Yu, Hua Yang, Shupeng Wu, Yanhou Geng, and Yanchun Han*

State Key Laboratory of Polymer Physics and Chemistry, Changchun Institute of Applied Chemistry, Chinese Academy of Sciences, 5625 Renmin Street, Changchun 130022, People's Republic of China

Supporting Information

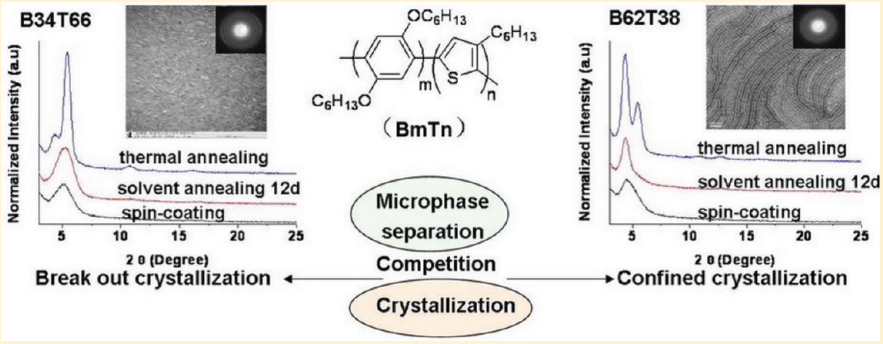

ABSTRACT: Microphase separation and crystallization in thin films of all-conjugated diblock copolymers poly(2,5-dihexyloxy-*p*-phenylene)-*block*-(3-hexylthiophene) (PPP-*b*-P3HT) with various main chain lengths were investigated under solvent vapor annealing or thermal annealing. It is shown that crystallization and microphase separation coexisted during thin film forming process due to the incompatibility and crystallization of the two conjugated blocks. When the B34T66 copolymer film was annealed in chlorobenzene vapor or at high temperature, crystallization broke out the microphase-separated structure. On the other hand, upon annealing of the films of B62T38 and B75T25 with higher PPP ratio, crystallization was confined in the microphase-separated domains. The copolymer composition plays a key role in determining the crystallization and the final morphology of the thin films.

INTRODUCTION

Conjugated polymers have been attracting much attention as new electronic and optoelectronic substances mainly used for active semiconducting layers in low-cost electronic devices.[1−4] The orientation and nanostructures of semiconducting polymers in solid state play an important role in determining the device performance.[5−7] To precisely control the organization and the nanostructure in the thin films of rod-like conjugated semiconductor polymer, a fascinating route is to covalently link with coil-like polymers.[8−15] Block copolymers containing polymeric semiconducting blocks can self-organize into well-defined microphase-separated structures driven by factors such as immiscibility or crystallizability difference between the blocks. There have been several reports on semiconducting polymer-based block copolymers containing a conjugated block and a nonconjugated block such as polystyrene (PS), polyisoprene (PI), poly(methyl acrylate) (PMMA),[12,16] etc. The addition of such "coil-like segments" has an effect on the crystallinity and leads to new morphological behavior. However, the coil segments are generally insulating and could dilute the concentration of the semiconducting blocks in the films and further limit the opotoelectronic properties.[17]

All-conjugated block copolymers of the rod–rod type have become a focus of interest due to the strong self-assembly induced by $\pi-\pi$ interactions and the unique ordered morphologies compared with those of rod–coil block copolymers.[18,19] Several all-conjugated thiophene-based rod–rod block copolymers have been synthesized because of their excellent charge-transporting mobility and high regioregular structure.[20−31] Hashimoto and co-workers synthesized all-conjugated diblock copolymer of P3HT-*block*-poly[3-(2-ethylhexyl)thiophene] (P3EHT) and discovered that the less crystalline P3EHT segment could promote the self-organization of P3HT domains in film.[23] Fully conjugated block polythiophenes in which each block contains a unique alkyl side chain have been synthesized.[24,25] Qiu and co-workers confirmed that diblock copolythiophenes with alkyl side-chain length different by two carbon atoms cocrystallized into a uniform crystal and, when the side chain lengths were different by more than two carbon atoms, preferred to microphase-separate into two independently crystallized domains of each block.[25] Side chain mainly interferes with intermolecular interactions; Seferos and co-workers synthesized selenophene–thiophene block copolymers with blocks of distinct

Received: May 5, 2011
Revised: November 30, 2011
Published: December 22, 2011

heterocycles and discovered that phase separation as well as the optical properties can be controlled by the heterocycle in the polymer chain.[26]

In contrast to the microphase separation of coil−coil block copolymers, most previous reports on all-conjugated diblock copolymers mainly focused on the crystallization instead of microphase separation of them. Crystallization of one block was a major drive to the nanowire formation. Additional contributions from the rigidity and the interchain overlapping of the conjugated orbits complicated the self-assembling behavior.[18,19] Microphase separation and crystallization are two kinds of phase transitions in polymer systems.[32−34] The final phase structure depends on the competition between microphase separation and crystallization.[32] With respect to new all-conjugated diblock copolymers, the superstructure and growth have yet to be investigated systematically. Although nanowires composed of microphase-separated crystal domains are always obtained in conjugated diblock copolymers, the crystalline structure and growth mechanism remain unrevealed and need extensive investigation.

In this article, we take a family of fire-new crystalline−crystalline all-conjugated diblock copolymers, poly(2,5-dihexyloxy-*p*-phenylene)-*block*-(3-hexylthiophene) (PPP-*b*-P3HT), as the research objects and systematically explore their crystallization behavior and nanoscale morphology with different main chain block ratios. We studied the effects of block ratio and annealing process on the transition between microphase separation and crystallization of the diblock copolymer thin films. Through the modulation of the block composition and annealing process, the competition between the microphase separation and crystallization was tuned, leading to observations of confined crystallization and breakout crystallization.

EXPERIMENTAL SECTION

Materials. Conjugated diblock copolymers PPP-*b*-P3HT with PPP:P3HT molar ratios of 16:84, 34:66, 62:38, and 75:25 were synthesized by Grignard metathesis (GRIM) polymerization method according to our previous report.[35] The molecular weights and thermal behavior of these diblock copolymers are listed in Tables 1 and 2. The molecular weights of different blocks in PPP-*b*-P3HT were well-controlled through the feed ratio of the monomers and the initiator, according to our previous report. The number-average molecular weights (M_n) of the studied PPP-*b*-P3HT estimated from GPC were around 28 400, 29 700, 32 400, and 41 100, with polydispersity index of 1.46, 1.34, 1.30, and 1.36. The degree of polymerization of PPP and P3HT segments estimated from the ^{1}H NMR spectrum were 27/140, 41/80, 69/43, and 138/45, respectively. Chlorobenzene (ClB) was purchased from Beijing Chemical Reagent Co.

Table 1. Summary of Composition and Molecular Weight of PPP-*b*-P3HT Diblock Copolymers[a]

polymer	*m*	*n*	*m*/*n* (%)	M_n	PDI
B16T84	27	140	16:84	28 400	1.46
B34T66	41	80	34:66	29 700	1.34
B62T38	69	43	62:38	32 400	1.30
B75T25	138	45	75:25	41 100	1.36

[a] *m*, *n*: the estimated degree of polymerization of PPP (B) and P3HT (T) block in the synthesized diblock copolymers; M_n: number-average molecular weight; PDI: polydispersity index.

Table 2. Summary of DSC Measurements of the Series of Diblock Copolymers[a]

polymer	$T_{m(P3HT)}$ [°C]	$T_{m(PPP)}$ [°C]	$T_{c(P3HT)}$ [°C]	$T_{c(PPP)}$ [°C]
B16T84	237.7		201.4	
B34T66	239.0	88.1	224.8	
B62T38	231.0	96.6	185.7	81.2
B75T25	219.3	99.2	172.8	84.4

[a] T_m: melting point; T_c: crystallization temperature.

Sample Preparation. The diblock copolymers were dissolved in chlorobenzene (a nonselective solvent) with concentration of 5 mg/mL. The solutions were heated up to 80 °C for complete dissolution. After cooling to room temperature, the solutions were standing in dark and vibration-free environment over 24 h at room temperature (the aging process has a negligible effect on the film morphologies) to obtain homogeneous samples. The films of diblock copolymers were prepared by spin-coating solutions onto precleaned silicon wafers at 1500 rpm for 30 s using a commercial spin-coater (KW-4A, chemat Technology Inc.). Prior to spin-coating, the wafers were cleaned with a 70/30 v/v solution of 98% H_2SO_4/30% H_2O_2 at 80 °C for 30 min, then thoroughly rinsed with deionized water, and finally blown dry in nitrogen.

For the solvent vapor treatment, the spin-coated samples were exposed to saturated chlorobenzene vapor in closed vessels at room temperature (20 °C) for different periods. Then, the samples were removed from the vessels quickly for fast drying.

Prior to the heat treatment, the spin-coated thin films were vacuum-dried to remove the residual solvents. The films were first melt at 280 °C (a temperature higher than the melting points of PPP and P3HT blocks) for 1 h and then cooled to room temperature slowly.

Characterization. Transmission electron microscopy (TEM), selected area electron diffraction (SAED), high-resolution transmission electron microscopy (HRTEM), atomic force microscopy (AFM), X-ray diffraction (XRD), differential scanning calorimetry (DSC), and two-dimensional grazing incident X-ray diffraction (2D GIXRD) techniques were applied to characterize the morphology and structure of diblock copolymer thin films.

AFM characterization was performed in tapping mode, using a SPA300HV with a SPI3800 N controller (Seiko Instruments Inc., Japan). A silicon microcantilever with spring constant 2 N/m and resonance frequency ∼70 kHz, (Olympus Co., Japan) with an etched conical tip was used for scanning.

TEM images and SAED patterns were obtained with a JEM-1011 transmission electron microscope (JEOL Inc., Japan) operated at 100 kV accelerating voltage. Samples for TEM were prepared by floating thin film on a carbon-coated copper grid. The samples were dried at room temperature for 24 h before TEM experiments. HRTEM was carried out on a FEI Tecnai G2 microscope operated at an accelerating voltage of 200 kV.

XRD profiles were obtained by using a Bruker D8 Discover Reflector with X-ray generation power of 40 kV tube voltage and 40 mA tube current. The measurements were obtained in a scanning interval of 2θ between 3° and 30°. To increase XRD peak intensity for investigating the crystallinity and orientation that prevail throughout the film, we employed an incident angle (α = 0.2°) slightly above the critical angle (α_c = 0.18°).

DSC curves were performed using a Perkin-Elmer DSC7 at a heating/cooling rate of 10/−10 °C min^{-1} under a nitrogen flow.

2D GIXRD was measured at Beijing Synchrotron Radiation Facility on beamline 1W1A with the incident energy of 8 keV (λ = 0.154 nm). The thin films were aligned using a Huber 5-circle diffractometer and point detector, and then their 2D GIXRD patterns were recorded by a Mar345 area detector.

RESULTS AND DISCUSSION

The thermodynamic incompatibility between the blocks makes the films prone to phase separate into domains of each block. Meanwhile, the conjugated polymer with a regular end-to-end arrangement of side chains allows for efficient $\pi-\pi$ stacking of the conjugated backbone to form crystalline supramolecular

dx.doi.org/10.1021/ma201024z | Macromolecules 2012, 45, 266−274

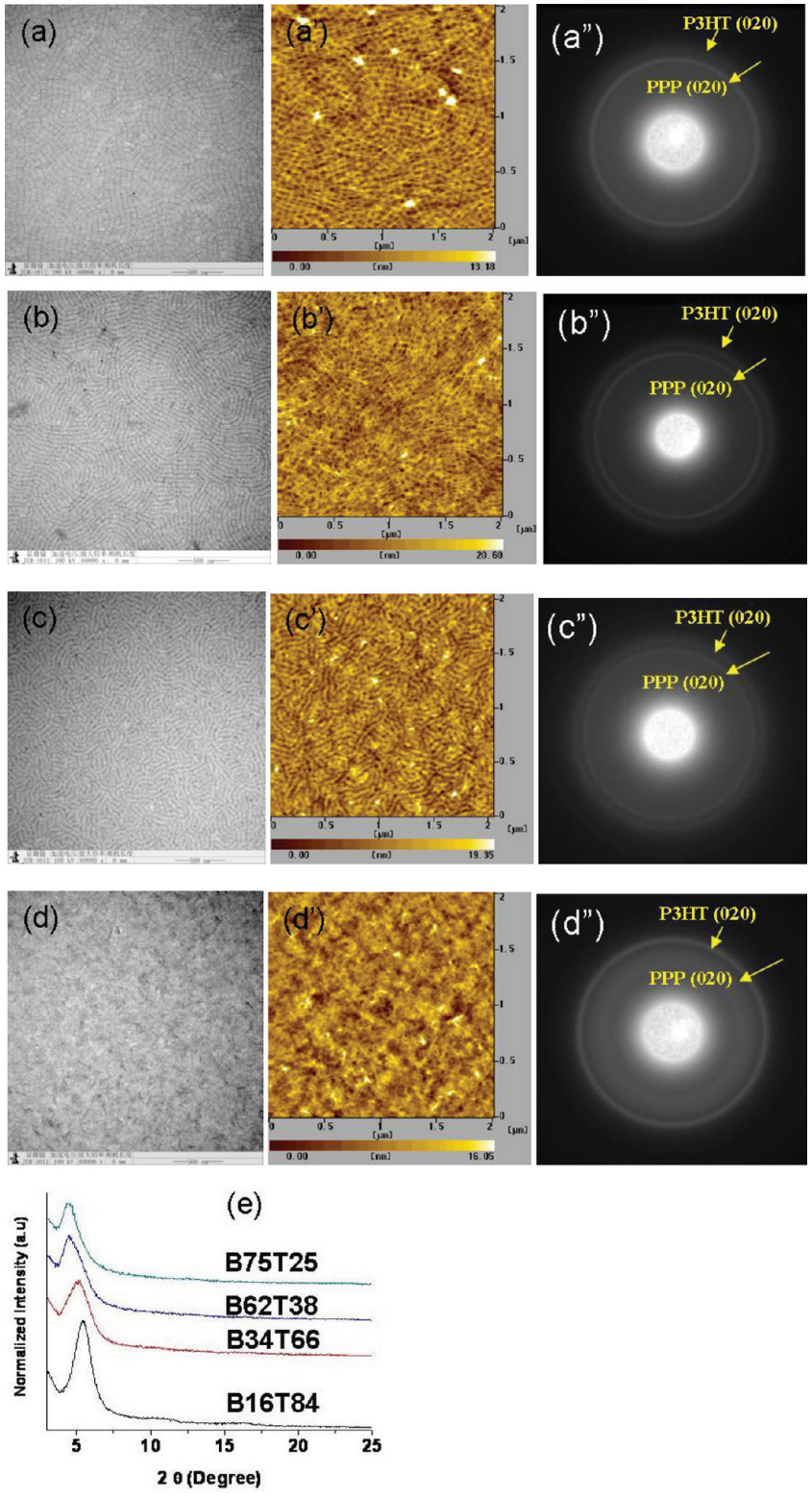

Figure 1. (a–d) TEM images (bar length: 500 nm), (a′–d′) AFM topographic images, and (a″–d″) SAED patterns of PPP-*b*-P3HT films with different block ratios: (a, a′, a″) B75T25, (b, b′, b″) B62T38, (c, c′, c″) B34T66, (d, d′, d″) B16T84. Thin films were prepared by spin-coating from 5 mg/mL chlorobenzene solutions. (e) XRD patterns of PPP-*b*-P3HT films with different block ratios.

structure.[36] The final phase structure in crystalline diblock conjugated copolymers depends on the competition between these two processes.

3.1. Competition of Crystallization and Microphase Separation in the Thin Film Forming Process. Figure 1 shows the morphologies of PPP-*b*-P3HT films (B75T25, B62T38, B34T66, B16T84) spin-coated from 5 mg/mL chlorobenzene solutions on Si substrate. TEM images (Figure 1a–c) show disordered spinodal-like morphologies in the as-cast B75T25, B62T38, and B34T66 films, respectively. The TEM contrast

dx.doi.org/10.1021/ma201024z | *Macromolecules* 2012, 45, 266–274

originates from the electron density of projected objects. Here, the sulfur atoms in P3HT should provide more electron scattering and thus appear darker. The sizes of the bright and dark domains in the TEM images can be approximately scaled with the degree of polymerization of both blocks in the diblock copolymers. B75T25 showed bright domains with a width of about 50 nm, while B62T38 and B34T66 showed narrower bright domains. Meanwhile, B75T25 and B62T38 showed dark domains with similar widths of around 10 nm, while B34T66 showed broader dark domains. B75T25 and B62T38 show similar widths of dark domains, probably due to the similar degree of polymerization of P3HT block in both copolymers. This difference in images also suggests that the bright and dark domains may correspond to the PPP and P3HT blocks, respectively. The AFM images of the prepared block copolymer films could provide further details of the surface structures. AFM images give microphase-separated structures consistent with the TEM images. As for the PPP-*b*-P3HT with the block ratio of 16:84, fiber structures dominate the whole film instead of the spinodal-like morphology observed in other systems (Figure 1d,d′).

The crystal structures of the films were investigated by SAED (Figure 1a″−d″). For B62T38 and B34T66, the SAED patterns show two blur diffraction rings. The outer rings in these SAED patterns are indexed as the diffractions from crystallographic (020) planes, corresponding to a $\pi-\pi$ stacking distance of 0.38−0.39 nm, which is in good agreement with the previously reported value of 0.38 nm in films of poly(alkylthiophene) homopolymers.[37] The inner ring is due to the diffraction of PPP, with a *d*-spacing of 0.43−0.44 nm, which is comparable to that in films of poly(*p*-phenylene) homopolymers (not shown here). On the other hand, SAED patterns for B75T25 and B16T84 give an intensive ring and a diffusive ring. For B75T25, the intensive ring is caused by the diffraction from crystallographic plane associated with PPP, and the diffusive ring is due to the diffraction of P3HT. For B16T84, the intensive ring and the diffusive ring are due to the diffraction of P3HT and PPP, respectively.

XRD was also used to investigate the crystal structures of the thin films (Figure 1e). The B75T25 shows a diffraction peak at $2\theta \approx 4.37°$, which is comparable with the diffraction of PPP homopolymer (shown in Figure S1). With the increase of P3HT block, the XRD spectra of the films of B62T38 and B34T66 show much broader nonsymmetric diffraction peaks, which are caused by the overlap of the diffraction peaks of PPP and P3HT. It is consistent with the SAED profiles, which show two diffraction rings. We used 2D GIXRD measurements with higher beam energy to resolve the diffractions of the spin-coated films before and after thermal annealing. The results showed excellent consistency to the XRD data (shown in Figures S2 and S3). As for B16T84, the peak at $2\theta \approx 5.4°$ corresponds to an interlayer *d*-spacing of 1.61 nm, and the other two diffraction peaks at around 10.8° and 16.2° represent second- and third-order diffractions of the lamella. The values are close to those reported for P3HT thin films and suggest the crystalline P3HT lamellae orient parallel to the substrate. No diffraction peaks associated with PPP are observed, which indicates that its diffraction peak may be too weak and overlapped by P3HT diffractions.

3.2. Breakout Crystallization in Block Copolymers B34T66 with a Higher Block Ratio of P3HT. The competition between crystallization and microphase separation determined the final film morphology. Therefore, we can tune the film morphology by the modulation of the extent of crystallization and microphase separation. Here we choose solvent vapor annealing and thermal annealing to promote the crystallization of both blocks. When the as-prepared B34T66 film with a relatively high P3HT content was annealed in chlorobenzene vapor or at high temperature, crystallization broke out the microphase-separated structure, yielding a transition from microphase-separated structure into crystalline structure.[32]

The evolution of microdomain structure in the B34T66 thin films was investigated by varying the annealing time in chlorobenzene vapor. Exposed to chlorobenzene vapor, the spinodal-like morphology disappeared gradually. With annealing time increasing to 5 h (Figure 2a,a′), fibrillar aggregates were generated on the film surface. The amount of the fibrillar aggregates increased with the extended annealing time (12 days) and covered the whole film eventually (Figure 2b,b′).

In the thermal annealing process, the spin-coated diblock copolymer thin films were heated above the melt point of two blocks and slowly cooled down to room temperature. Typical AFM images of B34T66 thin films after thermal annealing show network-like fibrillar crystals with lengths on the order of micrometers (Figure 2c). The TEM images confirmed the morphology observed in AFM images (Figure 2c′). That is to say, upon thermal annealing, the spinodal-like microphase-separated morphology disappears, and crystals dominate the film structure.

The crystallinity and molecule packing in the diblock copolymer thin films after different annealing processes were further examined by SAED and XRD spectra shown in Figure 2. The SAED patterns (in the insets of Figure 2b,c′) show two diffraction rings corresponding to P3HT and PPP block, respectively. So in such fibrils, the crystals of P3HT and PPP coexist. Compared with the as-prepared thin film, the diffraction peak in XRD spectra (Figure 2d) shifts to higher angle after solvent vapor treatment. As for thin films of diblock copolymer after annealing at 280 °C, the fibers of B34T66 show diffraction peaks that are characteristic of PPP and P3HT blocks. A prominent peak appears at $2\theta \approx 5.4°$, corresponding to an *d*-spacing of 1.61 nm of the well-organized lamellar structure of P3HT block. A shoulder peak at $2\theta \approx 4.37°$corresponds to the PPP block with a *d*-spacing of 2.02 nm. Such characteristic crystallographic structures of the block copolymer fibers is confirmed by the SAED patterns shown in the inset of Figure 2c′. The SAED patterns show a clear outer diffraction ring with a *d*-spacing of 0.38−0.39 nm, corresponding to the P3HT block and a inner diffraction ring with a *d*-spacing of 0.43−0.44 nm from the diffraction of PPP.

3.3. Confined Crystallization in Block Copolymers B62T38 and B75T25 with a Higher Block Ratio of PPP. Confined crystallization occurred in the films of B62T38 and B75T25 with higher PPP block ratios when the films are annealed in chlorobenzene vapor or at high temperature, as shown in Figure 3. When B62T38 and B75T25 thin films were annealed in chlorobenzene vapor, the morphology of the thin films changed from netlike to string of beads (Figure 3a,b). Meanwhile, the spinodal-like morphology can be obtained regardless of the treating time (Figure 3a′,b′). Figure 3c,c′,d,d′ shows the morphologies of B62T38 and B75T25 thin films after thermal annealing. Large fibers with several micrometers in length can be resolved in AFM images (Figure 3c,d). With further observation at higher magnification by TEM, each fiber is composed of several nanoscale ribbons (Figure 3c′,d′).

dx.doi.org/10.1021/ma201024z | *Macromolecules* 2012, 45, 266−274

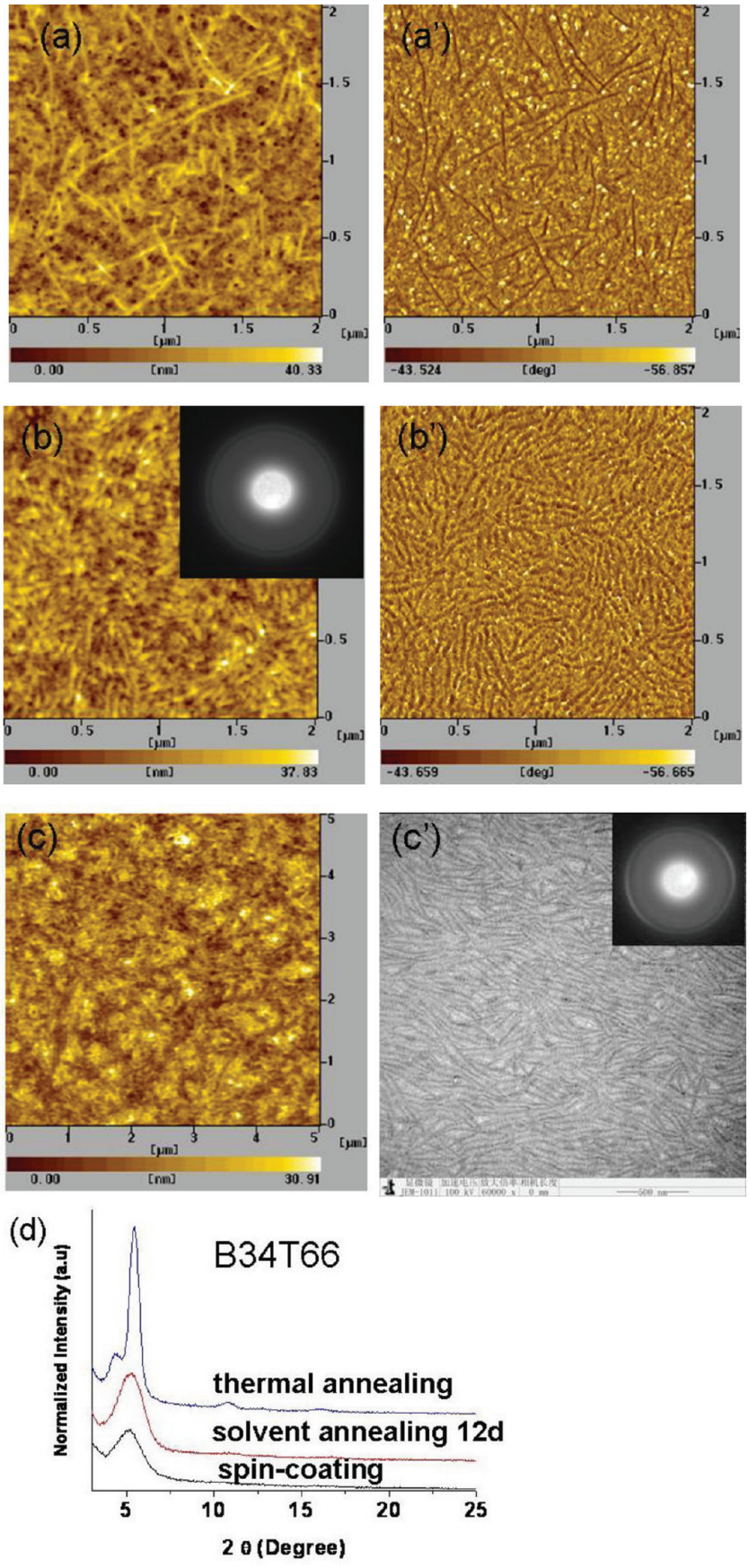

Figure 2. AFM topographic and phase images of thin B34T66 films with a higher block ratio of P3HT exposed to chlorobenzene vapor for different times: (a, a′) 5 h, (b, b′) 12 days (inset: SAED pattern), (c) AFM, and (c′) TEM images of thin B34T66 films annealed at 280 °C for 1 h (bar length: 500 nm; inset: SAED pattern). (d) XRD patterns of B34T66 thin films treated with different conditions.

dx.doi.org/10.1021/ma201024z | *Macromolecules* 2012, 45, 266−274

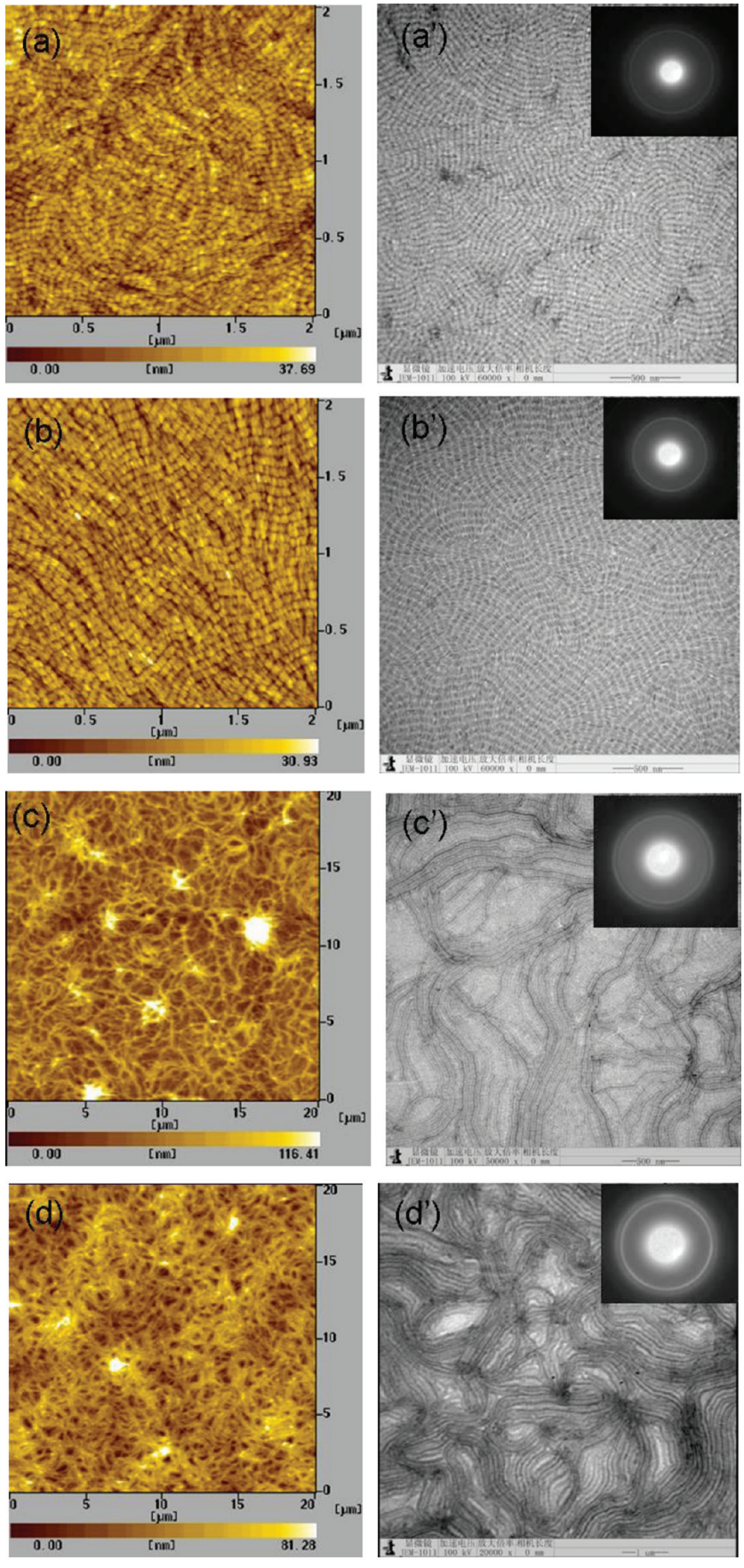

Figure 3. AFM and TEM images of thin films of block copolymers upon different annealing process: (a, a′) B62T38 and (b, b′) B75T25 exposed to chlorobenzene vapor for 12 days, (c, c′) B62T38 and (d, d′) B75T25 annealed at 280 °C for 1 h. (a′–c′) Bar length: 500 nm; (d′) bar length: 1 μm.

dx.doi.org/10.1021/ma201024z | *Macromolecules* 2012, 45, 266–274

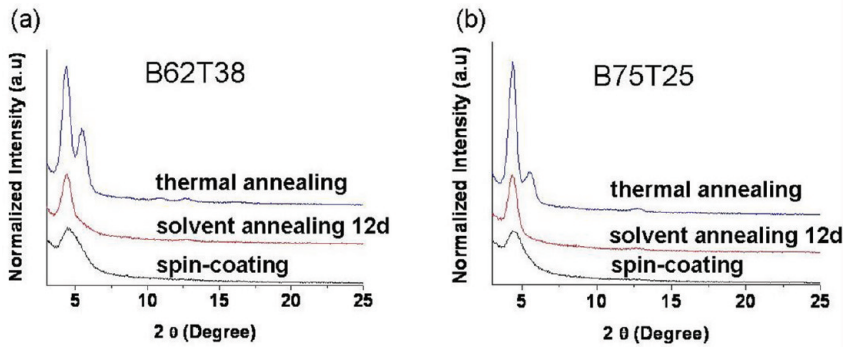

Figure 4. XRD patterns of (a) B62T38 and (b) B75T25 films treated with different conditions.

We speculate that thermal annealing yielded phase-separated nanoribbons, where the PPP and P3HT blocks crystallized within microphase-separated domains.

The crystal structures of the thin films were also checked with SAED (inset in Figure 3a′−d′).The inner diffraction ring with a *d*-spacing of 0.43−0.44 nm corresponding to the PPP block became clearer in B62T38 and B75T25 films after solvent vapor treatment. Meanwhile, two clear diffraction rings with a *d*-spacing of 0.38−0.39 nm and 0.43−0.44 nm from the diffraction of P3HT and PPP are obtained after thermal annealing. XRD measurements were performed on the thin films of diblock copolymers with higher PPP content after different annealing processes (Figure 4). Compared with the as-prepared films, the diffraction peak shifted to lower angle after treated with nonselective solvent vapor. Upon slow cooling from the melt, the PPP-*b*-P3HT copolymers clearly showed two distinct crystalline domains with relative intensities of X-ray diffraction peaks from the PPP- and P3HT-rich domains approximately scaling with the block ratio. A prominent peak corresponding to the PPP block was observed with a *d*-spacing of 2.02 nm, while a shoulder at $2\theta \approx 5.4^\circ$ is characteristic of P3HT block. These results show that the crystals are composed of two different crystalline domains formed by segregated PPP and P3HT blocks. The results are consistent with the thermal behaviors of block copolymers that two endothermic peaks and two exothermic peaks were observed during the heating and cooling process.

3.4. Theoretical Consideration of the Transition between Crystallization and Microphase Separation. For PPP-*b*-P3HT block copolymer system, crystallization and microphase separation coexist during the thin film forming process. Here we choose chlorobenzene as the nonselective solvent; the slow solvent evaporation speed during spin-coating facilitates the growth of crystalline domains in thin films. So a weak laterally microphase-separated structure due to incompatibility between PPP and P3HT and the crystallization of blocks is observed. In block copolymer B16T84 with a higher block ratio of P3HT, the crystallization of P3HT blocks dominates the surface morphology of the thin film, possibly because the priority crystallization of P3HT blocks breaks the microphase separation. These results also lead to a hypothesis that the crystallization ability of P3HT blocks is higher than PPP blocks probably because of the steric hindrance of more alkyl side chains in PPP. Similar behavior has been observed in other diblock copolymer systems.[23]

The diblock copolymer film absorbs chlorobenzene during annealing in chlorobenzene vapor; thus, the mobility of block copolymer molecules is enhanced, which assists the conjugated molecular chains to form crystals through $\pi-\pi$ stacking. For block copolymers with longer P3HT block, the P3HT chains can gradually diffuse to the neighbor chains and allow for efficient $\pi-\pi$ stacking of P3HT conjugated backbones to form crystalline supramolecular structures.[38] Because of the large amount of P3HT chains, crystals can develop into connected fibers, destroying the spinodal-like morphologies. In block copolymers with longer PPP block, the diffusion of P3HT chains is obstructed by the majority PPP block. Thus, the P3HT crystallization is confined in the microphase-separated domains.

In the case of thermal annealing process, the microphase-separated morphology prevails in the thin film at the molten state. Upon slow cooling down to the crystallization temperature of P3HT, the PPP blocks remain a coiled conformation due to its low melting point. The molten PPP blocks are mobile. Therefore, during the slow-cooling process, the P3HT blocks tend to form a thermodynamically favorable crystal structure consisting of edge-on side chains and parallel $\pi-\pi$ stacking planes of P3HT with respect to the substrate. For block copolymers with longer P3HT block, the majority P3HT chains can crystallize and break out the preformed microphase separation structure. When the temperature further reduced to the crystallization temperature of PPP block, the PPP block also form crystals. The crystallinity of the PPP block is restricted by the crystallization of P3HT block due to limited mobility of the P3HT blocks frozen in the lattice.[22,23] It therefore results in a larger ratio of the intensities of the two diffraction peaks in XRD patterns (Figure 2) from the P3HT- and PPP-rich domains than the block ratio. This result is further confirmed by the missing of the recrystallization peak of PPP block in the cooling process. In the case of block copolymers with longer PPP block, the preferential P3HT crystallization is confined in the microphase-separated domains. In turn, the majority block of PPP self-organize into crystals under the restriction of the crystallization of P3HT block. The crystallization ability of the P3HT plays a key role in determining the final morphology of the thin films.

We further investigated the nanometer scale morphologies in the nanoribbons of B62T38 and B75T25 with HRTEM. As shown in Figure 5, each nanoribbon composed of one main line and lots of short fibers perpendicular at both sides of the main line. More details were available from dark-field scanning transmission electron microscopy (STEM) measurements where bright features represent domains with a high electron scattering ability and are most likely due to the P3HT-rich phases. Topographic elemental mapping demonstrates that the sulfur is rich in the main line regions and decays rapidly in the

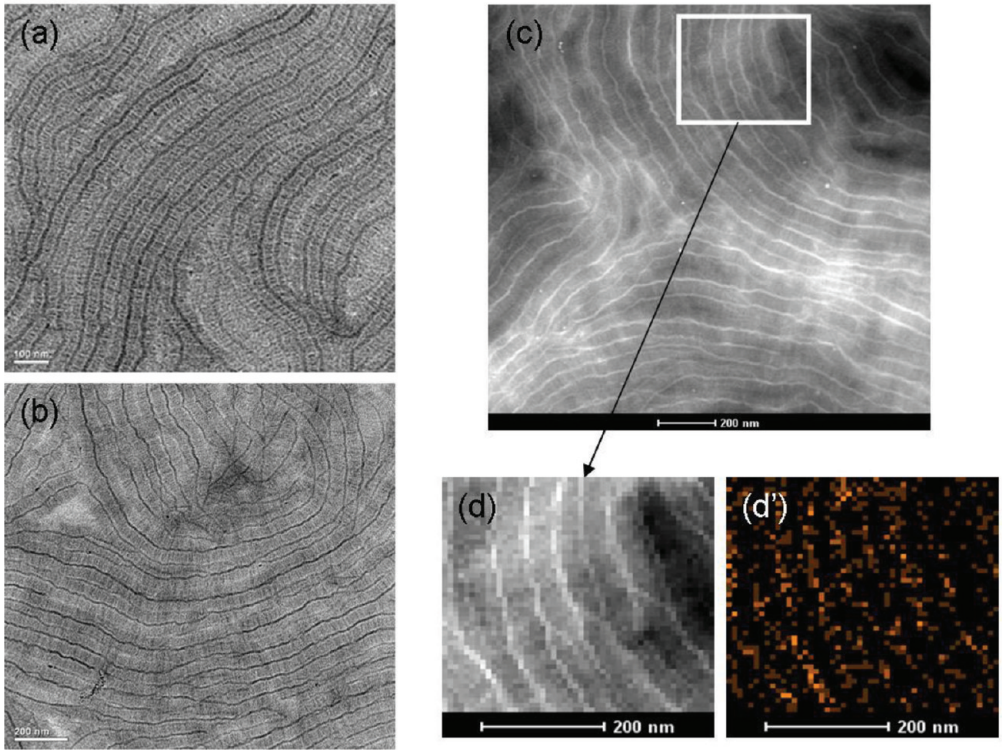

Figure 5. (a, b) HRTEM images of B62T38 and B75T25 after annealing at 280 °C for 1 h. (c) Dark-field STEM image of B75T25 thin films. In (c), electron-dense regions appear brighter. (d, d') STEM image and elemental mapping of sulfur content as a function of position.

surrounding area. This indicates the distribution of P3HT chains in such self-assembled structures concentrated in the main line area relatively. Such a structure further confirms the overwhelming of phase separation over crystallization.

CONCLUSION

In conclusion, we investigated the crystallization and microphase separation of crystalline−crystalline conjugated diblock copolymers with different main chains. There exists a competition between the crystallization and microphase separation in crystalline−crystalline conjugated block copolymers. We further tune the thin film morphology through the modulation of the competition between crystallization and microphase separation. It is the crystallization ability of the P3HT determines the final morphology of the thin film. Break-out crystallization and confined crystallization have been observed in block copolymers with a higher and lower block ratio of P3HT, respectively.

ASSOCIATED CONTENT

Supporting Information

Figures S1−S3. This material is available free of charge via the Internet at http://pubs.acs.org.

AUTHOR INFORMATION

Corresponding Author

*Tel 86-431-85262175; Fax 86-431-85262126; e-mail ychan@ciac.jl.cn.

ACKNOWLEDGMENTS

This work was subsidized by the National Natural Science Foundation of China (20923003, 21004064, and 20834005) and the Ministry of Science and Technology of China (2009CB623604). A portion of this work is based on the data obtained at 1W1A, BSRF. The authors gratefully acknowledge the assistance of scientists of Diffuse X-ray Scattering Station during the experiments.

REFERENCES

(1) McCullough, R. D. *Adv. Mater.* **1998**, *10*, 93−116.
(2) Sirringhaus, H.; Tessler, N.; Friend, R. H. *Science* **1998**, *280*, 1741−1744.
(3) Sirringhaus, H. *Adv. Mater.* **2005**, *17*, 2411−2425.
(4) Grimsdale, A. C.; Chan, K. L.; Martin, R. E.; Jokisz, P. G.; Holmes, A. B. *Chem. Rev.* **2009**, *109*, 897−1091.
(5) Bao, Z.; Dodabalapur, A.; Lovinger, A. J. *Appl. Phys. Lett.* **1996**, *69*, 4108−4110.
(6) Yang, H.; Shin, T. J.; Yang, L.; Cho, K.; Ryu, C. Y.; Bao, Z. *Adv. Funct. Mater.* **2005**, *15*, 671−676.
(7) Kline, R. J.; McGehee, M. D.; Kadnikova, E. N.; Liu, J.; Frchet, J. M. J.; Toney, M. F. *Macromolecules* **2005**, *38*, 3312−3319.
(8) Dai, C. A.; Yen, W. C.; Lee, Y. H.; Ho, C. C.; Su, W. F. *J. Am. Chem. Soc.* **2007**, *129*, 11036−11038.
(9) Shah, M.; Ganesan, V. *Macromolecules* **2010**, *43*, 543−552.
(10) Liu, J. S.; Sheina, E.; Kowalewski, T.; McCullough, R. D. *Angew. Chem., Int. Ed.* **2002**, *41*, 329−322.
(11) Ho, C. C.; Lee, Y. H.; Dai, C. A.; Segalman, R. A.; Su, W. F. *Macromolecules* **2009**, *42*, 4208−4219.
(12) Iovu, M. C.; Craley, C. R.; Jeffries-EL, M.; Krankowski, A. B.; Zhang, R.; Kowalewski, T.; McCullough, R. D. *Macromolecules* **2007**, *40*, 4733−4735.
(13) Leclère, P.; Calderone, A.; Marsitzky, D.; Francke, V.; Geerts, Y.; Müllen, K.; Brédas, J. L.; Lazzaroni, R. *Adv. Mater.* **2000**, *12*, 1042−1046.
(14) Lee, M.; Cho, B. K.; Zin, W. C. *Chem. Rev.* **2001**, *101*, 3869−3892.

(15) Iovu, M. C.; Zhang, R.; Cooper, J. R.; Smilgies, D. M.; Javier, A. E.; Sheina, E. E.; Kowalewski, T.; McCullough, R. D. *Macromol. Rapid Commun.* **2007**, *28*, 1816−1824.
(16) Li, B.; Sauve, G.; Iovu, M. C.; Jeffries-El, M.; Zhang, R.; Cooper, J.; Santhanam, S.; Schultz, L.; Revelli, J. C.; Kusne, A. G.; Kowalewski, T.; Snyder, J. L.; Weiss, L. E.; Fedder, G. K.; McCullough, R. D.; Lambeth, D. N. *Nano Lett.* **2006**, *6*, 1598−1602.
(17) Sauve, G.; McCullough, R. D. *Adv. Mater.* **2007**, *19*, 1822−1825.
(18) Scherf, U.; Gutacker, A.; Koenen, N. *Acc. Chem. Res.* **2008**, *41*, 1086−1097.
(19) Scherf, U.; Adamczyk, S.; Gutacker, A.; Koenen, N. *Macromol. Rapid Commun.* **2009**, *30*, 1059−1065.
(20) Wang, H. B.; Ng, M.; Wang, L.; Yu, L.; Lin, B. H.; Meron, M.; Xiao, Y. N. *Chem.—Eur. J.* **2002**, *8*, 3246−3253.
(21) He, M.; Zhao, L.; Wang, J.; Han, W.; Yang, Y. L.; Qiu, F.; Lin, Z. Q. *ACS Nano* **2010**, *4*, 3241−3247.
(22) Zhang, Y.; Tajima, K.; Hirota, K.; Hashimoto, K. *J. Am. Chem. Soc.* **2008**, *130*, 7812−7813.
(23) Zhang, Y.; Tajima, K.; Hashimoto, K. *Macromolecules* **2009**, *42*, 7008−7015.
(24) Wu, P. T.; Ren, G. Q.; Li, C. X.; Mezzenga, R.; Jenekhe, S. A. *Macromolecules* **2009**, *42*, 2317−2320.
(25) Ge, J.; He, M.; Qiu, F.; Yang, Y. L. *Macromolecules* **2010**, *43*, 6422−6428.
(26) Hollinger, J.; Jahnke, A. A.; Coombs, N.; Seferos, D. S. *J. Am. Chem. Soc.* **2010**, *132*, 8546−8547.
(27) Tu, G. L.; Li, H. B.; Forster, M.; Heiderhoff, R.; Balk, L. J.; Sigel, R.; Scherf, U. *Small* **2007**, *3*, 1001−1006.
(28) Park, J. Y.; Koene, N.; Forster, M.; Ponnapati, R.; Scherf, U.; Advincula, R. *Macromolecules* **2008**, *41*, 6169−6175.
(29) Chueh, C. C.; Higashihara, T.; Tsai, J. H.; Ueda, M.; Chen, W. C. *Org. Electron.* **2009**, *10*, 1541−1548.
(30) Wu, P. T.; Ren, G. Q.; Kim, F. S.; Li, C. X.; Mezzenga, R.; Jenekhe, S. A. *J. Polym. Sci., Polym. Chem.* **2010**, *48*, 614−626.
(31) Ren, G. Q.; Wu, P. T.; Jenekhe, S. A. *Chem. Mater.* **2010**, *22*, 2020−2026.
(32) Loo, Y. L.; Register, R. A.; Ryan, A. J. *Macromolecules* **2002**, *35*, 2365−2374.
(33) Loo, Y. L.; Register, R. A.; Ryan, A. J. *Phys. Rev. Lett.* **2000**, *84*, 4120−4123.
(34) Quiram, D. J.; Register, R. A.; Marchand, G. R. *Macromolecules* **1997**, *30*, 4551−4558.
(35) Wu, S. P.; Bu, L. J.; Huang, L.; Yu, X. H.; Han, Y. C.; Geng, Y. H.; Wang, F. S. *Polymer* **2009**, *50*, 6245−6251.
(36) Yamamoto, T.; Komarudin, D.; Arai, M.; Lee, B.; Suganuma, H.; Asakawa, N.; Inoue, Y.; Kubota, K.; Sasaki, S.; Fukuda, T.; Matsuda, H. *J. Am. Chem. Soc.* **1998**, *120*, 2047−2058.
(37) Prosa, T. J.; Winokur, M. J.; Moulton, J.; Smith, P.; Heeger, A. J. *Macromolecules* **1992**, *25*, 4364−4372.
(38) Lu, G. H.; Li, L. G.; Li, S. J.; Qu, Y. P.; Tang, H. W.; Yang, X. N. *Langmuir* **2009**, *25*, 3763−3768.

Macromolecules

Article

pubs.acs.org/Macromolecules

Block Copolymer Supramolecular Assembly beyond Hydrogen Bonding

Daniel Hagaman, Timothy P. Enright, and Alexander Sidorenko*

Department of Chemistry & Biochemistry, University of the Sciences, Philadelphia, Pennsylvania 19104, United States

Supporting Information

ABSTRACT: Supramolecular assemblies of block copolymers (BSAs) with low molecular weight additives require preferential interactions between the additive and one of the blocks. So far, only hydrogen bonds (HB) were explored to obtain BSAs. We report on three novel BSAs of block copolymer PS-*block*-P4VP with commercially valuable additives of the EDOT family. Two of the additives ((3,4-ethylenedioxythiophene) (EDOT) and 3,4-(2,2-dimethylpropylenedioxy)thiophene (ProDOT)) form the BSAs based on interactions others than HB. The morphology and some properties of the BSAs were studied by means of AFM, FTIR, and spectroscopic ellipsometry. The BSAs reveal cylindrical morphology with periodicity of ~30 nm. In thin films the orientation of the cylinders can be switched from perpendicular to parallel by annealing in vapors of a suitable solvent. Extraction with a selective solvent results in porous films with porosity of ~15%. These non-HB BSAs were compared with the HB BSA of HMeDOT as well as HABA BSA reported recently. The nature of the non-HB interactions is briefly discussed.

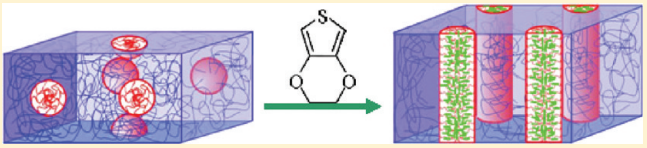

INTRODUCTION

The phenomenon of microphase separation in block copolymers (BCP) is a classic example and illustration of self-assembly in complex systems. A single molecule of BCP contains two or more different polymer chains, or blocks, connected by a covalent bond. The covalent linkage between immiscible blocks defeats macrophase separation caused by the entropy of mixing of polymer blends.[1,2] As a result, the blocks of one type segregate into domains with dimensions between 5 and 100 nm and several specific patterns. In the simplest case of diblock copolymers the gradual increase of volume fraction of one of the blocksproduces the following evolution of morphologies: body-centered spheres, hexagonally packed cylinders, bicontinuous double gyroid, and lamellae, with the same pattern repeating in inverse order.[1,3]

Ikkala et al.[4,5] have developed a new class of metamaterials, i.e., block copolymer supramolecular assemblies (BSA). One of the blocks of a BCP is selectively modified by a hydrogen-bonded additive of low molecular mass. The classic example is poly(styrene-*block*-4-vinylpyridine), PS-*block*-P4VP, with *n*-pentadecylphenol (PDP) reversibly attached to the P4VP block by H-bond formed between the nitrogen of pyridine and the hydroxyl group of PDP. Other examples include octyl gallate,[6,7] 1,5-dihydroxynaphthalene,[8] 2-(4′-hydroxybenzeneazo)-benzoic acid (HABA),[9,10] azo-dye DR1,[11] 1-pyrenebutyric acid,[12] quaterthiophene,[13] resorcinol,[14] carbohydrates,[15] dodecylbenzenesulfonic acid,[16] and bent-core additives.[17] Several special cases describe self-assembly in BSAs of triblock copolymers[18] and H-bonded carboxylthiophene attached to side-chain pyridine-terminated dendrimers.[19]

It is worth to define in greater detail the term "block copolymer supramolecular assembly". It is used to define the system of a block copolymer and a low molecular weight additive formed via selective noncovalent interactions between the additive and one of the blocks of the parent BCP. We use this term to distinguish our system from supramolecular assemblies of small molecules as well as mixtures of block copolymers and homopolymers recently developed by Russell et al.[20] The term itself and the abbreviation BSA stress the dualistic nature of the system: polymer basis (block copolymer) and small molecules (supramolecular) as an additive to form the entire system (assembly).

The presence of a weakly attached additive in one of the domains can qualitatively alter its morphology and properties. First, the morphology changes occur due to bulky additives selectively associated with one of the blocks. Second, BSAs eventually reveal hierarchical "structure-within-structure" morphologies due to smaller length-scale organization of additives (e.g., PDP) within one of the domains (P4VP + PDP).[21] Moreover, because of the high mobility of H-bonded molecules of the additive, the microphase separation in BSAs occurs quicker and can result in better ordering compared to neat BCPs. Third, a universal and practically valuable feature of BSAs is a possibility to extract the additive from the BSA bulk or film. Being attached by weak H-bonds, they can be easily removed by selective solvents, leaving nanoporous materials.[4,9] The latter can be used as nanotemplates for sol–gel reaction,[22] metal decoration,[23−25] and reactive deposition of metal nanoparticles[9,10] and polyaniline.[26]

Self-assembly in thin films of BSA is of particular interest and challenge. The presence of a distinguishing dimension, i.e.,

Received: May 24, 2011
Revised: November 1, 2011
Published: December 12, 2011

   dx.doi.org/10.1021/ma2011798 | *Macromolecules* 2012, 45, 275−282

height as opposed to lateral dimensions, allows us to consider orientation of cylinders and lamellae as perpendicular or parallel to the substrate surface plane. Two interfaces—free surface (air−BSA) and substrate−BSA interface—play a critical role in pattern formation. The effect of preferential interaction of one or more blocks with the interfaces in many cases makes the parallel orientation of BCP in thin films more favorable.[27] In the context of this article it is worth to mention the phenomenon of terrace formation which is typically observed in the case of parallel oriented domains, both cylinders and lamellae.[9,10,28] The thickness of the BSA films is another important factor that governs thermodynamics of the layers. Ideally, the domains confined between two interfaces will either form the terraces or adopt the perpendicular orientation.[29] The additive can significantly modify the BSA morphology if it preferentially occupies either surface of the film.[8−10,28,30]

The unique properties of BSAs originate from mobile additives attached by reversible hydrogen bonds (HB)[31] and other weak interactions including Coulombic and solvophobic ones.[32] In order to extend the range of available additives, other weak interactions can be explored as well. In this paper we test the hypothesis that non-HB interactions can serve as a basis to form the BSA instead of HB. We have chosen PS-*block*-P4VP as a parent BCP. Being potentially rich in different intermolecular interactions (HB, π-stacking, dipole−dipole, donor−acceptor), the block of P4VP is a very promising model for our needs. The choice of the counterpart (low molecular weight additive) is based on possible complementarities to P4VP and prospective applications. Taking into account the growing commercial importance of (3,4-ethylenedioxythiophene) (EDOT) as a precursor for the electroconductive polymer PEDOT,[33,34] our natural choice was EDOT and the family of commercially available EDOT-like compounds. The two dioxythiophene derivatives, namely 3,4-(2,2-dimethylpropylenedioxy)thiophene (ProDOT) and hydroxymethyl-3,4-ethylenedioxythiophene (HMeDOT), were used as the additives to form either the HB BSA (HMeDOT) or the non-HB BSA (EDOT, ProDOT) (Figure 1).[35−38] In both cases we assumed selective interactions

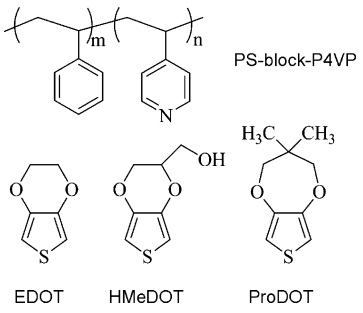

Figure 1. Parent BCP and the low molecular weight additives of the EDOT family: (3,4-ethylenedioxythiophene) (EDOT), 3,4-(2,2-dimethylpropylenedioxy)thiophene (ProDOT), and hydroxymethyl-3,4-ethylenedioxythiophene (HMeDOT) used in this work as the model compounds.

between the additive and the 4-vinylpyridine units of the of the parent BCP.

RESULTS

FTIR Spectroscopy. We begin our discussion with the analysis of the FTIR spectra of the BSAs and the corresponding low molecular weight additives. The survey FTIR spectra of an equimolar (with respect to P4VP content) compositions with ProDOT and HMeDOT are shown in the Figure 2a.

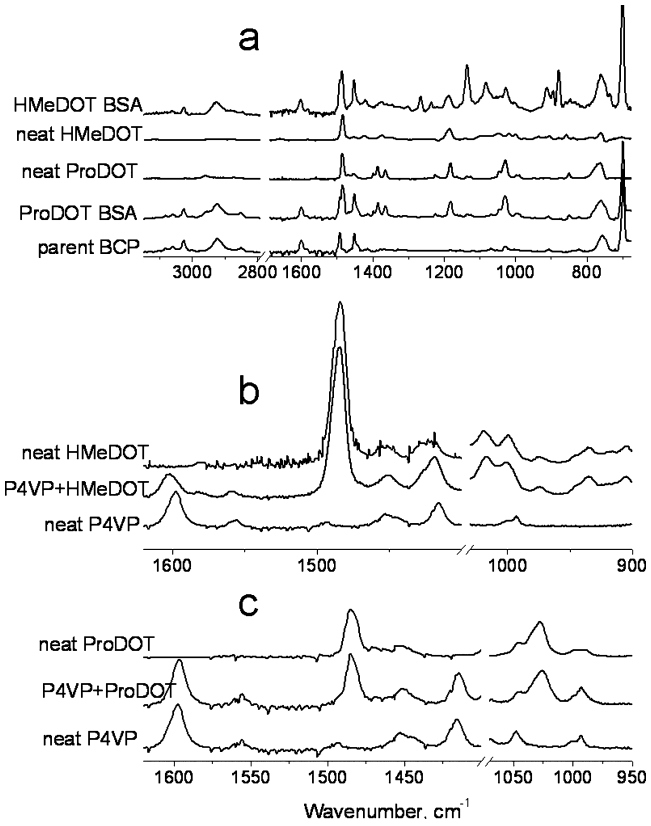

Figure 2. FTIR (ATR) spectra of neat HMeDOT, neat ProDOT, and corresponding BSAs with the parent BCP (survey spectra, a), HMeDOT associated with P4VP homopolymer (b), and ProDOT associated with P4VP (c).

The spectra were obtained from films of the compositions deposited by drop-casting with an ATR accessory. Both compositions formed homogeneous films with no signs of the macrophase separation of the additives. This provides evidence for the formation of some kind of molecular association of both additives with the BCP.[39] In the case of HMeDOT we anticipated the formation of a hydrogen bond between −OH group of the additive and the pyridine ring of the P4VP block.

On the basis of previous publications[40−43] and their own previous experiments, Ikkala et al.[5] identified three absorption bands of P4VP affected by HB formation, i.e., 1597, 1415, and 993 cm^{-1}. In spite of our expectations, we were not able to observe shifts in the pyridine ring absorption bands. The same observations were made for ProDOT. The detailed consideration of the spectra showed that the P4VP peak at 1597 cm^{-1} was masked by the overlapping PS peak at 1600 cm^{-1} (and PS constitutes the vast majority of the composition). Also, the peaks at 1415 and 993 cm^{-1}, being weak themselves, are complicated by the peaks of the additives. Apparently, the presence of the PS block makes further analysis unreliable. Therefore, we have performed more detailed analysis using two model systems: comblike homopolymers of P4VP/HMeDOT (Figure 2b) and P4VP/ProDOT (Figure 2c). (Here we adopt the terminology used by Ikkala and other researchers to refer to the homopolymers with side-chain additives attached by weak interactions, i.e., HB as opposed to comb-shaped polymers

dx.doi.org/10.1021/ma2011798 | *Macromolecules* 2012, 45, 275−282

carrying covalently attached mesogenic side groups according to ref 44.)

Similarly to previously reported examples with phenols, amines, alcohols, and carboxy acids,[5,45] formation of a HB with P4VP results in a significant shift of the IR absorption bands responsible for the pyridine ring vibrations. As shown in the Figure 2b, hydrogen bonding with HMeDOT results in a shift of the bands. Being the least screened out, the peak at 1597 cm^{-1} reveals a clear shift to 1604 cm^{-1}. Also, the peak at 1415 cm^{-1} shifts to 1419 cm^{-1}. The peak around 1000 cm^{-1} overlaps with the two IR bands of HMeDOT as well as ProDOT. However, the detailed analysis reveals the shift of the pyridine peak from 993 to 1009 cm^{-1} in the HMeDOT BSA (see Supporting Information). These shifts clearly indicate the formation of a HB between HMeDOT and the P4VP units. On the contrary, ProDOT assembly shows no shifts in the characteristic IR absorption bands of the P4VP block (Figure 2c). This observation proves our *a priori* assumption based on the absence of polar group; i.e., ProDOT cannot form HB with P4VP.

Spectroscopic ellipsometry was routinely used as a method of film thickness measurements together with the AFM scratch test. Besides that, we used both methods for analysis of the porosity of the films upon extraction of the additives (HMeDOT and ProDOT) by methanol. Being associated with P4VP blocks either by HB or non-HB interactions, we assumed that the additives can be easily removed by selective solvent, i.e., methanol. Indeed, ellipsometry demonstrated a significant shift in both Ψ (Figure 3) and Δ spectra of HMeDOT and ProDOT

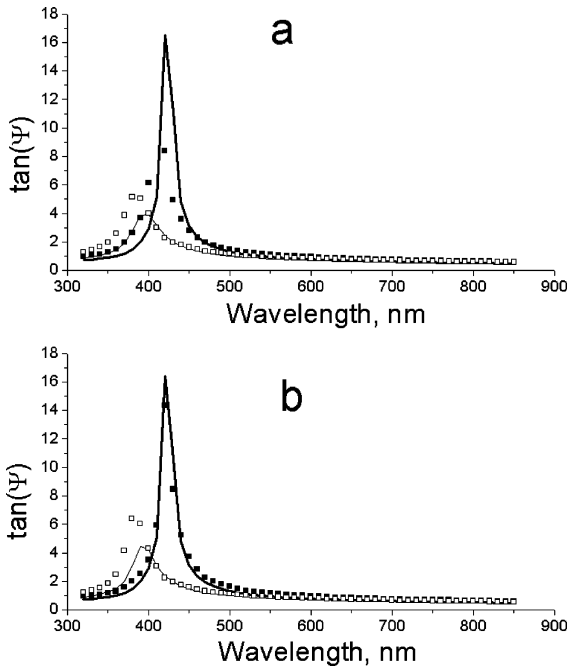

Figure 3. BSA films and corresponding porous films upon extraction with methanol as revealed by spectroscopic ellipsometry (tan(Ψ) spectra): HMeDOT (a) and ProDOT (b) BSAs. The best model fit is shown by the solid line, and the experimental data are represented by dots.

BSAs upon extraction with methanol. Concurrently, we performed a scratch test by AFM and found that the thickness of the films revealed only minor change (within 3% difference). This was evidence for the formation of porous films of the neat BCP. Using the Maxwell−Garnett effective media approximation

$$\frac{\varepsilon_{eff} - \varepsilon_2}{\varepsilon_{eff} + 2\varepsilon_2} = \varphi_1\left(\frac{\varepsilon_{eff} - \varepsilon_1}{\varepsilon_{eff} + 2\varepsilon_1}\right) \quad (1)$$

where ε_{eff}, ε_1, and ε_2 are effective dielectric constant and dielectric constant of phase 1 and phase 2, respectively, and φ_1 is the volume fraction of phase 1; we performed estimation of the porosity and compared them with the results of the calculations based on the amounts of the additive in the BSAs. The BSAs of HMeDOT and ProDOT contain 15.3 and 13.8 mass % of additives, respectively. Assuming the density of the P4VP-additive associate to be 1 g/cm^3, the porosity of the films resulting from methanol extraction is to be the same. Ellipsometry reveals significant porosity values in both films: 14.8% and 12.6% for HMeDOT and ProDOT BSA films of about 80 nm in thickness, respectively.

Atomic Force Microscopy. The morphology of thin films of the compositions provides important information about the BSA formation. This is due to the phenomenon of microphase separation in BSAs similarly to neat BCPs.[1] The morphology depends on Flory's immiscibility of the polymer blocks and the volume ratio of the blocks constituting the BCP. In the case of BSA, its morphology can change qualitatively compared to the parent BCP. This is due to the increasing volume fraction of one of the blocks if a selective interaction of the additive takes place (Figure 4). In particular, we have observed formation of

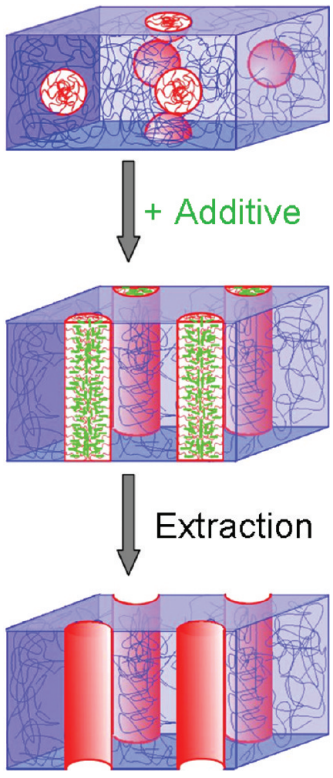

Figure 4. Concept of the morphology changes upon formation of BSA: spherical bcc morphology of the parent BCP (top) undergoes transformation to cylinders upon formation of the assembly with an additive. Successive extraction of the additive with a selective solvent results in porous film (bottom).

BSA of PS-P4VP + HABA[10] with AFM supported by other methods. The parent BCP with about 10% volume fraction of

dx.doi.org/10.1021/ma2011798 | *Macromolecules* 2012, 45, 275−282

P4VP revealed spherical bcc morphology. Selective interaction with a bulky additive HABA resulted in increase of the fraction of P4VP + HABA up to 25%. The cylindrical morphology is characteristic for such volume fraction of minor component; this has been proven by the extensive AFM studies.[9,10] Here we compare the morphology of thin films of two compositions, i.e., PS-P4VP + HMeDOT and PS-P4VP + ProDOT, with parent PS-P4VP. The AFM images of thin films of the parent BCP reveal spherical bcc morphology with the periodicity of 23 nm; the representative images of the height and phase signals along with the FFT and the power spectrum density plot of the parent BCP film are shown in the Supporting Information.

Thin films of BSA of HMeDOT deposited from its solution in 1,4-dioxane are microscopically smooth with rms roughness of 0.5 nm on a 1 × 1 μm^2 scale. However, the phase signal in tapping mode resolves the surface pattern of quasi-hexagonally ordered features. FFT conversion of the phase image clearly reveals the periodicity of 28.5 ± 1.0 nm. (Both images and the power spectrum density plot of the composition are provided in the Supporting Information.) Subsequent extraction of HMeDOT by methanol reveals quasi-hexagonal order of nanoscopic wells (Figure 5a) with the periodicity of 28.5 ± 1.0 nm. Apparently, being a selective solvent, methanol dissolves HMeDOT, leaving PS matrix of the BSA film unaffected. Similarly to the HABA-based BSA, vapor annealing in 1,4-dioxane improves the ordering (Figure 5b). The insets show FFT images of HMeDOT BSA films "as is" and upon vapor annealing. The FFT image in Figure 5a ("as is") reveals a halo corresponding to the periodicity of 28.5 nm. The FFT image of the BSA film upon vapor annealing demonstrates six sharp first-order peaks corresponding to the periodicity of 32.0 nm and the higher-order peaks spaced at $\sqrt{3}$ of main peak revealing the hexagonal order.

The hexagonal pattern of the film surface observed by AFM can reflect either spherical bcc morphology or perpendicular cylinders of P4VP + HMeDOT. Assuming the latter case, we have performed vapor annealing of the BSA film in chloroform. Indeed, AFM demonstrates the fingerprint-like pattern. Some regions with mixed orientation are also seen revealing incomplete switching of the orientation (Figure 5c). Similarly to the HABA BSA, periodicity of the parallel oriented cylinders is higher than in perpendicular orientation and is equal to 33.8 nm. We explain this apparent discrepancy by fast drying of the swollen film, which results in a distorted hexagonal matrix.[10]

The BSA of EDOT with PS-P4VP is a challenge to characterize. From spectroscopic ellipsometry time-resolved serial measurements we have found that liquid EDOT evaporates from thin films of its BSA within 3−5 min. Its evaporation results in collapse of the polystyrene matrix, leaving the morphology almost identical to the parent BCP (Supporting Information). Therefore, it is very difficult to characterize and manipulate thin films of EDOT BSA. However, we succeeded in AFM imaging a thin film of the BSA with EDOT. Immediately upon deposition by spin-coating, the film was immersed in methanol. Being insoluble in methanol, the morphology of the matrix was preserved and available for AFM characterization. The result is shown in Figure 6. It reveals a combination of dots and short stripes. Usually this is associated with weakly ordered cylinders of mixed orientation. The periodicity of the BSA with EDOT (~34 nm) overwhelmingly exceeds the periodicity of the parent BCP. These are the signs of the BSA formation, although the lack of direct evidence is apparent. Therefore, we have chosen a solid-state analogue of EDOT, i.e., ProDOT, as a model compound to investigate non-HB BSAs based on thiophenes and pyridines.

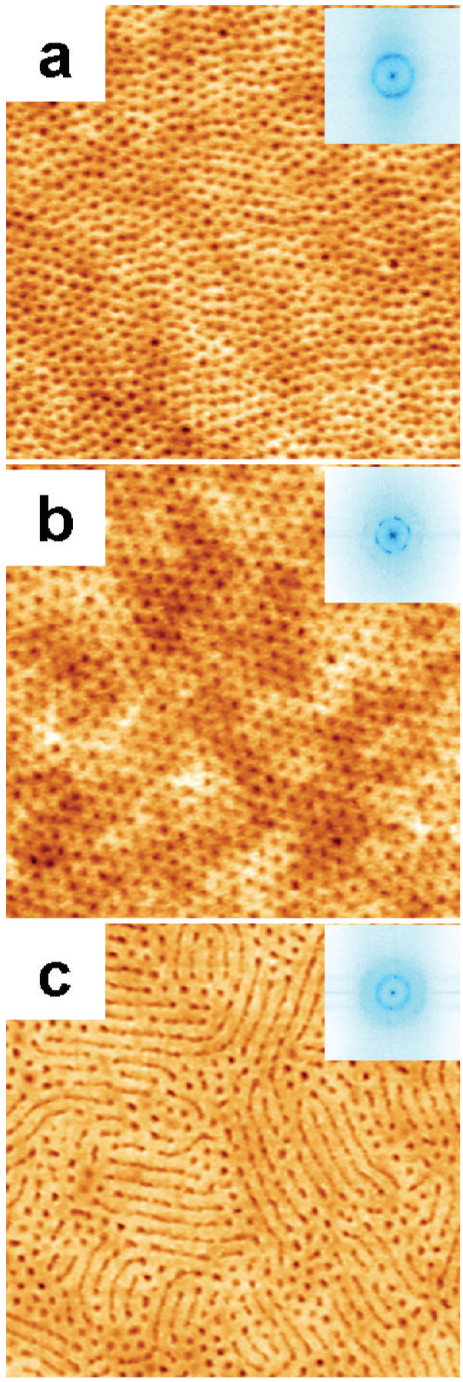

Figure 5. AFM images (topography) of thin films of HMeDOT BSA upon deposition (a), vapor annealing in 1,4-dioxane (b), and vapor annealing in chloroform (c). All images are 1 × 1 μm^2 scan size. The additive is extracted by methanol to reveal the structure. Insets: corresponding FFT images.

The BSA of ProDOT with PS-P4VP demonstrates good ability to form thin films with no signs of ProDOT macrophase separation (crystallization). This is the first indication of the formation of the BSA. The AFM image of ProDOT BSA reveals mixed morphology (Figure 7). We found that thinner films (30−50 nm in thickness) demonstrate preferentially hexagonal patterns with only a few elongated features (Figure 7a). The surface of the thicker films (50−80 nm in thickness) is

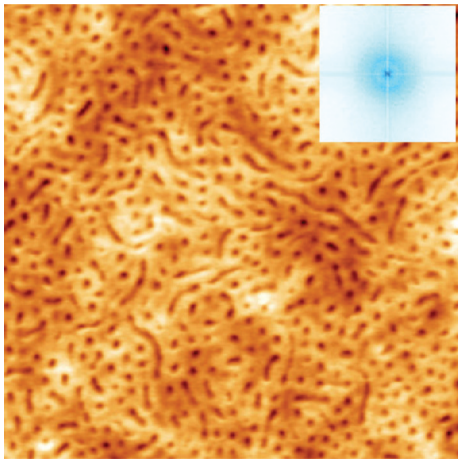

Figure 6. AFM image (topography) of thin films of EDOT BSA, 1 × 1 μm^2 scan size. The additive is extracted by methanol instantly upon deposition to preserve the structure and to reveal the features. Inset: corresponding FFT image.

dominated by elongated features (parallel cylinders) with a small number of dots (Figure 7b). Although the classical fingerprint-like morphology is absent, the presence of elongated features clearly indicates cylindrical morphology of the BSA in mixed orientation. The comparison of the periodicity observed in thin films of the parent BCP (23 nm, Supporting Information) and the films of the BSA with ProDOT (29−34 nm, Figure 7c) is further evidence for the BSA formation. Compared to the spherical morphology of the BCP, it clearly shows preferential interaction of ProDOT with the block of P4VP. Apparently, it can result in an increase of the volume fraction of the minor phase (P4VP) in the BCP from 0.110 up to 0.254 in the BSA, taking into account the equimolar composition (ProDOT vs P4VP) and assuming density of both blocks about 1 g/cm^3.

The fingerprint-like pattern would clearly indicate the formation of cylindrical morphology of parallel orientation. Formerly, we have used vapor annealing to switch the orientation of the BSA with HABA. Depending on selectivity of the solvent used for vapor annealing, either perpendicular (hexagonal pattern, 1,4-dioxane) or parallel (fingerprint-like, chloroform) orientations have been documented. Therefore, we applied a similar procedure to the BSA with ProDOT. However, vapor annealing in chloroform resulted in separation of ProDOT from the film in the form of crystals. AFM analysis of the surface revealed the morphology identical to the parent BCP. The rinse with methanol led to no changes in the surface morphology. Similar results were observed for vapors of 1,4-dioxane and THF. We concluded therefore that vapors of polar solvents have a destructive effect on the ProDOT interactions with the pyridines as they can replace the molecules of the additive in the BSA with non-HB interactions.

EDOT and its analogues are well-known as precursors for intrinsically conducting polymers (ICP). We have succeeded in oxidative polymerization of ProDOT *in situ* in the template of its BSA. In order to realize it, we have altered the approach of oxidative chemical vapor deposition designed by Gleason[46] to thin films of ProDOT BSA. We exposed the BSA films to I_2 vapors at room temperature overnight. The samples were then placed in a vacuum oven at 60 °C for 1 h to remove excess I_2. Because of higher optical density of poly(ProDOT), the films revealed more dense color though the thickness remained the same before and after polymerization as measured by the AFM

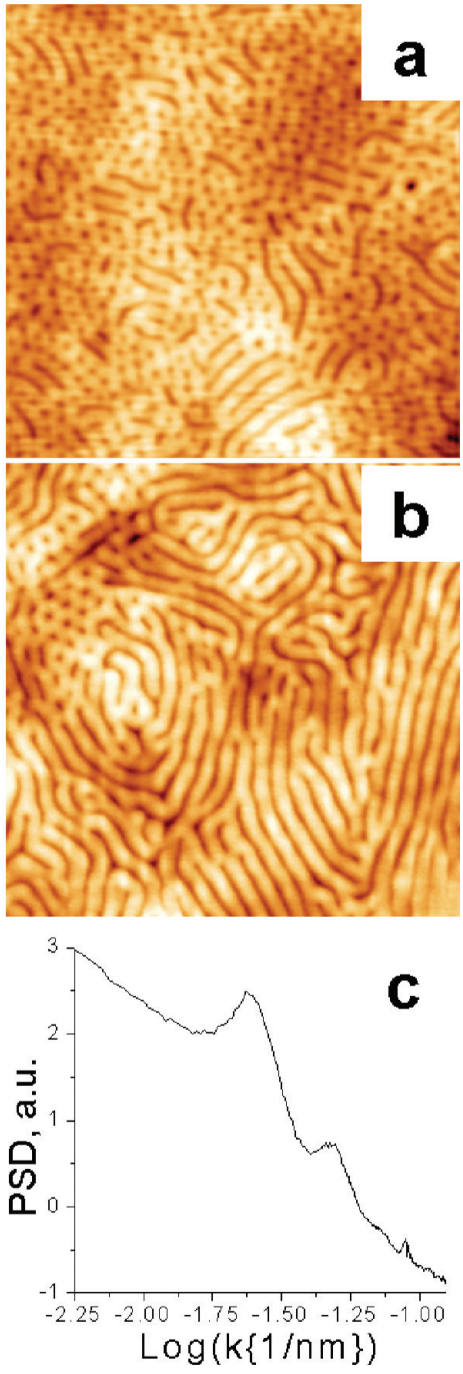

Figure 7. AFM image (topography) of thin films of ProDOT BSA revealing diversity of the patterns: majority of dots (thickness 50 nm, a) and majority of stripes (thickness 70 nm, b). 1 × 1 μm^2 scan size. A representative power spectrum density plot (c) reveals typical periodicity of ∼32 nm. The additive is extracted by methanol to reveal the structure.

scratch test. Selective plasma etching allowed us to reveal the composition as shown in Figure 8a. The features protruding through the film surface are the columns of the poly(ProDOT) while the PS matrix is partially etched away. The remaining films are insoluble in good solvents as a result of partial cross-linking of PS matrix and strong entanglement of poly(ProDOT) domains with chains of P4VP. Such films demonstrate modest conductivity as was revealed by a conductive AFM (Figure 8b).

dx.doi.org/10.1021/ma2011798 | *Macromolecules* 2012, 45, 275−282

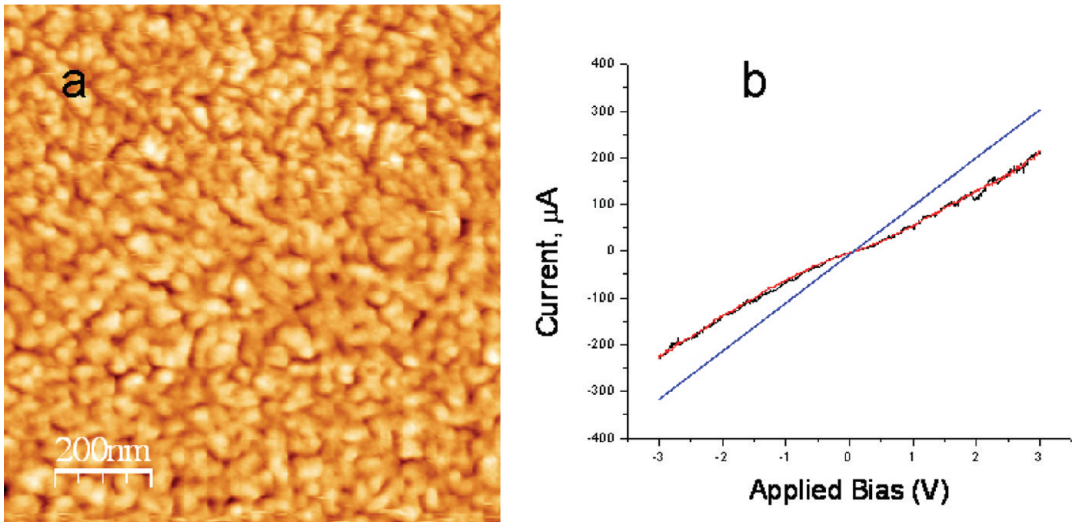

Figure 8. AFM image (topography) of partially etched sample with ProDOT BSA upon oxidative polymerization, 1 × 1 μm^2 scan size (a). Conductivity scan (C-AFM) between 3 and −3 V, forward (black) and backward (red); shunt 10 kohm resistor in the circuit. Blue line: reference scan of bare gold film (b).

DISCUSSION

The results presented above clearly indicate the fact of formation of a non-HB BSA. There are two important questions to be discussed. First, how does the energy of non-HB interactions between an additive and the units of BCP affect the stability and behavior of the BSA? Second, what is the nature of the interactions we observe in the BSA of PS-P4VP + ProDOT?

The first sign of the formation of the ProDOT was the change in the periodicity of the hexagonal pattern compared to the neat BCP of PS−PVP. Indeed, increase of the periodicity from 23 nm (parent BCP) to ∼30 nm (BSA) is quite substantial. Is the change in the periodicity enough to unambiguously conclude that the BSA is formed, though? It is probably true for relatively strong interactions, for instance when hydrogen bonds are formed: the preferential interactions of the components of the HABA and PDP BSAs are obvious from their molecular structures. However, in the case of non-HB interactions, the selectivity becomes an important factor, and concurrent interactions can play an important role. In particular, increased periodicity observed in the case of PS−P4VP + ProDOT (Figure 9a) can be explained by either (i) nonselective incorporation of molecules of the additive into both domains of the BCP, or (ii) preferential interaction with the major component (matrix), or (iii) preferential interaction with the minor component to an extent that the cylindrical morphology is achieved. In the two former cases the morphology is bcc spheres, and AFM would reveal hexagonally ordered dots. In the latter case either hexagonal arrays of dots (perpendicular orientation) or fingerprint-like patterns (parallel to surface orientation) are to be observed. Also, parallel oriented cylinders are usually associated with terraces; their height is commensurable with the cylinders' size. The formation of terraces allows one to distinguish between parallel oriented cylinders and perpendicular lamellae.

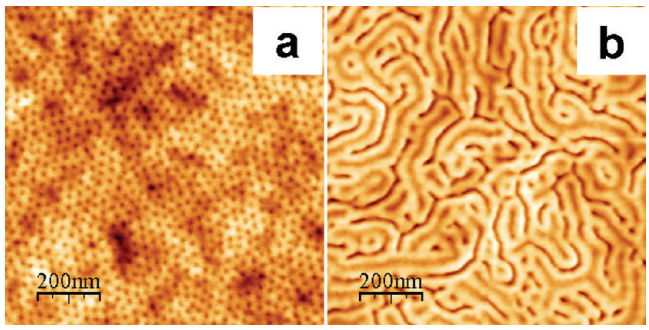

Figure 9. Vapor annealing of ProDOT BSA films in benzyl alcohol results in surface reconstruction from perpendicular cylinders (a) to parallel cylinders (b).

This reasoning led us to find conditions when both parallel and perpendicular orientations of cylinders can be observed using the AFM. This situation was observed for ProDOT BSA (Figure 7a,b) when, depending on the thickness, either preferentially perpendicular or preferentially parallel cylinders were observed. However, the switching of the orientation seemed to be the most unequivocal proof of the cylindrical morphology and thus selective interaction of the additive with P4VP block of the BCP. Our efforts to find the condition of orientation control of the BSA with ProDOT together with reasoning about the fine balance of polar and nonpolar interactions with the different components of the BSA resulted in such compound. The annealing of the BSA films in vapors of benzyl alcohol resulted in well-developed stripe patterns typical for parallel cylinders[47] (Figure 9b). Noteworthy, the starting morphology was perpendicular cylinders (hexagonal, Figure 9a). No signs of the destruction of the BSA (crystals, dewetting) were observed.

The second question relates to the nature of the interactions and requires consideration of possible interactions on the molecular level. As two model compounds we use EDOT and 4-ethylpyridine (4EP). The results of the partial charge distribution (Mulliken charges) calculated using DFT with basis set B3LYP/6-31G (open shell) are shown in Figure 10. First, they clearly indicate the possibility of strong Coulomb interactions between the positively charged sulfur of EDOT (+0.41) and the negatively charged nitrogen of pyridine ring (−0.37). Assuming head-to-head alignment of the donor (EDOT) and acceptor (4EP) and a distance between sites of 0.3 nm, we obtain the energy of Coulomb interaction about 10 kT for PS as media

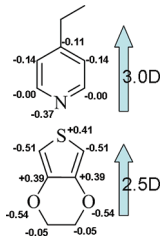

Figure 10. Two model compounds used for molecular simulation: 4-ethylpyridine (top) and EDOT (bottom). Results of DFT (B3LYP/6-31G) calculations in terms of Mulliken partial charges.

(ε = 2.6):

$$w(r) = -\frac{Q_S Q_N}{4\pi\varepsilon_0 \varepsilon r} \quad (2)$$

Second, both molecules have a substantial dipole moment of 2.98 D (4-ethylpyridine) and 2.47 D (EDOT). Using the Keesom equation for angle-averaged dipole−dipole interaction[48]

$$w(r) = -\frac{u_{\mathrm{EDOT}}^{2} u_{\mathrm{4EP}}^{2}}{3(4\pi\varepsilon_0)^2 kTr^6} \quad (3)$$

we obtain 230 kT for vacuum at r = 0.3 nm. Taking into account the dielectric constant of PS of 2.6, the energy value decreases to 34 kT. Therefore, both the Coulomb attraction between donor and acceptor sites and the dipole−dipole Keesom interaction seem to be substantial for stable non-HB BSA at room temperature.

Apparently, further analysis of the molecular interactions is required; both experimental aspects and high-level molecular simulations are expected to provide more details on the BSA formation. This work is ongoing, and the results will be reported elsewhere.

CONCLUSION

In this paper we report three new BSAs based on PS−P4VP and low molecular weight additives of the EDOT family: EDOT, ProDOT, and HMeDOT. The latter additive selectively interacts with pyridine rings of the P4VP block through the formation of hydrogen bonds. Conversely, the other two additives form BSAs in spite of the fact that they are not capable of hydrogen bonding with P4VP. Further comparison of HB and non-HB BSAs shows that non-HB BSAs are less stable. However, they can produce thin films with cylindrical morphology. The orientation of the cylinders can be switched by annealing in vapors of a suitable solvent. Extraction of the additive by a selective solvent (methanol) results in porous films. This allowed us to investigate their morphology by AFM and spectroscopic ellipsometry. On the other hand, gas phase oxidative polymerization *in situ* in the BSA template results in conductive polymer domains distributed in the matrix of parent polymer. Further studies on the nature of the interactions and manipulations are ongoing.

EXPERIMENTAL SECTION

Materials. Polystyrene-*block*-poly(4-vinylpyridine) (PS−P4VP), with the molecular masses (M_n) of PS 35 500 g mol^{-1}, P4VP 4400 g mol^{-1}, M_w/M_n = 1.09 for both blocks, and poly(4-vinylpyridine) with M_n 3200 g mol^{-1}, M_w/M_n = 1.20 were purchased from Polymer Source, Inc. 3,4-Ethylenedioxythiophene (EDOT), hydroxymethyl EDOT (HMeDOT), and 3,4-(2,2-dimethylpropylenedioxy)thiophene (ProDOT) were purchased from Sigma-Aldrich. Solvents chloroform, dichloromethane, 1,4-dioxane, benzyl alcohol, and methanol were purchased from Sigma-Aldrich and used as supplied. Silicon wafers {100} were cleaned successively in an ultrasonic bath (dichloromethane, methanol, Millipore water) for 15 min each and then in 2:1:1 alkali "piranha" solution (H_2O:H_2O_2:NH_4OH) at 82 °C for 40 min. The wafers were then rinsed thoroughly with Millipore water and dried by blowing with an argon stream.

Instrumentation. A Thermo Nicolet Avatar 370 spectrometer was used to collect the FTIR spectra. The spectra were taken using an ATR Smart Performer accessory (Ge crystal) from 4000 to 400 cm^{-1} at 1 or 4 cm^{-1} resolution and 32 or 64 scans.

Atomic force microscopy (AFM) images were obtained using a Veeco diInnova scanning probe microscope in tapping mode. The AFM probes (Budget Sensors) used have the following features: resonant frequency of 160−180 kHz and spring constant of about 48 N/m. The AFM images were treated (linear flattening) and analyzed using WsXM software (Nanotec Electronica).[49] Conductive AFM probing was done using CONTPt probes (NanoWorld, Inc.) on samples deposited on 100 nm thick film of Au. The sample holder was equipped with 10 kohm resistor (shunt) to prevent circuit shortage.

Psi and Delta profiles were obtained using a PHE-102 spectroscopic ellipsometer (Angstrom Advanced Inc.). Measurements were per formed at an incident angle of 70° in the wavelength range 320−850 nm.

Sample Preparation. The equimolar BSAs of PS−P4VP and the additives (with respect to P4VP units) were used throughout. The parent BCP and the additive were dissolved separately in 1,4-dioxane. The BCP solution was then added dropwise to the additive solution while it was kept in an ultrasonic bath and being mildly heated (40 °C). The BSA solution containing HMeDOT was aged at least 48 h prior to thin film deposition. The solutions of EDOT and ProDOT were aged at least 1 week prior to deposition to establish equilibrium and complete BSA formation.

Ellipsometry and AFM measurements were done on thin films deposited from the BSA solutions. They were deposited by either dip-coating or spin-coating techniques. Dip-coating was used to produce films between 30 and 60 nm. Spin-coating was used to deposit thicker films, 60−120 nm. Before depositions, all solutions were filtered using 0.2 μm PTFE filters.

Annealing in vapors of 1,4-dioxane, chloroform, and benzyl alcohol: the samples were exposed to the solvent vapor so that film thickness increased ~3 times. This was estimated by the color (interference) of the film. They were left in the swollen state for about 30 min and then immediately removed from the chamber.

ASSOCIATED CONTENT

Supporting Information

AFM images of thin films of neat (parent) BCP (Figure S1) and HMeDOT BSA as deposited (no extraction) (Figure S3) as reference materials; details for FTIR spectra of P4VP−HMEDOT associate (Figure S2). This material is available free of charge via the Internet at http://pubs.acs.org.

AUTHOR INFORMATION

Corresponding Author

*Tel (215) 596 8836; e-mail a.sidorenko@usp.edu.

ACKNOWLEDGMENTS

This work was funded by National Science Foundation (DMR 0947897) and in part by the Center for Drug Design and Delivery (KISK grant of the Department of Community and Economic Development, Commonwealth of Pennsylvania). The authors acknowledge helpful discussions with Dr. J. D. Tovar, Johns Hopkins University, Dr. V. Pophristic, University of the Sciences, Dr. I. Tokarev, and Prof. S. S. Minko, Clarkson University. T. P. Enright acknowledges financial support of his fellowship at NIST (SURF Award).

REFERENCES

(1) Bates, F. S.; Fredrickson, G. H. *Annu. Rev. Phys. Chem.* **1990**, *41*, 525−557.
(2) Muthukumar, M.; Ober, C. K.; Thomas, E. L. *Science* **1997**, *277*, 1225−1232.
(3) Matsen, M. W.; Bates, F. S. *Macromolecules* **1996**, *29*, 1091−1098.
(4) Ruokolainen, J.; Makinen, R.; Torkkeli, M.; Makela, T.; Serimaa, R.; ten Brinke, G.; Ikkala, O. *Science* **1998**, *280*, 557−560.
(5) Ruokolainen, J.; ten Brinke, G.; Ikkala, O.; Torkkeli, M.; Serimaa, R. *Macromolecules* **1996**, *29* (10), 3409−3415.
(6) Bondzic, S.; De Wit, J.; Polushkin, E.; Schouten, A. J.; Ten Brinke, G.; Ruokolainen, J.; Ikkala, O.; Dolbnya, I.; Bras, W. *Macromolecules* **2004**, *37* (25), 9517−9524.
(7) Polushkin, E.; Bondzic, S.; de Wit, J.; van Ekenstein, G. A.; Dolbnya, I.; Bras, W.; Ikkala, O.; ten Brinke, G. *Macromolecules* **2005**, *38* (5), 1804−1813.
(8) Laforgue, A.; Bazuin, C. G.; Prud'homme, R. E. *Macromolecules* **2006**, *39* (19), 6473−6482.
(9) Sidorenko, A.; Tokarev, I.; Minko, S.; Stamm, M. *J. Am. Chem. Soc.* **2003**, *125* (40), 12211−12216.
(10) Tokarev, I.; Krenek, R.; Burkov, Y.; Schmeisser, D.; Sidorenko, A.; Minko, S.; Stamm, M. *Macromolecules* **2005**, *38* (2), 507−516.
(11) Ali, N.; Park, S.-Y. *Langmuir* **2009**, *25* (23), 13426−13431.
(12) Kuila, B. K.; Gowd, E. B.; Stamm, M. *Macromolecules* **2010**, *43* (18), 7713−7721.
(13) Rancatore, B. J.; Mauldin, C. E.; Tung, S.-H.; Wang, C.; Hexemer, A.; Strzalka, J.; Frechet, J. M. J.; Xu, T. *ACS Nano* **2010**, *4* (5), 2721−2729.
(14) Tata, J.; Scalarone, D.; Lazzari, M.; Chiantore, O. *Eur. Polym. J.* **2009**, *45* (9), 2520−2528.
(15) Rodriguez, A. T.; Li, X.; Wang, J.; Steen, W. A.; Fan, H. *Adv. Funct. Mater.* **2007**, *17* (15), 2710−2716.
(16) Lee, J.-W.; Lee, C.-S.; Choi, S.-Y.; Kim, S.-H. *Macromolecules* **2010**, *43* (1), 442−447.
(17) Tenneti, K. K.; Chen, X.; Li, C. Y.; Wan, X.; Fan, X.; Zhou, Q.-F.; Rong, L.; Hsiao, B. S. *Macromolecules* **2007**, *40* (14), 5095−510.
(18) du Sart, G. G.; Vukovic, I.; Vukovic, Z.; Polushkin, E.; Hiekkataipale, P.; Ruokolainen, J.; Loos, K.; ten Brinke, G. *Macromol. Rapid Commun.* **2011**, *32* (4), 366−370.
(19) Leolukman, M.; Paoprasert, P.; Mandel, I.; Diaz, S. J.; McGee, D. J.; Gopalan, P. *J. Polym. Sci., Part A: Polym. Chem.* **2009**, *47* (19), 5017−5026.
(20) Jeong, U.; Kim, H. C.; Rodriguez, R. L.; Tsai, I. Y.; Stafford, C. M.; Kim, J. K.; Hawker, C. J.; Russell, T. P. *Adv. Mater.* **2002**, *14*, 274−276.
(21) Ruokolainen, J.; Ten Binke, G.; Ikkala, O. *Adv. Mater.* **1999**, *11* (9), 777−780.
(22) Sun, Z.; Bai, F.; Wu, H.; Schmitt, S. K.; Boye, D. M.; Fan, H. *J. Am. Chem. Soc.* **2009**, *131* (38), 13594−13595.
(23) Seifarth, O.; Schmeisser, D.; Krenek, R.; Sydorenko, A.; Stamm, M. *Prog. Solid State Chem.* **2006**, *34* (2−4), 111−119.
(24) Krenek, R.; Stamm, M.; Cimrova, V. *J. Appl. Phys.* **2008**, *103* (4), 044306/1−044306/16.
(25) Gowd, E. B.; Nandan, B.; Vyas, M. K.; Bigall, N. C.; Eychmueller, A.; Schloerb, H.; Stamm, M. *Nanotechnology* **2009**, *20* (41), 415302/1−415302/10.
(26) Kuila, B. K.; Stamm, M. *J. Mater. Chem.* **2010**, *20* (29), 6086−6094.
(27) Schwark, D.; Vezie, D.; Reffner, J.; Annis, B.; Thomas, E. *J. Mater. Sci. Lett.* **1992**, *11*, 352−355.
(28) van Zoelen, W.; Polushkin, E.; ten Brinke, G. *Macromolecules* **2008**, *41* (22), 8807−8814.
(29) Zettl, U.; Knoll, A.; Tsarkova, L. *Langmuir* **2010**, *26* (9), 6610−6617.
(30) Kriksin, Y. A.; Khalatur, P. G.; Erukhimovich, I. Ya.; ten Brinke, G.; Khokhlov, A. R. *Soft Matter* **2009**, *5* (15), 2896−2904. van Zoelen, W.; ten Brinke, G. *Soft Matter* **2009**, *5* (8), 1568−1582.
(31) Supramolecular materials based on hydrogen-bonded polymers: ten Brinke, G.; Ruokolainen, J.; Ikkala, O. *Adv. Polym. Sci.* **2007**, *207*, 113−177.
(32) Ligthart, G. B. W. L.; Scherman, O. A.; Sijbesma, R. P.; Meijer, E. W. *Macromol. Eng.* **2007**, *1*, 351−399.
(33) Heywang, G.; Jonas, F. *Adv. Mater.* **1992**, *4* (2), 116−18.
(34) Sun, J.; Zhang, B.; Katz, H. E. *Adv. Funct. Mater.* **2011**, *21* (1), 29−45.
(35) Roncali, J. *Electrochem. Commun.* **2000**, *2*, 72−76.
(36) Stephan, O.; Schottland, P.; Le Gall, P.-Y.; Chevrot, C.; Mariet, C.; Carrier, M. *J. Electroanal. Chem.* **1998**, *443* (2), 217−22.
(37) Kim, S.; Taya, M. *Electrochim. Acta* **2010**, *55* (19), 5307−5311.
(38) Welsh, D. M.; Kumar, A.; Meijer, E. W.; Reynolds, J. R. *Adv. Mater.* **1999**, *11* (16), 1379−1382.
(39) Coleman, M. M.; Graf, J. F.; Painter, P. C. *Specific Interactions and the Miscibility of Polymer Blends*; Technomic: Lancaster, PA, 1991.
(40) Cesteros, L. C.; Meaurio, E.; Katime, I. *Macromolecules* **1993**, *26*, 2323.
(41) Cesteros, L. C.; Isasi, J. R.; Katime, I. *Macromolecules* **1993**, *26*, 7256.
(42) Cesteros, L. C.; Jose', L.; Katime, I. *Polymer* **1995**, *36*, 3183.
(43) Takahashi, H.; Mamola, K.; Plyler, E. K. *J. Mol. Spectrosc.* **1966**, *21*, 217.
(44) Plate, N. A.; Shibaev, V. P. *Comb-Shaped Polymers and Liquid Crystals*; Plenum Press: New York, 1987.
(45) Ruokolainen, J.; Torkkeli, M.; Serimaa, R.; Vahvaselkae, S.; Saariaho, M.; ten Brinke, G.; Ikkala, O. *Macromolecules* **1996**, *29* (20), 6621−6628.
(46) Lock, J. P.; Im, S. G.; Gleason, K. K. *Macromolecules* **2006**, *39* (16), 5326−5329.
(47) Hamley, I. W. Introduction to Block Copolymers. In *Developments in Block Copolymer Science and Technology*; Hamley, I. W., Ed.; John Wiley & Sons: New York, 2004.
(48) Israelachvili, J. *Intermolecular and Surface Forces*, 2nd ed.; Academic Press: New York, 1991; pp 57−63.
(49) Horcas, I.; Fernandez, R.; Gomez-Rodriguez, J. M.; Colchero, J.; Gomez-Herrero, J.; Baro, A. M. *Rev. Sci. Instrum.* **2007**, *78*, 013705.

Macromolecules

Article

pubs.acs.org/Macromolecules

Thermodynamic and Structural Changes in Ion-Containing Symmetric Diblock Copolymers: A Small-Angle X-ray Scattering Study

Ilja Gunkel and Thomas Thurn-Albrecht*

Institut für Physik, Martin-Luther-Universität Halle-Wittenberg, 06099 Halle, Germany

Supporting Information

ABSTRACT: We present temperature-dependent SAXS measurements on symmetric poly(styrene-*block*-2-vinylpyridine) and poly(styrene-*block*-ethylene oxide) with added lithium triflate. Salt doping led to a strong increase of the order−disorder transition temperatures and increased domain spacings. Based on a detailed analysis of the scattering data close to the order−disorder transition, three contributions to the structural changes can be distinguished: an increased incompatibility between the different monomers, the additional volume of the added salt, and chain stretching due to coordination between polymer and salt. At the phase transition, i.e. at constant interaction parameter χ, for low concentrations the increase in domain size is quantitatively explained by the volume of the added salt, and at higher concentrations chain stretching sets in. Structural and thermodynamic effects are considerably stronger in PEO than in P2VP.

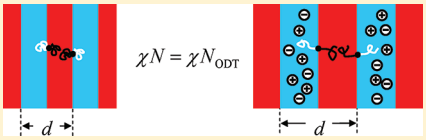

INTRODUCTION

Block copolymers with added ions which selectively dissolve in one block became of interest recently as nanostructured polymer electrolytes for use in batteries or fuel cells.[1−3] In the microphase-separated state such a system offers the possibility to simultaneously optimize different properties which would normally exclude each other. One block, being in a solid state, can give mechanical strength while the other block, typically in the liquid state, can be designed to achieve good ion transport.[4,5] Several studies on different ion-containing block copolymers have shown that the addition of salt also strongly changed the thermodynamic and structural properties. In the ordered state addition of salt induced modifications of the phase behavior and large increases in domain spacing.[6−11] These changes were attributed to an increased value of the interaction parameter χ due to the added salt, based on the established relation $d \sim aN^{2/3}\chi^{1/6}$ which relates domain spacing d with χ and is valid in the strong segregation limit.[6−8,11] Here N is the degree of polymerization and a the segment length. Similar conclusions were drawn from temperature-dependent studies in the weak segregation regime showing strongly increased order-to-disorder transition temperatures and again increased domain spacings.[6,7,12−15] Wang et al.[16] quantitatively analyzed the temperature dependence of χ from scattering experiments on ion-complexed block copolymers in the disordered state in the framework of the Leibler theory.[17] For their analysis, which confirmed the salt-induced increase of χ, they also had to assume salt-induced changes of the segment lengths. For pure block copolymers it is well-known that also in the weak segregation regime the domain spacing respectively the position of the peak in the structure factor depends on the incompatibility. Thus, an increase of N[18,19] and a decrease in temperature, leading to an increase of χ, were found to result in chain stretching.[20−26] Recently, in a theoretical study[27] significant changes in χ were predicted also for polymer blends with added ions. On the other hand, changes in structure can also be related to changes in conformation directly caused by coordination of ions with polymer chains. Lee et al.[13,28] presented direct evidence for such an effect. They demonstrated that coordination can either induce an increase or a decrease of the domain spacing depending on the type of coordination (inter- vs intramolecular coordination). Also, as a third point it should be taken into account that the additional volume of the added salt leads to an increase of the domain spacing. In general, separation of the above-mentioned different possible causes for chain stretching is difficult.

We here present detailed measurements of two block copolymers, poly(styrene-*block*-2-vinylpyridine) (PS−P2VP) and poly(styrene-*block*-ethylene oxide) (PS−PEO), both doped with $LiCF_3SO_3$, in the vicinity of the order−disorder transition, together with an analysis of the scattering data which allows partial separation of the different salt-induced effects. As a starting point we assume that also for ion-containing block copolymers the value of the incompatibility at the order−disorder transition is constant and, in particular, independent of salt concentration. We will show experimental evidence that this a reasonable assumption. On the basis of this approach, we were able to separate chain stretching originating from an increased incompatibility from the other effects by comparing values of the domain spacing directly at the order−disorder transition. As we will show, for low concentrations the increase in domain size can be quantitatively explained by the volume of the added salt, while at higher concentrations additional chain stretching sets in. The analysis of the transition temperatures as a function of

Received: June 19, 2011
Revised: November 5, 2011
Published: December 16, 2011

salt concentration shows that the salt-induced changes in χ are much larger for PEO than for P2VP.

THEORY

Ordering Transition. The local interactions in block copolymer melts are described by an interaction parameter χ with a temperature dependence

$$\chi = \frac{A}{T} + B \tag{1}$$

For ion-containing block copolymers it is often assumed that the ions, which are dissolved in only one of the blocks, simply modify the segmental interactions such that the whole system can still be described as a binary system with a new effective interaction parameter χ_{eff}

$$\chi_{\mathrm{eff}}(x_{\mathrm{m}}) = \frac{A(x_{\mathrm{m}})}{T} + B(x_{\mathrm{m}}) \tag{2}$$

where x_{m} denotes the molar ratio between ions and the monomers of the ion-containing block. As already mentioned in the Introduction, an increased value of $\chi_{\mathrm{eff}} > \chi$ should lead to an increased value of domain spacing $d(\chi_{\mathrm{eff}})$, even at constant temperature. Generally, the domain spacing d in ion-containing symmetric block copolymers should therefore depend on the salt concentration (molar ratio) x_{m} as follows:

$$d = d(\chi_{\mathrm{eff}}(x_{\mathrm{m}}), x_{\mathrm{m}}) \tag{3}$$

On the one hand, there is an explicit dependence on x_{m} originating from either conformational changes or from the additional volume of the salt. On the other hand, d implicitly depends on x_{m} via the modified segmental interactions in the ion-containing block copolymer that are described by $\chi_{\mathrm{eff}}(x_{\mathrm{m}})$. We propose to separate implicit and explicit effects based on simple arguments from the thermodynamics of block copolymers. As originally shown by Leibler,[17] there is a critical point at $(\chi N)_{\mathrm{ODT}} = 10.495$ at which a symmetric diblock copolymer melt undergoes a second-order phase transition from the disordered to a lamellar phase. This scenario was later modified by Fredrickson and Helfand,[29] who showed that fluctuations induce a weakly first-order phase transition and shift the transition to a larger $(\chi N)_{\mathrm{ODT}} = 10.495 + 41.022\bar{N}^{-1/3}$, where $\bar{N} \equiv Na^6v^{-2}$ is the invariant polymerization index (a and v are the statistical segment length and volume, respectively). In any case, if the added salt only changes χ, the value of $(\chi N)_{\mathrm{ODT}}$, i.e., the incompatibility at the order−disorder transition, remains unchanged and independent of salt concentration.

$$(\chi_{\mathrm{eff}}N)_{\mathrm{ODT}} = \mathrm{const} \tag{4}$$

Consequently, salt-induced changes of the domain spacing at the order−disorder transition should obey the following equation:

$$\begin{aligned}
&\frac{\mathrm{d}}{\mathrm{d}x_{\mathrm{m}}} d(\chi_{\mathrm{eff}}(x_{\mathrm{m}}), x_{\mathrm{m}})\Big|_{\mathrm{ODT}} \\
&= \frac{\partial}{\partial \chi_{\mathrm{eff}}} \mathrm{d} \frac{\partial}{\partial x_m} \chi_{\mathrm{eff}}\Big|_{\mathrm{ODT}} + \frac{\partial}{\partial x_{\mathrm{m}}} \mathrm{d}\Big|_{\mathrm{ODT}} \\
&\equiv \frac{\partial}{\partial x_{\mathrm{m}}} \mathrm{d}(x_{\mathrm{m}})\Big|_{\mathrm{ODT}}
\end{aligned} \tag{5}$$

Here $(\partial \chi_{\mathrm{eff}}/\partial x_{\mathrm{m}})|_{\mathrm{ODT}} = 0$ according to eq 4. The remaining contribution $(\partial/\partial x_{\mathrm{m}})\mathrm{d}(x_m)|_{\mathrm{ODT}}$ represents both changes of the domain spacing related to conformational changes of the ion-containing blocks and changes due to the additional volume of the salt.

Structure Factor of Block Copolymers in the Disordered State. According to Leibler,[17] in the mean-field approximation the structure factor $S(q)$ in the disordered state is given by

$$S^{-1}(q) = N^{-1}F(x, f) - 2\chi \tag{6}$$

where $f = N_{\mathrm{A}}/N$ describes the composition of the copolymer and $x = q^2R_{\mathrm{g}}^2$ with R_{g} denoting the radius of gyration of a Gaussian chain. The function $F(x,f)$ was calculated by Leibler in the framework of the random phase approximation and is given in terms of Debye functions. The function $F(x,f)$ has a minimum at x^*, corresponding to a maximum in the structure factor $S(q)$ at a scattering vector q^*. The maximum of the structure factor diverges at the spinodal where $F(x^*,f) = 2(\chi N)_{\mathrm{s}}$. In case of a symmetric ($f = 1/2$) composition $x^* = 3.7852$ and $(\chi N)_{\mathrm{s}} = 10.495$. The period of the lamellar phase ($d = 2\pi/q^*$) is predicted to be $d \approx 3.23R_{\mathrm{g}}$.

Accounting for composition fluctuations, Fredrickson and Helfand[29] corrected the structure factor $S(q)$ in a Hartree approximation. The corrected structure factor $S(q)$ possesses the same form as Leibler's structure factor and satisfies[30]

$$S^{-1}(q) = N^{-1}F(x, f) - 2\chi_{\mathrm{ren}} \tag{7}$$

with a renormalized interaction parameter χ_{ren}, given by

$$\chi_{\mathrm{ren}} = \chi - \frac{v}{2b^3} c^3 g \lambda N^{-2} [N^{-1}F(x^*, f) - 2\chi_{\mathrm{ren}}]^{-1/2} \tag{8}$$

where c, g, and λ are constants. In case of a symmetric composition these constants attain the following values[29]

$$\begin{aligned}
g &= \frac{3x^*}{2\pi} = 1.8073, \\
c &= \left[\frac{1}{3} x \frac{\partial^2 F}{\partial x^2}\right]^{1/2}_{x=x*} = 1.1019, \\
\lambda &= 106.19
\end{aligned} \tag{9}$$

Please note that the shape of the scattering curve and the position of the maximum q^* remain unchanged. The parameter χN, however, is renormalized, and thus the peak height changes such that $S(q^*)$ is finite at the transition. Please note that neither in eq 6 nor in eq 7 the value x^* depends on χ. Hence, a change in peak position due to chain stretching is not described within the framework of these theories.

Expanding the function $F(x,f)$ in eq 6 around its extremum at q^* the structure factor $S(q)$ can be approximated as[21,31]

$$S(q) \approx \frac{S(q^*)}{1 + \xi^2(q - q^*)^2} \tag{10}$$

dx.doi.org/10.1021/ma201334h | Macromolecules 2012, 45, 283−291

where the correlation length ξ and the peak height $S(q^*)$ are given by

$$\xi^2 = \frac{c^2 N b^2}{2[(\chi N)_s - \chi N]}, \quad S(q^*) = \frac{N}{2[(\chi N)_s - \chi N]} \tag{11}$$

Inserting the temperature dependence of the Flory–Huggins interaction parameter χ, which is given by eq 1, leads to the following relations:

$$\frac{1}{\xi^2} \sim \frac{1}{T_s} - \frac{1}{T}, \quad \frac{1}{S(q^*)} \sim \frac{1}{T_s} - \frac{1}{T} \tag{12}$$

ξ^{-2} and $S^{-1}(q^*)$ show the same linear dependence on $1/T$ (T_s denotes the spinodal temperature). In the vicinity of the phase transition, however, one expects deviations from the linear dependence on $1/T$ because of the fluctuation correction according to eqs 7 and 8.

Model Function. All scattering data were fitted at temperatures $T \geq T_{ODT}$ as well as $T < T_{ODT}$ to the following function:

$$y = y_0 + \frac{2A}{\pi} \frac{w}{4(x - x_c)^2 + w^2} + bx^c \tag{13}$$

In addition to a Lorentzian function, we used a power law in eq 13 to take the background scattering at low angles into account.[21] The fit parameters were the offset y_0, the area A of the Lorentz peak, the width w of the peak, its position x_c, the power law amplitude b, and the exponent c.

Comparing eq 13 with eq 11, one finds the following relations:

$$\frac{w^2}{4} = \frac{2[(\chi N)_s - (\chi N)]}{c^2 N b^2}, \quad \frac{\pi w}{2A} = \frac{2[(\chi N)_s - (\chi N)]}{N} \tag{14}$$

So the interaction parameter χN is essentially given by the inverse peak height $(2A/\pi w)^{-1}$ and width squared w^2 while the radius of gyration of the chain R_g is given by the inverse peak position x_c^{-1}.

EXPERIMENTAL SECTION

Materials. We used symmetric poly(styrene-*block*-2-vinylpyridine) (PS–P2VP) block copolymers and symmetric poly(styrene-*block*-ethylene oxide) (PS–PEO) block copolymers from Polymer Source. The molecular and thermodynamic characteristics of PS–P2VP and PS–PEO are shown in Table 1. SAXS patterns of both materials at room temperature in the ordered state show higher order reflections indicative of lamellar structures (see Supporting Information). Propylene glycol methyl ether acetate (PGMEA) obtained from Aldrich was filtered using 0.2 μm syringe filters. Lithium triflate ($LiCF_3SO_3$) from Aldrich was dried at 170 °C under vacuum for 24 h before use.

Table 1. Characteristics of the Block Polymers Used in This Study[a]

polymer	M_n [g mol^{-1}]	f_{PS}	PDI	T_{ODT} [°C]	d_{ODT} [nm]
PS–PEO	9500–8000	0.54	1.07	145 ± 2	16.7
PS–P2VP	8200–8300	0.50	1.09	161 ± 3	13.8

[a]The values of the number-average molecular weight (M_n) and the polydispersity index (PDI) were provided by the supplier. f_{PS} denotes the composition of the block copolymer. The order–disorder transition temperature (T_{ODT}) and the corresponding value of the domain spacing (d_{ODT}) were determined using small-angle X-ray scattering (data shown in Figures 2 and 3). Scattering patterns in the ordered state indicative of a lamellar microstructure are shown in the Supporting Information.

Sample Preparation. To prepare ion-containing block copolymers, we at first dissolved block copolymer (PS–P2VP/PS–PEO) and lithium triflate in PGMEA, followed by continuous stirring and moderate heating at 70 °C until the solutions became clear. Polymer and salt solutions were then mixed at a given ratio. Subsequently, most of the PGMEA was evaporated by heating again to 70 °C for several days. During this process precipitation of the salt did not occur. Before the SAXS measurements the samples were heated to 140 °C under vacuum for 24 h to remove remaining PGMEA and water. PS–P2VP was $LiCF_3SO_3$-doped at mass ratios from 5.3×10^{-3} to 4.3×10^{-2} and PS–PEO at mass ratios from 2.0×10^{-3} to 2.3×10^{-2}. Assuming that no salt was dissolved in PS, these values correspond to molar ratios of $[LiCF_3SO_3]$:[2VP] = 1.32–5.83% and $[LiCF_3SO_3]$:[EO] = 0.23–1.31%. We used different methods to keep the samples in the X-ray beam during the SAXS experiments. In the case of PS–P2VP the sample (thickness some 10 μm) was held on a simple aluminum foil with a thickness of 12.5 μm. In the case of PS–PEO aluminum disks with holes of 1 mm and a thickness of 2 mm were used to carry the samples.

Small-Angle X-ray Scattering (SAXS). All SAXS measurements were performed using an X-ray generator of rotating anode type with Cu target from Rigaku, operated at 2.4 kW. A confocal optics from Osmic provided monochromatic Cu Kα radiation. The X-ray beam was collimated by a system of three pinholes. At the position of the sample the size of the beam was ~350 μm. The flight path was fully evacuated, and the scattered radiation was detected by a Bruker Hi-Star multiwire proportional chamber. The data were collected as frames of 1024 × 1024 pixels and later on calibrated using silver behenate. The accessible q-range was 0.01 Å^{-1} < q < 0.14 Å^{-1}. To control the temperature of the samples, a hot stage from Linkam was used. Heat conduction paste was used for good thermal contact between the holder and the hot stage in vacuum. Exposure times were 500 s for PS–P2VP and 1200 s in the case of PS–PEO. Before every measurement the samples were given 60 s (PS–P2VP) and 300 s (PS–PEO) at the new temperature to equilibrate. Scattering data for the different ion-containing block copolymer samples were taken within a temperature range of about ±20 °C around the respective $T_{ODT}(x_m)$. Here $T_{ODT}(x_m)$ denotes the salt concentration-dependent temperature of the order–disorder transition. Measurements were generally taken during cooling runs. After each measurement the temperature was reduced by 3 K at a rate of 5 K min^{-1} (neat PS–P2VP was exceptionally measured in 5 K steps).

RESULTS AND DISCUSSION

Neat PS–P2VP and PS–PEO. Figure 1a shows SAXS profiles obtained for neat PS–P2VP at different temperatures during stepwise cooling. At the ordering transition the peak width decreased discontinuously accompanied by an increase of the peak intensity. For a quantitative analysis of the scattering data we fitted the SAXS profiles to eq 13 as can be seen exemplarily in Figure 1b for two curves in the immediate vicinity of the transition. To determine T_{ODT}, the peak width squared and the reciprocal peak intensity were plotted as a function of the reciprocal temperature as can be seen in Figure 2a for neat PS–P2VP. The discontinuity similarly observed in both curves corresponds to T_{ODT}.[20] We found T_{ODT} = 161 ± 3 °C for neat PS–P2VP, which is consistent with reported values for PS–P2VP of similar molecular weight.[32] The peak position decreased continuously with decreasing temperature. This known phenomenon of an increased domain spacing at lower temperatures[20−26] can be attributed to chain stretching caused by an increasing segmental interaction parameter χ. Figure 3a shows the peak width squared and the reciprocal peak intensity versus the reciprocal temperature for neat PS–PEO with T_{ODT}

dx.doi.org/10.1021/ma201334h | Macromolecules 2012, 45, 283–291

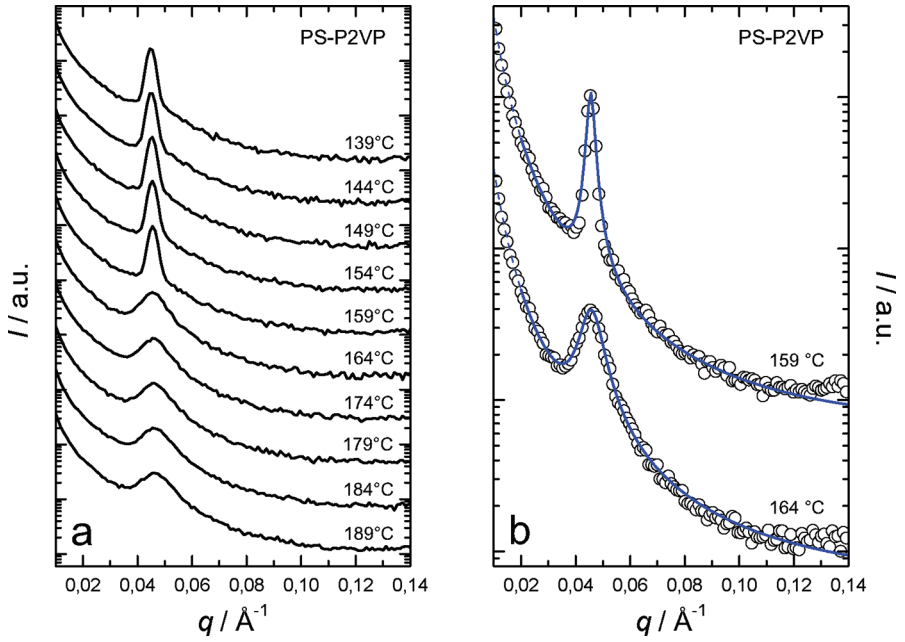

Figure 1. (a) Temperature dependence of the SAXS profiles for neat PS−P2VP in the vicinity of the order−disorder transition. (b) SAXS profiles (open circles) of neat PS−P2VP in the disordered (T = 164 °C) and the ordered state (T = 159 °C). The solid lines were obtained by curve fitting SAXS profiles to eq 13. Curves are shifted vertically for clarity.

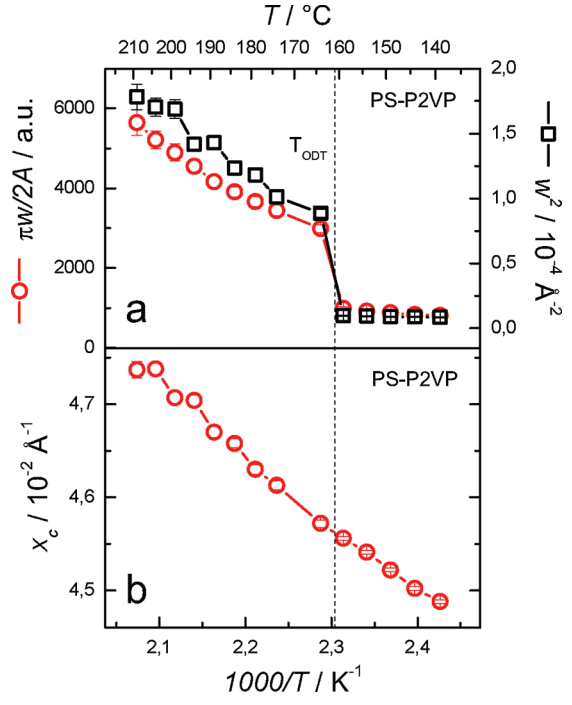

Figure 2. Scattering parameters as obtained from curve fitting SAXS profiles to eq 13 for neat PS−P2VP. (a) Square of peak width w^2 and reciprocal peak height $\pi w/2A$ as a function of reciprocal temperature. (b) Peak position x_c versus reciprocal temperature. Error bars represent fitting errors.

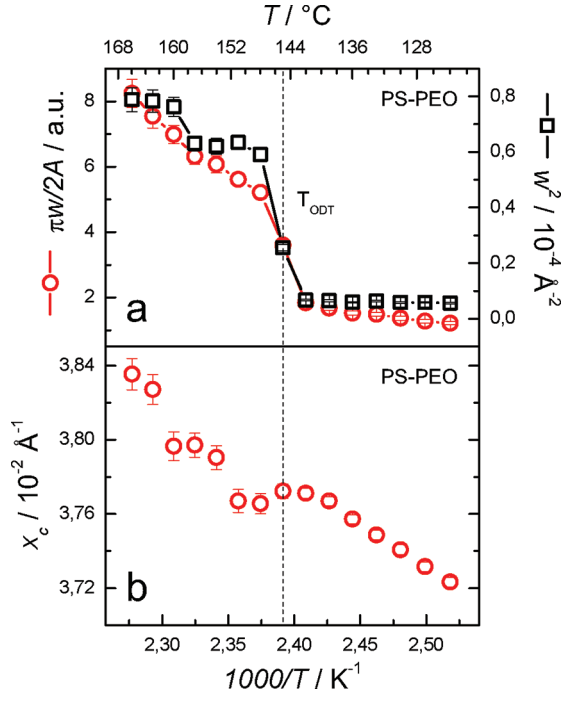

Figure 3. (a) Neat PS−PEO. Square of peak width w and inverse peak maximum $\pi w/2A$ vs inverse temperature. (b) Peak position x_c vs inverse temperature. Error bars represent fitting errors.

at 145 ± 2 °C. For neat PS−PEO we also found a decreasing peak position with decreasing temperature as can be seen in Figure 3b. For both systems the value of the peak width w in the ordered phase corresponds to the resolution of the scattering setup. Please note that the fitting errors of the parameters shown in Figures 2 and 3 are smaller than the statistical uncertainties of each measurement and will be omitted in the following.

PS−P2VP with $LiCF_3SO_3$. Figure 4 shows the SAXS results for $LiCF_3SO_3$-doped PS−P2VP with molar ratios between 1.32% and 5.83%. In Figure 4a, the peak width squared is plotted as a function of the reciprocal temperature. Here and in the following we only consider the peak width since this parameter is more robust than the peak intensity. For each sample T_{ODT} was determined as shown in Figure 2. The value of the squared width at the order−disorder transition is independent of the salt concentration. The strong increase of T_{ODT} with

dx.doi.org/10.1021/ma201334h | Macromolecules 2012, 45, 283−291

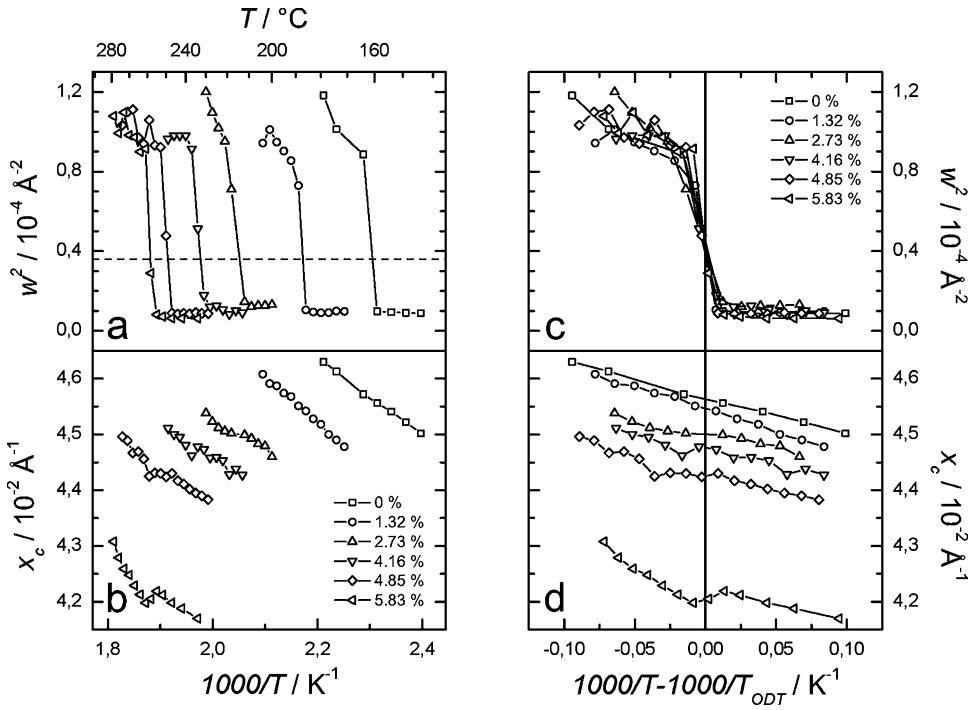

Figure 4. Results of SAXS data analysis for $LiCF_3SO_3$-doped PS−P2VP (molar ratios given in the legend). (a) Peak width squared w^2 as a function of reciprocal temperature. The dashed line indicates the value of w^2 at ODT. (b) Peak position x_c versus reciprocal temperature. (c) Peak width squared w^2 versus reduced reciprocal temperature $1000/T - 1000/T_{ODT}$. (d) Peak position x_c versus reduced reciprocal temperature.

increasing salt content can be attributed to the stronger incompatibility between the PS blocks and the ion-containing P2VP blocks. Figure 4b shows the peak position x_c versus the reciprocal temperature. For all salt concentrations the peak position decreased with decreasing temperature. The x_c curves run approximately parallel to each other with curves of higher salt concentrations at lower x_c values. To analyze the salt-induced changes further, we compare the values of the domain spacing at the order−disorder transition d_{ODT} as discussed above (cf. eqs 3−5). We replotted the squared widths from Figure 4a versus a reduced reciprocal temperature $1000/T - 1000/T_{ODT}$ as shown in Figure 4c. Please note the reduced reciprocal temperature $1000/T - 1000/T_{ODT}$ corresponds to $\chi N - (\chi N)_{ODT}$ according to eqs 1 and 2. In Figure 4c, the curves of the squared widths coincide—in particular at T_{ODT}—indicating a constant value of χN at the transition (cf. eq 14). This result confirms our assumption that $LiCF_3SO_3$-doped PS−P2VP can be treated as a block copolymer with an effective interaction parameter χ_{eff} in the range of salt concentrations studied here. In Figure 4d, the peak positions x_c from Figure 4b were replotted versus $1000/T - 1000/T_{ODT}$. The x_c curves do not overlap. According to eqs 4 and 5, the remaining differences in the domain spacings d_{ODT} at T_{ODT} should originate from direct effects of the salt, i.e., coordination or effect of added volume. For a discussion of these direct effects, we plotted T_{ODT} and d_{ODT} in Figure 5 vs x_m. Both parameters increase with increasing salt concentration. To distinguish between coordination and volume effects, we assumed in a first approximation that the volume of the polymer and the volume of the salt simply add up in the mixture. In this case the increase of the domain spacing d_{ODT} due to the volume of the added salt can be estimated as follows:

$$\frac{d}{d_{BCP}} = 1 + \frac{V_{salt}}{V_{BCP}} = 1 + x_m \frac{\rho_{BCP}}{\rho_{salt}} \qquad (15)$$

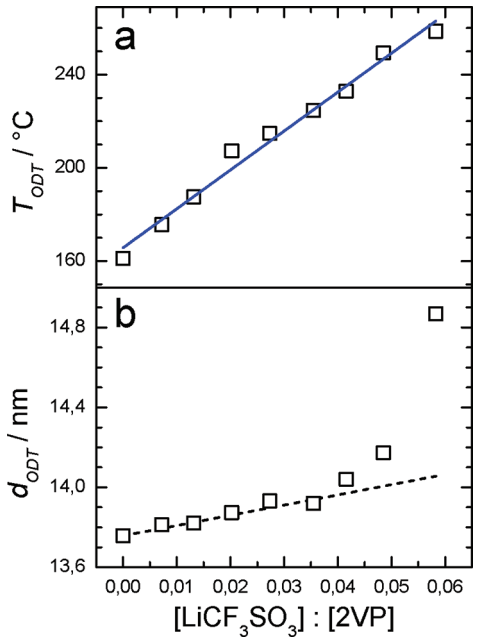

Figure 5. (a) The order−disorder transition temperature T_{ODT} (as shown by the open circles) for $LiCF_3SO_3$-doped PS−P2VP as a function of the molar ratio between $LiCF_3SO_3$ molecules and 2VP monomers. The corresponding linear fit is shown by the straight line and yields $T_{ODT} = 166 \pm 3$ °C + 1669 ± 78 °C × x_m, where x_m denotes the molar ratio. (b) The domain spacings $d = 2\pi/x_c$ (open squares) at the corresponding T_{ODT} are shown versus the molar ratio. The dashed line represents the estimated increase of the domain spacing due to the volume of the added salt.

Here d_{BCP} denotes the domain spacing in the neat block copolymer, V_{BCP} its volume, and x_m the mass ratio known from the sample preparation. For the densities of $LiCF_3SO_3$[33] and

dx.doi.org/10.1021/ma201334h | Macromolecules 2012, 45, 283−291

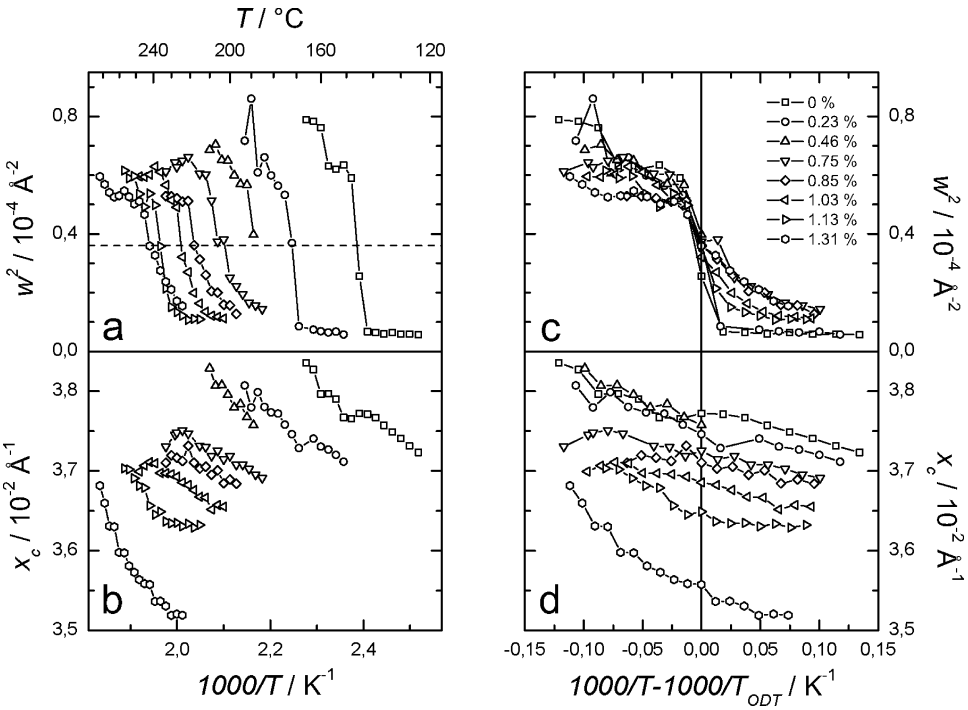

Figure 6. Results of SAXS data analysis for $LiCF_3SO_3$-doped PS−PEO (molar ratios given in the legend). (a) Peak width squared w^2 as a function of reciprocal temperature. The dashed line indicates the value of w^2 at ODT. (b) Peak position x_c versus reciprocal temperature. (c) Peak width squared w^2 versus reduced reciprocal temperature $1000/T - 1000/T_{ODT}$. (d) Peak position x_c versus reduced reciprocal temperature.

PS−P2VP[a] we used the values ρ_{salt} = 1.9 g cm^{-3} and ρ_{BCP} = 0.96 g cm^{-3}. At low salt concentrations up to ≈4% the values of d_{ODT} coincide with the increase of d according to eq 15 and above the increase is stronger. We attribute this effect to changes of chain conformation which could e.g. arise from coordination of 2VP with lithium ions.

PS−PEO with $LiCF_3SO_3$. Generally, adding $LiCF_3SO_3$ to PS−PEO induced qualitatively quite similar effects as in PS−P2VP. For example, in Figure 6a,b the SAXS results for $LiCF_3SO_3$-doped PS−PEO show an increase of T_{ODT} as well as an increase of the domain spacing with increasing salt concentration. However, the corresponding changes of T_{ODT} in PS−PEO occurred at lower salt concentrations than in PS−P2VP. For a well-defined analysis of salt-induced thermodynamic and conformational changes in PS−PEO we again plotted the SAXS data as a function of a reduced reciprocal temperature $1000/T - 1000/T_{ODT}$ as shown in Figure 6c,d. In Figure 6c, the peak widths squared showed a common value at T_{ODT}, $w^2(T_{ODT})$ = 3.6 × 10^{-5} Å^2, for all salt concentrations. This in particular corresponds to the value of $w^2(T_{ODT})$ for PS−P2VP. In Figure 6c the peak widths squared again overlapped above and at T_{ODT}, while below T_{ODT} the curves deviate from each other. It seems that for the salt containing systems the size of the ordered domain is limited. These last effects are beyond the scope of this work. Figure 6d shows that the values of the peak center x_c at T_{ODT} decrease with increasing salt concentration—analogously to the behavior in PS−P2VP. Figure 7 shows T_{ODT} and d_{ODT} vs x_m. The increase of T_{ODT} with x_m is about 4 times stronger in PS−PEO than in PS−P2VP. Figure 7b shows again d_{ODT} as a function of the molar ratio $[LiCF_3SO_3]$:[EO] together with the estimated effect of added salt volume (ρ_{salt} = 1.9 g cm^{-3} and ρ_{BCP} = 0.97 g cm^{-3})[b].[33] Now, at molar ratios above ≈1% the values of the domain spacing significantly deviate from the trivial volume

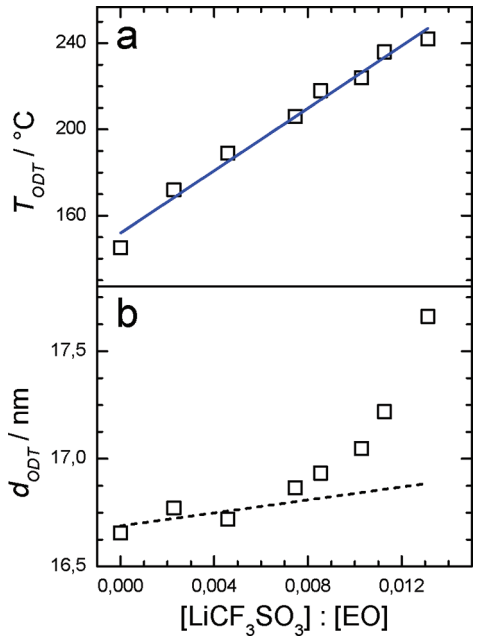

Figure 7. (a) Order−disorder transition temperature T_{ODT} for $LiCF_3SO_3$-doped PS−PEO as a function of the molar ratio between $LiCF_3SO_3$ molecules and EO monomers. Linear fit is shown by the straight line and yields T_{ODT} = 152 ± 3 °C + 7247 ± 386 °C × x_m where x_m denotes the molar ratio between the $LiCF_3SO_3$ molecules and the EO monomers. (b) The domain spacings $d = 2\pi/x_c$ at the corresponding T_{ODT} are shown versus the molar ratio between $LiCF_3SO_3$ and the EO monomers. The dashed line represents the increase of the domain spacing due to the volume of the added salt.

increase, indicating salt-induced chain stretching.[c] It might be surprising that also in PS−PEO changes of the chain conformation due to coordination with lithium ions should

dx.doi.org/10.1021/ma201334h | Macromolecules 2012, 45, 283−291

increase the domain spacing. From molecular dynamics simulations as well as small-angle neutron scattering experiments on PEO/LiI melts it was shown that the (overall) radius of gyration of PEO chains decreased due to coordination with lithium ions.[35,36] However, the detailed simulation analysis revealed that those chains with one to three EO-monomers coordinating with lithium ions can actually increase the radius of gyration while for numbers beyond three the radius of gyration decreased. Our results indicate that in PS−PEO block copolymers changes of the chain conformation due to coordination with lithium ions are different than in PEO homopolymers (suggesting e.g. a multichain coordination in block copolymers instead of the homopolymer single-chain coordination). Further (theoretical) work is needed to elaborate these differences between block copolymers and homopolymers. Interestingly, Gomez et al.[37] showed that a change of the chain conformation also influences the coordination between lithium ions and PEO in mixtures of PS−PEO and LiTFSI. By means of energy filtered transmission electron microscopy, they observed that lithium ions were increasingly confined to the middle of the PEO lamellae with increasing values of χN. Please note, though, that our observations were performed at constant χN.

The direct comparison of the salt-induced changes of T_{ODT} shown in Figure 8 suggests that the interaction with the salt is

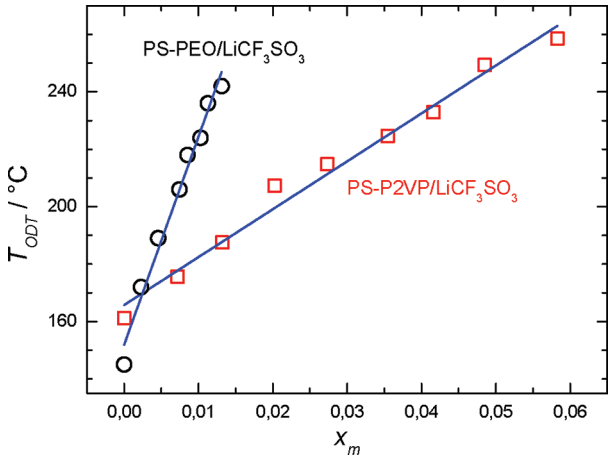

Figure 8. The order−disorder transition temperature T_{ODT} as a function of the molar ratio x_m in $LiCF_3SO_3$-doped PS−P2VP and PS−PEO block copolymers.

much stronger in the PEO-containing block copolymer than in the other system. To further analyze this effect, we suggest an approximation which eliminates the effect of molecular weight and allows an approximate determination of the effect of the salt on the interaction parameter χ. Assuming that N is constant, eqs 1, 2, and 4 reduce to the following relation

$$\frac{A}{T^0_{ODT}} + B = \frac{A(x_m)}{T_{ODT}(x_m)} + B(x_m) \tag{16}$$

where $T^0_{ODT} \equiv T_{ODT}(x_m = 0)$ denotes the order−disorder transition temperature of the neat block copolymers. The values of A and B for the neat block copolymers are known from the literature:[32,34] $\chi_{S-EO} = -7.03 \times 10^{-3} + 21.3/T$ and $\chi_{S-2VP} = V_{ref}(T)(-1.791 \times 10^{-4} + 0.478/T)$. Here $V_{ref}(T)$ denotes a temperature-dependent reference molar volume. For both systems we obtained a linear dependence of T_{ODT} on salt concentration:

$$T_{ODT}(x_m) = T^0_{ODT} + mx_m \tag{17}$$

To determine the values for $\chi_{eff}(x_m)$, we assume that the enthalpic changes in $\chi_{eff}(x_m)$ dominate and therefore set the entropic contribution as constant, i.e., $B(x_m) \equiv B$ in eq 16. This is certainly an approximation, but it is clear that there must be large changes in solvation energy[27] of $LiCF_3SO_3$ in the mixed and demixed state of the block copolymer which should show up in $A(x_m)$. Equation 16 then reduces to

$$A(x_m) = A\frac{T_{ODT}(x_m)}{T^0_{ODT}} \tag{18}$$

Inserting eq 18 into eq 2 leads to the following expression for $\chi_{eff}(x_m)$

$$\chi_{eff}(x_m) = \frac{A}{T}\left(\frac{T_{ODT}(x_m)}{T^0_{ODT}}\right) + B = \chi^0 + \frac{A}{T}\left(\frac{mx_m}{T^0_{ODT}}\right) \tag{19}$$

Above, eqs 1 and 17 were inserted to obtain the final expression for $\chi_{eff}(x_m)$. The change of the interaction parameter $\Delta\chi = \chi_{eff} - \chi^0$ is then given by

$$\Delta\chi(x_m) = \frac{A}{T}\left(\frac{mx_m}{T^0_{ODT}}\right) \tag{20}$$

$\Delta\chi$ is shown in Figure 9 for the systems studied here.[d] Indeed, the interaction parameter in PS−PEO increases stronger with

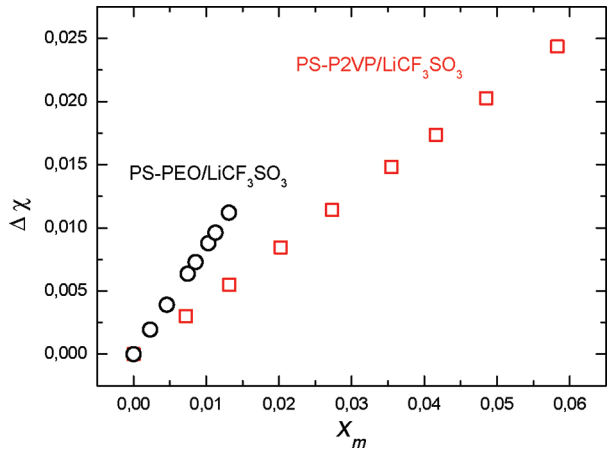

Figure 9. The change $\Delta\chi$ of the interaction parameter at $T = T^0_{ODT}$ due to $LiCF_3SO_3$ doping as a function of the molar ratio x_m in PS−P2VP and PS−PEO block copolymers.

increasing $LiCF_3SO_3$ concentration than in case of PS−P2VP. This result reflects the strong coordination of lithium ions with oxygen in PEO. Our values for $\Delta\chi$ are significantly smaller than values in previous publications.[10,11] Young et al.[11] calculated $\Delta\chi$ based on domain spacing data and the relationship between domain spacing and $\Delta\chi$ in the strong segregation regime. As we have shown in the present work, the domain spacing also contains contributions from coordination and salt volume which could account for larger values in $\Delta\chi$. Note that the analysis presented here is different from the analysis by

dx.doi.org/10.1021/ma201334h | Macromolecules 2012, 45, 283−291

Wanakule et al.[10,15] As mentioned, the addition of salt that selectively dissolves in one block changes the volume fraction of the copolymer system. As the value of $(\chi N)_{ODT}$, the incompatibility at the order−disorder transition, depends on the volume fraction,[17] the addition of salt also changes $(\chi N)_{ODT}$. Wanakule et al.[10,15] calculated these changes of $(\chi N)_{ODT}$ and χ_{ODT} in the framework of the Leibler theory.[17] Asymmetric block copolymers can show large changes of $(\chi N)_{ODT}$; for symmetric block copolymers, as they are used here, this effect is negligible. The effect on the value of $\Delta\chi$ in Figure 9 would be on the order 3×10^{-4} for the highest x_m considered here.

CONCLUSIONS

We analyzed the effect of salt doping on the order−disorder transition in two symmetric block copolymers, PS−P2VP and PS−PEO. Both systems can be described as effective binary systems with an an effective interaction parameter χ_{eff} which depends on the salt concentration. The results indicate that the interaction of $LiCF_3SO_3$ with PEO is considerably stronger than with P2VP. Furthermore, both block copolymers show a salt-induced change in domain spacing at the transition which was determined from the position of the peak of the structure factor. Comparing the domain spacing at the transition removes effects of χ on the chain conformation and singles out direct salt-induced effects like the volume of the added salt and additional conformational changes due to the coordination with the salt. In first order the changes in domain spacing could be quantitatively explained by the added volume of the salt, assuming volume additivity during mixing. Additional conformational effects set in only at somewhat higher concentrations (molar ratio ~1%) and are indicative of additional chain stretching. Further work is necessary to develop a theoretical understanding of this behavior. The method of analysis we propose seems generally applicable to study the effect of strongly selective additives on structure and thermodynamics of block copolymers. Examples could be ionic liquids or other strongly polar compounds.[38,39]

ASSOCIATED CONTENT

Supporting Information

Additional SAXS results and DSC analyis of the transitions occurring in the investigated materials. This material is available free of charge via the Internet at http://pubs.acs.org.

AUTHOR INFORMATION

Corresponding Author

*E-mail: thomas.thurn-albrecht@physik.uni-halle.de.

ACKNOWLEDGMENTS

This work was supported by the state Sachsen-Anhalt (research network nanostructured materials) and the International Max Planck Research School for Science and Technology of Nanostructures.

ADDITIONAL NOTES

[a]The density of PS−P2VP was approximated by its value for PS at 200 °C.[34]

[b]The density of PS−PEO was calculated using the values for PS respectively PEO at 200 °C.[34]

[c]Please note that degradation of PEO could not induce this effect since a lower molecular weight would lead to lower values of the domain spacing. GPC analysis of PS−PEO up to 200 °C did not show any indication of substantial degradation.

[d]To determine $\Delta\chi$ for PS−P2VP, $V_{ref}(T^0_{ODT} = 166\ °C) \approx 101$ mol cm^{-3} was used.

REFERENCES

(1) Armand, M.; Tarascon, J. M. *Nature* **2008**, *451*, 652−657.
(2) Deluca, N. W.; Elabd, Y. A. *J. Polym. Sci., Part B: Polym. Phys.* **2006**, *44*, 2201−2225.
(3) Soo, P.; Huang, B.; Jang, Y.; Chiang, Y.; Sadoway, D.; Mayes, A. *J. Electrochem. Soc.* **1999**, *146*, 32−37.
(4) Gray, F.; MacCallum, J.; Vincent, C.; Giles, J. *Macromolecules* **1988**, *21*, 392−397.
(5) Singh, M.; Odusanya, O.; Wilmes, G. M.; Eitouni, H. B.; Gomez, E. D.; Patel, A. J.; Chen, V. L.; Park, M. J.; Fragouli, P.; Iatrou, H.; Hadjichristidis, N.; Cookson, D.; Balsara, N. P. *Macromolecules* **2007**, *40*, 4578−4585.
(6) Epps, T.; Bailey, T.; Pham, H.; Bates, F. *Chem. Mater.* **2002**, *14*, 1706−1714.
(7) Epps, T.; Bailey, T.; Waletzko, R.; Bates, F. *Macromolecules* **2003**, *36*, 2873−2881.
(8) Wang, J.-Y.; Leiston-Belanger, J. M.; Sievert, J. D.; Russell, T. P. *Macromolecules* **2006**, *39*, 8487−8491.
(9) Wang, J.-Y.; Chen, W.; Roy, C.; Sievert, J. D.; Russell, T. P. *Macromolecules* **2008**, *41*, 963−969.
(10) Wanakule, N. S.; Virgili, J. M.; Teran, A. A.; Wang, Z.-G.; Balsara, N. P. *Macromolecules* **2010**, *43*, 8282−8289.
(11) Young, W.-S.; Epps, T. H. III *Macromolecules* **2009**, *42*, 2672−2678.
(12) Ruzette, A.; Soo, P.; Sadoway, D.; Mayes, A. *J. Electrochem. Soc.* **2001**, *148*, A537−A543.
(13) Lee, D.; Kim, H.; Kim, J.; Huh, J.; Ryu, D. *Macromolecules* **2006**, *39*, 2027−2030.
(14) Kim, B.; Ahn, H.; Kim, J. H.; Ryu, D. Y.; Kim, J. *Polymer* **2009**, *50*, 3822−3827.
(15) Wanakule, N. S.; Panday, A.; Mullin, S. A.; Gann, E.; Hexemer, A.; Balsara, N. P. *Macromolecules* **2009**, *42*, 5642−5651.
(16) Wang, J.-Y.; Chen, W.; Russell, T. P. *Macromolecules* **2008**, *41*, 4904−4907.
(17) Leibler, L. *Macromolecules* **1980**, *13*, 1602−1617.
(18) Almdal, K.; Rosedale, J.; Bates, F.; Wignall, G.; Fredrickson, G. *Phys. Rev. Lett.* **1990**, *65*, 1112−1115.
(19) Papadakis, C. M.; Almdal, K.; Mortensen, K.; Posselt, D. *Europhys. Lett.* **1996**, *36*, 289.
(20) Bates, F.; Rosedale, J.; Fredrickson, G. *J. Chem. Phys.* **1990**, *92*, 6255−6270.
(21) Holzer, B.; Lehmann, A.; Stuhn, B.; Kowalski, M. *Polymer* **1991**, *32*, 1935−1942.
(22) Stuhn, B.; Mutter, R.; Albrecht, T. *Europhys. Lett.* **1992**, *18*, 427−432.
(23) Almdal, K.; Bates, F. S.; Mortensen, K. *J. Chem. Phys.* **1992**, *96*, 9122−9132.
(24) Rosedale, J. H.; Bates, F. S.; Almdal, K.; Mortensen, K.; Wignall, G. D. *Macromolecules* **1995**, *28*, 1429−1443.
(25) Sakamoto, N.; Hashimoto, T. *Macromolecules* **1995**, *28*, 6825−6834.
(26) Almdal, K.; Mortensen, K.; Ryan, A. J.; Bates, F. S. *Macromolecules* **1996**, *29*, 5940−5947.
(27) Wang, Z.-G. *J. Phys. Chem. B* **2008**, *112*, 16205−16213.
(28) Lee, D. H.; Han, S. H.; Joo, W.; Kim, J. K.; Huh, J. *Macromolecules* **2008**, *41*, 2577−2583.
(29) Fredrickson, G.; Helfand, E. *J. Chem. Phys.* **1987**, *87*, 697−705.
(30) Bates, F. S.; Rosedale, J. H.; Fredrickson, G. H.; Glinka, C. J. *Phys. Rev. Lett.* **1988**, *61*, 2229−2232.
(31) Delacruz, M.; Sanchez, I. *Macromolecules* **1986**, *19*, 2501−2508.
(32) Zha, W.; Han, C. D.; Lee, D. H.; Han, S. H.; Kim, J. K.; Kang, J. H.; Park, C. *Macromolecules* **2007**, *40*, 2109−2119.

(33) Dinnebier, R.; Sofina, N.; Jansen, M. *Z. Anorg. Allg. Chem.* **2004**, *630*, 1613−1616.
(34) Zhu, L.; Cheng, S. Z. D.; Calhoun, B. H.; Ge, Q.; Quirk, R. P.; Thomas, E. L.; Hsiao, B. S.; Yeh, F.; Lotz, B. *Polymer* **2001**, *42*, 5829−5839.
(35) Borodin, O.; Smith, G. *Macromolecules* **1998**, *31*, 8396−8406.
(36) Annis, B.; Kim, M.; Wignall, G.; Borodin, O.; Smith, G. *Macromolecules* **2000**, *33*, 7544−7548.
(37) Gomez, E. D.; Panday, A.; Feng, E. H.; Chen, V.; Stone, G. M.; Minor, A. M.; Kisielowski, C.; Downing, K. H.; Borodin, O.; Smith, G. D.; Balsara, N. P. *Nano Lett.* **2009**, *9*, 1212−1216.
(38) Simone, P. M.; Lodge, T. P. *ACS Appl. Mater. Interfaces* **2009**, *1*, 2812−2820.
(39) Virgili, J. M.; Nedoma, A. J.; Segalman, R. A.; Balsara, N. P. *Macromolecules* **2010**, *43*, 3750−3756.

Macromolecules

Article

pubs.acs.org/Macromolecules

Directed Self-Assembly of POSS Containing Block Copolymer on Lithographically Defined Chemical Template with Morphology Control by Solvent Vapor

Yasuhiko Tada,[†,‡] Hiroshi Yoshida,[‡] Yoshihito, Ishida,[§] Tomoyasu Hirai,[§] Joan K. Bosworth,[⊥] Elizabeth Dobisz,[⊥] Ricardo Ruiz,[⊥] Mikihito Takenaka,[†] Teruaki Hayakawa,[§] and Hirokazu Hasegawa*[,†]

[†]Department of Polymer Chemistry, Graduate School of Engineering, Kyoto University, Nishikyo-ku, Kyoto 615-8510, Japan

[‡]Hitachi Research Laboratory, Hitachi Ltd., Hitachi, Ibaraki 319-1292, Japan

[§]Department of Organic and Polymeric Materials, Tokyo Institute of Technology, 2-12-1-S8-36 O-okayama, Meguro-ku, Tokyo 152-8552, Japan

[⊥]San Jose Research Center, Hitachi Global Storage Technologies, 3403 Yerba Buena Rd., San Jose, California 95135, United States

Supporting Information

ABSTRACT: Strongly segregating block copolymers (BCPs) are attractive as a means of forming 10 nm scale lithographic features. Here, we report directed self-assembly of polyhedral oligomeric silsesquioxane containing block copolymers (PMMA-*b*-PMAPOSS) with feature density multiplication to form long-range ordered arrays of dots having areal densities of ~4 tera dots per square inch via controlled solvent annealing. The degree of swelling of PMMA-*b*-PMAPOSS thin film during the carbon disulfide solvent annealing was optimized to give the polymer chain mobility to form the desired microdomain structure. Because the annealing solvent is not fully neutral to the components of the BCP, the types of microstructures formed depend strongly on the degree of swelling. We demonstrated that the directed self-assembly with 4× density multiplication of the chemically patterned template can be performed successfully under the optimized condition of solvent annealing and hexagonally packed dots array with 12 nm lattice spacing was produced. We also showed that the microdomain structures formed by solvent-annealing the BCP on the chemically patterned template could tolerate several percent of mismatch between the lattice spacing of the BCP and that of the template. In this study the morphology was limited to hexagonally packed dots. However, the results strongly support the potential application of the technique to form 10 nm scale features of other desired geometries.

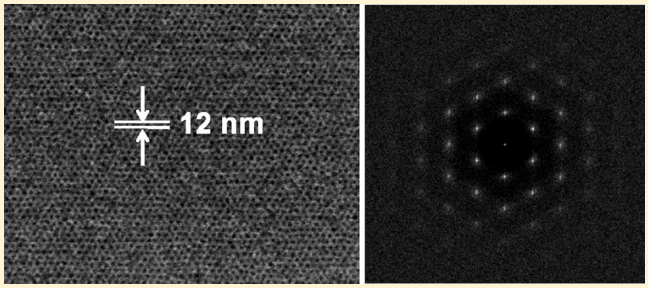

INTRODUCTION

Advances in directed assembly of block copolymer (BCP) thin films are quickly positioning self-assembly as a next-generation lithographic technique.[1−3] BCPs self-assemble via microphase separation to form periodic nanometer-scale structures in the range 5−100 nm. The most commonly observed morphologies of diblock copolymers are spherical domains in a body-centered lattice, hexagonally packed cylinders, or alternating lamellae.[4−8] The particular morphology of the self-assembled structure is determined by the relative volume fraction of the constituent blocks. The lattice length parameter of the phase-separated structure depends on the degree of polymerization, N. In order to assemble, the polymer chains must obtain sufficient mobility either by heating above their glass transition temperature, T_g, or by plasticizing with a solvent. However, both thermal and solvent annealing lowers the strength of block copolymer segregation, referred to as Flory−Huggins interaction parameter, χ. Therefore, both annealing conditions must be tuned to allow sufficient mobility for assembly but still fall below conditions that lead to the order−disorder transition (ODT). When annealing between T_g and ODT, the amount of microphase separation is limited by molecular diffusion. Because of the slow mechanism of diffusion, the self-assembled phase lattices form with localized order into numerous polycrystalline type structures with grain boundaries between them. For this reason, the first demonstrations of BCP phase separation as a form of lithography focused on the high pattern densities that could be attained and ignored the issues of pattern registration and long-range order.[1] More demanding applications such as magnetic storage or semiconductor devices require both registration and long-range ordering. Potential manufacturing applications have fueled extensive research to attain long-range ordering, good feature registration, and accurate placement with a very low number of defects. The BCP self-assembly can be

Received: August 9, 2011
Revised: November 5, 2011
Published: December 20, 2011

directed by graphoepitaxy (lithographically predefined templates with topographic relief)[9−16] or chemical heteroepitaxy (chemically prepatterned substrates).[17−24] Recent studies have demonstrated that directed self-assembly can have long-range ordering, with a multiple of the density and improved feature placement compared to the original lithographic templates.[9,21−27] Recently reports in which chemical heteroepitaxy was combined with nanofabrication techniques have shown much more complex patterns such as jogs, bends, junctions, chevrons, dashes, rectangular features, and even three-dimensional structures.[28−31]

A vast majority of research work on directed self-assembly has been devoted to polystyrene-*block*-poly(methyl methacrylate) (PS-*b*-PMMA), a model material that can be thermally annealed and, because of its PMMA content, may be used as a lithographic photoresist.[10,12,15−24] However, it is difficult for PS-*b*-PMMA to form features with a full pitch below 20 nm because of its small Flory−Huggins interaction parameter. More strongly segregating BCPs have been reported with ≤10 nm scale features.[25,26,32−36] However, achieving long-range order of some highly desirable BCP materials by thermal annealing is not possible because T_g exceeds the thermal degradation temperature of the BCP. In such cases solvent annealing offers an attractive alternative to thermal annealing to order the BCP. Here the solvent vapors dissolve in the BCP and act as a plasticizer. The swollen polymer chains attain sufficient mobility to order at temperatures (commonly at room temperature) well below their degradation temperature.[37] Solvent annealing can be applied to most types of self-assembling BCPs, opening many opportunities to extend directed self-assembly to the sub-10 nm scale.

Solvent annealing also offers the possibility of ordered structures not attainable with thermal annealing. By controlling the degree of swelling of each block, it is possible to reversibly tune the microdomain morphology (i.e., from spherical to cylindrical morphology and vice versa) through order−order transitions.[32,33,38,39] A solvent annealing process is described as follows: first, the as-spun BCP thin film is exposed to solvent vapor. Solvent vapor infiltrates into the BCP and swells the film, creating more free volume in the structure and a different conformational structure for the polymer chains, depending on solubility. In the swollen state, the BCP molecules have the mobility to form the self-assembled patterns.[40,41] After the solvent evaporates, the BCP molecules become frozen in the ordered structure. The morphology of the ordered structure depends on the solubility of the solvent vapor in the polymer blocks and on the degree of swelling during annealing. In fact, the morphologies of BCPs such as polystylene-*block*-polydimethylsiloxane and poly(α-methylstylene)-*block*-poly(4-vinylpyridine) have been engineered over a wide range of structures by controlling the amount and mixture of solvent vapors.[32,38] Bosworth et al.[42] reported that the self-assembled structure of poly(α-methylstyrene)-*block*-poly(4-vinylpyridine) ordered by solvent annealing can multiply the areal density of the chemically patterned template with a hexagonal array by a factor of 4.

In this work, we focus on polyhedral oligomeric silsesquioxane (POSS) containing BCPs. POSS is an attractive organic−inorganic hybrid material because of its molecular cage structure, the flexible functionality based on the substituents on the silicon atoms, and the high etch resistance to oxygen plasma. Hirai et al.[43−45] reported that POSS-containing BCPs, such as polystyrene-*block*-poly(methyl acrylate) POSS (PS-*b*-PMAPOSS) and poly(methyl methacrylate)-*block*-PMAPOSS (PMMA-*b*-PMAPOSS), can be synthesized by living anionic polymerization. They may offer a number of remarkable advantages for self-assembling lithography materials. In particular, the POSS-containing BCPs can self-assemble to well-defined features of a 10 nm scale in the thin films by solvent annealing under carbon disulfide (CS_2) vapor, and the resulting films show impressive structural stability without dewetting structures even in low molecular weight polymers around 10 K compared with other silicon-containing BCPs such as polystyrene-*block*-polydimethylsiloxane because of the high T_g of PMAPOSSs. Furthermore, POSS-containing domains have significantly higher etch resistance compared with the organic domains to oxygen reactive ion etching, resulting in promising formation of well-defined nanoporous films as lithography template by the dry etching process.

A solvent annealing process provides a much wider range of parameters that control the ordering of the BCP than a thermal annealing process. Therefore, it is important to characterize the solvent annealing process in detail and understand the effects of each parameter on the ordering process. We show that PMMA-*b*-PMAPOSS thin films annealed in CS_2 vapor undergo an order−order transition from cylindrical domains to spherical domains, with an increase in the degree of swelling. We also show that higher swelling is required for higher molecular weight BCPs to undergo the transition. The results are interpreted in terms of the relative solubility of the solvent vapor in each copolymer and the change in the effective Flory−Huggins parameter in the swollen state, the rate of the solvent evaporation on quenching the film and trapping the structure, and so on. The controlled solvent annealing is applied to the directed self-assembly of PMMA-*b*-PMAPOSS on chemically patterned substrates. We show the feature density multiplication over that of the original chemical pattern via controlled solvent annealing and the effect of the degree of swelling on the uniformity of the density multiplication. We report the long-range ordering and a density gain of 4 times of PMMA-*b*-PMAPOSS BCP films on the chemically patterned substrates to produce 3.7 Tdot/in.^{2} by the optimized solvent annealing process. We would like to emphasize how critical the precise control of the degree of swelling is to obtain the long-range ordering.

EXPERIMENTAL SECTION

Materials. Figure 1 shows the chemical structures of the polymers examined. Five PMMA-*b*-PMAPOSS diblock copolymers and a PMAPOSS homopolymer (hPMAPOSS) were synthesized by living anionic polymerization.[43] A hydroxy-terminated PMAPOSS (PMAPOSS-OH) was synthesized according to the method described in the Supporting Information. A hydroxy-terminated polystyrene (PS-OH) and a PMMA homopolymer (hPMMA) were purchased from Polymer Source Inc., Quebec, Canada, and Sigma-Aldrich, respectively.

The characteristics of the polymers are listed in Table 1. The volume fractions of the PMAPOSS blocks in the PMMA-*b*-PMAPOSS samples used in this study were in the range 83−87%.

Substrates. The Si wafer substrates were cleaned by immersion in a 7:3 mixture of sulfuric acid and hydrogen peroxide (*piranha solution*) at 80 °C for 10 min and washed with deionized water before using in each experiment.

Preparation of Chemically Patterned Templates. The piranha solution-cleaned Si substrates were spin-coated with PS-OH or PMAPOSS-OH dissolved in toluene. The PS or PMAPOSS was grafted onto the Si substrate by annealing the substrates in vacuum at 170 °C for 72 h. After the thermal treatment, the substrates were rinsed twice with toluene to remove any unreacted polymers.

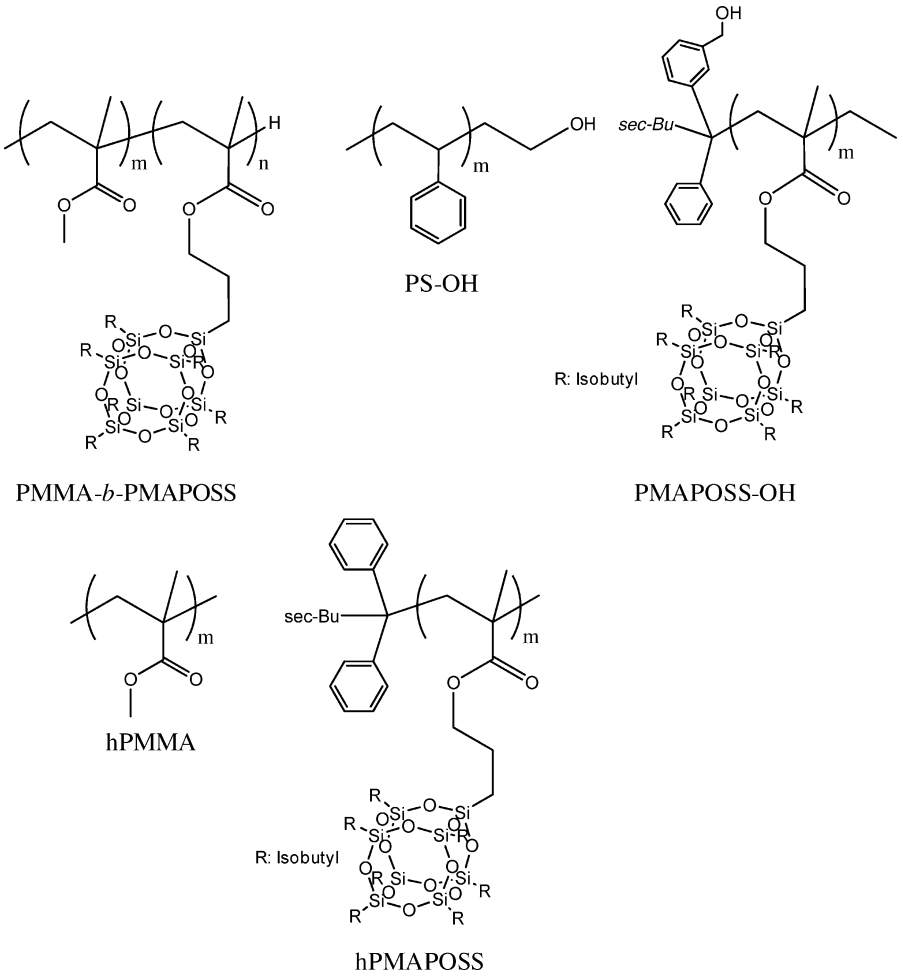

Figure 1. Representation of the polymer structures used in this study.

Table 1. Characterization of Polymers Used in This Study

composition[a]	M_n[b] (kg/mol)	M_w/M_n	PMAPOSS vol fraction[c]	d_0[d] (nm)
$PMMA_{49}$-*b*-$PMAPOSS_{34}$	37.4	1.08	0.87	30.0
$PMMA_{41}$-*b*-$PMAPOSS_{29}$	31.3	1.03	0.87	23.7
$PMMA_{34}$-*b*-$PMAPOSS_{18}$	20.9	1.06	0.83	18.3
$PMMA_{27}$-*b*-$PMAPOSS_{14}$	16.2	1.04	0.84	14.0
$PMMA_{25}$-*b*-$PMAPOSS_{13}$	14.9	1.04	0.83	12.4
PMAPOSS-OH	16.5	1.09		
PS-OH	3.7	1.08		
hPMMA	4.0	<1.1		
hPMAPOSS	29.8	1.04		

[a]The subscript numbers refer to the final composition in terms of the degree of polymerization of each component determined from the gel permeation chromatography (GPC) results and integration from ^{1}H NMR spectra. [b]Determined by GPC, calibrated against PS standards with THF as an eluent. [c]Determined by integration from ^{1}H NMR spectra and PMMA and PMAPOSS density of 1.15 and 1.13 g/cm^3, respectively, measured by the density gradient tube method. [d]Calculated from the 2D-FFT image of the SEM image of PMMA-*b*-PMAPOSS film solvent-annealed on the Si substrate at a certain t_{DS}.

The characteristics of the PS and PMMAPOSS layers grafted on the Si substrate are listed in Table 2. The average thicknesses of the grafted layers were measured by a ULVAC ESM-4500 ellipsometer. The coverage of the substrate surface was determined by the amount of carbon in a X-ray photoelectron spectroscopy, and the contact angle of PMMA to the polymer grafted surfaces was measured by a Kyowa

Table 2. Characteristics of the Surfaces of the Si Substrate and the Substrates with a Polymer-Grafted Layer Treated by Oxygen Plasma

surface	thickness of grafted layer[a] (nm)	XPS C_{1s} (CPS)	contact angle of hPMMA at 170 °C (deg)	
			before oxygen plasma	after oxygen plasma
Si treated by oxygen plasma		1.2×10^3		
PS-OH	5.1	2.7×10^4	25	0
PMAPOSS-OH	3.9	1.2×10^4	66	0

[a]Measured by ellipsometry.

Interface Science contact angle meter. A method to measure the contact angle of PMMA with the substrate was described previously.[47]

The PS- or PMAPOSS-grafted layer was patterned by e-beam lithography. A 50 nm PMMA e-beam resist layer was spin-coated onto the PS- or PMAPOSS-grafted Si substrate. The PMMA e-beam resist layer was exposed with a 100 kV electron beam in a Vistec VB6 system. Arrays of hexagonal dots were exposed, and the resist was developed in a 3:1 isopropanol and deionized water mixture at 2 °C, under ultrasonic agitation. The lattice spacings of the lithographically defined hexagonal arrays of dots, d_S, were set close to equal or twice the lattice spacing, d_0, of the hexagonal array formed by the PMMA-*b*-PMAPOSS. The developed PMMA resist pattern was used to selectively etch the underlying PS- or PMAPOSS-grafted layer by 5 s exposure to oxygen plasma. The surrounding PMMA film was

dx.doi.org/10.1021/ma201822a | *Macromolecules* 2012, 45, 292–304

sufficient to mask the matrix of the underlying brush layer during the 5 s etch. After the plasma etching the PMMA was removed with *N*-methyl-2-pyrolidone and toluene, leaving the chemically patterned PS- or PMAPOSS-grafted layer on the Si substrate.

Solvent Annealing. Thin films of PMMA-*b*-PMAPOSS were spin-cast on the Si substrates or the chemically patterned templates from the dilute solutions in either cyclohexane or chloroform. Cyclohexane and chloroform were used for dissolving $PMMA_{41}$-*b*-$PMAPOSS_{29}$ and the other PMMA-*b*-PMAPOSS, respectively. The film thickness was controlled by the concentration of the solutions and the spinning speed. The film thicknesses were determined by measuring the step height of the film scratched with a sharp knife with a Veeco Dimension 5000 atomic force microscope (AFM).

Figure 2 schematically illustrates the solvent annealing apparatus to expose the spin-cast films to CS_2 vapor. The concentration (or partial pressure) of CS_2 vapor was controlled indirectly with nitrogen counterflow in a sealed stainless steel chamber. The flow rates of the nitrogen were adjusted by using a flowmeter. As the reference sample, a PMMA-*b*-PMAPOSS film of thickness of 100 nm was always placed in the solvent annealing chamber along with the test samples, and its thickness change was monitored *in situ* with a Filmetrics F20 spectroscopic reflectometer. The degree of swelling (or swelling factor) of PMMA-*b*-PMAPOSS film, t_{DS}, is defined as the thickness of the reference sample in the swollen state divided by the initial film thickness. t_{DS} can be precisely controlled by the counterflow rate as shown in Figure S1. The test samples of $PMMA_{41}$-*b*-$PMAPOSS_{29}$ films had a thickness of 35 nm before the solvent annealing. The $PMMA_{41}$-*b*-$PMAPOSS_{29}$ films on the Si substrates were solvent-annealed at various t_{DS} for 1 h. The microstructures of the test samples were determined after the removal of the solvent in less than 30 s by excess nitrogen counterflow.

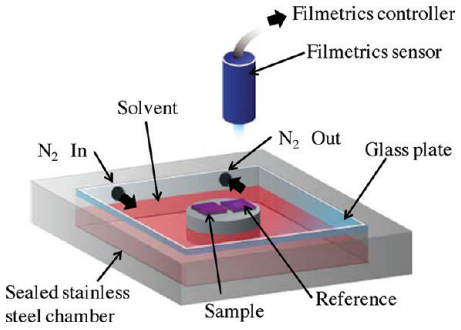

Figure 2. Schematic illustration of solvent annealing with an *in situ* film thickness monitor. The swollen state of the sample film is controlled by N_2 counterflow rate.

In general, the structures of the as-spun films, which depend on the casting solvent, can affect the morphologies after solvent annealing. However, in our experiments, no difference was observed between the two different casting solvents because the mobility of the PMMA-*b*-PMAPOSS chains is sufficient to erase the thermal history of the phase-separated structures in the as-spun films.

Microscopy. We examined the structures of the self-assembled PMMA-*b*-PMAPOSS films in a Hitachi S-4800 field-emission scanning electron microscope (SEM) operated with an acceleration voltage of 1.5 kV. Since the microdomains of the PMAPOSS blocks contain Si atoms, they discharge more secondary electrons than the microdomains of the PMMA blocks. Therefore, the dark and bright parts of the SEM images correspond to PMMA and PMAPOSS microdomains, respectively. We observed the surface of the self-assembled PMMA-*b*-PMAPOSS films by a Veeco Dimension 5000 AFM instrument to investigate their surface structure.

RESULTS AND DISCUSSION

Solvent-Annealed Structures of PMMA-*b*-PMAPOSS Thin Films on Si Substrates without Chemically Patterned Templates. Hirai et al.[43−45] reported that PMMA-*b*-PMAPOSS can form well-ordered microdomain structures by solvent annealing under CS_2 vapor. We focused our experiments on the effect of the degree of swelling of the BCP on the self-assembled structures during solvent annealing and observed the microdomain structures of the quenched films. Figure 3 shows the SEM images of the thin films of $PMMA_{41}$-*b*-$PMAPOSS_{29}$ after solvent evaporation. The dark and bright parts of SEM images correspond to the PMMA and the PMAPOSS domains, respectively. The as-spun film, shown in Figure 3a, did not exhibit a regular structure, although we can distinguish the PMMA domains from the PMAPOSS domains. The rapid evaporation of solvent during spin-coating of the BCP did not allow sufficient molecular mobility for the complete microphase separation of $PMMA_{41}$-*b*-$PMAPOSS_{29}$. In Figure 3b, line structures of the PMMA domains were observed in the films annealed with the swelling factor, t_{DS} = 125%.

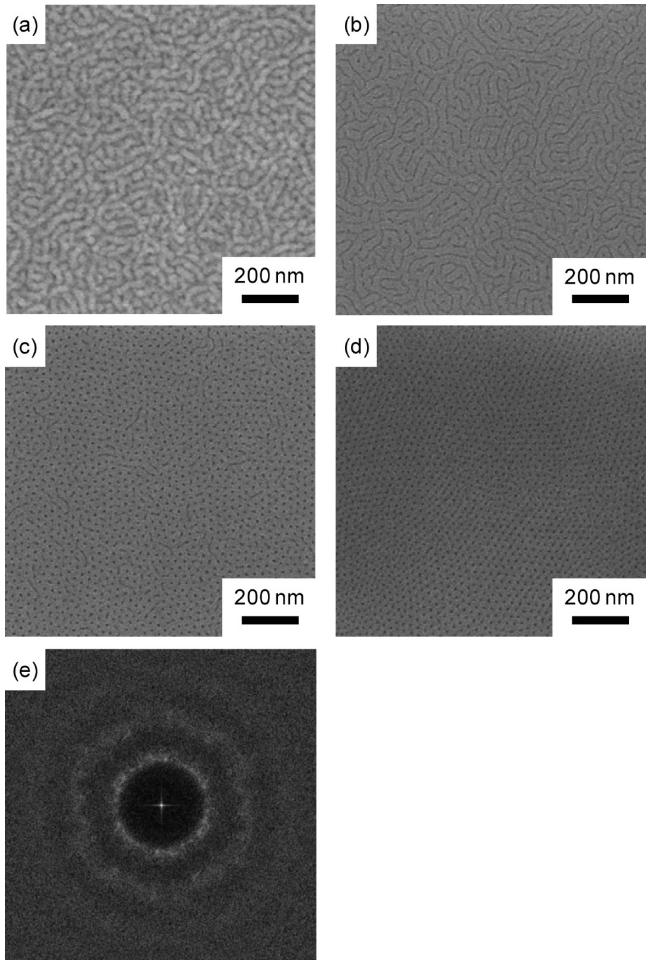

Figure 3. SEM images of the $PMMA_{41}$-*b*-$PMAPOSS_{29}$ films on the Si substrates. (a) As-spun film. (b−d) Solvent-annealed films. The films were solvent-annealed under CS_2 vapor for 1 h at three different degrees of swelling, t_{DS} of (b) 125%, (c) 150%, and (d) 175%. (e) The 2D-FFT image of the SEM image (c). The dark and bright parts of the SEM images correspond to the PMMA and PMAPOSS domains, respectively.

dx.doi.org/10.1021/ma201822a | *Macromolecules* 2012, 45, 292−304

Figure 3c shows the coexistence of line and dot structures of the PMMA domains after solvent annealing with the swelling factor, t_{DS} = 150%. The film annealed with the swelling factor, t_{DS} = 175%, shown in Figure 3d, exhibited only the dot structures, where the dots formed hexagonal lattices in the polycrystalline structure. Figure 3e shows a 2-dimensional fast Fourier transform (2D-FFT)[48] image of the hexagonally packed dot structure shown in Figure 3d. The 2D-FFT image exhibited isotropic halos with some spots. From the radius of the circular average of the intensity profile of the first halo in the 2D-FFT image, the lattice spacing of the self-assembled of $PMMA_{41}$-*b*-$PMAPOSS_{29}$ structure, d_0, was calculated to be 23.7 nm. The average radial distribution of the intensity was fitted to a Gaussian function.

To reveal the morphology of the PMMA domains forming the dot images, as in Figure 3c,d, a cross section of the PMMA-*b*-PMAPOSS film was observed with a transmission electron microscope (TEM). We used a thicker film of the higher molecular weight sample, $PMMA_{49}$-*b*-$PMAPOSS_{34}$, with a larger d_0 of 30.0 nm compared to that of the $PMMA_{41}$-*b*-$PMAPOSS_{29}$ for the purpose of observing the self-assembled structure clearly under TEM. The film was solvent-annealed with the swelling factor, t_{DS} = 185%. The initial film thickness was about 170 nm and the swollen film thickness was 315 nm, which corresponds to about 11d_0 of $PMMA_{49}$-*b*-$PMAPOSS_{34}$. In the cross section, the PMAPOSS domains were preferentially stained with RuO_4. In the TEM image, shown in Figure S2, the bright PMMA domains were observed as the dot structures. Since the top-down SEM image also showed the images with a matrix of spheres, we conclude that the PMMA domains are spherical in the solvent annealed $PMMA_{49}$-*b*-$PMAPOSS_{34}$ (t_{DS} = 185%). We further suggest that since the PMAPOSS volume fractions in the $PMMA_{49}$-*b*-$PMAPOSS_{34}$ BCP and the $PMMA_{41}$-*b*-$PMAPOSS_{29}$ BCP are the same and the swelling factors are similar, the morphology of the PMMA polymer in Figure 3c,d is also spherical. In this case the polymer morphology changed from cylindrical to spherical as the swell factor increased.

A morphology change could be explained by a change in relative volume fraction of the constituent blocks of the BCP in the swollen state. Since the block copolymer comprises two immiscible chains, we would expect the solvent molecules to have different affinities for the microdomains with the different blocks.[38] To investigate the relative solubility of the PMMA and PMAPOSS block chains with CS_2, we evaluated the swelling behaviors of the single-component films of hPMMA and hPMAPOSS. Each of the hPMMA and hPMAPOSS films spun on the Si substrates was exposed to CS_2 vapor under a N_2 counterflow adjusted to 20 mL/min, and t_{DS} was measured as a function of time until it reached a constant value. Under this flow condition, the degree of swelling, t_{DS}, was 123% for hPMMA and 139% for hPMAPOSS (Figure S3). This result suggests that

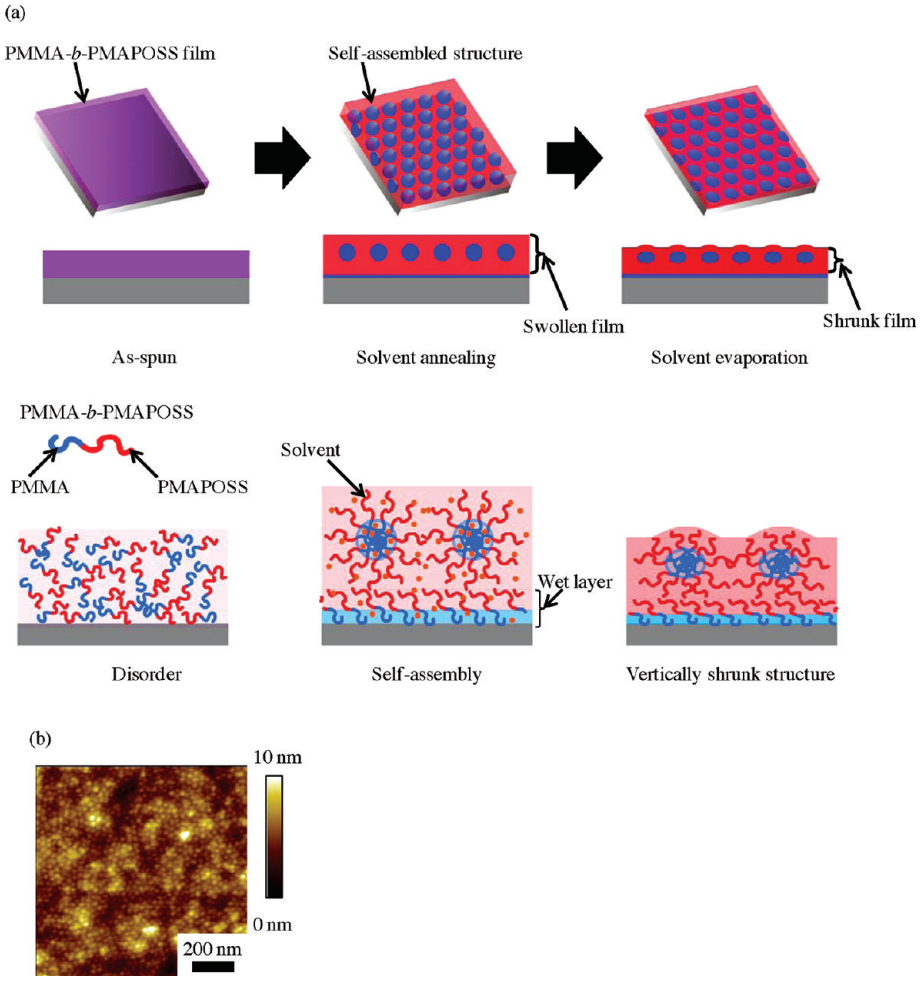

Figure 4. (a) Schematic illustrations of the solvent annealing process and the possible cross-sectional structures at each stage of the process. Red and blue chains represent the PMAPOSS and PMMA chains, respectively. Orange dots represent the CS_2 solvent molecules. (b) AFM topographic image of the $PMMA_{41}$-*b*-$PMAPOSS_{29}$ film solvent-annealed at t_{DS} = 185% for 1 h on the Si substrate.

dx.doi.org/10.1021/ma201822a | *Macromolecules* 2012, 45, 292–304

CS_2 is slightly selective to PMAPOSS. Thus, preferential partitioning of CS_2 into the PMAPOSS domains is expected in the solvent annealing of the PMMA-*b*-PMAPOSS films. We propose that the solvent annealing induces a change in the effective volume fractions of the two constituent blocks and can change the microdomain morphology from cylinders to spheres in this case.

We can further explain the morphologies in Figure 3 and Figure S2 in terms of the surface energies. Figure 4a shows the schematic illustrations of the solvent annealing process and the possible cross-sectional structure of the PMMA-*b*-PMAPOSS film at each stage. At the as-spun stage, PMMA-*b*-PMAPOSS is mostly in the disordered state although there may be slightly phase-separated regions. At the swollen stage, the solvent-swollen PMMA-*b*-PMAPOSS chains gain the mobility to diffuse and undergo microphase separation to form the self-assembled structure in thermodynamic equilibrium. If t_{DS} is large enough to induce the order−order transition, the morphology of the PMMA domains might change from cylinders to spheres. Since the surface tension of PMMA against the Si surface is smaller than that of PMAPOSS,[47] a thin wetting layer of PMMA may be formed adjoining to the Si surface. In contrast, the CS_2 vapor at the surface of the film has preference to PMAPOSS. On the solvent evaporation after the solvent annealing, the PMMA-*b*-PMAPOSS film may shrink in the thickness while the lateral size of the film remains unchanged. Therefore, the shape of the PMMA domains in the dried film may not be spherical but ellipsoidal. This expectation was confirmed by the TEM observation of the cross-sectional images of the dried film (Figure S2). Figure 4b shows the AFM height image of the thin film of $PMMA_{41}$-*b*-$PMAPOSS_{29}$ solvent-annealed at t_{DS} = 185%. The hexagonally packed bright dots of the PMMA domains were observed under the topographical contrast, and the dots were found to be 2−3 nm thicker than the PMAPOSS matrix. This result suggests that the degree of shrinkage of the PMMA domains is less than that of the PMAPOSS matrix, which is consistent with the higher solubility of CS_2 in PMAPOSS. Final confirmation of the above model would require *in situ* observation of the swollen films by grazing incidence small-angle X-ray scattering (GI-SAXS) with synchrotron radiation, which is beyond the scope of this work.

Effect of Molecular Weight of PMMA-*b*-PMAPOSS on Self-Assembled Structures. We further examined the CS_2 solvent annealing behavior of other molecular weights of PMMA-*b*-PMAPOSS.

Figure 5 shows the SEM images of the 15 nm thick, as-spun, films of $PMMA_{25}$-*b*-$PMAPOSS_{13}$ solvent annealed for 1 h under different swelling factors. As expected in Figure 5a, the as-spun film did not exhibit a periodic structure. Figure 5b shows coexistence of line and dot structures of the PMMA domains when the swelling factor was t_{DS} = 120% during annealing. The line structures are derived from the cylindrical PMMA microdomains oriented parallel to the Si substrate. The dot structures are most likely the spherical PMMA microdomains. When the swelling factor was increased to t_{DS} = 130%, the PMMA domains exhibited a disordered dot structure as shown in Figure 5c. This result suggests that with the 130% swelling factor the PMMA-*b*-PMAPOSS chains do not gain sufficient mobility to form a single hexagonal lattice. However, as the degree of swelling of the film increased to t_{DS} = 140% and 150%, a regular hexagonal array of dots formed as shown in Figure 5d,e. From the position of the first-order halo observed in the 2D-FFT image of Figure 5g obtained from the SEM image in Figure 5d, d_0 of the self-assembled structure of $PMMA_{25}$-*b*-$PMAPOSS_{13}$ at t_{DS} = 140% was determined to be 12.4 nm. In the same way, d_0 at t_{DS} = 150% was calculated to be 12.7 nm. Conversely, as the degree of swelling of the film further increased to t_{DS} = 175%, the hexagonally packed dot pattern did not exhibit the extent of order observed in the samples annealed with the swelling factors of t_{DS} = 140% and 150%, as shown in Figure 5f. According to Lodge et al.,[49] swelling of cylinder-forming BCP systems with a neutral solvent lowers the effective Flory−Huggins interaction parameter of the copolymers. In addition, greater swelling of one component

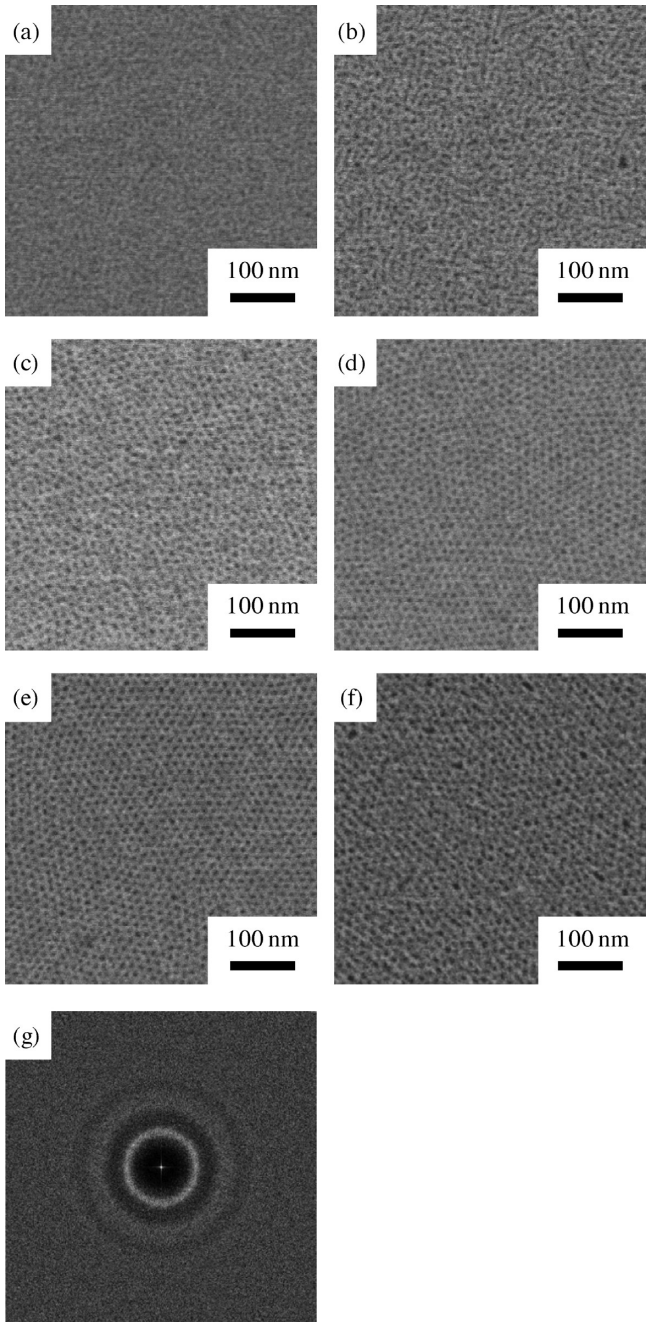

Figure 5. SEM images of the $PMMA_{25}$-*b*-$PMAPOSS_{13}$ films. (a) As-spun film. (b−f) Solvent-annealed films. The films were solvent-annealed on the Si substrates at various t_{DS} of (b) 120%, (c) 130%, (d) 140%, (e) 150%, and (f) 175%. (g) The 2D-FFT image of the SEM image (d). The dark and bright parts of the SEM images correspond to the PMMA and PMAPOSS domains, respectively.

dx.doi.org/10.1021/ma201822a | *Macromolecules* 2012, 45, 292−304

of the BCP that has a slightly greater affinity for the solvent can increase the volume fraction of the corresponding microdomains in the swollen state. CS_2 is slightly selective for PMAPOSS over PMMA, and the solvent annealing can increase $\phi_{PMAPOSS}$ and decrease χ in the swollen state.[43] The effects of the solvent annealing can be described with a schematic phase diagram of the microdomain morphology in $\chi_{eff}N$ vs $\phi_{PMAPOSS,eff}$ space as shown in Figure 6, where χ_{eff}, N, and $\phi_{PMAPOSS,eff}$ are

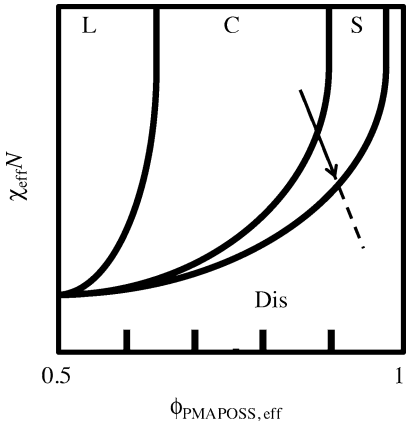

Figure 6. Right half of the schematic phase diagram of $\chi_{eff}N$ vs $\phi_{PMAPOSS,eff}$ for PMMA-*b*-PMAPOSS/CS_2 system. PMMA is the minor component and forms the dispersed domains in the cylindrical (C) and spherical (S) morphologies. The $\chi_{eff}N$ value of the BCP decreases with the infiltration of the solvent into the film. Since CS_2 swells the PMAPOSS matrix more than the PMMA domains, the effective volume fraction of PMAPOSS, $\phi_{PMAPOSS,eff}$, increases on swelling. The phase behavior of the BCP with increasing t_{DS} on solvent annealing is represented by the solid arrow, which predicts the morphological transition from cylinders to spheres upon swelling. The dashed line predicts the order−disorder transition at excess t_{DS}. The behavior of the BCP with a higher M_n on solvent-annealing is represented by the dotted arrow, which is obtained by the vertical shift of the solid arrow.

the effective Flory−Huggins interaction parameter in the swollen state, the degree of polymerization, and the effective volume fraction of the PMAPOSS blocks in the swollen state, respectively.[38,49,50] The morphological change with increasing t_{DS} can be recognized as a diagonal shift in the phase diagram along the solid arrow in Figure 6. Therefore, the morphology of the PMMA domains changes from cylindrical to spherical with increasing t_{DS}. Furthermore, the phase-separated structure may become unstable and the long-range order may become worse on the solvent annealing at t_{DS} > 175% because of the transition from the spherical microdomain morphology to the disorder state. This case is represented by a further diagonal shift on the dashed line in the phase diagram. Our results show that the optimum swelling factor to form a well-defined hexagonally packed dot pattern with $PMMA_{25}$-*b*-$PMAPOSS_{13}$ is in the range between 140 and 150%.

Similarly, we investigated the effect of t_{DS} on the self-assembled structures of $PMMA_{34}$-*b*-$PMAPOSS_{18}$ and $PMMA_{27}$-*b*-$PMAPOSS_{14}$ possessing the $\phi_{PMAPOSS}$ values of 83% and 84%, respectively, which are similar to the $\phi_{PMAPOSS}$ values for $PMMA_{41}$-*b*-$PMAPOSS_{29}$ and $PMMA_{25}$-*b*-$PMAPOSS_{13}$ (see Figures S4 and S5). The results are summarized in Figure 7, which presents the phase diagram of the self-assembled structures of the solvent annealed PMMA-*b*-PMAPOSS. The open circles and diamonds denote the spherical and cylindrical morphologies, respectively, while the open triangles indicate coexistence of the

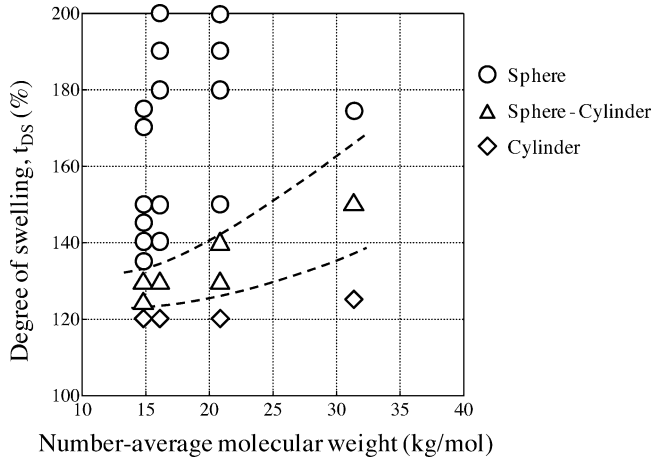

Figure 7. Phase diagram showing the morphologies of PMMA-*b*-PMAPOSS assembled via solvent-annealing with CS_2 vapor as a function of degree of swelling, t_{DS}, and number-average molecular weight of PMMA-*b*-PMAPOSS. The volume fraction of PMAPOSS in the PMMA-*b*-PMAPOSS samples, $\phi_{PMAPOSS}$, was in the range 83−87%. Open circles, triangles, and diamonds represent sphere, mixtures of sphere and cylinder, and cylinder morphologies of the PMMA domains, respectively.

spheres and cylinders. Figure 7 shows that the phase boundary for the cylinder-to-sphere transition shifts toward the higher values of t_{DS} with increasing M_n of PMMA-*b*-PMAPOSS. This can be understood qualitatively in terms of $\chi_{eff}N$ and $\phi_{PMAPOSS,eff}$ in the swollen state using Figure 6. As t_{DS} increases on swelling with CS_2, χ_{eff} decreases while $\phi_{PMAPOSS,eff}$ increases due to the higher affinity of CS_2 for PMAPOSS. It eventually induces the morphology transition from cylinders to spheres as represented by the arrow in Figure 6 for the PMMA-*b*-PMAPOSS with a smaller M_n. On the other hand, an increase in M_n of PMMA-*b*-PMAPOSS increases $\chi_{eff}N$ and prompts the backward shift along the arrow. Thus, a larger t_{DS}, which further reduces the χ_{eff} value, is necessary for the PMMA-*b*-PMAPOSS with a larger M_n to undergo the morphological transition from cylinders to spheres. Consequently, the phase boundary for the cylinder-to-sphere transition shifts toward the higher values of t_{DS} with increasing M_n of PMMA-*b*-PMAPOSS as shown in Figure 7. Although the discussion given above is qualitative, it suggests that we need to optimize the degree of swelling in the solvent annealing to obtain the desired hexagonally packed dot pattern depending on the M_n of PMMA-*b*-PMAPOSS.

Characteristics of Chemically Patterned Template Surface. In the previous section, we have determined the optimized solvent-annealing conditions to prepare well-defined highly ordered arrays of dots of PMMA-*b*-PMAPOSS BCPs on the Si substrates. We now consider directing the self-assembly process during the solvent annealing with chemical heteroepitaxy. Figure 8 shows a schematic illustration of the directed self-assembly process of PMMA-*b*-PMAPOSS, which forms PMMA spheres in PMAPOSS matrix on a chemically patterned template. The template with chemical contrast was composed of a hexagonal array of circular dots preferentially wetted by PMMA surrounded by a background matrix with higher affinity for PMAPOSS. The lattice spacing, the distance between adjacent planes, is denoted as d_s while the lattice constant, the distance between nearest neighbors, is represented as L_s. The preparation of the chemically patterned grafted film was described above. The patterned template had an array of etched dots that had surface

dx.doi.org/10.1021/ma201822a | *Macromolecules* 2012, 45, 292−304

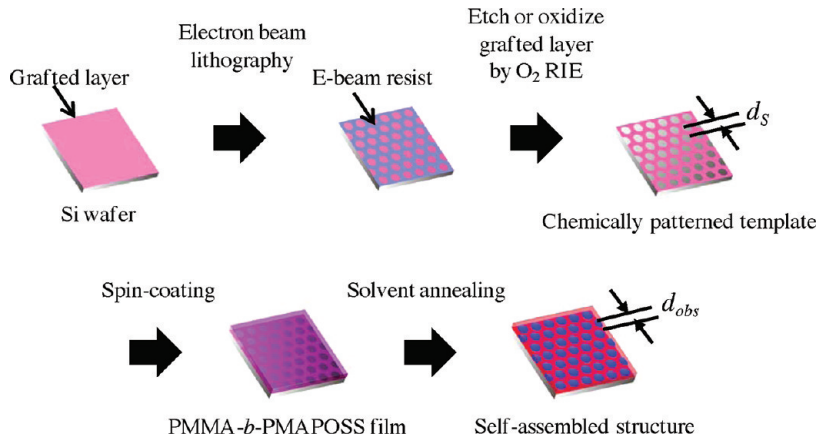

Figure 8. Schematic illustration of the directed self-assembly process with a chemically patterned template.

affinity for the PMMA component of the BCP. The surrounding matrix of unetched surface favored the PMAPOSS component of the BCP.

The geometric components of the e-beam lithography defined chemically patterned templates, d_s and L_s, are listed in Table 3. To evaluate the pattern quality of the chemically patterned templates, we evaluated the PMMA e-beam resist patterns on the PS brush after development. The surface of the PMMA e-beam resist was sputter coated with about 1 nm thick layer of Pt prior to SEM observations. Figure 9 shows the SEM images of the resist layer. The dark and bright parts of the SEM images correspond to the patterned holes in the PMMA e-beam resist layer and the remaining PMMA resist layer, respectively. As shown in Figure 9, there were several defects in the patterns with d_s = 23 nm (part a), while there were almost no defects in the patterns with d_s = 24, 26, and 28 nm (parts b, c, and d, respectively). The summary of the characteristics of the observed patterns in Figure 9 is given in Table 3. The average lattice spacing of the patterns, as measured by our SEM, are denoted as d_{eb} and its standard deviation σ_{eb}. The method employed to evaluate d_{eb} and σ_{eb} was described in the previous study.[23] The d_{eb} values almost agreed with the designed values, d_s. The pattern with d_s = 23 nm showed the largest σ_{eb} value of 3.4 nm, but the σ_{eb} values of the other patterns were less than 3 nm.

Table 3. Characteristics of the Patterns Formed with EB Lithography

d_s (nm)	L_s (nm)	d_{eb} (nm)	σ_{eb} (nm)
23	26	23.3	3.4
24	28	24.6	2.1
26	30	26.3	2.2
28	32	28.4	2.7

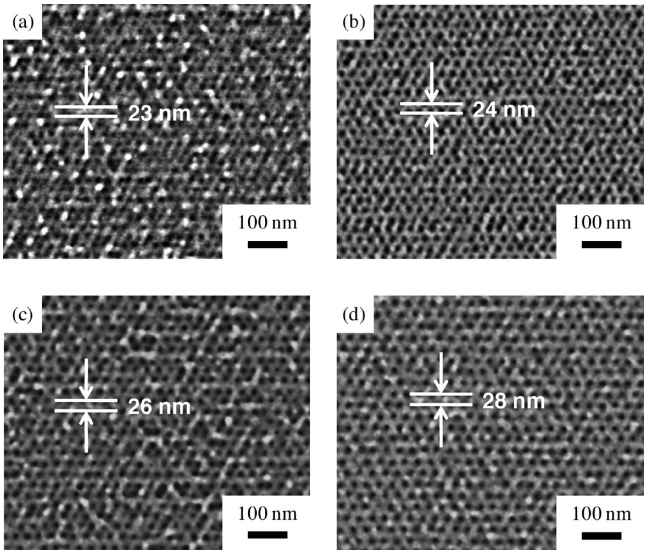

Figure 9. SEM images of the PMMA e-beam resist layer formed by e-beam lithography, which was employed to prepare the chemically patterned substrates. The resist pattern was etched with the oxygen plasma required to change the chemistry of the substrate. (a) d_s = 23 nm, (b) d_s = 24 nm, (c) d_s = 26 nm, and (d) d_s = 28 nm.

Chemical Heteroepitaxy with Chain Mobility from Solvent Annealing. We investigated the effect of the solvent annealing on the chemical heteroepitaxy for the thin films of PMMA-*b*-PMAPOSS on the chemically patterned templates of grafted PS-OH on the Si substrates. Thin films of $PMMA_{41}$-*b*-$PMAPOSS_{29}$ with d_0 = 23.7 nm were spin-coated onto the chemically patterned substrates and solvent-annealed for 3 h. The solvent annealing was performed with a swelling factor of t_{DS} = 185% so that $PMMA_{41}$-*b*-$PMAPOSS_{29}$ self-assembled in the well-defined hexagonal array of dots. The thickness of the $PMMA_{41}$-*b*-$PMAPOSS_{29}$ film was optimized to 12 nm to prevent the spherical PMMA domains from forming two layers upon swelling. At t_{DS} = 185%, the thickness of the film is expected to increase by swelling from 12 to 22 nm, which is nearly equal to d_0 inherent to $PMMA_{41}$-*b*-$PMAPOSS_{29}$.

Figure 10 shows that chemical epitaxial direction can be achieved with the sphere forming block copolymer solvent annealing conditions. The SEM image and the corresponding 2D-FFT image of a thin film of $PMMA_{41}$-*b*-$PMAPOSS_{29}$ self-assembled on the chemically patterned template with d_s = 23 nm are shown in Figure 10a. The self-assembled structure on the template with d_s = 23 nm resulted in a single hexagonal lattice with almost no point defects, in contrast to the relatively poor quality of the chemically patterned template shown in Figure 9a. The 2D-FFT image exhibits only spots as expected from the single hexagonal lattice, with the peaks to at least the fifth order. The lattice spacing of the self-assembled structure on the template, denoted as d_{obs}, calculated from the 2D-FFT image was 23.2 nm, which is the same as that of the underlying template, d_s = 23 nm. This result demonstrates that with appropriate solvent annealing conditions PMMA-*b*-PMAPOSS can self-assemble to

dx.doi.org/10.1021/ma201822a | *Macromolecules* 2012, 45, 292–304

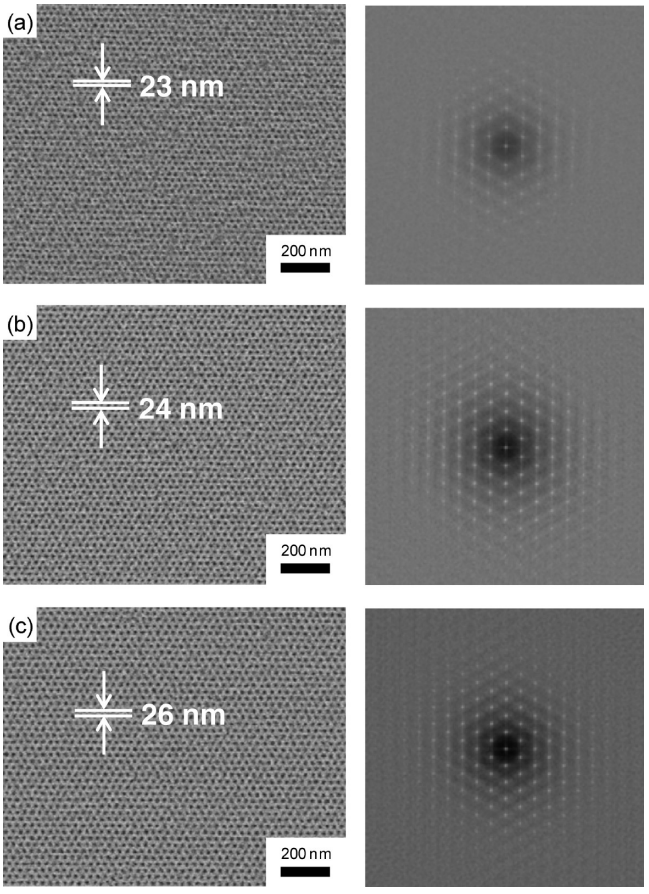

Figure 10. SEM images and the corresponding 2D-FFT images of the $PMMA_{41}$-*b*-$PMAPOSS_{29}$ thin films solvent-annealed on the chemically patterned templates composed of the PS-OH grafted layer. (a) d_s = 23 nm, (b) d_s = 24 nm, and (c) d_s = 26 nm. The film thickness is 12 nm.

form a well-oriented hexagonal lattice pattern with a long-range order along the chemically patterned template and rectify the defects of the chemically patterned template as can thermally annealed PS-*b*-PMMA.[23]

In Figure 10b,c, we examined the effect of the lattice mismatch of the chemically patterned template on the quality of the self-assembled structure. As shown in Figure 10b,c, single hexagonal lattices were also observed on the templates with d_s = 24 and 26 nm, which were both slightly larger than the d_0 (= 23.7 nm) of $PMMA_{41}$-*b*-$PMAPOSS_{29}$. The corresponding 2D-FFT images exhibited only spots, with the peaks at least to the sixth order. The d_{obs} values of the self-assembled structures for parts b and c of Figure 10 were 24.3 and 26.5 nm, respectively, which agreed with the d_s values of the template patterns. This result suggests that the lattice spacing d_{obs} of the self-assembled structures can be stretched to match the d_s of the underlying templates, at least up to 12% (d_{obs}/d_0 = 26.5/23.7 = 1.12) larger than d_0. This finding implies some extended flexibility in the chemically patterned template design.

Xiao et al.[25] proposed that the spherical microdomains of a BCP formed on the chemically patterned templates could be spherical, hemispherical, or disklike, depending on the relative size of the patterned features with respect to the inherent size of the BCP spherical domains. We also believe that the morphology of the spherical microdomains on the patterned template might have been deformed by the favorable interaction between the PMMA blocks and the Si substrate of the patterned template. However, confirming such a hypothesis requires a direct observation of the cross-sectional images of the BCP thin films by SEM or TEM, which is beyond the scope of this work.

The limit of the commensurability may be determined by the two competing thermodynamic factors: the interfacial free energy reduction by the lattice matching between the BCP microdomains and the template patterns and the conformational entropy loss as the chains stretch or shrink to achieve the template lattice spacing.

Effect of PMAPOSS Grafted Surface of the Chemically Patterned Template. Next, we examined the use of a PMAPOSS-OH chemically patterned template for the ordering of a thin film of $PMMA_{41}$-*b*-$PMAPOSS_{29}$ with solvent annealing, again with chemical pattern pitch 23, 24, and 26 nm. The samples were solvent annealed under conditions for a swelling factor of t_{DS} = 185% for 3 h.

Figure 11 shows the SEM images and the corresponding 2D-FFT images of the self-assembled structures on the templates

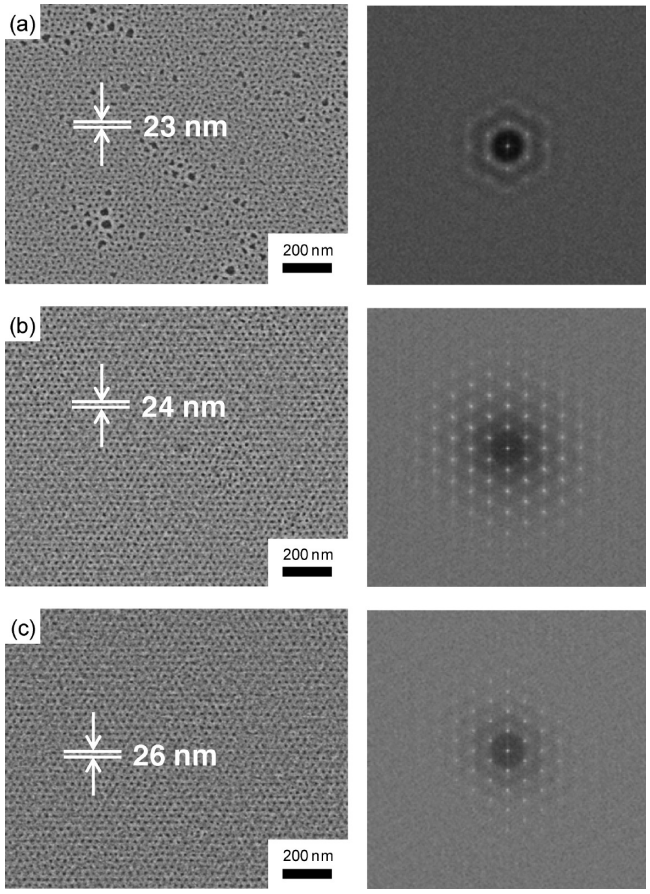

Figure 11. SEM images and the corresponding 2D-FFT images of the $PMMA_{41}$-*b*-$PMAPOSS_{29}$ thin films solvent-annealed on the chemically patterned templates composed of PMAPOSS-OH grafted layer. (a) d_s = 23 nm, (b) d_s = 24 nm, and (c) d_s = 26 nm. The film thickness is 12 nm.

prepared with PMAPOSS-grafted surface. Ordering on the d_s = 23 nm template pattern, shown in Figure 11a, gave mixed results. Some grains of the BCP self-assembled structure matched their lattice to that of the underlying template with d_s = 23 nm, but large dark regions were also observed, differing from the case of the PS-grafted template. The 2D-FFT image presented in Figure 11a exhibited a spot and halo pattern. Better results were obtained from the chemically patterned

dx.doi.org/10.1021/ma201822a | *Macromolecules* 2012, 45, 292–304

template patterns with d_s = 24 and 26 nm. Single well-ordered hexagonal lattices were observed as shown in Figure 11b,c. The accompanying 2D-FFT images exhibit only spots, with peaks up to fourth order. Thus, well-ordered self-assembled structures formed on chemically patterned templates of PMAPOSS-OH patterned with d_s = 24 and 26 nm. However, the d_s = 23 nm lattice clearly formed more readily on the chemically patterned PS-OH template than on the chemically patterned PMAPOSS-OH template. Table 2 shows a comparison of the wettability of a PMMA homopolymer to a PS-grafted surface and to a PMAPOSS-grafted surface. The interfacial energy of the PMMA component of the block copolymer to the PS grafted surface is less than that on the PMAPOSS-grafted surface. The lower chemical contrast of the PS surface could explain the wider latitude in lattice spacing on the PS grafted surface. These results may imply that the template prepared by patterning the PS-grafted layer is more suitable for the directed self-assembly of PMMA-*b*-PMAPOSS compared to that fabricated employing the substrate with the PMAPOSS-grafted layer. However, for thorough understanding of the effect, the dependences on M_n and/or grafting density of the grafted polymer have to be studied.

Directed Self-Assembly of PMMA-*b*-PMAPOSS with Density Multiplication. The primary motivation for use directed BCP self-assembly is to enhance the achievable lithographic resolution. With the use of lower molecular weight BCPs, we examine the ability to multiply the density of the lithographic chemical pattern arrays. We examined the directed self-assembly of $PMMA_{25}$-*b*-$PMAPOSS_{13}$ with d_0 = 12.4 nm on the chemically patterned PS-OH templates with d_s = 26 nm under CS_2 solvent annealing. $PMMA_{25}$-*b*-$PMAPOSS_{13}$ films, of 9 nm thickness, were annealed under CS_2 vapor with swelling factors of t_{DS} = 130, 140, and 150%. In the swollen state, the film thicknesses were expected to be about 12, 13, and 14 nm at t_{DS} = 130, 140, and 150%, respectively, which nearly correspond to d_0 of the $PMMA_{25}$-*b*-$PMAPOSS_{13}$ BCP.

Parts a, b, and c of Figure 12 present the SEM images and the corresponding 2D-FFT images of the thin films of $PMMA_{25}$-*b*-$PMAPOSS_{13}$ solvent-annealed on chemically patterned templates with d_s = 26 nm ≈ $2d_0$ at t_{DS} = 130, 140, and 150%, respectively. Figure 12a shows the film annealed at t_{DS} = 130%. Here the $PMMA_{25}$-*b*-$PMAPOSS_{13}$ self-assembled to form a dot structure of PMMA, but the accompanying 2D-FFT image shows on halos indicating the lack of long-range order in the array. Under solvent annealing a swell factor of t_{DS} = 130% components did not have sufficient mobility to fully order. Figure 12b shows the $PMMA_{25}$-*b*-$PMAPOSS_{13}$ film on the PS chemically patterned substrate, with d_s = 26 nm, annealed with a swelling factor t_{DS} = 140%. Both the SEM image on the left and the 2D-FFT of the image on the right show a long-range ordered hexagonal array of dots with lattice spacing of 13.4 nm, which was a almost half of the d_s value (= 26 nm) of the template. In contrast, the film annealed with a swelling factor of t_{DS} = 150%, shown in Figure 12c, shows a distorted hexagonal lattice pattern and streaks on the spots in the accompanying 2D-FFT of the image. These results show that solvent annealing with a swell factor of t_{DS} = 140% is optimal for the directed self-assembly of $PMMA_{25}$-*b*-$PMAPOSS_{13}$ with density multiplication by a factor of 4.

To evaluate the orientation distribution of the lattice patterns in Figure 12, we examined the azimuthal distribution of the first-order peak in the 2D autocorrelation pattern from the 2D-FFT image. Figure 13 shows the azimuthal angle, ψ,

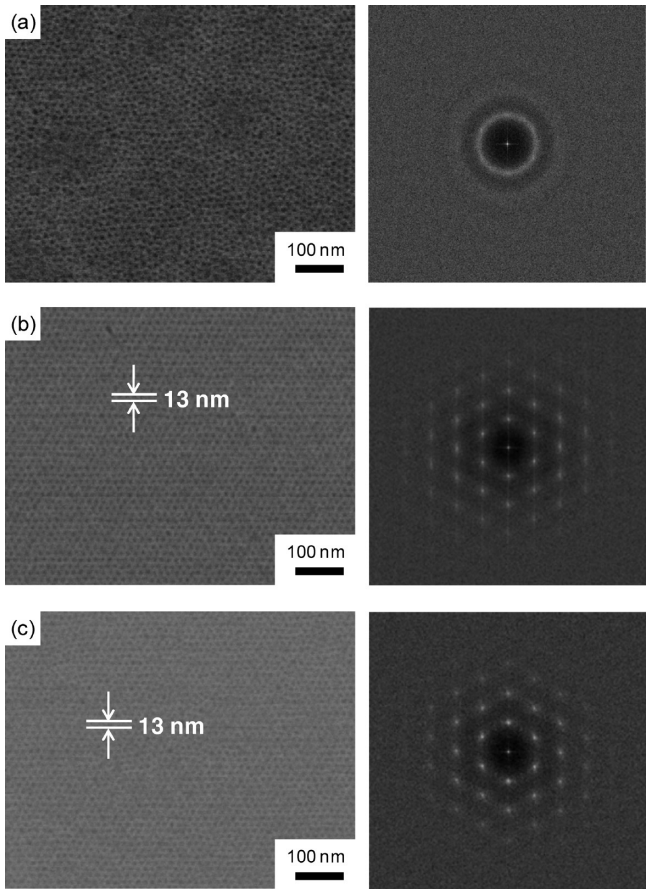

Figure 12. SEM images and the corresponding 2D-FFT images of the $PMMA_{25}$-*b*-$PMAPOSS_{13}$ thin films solvent-annealed on the chemically patterned template with d_s = $2d_0$ = 26 nm at various t_{DS}. (a) t_{DS} = 130%, (b) t_{DS} = 140%, and (c) t_{DS} = 150%. The film thickness is 9 nm. The chemically patterned templates were fabricated employing PS-OH grafted layer.

dependence of the intensity, I, of the first-order peak positions in the in the 2D autocorrelation pattern from the 2D-FFT images shown in Figure 12. Peaks were observed at every 60° of the azimuthal angle the samples annealed with swelling factors t_{DS} = 140% and 150%. Little or no azimuthal variation in intensity of the first-order ring was observed from the sample annealed with swelling factor, t_{DS} = 130%. The azimuthal angular widths of the peaks of the sample annealed with a t_{DS} = 140% swelling factor were narrower than those of the sample annealed with a swelling factor of t_{DS} = 150%. The widths, w, obtained by fitting the peaks at 180° with Gaussian function

$$I = I_0 + A \exp\left\{ -\left(\frac{\psi - \psi_0}{w}\right)^2 \right\}$$

were 5.8° and 9.2° for the samples annealed with swelling factors of t_{DS} = 140% and 150%, respectively. The results of the $PMMA_{25}$-*b*-$PMAPOSS_{13}$ ordering on the chemically patterned PS-OH template are summarized in Table 4. The length scale of the lithographically directed patterns lattice spacing was 13.4 nm as compared to a 12.4 nm length scale of the unguided block copolymer lattice spacing on the substrates. The standard deviation, σ, of the center-to-center distance of the dots in the self-assembled structures can be compared with that for the template pattern, σ_{eb}, listed in Table 3. The spacing σ values of

dx.doi.org/10.1021/ma201822a | *Macromolecules* 2012, 45, 292–304

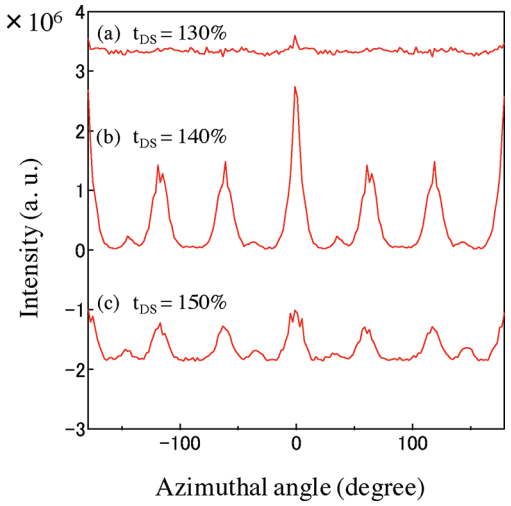

Figure 13. Azimuthal angle dependence of the first-order peak intensity of the 2D autocorrelation pattern from the 2D-FFT images of the $PMMA_{25}$-*b*-$PMAPOSS_{13}$ thin films solvent-annealed on the chemically patterned templates with $d_s = 2d_0 = 26$ nm at various t_{DS}. (a) $t_{DS} = 130\%$, (b) $t_{DS} = 140\%$, and (c)$t_{DS} = 150\%$.

Table 4. Quantitative Comparison of *d*, *σ*, and *w* among the Self-Assembled Structures of $PMMA_{25}$-*b*-$PMAPOSS_{13}$ on the Chemically Patterned Templates with $d_s = 2d_0 = 26$ nm

	self-assembled structure		
t_{DS} (%)	d_{obs} (nm)	σ (nm)	w (deg)
130	13.4		
140	13.4	1.5	5.8
150	13.0	1.7	9.2

the solvent-annealed lattices with swelling factors of $t_{DS} = 140\%$ and 150% were calculated to be 1.5 and 1.7 nm, respectively. The self-assembled lattice spacing σ's were 20−30% smaller than the σ_{eb} values of the chemically patterned template (d_s = 26 nm), which was 2.2 nm. As can be expected, σ values at t_{DS} = 140% were found to be the smallest and significantly smaller than the σ_{eb} value of the underlying chemically patterned template at one-quarter the BCP pattern density. The lower perfection exhibited by the BCP annealed with a swelling factor of t_{DS} = 150% than that of the BCP annealed with a swelling factor of t_{DS} = 140% may be caused by a slight difference in the lattice spacing of the self-assembled structure at the swollen state. Further work, such as *in situ* grazing incidence small-angle X-ray scattering in the swollen BCP may elucidate the result.

The density multiplication occurs with PMMA dots interpolating between dots in the substrate chemically patterned template pattern, and the placement accuracy of the quadruple density pattern is 20−30% better than that of the original lithographic pattern on the template. The pattern density multiplication can be achieved by careful optimization of the amount of BCP swelling during solvent annealing

Effects of the Lattice Mismatch between d_s and d_0 on Density Multiplication. Next, we investigated the effect of lattice mismatch between the $PMMA_{25}$-*b*-$PMAPOSS_{13}$ BCP length scale and that of the original lithographic chemically patterned template pattern. The lattice spacing of $PMMA_{25}$-*b*-$PMAPOSS_{13}$ self-assembled on the Si substrate without a chemically patterned template was found to be $d_0 = 12.4$ nm. We examined the directed assembly of the $PMMA_{25}$-*b*-$PMAPOSS_{13}$ with CS_2 solvent annealing with chemically patterned template prepatterns slightly above and below the value of $2d_0$ for 4× density multiplication. The $PMMA_{25}$-*b*-$PMAPOSS_{13}$ films were spun on chemically patterned PS-OH layers on Si substrates and annealed in CS_2 with a swelling factor of 140%. The length scales of the hexagonal lattices on the chemically patterned templates were d_s = 23, 24, and 28 nm. The SEM images and

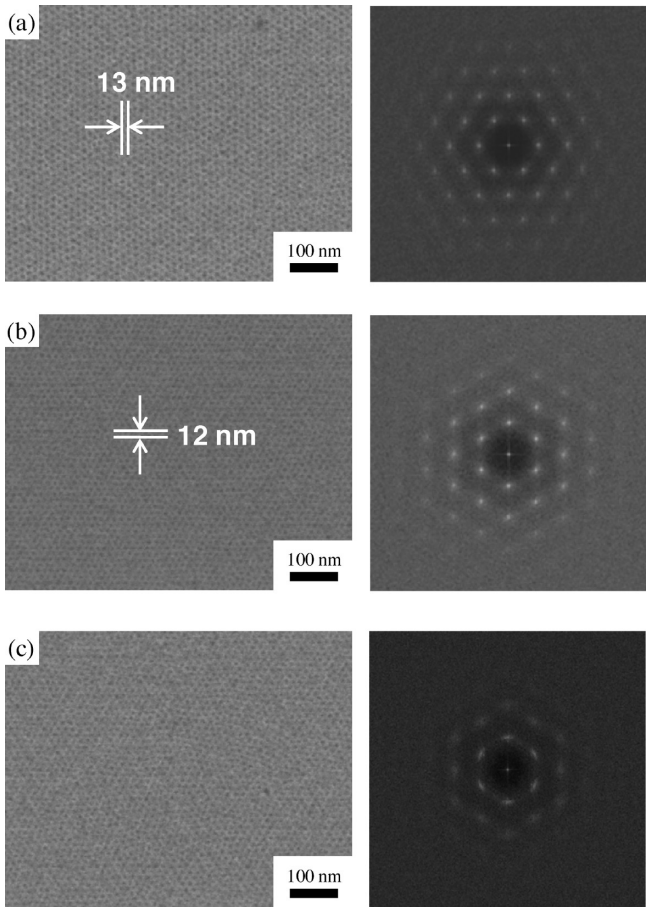

Figure 14. SEM images and the corresponding 2D-FFT images of the $PMMA_{25}$-*b*-$PMAPOSS_{13}$ thin films solvent-annealed at $t_{DS} = 140\%$ on the chemically patterned template with $d_s \approx 2d_0$. (a) d_s = 23 nm, (b) d_s = 24 nm, and (c) d_s = 28 nm. The film thickness is 9 nm. The chemically patterned templates were fabricated employing the PS-OH grafted layer.

the associated 2D-FFT images of the resulting ordered BCP are shown in Figure 14.

In Figure 14a is the resulting directed self-assembled BCP lattice on a chemically patterned template with a single hexagonal lattice pattern spacing of d_s = 23 nm. From the first-order peak positions in the circular-averaged 2D-FFT image, the dot lattice spacing of the self-assembled structures on the template was determined d_{obs} = 13.2 nm. Also note that the orientation of the BCP self-assembled lattice pattern was rotated by 30° with respect to that of the template pattern as schematically illustrated in Figure 15. Therefore, the interpolation of the dots occurred as illustrated in Figure 15, resulting in the hexagonal lattice with the orientation rotated by 30° with respect to the chemical pattern, and the density of the

dx.doi.org/10.1021/ma201822a | *Macromolecules* 2012, 45, 292−304

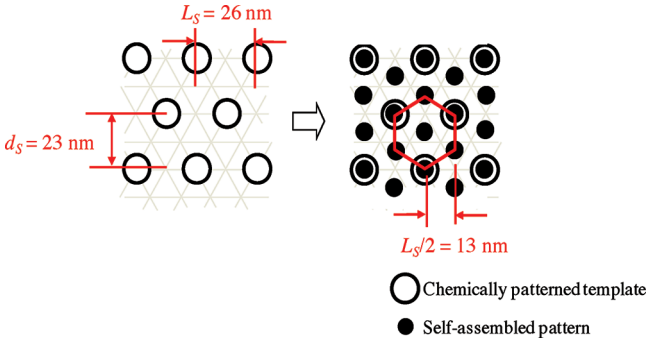

Figure 15. Schematic illustration of the density multiplication for the case shown in Figure 14a. The orientation of the hexagonal lattice of the self-assembled structure (filled circles) is rotated by 30° with respect to that of the chemically patterned template with d_s = 23 nm (open circles). The lattice spacing of the self-assembled structure, d_{obs}, corresponds to a half of the nearest center-to-center spacing of the dotlike holes (open circles) in the chemically patterned template, L_s.

self-assembled BCP is 3 times the density of the underlying chemically patterned template.[25]

In Figure 14b, the underlying chemically patterned template pattern was 24 nm in interplane spacing and 28 nm in the dot-to-dot spacing on axis. The directed BCP assembled in a single hexagonal lattice as shown Figure 14b. The corresponding 2D-FFT image exhibits a spotlike pattern with 3 orders of peaks. Analysis of the first-order peaks gave an average lattice inter-row spacing of d_{obs} = 12.3 nm, which was a half of the value of the lithographically defined chemical pattern, d_s = 24 nm. As determined above, the lattice spacing of the BCP self-assembled structure on the Si, d_0, was 12.4 nm. In this case, the directed BCP lattice had the same spacing as the spacing of the BCP lattice on Si. Areal density of hexagonal lattice pattern with lattice inter-row spacing of d_{obs} = 12.3 nm achieved in this study corresponds to 3.7 Tdot/in.^{2}. Most importantly we have demonstrated successful template pattern density multiplication with a PMMA-*b*-PMAPOSS BCP to an ultrahigh pattern density.

Figure 14c shows the directed self-assembled $PMMA_{25}$-*b*-$PMAPOSS_{13}$ BCP and its 2D-FFT image on a chemically patterned template with d_s = 28 nm. The mismatch chemical pattern on the substrate is further from the period of the $PMMA_{25}$-*b*-$PMAPOSS_{13}$ BCP lattice on Si than the sample in Figure 14a,b, and the long-range order of the self-assembled structure looks worse. However, the closer observation of the 2D-FFT image in Figure 14c shows the superposition of two different hexagonal lattices different lattice spacings (see Figure S6), namely d_{obs} = 12.3 and 13.8 nm. The first-order peaks for lattice spacing d_{obs} = 12.3 nm contain streaks, which suggest much broader orientation distribution of the hexagonal lattice than those shown in Figure 14a,b. This result suggests that a number of hexagonal lattice of the self-assembled structure with d_{obs} = 12.3 nm with slightly different orientations give rise to the arclike peaks. It should be noted that d_{obs} = 12.3 nm is almost identical to d_0 = 12.4 nm of the self-assembled structure on the Si substrate, suggesting that the lattice spacing of the majority of the self-assembled structures was not affected by the template lattice spacing. The first-order peaks of the lattice pattern with d_{obs} = 13.8 nm appear as the sharp points in the 2D-FFT image (Figure S6). In the latter lattice the spacing is ~2× the lithographic pattern spacing, and the BCP matrix stretched by 11% (d_{obs}/d_0 = 13.8/12.4 = 1.11) relative to lattice spacing of the self-assembled structure on the Si substrate as the result of the chemically patterned template with d_s = 28 nm. Thus, Figures 12b and 14 show one region where the self-assembled BCP is directed by the template with d_s = 26 nm and another which is directed by d_s = 23 nm. Both lattices formed an ~4× density multiplication of the original lithographic pattern, but the orientation in the d_{obs} = 13.8 nm is better controlled.

From these results, the reduction of the interface interaction enthalpy between the template surface and the polymer can overcome the loss of the conformational entropy of the block chains up to a 8% (d_{obs}/d_0 = 13.4/12.4 = 1.11) stretch in terms of d_{obs}/d_0 induced by the template pattern with d_s.

■ CONCLUSIONS

We have demonstrated that the directed self-assembly of POSS containing BCP, PMMA-*b*-PMAPOSS, can realize a 4× density multiplication over the chemically patterned substrate by solvent annealing with CS_2, thereby achieving the dot density of about 4 Tbit/in.^{2}. The key factor for the successful density multiplication with a sufficient long-range order is to control the degree of swelling during the solvent annealing process because the lattice spacing of the self-assembled structure of the PMMA-*b*-PMAPOSS film is sensitive to the degree of swelling. It was observed that the lattice spacing of the self-assembled structure changed slightly depending on the degree of swelling even if the same chemically patterned substrate with the hexagonally packed dot pattern was used. The mismatch in the lattice spacing between the template pattern and the BCP microdomains causes a reduction in the long-range order of the self-assembled structure. The swelling with CS_2 is necessary also to provide sufficient mobility to PMMA-*b*-PMAPOSS for self-assembling. Therefore, control of the degree of swelling during the solvent annealing process under the optimum condition is critical.

Furthermore, we showed that the PMMA-*b*-PMAPOSS thin film could undergo morphological transition from cylinders to spheres depending on the degree of swelling as well as the molecular weight of PMMA-*b*-PMAPOSS due to the selectivity of CS_2 to PMAPOSS. It was found that the choice of the material for the grafting layer in the chemical heteroepitaxy was also important. PS-OH was found to be more suitable than PMAPOSS-OH as a chemically patterned template layer for making the defect-free self-assembled structures of PMMA-*b*-PMAPOSS. The self-assembled structure of PMMA-*b*-PMAPOSS can tolerate 12% and 8% mismatch between the lattice spacing of the chemically patterned template and the inherent lattice spacing of the BCP with and without a 4× density multiplication, respectively.

The results show that solvent annealing can be applied to the directed self-assembly with a density multiplication under a controlled annealing environment. With solvent annealing, a wider variety of BCPs can be utilized in the lithographic applications than thermal annealing. The relative selectivity of the solvent for each of the two blocks allows further control of the morphology. In this study, we have limited the study to apply the technique only to the hexagonally packed dot pattern, but the results strongly support the possibility to adapt the technique to other domain structures as well as to more complex features.

dx.doi.org/10.1021/ma201822a | *Macromolecules* 2012, 45, 292–304

■ ASSOCIATED CONTENT

Supporting Information

Experimental details, Schemes S1 and S2, and Figures S1−S7. This material is available free of charge via the Internet at http://pubs.acs.org.

■ AUTHOR INFORMATION

Corresponding Author

*Tel +81 075-383-2620; Fax +81 075-383-2623; e-mail hasegawa@alloy.polym.kyoto-u.ac.jp.

■ ACKNOWLEDGMENTS

T.H. gratefully thanks Prof. Padma Gopalan (University of Wisconsin—Madison) for her helpful discussions on the synthesis of PMMA-*b*-PMAPOSSs. This work was partially supported by New Energy and Industrial Technology Development Organization (NEDO), Japan.

■ REFERENCES

(1) Park, M.; Harrison, C.; Chailin, P. M.; Register, R. A.; Adamson, D. H. *Science* **1997**, *276*, 1401.
(2) Kim, H.-C.; Park, S.-M.; Hinsberg, W. D. *Chem. Rev.* **2010**, *110*, 146.
(3) Galatsis, K.; Wang, K. L.; Ozkan, M.; Ozkan, C. S.; Huang, Y.; Chang, J. P.; Monbouquette, H. G.; Chen, Y.; Nealey, P. F.; Botros, Y. *Adv. Mater.* **2010**, *22*, 769.
(4) Khandpur, A. K.; Forster, S.; Bates, F. S.; Hamely, I. W.; Ryan, A. J.; Bras, W.; Almdal, K.; Mortensen, K. *Macromolecules* **1995**, *28*, 8796.
(5) Bate, F. S.; Fredrickson, G. H. *Annu. Rev. Phys. Chem.* **1990**, *41*, 525.
(6) Hashimoto, T. In *Thermoplastic Elastmers*; Legge, N. R., Holden, G., Schroeder, H. E., Eds.; Hanser: Vienna, 1996.
(7) Matsen, M. W.; Schick, M. *Phys. Rev. Lett.* **1994**, *72*, 2660.
(8) Takenaka, M.; Wakada, T.; Akasaka, S.; Nishitsuji, S.; Saijo, K.; Shimizu, H.; Kim, M. I.; Hasegawa, H. *Macromolecules* **2007**, *40*, 4399.
(9) Bita, I.; Yang, J. K. W.; Jung, Y. S.; Ross, C. A.; Thomas, E. L.; Berggren, K. K. *Science* **2008**, *321*, 939.
(10) Black, C. T.; Guarini, K. W.; Milkove, K. R.; Baker, S. M.; Russell, T. P.; Tuominen, M. T. *Appl. Phys. Lett.* **2001**, *79*, 409.
(11) Segalman, R. A.; Yokoyama, H.; Kramer, E. J. *Adv. Mater.* **2001**, *13*, 1152.
(12) Sundrani, D.; Sibener, S. J. *Macromolecules* **2002**, *35*, 8531.
(13) Cheng, J. Y.; Ross, C. A.; Thomas, E. L.; Smith, H. I.; Vancso, G. J. *Appl. Phys. Lett.* **2002**, *81*, 3657.
(14) Cheng, J. Y.; Mayes, A. M. *Nature Mater.* **2004**, *3*, 823.
(15) Xiao, S. G.; Yang, X. M.; Edwards, E. W.; La, Y. H.; Nealey, P. F. *Nanotechnology* **2005**, *16*, S324.
(16) Chen, F.; Akasaka, S.; Inoue, T.; Takenaka, M.; Hasegawa, H.; Yoshida, H. *Macromol. Rapid Commun.* **2007**, *28*, 2137.
(17) Rockford, L.; Liu, Y.; Mansky, P.; Russell, T. P.; Yoon, M.; Mochrie, S. G. J. *Phys. Rev. Lett.* **1999**, *82*, 2602.
(18) Kim, S. O.; Solak, H. H.; Stoykovich, M. P.; Ferrier, N. J.; de Pablo, J. J.; Nealey, P. F. *Nature* **2003**, *424*, 411.
(19) Edwards, E. W.; Stoykovich, M. P.; Solak, H. H.; Nealey, P. F. *Macromolecules* **2006**, *39*, 3598.
(20) Welander, A. M.; Kang, H.; Stuen, K. O.; Solak, H. H.; Müller, M.; de Pablo, J. J.; Nealey, P. F. *Macromolecules* **2008**, *41*, 2759.
(21) Ruiz, R.; Kang, H.; Detcheverry, F. A.; Dobisz, E.; Kercher, D. S.; Alberecht, T. R.; de Pablo, J. J.; Nealey, P. F. *Science* **2008**, *321*, 936.
(22) Cheng, J. Y.; Rettner, C. T.; Snaders, D. P.; Kim, H. C.; Hinsberg, W. D. *Adv. Mater.* **2008**, *20*, 3155.
(23) Tada, Y.; Akasaka, S.; Yoshida, H.; Hasegawa, H.; Dobisz, E.; Kercher, D.; Takenaka, M. *Macromolecules* **2008**, *41*, 9267.
(24) Tada, Y.; Akasaka, S.; Takenaka, M.; Yoshida, H.; Ruiz, R.; Dobisz, E.; Hasegawa, H. *Polymer* **2009**, *50*, 4250.
(25) Xiao, S.; Yang, X. M.; Park, S.; Weller, D.; Russell, T. P. *Adv. Mater.* **2009**, *21*, 2516.
(26) Wan., L.; Yang, X. M. *Langmuir* **2009**, *25*, 12408.
(27) Cheng, J. Y.; Snaders, D. P.; Truong, H. D.; Harrer, S.; Friz, A.; Holmes, S.; Colburn, M.; Hinsberg, W. D. *ACS Nano* **2010**, *4*, 4815.
(28) Stoykovich, M. P.; Kang, H.; Daoulas, K. C.; Liu, G.; Liu, C.-C.; Pablo, J. J.; Muller, M.; Nealey, P. F. *ACS Nano* **2007**, *1*, 168.
(29) Ruiz, R.; Dobisz, E.; Albrecht, T. R. *ACS Nano* **2011**, *5*, 79.
(30) Kang, H.; Crag, G. S. W.; Nealey, P. F. *J. Vac. Sci. Technol., B* **2008**, *26*, 2495.
(31) Liu, G.; Thomas, C. S.; Craig, G. S. W.; Nealey, P. F. *Adv. Funct. Mater.* **2010**, *20*, 1251.
(32) Jung, Y. S.; Ross, C. A. *Adv. Mater.* **2009**, *21*, 2540.
(33) Jung, Y. S.; Ross, C. A. *Nano Lett.* **2007**, *7*, 2046.
(34) Jung, Y. S.; Chang, J. B.; Verploegen, E.; Berggren, K. K.; Ross, C. A. *Nano Lett.* **2010**, *10*, 1000.
(35) Park, S.; Lee, D. H.; Xu, J.; Kim, B.; Hong, S. W.; Jeong, U.; Xu, T.; Russell, T. P. *Science* **2009**, *323*, 1030.
(36) Takenaka, M.; Aburaya, S.; Akasaka, S.; Hasegawa, H.; Hadjichristidis, N.; Sakellariou, G.; Tada, Y.; Yoshida, H. *J. Polym. Sci., Part B: Polym. Phys.* **2010**, *48*, 2297.
(37) Mori, K.; Hasegawa, H.; Hashimoto, T. *Polymer* **1990**, *31*, 2368.
(38) Bosworth, J. K.; Paik, M. Y.; Ruiz, R.; Schwartz, E. L.; Huang, J. Q.; Ko, A. W.; Smilgies, D.-M.; Black, C. T.; Ober, C. K. *ACS Nano* **2008**, *2*, 1396.
(39) Paik, M. Y.; Bosworth, J. K.; Smilges, D.-M.; Schwartz, E. L.; Andre, X.; Ober, C. K. *Macromolecules* **2010**, *43*, 4253.
(40) Saraf, R. F.; Niu, S.; Stumb, E. *Appl. Phys. Lett.* **2002**, *80*, 4425.
(41) Niu, S.; Saraf, R. F. *Macromolecules* **2003**, *36*, 2428.
(42) Bosworth, J. K.; Dobisz, E.; Ruiz, R. *J. Photopolym. Sci. Technol.* **2010**, *23*, 145.
(43) Hirai, T.; Leolukman, M.; Hayakawa, T.; Kakimoto, M.; Gopalan, P. *Macromolecules* **2008**, *41*, 4558.
(44) Hirai, T.; Leolukman, M.; Jin, S.; Goseki, R.; Ishida, Y.; Kakimoto, M.; Hayakawa, T.; Ree, M.; Gopalan, P. *Macromolecules* **2009**, *42*, 8835.
(45) Hirai, T.; Leolukman, M.; Jin, S.; Liu, C. C.; Han, E.; Kim, Y. J.; Ishida, Y.; Hayakawa, T.; Kakimoto, M.; Nealey, P. F.; Gopalan, P. *Adv. Mater.* **2009**, *21*, 4334.
(46) Kim, B.; Ryu, D. Y.; Pryamitsyn, V.; Ganesan, V. *Macromolecules* **2009**, *42*, 7919.
(47) Ishida, Y.; Tada, Y.; Hirai, T.; Goseki, R.; Kakimoto, M.; Yoshida, H.; Hayakawa, T. *J. Photopolym. Sci. Technol.* **2010**, *23*, 155.
(48) Fourier transfer of a real space image results in a matrix of complex number, which cannot be plotted in a 2D plane. Therefore, its 2D power spectrum density function was plotted and defined as a 2D-FFT image.
(49) Hanley, K. J.; Lodge, T. P.; Huang, C.-I. *Macromolecules* **2000**, *33*, 5918.
(50) Tokarev, I.; Krenek, R.; Burkov, Y.; Schmeisser, D.; Sidorenko, A.; Minko, S.; Stamm, M. *Macromolecules* **2005**, *38*, 507.

Macromolecules

Article

pubs.acs.org/Macromolecules

Structure of pH-Responsive Polymer Brushes Grown at the Gold–Water Interface: Dependence on Grafting Density and Temperature

Haidong Jia,[†] Andrew Wildes,[‡] and Simon Titmuss*[,§]

[†]Department of Chemistry, Physical & Theoretical Chemistry Laboratory, University of Oxford, South Parks Road, Oxford OX1 3QZ, U.K.

[‡]Institut Laue-Langevin, BP 156, 38402 Grenoble Cedex 9, France

[§]School of Physics & Astronomy, University of Edinburgh, Edinburgh EH9 3JZ, U.K.

Supporting Information

ABSTRACT: Poly(2-(dimethylamino)ethyl methacrylate) (PDMAEMA) brushes have been grown by surface-initiated atom transfer radical polymerization (SI-ATRP) from the gold–water interface at different grafting densities, and neutron reflectivity has been used to characterize the response of the brush structures to changes in pH and temperature. Low-density brushes show the greatest response to changes in pH, with the swelling of the highest density brushes essentially independent of pH. The scaling exponent of the swelling ratio with grafting density changes from $\beta \sim -0.7$, which is typical for neutral brushes, at pH 10, to $\beta \sim -1.4$, at pH 3, reflecting the change in the dominant contribution to the osmotic pressure in the brush. At low pH, the osmotic pressure due to the counterions of the charged segments exceeds that of the segmental excluded volume, except in the highest density brushes, resulting in the pH-dependent swelling response of all but the highest density brushes. At pH 10, increasing temperature causes a partial collapse of the brushes with a transition temperature in the range 30–40 °C. The transition is associated with the dehydration of the hydrophilic segments. The magnitude of the deswelling decreases with increasing grafting density, reflecting the decreasing volume fraction of water in the brush.

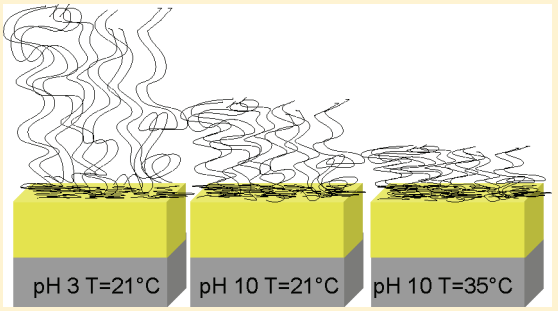

1. INTRODUCTION

Polymer brushes are layers of polymer chains grafted to an interface at a sufficiently high density that, in a good solvent, there is an osmotic driving force for the chains to stretch away from the interface.[1] This extended conformation makes brush layers useful for the steric stabilization of colloidal dispersions[2] as well as tuning the functional properties of interfaces.[3,4] Recently, attention has focused on forming brushes from polymers that respond to physicochemical stimuli, such as pH and temperature, with the aim of producing smart or responsive interfaces, that have potential applications as actuators, sensors, and in control of wetting properties.[5] Control over interfacial wetting of nanoparticles is key in the use of such particles to stabilize Pickering emulsions of immiscible liquids.[6,7]

Dense polymer brushes can be formed by grafting from both planar or nanoparticle interfaces by surface-initiated polymerization either from a small molecule initiator, anchored via thiol or silane chemistry at gold or silica interfaces, respectively,[8] or from polyelectrolytic macroinitiators, adsorbed at charged interfaces.[9] Both approaches have been used in the preparation of stimulus-responsive brushes, which have been characterized by neutron reflectivity measurements.[10−15]

PDMAEMA is a weak polyelectrolyte that exhibits conformational changes in response to both pH and temperature.[11,14] We have used SI-ATRP to functionalize gold nanoparticles with layers of responsive PDMAEMA brushes.[16] These functionalized nanoparticles stabilize Pickering emulsions that can be reversibly broken by altering the pH, giving potential applications in controlled release.[16]

Our overall goal is to relate the microscopic changes in the conformation of the PDMAEMA layer to the macroscopic response of dispersions of gold nanoparticles functionalized with the same responsive polymer layers.[16] Here we focus on the characterization of the brushes and how their swelling behavior varies with grafting density, solution pH, and temperature. By using a planar geometry and neutron reflectivity, attention is focused on the conformational changes that occur in the polymer layer, without the complicating effects of a change in structure factor that occur in small-angle scattering measurements of the dispersions. The effect of interfacial curvature on layer structure and the microscopic and macroscopic structural response of the nanoparticle dispersions will be described in a future publication.

2. EXPERIMENTAL SECTION

2.1. Materials and Sample Preparation. *2.1.1. Materials.* DMAEMA was purchased from Aldrich and purified by passing it through a basic alumina column (150 mesh) also from Aldrich.

Received: August 11, 2011
Revised: December 7, 2011
Published: December 14, 2011

Table 1. Dry Thicknesses, Grafting Densities, and Swollen Thicknesses for the PDMAEMA Brushes

sample	G4	G2	G7	G5
initiator/%	10	10	25	100
polymerization time/h	1	2	1	1
h_{dry}/Å	50 ± 3	90 ± 5	100 ± 5	190 ± 5
σ/Å^{-2}	0.0015 ± 0.0001	0.0014 ± 0.0001	0.003 ± 0.0001	0.0057 ± 0.0001
$L_{pH\ 3}$/Å	234	564	340	360
$L_{pH\ 7}$/Å	142	338	271	342
$L_{pH\ 10}$/Å	127	271	246	342
T_{spike}/Å	24	20	16	5
ϕ_{spike}	0.94	0.94	0.94	0.94
N	148	286	148	148
f_{brush}	0.57	0.76	0.86	0.98

Cu(I)Br, Cu(II)Br_2, 1,1,4,7,10,10-hexamethyltriethylenetetramine (HMTETA), 11-mercapto-1-undecanethiol (MUT), dichlorobenzene, propan-2-ol, iodine (I_2), tetrahydrofuran (THF), and dichloromethane (CH_2Cl_2) were purchased from Aldrich and used without further purification; mercaptoundecyl bromisobutyrate (MUBB) was purchased from Prochimia and used without further purification.

2.1.2. Preparation of Gold-Coated Quartz Blocks. One-side polished quartz blocks (Crystran) with dimensions 50 × 60 × 11 mm were used as the superphase, through which the neutrons are incident on the interface. Before deposition of gold, the quartz blocks were first washed for 10 min with a 2% Hellmanex solution at 60 °C and then immersed in aqua regia (3:1 mixture of HCl and HNO_3) for 2 h. The blocks were then successively rinsed with 18 MΩ cm conductivity water and ethanol, before drying under a nitrogen stream. The blocks were then subjected to 30 min of UV/ozone cleaning. The coating procedure was carried out in the Thin Film Facility at the Department of Physics, University of Oxford, using a Leybold L560 coating plant. The blocks were first coated with a ∼10 nm titanium adhesion layer, followed by a ∼10 nm gold layer.

2.1.3. Self-Assembly of the Initiator Monolayer. The gold-coated quartz blocks were immersed in a 5 mM solution of the initiator (MUBB) in dichlorobenzene for 12 h at room temperature, forming a self-assembled monolayer (SAM) with a thickness of 0.8 nm, as determined by ellipsometry and neutron reflectivity (data shown in Figure S2 and fit parameters in Table S1, in the Supporting Information). The grafting density of the polymer brushes was controlled by varying the molar ratio of the initiator (MUBB) to dilutant (MUT), an approach previously demonstrated by Jones et al.[17] SAMs comprising 10%, 25%, and 100% MUBB have been used in this study.

2.1.4. Surface-Inititiated Atom Transfer Radical Polymerization. In a flask, 80 mL of a reaction mixture comprising DMAEMA (335 mmol), CuBr (1.34 mmol), $CuBr_2$ (0.15 mmol), HMTETA (3.2 mmol), and 20 mL of propan-2-ol/water (8:2) was degassed by purging with nitrogen for 30 min. The mixture in the flask was then transferred under nitrogen to a reaction chamber containing the initiator-functionalized gold-coated quartz blocks. To obtain brushes comprising chains of similar molecular weights, the polymerizations on blocks G4, G5, and G7 (see Table 1) were performed under identical conditions for 1 h; for block G2, the polymerization time was doubled.

2.1.5. Fourier Transform Infrared Attenuated Total Reflection (FTIR-ATR). FTIR-ATR spectra were measured using a Bio-Rad FTS 7000 spectrometer, in which the infrared light is reflected back through an objective onto a liquid-nitrogen-cooled narrow-band mercury–cadmium–telluride (MCT) detector. The spectra comprise 256 scans at a resolution of 2 cm^{-1}.

2.1.6. Matrix-Assisted Laser Desorption Ionization Mass Spectrometry (MALDI-MS). To determine the molecular weight of the PDMAEMA chains making up the brushes, the thiol bond was cleaved by oxidation following overnight incubation in a 4 mM solution of iodine in dichloromethane. The iodine/dichloromethane was then removed by reduced pressure evaporation, and the remaining polymer was dissolved in THF and analyzed by MALDI-MS.

MALDI-MS was performed on a Bruker time-of-flight spectrometer. The PDMAEMA cleaved from the interface (∼1 mg) was dissolved in 100 μL of THF, and 2 μL of this was mixed with 10 μL of a matrix solution comprising 0.1 M 2,5-dihydroxybenzoic acid (DHA) in a 1:1 (v/v) water/acetonitrile mixture, to which 2 μL of 0.1 M NaCl was added. Approximately 4 μL of this mixture was placed on the sample plate and dried. The sample was irradiated at λ = 337 nm at 5 Hz with a total accumulation of 200 shots per spectrum at a power slightly above the threshold for ion formation. The molecular weight was determined by numerical integration of the resulting peak area.

2.1.7. Ellipsometry. The dry thickness of the polymer layer was measured using a Beaglehole ellipsometer. The relative change in the phase shift and amplitude of the two perpendicular components of polarized incident light (λ = 632.8 nm) upon reflection from an interfacial layer are used to determine the mean refractive index and average thickness of the film.[18] The dry polymer layer was modeled as a single layer sandwiched between gold and air and the refractive index of the PDMAEMA polymer was assumed to be described by Cauchy parameters A_n = 1.52 and B_n = 0.01. Measurements made at five different points yielded identical dry thicknesses.

2.1.8. Neutron Reflectivity. Specular neutron reflectivity measurements were made in time-of-flight mode using the D17 reflectometer at ILL.[19] Reflectivity profiles presented in this work are plots of RQ^4, where R is the specular reflectivity and $Q = 4\pi \sin\theta/\lambda$, with θ the glancing angle of incidence and λ the neutron wavelength, is the momentum transfer. Plotting and fitting the data in Porod form (RQ^4) removes the effect of the reflectivity decreasing as $R \sim Q^{-4}$ at $Q \gg Q_c$ expected for a sharp interface, highlighting the effects of small changes in reflectivity across the whole Q-range. Glancing angles of incidence of 0.3° and 2.3° were used giving a Q-range of 0.0033–0.22 Å^{-1}. The reflected intensity was normalized to the incident beam spectral distribution and detector efficiency and established on an absolute reflectivity scale with a resolution $\Delta Q/Q$ = 5%. The reflectivity at $Q >$ 0.2 Å^{-1} is dominated by sample-dependent background, which arises primarily from the incoherent scattering from the bulk solution. To remove this contribution, a background measured to the side of the specular ridge was subtracted before evaluating the reflectivity.

The thickness and roughness of the gold and titanium layers were first determined by neutron reflectivity measurements from a quartz block (coated with the metal layers during the same deposition as those used to prepare the brush layers) with D_2O and cmAu subphases. Typical reflectivity profiles and the metal layer thicknesses are shown in Figure S2 of the Supporting Information.

The MOTOFIT package[20] was used to fit the reflectivity profiles to model scattering length density profiles. The model comprises a layer of Ti between the quartz superphase and a layer of Au (layer thicknesses and roughnesses given in Table S1) capped by a 8 Å initiator layer (common to all models), followed by two layers with scattering length densities corresponding to mixtures of polymer and solvent to represent the brush region.

Quartz was chosen as the superphase (through which the neutrons are incident on the interface) as its scattering length density is close to that of gold, which means that with a subphase that is contrast-

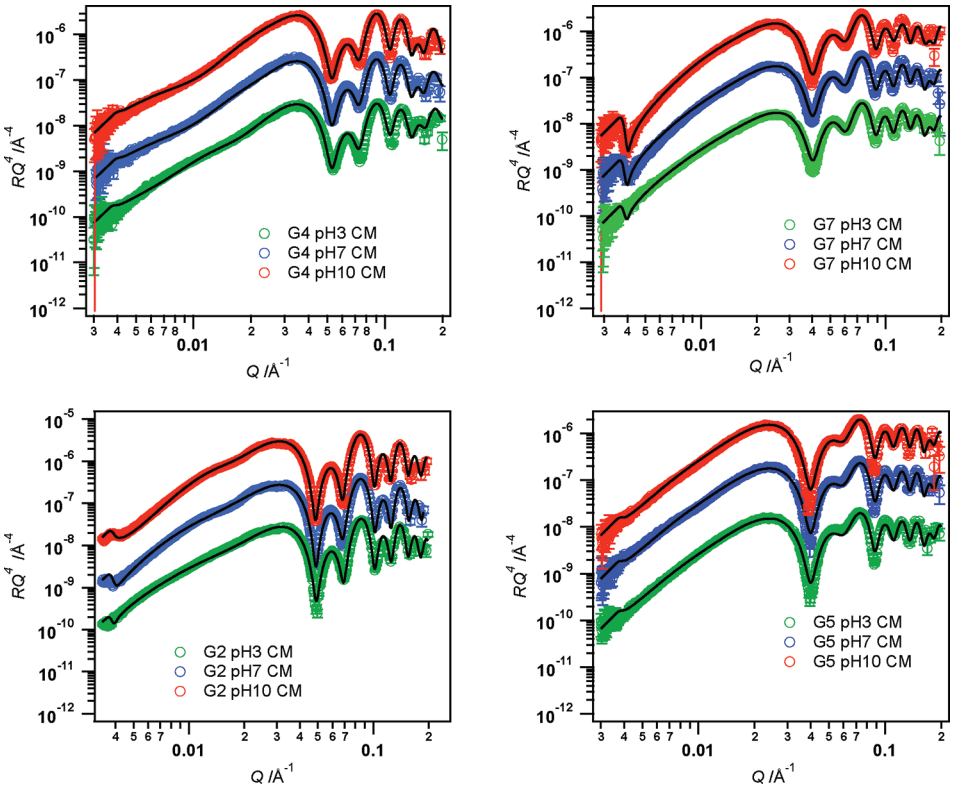

Figure 1. Porod plots of specular neutron reflectivity measured from PDMAEMA brushes (as in Table 1) at the quartz|Ti|gold−water (cmAu) interface at a temperature of 21 °C; solid lines give best fits to the reflectivities. The plots measured at pH 3 are on the correct absolute scale, whereas those measured at pH 7 and pH 10 are offset by scaling factors of 10 and 100, respectively.

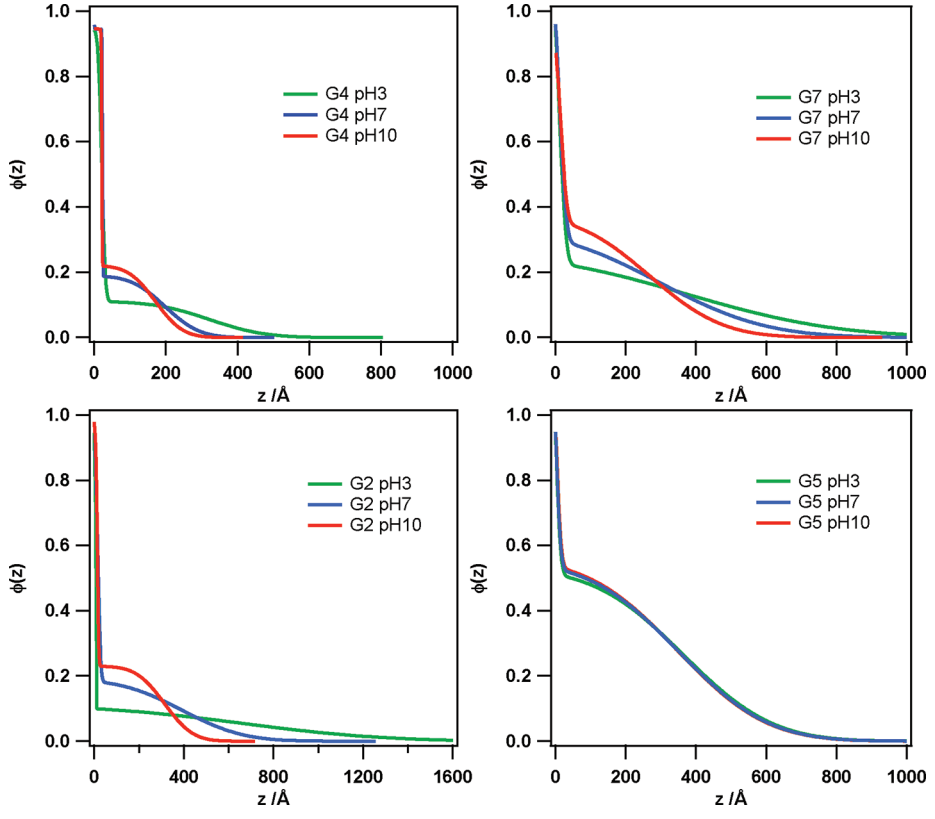

Figure 2. Interfacial volume fraction profiles determined for the PDMAEMA brushes (as in Table 1) at pH 3, pH 7, and pH 10.

matched to gold (cmAu), a buildup of hydrogenous material at the gold interface creates a well in the scattering potential between the gold interface and the bulk cmAu phase, as illustrated by Figure S1 of the Supporting Information. This makes the curvature of the Porod

dx.doi.org/10.1021/ma201839y | *Macromolecules* 2012, 45, 305−312

plot in the range $0.004 < Q < 0.05$ Å^{-1} sensitive to the shape of the polymer volume fraction profile.

The scattering length density profiles of the brush region, $\rho(z)$, were optimized using a genetic algorithm in which the layer thicknesses, scattering length densities and roughnesses are varied to minimize the χ^2 between the measured and calculated reflectivities. The monomer volume fraction profiles were then determined as

$$\varphi(z) = \frac{\rho(z) - \rho_{sub}}{\rho_{DMAEMA} - \rho_{sub}} \quad (1)$$

where ρ_{sub} is the scattering length density of the D_2O ($\rho_{D_2O} = 6.35 \times 10^{-6}$ Å^{-2}) or cmAu ($\rho_{cmAu} = 4.5 \times 10^{-6}$ Å^{-2}) subphase and ρ_{DMAEMA}(= 0.8×10^{-6} Å^{-2}) is the scattering length density of the polymer.[21]

From the volume fraction profile, we evaluate the surface excess of polymer grafted to the interface, $\gamma = \int_0^\infty \phi(z)\, dz$, and a measure of the swollen thickness of the layer, L[22,23]

$$L = \frac{2\int_0^\infty z\varphi(z)\, dz}{\int_0^\infty \varphi(z)\, dz} \quad (2)$$

Neutron reflectivity was measured with both D_2O and cmAu subphases at pH 7. The covalent grafting of the polymer means that the total amount of polymer at the interface must be the same in each of these measurements and should be consistent with the dry thickness measured by ellipsometry, h_{dry}, before the neutron reflectivity experiment. The total amount of polymer obtained from these measurements was used to constrain the fitting of the reflectivities measured, at different pHs and temperatures, with a single cmAu subphase.

3. RESULTS AND DISCUSSION

3.1. Polymer Brush Growth and Characterization.

Four different brushes, characterized by three different grafting densities and two different degrees of polymerization, have been prepared, and their properties are summarized in Table 1. Figure S3 of the Supporting Information shows the FTIR-ATR spectrum of a PDMAEMA (100% MUBB, 1 h polymerization, dry thickness = 19 nm) brush grown from a gold–water

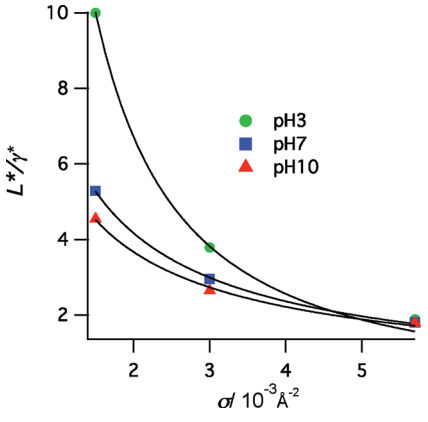

Figure 3. Plots of swelling ratio for the swellable part of the brush as a function of grafting density at different pHs.

Table 2. Scaling Exponents for Brush Swelling Ratio with Degree of Polymerization (α) and Grafting Density (β)

pH	prefactor	α	β
3	0.001	−0.19	−1.39
7	0.03	−0.05	−0.82
10	0.04	−0.06	−0.73

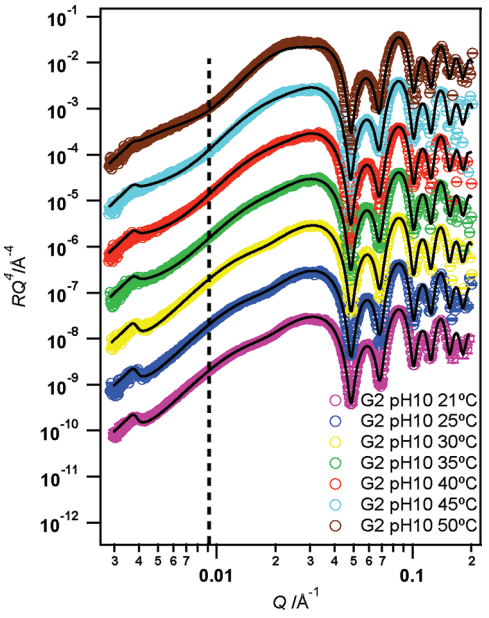

Figure 4. Porod plots of specular neutron reflectivity measured from PDMAEMA brush G2 (see Table 1) at the quartz|Tilgold–water (cmAu) interface at pH 10 with increasing temperature; solid lines give best fits to the reflectivities. The plot measured at 21 °C is on the correct absolute scale, whereas those measured at increasing temperatures are offset by a constant scaling factor of 10.

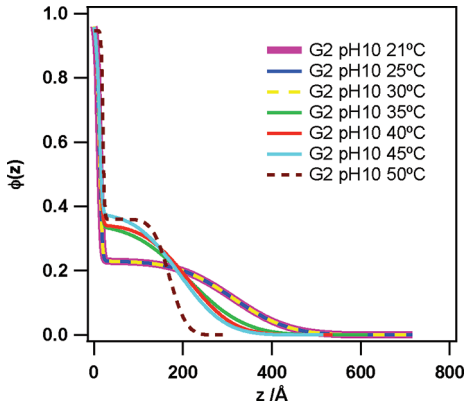

Figure 5. Interfacial volume fraction profiles determined for the PDMAEMA brush G2 (see Table 1) at pH 10 with increasing temperature.

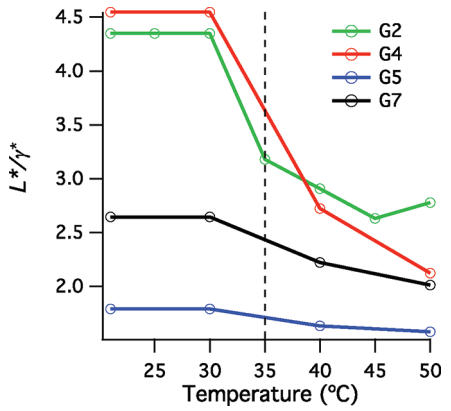

Figure 6. Temperature dependence of the swelling ratio for the PDMAEMA brushes.

dx.doi.org/10.1021/ma201839y | Macromolecules 2012, 45, 305–312

interface. The appearance of C−H stretches at 2700−3000 cm^{-1}, ester carbonyl stretch at 1729 cm^{-1}, and tertiary amine peak at 1150 cm^{-1} demonstrates the successful growth of PDMAEMA brushes from the gold−water interface. To obtain the molecular weight of the grafted PDMAEMA chains, the chains were first oxidatively cleaved from gold interface using iodine, resulting in the disappearance of these characteristic infrared absorption peaks. MALDI-MS was used to determine the molecular weight. A typical mass spectrum obtained from PDMAEMA cleaved from a gold interface following a 1 h polymerization is shown in Figure S4 of the Supporting Information. Numerical integration of the highest intensity peak (27 463 Da) gives the number-average molecular weight M_n = 26 360 Da; the mass spectrum also shows dimer and trimer peaks at 54 733 and 82 102 Da, respectively. The dry thickness measured by ellipsometry at a given grafting density was found to increase linearly with polymerization time unless the polymerization time exceeded 2 h, meaning that polymerization time can reliably be used to control the degree of polymerization. For each brush, ellipsometry measurements at five different positions yielded the same dry thickness. The grafting density can be controlled by choosing the appropriate ratio of initiator to dilutant thiol: in this study solution compositions of 10%, 25%, and 100% MUBB have been used. The grafting density was evaluated from the measured dry thickness h and grafted chain molecular weight (M) as

$$\sigma = \frac{\rho_m h N_A}{M} \tag{3}$$

where ρ_m is the mass density of the DMEAMA. We found that it was not possible to obtain brushes with a grafting density $\sigma >$ 0.006 $Å^{-2}$ even for an incubation solution composition of 100% MUBB and incubation times in excess of 24 h. Although the grafting density increases with the mole fraction of MUBB in the incubation solution, the increase is nonlinear, which raises the possibility that the chain initiation efficiency is dependent on the fractional coverage of initiators in the thiol monolayer. It appears that the initiation efficiency decreases with increasing density of grafted chains. At high chain density, crowding within the polymer layer will affect the local concentration of reactants and hence the relative reaction rates of initiation, propagation, and termination.[24] This is likely to exert the greatest influence on reactions between grafted chains, such as termination between grafted radicals and degenarative chain transfer between a grafted chain and a grafted radical.

3.2. pH Response of PDMAEMA Brushes. Figure 1 shows Porod plots of the neutron reflectivity measured from the brushes listed in Table 1 as a function of pH. In all cases the reflectivity at $Q > 0.04$ $Å^{-1}$ is dominated by the Kiessig fringes that result from the well-defined titanium, gold, and initiator layers that are sandwiched between the quartz and the PDMAEMA−water interface. Comparison of the high-Q regions for G5/G7 indicate that this fringe structure is modulated by changes in the polymer layer, although it is in the low-Q region, just above the critical edge, that changes in brush structure with pH lead to the most obvious changes in reflectivity. Figure 2 shows the volume fraction profiles that give the best fits to the Porod plots. The volume fraction profiles comprise a thin (layer thickness T_{spike}), high volume fraction (ϕ_{spike}) layer or spike, at the solid−liquid interface, that is independent of pH, followed by a Gaussian-like decay into the liquid phase. From Figure S1, it can be seen that the spike layer is associated with the polymer layer rather than the initiator monolayer.

We have previously observed a similar spike layer in our study of PDMAEMA brushes grown from a macroinitiator adsorbed on sapphire,[14] and similar density profiles have been observed for PDMAEMA brushes formed by a Langmuir−Schaefer transfer of diblock copolymers, with a hydrophobic PMMA anchoring block, from the air−water interface onto a hydrophobized silicon substrate.[25] The spike layer is required to ensure that a good fit is obtained across the complete Q-range of the Porod plots for models consistent with the total amount of polymer at the interface determined by ellipsometry. The absence of such a spike from the density profiles determined for PDMAEMA brushes grown from silica interfaces could be associated with the more limited Q-range employed in their neutron reflectivity measurements,[11] as it is the high Q-range that will offer the greatest sensitivity to thin interfacial layers; furthermore, our approach of fitting to a Porod plot treats the high Q-range with a comparable weight to the low Q-range, which is predominantly sensitive to the overall shape of the density profile and total amount of polymer at the interface.

As this spike layer is independent of pH, the segments comprising it are clearly not involved in the swelling of the brush. We suggest that an attractive interaction either between the DMAEMA segments and the initiator-coated gold interface or between DMAEMA segments in the lower part of the brush is sufficient to overcome the swelling effect of the osmotic pressure due to the segment excluded volume and the counterions. An increase in either of these contributions to the free energy of the chain will lead to an increase in the swelling force that is exerted on the adsorbed segments comprising the spike. From Table 1 it is clear that as the grafting density, σ, increases the fraction (and total number) of segments that are adsorbed at the initiator−water interface decreases.

For a weak polyelectrolyte, there are two osmotic contributions to the free energy of the brush that favor stretching of an individual chain, against the entropic elasticity, driving brush swelling. Within a Flory−Huggins approach, the combinatorial excluded volume contribution to the osmotic pressure scales as $\Pi_{mix} \sim \phi^2$. When the segments are charged, the condition of local electroneutrality means there will also be an osmotic pressure due to counterions confined within the brush, $\Pi_{counter} \sim N\sigma$, which implies that the osmotic stretching force on each chain due to the counterions is independent of the grafting density. This means that the increased swelling force that pulls segments out of the spike layer of adsorbed PDMAEMA must be a consequence of the increased excluded volume contribution to the osmotic pressure at high grafting density.

It is the Gaussian part of the brush distribution which changes in response to changes in pH, causing the changes in reflectivity at low-Q, that are associated with changes in the overall shape of the scattering potential well between the quartz|Ti|Au superphase and the cmAu subphase.

The response of the outer part of the brush distribution to changes in pH is characterized by the degree of swelling (L^*/γ^*), where $\gamma^* = h_{dry} - \phi_{spike}T_{spike}$ is the amount of polymer in the swollen Gaussian part of the distribution and L^* is a measure of the swollen thickness of this part of the distribution, determined by evaluating the moment of the outer part of the brush (i.e., excluding the spike) relative to the base of the

dx.doi.org/10.1021/ma201839y | Macromolecules 2012, 45, 305−312

swellable brush region at the outer edge of the spike.[26] Figure 3 shows a plot of the degree of swelling as a function of grafting density for the three lower molecular weight brushes at the three pHs. From the volume fraction profiles in Figure 2 and the degrees of swelling plotted in Figure 3, it is clear that the low density brushes (G4 and G2) display the greatest pH response and that the response (degree of swelling) depends only weakly on the degree of polymerization. The swelling follows a well-defined power law dependence on the grafting density, σ

$$\frac{L^*}{\gamma^*} \sim (fN)^{\alpha}\sigma^{\beta} \tag{4}$$

where f is the fraction of the N monomers of the polymer that are in the swollen Gaussian part of the distribution.

There is a clear change in the scaling exponent β from $\beta = -0.82$ at pH 7 to $\beta = -1.4$ at pH 3. These values are comparable to the $\beta = -0.7$ obtained for uncharged PDMAEMA in methanol and $\beta = -0.95$ obtained for PTMAEMA, the quaternized strong polyelectrolyte analogue, in water.[11] From the small differences in the degrees of swelling observed for the two brushes with different degrees of polymerization (G2 and G4), the scaling parameter α has been evaluated at the three pHs and is tabulated in Table 2.

The classic scaling approach to weak polyelectrolyte brushes predicts[27]

$$\frac{L^*}{\gamma^*} \sim N^0\sigma^{-4/3}c_s^{-1/3} \tag{5}$$

where c_s is the concentration of added salt (i.e., ions that cannot participate in the acid−base equilibrium). Using a continuum numerical SCF approach, Witte et al. explicitly demonstrated that such a scaling law is only obtained when the compressibility constraint is removed, i.e., in the limit that the effective segment volume tends to zero.[28] For a finite segmental excluded volume they obtain a range of scaling exponents for brush height with grafting density ($L \sim \sigma^l$) from $l = 0.14$ to $l = 0.3$, depending on the solvent quality, segmental excluded volume, pH, and ionic strength. As $\gamma^* \sim N\sigma$, the corresponding values of β lie in the range −0.86 to −0.7. The values of β obtained experimentally here, shown in Table 2, range from close to the classic scaling result of eq 5 at pH 3 to the results of the numerical SCF study at pH 7 and 10. In particular, the value of $\beta_{\mathrm{pH}\ 3} = -1.4$ implies that the brush height at pH 3 scales only weakly with grafting density ($l = -0.4$). The small negative scaling exponent indicates that the brush is truly in the osmotic regime in which the osmotic pressure due to the counterions dominates over that due to the segmental excluded volume. This explains the low prefactor observed at pH 3: the osmotic pressure due to the counterions is sufficiently high that the average volume occupied by each segment in the swollen brush is greater than the excluded volume of the segment, which is equivalent to relaxing the incompressibility constraint described by Witte et al.[28] The nonzero scaling exponent with grafting density is a result of the increase in the local concentration of monomers, with increasing σ, which shifts the acid−base equilibrium toward the reactants (i.e., unprotonated monomers), decreasing the average degree of charging, lowering the osmotic pressure of the confined counterions, leading to a less swollen brush compared to a lower grafted density brush. The weak scaling dependence of the degree of swelling on degree of polymerization, which is evident from the values of α in Table 2, was also observed in the SCF study for brushes comprising chains of less than 10^2 Kuhn segments.[28]

When designing polymer layers to be responsive to changes in pH, it is clear from Figure 3 that the highest grafting density measured (G5 corresponding to 100% MUBB) is not suitable. At this grafting density, the volume fraction of polymer is sufficiently high that the osmotic pressure due to the segments exceeds that due to the counterions of the charged segments, even at pH 3, resulting in a degree of swelling is essentially independent of pH.

It was noted above that the observation of a spike layer at the base of the brush is suggestive of either an attractive interaction between the DMAEMA segments and the initiator-coated gold interface or between DMAEMA segments in the lower part of the brush. Although PDMAEMA has been used to anchor diblock polymers to the interfaces of bare gold nanoparticles,[29] in the system studied here, the gold interface is covered by a dense thiol layer, so the electrostatic anchoring mechanism suggested for the PDMAEMA on bare gold nanoparticles is unlikely to be applicable. We suggest two alternative mechanisms for this attractive interaction, depending on the charge on the segments at the base of the brush, closest to the interface. In the case that these segments are either charged or exist as a dipole comprising ionized segment and a bound counterion, a charge−image−charge or dipole−image−dipole interaction at the dielectric discontinuity of the thiol-coated gold−water interface could lead to an attraction between the segment and the interface. In the case that the segments at the base of the brush are uncharged, then the effective solvent quality of these segments will be poorer, resulting in a net attraction for the hydrophobic thiol layer. For sufficiently dense brushes, SCF calculations have predicted that a large fraction of segments nearest the grafting interface of weak polyelectrolyte brushes might be uncharged, as the high local concentration of segments, coupled to a long screening length, shifts the chemical equilbrium of the acid−base ionization toward the uncharged segments.[28,30] In addition to driving attraction between the uncharged segments and the hydrophobic thiol-coated interface, this will also favor an attraction between uncharged DMAEMA segments, which will also result in a dense inner layer.

Recently, experimental[31,32] and theoretical[30,33] studies have suggested that weak polyelectrolyte brush systems can be unstable with respect to the formation of lateral inhomogeneities. The driving force for this instability is the existence of a minimum in the chain chemical potential with coverage, caused by the coupling between the chemical equilibrium between charged and uncharged segments, the solvent quality, and the local segment density, which drives the tethered chains to microphase separate into high- and low-density domains.[30] The experimental observations were made by AFM on PDMAEMA brushes formed from diblock copolymers transferred from an air−water interface by Langmuir−Blodgett deposition.[31,32] The conformational degrees of freedom that are responsible for determining the length scale of the lateral inhomogeneities are absent from the covalently grafted chains that form the brushes that we studied. Furthermore, the brushes studied here are at grafting densities that exceed those in the AFM studies and so outside the lateral instability region. Nevertheless, the authors of the AFM study point out that that in the case of immobile chains the instability that drives the lateral microphase separation in their system will result in a microscopic

reorganization of the chain conformation in both the lateral and vertical directions.[32] The specular neutron reflectivity measurements we present provide a laterally averaged density profile. The dense spike layer could be a manifestation of a vertical reorganization into a dense inner layer and a dilute outer layer, consistent with the prediction of SCF calculations, which predict a low fraction of charged segments in the dense inner region even at low pH.[28]

3.3. Temperature Response of PDMAEMA Brushes.

PDMAEMA is also responsive to changes in temperature, and the thermoresponsive properties are dependent on pH, with the cloud point decreasing from 76 °C at pH 7 to around 38 °C at pH 10, for solutions of a linear PDMAEMA of comparable molecular weight to the chains forming the brushes in this study.[34] Figure 4 shows the variation in the neutron reflectivity from brush G2 at pH 10 as the temperature is changed (temperature-dependent neutron reflectivities for the other brushes are given in Figure S5 of the Supporting Information). The corresponding volume fraction profiles that give the best fits to the measured reflectivities are shown in Figure 5 for G2 and in Figure S6 in the Supporting Information for the other brushes. There is a clear change in the curvature of the Porod plots that occurs at $Q \sim 0.009$ Å^{-1} at a temperature between 30 and 35 °C. (Figure S7 in the Supporting Information highlights this region of the experimental reflectivity profiles.) This can be attributed to a pronounced increase in the volume fraction of polymer just beyond the interfacial spike that is accompanied by a more rapid decay into the solution phase, resulting in a less swollen layer. For the other brushes, fewer measurements were possible due to time constraints, so it is only possible to identify that the transition occurs between 30 and 40 °C. The volume fraction profiles have some similarities with those determined by Yim et al. in their neutron reflectivity study of PNIPAM brushes.[13,35,36] They attribute the bilayer structure to a vertical phase separation into an inner dense phase and an outer dilute phase, as has been predicted for brushes formed from chains that are at a temperature above the LCST.[37]

The response of the brushes to temperature is summarized in Figure 6, which plots L^*/γ^* as a function of temperature; the amount of polymer in the spike layer adjacent to initiator-coated gold interface does not change with temperature, so L^*/γ^* is again evaluated for the swollen part of the distribution, excluding the spike. As is evident from Table 1 at 21 °C, the spike layer is most pronounced for the low grafting density brushes (G2 and G4). For the higher density brushes, in which the average volume fraction is higher, there is a smoother transition between the inner spike layer and the swollen Gaussian part of the distribution. As the temperature increases beyond the partial collapse transition, and the average volume fraction increases in the less swollen low-density brushes, the overall shape of the distributions become more similar to those of the higher-density brushes.

For G2 a second transition occurs between 45 and 50 °C, although this is associated with a loss of 16% of the polymer from the interface, which means that unlike the other brushes, the temperature response would not be fully reversible on cooling. The loss of chains from the interface is a consequence of the unstable nature of the gold−thiol bond at elevated temperatures.[38] That degrafting is only observed for the highest molecular weight chains is easily understood for the case of a good solvent, as there is an osmotic driving force pulling the chain out of the high density brush that will increase with chain length. That it is observed for chains in a brush that is above the temperature-induced collapse transition highlights the two-phase nature of these brushes in this regime and the volume fraction dependence of the Flory χ parameter.[37,39,40] The dependence of solvent quality on volume fraction results in incomplete brush collapse, occurring first at the base of the brush where the monomer density is highest. We suggest that it is the swelling of the low-density outer region of the brush that provides an osmotic force pulling the chain out of the brush. Only for the brush formed from high molecular weight chains is this force sufficiently large for chains to desorb from the gold interface.

The origin of the volume fraction and temperature dependence of the χ parameter that is manifested as a lower critical solution temperature has been explained in terms of a hydrophilic/hydrophobic two-state model,[39] in which hydrogen-bonding interactions and the translational entropy of water play a key role. As the temperature increases, dehydration of the DMAEMA monomers is favored, provided that the volume fraction of monomers is sufficiently high for water−monomer hydrogen bonds to be replaced by monomer−monomer hydrogen bonds. The high average volume fraction of polymer in the densest brush means that the monomers are already less hydrated than in the lower density brushes, so the decrease in hydration that occurs on increasing the temperature above the transition results in a smaller decrease in the excluded volume and hence a smaller deswelling than in the lower density brushes.

4. CONCLUSIONS

SI-ATRP has been used to graft PDMAEMA brushes from thiol initiators at different grafting densities at the gold−water interface. The swelling ratio of these layers display different scalings with grafting density at pH 3 compared with pH 7 and 10, which can be attributed to a switch in the dominant contribution to the osmotic pressure within the brush from the counterions of the charged segments at pH 3 to the segment excluded volume at pH 7 and 10. The highest density brush (corresponding to 0.006 chains/Å^2) displays the weakest response to changes in pH. At pH 10, the brushes undergo a partial collapse when a transition temperature in the range 30−40 °C is exceeded. Above this transition temperature a two-phase brush develops, with a dense inner region and a dilute outer region. The observation that the dense inner region of this two-phase brush region does not reach the very high density of the thin spike layer, which is always present independent of pH or temperature, suggests that in the spike layer there is an attractive interaction for the hydrophobic thiol-coated interface in addition to the volume-fraction-dependent solvent quality driven interaction between DMAEMA segments that is present in the dense region that forms following temperature-induced partial collapse. The temperature response is also greatest for the lowest density brushes, which contain the highest volume fraction of water and so are the most sensitive to dehydration of the hydrophilic segments.

These quantitative observations of the response of PDMAEMA brush conformation to changes in pH and temperature have helped in the formulation of design rules for the functionalization of gold nanoparticles to act as temperature and pH controllable emulsifiers.[16]

■ ASSOCIATED CONTENT

Supporting Information

Table S1 and Figures S1−S7. This material is available free of charge via the Internet at http://pubs.acs.org.

■ AUTHOR INFORMATION

Corresponding Author

*E-mail: simon.titmuss@ed.ac.uk.

■ ACKNOWLEDGMENTS

H.J. acknowledges the EPSRC & Royal-Dutch Shell for the award of a Dorothy Hodgkin Postgraduate Award (EP/P501954/1), and S.T. thanks the Royal Society for a University Research Fellowship, the Scottish Universities Physics Alliance (SUPA), and the National Physical Laboratory's Strategic Research Programme. We thank the Institut Laue Langevin (France) for the award of beam-time, ISIS (Rutherford Appleton Laboratory, STFC) for consumables support, and Mr. Rick Makin (Department of Physics, Thin Film Facility, University of Oxford) for depositing the gold/titanium layers.

■ REFERENCES

(1) Toomey, R.; Tirrell, M. *Annu. Rev. Phys. Chem.* **2008**, *59*, 493−517.

(2) Jia, H.; Grillo, I.; Titmuss, S. *Langmuir* **2010**, *26*, 7482−7488.

(3) La Spina, R.; Tomlinson, M. R.; Ruiz-Pérez, L.; Chiche, A.; Langridge, S.; Geoghegan, M. *Angew. Chem., Int. Ed.* **2007**, *46*, 6460−6463.

(4) Jia, H.; Titmuss, S. *Nanomedicine* **2009**, *4*, 951−966.

(5) Chen, T.; Ferris, R.; Zhang, J.; Ducker, R.; Zauscher, S. *Prog. Polym. Sci.* **2010**, 94−112.

(6) Haase, M. F.; Grigoriev, D.; Moehwald, H.; Tiersch, B.; Shchukin, D. G. *Langmuir* **2011**, *27*, 74−82.

(7) Saigal, T.; Dong, H.; Matyjaszewski, K.; Tilton, R. D. *Langmuir* **2010**, *26*, 15200−15209.

(8) Edmondson, S.; Osbourne, V. L.; Huck, W. T. S. *Chem. Soc. Rev.* **2004**, *33*, 14−22.

(9) Edmondson, S.; Armes, S. P. *Polym. Int.* **2009**, *58*, 307−316.

(10) Geoghegan, M.; Ruiz-Pérez, L.; Dang, C. C.; Parnell, A. J.; Martin, S. J.; Howse, J. R.; Jones, R. A. L.; Golestanian, R.; Topham, P. D.; Crook, C. J.; Ryan, A. J.; Sivia, D. S.; Webster, J. R. P.; Menelle, A. *Soft Matter* **2006**, *2*, 1070−1080.

(11) Sanjuan, S.; Perrin, P.; Pantoustier, N.; Tran, Y. *Langmuir* **2007**, *23*, 5769−5778.

(12) Zhang, J.; Nylander, T.; Campbell, R. A.; Rennie, A. R.; Zauscher, S.; Linse, P. *Soft Matter* **2008**, *4*, 500−509.

(13) Yim, H.; Kent, M. S.; Mendez, S.; Lopez, G. P.; Satija, S.; Seo, Y. *Macromolecules* **2006**, *39*, 3420−3426.

(14) Moglianetti, M.; Webster, J. R. P.; Edmondson, S.; Armes, S. P.; Titmuss, S. *Langmuir* **2010**, *26*, 12684−12689.

(15) Moglianetti, M.; Webster, J. R. P.; Edmondson, S.; Armes, S. P.; Titmuss, S. *Langmuir* **2011**, *27*, 4489−4496.

(16) Jia, H. Ph.D. Thesis, University of Oxford, 2010.

(17) Jones, D. M.; Brown, A. A.; Huck, W. T. S. *Langmuir* **2002**, *18*, 1265−1269.

(18) Azzam, R, M. A.; Bashara, N. M. *Ellipsometry and Polarized Light*; North-Holland: Amsterdam, 1989.

(19) Cubbitt, R.; Fragneto, G. *Appl. Phys. A: Mater. Sci. Process.* **2002**, *74*, S329−S331.

(20) Nelson, A. *J. Appl. Crystallogr.* **2006**, *39*, 273−276.

(21) An, S. W.; Thirtle, P. N.; Thomas, R. K.; Baines, F. L.; Billingham, N. C.; Armes, S. P.; Penfold, J. *Macromolecules* **1999**, *32*, 2731−2738.

(22) Mir, Y.; Auroy, P.; Auvray, L. *Phys. Rev. Lett.* **1995**, *75*, 2863.

(23) Tran, Y.; Auroy, P.; Lee, L. T. *Macromolecules* **1999**, *32*, 8952−8964.

(24) Edmondson, S. Ph.D. Thesis, University of Cambridge, 2006.

(25) Tomlinson, M. R.; Cousin, F.; Geoghegan, M. *Polymer* **2009**, *50*, 4829−4836.

(26) $L^* = [2\int_{T_{spike}}^{\infty}(z - T_{spike})\phi(z)\ dz]/[\int_{T_{spike}}^{\infty}\phi(z)\ dz]$.

(27) Zhulina, E. B.; Birshtein, T. M.; Borisov, O. V. *Macromolecules* **1995**, *28*, 1491−1499.

(28) Witte, K. N.; Sangtae, K.; Won, Y.-Y. *J. Phys. Chem. B* **2009**, *113*, 11076−11084.

(29) Yuan, J.-J.; Schmid, A.; Armes, S. P.; Lewis, A. L. *Langmuir* **2006**, *22*, 11022−11027.

(30) Gong, P.; Genzer, J.; Szleifer, I. *Phys. Rev. Lett.* **2007**, *98*, 018302.

(31) Witte, K. N.; Hur, J.; Sun, W.; Kim, S.; Won, Y.-Y. *Macromolecules* **2008**, *41*, 8960−8963.

(32) Hur, J.; Witte, K. N.; Sun, W.; Won, Y.-Y. *Langmuir* **2009**, *26*, 2021−2034.

(33) Tagliazucchi, M.; de la Cruz, M. O.; Szleifer, I. *Proc. Natl. Acad. Sci. U. S. A.* **2010**, *107*, 5300−5305.

(34) Plamper, F. A.; Ruppel, M.; Schmalz, A.; Borisov, O.; Ballauff, M.; Müller, A. H. E. *Macromolecules* **2007**, *40*, 8361−8366.

(35) Yim, H.; Kent, M. S.; Mendez, S.; Balamurugan, S. S.; Balamurugan, S.; Lopez, G. P.; Satija, S. *Macromolecules* **2004**, *37*, 1994−1997.

(36) Yim, H.; Kent, M. S.; Datija, S.; Mendez, S.; Balamurugan, S.; Lopez, G. P. *Phys. Rev. E* **2005**, *72*, 051801.

(37) Baulin, V. A.; Zhulina, E. B.; Halperin, A. *J. Chem. Phys.* **2003**, *119*, 10977−10988.

(38) Kim, J.-B.; Bruening, M. L.; Baker, G. L. *J. Am. Chem. Soc.* **2000**, *122*, 7616−7617.

(39) Baulin, V. A.; Halperin, A. *Macromolecules* **2002**, *35*, 6432−6438.

(40) Mendez, S.; Curro, J. G.; McCoy, J. D.; Lopez, G. P. *Macromolecules* **2005**, *38*, 174−181.

Macromolecules

Article

pubs.acs.org/Macromolecules

Multistep Crystallization Process Involving Sequential Formations of Density Fluctuations, "Intermediate Structures", and Lamellar Crystallites: Poly(3-hydroxybutyrate) As Investigated by Time-Resolved Synchrotron SAXS and WAXD

Longhai Guo,[†] Nicolas Spegazzini,[†] Harumi Sato,*[,†] Takeji Hashimoto,[†,‡] Hiroyasu Masunaga,[§] Sono Sasaki,[§,⊥] Masaki Takata,[§] and Yukihiro Ozaki*[,†]

[†]Department of Chemistry, School of Science and Technology and Research Center of Environmental Friendly Polymer, Kwansei-Gakuin University, Gakuen 2-1, Sanda, Hyogo 669-1545, Japan

[‡]Professor Emeritus, Kyoto University, Kyoto 606-8501, Japan, and Honorary Chair Professor, National Tsing Hua University, Hsinchu 30013, Taiwan

[§]Japan Synchrotron Radiation Research Institute, 1-1-1, Kouto, Sayo-cho, Sayo-gun, Hyogo 679-5198, Japan

[⊥]Kyoto Institute of Technology, Matsugasaki, Sakyo-ku, Kyoto 606-8585, Japan

Supporting Information

ABSTRACT: We explored the isothermal crystallization process of poly(3-hydroxybutyrate) by means of simultaneous measurements of time-resolved wide-angle X-ray diffraction (tr-WAXD) and small-angle X-ray scattering (tr-SAXS) methods. The tr-WAXD analyses involve not only (1) a precise analysis of the integral widths but also the analyses such as (2) two-dimensional correlation spectroscopy (2D-COS) and (3) multivariate curve resolution–alternating least squares (MCR-ALS). The tr-SAXS analyses involve not only (4) the conventional one-dimensional correlation function analysis but also the analyses such as (5) 2D-COS between tr-SAXS and tr-WAXD profiles and (6) 2D-COS of tr-SAXS profiles themselves. These analyses elucidated a multistep crystallization process as classified by region I to III in order of the increasing time. In region I, the density fluctuations are first built up in the amorphous matrix, and then the density-rich regions locally develop "intermediate structures" having the mesomorphic orders between pure amorphous melts and pure crystals [lamellar crystallites (LC)], which then grow into layers of the intermediate structures [defined as mesomorphic layers (ML)] with the long spacings. These results were elucidated by analysis (5) and (6). In region II, LC start to be created from ML, which was elucidated by analysis (1) to (4), and both of the weight fractions of ML (X_{inter}) and LC (X_{crys}) increase with time [analysis (3)]. In region III, X_{inter} and X_{crys} decreases and increases with time, respectively [analysis (3)], because the transformation form ML to LC dominates the transformation from the density fluctuations to ML. The WAXD profiles due to ML in region I was identified by analysis (1), while those in regions II and III were identified by analysis (3).

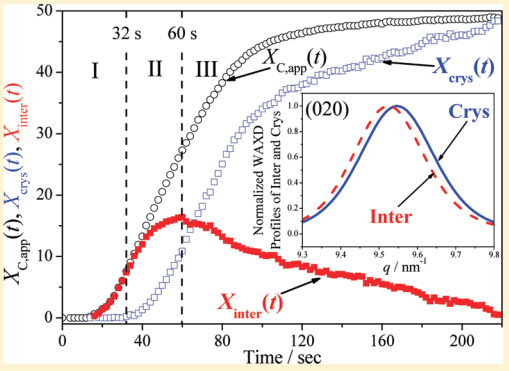

I. INTRODUCTION

Semicrystalline polymers constitute the largest group of commercially useful polymers, and their crystallization process transforming entangled melts into semicrystalline superstructures has been one of important scientific themes in polymer physics.[1−3] In this work, we aim to explore the isothermal crystallization process of molten bulk polymers with a particular focus on its early stage, which may involve formation of a various range of mesomorphic orders before formation of well-ordered crystallites, by using simultaneous measurements of time-resolved synchrotron small-angle X-ray scattering (tr-SAXS) and wide-angle X-ray diffraction (tr-WAXD) on a given specimen undergoing crystallization. The polymer to be studied is poly(3-hydroxybutyrate) (PHB), which is a kind of biodegradable semicrystalline polymer,[4−9] with orthorhombic crystal structure, $P2_12_12_1$-D_2^4, and lattice parameters a = 5.76 Å, b = 13.2 Å, and c = 5.96 Å (fiber repeat distance).[5] The thermal and melting behavior of PHB and PHB-based copolymers and their blends have been investigated by us[10−17] and several other research groups.[18,19] An intramolecular hydrogen bonding (HB) −C═O···H−C− between the −C═O group in one helix and one of the −C−H group in the $-CH_3$ group in the other helix along the a-axis has been clarified to stabilize the chain folding in PHB lamellar

Received: June 29, 2011
Revised: October 21, 2011
Published: December 19, 2011

crystallites.[11−14] The effects of HBs were reported also on the cold crystallization[16] and isothermal crystallization behaviors.[20,21]

Recently, Zhang et al.[20] reported a transient appearance of the IR band around 1731 cm^{-1} with respect to its second derivative spectra during the course of the isothermal crystallization process of PHB and the variation of this band prior to that of the crystalline −C═O band of PHB (1722 cm^{-1}) by means of the two-dimensional correlation spectroscopy (2D-COS) of the IR bands. Therefore, this 1731 cm^{-1} band was assumed to be due to the "intermediate structures" which are neither pure amorphous melts nor true crystals but rather structures having mesomorphic orders between the melts and the true crystals (well-ordered lamellar crystallites). Suttiwijitpukdee et al.[21] further reported the transformation of the intermediate structures to the lamellar crystallites without the HBs and then to those with the HBs during the isothermal crystallization process by means of the FTIR analyses. Nevertheless, the structural entity of the intermediate structures was not identified at all in these works. In this work, we define the "intermediate structures" in the same meaning as described above and aim to separate them from the true crystals and identify their diffraction profiles.

The intermediate structures have been generally found for some polymers such as syndiotactic polypropylene (s-PP), isotactic polypropylene (i-PP), polyethylene (PE), poly(ethylene terephthalate) (PET), polycaprolactone (PCL), *cis*-1,4-polybutadiene (PB), etc. Therefore, the identification of them and their WAXD profiles for PHB are quite important to gain deep insights into crystallization from molten polymers in general and to study universality of their existence leading to the well-ordered lamellar crystallites.

Through FTIR study of the isothermal crystallization of PE, Tashiro et al.[22] found that the IR band attributed to the mesomorphic phase shows up prior to the appearance of the crystal band. In the early stage of the crystallization process of PE, Kanig[23] reported the existence of intermediate stages during the formation of the lamellar crystallites by means of the transmission electron microscopy with the special staining method. The tr-SAXS and tr-WAXD studies of the isothermal crystallization at varying crystallization temperatures T_c for the cross-linked PB melts drawn by fixed draw ratios λ[24,25] revealed that the periodic density fluctuations as observed by the SAXS invariant $Q(t)$ evolve much earlier than the evolution of the crystallinity as observed by tr-WAXD. Moreover, the reports elucidated that the WAXD crystallinity starts to increase with t after the increase of $Q(t)$ with t and that the time lag of the two quantities depends on T_c and λ. This trend was found to be especially remarkable in the case when λ is large and T_c is high. These results may well indicate formation of the intermediate structures prior to formation of the well-developed crystallites, although existence of the intermediate structures was not explicitly mentioned and identified in the reports.[24,25] Through the investigation of i-PP by time-resolved light scattering, Okada et al.[26] and Pogodina et al.[27] reported that the development of crystallites occurs much more slowly and appears at much later stages of the crystallization process than that of the density fluctuations. Evolutions of light scattering patterns as well as SAXS profiles preceding the crystallization were also reported by Matsuba et al. for PET.[28] Strobl[29] proposed the concept of the multistep crystallization process of polymers from melts to homogeneous lamellar crystallites via formation of the following intermediate states: first the mesomorphic layers and then the granular crystalline layers. Sajkiewicz et al.[30] proposed the existence of the intermediate phase in addition to the crystalline and amorphous phases and identified its WAXD profiles during the isothermal and nonisothermal crystallization processes of various PEs by precisely analyzing tr-WAXD profiles.

In this study, we aim to analyze the tr-SAXS and tr-WAXD profiles during the isothermal crystallization process to investigate whether or not PHB develops the density fluctuations and the intermediate structures prior to formation of the lamellar crystallites. If it does, we will try to identify the WAXD profiles attributed to the intermediate structures. The identification of the profiles in turn will stimulate an identification of the corresponding structures. The time variations of SAXS and WAXD profiles are quite similar to those of near-infrared (NIR) and FTIR in the point that the time variations of the various elemental profiles or spectra, which contribute to those of the observed ones, are considerably or heavily superposed each other. It is often difficult to directly decompose the observed profiles or spectra into the elemental ones through the conventional analytical method.

In order to overcome the difficulty described above, we applied the 2D-COS and the multivariate curve resolution−alternating least squares (MCR-ALS) analyses to the tr-WAXD profiles, both of which have widely been used for the analysis of NIR and FTIR spectra with superposed bands. The 2D-COS, proposed by Noda,[31−33] is a powerful and versatile method for elucidating not only subtle variations of spectra composed of overlapped peaks by spreading the peaks along the second dimension but also a sequential order in the time variation of the elemental spectra induced by an external perturbation such as temperature and time. The MCR-ALS is a powerful tool, which can extract information on the time variation of each of the elemental spectra from the time variation of the observed spectra.[34−41] These two techniques applied to the tr-WAXD are very ideally suited for investigating the time evolutions of the elemental WAXD profiles, while the 2D-COS between tr-SAXS and tr-WAXD profiles and the 2D-COS of tr-SAXS profiles themselves are useful to investigate the evolutions of the density fluctuations and the intermediate structures, and their sequential order with time, if they exist, as will be detailed in the text. We would like to stress here that precise analyses of the 2D-COS between the tr-SAXS and tr-WAXD and between tr-SAXS themselves enable us to resolve definitely a time difference between evolution of the true crystals via WAXD and that of the long period via SAXS, as will be discussed in section IV-8, although the direct comparisons of the time evolutions between WAXD and SAXS hardly enable us to discern this time difference, as will be elucidated in sections III-2, IV-1, and IV-2.

II. EXPERIMENTAL METHODS

II-1. Materials and Sample Preparation. PHB, which was obtained from the Aldrich Corp., has a number-averaged molecular weight $M_n = 6.5 \times 10^5$, a melting point (T_m) at 175 °C, and a glass transition temperature (T_g) at 0 °C. The sample was hot pressed in a sample holder having its inner diameter of 3 mm and thickness of 0.5 mm at 100 °C with 5 MPa for 1 min and then rapidly cooled down in air to room temperature. Subsequently, the sample was sealed by a polyimide film on the two sides of the sample holder. The as-prepared sample was used for the measurements of synchrotron radiation SAXS and WAXD.

II-2. Time-Resolved Synchrotron SAXS and WAXD Measurements. The time-resolved SAXS and WAXD experiments were performed in the BL03XU beamline with wavelength λ = 1.0 Å at

SPring-8, Harima, Japan. The sample-to-detector distances for SAXS and WAXD measurements were set to be 1780 and 60 mm, respectively. The two-dimensional SAXS and WAXD patterns were simultaneously recorded every 2 s with the exposure times of 0.8 and 1 s with a CCD camera (Hamamatsu Photonics, Shizuoka, Japan, V7739P+ORCA R2) and an imaging plate (IP) system (Rigaku, Tokyo, Japan, RAXIS VII), respectively. The SAXS and WAXD profiles were obtained by circularly averaging their two-dimensional patterns as a function of magnitude of the scattering vector, q (0.1−1.7 and 6−27 nm^{-1}, respectively), where $q = (4\pi/\lambda) \sin\theta$, and 2θ is the scattering angle of SAXS or Bragg angle for WAXD, respectively, and λ is wavelength of the incident X-ray beam.

The sample holder was placed in a sample cell made out of copper with a temperature sensor to record the real sample temperature during the experiments. The isothermal crystallization experiments were conducted at 120 °C. For this purpose, a homemade temperature enclosure with two heating chambers (designed hereafter as HC1 and HC2, respectively) was employed for a temperature jump (T-jump) from a temperature above T_m (T_i) to the isothermal crystallization temperature (T_c).[42] In this experiment, HC1 and HC2 were maintained at T_i = 180 °C and T_c = 120 °C, respectively. Upon moving synchronously HC1 and HC2 with respect to the sample cell fixed at the center of the incident beam, the sample can be heated by one of these two heating chambers. After 1 min heating of the sample with HC1 to completely erase the thermal history of the sample via melting at T_i, HC1 and HC2 were synchronously moved within 2 s so that HC1 goes out of the sample cell and HC2 comes into the sample cell, and then the sample was controlled at T_c = 120 °C with the temperature fluctuation less than ±0.5 °C during the isothermal crystallization process.

II-3. Analysis of WAXD Profiles. The WAXD profiles observed as a function of q and t, $I^{obs}_{WAXD}(q; t)$, during the isothermal crystallization process are composed of the diffraction profiles from "pure amorphous phase" (disordered liquid phase), $I^{am}_{WAXD}(q; t)$, and those from "nonamorphous phase", $I^{c,app}_{WAXD}(q; t)$, which include the diffraction profiles from not only the lamellar crystallites but also the "intermediate structures" having varying degrees of mesomorphic orders between the pure amorphous phase and crystallites. Hence, $I^{obs}_{WAXD}(q; t)$ is given by

$$I^{obs}_{WAXD}(q; t) = I^{am}_{WAXD}(q; t) + I^{c,app}_{WAXD}(q; t) \quad (1)$$

where $I^{am}_{WAXD}(q; t)$ is obtained in this experiment from the observed profile at 10 s, $I^{obs}_{WAXD}(q; t = 10\ s)$, before the onset of the crystallization after the T-jump to T_c. The superscript "c,app" in $I^{c,app}_{WAXD}(q; t)$ designates an "apparent crystalline" phase or the nonamorphous phase because it comprises not only the crystallites but also the intermediate structures. In this work, we aim to explore the ordering process of PHB in its early stage of the isothermal crystallization process through the time evolution of $I^{c,app}_{WAXD}(q; t)$.

II-4. Analysis of SAXS Profiles. The time evolution of the characteristic morphological parameters such as average layer thickness of the intermediate structures or the lamellar crystals thickness $[l_c(t)]$, average amorphous layer thickness $[l_a(t)]$, and average long period $[L(t)]$ of the intermediate structures or the lamellar crystals can be evaluated from the one-dimensional correlation function,[43] $\gamma(z; t)$, defined by

$$\gamma(z; t) = \int_0^\infty q^2 I_{SAXS,C}(q; t) \cos(qz)\, dq/Q(t) \quad (2)$$

where z is the direction along which the layer or/and lamellae are stacked with their normals parallel to the z-axis and $Q(t)$ is the scattering invariant

$$Q(t) = \int_0^\infty q^2 I_{SAXS,C}(q; t)\, dq \quad (3)$$

where $I_{SAXS,C}(q; t)$ is the measured SAXS profiles corrected for the thermal diffuse scattering (TDS), I_{TDS}, to be described below. Since the observed SAXS profiles, $I_{SAXS}(q; t)$, can be collected only over the accessible finite q rang, it is necessary to extrapolate them to both high and low q values for the integration. The extrapolation of the profiles to q = 0 is accomplished by using the Guinier law:[44,45]

$$I_{SAXS}(q; t) = A(t) \exp[-q^2 R_g(t)^2/3] \quad (4)$$

where $A(t)$ is a proportionality constant independent of q, and $R_g(t)$ is the radius of gyration of the structural unit relevant to the small q range investigated at time t. The values of $A(t)$ and $R_g(t)$ can be determined through the so-called Guinier plot, $\ln[I_{SAXS}(q; t)]$ vs q^2, using the intensity data in a sufficiently low q region. The extrapolation of the profiles to the large q can be conducted on the basis of the Porod law:[46,47]

$$I_{SAXS}(q; t) = I_{TDS} + K_p q^{-4} \quad (5)$$

where K_p is the Porod constant and I_{TDS} is the thermal diffuse scattering which is assumed to be independent of q over the narrow q range covered in this experiment. The values of K_p and I_{TDS} can be determined through the Porod plot, $I_{SAXS}(q; t)q^4$ vs q^4, using the intensity data in a sufficiently large q region. The I_{TDS} thus evaluated were subtracted from $I_{SAXS}(q; t)$ to obtain $I_{SAXS,C}(q; t)$ and then multiplied by q^2 to correct for the Lorentz factor. The determination of the characteristic parameters (L, l_a, l_c) from the one-dimensional correlation function is shown in detail in Supporting Information 1.

II-5. 2D Correlation Analyses of Time-Resolved WAXD and SAXS Profiles. The Lorentz-corrected SAXS profiles, $q^2 I_{SAXS,C}(q; t)$, as well as the WAXD profiles corrected for the amorphous halo, $I^{c,app}_{WAXD}(q; t)$, taken from 16 s after the induction period, t_0 (t_0 = 14 s to be described later in section III in conjunction with Figure 6), during the isothermal crystallization process were selected not only for the homospectral 2D-COS of the WAXD profiles themselves and that of the SAXS profiles themselves but also for the heterospectral 2D-COS between the WAXD and SAXS profiles by using the homemade software. In the synchronous and asynchronous 2D correlation maps, the cross-peaks can be observed with positive or negative intensities. The positive synchronous cross-peak, $\Phi(\nu_1, \nu_2)$, means that the intensity at ν_1 and ν_2 synchronously increases or decreases with time. The negative $\Phi(\nu_1, \nu_2)$ suggests that one of the spectral intensities at ν_1 and ν_2 is increasing with time, while the other is decreasing. When $\Phi(\nu_1, \nu_2)$ is positive, the asynchronous cross-peak, $\Psi(\nu_1, \nu_2)$, becomes positive if the intensity at ν_1 changes before that at ν_2 in the sequential order of time, or $\Psi(\nu_1, \nu_2)$ becomes negative if the intensity at ν_1 changes after that at ν_2. However, this rule[31−33] is reversed if $\Phi(\nu_1, \nu_2) < 0$.

II-6. MCR-ALS Analysis of WAXD Profiles. The WAXD profiles, $I^{c,app}_{WAXD}(q; t)$, taken from t = 16 to 218 s were selected for the MCR-ALS analysis by using the homemade software. The experimental data $I^{c,app}_{WAXD}(q; t)$ were arranged in a matrix $\mathbf{D} = (D_{ij})$ with i = 1 to n and j = 1 to m, in which $D_{ij} \equiv I^{c,app}_{WAXD}(q_j; t_i)$, so that the jth column represents the time dependence of WAXD intensity at a given q_j and the ith row represents the WAXD intensity profile at a given time t_i. The MCR-ALS analysis allows mathematically the decomposition of the experimental data matrix $\mathbf{D}$ into the product of two data matrices $\mathbf{C}$ and $\mathbf{S}^T$ given as follows

$$\mathbf{D} = \mathbf{C}\mathbf{S}^T + \mathbf{E} \quad (6)$$

where the column vector of matrix $\mathbf{C} = (C_{ik})$, $C_{ik} = W_k(t_i)$ with i = 1 to n and k = 1 to l, l being the number of elemental diffraction profiles $I_k(q)$, corresponds to the time dependence of the weight fraction of the kth elemental profile $I_k(q_j)$ with j = 1 to m, while the kth row vector of matrix $\mathbf{S}^T = (S^T_{kj})$, $S^T_{kj} = I_k(q_j)$ with k = 1 to l and j = 1 to m, corresponds to the kth elemental diffraction profile, and $\mathbf{E}$ is the residual matrix. A more detailed description of this method is provided in Supporting Information 2.

III. RESULTS

III-1. Time-Resolved WAXD. Figure 1a shows some typical WAXD profiles, $I^{obs}_{WAXD}(q; t)$ (black lines), at 10, 30, and 100 s, each of which is vertically shifted relative to the

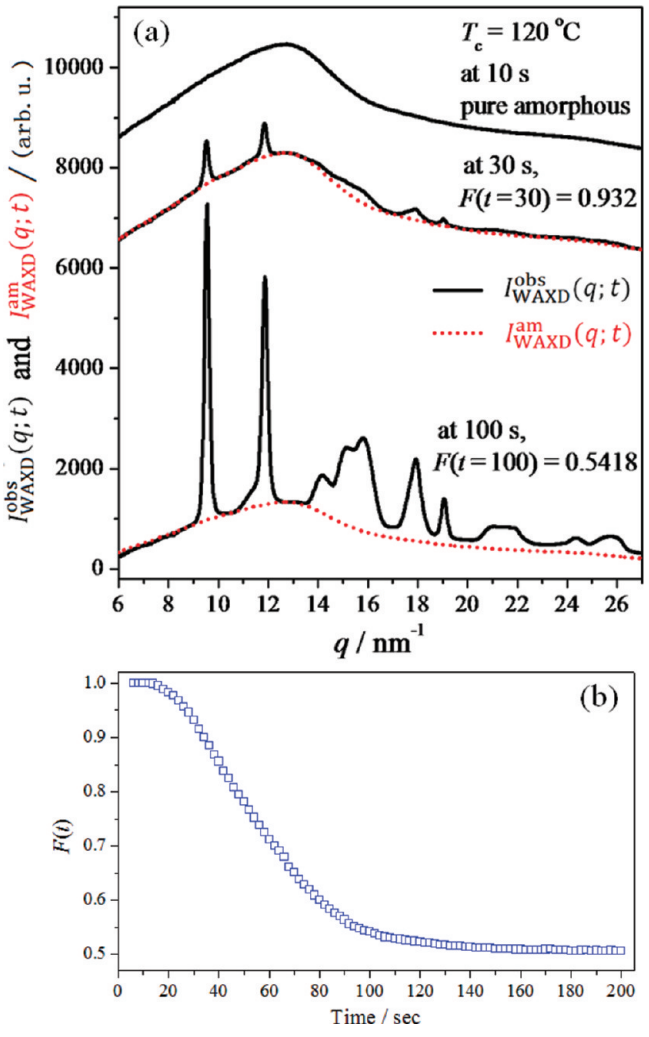

Figure 1. (a) Representative WAXD profiles for PHB observed at 10, 30, and 100 s, $I^{obs}_{WAXD}(q; t)$ (black solid lines), and the profiles for the amorphous halos, $I^{am}_{WAXD}(q; t)$, at 30 and 100 s (red dotted lines). $I^{am}_{WAXD}(q; t)$ was determined from the observed profile $I^{obs}_{WAXD}(q; t = 10\ s)$ before the crystallization as follows: $I^{am}_{WAXD}(q; t) = F(t)I^{obs}_{WAXD}(q; t = 10\ s)$ with $F(t)$ being the reduction factor at time t. (b) $F(t)$ as a function of crystallization time.

bottom profile by the amount of 8000, 6000, and 0 arbitrary units, respectively, to avoid the overlapping of the profiles. Moreover, the figure also displays the best-fitted amorphous halos, $I^{am}_{WAXD}(q; t)$ (red dotted lines), together with the factors $F(t)$. $I^{am}_{WAXD}(q; t)$ was determined as follows:

$$I^{am}_{WAXD}(q; t) = F(t)I^{obs}_{WAXD}(q; t = 10\ s) \quad (7)$$

Here the factor $F(t)$ is defined on the basis of the following concept. The q dependence of the amorphous profile $I^{am}_{WAXD}(q; t)$ at a given time t after the isothermal crystallization is equal to that of $I^{obs}_{WAXD}(q; t = 10\ s)$ for the observed profile at $t = 10$ s before the onset of crystallization. However, the absolute intensity of $I^{am}_{WAXD}(q; t)$ decrease with time t by a factor $F(t)$ because of the conversion of the pure amorphous phase to the nonamorphous phase. The concept introduced here is legitimate without any problems, especially in the early stage where a spatial arrangement of atoms in the amorphous phase hardly changes with time. In this work, we determined $F(t)$ so that $I^{obs}_{WAXD}(q; t = 10\ s)$ is best-fitted with the baseline of $I^{obs}_{WAXD}(q; t)$, as shown in Figure 1a, and the factor $F(t)$ thus evaluated as a function of t is shown in Figure 1b. Figure 2 shows the temperature protocol for the T-jump from

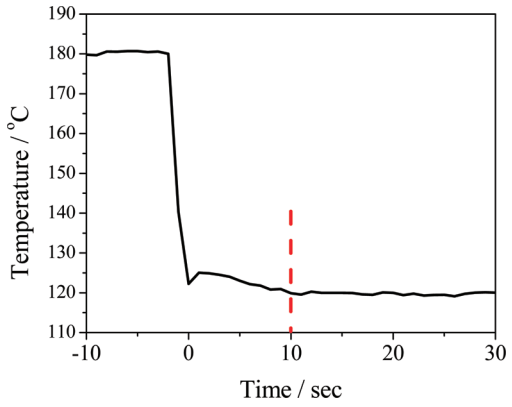

Figure 2. Temperature protocol for the T-jump from 180 to 120 °C.

180 to 120 °C, which was recorded by a sensor embedded in the sample. As shown in the figure, the sample at 10 s has already reached at 120 °C, and local spatial arrangements of atoms in the sample are expected to be equilibrated, judging from the time dependence of the WAXD profile at t around 10 s.

The WAXD profiles of the nonamorphous phase, $I^{c,app}_{WAXD}(q; t)$, were obtained by

$$I^{c,app}_{WAXD}(q; t) = I^{obs}_{WAXD}(q; t) - I^{am}_{WAXD}(q; t) \quad (8)$$

The time-resolved profiles from 16 to 200 s are shown in Figure 3 together with the assignment of the lattice plane (hkl)

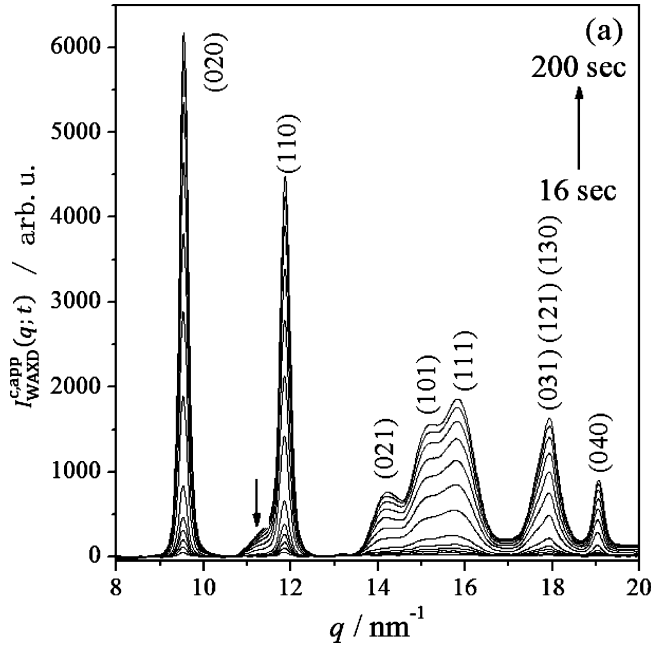

Figure 3. Apparent WAXD diffraction profiles corrected for the amorphous halo, $I^{c,app}_{WAXD}(q; t)$.

for each diffraction peak. The profiles in the q regions of 13−17 and 17−18.5 nm^{-1} comprise multiple diffraction peaks. It can be clearly seen from Figure 3 that the areas under the diffraction peaks and their heights increase with time due to the increasing ordering and crystallinity.

dx.doi.org/10.1021/ma201475t | Macromolecules 2012, 45, 313−328

The apparent crystallinity $X_{C,app}(t)$ was calculated from profiles shown in Figures 1 and 3 by using the following equation

$$X_{C,app}(t) = \frac{\int_{q_{min}}^{q_{max}} I_{WAXD}^{c,app}(q;\, t) q^2 \, dq}{\int_{q_{min}}^{q_{max}} I_{WAXD}^{obs}(q;\, t) q^2 \, dq} \quad (9)$$

where q_{min} = 6 nm^{-1} and q_{max} = 27 nm^{-1}. It should be noted that the nonamorphous phase is composed of the intermediate structures with the mesomorphic orders and the lamellar crystallites. Their weight fractions are defined as $X_{int}(t)$ and $X_{crys}(t)$, respectively. Thus, $X_{C,app}(t)$ is a sum of the corresponding two contributions, $X_{int}(t)$ and $X_{crys}(t)$, respectively. The result on $X_{C,app}(t)$ will be discussed later in section IV-1 in conjunction with Figure 6. The integral widths, $\beta_i(t)$, of the diffraction peaks 020 and 110 and the multiple diffraction peaks in the q ranges of 13−17 and 17−18.5 nm^{-1} were calculated from the profiles shown in Figure 3 by using the following equation[48]

$$\beta_i(t) = \frac{\int_{q_{i,min}}^{q_{i,max}} I_{WAXD}^{c,app}(q;\, t) q^2 \, dq}{I_{WAXD}^{c,app}(q = q_{p,i};\, t) {q_{p,i}}^2(t)} \quad (10)$$

where i refers to the ith diffraction peak [i = (020), (110), and the two multiple diffraction peaks]; $q_{i,min}$ and $q_{i,max}$ denote the limits of the q's where the ith diffraction intensity for $I_{WAXD}^{c,app}$ drops to zero; $q_{p,i}$ is the q value at the ith diffraction peak. As shown in Figure 3, the diffraction peak from the (110) lattice plane is overlapped with the weak diffraction peak as marked by the arrow which exists at $q \approx 11.6$ nm^{-1}. The 110 diffraction peak which was separated from the weak diffraction peak was used to evaluate β_{110}. Moreover, the third derivatives of the WAXD profiles were employed to determine the diffraction peak positions of the lattice planes (020) and (110) to calculate lattice parameters $a(t)$ and $b(t)$. The results on $\beta_i(t)$, $a(t)$, and $b(t)$ will be discussed in section IV-2 in conjunction with Figure 8.

III-2. Time-Resolved SAXS. Figure 4a shows time-resolved Lorentz-corrected SAXS profiles during the isothermal crystallization process from 0 to 200 s. Each profile is vertically shifted relatively to its preceding profile with a constant incremental value (0.2 and 0.05 arbitrary units for part a and b, respectively). It is found that a scattering peak appears after some induction period and it increases its intensity and shifts to a large q value with time, which is a common phenomenon observed for isothermal crystallization processes of polymers.[24,25,49−53] Figure 4b highlights particularly the time evolution of the representative SAXS profiles in the very early stage of the crystallization process from 0 to 36 s, corresponding essentially to time region I defined in section IV-2 in conjunction with Figure 8. It is noteworthy that the SAXS intensity tends to increase, especially at small q regions, even in the time t < 24 s before the appearance of clear SAXS peak.

Figure 5 shows some representative one-dimensional correlation functions $\gamma(z;\, t)$, which were obtained by using eq 2 from the Lorentz-corrected tr-SAXS profiles shown in Figure 4. Through the analysis of the one-dimensional correlation functions, the time evolutions of the characteristic parameters $L(t)$, $l_c(t)$, $l_a(t)$, and Q were obtained, the results of which are shown in Figure 13a, together with the "local apparent crystallinity" $l_c(t)/L(t)$ shown in Figure 13b. Here the word "local" is used because the SAXS tends to evaluate apparent crystallinity within grains,[24,25] when the grains composed of amorphous layers, the mesomorphic layers, and/or the lamellar crystallites are dispersed in the amorphous matrix. The curve 1 at 20 s representative to the early part in region I shows almost a monotonic decrease from 1 to 0 with z,

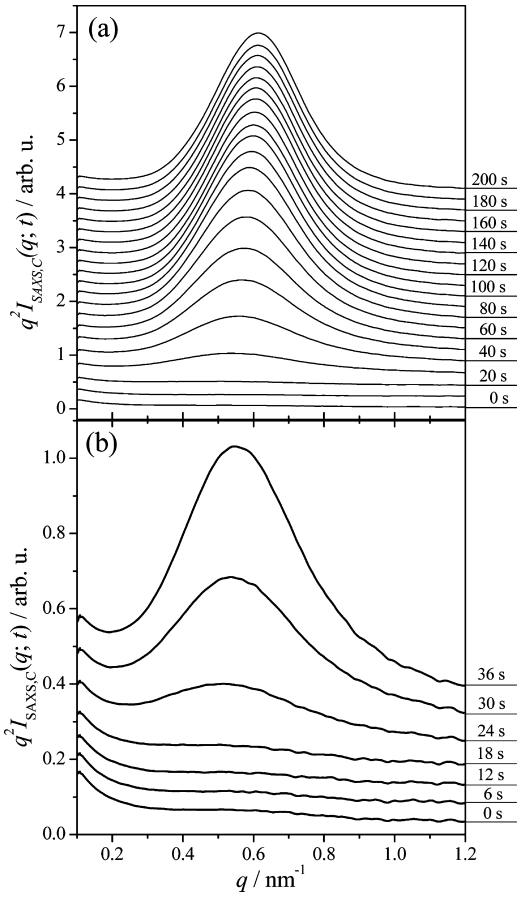

Figure 4. (a) Lorentz-corrected SAXS profiles of PHB obtained during the isothermal crystallization process at 120 °C from 0 to 200 s and (b) from 0 to 36 s. Each profile at a given time is vertically shifted by a constant incremental value [0.2 arbitrary units for (a) and 0.05 arbitrary units for (b)] relative to its preceding profile.

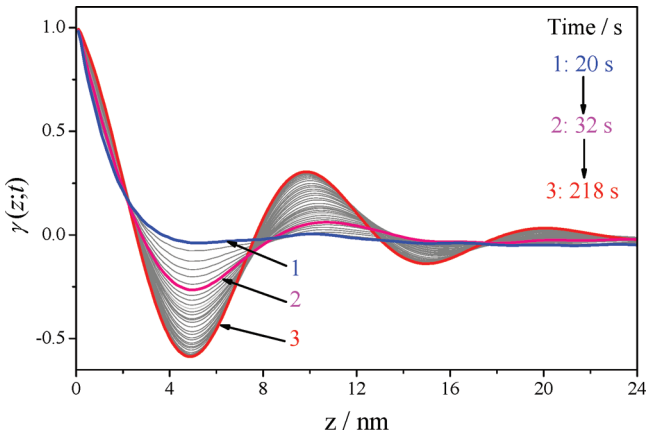

Figure 5. One-dimensional correlation function $\gamma(z;\, t)$ obtained from the Lorentz-corrected SAXS intensity profiles. The profiles at 20 (blue), 32 (pink), and 218 s (red) are highlighted with thick lines numbered by 1 to 3, respectively.

dx.doi.org/10.1021/ma201475t | Macromolecules 2012, 45, 313−328

which implies the correlation functions characteristic to isolated layers. As time elapses, the correlation function shows an oscillation around zero value with sharper minima and maxima with time, suggesting an increasing order with respect to a periodic arrangement of the mesomorphic layers or/and the lamellar crystallites. The SAXS results will be further analyzed and discussed in sections IV-6 to IV-8 in conjunction with Figures 13 and 14.

IV. ANALYSES AND DISCUSSION

IV-1. Time Evolution of Apparent Crystallinity $X_{C,app}(t)$. The time evolution of apparent crystallinity $X_{C,app}(t)$ was evaluated by using eq 9, and the result is shown in Figure 6

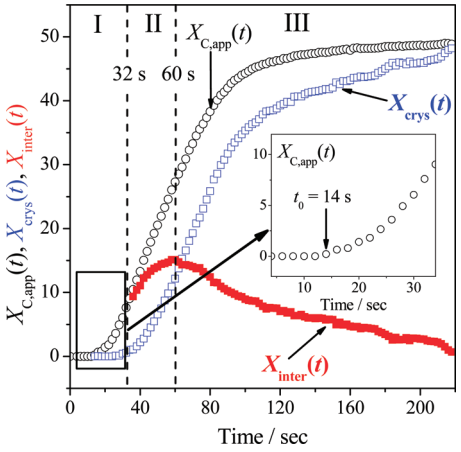

Figure 6. Time-resolved apparent crystallinity, $X_{C,app}(t)$, obtained from the WAXD profiles corrected for the amorphous halo, $X_{inter}(t)$ (the intermediate structures), and $X_{crys}(t)$ (the lamellar crystallites). The inset identifies the induction period t_0 = 14 s for the onset of the increasing $X_{C,app}(t)$.

(black symbol) together with $X_{crys}(t)$ and $X_{inter}(t)$. The separation of $X_{C,app}(t)$ into $X_{crys}(t)$ and $X_{int}(t)$ will be discussed later in section IV-4. It can be seen from Figure 6 that $X_{C,app}(t)$ starts to increase from 14 s, indicating that the transformation from pure amorphous phase to the nonamorphous phase starts to occur after the induction period of t_0 = 14 s. The figure indicates a classification of the whole time span into the three regions, region I to III, which will be discussed later in conjunctions with Figures 8, 11, and 13.

The evolution of $X_{C,app}(t)$ is sigmoidal with an inflection point around 60 s where the curvature changes from the downward concave curvature to the upward convex curvature. $[\partial X_{C,app}(t)/\partial t]_T$ increases with t in time region I and II and slow down in time region III: It is slowed down especially at $t >$ 100 s, seemingly in the secondary crystallization regime in the light of the Avrami plots, $\ln\{-\ln[1 - X_{C,app}(t - t_0)]\}$ vs $\ln(t - t_0)$ and $\ln\{-\ln[1 - X_{crys}(t - t_1)]\}$ vs $\ln(t - t_1)$, where $X_{crys}(t)$ is defined in section IV-4 (eq 12), as indicated in Supporting Information 3.

IV-2. Time Evolution of WAXD Profiles: Elucidation of Multistep Crystallization Process via Intermediate Structures with Mesomorphic Orders. Time-resolved WAXD profiles corrected for the amorphous halo $I^{c,app}_{WAXD}(q; t)$ shown in Figure 3 are enlarged and highlighted around 020 and 110 diffraction peaks in Figure 7a and around the multiple diffraction peaks composed of 021, 101, and 111 in Figure 7b, where we focus on the profiles only up to 100 s, corresponding

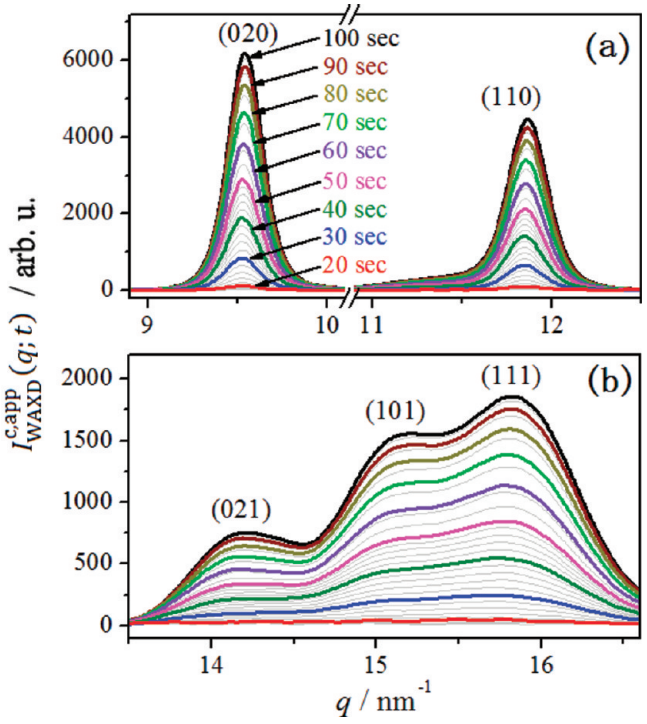

Figure 7. Time-resolved WAXD profiles corrected for the amorphous halo, $I^{c,app}_{WAXD}(q; t)$, in the region of q = 9−13 nm^{-1} (a) and 13−17 nm^{-1} (b) focused on the isothermal crystallization process at 120 °C from 16 to 100 s, where the thickened lines are recorded at 20 (red), 30

to roughly the primary stage of the crystallization as inferred from Figure 6. As displayed in the figure, the diffraction peaks are obviously narrowing and becoming intense with time. Figure 8 shows the integral widths of 020 and 110 diffraction peaks, β_{020} and β_{110}, respectively (part a), and the integral widths of the multiple diffraction peak composed of 021, 101, and 111, $\beta_{021,101,111}$, and that composed of 031, 121, and 130, $\beta_{031,121,130}$ (part b), as a function of the crystallization time. The solid lines indicate the integral widths calculated from the MCR-ALS analyses to be discussed later in section IV-4.

The variations of the integral widths with time can be classified into three time regions across the two critical times as indicated by the broken lines around 32 and 60 s. All the integral widths rapidly decrease with time in region I; β_{020} and β_{110} reach a minimum value, while the rates of the decrease of $\beta_{021,101,111}$ and $\beta_{031,121,130}$ with time tend to slow down at the end of region I. In region II, β_{020} and β_{110} increase with time, the rate of which tends to slow down at the end of this region, while the integral widths for the two multiple diffraction peaks keep decreasing with time at the rates much slower than those in region I. All the integral widths remain almost constant at $t >$ 100 s in region III.

In order to more clearly investigate the time evolutions of the WAXD profiles in region I, the profiles from 16 to 32 s are more closely investigated with the enlarged Figure 9a, b, in which the profile at 218 s (the black line) is also shown with the intensity reduced by a factor of 0.25 as a reference for the profile relevant to the well crystallized lamellae. It is interesting to note the followings: each of the 020 and 110 diffraction profiles at 218 s has a peak position slightly larger than those up to 32 s. The multiple diffraction profile at 218 s shows the three distinct diffraction peaks around q = 14.2, 15.1, and 15.9 nm^{-1} as shown by the arrows together with the corresponding lattice

dx.doi.org/10.1021/ma201475t | Macromolecules 2012, 45, 313−328

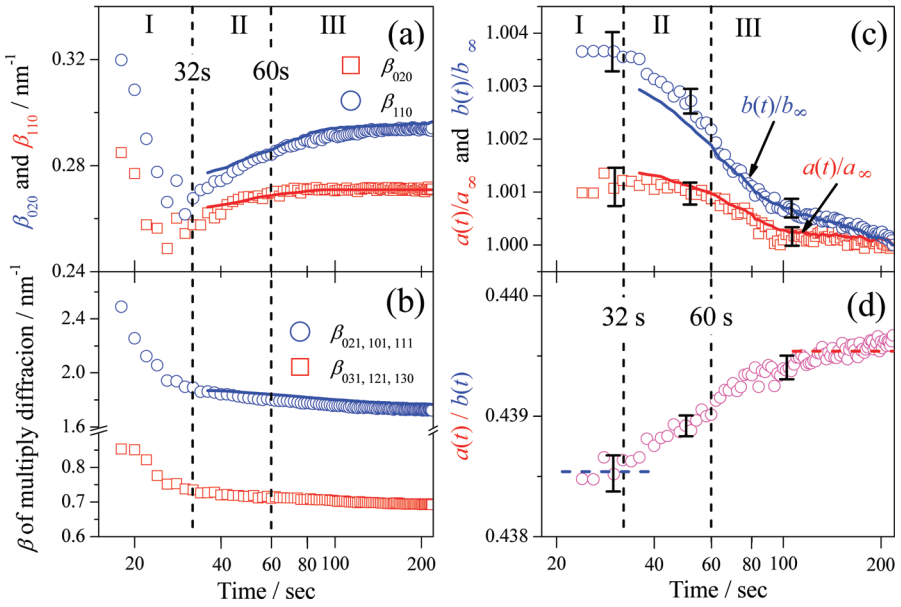

Figure 8. Apparent integral widths of the 020 and 110 diffraction peaks, β_{020} and β_{110}, respectively (a); apparent integral width of the multiple diffraction profile from 021, 101, and 111 peaks, $\beta_{021,101,111}$; that from 031, 121, and 130 peaks, $\beta_{031,121,130}$ (b); the apparent lattice parameters $a(t)$ and $b(t)$ normalized by the respective lattice parameters determined at the long time limit of the crystallization a_∞ and b_∞ (c); the time evolution of the ratio $a(t)/b(t)$ (d). The solid lines were determined from the reconstructed WAXD profiles by using the MCR-ALS analyses.

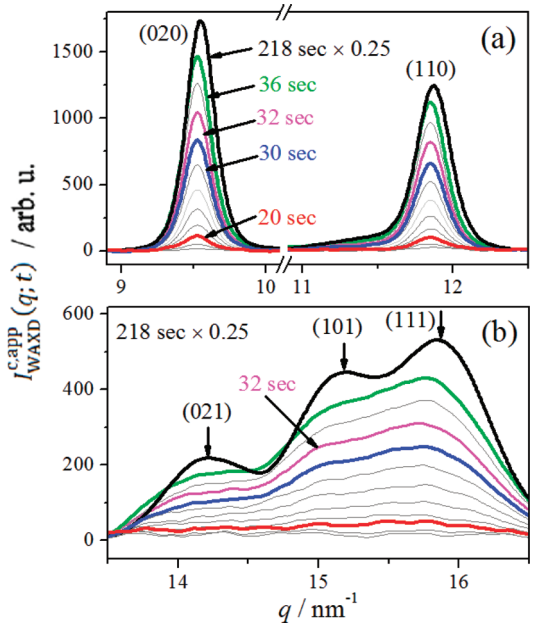

Figure 9. Time-resolved WAXD profiles corrected for the amorphous halo in the region of q = 9−13 nm^{-1} (a) and 13−17 nm^{-1} (b) focused on in the early stage of the isothermal crystallization process from 16 to 32 s (in time region I), where the thick lines are recorded at 20 (red), 30 (blue), 32 (purple), and 36 s (green). The WAXD profile at 218 s (black) with a reduced intensity by a factor of 0.25 is shown as a reference for the profiles from the well-developed crystallites.

planes (021), (101), and (111), respectively, whereas these three diffraction peaks in region I are heavily superposed each other, and only the very broad diffraction peaks, if there are, can be observed at q's smaller than those at 218 s.

Time Region I. The time evolution of the WAXD profiles in region I may be interpreted on the basis of the following two models: (a) formation of "imperfect crystals" with a large lattice strain or (b) the "intermediate structures" with the mesomorphic orders. An important question to be addressed here is which model is more plausible: In either case, the decrease of the peak width can be accounted for by the increase of the crystallite size and the lattice perfection in model (a) or by the increase of the intermediate-structure size and the mesomorphic orders in model (b). Thus, both models seem to be feasible on the basis of the WAXD results only. Our previous time-resolved FTIR (tr-FTIR) results on the isothermal crystallization of PHB with a different M_n (2.9×10^5) at a similar temperature (117 °C)[21] provided the following piece of evidence in favor of model (b) as will be described below.

The tr-FTIR showed the evolution of the band at ∼1732 cm^{-1} in the C═O stretching vibration region, which was assigned to be the so-called intermediate structures,[20] though details of the structures were left totally unsolved yet. This band was found to appear definitely before the appearance of the crystalline bands at ∼1722 cm^{-1} in the C═O stretching vibration region and at ∼1229, ∼895, and ∼825 cm^{-1} in the C−H bending and C−O−C stretching vibration region [see Scheme 1 in ref 21]. Moreover, the amorphous bands at ∼1740 and ∼1184 cm^{-1} were found to decrease their absorbances with time only after the onset of the appearance of the band ∼1732 cm^{-1}. These results reveal that there is a time span in which the structures as observed by FTIR are neither pure amorphous states nor crystalline states. If this time span found in tr-FTIR experiments corresponds to region I found in the tr-WAXD experiments, the WAXD profiles in region I is expected to reflect the "intermediate structures" rather the "imperfect crystals". To further confirm this hypothesis, it is crucial to conduct a simultaneous measurement of tr-WAXD, tr-SAXS, and tr-FTIR. Hereafter, we shall advance our discussion based on model (b). However, the discussion to be developed is valid even in the case when the terminology of the "intermediate structures" is read as that of the "imperfect crystals".

Those phenomena described above in conjunction with Figures 8 and 9 reveal that, in region I, the isothermal crystallization involves first the transformation of the

dx.doi.org/10.1021/ma201475t | *Macromolecules* 2012, 45, 313−328

amorphous melts into the intermediate structures which have orders between the amorphous melts and the lamellar crystallites. The intermediate structures with the mesomorphic orders give rise to the 020 and 110 diffraction profiles with the larger characteristic spacings and broader widths than those from the well-developed lamellar crystallites formed at 218 s, as shown in Figure 9a. It also gives rise to the multiple diffraction profile with a broader and ill-defined profile than that from the lamellar crystallites at 218 s, as shown in Figure 9b. In Region I, the intermediate structures continuously grow in size and order with time, so that the integral widths keep decreasing, although the characteristic spacings are kept constant.

Time Regions II and III. The increase of β_{020}, β_{110} in region II is due to the onset of the transformation from the mesomorphic orders to the lamellar crystallites with the lattice spacings slightly smaller than those of the mesomorphic orders under such a condition that both the lamellar crystallites and the mesomorphic orders increase in their amount with time. The disparity in the peak positions of these two diffraction profiles and thereby in the respective spacings causes the broadening of the integral widths. In region III, the weight fraction of the lamellar crystallites may further increase at the expense of the mesomorphic orders, thereby giving rise to the almost constant β_{020} and β_{110} or decreasing $\beta_{021,101,111}$ and $\beta_{031,121,130}$. The different time-evolution behavior of the integral widths β_{020} and β_{110} in comparison with that of the multipeaks $\beta_{021,101,111}$ and $\beta_{031,121,130}$ may be due to a heavy overlap of the multipeaks, which may hide the minimum observed in the time evolution of β_{020} and β_{110} at the end of region I. It may depend also on *hkl*-dependent distribution of the mesomorphic orders [in the case of model (b)] or the lattice strain [in the case of model (a)] in the light of the fact that the (020) and (110) lattice planes are parallel to *c*-axis, while the multiple peaks are not.

Figure 8c shows the time evolution of the normalized "apparent lattice parameters" $a(t)/a_\infty$ and $b(t)/b_\infty$ as determined from the diffraction peak positions of the (020) and (110) lattice planes by assuming orthorhombic crystal structure, where a_∞ and b_∞ are the apparent lattice parameters at the long time limit of this experiment (218 s) and those obtained with MCR-ALS analysis (the solid lines) to be discussed later. The spacings $a(t)$ and $b(t)$ in region I are the spacings for the intermediate structures with the mesomorphic orders, while those in region II and III are the weight-averaged spacings between the intermediate structures and the lamellar crystallites. The word "apparent" is used here to note that the spacings are not those only from the well-developed lamellar crystallites themselves. In region I, the apparent spacings $a(t)$ and $b(t)$ of the intermediate structures remain essentially constant with time, while in region II, the apparent spacings are expected to decrease with time because of the onset of formation of the lamellar crystallites with the smaller lattice spacings. The apparent spacings keep decreasing in time region III also because of the increasing amount of the lamellar crystallites with time, though the rate of the decrease tends to slow down at $t > 100$ s in the seemingly secondary crystallization regime, where the hydrogen bondings −C═O···H−C− between −C═O groups and one of −C−H groups of $-CH_3$ of PHB starts to form along the *a*-axis of the lamellar crystallites.[11,21] Figure 8d presents the time evolution of the ratio $a(t)/b(t)$ again based on the assumption of orthorhombic crystal structure. The ratio is constant in region I as shown by the dashed line within the experimental accuracy, then increases with time in regions II and III, and finally reaches a steady value at the end of region III as also shown by the dashed line.

In order to confirm the above conclusion inferred from the direct analyses of the tr-WAXD profiles, we further conducted the 2D-COS and MCR-ALS analyses on $I^{c,app}_{WAXD}(q; t)$.

IV-3. 2D Correlation Analyses of WAXD Profiles. The crystal structure of PHB is known, and the observed WAXD peaks are related to each other in accordance with the crystal structure. It is needless to say that the 2D correlation analysis to be presented here is based on this basic principle. Within this framework, however, it further adds the following basic information. In the case when the observed diffraction peaks are composed of some elemental peaks which may have different time evolutions, the 2D correlation analysis elucidates in principle existence of the elemental peaks which evolve asynchronously (with time differences) each other.

Consequently, in order to extract more precise and direct pieces of evidence about the evolution of the intermediate structures, we employed the 2D-COS analysis for the time-resolved WAXD profiles corrected for the amorphous halo, which enables one to further explore the time sequences of the evolution of the WAXD profiles due to the intermediate structures and those due to the lamellar crystallites. Figures 10a and 10b display the synchronous 2D correlation maps $\Phi(q_1, q_2)$ and asynchronous 2D correlation map $\Psi(q_1, q_2)$, respectively, generated from the tr-WAXD profiles in the q region of 13−17 nm^{-1} obtained in the time span from 16 to 60 s in time region I and II. Figures 10c and 10d show the three-dimensional display of $\Phi(q_1, q_2)$ and $\Psi(q_1, q_2)$, respectively.

In the synchronous 2D correlation map, three autopeaks are clearly seen to develop around 14.2, 15.2, and 15.9 nm^{-1} (at positions 1, 2, and 3, respectively) together with positive cross-peaks around (15.9, 15.2), (15.9, 14.2), and (15.2, 14.2) nm^{-1} (at positions 4, 5, and 6, respectively), indicating that these three diffraction peaks are simultaneously increasing with time. These peak positions are identical to those observed in $I^{c,app}_{WAXD}(q; t)$ at $t = 218$ s [the three arrows on the black line shown in Figure 9b] and expected to be consistent with the PHB orthorhombic crystal structures with the lattice spacings of $a = 5.78$, $b = 13.16$, and $c = 6.027$ Å within the context that the peak positions, and hence the lattice parameters vary with the crystallization conditions. However, in the asynchronous 2D correlation map, in addition to these three diffraction peaks, three diffraction peaks are newly observed remarkably around 13.9, 14.7, and 15.5 nm^{-1}, whose peak positions are smaller than those found in $\Phi(q_1, q_2)$, indicating that the lattice (or apparent lattice) spacings of these three peaks found in $\Psi(q_1, q_2)$ are larger than those observed in $\Phi(q_1, q_2)$. Whether these new peaks can be assigned to the intermediate structures or the imperfect crystals is not clear only from the tr-WAXD results, as discussed in section IV-2. Nevertheless, the 2D synchronous and asynchronous correlation maps unveil the fact that there are at least two kinds of structures relevant to the WAXD profiles developed asynchronously during the isothermal crystallization process: the lamellar crystallites with orthorhombic crystal structure and either the intermediate structures or the imperfect crystals having the apparent lattice spacings larger than the lamellar crystallites. We proposed that the intermediate structures are more plausible than the imperfect crystals with the information obtained from the tr-FTIR as discussed in section IV-2.

If the two diffraction peaks exist in the asynchronous 2D correlation map, the synchronous 2D correlation map should show the cross-peaks between them also. However, the strong overlapping between the two diffraction profiles with the peak

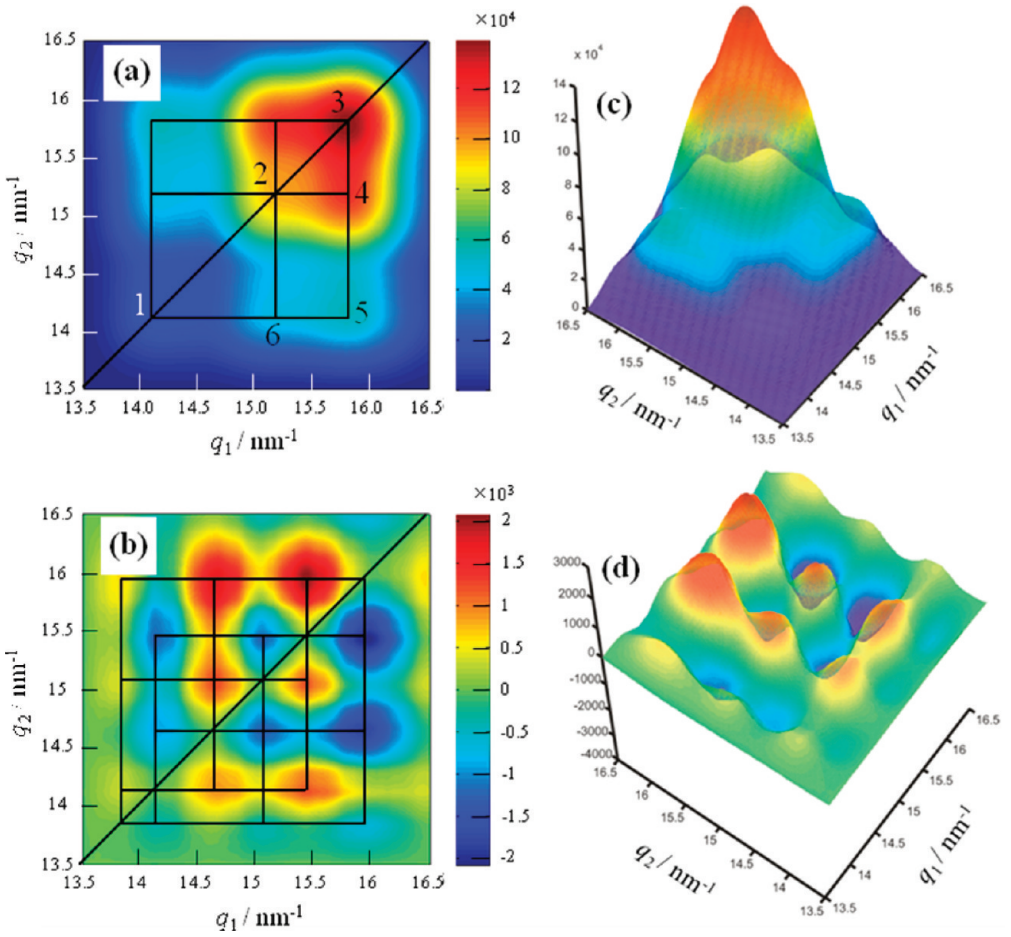

Figure 10. Synchronous (a) and asynchronous (b) 2D correlation maps calculated from the WAXD profiles corrected for the amorphous halo (13.5−16.5 nm^{-1}) obtained during the isothermal crystallization process (16−60 s) at 120 °C. Parts (c) and (d) show the bird's-eye views of (a) and (b), respectively.

Table 1. Synchronous and Asynchronous 2D Correlation Intensities, $\Phi(k, l)$ and $\Psi(k, l)$, Respectively, with k and l Being the Diffraction-Peak Wavenumber of the Lamellar Crystallites (Denoted L at 14.2, 15.2, 15.9 nm^{-1}) or the Intermediate Structures (Denoted I at 13.9, 14.7, 15.5 nm^{-1}) and the Sequential Order in the Time Variations of the Two Diffraction Peaks at k and l

no.	$\Phi(k, l)$	$\Psi(k, l)$	assign[a]	time sequence
1	$\Phi(15.9, 13.9) > 0$	$\Psi(15.9, 13.9) < 0$	(L, I)	15.9 after 13.9
2	$\Phi(15.9, 14.7) > 0$	$\Psi(15.9, 14.7) < 0$	(L, I)	15.9 after 14.7
3	$\Phi(15.9, 15.5) > 0$	$\Psi(15.9, 15.5) < 0$	(L, I)	15.9 after 15.5
4	$\Phi(15.5, 14.2) > 0$	$\Psi(15.5, 14.2) > 0$	(I, L)	15.5 before 14.2
5	$\Phi(15.5, 15.2) > 0$	$\Psi(15.5, 15.2) > 0$	(I, L)	15.5 before 15.2
6	$\Phi(15.2, 13.9) > 0$	$\Psi(15.2, 13.9) < 0$	(L, I)	15.2 after 13.9
7	$\Phi(15.2, 14.7) > 0$	$\Psi(15.2, 14.7) < 0$	(L, I)	15.2 after 14.7
8	$\Phi(14.7, 14.2) > 0$	$\Psi(14.7, 14.2) > 0$	(I, L)	14.7 before 14.2
9	$\Phi(14.2, 13.9) > 0$	$\Psi(14.2, 13.9) < 0$	(L, I)	14.2 after 13.9

[a]L and I designate the lamellar crystallites and the intermediate structures with the mesomorphic orders.

intensities at the small q values being much weak than those at the large q values makes the synchronous 2D correlation map hardly distinguish the cross-peaks arising from these two structures. Table 1 summarizes signs of various cross-correlation peaks which are expected to exist in the synchronous map $\Phi(k, l)$ and which are actually observed clearly to exist in the asynchronous map $\Psi(k, l)$ with k and l being the diffraction peak positions belonging to either the lamellar crystallites or the intermediate structures, designated as L or I, respectively. According to the Noda's rule[33] in the 2D correlation analysis, the case of $\Phi(k, l) > 0$ and $\Psi(k, l) < 0$ suggests that the lth diffraction peak appears prior to the kth diffraction peak, while the case of $\Phi(k, l) > 0$ and $\Psi(k, l) > 0$ suggests that the kth diffraction peak appears prior to the lth diffraction peak. According to this rule, the cross-correlation peaks no. 1 in Table 1, which satisfies $\Phi(15.9, 13.9) > 0$ and $\Psi(15.9, 13.9) < 0$, suggest that the peak at $q = 13.9$ nm^{-1} appears prior to the peak at $q = 15.9$ nm^{-1}, thereby the intermediate structures (I) appear prior to the lamellar crystallites (L). All the cross-correlation peaks of Φ and Ψ labeled no. 1 to 9 consistently elucidate that, after the induction period, the intermediate structures develop prior to the lamellar crystallites, which is physically reasonable and supports the validity of the Noda's rule in this case.

dx.doi.org/10.1021/ma201475t | *Macromolecules* 2012, 45, 313−328

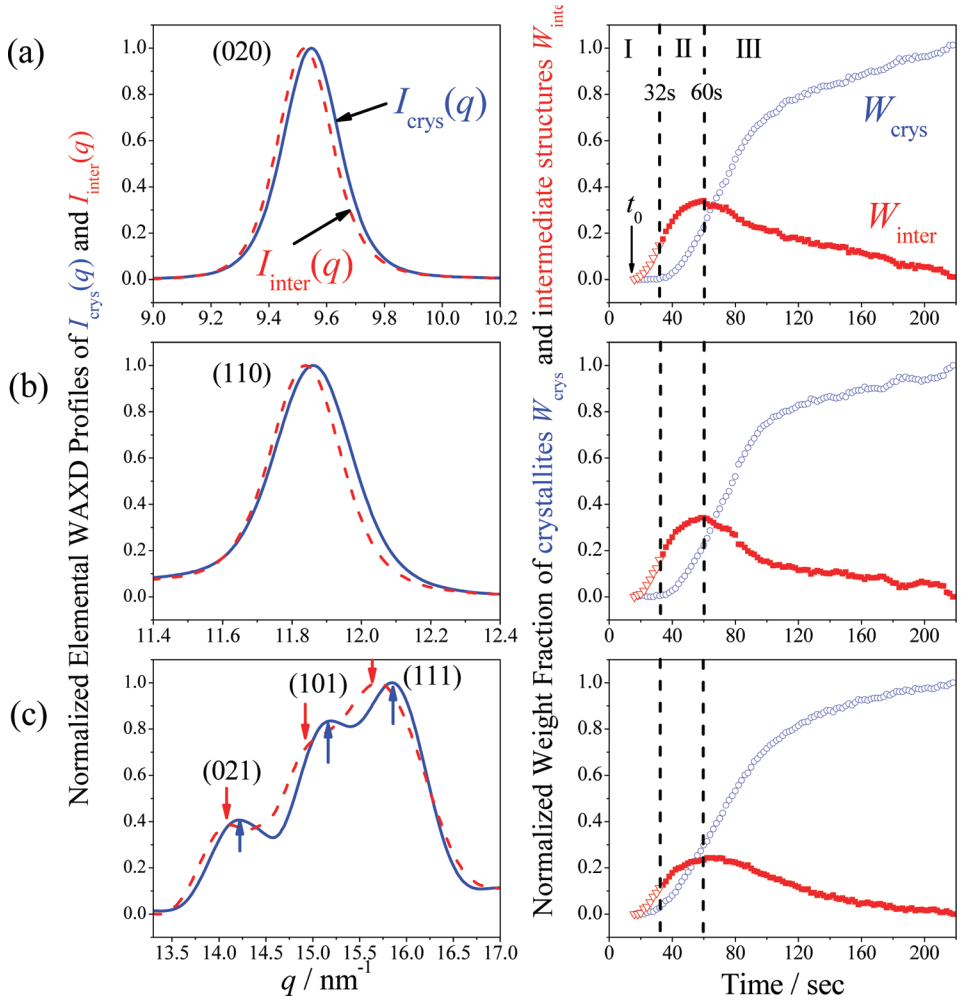

Figure 11. Decomposed elemental WAXD profiles for the intermediate structures [the red dotted lines, $I_{inter}(q)$] and the lamellar crystallites [the blue solid lines, $I_{crys}(q)$] (left half) and time evolution of the weight fractions of the intermediate structures (red filled symbols, W_{inter}) and lamellar crystallites (blue unfilled symbols, W_{crys}) in time region II and III during the isothermal crystallization process as determined by the application of MCR-ALS to the following observed profiles: (a) 020; (b) 110; (c) the multiple diffraction peaks composed of 021, 101, and 111. The W_{inter} in time region I is equal to $X_{C,app}(t)$ shown in Figure 6 which was directly determined from $I^{c,app}_{WAXD}(q; t)$ shown in Figure 9.

Consequently, we succeeded in unequivocally verifying or confirming the conjecture given in section IV-2 concerning existence of the diffraction peaks due to the intermediate structures and its evolution prior to the evolution of the diffraction peaks due to the lamellar crystallites. We would like to stress here that the 2D-COS enables this unequivocal verification or confirmation even under the condition that the two diffraction peaks are superposed each other so that the difference in the time evolution of the two diffraction peaks are unable to be captured directly in time region II and III, as defined in Figure 8 and as shown in Figure 9b.

IV-4. MCR-ALS Analyses of WAXD Profiles. We applied the MCR-ALS analysis to decompose the net WAXD profiles into those from the intermediate structures and the lamellar crystallites in the time region II and III. The two diffraction profiles so closely overlapped each other that there are no other effective methods to decompose the observed profiles into the two diffraction profiles. Before the MCR-ALS analysis, the number of components (the number of the elemental diffraction profiles in the observed WAXD profiles in our particular case) was first determined by using the evolving factor analysis (EFA),[34,54,55] which is outlined in the Supporting Information 2. On the basis of the EFA analyses, we determined the two components, which will be assigned later to be the diffraction due to the intermediate structures and that due to the lamellar crystallites, for the MCR-ALS analyses of the WAXD profiles in the q regions of 9.0−10.2, 11.4−12.4, and 13.0−17.0 nm^{-1}. The results are shown in parts a, b, and c of Figure 11, respectively. Through the MCR-ALS analyses in the different q regions, we obtained the two elemental WAXD profiles, $I_{inter}(q)$ for the intermediate structures and $I_{crys}(q)$ for the lamellar crystallites, as shown by the red broken lines and blue solid lines, respectively, in the left half of Figure 11. Each of the elemental profiles is normalized in such a way that its maximum intensity is equal to 1. The time evolution of the weight fraction of the lamellar crystallites and the intermediate structures, defined as W_{crys} and W_{inter}, respectively, are plotted as a function of time with the blue and red symbols in the right half of Figure 11. The weight fractions are adjustable parameters to attain the best fit of the observed profiles $I^{c,app}_{WAXD}(q; t)$ with the reconstructed profiles $I^{recon}_{WAXD}(q; t)$

$$I^{recon}_{WAXD}(q; t) = W_{inter}(t)I_{inter}(q) + W_{crys}(t)I_{crys}(q) \quad (11)$$

obtained by the MCR-ALS analysis. It should be noted that $I_k(q)$ (k = inter or crys) is assumed to be independent of time but only $W_k(t)$ (k = inter or crys) changes with time in region II

dx.doi.org/10.1021/ma201475t | Macromolecules 2012, 45, 313−328

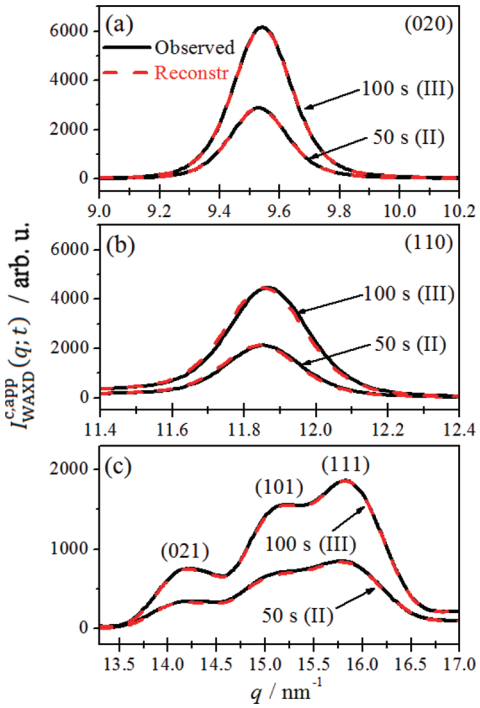

Figure 12. Comparisons of the observed WAXD profiles, $I^{c,app}_{WAXD}(q; t)$ (black solid lines), and the reconstructed WAXD profiles, $I^{recon}_{WAXD}(q; t)$ (red broken lines), obtained after the MCR-ALS analyses: (a) 020; (b) 110; (c) the multiple diffraction peaks composed of 021, 101, and 111.

and III. The reconstructed profiles after the MCR-ALS analyses of diffraction peaks 020 and 110 as well as the multiple diffraction peaks composed of 021, 101, and 111 at 50 and 100 s are shown in parts a, b, and c of Figure 12, respectively. A good agreement was found between the observed profiles (shown by the black solid lines) and the reconstructed profiles (shown by the red broken lines). Although it is natural to attain the good agreement, the agreement supports the validity of the MCR-ALS analysis in this work. Consequently, the WAXD profiles from the intermediate structures of PHB are clarified for the first time to be given directly by $I^{c,app}_{WAXD}(q; t)$ in region I and by $I_{inter}(q)$ in eq 11 together with the results show in Figure 11 in regions II and III.

Let us first discuss the normalized diffraction profiles shown in the left half of Figure 11. Comparisons between the two elemental profiles $I_{inter}(q)$ and $I_{crys}(q)$ clearly indicate that all the profiles of the former have a peak or peaks at smaller q or q's than those of the latter, indicating that the characteristic spacings of the intermediate structures are larger than those of the lamellar crystallites, and hence the intermediate structures are less perfect than the lamellar crystallites. Moreover, in the q region of 13−17 nm^{-1} shown in the left half of Figure 11c, the profile of $I_{inter}(q)$ consists of three diffraction peaks at q = 14.0, 14.7, and 15.5 nm^{-1} (shown by the red arrows), while that of $I_{crys}(q)$ consists of those at 14.3, 15.2, and 15.8 nm^{-1} (shown by the blue arrows), which are almost equal to the q values where the peaks are found for the 2D asynchronous and synchronous maps in parts b and a of Figure 10, respectively. Consequently, the small q-shift in the peak positions of the diffraction profiles due to the intermediate structures is consistently found not only in the WAXD profiles themselves shown in Figure 9 but also in 2D asynchronous map shown in Figure 10b and in the elemental profiles decomposed by MCR-ALS analyses shown in the left half of Figure 11. These results reinforce each other for unequivocal identification of existence of the intermediate structures.

Now let us discuss the variation of relative weight fractions $W_{inter}(t)$ and $W_{crys}(t)$ shown in the right half of Figure 11. They are actually evaluated in regions II and III only: The value $W_{inter}(t)$ in region I is equal to $X_{c,app}(t)$: $W_{inter}(t = 32\ s) = X_{c,app}(t = 32\ s)$. It is found that all of the $W_{inter}(t)$ and $W_{crys}(t)$ obtained in the different q regions show the very similar trends as follows: (1) The $W_{inter}(t)$ increases from zero to a maximum value with time from 14 s (the induction time t_0) to 60 s, followed by the decrease from the maximum values to zero with a further increase of the time. Meanwhile, (2) the $W_{crys}(t)$ begins to increase from zero at around 32 s and rapidly increase with the time until 100 s, followed by the slow increase with a further increase of the time, seemingly due to the secondary crystallization process.

Thus, we can conclude that (1) only the intermediate structures grow via the transformation from the amorphous phase to the mesomorphic phase (designated as $T_{am\text{-}meso}$) after the induction time t_0 in region I, (2) both the intermediate structures and the lamellar crystallites grow via $T_{am\text{-}meso}$ and the transformation from the intermediate structures to the lamellar crystallites (designated as $T_{meso\text{-}crys}$) in region II, and (3) in region II, the rate of $T_{am\text{-}meso}$ is anticipated to be larger than that of $T_{meso\text{-}crys}$, so that W_{inter} increases with time, while in region III, the rate of $T_{am\text{-}meso}$ is anticipated to be smaller than that of $T_{meso\text{-}crys}$, so that W_{inter} decreases with time, thereby giving rise to the maximum value of W_{inter} at the boundary between II and III.

The results revealed in Figure 11 with MCR-ALS analyses are consistent with the results revealed in Figure 8 obtained by the direct observations of the WAXD profiles. The reduction of the integral widths of "apparent 020 and 110 diffraction peaks" in region I is due to the growth and ordering of the intermediate structures. The word "apparent" was used because the diffractions in this time span are from the mesomorphic orders but not from crystals. In region II, both the intermediate structures and lamellar crystallites having different spacings grow and give rise to the diffraction peaks at slightly different q's, which accounts for the increase of the "apparent integral widths" β_{020} and β_{110}. The word "apparent" was used again because the observed diffractions comprised the two elemental profiles.

The results of MCR-ALS analyses revealed in Figure 11 provide a profound interpretation for the results shown in Figure 8c also on the time dependence of the apparent lattice spacings directly obtained from the observed WAXD profiles $I^{c,app}_{WAXD}(q; t)$. The apparent lattice spacings $a(t)$ and $b(t)$ in time region I reflect those from the intermediate structures only which is independent of time and larger than those from the lamellar crystallites to be developed in regions II and III. The growth of the lamellar crystallites via $T_{meso\text{-}crys}$ in regions II and III decreases $a(t)$ and $b(t)$. The results in Figures 8c and 11 are consistent and reinforce each other with respect to the concept of the multistep crystallization process via formation of the intermediate structures.

The time difference between the onsets of the intermediate mesomorphic structures and the lamellar crystallites as elucidated by MCR-ALS analyses of $W_{inter}(t)$ and $W_{crys}(t)$ in Figure 11 is consistent with that elucidated from the 2D-COS analyses shown in Figure 10 and Table 1, supporting here again the Noda's rule. The time evolution of the apparent crystallinity

dx.doi.org/10.1021/ma201475t | Macromolecules 2012, 45, 313−328

$X_{C,app}(t)$ shown in Figure 6 can be analyzed more deeply by using the pieces of information on $W_{crys}(t)$ and $W_{inter}(t)$ shown in Figure 11: the apparent $X_{C,app}(t)$ can be decomposed into the true crystallinity $X_{crys}(t)$ and the weight fraction of the mesomorphic orders $X_{inter}(t)$ as follows:

$$X_{crys}(t) = \frac{X_{C,app}(t)W_{crys}(t)}{W_{crys}(t) + W_{inter}(t)} \quad (12)$$

and

$$X_{inter}(t) = X_{C,app}(t) - X_{crys}(t) \quad (13)$$

The results are also shown in Figure 6 by the blue and red symbol, respectively. $X_{inter}(t)$ increases with time from 0 at 14 s to ~10 wt % at the end of region I, to a maximum value of ~15 wt % at the end of region II, and then decreases to zero at 218 s, while $X_{crys}(t)$ increases with time from zero at the end of region I to ~12 wt % at the end of region II and to ~50 wt % at 218 s.

IV-5. Comparisons with Time-Resolved FTIR Analyses. At this stage, we shall compare the results obtained in this work with those previously obtained on the isothermal crystallization process of PHB by using the tr-FTIR methods,[20,21] with a particular emphasis of the intermediate structures. Zhang et al.[20] conducted the 2D-COS analysis of the time-resolved IR bands of PHB in the −C═O stretching vibration region and found the sequential changes of the characteristic bands in the order of 1743, 1731, and 1722 cm^{-1} with time. By assuming the band at 1731 cm^{-1} is due to the intermediate structures, they speculated that the sequential changes of the bands suggest transformations first from the amorphous melts to the intermediate structures and then to the lamellar crystallites with the HBs −C═O···H−C− between the −C═O groups and one of −C−H groups in $-CH_3$ along the *a*-axis. Suttiwijitpukdee et al.[21] studied the time-resolved IR bands not only in the −C═O stretching vibration region but also in the −C−H bending and −C−O−C stretching vibration regions and further elaborated such a multistep crystallization process as given by the following sequential orders: from the amorphous melts to the intermediate structures, then to the lamellar crystallites without the HBs, and finally to the lamellar crystallites with the HBs.

The present works provide a piece of solid evidence on the intermediate structures responsible for the IR band at 1731 or 1732 cm^{-1} and further elucidate the corresponding WAXD profiles (as shown by the profiles up to 32 s in Figure 9) with broad widths and the larger characteristic spacings as characterized by the results shown in region I in Figure 8 and the profiles $I_{inter}(q)$ on the left half in Figure 11 in regions II and III. The decrease of the lattice parameters $a(t)$ and $b(t)$ in regions II and III are clearly due to the formation of the well-developed lamellar crystallites in these regions. However, it is not clear yet where the HBs begin to form in the crystallization process. It may be possible to speculate the considerable amount of the HBs are formed at $t > 100$ s, beyond which $a(t)/a_\infty$ hardly changes with time and $b(t)/b_\infty$ decreases slowly with time. This time region may be the one where the secondary crystallization seems to occur as pointed out earlier in conjunction with Figure 6. Our earlier work[21] also elucidated the HBs are formed predominantly in the secondary crystallization process. It is crucial to simultaneously investigate tr-WAXD and tr-SAXS with tr-FTIR on the same specimens in order to further clarify the time span for the evolution of the intermediate structures and HBs, which deserves future works.

IV-6. Evolutions of High-Order Self-Assembly As Observed by SAXS Analysis. Up to this stage, we discussed the time evolution of the individual intermediate structures and crystallites from the amorphous melts. Here in this section, we shall discuss space-time organization of a higher order self-assembly (or a texture) composed of amorphous regions, intermediate structures, and crystallites in the crystallization process. The tr-SAXS profiles employed in this work enable us to explore the space-time organization of these elemental structural units in the length scale of ~50 nm.

From the one-dimensional correlation function shown in Figure 5, we determined the characteristic parameters $L(t)$, $l_c(t)$, $l_a(t)$, and $Q(t)$ as well as the local apparent crystallinity $l_c(t)/L(t)$ within the grains, which are composed of the mesomorphic layers and/or the lamellar crystallites and the intervening amorphous layers between them. The grains in turn are dispersed in the amorphous matrix. The results are shown in Figure 13 which reveal the several interesting features: (1) After

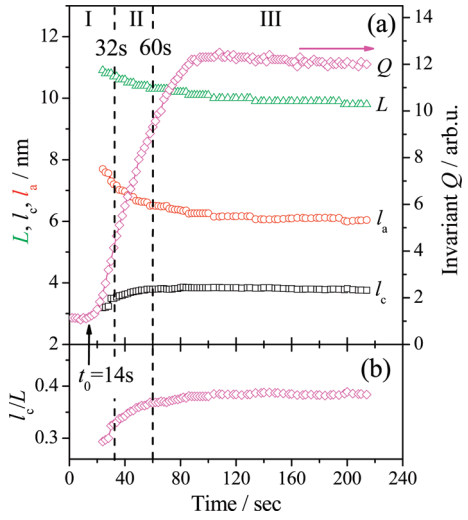

Figure 13. (a) Variations of characteristic parameters obtained from the one-dimensional correlation function such as the long period L, the mesomorphic-layer or lamellar-crystal thickness l_c, the amorphous-layer thickness l_a, and invariants Q (a) and (b) the local apparent crystallinity l_c/L as a function of time.

the induction period of t_0 = 14 s, the invariant Q starts to sigmoidally increase with time with an inflection point at $t \sim 60$ s as in the case of $X_{C,app}(t)$ vs t in Figure 6: it increases very rapidly in regions I and II and then slows down in region III. (2) There is only a single characteristic long spacing $L(t)$ evolved throughout the whole crystallization process, and the spacing slightly decreases with time at a relatively larger rate in regions I and II than in region III and reaches an almost constant value at $t > 100$ s in region III (seemingly in the secondary crystallization regime). (3) There is only a single thickness l_c of either the layers composed of the intermediate structures or the lamellar crystallites which continuously increases slightly with time throughout the whole crystallization process at a largest rate in region I, followed by the decreasing rate in the order of regions II and III, and eventually reaches a constant value at $t > 100$ s. (4) The value $l_a(t)$ decreases more largely with time as a consequence of the increasing $l_c(t)$ and decreasing $L(t)$.

dx.doi.org/10.1021/ma201475t | *Macromolecules* 2012, 45, 313−328

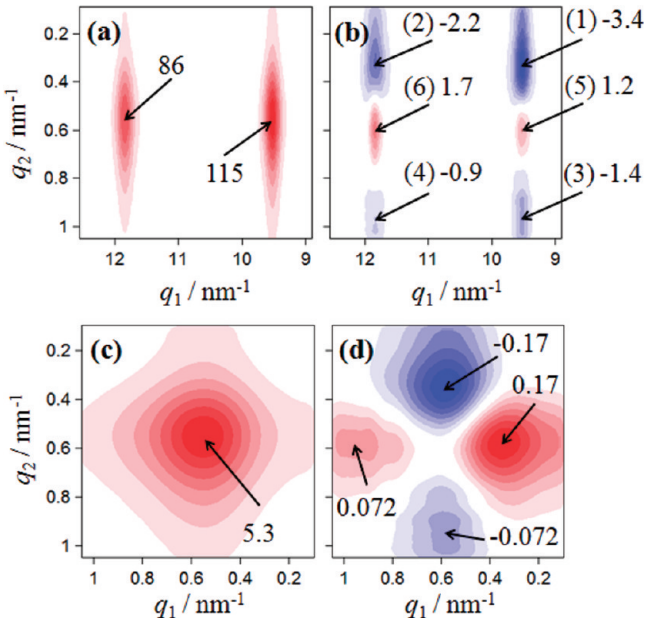

Figure 14. 2D-COS between the tr-WAXD and tr-SAXS profiles in region I form 16 to 32 s: (a) synchronous map $\Phi(q_1, q_2)$ and (b) asynchronous map $\Psi(q_1, q_2)$; and the 2D-COS between the tr-SAXS profiles themselves: (c) synchronous map $\Phi(q_1, q_2)$ and (d) asynchronous map $\Psi(q_1, q_2)$. The red and blue areas indicate the positive and negative correlation intensities, respectively. The number attached to each arrow indicates the maximum or minimum intensity of the positive or negative correlation peak, respectively.

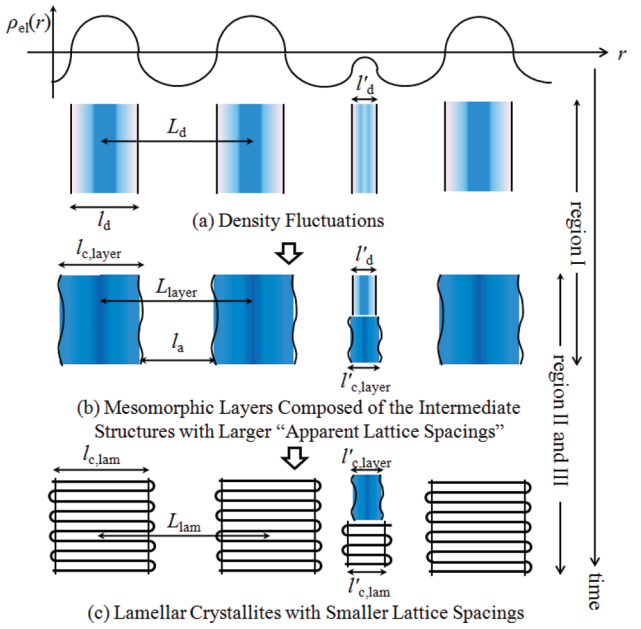

Figure 15. Schematic illustration of the multistep crystallization process involving the continuous transformation of first (a) the density-rich regions to (b) the mesomorphic layers and then from the mesomorphic layers to (c) the lamellar crystallites, which involves also the continuous increase of the size of the fundamental structural units from l_d to $l_{c,layer}$ and from $l_{c,layer}$ to $l_{c,lam}$.

Evidence (2) and (3) described above reveal themselves that the intermediate structures developed in region I grow into the layers with mesomorphic orders (defined as layers or mesomorphic layers) periodically arranged in space with amorphous melt layers intervening between them and that the mesomorphic layers are continuously transformed into the lamellar crystallites in regions II and III. The small decreases of L [evidence (2)] may be interpreted as a consequence of insertions of new mesomorphic layers or lamellar crystallites in the space between the as-grown mesomorphic layers or lamellar crystallites ("car-parking problems" in fixed parking area).[1,24,25] In region I, only the mesomorphic layers grow, and its thickness $l_c(t)$ increases with t, implying that the chains in the layers tend to have more stretched conformations (helical conformations) with increasing degree of mesomorphic orders compared with random-coil conformations in the melt. The $l_c(t)$ further increases in region II to reach the critical thickness, followed by the transformation from the mesomorphic layers to the lamellar crystallites as proposed by Strobl.[29] This means that the chains tend to have even more stretched conformation accompanied by the transformation. We will present a schematic illustration for the assembly of the mesomorphic layers, the lamellar crystallites, and the amorphous layers formed in the crystallization process in Figure 15 in section V.

IV-7. 2D Correlation Analyses between SAXS and WAXD Profiles. Since the SAXS and WAXD profiles were collected simultaneously, they can be used to analyze the time sequence on the evolution of these two profiles by means of the heterospectral 2D-COS analysis between the Lorentz-corrected SAXS profiles $q^2I_{SAXS,C}(q; t)$ and the WAXD profiles $I^{c,app}_{WAXD}(q; t)$ corrected for the amorphous halo. We have already clarified from the 2D-COS analysis (IV-3) and MCR-ALS analysis (IV-4) of the tr-WAXD profiles that only the intermediate structures form in region I; both the intermediate structures and the lamellar crystallites grow in region II. Consequently, in this section we will focus on the 2D-COS analysis between $q^2I_{SAXS,C}(q; t)$ and $I^{c,app}_{WAXD}(q; t)$ in time region I (from 16 to 32 s) in order to confirm the evolution of the intermediate structures with respect to tr-SAXS in this time region.

As shown in Figure 4b, $q^2I_{SAXS,C}(q; t)$ from 16 to 32 s shows the shift of the peak position from q = 0.50 to 0.55 nm^{-1}. One may worry about the effect of this peak shift on the 2D-COS analysis. However, we believe that this shift ~10% is small enough so that it will not cause any serious errors. We confirmed this fact by taking 2D-COS with the reduced SAXS profiles $I_{SAXS,C}(q/q_{max}; t)$, where q is reduced by the time-dependent peak position $q_{max}(t)$ so that the reduced SAXS profiles do not show the peak shift (see Figures S4-1 and S4-2 in Supporting Information 4).

Figures 14a and 14b show the synchronous $\Phi(q_1, q_2)$ and asynchronous $\Psi(q_1, q_2)$ 2D correlation maps obtained during the isothermal crystallization process from 16 to 32 s (in region I), respectively. The red and blue areas indicate the regions with the positive and negative correlation intensities, respectively. In the synchronous map (part a), there are two positive peaks: Φ(9.5, 0.6) > 0 and Φ(11.9, 0.6) > 0, while in the asynchronous map (part b), there are two strongly negative peaks: (1) Ψ(9.5, 0.36) < 0 and (2) Ψ(11.9, 0.36) < 0, two weakly negative peaks: (3) Ψ(9.5, 0.97) < 0 and (4) Ψ(11.9, 0.97) < 0, and two weakly positive peaks: (5) Ψ(9.5, 0.6) > 0 and (6) Ψ(11.9, 0.6) > 0. If the time evolution of the SAXS peak around q = 0.6 nm^{-1} and those of the 020 WAXD peak around q = 9.5 nm^{-1} and the 110 WAXD peak around q = 11.9 nm^{-1} have the common time evolution process, involving only formation of the intermediate structures, we will not be able to observe the cross-peaks in the asynchronous map as shown in Figure 14b. Existence of the asynchronous cross-peaks thereby implies clearly a piece of solid evidence that there

dx.doi.org/10.1021/ma201475t | Macromolecules 2012, 45, 313–328

must be at least another component, which influences the time-evolution of the SAXS profiles at a different rate, in addition to the evolution of the intermediate structures as observed by the WAXD profiles, although the time evolution of the SAXS profiles (Figures 4b and 13) and that of WAXD profiles (Figures 6 and 9) are very similar, and thereby they do not suggest directly existence of the another component.

Let us first take a look at the 2D-COS and find out a possible additional component. The negative asynchronous peaks labeled by (1) to (4) in Figure 14b together with the positive synchronous correlation intensities at the respective peak positions shown in Figure 14a suggest such a sequential order as follows: The SAXS intensities at q = 0.36 and 0.97 nm^{-1} evolve faster than the WAXD peak intensities at q = 9.5 and 11.9 nm^{-1}[defined hereafter as sequential order (1)], if the Noda's rule is applicable to the 2D-COS between tr-SAXS and tr-WAXD profiles. Let us next consider below if there are any plausible models to explain the above sequential order (1) attained by this rule. We conjecture that the additional component described above must be the density fluctuations which are built up in the homogeneous amorphous matrix prior to the formation of the intermediate structures. The mesomorphic layers composed of the intermediate structures, which are periodically developed in space, give rise to $I_{SAXS}^{interm}(q; t)$ with a peak at $q \sim 0.6$ nm^{-1}. The density fluctuations give rise to $I_{SAXS}^{density}(q; t)$ which has an intensity distribution with q much broader than $I_{SAXS}^{interm}(q; t)$, so that the observed intensity at $q \sim 0.6$ nm^{-1} is dominated by $I_{SAXS}^{interm}(q; t)$ but that at $q \sim 0.36$ or 0.97 nm^{-1} is dominated by $I_{SAXS}^{density}(q; t)$. Under this condition if the density fluctuations evolve faster than the periodic mesomorphic layers, the sequential order (1) found above can be accounted for. Thus, this sequential order (1) is unveiled only by the precise analysis of the 2D-COS.

Let us next consider the asynchronous peaks (5) Ψ(9.5, 0.6) and (6) Ψ(11.9, 0.6) in Figure 14b having a weak positive intensity. The small absolute intensity of these two asynchronous peaks compared with the large absolute intensity of the asynchronous peaks (1) and (2) must imply that the evolution of the peaks at q = 0.6 and 9.5 or 11.9 nm^{-1} is less asynchronous (or more synchronous) than the evolution of the peaks at q = 0.36 and 9.5 or 11.9 nm^{-1}. The small positive intensity of the asynchronous peak (5) and peak (6) together with the positive synchronous intensity at the respective positions imply such a sequential order as follows: The WAXD intensities at q = 9.5 and 11.9 nm^{-1} evolve slightly faster than the evolution of the SAXS peak at q = 0.6 nm^{-1} according to the Noda's rule [defined hereafter as sequential order (2)]. This sequential order may infer that the intermediate structures first locally developed in the as-formed density-rich region [stage (i)]; then the locally developed intermediate structures grow and order into the mesomorphic layers composed of the intermediate structures [stage (ii)]. Consequently, this sequential order (2) occurs after the sequential order (1). One should note that the WAXD peaks at q = 9.5 and 11.9 nm^{-1} are sensitive to the locally developed intermediate structures, while the SAXS peak at q = 0.6 nm^{-1} is sensitive to the periodic mesomorphic layers. In stage (i), the SAXS peak due to the density fluctuations may not exist or even if it exists, it may not be remarkable at least, thereby satisfying the condition of $I_{SAXS}^{density}(q = 0.6 \text{ nm}^{-1}; t) < I_{SAXS}^{interm}(q = 0.6 \text{ nm}^{-1}; t)$, while in stage (ii) the SAXS peak due to the periodic mesomorphic layers must be increasingly remarkable with time. Thus, we would like to stress that this information also is unveiled only by the precise analysis of the 2D-COS but cannot be ever obtained at all by the direct comparisons of the tr-SAXS and the tr-WAXD. Consequently, the Noda's rule applied to the 2D-COS between the tr-SAXS and tr-WAXD profiles seems to provide a physically reasonable model.

On the basis of this heterospectral 2D-COS analysis described above together with the previous FTIR results,[21] we propose that the density fluctuations are first formed in the homogeneous melts; then the density-rich regions locally develop the intermediate structures with the mesomorphic orders. Upon a further elapse of time, the locally developed intermediate structures grow into the mesomorphic layers; the mesomorphic layers are then transformed first into the lamellar crystallites without HBs and eventually those with HBs.

IV-8. 2D Correlation Analyses between SAXS Profiles. If the time changes in the SAXS profiles in region I are composed of $I_{SAXS}^{density}(q; t)$ and $I_{SAXS}^{interm}(q; t)$ which evolve at different rates as elucidated in section IV-7, the 2D-COS of tr-SAXS profiles themselves taken in region I are expected to give rise to the asynchronous 2D cross-peaks. Figures 14c and 14d show the synchronous and asynchronous 2D correlation maps, $\Phi(q_1, q_2)$ and $\Psi(q_1, q_2)$, respectively, taken from the Lorentz-corrected SAXS profiles from 16 to 32 s (corresponding to region I only). The red and blue areas indicate the positive and negative correlation intensities, respectively. The data shows that Φ(0.6, 0.36) > 0 and Ψ(0.6, 0.36) < 0; Φ(0.97, 0.6) > 0 and Ψ(0.97, 0.6) > 0, implying such a sequential order as the intensity at q = 0.36 and 0.97 nm^{-1} changing faster than the intensity at q = 0.6 nm^{-1} according to the Noda's rule. This suggests that the density fluctuations are built up faster than formation of the mesomorphic layers. This result seems to be reasonable and is consistent with the results obtained in section IV-7, thereby supporting the Noda's rule. We would like to stress again that this conclusion is obtained by the 2D-COS analysis only but not by the direct observations of the tr-SAXS results shown in Figures 4b and 13.

V. CONCLUSION

The multistep crystallization process as revealed by tr-SAXS and tr-WAXD investigations of PHB is partially presented by schematic illustration shown in Figure 15. The density fluctuations are first built up in the molten bulk PHB (a), density-rich regions are then transformed into the layers composed of the intermediate structures with the mesomorphic orders between the melts and well-developed lamellar crystallites (b), and the mesomorphic layers are eventually transformed into the well-ordered lamellar crystallites (c). We think that the structural transformation process from (b) to (c) may involve the process proposed by Strobl (see Figures 1 and 2 of ref 29): a spontaneous thickening of the mesomorphic layer up to a critical value, followed by the transformation into a granular crystalline layer, and finally the transformation into homogeneous lamellar crystallites. Our work captures the trend of these detail processes in the process from (b) to (c), as already discussed in the last part of the last paragraph in section IV-6 in conjunction with increasing $l_c(t)$ in regions I and II. We believe that our model is consistent with the Strobl's model and further reinforce it by adding new pieces of evidence as summarized below.

The transformation from (a) to (b) occurs in time region I, which was clarified by (1) 2D-COS between tr-SAXS and tr-WAXD profiles (section IV-7, Figure 14a,b) and (2) 2D-COS of tr-SAXS profiles themselves (section IV-8, Figure 14c,d).

The transformation from (b) to (c) occurs in time region II and III, which was clarified by (3) the precise analysis of the integral widths (section IV-2, Figure 8), (4) the 2D-COS of the tr-WAXD profiles (section IV-3, Figure 10), (5) the MCR-ALS of the tr-WAXD profiles (section IV-4, Figure 11), and (6) the conventional one-dimensional correlation function analysis of tr-SAXS profiles (section IV-6, Figure 13). The analysis (1) elucidates that the density fluctuations are first built up in a homogeneous amorphous melt; then the density-rich regions locally develop the intermediate structures with the mesomorphic orders; the locally developed intermediate structures grow into the layer with the long spacing. The analysis (5) further distinguishes region II and III as follows: in region II, relative weight factions of both the intermediate structures comprising the mesomorphic orders (W_{inter}) and the well-developed lamellar crystallites (W_{crys}) increase with time; while in region III, W_{inter} decreases and W_{crys} increases with time. The difference in the time dependence of W_{inter} and W_{crys} in regions II and III is attributed to the difference in transformation rate from (a) to (b) ($T_{am\text{-}meso}$) and from (b) to (c) ($T_{meso\text{-}crys}$) in these two regions: the rate $T_{am\text{-}meso}$ > the rate $T_{meso\text{-}crys}$ in region II and opposite is the case in region III, as discussed in section IV-4. The analysis (5) identified the diffraction profiles from the intermediate structures and well-developed lamellar crystallites in regions II and III, while the diffraction profiles from the intermediate structures in region I was directly identified by the analysis (3). The analyses (3) to (5) elucidated that the "apparent lattice spacings" of the intermediate structures are larger than the lattice spacings of the lamellar crystallites.

The analysis (6) elucidated the time evolution of the characteristic parameters such as the scattering invariant $Q(t)$, the long spacing $L(t)$ of the mesomorphic layers $[L_{layer}(t)]$ and/or the lamellar crystallites $[L_{lam}(t)]$, the thickness $l_c(t)$ of the mesomorphic layers $[l_{c,layer}(t)]$ and/or the lamellar crystallites $[l_{c,lam}(t)]$, and the local volume fraction of the mesomorphic layers or the lamellar crystallites within their grains, $l_c(t)/L(t)$, which are dispersed in the matrix of the amorphous melts (see Figure 15). The results shown in Figure 13 revealed that the mesomorphic layers are continuously transformed into the lamellar crystallites, giving rise to continuous variations of $L(t)$ from $L_{layer}(t)$ to $L_{lam}(t)$ and $l_c(t)$ from $l_{c,layer}(t)$ to $l_{c,lam}(t)$ with time.

The small decrease of $L(t)$ with t may be due to the evolution of new density-rich regions with thickness l'_d and their transformations first into the mesomorphic layers and then to lamellar crystallites with the thicknesses $l'_{c,layer}(t)$ and $l'_{c,lam}(t)$, respectively, in the amorphous regions between the as-developed density-rich regions, layers, or crystallites, as illustrated in the third column of Figure 15a–c. The thickness l'_d, $l'_{c,layer}$, and $l'_{c,lam}$ may be smaller than l_d, $l_{c,layer}$, and $l_{c,lam}$, respectively, in the case when the thickness $l_a(t)$ is not sufficiently large for the newly inserted density-rich regions, layers, and/or crystallites. The density-rich regions with l'_d in part (a) are expected to increase its density to a sufficiently high level before they are transformed into the mesomorphic layers with $l'_{c,layer}$ as illustrated in part (b).

The increase of $l_c(t)$ and $l_c(t)/L(t)$ was discussed in section IV-6. The transformation from (a) to (b) must involve a change in the single chain conformations from more or less random coil conformations to the stretched chain conformations (or increasing fraction of helical conformations) in order for the chains to be incorporated in the mesomorphic orders. This may involves an increase of the thickness in the density-rich regions from l_d (or l'_d) to the thickness of the mesomorphic layers $l_{c,layer}$ (or $l'_{c,layer}$), while the characteristic spacing for the density fluctuations L_d may be almost the same as L_{layer}.

Finally, we would like to stress that the conclusions achieved in this work solidify those reported by the earlier works and strengthen the universal features of the multistep crystallization process for bulk polymer melts. We would like to remark also the point that the isothermal crystallization at the same temperature from glassy states is quite intriguing in comparison with that from melts. This deserves future works.

■ ASSOCIATED CONTENT

Supporting Information

(1) One-dimensional correlation function analysis; (2) MCR-ALS and EFA algorithm and their results; (3) Avrami plots on $X_{C,app}(t)$ and $X_{crys}(t)$; (4) heterospectral and homospectral 2D-COS analyses with tr-SAXS profiles and their results. This material is available free of charge via the Internet at http://pubs.acs.org.

■ AUTHOR INFORMATION

Corresponding Author

*E-mail: ozaki@kwansei.ac.jp (Y.O.); hsato@kwansei.ac.jp (H.S.).

■ ACKNOWLEDGMENTS

This work was supported by Grant-in-Aid for Scientific Research (C) from MEXT (No. 20550026, No. 20550197), Grant-in-Aid for Scientific Research on Innovative Areas from MEXT (No. 21106521), and Shiseido Female Researcher Science Grant 2009. This works was supported also by Kwansei-Gakuin University "Special Research" project 2009–2014. The authors thank beam time during experiments at Frontier Softmaterial Beamline: FSBL 03XU in SPring-8.

■ REFERENCES

(1) Strobl, G. R. *The Physics of Polymers*; Springer-Verlag: Berlin, 1997.
(2) Lotz, B. *Eur. Phys. J. E* **2000**, *3*, 185–1894.
(3) Wunderlich, B. *Prog. Polym. Sci.* **2003**, *28*, 383–450.
(4) Cornibert, J.; Marchessault, R. H. *J. Mol. Biol.* **1972**, *71*, 735–756.
(5) Yokouchi, M.; Chatani, Y.; Tadokoro, H.; Teranishi, K.; Tani, H. *Polymer* **1973**, *14*, 267–272.
(6) Doi, Y. *Microbial Polyester*; VCH Publishers: New York, 1990.
(7) Anderson, A. J.; Dawes, E. A. *Mirobiol. Rev.* **1990**, *54*, 450–472.
(8) Lara, M. L.; Gjalt, H. W. *Microbiol. Mol. Biol. Rev.* **1999**, *63*, 21–53.
(9) Iwata, T.; Doi, Y. *Macromol. Chem. Phys.* **1999**, *200*, 2429–2442.
(10) Sato, H.; Nakamura, M.; Padermshoke, A.; Yamaguchi, H.; Terauchi, H.; Ekgasit, S.; Noda, I.; Ozaki, Y. *Macromolecules* **2004**, *37*, 3763–3769.
(11) Sato, H.; Murakami, R.; Padermshoke, A.; Hirose, F.; Senda, K.; Noda, I.; Ozaki, Y. *Macromolecules* **2004**, *37*, 7203–7213.
(12) Sato, H.; Murakami, R.; Zhang, J.; Mori, K.; Takahashi, I.; Terauchi, H.; Noda, I.; Ozaki, Y. *Macromol. Symp.* **2005**, *230*, 158–166.
(13) Sato, H.; Mori, K.; Murakami, R.; Ando, Y.; Takahashi, I.; Zhang, J.; Terauchi, H.; Hirose, F.; Senda, K.; Tashiro, K.; Noda, I.; Ozaki, Y. *Macromolecules* **2006**, *39*, 1525–1531.
(14) Sato, H.; Ando, Y.; Dybal, J.; Iwata, T.; Noda, I.; Ozaki, Y. *Macromolecules* **2008**, *41*, 4305–4312.
(15) Guo, L. H.; Sato, H.; Hashimoto, T.; Ozaki, Y. *Macromolecules* **2010**, *43*, 3897–3902.
(16) Guo, L. H.; Sato, H.; Hashimoto, T.; Ozaki, Y. *Macromolecules* **2011**, *44*, 2229–2239.

(17) Suttiwijitpukdee, N.; Sato, H.; Zhang, J.; Hashimoto, T.; Ozaki, Y. *Polymer* **2011**, *52*, 461−471.
(18) An, Y.; Dong, L.; Li, L.; Mo, Z.; Feng, Z. *Eur. Polym. J.* **1999**, *35*, 365−369.
(19) Androsch, R. *Polymer* **2008**, *49*, 4673−4679.
(20) Zhang, J.; Sato, H.; Noda, I.; Ozaki, Y. *Macromolecules* **2005**, *38*, 4274−4281.
(21) Suttiwijitpukdee, N.; Sato, H.; Zhang, J.; Hashimoto, T. *Macromolecules* **2011**, *44*, 3467−3477.
(22) Tashiro, K.; Sasaki, S.; Gose, N.; Kobayashi, M. *Polym. J.* **1998**, *30*, 485−491.
(23) Kanig, G. *Colloid Polym. Sci.* **1991**, *269*, 1118−1125.
(24) Saijo, K.; Hashimoto, T. *Mater. Res. Soc. Symp. Proc.* **1986**, *79*, 267−276.
(25) Saijo, K.; Zhu, Y. P.; Hashimoto, T.; Wasiak, A.; Brzostowski, N. *J. Appl. Polym. Sci.* **2007**, *105*, 137−157.
(26) Okada, T.; Saito, H.; Inoue, T. *Macromolecules* **1992**, *25*, 1908−1911.
(27) Pogodina, N. V.; Siddiquee, S. K.; van Egmond, J. W.; Winter, H. H. *Macromolecules* **1999**, *32*, 1167−1174.
(28) Matsuba, G.; Kaji, K.; Nishida, K.; Kanaya, T.; Imai, M. *Polym. J.* **1999**, *31*, 722−727.
(29) Strobl, G. R. *Eur. Phys. J. E* **2000**, *3*, 165−183.
(30) Sajkiewicz, P.; Hashimoto, T.; Saijo, K.; Gradys, A. *Polymer* **2005**, *46*, 513−521.
(31) Noda, I. *Appl. Spectrosc.* **1993**, *47*, 1329−1336.
(32) Noda, I.; Dowrey, A. E.; Marott, C.; Story, G. M.; Ozaki, Y. *Appl. Spectrosc.* **2000**, *54*, 236A−248A.
(33) Noda, I.; Ozaki, Y. *Two-Dimensional Correlation Spectroscopy*; John Wiley & Sons: Chichester, UK, 2004.
(34) Marquez-Alvarez, C.; Rodriguez-Ramos, I.; Guerrero-Ruiz, A.; Haller, G. L.; Fernandez-Garcia, M. *J. Am. Chem. Soc.* **1997**, *119*, 2905−2914.
(35) Larrechi, S. M.; Rius, X. F. *Appl. Spectrosc.* **2004**, *58*, 47−53.
(36) Garrido, M.; Lazaro, I.; Larrechi, S. M.; Rius, X. F. *Anal. Chim. Acta* **2004**, *515*, 65−73.
(37) Spegazzini, N.; Ruisanchez, I.; Larrechi, S. M.; Cadiz, V.; Canadell, J. *Analyst* **2008**, *133*, 1028−1035.
(38) Perera, P.; Wyche, M.; Loethen, Y.; Ben-Amotz, D. *J. Am. Chem. Soc.* **2008**, *130*, 4576−4577.
(39) Spegazzini, N.; Ruisanchez, I.; Larrechi, S. M. *Anal. Chim. Acta* **2009**, *642*, 155−162.
(40) Blobel, J.; Bernado, P.; Svergun, I. D.; Tauler, R.; Pons, M. *J. Am. Chem. Soc.* **2009**, *131*, 4378−4386.
(41) Iglesias-Juez, A.; Kubacka, A.; Fernandez-Garcia, M.; Michiel, M. D.; Newton, M. A. *J. Am. Chem. Soc.* **2011**, *133*, 4484−4489.
(42) Sasaki, S.; Sato, H.; Funatsu, R.; Yoshimoto, J.; Masunaga, H.; Ogawa, H. *SPring-8 User Experiment Report* **2008B**, 2026. Masunaga, H.; Ogawa, H.; Sasaki, S. *SPring-8 User Experiment Report* **2010B**, 1068.
(43) Strobl, G. R.; Schneider, M. *J. Polym. Sci., Polym. Phys. Ed.* **1980**, *18*, 1343−1359.
(44) Guinier, A. *Ann. Phys.* **1939**, *12*, 161−237.
(45) Guinier, A.; Fournet, G. *Small Angle X-ray Scattering*; John Wiley & Sons, Inc.: London, 1955.
(46) Porod, G. *Kolloidn. Zh.* **1951**, *124*, 83−111.
(47) Porod, G. *Kolloidn. Zh.* **1952**, *125*, 51−57.
(48) The integral of $[I(q)q^2]$ in the equation means the integration of the relevant diffraction peak intensity (with the spherically symmetric distribution for the powder patterns) overall reciprocal space. For systems having a spherically symmetric diffraction intensity distribution in the reciprocal space, this definition of the integral width is physically more reasonable than the conventional definition of β = [integral of $I(q)$]/$I_{max}(q)$.
(49) Hsiao, B. S.; Wang, Z.; Yeh, F.; Gao, Y.; Sheth, C. K. *Polymer* **1999**, *40*, 3515−3523.
(50) Sasaki, S.; Tashiro, K.; Kobayashi, M.; Izumi, Y.; Kobayashi, K. *Polymer* **1999**, *40*, 7125−7135.
(51) Lisowski, S. M.; Liu, Q.; Cho, J.; Runt, J.; Yeh, F.; Hsiao, B. S. *Macromolecules* **2000**, *33*, 4842−4849.
(52) Hama, H.; Tashiro, K. *Polymer* **2003**, *44*, 6973−6988.
(53) Reddy, R. K.; Tashiro, K.; Sakurai, T.; Yamaguchi, N.; Sasaki, S.; Masunaga, H.; Takata, M. *Macromolecules* **2009**, *42*, 4191−4199.
(54) Maeder, M. *Anal. Chem.* **1987**, *59*, 527−530.
(55) II'ichev, Y. V.; Schworer, M. A.; Wirz, J. *J. Am. Chem. Soc.* **2004**, *126*, 4581−4595.

Macromolecules

ARTICLE

pubs.acs.org/Macromolecules

Fluorescence Behavior of Dyes in Thin Films of Various Polymers

Atsuomi Shundo,[†] Yohei Okada,[†] Fuyuki Ito,[‡] and Keiji Tanaka*[,†]

[†]Department of Applied Chemistry, Kyushu University, Fukuoka 819-0395, Japan

[‡]Department of Chemistry, Shinshu University, Nagano 380-8544, Japan

ABSTRACT: We have studied the fluorescence behavior of a dye, 6-(*N*-(7-nitrobenz-2-oxa-1,3-diazol-4-yl)amino)hexanoic acid (NBD), in thin films of polymers with various polarities, such as poly(methyl methacrylate) (PMMA), Arton, poly(styrene) (PS), hydrogenated polystyrene (H-PS), and Zeonex. In the case of well-dispersed systems, the fluorescence behavior of NBD could be explained in terms of the mobility of the polymer matrix. This was the case for PMMA, Arton, and PS. On the other hand, when H-PS or Zeonex was used, NBD aggregated in the films, leading to unusual fluorescence behavior: the fluorescence lifetime and maximum wavelength increased with a decrease in the film thickness. Time- and space-resolved fluorescence spectroscopy using an evanescent wave excitation revealed that the aggregation states of NBD near the interface varied with the film thickness. While NBD molecules near the interface aggregated in a thick film, such was not the case in a thin film. Angular-dependent X-ray photoelectron spectroscopy (ADXPS) structurally confirmed the above observations; that is, the film thickness greatly influenced the depth profile of the NBD composition in the polymer films.

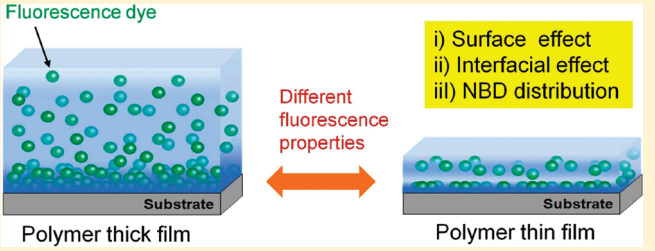

1. INTRODUCTION

The idea of incorporating dyes into a polymer matrix has attracted a great deal of interest as a simple fabrication scheme for functional devices. For example, thin polymer films containing fluorescence dyes have been extensively studied for sensors,[1−3] image patterning,[4−6] optical storage media,[7−9] and solar cells.[10−12] In these applications, one of the crucial points is to control the dispersion state of dyes in the polymer films. This is simply because aggregation formation of the dyes often alters the original fluorescence properties, such as the emission band position and lifetime.[13−16] In general, the dispersion state of dye molecules in a polymer is closely related to their miscibility. Hence, an effect of polymer polarity on the fluorescence behavior of the dye, especially in thin films, should be studied as the first benchmark for developing the functional materials mentioned above.

It has been widely accepted that the fluorescence properties of a dye that is molecularly dispersed in a polymer matrix are influenced by the mobility of the surrounding polymer chains.[17−19] This feature makes it possible to determine the glass transition temperature (T_g) of the matrix polymer by measuring the temperature-induced change in the fluorescence emission.[20−25] Recently, this notion was applied to study the spatial distribution of T_g in thin polymer films. Torkelson and co-workers presented clear evidence for a mobility gradient in thin polymer films, in which a dye labeled-layer was inserted at an arbitrary position.[21,22,24] As a result, the segmental dynamics at the surface were much faster than that in the corresponding bulk. We also investigated the polymer dynamics at the interface with inorganic solids using evanescent wave excitation, showing that the interfacial segmental dynamics was much slower than that in the bulk.[23,25]

As mentioned above, fluorescence spectroscopy enables us to gain direct access to local dynamics in polymer films. However, fluorescence properties are dependent on the place where the dye molecules exist. For instance, in general, the fluorescence lifetime, which determines the intensity, at the interface is not the same as that in the bulk. Thus, as long as the spectroscopy is applied to determine the local T_g, the absolute value of the fluorescence lifetime, as well as the emission wavelength, is not so important. This is because the T_g can be defined as a temperature at which the decrement of fluorescence lifetime, or intensity, changes with increasing temperature. In this case, although the extent to which the fluorescence lifetime changes with temperature is important, the absolute lifetime of the fluorescence is not necessary. However, to apply fluorescence spectroscopy further in order to study the physical properties of polymers, especially in confined spaces, we require a better understanding of the factors that control the fluorescence behavior of dyes in a confined space. The knowledge can be also useful for the fabrication of the aforementioned functional devices.

This study revealed the fluorescence behavior of dyes in a polymer film as the film thickness decreases. We propose a possible explanation for the peculiar thickness dependence seen in some polymers on the basis of space-resolved fluorescence spectroscopy using evanescent wave excitation, in conjunction with X-ray photoelectron spectroscopy to provide structural information.

Received: August 20, 2011
Revised: October 29, 2011
Published: December 05, 2011

Table 1. Characteristics of Polymers Used in This Study[a]

	PMMA	Arton®	PS	H-PS	Zeonex®
	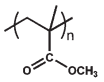	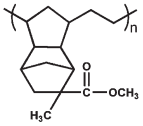	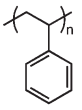	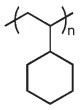	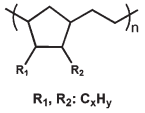
M_n	41.5k	44.7k	53.4k	91.6k	20k
M_w/M_n	1.08	2.2	1.03	1.2	2.0
T_g / K	393	422	376	418	412
ε (at 1 Hz)	2.8	2.7	2.5~2.6	2.3	2.3
n (at 430 nm)	1.496	1.523	1.585	1.506	1.525
θ_c (with SLAH-79) / °	46.9	48.0	50.6	47.3	48.1

[a] Chemical structures, number-average molecular weights (M_n), molecular weight distribution (M_w/M_n), glass-transition temperatures (T_g), dielectric constants at 1 MHz (ε), refractive indices at 430 nm (n), and critical angles against a SLAH-79 substrate with a refractive index of 2.05 (θ_c).

2. EXPERIMENTAL SECTION

2.1. Sample and Film Preparation. Poly(methyl methacrylate) (PMMA), Arton, polystyrene (PS), hydrogenated polystyrene (H-PS), and Zeonex were used as matrix polymers. PMMA and PS were purchased from Polymer Source Inc. and were used as received. Arton was kindly supplied from JSR Co. H-PS and Zeonex were also kindly supplied from Zeon Co. Arton, H-PS, and Zeonex were purified by reprecipitation. Table 1 summarizes the chemical structure, the number-average molecular weight (M_n), and molecular weight distribution (M_w/M_n), where M_w is the weight-average molecular weight, and the glass transition temperature (T_g), together with the dielectric constant (ε) at 1 MHz, the refractive index (n) at a wavelength of 430 nm, and the critical angle calculated against a glass substrate (SLAH-79) with a refractive index of 2.05. M_n and M_w/M_n were determined by gel permeation chromatography (Tosoh HLC-8220) with Shodex KF-804L and KF-805L columns against PS standards. The bulk T_g was measured by differential scanning calorimetry (Extra6000 DSC6220, SII Co., Ltd.). As a fluorescent probe, 6-(*N*-(7-nitrobenz-2-oxa-1,3-diazol-4-yl)amino)hexanoic acid (NBD) was purchased from Sigma-Aldrich Co. and used as received. The chemical structure of NBD is shown in Figure 1a. Thin polymer films containing NBD were prepared on a SLAH-79 substrate by a spin-coating method. The molar ratio of NBD to a repeating unit of polymer was fixed to be ~0.1%. All films were dried under vacuum at room temperature for 24 h. The thickness of the films was determined by ellipsometry (M-150, Jasco Co., Ltd.).

2.2. Characterizations. Ultraviolet (UV)−visible (vis) and fluorescence spectra for a tetrahydrofuran (THF) solution of NBD were recorded by a U-4100 spectrophotometer (Hitachi High-Technologies Co.) and a F-4500 fluorescence spectrophotometer (Hitachi High-Technologies Co.), respectively. For the time-resolved fluorescence spectroscopy, NBD dyes were excited with the second-harmonic generation of a mode-locked titanium:sapphire laser (Spectra Physics, Tsunami; full width at half-maximum (fwhm) = 1.5 ps; wavelength = 430 nm) equipped with a pulse selector and a harmonic generator. A streak scope (Hamamatsu Photonics, C4334-01) was used to detect the time-resolved fluorescence from excited NBD molecules. An excitation pulse was irradiated on the film from the substrate side via a prism at a certain angle. When the incident angle (θ) is larger than the critical angle (θ_c), the excitation pulse is totally reflected at the interface between the polymer and the substrate. In this case, an evanescent wave, where the electric field exponentially decays along the direction normal to the interface, is generated at the polymer interface. Information near the substrate interface was selectively extracted on the basis of this evanescent wave excitation. The θ_c values for the matrix polymers are summarized in Table 1. In the case of $\theta < \theta_c$, the excitation pulse went through the internal bulk phase of the film, meaning that the data so obtained reflects bulk information. For the bulk measurements, a θ value of 45° was used for all polymers. The chemical composition at the film surface of the polymers containing NBD was examined by X-ray photoelectron spectroscopy (XPS, PHI 5800 ESCA system, Physical Electonics, Co., Ltd.) with a monochromatized Al K_α source operated at 14 kV and 24 mA. The C_{1s} peak was calibrated to a binding energy of 285.0 eV for the neutral carbons to correct the charging energy shifts. The analytical depth (d_{XPS}) of XPS from the outermost surface is defined by $3\lambda_e \sin\theta_e$, where λ_e and θ_e are the inelastic mean-free path of photoelectrons in the solid and the emission angle of photoelectrons, respectively. The λ_e for C_{1s} photoelectrons was taken to be 3.1 nm, calculated by Ashley's equation.[26]

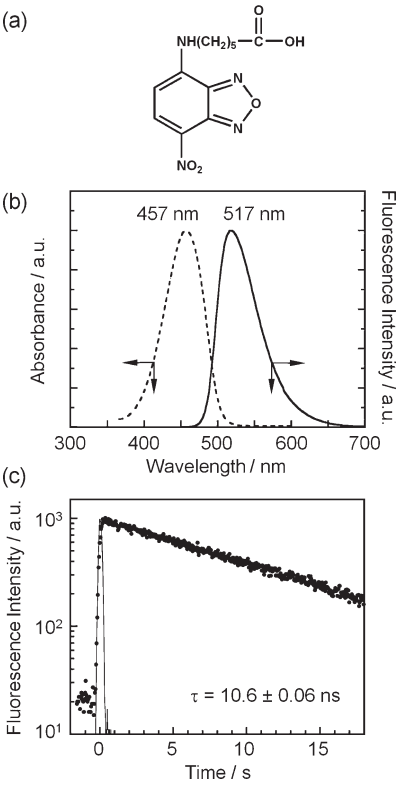

Figure 1. (a) Chemical structure of 6-(*N*-(7-nitrobenz-2-oxa-1,3-diazol-4-yl)amino)hexanoic acid, NBD, (b) UV−vis and fluorescence spectra for a THF solution of NBD with a concentration of 10 μM, and (c) fluorescence decay curve for the solution.

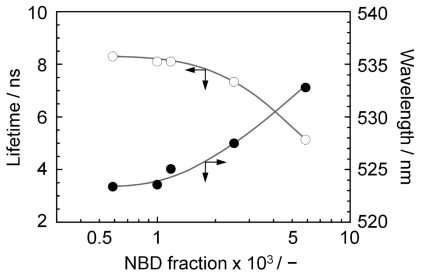

Figure 2. NBD fraction dependence of the fluorescence lifetime and maximum wavelength for NBD dispersed in a PMMA film with a thickness of 2 μm. Solid lines are guides to the eye.

The depth profile of NBD composition in the vicinity of the film surface was analyzed by angular-dependent XPS (ADXPS)[27] over a range of θ_e from 15° to 90°. Also, the depth profile of NBD composition in the films near the substrate interface was also obtained. To do so, the films were floated off on a water surface and then picked up by attaching the substrate from the air side.[28]

3. RESULTS AND DISCUSSION

3.1. Fundamental Fluorescence Behavior of NBD. Figure 1b shows the UV−vis and fluorescence spectra for NBD in THF with a concentration of 10 μM. The maximum wavelengths in absorption (λ_{max}) and fluorescence emission (λ_{em}) were 457 and 517 nm, respectively. Since the emission band slightly overlapped with the absorption at 457 nm, a wavelength of 430 nm was selected to excite NBD for the fluorescence study. Figure 1c shows the time (t) dependence of fluorescence intensity (I) for NBD excited at 430 nm. The decay curve was fitted by the following double-exponential equation with two time constants, τ_{fast} and τ_{slow}:

$$I = I_0\{(1-x)\exp(-t/\tau_{fast}) + x\exp(-t/\tau_{slow})\} \quad (1)$$

where I_0 and x are the fluorescence intensity right after the excitation and the fraction of the slow component, respectively. The overall lifetime of the emission (τ) was defined as

$$\tau = (1-x)\tau_{fast} + x\tau_{slow} \quad (2)$$

The lifetime for NBD in THF was 10.6 ± 0.06 ns.

In general, the fluorescence behavior of a dye in a solid is not the same as that in a solution because the surrounding environment of the dye differs in the two states. Thus, as a typical polymer solid, τ and λ_{em} for NBD dispersed in the PMMA film with a thickness of ~2 μm were examined. Figure 2 shows the NBD concentration dependence of the τ and λ_{em} values. In the case of a NBD concentration lower than 0.1 mol % in the 2 μm thick film, both τ and λ_{em} values were almost constant, and no signature for the aggregation of NBD was observed. When the NBD concentration went beyond 0.1 mol %, the τ and λ_{em} became shorter and longer, respectively. This might be due to an energy transfer from the monomers to the aggregate sites or to the excimers.[16,29] Thus, hereafter, the NBD concentration in the polymer films was fixed to be 0.1 mol % unless otherwise stated.

3.2. Film Thickness Dependence of Fluorescence Behavior. Figure 3a shows the thickness dependence of the fluorescence lifetime for NBD dispersed in films of PMMA, Arton, PS, H-PS, and Zeonex. The τ values of NBD in the polymer films were in the range from 3 to 9 ns, which were smaller than that obtained in the THF solution. In a thick region of a few hundreds of nanometers,

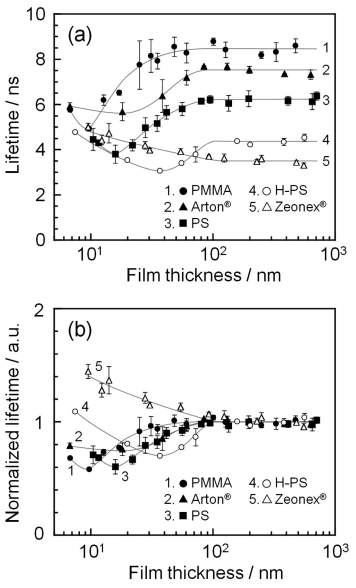

Figure 3. Film thickness dependence of (a) fluorescence lifetime and (b) normalized lifetime for NBD dispersed into various polymers: PMMA, Arton, PS, H-PS, and Zeonex. The molar ratio of NBD to a monomer unit in polymer is 1.0×10^{-3}. Solid lines are guides to the eye.

the τ value was longer in the order of PMMA, Arton, PS, H-PS, and Zeonex. This order agreed with that for the dielectric constant (ε) collected in Table 1, implying that the τ for NBD is a function of the polarity of the matrix polymer. This is because the dipole moment of NBD in the excited state is quite different from that in the ground state.[30] When the film became thinner than ~100 nm, the τ value was dependent on the thickness. To make a comparison among polymers easier, τ was normalized by the average value for the thick films, as shown in panel b of Figure 3. When PMMA was used as a matrix polymer, τ first decreased with decreasing thickness. However, in an ultrathin region thinner than 10 nm, the trend reversed and τ started to increase. Similar behavior could be seen for the Arton and PS films. In the case of H-PS, the trend was also similar to that for PMMA, Arton, and PS. However, the minimum lifetime was observed at a thickness of ca. 40 nm, which was thicker than for the others. The curve for H-PS was just like that for one of the others but shifted toward a thicker region. On the other hand, τ simply increased with decreasing thickness for the Zeonex film.

To discuss the possibility of aggregation formation of NBD in the thinner films, fluorescence spectra were collected. Figure 4 shows the spectra for NBD in five different polymer films with thicknesses of approximately 200 and 10 nm. The fluorescence spectra for NBD in PMMA and Arton films were insensitive to the thickness. Also, the spectrum for NBD in a 10 nm thick PS film was slightly shifted to a higher wavelength side from the original, but the extent was actually trivial. On the other hand, a thinning-induced red shift of the spectrum was observed for the H-PS and Zeonex films. Thus, although it can be hardly claimed solely from Figure 4 that NBD was homogeneously distributed in thin PMMA and Arton films, it is apparent that the distribution of NBD was inhomogeneous, that is, aggregation of NBD occurred, in the H-PS and Zeonex films.

Next, we revisit the thickness dependence of the fluorescence lifetime for NBD shown in Figure 3. The fluorescence lifetime of NBD decreased with decreasing film thickness except in Zeonex.

dx.doi.org/10.1021/ma201901x |*Macromolecules* 2012, 45, 329–335

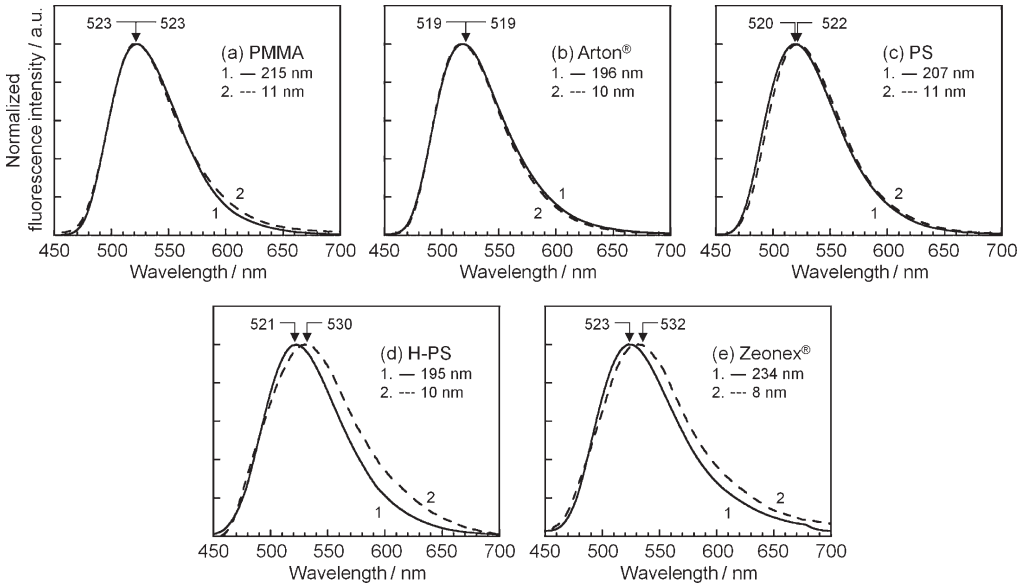

Figure 4. Fluorescence spectra for NBD dispersed into the films of (a) PMMA, (b) Arton, (c) PS, (d) H-PS, and (e) Zeonex, with film thicknesses of ca. 200 and 10 nm. The molar ratio of NBD to a monomer unit in polymer is 1.0×10^{-3}.

This might be rationalized by two factors. First, the local concentration of NBD starts to fluctuate in the films with decreasing thickness. This means that the concentration of NBD increases and decreases depending on the position. At a position where the local concentration is higher, the lifetime decreases, as seen in Figure 2, indicating that the energy transfers from the monomers to the aggregate sites. Second, the molecular motion of polymer chains alters the fluorescence lifetime of NBD. In general, the polymer mobility at the surface and substrate interfaces is respectively enhanced and depressed in comparison with that in the internal region of the film.[31−34] Hence, the fluorescence lifetime should be shorter at the surface region than in the bulk because the fractional amount of nonradiative pathways to the ground state increases due to the enhanced mobility of the matrix polymer. Since the ratio of the surface area to the total volume increases with decreasing film thickness, the surface effect becomes more striking with decreasing thickness. That is, the fluorescence lifetime decreases with decreasing thickness. However, an increase in the lifetime was observed in the ultrathin films as well as in Zeonex films. This cannot be simply explained in terms of these two factors. Such a discrepancy motivates us to examine the fluorescence dynamics of NBD at the substrate interface.

3.3. Fluorescence Behavior at the Substrate Interface. The fluorescence spectrum and lifetime of NBD at the interface with the solid substrate can be selectively obtained by evanescent wave excitation.[23,25] To compare the interfacial fluorescence behavior with that in the internal bulk, the measurements were made at two different θs being smaller and larger than the θ_c. The penetration depth (d_p) of the evanescent wave is given by[35]

$$d_p = \lambda(\sin^2 \theta - \sin^2 \theta_c)^{-1/2}/2\pi n \quad (3)$$

where λ is the wavelength of the excitation. In fact, the relation between the depth and the electric field intensity (I_{ev}) is much more important for the interfacial selectivity than the d_p value.[35]

$$I_{ev} = I_{ev,0} \exp(-2z/d_p) \quad (4)$$

Here, z is the depth from the interface. The analytical depth (d) is defined as the position at which I_{ev} becomes $I_{ev,0}/e$, namely, the value of I_{ev} corresponding to $d_p/2$. Equations 3 and 4 indicate that the d value can be regulated by changing θ. For the interfacial measurements, the d value was kept to be 35 nm, which corresponded to θs of 60.7° for PMMA and 62.0° for Zeonex. The d value of 35 nm is larger than the thickness of the thin films studied here (<20 nm). However, taking into account the fact that the electric field intensity of the evanescent light is the strongest at the interface and exponentially decays with increasing depth, the fluorescence emission obtained by this method would mostly reflect that near the interface. In fact, differences in the fluorescent spectra and the lifetimes of NBD were observed between the two measurements carried out under the conditions of $\theta < \theta_c$ and $\theta > \theta_c$.

Figures 5 and 6 show the fluorescence decay curves and spectra for NBD in the films of PMMA and Zeonex, which represent typical polar and nonpolar cases, respectively. The data for approximately 200 and 20 nm thick films are presented. To excite NBD dyes, transmitted pulses and evanescent waves were used to obtain the information in the bulk and at the interface, respectively. In the case of PMMA, the lifetime was longer at the interface than in the bulk. On the other hand, the λ_{em} for NBD at the interface was almost the same as that in the bulk, indicating that the NBD dyes were well-dispersed even in the interfacial region. So far, many researchers have reported that the segmental motion of PMMA at the interface with hydrophilic substrates was less active than that in the bulk.[25,36−38] If this is the case, since the fractional amount of nonradiative pathways to the ground state for excited NBD decreases at the interface thanks to the less active molecular motion, it is reasonable that the lifetime for NBD at the interface became longer, as shown in panels a and c of Figure 5.

The fluorescence behavior of NBD in the Zeonex films definitely differed from those in PMMA. In the case of the thick film, the τ and λ_{em} at the interface were respectively shorter and longer than the bulk values. The red shift of λ_{em} in panel b of Figure 6 means that aggregate formation of NBD dyes was more striking in the interfacial region than in the bulk. Thus, it is

dx.doi.org/10.1021/ma201901x |*Macromolecules* 2012, 45, 329–335

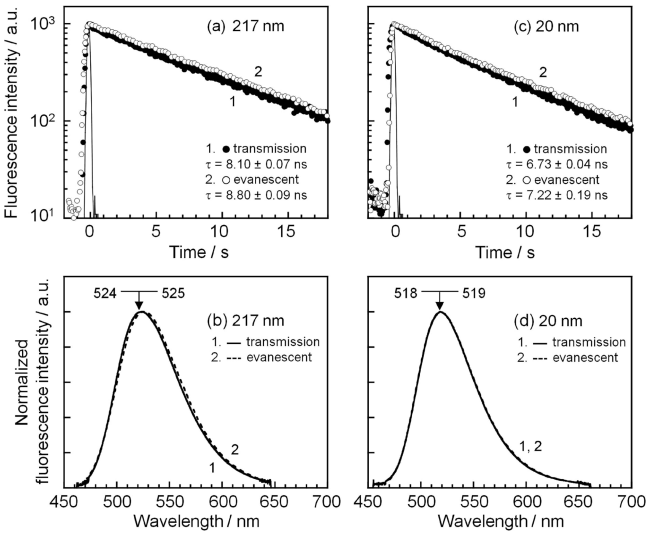

Figure 5. Fluorescence decay curve and spectra for NBD dispersed in the PMMA films with a thickness of (a, b) 217 nm and (c, d) 20 nm. The data indicated by transmission and evanescent correspond to those obtained by excitation of NBD at $\theta < \theta_c$ and $\theta > \theta_c$, respectively. The molar ratio of NBD to a monomer unit in PMMA is 1.0×10^{-3}.

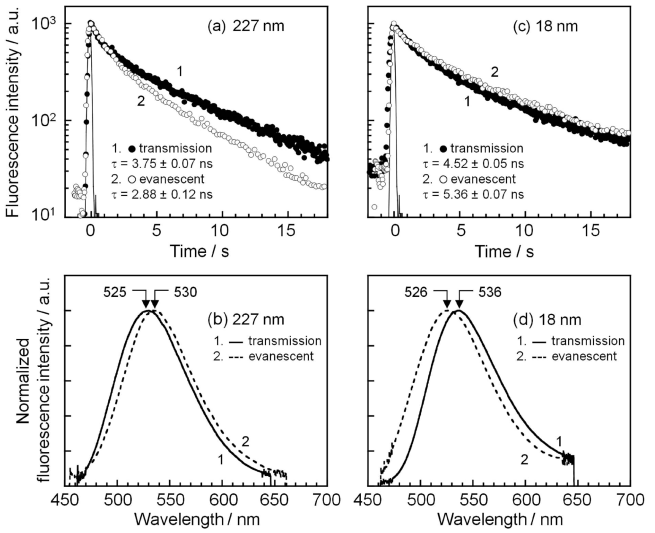

Figure 6. Fluorescence decay curve and spectra for NBD dispersed in the Zeonex films with thicknesses of (a, b) 227 nm and (c, d) 18 nm. The data indicated by transmission and evanescent correspond to those obtained by excitation of NBD at $\theta < \theta_c$ and $\theta > \theta_c$, respectively. The molar ratio of NBD to a monomer unit in Zeonex is 1.0×10^{-3}.

conceivable that the effect of aggregation for NBD on its lifetime was dominant over the effect of the interfacial chain mobility. When the Zeonex film became thinner at ca. 20 nm, the trend reversed. That is, the interfacial τ was larger than the bulk value. Currently, the NBD concentration in the sample was fixed, meaning that the total number of NBD molecules was smaller in the thin film than in the thick film. Hence, it would be possible that the NBD concentration at the interface was smaller in the thin film than in the thick film, resulting in a lesser extent of aggregate formation at the interface of the thin film because a sufficient amount of NBD could not be partitioned to the

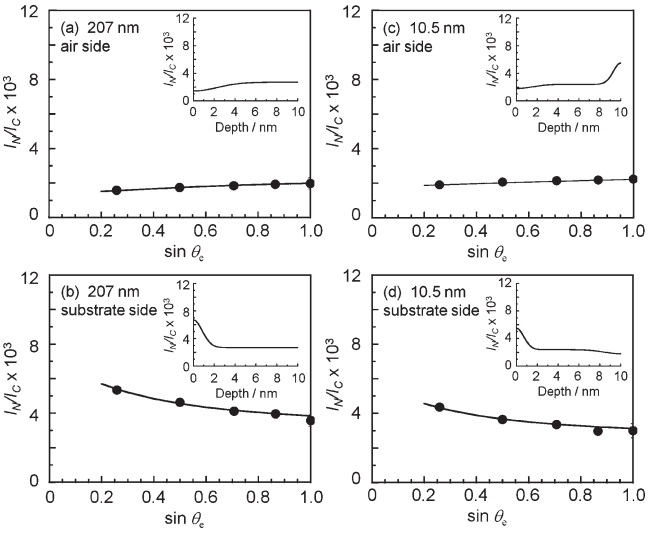

Figure 7. Sin θ_e dependence of the ratio of peak intensity due to N_{1s} and C_{1s} (I_N/I_C) in XPS spectra for the PMMA films with thicknesses of (a, b) 207 nm and (c, d) 10.5 nm. The solid circles are the experimental data. The insets show the model depth profiles of atomic ratio of nitrogen to carbon to obtain the best fit to the data. The molar ratio of NBD to a monomer unit in PMMA is 1.0×10^{-3}.

interfacial region due to a lack of NBD molecules. Hence, in the case of the thin film, the effect of the interfacial chain mobility was more dominant than the effect of aggregate formation on the lifetime of NBD. Interestingly, the λ_{em} value at the interface was shorter than that in the bulk for the thin film. This implies that in the case of the thin Zeonex film the extent of NBD aggregate formation was more marked in the bulk region than in the interfacial region.

3.4. Depth Profile of NBD in Films. We finally come to the distribution of NBD dyes in the films along the direction normal to the interface determined by XPS. Here, the films of PMMA and Zeonex were again examined as typical polar and nonpolar cases, respectively. To analyze the NBD concentration at the substrate interface, the films prepared on the substrates were floated off onto the water surface, and then they were attached to different substrates from the air side, resulting in an upside-down version of the films.[28] Since nitrogen atoms exist only in NBD, the intensity ratio of XPS N_{1s} to C_{1s} peaks (I_N/I_C) reflects the NBD composition. Figure 7 shows the sin θ_e dependence of I_N/I_C for 207 and 10.5 nm thick PMMA films. As stated in the Experimental Section, sin θ_e corresponds to the analytical depth; a smaller θ_e corresponds to a shallower depth from the outermost region. While panels a and c show the data for the surface side, panels b and d show the data for the substrate interface side. The I_N/I_C slightly decreased with decreasing sin θ_e, meaning that the concentration of NBD dyes was a little lower in proximity to the surface. In general, a component with lower surface energy is enriched at the surface due to the requirement for the minimization of the total free energy of the system.[39−42] Hence, it is reasonable that the higher surface energy component, namely NBD, prefers to be outermost in the surface region.[43] In the case of the interfacial region, on the contrary, the value of I_N/I_C increased with decreasing sin θ_e. Thus, it can be claimed that NBD dyes were enriched at the substrate interface because of an attractive interaction between NBD and the hydrophilic substrate.

dx.doi.org/10.1021/ma201901x |*Macromolecules* 2012, 45, 329–335

In XPS, the photoelectron intensity for the j-core level at θ_e is expressed as[27]

$$I_j(\theta) = Fk \int_0^\infty n_j(z) \exp\{-z/(\lambda_j \sin \theta_e)\}\, dz \quad (5)$$

where z and $n_j(z)$ represent the depth and the composition at z, respectively. F and k are the transmission function and a factor related to the sensitivity, respectively. Hence, even though the analytical depth is z, photoelectrons are not uniformly emitted from the depth region from the surface to z. Instead, the detected amount of photoelectrons exponentially decays with increasing depth to z. This means that the dependence of surface composition on sin θ_e, as in Figure 7, cannot be simply regarded as the compositional depth profile. Thus, the following treatment was made to extract a plausible composition profile near the surface in the real space. The NBD composition in a polymer film $f(z)$ was assumed to be expressed by the Gaussian function

$$f(z) = a \exp(-z^2/b^2) + c \quad (6)$$

where a, b, and c were constants and were the fitting parameters. Moreover, I_N/I_C obtained by XPS at a given θ_e can be expressed by

$$I_N/I_C = \int_0^\infty f(z) \exp(-z/\lambda_j \sin \theta_e)\, dz \Big/ \int_0^\infty \exp(-z/\lambda_j \sin \theta_e)\, dz \quad (7)$$

Accordingly, the sin θ_e−I_N/I_C curve was fitted with eqs 6 and 7 using a, b, and c parameters.

Solid curves in Figure 7 denote the best-fitted curves obtained on the basis of the procedure mentioned above. Insets in Figure 7 show the model depth profiles of I_N/I_C for the best fits. In the case of a 207 nm thick PMMA film, NBD was slightly depleted at the film surface. On the other hand, the concentration of NBD at the outermost interfacial region with the substrate was approximately twice that introduced due to the favorable interaction between NBD and the hydrophilic substrate. We have already examined the concentration dependence of the lifetime for NBD shown in Figure 2. Even though the NBD concentration doubles to 0.2 mol %, the lifetime will remain unchanged. Thus, the effect of depressed molecular motion of PMMA in the interfacial region overcomes the effect of the concentration increment on the fluorescence behavior. In the case of a 10.5 nm thick PMMA film, since the analytical depth was comparable to the film thickness, the insets of panels c and d possess bilateral symmetry. That is, the NBD concentration profile from the surface can be superimposed on that from the substrate interface after reversing one of them from right to left. This is a signature that our fitting process was reliable. The NBD concentration profile in the thin film was essentially the same as that in the thick one. Nevertheless, the lifetime of NBD in the thin film was shorter than that in the thick film. This was the case in not only in the bulk but also at the interface, as shown in Figure 5. This can be explained in terms of a surface effect. The segmental mobility of polymer at the surface is enhanced in comparison with that in the bulk. This makes the lifetime of dyes in the surface region shorter. When a film becomes thinner, the surface and interfacial ratio to the total volume increases. Eventually, the effect of the surface mobility interferes with that of the interfacial mobility.

Figure 8 shows the sin θ_e dependence of I_N/I_C for 189 and 11.2 nm thick Zeonex films. Similarly to Figure 7, the upper and lower panels show the data for the surface and substrate interfacial sides, respectively. Insets denote the depth dependence of I_N/I_C to reproduce the experimental relation between sin θ_e and I_N/I_C. In the case of the 189 nm thick film, the NBD was preferentially segregated at the substrate interface, and the NBD concentration at the outermost region was roughly 3 times that of the bulk. Given that the NBD molecules were heterogeneously dispersed in the interfacial plane as well, aggregation can be serious, leading to an obvious reduction of the NBD lifetime via overcoming the effect of the depressed chain mobility at the interface. The concentration profile was quite unique for the 11.2 nm thick film. In this case, the NBD concentration at the outermost interface with a substrate was almost the same as that at the surface side. In addition, a depletion layer of NBD existed in the depth region from 6 to 8 nm from the air surface. This implies that the aggregation of NBD near to the interface had been suppressed. The information about the NBD composition obtained by XPS is in good accord with the discussion of the fluorescence behavior of NBD.

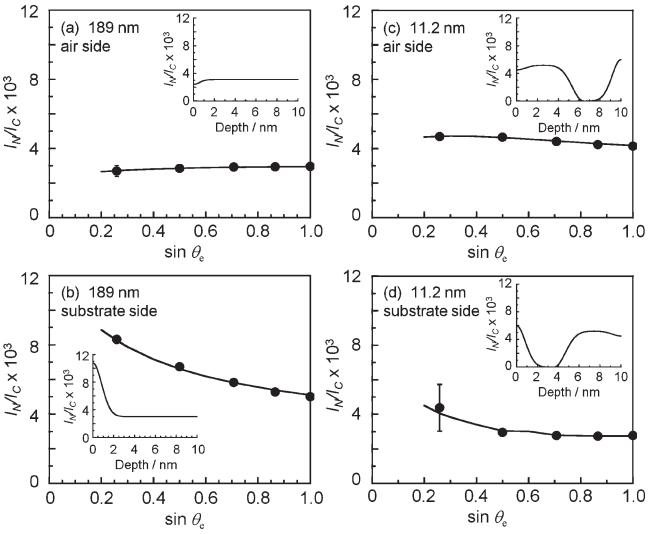

Figure 8. Sin θ_e dependence of the ratio of peak intensity due to N_{1s} and C_{1s} (I_N/I_C) in XPS spectra for the Zeonex films with thicknesses of (a, b) 189 nm and (c, d) 11.2 nm. The solid circles are the experimental data. The insets show the model depth profiles of atomic ratio of nitrogen to carbon to obtain the best fit to the data. The molar ratio of NBD to a monomer unit in Zeonex is 1.0×10^{-3}.

4. CONCLUSIONS

We have studied the fluorescence behavior of NBD dye dispersed in thin films of polymers with various polarities, which regulate the interaction with the NBD. The fluorescence behavior of NBD in thick films of a polymer depended on which kind of a polymer was used as a matrix. When a polymer film becomes thinner, the ratio of surface and interfacial areas to the total volume increases. Thus, to understand the fluorescence behavior of a dye in a thin polymer film, the surface and interfacial effects should be taken into account. The segmental mobility of polymers at the surface and the substrate interface are respectively enhanced and depressed in comparison with that in the internal bulk phase. Since the fractional amount of nonradiative pathways to the ground state of excited NBD molecules is closely related to the polymer mobility, the fluorescence lifetime at the surface and interface should be shorter and longer than that in the bulk,

respectively. Such an idea was applicable to explain the fluorescence behavior of NBD, which was well-dispersed in thin films of PMMA and Arton, and probably PS as well. However, this was not the case for H-PS and Zeonex. The distribution of NBD in the surface and interfacial regions is extremely inhomogeneous, leading to the aggregation of NBD molecules. The aggregation formation of dye molecules make the fluorescence lifetime shorter. Thus, in addition to the surface and interfacial effects related to polymer mobility, the dispersion state of dye molecules should be also taken into account. In other words, estimating precisely the surface and interfacial effects associated with the dispersion state of dye helps us to design and construct thin polymer films containing fluorescence dyes with desired properties.

AUTHOR INFORMATION

Corresponding Author

*Tel +81-92-802-2878, Fax +81-92-802-2880, e-mail k-tanaka@cstf.kyushu-u.ac.jp.

ACKNOWLEDGMENT

We thank Prof. Toshihiko Nagamura at Kyushu University for his fruitful discussions. This research was partly supported by Grant-in-Aid for Young Scientists A (No. 21685013), for Scientific Research on Innovative Areas "Molecular Soft-Interface Science" (No. 21106516), and for the Global COE Program "Science for Future Molecular Systems" from the Ministry of Education, Culture, Sports, Science and Technology, Japan.

REFERENCES

(1) Crenshaw, B. R.; Weder, C. *Adv. Mater.* **2005**, *17*, 1471–1476.
(2) Greene, N. T.; Shimizu, K. D. *J. Am. Chem. Soc.* **2005**, *127*, 5695–5700.
(3) Thomas, S. W.; Joly, G. D.; Swager, T. M. *Chem. Rev.* **2007**, *107*, 1339–1386.
(4) Aoki, A.; Ghosh, P.; Crooks, R. M. *Langmuir* **1999**, *15*, 7418–7421.
(5) Onoda, M.; Tada, K. *Curr. Appl. Phys.* **2006**, *6*, 887–890.
(6) Kim, J.-M. *Macromol. Rapid Commun.* **2007**, *28*, 1191–1212.
(7) Wang, G.; Hou, L.; Gan, F. *Phys. Status Solidi A* **1999**, *174*, 269–275.
(8) Na, H.-S.; Kim, J.-H.; Hong, K.-M.; Ko, B.-S.; Kim, B.-C.; Han, Y.-K. *Mol. Cryst. Liq. Cryst.* **2000**, *349*, 35–38.
(9) Maeda, M.; Ishitobi, H.; Sekkat, Z.; Kawata, S. *Appl. Phys. Lett.* **2004**, *85*, 351–353.
(10) Wang, P.; Zakeeruddin, S. M.; Moser, J. E.; Nazeeruddin, M. K.; Sekiguchi, T.; Grätzel, M. *Nature Mater.* **2003**, *2*, 402–407.
(11) Nogueira, A. F.; Longo, C.; Paoli, M. A. D. *Coord. Chem. Rev.* **2004**, *248*, 1455–1468.
(12) Zhang, W.; Cheng, Y. M.; Yin, X. O.; Liu, B. *Macromol. Chem. Phys.* **2011**, *212*, 15–23.
(13) Birks, J. B. *Photophysis of Aromatic Molecules*; Wiley-Interscience: London, 1970.
(14) Wang, Y. *Chem. Phys. Lett.* **1986**, *126*, 209–214.
(15) Shimizu, M.; Mochida, K.; Katoh, M.; Hiyama, T. *J. Phys. Chem. C* **2010**, *114*, 10004–10014.
(16) Ito, F.; Kakiuchi, T.; Sakano, T.; Nagamura, T. *Phys. Chem. Chem. Phys.* **2010**, *12*, 10923–10927.
(17) Nishijima, Y. *Ber. Bunsenges. Phys. Chem.* **1970**, *74*, 778–784.
(18) Bokobza, L.; Pajot, E.; Monnerie, L.; Bouas-Laurent, H.; Castellan, A. *Polymer* **1981**, *22*, 1309–1311.
(19) Anwand, D.; Müller, W.; Strehmel, B.; Schiller, K. *Makromol. Chem.* **1991**, *192*, 1981–1991.
(20) White, C. C.; Migler, K. B.; Wu, W. L. *Polym. Eng. Sci.* **2001**, *41*, 1497–1505.
(21) Ellison, C. J.; Torkelson, J. M. *Nature Mater.* **2003**, *2*, 695–700.
(22) Priestly, R. D.; Ellison, C. J.; Broadbelt, L. J.; Torkelson, J. M. *Science* **2005**, *309*, 456–459.
(23) Tanaka, K.; Tsuchimura, Y.; Akabori, K.; Ito, F.; Nagamura, T. *Appl. Phys. Lett.* **2006**, *89*, 061916–1−2.
(24) Roth, C. B.; McNerny, K. L.; Jager, W. F.; Torkelson, J. M. *Macromolecules* **2007**, *40*, 2568–2574.
(25) Tanaka, K.; Tateishi, Y.; Okada, Y.; Nagamura, T.; Doi, M.; Morita, H. *J. Phys. Chem. B* **2009**, *113*, 4571–4577.
(26) Ashley, J. C. *IEEE Trans. Nucl. Sci.* **1980**, *NS-27*, 1454–1458.
(27) Andrade, J. D. In *Surface and Interfacial Aspects of Biomedical Polymers*; Andrade, J. D., Ed.; Plenum Press: New York, 1985; Vol. 1, Chapter 6, p 105.
(28) Kawaguchi, D.; Tanaka, K.; Takahara, A.; Kajiyama, T. *Macromolecules* **2001**, *34*, 6164–6166.
(29) Phillips, D.; Rumbles, G. *Polym. Photochem.* **1984**, *5*, 153–170.
(30) Mukherjee, S.; Chattopadhyay, A.; Samanta, A.; Soujanya, T. *J. Phys. Chem.* **1994**, *98*, 2809–2812.
(31) Forrest, J. A.; Jones, R. A. L. In *Polymer Surfaces, Interfaces and Thin Films*; Karim, A., Kumar, S., Eds.; World Scientific: Singapore, 2000; Chapter 7, p 251.
(32) Keddie, J. L.; Jones, R.; Cory, R. A. *Europhys. Lett.* **1994**, *27*, 59–64.
(33) Forrest, J. A.; Dalnoki-Veress, K.; Stevens, J. R.; Dutcher, J. R. *Phys. Rev. Lett.* **1996**, *77*, 2809–2005.
(34) Tanaka, K.; Hashimoto, K.; Kajiyama, T.; Takahara, A. *Langmuir* **2003**, *19*, 6573–6575.
(35) Matsuoka, H. *Macromol. Rapid Commun.* **2001**, *22*, 51–67.
(36) Wallace, W. E.; van Zanten, J. H.; Wu, W. L. *Phys. Rev. E* **1995**, *52*, R3329–R3332.
(37) Miyazaki, T.; Nishida, K.; Kanaya, T. *Phys. Rev. E* **2004**, *69*, 061803–1−5.
(38) Rittigstein, P.; Torkelson, J. M. *J. Polym. Sci., Part B: Polym. Phys.* **2006**, *44*, 2953–2943.
(39) Bhatia, Q. S.; Pan, D. H.; Koberstein, J. T. *Macromolecules* **1988**, *21*, 2166–2175.
(40) Jones, R. A. L.; Kramer, E. J.; Rafailovich, M. H.; Sokolov, J.; Schwarz, S. A. *Phys. Rev. Lett.* **1989**, *62*, 280–283.
(41) Tanaka, K.; Kajiyama, T.; Takahara, A.; Tasaki, S. *Macromolecules* **2002**, *35*, 4702–4706.
(42) Geoghegan, M.; Krausch, G. *Prog. Polym. Sci.* **2003**, *28*, 261–302.
(43) The surface energy of NBD was estimated to be 66 mJ m^{-2}, being higher than that for PMMA of 43 mJ m^{-2}, on the basis of an atomic group contribution method by van Krevelen.

Macromolecules

ARTICLE

pubs.acs.org/Macromolecules

Dynamic Competition between Crystallization and Phase Separation at the Growth Interface of a PMMA/PEO Blend

Weichao Shi[†,‡] and Charles C. Han[†,*]

[†]Beijing National Laboratory for Molecular Sciences, Joint Laboratory of Polymer Science and Materials, Institute of Chemistry, Chinese Academy of Sciences, Beijing 100190, China

[‡]Graduate School of the Chinese Academy of Sciences, Beijing 100190, China

ABSTRACT: We investigated the dynamic competition between crystallization and phase separation in a dynamically asymmetric blend of poly(methyl methacrylate) (PMMA) and poly(ethylene oxide) (PEO). Because of a large difference in glass transition temperatures between these two components, the phase transition dynamics is slowed down and can be observed in more detail. There is a morphological inversion from spherulitic to concentric ring patterns by adjusting the quench depth. Under deep quench, phase separation tends to be enhanced by the large concentration deviation at the growth interface of crystals, and propagates outward with convective concentration waves. Meanwhile, short needle-like crystals appear in the phase separated domains, compared with long crystal strips in a spherulitic pattern. A general dynamic competition model is proposed to qualitatively interpret the complex interplay between crystallization and phase separation. On the basis of this model, various morphologies are observed and predicted.

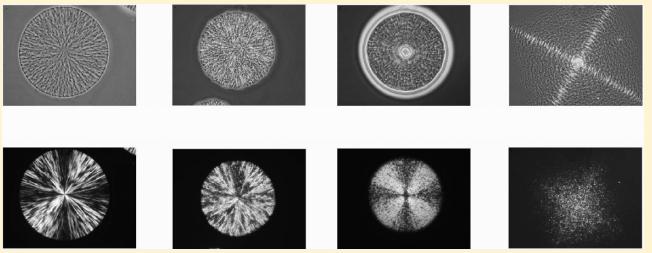

INTRODUCTION

Crystalline plastics (such as polyolefin), as well as amorphous resins (such as poly(methyl methacrylate) and polystyrene), are widely used in our daily life. Crystallization,[1−3] as well as phase separation,[4−9] has been well studied for decades. However, in a practical process, several phase transitions may take place simultaneously, leading to complex structures and affecting the final properties of material. So, investigation on the interplay between crystallization and phase separation has been in the spotlight recently.[10−18]

Much effort has been made to clarify the crystallization process,[19,20] particularly on the growth stage.[21−24] In a classical picture, this solid−liquid transition takes place below the equilibrium melting temperature via primary nucleation and successive growth. For a liquid−liquid phase separation process, the nucleation and growth type of phase separation takes place in the metastable region. The spinodal decomposition undergoes within unstable region, signified by a cocontinuous morphology. In conventional studies (like solutions of small molecules or polyolefin copolymer blends), component molecules have equal mobility, which response immediately to phase separation behavior. We refer to this kind of phase separation as normal phase separation, or dynamically symmetric phase separation. However, different chain sizes or other transitions, like gelation or glass transition, may enhance the dynamical asymmetry between the two components, resulting in a new type of phase separation, known as viscoelastic phase separation.[25−27]

Take the phase separation with an upper critical solution temperature (UCST) for example. Two types of phase diagram may be considered when crystallization couples with phase separation. For the first type, the melting depression line and binodal line intersect. So, only phase separation occurs in the upper region. And crystallization and phase separation take place simultaneously in the bottom region. The second type of phase diagram, which will be investigated in this study, is that the phase separation binodal line is located fully below the crystal melting line. Accordingly, crystallization takes place under shallow quench and the coupled transitions under deep quench.

It has been noted in experiments that primary nucleation of crystallization can be assisted by concentration fluctuation, especially at the interface boundaries of phase separated domains.[28−32] The physical origin can be ascribed to two factors. One is the decrease of surface energy of crystallizing embryos via heterogeneous nucleation on the interface. The second reason is ascribed to fluctuation-assisted molecular ordering by active interdiffusion at the interfaces. The former has been tested theoretically[33] but the latter still remain as a challenge. There also have been reports that nucleation and growth type of phase separation may be induced at the growth front of spherulites.[34] The concentration profile at the growth front changes as spherulites grow and may transverse from the original miscible state to the metastable state. As there is energy barrier for nucleation, this coupling process could occur after a long time.

In spite that much progress has been achieved until present, some essential problems are still unsettled: Is the phase separation dynamics the same everywhere, near or away from the

Received: August 25, 2011
Revised: October 20, 2011
Published: December 01, 2011

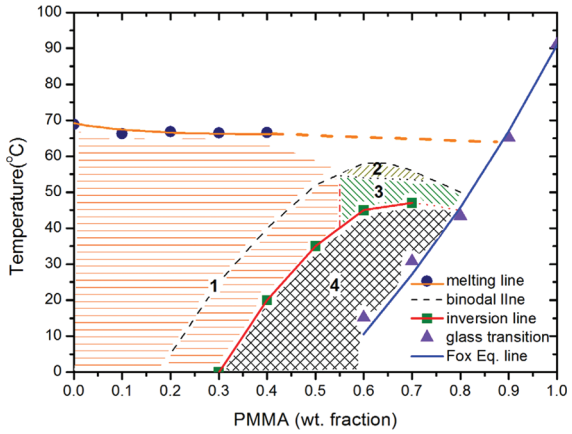

Figure 1. Phase and morphology diagram of PMMA/PEO blend. Compact spherulitic morphology forms are shown in region 1, and nucleation and growth type of phase separation are observed in region 2, a loose spherulitic morphology in region 3, and a concentric ring pattern in region 4.

crystals? How will the crystal growth be affected by phase separation? Is there universal law behind these complex dual transitions? In this study, we intend to provide some explicit answers to some of these questions. We used poly(methyl methacrylate) (PMMA)/poly(ethylene oxide) (PEO) blend for investigation. Although the miscibility of PMMA/PEO blend is unsettled for a long time,[35,36] we have confirmed the UCST phase separation behavior. Because of a great difference in glass transition temperatures between PMMA (about 100 °C) and PEO (about −60 °C), the blend undergoes phase separation as viscoelastic model predicts. With this dynamically asymmetric property, we directly confirmed the faster phase separation dynamics at the growth interface of crystals on macroscopic scale. And the propagating concentration waves led to quadratic or circular alternating structures of phase separated patterns. This phenomenon can be qualitatively interpreted by a general dynamic competition model between crystallization and phase separation.

EXPERIMENTAL SECTION

Materials. PMMA and PEO were purchased from Aldrich Chemicals and Beijing Chemcal Co., respectively. The molecular weight was determined by gel permeation chromatography. For PMMA, the weight-average molecular weight M_w = 15000 and M_w/M_n = 1.73 where M_n stands for number-average molecular weight. For PEO, M_w = 20000 and M_w/M_n = 1.08. The materials were used after purification. The glass transition temperatures of PMMA and PEO were found to be about 91 °C and −60 °C, respectively, using a differential scanning calorimeter (DSC, MettlerToledo-822e) at a heating rate of 10 °C/min.

Film Preparation. PMMA and PEO were dissolved in chloroform with 5% of polymer by weight. The solution was stirred at room temperature over 24 h, then casted on a clean glass plate. The solvent was quickly evaporated and further dried until constant weight. The film thickness is kept at about 20 μm.

Optical Microscopy. The phase contrast optical microscopy (PCOM) and polarized optical microscopy (POM) were carried out using an Olympus (BX51) optical microscope and Olympus (C-5050ZOOM) camera. The experimental temperature was controlled by a Linkam (LTS350) hot stage.

Scanning Electron Microscopy. Samples were coated by platinum before observation under SEM (JEOL JSM 6700F).

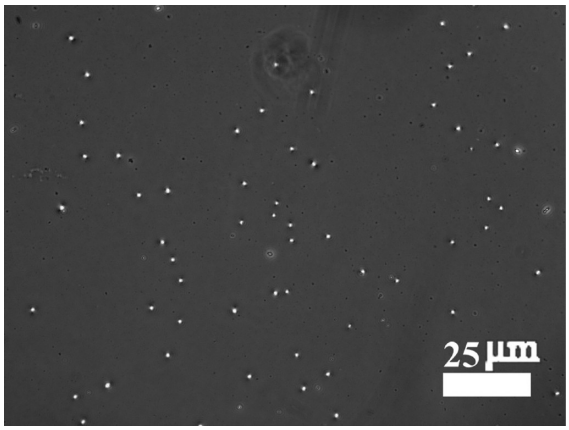

Figure 2. Nucleation and growth type phase separation of the blend with PMMA content at 0.6 annealed at 55 °C. The picture was taken under PCOM with slight artificial modification to enhance the contrast.

RESULTS AND DISCUSSION

Phase and Morphology Diagram. We illustrated the phase and morphology diagram of the blend in Figure 1.[37] The melting temperatures of PEO crystals were measured by DSC with a heating rate of 10 °C/min. The equilibrium melting temperatures at different fractions were determined using Hoffman—Weeks extrapolation. The final equilibrium curve shown in the phase diagram is often called melting depression line. The equilibrium temperature decreases as PMMA content increases. This may be caused by two factors: one is thermodynamic factor and the other is dynamic. Blending with small amount of PMMA lowers the chemical potential of PEO in the melt. So the corresponding equilibrium crystals appear at lower temperatures from thermodynamic sense. Also, amorphous PMMA molecules diffuse much slower than crystallizable PEO, therefore, it is more difficult to form regular array of PEO chains at the growth front as PMMA content increases. This dynamic process leads to more defects, thus the resulting PEO crystals melt at a lower temperature.

The glass transition temperatures of the blend were also determined by DSC with a heating rate of 10 °C/min. The glass transition temperatures were not tested at the contents of PMMA weight fractions less than 0.4 because of the effect from PEO crystallization. The measured temperatures at higher PMMA fractions were well fitted by Fox equation. It needs to be pointed out that this cannot be a criterion to determine the miscibility between these two components, although the application of the Fox equation should be confined within miscible condition.

Strictly speaking, the binodal line beneath the melting depression line cannot be quantitatively determined because of the interplay between crystallization and phase separation. So, we just schematically showed a boundary line, assuming the two transitions are independent. However, we will introduce an inversion line to indicate the dynamic inversion from the crystallization dominant to phase separation dominant. The determination of this dynamic inversion line will be given later.

Phase Separation at the Growth Interface. In conventional spinodal decomposition, cocontinuous structures grow randomly in full space. However, we find a spinodal may be induced by crystal growth and propagate concentrically in the radial direction. We would like to give detailed information on morphology and phase separation dynamics in this section.

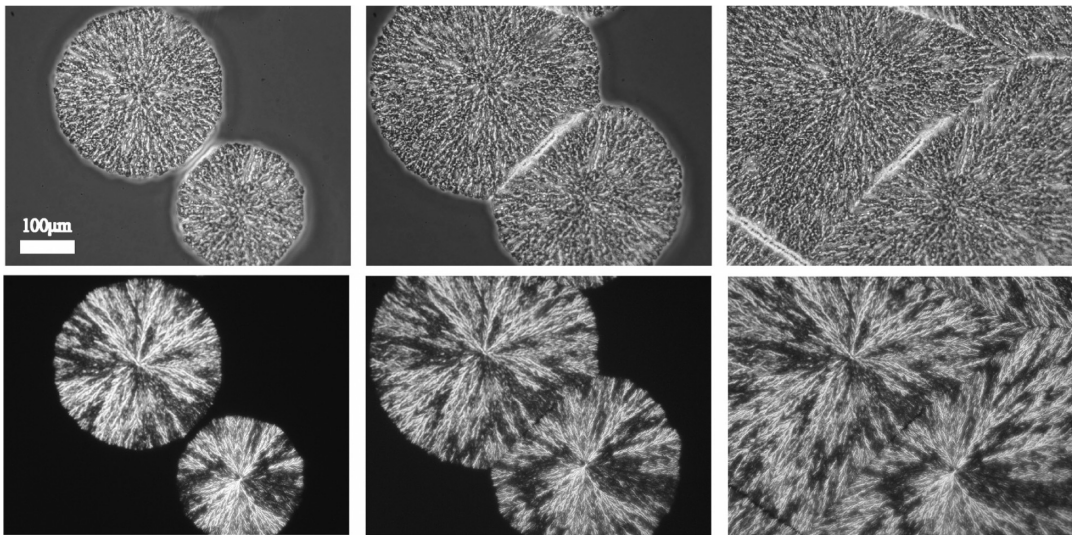

Figure 3. Time evolution of the loose spherulitic pattern of the blend with PMMA content at 0.6 annealed at 45 °C for 14.5, 18.5, and 36 h. The observation was carried out at nearly the same time under PCOM (upper row) and POM (lower row).

The critical composition is between 0.6 and 0.7 of PMMA weight fraction (estimated about 0.68 via $\phi_{c,PMMA} = (N_{PEO})^{1/2}/((N_{PEO})^{1/2} + (N_{PAMMA})^{1/2})$). Although the dynamics of the blend with PMMA weight fraction 0.7 is much slower, it has similar morphologies with the blend with PMMA weight fraction 0.6. So we only show the experimental results for PMMA content at 0.6.

Figure 2 (region 2 in the phase and morphology diagram) shows the liquid−liquid phase separation at 55 °C after a long annealing time of 10 days. Crystallization at this low quench depth seemed difficult to occur through homogeneous nucleation. But sparsely distributed PMMA particles appeared. So we infer that the nucleation and growth type of liquid−liquid phase separation took place between spinodal and binodal line in this case. As temperature decreases, the kinetics of crystallization speeds up more than that of phase separation.

Figure 3 (region 3 in the phase and morphology diagram) shows the growth of PEO spherulites at 45 °C with PMMA weight fraction of 0.6. Loose spherulites grew isotropically. It is clear that amorphous domains were intercalated in the interfibrillar regions. Fibrillar crystals grew in the radial direction with short branches. The whole spherulites lost the regular Maltese cross. These phenomena may be ascribed to the slow diffusion of PMMA and weak phase separation effect.

The kinetics of phase separation became dominated below 45 °C. Figure 4a (region 4 in the phase and morphology diagram) shows the characteristic morphologies at 42 °C. It clearly shows a trend from spherulitic pattern to concentric alternating phase separation rings. Note that small spherulites still located at the centers. There was clearly a size difference between phase separating and crystallizing areas at nearly the same time. Furthermore, short lamellar stacks, instead of long crystal stripes, arrayed regularly in the tangential directions and showed a Maltese-like cross, which was clearly revealed in Figure 4b. The detailed investigation on the crystal structures will be given in a subsequent paper.

Figure 5 (region 4 in the phase and morphology diagram) shows the morphological evolution of the blend at 35 °C. All

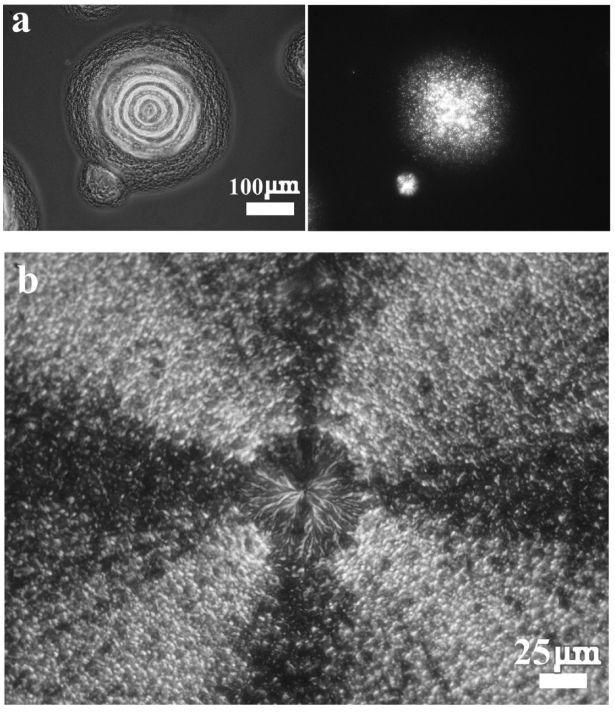

Figure 4. Characteristic morphology of the blend with PMMA content at 0.6 annealed at 42 °C. (a) The observation was carried out at nearly the same time under PCOM (right) and POM (left). (b) Crystal order was observed under POM in the concentric alternating pattern.

the photographs were taken by quickly transferring from a phase-contrast mode to polarized mode. Alternating quadratic domain emerged initially while there was not much information from crystal growth. After a certain time, bright spotlights appeared first at the center of the domain and then grew outward into the phase separated regions. Note that the size differences between PCOM and POM pictures were more obviously revealed in this condition. It can be concluded that the kinetics of phase separation was faster than the growth of crystallization.

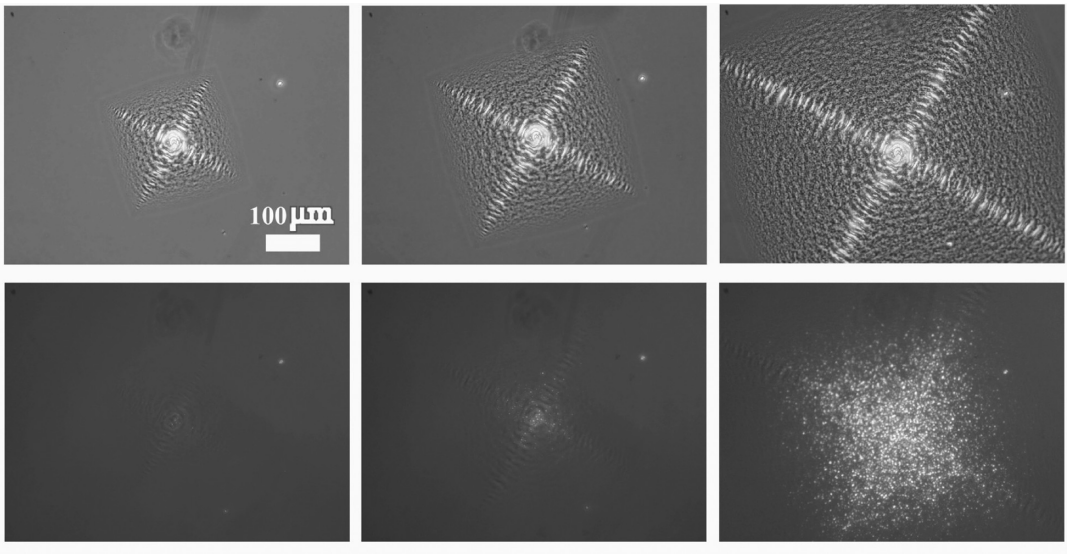

Figure 5. Time evolution of the concentric pattern of the blend with PMMA content at 0.6 annealed at 35 °C for 40, 55, and 90 min. The observation was carried out at nearly the same time under PCOM (upper row) and POM (lower row).

Closer observation of the square-like structure indicates that the sparsely distributed crystals were short needle-like, as shown in Figure 6. Moreover, the needle-like crystals lost regular arrangement and oriented randomly in phase separated domains.

A characteristic feature of this square shape is the four arms in the diagonal directions, consisting of alternating phase separated domains. Sometimes more arms appeared or one arm might split into two, leading to the distorted shape. But shapes with fewer arms were never seen. In addition, the square shape maintained quite well from initial until impingement between domains. It should be stressed that the four arms are not the result of birefringence, but signifies larger concentration deviations in the directions. This can be ascertained under SEM, which will be shown later.

Traditional spinodal decomposition takes place in full space because of no energy barrier. However, as revealed in Figure 5, when phase separation is coupled with crystallization, a phase separation showing square-like shape is reported for the first time. There have been a lot of reports on PEO crystals with quadratic form,[38−40] and we consider the square-like phase separated pattern is the magnified reflection of the original crystal shape. A detailed discussion on this will be given later. We may test this assumption by a simple double quench experiment. The sample was first annealed at 43 °C for 12 h and quenched to 35 °C subsequently. The temporal evolution is revealed in Figure 7. The initial structure was nearly isotropic when the annealing temperature was 43 °C. After quenching to 35 °C, concentric alternating structure appeared at the growth interface with many more arms. Regular square-like pattern was not observed. Phase separation in the arm direction seemed to grow faster. However, lateral crystallization did not begin until a long time interval later. This experiment may give us two clues: phase separation pattern is affected by the initial structure; phase separation kinetics is faster than crystallization under deep quench.

As stated above, phase separating domains grew anisotropically, faster in the diagonal direction. However, the concentration waves propagate with constant velocity in all directions. The linear growth of the phase separating domains is shown in Figure 8. The size of the spherulites was determined by the diameter, and the square

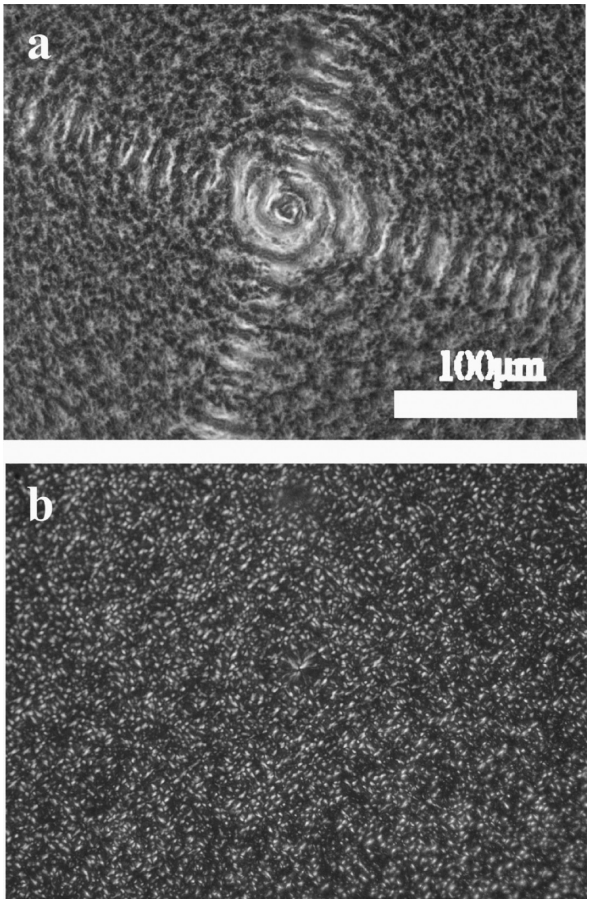

Figure 6. Close observation of the square-like concentric structure under PCOM (a) and POM (b). The blend with PMMA content at 0.6 annealed at 35 °C after 48 h.

domains were determined by the average length of each side. The linear growth of spherulite is usually determined by the secondary nucleation rate. However, this linear growth of phase separating

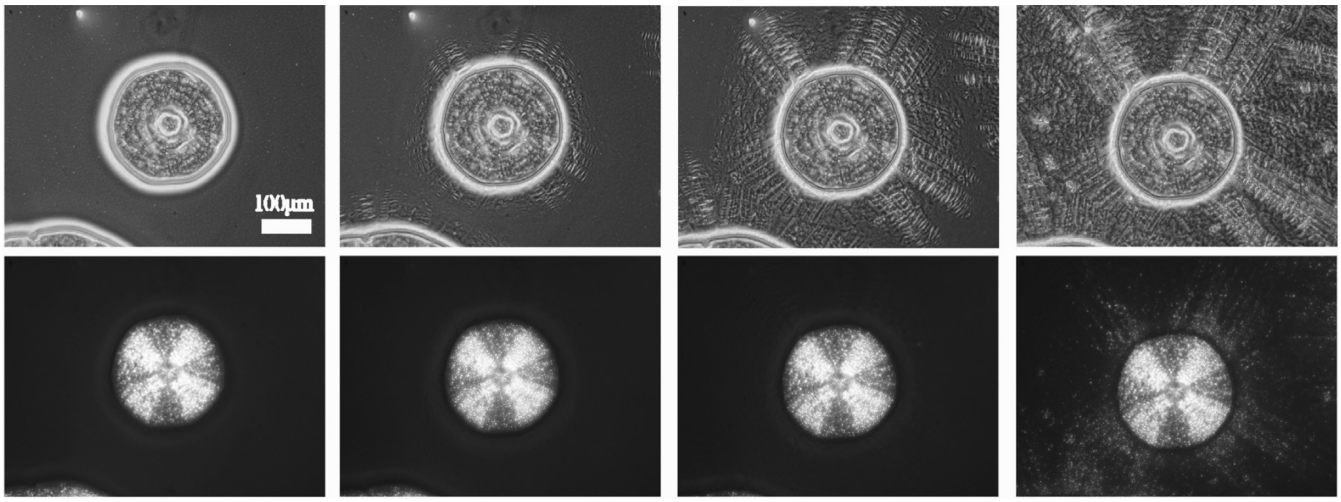

Figure 7. Time evolution of the characteristic pattern of the blend with PMMA content at 0.6 quenched to 35 °C for 0, 30, 60, and 120 min after annealing at 43 °C for 12 h. The observation was carried out at nearly the same time under PCOM (upper row) and POM (lower row).

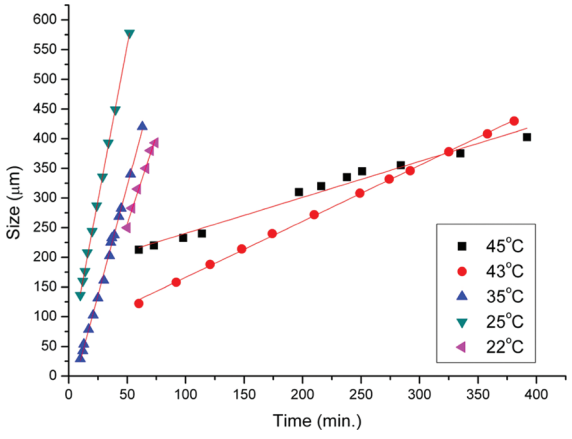

Figure 8. Size versus time plot of the blend with PMMA content at 0.6. The onset times are shifted.

domains is determined by the phase separation dynamics, since concentration growth from initial fraction to glassy fraction should have kept constant at a specific temperature.

When the PMMA weight fraction was decreased to 0.5, square-like morphology could not form but new features appeared. At this off-critical composition, phase separation did not take strong effect until the temperature was below 35 °C. So crystallization process dominated above 35 °C. Figure 9 (region 1 in the phase and morphology diagram) shows the typical morphology at 45 °C. Compact spherulites grew with long fibrillar crystals in the radial direction. We also see the isolated amorphous domains trapped inside the interfibrillar regions from phase contrast mode and the regular Maltese cross from polarized mode. Compared with the loose structure formed with PMMA weight fraction at 0.6, formation of compact structure mainly dues to the higher PEO content and lower viscosity.

Phase separation process became dominated when the temperature was lowered to below 35 °C. The morphological evolution at 30 °C is shown in Figure 10 (region 4 in the phase and morphology diagram). Here we can see crystallization-initiated phase separation more clearly. Compact spherulites grew initially, and phase

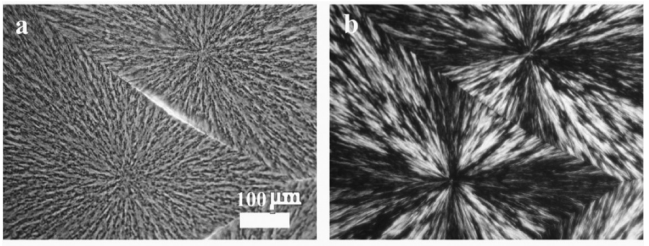

Figure 9. Characteristic morphology observed under PCOM (a) and POM (b) at 45 °C for the sample with PMMA content at 0.5.

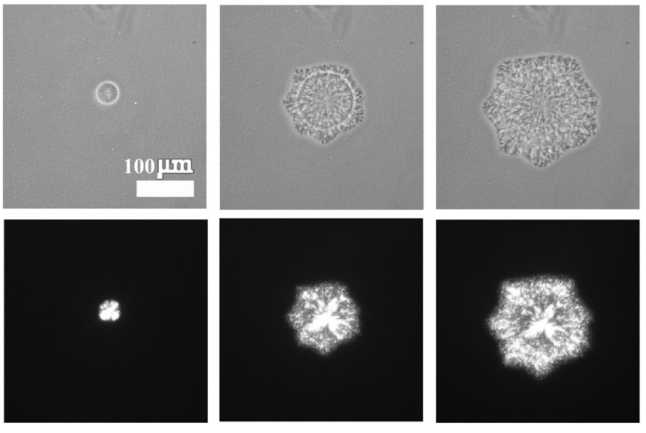

Figure 10. Time evolution of the characteristic pattern of the blend with PMMA content at 0.5 quenched to 30 °C for 13, 20, and 30 min. The observation was carried out at nearly the same time under PCOM (upper row) and POM (lower row).

separation became dominating at the growing interface subsequently. The initial spherulite was consisted of long crystalline strips, but small crystals were isolated within phase separated domains laterally afterward. Furthermore, by comparing the pictures in the top and bottom rows, we see the equal size of the growing domains in the initial time (pictures in the

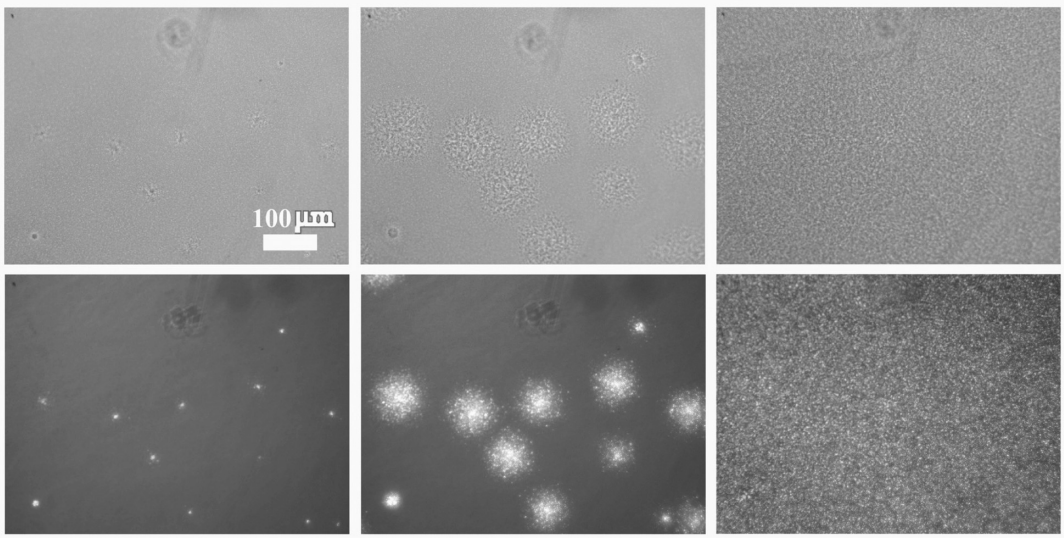

Figure 11. Time evolution of the characteristic pattern of the blend with PMMA content at 0.5 quenched to 10 °C for 10, 20, and 50 min. The observation was carried out at nearly the same time under PCOM (upper row) and POM (lower row).

first column), and size contrast emerged at later times. This indicates that the dominant factor was transformed from crystallization to phase separation.

The competing dynamics was similar when we carried out experiment at an even lower temperature. Figure 11 (region 4 in the phase and morphology diagram) displays the morphological evolution at 10 °C. In this case, phase separation occurred following the formation of some small crystallites. Phase-separated regions showed low contrast under phase contrast mode, compared with morphologies at higher temperatures. This conveys that smaller concentration deviation was induced by phase separation. Because of this very low temperature, a small concentration growth of PMMA may already reach the glassy fraction, thus leading to a drastic pinning of any further concentration increase. We also notice the size difference in pictures under PCOM and POM taken at nearly the same time.

When the PMMA weight fraction was decreased to less than 0.4, the size difference between phase contrast mode and polarized mode could not be clearly observed. That was, crystallization and phase separation underwent "neck and neck". The reason could be attributed to the faster crystallization kinetics and lower binodal temperatures when PMMA content decreases. However, concentration distribution was rearranged under the perturbation of phase separation, which will be shown in the next section.

Concentric Alternating Patterns. Under deep quench, phase separation propagates outward from the growth interface with the initial crystal structure as template. We will further investigate the characteristic pattern formed in this condition with SEM.

Figure 12 shows the surface character of the blends with PMMA weight fraction of 0.6 at different temperatures. At 42 °C, alternating circular rings appeared at the center but dissipated when propagated further away. However, alternating quadratic rings appeared in the center at 35 °C. In addition, 'arms' appeared mainly in the diagonal directions and propagated from the center. This coincides with the appearance under PCOM (Figure 4 and 5) and may be a good indication that the amplitude of concentration fluctuation is greater near the center and in the diagonal directions.

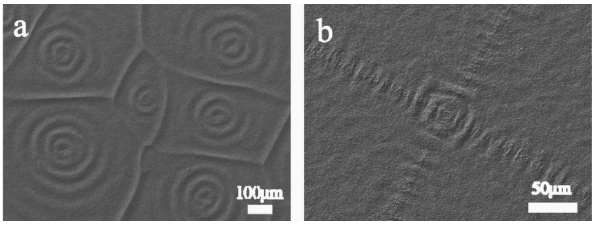

Figure 12. Surface morphology observed under SEM for the blend with PMMA content at 0.6 annealed at (a) 42 °C and (b) 35 °C.

Figure 13 shows the characteristic morphologies at different temperatures with PMMA weight fraction of 0.6. All samples were etched by acetone to take the amorphous-rich phase away before observation. At 47 °C, amorphous domains were mainly engulfed into the interfibrillar regions in the radial direction. However, the etched samples showed concentric alternating patterns at lower temperatures. The alternating phase separated domains arrayed regularly in the tangential direction, normal to the propagation waves. So there was a morphological inversion at about 45 °C.

When PMMA weight fraction decreased to 0.5, the characteristic morphologies also changed from spherulitic to alternating ring patterns as temperature decreased. In Figure 14, the morphology at 40 °C showed the regular spherulitic pattern. The PMMA-rich domains were distributed along the radial direction. Concentric alternating patterns were shown for samples prepared at 30 and 25 °C. Most amorphous domains located alternatively normal to the propagation direction. However, concentric rings broke up at even lower temperatures. The morphological inversion from spherulitic to concentric structure occurred near 35 °C at this composition.

When PMMA content was at 0.4, we cannot observe phase separation at the growth interface directly under optical microscopy. However, when observed under SEM after etching by xylene, we can see a similar morphological inversion near 20 °C from Figure 15.

It should be noted that these concentric structures may show spherulitic-like growth, especially when PMMA content is low.

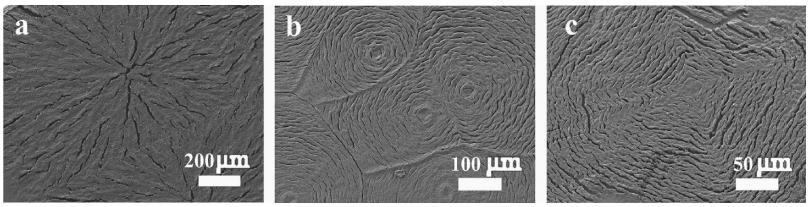

Figure 13. Characteristic structures of the blend with PMMA content at 0.6 annealed at (a) 47, (b) 42, and (c) 40 °C. All samples were etched by acetone to take the amorphous-rich phase away before observation.

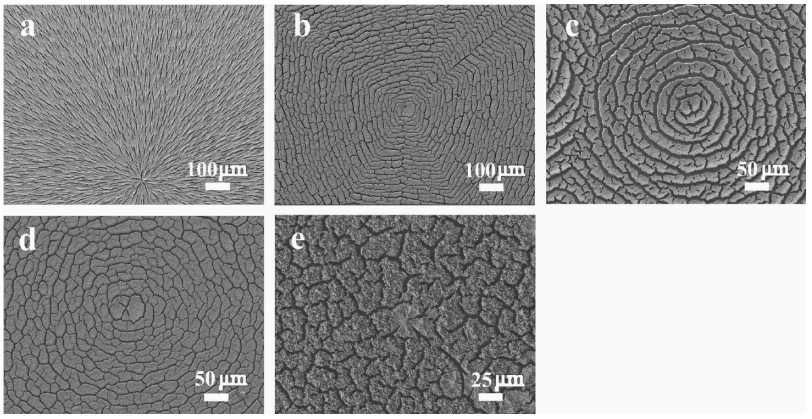

Figure 14. Characteristic structures of the blend with PMMA content at 0.5 annealed at (a) 40, (b) 30, (c) 25, (d) 20, and (e) 10 °C. The first four samples were etched by xylene and the last one by THF to take the amorphous-rich phase away before observation.

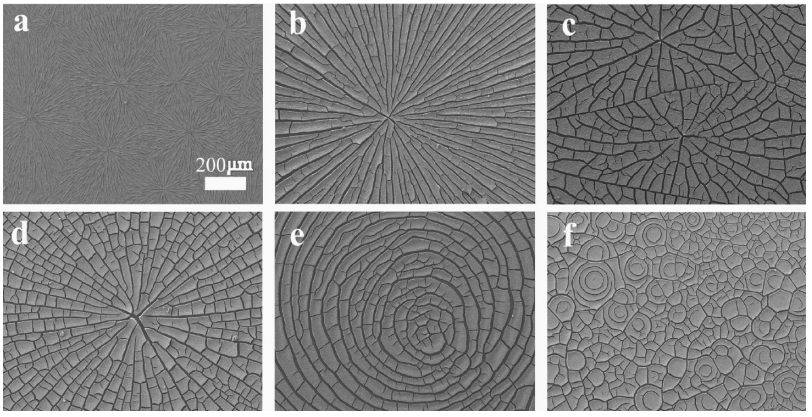

Figure 15. Characteristic structures of the blend with PMMA content at 0.4 annealed at (a) 40, (b) 25, (c) 20, (d) 15, (e) 10, and (f) 5 °C. All samples were etched by xylene to take the amorphous-rich phase away before observation.

However, the spatial distribution of concentration, as stated above, will change drastically when phase separation is intervening into the crystal growth kinetics. This will also affect lamellar orientation and macroscopic birefringence, which will be discussed in a separate paper later.

Crystallization Assisted Phase Separation at the Growth Interface. Because of the large difference in glass transition temperatures, the two components of PEO and PMMA behave differently. The PMMA molecules relax very slowly when a driving force is applied, while PEO molecules response immediately to an applied force. In order to provide a better explanation to this phase separation mechanism, we employed the viscoelastic phase separation model proposed by Tanaka.[27]

The dynamics of a viscoelastic phase separation process can be briefly summarized as follows. There is usually a long "frozen" stage in the initial time of phase separation. On one hand, the initial concentration fluctuation is always depressed within the viscoelastic length.[27,41] On the other hand, the coupled velocity field is negligible because of a small concentration deviation between the two phases. As phase separation continues, the concentration deviation becomes intensified and the induced velocity field gets significant, thus the conditions are created for an enhanced phase separation dynamics. We may call this stage as fast growth stage. Then, the relaxation process of the network stress becomes the controlling factor as phases get more and more concentrated. In the late stage, the dynamics can be

described by the hydrodynamic coarsening process as in the normal phase separation.

When viscoelastic phase separation is the only transition in a system, this process occurs homogeneously in full space. However, when crystallization process is also happening, a phase separation process may be affected inhomogeneously. Here we employed a simplified model to describe the crystallization process in a fully miscible blend, which consists of a crystalline component and an amorphous component. Successive growth of the crystal after primary nucleation occurs by absorbing crystallizable molecules onto the growth front and rejecting the amorphous ones away. Assume further that the amorphous component can be completely excluded. Then the amorphous concentration profile at the growth front in the radial direction can be described by an exponential decay function:[2]

$$\varphi(r,t) = \varphi(0,t)\exp[-(G/D)r] + \varphi_0 \quad (1)$$

$\varphi(0,t)$ is also expressed as $\varphi(0,t) \sim GR(t)/D$. Here $\varphi(0,t)$ is the amorphous concentration at crystallizing front; φ_0 is the average concentration in the original melt; $R(t)$ is the radius of the spherulite; G is the growth rate, and D the diffusion coefficient of the amorphous component. So the concentration deviation at the growth front is intensified as crystals grow. However, in the practical case, amorphous molecules are partially rejected and partially intercalated into the interlamellar or interfibrillar regions.

When crystallization and phase separation occur simultaneously, spherulitic morphology cannot be destructed under a shallow quench. This is mainly attributed to a smaller thermodynamic driving force of phase separation than that of crystallization. Under a deep quench within the spinodal region (region 4 in Figure 1), phase separation will occur under viscoelastic effect. Crystal nuclei may form randomly in space when short-range density fluctuation overcomes an energy barrier. Then, crystals can grow and become larger. Meanwhile, the dynamics of phase separation was kept slow because of the long-range viscoelastic depression. Therefore, most areas stay "frozen" in the initial stage. The dynamics will be enhanced only when concentration gradient and velocity field are slowly built up after a long time. However, as crystals grow, the amorphous-rich phase is built up first at the growth interface of crystals (eq 1). Thus, the thermodynamic instability is intensified and the coupled velocity field will accelerate the phase separation dynamics. In other words, the dynamics of phase separation is greatly enhanced at the growth interface assisted by the crystallization, as if pushed into the fast growth stage, when other regions are still frozen. As the amorphous-rich phase gets more and more concentrated, the slow relaxation process turned to be the controlling factor, and further coarsening is slowed down. But the induced concentration waves propagate farther away, enhancing the dynamics of phase separation in the neighboring regions. If the lateral phase separation dynamics is faster than the original crystal growth, further propagation may be maintained by concentration deviation induced by phase separation itself. Regular concentric alternating structures will be kept as long as regular concentration deviation profiles are reserved. Concentric patterns were previously reported in spiral spherulites,[42,43] or when phase separation is coupled with gelation,[44,45] or affected by adding nanoparticles.[46] Simulation work[47] revealed that concentration deviation may assist thermodynamic instability based on Cahn−Hilliard model, without taking into account of the velocity field in actual case. In this study, the concentric pattern, formed under the competition between crystallization and phase separation, is reported for the first time.

It should be noted that phase separation has different sensitivity to concentration deviation at the growth interface, depending on location in the phase and morphology diagram. As stated previously, crystallization dominates the whole process at relatively high temperatures and overwhelms only in the initial stage at low temperatures. That is, phase separation is sensitive to small concentration deviation induced by crystallization when temperature is low. At higher temperatures, due to small thermodynamic driving force, phase separation occurs only when large concentration deviation is built up at the growth interface. So, at particular intermediate temperatures, phase separation does not take charge until spherulites grew to a large size. But when PMMA content is even lower (below 0.4), it is difficult to observe phase separation at the growth interface. On one hand, the binodal temperatures become lower. On the other hand, growth rate of crystallization increases dramatically. Fast growth of spherulites enclosed amorphous molecules into the interlamellar or interfibrillar regions, thus preventing the establishment of concentration profile in the radial direction.

The observed square-like morphology is quite interesting. Then, let us look for the formation mechanism of this featured pattern. PEO crystals with quadratic shapes prepared in PMMA/PEO blend have been reported in many articles. We speculate that the square-like phase separating domain is the macroscopic reflection of concentration profile created by the initial crystallization. The initial dendritic nuclei grow anisotropically in the four-arm directions. Loose branches from these arms usually appear later. Crystallization in each arm is more regular than that in branches. So, concentration deviation is anisotropically distributed around, higher at the front of each vortex and lower at farther regions between vortices. The laterally assisted phase separation inherited this character and retained the high concentration deviation in the diagonal directions, forming four arms consisted of alternating phase separated domains.

General Dynamic Competition Model. In this section, we would like to first reconsider the crystallization and phase separation independently, and then expand to the coupled phase transitions.

In fully miscible blend, crystal growth involves two processes: secondary nucleation at the crystallizing front and transport of the crystallizable molecules. Here we choose two characteristic times to denote each process, respectively. The induction time for preparing secondary critical nuclei near growth front is denoted as τ_i hereafter. The time for a crystalline polymer crossing the amorphous-rich barrier regions to get to the original crystallizing front, which is denoted as τ_c. Although τ_i is determined by the thermodynamic property of the blend ($\tau_i \sim \exp(\Delta G/kT)$ where ΔG is the energy barrier), it can be comparatively displayed in a dynamic manner as $\tau_i \sim l/G$, where $l \sim D/G$ gives characteristic length of the amorphous-rich regions. D is the diffusion coefficient of the amorphous molecules and G the growth rate of the crystallizing front. On the basis of "Vogel−Fulcher law", τ_c can be predicted as $\tau_c \sim l^2/D'(\varphi)$, where $D'(\varphi) \sim \exp[-B/(\varphi_g-\varphi)]$. D' is the diffusion coefficient of the crystalline molecules. B is a constant and φ_g is the glassy fraction of the blend at the temperature. We note that τ_c has strong concentration dependence if the components have large glass transition temperature

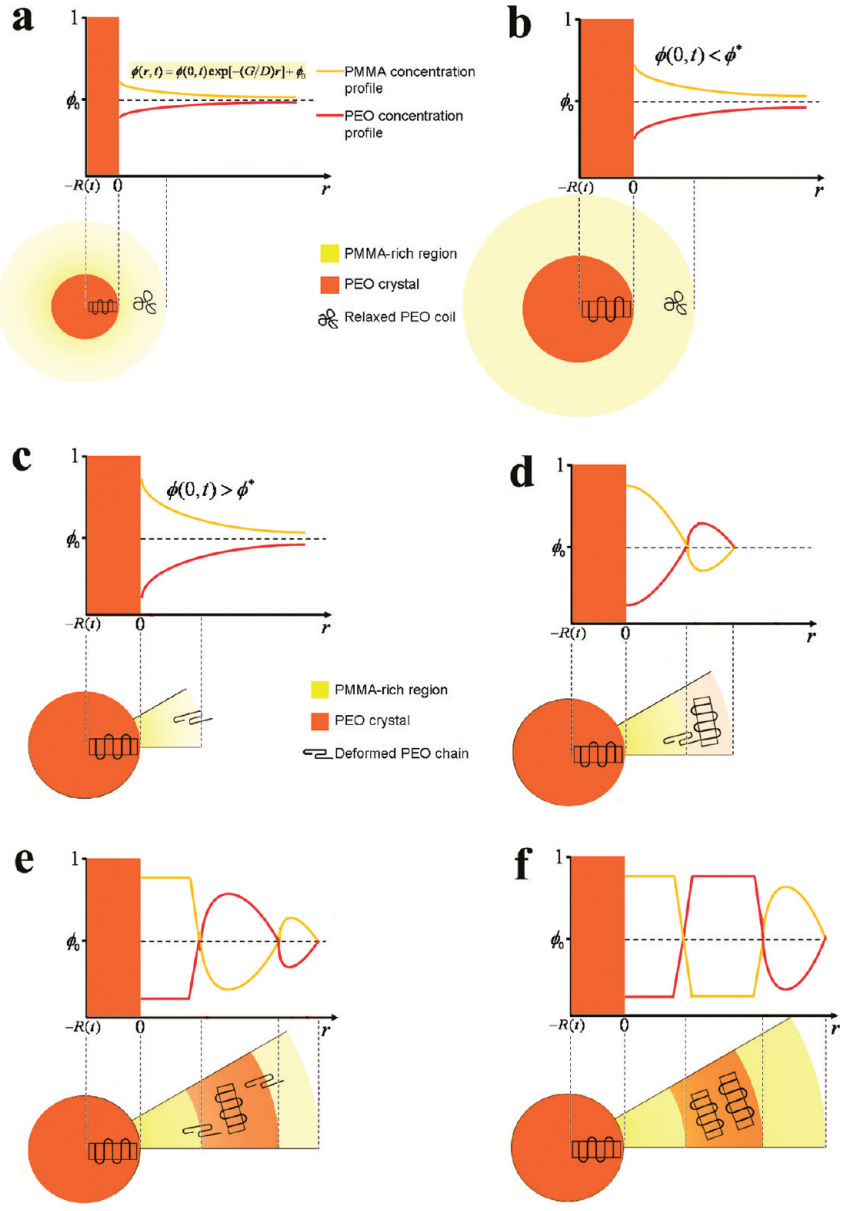

Figure 16. Schematic representation of the formation mechanism of spherulitic growth (a, b) and concentric alternating pattern (c−f). $\varphi(0,t)$ is the PMMA concentration at the growth front of PEO crystals. φ^* is defined as a critical concentration when $\tau_i \approx \tau_d$.

difference. If the components are dynamically symmetric, then τ_c is only controlled by the distance.

If the two processes compete with each other when crystallization proceeds in a fully miscible blend, then two kinds of characteristic morphologies can be predicted. If $\tau_c < \tau_i$, crystalline molecules can always cross over the amorphous-rich regions and crystallize at the growth front, forming compact spherulitc morphology. Crystalline molecules crystallizing in dilute solution is a good example ($\tau_c \ll \tau_i$). If $\tau_i < \tau_c$, then the original crystallizing front may stop and a new crystallite may form, trapping the amorphous-rich regions between lamellae or lamellar stacks. In this case, loose spherulitic morphology forms. Crystallization of a blend near but above the glass transition temperature follows this condition ($\tau_i \ll \tau_c$).

When phase separation intervenes into the crystallization, a third characteristic time τ_d enforced into the mechanism, which denotes the deformation rate of phase separated domains. This concept was first proposed by H. Tanaka to qualitatively describe phase separation dynamics.[27] The deformation rate is mainly determined by osmotic pressure in the initial stage which is estimated as $\tau_d \sim l/\Delta\varphi(t)^2$, and controlled by the interfacial tension in the late stage which is estimated as $\tau_d \sim l\eta/\sigma$ (Siggia's coarsening mechanism).[27] η denotes the viscosity and σ the surface tension. In addition, if we generalize τ_c as the relaxation controlled process in a phase separation, we note that $\tau_d > \tau_c$ all through a symmetric phase separation process. However, in a dynamically asymmetric phase separation, the controlling factor switches from τ_d in the initial stage ($\tau_d > \tau_c$) to τ_c in the intermediate stage ($\tau_d < \tau_c$), and finally returns to τ_d in the late stage ($\tau_d > \tau_c$).

In the coupled transitions of crystallization and phase separation, the formation of various morphologies may form on the

dx.doi.org/10.1021/ma201940m |*Macromolecules* 2012, 45, 336–346

relative scale of τ_i, τ_c, and τ_d. By a detailed analysis, we give the following results:

I $\tau_c < \tau_i < \tau_d$: Compact spherulites always form, and the amorphous-rich phase is all repelled into the interspherulitic regions.

II $\tau_c < \tau_d < \tau_i$: Phase separation occurs faster than crystallization, but subsequently formed compact spherulites may distort the phase-separated pattern. The amorphous-rich phase may be pushed into the interspherulitic regions.

III $\tau_i < \tau_c < \tau_d$: Loose spherulites forms, trapping the amorphous-rich regions in the interlamellar or interfibrillar regions.

IV $\tau_i < \tau_d < \tau_c$: The situation is similar to III, but only appears in dynamically asymmetric systems.

V $\tau_d < \tau_c < \tau_i$: The situation is similar to II, but only appears in dynamically asymmetric systems.

VI $\tau_d < \tau_i < \tau_c$: phase separation occurs faster than crystallization, and the subsequently formed loose crystallites are confined in the phase-separated crystalline-rich regions. This case only appears in dynamically asymmetric systems.

Furthermore, the time interval between each two characteristic times, $\tau_i - \tau_c$, $\tau_i - \tau_d$ and $\tau_c - \tau_d$, may reflect the correlation between a new crystal and the original crystal, the correlation between crystallization and phase separation, or asymmetry criterion, respectively. This part of work will be discussed in a following paper.

Some researchers consider the size contrast between spherulites and phase separated domains may also affect the morphology. However, this scenario has been explicitly included in the classifications above. The situations stated above are considered based on the assumption that crystallization and phase separation are independent in simultaneous phase transitions. Very few theoretical solutions are available based on the final equilibrium state, more accurate predictions merit further consideration which should include the interface conditions between the crystalline front and the amorphous-rich phase.

In a real situation, it may be more complex which could involve several cases stated before in a whole dynamic process. We may apply this general model to the crystallization assisted phase separation growth in this study. When temperature is quenched under binodal line, crystallization occurs first. Because of nearly homogeneous composition, $\tau_d \sim l/\Delta\varphi(t)^2$ is very large. So, $\tau_c < \tau_i < \tau_d$ or $\tau_i < \tau_c < \tau_d$, depending on the initial composition. Only spherulites form in this stage. As spherulites grow larger, concentration deviation at the growth interface becomes significant, thus enhancing phase separation. Meanwhile, the amorphous-rich layer at the growth interface depresses interdiffusion drastically. So, three choices are possible: if $\tau_i < \tau_d < \tau_c$, then crystallization and phase separation propagate "neck and neck" and the original spherulitic structure is kept; if $\tau_d < \tau_c < \tau_i$, then phase separation goes ahead of crystallization, leading to concentric structures and compact crystals in phase separated regions (for example, when PMMA content is at 0.4); if $\tau_d < \tau_i < \tau_c$, also phase separation leading concentric structure forms with open crystals in phase separated domains (when PMMA content is at 0.6). The spherulitic growth is schematically illustrated in Figure 16, parts a and b. The formation mechanism of the concentric alternating pattern is shown in Figure 16, parts c–f.

We can also give a rough estimation of the characteristic length in the concentric structures via this model. Suppose the growth of PMMA-rich regions is pinned until glass transition, then the deformation time $\tau_d \sim l/(\varphi_g - \varphi)^2$. This time interval should equal the rheological time of the same domain. So the length of the amorphous-rich domain should be $l \sim \exp[-B/(\varphi_g - \varphi)]/(\varphi_g - \varphi)^2$. When shallower quench is applied and phase separation is quite weak, the size of the PEO-rich domain can be roughly estimated as $l' \sim Gl/\Delta\varphi(t)^2 \sim D/\Delta\varphi(t)^2 \sim D^3/G^2R(t)^2 \sim D^3/G^2l'^2$, leading to $l' \sim G^{-2/3}$.

CONCLUSIONS

We investigated the morphology and phase separation behavior under the effect of the dynamic coupling between crystallization and phase separation processes. Crystallization dynamics is slightly affected by phase separation, showing spherulitic shape, when shallow quench is applied. In deep quench, concentric alternating pattern forms under the competition between these two transitions. The detailed process can be described as follows. Crystallization always occurs ahead of phase separation, due to larger thermodynamic driving force exerted for a temperature quench in our system. As the amorphous-rich layer becomes concentrated enough as crystals grow larger, phase separation takes place first at the growth interface, then concentration waves propagate farther away with constant velocity until impingement. A general dynamic competition model is proposed to qualitatively interpret the nonequilibrium process in both miscible and phase separating blends. Various morphologies can be predicted and observed based on this model.

It should be stressed that phase separation tends to be assisted by crystallization at the growth interface. This should be a general phenomenon in simultaneous phase transitions, if the generality of a viscoelastic phase separation model can be held. However, phase separation dynamics at the growth interface may be smeared or destructed in dynamically symmetric systems (like polyolefin blends), because of the lack of dynamic depression within viscoelastic length in the initial stage and hydrodynamic coarsening in the late stage.

AUTHOR INFORMATION

Corresponding Author

*Telephone: +86 10 82618089. Fax: +86 10 62521519. E-mail: c.c.han@iccas.ac.cn.

ACKNOWLEDGMENT

This work is supported by National Natural Science Foundation of China (No. 50930003) and the Ministry of Science and Technology of China Special Funds for Innovation in 2009 (2009IM031000).

REFERENCES

(1) Paul, D. R.; Newman, S. *Polymer blends*; Academic Press: New York, 1978.

(2) Wunderlich, B. *Macromolecular Physics*; Academic Press: New York, 1973; Vol. 1, p 300.

(3) Cheng, S. Z. D. *Phase transitions in polymers: the role of metastable states*; Elsevier: Amsterdam and Boston, MA, 2008).

(4) Han, C. C.; Akcasu, A. Z. *Annu. Rev. Phys. Chem.* **1992**, *43*, 61.

(5) de Gennes, P. G. *J. Chem. Phys.* **1980**, *72*, 4756.

(6) Pincus *J. Chem. Phys.* **1981**, *75*, 1996.

(7) Binder, K. *J. Chem. Phys.* **1983**, *79*, 6387.

(8) Bates, F. S.; Wiltzius, P. *J. Chem. Phys.* **1989**, *91*, 3258.

(9) Hashimoto, T. *Phase Transitions* **1988**, *12*, 47.
(10) Wang, H.; Shimizu, K.; Kim, H.; Hobbie, E. K.; Wang, Z. G.; Han, C. C. *J. Chem. Phys.* **2002**, *116*, 7311.
(11) Tsuburaya, M.; Saito, H. *Polymer* **2004**, *45*, 1027.
(12) Chuang, W. T.; Jeng, U. S.; Hong, P. D.; Sheu, H. S.; Lai, Y. H.; Shih, K. S. *Polymer* **2007**, *48*, 2919.
(13) Lee, J. K.; Choi, W. S.; Kwon, Y. K.; Lee, K. H. *Polymer* **2002**, *43*, 2827.
(14) Zhou, D.; Shi, A. C.; Zhang, P. *J. Chem. Phys.* **2008**, *129*, 154901.
(15) Shabana, H. M.; Olley, R. H.; Bassett, D. C.; Jungnickelb, B. J. *Polymer* **2000**, *41*, 5513.
(16) Tanaka, S.; Yamamoto, M.; Ito, K.; Hayakawa, R. *Phys. Rev. E* **1997**, *56*, R67.
(17) Wang, Z.; Wang, H.; Shimizu, K.; Dong, J. Y.; Hsiao, B. S.; Han, C. C. *Polymer* **2005**, *46*, 2675.
(18) Wang, H.; Shimizu, K.; Hobbie, E. K.; Wang, Z. G.; Meredith, J. C.; Karim, A.; Amis, E. J.; Hsiao, B. S.; Hsieh, E. T.; Han, C. C. *Macromolecules* **2002**, *35*, 1072.
(19) Muthukumar, M. *Philos. Trans. R. Soc. London A* **2003**, *361*, 539.
(20) Olmsted, P. D.; Poon, W. C. K.; McLeish, T. C. B.; Terrill, N. J.; Ryan, A. J. *Phys. Rev. Lett.* **1998**, *81*, 373.
(21) Lorenzo, M. L. D. *Prog. Polym. Sci.* **2003**, *28*, 663.
(22) Keller, A.; Cheng, S. D. Z. *Polymer* **1998**, *39*, 4461.
(23) Hoffman, J. D.; Miller, R. *Polymer* **1997**, *38*, 3151.
(24) Strobl, G. *Prog. Polym. Sci.* **2006**, *31*, 398.
(25) Tanaka, H. *Macromolecules* **1992**, *25*, 6377.
(26) Tanaka, H. *Phys. Rev. Lett.* **1996**, *76*, 787.
(27) Tanaka, H. *J. Phys.: Condens. Matter* **2000**, *12*, R207.
(28) Zhang, X.; Wang, Z.; Zhang, R.; Han, C. C. *Macromolecules* **2006**, *39*, 9285.
(29) Zhang, X.; Wang, Z.; Muthukumar, M.; Han, C. C. *Macromol. Rapid Commun.* **2005**, *26*, 1285.
(30) Du, J.; Niu, H.; Dong, J. Y.; Dong, X.; Wang, D. J.; He, A.; Han, C. C. *Macromolecules* **2008**, *41*, 1421.
(31) Zhang, X.; Wang, Z.; Dong, X.; Wang, D.; Han, C. C. *J. Chem. Phys.* **2006**, *125*, 024907.
(32) Hong, S.; Zhang, X.; Zhang, R.; Wang, L.; Zhao, J.; Han, C. C. *Macromolecules* **2008**, *41*, 2311.
(33) Mitra, M. K.; Muthukumar, M. *J. Chem. Phys.* **2010**, *132*, 184908.
(34) Tanaka, H.; Nishi, T. *Phys. Rev. Lett.* **1985**, *55*, 1102.
(35) Woo, E. M.; Barlow, J. W.; Paul, D. R. *J. Polym. Sci., Polym. Symp. Ed.* **1984**, *71*, 137.
(36) Suvorova, A. I.; Hassanova, A. H.; Tujkova, I. S. *Polym. Int.* **2000**, *49*, 1014.
(37) Shi, W.; Cheng, H.; Chen, F.; Liang, Y.; Xie, X.; Han, C. C. *Macromol. Rapid. Commun.* DOI: 10.1002/marc.201100490.
(38) Grozev, N.; Botiz, I.; Reiter, G. *Eur. Phys. J. E* **2008**, *27*, 63.
(39) Ferreiro, V.; Douglas, J. F.; Warren, J.; Karim, A. *Phys. Rev. E* **2002**, *65*, 051606.
(40) Okerberg, B. C.; Marand, H. *J. Mater. Sci.* **2007**, *42*, 4521.
(41) Toyoda, N.; Takenaka, M.; Saito, S.; Hashimoto, T. *Polymer* **2001**, *42*, 9193.
(42) Okabe, Y.; Kyu, T. *Polymer* **2004**, *45*, 8485.
(43) Kyu, T.; Chiu, H.-W.; Guenthner, A. J.; Okabe, Y.; Saito, H.; Inoue, T. *Phys. Rev. Lett.* **1999**, *83*, 2749.
(44) Harada, A.; Qui, T. C. *Macromolecules* **1997**, *30*, 1643.
(45) Qui, T. C.; Harada, A. *Phys. Rev. Lett.* **1996**, *76*, 1162.
(46) Karim, A.; Douglas, J. F.; Nisato, G.; Liu, D.-W.; Amis, E. J. *Macromolecules* **1999**, *32*, 5917.
(47) Lee, B. P.; Douglas, J. F.; Glotzer, S. C. *Phys. Rev. E* **1999**, *60*, 5812.

NOTE ADDED AFTER ASAP PUBLICATION

This article posted ASAP on December 1, 2011. There is a correction to the equation describing the length of the amorphous-rich domain in the last paragraph of the Results and Discussion. The correct version posted on December 5, 2011.

Macromolecules

Article

pubs.acs.org/Macromolecules

Strategies for Hydrogen Bonding Based Layer-by-Layer Assembly of Poly(vinyl alcohol) with Weak Polyacids

Hyomin Lee,[†] Remy Mensire,[†,§] Robert E. Cohen,*[,†] and Michael F. Rubner*[,‡]

[†]Department of Chemical Engineering, Massachusetts Institute of Technology, Cambridge, Massachusetts 02139, United States

[‡]Department of Materials Science and Engineering, Massachusetts Institute of Technology, Cambridge, Massachusetts 02139, United States

[§]Department of Mechanics, Ecole Polytechnique, Palaiseau 91120, France

Supporting Information

ABSTRACT: Multilayer thin films that consist of poly(vinyl alcohol) (PVA) and weak polyacids such as poly(acrylic acid) (PAA) and poly(methacrylic acid) (PMAA) were prepared by hydrogen bonding interactions. Both the degree of hydrolysis and molecular weight of PVA were investigated in terms of their influence on growth behavior and pH stability. Multilayer films containing PVA and PAA could be assembled successfully only by using partially hydrolyzed PVA and low-pH solutions. By comparing films containing PAA with those containing a more strongly interacting partner, PMAA, it was shown that the extent of PVA hydrolysis becomes significant only when weak hydrogen bonding pairs such as PVA and PAA were used. pH-triggered dissolution experiments demonstrated that the degree of hydrolysis can be used as an additional parameter by which to tune the pH stability of the film. Also, the presence of an abundance of free hydroxyl and carboxylic acid groups in the multilayer allowed enhanced pH stability to be obtained by thermal and chemical methods as well as numerous opportunities for postassembly functionalization.

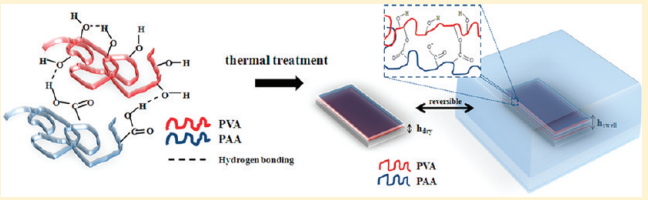

1. INTRODUCTION

Poly(vinyl alcohol) (PVA) is extensively utilized in many important technologies due to its wide ranging attributes including, for example, a high level of biocompatibility and hydrophilicity, excellent barrier properties and ease of chemical functionalization, cross-linking, and crystallization. The incorporation of this important water-soluble polymer into layer-by-layer (LbL) assembled multilayer thin films, however, remains limited to only a few material combinations that tend to exploit the strong hydrogen bonding ability and often limited water solubility of the PVA assembly partner. Previous hydrogen bonding partners used to form LbL multilayers with PVA include polyaniline[1] and clay particles.[2,3] Although these multilayer systems provide unique property combinations, they clearly lack the level of versatility and postassembly chemical and physical manipulation that is now well established with polyelectrolyte multilayers based on weak polyelectrolytes such as poly(acrylic acid) (PAA). In fact, it is quite interesting to note that PVA stands out as one of the few water-soluble, hydrogen-bonding polymers that has not been successfully assembled into a multilayer thin film with suitable polyacids or other often-utilized hydrogen bonding partners. This is in contrast to poly(ethylene oxide) (PEO), which readily forms LbL assembled polymer multilayers with PAA. It should also be noted that others have assembled PVA multilayers using a borax complex,[4] hydrophobic interactions,[5] covalent bonding,[6] and polymer mixtures.[7]

In this paper, we demonstrate that it is possible to fabricate high quality, hydrogen-bonded multilayer films from PVA and PAA or poly(methacrylic acid) (PMAA). As expected, it was found that the assembly solution pH must be low enough to avoid ionization of the carboxylic acid groups of PAA. However, it will be demonstrated that the degree of hydrolysis of PVA and its molecular weight are also critical parameters that determine whether hydrogen-bonded LbL assembly is possible. To realize high quality multilayer thin films, it is also necessary to utilize suitable surface chemistry to anchor the first layer of PVA. It will be further shown that the pH stability of the resultant multilayer thin films can be enhanced significantly with a short heat treatment that introduces ester cross-links between PVA and PAA. Thus, with suitable heat treatment, robust multilayer thin film hydrogels with reversible swelling behavior can be created that are stable at physiological pH. The presence of an abundance of free alcohol and carboxylic acid groups in the lightly cross-linked films provides numerous opportunities for postassembly functionalization as will be demonstrated by the covalent attachment of a protein to the acid groups and a PEO-modified dye to the alcohol groups. This PVA based multilayer system represents a new, stable, and quite versatile platform for applications ranging from biological to optical. For example, in a future publication, we will show

Received: September 14, 2011
Revised: November 4, 2011
Published: December 9, 2011

that suitably functionalized optical quality coatings with outstanding antifog properties can be fabricated from this system.

2. MATERIALS AND METHODS

2.1. Materials. To investigate the effect of degree of hydrolysis and molecular weight on the interpolymer complexation behavior and thus on growth behavior and stability of films, a number of PVA samples were obtained from Sigma-Aldrich (P1: M_w = 24 500 g/mol, PDI = 1.99, 87−89% hydrolyzed; P2: M_w = 88 400 g/mol, PDI = 1.18, 87−89% hydrolyzed; P3: M_w = 131 000 g/mol, PDI = 1.50, 87−89% hydrolyzed; F1: M_w = 21 400 g/mol, PDI = 1.22, 98−99% hydrolyzed; F2: M_w = 144 000 g/mol, PDI = 1.34, 98−99% hydrolyzed). The codes P and F indicate partial versus full hydrolysis while molecular weight increases with the integer in the sample code. Each sample was dissolved in a pH 7.0 buffer solution (0.2 M sodium nitrate, 0.01 M sodium phosphate) at a concentration of 2 mg/mL and characterized using gel permeation chromatography (GPC) (Agilent Technology 1260 Infinity, Wyatt Optilab T-rEX detector, PL Aquagel -OH column). The resulting molecular weight and polydispersity values are summarized in Table 1.

Table 1. Number-Average Molecular Weight (M_n), Weight-Average Molecular Weight (M_w), and the Polydispersity Index (PDI = M_w/M_n) of the PVA Samples[a] Used in This Work

PVA samples	M_n (10^4 g/mol)	M_w (10^4 g/mol)	PDI (M_w/M_n)
P1	1.23	2.44	1.99
P2	7.50	8.84	1.18
P3	8.73	13.1	1.50
F1	1.76	2.14	1.22
F2	10.8	14.4	1.34

[a]P: partially hydrolyzed (87−89%) PVA; F: fully hydrolyzed (98−99%) PVA.

2-Butanone (MEK, 99+% ACS reagent), methylene blue dye, albumin−fluorescein isothiocyanate conjugate (FITC-BSA), glutaraldehyde solution (Grade II, 25% in H_2O), *N*-(3-(dimethylamino)propyl)-*N*′-ethylcarbodiimide hydrochloride (EDC), *N*-hydroxysulfosuccinimide sodium salt (NHS), MES sodium salt, and Tween-20 were obtained from Sigma-Aldrich. Poly(acrylic acid) (PAA, M_w = 225 000 g/mol, 20% aqueous solution), poly(methacrylic acid) (PMAA, M_w = 100 000 g/mol), and poly(glycidyl methacrylate) (PGMA, M_w = 25 000 g/mol, 10% solution in MEK) were obtained from Polysciences. Rhodamine B labeled poly(ethylene glycol) (RB-PEG) was obtained from Nanocs. Standard (soda lime) glass microscope slides and phosphate buffer saline (PBS) were obtained from VWR. Deionized water (DI, 18.2 MΩ·cm, Milli-Q) was used in all aqueous polymer solutions and rinsing procedures.

2.2. Methods. *2.2.1. PGMA Surface Anchoring Chemistry.* The glass substrates were degreased by sonication in a 4% (v/v) solution of Micro-90 (International Products Co.) for 15 min and subsequently sonicated twice in DI water for 15 min and dried with compressed air. They were then treated with oxygen plasma (PDC-32G, Harrick Scientific Products, Inc.) for 2 min at 150 mTorr. A plasma-treated glass slide was immediately immersed in a 0.1% (w/v) PGMA/MEK solution for 20 s and then placed in a 110 °C oven for 30 min to covalently bond PGMA to the glass substrate. After cooling to ambient temperature, the PGMA-coated glass substrate was immersed in a 1 mg/mL aqueous solution of PVA (pH 2.0) for 20 min. The PVA-coated substrate was then dried at ambient temperature and again placed in the oven at 110 °C for 30 min to induce a chemical reaction between the residual epoxy groups present in PGMA and the PVA hydroxyl groups. Silicon wafers were treated using the same protocol.[8]

2.2.2. Thin Film Assembly. Films were constructed using a Stratosequence VI spin dipper (Nanostrata Inc.) controlled using StratoSmart v6.2 software. PGMA-treated substrates that were reacted with a layer of PVA were first rinsed three times using DI water of the same pH as the preceding PVA solutions to remove loosely bound PVA from the substrate. LbL assembly was then commenced with dipping times of 10 min for the polymer solutions, followed by three rinses of 2, 1, and 1 min. The concentration of the polymer solutions used was 1 mg/mL, and the pH of these solutions and the rinse water were adjusted with 0.1 M HCl or 0.1 M NaOH. PVA/PAA films were also produced by spray assembly using automated equipment described in a previous publication.[9] For the spray assembly, we used the same concentrations and pH conditions as employed in the dip assembly, but the cycle times (polymer solution 12 s/delay time 6 s/rinsing 20 s twice) to produce a bilayer were significantly smaller. The nomenclature for LbL films follows the convention (hydrogen bonding acceptor/donor)$_Z$, where Z is the total number of bilayers deposited. Typically the pH conditions are specified for individual polymer solutions, but here all the LbL films were assembled at pH 2.0 conditions and were omitted for simplicity.

2.2.3. Functional Modification with FITC-BSA/RB-PEG. $(PVA_{P3}/PAA)_{30}$ films on glass substrates were heated for 5 min at 140 °C. Then the film was immersed in 0.1 M EDC and 0.1 M NHS solution in 50 mM MES buffer (pH 5.0) for 30 min. The sample was then rinsed with 50 mM MES buffer (pH 5.0) for 10 s and immediately immersed in 1 mg/mL FITC-BSA in MES buffer (pH 6.0) for 2 h. After rinsing with DI water, the sample was soaked in 0.1% (v/v) Tween-20 in PBS (pH 6.0) for either 3 or 15 h on the shaker plate set at 100 rpm. Samples were rinsed thoroughly with DI water and dried with compressed air. Control samples were prepared with the exact same protocol without the EDC/NHS. After FITC-BSA was attached to the film, sample was immersed in 0.5 mg/mL RB-PEG solution for 30 min. Then the sample was soaked in 30 °C 0.13% (w/w) glutaraldehyde in PBS for 10 min, rinsed with DI water, and dried with compressed air. Similarly, a control sample was prepared without the glutaraldehyde cross-linking.

2.2.4. Characterization. Dry film thicknesses were measured using a Tencor P16 surface profilometer with a 2 μm stylus tip, 2 mg stylus force, and a scanning rate of 50 μm/s. To determine wet film thicknesses *in situ*, a custom-built quartz cell was used in conjunction with a J.A. Woollam XLS-100 spectroscopic ellipsometer as described previously.[9,10] Data were collected between 400 and 1000 nm at a 70° incidence angle and analyzed with WVASE32 software. To measure the extent of reversible swelling, the thickness of each film was measured first when immersed for 10 min in water of a designated pH and then after drying with compressed air. Topographical images of the multilayers were obtained using a Veeco Nanoscope V Dimension 3100 AFM microscope in tapping mode.

The extent of polymer complexation in various pH conditions was determined by measuring the attenuation of light using UV−vis spectroscopy (Varian Cary 50 Bio) over the 370−750 nm range 10 min after the mixing of two hydrogen bonding polymer solutions. IR spectra of films deposited on ZnSe plates were taken using a Nicolet 4700 FT-IR spectrometer (Thermo Scientific). The extent of pH-triggered disintegration was determined by measuring the ratio of the dry film thickness before and after 2 h incubation in pH-adjusted DI water. NMR spectra of samples dissolved in deuterated water were obtained on a Varian Mercury-300 spectrometer. The degree of hydrolysis for the fully hydrolyzed and partially hydrolyzed PVA samples of similar molecular weight was determined by the analysis of NMR spectra. Peak areas of hydrogen atoms attached to the α carbon (H_b' and H_b'': peaks near 4.0 ppm) in PVA were set to 1.00. The peak area near 2.1 ppm which corresponds to the acetate hydrogen H_c was then used to calculate the fraction of acetate groups in the overall PVA chain. The amount of each polymer within the freestanding $(PVA_{P3}/PAA)_{100}$ film was calculated by normalizing with respect to the peaks associated with the hydrogen atoms on the α carbon (H_b' and H_b'') and subtracting out the contribution of PVA in the upfield region (1.0−2.5 ppm) where only the hydrogen atoms of PAA appear. The presence of carboxylic acid groups was probed using methylene blue as described previously.[11] The emission spectra of the films that contained fluorescent dyes were obtained from Horiba Fluorolog-3 spectrofluorometer. The fluorescence emission was visualized with

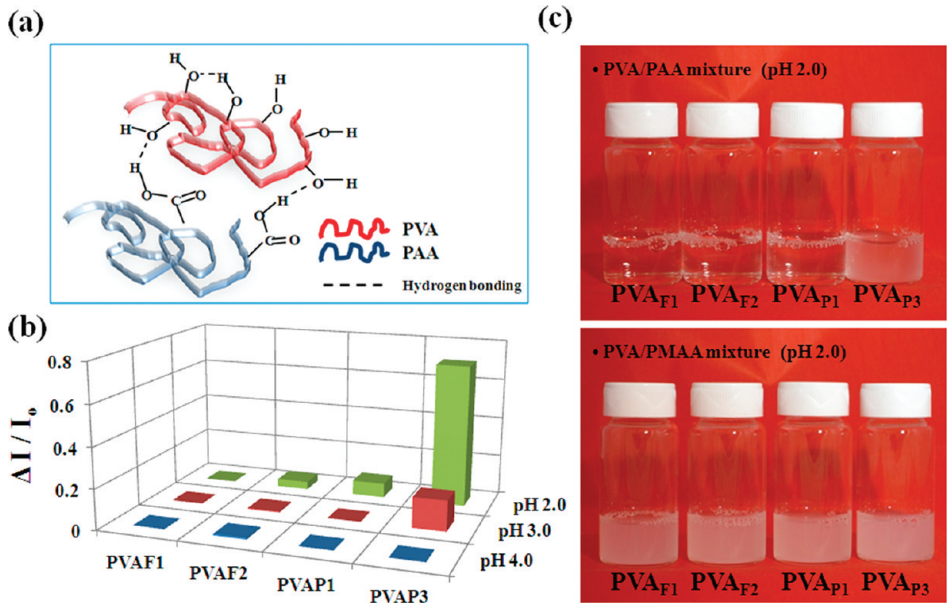

Figure 1. (a) Cartoon showing interpolymer complexation of PVA and PAA. (b) pH/PVA matrix showing the attenuation of transmitted light (I) expressed as $\Delta I/I_0$ where $\Delta I = I_0 - I$ and I_0 is the incident light intensity averaged over the 370−750 nm range. (c) Photographs of PVA/PAA and PVA/PMAA mixtures. PVA and PAA were mixed in equal volume ratios. The concentration of each solution before mixing was 1 mg/mL, and the pH was adjusted to 2.0 using HCl. All solutions were transparent before mixing, and the light transmittance was measured 10 min after mixing for (b).

Zeiss LSM 510 confocal laser scanning microscopy (CLSM) with the excitation wavelengths set at 488 and 543 nm.

3. RESULTS AND DISCUSSION

3.1. Interpolymer Complexes of PVA in Aqueous Solution. In order to identify solution assembly conditions that would favor robust multilayer growth, we first studied interpolymer complex formation between a variety of PVA samples and the complementary polyacids PAA and PMAA. Others have reported that poly(carboxylic acid)s and proton-accepting polymers can form interpolymer complexes through hydrogen bonding interactions.[12] These water-insoluble complexes are often readily detected by simple turbidity, transmission measurements, or visual inspection of the mixed solutions. These simple tests are known to be a helpful predictor of the ability of complementary polymer pairs to assemble into LbL films.[13] Mixing PAA and proton-accepting polymers such as PEO in suitable aqueous solutions, for example, leads to interpolymer hydrogen bonding interactions that screen the hydrophilic functional groups and result in insoluble polymer complexes.[14] Conditions that favor the formation of these water-insoluble complexes are good candidates for successful LbL assembly.

Although the repeat unit of PVA is isomeric with that of PEO, its hydrogen bonding properties are very different due to the presence of hydroxyl groups. The hydroxyl groups of PVA can form hydrogen bonds with other hydroxyl groups within the same chain (intrachain hydrogen bonding) or on other PVA chains (interchain hydrogen bonding). PVA is made by the hydrolysis of poly(vinyl acetate), and the fraction of residual acetate groups along the chain typically varies from as high 15% to as low as 1%. Since the degree of hydrolysis determines the linear density of hydroxyl groups along the chain, it will also affect the behavior of PVA in solution and its ability to engage in inter- and intramolecular hydrogen bonds. As might be expected, polymer complex formation is also strongly influenced by the molecular weight of the interacting polymers.

To explore these different parameters, various PVA samples with different degrees of hydrolysis and different molecular weights were mixed with complementary hydrogen bond donors (PAA and PMAA) to test for interpolymer complex formation.

Figure 1b displays the fractional attenuation of light ($\Delta I/I_0$) of various solutions of PVA and PAA. When PAA is the proton-donating polymer, complexation with PVA depends strongly on the pH of the aqueous solution. While turbidity is observed in several cases at pH 2.0, as the pH increases, hydrogen bonding decreases due to the increased ionization of the PAA chains, and consequently, the measured light attenuation decreases toward zero. The results show that even in pH 2.0 DI water where PAA is known to be fully protonated, complexes are not formed readily for both low and high molecular weight fully hydrolyzed PVA (F1 and F2). However, for partially hydrolyzed PVA (P1 and P3) and especially for the high molecular weight sample PVA_{P3}, there is a noticeable change in solution turbidity upon mixing the polymer solutions. For PVA_{P3}/PAA, the solution turbidity is also apparent even at pH 3.0, where PAA starts to ionize. These results clearly show that the degree of hydrolysis and molecular weight of PVA are important parameters controlling polymer complexation with PAA. PMAA was also used to evaluate the effect of the degree of hydrolysis on interpolymer complexation. Others have reported that PEO/PMAA complexes are more stable and more strongly interacting than PEO/PAA complexes due to the α-methyl group of PMAA.[15] As shown in Figure 1c, all PVA solutions became turbid upon mixing with PMAA. From this, we conclude that the effect of the extent of PVA hydrolysis is significant only for weakly interacting polymer pairs such as PVA and PAA. The analogue of Figure 1b for PVA/PMAA was also produced and is included in the Supporting Information (Figure S1).

dx.doi.org/10.1021/ma202092w | *Macromolecules* 2012, 45, 347−355

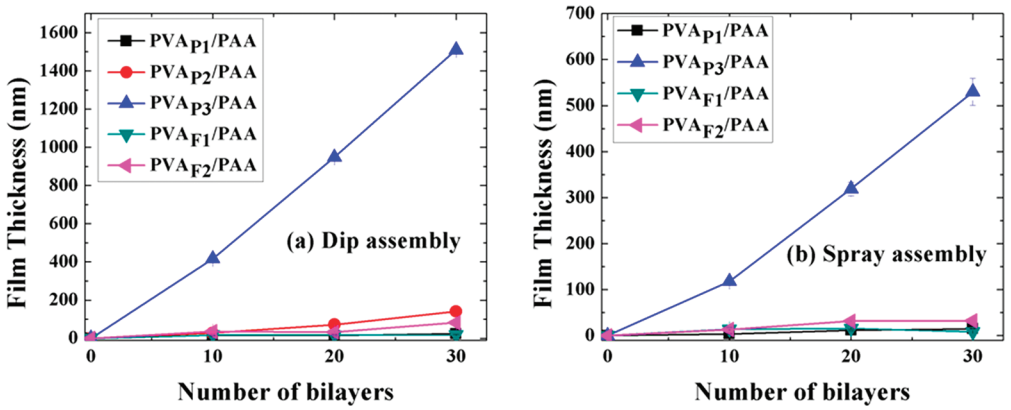

Figure 2. Growth behavior of (PVA$_{P1}$/PAA) (black squares), (PVA$_{P2}$/PAA) (red circles), (PVA$_{P3}$/PAA) (blue triangles), (PVA$_{F1}$/PAA) (green triangles), and (PVA$_{F2}$/PAA) (pink triangles) systems assembled at pH 2.0 on glass substrates modified with PGMA. (a) shows results obtained by dip assembly, and (b) shows data obtained on films produced by spray assembly.

Table 2. Average Thickness Increment per Bilayer, Roughness, and Time Required To Obtain a 500 nm Film Using Two Different LbL Methods for (PVA$_{P1}$/PAA), (PVA$_{P2}$/PAA), and (PVA$_{P3}$/PAA)[a]

	thickness per bilayer (nm)		roughness (nm)[b] R_a		time required to obtain a 500 nm film (min)	
system	dip assembly	spray assembly	dip assembly	spray assembly	dip assembly	spray assembly
(PVA$_{P1}$/PAA)	0.4	0.6	1.3	2.1		
(PVA$_{P2}$/PAA)	5.7		0.8			
(PVA$_{P3}$/PAA)	54.7	20.6	0.6	7.6	323	67

[a]The linear regime was considered to be from 10 to 30 bilayers. [b]Roughness was measured using profilometry.

3.2. Layer-by-Layer Assembly of PVA with PAA or PMAA. *3.2.1. LbL Assembly on Substrates Modified with PGMA Anchoring Chemistry.* With the insight gained from the interpolymer complex formation screening test, we explored how complex formation relates to the LbL assembly process. It should be noted at this point that high-quality LbL films were obtained only if suitable surface chemistry was applied to the substrate prior to the deposition of the first PVA layer. In the case of PEO/PAA hydrogen-bonded films, it has been reported[16] that reproducibility issues exist as well as batch-to-batch variability even for carefully controlled assembly conditions. We observed similar behavior in our preliminary experiments with the PVA/PAA system in which the only pretreatment of the glass substrate was oxygen plasma. In particular, overall film quality was poor, exhibiting agglomerates and nonuniform thickness across the film. Luzinov's group[8,17] recently introduced a robust method to anchor various polymers to surfaces by attaching a macromolecular anchoring layer rich in epoxy functional groups to the substrate. PGMA serves as an anchoring interlayer to attach functional polymers, providing a strong bond between the grafted layer and the substrate. Using this method, the first layer of PVA was covalently bonded to the substrate. The film subsequently assembled on top of this layer showed enhanced thickness reproducibility and increased smoothness as shown in Supporting Information (Figure S2). The enhanced adhesion of the LbL films to the substrates greatly simplified the swelling characterization and spectroscopy analysis. Because of these many advantages, all multilayers were assembled from aqueous solutions of pH 2.0 with no added salt onto PGMA-modified glass substrates with the first layer of PVA covalently attached as described above. Both dip and spray assembly were utilized to fabricate the multilayer thin films.

3.2.2. Layer- by-Layer Assembly of PVA with PAA. Figure 2 shows the growth profiles of the various PVA/PAA multilayers examined in this work. As predicted by the solution complexation studies, multilayer growth was dramatically dependent on the molecular weight and degree of hydrolysis of PVA. Whereas the PVA$_{Fx}$/PAA systems (fully hydrolyzed PVA) exhibited very small thickness increments per deposition cycle even with the higher molecular weight PVA, multilayer growth of the PVA$_{Px}$/PAA systems (partially hydrolyzed PVA) was strongly dependent on the molecular weight of PVA. Only multilayers created from the highest molecular weight PVA showed high thickness increments per bilayer. Table 2 presents the average thickness increment per bilayer for all of the PVA$_{Px}$/PAA systems assembled in this study.

For PVA/PAA multilayers assembled at pH 2.0 with fully hydrolyzed PVA, small incremental thicknesses were observed, and the multilayers were generally rough compared to the film thicknesses. In sharp contrast, a large bilayer thickness was observed for the PVA$_{P3}$/PAA system with an average value of 54.7 nm obtained by using the dip assembly process and 20.6 nm obtained by using the spray LbL assembly process. The former bilayer thickness is comparable to the ~80 nm per bilayer value reported for dip assembled PEO/PAA,[16,18] which also features weak intermolecular hydrogen bonding. For the multilayers assembled with partially hydrolyzed PVA, the average bilayer thickness depends strongly on the molecular weight of the PVA used in the assembly process. Similar observation have been reported previously for the PEO/PAA system, where a 7-fold increase in bilayer thickness was observed when the molecular weight of PEO was increased from 1.5 to 20 kDa.[16] However, as seen in Figure 2 and Table 2, the average bilayer thickness observed for the dip assembled PVA/PAA system increases by a factor of about 100 when the molecular weight (M_n) of partially hydrolyzed PVA increased

dx.doi.org/10.1021/ma202092w | Macromolecules 2012, 45, 347–355

from 12 to 87 kDa. The spray assembly results show that this multilayer system can be fabricated by using spray approaches. In these preliminary studies, the dip assembled multilayers exhibited a larger thickness per bilayer compared to spray assembled films and lower roughness values. We anticipate that further optimization of the spray assembly process will result in more comparable films. In any event, it is clear that, if needed, it will be possible to take advantage of the faster processing times inherent in the spray assembly process (see Table 2).

3.2.3. Layer-by-Layer Assembly of PVA with PMAA. As anticipated by the complexation experiments, in the case of the PVA/PMAA multilayer system, reasonable multilayer growth was obtained for all PVA samples examined (Figure 3). The use

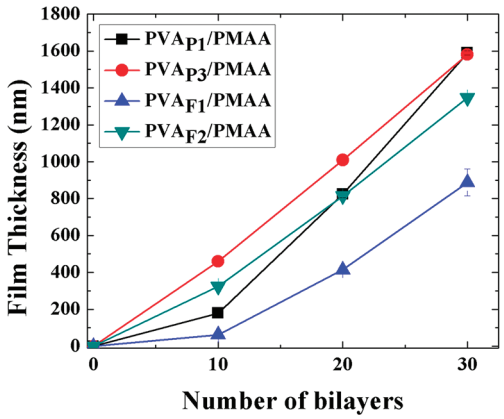

Figure 3. Growth behavior of (PVA$_{P1}$/PMAA) (black squares), (PVA$_{P3}$/PMAA) (red circles), (PVA$_{F1}$/PMAA) (blue triangles), and (PVA$_{F2}$/PMAA) (green triangles) systems dip-assembled at pH 2.0 on glass substrates modified with PGMA.

of the more strongly interacting polyacid PMAA results in average thickness increments comparable to the best PVA/PAA system, regardless of the molecular weight and the degree of hydrolysis of the PVA utilized to fabricate the multilayer.

3.2.4. pH-Triggered Disintegration of Hydrogen-Bonded PVA/PAA or PVA/PMAA Multilayers. As mentioned briefly in the Introduction, poly(carboxylic acid)s incorporated into a hydrogen-bonded multilayer become ionized when exposed to pH conditions higher than the assembly pH. When multilayer films are exposed to this critical higher pH, the hydrogen bonds are disrupted and the film dissolves. The critical pH at which film disintegration occurs depends upon the strength of the hydrogen bonding interactions within the multilayer film, with weaker interactions resulting in lower critical pH values.[19,20] Among the pH-degradable hydrogen-bonded multilayer systems reported so far, the PEO/PAA system is known to be one of the weakest, with a critical dissolution pH of 3.5.[16] When PMAA was used as the hydrogen bonding partner with PEO, the critical pH shifted to a slightly higher value of 4.6.[19]

In order to determine the critical film dissolution pH, multilayer films were immersed into a pH-adjusted solution for 2 h and the dry film thickness was measured and compared to the original thickness. As shown in Figure 4, (PVA$_{P3}$/PAA) multilayers start to dissolve between pH 2.5 and 3.0, well below the value of 3.5 observed for PEO/PAA. When PVA is assembled with the more strongly interacting polymer PMAA, the critical pH shifts to higher values as expected. In contrast to the PEO/PAA multilayer system (~1.1 pH units[16,19]), a more substantial increase of 3.75 pH units is observed when

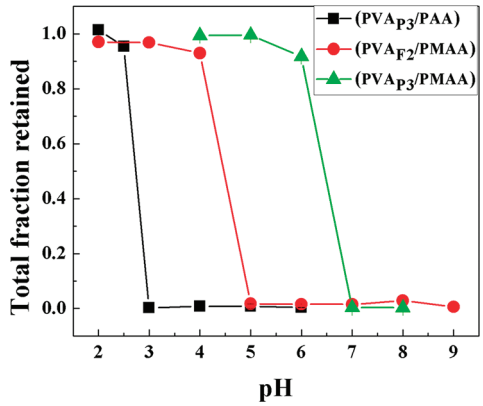

Figure 4. pH-triggered disintegration of hydrogen-bonded systems without any post-treatment: (PVA$_{P3}$/PAA) (black squares), (PVA$_{F2}$/PMAA$_{100K}$) (red circles), and (PVA$_{P3}$/PMAA$_{100K}$) (green triangles).

comparing PVA$_{P3}$/PAA to PVA$_{P3}$/PMAA. The enhanced pH stability of PVA$_{P3}$/PMAA is attributed to the presence of the methyl groups in PMAA, which, along with the acetate moieties in the PVA, lead to stronger hydrophobic interactions that stabilize the film.[21] Figure 4 shows that it is possible to tune the critical pH value of PVA containing multilayers from a very low value (about 2.5, (PVA$_{P3}$/PAA)) to as high as about 6.5 (PVA$_{P3}$/PMAA) by simply changing the hydrogen bonding polyacid partner or by using PVA materials with different degrees of hydrolysis.

The effect of PVA molecular weight on film disintegration was also examined. Although the molecular weight of the depositing polymer significantly affects the film growth behavior as shown in Figure 2, we observed that films containing PVA chains of different molecular weights exhibit essentially the same critical pH value, consistent with results reported for other hydrogen-bonded systems.[19,22] Indeed, as shown in the Supporting Information (Figure S3), the PVA$_{P2}$/PAA and PVA$_{P3}$/PAA multilayers show similar critical pH values even though the film growth behavior is significantly different for these two systems. Dissociation of polymer segments is apparently governed by the destruction of cooperative sequences of associating functional groups, and with sufficiently long exposure to a solution, the molecular weight has only a kinetic effect.

3.3. Composition Analysis and Heat-Induced Cross-Linking Studies of (PVA$_{P3}$/PAA)$_{100}$. *3.3.1. Composition Analysis Using ^{1}H NMR.* The chemical composition of (PVA$_{P3}$/PAA)$_{100}$ multilayer films was characterized by dissolving free-standing films in a deutrated solvent (D_2O) and carrying out ^{1}H NMR spectroscopy on the solutions as shown in Supporting Information (Figure S4). As a baseline, the degree of hydrolysis for the fully hydrolyzed and partially hydrolyzed PVA samples of similar molecular weight was determined. NMR analysis revealed that the fully hydrolyzed PVA sample has a degree of hydrolysis of 97%, whereas the partially hydrolyzed PVA sample is 84% hydrolyzed; both of these values agree well with the manufacturers' stated values. Using the determined degree of hydrolysis and the PAA spectrum as a reference, the overall composition of a (PVA$_{P3}$/PAA)$_{100}$ multilayer film was determined to be approximately 47% PVA and 53% PAA.

3.3.2. Heat-Induced Cross-Linking and Its Effect on Multilayer pH Stability. Several methods have been developed in the literature to extend the pH stability of hydrogen-bonded

dx.doi.org/10.1021/ma202092w | *Macromolecules* 2012, 45, 347–355

films to physiological conditions.[19] These methods include blending hydrogen-bonded films with an electrostatically interacting pair[23,24] and cross-linking of the constituent polymers.[25,26] In the case of the PVA/PAA multilayer films, the presence of both carboxylic acid and alcohol groups makes it possible to form cross-links via a simple thermally induced esterification reaction.[27,28] Figure 5 shows how pH-dependent

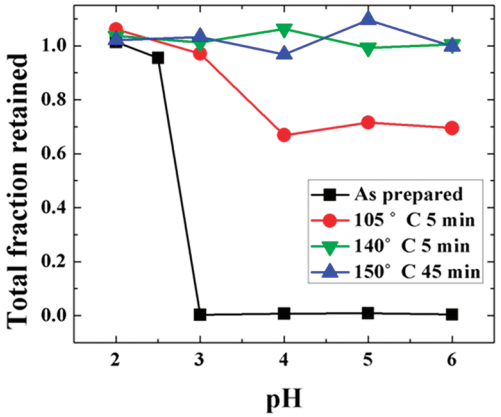

Figure 5. pH-triggered disintegration of hydrogen-bonded $(PVA_{P3}/PAA)_{30}$ film after heat-induced esterification. Subjecting the film to heat treatment allows control of the disintegration pH.

film stability varies with the extent of heat treatment for the PVA_{P3}/PAA system. As-prepared films had a critical pH between 2.0 and 3.0 and dissolved completely at higher pH values. When a $(PVA_{P3}/PAA)_{30}$ multilayer film was subjected to 105 °C for 5 min, the film became somewhat more stable than the as-prepared films but still exhibited partial dissolution. For reference, the glass transition temperatures of PVA[29] and PAA[18] are 55−65 and 90−100 °C, respectively. When samples were heated for 5 min at 140 °C and for 45 min at 150 °C, however, they were rendered completely stable over a wide range of pH values for up to 1 week. FT-IR analysis confirmed that heat treatment at these higher temperatures results in the formation of ester cross-links (see Figure S5).

3.3.3. Effect of Solution pH on the Swelling of Various Heat-Treated Samples. The pH-dependent swelling behavior of heat-treated multilayer films was monitored using *in situ* ellipsometry. The swelling ratio is defined here as the ratio of the thickness of a film in contact with excess water at stated conditions to that of a dry film, both thicknesses measured via ellipsometry. Figure 6a shows the swelling ratio in pH 2.0 DI water versus time for a series of $(PVA_{P3}/PAA)_{30}$ films subjected to a variety of heat treatment protocols. For the untreated sample, the swelling ratio was ∼5.5, and as the heating temperature (and time) increased from 105 °C (5 min) to 140 °C (5 min) to 150 °C (45 min), a decrease in swelling ratio was observed: the corresponding values of swelling ratio were ∼3.2, ∼2.3, and ∼1.4, respectively. This gradual decrease in swelling ratio is consistent with increased esterification cross-linking. Comparing the swelling of $(PVA_{P3}/PAA)_{30}$ films subjected to different heat treatments in pH 7.4 phosphate buffer saline-(PBS), it is evident from Figure 6b that only those films heated for 5 min at 140 °C and for 45 min at 150 °C were stable at physiological pH. Interestingly, a comparison of the swelling ratio at the extremes of the pH range investigated revealed that the swelling ratio of films in pH 2.0 DI water and pH 7.4 PBS were ∼1.4 and ∼1.8, respectively, for multilayer films treated for 45 min at 150 °C. However, for the multilayer films heated for 5 min at 140 °C, a significant difference in swelling ratio was observed with a value of ∼2.3 for pH 2.0 DI water and a value of ∼4.3 for pH 7.4 PBS. Similar behavior was observed previously for a bicomponent hydrogel consisting of PVA and PAA prepared by solvent casting and heat treated to give pH-responsive hydrogels. It was reported that the amount of pH-responsive swelling was reduced by increase of heating time due to enhanced cross-linking in these blends.[27,28]

3.3.4. Reversibility of pH-Triggered Swelling. The thickness of a $(PVA_{P3}/PAA)_{30}$ film heated for 5 min at 140 °C was monitored by *in situ* ellipsometry over five cycles of immersion in either pH 2.0 DI water or pH 7.4 PBS with drying after each step (Figure 7a). Each film was immersed in solution for 10 min and dried at room temperature for several minutes with N_2 before measurements. The thickness increases and decreases observed using *in situ* ellipsometry were accompanied by commensurate decreases and increases of the refractive index, indicating that film loss was negligible during pH cycling. These results confirm the excellent pH stability that results from the thermal cross-linking step. Figure 7b is a schematic of the key features of a heat-treated multilayer film including covalent linkages in the form of ester bonds, ionized carboxylic acid groups, and hydroxyl groups. Changes in the degree of ionization of the acid groups primarily drive the pH-responsive swelling behavior.

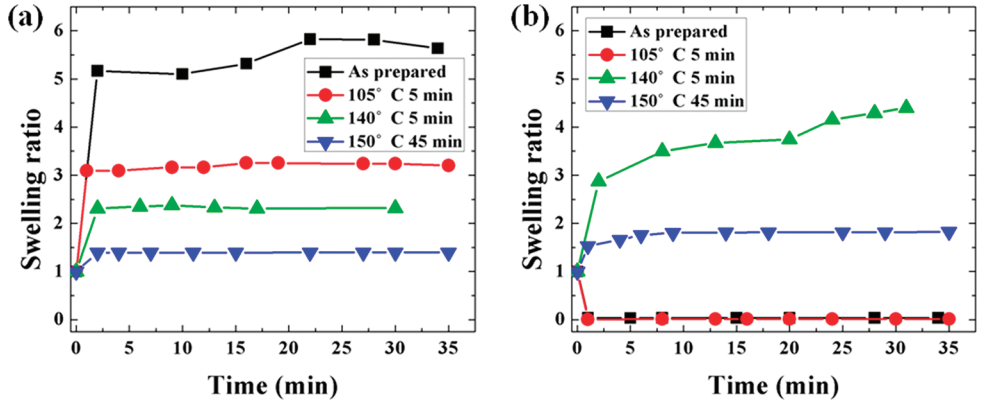

Figure 6. Swelling experiments using *in situ* ellipsometry measurements of $(PVA_{P3}/PAA)_{30}$ films to verify the effect of thermal cross-linking: (a) pH 2.0 DI water, (b) pH 7.4 PBS buffer.

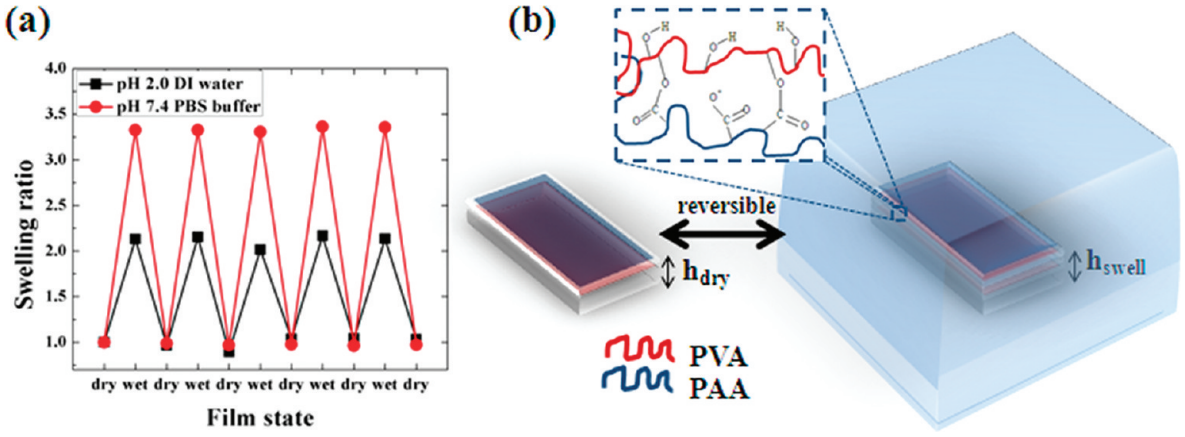

Figure 7. (a) pH-dependent reversible swelling behavior of a $(PVA_{P3}/PAA)_{30}$ film heated for 5 min at 140 °C in pH 2.0 DI water and pH 7.4 PBS. Films were immersed in the solution for 10 min and dried with N_2. (b) Cartoon showing a pH-dependent reversible swelling.

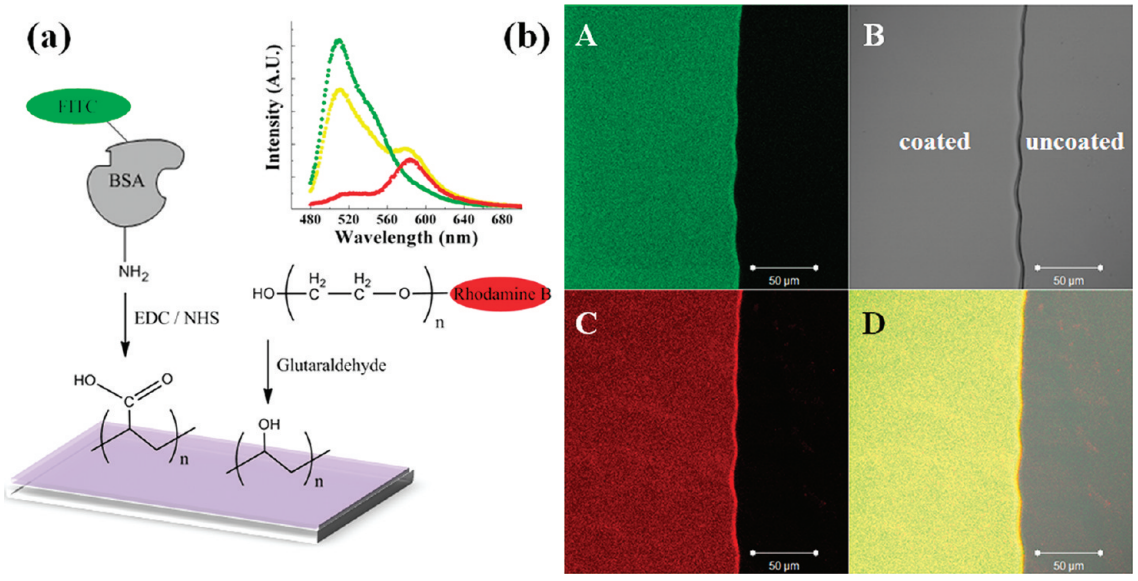

Figure 8. (a) Scheme of a film being functionalized with FITC-BSA and RB-PEG. Upper-right-hand corner shows the emission spectra of three individual samples excited at a single wavelength of 440 nm (green: FITC-BSA only; red: RB-PEG only; yellow: both). (b) A, C: Confocal microscopy image of the film functionalized with both FITC-BSA and RB-PEG measured at two different excitation wavelengths of 488 nm (for FITC) and 543 nm (for RB), respectively. B: Plain image to distinguish the coated area. D: Overlay image excited at both wavelengths (488 and 543 nm).

We used methylene blue adsorption[11] to verify the presence of ionized carboxylic acids existing in the film. The procedure simply involved adsorbing positively charged methylene blue dye into the film and observing whether the film remained stained after thorough rinsing. Figure S7 in the Supporting Information shows that a significant amount of ionized carboxylic acid groups is present in the film even after rigorous rinsing with PBS.

3.4. Biofunctionalization with FITC-BSA and RB-PEG.

Cross-linked $(PVA_{P3}/PAA)_x$ multilayers are essentially swellable thin film hydrogels, replete with free carboxylic acid and alcohol groups. This combination of properties and functionality makes this multilayer system an extremely versatile platform for exploring various types of bioengineered surfaces. To demonstrate that the hydroxyl and carboxylic acid groups can be utilized to add additional functionality to the multilayer, specific postfunctionalization chemistries were examined. By selective targeting of these functional groups, it is possible to covalently attach multiple synthetic and biological molecules to the multilayer in a controlled fashion. To accomplish this, a model protein, BSA-labeled FITC (FITC-BSA) end-functionalized with a primary amine, and a PEG-labeled Rhodamine B (RB-PEG) molecule end-functionalized with a hydroxyl group were used as probe molecules. PEG molecules are known to confirm biocompatibility to thin films. As shown in Figure 8a, the multilayer film was first functionalized with FITC-BSA using carbodiimide chemistry. In this case, the carboxylic acid groups embedded in the film were first activated by EDC/NHS chemistry and subsequently reacted with the amine terminated FITC-BSA. To confirm that the FITC-BSA was covalently attached and not simply physically absorbed, a control experiment was done by placing samples with and without the EDC/NHS treatment in a 0.1% (v/v) Tween-20 PBS solution for 3 h on a shaker plate. Tween-20 is known to facilitate the removal of physically absorbed proteins.[30] The results shown in Figure S8a in the Supporting Information confirm that in the case of samples activated with EDC/NHS chemistry a significant fraction of the FITC-BSA is covalently

dx.doi.org/10.1021/ma202092w | Macromolecules 2012, 45, 347–355

attached to the multilayer and hence not removed by treatment in the Tween solution.

After FITC-BSA attachment, the film was immersed for 30 min into a 0.5 mg/mL RB-PEG solution. The film was then immersed into a 30 °C, 0.13% (w/w) glutaraldehyde containing PBS solution for 10 min, rinsed with DI water, and dried. When the film is introduced into the 0.13% (w/w) glutaraldehyde PBS solution, it is expected that reactions with both the hydroxyl-terminated RB-PEG molecules and the hydroxyl groups of the PVA chains are possible. In the latter case, further chemical cross-linking of the multilayer would occur. Also, given the positive charge of the RB-PEG molecules, one would expect an uptake of dye due to electrostatic binding with the free carboxylic acid groups of PAA. This was confirmed by control experiments in which multilayer films without the FITC-BSA attached were exposed to solutions of RB-PEG and subsequently treated for 15 h in a Tween-20 solution (in Figure S8b in the Supporting Information). Even after the extensive Tween treatment, about half of the dye initially loaded onto the film remained. Thus, it is also possible to use electrostatic binding to add functional molecules to this multilayer. This might be desirable if pH triggered release of the functional molecule is important. For films prior loaded with FITC-BSA, there would be fewer acid groups available for electrostatic binding of the RB-PEG.

Figure 8 shows the emission spectra of multilayer films functionalized with the various molecules as well as confocal microscopy images of a multilayer film functionalized with both FITC-BSA and RB-PEG. In the case of the emission spectra, samples excited at a wavelength of 440 nm that have been treated only with FITC-BSA, only with RB-PEG, and with both molecules reveal the characteristic emission of each dye (green curve, FITC-BSA only; red curve, RB-PEG only) and the combination spectrum expected when both dyes are present (yellow curve). The confocal microscopy images of the film functionalized with both FITC-BSA and RB-PEG also clearly reveal that the multilayer is emitting both a green and red signal, indicating that both molecules are present in the film.

4. CONCLUSIONS

In summary, we have demonstrated that hydrogen-bonded LbL films containing PVA and PAA can be assembled successfully at low pH by using a relatively high molecular weight sample of partially hydrolyzed PVA. By comparing films containing PAA with those containing a more strongly interacting polyacid, PMAA, it was demonstrated that the extent of PVA hydrolysis becomes a significant factor only when weak hydrogen bonding pairs such as PVA and PAA are used. We also demonstrated by pH-triggered dissolution experiments that the degree of hydrolysis can be used as an additional parameter by which to tune the pH stability of the film. This feature may be very useful in the fabrication of sacrificial multilayers for controlled release of overlying multilayers or of therapeutic agents. Thermal treatment of the PVA/PAA multilayer system was found to introduce covalent ester cross-links that stabilize the film to physiological conditions. These heat-treated films were stable to repeated exposure to aqueous solutions of wide ranging pH and swelled reversibly in response to these pH changes. Also, suitably end-functionalized biologically relevant molecules (FITC-BSA and RB-PEG) were successfully covalently attached to the PVA/PAA multilayer to validate that this system is a stable platform, suitable for further functionalization. This new multilayer systems opens the door to the exploration of a wide variety of biofunctional thin films and optical coatings.

■ ASSOCIATED CONTENT

Supporting Information

Interpolymer complexation of PVA/PMAA, AFM image of $(PVA_{P3}/PAA)_{30}$ film, pH-triggered dissolution of different molecular weight PVA/PAA films, ^1H NMR spectra, FT-IR analysis, methylene blue adsorption test, and emission spectra of films coated with either FITC or RB. This material is available free of charge via the Internet at http://pubs.acs.org.

■ AUTHOR INFORMATION

Corresponding Author

*E-mail: recohen@mit.edu (R.E.C); rubner@mit.edu (M.F.R).

■ ACKNOWLEDGMENTS

We thank the Center for Materials Science and Engineering (CMSE), the Institute for Soldier Nanotechnologies (ISN), Prof. Michael Strano, and Prof. Bradley Olsen for use of their characterization facilities and Dr. Jonathan DeRocher for helpful discussions during the preparation of this manuscript and Mr. Jonathan Gilbert for assistance with the CLSM measurements. This work was partially supported by a Samsung Scholarship and in part by the MRSEC Program of the National Science Foundation under Award DMR-0819762.

■ REFERENCES

(1) Stockton, W. B.; Rubner, M. F. *Macromolecules* **1997**, *30*, 2717−2725.
(2) Podsiadlo, P.; Kaushik, A. K.; Arruda, E. M.; Waas, A. M.; Shim, B. S.; Xu, J.; Nandivada, H.; Pumplin, B. G.; Lahann, J.; Ramamoorthy, A.; Kotov, N. A. *Science* **2007**, *318*, 80−83.
(3) Huang, S.; Cen, X.; Peng, H.; Guo, S.; Wang, W.; Liu, T. *J. Phys. Chem. B* **2009**, *113*, 15225−15230.
(4) Manna, U.; Patil, S. *J. Phys. Chem. B* **2009**, *113*, 9137−9142.
(5) K, J.; Hsu, S. L.; McCarthy, T. J. *Langmuir* **2007**, *23*, 3260−3264.
(6) Chevallier, P.; Turgeon, S. p.; Sarra-Bournet, C.; Turcotte, R. l.; Laroche, G. t. *ACS Appl. Mater. Interfaces* **2011**, *3*, 750−758.
(7) Matsuda, M.; Shiratori, S. *Langmuir* **2011**, *27*, 4271−4277.
(8) Zdyrko, B.; Swaminatha Iyer, K.; Luzinov, I. *Polymer* **2006**, *47*, 272−279.
(9) Nogueira, G. M.; Banerjee, D.; Cohen, R. E.; Rubner, M. F. *Langmuir* **2011**, *27*, 7860−7867.
(10) Lee, D.; Rubner, M. F.; Cohen, R. E. *Nano Lett.* **2006**, *6*, 2305−2312.
(11) Yoo, D.; Shiratori, S. S.; Rubner, M. F. *Macromolecules* **1998**, *31*, 4309−4318.
(12) Bailey, F. E.; Callard, R. W.; Lundberg, R. D. *J. Polym. Sci., Part A* **1964**, *2*, 845−&.
(13) Kharlampieva, E.; Kozlovskaya, V.; Sukhishvili, S. A. *Adv. Mater.* **2009**, *21*, 3053−3065.
(14) Chen, Y.; Pang, Y.; Wu, J.; Su, Y.; Liu, J.; Wang, R.; Zhu, B.; Yao, Y.; Yan, D.; Zhu, X.; Chen, Q. *Langmuir* **2010**, *26*, 9011−9016.
(15) Jeon, S. H.; Ree, T. *J. Polym. Sci., Part A1* **1988**, *26*, 1419−1428.
(16) DeLongchamp, D. M.; Hammond, P. T. *Langmuir* **2004**, *20*, 5403−5411.
(17) Iyer, K. S.; Zdyrko, B.; Malz, H.; Pionteck, J.; Luzinov, I. *Macromolecules* **2003**, *36*, 6519−6526.
(18) Lutkenhaus, J. L.; Hrabak, K. D.; McEnnis, K.; Hammond, P. T. *J. Am. Chem. Soc.* **2005**, *127*, 17228−17234.
(19) Kharlampieva, E.; Sukhishvili, S. A. *Polym. Rev.* **2006**, *46*, 377−395.
(20) Sukhishvili, S. A.; Granick, S. *J. Am. Chem. Soc.* **2000**, *122*, 9550−9551.

(21) Kharlampieva, E.; Kozlovskaya, V.; Tyutina, J.; Sukhishvili, S. A. *Macromolecules* **2005**, *38*, 10523−10531.
(22) Sukhishvili, S. A.; Granick, S. *Macromolecules* **2001**, *35*, 301−310.
(23) Cho, J.; Caruso, F. *Macromolecules* **2003**, *36*, 2845−2851.
(24) Kharlampieva, E.; Sukhishvili, S. A. *Langmuir* **2004**, *20*, 10712−10717.
(25) Yang, S. Y.; Rubner, M. F. *J. Am. Chem. Soc.* **2002**, *124*, 2100−2101.
(26) Yang, S. Y.; Lee, D.; Cohen, R. E.; Rubner, M. F. *Langmuir* **2004**, *20*, 5978−5981.
(27) Jin, X.; Hsieh, Y.-L. *Polymer* **2005**, *46*, 5149−5160.
(28) Vázquez-Torres, H.; Cauich-Rodríguez, J. V.; Cruz-Ramos, C. A. *J. Appl. Polym. Sci.* **1993**, *50*, 777−792.
(29) Marten, F. L. In *Kirk-Othmer Encyclopedia of Chemical Technology*; John Wiley & Sons, Inc.: New York, 2002.
(30) Cui, R.; Huang, H.; Yin, Z.; Gao, D.; Zhu, J.-J. *Biosens. Bioelectron.* **2008**, *23*, 1666−1673.

Macromolecules

Article

pubs.acs.org/Macromolecules

On the Use of Bis(cyclopentadienyl)titanium(IV) Dichloride in Visible-Light-Induced Ring-Opening Photopolymerization

Mohamad-Ali Tehfe,[†] Jacques Lalevée,[†,*] Fabrice Morlet-Savary,[†,*] Bernadette Graff,[†] and Jean-Pierre Fouassier[‡]

[†]Institut de Science des Matériaux de Mulhouse, LRC CNRS 7228, ENSCMu-UHA

15, rue Jean Starcky, 68057 Mulhouse Cedex, France

[‡]University of Haute Alsace, 68057 Mulhouse Cedex, France

ABSTRACT: A titanocene derivative (bis(cyclopentadienyl)titanium(IV) dichloride $\mathbf{Cp_2TiCl_2}$), for visible light induced polymerization of cationic resins working through a free radical promoted process is presented. This new photoinitiating system is based on the $\mathbf{Cp_2TiCl_2}$ free radical initiator, a silane (tris(trimethylsilyl)silane: TTMSS), and an onium salt (diphenyliodonium hexafluorophosphate: Ph_2I^+) and appears suitable under long wavelength irradiation ($\lambda > 400$ nm). The polymerization reaction is highly efficient in aerated conditions (almost 100% conversion) and dramatically better than in laminate. The system works under exposure to a Xe lamp, a diode laser or a household LED bulb. The mechanisms are investigated by ESR experiments. The specific role of the generated free radicals is highlighted.

$Cp_2TiCl_2 \rightarrow CpTi^{\bullet}Cl_2 + Cp^{\bullet}$ (visible light)

↓ (silane, iodonium)

$R_3Si^{\bullet} + R_3Si^+$ ROP of epoxides

INTRODUCTION

Bis(cyclopentadienyl)titanium(IV) dichloride ($\mathbf{Cp_2TiC1_2}$) (Scheme 1) was prepared in 1954 by Wilkinson and Birmingham.[1] This titanium-based compound is one of the simplest, cheapest, and most commercially available transition metals; this product is also nontoxic and environmentally friendly. This latter property strongly contrasts with the high toxicity of many transition metals[2a−e] and has allowed the use of $\mathbf{Cp_2TiC1_2}$ in different medical applications,[2f,g] removal of toxic metals[2h] and prostheses.[2i] The present paper aims at introducing $\mathbf{Cp_2TiCl_2}$ in the photopolymerization area where it could be used for applications requiring safe conditions. Its performance will be compared to that of the known titanocene derivative bis(cyclopentadienyl)-bis[2,6-difluoro-3-(1-pyrryl)-phenyl]titanium (Irgacure 784).

Ring-opening photopolymerization is actually well-known in radiation curing.[3] However, a known drawback is related to the lack of absorption of cationic photoinitiators in the emission spectral range of classical UV lamps ($\lambda > 300$ nm). Photosensitization of these salts has long been recognized[4] and some recent works have shown an important progress for the development of photoinitiating systems that are able to efficiently start the reaction under visible lights (refs 5 and 6; see also a recent review in ref 3h). An elegant sensitization process is the free radical promoted cationic photopolymerization (FRPCP):[4a−f] the basic idea is to produce a radical (from a photoinitiating system) which in turn should be oxidized by the iodonium salt 1. In this process, the resulting cation (R^+) is considered as the polymerization initiating structure.[4a−h,5a,b,d,e,7−10] A suitable selection of the radical source obviously allows to tune the absorption in the near UV or/and visible wavelength range (e.g., using benzoin ethers, phosphine oxides, acridine diones, thiopyrylium salts, metallocenes, ...).[11]

$$R^{\bullet} + Ph_2I^+ \rightarrow R^+ + Ph^{\bullet} + PhI \quad (1)$$

Another drawback in FRPCP remains the oxygen sensitivity[5d,e,6a,b,12,13] of the system as the addition of radicals to oxygen generating hardly oxidable peroxyls is usually highly efficient, i.e., the rate constant for this reaction is usually close to the diffusion limit.[14] FRPCP is usually rather inhibited in aerated conditions.[5a,e,6a,12] Recently, it has been reported that the incorporation of silyl radicals in new photoinitiating systems can be highly worthwhile to overcome this oxygen inhibition.[6] This prompted us to investigate the efficiency of the $\mathbf{Cp_2TiCl_2}$/silane (TTMSS)/iodonium salt (Ph_2I^+) photoinitiating system in the FRPCP of an epoxide monomer (EPOX) upon long wavelength excitation (under visible LED bulbs, xenon lamp and laser diodes). The overall mechanism will be discussed using ESR and ESR spin trapping experiments (ESR-ST).

EXPERIMENTAL SECTION

The compounds investigated here are presented in Scheme 1 and used with the best purity available. Bis(cyclopentadienyl)titanium(IV) dichloride ($\mathbf{Cp_2TiCl_2}$), tris(trimethylsilyl)silane (TTMSS) and diphenyl iodonium hexafluorophosphate (Ph_2I^+) were obtained from Aldrich. The monomer (3,4-epoxycyclohexane)methyl 3,4-epoxycyclohexylcarboxylate (EPOX or UVACURE 1500) was obtained from Cytec.

i. Free Radical Promoted Cationic Polymerization Processes. The two- and three-component photoinitiating systems are based on $\mathbf{Cp_2TiCl_2}$/Ph_2I^+ (1%/2% w/w) and $\mathbf{Cp_2TiCl_2}$/TTMSS/Ph_2I^+ (1%/3%/2% w/w). The experimental conditions are given in the figure captions.

As in ref 6a, the laminated or aerated films (25 μm thick) deposited on a BaF_2 pellet were irradiated with the polychromatic light (incident

Received: October 14, 2011
Revised: November 17, 2011
Published: December 9, 2011

Scheme 1. Investigated Compounds

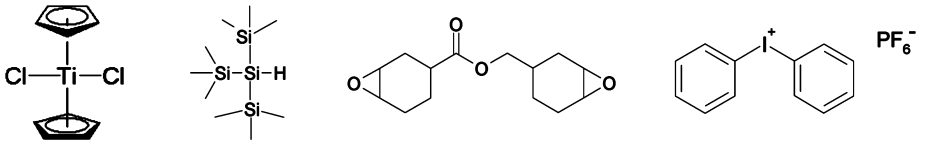

Cp_2TiCl_2 TTMSS EPOX Ph_2I^+

light intensity: $I_0 \approx 60$ mW cm^{-2}; 400 nm < λ < 800 nm) of a xenon lamp (Hamamatsu, L8253, 150 W). To ensure a visible light irradiation, a cut off filter has been used to select λ > 400 nm. The evolution of the epoxy group content is continuously followed by real time FTIR spectroscopy (Nexus 870, Nicolet) as reported in.[6a,15] The absorbance of the epoxy group was monitored at about 790 cm^{-1}. The Si−H conversion for TTMSS is followed at about 2050 cm^{-1}. Some experiments using a diode laser (473 nm; MGL-III-473-Bfioptilas; $I_0 \sim$ 100 mW/cm^2) and a blue LED bulb (I_0 = 15 mW/cm^2 at a distance of 4 cm) irradiation are also presented.

ii. ESR and ESR Spin Trapping (ESR-ST) Experiments. The ESR experiments were carried out here using a X-Band spectrometer (MS 200 from Magnettech-Berlin, Berlin, Germany) at room temperature. The radicals were generated through photolysis (xenon lamp) under argon or under air in an inert solvent (*tert*-butylbenzene). In ESR-ST, the generated radicals were trapped by phenyl-*N*-tbutylnitrone (PBN); this procedure is also described in detail in ref 16:

$$R^{\bullet} + PhCH{=}N^{+}(tBu)O^{-} \rightarrow PhCHR - N(tBu)O^{\bullet}$$

RESULTS AND DISCUSSION

1. Photopolymerization Experiments. Because of its absorption spectrum and molar extinction coefficients (Figure 1), Cp_2TiCl_2 allows a large and efficient covering of the emission spectrum of the blue LED bulb (λ_{max} = 462 nm), Xe lamp and the line of the high energy diode laser (473 nm).

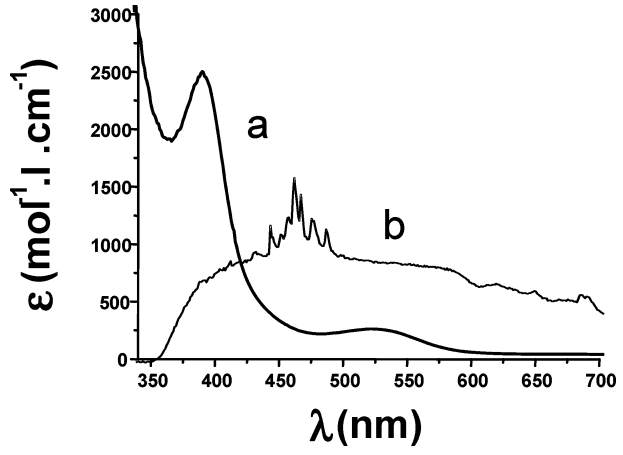

Figure 1. (a) UV−visible absorption spectra of Cp_2TiCl_2 in acetonitrile. (b) Emission spectrum of the Xe lamp.

Some examples of polymerization kinetics obtained with photoinitiating systems based on Cp_2TiCl_2 are given in Figures 2 and 3. For the TTMSS/Ph_2I^+ initiating system, no polymerization is observed: the presence of Cp_2TiCl_2 is requested for visible light absorption. The presence of TTMSS in the photoinitiating system is decisive as the starting system (Cp_2TiCl_2/Ph_2I^+) does not work (Figure 3 curve 1 vs curve 2): conversion close to 100% in presence of TTMSS vs

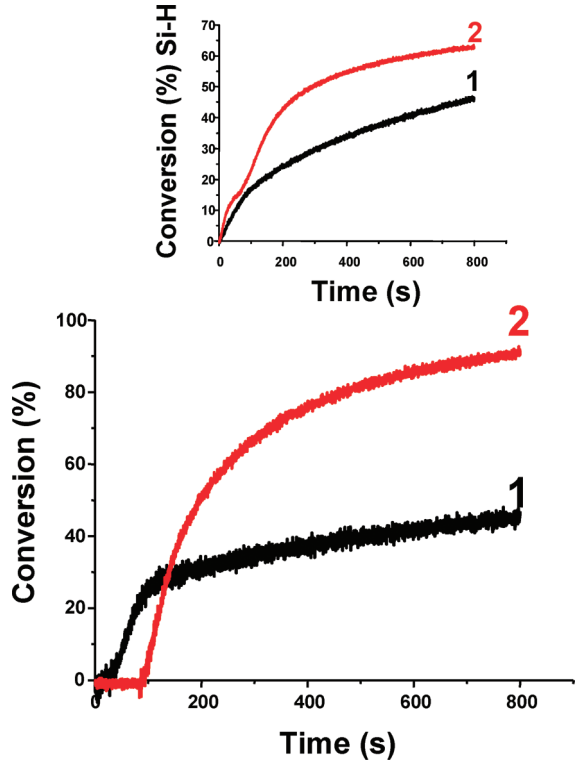

Figure 2. Polymerization profiles of (3,4-epoxycyclohexane)methyl 3,4-epoxycyclohexylcarboxylate (**EPOX**) upon a Xe lamp irradiation (λ > 390 nm) in the presence of bis(cyclopentadienyl)titanium(IV) dichloride (Cp_2TiCl_2)/tris(trimethylsilyl)silane (TTMSS)/diphenyl iodonium hexafluorophosphate (Ph_2I^+) (1%/3%/ 2% w/w) photoinitiating system. Inset: Conversion of the Si−H functions, in laminate (1) and under air (2).

<30% in absence of this compound. Therefore, the presence of TTMSS drastically improves both the polymerization rate and the final conversion of EPOX upon the Xe lamp exposure under air. Remarkably, a final conversion very close to 100% is found for the Cp_2TiCl_2/TTMSS/Ph_2I^+ three-component initiating system; i.e., such a complete conversion can hardly be obtained with conventional systems.[11a]

In Figure 2, it can be noted that the polymerization is dramatically better under air (curve 2; final conversion ∼100%) than in laminate (curve 1; final conversion ∼50%): this is an unusual behavior. The polymerization rates using this Cp_2TiCl_2/TTMSS/Ph_2I^+ system are also higher under air than in laminate. The Si−H conversion is also more important under air: this demonstrates that the Si−H conversion is directly related to the overall efficiency of the system. For diode laser irradiation (473 nm), an excellent polymerization profile is also obtained for the three-component system.

A similar behavior is found with a low light intensity when using a blue LED bulb irradiation: in the presence of Cp_2TiCl_2/Ph_2I^+, no polymerization is observed. Interestingly,

dx.doi.org/10.1021/ma202307x | *Macromolecules* 2012, 45, 356−361

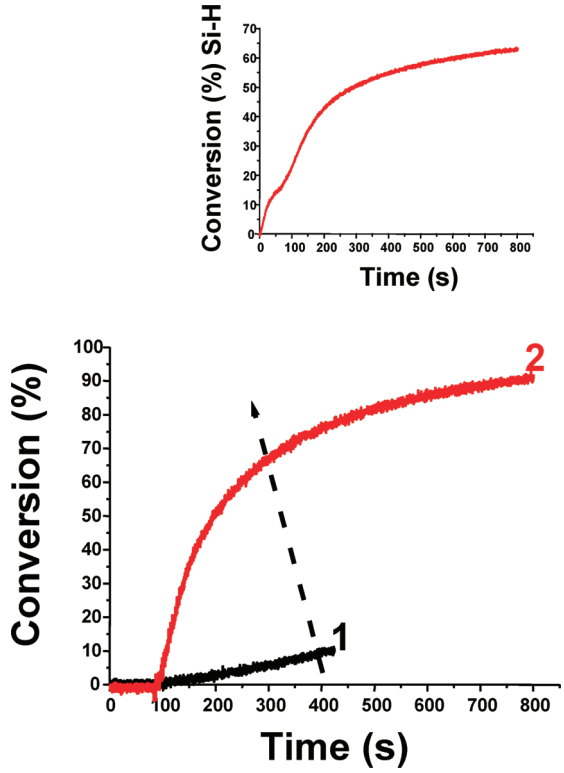

Figure 3. Compared polymerization profiles of (3,4-epoxycyclohexane)methyl 3,4-epoxycyclohexylcarboxylate (**EPOX**) upon a Xe lamp irradiation (λ > 390 nm) in the presence of two photoinitiating systems **under air**: (1) bis(cyclopentadienyl)titanium-(IV) dichloride (**Cp_2TiCl_2**)/diphenyl iodonium hexafluorophosphate (Ph_2I^+) (1%/2% w/w); (2) bis(cyclopentadienyl)titanium(IV) dichloride (**Cp_2TiCl_2**)/tris(trimethylsilyl)silane (TTMSS)/ diphenyl iodonium hexafluorophosphate (Ph_2I^+) (1%/3%/ 2% w/w). Inset: conversion of the Si−H content in case 2.

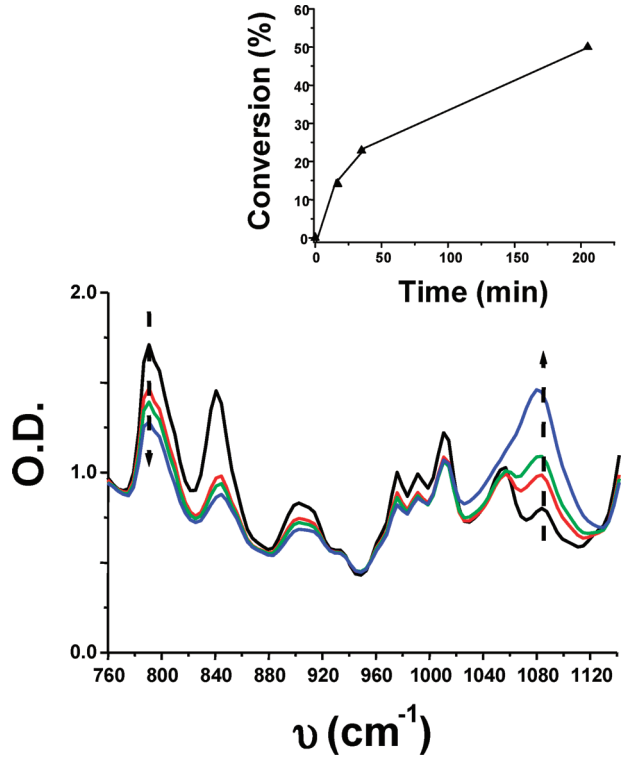

Figure 4. IR spectra recorded during the photopolymerization of (3,4-epoxycyclohexane)methyl 3,4-epoxycyclohexylcarboxylate under a blue LED bulb irradiation in the presence of bis(cyclopentadienyl)-titanium(IV) dichloride (**Cp_2TiCl_2**)/ tris(trimethylsilyl)silane (TTMSS)/ diphenyl iodonium hexafluorophosphate (Ph_2I^+) (1%/ 3%/ 2% w/w). Inset: monomer conversion vs time profile, under air.

the **Cp_2TiCl_2**/TTMSS/Ph_2I^+ system leads to a good polymerization (Figure 4); i.e., a conversion >55% is reached within 180 min of irradiation, and a completely tack free coating is formed after 20 h of irradiation. The formed polyether network is easily characterized by its absorption band at 1080 cm^{-1}.

For this new proposed system, a complete conversion can be achieved (>95%), this was not the case for a previous system based on a bis(cyclopentadienyl)-bis[2,6-difluoro-3-(1-pyrryl)-phenyl]titanium with about 60% of final conversion.[6c]

2. Chemical Mechanisms. The mechanism for the photolysis of **Cp_2TiCl_2** has been investigated in few works. Photoproduct analysis have been reported in.[17] The cyclopentadienyl derivatives of a variety of transition metals have been shown to undergo a homolysis of the Cp-metal bond under visible lights:[17] this reaction has been exploited as a source of substituted cyclopentadienyl radicals ($Cp^\bullet$) and/or metal-centered radicals in ESR studies.[17e−h]

As expected from,[17b] different free radicals are observed here by ESR spectroscopy during the photolysis of **Cp_2TiCl_2** under argon (Figures 5A and 5C): two titanium radicals (singlet spectra at g ∼ 1.97 and g ∼ 1.98) and $Cp^\bullet$ (Figure 5A). For ESR-spin trapping experiments, the PBN spin adduct of $Cp^\bullet$ is characterized by a_H = 3.1 G; a_N = 14.6 G (Figure 5C). The main titanium radical is $CpTi^\bullet Cl_2$ in agreement with Scheme 2. The second $Ti^\bullet$ species was not clearly ascribed.[17b] $CpTi^\bullet Cl_2$ is a rather long-lived species (>10 s under argon). From the calculated singly occuped molecular orbital (SOMO), it can be observed that this radical is clearly centered on the titanium (spin density =1.09; spin density for the other atoms <0.01) (Figure 6). The SOMO clearly corresponds to a d orbital of Ti. In aerated conditions, the singlet ESR spectrum observed at g ∼ 2.0129 (Figure 5B) is ascribed to $CpCl_2Ti{-}OO^\bullet$ in agreement with[17] thereby outlining the reactivity of $CpTi^\bullet Cl_2$ toward O_2. This is also confirmed by a highly exothermic process for this $CpTi^\bullet Cl_2/O_2$ interaction (−129 kJ/mol at UB3LYP/LANL2DZ level): $CpTi^\bullet Cl_2$ is highly efficient to consume oxygen in the polymer media.

Considering the very low efficiency of **Cp_2TiCl_2**/Ph_2I^+ to initiate the ring-opening photopolymerization of EPOX, it can be assumed that $CpTi^\bullet Cl_2$ and $Cp^\bullet$ (i) are not efficiently oxidize by Ph_2I^+ or/and (ii) the resulting cations are not active structures in the cationic photoinitiation process.

In the presence of TTMSS, $Cp^\bullet$ can rapidly react by hydrogen abstraction with the silane and generates a silyl radical (2).[6c] Titanium centered radicals are not affected by the presence of TTMSS.[6c] The tris(trimethylsilyl)silyl radical is easily oxidized by Ph_2I^+ (3) with a rate constant of 2.6 × 10^6 M^{-1} s^{-1},[6a] leading to the formation of a silylium cation which can initiate the cationic polymerization (4) as noted in many other systems.[6] The formed $Ph^\bullet$ (3) should also react with TTMSS to form a new silyl radical (5). This latter process contributes to the observed high Si−H conversion (see again Figure 3).

$$Cp^\bullet + (TMS)_3Si - H \rightarrow Cp - H + (TMS)_3Si^\bullet \quad (2)$$

$$(TMS)_3Si^\bullet + Ph_2I^+ \rightarrow (TMS)_3Si^+ + Ph^\bullet + PhI \quad (3)$$

dx.doi.org/10.1021/ma202307x | *Macromolecules* 2012, 45, 356−361

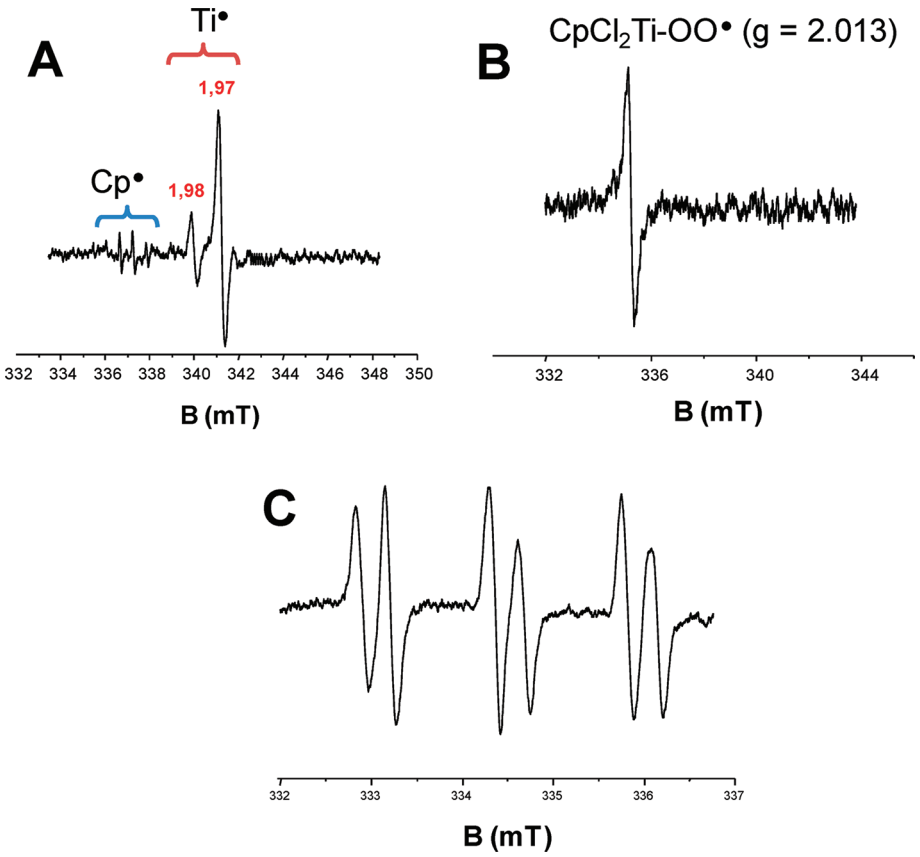

Figure 5. (A) ESR spectra obtained during irradiation (under argon) of bis(cyclopentadienyl)titanium(IV) dichloride (**Cp_2TiCl_2**) in *tert*-butylbenzene under visible light (irradiation with a Xenon Lamp; $\lambda > 400$ nm). (B) ESR spectra obtained during irradiation (under air) of bis(cyclopentadienyl)titanium(IV) dichloride (**Cp_2TiCl_2**) in *tert*-butylbenzene under visible light (irradiation with a Xe Lamp; $\lambda > 400$ nm). (C) ESR Spin Trapping spectrum obtained after irradiation of bis(cyclopentadienyl)titanium(IV) dichloride (**Cp_2TiCl_2**) in *tert*-butylbenzene under visible light (under argon) (Xe Lamp exposure; PBN 0.05 M; $\lambda > 400$ nm). See text.

Scheme 2

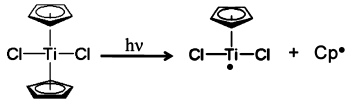

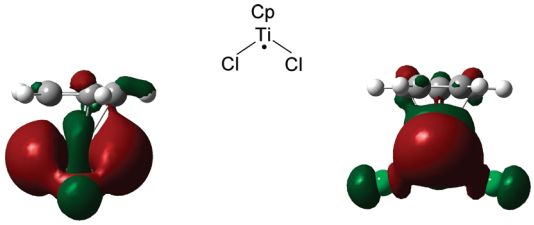

Figure 6. SOMO for $CpTi^{\bullet}Cl_2$ for two different views (UB3LYP/LANL2DZ geometry optimization).

$$(TMS)_3Si^{+} + M \rightarrow \text{polymer} \quad (4)$$

$$Ph^{\bullet} + (TMS)_3Si - H \rightarrow Ph - H + (TMS)_3Si^{\bullet} \quad (5)$$

In aerated media, the different radicals generated ($Cp^{\bullet}$, $CpTi^{\bullet}Cl_2$, and $Ph^{\bullet}$) are easily converted into peroxyl radicals (see also above for the $CpTi^{\bullet}Cl_2/O_2$ interaction) (6) and then into silyl radicals by hydrogen abstraction with TTMSS (7): this is a general behavior of the peroxyl/silane couple.[18] These reactions explain the higher Si–H conversion in aerated media compared to laminated conditions. The fast peroxidation reaction avoids the recombination processes (which are much slower for peroxyl radicals)[19] and increases the global free radical yield: this is in agreement with the better behavior observed when using the three-component system in photopolymerization in aerated conditions.

$$Cp^{\bullet}, CpTi^{\bullet}Cl_2, Ph^{\bullet} + O_2 \rightarrow CpOO^{\bullet}, CpTiCl_2OO^{\bullet}, PhOO^{\bullet} \quad (6)$$

$$CpOO^{\bullet}, CpTiCl_2OO^{\bullet}, PhOO^{\bullet} + (TMS)_3Si{-}H \rightarrow CpOOH, PhOOH, CpTiCl_2OOH + (TMS)_3Si^{\bullet} \quad (7)$$

The specific behavior of the silyl radicals under air has been investigated in different works:[6a,12] these structures can efficiently generate siliylium cations without oxygen inhibition. A complete reaction scheme was given in ref 11a.

The formation of free radicals in Scheme 2 is also in full agreement with the photoinitiator ability of **Cp_2TiCl_2** in free radical polymerization FRP of trimethylolpropane triacrylate TMPTA (Figure 7). $Cp^{\bullet}$ and $CpTi^{\bullet}Cl_2$ can be considered as interesting potential initiating radicals in FRP.

dx.doi.org/10.1021/ma202307x | *Macromolecules* 2012, 45, 356–361

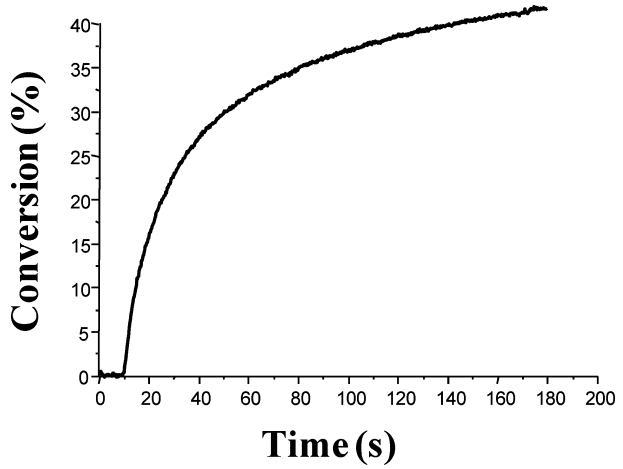

Figure 7. Conversion vs time curves for the photopolymerization of trimethylolpropane triacrylate (TMPTA) in laminate) using Cp_2TiCl_2 (1% w/w). Sample thickness = 20 μm; Xe lamp (λ > 390 nm) irradiation.

CONCLUSION

Compared to previous systems proposed for FRPCP, the proposed Cp_2TiCl_2/TTMSS/diphenyl iodonium salt system exhibits an excellent performance in aerated media and a remarkable final conversion close to 100%. This compound is also nontoxic and can be used for medical applications. Other monomers (limonene dioxide, epoxidized soybean oil) can also be polymerized by the presented approach. It also opens up a way to carry out cationic photopolymerization under air and upon visible wavelengths, e.g., for laser imaging area or formation of holographic optical elements (in this last case, the lower shrinkage of the cationically cured polymers could be an advantage compared to free radical polymerization reactions).

AUTHOR INFORMATION

Corresponding Author

*E-mail: (J.L.) j.lalevee@uha.fr; (F.M.-S.) fabrice.morlet-savary@uha.fr.

ACKNOWLEDGMENTS

J.L. thanks the Institut Universitaire de France; all the authors thank the French Agency for Research ANR (ANR-BLAN-0802; ANR SILICIUM).

REFERENCES

(1) Wilkinson, G.; Birmingham, J. M. *J. Am. Chem. Soc.* **1954**, *76*, 4281−4286.

(2) (a) England, M. W.; Turner, J. E.; Hingerty, B. E.; Jacobson, K. B. *Health Phys.* **1989**, *57*, 115−119. (b) Pandey, A. K.; Pandey, S. D.; Misra, V. *Ecotoxicol. EnViron. Saf.* **2002**, *52*, 92−96. (c) Wah, K.; Chow, K. L. *Aquat. Toxicol.* **2002**, *61*, 53−64. (d) Petrauskienè, L. *Environ. Toxicol.* **2004**, *19*, 336−341. (e) Montvydienè, D.; Marèiulionienè, D. *Environ. Toxicol.* **2004**, *19*, 351−358. (f) Bermudez, E.; Mangum, J. B.; Asghariam, B.; Wong, B. A.; Reverdy, E. E.; Janszen, D. B.; Hext, P. M.; Warheit, D. B.; Everitt, J. I. *Toxicol. Sci.* **2002**, *70*, 86−97. (g) Lademann, J.; Weigmann, H.-J.; Schafer, H.; Muller, G.; Sterry, W. *Skin Pharmacol. Appl.* **2000**, *13*, 258−264. (h) Clearfield, A.; Bortun, A. I.; Khainakov, S. A.; Bortun., L. N.; Strelko, V. V.; Khryaschevskii, V. N. *Waste Manage.* **1998**, *18*, 203−210. (i) Niinomi, M. *Sci. Technol. AdV. Mater.* **2003**, *4*, 445−454.

(3) (a) Crivello, J. V. *Photoinitiators for Free Radical, Cationic and Anionic Photopolymerization*, 2nd ed.; Bradley, G., Ed.; New York, 1998; (b) Crivello, J. V. *Ring-Opening Polymerization*; Brunelle, D. J., Ed.; Hanser: Munich, Germany, , 1993; (c) Fouassier, J. P. *Photoinitiation, Photopolymerization and Photocuring: Fundamental and Applications*; Hanser Publishers: New York, 1995; (d) *Photochemistry and UV Curing*, Fouassier, J. P., Ed., Research Signpost: Trivandrum, India, 2006; (e) *Photoinitiated polymerization*; Belfield, K. D., Crivello, J. V., Eds., ASC Symposium Series 847; American Chemical Society: Washington, DC, 2003; (f) *Radiation Curing in Polymer Science and Technology*; Fouassier, J. P., Rabek, J. F., Eds., Elsevier Science Publishers Ltd.: London, 1993; (g) *Basics of Photopolymerization Reactions*; Fouassier, J. P., Allonas, X., Eds., Research Signpost: Trivandrum, India, 2010; (h) Fouassier, J. P.; Lalevée, J. *Photoinitiators for Polymer Synthesis: Scope, Reactivity and Efficiency*; Wiley-VCH: New York, in press

(4) (a) Ledwith, A. *Polymer* **1978**, *19*, 1217−1219. (b) Crivello, J. V.; Lam, J. H. W. *J. Polym. Sci., Polym. Chem. Ed.* **1979**, *17*, 1059−1065. (c) Crivello, J. V.; Lee, J. L. *Macromolecules* **1981**, *14*, 1141−1147. (d) Baumann, H.; Timpe, H. J. *Z. Chem.* **1984**, *24*, 18−19. (e) Yagci, Y.; Schnabel, W. *Makromol. Chem. Rapid Commun.* **1987**, *8*, 209−213. (f) Yagci, Y.; Pappas, S. P.; Schnabel, W. *Z. Naturforsch.* **1987**, *42A*, 1425−1428. (g) Saeva, F. D.; Breslin, D. T.; Martic, P. A. *J. Am. Chem. Soc.* **1989**, *111*, 1328−1330. (h) Bi, Y.; Neckers, D. C. *Macromolecules* **1994**, *27*, 3683−3693. (i) Allen, N. S. *J. Photochem. Photobiol. A: Chem.* **1996**, *100*, 101−111. (j) Yagci, Y.; Hepuzer, Y. *Macromolecules* **1999**, *32*, 6367−6370.

(5) (a) Crivello, J. V.; Sangermano, M. *J. Polym. Sci., Part A: Polym. Chem.* **2001**, *39*, 343−356. (b) Dursun, C.; Degirmenci, M.; Yagci, Y.; Jockusch, S.; Turro, N. J. *Polymer* **2003**, *44*, 7389−7396. (c) Crivello, J. V.; Bulut, U. *J. Polym. Sci., Part A: Polym. Chem.* **2005**, *43*, 5217−5321. (d) Crivello, J. V. *J. Polym. Sci., Part A: Polym. Chem.* **2009**, *47*, 866−875. (e) Crivello, J. V. *J. Macromol. Sci. Part A* **2009**, *46*, 474−483. (f) Bulut, U.; Gunbas, G. E.; Topare, L. *J. Polym. Sci., Part A: Polym. Chem.* **2009**, *48*, 209−213. (g) Aydogan, B.; Gunbas, G. E.; Durmus, A.; Toppare, L.; Yagci, Y. *Macromolecules* **2010**, *43*, 101−106.

(6) (a) Lalevée, J.; El-Roz, M.; Allonas, X.; Fouassier, J. P. *J. Polym. Sci., Part A: Polym. Chem.* **2008**, *46*, 2008−2014. (b) Lalevée, J.; Dirani, A.; El-Roz, M.; Allonas, X.; Fouassier, J. P. *J. Polym. Sci., Part A: Polym. Chem.* **2008**, *46*, 3042−3047. (c) Tehfe, M. A.; Lalevée, J.; Allonas, X.; Fouassier, J. P. *Macromolecules* **2009**, *42*, 8669−8674. (d) Tehfe, M. A.; Lalevée, J.; Gigmes, D.; Fouassier, J. P. *Macromolecules* **2010**, *43*, 1364−1370. (e) Souane, R.; Tehfe, M. A.; Lalevée, J.; Gigmes, D.; Fouassier, J. P. *Macromol. Chem. Phys.* **2010**, *211*, 1441−1445. (f) Tehfe, M. A.; Lalevée, J.; Gigmes, D.; Fouassier, J. P. *J. Polym. Sci. Part A: Polym. Chem* **2010**, *48*, 1830−1837.

(7) (a) Yagci, Y.; Ledwith, A. *J. Polym. Sci., Part A: Polym. Chem.* **1988**, *26*, 1911−1918. (b) Baumann, H.; Timpe, H. J. *Z. Chem.* **1984**, *24*, 18−19. (c) Yagci, Y.; Kminek, I.; Schnabel, W. *Polymer* **1993**, *34*, 426−428.

(8) (a) Arsu, N.; Hizai, G.; Yagci, Y. *Macromol. Rep.* **1995**, 1257−1262. (b) Yagci, Y.; Reetz, I. *Prog. Polym. Sci.* **1998**, *23*, 1485−1538.

(9) Durmaz, Y. Y.; Moszner, N.; Yagci, Y. *Macromolecules* **2008**, *41*, 6714−6718.

(10) Degirmenci, M.; Onen, A.; Yagci, Y.; Pappas, S. P. *Polym. Bull.* **2001**, *46*, 443−449.

(11) (a) Lalevée, J.; Tehfe, M. A.; Morlet-Savary, F.; Graff, B.; Allonas, X.; Fouassier, J. P. *Prog. Org. Coatings* **2011**, *70*, 23−31. (b) Tehfe, M. A.; Lalevée, J.; Morlet-Savary, F.; Blanchard, N.; Fries, C.; Graff, B.; Allonas, X.; Louërat, F.; Fouassier, J. P. *Eur. Polym. J.* **2010**, *46*, 2138−2144.

(12) Lalevée, J.; Blanchard, N.; El-Roz, M.; Graff, B.; Allonas, X.; Fouassier, J. P. *Macromolecules* **2008**, *41*, 4180−4186.

(13) Lalevée, J.; Allonas, X.; Fouassier, J. P. *Chem. Phys. Lett.* **2009**, *469*, 298−303.

(14) Maillard, B.; Ingold, K. U.; Scaiano, J. C. *J. Am. Chem. Soc.* **1983**, *105*, 5095−5099.

(15) (a) Lalevée, J.; Allonas, X.; Jradi, S.; Fouassier, J. P. *Macromolecules* **2006**, *39*, 1872−1879. (b) Lalevée, J.; Zadoina, L.;

Allonas, X.; Fouassier, J. P. *J. Polym. Sci. Part A: Chem* **2007**, *45*, 2494−2502.
(16) (a) Tordo, P. *Spin-trapping: recent developments and applications*; Atherton, N. M., Davies, M. J., Gilbert, B. C., Eds.; Electron Spin Resonance 16, The Royal Society Of Chemistry: Cambridge, U.K.,1998. (b) Criqui, A.; Lalevée, J.; Allonas, X.; Fouassier, J. P. *Macromol. Chem. Phys.* **2008**, *209*, 2223−2231.
(17) (a) Roloff, A.; Meier, K.; Riediker, M. *Pure Appl. Chem.* **1986**, *58*, 1267−1272. (b) Davies, G. A.; Hawari, A.-A. J. *J. Organomet. Chem.* **1983**, *250*, 247−256. (c) Vitz, E.; Brubaker, C. H. *J. Organomet. Chem.* **1974**, *82*, C16−C27. (d) Vita, E.; Wagner, P. J.; Brubaker, C. H. *J. Organomet. Chem.* **1976**, *104*, C33−C40. (e) Barker, P. J.; Davies, A. G.; Tse, M.-W. *J. Chem. Soc., Perkin Trans. II* **1980**, 941−946. (f) Barker, P. J.; Davies, A. G.; Hawari, J-A.-A.; Tse, M.-W. *J. Chem. Soc., Perkin Trans. II* **1980**, 1488−1492. (g) Davies, A. G.; Hawari, J.A.-A. *J. Organomet. Chem.* **1980**, 201−221. (h) Davies, A. G.; Gaffney, C.; Harrison, P. G.; Hawari, J.A.-A. *J. Chem. Soc., Perkin Trans. II* **1982**, 631−637.
(18) Lalevée, J.; Blanchard, N.; Graff, B.; Allonas, X.; Fouassier, J. P. *J. Organomet. Chem.* **2008**, *693*, 3643−3649.
(19) Alfassi, Z. *Peroxyl Radicals*: Wiley-VCH: Chichester, U.K., 1997.

Macromolecules

Article

pubs.acs.org/Macromolecules

Torsional Entropy at the Origin of the Reversible Temperature-Induced Phase Transition of Cellulose

Pan Chen, Yoshiharu Nishiyama,* and Karim Mazeau

Centre de Recherches sur les Macromolécules Végétales (CERMAV-CNRS), BP 53, F-38041 Grenoble cedex 9, France

Supporting Information

ABSTRACT: The temperature-induced phase transition of native cellulose was studied by X-ray diffraction and molecular dynamics (MD) simulation. Upon heating, this transition is characterized by an important expansion of the distance between the planes of glucopyranose rings, which is observed both experimentally and in MD. Computed trajectories suggest that this expansion is caused by a rotation of the exocyclic hydroxymethyl groups. Upon cooling, the phase transition, experimentally known as reversible, was found to be irreversible in the MD simulation when using current GROMOS 53a6 force field parameters. By varying one of these, related to the potential energy of the hydroxymethyl conformers, a reversible phase transition could be observed *in silico*. From the linear dependence of the transition temperature on the dihedral energy of the different conformers, the entropy change due to the phase transition could be estimated to be about 26 JK^{-1} mol^{-1}. This value essentially reflects the additive contribution of the torsional entropies of the exocyclic moieties, as other conformational parameters appeared to have little effect on the phase transition.

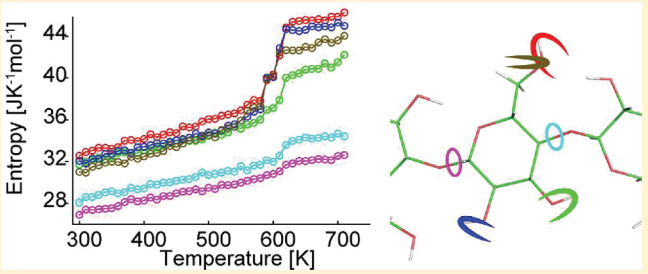

1. INTRODUCTION

Cellulose, like many other polysaccharides, has limited conformational freedom, and thus predicting the gross structure of its crystal should appear straightforward. Indeed, its repeat unit, namely the β-glucopyranosyl ring, rarely departs from the $^4C_1$ chair conformation. In addition, the two bonds involving the bridge oxygen linking subsequent units have some degree of torsional freedom, but one particular pair of torsion angles giving an extended chain trajectory is much favored over the other regions of conformational space, at least for condensed-phase structures. In opposition to this rigidity, each residue has a degree of torsional freedom determining the orientation of the exocyclic hydroxymethyl group, a feature which is therefore susceptible to modify the overall sugar molecular shape. This group can adopt three stable staggered orientations, named *tg*, *gt*, and *gg*, depending on the position of the O6 atom, whether it is in trans (*t*) or gauche (*g*), with respect to the ring oxygen O5 and carbon C4.[1]

The conformational preference of the exocyclic hydroxymethyl group of sugar has been studied for many decades using crystal structure determination,[2] *J*-coupling in solution NMR,[3−6] and theoretical calculation based on quantum mechanics.[7−9] Some recent studies involve infrared spectroscopy on isolated molecules in vacuum[10] and neutron wide-angle scattering analysis of aqueous solutions.[11] It is generally accepted that the *tg* conformation is of very little importance in solution for both glucose and its analogues: in aqueous solution, *gg* and *gt* conformations are dominant, but the *gg* case is slightly favored over that of the *gt*.[3] Finally, the *tg* conformation can seldom be seen in crystal structures that contain glucosyl residues. Yet, the energy difference among the different conformations as well as the origin of stabilization of one conformer over another is still controversial.

Native cellulose is one of the rare glucosyl-based structures that have the *tg* conformation. This conformation was first proposed by linked atom structure refinement using X-ray fiber diffraction data[12] and later confirmed by empirical relationship between ^{13}C NMR chemical shift of C6 and its conformation.[13] More recently, the oxygen atom O6 in the *tg* position was directly visualized in Fourier omit map using high-resolution X-ray diffraction data for both allomorphs of native cellulose.[14,15]

Upon heating at about 500 K, crystalline cellulose undergoes a phase transition, yielding the so-called "high temperature phase",[16−18] identified by an expansion of the unit cell volume that increases discontinuously by a few percent when this temperature is reached. The modeling of this transition by molecular dynamics (MD) has been investigated using different force fields.[19,20] These MD simulations were able to reproduce the unit cell expansion during the phase transition and showed that upon heating the hydroxymethyl groups of crystalline cellulose shifted from the *tg* conformation toward the *gt* and *gg* situations. Experimentally, the high temperature phase reverts to its initial low temperature counterpart upon cooling. This can be deduced from the comparison of the X-ray diagrams of cellulose before and after annealing, which shows that initial unit cell is restored,[14] while ^{13}C NMR data[22] together with

Received: August 26, 2011
Revised: December 9, 2011
Published: December 22, 2011

crystal structure refinement[14] indicate that the *tg* conformation of the hydroxymethyl groups is also recovered in the cooled specimens. In the MD calculations, however, the sample recovery was not obtained upon cooling, as mentioned briefly in the recent paper by Zhang et al.[20] based on the use of the GLYCAM force field. When using the GROMOS 53a6 force field, we also noticed that the hydroxymethyl group of the cooled cellulose structure did not go back to the experimentally determined *tg* conformation. For cellulose, the tendency of favoring the calculated *gt* and *gg* conformations instead of the experimental *tg* is also seen in several room temperature MD studies[23] as well as in structure predictions studies.[24]

In this paper, we have systematically varied the relative energy of the three staggered positions of the exocyclic hydroxymethyl group in order to reproduce the experimentally observed reversible phase transition and to obtain insights into its molecular origin.

2. EXPERIMENTAL SECTION

X-ray fiber diffraction patterns of cellulose during a heating and cooling cycle were measured at D2AM beamline of the European Synchrotron Radiation Facilities. An oriented fiber of tunicin microcrystals embedded in PVA[25] was used as sample, and the experimental setup was as described in a previous paper,[26] except that the sample environment was helium gas. The heating rate was 8 K/min up to 473 and 4 K/min up to 573 K while the cooling rate was 8 K/min down to 500 and 4 K/min below. A diffraction image was recorded every 30 s with exposure times of 10 s.

3. SIMULATION PROCEDURE

The GROMACS software package,[27] version 4.5, was used for molecular dynamics simulation and analysis. A united atom force field, GROMOS 53a6[28] (FFG53a6), was used, if not specified otherwise. In this force field, CH and CH_2 groups are treated as single united particles. Molecular dynamics calculations were based on the canonical NPT ensemble (constant number of particles, pressure and temperature). The equations of motion were solved using the standard leapfrog algorithm[29] using time steps of 1 fs. The cutoff distance for short-range Coulomb interaction and Lennard-Jones nonboned interactions were set to 0.9 nm. The long-range dispersion forces were corrected for energy and pressure. Particle mesh Ewald summation[30] was used for the long-range Coulomb interactions. Pressure of the system was regulated using the Berendsen algorithm,[31] and temperature was regulated by the velocity rescaling algorithm.[32] All bond lengths were constrained using the LINCS algorithm,[33] and molecular dynamics frames were saved every picosecond. Molecular trajectories were visualized using VMD software.[34]

3.1. Construction of the Initial Structures. Cellulose Iβ was considered in this study, and its coordinates deduced from X-ray diffraction data[14] were used as a starting model. Its basic crystal features are represented in Figure 1.

To model the bulk properties, the infinite crystal approach was chosen to avoid the surface effects characteristics of the finite crystal models immersed in aqueous solution. The asymmetric units in the cells were duplicated to construct P_1 supercells having an almost cubic shape with about 4 nm in each dimension. Each individual cellulose chain consisted of 8 glucosyl units and was covalently bonded to its own periodic image to simulate infinite chain length. Two types of supercells were generated, one with the periodic boundaries *xz*, *yz*, and *xy* parallel to (100), (010), and (001) planes and the other with the boundaries parallel to (110), (1$\bar{1}$0), and (001) planes. As both gave similar results, the systematic studies were performed with the second supercell.

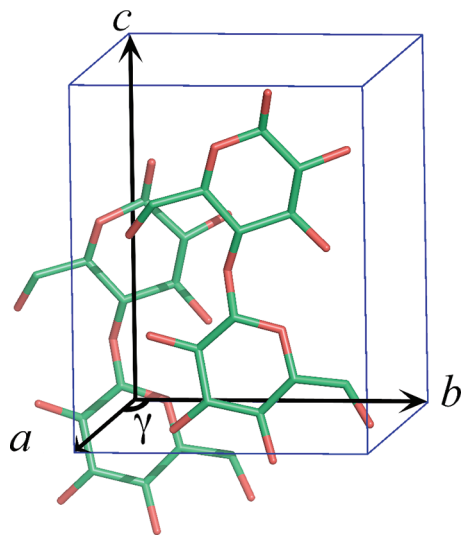

Figure 1. Unit cell of cellulose I$_\beta$.

The structures were then optimized by the steepest-descent method followed by the conjugate gradient method. The convergence criterion to stop minimization was a maximum force of 1 kJ mol^{-1} Å^{-1}. The structures were then equilibrated at 300 K and 1 atm, allowing their periodic boxes to deform in size and shape, involving six degrees of freedom. The compressibility (diagonal element of compliance tensor) of the box was estimated by following the box deformation at various pressure conditions as 2.5×10^{-5}, 2.2×10^{-5}, 7.9×10^{-7}, 1.2×10^{-5}, 4.2×10^{-5}, 4.4×10^{-5} (bar^{-1}) for the *xx*, *yy*, *zz*, *xy*, *yz*, *zx* components and used for the subsequent calculation.

3.2. Simulated Annealing and Structural Characteristics. The system was then heated in a stepwise manner typically with 10 K increments followed by a short equilibration of 100 ps. Heating and cooling rates were varied from 100 to 1 K/ns. Total duration of the annealing process was typically of the order of 100 ns; the slow cooling was only applied for temperature ranges where the transition was expected.

The unit cell parameters were calculated from the total box size at each temperature. Conformational parameters such as the puckering parameters (Q,Θ,Φ) of the pyranose rings,[35] the torsion angles φ and ψ[36] across the glycosidic linkages, and the torsion angle ω[36] describing the orientation of the exocyclic hydroxymethyl groups were calculated for all residues from the coordinates in the trajectory file.

4. RESULTS AND DISCUSSION

Figure 2 shows the experimental *a*-axis parameter determined from the peak positions of the 1$\bar{1}$0, 110, and 200 reflections measured on oriented tunicin fiber in a helium atmosphere as a function of temperature during heating and cooling. There is a sharp transition at 500 K during the heating with a sudden increase in the *a*-axis as already observed.[17] In this study we also followed the cooling, where a similar transition, although broader, could be observed as well at a slightly lower temperature. The transition was essentially reversible. The temperature difference at which the transition occurs between cooling and heating is probably due to the loss in crystallinity associated with the phase transition as the peak widths were

dx.doi.org/10.1021/ma201954s | *Macromolecules* 2012, 45, 362–368

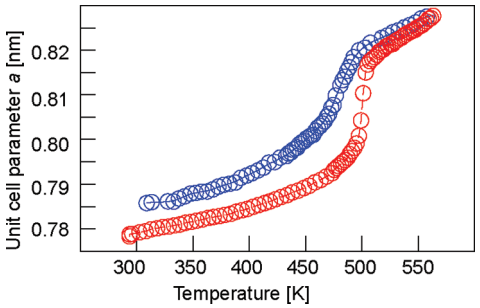

Figure 2. Experimental variation of the crystal cell parameter *a* during heating (red) and cooling (blue).

slightly larger after the annealing in a helium environment. Indeed, the phase transition during heating of a cellulose sample with thinner crystallite occurs at lower temperature and is less abrupt.[36]

4.1. Simulated Annealing with the Standard Force-Field Parameters. The variation of the unit cell parameters of the simulated crystal as a function of temperature during the heating phase is shown in Figure 3. Already at low temperature,

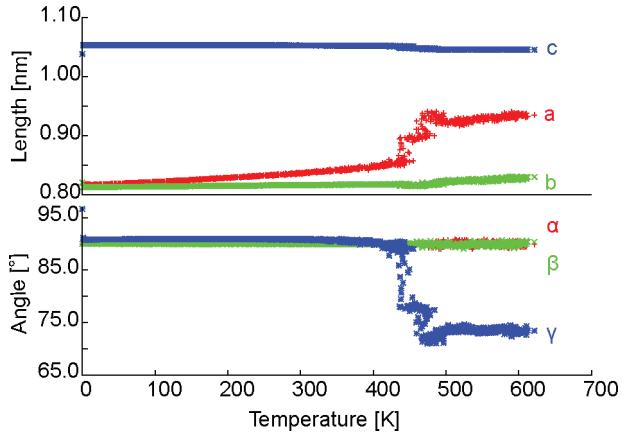

Figure 3. Simulated unit cell parameters as a function of temperature during heating.

the absolute value of the *a*-axis was significantly larger than the experimental value and the γ angle was much closer to rectangular (γ = 90.91°). These tendencies are similar to the results already reported by several authors.[19−21] The discrepancies between the simulated and experimental parameters will be treated in a separate paper.

Figure 4 shows the histogram of the ω torsion angle as a function of temperature during heating. At room temperature, the individual chains adopt the expected conformation (Figure S1). Importantly, the ω torsion angle is narrowly distributed at around 180° (Figure 4), meaning that the hydroxymethyl groups remain close to the ideal *tg* conformation. The spatial organization of the chains is also consistent with the experimental data[14] and earlier modeling.[19]

As the temperature increases, a phase transition occurs; it is characterized by a departure from linearity of the thermal expansion in the *a*-axis (Figure 3) and by a rotation of the hydroxymethyl groups (Figure 4). This aspect of transition during heating agrees with the results of other groups.[19−21] Note that the *gg* orientation appears prior to the *gt* counterpart. The phase transition occurs at 450 K, which is reasonably close to the experimental measure of about 500 K. The relative

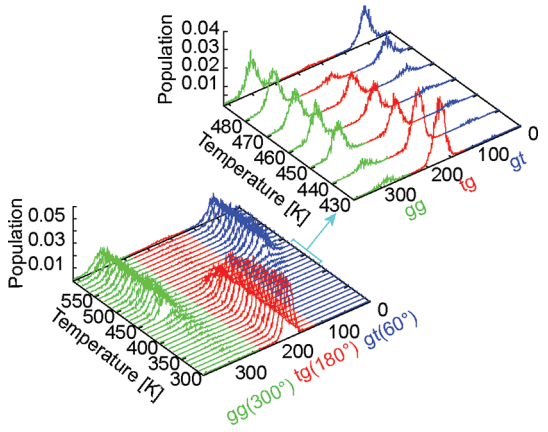

Figure 4. Hydroxymethyl torsion (ω) distibution as a function of temperature. The top right figure is an enlargement around the phase transition in the temperature range 430−490 K.

populations of *gt* and *gg* conformers at high temperature vary according to the force field used, but the significant diminution of *tg* population was common to all previous reports.

The monoclinic angle also drastically changed to an acute angle, in other terms, according to the standard definition,[37] the parallel-up structure changed to a parallel-down structure. This behavior was independent of the box size or the choice of box boundary. On the other hand, we reproduced earlier results[19] by using the same simulation box together with the shear compressibilities set to 0. Zero shear compressibility is normally applied for simulation of protein in water solution, as the protein would anyway have the freedom to deform due to the water molecules. However, in the case of our infinite crystal, the shear compressibilities must be given a finite value to permit adoption of the most stable intermolecular organization. We think that the result in the previous report was biased by the fixed angle of the periodic box due to the shear compressibility of zero.

At high temperature (550 K), the distribution of the torsion angle around the glycosidic linkage φ and ψ was wider than that at room temperature, but the average values remained almost unchanged (Figures S2a,b and S3a,b). The sugar puckering parameters also indicated that the sugar conformation did not change throughout the whole temperature range (Figures S4a,b and S5a,b). This was not true for the exocylic hydroxymethyl group orientation (Figures S2c,d and S3c,d).

When the system was cooled to room temperature, the ω torsion angle remained mainly the *gt* and *gg* conformation without any trace of *tg* (see the red curve in Figure 5, bottom). In addition, no discontinuous event was observed for the unit cell parameters (see the green curve in Figure 6, top). This is obviously a discrepancy with respect to the experiments as seen in Figure 2. Comparing the potential energies at 300 K before and after annealing revealed that the total enthalpy was lowest for the annealed structure with *gt* and *gg* conformers (Table 1). Thus, we can conclude that the irreversible behavior is not a consequence of the limited cooling rate but is due to the force field parameters that describe the energy profile for rotation of the hydroxymethyl group.

4.2. Torsional Bias Energy Profile of the Hydroxymethyl Group in FFG53a6. The distribution of the ω torsion angle is directly related to the "proper dihedral" term of the potential energy function in the GROMACS program.[28] The dihedral energy (E_{dih}) of exocyclic hydroxymethyl group

dx.doi.org/10.1021/ma201954s | *Macromolecules* 2012, 45, 362−368

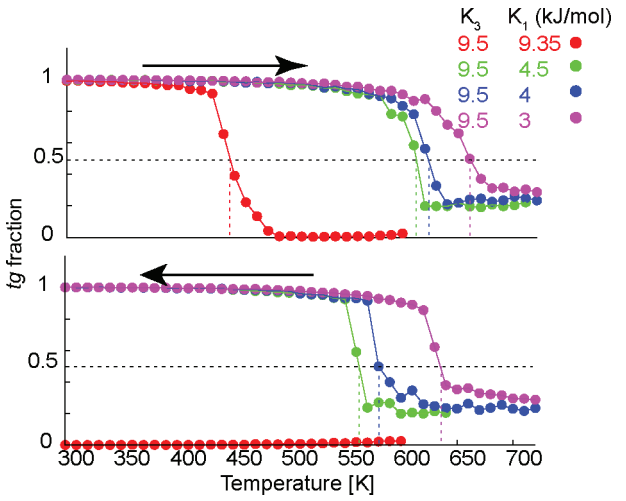

Figure 5. Amount of *tg* conformation during the heating (top) and cooling (bottom) processes for different K_1 values.

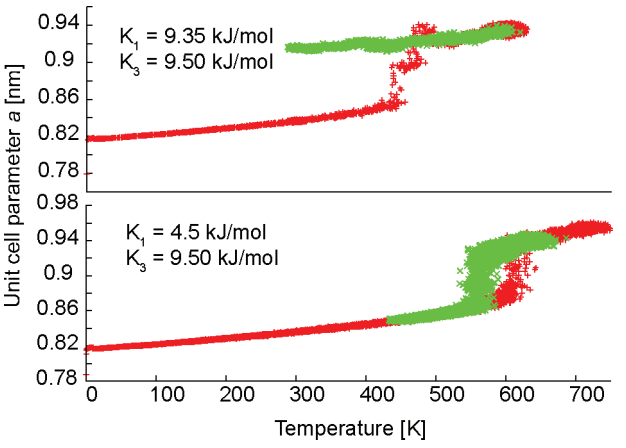

Figure 6. Unit cell parameter *a* as a function of temperature with the standard parameter K_1 = 9.35 kJ/mol (top) and with modified torsional parameter K_1 = 4.5 kJ/mol (bottom). Heating is in red, and cooling is in green.

Table 1. Energy per Glucose of Cellulose Iβ at 300 K at the Beginning of the Simulation (Quoted Heating) and after Annealing (Quoted Cooling) Calculated with the Original and Modified Values of the K_1 and K_3 Parameters

		E (kJ/mol)	
K_1 (kJ/mol)	K_3 (kJ/mol)	heating	cooling
9.35	9.50	352.69	350.85
4.50	9.50	342.89	342.92
4.00	9.50	341.90	340.91
3.00	9.50	339.88	339.90

takes the following analytical form:

$$E_{dih} = K_1(1 - \cos \omega) + K_3(1 + \cos 3\omega)$$

where ω is the torsion angle and K_1 and K_3 are force constants which respectively have the values of 9.35 and 9.5 kJ/mol in the FFG53a6 force field. K_1 adds an energy penalty to the *tg* conformation, and K_3 defines the height of the energy barriers between the three staggered positions. These values are based on quantum mechanic (QM) calculation of isolated methyl-glucoside, considering only two arrangements of the secondary hydroxyl groups. The resulting E_{dih} profile around the dihedral angle ω is shown in Figure 7.

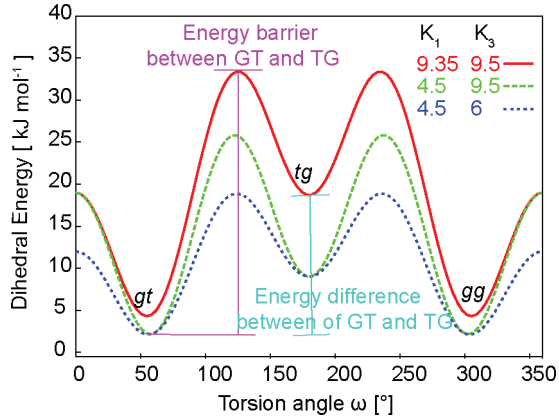

Figure 7. Dihedral energy profile of the rotation of the hydroxymethyl group, continuous red curve: original parameters K_3 = 9.5 kJ/mol, K_1 = 9.35 kJ/mol, green stippled line: modifyed parameters K_3 = 9.5 kJ/mol, K_1 = 4.5 kJ/mol, blue stippled line: K_3 = 6 kJ/mol, K_1 = 4.5 kJ/mol.

Close inspection of the published energy profiles as a function of the torsion angle ω of glucose reveals a strong dependence on the orientation of the secondary hydroxyl groups: clockwise and counterclockwise. Also, noticeable differences can be seen between the reference energy curves, calculated using QM, and the predicted one using the 45a4 parameters.[38] The torsion energy estimated with the molecular mechanics method was 10 kJ/mol higher than the one using the QM method for some values of ω. Furthermore, in native cellulose, the orientation of the secondary hydroxyl groups is neither clockwise nor counterclockwise, which are the only arrangements, considered in the QM calculation.

The 20 ns simulation of β-D-glucopyranose in explicit water system showed 0% *tg* conformers.[38] Analysis of the NMR coupling constants using Karplus type equations predicts a population of *tg* ranging from negative value[39] to 9%.[3] Thus, the dihedral parameters are still far from being established.

4.4. Modification of the Parameters. We systematically modified the two force constants K_1 and K_3 of the dihedral energy term to study their effect on the thermal behavior of the crystal. The values chosen did not affect the distribution of glycosidic angles and puckering parameters.

Table 2 summarizes the reversibility of the transition for different combinations of the two parameters. When the barrier parameter K_3 was kept to its original value, reversibility was observed when K_1 was lower than or equal to 4.5 kJ/mol. By lowering K_3, a higher K_1 also became acceptable.

The simulated variation of the *a* parameter as a function of temperature during heating (red traces) and cooling (green traces) is shown in Figure 6. Whereas Figure 6 (top) is obtained with the standard values of K_1 = 9.35 kJ/mol and K_3 = 9.50 kJ/mol, Figure 6 (bottom) results from the lowering of K_1 to 4.5 kJ/mol. When shifting to this last K_1 value, one sees that during the cooling the unit cell parameter *a*, which remained constant in the standard situation, decreased discontinuously to reach its starting preheating value, indicating a reversibility of the process. All other unit cell parameters showed similar reversibility (Figure S6). The corresponding torsional bias profile, E_{dih}, is given in Figure 7: lowering K_1 to 4.5 kJ/mol

dx.doi.org/10.1021/ma201954s | *Macromolecules* 2012, 45, 362–368

Table 2. Reversibility of the Transition for Selected Values of K_1 and K_3[a]

K_3 (kJ/mol)	K_1 (kJ/mol) 9.35	8	7	6	5	4.5	4	3
9.5	×	×	×	×	×	○	○	○
8					×	○	○	○
7					×	○	○	○
6	×			×	○	○	○	○
5	×			×	○	○	○	
4	×				○			
3	×							

[a]The symbol × was used when the transition was irreversible; ○: the transition was reversible; blank: not tested. The slowest cooling rate is 1 K/ns.

decreases the relative energy of the *tg* conformer and lowers the energy barrier for the *gg* or *gt* to *tg* transition.

Figure 5 shows the population of the *tg* conformer as a function of temperature with different values of K_1. Upon heating, the lower the value of K_1, the higher the transition temperature. Furthermore, only low values of K_1 allow the hydroxymethyl groups to rotate back to its original *tg* orientation upon cooling.

In both the modeling and the experiments, the transition temperature showed a significant hysteresis (see Figures 2, 5, and 6). The transition temperature was systematically higher in the heating phase than in the cooling one. However, the hysteresis is predicted to be larger by modeling than observed by experiment. This is probably due to the very fast heating and cooling rates in the MD compared to the standard experimental time frame. However, lowering the heating and cooling rates down to 1 K/ns did not significantly reduce the hysteresis. The phase transition temperature, defined as the point where the *tg* population becomes 50%, is plotted as a function of K_1 parameter in Figure 8. The phase transition temperature

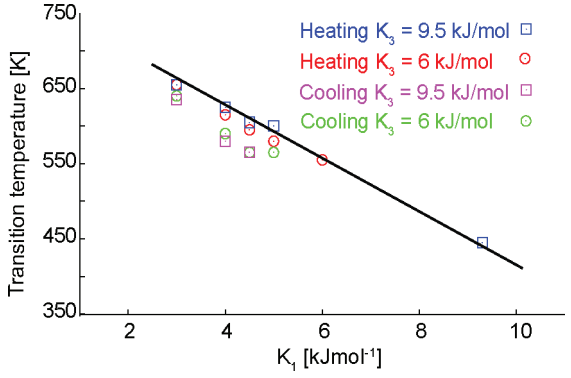

Figure 8. Variations of the transition temperature as a function of K_1.

increased linearly with the decrease in K_1 value. Therefore, the experimentally observed transition temperature, 500 K, corresponds to a K_1 value of about 7 kJ/mol.

Since the temperature induced allomorphic conversion is reversible, it can be explained as a thermodynamic phase transition. A system exploring all the accessible conformational space at constant pressure should minimize its Gibbs free energy:

$$G = H - TS$$

where H is the enthalpy of the system corresponding to the potential energy and S is the entropy. The phase transition should occur when

$$G_{RT} = G_{HT}$$

$$T = \frac{H_{RT} - H_{HT}}{S_{RT} - S_{HT}}$$

where the subscripts RT and HT refer to the room and high temperature phases, respectively.

K_1 directly adds to $H_{RT} - H_{HT}$, thus decreasing the phase transition temperature. Figure 8 shows that the transition temperature, deduced from Figure 5, varies almost linearly with K_1, which suggests that $S_{RT} - S_{HT}$ is constant and independent of K_1. $S_{RT} - S_{HT}$ is negative, which means that there should be an entropy gain by adopting the *gg/gt* conformations (HT structure) instead of the *tg* conformation (RT), which is not very dependent on the local force-field parameters that we have modified. From the slope of the curves in Figure 8 the entropy of transition to the high-temperature phase can be estimated roughly at 26 JK^{-1} mol^{-1}. The slope was almost the same when K_3 = 6 kJ/mol or K_3 = 9.5 kJ/mol, but the hysteresis was smaller when K_3 = 6 kJ/mol.

At the temperature of 500 K, the variation in entropy associated with the deformations of the bond lengths and bond angles is negligible. Similarly, the glucosyl ring geometry remains constant during the phase transition. Thus, the variation in entropy can be attributed only to variations in exocyclic torsion angles. The torsional entropies S can be defined as follows:[40]

$$S = -k_B \int_0^{2\pi} P(\chi) \ln(P(\chi))\, d\chi$$

where k_B is the Boltzmann constant and $P(\chi)$ is the probability to find the torsional angle at χ. In practice, this was done by constructing a histogram (1° step) of torsion angles at each temperature and by performing simple summation according to

$$S = \sum_0^{360} P(\chi) \ln(P(\chi))$$

The entropies of the different torsion angles in cellulose $\tau 2$, $\tau 3$, $\tau 6$, φ, ψ, and ω[36] as a function of temperature are shown in Figure 9. The entropy gain of ω during the transition was 6 J

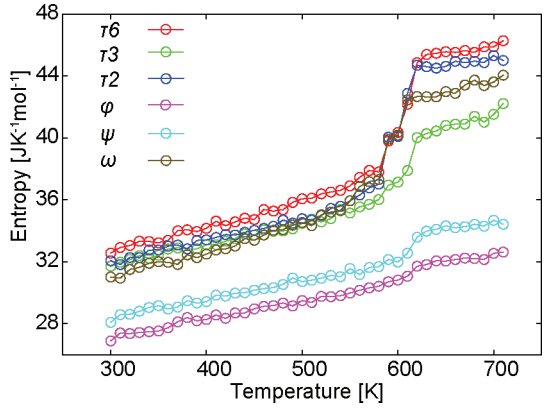

Figure 9. Entropies of dihedral angles[36] as a function of temperature with K_1 = 4.5 kJ/mol.

dx.doi.org/10.1021/ma201954s | *Macromolecules* 2012, 45, 362–368

K^{-1} mol^{-1} . This value is in the same range as the entropy gains of $\tau 2$, $\tau 3$, $\tau 6$ (8, 4, and 8 J K^{-1} mol^{-1}, respectively), whereas that of the φ, ψ torsion angles is negligible. Note that the sum of these four significant components corresponds to the expected entropy gain from the slope of Figure 8.

The transition frequency among different staggered positions of the hydroxymethyl groups increased almost exponentially with temperature in the temperature range 300−600 K (Figure 10). Even at room temperature, the frequency of the order of one transition every 1−10 ns is still faster than the NMR time scale. The conformation is predominantly *tg* (Figure 4) until the phase transition temperature, so the residence times for conformations other than *tg* are even shorter. This dynamic picture is different from the frozen microdomain structure proposed earlier based on shorter simulation time of 1 ns using PCFF as force field.[41]

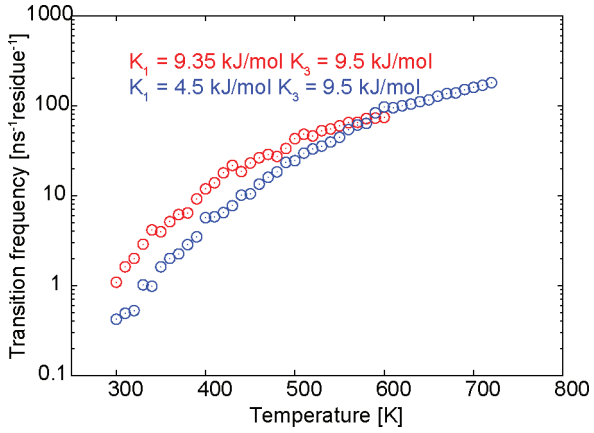

Figure 10. Transition frequency of ω as a function of temperature.

The reasonable number of transitions during the simulation is another indication that the simulation is reflecting thermodynamic aspects of the system that governs the reversible phase transition. In the real system, the cellulose chains are closer and the energy barrier between different staggered O6 positions may be different than indicated by the force field that we have used. However, we observed here a frequency range over 3 orders of magnitude and a temperature range of 300 K. A few kJ difference in energy profile would not modify this general behavior.

After we submitted the first draft of the manuscript, one of the reviewers pointed out the existence of a new GROMOS force field optimized for carbohydrates, $56A_{CARBO}$.[42] We duplicated the simulation annealing with this new force field and found the same irreversibility where the high-temperature phase had lower total energy. The high temperature phase using $56A_{CARBO}$ was characterized by dominance of *gt* conformation for the hydroxymethyl groups instead of a mixture of gt/gg observed with the 53A6. We cannot tell the preference between these two force fields due to the lack of experimental determination of the high-temperature structure, but we believe that the $56A_{CARBO}$ also has to be further tuned to reproduce the reversible phase transition.

5. CONCLUSIONS

By choosing a range of alternative parameters for the torsion energy of the exocyclic hydroxymethyl groups, we could roughly reproduce the experimentally observed reversible phase transition of native cellulose, although some of the calculated unit cell parameters were substantially different from the experimental ones. This means that the thermal phase transition phenomena can be partly decoupled from the packing of cellulose chains. The ring conformation and glycosidic torsion angle globally did not change as a function of temperature. Thus, the thermal behavior of cellulose crystals can be understood as a phase transition phenomena of a fairly rigid backbone with flexible side groups that induce the transition. A systematic variation of the torsion energy profile allowed us to understand the phase transition as a gain in entropy that stabilizes a new structure at high temperature. This means that the cellulose behavior at time scale longer than picoseconds can be probably described in a fairly large temperature range, using rigid backbone with one flexible group. Such discrepancy drastically reduces the number of effective parameters. The torsion energy profile of the exocyclic hydroxymethyl group appears to be the key aspect in determining the phase behavior of the cellulose crystal in thermally induced phase transition of cellulose Iβ. This work gives an explanation to the thermodynamic behavior of solid−solid phase transition using molecular dynamics simulation coupled with force field parameter modulation and is not intended to give new force field parameters.

■ ASSOCIATED CONTENT

Ⓢ Supporting Information

Unit cell parameters and conformational parameters as a function of temperature in the heating phase using the 53A6 and after modification of torsional parameter. This material is available free of charge via the Internet at http://pubs.acs.org.

■ ACKNOWLEDGMENTS

Part of the study was financed by the Agence National de la Recherche (ANR-07-JCJC-21). We thank H. Chanzy and Alfred D. French for valuable comments during the writing of this work.

■ REFERENCES

(1) French, A. D.; Johnson, G. P. *Can. J. Chem.* **2006**, *84*, 603−612.
(2) Marchessault, R. H.; Pérez, S. *Biopolymers* **1979**, *18*, 2369−2374.
(3) Thibaudeau, C.; Stenutz, R.; Hertz, B.; Klepach, T.; Zhao, S.; Wu, Q.; Carmichael, I.; Serianni, A. S. *J. Am. Chem. Soc.* **2004**, *126*, 15668−15685.
(4) Corchado, J. C.; Sanchez, M. L.; Aguilar, M. A. *J. Am. Chem. Soc.* **2004**, *126*, 7311−7319.
(5) Stenutz, R.; Carmichael, I.; Widmalm, G.; Serianni, A. S. *J. Org. Chem.* **2002**, *67*, 949−958.
(6) Rockwell, G. D.; Grindley, T. B. *J. Am. Chem. Soc.* **1998**, *120*, 10953−10963.
(7) Cramer, C. J.; Truhlar, D. G. *J. Am. Chem. Soc.* **1993**, *115*, 5745−5753.
(8) Brown, J. W.; Wladkowski, B. D. *J. Am. Chem. Soc.* **1996**, *118*, 1190−1193.
(9) Wladkowski, B. D.; Chenoweth, S. A.; Jones, K. E.; Brown, J. W. *J. Phys. Chem. A* **1998**, *102*, 5086−5092.
(10) Cocinero, E. J.; Stanca-Kaposta, E. C.; Dethlefsen, M.; Liu, B.; Gamblin, D. P.; Davis, B. G.; Simons, J. P. *Chem.—Eur. J.* **2009**, *15*, 13427−13434.
(11) Mason, P. E.; Neilson, G. W.; Enderby, J. E.; Saboungi, M.-L.; Cuello, G.; Brady, J. W. *J. Chem. Phys.* **2006**, *125*, 224505−224514.
(12) Gardner, K. H.; Blackwell, J. *Biopolymers* **1974**, *13*, 1975−2001.
(13) Horii, F.; Hirai, A.; Kitamaru, R. *Polym. Bull.* **1983**, *10*, 357−361.

(14) Nishiyama, Y.; Langan, P.; Chanzy, H. *J. Am. Chem. Soc.* **2002**, *124*, 9074−9082.
(15) Nishiyama, Y.; Sugiyama, J.; Chanzy, H.; Langan, P. *J. Am. Chem. Soc.* **2003**, *125*, 14300−14306.
(16) Wada, M. *J. Polym. Sci., Part B: Polym. Phys.* **2002**, *40*, 1095−1102.
(17) Hori, R.; Wada, M. *Cellulose* **2005**, *12*, 479−484.
(18) Wada, M.; Hori, R.; Kim, U.-J.; Sasaki, S. *Polym. Degrad. Stab.* **2010**, *95*, 1330−1334.
(19) Bergenstråhle, M.; Berglund, L. A.; Mazeau, K. *J. Phys. Chem. B* **2007**, *111*, 9138−9145.
(20) Zhang, Q.; Bulone, V.; Agren, H.; Tu, Y. *Cellulose* **2011**, *18*, 207−221.
(21) Matthews, J. F.; Bergenstråhle, M.; Beckham, G. T.; Himmel, M. E.; Nimlos, M. R.; Brady, J. W.; Crowley, M. F. *J. Phys. Chem. B* **2011**, *115*, 2155−2166.
(22) Horii, F.; Yamamoto, H.; Kitamaru, R.; Tanahashi, M.; Higuchi, T. *Macromolecules* **1987**, *20*, 2946−2949.
(23) Mathews, J. F.; Skopec, C. E.; Mason, P. E.; Zuccato, P.; Torget, R. W.; Sugiyama, J.; Himmel, M. E.; Brady, J. W. *J. Carbohydr. Res.* **2006**, *341*, 138−152.
(24) Viëtor, R. J.; Mazeau, K.; Lakin, M.; Pérez, S. *Biopolymers* **2000**, *54*, 342−354.
(25) Nishiyama, Y.; Johnson, G. P.; French, A. D.; Forsyth, V. T.; Langan, P. *Biomacromolecules* **2008**, *9*, 3133−3140.
(26) Nishiyama, Y.; Putaux, J.-L.; Montesanti, N.; Hazemann, J.-L.; Rochas, C. *Biomacromolecules* **2010**, *11*, 76−87.
(27) Hess, B.; Kutzner, C.; Van der Spoel, D.; Lindahl, E. *J. Chem. Theory Comput.* **2008**, *4*, 435−447.
(28) Oostenbrink, C.; Villa, A.; Mark, A. E.; Van Gusteren, W. F. *J. Comput. Chem.* **2004**, *25*, 1656−1676.
(29) Hockney, R. W.; Goel, S. P. *J. Comput. Phys.* **1974**, *14*, 148−158.
(30) Darden, T.; York, D.; Pedersen, L. *J. Chem. Phys.* **1993**, *98*, 10089−10092.
(31) Berendsen, H. J. C.; Postma, J. P. M.; Van Gunsteren, W. F.; DiNola, A.; Haak, J. R. *J. Chem. Phys.* **1984**, *81*, 3684−3690.
(32) Bussi, G.; Parrinello, M. *J. Chem. Phys.* **2007**, *126*, 14101−14107.
(33) Hess, B.; Bekker, H.; Berendsen, H. J. C.; Fraaije, J. G. E. M. *J. Comput. Chem.* **1997**, *18*, 1463−1472.
(34) Humphrey, W.; Dalke, A.; Schulten, K. *J. Mol. Graphics* **1996**, *14*, 33−38.
(35) Cremer, D.; Pople, J. A. *J. Am. Chem. Soc.* **1975**, *97*, 1354−1358.
(36) The torsion angle φ is defined as O5−C1−O1−C4, ψ as C1−O1−C4−C5, ω as O5−C5−C6−O6, $\tau 2$ as C1−C2−O2−HO2, $\tau 3$ as C4−C3−O3−OH3, and $\tau 6$ as C5−C6−O6−HO6.
(37) French, A. D.; Howley, P. S. In *Cellulose and Wood, Chemistry and Technology*; Schuerch, C., Ed.; Wiley: New York, 1989; pp 159−167.
(38) Lins, R. D.; Hünenberger, P. H. *J. Comput. Chem.* **2005**, *26*, 1400−1412.
(39) Bock, K.; Duus, J. *J. Carbohydr. Chem.* **1994**, *13*, 1400−1412.
(40) Li, D.-W.; Brüschweiler, R. *Phys. Rev. Lett.* **2009**, *102*, 118108.
(41) Mazeau, K. *Cellulose* **2005**, *12*, 339−349.
(42) Hansen, H.; Hünenberger, P. *J. Comput. Chem.* **2011**, *32*, 998−1032.

Macromolecules

Article

pubs.acs.org/Macromolecules

Radii of Gyration of Ring-Shaped Polystyrenes with High Purity in Dilute Solutions.

Atsushi Takano,[†,*] Yutaka Ohta,[†] Keisuke Masuoka,[†] Kazuki Matsubara,[†] Tomohiro Nakano,[†] Atsushi Hieno,[†] Masanao Itakura,[‡] Kayori Takahashi,[‡] Shinichi Kinugasa,[‡] Daisuke Kawaguchi,[†] Yoshiaki Takahashi,[§] and Yushu Matsushita[†]

[†]Department of Applied Chemistry, Nagoya University, Furo-cho, Chikusa-ku, Nagoya, 464-8603, Japan

[‡]National Metrology Institute of Japan, National Institute of Advanced Industrial Science and Technology, 1-1-1 Higashi, Tsukuba, Ibaraki 305-8565, Japan

[§]Institute for Materials Chemistry and Engineering, Kyushu University, 6-1, Kasuga-koen, Kasuga-city, Fukuoka 816-8580, Japan

ABSTRACT: Ring polystyrenes (PSs) were synthesized by anionic polymerization technique and purified with preparative size-exclusion chromatography (SEC). Seven ring PSs with their weight-average molecular weight (M_w) ranging from 17k to 570k were prepared and they were confirmed to have high purities all over 96% by liquid chromatography at the chromatographic critical condition (LCCC) analyses. Their radii of gyration (R_gs) were determined in benzene-d_6 as a good solvent and in cyclohexane-d_{12} or cyclohexane-h_{12} as Θ solvents by small-angle neutron scattering (SANS) or light scattering (LS). It has been found that R_gs of ring polymers are scaled with M_w as $R_g \propto M_w^{0.60}$ in a good solvent and as $R_g \propto M_w^{0.53}$ in Θ solvents. Moreover it was confirmed that g factors, $\langle R_g^2\rangle_{(Ring)}/\langle R_g^2\rangle_{(Linear)}$, obtained in Θ solvents are meaningfully larger than theoretically predicted values owing to the topological effect stored in ring molecules.

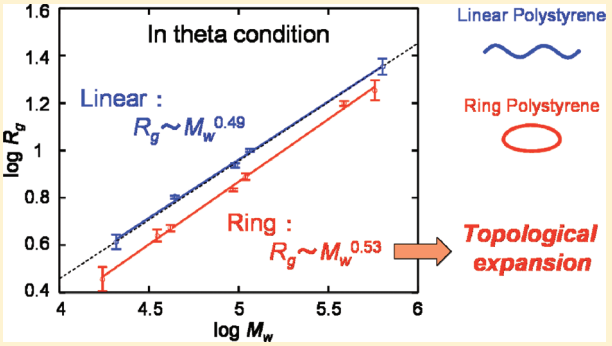

INTRODUCTION

A ring polymer has topologically appealing structure with no chain ends and it is considered as a model polymer to clarify the topological effect on physical properties such as chain dimensions, viscoelastic properties, diffusion properties and so on. Various properties of ring polymers have been predicted by theoretical studies,[1−7] computer simulations,[8−24] while they have been examined by experimental studies.[25−46] One of the fundamental properties representing ring polymers is their chain dimensions in solutions.

Theoretically, the radius of gyration (R_g) of a ring polymer in a Θ solvent was calculated on the basis of Gaussian approximation by Zimm and Stockmayer[2] as $\langle R_g^2\rangle_{ring} = nb^2/12$, where n and b denote the number of segment per chain and segment length, respectively. From this equation, it is easily understood that the scaling relationship between R_g and M_w is represented as $R_g \propto M_w^{0.5}$, which is the same molecular weight dependence as that for a linear polymer at the unperturbed state. On the other hand, under good solvent condition, Douglas and Freed calculated R_gs of ring polymers by a renormalized two-parameter theory[6] and proposed scaling relationship $R_g \propto M_w^{0.6}$, whose exponent is also the same as that for a linear polymer.

Recently many simulation approaches were actively carried out for predicting chain dimensions of trivial (unknotted) rings and also knotted ones. The arguments here should be focused on the scaling exponent ν for the relationship, $R_g \propto M_w^{\nu}$. Deustch has predicted a scaling equation, $R_g \propto M_w^{0.585}$ for trivial ring polymers under the condition with no excluded volume,[8] while $\nu = 0.588$ by Grosberg et al.,[9] $\nu = 0.588$ by Dobay et al.,[10] $\nu = 0.555-0.58$ by Matsuda et al.,[11] and $\nu = 0.58$ by Moore et al.,[12] are all predicting higher exponents, close to 0.6. To the contrary, Deguchi et al. predicted the relationship $R_g \propto M_w^{0.5}$, which is having a very low ν value.[13]

Not only scaling exponents, but g-factors, $\langle R_g^2\rangle_{(Ring)}/\langle R_g^2\rangle_{(Linear)}$, which are the ratio of mean square radii of gyration (R_gs) of ring and linear polymers were also discussed. Zimm and Stockmayer have calculated the g-factor as 0.5 for Gaussian ring.[2] Prentice has predicted the higher value, 0.568, for g-factor by one-loop renormalization group calculation,[5] whereas Douglas and Freed have calculated to have $g = 0.516$ by a renormalized two-parameter theory in a good solvent.[6] Simulations also predicted the g-factors. Zifferer et al. have predicted $g = 0.536$,[15] and Chen et al. obtained $g = 0.563$[16] by Monte Carlo method, while Kanaeda et al. have predicted $g = 0.539$ by Brownian dynamics.[17] Thus, most of works conjectured the larger values than 0.5, which is naturally given under the assumption of Gaussian statictics.

Received: September 7, 2011
Revised: December 2, 2011
Published: December 19, 2011

In the experimental studies, Lutz et al. measured the R_gs of ring polystyrenes in cyclohexane-d_{12} at 34.5 °C and obtained 0.5 for g, which being in good agreement with the theoretical prediction.[33] Hadziioannou et al. measured the R_gs of ring polystyrenes in cyclohexane-d_{12} at 33 °C and reported $g = 0.5$.[35] Moreover Roovers summarized his own data combined with Hadziioannou's and concluded that the g-factor of polystyrenes in cyclohexane should be 0.50_3.[41] Raganetti et al. measured the R_gs of ring polystyrenes in toluene-d_8 (good solvent) and obtained 0.55 for g,[32] whereas Lutz et al. reported a somewhat different value, 0.53[33], for the same system. Furthermore, Higgins et al. measured the R_gs of ring/linear polydimethylsiloxane in benzene-d_6 (good solvent) and the g-factor was found to be 0.53.[25]

Thus, the experimental results on g-factor under Θ condition support that they are in good agreement with Gaussian approximation, while those under good condition indicate that they are slightly larger values than that predicted by renormalization group calculation. However the chain contraction manner of ring polymers has not been concluded yet, possibly due to the fact that the ring samples synthesized so far have relatively low molecular weights, and hence, the molecular weight range is fairly narrow so as not to give a statistically meaningful conclusion. In addition to this fact, more seriously, the purity of the samples was not fully clarified for most of the experimental studies.

Thanks to the development of recent HPLC techniques, several ring polymer samples were analyzed by a new HPLC technique, called liquid chromatography at the chromatographic critical condition (LCCC). For example it was quantitatively confirmed that the ring samples synthesized by Roovers et al. were contaminated with as much as 10−20% linear polymers.[47] Along this line well-characterized ring samples with high purity are strongly required for rigorous investigation of physical properties of ring polymers.

In this paper, we prepared highly purified ring polystyrene samples with wide molecular weight range by anionic polymerizations and HPLC separation techniques. Then the R_gs of the ring samples were measured in cyclohexane-h_8/-d_8 as Θ solvents and in benzene as a good solvent by small-angle neutron scattering (SANS) and light scattering (LS), and the molecular weight dependence of R_gs and the corresponding g-factors in both solvents were compared.

EXPERIMENTAL SECTION

Sample Preparation and Characterizations. Synthesis of linear telechelic PSs, end-to-end ring closure reactions of the telechelic polymers and purification of ring polymers by SEC were carried out in the same manner as reported previously.[46] Weight-average molecular weights, M_ws, of all the samples were measured by light scattering in THF at 35 °C using DAWN EOS enhanced optical system of Wyatt Technology, where the wavelength of the laser light adopted is 690 nm. Polydispersity index, M_w/M_n, of each sample was determined by SEC, which is composed of a set of pump, the DP-8020, and a UV detector, the UV-8020 (wavelength 254 nm) of Tosoh Co. Ltd. SEC experiments were performed a typical isocratic HPLC system equipped with three polystyrene gel columns, TSK-gel G4000H_{HR} (10 nm pore, 4.6 mm φ × 30 mm, 5 μm particle size) of Tosoh Ltd., operated at 40 °C. The eluent was THF and the flow rate was 1.0 mL/min. LCCC experiments were conducted by the same HPLC system as used for SEC experiments equipped with two C18-bonded silica gel columns, ODS-80TsQA (10 nm pore, 6 mm φ × 150 mm, 3 μm particle size) of Tosoh Ltd. The eluent was a mixture of CH_2Cl_2 and CH_3CN (HPLC grade, 57/43 in volume), and the flow rate was 0.5 mL/min. The column temperature was adjusted at 25−38 °C by a programmable bath/circulator, HAAKE phoenix II.

SANS and LS Measurements. SANS measurements were performed using the SANS-U spectrometer with a two-dimensional position-sensitive detector at the Institute for Solid State Physics, the University of Tokyo. Monochromated neutron beam with wavelength of 0.70 nm was used. The sample−to-detector distances adopted are 4.0 m for samples with molecular weight of 20k, 8.0 m for samples with molecular weight of 30k, 40k, 90k, 110k and 380k. The applied temperature of the SANS measurements of the linear and ring polymers in cyclohexane-d_{12} as a Θ solvent was 40 °C, because 40.2 °C was reported as the Θ temperature for linear polystyrene in cyclohexane-d_{12} by Strazielle et al,[48] while SANS measurements for the linear and ring polymers in benzene-d_6 as a good solvent were carried out at 25 °C.

LS measurements were performed using a DLS-8000 of Otsuka Electronics Co. for the samples with molecular weight of 600k, He−Ne laser (wavelength 632.8 nm) being used as a light source. Selected temperature in chclohexane-h_{12} as a Θ solvent was 34.5 °C, while 25 °C was adopted for experiments in benzene-d_6 as a good solvent.

RESULTS AND DISCUSSION

Since telechlic polymers were cyclized by end-to-end ring-closure reaction in a good solvent (THF) where the polymer chains are sufficiently expanded, the formed ring polymers might hardly be self-entangled, hence the topology type of the rings employed in this study should be trivial (unknotted) rings. A computer simulation predicted that a trivial ring polymer is preferentially formed in cyclization of linear precursor under a good solvent condition unless chain length is extremely long.[50]

Figure 1a compares an example of SEC chromatograms of the fractionated ring PS with molecular weight of 90k expressed

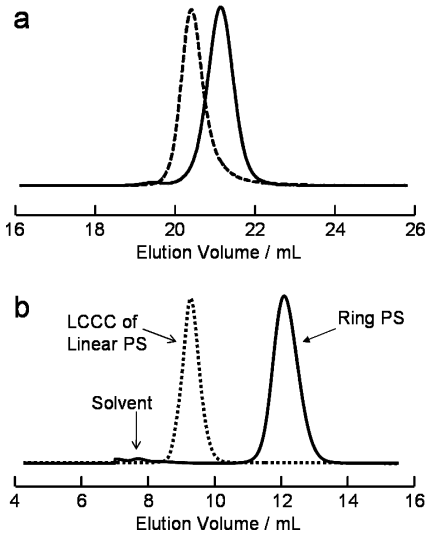

Figure 1. (a) SEC chromatograms and (b) LCCC chromatograms of fractionated rings (solid lines) and the linear precursor (dashed lines) with molecular weight of 90k.

by a solid line and that of the linear precursor by a dashed line, whereas Figure1b displays two LCCC chromatograms at the critical condition of linear polystyrenes with corresponding lines. From the SEC chromatograms shown in Figure 1a, it is evident that apparent molecular weight of the ring polymer is ca. 70% comparing with the corresponding linear one; however, the difference in the hydrodynamic volume between linear and ring PS is not sufficiently large to provide the complete

dx.doi.org/10.1021/ma202031w | Macromolecules 2012, 45, 369−373

separation in SEC. From LCCC chromatograms shown in Figure 1b; however, it is confirmed that the difference in the elution volume between linear and ring PS is large enough to provide the complete separation, and hence it enable to estimate the purity of ring molecule in the fractionated sample quantitatively.

Molecular characteristics of linear polymer samples are listed in Table 1 and those of the corresponding ring counterparts are

Table 1. Molecular Characteristics and Chain Dimensions of Linear Telechelic Polystyrenes

sample	$10^{-3}M_w$ [a]	M_w/M_n [b]	$R_{g,g}$ (nm)[c]	$R_{g,0}$ (nm)
L-20	20.7	1.02	4.36 ± 0.45	4.10 ± 0.30[d]
L-30	39.6	1.05	–	–
L-40	44.2	1.03	7.23 ± 0.32	6.39 ± 0.04[d]
L-90	95.9	1.03	–	8.64 ± 0.18[d]
L-110	115	1.04	12.8 ± 0.29	10.0 ± 0.10[d]
L-380	376	1.04	–	–
L-600	635	1.01	36.2 ± 1.5	22.6 ± 1.8[e]

[a]Determined by light scattering in THF at 35 °C. [b]Determined by SEC. [c]Measured in benzene-d_6 at 25 °C. [d]Measured in cyclohexane-d_{12} at 40 °C. [e]Measured in cyclohexane-h_{12} at 34.5 °C.

Table 2. Molecular Characteristics and Chain Dimensions of Ring Polystyrenes

sample	$10^{-3}M_w$ [a]	M_w/M_n [b]	purity (%)[c]	$R_{g,g}$ (nm)[d]	$R_{g,0}$ (nm)
R-20	17.4	1.02	$99._0$	2.90 ± 0.35	2.86 ± 0.35[e]
R-30	35.2	1.04	$99._7$	5.44 ± 0.48	4.37 ± 0.27[e]
R-40	41.7	1.02	$96._6$	5.70 ± 0.25	4.72 ± 0.15[e]
R-90	93.0	1.02	$99._5$	–	6.83 ± 0.07[e]
R-110	109	1.01	$99._0$	9.36 ± 0.15	7.72 ± 0.26[e]
R-380	386	1.02	99.6	–	15.8 ± 0.38[e]
R-600	573	1.02	$98._0$	25.9 ± 1.5	17.9 ± 1.8[f]

[a]Determined by light scattering in THF at 35 °C. [b]Determined by SEC. [c]Estimated from LCCC and IC. [d]Measured in benzene-d_6 at 25 °C. [e]Measured in cyclohexane-d_{12} at 40 °C. [f]Measured in cyclohexane-h_{12} at 34.5 °C.

shown in Table 2, where purities of all the ring polymers are listed. It was confirmed by LCCC or IC analyses that all the ring samples have high purity, being higher than 96%.

Figure 2a shows example of so-called square-root plots of the scattered SANS intensities for the sample R-110 for three benzene-d_6 solutions with different concentrations according to eq 1,

$$1/I^{1/2} = 1/(KcM_w)^{1/2} + q^2R_g{}^2/6(KcM_w)^{1/2} \quad (1)$$

From the eq 1 and the correspondent $1/I^{1/2}$ vs q^2 plots, it is evident that the ratio of the initial slope and the intercept gives apparent R_g at finite concentration. Figure 2b shows the extrapolation of the apparent radii of gyration thus estimated to infinite dilution by least-squares fitting. The radii of gyration obtained by this procedure are listed in Table 1 and Table 2. $R_{g,g}$s denote the radii of gyration for linear and ring polymers in benzene-d_6 at 25 °C, while $R_{g,0}$s express the R_g in cyclohexane-h_{12} at 34.5 °C or in cyclohexane-d_{12} at 40 °C.

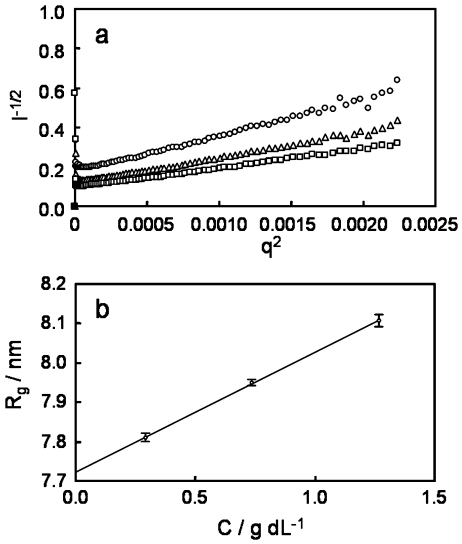

Figure 2. (a) $I^{-1/2}$–q^2 plot for ring PS with molecular weight of 110k in cyclohexane-d_{12} at 40 °C. Polymer concentrations: 0.29 g/dL (circles), 0.74 g/dL (triangles), and 1.27 g/dL (squares). (b) Extrapolation of R_g values obtained from data in part a taken to infinite dilution.

The radii of gyration, $R_{g,g}$s, for linear and ring polymers in benzene-d_6 at 25 °C are double–logarithmically plotted against molecular weight, M_w, in Figure 3.

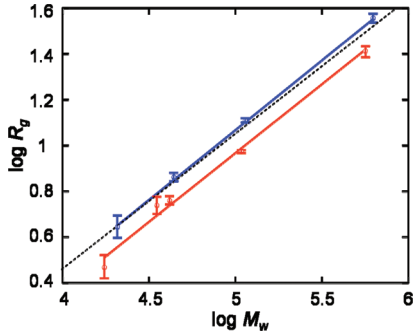

Figure 3. Double logarithmical plots of the radii of gyration against molecular weight for ring (red line) and linear polymers (blue line) in benzene-d_6. A dashed line shows R_g–M_w relationship for linear polystyrenes in benzene reported by Miyaki et al.[49]

This figure also includes R_g–M_w relationship for linear polystyrenes for wide molecular weight range in benzene reported by Miyaki et al.[49] according to the eq 2,

$$R_g = 0.0121M_w{}^{0.595} \quad (\text{in nm, linear PS, in benzene}) \quad (2)$$

as a dashed line for a reference, which is considered to be the most reliable data. Present data of the linear polystyrenes in benzene-d_6 are closely located on the dashed line, and the scaling relationship obtained by the least-squares fitting is as follows,

$$R_{g,g} = (0.0099 \pm 0.0008)M_w{}^{0.61\pm0.02} \quad (\text{in nm, linear PS, in benzene-}d_6) \quad (3)$$

dx.doi.org/10.1021/ma202031w | Macromolecules 2012, 45, 369–373

On the other hand data for the ring polystyrenes in benzene-d_6 were also shown in Figure 3, and it is apparent that the R_{gg} values for rings are evidently smaller than those for the linear ones. The slope of the fitted straight line is close to that for the linear polystyrenes, and the scaling relationship obtained by the least-squares fitting is as follows,

$$R_g = (0.0090 \pm 0.0008)M_w^{0.60\pm0.02}$$

$$(\text{in nm, ring PS, in benzene-}d_6) \quad (4)$$

This exponent, 0.60, is close enough to the empirical scaling exponent of 0.61 for the linear polymers in benzene as shown in eq 3.

From the eq 3 and 4, g-factors can be calculated as $0.589 \leq g \leq 0.647$ in the molecular weight range of present work, $17k \leq M_w \leq 570k$, which are slightly larger than the predicted value by renormalized two-parameter theory,[6] 0.516, throughout the molecular weight range adopted, whereas the present results gives almost the same values reported previously by Ragnetti et al.(0.55), Lutz et al. (0.53) and Higgins et al. (0.53).

On the other hand, the $R_{g,0}$s for linear and ring polymers in cyclohexane-h_{12}/-d_{12} are double−logarithmically plotted against molecular weight in Figure 4.

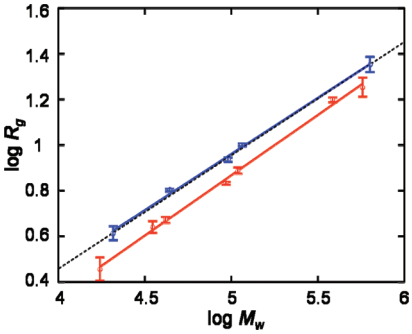

Figure 4. Double logarithmic plots of radii of gyration against molecular weight for ring (red line) and linear polymers (blue line) in cyclohexane-d_{12}/h_{12}. A dashed line shows R_g−M_w relationship for linear polystyrenes in benzene reported by Miyaki et al.[49]

This graph also includes R_g−M_w relationship for linear polystyrenes in cyclohexane reported by Miyaki et al.[49] according to the eq 5

$$R_{g,0} = 0.029_7 M_w^{0.50} \quad (5)$$

as a dashed line as a reference. Present data for the linear polystyrenes in cyclohexane-h_{12}/-d_{12} shown as open circles mostly fall on the dashed line, and the scaling relationship obtained by the least-squares fitting is as follows:

$$R_{g,0} = (0.0315 \pm 0.0018)M_w^{0.49\pm0.01}$$

$$(\text{in nm, linear PS, in cyclohexane-}h_{12}/\text{-}d_{12}) \quad (6)$$

From eq 6, it is evident that the present data are in good agreement with those in the literature. Data for the ring polystyrenes in cyclohexane-h_{12}/-d_{12} were also shown as open circles in Figure 4, it is evident that the absolute $R_{g,0}$s values for rings are clearly smaller than those for the linear ones. The least-squares fitting gives the R_g−M_w scaling relationship as follows:

$$R_{g,0} = (0.0168 \pm 0.0013)M_w^{0.53\pm0.02}$$

$$(\text{in nm, ring PS, in cyclohexane-}h_{12}/\text{-}d_{12}) \quad (7)$$

The scaling exponent in eq 7, 0.53, is rather larger than that in eq 6, and this difference seems to be meaningful beyond experimental errors. This experimental result suggests that there exists cirtain repulsive forces between segments on a ring molecules at the Θ condition for linear polystyrene. This might be attributed to the "topological expansion effect" or the "topological swelling effect", which is predicted by Deustch et al.,[8] Grosberg et al.,[9] Dobay et al.,[10] Matsuda et al.,[11] and Moore et al.[12]

If we look at this phenomenon from the other side of physical chemistry of polymers, this result can be regarded as "Θ-temperature depression" for ring molecules, assuming that the definition of Θ-temperature is "the temperature at which the exponent ν in R_g−M^ν relation becomes 0.5". Along this line, present result is consistent with experimental data of Θ-temperature depression for ring polystyrenes in cyclohexane by Roovers et al.[51] and Takano et al.,[52] and also with a simulation result by Suzuki et al.[53]

Since the scaling exponent for linear and ring polymers in cyclohexane is different, g-factor should have molecular weight dependence. As a matter of fact g-factors can be calculated within the molecular weight range of the present work ($17k \leq M_w \leq 570k$) from the eqs 4 and 5 as $0.557 \leq g \leq 0.730$, which are apparently larger than the predicted value for Gaussian chain, 0.5. This is contradictory to the previous experimental results by Lutz,[33] Hadziioannou,[35] and Roovers.[41]

Thus, experimentally obtained g-factors for the trivial ring polymers in Θ solvents, which are larger than the theoretically predicted values for Gaussian chain, indicate that the trivial rings are more expanded than the theoretically predicted values in the solvent.

CONCLUSION

The radii of gyration of trivial ring polymers were measured by neutron or light scattering under good condition and also under Θ condition for linear PS. It was confirmed that ring polymers give almost the same scaling exponent, ν, for the relationship $R_g \propto M_w^\nu$ under good condition however the exponent of ring polymers under Θ condition is a little larger than that for linear ones, this leads larger g-factors than the theoretically predicted values under Θ condition, possibly due to the topological interactions of ring polymers in solutions, which is evident in a Θ solvent.

AUTHOR INFORMATION

Corresponding Author

*Telephone: +81-52-789-3211. Fax: +81-52-789-3210. E-mail: atakano@apchem.nagoya-u.ac.jp.

ACKNOWLEDGMENTS

We gratefully thank to Prof. Y. Nakamura at Department of Polymer Chemistry in Kyoto University for data analyses of SANS. A.T. acknowledges to Prof. T.Deguchi at Department of Physics in Ochanomizu University for fruitful discussion. This work was carried out under the Joint-use Research Program for Neutron Scattering, Institute for Solid State Physics (ISSP), the University of Tokyo, at the Research Reactor JRR-3, JAEA (Proposal Nos. 5553, 6567, 7633, 8852K, and 9605).

REFERENCES

(1) Kramers, H. A. *J. Chem. Phys.* **1946**, *14*, 415−424.
(2) Zimm, B. H.; Stockmayer, W. H. *J. Chem. Phys.* **1949**, *17*, 1301−1314.
(3) Casassa, E. F. *J. Polym. Sci., Part A* **1965**, *3*, 605−614.
(4) Burchard, W.; Schmidt, M. *Polymer* **1980**, *21*, 745−749.
(5) Prentis, J. J. *J. Chem. Phys.* **1982**, *76*, 1574−1583.
(6) Douglas, J. F.; Freed, K. F. *Macromolecules* **1984**, *17*, 2344−2354.
(7) Cates, M. E.; Deutsch, J. M. *J. Phys. (Paris)* **1986**, *47*, 2121−2128.
(8) Deutsch, J. M. *Phys. Rev. E* **1999**, *59*, R2539−R2541.
(9) Grosberg, A. Y. *Phys. Rev. Lett.* **2000**, *85*, 3858−3861.
(10) Dobay, A.; Dubochet, J.; Millett, K.; Edouarrd, P.; Stasiak, A. *Proc. Natl. Acad. Sci. U.S.A.* **2003**, *100*, 5611−5615.
(11) Matsuda, H.; Yao, A.; Tsukahara, H.; Deguchi, T.; Furuta, T.; Inami, T. *Phys. Rev. E* **2003**, *68*, 011102.
(12) Moore, N. T.; Grosberg, A. Y. *Phys. Rev. E* **2005**, *72*, 061803.
(13) Shimamura, M. K.; Deguchi, T. *Phys. Lett. A* **2000**, *25*, 184−191.
(14) Shimamura, M. K.; Deguchi, T. *Phys. Rev. E* **2001**, *64*, 020801.
(15) Zifferer, G.; Preusser, W. *Macromol. Theory Simul.* **2001**, *10*, 397−407.
(16) Chen, Y. −D. *J. Chem. Phys.* **1983**, *78*, 5191−5196.
(17) Kanaeda, N.; Deguchi, T. *J.Phys. A: Math. Theor.* **2008**, *41*, 145004.
(18) Naghizadeh, J.; Sotobayashi, A. *J. Chem. Phys.* **1974**, *60*, 3104−3108.
(19) Baumgartner, W. *J. Chem. Phys.* **1982**, *76*, 4275−4280.
(20) Garcia Bernal, J. M.; Tirado, J. J.; Freire, M. M.; Garcia de la Torre, J. *Macromolecules* **1990**, *23*, 3357−3362.
(21) Garcia Bernal, J. M.; Tirado, J. J.; Freire, M. M.; Garcia de la Torre, J. *Macromolecules* **1991**, *24*, 593−598.
(22) Muller, M.; Wittner, J. P.; Cates, M. E. *Phys. Rev. E* **1996**, *53*, 5063−5074.
(23) Brown, S.; Szamel, G. *J. Chem. Phys.* **1998**, *108*, 4705−4708.
(24) Brown, S.; Szamel, G. *J. Chem. Phys.* **1998**, *109*, 6184−6192.
(25) Higgins, J. S.; Dodgson, K.; Semlyen, A. *Polymer* **1979**, *20*, 553−558.
(26) Hild, G.; Kohler, A.; Rempp, P. *Eur. Polym. J.* **1980**, *16*, 525−527.
(27) Geiser, D.; Hocker, H. *Macromolecules* **1980**, *13*, 653−656.
(28) Vollmert, B.; Huang, J. X. *Macromol. Chem. Rapid Commun.* **1980**, *1*, 333−339.
(29) Vollmert, B.; Huang, J. X. *Macromol. Chem. Rapid Commun.* **1981**, *2*, 467−472.
(30) Roovers, J.; Toporowski, P. M. *Macromolecules* **1983**, *16*, 843−849.
(31) Roovers, J. *Macromolecules* **1985**, *18*, 1359−1361.
(32) Ragnetti, M.; Geiser, D.; Hocker, H.; Oberthur, R. C. *Macromol. Chem.* **1985**, *186*, 1701−1709.
(33) Lutz, P.; McKenna, G. B.; Rempp, P.; Strazielle, C. *Macromol. Chem. Rapid Commun.* **1986**, *7*, 599−605.
(34) Roovers, J. *J. Polym. Sci. Polym. Phys. Ed.* **1985**, *23*, 1117−1126.
(35) Hadziioannou, G.; Cotts, P. M.; ten Brinke, G.; Han, C. C.; Lutz, P.; Strazielle, C.; Rempp, P.; Kovacs, A. J. *Macromolecules* **1987**, *20*, 493−497.
(36) Mills, P. J.; Mayer, J. W.; Kramer, E. J.; Hadziioannou, G.; Lutz, P.; Strazielle, C.; Remmp, P.; Kovacs, A. J. *Macromolecules* **1987**, *20*, 513−518.
(37) Roovers, J. *Macromolecules* **1988**, *21*, 1517−1521.
(38) Roovers, J.; Toporowski, P. M. *J. Polym. Sci., Part B: Polym. Phys.* **1988**, *26*, 1251−1259.
(39) Rique-Lurbet, L.; Schappacher, M.; Deffieux, A. *Macromolecules* **1994**, *27*, 6318−6324.
(40) Kubo, M.; Hayashi, T.; Kobayashi, H.; Tsuboi, K.; Itoh, T. *Macromolecules* **1997**, *30*, 2805−2807.
(41) Roovers, J. *Cyclic Polymers*, 2nd ed.; Semlyen, J. A., Ed., Kluwer: Dorderecht, The Netherlands, 2000, Chapter 10.
(42) Dong, D.; Hogen-Esch, T. E. *e-Polym.* **2001**, 007.
(43) Lepoittevin, B.; Perrot, X.; Masure, M.; Hemery, P. *Macromolecules* **2001**, *34*, 425−429.
(44) Takano, A.; Nonaka, A.; Kadoi, O.; Hirahara, K.; Kawahara, S.; Isono, Y.; Torikai, N.; Matsushita, Y. *J. Polym. Sci., Part B, Polym. Phys* **2002**, *40*, 1582−1589.
(45) Arrighi, V.; Gagliardi, S.; Dagger, A. C.; Semlyen, J. A.; Higgins, J. S.; Shenton, M. J. *Macromolecules* **2004**, *37*, 8057−8065.
(46) Cho, D.; Masuoka, K.; Koguchi, K.; Asari, T.; Takano, A.; Matsushita, Y. *Polym. J.* **2005**, *37*, 506−511.
(47) Lee, H. C.; Lee, H.; Lee, W.; Chang, T.; Roovers, J. *Macromolecules* **2000**, *33*, 8119−8121.
(48) Strazielle, C.; Benoit, H. *Macromolecules* **1975**, *8*, 203−205.
(49) Miyaki, Y.; Einaga, Y.; Fujita, H. *Macromolecules* **1978**, *11*, 1180−1186.
(50) Deguchi, T.; Tsurusaki, K. *Phys Rev E* **1997**, *55*, 6245−6248.
(51) Roovers, J. *J. Polym. Sci., Polym. Phys. Ed.* **1985**, *23*, 1117−1126.
(52) Takano, A.; Kushida, Y.; Ohta, Y.; Masuoka, K.; Matsushita, Y. *Polymer* **2009**, *50*, 1300−1303.
(53) Suzuki, J.; Takano, A.; Matsushita, Y. *J. Chem. Phys.* **2011**, *135*, 204903.

Macromolecules

ARTICLE

pubs.acs.org/Macromolecules

Upper Critical Solution Temperature of Poly(*N*-acryloyl glycinamide) in Water: A Concealed Property

Jan Seuring,[†] Frank M. Bayer,[‡] Klaus Huber,[‡] and Seema Agarwal*[,†]

[†]Fachbereich Chemie, Philipps-Universität Marburg, Hans-Meerwein Straße, D-35032 Marburg, Germany

[‡]Department Chemie—Physikalische Chemie,Universität Paderborn,Warburger Straße 100, D-33098 Paderborn, Germany

Supporting Information Web-Enhanced

ABSTRACT: Polymers showing an upper critical solution temperature (UCST) in water are rare. Recently, the nonionic homopolymer poly(*N*-acryloyl glycinamide) (poly(NAGA)) has been shown to exhibit a sharp upper critical solution temperature in pure water as well as in electrolyte solution. Although poly(NAGA) is known for decades the UCST behavior had not been reported. The first controlled radical polymerization of poly(NAGA) by the RAFT (reversible addition−fragmentation transfer) process was also achieved recently, but no UCST was observed. The present study shows that traces of ionic groups in the polymer prevent phase separation. Failure to notice the UCST in the past was because ionic groups have been introduced unintentionally by either acrylate impurities in the monomer, hydrolysis of the polymer side chains, and/or usage of ionic initiators or chain transfer agents. A synthetic procedure for high purity NAGA monomer free of ionic impurities is reported. It is also shown how to obtain stable aqueous solutions of nonionic poly(NAGA) so that the UCST behavior can be exploited in pure water as well as in a physiological milieu. Further, ultrasensitive differential scanning calorimetry and light scattering were used to get insights into the phase separation mechanism. We believe that this knowledge is transferable to other systems and will greatly accelerate research in the field of macromolecules that feature thermally reversible hydrogen bonding.

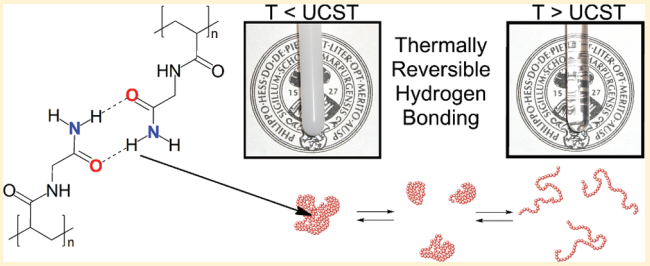

1. INTRODUCTION

Stimuli-responsive polymers or "smart" polymers exhibit a predictive and sharp change in properties upon only small changes in the environment (e.g., temperature, pH, ionic strength, radiation, mechanical stimuli).[1] These changes can result in phase separation from aqueous solution or order-of-magnitude changes of hydrogel size and water content. One class of smart polymers are thermoresponsive polymers, the best known example being Poly(*N*,*N*-isopropylacrylamide) (PNiPAAm) which shows a lower critical solution temperature (LCST). It undergoes phase separation from dilute aqueous solution at approximately 33 °C.[2] Above this temperature the dissolved polymer changes from the coil to the globule conformation. PNiPAAm and related polymer systems have been well characterized and are widely used to design smart materials.[3] Current applications are bioseparation and drug delivery, the development of new biocatalysts, biomimetic actuators, and surfaces with switchable hydrophobic−hydrophilic properties.[1,4,5]

In contrast to the LCST polymers, only a few polymeric materials with an upper critical solution temperature (UCST) in water are known.[6−13] In most cases, the UCST is based on either ionic interactions or hydrogen bonding. The first is observed for some polybetaines.[11−13] However, the electrostatic interactions of polyelectrolytes (e.g., polybetaines) are disturbed by the presence of salts which makes them unsuitable for the application under physiological conditions. For this reason, novel nonionic polymer systems showing sharp UCST-type phase transitions over a wide range of concentrations and being tolerant to electrolytes are highly desirable. Despite the high potential of such systems, research had been limited to a few scattered publications and patents that focused on the application instead on the phase transition itself and lacked important aspects concerning sample preparation and stability.[6,14−17] We believe that progress has been hindered because of poor reproducibility. In this study, drawing on the example of poly(*N*-acryloyl glycinamide) (poly(NAGA)), sample preparation, sample stability and the basic features of its thermoresponsive behavior are discussed in particular.

Poly(*N*-acryloyl glycinamide) (Chart 1) is long known. It has first been synthesized by Haas and Schuler in 1964.[18] They found that poly(NAGA) can form thermoreversible gels in concentrated aqueous solutions.[18−23] Haas and Schuler showed that hydrogen bond interrupting agents like thiocyanate or urea can prevent the formation of the gel.[19] Furthermore, they calculated that the average number of groups involved in a cross-link is too low to form crystallites.[20] This was supported by the extremely low heat of formation per cross-link. They estimated it to be −5 to −12 kcal/mol of cross-links.[22] They concluded that the cross-linking is based on randomly distributed hydrogen bonds.

Received: September 9, 2011
Revised: November 14, 2011
Published: December 16, 2011

Chart 1. Poly(NAGA) Bearing H-Donor and H-Acceptor Sites (Left) That Can Be Blocked by Thiocyanate Salts (Right)

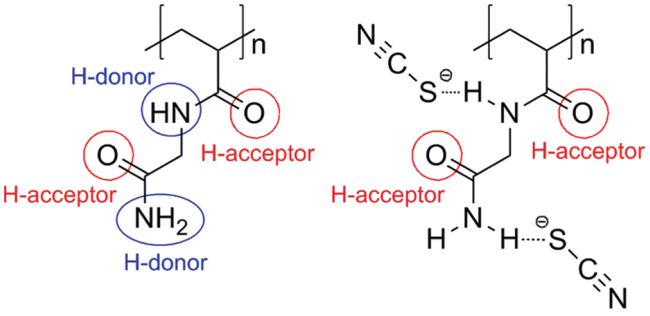

In dilute solutions, poly(NAGA) does not show thermoreversible gelation. However, despite looking transparent and homogeneous, the solution contains polymer aggregates. This was first evidenced by a nonlinear dependency of the reduced viscosity from the polymer concentration in pure water and the fact that the viscosity dropped significantly upon addition of sodium thiocyanate.[19] Later, the conclusions of Haas and Schuler were confirmed by light scattering[24] and Raman spectroscopy.[25]

Despite studying the thermoreversible gelation of poly(NAGA) an upper critical solution temperature has not been reported in the publications mentioned above. The UCST of poly(NAGA) and derivatives like poly(*N*-asparagine amide) was first mentioned in some patents by Ohnishi et al.[15−17] On the basis of these patents we published the first study on the UCST behavior of poly(NAGA) and its copolymers with *N*-acetyl acrylamide as a comonomer.[26] The copolymerization parameters as well as the correlation between the cloud point and the copolymer composition, polymer concentration and presence of electrolytes were examined.

The first controlled radical polymerization of poly(NAGA) and poly(*N*-asparagine amide) by the RAFT process was achieved by Lutz et al. but no UCST was observed for poly(NAGA)[27] and a strong positive molecular weight dependence for poly(*N*-asparagine amide).[28] Both phenomena will be discussed and explained in this study.

We were surprised by the fact that the UCST behavior of poly(NAGA) has not been reported in open literature although the polymer is known since 1964. In this work we demonstrate that the upper critical solution behavior in water of poly(NAGA) is suppressed by traces of ionic groups that can be introduced unintentionally by monomer impurities prior to polymerization, by polymer hydrolysis, by the use of ionic radical initiators or ionic chain transfer agents. We believe that poly(NAGA) used in previous studies contained traces of ionic groups that were responsible for the absence or irreproducible UCST behavior, thus explaining why this key feature remained unpublished. In this work, it is shown how to obtain stable aqueous solutions of nonionic poly(NAGA) including the monomer synthesis, polymer synthesis and the dissolution of the polymer in water. From the dissolution conditions the temperature, time and the surprisingly strong influence of the material of the vessel used for dissolution are highlighted. It is also shown that these findings do not interfere with the applicability in aqueous solution or biological fluids. Finally, it is demonstrated how the phase transition can be analyzed by employing powerful methods such as microcalorimetry or light scattering.

Scheme 1. Synthesis for *N*-Acryloyl Glycinamide According to Haas et al.[18] [a]

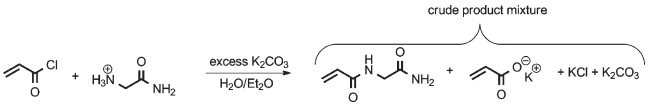

[a] The crude product mixture contains potassium acrylate as a side product.

2. RESULTS AND DISCUSSION

2.1. Synthesis of Acrylate Free *N*-Acryloyl Glycinamide. The procedure used for the synthesis of NAGA had crucial influence on the UCST behavior of the corresponding polymer (poly(NAGA)). The conventional synthesis of the monomer *N*-acryloyl glycinamide as reported many years ago by Haas and Schuler followed by others is troubled by the fact that potassium acrylate is a side product of the synthesis (Scheme 1).[18,25,27]

If residues of potassium acrylate remain in the monomer subsequent polymerization leads to the incorporation of acrylic acid units into the polymer backbone. Even small amounts of carboxyl groups in the resulting polymers caused a dramatic suppression of the UCST (further discussion in the section Suppression of the UCST by Ionic Groups in the Polymer). Also, the formation of readily polymerizable potassium acrylate during synthesis bears a high risk of premature polymerization during synthesis and work-up. To prevent the formation of large amounts of potassium acrylate during synthesis and to minimize the risk of premature polymerization a new modified synthetic procedure is developed. Acryloyl chloride should not be used in excess as done in previously reported procedures because it is not necessary for obtaining good yields. An excess would result in quantitative formation of potassium acrylate. The potassium carbonate solution should not be added to a solution of glycinamide hydrochloride and acryloyl chloride as done by Haas and Schuler. This facilitates the hydrolysis of acryloyl chloride to potassium acrylate, and in our experiments, we experienced premature polymerization 4 times out of 7 during synthesis. Instead, acryloyl chloride should be added dropwise to the glycinamide solution. Another critical step of the synthesis is the removal of water from the crude product mixture during work-up. To prevent unwanted polymerization water should be removed by lyophilization instead of rotary evaporation. Also, recrystallization alone is not sufficient to obtain an acrylate free monomer. Suitable methods are the Soxhlet extraction with diethyl ether or column chromatrography. Soxhlet extraction, however, is inconvenient because of long extraction times, varying yields due to poor penetration of the crude product mixture and the formation of polymeric impurities. Extraction with acetone followed by column chromatography and subsequent recrystallization from a mixture of methanol and acetone was found to yield an acrylate free monomer as colorless, transparent crystals in a reproducible good yield (75%). Recently, we published the crystal structure of NAGA.[29] Standard methods such as NMR, IR, TLC, and CHN analysis are not sensitive enough to detect significant differences in monomer purity. Separation by liquid chromatography using a conventional C18 column was also unsuccessful. Instead, the determination of the melting point by DSC (Figure 1), determination of residual potassium by flame atomic absorption spectroscopy and direct quantification of acrylate by capillary electrophoresis

dx.doi.org/10.1021/ma202059t |*Macromolecules* 2012, 45, 374–384

(Figure 2) proved to be useful. Table 1 compares the conventional method of preparation with our newly modified method in terms of product purity. Previously reported melting points (129,[18] 140−141,[21] and 136−136.5 °C[30]) were lower than observed for NAGA made in this work. A direct proof for the presence of acrylate impurities in conventionally synthesized NAGA could be obtained by capillary electrophoresis. In contrast, NAGA synthesized by our method did not show an acrylate signal. As the majority of impurities are potassium salts (Scheme 1) determination of the residual potassium content by flame atomic absorption spectroscopy is also suitable for controlling the product purity. The residual potassium content of NAGA synthesized by our method was 4.6 ppm and negligible in comparison to NAGA made by the conventional procedure (9700 ppm). Both NAGAs were polymerized under similar reaction conditions i.e. in DMSO using AIBN as initiator at 70 °C. The poly(NAGA) made from monomer that was synthesized according to the conventional literature procedure showed no UCST while acrylate free NAGA (this work) showed an UCST.

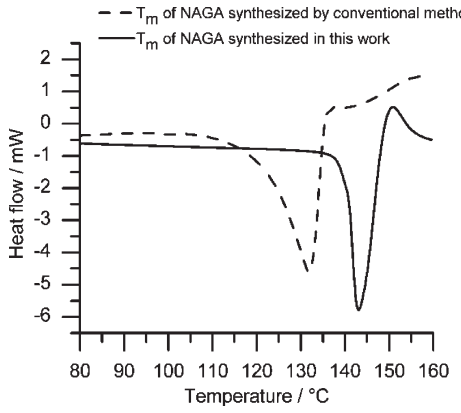

Figure 1. Melting point of *N*-acryloyl glycinamide determined by differential scanning calorimetry at a heating rate of 10 K/min. After melting, the monomer polymerizes, causing an exothermic heat flow.

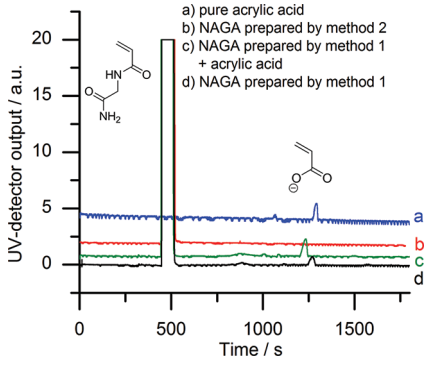

Figure 2. Capillary electrophoresis for the detection and quantification of acrylate impurities in *N*-acrylate glycinamide after different methods of preparation.

2.2. Turbidity Curve of Poly(NAGA) in Water: Basic Considerations. To follow changes in the UCST behavior, the cloud points upon cooling and heating were determined using turbidimitry as a major tool (a movie of the UCST transition is available in the HTML version of this paper). Therefore, it is necessary to discuss the basic features and major influences on the turbidity curve. The turbidity curve of poly(NAGA) shows a large hysteresis (Figure 3). At a polymer concentration of 1.0 wt % and a heating rate of 1.0 °C/min it is 10 °C. From a thermodynamic point of view the cloud point upon cooling and heating must be identical when the system has got sufficient time for relaxation. Indeed, the hysteresis observed is a kinetic phenomenon. According to our synthesis and sample preparation the phase transition temperature of a 1.0 wt % poly(NAGA) solution is about 22−23 °C. Cooling at a rate of 1.0 °C/min led to a cloud point of 13.7 °C. Between the phase transition temperature and the cloud point upon cooling the solution is thermodynamically instable although relaxation occurs very slowly. When cooled from 50 to 18.5 °C followed by keeping the temperature constant for 5 d, the slow growing of aggregates could be followed by conventional dynamic light scattering and turbidimetry (Figure 4). In another experiment, the same solution was cooled and kept constant at 22 °C. Still phase separation took place, although it proceeded extremely slowly. The transmittance

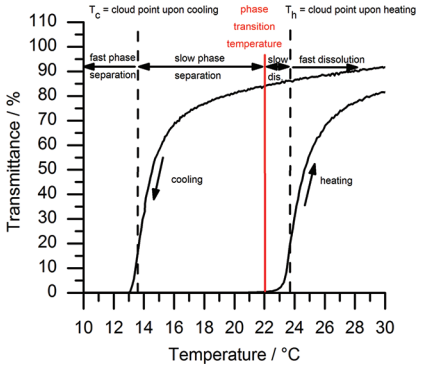

Figure 3. Turbidity curve of a 1.0 wt % poly(NAGA) solution in pure water at a heating rate of 1.0 °C/min.

Table 1. Comparison of the Purity of N-Acryloyl Glycinamide after Two Different Methods of Preparation

method	1 (conventional procedure)	2 (this work)
eq acryloyl chloride used in synthesis[a]	1.20	0.98
purification[b]	extraction with methanol/acetone (v/v = 1/2) + recrystallization therefrom[b]	extraction with acetone + column chromatography + recrystallization from methanol/acetone (v/v = 1/2)
T_m (DSC)/°C[c]	132	143
K-content/ppm	9700 (acrylate <0.7 mol %)	4.6 (acrylate <0.00033 mol %)
acrylate content (capillary electrophoresis)/wt %	0.12	<0.01
UCST behavior of resulting polymers?[d]	no	yes

[a] 1.20 equiv were used in all previous publications.[18,25,27] [b] Haas and Schuler recrystallized from methanol/acetone (v/v = 1/2), Marstokk et al. from methanol/acetone (v/v = 1/1) and Lutz et al. from pure acetone. [c] Previously reported melting points: 129, 140−141, and 136−136.5 °C.[18,21,30] [d] No UCST = no phase separation of a 1.0 wt % solution in pure water upon cooling in an ice bath.

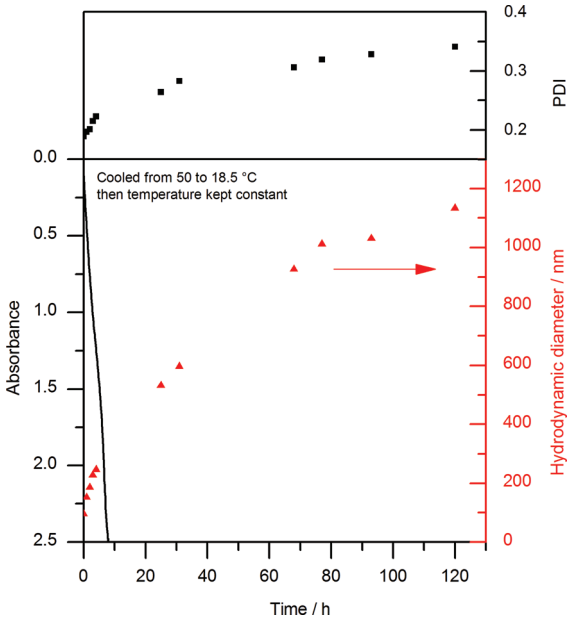

Figure 4. Slow formation of aggregates in a 1.0 wt % aqueous solution of poly(NAGA) after a drop of temperature from 50 to 18.5 °C. The temperature was kept constant for 120 h.

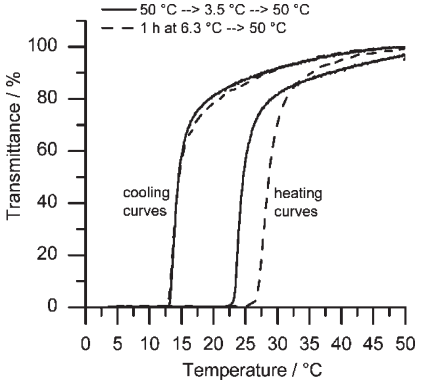

Figure 5. Influence of thermal history on the cloud point upon heating. Two turbidity measurements of the same 1.0 wt % aqueous solution of poly(*N*-acryloyl glycinamide) at a heating rate of 1.0 °C/min. Solid curve = cooled from 50 to 3.5 °C and heated back to 50 °C. Dashed curve = sample was tempered at 6.3 °C for 1 h before heating to 50 °C followed by cooling to 3.5 °C.

dropped to 7% (absorbance of 1.1) within 37 h and was still decreasing when the experiment was aborted. From this experiment and the fact that the phase transition temperature must be below the cloud point upon heating it was concluded that the phase transition temperature is between 22 and 23 °C. When the complementary experiment was performed involving heating from 4 to 18.5 °C, no dissolution was observed. This showed the cloud point upon cooling being dependent on the cooling rate. The cloud point upon heating, on the other hand, is dependent on the thermal history below the phase transition temperature and thereby indirectly dependent on the heating rate. In a separate experiment, we could show that the cloud point upon heating is shifted to higher values when the sample is tempered for longer time intervals below the phase transition temperature (Figure 5).

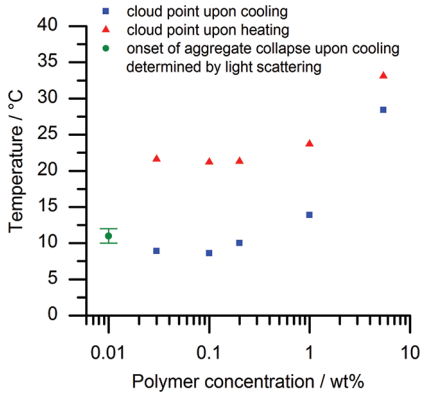

Figure 6. Phase transition temperature as a function of concentration (note the logarithmic scale) of poly(NAGA) in pure water. The heating rate for the cloud point measurements was 1.0 °C/min except for c = 0.03 wt % where it was 0.1 °C/min.

Recently, we have shown that the cloud point of aqueous poly(NAGA) solutions increases with increasing polymer concentration[26] as it is expected for polymers showing UCST behavior. In dilute solutions the concentration dependence of the cloud point is less prominent (Figure 6, note the logarithmic scale). This observation is similar to the phase transition behavior of PNiPAAm.[31,32]

For all the reasons mentioned above it is important to keep the polymer concentration as well as the heating program constant when comparing the UCST behavior of different polymers. In respect to time exposure and sensitivity a concentration of 1.0 wt % and a heating rate of 1.0 °C/min were considered most appropriate for the majority of turbidity measurements.

2.3. Suppression of the UCST by Ionic Groups in the Polymer. The role of ionic groups in suppressing the UCST of poly(NAGA) was confirmed by deliberately adding acrylic acid prior to polymerization of NAGA. The corresponding polymers were designated according to the acrylic acid content in the feed in mol %, i.e., AA0.01, AA0.10, AA0.21, AA1.00, and AA5.00. It was found that just small amounts of carboxyl groups dramatically suppress the UCST (Table 2).

Poly(NAGA) sythesized from acrylate free monomer (acrylate content <4 ppm) showed a cloud point at 13.7 and 23.5 °C in cooling and heating cycles, respectively. The addition of acrylic acid in even very low amounts (AA0.01 and AA0.10) led to a decrease in UCST. The UCST disappeared completely on increasing the amount of acrylic acid to 0.21 mol % and beyond. The shielding of the carboxylate groups by electrolytes counteracts these effects. In phosphate buffered saline the cloud point of the polymers AA0.01 and AA0.1 with low carboxylate content recovers to the level of the cloud point of nonionic poly(NAGA). Having no cloud point in pure water AA1.00 shows a cloud point in PBS, although it is slightly lower than this of nonionic poly(NAGA). If the acrylic acid content is further increased to 5.0 mol % the cloud point is absent even in PBS showing that carboxyl contents higher than 1 mol % started to influence the hydrophilic−lipohilic balance in a significant manner.

This fact of suppression of UCST by ionic groups was further supported by functionalization of the chain end groups by using chain transfer agents or ionic initiators. The results showed that ionic groups in general are the cause of cloud point/UCST suppression. Recently, Lutz et al. performed RAFT polymerization

dx.doi.org/10.1021/ma202059t |*Macromolecules* 2012, 45, 374–384

Table 2. Influence of Ionic Groups on the Cloud Point of 1.0 wt % Poly(NAGA) in Pure Water and Phosphate Buffered Saline, Respectively[a]

					cloud point/°C			
					pure water		phosphate buffered saline	
polymer code	CTA	acrylic acid in feed/mol %	polymerization medium	initiator	cooling	heating	cooling	heating
poly(NAGA)-std	-	<4 ppm[b]	DMSO	AIBN	13.7	23.5	10.2	21.3
AA0.01	-	**0.01**	DMSO	AIBN	11.4	19.9	9.7	20.4
AA0.10	-	**0.10**	DMSO	AIBN	2.5	13.0	10.0	20.9
AA0.21[c]	-	**0.21**[c]	DMSO	AIBN	none	none	n.d.	n.d.
AA1.00	-	**1.00**	DMSO	AIBN	none	none	8.1	19.1
AA5.00	-	**5.0**	DMSO	AIBN	none	none	none	none
RAFT_1	**BCPS**[d]	<4 ppm[b]	DMSO	AIBN	none	none	3.8	10.5
RAFT_2	DBTC[f]	<4 ppm[b]	DMSO	**VA-044**[e]	none	none	13.4	22.2
RAFT_3	DBTC[f]	<4 ppm[b]	DMSO	AIBN	15.7	25.7	11.4	22.6
poly(NAGA)-KPS	-	<4 ppm[b]	water/isopropanol	**KPS**[g]	11.8	22.1	8.1	18.9

[a] The source of ionic groups that caused depression or absence of the cloud point was printed in bold letters. [b] Acrylic acid originating from the monomer synthesis is present in the form of potassium acrylate. According to flame atomic absorption spectroscopy the potassium content was 4.6 ppm; hence, the potassium acrylate content is below 4 ppm. [c] Polymer resulting from the polymerization of NAGA that was synthesized using method 2 (Table 1). Acrylic acid is present in the form of a potassium acrylate impurity that was quantified by capillary electrophoresis. [d] BCPS = sodium 3-(((benzylthio)-carbonothioyl)thio)propane-1-sulfonate. [e] 2,2′-Azobis[2-(2-imidazolin-2-yl)propane]dihydrochloride. [f] DBTC = dibenzyl trithiocarbonate. [g] KPS = potassium persulfate.

of NAGA in water using sodium 3-(((benzylthio)carbonothioyl)-thio)propane-1-sulfonate as CTA and VA-044 as initiator.[27] The resulting polymers possessed sulfonate groups at the ω chain ends and partly imidazolium chloride moieties at the α chain ends originating from the initiator VA-044 which was used in the ratio CTA/initiator = 3/1. These polymers did not display a cloud point in pure water at least up to a degree of polymerization of 500. The absence of an UCST could be due to acrylate impurities in the monomer as the monomer was synthesized by the conventional monomer synthesis or hydrolysis during the polymerization in water (overnight at 60 °C). For this reasons the polymer synthesis reported by them was repeated with acrylate free monomer in DMSO as a solvent with substitution of either the CTA and/or the initiator with a nonionic compound (polymers RAFT_1, RAFT_2, and RAFT_3 in Table 2). In all cases the chain ends were functionalized by the RAFT agent as determined by NMR spectroscopy. The average degree of polymerization (P_n) was estimated from the integral ratio of the phenylic protons compared to the methylene protons adjacent to the nitrogen (NMR sepctra in the Supporting Information). It was calculated to be 189, 160, and 118 for RAFT_1, RAFT_2, and RAFT_3, respectively. Some of the α chain ends were functionalized by the initiator. Since the initiator signals overlap with polymer signals it was not possible to estimate the amount iniator derived chain ends. Hence, the real P_n will be slightly lower than calculated. However, for the conclusions drawn it is sufficient to know that the P_n was in the range of 100 to 200. If the ω chain end was functionalized with sulfonate (RAFT_1) the cloud point was absent in pure water. Switching to nonionic dibenzyl trithiocarbonate as CTA while using the ionic initiator VA-044 led to the same observation. This demonstrates that, despite being commonly neglected, a considerable amount of α chain ends was derived from the initiator in the RAFT process. At P_n = 100−200 the chain end counts for 0.5−1.0% in respect to NAGA units. Thus, the absence of a cloud point in pure water is in agreement with the findings for carboxyl groups where cloud points are absent for contents >0.10%. If the initiator as well as the transfer agent are nonionic (RAFT_3) a cloud point could be observed. Free radical polymerization of NAGA in a water/isopropanol mixture using potassium persulfate as initiator leads to a polymer with a molecular weight of 230 kDa (P_n = 1800).[25] This corresponds to only 0.06% in respect to NAGA units and explains why the cloud point is just slightly depressed compared to nonionic poly(NAGA).

2.4. Suppression of the UCST by the Hydrolysis of Amide Bonds of NAGA. Amides are relatively stable against hydrolysis, especially at neutral pH. However, despite proceeding slowly hydrolysis does occurr as shown for poly(acrylamide).[33,34] Hence, hydrolysis must be taken into account and it is necessary to choose the dissolution conditions carefully. Bringing the solid nonionic polymer into aqueous solution is not trivial. Temperatures greater 60 °C were necessary. On the other hand, higher temperatures accelerate the hydrolysis, which may result in loss of the UCST behavior. The influence of the temperature on the dissolution state and UCST behavior was investigated qualitatively (Table 3). On the basis of our observations the process of dissolution at elevated temperatures was categorized as follows: Category 1: swollen physically cross-linked hydrogel particles exist along with dissolved polymer. Category 2: the solution is clear and homogeneous above the cloud point and complete phase separation occurs below the cloud point. When the polymer precipitates an intransparent (path length = 1 cm) milk is formed. Within minutes further flocculation leads to visible particles that slowly sediment. Category 3: the solution shows decreasing turbidity upon cooling and decreasing tendency to flocculate. Category 4: the cloud point has disappeared, and the solution is clear over the whole temperature range. At 60 °C the polymer did not completely dissolve (category 1). At 70, 80, and 90 °C all four categories of dissolution are observed depending on the time of heating. At 70 °C in PP-tubes the cloud point

dx.doi.org/10.1021/ma202059t |*Macromolecules* 2012, 45, 374–384

Table 3. Influence of the Temperature and the Surface of the Used Vessel on the Progress of Dissolution and the Cloud Point of Poly(NAGA) in Pure Water[a]

		category of dissolution								
temperature/°C	vessel material	0.25 h	0.5 h	1 h	2 h	3 h	4.5 h	7 h	12 h	18 h
60	PP	1	1	1	1	1	1	1	1	1 + 4[b]
70	PP	1	1	1	1	2	2	3	4	4
80	PP	1	2	2	3	3	3	4	4	4
90	PP	1	2	2	3	4	4	4	4	4
80	borosilicate glass[c] (acidic)	1	3	3	3	4	4	4	4	4
80	borosilicate glass[c] (neutral)	1	3	4	4	4	4	4	4	4
80	borosilicate glass[c] (basic)	1	3	4	4	4	4	4	4	4
80	fused silica (neutral)	1	2	2	3	3	3	4	4	4

[a] All samples were dissolved without agitation at a concentration of 1.0 wt %. The temperature stated is the temperature inside the vessels. The dissolution process was divided into four categories. 1 = swollen physically crosslinked hydrogel particles exist along with dissolved polymer, the dissolved fraction shows thermoresponsivity. 2 = the solution is clear and homogeneous above the cloud point and complete phase separation occurs below the cloud point. When the polymer precipitates an intransparent (path length =1 cm) milk is formed. Within 10 min further flocculation leads to visible particles that slowly sediment. 3 = the solution shows decreasing turbidity upon cooling and decreasing tendency to flocculate. 4 = the cloud point has disappeared, and the solution is clear over the whole temperature range. [b] The cloud point of the dissolved polymer fraction disappeared. [c] Two borosilicate glass vials (Macherey-Nagel, N8−425, 1.5 mL, 11.6 × 32 mm, hydrolytic class I) were filled with either 1 M hydrochloric acid or pure water or 1 M sodium hydroxide and let to stand for 1 h. Thereafter all vials where rinsed 10 times with pure water, dried at 80 °C for 1 h, and used the same day. The results of both experiments were identical.

Table 4. Influence of the Hydrolysis at 75 °C on the Cloud Point of Poly(NAGA)

		cloud point/°C	
time/h[a]	additive	cooling	heating
0.5	-	11	21
1.5	-	7	17
3.0	-	4	14
5.0	-	0−3[b]	n.d.
5.0	9 mM NaCl	9.4	20.7
5.0	100 mM NaCl	9.0	20.4
8.5	100 mM NaCl	6.0	16.7

[a] Time that the polymer dispersion or solution was held at 75 °C. A 30 mg sample of dry polymer was dissolved in the measuring cuvette (Hellma, Suprasil, fused silica) at 75 °C in 2970 mg of pure water with magnetic stirring at 300 rpm to obtain a 1.0 wt % polymer solution. After 0.5 h, the solution appeared clear and the first measurement was conducted. [b] The cloud point was below the cooling limit of the turbidity photometer. The sample showed a cloud point when cooled in an ice bath for 5 min.

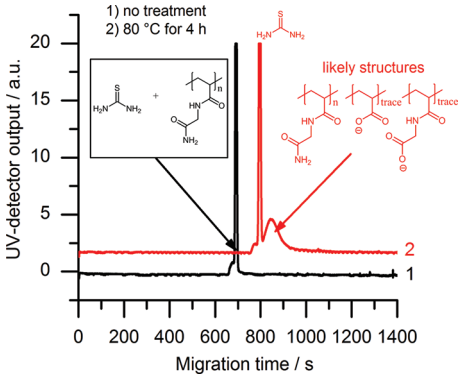

Figure 7. Proof for the formation of anionic units in poly(*N*-acryloyl glycinamide) by capillary electrophorsis. Curve 1 = electrophoresis of a 1 g/L solution of poly(NAGA) in 10 mM phosphate buffer. Curve 2 = electrophoresis of the same solution after heating it to 80 °C for 4 h in a glass vessel of hydrolytic class III. The migration time of the heat treated polymer is increased compared to the nonionic standard, hence indicating hydrolysis.

disappeared after 12 h, at 80 °C after 7 h and at 90 °C after 3 h. In fused silica vessels, the speed of hydrolysis is approximately the same whereas in borosilicate glass vessels the hydrolysis is much faster and the cloud point disappeared after 1 h at 80 °C. In addition to these qualitative results the proceeding decrease of the cloud point with prolonged heating was analyzed by turbidity measurements (Table 4).

As expected the thermoresponsivity could be recovered by adding a salt as long as the carboxyl content is low. Because of the small degree of hydrolysis a quantification of carboxyl groups was not possible. The presence of anionic moieties in the polymer backbone, however, could be proven by capillary electrophoresis (Figure 7). The migration time of a heat treated polymer solution (4 mL class vial, hydrolytic glass III, 4 h, 80 °C) was increased compared to a nonionic internal standard. The absolute migration times of the nonionic standard are not identical because the polymers get partially adsorbed at the capillary walls.

2.5. Influence of Surfaces on the Hydrolysis. The reproducible preparation of aqueous solutions of poly(NAGA) is complicated by the fact that the speed of hydrolysis is a function of many parameters. Apart from the temperature the surface of the vessel used for dissolution is of importance. For instance, the degradation of gelatin has been observed to proceed faster in glass vessels than in poly(propylene) vessels.[35] Gelatin is a biopolymer that contains amide bonds between its amino acid units and also shows a similar thermoreversible gelation, providing a good comparison to poly(NAGA). The authors argued that gelatin adsorbs at the glass wall causing an unfolding of the macromolecule. An effect that has been described by others.[36] It was assumed that gelatin is more prone to hydrolysis in its unfolded state. Our findings suggest a different conclusion.

dx.doi.org/10.1021/ma202059t |*Macromolecules* 2012, 45, 374–384

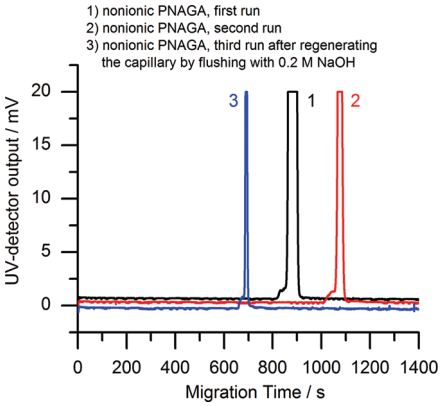

Figure 8. Capillary electrophoresis of nonionic poly(NAGA). In all runs, thiourea was used as nonionic internal standard. From run one to run two the migration time increased due to polymer adsorption to the wall of the fused silica capillary.

Indeed, poly(NAGA) adsorbs at glass walls which could be well observed in capillary electrophoresis experiments where capillaries from fused silica are used (Figure 8). The migration time of the neutral polymer increased strongly from one measurement to the next. This effect is well-known and a consequence of polymer adsorption.[37] Adsorbed polymer could be washed off with sodium hydroxide solution to regenerate an uncoated silica surface. However, the speed of hydrolysis which is indicated by the loss of the cloud point was not faster in fused silica vessels compared to poly(propylene) vessels (Table 2). In both vessels it took 7 h at 80 °C for the cloud point to disappear. Instead, hydrolysis was greatly accelerated in glass vessels containing alkali and alkaline earth metal oxides. The borosilicate vials used were of hydrolytic class I (alkaline release = 0.35 ± 0.05 mL 0.02 N H_2SO_4/10 g of glass, measured according to USP 25) and it took only 1 h until the cloud point disappeared at 80 °C. This conclusion is supported by the fact that acid treatment of these glasses prior to the test increased the time until cloud point loss to 4 h while neutral and basic treatment had no effect. The pH increase in the bulk solution by the leaching of alkali bases is not significant. The polymer, however, is crowded at the source of alkali base formation, namely the interfacial area with a high local pH. Thus, it is most likely the combination of adhesion and basic glass components that is responsible for this surprising acceleration of hydrolysis.

Along with surface effects goes an influence of the polymer concentration and volume to surface ratio (not investigated in this study). The real surface area in turn strongly depends on the surface roughness which further complicates the matter. The results described above show that the choice of vessel and dissolution conditions is essential and needs to be stated in great detail in order to conduct reproducible and comparable experiments. Poly(propylene) vessels seem to be most appropriate for the handling of poly(NAGA) solutions. Paying attention to all relevant dissolution conditions previeously discussed a reproducibility of sd(cloud point, four samples) = ± 0.2 °C for a 1.0 wt % solution of nonionic poly(NAGA) in pure water was achieved.

2.6. UCST in Human Blood Serum. The cloud point of poly(*N*-acryloyl glycinamide) can be influenced by additives. Chaotropic agents or hydrogen bond breaking agents like sodium thiocyanate reduce the cloud point[26] whereas kosmotropic agents like sulfate salt increase the cloud point. The question whether

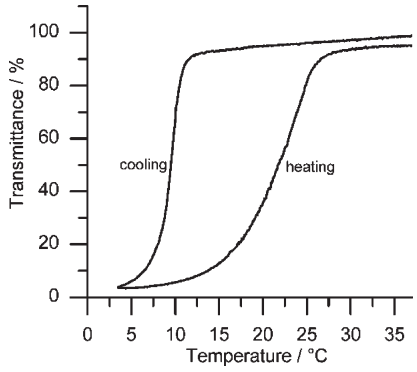

Figure 9. Turbidity curve of a 0.1 wt % solution of nonionic poly(*N*-acryloyl glycinamide) in 90 vol % human blood serum. Heating rate = 1.0 °C/min.

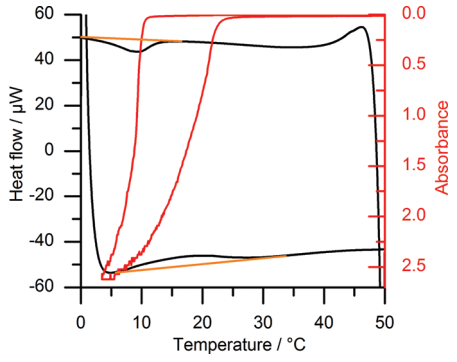

Figure 10. Differential scanning microcalorimetry (black curve) of a 1.0 wt % aqueous solution of poly(*N*-acryloyl glycinamide) overlaid with the turbidimetry curve (red curve) of a 0.2 wt % aqueous solution of the same polymer. A straight baseline (orange) has been added to the DSC curve for clarity. For both measurements, the heating rate was 1.0 °C/min. Measurement ranges of DSC: 50 to 0 °C, 10 min at 0 °C, and then 0 to 50 °C. Measurement ranges of turbidimetry: 50 to 3.5 °C, 3.5 to 50 °C. Note that the heat flow is scaled in µW.

the UCST transition of poly(NAGA) could be exploited in biomedical applications is of great interest and its answer will govern the path of further research in this field. As biological fluids are a complex mixture of compounds simple models like phosphate buffered saline are inadequate and tests in real biological fluids are necessary. For this purpose the human human blood serum was chosen. Figure 9 shows that poly(NAGA) displays a cloud point at 9.8 °C upon cooling and 24 °C upon heating at a heating rate of 1.0 °C/min despite the complex environment of blood serum. Although for specific applications the kinetics of the UCST transition need to be considered the results shown here are highly encouraging for further research in this direction.

2.7. Ultrasensitive Differential Scanning Calorimetry. For simplicity, we assume that the polymer solution separates into pure polymer and pure solvent phases. On this assumption, a polymer dissolves in a solvent when the change of the free enthalpy of dissolution ΔG is negative (eq 1).

$$\Delta G = \Delta H - T\Delta S \quad (1)$$

The LCST of PNiPAAm is due to the fact that both the change of enthalpy (ΔH) and the change of entropy (ΔS) are negative.

dx.doi.org/10.1021/ma202059t |*Macromolecules* 2012, 45, 374–384

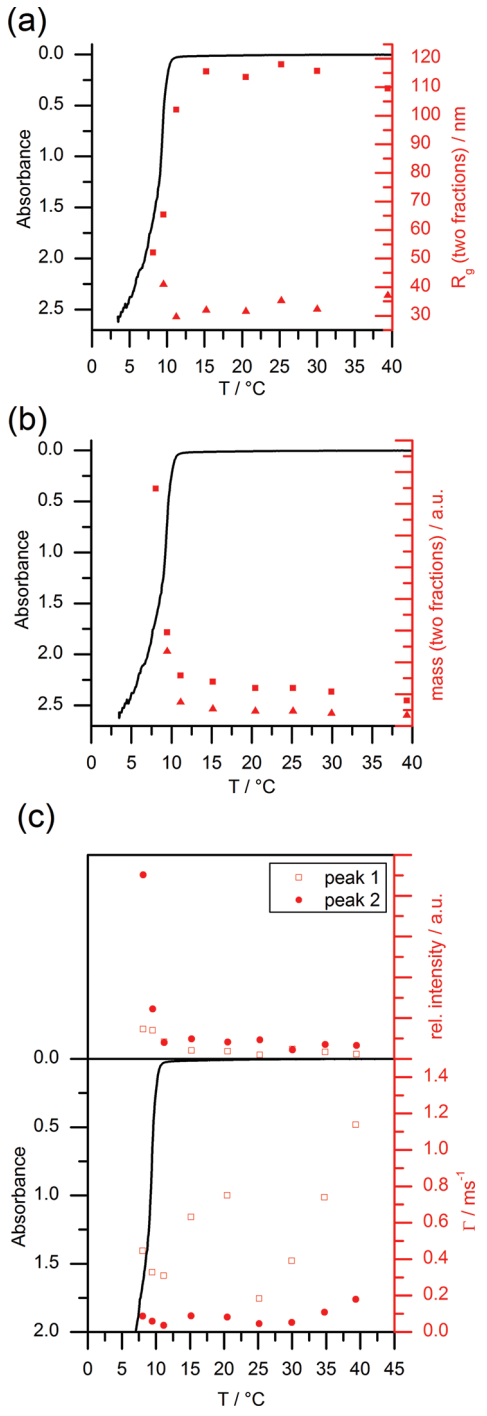

Figure 11. Light scattering results from a 0.01 wt % solution of poly(NAGA) in pure water. (a) Radii of gyration from static light scattering reveal two separable fractions (squares and triangles) which are plotted versus temperature. (b) Respective relative mass data are plotted for both fractions from static light scattering. (c) The inverse relaxation time of the fast mode (hollow squares) and the slow mode (solid circles) and their contribution to the overall scattering intensity are plotted versus temperature.

The negative change of entropy is explained by the highly ordered hydration shell of the isopropyl groups when the polymer is in solution (hydrophobic effect). With increasing temperature this effect contributes more to the change of free enthalpy until a critical temperature is reached where ΔG gets positive.

Scheme 2. Effect of Carboxyl Content on the UCST of Poly(*N*-acryloyl glycinamide) Solutions in Pure Water or Phosphate Buffered Saline, Respectively

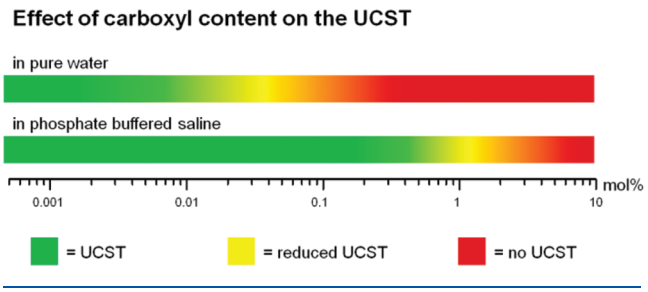

The polymer precipitates. For a polymer showing an UCST the opposite situation is expected. Both ΔH and ΔS should be positive. Poly(NAGA) does not contain a hydrophobic side chain as PNiPAAm. Therefore, the hydrophobic effect is small and the entropy change is dominated by the random distribution of chains in solution and the increased chain flexibility. In the solid state poly(NAGA) is stabilized by hydrogen bonding which is indicated by the very high glass transition temperature of 186 °C.[26] In order to bring the polymer into solution, these hydrogen bonds have to be cleaved. While the cleavage of the interpolymer amide−amide hydrogen bonds is an endothermic process the simultaneous formation of amide−water hydrogen bonds is exothermic. This greatly diminishes the overall observable change of enthalpy. For low molecular weight amides in water, the heat of formation of hydrogen bonds has been shown to be close to zero.[38]

Previous experiments to detect an enthalpy change by conventional differential scanning calorimetry have not been successful. In this study we used a calorimeter of much higher sensitivity in order to detect the assumed transition. Indeed we observed an exothermic peak upon precipitation and an endothermic peak upon dissolution (Figure 10). The heat of transition was determined to be 0.7 ± 0.4 J/g. The transitions were broad and close to the turning point of the heating profile which made it difficult to apply a reliable baseline. Therefore, a relatively large error has been introduced. To the best of our knowledge this is the first calorimetric evidence of a UCST transition of a poly(acrylamide) derivative. The ΔH values calculated from the cooling and heating curves are identical, indicating that the transition is fully reversible. Over nine consecutive DSC runs, there is no significant decrease in ΔH values. This is another indication for a good reversibility of the UCST transition.

2.8. Static and Dynamic Light Scattering. Polymers exhibiting a LCST like PNiPAAm undergo a coil-to-globule transition at a molecular level. The coil-to-globule transition of a single chain can be detected by dynamic and static light scattering.[39] Marstokk et al. have shown that poly(NAGA) does not molecularly dissolve in pure water.[25] Aggregates are present even at low concentrations. Only a 2 M solution of sodium thiocyanate was capable of breaking up the aggregates producing a molecular dispersion. Under these conditions, however, the UCST transition would also be suppressed. Although we were forced to accept the presence of aggregates, we will outline a brief qualitative discussion of our prelimenary light scattering results referring to a temperature series in pure water at a poly(NAGA) concentration of 0.01 wt %. Below the cloud point curve key parameters like the radius of gyration and the molecular mass of

dx.doi.org/10.1021/ma202059t |*Macromolecules* 2012, 45, 374–384

Scheme 3. Ionic Groups in Poly(NAGA) Reduce or Prevent the UCST in Pure Water[a]

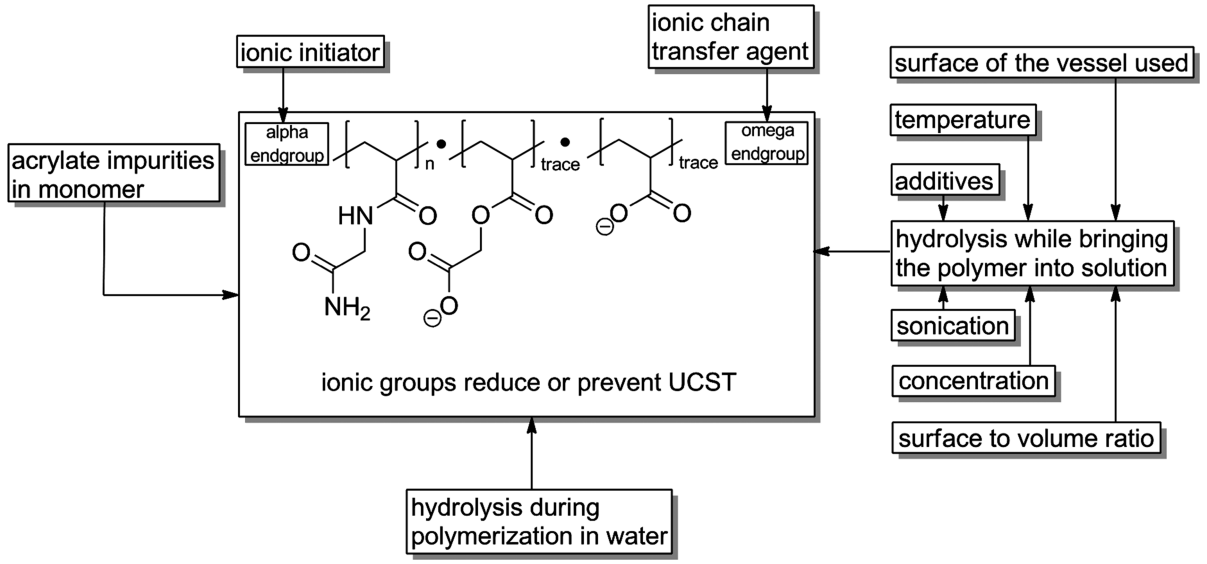

[a] The introduction of such groups can occur prior to polymerization, during polymerization or after polymerization by hydrolysis. The kinetics of hydrolysis are influenced by a multitude of parameters.

the present polymer particles changed drastically. At 40 °C we observed two well separated slopes in static light scattering curves (Supporting Information), each revealing a radius of gyration (Figure 11, a and b). One is close to R_g = 110 nm and a second one lies close to R_g = 37 nm with a relative mass of 1.0 and 2.4, respectively. The two separable values correspond to two different species and may be attributed to a single coil fraction and to an aggregate fraction. The dispersion was stable for at least 24 h. Over a period of 8 h, the temperature was successively decreased stepwise. Once the temperature dropped below 15 °C the size of the larger fraction shrank drastically until the two fractions merged at 8 °C with R_g = 52 nm. Simultaneously the relative mass of the aggregate fraction increased to 37, indicating that the polymer aggregates collapsed and became very compact. One can estimate that the density of the particles increased by more than 2 orders of magnitude during this temperature drop. To shed further light on this process and its participating species, we performed an inverse Laplace Transformation of the normalized electric field correlation function from dynamic light scattering at a scattering angle of 30°, where the signal-to-noise ratio is expected to be good enough. The transformation was based on the CONTIN routine representing the inverse relaxation times Γ of the contributing species and their intensity contributions (Figure 11c). In close agreement with the strongly bended curves from static light scattering, two well separated modes became discernible. As expected, the scattering intensity of the aggregates emphasized at this point that an evaluation of clear-cut trends from the CONTIN analysis always requires high precision data. Nevertheless, even with a prelimenary analysis at a single angle a decrease to 1/3 occurs for Γ from the fast mode (1.2/ms to 0.4/ms) which indicates a significant contraction of the species identified as the single chains. The slow mode seems to follow a similar trend. However, it is difficult to attribute any mechanistic features to these variations since aggregation is certainly overlaid by a condensation/collapse of the constituent chains. The overlay of such trends may even result in a minimum. Considering the uncertainty of the CONTIN analysis, such a minimum is also compatible with the trend in Γ of the slow mode.

3. CONCLUSION

Nonionic polymers bearing primary amide moieties, like poly(NAGA), can display an UCST in aqueous solution due to thermally reversible hydrogen bonding. In this study it was shown that traces of ionic groups in the polymer prevent phase separation of poly(NAGA) (Scheme 2). In the past, the UCST of poly(*N*-acryloyl glycinamide) had not been reported because ionic groups were introduced accidentally by either acrylate impurities in the monomer, hydrolysis of the polymer side chains and/or usage of ionic initiators (Scheme 3).

Monomer purity must be proven by stating physical properties and analytical data like the melting point and residual potassium content. The ionic groups can be shielded by counterions so that the addition of salts largely compensates the ionic groups UCST lowering effects. Nevertheless, the ability to control the electrostatics of the polymers is crucial. To avoid ionic groups in the polymer, some guidelines should be followed. During monomer synthesis acryloyl chloride should be used in deficit and acrylate impurities need to be thoroughly removed from the product, e.g., by column chromatography. To prevent hydrolysis of the polymer side chains polymerization should be performed in non-aqueous media or at lower temperatures. Also, when preparing aqueous solutions of poly(NAGA) the dissolution conditions have to be chosen with care. Prolonged heating to higher temperatures (T > 70 °C, t > 3 h) should be avoided to retain thermoresponsivity. In any case the dissolution conditions like temperature, time, concentration, material and dimensions of the vessel used and agitation should be stated in detail to ensure reproducibility. We believe that this knowledge is transferable to other systems and will greatly accelerate research in the field of UCST polymers.

Turbidity and DLS studies revealed that the phase transition temperature of a 1.0 wt % solution of poly(NAGA) in pure water

(according to our synthesis and sample preparation) is 22–23 °C. However, at conventional heating rates such as 1.0 or 0.1 °C/min, the turbidity curve displayed a large hysteresis. There was a temperature interval around the phase transition temperature where equilibration of the system was extremely slow. In dilute solutions (0.01 to 1.0 wt %) the phase transition temperature showed little concentration dependence. A combined static and dynamic light scattering goniometer was used in order to study the UCST transition on a molecular level. Solutions of poly(NAGA) in pure water contained aggregates even at 40 °C and very low concentrations such as 0.01 wt %. Below the phase transition temperature the radius of gyration of the aggregate fraction decreased, whereas its relative mass still increased. Hence, the density of the particles increased more than 2 orders of magnitude indicating that further aggregation took place simultaneously with a drastic shrinking of the aggregate dimensions.

We measured the first DSC trace of the UCST transition of this polymer class by employing an ultrasensitive calorimeter. As anticipated from basic thermodynamic considerations we found an endothermic heat of transition upon heating and an exothermic heat of transition upon cooling which corresponds to the cleavage and formation of polymer–polymer hydrogen bonds, respectively. The heat of transition is extremely low and was determined to be 0.7 ± 0.4 J/g. The transition appeared to be fully reversible over a number of at least 9 consecutive runs which involved heating up to 50 °C.

The sum of experiments showed that polymers featuring primary amide groups, like poly(*N*-acryloyl glycinamide), represent a powerful tool for the preparation of responsive materials that retain their function under physiological conditions. With its upper critical solution temperature in water poly(*N*-acryloyl glycinamide) complements the well investigated polymers with lower critical solution temperature in water such as poly(*N*-isopropylacrylamide). This work has established the synthetic and analytical base needed to exploit the inherent thermoresponsive properties of poly(NAGA).

■ ASSOCIATED CONTENT

Supporting Information. Materials, methods, experimental, and characterization details. **Web enhanced object.** A video of the UCST transition of two polymer samples with different cloud points is available online. This material is available free of charge via the Internet at http://pubs.acs.org.

Web Enhanced Feature. A movie of the UCST transition is available in the HTML version of this paper.

■ AUTHOR INFORMATION

Corresponding Author

*E-mail: agarwal@staff.uni-marburg.de.

■ ACKNOWLEDGMENT

The authors would like to thank the Philipps-University of Marburg for funding and the group of Prof. Barner-Kowollik (KIT) for the provision of dibenzyltrithiocarbonate. Also, we would like to express our gratitude to Christian Ortmann from TA Instruments and Prof. Ute Pyell from the University of Marburg for providing the experimental setup and assistance for ultra sensitive differential scanning calorimetry and capillary electrophoresis, respectively.

■ ABBREVIATIONS

BCPS, sodium 3-(((benzylthio)carbonothioyl)thio)propane-1-sulfonate; CTA, chain transfer agent; DBTC, dibenzyltrithiocarbonate; DLS, dynamic light scattering; DSC, differential scanning calorimetry; KPS, potassium persulfate; LCST, lower critical solution temperature; NAGA, *N*-acryloyl glycinamide; PNiPAAm, poly(*N*-isopropylacrylamide); UCST, upper critical solution temperature; USP, United States Pharmacopeia; RAFT, reversible addition–fragmentation chain transfer polymerization; TLC, thin layer chromatography

■ REFERENCES

(1) Cameron, A.; Shakesheff, K. M. *Adv. Mater.* **2006**, *18*, 3321–3328.
(2) Schild, H. G. *Prog. Polym. Sci.* **1992**, *17*, 163–249.
(3) Ren, L.; Agarwal, S. *Macromol. Chem. Phys.* **2007**, *208*, 245–253.
(4) Jun, L.; Bochu, W.; Yazhou, W. *Int. J. Pharm.* **2006**, *2*, 513–519.
(5) Kobayashi, J.; Okano, T. *Sci. Technol. Adv. Mater.* **2010**, *11*, 014111.
(6) Aoki, T.; Nakamura, K.; Sanui, K.; Kikuchi, A.; Okano, T.; Sakurai, Y.; Ogata, N. *Polym. J.* **1999**, *31*, 1185–1188.
(7) Katono, H.; Kohei, S.; Ogata, N.; Okano, T.; Sakurai, Y. *Polym. J.* **1991**, *23*, 1179–1178.
(8) Aoki, T.; Kawashima, M.; Katono, H.; Sanui, K.; Ogata, N.; Okano, T.; Sakurai, Y. *Macromolecules* **1994**, *27*, 947–952.
(9) Katono, H.; Maruyama, A.; Sanui, K.; Ogata, N.; Okano, T.; Sakurai, Y. *J. Controlled Release* **1991**, *16*, 215–228.
(10) Jiang, Z.; You, Y.; Gu, Q.; Hao, J.; Deng, X. *Macromol. Rapid Commun.* **2008**, *29*, 1264–1268.
(11) Zhang, Z.; Chao, T.; Chen, S.; Jiang, S. *Langmuir* **2006**, *22*, 10072–10077.
(12) Lowe, A. B.; Mc Cormick, C. L. *Chem. Rev.* **2002**, *102*, 4177–4190.
(13) Arotcarena, M.; Heise, B.; Ishaya, S.; Laschewsky, A. *J. Am. Chem. Soc.* **2002**, *124*, 3787–3793.
(14) Ohnishi, N.; Aoshima, K.; Kataoka, K., Ueno, K., *Stimuli-responsive polymer utilizing keto-enol tautomerization*. EP 0 922 715 A2, June 16, 1999.
(15) Ohnishi, N.; Furukawa, H.; Kataoka, K., Ueno, K., *Polymer Having An Upper Critical Solution Temperature*. US 7,195,925 B2, March 27, 2007.
(16) Nagaoka, H.; Ohnishi, N., Eguchi, M., *Thermoresponsive Polymer and Production Method Thereof*. US 2007/0203313 A1, August 30, 2007.
(17) Eguchi, M.; Ohnishi, N.; *Aqueous Solution of Polymer Having Upper Critical Solution Temperature, Aqueous Dispersion of Particle Modified with the Polymer and Method of Storing the Same*. EP 2 009 044 A1, December 31, 2008.
(18) Haas, H. C.; Schuler, N. W. *J. Polym. Sci., Part C: Polym. Lett.* **1964**, *2*, 1095–1096.
(19) Haas, H. C.; Moreau, R. D.; Schuler, N. W. *J. Polym. Sci., Part A-2* **1967**, *5*, 915–927.
(20) Haas, H. C.; Chiklis, C. K.; Moreau, R. D. *J. Polym. Sci., Part A-1* **1970**, *8*, 1131–1145.
(21) Haas, H. C.; MacDonald, R. L.; Schuler, A. N. *J. Polym. Sci., Part A-1* **1970**, *8*, 1213–1226.
(22) Haas, H. C.; Manning, M. J.; Mach, M. H. *J. Polym. Sci., Part A-1* **1970**, *8*, 1725–1730.
(23) Haas, H. C.; MacDonald, R. L.; Schuler, A. N. *J. Polym. Sci., Part A-1* **1970**, *8*, 3405–3415.
(24) Ostrovskii, D.; Jacobsson, P.; Nyström, B.; Marstokk, O.; Kopperud, H. B. M. *Macromolecules* **1999**, *32*, 5552–5560.
(25) Marstokk, O.; Nyström, B.; Roots, J. *Macromolecules* **1998**, *31*, 4205–4212.
(26) Seuring, J.; Agarwal, S. *Macromol. Chem. Phys.* **2010**, *211*, 2109–2117.
(27) Glatzel, S.; Badi, N.; Päch, M.; Laschewsky, A.; Lutz, J. *Chem. Commun.* **2010**, *46*, 4517–4519.

(28) Glatzel, S.; Laschewsky, A.; Lutz, J. *Macromolecules* **2011**, *44*, 413–415.
(29) Seuring, J.; Agarwal, S.; Harms, K. *Acta Crystallogr., Sect. E: Struct. Rep. Online* **2011**, *67*, o2170.
(30) Heilmann, S. M.; Smith, H. K. *J. Appl. Polym. Sci.* **1979**, *24*, 1551–1564.
(31) Fujishige, S.; Kubota, K.; Ando, I. *J. Phys. Chem.* **1989**, *93*, 3311–3313.
(32) Winnik, F. M. *Macromolecules* **1990**, *23*, 233–242.
(33) Kheradmand, H.; Francois, J. *Polymer* **1988**, *29*, 860–870.
(34) Muller, G. *Polym. Bull.* **1981**, *5*, 31–37.
(35) van den Bosch, E.; Gielens, C. *Int. J. Biol. Macromol.* **2003**, *32*, 129–138.
(36) Egger, D. K.; Valentine, J. S. *J. Mol. Biol.* **2001**, *314*, 911–922.
(37) Lucy, C. A.; MacDonald, A. M.; Glucev, M. D. *J. Chromatogr., A* **2008**, *1184*, 81–105.
(38) Mitchell, J. B. *Chem. Phys. Lett.* **1991**, *180*, 517–523.
(39) Wu, C.; Wang, X. *Phys. Rev. Lett.* **1998**, *80*, 4092–4094.

Macromolecules

Article

pubs.acs.org/Macromolecules

Stimuli-Responsive Nanocomposite Gels and Soft Nanocomposites Consisting of Inorganic Clays and Copolymers with Different Chemical Affinities

Kazutoshi Haraguchi,* Kazutaka Murata, and Toru Takehisa

Material Chemistry Laboratory, Kawamura Institute of Chemical Research, 631 Sakado, Sakura, Chiba 285-0078, Japan

ABSTRACT: A novel series of nanocomposite hydrogels (MD-NC gels), consisting of inorganic clay (hectorite) and specific copolymers with different chemical affinities for water, i.e., copolymers composed of hydrophobic (2-methoxyethyl acrylate: MEA) and hydrophilic (*N*,*N*-dimethylacrylamide: DMAA) units, were prepared by *in situ* free-radical polymerization in aqueous media at 20 °C. MD-NC gels showed outstanding stimuli sensitivities in response to changes in temperature, pH, salt concentration, and solvents in the surrounding aqueous solution as well as excellent, composition-dependent mechanical properties, such as a large elongations at break (≥1000%) and high strengths and moduli. After drying, the gels were changed into transparent, soft nanocomposites (MD-NCs) with high mechanical toughness and safety in *in vitro* cytotoxicity tests. The clay morphology in MD-NCs gradually changed on increasing the molar ratio of DMAA from a clay shell network of 20 nm thickness to a uniform dispersion of exfoliated clay platelets in a polymer matrix.

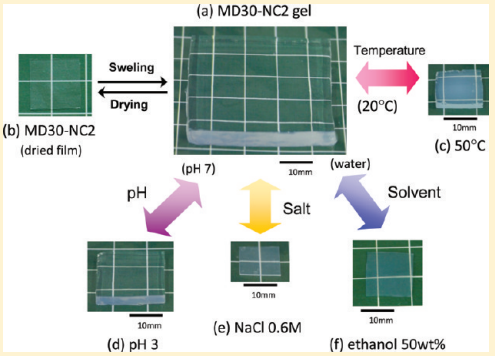

INTRODUCTION

Stimuli-responsive polymer hydrogels have attracted considerable attention as one of the most promising types of functional soft materials available because of their ability to undergo significant changes in volume and properties (e.g., transparency, modulus, absorption/desorption of solute, surface properties, etc.) in response to external stimuli or environmental changes.[1,2] So far, various kinds and/or forms of smart hydrogels have been studied for applications in intelligent devices such as sensors and actuators,[3] artificial insulin-control systems,[4] efficient bioseparation devices,[5] and biotechnological and tissue engineering devices[6,7] using different kinds of stimuli-sensitive polymers. Among them, poly(*N*-isopropylacrylamide) (PNIPA) and its corresponding hydrogels have been most intensively studied, since they exhibit a well-defined phase transition at a lower critical solution temperature (LCST)[8] that is experimentally convenient (around 32 °C) for the above-mentioned targets. However, in most cases, the PNIPA hydrogels, with conventional randomly cross-linked network structures, fracture easily at low stresses and deformations because polymer chains with a broad distribution of chain length between cross-linking points are successively broken due to the stress localization in the shorter chains present at any instant.[9] Therefore, for practical applications, it is difficult to handle them under conditions involving substantial stress and strain or to use them in macroscopic forms such as thin films, sheets, rods, and tubes. Also, the hydrogels become very hard, brittle solids when they are dried. Consequently, there was a need to create new hydrogels with good mechanical properties and high sensitivity and response to stimuli.

In 2002, a new class of polymer hydrogels, i.e., nanocomposite hydrogels (NC gels), with a unique organic (polymer)−inorganic (clay) network structure that satisfied both requirements was reported.[10] As an example, NC gels consisting of PNIPA and clay (hectorite) exhibited greatly improved mechanical, optical, and swelling−deswelling properties compared with those of chemically cross-linked hydrogels (OR gels) prepared using organic cross-linkers.[11,12] In addition, it was found that NC gels have a number of new functions related to optical anisotropy, biocompatibility, micropatterning, gel−air interfacing, and control of morphology.[13] Thus, the disadvantages of conventional OR gels, such as mechanical fragility, structural heterogeneity, low degrees of swelling, and low rates of shrinking, were simultaneously overcome by the introduction of NC gels. Thereafter, extensive studies were undertaken to improve their properties,[14,15] find new characteristics,[16] clarify the details of the polymer/clay network structure,[17,18] find new synthetic methods,[19] and create new kinds of NC gels.[20,21]

The extension of the synthesis of NC gels to a system composed of hydrophilic clay and hydrophobic polymer (poly(2-methoxyethyl acrylate): PMEA) results in micro- and macrophase separations during polymerization in the presence of the exfoliated clay, whereby a new class of soft nanocomposite (solid: M-NC) was developed.[22] M-NCs exhibit excellent transparency (structural uniformity) and tough

Received: September 20, 2011
Revised: December 6, 2011
Published: December 14, 2011

mechanical properties, despite their high clay content (10−50 wt %), due to their unique clay network morphology.

In the present paper, we report a novel NC gel consisting of inorganic clay (hectorite) and specific copolymers with different chemical affinities for water, i.e., copolymers composed of hydrophilic and hydrophobic monomers. These new NC gels show high mechanical toughness and outstanding stimuli-sensitivities in response to changes in temperature, pH, salt concentration, and solvents in the surrounding aqueous solution. In addition, after subsequent drying, the NC gels form transparent, functional, soft nanocomposites.

EXPERIMENTAL SECTION

Raw Materials. 2-Methoxyethyl acrylate (MEA) and *N,N*-dimethylacrylamide (DMAA), provided by Toagosei Co., Japan and Kohjin Co., Japan, respectively, were purified by filtering through activated alumina. Other reagents, initiator (potassium peroxodisulfate: KPS), and catalyst (*N,N,N′,N′*-tetramethylethylenediamine: TEMED) were purchased from Wako Pure Chemical Industries, Japan, and used without further purification. The water used for all experiments was ultrapure water supplied by a Puric-Mx system (Organo Co., Japan). Oxygen dissolved in the pure water was removed by bubbling N_2 gas for longer than 3 h prior to use, and oxygen was excluded from the system throughout the synthesis. The inorganic clay, synthetic hectorite "Laponite XLG" (Rockwood Ltd., U.K.; $[Mg_{5.34}Li_{0.66}Si_8O_{20}(OH)_4]Na_{0.66}$: layer size = 30 nm in diameter × 1 nm in thickness; cation exchange capacity = 104 mequiv/100 g), was used after washing and freeze-drying.

Synthesis of NC Gels and NCs Therefrom. Uniform aqueous solutions consisting of two kinds of monomers (MEA and DMAA), clay (Laponite XLG), KPS, and TEMED were prepared at 1 °C. The total concentration of monomers was fixed at 1 M. The molar ratio of the monomers, initiator, and catalyst was 100:0.426:0.735. Redox polymerization was carried out at 20 °C for 24 h. The resulting NC gels are termed MD-NC gels according to the specific comonomers (MEA and DMAA) used. The MD-NC gels with different compositions are represented as MD*x*-NC*n* gels, where x is the content of DMAA represented by $x = 100 \times [DMAA]/([DMAA] + [MEA])$ and n is the clay concentration ($C_{clay} = n$ mol/L H_2O) in the reaction solution. In this study, values of x and n were varied between 10 and 80 and between 1 and 7, respectively. The resulting gels (MD-NC gels) were subsequently dried at dried at room temperature for 2 days followed by drying for 24 h at 80 °C under vacuum in order to obtain the nanocomposites (MD-NCs). Solid MD-NCs with different compositions were similarly defined as MD*x*-NC*n*. Furthermore, the MD-NCs were subsequently immersed in water for 24 h to obtain the reswollen MD-NC gels.

Measurements. Thermogravimetric analysis (TGA): 10 °C/min, ∼600 °C, N_2 flow. Differential scanning calorimetry (DSC): 1 °C/min, −100 to 50 °C. Transmission electron microscopy (TEM): 50 nm thin film, 100 kV. Tensile mechanical tests: sample size 5.5 mm in diameter (for the gel) × 70 mm, 30 mm gauge length, 100 mm/min head speed. For NCs, the corresponding gel samples were dried before use. Swelling tests: sample size 5.5 mm in diameter × 30 mm length (of as-prepared gel), 2−80 °C for 24−100 h in water and aqueous solutions at pH 3, with 0.6 M NaCl and 50 wt % ethanol.

Cytotoxicity Tests. *In vitro* cytotoxicity tests of MD30-NC2, MD10-NC5, MD10-NC10, and M-NC2 were performed according to ISO 10993-5 (1999) guidelines in "Biological Evaluation of Medical Devices". Test conditions were as follows. Sample solutions were extracted in MEM (Minimum Essential Medium) culture medium for 24 h at 37 °C. Cell lines V79 from Chinese hamster lung fibroblast were obtained from Health Science Research Resources Bank (Japan). Cell lines with different concentrations of sample extracts (0−100%) were incubated for 7 days at 37 °C in air with 5% carbon dioxide. The cytotoxicity of each sample was determined quantitatively by measuring the number of living colonies after cultivation, using colony counter ProtoCOL System (Synoptics Ltd., Japan).

RESULTS AND DISCUSSION

Synthesis of MD-NC Gels (Hydrogel) and MD-NCs (Solid). Uniform nanocomposite hydrogels (MD-NC gels) were prepared by *in situ* free-radical copolymerization of two different types of monomers (MEA and DMAA) in the presence of exfoliated clay (hectorite: Laponite XLG) platelets in aqueous media. Since polymerization yields were greater than 98%, and the clay was completely incorporated into the hydrogel (Table 1), the compositions of the resulting MD-NC gels were virtually the same as those of the initial reaction solutions. MD-NC gels with different compositions are described as MD*x*-NC*n* gels where x is the mole percentage of [DMAA] and n is the clay concentration in mol/L H_2O. Here, it should be noted that homopolymers of each monomer show completely different characteristics: PMEA is water-insoluble and has a glass transition temperature (T_g) of −34 °C,[22] while PDMAA is water-soluble and has a T_g of 124 °C.[23] Therefore, in MEA/DMAA copolymer, the chemical affinity toward water should change from attractive (hydrophilic) to repulsive (hydrophobic) according to the composition of the polymer, i.e., the ratio of monomers used.

Table 1. Yield of Nanocomposite, Glass Transition Temperature (T_g), and Clay Content of MD*x*-NC*n*

			clay content (wt %)	
sample	yield[a] (%)	T_g (°C)	obs[b]	calc
MD10-NC2	98	−30	10.9	10.7
MD30-NC2	99	−10	11.0	11.2
MD50-NC2	98	14	11.2	11.7
MD80-NC2	99	67	12.0	12.3
MD10-NC5	98	−31	23.0	23.1
MD30-NC5	99	−10	23.5	23.9
MD50-NC5	99	16	24.5	24.9

[a]Yields were determined from the weights of dried material. [b]The clay content was evaluated by TGA.

A typical MD-NC gel (MD30-NC2 gel) is shown in Figure 1a. MD*x*-NC*n* gels were always uniform and mostly transparent for $x \geq 30$ regardless of the value of n, whereas at lower values of x, the transparency decreased with x; the gels were translucent at $x = 20$ and opaque for $x \leq 10$. The fact that uniform hydrogels were obtained without using any organic cross-linkers indicates that three-dimensional networks are formed throughout the MD-NC gel samples with the clay platelets acting as cross-linkers. Where $x \leq 20$, the transparencies of MDx-NC2 gels were low, probably due to the partially aggregated morphology of clay, as shown later.

Subsequently, transparent nanocomposites (solid: MD-NCs) were obtained by drying the as-prepared MD-NC gels, as shown in Figure 1b (MD30-NC2). The MD*x*-NC*n* were all transparent regardless of the values of x (even at $x \leq 20$) and n and showed a variety of mechanical properties including soft and flexible to hard and rigid, depending on the values of x and n. Also, it was observed that all MD*x*-NC*n* revert to hydrogels when immersed in water (Figure 1b → 1a). This behavior is completely different from that of soft nanocomposites, M-NC*n* (i.e., MD*x*-NC*n* where $x = 0$), which never revert to a hydrogel state.[22] Thus, by *in situ* free-radical polymerization at ambient temperature, MD-NC gels, and therefore, MD-NCs, can be readily prepared in various forms such as films, sheets, fibers, tubes, and bulk with uneven surfaces.

dx.doi.org/10.1021/ma202114z | *Macromolecules* 2012, 45, 385−391

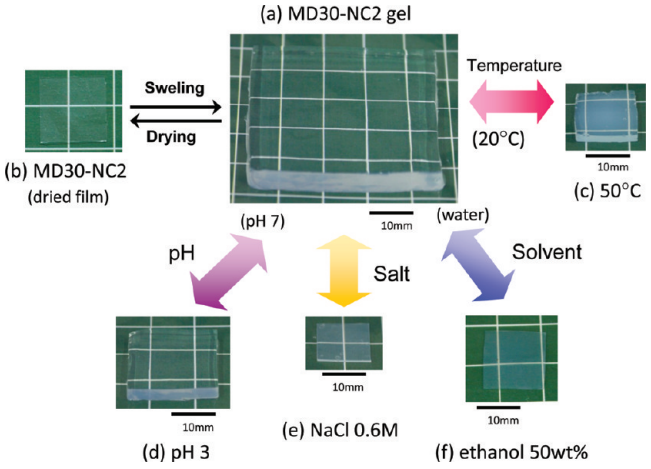

Figure 1. (a) Transparent and mechanically tough MD30-NC2 gel and (b) the soft nanocomposite (MD30-NC2) dried therefrom. The MD30-NC2 gel exhibits stimuli sensitivity in response to (c) temperature (20 ↔ 50 °C), (d) pH (7 ↔ 3), (e) salt concentration (NaCl, 0 ↔ 0.6 M), and (f) solvent (ethanol, 0 ↔ 50 wt %) in the surrounding aqueous solution. Here, images in (a)−(f) are different views of the same sample under different conditions.

Mechanical Properties of MD-NC Gels and MD-NCs. It was found that MD-NC gels show high mechanical toughness and withstand extensive deformation such as elongation, compression, bending, and tearing. Figure 2 (black lines)

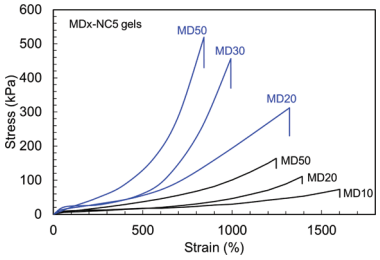

Figure 2. Tensile stress−strain curves for as-prepared MD*x*-NC5 gels (x = 10−50) (black lines). The blue lines represent the once-dried and reswollen MD*x*-NC5 gels (W_{H_2O}/W_{dry} = 400%).

shows tensile stress−strain curves for as-prepared MD*x*-NC5 gels (x = 10−50). The gels could be stretched to 1200−1600% (ε_b: elongation at break), and the ultimate tensile stress (σ) increased with x, e.g., 70 kPa (MD10-NC5 gel) and 165 kPa (MD50-NC5 gel). Similar changes in stress−strain curves were also observed by increasing the value of n at constant x. These characteristics of MD-NC gels were quite similar to those of NC gels consisting of hydrophilic homopolymers (e.g., PDMAA or PNIPA) and clay.[11,23]

It was also observed that the mechanical properties of nanocomposites (MD*x*-NC*n*), prepared by drying MD*x*-NC*n* gels, vary according to the values of x and n. In particular, at relatively low x (≤50) and n (≤5), the transparent MD*x*-NC*n* films exhibited remarkable toughness. Tensile stress−strain curves for MD*x*-NC2 and MD*x*-NC5 are shown in Figure 3 (blue and red lines). σ (ε_b) was 6.5 MPa (1000%), 9.5 MPa (650%), and 15 MPa (350%) for MD10-NC2, MD30-NC2, and MD30-NC5, respectively. Thus, at constant n, the initial modulus (E) and σ increased and ε_b decreased with increasing x. Accordingly, at constant x, the same tendency was observed with increasing n. In addition, analogous to M-NC*n* (x = 0)

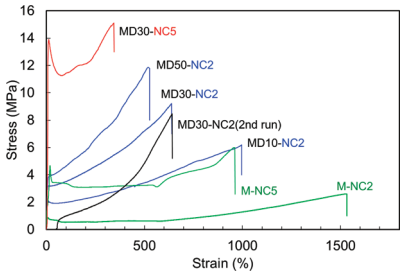

Figure 3. Tensile stress−strain curves for MD*x*-NC2 and MD*x*-NC5 (x = 10−50) (blue and red lines). The green lines represent M-NC2 (x = 0) and M-NC5 (x = 0). The black line shows the second run for MD30-NC2.

(green lines in Figure 3: M-NC2, M-NC5), MD*x*-NC*n* showed a tendency toward a yielding behavior with a maximum stress at a very low strain (about 10%) followed by significant elongation, although a definite necking phenomenon was not clearly observed since the stress increased more rapidly after the yield point compared with that for M-NC*n*. Further, it was observed that MD*x*-NC*n* exhibit different stress−strain curves on repeated cycling, as shown in Figure 3 (black line: the second run for MD30-NC2). Here, a simpler and reversible stress−strain curve was observed on repeated cycling, while σ and ε_b were almost constant in successive cycles. Thus, it was concluded that all MD*x*-NC*n* in the range of $1 \leq n \leq 5$ and $x \leq 50$ showed very tough mechanical properties despite their relatively high clay content (ca. 5−25 wt %), and their mechanical properties vary markedly depending on their composition (x, n) between the two types of NCs, i.e., M-NC*n* (x = 0, soft NC with $\varepsilon_b \geq 1000\%$) and D-NC*n* ($x$ = 100, hard NC with $\varepsilon_b < 30\%$).

In addition, MD-NCs when immersed in water can revert to MD-NC gels by absorbing water. It was found that reswollen MD-NC gels show tensile properties different to those of as-prepared samples, as shown in Figure 2 (black lines represent as-prepared MD*x*-NC5 gels and blue lines once dried and reswollen MD*x*-NC5 gels). Here, values of σ and E for the reswollen gels increased to approximately 2−4 times those of the as-prepared gel, while values of ε_b decreased to one-half or one-third of those of the as-prepared gels. This is because the cross-link density increased during the drying process. It was reported that the polymer−clay network structure of NC gels is changed irreversibly by drying due to the formation of additional cross-links (hydrogen bonds) between the clay and the polymer in the condensed (dried) state.[24] Similar phenomena should occur during the drying process of MD-NC gels.

Additional drying-swelling treatments produced no further changes in the tensile properties. This indicates that the network structure of MD-NC gels is only modified during the first drying process and that the network is then stable against repeated drying treatments. These results are also consistent with those observed for NC gels.[24]

Swelling Properties of MD-NC Gels. MD*x*-NC*n* gels showed equilibrium degrees of swelling (EDS) in water. It was found that values of EDS largely depended on the values of x and n, which serve to increase and decrease EDS, respectively, because of the high hydrophilicity of DMAA units, high hydrophobicity of MEA units, and the role of clay as a cross-linker. Figure 4 shows the dependence of EDS on x for MD*x*-NC*n* gels reswollen in water at 20 °C. Values of EDS, at

dx.doi.org/10.1021/ma202114z | Macromolecules 2012, 45, 385−391

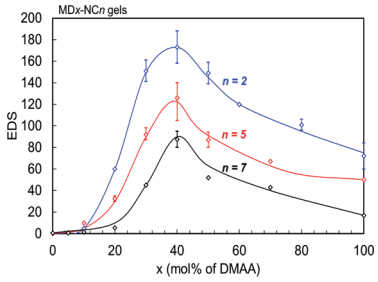

Figure 4. Effect of x on the degree of swelling for MDx-NCn gels (n = 2−7). Swelling conditions: water at 20 °C for 100 h.

constant n were maximal at x = 40. This is attributed to the combined effects of the hydrophilicity and cross-linking capability of the DMAA units because hydrophilic PDMAA[23] is more capable of forming cross-links with clay platelets than is PMEA.[22] Therefore, at low x (≤40), the degree of swelling increased with increasing x due to the increase in the system's hydrophilicity. However, at high x (>40), the degree of swelling decreased with increasing x because the formation of cross-links between PDMAA and clay becomes predominant. In contrast, at constant x, EDS decreased monotonically with increasing n due to increased cross-link density (Figure 4).

Sensitivity to Stimuli. It was found that MD-NC gels show thermosensitive swelling behaviors. For example, as shown in Figure 5a, reswollen MDx-NC2 gels exhibited

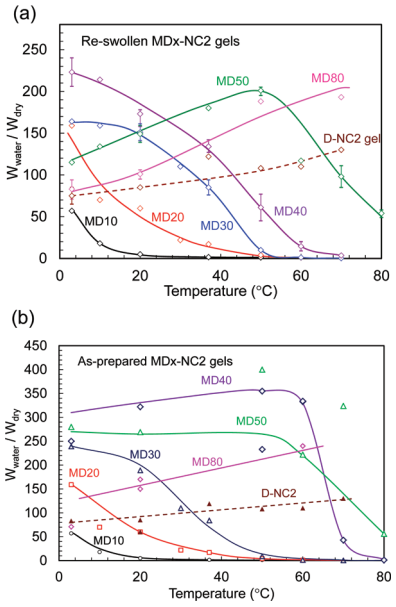

Figure 5. Temperature dependencies of the degree of swelling for the MDx-NC2 gels (x = 10−80). D-NC2 gel (x = 100) is indicated by a dotted line. (a) Once-dried and reswollen state. (b) As-prepared state.

remarkable changes in swelling behavior with temperature. This was particularly evident in gels with intermediate x, such as MD30-NC2 and MD50-NC2 gels. In both cases, the degree of swelling decreased markedly at high temperatures. Essentially, the temperature above which the swelling of gels decreased rapidly increased with x. On the other hand, at high values of x (>50), the temperature-induced deswelling decreased greatly with increasing x and did not occur in the case of the D-NC2 gel (x = 100) (Figure 5a: dotted lines). Thermosensitive swelling−deswelling behaviors were also observed in other MDx-NCn gels with different n; in general, the degree of swelling decreased with increasing n. Similar thermosensitive swelling behaviors were observed for as-prepared gels (Figure 5b: as-prepared MDx-NC2 gels), although the degree of swelling is generally higher than that of once-dried and reswollen MDx-NC2 gels (Figure 5a) due to the lower cross-link density of the undried samples. Thus, MDx-NCn gels showed well-defined thermosensitive swelling in addition to excellent mechanical and optical properties. Here, it should be noted that the pure constituents (PMEA, PDMAA, and clay) and the nanocomposite gel (D-NC gel) do not show thermosensitivity. The thermosensitivity and mechanical toughness that characterize MD-NC gels are attributed to the copolymerization of two monomers (MEA and DMAA) with different chemical affinities and the network-forming capability of the clay. Because MEA and DMAA have completely different properties, i.e., they are hydrophobic and hydrophilic, respectively, the solubility of their copolymers, MD, in water changes according to the ratio of the two monomers, which induces a large temperature dependence of the solubility due to the individual contributions of the two units. That is, at low temperatures, the MD copolymers dissolve in water due to strong hydrogen bonding between the hydrophilic DMAA units and water. At higher temperatures above LCST, the hydrogen bonding weakens and hydrophobic interactions with the MEA units become dominant. The temperature above which the deswelling of the MD-NC gels occurs is determined by the balance of hydrophilic and hydrophobic units in the copolymers. This is consistent with the results reported so far on copolymers comprising hydrophilic and hydrophobic monomers such as DMA and *N*-*tert*-butylacrylamide,[25] DMAA and MEA,[26−28] and their hydrogels.[26] In the case of the MD system, it was reported that MD copolymers form aqueous solutions with different cloud points depending on their compositions and that MD gels with weak chemical cross-links exhibit volume shrinkage with rising temperature even though they should be mechanically very weak.

It was also observed that MD-NC gels exhibit thermoreversible changes in gel volume and transparency. Figures 6a (MD20-NC2) and 6b (MD30-NC5) show the repeated changes in gel size (length) and transparency, respectively, by alternating the temperature between 20 and 50 °C. Furthermore, it was observed that MD-NC gels showed stimuli sensitivity in response to other stimuli such as pH, salt (NaCl) concentration, and solvent (ethanol) concentration in the surrounding aqueous solution (Figures 1d−f). For example, the reversible swelling−deswelling behaviors in response to changes of the NaCl concentration (0 ↔ 0.6 M) in the surrounding medium are shown in Figure 6c (MD30-NC2 gel). Thus, it was revealed that MD-NC gels exhibit reversible volume and transparency changes in response to various external stimuli in addition to having good mechanical toughness. The reasons why the MD-NC gels show the stimuli sensitivities in response to changes in pH, solvent, and salt concentrations, in addition to temperature, are attributed to the combined effects of clay and MD copolymer. As shown in a previous paper[29] (PDMAA or PNIPA), NC gels exhibit swelling behaviors characteristic of a polyelectrolyte gel due to the ionic nature of exfoliated clay incorporated in the network, where the degree of swelling changed with pH and salt (e.g., NaCl) concentration in the surrounding aqueous solution. MD-NC gels exhibit analogous changes in swelling with changes in pH and salt concentration. On the other hand,

dx.doi.org/10.1021/ma202114z | *Macromolecules* 2012, 45, 385−391

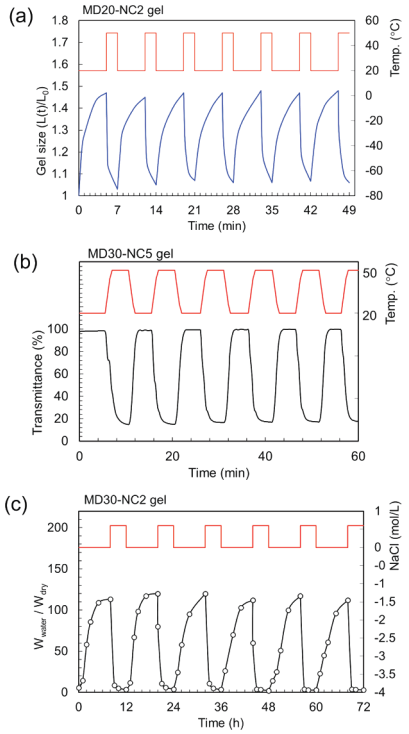

Figure 6. (a) Thermoreversible change in the gel size (length) of an MD20-NC2 gel by alternating the temperature between 20 and 50 °C. The initial dried gel size: 0.6 mm (width) × 0.09 mm (thickness) × 30 mm length. (b) Thermoreversible change in the transparency for MD30-NC5 gel by alternating the temperature between 25 and 50 °C. (c) Salt-induced swelling–deswelling behavior of a MD30-NC2 gel. The gels used in (a)–(c) are all reswollen after being dried once.

MD-NC gels exhibit deswelling behavior with increasing temperature, and the temperature above which deswelling occurs changes strongly depending on the copolymer composition (i.e., on the molar ratio of D), as shown in Figure 5. It is known that PNIPA hydrogels containing both hydrophilic (amide) and hydrophobic (isopropyl) groups in the same monomer unit undergo deswelling at temperatures above the LCST and that the swelling/deswelling behavior is strongly influenced by additives such as salt and solvent in the surrounding aqueous solution.[30,31] Because MD copolymers also consist of hydrophilic (DMAA) and hydrophobic (MEA) monomer units, their hydrogels (MD-NC gels) are expected to show similar effects of salt and solvent on their swelling/deswelling behavior, by analogy with PNIPA gels. The temperature-induced deswelling of MD-NC gels may be attributed to conformational changes in MD copolymers from hydrophilic (coil) to hydrophobic (globule) states with increasing temperature in a similar manner to that of PNIPA due to the hydrophobic hydration and dehydration.[32]

Network Structure of MD-NC Gels. All the characteristics of MD-NC gels, including excellent mechanical and optical properties and sensitivity to various stimuli, are a consequence of their network structure, consisting of clay and MD copolymer. It was reported that M-NC and D-NC gels, individually, show unique network structures; i.e., the M-NC clay–network morphology[22] consists of a large number of hollow spheres of aggregated clay platelets with PMEA chains packed inside, while the polymer–clay network structure of NC gels[10,11,17,18,23] consists of exfoliated clay platelets uniformly dispersed in aqueous media with a number of flexible polymer chains linking them together. In the present case of MD-NC gels, TEM observations revealed that the dried gels have clay morphologies intermediate between those of M-NCn (x = 0) and D-NCn (x = 100). For example, in MDx-NC2, the clay morphology changed with the value of x (10–30); as shown in Figure 7, the proportion of exfoliated clay platelets gradually

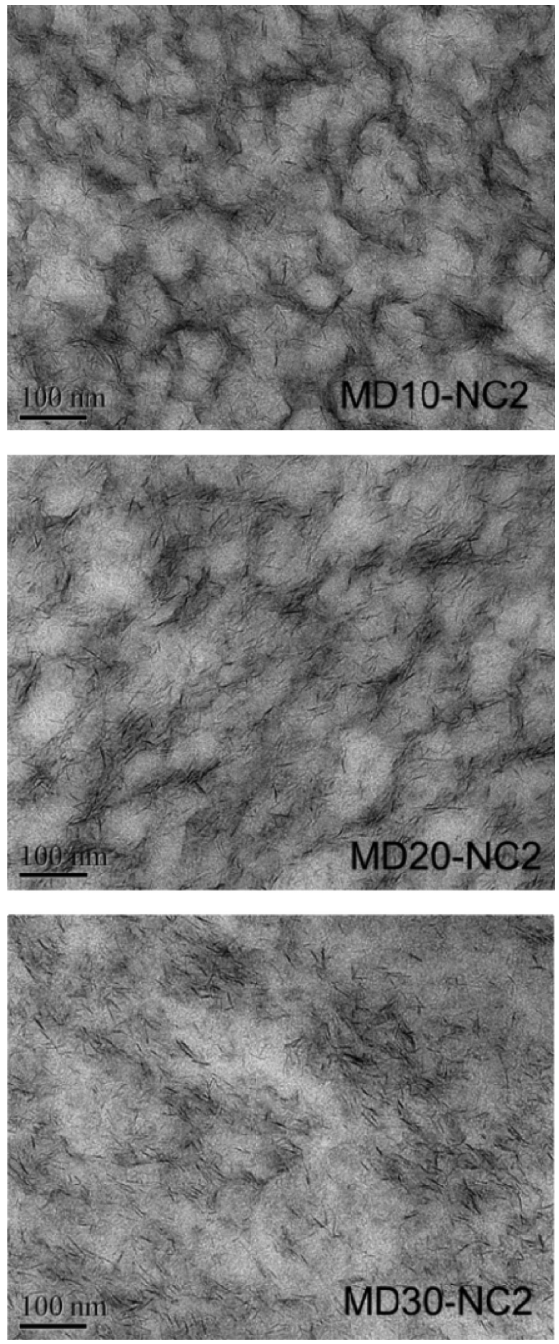

Figure 7. TEM images of MDx-NC2: (a) MD10-NC2, (b) MD20-NC2, and (c) MD30-NC2.

increased and the clay network morphology consisting of a clay shell 20 nm thick was destroyed with increasing x. For x > 30, most of clay was uniformly dispersed in an exfoliated state and formed polymer–clay network structures characteristic of normal NC gels consisting of PDMAA or PNIPA homopolymers. In addition, it was observed from DSC data that MDx-

dx.doi.org/10.1021/ma202114z | Macromolecules 2012, 45, 385–391

NC2 and MD*x*-NC5 always showed one T_g and that T_gs of MD*x*-NC2 changed from −30 °C to above 50 °C almost linearly with values of *x* (Table 1). Therefore, MD*x*-NC2 ($x \leq 50$) can be soft nanocomposites at ambient temperature, despite their fairly high clay content, due to the low T_gs of the constituent copolymers.

Thus, MD-NC gels and MD-NCs may be used as new stimuli-responsive hydrogels and soft nanocomposites, respectively, in various research fields and applications. All their constituents, including PMEA, PDMAA, clay, and water, are biologically safe materials; e.g., PMEA is used in medical devices such as cardiopulmonary bypass devices[33] due to its antithrombogenicity,[34] PDMAA is used as an ingredient in copolymers for contact lenses, and clay (synthetic hectorite) is used as a component of cosmetics. Therefore, it is expected that MD-NCs and their gels will be useful in biomedical applications. Accordingly, the safety of the MD*x*-NC*n* gels and M-NC*n* was confirmed by *in vitro* cytotoxicity tests using V79 cells. Figure 8 shows the percentage change in number of colonies on varying the concentration of extract added in culture medium, relative to the number of colonies obtained without adding any sample extract. It was observed that, in all samples, MD30-NC2, MD10-NC5, MD10-NC10, and M-NC2, the number of colonies remained constant (>80%) regardless the concentration of extract. These results indicate that MD*x*-NC*n* and M-NC*n* are safe materials in terms of *in vitro* cytotoxicity tests. The usefulness of MD-NCs and MD-NC gels in biomedical applications such as implantation in living animals and substrata for cell culture and thermoresponsive cell detachment will be reported in subsequent papers.

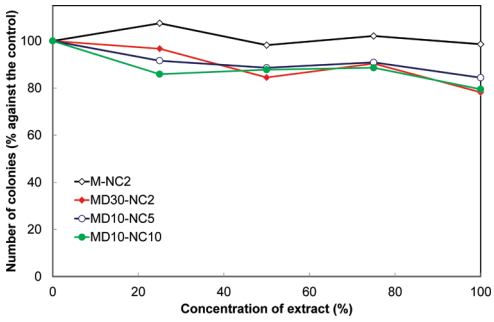

Figure 8. *In vitro* cytotoxicity tests of MD30-NC2, MD10-NC5, MD10-NC10, and M-NC2 using V79 cells. The change in number of colonies by altering the concentration (0−100%) of extract added in culture medium was represented in percentage against the number of colonies obtained in culture medium without sample extract (0%).

CONCLUSION

MD-NC gels (hydrogels) and MD-NCs (solids) are both soft nanocomposite materials that exhibit excellent mechanical properties in addition to excellent optical and swelling properties. Additionally, MD-NC gels show remarkable stimuli sensitivities in response to various external stimuli such as temperature, solvent, pH, and salt concentration in the surrounding aqueous solution due to the balance of hydrophilic and hydrophobic units in the polymer constituents. The clay morphology in MD*x*-NC*n* changed with the value of *x* from an aggregated clay network consisting of clay shells 20 nm thick ($x = 0$) to uniform dispersions of exfoliated clay platelets in polymer matrices ($x > 30$). In addition, since MD-NC gels and MD-NCs derived therefrom can be readily prepared in various forms including films, sheets, fibers, and tubes, they could be widely utilized as soft, stimuli-responsive materials for a broad variety of applications.

AUTHOR INFORMATION

Corresponding Author

*E-mail hara@kicr.or.jp; Fax (+81) 43-498-2202; Tel (+81) 43-498-2111.

ACKNOWLEDGMENTS

We thank Mr. M. Uota (DIC Co.) for TEM observation. This work was supported by the Ministry of Education, Science, Sports and Culture of Japan (Grant-in-Aid 23350117), and NEDO, Japan.

REFERENCES

(1) Osada, Y., Khokhlov, A. R., Eds.; *Polymer Gels and Networks*; Marcel Dekker: New York, 2002.
(2) S. Chaterji, S.; Kwon, I. K.; Park, K. *Prog. Polym. Sci.* **2007**, *32*, 1083−1122.
(3) Jeong, B.; Gutowska, A. *Trends Biotechnol.* **2002**, *20*, 305−311.
(4) Matsumoto, A.; Yoshida, R.; Kataoka, K. *Biomacromolecules* **2004**, *5*, 1038−1045.
(5) Cai, W.; Anderson, E. C.; Gupta, R. B. *Ind. Eng. Chem. Res.* **2001**, *40*, 2283−2288.
(6) Yamato, M.; Okano, T. *Mater. Today* **2004**, *7*, 42−47.
(7) Grove, T. Z.; Osuji, C. O.; Forster, J. D.; Dufresne, E. R.; Regan, L. *J. Am. Chem. Soc.* **2010**, *132*, 14024−14026.
(8) Schild, H. G. *Prog. Polym. Sci.* **1992**, *17*, 163−249.
(9) Haraguchi, K. *Macromol. Symp.* **2007**, *256*, 120−130.
(10) Haraguchi, K.; Takehisa, T. *Adv. Mater.* **2002**, *14*, 1120−1124.
(11) Haraguchi, K.; Takehisa, T.; Fan, S. *Macromolecules* **2002**, *35*, 10162−10171.
(12) Haraguchi, K.; Li, H. J. *Angew. Chem., Int. Ed.* **2005**, *44*, 6500−6504.
(13) Haraguchi, K. *Polym. J.* **2011**, *43*, 223−241.
(14) Haraguchi, K.; Li, H. J. *Macromolecules* **2006**, *39*, 1898−1905.
(15) Zhu, M.; Liu, Y.; Sun, B.; Zhang, W.; Liu, X.; Yu., H.; Zhang, Y.; Kuckling, D.; Adler, H. P. *Macromol. Rapid Commun.* **2006**, *27*, 1023−1028.
(16) Haraguchi, K.; Uyama, K.; Tanimoto, H. *Macromol. Rapid Commun.* **2011**, *32*, 1253−1258.
(17) Miyazaki, S.; Endo, H.; Karino, T.; Haraguchi, K.; Shibayama, M. *Macromolecules* **2007**, *40*, 4287−4295.
(18) Haraguchi, K.; Xu, Y.; Li, G. *Macromol. Rapid Commun.* **2010**, *31*, 718−723.
(19) Haraguchi, K.; Takada, T. *Macromolecules* **2010**, *43*, 4294−4299.
(20) Mu, J.; Zheng, X. *J. Colloid Interface Sci.* **2007**, *307*, 377−385.
(21) Fukasawa, M.; Sakai, T.; Chung, U. I.; Haraguchi, K. *Macromolecules* **2010**, *43*, 4370−4378.
(22) Haraguchi, K.; Ebato, M.; Takehisa, T. *Adv. Mater.* **2006**, *18*, 2250−2254.
(23) Haraguchi, K.; Farnworth, R.; Ohbayashi, A.; Takehisa, T. *Macromolecules* **2003**, *36*, 5732−5741.
(24) Haraguchi, K.; Li, H. J.; Ren, H.; Zhu, M. *Macromolecules* **2010**, *43*, 9848−9853.
(25) Liu, H. Y.; Zhu, X. X. *Polymer* **1999**, *40*, 6985−6990.
(26) Mueller, K. F. *Polymer* **1992**, *33*, 3470−3476.
(27) EI-Ejmi, A. S.; Huglin, M. B. *Polym. Int.* **1996**, *39*, 113−119.
(28) El-Ejimi, A. S.; Huglin, M. B. *Eur. Polym. J.* **1997**, *33*, 1281−1284.
(29) Ren, H.-Y.; Zhu, M.; Haraguchi, K. *Macromolecules* **2011**, *44*, 8516−8526.
(30) Otake, K.; Inomata, H.; Konno, M.; Saito, S. *Macromolecules* **1990**, *23*, 283−289.

(31) Inomata, H.; Goto, S.; Otake, K.; Saito, S. *Langmuir* **1992**, *8*, 687−690.
(32) Annaka, M.; Motokawa, K.; Sasaki, S.; Nakahira, T.; Kawasaki, H.; Maeda, H.; Amo, Y.; Tominaga, Y. *J. Chem. Phys.* **2000**, *113*, 5980−5985.
(33) Saito, N.; Motoyama, S.; Sawamoto, J. *Artif. Organs* **2000**, *24*, 547−554.
(34) Tanaka, M.; Mochizuki, A. *J. Biomed. Mater. Res.* **2004**, *43*, 684−695.

Macromolecules

ARTICLE

pubs.acs.org/Macromolecules

Complex Formation of Collagen Model Peptides with Polyelectrolytes and Stabilization of the Triple Helical Structure

Ken Terao,*[,†,‡] Ryoko Kanenaga,[†] Takahiro Sato,[†] Kazunori Mizuno,[‡] and Hans Peter Bächinger*[,‡,§]

[†]Department of Macromolecular Science, Osaka University, 1-1, Machikaneyama-cho, Toyonaka, Osaka, 560-0043, Japan

[‡]Research Department, Shriners Hospital for Children, Portland, Oregon 97239, United States

[§]Department of Biochemistry and Molecular Biology, Oregon Health & Science University, Portland, Oregon 97239, United States

Supporting Information

ABSTRACT: Small-angle X-ray scattering (SAXS) measurements were made for three collagen model peptides, H−(Gly-Pro-4-(*R*)-Hyp)$_9$−OH, H−(Pro-4-(*R*)-Hyp-Gly)$_9$−OH, and H−(Gly-4-(*R*)-Hyp-4-(*R*)-Hyp)$_9$−OH with or without sodium polyacrylate (NaPAA) in 20 mM and 100 mM aqueous NaCl at 15 and 75 °C. At 15 °C, almost all triple helical peptides form a complex with NaPAA when the molar ratio of acrylic acid unit to peptide molecules is larger than 10 whereas they are molecularly dispersed at 75 °C. Furthermore, the attached triple helices appreciably extend the main chain of NaPAA, and the radius of gyration for the complex is at most twice larger than the single NaPAA chain. Circular dichroism measurements demonstrated that the complexation noticeably stabilizes the triple helical structure and the melting midpoint temperature T_m is 2−10 °C higher than that for the solution without NaPAA. This stabilization was also observed for negatively charged sodium carboxymethylamylose and sodium hyaluronate as well as for positively charged poly(vinyl ammonium) chloride, but no appreciable stabilization of the triple helical structure by the polyelectrolytes was observed for an end-capped peptide Ac−(Gly-Pro-4-(*R*)-Hyp)$_9$-NH$_2$. These results indicate that the complex formation is due to the electrostatic attraction between polyelectrolytes and the opposite charges at the end of uncapped triple helical peptides.

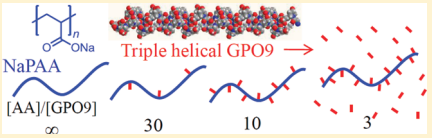

INTRODUCTION

Some synthetic oligo-peptides having Gly-Xaa-Yaa triplet repeats, whose Xaa and Yaa are often composed of proline or 4-(*R*)-hydroxyproline, form a triple helix in solution at low temperature. Since this helical structure and sequences are similar to the triple helical part of natural collagen molecules, they are so-called collagen model (or mimic) peptides[1] (CMP) or triple-helical peptides.[2] This triple helical structure dissociates with raising temperature and the conformational change between triple helix and single-chain random coil is fully reversible, which is different from native collagen helices. Thus, these collagen model peptides have been well studied to determine the detailed conformation as well as to investigate the origin of thermal stability of the triple helices.[1−6]

The amine and carboxylic acid groups at the N- and C-termini of the CMP are ionizable at acidic and basic pH, so that the CMP triple helix and single-chain random coil are viewed as a trivalent and monovalent cationic (anionic) species, respectively at acidic (basic) pH. Furthermore, the ionization at the chain end destabilizes the triple helix. Therefore, the electrolytic character of the CMP provides interesting phenomena at interacting with polyelectrolytes. For example, since the attractive interaction between the polyelectrolyte and counterions is definitively affectable by the ionic valence of the counterions, polyelectrolytes should interact with triple helical CMPs much stronger than single chain CMPs. The complexation with triple-helical CMPs may change the conformation of the polyelectrolyte because the triple helices act as rigid graft chains of the polyelectrolyte main chain. On the other hand, the CMP triple helix may be stabilized by the neutralization of the end charges in the complex with the polyelectrolyte.

Recently, we found that the methanol solution of H−(Pro-Pro-Gly)$_5$−OH (PPG5) became turbid by addition of poly(acrylic acid)(PAA), indicating the formation of poorly soluble complexes due to the attractive force between three N-termini and COOH groups of PAA.[7] Furthermore, the addition of PAA into the methanol solution increased the thermal stability of the triple helix of this CMP as high as 30 °C. Similar stabilization was also reported for trimerized CMPs by covalent bonds or interaction among noncollagenous domains.[1,2,8−11] This is thus most likely due to the reduction of electrostatic repulsion force among the *N*-termini. However, this CMP−PAA complex was hardly dissolved in methanol; it was thus difficult to study this complex more extensively.

After some attempts, we found that thermal stability of triple helix for more hydrophilic CMPs, that is, H−(Gly-Pro-4-(*R*)-Hyp)$_9$−OH (GPO9) (**1** in Chart 1), H−(Pro-4-(*R*)-Hyp-Gly)$_9$−OH (POG9) (**2**), and H−(Gly-4-(*R*)-Hyp-4-(*R*)-Hyp)$_9$−OH

Received: September 26, 2011
Revised: November 12, 2011
Published: December 07, 2011

Chart 1. Chemical Structures of the Investigated Samples

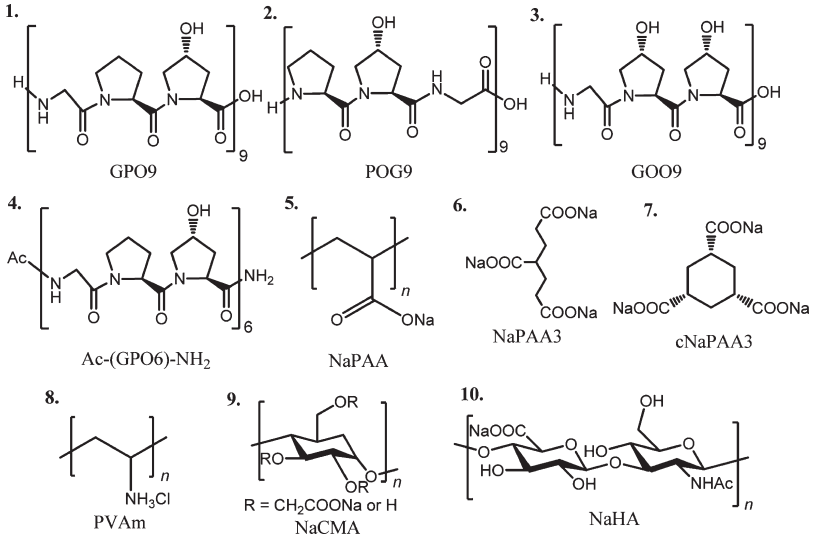

(GOO9) (**3**) in pure water significantly increases with the content of sodium poly(acrylic acid)(NaPAA) (**5**) and the mixtures were completely transparent at any composition of the two solutes, suggesting that the complexes have good solubility in water. We thus determined the molar mass and the dimensional properties of the complex consisting mainly of GPO9 and NaPAA by small-angle X-ray scattering (SAXS) at different temperatures. The thermal stability of the triple helices was also examined for these systems as well as those consisting of some other polyelectrolytes and low molecular-weight electrolytes shown in Chart 1 (**6**−**10**) to estimate the dominant effect of complex formation. As the reference, an end-capped peptide, acetyl−(Gly-Pro-4-(*R*)-Hyp)$_6$−NH$_2$ (Ac−(GPO6)−NH$_2$) (**4**), in which both end groups are not ionized in aqueous solution, was also studied to clarify the end effect.

EXPERIMENTAL SECTION

Samples. Four peptide samples GPO9, POG9, GOO9, and Ac−(GPO6)−NH$_2$ were synthesized with an ABI 433A synthesizer (Applied Biosynthesis, Foster, CA) using Fmoc amide acids and purified by solvent gradient HPLC; details including Mass spec characterization are described elsewhere.[12] Molecular weights of the samples GPO9, POG9, GOO9, and Ac-(GPO6)-NH$_2$ are 2423, 2423, 2567, and, 1663, respectively. Two NaPAA samples were prepared by neutralization of narrow dispersed PAA samples (Polymer Source) with aqueous sodium hydroxide. Their weight-average molecular weights M_w's were estimated to be 3.04×10^4 and 2.51×10^4 for NaPAA323 and NaPAA267, respectively, from the sedimentation equilibrium data for the corresponding PAA samples.[7,13] Their ratios of *z*-average molecular weight M_z to M_w, a polydispersity index, were also estimated to be ca. 1.05. Commercially available 1,3,5-pentanetricarboxylic acid and 1,3,5-cyclohexanetricarboxylic acid were neutralized by NaOH and used as oligo NaPAA. They are designated as NaPAA3 (**6**) and cNaPAA3 (**7**), respectively. A sodium carboxymethyl amylose sample NaCMA26K was prepared from enzymatically synthesized amylose[14] by a known method,[15] and the M_w and M_z/M_w values were determined from the sedimentation equilibrium to be 2.57×10^4 and 1.04, respectively. Molar fraction of carboxymethyl groups was estimated to be 0.40, 0.03, and 0.21 for 2-, 3-, and 6-position, respectively, from a ^{1}H NMR measurement for fully hydrolyzed sample in deuterated sulfuric acid (5 M),[16] and hence, the degree of substitution is 0.64. A polyvinyl amine hydrochloric acid sample PVAm310 K was synthesized by free radical polymerization and purified by fractional precipitation. The M_w and the ratio of M_w to the number-average molecular weight of the sample was determined to be 3.1×10^4 and 1.18 from multiangle laser light scattering equipped with size exclusion chromatography.[17] A native sodium hyaluronic acid (NaHA) sample from rooster comb purchased from Wako was also used in this study.

Small-Angle X-ray Scattering (SAXS). SAXS measurements were made for GPO9, NaPAA (NaPAA323 or NaPAA267), and their mixtures, dissolved in 20 mM or 100 mM aqueous sodium chloride all at 15 and 75 °C. The composition of each solution is specified in terms of the total solute mass concentration c and the molar ratio α of the NaPAA monomer unit to the collagen model peptide in what follows. The latter was chosen to be 3, 10, and 30, in the SAXS measurements. Scattering intensities $I(q)$ at the absolute value q of the scattering vector were measured on Rigaku R-AXIS VII imaging plates at the BL40B2 beamline in SPring-8 (Hyogo, Japan) or the BL-10C beamline in KEK-PF (Ibaraki, Japan). Intensity of the direct beam was measured by using ionic chambers at the upper and lower ends of the capillary to correct the $I(q)$ data. The wavelength, the camera length, and the accumulation time were chosen to be 0.10−0.15 nm, 1500−2000 mm, and 300 s, respectively. The actual camera length and the center of the beam on the Imaging plates were determined by powder diffraction of the silver behenate. Solvent and four solutions with different c were filled in a 1.5 mm quartz capillary and measured to determine the excess scattering intensity $\Delta I(q)$ as the difference in $I(q)$ between the solution and solvent. The SAXS measurements were also made for POG9, GOO9, and their mixtures with NaPAA267 at the ratio α of 30 in 20 mM aqueous NaCl at 15 and 75 °C.

In the aqueous solution, NaPAA and CMP may form complexes with different aggregation numbers, but here the complexes are regarded as a single scattering component for simplicity. Then, the solution of the mixture of NaPAA and CMP contains three scattering components, CMP (component 1), NaPAA (component 2), and their complex (component 3) in general. Component 1 is the triple helix or single-chain random coil of CMP, and the coexistence of the

dx.doi.org/10.1021/ma202176w |*Macromolecules* 2012, 45, 392–400

two species is not considered in what follows. According to the SAXS theory,[18] $\Delta I(q)/c$ for a solution containing three scattering components at infinite dilution is written as

$$\left[\frac{\Delta I(q)}{Kc}\right]_{c=0} = w_1\Delta z_1{}^2 M_1 P_1(q) + w_2\Delta z_2{}^2 M_2 P_2(q) + w_3\Delta z_3{}^2 M_3 P_3(q) \quad (1)$$

where w_i, Δz_i, M_i, and $P_i(q)$ are the weight fraction in the total solute, excess electron density, molar mass, and particle scattering function of the component i, respectively, and K is the optical constant which is independent of the solute. The excess electron density Δz_i is given by

$$\Delta z_i = z_i - v_i\rho_{e,s} \quad (2)$$

Here, z_i is the number of moles of electrons per unit mass of the component i, $\rho_{e,s}$ the electron density of the solvent, and v_i the partial specific volume of the component i. The value of v_2 was determined from the specific density increment $(\partial\rho/\partial c_i)_\mu$ at fixed chemical potential of diffusible components for NaPAA in 20 mM and 100 mM aqueous NaCl at 15 and 75 °C. On the other hand, v_1 for the peptide samples were used for the previously obtained values[19] in pure water because it is infeasible to determine v_1 for dialyzed small peptide solutions; this may not cause a significant error because of the low saline concentrations (20 mM and 100 mM) in the present study. The value of v_3 was calculated from v_1 and v_2 (see below). The optical constant K was determined by using the scattering data for aqueous solutions of NaPAA323, NaPAA267, GOO9, or GPO9.

Circular Dichroism (CD). Circular dichroism measurements were made for GPO9, Ac−(GPO9)−NH_2, POG9, GOO9 with or without NaPAA323, NaPAA267, NaPAA3, cNaPAA3, NaCMA26K, PVAm310 K, or NaHA, in 0, 20, or 100 mM aqueous NaCl using a JASCO J720WO or AVIV 202 spectropolarimeter both equipped with a Peltier thermostated cell holder and a 1 mm path length rectangular quartz cell. Temperature scans were recorded at fixed wavelength and at 6 or 10 °C h^{-1} to determine the molar ellipticity $[\theta]$ to estimate the melting midpoint temperature T_m of the triple helices; wavelength scans were evaluated in the range of wavelength between 210 and 260 nm at fixed temperatures.

RESULTS AND DISCUSSION

Complex Formation of NaPAA and GPO9. As indicated by eq 1, $Kc/\Delta I(q)$ at $c = 0$ and $q = 0$ is directly related with the complex formation. To obtain the limiting scattering function, we analyzed the scattering data using the Berry square root plot. Figure 1 is an example of $[Kc/\Delta I(q)]^{1/2}$ vs q^2 plots[20] for the mixture of GPO9 and NaPAA267 ($\alpha = 10$) in 100 mM aqueous NaCl at 75 and 15 °C. Filled circles indicate $[Kc/\Delta I(q)]^{1/2}$ at infinite dilution, $[Kc/\Delta I(q)]_{c=0}{}^{1/2}$, determined using plots of $[Kc/\Delta I(q)]^{1/2}$ vs c. The obtained data points were extrapolated to $q^2 = 0$ by a straight line to determine $[Kc/\Delta I(0)]_{c=0}{}^{1/2}$, $P(q)$, and the z-average radius of gyration $\langle S^2\rangle_z$. We note that the data for pure NaPAA in 20 mM NaCl were not analyzed because the extrapolation of the scattering intensity to zero angle was infeasible probably due to the significant intramolecular electrostatic interactions.

The obtained $[Kc/\Delta I(0)]_{c=0}{}^{1/2}$ at 15 °C are 0.404 times smaller than that at 75 °C, corresponding to 6.1 times larger scattering intensity at 15 °C, indicating complex formation between NaPAA and GPO9.

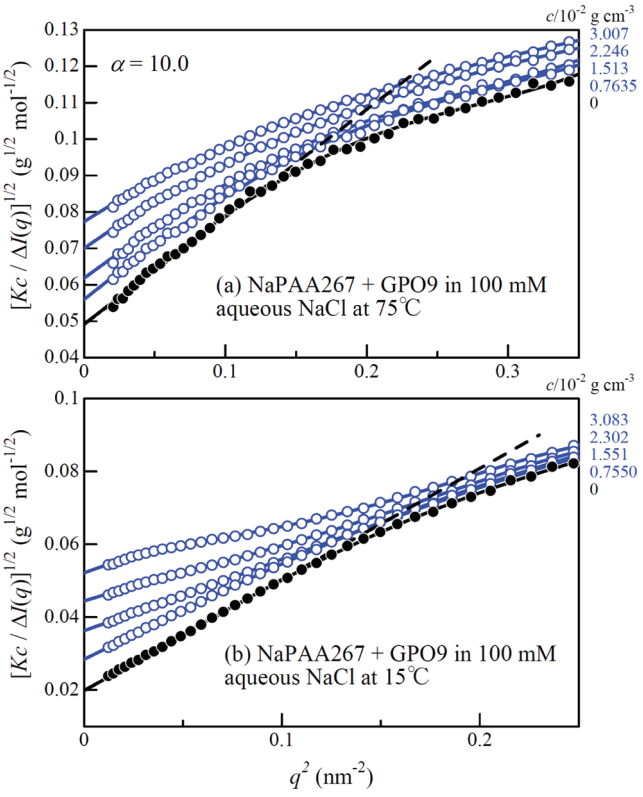

Figure 1. Plots of $[Kc/\Delta I(q)]^{1/2}$ vs q^2 for NaPAA267 + GPO9 (α = 10.0) in 100 mM aqueous NaCl at 75 (a) and 15 °C (b). Filled symbols indicate the data extrapolated to $c = 0$.

If the CMP and NaPAA exist in the mixture solution independently without complexation, eq 1 reduces in the limit of $q = 0$ to

$$\left(\frac{M_c}{\alpha} + \frac{M_2}{n}\right)\left[\frac{\Delta I(0)}{Kc}\right]_{c=0} = \frac{\Delta z_1{}^2 M_c M_1}{\alpha} + \frac{\Delta z_2{}^2 M_2{}^2}{n} \quad \text{(no complexation)} \quad (3)$$

where n is the degree of polymerization of NaPAA, M_c the molar mass of GPO9, and M_1 is equal to M_c and $3M_c$ when the component 1 is the single-chain and triple helix, respectively. Figure 2 thus illustrates the experimental $\{[(M_c/\alpha) + (M_2/n)][\Delta I(0)/Kc]_{c=0}\}^{1/2}$ plotted against α^{-1} and that at 75 °C (red symbols) are close to the red solid lines indicating values calculated by eq 3 with $M_1 = M_c$, demonstrating the all components are molecularly dispersed at the temperature. This is reasonable because CD spectra for GPO9 with and without NaPAA showed that all GPO9 chains take the random coil conformation at 75 °C (see Supporting Information).

On the other hand, the experimental data at 15 °C (blue symbols) are significantly larger than the calculated values from eq 3 with $M_1 = M_c$ and $3M_c$ (the red solid and dashed lines), definitely indicating the complex formation between NaPAA and GPO9, although the CD spectra at 15 °C shown in Supporting Information does not change by addition of NaPAA. The CD spectra rather indicate that the triple helix of GPO9 is stable even in the complex with NaPAA at 15 °C.

If all CMP triple helices form complexes with NaPAA chains in the solution at 15 °C, the degree of complexation of each NaPAA

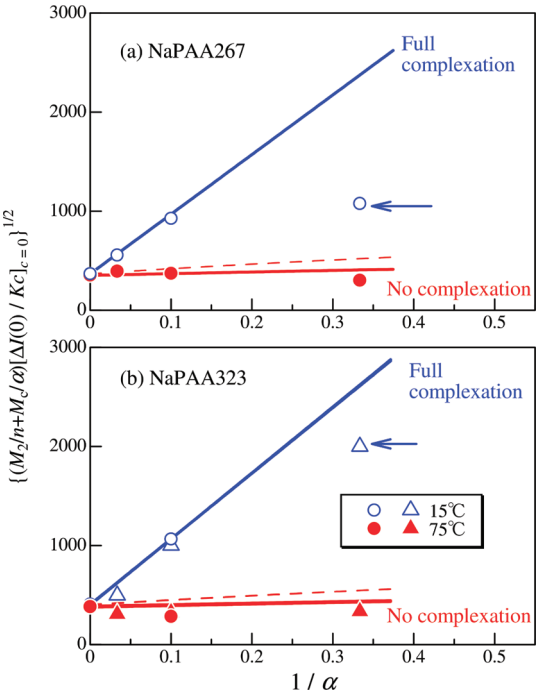

Figure 2. Plots of $\{[(M_c/\alpha) + (M_2/n)]\,[\Delta I(0)/Kc]_{c=0}\}^{1/2}$ vs $1/\alpha$ for NaPAA267 (a) and NaPAA323 (b) in 100 mM (circles) and 20 mM (triangles) aqueous NaCl at 75 °C (red filled symbols) and 15 °C (blue open symbols). Solid blue lines, dashed red lines, and solid red lines indicate the calculated values by using eq 4 (all peptide form a complex with NaPAA), eq 3 with $M_1 = 3M_c$ (triple helix + NaPAA), and eq 3 with $M_1 = M_c$ (molecularly dispersed), respectively.

chain becomes α^{-1} ($\alpha \geq 1$), and eq 1 is simplified as

$$\left(\frac{M_c}{\alpha} + \frac{M_2}{n}\right)\left[\frac{\Delta I(0)}{Kc}\right]_{c=0} = n\left(\Delta z_1\frac{M_c}{\alpha} + \Delta z_2\frac{M_2}{n}\right)^2 \quad \text{(full complexation)} \qquad (4)$$

This equation shows that $\{[(M_c/\alpha) + (M_2/n)][\Delta I(0)/Kc]_{c=0}\}^{1/2}$ increases as a linear function of α^{-1}. The solid blue lines in Figure 2 indicate theoretical values in the case of the full complexation, calculated from eq 4, which excellently fit the experimental data at α = 30 and 10. This demonstrates that almost all GPO9 chains form complexes with both NaPAA of different molecular weights. Similar results were obtained for POG9 and GOO9 with NaPAA at α = 30.

On the contrary, solutions including larger amounts of GPO9 compared to NaPAA, that is, α = 3, have intermediate scattering intensity between those calculated from eqs 3 and 4. This indicates that not all GPO9 molecules form a complex with NaPAA, though the number of negative charges of NaPAA in solution is three times larger than that of GPO9 molecules. If the degree of complexation of each NaPAA chain is f ($\leq\alpha^{-1}$), eq 1 can be rewritten as

$$\left(\frac{M_c}{\alpha} + \frac{M_2}{n}\right)\left[\frac{\Delta I(0)}{Kc}\right]_{c=0} = n\left(\Delta z_1 M_c f + \Delta z_2\frac{M_2}{n}\right)^2 + 3\Delta z_1{}^2 M_c{}^2\left(\frac{1}{\alpha} - f\right) \quad \text{(partial complexation)} \qquad (5)$$

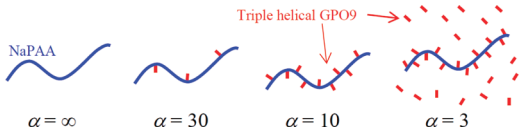

Figure 3. Schematic representation of complex formation for investigated α at 15 °C.

since all GPO9 molecules take triple helices at 15 °C. When the experimental results at α = 3 are substituted into the left-hand side of eq 5, the f values were estimated to be 0.12 in 100 mM aqueous NaCl and 0.24 in 20 mM, which correspond to that 36% and 72% of the GPO9 triple helix form complexes with NaPAA in 100 and 20 mM aqueous NaCl, respectively: The degree of complexation (or the binding constant) is higher in lower ionic strength. This complex formation is therefore most likely due to the electrostatic attraction between COO^- groups of NaPAA and three N termini of GPO9 triple helices. It seems that the triple helical GPO9's attach rather regularly along the NaPAA chain because of the electrostatic repulsion and steric hindrance between neighboring GPO9 triple helices (cf. Figure 3).

Strictly speaking, f depends on c, if the solution is in the association−dissociation equilibrium. Although the SAXS data were extrapolated to the zero c, f obtained above are probably the values in the vicinity of 5×10^{-3} g cm^{-3}, that is the lowest c where the SAXS measurements were made.

Global Conformation of the Complex. The shape of the complex in Figure 3 looks like comb polymers. Since the main chain of regular comblike polymers can be extended in a good solvent[21] and even in theta solvents[22] compared with the corresponding linear polymer without the side chains, NaPAA main chains of the current complex would have larger dimensions than the free NaPAA chains.

Here, we only consider the conformation of the complex at the full complexation at α = 10 and 30 at 15 °C. In this case, eq 1 is reduced to

$$\left[\frac{\Delta I(q)}{Kc}\right]_{c=0} = \frac{n[\Delta z_1(M_c/\alpha) + \Delta z_2(M_2/n)]^2}{(M_c/\alpha) + (M_2/n)}P_3(q) = \frac{n[\Delta z_1(M_c/\alpha) + \Delta z_2(M_2/n)]^2}{(M_c/\alpha) + (M_2/n)} \times \left(1 - \frac{1}{3}\langle S^2\rangle_{z,3}q^2 + \cdots\right) \quad \text{(full complexation)} \qquad (6)$$

and we can obtain the radius of gyration $\langle S^2\rangle_{z,3}{}^{1/2}$ of the complex from the angular dependence of $[\Delta I(q)/Kc]_{c=0}$.

As shown in Table 1, the radii of gyration $\langle S^2\rangle_{z,3}{}^{1/2}$ for α = 10 and 30 at 15 °C are appreciably larger than that $\langle S^2\rangle_{z,2}{}^{1/2}$ for corresponding NaPAA without complexation (at $\alpha = \infty$). Considering the contour length of NaPAA is 8 to 10 times longer than the triple helical GPO9, this high $\langle S^2\rangle_{z,3}{}^{1/2}$ is most likely due to the extension of the main chain. Furthermore, Kratky plots $[q^2P_2(q)$ or $q^2P_3(q)$ vs $q]$ for pure NaPAA, α = 10, and α = 30 illustrated in Figure 4 indicates the $q^2P_2(q)$ or $q^2P_3(q)$ value in finite q range remarkably decreases with decreasing α. It should be noted that the $P_3(q)$ and then $\langle S^2\rangle_{z,3}{}^{1/2}$ for α = 30 mixtures of GOO9 and POG9 are essentially the same as those for GPO9 and hence omit them in the following analysis.

First, we analyzed $P_2(q)$ for pure NaPAA267 and NaPAA323 in 100 mM aqueous NaCl (shown by red circles in panels a and b in Figure 4) by the wormlike cylinder model, characterized by the

dx.doi.org/10.1021/ma202176w |Macromolecules 2012, 45, 392–400

Table 1. Radii of Gyration for NaPAA and NaPAA−GPO9 Complex in 100 mM and 20 mM Aqueous NaCl at 15 °C

	$\langle S^2\rangle_{z,2}^{1/2}$, $\langle S^2\rangle_{z,3}^{1/2}$ (nm)		
α	NaPAA267 in 100 mM NaCl	NaPAA323 in 100 mM NaCl	NaPAA323 in 20 mM NaCl
∞ (pure NaPAA)	5.7	6.7	
30	7.3		6.4
10	9.6	10.9	10.3

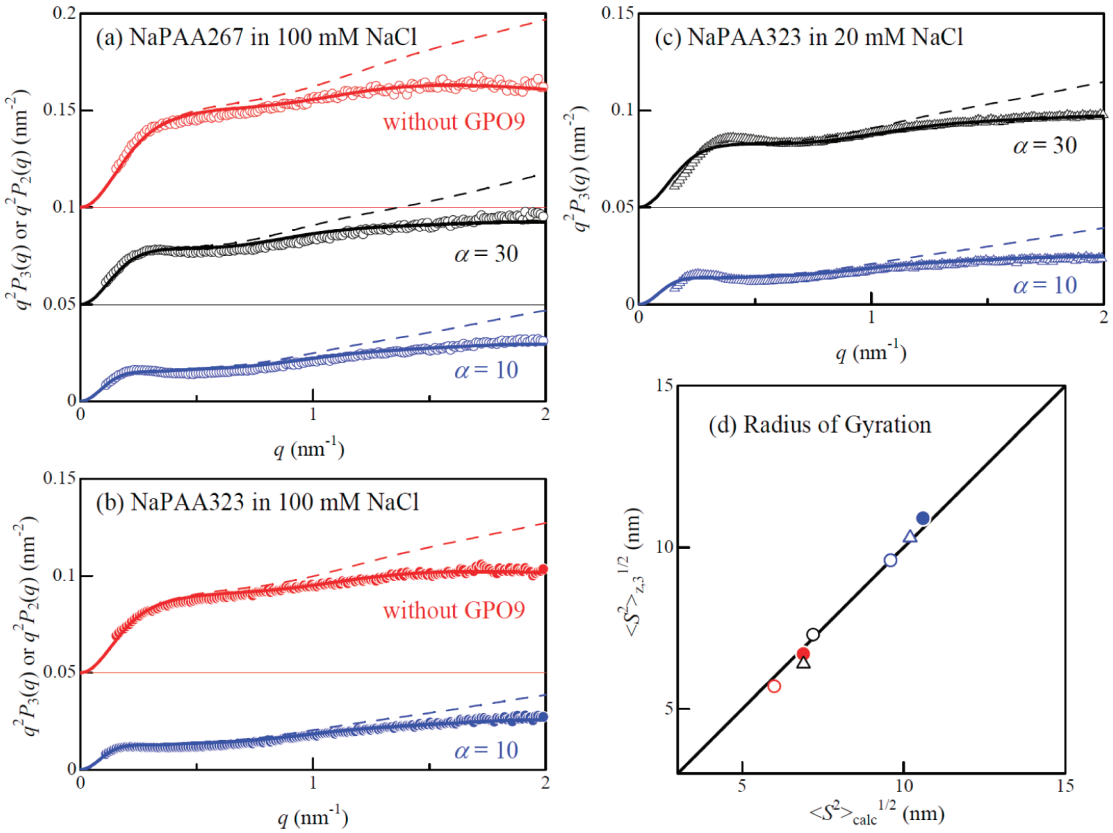

Figure 4. Kratky plots for (a) NaPAA267 and (b) NaPAA323, both in 100 mM aqueous NaCl, and (c) NaPAA323 in 20 mM aqueous NaCl with or without indicated GPO9 all at 15 °C. Solid curves are the theoretical values calculated for the wormlike combs with the parameters listed in the text. Dashed curve is those for infinite thin chains ($d_B = 0$). (d) Comparison between the experimental radius of gyration $\langle S^2\rangle_{z,3}^{1/2}$ and calculated one $\langle S^2\rangle_{calc}^{1/2}$ from the wormlike chain parameters estimated from the scattering functions. Symbols are the same as those in panels a−c.

contour length L_m, the Kuhn segment length λ_m^{-1} (stiffness parameter), and the cylinder diameter d.[23] The fitting results are indicated by red solid curves in the panels, and the three parameters, h_m ($\equiv L_m/n$), λ_m^{-1}, and d obtained by the fitting were 0.26 ± 0.01 nm, 3.3 ± 0.3 nm, and 1.5 ± 0.1 nm, respectively; the chain stiffness is fairly comparable with the previously estimated values.[24]

Assuming that the GPO9 attaches at regular intervals, the NaPAA-GPO9 complex may be modeled by the wormlike comb model (see Appendix). When the contour length L_s and the Kuhn segmtent length λ_s^{-1} for the side groups are reasonably assumed to be 8.2 nm and ∞ from our recent SAXS data for GPO9,[19] $P_3(q)$ may be calculated with the remaining parameters L_m, λ_m^{-1}, and the chain thickness parameter d_B. A curve fitting procedure was employed to determine those parameters. Theoretical curves thus obtained (black and blue solid curves in panels a−c in Figure 4) fit the experimental data well, indicating that the regularly branched wormlike comb model is suitable to describe the shape of the complex in solution. The obtained parameters also explain the experimental $\langle S^2\rangle_{z,3}$ data since they

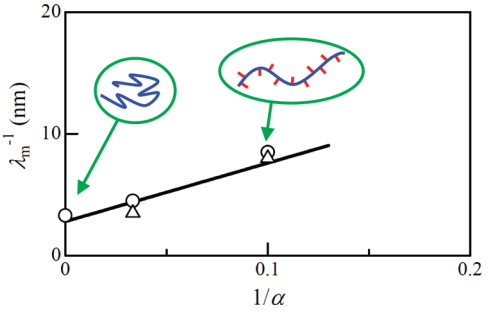

Figure 5. Composition ($1/\alpha$) dependence of the main chain stiffness λ_m^{-1} for NaPAA and GPO9 complexes in 100 mM (open circles) and 20 mM (triangles) at 15 °C.

dx.doi.org/10.1021/ma202176w |*Macromolecules* 2012, 45, 392–400

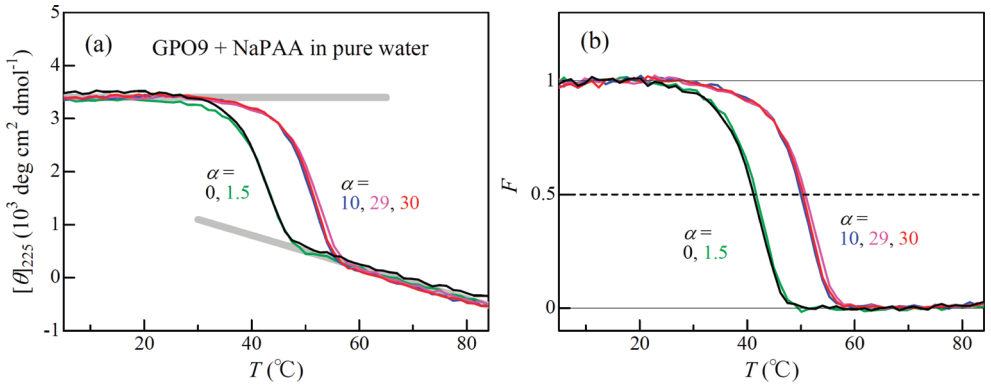

Figure 6. Temperature dependence of molar ellipticity $[\theta]_{225}$ at λ_0 = 225 nm (a) and helix content F (b) for GPO9 without or with NaPAA in pure water. Heating rates were 6 °C/h and CMP mass concentration was set to be 3.0×10^{-4} g cm^{-3}. Curves are the data points for different α: α = 0 (black), α = 1.5 (green), α = 10 (blue), α = 29 (magenta), α = 30 (red).

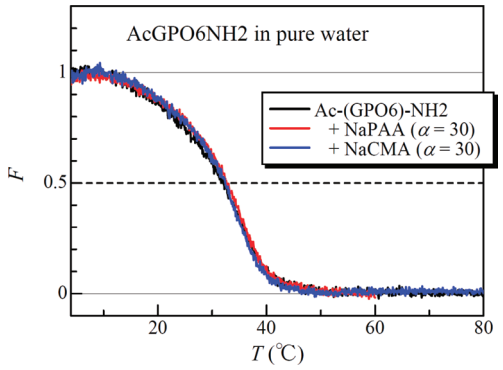

Figure 7. Temperature dependence of F for Ac−(GPO6)−NH_2 (black), along with those mixed with NaPAA323 (red) or NaCMA (blue) in pure water. Heating rates were 10 °C/h, CMP mass concentration and α were set to be 3.0×10^{-4} g cm^{-3} and 30, respectively.

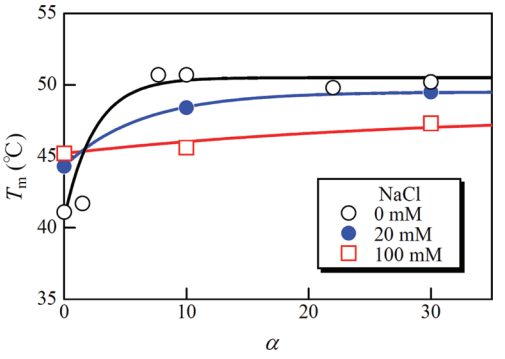

Figure 8. Composition dependence of T_m for GPO9 including NaPAA in pure water (open circles), 20 mM aqueous NaCl (filled circles), and 100 mM (squares) aqueous NaCl at a temperature increasing rate of 6 °C h^{-1}.

are fitted by the theoretical radius of gyration $\langle S^2 \rangle_{calc}$ calculated by eq 10 with the parameters obtained from $P_3(q)$ as shown in panel d in Figure 4. Whereas almost the same h_m (= 0.26 ± 0.01 nm) and d_B (=0.15 ± 0.01 nm) as those for pure NaPAA were obtained for all systems shown in Figure 4, λ_m^{-1}'s at α = 10 and 30 are appreciably larger than that for NaPAA. Figure 5 displays the plot of λ_m^{-1} against $1/\alpha$ for the complexes in 100 and 20 mM NaCl at 15 °C. The stiffness of the main chain increases linearly with $1/\alpha$ and reaches twice the value than that for NaPAA. This is most likely due to the interaction between the side GPO9 chains and the main NaPAA chain. On the one hand, λ_m^{-1} does not appreciably depend on the ionic strength whereas the intrinsic viscosities for NaPAA increase significantly with decreases the ionic strength.[25] This seems to be rather unusual but possibly because the interaction between triple helical GPO9 and NaPAA becomes more attractive with decreasing NaCl concentration and compensates the increase of the electrostatic excluded-volume effects.

Stabilization of Triple Helical Structure of GPO9 in the Presence of NaPAA. The molar ellipticity $[\theta]_{225}$ at λ_0 = 225 nm remarkably reflects the conformation of peptide chain. Figure 6 thus displays those for GPO9 triple helices in the presence of various amounts of NaPAA in pure water at 225 nm wavelength plotted against temperature. Except for the conformational transition region (35−55 °C), $[\theta]_{225}$ obey straight lines. Thus, those for triple helices ($[\theta]_{helix}$) and single coil ($[\theta]_{coil}$) can be estimated as shown in the figure and therefore the helix content F defined by

$$[\theta(T)] = F(T)[\theta(T)]_{helix} + [1 - F(T)][\theta(T)]_{coil} \quad (7)$$

are plotted against temperature in the panel (b) of the figure. The melting midpoint temperatures T_m's are determined as the temperature at F = 0.5. Although the T_m value at α = 1.5 is close to that without NaPAA, T_m increases rapidly with α and reaches ca. 8 °C higher for α = 10 − 30 mixtures. Similar stabilization of triple helical structure was also seen for POG9 and GOO9. It should be noted that although $[\theta]_{225}$ around T_m slightly depend on the temperature changing rate r_T,[26] but the difference of T_m between the mixtures and pure GPO9 are essentially the same for the two r_T's, that is 6 and 10 °C h^{-1}. Considering the low mass concentration of these two components, triple helical GPO9 chains should strongly interact with NaPAA even at the T_m. Another interesting point is that no detectable T_m change was observed in pure water when trimer models of NaPAA (NaPAA3 and cNaPAA3 in Chart 1) were added ($\alpha \sim 30$), showing that "poly"electrolyte is mandatory to stabilize triple helices and suggesting that GPO9 does not form a complex with trivalent electrolytes.

dx.doi.org/10.1021/ma202176w |*Macromolecules* 2012, 45, 392–400

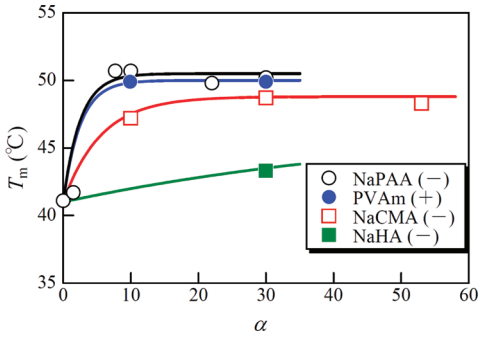

Figure 9. Composition dependence of T_m for GPO9 with NaPAA (open circles), sodium carboxymethylamylose (NaCMA, open squares), sodium hyaluronate (NaHA, filled squares), and polyvinylamine hydrochloride (PVAm, filled circles) in pure water at a temperature raising rate of 0.1 °C/min. Key: (−) polyanion; (+) polycation.

If the thermal stabilization of triple helices with the presence of NaPAA is mainly due to the reduction of electrostatic repulsion force between three N-termini, significant thermal stabilization is no more seen for an N-terminal capped collagen model peptide with NaPAA. A noncharged peptide Ac-(GPO6)-NH_2 (**4** in Chart 1) is thus used instead of GPO9 and the measured temperature dependence of F as shown in Figure 7. Though a relatively high α is chosen, the obtained T_m's when including polyelectrolytes are essentially the same as that for pure Ac−(GPO6)−NH_2, indicating that electrostatic repulsion between N-termini of GPO9, GOO9, and POG9 is screened by the anionic groups of NaPAA to increase T_m. This is reasonable because T_m for GPO9 raises with increasing the saline concentration and that at 100 mM is 4 °C higher than that in pure water (see Figure 8).

Figure 8 illustrates the α dependence of T_m for the GPO9-NaPAA system with or without NaCl. In pure water, T_m rapidly increases with increasing α and reaches an asymptotic temperature when $\alpha \geq 10$. With increasing ionic strength, the α dependence of T_m becomes weaker, because the triple helix is appreciably stabilized even at $\alpha = 0$. In 100 mM aqueous NaCl, the stabilization is no more significant whereas almost all GPO9 triple helices form a complex with NaPAA in the solution. A similar trend was also obtained for mixtures of 10 times higher concentration (not shown here) being comparable to that for SAXS. Therefore, an increase in T_m in dilute solution is consistent with the complex formation, but the complex formation does not always show the increase of T_m. This is probably due to the counterions condensing around the polyelectrolyte. Consequently, it is reasonably supposed that the attractive force between GPO9 and NaPAA may weaken with increasing the ionic strength. This is consistent with the fact that the degree of complexation f estimated from SAXS at $\alpha = 3$ becomes lower with increasing ionic strength.

The stabilization of the CMP triple helix was also observed by addition of polyelectrolytes other than NaPAA, listed in Chart 1. Figure 9 compares T_m of GPO9 by addition of three different polyelectrolytes. Here, linear charge densities c_d of the polyelectrolytes added are ca. 3.8 nm^{-1} for NaPAA, ca. 1.9 nm^{-1} for NaCMA (when assuming helix pitch per residue of NaCMA is 0.32 nm),[27,28] and ca. 0.80 nm^{-1} for NaHA[29] T_m is an increasing function of α in presence of the three polyelectrolytes, that is probably due to the complex formation. However, T_m increases less rapidly with decreasing c_d and the asymptotic value becomes smaller for smaller c_d polymer, indicating that not only ionic strength but also charge density of the polyelectrolytes play an important role to stabilize the triple helices of oligopeptides in the complex. It should be added that the GPO9 has COO^- group at the C-termini, which may interact with cationic groups of the polycations. Indeed, poly(vinyl ammonium) chloride (**8** in Chart 1) whose c_d is essentially the same as NaPAA stabilizes triple helices almost to the same extent as the NaPAA case (see filled circles in Figure 9).

■ CONCLUSIONS

Triple helical GPO9, POG9, and GOO9 form a complex with NaPAA at 15 °C whereas they are molecularly dispersed above the helix−coil transition temperature (75 °C). This is most likely due to the electrostatic attraction between ionized N-termini of the peptide and anionic groups of NaPAA. Indeed, this trend is more significant at lower ionic strength. Dimensional properties of the complex were successfully explained by the wormlike comb model and the NaPAA chain is found to be extended by the grafted peptide molecules. A further important point is that the triple helical structure of the peptides is stabilized by this complexation, possibly because the free positive charges at the three N-termini destabilize the triple helical structure. This stabilization strengthens with decreasing ionic strength of solvent or increasing line charge density of polyelectrolytes. Similar stabilization was also found for GPO9 and a positively charged polyelectrolyte, indicating that ionized N-termini as well as C-termini of the triple helices may form the complex with polyelectrolytes having opposite charge.

■ APPENDIX: PARTICLE SCATTERING FUNCTION AND GYRATION RADIUS OF WORMLIKE COMBS WITH DIFFERENT ELECTRON DENSITY

Nakamura and Norisuye[21,30] derived the scattering function $P_0(q)$ for the semiflexible brushes whose side chain of the contour length L_s is linked to the main chain of the contour length L_m by a universal joint in the same manner as Huber and Burchard's for wormlike stars.[31]

$$P_0(q) = \frac{1}{(L_m + pL_s)^2} \sum_i \sum_j \int ds_i \int ds_i \langle \exp[iq \cdot R(si, sj)] \rangle$$
$$= \frac{2[J_1(k; L_m, \lambda_m) + J_2(k; p, L_s, \lambda_s) + J_3(k; p, L_s, L_m, \lambda_s, \lambda_m) + J_4(k; p, L_s, L_m, \lambda_s, \lambda_m)]}{(L_m + pL_s)^2} \quad (8)$$

Here, p is the number of side chains ($=n/3\alpha$), $\mathbf{q}$ is the scattering vector, and $\mathbf{R}(s_i, s_j)$ is the vector between the contour points $\mathbf{R}(s_i)$ and $\mathbf{R}(s_j)$ on the subchains i and j, respectively, at the contour distances s_i and s_j, measured from one ends of the subchains.

dx.doi.org/10.1021/ma202176w |Macromolecules 2012, 45, 392–400

The subchain is a side chain or a portion of the main chain lain between neighboring junction points. The summation can be decomposed into the four terms, J_1 (both $\mathbf{R}(s_i)$ and $\mathbf{R}(s_j)$ are on the main chain), J_2 (both $\mathbf{R}(s_i)$ and $\mathbf{R}(s_j)$ are on the same side chain), J_3 ($\mathbf{R}(s_i)$ is on the main chain and $\mathbf{R}(s_j)$ is on a side chain), and J_4 ($\mathbf{R}(s_i)$ and $\mathbf{R}(s_j)$ are on different side chains) (see eqs 79−82 in ref30 for the details on J_1, J_2, J_3, and J_4). Here, λ_s^{-1} and λ_m^{-1} are the Kuhn segment lengths of the side chain (i.e., CMP) and main chain (NaPAA), respectively.

Equation 8 is however applicable only when the SAXS contrast factors per unit contour length of the side chain $\Delta z_s M_{L,s}$ and of the main chain $\Delta z_m M_{L,m}$ are the same, where, $M_{L,s}$ ($\equiv M_s/L_s$) and $M_{L,m}$ ($\equiv M_m/L_m$) are the molar masses per unit contour length of the side chain and main chain, respectively. In our case, the value $\Delta z_s M_{L,s}$ for the triple helical GPO9 is 46% larger than that $\Delta z_m M_{L,m}$ for NaPAA, so that we extend eq 8 as

$$P_0(q) = \frac{1}{(\Delta z_m M_m + p\Delta z_s M_s)^2} \sum_i \sum_j \int ds_i \int ds_j \, \Delta z_i M_{L,i} \Delta z_j M_{L,j} \langle \exp[iq \cdot \mathbf{R}(s_i, s_j)] \rangle$$

$$= \frac{2[(\Delta z_m M_{L,m})^2 J_1(k; L_m, \lambda_m) + (\Delta z_s M_{L,s})^2 J_2(k; p, L_s, \lambda_s) + \Delta z_s \Delta z_m M_{L,s} M_{L,m} J_3(k; p, L_s, L_m, \lambda_s, \lambda_m) + (\Delta z_s M_{L,s})^2 J_4(k; p, L_s, L_m, \lambda_s, \lambda_m)]}{(\Delta z_m M_m + p\Delta z_s M_s)^2} \quad (9)$$

to calculate $P_3(q)$ for the GPO9-NaPAA complex. Likewise, the radius of gyration for the complex can be calculated by

$$\langle S^2 \rangle = \frac{[(\Delta z_m M_{L,m})^2 I_1(L_m, \lambda_m) + (\Delta z_s M_{L,s})^2 I_2(p, L_s, \lambda_s) + \Delta z_s \Delta z_m M_{L,s} M_{L,m} I_3(p, L_s, L_m, \lambda_s, \lambda_m) + (\Delta z_s M_{L,s})^2 I_4(p, L_s, L_m, \lambda_s, \lambda_m)]}{(\Delta z_m M_m + p\Delta z_s M_s)^2} \quad (10)$$

where I_1, I_2, I_3, and I_4 are listed as eqs 69 − 72 in ref 30.

In the case of the GPO9-NaPAA complex, the chain diameter d (= 1.6 nm) of NaPAA is almost equivalent to that for triple helical GPO9,[19] the chain thickness for the complex can be considered according to the following equation for the touched-bead model with the same bead diameter d_B both for NaPAA and triple helical GPO9.[32]

$$P_3(q) = 9\left(\frac{2}{qd_B}\right)^6 [\sin(qd_B/2) - (qd_B/2)\cos(qd_B/2)]^2 P_0(q) \quad (11)$$

It should be noted that this chain thickness is not appreciable for $\langle S^2 \rangle$ when we estimate the contribution in $\langle S^2 \rangle$ by $d^2/8$.[33]

■ ASSOCIATED CONTENT

Ⓢ Supporting Information. Circular dichroism spectra for GPO9 with or without NaPAA. This material is available free of charge via the Internet at http://pubs.acs.org.

■ AUTHOR INFORMATION

Corresponding Author

*E-mail: (K.T.) kterao@chem.sci.osaka-u.ac.jp; (H.P.B.) hpb@shcc.org.

■ ACKNOWLEDGMENT

The synchrotron radiation experiments were performed at the BL40B2 in SPring-8 with the approval of the Japan Synchrotron Radiation Research Institute (JASRI) (Proposal No. 2010B1126) and at the BL-10C in KEK-PF under the approval of the Photon Factory Program Advisory Committee (No. 2010G080). The authors thank Prof. Yoji Inoko (Osaka Univ.) for SAXS measurements in KEK-PF and Prof. Shinichi Kitamura (Osaka Pref. Univ.) for supplying an enzymatically synthesized amylose sample. K.T. is indebted to the Institutional Program for Young Researcher Overseas Visits, Japan Society of the Promotion of Science (JSPS).

■ REFERENCES

(1) Fallas, J. A.; O'Leary, L. E. R.; Hartgerink, J. D. *Chem. Soc. Rev.* **2010**, *39*, 3510–3527.
(2) Fields, G. B. *Org. Biomol. Chem.* **2010**, *8*, 1237–1258.
(3) Shoulders, M. D.; Raines, R. T. *Annu. Rev. Biochem.* **2009**, *78*, 929–958.
(4) Berisio, R.; De Simone, A.; Ruggiero, A.; Improta, R.; Vitagliano, L. *J. Peptide Sci.* **2009**, *15*, 131–140.
(5) Okuyama, K.; Kawaguchi, T. *Kobunshi Ronbunshu* **2010**, *67*, 229–247.
(6) Okuyama, K. *Connect. Tissue Res.* **2008**, *49*, 299–310.
(7) Kita, Y.; Terao, K.; Sato, T. *Kobunshi Ronbunshu* **2010**, *67*, 686–689.
(8) Feng, Y.; Melacini, G.; Taulane, J. P.; Goodman, M. *J. Am. Chem. Soc.* **1996**, *118*, 10351–10358.
(9) Locardi, E.; Kwak, J.; Scheraga, H. A.; Goodman, M. *J. Phys. Chem. A.* **1999**, *103*, 10561–10566.
(10) Frank, S.; Boudko, S.; Mizuno, K.; Schulthess, T.; Engel, J.; Bächinger, H. P. *J. Biol. Chem.* **2003**, *278*, 7747–7750.
(11) Suehiro, T.; Tada, T.; Waku, T.; Tanaka, N.; Hongo, C.; Yamamoto, S.; Nakahira, A.; Kojima, C. *Biopolymers* **2011**, *95*, 270–277.
(12) Mizuno, K.; Hayashi, T.; Peyton, D. H.; Bächinger, H. P. *J. Biol. Chem.* **2004**, *279*, 38072–38078.
(13) Mizuse, M. M.S. Thesis, Osaka University: Osaka, Japan, 2010.
(14) (a) Kitamura, S.; Yunokawa, H.; Mitsuie, S.; Kuge, T. *Polym. J.* **1982**, *14*, 93–99. (b) Waldmann, H.; Gygax, D.; Bednarski, M. D.; Shangraw, W. R.; Whitesides, G. M. *Carbohydr. Res.* **1986**, *157*, c4–c7.
(15) Dubin, P.; Brant, D. A. *Macromolecules* **1975**, *8*, 831–842.
(16) Heinze, T.; Pfeiffer, K.; Lazik, W. *J. Appl. Polym. Sci.* **2001**, *81*, 2036–2044.
(17) Ueno, K.; Ueno, H.; Sato, T. *Polym. J.* **2011**, DOI: 10.1038/pj.2011.65.
(18) Glatter, O.; Kratky, O. *Small Angle X-ray Scattering*; Academic Press: London, 1982.
(19) Terao, K.; Mizuno, K.; Murashima, M.; Kita, Y.; Hongo, C.; Okuyama, K.; Norisuye, T.; Bächinger, H. P. *Macromolecules* **2008**, *41*, 7203–7210.

(20) Berry, G. C. *J. Chem. Phys.* **1966**, *44*, 4550–4564.
(21) Nakamura, Y.; Wan, Y.; Mays, J. W.; Iatrou, H.; Hadjichristidis, N. *Macromolecules* **2000**, *33*, 8323–8328.
(22) Terao, K.; Farmer, B. S.; Nakamura, Y.; Iatrou, H.; Hong, K.; Mays, J. W. *Macromolecules* **2005**, *38*, 1447–1450.
(23) Nakamura, Y.; Norisuye, T. *J. Polym. Sci., Part B: Polym. Phys.* **2004**, *42*, 1398–1407.
(24) (a) Schweins, R.; Hollmann, J.; Huber, K. *Polymer* **2003**, *44*, 7131–7141. (b) Muroga, Y.; Noda, I.; Nagasawa, I. *Macromolecules* **1985**, *18*, 1576–1579. (c) Knappe, P.; Bienert, R.; Weidner, S.; Thünemann, A. F. *Macromol. Chem. Phys.* **2010**, *211*, 2148–2153.
(25) Noda, I.; Tsuge, T.; Nagasawa, M. *J. Phys. Chem.* **1970**, *74*, 710–719.
(26) Mizuno, K.; Boudko, S.; Engel, J.; Bächinger, H. P. *Biophys. J.* **2010**, *98*, 3004–3014.
(27) Nakanishi, Y.; Norisuye, T.; Teramoto, A.; Kitamura, S. *Macromolecules* **1993**, *26*, 4220–4225.
(28) Norisuye, T. *Polym. J.* **1994**, *26*, 1303–1307.
(29) Hayashi, K.; Tsutsumi, K.; Nakajima, F.; Norisuye, T.; Teramoto, A. *Macromolecules* **1995**, *28*, 3824–3830.
(30) Nakamura, Y.; Norisuye, T. In *Soft-Matter Characterization*; Borsali, R., Pecora, R., Eds.; Springer: Berlin, 2008; Vol. 1, p 236−286.
(31) Huber, K.; Burchard, W. *Macromolecules* **1989**, *22*, 3332–3336.
(32) Burchard, W.; Kajiwara, K. *Proc. R. Soc. London, Ser. A.* **1970**, *316*, 185–199.
(33) Konishi, T.; Yoshizaki, T.; Saito, T.; Einaga, Y.; Yamakawa, H. *Macromolecules* **1990**, *23*, 290–297.

Macromolecules

Article

pubs.acs.org/Macromolecules

Polymer Actuators Using Ion-Gel Electrolytes Prepared by Self-Assembly of ABA-Triblock Copolymers

Satoru Imaizumi, Hisashi Kokubo, and Masayoshi Watanabe*

Department of Chemistry and Biotechnology, Yokohama National University, Tokiwadai, Hodogaya-ku, Yokohama 240-8501, Japan

Supporting Information

ABSTRACT: Well-defined ABA-triblock copolymers, polystyrene-*block*-poly(methyl methacrylate)-*block*-polystyrene (SMS), which have two different polystyrene (PSt) weight fractions (f_{PSt}), were synthesized by successive atom-transfer radical polymerizations. Ion gels consisting of SMS and an ionic liquid, (1-ethyl-3-methylimidazolium bis(trifluoromethanesulfonyl)amide [C_2mim][NTf_2]), were prepared using the cosolvent evaporation method with tetrahydrofuran. Atomic force microscope images of the ion gels indicated that PSt is phase-separated to form sphere domains that serve as physical cross-linking points because PSt is not compatible with [C_2mim][NTf_2], while a continuous poly(methyl methacrylate) (PMMA) phase with dissolved [C_2mim][NTf_2] is formed to serve as ion conduction paths. Accordingly, the ion gels are formed by the self-assembly of SMS and the preferential dissolution of [C_2mim][NTf_2] into the PMMA phase. The viscoelastic properties of the gels can be easily controlled by changing f_{PSt} in SMS and [C_2mim][NTf_2] concentration in the ion gels. The ion gels that exhibit high ionic conductivities (>10^{-3} S cm^{-1}) at room temperature were used as an electrolyte of an ionic polymer actuator, which has a trilaminar structure consisting of the ion-gel electrolyte sandwiched between two composite carbon electrodes containing high-surface-area activated carbon powders. By applying low voltages (<3.0 V) to the electrodes, the actuator exhibited a soft bending motion toward the anodic side.

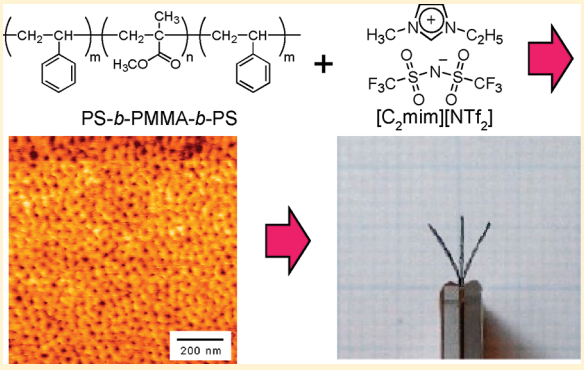

1. INTRODUCTION

Ionic liquids (ILs) exhibit unique properties such as thermal and (electro)chemical stability, nonvolatility, nonflammability, and high ionic conductivity; consequently, they have been an area of intense interest.[1] ILs have received much attention since Wilkes et al. reported air- and water-stable ILs containing the tetrafluoroborate anion in 1992.[2] ILs are generally regarded as environmentally benign green solvents and a promising class of functional materials. The properties of ILs can be adjusted widely because an infinite number of possible combinations of cations and anions can be achieved. For this reason, ILs are sometimes referred to as "designer solvents" and "third solvents" following water and organic solvents.

From the standpoint of materials science, the combination of ILs and polymers is promising for the development of novel materials because certain polymers are compatible with ILs.[3−5] The development of polymer electrolytes with unique properties such as thin-film formability, flexibility, and transparency in addition to high ionic conductivity has been an intensive topic of many researchers attempting to realize novel electrochemical devices.[6] In 1993, we published the first report on a polymer electrolyte containing an IL with an exceptionally high ionic conductivity.[7] This electrolyte was molecular composites consisting of a chloroaluminate IL and a polymer. Subsequently, we found that common vinyl monomers are widely soluble in air- and water-stable ILs and that they can be polymerized in ILs by free-radical polymerization.[8] In certain cases, good compatibility of the resulting polymers with the ILs can be achieved, regardless of the polymer concentration and temperature. Network polymers containing ILs (ion gels) can be obtained in such cases.[8] During the same time as our above research, many other studies investigated the solidification or gelation of ILs to obtain solid electrolytes by utilizing crystalline fluorinated copolymers,[9] stereocomplex formations of poly(methyl methacrylate)s,[10] and self-organization of amphiphilic block copolymers,[11] as well as the addition of colloidal nanoparticles[12−14] and low molecular weight gelators.[15,16] Among them, the utilization of block copolymers is of great interest since this methodology may have the potential to afford easily processable and mechanically strong ion gels by utilizing self-assembly of the block copolymers. Lodge et al. have been conducting systematic studies of the preparation, structure, rheology, and application of ions gels consisting of block copolymers and ILs.[11,17]

Applicable fields of ion gels are diverse, e.g., solid electrolytes of electrochemical devices such as capacitors,[18] batteries,[19] fuel cells,[20] solar cells,[21] and actuators;[22−24] membranes for gas separation[25] and catalytic reactions;[26] and dielectric layers of

Received: October 3, 2011
Revised: November 25, 2011
Published: December 15, 2011

Scheme 1. Synthesis of SMSs by Successive ATRPs

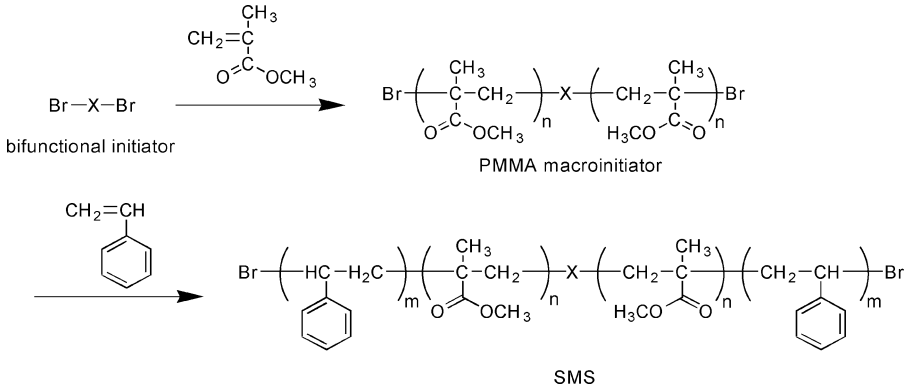

organic transistors.[27] We have been especially interested in polymer actuators as an application of ion gels. As a material for manufacturing artificial muscles with biomimetic soft motion, polymer actuators using electroactive polymer (EAP) have been applied to manipulators and robotic devices.[28−32] Ionic EAP actuators[30−32] driven by diffusion or migration of ions can exhibit relatively large deformation in response to application of low voltages. However, these actuators have a serious problem with regard to their durability under atmospheric conditions owing to evaporation of solvents, which are necessary to provide environments that permit the movement of ions. To overcome such problems, ILs have been applied to the electrolytes of ionic EAPs.[22−24] Most research in this field has focused on optimization of the electrolytes by changing the IL structures,[33] but very few studies have focused on matrix polymers for ILs. Indeed, poly(vinylidene fluoride-*co*-hexafluoropropylene) (P(VDF-*co*-HFP))[24,33a−d] and Nafion[23,33e] have been mainly investigated in this context. Thus, additional knowledge regarding the effects of the polymer structure and properties on the performance of actuators is needed.

In this study, we investigated the microstructures, rheological properties, and ionic conductivity of ion gels formed by self-assembly of polystyrene-*block*-poly(methyl methacrylate)-*block*-polystyrene (SMS) triblock copolymers,[11c] prepared by successive atom-transfer radical polymerizations (ATRP).[34,35] Our previous study showed that polystyrene (PSt) and poly(methyl methacrylate) (PMMA) were insoluble and soluble, respectively, in 1-ethyl-3-methylimidazolium bis(trifluoromethanesulfonyl)amide ($[C_2mim][NTf_2]$);[36] thus, preferential dissolution of $[C_2mim][NTf_2]$ in the PMMA phase was expected, which was also confirmed by the study by Frisbie and Lodge et al.[11c] The continuous PMMA phase with dissolved $[C_2mim][NTf_2]$ may serve as conduction paths for the IL, while the phase-separated PSt phase may serve as physical cross-linking points. Furthermore, we report the performance of the polymer actuators using ion-gel electrolytes consisting of SMS and $[C_2mim][NTf_2]$. Chemically deposited noble-metal electrodes[23,30] and carbon nanotubes,[24,37] have been widely used as electrode materials for ionic EAPs. We have proposed that inexpensive and ubiquitous carbon materials such as activated carbon can be used as electrode material of the actuators.[38] Here, we demonstrate an ionic EAP actuator with a trilamellar structure consisting of an ion-gel electrolyte sandwiched between two composite carbon electrodes containing high-surface-area activated carbon powders. The correlation between the actuator performance and the properties of the ion gels is also discussed.

2. EXPERIMENTAL SECTION

Materials. An ionic liquid, $[C_2mim][NTf_2]$, was prepared according to the literature with slight modification[39] and dried under vacuum at 100 °C for 24 h. The water content in $[C_2mim][NTf_2]$ determined by Karl Fischer titration was less than 10 ppm. 2-Bromoisobutyl bromide, dehydrated anisole, and 4,4′-dinonyl-2,2′-bipyridine (dNbpy) were purchased from Aldrich and used without further purification. CuBr and $CuBr_2$ were purchased from Wako Chemical. CuBr was washed with glacial acetic acid, dehydrated ethanol, and diethyl ether, dried under vacuum, and then stored in an argon-atmosphere glovebox (VAC). $CuBr_2$ was dried under vacuum and stored in the same drybox. Ethylene glycol, triethylamine and *N*,*N*,*N*′,*N*′,*N*″-pentamethyldiethylenetriamine (PMDETA) were purchased from Tokyo Chemical Industry, and were dried by molecular sieves. Methyl methacrylate (MMA) and styrene (both from Wako Chemical) were dried by calcium hydride overnight and vacuum-distilled prior to use.

Synthesis of a Bifunctional Initiator. A bifunctional initiator, ethylene glycol bis(2-bromoisobutyrate), was synthesized according to the literature.[40] To accomplish this, ethylene glycol (5.6 mL, 0.10 mol) and triethylamine (34 mL, 0.24 mol) were dissolved in 300 mL of diethyl ether in a three-necked flask under a N_2 atmosphere, after which the solution was cooled to 0 °C in an ice bath. Next, 2-bromoisobutyl bromide (30 mL, 0.24 mol) was dropped into the solution, and the solution was stirred overnight. The reaction solution was then filtered, after which the filtrate was washed with water three times. Finally, white needle crystals (14 g, 39 mmol, yield 39%) were obtained by recrystallization from ethanol/H_2O. ^1H NMR of the bifunctional initiator (400 MHz, $CDCl_3$): δ (ppm) = 1.94 (s, $(CH_3)_2C$, 12H), 4.44 (s, OCH_2, 4H). (The spectrum is shown in Supporting Information, Figure S-1)

Synthesis of PMMA Macroinitiator. The bifunctional initiator (1.7 g, 4.8 mmol) and $CuBr_2$ (2.5 mg, 0.24 mmol) were dried under reduced pressure in a three-necked flask. Anisole (200 mL) and PMDETA (0.63 μL, 3.0 mmol) were then added to the flask. To dissolve $CuBr_2$ by complex formation with PMDETA, the solution was stirred overnight at 60 °C under a N_2 atmosphere. After cooling the solution, CuBr (0.34 mg, 2.4 mmol) and MMA (200 mL, 1.9 mol) were added to the flask. The reaction mixture was then degassed by sonication under reduced pressure and successive N_2 replacement three times. A polymerization reaction was subsequently conducted at 60 °C for 6 h with stirring (Scheme 1). Next, the reaction was quenched by cooling to 0 °C, after which the crude polymer was isolated by precipitation into an excess amount of methanol and collected by suction filtration. The polymer was then dissolved again in ethyl acetate and the solution was purified by column chromatography (alumina) to remove the Cu complexes from the PMMA. The eluted ethyl acetate solution of the PMMA was poured into a large excess of hexane, and the precipitates were filtered and dried under vacuum. The purified PMMA macroinitiator was obtained as white powder (Yield: 90 g). The molecular characterization results are shown in Table 1.

dx.doi.org/10.1021/ma2022138 | *Macromolecules* 2012, 45, 401−409

Table 1. Monomer Conversion, Molecular Weight, Molecular Weight Distribution, and Composition of PMMA and SMSs

	convn[a]	$M_{n,theo}$ ($\times 10^{-4}$)[b]	M_n ($\times 10^{-4}$)	M_w/M_n[c]	f_{PSt} (wt %)[d]
PMMA[e]	0.47[f]	1.9	1.89[c]	1.12	–
SMS-18	0.1[g]	2	2.31[f]	1.11	18.3[f]
SMS-48	0.3[g]	4	3.65[f]	1.16	48.2[f]

[a]Monomer conversion. [b]Calculated from monomer conversion. [c]Evaluated by GPC analysis using PMMA standard. [d]Weight fraction of PSt in the SMS. [e]Utilized as a macroinitiator for SMSs. [f]Calculated by ^{1}H NMR analysis. [g]Calculated from polymer yield.

Synthesis of ABA-Triblock Copolymers. The synthesized PMMA macroinitiator (20 g, 1.1 mmol), CuBr (0.13 g, 0.87 mmol), $CuBr_2$ (5.8 mg, 0.026 mmol), and dNbpy (0.76 g, 1.9 mmol) were added into a dried round-bottom flask. Styrene (80 mL, 0.69 mol), which is not only a monomer but also a reaction solvent, was then poured into the flask. The polymerization reaction was then allowed to proceed at 100 °C. At 26 and 45 h from the initiation of the polymerization, heating was stopped. The obtained polymer was then isolated and purified by reprecipitation using a similar method as that used for the PMMA macroinitiator. The weight fractions of PSt in SMS-18 and SMS-48 were evaluated from ^{1}H NMR spectra shown in Figure S-2, Supporting Information. The molecular characterization results of the block copolymers are shown in Table 1. Gel permeation chromatograms (GPC) of the PMMA macroinitiator and ABA-triblock copolymers (Figure 1) indicated that well-defined block copolymers were prepared by the successive ATRP method.

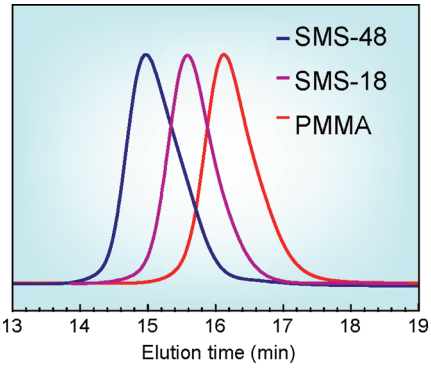

Figure 1. Gel permeation chromatograms of PMMA macroinitiator and SMS block copolymers.

Material Characterization. Viscoelastic measurements were conducted using a Physica MCR301 (Anton Paar) rotary rheometer with an H-PTD200 temperature controller. A parallel plate (25 or 50 mm diameter) was installed, depending on the modulus of each sample. The frequency dispersion was measured in the frequency range of 0.1 to 100 rad s^{-1} and in the temperature range from 120 to 0 °C by 10 °C steps. The samples were thermally equilibrated at each temperature for at least 1 h before the measurements. Differential scanning calorimetry (DSC) was conducted using a Seiko Instruments DSC 6220 under a nitrogen atmosphere. The samples were tightly sealed in aluminum pans in the dry glovebox. The DSC measurements were conducted by heating to +150 °C, cooling to −150 °C, and then heating to +150 °C at a cooling and heating rate of 10 °C min^{-1}. The glass transition temperatures (T_g) were determined from the mid points of heat capacity changes in the DSC thermograms during the programmed reheating scans. Atomic force microscope (AFM) images were recorded at room temperature by an SPA-400 microscope unit and a SPI3800N probe controller (Seiko Instruments Inc.) in tapping mode, using a silicon cantilever with a spring constant of 15 N m^{-1}. A lump of the ion gel sample was frozen with liquid N_2, cleaved, and sliced into a thin film to expose the cleaved face for the AFM observation. The ionic conductivity of the ion gels was determined from complex impedance measurements using a Hewlett-Packard 4192A LF impedance analyzer over a frequency range of 5 Hz to 13 MHz. The ion gel samples were then placed between two stainless steel disk electrodes separated by a polytetrafluoroethylene spacer with an inner diameter of 8.5 mm and a height of 3 mm. The cell constant was determined using a 0.01 M KCl standard aqueous solution. The sample cell was placed in a thermo-regulated bath and thermally equilibrated at each temperature for at least 1 h before taking the measurements.

Preparation and Measurement of Ion Gel Actuators. Preweighed amounts of SMS and $[C_2mim][NTf_2]$ were dissolved in tetrahydrofuran (THF) as a cosolvent. After casting the THF solution in a flat Petri dish, the THF was gradually removed from the solution at ambient temperatures and then dried under vacuum for more than 12 h. Transparent and flexible ion gel membranes (SMS/$[C_2mim][NTf_2]$ composites) were obtained by this procedure.

Ion gel actuators have a trilaminar structure consisting of an ion-gel electrolyte membrane sandwiched between two carbon electrodes. The carbon electrodes were prepared by mixing activated carbon (24 wt %, Kuraray Co. Ltd.), Ketjen black (3 wt %, Lion Corp.), P(VDF-*co*-HFP) (8 wt %, Arkema Inc.), and $[C_2mim][NTf_2]$(65 wt %) using a conditioning mixer (AR-250, Thinky). The mixture was then hot pressed with a polyimide spacer (50 μm) at 130 °C. Next, ion gel membranes with a thickness of 100 μm were fabricated by hot pressing at 130−160 °C, and the electrode membranes were attached to both sides of the ion-gel electrolyte by hot pressing at 80−130 °C to fabricate a monolithic trilaminar membrane. The thickness of the actuators became a little thinner (ca. 10 μm) than the total thickness of the electrodes and the electrolyte by the final hot pressing. Rectangular pieces (width of 2 mm and length of 7 mm) were cut from the monolithic membrane and clipped between Cu tapes connected to a potentiostat (HA-301, Hokuto Denko) and a function generator (HB-104, Hokuto Denko). Displacement of the actuator was measured at room temperature by a laser displacement meter (LC-2440, Keyence) at 4 mm from the clamped end.

3. RESULTS AND DISCUSSION

Formation of Ion Gels. It is interesting to explore how effectively $[C_2mim][NTf_2]$ gelates with the addition of SMS block copolymers. The gelation point of the SMS and $[C_2mim][NTf_2]$ binary systems was evaluated by dynamic viscoelastic measurement. The dynamic rheological properties measured under a constant strain amplitude within a linear viscoelastic regime are shown in Figure 2. The 7 wt % dispersions are liquids for both SMS block copolymer systems; the viscous modulus (G'') exceeds the elastic modulus (G') over the entire frequency range, and both moduli exhibit dependence on frequency. The dispersions show a complicated response at 9 wt % for SMS-18 and at 8 wt % for SMS-48. Specifically, the moduli exhibit a crossover at a high frequency. However, G' is dominant and the moduli become relatively independent of frequency toward the low end of the frequency spectrum. At 9 wt % for SMS-48, G' is larger than G'' and becomes less dependent on frequency over the entire measured range. These findings indicate that dispersions containing greater than 9 wt % for SMS-18 and more than 8 wt % for SMS-48 behave as soft solid materials (ion gels). In appearance, binary systems containing SMS at levels just below the gelation concentrations were bluish viscous liquids because of Rayleigh scattering, and these systems became extremely viscous as they approached gelation. Binary systems containing SMS at levels higher than the gelation concentrations became transparent and colorless gels.

dx.doi.org/10.1021/ma2022138 | *Macromolecules* 2012, 45, 401−409

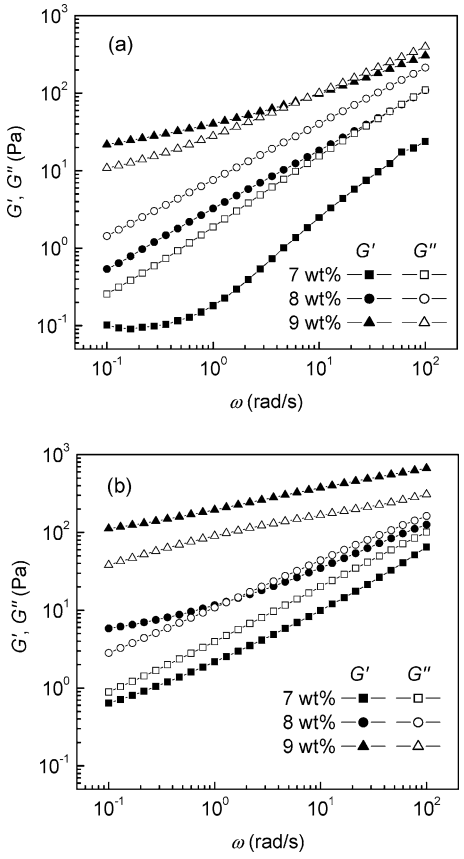

Figure 2. Storage (G') and loss (G'') moduli as a function of frequency for binary systems consisting of $[C_2mim][NTf_2]$ and SMS-18 (a) or SMS-48 (b) at 20 °C.

Lodge et al. reported that gelation of an IL, 1-butyl-3-methylimidazolium hexafluorophosphate ($[C_4mim]PF_6$), could be achieved by the self-assembly of as little as 5 wt % of a triblock copolymer, PSt-*block*-poly(ethylene oxide)(PEO)-*block*-PSt (SOS), where M_n of the each terminal PSt is 4760 Da, M_n of the middle PEO is 25 500 Da, the polydispersity index (M_w/M_n) is 1.36, and the PSt weight fraction (f_{PSt}) is 0.28.[11a] Although there are differences in the IL-philic segment structure; PEO against PMMA, and in the IL structures; $[C_4mim]PF_6$ against $[C_2mim][NTf_2]$, the critical gelation concentrations of these block copolymers are comparable. The somewhat lower gelation concentration of SOS than that of SMS may be ascribed to its higher M_n of the IL-philic PEO segment. They also recently reported physical properties of $[C_2mim][NTf_2]$ ion-gels with the 10 wt % addition of an SMS block copolymer (M_n of the SMS = 121 kDa, f_{PSt} = 0.29).[11c]

Figure 3 shows the viscoelastic moduli (G' and G'') of the ion gels containing 10 wt % SMSs as a function of temperature in the range of 0 to 120 °C at a frequency of 1 rad/s. The SMS-18 ion gel exhibits a crossing of G' and G'' at around 50 °C, where the sol−gel transition occurs. This sol−gel transition temperature is almost the same as T_g of PSt (= ca. 50 °C) with molecular weight of 2 kDa,[41] however, it depends on the angular frequency, as shown in Figure S-3, Supporting Information. SMS concentrations also affect the sol−gel transition temperatures (Figure S-4, Supporting Information). These results indicate that the stability of PSt cross-linking points cannot be explained only by the magnitude of T_g. The higher is the concentration or angular frequency, the higher

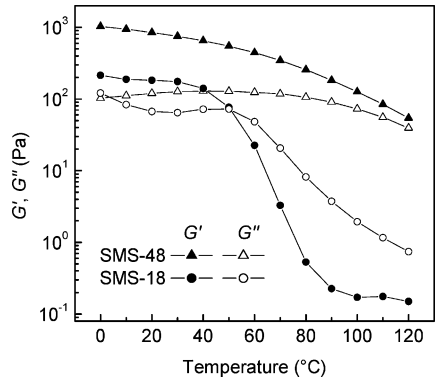

Figure 3. Temperature dependence of G' and G'' of ion gels based on SMS-48 (10 wt %) and SMS-18 (10 wt %) at 1 rad/s.

appears the sol−gel transition temperature. Conversely, the SMS-48 ion gel displays no transition over the measured temperature (0−120 °C). This phenomenon indicates that the PSt domain remains aggregated even above its T_g (=ca. 90 °C) with molecular weight of 9 kDa,[41] because PSt is less compatible with $[C_2mim][NTf_2]$. The difference in the sol−gel transition behavior of SMS-18 and SMS-48 appears to be caused by the difference in the incompatibility between PSt and $[C_2mim][NTf_2]$, which strongly depends on the molecular weight of PSt blocks. Strain dependencies of the viscoelastic moduli are shown in Figure 4. A linear regime was maintained

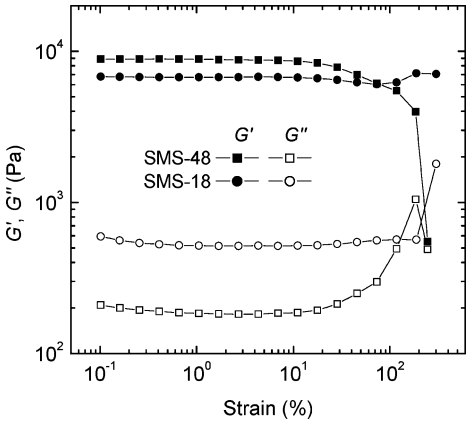

Figure 4. G' and G'' as a function of strain for ion gels containing 15 wt % of SMS-18 or SMS-48 at 25 °C and 1 Hz.

for up to 10% strain for each ion gel. By applying larger strain, the polymer networks were broken, possibly because of slipping-off of PSt chains from PSt domains that serve as physical cross-linking points of the ion gels. The plateau G' of the SMS-18 composite and SMS-48 composite are 7 and 9 kPa, respectively. The higher tan δ (=G''/G') value of the SMS-18 composite than that of the SMS-48 composite suggests that the number of looped chains, which are dominant in the sol state and ineffective in the formation of the gels, remains in a larger quantity in the SMS-18 composite. This is supported by the fact that deviation from the G' values of ideal gels is larger for SMS-18 than that for SMS-48 (Figure S-5, Supporting Information). The ion gel formed by SMS-48 has a higher cross-linking density than that formed by SMS-18, resulting in a hard and brittle gel.

dx.doi.org/10.1021/ma2022138 | *Macromolecules* 2012, 45, 401−409

Microstructure and Ionic Conductivity of Ion Gels. To confirm selective dissolution of $[C_2mim][NTf_2]$ in PMMA segments, which was expected from the observations in the rheological measurements (*vide supra*), we conducted DSC measurements of the ion gels. The DSC thermograms for SMS-48/$[C_2mim][NTf_2]$ are shown in Figure S-6, Supporting Information. The T_g values and the transition widths determined from the onsets and ends of heat capacity changes are listed in Table S-1, Supporting Information. Figure 5 shows

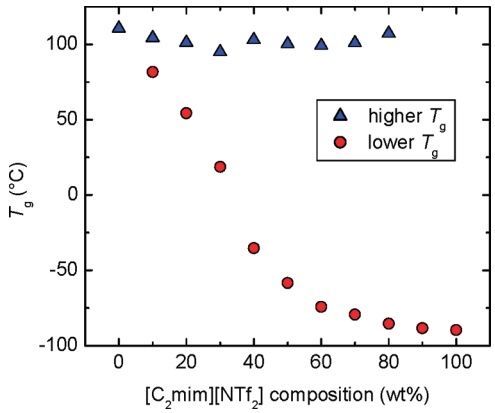

Figure 5. T_g of ion gels based on SMS-48 as a function of weight fraction of $[C_2mim][NTf_2]$.

the T_g values of ion gels based on SMS-48 plotted against $[C_2mim][NTf_2]$ weight fractions. In the case of neat SMS-48, only one T_g is observed at ca. 100 °C. We can not distinguish T_g values of PSt and PMMA because they are close together. As the weight fraction of $[C_2mim][NTf_2]$ increases, one T_g is still retained at ca. 100 °C, whereas another T_g appears at lower temperatures. In $[C_2mim][NTf_2]$ composition range of 30−50 wt %, the heat capacity changes corresponding to the lower T_gs are broadened (Figure S-6 and Table S-1, Supporting Information). Lodge et al. recently reported that PMMA/$[C_2mim][NTf_2]$ solutions have two apparent glass transitions at intermediate compositions, even if the binary systems are good solvent solutions.[42] We also observed similar phenomena in the network PMMA with dissolved $[C_2mim][NTf_2]$.[8b,c] In the present case, the broadening may also be caused by the coexistence of PMMA-rich region and $[C_2mim][NTf_2]$-rich region. When the weight fraction of $[C_2mim][NTf_2]$ becomes higher than 0.8, T_g at ca. 100 °C disappears and only one T_g appears at low temperature. When the weight fraction of $[C_2mim][NTf_2]$ becomes high, T_g of PSt cannot be observed because of a small heat capacity change accompanied by glass transition of PSt.

Figure 6 shows a tapping-mode AFM phase image of an ion gel containing 30 wt % of SMS-48. In this image, the bright region indicates a softer and more attractive surface, while the dark region indicates a harder and less-attractive surface. As expected, the image clearly shows that the ion gel is phase-separated between soft and hard domains.[43] The continuous bright portions and spherical dark portions correspond to PMMA(15 wt %) with dissolved $[C_2mim][NTf_2]$(70 wt %) domains and PSt(15 wt %) domains, respectively. In this case, the PSt spheres did not appear to form a fully ordered structure from the AFM image. Figure S-7 (Supporting Information) shows a two-dimensional (2D) Fourier power spectrum corresponding to the AFM image (Figure 6). An obscurely

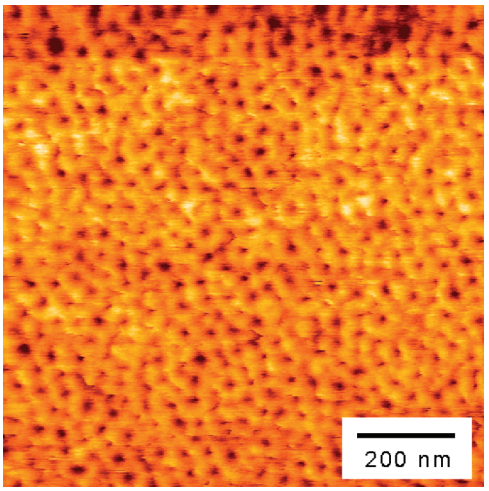

Figure 6. Tapping-mode AFM phase image of an ion gel based on SMS-48 (30 wt %).

ring-shaped 2D Fourier power spectrum is obtained, which indicates that the microphase separated structure of the ion gel does not have a fully ordered cubic structure, but rather a short-range ordered structure. Since phase diagram of block copolymers is well understood,[43] it is interesting to know the factors that determine the phase behavior and ordered/disordered structures. In the case of ordinary block copolymers, the ordered/disordered structures depend on the compatibility and segment size of each block.[43] Strongly segregated systems with less compatible blocks with large segment size take ordered structures. In the present case, quantitative compatibility of $[C_2mim][NTf_2]$ with PMMA and further that between PSt and PMMA with dissolved $[C_2mim][NTf_2]$ remains unexplored at a fundamental level.[5b] We just speculate now that the segregation between PSt and PMMA with dissolved $[C_2mim][NTf_2]$ is not strong enough to form a fully ordered structure.

Figure 7 shows the Arrhenius plot of ionic conductivities for the ion gels. The conductivity values were calculated from a cell

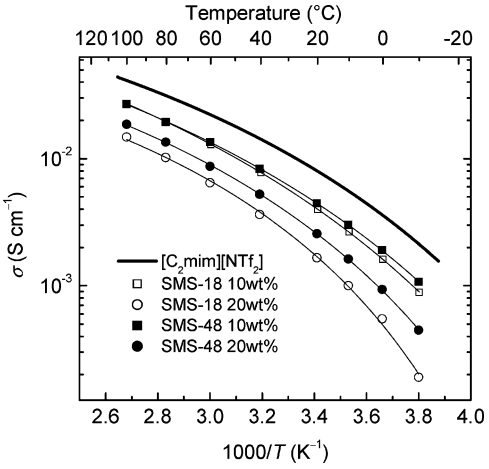

Figure 7. Arrhenius plots of ionic conductivity for the ion gels based on the SMS block copolymers with dissolved $[C_2mim][NTf_2]$.

constant and the real part of cell impedance value (Z') where the imaginary part of cell impedance ($-Z''$) takes a minimum in the Nyquist plots (Z' vs $-Z''$ plots). Typical Nyquist plots are

dx.doi.org/10.1021/ma2022138 | *Macromolecules* 2012, 45, 401−409

as shown in Figure S-8, Supporting Information, which consist of a low frequency spur corresponding to the interfacial impedance and a high frequency arc corresponding to the bulk impedance. There were no significant changes in the shape of the Nyquist plots with temperature, polymer concentration, and f_{PS} of SMS. Room temperature ionic conductivities of the gels reach 10^{-3} S cm^{-1}, and the temperature dependencies can be represented by the Vogel–Fulcher–Tammann (VFT) equation. On the basis of the VFT equation and the best-fit parameters (Supporting Information, Table S-2), the lines on the plots reproduce the experimental data well. It is also interesting to note that the ion gel based on SMS-18 exhibits continuous conductivities expressed by the VFT equation from −10 to +100 °C, even though the binary system undergoes a sol–gel transition at ca. 50 °C, as shown in Figure 3. This is contrasted by the previous observation that gel electrolytes based on ABA block copolymers, polyethylene-*block*-poly(ethylene oxide-*co*-propylene oxide)-*block*-polyethylene, and a 1 M Li[NTf$_2$] solution in γ-butyrolactone.[44] The gel electrolytes exhibit discontinuous conductivity changes at the sol–gel transition temperatures owing to melting of the end-polyethylene-blocks. In this case, there should be certain interactions between the Li salts and the midpolyether-blocks, which result in discontinuous conductivity increases at gel-to-sol transitions owing to melting of the end-blocks. Conversely, the [C$_2$mim][NTf$_2$] consists of extremely weak Lewis acidic cations and Lewis basic anions.[45] Thus, the motion of [C$_2$mim][NTf$_2$] is relatively decoupled from the motion of PMMA segments,[8c] and the melting of end-PSt-blocks does not contribute to acceleration of the transport of [C$_2$mim][NTf$_2$].

The ionic conductivities of the SMS-48 ion gels are higher than those of SMS-18 ion gels at the same block copolymer compositions. Since we have reported the ionic conductivities of loosely cross-linked PMMA networks with dissolved [C$_2$mim][NTf$_2$],[8b] we simulated the ionic conductivities of SMS ion gels based on a two-phase model composed of continuous PMMA domains with dissolved [C$_2$mim][NTf$_2$] and isolated PSt domains. This two-phase model assumes complete phase separation between these two phases. The conductivity can be written as

$$\sigma = \phi\sigma(\text{PMMA} + [\text{C}_2\text{mim}][\text{NTf}_2]) + (1 - \phi)\sigma(\text{PSt})$$

where ϕ is the volume fraction of the PMMA domains with dissolved [C$_2$mim][NTf$_2$]. Because of the negligibly low conductivity of σ(PSt), the above equation can be rewritten as

$$\sigma = \phi\sigma(\text{PMMA} + [\text{C}_2\text{mim}][\text{NTf}_2])$$

The broken lines in Figure 8 show σ(PMMA + [C$_2$mim][NTf$_2$]) determined from our data,[8b] and the solid lines represent ϕ σ(PMMA + [C$_2$mim][NTf$_2$]). Both of these values are plotted against the weight fraction of SMS in the ion gels. As shown in the figure, the ϕ (volume fraction of the PMMA/[C$_2$mim][NTf$_2$]) has little effect on the σ values. The experimental data shown by solid plots are reasonably located along the solid lines, and interference of the ion transport by the PSt domains appears to be very small. The higher conductivity for the SMS-48 ion gels than the SMS-18 ion gels shown in Figure 7 simply comes from the fact that the PMMA phase in the SMS-48 ion gel contains larger amounts of [C$_2$mim][NTf$_2$] at the same SMS weight fraction and thus exhibits higher σ(PMMA + [C$_2$mim][NTf$_2$]). This effect overwhelms the small ϕ for the SMS-48 ion gels. Since the ionic diffusion of [C$_2$mim][NTf$_2$] is interrupted by the

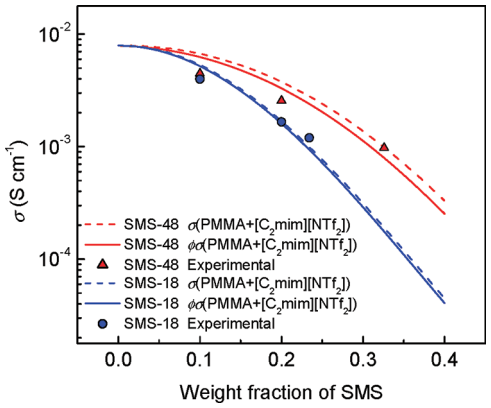

Figure 8. Ionic conductivity at 20 °C as a function of weight fraction of SMS for the ion gels containing [C$_2$mim][NTf$_2$]. Broken line: σ(PMMA + [C$_2$mim][NTf$_2$]) from ref8b; Solid line: ϕ σ(PMMA +[C$_2$mim][NTf$_2$]). Solid plots: experimental data.

interaction with PMMA chains,[8b] the ionic mobility is mainly determined by the PMMA/[C$_2$mim][NTf$_2$] compositions.

Performance of Polymer Actuator Using Ion Gels. The self-assembly of the SMS block copolymers in an IL was shown to form highly ion-conductive and nonvolatile soft-materials (ion gels). Here, we show an application of the ion gels to ionic EAP actuators. Figure 9 shows the current and bending

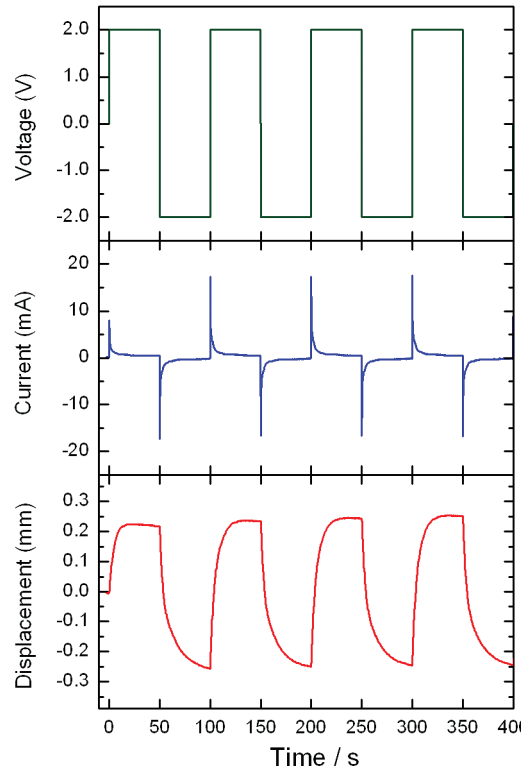

Figure 9. Current and displacement responses of an ion gel actuator based on SMS-18 (20 wt %) against application of ±2.0 V rectangular voltage with a cycle of 100 s.

displacement responses of an ion gel actuator against a rectangular voltage application (see also Figure S-9, Supporting Information). When voltage is applied to the actuator, charging current is observed, but this current decays exponentially with time. No faradaic current was observed in the cyclic

dx.doi.org/10.1021/ma2022138 | *Macromolecules* 2012, 45, 401–409

voltammetry within the voltage range of ±2.0 V. These phenomena indicate that charging and discharging of the electric double layer formed at the interface between the activated carbon and $[C_2mim][NTf_2]$ in the electrode layer is responsible for displacement of the actuator. It should be noted that the bending displacement is always directed toward the anodic side. In other words, the actuator bends toward the positively polarized electrode direction. This behavior has been widely observed in ionic EAP actuators using ILs.[23,24,33,46] We have investigated the transport properties of common ionic liquids in detail, especially imidazolium-based ILs.[47] Interestingly, the diffusivity of the cations is larger than that of anions in most cases, even if the van der Waals radius of the cations is larger than that of the anion.[47c] Typically, the cationic and anionic diffusivity of $[C_2mim][NTf_2]$ is clarified to be 4.4×10^{-7} and 2.5×10^{-7} cm^2 s^{-1}, respectively, at 20 °C,[47c] which corresponds to a cationic transference number of 0.64. The cationic transference number in the PMMA-based ion gels also becomes larger as the mole fraction of $[C_2mim][NTf_2]$ decreases (increasing the mole fraction of PMMA) owing to preferential interaction of the $[NTf_2]$ anion with PMMA chains.[8b] Such imbalanced transport between the cation and anion induces concentration polarization of $[C_2mim][NTf_2]$ inside the polymers (PMMA in the electrolyte layer and P(VDF-*co*-HFP) in the electrode layer) via electrochemical polarization of the actuators. On the anodic side, the concentration becomes lower than that in the bulk, while on the cathodic side, it becomes larger than that in the bulk. This concentration polarization causes swelling of the cathodic electrode layer and deswelling of the anodic electrode layer, which appears to explain such displacement. The actuation mechanism will be discussed in detail in a forthcoming paper.

The applied voltage dependence of the displacement of the ion gel actuators is shown in Figure 10. As the applied voltages

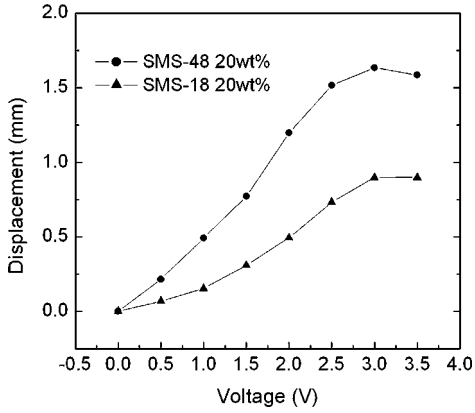

Figure 10. Displacement of ion gel actuators based on SMS block copolymers as a function of the magnitude of rectangular-wave voltages at a cycle of 100 s.

increase, electric charges stored in the electric double layer increase, resulting in an increase in displacement up to ca. 1.6 mm at 3.0 V, which is 40% of its length. However, when a voltage of 3.5 V is applied, the displacement does not change or decreases slightly, despite an increase in the flowing current. Reversibility of motion of the actuators also deteriorated at an applied voltage of 3.5 V. This is due to certain irreversible faradaic reactions. Although the electrochemical potential window $[C_2mim][NTf_2]$ is reported to be wider than 4 V,[39,48] the actuator experiments were conducted under atmospheric conditions and the contamination by water and oxygen could cause to reduce the electrochemical stability of the actuator. Figure 11 shows the displacement amplitude of

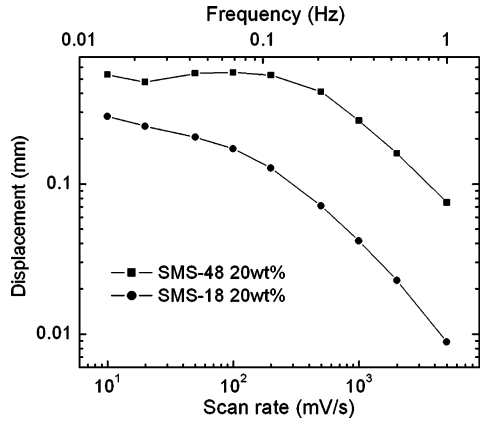

Figure 11. Scan rate dependence of the displacement amplitude for ion gel actuators based on SMS block copolymers with the application of ±1.5 V triangular wave voltage.

the actuators with the application of ±1.5 V triangular wave voltage as a function of the scan rate and a function of the frequency (upper horizontal axis). The actuator based on SMS-48 demonstrates superior performance in terms of displacement amplitude and speed. These results reflect the difference in the electrolyte properties. Specifically, the ionic conductivities of the ion gels containing 20 wt % of SMS-48 and SMS-18 at 20 °C are 2.4×10^{-3} and 1.7×10^{-3} S cm^{-1}, respectively. Higher conductivity makes the time constants of the actuators smaller, which enhances the amount of electricity stored at the electric double layers and the magnitude of concentration polarization of $[C_2mim][NTf_2]$ at a constant voltage scan rate. The simplest equivalent circuit for the actuators is the series connection of a resistance and a capacitance. The resistance (R) correlates with the conductivity and shape of ion gels and the capacitance (C) corresponds to the double layer capacitance between the ion gel and carbon electrodes. Actual R and C values of the actuator were estimated to be R = 40 Ω and C = 0.1 F for an ion gel actuator based on SMS-18 (20 wt %), which is shown in Figure 9. In this case, the time constant becomes 4 s. However, the displacement in Figure 9 continues to increase for several tens of seconds. In the actuation experiments, one end of a rectangular trilaminar-specimen was clipped between Cu current-collectors. The carbon electrode layer is much more resistive compared with the metal. Consequently, the potential drop along longitudinal direction of the actuator specimen cannot be neglected. This is the main reason why the time constant of the actuator during actuation becomes longer than that estimated from the R and C values. However, for fast and large movement of the actuators, reduction of the time constant by the achievement of high ionic conductivity of the ions gels and large double-layer capacitance as well as the achievement of high electronic conductivity of the carbon electrodes appears to be the most crucial requirements.

■ CONCLUSION

We investigated the gelation of an IL, $[C_2mim][NTf_2]$, by self-assembly of SMS block copolymers. The rheological properties, AFM images, and ionic conductivity of the SMS/$[C_2mim]$-

dx.doi.org/10.1021/ma2022138 | *Macromolecules* 2012, 45, 401–409

[NTf_2] binary systems are reasonable if we assume that the gelation occurs via aggregation of the PSt segments in the IL owing to incompatibility with [C_2mim][NTf_2] and that the resulting ion gels have two-phase structures consisting of continuous PMMA phases with preferentially dissolved [C_2mim][NTf_2] and isolated PSt phases. The aggregated PSt phases serve as physical cross-linking points of the ion gels.

Moreover, we fabricated ionic EAP actuators using SMS/[C_2mim][NTf_2] ion gels. The ion gel actuators have a trilaminar structure composed of the ion-gel electrolyte sandwiched between two composite carbon electrodes containing high-surface-area activated carbon powders. By applying low voltages (<3.0 V) to the electrodes, the actuator exhibited soft bending motion toward the anodic side. The displacement of the actuator increased with an increase in the charge stored at the electric double layer between the activated carbon and the IL, eventually increasing to 40% of its length. The ionic conductivity of the ion gels was closely correlated with the performance of the actuators.

■ ASSOCIATED CONTENT

Supporting Information

Characterization of materials (Figure S-1 and S-2), rheological properties (Figure S-3, S-4, and S-5), thermal properties (Table S-1 and Figure S-6), two-dimensional Fourier power spectrum of a tapping mode AFM phase image (Figure S-7), ionic conductivity (Figure S-8 and Table S-2), and photographs of the movement of an ion gel actuator (Figure S-9). This material is available free of charge via the Internet at http://pubs.acs.org.

■ AUTHOR INFORMATION

Corresponding Author

*Telephone and fax: +81-45-339-3955. E-mail: mwatanab@ynu.ac.jp.

■ ACKNOWLEDGMENTS

This work was supported in part by Grants-in-aid for Scientific Research on Priority Areas (No. 438-19016014 and No. 452-17073009) from the MEXT of Japan.

■ REFERENCES

(1) (a) Welton, T. *Chem. Rev.* **1999**, *99*, 2071. (b) Holbrey, J. D.; Seddon, K. R. *Clean Prod. Process* **1999**, *1*, 223. (c) Wasserscheid, P.; Keim, W. *Angew. Chem., Int. Ed.* **2000**, *39*, 3772. (d) Wilkes, J. S. *Green Chem.* **2002**, *4*, 73. (e) Seddon, K. R. *Nat. Mater.* **2003**, *2*, 363. (f) Plechkova, N. V.; Seddon, K. R. *Chem. Soc. Rev.* **2008**, *37*, 123.

(2) Wilkes, J. S.; Zaworotko, M. J. *J. Chem. Soc., Chem. Commun.* **1992**, 965.

(3) *Ionic liquids in Polymer Systems: Solvents, Additives, and Novel Applications*; ACS Symposium Series 913; Brazel, C. S., Rogers, R. D., Eds.; American Chemical Society: Washington DC, 2005.

(4) Winterton, N. *J. Mater. Chem.* **2006**, *16*, 4281.

(5) (a) Ueki, T.; Watanabe, M. *Macromolecules* **2008**, *41*, 3739. (b) Ueki, T.; Watanabe, M. *Bull. Chem. Soc. Jpn.* **2011**, DOI: 10.1246/bcsj.20110225.

(6) (a) *Polymer Electrolyte Reviews 1 and 2*; MacCallum, J. R., Vincent, C. A., Eds.; Elsevier: London, 1987 and 1989. (b) Gray, F. M. *Solid Polymer Electrolytes*; VCH Publishers: New York, 1991. (c) *Application of Electroactive Polymers*; Scrosati, B., Ed.; Chapman & Hall: London, 1993.

(7) Watanabe, M.; Yamada,, S.-I.; Sanui, K.; Ogata, N. *J. Chem. Soc., Chem. Commun.* **1993**, 929.

(8) (a) Noda, A.; Watanabe, M. *Electrochim. Acta* **2000**, *45*, 1265. (b) Susan, M. A. B. H.; Kaneko, T.; Noda, A.; Watanabe, M. *J. Am. Chem. Soc.* **2005**, *127*, 4976. (c) Seki, S.; Susan, M. A. B. H.; Kaneko, T.; Tokuda, H.; Noda, A.; Watanabe, M. *J. Phys. Chem. B* **2005**, *109*, 3886.

(9) (a) Carlin, R. T.; Fuller, J. *Chem. Commun.* **1997**, 1345. (b) Fuller, J.; Breda, A. C.; Carlin, R. T. *J. Electrochem. Soc.* **1997**, *144*, L67. (c) Fuller, J.; Breda, A. C.; Carlin, R. T. *J. Electroanal. Chem.* **1998**, *459*, 29.

(10) Kawauchi, T.; Kumaki, J.; Okoshi, K.; Yashima, E. *Macromolecules* **2005**, *38*, 9155.

(11) (a) He, Y.; Boswell, P. G.; Bühlmann, P.; Lodge, T. P. *J. Phys. Chem. B* **2007**, *111*, 4645. (b) Lodge, T. P. *Science* **2008**, *321*, 50. (c) Zhang, S.; Lee, K. H.; Frisbie, C. D.; Lodge, T. P. *Macromolecules* **2011**, *44*, 940.

(12) (a) Hasegawa, K.; Tatsumisago, M.; Minami, T. *J. Electrochem. Soc.* **1999**, *146*, 3359. (b) Wang, P.; Zakeeruddin, S. M.; Comte, P.; Exner, I.; Grätzel, M. *J. Am. Chem. Soc.* **2003**, *125*, 1166. (c) Usui, H.; Matusi, H.; Tanabe, N.; Yanagida, S. *J. Photochem. Photobiol. A* **2004**, *164*, 97. (d) Katakabe, T.; Kawano, R.; Watanabe, M. *Electrochem. Solid-State Lett.* **2007**, *10*, F23.

(13) (a) Ueno, K.; Inaba, A.; Kondoh, M.; Watanabe, M. *Langmuir* **2008**, *24*, 5253. (b) Ueno, K.; Hata, K.; Katakabe, T.; Kondoh, M.; Watanabe, M. *J. Phys. Chem. B* **2008**, *112*, 9013. (c) Ueno, K.; Imaizumi, S.; Hata, K.; Watanabe, M. *Langmuir* **2009**, *25*, 825. (d) Ueno, K.; Inaba, A.; Sano, Y.; Kondoh, M.; Watanabe, M. *Chem. Commun.* **2009**, 3603. (e) Ueno, K.; Sano, Y.; Inaba, A.; Kondoh, M.; Watanabe, M. *J. Phys.Chem. B* **2010**, *114*, 13095. (e) Ueno, K.; Watanabe, M. *Langmuir* **2011**, *27*, 9105.

(14) (a) Shimano, S.; Zhou, H.; Honma, I. *Chem. Mater.* **2007**, *19*, 5216. (b) Lee, U.-H.; Kudo, T.; Honma, I. *Chem. Commun.* **2009**, 3068.

(15) Hanabusa, K.; Fukui, H.; Suzuki, M.; Shirai, H. *Langmuir* **2005**, *21*, 10383.

(16) (a) Kimizuka, N.; Nakashima, T. *Langmuir* **2001**, *17*, 6759. (b) Ikeda, A.; Sonoda, K.; Ayabe, M.; Tamaru, S.; Nakashima, T.; Kimizuka, N.; Shinkai, S. *Chem. Lett.* **2001**, 1154.

(17) (a) He, Y.; Lodge, T. P. *Chem Cmmun.* **2007**, 2732. (b) He, Y.; Lodge, T. P. *Macromolecules* **2008**, *41*, 167.

(18) (a) Lewandowski, A.; Świderska, A. *Solid State Ionics* **2003**, *161*, 243. (b) Isshiki, Y.; Nakamura, M.; Tabata, S.; Dokko, K.; Watanabe, M. *Polym. Adv. Tech.* **2011**, *22*, 1254.

(19) (a) Shobukawa, H.; Tokuda, H.; Susan, M.; Watanabe, M. *Electrochim. Acta* **2005**, *50*, 3872. (b) Shin, J.-H.; Henderson, W. A.; Passerini, S. *J. Electrochem. Soc.* **2005**, *152*, A978. (c) Ye, H.; Huang, J.; Xu, J. J.; Khalfan, A.; Greenbaum, S. G. *J. Electrochem. Soc.* **2007**, *154*, A1048.

(20) (a) Lee, S.-Y.; Yasuda, T.; Watanabe, M. *J. Power Sources* **2010**, *195*, 5909. (b) Lee, S.-Y.; Ogawa, A.; Kanno, M.; Nakamoto, H.; Yasuda, T.; Watanabe, M. *J. Am. Chem. Soc.* **2010**, *132*, 9764.

(21) (a) Wang, P.; Zakeeruddin, S. M.; Exnar, I.; Grätzel, M. *Chem. Commun.* **2002**, 2972. (b) Kawano, R.; Katakabe, T.; Shimosawa, H.; Nazeeruddin, M. K.; Grätzel, M.; Matsui, H.; Kitamura, T.; Tanabe, N.; Watanabe, M. *Phys. Chem. Chem. Phys.* **2010**, *12*, 1916.

(22) (a) Lu, W.; Fadeev, A. G.; Qi, E.; Smela, B. H.; Mattes, B. R.; Ding, J.; Spinks, G. M.; Mazurkiewicz, J.; Zhou, D. Z.; Wallace, G. G.; MacFarlane, D. R.; Forsyth, S. A.; Forsyth, M. *Science* **2002**, *297*, 983. (b) Zhou, D.; Spinks, G.; M. Wallace, G. G.; Tiyapiboonchaiya, C.; MacFarlane, D. R.; Forsyth, M.; Sun, J. *Electrochim. Acta* **2003**, *48*, 2355.

(23) (a) Bennett, M. D.; Leo, D. J. *Sens. Actuators A* **2004**, *115*, 79. (b) Akle, B. J.; Bennett, M. D.; Leo, D. J. *Sens. Actuators A* **2006**, *126*, 173.

(24) (a) Fukushima, T.; Asaka, K.; Kosaka, A.; Aida, T. *Angew. Chem., Int. Ed.* **2005**, *44*, 2410. (b) Mukai, K.; Asaka, K.; Kiyohara, K.; Sugino, T.; Takeuchi, I.; Fukushima, T.; Aida, T. *Electrochim. Acta* **2008**, *53*, 5555.

(25) (a) Bara, J. E.; Camper, D. E.; Gin, D. L.; Noble, R. D. *Acc. Chem. Res.* **2010**, *43*, 152. (b) Bara, J. E.; Hatakeyama, E. S.; Gabriel, C. J.; Zeng, X.; Lessmann, S.; Noble, R. D. *J. Membr. Sci.* **2008**, *316*, 186.

(26) Scott, K.; Basov, N.; Jachuck, R.; Winterton, N.; Cooper, A.; Davies, C. *Chem. Eng. Res. Des.* **2005**, *83*, 1179.
(27) (a) Lee, J.; Panzer, M. J.; He, Y.; Lodge, T. P.; Frisbie, C. D. *J. Am. Chem. Soc.* **2007**, *129*, 4532. (b) Cho, J. H.; Lee, J.; Xia, Y.; Kim, B.; He, Y.; Renn, M. J.; Lodge, T. P.; Frisbie, C. D. *Nat. Mater.* **2008**, *7*, 900. (c) Lee, J.; Kaake., L. G.; Cho, J. H.; Zhu, X.-Y.; Lodge, T. P.; Frisbie, C. D. *J. Phys. Chem. C* **2009**, *113*, 8972.
(28) *Electroactive Polymer (EAP) Actuators as Artificial Muscles*; Bar-Cohen, Y., Ed.; SPIE Press: Bellingham, WA, 2001.
(29) Pelrine, R.; Kombluh, R.; Pei, Q.; Joseph, J. *Science* **2000**, *287*, 836.
(30) (a) Asaka, K.; Oguro, K.; Nishimura, Y.; Mizuhata, M.; Takenaka, H. *Polym. J.* **1995**, *27*, 436. (b) Shahinpoor, M. *Electrochim. Acta* **2003**, *48*, 2343.
(31) (a) Kaneto, K.; Kaneko, M.; Min, Y.; MacDiarmid, A. G. *Synth. Met.* **1995**, *71*, 2211. (b) Baughman, R. H. *Synth. Met.* **1996**, *78*, 339. (c) Smela, E. *Adv. Mater.* **2003**, *15*, 48.
(32) Osada, Y.; Okuzaki, H.; Hori, H. *Nature* **1992**, *355*, 242.
(33) (a) Takeuchi, I.; Asaka, K.; Kiyohara, K.; Sugino, T.; Terasawa, N.; Mukai, K.; Shiraishi, S. *Carbon* **2009**, *47*, 1373. (b) Takeuchi, I.; Asaka, K.; Kiyohara, K.; Sugino, T.; Terasawa, N.; Mukai, K.; Fukushima, T.; Aida, T. *Electrochim. Acta* **2009**, *54*, 1762. (c) Terasawa, N.; Takeuchi, I.; Matsumoto, H. *Sens. Actuators, B* **2009**, *139*, 624. (d) Terasawa, N.; Takeuchi, I.; Matsumoto, H.; Mukai, K.; Asaka, K. *Sens. Actuators B* **2011**, *156*, 539. (e) Lee, J.-W.; Yoo, Y.-T. *Sens. Actuators B* **2009**, *137*, 539.
(34) (a) Wang, J.-S.; Matyjaszewski, K. *Macromolecules* **1995**, *28*, 7901. (b) Matyjaszewski, K.; Xia, J. *Chem. Rev.* **2001**, *101*, 2921. (c) Matyjaswewski, K.; Tsarevsky, N. V. *Nat. Chem.* **2009**, *1*, 276. (d) Tsarevsky, N. V.; Matyjaszewski, K. *Chem. Rev.* **2007**, *107*, 2270. (e) Patten, T. E.; Xia, J.; Abernathy, T.; Matyjaszewski, K. *Science* **1996**, *272*, 866.
(35) (a) Kato, M.; Kamigaito, M.; Sawamoto, M.; Higashimura, T. *Macromolecules* **1995**, *28*, 1721. (b) Kamigaito, M.; Ando, T.; Sawamoto, M. *Chem. Rev.* **2001**, *101*, 3689.
(36) Ueki, T.; Karino, T.; Kobayashi, Y.; Shibayama, M.; Watanabe, M. *J. Phys. Chem. B.* **2007**, *111*, 4750.
(37) Baughman, R. H.; Cui, C.; Zakhidov, A. A.; Iqbal, Z.; Barisci, J. N.; Spinks, G. M.; Wallace, G. G.; Mazzoldi, A.; Rossi, D. D.; Rinzler, A. G.; Jaschinski, O.; Roth, S.; Kertesz, M. *Science* **1999**, *284*, 1340.
(38) (a) Nanjo, S.; Watanabe, M.; Asai, K.; Yokoyama, K.; Yamamoto, M. *Abst. 71st Annu. Meet. Electrochem. Soc. Jpn.* **2004**, 263. (b) Okuno, T.; Sugoh, N.; Kato, T.; Ohgi, H.; Watanabe, M. *PCT Int. Appl.* WO2008123064, 2008.
(39) Bonhôte, P.; Dias, A.-P.; Papageorgiou, N.; Kalyanasundaram, K.; Grätzel, M. *Inorg. Chem.* **1996**, *35*, 1168.
(40) Karanam, S.; Goossens, H.; Klumperman, B.; Lemstra, P. *Macromolecules* **2003**, *36*, 3051.
(41) Santangelo, P. G.; Roland, C. M. *Macromolecules* **1998**, *31*, 4581.
(42) Mok, M. M.; Liu, X.; Bai, Z.; Lei, Y.; Lodge, T. P. *Macromolecules* **2011**, *44*, 1016.
(43) Bates, F. S. *Science* **1991**, *251*, 898.
(44) Jannasch, P. *Polymer* **2002**, *43*, 6449.
(45) (a) Tokuda, H.; Tsuzuki, S.; Susan, M. A. B. H.; Hayamizu, K.; Watanabe, M. *J. Phys. Chem. B* **2006**, *110*, 19593. (b) Ueno, K.; Tokuda, H.; Watanabe, M. *Phys. Chem. Chem. Phys.* **2010**, *12*, 1649.
(46) (a) Palmre, V.; Brandell, D.; Mäeorg, U.; Torop, J.; Volobujeva, O.; Punning, A.; Johanson, U.; Kruusmaa, M.; Aabloo, A. *Smart Mater. Struct.* **2009**, *18*, 095028. (b) Torop, J.; Palmre, V.; Arulepp, M.; Sugino, T.; Asaka, K.; Aabloo, A. *Carbon* **2011**, *49*, 3113. (c) Terasawa, N.; Takeuchi, I. *Sens. Actuators B* **2010**, *145*, 775.
(47) (a) Noda, A.; Hayamizu, K.; Watanabe, M. *J. Phys. Chem. B* **2001**, *105*, 4603. (b) Tokuda, H.; Hayamizu, K.; Ishii, K.; Susan, M. A. B. H.; Watanabe, M. *J. Phys. Chem B* **2004**, *108*, 16593. (c) Tokuda, H.; Hayamizu, K.; Ishii, K.; Susan, M. A. B. H.; Watanabe, M. *J. Phys. Chem B* **2005**, *109*, 6103. (d) Tokuda, H.; Ishii, K.; Susan, M. A. B. H.; Tsuzuki, S.; Hayamizu, K.; Watanabe, M. *J. Phys. Chem. B* **2006**, *110*, 2833. (e) Tsuzuki, S.; Shinoda, W.; Saito, H.; Mikami, M.; Tokuda, H.; Watanabe, M. *J. Phys. Chem. B* **2009**, *113*, 10641.
(48) Wang, C. S.; Zhang, X. B.; Yang, H. S.; Qi, Z. F.; He, P. M.; Li, W. Z. *J. Electrochem. Soc.* **1999**, *146*, 1696.

NOTE ADDED AFTER ASAP PUBLICATION

This article was published ASAP on December 15, 2001. Due to a production error, various revisions to Table 1, equations, and several places throughout the text were not present. The correct version posted on December 22, 2011.

Macromolecules

ARTICLE

pubs.acs.org/Macromolecules

Synthesis of Flower-Like Poly(Ethylene Oxide) Based Macromolecular Architectures by Photo-Cross-Linking of Block Copolymers Self-Assemblies

Vijay S. Kadam,[†] Erwan Nicol,[†,*] and Cédric Gaillard[‡]

[†]Polymères, Colloïdes, Interfaces, UMR CNRS 6120, Université du Maine, 72085 Le Mans, France

[‡]Laboratoire de Microscopie BIBS, INRA, UR1268 Biopolymères Interactions Assemblages, F-44316 Nantes, France

ABSTRACT: A triblock poly(2-methacryloyloxyethyl acrylate)-*b*-poly(ethylene oxide)-*b*-poly(2-methacryloyloxyethyl acrylate) (PMEA-*b*-PEO-*b*-PMEA) copolymer bearing polymerizable groups on the hydrophobic blocks was synthesized and self-assembled in water. The transient micellar structures formed in selective solvent were permanently fixed by cross-linking the methacrylate moieties in the micelles cores under UV light. The structures obtained after cross-linking were characterized by static and dynamic light scattering (SLS and DLS), size exclusion chromatography (SEC), and electron microscopy (TEM and cryoTEM). SLS measurements showed an increase of the aggregation number of the micelles during the photo-cross-linking process. This result was discussed in terms of competition between the micelles polymerization rate and the unimers exchange rate. At low concentration, mainly flower-like architectures were obtained. As the concentration of the cross-linked solutions increased, more complex aggregates, in which the "flower" is the basic unit, were obtained.

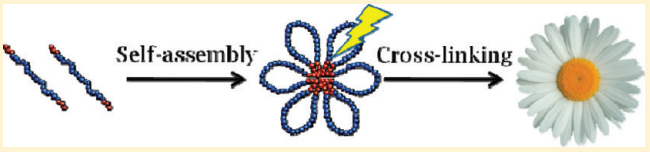

INTRODUCTION

Complex macromolecular architectures are of great interest mainly because their properties, either in solution or in bulk, differ from those of their linear analogues. Accordingly, various macromolecular architectures based on poly(ethylene oxide) (PEO) were synthesized for potential applications as thickeners or in the biomedical field. G. Lapienis recently reviewed the syntheses of star-shaped polymers having PEO arms.[1] Multiarms PEO stars were initially synthesized using the so-called "core-first" method but the "arm-first" strategies was also extensively utilized. However, the number of arms per star was not well controlled in the case of arm-first method. The arms polydispersity can be narrowed using self-associative properties of PEO based amphiphilic block copolymers in a selective solvent such as water. Core cross-linking of micelles made of asymmetric PEO-based copolymers resulted in well-defined star-like copolymers.[2−4] More complex branched architectures such as combs,[5] dendrimers,[6,7] hyperbranched polymers,[8,9] or "pom-pom"[10] were also synthesized from PEO.

The development of the so-called "topological polymer chemistry" brings to light the role that ring polymers could play, i.e., polymers exhibiting no chain-end, in finding new properties and applications.[11] For these reasons, cyclic polymers synthesis has attracted more and more attention. For instance, PEO based cyclic polymers were elaborated by intramolecular chain-ends coupling in dilute solution.[12−14] Although the macromolecular architectures, for which literature reports the synthesis, are numerous, very few articles deal with the elaboration of flower-like structures. Thus, the physical properties of these original macromolecular architectures are almost unknown because of the lack of materials available for studies. Their dynamic properties in the bulk could be original and interesting from an academic point of view. The differences of behaviors of linear, star[15] and cyclic[16] polymers are well-known and theoretically predicted. The behavior of entangled flower-like polymers in bulk could be an intermediate between stars and macrocycles. The diffusion properties of these structures in heterogeneous matrices could also be of interest if one considers the potential applications as drug carriers. The diffusion process of (macro)molecules or particles in gels or biological matrices is a complicated process that depend on the matrix, the solvent and the diffusants.[17] The size and architecture of the diffusing particles have an influence on the diffusion rate and accessibility to certain parts of the matrix. Flower-like nanocarriers could exhibit diffusion properties different to those of star-like micelles commonly used for drug delivery. Furthermore, as presented below, oligomers of flowers (dimers, trimers, etc..) can be synthesized. These structures could give access to a broader range of diffusion coefficients allowing a control over the time of drug delivery.

Saito et al. reported the synthesis of flower-like polymers based on poly(2-vinylpyridine)/polystyrene,[18] poly(vinyl alcohol)/polystyrene[19] and poly(2-hydroxyethyl methacrylate)/polystyrene.[20] All these original architectures were synthesized by covalently cross-linking the core of self-assembled triblock copolymers in selective solvent. This strategy consisting in cross-linking block copolymers self-assemblies in solution has already been widely applied in the literature to synthesize star-like architectures,[2,3,21−30] shell cross-linked particles[31−37] or more original structures. For instance, cross-linked vesicles,[38−42] nanocylinders,[29,43−45] tadpoles[46,47]

Received: October 13, 2011
Revised: November 16, 2011
Published: December 01, 2011

or "hamburger-like" structures[48] can be synthesized. In Saito et al.'s flowers synthesis, the triblock copolymers were self-assembled in organic media and the blocks constituting the micelles core were sometimes long leading to large microgel cores.[18,20] Di Biase et al.[49] photo-cross-linked Pluronic F127 diacrylate triblock copolymers that fixed the structures in a colloidal state. However, the copolymers were functionalized at the end of the hydrophilic blocks, so, the reactive moieties were not gathered into the micelle cores and the particles obtained after cross-linking did not exhibit flower-like structures. Hu et al.,[50] recently, reported the photo-cross-linking of symmetrical associative ABCBA pentablock copolymers in solution. The aim of their work was the synthesis of well-defined macrocycles but the same copolymer could have been used to synthesize flower-like polymers. To the best of our knowledge, neither the synthesis of flower-like polymers in aqueous medium nor that of poly(ethylene oxide) based flowers have been reported in the literature.

This article reports the synthesis of flower-like PEO architectures using Saito et al. strategy. A triblock copolymer having hydrophobic blocks bearing polymerizable groups was synthesized by atom transfer radical polymerization (ATRP). This copolymer was self-assembled in aqueous solution at various concentrations to give various transient flower-like objects depending on the concentration and the micelle cores were photo-cross-linked to permanently fix the structures. The resulting architectures were analyzed using static light scattering (SLS), dynamic light scattering (DLS), size exclusion chromatography (SEC), and transmission electron microscopy (TEM and cryoTEM).

EXPERIMENTAL SECTION

Materials. In this study, 2-bromoisobutyryl bromide (Aldrich, 99%), poly(ethylene oxide) (α,ω-PEO, Fluka, $M_w = 10^5$ g·mol^{-1}), *N*,*N*,*N*′,*N*″,*N*″-pentamethyldiethylenetriamine (PMDETA, Aldrich, 99%), $Cu^{I}Br$ and $Cu^{II}Br$ (Aldrich, 99.99%), dimethylformamide (DMF) (Aldrich, 99.8%), lithium bromide (Aldrich, 99.99%), triethylamine (Aldrich 99%), 4-(dimethylamino)pyridine (DMAP, 99%), and 2,2-dimethoxy-2-phenylacetophenone (DMPA, Aldrich) were used as received. Toluene (Aldrich 99.8%) was dried over CaH_2 and distilled off. Methacryloyl chloride was purified by distillation. 2-Hydroxyethyl acrylate (HEA, Aldrich, 96%) was purified by initially dissolving the monomer in water (25 vol %). Hydroquinone (0.1 wt %) was then added to the solution to avoid polymerization. The solution was extracted 10 times with hexane to remove diacrylates and the aqueous solution was salted (NaCl: 200 g·L^{-1}). The monomer was then separated from the aqueous phase by ether extraction (4 times) to remove acrylic acid. Hydroquinone (0.05 wt %) was added to ether phase, and it was dried over MgSO4 (3 wt %). The ether phase was then evaporated-off over the rotary evaporator. Finally, purified monomer was distilled under reduced pressure (70 °C/3 mmHg) just before the polymerization and passed through a short column of basic alumina to remove traces of acidic impurities.

Synthesis of PEO Macroinitiator. A dibromide functionalized PEO macroinitiator (Br-PEO-Br) was synthesized using a procedure described previously.[4]

ATRP of Hydroxyethyl Acrylate from Br−PEO−Br Macroinitiator. In a typical ATRP reaction, 10 mL of HEA (87 mmol, 100 equiv) and 40 mL of toluene (80% v/v) were charged into 100 mL Schlenk tube. The solution was freeze−pump−thawed for three times and then kept under argon. α,ω-PEO macroinitiator (8.968 g, 0.87 mmol), $Cu^{I}Br$ (62.45 mg, 0.435 mmol) and $Cu^{II}Br$ (9.72 mg, 0.0435 mmol) were introduced in another Schlenk tube, degassed, and backfilled with argon for three times. Previously freeze−pump−thawed solution was transferred to latter Schlenk under argon using a cannula. The reaction mixture was heated to 35 °C under stirring until all of the $Cu^{II}Br$ dissolved and the solution became homogeneous. The solution was freeze−pump−thawed for three times again, backfilled with argon, and placed in an oil bath thermo-stated at 50 °C. Finally, a previously argon purged (15 min) 91 μL (0.435 mmol, 0.5 equiv) sample of PMDETA was added under argon. The reaction medium was kept at 50 °C during 5 h to reach the desired conversion. At the end, the solution was diluted with THF, passed through a column of neutral alumina to remove Cu-catalyst, concentrated, and precipitated twice in ether. The resulting polymer was dissolved in distilled water, dialyzed (molecular weight cutoff: 3500 g/mol) for 2 days, and recovered by freeze-drying.

End Functionalization of Triblock Copolymer. A dried round-bottom flask equipped with stirrer and pressure equalizing addition funnel was charged with 10 g of PHEA-*b*-PEO-*b*-PHEA (0.85 mmol), 50 mg of DMAP, 50 mg of hydroquinone, and 200 mL of dry toluene. The flask was warmed to 35 °C to dissolve all the solids under stirring. The flask was flushed with argon, and 3.6 mL of triethyl amine (25.6 mmol, 30 equiv) was added and kept stirring for 10 min. Finally, methacryloyl chloride, 2.5 mL (25.6 mmol, 30 equiv), was diluted with 25 mL of dry toluene and added dropwise. The reaction mixture was kept stirring at room temperature for 2 days under argon atmosphere. The reaction mixture was filtered carefully to remove triethylamine hydrochloride salt, concentrated, and precipitated twice in ether.

Photo-Cross-Linking. For photo-cross-linking experiments, a solution of DMPA photoinitiator (0.01M) was prepared in THF. The molar ratio of DMPA to polymer was fixed at 0.17, which corresponds to on average to about three molecules per micelle considering that the average number of hydrophobic groups per micelle is 33. The required amount of solution of DMPA was placed on the walls of a glass vial, and THF was evaporated off under a gentle flow of argon, after which the polymer solution was introduced into the vial that was sealed with a rubber septum. The vial was rotated overnight on a roller stirrer. Just before the photo-cross-linking experiment, the solution was bubbled by purging argon for 15 min to remove traces of dissolved oxygen. The samples were photo-cross-linked in a glass vial by irradiating with UV-light at 365 nm (Dymax BlueWave 200 UV Lamp).

Size Exclusion Chromatography. SEC observations in THF were done with a system consisting of a Spectra SYSTEM AS100 auto sampler, a column (JORDI gel 500 Å, 5 μm, 50 cm) followed by a Spectra Physics RI-71 refractive index detector, and a Spectra Physics UV detector (λ = 254 nm). The flow rate of the eluent was 1 mL·min^{-1} at room temperature. The column was calibrated with PEO standards.

SEC in DMF containing 0.01 M LiBr were done on a system consisting of a Waters 510 pump, with a Guard column (Polymer Laboratories, PL gel 5 μm Guard column, 50 × 7.5 mm) followed by two columns (Polymer Laboratories (PL), 2 PL gel 5 μm MIXED-D columns, 2 × 300 × 7.5), with a Waters 410 RI detector. The flow rate of eluent was 1 mL·min^{-1} at 30 °C.

Fluorescence Measurements. Fluorescence spectra were recorded with a Horiba-Jobin Yvon fluorescence spectrophotometer in the right-angle geometry. For the fluorescence measurements, 3 mL of each sample were placed in a 1 cm square quartz cell. The emission spectra, were recorded using the excitation wavelength at 329 nm and the excitation spectra, were recorded using the emission wavelength at 371 nm. The slit widths were set at 2 nm for both excitation and emission fluorescent measurements. Samples were prepared as follows. Eighteen μL of a pyrene solution in THF (10^{-4} M) was placed on the wall of a glass vial and rotated under gentle flow of N_2 to evaporate the THF and to form a film of pyrene. Aqueous polymer solutions were prepared in Milli-Q water by diluting stock solutions to the desired polymer concentration (from 10^{-4} to 10 g·L^{-1}). Three mL of polymer solution was added to the vial to yield a final pyrene concentration of 6×10^{-7} M for each sample. The pyrene-containing samples were stirred for 2 days in the dark at room temperature.

Scheme 1. Synthesis Route to the PMEA-*b*-PEO-*b*-PMEA Triblock Copolymer

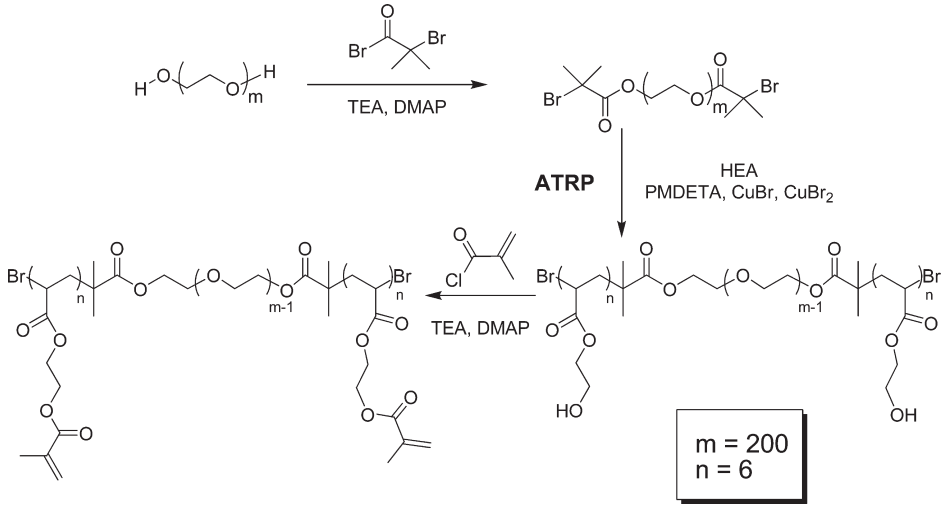

Light Scattering (LS). Static and dynamic light scattering measurements were performed using commercial equipment (ALV-Langen, Germany) equipped with an He−Ne laser emitting vertically polarized light at $\lambda = 632$ nm. The temperature was set at 20 °C and controlled by a thermostat bath (±0.1 °C). Measurements were made at angles of observation (θ) ranging between 12 and 150 deg at concentrations specified in the text. Prior to measurements, the polymer solutions were filtered to 0.2−0.45 μm using inorganic membrane filter. The refractive index increment of the copolymer in water was assumed to be that of pure PEO in water, i.e., $(dn/dC) = 0.135\ mL \cdot g^{-1}$. It has been measured for PEO in DMF + LiBr: $(dn/dC) = 0.044\ mL \cdot g^{-1}$ using Optilab rEX refractive index detector. These values were assumed constant for all the experiments meaning that the effect of photoinitiator and photo-cross-linking was neglected. This assumption seemed reasonable since the PEO corona represented 82% (w/w) of the copolymer and was not affected by the photo-cross-linking. Furthermore, the (dn/dC) values of poly(alkyl acrylate)s are very close to those of PEO in various solvents.[51]

A more detailed description of the data treatment was given previously.[4]

Microscopy. *TEM.* A drop of each aqueous dispersion specimen was first placed on a carbon-coated TEM copper grid (Quantifoil, Germany) and let to air-drying. The sample was then negatively stained with uranyl acetate (Merck, Germany). For that, the sample-coated TEM grid was successively placed on a drop of an aqueous solution of uranyl acetate (2% w/w) and on a drop of distilled water. The grid was then air-dried before introducing them in the electron microscope. The short contact time between uranyl acetate solution and the sample does not allow the diffusion of the salt into the micelles corona.

CryoTEM. Specimens for cryoTEM observation were prepared using a cryoplunge cryo-fixation device (Gatan, USA) in which a drop of the aqueous suspension was deposited onto glow-discharged holey-type carbon-coated grids (Ted Pella Inc., USA). The TEM grid was then prepared by blotting the drop containing the specimen to a thin liquid layer remained across the holes in the support carbon film. The liquid film was vitrified by rapidly plunging the grid into liquid ethane cooled by liquid nitrogen. The vitrified specimens were mounted in a Gatan 910 specimen holder (Gatan, USA) that was inserted in the microscope using a CT-3500-cryotransfer system (Gatan, USA) and cooled with liquid nitrogen. TEM images were then obtained from specimens preserved in vitreous ice and suspended across a hole in the supporting carbon substrate.

All the samples were observed using a JEM 1230 'Cryo' microscope (Jeol, Japan) operated at 80 kV and equipped with a LaB_6 filament. For the cryo-TEM experiments, the microscope was operated under low dose conditions (<10 e^-/A^2), at −178 °C. The micrographs were recorded on a Gatan 1.35K × 1.04K × 12 bit ES500W CCD camera.

Image Analysis. The software ImageJ (Research Services Branch NIMH & NINDS) has been used to determine particle size distributions and apply a contrast enhancement of the cryoTEM images.

RESULTS AND DISCUSSION

The synthesis of flower-like polymers is based on the self-assembly of amphiphilic triblock copolymers. As previously suggested, associative telechelic polymers or amphiphilic triblock copolymers form flower-like micelles at concentration above the cmc.[52] As concentration increases, flowers interconnect to form more complex structures until the percolation threshold is reached and a physical gel is formed. However, simple telechelic polymers form transient objects and any modification of the environment (temperature, concentration, ...) can affect the structure. Direct and accurate analyses of the structures, size distributions and molecular weights of the flower-like architectures are thus very complicated. Furthermore, isolation of these objects to study, individually, their properties is almost impossible without modification of the structures. In order to avoid these drawbacks, triblock copolymers that can be cross-linked in the micellar state were synthesized. The synthetic pathway leading to the triblock copolymer bearing polymerizable moieties is described in Scheme 1. Br−PEO−Br macroinitiator was synthesized by esterification of α,ω-hydroxyl end-capped PEO with 2-bromoisobutyryl bromide. The quantitative functionalization of the hydroxyl groups was checked by ^{1}H NMR. The precursor triblock PHEA-*b*-PEO-*b*-PHEA copolymer was obtained by atom transfer radical polymerization (ATRP) of hydroxyl ethyl acrylate (HEA) initiated by the Br-PEO-Br macroinitiator in toluene at 50 °C in the presence of CuBr/$CuBr_2$/PMDETA as a catalytic system. The following molar ratio was used: $[HEA]_0/[Br-PEO-Br]_0/[CuBr]_0/[CuBr_2]_0/[PMDETA]_0 = 100/1/0.5/0.05/0.55$ with a HEA concentration of 20% v/v in toluene. The kinetics of the polymerization was monitored by ^{1}H NMR and the reaction was stopped at 11% conversion after 5 h. SEC trace shows a small increase of molecular weight (M_n = 10600 $g \cdot mol^{-1}$) and the polydispersity index remains low (PDI = 1.07) (Figure 1). The hydroxyl groups of the copolymer were then esterified with methacryloyl chloride in toluene. Proton NMR spectrum of the resulting PMEA-*b*-PEO-*b*-PMEA indicates a quantitative functionalization of the alcohol groups (Figure 2). By comparing

dx.doi.org/10.1021/ma2022937 |*Macromolecules* 2012, 45, 410–419

the integrals of the methyl protons (a, a′) and those of the MEA peaks, the degree of polymerization of 6 was estimated for each PMEA block. SEC trace shows a bimodal distribution indicating that a small fraction (10%) of chains coupled during the esterification step (Figure 1). However the molar mass distribution remains narrow (PDI = 1.08) for a number-average molecular weight of 11500 g·mol^{-1}.

In order to form the flower-like structures, the triblock copolymers were self-assembled in water. The onset of formation of the micelles was evaluated using steady-state fluorescence of pyrene. The evolution of the intensity ratio of the pyrene excitation bands at 337.6 and 333.8 nm as a function of $PMEA_6$-*b*-PEO_{200}-*b*-$PMEA_6$ copolymer concentration is shown in Figure 3a. As demonstrated by Wilhelm et al.,[53] the ratio of the pyrene concentration in the aqueous phase $[Py]_w$ to that in the micellar cores $[Py]_m$, for $C >$ cmc, is given by:

$$\frac{[Py]_w}{[Py]_m} = \frac{F_{max} - F}{F - F_{min}} = \frac{1000\rho_{PMEA}}{K.\chi_{PMEA}(C - CMC)} \quad (1)$$

where F is the ratio $I_{337.6\ nm}/I_{333.8\ nm}$, K is the partition coefficient of pyrene between the micellar and the aqueous phase, χ_{PMEA} is the weight fraction of the PMEA block in the copolymer, and ρ_{PMEA} is the density of the PMEA.

Figure 3b shows the evolution of $(F_{max} - F)/(F - F_{min})$ as a function of $1/(C -$ cmc). The best fit was obtained for cmc = 0.05 g·L^{-1}. Assuming a PMEA weight fraction and density of, respectively, $\chi_{PMEA} = 0.17$ and $\rho_{PMEA} = 1.1$ (approximated by the value of pure poly(alkyl acrylate) taken from the literature), the partition coefficient of pyrene between the micellar and the aqueous phase (K) was evaluated to 1.7×10^4.

Triblock $PMEA_6$-*b*-PEO_{200}-*b*-$PMEA_6$ copolymer was dissolved in water at concentrations ranging from 1 to 12 g·L^{-1}. The self-assembly was shown to be in thermodynamic equilibrium and the terminal relaxation time of a network formed at high concentration and usually associated with the lifetime of a hydrophobic block into the micelle core was estimated at 0.2 s. at 20 °C.[54] Before UV irradiation, the weight-average molar mass of the micelles was estimated by SLS to 2.2×10^5 g mol^{-1} at low concentration, leading to an aggregation number of 33 hydrophobic blocks per micelle. The photoinitiator was added to the micelles cores and UV irradiation (λ_{max} = 365 nm, I = 180 mW·cm^{-2}) was applied to initiate the polymerization of methacrylate moieties in the core (Scheme 2).

The rate of photopolymerization was monitored by ^{1}H NMR by following the decrease of the ethylenic protons signals (5.6 and 6.0 ppm). As previously shown on similar diblock copolymers,[27] the photopolymerization proceeded very rapidly and a complete conversion of the double bonds was reached within 60 s for a UV intensity of 180 mW/cm^2.

Surprisingly, the molar mass of the flower-like micelles increased during the photo-cross-linking process when small amounts of photoinitiator were used (Figure 4). A huge amount of photoinitiator (around 120 DMPA molecules per micelle) was necessary not to observe this increase of aggregation number of micelles during the cross-linking step. Of course, even before UV irradiation, the incorporation of such a large quantity of organic molecules into the micelle core was accompanied by an increase of the aggregation number by comparison with micelles free of DMPA and a fraction of large aggregates appearing after UV irradiation complicated the analysis of light scattering data.

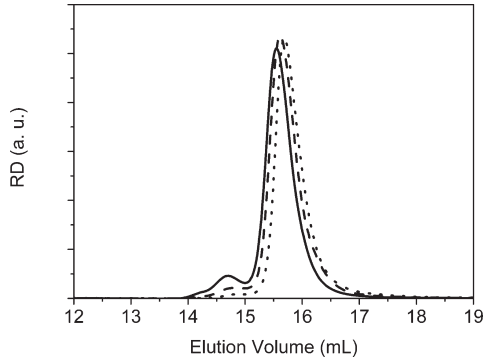

Figure 1. SEC traces of Br−PEO_{200}−Br macroinitiator (dot line), $PHEA_6$-*b*-PEO_{200}-*b*-$PHEA_6$ (dashed line) and $PMEA_6$-*b*-PEO_{200}-*b*-$PMEA_6$ (straight line) block copolymers in THF.

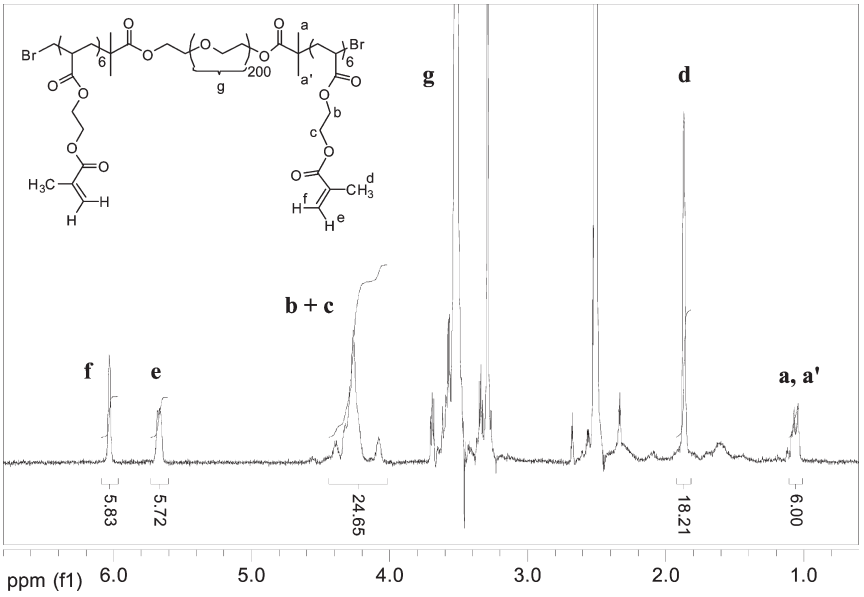

Figure 2. ^{1}H NMR spectrum of $PMEA_6$-*b*-PEO_{200}-*b*-$PMEA_6$ block copolymer in $CDCl_3$.

dx.doi.org/10.1021/ma2022937 |*Macromolecules* 2012, 45, 410–419

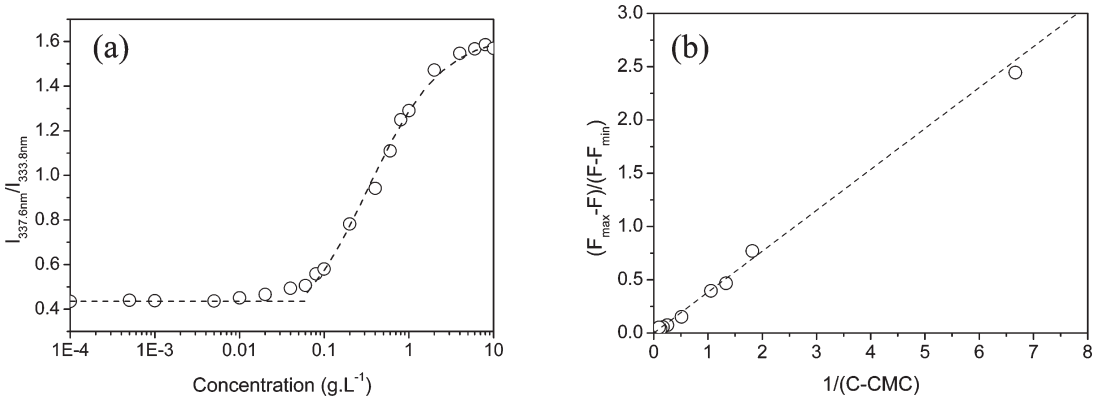

Figure 3. (a) Fluorescence intensity ratio $I_{337.6\ nm}/I_{333.8\ nm}$ (from pyrene excitation spectra) as a function of $PMEA_6$-*b*-PEO_{200}-*b*-$PMEA_6$ copolymer concentration. The dashed line is the fit to eq 1. (b) Evolution of $(F_{max} - F)/(F - F_{min})$ as a function of $1/(C - cmc)$ with cmc = 0.05 g·L^{-1}.

Scheme 2. Elaboration of Flower-Like POE Architectures by Self-Assembly of Triblock Copolymers in Water and Core Photo-Cross-Linking

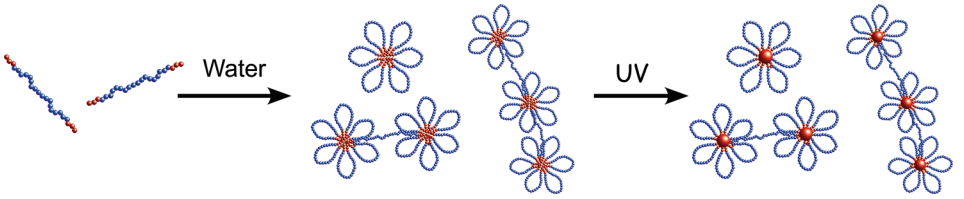

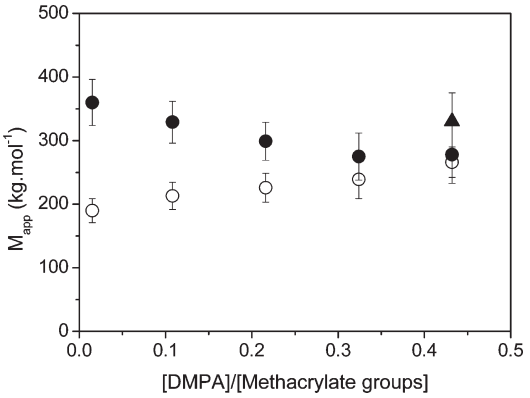

Figure 4. Evolution of the apparent molar mass M_{app} (measured by SLS in water at 1 g·L^{-1}) of the flower-like micelles as a function of the [DMPA]/[methacrylate groups] ratio, before (open circles) and after UV irradiation (60s. at 180 mW·cm^{-2}) (filled circles). The triangle corresponds to M_{app} measured after UV irradiation and dispersion at 1 g·L^{-1} in DMF + LiBr.

One might fear, with such a high [DMPA]/[methacrylate groups] ratio, that the termination reactions are predominant and that the cross-linking efficiency is low. However, the size and aggregation number of the resulting micelles dispersed in DMF+LiBr remained almost unchanged indicating a good efficiency of the cross-linking process.

The increase of aggregation number took place very rapidly when the UV lamp was lighted. Figure 5a shows the evolution of the ratio between the apparent molar mass $(M_a(t))$ measured after an irradiation time (t) over the initial apparent molar mass before irradiation $(M_a(0))$ as a function of the UV exposure time (I = 180 mW·cm^{-2}). This experiment was performed at 1 g·L^{-1} with a [DMPA]/[methacrylate groups] ratio set to 1.5%, corresponding to, in average, three DMPA molecules per micelle. It clearly showed an increase of the molar mass of around 70% within a few seconds of UV irradiation. However, this increase is not due to micelles coupling because SEC trace in DMF exhibits only a small fraction of dimers (see below) and no difference in the hydrodynamic radius (13 nm) and size distributions measured by DLS could be detected before and after UV exposure (Figure 5b). Changing the UV light intensity by a factor of 2 did not modify significantly this tendency. This increase of molar mass can thus be only attributed to an increase of aggregation number of the flowers.

Three hypotheses can be made to explain these observations: (1) The DMPA molecules are not homogeneously distributed between all the micelles and photoinitiation cannot take place in a non negligible part of them. This could be observed if the number of photoinitiator molecules is close to the number of micelles. Thus, uncross-linked micelles will feed initiated ones.[3] (2) The photoinitiation rate is too small compared to the unimers exchange rate and noninitiated micelles empty on behalf to initiated ones. (3) The rate of termination reactions is very high and many DMPA molecules are necessary to reinitiate the polymerization of the core after it is stopped.

This behavior is usual in the case of polymerizable surfactants and Cochin et al.[55,56] explained it by hypothesis 2. It is much more unexpected in the present case because analogous diblock copolymers did not show any significant structural modification during the photo-cross-linking process even when initiated by small amounts of DMPA (around 3 molecules per micelle).[3,27] Hypothesis 1 seems improbable because the size increase is

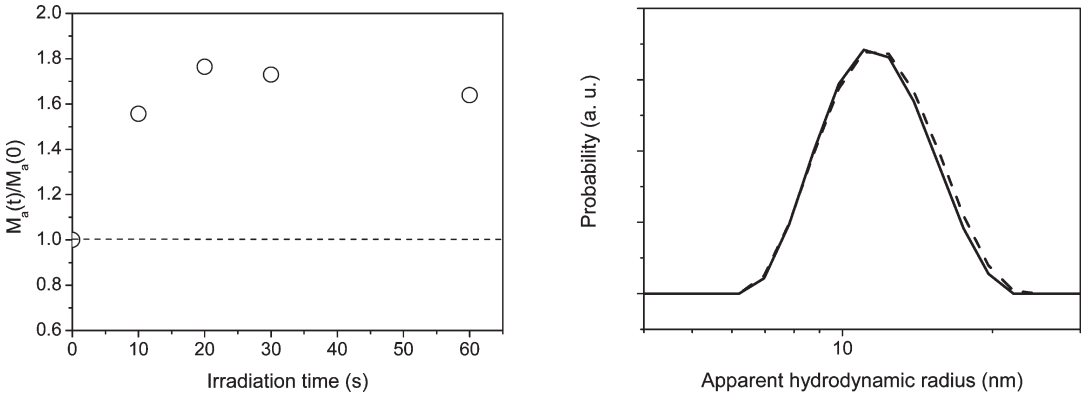

Figure 5. (a) Evolution of the ratio $M_a(t)/M_a(0)$ as a function of UV irradiation time at 180 mW·cm^{-2}. (b) Apparent size distribution of the S1 sample before (dashed line) and after UV irradiation (straight line) measured by DLS at 1 g·L^{-1}.

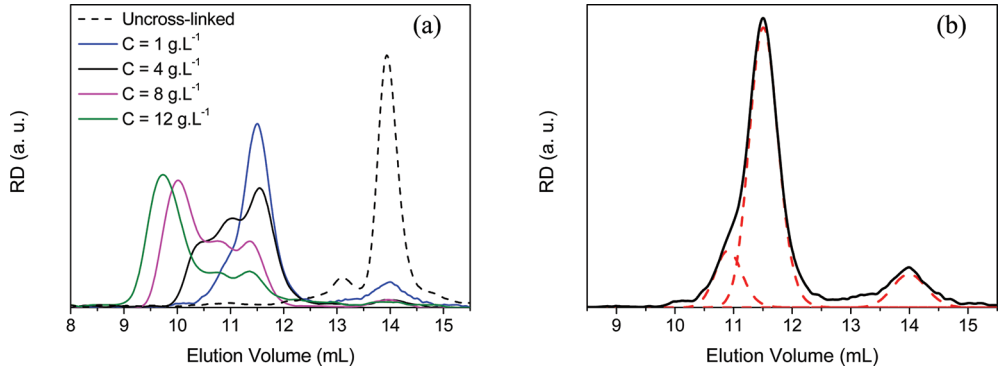

Figure 6. (a) SEC traces (in DMF + LiBr) of PMEA$_6$-*b*-PEO$_{200}$-*b*-PMEA$_6$ unimer and samples cross-linked at 1, 4, 8, and 12 g·L^{-1}. (b) Deconvolution of the SEC trace of the sample cross-linked at 1 g·L^{-1}.

observed even in the case of large [DMPA]/[methacrylate groups] ratio leading, in average, to tens of DMPA molecules per micelle. Yet, it is difficult to decide between the last two hypotheses and even more to figure out why diblock and triblock copolymers, having roughly the same hydrophilic−lipophilic balance (HLB) and the same associative properties, behave differently during the photo-cross-linking process. La Flèche et al.[57] showed that the architecture (two (linear)-, three- and four-armed star) of PEO end-capped with dodecyl moieties has no influence on the lifetime of the hydrophobic block in the micelle core. As far as we are aware, a direct comparison of the unimer exchange rates of diblock A_n-B_m and analogous triblock ($A_n-B_{2m}-A_n$) copolymers has never been reported (A and B being the hydrophobic and hydrophilic block, respectively). Differences in the unimers exchange rates depending on the macromolecular architectures could explain the differences observed during the photo-cross-linking step.

Despite the increase of aggregation number, we choose to work with a small amount of photoinitiator, as was studied with diblock copolymers, in order to overcome the problems of big cores swollen with DMPA and those of aggregates generated during the photo-cross-linking process. The size distributions of structures cross-linked at various concentrations (ranging from 1 to 12 g·L^{-1}) were analyzed by SEC in DMF containing LiBr (10^{-2} mol·L^{-1}) (Figure 6). DMF is a good solvent of both blocks leading to the dissociation of uncross-linked micelles and, as previously reported,[27] addition of LiBr salt avoids the physical

Table 1. Characteristics of the Structures Obtained by Cross-Linking PMEA$_6$-*b*-PEO$_{200}$-*b*-PMEA$_6$ in Water at Various Concentrations

sample	cross-linking concentration, g·L^{-1}	M_w (g·mol^{-1})[a]	R_{hz} (nm)[b]	R_{gz} (nm)[a]
S1	1	3.60×10^5	13	-
S2	2	3.80×10^5	14	-
S4	4	5.90×10^5	17	-
S8	8	4.61×10^6	55	65
S10	10	1.48×10^7	74	103
S12	12	2.85×10^7	95	144

[a] Measured by SLS by extrapolating KC/R to $q \rightarrow 0$ and $C \rightarrow 0$. [b] Measured by DLS at $q \rightarrow 0$ and $C \rightarrow 0$.

aggregation of micelles. A shift of the main peak to the lower elution volume is clearly observed after photo-cross-linking indicating an efficient stabilization of the micellar architectures. The fraction of polymer eluted at V_{el} = 11.5 mL was attributed to the stabilized flower-like polymers. As the concentration of polymer in the cross-linked solutions increased, dimers of flowers (at V_{el} = 10.9 mL), trimers of flowers and bigger and more complex aggregates appeared. For the highest concentrations (12 g·L^{-1}), the separation of the biggest structures became impossible because they were eluted below the total exclusion limit of the column. Deconvolution of the SEC trace of the sample cross-linked at 1 g·L^{-1} revealed a large fraction of "flowers", a fraction

dx.doi.org/10.1021/ma2022937 |*Macromolecules* 2012, 45, 410–419

of dimers around 13% and a fraction of remaining unimers of 10% (Figure 6b). This amount of uncross-linked unimers can be explained by the effect of cmc. Indeed, it is usually admitted that the concentration of nonassociated chains in the medium is equal to the cmc. Thus, at $C = 1\ g \cdot L^{-1}$, assuming a cmc = $0.05\ g \cdot L^{-1}$, the percentage of nonassociated chains should be around 5%. So, either the cmc is a little underestimated (maybe due to association of pyrene with the hydrophobic block below the cmc) or a small fraction of the chains, around 5%, is not fully functionalized or is not covalently incorporated into the micelles due to termination reactions. The analysis of SEC traces of samples cross-linked at higher concentrations tends to privilege the first hypothesis because the remaining uncross-linked population for the sample cross-linked at $12\ g \cdot L^{-1}$, is around 1% not 5%.

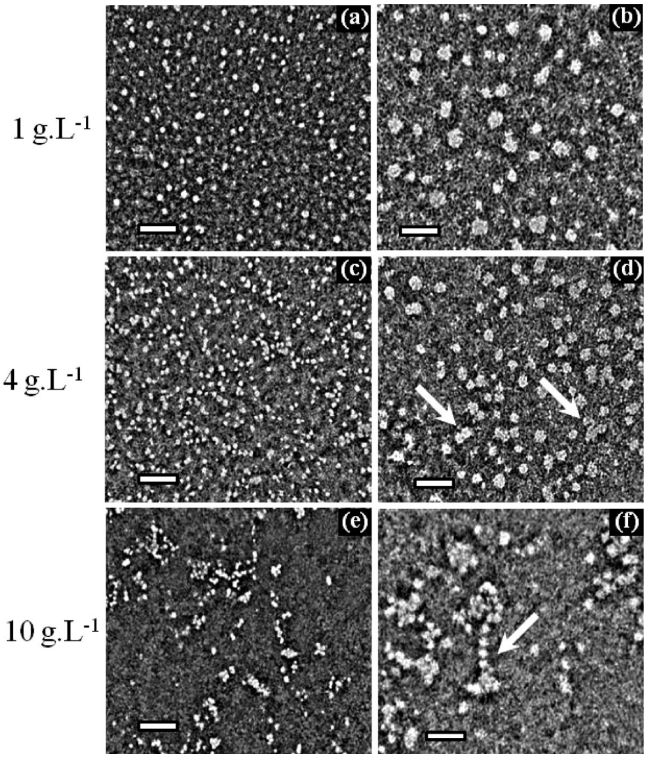

Figure 7. Negatively stained TEM images of (a, b) S1, (c, d) S4, and (e, f) S10 samples. Databars correspond to 200 and 100 nm for, respectively, the left and right images.

The weight-average molar masses (M_w), hydrodynamic radius (R_h), and radius of gyration (R_g) of the structures formed at various concentrations were analyzed by static and dynamic light scattering (Table 1). Such analysis is impossible for the uncross-linked systems because, only apparent molar masses are measured due to excluded volume interactions between chains at high concentration and dilution modifies the reversible structures. This analysis was, thus, performed on cross-linked systems that can be diluted without modification of sizes and distributions. At low concentration, triblock copolymers were fixed into flower-like architectures exhibiting an aggregation number around 54 hydrophobic groups per micelle. The evolution of M_w, R_h, and R_g confirmed that more and larger aggregates of flowers were formed when concentration increased. Close to the percolation threshold a sharp increase of the molar mass and radii was observed. Between 13 and 14 $g \cdot mol^{-1}$, the system percolated and a chemical gel was obtained after cross-linking.

Samples S1, S4, and S10 were analyzed by transmission electron microscopy (TEM) and cryoTEM after cross-linking. Figure 7 shows cross-linked micelles negatively stained by uranyl acetate. Using this technique, particles appear white on a dark background. Sample S1 exhibited rather monodisperse spherical particles (flower-like micelles) in agreement with SEC and light scattering measurements. Sample S4 clearly showed higher fraction of connected micelles (dimers or trimers) as indicated by arrows in Figure 7d. As expected, the fraction of connected micelles into large aggregates became predominant in sample

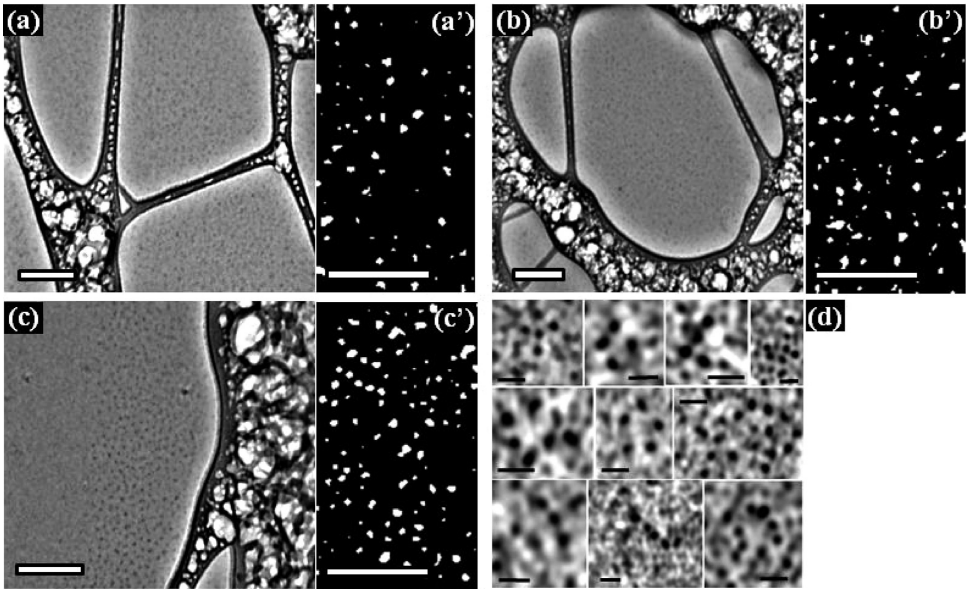

Figure 8. Cryo-TEM images of (a, a′) S1, (b, b′) S4 and (c, c′) S10 samples. Images a′, b′, and c′ correspond to contrast-enhanced higher magnification cryoTEM views of samples S1, S4 and S10, respectively. Typical self-assembled structures viewed on the cryoTEM images of S10 samples are shown in part d. Databars correspond to 200 nm for images a, b, c/a′, b′, c′ and to 20 nm for image d.

dx.doi.org/10.1021/ma2022937 |*Macromolecules* 2012, 45, 410–419

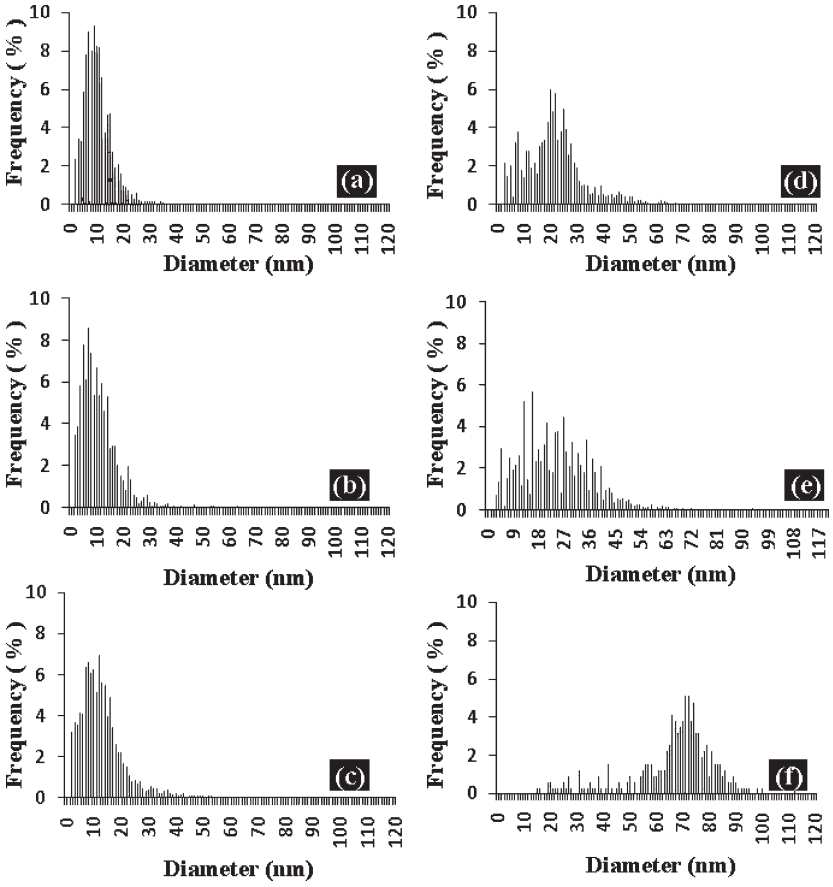

Figure 9. Histograms deduced from cryoTEM images of (a) S1, (b) S4, and (c) S10 samples and from TEM images of (d) S1, (e) S4, and (f) S10 samples.

S10 for which various morphologies going from compact to garland-like aggregates (see arrow in Figure 7f) were observable.

CryoTEM analyses were performed on the cross-linked flower-like objects in a vitrified aqueous environment (Figure 8). Although the resolution is lower than that of TEM analyses, the structures observed resembled those shown in Figure 7 indicating that the drying and coloration processes used for TEM imaging did not modify significantly the architectures. CryoTEM images showed dark particles. As no contrast agent was used, only the parts of the objects having the highest electronic density were clearly viewed, i.e., mainly the PMEA micelles cores. The PEO corona was very difficult to visualize because of its high hydration rate leading to a low contrast with water. Thus, connected micelles were not easily distinguished from single flowers even after contrast enhancement (Figure 8, parts b′ and c′). However, a regular distance between single flowers was systematically observed in the flowers assemblies (Figures 8c′ and d′). Yet, cryoTEM images of sample S1 exhibited mainly single particles while S10 showed structures, having roughly the same characteristic distance between dark particles (Figure 8d), which can be attributed to micelles aggregates. The same diversity of compact (top of Figure 8d) and garland-like (bottom of Figure 8d) aggregates could be observed.

The quantitative analysis of the particles sizes was performed on both cryoTEM and TEM images using ImageJ (Figure 9). The number-averaged and z-averaged values of the diameters are gathered in Table 2. As shown previously, only the micellar cores had sufficient contrast with water for being observed by cryoTEM. This explains the very weak differences between the samples and the

Table 2. Mean Diameter (D_{mean}) and *z*-Averaged Diameter (D_z) Values from Statistical Analysis of CryoTEM and Conventional TEM Images

	cryoTEM			conventional TEM		
	S1	S4	S10[b]	S1	S4	S10[c]
D_{mean} (nm)	10.5	11.2	13.2	21.8	24.6	66.5
D_z (nm)	17.5	22.9	27.8	35.1	38.2	74.5
N[a]	2525	2047	3477	2272	3286	314

[a] Number of particles counted for statistical analysis. [b] Only elemental particles have been counted. [c] Assembled structures have been counted.

low diameters values. These values were, however, very similar to those measured by cryoTEM on PEO-*b*-Poly(ethyl acrylate) (PEA) star-like micelles exhibiting the same aggregation number[4] but twice higher than those measured by small angle neutron scattering on PEO-*b*-PEA micelles[27] indicating that part of the PEO corona was visible. Conventional TEM showed the whole particles and aggregates but in a dried state and deposited onto a surface. Nevertheless, the population distributions of S1, S4, and S10 were consistent with those measured by SEC in DMF. In order to compare TEM images analyses and DLS measurements, *z*-averaged diameters (D_z) were calculated. Diameters of S1 and S4 samples were in good agreement with the corresponding R_{hz} measured by DLS. Small differences observed could be attributed to the flattening of the micelles onto the surface that

dx.doi.org/10.1021/ma2022937 |*Macromolecules* 2012, 45, 410–419

counterbalanced the dehydration of the PEO corona and the shrinking of the particles. This led to slightly higher values of D_z. The apparent discrepancy between R_{hz} and D_z for sample S10 was probably due to the poor statistics of the TEM image analysis (only 314 micelles-assembled structures) and due to the fact that R_{hz} is very sensitive to the biggest aggregates that may not be observed on the TEM images because of their very small fraction.

CONCLUSION

A triblock poly(2-methacryloyloxyethyl acrylate)-*b*-poly(ethylene oxide)-*b*-poly(2-methacryloyloxyethyl acrylate) (PMEA-*b*-PEO-*b*-PMEA) copolymer bearing polymerizable groups on the hydrophobic blocks was synthesized using ATRP technique. Its self-assembly in water led to various transient flower-like micellar architectures that could be efficiently and rapidly stabilized by photo-cross-linking of the hydrophobic cores. The molar masses, sizes, and population distributions were analyzed by light scattering in water, TEM, cryoTEM, and SEC in DMF, a good solvent for both blocks. At low concentration, mainly single flowers were observed. Increasing the solution concentration led to bridging of the micelles. More and bigger aggregates, for which the flower-like micelle is the basic unit, were formed. When reasonable amounts of photoinitiator were used, the photo-cross-linking process induced an increase of the aggregation number of the flower-like micelles without additional coupling of the flowers. This behavior is different of that of analogous diblock copolymer micelles for which no significant increase of size or aggregation number was observed after cross-linking. Further investigations, such as hybridization techniques, will be implemented to understand the influence of block copolymer architecture on the dynamics of the self-assemblies and on the cross-linking process. Anyway, this self-assembly/photo-cross-linking technique led to well-defined flower-like PEO architectures and could be applied to synthesize "flower" polymers of various chemical nature. Furthermore, as reported by Nasongkla et al.,[58] the topology effect of ring polymers induces a longer retention time in body compared to linear analogous. The same behavior could be anticipated for flower-like amphiphilic polymers that exhibit, in addition, the capacity of loading and carrying drugs. This peculiar property could be exploited in the aim of designing new vectors for drug delivery.

AUTHOR INFORMATION

Corresponding Author

*E-mail: erwan.nicol@univ-lemans.fr.

ACKNOWLEDGMENT

The authors thank the National Research Agency (ANR, program HYPARC) for their financial support. Sagrario Pascual, Taco Nicolai, and Lazhar Benyahia are greatly thanks for fruitful discussions. Hien The Ho is acknowledged for SEC analyses in DMF.

REFERENCES

(1) Lapienis, G. *Prog. Polym. Sci.* **2009**, *34*, 852–892.
(2) Li, W. W.; Matyjaszewski, K. *J. Am. Chem. Soc.* **2009**, *131*, 10378–10379.
(3) Nicol, E.; Niepceron, F.; Bonnans-Plaisance, C.; Durand, D. *Polymer* **2005**, *46*, 2020–2028.
(4) Piogé, S.; Fontaine, L.; Gaillard, C.; Nicol, E.; Pascual, S. *Macromolecules* **2009**, *42*, 4262–4272.
(5) Naraghi, K. S.; Meneghetti, S. P.; Lutz, P. J. *Macromol. Rapid Com.* **1999**, *20*, 122–126.
(6) Feng, X.; Taton, D.; Ibarboure, E.; Chaikof, E. L.; Gnanou, Y. *J. Am. Chem. Soc.* **2008**, *130*, 11662–11676.
(7) Feng, X. S.; Taton, D.; Chaikof, E. L.; Gnanou, Y. *J. Am. Chem. Soc.* **2005**, *127*, 10956–10966.
(8) Walach, W.; Trzebicka, B.; Justynska, J.; Dworak, A. *Polymer* **2004**, *45*, 1755–1762.
(9) Wilms, D.; Schomer, M.; Wurm, F.; Hermanns, M. I.; Kirkpatrick, C. J.; Frey, H. *Macromol. Rapid Com.* **2010**, *31*, 1811–1815.
(10) Truelsen, J. H.; Kops, J.; Batsberg, W.; Armes, S. P. *Polym. Bull.* **2002**, *49*, 235–242.
(11) Yamamoto, T.; Tezuka, Y. *Polym. Chem.* **2011**, *2*, 1930–1941.
(12) Pang, X. C.; Wang, G. W.; Jia, Z. F.; Liu, C.; Huang, J. L. *J. Polym. Sci., Part A: Polym. Chem.* **2007**, *45*, 5824–5837.
(13) Sun, T.; Yu, G. E.; Price, C.; Booth, C.; Cooke, J.; Ryan, A. J. *Polymer* **1995**, *36*, 3775–3778.
(14) Yan, Z. G.; Yang, Z.; Price, C.; Booth, C. *Makromol. Chem., Rapid Commun.* **1993**, *14*, 725–732.
(15) McLeish, T. C. B.; Milner, S. T. Entangled dynamics and melt flow of branched polymers. In *Branched Polymers II*; Roovers, J., Ed.; Springer-Verlag: Berlin: Berlin, 1999; Vol. 143, pp 195−256.
(16) Kapnistos, M.; Lang, M.; Vlassopoulos, D.; Pyckhout-Hintzen, W.; Richter, D.; Cho, D.; Chang, T.; Rubinstein, M. *Nature Mater.* **2008**, *7*, 997–1002.
(17) Masaro, L.; Zhu, X. X. *Prog. Polym. Sci.* **1999**, *24*, 731–775.
(18) Saito, R.; Ishizu, K. *Polymer* **1997**, *38*, 225–229.
(19) Saito, R.; Yoshida, S.; Ishizu, K. *J. Appl. Polym. Sci.* **1997**, *63*, 849–854.
(20) Saito, R.; Akiyama, Y.; Ishizu, K. *Polymer* **1999**, *40*, 655–660.
(21) Ding, J.; Liu, G. *Macromolecules* **1998**, *31*, 6554–6558.
(22) Gao, H.; Jones, M.-C.; Chen, J.; Prud'homme, R. E.; Leroux, J.-C. *Chem. Mater.* **2008**, *20*, 3063–3067.
(23) Guo, A.; Liu, G.; Tao, J. *Macromolecules* **1996**, *29*, 2487–2493.
(24) Henselwood, F.; Liu, G. *Macromolecules* **1997**, *30*, 488–493.
(25) Jiang, J.; Qi, B.; M., L.; Zhao, Y. *Macromolecules* **2007**, *40*, 790–792.
(26) Kakizawa, Y.; Harada, A.; Kataoka, K. *J. Am. Chem. Soc.* **1999**, *121*, 11247–11248.
(27) Piogé, S.; Nesterenko, A.; Brotons, G.; Pascual, S.; Fontaine, L.; Gaillard, C.; Nicol, E. *Macromolecules* **2011**, *44*, 594–603.
(28) Rheingans, O.; Hugenberg, N.; Harris, J. R.; Fischer, K.; Maskos, M. *Macromolecules* **2000**, *33*, 4780–4790.
(29) Tao, J.; Stewart, S.; Liu, G.; Yang, M. *Macromolecules* **1997**, *30*, 2738–2745.
(30) Wilson, D. J.; Riess, G. *Eur. Polym. J.* **1988**, *24*, 617–621.
(31) Fujii, S.; Cai, Y.; Weaver, J. V. M.; Armes, S. P. *J. Am. Chem. Soc.* **2005**, No. 127, 7304–7305.
(32) Huang, H.; Kowalewski, T.; Remsen, E. E.; Gertzmann, R.; Wooley, K. L. *J. Am. Chem. Soc.* **1997**, *119*, 11653–11659.
(33) Liu, S.; Weaver, J. V. M.; Save, M.; Armes, S. P. *Langmuir* **2002**, No. 18, 8350–8357.
(34) O'Reilly, R. K.; Hawker, C. J.; Wooley, K. L. *Chem. Soc. Rev.* **2006**, *35*, 1068–1083.
(35) Thurmond, K. B., II; Kowalewski, T.; Wooley, K. L. *J. Am. Chem. Soc.* **1996**, *118*, 7239–7240.
(36) Thurmond, K. B., II; Kowalewski, T.; Wooley, K. L. *J. Am. Chem. Soc.* **1997**, *119*, 6656–6665.
(37) Zhang, Q.; Remsen, E. E.; Wooley, K. L. *J. Am. Chem. Soc.* **2000**, *122*, 3642–3651.
(38) Ding, J.; Liu, G. *J. Phys. Chem. B* **1998**, *102*, 6107–6113.
(39) Discher, B. M.; Bermudez, H.; Hammer, D. A.; Discher, D. E.; Won, Y.-Y.; Bates, F. S. *J. Phys. Chem. B* **2002**, *106*, 2848–2854.
(40) He, J.; Tong, X.; Tremblay, L.; Zhao, Y. *Macromolecules* **2009**, *42*, 7267–7270.
(41) Maskos, M.; Harris, J. R. *Macromol. Rapid Com.* **2001**, *22*, 271–273.

(42) Park, C. W.; Lee, H. J.; Yang, H.-m.; Woo, M.-a.; Park, H. g.; Kim, J.-D. *J. Polym. Sci., Part A: Polym. Chem.* **2010**, *49*, 203–210.
(43) Ishizu, K. H., K. *J. Polym. Sci., Part A: Polym. Chem.* **2005**, *43*, 63–70.
(44) Liu, G.; Yan, X.; Duncan, S. *Macromolecules* **2002**, *35*, 9788–9793.
(45) Rupar, P. A.; Cambridge, G.; Winnik, M. A.; Manners, I. *J. Am. Chem. Soc.* **2011**, *133*, 16947–16957.
(46) Njikang, G.; Liu, G.; Curda, S. A. *Macromolecules* **2008**, *41*, 5697–5702.
(47) Tao, J.; Liu, G. *Macromolecules* **1997**, *30*, 2408–2411.
(48) Dupont, J.; Liu, G. *Soft Matter* **2010**, *6*, 3654–3661.
(49) Di Biase, M.; de Leonardis, P.; Castelletto, V.; Hamley, I. W.; Derby, B.; Tirelli, N. *Soft Matter* **2011**, *7*, 4928–4937.
(50) Hu, J.; Zheng, R.; Wang, J.; Hong, L.; Liu, G. *Macromolecules* **2009**, *42*, 4638–4645.
(51) Michielsen, S. Specific index increments of polymers in dilute solution. In *Polymer Handbook*, 4th ed.; Brandrup, J. I., Immergut, E. H., Grulke, E. A., Ed. John Wiley and Sons, Inc.: New York, 1999; pp 594−595.
(52) Yekta, A.; Duhamel, J.; Adiwidjaja, H.; Brochard, P.; Winnik, M. A. *Langmuir* **1993**, *9*, 881–883.
(53) Wilhelm, M.; Zhao, C.-L.; Wang, Y.; Xu, R.; Winnik, M. A.; Mura, J.-L.; Riess, G.; Croucher, M. D. *Macromolecules* **1991**, *24*, 1033–1040.
(54) Kadam, V.; Nicolai, T.; Nicol, E.; Benyahia, L. *Macromolecules* **2011**, *44*, 8225–8232.
(55) Cochin, D.; Candau, F.; Zana, R. *Macromolecules* **1993**, *26*, 5755–5764.
(56) Cochin, D.; Zana, R.; Candau, F. *Macromolecules* **1993**, *26*, 5765–5771.
(57) Laflèche, F.; Durand, D.; Nicolai, T.; Gnanou, Y.; Taton, D. *Macromolecules* **2003**, *36*, 1341–1348.
(58) Nasongkla, N.; Chen, B.; Macaraeg, N.; Fox, M. E.; Fréchet, J. M. J.; Szoka, F. C. *J. Am. Chem. Soc.* **2009**, *131*, 3842–3843.

Macromolecules

Article

pubs.acs.org/Macromolecules

A Spectroscopic Analysis of the Role of Side Chains in Controlling Thermochromic Transitions in Polydiacetylenes

Lei Yu and Shaw Ling Hsu*

Polymer Science and Engineering, University of Massachusetts (Amherst), and NSF Materials Research Science & Engineering Center, Amherst, Massachusetts 01003, United States

ABSTRACT: A systematic study has been carried out to investigate the role of the side chains in lowering the reversible thermochromic transition temperature of polydiacetylenes. The type of interacting groups also proved to be crucial. Polymers with hydrogen-bonded side chains have consistently behaved differently as compared to polymers with less specific interactions associated with metallic ions. The most striking factor is the orderliness of the polymethylene portion of the side chains. The length of the side chains is critical in determining the transition temperature. In some cases, the packing order of the side chains is of sufficient order to crystallize. When high order exists, a reversible thermochromic transition is difficult to achieve. Conversely, if the side chains are disordered at any temperature, the transition temperatures are low and the transition is always reversible. This is the case for side chains stabilized by the presence of metallic ions. It is apparent that the presence of long-range nonspecific electrostatic interactions is important in determining reversible thermochromic transitions. These structural features are most easily observed using infrared spectroscopy and Raman scattering. Supporting evidence have been obtained using thermal analysis and X-ray diffraction.

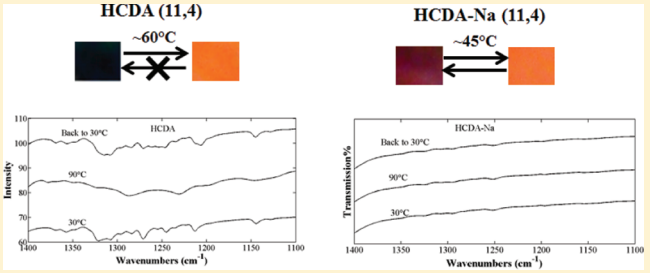

INTRODUCTION

Thermochromic polymers, narrowly defined as polymers that can change in color as a function of temperature, have always been fascinating subjects of study from a fundamental perspective.[1−3] There are also very useful properties associated with this class of polymers or polymer/molecular blends.[4−11] The structure of the main chain responsible for the color needs to be conjugated. Polydiacetylene (PDA), shown schematically in Scheme 1, is an ideal model. It is generally polymerized from molecular solids by ultraviolet (UV) irradiation with no need for initiator and catalysts.[12] Therefore, they are fully crystalline with well-defined structure without the perturbing effects from conformational disorder of the main chain. PDA, shown in Scheme 1, is composed of three parts: conjugated backbone, alkyl side chain, and headgroup.

Scheme 1. Schematic Structure of Model PDA

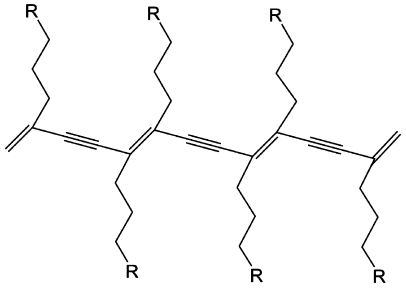

The main focus of the current study deals with controlling the temperature at which thermochromic transition occurs, T_t. PDAs are well-known for its classic blue-to-red color transition when temperature increases above T_t. The reduction of "conjugation length" is the most popular explanation for the classic blue-to-red color transition. Earlier studies have suggested[13−15] that the blue phase has a planar structure and the red phase is nonplanar with a reduction of the main chain "conjugation length". An alternative explanation suggests that the red phase may have a different geometry as compared to the blue phase.[16,17] There is abundant evidence showing that the color change is intimately connected to the structure of the side chain. For example, it has been shown that the torsion of the methyl-terminated side chains can induce both color and Raman frequency shift in PDA with changes proportional to the torsion angle.[18] A rotation as small as 15° of the $-CH_3$ group can shift the color from blue to red with a decrease of the maximum absorption wavelength from the blue ($\lambda_{max} \sim 640$ nm) to the red ($\lambda_{max} \sim 550$ nm).

The central focus of this current study is to elucidate the structural features that would influence the transition temperature and the reversibility of the thermochromic transition. Earlier studies have demonstrated that the length of the alkyl side chains is important.[19−22] Most of the studies have demonstrated that shorter side chains result in higher temperature sensitivity or lower T_t. But the symmetry of the

Received: July 4, 2011
Revised: November 23, 2011
Published: December 7, 2011

Table 1. PDAs and PDA-Na and the Corresponding Length of the Alkyl Side Chain

name	PCDA	HCDA	ODDA-1	ODDA-2	DCDDA	PCDA-Na	HCDA-Na
(*n*,*m*)	(11,8)	(11,4)	(4,8)	(9,3)	(8,8)	(11,8)	(11,4)

side chains, i.e., the length of side chains on each side of the main chain, on the transition is not discussed. Length of alkyl side chain is not the only factor that can affect the color transition temperature; different interacting groups and strength of interaction may also affect T_t. Even the earliest studies have shown that the formation and dissociation of the hydrogen bonds associated with R serves as a "switch" for the color change.[1] The stability of the interaction and the orderliness of the localized molecular architecture determine the reversibility of the transition in 10,12-pentacosadiynoic acid (PCDA).[19] The introduction of metallic ions (Na, Li, or Zn) and associated electrostatic interactions can also affect the reversibility of the transition in PCDAs.[23−25] Variations of this method such as the introduction of covalent bonds or shortening the interaction using nanoparticles or Langmuir−Blodgett films have also been investigated.[25−27]

Although the studies cited above have shown interesting possibilities for controlling thermochromic transitions in PDAs, details of the structural features are missing.[13,28−30] Earlier NMR studies have suggested that the restriction of side chains should result in better reversibility.[29] Others have suggested the strength of interaction is the key to reversibility.[30] In this current study, a combination of characterization techniques is employed to analyze the structures needed to control the transition temperature and the reversibility of the thermochromic transition. The well-known PCDA-alike PDAs and the corresponding PDA−Na system with different length of alkyl side chains have been analyzed. The mechanisms of the irreversible and reversible color transition in these two PDA systems are discussed.

EXPERIMENTAL SECTION

Materials. All the materials used in this study are tabulated in Table 1. The model diacetylenes (DA), purchased from GFS Chemicals, include 10,12-pentacosdiynoic acid (PCDA), 6,8-heneicosadiynoic acid (HCDA), 10,12-octadecadiynoic acid (ODDA-1), 5,7-octadecadiynoic acid (ODDA-2), and 10,12-docosadiynedioic acid (DCDDA). *n* and *m* indicate the carbon number of the tail and internal alkyl side chains. PCDA-Na and HCDA-Na have been synthesized as shown previously.[23] The diacetylene monomers were dissolved in tetrahydrofuran (THF). Solution was then deposited on a glass slide. After the evaporation of the solvent, the monomers were set ∼2 cm from the 254 nm UV light to be polymerized. The monomers became blue after several seconds, indicating the success of polymerization. After being scratched from the glass slide, the small powder-like crystals were analyzed. All of the DA monomers were polymerized using the model UVGL-25 MINERALIGHT lamp (254 nm UV light; 18.4 W). Unlike other derivatives, ODDA-1-Na(4,8) cannot be polymerized by the 254 nm UV radiation.

Characterization. The PDAs and PDA-Na were characterized by Fourier transform infrared (FTIR) spectroscopy (PerkinElmer Spectrum 100), differential scanning calorimetry (DSC, TA Instruments Q100, heating/cooling rate 10 °C/min, nitrogen flow rate 50 mL/min), Raman spectroscopy (HORIBA Jobin Yvon, excitation wavelength λ = 632.8 nm), and X-ray diffraction (PANalytical X'PertPert Material Research diffractometer). The custom-made hot stage, which is connected to a temperature control system made by OMEGA, was used to observe the thermochromic transitions of the samples. Immediately after UV polymerization, PCDA-Na exhibits a red color corresponding to a metastable structure as reported previously.[23] When heated to above 50 °C, it becomes a stable blue phase. In our study, we studied the classic blue-to-red transition from the blue phase. We have also fabricated a variable temperature (−160 to 300 °C) sample cell capable of being used in either Raman or infrared experiments.

RESULTS AND DISCUSSION

The PCDA polydiacetylenes and their derivatives are the principal focus of this study. Different alkyl side chain length and two types of interacting functional groups are studied. The polymers studied are shown schematically in Figure 1. Figure 1a shows the PCDA with −COOH as the headgroup on one side of the conjugated polymer backbone. The alkyl chain with *m* carbons connects the headgroup with the polymer backbone, and those with *n* carbons are on the other side of the backbone. This study focuses on the effects of hydrogen bonds, not necessarily the types of hydrogen bonds present.[17,31−35] Figure 1b presents the PDA−Na system, which can be obtained by reacting PDA (e.g., PCDA and HCDA) with NaOH as described previously.[23] Figure 1c shows a DCDDA with −COOH at both sides of the conjugated backbone.

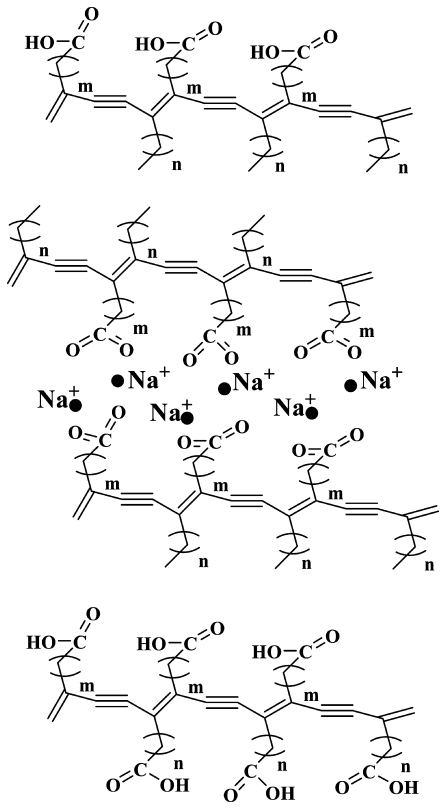

Figure 1. Schematic structures of the three types of polydiacetylenes studied: (a) possibility of hydrogen bonds on one side; (b) possibility of electrostatic interactions; (c) possibility of hydrogen bonds on both side of the main chain.

Thermochromic Transitions Observed. The thermochromic response of the various PDA's and the transition temperature, T_t, measured are summarized in Figure 2. They can be divided into two groups: one with reversible transitions (one stabilized with metallic salts) and the other with

dx.doi.org/10.1021/ma201519v | Macromolecules 2012, 45, 420−429

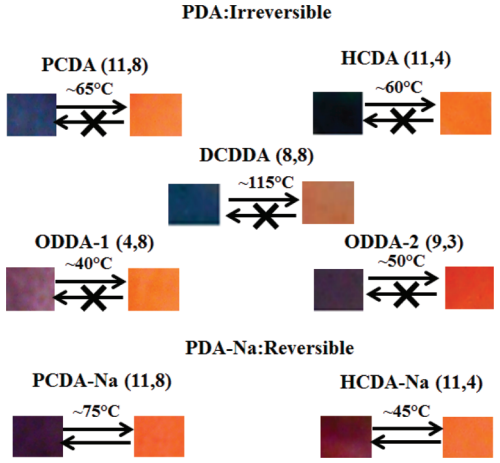

Figure 2. Thermochromic response and color transition temperature (T_t) for several PDAs and PDA-Na.

irreversible transitions (containing hydrogen bond interactions). It is clear that the length of the alkyl chains, both n and m, are important in determining T_t. The T_t values of PCDA(11,8), HCDA(11,4), and ODDA-1(4,8) demonstrate that a decrease of either n or m can depress T_t. n is found to be moderately more effective than m in affecting the T_t. ODDA-2(9,3) has a higher T_t than ODDA-1(4,8) even though they have the same $n + m$ value. HCDA-Na(11,4) shows a lower T_t than PCDA-Na(11,8) as expected. DCDDA(8,8), which has COOH groups on both sides of the conjugated backbone, exhibits irreversible color transition and a much higher T_t even for PCDA(11,8) with long alkyl side chains. The length of the alkyl side chain is not the only factor that affects T_t. Clearly, the more stable molecular structure due to the hydrogen bonds formed on both sides of the main chain in DCDDA makes a significant difference. PCDA-Na shows higher T_t while HCDA-Na has a lower T_t than their neat derivatives. This difference demonstrates that long-range electrostatic interactions between headgroups do not necessarily results in higher T_t.

Analysis of Associated Structural Transitions. Characterization of the structural changes associated with the thermochromic transition is our principal interest. UV−VIS absorption can be used directly to characterize the transition. The specific Raman signatures representing the conjugated backbone are also well assigned.[36,37] In this study we have also employed infrared absorption and thermal analysis to elucidate the structural transformation associated with the thermochromic transition. Wide-angle X-ray diffraction is used to supplement our spectroscopic interpretation. In this study, Raman and infrared spectroscopy are given particular emphasis is because of their sensitivity to localized order or disorder not requiring the long-range coherence as required for diffraction.

The intensity of the Raman-active C═C (1400 cm^{-1}) and C≡C (2200 cm^{-1}) bond stretching vibrations associated with the conjugated backbone is strongly enhanced because of the low-lying electronic transitions associated with the conjugated backbone.[18,36−40] These vibrations are representative of the backbone structure. The frequency changes in these bands as a function of temperature of the various PCDA samples are

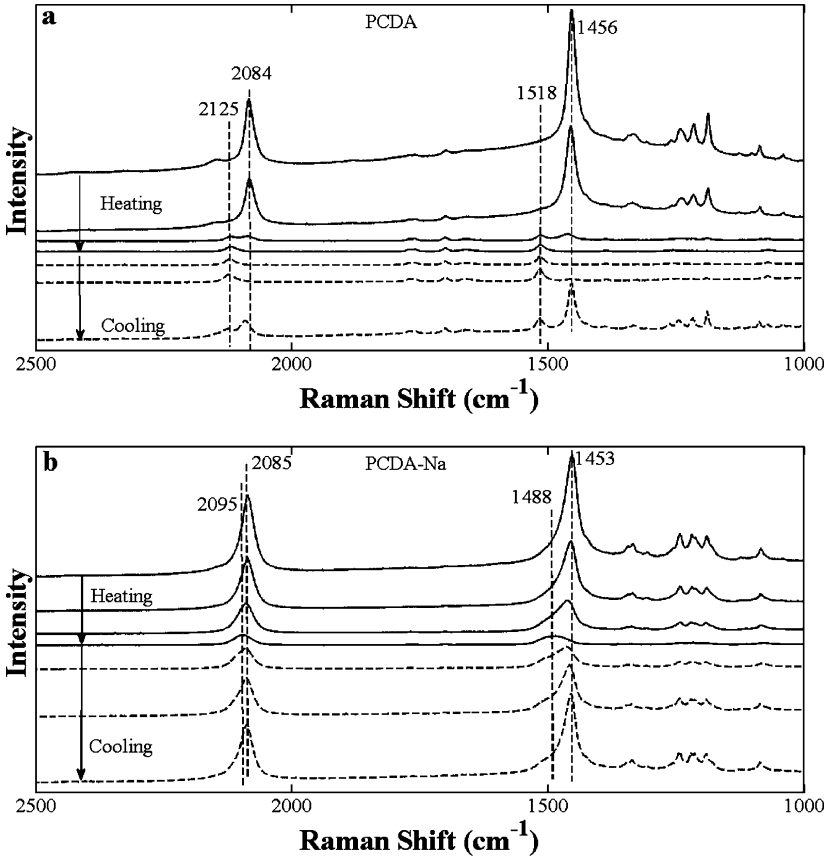

Figure 3. Temperature-dependent Raman spectra of (a) PCDA and (b) PCDA-Na during the heating and cooling between 30 and 90 °C. The temperature difference between any two adjacent plots is 20 °C.

dx.doi.org/10.1021/ma201519v | *Macromolecules* 2012, 45, 420−429

shown in Figure 3a. As the temperature cycles from 30 to 90 °C, the intensity of the vibrations at 1456 and 2084 cm^{-1} assigned to C═C and C≡C, respectively, change and are replaced by a vibration at 1518 and 2125 cm^{-1}, respectively. As temperature increases, the 1456 cm^{-1} peak decreases and another band at 1518 cm^{-1} grows. At 90 °C, above the thermochromic transition, only the 1518 cm^{-1} peak exists. Similarly, for the C≡C vibration, the original peak at 2084 cm^{-1} is replaced by a new peak located at 2125 cm^{-1} at elevated temperatures. It is interesting to note that at 70 °C a coexistence of the four peaks 1456, 1518, 2084, and 2125 cm^{-1} is observed. The vibrations that disappeared at elevated temperatures remerged, only partially, when the sample temperature is lowered. Even when sample temperature is lowered back to 30 °C, the vibrations at 1518 and 2125 cm^{-1} remained. After cooling back to 30 °C, the C≡C vibration emerged at a new position at 2091 cm^{-1}, which is 7 cm^{-1} higher than the original position. In this case, somewhat different from the color change observed, the Raman shifts do not follow the color change exactly. The frequency differences observed represents an irreversible change in the structure as temperature is cycled up and down.

In contrast to the PDAs with hydrogen-bonding possibilities, the Raman data obtained for the samples with metallic salts are clearly reversible as shown in Figure 3b. At low temperatures, two peaks at 1453 and 2085 cm^{-1}, assigned to C═C and C≡C stretching vibrations, are observed. When heated to 90 °C, the two vibrations shift to 1488 and 2095 cm^{-1}, respectively. As the sample temperature decreases back to 30 °C, the two peaks shift reversibly back to the original positions at 1453 and 2085 cm^{-1}. This process is totally different from that in PCDA, which involves the appearance and disappearance of new bands and some hysteresis.

For comparison, UV−VIS spectroscopy was used to investigate the two types of irreversible and reversible thermochromic transitions. Our data are identical to the ones shown previously.[23] The absorption data showed a simultaneous decrease of the absorption at 640 nm, an increase at 550 nm for PCDA, and a gradual shift of absorption peak for a PCDA-derived PDA with reversible color transition. The result from the UV−VIS spectra is consistent with our Raman results except that when temperature returns to 30 °C in PCDA, the UV−VIS did not show a complete recovery of the absorption peak at longer wavelength (lower energy).

In PDAs, the intermolecular interaction arises from hydrogen bonds, while in PDA-Na, it is the electrostatic interactions. Because both of them involve the C═O bond in the carboxylate group, infrared spectroscopy was used to investigate the behavior of headgroups by observing the behavior of C═O stretching vibration during color transition in both PDA and PDA-Na systems. Infrared data (Figure 4) were obtained for both PCDA(11,8) and HCDA(11,4) as when they were heated and cooled. At 30 °C, the C═O vibration band in PCDA appears at 1693 cm^{-1}. As temperature increases, this peak intensity starts to decrease at ~65 °C replaced by a peak at 1712 cm^{-1}. At 80 °C, only the 1712 cm^{-1} peak can be seen. When the temperature returns to 30 °C, the C═O vibration shifts back partially to the original position ending at 1699 cm^{-1}, slightly higher than the original position. In HCDA-(11,4), when heated, the C═O vibration band shifts from 1693 cm^{-1} at 30 °C to 1712 cm^{-1} at 65 °C. The band stays at 1712 cm^{-1} even when the temperature is raised further to 85 °C. When the temperature is lowered back, the band at 1712 cm^{-1}

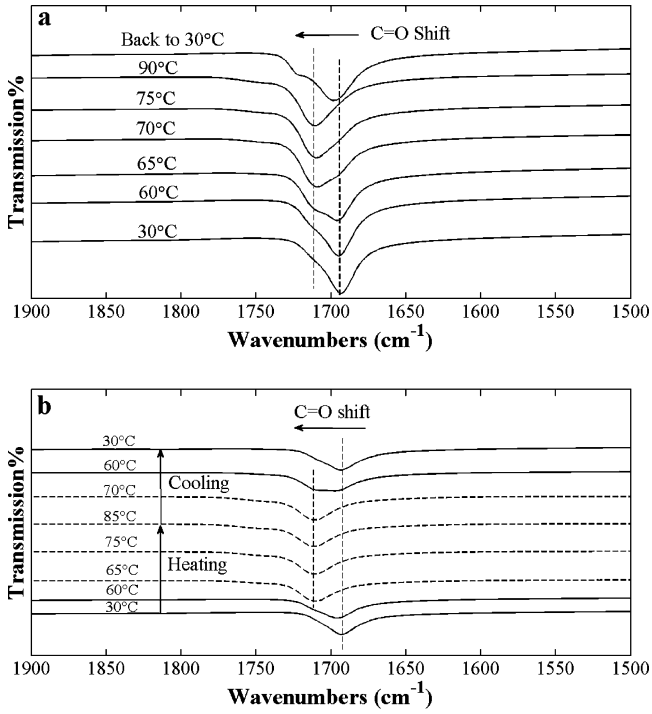

Figure 4. Infrared spectra obtained for PCDA and HCDA as a function of temperature: (a) PCDA (n = 11, m = 8); (b) HCDA (n = 11, m = 4). The temperature was cycled from 30 to 90 °C and back to 30 °C.

disappeared, gradually leaving only the band at 1693 cm^{-1}. These observations are somewhat different as compared to the complete reversibility reported previously.[19,41]

The infrared spectra obtained for the salt derivatives are shown in Figure 5. The C═O stretching is at a lower value as compared to the acid form. This vibration in PCDA-Na and HCDA-Na was observed at 1556 and 1559 cm^{-1}, respectively. These vibrations do not change in position as a function of temperature.

In contrast to the two different systems shown above, the infrared data at various temperatures obtained for DCDDA-(8,8) with COOH headgroup on both sides of the conjugated backbone are shown in Figure 6. The C═O vibration band shifts from 1693 cm^{-1} at 30 °C to 1711 cm^{-1} at 110 °C and then return to 1699 cm^{-1} when sample is cooled back to 30 °C. The structure due to the presence of hydrogen bonds on both side of the main chain is more stable as compared to polydiacetylene with hydrogen bond only at one side. This structure requires more energy and therefore higher temperature to weaken the hydrogen bonds formed.

What Do Side Chains Tell Us? The UV−VIS absorptions, Raman-active backbone stretching vibrations, and infrared-active C═O stretching bands all provide a consistent picture. When the change in frequency is reversible, we would assume that the original environment is recovered. When irreversible changes are observed, it can be deduced that interaction or the structure does not recover the original state, at least at the time scale that we carried out the spectroscopic experiments. The thermal properties of various PDAs and PDA-Na have been obtained using DSC (Figure 7). These provide a somewhat different picture. Virtually all of the endothermic peaks found for the PDAs occur at or near T_t, except for HCDA. In that case, the observed T_t for HCDA is at 55−60 °C, lower than the

dx.doi.org/10.1021/ma201519v | Macromolecules 2012, 45, 420−429

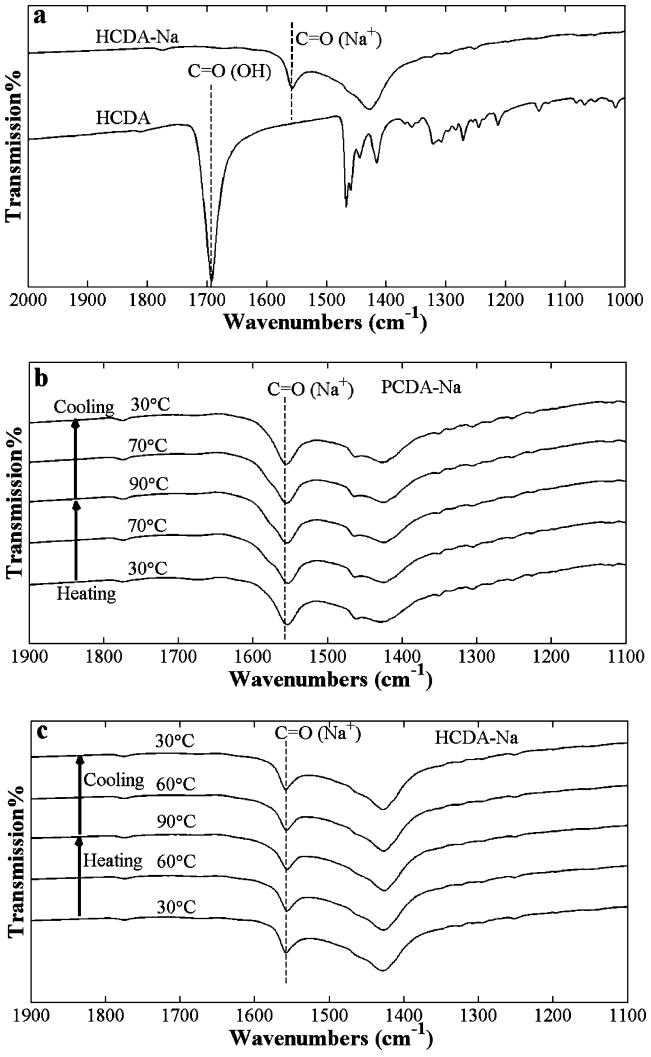

Figure 5. (a) Comparison of C=O vibration band of HCDA and HCDA-Na in FTIR spectra. Temperature-dependent infrared spectra of (b) PCDA-Na and (c) HCDA-Na. The samples were heated from 30 to 90 °C and cooled back to 30 °C.

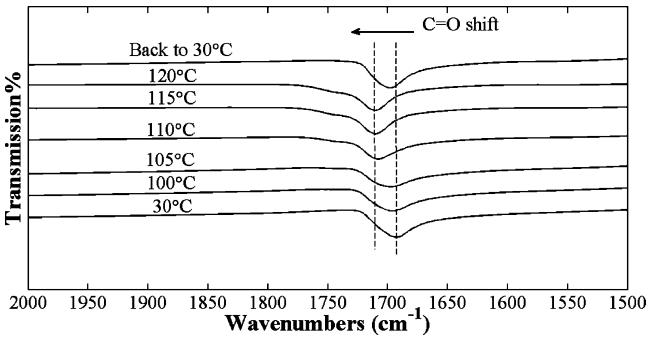

Figure 6. Temperature-dependent infrared spectra obtained for DCDDA. The temperature increases from 30 to 120 °C and then returns to 30 °C.

73.5 °C peak found in DSC. There is also a tremendous difference between the transition temperature, T_t, and endotherms found in the salt derivatives. The observed color transition temperature of PCDA-Na and HCDA-Na is at 75–80 and 45–55 °C, respectively. These are substantially lower

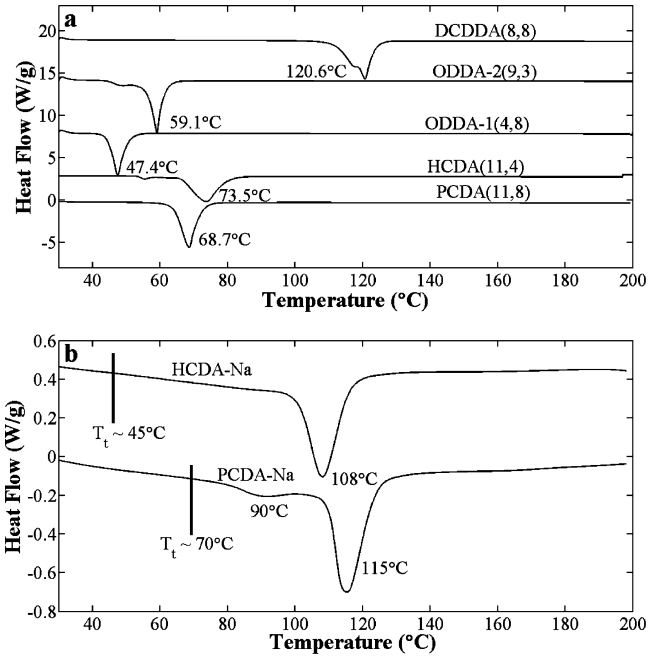

Figure 7. DSC results of (a) PDAs and (b) PCDA-Na and HCDA-Na.

than the main endotherms [108 °C (HCDA-Na) and 115 °C (PCDA-Na)] measured by DSC (Figure 7b).

The thermal data obtained for the various PDA's present an additional aspect of the structure transformation. The tremendous differences between T_t and endotherms observed in DSC for the salt derivatives can be explained by the presence of nonspecific long-range electrostatic interactions present in those samples. The heats of melting associated with those endotherms are relatively small in comparison to most other PDAs with hydrogen bonds present. On the basis of the infrared absorptions, it is clear that the difficulty in controlling the reversibility of the blue–red transition is due to the difficulties in the recovery of hydrogen bond geometry. Unlike previous studies involving PDAs that are soluble,[1] once broken, the hydrogen bonds are difficult to re-form in the solid state. It is well-known that the strength of hydrogen bonds is highly dependent on the directionality and distance of the functional groups involved.[42] This is in direct contrast to the ionic derivative. In that case, the electrostatic interactions are nonspecific but have a long range. Therefore, two-dimensional or even three-dimensional structures can be maintained even when main chain conjugation is interrupted. This accounts for the lack of correlation between T_t and the peak temperature of the endotherms observed. Although the heat of melting in the salt derivatives is rather small (1/10 of the hydrogen-bonded derivatives), the structure may be extremely stable possessing a reversible thermochromic transition.

We then focus on the structure necessary to control the transition temperature. It is apparent that the length of the alkyl chains certainly should be considered. As mentioned previously, the structure of the side chain can affect the main chain conjugation and thus sample color.[18] On the basis of the T_t's observed for all PDAs, it is clear that the length of the side chains matters. We were intrigued by the disordering process of these side chains as a function of temperature. As mentioned above, the interaction of the head groups provides structural constraints for the alkyl chains limiting their ability to seek an equilibrium conformation. Conversely, the alkyl chains may

dx.doi.org/10.1021/ma201519v | Macromolecules 2012, 45, 420–429

limit the mobility of the head groups to seek the strongest possible interaction, especially for the formation of hydrogen bonds. It has already been demonstrated above that the lack of reversibility of the thermochromic transition is directly related to the lack of recovery of C═O stretching frequency. It has also been shown that length of the alkyl chains is an important parameter (Figure 2). Based on these observations, two questions were raised: (1) Although these PDAs were polymerized from highly ordered molecular crystals, do the polymers obtained represent the global minimum of the crystalline form? (2) Although head groups are important, can the irreversibility of thermochromic transition be correlated to the disordering process of the alkyl chains?

Infrared signatures associated with conformational order of polymethylene chains are well established.[43] Because of the coupling along the chain, a set of progression bands usually can be found. The frequency of these bands is indicative of the chain length. The relative intensity of the bands observed is characteristic of the chain conformation order. We have focused on the progression bands in the ~1100−1400 cm^{-1} region assignable to the CH_2 wagging vibration.[44,45] The infrared data obtained for various PDAs are shown in Figure 8. Even with the

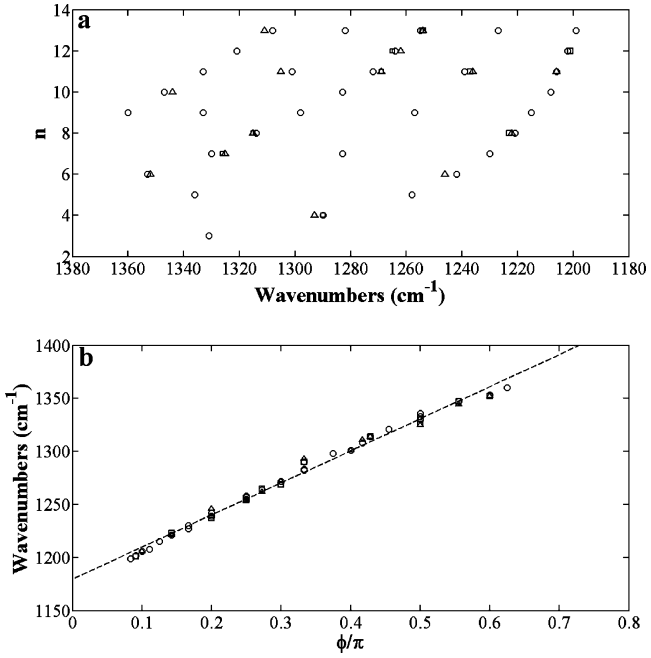

Figure 8. (a) Polymethylene wagging modes and (b) wavenumbers phase curve for *n*-paraffins (circle), blue phase PCDA (square), and red phase PCDA (triangle). n = 3−13. The dashed line is a fitted straight line through all the data.

different side groups and significant variation in chain length, the weak but well-defined peaks found in the CH_2 wagging region agree well with the ones found for *n*-alkanes. This is shown in Table 2 (data obtained from Figure 10). In addition, the CH_2 rocking vibration is also of great interest. In the unit cells with more than one chain, crystal field splitting can be found.[46]

All the observed methylene wagging bands shown in Table 2 are displayed in Figure 8a. Based on the coupled oscillator model,[43] ϕ, the phase difference between the wagging motion of adjacent CH_2 group, is given by

Table 2. Comparison of CH_2 Wagging Peaks Position (in cm^{-1}) of Alkyl Side Chains in PCDA and PCDA-Na with *n*-Alkane with Same Length[a]

reference	PCDA(B)	PCDA(R)	PCDA-Na
1199 **(w)**			1192 (vw)
1202 **(w)**	1201 (w)		
1206 **(w)**		1206 (w)	
1208 (w)			
1215 (m)			
1221 (m)	1223 (w)	1222 (m)	
1227 **(w)**			1225 (vw)
1230 (m)			
1239 **(vw)**	1237 (w)	1236 (m)	
1242 (m)		1246 (w)	
1255 **(m)**	1254 (w)	1254 (w)	1253 (vw)
1257 (w)			
1258 (m)			
1264 **(w)**	1265 (vw)	1262 (w)	
1272 **(w)**	1269 (vw)	1269 (m)	
1282 **(w)**			
1283 (w)			1283 (vw)
1293 (m)	1290 (w)	1293 (m)	
1298 (m)			
1301 **(vw)**		1305 (w)	
1308 **(m)**		1311 (w)	1306 (vw)
1314 (m)	1315 (vw)	1315 (m)	
1321 **(w)**			
1330 (w)	1326 (vw)	1325 (m)	
1331 (w)			
1333 **(vw)**			
1336 (w)			
1347 (w)	1344 (vw)	1344 (w)	
1350 **(w)**			1350 (vw)
1353 (w)	1352 (vw)	1352 (w)	
1360 (w)	1365 (w)	1365 (w)	1385 (vw)

[a]"Reference" is the *n*-alkane with same length as that in alkyl side chain of PCDA; "(B)" and "(R)" mean blue and red phase of PCDA. The bold and italic numbers correspond to the CH_2 wagging bands that can only be found in *n*-alkane with carbon number n = 11, 12, 13. The relative intensities of the CH_2 wagging modes are designated as strong, s; medium, m; or weak, w.

$$\phi_k = \frac{k\pi}{m+1} \quad (k = 1, 2, 3, ..., m) \tag{1}$$

where $m = n - 2$ is the number of CH_2 groups. For odd-numbered *n*-paraffins, the k can be odd and even, while for even-numbered *n*-paraffins, only k-odd wagging bands are infrared-active.[43] The wagging bands wavenumbers are known to be dependent only on ϕ_k. The phase dependence of the wagging modes of hydrocarbon chains in *n*-paraffin, blue phase PCDA, and red phase PCDA is shown in Figure 8b. In Figure 8, the circle, square, and triangle are associated with the *n*-paraffin, blue phase PCDA, and red phase PCDA, respectively. Figure 8b shows that all the points fall very close to a fitted straight line as expected.[43]

It can be seen that the conformational order (Figure 9) of all PDAs, e.g. PCDA, HCDA, or DCDDA, with acid head groups is high. All these samples exhibit irreversible thermochromic transitions. There are well-defined features assignable to CH_2 wagging progression. These features are sensitive to temperature disappearing above T_t. In contrast, the total absence of order is seen in the Na derivative, independent of sample

dx.doi.org/10.1021/ma201519v | Macromolecules 2012, 45, 420−429

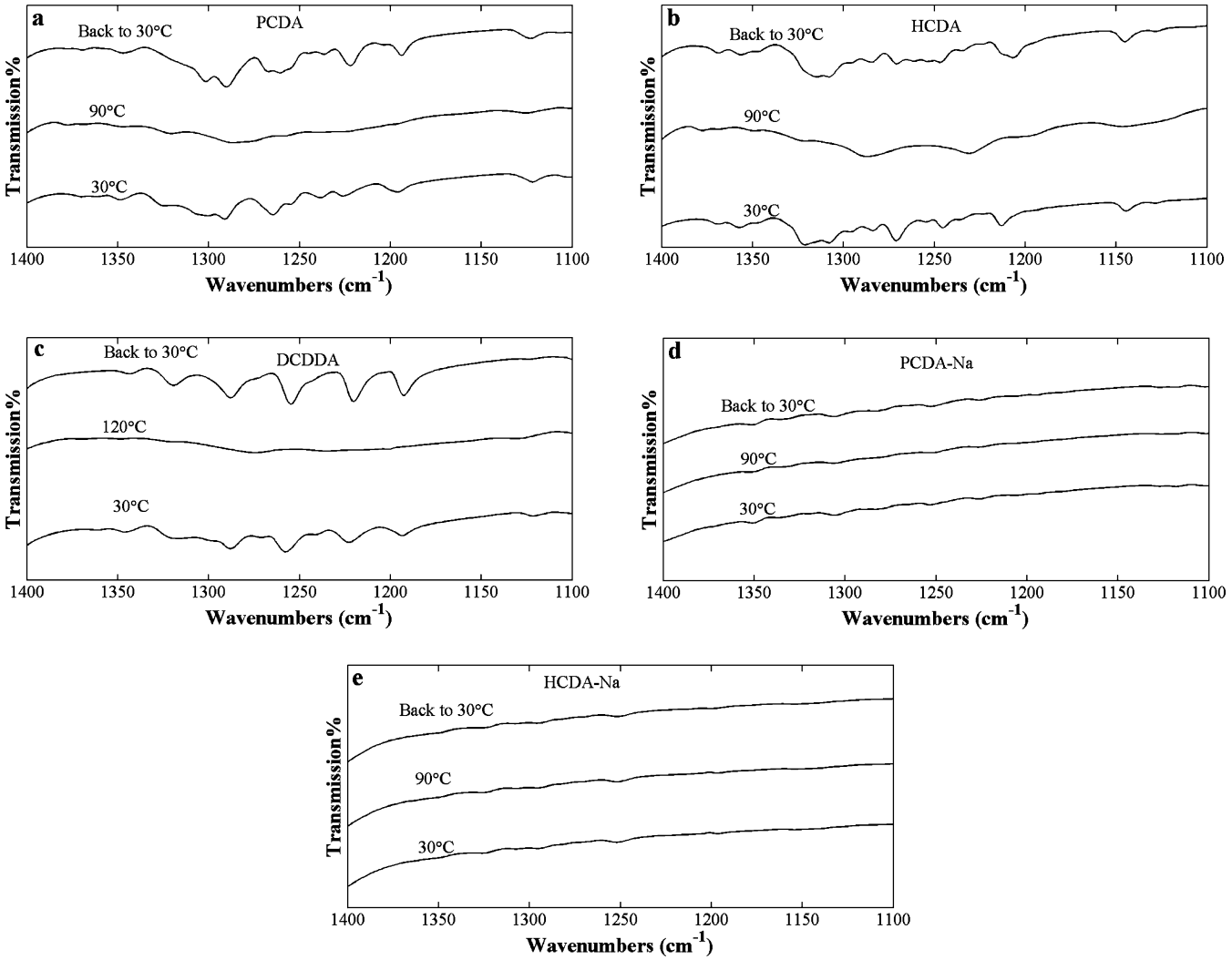

Figure 9. Temperature-dependent FTIR spectra of (a) PCDA, (b) HCDA, (c) DCDDA, (d) PCDA-Na, and (e) HCDA-Na; (f) comparison of HCDA and HCDA-Na in the CH_2 wagging vibration region.

temperature. These observations would suggest that conformational order in hydrogen-bonded PDAs is strongly correlated to the thermochromic transition and to the hydrogen bond formation. The most surprising fact is that the corresponding alkyl chains in the Na derivatives are disordered at any temperature. Perhaps the large size of the interacting metallic ions prevents the alkyl chains to pack as well as in other PDA samples. Obviously, the thermochromic transition necessarily be associated with the conjugation of the backbone.

It is then interesting to examine the other point; i.e., do the alkyl chains exist in the global minimum in the as polymerized PDAs? Each of these samples was annealed by cycling them to above the T_t and then lowering back to ambient temperature. In addition, we examined each of the samples before and after annealing at liquid nitrogen temperature. At the low temperatures, vibrations sharpen, making them easier to be observed. These data are shown in Figure 10. There is no question that conformational order is far from perfect in the samples exhibiting irreversible thermochromic transitions. But after cycling up through the transition temperature, the conformation of the alkyl chains achieved a more ordered state as shown in the CH_2 wagging region. The relative intensity is labeled in Table 2 after each wagging band, indicating the perfection of side-chain packing. In contrast, evidence of conformation order is difficult to find in the Na derivative. There is no measurable change for this sample as a function of time and thermal history. The molecular environment of the hydrogen-bonded acid groups also exhibit irreversible changes after annealing as shown in Figure 10c. The peaks seen in the as polymerized PDA sample (1815, 1773, 1720, and 1699 cm^{-1}) shift to new positions (1810, 1772, 1724, and 1700 cm^{-1}) after the first temperature cycle and remain unchanged afterward. Small C═O coupling peaks can be seen in PCDA-Na as shown in Figure 10d, and they are unchanged before and after color transition, which indicates that the molecular environment returned completely when color recovered.

The wide-angle X-ray diffraction pattern of PCDA in Figure 11 shows the spacing between the (00*l*) plane, which is proportional to the distance perpendicular between two conjugated backbones, decreases after color transition because of the structural change in the alkyl side chain. As reported previously, that is not the case for the PCDA-Na sample.[23] These diffraction results are consistent with the interpretation of the infrared spectra, illustrating the correlation between alkyl chain conformation and corresponding color transitions.

dx.doi.org/10.1021/ma201519v | *Macromolecules* 2012, 45, 420−429

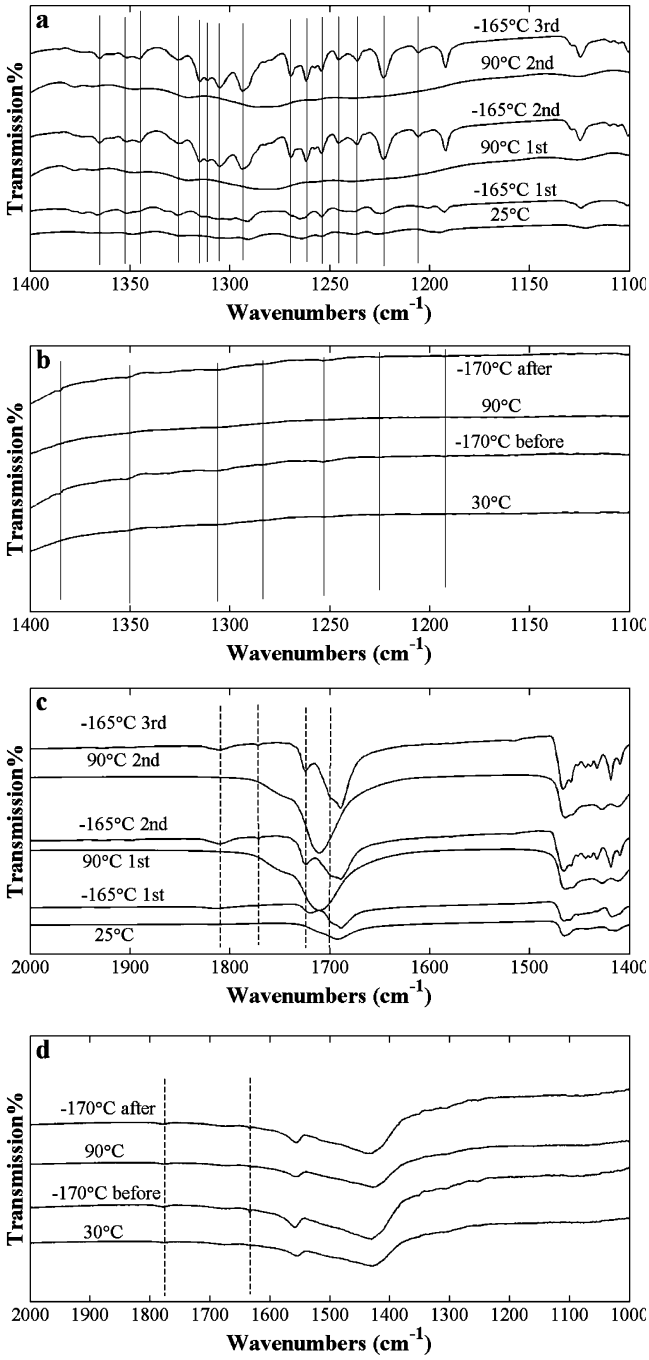

Figure 10. FTIR spectra of the CH_2 wagging peaks in (a) PCDA during the thermal treatment 25 °C → −165 °C → 90 °C → −165 °C → 90 °C → −165 °C, (b) PCDA-Na during thermal treatment 30 °C → −170 °C → 90 °C → −170 °C, (c) C═O coupling vibration of PCDA during the same thermal treatment as in (a), and (d) C═O coupling vibration of PCDA-Na during the same thermal treatment as in (b).

Based on the results reported above, the possible mechanisms for the thermochromic transition in PCDA and PCDA-Na are shown schematically in Figure 12. For PCDA with irreversible color transition, at room temperature, most of the alkyl side chains are in ordered crystalline structure and "locked" by specific intermolecular interactions. When temperature increases to T_t, the alkyl side chain becomes disordered and perturbs the conjugated backbone; thus, the color changes. The disordering process and the possible rotation of the side

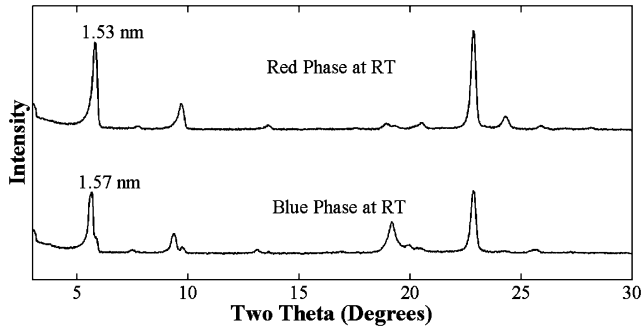

Figure 11. XRD pattern of PCDA blue phase and red phase at room temperature.

chain can break the hydrogen bond, which is largely dependent on the relative position of C═O and O−H bonds. When temperature lowers back, the alkyl side chains adopt a more stable ordered structure. However, most of the C═O may form hydrogen bonds with O−H differently as before so the blue color cannot recover. In PCDA-Na, the alkyl side chains are disordered at any temperature. The nonspecific electrostatic bonds between headgroups are sufficiently stable, allowing the alkyl side chains to recover to its original position thus a reversible thermochromic transition.

■ CONCLUSIONS

Several characterization techniques in conjunction were used to elucidate the structural elements and their changes associated with the thermochromic transition (blue−red) in various polydiacetylenes and their derivatives. The thermochromic transition can be observed easily in terms of the sample color change (blue−red), DSC, Raman features associated with the conjugated backbone, or infrared spectroscopy. The intermolecular interactions of the headgroups were clearly important in determining the transition temperature and the reversibility of the transition. Although hydrogen bonds have been shown to be successful in controlling the reversible transition of soluble PDAs,[1] that is not the case in the condensed state. In this study, all side chains involving strong hydrogen bonds exhibit irreversible thermochromic transitions. The introduction of metallic ions and associated electrostatic interactions is the easier route to control the transition. The thermal data from DSC have shown that the heat of melting of the Na derivative is only one-tenth of the hydrogen-bonded derivative. But the reversibility can be achieved because the electrostatic interaction is long-range and nonspecific and can easily accommodate the structural changes as a function of temperature. In contrast, the irreversibility of the hydrogen bonds formation in the condensed state impedes the reversibility of the thermochromic transition. Not only is the role of the headgroup important, infrared technique also provided compelling evidence that the conformation order of the alkyl side chains is directly associated with the main chain conjugation. The length of the alkyl side chain definitely affects the transition temperature. Increasing the side chain length and alteration of the symmetry of the two sides of the main chain can also change the T_t. There is little evidence showing the alkyl side chains are ordered in the Na derivatives. The forgiving disordered side chains together with the nonspecific long-range electrostatic of the metallic ions always yielded reversible thermochromic transitions. Lastly, although PDAs are directly polymerized from molecular crystals, we

dx.doi.org/10.1021/ma201519v | Macromolecules 2012, 45, 420−429

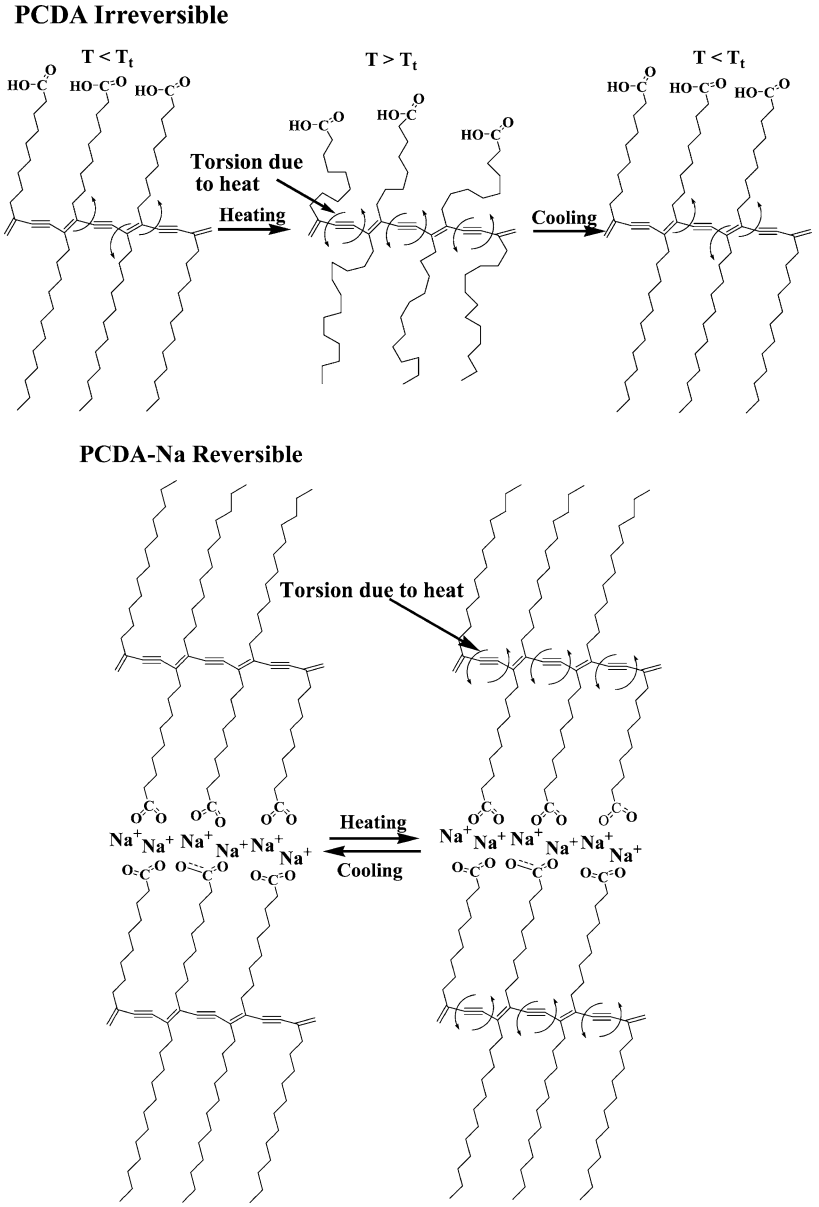

Figure 12. Schematic illustrations of the mechanisms of color transitions of (a) PCDA and (b) PCDA-Na.

found that side chains are not in the equilibrium state and can further evolve into a more ordered state after annealing, further complicating the thermochromic transition.

AUTHOR INFORMATION

Corresponding Author

*Tel (413-577-1411); e-mail slhsu@polysci.umass.edu.

ACKNOWLEDGMENTS

We are grateful for a grant from Saint Gobain Habitat group to support this study. In addition, the facility support from the NSF Materials Research Science and Engineering Center at the University of Massachusetts is greatly appreciated.

REFERENCES

(1) Chang, C.; Hsu, S. L. *Makromol. Chem. Macromol Chem. Phys.* **1985**, *186*, 2557−2567.
(2) Okada, S.; Peng, S.; Spevak, W.; Charych, D. *Acc. Chem. Res.* **1998**, *31*, 229−239.
(3) Chance, R. R.; Baughman, R. H.; Muller, H.; Eckhardt, C. J. *J. Chem. Phys.* **1977**, *67*, 3616−3618.
(4) Pires, A. C. S.; Soares, N. D. F.; da Silva, L. H. M.; da Silva, M. C. H.; Mageste, A. B.; Soares, R. F.; Teixeira, A. V. N. C.; Andrade, N. J. *J. Phys. Chem. B* **2010**, *114*, 13365−13371.
(5) Chance, R. R. *Macromolecules* **1980**, *13*, 396−398.
(6) Yoon, J.; Chae, S. K.; Kim, J. M. *J. Am. Chem. Soc.* **2007**, *129*, 3038−3039.
(7) Lee, S.; Kim, J. M. *Macromolecules* **2007**, *40*, 9201−9204.
(8) Charych, D. H.; Nagy, J. O.; Spevak, W.; Bednarski, M. D. *Science* **1993**, *261*, 585−588.
(9) Pan, J. J.; Charych, D. *Langmuir* **1997**, *13*, 1365−1367.
(10) Nallicheri, R. A.; Rubner, M. F. *Macromolecules* **1991**, *24*, 517−525.
(11) Carpick, R. W.; Sasaki, D. Y.; Burns, A. R. *Langmuir* **2000**, *16*, 1270−1278.
(12) Sun, X. M.; Chen, T.; Huang, S. Q.; Li, L.; Peng, H. S. *Chem. Soc. Rev.* **2010**, *39*, 4244−4257.
(13) Beckham, H. W.; Rubner, M. F. *Macromolecules* **1993**, *26*, 5192−5197.
(14) Enkelmann, V. *Adv. Polym. Sci.* **1984**, *63*, 91−136.

(15) Saito, A.; Urai, Y.; Itoh, K. *Langmuir* **1996**, *12*, 3938−3944.
(16) Schott, M. *J. Phys. Chem. B* **2006**, *110*, 15864−15868.
(17) Yoon, B.; Lee, S.; Kim, J. M. *Chem. Soc. Rev.* **2009**, *38*, 1958−1968.
(18) Filhol, J. S.; Deschamps, J.; Dutremez, S. G.; Boury, B.; Barisien, T.; Legrand, L.; Schott, M. *J. Am. Chem. Soc.* **2009**, *131*, 6976−6988.
(19) Kim, J. M.; Lee, J. S.; Choi, H.; Sohn, D.; Ahn, D. J. *Macromolecules* **2005**, *38*, 9366−9376.
(20) Ma, Z. F.; Li, J. R.; Jiang, L.; Cao, J.; Boullanger, P. *Langmuir* **2000**, *16*, 7801−7804.
(21) Phollookin, C.; Wacharasindhu, S.; Ajavakom, A.; Tumcharern, G.; Ampornpun, S.; Eaidkong, T.; Sukwattanasinitt, M. *Macromolecules* **2010**, *43*, 7540−7548.
(22) Wacharasindhu, S.; Montha, S.; Boonyiseng, J.; Potisatityuenyong, A.; Phollookin, C.; Tumcharern, G.; Sukwattanasinitt, M. *Macromolecules* **2010**, *43*, 716−724.
(23) Pang, J. B.; Yang, L.; McCaughey, B. F.; Peng, H. S.; Ashbaugh, H. S.; Brinker, C. J.; Lu, Y. F. *J. Phys. Chem. B* **2006**, *110*, 7221−7225.
(24) Balakrishnan, S.; Lee, S.; Kim, J. M. *J. Mater. Chem* **2010**, *20*, 2302−2304.
(25) Huang, X.; Jiang, S. G.; Liu, M. H. *J. Phys. Chem. B* **2005**, *109*, 114−119.
(26) Peng, H. S.; Tang, J.; Pang, J. B.; Chen, D. Y.; Yang, L.; Ashbaugh, H. S.; Brinker, C. J.; Yang, Z. Z.; Lu, Y. F. *J. Am. Chem. Soc.* **2005**, *127*, 12782−12783.
(27) Peng, H. S.; Tang, J.; Yang, L.; Pang, J. B.; Ashbaugh, H. S.; Brinker, C. J.; Yang, Z. Z.; Lu, Y. F. *J. Am. Chem. Soc.* **2006**, *128*, 5304−5305.
(28) Beckham, H. W.; Rubner, M. F. *Macromolecules* **1993**, *26*, 5198−5201.
(29) Lee, D. C.; Sahoo, S. K.; Cholli, A. L.; Sandman, D. J. *Macromolecules* **2002**, *35*, 4347−4355.
(30) Ahn, D. J.; Lee, S.; Kim, J. M. *Adv. Funct. Mater.* **2009**, *19*, 1483−1496.
(31) Tieke, B.; Bloor, D.; Young, R. J. *J. Mater. Sci.* **1982**, *17*, 1156−1166.
(32) Gentle, I. R.; Peng, J. B.; Barnes, G. T. *Adv. Colloid Interface Sci.* **2001**, *91*, 163−219.
(33) Jeffrey, G. A.; Saenger, W. *Hydrogen Bonding in Biological Structures*; Springer-Verlag: Berlin, 1991.
(34) Jeffrey, G. A. *An Introduction to Hydrogen Bonding*; Oxford University Press: New York, 1997.
(35) Steiner, T. *Angew. Chem., Int. Ed.* **2002**, *41*, 48−76.
(36) Colthup, N. B.; Daly, L. H.; Wiberly, S. E. *Introduction to Infrared and Raman Spectroscopy*, 3rd ed.; Academic Press, Inc.: Boston, 1990.
(37) Exarhos, G. J.; Risen, W. M.; Baughman, R. H. *J. Am. Chem. Soc.* **1976**, *98*, 481−487.
(38) Baughman, R. H.; Witt, J. D.; Yee, K. C. *J. Chem. Phys.* **1974**, *60*, 4755−4759.
(39) Koshihara, S.; Tokura, Y.; Takeda, K.; Koda, T.; Kobayashi, A. *J. Chem. Phys.* **1990**, *92*, 7581−7588.
(40) Batchelder, D. N.; Evans, S. D.; Freeman, T. L.; Haussling, L.; Ringsdorf, H.; Wolf, H. *J. Am. Chem. Soc.* **1994**, *116*, 1050−1053.
(41) Ahn, D. J.; Chae, E. H.; Lee, G. S.; Shim, H. Y.; Chang, T. E.; Ahn, K. D.; Kim, J. M. *J. Am. Chem. Soc.* **2003**, *125*, 8976−8977.
(42) Kollman, P. A. *J. Am. Chem. Soc.* **1972**, *94*, 1837−&.
(43) Snyder, R. G.; Schachtschneider, J. H. *Spectrochim. Acta* **1963**, *19*, 85−116.
(44) Zbinden, R. *Infrared Spectroscopy of High Polymers*; Academic Press: New York, 1964; p 264.
(45) Snyder, R. G. *J. Mol. Spectrosc.* **1960**, *4*, 411−434.
(46) Stein, R. S. *J. Chem. Phys.* **1955**, *23*, 734−736.

Macromolecules

Article

pubs.acs.org/Macromolecules

Structures of PEP–PEO Block Copolymer Micelles: Effects of Changing Solvent and PEO Length and Comparison to a Thermodynamic Model

Grethe Vestergaard Jensen,[†] Qing Shi,[†] G. Roshan Deen,[†,§] Kristoffer Almdal,[‡] and Jan Skov Pedersen*[,†]

[†]Department of Chemistry & Interdisciplinary Nanoscience Center (iNANO), Aarhus University, Langelandsgade 140, DK-8000 Aarhus C., Denmark

[‡]DTU Nanotech, Department of Micro- and Nanotechnology, Technical University of Denmark, Building 345Ø, DK-2800 Kongens Lyngby, Denmark

Supporting Information

ABSTRACT: Structures of poly(ethylene propylene)–poly(ethylene oxide) (PEP–PEO) block copolymer micelles were determined from small-angle X-ray scattering and static light scattering and compared to predictions from a thermodynamic model. Both the corona block length and the solvent water–ethanol ratio were changed, leading to a thorough test of this model. With increasing ethanol fraction, the PEP core–solvent interfacial tension decreases, and the solvent quality for PEO changes. The weight-average block masses were 5.0 kDa for PEP and 2.8–49 kDa for PEO. For the lowest PEO molar mass and samples in pure water (except for the highest PEO molar mass), the micelles were cylindrical; for other conditions they were spherical. The structural parameters can be reasonably well described by the thermodynamic model by Zhulina et al. [*Macromolecules* **2005**, *38* (12), 5330–5351]; however, they have a stronger dependence on solvent composition and PEO molar mass than predicted.

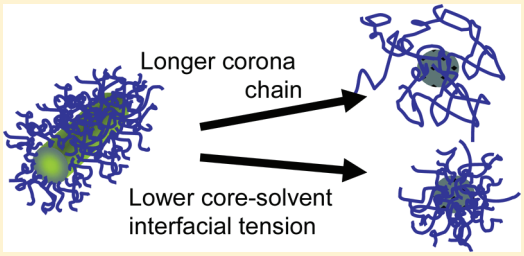

INTRODUCTION

Block copolymers and their micelles have many applications, as e.g. synthesis templates,[1,2] photonic crystals,[3,4] drug delivery systems,[5,6] emulsion stabilizers,[7] and epoxy tougheners.[8,9] The wide variety of block copolymer that can be synthesized allows for fine-tuning of these systems to meet the demands of specific applications.[10]

To understand and be able to predict micelle structures, numerous theoretical thermodynamic models have been suggested.[11−17] They include different contributions to the free energy of micelle formation, such as the surface energy of the micelle core, the interaction energy of chains in the corona, both with other chains and with the solvent, conformational entropy of the core and corona chains (related to chain stretching or compression), and mixing entropy of the micelles with the solvent. The final micelle structures are a result of the fine balance between all these contributions and are thus highly sensitive to small changes in conditions. The model by Zhulina et al.[17] has proven to be able to describe structural transitions in different systems upon variation of block length of the solvophilic block,[17] temperature,[18] and solvent selectivity for block copolymers with comparable lengths of the two blocks.[19,20]

In the present work, micelles of the block copolymer poly(ethylene propylene)–poly(ethylene oxide) (PEP–PEO) in different water–ethanol mixtures are studied. Several studies in the literature show how micelles of this polymer change their structure upon variation of solvent or block lengths.[21−23] In the present work the fraction of ethanol in the solvent, ϕ_{eth}, is changed, which leads to variation of both the interactions with the core (via the PEP–solvent interfacial tension) and with the corona chains (via the solvent quality for PEO, quantified by the second virial coefficient). These changes lead to a change in the preferred curvature of the micelle core and thus to a change of micellar size or shape. All the block copolymers have a PEP chain of 5.0 kDa weight-average molar mass, whereas the PEO weight-average molar mass, M_{PEO}, is varied from 2.8 to 49 kDa. The smaller M_{PEO} allow for a lower micelle core curvature. However, the core size is limited by the PEP stretching. Thus, for small PEO chains and high PEP–solvent interfacial tensions, a shape transition from spherical to cylindrical micelles might occur in order to reach the most favorable core surface curvature without stretching the PEP chain excessively.

The micelle structures were determined by simultaneous fits of an advanced structural model to small-angle X-ray scattering (SAXS) and static light scattering (SLS) data, taking the different scattering contrasts for the two techniques into account as previously described.[24] The results for the experimentally determined micelle core and corona sizes are compared to the predictions by the model of Zhulina et al.[17] Both the solvent and the length of the lyophilic block are varied, leading to an

Received: July 16, 2011
Revised: November 23, 2011
Published: December 12, 2011

extensive test of the thermodynamic model. The fact that more than one system parameter is varied is especially important, as the thermodynamic model contains two numerical prefactors which are system dependent, as they are related to the interactions between polymer chains in the corona. These prefactors are determined from the optimal fit of the model predictions to the experimentally determined core and corona sizes. Thus, if the model was only compared to micelle structures upon variation of one system parameter, a set of prefactors might be found that could give a good fit without necessarily being able to predict the structures at other system conditions. The variation of more system parameters thus adds further constraints to the values of the prefactors. By checking whether a consistent set of prefactors can give a good agreement of the model with all the observed micellar sizes, the thermodynamic model can be validated on a solid ground.

MATERIALS AND METHODS

The polymers were synthesized by anionic living polymerization.[25,26] Polyisoprene polymerized in apolar solvent was terminated by ethylene oxide. The hydroxyl-terminated polyisoprene was saturated over $Pd/CaCO_3$ catalyst to obtain hydroxyl-terminated PEP (PEP-OH). Ethylene oxide was polymerized in tetrahydrofurane (THF) after reinitiation of the PEP-OH by potassium naphthalide in THF. The same batch of PEP-OH was used for all the studied PEP−PEO samples, and thus the PEP block is exactly the same apart for minute differences in the content of PEP homopolymer. The PEP homopolymer content was estimated from the size exclusion chromatography (SEC) trace to less than 2%. The molar mass of the polymers were determined by SEC and matrix-assisted laser desorption/ionization time of flight mass spectrometry.[27] In the modeling we have used the weight-average molar values 5.0 kDa for the PEP block, whereas the weight-average molar mass of the PEO blocks used are 2.8, 4.9, 10, 20, and 49 kDa. The polydispersity indices of the block copolymers were determined to 1.07, 1.03, 1.11, 1.12, and 1.20, respectively. The block copolymers will be denoted $PEP_{5.0}$−PEO_x with subscripts indicating their block molar masses in kDa. Further synthesis and characterization details are discussed in the Supporting Information.

The solvents used are pure water, 30 wt % ethanol, 50 wt % ethanol, 70 wt % ethanol, and pure ethanol, where the percentages refers to the fraction of 96% ethanol as supplied by Aldrich.

All five polymers were dissolved in all five solvents; however, $PEP_{5.0}$−$PEO_{2.8}$ could not be dissolved in water. It was also difficult to dissolve in 30 wt % ethanol, and it required stirring, which also leads to slight heating, to obtain a homogeneous sample for SAXS and SLS. The solutions in pure water were heated to 90 °C for 2 h and then left to cool slowly to ambient temperature, in order to obtain a state which is closer to equilibrium since the PEP core is kinetically frozen in water at room temperature.[28,29]

SAXS data were collected on the prototype of the three-pinhole NanoStar Bruker AXS camera equipped with a rotating Cu anode giving Cu Kα X-rays with a wavelength λ of 1.54 Å, and a two-dimensional HiSTAR gas detector.[30] The polymer concentration was 1 wt %. The sample−detector distance was maximized to 108 cm, giving access to scattered intensities at scattering vector lengths, q, from 0.004 to 0.2 $Å^{-1}$ for a set of small pinholes. The scattering vector length is $q = 4\pi \sin\theta/\lambda$, where 2θ is the scattering angle. Samples were kept in thermostated (T = 23 °C) reusable home-built quartz capillary holders. The solvents were measured in the same capillaries, and the scattering was subtracted from the sample scattering. The data were converted to absolute scale using the scattering from a pure water sample as primary standard.

SAXS data were also collected for solutions of PEO homopolymers (weight-average molar mass of 2.15, 5.40, 10.5, 20.4, and 40.0 kDa and polydispersity indices of 1.04, 1.08, 1.05, 1.07, and 1.15, respectively, Polymer Source, Canada) in each solvent. The second virial coefficients, $A_{2,PEO}$, for the PEO chains was retrieved for each solvent, from fits of a Zimm−RPA polymer model[31,32] to these data:

$$I(q) = \frac{cM_{PEO}\Delta\rho_{PEO}{}^2}{N_{Avo}\rho_{PEO}{}^2}\frac{P_{chain}(q)}{1 + \nu_{RGT}P_{chain}(q)} \quad (1)$$

where c is the polymer concentration in mass per unit volume, M_{PEO} is the weight-average polymer molar mass, $\Delta\rho_{PEO}$ is the excess scattering length density of PEO (see details below), N_{Avo} is Avogadro's number, ρ_{PEO} is the PEO partial specific density, and $P_{chain}(q)$ is the polymer form factor of excluded volume chains, which was taken from refs 33 and 34. ν_{RGT} is an interaction parameter which was calculated by renormalization group theory[35] as a function of the product $M_{PEO}A_{2,PEO}c$. The resulting numerical expression for ν_{RGT} includes both second- and higher-order interactions between the chains. The determined values of $A_{2,PEO}$ turned out to depend on the PEO molar mass as $A_{2,PEO} = A_{2,PEO1}M_{PEO}{}^{-0.324}$. A power law is expected for this dependency; however, this exponent is rather high compared to the exponent of −0.2, which is predicted in the limit of high molar mass.[36] At lower molar mass, a deviation toward a larger slope in a log−log plot of A_2 vs M_{PEO} has been observed.[37] Thus, using a power law for parametrizing the A_2 dependence of M_{PEO} gives an exponent of −0.324 for the interval of M_{PEO} that also corresponds to the M_{PEO} masses of the block copolymers.

SLS was measured using a He/Ne diode laser of 25 mW of wavelength λ_0 = 632.8 nm (JDS Uniphase) and an ALV/CGS-8F goniometer (ALV GmbH, Germany) with an ALV-Static & Dynamic enhancer with fiber splitting for detection in pseudo-cross-correlation mode. The incident light was orthogonally polarized with respect to the horizontal scattering plane, and the light intensity was regulated with an ALV/8 steps attenuator. The scattered intensity was detected at angles from 15° to 160°, corresponding to values of q of 0.00035 to 0.0026 $Å^{-1}$, taking into account that the wavelength in the sample λ differs by the laser vacuum wavelength, λ_0, according to $\lambda = \lambda_0/n_s$, where n_s is the refractive index of the solution. The samples were kept at T = 23 °C using a circulating water thermostat. The 1% samples for SAXS were diluted by a factor of 100 for the SLS measurements in order to avoid multiple scattering. The micelle structure is not expected to change upon dilution, as the samples for SAXS were already dilute, and it is the interactions with the solvent of PEP and PEO that determine the micelle shapes in this dilute regime. For cylindrical micelles, however, the length is expected to depend on the concentration for samples at equilibrium at room temperature.[38] As the length is mainly determined from the SLS data, the values correspond to the concentrations of the diluted SLS samples. To reduce scattering from dust and impurities, the SLS samples were filtered multiple times. Thus, the final sample concentrations of the SLS samples are not precisely known. Scattering data from pure solvents were subtracted from the solution data. The resulting

dx.doi.org/10.1021/ma2016369 | Macromolecules 2012, 45, 430−440

Table 1. Input Parameters and Calculated Values for Scattering Contrasts[a]

ϕ_{eth}	$dn_s/dc_{PEP_5,PEO_{4.8}}$ (mL/g)	$dn_s/dc_{PEO_{4.6}}$ (mL/g)	$dn_s/dc_{PEP_{5\ app}}$ (mL/g)	$\Delta\rho_{PEP,SLS}$ (10^8 cm^{-2})	$\Delta\rho_{PEO,SLS}$ (10^8 cm^{-2})	$\rho_{PEO_{4.6}}$ (g/cm^3)	$\rho_{solvent}$ (g/cm^3)	$\Delta\rho_{PEP,SAXS}$ (10^{10} cm^{-2})	$\Delta\rho_{PEO,SAXS}$ (10^{10} cm^{-2})
0	0.161	0.135	0.187	3.34	3.38	1.198	0.9976	−1.139	1.640
0.3	0.122	0.124	0.121	2.15	3.12	1.204	0.9557	−1.185	1.650
0.5	0.138	0.111	0.145	2.59	2.73	1.172	0.9183	−0.4623	2.078
0.7	0.135	0.109	0.161	2.87	2.65	1.168	0.8760	−0.0875	2.416
1	0.130	0.125	0.134	2.38	3.00	1.149	0.8056	0.5467	2.871

[a] ϕ_{eth}: fraction of ethanol in mixed water/ethanol solvent. dn_s/dc_i: refractive index increments for species i. The value for PEP is an apparent value calculated from the values for PEP−PEO and PEO. $\Delta\rho_{i,SLS}$: scattering contrasts for SLS of species i, calculated from eq 4. ρ_i: apparent specific densities for species i. $\Delta\rho_{i,SAXS}$: scattering contrasts for SAXS of species i. A density of PEP of 0.853 g/cm^3 was applied for the contrast calculations.

intensities were converted to absolute scale using the scattering from toluene as a standard.

PEP−solvent interfacial tensions were measured for each of the solvents using a PEP homopolymer synthesized by living anionic polymerization of isoprene. The synthesis procedure was the same as for the PEP block of the block copolymer. However, the polyisoprene was terminated by methanol in order to obtain a hydrogen end group rather than a hydroxyl group. As for the block copolymer, the polyisoprene was saturated over Pd/$CaCO_3$ catalyst to obtain the final PEP product. The PEP molar mass was 7.4 kDa and its polydispersity index 1.01, as determined by size exclusion chromatography. The interfacial tensions were measured by the sitting drop technique, using a KLV CAM101 tensiometer and software for drop shape analysis applying the Young−Laplace equations for determining the interfacial tension on the basis of the drop shape and size as well as the densities of the solvent and of the PEP. The density of the sticky PEP oil was measured by weighing 5.00 mL of the substance, which gives a value of 0.853 g/cm^3.

Measurements of partial specific densities of $PEP_{5.0}$−$PEO_{4.9}$ and a PEO homopolymer (4.60 kDa, Aldrich) were performed to obtain the apparent partial specific densities of each of the blocks from which the X-ray scattering contrasts were calculated. The scattering contrasts for the light scattering were calculated on the basis of measurements of the refractive index increments for $PEP_{5.0}$−$PEO_{4.9}$ and for the 4.6 kDa PEO homopolymer in each of the solvents. The contrast calculations for both techniques are described in detail in ref 24. The measured values of the refractive index increments and densities of $PEP_{5.0}$−$PEO_{4.9}$ and $PEO_{4.6}$ in the different solvents are given in Table 1. From these the corresponding apparent values for $PEP_{5.0}$ can be calculated. These numbers are also given in Table 1 together with the SLS and SAXS contrasts, $\Delta\rho_{SLS}$ and $\Delta\rho_{SAXS}$, calculated as respectively

$$\Delta\rho_{SLS,i} = \frac{2\pi n_s}{\lambda_0^2}\frac{dn_s}{dc_i}\rho_i \tag{2}$$

and

$$\Delta\rho_{SAXS,i} = b_e(\rho_{e,i} - \rho_{e,solvent}) \tag{3}$$

where n_s is the solution refractive index, λ_0 is the laser wavelength in vacuum, dn_s/dc_i is the refractive index increment of species i, ρ_i is the mass density of species i, b_e is the scattering length of an electron, $b_e = 2.82 \times 10^{-13}$ cm, and $\rho_{e,i}$ is the number density of electrons of species i per unit volume. The refractive index increment of PEP cannot be measured directly, since PEP cannot be dissolved in the solvents. Instead, we used the relation[24]

$$\frac{dn_s}{dc_{polymer}} = \frac{1}{\rho_{polymer}}\left(x\frac{dn_s}{dc_{PEO}}\rho_{PEO} + (1-x)\frac{dn_s}{dc_{PEP}}\rho_{PEP}\right) \tag{4}$$

where c_i is the mass concentration of species i and $dn/dc_{polymer}$ and dn/dc_{PEO} are the refractive index increment of respectively the block polymer solutions and the solutions with the PEO homopolymer. The values in Table 1 are calculated under the assumption that the density of PEP is equal to the measured value of the bulk homopolymer, $\rho_{PEP} = 0.853$ g/cm^3.

Structural Models. A structural model[39−41] was fitted simultaneously to the SLS and SAXS data, taking into account the different scattering contrasts for the two techniques, as previously described.[24] For spherical micelles the form factor is

$$\begin{aligned} P_{sph-mic}(q) = {} & (pV_{PEP}\Delta\rho_{PEP}A_{sph}(qR_{core}, \sigma_{core}))^2 \\ & + p[p - P'_{chain}(0)] \\ & \times (V_{PEO}\Delta\rho_{PEO}A_{sph-shell}(q, R_{core}, R_{mic}))^2 \\ & + 2p^2V_{PEP}\Delta\rho_{PEP}A_{sph}(qR_{core}, \sigma_{core}) \\ & \times V_{PEO}\Delta\rho_{PEO}A_{sph-shell}(q, R_{core}, R_{mic}) \\ & + p(V_{PEO}\Delta\rho_{PEO})^2P'_{chain}(q) \end{aligned} \tag{5}$$

where p is the aggregation number, V_{PEP} and V_{PEO} are the volumes of the PEP and PEO block, respectively, and

$$\begin{aligned} A_{sph}(qR_{core}, \sigma_{core}) = {} & \frac{3[\sin(qR_{core}) - qR_{core}\cos(qR_{core})]}{(qR_{core})^3} \\ & \exp(-q^2{\sigma_{core}}^2) \end{aligned} \tag{6}$$

is form factor amplitude of the spherical core with radius R_{core} and a surface with a graded interface described by the width σ_{core}. Furthermore

$$\begin{aligned} & A_{sph-shell}(q, R_{core}, R_{mic}, \sigma_{core}, \sigma_{corona}) \\ & = [A_{sph}(qR_{mic}){R_{mic}}^3\exp(-q^2{\sigma_{core}}^2) \\ & \quad - A_{sph}(qR_{core}){R_{core}}^3\exp(-q^2{\sigma_{corona}}^2)] \\ & \quad /({R_{mic}}^3 - {R_{core}}^3) \end{aligned} \tag{7}$$

is the normalized form factor amplitude of the corona with an outer radius R_{mic} with a graded interface given by the width σ_{corona}. Finally

$$P'_{chain}(q) = \frac{P_{chain}(q)}{1 + \nu P_{chain}(q)} \tag{8}$$

dx.doi.org/10.1021/ma2016369 | Macromolecules 2012, 45, 430−440

is the effective single chain form factor of a chain in the corona. The parameter ν is a concentration parameter which is an increasing function of the reduced surface coverage Σ/Σ^* of the micelles:

$$\Sigma/\Sigma^* = \frac{pR_{g,PEO}{}^2}{4(R_{core} + R_{g,PEO})^2} \quad (9)$$

where $R_{g,PEO}$ is the radius of gyration of the PEO chains in the corona. Monte Carlo simulations[40] have shown that the interaction parameter is $\nu = 1.42(\Sigma/\Sigma^*)^{1.04}$ for corona polymer chains in a good solvent. The measurements on PEO polymers in the various solvents and the determination of their second virial coefficients allowed an adjustment of the constant in the expression for ν so that the interaction effects in the micelle model corresponds to the actual solvent quality of the corona chains.

For the long cylindrical micelles with length $L \gg R_{mic}$, where R_{mic} is the outer radius of the core−shell structure, the scattering form factor is

$$\begin{aligned} P_{cyl-mic}(q) = {} & P_{length}(qL)[(pV_{PEP}\Delta\rho_{PEP}A_{cs}(qR_{core}, \sigma_{core}))^2 \\ & + p[p - P'_{chain}(0)] \\ & \times (V_{PEO}\Delta\rho_{PEO}A_{cs-shell}(q, R_{core}, R_{mic}, \sigma_{core}, \sigma_{corona}))^2 \\ & + 2p^2V_{PEP}\Delta\rho_{PEP}A_{cs}(qR_{core}, \sigma_{core})V_{PEO}\Delta\rho_{PEO} \\ & \times A_{cs-shell}(q, R_{core}, R_{mic}, \sigma_{core}, \sigma_{corona})] \\ & + p(V_{PEO}\Delta\rho_{PEO})^2P'_{chain}(q) \end{aligned} \quad (10)$$

with the length form factor

$$P_{length}(qL) = 2\mathrm{Si}(qL)/(qL) - 4(\sin(qL/2)/(qL))^2 \quad (11)$$

where $\mathrm{Si}(x) = \int_0^x t^{-1} \sin t \, dt$.[42] The core form factor amplitude including a graded interface described by the width σ_{core} is

$$A_{cs}(qR_{core}, \sigma_{core}) = \frac{2J_1(qR_{core})}{qR_{core}}\exp(-q^2\sigma_{core}{}^2) \quad (12)$$

where $J_1(x)$ is a first-order Bessel function of first kind. The corona form factor amplitude is, for a structure where also the outer interface is graded:

$$\begin{aligned} & A_{cs-shell}(q, R_{core}, R_{mic}\sigma_{core}, \sigma_{corona}) \\ & = [A_{cs}(qR_{mic})R_{mic}{}^2\exp(-q^2\sigma_{core}{}^2) \\ & \quad - A_{cs}(qR_{core})R_{core}{}^2\exp(-q^2\sigma_{corona}{}^2)] \\ & \quad /(R_{mic}{}^2 - R_{core}{}^2) \end{aligned} \quad (13)$$

For cylindrical micelles the reduced surface coverage is

$$\Sigma/\Sigma^* = \frac{pR_{g,PEO}{}^2}{2(R_{core} + R_{g,PEO})L} \quad (14)$$

Size polydispersity of the micelles was included in the models by a Gaussian distribution of core radii. For the cylindrical micelles an exponential distribution was applied for the length.[38] This distribution was cut at a minimum value of $4R_{core}$ and at a maximum value of $3L$.

The intensity expression fitted to the scattering data was

$$I(q) = n\langle P(q)\rangle \quad (15)$$

where n is the micelle number density $n = c/(\langle p\rangle M)$, where c is the mass concentration, $\langle p\rangle$ is the number-average aggregation number, M is the molar mass of the block polymer, and $\langle P(q)\rangle$ is the average form factor for normalized size distributions. A hard-sphere structure factor[43] was included for the SAXS data for spherical micelles to account for concentration effects. The ratio between the hard-sphere radius and the outer micelle radius was added as a fit parameter. From the hard-sphere radius and the micelle concentration (calculated from the sample concentration and the micelle aggregation number) the volume fraction of the hard spheres, which is also required for the calculation of the structure factor, can be determined. As the SLS data were collected at much lower concentration where the concentration effects are expected to be negligibly small, no structure factor was included in the corresponding q range. For the cylindrical micelles there is no simple way of describing concentration effects. As the structural model agrees well with the SAXS data at low q, any concentration effects are expected to be small. Thus, no structure factor was included for the cylindrical micelles.

The model was fitted simultaneously to the SAXS and SLS data using standard least-squares methods.[44] For the SAXS data, the model was convoluted by the instrumental resolution function to take into account the instrumental smearing.[45] The parameters of the resolution function were determined from the width of the beam at the detector.[46]

The structural model describing either spherical or cylindrical core−shell particles was fitted to each of the data sets. The fits were performed on absolute scale, including all the calculated contrasts. The fit parameters of the models are described in the following. The radius of the PEP core, R_{core} (and length L for the cylindrical micelles), was fitted, and the core was assumed to be dense containing no solvent. Thus, the aggregation number of the micelle can be calculated as $p = V_{core}/V_{PEP}$, where V_{core} is the core volume ($V_{core} = 4\pi R_{core}{}^3/3$ for spheres and $V_{core} = \pi R_{core}{}^2L$ for cylinders) and V_{PEP} is the volume of a single PEP chain given by its molar mass and density as $V_{PEP} = M_{PEP}/(\rho_{PEP}N_{Avo})$, where M_{PEP} is the molar mass for PEP and ρ_{PEP} is its apparent specific density. It turned out to be necessary to fit the value of ρ_{PEP} when fitting the structural model to the data. The fitted values fall within ±0.05 g/cm^3 of the measured density of bulk PEP. This *apparent* change in core density might include solvation effects of the micelle cores as well as minor errors in the determined value of the molar mass of the copolymer blocks leading to discrepancies in the copolymer compositions. For the Gaussian size distribution of the radii, a relative width of 8% was applied.

The corona thickness is defined as $T_{corona} = R_{mic} - R_{core}$, and the corona volume is $V_{corona} = 4\pi(R_{mic}{}^3 - R_{core}{}^3)/3$ for spherical micelles and $V_{corona} = \pi L(R_{mic}{}^2 - R_{core}{}^2)$ for cylindrical micelles. From this, a swelling factor of the corona, given by $V_{corona}/(pV_{PEO})$ ($\geq$1), where V_{PEO} is the volume of a single PEO chain, can also be calculated.

Both the core−corona interface and the corona surface were graded in the model. For the core−corona interface, the width was fixed at σ_{core} = 5 Å, whereas the width of the corona, σ_{corona}, was in general much larger, showing that the corona is not homogeneous, but rather has a density that decreases with distance from the core. However, in the fits σ_{corona} is limited to be below $T_{corona}/3$ to avoid problems with conservation of volume in the model. Because of the grading of the corona surface, the corona spans a larger region than defined by T_{corona}, and to include this, the total corona thickness is set to $D_{corona} = T_{corona} + \sigma_{corona}$.

dx.doi.org/10.1021/ma2016369 | Macromolecules 2012, 45, 430−440

The micelle form factors (eqs 5 and 10) contain the scattering contribution from the chains within the corona (eq 8). The effective form factor depends on the PEO contour length, the PEO statistical Kuhn length (taken as 10 Å[47]), and the interaction paramter, ν, determined from fits of the Zimm/RPA chain model to SAXS data from solutions of PEO homopolymers of varying molar masses as described in Materials and Methods. As mentioned above, the scale factor for ν for the corona chains in the various solvents was obtained by comparison of the fits to simulation data of chains in a good solvent as was also done in ref 24. The free fit parameters are then R_{core}, T_{corona}, σ_{corona}, and ρ_{PEP}, for the cylinders a length, L, and for the spheres a scale factor giving the ratio between the hard-sphere radius and the micelle radius, R_{mic}. Furthermore, a scale factor for SLS and one for SAXS were fitted to account for errors in the sample concentrations. They will also account for minor errors in the intensity normalization (incoming intensity, sample transmission, and sample thickness). For SAXS a flat background was also added.

THEORETICAL BASIS

Thermodynamic Model. The thermodynamic model for micelles by Zhulina et al.[17] contains three contributions to the free energy of a block copolymer molecule in a micelle:

$$F_{mic} = F_{int} + F_{core} + F_{corona} \tag{16}$$

F_{int} is the energy of the core interface associated with each chain and is given as

$$F_{int} = \frac{\gamma s_0}{k_B T} \tag{17}$$

where γ is the core−solvent interfacial tension and s_0 is the core surface area per polymer molecule. For spheres we have $s_{0,sph} = 3V_{PEP}/R_{core}$ and for cylinders $s_{0,cyl} = 2V_{PEP}/R_{core}$ (assuming that the area of the cylinder ends is negligible). k_B is the Boltzmann constant, and T is the absolute temperature. Thus, the energy is given in units of k_BT.

F_{core} is the conformation entropy related to stretching of the chains in the core. It is expressed as

$$F_{core} = k_j \frac{R_{core}^2}{\langle r_{ee}^2 \rangle} \tag{18}$$

where $\langle r_{ee}^2 \rangle$ is the mean-square end-to-end distance of the core polymer. It is calculated as $\langle r_{ee}^2 \rangle = L_{PEP} l_{k,PEP}$, where L_{PEP} is the PEP contour length and $l_{k,PEP}$ it the PEP Kuhn length. The parameter k_j depends on the morphology of the micelles. For spheres one has $k_{sph} = \pi^2/16$ and for cylinders $k_{cyl} = 3\pi^2/80$.[48] The term F_{core} only describes the energy contribution for PEP stretching and is not valid if the PEP chains are compressed rather than stretched. For the present PEP−PEO micelles, we do not expect any significant energy contribution from PEP compression, as the root-mean-square end-to-end distance $\langle r_{ee}^2 \rangle^{1/2}$ for the PEP chains ($\langle r_{ee}^2 \rangle^{1/2} = (N_{PEP} l_{PEP} l_{k,PEP})^{1/2}$ = 72.8 Å) is only slightly larger than the smallest obtained values for R_{core} (for $PEP_{2.8}$−PEO_{49} in 70% ethanol and for $PEP_{2.8}$−PEO_{20} and $PEP_{2.8}$−PEO_{49} in ethanol, see Table 2), corresponding to only a slight compression for these samples. Thus, we do not expect any significant energy contribution from compression of the PEP chains for any of the samples.

F_{corona} is the energy of the corona chains and includes both conformational entropy of chain stretching and effective repulsive interaction between the chains. It is based on a blob model for the corona chains, taking the grafting density of the chains on the micelle core into account. Furthermore, the increased area per chain with increasing distance from the core is accounted for. This gives expressions for F_{corona} that depend on the micelle geometry.

Table 2. Micelle Core Radius, R_{core} (Å), Determined from SAXS and SLS

M_{PEO} (kDa)	$\phi_{eth} = 0$	$\phi_{eth} = 0.3$	$\phi_{eth} = 0.5$	$\phi_{eth} = 0.7$	$\phi_{eth} = 1$
2.8		115(10)	99(2)	94(6)	80(8)
4.9	168(17)	151(1)	136(2)	118(2)	101(4)
10	134(4)	134(3)	100(2)	110(18)	72(1)
20	129(4)	118(2)	100(3)	91(8)	68(1)
49	95(9)	96(4)	85(4)	56(10)	51(3)

For chains grafted to a planar surface under good solvent conditions with a surface area s per chain, the blob dimension normal to the surface will be $s^{1/2}$. As each blob has the energy k_BT, the energy density will be $\psi(s) = C_F k_B T/s^{3/2}$. C_F is a numerical constant of order unity. For a curved micelle core, the surface area s per corona chain will increase with distance x from the micelle center (for $x \geq R_{core}$):

$$s(x) = \frac{s_0 x}{R_{core}} \quad \text{for cylinders}$$
$$s(x) = \frac{s_0 x^2}{R_{core}^2} \quad \text{for spheres} \tag{19}$$

The total energy for the corona chain is obtained by integrating $\psi(s)$ over the entire corona volume, that is, from $x = R_{core}$ to $x = R_{core} + D_{corona}$:

$$F_{corona} = \int_{R_{core}}^{R_{core}+D_{corona}} \frac{\psi(s)}{k_B T} s(x)\, dx = C_F \int_{R_{core}}^{R_{core}+D_{corona}} s(x)^{-1/2}\, dx \tag{20}$$

Zhulina et al.[17] showed that the corona thickness D_{corona} could be written as

$$D_{corona} = R_{core}\left\{\left[1 + \frac{1}{\bar{\nu}} C_H N_{PEO} s_0^{(\bar{\nu}-1)/(2\bar{\nu})} l_{PEO}^{1/\bar{\nu}}/R_{core}\right]^{\bar{\nu}} - 1\right\} \tag{21}$$

for spheres and

$$D_{corona} = R_{core}\left\{\left[1 + \frac{1+\bar{\nu}}{2\bar{\nu}} C_H N_{PEO} s_0^{(\bar{\nu}-1)/(2\bar{\nu})} l_{PEO}^{1/\bar{\nu}}/R_{core}\right]^{2\bar{\nu}/(1+\bar{\nu})} - 1\right\} \tag{22}$$

for cylinders. $\bar{\nu}$ is the excluded volume scaling exponent taking the value 0.588 in good solvents, N_{PEO} is the number of monomers in the corona chain, and l_{PEO} is the length of an ethylene oxide monomer. C_H is another solvent-dependent numerical constant which is proportional to $A_{2,PEO}^{1/3}$ under good solvent conditions for the corona block ($A_{2,PEO}$ is the second virial coefficient of the corona polymer in the solvent). Under these conditions C_F is expected to take a constant value

dx.doi.org/10.1021/ma2016369 | Macromolecules 2012, 45, 430−440

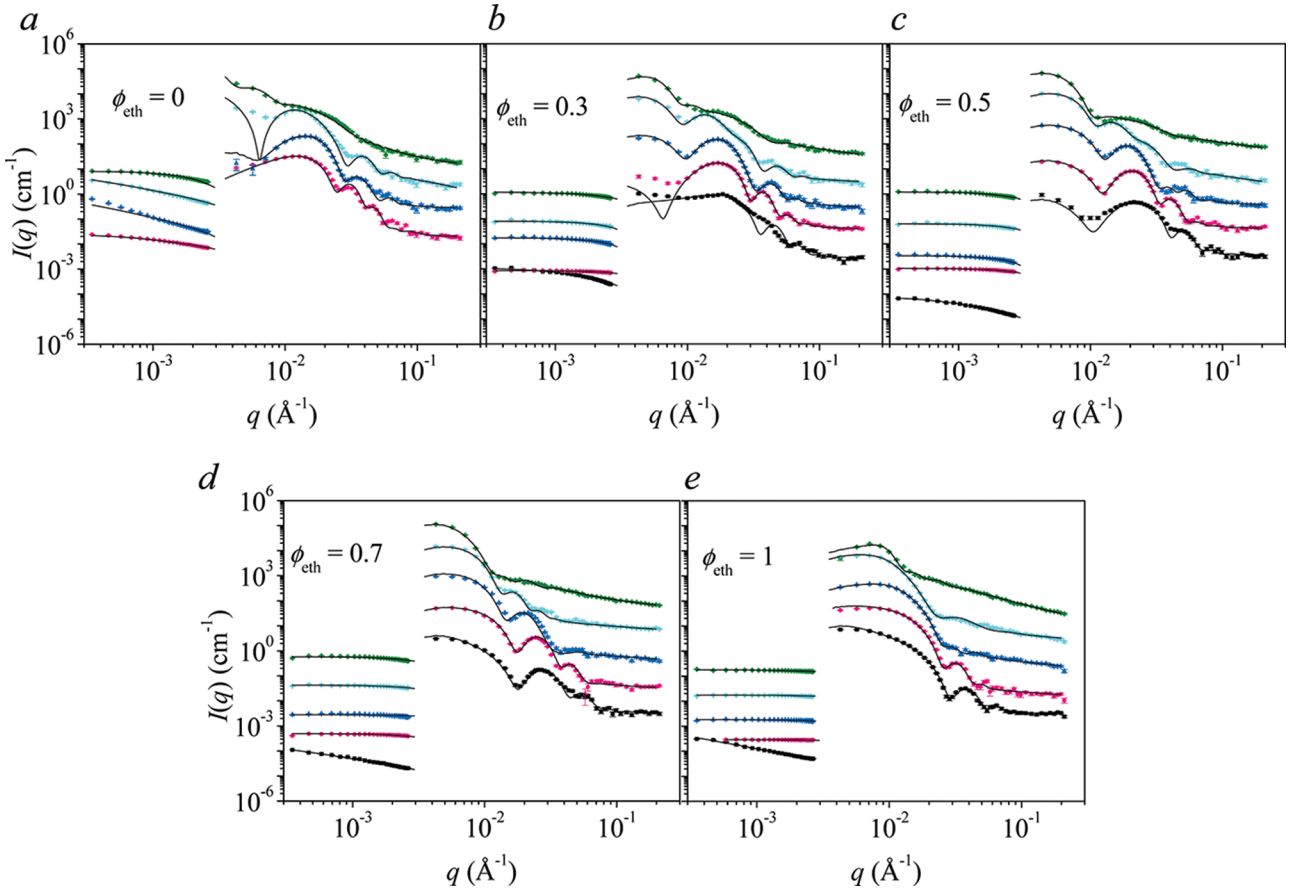

Figure 1. SLS (low q) and SAXS data (high q) for PEP−PEO solutions with M_{PEP} = 5.0 kDa and varying M_{PEO} in water−ethanol mixtures of different ethanol fractions, ϕ_{eth}. Each graph corresponds to one value of ϕ_{eth}: (a) ϕ_{eth} = 0, (b) ϕ_{eth} = 0.3, (c) ϕ_{eth} = 0.5, (d) ϕ_{eth} = 0.7,[24] and (e) ϕ_{eth} = 1. From the bottom in each graph: M_{PEO} (kDa) = 2.8 (squares), 4.9 (circles), 10 (upward triangles), 20 (downward triangles), and 49 kDa (diamonds). The data for samples of M_{PEO} = 2.8 kDa are shown on absolute scale. The remaining data sets are scaled by a factor of 10 for each consecutive data set. The lines are fits of the structural models performed simultaneously to the SLS and SAXS data. A model of cylindrical micelles was applied for all samples of M_{PEO} = 2.8 kDa and for samples in pure water (ϕ_{eth} = 0) for M_{PEO} = 4.9, 10, and 20 kDa.

for all solvents. The energy F_{corona} was shown to be given by

$$F_{corona} = \bar{\nu} C_F R_{core} s_0^{-1/2} \times \ln\left[1 + \frac{1}{\bar{\nu}} C_H N_{PEO} s_0^{(\bar{\nu}-1)/(2\bar{\nu})} l_{PEO}^{1/\bar{\nu}} / R_{core}\right] \quad (23)$$

for spheres and

$$F_{corona} = 2 C_F R_{core} s_0^{-1/2} \left\{\left[1 + \frac{1+\bar{\nu}}{2\bar{\nu}} C_H N_{PEO} s_0^{(\bar{\nu}-1)/(2\bar{\nu})} l_{PEO}^{1/\bar{\nu}} / R_{core}\right]^{\bar{\nu}/(1+\bar{\nu})} - 1\right\} \quad (24)$$

for cylinders.

RESULTS

Structural Results. SLS and SAXS data together with structural model fits are shown in Figure 1. The SLS data cover the smallest q values and thus contain information on large length scales. The SAXS data cover higher values of q than the SLS data, and thus mainly contain information on smaller length scales, in the present case on the structure of the micelle cross section. Thus, spheres and cylinders are not easily distinguished from the SAXS data. Furthermore, the opposite signs of the SAXS scattering contrast for PEP and PEO in several of the solvents (see Table 1) lead to suppression of the scattered intensity at low q, which further complicates the extraction of structural information at larger length scales from the SAXS data. For SLS, however, all contrasts are positive, and the data cover lower q values, leading to a clear distinction between spheres and cylinders. For rodlike particles, such as cylinders, the scattered intensity follows at low to intermediate q a power law $I \sim q^{-1}$, which is clearly observed for all samples with $PEP_{5.0}$−$PEO_{2.8}$ and for the samples in pure water, except for

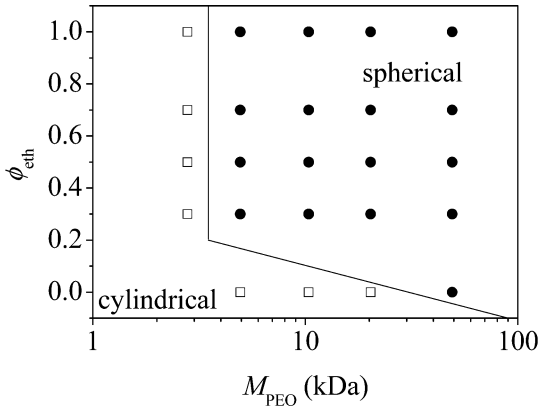

Figure 2. Indications of micelle shape (spherical or cylindrical) for different values of ethanol fraction in solvent, ϕ_{eth}, and PEO molar mass, M_{PEO}, for PEP−PEO solutions with M_{PEP} = 5.0 kDa. The shapes are determined by comparison of a structural model with SLS and SAXS data from the solutions.

dx.doi.org/10.1021/ma2016369 | Macromolecules 2012, 45, 430−440

Table 3. Micelle Corona Thickness, D_{corona} (Å), Determined from SAXS and SLS

M_{PEO} (kDa)	ϕ_{eth} = 0	ϕ_{eth} = 0.3	ϕ_{eth} = 0.5	ϕ_{eth} = 0.7	ϕ_{eth} = 1
2.8		75(3)	79(2)	73(10)	57(7)
4.9	105(2)	113(2)	113(3)	107(4)	97(4)
10	166(8)	280(5)	199(2)	218(28)	147(1)
20	265(195)	344(3)	371(3)	279(1)	224(1)
49	651(8)	630(7)	529(7)	418(10)	377(1)

Table 4. Input Parameters for Thermodynamic Model[a]

ϕ_{eth}	$\gamma_{PEP\text{-}solv}$ (mN/m)	$A_{2,PEO1}$ (mm^3 mol/g^2)	C_F
0	42.4	3.6(0.1)	0.55
0.3	16.3	5.1(0.3)	0.6
0.5	11.9	5.1(0.2)	0.65
0.7	11.7	4.3(0.2)	0.9
1	6.4	3.1(0.1)	1

[a] ϕ_{eth}: fraction of ethanol in mixed water/ethanol solvent. $\gamma_{PEP\text{-}solv}$: PEP/solvent interfacial tension. $A_{2,PEO1}$: the second virial coefficient of PEO, $A_{2,PEO}$, for any molar mass M_{PEO} according to $A_{2,PEO} = A_{2,PEO1}(M_{PEO}/1\ kDa)^{-0.324}$. The exponent was determined experimentally (see Materials and Methods). C_F: numerical input parameter for the thermodynamic model.

$PEP_{5.0}$–PEO_{49}. Thus, for these samples the model for cylindrical micelles is applied, whereas the model for spherical micelles is applied for the remaining samples. An overview of the micelle shapes observed for different values of ϕ_{eth} and M_{PEO} is given in Figure 2. Zimm plots of the SLS data are given in the Supporting Information, more clearly showing the fit qualities and giving radii of gyration deducted from the SLS data.

The micelle structures change as the PEO molar mass, M_{PEO}, increases or as the fraction of ethanol in the solvent, ϕ_{eth}, is varied. Changing ϕ_{eth} has two effects: Most importantly, the core–solvent interfacial tension, $\gamma_{PEP\text{-}solv}$, decreases with increasing ϕ_{eth} (see Table 4). Second, the solvent quality for the PEO chains is changed, which can be quantified by the change in the second virial coefficient, $A_{2,PEO} = A_{2,PEO1}M_{PEO}^{-0.324}$. The values of $A_{2,PEO1}$ for each solvent are given in Table 4 and show that the solvent quality is best at around ϕ_{eth} = 0.5.

The values for R_{core} and $D_{corona} = T_{corona} + \sigma_{corona}$ resulting from the fits of the structural models are plotted in Figure 3. As expected, R_{core} decreases with increasing M_{PEO} due to the larger size of the chains in the corona and the corresponding increase of the chain–chain interactions, leading to a larger core curvature. It also decreases with increasing ϕ_{eth}, as the cost of increasing the total core surface area (the interfacial tension) becomes smaller. The smaller cores are favored by less stretching of the PEP chains in the core and lower degree of PEO interactions. The fitted values of the PEP density, ρ_{PEP}, fall within the interval 0.814–0.899 g/cm^3. The experimentally determined density of bulk PEP was 0.853 g/cm^3.

The lengths of the cylindrical micelles of the $PEP_{5.0}$–$PEO_{2.8}$ samples are L = 1200, 1945, and 5794 Å in solvents of ϕ_{eth} = 0.3, 0.5, and 0.7, respectively. For ϕ_{eth} = 1, the length was larger than what could be resolved by SLS, and it was fixed at L = 50 000 Å. For ϕ_{eth} = 0, the lengths are L = 1750, 50 000 (also fixed because it was too large), and 11 650 Å for M_{PEO} = 4.9, 10, and 20 kDa, respectively. As the information on the length is contained in the SLS data, the determined values correspond to the lengths for the dilute samples used for SLS measurements as previously mentioned.

The scale factor for the SAXS intensity was close to unity for all samples, which corresponds to well-determined values for the sample concentrations and contrasts. The scale factors for SLS were all smaller than unity. This is ascribed to the repeated filtration of these samples, leading to a decrease in the actual concentration by 10–55%, giving scale factors in the interval 0.45–0.9. The spherical micelles are relatively monodisperse, and the loss of sample and possible fractionation caused by the filtration is not expected to influence the samples. The cylinders are polydisperse in length, and any fractionation of the sample that might occur during filtration will influence the length of the micelles as obtained from the SLS data. As the cylinder length is much larger than the cross-sectional diameter, the decoupling of scattering contributions from the micelle cross section and length is valid, and a change of length will not influence the data in the SAXS region that mainly contain the contributions from the micelle cross section. Thus, even if the length distribution has changed by the filtration, it is valid

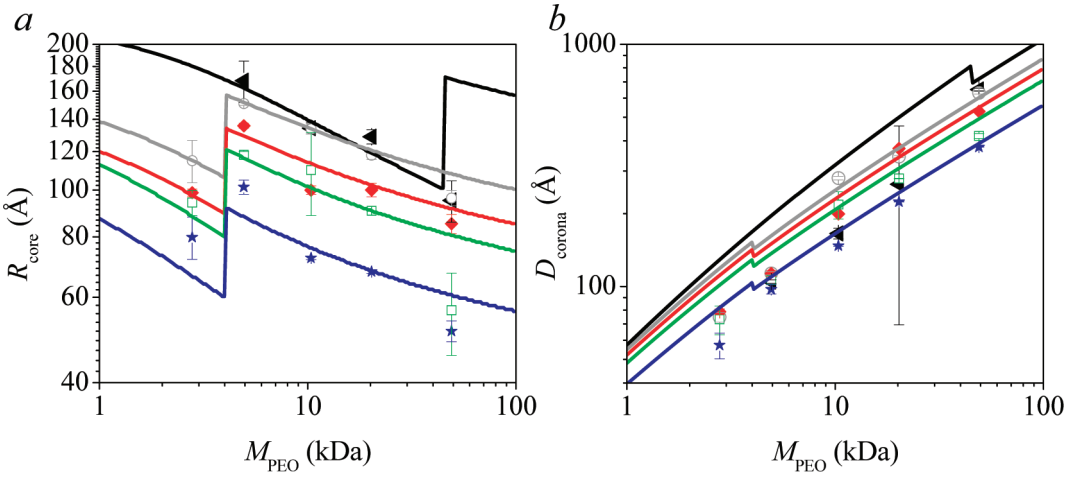

Figure 3. Structural parameters obtained by fitting a structural model (see text) to SLS and SAXS data (points). Core radius (*a*) and corona thickness (*b*) of the spherical or cylindrical micelles (shapes indicated in Figure 2) plotted against M_{PEO} for PEP–PEO solutions in water–ethanol mixtures of different fractions of ethanol, ϕ_{eth}. ϕ_{eth} = 0 (black left triangles), 0.3 (gray open circles), 0.5 (red diamonds), 0.7 (green open squares), and 1 (blue stars). The lines are predictions from the thermodynamic model for the same values of ϕ_{eth}. ϕ_{eth} increases when going from the top and downward in the plots.

dx.doi.org/10.1021/ma2016369 | *Macromolecules* 2012, 45, 430–440

to use the SLS data together with SAXS data collected from samples at a higher concentration.

The surface coverage of the micelle core by the PEO chains is in general very high for these micelles. This is clearly seen in the plot of the reduced surface coverage, Σ/Σ^*, in Figure 4.

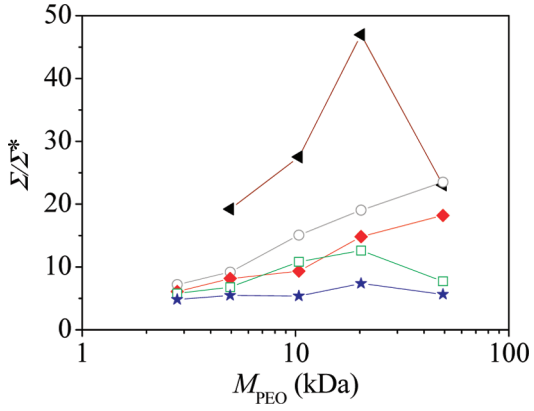

Figure 4. Reduced surface coverage for the micelles calculated from the core dimensions and the radius of gyration of the PEO chains (eqs 9 and 14) plotted against M_{PEO} for PEP−PEO solutions in water−ethanol mixtures of different fractions of ethanol, ϕ_{eth}. ϕ_{eth} = 0 (black left triangles), 0.3 (gray open circles), 0.5 (red diamonds), 0.7 (green open squares), and 1 (blue stars).

Σ/Σ^* decreases with increasing ethanol content in the solvent. It increases with molar mass of the PEO but for water, 70% ethanol, and ethanol decreases again at the highest PEO molar mass.

Comparison to Thermodynamic Model. The free energy expression of the model F_{mic} (eq 16) contains two unknown parameters, namely the numerical prefactors C_F and C_H. We have set C_F and C_H so that the best possible fits were obtained between the experimentally determined values of R_{core} and D_{corona} with the values minimizing F_{mic}. That is, for a given set of C_F and C_H, F_{mic} was minimized with respect to R_{core} and D_{corona} to find the optimal values of R_{core} and D_{corona}, which were then compared with the ones determined by the fits to the SAXS and SLS data. As the free energies of spherical and cylindrical micelles, as calculated by the model, are very close, we do not at this stage use the model for predicting the micelle morphology. Rather, we apply the experimentally observed morphology for each sample when performing the calculations and minimizations of F_{mic}, in agreement with the approach used by Lund et al.[19] This point is discussed further below. The energy minimization was thus done for spherical or cylindrical micelles for the relevant solvents and regions of M_{PEO}. Thus, the calculations were performed for cylindrical micelles for the samples in pure water, except for $PEP_{5.0}$−PEO_{49}, and for all $PEP_{5.0}$−$PEO_{2.8}$ samples. For the remaining samples, calculations were performed for spherical micelles.

In the expression for the model free energy, the molar masses, the interfacial tensions, $\gamma_{PEP\text{-}solv}$, and the second virial coefficient of PEO, $A_{2,PEO} = A_{2,PEO1}M_{PEO}^{-0.324}$, are experimentally determined (see Materials and Methods). Literature values are applied for the monomer length l of PEP and PEO, l_{PEO} = 5.8 Å[49] and l_{PEP} = 8.4 Å,[19,50] and for their Kuhn lengths, $l_{k,PEP}$ = 12 Å[51] and $l_{k,PEO}$ = 10 Å.[47]

According to the thermodynamic model, C_F should take a constant value for all good solvents. However, to obtain a satisfactory fit of the model to the experimentally determined structural parameters, it was necessary to have different values for C_F for each of the solvents. Lund et al. managed to describe the micelle dimensions for the polymer PEP_1−PEO_1 upon changing the solvent (the mixing ratio in a water−dimethylformamide mixture) with only one value of C_F.[19] In that study it was necessary to use different values of C_F and C_H for spherical and cylindrical micelles, respectively. Here we use the same value of C_F for spheres and cylinders (as also suggested in the original model by Zhulina et al.), but, as mentioned, different values of C_F for the different water−ethanol mixing ratios. If a constant value for C_F was applied, the predicted dependence of R_{core} on ϕ_{eth} was not as strong as the experimental values suggest.

C_H is expected to take different values as it is proportional to $A_{2,PEO}^{1/3}$. Hence, if $C_{H,wt,1}$ is the value of C_H for a PEO chain of molar mass 1 kDa in pure water, C_H can be given as $C_H = C_{H,wt,1}[A_{2,PEO1}M_{PEO}^{-0.324}/A_{2,PEO1}(\phi_{eth} = 0)]^{1/3}$ (where M_{PEO} is the molar mass in kDa inserted unit-less). Using this, it was only necessary to have one free parameter, $C_{H,wt,1}$, from which the value of C_H of all the solutions could be calculated. $C_{H,wt}$ and a set of C_F values (one for each solvent) were then given values to obtain the best possible simultaneous fit of the theoretically predicted values of R_{core} and D_{corona} to the experimentally determined values. The resulting value of $C_{H,wt}$ is 0.66. The values of C_F are given in Table 4, and one sees that the values are increasing with ethanol fraction.

The resulting theoretically expected equilibrium values of R_{core} and D_{corona} as a function of M_{PEO} are also plotted in Figure 3 (as lines). They agree reasonably well with the values determined by SAXS and SLS. However, the slopes of the decrease of R_{core} and increase of D_{corona} with M_{PEO} are underestimated. Especially, R_{core} is overestimated by the model for the highest value of M_{PEO}. Furthermore, D_{corona} is overestimated for the cylindrical micelles.

For the samples in pure water, the core−solvent interfacial tension is very high, resulting in that the micelles in these samples are not equilibrated as there is no exchange of molecules at room temperature. In an attempt to obtain structures closer to equilibrium, these samples were, as already mentioned, heated to 90 °C for 2 h followed by a slow cooling to room temperature. The interfacial tension between PEP and water is changing with temperature. For polyethylene the change with the temperature is −0.022 mN m^{-1} $°C^{-1}$.[52] Assuming that this value also applies for PEP, the interfacial tension at 90 °C can be calculated from the known value at 23 °C. This gives a value of 41 mN/m. Thus, even at 90 °C the PEP−water interfacial tension is very high, and the system cannot be expected to reach equilibrium within 2 h. It can therefore also not be expected that the determined structural parameters coincide with the predictions from the thermodynamic model. However, the accordance with the experimentally determined values for the core radius is reasonable, except for the highest PEO molar mass, as it is also the case for the ethanol containing solvents.

The corona thickness, D_{corona}, is overestimated for *all* the cylindrical micelles. Thus, the discrepancy in pure water might not (just) arise because of kinetically trapped states. It could also be that the experimental value for the corona thickness should not be defined as $T_{corona} + \sigma_{corona}$, but rather, that several σ_{corona} should be included to account for the total extension of the corona. This might especially be the case when the PEO density in the corona is high. As the core surface curvature is low for the cylindrical micelles, this applies in this case. Attempts were made to redefine the experimental D_{corona} as the radial distance from the core interface to the point where the PEO fraction in the corona reaches a certain absolute level.

dx.doi.org/10.1021/ma2016369 | *Macromolecules* 2012, 45, 430−440

However, this did not improve the fits as it gave a too weak dependence of D_{corona} on M_{PEO}. The thermodynamic model overestimates D_{corona} with approximately a factor of 2 for the cylindrical micelles in water. Thus, a redefinition of the experimental value of D_{corona} is not enough to explain the discrepancy.

Sphere-to-Cylinder Transition. Having determined the unknown parameters C_F and C_H, entering the free energy expressions, one can now also compare the energies of spherical and cylindrical micelles to see which morphology is predicted by the model. For each solvent and each value of M_{PEO}, the obtained values of the minimum energy, $F_{mic,min}$ for the spherical and cylindrical micelles are compared. The morphology giving the lowest value of $F_{mic,min}$ is then the micelle morphology predicted by the thermodynamic model. $F_{mic,min}$ is plotted against M_{PEO} for each of the different solvents in Figure 5.

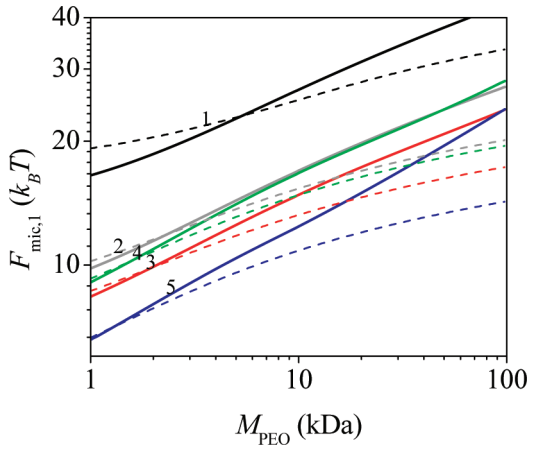

Figure 5. Equilibrium free energy per copolymer molecule in the micelles plotted against M_{PEO} for spherical (full lines) or cylindrical (dashed lines) micelles. They are obtained by minimizing the expression for F_{mic} (eq 16) with respect to the core radius, R_{core}, and corona thickness, D_{corona}, using the input parameters given in the text for the different ethanol fractions in the solvent, ϕ_{eth} = 0 (no. 1, black lines), 0.3 (no. 2, gray lines), 0.5 (no. 3, red lines), 0.7 (no. 4, green lines), and 1 (no. 5, blue lines).

The results suggest that cylindrical micelles should only be favored in pure water for M_{PEO} = 4.9 kDa, and in ϕ_{eth} = 0.3 for M_{PEO} = 2.8 kDa. However, for all $PEP_{5.0}$–$PEO_{2.8}$ samples, the energies for the spherical and cylindrical micelles are very close, and a small positive offset of the energy for the spherical relative to the cylindrical morphology would give predictions of cylindrical micelles for all solvents for this polymer.

For the samples in pure water, cylindrical micelles were observed for all samples, except for the highest value of M_{PEO}. Cylindrical micelles are only predicted for $PEP_{5.0}$–$PEO_{4.9}$. Thus, according to the thermodynamic model, the remaining observed cylindrical micelles must be kinetically trapped structures.

DISCUSSION

Small-angle X-ray scattering and static light scattering have provided extensive results on the morphology and structure of micelles of a series of block copolymers of PEP–PEO in mixtures of water and ethanol. The broad span of PEO block mass from 2.8 to 49 kDa for a constant PEP block mass of 5.0 kDa leads to a large variation in corona thickness relative to core, which simultaneously leads to variation of the importance of chain interaction within the corona. This results for all solvents in a morphology change from cylindrical to spherical micelles for increasing molar mass.

The variation of the solvents by mixing water and ethanol has two effects. It both changes the surface energy of the PEP–solvent interface and the interaction between the PEO chains in the corona. The change in the surface energy of the PEP–solvent interface results in that the solvent selectivity decreases for increasing amounts of ethanol. The introduction of 30% ethanol and more into the solvent has the consequence that molecular exchange sets in and that the micelles obtain their equilibrium structure, which was not the case in pure water. The lower surface energy allows for larger PEP–solvent interfaces and therefore smaller micellar cores and aggregation numbers. For the large surface energies, the growth in size of the cores leads to stretching of the PEP chains and an associated cost in conformational entropy.

The measurements on homopolymers of PEO in the various solvents show that interchain interactions within the corona are most important for a solvent with about 50% ethanol, as the second virial coefficient is larger for this solvent composition. This means that the energy cost of having a high chain density in the corona is largest for this solvent composition. In addition to the energy cost due to interchain interactions, there is an associated PEO chain stretching that gives a cost of conformational entropy for the chains.

The thermodynamic model by Zhulina et al. constitutes an attempt to take the various effects into account to describe the changes in micelle morphology and to predict structural parameters such as aggregation number/core size and corona thickness. By optimizing the free parameters of the model, it was possible to fit it to structural parameters of the micelles observed upon variation of both the core–solvent surface energy $\gamma_{PEP-solvent}$, the strength of the interchain interactions of the corona polymer as described by $A_{2,PEO}$, and length of the corona polymers. This demonstrates that the model includes the most important terms describing the thermodynamics of the self-assembly of the block copolymers and that it has potential for being applied for prediction purposes.

For the largest M_{PEO} the model systematically overestimated the core radius. This fact points toward that some strong interchain interactions in the corona are not taken into account by the model. It has been shown that such corona interactions depend on the structural parameters via the reduced surface coverage,[40] Σ/Σ^*. The decrease of R_{core} for the highest M_{PEO} leads to a relaxation in Σ/Σ^* (Figure 4), which is energetically favorable. This indicates that inclusion of the (strong) dependency on Σ/Σ^* directly in the thermodynamic model might lead to a better prediction of the decrease of R_{core}.

In general, the weakness of the model is the inclusion of the system dependent parameters C_H and C_F. They do have some physical interpretation as they set the scale for the dependence of the corona thickness on polymerization degree and for the energy scale of the blobs within the corona. As C_F and C_H change depending on the system, the model loses its predictive power unless one can establish their dependence on measurable system properties. In the present work we were able to use the expected dependency of C_H on $A_{2,PEO}$ to use only one free parameter to give the values of C_H for all solutions, which reflects the physical significance of C_H. For C_F, a systematic increase with ethanol content in the solvent was observed. The origin of this dependence is not clear to us. According to

dx.doi.org/10.1021/ma2016369 | Macromolecules 2012, 45, 430–440

Zhulina et al., C_F should take a constant value for good solvent conditions for the corona block, whereas it is dependent on a three-body interaction parameter for a theta solvent. However, if higher order effects give significant contributions, one might expect a dependency of C_F on the solvent, also under good solvent conditions. Another important point is that the corona profiles are not perfectly described by the expressions given in eq 19.[40] Any deviation from the profiles applied in the thermodynamic model might be "corrected" by a different effective value of C_F. Such deviations would depend on the fraction of ethanol in the solvent and might lead to chain interactions in the corona different from those in the model and hence give different values of C_F.

By comparing energies of cylindrical and spherical micelles, the model should in principle also be able to predict the micelle morphology. As mentioned above, the model does not predict perfectly the experimentally obtained shapes although it does indeed predict transformations between cylindrical and spherical shapes for conditions close to where they are observed. The cylindrical shape observed for all $PEP_5-PEO_{2.8}$ samples is only predicted for the 30% ethanol sample. In pure water cylinders were observed for all samples except for the PEP_5-PEO_{49} sample. It was only predicted for the $PEP_5-PEO_{4.9}$ sample. However, as these samples cannot be expected to be equilibrated, this discrepancy might arise because the micelles are kinetically frozen.

We also tried to adjust the values of the system dependent model parameters C_H and C_F in order to force the model to predict the morphology changes on the expense of having worse agreement with the structural parameters. This led to a significantly worse agreement of the structural parameters, and we conclude that this is not a good approach. It is therefore that we in this paper present the results from primarily optimizing the model parameters against the structural parameters.

CONCLUSIONS

By combining SLS and SAXS, structures have been determined for micelles in five different water−ethanol mixtures of the block copolymer PEP−PEO for a 5.0 kDa PEP and five different PEO molar masses from 2.8 to 49 kDa. For most of the samples, spherical micelles were observed with a core radius decreasing with M_{PEO} and ϕ_{eth}. For the lowest value of M_{PEO} as well as for the samples in pure water (except for the highest value of M_{PEO}) cylindrical micelles were observed.

A thermodynamic model by Zhulina et al.[17] was used for comparison with the obtained structural parameters and can provide reasonable fits to them. However, the predicted transitions between cylindrical and spherical micelles occurred at too low M_{PEO} values. The slope of the decrease of R_{core} and increase of D_{corona} with M_{PEO} is underestimated, and for the largest M_{PEO}, the model overestimates the core radii and thus the aggregation number of the micelles.

We challenged the thermodynamic model by using it to describe structural parameters and shape transitions when two parameters are varied, namely, the corona chain molar mass and the solvent properties. Although the predictions are not perfect, the comparison has shown that the model contains the main ingredients although the individual terms might have to be changed in order to obtain better agreement. Especially, the core radii were overestimated for the highest M_{PEO}. This might be related to the dependency of the micelle structure on the reduced surface coverage of the core by the PEO blocks in the corona, as this parameter relaxes for the highest M_{PEO}. Furthermore, it was necessary to include a solvent dependence of the model parameter C_F. C_F determines the strength of the interactions between the chains in the corona and was by the model predicted to take a constant value. This discrepancy could be related to the fact that the rather simple corona profiles suggested by the thermodynamic model might have to be altered in order to describe the actual profiles.[40]

ASSOCIATED CONTENT

Supporting Information

Details on the polymer synthesis and characterization; Zimm plots of the SLS data and the corresponding calculated radii of gyration of the spherical micelles. This material is available free of charge via the Internet at http://pubs.acs.org.

AUTHOR INFORMATION

Corresponding Author

*Tel +45 87155921; e-mail jsp@chem.au.dk.

Present Address

[§]Natural Science and Science Education, National Institute of Education, Nanyang Technological University, 1-Nanyang Walk, Singapore.

ACKNOWLEDGMENTS

We thank the Danish Natural Science Council for a grant supporting this work.

REFERENCES

(1) Feng, P.; Bu, X.; Pine, D. J. *Langmuir* **2000**, *16* (12), 5304−5310.
(2) Sundblom, A.; Palmqvist, A. E. C.; Holmberg, K. *Langmuir* **2009**, *26* (3), 1983−1990.
(3) Fink, Y.; Urbas, A. M.; Bawendi, M. G.; Joannopoulos, J. D.; Thomas, E. L. *J. Lightwave Technol.* **1999**, *17* (11), 1963−1969.
(4) Edrington, A. C.; Urbas, A. M.; DeRege, P.; Chen, C. X.; Swager, T. M.; Hadjichristidis, N.; Xenidou, M.; Fetters, L. J.; Joannopoulos, J. D.; Fink, Y.; Thomas, E. L. *Adv. Mater.* **2001**, *13* (6), 421−425.
(5) Kwon, G. S.; Kataoka, K. *Adv. Drug Delivery Rev.* **1995**, *16* (2−3), 295−309.
(6) Kataoka, K.; Harada, A.; Nagasaki, Y. *Adv. Drug Delivery Rev.* **2001**, *47* (1), 113−131.
(7) Müller, H.; Leube, W.; Tauer, K.; Förster, S.; Antonietti, M. *Macromolecules* **1997**, *30* (8), 2288−2293.
(8) Liu, J.; Sue, H.-J.; Thompson, Z. J.; Bates, F. S.; Dettloff, M.; Jacob, G.; Verghese, N.; Pham, H. *Acta Mater.* **2009**, *57* (9), 2691−2701.
(9) Thio, Y. S.; Wu, J.; Bates, F. S. *J. Polym. Sci., Part B: Polym. Phys.* **2009**, *47* (11), 1125−1129.
(10) Lodge, T. P. *Macromol. Chem. Phys.* **2003**, *204* (2), 265−273.
(11) Förster, S.; Zisenis, M.; Wenz, E.; Antonietti, M. *J. Chem. Phys.* **1996**, *104* (24), 9956−9970.
(12) Noolandi, J.; Hong, K. M. *Macromolecules* **1983**, *16* (9), 1443−1448.
(13) Nagarajan, R.; Ganesh, K. *J. Chem. Phys.* **1989**, *90* (10), 5843−5856.
(14) Halperin, A. *Macromolecules* **1987**, *20* (11), 2943−2946.
(15) Leibler, L.; Orland, H.; Wheeler, J. C. *J. Chem. Phys.* **1983**, *79* (7), 3550−3557.
(16) Birshtein, T. M.; Zhulina, E. B. *Polymer* **1989**, *30* (1), 170−177.
(17) Zhulina, E. B.; Adam, M.; LaRue, I.; Sheiko, S. S.; Rubinstein, M. *Macromolecules* **2005**, *38* (12), 5330−5351.
(18) LaRue, I.; Adam, M.; Pitsikalis, M.; Hadjichristidis, N.; Rubinstein, M.; Sheiko, S. S. *Macromolecules* **2006**, *39* (1), 309−314.
(19) Lund, R.; Pipich, V.; Willner, L.; Radulescu, A.; Colmenero, J.; Richter, D. *Soft Matter* **2011**, *7* (4), 1491−1500.

(20) Lonetti, B.; Tsigkri, A.; Lang, P. R.; Stellbrink, J.; Willner, L.; Kohlbrecher, J.; Lettinga, M. P. *Macromolecules* **2011**, *44* (9), 3583−3593.
(21) Willner, L.; et al. *Europhys. Lett.* **2000**, *51* (6), 628.
(22) Kaya, H.; Willner, L.; Allgaier, J.; Stellbrink, J.; Richter, D. *Appl. Phys. A: Mater. Sci. Process.* **2002**, *74* (0), s499−s501.
(23) Lund, R.; Willner, L.; Stellbrink, J.; Radulescu, A.; Richter, D. *Macromolecules* **2004**, *37* (26), 9984−9993.
(24) Jensen, G. V.; Shi, Q.; Hernansanz, M. J.; Oliveira, C. L. P.; Deen, G. R.; Almdal, K.; Pedersen, J. S. *J. Appl. Crystallogr.* **2011**, *44*, 473−482.
(25) Ndoni, S.; Papadakis, C. M.; Bates, F. S.; Almdal, K. *Rev. Sci. Instrum.* **1995**, *66* (2), 1090−1095.
(26) Hillmyer, M. A.; Bates, F. S. *Macromolecules* **1996**, *29* (22), 6994−7002.
(27) Shi, Q. Study of Micelle Formation of PEP-PEO Diblock Copolymers in Water, Ethanol, and Water-Ethanol Mixtures by SAXS. Master Thesis, Aarhus University, Aarhus, 2004.
(28) Willner, L.; et al. *Europhys. Lett.* **2001**, *55* (5), 667.
(29) Lund, R.; Willner, L.; Richter, D.; Dormidontova, E. E. *Macromolecules* **2006**, *39* (13), 4566−4575.
(30) Pedersen, J. *J. Appl. Crystallogr.* **2004**, *37* (3), 369−380.
(31) Pedersen, J. S.; Schurtenberger, P. *Europhys. Lett.* **1999**, *45* (6), 666.
(32) Pedersen, J. S.; Schurtenberger, P. *J. Polym. Sci., Part B: Polym. Phys.* **2004**, *42* (17), 3081−3094.
(33) Pedersen, J. S.; Schurtenberger, P. *Macromolecules* **1996**, *29* (23), 7602−7612.
(34) Pedersen, J. S.; Laso, M.; Schurtenberger, P. *Phys. Rev. E* **1996**, *54* (6), R5917.
(35) Ohta, T.; Oono, Y. *Phys. Lett. A* **1982**, *89* (9), 460−464.
(36) Wang, S.-C.; Wang, C.-K.; Chang, F.-M.; Tsao, H.-K. *Macromolecules* **2002**, *35* (25), 9551−9555.
(37) Kawaguchi, S.; Imai, G.; Suzuki, J.; Miyahara, A.; Kitano, T.; Ito, K. *Polymer* **1997**, *38* (12), 2885−2891.
(38) Cates, M. E. *Macromolecules* **1987**, *20* (9), 2289−2296.
(39) Pedersen, J. S.; Svaneborg, C. *Curr. Opin. Colloid Interface Sci.* **2002**, *7* (3−4), 158−166.
(40) Svaneborg, C.; Pedersen, J. S. *Macromolecules* **2002**, *35* (3), 1028−1037.
(41) Pedersen, J. S.; Svaneborg, C.; Almdal, K.; Hamley, I. W.; Young, R. N. *Macromolecules* **2003**, *36* (2), 416−433.
(42) Neugebauer, T. *Ann. Phys.* **1943**, *42* (7/8), 509−533.
(43) Kinning, D. J.; Thomas, E. L. *Macromolecules* **1984**, *17* (9), 1712−1718.
(44) Pedersen, J. S. *Adv. Colloid Interface Sci.* **1997**, *70*, 171−210.
(45) Pedersen, J. S.; Posselt, D.; Mortensen, K. *J. Appl. Crystallogr.* **1990**, *23*, 321−333.
(46) Pedersen, J. S. *J. Phys. IV* **1993**, *3* (C8), 491−498.
(47) Pedersen, J. S.; Gerstenberg, M. C. *Macromolecules* **1996**, *29* (4), 1363−1365.
(48) Semenov, A. N. *Sov. Phys., JETP* **1985**, *61* (4), 733−742.
(49) Hammouda, B.; Ho, D. L. *J. Polym. Sci., Part B: Polym. Phys.* **2007**, *45* (16), 2196−2200.
(50) Richter, D.; Monkenbusch, M.; Arbe, A.; Colmenero, J. Neutron Spin Echo in Polymer Systems. In *Neutron Spin Echo in Polymer Systems*; Springer: Berlin, 2005; Vol. *174*, pp 1−221.
(51) Aharoni, S. M. *Macromolecules* **1983**, *16* (11), 1722−1728.
(52) Petke, F. D.; Ray, B. R. *J. Colloid Interface Sci.* **1969**, *31* (2), 216−227.

Macromolecules

ARTICLE

pubs.acs.org/Macromolecules

2D Encapsulation in Multiphase Polymers: Role of Viscoelastic, Geometrical and Interfacial Properties

Khalid Lamnawar,[†] Mosto Bousmina,[§] and Abderrahim Maazouz*[,‡,§]

[†]Laboratoire de Mécanique des Contacts et des Structures, Université de Lyon, CNRS, INSA-Lyon, LaMCoS UMR CNRS#5259, Groupe de Recherche Pluridisciplinaire en Plasturgie, F69621, France

[‡]Université de Lyon, F-69361 Lyon, and CNRS, UMR 5223, Ingénierie des Matériaux Polymères, INSA Lyon, F-69621 Villeurbanne, France

[§]Hassan II Academy of Science and Technology, Postal Code 10 100, Rabat, Morocco

ABSTRACT: The aim of the present work has been to gain a fundamental understanding of the mechanisms governing encapsulation in the multiphase systems as a blend or multilayer structures. The model systems chosen for this study are based on (i) Newtonian poly(dimethylsiloxane) polymers of varying molar masses and (ii) high molecular weight, viscoelastic, and compatible pair polymers of PVDF and PMMA. The same approach was applied to functionalized polymers to investigate the effect of physicochemical affinity on two pairs of asymmetrical reactive polymers based on PE-GMA (glycidyl methacrylate)/PVDF-*g*-MA (maleic anhydride) and a PE/PVDF as a reference. The linear viscoelastic and surface properties of the neat and bilayer model systems structures have been investigated. The optical obeservations of the encapsulation kinetic of two drops were recorded using a homemade device. Specific experiments were carried out to follow up the kinetic of encapsulation, and the results were rationalized as a function of the effect of the viscosity, elasticity ratios, drop geometry, the interfacial tension, and the physicochemical affinity. Throughout all the experiment, the mechanisms were purposed for each system and discussed based on the theories of molecular forces or Brownian motion governing diffusion and Ostwald ripening, in contrast to the theories of coalescence. The viscosity ratio coupled to the drop geometry of the material was found to be a key parameter and that it has to be linked to the interfacial tension and spreading parameters. Furthermore, the encapsulation appeared to be hindered by the interdiffusion process in the case of compatible pair system despite their elasticity and surface tension contrast. Finally, the encapsulation kinetic could be reduced or eliminated by the creation of a copolymer at the interface for a reactive system. The results obtained by the optical investigation of two drops corroborated the rheological data of the bilayer systems. Hence, the obtained results rendered it possible to decouple the influence of the viscoelastic parameters to flow, interfacial tension, thereby highlighting a number of macroscopic effects that were governed by the interdiffusion or reaction of macromolecular chains at the interface to give a better understanding of encapsulation phenomenon in multiphase systems.

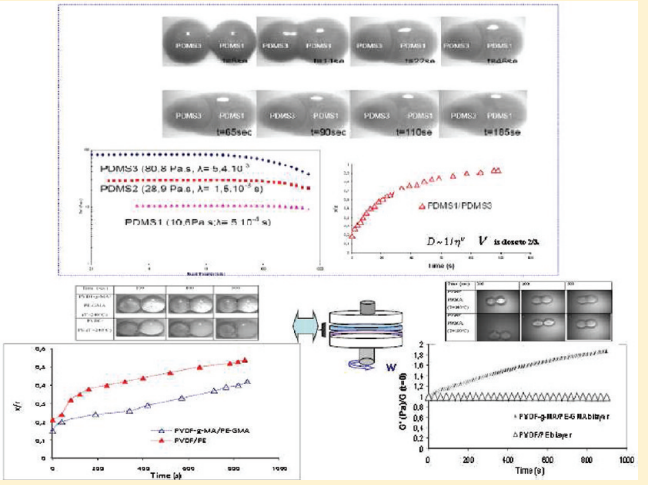

1. INTRODUCTION

Encapsulation phenomena has been observed in experiments involving a wide range of materials from oil and water to polymer melts for both high and low Reynolds numbers. It can also used as a technique in the food, biomedical, and pharmaceutical industry where small particles, cells, and cell agglomerates are produced and dispersed in an ambient medium. Encapsulation efficiency is also of primary importance in the biomedical industry, as reviewed by Orive et al.[1] The phenomenon has been also observed in other systems as in bubblesand cells.[2,3] The subject is vast, and hence it is a daunting task to summarize this remarkably rich and multifaceted area. The encapsulation subject is old in principle; the pioneering works show that lower viscosity material will eventually encapsulate the higher viscosity fluid.[4] In the case of multiphase polymer system, we shall quickly list some investigations of close relevance to the present study:

a. Encapsulation in Multilayer Structure. Previous work on layer thickness uniformity has primarily been devoted to the effects of differing polymer viscosities in the individual layers under shear.[5−9] These differences in viscosities give rise to a phenomenon known as "viscous encapsulation" in producing nonuniform layer thicknesses. There has only been performed a very limited number of experimental studies dealing with encapsulation phenomena,[10−12] and most of these research efforts

Received: May 20, 2011
Revised: September 20, 2011
Published: December 22, 2011

have suggested that, irrespective of the stability of the interface, the more viscous fluid tends to push into its less viscous counterpart, eventually leading to the less viscous fluid encapsulating the more viscous components. In other words, encapsulation is caused by the tendency of the less viscous polymer to enter the region of high shear (i.e., the wall with a highest shear stress).[13] Differences in wall adhesion and viscoelastic characteristics of polymers and weak secondary flows caused by viscoelastic effects have been demonstrated to be the contributing factors.[14] In an early study, White et al.[15] argued that the shape of the interface can also be influenced by the jump in secondary normal stress difference. Recently, it was demonstrated that this phenomenon is mainly driven by a jump in viscosity but also by a difference in elasticity between the two fluids.[16] These experimental observations are consistent with numerical studies with Newtonian and purely inelastic constitutive equations.[17,18] However, examples of coextruded structures with nonuniform layer thicknesses have been observed even when the viscoelastic properties of the materials are very similar.[19] This implies that another factor affects the flow of the materials during process. An investigation of the effect of polymer viscoelasticity and physicochemical affinity on the layer thickness uniformity of multilayer coextruded structures would thus be of great interest.

b. Encapsulation in Blend. In studies of multicomponent polymer blends of more than two phases, papers dedicated to this subject have shown that the morphology resulting from the competition between drops collision under flow followed by coalescence/encapsulation or drop breakup depends mainly on the interfacial and rheological properties.[20,21] The final droplet size distribution, under mixing, results from the balance between the present phenomena.[22] Recently, the effect of compatibilization on the deformation and breakup of drops in stepwise increasing shear flow has been investigated.[23]

Hobbs et al.[24] first reported the encapsulation concept on the spontaneous development of the composite droplet morphology in immiscible systems. They suggested that, under equilibrium mixing conditions, interfacial forces might play an important role in establishing the phase morphology of multiphase polymer blends. By using the concept of a spreading coefficient, they rewrote the Harkin equation (eq 1) in which two dissimilar phases are dispersed within a third matrix material by substituting the appropriate interfacial tensions for the surface tension values

$$\lambda_{31} = \sigma_{12} - \sigma_{31} - \sigma_{13} \quad (1)$$

Here, σ_{12}, σ_{32}, and σ_{13} are the interfacial tensions for each component pair, and λ_{31} is defined as the spreading coefficient for the case of component 3 encapsulating component 1. The index 2 refers to the matrix. λ_{31} must be positive for component 1 to be encapsulated by component 3. The authors successfully demonstrated the usefulness of the spreading coefficient concept for predicting the various morphologies that were formed and in particular the encapsulation effect.

Recently, a numerical simulation of particle encapsulation due to liquid thread breakup has been published to investigate the effect of the particle spacing, viscosity ratio, Reynolds number, and waveform of interfacial perturbations.[25]

Recent papers on ternary systems have suggested that composite droplet formation may be related to the viscosity of the dispersed components.[26] Nemirovski et al.[27] studied the phase morphology of a number of three-component (thermoplastic/thermotropic) systems and suggested that the dispersed component A would encapsulate the dispersed component B (in a matrix C) when both the thermodynamics, expressed by means of a positive $\lambda_{A/B}$ spreading coefficient, and the kinetic effects, expressed by means of a dispersed phase viscosity ratio smaller than 1, acted cooperatively. However, in some cases, a dispersed phase viscosity ratio greater than 1 was found to hinder the development of the core−shell structure (A encapsulating B) even though encapsulation had been predicted by a positive $\lambda_{A/B}$ spreading coefficient.

The reverse effect was observed by Gupta and Srinivasan[28] for ternary blends of styrene−ethylene−butylene terpolymer (SEBS) and polycarbonate (PC) dispersed within a PP matrix. The SEBS component formed a boundary layer at the surface of the PC droplets when PC was less viscous than SEBS, whereas the minor components were separately dispersed when PC was more viscous than SEBS. However, most authors have failed to find any influence of the dispersed phase core−shell viscosity ratio on the composite droplet structure.[29,48]

Recently, Reignier et al.[30] investigated the influence of the molecular weight of the dispersed phase components on encapsulation effects in the composite droplet phase for a ternary blend composed of PS and PMMA dispersed in HDPE. Hence, it was found that arguments based on the effect of viscosity ratio or the absolute viscosities of the different dispersed phases do not explain the obtained results concerning the composite droplet morphology, from PMMA encapsulating PS to PS encapsulating PMMA. This morphology depends on the molecular weight of the each polymer and the mixing and annealing times. Considering all the above, a conceptual model has been developed to predict encapsulation effects in composite droplet type systems based on the use of a dynamic interfacial tension (i.e., taking into account then elasticity of the polymer components). Calculations based on the dynamic interfacial tension model, using elasticities based on constant shear stress (first normal stress coefficient based on Laun's law), were able to account for all of the observed encapsulation effects in this work.

Finally, as briefly summarized above, significant progress in understanding the encapsulation phenomenon in multiphase systems has been obtained over the past decades. Few papers have been dedicated to polymer systems. To the best of our knowledge, few research efforts have, with regard to fundamental and experimental aspects, been dedicated to this subject. Despite the interesting nature of this kind of research, it is of no help when attempting to comprehend either the generation of the encapsulation decoupled to shear or their connection with the physicochemical affinity and viscoelasticity.

A thorough understanding of physicochemical aspects as well as of the full rheological parameters of the encapsulation phenomena has yet to be established. In order to attain this, the attention of the present study has been focused on performing original experiments with well-characterized model polymer fluids with different molar masses and functionalities. The aim of this work thus involved decoupling the influence of viscoelastic parameters and flow, thereby highlighting a number of macroscopic effects coupled to the physicochemical affinity which can affect the encapsulation phenomenon. The purpose of the investigation has been to present simples experimental studies in an attempt to gain an understanding of the mechanisms governing encapsulation decoupled to these parameters. The obtained optical results will be analyzed based on the surface properties and rheological properties of mono- and bilayer systems. The details of the experimental procedures

are presented in the next section, followed by the main results and a discussion.

2. EXPERIMENTAL SECTION

2.1. Base Materials. *a. The Model Fluids.* Three types of poly(dimethylsiloxane) (PDMS) with varying viscosities and molecular weight were chosen, and their designations and viscosities are listed in Table 1. Moreover, a complete investigation of the rheological properties of the materials was carried out.

b. High Molecular Weight Model Polymers. Two systems were kindly supplied by Arkema (Serquigny, France): (i) The first pair was based on PVDF/PMMA and was completely miscible. (ii) The second system was based on two pairs of reactive polymers at interfaces of PE-GMA (glycidyl methacrylate)/PVDF-*g*-MA (maleic anhydride). A pair consisting of PE/PVDF was used as a nonreactive system.

Table 1. Designations of the Three PDMS Materials and Their Respective Viscosities and Molecular Weights (Values Given by Sigma-Aldrich)

fluid	Newtonian viscosity (Pa·s)	M_w (g/mol)
PDMS1	10.6	76 000
PDMS2	28.9	94 000
PDMS3	80.8	130 000

Table 2. High Molecular Weight Polymers Used and Their Main Characteristics

sample code	supplier	characteristic functions	$\overline{M}_w$[a] (g/mol)	I_p[a]	T_m[b] (°C)
PVDF	Arkema	–	210 000	2	169.4
PVDF-*g*-MA	Arkema	maleic anhydride	200 000	2.2	168.5
PMMA	Arkema		195 000	1.994	120
PE	Arkema	–	240 000	9.9	114
PE-GMA	Arkema	(glycidyl methacrylate)	207 000	10	107

[a] Measured in our laboratory by gel permeation chromatography (GPC) with tetrahydrofuran (THF) as solvent for PMMA, dimethylformamide (DMF) for PVDF, and PVDF-*g*-MA and trichlorobenzene (TCB) at 135 °C for PE and PE-GMA (universal calibration). [b] Measured in our laboratory by a DSC Q20 (TA Instruments) at heating and cooling rate of 10 °C/min.

Table 2 reports all the high molecular weight polymers used in this study along with their source and some of their characteristics.

2.2. Rheological Investigations in Linear Viscoelasticity Regime. *a. Rheological Properties of the Pure Polymers.* All rheological measurements were carried out in the linear viscoelastic region in small-amplitude oscillatory shear mode as was verified by preliminary strain sweep measurements. Polymer degradation was avoided by continuously purging the oven with nitrogen. The measured rheological functions included the complex viscosity η^*, its real and imaginary components η' and η'', and the elastic modulus G' and loss modulus G'':

The rheological behavior of model fluids was studied. Flow tests were performed with a stress-controlled rotational rheometer AR100 from TA Instruments, with a cone and plate geometry (D = 60 mm, $\alpha = 2° \approx 0.035$ rad, gap = 66 μm). To obtain the largest possible range of frequencies, the tests were carried out from 25 to 65 °C. A master curve was plotted for a reference temperature of 25 °C using a time–temperature superposition procedure. Figure 1 depicts the rheological

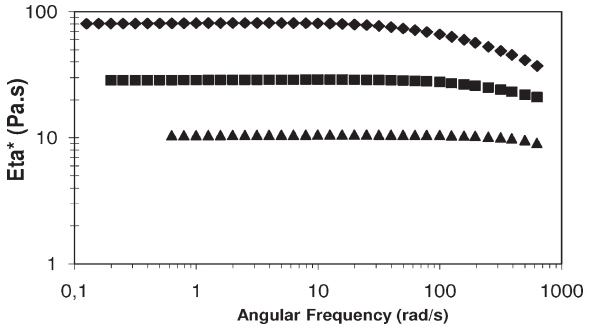

Figure 1. Complex viscosity modulus vs the frequency for PDMS1 (triangle), PDMS2 (square), and PDMS3 (diamond) at 25 °C.

Table 3. Rheological Characteristics for PDMS at 25 °C[a]

fluid	η_0 (Pa·s)	λ (s)
PDMS1	10.6	1.5×10^{-4}
PDMS2	28.9	1.5×10^{-3}
PDMS3	80.8	3.1×10^{-3}

[a] Relaxation times are calculated by the Cole–Cole method.

Table 4. Zero-Shear Viscosities η_0, Activation Energies E_a, and Relaxation Times λ for PE, PE-GMA, PVDF, PMMA, and PVDF-*g*-MA at 240 °C

polymer	η_0 (Pa·s)	E_a (kJ/mol)	λ (s)
PE	7400	53	0.9
PE-GMA	5010	56	0.79
PVDF-MA	2950	58.5	0.39
PVDF	1820	51.5	0.31
PMMA	1800	70	0.25

curves for PDMS1, PDMS2, and PDMS3. However, all polymers exhibit Newtonian behavior in the expected range of the investigation with a constant viscosity and zero first normal stress difference. Viscosity is constant, and G' is almost zero. PDMS3 does show some traces of the first normal stress difference but only at high angular frequency that are well above the maximum angular frequency used in the work. Newtonian viscosities and relaxation times at 25 °C for each fluid were then deduced from this curve (the same results have been obtained in the work of Muller et al.[31]).

Table 3 regroups these later results. Relaxation times are calculated by the Cole–Cole method. When plotting the real and imaginary parts of viscosity in the complex plan, the obtained curve presents a maximum for $\lambda\omega = 1$. We can directly deduce the value of λ. Meanwhile, the relaxation times are very small and increase with the viscosity (i.e., molar mass).

Rheological measurements for the high molecular weight polymers were performed using a strain-controlled rotational rheometer ARES (Advanced Rheometrics Expansion System, Rheometrics Co.) with a parallel plate–plate geometry. All film of PE, PE-GMA, PMMA, PVDF, and PVDF-*g*-MA were previously fabricated under identical processing conditions in order to eliminate sample-to-sample errors. All the resin granules were dried at 80 °C under vacuum to remove the moistures before use. Samples for rheological measurements were prepared by compression molding at 180 °C with a pressure of 200 bar between two Teflon films to obtain a smooth surface. During heating and cooling stages of compression, nitrogen purging was introduced to protect polymers from oxidation. All samples were prepared under the same processing conditions to eliminate samples to samples errors. These round samples were subsequently annealed at 65 °C under vacuum for 1 week to remove possible surface contaminants

dx.doi.org/10.1021/ma201151k |*Macromolecules* 2012, 45, 441–454

and to allow the relaxation of chains at the surface having become oriented as a result of shear and elongation during the film preparation.

Rheological properties were then explored within a range of temperatures spanning from 180 to 240 °C. Their master curves obtained by Arrhenius rule at a reference temperature of 240 °C. The corresponding activation energies of viscous flow calculated from the master curve at such a reference temperature are reported in Table 4.

For the sake of clarity, only the rheological results at 240 °C are presented. For example, Figure 2a confirms that PVDF and PMMA presented equivalent rheological behaviors of viscosity at 240 °C. On the basis of storage modulus values, PVDF is more elastic than PMMA at this reference temperature. In addition, Figure 2b depicts a comparison of rheological behavior (viscosity and storage modulus) of PVDF, PE, PVDF-*g*-MA, and PE-GMA at 240 °C. PMMA is not present here because it is shows the same behavior as PVDF. All the materials exhibit a Newtonian behavior at low frequencies. The viscosity curves of the PE and PE-GMA displayed a noticeable pseudoplastic behavior above 0.5 rad/s, whereas 1 rad/s for PVDF and PVDF-*g*-MA. Based on their storage modulus, PE and PE-GMA are more elastic than PVDF-*g*-MA and PVDF, respectively. This result also supported by the measurement of the first normal stress difference. These results thus confirmed that these polymers were significantly different with respect to their viscous and elastic flow properties and their high molar masses.

Table 4 summarizes also the obtained zero shear viscosities and the relaxation times calculated based on the Cole−Cole method at 240 °C. Furthermore, the comparison of the relaxations times corroborates the above obtained results based on the storage modulus. All of these studied polymers are highly viscous and elastic in comparison with PDMS.

Hence, based on these rheological investigations, the zero-shear viscosity ratios for the studied temperatures were evaluated as presented in Table 5.

b. Rheological Properties of Bilayer Systems in Linear Viscoelastic Regime. Rheological measurements of the bilayer systems (based on PVDF, PMMA, PVDF-*g*-MA, PE, and PE-GMA with symmetrical and asymmetrical configurations) were carried out under a strain-controlled rheometer: ARES (Advanced Rheometrics Expansion System) using a parallel-plate geometry (Φ = 25 mm) at different temperatures from 180 to 240 °C. Polymer degradation was avoided by continuously purging the oven with nitrogen.

The bilayer assembly for diffusion process was prepared by bringing the polymers round disks into intimate contact at room temperature with a desirable configuration before loaded between the plates and then annealed in the oven detected by a mode of the experiments. (For the sake clarity of this paper, only the experiments with dynamic time sweep test will be presented.) The zero time was defined as the time when the heating chamber of the rheometer was closed and the healing time was the contact time after having reached the plate temperature. The polymer sandwich was slightly compressed to ensure contact and obtain a desired gap. Indeed, the pressure was expected to affect the diffusion process and thus also the interpenetration of chains at the interface.

Prior experiments have been carried out by both reverse configurations, and the errors observed between the results of these two configurations were minimized through selecting a better gap between upper plate and lower plate (which is equal to the total thickness of bilayer). It is noticed that the gap was set to be equal to the total thickness of bilayer in this part of experiments is for the sake of avoiding the effects of external compression pressures, making the investigation more complicated. A prestudy was led to obtain a better gap in order to provide an improved reproducibility. Indeed, in that context, three configurations and sample thicknesses were studied: (i) 1 mm: 500 μm/500 μm; (ii) 1.2 mm: 600 μm/600 μm; (iii) 1.4 mm: 700 μm/700 μm. Nevertheless, in the present investigation, the lower viscous material was, in the case of the bilayer structure, placed close to the motor to obtain a good dissipation of strain. The most viscous material was placed at the top near the transducer. Moreover, despite reversing the position

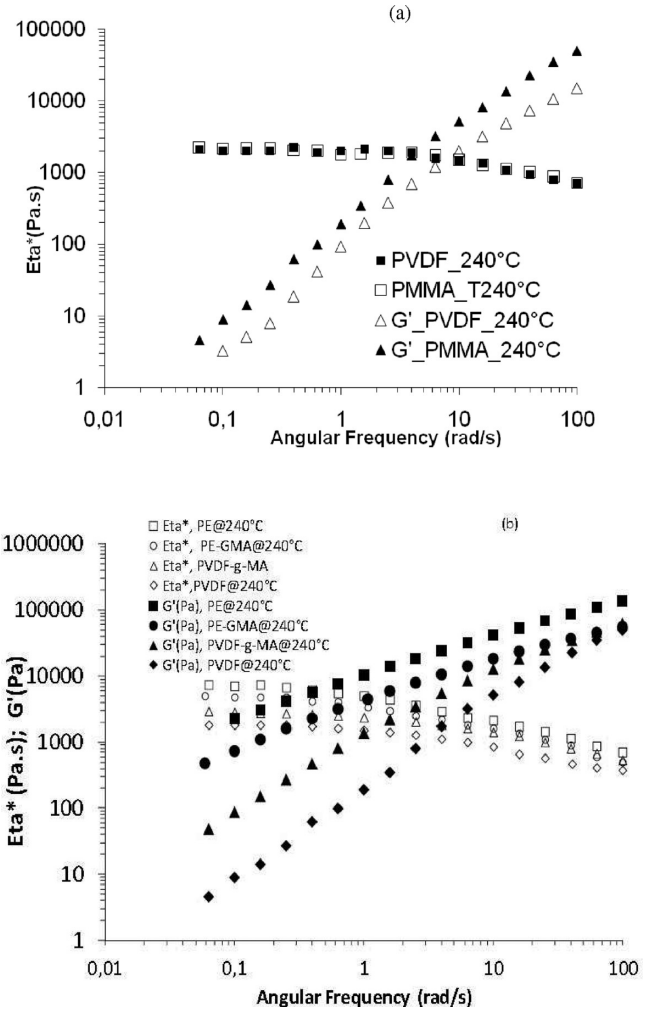

Figure 2. (a) An example of the storage and complex viscosity modulus vs the frequency of PVDF and PMMA at 240 °C. (b) Comparison of the complex viscosity modulus and storage modulus vs the angular frequency of PE, PE-GMA, PVDF, and PVDF-*g*-MA at 240 °C.

Table 5. Zero-Shear Viscosity Ratios at Different Temperatures of the the Used Polymer Pairs

	zero-shear viscosity ratio			
T (°C)	PVDF/PMMA	PE-GMA/PVDF-*g*-AM	PE/PVDF	PDMS3/PDMS1
25				8
190	1.15	2	3.8	
210	1.03	1.7	3.5	
240	1	1.5	3.2	

of the two polymer plates, equivalent results were obtained with the reactive and nonreactive systems regardless of these three thicknesses. For the sake of clarity and in order to reduce the number of samples, only the results concerning 600 μm/600 μm of bilayer are presented.

To make sure all the oscillatory measurements being performed for each configuration within the linear viscoelastic regime, a prior dynamic strain sweep test was conducted ranging from 0.1% to 100% with a maximum angular frequency (ω) amplitude of 100 rad/s. At a fixed

dx.doi.org/10.1021/ma201151k |*Macromolecules* 2012, 45, 441–454

Table 6. Surface Tension Values for Model Fluids Obtained with Three Substrates (Columns 2−4) as Well as Merely One Nonpolar Substrate (Column 6)[a]

	measurements with 3 substrates: PTFE, aluminum, and glass at 25 °C				measurements with only PTFE at 25 °C
sample	γ_L^p (mN/m)	γ_L^d (mN/m)	γ_L (mN/m)	contribution of polar part γ_L^p/γ_L (%)	γ_L^p (mN/m)
PDMS1	0.5	22.4	23.0	2.8	23.3
PDMS2	0.6	23.1	23.6	2.3	23.6
PDMS3	0.6	22.7	23.3	2.6	23.8

[a] The contribution of the polar component to the surface tension is displayed in column 5.

temperature, the dynamic time sweep tests were implemented at a 5% of fixed strain that lies in linear viscoelastic region and a given angular frequency of 1 rad/s amplitude. All measurements, whether conducted were performed with a 200 FRTN1 transducer with a lower limit of 0.02 g·cm. We considered only torques's that were 4 times higher than the lower limit of 0.02 g·cm given by the rheometer. Measurements were taken once the sample had reached a fully relaxed state and without any squeeze flow (with an axial force more than 10%). Finally, additional details of the experimental procedure can be found in previous articles of Qiu and Bousmina[32] as well as Lamnawar and Maazouz.[19,33−35]

2.3. Surface Tension Properties. The surface tension was evaluated for all samples. The contact angles between the liquids and three substrates were measured to determine the polar, γ_L^p, and the dispersive, γ_L^d, components of the liquid surface tension. When considering a liquid drop of surface tension γ_L on a solid substrate of surface tension γ_S, the equilibrium at the triple point can be written as

$$\gamma_S = \gamma_{SL} + \gamma_L \cos\alpha \quad (2)$$

where γ_{SL} is the interfacial tension between the liquid and the substrate and α is the contact angle. According to Owens and Wendt,[36] γ_{SL} can be expressed as

$$\gamma_{SL} = \gamma_S + \gamma_L - 2(\gamma_S^d\gamma_L^d)^{1/2} - 2(\gamma_S^p\gamma_L^p)^{1/2} \quad (3)$$

Taking into account eqs 2 and 3, this leads to

$$\gamma_L(1 + \cos\alpha) = 2(\gamma_S^d\gamma_L^d)^{1/2} + 2(\gamma_S^p\gamma_L^p)^{1/2} \quad (4)$$

In the above equation, the values of γ_S^d, γ_S^p, and α are known for each used substrate. This equation can be rewritten as follows:

$$\frac{1 + \cos\alpha}{2\sqrt{\gamma_S^d}} = \frac{1}{\gamma_L}\sqrt{\gamma_L^p}\sqrt{\frac{\gamma_S^p}{\gamma_S^d}} + \frac{1}{\gamma_L}\sqrt{\gamma_L^d} \quad (5)$$

By plotting

$$\frac{1 + \cos\alpha_i}{2\sqrt{\gamma_{S_i}^d}} = f\left(\sqrt{\frac{\gamma_{S_i}^p}{\gamma_{S_i}^d}}\right) \quad (6)$$

where i is the number of substrates, the polar and the dispersive components of the liquid can be easily determined from the above expressions. The obtained results are given with an average error of ±0.2 mN/m.

The surface tension can be simply estimated by

$$\gamma_L = \frac{4\gamma_S}{(1 + \cos\alpha)^2} \quad (7)$$

Table 6 summarizes the surface tension measured for model fluids on the PTFE substrate. In fact, the PTFE substrate had a surface tension γ_S of about 22.5 mN/m, and as can be seen in column 5, polar parts can be neglected. Measurements could be achieved on a single nonpolar substrate (PTFE), which improved their accuracy.

Table 7. Surface Tension Values at Several Temperatures for PE

temp (°C)	183	190	194	199	207	213	220	240
surface tension (mN/m)	22.8	22.4	21.9	21.4	20.9	20.3	20.2	19.6

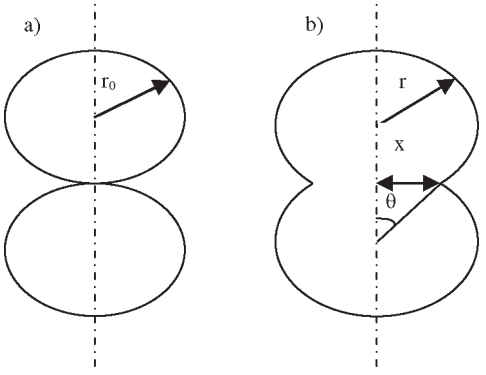

Figure 3. Geometrical illustration of the coalescence/encapsulation process of two drops at (a) $t = 0$ s and (b) $t > 0$ s. The parameters r, x, and θ represent the radius, the neck radius, and the coalescence angle, respectively.

On the other hand, the surface tension of the high molecular polymers on a PTFE substrate was calculated at each test temperature according to eq 7. A small flow of an inert gas was necessary to prevent thermal degradation of the material. As an example, Table 7 gives an example of the results obtained for PE. The surface tension varied from 22.8 mN/m at 180 °C to 19.6 mN/m at 240 °C.

The surface tension decreased linearly with the increase of the temperature with a small slope as $d\gamma/dT = -0.08$ mN/(m °C) for all studied polymers (PE, PE-GMA, PVDF, PVDF-*g*-MA, and PMMA). Similar values are found in the literature for numerous polymers and corroborate our experimental results. Indeed, Kwak et al.[37] have measured the surface tension of a PE and obtained a value of 18.3 mN/m at 240 °C. According to Wu,[38] the surface tension of a grafted PE was 20.1 mN/m at 240 °C, which was comparable to our result for PE-GMA. The values found for PVDF and PMMA, respectively 16.5 mN/m and 31.8 mN/m at 240 °C, were in agreement with those presented by Wu.[38] On the other hand, the obtained value of PVDF-*g*-MA is quietly the same as PVDF.

2.4. Optical Observations. The optical experiments were recorded on the homemade systems especially developed for this study. They were conducted on a regulated hot stage on which the drops or the particles were deposited. A Zeiss binocular and a Pantera CCD camera linked to a computer rendered it possible to record images at regular intervals. Drops were deposited on the substrate (Figure 3), and the entire process of coalescence and encapsulation was recorded. At short times, i.e., when the neck radius grew quickly, all images were analyzed.

dx.doi.org/10.1021/ma201151k |*Macromolecules* 2012, 45, 441–454

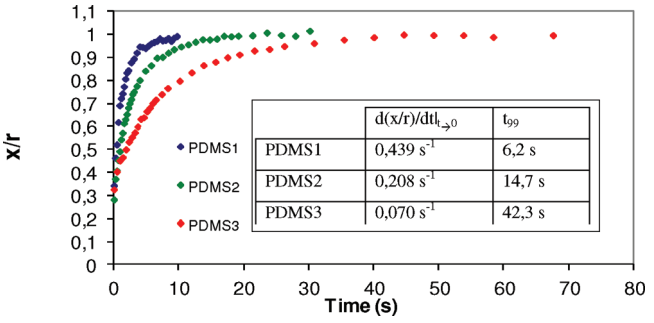

Figure 4. Coalescence/encapsulation curves for PDMS1/PDMS1, PDMS2/PDMS2, and PDMS3/PDMS3 pairs at 25 °C (r and x are the radius and neck radius, respectively).

When the encapsulation rate decreased, data were exploited every 5 or 10 images. All tests were repeated at least 3 times to ensure reproducibility. The presented results correspond to mean values of the 3 tests since this decreased the experimental error (4%).

3. RESULTS AND DISCUSSION

3.1. Primary Investigations of the Coalescence Kinetics. *a. Model Fluids.* The experiments were carried out at 25 °C for the model fluids. Only one substrate based on PTFE. To increase the contrast between the drops and the substrate, the model fluids were colored with a silicon carbide SiC powder. The amount of SiC in each fluid was ∼1%, and the size of the particles was 5 μm. The droplet size is around 8100 μm on diameter in all of measurements. (The half of this size has been used in the case of the smaller droplet in the investigation of the drop geometry effect.) Hence, the SiC particle size can be neglected compared to droplet geometry. It was experimentally verified that the addition of SiC to the fluids did not modify their rheological and interfacial properties. Drops were deposited on the substrate, and because of their low or relatively low viscosities, the fluids adopted a spherical shape more or less instantaneously. The entire process of encapsulation on 2D was recorded. At short times, i.e., when the neck radius grew rapidly, all images were analyzed.

Influence of Viscosity and the Interfacial Tension. i. Influence of Viscosity. Figure 4 compares the coalescence/encapsulation experiments for the three PDMS materials, and as can be seen, PDMS1 coalesced faster than PDMS2 and PDMS3. This was quantitatively confirmed by t_{99}, which was the time required to reach 99% of completion, and the initial slope. The experimental results corroborate those of Muller et al.[31] PDMS1 required 6.2 s to coalesce while 42.3 s was necessary for PDMS3. The initial slope also provided an indication of the encapsulation rate: from 0.439 s^{-1} for PDMS1, this value decreased to 0.070 s^{-1} for PDMS3.

The coalescence is governed by two contributions: (1) the wetting capacity and (2) the diffusion at the interface. The main driving force for particles coalescence is the surface tension, while viscous flow (according to the mobility of particles) is the opposing factor. The emphasis of lot work in the literature is on the development of a simple or general models which further could be adapted in simulating industrial process of ceramics, metals, and more complicated systems based on polymers. Frenkels models,[39] which is dedicated in the first time to metals, is based on Newtonian viscous flow under the action of surface tension. More recently, the mechanisms purposed in the literature are based on the balance of the work of surface tension and the viscous dissipation (the rate of coalescence occurring by viscous flow promoted by surface tension). All the other forces including gravity are neglected. Many authors have suggested that not only the viscous flow is acting on the coalescence but also the viscoelasticity of the material.[40] The coalescence mechanism can be explained following three steps: (1) elastic adhesive contact, (2) zipping contact growth, and (3) stretching contact. The phase 1 happens in short times. When particles are brought into contact, they deform to create a finite contact surface. The theory to describe this phase is also well-known as JKR theory.[41] The neck radius is proportional to $t^{1/3}$. The second phase (elastic driven response) occurs after the elastic adhesive contact but before the stretching contact. The neck radius growth is driven by adhesive intersurface forces and resisted by viscoelastic deformation. x/r is proportional to $t^{1/7}$. The Newtonian approach proposed by Frenkel can be used for long times. The neck radius is also proportional to $t^{1/2}$. Mazur and Plazek[42] found that the coalescence can be viewed as the sum of the elastic adhesive contact and the Newtonian contributions. Recently, Lin et al.[43] modeled sintering by adding the three contributions. They gave a good description and analysis of these three steps in their article.

In our experiments using the model polymer fluids, the observed process in the beginning times was governed by diffusion at the interface between the two drops placed in close vicinity of each other. The physical parameter responsible of interfacial tension's decreasing (i.e., compatibilization) is the interdiffusion between the neighboring phases. The theory for molecular forces or Brownian motion induced coalescence can be derived. Once the initial barrier energy was overcome (according to the interfacial energy), the two drops started to coalesce due to self-diffusion of the polymeric chains on both sides of the interface. The self-diffusion coefficient in a polymer networks is scaled as the inverse of the viscosity, $D \sim 1/\eta^{\nu}$ where the exponent ν is close to 2/3. The time of diffusion over a distance L is scaled as the inverse of the diffusion coefficient, $t = L^2/D$, and therefore increases proportionally to the viscosity $t \sim \eta^{\nu}$. For instance, PDMS3 was ∼2.8 times more viscous than PDMS2. The diffusion time in the two samples should scale with a power ν in the same proportion. An indirect way to confirm such proportionality was to compare the viscosity ratio η-(PDMS3)/η(PDMS2) with the ratio of the experimental characteristic times t_{99}(PDMS3)/t_{99}(PDMS2). Such a ratio was 2.87 for t_{99}. Similarly, the proportionality was also reasonably confirmed for PDMS2/PDMS1 and PDMS3/PDMS1.

ii. Influence of the Interfacial Tension. According to the results given in Table 6, the three values of surface tension for PDMS3 were slightly higher than for PDMS1 and PDMS2. For PDMS1, which had a low viscosity and was Newtonian, the coalescence was fast as confirmed in the last paragraph. It was possible to calculate the spreading parameter S of the fluids on the PTFE thanks to $S = \gamma_S - (\gamma_L + \gamma_{SL})$.

Table 8 gives interfacial tensions and spreading parameters for all fluids.

For $S > 0$, the wetting was complete and the fluid spread on the substrate. Contrarily, for $S < 0$, the wetting was partial, and the fluid remained a drop. For PDMS1, the spreading parameter was higher as compared to that of PDMS3 ($S = -1.34$ mN/m). The configuration was unfavorable, and the fluid had a tendency not to wet the substrate. Negative spreading parameters were also found for the other PDMS samples. PDMS1 spread better on PTFE, and a hypothesis was that the low viscosity of this fluid

dx.doi.org/10.1021/ma201151k |*Macromolecules* 2012, 45, 441–454

Table 8. Interfacial Tension of the Three PDMS Fluids on PTFE as Well as Their Spreading Parameter on PTFE

fluid	interfacial tension with PTFE (mN/m)	spreading parameter on PTFE (mN/m)
PDMS1	8×10^{-3}	−0.84
PDMS2	1.2×10^{-2}	−1.06
PDMS3	1.9×10^{-2}	−1.34

allowed a faster spreading and coalescence as opposed to for PDMS3.

The present results can also explained based on the theories of Ostwald ripening which predict a decrease in the droplet growth rate with increasing interfacial tension in contrast to the theories of coalescence.[40,44] In the literature, Ostwald ripening is a physical process in which molecules from a droplet diffuse into other phase (matrix in blend for example) due to the differences in capillary pressures between large and small droplet. Meanwhile, the calculation of the spreading parameters based on the surface tension measurements show that this parameter was higher for PDMS1 compared to PDMS2 and PDMS3 even its lower viscosity. Note that S is also negative for the three PDMS.

The Ostwald ripening predicts a decrease on the droplet growth rate with a higher interfacial tension:[44] $[\gamma_{PDMS3} > \gamma_{PDMS2} > \gamma_{PDMS1}] \Rightarrow [S_{PDMS1} > S_{PDMS2} > S_{PDMS3}]$). Indeed, PDMS1 coalescence faster than PDMS2 and PDMS3, respectively $(d(x/r)/dt|_{t\to 0} = 0.439\ s^{-1}$ for PDMS1 compared to $d(x/r)/dt|_{t\to 0} = 0.07\ s^{-1}$ for PDMS3). For PDMS3, the wetting is unfavorable, and the diffusion is slowed down because of its high viscosity. For PDMS 1, for example, despite a negative spreading parameter, the diffusion is higher and this effect seems not to be affected by a low wetting capacity.

In fact, t_{99} evaluated in Figure 4 can be reduced in order to take into account the zero-shear viscosity, the surface tension, and the initial particle radius: $t_r = t_{99}\gamma/\eta_0 r_0$. They are respectively 3.15, 3.03, and 3.09 for the PDMS1, PDMS2, and PDMS3. The calculated values are similar for the three polymers on the same substrate. This indicates that the viscosity, surface tension, and the droplet geometry radii play a combined role. Furthermore, we can scale also the graphs with dimensionless time of Pokluda et al.[45] given by $t\gamma/\eta r_0$where γ is the surface tension and r_0 and η are the initial particle and the viscosity, respectively. However, on the contrary of our in which we have taken into account the real radius versus time (it was evaluated in situ with our special optical device), Pokluda et al.[45] assumed as Frenken that the particle radius is constant $[r(t) = r_0]$ and made an approximation for small angles $\cos(\theta) = 1 - (\theta^2/2)$. In our case, only the second assumption is taken into account. The work is in progress to modeless with numerical simulation this phenomenon, and this dimensionless time to verify the limits of Frenkel, Belluhumeur, and Pokluda models.

Furthermore, the effect of surface tension is highlighted through this investigation and should be taken into account especially for the high viscous materials. The interfacial tension plays a role for the more viscous materials at a same temperature and may accelerate or slow down the kinetics depending on the wetting of the substrate (i.e., spreading parameter). Hence, the effect of the viscous forces than initially supposed was more complex and should be coupled to the interfacial forces.

b. High Molecular Weight Polymers. The optical observations of the high molecular polymers were performed on the PTFE substrate at a variety of temperatures ranging from 180 to 240 °C. All of the measurements were carried out under nitrogen to avoid degradation. Similar to the model fluids, the spreading parameters seemed to be $S < 0$. Hence, theses investigations rendered it possible to examine the effects of viscosities, relaxation times, and interfacial reaction in the case of the reactive system. For the sake of clarity, all of these results are discussed in the next paragraph.

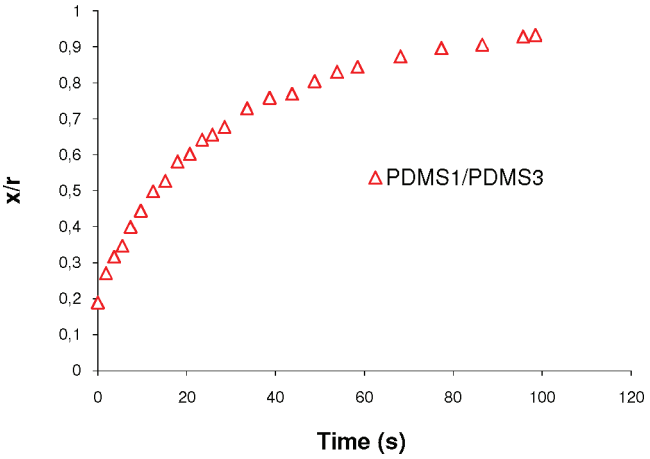

Figure 5. A coalescence/encapsulation curve of PDMS1/PDMS3 drops at 25 °C (r and x are the radius and neck radius, respectively).

3.2. Highlights of the Encapsulation Kinetics of the Model Fluids. *a. Influence of the Viscosity Ratio and the Surface Tension.* The encapsulation phenomenon was recorded by optical observations as a function of the viscosity ratio and the polymer/substrate interfacial tension. The relaxation times of PDMS are smaller and can be neglected. Figure 5 displays an illustration of the coalescence evolution of the PDMS1/PDMS3 pair, for which the viscosity ratio reached a value of 8. As symmetrical polymers, the first step of the observed encapsulation process was governed by diffusion at the interface between the two drops placed in close vicinity of each other. The theory for molecular forces or Brownian motion induced coalescence can be derived. Once the initial barrier energy was overcome, the two drops started to coalesce due to self-diffusion of the polymeric chains on both sides of the interface. Moreover, the relaxation times of PDMS(s) are neglected. In addition, it should be kept in mind that the interfacial tension of PDMS1 and PDMS3 with the PTFE substrate was 8×10^{-3} and 1.2×10^{-2} mN/m, respectively. PDMS1 spread better than PDMS3 because it is higher spreading parameter. The calculation of capillary number $Ca = \sigma R/\gamma_{12} = \eta\dot{\gamma}/(\gamma_{12}/R)$, which represents the ratio between viscous stresses (shear for example), $\sigma = \eta\dot{\gamma}$, that tend to deform the drops and interfacial stresses, γ_{12}/R, that resist to the deformation and tend to restore the initial shape of the drop, R being the drop radius and γ_{12} the interfacial tension. Indeed, the capillary numbers calculated (at lower shear rate $\dot{\gamma} = 1\ s^{-1}$, for example) are as follows: $Ca_{PDMS1} = 10.6/1.97 \Rightarrow 10.6 \gg 1.97$; $Ca_{PDMS3} = 80.8/4.68 \Rightarrow 80.8 \gg 4.68$. Considering PDMS3 as a matrix: $Ca_{PDMS1\to PDMS3} = 80.8/7.4 \times 10^{-1} \Rightarrow 80.8 \gg 7.4 \times 10^{-1}$. The PDMS1/PDMS3 interfacial tension $(= 3 \times 10^{-3}$ mN/m) was calculated using the generic-mean equation given in ref 38 from the surface tension values given in Table 7 and neglecting the polar interaction. Hence, the viscous forces appeared to be very higher in comparison to their capillary counterparts.

dx.doi.org/10.1021/ma201151k |*Macromolecules* 2012, 45, 441–454

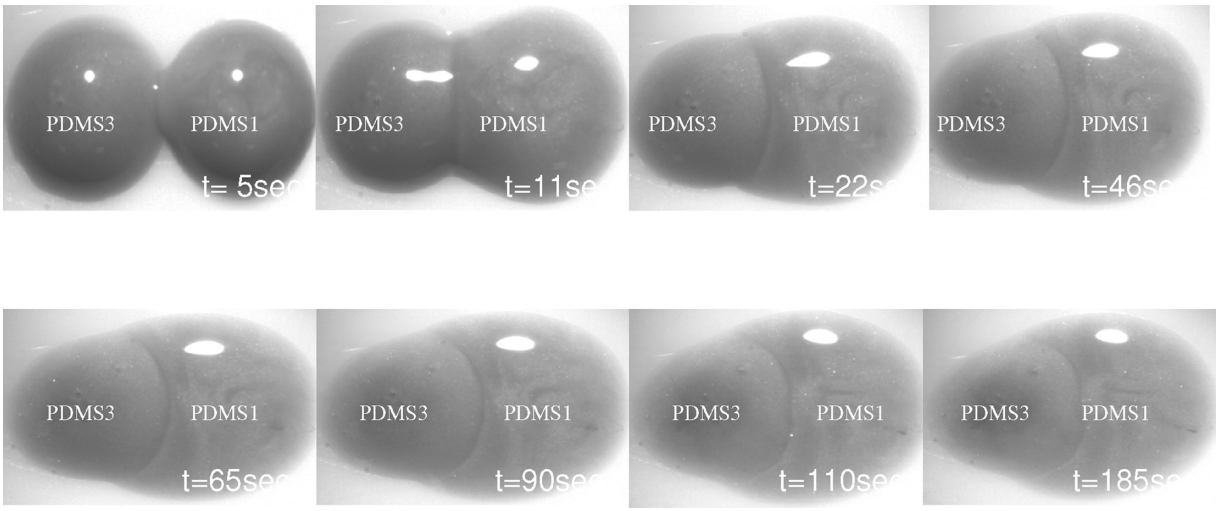

Figure 6. An illustration of the encapsulation at 25 °C in the case of the PDMS1/PDMS3 pair.

Furthermore, Figure 6 provides an experimental illustration of the fact that the less viscous polymer tended to encapsulate its more viscous counterpart but at a low shear rate.

We remind that the digital image analysis software was used to analyze the obtained pictures. A neck radius x can be calculated in situ by our special optical device and mathematical program. Images of neck growth evolution were taken as a function of time to obtain the dimensionless neck radius (x/r), where x is the length of the neck between the two particles and r is the mean radius of the droplet. In the short time, when the neck radius grew quickly, all images were analyzed. It is get of easy process. When the encapsulation is more pronounced, a special tool in the Matlab program is developed here to evaluate with accuracy the boundary between the two drops and also the real angle θ. At longer time, it is difficult to provide a clear distinction of the thinner neck radius; a lot of experiments have been carried out and repeated to have a reproduction of the measurements. These details are included in the text.

To illustrate this phenomenon, the initial encapsulation strain rate between t_1 and t_2 can be calculated from the results of Figure 4 by

$$\dot{\varepsilon}_i = \frac{x_2 - x_1}{x_2} \frac{1}{t_2 - t_1} \tag{8}$$

The initial strain rate between two times can be calculated. x_1 and x_2 are respectively the neck radius at t_1 and t_2, respectively. It appeared that $\dot{\varepsilon}_i$ was 0.07 and 0.43 s^{-1} for PDMS3 and PDMS1, respectively.

According to Frenkel, the strain rate is assumed to be constant throughout the complete domain. The obtained lower values of $\dot{\varepsilon}_i$ in our experiments allowed us to confirm that the observed encapsulation proven also at low strain and stress rate. In the literature of coextrusion process, a lot of papers accord this phenomenon only to the effect of higher shear rate in which the lower viscous polymer is forced to encapsulate the higher viscous one (viscous dissipation). The obtained results confirmed that this phenomenon is not the sole mechanism; it is shown here, experimentally, that encapsulation can occur at low shear or strain rate, and it is governed by surface and viscous forces.

Moreover, the higher viscosity ratio between PDMS3 and PDMS1 seems to be the principal parameter and the motor of the encapsulation phenomena (confirmed previously by the calculated *Ca* number: viscous forces are very higher compared to capillary forces). For the clarity purpose of our paper, only the experiments of PDMS1/PDMS3 are presented. The same conclusions were noted in the experiment observations of PDMS1/PDMS2 and PDMS2/PDMS1 couples.

b. Influence of Drop Geometry. Figure 7 illustrates the role of the drop geometry in the kinetics of encapsulation of model fluids. PDMS3 was chosen to investigate the role of the drop geometry. The encapsulation kinetics were recorded with two drops of different shape (the diameter of the smaller drop is one-half of the bigger one) (Figure 8), and their kinetics were compared to the PDMS3/PDMS3 evolution with identical drops. The slow kinetics of the (x/r) evolution could be noted with PDMS3/PDMS3 using a different drop shape.

We aware that it is very difficult to find, in the first times, if there is encapsulation of small droplet by the bigger one. However, a special numerical program using Matlab allowing finding the real boundary and distinction between two drops observed by the polarized microscope coupled to the CCD camera. It is important to note that the concentration of SiC was varied in each drop to make a clear distinction between drops. We have also thanked to use a pigment colorant for each drops, but it is too difficult to choose a suitable miscible colorant which cannot change the rheological behavior and the surface tension properties.

In conclusion, these simple experiments provided an illustration to the fact that the drop geometry was also a key parameter that needed to be taken into account. At a small shear rate, the small drop was encapsulated by the bigger one. When the drops had the same geometry, a high surface contact area interfacial area/volume allowed the chains to diffuse, thus increasing the density across the interface/interphase.

This was quantitatively confirmed with the parameter t_{99}. PDMS3/PDMS3 drops of equal shape required 42.3 s to coalesce while 140 s was necessary for the second system. However, the initial slope was quite similar for both of the studied systems (0.07 s^{-1} for the first as compared to 0.067 s^{-1} for the second).

3.3. Experimental Investigation of the Encapsulation Phenomenon of High Molecular Weight Model Polymers. *a. Effect of Elasticity and Interfacial Tension.* In order to investigate

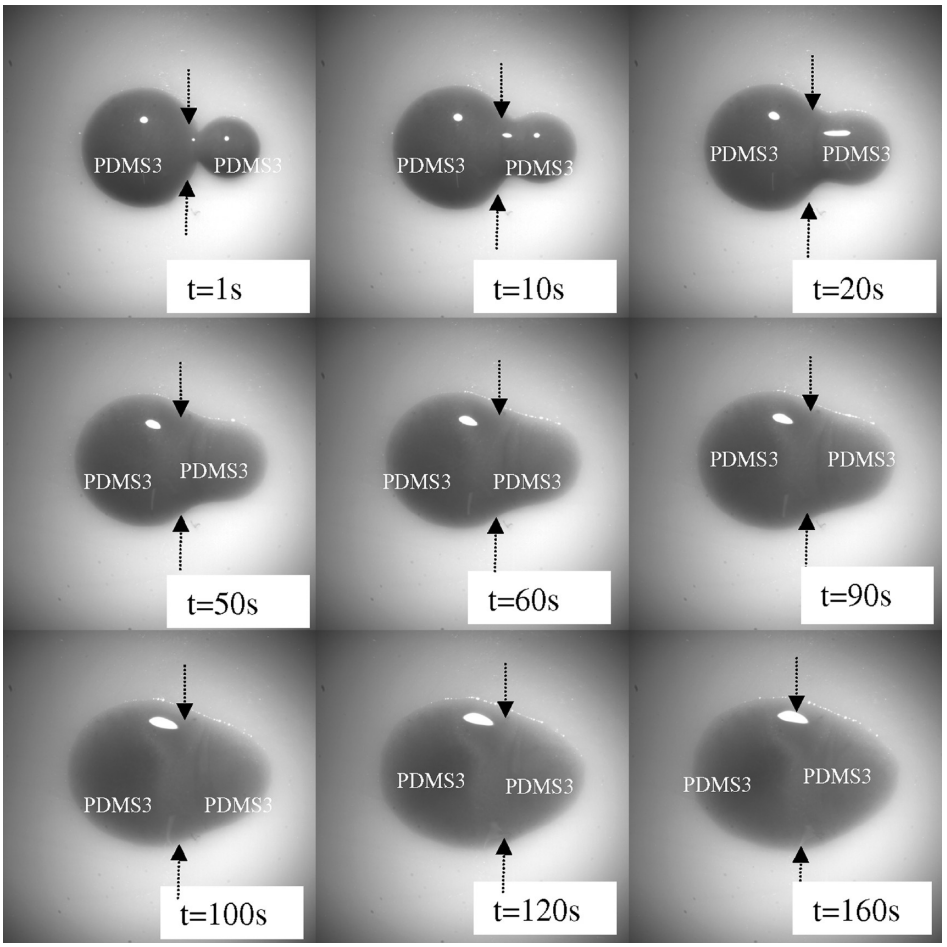

Figure 7. An illustration of the encapsulation at 25 °C in the case of two PDMS3/PDMS3 pairs differing in geometry.

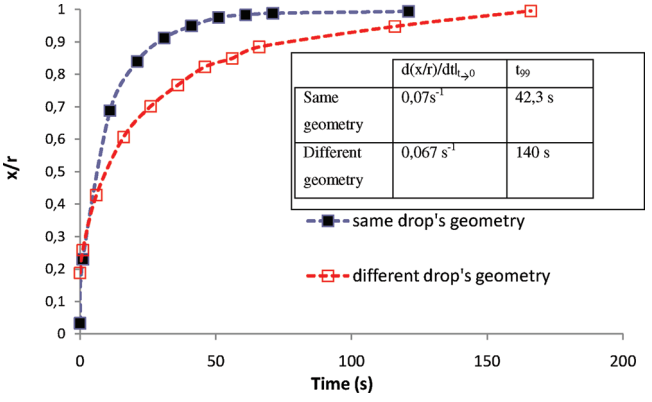

Figure 8. Influence of the drop geometry effect on the PDMS3/PDMS3 encapsulation phenomenon at 25 °C (r and x are the radius and neck radius, respectively).

the effect of the elasticity and interfacial tension on the encapsulation phenomenon, studies were performed on completely miscible, high molecular materials based on PVDF/PMMA which they present close viscosities. Poly(vinylidene fluoride) (PVDF)/poly(methyl methacrylate) (PMMA) multiphase systems, as an example of crystalline/amorphous polymers, are miscible in the molten state. Furthermore, and according to their rheological behavior, the chosen materials present the same viscosity ratio especially at 240 °C. The following investigation allows us also to probe the effect of elasticity and interfacial tension on the encapsulation kinetic.

Numerous studies of this blend have been carried out from scientific and technological view points. The miscibility of PVDF/PMMA couple is thought to be the result of an interaction between oxygen and carboxyl groups of PMMA and hydrogen atom of PVDF. Their lower Flory−Huggins parameter confirmed this purpose ($\chi \cong -0.07$).[46,47]

Furthermore, the kinetic of coalescence was assessed at several temperatures and the comparison between the encapsulation kinetics of PVDF/PVDF, PMMA/PMMA, and PVDF/PMMA are given in Figure 9a,b.

Meanwhile, it is important to note that the radius of drops is calculated here in situ with time, and it is not constant on the contrary of the assumptions of Frenkel. The different curves given the x/r versus time do not start at the same x/r. First of all, even that all images are treated, not all the points are in the represented in the plotted figures for the clarity purpose and to make distinction when we compare the kinetics in the beginning times. Moreover, the difference is around 0.05 in the majority of measurements. This is an experimental error because it was too difficult to prepare the same drops with identical size (r = 4054 μm). The granulate diameter can be varied slightly in the preparation of high molecular weight polymer or with 2D wetting

dx.doi.org/10.1021/ma201151k |*Macromolecules* 2012, 45, 441–454

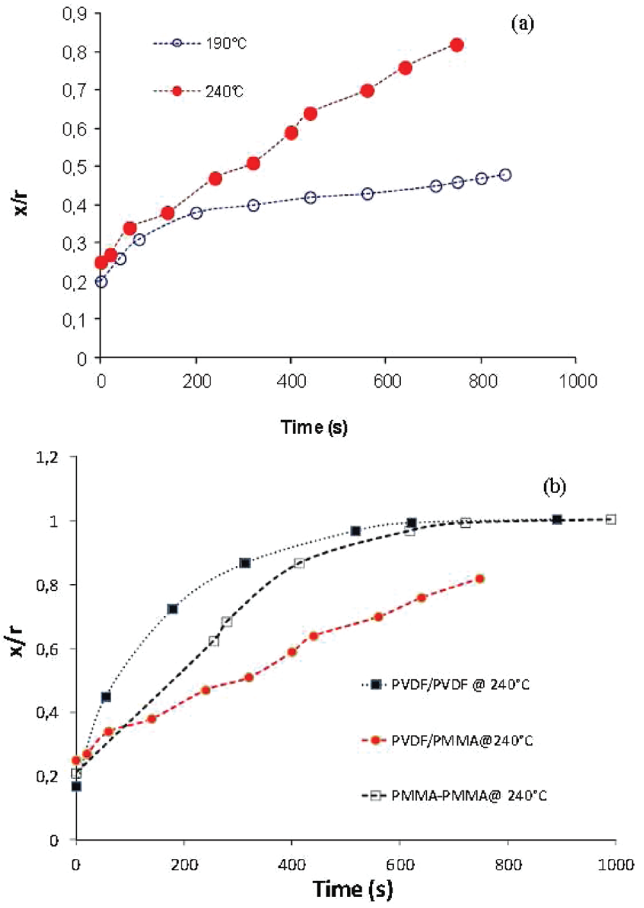

Figure 9. (a) Encapsulation kinetic curves of PVDF/PMMA drops at 190 and 240 °C (r and x are the radius and neck radius, respectively). (b) Comparison of the encapsulation kinetics at 240 °C between PVDF/PVDF, PMMA/PMMA, and PVDF/PMMA.

on the PTFE substrate of PDMS depending on their spreading parameter. This small difference in the initial size does not affect any way the kinetics of encapsulation, and the radius and neck radius are calculated with accuracy.

As reported in the rheological part, both of PVDF and PMMA are more viscous at 190 °C compared to 240 °C. We note that the kinetic of coalescence in Figure 9a is slower at 190 °C. The faster kinetics at this higher temperature is attributed to higher mobility of chains which can be represented by the lower viscosity. The coalescence at the 240 °C is nearly complete (x/r = 0.9) compared to 190 °C.

In this part dedicated to high molecular polymers based on PVDF and PMMA, it is of the interesting case which the materials have a close viscosity and the contrast of elasticity and the surface tension with PTFE We remind that the viscosity ratio is close to 1 despite the increasing of temperature from 190 to 240 °C (from 1.15 to 1, respectively). The only discriminating parameter between these two fluids which is not taken into account in the reduced time (t_r) is their elasticity.

Figure 9b shows that the PVDF/PMMA coalescence kinetics is less pronounced as compared to those of PVDF/PVDF and PMMA/PMMA. The relaxation times are respectively 0.31 and 0.25 s for PMMA and PVDF. They are more elastic compared to PDMS. The values of interfacial tension of PVDF and PMMA with PTFE are 16.5 and 31.8 mN/m at 240 °C, respectively. This large difference of interfacial tension has also a role here. The spreading parameter of PVDF is then more higher compared to PMMA. They are also negative allowing the partially wetting PDMS and to not accelerate the coalescence. However, they coalescence totally and their x/r reach the value x/r = 1.

Despite the close viscosities of the two materials, it is clearly shown here that driving interfacial forces can be counterparts by the elastic forces according to the higher relaxation times of PVDF and PMMA, respectively.

Muller et al.[31] observed an increase of the elasticity lead to an increase of the reduced time in the case of Boger fluids. Indeed, it appears that the higher interfacial tension and relaxation time of PVDF and PMMA attenuated the rate of coalescence as it was confirmed experimentally of PMMA/PMMA in comparison with PVDF/PVDF system. It is too surprising also that the calculated t_{99} are very close for the two couples even the lower kinetic coalescence of PMMA/PMMA. The corresponding x/r reaches the value 1 beyond 600 s even though the coalescence rate of PMMA/PMMA is less than PVDF/PVDF before this time. The lower relaxation time (i.e., elasticity) of PMMA seems to be the principal parameter at longer time which can explain the counterbalance of its higher interfacial tension.

In addition, PVDF/PMMA represents the lower coalescence kinetics, and its t_{99} is much longer than those of PVDF/PVDF and PMMA/PMMA. Furthermore, no encapsulation phenomenon could be seen in the different experimental conditions as demonstrated by Figure 10, despite the difference in elasticity and surface tension.

The observed development represented the signature of the kinetics of diffusion where the macromolecular chains intertwined and gradually became replaced by a more robust interphase. This result can be explained on the basis of the diffusion mechanism which was significant in the case of symmetrical polymer/polymer interface. The encapsulation appeared to be hindered by the interdiffusion process in the case of miscible pair system despite their elasticity and surface tension contrast. In conclusion, the viscosity ratio seems to be a motor of encapsulation mechanism, and its role is very complicated and should be coupled to the elasticity and interfacial tension.

Furthermore, the results from an optical investigation of the coalescence kinetics of two drops corroborated those obtained through rheology of the bilayer systems according to the procedure given in our previous work in the PE/PA6 reactive pair system. For the sake of clarity, additional details of the experimental procedure can be found in previous articles of Qiu and Bousmina[32] as well as Lamnawar and Maazouz.[19,33−35]

In the present work, the rheological measurements were carried out under small amplitude of deformations (linear viscoelastic region) to rule out the effect of flow brought by large deformation on the diffusion process, to obtain the linear viscoelastic region; a prior dynamic strain sweep test was accomplished. The strain amplitude was chosen (5%).

An example of the evolution of G' and $G'(t)/G'(0)$ of bilayer with healing time at 190 and 240 °C is depicted in Figure 11. The noticeable G' increment of bilayer with time is attributed to the diffusion process taking place at the polymer−polymer interface. The present interface will be replaced by the robust interphase between the neighboring layers according to the mutual diffusion of chains. For more clarity, the increment with time is disposed in a form of $G'(t)/G'(0)$ compared with neat polymers, where the near linearity of $G'(t)/G'(0)$ to 1.0 of the neat polymers through the whole measuring time indicates their stability at the

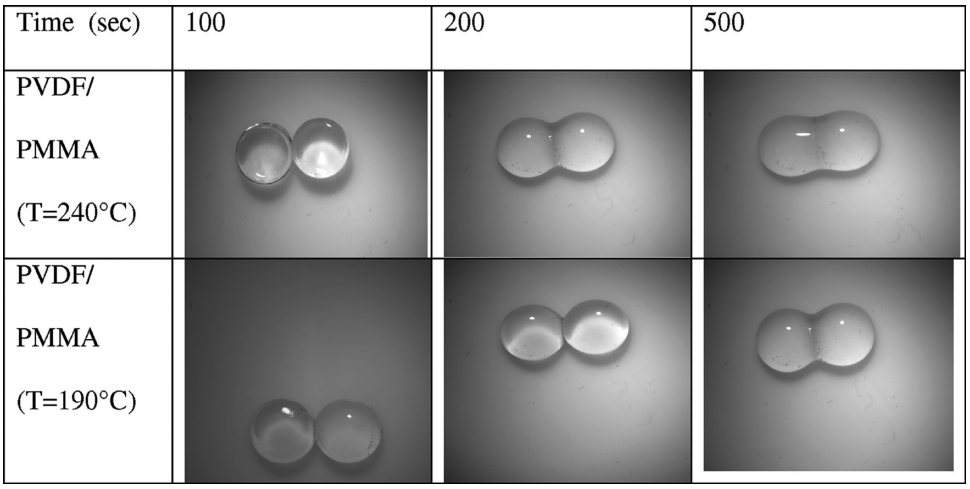

Figure 10. Illustration of the coalescence/encapsulation kinetics of PVDF/PMMA drops at 190 and 240 °C.

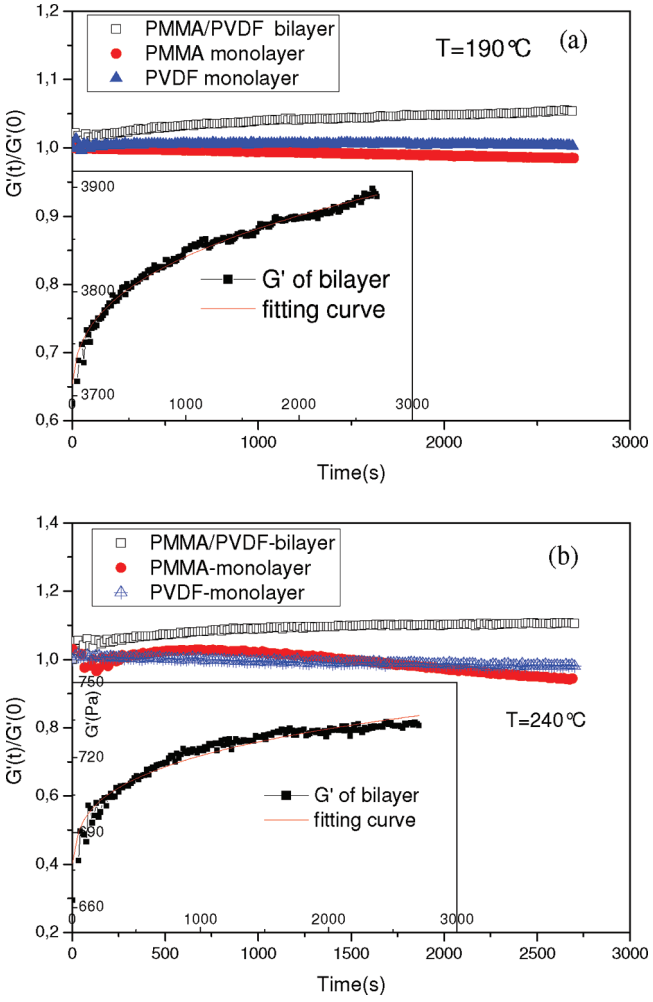

Figure 11. Evolution of G' and $G'(t)/G'(0)$ of PVDF/PMMA bilayer with healing time and corresponding fit curve at ω = 1 rad/s under different temperatures: (a) 190 °C; (b) 240 °C.

temperature measuring. The increase in storage modulus is a signature of the diffusion processes across the interface. As the mass transport proceeds, the initial weak interface strengthens

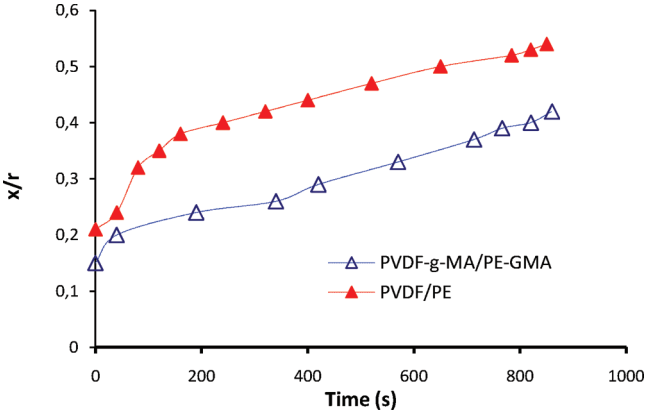

Figure 12. Comparison of encapsulation curves at 240 °C featuring PVDF-*g*-AM/PE-GMA and PVDF/PE drop systems (r and x are the radius and neck radius, respectively).

with time due to the interpenetration of polymer chains that are continuously delivered by the polymer bulk reservoirs of the two sides of the interface. Hence, the kinetics of diffusion is very fast at 240 °C compared to 190 °C according to the increase of chains mobility with temperature.

In conclusion, the rheological investigation confirmed that the kinetic of diffusion can be followed and demonstrated with the increasing of storage modulus. This observation is corroborated with optical observations which the slop of the neck radius increase significantly at 240 °C according to higher mobility of chains and the decreasing of the relaxation time compared to 190 °C. Hence, we can note a perfect ad equation between rheological and optical observations.

b. Effect of Chemical Compatibilization. Moreover, the same approach was applied to functionalized polymers in order to investigate the effect of reactive compatibilization on the encapsulation phenomenon. Two pairs of reactive polymers at interfaces based on PE-GMA (glycidyl methacrylate)/PVDF-*g*-MA (maleic anhydride) as well as a nonreactive material at an interface based on PVDF/PE were selected. The kinetics of coalescence were evaluated at several temperatures. For example, Figure 12 shows a comparison of the encapsulation kinetics of these systems at 240 °C.

dx.doi.org/10.1021/ma201151k |*Macromolecules* 2012, 45, 441–454

The interfacial reaction between MA and GMA functions certainly attenuated the coalescence kinetics.

As shown in Figure 2, the viscosities of PE-GMA are smaller than PE. On the contrary, this of PVDF-*g*-MA is more higher compared to PVDF. Meanwhile, it is also important to note that the viscosity ratio of PE-GMA/PVDF-*g*-MA is lower compared to PE/PVDF, allowing a higher mobility of chains before reaction (diffusion-controlled reaction mechanisms). Furthermore, results from an optical investigation of the coalescence kinetics of two drops corroborated those obtained through rheology of the bilayer systems. Indeed, the observed phenomena and the results can be analyzed based on the physicochemical mechanisms involved in the diffusion/reaction interfaces. As can be seen from Figure 13, the elastic modulus of PE-GMA/PVDF-*g*-MA increased with time as compared to the nonreactive system based on PE/PVDF. In fact, no significant increase in viscosity was found in the case of the latter, thus confirming that the observed phenomenon was caused by the reactivity at the interface at a low oscillation frequency.

In addition, the viscosity ratio at 240 °C of PE/PVDF is much higher compared to PE-GMA/PVDF-MA. It is decreased to 1.5 from 3.2 (half that of the nonreactive system). Note that the reactive system stay having a higher viscosity ratio, but this value is more close to 1 than this of the nonreactive system. The lower viscosities of functionalized polymer allow a higher mobility of chains to move for reaction (diffusion-controlled reaction).

Since a reactive polymer bilayer generates graft or block copolymers near the interface, each block (or graft) component can easily entangle with (or stick to) the corresponding homopolymer located near the interface. Thus, such an interface should be strengthened as compared to an interface without graft or block copolymers. This could increase the viscosity of the reactive polymer bilayer as opposed to that of a nonreactive polymer bilayer. Consequently, such a behavior was evidence of the formation of a copolymer from the reaction of PE-GMA and the carboxylic and maleic anhydride functions of functionalized PVDF.

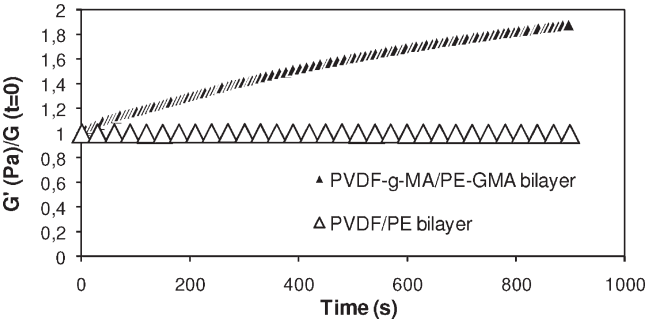

Figure 13. Comparison of the evolution of $G'(\mathrm{Pa})/G'(t=0)$ vs time at 240 °C for a reactive bilayer PE-GMA/PVDF-*g* system and a nonreactive one based on PE/PVDF.

Finally, no encapsulation was noted in these cases despite that the zero shear viscosity ratio of PE-GMA/PVDF-*g* MA was close to 1.5 (Figure 14). The triggered copolymer at the interface hinders the encapsulation kinetic. On the contrary, the nonreactive system as PE/PVDF with a higher viscosity ratio (close 3.2) confirms that the PVDF tend to encapsulate the PE. This reaction was confirmed by the rheological tool, and no encapsulation between the reactive drops is noted at this temperature on the contrary of PE/PVDF pair.

This seemed to confirm that it was essential to couple the viscosity ratio to the physicochemical affinity and viscoelastic parameters in order to gain a better understanding of the encapsulation phenomenon in multiphase systems. In addition, the role of the viscosity ratio, elasticity ratio, and layer ratio should also be investigated, thereby coupling to the reaction rate/compatibilization phenomena of the polymer/polymer interface. Indeed, for a reactive system, the encapsulation phenomenon could be reduced or eliminated by the creation of a copolymer at the interface. Finally, this system is more complex which it is essential to couple the role of viscoelasticity and the physicochemical affinity. More investigations are in progress to decouple the role of these parameters.

4. CONCLUSIONS

Throughout the investigation, the encapsulation phenomenon was recorded by optical observations as a function of the viscosity ratio, elasticity, and the polymer/substrate interfacial tension. All the experiments are conducted on a PTFE substrate. The effects of viscosity, surface tension, and relaxation time are highlighted. The model experiments do not require any labeling, and the spirit here is based on the decoupling between flow or shear and the physical parameters.

1. The investigation of model Newtonian polymers based on poly(dimethylsiloxane) of varying molar masses showed that the viscosity ratio of the material was a key parameter and that it had a considerable influence on the kinetic of encapsulation phenomenon. The used polymers are fluids at room temperature. One can perfectly control their rheological behavior and surface tension. The coalescence experiments are conducted on a PTFE substrate. The encapsulation of two drops or molten particles placed in close vicinity of each other was monitored with a CCD camera at regular intervals time. An experimental illustration was

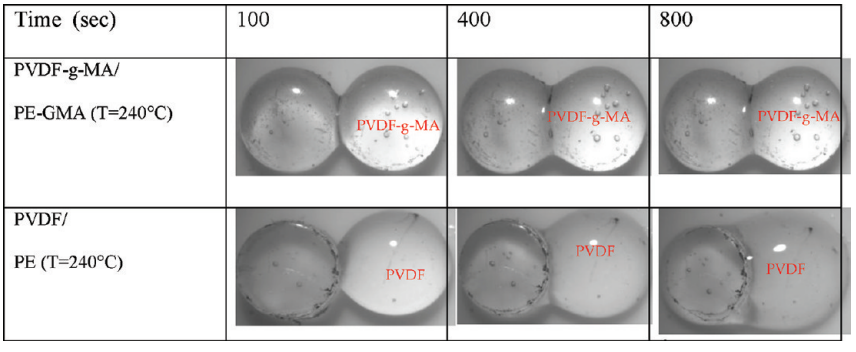

Figure 14. Illustration of the encapsulation kinetics of PVDF-*g*-MA/PE-GMA and PVDF/PE drops at 240 °C.

given to confirm that the less viscous polymer tended to encapsulate its more viscous counterpart but at low strain and shear rate. Throughout all the experiment, the mechanisms were purposed for each system and discussed based on the theories of molecular forces or Brownian motion governing diffusion at the polymer polymer interfaces. Furthermore, the effect of surface tension is highlighted through this investigation and should be taken into account especially for the high viscous materials. The interfacial tension played a role for the more viscous materials at the same temperature and was found to accelerate or slow down the kinetics depending on the spreading parameters. The results can also explained based on the theories of Ostwald ripening which predict a decrease in the droplet growth rate with increasing interfacial tension in contrast to the theories of coalescence. We demonstrated that the encapsulation phenomenon for these model fluids governed by two contributions: (i) the wetting capacity and (ii) the diffusion at the interface.

On the other hand, this work showed that the viscosity ratio coupled to drop geometry and of the material was a key parameter and that it had a considerable influence on the encapsulation kinetics. At a low shear rate, the small drop was encapsulated by the bigger one. A high surface contact/volume allowed the chains to diffuse, thus increasing the density across the interface/interphase. Meanwhile, these results also confirmed that the viscous dissipation mechanism (encapsulation at high shear rate) given in the literature was not the sole mechanism present to explain the phenomenon. On the basis of these results, we demonstrate that the viscosity ratio seems to be a motor of encapsulation mechanism, and its role is very complicated and should be coupled to the elasticity and interfacial tension.

2. In a second step, the kinetics of encapsulation of the high molecular weight based on PVDF/PMMA were assessed at several temperatures and compared to the corresponding results for PVDF/PVDF and PMMA/PMMA used as references. The present asymmetric, viscoelastic system is completely compatible and fully characterized. PVDF and PMMA have the same viscosity behavior. Indeed, the effect of elasticity and interfacial tension was highlighted. Furthermore, no encapsulation phenomenon was seen despite the difference in elasticity and surface tension for PVDF/PMMA with the same viscosity as compared to the symmetrical references. The encapsulation appeared to be hindered by the interdiffusion process in the case of compatible pair system despite their elasticity and surface tension contrast. The observed development represented the signature of the kinetics of diffusion where the macromolecular chains intertwined and gradually became replaced by a more robust interphase. The present phenomenon has been confirmed by the rheological investigation of the present bilayer systems.

3. Finally, the same approach was applied to functionalized polymers. Two pairs of reactive polymers at interfaces based on PE-GMA (glycidyl methacrylate)/PVDF-*g*-MA (maleic anhydride) as well as a nonreactive material at an interface based on PE/PVDF were selected.

In addition, the viscosity ratio at 240 °C of PE/PVDF is much higher compared to PE-GMA/PVDF-MA. It is decreased to 1.5 from 3.2 (half that of the nonreactive system). Note that the reactive system stay having a higher viscosity ratio, but this value is more close to 1 than this of the nonreactive system. The lower viscosities of functionalized polymer allow a higher mobility of chains to move for reaction (diffusion-controlled reaction). This reaction was confirmed by the rheological tool, and no encapsulation between the reactive drops is noted at this temperature on the contrary of PE/PVDF pair. The triggered copolymer at the interface hinders the encapsulation kinetic. On the contrary, PE/PVDF with a higher viscosity ratio (close 3.2) confirms that the PVDF tend to encapsulate the PE. The results obtained by an optical investigation of the encapsulation kinetics of two drops corroborated rheological data of the bilayer systems. The observed phenomena and the results were analyzed based on the physicochemical mechanisms involved in the diffusion/reaction interfaces. This seemed to confirm that the parameter should be coupled to the physicochemical affinity and viscoelastic parameters in order to give a better understanding of encapsulation phenomenon in multiphase systems. Meanwhile, the present system is more complex which it is essential to couple the role of viscoelasticity and the physicochemical affinity. More investigations are in progress to decouple the role of these parameters. Finally, the role of the viscosity ratio, elasticity ratio, and the interfacial tension should also be investigated, thereby coupling to the reaction rate/compatibilization phenomenon at the polymer/polymer interface. Indeed, for a reactive system, the encapsulation defect could be reduced or eliminated by the creation of a copolymer at the interface.

Hence, the obtained results rendered it possible to decouple the influence of the viscoelastic parameters to flow, interfacial tension, thereby highlighting a number of macroscopic effects that were governed by the interdiffusion or reaction of macromolecular chains at the interface to give a better understanding of encapsulation phenomenon in multiphase systems.

AUTHOR INFORMATION

Corresponding Author

*E-mail: abderrahim.maazouz@insa-lyon.fr (A.M.).

ACKNOWLEDGMENT

The authors express their appreciation to the reviewers for their constructive and meticulous assessment of this work. They thank Arkema for providing samples and their help to progress this work.

REFERENCES

(1) Orive, G.; Hernandez, R. M.; Gascon, A. R.; Callafiore, R.; Chang, T. M. S.; Hortelano, G. *Nature Med.* **2003**, *9*, 104–107.
(2) Goosen, M. F. A.; O'Shea, G. M.; Gharapetian, H. M.; Chou, S.; Sun, A. M. *Biotechnol. Bioeng.* **1985**, *27* (2), 146–150.
(3) Deng, Q.; Anilkumar, A. V.; Wang, T. G. *J. Fluid Mech.* **2007**, *578*, 119–138.
(4) Tomotika, S. *Proc. R. Soc. London, A* **1935**, *150*, 322–337.
(5) Southern, J. H.; Ballman, R. L. *J. Appl. Polym. Sci.* **1973**, *20*, 175.
(6) Everage, A. E. *Trans. Soc. Rheol.* **1973**, *17*, 629.
(7) Lee, B. L.; White, J. L. *Trans. Soc. Rheol.* **1974**, *18*, 467.
(8) Southern, J. H.; Ballman, R. L. *J. Polym. Sci.* **1975**, *13*, 863.
(9) Dooley, J.; Hyun, K. S.; Hughes, K. *Polym. Eng. Sci.* **1998**, *38*, 1060–1071.
(10) Wilson, G. M.; Khomami, B. *J. Non-Newtonian Fluid Mech.* **1992**, *45*, 355–384.
(11) Theofanous, G.; Nourgaliev, R.; Khomami, B. *J. Non-Newtonian Fluid Mech.* **2007**, *143*, 131–132.
(12) Yih, C. S. *J. Fluid Mech.* **1967**, *27*, 337–352.
(13) Zhao, R.; Macosko, C. W. *J. Rheol.* **2002**, *46* (1), 145–167.
(14) Schrenk, W. J.; Bradley, N. L.; Alfrey, T. J.; Maack, H. *Polym. Eng. Sci.* **1978**, *18* (08), 620.

(15) White, J. L.; Ufford, R. C.; Dharod, K. R.; Price, R. L. *J. Appl. Polym. Sci.* **1972**, *16*, 1313–1330.
(16) Khomami, B. *J. Non-Newtonian Fluid Mech.* **1990**, *37*, 19–36.
(17) Joseph, D. D. *Fluid Dynamics of Viscoelastic Liquids*; Springer : New York, 1990.
(18) Karagianis, H. A. N.; Vlachopoulos, J. *Rheol. Acta* **1990**, *29*, 71–81.
(19) Lamnawar, K.; Maazouz, A. *Polym. Eng. Sci.* **2009**, *49*, 727–739.
(20) Boonen, E.; Van Puyvelde, P.; Moldenaers, P. *J. Rheol.* **2010**, *54* (6), 1285–1306.
(21) Boonen, E.; Van Puyvelde, P.; Moldenaers, P. *ACS Appl. Mater. Interfaces* **2010**, *2* (7), 2140–2146.
(22) Jeelani, S. A. K.; Windhab, E. J. *Chem. Eng. Sci.* **2009**, *64*, 2718–2722.
(23) Sourki, A. F.; Huneault, M. A.; Bousmina, M. *Polymer* **2009**, *50*, 645–653.
(24) Hobbs, S. Y.; Dekkers, M. E. J.; Watkins, W. H. *J. Mater. Sci.* **1988**, *23*, 1225–1230.
(25) Luo, H.; Pozrikidis, C. *Comput. Fluids* **2009**, *38*, 564–571.
(26) Scribben, E.; Aaron, P. R.; Baird, G. D. *J. Rheol.* **2005**, *49*, 1159.
(27) Nemirovski, N.; Siegmann, A.; Narkis, M. *J. Macromol. Sci., Part B: Phys.* **1995**, *34*, 459–475.
(28) Gupta, A. K.; Srinivasan, K. R. *J. Appl. Polym. Sci.* **1993**, *47*, 167–184.
(29) Hemmati, M.; Nazokdast, H.; Panahi, H. S. *J. Appl. Polym. Sci.* **2001**, *82*, 1129–1137.
(30) Reignier, J.; Favis, B. D.; Heuzey, M.-C. *Polymer* **2003**, *44*, 49–59.
(31) Muller, J.-D.; Bousmina, M.; Maazouz, A. *Macromolecules* **2008**, *41*, 2096–2103.
(32) Qiu, H.; Bousmina, M. *Macromolecules* **2000**, *33*, 6588–6594.
(33) Lamnawar, K.; Maazouz, A. *Rheol. Acta* **2006**, *45*, 411–424.
(34) Lamnawar, K.; Maazouz, A. *Rheol. Acta* **2008**, *47*, 383–397.
(35) Lamnawar, K.; Baudoin, A.; Maazouz, A. *Eur. Polym. J.* **2010**, *46*, 1604–1622.
(36) Owens, D. K.; Wendt, R. C. *J. Appl. Polym. Sci.* **1969**, *13*, 1741–1747.
(37) Kwak, D. Y.; Cheung, L. K.; Park, C. B.; Neumann, A. W. *Polym. Eng. Sci.* **1998**, *38*, 757–764.
(38) Wu, S. *Polymer Interface and Adhesion*; Marcel Dekker: New York, 1982.
(39) Frenkel, J. *J. Phys.* **1945**, *9*, 385.
(40) Bellehumeur, C. T.; Kontopoulou, M.; Vlachopoulos, J. *Rheol. Acta* **1998**, *37*, 270.
(41) Johnson, K. L.; Kendall, K.; Roberts, A. D. *Proc. R. Soc. London., Ser. A* **1971**, *324*, 301–313.
(42) Mazur, S.; Plazek, D. J. *Prog. Org. Coat.* **1994**, *24*, 225–236.
(43) Lin, Y. Y.; Hui, C. Y.; Jagota, A. *J. Colloid Interface Sci.* **2001**, *273*, 267–282.
(44) Fortelný, I.; Živný, A.; Jůza, J. *J. Polym. Sci., Part B: Polym. Phys.* **1999**, *37*, 181–187.
(45) Pokluda, O.; Bellehumeur, C. T.; Vlachopoulos, J. *AIChE J.* **1997**, *43*, 3253.
(46) Chang, D.-H.; Kim, J.-K. *Macromolecules* **1989**, *22*, 1914–1921.
(47) Yang, H.-H.; Chang, D.-H.; Kim, J.-K. *Polymer* **1994**, *35* (7), 1503–1511.
(48) Becu, L.; Sautereau , H.; Maazouz, A.; et al. *Polym. Adv. Technol.* **1995**, *6*, (5), 316−325.

Macromolecules

Article

pubs.acs.org/Macromolecules

New Insight to the Mechanism of the Shear-Induced Macroscopic Alignment of Diblock Copolymer Melts by a Unique and Newly Developed Rheo−SAXS Combination

T. Meins,[†] K. Hyun,[‡] N. Dingenouts,[†] M. Fotouhi Ardakani,[§] B. Struth,[∥] and M. Wilhelm*[,†]

[†]Institute for Chemical Technology and Polymer Chemistry, Karlsruhe Institute of Technology (KIT), Engesserstraße 18, 76128 Karlsruhe, Germany

[‡]School of Chemical and Biomolecular Engineering, Pusan National University, Jangjeon-Dong 30, Busan 609-735, Korea

[§]Laboratory for Electron Microscopy, Karlsruhe Institute of Technology (KIT), Engesserstraße 7, 76131 Karlsruhe

[∥]DESY, Notkestrasse 85, D-22607 Hamburg, Germany

ABSTRACT: In-situ flow alignment kinetics of a self-assembled lamellar phase polystyrene-*block*-polyisoprene (PS-*b*-PI, M_w = 26 500 g/mol, f_{PS} = 51%) diblock copolymer melt has been investigated in detail under mechanical large amplitude oscillatory shear (LAOS) utilizing a unique Rheo−SAXS combination developed in cooperation with the German Electron Synchrotron (DESY) in Hamburg. This marks the first time that the strain and time dependence of the shear-induced macroscopic perpendicular orientation of the lamellar microstructure could be monitored with a time resolution of 10 s per frame. Two mechanical parameters were used to compare the structural evolution and dynamics with the mechanical response of the sample. The mechanical loss modulus G″, which was directly obtained from the in situ Rheo−SAXS experiments performed with a stress controlled rheometer, and the nonlinear parameter $I_{3/1}$, which was calculated by Fourier-transform-rheology (FT-rheology) from the raw stress data obtained from a strain controlled rheometer. Significant correlations between the mechanical response and the structural changes of the sample were detected. For example, the orientation times τ calculated from both the X-ray and the mechanical measurements showed a power law dependence with $\tau \sim \gamma_0^{-1.6}$ (in situ SAXS) and $\sim \gamma_0^{-2}$ (FT-rheology). Furthermore, the quality of the macroscopic orientation at large shear amplitudes (γ_0 = 2 and γ_0 = 3) was found to be a function of the mechanical excitation time. A better macroscopic orientation for shorter mechanical excitation times was achieved, while longer experimental times caused an unexpected reduction in the degree of orientation. In these situations, ex-situ SAXS and TEM studies indicated that a stable biaxial distribution of the lamellar microstructure that was preferentially orientated both parallel and perpendicular was formed, causing a drastic change in the response of both the mechanical quantities $G''(t)$ and $I_{3/1}(t)$.

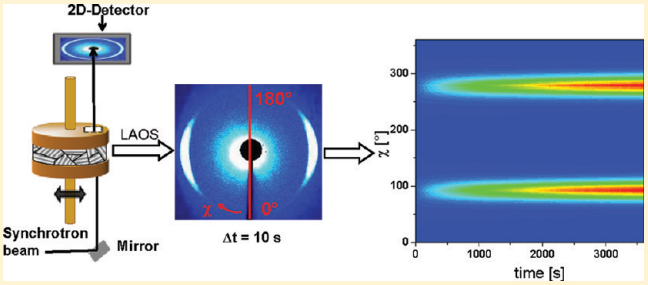

INTRODUCTION

Certain types of soft matter, such as liquid crystals, amphiphiles, and block copolymers, self-assemble into nanostructured morphologies below their order−disorder transition temperature (T_{ODT}) as a way to minimize highly unfavorable enthalpic contributions to the free energy. Self-assembly usually leads to a polydomain structure with locally anisotropic ordered domains (grains) that are randomly orientated throughout the whole sample, resulting in a macroscopically isotropic material.[1,2] However, many practical applications including functional membranes, anisotropically charged materials and photon conductors require that the final material is macroscopically anisotropic.

Application of an external stimulus, such as an electric, magnetic, or mechanical field, can then be used to obtain the preferred macroscopic alignment.[3−9] As an example of this, shear flow was shown to be a feasible method for macroscopically aligning symmetric block copolymers and liquid crystals, see refs 10−17 and citations within. Therefore, it is important to understand the mechanism and kinetics of mechanically induced macroscopic orientation as a way to optimize this alignment and to tailor processing conditions for specific applications. This would result in, for example, new functional materials that could be used as templates for nanoparticles in certain advanced applications[18−20] as well as a way to improve nonequilibrium molecular dynamics simulations.[21−24] Furthermore, controlling the kinetic pathway of the macroscopic alignment by varying the mechanical shear field enables the exploitation of nonequilibrium or transient morphologies as first shown in a recent study[25] on low molecular weight liquid

Received: June 30, 2011
Revised: November 21, 2011
Published: December 19, 2011

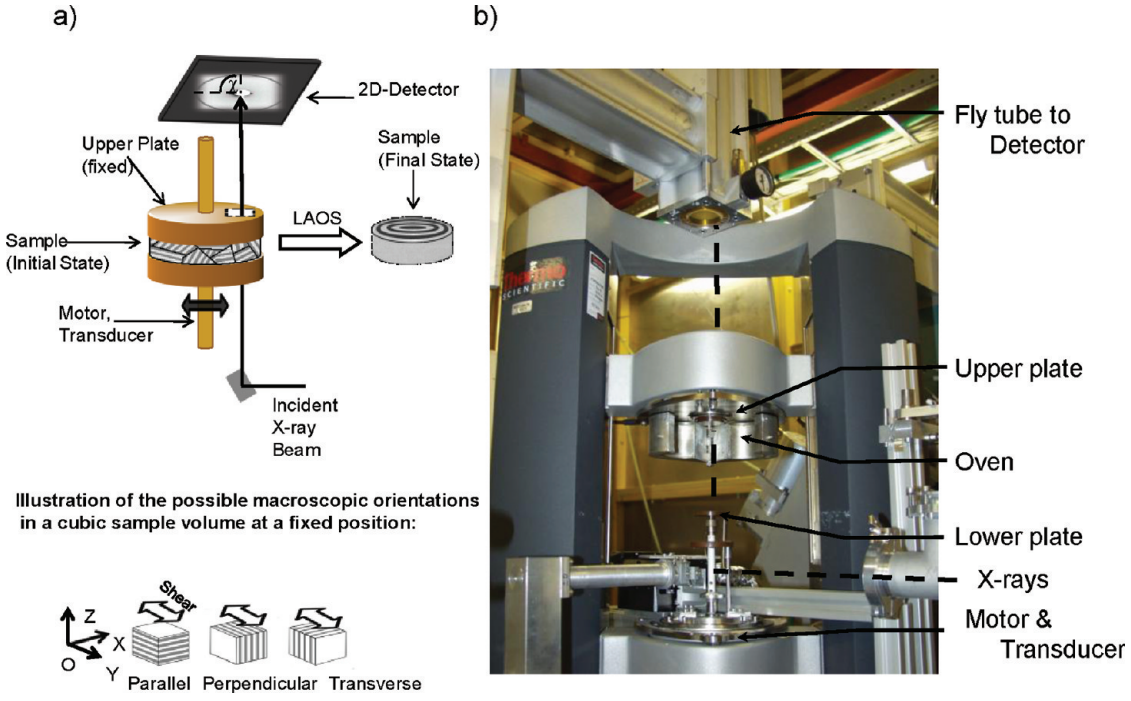

Figure 1. Unique Rheo−SAXS apparatus used in this work, where a Pilatus 100k was used as a 2D-Detector. (a) Schematic representation of the experimental setup, the Cartesian coordinate *OXYZ* is defined such that the vertically reflected X-ray beam is parallel to the *OZ* axis. Oscillatory shear is applied by the lower sample plate which is where the transducer is located. The upper sample plate remains fixed during the experiments. (b) Picture of the real setup, which is located at the beamline BW1 at the HasyLab.

crystals. Additionally, processing conditions can be optimized with respect to the quality of the alignment and the shear duration.

For the macroscopic orientation of symmetric block copolymers, large amplitude oscillatory shear (LAOS) was shown to be the preferred method because it allows for different orientations of the unit normal of the lamellae.[26] In most studies, the morphological characterization of a shear-oriented block copolymer was performed ex-situ, making it difficult to study the kinetic processes involved in the alignment.[27−32] While birefringence is a powerful tool to follow the progress of orientation online,[31,32] enabling data processing on a microsecond scale, it unfortunately provides no direct information on nanometer length scale structural changes and requires ex-situ experiments to provide reliable morphological information. Therefore, there would be a clear advantage to have online SAXS or SANS measurements instead.

It is also important to note that ex-situ measurements are more difficult to interpret due to variations caused by sample preparation, loading, thermal history of the sample and possible distortion of the aligned structures caused by cooling, unloading, and trimming. Furthermore, only a limited amount of kinetic data is then available. On the other hand, these ex-situ measurements provide information about structural properties along all three directions, which is not accessible by currently available in situ methods.[33] Nevertheless, there is a pressing need to develop an in situ measurement technique with adequate time resolution that can correlate induced structural changes in the melt state with the mechanical response and that can also follow the kinetic pathway of the macroscopic orientation process under precise experimental conditions. In this context SAXS[34,35] and SANS[36−40] experiments were shown to be the method of choice for evaluating the mechanism and kinetics of the orientation process on a length scale corresponding to the molecular dimension and for also providing an average over the representative sample volume.

In recent years, much effort has been devoted to online monitoring of the influence of nonlinear mechanical excitations on various phase separated systems.[41,42] Different approaches and experimental setups were developed for in situ experiments utilizing a variety of shear cells. An example of this is the Couette geometry,[34,40,43] which was used to generate macroscopic orientation in block copolymer solutions under defined mechanical conditions. While this setup has the advantage of investigating the alignment along two distinct trajectories, it is mainly limited to polymer solutions. In addition, capillary[44] and multipass[45] rheometers were used to mimic the influence of high shear rates to the macroscopic alignment under processing conditions.

Nevertheless, parallel plate (or cone plate) geometries are preferred for examining the underlying kinetic pathway of the block copolymer melt orientation process as a function of shear frequency, strain amplitude, temperature, and the duration of shear. The advantages of this approach include precise dynamic mechanical measurements, simple sample preparation, ease of temperature control and the appropriate range of frequencies and strain amplitudes required for polymer melts having glass transition temperatures below and above room temperature. A disadvantage of this approach is that the sample volume may become too large, resulting in an undesired absorption phenomenon that may interfere with the scattering experiments. In recent years, there have been new developments using parallel plate geometries where precise rheological measurements and simultaneous characterization of mechanically induced structural changes via X-ray scattering were obtained. With this approach, Polushkin et al.[46,47] and Garcia-Gutierrez et al.[48] were able to investigate two distinct directions, but could only perform these experiments on a

dx.doi.org/10.1021/ma201492n | *Macromolecules* 2012, 45, 455−472

very small sample volume, which unfortunately limits the use of large amplitude oscillatory shear (LAOS).

To overcome this drawback, a new and unique Rheo−SAXS combination[25] was developed. This setup (see Figure 1) enables full rheological characterization of polymer melts while simultaneously probing mechanically induced structural changes on a nanometer length scale. In contrast to other experimental parallel plate setups where the primary X-ray beam is directed through the rheometer gap along the shear vector direction,[1,47,49] the primary synchrotron X-ray beam is directed through the sample along the shear gradient (*OZ* axis)[25] (see Figure 1a).

Previous in situ experiments published in the literature focused on the influence of the applied shear flow on the hierarchically structured material, but did not associate these effects with the underlying mechanical response under nonlinear flow. The aim of this work is to study in situ the effect of large amplitude oscillatory shear (LAOS) using varying strain amplitudes on the macroscopic alignment kinetics of a symmetric PS-*b*-PI diblock copolymer (M_w = 26 500 g/mol, f_{Ps} = 51%, PDI = 1.04) and then to compare the mechanical response with the changing structural dynamics.

This is the first time that the macroscopic perpendicular orientation could be studied in situ. In these experiments, the mechanical response of the diblock copolymer melt was monitored and characterized in situ using the time dependence of the mechanical loss modulus G''. As a measure of the degree of mechanical nonlinearity, the time dependence of the intensity of the third harmonic $I(3\omega_1)$ to the fundamental $I(\omega_1)$ as determined by Fourier-transform-rheology (FT-rheology)[50,51] was examined, where $I(3\omega_1)/I(\omega_1)$ is here denoted as $I_{3/1}$. As FT-rheology is one of the most sensitive methods for determining mechanical nonlinearity,[52] $I_{3/1}$ was used to guide additional ex-situ SAXS experiments, acting as a "mechanical" monitor for the progress of macroscopic orientation.

In this publication, the first results generated from the new in situ Rheo−SAXS setup to correlate mechanical and structural responses of a block copolymer melt under mechanical excitation are reported. New information on the kinetic pathway of a lamellar perpendicular orientation process is reported. Specifically, it was found that increasing the shear amplitude significantly affects the orientation time τ, but, as the mechanical excitation exceeds a certain level, the overall degree of alignment is actually reduced as a deordering process starts to occur for γ_0 = 2 and γ_0 = 3. Additionally, a first explanation of the structural dynamics involved during this process is presented based on the nonlinear mechanical response of the sample. The orientation time calculated for all LAOS-experiments exhibited a power law dependence on the strain amplitude.

EXPERIMENTAL METHODS

Materials and Sample Preparation. The polystyrene-*block*-polyisoprene (PS-*b*-PI) diblock copolymer was synthesized via sequential anionic polymerization of styrene followed by isoprene under high vacuum at room temperature using toluene as the solvent and *sec*-butyllithium as the initiator. Aliquots of the PS precursor were taken for molecular characterization. The purification of the solvents and monomers is described in detail elsewhere.[53] The final PS-*b*-PI anion was terminated with a small amount of methanol. The synthesized polymer was stabilized with 0.1 wt % 2,6-di-*tert*-butyl-4-methylphenol to avoid oxidation of the unsaturated PI block. The terminated diblock copolymer was participated in methanol.

The PS-*b*-PI sample and its precursor were characterized by GPC equipped with a refractive index monitor and an UV-detector. The elution solvent was THF and calibrated with commercially available monodisperse PS standards (Polymer Standard Service). With the molecular weight of the precursor determined by GPC the PS-*b*-PI composition was calculated from the ^{1}H NMR (M_w = 26 500 g/mol, PDI = 1.04 and f_{PS} = 51%).

The resulting PS-*b*-PI was freeze-dried from a cyclohexene solution (10 wt %) under high vacuum for 10 h. The obtained pure powder was hot pressed under vacuum at 140 °C into sample discs with diameters of 13 respectively 36 mm and a thickness of approximately 1 mm. The pressure applied to the block copolymer melt was adjusted to 3 bar. The obtained discs were used without a further annealing step.

External Rheology. Additional rheological measurements were conducted using oscillatory shear flow and a parallel plate geometry (diameter of 13 mm and gap of 1 mm) on a shear strain controlled ARES rotational rheometer from TA Instruments. All rheological tests were performed under direct strain oscillation (DSO).

The order−disorder transition temperature (T_{ODT}) was 205 °C as detected by a drastic decrease in the temperature dependence of the low frequency ($\omega_1/2\pi$ = 1 Hz) mechanical storage (G') and loss (G'') moduli when applying a heating rate of 0.5 K/min. The dynamic frequency sweeps were performed using a frequency range from 0.1 to 10 Hz while applying a strain amplitude of γ_0 = 0.02. These conditions ensured a linear mechanical response of the sample.

The LAOS experiments were conducted using the same conditions as the in situ LAOS experiments performed with the Rheo−SAXS combination. The nonlinear parameter $I_{3/1}$ was calculated from the mechanical raw data utilizing a custom-made experimental setup described elsewhere.[51]

External SAXS Measurements. The morphology of the synthesized PS-*b*-PI was determined by ex-situ 2D-SAXS measurements (Hecus S3-Micro X-ray system) using a point microfocus source, 2D-X-ray mirrors and a two-dimensional CCD-Detector from Photonic Science. In addition, a block collimator system was used to ensure low back ground scattering. With this system, the $\vec{q}$ vector that can be detected varies from 0.08 to 4.7 nm^{-1}.

To follow the time evolution of the nonlinear parameter, the LAOS experiments were stopped at specific times to examine ex-situ the state of orientation. The samples were rapidly cooled to room temperature (within 10 min) and the normal force was thoroughly adjusted to compensate for thermal shrinking until the state of orientation was frozen by the glassy PS blocks. At this point, the sample was removed from the shear geometries. For each state of orientation, the macroscopic orientation along each of the three major directions was determined at three points in the sample, i.e., at a radius of 2 mm (position c, γ_{local} = 0.31 γ_0), 4 mm (position b, γ_{local} = 0.62γ_0) and 5.5 mm (position a, γ_{local} = 0.85γ_0). The investigation of these three different positions revealed the influence of the strain gradient caused by the parallel plate geometry on the macroscopic orientation.

Transmission Electron Microscopy. For TEM material was taken at a radius of 5.5 mm from the center of the sample disk. A 1 mm × 1 mm piece was cut from the sample disk at room temperature, while it was ensured the orientation of each of the axes of the piece corresponds to the (*OX*, *OY*, *OZ*) direction of the flow cell. For the cutting the sample was embedded into a epoxy resin and cut with a cryomicrotome (Ultracut E + Leica FC4) at a temperatures of −160 °C with a thickness of approximately 60 nm. First 100 μm were cut into the sample to obtain a clean face and avoid any surface artifacts. For all three spacial direction (normal, radial and tangential) two slices were prepared with a cutting speed of 0.05 mm/s and placed on copper grids. Prior the TEM investigations, the samples were stained by exposing them to vapor over OsO_4 for 40 min. Images are recorded using a Zeiss LEO 912 Ω (120 keV) microscope.

Rheo−SAXS Setup. In-situ Rheo−SAXS measurements were carried out at the beamline BW1 of the DORIS III storage ring at HASYLAB (DESY, Hamburg, Germany). The selected wavelength was 0.1267 nm.

In order to achieve a well-defined mechanical excitation as well as to precisely detect the mechanical response, the beamline is equipped

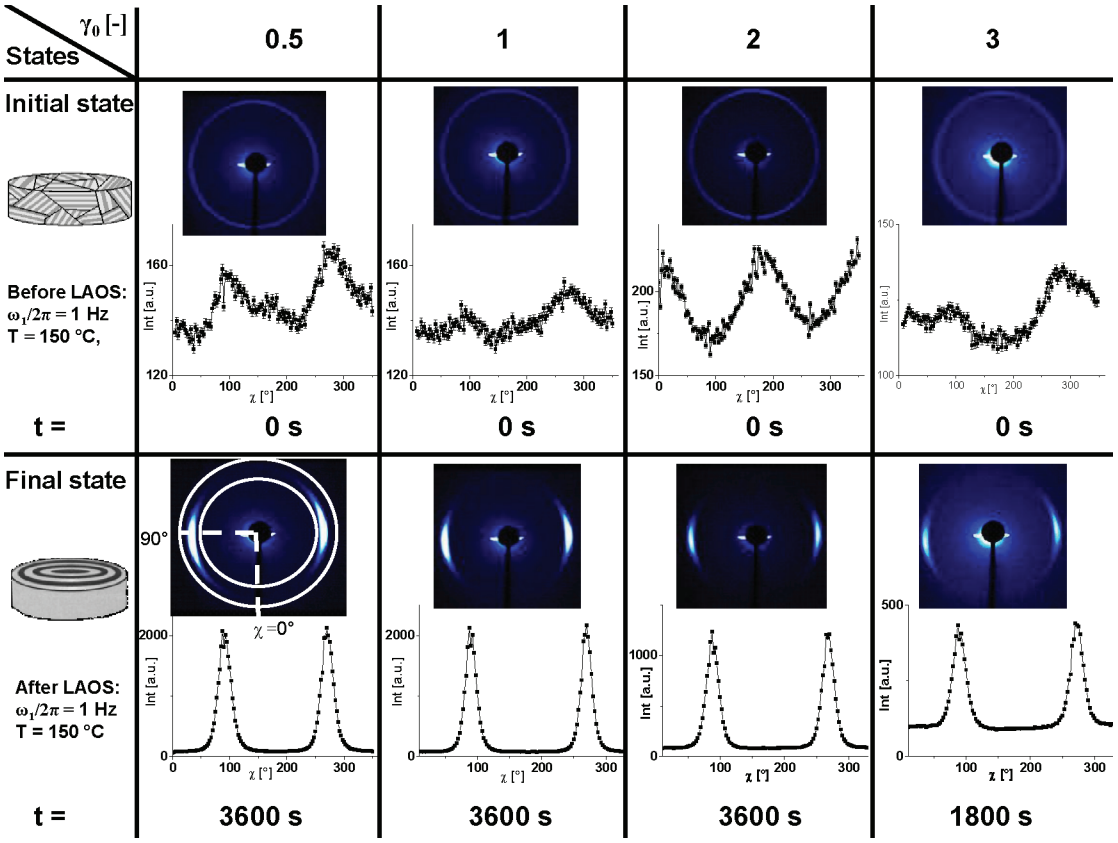

Figure 2. Summary of the applied experimental conditions, including 2D-SAXS images and azimuthally averaged 1D-plots of the first order reflection representing the orientation of the sample before and after shear was imposed. The peak width of the azimuthally averaged reflections at 90° and 270° were taken to monitor the alignment process during LAOS.

with a specially modified stress controlled rheometer (Mars II, Thermo Scientific). For this rheometer, custom-made Vespel comprised parallel plate geometries were made with a diameter of 36 mm. These geometries contain thin windows of 0.3 mm thickness at 15.5 mm distance from the center of the plate (γ_{local} = 0.86 γ_0) to minimize scattering and absorbance effects which reduce the beam intensity. The rheometer is equipped with a custom-made cylindrical heating cell operating with nitrogen as an inert gas to avoid oxidative decomposition of the polymer melts. The accessible temperature range lies between room temperature and 250 °C, with an accuracy of ±0.5 °C.

To redirect the intrinsically horizontal synchrotron X-ray beam by 90°, a diamond (004) reflection (see Figure 1) was used.[25] The scattered intensities were recorded by a 2D detector (Pilatus 100k) positioned at a distance of 2.54 m above the sample. The acquisition time between each 2D-SAXS frame was adjusted to 11 s corresponding to 10 s exposure and 1 s delay time for data storage and triggering. The data were evaluated by the commercially available Datasqueeze software and self-written MatLab routines.

In-situ Rheo–SAXS Sample Loading and Experimental Procedure. The parallel plate geometries were tempered at 150 °C for 1 h before zero fixture was performed. The sample disk was mounted between the plates and slightly squeezed until the whole geometry surface was covered with the polymer melt. All rheological measurements were performed using the controlled stress deformation mode (CD) of the Mars rheometer.

After annealing the sample for 20 min, a strain sweep test (0.001 < γ_0 < 7) was conducted ($\omega_1/2\pi$ = 1 Hz, T = 150 °C) to determine the mechanical linear and nonlinear regimes. Afterward, and prior to each orientation experiment, the block copolymer melt was heated to 225 °C, which is 20 °C above the order–disorder transition temperature, and then tempered for at least 20 min to remove previous thermal and deformation history. The sample was then cooled to the measurement temperature while constantly adjusting the gap to control for thermal shrinkage of the sample and the sample geometries. To avoid squeeze flow induced orientation, a normal force of less than 0.05 N (~50 Pa) was applied. At the measurement temperature, the sample was allowed to temper for another 20 min. Before and after each LAOS experiment, mechanical frequency sweeps in the linear regime were preformed and SAXS images of the initial state were recorded.

RESULTS

A detailed understanding of the kinetic pathway for the overall alignment of self-assembled block copolymers under mechanical shear flow is an essential factor for the optimized fabrication of nanoscaled, hierarchical anisotropoic ordered systems. Moreover, precise information about the optimum processing parameters (temperature, frequency, deformation and shear duration) could improve production processes for other advanced functional materials. Therefore, the shear-induced macroscopic perpendicular orientation of a well-defined symmetric PS-*b*-PI diblock was studied by applying large amplitude oscillatory shear (LAOS) excitations.

In-Situ SAXS Studies. In-situ synchrotron X-ray investigations were performed to clarify the time dependent orientation evolution at varying strain amplitudes γ_0 for the macroscopic alignment process of the lamellar microstructure using a 10 s time resolution for each 2D-SAXS frame. The mechanical excitation frequency was fixed at 1 Hz for all measurements, meaning that every 2D-SAXS image averaged only 10 mechanical oscillation cycles. According to the sample loading procedure described in the Experimental Methods, the following strain amplitudes of γ_0 = 0.5, γ_0 = 1, γ_0 = 2, and γ_0 = 3

dx.doi.org/10.1021/ma201492n | *Macromolecules* 2012, 45, 455–472

were analyzed with a constant shear frequency of 1 Hz at T = 150 °C.

The applied experimental conditions are summarized in Figure 2. Additionally, representative 2D-SAXS patterns for undeformed PS-*b*-PI and for the final state of orientation after LAOS experiments are shown (see Figure 2). The initial, unaligned state shows ringlike images, which are typical for multidomain macroscopically isotropic morphologies. However, after the LAOS experiment, the appearance of anisotropic SAXS patterns with pronounced reflections at 90° and 270° indicated a macroscopic perpendicular alignment of the lamellae.

The azimuthally averaged SAXS patterns are displayed beneath each 2D-image where these images show a slight anisotropy in the scattering pattern even for the undeformed samples. These small amounts of preorientation are due to slight squeeze flow alignments, which could not be avoided even by restricting the normal force to values below 0.05 N (~50 Pa) and adjusting the measurement gap. As this preorientation is weak compared to the strong reflections caused by the mechanical excitation, it was assumed that the effect of these prealignments did not dominate the experimental results.

A representative contour plot (γ_0 = 0.5) of all 354 azimuthally averaged 2D-SAXS patterns recorded during a macroscopic orientation experiment ($t_{experiment}$ = 3600 s) of the PS-*b*-PI is shown in Figure 3. From this representation, the

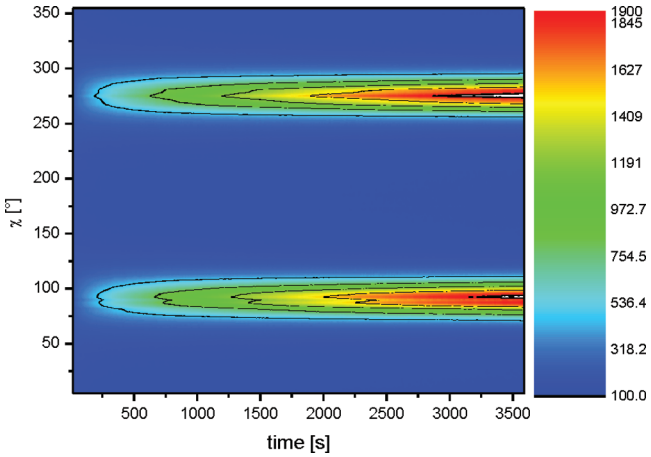

Figure 3. Contour plot of the azimuthally averaged 2D-SAXS patterns recorded during the macroscopic orientation of PS-*b*-PI under large amplitude oscillatory shear (LAOS: $\omega_1/2\pi$ = 1 Hz, γ_0 = 0.5, T = 150 °C).

development of scattered reflections in an interval corresponding to a minimum scattered wave vector of $|\vec{q}|$ = 0.25 nm^{-1} and an upper boundary of $|\vec{q}|$ = 0.35 nm^{-1} is clearly seen. It is interesting to note that during the entire mechanical excitation only the scattered reflections at 90° and 270° appeared, which indicate the development of a macroscopic perpendicular orientation with the unit normal of the lamellae preferentially orientated along the *OX* axis. In addition, there were no detectable scattered reflections at 180° and 360° corresponding to a transverse orientation for all experiments carried out in this work.

These results were the first obtained for block copolymer melts using a newly developed prototype Rheo−SAXS combination located at the storage ring DORIS III. At this stage of development, it was not possible to precisely determine the primary beam intensity throughout the experiment. However, selective measurements of the primary beam intensity were performed before and after each dynamic shear experiment. These measurements do not, however, reveal primary beam intensity fluctuations, which may also occur during the in situ experiments due to fluctuations in the beam-orbit.

Therefore, at this stage, the evolution of the azimuthally averaged peak width was taken as a measure for the kinetics of the alignment process. As it showed a stronger variation (by a factor of 3) between its initial and final values during the macroscopic alignment process, the χ-dependence of the peak width was chosen for study instead of the radial averaged (θ-dependence) peak width. By fitting the scattering reflection centered around 90° in the 2D-SAXS images for all measurement times with a Gaussian function, the standard deviation σ_{SAXS} was calculated and used to quantify the shear induced changes for the orientation distribution of the lamellae with unit normal parallel in the (*OX*, *OY*) plane.

For all four strain amplitudes used in this study, a drastic decrease in the peak width occurred in the first 100 to 250 s of the experiment (see Figure 4). The starting values for the standard deviation vary between approximately σ_{SAXS} = 19° for the two lowest strain amplitudes (γ_0 = 0.5 and γ_0 = 1), σ_{SAXS} = 15° for γ_0 = 2, and σ_{SAXS} = 12° for γ_0 = 3. For γ_0 = 0.5 and γ_0 = 1, the decrease of the peak width of the azimuthally averaged first order reflection occurred throughout the whole mechanical excitation, but reached a plateau after 2000 and 1300 s, respectively. There was only a slight deviation from the plateau value of σ_{SAXS} = 10.5° to σ_{SAXS} = 10.7° for γ_0 = 1 after 2000 s, while for γ_0 = 0.5, there was no observable deviation from the plateau value with time. The appearance of a plateau indicated that a stable macroscopic orientation was formed despite the continuing dynamic mechanical excitation.

The two higher strain amplitudes (γ_0 = 2 and γ_0 = 3) exhibited similar behavior in the beginning of the experiment, i.e. showed a rapid decrease in σ_{SAXS}, but, instead of reaching a plateau, formed a minimum after t = 240 s (γ_0 = 2) and t = 100 s (γ_0 = 3). This behavior was in strong contrast to the LAOS experiments at lower strain amplitudes ($\gamma_0 \leq 1$) and indicated that this state of macroscopic orientation was not stable under continuing mechanical stimulus. For both of these strain amplitudes ($\gamma_0 \geq 1$), the peak width began to increase from its minimum value of σ_{SAXS} = 9° (γ_0 = 2) and σ_{SAXS} = 8° (γ_0 = 3) at t = 350 s and t = 150 s, respectively. The insets in Figure 4 display this broadening of the scattering reflections, after reaching the minimum, at characteristic time intervals. For a strain amplitude of γ_0 = 3, σ_{SAXS} developed exponentially toward a stable less orientated but, however, value of σ_{SAXS} = 9.8° approximately 1000 s after passing through the minimum, while for γ_0 = 2, an overshoot was detected instead.

The deordering process for γ_0 = 2 began with a rapid increase in σ_{SAXS} in the first 300 s after the minimum was reached, followed by a pseudo plateau with $\sigma_{SAXS} \approx$ 12°. This state of reduced orientation was not stable and the block copolymer lamellae began to reorientate after 1700 s as the LAOS experiment continued. As a consequence, σ_{SAXS} decreased over the observed experimental time until a final value of $\sigma_{SAXS} \approx$ 10° was reached.

These first results obtained from the in situ Rheo−SAXS measurements indicate that, for higher strain amplitudes ($\gamma_0 >$ 1), the quality of the macroscopic orientation is a complex

dx.doi.org/10.1021/ma201492n | *Macromolecules* 2012, 45, 455−472

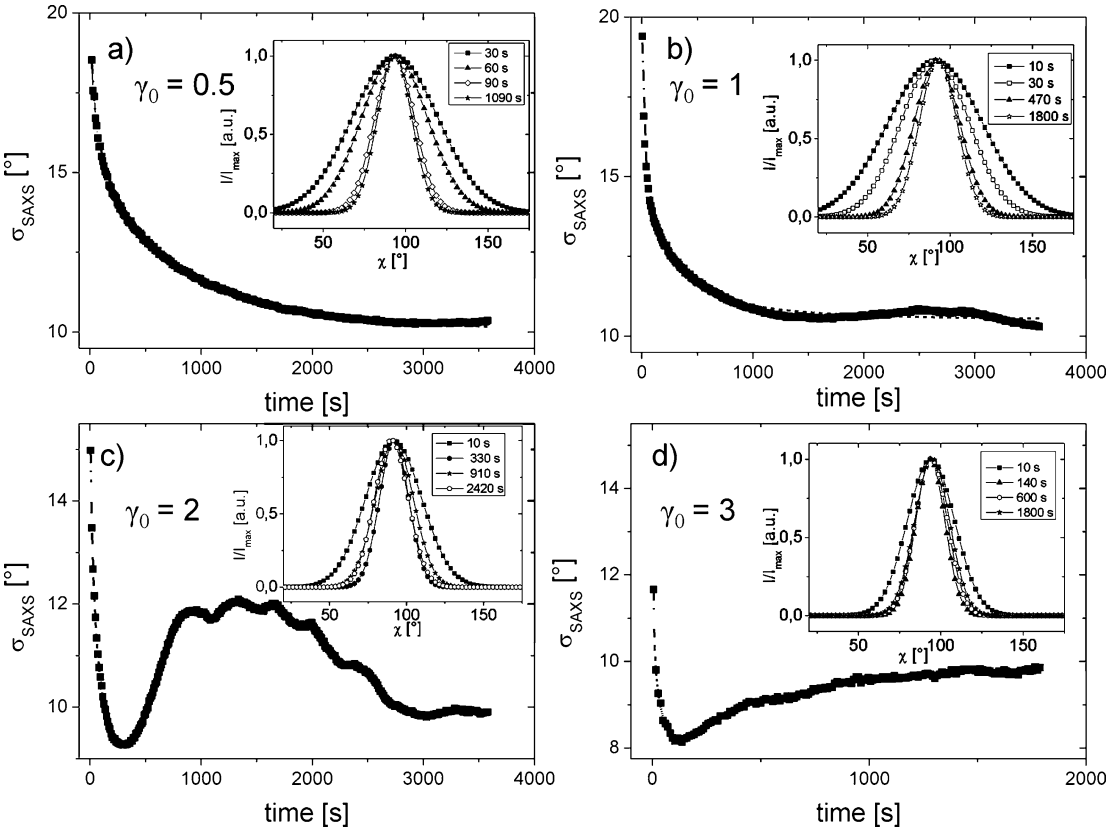

Figure 4. Time dependence of the standard deviation σ_{SAXS} calculated by fitting the first order scattered reflections at 90° (2D-SAXS images) with a Gaussian function. The dotted lines represent the stretched exponential fit (see text). The insets represent the azimuthally averaged first order scattered reflections at characteristic times during the mechanical excitation. (a) γ_0 = 0.5, (b) γ_0 = 1, (c) γ_0 = 2, and (d) γ_0 = 3.

process, the state and degree of orientation is strongly affected by the duration of the applied mechanical shear field.

Rheological Studies. As the goal of this study was to compare structural dynamics caused by the applied mechanical excitation with the viscoelastic response of the polymer melt, the mechanical response of the block copolymer melt was analyzed in terms of the mechanical loss modulus $G''(t)$ and a qualitative measure of the mechanical nonlinearities via the parameter $I_{3/1}(t)$. The nonlinear parameter could only be determined accurately, utilizing a special experimental setup[54] that included a strain controlled rheometer for the evaluation of the stress−strain raw data. For all rheological measurements, a data point was collected every 10 s to ensure a similar time resolution as the in situ 2D-SAXS data.

It is important to note that the mechanical measurements utilizing the in situ Rheo−SAXS setup were performed within the controlled deformation mode (CD) of the Mars rheometer. The experimental data obtained with the ARES rheometer were performed by controlling the strain position during an oscillation cycle (separated motor and transducer technology, direct strain oscillation, DSO).[55]

a. Mechanical Quantities (G′, G″). Figure 5 displays the time behavior of the mechanical storage modulus G′ and loss modulus G″ for γ_0 = 0.5 at T = 150 °C and $\omega_1/2\pi$ = 1. At the chosen experimental conditions, the in situ measured mechanical viscoelastic behavior in the nonlinear regime was dominated by the viscous (G'') rather than the elastic (G') modulus (tan δ = 3−4). This ratio increased at the end of the LAOS experiment where tan δ = 6. Because of the dominance of the mechanical loss modulus under the chosen experimental

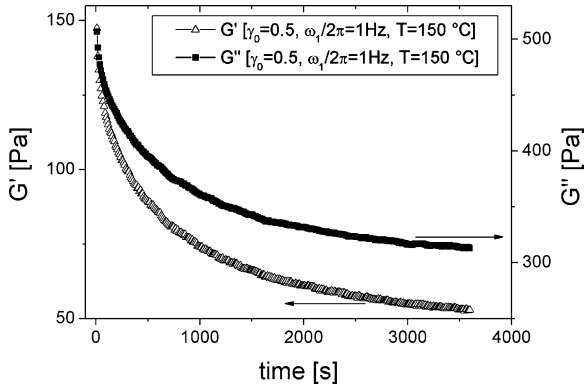

Figure 5. Time dependence of the mechanical viscoelastic properties G' (open triangle) and G'' (squares) under LAOS ($\omega_1/2\pi$ = 1 Hz, γ_0 = 0.5, T = 150 °C). As the loss modulus G'' dominates the mechanical response under the applied conditions, it was chosen to online monitor the alignment process.

conditions, $G''(t)$ was chosen to monitor the macroscopic orientation process.

Before further discussing the time evolution of G'' during LAOS, the linear dynamic mechanical response is examined for both the CD and DSO measurements of the undeformed macroscopically isotropic and for the perpendicular macroscopically anisotropic block copolymer melt (γ_0 = 0.5) under small amplitude oscillatory shear (SAOS) (see Figure 6).

The storage and loss moduli are plotted as a function of frequency. The data for the LAOS experiments at higher strain amplitudes were not included here as they showed similar

dx.doi.org/10.1021/ma201492n | *Macromolecules* 2012, 45, 455−472

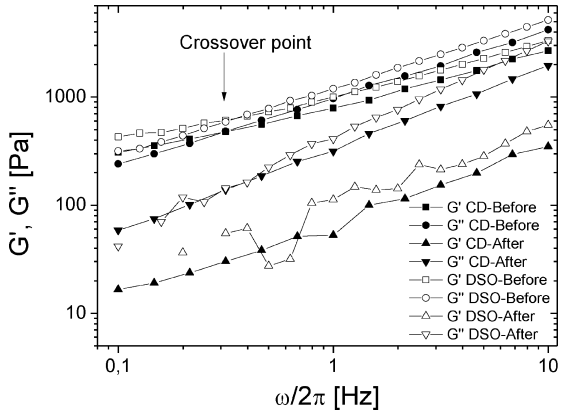

Figure 6. Linear dynamic mechanical response under SAOS (T = 150 °C, γ_0 = 0.02) before and after LAOS ($\omega_1/2\pi$ = 1 Hz, T = 150 °C, γ_0 = 0.02). The linear viscoelastic response obtained by CD (filled symbols) and DSO (open symbols) measurements show the same trend and a crossover point between $G'(\omega/2\pi)$ and $G''(\omega/2\pi)$ at $\omega/2\pi$ = 0.32 Hz. The linear mechanical moduli determined under CD respectively DSO differed by a factor of 1.5.

behavior and, thus, did not seem to depend on the applied strain amplitude. In the frequency sweep test, a clear crossover point (tan δ = 1) at $\omega/2\pi$ = 0.32 Hz was observed for the randomly orientated sample measured by CD and DSO measurements. This crossover indicates that a transition between the mechanical response being dominated by the microstructure (tan $\delta \leq 1$) and the so-called transition zone II[27] (tan $\delta \geq 1$), where the viscous flow dominates the viscoelasticity of PS-*b*-PI diblock copolymers, occurred.

The slope of $G''(\omega/2\pi)$ in the low frequency region of the undeformed sample was approximately equal to 0.5. This value is typical for lamellar self-assembled block copolymers.[49,56,57] For the oriented sample, the slope of G'' increased to about 0.8 and the crossover point did not appear within the investigated frequency region. Furthermore, the values for the storage and loss moduli in the low frequency region were significant reduced at lower frequencies after the sample melt was macroscopically aligned. This trend was obtained for both types of oscillatory shear tests CD and DSO. The reduction in the moduli for the orientated samples was verified for all achieved perpendicular alignments. The reduction in the linear dynamic shear moduli for the macroscopic aligned diblock copolymer melt has also been reported by Gupta et al.[32] for an overall parallel alignment.

However, there is a difference in the values of $G''(\omega/2\pi)$ and $G''(\omega/2\pi)$ determined with the stress controlled (CD measurements) and strain controlled rheometer (DSO measurements). These differences were also detected for $G''(t)$ during the LAOS experiments where $G''(t)$ measured with the strain controlled rheometer was always higher (approximately by a factor 1.5) than the $G''(t)$ determined with the stress controlled rheometer. On the one hand, these differences might be explained by the varying experimental equipments, such as different geometry materials (Vespel used with the stress controlled rheometer and Invar with the strain controlled rheometer) and diameters leading to different moments of

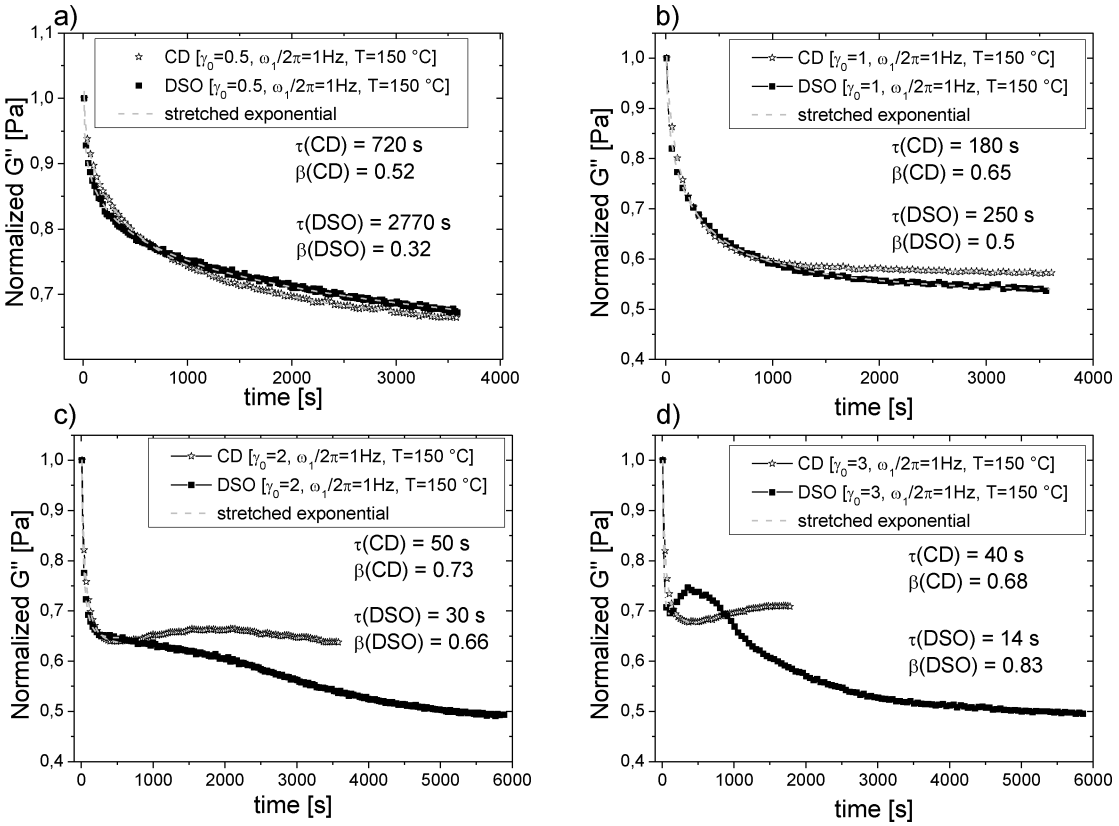

Figure 7. Time dependence of the mechanical loss modulus G' at (a) γ_0 = 0.5, (b) γ_0 = 1, (c) γ_0 = 2, and (d) γ_0 = 3. The controlled deformation CD (open stars) and the direct strain oscillation DSO (filled squares) show a similar time behavior for γ_0 = 0.5, γ_0 = 1 and in the beginning of the LAOS experiment for γ_0 = 2 and γ_0 = 3. For the two higher strain amplitudes the time progression of $G''(t)$ for the CD and DSO measurements show different trends as the deordering process occurs.

dx.doi.org/10.1021/ma201492n | *Macromolecules* 2012, 45, 455−472

inertia. Furthermore, the initial state of alignment of the diblock copolymer melts could not be detected for the rheological measurements performed with the strain controlled rheometer. Therefore, these differences in the initial state which can be caused by squeeze flow also affect the mechanical shear response of the sample melt.

For a better comparison of the LAOS experiments using CD and DSO, the obtained $G''(t)$ data were normalized. Parts a–d of Figure 7 show the mechanical loss modulus $G''(t)$ obtained from the CD and DSO measurements for all applied strain amplitudes. It can be seen that $G''(t)$ was reduced during the LAOS experiments by approximately 30% to 40% for $\gamma_0 = 0.5$ and $\gamma_0 = 1$, respectively. The time progression of G'' showed a similar stretched exponential decay in the beginning of the LAOS experiments for all four strain amplitudes measured by CD and DSO methods. For the two lowest strain amplitudes only small deviations between the $G''(t)$ data of the CD and DSO measurements were observed, mainly attributed to differences in the orientation time τ which differed by approximately a factor of 4 (for $\gamma_0 = 0.5$). Nevertheless, the total trend of the $G''(t)$ for $\gamma_0 = 0.5$ and $\gamma_0 = 1$ was similar.

In contrast, for $\gamma_0 = 2$ and $\gamma_0 = 3$ strong derivations occurred after both measurements (CD and DSO) revealed a similar stretched exponential decay in the beginning of the LAOS experiment. For $\gamma_0 = 2$ the time progression of G″ for the CD measurements showed an increase after approximately 800 s while the G″(t) data obtained from the DSO measurements showed a monotonic decrease which reached a plateau value after 4700 s. However, the G″(t) obtained from the in situ Rheo–SAXS investigations (CD) also decreased again after $t \approx$ 2200 s. For the highest strain amplitude ($\gamma_0 = 3$) the differences between the CD and DSO data of $G''(t)$ were more pronounced. In the first 100 s the stretched exponential time progression of $G''(t)$ was similar and exhibited a rapid decrease of approximately 30%. After this point the $G''(t)$ data obtained by DSO showed an overshoot after which $G''(t)$ monotonically decayed to approximately 50% of its initial value. In contrast, for the CD measurements $G''(t)$ stayed nearly constant in its minimum value over a period of 300 s after which a monotonic increase was observed.

It has to be noted that these were the first experiments carried out with the in situ Rheo–SAXS setup which implied restrictions in the experimental time. Therefore, in the present state, it is not possible to conclusively address the observed differences in the time progression of the $G''(t)$ data measured by CD and DSO. However, it can be clearly seen that the strongest discrepancy occurred after a duration of shear which causes a deordering of the preferentially perpendicular aligned block copolymer grains as observed from the in situ 2D-SAXS patterns for $\gamma_0 = 2$ and $\gamma_0 = 3$ (see Figure 4). It is assumed that the deordering process causes the deviation of $G''(t)$ from the simple stretched exponential decay.

As already mentioned above, the initial state for the DSO alignment experiments could not be observed in situ. Therefore, squeezing effects could probably affect the mechanical response during LAOS. Another factor for the diversities in the nonlinear mechanical response during LAOS could be caused by the two different ways the oscillatory experiments were performed (CD and DSO). Läuger et. al[55] reported significant differences between stress and strain control in the nonlinear mechanical response of complex fluids influencing the G'' data of the measurements. Therefore, additional FT-rheological measurements were performed to precisely follow the mechanical nonlinear response.

b. Nonlinear Mechanical Response Studied by FT-Rheology. For the rheological measurements, a strain controlled rheometer was used to calculate the nonlinear parameter $I_{3/1}(t)$ from the raw stress data via FT-rheology.[51,52] Shear-induced macroscopic alignment of the lamellar self-assembled block copolymer microstructure was achieved by large amplitude oscillatory shear using DSO. Consequently, the measured mechanical response to large deformations fell within the nonlinear regime and consisted of the odd higher harmonics of the applied mechanical excitation frequency ($\omega_1/2\pi = 1$ Hz). By examining the mechanical raw data using the ideas developed in FT-rheology,[51,54,58−61] it was possible to analyze the resulting signal additional with respect to both the phase and intensities of the higher harmonics (e.g., $I_{3/1}(t)$, $I_{5/1}(t)$, $I_{7/1}(t)$, ...) that are within the stress response.

As the relative intensity of the third harmonic $I_{3/1}$ was the dominant signal in the calculated FT-Spectra (see Figure 8),

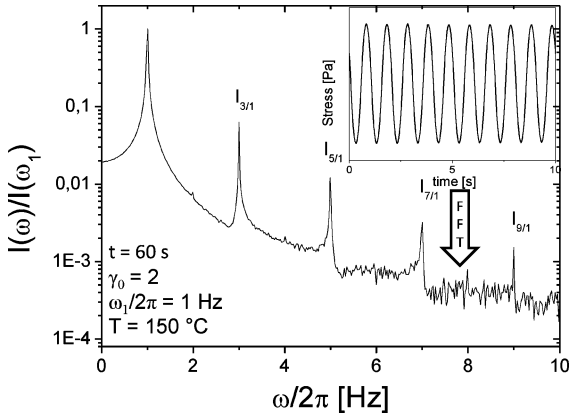

Figure 8. FT-spectrum of the time dependent torque calculated from the mechanical raw data after 60 s for PS-*b*-PI-13k-13k ($\omega_1/2\pi = 1$ Hz, $\gamma_0 = 2$, $T = 150$ °C). All peaks are normalized to the fundamental peak at $\omega_1/2\pi = 1$ Hz. The inset represents the raw data of the stress response from which the magnitude spectrum was calculated.

the time evolution of the intensity of $I_{3/1}(t)$ was used to quantify and follow the nonlinear response. Previous investigations of $I_{3/1}(t)$,[52,62,63] with respect to the mechanical excitation of block copolymers,[33,64,65] have shown that it is reasonable to utilize this quantity for monitoring and assessing the macroscopic orientation process.

Figure 9 shows $I_{3/1}(t)$ for strain amplitudes between $\gamma_0 = 0.5$ and $\gamma_0 = 3$. For all strain amplitudes, the dynamic mechanical nonlinear quantity showed first a rapid decay in the beginning of the experiments. At the two lowest strain amplitudes $I_{3/1}(t)$ exhibited similar behavior as the $G''(t)$ data (see Figure 7) in that there was a rapid decrease of $G''(t)$ and $I_{3/1}(t)$ in the first 1000 s followed by a slower decay, which finally leveled off into a plateau value (for $\gamma_0 = 1$) of $I_{3/1}(t) = 0.012$. For $\gamma_0 = 0.5$, these plateau values were higher than those measured for $\gamma_0 = 1$ ($I_{3/1}(t) = 0.016$). For the two largest strain amplitudes ($\gamma_0 = 2$ and $\gamma_0 = 3$), the time dependence of $I_{3/1}$ differed significantly from the stretched exponential trend in the first 100 s of the experiments.

However, $I_{3/1}(t)$ was nearly constant over a period of 800 s, after which it began to increase again until it reached a final stable value of approximately $I_{3/1}(t) = 0.025$ at $t = 4800$ s and t

dx.doi.org/10.1021/ma201492n | *Macromolecules* 2012, 45, 455–472

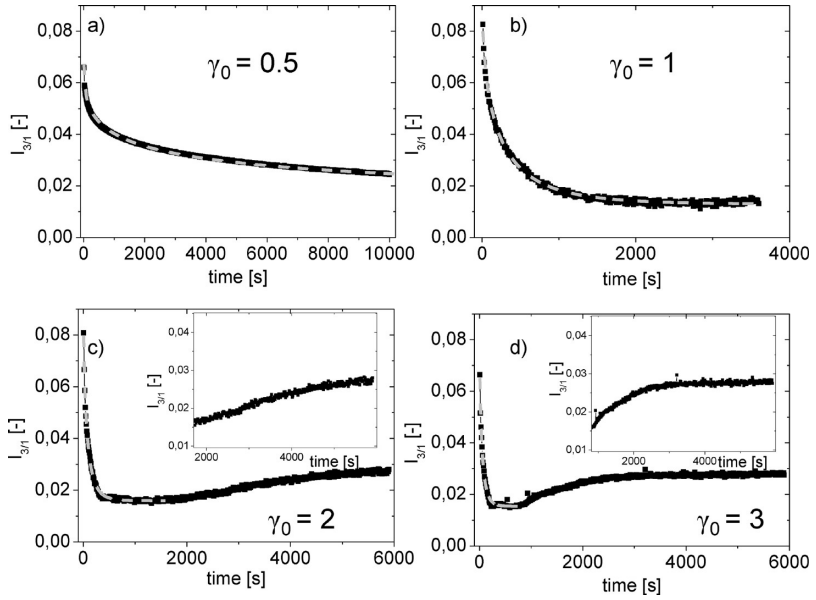

Figure 9. Time dependence of the relative intensities of the nonlinear parameter $I_{3/1}$ measured with a strain controlled rheometer for (a) $\gamma_0 = 0.5$, (b) $\gamma_0 = 1$, (c) $\gamma_0 = 2$, and (d) $\gamma_0 = 3$. The dotted lines represent the stretched exponential fit (see text). Insets display an enlargement of the region were the deordering of the perpendicular alignment occurs as detected by the mechanical response.

= 2500 s for γ_0 = 2 and 3, respectively. Interestingly, the detected time evolution of $I_{3/1}$ was more similar to the observed $G''(t)$ (CD) data and structural alignments as detected by in situ Rheo−SAXS than to the simultaneously obtained $G''(t)$ using DSO. The data of $I_{3/1}(t)$ showed a stretched exponential decay as the perpendicular orientation occurred as well as an increase in the mechanical nonlinear response as the deordering of the macroscopic perpendicular aligned sample melt proceeded. This was also proven by ex-situ SAXS studies (see text below).

To illustrate the reproducibility of the mechanical measurements performed with the strain controlled rheometer (DSO), the time evolution for G'' and $I_{3/1}$ for $\gamma_0 = 3$ is represented with error bars in Figure 10. The error bars were determined from

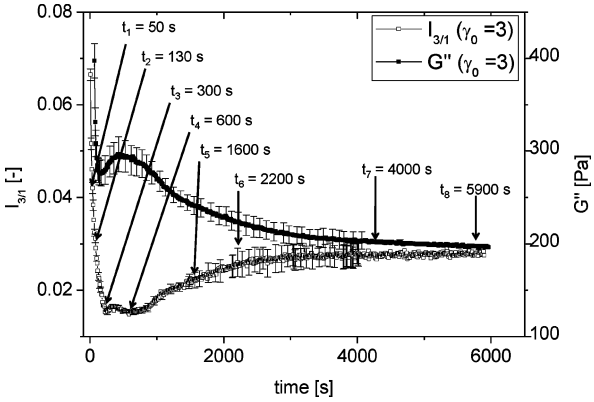

Figure 10. Time dependence of the dynamic mechanical quantities G'' (filled squares) and $I_{3/1}$ (open squares). G'' was shifted by 50 s to avoid an overlay of the data points. The arrows indicate the specific points that were chosen for ex-situ probing of the macroscopic structure. The error bars shown up to 2000 s were calculated from four fully independent measurements.

four different measurements that included new sample loading and heating above the T_{ODT}. It can be seen that the statistical error for $G''(t)$ was below 10%, while for $I_{3/1}(t)$, the relative error was even below 3%, at least until the deordering process began.

c. Ex-Situ Structural Studies. To follow the progress of macroscopic orientation during the LAOS experiments realized with a strain controlled rheometer, the nonlinear parameter $I_{3/1}(t)$ was selected as a trajectory. To examine the structure present at a specific time, the samples were cooled to room temperature and removed from the shear geometries without subjecting them to any further shear. The degree of alignment for the mechanically induced anisotropic orientation distribution of the lamellar microdomains was analyzed at three different positions along the radial vector of the sample discs, as described in the section Experimental Methods. For each applied strain amplitude, at least three different states of alignment were characterized by 2D-SAXS along the radial (*OX* axis), the normal (*OZ* axis) and the tangential (*OY* axis) as described in the literature.[33] In addition TEM images were obtained for the minimum value (t_3 = 300 s) and the plateau value (t_8 = 5900 s) of $I_{3/1}$ to verify the developed macroscopic orientation in real space.

The resulting final structures for all LAOS experiments with $\gamma_0 = 0.5$, $\gamma_0 = 1$, $\gamma_0 = 2$, and $\gamma_0 = 3$ are summarized in Tab. 1. To

Table 1. Summary of the Ex-Situ Determined Final State of Macroscopic Orientation for All Four Applied Strain Amplitudes at T = 150 °C and $\omega_1/2\pi$ = 1 Hz[a]

γ_0 [−] macroscopic orientation	0.5	1	2	3
parallel			XX	XX
perpendicular	X	X	XX	XX

[a]The X's indicate the type of macroscopic orientation observed while two X's at a given strain amplitude indicate a biaxial orientation.

explore the deordering process for $\gamma_0 > 1$, as first detected with in situ 2D-SAXS measurements, only the data for the structural development at $\gamma_0 = 3$ was presented here because the dynamic mechanical parameters ($G''(t)$ and $I_{3/1}(t)$) showed the largest

dx.doi.org/10.1021/ma201492n | *Macromolecules* 2012, 45, 455−472

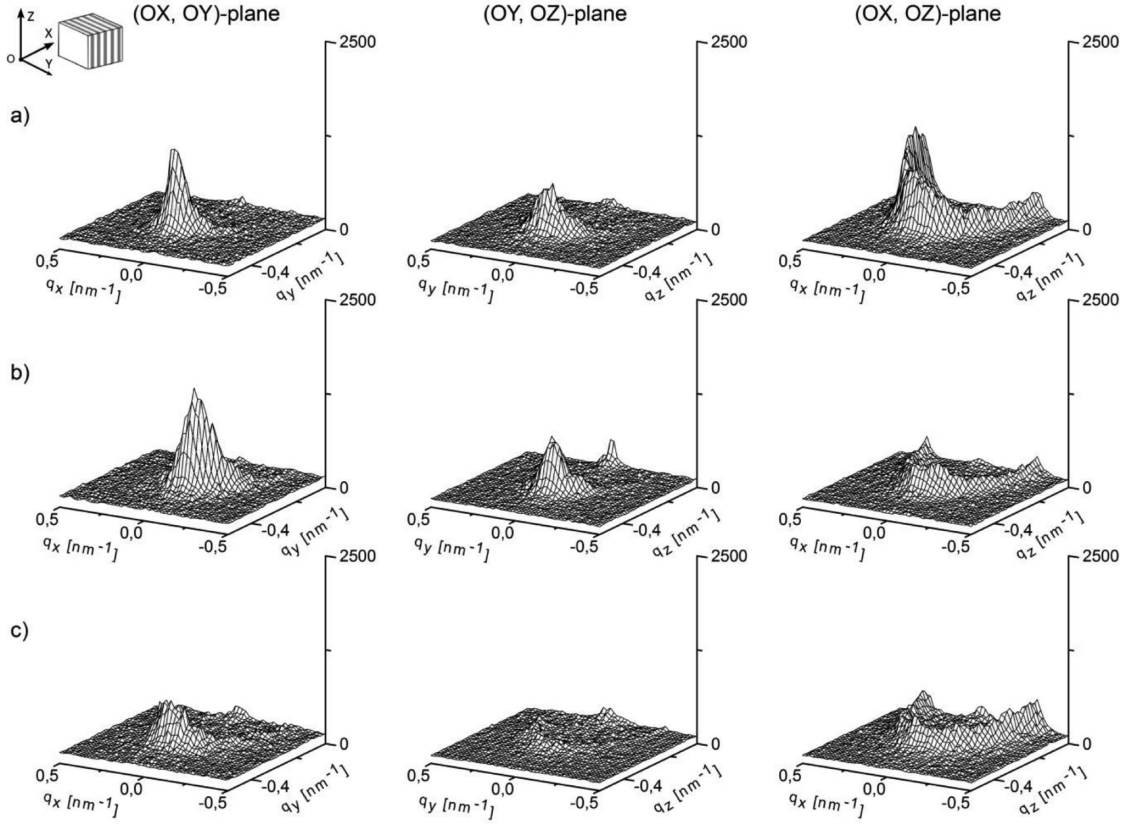

Figure 11. 2D-SAXS patterns after t_1 = 50 s along the normal (*OX, OY*) plane, radial (*OY, OZ*) plane and the tangential (*OX, OZ*) plane at three different positions with respect to the center of the sample disk: (a) r = 5.5 mm, (b) r = 4 mm, and (c) r = 2 mm. The ex-situ measured patterns indicate that the alignment of the block copolymer grains occurs in the beginning over a reduction of unfavorable transverse aligned lamellae.

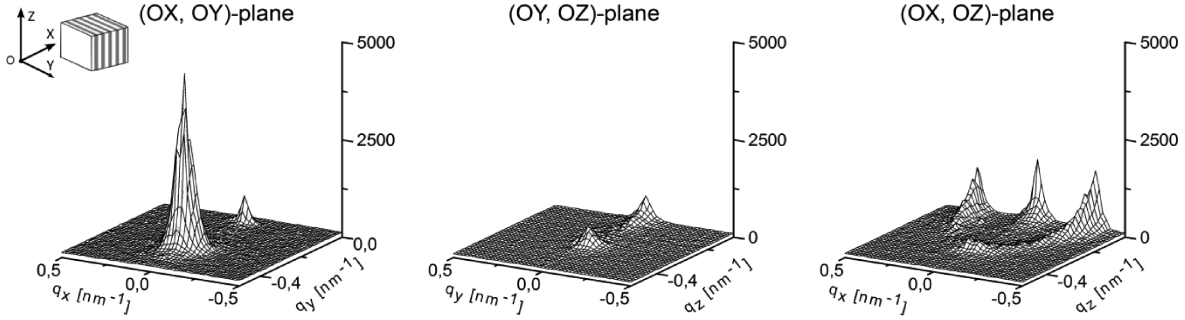

Figure 12. 2D-SAXS patterns after t_3 = 300 s along the normal (*OX, OY*) plane, radial (*OY, OZ*) plane and the tangential (*OX, OZ*) plane at the edge of the sample (r = 5.5 mm). Ex-situ 2D-SAXS measurements indicated that in the plateau region of $I_{3/1}(t)$ a stable macroscopic orientation with primarily well ordered perpendicular alignment is achieved.

deviations from a monotonic decrease under these conditions. Apart from the initial state (t = 0 s), which featured the ringlike structure in all three directions expected for the isotropic initial state of the sample, an anisotropic orientation distribution was seen at all eight different preshear times (see Figure 10) analyzed by ex-situ 2D-SAXS measurements.

After 50 s, which corresponded to the regime in which $G''(t)$ and $I_{3/1}(t)$ experienced a rapid drop, a complex texture in the microstructure (see Figure 11) was obtained for $\gamma_0 > 1$. At positions close to the edge of the sample geometries, the unit normal of the lamellae were orientated perpendicular (peak in the (*OX, OY*) plane), parallel (smaller reflection in the (*OY, OZ*) plane) and all orientations in between (ringlike pattern in the (*OX, OZ*) plane). This finding is consistent with the results reported by Chen et al.[29] After moving closer to the center of the sample geometry, the orientation distribution with its perpendicular and parallel projections decreased as the peaks in the (*OX, OY*) and (*OY, OZ*) planes broadened and decreased in intensity. This behavior is consistent with the experiments at lower strain amplitudes (γ_0 = 0.5, γ_0 = 1, γ_0 = 2) where the different positions along the radial vector for parallel plate geometries corresponded to lower strain amplitudes.

As γ_0 varies from 2 to 0.5, it was found that the development of the peak in the parallel direction became less pronounced. As the mechanical excitation persisted, the degree of perpendicular alignment was significantly enhanced as indicated by the increased intensity and narrowed scattered peak in the (*OX, OY*) plane (results not shown here). The scattering patterns for each state of orientation measured at different positions between the center and the edge of the sample disk

dx.doi.org/10.1021/ma201492n | *Macromolecules* 2012, 45, 455–472

(corresponding to different γ_0) clarified that the macroscopic alignment improved closer to the edge of the parallel plates.

At the onset of the plateau at t_3 = 300 s (γ_0 = 3), the orientation distribution was dominated by the perpendicular alignment and only at a position near the edge of the parallel plate geometries (r = 5.5 mm) a small amount of parallel orientation (reflection in the (OY, OZ)-plane) that could still be detected (see Figure 12).

Furthermore, TEM measurements verified the well aligned macroscopic perpendicular orientation of the lamellar at the minimum of $I_{3/1}(t)$. In Figure 13, the TEM image obtained in the (OX, OY) plane nicely reveals the high macroscopic alignment of the lamellar microstrucutre.

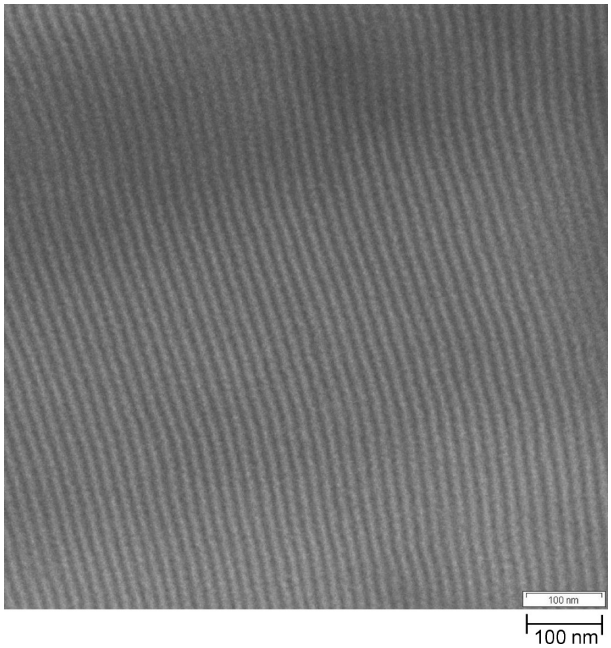

Figure 13. Structure of the macroscopic perpendicular aligned PS-*b*-PI-13−13 diblock copolymer obtained at the minimum of $I_{3/1}(t)$ (t_3 = 300 s) along the (OX, OY) plane (normal direction) at the edge of the sample (r = 5.5 mm).

Further investigation at t_4 = 600 s, indicated that the plateau region of the dynamic mechanical parameter $I_{3/1}(t)$ corresponded to a stable state of macroscopic orientation under LAOS. For all other strain amplitudes, it was also found that, at the minimum of $I_{3/1}(t)$, the orientation distribution of the lamellar microstructures showed an overall perpendicular orientation (results not shown here).

As the value of $I_{3/1}(t)$ began to rise, the scattering patterns at t_5 = 1600 s indicated that the well ordered macroscopic perpendicular alignment obtained in the plateau region of $I_{3/1}(t)$ became less ordered and showed a significant increase in the number of microdomains preferentially orientated in the parallel direction (see Figure 14). It can be seen that the extent of this orientation decreased traveling from the outer edge to the center of the geometries, while the perpendicular projection was the dominant orientation near the middle of the sample plates. These findings were consistent with the one obtained for γ_0 = 2.

The deordering process was only detected for γ_0 > 1, while the achieved perpendicular orientation distribution remained unchanged as the mechanical stimulus proceeded for the two lower strain amplitudes. Interestingly, at the end of the experiment for γ_0 = 3 (t_8 = 5900 s) (see Figure 15) and also for the final macroscopic alignment for γ_0 = 2, the scattering patterns in the (OX, OY) and (OY, OZ) planes showed an anomalous biaxial orientation with approximately similar amounts of perpendicular and parallel orientation in the region where G''(t) and $I_{3/1}(t)$ exhibited constant values (results not shown here). These findings could also be confirmed by the real space investigations of the aligned microstructures utilizing TEM measurements. It is important to note that the TEM images nicely reveals the polymer grains which are preferentially orientated along the parallel and the perpendicular direction with respect to the applied shear field.

The discovery of a stable biaxial orientation of the lamellae unit normal under shear flow was first described by Okamoto et al.,[49] utilizing in situ Rheo−SAXS measurements with a custom-made shear cell. This setup was, however, limited to a sawtooth type shear strain with γ_{max} = 0.5 and a time resolution of several hundred seconds. In that work,[49] the specimens initially had an uniaxial parallel orientation and the biaxial alignment was achieved by reorientating the macroscopically aligned structures. Therefore, the biaxial orientation was achieved by applying two different mechanical experimental conditions, one to initially macroscopically align the randomly orientated sample and the second to reorientate the aligned system.

To the best of our knowledge, the results described here showed, for the first time, the development of an anomalous macroscopic biaxial orientation developed from an unoriented macroscopic isotropic melt by applying a single set of experimental parameters ($\omega_1/2\pi$ = 1 Hz, γ_0 = 2 and γ_0 = 3, T = 150 °C) throughout the experiment. Therefore, it could be shown that the appearance of a biaxial macroscopic orientation along the parallel and perpendicular directions for strain amplitudes γ_0 > 1 is only a function of the duration of shear.

It is important to note that Wang et al.[40] already reported a disordering phenomenon utilizing an in situ SANS setup with a shear cell which consists of two concentric cylinders. Their experiments were carried out by applying a reciprocating shear field.[66] In that work[40] a concentrated PS-*b*-PI (M_w = 33 400 g/mol, PDI = 1.07, f_{PS} = 47%) solution first aligned macroscopically perpendicular while after a certain duration of shear was exceeded a disordering toward a poorly defined overall parallel alignment occurred. However, the main differences between our results shown here were that Wang et al.[40] studied concentrated polymer solutions and that no stable biaxial orientation was obtained. Furthermore, the maximum time resolution of the in situ SANS experiments was limited to several minutes. Nevertheless, the results obtained by Wang et al.[40] confirmed the existence of transient well aligned macroscopic orientated diblock copolymer melts which become unstable as the mechanical stimulus proceeds.

To summarize the ex-situ determined structural changes for γ_0 = 3, the time dependence of the ex-situ calculated standard deviation of the azimuthally averaged first order reflection in the (OX, OY)-plane (perpendicular) and the (OY, OZ)-plane (parallel) are shown in Figure 16. The measurements were performed at a position along the radial vector of r = 5.5 mm, corresponding to a local strain amplitude of $\gamma_{0\text{-loc}}$ = 0.85*γ_0. It can be seen that this trend, which was also present in the time dependence of the mechanical nonlinear parameter $I_{3/1}$, was reflected by the peak width of the developing macroscopic perpendicular and parallel alignments.

dx.doi.org/10.1021/ma201492n | *Macromolecules* 2012, 45, 455−472

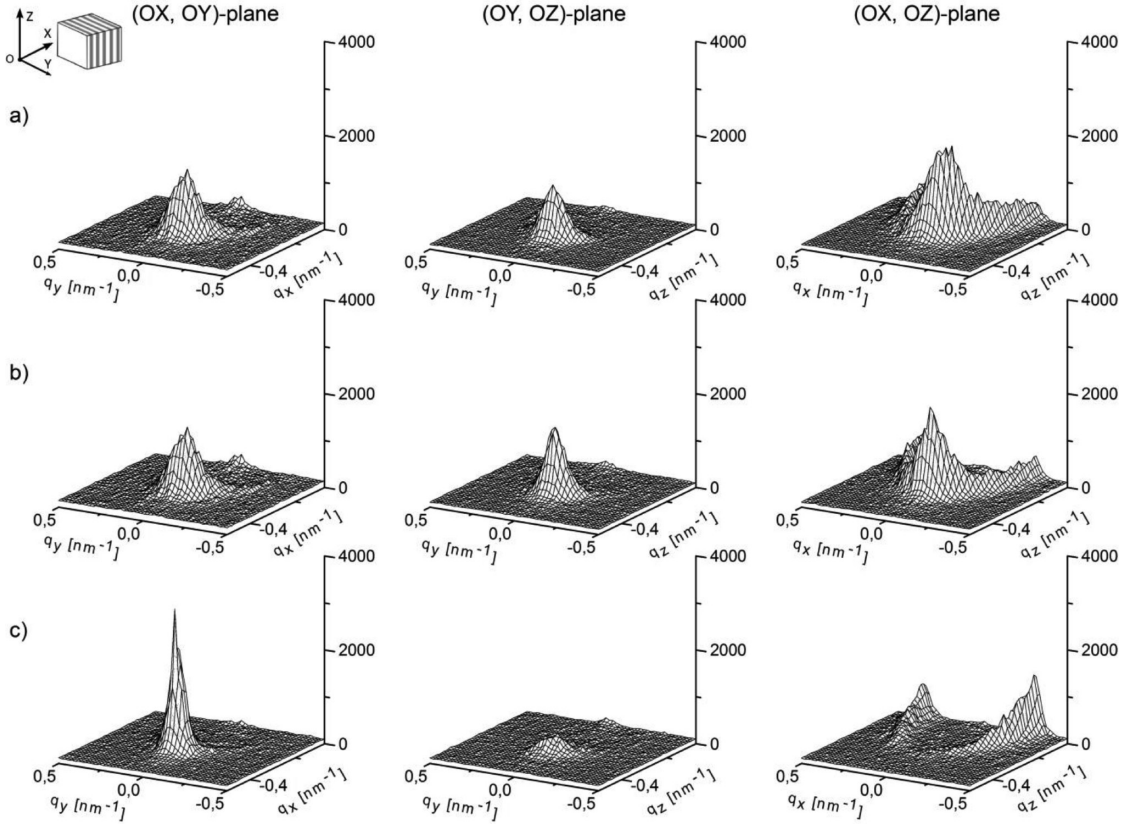

Figure 14. 2D-SAXS patterns after t_S = 1600 s along the normal (*OX, OY*) plane, radial (*OY, OZ*) plane and the tangential (*OX, OZ*) plane at three different positions with respect to the center of the sample disk: (a) r = 5.5 mm, (b) r = 4 mm, and (c) r = 2 mm. The deordering process is indicated by the beginning development of a biaxial orientation with the unit normal of the lamellae being preferentially directed along the *OX* and *OZ* axis.

Furthermore, no precise explanation for the correlation between the observed overshoot in the time dependence of G'' (DSO measurements) and changes in the alignment of the lamellar microdomains was found. However, the results indicate that the time progression of the nonlinear response as quantified by $I_{3/1}(t)$, is directly correlated to the kinetic pathway of the macroscopic alignment and the following deordering process in the block copolymer melt. A possible explanation for those observations will be discussed in the following section.

■ DISCUSSION

a. Implication for the Alignment Mechanism. The results obtained by in situ Rheo−SAXS measurements indicated a significant correlation between the time dependence of the structural changes and the dynamic mechanical response of the sample melt. The former were quantified by the time evolution of the standard deviation σ_{SAXS} calculated from the azimuthally averaged first order reflection in the 2D scattering pattern. The latter by the dominant viscoelastic property, the mechanical loss modulus $G''(t)$, and the nonlinear parameter $I_{3/1}(t)$.

The applied strain amplitudes caused in all cases a rapid drop in the measured quantities, reflecting the increasing orientation of the lamellar microstructures. With increasing strain amplitude, this process was accelerated, meaning that the rapid drop in the observed mechanical and structural parameters became even more pronounced during the LAOS experiments at higher γ_0 (see Figure 4, Figure 7 and Figure 9). These findings are consistent with the results obtained by Chen et al., who used in situ birefringence and ex-situ SAXS studies to monitor the progress of macroscopic orientation.[29]

From the agreement between the shear-induced structural changes determined via 2D-SAXS and the mechanical no-linear response quantified by $I_{3/1}(t)$ (see Figure 16), it can be seen that there is a correlation between the time dependent nonlinear mechanical response and the development of the aligned macroscopic structure.

Furthermore, it was confirmed that the perpendicular orientation process began with an elimination of the orientation distribution with the unit normal of the lamellae being orientated preferentially along the transverse (*OY* axis) direction. This elimination process was more pronounced at higher strain amplitudes ($\gamma_0 > 1$) and was reduced traveling from the outside edge of the parallel plate to its center. Next, the remaining orientation distribution was converted into a macroscopic system with preferentially perpendicularly orientated lamellar microstructures. It could be shown that the plateau values of the nonlinear mechanical parameter corresponded to a temporally stable state of macroscopic alignment that remained constant for $\gamma_0 \leq 1$.

The best macroscopic alignment of $\sigma_{Min\text{-}SAXS} = 8°$ observed during the in situ Rheo−SAXS measurements was achieved for $\gamma_0 = 3$, $\omega_1/2\pi = 1$ Hz at $T = 150$ °C and a duration of shear of approximately $t_{shear} = 130$ s.

For the first time, however, it was shown that for deformation amplitudes higher than 1 ($\gamma_0 > 1$), the achieved degree of macroscopic orientation was not stable as the

dx.doi.org/10.1021/ma201492n | *Macromolecules* 2012, 45, 455−472

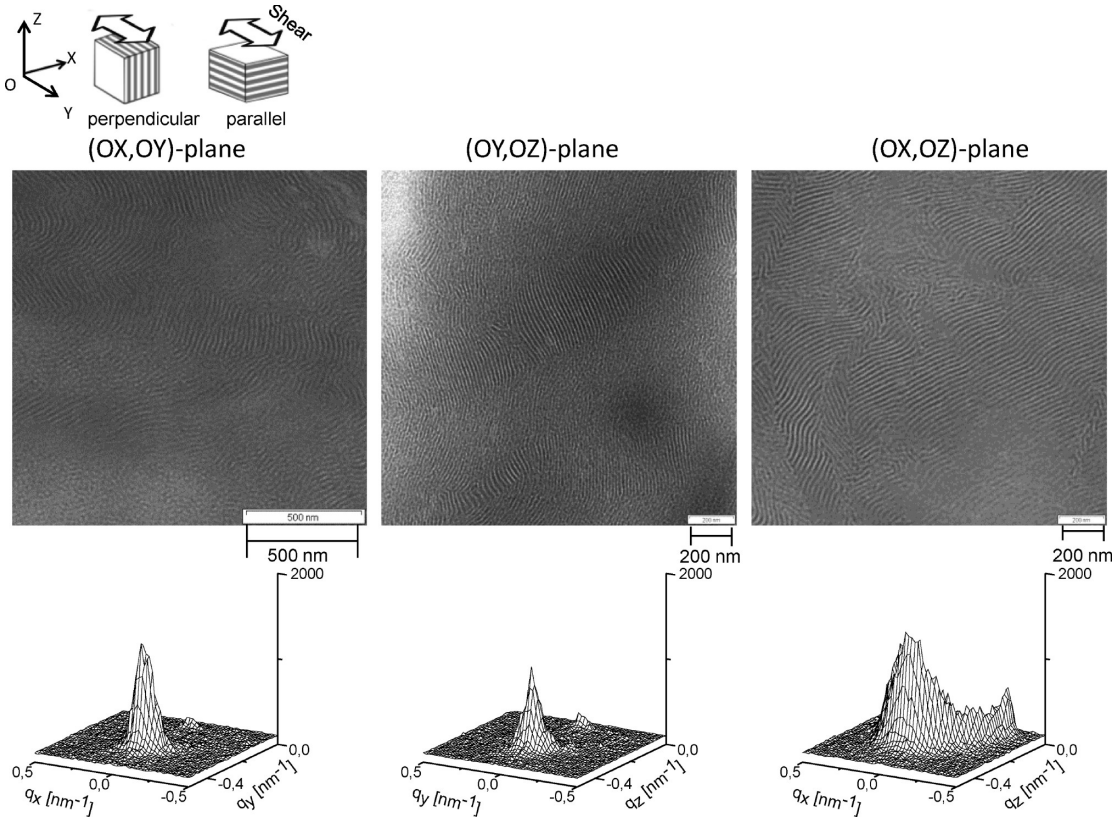

Figure 15. Real space information and 2D-SAXS patterns after t_8 = 5900 s along the normal (*OX, OY*) plane, radial (*OY, OZ*) plane and the tangential (*OX, OZ*) plane at the edge of the sample (r = 5.5 mm). In the final region where $I_{3/1}(t)$ is constant, a macroscopic stable biaxial orientation is achieved.

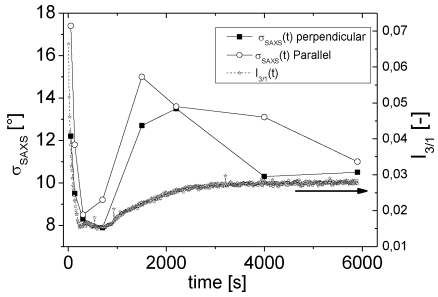

Figure 16. Time evolution of the standard deviation as measured by ex-situ 2D-SAXS close to the edge of the sample disk (r = 5.5 mm) for the macroscopic perpendicular (filled squares) and parallel (open circles) alignments. The open stars represent the time dependence of the nonlinear parameter.

mechanical excitation continued above a certain point. This state of orientation then became deordered under further mechanical stimulus, resulting in a broadening of the orientation distribution and the development of a biaxial distribution with approximately equal amounts of locally anisotropic lamellar ordered diblock copolymer microdomains having parallel and perpendicular orientations for $\gamma_0 > 1$. This phenomenon was also observed for various other symmetric PS-*b*-PI diblock copolymer melts with different molecular weights between 26 500 g/mol and 40 000 g/mol.

The ex-situ 2D-SAXS measurements revealed that $I_{3/1}(t)$ characterizes the progress of macroscopic orientation in a reasonable and reproducible way. Furthermore, $I_{3/1}(t)$ was sensitive to the deordering process by exhibiting a significant increase as the deordering takes place. This trend was also observed for the $G''(t)$ obtained from the in situ Rheo−SAXS (CD) experiments (see Figure 7). It must be noted that the mechanical loss modulus $G''(t)$ obtained from large amplitude oscillatory shear experiments using DSO method also showed variations from a stretched exponential decaying trend. However, the time progression of G″(t) obtained from CD measurements and DSO measurements exhibited different time progression, especially as the deordering process occurred (see Figure 7). The ex-situ 2D-SAXS investigations revealed no information about the different time progression of the $G''(t)$ such as the observed overshoot for γ_0 = 3.

Following previous work,[33,65] we suggest that nonlinear mechanical characterization as determined via FT-Rheology was able to follow macroscopic alignment processes in real time because it is also sensitive to complex structural dynamics. This agreement is consistent with a proposed rotational orientation mechanism instead of a selective layer melting mechanism, as another possible pathway for the perpendicular alignment and the deordering process.[22,26,67,68] Even though, Gupta et al.[32] concluded by the examined strain dependency of the macroscopic alignment at a fixed frequency and temperature that the kinetic pathway of the macroscopic orientation cannot be satisfactorily explained by either of the mechanisms suggested above.

Interestingly, for a strain amplitude of γ_0 = 2 and γ_0 = 3, the shear-induced macroscopic orientation was a function of the shear duration. After a critical shear duration deordering was observed which resulted in a biaxial alignment with parallel and perpendicular fractions. It is important to note that this was achieved under isothermal conditions by applying a single

dx.doi.org/10.1021/ma201492n | *Macromolecules* 2012, 45, 455−472

excitation frequency and deformation amplitude. If it is assumed that the applied experimental conditions were at the vicinity of the transition point between the perpendicular (selective layer melting) and parallel (rotational mechanisms) alignment,[26] then the dynamic shear field would lead directly to a biaxial orientation, as neither the parallel nor the perpendicular alignment would be preferred. However, the results shown above indicate that the pathway to the biaxial orientation developed instead in two steps. First, a well-aligned perpendicular state was observed, which became unstable as the oscillating mechanical stimulus continued, and then, finally, deordered to create the final stable biaxial orientation.

On the basis of these results, a rotation mechanism of the locally ordered block copolymer grains is proposed for these experimental conditions. In the following section, a detailed discussion on the kinetics of the rotation mechanism and its effect on the nonlinear response as quantified by $I_{3/1}(t)$ is provided. It should be noted that these assumptions are based on the results obtained by in situ Rheo−SAXS measurements, which confirmed that the deordering process occurred in the melt state and led directly to a broadening of the azimuthally averaged first order scattered reflection and was, therefore, not a result of factors necessary for ex-situ studies, such as cooling and sample preparation. On the other hand, additional FT-rheology and ex-situ 2D-SAXS measurements provided insight into the mechanical nonlinear response and also structural changes along all three spatial directions.

b. Correlation between Structural Changes and Mechanical Response. A schematic sketch of the proposed macroscopic perpendicular alignment process under the applied conditions is provided in Figure 17. This sketch represents the orientation process until the overall perpendicular alignment was achieved, i.e., until $I_{3/1}(t)$ reached its minimum, not considering the deordering process. The direction of the unit normal of the lamellae in one locally ordered block copolymer grain is represented as a vector.

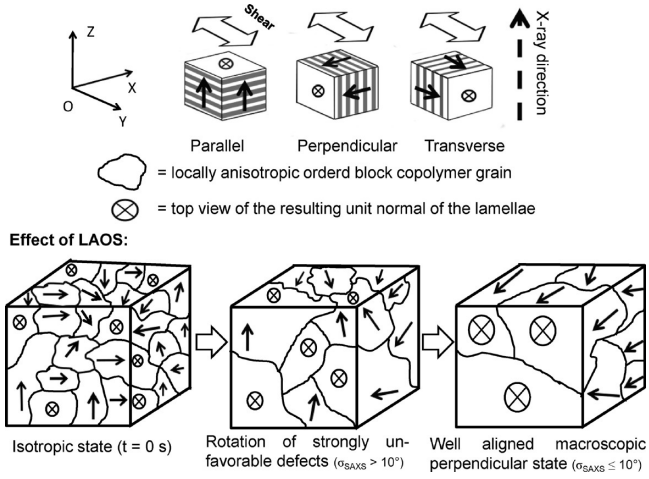

Figure 17. Schematic representation of the shear-induced alignment of a PS-*b*-PI diblock copolymer melt. The unit normal of the lamellae of the locally ordered isotropic block copolymer grains are indicated by arrows and on the top view by circles with a cross. For further explanation, see the text.

We propose that the applied large amplitude oscillatory shear caused a rotation of the microdomains. Therefore, the various locally anisotropically ordered microdomains with their unit normal pointing statistically into all spatial directions can be regarded in terms of defects and nucleation points. Specifically, the grains possessing a unit normal of the lamellae with a spatial orientation that is different than the energetically favored macroscopic aligned final state, i.e., the perpendicular alignment, were considered as defects. Grains with the unit normal of their lamellae microdomains orientated in approximately the perpendicular direction (parallel to the *OX* axis) were instead regarded as nucleation points.

The initial macroscopically isotropic sample melt had randomly orientated unit normal of the locally isotropic ordered microdomain grains. Each orientation has a different energy level with respect to the shear direction, which depends on the spatial orientation of the unit normal of the lamellae and the size and shape of the locally ordered block copolymer grain.

By applying large amplitude oscillatory shear to the polymer melt, the grains which possess the most unfavorable energy levels will be rotated into the perpendicular orientation first. As the macroscopic alignment proceeds, the number of grains which do not have the favorable orientation is reduced. This process led to the final macroscopically perpendicular aligned sample melt, which was proven by in- and ex-situ 2D-SAXS studies.

As the grains were rotated into the preferred perpendicular alignment ((*OX*, *OY*) plane), some grain interfaces will vanish and larger grains will develop. The time evolution of the radial averaged first order reflection (not shown here), indicated that the development of larger grains was not significant during the orientation process as this value varied from only 4% ($\gamma_0 = 0.5$) to 14% ($\gamma_0 = 3$) with respect to its initial and final value.

To derive a dependency between the structural changes and the mechanical response, it was assumed that the locally ordered grains in the block copolymer melt have a size in the submicrometer range (see Figure 15). These grains are surrounded by an interface which separates each block copolymer grain. In a recent study, it was shown that the non linear response even for two Newtonian fluids in an emulsion is caused by interfacial tension and size.[69,70] Therefore, in our case $I_{3/1}$ most probably originates as interfaces are deformed during mechanical stimulus.

The rotation of the locally anisotropic ordered grains by LAOS will cause a deformation of the surrounding interfaces where this deformation results in a mechanical nonlinear response that can be monitored and quantified using the nonlinear parameter $I_{3/1}(t)$. As the LAOS experiment proceeded, the amount of defects was reduced and, therefore, the number and extent of deformed microdomain surfaces was also reduced causing a decrease in the nonlinear mechanical response. This idea is supported by the result that the observed low value plateau for $I_{3/1}(t)$ which was evident at all four measured strain amplitudes, corresponded to a well-aligned perpendicular orientation as confirmed by 2D-SAXS measurements.

These results support the assumption that the nonlinear response during shear-induced orientation of block copolymer melts was primarily caused by the deformation of the grain interfaces during rotational alignment. The above suggested mechanism may also explain the detected increase of $I_{3/1}$ for strain amplitudes $\gamma_0 > 1$. As the in situ Rheo−SAXS studies showed, the development of the biaxial orientation occurred along a broadening of the orientation distribution in the (*OX*, *OY*) plane (see Figure 4). This would cause a further mechanically induced rotation of the block copolymer grains

and an increase in the value of the nonlinear response, which was, in fact, seen in the ex-situ measurements.

It is important to note that the results presented here do not allow a precise prediction about the origin of the observed deordering process. As these were the first results with respect to the observed deordering phenomenon, a possible explanation of the underlying microstructural processes will be examined in more detailed future works. For this purpose, we are aiming to perform detailed investigation including the molecular weight dependence of the deordering process and applying high sensitive in situ Rheo−dielectric combination.[71,72]

c). Quantitative Orientation Kinetics. On the basis of the results above for the correlation between the nonlinear mechanical response and the structural dynamics in the sample melt, it is possible to evaluate the kinetics of the alignment process by comparing the orientation time determined for each method (2D-SAXS, rheology, and FT-rheology). To do this, it must first be clarified how this orientation time can be calculated and to assess whether this method corresponds to a reasonable model for the experimental data.

A simple theoretical approach is presented here to deduce a mathematical expression for the rotation kinetics. The main idea of this approach is to use a first order scheme for the kinetics. With the assumption that $I_{3/1}(t)$ is proportional to the number of defects $N_D(t)$ or intergrain area at a specific time, i.e., that

$$I_{3/1}(t) \sim N_D(t) \tag{1}$$

the following first order kinetic expression for the time evolution under constant shear conditions (γ_0, T, $\omega_1/2\pi$) is then obtained:

$$\frac{dN_D(t)}{dt} \sim kN_D(t) \tag{2}$$

where k is proportional to the inverse of the orientation time τ ($k \sim 1/\tau$).

In the discussion above, it was assumed that the nonlinear response quantified by $I_{3/1}$ is caused by the rotational deformation of the interfaces of the grains, the so-called defects. Because of heterogeneities in the size distribution, shape and orientation of these locally anisotropic ordered domains, the orientation times τ for the rotation of these grains will be covered by certain distribution. These heterogeneities were accounted for by introducing a "heterogeneity-index" β, to broaden the single exponential. The most simple and less parameter intense description is given by a stretched exponential function. This leads to the final expression:

$$I_{3/1}(t) = A + Be^{-(t/\tau)^{\beta}} \tag{3}$$

The latter term of eq 3 is the well-known expression for the stretched exponential function, as discussed in the literature.[73,74]

It is important to note that the stretched exponential function has already been used to describe the experimental time evolution during the shear-induced alignment process of block copolymers.[65] However, this function was used without providing further explanations for the stretched exponential time progression of the shear-induced orientation.

Using a stretched exponential provides a simple method for describing the macroscopic orientation of block copolymer grains by a rotation mechanism after taking into account that the orientation times τ possess a broad and continuous distribution that cannot be described by a single exponential decay ($\beta = 1$).

In addition to the above-mentioned heterogeneity in the size distribution of the block copolymer grains, the stretched exponential takes into account the appearance of a strain gradient, which in parallel plate−plate geometries, is a function of the radial distance as well as of any small preorientations distributed within the block copolymer melt. The broadened orientation time distribution is then expressed in terms of the deviance of β ($0 < \beta \leq 1$) from an ideal exponential function where $\beta = 1$.

The fitted curves for time evolution of σ_{SAXS}, G'' and $I_{3/1}$ are shown in Figure 4, Figure 7 and Figure 9, respectively, as dotted lines. It can be seen in these Figures that this approach for analyzing the kinetics of shear-induced macroscopic orientation using a rotation mechanism is reasonable. The calculated fit parameters are summarized in Table 2 for all three quantities ($\sigma_{SAXS}(t)$, $G''(t)$, $I_{3/1}(t)$).

Table 2. Calculated Parameters as Orientation Time τ and β-Parameter by Fitting the Time Data of (a) σ_{SAXS}, (b) G'' Obtained under CD, and (c) the Nonlinear Parameter $I_{3/1}$ under DSO for all Four Strain Amplitudes with a Stretched Exponential $y = y_0 + Ae^{-((t-t_0)/(\tau))^{\beta}}$

a				
strain (in situ SAXS)	y_0 [deg]	τ [s]	β [−]	A [deg]
0.5	10.2	430	0.58	10
1	10.5	110	0.50	10
2	9.4	60	0.80	7
3	7.7	20	0.60	4
b				
strain (G''-CD)	y_0 [Pa]	τ [s]	β [−]	A [Pa]
0.5	355	720	0.52	214
1	240	190	0.67	180
2	210	50	0.73	120
3	130	40	0.72	60
c				
strain ($I_{3/1}$)	y_0 [−]	τ [s]	β [−]	A [−]
0.5	0.016	2100	0.38	0.051
1	0.012	250	0.67	0.065
2	0.016	75	0.80	0.062
3	0.015	50	0.75	0.052

It is clear, however, that the orientation times τ differ between the mechanical and 2D-SAXS measurements. This difference became more pronounced at the two lowest strain amplitudes ($\gamma_0 = 0.5$ and $\gamma_0 = 1$). The deviance of β from the ideal case $\beta = 1$ indicated that a broadened distribution in the dynamic orientation process occurred, which is often observed in disordered systems like polymers due to e.g. grain size distribution.

Interestingly, the plateau values γ_0 of the nonlinear parameter $I_{3/1}(t)$ and the peak width determined by the standard deviation $\sigma_{SAXS}(t)$ of the 2D-SAXS scattering pattern, were much less strain or method dependent compared to the plateau value of the mechanical loss modulus $G''(t)$, which showed a much larger deviation. By plotting the strain amplitude as a function of the calculated orientation times for each measurement method on a double logarithmic scale, shown in Figure 18, a scaling dependence of the macroscopic orientation on the

dx.doi.org/10.1021/ma201492n | Macromolecules 2012, 45, 455−472

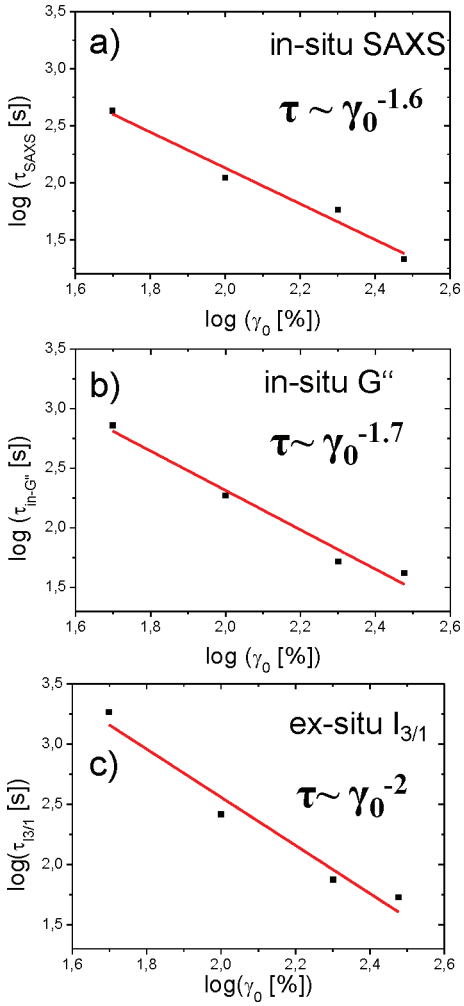

Figure 18. Double logarithmic plot of the orientation time τ as a function of the strain amplitude γ_0. The solid lines represent a linear regression revealing a slope of approximately −1.6 for (a) σ_{SAXS} (calculated from in situ SAXS), (b) G″ (CD), and (c) $I_{3/1}$ (calculated from the raw data obtained under DSO).

applied strain amplitude was obtained. For all measurements presented here, it was found that the orientation time could be described by a power law dependence on the strain amplitude ranging from $\tau \sim \gamma_0^{-1.6}$ and $\tau \sim \gamma_0^{-2}$ where this result has not been previously reported to the best of our knowledge. The strain dependence of G″(t) measured under DSO showed a power law dependence of $\tau \sim \gamma_0^{-3}$ (results not shown here).

The difference between the results obtained in a previous work on polystyrene-*b*-polybutadiene diblock copolymers[65] that revealed a forth power dependence ($\tau \sim \gamma_0^{-4}$) on the strain amplitude, are not in contrast with the results reported here. The investigations preformed by C. Oelschlaeger et al. considered the orientation of the unit normal of the lamellae parallel to *OZ* axis, corresponding to a parallel overall orientation instead of a perpendicular alignment. This orientation was achieved at elevated temperatures near T_{ODT} where microstructure dominates the rheological response of the sample, resulting in $G'(\omega/2\pi)$ values that are higher than those for $G''(\omega/2\pi)$. Therefore, it can be assumed that this high elasticity also affected the macroscopic orientation dynamics in the polymer melt.

CONCLUSIONS

The combination of a rheometer for precise mechanical measurements and a powerful X-ray source, provided by the German Electron Synchrotron in Hamburg (DESY), enabled the in situ analysis of the overall mechanical alignment of hierarchical ordered systems on a nanometer length scale. With the unique Rheo−SAXS-combination, located at the beamline BW1 at HasyLab, it was possible to monitor online, with a time resolution of 10 s, the structural evolution during flow-induced alignment of a symmetric diblock copolymer using a variety of large amplitude oscillatory shear conditions. By changing the strain amplitude, the kinetic pathways involved in the macroscopic perpendicular orientation of the PS-*b*-PI (M_w = 26 500 g/mol, f_{PS} = 51%) diblock copolymer melts were studied in detail.

For the first time, it was shown that, for high strain amplitudes (γ_0 = 2 and 3), an optimal degree of macroscopic orientation was achieved at short mechanical excitation times (t_{shear} < 500 s). During the in situ Rheo−SAXS measurements the best macroscopic alignment ($\sigma_{Min\text{-}SAXS}$ = 8°) was achieved for γ_0 =3, $\omega_1/2\pi$ = 1 Hz at T = 150 °C and a duration of shear of t_{shear} = 130 s. Surprisingly, as the LAOS experiment continued after reaching a primary minimum of σ_{SAXS} = 9° for γ_0 = 2 and σ_{SAXS} = 8° for γ_0 = 3, a less ordered overall orientation developed of approximately σ_{SAXS} = 10° for γ_0 = 2 and γ_0 = 3. This was indicated by a broadening of the azimuthally averaged scattered peak in the (*OX*, *OY*) plane detected by in situ Rheo−SAXS measurements and also confirmed by ex-situ SAXS studies, which revealed a heterogeneous biaxial distribution with both parallel and perpendicular fractions. Additional real space verification, using transmission electron microscopy (TEM), confirmed our assumption of a final less ordered structure.

By comparing the structural changes with the mechanical responses, it was found that the deordering process was also visible in the time evolution of the mechanical properties G'' and $I_{3/1}$. However, significant differences between stress and strain control in the nonlinear behavior of $G''(t)$ were obtained as the deordering process occurred. In contrast, the time progression of the mechanical response for G″ detected by the controlled stress deformation (CD) measurements and $I_{3/1}(t)$ calculated from the raw data of the strain controlled measurements, both showed a similar stretched exponential decay in the beginning of the mechanical excitation as well as an increase in $G''(t)$ and $I_{3/1}(t)$ from their plateau values at higher strain amplitudes. This increase in the mechanical properties indicated that deordering of the unit normal of the lamellae in the block copolymer melt occurred. Therefore, it was assumed that a higher degree of disorder in the sample caused a higher nonlinear response as measured by FT-rheology due to the interfacial tension between the locally anisotropic ordered microdomain grains.

From these findings, we proposed an orientation mechanism that is mainly dominated by the rotation of the locally ordered lamellar block copolymer grains. Furthermore, the kinetics of the orientation process as measured by 2D-SAXS revealed that the overall orientation of the lamellae is a function of the applied mechanical strain amplitude γ_0 where the orientation time τ had a power law dependence ranging between $\tau \sim \gamma_0^{-1.6}$ and γ_0^{-2}. However, by comparing the in situ time data calculated from the 2D-SAXS patterns with the in situ measured mechanical response quantified by the mechanical

dx.doi.org/10.1021/ma201492n | *Macromolecules* 2012, 45, 455−472

loss $G''(t)$ and the nonlinear parameter $I_{3/1}(t)$, the same power law dependence for the orientation time was confirmed.

These first results obtained by our unique Rheo−SAXS setup demonstrate the connectivity between structural dynamics in PS-*b*-PI diblock copolymer melts and the mechanical nonlinear response of the sample under large amplitude oscillatory shear. Furthermore, new insight into the stability and the evolution of the macroscopic perpendicular orientation were obtained. On the basis of these first experiments, this approach will be extended to more detailed investigations on a variety of PS-*b*-PI systems, including in situ Rheo−dielectric studies, to gain more information on the dynamics governing the alignment process and the, for the first time, observed deordering process.

■ ACKNOWLEDGMENTS

This research was carried out with the support of the HasyLab at the German Synchrotron (DESY) in Hamburg. Kyu Hyun acknowledges support by Basic Science Research Program through the National Research Foundation of Korea (NRF) funded by the Ministry of Education, Science and Technology (No. 2010-0024466) and Pusan National University Research Grant, 20100173. We thank André H. Gröschel from the University of Bayreuth for preparing the TEM cuts. Furthermore, the authors would like to thank Ingo Naue and Deepak Ahirwal for their valuable discussions on data fitting and the supply of accurate MatLab fit routines as well as Jennifer Kübel for proofreading the manuscript.

■ REFERENCES

(1) Laiho, A.; Ikkala, O. *Rev. Sci. Instrum.* **2007**, *78*, 1218.
(2) Hamley, I. W. *The physics of block copolymers*; Repr. ed.; Oxford Univ. Press: Oxford, U.K., 2003.
(3) Chen, Z. R.; Kornfield, J. A.; Smith, S. D.; Grothaus, J. T.; Satkowski, M. M. *Science* **1997**, *277*, 1248.
(4) Wang, J. Y.; Leiston-Belanger, J. M.; Sievert, J. D.; Russell, T. P. *Macromolecules* **2006**, *39*, 8487.
(5) Thurn-Albrecht, T.; Schotter, J.; Kastle, C. A.; Emley, N.; Shibauchi, T.; Krusin-Elbaum, L.; Guarini, K.; Black, C. T.; Tuominen, M. T.; Russell, T. P. *Science* **2000**, *290*, 2126.
(6) Böker, A.; Knoll, A.; Elbs, H.; Abetz, V.; Müller, A. H. E.; Krausch, G. *Macromolecules* **2002**, *35*, 1319.
(7) Sanger, J.; Gronski, W.; Leist, H.; Wiesner, U. *Macromolecules* **1997**, *30*, 7621.
(8) Schmidt, K.; Schoberth, H. G.; Ruppel, M.; Zettl, H.; Hansel, H.; Weiss, T. M.; Urban, V.; Krausch, G.; Böker, A. *Nat. Mater.* **2008**, *7*, 142.
(9) Olszowka, V.; Hund, M.; Kuntermann, V.; Scherdel, S.; Tsarkova, L.; Böker, A. *ACS Nano* **2009**, *3*, 1091.
(10) Winter, H. H.; Scott, D. B.; Gronski, W.; Okamoto, S.; Hashimoto, T. *Abstr. Pap. Am. Chem. Soc.* **1993**, *206*, 407.
(11) Sakurai, S. *Polymer* **2008**, *49*, 2781.
(12) Mori, K.; Hasegawa, H.; Hashimoto, T. *Polymer* **2001**, *42*, 3009.
(13) Koppi, K. A.; Tirrell, M.; Bates, F. S.; Almdal, K.; Colby, R. H. *J. Phys. II* **1992**, *2*, 1941.
(14) Colby, R. H. *Curr. Opin. Colloid Interface Sci.* **1996**, *1*, 454.
(15) Darling, S. B. *Prog. Polym. Sci.* **2007**, *32*, 1152.
(16) Hamley, I. W. *J. Phys.: Cond. Mat.* **2001**, *13*, R643.
(17) Bates, F. S.; Rosedale, J. H.; Fredrickson, G. H. *J. Chem. Phys.* **1990**, *92*, 6255.
(18) Mendoza, C.; Pietsch, T.; Gindy, N.; Fahmi, A. *Adv. Mater.* **2008**, *20*, 1179.
(19) Mendoza, C.; Pietsch, T.; Gutmann, J. S.; Jehnichen, D.; Gindy, N.; Fahmi, A. *Macromolecules* **2009**, *42*, 1203.
(20) Bockstaller, M. R.; Mickiewicz, R. A.; Thomas, E. L. *Adv. Mater.* **2005**, *17*, 1331.
(21) Fredrickson, G. H.; Helfand, E. *J. Chem. Phys.* **1987**, *87*, 697.
(22) Frederickson, G. H. *J. Rheol.* **1994**, *38*, 1045.
(23) Guo, H. X. *J. Chem. Phys.* **2006**, *125*, 214902.
(24) Chen, P. L. *Phys. Rev. E* **2005**, 71.
(25) Struth, B.; Hyun, K.; Kats, E.; Meins, T.; Walther, M.; Wilhelm, M.; Grübel, G. *Langmuir* **2011**, 2880.
(26) Wiesner, U. *Macromol. Chem. Phys.* **1997**, *198*, 3319.
(27) Zhang, Y. M.; Wiesner, U. *Macromol. Chem. Phys.* **1998**, *199*, 1771.
(28) Winter, H. H.; Scott, D. B.; Waddon, A. J.; Lin, Y. G.; Karasz, F. E. *Theor. Appl. Rheol.* **1992**, *1 and 2*, 405.
(29) Chen, Z. R.; Issaian, A. M.; Kornfield, J. A.; Smith, S. D.; Grothaus, J. T.; Satkowski, M. M. *Macromolecules* **1997**, *30*, 7096.
(30) Winey, K. I.; Patel, S. S.; Larson, R. G.; Watanabe, H. *Macromolecules* **1993**, *26*, 2542.
(31) Gupta, V. K.; Krishnamoorti, R.; Chen, Z. R.; Kornfield, J. A.; Smith, S. D.; Satkowski, M. M.; Grothaus, J. T. *Macromolecules* **1996**, *29*, 875.
(32) Gupta, V. K.; Krishnamoorti, R.; Kornfield, J. A.; Smith, S. D. *Macromolecules* **1995**, *28*, 4464.
(33) Langela, M.; Wiesner, U.; Spiess, H. W.; Wilhelm, M. *Macromolecules* **2002**, *35*, 3198.
(34) Di Cola, E.; Fleury, C.; Panine, P.; Cloitre, M. *Macromolecules* **2008**, *41*, 3627.
(35) Okamoto, S.; Saijo, K.; Hashimoto, T. *Macromolecules* **1994**, *27*, 3753.
(36) Balsara, N. P.; Hammouda, B.; Kesani, P. K.; Jonnalagadda, S. V.; Straty, G. C. *Macromolecules* **1994**, *27*, 2566.
(37) Terashima, T.; Motokawa, R.; Koizumi, S.; Sawamoto, M.; Kamigaito, M.; Ando, T.; Hashimoto, T. *Macromolecules* **2010**, *43*, 8218.
(38) Zipfel, J.; Berghausen, J.; Schmidt, G.; Lindner, P.; Alexandridis, P.; Richtering, W. *Macromolecules* **2002**, *35*, 4064.
(39) Habas, J. P.; Pavie, E.; Perreur, C.; Lapp, A.; Peyrelasse, J. *Phys. Rev. E.* **2004**, *70*, 061802.
(40) Wang, H.; Kesani, P. K.; Balsara, N. P.; Hammouda, B. *Macromolecules* **1997**, *30*, 982.
(41) Abuzaina, F. M.; Garetz, B. A.; Mody, J. U.; Newstein, M. C.; Balsara, N. P. *Macromolecules* **2004**, *37*, 4185.
(42) Hamley, I. W.; Pople, J. A.; Booth, C.; Derici, L.; Imperor-Clerc, M.; Davidson, P. *Phys. Rev. E* **1998**, *58*, 7620.
(43) Berghausen, J.; Zipfel, J.; Diat, O.; Narayanan, T.; Richtering, W. *Phys. Chem. Chem. Phys.* **2000**, *2*, 3623.
(44) Carreras, E. S.; Piau, J.-M.; El Kissi, N.; Pignon, F.; Panine, P. *J. Rheol.* **2006**, *50*, 803.
(45) Stasiak, J.; Mackley, M. R.; Squires, A. M.; Castelletto, V.; Hamley, I. W.; Moggridge, G. D. *Soft Matter* **2010**, *6*, 1941.
(46) Polushkin, E.; van Ekenstein, G. A.; Ikkala, O.; ten Brinke, G. *Rheol. Acta* **2004**, *43*, 364.
(47) Polushkin, E.; Bondzic, S.; de Wit, J.; van Ekenstein, G. A.; Dolbnya, I.; Bras, W.; Ikkala, O.; ten Brinke, G. *Macromolecules* **2005**, *38*, 1804.
(48) Garcia-Gutierrez, M. C.; Hernandez, J. J.; Nogales, A.; Pantine, P.; Rueda, D. R.; Ezquerra, T. A. *Macromolecules* **2008**, *41*, 844.
(49) Okamoto, S.; Saijo, K.; Hashimoto, T. *Macromolecules* **1994**, *27*, 5547.
(50) Wilhelm, M.; Maring, D.; Spiess, H. W. *Rheol. Acta* **1998**, *37*, 399.
(51) Wilhelm, M. *Macromol. Mater. Eng.* **2002**, *287*, 83.
(52) Hyun, K.; Wilhelm, M. *Macromolecules* **2009**, *42*, 411.
(53) Hadjichristidis, N.; Iatrou, H.; Pispas, S.; Pitsikalis, M. *J. Polym. Sci., Part A: Polym. Chem.* **2000**, *38*, 3211.
(54) Hyun, K.; Wilhelm, M.; Klein, C. O.; Cho, K. S.; Nam, J. G.; Ahn, K. H.; Lee, S. J.; Ewoldt, R. H.; McKinley, G. H. *Prog. Polym. Sci.* **2011**, DOI: 10.1016/j.progpolymsci.2011.02.002.
(55) Lauger, J.; Stettin, H. *Rheol. Acta* **2010**, *49*, 909.
(56) Bates, F. S. *Macromolecules* **1984**, *17*, 2607.
(57) Larson, R. G.; Winey, K. I.; Patel, S. S.; Watanabe, H.; Bruinsma, R. *Rheol. Acta* **1993**, *32*, 245.

(58) Daniel, C.; Hamley, I. W.; Wilhelm, M.; Mingvanish, W. *Rheol. Acta* **2001**, *40*, 39.
(59) Flory, P. J. *Principles of polymer chemistry*; Cornell Univ. Press: Ithaca, NY, 2006.
(60) Reimers, M. J.; Dealy, J. M. *J. Rheol.* **1996**, *40*, 167.
(61) Ramirez, R. W. *The FFT: fundamentals and concepts*; Prentice-Hall: Englewood Cliffs, NJ, 1985.
(62) Neidhofer, T.; Sioula, S.; Hadjichristidis, N.; Wilhelm, M. *Macromol. Rapid Commun.* **2004**, *25*, 1921.
(63) Klein, C. O.; Spiess, H. W.; Calin, A.; Balan, C.; Wilhelm, M. *Macromolecules* **2007**, *40*, 4250.
(64) Hyun, K.; Nam, J.; Wilhelm, M.; Ahn, K.; Lee, S. *Rheol. Acta* **2006**, *45*, 239.
(65) Oelschlaeger, C.; Gutmann, J. S.; Wolkenhauer, M.; Spiess, H. W.; Knoll, K.; Wilhelm, M. *Macromol. Chem. Phys.* **2007**, *208*, 1719.
(66) Koppi, K. A.; Tirrell, M.; Bates, F. S.; Almdal, K.; Colby, R. H. *J. Phys. II* **1992**, *2*, 1941.
(67) Cates, M. E.; Milner, S. T. *Phys. Rev. Lett.* **1989**, *62*, 1856.
(68) Hadziioannou, G.; Mathis, A.; Skoulios, A. *Colloid Polym. Sci.* **1979**, *257*, 136.
(69) Carotenuto, C.; Grosso, M.; Maffettone, P. L. *Macromolecules* **2008**, *41*, 4492.
(70) Reinheimer, K.; Massimiliano, G.; Wilhelm, M. *J. Colloid Interface Sci.* **2011**, 818.
(71) Höfl, S.; Kremer, F.; Spiess, H. W.; Wilhelm, M.; Kahle, S. *Polymer* **2006**, *47*, 7282.
(72) Hyun, K.; Höfl, S.; Kahle, S.; Wilhelm, M. *J. Non-Newtonian Fluid Mech.* **2009**, *160*, 93.
(73) Alvarez, F.; Alegria, A.; Colmenero, J. *Phys. Rev. B* **1991**, *44*, 7306.
(74) Williams, G.; Watts, D. C. *Trans. Faraday Soc.* **1970**, *66*, 80.

Macromolecules

ARTICLE

pubs.acs.org/Macromolecules

Influence of Metal Ion and Polymer Core on the Melt Rheology of Metallosupramolecular Films

Justin R. Kumpfer,[†] Jeong J. Wie,[‡] John P. Swanson,[∥] Frederick L. Beyer,[⊥] Michael E. Mackay,[*,‡,§] and Stuart J. Rowan[*,†]

[†]Department of Macromolecular Science & Engineering, Case Western Reserve University, 2100 Adelbert Rd., Cleveland, Ohio 44106-7202, United States

[‡]Department of Chemical Engineering, University of Delaware, 150 Academy St., Newark, Delaware 19716, United States

[§]Department of Materials Science & Engineering, University of Delaware, 201 DuPont Hall, Newark, Delaware 19716, United States

[∥]Department of Chemistry and Biochemistry, California Polytechnic State University, San Luis Obispo, California 93407-0402, United States

[⊥]U.S. Army Research Laboratory, Aberdeen Proving Ground, Maryland 21005-5069, United States

Supporting Information

ABSTRACT:

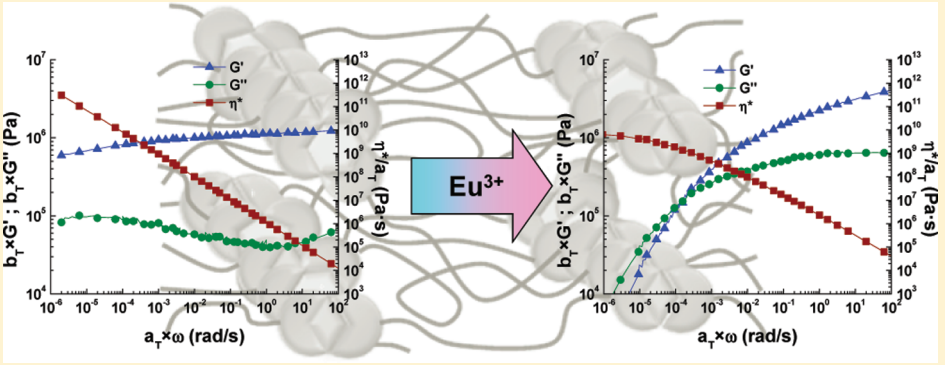

Detailed rheological studies of metallosupramolecular polymer films in the melt were performed to elucidate the influence of the metal ion and polymer components on their mechanical and structural properties. 4-Oxy-2,6-bis(*N*-methylbenzimidazolyl)pyridine telechelic end-capped polymers with a low-T_g core, either poly(tetrahydrofuran) or poly(ethylene-*co*-butylene), were prepared with differing ratios of Zn^{2+} and Eu^{3+} to determine the influence of polymer chain chemistry and metal ion on the properties. Increasing the amount of the weaker binding europium yielded more thermoresponsive films in both systems, and results show that the nature of the polymer core dramatically affected the films mechanical properties. All of the films studied exhibited large relaxation times, and we use this to explain the pure sinusoidal behavior found in the "nonlinear" viscoelastic region. Basically, the system cannot relax during a strain cycle, allowing us to assume the network destruction and creation rates to be only a function of the strain amplitude in a simplified network model used to rationalize the observed behavior.

INTRODUCTION

Supramolecular polymers utilize reversible, noncovalent interactions to achieve high molecular weight materials that combine the properties of typical covalent polymers with those of low molecular weight molecules.[1−6] These polymers have gained increasing interest from a materials' properties standpoint as they can have mechanical properties similar to covalent polymers but have much greater temperature-dependent viscosities as a result of the reversible interactions, which allows easy processing and/or the material to exhibit stimuli-responsive behaviors.[7−11] An additional benefit of these types of polymers is that their properties are widely tailorable simply by modifying the reversible interaction used. A number of noncovalent interactions have been utilized to access such materials, with the largest focus being on hydrogen bonding.[12−15] Another type of interaction that has become popular is metal−ligand coordination[16−20] which allows for a wide range of properties as many different ligands and metal ions can be used. While detailed studies of the melt rheological properties of supramolecular polymers assembled with hydrogen bonds have been carried out,[21−26] the same is not the case for metallosupramolecular polymers. In-depth solution rheological studies of metal-coordination polymers

Received: July 19, 2011
Revised: November 14, 2011
Published: December 01, 2011

Scheme 1. Chemical Structures of Mebip End-Capped Macromonomers Studied with Poly(tetrahydrofuran) (1) and Poly(ethylene-*co*-butylene) (2) Cores[a]

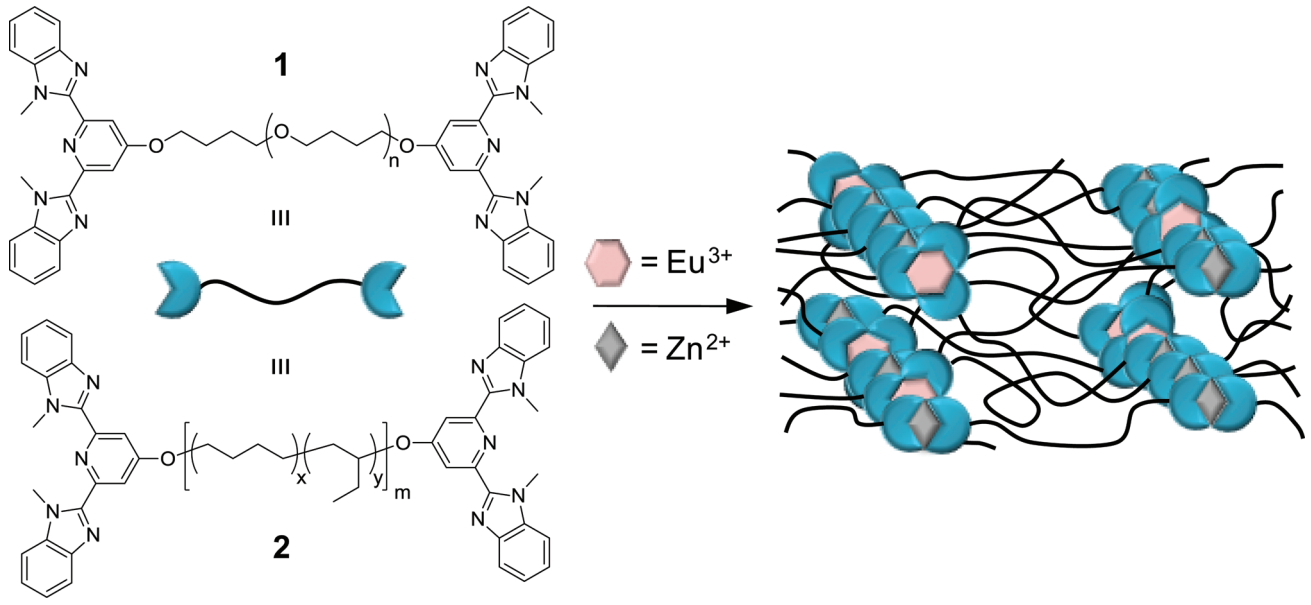

[a] These macromonomers self-assemble with zinc and europium salts to yield stimuli-responsive, phase-separated network structures.

have been reported,[27−29] and similarly some of us have performed investigations into the rheological and stimuli-responsiveness of metallosupramolecular gels.[30−33] However, to date there have been no studies performed exploring the solid-state rheological properties of metallosupramolecular polymer films.

We have shown previously that elastomeric films can be prepared from ligand end-capped low-T_g polymers assembled with zinc and/or lanthanides and that these films show interesting stimuli-responsive properties that are highly dependent on the metal ion content. In particular, metallosupramolecular polymers prepared from a 2,6-bis(*N*-methylbenzimidazoyl) pyridine (MeBip) end-capped poly(tetrahydrofuran) (**1**) with zinc and europium ions yield temperature- and chemo-responsive films,[34,35] while those prepared with MeBip end-capped poly(ethylene-*co*-butylene) (**2**) yield thermo- and photo-responsive rehealable elastomers with either zinc or lanthanide ions.[36] In order to achieve a better understanding of these metallosupramolecular polymers, we report a detailed rheological study of both these materials to examine the role of the metal ions and the nature of the polymer backbone on the materials' properties.

EXPERIMENTAL METHODS

Materials Used. Compounds **1** and **2** were synthesized according to previously published methods[34−36] with molecular weights of 4200 and 4000 g/mol, respectively. All reagents and solvents were purchased from Aldrich Chemical Co. and used without further purification. Spectrophotometric grade chloroform and acetonitrile were used for all experiments.

Sample Film Preparation. Example procedure for **1** with Zn^{2+}:Eu^{3+} 70:30. 952 μL (0.01 mmol) of a $Eu(ClO_4)_3$ solution in acetonitrile (10 mM) and 1666.7 μL (0.03 mmol) of a $Zn(ClO_4)_2$ solution in acetonitrile (20 mM) were mixed with 200 mg (0.05 mmol) of **1** in 5 mL of chloroform. The solvent was removed under vacuum, and the metallosupramolecular polymer was redissolved in 2 mL of chloroform, cast into an aluminum-walled casting dish with a Teflon base, and allowed to air-dry overnight. The films were further dried in a vacuum oven at 40 °C for 6 h to remove any residual solvent before use. Films of other metal ratios were prepared by varying the amounts of $Eu(ClO_4)_3$ and $Zn(ClO_4)_2$ appropriately. Typical film thicknesses were 0.25 ± 0.05 mm.

Rheological Measurements. All experiments were carried out on a TA Instruments ARES G2 rheometer with 8 mm parallel plates. Circular disks of the films were obtained using an 8 mm diameter steel punch. Prior to each experiment, the samples were heated under compression for short periods of time (5 min, see below for more details) before cooling to 30 °C. This step is required for good adhesion between the films and the plates. It also erases any thermal history that may have resulted from crystallization of the poly(tetrahydrofuran) core of macromonomer **1**. Films of composition Zn^{2+}:Eu^{3+} 100:0 to 80:20 were heated to 130 °C under a normal force of 5 N. Films with higher europium contents required slightly lower temperatures and pressures to prevent the film from flowing out of the plates. As such, the 70:30 film was pressed at 110 °C and 5 N, the 60:40 film at 90 °C and 3 N, and the 50:50 film was pressed at 70 °C and 3 N. Strain sweeps were performed in order to determine the linear viscoelastic region for each film. Samples were strained at a constant frequency of 10 rad/s and ramped from 0.1% strain until the samples lost adhesion, which was typically at strains larger than 30%. All frequency sweep experiments were performed at 1% strain to ensure that all responses were in the viscoelastic region. Frequency sweeps were carried out over a frequency range of 0.1−100 rad/s with temperatures from 30 to 110 °C in 20 °C increments. Temperatures never exceeded 130 °C to avoid decomposition of the metal salts. The frequency sweeps for each film were then combined using time−temperature superposition to generate master curves. The reference temperature was 30 °C for all master curves.

Small-Angle X-ray Scattering (SAXS) Characterization. SAXS data were collected using a customized, pinhole collimated SAXS camera. X-rays having wavelength (λ) of 1.542 Å were generated at 45 kV and 100 mA with a Rigaku Ultrax18 rotating Cu anode and filtered using Ni foil. Two-dimensional data sets were collected using a Molecular Metrology 120 mm diameter area detector and then

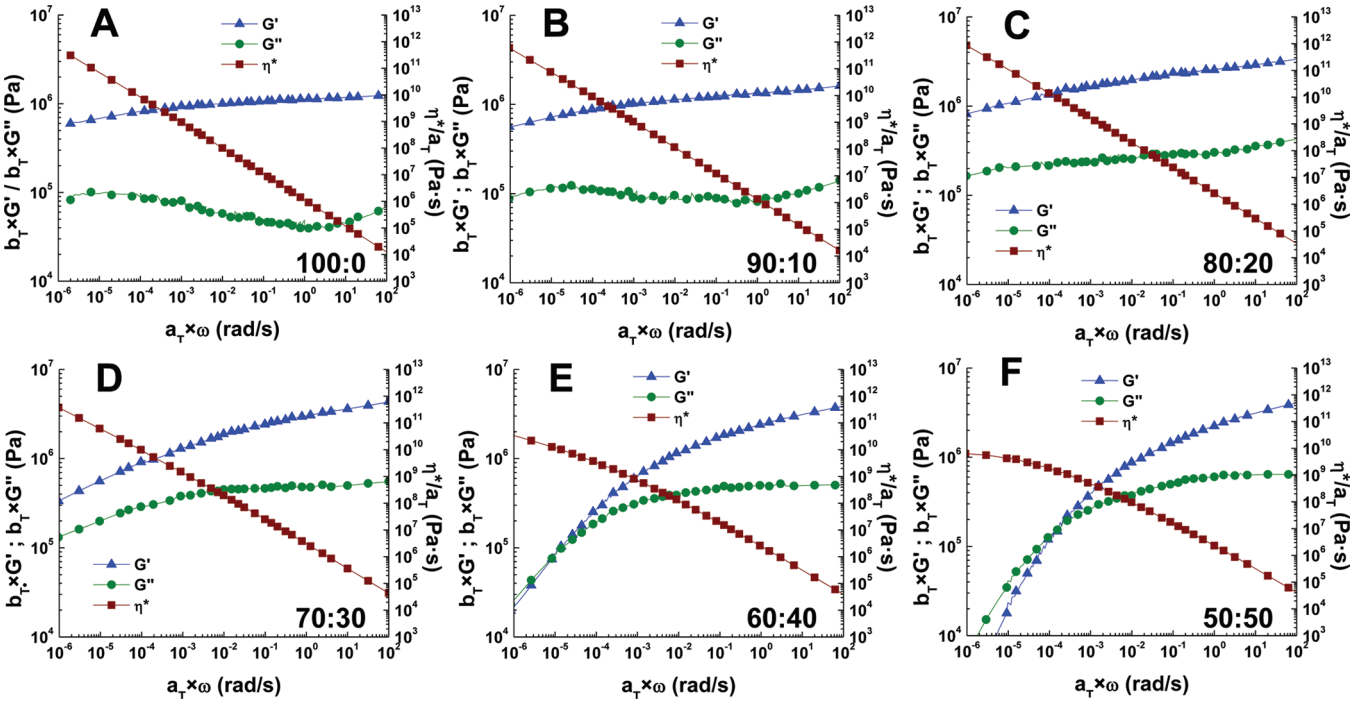

Figure 1. Master curves of films of **1** prepared with varying ratios of Zn^{2+}:Eu^{3+}. (A) 100:0, (B) 90:10, (C) 80:20, (D) 70:30, (E) 60:40, (F) 50:50. Storage modulus (triangles), loss modulus (circles), and complex viscosity (squares) vs oscillatory angular frequency. T_{ref} = 30 °C.

corrected for background noise and sample absorption. The corrected data were then azimuthally averaged to yield one-dimensional intensity, I, as a function of scattering vector magnitude, q, where $q = 4\pi \sin(\theta)/\lambda$ and 2θ is the scattering angle. The instrument was calibrated using Ag behenate, and the data were placed on an absolute scale (cm^{-1}) using type 2 glassy carbon, previously calibrated at the Advanced Photon Source, Argonne National Laboratory, as a secondary intensity standard. Each sample was characterized at two sample-to-detector distances, 150 and 50 cm, and the reduced data were combined into one continuous data set. All SAXS data processing, manipulation, and analysis were performed using Wavemetrics IGOR Pro and procedures available from Argonne National Laboratory.[37]

RESULTS AND DISCUSSION

Macromonomers **1** and **2** were prepared using methods we have previously reported.[34−36] These macromonomers were then self-assembled in solution with Zn^{2+} and Eu^{3+} perchlorate salts to yield the metallosupramolecular polymers which were then solution cast to yield elastomeric films. For mixed metal ion systems the percentages reported represent the idealized percentage of the total MeBip ligands that are coordinated with each metal ion, assuming a 2:1 Mebip:Zn^{2+} binding and a 3:1 Mebip:Eu^{3+}. For example, in a mixed Zn^{2+}:Eu^{3+} film of 70:30, 70% of the MeBip ligands can be bound to a Zn^{2+} ion and 30% of the ligand can bind to the Eu^{3+}. The metal:macromonomer ratio was calculated to ensure all ligands can bind to a metal ion and all metal ions are fully coordinated. Specifically in this study we were interested in examining the effect of two different parameters on the rheological properties of these materials, namely the effect of Zn^{2+} ions versus Eu^{3+} ions and the effect of the macromonomer core.

Influence of Eu^{3+} Content. We have previously reported,[35] using dynamic mechanical thermal analysis (DMTA), that films of the metallosupramolecular polymers of **1** with higher ratios of the Eu^{3+} to Zn^{2+} exhibit enhanced temperature sensitivity which leads to more sensitive stimuli-responsive films. Thus, to examine this effect in more detail a series of films of **1** with varying Zn^{2+}:Eu^{3+} ratios, shown in Scheme 1, were prepared ranging from 100:0 to 50:50. Metallosupramolecular polymers of **1** with less than 50% of the ligand bound to Zn^{2+} ions did not form mechanical stable films, yielding instead only oils.

The master curves obtained for the films (Figure 1) help to give insight into the structure of these metallosupramolecular polymers. From the master curves it can be concluded that there is a change in the structure as the ratio of Zn^{2+} to Eu^{3+} decreases. Films composed of 100% Zn^{2+} display typical rheological behavior of high molecular weight polymers after observation of the low-frequency region. In the case of the high Zn^{2+} content films (100:0−70:30), the terminal (flow) region cannot be reached over the range of temperatures and frequencies studied, and only the plateau region can be observed. Surprisingly, no minimum in the tan δ curve (vs ω) is observed that would correlate to a plateau modulus (see Supporting Information). Even at lower temperatures, ca. −30 °C, no minimum is found for tan δ which may result from the fact that even at −30 °C the polymer is still well above T_g of the poly(tetrahydrofuran) core (ca. −80 °C).

As the Eu^{3+} content in the films increases, the frequency at which the behavior changes from the plateau region to the terminal region shifts to higher values. This is indicative of a decrease in the effective molecular weight of the assembled macromonomers and/or a reduction of entanglements as a result of the molecular weight reduction. This gives insight into what is changing structurally as the Eu^{3+} content is increased. For a Zn^{2+}:Eu^{3+} 100:0 film, it would be expected to form a linear, high molecular weight polymer as the 2:1 Mebip:Zn^{2+} complex will just yield chain extension. Once Eu^{3+} is added, it can bind in a 3:1 Mebip:Eu^{3+} ratio which can act as a branching point. Thus, as

dx.doi.org/10.1021/ma201659d |*Macromolecules* 2012, 45, 473–480

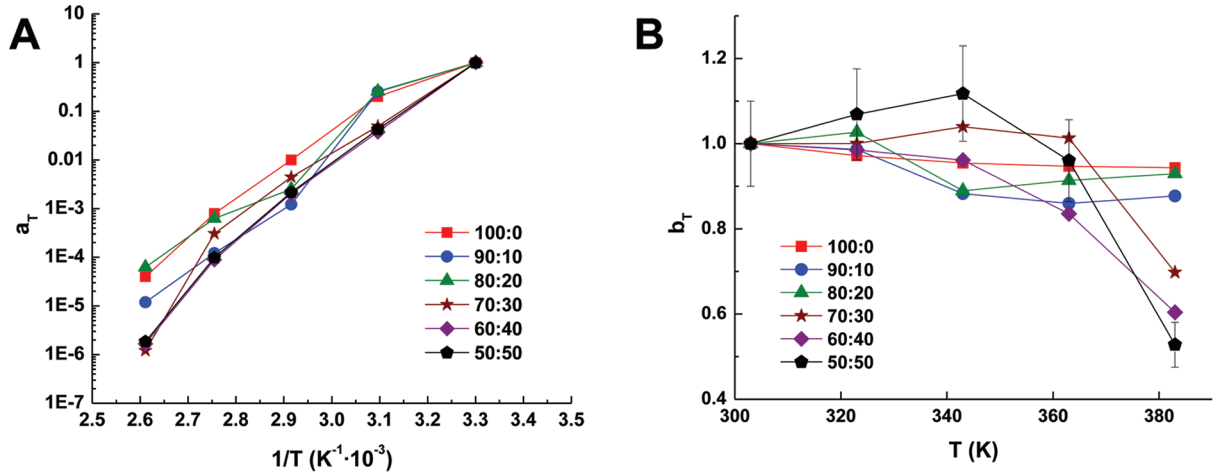

Figure 2. Horizontal (A) and vertical (B) shift factors of the series of films prepared with **1**. The difference in a_T at high temperatures suggests these films are relatively frequency dependent, whereas changes in b_T with increasing Eu^{3+} display the increased temperature sensitivity. Error bars are shown for the Zn^{2+}:Eu^{3+} 50:50 sample only for clarity; however, they apply to all of the data sets in (B). The error results from a curve fit minimizing an objective function to overlay the curves.

more Eu^{3+} is introduced, the amount of branching will increase, which will effectively reduce the molecular weight of the linear polymer segments, which are formed by chain extension with Zn^{2+} complexes between cross-links, since the amount of the Zn^{2+} is reduced, while the total molecular weight increases. Concordantly, it can be expected that the polydispersity of the linear polymer segments formed with Zn^{2+} will also increase as the Eu^{3+} content is increased, which is backed up by examination of the G'' vs ω curves. In the high content Zn^{2+} materials (100:0 and 90:10) both a minima and maxima are observed as ω is decreased in the G'' curve; however, this behavior is replaced by a more linear one as more Eu^{3+} is added, consistent with an increase in the polydispersity of the material.[38]

The relaxation time, which is roughly defined as the terminal viscosity divided by the plateau modulus, is also greatly dependent on the Eu^{3+} content within the films. It is not possible to determine the terminal viscosity for films containing 0%−30% Eu^{3+}, as the terminal region was not reached, but it is obvious that there is a trend of increasing relaxation times with decreasing Eu^{3+} content. For the films containing 40% and 50% Eu^{3+}, the terminal viscosities, which were estimated at 3.3×10^{10} and 6.3×10^{9} Pa·s, are used with estimations of the plateau modulus (3.79 and 3.97 MPa) to give relaxation times of 8700 and 1600 s, respectively. As mentioned earlier, no minimum in tan δ was observed in these films so the estimations of the plateau modulus were taken from the lowest measured tan δ value. Thus, for these two films the estimated plateau modulus is lower than the real value. The increase in the estimated plateau modulus from the 40%−50% Eu^{3+} is only 5%, which is within experimental error. Nonetheless, these results show that the relaxation times of these films are extremely dependent on the metal ratios, where a 10% increase in Eu^{3+} leads to a 5-fold decrease in relaxation time. This suggests that the decreasing terminal viscosity is primarily responsible for the dramatic decrease in relaxation times as more Eu^{3+} is added. This is likely on account of the increasing amount of Eu^{3+} increasing branching which will play a role in decreasing the viscosity. It is also possible that the decrease in terminal viscosity in the higher concentration Eu^{3+} materials is on account of the easier decomplexation of the weaker bound Eu^{3+} complexes relative to the Zn^{2+} complexes, resulting in more facile depolymerization in the system.

The effect on the temperature sensitivity with changing metal ratios can be elucidated by examining the master curve shift factors shown in Figure 2. The horizontal shift factors (Figure 2A) change in both slope and intensity which implies that these materials are quite temperature dependent. The vertical shift factors (Figure 2B) also show the dramatic change in the temperature sensitivity, particularly at high temperature, with decreasing the Zn^{2+}:Eu^{3+} ratio. For example, the shift factors for the Zn^{2+}:Eu^{3+} 100:0 film change little with temperature, while the Zn^{2+}:Eu^{3+} 50:50 film exhibits much different behavior in the temperature range studied. A trend is observed with changing metal ratio, and as the amount of Eu^{3+} is increased, the vertical shift factors move from a linear response to a larger and larger nonlinear response with temperature. This data is consistent with the previously published DMTA results[35] which show the increasing temperature sensitivity of the films with increasing amounts of Eu^{3+}.

While the temperature dependence of the vertical shift factor b_T may seem unusual, it can be explained quite simply by remembering its origin. Consider network theory[39] where the storage and loss modulus can both be written as $nk_BTf(\lambda\omega)$, where n is the number of cross-links per unit volume, k_B is Boltzmann's constant, T is temperature, and $f(\lambda\omega)$ is a function describing the modulus frequency dependence (ω) which is normalized by a relaxation time (λ). Of course, the functional form is different for the two moduli. The number of cross-links can be interpreted as the number of molecules per unit volume or entanglements per unit volume depending on model specifics for the system at hand. For linear polymer melts n can be written as $\rho N_A/M$ where ρ is the mass density, N_A is Avogadro's number, and M is molecular weight, allowing one to write the vertical shift factor as

$$b_T = \frac{[\rho N_A/M]k_BT}{[\rho_0 N_A/M_0]k_BT_0} = \frac{\rho T}{\rho_0 T_0} \quad (1)$$

where the subscript 0 is used to denote "at the reference temperature" and the molecular weight is assumed constant in

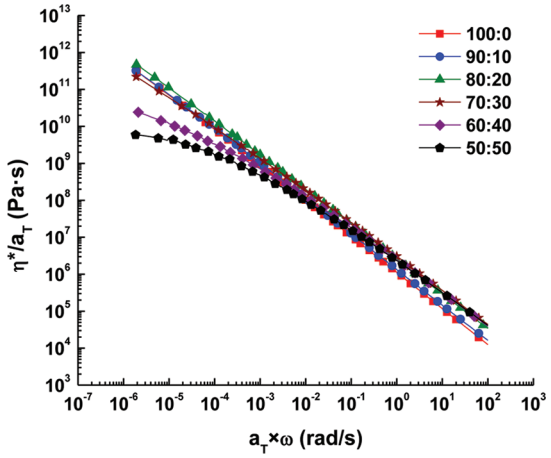

Figure 3. Time−temperature superposition plot of complex viscosity vs oscillatory angular frequency. Films of **1** with Zn^{2+}:Eu^{3+} ratios of 60:40 and 50:50 approach terminal viscosities while films containing less Eu^{3+} have nonterminal viscosities of order 10^{12} Pa·s, which is near the defined viscosity of a glass. The temperature range studied was 30−110 °C.

the later form of the equation. Since the melt density does not change very much with temperature and the absolute temperature similarly changes little, plus as temperature rises the density falls, b_T will typically change by at most 10%.

The metallosupramolecular materials studied here have a higher temperature sensitivity, especially those containing larger amounts of Eu^{3+}. This is consistent with Eu^{3+} decomplexing from the Mebip end groups as the temperature is increased. This leads to b_T falling by a factor of 2 in the case of the 50:50 material, suggesting the effective molecular weight changes with temperature. This may violate the inherent assumption of thermorheological simplicity, invalidating the use of shift factors; however, the effect is relatively mild in that the entire material does not decomplex and we believe that one can use shift factors to obtain an approximation to the full rheological response for the extended frequency range. Yet, this caveat should be kept in mind; the higher Eu^{3+} content materials may change in effective molecular weight, and the terminal region, obtained from higher temperature data, may have a smaller molecular weight than data collected at lower temperatures. Indeed, we should expect this since at higher temperatures the materials obtain low viscosity through more complete decomplexation, allowing them to heal if need be.[36]

The complex viscosity is also directly affected by the metal ion composition of the films. As the ratio of Zn^{2+}:Eu^{3+} is decreased, the viscosity is observed to decrease, most noticeably upon approaching the terminal region. As mentioned before, the transition to the terminal region is only observed for the films comprised of Zn^{2+}:Eu^{3+} 60:40 and 50:50 which can also be seen in the complex viscosity data. It is necessary to remember that the effective molecular weight for these films should be reduced as temperature is increased as a result of metal−ligand decomplexation of the more thermally responsive Eu^{3+} complexes. This suggests that the viscosity decrease is most likely a result of depolymerization at high temperatures. The probably of forming rings should also increase with increasing Eu^{3+} which may also contribute to the reduction in viscosity, although we have no evidence to directly support this idea. The film with the lowest complex viscosity (Zn^{2+}:Eu^{3+} 50:50) has a terminal viscosity of ∼5×10^9 Pa·s. This value is higher than any previously reported for a supramolecular polymer and may in part be related to the microphase-separated morphology of these materials (vide infra). Figure 3 shows that the complex viscosities are also shown to increase dramatically as the Eu^{3+} content is decreased as there is a 5-fold estimated increase in the terminal viscosity of the 60:40 over the 50:50 film. For films consisting of Zn^{2+}:Eu^{3+} ratios of 100:0 to 70:30, a terminal viscosity is not reached in the temperature −frequency range studied. All of these films show viscosities ranging from 5×10^{11} to 1×10^{12} Pa·s with terminal viscosities expected to be even larger. This is extremely surprising for thermoplastic elastomers, as one definition of a glass is a material exhibiting a viscosity of 1×10^{12} Pa·s.[40] These films show viscosities just below that defined transition, suggesting that these films are behaving as extremely viscous liquids.

Influence of the Core Polymer. In order to study the impact of the polymer backbone on the melt rheology behavior of these metallosupramolecular polymers, select films (Zn^{2+}:Eu^{3+} 100:0 and 50:50) were prepared from the end-capped poly(ethylene-*co*-butylene) (**2**) and compared with the previous results. Both cores have low glass transition temperatures (ca. −80 and −25 °C for **1** and **2**, respectively); however, the poly(tetrahydrofuran) core is more polar, and the oxygen atoms in the backbone have the potential to act as weak metal ion coordinating sites, which is not possible in the hydrocarbon core of **2**.

Meijer and co-workers[41] have shown that the polarity of the core polymer in telechelic supramolecular polymers assembled using hydrogen-bonding motifs influences the self-assembly process. Polar polymers were found to disrupt hydrogen bonding and dramatically reduce the mechanical properties compared to the nonpolar polymers which yielded highly phase-separated materials. Thus, it was expected in these metallosupramolecular polymers that the poly(ethylene-*co*-butylene) core would enhance the material properties of the films as it should allow for greater phase separation from the charged metal−ligand complexes, whereas the poly(tetrahydrofuran) monomer would be more miscible with the complexes and has the potential to weakly coordinate the metal ions, especially with the Eu^{3+} ions.

This anticipated difference in the microphase separation behaviors of **1** and **2** was studied using small-angle X-ray scattering (SAXS) on films of the different materials, as was recently shown for solution-cast films of **2** with Zn^{2+}.[36] Microphase-separated morphologies with appreciable long-range order give rise to constructive interference between scattered X-rays producing Bragg diffraction maxima; materials with good long-range order exhibit a higher number of Bragg maxima than those with poor long-range order. Figure 4A shows SAXS data for the series of films prepared with **1**. For all samples, two Bragg diffraction maxima are observed, characteristic of moderate long-range order. The second-order peaks are located at twice the spacing of the primary maxima (q^*), indicative of a lamellar morphology in which the poly(tetrahydrofuran) core and metal−ligand complexes form alternating layers of soft and hard phases, respectively, and consistent with those reported previously for metallosupramolecular polymers.[36] The lamellar period, d, where $d = 2\pi/q^*$, is ∼8.2 nm for all samples and gives the center-to-center distance between hard phases in the case of a lamellar morphology.

When compared to the films prepared with **2**,[36] which all showed at least three Bragg diffraction maxima, it is apparent

dx.doi.org/10.1021/ma201659d |*Macromolecules* 2012, 45, 473–480

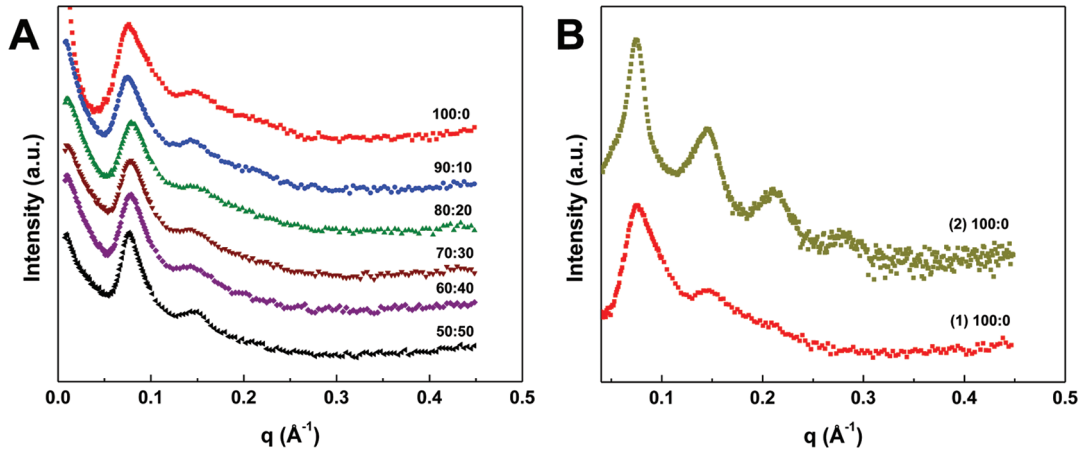

Figure 4. (A) SAXS data of films prepared with **1**. (B) Comparison of Zn^{2+}:Eu^{3+} 100:0 films prepared with **1** and **2**. Films prepared with **2** show greater long-range ordering as a result of better phase separation.

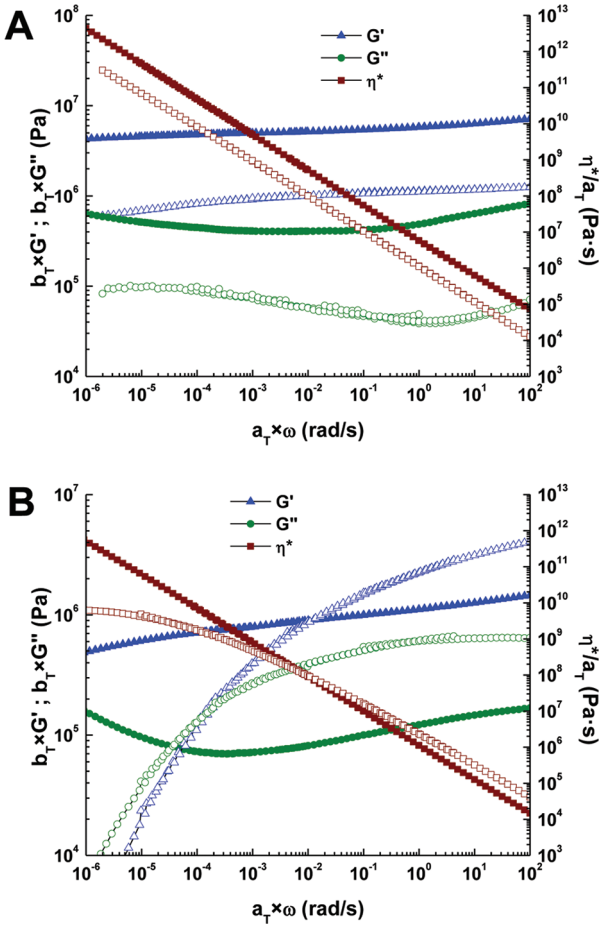

Figure 5. Direct comparison of the master curves obtained for films prepared with **1** (open) vs **2** (closed) containing various Zn^{2+}:Eu^{3+} ratios. (A) 100:0 (B) 50:50. Films prepared with **2** show enhancement in G' (triangles), G'' (circles), and η^* (squares), which is a result of better phase separation between the polymer core and metal−ligand complexes.

that the degree of ordering in the films based on **1** is significantly reduced (Figure 4B). This is consistent with the more polar poly(tetrahydrofuran) being able to interfere with the ability of the Zn^{2+} to form metal−ligand complexes with the Mebip ligand, resulting in reduced long-range order relative to the 100% Zn^{2+} sample based on poly(ethylene-*co*-butylene). Furthermore, the degree of long-range order is unaffected by the replacement of Zn^{2+} with Eu^{3+} in the materials based on poly(tetrahydrofuran). Therefore, in the case of the polar poly(tetrahydrofuran) cores, the effect of the polar core on the long-range order strongly dominates over the effect of metal ion.

As expected, the films prepared with **2** show dramatic enhancements in material properties over films prepared with **1** as shown in Figure 5. A direct comparison of the Zn^{2+}:Eu^{3+} 100:0 materials (Figure 5A) shows an order of magnitude enhancement in the modulus and viscosity just by changing the polymer core from **1** to **2**. The mechanical enhancement is most obvious when comparing the 50:50 films, focusing primarily on the lower frequency behavior. As shown earlier, films made with **1** at this metal ratio essentially displayed a terminal region, whereas films of the same metal ratio with **2** are still in the plateau region at the same frequencies and temperatures. In fact, the Zn^{2+}:Eu^{3+} 50:50 film with **2** demonstrates very similar behavior with the 100:0 film prepared with **1**, suggesting that the polymer core plays a larger role in determining the materials' properties than the two different metal ions in the mixed Zn^{2+} and Eu^{3+} films. This effect can, in part, be explained by the increased microphase separation and long-range morphology observed in the metallosupramolecular polymers of **2** when compared to **1**. As mentioned earlier, films of **1** with Zn^{2+}:Eu^{3+} 0:100 do not form stable films and result in oils. Interestingly, however, films prepared with 100% Eu^{3+} and **2** do form mechanically stable films. This is consistent with the increased phase separation imparted by the nonpolar core of macromonomer **2** and/or the ability of the poly(tetrahydrofuran) oxygens in **1** to weakly coordinate with the Eu^{3+} and compete with the ligand complexes.

Response at High Strain. Strain sweeps are generally used to determine what strain magnitude can be used in order to stay within the linear viscoelastic region which is verified as a linear response in G', G'', and tan δ. Once the stress no longer follows a linear trend, the material is said to be outside of the viscoelastic region. This can also be seen in the stress waveform which follows a sinusoidal pattern within the linear viscoelastic region while outside of this region the waveform becomes nonsinusoidal, having multiple frequency components easily visualized by a

dx.doi.org/10.1021/ma201659d |*Macromolecules* 2012, 45, 473–480

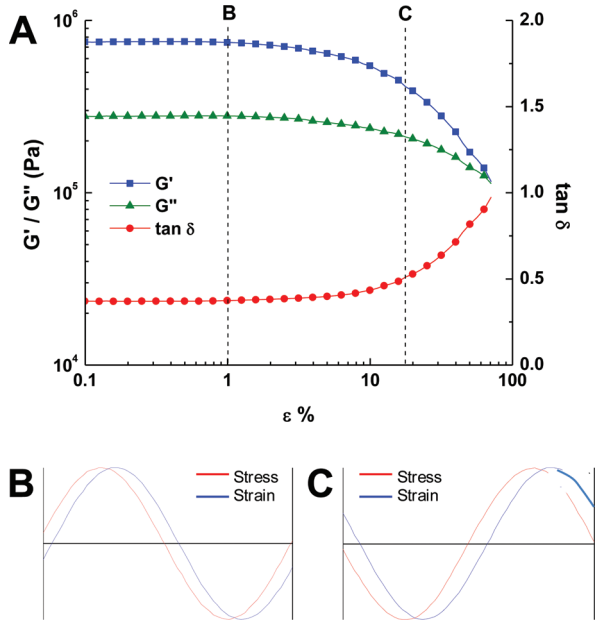

Figure 6. Strain sweep of a representative film of **1** with Zn^{2+}:Eu^{3+} 70:30. The waveform at 1% strain (B) shows a typical response in the linear region of the strain sweep. At 17.7% strain (C) the material is no longer in the viscoelastic region; however, the waveform still shows a linear response as a result of the extremely long relaxation times which prevent them from relaxing within the experiment time frame.

Fourier transform of the stress wave. Interestingly, for all Zn^{2+}:Eu^{3+} films a sinusoidal waveform is observed even though the material is no longer in the linear viscoelastic region as shown in Figure 6. The large-amplitude oscillatory strain experiments were performed with a sampling frequency of 500 data points per second, which will not influence data analysis since the frequency used in the experiments shown in Figure 6, 10 rad/s, is well below the sampling rate (as are all frequencies used in this study). Furthermore, a Fourier transform of the output torque showed no higher order harmonics, which is consistent with the model proposed below. A strain of 17.7% is well within the apparent nonlinear region as the storage modulus has decreased by a factor of ~2; however, a linear stress (torque) response is still seen. We believe this is a result of the extremely long relaxation times that are observed for these materials.

As mentioned above, the relaxation times for the two samples that displayed a terminal region were 1000−10 000 s in value. These are quite large, and because of this we do not believe the system can relax during a strain cycle. This is expected because of the phase-separated morphology prohibiting molecular motion greatly affects the destruction or creation of the network segment terms in the network theory frequently used to describe nonlinear rheological behavior.[42] The term can be written as a function of the strain or stress, which are both functions of time, exemplifying that as the strain or stress is increased, the rate of segment destruction increases and the segment creation decreases, but they are also functions of time. Here we assume the network creation rate, L, can be written as $L_0 \exp(a\gamma^0)$, where L_0 and a are constants and γ^0 is the strain amplitude, making the creation rate only a function of the strain amplitude and not time. Similarly the destruction rate, $1/\lambda$, is given by $1/\lambda_0 \exp(b\gamma^0)$, again which is dependent on the strain amplitude and not time. Of course, the strain in this experiment is given by $\gamma(t) = \gamma^0 \sin(\omega t)$, where ω is the frequency.

Since the relaxation times are so large in these materials, we hypothesize there is minimal relaxation during a strain cycle, as mentioned above, and so assume the destruction and creation rates are related to the strain amplitude. When this is done, the equations developed by Ahn and co-workers[42] are remarkably simple to solve, and the stress is a pure sinusoid of the form $\sin(\omega t + \delta)$, where δ is the phase lag, one easily finds for a singular relaxation mode

$$G' = \frac{e^{[a-b]\gamma^0}\omega^2}{e^{2b\gamma^0} + \omega^2} \quad (2)$$

$$G'' = \frac{e^{a\gamma^0}\omega}{e^{2b\gamma^0} + \omega^2} \quad (3)$$

If the material is a linear viscoelastic liquid, then a and b are zero. Note that we have written the two moduli in dimensionless form normalized by the number of network segments per unit volume, Boltzmann's constant, and temperature. It is possible to assume multiple relaxation modes and fit this nonlinear generalized Maxwell model to the data at hand. However, little is gained. Instead, we draw two conclusions from this model. First, it is possible to have a pure sinusoid in the "nonlinear" viscoelastic region. Our hypothesis is that the material cannot relax during a period of oscillation. In true polymeric materials relaxation occurs via segmental Brownian motion. Obviously, this does not occur in our materials, and structural recovery is slow and related to the materials' morphology, the metal ions coordinating with the end groups and in the case of **1** with the oxygen atoms present in the polymeric backbone. The thermal energy is obviously insufficient to allow rapid recovery for the conditions we have chosen to use.

Second, eqs 2 and 3 are extremely robust in their predictions. The relative magnitude of a and b can change the strain response of the material to generate rheological phase diagrams suggested by Ahn and co-workers. The results in Figure 6 suggest $a > b$ since both G' and G'' decrease with γ^0. Of course, detailed modeling would be required to satisfactorily fit the moduli data over all frequencies and strains.

As stated above, we would learn little in performing this exercise since arbitrary assumptions would have to be made. For example, many relaxation modes are required to fit the data over the entire frequency range. Would only the first mode be represented by eqs 2 and 3, or would all modes? Would the network creation and destruction parameters a and b be different for each mode? Either or both of these assumptions could generate satisfactory data representations, and so we do not do so. This model is very powerful though and rich in its predictions and lends credence to our hypothesis that relaxation during a deformation cycle does not occur.

As far as we know, this is the first observation of this effect where a pure sinusoid is observed in the so-called nonlinear region. The materials synthesized in this work are obviously unusual when compared to conventional covalent polymers; however, we do not believe that this effect is unique. If another system cannot relax during an oscillation period, then similar behavior could be observed. Obviously, our system has extremely large relaxation times, allowing us to demonstrate this behavior.

dx.doi.org/10.1021/ma201659d |*Macromolecules* 2012, 45, 473–480

CONCLUSIONS

A detailed study of the rheological behavior of a series of metallosupramolecular films in the melt was carried out to determine the impact of changing metals and the macromonomers. It was found that in films with varying ratios of zinc and europium increasing the europium content resulted in a dramatic change in the temperature response which allowed the films to reach the terminal region. It was also determined that the polymeric core plays a significant role in the materials' properties where a nonpolar poly(ethylene-*co*-butylene) core displayed dramatic enhancement of G', G'', and η^* relative to the more polar poly(tetrahydrofuran) core. All of the films studied had terminal complex viscosities greater than 1×10^9 Pa·s, which is higher than any previously reported for a supramolecular polymer and near to the value that defines a glass (1×10^{12} Pa·s). The films exhibited a sinusoidal waveform in the "nonlinear" viscoelastic region of the strain sweeps as a result of extremely long relaxation times which prevents the material from relaxing during a period of oscillation. We used this to develop a simplified network model which can be applied to other materials that are unable to relax during an oscillation period.

ASSOCIATED CONTENT

Supporting Information. Master curves of Zn^{2+}:Eu^{3+} 0:100 with **1** and **2**; tan δ curves of films with **1**; strain sweeps of films with **1**; shift factors of films with **2**. This material is available free of charge via the Internet at http://pubs.acs.org.

AUTHOR INFORMATION

Corresponding Author

*E-mail: stuart.rowan@case.edu (S.J.R.); mem@udel.edu (M.E.M.).

ACKNOWLEDGMENT

This material is based upon work supported by the U.S. Army Research Office (W911NF-09-1-0288), the National Science Foundation under Grants CHE-0704026, DMR-0602869, and MRI-0821515 (for the purchase of the MALDI-TOF/TOF), and the Case School of Engineering.

REFERENCES

(1) Fox, J. D.; Rowan, S. J. *Macromolecules* **2009**, *42*, 6823–6835.
(2) De Greef, T. F. A.; Smulders, M. M. J.; Wolffs, M.; Schenning, A. P. H. J.; Sijbesma, R. P.; Meijer, E. W. *Chem. Rev.* **2009**, *109*, 5687–5754.
(3) Lehn, J.-M. *Prog. Polym. Sci.* **2005**, *30*, 814–831.
(4) Weck, M. *Polym. Int.* **2007**, *56*, 453–460.
(5) Harada, A.; Takashima, Y.; Yamaguchi, H. *Chem. Soc. Rev.* **2009**, *38*, 875–882.
(6) Courtois, J.; Baroudi, I.; Nouvel, N.; Degrandi, E.; Pensen, S.; Ducouret, G.; Chanéac, C.; Bouteiller, L.; Creton, C. *Adv. Funct. Mater.* **2010**, *20*, 1803–1811.
(7) Wojtecki, R. J.; Meador, M. A.; Rowan, S. J. *Nature Mater.* **2011**, *10*, 14.
(8) Kim, H.-J.; Lim, Y.-B.; Lee, M. *J. Polym. Sci., Part A: Polym. Chem.* **2008**, *46*, 1925–1935.
(9) Rieth, S.; Baddeley, C.; Badjić, J. D. *Soft Matter* **2007**, *3*, 137–154.
(10) Nair, K. P.; Breedveld, V.; Weck, M. *Macromolecules* **2011**, *44*, 3346–3357.
(11) For additional examples see: (a) Yuen, F.; Tam, K. C. *Soft Matter* **2010**, *6*, 4613–4630. (b) Liu, J.; Chen, G.; Goo, M.; Jiang, M. *Macromolecules* **2010**, *43*, 8086–8093. (c) Sholrollahi, P.; Mirzadeh, H.; Scherman, O. A.; Huck, W. T. S. *J. Biomed. Mater. Res., Part A* **2010**, *95A*, 209–221. (d) Matsumoto, S.; Yamaguchi, S.; Ueno, S.; Komatsu, H.; Ikeda, M.; Ishizuka, K.; Iko, Y.; Tabata, K. V.; Aoki, H.; Ito, S.; Noji, H.; Hamachi, I. *Chem.—Eur. J.* **2008**, *14*, 3977–3986.
(12) Shimizu, L. S. *Polym. Int.* **2007**, *56*, 444–452.
(13) Bouteiller, L. *Adv. Polym. Sci.* **2007**, *207*, 79–112.
(14) Armstrong, G.; Buggy, M. *J. Mater. Sci.* **2005**, *40*, 547–559.
(15) Binder, W. H.; Zirbs, R. *Adv. Polym. Sci.* **2007**, *207*, 1–78.
(16) Chiper, M.; Hoogenboom, R.; Schubert, U. S. *Macromol. Rapid Commun.* **2009**, *30*, 565–578.
(17) Moughton, A. O.; O'Reilly, R. K. *Macromol. Rapid Commun.* **2010**, *31*, 37–52.
(18) McKenzie, B. M.; Rowan, S. J. *Molecular Recognition and Polymers*; Rotello, V. M., Thayumanavan, S., Eds.; John Wiley and Sons: Hoboken, NJ, 2008; Chapter 7, p 157.
(19) Li, Z.; Djohari, H.; Dormidontova, E. E. *J. Chem. Phys.* **2010**, *133*, 184904–1–9.
(20) Xu, D.; Craig, S. L. *Macromolecules* **2011**, *44*, 5465–5472.
(21) van Beek, D. J. M.; Spiering, A. J. H.; Peters, G. W. M.; te Nijenhuis, K.; Sijbesma, R. P. *Macromolecules* **2007**, *40*, 8464–8475.
(22) Sivakova, S.; Bohnsack, D. A.; Mackay, M. E.; Suwanmala, P.; Rowan, S. J. *J. Am. Chem. Soc.* **2005**, *127*, 18202–18211.
(23) Elkins, C. L.; Park, T.; Mckee, M. G.; Long, T. E. *J. Polym. Sci., Part A: Polym. Chem.* **2005**, *43*, 4618–4631.
(24) Herbst, F.; Schröter, K.; Gunkel, I.; Gröger, S.; Thurn-Albrecht, T.; Balbach, J.; Binder, W. H. *Macromolecules* **2010**, *43*, 10006–10016.
(25) Wietor, J.-L.; van Beek, D. J. M.; Peters, G. W.; Mendes, E.; Sijbesma, R. P. *Macromolecules* **2011**, *44*, 1211–1219.
(26) Woodward, P. J.; Merino, D. H.; Greenland, B. W.; Hamley, I. W.; Light, Z.; Slark, A. T.; Hayes, W. *Macromolecules* **2010**, *43*, 2512–2517.
(27) Xu, D.; Craig, S. L. *J. Phys. Chem. Lett.* **2010**, *1*, 1683–1686.
(28) Vermonden, T.; van Steenbergen, J.; Besseling, N. A. M.; Marcelis, A. T. M.; Hennink, W. E.; Sudhölter, E. J. R.; Cohen Stuart, M. A. *J. Am. Chem. Soc.* **2004**, *126*, 15802–15808.
(29) Serpe, M. J.; Craig, S. L. *Langmuir* **2007**, *23*, 1626–1634.
(30) Weng, W.; Li, Z.; Jamieson, A. M.; Rowan, S. J. *Soft Matter* **2009**, *5*, 4647–4657.
(31) Lee, J. H.; Lee, H.; Seo, S.; Jaworski, J.; Seo, M. L.; Kang, S.; Lee, J. Y.; Jung, J. H. *New J. Chem.* **2011**, *35*, 1054–1059.
(32) Adarsh, N. N.; Dastidar, P. *Cryst. Growth. Des.* **2011**, *11*, 328–336.
(33) For other examples see: (a) Zhao, Y.; Beck, J. B.; Rowan, S. J.; Jamieson, A. M. *Macromolecules* **2004**, *37*, 3529–3531. (b) Batabyal, S. K.; Leong, W. L.; Vittal, J. J. *Langmuir* **2010**, *26*, 7464–7468. (c) Grondin, P.; Roubeau, O.; Castro, M.; Saadaoui, H.; Colin, A.; Clérac, R. *Langmuir* **2010**, *26*, 5184–5195. (d) Weng, W.; Beck, J. B.; Jamieson, A. M.; Rowan, S. J. *J. Am. Chem. Soc.* **2006**, *128*, 1163–11672.
(34) Beck, J. B.; Ineman, J. M.; Rowan, S. J. *Macromolecules* **2005**, *38*, 5060–5068.
(35) Kumpfer, J. R.; Jin, J.; Rowan, S. J. *J. Mater. Chem.* **2010**, *20*, 145–151.
(36) Burnworth, M.; Tang, L.; Kumpfer, J. R.; Duncan, A. J.; Beyer, F. L.; Fiore, G. L.; Rowan, S. J.; Weder, C. *Nature* **2011**, *472*, 334–337.
(37) Ilavsky, J.; Jemian, P. R. *J. Appl. Cyrstallogr.* **2009**, *42*, 347.
(38) Ferry, J. D. *Viscoelastic Properties of Polymers*, 3rd ed.; John Wiley & Sons, Inc.: New York, 1980.
(39) Larson, R. G. *Constitutive Equations for Polymer Melts and Solutions*; Butterworths: Boston, 1988.
(40) Fluegel, A.; Varshneya, A. K.; Earl, D. A.; Seward, T. P.; Oksoy, D. *Ceram. Trans.* **2005**, *170*, 129–143.
(41) Mes, T.; Smulders, M. M. J.; Palmans, A. R. A.; Meijer, E. W. *Macromolecules* **2010**, *43*, 1981–1991.
(42) Sim, H. G.; Ahn, K. H.; Lee, S. J. *J. Non-Newtonian Fluid Mech.* **2003**, *112*, 237–250.

Macromolecules

Article

pubs.acs.org/Macromolecules

Linear Viscoelastic and Uniaxial Extensional Rheology of Alkali Metal Neutralized Sulfonated Oligostyrene Ionomer Melts

Gerald H. Ling,[†] Yangyang Wang,[‡] and R. A. Weiss*[,†]

[†]Department of Polymer Engineering and [‡]Department of Polymer Science, University of Akron, Akron, Ohio 44325, United States

ABSTRACT: The linear viscoelastic and nonlinear extensional behavior of melts of alkali metal salts of oligomeric sulfonated polystyrene (SPS) ionomers were characterized by dynamic shear and nonlinear, uniaxial extensional flow experiments. The oligomeric SPS had a weight-average molecular weight of 4000 g/mol, a polydispersity index of 1.06, and a degree of sulfonation of 6.5 mol %. The molecular weight was below the entanglement molecular weight of PS, so all rheological effects were due to association of the ionic dipoles and nanophase separation of the ionic species that provides a transient elastic network. The SPS salts exhibited linear viscoelastic properties similar to well-entangled polystyrene (PS) melts, with a distinct rubbery region that had a shear modulus comparable to that of high molecular weight PS. Time−temperature superposition failed as a consequence of overlapping relaxations for the terminal response of the chain and ion hopping of the ionic dipoles. Unlike entangled PS melts, the modulus of the ionomer increased with increasing extensional strain rate, and a maximum in the stress occurred at a relatively low Hencky strain that was nearly independent of strain rate. The maximum in the stress during stretching was attributed to a catastrophic failure of the physical ionic network. At sufficiently high stress, the chains can pull the ionic groups out of nanophase-separated ionic domains, which significantly disrupts the network microstructure.

INTRODUCTION

Ionomers are a special class of polymers with a relatively small concentration of ionic groups attached to the backbone. The ionic groups are typically salts of sulfonic, phosphonic, or carboxylic acid neutralized usually with metal, ammonium, or phosphonium counterions which assures overall electrical charge neutrality.[1] Depending on the ion concentration, degree of neutralization, and choice of counterion, the rheological properties can be significantly different from that of the parent polymer chain. That is due to interchain associations that leads to physical cross-linking[2,3] and may also produce microphase separation of nanometer-sized ionic aggregates, often called *ionic clusters*. Flow at elevated temperatures is still possible, even in the presence of these physical cross-links, due to "*ion hopping*",[4] whereby ion pairs diffuse from one ionic cluster to another at a characteristic relaxation time. However, the relaxation times are typically long and require many ion pairs to "hop" from ionic cluster to another ionic cluster in order for the center of mass of the chain to diffuse through the matrix.[5] Consequently, the melt viscosity and relaxation times of ionomers are significantly higher and longer, respectively, than those of the nonionic parent polymer.

The characterization of the rheological behavior of ionomers is complicated for a variety of reasons. Ionomers with well-entangled polymer backbone chains tend to have extremely long relaxation times due to temporary cross-links that can persist well above the degradation temperature,[6,7] making them essentially impossible to characterize using conventional instrumentation and techniques. In addition, it is difficult to separate the relaxation mechanisms due to molecular entanglements, trapped entanglements, and ionic interactions in ionomers. Rubber elasticity models that treat the ionic interactions as simple molecular cross-links tend to underestimate the cross-link density of ionomer melts because of the supramolecular structure of the ionic clusters, and the calculated contribution to the viscoelastic properties of trapped entanglements in ionomers is similar to that of the ionic cross-links.[7] Experimental efforts to understand the dynamics in such systems have involved diffusion and stress relaxation experiments, and models of the rheology have focused mainly on modified reptation models.[8−10]

The majority of work in the field of ionomers has concerned the linear viscoelastic response attained using dynamic methods because of the long relaxation times and high viscosities of the ionomer melts. Recently, Weiss and Zhao[11] reported the steady shear and linear viscoelastic properties of a sulfonated polystyrene ionomer (SPS) and its alkali metal salt derivatives. That study used low molecular weight (4 kg/mol) oligomeric SPS, which facilitated steady shear measurements using conventional parallel and cone and plate geometries. In addition, the effect of ionic interactions on the viscoelastic properties of the ionomers was isolated, since the polymer chain length used was far below the entanglement molecular weight of polystyrene. Thus, the effects of molecular entanglements were eliminated, and the changes in the flow properties of the ionomers were due solely to the effective lengthening of the

Received: August 13, 2011
Revised: November 30, 2011
Published: December 19, 2011

polymer chains and the formation of branched and physically cross-linked structures by interchain dipolar associations.

The linear and nonlinear viscoelastic properties of those low molecular weight SPS ionomers under shear were comparable to those of a polystyrene with molecular weights as high as 1.5M g/mol. However, little is known about the effect of dipolar associations in ionomers on extensional properties, especially nonlinear behavior, which provided the incentive for the research described in this paper.

While there has been considerable interest in the elongational properties of classical polymers,[12−15] little work has been done on ionomers. To the best of our knowledge, the only other study of the elongational properties of random ionomers was published almost three decades ago,[16] and more recently, Stadler et al.[17] described the elongational behavior of telechelic polybutadiene ionomers. Those papers reported extensional viscosities that exceeded the values of the linear viscoelastic envelope predicted from shear experiments. Connelly et al.[16] reported that the degree and onset of this deviation, which is often referred to as "*strain hardening*", increased as a function of ion concentration, which is unlike the "universal" onset exhibited by typical polymers at a Hencky strain of ∼0.7−1. Stadler et al.[17] also reported that the deviation from LVE behavior had an ion concentration dependence but that dependence was not resolved due to the low elongation at break for their ionomers.

This paper describes the linear viscoelastic behavior and nonlinear extensional flow behavior of a low molecular weight sulfonated polystyrene ionomer. As with the earlier work on shear behavior,[11] a low molecular weight ionomer was used to eliminate the effects of chain entanglements. Although the polystyrene was the same as used in that previous study, the sulfonation level used in the current work was higher.

EXPERIMENTAL SECTION

Materials. Low molecular weight polystyrene (PS), M_w = 4 kg/mol, with a polydispersity index, PDI = 1.06, was obtained from Pressure Chemical Co. The PS was converted into a lightly sulfonated polystyrene (SPS) ionomer by reaction with acetyl sulfate in a dichloroethylene solution, according to the procedure of Makowski et al.[18] The SPS samples were converted to alkali metal salts by neutralization with an appropriate metal acetate or hydroxide.[11] The degree of sulfonation, DS, was 6.5 mol % (defined as the average number of sulfonate groups in 100 styrene repeat units), which corresponds to an average of 2.5 sulfonate groups per chain. However, because the sulfonation reaction occurs randomly, the product actually includes a distribution of PS chains with varying sulfonation levels. This ionomer will heretofore be referred to as SPS6.5, and the notation for the ionomers is MSPS6.5, where M is the alkali metal used for the cation. The samples used in this research and their characteristics are listed in Table 1.

Table 1. MSPS6.5 Ionomer Charge Densities and Glass Transition Temperatures[a]

	PS	Na	K	Rb	Cs
a, pm		102	138	149	170
q/a, pm^{-1}		0.0098	0.0072	0.0067	0.0059
cq/a, nm^{-1}		0.64	0.47	0.44	0.38
T_g, °C	80	98	99	100	97

[a] c = sulfonate concentration (mol SO_3/100 mol styrene), q = cation charge, and a = cation radius.

Materials Characterization. The glass transition temperatures (T_g) of the parent PS and the ionomers were measured by differential scanning calorimetry (DSC) using a TA Instruments Q200 DSC, a heating rate of 20 °C/min, and a nitrogen atmosphere. The DS of the SPS was determined by elemental sulfur analysis (Galbraith Laboratories, Inc.) and ^{1}H NMR using the procedure described by Baigl et al.[19] The DS values calculated from the two methods agreed within 10%.

Rheology. Dynamic and steady-shear experiments were performed with a TA Instruments ARES-G2 rheometer equipped with 25 or 8 mm parallel plates. Temperature control was achieved using a convection oven with a dehumidified-air gas source. The SPS samples were prepared by compression molding at 200 °C under vacuum prior to being tested. Frequency sweeps spanning 0.1 to 100 rad/s at temperatures of 120, 140, 160, and 180 °C were performed in the linear viscoelastic (LVE) region to construct a master curve using the time−temperature superposition (TTS) principle. Step shear rates of 0.001−20 s^{-1} were used to determine the transient stress growth and steady-state properties of the SPS samples.

Uniaxial extension measurements were made with a TA Instruments ARES-G2 rheometer equipped with a Sentmanat extensional rheometer (SER) fixture[20,21] purchased from Xpansion Instruments. Temperature control was achieved using the same convection oven described above. Attempts to prepare conventional rectangular ionomer samples using a heat press were unsuccessful since the thin samples were too brittle to handle once cooled to room temperature. Furthermore, the samples tend to crack upon cooling as the thermal expansion coefficient of the ionomer and mold linear sheets (polyester, polyimide, or aluminum) were sufficiently different to cause uneven deformation upon cooling. Instead, the ionomers were extruded using a Monsanto capillary viscometer into cylindrical specimens with an average diameter and length of 0.75 mm and 25 mm, respectively. The samples were stored in a desiccator overnight at 50 °C in a vacuum oven prior to being tested to prevent the absorption of water and to establish a constant thermal history for all the samples. Step Hencky strain rates of 0.01−3 s^{-1} were used to determine the transient stress growth behavior of the SPS samples at 120, 140, and 160 °C.

RESULTS AND DISCUSSION

Linear Viscoelasticity. Figure 1 shows the LVE master curves of the alkali metal salts of SPS as a function of angular frequency, ω. TTS failed for the alkali metal salts, principally in the midrange of reduced frequency, especially for G''. Failure of TTS became more apparent as the Coulomb energy of the ion pair increased (i.e., Na > K > Rb > Cs), as was observed previously for oligomeric SPS with lower DS[11] and for telechelic polybutadiene[22] ionomers. The failure of TTS for the low-molecular-weight SPS ionomers contrasts with the observations for high-molecular-weight SPS ionomers[7,23,24] and ethylene−methacrylate ionomers[5,25] where TTS worked reasonably well. The success of TTS in the latter systems is essentially an artifact due to the large separation between the relaxation times of ion hopping and the terminal behavior of the polymer chain.[2] The appearance of a rheologically simple system is a consequence of only one relaxation mechanism being accessed in the time frame of a single experiment. A more complete discussion of this phenomenon is provided by Register and Prud'homme.[3]

Neutralization of the sulfonate groups produces a substantial change in the rheological properties of the SPS ionomer melts. The most distinct change is the appearance of a rubbery region indicated by a plateau in the storage modulus, G', and loss modulus, G'', while the transition region ($\omega \sim 10^3$) was essentially unchanged. The breadth of the rubbery plateau increased as the Coulomb energy of the ion pair increased from Cs to Na, and the first crossover frequency (ω_c), where the values of G' and G'' cross, was suppressed by almost 3 decades for the Na salt compared with the Cs salt ionomer (Figure 2). The magnitude of the plateau modulus, G_N^0, however, was relatively insensitive to

dx.doi.org/10.1021/ma201854w | Macromolecules 2012, 45, 481−490

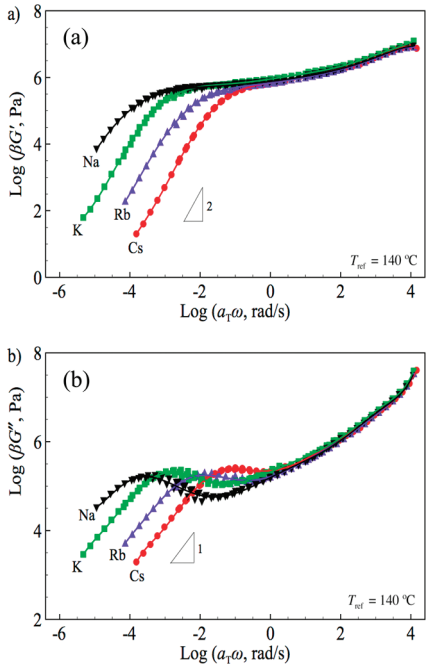

Figure 1. Linear viscoelastic master curves of the alkali metal salts of MSPS6.5 shifted to T_{ref} = 140 °C: (a) G'; (b) G''. The vertical shift factor, β, used to construct the master curves was close to unity (±3%) and did not have a significant impact on the master curve construction.

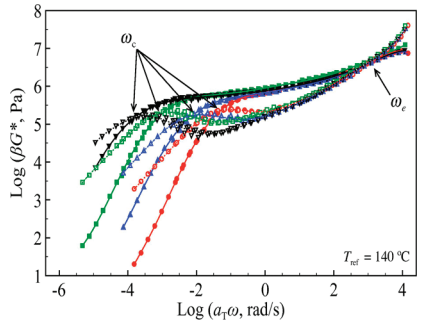

Figure 2. Linear viscoelastic master curves of the alkali metal salts of MSPS6.5 shifted to T_{ref} = 140 °C. Filled symbols represent G' while the open symbols represents G'' of CsSPS (●), RbSPS (▲), KSPS (■), and NaSPS (▼).

the choice of the cation, which indicates that the network structure formed was only dependent on the concentration of ionic groups, which controls the network microstructure of the ionomer. That observation is also consistent with the previous study of low-molecular-weight SPS ionomers with lower DS.[11]

The failure of TTS for these SPS ionomers occurred at the intermediate frequencies. The pseudo-master curves shown in Figure 1 were constructed by superimposing the data at low frequencies, i.e., the elastic response, and these pseudo-master curves were used to extract rheological information to help better understand the uniaxial extensional response. The terminal relaxation time, τ, was calculated from the inverse of ω_c, and the internal equilibration time, τ_e, was calculated from the inverse of the second crossover frequency, ω_e (see Figure 2). For these materials τ is a consequence of the dynamics of the physical cross-links derived from the nanodomain network, and τ_e arises from relaxation of the oligomer chain, which, i.e., the network chains. For these materials, the rubbery plateau seen in Figure 1 is not due to covalent cross-links or to molecular entanglements (the molecular weight of these ionomers was far below the entanglement molecular weight of PS), as is common in cross-linked or high-molecular-weight neutral polymers. In this case, the plateau in the modulus is a consequence of the temporary cross-links formed by ionic interactions or the supramolecular cluster microstructure. An apparent molecular weight between the ionic cross-links, $M_{e,app}$ was estimated from G_N^0, i.e., the value of G' at the inflection point in the rubbery plateau region, using the following relationship:[26]

$$G_N^0 = \frac{\rho RT}{M_{e,app}} \quad (1)$$

where ρ is the mass density of the polymer, R is the ideal gas constant, and T is the absolute temperature. Note that in this context the term entanglement is used herein to represent the physical impediments to translation of the chains, which for the ionomers are the physical, temporary cross-links between ionic groups on different chains. The apparent molecular weight of the SPS ionomer, M_{app}, and the number of entanglements per chain, Z, were calculated using eq 2[27] with the assumption that $\tau \propto M^{3.4}$.

$$\frac{\tau}{\tau_e} \approx \left(\frac{M_{app}}{M_{e,app}}\right)^{3.4} = Z^{3.4} \quad (2)$$

The parent polystyrene exhibits Rouse dynamics. For entangled chains, the Rouse model is usually valid due to small fluctuations along the contour between entanglements,[28] and a crossover time, τ_R, can be defined from eq 3.[29]

$$\tau_R = \tau/Z^{1.4} \quad (3)$$

For times longer than τ_R, linear entangled chains relax by reptation. The ionomers described in this paper are not entangled polymers. For a first approximation, the dynamics associated with the physical associations of the ionic groups might be thought of as entanglements in the sense that they are transient. Although it is tempting to assume similar dynamics for the relaxation behavior of these two types of temporary restraints, because of the microphase separation of the associated dipoles into nanodomains, the relaxation behavior restraints in the ionomer are likely to be much different than for molecular entanglements. The terminal response of the system is expected to be a cooperative cascade of motions, whereby an individual ion pair pulls out of a nanodomains and "hops" to another nanodomain, allowing the chain between ionic groups to relax. Thus, translation of chains involves discrete steps wherein the chain moves by sequential *ion hopping*. This cascade is responsible for the terminal relaxation τ.

Little theory exists for the viscoelastic behavior of ionomers and it is not apparent whether large-scale contour fluctuations or a crossover time are applicable to the ionomer melts. For the sake of discussion, τ_R was calculated for each material using eq 3, and the three regions of viscoelastic behavior that are usually found in entangled systems were determined from the three relaxation times found in eqs 2 and 3. The following discussion analyzes the experimental rheology data for these systems in the context of that of an entangled polymer. No claim is made that this is the proper framework for considering ionomer dynamics, and in fact, it is doubtful that it is. However, it does provide a means to identify the similarities and differences between the melt rheology of an ionomer and that of a molecularly entangled system.

dx.doi.org/10.1021/ma201854w | *Macromolecules* 2012, 45, 481–490

The LVE parameters for all the SPS ionomers estimated from the data shifted to different temperatures are listed in Tables 2−5.

Table 2. Material Properties of MSPS6.5 at 180 °C

sample	τ, s	τ_e, μs	τ_R, ms	G_N^0, MPa	Z	$M_{e,app}$, kg/mol	M_{app}, kg/mol
CsSPS	0.03	2	0.6	0.75	17	4.8	81
RbSPS	0.1	1.2	0.9	0.63	28	5.7	159
KSPS	0.6	1	2.5	0.68	51	5.3	266
NaSPS	6.5	1.6	120	0.59	88	6.1	532

Table 3. Material Properties of MSPS6.5 at 160 °C

sample	τ, s	τ_e, μs	τ_R, ms	G_N^0, MPa	Z	$M_{e,app}$, kg/mol	M_{app}, kg/mol
CsSPS	0.5	34	9.6	0.67	17	5.3	90
RbSPS	2.5	28	23	0.60	29	6.0	170
KSPS	13	19	510	0.63	52	5.7	295
NaSPS	130	31	2400	0.60	89	6.0	528

Table 4. Material Properties of MSPS6.5 at 140 °C

sample	τ, s	τ_e, ms	τ_R, s	G_N^0, MPa	Z	$M_{e,app}$, kg/mol	M_{app}, kg/mol
CsSPS	20	1.2	1	0.68	13	7.1	92
RbSPS	150	1.3	5	0.57	24	7.9	190
KSPS	690	1	13	0.59	40	8.0	320
NaSPS	5500	1.3	62	0.56	68	8.4	570

Table 5. Material Properties of MSPS6.5 at 120 °C

sample	τ, ks	τ_e, s	τ_R, ks	G_N^0, MPa	Z	$M_{e,app}$, kg/mol	M_{app}, kg/mol
CsSPS	2.2	0.2	0.1	0.54	12	6.3	76
RbSPS	8.2	0.2	0.4	0.54	17	6.5	110
KSPS	85	0.1	1.5	0.57	42	6.0	250
NaSPS	660	0.1	6.5	0.51	77	6.6	510

The average values of G_N^0 and $M_{e,app}$ for the SPS ionomer salts with three different levels of sulfonation are listed in Table 6 (the data for DS = 2.5 and 4.8 mol % are from Weiss and Zhao[11]). The average value of $M_{e,app}$ estimated from the LVE data using eq 1 for the SPS ionomer salts with DS = 4.8% is identical to the value reported for PS, M_e = 17 kg/mol. However, the corresponding values of $M_{e,app}$ for the SPS ionomer salts with DS = 2.5% and DS = 6.52% were significantly higher and lower, respectively. The two lower sulfonation levels have an average of one and two sulfonate groups per chain, which should only produce chain extension as a consequence of the ionic interactions. The larger than expected $M_{e,app}$ value for DS = 2.5% was attributed to the random sulfonation process and low sulfonation levels.[11]

Table 6. Average Plateau Modulus, G_N^0, and Molecular Weight between Entanglements, $M_{e,app}$, for SPS Ionomers with Different Degrees of Sulfonation, DS, at 140 °C[a]

DS, %	G_N^0, MPa	$M_{e,app}$, kg/mol
2.5	0.016	220
4.8	0.21	17
6.5	0.60	8

[a]Values for DS = 2.5 and 4.8% are from ref 11.

The high value of $M_{e,app}$ (i.e., a low value of G_N^0) is due to the fact that close to 70% of the PS chains were either unsulfonated or had only one sulfonate group. The unsulfonated and monosulfonated chains are mechanically inactive and do not contribute to the elastic response. On the other hand, a DS of 6.52% corresponds to an average of 2.5 sulfonate groups per chain, which produces a physically cross-linked network in addition to chain extension, thus decreasing $M_{e,app}$.

Uniaxial Extension. Extensional experiments were only performed on the CsSPS and RbSPS ionomers. The acid precursor of SPS did not hold its shape during an extensional test due to its relatively low viscosity and elasticity. The viscosities of the Na and K salts were very high, and those samples could not be extruded at a reasonable rate to fabricate useful specimens. A single 25 mm cylinder of the NaSPS or KSPS required ∼4 h to extrude, and increasing the extrusion pressure to accelerate the extrusion produced melt fracture of the strands (Figure 3). The stress for this sample was ∼0.05 MPa.

Figure 3. Example of melt fracture (top strand) exhibited by KSPS and NaSPS when the extrusion process was accelerated. The bottom strand is an example of the strands used for the extensional tests.

It is remarkable that these low-molecular-weight, unentangled polymers exhibited such behavior. The melt fracture stress for these ionomers was comparable to that reported by Vlachopoulos and Lidorikis[30] for very high-molecular-weight poly styrene ($M > 10^6$ g/mol), although the latter polymer is highly entangled and the ionomers had no molecular entanglements. For the ionomers, the dipole−dipole associations of the ionic species play a role similar to that of entanglements with regard to the rheological behavior, but as discussed in the sections that follow, the nonlinear behavior, especially with regard to fracture or failure, is very much different for the two systems.

The long extrusion times used to extrude the samples also led to some water absorption by the extruded strand from the ambient atmosphere. The amount of water uptake of SPS varied depending on the DS and the choice of the cation used,[31] and for some samples, the amount of absorbed water was significant. Although that water could be removed by drying the specimen after extrusion, this produced a slight deformation of the cylindrical sample, which affects the accuracy of the values reported herein for the extensional experiments. However, while the experimental errors are relatively high, the qualitative aspects of the results reported are believed to be valid.

The terminal flow, viscoelastic, and rubbery regions of the rheological response of the ionomers can be calculated for the Hencky strain rates applied during uniaxial extension using the relaxation times calculated from the LVE data. The three regions are distinguished by the Weissenberg number, Wi, which defines the degree of nonlinearity of the flow. For simple uniaxial extension, it is defined as the product of the extension rate and a characteristic relaxation time of the fluid

dx.doi.org/10.1021/ma201854w | Macromolecules 2012, 45, 481−490

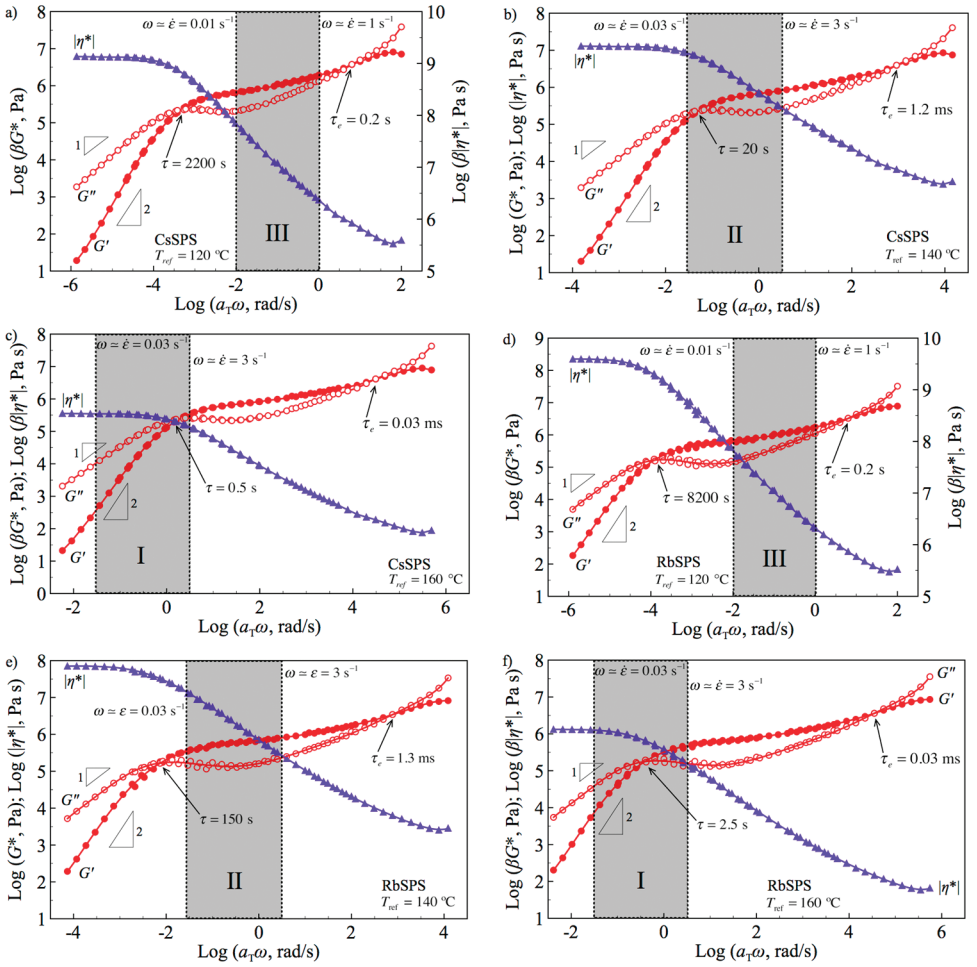

Figure 4. Linear viscoelastic master curves of CsSPS and RbSPS shifted to (a, d) 120 °C, (b, e) 140 °C, and (c, f) 160 °C. The dotted lines indicate the terminal flow (I), viscoelastic (II), and rubbery (III) regions probed in the uniaxial extensional experiments.

(see Figure 4). The terminal flow region (I) is defined by $Wi = \dot{\varepsilon}\tau < 1$, the rubbery region (II) by $Wi = \dot{\varepsilon}\tau_R > 1$, and the intermediate viscoelastic region (III) by $\tau_R^{-1} > \dot{\varepsilon} > \tau^{-1}$.[32] These regions are shown on the master curves of CsSPS and RbSPS at 120, 140, and 160 °C in Figure 4. The significance of the one region shown on each master curve is that this is the region experimentally accessible at the reference temperature.

Figure 5 shows the transient extensional viscosities, $\eta_e^+(t)$, of CsSPS and RbSPS as a function of time for different Hencky strain rates and temperatures. Note that $\eta_e^+(t)$ do not overlap or fall on the LVE envelope. The reason for this anomalous behavior is believed to be related to a rate-dependent network structure that forms due to the dipolar interactions between ionic groups. Even poorer overlap was observed when the isothermal data were shifted using the shift factors obtained from the LVE data, which further emphasizes the breakdown of TTS for these ionomers.

The LVE envelope identified by the dotted lines in Figure 5 was not determined from start-up flow measurements, but from the $\eta_e^+(t) = 3\int_0^t G(t')\,dt'$ relationship using the relaxation modulus, $G(t)$, obtained from the dynamic modulus, $G^*(t)$. The best agreement was obtained for the Rb salt ionomer at the highest temperature used, 160 °C (see Figure 5f), where the solid line corresponds to the product of Tr and the transient shear viscosity, $\eta^+(t)$, obtained using a shear rate of 0.01 s^{-1}. In general, the extensional viscosity data deviate from these results. The Cs salt ionomer had the weakest Coulomb force for the ion pair and exhibited the weakest intermolecular interactions of the different salts evaluated, and at elevated temperatures, it is expected to behave rheologically most like the parent polystyrene.

Typically, $\eta_e^+(t)$ never exceeds the LVE envelope at low strains or strain rates. However, when the strain or strain rate increases substantially, Tr can deviate from the usual value of three for uniaxial elongation.[33] From a comparison of the $\eta_e^+(t)$ data in Figure 5, it is apparent that the choice of counterion affects the deviation of the SPS ionomer data. RbSPS, which has a higher charge density than CsSPS, exhibited $Tr > 3$ at all Hencky strain rates and temperatures tested, whereas CsSPS primarily only exhibited $Tr > 3$ at the lowest temperature and highest Hencky strain rate tested.

Stadler et al.[17] recently reported that a similar deviation of Tr also occurred for polybutadiene telechelic carboxylate ionomers neutralized with Rb, Na, K, and Li. The degree of the deviation that they observed also increased with the Coulomb energy of the ion pair and extension rate, though they also observed an additional anomalous deviation in their Rb salt ionomer at low strain rates. Those authors attributed their observations to two competing mechanisms: one typical of most polymers that occurs at high strain rates and a second one that occurs at low Hencky strain rates whereby $\eta_e^+(t)$ increases as the rate decreases. The latter effect is analogous to the behavior usually

dx.doi.org/10.1021/ma201854w | Macromolecules 2012, 45, 481−490

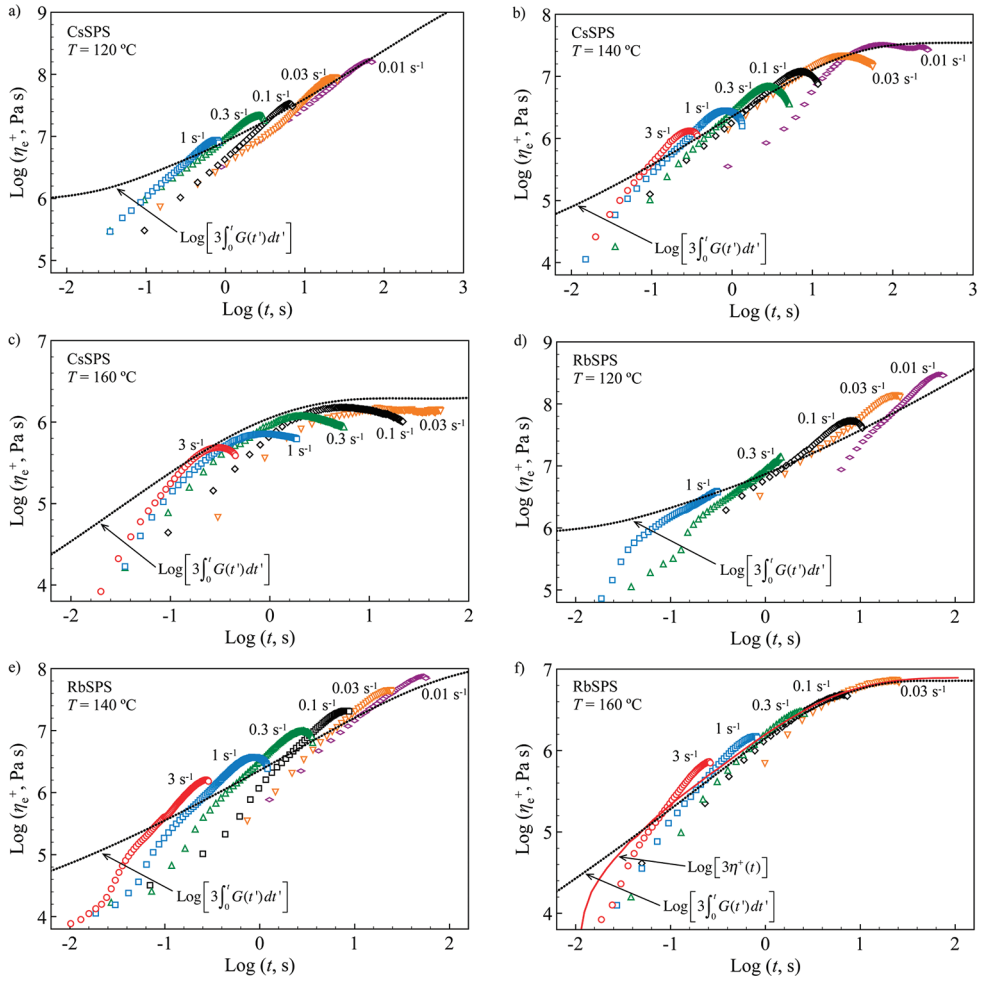

Figure 5. Transient extensional viscosities at different Hencky rates of CsSPS and RbSPS as a function of time at (a, d) 120 °C, (b, e) 140 °C, and (c, f) 160 °C. The dotted curve corresponds to the LVE data measured from shear.

found in lightly branched systems with long segmental relaxation times, such as metallocene polyethylenes with long-chain branching.[34,35]

The strain hardening behavior ($Tr > 3$) observed for the SPS ionomers appears to be more characteristic of the first mechanism described by Stadler et al.,[17] though it was poorly developed due to the low extensions at which the sample ruptured. The absence of Stadler et al.'s second mechanism for the SPS ionomers may be due to the much stronger intermolecular interactions of the sulfonate dipoles compared with carboxylate dipoles which produces a higher cohesive strength of the sulfonate ionic clusters, or it may be a result of the absence of chain entanglements, which are present in the polybutadiene ionomers described in ref 17. The higher cohesive strength of the SPS ionic clusters contributes to longer segmental relaxation times, since the chains need to disengage from one cluster and diffuse to another for relaxation of the segment of the chain that includes the ionic group. That effect would also explain the more apparent strain hardening in the SPS ionomer system. The failure to observe the low-rate strain hardening may be due to the inability to extend the SPS filaments sufficiently to achieve steady state.

The transient extensional stress data are plotted in Figure 6. The extensional stress, σ, for the SPS ionomer melts only reached steady state for the lowest Hencky strain rates. The solid curve shown in Figure 6b is the locus of the maximum stresses predicted from shear data and was constructed from a quadratic fit to the shear stress data over the range of 0.01–20 s^{-1}. The maximum stress predictions using the shear data agreed well with experimental values obtained from uniaxial extension. That behavior is expected in conventional entangled polymers, and it suggests that even though the elasticity developed in these low-molecular-weight ionomers is due to physical, dipolar interactions between metal sulfonate groups, the dynamics of these chains has some resemblance to that of entangled chains.

The maximum stress should occur when the chains pull out of the ionic clusters, which should correspond to the cohesive strength of the aggregates. The dotted curve shown in Figure 6b corresponds to the stress for G_N^0 obtained from LVE shear data. Note that σ significantly exceeded that value at high Hencky strain rates, which indicates that the effect of the ionic aggregates on the rheological behavior was actually greater than that of entanglements.

When the engineering stress, σ_{eng}, is plotted as a function of Hencky strain, ε, a stress maximum that is relatively independent of ε is observed (Figure 7). The maximum occurs at a relatively low value of ε and in most cases, below the theoretical maximum Hencky strain, ε_{max}. These results suggest that there is a limiting value of ε corresponding to extension of the chain between the ionic "entanglements", i.e., the clusters. During the extensional experiment, the load bearing chains are

dx.doi.org/10.1021/ma201854w | Macromolecules 2012, 45, 481–490

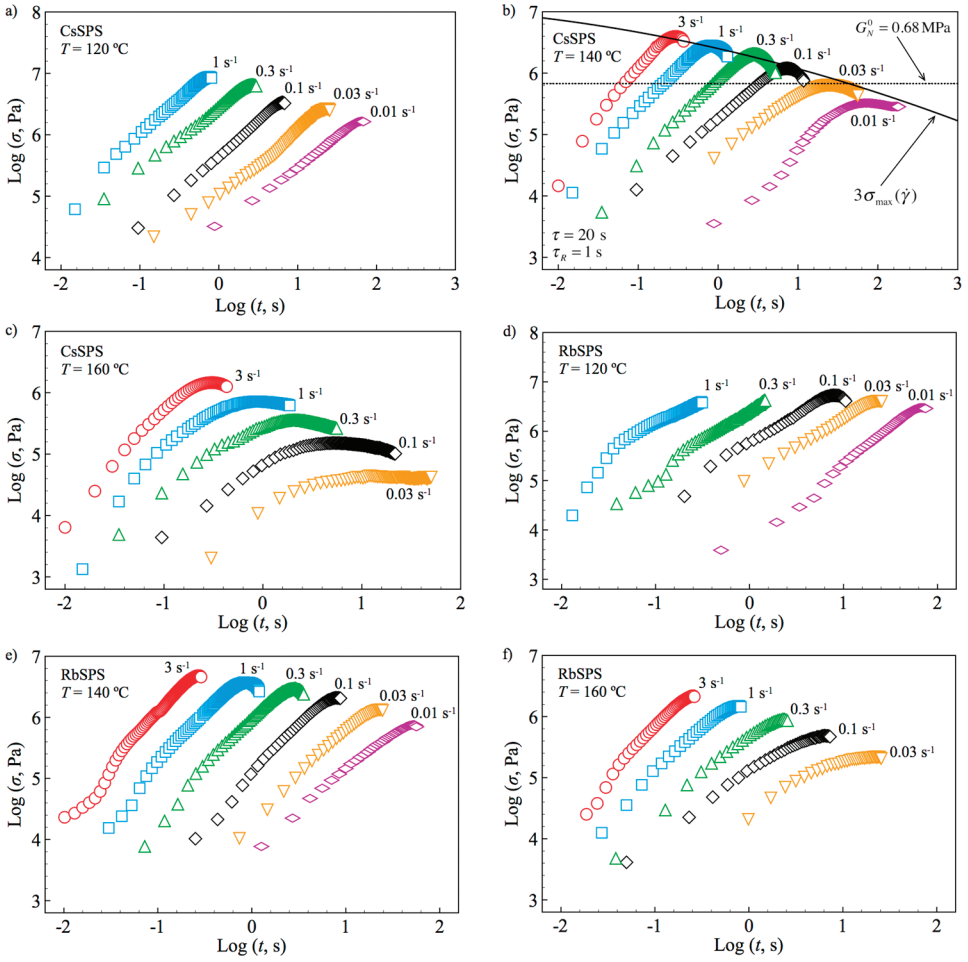

Figure 6. Transient extensional stresses at different Hencky strain rates of CsSPS and RbSPS as a function of time at (a, d) 120, (b, e) 140, and (c, f) 160 °C.

stretched until the elastic restoring stress equals the cohesive strength of the ionic clusters. Upon further extension, the chain segment containing the ionic group mechanically pulls out of the ionic clusters just prior to full chain extension, which explains the premature maximum relative to ε_{max} and subsequently produces the rapid drop in σ_{eng}. This behavior is distinct from that of strain softening of a physically entangled polymer melt, e.g., polystyrene or poly(styrene-*co*-*ran*-butadiene).[31] Although the isothermal stress maximum values for a 400 kg/mol PS and the SPS ionomers were similar, the Hencky strain for PS was more than twice that of the SPS ionomers.

The stress predictions for the CsSPS and RbSPS from calculated from the classical theory of rubber elasticity (RE)

$$\sigma_{eng} = G_N^0\left(\nu - \frac{1}{\nu^2}\right) \tag{4}$$

and from the Doi–Edwards model (DE)[35]

$$\sigma_{eng} = \frac{5G_N^0}{2(\nu^3 - 1)\nu}\left[2\nu^3 + 1 - 3\nu^3\frac{\tan^{-1}(\sqrt{\nu^3 - 1})}{\sqrt{\nu^3 - 1}}\right] \tag{5}$$

where $\nu = e^{\varepsilon}$, are plotted in Figure 7. The RE model does not have any built-in cohesive failure mechanism, and therefore, σ_{eng} grows without bound. The DE model does predict a maximum in σ_{eng}, but this is due to an elastic mechanical instability such as necking. The DE model, however, did not fit the data in Figure 7 well. Deviation above the DE limit is not uncommon for polymers and is usually a signature of substantial chain stretching,[12,13] which is consistent with the failure mechanism proposed above for the ionomers in extension.

For some values of the Hencky strain rates and temperatures, the extensional stress measured for the ionomers was higher than the prediction from RE theory (Figure 7), which is puzzling since one expects the RE prediction to represent an upper limit of the stress. The reason for this behavior is not understood, but several speculative explanations come to mind. One is that the result is a consequence of the difference in the effects of shear and extension on the viscoelastic behavior of ionomers. The elastic network in this case derives from the properties of the nanodomains which act as multifunctional temporary cross-links (or, in the nomenclature used in this paper, entanglements). The RE stress predictions were based on a entanglement density calculated from the shear modulus data, and as shown in Figure 5, the Trouton ratio for these polymers can be greater than three. A Tr > 3 is consistent with a value of $\sigma > \sigma_{RE}$ when the latter is calculated from the shear modulus.

The abnormally high extensional stress of the ionomer melts is more pronounced at higher Hencky strain rates and lower temperatures, which also suggests that it may arise from glassy contributions due to the ionic clusters. Another possible explanation for this behavior could be a rate-dependent ionic network structure whereby the ionic interactions switch from

dx.doi.org/10.1021/ma201854w | *Macromolecules* 2012, 45, 481–490

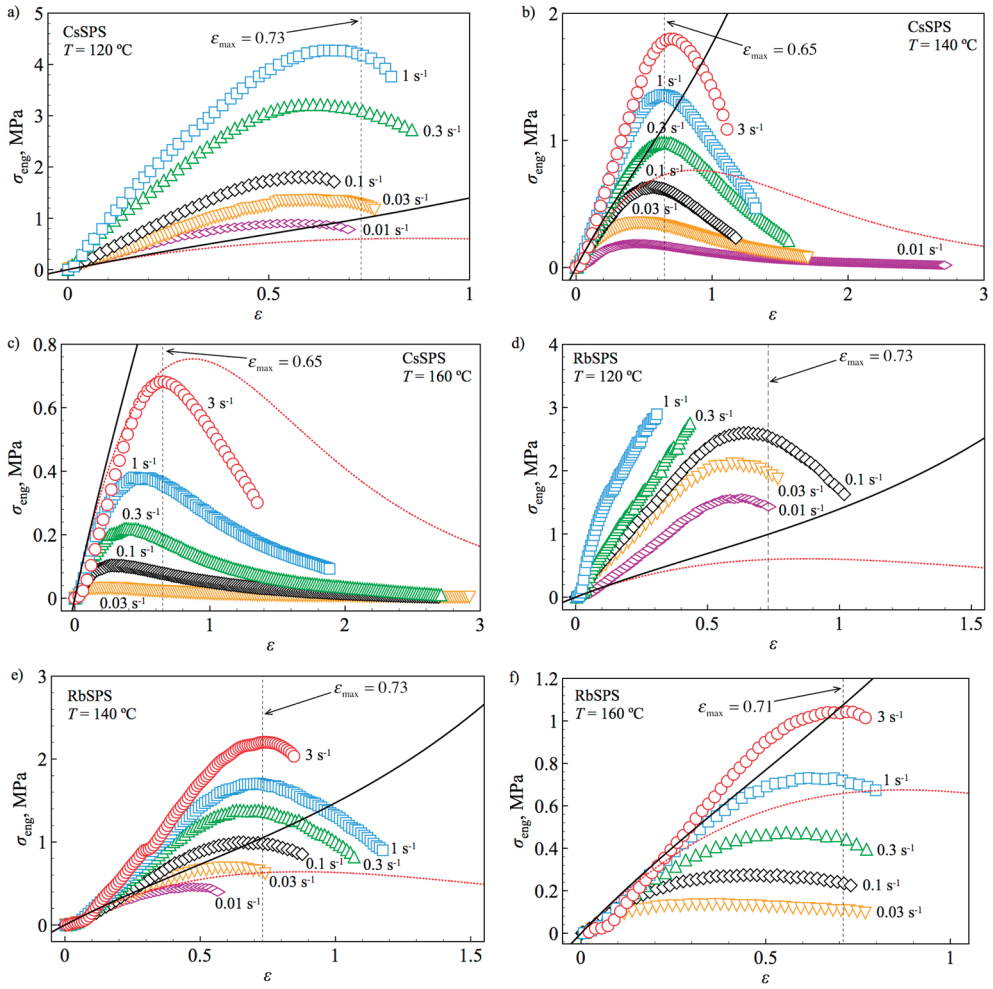

Figure 7. Engineering stress at different Hencky rates for CsSPS and RbSPS as a function of Hencky strain at 120, 140, and 160 °C. The solid lines denote the calculation from the classical rubber elasticity theory while the dotted curves are based on the Doi–Edwards model.[36]

intra- to interchain associations. That mechanism has been used to explain the dilatant behavior of ionomer solutions[37−39] and, more recently, SPS melts.[11] Witten and Cohen[40] proposed that the dilatancy is due to the unraveling of polymer chains due to deformation, which results in an increased number of interchain associations at the expense of intrachain associations. Thus, a higher concentration of intermolecular complexes may be formed at higher extension rates leading to higher than expected stresses. At this point, all these explanations are unproven, and more investigation of this phenomenon is needed to identify the origin of the high stress.

The maximum σ_{eng} normalized by G_N^0 and temperature for CsSPS and RbSPS is plotted as a function of *Wi* in Figure 8. All the data collapsed onto a single curve, which indicates that the network structure formed by the ionic clusters and the time constant for the underlying dynamics are independent of the neutralizing cation. The nonlinear scaling of the stress with temperature, however, underscores the competing relaxation times of the ion hopping (τ) and the backbone chain dynamics, where τ_e is the longest relaxation time. This is consistent with the earlier observation from the LVE data that TTS broke down primarily in G'' due to overlap of the two relaxation processes.

The effect is more evident when the Hencky strain at the engineering stress maximum, ε_{max}, is plotted as a function of *Wi* (Figure 9). The data for each of the three temperatures can be separated into distinct plots with differing slopes, and the slope

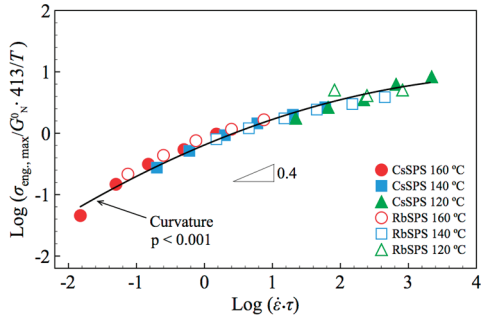

Figure 8. Engineering stress maximum for CsSPS and RbSPS as a function of *Wi*. The engineering stress was normalized with the plateau modulus and temperature. A linear regression suggests that there is slight curvature to the line through the data points.

approaches zero at the lowest temperature (120 °C). This result suggests that the failure mode may be different at each temperature, which is consistent with the three different viscoelastic regimes probed: (1) terminal flow (160 °C), (2) viscoelastic behavior (140 °C), and (3) rubber-like elasticity (120 °C). At higher temperatures, the chains can relax and flow prior to the point of failure leading to a rate-dependent ε_{max}. Higher temperatures also weaken the cohesive strength of the clusters, which allows sufficient chain pull-out to provide the mobility for the chain relaxation. However, as the temperature

dx.doi.org/10.1021/ma201854w | *Macromolecules* 2012, 45, 481−490

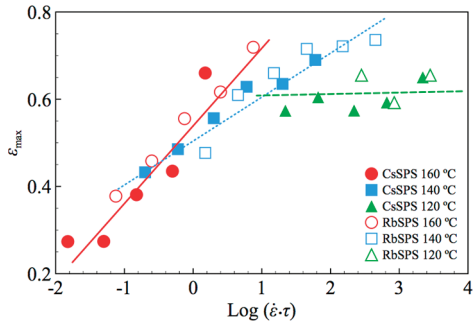

Figure 9. Hencky strain corresponding to the maximum in the engineering stress for CsSPS and RbSPS as a function of *Wi*.

decreases and approaches T_g, segmental chain motion is restricted and the point of failure becomes relatively independent of *Wi* as seen ε_{max} data for 120 °C for both CsSPS and RbSPS. Hence, the network fails catastrophically as chains pull out of the ionic clusters to accommodate the elevated stresses.

CONCLUSIONS

The incorporation of a small concentration of alkali-metal-neutralized sulfonate groups onto unentangled PS chains produced a significant increase in the melt viscosity and the development of significant elasticity. A rubbery plateau was evident in the linear viscoelastic behavior, which indicates the presence of an elastic network, which was due to intermolecular association of ionic dipoles and microphase separation of ion-rich nanodomains that provides a physically cross-linked, transient network. T_g of the ionomers was independent of the cation used, which indicates that the network structures of the different salts were identical. Viscous flow of these ionomers is thought to be due to an ion-hopping mechanism, whereby the stress in the network chains relaxes by pulling an ionic segment out of one ionic domain and allowing it to diffuse to another domain.

The breadth of the rubbery region and the corresponding terminal relaxation time increased as the size of the cation decreased, which indicates that the strength of the network, or the ion-hopping dynamics, increased with Coulomb energy of the ion pair. Like T_g, however, the magnitude of G_N^0 was relatively insensitive to the choice of the cation. TTS failed for these materials, which is believed to be a consequence of overlapping relaxation processes, one involving terminal flow of the backbone chain and the other ion hopping of the ionic segments.

The uniaxial extension behavior of CsSPS and RbSPS melts differed from that of a molecularly entangled polymer. The isothermal extensional viscosity, $\eta_e^+(t)$, measured at different strain rates did not overlap or fall on the linear viscoelastic envelope. In addition, *Tr* exceeded the LVE value of 3 at high strain rates and low temperatures for both the Cs and Rb salts, and the amount of that deviation increased with increasing Coulomb energy and decreasing temperature. The origin of that deviation was not determined but may be a consequence of effects such as a rate-dependent ionic network structure or some glassy response of the ionic domains. Further investigation is needed to isolate the source of this anomaly.

The maximum stress levels achieved under extension were similar to that of a well-entangled high-molecular-weight PS homopolymer at comparable temperatures and Hencky extension rates. That result indicates that the absolute strength of the transient elastic network formed by ionic dipolar interactions can be at least as strong as that produced by molecular entanglements. The strain at the stress maximum, however, for the ionomers was considerably lower than that for entangled PS melts. For high-molecular-weight PS, the stress maximum is a yield point resulting from plastic flow of the melt, while for the ionomers the stress maximum is a catastrophic destruction of the ionic network. Thus, although relatively strong transient networks can be achieved by ionic interactions, they behave in a much more brittle fashion than molecular entanglements. The main difference here is that the ionomer melt network lacks the relaxation process and energy dissipation mechanism that is provided by diffusional motions of disentanglement of polymer chains. That finding could be important in the design of supramolecular polymer systems using ionic or other intermolecular interactions such as hydrogen bonding or transition metal complexes. On the basis of the results described in this paper, one might expect that the development of elastomeric properties is possible with such supramolecular polymers, but the allowable strains may be deficient.

As was indicated earlier in this paper, the extensional and nonlinear viscoelastic behavior of ionomers has not been widely studied, and the current understanding is poor. The results described in this paper shows that ionomer melts have some characteristics similar to those of high-molecular-weight, highly entangled polymers. For example, the ionomers described herein had melt viscosities comparable to PS homopolymers with molecular weights in excess of 10^6 g/mol, and they exhibited transient elastic effects that are commonly observed in entangled polymer melts. The observation of melt fracture of these oligomeric ionomer melts reinforces the similarity to high-molecular-weight polymers. However, the nature of the network structure and how it fails for the ionomers are distinct from those of entangled polymer melts.

Many observations reported in this paper need further characterization and definitely would benefit from theoretical advances in the field. It is clear from the nonlinear extensional response that as currently formulated, entanglement or other transient network models cannot describe the behavior of ionomer melts.

AUTHOR INFORMATION

Corresponding Author

*E-mail: rweiss@uakron.edu.

ACKNOWLEDGMENTS

This research was supported in part by a grant from the Polymer Division of the National Science Foundation, Grant 0960461.

REFERENCES

(1) Jérôme, R.; Mazurek, M. In *Ionomers*; Tant, M. R., Mauritz, K. A., Wilkes, G. L., Eds.; Blackie Academic: London, 1997; pp 3−40.
(2) Earnest, T. R.; MacKnight, W. J. *J. Polym. Sci., Polym. Phys. Ed.* **1978**, *16*, 143−157.
(3) Register, R. A.; Prud'homme, R. K. In *Ionomers*, Tant, M. R., Mauritz, K. A., Wilkes, G. L., Eds.; Blackie Academic: London, 1997; pp 208−260.
(4) Cooper, W. *J. Polym. Sci.* **1958**, *28*, 195−206.
(5) Vanhoorne, P.; Register, R. A. *Macromolecules* **1996**, *29*, 598−604.
(6) Weiss, R. A.; Lefelar, J. A. *Polymer* **1986**, *27*, 3−10.
(7) Weiss, R. A.; Fitzgerald, J. J.; Kim, D. *Macromolecules* **1991**, *24*, 1071−1076.

(8) González, A. E. *Polymer* **1983**, *24*, 77−80.
(9) González, A. E. *Polymer* **1984**, *25*, 1469−1474.
(10) Leibler, L.; Rubinstein, M.; Colby, R. H. *Macromolecules* **1991**, *24*, 4701−4707.
(11) Weiss, R. A.; Zhao, H.-Y. *J. Rheol.* **2009**, *53*, 191−213.
(12) Bach, A.; Almdal, K.; Rasmussen, H. K.; Hassager, O. *Macromolecules* **2003**, *36*, 5174−5179.
(13) Bach, A.; Rasmussen, H. K.; Hassager, O. *J. Rheol.* **2003**, *47*, 429−441.
(14) Nielsen, J. K.; Rasmussen, H. K.; Hassager, O.; McKinley, G. H. *J. Rheol.* **2006**, *50*, 453−476.
(15) Wang, Y.; Boukany, P.; Wang, S.-Q.; Wang, X. *Phys. Rev. Lett.* **2007**, *99*, 237801/1−4.
(16) Connelly, R. W.; Mcconkey, R. C.; Noonan, J. M.; Pearson, G. H. *J. Polym. Sci., Part B: Polym. Phys.* **1982**, *20*, 259−268.
(17) Stadler, F. J.; Still, T.; Fytas, G.; Bailly, C. *Macromolecules* **2010**, *43*, 7771−7778.
(18) Makowski, H. S.; Lundberg, R. D.; Singhal, G. H. U.S. Patent, 3,870,841, 1975.
(19) Baigl, D.; Seery, T. A. P.; Williams, C. E. *Macromolecules* **2002**, *35*, 2318−2326.
(20) Sentmanat, M.; Wang, B. N.; Mckinley, G. H. *J. Rheol.* **2005**, *49*, 585−606.
(21) Sentmanat, M. L. *Rheol. Acta* **2004**, *43*, 657−669.
(22) Stadler, F. J.; Pyckhout-Hintzen, W.; Schumers, J.-M.; Fustin, C.-A.; Gohy, J.-F. O.; Bailly, C. *Macromolecules* **2009**, *42*, 6181−6192.
(23) Colby, R. H.; Zheng, X.; Rafailovich, M. H.; Sokolov, J.; Peiffer, D. G.; Schwarz, S. A.; Strzhemechny, Y.; Nguyen, D. *Phys. Rev. Lett.* **1998**, *81*, 3876−3879.
(24) Weiss, R. A.; Yu, W.-C. *Macromolecules* **2007**, *40*, 3640−3643.
(25) Tierney, N. K.; Register, R. A. *Macromolecules* **2002**, *35*, 2358−2364.
(26) Rubinstein, M.; Colby, R. *Polymer Physics*; Oxford University Press: Oxford, 2003.
(27) Ferry, J. D. *Viscoelastic Properties of Polymers*, 3rd ed.; Wiley: New York, 1980.
(28) Milner, S. T.; McLeish, T. C. B. *Phys. Rev. Lett.* **1998**, *81*, 725−728.
(29) Osaki, K.; Inoue, T.; Isomura, T. *J. Polym. Sci., Part B: Polym. Phys* **2000**, *38*, 1917−1925.
(30) Vlachopoulos, J.; Lidorikis, S. *Polym. Eng. Sci.* **1971**, *11*, 1−5.
(31) Chun, C. Diffusion in sulfonated polystyrene ionomers. M.S. Thesis, Univ. Connecticut, 1978; p 153.
(32) Wang, Y.; Wang, S.-Q. *J. Rheol.* **2008**, *52*, 1275−1290.
(33) Meissner, J., S.; Stephenson, E.; Demarmels, A.; Portman, P. *J. Non-Newtonian Fluid Mech.* **1982**, *11*, 221−237.
(34) Auhl, D.; Stange, J.; Münstedt, H.; Krause, B.; Voigt, D.; Lederer, A.; Lappan, U.; Lunkwitz, K. *Macromolecules* **2004**, *37*, 9465−9472.
(35) Gabriel, C.; Munstedt, H. *J. Rheol.* **2003**, *47*, 619−630.
(36) McKinley, G. H.; Hassager, O. *J. Rheol.* **1999**, *43*, 1195−1212.
(37) Lundberg, R. D.; Duvdevani, I. In Polymers as Rheology Modifiers; Schulz, D. N., Glass, J. E., Eds.; *ACS Symp. Ser.* **1991**, *462*, 155−75.
(38) Peiffer, D. G.; Kaladas, J.; Duvdevani, I.; Higgins, J. S. *Macromolecules* **1987**, *20*, 1397−1400.
(39) Shao, L.; Weiss, R. A.; Lundberg, R. D. *J. Polym. Sci., Part B: Polym. Phys.* **1995**, *33*, 2083−2092.
(40) Witten, T. A. Jr.; Cohen, M. H. *Macromolecules* **1985**, *18*, 1915−1918.

Macromolecules

Article

pubs.acs.org/Macromolecules

Unexpected PDMS Behavior in Segregated Cylindrical and Spherical Nanophases of PS–PDMS Asymmetric Diblock Copolymers

Lourdes del Valle-Carrandi,[†,‡] Angel Alegría,*[,†,‡] Arantxa Arbe,[‡] and Juan Colmenero[†,‡,§]

[†]Departamento de Física de Materiales, Universidad del País Vasco (UPV/EHU), Apartado 1072, 20080 San Sebastián, Spain

[‡]Materials Physics Center (MPC), Centro de Física de Materiales (CSIC-UPV/EHU), Paseo Manuel de Lardizabal 5, 20018 San Sebastián, Spain

[§]Donostia International Physics Center, Paseo Manuel de Lardizabal 4, 20018 San Sebastián, Spain

ABSTRACT: The structure and dynamics of the poly(dimethylsiloxane) (PDMS) segregated nanophase in block copolymers with polystyrene (PS) has been analyzed in detail by combining wide- and small-angle X-ray diffraction, infrared absorption, differential scanning calorimetry, and dielectric relaxation spectroscopy. In particular, we have investigated PS-rich PS–PDMS diblocks where the minority PDMS phase is segregated into cylindrical and spherical regions with diameter in the range 10–20 nm and compared the results with those previously reported on symmetric diblocks with lamellar phases of similar size. It is found that in these highly segregated cylindrical and spherical regions in the copolymers PDMS presents a rather unexpected behavior as probed by X-ray diffraction, infrared absorption, differential scanning calorimetry, and dielectric relaxation spectroscopy. Structural techniques indicate poor packing of the PDMS segments, whereas calorimetric experiments evidence both strong suppression of PDMS crystallization and significant reduction of the glass transition temperature range. Connected with that, the dielectric relaxation probing the PDMS segmental dynamics is much more heterogeneous and markedly faster not only than that observed for PDMS in lamellar nanophases but more strikingly than that of PDMS melt.

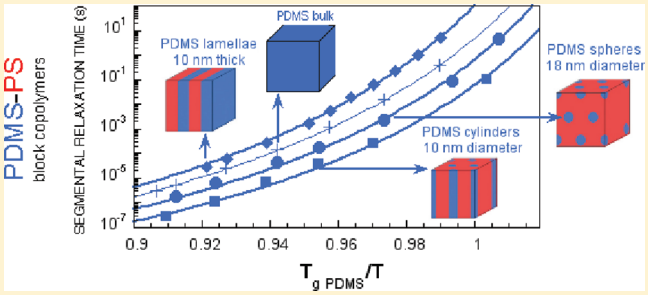

INTRODUCTION

Block copolymers offer an attractive route to generate new nanostructured materials because the large variety of structural arrangements they give rise by spontaneous self-assembly into a diversity of mesophases.[1−4] Both the structure and size of the domains can be in principle carefully tuned by controlling the molecular weight of each of the blocks and the specific interactions between them and with the substrate. These ordered structures range from spherical, cylindrical, lamellar, to bicontinuous geometries.[2,3] For symmetric block copolymers, i.e., when the fraction of the two blocks is similar, the lamellar structure is commonly preferred. However, by decreasing the fraction of one of the blocks, highly curved surfaces are favored, leading to segregated phases of cylindrical or spherical shape where the chains of that block are restricted in two or three dimensions, respectively. Despite the evident interest of the impact of this confinement on the dynamics, most of the attention on the diblock copolymer systems has been focused on the structural features.

In addition to the applied interest, the structural arrangements of diblock copolymers can also provide a way to investigate the properties of the components in circumstances that can be very different from those of the bulk material. In particular, the nanometer size of these structures might cause the emergence of confinement-related effects.[5,6] Moreover, the interfacial effects[7,8] can become prominent because the strong increase of the surface-to-volume ratio. Results in the literature report on the confinement-related effects on the component chain dynamics.[9−21] Particularly, it has been found that the chain dynamics of polyisoprene (PI) in lamellar mesophases formed by PS–PI–PS (PS: polystyrene) triblock is dramatically disturbed.[22] On the other hand, the PI chain dynamics in diblocks PI–PDMS (PDMS: polydimethylsiloxane) with micelle-like structures resulted to be speeded-up with respect to that of bulk PI and significantly more heterogeneous.[23] In both cases, the fluctuations at the interfaces seemed to play a major role. When considering the segmental dynamics, the number of reported results is also rather limited.[11,13,14,16−19,21,24−26]

In general, all these studies reported a relatively minor effect of the nanostructure on the component segmental dynamics. This is the case even when the size of the segregated phase is reduced to tens of nanometers. In fact, most of the results have been interpreted as a consequence of the presence of the interface. For example, for triblock PS–PI–PS and diblock PS–PI a small slowing down of the PI segmental dynamics has been detected.[22,25] Contrarily, in the PI–PDMS micellar structures it was evident that the PI segmental dynamics is significantly faster than that of the bulk state.[23] This latter effect was

Received: September 16, 2011
Revised: November 24, 2011
Published: December 12, 2011

rationalized quantitatively as induced by the high mobility of the fast-moving PDMS chain surrounding the PI micelle core coupled with the presence of interfacial capillary waves.

The linear block copolymers based on PS and PDMS chains have been considered as good candidates for both technological applications and model systems.[27,28] In this particular system, the two components are highly immiscible and the Flory–Huggins interaction parameter increases on cooling. Thus, the strong segregation limit can be achieved even with moderately molar mass blocks as evidenced in ref 27. The segmental dynamics of PDMS in symmetric diblocks and triblocks with PS was investigated in the past showing a noticeable effect of the nanostructure.[16] In particular, it was reported that the PDMS segments attached to the interface present a distinct slower dynamics and there was a gradient of increasing mobility to the bulklike behavior. More recently, molecular dynamics simulations showed that this gradient of mobility occurs essentially at the interface.[21] One of the particularities of the PS–PDMS system is the extremely large difference in chain flexibility of the blocks, PDMS being one of the most flexible polymers whereas PS is a relatively stiff one. Although this feature seems to have no remarkable effects in the behavior of PDMS nanosegregated in lamellar phase as in symmetric diblock PS–PDMS copolymers,[16] the situation could be different in asymmetric diblocks where the segregated and highly flexible PDMS phase would be completely surrounded by a relatively rigid matrix. In that situation the combination of interfacial tension and packing frustration could imply a higher degree of constrains and therefore might have a profound impact in the segregated PDMS behavior. Noticeably, preliminary results evidenced that in these asymmetric diblocks with highly segregated PDMS phase PDMS crystallization seems to be strongly suppressed.[19]

In this work, we present new results on the effect of the nanostructure in the PDMS behavior in highly segregated nanophases of PS–PDMS diblock copolymers presenting different mesophase geometries. Particularly, we have investigated PS-rich PS–PDMS diblocks where the minority PDMS phase is segregated into cylindrical and spherical regions with diameters in the range 10–20 nm. It is found that in these highly segregated copolymers PDMS presents a rather unexpected behavior as probed by wide- and small-angle X-ray scattering (WAXS and SAXS), infrared spectroscopy (FTIR), differential scanning calorimetry (DSC), and broadband dielectric relaxation spectroscopy (BDS). In addition to a strong suppression of PDMS crystallization, confirmed by DSC, FTIR, and WAXS, the PDMS segments present a dynamics that is markedly different from that of the bulk melt and much more heterogeneous. Furthermore, the PDMS segments at the interface of these segregated phases seem to be highly constrained, as it was already reported for the symmetric PS–PDMS diblock in lamellar mesophase. These results are interpreted as mainly originated by the packing frustration of the segregated PDMS segments.

EXPERIMENTAL SECTION

Samples. The main characteristics of the copolymers investigated are shown in Table 1. For comparative reasons, measurements were also performed on PS and PDMS homopolymers with similar molecular weight than the respective component of the copolymers. The materials were all purchased from Polymer Source Inc.

When preparing the samples for the different setups, the block copolymers and PS homopolymers were solved in toluene with a 4% weight concentration and deposited in the proper holder for each experiment. Then, the samples were heated to 390 K and maintained for 12 h in a vacuum oven before heating to 450 K for 2 h in order to allow the complete development of the preferred morphology. Finally, the sample was allowed to cool under vacuum at room temperature.

Table 1. Molecular Characteristics of the Copolymers Investigated[a]

product ID	M_n PS (g/mol)	M_n PDMS (g/mol)	M_w/M_n	N	ϕ_{PDMS}	χN (room temp)
22PDMS7500	30 000	7500	1.10	428	0.22	140
25PDMS4000	13 500	4000	1.07	184	0.25	66

[a]Number-average molecular weights (M_n), polydispersity index (M_w/M_n), overall degree of polymerization (N), PDMS volume fraction (ϕ_{PDMS}),[29] and the interblock segregation strength (χN).[30]

Transmission Electron Microscopy. The measurements were carried out at room temperature by means of a JEOL JEM 1010 transmission electron microscope operating at an acceleration voltage of 100 kV. Samples were prepared on a copper grid (400 mesh) covered only with carbon (purchased from Fedelco). A drop of the previously prepared solutions was deposited, and the excess was removed in order to obtain a thin layer. Then, the thermal treatment mentioned previously was followed.

Small-Angle X-ray Scattering (SAXS). For the SAXS characterization of the samples, the same copolymer solution was added drop by drop over Kapton. After that, the same thermal treatment mentioned above was followed, and finally the sample was separated carefully from the support. SAXS diffraction experiments were performed on a Rigaku PSAXS-L equipment operating at 45 kV and 0.88 mA. The MicroMax-002+ X-ray generator system is composed by a microfocus sealed tube source module and an integrated X-ray generator unit which produces Cu Kα transition photons of wavelength λ = 1.54 Å. The flight path and the sample chamber in this equipment are under vacuum. The scattered X-rays are detected on a two-dimensional multiwire detector (2D-200X) of 200 mm diameter active area with ca. 200 μm resolution and converted to one-dimensional scattering curves by radial averaging. The scattered intensities are represented as a function of momentum transfer Q, $Q = 4\pi\lambda^{-1} \sin\theta$, where θ is half the scattering angle. Reciprocal space calibration was done using silver behenate as standard. The sample-to-detector distance was 2 m, covering a Q range from 0.008 to 0.2 Å^{-1}.

The measurements as a function of temperature were performed by means of a Linkam Scientific Instruments THMS600 temperature controller. This setup allows measurements in the range from 77 to 873 K with a temperature stability of ±0.1 K. In our case, measurements from 100 to 450 K were carried out in steps of 25 K. The measuring time was 1 h at each temperature. The measurements were corrected (subtraction) for the very low-Q scattering tail likely due to voids and impurities in the samples.

Wide-Angle X-ray Scattering (WAXS). The WAXS measurements of the copolymers were carried out by a Bruker D8 Advance diffractometer operating at 30 kV and 20 mA equipped with Cu Kα source and a Vantec-1 PSD detector. The Q range covered was between 0.36 and 2.1 Å^{-1}. A MRI wide range low-temperature chamber was used in order to cover the temperature range from 110 to 300 K. In the case of the reference PDMS homopolymer, we used the Rigaku PSAXS-L equipment supplied with a WAXS image plate chamber. In this case a Q range from approximately 0.7 up to 5 Å^{-1} was covered. The same temperature control than in the case of the SAXS measurements was used. The PDMS homopolymer that is liquid at room temperature was placed in sealed boron-rich capillaries with an outside diameter of 1 mm and wall thickness of 0.01 mm.

Fourier Transform Infrared Spectroscopy. Fourier transform infrared (FTIR) analysis was carried out by means of a JASCO 6500 spectrometer. The measurements were done by using a low-temperature diamond ATR system (Golden Gate-Specac) purged with nitrogen. The high thermal conductivity provides rather rapid cooling and temperature stabilization. Spectra were obtained by using 50 scans with a 4 cm^{-1} resolution. The experiments were performed at

dx.doi.org/10.1021/ma202107m | Macromolecules 2012, 45, 491–502

room temperature and at 140 K, which is the lowest temperature achieved with our setup.

Differential Scanning Calorimetry. The samples were prepared from the copolymer−toluene solutions added drop by drop on a gold-plated stainless steel electrode disk of 40 mm diameter used for further dielectric measurements. After the thermal treatment mentioned before, 5−10 mg of sample was taken and encapsulated in an aluminum pan. The DSC measurements were carried out using a Q2000 set up from TA Instruments with a liquid nitrogen cooling system (He gas was used for thermalization). The sample pan was inserted rapidly into the instrument sample holder after temperature stabilization at 100 K. In this way, the cooling rate from room temperature was higher than 100 K/min (sufficient to avoid possible PDMS melt crystallization).

The calorimetric results were obtained using a rate of 3 K/min by temperature-modulated experiments, 60 s period and 0.5 K amplitude, during heating from 100 to 400 K, cooling back to 100 K at the same rate, and finally heating again to 400 K.

Broadband Dielectric Spectroscopy. Measurements of the complex dielectric permittivity ($\varepsilon^* = \varepsilon' - i\varepsilon''$) vs frequency were performed in the range 10^{-1}−10^{6} Hz, using a Novocontrol high-resolution dielectric analyzer (Alpha-N analyzer). As was mentioned above, the sample preparation for calorimetric and dielectric measurements was done simultaneously. An upper electrode of 20 mm was placed on the previously prepared film over the gold-coated disk, and a separation of 100 μm between both electrodes was maintained by using a cross-shaped Teflon spacer of small area. Then, the sample cell was set in a cryostat, and its temperature was controlled via a nitrogen gas jet stream coupled with the Novocontrol Quatro controller.

Before the dielectric measurements, the sample cell was quenched in liquid nitrogen to avoid possible crystallization of PDMS during the first cooling. The dielectric experiments were performed isothermally from 120 to 140 K in steps of 5 K, from 140 to 160 K in steps of 2.5 K, from 160 to 180 K in steps of 10 K, and from 180 to 270 K in steps of 10 K. Then, the sample was cooled back to 120 K at a rate of 3 K/min and finally heated again to 270 K with the same steps mentioned for the first heating program.

RESULTS

TEM. In order to characterize the morphology/nanostructure of the diblock copolymers, we have combined TEM and SAXS measurements. We will start describing TEM results. Figure 1 shows representative images obtained by TEM at room temperature after the thermal treatment of the samples described in the previous section. Patterns typical of phase-segregated block copolymer domains can be clearly seen for both copolymer systems, with dark areas corresponding to PDMS rich regions due to the higher electronic density of the silicon atoms.

According to the theoretical phase diagram, from the PDMS volume fractions and the segregation strengths (see Table 1) we would expect cylindrical PDMS phases for both copolymers. However, in the case of the 22PDMS7500 sample—the lowest PDMS volume fraction—the pattern suggests a nanostructure of PDMS spheres, with radii of about 10 nm, embedded in a PS matrix. This result, which will be confirmed by SAXS, is in line with the reported strong skewed toward low styrene volume fractions of the PS−PDMS experimentally determined phase diagram.[31] These spheres seem to be ordered in a BCC (body-centered cubic)-like disturbed lattice. In the case of the 25PDMS4000 sample, the TEM image seems to be more compatible with the expected cylindrical PDMS regions with radii of about 5 nm.

SAXS. A better insight into the nanostructure of our diblock copolymers can be obtained by SAXS experiments. Note that

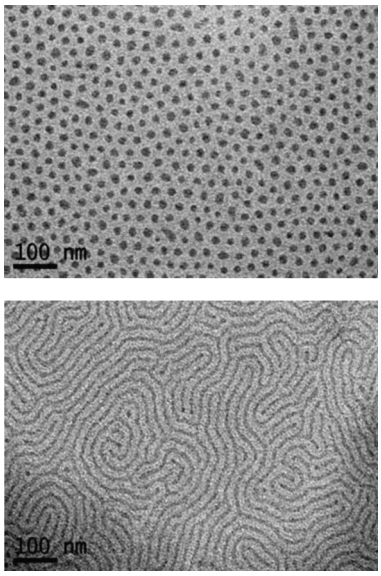

Figure 1. TEM micrographs from 22PDMS7500 (upper frame) and 25PDMS4000 (bottom frame). The dark areas correspond to the PDMS-rich phase.

contrary to the TEM case where extremely thin films are imaged, the sample thickness used for these experiments is of the same order than that used afterward for further investigation. The results obtained at 175 K for 22PDMS7500 and 25PDMS4000 samples are shown in Figure 2 as a

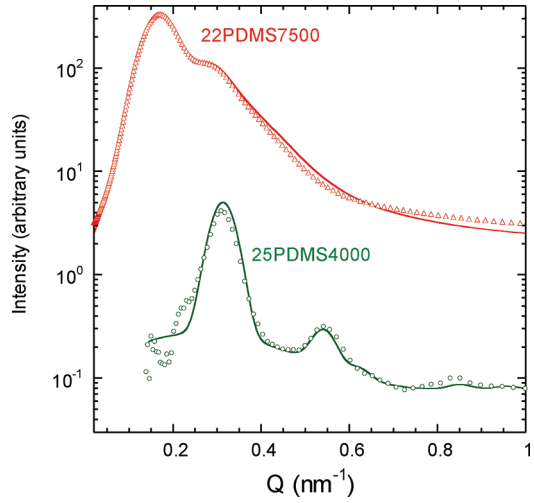

Figure 2. SAXS intensities as a function of the scattering vector for the two diblock copolymers studied here: 22PDMS7500 (red) and 25PDMS4000 (green) at 175 K. The solid lines represent the proposed fits.

representative example. The SAXS intensity of both samples shows both primary and secondary defined peaks at low Q, suggesting ordered structures. A quantitative analysis of the SAXS profiles at the different temperatures was carried out by fitting the experimental curves to analytical expressions for the scattering functions, which contain contributions from both structure and form factors.[32] The calculations were done by using the Scatter software developed by S. Förster and L. Apostol [http://www.chemie.uni-hamburg.de/pc/polymer/software.html].[33,34]

dx.doi.org/10.1021/ma202107m | *Macromolecules* 2012, 45, 491−502

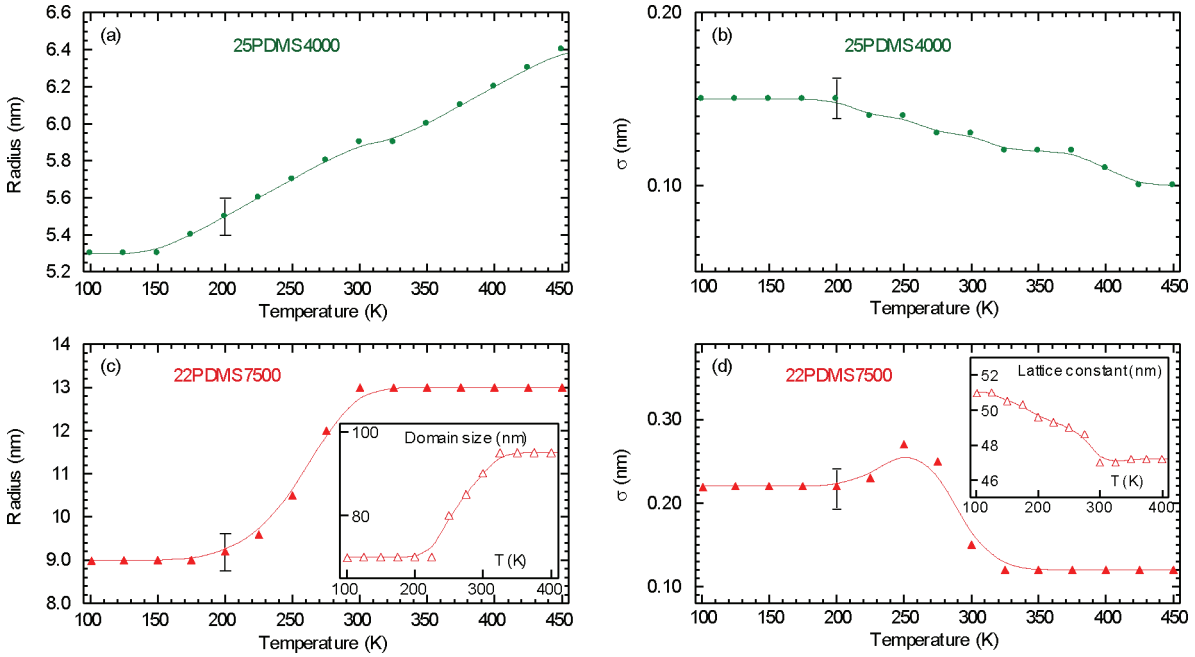

Figure 3. Fitting parameters, radius (left) and its distribution σ (right), for SAXS experimental data: upper frames 25PDMS4000 and lower frames 22PDMS7500. Insets in (c) and (d) show the temperature variation of the domain size and lattice constant obtained for the 22PDMS7500 copolymer. The vertical bars correspond to the typical estimated uncertainty. The lines are only guides for the eyes.

In the case of the 22PDMS7500 copolymer, the best simple model results to be a nanostructure of PDMS spheres ordered in a BCC lattice, in agreement with TEM observations. The SAXS data corresponding to the sample 25PDMS4000 were well described with a simple model of cylinders of PDMS in a HCP (hexagonally close packing) lattice, also in agreement with the features observed by TEM. The disorder scattering was taken into account by considering a Gaussian displacement from the ideal lattice point distribution[33] with zero average and relative mean-squared value of 2 nm. The fitting curves corresponding to 175 K are shown in Figure 2 as an example. The temperature dependence of the parameters characterizing the PDMS nanosegregated phase, namely the radius of the sphere/cylinder and its relative standard deviation, σ, are depicted in Figure 3a−d.

When fitting the SAXS patterns for the 25PDMS4000, it was possible to keep constant the domain size (90 nm), length of the cylinders (300 nm), and lattice constant (22.9 nm) for the full range of temperatures investigated. Contrary, for the 22PDMS7500 copolymer, the required lattice constant and domain size are temperature dependent (see insets in Figure 3c,d). It is worthy of remark that the values of the radii obtained at room temperature (5.9 nm for 25PDMS4000 sample and 13 nm for 22PDMS7500 sample) agree rather well with those estimated from those TEM micrographs. Moreover, the rather pronounced distortion of the BCC lattice observed by TEM is also consistent with a relatively small domain size as obtained from SAXS in the case of the 22PDMS7500 sample. This feature becomes more pronounced at lower temperatures.

Figure 3 shows that in the low-temperature range below about 200 K the main structural parameters corresponding to both copolymers tend to a plateau value, indicating that the nanostructural features are essentially temperature independent in this range. It is noteworthy that this is the range of the dynamics studies carried out by us (see below). However, at higher temperatures systematic changes are apparent in both copolymers. Whereas the radius of the cylinders increases rather moderately and monotonously, the radius of the spheres presents an important increase in a relatively narrow range and becomes essentially constant above room temperature. Noticeably, as far as the average radius increases with temperature, the width of the distribution diminishes accordingly for both copolymers.

WAXS. Figure 4a shows the X-ray intensity scattered by the two reference homopolymers, namely PS (M_n = 33 000 g/mol and M_w/M_n = 1.06) coded PS33000 and PDMS (M_n = 7000 g/mol and M_w/M_n = 1.14) coded PDMS7000. In the case of PDMS7000 at 250 K, only one broad peak is mainly visible, centered at about 0.85 Å^{-1}. Based on MD simulations, this peak has been attributed to PDMS intermacromolecular correlations in the liquidlike state with an average interchain distance of z8.4 Å.[35] Such an interpretation is supported by the observation of a shift of this peak toward lower Q values with increasing temperature (see the arrow in Figure 4a). At 110 K, sharp peaks evidence the crystalline structure of this sample. In the case of the PS33000 homopolymer, the diffraction pattern reveals a broad peak centered at around 1.4 Å^{-1}. The position of this peak does not vary with temperature, hinting its intramolecular character. MD simulations point also to this origin and show that it is predominantly controlled by the relative position of phenyl rings.[36−38] The increasing intensity at low Q of the PS33000 diffraction pattern is due to the presence of a low-Q peak centered at $Q_{max} \approx 0.5$ Å^{-1}, likely reflecting intermolecular distances either between phenyl rings or main-chain atoms.[37] The WAXS intensities corresponding to the two copolymers are shown in Figure 4b,c. At room temperature two main peaks are evident for the two copolymers. By direct comparison with the homopolymer intensities (Figure 4a), we can attribute the peak at $Q \sim 0.85$ Å^{-1} in the copolymers to the intermolecular correlations of PDMS in the segregated PDMS phases. It appears at the same Q value as the corresponding peak of pure PDMS, and in addition, the PS X-ray diffraction curve does not

dx.doi.org/10.1021/ma202107m | Macromolecules 2012, 45, 491−502

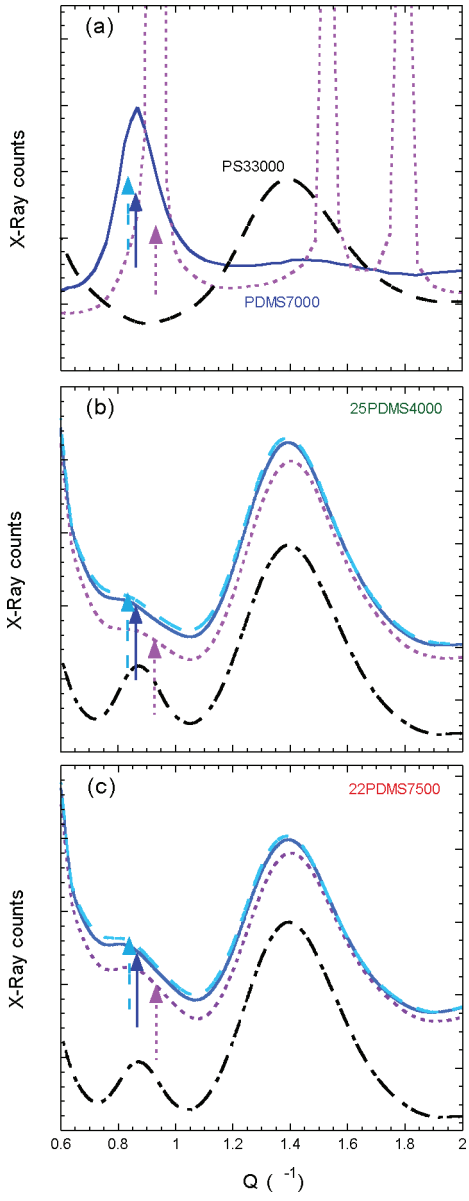

Figure 4. WAXS curves for (a) PDMS7000 (solid line at 250 K, dotted line at 110 K) and PS33000 at 250 K (dashed line), (b) 25PDMS4000, and (c) 22PDMS7500. In (b) and (c) the experimental data are shown as a dashed line at room temperature, as a solid line at 250 K, and as a dotted line at 110 K. The vertical arrows represent the position of the peaks for the PDMS7000 homopolymer at 300 K (dashed arrows), 250 K (full arrows), and 110 K (dotted arrows). Dashed-dotted lines are the expected result of a simple superposition from the homopolymer WAXS curves at 250 K (shifted down vertically for clarity).

show any peak in this Q range. Just for comparison, and underlining the intermacromolecular character of this peak, we have included in Figure 4b,c as vertical lines, the position of the peak of pure PDMS for different temperatures. On the other hand, the main peak at about 1.4 $Å^{-1}$ in the copolymers must be dominated by the intramolecular phenyl−phenyl correlations of the PS phase above-described, and the increasing intensity toward lower Q values can be assigned to the intermolecular PS low-Q peak.

The dashed lines in Figure 4b,c correspond to the patterns obtained by simple addition of the diffraction curves of the two components at 250 K, properly weighted. A rather dramatic difference is observed when the diffraction curves measured for the two samples at the same temperature are compared with the so calculated ones. The peak maximum characteristic of the PDMS interchain distances is located at distinctly lower Q values for both copolymers. Furthermore, the peaks in the copolymers are poorly defined, which suggests that the PDMS local order in the copolymers is considerably lost. Noticeably, the PDMS peak intensity of the copolymer with cylindrical morphology (25PDMS4000) is smaller than that of the copolymer with spherical morphology despite the larger PDMS content.

The WAXS results at 250 K can be interpreted as due to the fact that PDMS segments in the copolymers reach a poor packing level. At room temperature the maximum of this peak in all the samples, as well as in the reference one, is slightly shifted toward lower Q values without much change of intensity and shape, which would just be indicative of expansion on heating. At the lowest temperature (110 K), Figure 4b,c shows that no peak signature of crystalline PDMS is observed in the copolymers where the PDMS is nanosegregated in spheres or cylinders. Here the crystallization seems to be frustrated. Even at 110 K the broad peak characteristic of the amorphous state remains and is located at much smaller Q values than the crystalline diffraction peak of PDMS, which again indicates a poor packing level. Surprisingly, the peak position is not strongly affected by decreasing the temperature from 250 to 110 K (i.e., a 140 K jump). All this clearly evidences the presence of constraints imposed by the rigid PS matrix in the segregated PDMS spheres and cylinders that likely prevents the expected PDMS densification.

FTIR. The vibrational properties of PDMS in the copolymers were studied by FTIR as a complementary technique. Analyzing both PS33000 and PDMS7000 homopolymers, we concluded that the region where the Si−O−Si asymmetric stretching bands are located (940−1140 cm^{-1}) could be suitable for selectively characterize PDMS because only two weak bands from PS appear, namely around 1068 and 1028 cm^{-1} (see Figure 5a). Then, for the study of these PS−PDMS diblock copolymers the Si−O−Si asymmetric stretching bands will be analyzed in detail. In Figure 5b, the results obtained for the two diblock copolymers under study are depicted. The vertical lines represent the position of the two main peaks of the PDMS homopolymer at around 1011 and 1083 cm^{-1}. At room temperature, the spectra observed in the 22PDMS7500 and 25PDMS4000 samples are rather similar to each other. The positions of the maxima of their absorption peaks match almost perfectly among them and are close to those observed in the PDMS homopolymer. Nevertheless, the shape of the whole band is different from that observed in the homopolymer; for example, the two prominent peaks present some kind of shoulder at around 1020 and 1065 cm^{-1} that, however, might be related to the contributions expected from weak PS vibration bands mentioned before. For PDMS homopolymer at low temperature, which has crystallized, the high wavenumber peak becomes better defined, without detectable changes in the two main peak frequencies. Contrarily, for the two copolymers the intensities of both peaks increase at low temperature, and both experience a noticeable red shift.

The previous results can be more quantitatively examined by performing a band analysis based on a description in terms of a few sub-bands. By this approach the PS absorption is well accounted for with only two Gaussian sub-bands at 1068.8 and

dx.doi.org/10.1021/ma202107m | *Macromolecules* 2012, 45, 491−502

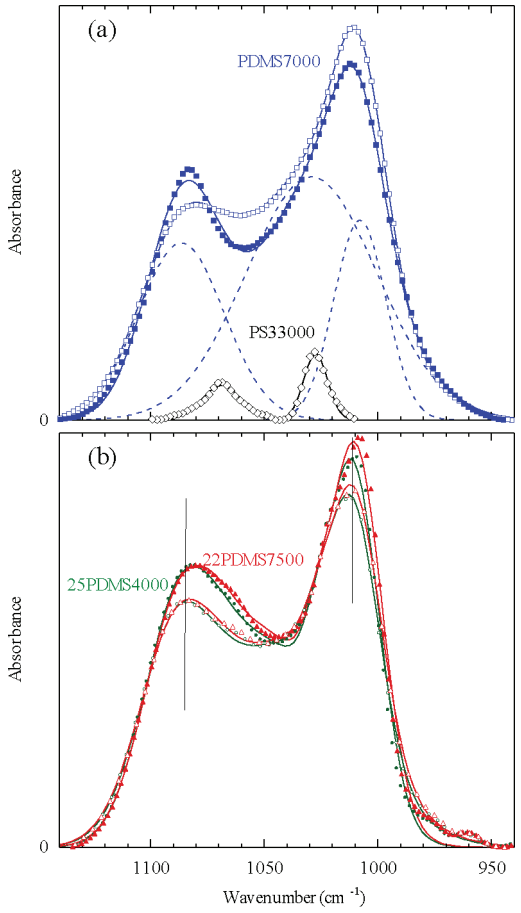

Figure 5. FTIR spectra of the reference polymers (a) and copolymers (b): PDMS7000 (open squares at room temperature, solid squares at 140 K), PS33000 at room temperature (diamonds), 22PDMS7500 (open triangles at room temperature, filled triangles at 140 K), and 25PDMS4000 (open circles at room temperature, filled circles at 140 K). Intensities of the copolymers are scaled to match at 1100 cm^{-1}. The vertical lines represent the peak position of the reference PDMS. The solid thin lines correspond to the fitting according with Gaussian sub-bands superposition. The dashed thin lines in (a) correspond to the Gaussian PDMS components at room temperature.

1027.4 cm^{-1} with relative areas of 35% and 65%, respectively. For PDMS, three Gaussian sub-bands at 1086.7, 1029.7, and 1008.0 cm^{-1} with relative areas of 26%. 55%, and 19% are required at room temperature. It is worth mentioning that the central sub-band is somehow hidden but accounts for most of the IR absorption. Upon crystallization, at the lowest temperature there are minor changes in relative areas and sub-band positions: namely, sub-bands move to 1085.7, 1025.4, and 1008.9 cm^{-1}, respectively, with areas 29%, 57%, and 17%. Since the whole band transforms clearly, the changes in width of the sub-bands is the major effect, particularly the sub-band at around 1086 cm^{-1} becomes notably narrower.

A rather good description of the absorption band is obtained for the two copolymers (see Figure 5b) by simply maintaining the characteristics of the two PS sub-bands and allowing those of PDMS to change. However, the resulting line is not able to capture the details, and particularly it does not account for the shoulders appearing close to the PS sub-band positions. All this suggests that these features are characteristics of the PDMS vibrations and particularly could be related with the chain segments anchorage to the PS interface. However, a more detail analysis of these features is out of the scope of the present work.

When considering the output of the fitting procedure followed in the copolymers, at room temperature the obtained PDMS sub-bands positions for 22PDMS7500 and 25PDMS4000 are 1089.3, 1040.8, and 1009.9 cm^{-1}, with relative areas around 25%, 53%, and 22%, respectively, and 1089.7, 1042.3, and 1010.8 cm^{-1}, with relative areas around 23%, 55%, and 22%, respectively. By comparing these values with those from pure PDMS, a remarkable blue shift of the central (hidden) sub-band is very apparent. Furthermore, this sub-band is further blue-shifted to 1050 when fitting the low-temperature data. Noticeably, the shape of the whole band at low temperature is not much different from that at high temperature, which is in marked contrast with the evident changes associated with PDMS crystallization. This result is in agreement with the strong crystallization suppression detected by WAXS in the copolymers. Particularly, any significant narrowing of the sub-band centered around 1087 cm^{-1} is detected in the copolymers, this precise sub-band being clearly narrower in crystallized PDMS.

DSC. DSC measurements provide insight into the thermodynamical behavior of the copolymers studied here. In Figure 6a,

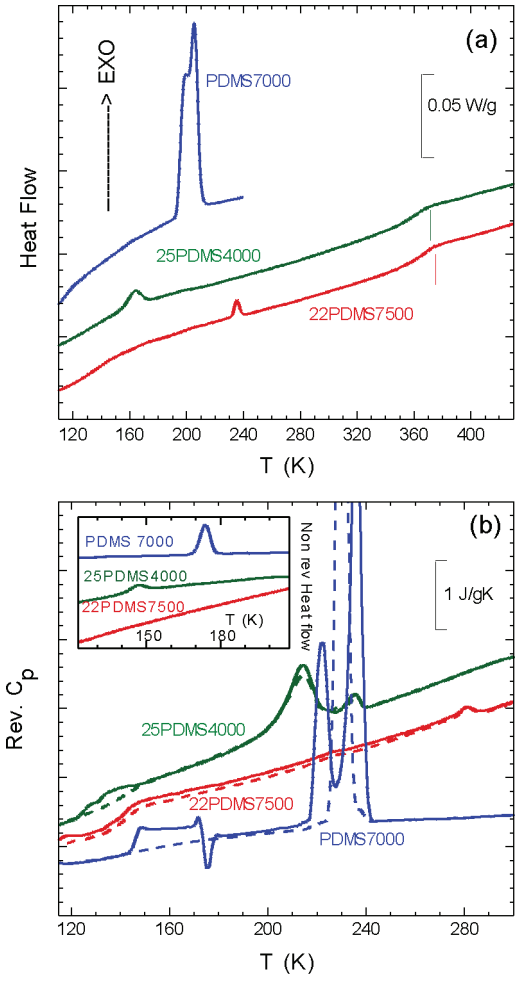

Figure 6. DSC scans during (a) the cooling and (b) heating runs after being rapidly (solid lines) and slowly cooled (dashed lines) for the copolymers and the reference PDMS7000 homopolymer. The vertical lines correspond to the T_g values of linear PS[39] with the same molecular weight than that of the PS blocks. The inset in (b) represents the nonreversing signal during the first heating run.

dx.doi.org/10.1021/ma202107m | *Macromolecules* 2012, 45, 491–502

we present the heat flow during a cooling run at 3 K/min. The step at high temperatures in the data of the copolymers corresponds to the glass-transition temperature T_g of the PS phase. In both cases this T_g step is very visible—due to the high weight content of the PS component—and located at distinctly lower temperatures than linear PS with the same molecular mass than the PS block (see vertical lines[39]), in agreement with earlier literature results.[40] This suggests that the presence of the PDMS segregated phase in the copolymer causes a small plasticization effect on the PS matrix. The presence of a large interface associated with the segregated PDMS phase could also play a significant role.[41] One additional remarkable feature observed in this cooling run is the presence of exothermic peaks. In pure PDMS a very prominent exothermic peak in the range 200−215 K reflects the PDMS crystallization, taking place during cooling at moderate rates. The copolymers present a rather small exothermic peak, taking place at about 230 K for 22PDMS7500 and at about 160 K for 25PDMS4000. These features might be attributed to a crystallization process in the PDMS phase, but considering the WAXS and FTIR results mentioned before where no signatures of PDMS crystallization were present, the situation is unclear. By quantifying the energy of the exothermic peaks, it is clear that PDMS crystallization, if any, is strongly suppressed in the copolymers, the energetic reduction with respect to pure PDMS being 65% for 25PDMS4000 and 85% for 22PDMS7500.

In Figure 6b, we depict two heating runs at 3 K/min after a fast (solid line) and a slow (dashed line) cooling rate, of about 100 and 3 K/min, respectively, for the two copolymers and pure PDMS as a reference. Pure PDMS is completely amorphous at the beginning of the first run,[42] and consequently it shows a sharp increase of C_p at the glass transition temperature (147 K) followed by a cold crystallization occurring at around 170 K, resulting in a strong reduction of C_p. Increasing temperature further, a complex melting process is detectable in the range 220−240 K. Contrarily in the second run, PDMS has crystallized during cooling and presents a weak and broad C_p step in the range 150−200 K characteristic of a semicrystalline polymer, followed by a rather sharp melting event at around 230 K. All this is in perfect agreement with previous results.[42] When the thermal behavior of the 22PDMS7500 and 25PDMS4000 copolymers during the heating runs is considered, both present a prominent but broader T_g feature, detectable at much lower temperatures than that of the corresponding PDMS homopolymer. This decrease of T_g is a very surprising result taking into account that in the copolymers the PDMS segments are anchored to the frozen PS chains, and if any, one could more easily expect a shift of T_g to higher temperatures. It is also noticeable that the C_p jump during the second heating runs of the copolymers is not reduced (but slightly shifted to high temperatures, particularly for 25PDMS4000), which again indicates that PDMS crystallization is strongly suppressed in these copolymers. The nonreversing signal during the first heating run from the copolymers in this T range (see inset in Figure 6b) shows no detectable events for 22PDMS7500 and a weak feature just above the glass transition range for 25PDMS4000. By increasing temperature further, both copolymers evidence endothermic events in the reversing signal with nearly no effect of the cooling rate used before the heating run. These results again evidence that the conventional PDMS crystallization is inhibited in the strongly segregated copolymers. In fact, no changes around these temperatures were detectable in WAXS or FTIR experiments. Furthermore, SAXS patterns did not show any additional reflections when decreasing temperature as it is actually found in crystallized PDMS.[42]

On the other hand, the quantification of the C_p jump at T_g could provide additional insights. When the value from amorphous PDMS is considered and the "dilution effect" is taken into account, the comparison with the C_p jump in the copolymers evidence a reduction of about 7% for the 22PDMS7500 copolymer and of about 22% for 25PDMS4000. This detectable C_p jump reduction would be due, at least in part, to the significant reduction of the rotational degrees of freedom of the PDMS segments anchorage to the PS interface. The larger reduction found in the 25PDMS4000 copolymer would be naturally explained by the shorter PDMS chains. The fact that the C_p jump remains essentially the same for the samples quenched into liquid nitrogen and those cooled down at a moderate rate again indicates that, if any, the possible crystallinity in the PDMS segregated phase has to be small.

Broadband Dielectric Spectroscopy. The dielectric relaxation techniques allowed studying selectively the PDMS segmental dynamics within the diblock PS−PDMS copolymers since PDMS is the component contributing more to the dielectric relaxation, the PS relaxation strength being very weak. Furthermore, the contribution of PS to the dielectric losses in the temperature range relevant for PDMS is completely negligible. On the other hand, close to the T_g of the PS phase, the sample conductivity prevents a detailed analysis of the weak dielectric relaxation associated with PS. The dielectric behavior of the corresponding PDMS homopolymer with a chain length similar to that of the PDMS sequence in the diblocks will also be considered. In PDMS dielectric loss spectra, only the segmental motions (α-process) are observed, and no significant secondary relaxation processes can be detected.[42] The dielectric experiments on the copolymers after being fast cooled to the lowest temperature showed time-dependent results (mainly for 25PDMS4000) which, together to what was shown in the DSC scans of Figure 6b, suggest that the copolymer samples are in a highly unstable state when fast cooled. This was not the case for the samples cooled down at 3 K/min where well reproducible results were obtained. So we considered more reliable to analyze the dielectric loss of the copolymers in this latter situation. Moreover, this is the structural state characterized by SAXS, WAXS, and FTIR. Figure 7 shows the dielectric losses as recorded isothermally on the copolymers after being cooled at a rate of 3 K/min in the dielectric cell. For comparative reasons we have also included previously reported results from a symmetric PS−PDMS diblock copolymer with a lamellar nanostructure,[16] here coded 53PDMS11600 (Figure 7c). All ε'' values were normalized according to the high-frequency permittivity ε_∞ (around 2.7 for all samples), which was taken as the value of the ε' component at high frequency (1 MHz) and low temperature (120 K). In this way, the effect of small uncertainties in sample geometry on the signal (loss intensity) is minimized. In Figure 7a−c a prominent relaxation process is observed within the probed frequency window at temperatures between 145 and 160 K, which is straightforwardly related to the segmental mobility of PDMS component.

The dielectric losses in the copolymers are broader than those observed in amorphous PDMS. However, this effect is much more dramatic for the two copolymers with cylindrical and spherical PDMS nanophases than that previously reported for the symmetric copolymer with PDMS lamellar nanophase.

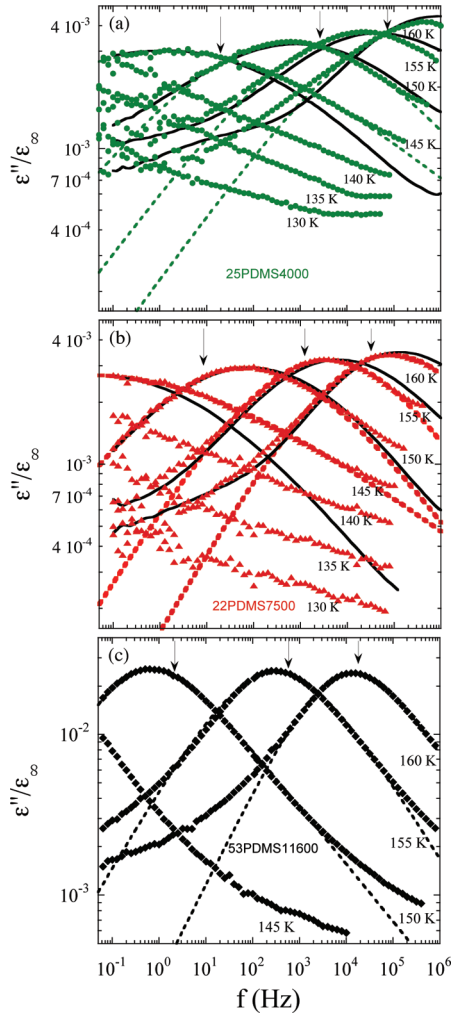

Figure 7. (a, b) Dielectric loss vs frequency for the two asymmetric diblock copolymers studied here at different temperatures. (c) Previously reported measurements on a symmetric diblock copolymer.[16] The vertical arrows show the position of the peak maximum of the corresponding PDMS homopolymers at 150, 155 and 160 K. Dashed lines correspond to HN fits according to eq 1. The solid lines present the description obtained for 145, 150, 155, and 160 K with a single distribution of the fragility parameter (see text for details).

It is worth mentioning that in the case of the cylindrical and spherical PDMS copolymers the loss peaks are also rather symmetric. In addition, and likely related with the T_g-depression detected by DSC, the dielectric relaxation in these two copolymers is notably faster than that in the corresponding PDMS homopolymers (see arrows in Figure 7). These results suggest a markedly different molecular environment of PDMS segments in the two copolymers with cylindrical and spherical PDMS nanophase. Note that for example in Figure 7b, contrary to the homopolymer and the 53PDMS11600 copolymer case (Figure 7c), the loss peak corresponding to 145 K already enters in the probed frequency window. Nevertheless, the three copolymers, irrespective of the phase morphology, share a low-frequency tail-like contribution in the dielectric losses indicative of the presence of a fraction of slowly moving PDMS segments, likely influenced by the PS rigid phase.

The main part of the dielectric losses from the copolymers (including 53PDMS11600) was fitted according to the empirical Havriliak–Negami (HN) equation:[43]

$$\varepsilon''(\omega) = \Delta\varepsilon\ \mathrm{Im}\left[\frac{-1}{(1 + [i\omega/\omega_c]^{\alpha})^{\gamma}}\right] \quad (1)$$

In this equation, α (γ) denotes the symmetric (asymmetric) broadening of the relaxation peak ($0 < \alpha, \gamma < 1$); $\Delta\varepsilon$ is its dielectric strength, and ω_c is a characteristic frequency related to the peak relaxation time τ by the equation

$$\omega_c\left[\sin\left(\frac{\alpha\pi}{2\gamma + 2}\right)\right]^{1/\alpha} = \tau^{-1}\left[\sin\left(\frac{\gamma\alpha\pi}{2\gamma + 2}\right)\right]^{1/\alpha} \quad (2)$$

This empirical description also allows to characterize the loss peak width by the full width at half-maximum (fwhm) that can be approximately calculated from the shape fitting parameters (α and γ) by means of the empirical equation[44]

$$\mathrm{fwhm}(\alpha, \gamma) = -0.516 + \frac{1.058}{\alpha} + \frac{0.039}{\gamma} + \frac{0.563}{\alpha\gamma} \quad (3)$$

For the copolymer samples 22PDMS7500 and 25PDMS4000, depicting both rather symmetric loss peaks, the parameter γ was fixed to 1 (Cole–Cole relaxation function) in order to reduce the coupling among fitting parameters. Representative fitting curves are shown as dashed lines in Figure 7. Although some discrepancies are apparent in the tails, at this point we consider the fitting satisfactory enough to be used for the comparison among the different systems.

First, in Figure 8a we can see the temperature dependence of the PDMS relaxation time as determined from the loss peak frequency. For a detailed comparison the trivial differences associated with changes in molecular weight of the PDMS blocks have to be considered, so the T_g values obtained from DSC on the corresponding homopolymers have been used for normalization of the temperature scale. While in the lamellar nanophase the PDMS segmental dynamics is slowed down with respect to that in the homopolymer, in the copolymers nanosegregated in spheres and cylinders we observe faster motions of the PDMS segments. As already mentioned, this behavior is completely unexpected *a priori* due to the presence of the essentially frozen PS component.

The dielectric strength obtained from the fits is represented in Figure 8b also as a function of $T_{g,PDMS}/T$, where the $\Delta\varepsilon$ values have been normalized to the PDMS fraction to remove the trivial dilution effect. For all copolymers the obtained values are lower than those of the pure PDMS, the difference being relatively small for the lamellar nanophase (ca. 90%). This discrepancy can be rationalized by a more detailed analysis[16] of the low-frequency background (see below). However, for the other two copolymers the difference is dramatic, ~50%, and can hardly be explained in a similar way. Moreover, for these two samples the temperature dependence of $\Delta\varepsilon$ is also markedly weaker.

Finally, in Figure 8c the width of the loss peak (fwhm) as a function of temperature for the different samples is compared. For the homopolymer and the copolymer with lamellar nanophase, this parameter shows a quite similar behavior, in the latter case being larger by less than half a decade. On the other hand, once again the behavior of the 22PDMS7500 and the 25PDMS4000 is clearly different, showing much larger values of fwhm, which could be anticipated from the direct inspection of the dielectric loss curves. Moreover, in these two copolymers a further sudden increase of the width at the lowest

dx.doi.org/10.1021/ma202107m | *Macromolecules* 2012, 45, 491–502

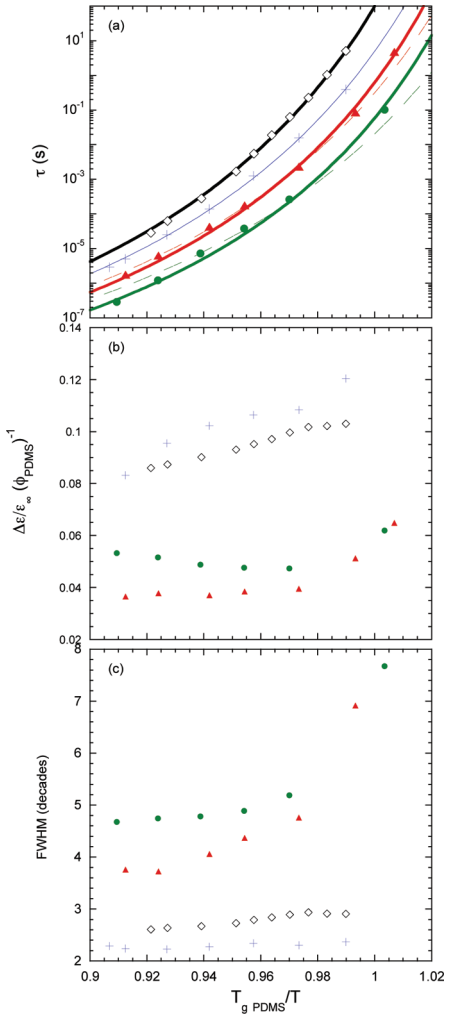

Figure 8. Characteristic relaxation time, deduced from the frequency of the dielectric loss maximum (a), dielectric strength (b), and fwhm of the loss peak (c) as a function of $T_{g,PDMS}/T$: 22PDMS7500 (triangles), 25PDMS4000 (circles), 53PDMS11600 (diamonds), and PDMS7000 (+). Lines in (a) correspond to data fitting curves; see text for details. The values of $T_{g,PDMS}$ were taken from ref 39.

temperatures is also apparent. Despite the similarities between these two copolymers, the sample 25PDMS4000 presents even larger values of fwhm, remaining very high (about 4.5 decades) even at the highest accessible temperatures.

DISCUSSION

First, let us comment on the calorimetric features detected in the 22PDMS7500 and 25PDMS4000 copolymers. As already mentioned, these features seem to suggest some crystallization process. However, no indication of PDMS crystallinity was detectable at low temperatures by WAXS or FTIR. Neither, crystallinity-related reflections were observed by SAXS. All this suggests that likely there is some structural reorganization in the copolymers distinct from conventional PDMS crystallization. The extent of this structural reorganization is much smaller for 22PDMS7500, but in both cases the energy involved corresponds to a relatively small fraction than that expected for PDMS phase crystallization. This suggests the possibility of formation of a minor fraction of extremely little PDMS crystals or some other PDMS mesophase. In any case the PDMS segmental degrees of freedom typical of a polymer melt remain active, as evidenced by the fact that the jump in C_p at T_g is relatively large, and it does not change noticeably when directly comparing the data from both runs, after quenching and after slow cooling, on the same sample.

The subsequent discussion will be mainly focused on the dynamical behavior of PDMS at low temperatures (ca. $T < 200$ K) where the nanostructural features of the systems are essentially temperature independent. All the previous results on the PDMS properties evidence that both structure and dynamics are considerably perturbed with respect to the usual PDMS melt when the cylindrical and spherical segregated phases are considered, the effects being qualitatively different and more pronounced than in the previously reported lamellar segregated phases. As the characteristic sizes of the different segregated phases are similar, the observed effects cannot straightforwardly be attributed to finite size effects. Noteworthy, the sphere diameter (~18 nm) is larger than the lamella thickness (~10 nm). As was already mentioned in the Introduction, in copolymers with lamellar segregated phases the properties of the PDMS block do not differ much from those of the corresponding homopolymer, most of the detected differences being ascribed to the PS−PDMS interfaces.[16] Furthermore, simulations on symmetric diblocks with components of distinct mobility[17] have recently confirmed this result. Taking this into account, the origin of the observed effects could be related with the balance between the degree of chain stretching, packing frustration, and interface curvature,[3] the latter being absent in lamellar phases. Because the high flexibility of PDMS blocks the preferred local structure in the bulk, it could not be the most favorable one in the segregated phase with large interfacial curvature. In addition, in these segregated phases the PDMS regions can become easily isolated and completely surrounded by the majority component forming the matrix. When considering such a situation with a matrix of high T_g, as is the case of PS, as soon as the sample temperature decreases and the matrix becomes frozen, the segregated phase is forced to fill the space as dictated by the thermal contraction of the matrix, which is rather limited. This would result in the emergence of stresses mainly at the interface and eventually to a "negative pressure" in the still very mobile segregated phase. This picture could explain the deep changes observed in the segregated PDMS phases of the copolymers 22PDMS7500 and the 25PDMS4000 both in the local structure and in the dynamical behavior. The WAXS patterns evidence the significant difference between the local order of PDMS in the curved segregated phases with respect to that of bulk PDMS, the packing in the asymmetric diblock system being relatively poor. This is also reflected in the noticeable changes of the PDMS vibrational modes as observed by ATR-FTIR, particularly the chain stretching could explain the blue shift of the central PDMS sub-band which is even stronger at lower temperatures. In addition to that, on cooling below the glass transition temperature of PS, strong stresses at the interfaces and negative pressure in the segregated PDMS phase could be expected. All this would explain the strong suppression of the PDMS phase crystallization at low temperature. Moreover, as a consequence of these structural changes the PDMS glass transition temperature would become lower and broader than that of the pure polymer. These effects are clearly reflected in the PDMS segmental dynamics as detected by the dielectric relaxation experiments, where the loss peak is extremely broad and presents its maximum at frequencies considerably higher

dx.doi.org/10.1021/ma202107m | Macromolecules 2012, 45, 491−502

than that in the homopolymer (see vertical arrows in Figure 3). Finally, the structural changes could also be at the origin of the markedly lower values of the dielectric strength of PDMS in these segregated phases. The suggested conformational and packing changes would also have consequences in the orientational correlation of neighboring dipole moments, modifying the Kirkwood correlation factor,[43] which could account for the observed changes in the dielectric strength, at least in part, and mainly its temperature dependence. All these local packing perturbations are expected to be more relevant as the size of the segregated nanophase decreases (and the curvature of the interfaces increases), which seems to be the case as both structurally and dynamically the PDMS behavior in the diblock with the shortest PDMS blocks is the most striking. In this copolymer 25PDMS4000 the WAXS pattern features from PDMS are much weaker (even if the PDMS relative amount is larger than in the 22PDMS7500 copolymer), and the PDMS segmental dynamics is more speeded up with respect to the corresponding homopolymer. Furthermore, when comparing the fwhm of the dielectric loss peaks for the two copolymers 25PDMS4000 and 22PDMS7500, it is evident that the former is larger. This difference is likely related with the greater structural heterogeneity as revealed in the WAXS patterns but could be also associated with the structural modifications detected in the DSC scan as exothermic peaks during cooling, these features being much more prominent for 25PDMS4000 copolymer. In connection with the possible residual crystallinity in the two copolymers, the values of the dielectric relaxation strength obtained in the two copolymers are rather similar, questioning again the direct relationship between the features detected by DSC and the occurrence of conventional PDMS crystallization in the segregated phase.

In spite of these differences between the PDMS behavior in the asymmetric PS−PDMS diblock copolymers here investigated and those previously reported for the lamellar case, some common features also exist. In all the PS−PDMS diblock copolymers the PDMS chains are anchored to rigid PS at the nanophase interface, and this fact has a noticeable impact in the dynamics of the neighboring PDMS segments. In our previous study of the symmetric PS−PDMS diblock copolymer with lamellar nanophase,[42] there was a rather well-resolved feature in the dielectric loss spectrum that was attributed to the anchorage effects. Namely, the dielectric losses at low frequencies and relatively high temperatures do not decrease to zero as in the PDMS melt but seem to tend to a low loss plateau-like behavior (see Figure 6 in ref 16). This part of the response was conveniently described by a contribution with the same characteristics as that observed experimentally in the constrained amorphous phase (CAP) of semicrystalline PDMS. This result was interpreted as indicative that the PDMS segments affected by anchorage at the interface with rigid PS behave in a similar way as the PDMS segments in the amorphous phase anchored to the rigid PDMS crystallite surface. Note that also in this latter case the disordered PDMS phase is in a nanosegregated lamellar phase with typical thickness of a few nanometers. Although this approach would be less justified for cylindrical and spherical PDMS nanosegregation, we found that it is still compatible with the experimental data. This is illustrated in Figure 9, where it can be seen that the low-frequency part of the data collected at 160 K in the two copolymers here investigated can be accounted for by the

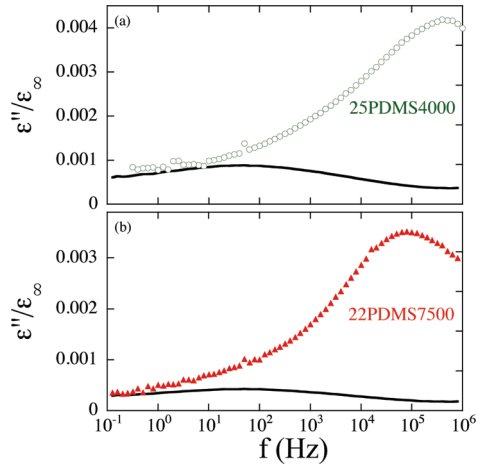

Figure 9. Dielectric losses at 160 K for the two copolymers, 25PDMS4000 (a) and 22PDMS7500 (b), as compared with the dielectric losses measured at the same temperature in semicrystalline PDMS after proper rescaling (solid line).

type of response measured in semicrystalline PDMS, properly scaled. Moreover, this comparison also puts in evidence that the CAP-like response extends also toward high frequencies, indicating that at the interface slow and fast PDMS segments can coexist. This hypothesis has been very recently confirmed by simulation results on diblock copolymers in the lamellar phase with components showing different dynamical properties.[17] The evaluation of this CAP-like background level for the different copolymers shows that, as it would be expected, it increases with the PDMS volume fraction. Nevertheless, the ratio of this signal to the PDMS volume fraction depends on the geometry of the nanosegregated phase, being the lowest for the spheres, whereas for the cylinders it is only marginally lower than for lamellas (with noncrystallized PDMS). Interestingly, the higher CAP-like background for the 25PDMS4000 would be directly related with the stronger reduction of the C_p jump at T_g detected by DSC.

A possible explanation for the behavior of the CAP-like background can be found by considering that the effect of the anchorage to the interface extends to a limited distance from the interface, which could depend on geometry. Moreover, the shortest the PDMS chains the largest the fraction of affected segments would be. From previous estimations[16] a layer of about 1 nm would be affected by anchorage in the lamella phase. Similar arguments using the present results yield a layer of about 0.5 nm thick for the cylindrical segregated PDMS phase and a layer of about 0.3 nm thick for the spherical segregated PDMS phase. These rough estimates clearly point to a strong effect of the interface curvature on the size of the highly constrain layer in the vicinity of the frozen interface.

When comparing the PDMS segmental dynamics in the PS−PDMS diblock copolymers with that of the corresponding homopolymers, the values of the main relaxation times obtained from the loss peak maxima (see Figure 8a) were in qualitative agreement with the significant T_g reduction observed in the DSC traces. However, the difference in the temperature dependence of the relaxation times cannot be completely accounted for by the corresponding T_g change.

dx.doi.org/10.1021/ma202107m | *Macromolecules* 2012, 45, 491−502

To illustrate this result, the relaxation time data in Figure 8a have been fitted by means of a Vogel−Fulcher−Tamman (VFT) equation:[45]

$$\tau(T) = \tau_\infty \exp\left(\frac{DT_0}{T - T_0}\right) \quad (4)$$

where T_0 is the characteristic Vogel temperature, τ_∞ is the high-temperature asymptotic value of the relaxation time, and D is the so-called fragility parameter. When the values of D and τ_∞ are fixed to those obtained for pure amorphous PDMS according to ref 16 (D = 3.8 and $\tau_\infty = 5.5 \times 10^{-13}$ s), a change in T_g directly corresponds to an equivalent change in T_0, assuming that the relaxation time at T_g remains the same. Dashed lines in Figure 8a represent the best possible fit of the data using this approach, i.e., with T_0 as single free parameter. As was previously shown,[16] this description works well for the PDMS in lamellar segregated phases, but the fits are not satisfactory for the two new diblocks considered here, mainly for 25PDMS4000. Remarkably, another simple approach that captures much better the experimental behavior is to fix the ratio T_0/T_g to that found in pure PDMS (T_0/T_g = 0.89) and use D as the single fitting parameter (see solid lines). The resulting values were D = 3.15 for 25PDMS4000 and D = 3.45 for 22PDMS7500. The values are significantly lower than that found in pure PDMS, and the difference is larger for the copolymer with shorter PDMS chains. This could be related to the larger perturbation of the PDMS properties expected as the size of the isolated nanophase becomes smaller. In the above-proposed framework, this suggests that the fragility parameter D could be intimately related with the structural and conformational state of the PDMS in the segregated phase, particularly taking into account that D is not expected to be much influenced by density changes[46,47] that might also exist.

As aforementioned, the dielectric losses evidence a very heterogeneous PDMS segmental dynamics in the two copolymers here considered, whereas the heterogeneity in the symmetric PS−PDMS diblock with lamellar nanostructure was relatively small. In this latter case it was found that the temperature dependence of the dielectric loss shape is conveniently captured by considering the superposition of pure PDMS-like responses with the relaxation time distributions originated by a single distribution of T_0 values in eq 4; i.e., the other parameters (D, τ_∞) were fixed to the values used when describing PDMS bulk behavior. Thus, we can question whether an analogous approach would also be valid for the asymmetric copolymers with PDMS nanosegregated in cylinders and spheres. In these cases, we have found that the temperature dependence of the main relaxation time can be well captured by allowing only the parameter D in eq 4 to change, the other parameters taken from the corresponding pure PDMS behavior. Consequently, we have assumed that the main dielectric losses in these diblocks would result from a distribution of pure PDMS-like responses with relaxation time distributions originated by a single distribution of D values in eq 4, i.e.

$$\varepsilon''(\omega) = \Delta\varepsilon \int_0^\infty \mathrm{Im}\left[\frac{-1}{(1 + [i\omega/\omega_c(D)]^\alpha)^\gamma}\right] g(D)\, \mathrm{d}D \quad (5)$$

As the loss peaks in Figure 7a,b look rather symmetric, we assumed a Gaussian distribution function $g(D)$, i.e.

$$g(D) = \frac{1}{\sqrt{2\pi}\sigma_D} \exp\left[-\frac{1}{2}\left(\frac{D - D_a}{\sigma_D}\right)^2\right] \quad (6)$$

with an average value D_a equal to that obtained above for the corresponding copolymer. In this way, only the standard deviation of the distribution, σ_D, determines the temperature-dependent width of the dielectric losses from PDMS in the copolymer, whereas the other parameters are fixed. The result of such description is included in Figure 7a,b as solid lines, where the CAP-like background with the intensity determined from the comparison made in Figure 9 has been also added. The values used for σ_D were 0.64 and 0.56 for 25PDMS4000 and 22PDMS7500, respectively. Overall, this description captures fairly well most of the experimental features, taking into account the simplicity of this approach. The main discrepancies are detected at the lowest temperatures, suggesting the presence of even faster contributions that are not well accounted by the Gaussian distribution.

CONCLUSIONS

The segregated cylindrical and spherical PDMS nanophases formed by self-assembly of asymmetric diblock PS−PDMS copolymers evidence both structural and dynamical anomalies when compared not only with bulk PDMS but also with PDMS in lamellar nanophases. Because the typical sizes of the PDMS lamellae are similar to those of the cylindrical and spherical PDMS nanophases, the effect cannot be directly attributed to size effects by geometrical confinement. The reported results can be considered as a result of the poor packing of the PDMS segments originated by the balance between the degree of chain stretching, packing frustration, and interface curvature in the segregated phases of asymmetric diblocks. This poor packing is evidenced in the WAXS pattern and also is the detectable by important changes in the PDMS vibrational modes. Moreover, in these cylindrical and spherical PDMS nanophases PDMS crystallization is strongly suppressed, if not inhibited, and the glass transition temperature appears considerably reduced. In agreement with this latter finding, the dielectric loss peak associated with the PDMS segmental dynamics is located at higher frequencies and is much broader than that of bulk PDMS. The temperature dependence of the main dielectric relaxation times can be well described using a VFT equation similar to that describing the results in bulk PDMS, but with a quite lower value of the fragility parameter D. The temperature-dependent shape of the dielectric loss peaks can be semi-quantitatively accounted by a T-independent distribution of D values leading to a distribution of relaxation processes with different times, each of the dielectric loss components having the shape of the segmental relaxation in PDMS melt.

Regardless of these dramatic differences between PDMS nanosegregated in cylinders and spheres when compared with PDMS nanosegregated in lamellas, in all cases the effects of chain anchorage is reflected in the dielectric losses as a broad and slow contribution with the same characteristics as the dielectric relaxation produced by the constrained amorphous phase in semicrystalline bulk PDMS. It is noteworthy that the presence of this component was a main effect detected in the lamellar case and was interpreted as a signature of the dominant influence of the interface in that case. Although this feature also

dx.doi.org/10.1021/ma202107m | Macromolecules 2012, 45, 491−502

results relevant for PDMS nanosegregated in cylinders and spheres, the major cause for the most dramatic changes observed would be the poor local packing of the PDMS segments, likely as a result of the presence of a highly curved interface.

A question that remains open is whether the results obtained depend on the chemical nature of the two polymer blocks here considered, or otherwise it is something that would be expected to occur to some extent in any strongly segregated block copolymer with highly curved interfaces. Work in this direction is currently in progress.

AUTHOR INFORMATION

Corresponding Author

*E-mail: angel.alegria@ehu.es.

ACKNOWLEDGMENTS

The authors acknowledge the University of the Basque Country and Basque Country Government (Ref. No. IT-436-07, Depto. Educación, Universidades e Investigación) and the Spanish Ministry of Science and Innovation (Grant No. MAT 2007-63681) for their support. We also thank SGIker UPV/EHU services for WAXS and TEM measurements and Silvia Barbosa-Fernandez (University of Vigo) for carrying out TEM measurements. L.V.C. particularly acknowledges the PhD grant support of the Basque Government.

REFERENCES

(1) Bates, F. S.; Fredrickson, G. H. *Annu. Rev. Phys. Chem.* **1990**, *41*, 525.
(2) Hamley, I. W. *The Physics of Block Copolymers*; Oxford University Press: Oxford, UK, 1998.
(3) Hadjichristidis, N.; Pispas, S.; Floudas, G. *Block Copolymers: Synthetic Strategies, Physical Properties, and Applications*; Wiley-IEEE: Hoboken, NJ, 2003.
(4) Meuler, A. J.; Hillmyer, M. A.; Bates, F. S. *Macromolecules* **2009**, *42*, 7221.
(5) Schönhals, A.; Goering, H.; Schick, Ch.; Frick, B.; Zorn, R. *J. Non-Cryst. Solids* **2005**, *351*, 2668.
(6) Sanz, A.; Nogales, A.; Ezquerra, T. A. *Soft Matter* **2011**, *7*, 6477.
(7) He, F.; Wang, L.-M.; Richert, R. *Eur. Phys. J.: Spec. Top.* **2007**, *141*, 3.
(8) Tsui, O. K. C.; Russell, T. P.; Hawker, C. J. *Macromolecules* **2001**, *34*, 5535.
(9) Yao, M. L.; Watanabe, H.; Adachi, K.; Kotaka, T. *Macromolecules* **1991**, *24*, 2955.
(10) Kaznessis, Y. N.; Hill, D. A.; Maginn, E. J. *Macromolecules* **1998**, *31*, 3116.
(11) Adachi, K.; Kotaka, T. *Pure Appl. Chem.* **1997**, *69*, 125.
(12) Tang, W. H. *Macromolecules* **2000**, *33*, 1370.
(13) Laredo, E.; Hernandez, M. C.; Bello, A. *Phys. Rev. E* **2002**, *65*, 021807.
(14) Zhukov, S.; Geppert, S.; Stuhn, B.; Staneva, R.; Gronski, W. *Macromolecules* **2002**, *35*, 8521.
(15) Zhukov, S.; Geppert, S.; Stuhn, B.; Staneva, R.; Gronski, W. *Macromolecules* **2003**, *36*, 6166.
(16) Lorthioir, C.; Alegría, A.; Colmenero, J.; Deloche, B. *Macromolecules* **2004**, *37*, 7808.
(17) Slimani, M. Z.; Moreno, A. J.; Colmenero, J. *Macromolecules* **2011**, *44*, 6952.
(18) Roth, C. B.; Torkelson, J. M. *Macromolecules* **2007**, *40*, 3328.
(19) del Valle-Carrandi, L.; Alegría, A.; Colmenero, J. *Eur. Phys. J.: Spec. Top.* **2010**, *189*, 257.
(20) Willner, L.; Lund, R.; Monkenbusch, M.; Holderer, O.; Colmenero, J.; Richter, D. *Soft Matter* **2010**, *6*, 1559.
(21) Moreno, S.; Rubio, R. G. *Macromolecules* **2002**, *35*, 5483.
(22) Alig, I.; Floudas, G.; Avgeropoulos, A.; Hadjichristidis, N. *Macromolecules* **1997**, *30*, 5004.
(23) Lund, R.; Willner, L.; Alegría, A.; Colmenero, J.; Richter, D. *Macromolecules* **2008**, *41*, 511.
(24) Gitsas, A.; Floudas, G.; Butt, H.-J.; Pakula, T.; Matyjaszewski, K. *Macromolecules* **2010**, *43*, 2453.
(25) Floudas, G.; Meramveliotaki, K.; Hadjichristidis, N. *Macromolecules* **1999**, *32*, 7496.
(26) Mok, M. M.; Masser, K. A.; Runt, J.; Torkelson, J. M. *Macromolecules* **2010**, *43*, 5740.
(27) Ninago, M. D.; Satti, A. J.; Ciolino, A. E.; Vallés, E. M.; Villar, M. A.; Vega, D. A.; Sanz, A.; Nogales, A.; Rueda, D. R. *J. Polym. Sci., Part B: Polym. Chem.* **2010**, *48*, 3119.
(28) Takenaka, M.; Aburaya, S.; Akasaka, S.; Hasegawa, H.; Hadjichristidis, N.; Sakellariou, G.; Tada, Y.; Yoshida, H. *J. Polym. Sci., Part B: Polym. Phys.* **2010**, *48*, 2297.
(29) Lichtenthaler, R. N.; Liu, D. D.; Prausnitz, J. M. *Macromolecules* **1978**, *11*, 192.
(30) Rosati, D.; Perrin, M.; Navard, P.; Harabagiu, V.; Pinteala, M.; Simionescu, B. C. *Macromolecules* **1998**, *31*, 4301.
(31) Chu, J. H.; Rangarajan, P.; Adams, J. L.; Register, R. A. *Polymer* **1995**, *36*, 1569.
(32) Hamley, I. W.; Castelletto, V. *Prog. Polym. Sci.* **2004**, *29*, 909.
(33) Förster, S.; Timmann, A.; Konrad, M.; Schellbach, C.; Meyer, A.; Funari, S. S.; Nakamura, H.; Mulvaney, P.; Knott, R. *J. Phys. Chem. B* **2005**, *109*, 1347.
(34) Förster, S.; Burger, C. *Macromolecules* **1998**, *31*, 879.
(35) Habenschuss, A.; Tsige, M.; Curro, J. G.; Grest, G. S.; Nath, S. K. *Macromolecules* **2007**, *40*, 7036.
(36) Furuya, H.; Mondello, M.; Yang, H.-J.; Roe, R.-J.; Erwin, R. W.; Han, C. C.; Smith, S. D. *Macromolecules* **1994**, *27*, 5674.
(37) Iradi, I.; Álvarez, F.; Colmenero, J.; Arbe, A. *Physica B* **2004**, *350*, 881.
(38) Álvarez, F.; Colmenero, J.; Arbe, A. *Int. Union Crystallogr. Newsl.* **2004**, *31*, 35.
(39) Ding, Y.; Kisliuk, A.; Sokolov, A. P. *Macromolecules* **2004**, *37*, 161.
(40) Lu, Z. H.; Krause, S. *Macromolecules* **1982**, *15*, 112.
(41) Boucher, V. M.; Cangialosi, D.; Alegría, A.; Colmenero, J.; Pastoriza-Santos, I.; Liz-Marzan, L. M. *Soft Matter* **2011**, *7*, 3607.
(42) Lund, R.; Alegría, A.; Goitandía, L.; Colmenero, J.; González, M. A.; Lindner, P. *Macromolecules* **2008**, *41*, 1364.
(43) Bottcher, C. J. F. *Theory of Dielectric Polarization*; Elsevier: Amsterdam, 1973.
(44) Schwartz, G. A.; Colmenero, J.; Alegría, A. *Macromolecules* **2007**, *40*, 3246.
(45) Vogel, H. *Phys. Z.* **1921**, *22*, 645. Fulcher, G. S. *J. Am. Ceram. Soc.* **1923**, *8*, 339. Tammann, G.; Hesse, W. *Z. Anorg. Allg. Chem.* **1926**, *156*, 245.
(46) Schwartz, G. A.; Colmenero, J.; Alegría, A. *Macromolecules* **2006**, *39*, 3931.
(47) Guo, J.; Simon, S. L. *J. Chem. Phys.* **2011**, *135*, 074901.

Macromolecules

Article

pubs.acs.org/Macromolecules

Emergence and Stability of Helical Superstructures in ABC Triblock Copolymers

Weihua Li* and Feng Qiu*

State Key Laboratory of Molecular Engineering of Polymers, Department of Macromolecular Science, Fudan University, Shanghai 200433, China

An-Chang Shi*

Department of Physics and Astronomy, McMaster University, Hamilton, Ontario, Canada, L8S 4M1

ABSTRACT: The emergence and stability of superstructured cylindrical phases in frustrated ABC linear triblock copolymers are investigated by the self-consistent field theory. Our results reveal that the complex single/double/triple helices-on-cylinder phases are formed when the straight cylinders-on-cylinder and rings-on-cylinder phases are frustrated due to packing constraints. A free energy comparison indicates that the double and triple helical phases are stable, whereas the other cylinders-on-cylinder phases are metastable. In addition, the chirality and rotation for the helical supercylinders are considered in our calculations. Our theoretical prediction is consistent with a number of experimental observations.

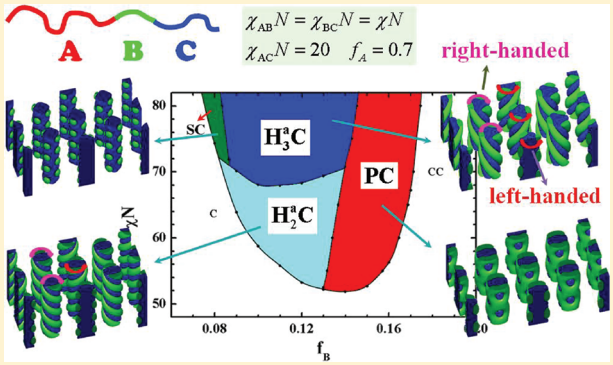

I. INTRODUCTION

The formation of helical structures is a fascinating yet generic behavior in nature. Besides the most well-known examples of α-helices in proteins and DNA double-strand helices, helices also arise in screws, springs, tendrils, vines, and so on.[1] The propensity of helices in nature has attracted tremendous attention to the origin of helical structures. Motivated by nature, polymer scientists have been searching for and studying helical structures formed from the self-assembly of synthetic polymers. Similar to the α-helices in proteins, chiral centers can be introduced into synthetic polymers. It has been shown that diblock copolymer composed of at least one chiral block can self-assemble into helical structures.[2−4] What is more fascinating is that helical structures can also spontaneously form in cylinder-forming achiral diblock copolymers confined in a cylindrical nanopore,[5−12] and in softly confined achiral ABC star[13] and linear triblock copolymers (or solution systems).[14] In addition, helical structures have also been observed in melts of complex block copolymers such as ABC linear triblock copolymers. Understanding the formation and stability of these helical superstructures from achiral block copolymers in bulk presents an interesting challenge in soft matter theory.

In the present paper we focus on the formation and stability of helical superstructures from linear ABC triblock copolymer melts. Because of the large number of controlling parameters and topological constraints, ABC triblock copolymers exhibit an extreme rich phase behavior.[15] Their sophisticated self-assembling capabilities have made ABC triblock copolymers an important platform for the engineering of new ordered phases, which may have potential applications for fabrication techniques of functional materials.[16,17] According to the relative strength of the three Flory−Huggins interaction parameters, χ_{AB}, χ_{BC}, and χ_{AC}, the phase behavior of triblock copolymer melts can be classified into "nonfrustrated" and "frustrated" cases.[18] In the nonfrustrated case, the repulsion between the two end-blocks, χ_{AC}, is comparable to or larger than the repulsion between the neighboring blocks, χ_{AB} and χ_{BC}, thus the A and C blocks prefer to be separated, forming distinct A/B and B/C interfaces. This type of structures do not frustrate the topology of the linear ABC chain architecture. In the frustrated case, the repulsion between the two end-blocks, χ_{AC}, is weaker than the repulsions between the neighboring blocks, χ_{AB} or χ_{BC}, thus the block copolymers prefer structures with larger A/C interfaces. However the formation of A/C interfaces is not commensurate with the topology of the linear ABC triblock copolymers, resulting in the formation of complex ordered phases to alleviate the topological frustration. The phase behaviors of triblock copolymers have been extensively studied by experiments and theories.[19]

Because of the simplicity of the core−shell or alternated structures, theoretical framework based on the spectral method for the study of the phase behavior of nonfrustrated ABC triblock copolymers has been well developed.[20−22] On the

Received: October 27, 2011
Revised: November 26, 2011
Published: December 12, 2011

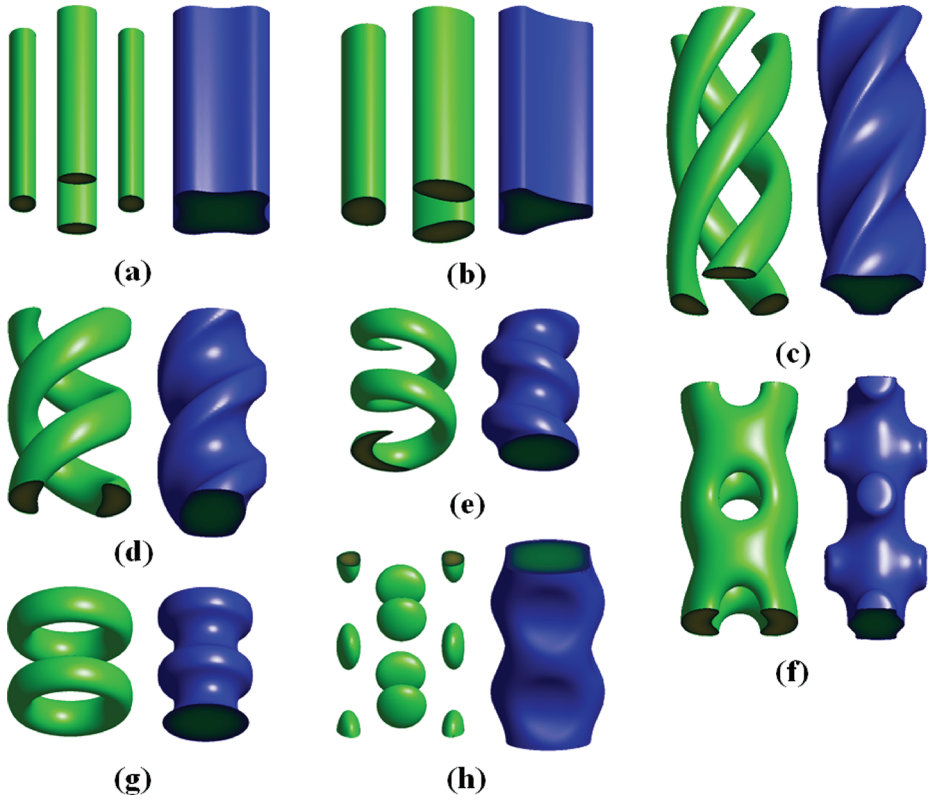

Figure 1. Isosurfaces for ϕ_B (green) and ϕ_C (blue) of superstructures formed in frustrated ABC linear triblock copolymers: (a) quadruple cylinders-on-cylinder (C_4C); (b) triple cylinders-on-cylinder (C_3C); (c) triple helices-on-cylinder (H_3C); (d) double helices-on-cylinder (H_2C); (e) single helix-on-cylinder (C_3C); (f) perforated-lamella-on-cylinder (PC); (g) rings-on-cylinder (RC); (h) spheres-on-cylinder (SC).

other hand, the ordered phases formed from frustrated triblock copolymers change from the core−shell type or alternating type to superstructured or hierarchical structures, such as cylinders-on-lamellae, spheres-on-lamellae, cylinders-on-cylinder, spheres-on-cylinder, and so on. Theoretical investigation of these complex structures has been carried out by a generic spectral method of the self-consistent field theory (SCFT).[23] The generic spectral method is an efficient tool for the search of possible ordered phases. However, the determination of precise phase diagrams using the spectral method requires a large number of basis functions. In the current study, we apply the pseudospectral method,[24−26] coupled with the knowledge of the symmetry of the ordered phases, to examine the formation and stability of complex ordered phases of frustrated triblock copolymers. We will focus on one type of complex ordered phases, i.e., hierarchical phases of hexagonal cylinders, where the large cylinders are decorated by various substructures. A number of supercylindrical phases, including cylinders-on-cylinder and spheres-on-cylinder, have been either observed or postulated in previous experiments or theories.[15,19,27−36] The cylinders-on-cylinder phases are of great interest because the substructures of cylinders can be straight cylinders, or helices, or rings. In addition, for the cases of straight cylinders and helices, the cylinder/helix number is another quantity to vary the supercylindrical phase. For example, the helical number of the helical supercylinders, formed in the poly(styrene-*b*-butadiene-*b*-methyl methacrylate) (PS−PB-PMMA) triblock copolymers, was proposed to be four,[29] and recently it was determined to be two by 3D transmission electron microtomography (TEMT).[34] To date, there is no direct proof to support that there is no other helical phase except for the double-helical one, such as single-helical, triple-helical, or four-helical phase. Furthermore, the relative stability of these helical phases to those straight cylinders-on-cylinder phases is unknown. Therefore, a theoretical study to explore the supercylindrical phase behaviors of frustrated ABC linear triblock copolymers is desirable. In this paper, we report a theoretical study of these complex superstructures within the framework of SCFT. Specifically, we use the pseudospectral method, coupled with special initial conditions, to compute the free energy of a number of candidate structures, thus determining the relative stability of these phases.

II. THEORY

We consider an incompressible melt of ABC linear triblock copolymers with a degree of polymerization N in a volume of V. The chain lengths of A, B and C blocks are specified by f_AN, f_BN, and f_CN ($f_A + f_B + f_C = 1$), respectively. The interactions between the three dissimilar monomers are characterized by three Flory−Huggins interaction parameters, χ_{AB}, χ_{AC}, and χ_{BC}. The radius of gyration of the polymer, R_g, is set as the unit of spatial lengths in our calculations. Within the mean-field approximation to statistical mechanics of the Edwards model of polymers,[26,37] the free energy functional F for n Gaussian triblock copolymer chains at a given temperature T is given by,

$$\frac{F}{nk_BT} = -\ln Q + \frac{1}{V}\int d\mathbf{r}\,\{\chi_{AB}N\phi_A(\mathbf{r})\phi_B(\mathbf{r}) + \chi_{AC}N\phi_A(\mathbf{r})\phi_C(\mathbf{r}) + \chi_{BC}N\phi_B(\mathbf{r})\phi_C(\mathbf{r}) - \omega_A(\mathbf{r})\phi_A(\mathbf{r}) - \omega_B(\mathbf{r})\phi_B(\mathbf{r}) - \omega_C(\mathbf{r})\phi_C(\mathbf{r}) - \eta(\mathbf{r})[1 - \phi_A(\mathbf{r}) - \phi_B(\mathbf{r}) - \phi_C(\mathbf{r})]\} \quad (1)$$

dx.doi.org/10.1021/ma2023952 | *Macromolecules* 2012, 45, 503−509

Here ϕ_A, ϕ_B, and ϕ_C are the monomer densities. The quantity Q is the partition function of a single polymer chain interacting with the mean fields ω_A, ω_B, and ω_C, which are produced by the surrounding chains. Minimization of the free energy with respect to the monomer densities and the mean fields leads to the following standard SCFT equations[26]

$$\omega_A(\mathbf{r}) = \chi_{AB}N\phi_B(\mathbf{r}) + \chi_{AC}N\phi_C(\mathbf{r}) + \eta(\mathbf{r})$$
$$\omega_B(\mathbf{r}) = \chi_{AB}N\phi_A(\mathbf{r}) + \chi_{BC}N\phi_C(\mathbf{r}) + \eta(\mathbf{r})$$
$$\omega_C(\mathbf{r}) = \chi_{AC}N\phi_A(\mathbf{r}) + \chi_{BC}N\phi_B(\mathbf{r}) + \eta(\mathbf{r})$$
$$\phi_A(\mathbf{r}) = \frac{1}{Q}\int_0^{f_A} \mathrm{d}s\, q(\mathbf{r}, s)q^{\dagger}(\mathbf{r}, s)$$
$$\phi_B(\mathbf{r}) = \frac{1}{Q}\int_{f_A}^{f_A+f_B} \mathrm{d}s\, q(\mathbf{r}, s)q^{\dagger}(\mathbf{r}, s)$$
$$\phi_C(\mathbf{r}) = \frac{1}{Q}\int_{1-f_C}^{1} \mathrm{d}s\, q(\mathbf{r}, s)q^{\dagger}(\mathbf{r}, s)$$
$$Q = \frac{1}{V}\int \mathrm{d}\mathbf{r}\, q(\mathbf{r}, s)q^{\dagger}(\mathbf{r}, s)$$
$$\phi_A(\mathbf{r}) + \phi_B(\mathbf{r}) + \phi_C(\mathbf{r}) = 1 \qquad (2)$$

In the above equations, $q(\mathbf{r},s)$ and $q^{\dagger}(\mathbf{r},s)$ are end-segment distribution functions.[26] These distribution functions satisfy the modified diffusion equations

$$\frac{\partial q(\mathbf{r}, s)}{\partial s} = \nabla^2 q(\mathbf{r}, s) - \omega(\mathbf{r}, s)q(\mathbf{r}, s) \qquad (3)$$

$$-\frac{\partial q^{\dagger}(\mathbf{r}, s)}{\partial s} = \nabla^2 q^{\dagger}(\mathbf{r}, s) - \omega(\mathbf{r}, s)q^{\dagger}(\mathbf{r}, s) \qquad (4)$$

where $\omega(\mathbf{r},s) = \omega_K(\mathbf{r})$ when s belongs to K blocks (K = A, B, C). The initial conditions are $q(\mathbf{r},0) = q^{\dagger}(\mathbf{r},1) = 1$. For numerical solutions, we employ the second-order operator-split method (or the pseudospectral method)[2425,] to solve the modified diffusion equations for the end-segment distribution functions.

III. RESULTS AND DISCUSSION

We assume that the A-block has the largest volume fraction thus the A-blocks form the matrix of the phases. The candidate ordered phases are formed by C-cylinders arranged in the A-matrix, where the A/C interfaces are decorated by B-substructures. Besides the simple cylinders (C) and B/C core−shell cylinders (CC), there are eight cylindrical superstructures examined in the current study (Figure 1): (a) quadruple straight cylinders-on-cylinder (C_4C), (b) triple straight cylinders-on-cylinder (C_3C), (c) triple helices-on-cylinder (H_3C), (d) double helices-on-cylinder (H_2C), (e) single helix-on-cylinder (H_1C), (f) perforated-lamella-on-cylinder (PC), (g) rings-on-cylinder (RC), and (h) spheres-on-cylinder (SC). These ordered phases are obtained from the SCFT calculations by using initial conditions bearing their symmetries. In practice, first we set the axial direction of cylinder along the z-direction, and the perpendicular cross-section to the xy-plane. Then the hexagonal symmetry is imposed on the arrangement of cylinders. We parallelize[38] the pseudospectral method to solve the modified diffusion equations for the end-segment distribution functions, using the fast-Fourier transform (FFTW) libraries.[39] Usually two unit cells for each structure are put into a cuboidal box which is discretized into a $N_x \times N_y \times N_z = 128 \times 128 \times 64$ lattice. We impose periodic boundary conditions on all edges of the cubic lattice. The free energy is minimized with respect to the size of the simulation box. The chain contour length for the copolymer is discretized with $\Delta s = 0.01$, and the trapezoidal scheme is used to carry out integration along s. During the iteration steps to solve the SCFT equations, a simple linear mixing scheme is used to update the fields for each iteration. The convergence is judged by ensuring the free energy and the incompressibility condition to an accuracy of about 10^{-7}.

As a typical example of frustrated triblock copolymers, we will use the parameter set such that $\chi_{AC}N \ll \chi_{AB}N = \chi_{BC}N = \chi N$. This assumption is reasonable for typical frustrated systems studied in experiments, such as poly(styrene-*b*-butadiene-*b*-methyl methacrylate) (PS−PB−PMMA),[28,29,31,34] poly(styrene-*b*-ethylene-*co*-butylene-*b*-methyl methacrylate)(PS−PEB−PMMA),[27,28] and poly(styrene-*b*-2-vinylpyridine-*b*-tert-butyl methacrylate) (PS−P2VP−PtBMA).[32,33] The phase behavior is presented by two typical phase diagrams. The first one is the portion of the supercylindrical phase region between $f_A = 0.68$ and $f_A = 0.76$ in the triangular phase diagram with $\chi N = 80$ and $\chi_{AC}N = 20$ (Figure 2). The choice of this composition

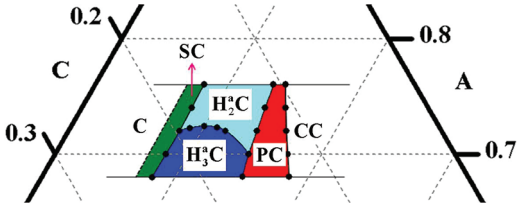

Figure 2. Portion of the supercylindrical phase region between f_A = 0.68 and f_A = 0.76 of the triangular phase diagram with given $\chi_{AB}N = \chi_{BC}N = \chi N = 80$ and $\chi_{AC} = 20$. The filled circles denote the points at which we have calculated the phase boundaries, the solid curves connecting these points are to guide the eyes, and the dashed curve without points is roughly estimated in our calculations.

region ensures that typical supercylindrical phases are obtained.[40] The second phase diagram (Figure 3) is

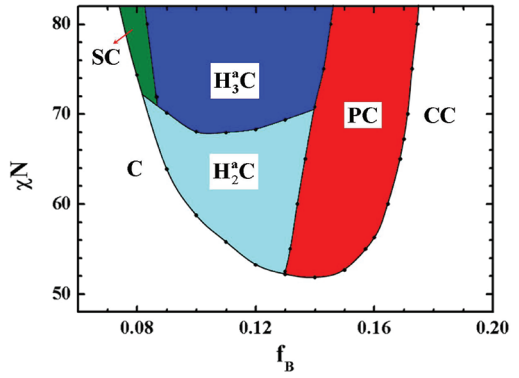

Figure 3. Portion of the phase diagram with respect to f_B and χN for fixed χ_{AC} = 20 and f_A = 0.70.

constructed for $\chi_{AC}N = 20$ and $f_A = 0.7$ ($f_B + f_C = 0.3$), showing the dependence on the interaction parameter χN. These phase diagrams are constructed by a careful comparison

dx.doi.org/10.1021/ma2023952 | *Macromolecules* 2012, 45, 503−509

of the free energies of the candidate structures. A typical plot of the free energy difference of these phases relative to the H_2C for f_A = 0.7 is given in Figure 4. This free-energy comparison

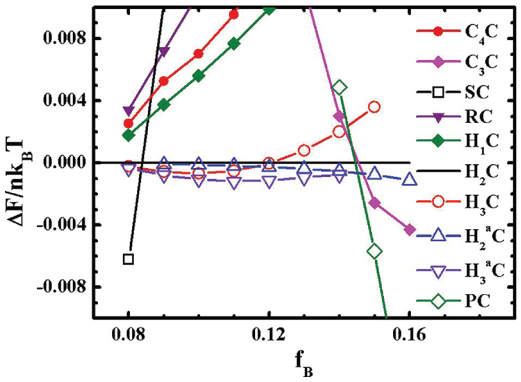

Figure 4. Free energy of various phases relative to that of H_2C, which is indicated by a solid line, as a function of f_B.

reveals that the stable phase sequence is SC, H_3^aC, PC, and CC when f_B increases (the free energy of CC is not shown for clarity). The free-energy differences between the types of double-helical and triple-helical phases are always small compared with those between the helical phases and other nonhelical ones. Both phase diagrams shown in Figures 2 and 3 suggest that only H_2^aC and H_3^aC are stable phases of the cylinders-on-cylinder type. The other two phases postulated previously by experiments or theories, C_4C and RC, are found to be metastable.

Comparing with cylinder-forming diblock copolymers under cylindrical confinement,[8,9] the B-cylinders in the current system can be considered as softly confined in the space between the concentric A and C domains. For a given set of volume fractions, both the B-cylinders and the C-cylinder have their preferred diameters because of their spontaneous curvature arising from the competition between the stretching energy and the interfacial energy. In general these preferred diameters will lead to different lengths of B- and C-cylinders. The packing of these cylinders of different lengths results in the formation of helical structures. The difference between the cylindrically confined system is that the screwing radius of the B-helices is determined by the volume fraction of the C-block in the present system, while it can be varied along with the helical pitch in the former system. For the case of straight B-cylinders, the restriction becomes stronger because the B/C-cylinders have to have equal length, and thus gives rise to a high packing frustration which results in a penalty of stretching energy. One way to release the high stretching energy is to add or remove one B-cylinder. As a consequence, the free-energy difference between two straight-cylinder phases, such as C_4C and C_3C, is rather large. For a given f_A, the change of f_B (or f_C) can significantly influence the sizes of both B-cylinders and C-cylinder, and thus influence the length ratio of the B- and C-cylinders which in turn determines the relative stability between C_4C and C_3C. When the B-cylinders are screwed onto the C-cylinder to form helices, the packing of the B-cylinders has more freedom, i.e., adjusting the pitch of helices, to reduce the packing frustration from the size mismatch. Despite this advantage, the number of helices is still a useful quantity to release the packing frustration. Similar as the transition between C_4C and C_3C, the packing of three B-helices in the reduced space becomes too crowded when the C-cylinder size is decreased, and thus, H_3^aC transfers to H_2^aC. However, the free-energy difference between the two helical phases becomes much smaller. Further analysis on this delicate transition is provided in the following content. As a special case of helices,

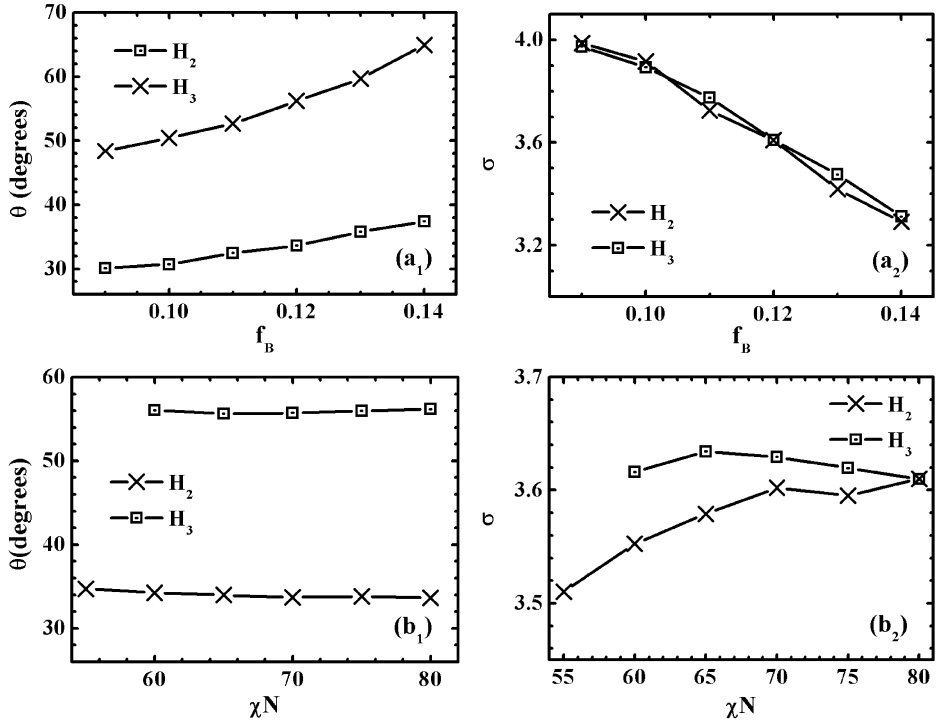

Figure 5. Pitch angle of helices and the length ratio of the B helices and the C cylinder as a function of f_B or χN for $\chi_{AC}N$ = 20. The upper row is for χN = 80 and f_A = 0.70, and the bottom row is for (f_A, f_B, f_C)= (0.70, 0.12, 0.18).

dx.doi.org/10.1021/ma2023952 | *Macromolecules* 2012, 45, 503−509

the supercylindrical phase of rings with zero pitch angle is an alternative candidate phase in which the C-cylinder can adjust its length freely to satisfy the B-cylinders. A comparison of the free-energy between RC and H_1C, reveals that RC has consistently higher free energy than the H_1C phase. This is because the bending energy of the rings in RC is higher than that of the helix in H_1C. However, the nonuniformity of chain stretching in H_1C is more pronounced compared with H_2C and H_3C, and thus it has higher free energy.

There are two notable features in the phase diagram of Figure 3. The first feature is that the B-substructure transfers from disorder (C),[41] to spheres (SC), to helices (curved cylinders), to perforated lamella (PC), and then to lamella (CC) as f_B increases. This behavior resembles the phase sequence of B/C diblock copolymers.[42] The second feature is that H_3^aC transfers to H_2^aC when χN decreases. This transition is mainly driven by the decreasing of the C-cylinder circumference which allows fewer helices to screw on it. To understand the delicate transition between H_3^aC and H_2^aC quantitatively, we calculate the length ratio between the B-cylinders (or helices) and C-cylinder, defined as $\sigma = k(1 + 1/(\tan\theta)^2)^{1/2}$, where k and θ are the number and the pitch angle of helices, respectively. The pitch angle is determined by $\theta = \tan^{-1}(L_0/2\pi r_0)$, where L_0 is the length of the supercylinder for one complete helix turn, and r_0 is the screwing radius of the helix, i.e., the distance between the maximum density point of B-helix and the center of the supercylinder. For helical phases, σ can be adjusted by varying the pitch angle to ensure that the B and C cylinders have near preferred sizes, while it is fixed as 3 or 4 for C_3C or C_4C. In Figure 5, the length ratio σ, as well as the pitch angle θ, as a function of χN or f_B, is presented. Parts a_1 and a_2 of Figure 5 are for the phase path of varying f_B for fixed parameters of $\chi N = 80$, $\chi_{AC}N = 20$, and $f_A = 0.70$ in Figure 2, and parts b_1 and b_2 are for that of varying χN for fixed compositions of (0.70, 0.12, 0.18) and interaction parameter of $\chi_{AC}N = 20$. When f_B is increased, the pitch angle of helices increases for both H_3^aC and H_2^aC, while the length ratio drops down. It is surprising that H_3^aC and H_2^aC has very close length ratios. This suggests that the two helical phases have a comparable strong capability of adjusting the sizes of both B- and C-cylinders to be close to their preferred values. This capability leads to large free-energy differences between them and those straight-cylinder phases, while small free-energy differences between themselves. When $f_B = 0.09$, the length ratio is close to 4, i.e., the length ratio of the phase C_4C. This is why the free-energy difference between C_4C and the two helical phases becomes reasonably small, but is still obviously larger than that between H_3^aC and H_2^aC. In the frustrated phases, there is a constraint arising from the architecture topology that each chain starting from the A matrix has to go through these distributed B domains, and then to enter the C domain. This means that the distribution of B domains in each phase, determining the uniformity degree of A and C chain stretching, is another factor influencing the phase stability besides the major factor of the length ratio. The phases of straight cylinders can release the chain stretching only in the plane of the cross section perpendicular to the axis of C-cylinder, while the helical phases have the third direction along the C-cylinder axis to do so. This advantage makes the helical phases have more favorable stretching energy than those of straight cylinders even when they have similar length ratio. As the length ratio drops down and deviates from 4, the free-energy difference between C_4C and the helical phases increases tremendously. Though the length ratios of the two helical phases are similar at the large value of f_B, the pitch angle of H_3^aC has been raised very large. At $f_B = 0.14$, the pitch angle is as high as 65 deg. According to this increasing tendency, we expect that the pitch angle would reach rapidly the maximum value of 90 deg for larger f_B. For the case of large pitch angles, the distribution of the B domains in H_3^aC becomes close to that of C_3C. This reason drives H_3^aC to transfer to H_2^aC which can lead to the similar length ratio but with smaller pitch angle and less constraint on the chain architecture. Besides the constraint on the chain stretching resulted by the distribution of the B-domains, the shape of the B domains can also influence the chain stretching, particularly for the B blocks. In the helical phases, the cross section perpendicular to the screwing axis is closer to an ideal shape for the B-cylinders, i.e., the preferred circle shape, for the phase with more helices (see Figure 1). The competition between the two minor factors of the distribution and the shape of the B-cylinders subtly determines the relative stability between H_3^aC and H_2^aC when they have similar length ratio. For $f_B \leq 0.14$, H_3^aC with reasonable low pitch angles is more favorable than H_2^aC. In the other case of parts b_1 and b_2, both the pitch angle and the length ratio have more moderate change as χN. Particularly the change of the pitch angle is smaller than one degree when χN varies between 55 to 80. This is because χN has similar influence on the sizes of the B- and C-cylinders. However, the B-cylinders have much larger curvature than the C-cylinder for the present asymmetric B/C composition. This fact results in increasing the size ratio of the B- and C-cylinders as χN is decreased, and thus decreasing their length ratio. Therefore, H_3^aC transfers to H_2^aC when χN is decreased.

Helices-on-cylinder have been observed in a number of experiments.[29,31−34] The compositions of the majority of these ABC triblock copolymers are located in the helical-phase regions of the current study. In particular, Jinnai et al. in a recent study have observed double-helical morphologies with antiferromagnetic arrangement of chirality by using the TEM tomography. For the composition of the PS−PB-PMMA (C: PS, B: PB, A: PMMA), i.e., (0.21, 0.09, 0.70) in their experiments, the value of χN for the stable double-helical phase is between 64 and 70 in the phase diagram of Figure 3. By taking the factor of different segment sizes into account that the PB block has relatively smaller segment size, the experimental phase point should be moved toward inside of the phase diagram.[43] In addition, a number of quantities about the superstructures and their varying tendency are comparable with our theoretical prediction. For example, the pitch and pitch angle decrease as the C block increases or the B block decreases (see Figure $5a_1$). The pitch angle, measured as 40 deg in the experiment, is different from the 30 deg estimated in our calculations. The discrepancy may be induced by the factor of the segment sizes and other uncontrollable experimental factors, such as measuring error for the pitch angle, small composition deviations, and polydispersity of polymers.

Because the helices are formed from achiral block copolymers, their chirality is not determined *a priori*. In principle we would have equal number of left-handed and right-handed helices in a given system. The arrangement of the different helices depends on the interaction between the left-handed and right-handed species. Similar to a magnetic system, the interactions can be ferromagnetic, favoring helices of the same handedness, or antiferromagnetic favoring helices of alternating handedness. Because the C-cylinders are arranged

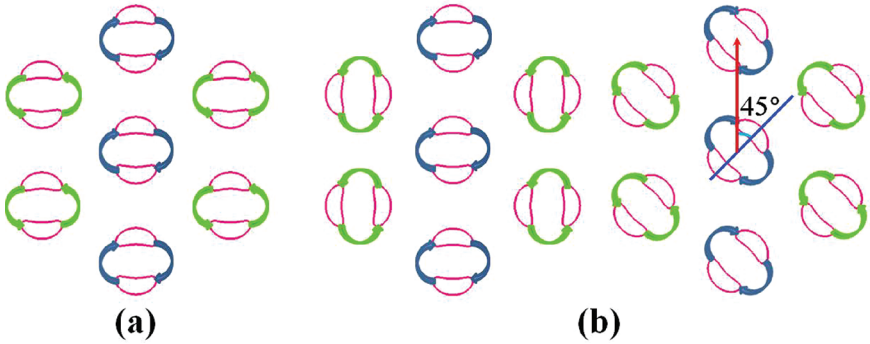

Figure 6. Schematic description of a simple arrangement of hexagonal helical supercylinders with different chiralities (indicated by various-color arrows) or rotations. (a) If the handedness is uniform, it presents as H_2C; otherwise, it presents as H_2^aC. (b) The left picture presents as $H_2^{90}C$ for uniform handedness where the helixes have a 90 deg difference of rotations between two neighbor rows; otherwise, it presents as $H_2^{a,45}$, whose cross-section with a shift of 45 deg pitch angle becomes the right picture.

on a hexagonal lattice, the state of an antiferromagnetic system is frustrated. In what follows we choose a simple arrangement for the double-helical phase illustrated in Figure 6a, i.e., the cylinders with left-handed and right-handed helices are arranged on alternative rows, which is termed as H_2^aC (the "anti" is denoted by the superscript "a"). In addition, there is a rotational freedom for each cylinder in the helical superstructures. In our calculations, we consider a number of double and triple helical phases including the two freedoms of chirality and rotation. Here we just present the free-energy comparisons of four typical double-helical phases as examples.

For a given set of parameters, $\chi_{AC}N = 20$, $\chi N = 80$, and $f_A = 0.7$, the free-energy difference, $\Delta F = F_k - F_{H_2C}$ (k indicates the other three phases, $H_2^{90}C$, $H_2^{a,45}C$, or H_2^aC), clearly shows that the antiferromagnetic H_2^aC phase among the four phases is the most favorable, and the second favorable phase, $H_2^{90}C$, has slightly higher free energy (Figure 7). The phase of $H_2^{90}C$ has

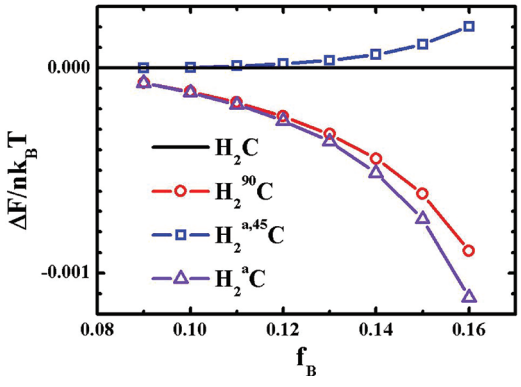

Figure 7. Free-energy of various double-helical supercylindrical phases, $H_2^{90}C$, $H_2^{a,45}C$, and H_2^aC, relative to H_2C, as a function of the volume fraction, f_B.

uniform chirality, but 90-deg rotation difference between neighbor rows of helical supercylinders. However, the free-energy difference between these phases is rather small, especially for relative small f_B. Similar to our previous results,[44] the free-energy difference between the helical phases with varying chirality and rotation is a second-order effective interaction between neighbor supercylinders, which is mainly induced by the packing of the chains.[34] This calculation provides a theoretical evidence for the observation of antiferromagnetic chiral arrangement in experiments.[32,34] Our further calculations suggest that similar conclusion can be made for the triple-helices, predicting an antiferromagnetic chiral arrangement (the H_3^aC phase).

IV. CONCLUSIONS

We have examined the formation and stability of supercylindrical phases, including quadruple/triple straight cylinders-on-cylinder, single/double/triple helices-on-cylinder, and rings-on-cylinder together with their competing phases of spheres-on-cylinder, perforated-lamella-on-cylinder, and core−shell cylinders, in frustrated ABC linear triblock copolymers. Careful comparisons of their free energy indicate that the double and triple helical phases are the stable supercylindrical phases, while the phases of single helix-on-cylinder, rings-on-cylinder, and quadruple/triple straight cylinders-on-cylinder, are metastable. The phase regions of the double/triple helical phases, surrounding by phases of spheres-on-cylinder, perforated-lamella-on-cylinder, and core−shell cylinder, are identified. Our results are well consistent with most of experimental observations of helical supercylinders, particularly with the most recent one by Jinnai et al.[34] The careful theoretical study is helpful to understand the self-assembling mechanism of these complex hierarchical phases, and is a useful guide for experiments to look for new phases, for example, the triple-helical supercylindrical phase.

The formation of the helical phases is induced by the mismatched lengths between the B- and C-cylinders because both of them have their preferred sizes for given parameters. Screwing B-cylinders around C-core-cylinder with a varying pitch angle is an efficient way to adjust the mismatched length ratio generally existing in the phases of straight cylinders. Through the analysis of the length ratio as well as the pitch angle, we find that the double and triple helical phases have similar capability on adjusting the length ratio, and thus their transition is very delicate, which has been shown by their tiny free-energy difference. Besides the major factor of the length ratio, there are two minor factors influencing the phase stability, i.e., the distribution and the shape of the B domains, which determine the uniformity degree of chain stretching. The role of the B-domain distribution arises from the constraint of the architecture topology that the polymer chain starting from A matrix has to go through B domains, and then enter C domain. When the helical phases have similar length ratio, the subtle competition between the two secondary factors determines their transition. This characteristics makes it more difficult to be

dx.doi.org/10.1021/ma2023952 | Macromolecules 2012, 45, 503−509

understood than those transitions among the helical phases in the system of cylindrically confined diblock copolymers.

In addition, we have examined the freedoms of handedness and rotation of these helical supercylinders arranged on the hexagonal lattice. By a simple arrangement of double-helical supercylinders with different chiralities, i.e., alternative rows of left-handed and right-handed helices, our calculations show that the introduction of antiferromagnetic chiralities onto neighboring helical supercylinders is preferred. In this case, the uniform rotation is most favorable, and this corresponding phase is referred as H_2^aC. In the other case of uniform chirality, $H_2^{90}C$ with a rotation difference of 90-degree on alternative rows of supercylinders is more stable than those with other values of rotation difference. However $H_2^{90}C$ consistently has slightly higher free energy than H_2^aC.

AUTHOR INFORMATION

Corresponding Author

*E-mail: weihuali@fudan.edu.cn (W.L.); fengqiu@fudan.edu.cn (F.Q.); shi@mcmaster.ca (A.-C.S.).

ACKNOWLEDGMENTS

This work is supported by the National Natural Science Foundation of China (Grants 20974026, 20990231), the National High Technology Research and Development Program of China (863 Grant No. 2008AA032101), and the Natural Science and Engineering Research Council (NSERC) of Canada. The computation was made by the facilities of SHARCNET (www.sharcnet.ca). Further computing resources were kindly provided by Dr. R. A. Wickham.

REFERENCES

(1) Chouaieb, N.; Goriely, A.; Maddocks, J. H. *Proc. Natl. Acad. Sci. U.S.A.* **2006**, *103*, 9398.
(2) Ho, R. M.; et al. *J. Am. Chem. Soc.* **2004**, *126*, 2704.
(3) Ho, R. M.; Chiang, Y. W.; Lin, S. C.; Chen, C. K. *Prog. Polym. Phys.* **2011**, *36*, 376.
(4) Ho, R. M.; et al. *J. Am. Chem. Soc.* **2009**, *131*, 18533.
(5) Wu, Y.; et al. *Nat. Mater.* **2004**, *3*, 816−822.
(6) Shin, K.; Xiang, H.; Moon, S. I.; Kim, T.; McCarthy, T. J.; Russell, T. P. *Science* **2004**, *306*, 76.
(7) Xiang, H.; Shin, K.; Kim, T.; Moon, S. I.; McCarthy, T. J.; Russell, T. P. *Macromolecules* **2005**, *38*, 1055−1056.
(8) Yu, B.; Sun, P.; Chen, P.; Jin, Q.; Ding, D.; Li, B.; Shi, A. C. *Phys. Rev. Lett.* **2006**, *96*, 138306.
(9) Li, W. H.; Wickham, R. A. *Macromolecules* **2006**, *39*, 8492.
(10) Feng, J.; Ruckenstein, E. *Macromolecules* **2006**, *39*, 4899−4906.
(11) Chen, P.; Liang, H. J.; Shi, A. C. *Macromolecules* **2007**, *40*, 7329.
(12) Sevink, G. J. A.; Zvelindovsky, A. V. *J. Chem. Phys.* **2008**, *128*, 084901.
(13) Kong, W. X.; Li, B. H.; Jin, Q. H.; Ding, D. T.; Shi, A. C. *J. Am. Chem. Soc.* **2009**, *131*, 8503.
(14) Wang, L. Q.; Lin, J. P. *Soft Matter* **2011**, *7*, 3383.
(15) Bates, F. S.; Fredrickson, G. H. *Annu. Rev. Phys. Chem.* **1990**, *41*, 525.
(16) Park, M.; Harrison, C.; Chaikin, P. M.; Register, R. A.; Adamson, D. H. *Science* **1997**, *276*, 1401.
(17) Park, C.; Yoon, J.; Thomas, E. L. *Polymer* **2003**, *44*, 6725.
(18) Bailey, T. S. *Morphological behavior spanning the symmetric AB and ABC block copolymer states*; Ph.D. Thesis, University of Minnesota, 2001.
(19) Abetz, V.; Simon, P. F. W. *Adv. Polym. Sci.* **2005**, *189*, 125.
(20) Matsen, M. W. *J. Chem. Phys.* **1998**, *108*, 785.
(21) Ranjan, A.; Morse, D. C. *Phys. Rev. E.* **2006**, *74*, 011803.
(22) Tyler, C. A.; Qin, J.; Bates, F. S.; Morse, D. C. *Macromolecules* **2007**, *40*, 4654.
(23) Guo, G.; Zhang, G.; Qiu, F.; Zhang, H.; Yang, Y.; Shi, A. C. *Phys. Rev. Lett.* **2008**, *101*, 028301.
(24) Rasmussen, K. Ø.; Kalosakas, G. J. *J. Polym. Sci., Part B: Polym. Phys.* **2002**, *40*, 1777.
(25) Tzeremes, G.; Rasmussen, K. Ø.; Lookman, T.; Saxena, A. *Phys. Rev. E.* **2002**, *65*, 041806.
(26) Fredrickson, G. H. *The Equilibrium Theory of Inhomogeneous Polymers*; Oxford University Press: Oxford, U.K., 2006.
(27) Auschra, C.; Stadler, R. *Macramolecules* **1993**, *26*, 2171.
(28) Stadler, R.; Auschra, C.; Beckmann, J.; Krappe, U.; Voigt-Martin, I.; Leibler, L. *Macromolecules* **1995**, *28*, 3080.
(29) Krappe, U.; Stadler, R.; Voigt-Martin, I. *Macromolecules* **1995**, *28*, 4558.
(30) Zheng, W.; Wang, Z. G. *Macromolecules* **1995**, *28*, 7215.
(31) Breiner, U.; Krappe, U.; Abetz, V.; Stadler, R. *Macromol. Chem. Phys.* **1997**, *198*, 1051.
(32) Elbs, H.; Abetz, V.; Hadziioannou, G.; Drummer, C.; Krausch, G. *Macromolecules* **2001**, *34*, 7917. Elbs, H.; et al. *Macromolecules* **2002**, *35*, 5570.
(33) Ludwigs, S.; Schmidt, K.; Stafford, C. M.; Amis, E. J.; Fasolka, M. J.; Karim, A.; Magerle, R.; Krausch, G. *Macromolecules* **2005**, *38*, 1850.
(34) Jinnai, H.; Kaneko, T.; Matsunaga, K.; Abetz, C.; Abetz, V. *Soft Matter* **2009**, *5*, 2042.
(35) Tang, P.; Qiu, F.; Zhang, H. D.; Yang, Y. L. *Phys. Rev. E.* **2004**, *69*, 031803.
(36) Sun, M. Z.; et al. *Phys. Rev. E.* **2008**, *77*, 016701.
(37) Shi, A.-C. *Development in Block Copolymer Science and Technology*; Hamley, I. W., Ed.; Wiley: New York, 2004).
(38) Sides, S. W.; Fredrickson, G. H. *Polymer* **2003**, *44*, 5859−5866.
(39) Frigo, M.; Johnson, S. G. FFTW: an adaptive software architecture for the FFT. *Proc. ICASSP* **1998**, *3*, 1381−1384.
(40) Abetz, V.; Goldacker, T. *Macromol. Rapid Commun.* **2000**, *21*, 16.
(41) The transition between C and CC phases is a continuous transition for varying B composition (not given in Figure 3). Even in the C phase, the B density is not uniform.
(42) Matsen, M. W.; Schick, M. *Phys. Rev. Lett.* **1994**, *72*, 2660−2663.
(43) Matsen, M. W.; Bates, F. S. *J. Polym. Sci., Part B: Polym. Phys.* **1997**, *35*, 945.
(44) Xu, Y.; et al. *J. Polym. Sci., Part B: Polym. Phys.* **2010**, *48*, 1101.

Macromolecules

Article

pubs.acs.org/Macromolecules

Exploring Lateral Microphase Separation in Mixed Polymer Brushes by Experiment and Self-Consistent Field Theory Simulations

Andrew D. Price,[†] Su-Mi Hur,[‡,§] Glenn H. Fredrickson,[‡,§,∥] Amalie L. Frischknecht,[†] and Dale L. Huber*[,†]

[†]Center for Integrated Nanotechnologies, Sandia National Laboratories, Albuquerque, New Mexico 87185, United States

[‡]Department of Chemical Engineering, [§]Materials Research Laboratory, and [∥]Department of Materials, University of California, Santa Barbara, Santa Barbara, California 93106, United States

Supporting Information

ABSTRACT: Similar to block copolymers, mixed polymer brushes are physically constrained and, upon annealing, microphase separate into nanodomains with morphologies largely dependent on the volume fractions of the polymers. A combination of experimental analysis of polystyrene (PS)/poly(methyl methacrylate) (PMMA) brushes and self-consistent field theory (SCFT) simulations is employed to determine the phases of annealed binary brushes. By annealing the brushes under conditions that maximize lateral versus vertical separation, a rich array of phases are observed with general agreement to predictions by SCFT simulations. The incorporation of random perturbations to the grafting density in SCFT simulations accounts for disorder in the arrangement of the polymer domains for the PS/PMMA brushes. Additionally, autocorrelation of the polymer domains yields an experimental domain spacing that is nearly 2 times greater than SCFT predictions, which is hypothesized to result from polydispersity in the PS/PMMA brushes. These findings should provide a basis for the improved fabrication of nanopatterned mixed polymer brushes with implications for the enhancement of biological surfaces, membranes, and nanolithography.

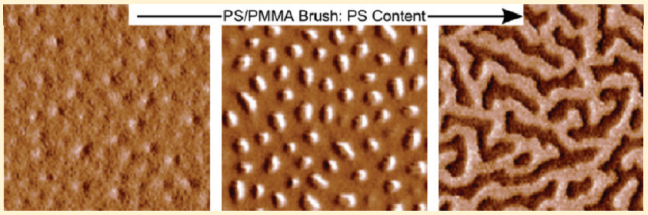

INTRODUCTION

Patterning surfaces by the self-assembly of polymers allows a high-throughput and inexpensive means for creating feature sizes below those easily accomplished by conventional photolithography.[1−10] Such nanoscale patterning can be achieved by spatially limited phase separation of two or more immiscible polymers. When macroscopic phase separation is prevented through the connectivity of the polymer molecules, the system compensates by arranging the polymers into ordered nanodomains to minimize the energy of the system.[11,12] This "microphase separation" has been definitively demonstrated with block copolymer systems by experiment, analytical theory, and simulation.[1,2,5,6,8−10,12−16] Selective deposition of materials into block copolymer patterns creates nanopatterned surfaces with electronic, biological, and membrane applications and is even being applied to the manufacture of computer chips.[2,10,17−20] The research possibilities and commercial promise of block copolymer lithography is substantial, but the need to coat surfaces with the copolymers using physical means (typically spin-coating) creates limitations. For example, block copolymers can be problematic when patterning nonplanar surfaces or creating composites where the polymer layer is a component of the final, permanent structure. Additionally, the directed assembly of block copolymers into complex geometries, such as sharp bends, is limited by energetically unfavorable polymer stretching except with the added complexity of a ternary system.[8] A complementary patterning technique that does not rely on the physical deposition of block copolymers has the potential to overcome such drawbacks.

As an alternative to block copolymers, the microphase separation of binary polymer brushes has been investigated.[21−26] Similar to block copolymers, immiscible polymers are limited to microphase separation by covalent linkages, in this instance by their attachment to the substrate surface. As polymer brushes can create dense and stable polymer coatings, they have been frequently investigated for surface modification of nanoparticles and planar substrates for use in biological systems, membranes, chromatography supports, and antifriction surfaces.[27−29] When applied as mixed brushes, they may become environmentally responsive whereby one polymer is attracted to the free surface while the other collapses away from it.[23,30−32] Properties including wettability, adhesion, and biocompatibility are largely dependent upon the polymer component at the free surface. On the other hand, lateral phase separation of mixed polymer brushes may occur when the surface is not selective for either polymer during annealing.[21,25,26] A number of theoretical and computational studies have predicted the equilibrium structure of phase-separated mixed polymer brushes as a function of factors such as grafting density, solvent selectivity, and polymer volume fraction, yet

Received: November 21, 2011
Published: December 12, 2011

scant evidence in the literature demonstrates experimental agreement with simulation.[24,26,32,33] Here, we aim to explore the phases in laterally segregated mixed brushes by minimizing polymer selectivity under annealing conditions, i.e., by minimizing the tendency for vertical segregation.

A combination of both vertical and lateral phase separation in binary polymer brushes occurs in response to solvent selectivity and is mediated by asymmetry in polymer chain lengths and grafting densities. Binary brushes of poly(methyl acrylate) (PMA) and poly(styrene-*co*-2,3,4,5,6-pentafluorostyrene) (PSF) vertically segregate in response to selective solvents with notable lateral segregation of PMA into depressions when PSF is selected for.[21] Nanomechanical mapping of the surfaces confirmed lateral segregation of the two polymers. A subsequent study by Minko and co-workers demonstrated the appearance of a ripple phase when polystyrene (PS)/poly(methyl methacrylate) (PMMA) brushes were exposed to a nonselective solvent.[34] Plasma etching of the PMMA component confirmed that the lateral segregation remained well into the polymer layer. Rühe and co-workers also examined PS/PMMA brushes showing laterally segregated domains when exposed to a nonselective solvent.[25] The proportion of PMMA vs PS measured at the top surface by AFM roughly corresponds to volume fractions of the polymers when the molecular weight and grafting density of the PMMA fraction are varied. The polymer domains exhibited a "memory" due to local fluctuations in brush composition with domain switching being harnessed to induce nanomotion in nano-objects.[35−37] Similar responsive surfaces were prepared by Zhao and co-workers with a narrow polydispersity by growing polymers from the surface via living radicals.[38] Despite addressing polydispersity, such brushes were typically thin and composed of low-molecular-weight polymers perhaps limiting their segregation potential. These studies give glimpses into the domain structure of mixed polymer brushes, but as discussed by Zhao and Zhu, the challenges of sample preparation and analysis have left the phase morphologies of mixed polymer brushes largely unexplored experimentally.[39]

Both theory and simulation have been used to study phase separation in grafted binary brushes. The behavior of ideal binary brushes with uniform grafting densities has been fairly comprehensively explored using field theoretic models and in particular self-consistent field theory (SCFT).[22,24,23,26] The most recent of these studies include calculations of the phase behavior of mixed brushes in both nonselective[24] and selective solvents[23,26] and a recent calculation for the phase behavior of a mixed brush in the melt state with no solvent.[40] In the melt or in nonselective solvent, a symmetric 50−50 mixture of two grafted homopolymers of equal molecular weight results in lateral phase separation of the brush into a "ripple" phase, with domains of each polymer extending in one lateral direction. More asymmetric compositions lead to various hexagonally packed or checkerboard phases. The SCFT results for brushes with uniform grafting density all exhibit a high degree of long-range order, similar to that seen in block copolymer thin films but not seen to date in mixed polymer brushes. Monte Carlo[41,42] and single-chain-in-mean-field[36,43] simulations have demonstrated that fluctuations in grafting density lead to a loss of long-range order in the laterally phase-separated morphologies.

Here, we explore the phase morphologies of PS/PMMA binary brushes when annealed under nonselective conditions using experiment and simulation. A free radical approach is used to grow the polymer brushes with the polymer volume fraction systematically varied by manipulation of the grafting density of the constituent polymers. The observed phases are compared with those predicted by full three-dimensional SCFT calculations assuming melt conditions. With a careful approach to brush preparation and annealing, we demonstrate that, similar to block copolymers, binary polymer brushes may self-assemble into different phases.

MATERIALS AND METHODS

Materials. Silicon wafers (Silicon Quest International) were test grade P-type, CZ silicon doped with boron. 2,2′-Azobis(2-methylpropionitrile) (AIBN, Aldrich, 98%) and 4,4′-azobis(4-cyanovaleric acid) (ACVA, Aldrich, ≥98%) were recrystallized twice from methanol. Methyl methacrylate (Aldrich, 99%) and styrene (Aldrich, ≥99%) were distilled under reduced pressure to remove inhibitor. Methylene chloride (Fisher, Certified ACS) and triethylamine (Alfa Aesar, ≥99%) were distilled from calcium hydride and stored over 3 Å molecular sieves. 1,4-Dioxane (Acros, 99.8%, extra dry), chloroform (Fisher, Certified ACS), thionyl chloride (Aldrich, 99.5%), tetrahydrofuran (THF, Fisher, HPLC), toluene (Fisher, Optima), heptane (Aldrich, 99.8%) benzene (Aldrich, 99.8%), and 3-aminopropylmethyldiethoxysilane (APMDES, Gelest) were used as received. Deionized water had a resistivity of greater than 18.2 MΩ·cm.

Methods. IR data were obtained using a Bruker IFS 66v/S FTIR in KBr. Growth from the surface was measured using a Nanofilm EP3 imaging ellipsometer operating with an internal solid-state laser at 532 nm and angle of incidence of 70°. Results were obtained from three different spots on the wafer with four measurements per spot. The refractive index was taken as 1.49 for PMMA and 1.59 for PS with the number varied according to the composition of the mixed polymer brush. The refractive indices for APMDES and ACVA were taken as 1.43 and 1.45, respectively. A liquid cell attachment was used for measuring the polymer brush swelling to THF vapor. The cell was used with an angle of incidence of 60° and attached to a temperature-controlled reservoir of THF and an empty syringe for drawing the vapor into the flow cell.

The phase and height morphologies of the polymer brushes were characterized by an Asylum MFP3D atomic force microscope (AFM). Tapping mode images were acquired with a silicon cantilever (Nanosensors) with a resonance frequency of ∼330 kHz, a force constant of ∼42 N/m, and a tip radius of less than 7 nm. All measurements were taken in the repulsive region of the Lennard-Jones interaction force curve (phase <90°). Instrument software and ImageJ were used for image analysis including a radically averaged autocorrelation macro for ImageJ.[44] The roughness of the surface as root-mean-square deviation from the mean plane (rms) was calculated over an area of 4 μm^2. Further characterization of the polymer brushes was taken on a high-resolution scanning electron microscope from the FEI Co. (Nova 600 Nanolab) using a electron beam voltage of 5 kV. Prior to imaging, the samples were stained with ruthenium(IV) tetraoxide to enhance contrast between the polymers.

Polymer molecular weight and polydispersity were measured by gel permeation chromatography (GPC) against polystyrene standards using THF as the mobile phase. A universal calibration was employed for the measurement of PMMA molecular weights using previously determined Mark−Houwink parameters.[54] The column was a Waters HR4 operated at room temperature with a flow rate of 1 mL/min. Polymers were detected using a refractive index detector with the addition of a fluorescence detector for PS (ex = 254 nm, em = 354 nm).

Amination of Silicon Surface. A 3 in. silicon wafer was rinsed with acetone and water then treated by piranha solution (concentrated H_2SO_4, 30% H_2O_2, 7/3 v/v) at 80 °C for 1 h. Subsequently, the wafer was rinsed extensively with water, dried under a stream of N_2, and exposed to UV/O_3 for 30 min. The silicon wafer was rinsed once more with water (to hydrate the surface) and dried for 5 min at 110 °C before silane deposition. A silane coating was applied to the wafer by exposing the wafer to APMDES vapor for 16 h. The wafer was

Scheme 1. Synthesis of PS/PMMA Mixed Brushes[a]

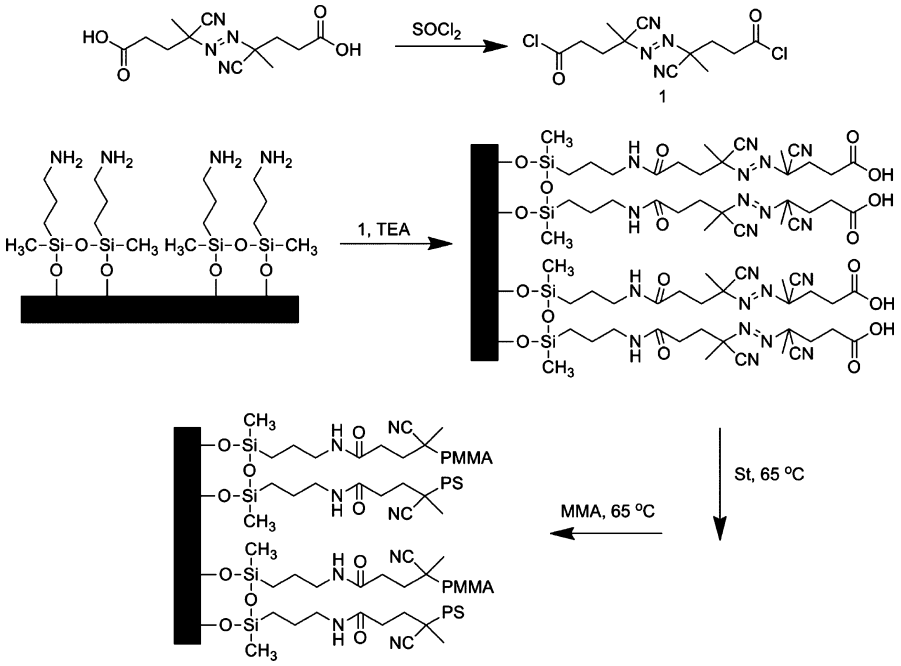

[a]The free radical initiator, ACVA, is converted into its acid chloride (**1**) by treatment with thionyl chloride. The initiator is covalently attached to a silicon surface by reacting with surface bound aminopropylsilanes in the presence of triethylamine (TEA). Styrene (St) is polymerized from the surface by thermal initiation of the immobilized ACVA. Subsequently, methyl methacrylate (MMA) is polymerized from noninitiated ACVA, forming a mixed brush of PS and PMMA.

suspended ~3 in. above a reservoir of APMDES in a vacuum chamber evacuated to a pressure of 100 mTorr. The silane coating was annealed for 30 min at 110 °C under vacuum and then rinsed with acetone, isopropanol, and water to remove noncovalently linked silane.

Initiator Attachment. 1.00 g of ACVA was dispersed into 25.0 mL of CH_2Cl_2 under an atmosphere of argon. To this mixture was added 2.5 mL of $SOCl_2$ and refluxed in a 40 °C oil bath until all solids were dissolved (~12 h). The initiator was recovered by removal of the liquid under reduced pressure, affording a light yellow solid. This was purified by recrystallization from heptane, yielding a white solid. Complete conversion of the carboxylic acid to acid chloride was confirmed by measuring the shift in the peak infrared adsorption of the carbonyl from 1712 to 1797 cm^{-1}. The aminated silicon was cut into 1 × 0.5 in. pieces and added to a solution of 32 mM of the acid chloride of ACVA in CH_2Cl_2. A catalytic amount of triethylamine was added, and the chip was sealed under an atmosphere of argon. The chip was slowly shaken at 320 rpm for 16 h to covalently attach the initiator to the aminated surface. To remove unbound initiator, the chip was rinsed with CH_2Cl_2, sonicated briefly in *N*,*N*-dimethylformamide, and finally rinsed with acetone, water, and isopropanol.

Surface-Initiated Polymerization. A solution of styrene in 1,4-dioxane (30% v/v styrene) containing AIBN varying between 0.6 and 3.0 mM was degassed by three cycles of freeze/pump/thaw. The monomer solution was added to a thick-walled glass vial containing the chip with immobilized initiator in a helium-purged glovebox containing less than 0.1 ppm of O_2 and fitted with a Teflon-coated silicone septum. A slight vacuum was pulled over the solution, and the solution was heated to 65 ± 0.5 °C in an aluminum block to thermally initiate polymerization. Noncovalently attached polymer was removed from the chip by continuously extracting with CH_2Cl_2 in a Soxhlet extractor for 12 h. Free polymer was precipitated into methanol for characterization by GPC. A second polymerization was the carried out in methyl methacrylate to grow PMMA chains from noninitiated ACVA on the silicon surface. A solution of methyl methacrylate in 1,4-dioxane (20% v/v methyl methacrylate) containing AIBN varying between 0.6 and 3.0 mM was degassed by three cycles of freeze/pump/thaw. The monomer solution was added to a thick-walled glass vial containing the chip with polystyrene brush in a helium-purged glovebox containing less than 0.1 ppm of O_2 and fitted with a Teflon-coated silicone septum. A vacuum was pulled over the solution, and the solution was heated to 65 °C ± 0.5 °C in an aluminum block to thermally initiate polymerization. Noncovalently attached polymer was removed from the chip by continuously extracting with chloroform in a Soxhlet extractor for 12 h. Free polymer was precipitated into methanol for characterization by GPC.

Polymer Annealing. Binary polymer brushes were annealed by exposure to an atmosphere of saturated solvent vapor. The brush surfaces were placed in a chamber that was pumped down to a pressure of 20 mTorr. To the evacuated chamber a small quantity of solvent (THF, toluene, or benzene) was introduced, creating an atmosphere of saturated vapor. Polymer annealing proceeded for a minimum of 24 h. Prior to bringing the chamber back up to atmosphere, solvent vapor was pumped out of the chamber so no liquid solvent condensed on the brush surface. In some instances the brushes were further annealed at 130 °C for 48 h in a vacuum oven with a pressure of 23 in.Hg below atmosphere.

Self-Consistent Field Simulations. The phase behavior and morphologies of mixed binary brushes in the melt state were calculated using a field theoretic model introduced in our previous work.[40] The polymers are modeled as continuous Gaussian chains tethered to the substrate, which is modeled as a hard, impenetrable wall. We assume that the free surface is neutral to both polymers and that there is a large polymer−air surface tension and so also treat the free surface as a flat, hard wall. We consider n_A and n_B monodisperse A and B tethered homopolymers, with equal chain lengths N. The number fraction of A chains is f_A, where $n_A = f_A n$ and $n_B = (1 - f_A)n$, and n is the total number of chains. The system volume is $V = L_x L_y L_z = (\bar{L}_x R_g)(\bar{L}_y R_g)(\bar{L}_z R \times_g) \equiv \bar{V} R_g^3$, where R_g is the unperturbed (melt) radius of gyration of the A or B homopolymers. Length scales in the simulation results are in units of R_g. Throughout this work, the mixed brush is assumed to have a height of $L_z = 3R_g$. Since the system is a melt, the height fixes the overall grafting density. Periodic boundary conditions are employed in the plane of the brush in the x and y directions.

dx.doi.org/10.1021/ma202542u | *Macromolecules* 2012, 45, 510−524

We use a standard Gaussian-chain model with harmonic stretching energy for both chains. The interaction energy is modeled with a Flory-type local contact interaction between dissimilar A and B polymer segments, denoted by the Flory parameter χ. In addition to the harmonic stretching energy of the Gaussian chain and the segmental interaction energy, a penalty for local density fluctuations away from the average density ρ_0 is modeled using the compressible Helfand model, characterized by a stiffness parameter ζ. Throughout our calculations we set $\zeta N = 100$, so the brush is relatively incompressible. The SCFT free energy functional has the form

$$\beta F \propto \int_{\bar{V}} d\mathbf{r}\left[\frac{1}{\chi N} W_-{}^2(\mathbf{r}) - \frac{2\zeta N}{\chi N + 2\zeta N} iW_+(\mathbf{r})\varphi(\mathbf{r}) - \frac{1}{\chi N + 2\zeta N}(iW_+(\mathbf{r}))^2\right] - \bar{V}\bar{\varphi}f_A \int d\mathbf{x}_\perp \times \int dz g_A(\mathbf{x}_\perp, z) \ln Q_A(\mathbf{x}_\perp, z; [W_A]) - \bar{V}\bar{\varphi}(1 - f_A) \times \int d\mathbf{x}_\perp \int dz\, g_B(\mathbf{x}_\perp, z) \ln Q_B(\mathbf{x}_\perp, z; [W_A])$$

Here $\beta = 1/kT$ is the inverse temperature, Q_A and Q_B are the single chain partition functions for A and B chains, and $\varphi(\mathbf{r})$ is the total polymer segment density in the brush with spatial average $\bar{\varphi}$. Potential fields, W_A and W_B, that act on A and B segments, respectively, are defined as $W_A = iW_+ - W_-$ and $W_B = iW_+ + W_-$, where W_+ is a pressure-like field that couples with total density fluctuations and W_- is an exchange potential field that couples to composition fluctuations. Each chain is grafted at a location $\mathbf{x}_\perp$ in the plane of the substrate, while the brush extends in the z direction. The functions $g_A(\mathbf{x}_\perp,z)$ and $g_B(\mathbf{x}_\perp,z)$ are normalized grafted end distribution functions for the A and B chains, respectively. These functions can describe laterally uniform distributions of grafting points or grafting densities that vary across the substrate.

The stationary condition of the free energy functional is found using the mean-field approximation. In this work we solve the SCFT equations using a pseudospectral method. Two types of SCFT calculations are performed. To calculate the phase diagram of the melt brush, only one unit cell of the morphology of interest is included. The optimal lateral system size is determined by box relaxation, resulting in a system with negligible internal stress. The phase diagram is constructed by comparing the free energies of the candidate phases. To compare morphologies to experimental AFM images, we employed large cell SCFT calculations subject to random initial field configurations. A detailed derivation of the SCFT and a description of our numerical methods can be found in our previous work.[40,45]

RESULTS AND DISCUSSION

Polymer Brush Formation. Binary polymer brushes of polystyrene (PS)/poly(methyl methacrylate) (PMMA) are synthesized as a variation of published protocols.[21,25,46] Surface attachment of a free radical initiator (ACVA) allows the consecutive growth of two different polymers. Attachment to the silicon surface is accomplished by covalently linking the acid chloride of ACVA to the silicon surface functionalized with a primary amine-terminated silane (Scheme 1). Particular attention is focused on creating a highly uniform initiator layer to minimize variations in the polymer brush density that may disrupt the phase morphology. To create a uniform surface of attachment sites, vapor deposition of APMDES was chosen. Compared to solution-based deposition techniques, vapor deposition of silanes has been shown to produce surfaces of superior uniformity.[47−49] Because of the complex kinetics of silane attachment to surface silanols, even silanes that cannot self-polymerize (monoalkoxy- and monochlorosilanes) can create inhomogeneous surfaces when deposited from solution due in part to solution impurities and inefficient mass transport. Additionally, nonuniformity in silanol presentation on the silicon surface will manifest itself in the silane layer when monofunctional silanes are used. As trialkoxysilanes have a tendency to extensively polymerize, a dialkoxysilane was chosen to provide high density coverage of primary amines while minimizing polymerization of the silane. APMDES deposition reliably produced coatings of 1.3 ± 0.2 nm, corresponding to a multilayer of ∼2 molecules with an rms roughness of 1.8 Å, which is only a slight increase in roughness over the underlying silicon surface ($rms_{silicon}$ = 1.1−1.3 Å).

The acid chloride of ACVA creates a highly reactive species that reacts readily with primary amines, forming an amide bond (Scheme 1). Surface attachment chemistry is strongly influenced by the sterics of the reaction. Many schemes for joining a carboxylic acid to an amine in solution, such as an active ester intermediate, do not efficiently occur at a surface due to the bulk of the leaving group. Possessing little steric hindrance, the acid chloride intermediate provides an ideal leaving group chemistry and has been shown to be capable of reacting with nearly quantitative yield at a surface.[50] This approach is ideal for creating a dense and uniform coverage of the initiator, and ACVA attachment to the surface reliably creates an initiator layer of 1.2 ± 0.2 nm in thickness. Of potential concern is whether the initiator is attached to the surface by one or both ends as it is likely a combination of the two exists on the surface.[46,51] Initiators attached by only one end will have a molecular fragment liberated upon initiation, causing polymerization in solution in addition to the surface. Considering that free initiator is intentionally added to solution in our reaction scheme, this is not a concern here. There is also the potential that the attachment may affect the decomposition rate of the initiator. We do not explicitly investigate this but assume this is likely to have minimal if any effect on the decomposition rate of ACVA as attachment occurs a number of atoms away from the metastable azo group.

A "grafting from" approach is chosen for polymer brush synthesis as this method has proven amenable to the formation of dense brushes.[29,52] Significant interaction between adjacently grafted polymers is a prerequisite for phase separation and likely not achievable by a "grafting to" approach. A number of studies have already detailed the growth of polymer brushes via free radical and controlled radical polymerization, so our description will be brief.[21,25,29,52,53] Binary polymer brushes are formed by thermal initiation of surface-immobilized initiators in the presence of monomer solution. ACVA is reported to have a half-life of ∼10 h at 65 °C, though this number can vary significantly depending on the environment of the initiator.[54] Thermal control allows for a two-step process whereby a significant number of uninitiated ACVA remains on the surface following the first polymerization (styrene) to allow for a second polymerization in the presence of a different monomer (methyl methacrylate). The grafting density of each polymer was calculated by measuring the thickness of the dry brush and the molecular weight of the ungrafted polymer following each polymerization. The (unperturbed) radius of gyration (R_g) was calculated from $r_0/\sqrt{6}$, where r_0 is the polymer end-to-end distance and is calculated as

$$\frac{r_0}{\sqrt{M_n}} = 0.0670 \text{ nm} \quad \text{for polystyrene}$$

dx.doi.org/10.1021/ma202542u | Macromolecules 2012, 45, 510−524

Table 1. Properties of the Binary Polymer Brushes of PS and PMMA

sample	polymer	M_n (g/mol)	PDI (M_w/M_n)	R_g (nm)	measured thickness (nm)[a]	grafting density (chains/nm^2)	grafting distance (nm)	vol fraction PS
A	PMMA	174 400	1.64	10.91	26.34	0.11	3.43	0.00
	PS	137 300	1.66	10.14	1.77	0.01	12.50	
B	PMMA	170 500	1.66	10.79	32.07	0.13	3.07	
	combined				33.84	0.14	2.98	0.05
	PS	135 400	1.71	10.06	5.57	0.03	7.00	
C	PMMA	170 500	1.66	10.79	28.48	0.12	3.26	
	combined				34.05	0.15	2.96	0.16
	PS	135 800	1.75	10.08	11.00	0.05	4.99	
D	PMMA	172 400	1.66	10.85	27.47	0.11	3.34	
	combined				38.47	0.17	2.77	0.29
	PS	117 400	1.97	9.37	11.42	0.06	4.55	
E	PMMA	132 600	2.20	9.51	18.55	0.10	3.56	
	combined				29.97	0.16	2.81	0.38
	PS	116 000	1.74	9.32	14.49	0.08	4.01	
F	PMMA	91 200	2.02	7.89	15.00	0.12	3.29	
	combined				29.49	0.20	2.54	0.49
	PS	92 500	1.95	8.32	19.05	0.13	3.13	
G	PMMA	82 300	2.43	7.50	18.20	0.16	2.83	
	combined				37.25	0.29	2.10	0.51
	PS	120 900	1.78	9.51	15.76	0.08	3.93	
H	PMMA	101 600	1.76	8.33	11.43	0.08	3.97	
	combined				27.19	0.16	2.79	0.58
	PS	133 600	1.73	10.00	20.79	0.10	3.60	
I	PMMA	101 600	1.76	8.33	9.81	0.07	4.29	
	combined				30.60	0.17	2.76	0.68
	PS	124 000	2.04	9.63	14.47	0.07	4.15	
J	PMMA	133 100	2.23	9.53	12.89	0.07	4.28	
	combined				27.36	0.14	2.98	0.53
	PS	103 100	2.02	8.78	18.25	0.11	3.37	
K	PMMA	136 300	2.24	9.65	12.36	0.06	4.43	
	combined				30.61	0.18	2.68	0.60

[a]Thickness of the dried brush measured by ellipsometry.

$$\frac{r_0}{\sqrt{M_n}} = 0.0640 \text{ nm} \quad \text{for poly(methyl methacrylate)}$$

where M_n is the number-average molecular weight of the polymer.[54] Following the method of Lemieux et al., grafting density (D, chains/nm^2) is calculated as

$$D = \frac{\rho t N_a}{M_n \times 10^{21}}$$

where t is thickness of the dry brush layer, N_a is Avogadro's number, and ρ is polymer density (ρ = 1.05 g/cm^3 for PS and ρ = 1.19 g/cm^3 for PMMA). The average distance between grafting points (l, nm) is calculated as $l = 2/(\pi D)^{1/2}$.[21] The properties of the polymer brushes presented in this paper are given in Table 1. As the grafting distances of the polymers are significantly less than their R_g values, it is clear that all of the samples are in the brush regime.

The dry brush thickness of polystyrene grown in monomer solution containing 1.8 mM free initiator is plotted versus polymerization time in Figure 1. Brush growth occurs nearly linearly at first, but around 20 h it begins to plateau. As monomer is in large excess, this result seems to indicate a depletion of initiator on the surface. However, if the sample is thoroughly washed by Soxhlet extraction in dichloromethane, brush growth continues when remaining surfaces initiators are activated. This phenomenon has been investigated and was explained by dividing the brush growth into two regimes.[53] In the first, polymer growth occurs via conventional brush growth from the surface. At a sufficient surface density, it is speculated that hindered mobility close to the surface increases the polymerization rate due to the Trommsdorff effect.[53] Nongrafted polymer forms a dense multilayer coating creating a large steric barrier to monomer addition. Removal of nongrafted polymer by Soxhlet extraction permits brush formation to continue.

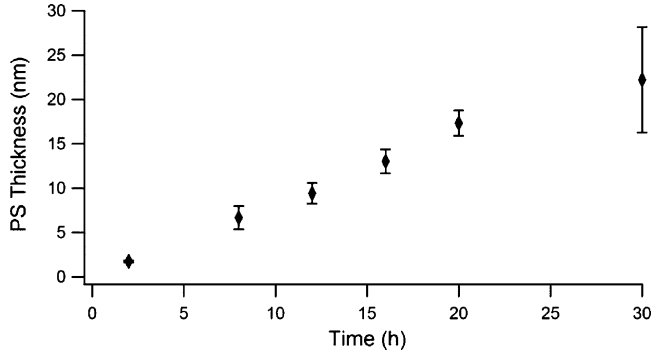

Figure 1. Dry brush thickness of polystyrene grown from the surface with attached initiator. Polymerization conditions: 30% styrene in 1,4-dioxane (v/v), 1.8 mM AIBN, 65 °C.

dx.doi.org/10.1021/ma202542u | Macromolecules 2012, 45, 510−524

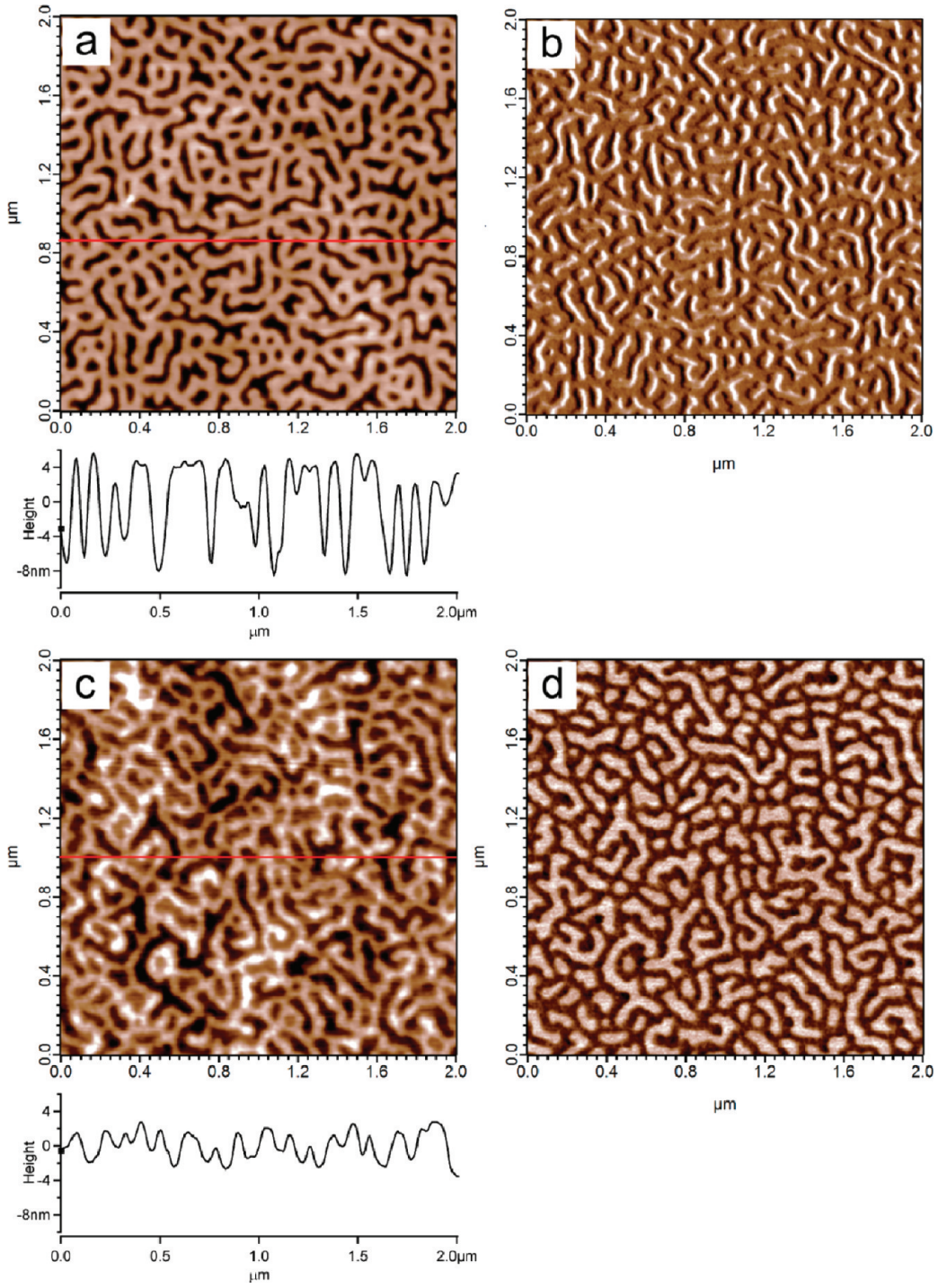

Figure 2. AFM (a) height and (b) phase images of sample G after annealing in THF vapor for 24 h. AFM (c) height and (d) phase images of the same sample subsequently heat annealed at 130 °C for 48 h. The red line in the height images indicates the cross-sectional height measurements of the accompanying graphs (phase range: b, 8°; d, 5°).

We would also like to comment on the addition of free initiator to monomer solution. In agreement with previous investigations, free initiator was necessary for brush growth. It is speculated that free initiator "mops up" trace impurities that inhibit polymerization.[55] The free initiator also serves to limit the molecular weight of the polymers by creating a constant source of free radicals.[31] Though large polymers are strongly segregating, they will also be highly entangled in the brush and significantly extend the annealing time. It is usually assumed that the molecular weight of the surface-bound polymers will be equivalent to those in solution.[51,53] We follow this assumption here as polymers growing on the surface are expected to terminate by the same mechanism as those grown in solution (i.e., by reaction with bulk free radicals or transfer to monomer or solvent molecules). Reaction with the surface or surface bound radicals is expected to be insignificant by comparison.

Polymer Annealing. Annealing provides the chain mobility necessary for incompatible polymers to demix. As the polymers are covalently linked to the surface, equilibrium will be reached where the entropy of mixing is balanced by chain

dx.doi.org/10.1021/ma202542u | *Macromolecules* 2012, 45, 510−524

stretching. An ideal anneal for lateral segregation occurs when the top surface of the brush is not selective for one of the two polymers. Under melt conditions, the surface tensions of PS and PMMA are relatively similar, so we adopt a procedure of heating the brush above its glass transition temperature while under a vacuum. In block copolymer thin films, the solid interface is often preferential to one of the components, creating a vertically segregated film.[1] To overcome this, the solid surface is often functionalized to create a nonpreferential interface (e.g., a random copolymer of identical chemistry to the thin film).[56−58] In binary polymer brushes, the covalent linkages create a mixture of the polymers at the surface whose surface energy resembles that of a random copolymer of the two components. Therefore, we do not expect the solid surface to be significantly preferential toward one of the polymers.

Following Soxhlet extraction in chloroform, binary brushes of PMMA and PS are analyzed by AFM, which shows a relatively flat topography with little phase differentiation (see Supporting Information). It is likely that either the polymers are vertically segregated or sufficiently mixed so that only minor evidence of segregation is observed. Initially, the brushes were annealed above their glass transition temperatures (T_g) in a 150 °C vacuum oven for 72 h. Interestingly, we observe a combination of microphase and macrophase separation of the polymer brush, leading us to conclude that some polymers are cleaved from the surface (see Supporting Information). The samples were subsequently washed by Soxhlet extraction with chloroform. Ellipsometric measurements confirmed a decrease in dry brush thickness by 10−30%, confirming detachment of some polymer. To our knowledge, this phenomenon has not been observed in previous studies. We speculate that during annealing local polymer stretching during demixing exceeds the bond energies in some instances, causing the breakage. The most likely points for this are the Si−O bonds anchoring the polymer to the surface though we cannot rule out scission within the polymer. We chose to defer an in depth investigation of this to future studies and overcome this obstacle by annealing the polymer brush with solvent vapor.

The addition of solvent molecules to polymer thin films increases the internal free volume until a critical polymer fraction is reached where the T_g is lowered below the ambient temperature.[59,60] The plasticizing effect of the solvent is expected to allow the polymer to anneal without becoming detached from the surface. Unlike annealing in liquid solvent, vapor will not leave drying artifacts and creates an environment that is more reminiscent of a melt than would occur in brushes highly swollen with solvent (i.e., brushes swollen in saturated solvent vapor are less than 1/2 the thickness of those solvated by liquid solvent). We chose a series of nonselective, good solvents for PS and PMMA (toluene, THF, benzene) for annealing to minimize the preference of the free surface and vertical segregation of the brush. In practice, a solvent will always have, to some extent, a preference for one polymer in a mixture as determined by the Flory−Huggins interaction parameter.[61,62] Under saturated THF vapor, PS and PMMA brushes were measured to swell by 69 ± 12% and 116 ± 11%, respectively, corresponding to a respective polymer fraction of 0.59 and 0.46. Under these conditions the polymer brush is expected to achieve the critical solvent fraction necessary to lower its T_g below room temperature while still being significantly less swollen than similar polymer brushes saturated with liquid solvent.[59,60]

Polymer brush samples were annealed in saturated THF vapor for 24 h and analyzed by AFM (Figure 2). Domains in both the topography and phase contrast (a measure of material properties) images are clearly evident. The morphology of the domain structure is in part dependent on the volume fraction of the comprising polymers and will be discussed in detail below. A striking result is the rather large height difference between the domains. In Figure 2a, PS domains (dark) are measured as depressions in a PMMA (light) continuous phase with an rms roughness of 4.40 nm. Localized heights following the red line are shown in the accompanying graph. Phase contrast between PS (light) and PMMA (dark) is also observed though artifacts at the edges of the domains are a result of the rather abrupt height differences. This height difference is not surprising as solvent becomes nearly irreversibly trapped in polymer films when it is dried to the point where it vitrifies.[60] From the measurements above we see that PMMA swells to a greater extent than PS, demonstrating its increased capacity for THF. It follows that upon drying PMMA will contain a greater amount of entrapped THF than PS assuming both polymers vitrify at similar polymer fractions, accounting for its greater thickness in the dried brush. Ideal lateral segregation assumes a perfectly flat free surface. The effect surface undulations have on domain morphology structure is unknown, but leveling of the brush surface does not appear to significantly alter the domain morphology (Figure 2c,d). Heating vapor annealed brushes above their T_g softens the polymer structure, allowing some entrapped solvent to be released. Indeed, we observe flatter topography with an rms roughness of 1.44 nm (Figure 2c), following an additional heat anneal at 130 °C for 48 h. Localized heights following the red line are shown in the accompanying graph. Additionally, the smoother brush eliminates artifacts in the phase image, allowing us to visualize discrete boundaries between microphase separated PS and PMMA (Figure 2d). Unlike heating the brush from a mixed state, heating the brush above the T_g of its components following vapor annealing does not cause polymer scission. It is probable that equilibrium domain structures have already been reached, and the heat simply enables the escape of trapped solvent and segmental rearrangements to flatten the surface. On the other hand, exposing the brush to a different solvent vapor causes reorganization of the nanodomains (as discussed below).

SCFT Phase Diagram. Previous SCFT investigations of mixed brushes have mostly focused on phase behavior in various solvents, both nonselective and selective.[24,23,26] Although our samples are solvent vapor annealed, the final morphology after the subsequent heat annealing is likely to be closer to the equilibrium melt morphology than to the morphology corresponding to exposure of the brush to liquid solvent. In particular, the rms roughness of the vapor and heat annealed brushes is much less than previously investigated, solvent-annealed brushes.[34] Therefore, we feel it is more appropriate to compare the experimental phase morphology to that of a melt mixed brush. We previously calculated the first mean-field phase diagram, showing phases as a function of f_A and χN, for a melt mixed polymer brush.[40] An extension of this phase diagram to $\chi N = 20$ is shown in Figure 3. We have assumed that the two grafted polymers have equal degrees of polymerization N, that the grafting density of both chains is uniform, and that the height of the brush is $3R_g$. The PS/PMMA brushes studied here approximately conform with these assumptions; in particular, the heights of the brushes are about $3R_g$ (see Table 1). The phases shown were calculated using unit

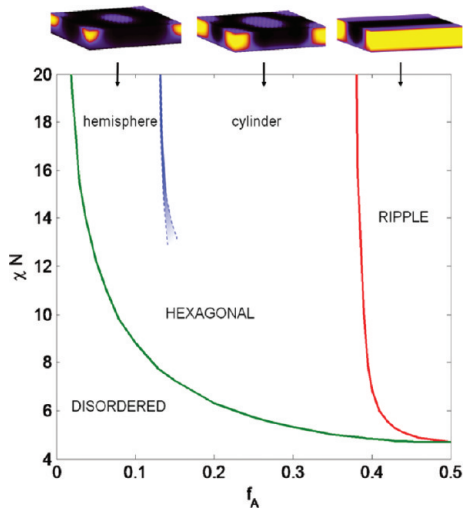

Figure 3. Mean-field phase diagram of the A–B mixed polymer brush as a function of the fraction of grafted A chains, f_A, and the segregation force, χN. Density profiles show the morphologies of the indicated phases. The width of the blue transition line between cylinders and hemispheres indicates the uncertainty in the location of this transition. (Adapted from Figure 1 in ref 40 with additional data.)

cell calculations and represent the equilibrium SCFT phases. Note that the phase diagram is symmetric about $f_A = 1/2$, and so only half is shown in Figure 3.

At low χN and for small f_A, the brush is in a mixed, disordered state. Above the order–disorder transition at $\chi N = 4.69$, the mixed brush laterally phase separates into a variety of phases depending on f_A. These phases are similar to those found in block copolymer thin films, although with some important differences. For symmetric compositions near $f_A = 1/2$, the brush forms a "ripple" phase, with A- and B-rich domains alternating in one lateral direction while the brush is uniformly homogeneous in the other direction. As the composition becomes more asymmetric, the morphology changes to hexagonally packed cylinders of the minority phase, with a first-order phase transition between the ripple phase and the cylindrical phase. In this phase, the cylinders extend throughout the brush nearly to the grafting surface (see inset to Figure 3). For smaller f_A, the morphology changes to a phase of hexagonally packed "hemispheres", in which the minority domain does not extend to the grafting surface but instead forms a hemispherical domain near the top of the brush. This phase is analogous to the spherical phase in diblock copolymers. However, the transition from cylinders to hemispheres is different in the mixed brush. At low χN, this transition is gradual, and there is apparently no thermodynamic transition between the two morphologies. As indicated in the phase diagram, our simulations suggest there is a critical point near $\chi N = 14$. For χN larger than the critical point, there is a weakly first-order transition between the cylinder and hemisphere phases.[40]

SCFT calculations above $\chi N = 20$ become increasingly difficult numerically. However, as in diblock copolymers, the mixed brush exhibits phase transitions which change little in f_A at large χN, so we expect the various transitions to be located at nearly the same values of f_A for the experimental systems. At $\chi N = 20$, the transitions are near $f_A = 0.019$ (disordered to hemispheres), $f_A = 0.13$ (hemispheres to cylinders), and $f_A = 0.38$ (cylinders to ripple).

Experimental Phase Morphology. A series of binary polymer brushes of PS and PMMA are prepared, systematically varying their grafting densities. We are therefore able to investigate the effect of the polymer volume fraction on the equilibrium phase morphology of PS/PMMA brushes following annealing. AFM phase images of annealed brushes with PS volume fractions increasing from 0 to 0.68 (samples A–I) are presented in Figure 4. The overall trend is not simply an increase in the amount of PS (light color) at the surface, but a rich array of phases. Of particular significance is a strong qualitative similarity between phases observed by experiment and those predicted by SCFT simulations. In this section we will detail characteristics of the phases observed, some of which deviate from the SCFT predictions but many of which are accurately predicted by our simple model. In later sections we will try to account for some of the differences.

The segregation force, χN, driving phase separation is quantitatively determined by the Flory–Huggins interaction parameter, χ, and the degree of polymerization, N. As just discussed, below a critical χN the polymer brush is expected to remain well mixed in a disordered phase regardless of the volume fraction of each polymer. Experimentally, the χN of our system, which ranges from 25 to 40, is well above the predicted value needed to cause phase separation. A disordered phase is also predicted when the fraction of one of the polymer components is very small. Experimentally, the disordered phase should be indistinguishable from a polymer brush composed solely of the dominant polymer as in Figure 4a, a PMMA brush. The large χN of our system quickly transitions the polymer brush into phase segregated domains with only small percentages of a mixed component.

Overall, the phase morphology of Figure 4 can be coarsely divided into round and elongated domains, i.e., the cylindrical (or hemispherical) and ripple phases, respectively. Figure 4b–e, with PS fractions increasing from 0.05 to 0.38, exhibits characteristics of the cylindrical and hemispherical phases. The transition between the two is a consequence of the local availability of the minority polymer. In Figure 4b,c, dimples in the phase images lack the contrast of the prominent circular features in Figure 4e. Figure 4d shows both features in coexistence. Hemispheres which contain significantly less PS than cylinders that extend the entire brush thickness could easily account for this difference in phase measurements. To gain a better look at the domains, the samples of Figure 4b,c,e are stained using ruthenium tetraoxide and imaged with SEM (Figure 5a,b,c, respectively). The ruthenium is known to selectively stain PS in mixtures with PMMA providing enhanced contrast.[63] However, the staining swells the PS domains possibly adding some degree of distortion to brush morphology. The hemispherical domains are clearly visible in Figure 5a,b with an apparent increase in size as PS fraction is increased from 0.05 to 0.16. The hemispheres do not show the clear-cut contrast of the cylindrical domains of Figure 5c with a PS fraction of 0.38.

In addition to the apparent existence of hemisphere and cylinder domains, a few other observations are worth mentioning. For PS fractions of 0.05 and 0.16 (samples B and C) few cylindrical domains appear over an area predominantly composed of hemispherical domains. We believe this is due to a local enrichment in PS from fluctuations in polymer grafting density and/or polydispersity. These disparities are less apparent for higher PS fractions when localized fluctuations are largely absorbed into the overall

dx.doi.org/10.1021/ma202542u | Macromolecules 2012, 45, 510–524

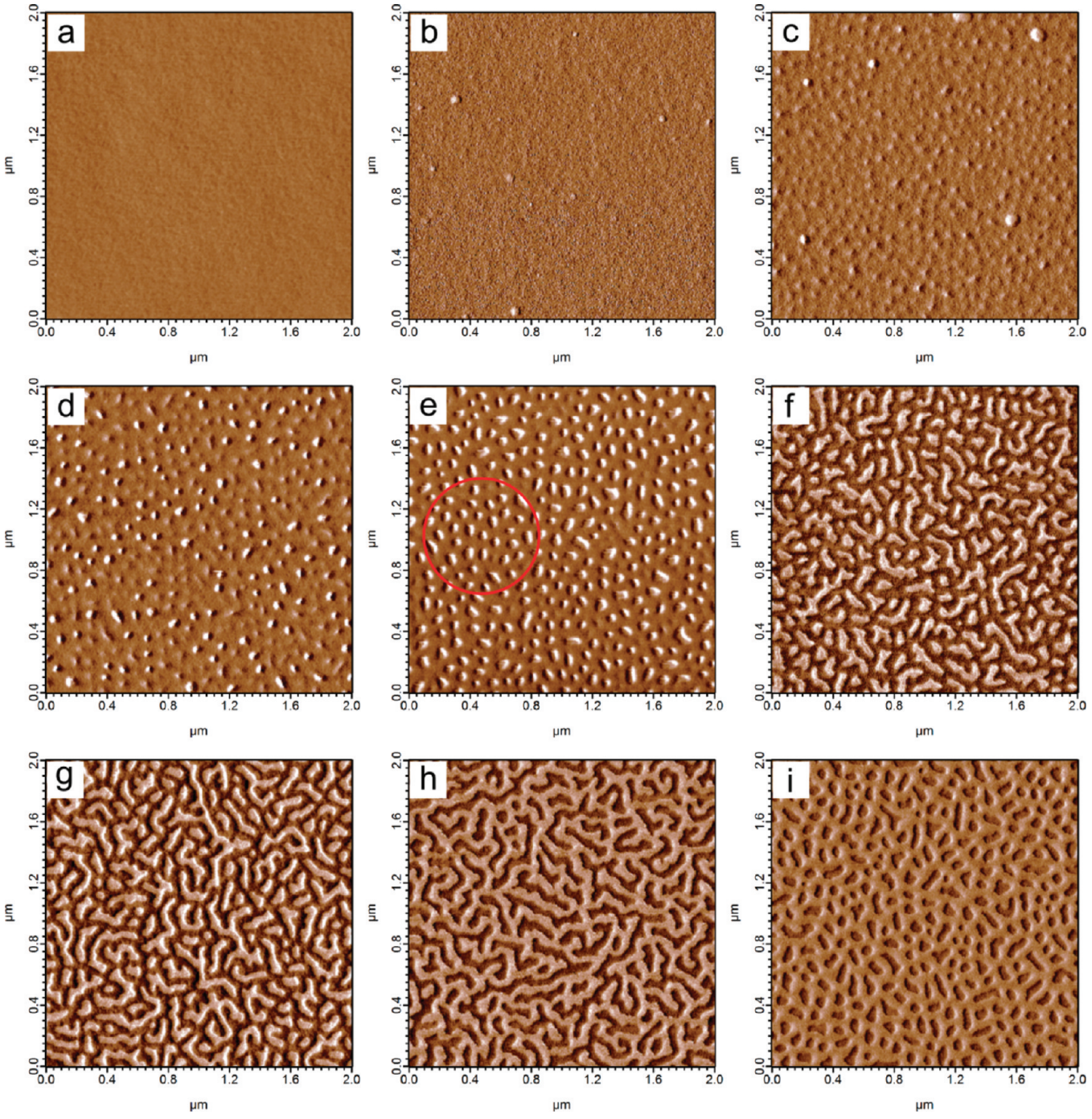

Figure 4. AFM phase images of polymer brushes annealed by THF vapor for 24 h followed by a heat anneal at 130 °C for 48 h. The PS volume fraction, sample, and phase ranges are as follows: (a) 0, sample A, 8°; (b) 0.05, sample B, 6°; (c) 0.16, sample C, 6°; (d) 0.29, sample D, 6°; (e) 0.38, sample E, 6°; (f) 0.49, sample F, 6°; (g) 0.51, sample G, 5°; (h) 0.58, sample H, 5°; (i) 0.68, sample I, 6°. The red circle in (e) outlines an area suggesting hexagonal ordering of the PS domains.

domain structure. From Figure 4d the coexistence between cylinders and hemispheres supports the notion of a weak first-order transition where metastable hemispheres exist in a region of cylinders. In Figure 4e, the morphology appears to be well entrenched in the cylindrical phase though the slight elongation of some domains hints at the emergence of the ripple morphology. It is quite possible that local fluctuations in the polymer fraction cause localized phase transitions. Of final note is the appearance of short-range ordering in the round domains of Figure 4c–e. In many instances there is evidence of a distorted hexagonal arrangement (see circled region in Figure 4e). The domains are not ordered enough to characterize by a Fourier transform yet hint at an underlying tendency of the system to arrange on length scales greater than the individual domains.

Figure 4f–h shows the existence of a ripple phase when the polymer fraction is nearly equal. This phase is characterized by elongated domains of one polymer in a continuous matrix of the other. In this example, elongated polystyrene domains with a PS fraction of 0.49 (Figure 4f) further elongate as the PS

dx.doi.org/10.1021/ma202542u | *Macromolecules* 2012, 45, 510–524

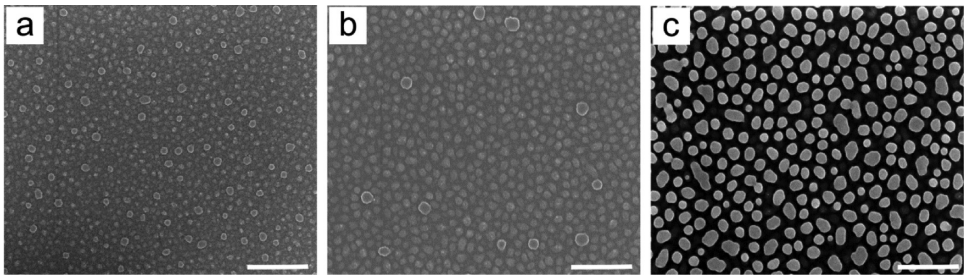

Figure 5. SEM images of annealed (a) sample B, (b) sample C, and (c) sample E stained with ruthenium tetraoxide to enhance the contrast of the PS domains. Electron beam voltage = 5 kV. Scale bar = 500 nm.

fraction increases to 0.51 (Figure 4g). The domains appear to grow only axially with a moderate occurrence of branching. The domain widths are measured to be 48 ± 5 nm and are expected to be a consequence of the polymer molecular weights of the brush. At a critical PS fraction there is a transition from PS domains in a continuous PMMA matrix to PMMA domains in a continuous PS matrix (Figure 4g,h). In this example this transition occurs between a PS fraction of 0.51 and 0.58. The fact that the transition does not occur at a 50/50 polymer fraction implies that other variables aside from polymer fraction may affect the phase morphology.

Ideally for equal length PS and PMMA chains, the phase diagram for the mixed brushes should be symmetrical; i.e., the phase progression for 0 to 0.5 PS volume fraction should be identical for 0.5 to 1.0 PS volume fraction except with PMMA as the minority component forming domains in a PS matrix. The elongated PMMA domains in Figure 4h progressively shorten so that at a PS fraction of 0.68 the PMMA domains are bordering on the cylindrical phase. If we were to continue increasing the PS fraction, we would expect PMMA cylinders to transition into hemispheres and finally into a disordered morphology as the PS fraction approaches 1.0. However, the phase diagram may be skewed by a variety of influences. In this study we focus on polymer fraction though, due to differences in molecular weights between the PS and PMMA components, the volume fraction does not necessarily equal the grafting density fraction of the polymers. The statistical segment lengths of PS and PMMA are also not equivalent as was assumed in the SCFT calculations. None of these variables were explicitly investigated in this study but may easily account for differences in phase morphology between two samples having similar polymer volume fractions. Furthermore, differences in polydispersity between samples may further complicate the situation. Finally, we expect the morphology of the brushes to be dependent on the annealing solvent.

There is a strong bias imparted by the annealing solvent to the equilibrium morphology of the mixed brush.[26] Despite our use of good solvents for PS and PMMA (THF, toluene, benzene), all have a selective preference as numerically predicted by the Hildebrand solubility parameters (Table 2). In the context of regular solution theory, the miscibility between a polymer and solvent inversely scales as the square of the difference between their solubility parameters.[54] Not only does this create miscibility differences in the brush but also a free surface that is slightly selective due to the solvent vapor. From Table 2, we can predict that the preference for PS will be toluene > THF > benzene, while the inverse holds for PMMA. Figure 6 demonstrates the phase morphologies of similar samples annealed in different solvent vapors. Samples J, K, and I are annealed in THF vapor and imaged by AFM and shown in parts a, c, and e of Figure 6, respectively. Following, the samples are washed with chloroform to mix the brushes, and sample J is reannealed in toluene vapor (Figure 6b) and samples K and I are reannealed in benzene vapor (parts d and f in Figure 6, respectively). Changing the annealing solvent from THF to toluene vapor has a similar effect to increasing the fraction of PS, and as a consequence, the PS domains in Figure 6a substantially elongate (Figure 6b). The AFM phase images are analyzed to quantify the extent of each polymer on the brush surface with the areal PS percentage of sample J increasing from 46% to 55%. Conversely, changing the annealing solvent from THF to benzene is analogous to increasing the fraction of PMMA, and as a consequence, the elongated PS domains in Figure 6c substantially shorten (Figure 6d). The areal percentage of PS presented on the brush surface of sample K decreases from 51% PS to 44% PS. Even more dramatic is when solvent annealing appears to drive a phase transition. In Figure 6e, sample I appears largely in a cylindrical phase when annealed in THF but clearly is in the ripple phase when annealed in benzene (Figure 6f). The areal percentage of PS at the brush surface dramatically decreases from 68% PS to 55% PS. While there is a clear trend between polymer fractions and annealing solvent, the polymer areal percentages of PS and PMMA measured do not always match overall volume fractions of the brush. We speculate that the solvents have a tendency to change the partitioning of the polymers, thereby altering the composition of polymer domains. In other words, the amount of minority polymer comprising a domain changes with the annealing solvent. It is also possible that the phase morphology presented on the top surface changes with depth; however, a previous study which etched into the polymer brush showed the composition changed little with depth.[34]

Table 2. Hildebrand Solubility Parameters of Polymers and Solvents[54]

	solubility parameter ($MPa^{1/2}$)
polymer	
PS	17.5−19.1[a]
PMMA	18.5−19.5[a]
solvent	
toluene	18.2
THF	18.6
benzene	18.8

[a]Range due to method of measurement.

Large Cell SCFT Morphologies. The lowest free energy morphologies predicted by the unit cell SCFT calculations exhibit perfect long-range order, while as is clear from this work and previous experimental work, long-range order has not been observed to date in mixed polymer brushes. Perfect long-range

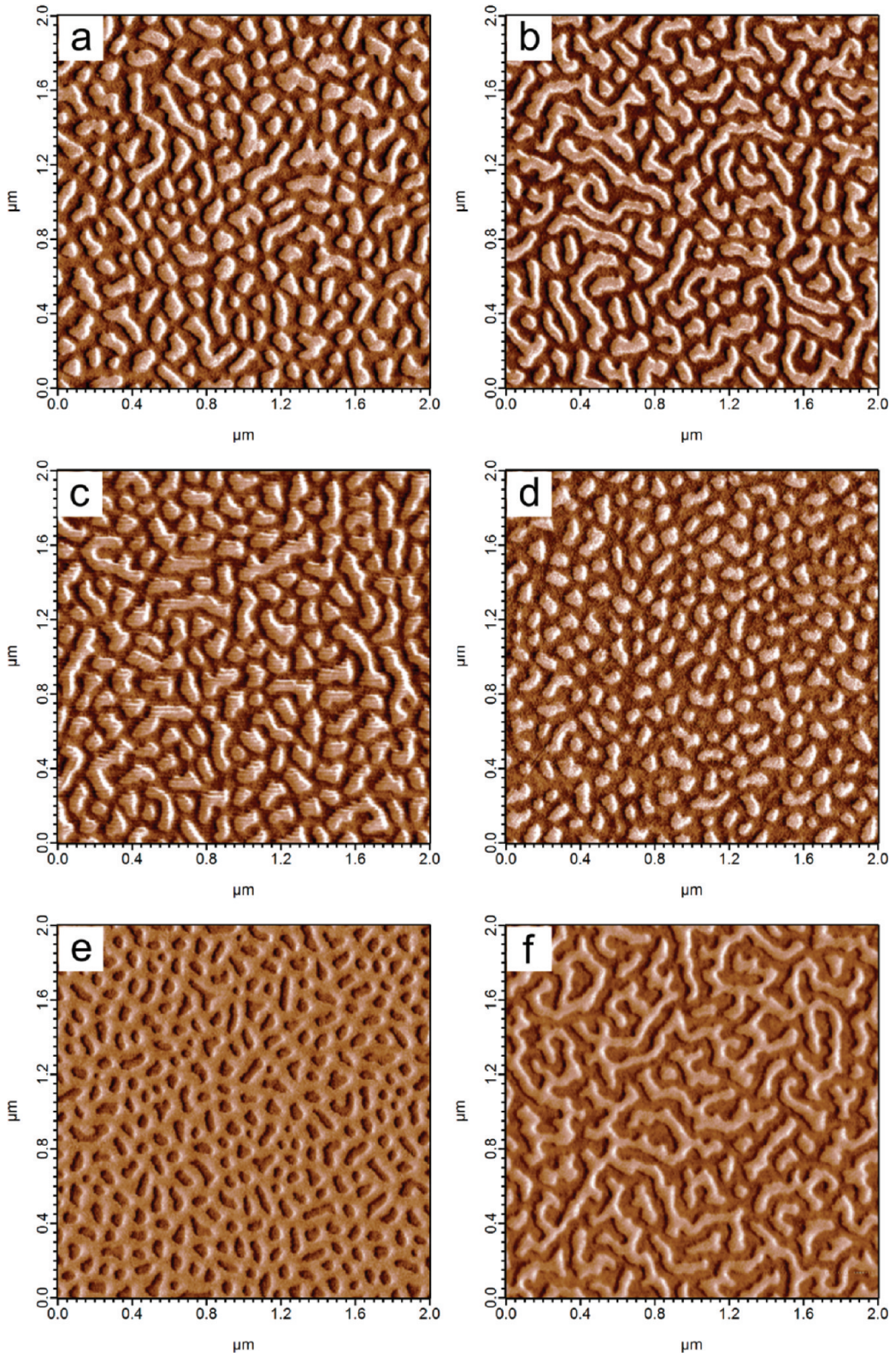

Figure 6. AFM phase images of (a, b) sample J, (c, d) sample K and (e, f) sample I annealed for 24 h in THF vapor (a, c, e), toluene vapor (b), and benzene vapor (d, f). Phase range = 6°.

order is difficult to achieve even in diblock copolymer thin films, which exhibit various defects unless efforts are made to align the domains. However, mixed brushes typically do not show as much order as copolymer films. Previous computational and experimental work proposed that the lack of long-range order in mixed brushes is due to heterogeneities in the grafting densities of the two polymers.[36,42,43] To explore this possibility, we performed large cell SCFT calculations in which the composition of the grafting density was not uniform. Instead, the grafting density of A polymers was generated using

correlated Gaussian random fields

$$\langle \varphi_A(\mathbf{x}_\perp)\varphi_A(\mathbf{x}'_\perp)\rangle = \lambda \exp\left[-\frac{|\mathbf{x}_\perp - \mathbf{x}'_\perp|^2}{2\sigma^2}\right]$$

with an average lateral A grafting density (normalized by the total grafting density) of $\langle \varphi_A(\mathbf{x}_\perp)\rangle = f_A$. The total grafting density of A and B polymers is kept fixed, so grafted B chains compensate accordingly for fluctuations in the A grafting density. Calculations are performed at $\chi N = 16$ for mixed brushes of height $3R_g$ as before, with lateral dimensions of $50R_g$. The amplitude of the correlations was fairly low, $\lambda = 0.02$, and the length scale (standard deviation) of the correlations in the grafting density was taken to be $\sigma = 0.5R_g$. Since the distance between grafting points is on the order of 2.5−3 nm, or around $(0.25-0.3)R_g$ (see Table 1), it seems reasonable to assume that experimental variations in grafting density would be at least this large but probably not much larger than R_g. We found that varying the length scale σ of the grafting density correlations between $0.35R_g$ and $0.7R_g$ resulted in very similar morphologies, so here we present results for $\sigma = 0.5R_g$.

The simulated morphologies of the brush with grafting density fluctuations are shown in Figure 7 for various values of f_A along with the corresponding morphologies assuming uniform grafting of both polymers. In these calculations, the SCFT fields W_- and W_+ are given random initial values, and the free energy is relaxed to its stationary value at $\chi N = 16$ using a steepest descent search method. This corresponds to a fairly rapid quenching of the brush from the disordered to an ordered state. For the cases with uniform grafting, the mixed brush forms well-ordered domains of the appropriate phase (as determined by the phase diagram), but there are still some defects present. The hemispherical and cylindrical phases display hexagonal ordering, and the ripple phases show the distinctive "fingerprint" texture commonly observed in lamellar-forming block copolymer thin films as we noted previously.[40] If the value of χN is slowly increased (annealed), the systems with uniform grafting will eventually converge to states with few or no defects.

Introducing fluctuations in the relative grafting density of the two species has a significant effect on the morphologies. As shown in Figure 7, all the morphologies show considerably less order. There are some elongated domains in the cylindrical phase at $f_A = 0.3$, and in all cases there is more variation in domain size than for the uniformly grafted brushes. The simulated morphologies appear qualitatively very similar to the AFM images in Figure 4. We note that for the cases with fluctuations in the grafting density annealing the systems slowly instead of quenching does not lead to significant differences in the morphologies of Figure 7.

Autocorrelation of Polymer Domains. An ideal binary brush is formed when the following are true: (1) monodisperse polymers, (2) linear polymers, and (3) uniform grafting density. When annealed in a melt, these ideal brushes are predicted to assemble into the phases of the left-hand column of Figure 7. Even minor variations in polymer grafting density disrupts the long- and short-range ordering predicted to form in melts from ideal binary brushes. It is certain that our experimental PS/PMMA brushes contain a combination of nonidealities that generate phase morphologies qualitatively similar to predicted SCFT simulations of binary brushes incorporating fluctuations in grafting density (Figure 7, right-hand column). Additionally, solvent annealing evidently does not create a fully equilibrated melt adding further deviation of our experiments from SCFT predictions. To gain a quantitative measurement of order and domain spacing in both our experiments and simulations, the autocorrelation of polymer domains was calculated as a function of radial distance, as shown in Figure 8.

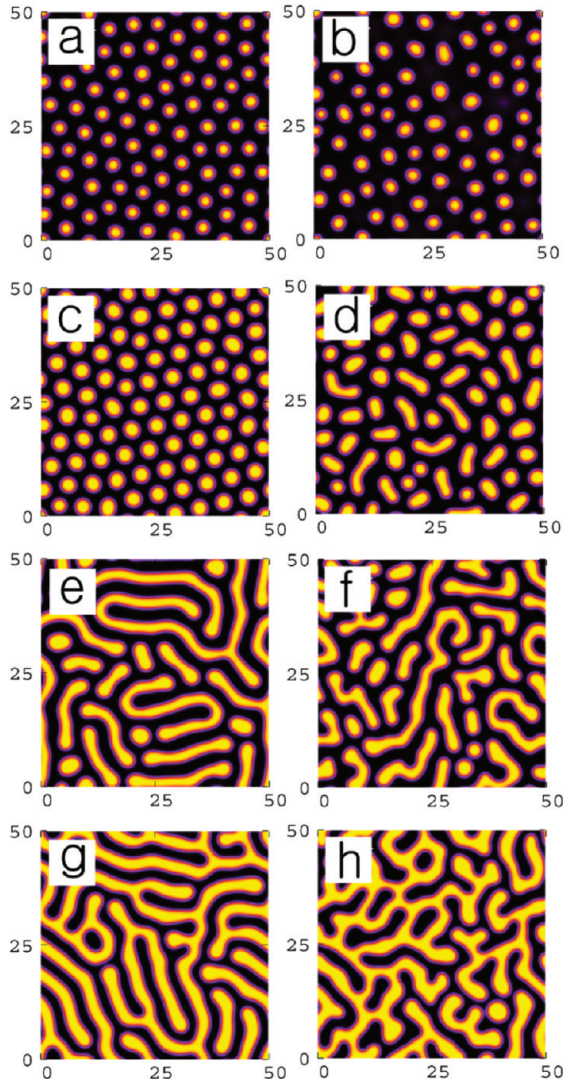

Figure 7. SCFT phase images (top surface) of a mixed polymer brush of height $3R_g$ and lateral dimensions of $(50 \times 50)R_g$ at $\chi N = 16$ for various f_A: (a, b) $f_A = 0.1$, (c, d) $f_A = 0.3$, (e, f) $f_A = 0.4$, and (g, h) $f_A = 0.5$. While (a, c, e, g) have uniform grafting density distributions, the normalized grafting density distributions of A chains in (b, d, f, h) are generated using correlated Gaussian random fields with a mean value of f_A. In all cases the total grafting density is uniform over the domain.

The autocorrelations in the experimental systems are significant and qualitatively similar to those predicted by the SCFT simulations. This is particularly true for the SCFT results with fluctuating grafting density. In that case, for both cylindrical and ripple phases, the amount of correlation among domains as measured by the magnitudes of the first trough and subsequent peak is similar in the experiments and the SCFT results, indicating a similar degree of order.

From Figure 8a we can discern five positive peaks beyond the radial center indicating at least a measurable long-range correlation distance of ∼480 nm. Additionally, we can obtain a nearest-neighbor distance of PS domains of 109 nm or

dx.doi.org/10.1021/ma202542u | Macromolecules 2012, 45, 510−524

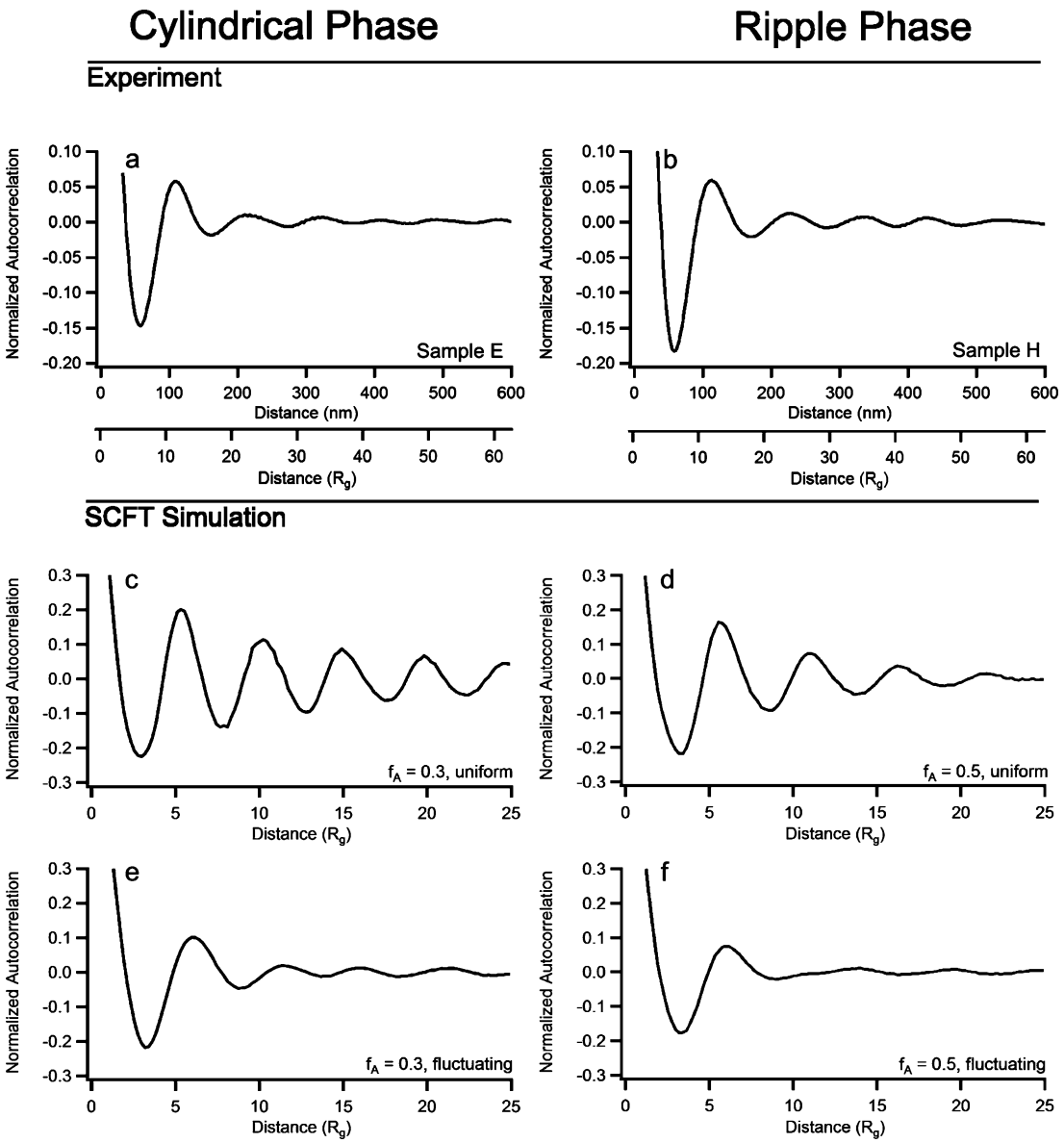

Figure 8. Radial autocorrelation functions calculated for the cylindrical morphology (a, c, e) and ripple morphology (b, d, f). Experimental samples: (a) sample E (PS fraction = 0.38) and (b) sample H (PS fraction = 0.58). SCFT Simulations with uniform grafting density distributions: (c) $f_A = 0.3$ and (d) $f_A = 0.5$. SCFT simulations with fluctuating grafting density distributions ($\lambda = 0.02$): (e) $f_A = 0.3$ and (f) $f_A = 0.5$.

$\sim 11.5R_g$ for sample E. Comparing to SCFT simulations with $f_A = 0.3$, we find nearest-neighbor distances of polymer A cylindrical domains to be $5.3R_g$ for uniform grafting density distributions and $6.15R_g$ for fluctuating grafting density distributions (Figure 8, parts c and e, respectively). The slightly greater R_g distances of nearest-neighbor cylindrical domains with fluctuating grafting density is a result of the disruption of domain packing. However, this small increase does not account for the almost 2 times increase in nearest-neighbor spacing measured for the experiments when compared to the SCFT simulations. The ripple morphology yields similar results. We can discern from Figure 8b four positive peaks beyond the radial center, indicating at least a measurable long-range correlation distance of ~450 nm. Additionally, we can obtain a nearest-neighbor distance of 112 nm or $\sim 12.5R_g$ for sample H. Comparing to SCFT simulations with $f_A = 0.5$, we find nearest-neighbor distances of polymer A ripple domains to be $5.7R_g$ for uniform grafting density distributions and $6.0R_g$ for fluctuating grafting density distributions (Figure 8, parts d and f, respectively).

There are several likely contributions to the discrepancy in domain spacing. The experimental systems are at higher χN values than the simulations, and we expect the domain spacing to increase with increasing χN. However, on the basis of the domain spacing for the hexagonal phases for $10 < \chi N < 20$,[40] we estimate the domain spacing at $\chi N = 35$ to be larger by only about 5%. The experimental systems are annealed in solvent vapor, which could lead to larger domain sizes than the SCFT results due to swelling in the solvent. Solvent could affect the various phases differently due to small differences in selectivity of the solvent for the PS as compared to the PMMA domains. Preliminary results indicate that the domain spacing also increases with increasing values of both λ and σ. In particular, increasing the amplitude of the grafting density correlations from $\lambda = 0.02$ to $\lambda = 0.1$ for the ripple phase leads to an increase in the domain spacing from $6.00R_g$ to $6.35R_g$. Details of the

dx.doi.org/10.1021/ma202542u | *Macromolecules* 2012, 45, 510−524

grafting density fluctuations are difficult to measure experimentally. We could in principle adjust λ and σ so that the SCFT calculations would fit the measured domain spacing, but this would lead to morphologies that look qualitatively different than the experimental morphologies. A detailed SCFT study of the effects of varying the grafting density fluctuations with a range of λ and σ values will be presented in a future manuscript.

Finally, unlike the simulations, the PS/PMMA brushes contain significant polydispersity in both polymers, and the average molecular weights of PS and PMMA are not exactly the same (see Table 1). Previous studies of microphase-separated block copolymer systems have observed similar increases in domain spacing with polydispersity for both lamellar and cylindrical structures.[64−67] In polydisperse systems, it is speculated that the overall stretching energy is reduced by recruiting larger polymers into the center of domain structures to minimize the stretching of the smaller ones. To the best of our knowledge, no study has characterized the influence of polydispersity on domain spacing in laterally separated binary polymer brushes, but on the basis of the results here, it is reasonable to anticipate a similar trend.

CONCLUSIONS

The phase morphologies of binary brushes annealed under nonselective conditions were explored by a combination of experiment and SCFT simulations. The phase morphologies were determined by varying the grafting density of one polymer while keeping the overall grafting density constant. To grow mixed polymer brushes of PS and PMMA, free radical initiators were immobilized on a surface and successively initiated in the presence of styrene followed by methyl methacrylate to form a series of samples with PS volume fractions ranging from 0.00 to 0.68. Careful attention was paid to the surface chemistry to create a uniform initiator layer and minimize heterogeneities in the final mixed brush. Additionally, the experimental setup was designed to minimize the effect of molecular weight differences on the equilibrium melt morphology.

SCFT simulations of a binary polymer brush annealed under melt conditions predicted disordered, hexagonal, and ripple phases above a critical χN value. At high χN values the phase transition boundaries change little with χN and provide guidance to the phase transition boundaries in our PS/PMMA brushes. Indeed, PS/PMMA brushes annealed under nonselective solvent vapor exhibited the domain structures predicted by SCFT. Our ability to achieve lateral versus vertical separation of the polymers allowed unambiguous visualization of the polymer phases as a function of polymer fraction. Observed were ripple and circular domains with the further subdivision of the circular domains into cylinders and hemispheres. The lack of long-range hexagonal packing by the circular domains, along with distortions in shape, suggests nonidealities in brush structure and annealing conditions.

To create an improved approximation of the experimental system through SCFT simulations, fluctuations in the grafting density of polymers were introduced which disrupted the hexagonal order of the circular domains. Visualizations of the polymer domains calculated using SCFT showed a qualitative similarity to our experiments. The calculated autocorrelation functions for the domain structures showed a similar degree of order in both the experiments and the SCFT simulations for systems with grafting density fluctuations. However, the experimental nearest-neighbor spacing of the polymer domains in both the cylindrical and ripple phases was approximately twice that predicted by SCFT simulations even with a fluctuating grafting density accounted for. As the simulations do not account for the full complexity of the experimentally generated brushes, it is reasonable to expect there to be this difference. Future experiments will seek to improve the convergence of experimentally observed phases with theoretical predictions. We anticipate the advancements presented here to provide a basis for improving both the physical fabrication and computational predictions of nanopatterned mixed polymer brushes. Like nanopatterned block copolymer surfaces which are coming into their own, this complementary technique has enormous potential to transition from a laboratory curiosity into a driver for technological innovation.

ASSOCIATED CONTENT

Supporting Information

AFM height and phase images of chloroform solvent annealed PS/PMMA brushes (Figure S1); AFM phase images of PS/PMMA brushes annealed from a melt (Figure S2). This material is available free of charge via the Internet at http://pubs.acs.org.

AUTHOR INFORMATION

Corresponding Author

*E-mail: dlhuber@sandia.gov.

ACKNOWLEDGMENTS

This work was performed, in part, at the Center for Integrated Nanotechnologies, a U.S. Department of Energy, Office of Basic Energy Sciences user facility. Sandia National Laboratories is a multiprogram laboratory managed and operated by Sandia Corporation, a wholly owned subsidiary of Lockheed Martin Corporation, for the U.S. Department of Energy's National Nuclear Security Administration under Contract DE-AC04-94AL85000. Partial support was also provided from the MARCO Center on Functional Engineered Nano Architectonics (FENA) and the Sandia National Laboratories LDRD program.

REFERENCES

(1) Albert, J. N. L.; Epps, T. H. *Mater. Today* **2010**, *13*, 24.
(2) Hamley, I. W. *Angew. Chem., Int. Ed.* **2003**, *42*, 1692.
(3) Jeong, U. Y.; Kim, H. C.; Rodriguez, R. L.; Tsai, I. Y.; Stafford, C. M.; Kim, J. K.; Hawker, C. J.; Russell, T. P. *Adv. Mater.* **2002**, *14*, 274.
(4) Kim, S. O.; Solak, H. H.; Stoykovich, M. P.; Ferrier, N. J.; de Pablo, J. J.; Nealey, P. F. *Nature* **2003**, *424*, 411.
(5) Park, M.; Harrison, C.; Chaikin, P. M.; Register, R. A.; Adamson, D. H. *Science* **1997**, *276*, 1401.
(6) Ruiz, R.; Kang, H. M.; Detcheverry, F. A.; Dobisz, E.; Kercher, D. S.; Albrecht, T. R.; de Pablo, J. J.; Nealey, P. F. *Science* **2008**, *321*, 936.
(7) Stoykovich, M. P.; Kang, H.; Daoulas, K. C.; Liu, G.; Liu, C. C.; de Pablo, J. J.; Mueller, M.; Nealey, P. F. *ACS Nano* **2007**, *1*, 168.
(8) Stoykovich, M. P.; Muller, M.; Kim, S. O.; Solak, H. H.; Edwards, E. W.; de Pablo, J. J.; Nealey, P. F. *Science* **2005**, *308*, 1442.
(9) Stoykovich, M. P.; Nealey, P. F. *Mater. Today* **2006**, *9*, 20.
(10) Tang, C. B.; Lennon, E. M.; Fredrickson, G. H.; Kramer, E. J.; Hawker, C. J. *Science* **2008**, *322*, 429.
(11) Bates, F. S.; Fredrickson, G. H. *Phys. Today* **1999**, *52*, 32.
(12) Fasolka, M. J.; Mayes, A. M. *Annu. Rev. Mater. Res.* **2001**, *31*, 323.
(13) Bang, J.; Jeong, U.; Ryu, D. Y.; Russell, T. P.; Hawker, C. J. *Adv. Mater.* **2009**, *21*, 4769.
(14) Cheng, J. Y.; Ross, C. A.; Smith, H. I.; Thomas, E. L. *Adv. Mater.* **2006**, *18*, 2505.
(15) Krausch, G.; Magerle, R. *Adv. Mater.* **2002**, *14*, 1579.

(16) Segalman, R. A. *Mater. Sci. Eng., R* **2005**, *48*, 191.
(17) Aizawa, M.; Buriak, J. M. *Chem. Mater.* **2007**, *19*, 5090.
(18) Black, C. T.; Ruiz, R.; Breyta, G.; Cheng, J. Y.; Colburn, M. E.; Guarini, K. W.; Kim, H. C.; Zhang, Y. *IBM J. Res. Dev.* **2007**, *51*, 605.
(19) Garber, L. *Computer* **2007**, *40*, 17.
(20) Li, L.; Chen, C. K.; Li, J.; Zhang, A. J.; Liu, X. Y.; Xu, B.; Gao, S. B.; Jin, G. H.; Ma, Z. *J. Mater. Chem.* **2009**, *19*, 2789.
(21) Lemieux, M.; Usov, D.; Minko, S.; Stamm, M.; Shulha, H.; Tsukruk, V. V. *Macromolecules* **2003**, *36*, 7244.
(22) Marko, J. F.; Witten, T. A. *Phys. Rev. Lett.* **1991**, *66*, 1541.
(23) Minko, S.; Muller, M.; Usov, D.; Scholl, A.; Froeck, C.; Stamm, M. *Phys. Rev. Lett.* **2002**, 88.
(24) Muller, M. *Phys. Rev. E: Stat., Nonlinear, Soft Matter Phys.* **2002**, 65.
(25) Santer, S.; Kopyshev, A.; Yang, H. K.; Ruhe, J. *Macromolecules* **2006**, *39*, 3056.
(26) Wang, J. F.; Muller, M. *J. Phys. Chem. B* **2009**, *113*, 11384.
(27) Luzinov, I.; Minko, S.; Tsukruk, V. V. *Prog. Polym. Sci.* **2004**, *29*, 635.
(28) Zhao, B.; Brittain, W. J. *Prog. Polym. Sci.* **2000**, *25*, 677.
(29) Barbey, R.; Lavanant, L.; Paripovic, D.; Schuwer, N.; Sugnaux, C.; Tugulu, S.; Klok, H. A. *Chem. Rev.* **2009**, *109*, 5437.
(30) Minko, S.; Usov, D.; Goreshnik, E.; Stamm, M. *Macromol. Rapid Commun.* **2001**, *22*, 206.
(31) Sidorenko, A.; Minko, S.; Schenk-Meuser, K.; Duschner, H.; Stamm, M. *Langmuir* **1999**, *15*, 8349.
(32) Xue, Y. H.; Liu, H.; Lu, Z. Y.; Liang, X. Z. *J. Chem. Phys.* **2010**, 132.
(33) He, G. L.; Merlitz, H.; Sommer, J. U.; Wu, C. X. *Macromolecules* **2009**, *42*, 7194.
(34) Usov, D.; Gruzdev, V.; Nitschke, M.; Stamm, M.; Hoy, O.; Luzinov, I.; Tokarev, I.; Minko, S. *Macromolecules* **2007**, *40*, 8774.
(35) Prokhorova, S. A.; Kopyshev, A.; Ramakrishnan, A.; Zhang, H.; Ruhe, J. *Nanotechnology* **2003**, *14*, 1098.
(36) Santer, S.; Kopyshev, A.; Donges, J.; Ruhe, J.; Jiang, X. G.; Zhao, B.; Muller, M. *Langmuir* **2007**, *23*, 279.
(37) Santer, S.; Kopyshev, A.; Donges, J.; Yang, H. K.; Ruhe, J. *Langmuir* **2006**, *22*, 4660.
(38) Zhao, B.; Haasch, R. T.; MacLaren, S. *J. Am. Chem. Soc.* **2004**, *126*, 6124.
(39) Zhao, B.; Zhu, L. *Macromolecules* **2009**, *42*, 9369.
(40) Hur, S.; Frischknecht, A. L.; Huber, D. L.; Fredrickson, G. H. *Soft Matter* **2011**, *7*, 8776.
(41) Brown, G.; Chakrabarti, A.; Marko, J. F. *Europhys. Lett.* **1994**, *25*, 239.
(42) Wenning, L.; Muller, M.; Binder, K. *Europhys. Lett.* **2005**, *71*, 639.
(43) Wang, J. F.; Muller, M. *Langmuir* **2010**, *26*, 1291.
(44) Radially Averaged Autocorrelation Function. http://imagejdocu.tudor.lu/doku.php?id=macro:radially_averaged_autocorrelation (accessed Aug 8, 2011).
(45) Chantawansri, T. L.; Hur, S. M.; Garcia-Cervera, C. J.; Ceniceros, H. D.; Fredrickson, G. H. *J. Chem. Phys.* **2011**, 134.
(46) Czaun, M.; Hevesi, L.; Takafuji, M.; Ihara, H. *Macromolecules* **2009**, *42*, 4539.
(47) Anderson, A. S.; Dattelbaum, A. M.; Montano, G. A.; Price, D. N.; Schmidt, J. G.; Martinez, J. S.; Grace, W. K.; Grace, K. M.; Swanson, B. I. *Langmuir* **2008**, *24*, 2240.
(48) Dorvel, B.; Reddy, B.; Block, I.; Mathias, P.; Clare, S. E.; Cunningham, B.; Bergstrom, D. E.; Bashir, R. *Adv. Funct. Mater.* **2010**, *20*, 87.
(49) Zhang, F.; Sautter, K.; Larsen, A. M.; Findley, D. A.; Davis, R. C.; Samha, H.; Linford, M. R. *Langmuir* **2010**, *26*, 14648.
(50) Orendorff, C. J.; Huber, D. L.; Bunker, B. C. *J. Phys. Chem. C* **2009**, *113*, 13723.
(51) Boven, G.; Oosterling, M. L. C. M.; Challa, G.; Schouten, A. J. *Polymer* **1990**, *31*, 2377.
(52) Edmondson, S.; Osborne, V. L.; Huck, W. T. S. *Chem. Soc. Rev.* **2004**, *33*, 14.
(53) Minko, S.; Sidorenko, A.; Stamm, M.; Gafijchuk, G.; Senkovsky, V.; Voronov, S. *Macromolecules* **1999**, *32*, 4532.
(54) Brandrup, J.; Immergut, E. H.; Grulke, E. A. *Polymer Handbook*, 4th ed.; John Wiley & Sons: New York, 1999.
(55) Baum, M.; Brittain, W. J. *Macromolecules* **2002**, *35*, 610.
(56) Huang, E.; Pruzinsky, S.; Russell, T. P.; Mays, J.; Hawker, C. J. *Macromolecules* **1999**, *32*, 5299.
(57) Huang, E.; Russell, T. P.; Harrison, C.; Chaikin, P. M.; Register, R. A.; Hawker, C. J.; Mays, J. *Macromolecules* **1998**, *31*, 7641.
(58) Mansky, P.; Liu, Y.; Huang, E.; Russell, T. P.; Hawker, C. J. *Science* **1997**, *275*, 1458.
(59) Elbs, H.; Krausch, G. *Polymer* **2004**, *45*, 7935.
(60) Laschitsch, A.; Bouchard, C.; Habicht, J.; Schimmel, M.; Ruhe, J.; Johannsmann, D. *Macromolecules* **1999**, *32*, 1244.
(61) Huang, C. I.; Chapman, B. R.; Lodge, T. P.; Balsara, N. P. *Macromolecules* **1998**, *31*, 9384.
(62) Peng, J.; Kim, D. H.; Knoll, W.; Xuan, Y.; Li, B. Y.; Han, Y. C. *J. Chem. Phys.* **2006**, 125.
(63) Trent, J. S.; Scheinbeim, J. I.; Couchman, P. R. *J. Polym. Sci., Part C: Polym. Lett.* **1981**, *19*, 315.
(64) Lynd, N. A.; Hillmyer, M. A. *Macromolecules* **2005**, *38*, 8803.
(65) Matsen, M. W. *Eur. Phys. J. E* **2006**, *21*, 199.
(66) Matsushita, Y.; Noro, A.; Iinuma, M.; Suzuki, J.; Ohtani, H.; Takano, A. *Macromolecules* **2003**, *36*, 8074.
(67) Ruzette, A. V.; Tence-Girault, S.; Leibler, L.; Chauvin, F.; Bertin, D.; Guerret, O.; Gerard, P. *Macromolecules* **2006**, *39*, 5804.

Macromolecules

Article

pubs.acs.org/Macromolecules

Simple and Complex Micelles in Amphiphilic Mixtures: A Coarse-Grained Mean-Field Study

Martin J. Greenall*[,†,‡] and Gerhard Gompper[†]

[†]Theoretical Soft Matter and Biophysics, Institute for Complex Systems, Forschungszentrum Jülich, 52425 Jülich, Germany

[‡]Institut Charles Sadron, 23, rue du Loess, 67034 Strasbourg, France

ABSTRACT: Binary mixtures of amphiphiles in solution can self-assemble into a wide range of structures when the two species individually form aggregates of different curvatures. In this paper, we focus on small, spherically symmetric aggregates in a solution of sphere-forming amphiphile mixed with a smaller amount of lamella-forming amphiphile. Using a coarse-grained mean-field model (self-consistent field theory, or SCFT), we scan the parameter space of this system and find a range of morphologies as the interaction strength, architecture, and mixing ratio of the amphiphiles are varied. When the two species are quite similar in architecture, or when only a small amount of lamella-former is added, we find simple spherical micelles with cores formed from a mixture of the hydrophobic blocks of the two amphiphiles. For more strongly mismatched amphiphiles and higher lamella-former concentrations, we instead find small vesicles and more complex micelles. In these latter structures, the lamella-forming species is encapsulated by the sphere-forming one. For certain interaction strengths and lamella-former architectures, the amount of lamella-forming copolymer encapsulated may be large, and the implications of this for the solubilization of hydrophobic chemicals are considered. The mechanisms behind the formation of the above structures are discussed, with a particular emphasis on the sorting of amphiphiles according to their preferred curvature.

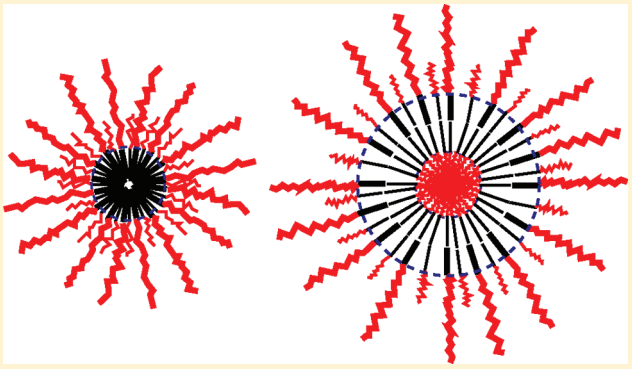

INTRODUCTION

Amphiphilic molecules such as block copolymers and lipids can self-assemble into many different structures when dissolved in solution.[1,2] This phenomenon has recently attracted a great deal of attention,[3,4] driven by both the potential applications of self-assembled amphiphile aggregates in the encapsulation and delivery of active chemicals such as drugs and genetic material[5,6] and the insights gained into biological systems.[7]

For solutions of a single type of simple amphiphile, such as a diblock copolymer or simple lipid, it is fairly straightforward to gain a basic understanding of which aggregate will form in a given system.[8,9] Although a variety of factors, such as the concentration[8,10] and size[11] of the amphiphilic molecules, may play a role, the shape of the aggregates is most easily controlled via the architecture of the amphiphile, that is, the relative sizes of its hydrophilic and hydrophobic blocks. If the hydrophilic component is large (or appears large due to its interaction with the solvent), then spherical micelles are seen. However, if the hydrophobic block is large, lamellar structures such as vesicles form. For intermediate architectures, cylindrical micelles are observed, as either isolated, wormlike structures[12] or branched networks.[13]

The experimental phenomenology is much richer in binary mixtures of amphiphiles,[14] especially those that individually self-assemble into different aggregates.[15−17] Novel structures are observed, such as undulating cylinders and branched, octopus-like aggregates.[15] Binary mixtures have been investigated in a wide variety of amphiphile systems. A great deal of work has been carried out on lipid−detergent systems,[18,19] and over the past few years lipid[7,20,21] and block copolymer[12,15] mixtures have been widely studied. Lipid mixtures are of interest due to their presence in cells and role in biological transport processes.[22] In the case of block copolymers, on the other hand, the motivation for the use of two amphiphiles is that it greatly increases the number of design parameters and gives finer control over the self-assembly. The architectures and concentrations of both species may now be varied, as may the stage in the self-assembly process at which they are blended.[12] A number of properties of the aggregates may be controlled, such as their shape,[12] stability,[23] and ability to solubilize hydrophobic compounds.[24] An interesting and recent example is the addition of lamella-forming copolymers with a short hydrophilic block to a solution of longer sphere-formers to increase the solubilization capacity of the resulting micelles while maintaining their compact and stable spherical shape.[23,24] In the current paper, we study a basic example of such a system: a solution of sphere-forming diblock copolymers to which an admixture of diblocks with a much shorter hydrophilic block is

Received: June 27, 2011
Revised: November 29, 2011
Published: December 19, 2011

added. To study the problem in as simple a form as possible, we consider two copolymer species that are formed of the same species A (hydrophilic) and B (hydrophobic) and have the same length hydrophobic blocks. We focus on the case where the sphere-formers remain in the majority and, using coarse-grained mean-field theory, investigate how the small spherical aggregates formed are modified by the presence of the shorter copolymers. We perform a broad scan of the system's parameter space and study how the core composition and radius of the micelles are affected by the interactions, concentrations, and architectures of the two polymers.

The paper is organized as follows. In the following section, we introduce the coarse-grained mean-field theory (self-consistent field theory) that will be used. We then present and discuss our theoretical results and give our conclusions in the final section.

SELF-CONSISTENT FIELD THEORY

Self-consistent field theory (SCFT)[25] is a coarse-grained mean-field model that has been used successfully to model equilibrium[26−28] and metastable[29,30] structures in polymer blends and melts. SCFT has several features that make it particularly suitable for the study of the current problem of small binary aggregates. First, its general advantages are that it is less computationally intensive than simulation techniques such as Monte Carlo yet, for sufficiently long amphiphiles,[31] provides comparably accurate predictions of micelle size and shape.[31−33] Second, as a relatively simple, coarse-grained theory, it will allow us to model the broad phenomenology of the system clearly and show how general the phenomena observed are likely to be. Furthermore, SCFT has a specific feature that is especially useful in the current problem: it makes no initial assumption about the segregation of two copolymers of different architecture within the micelle, provided the two amphiphile species are formed from the same types of monomer. This will enable us to demonstrate that effects such as the encapsulation of one polymer species by another within the micelle arise spontaneously and do not require further assumptions to be made.

To make our discussion more concrete, we now outline the mathematical structure and main assumptions of SCFT as applied to the current system. The theory considers an ensemble of many polymers, which are modeled as random walks in space.[34] The intermolecular interactions are modeled by assuming that the system is incompressible and introducing a contact potential between the molecules,[28] the strength of which is fixed by the Flory χ parameter.[35] The computational problem of solving the SCFT equations is then simplified by making a mean-field approximation[28] that corresponds to neglecting fluctuations.

SCFT can be used to study a wide variety of polymer systems, including simple homopolymers,[36] more complex copolymers,[37,38] and mixtures of these.[39] We model the system of two amphiphiles in a solvent by a simple mixture of two types of AB block copolymer with A homopolymer solvent. We take the lamella-forming species of copolymer to have a mean-squared end-to-end distance of a^2N, where a is the monomer length and N is the degree of polymerization.[28] This polymer contains N_B hydrophobic B monomers and $N_A = N - N_B$ hydrophilic A monomers. To consider the effect of different lamella-formers on the self-assembly, we vary the number of A monomers while keeping N_B fixed.

We note that our use of the term lamella-former to refer to amphiphiles with long hydrophobic blocks is not precise, as these molecules might precipitate rather than self-assemble in solution[40] if not mixed with an amphiphile with a larger hydrophilic block such as a sphere-former.[41] Furthermore, in aggregates formed from a mixture of sphere-formers and amphiphiles with a short hydrophilic block, the presence of these latter molecules might lead to the formation of regions of negative curvature rather than the zero-curvature regions that would be favored by a lamella-former.

All sphere-formers considered contain $N_{B2} \equiv N_B$ hydrophobic monomers, but their overall length is necessarily greater and is given by αN, where $\alpha > 1$. As above, the number of A monomers N_{A2} is varied with N_B fixed in order to investigate the effect of sphere-former architecture on the aggregate properties. For simplicity, the number N_S of A monomers in a homopolymer solvent molecule is also fixed at N_B. Since we focus on spherical aggregates, we assume spherical symmetry of the calculation box with reflecting boundary conditions at the origin and outer limit of the system. The validity of this assumption will be discussed in detail later.

In this paper, we keep the amounts of copolymer and homopolymer fixed; that is, we work in the canonical ensemble. Applying the procedure described above, we find that the SCFT approximation to the free energy of our system has the form

$$\begin{aligned}\frac{FN}{k_BT\rho_0V} = \frac{F_hN}{k_BT\rho_0V} - (\chi N/V) \\ \int d\mathbf{r}\,[(\varphi_A(\mathbf{r}) + \varphi_{A2}(\mathbf{r}) + \varphi_S(\mathbf{r}) - \bar{\varphi}_A \\ - \bar{\varphi}_{A2} - \bar{\varphi}_S)(\varphi_B(\mathbf{r}) + \varphi_{B2}(\mathbf{r}) - \bar{\varphi}_B \\ - \bar{\varphi}_{B2})] - (\bar{\varphi}_A + \bar{\varphi}_B)\ln(Q_{AB}/V) \\ - [(\bar{\varphi}_{A2} + \bar{\varphi}_{B2})/\alpha]\ln(Q_{AB2}/V) \\ - \bar{\varphi}_S\ln(Q_S/V) \qquad (1)\end{aligned}$$

where the $\bar{\varphi}_i$ are the mean volume fractions of the various components. The $\phi_i(\mathbf{r})$ are the local volume fractions, with i= A or A2 for the hydrophilic components of species 1 and 2, i = B or B2 for the hydrophobic components, and i = S for the A homopolymer solvent. The strength of the repulsive interaction between the A monomers (hydrophilic component and solvent) and B monomers (hydrophobic component) is determined by the Flory parameter χ. V is the total volume, $1/\rho_0$ is the volume of a monomer, and F_h is the SCFT free energy of a homogeneous system of the same composition. The architectures of the individual molecules enter through the single-chain partition functions Q_i, which are calculated from the propagators q and $q^\dagger$.[28] These latter quantities satisfy diffusion equations with a field term that incorporates the polymer interactions. The polymer density profiles are computed from integrals over the propagators.[28,42]

The derivation of the mean-field free energy F also generates a set of simultaneous equations linking the values of the fields and densities. In order to calculate the SCFT density profiles for a given set of polymer concentrations, we begin by making a initial guess for the fields $w_i(\mathbf{r})$ and solve the diffusion equations to calculate the propagators and then the densities corresponding to these fields. The new $\phi_i(\mathbf{r})$ are then substituted into the

dx.doi.org/10.1021/ma2014639 | Macromolecules 2012, 45, 525−535

simultaneous equations to calculate new values for the w_i.[43] The procedure is repeated until convergence is achieved.

The diffusion equations are solved using a finite difference method.[44] To resolve the more complex features of the micelle density profiles, it is necessary to use a relatively fine discretization: a spatial step size of $0.028aN_B^{1/2}$ (compared to a typical system size of $6-8aN_B^{1/2}$) and a step size for the curve parameter s of 0.0025.

Until now, we have only considered isolated spherical micelles. We must now link the thermodynamics of a single aggregate to those of a larger system containing many micelles. To do this, we proceed as follows.[45,46] First, we calculate the free energy density of a box containing a single spherical aggregate surrounded by solvent. Since we assume spherical symmetry, the calculation is effectively one-dimensional. The volume of the simulation box containing the aggregate is then varied, keeping the total volume fractions of both types of copolymer constant, until the box size with the minimum free energy density is found. Provided the system is dilute, so that micelle is surrounded by a large volume of solvent, this mimics the behavior of a larger system (of fixed volume and fixed copolymer volume fraction) containing many micelles. The reason for this is that such a system minimizes its total free energy by changing the number of micelles and therefore the volume ("box size") occupied by each. Minimizing the free energy density in this way locates the micelle that would have the lowest free energy and hence be most likely to be observed in a sample containing many aggregates. This approach allows many-micelle systems to be investigated using inexpensive one-dimensional calculations on single aggregates, and its predictions on micelle radii and shape transitions often agree well with experiment.[45,46] It can also be extended to cylindrical and lamellar aggregates.[46] We note that micellization can also be studied using SCFT in the grand canonical ensemble.[29,47] The present approach was introduced since it uses the total copolymer volume fraction as input, and this quantity can be directly measured in experiments.

RESULTS AND DISCUSSION

We divide the results section into five subsections. The first of these discusses the stability of spherically symmetric mixed aggregates with respect to other structures for the parameter range of interest. The following four sections focus on the effect on the micelle morphology of the lamella-former concentration, the strength of the interaction between the two species, the lamella-former architecture, and the sphere-former architecture.

Spherically Symmetric Mixed Aggregates. Motivated by the possibility of forming compact structures containing a large fraction of hydrophobic material,[23,24] we will focus in this paper on small, spherically symmetric mixed aggregates. Before presenting detailed calculations on these structures, we establish their stability. Most of our calculations employ a particular pair of strongly mismatched copolymers: a lamella-former with $N_A = N_B/4$ and a sphere-former with $N_{A2} = 7N_B$. In our calculations for spherical micelles and vesicles in the subsequent sections, we use a range of Flory parameters χ, but often concentrate on two values: $\chi N_B = 22.5$, where the interfaces between species A and B are relatively sharp, and $\chi N_B = 15$, where they are less well-defined. These polymer parameters could be obtained in, for example, a blend of polystyrene–polybutadiene copolymer and polystyrene homopolymer such as that considered by Kinning et al.[8] in their study of micelle shape transitions. Using the free energy minimization method described above, we now calculate the free energy densities of spherical, infinite cylindrical, and infinite bilayer structures for this polymer pair as the amount of lamella-former is increased from 0 to 40% of all copolymer by volume, the composition range we will consider in our later calculations. Figure 1a shows the results for $\chi N_B = 22.5$ and

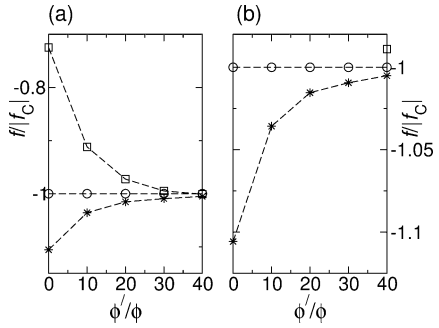

Figure 1. Free energy densities of spheres (marked with asterisks), cylinders (circles), and bilayers (squares) in blends of lamella-formers ($N_A = N_B/4$) and sphere-formers ($N_{A2} = 7N_B$) in homopolymer solvent as a function of the ratio ϕ'/ϕ of the volume fraction of lamella-formers ϕ' to the total volume fraction of copolymers ϕ. All free energy densites are normalized with respect to that of the cylinder.

Figure 1b those for $\chi N_B = 15$. In both cases, we see that the spherically symmetric structure has the lowest free energy density over the concentration range considered, even given the fact that our calculations overestimate the tendency toward the formation of cylinders and lamellae due to their neglect of end-cap and edge energy.[46] Indeed, for $\chi N_B = 15$ (Figure 1b), no bilayer can be found below the highest lamella-former concentration considered, 40%. These calculations do not explicitly rule out the formation of other small aggregates such as disks[48] and short rods,[12] which may indeed coexist with the spherical structures, especially at higher lamella-former concentrations. However, the fact that these aggregates contain significant cylindrical or bilayer sections, both of which are less energetically favorable than the sphere, means that they are unlikely to be the dominant structure. Indeed, recent Monte Carlo simulations[49] on a system such as those considered in this paper (mixtures of lamella- and micelle-forming amphiphiles with matched hydrophobic blocks) have found small spherical aggregates at even higher lamella-former concentrations than those considered here.

We have now confirmed that the sphere has the lowest free energy of the three simplest self-assembled structures for the mixture of lamella-formers with $N_A = N_B/4$ and sphere-formers with $N_{A2} = 7N_B$, the system studied in most detail in this paper. However, we will also explore the parameter space more fully, changing the architecture of both species and also the strength of the repulsion between their hydrophobic and hydrophilic blocks. Many of these changes, such as lengthening the hydrophilic block of the lamella-former, would be expected to lower the free energy of the sphere with respect to the other structures,[41] and in these cases we perform no further calculations. However, when we make changes that might make the cylindrical or lamellar aggregates more favorable, such as shortening the hydrophilic block of the sphere-former,[21] we check that the sphere still has the lowest free energy for the most extreme values of the parameters considered.

dx.doi.org/10.1021/ma2014639 | Macromolecules 2012, 45, 525–535

It is also possible that the two species will form aggregates containing only one type of amphiphile, rather than the mixed aggregates considered above. Unfortunately, this question is difficult to address directly using our current approach. However, a considerable number of experiments[50−52] have shown the formation of mixed aggregates in binary systems over a wide range of mixing ratios and copolymer architectures. This phenomenon has also been predicted from scaling theory.[53] In addition, it is also possible in some systems to encourage the formation of mixed aggregates through manipulation of the blending process,[12,15] even when one of the species precipitates in solution when not mixed with another amphiphile.[41]

Effect of Lamella-Former Concentration. We now focus in more detail on spherically symmetric morphologies. First, we consider the same pair of copolymers as in Figure 1a: a lamella-former with $N_A = N_B/4$ and a sphere-former with $N_{A2} = 7N_B$. The Flory parameter is set to the relatively high value of $\chi N_B = 22.5$. We fix the overall volume fraction of copolymer to 10%, to give a reasonable volume of solvent around the micelle without making the simulation box so large that the calculations become slow.

Figure 2 shows a series of radial cuts through the density profile of the optimum spherical aggregate as the volume

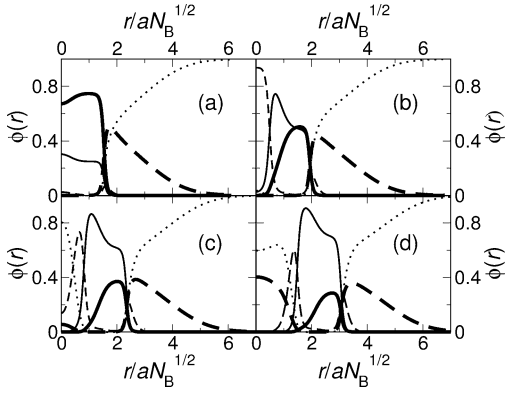

Figure 2. Cuts through the density profiles of the spherically symmetric aggregates formed in a solution of lamella-former with $N_A = N_B/4$ mixed with a sphere-former with $N_{A2} = 7N_B$. The Flory parameter is set to the relatively high value of $\chi N_B = 22.5$. The volume fractions of lamella-formers as a percentage of all copolymers are (a) 5%, (b) 15%, (c) 25%, and (d) 35%. Sphere-formers are shown with thick lines and lamella-formers with thin lines. The hydrophobic components are plotted with full lines, the hydrophilic components with dashed lines, and the solvent with a dotted line.

fraction of lamella-former is increased from 5% to 35% of all copolymers in steps of 10%. For the lowest of these lamella-former concentrations (Figure 2a), the sphere-formers and lamella-formers are homogeneously mixed in the core, and a simple mixed micelle, sketched in Figure 3, is formed. Note that this sketch, and the others in this paper, are intended to show the composition of the various layers of the micelle as clearly as possible, rather than to give a precise representation of the density profile. In particular, the density of the core is much more uniform in the radial direction than the sketch implies (see Figure 2a). This simple micelle is little different from that which would be formed in a system of pure sphere-forming amphiphiles: the concentration of lamella-formers is not yet sufficiently large to have a strong effect on the micelle morphology. Indeed, for such low lamella-former concentrations, mixed micelles may not be present,[53] with pure aggregates of the two species forming instead.

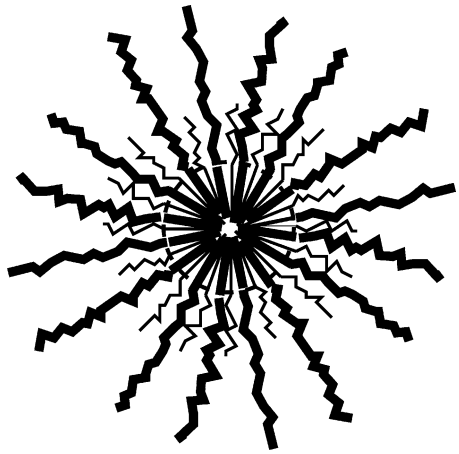

Figure 3. Sketch of a simple mixed micelle. Sphere-formers are shown with thick lines and lamella-formers with thin lines. The hydrophobic components are plotted with straight lines, the hydrophilic components with zigzag lines, and the boundary of the hydrophobic core is marked with a dashed circle. This structure is seen for weakly mismatched copolymers at all χ parameters considered. Note that this sketch is intended simply to show the composition of the various layers of the micelle and does not give a precise representation of the density profile.

However, as more lamella-forming molecules are added (Figure 2 b), their influence on the core composition of the micelle becomes clear. A polymer with a large hydrophobic component that naturally forms flat bilayers or even structures of negative curvature is in an energetically highly unfavorable state in a small, positively curved micelle. In consequence, these molecules segregate to the center of the aggregate, where they form a tightly wrapped bilayer. This structure is sketched in Figure 4. The polymers in the inner leaflet of this bilayer are in a more favorable negative curvature state, with their hydrophilic components pointing in toward the center of the micelle. Those in the outer leaflet are also in a more favorable state than at lower lamella-former concentrations: they are no longer forced into the core of a compact micelle but sit in a shell on the outside of the new core region. Here, they are mixed with the sphere-formers, which can no longer form their preferred simple micelle structure but strongly prefer the positively curved surface of the new spherical aggregate to its core. The new micelle therefore has an inner core of hydrophilic A blocks, an outer core of hydrophobic B blocks, and a hydrophilic A corona.

As the lamella-former concentration is increased still further, to 25% by volume of all copolymers (Figure 2c), solvent penetrates into the core of the micelle, as the inner bilayer of lamella-formers becomes more dominant in fixing the micelle morphology and expands toward the planar state. This process continues in Figure 2d, where 35% of all copolymers are lamella-forming. Here, a number of the sphere-formers have mixed with the inner leaflet of the lamella-former bilayer, meaning that the overall structure has the form of a (very) small bilayer vesicle (see the sketch in Figure 5).

These small vesicle structures have indeed been seen in recent Monte Carlo simulations by Ji and Ding[49] on systems of binary amphiphiles with different hydrophilic block lengths but matched hydrophobic blocks, the system considered in the current paper. They were found to form even when the shorter

dx.doi.org/10.1021/ma2014639 | Macromolecules 2012, 45, 525−535

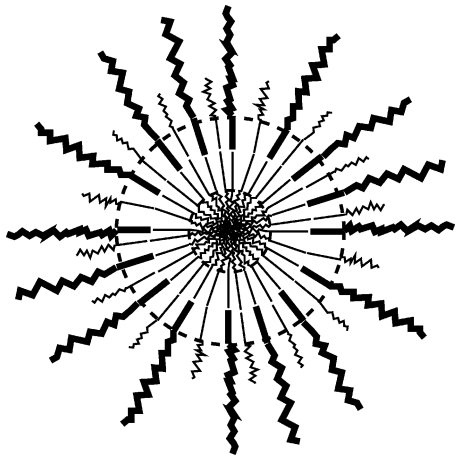

Figure 4. Sketch of a complex ABA mixed micelle with a hydrophilic A inner core, a hydrophobic B outer core, and a hydrophilic A corona. Sphere-formers are shown with thick lines and lamella-formers with thin lines. The hydrophobic components are plotted with straight lines, the hydrophilic components with zigzag lines, and the boundaries of the two cores are marked with dashed circles. This structure is seen for larger χ parameters. Note that this sketch is intended simply to show the composition of the various layers of the micelle and does not give a precise representation of the density profile.

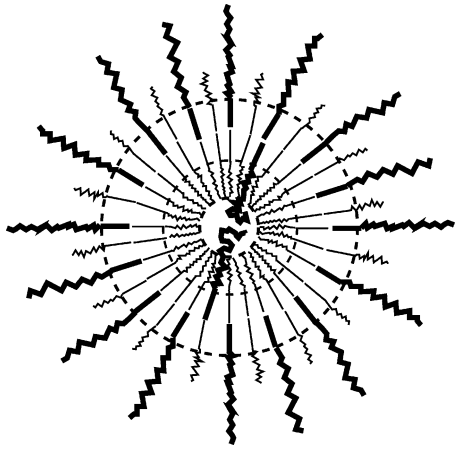

Figure 5. Sketch of a small vesicle composed of a solvent center, a layer of hydrophilic A blocks, a layer of hydrophobic B blocks, and a hydrophilic A corona. Sphere-formers are shown with thick lines and lamella-formers with thin lines. The hydrophobic components are plotted with straight lines, the hydrophilic components with zigzag lines, and the boundaries of the various regions are marked with dashed circles. This structure is seen for larger χ parameters. Note that this sketch is intended simply to show the composition of the various layers of the aggregate and does not give a precise representation of the density profile.

of the two copolymer species formed larger bilayer vesicles. Indeed, some of the small vesicles observed in these simulations contain such a small number of solvent molecules that they correspond more closely to the "ABA" structure sketched in Figure 4. The segregation of the two amphiphile species between the inner and outer leaflets shown in Figure 2b–d is also clearly visible in the results of Ji and Ding.[49]

Furthermore, small vesicles with a preferred radius have been seen in experiments on mixtures of sphere- and lamella-forming amphiphiles.[7,54] Their existence has also been predicted in recent lattice SCFT calculations by Li et al.[55] Our current work considers a different region of parameter space to these lattice-based calculations, which focus on weakly mismatched amphiphiles and (usually) higher lamella-former concentrations. In consequence, the mechanism by which the preferred vesicle radius is selected appears to be rather different in the two studies. In our work, strong segregation of the two species occurs, and the compositions of the inner and outler leaflets of the bilayer are quite different, as in the simulations of Ji and Ding.[49] The small vesicle structure forms as it accommodates both the preference of the shorter copolymers for a bilayer structure and that of the longer, sphere-forming amphiphiles for positively curved surfaces. This is in contrast to the results of Li et al.,[55] where the vesicles are larger and the two bilayer leaflets have similar compositions. The individual vesicles therefore have no preferred curvature, and coexistence with a high concentration of mixed micelles is found to be necessary for vesicle size selection to occur. Highly curved mixed bilayers may also be seen as the end sections of larger tubular vesicles[56] and have also been investigated using molecular dynamics simulations.[57] Our current work gives some broad guidance as to how the system parameters might be varied in order to encourage or discourage the formation of these structures.

We now turn our attention to a system in which the two polymer species have the same architectures as before ($N_A = N_B/4$ for the lamella-former and $N_{A2} = 7N_B$ for the sphere-former), but a significantly weaker interaction strength of $\chi N_B = 15$. The difference between the two systems can be seen even at only 5% lamella-former (Figure 6a). Here, the radial

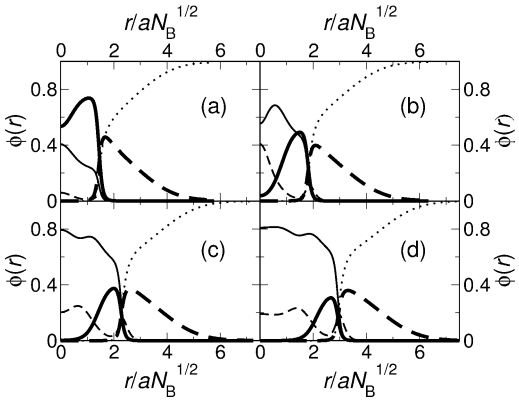

Figure 6. Cuts through the density profiles of the spherically symmetric aggregates formed in a solution of lamella-former with $N_A = N_B/4$ mixed with a sphere-former with $N_{A2} = 7N_B$. The Flory parameter is set to the relatively low value of $\chi N_B = 15$. The volume fractions of lamella-formers as a percentage of all copolymers are (a) 5%, (b) 15%, (c) 25%, and (d) 35%. Sphere-formers are shown with thick lines and lamella-formers with thin lines. The hydrophobic components are plotted with full lines, the hydrophilic components with dashed lines, and the solvent with a dotted line.

segregation of the two polymers according to their preferred curvatures is already clearly underway. Before, it was prevented at lower lamella-former concentrations by the energetic cost of mixing the hydrophilic A blocks with the hydrophobic B core. As more lamella-former is added to reach 15% (Figure 6b), the behavior of the two systems diverges still further. In the system with stronger repulsive interactions discussed earlier, the A and B blocks demix in the core, leading to the ABA structure seen in Figure 2b and sketched in Figure 4. In the current system, although some demixing does indeed occur (Figure 6b), the

dx.doi.org/10.1021/ma2014639 | Macromolecules 2012, 45, 525–535

effect is much weaker, and A- and B-rich regions can no longer be clearly separated. This structure is sketched in Figure 7. For

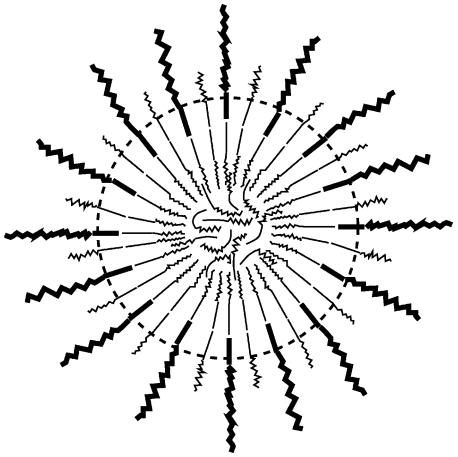

Figure 7. Sketch of a complex mixed micelle with a weakly structured core formed of lamella-formers and the hydrophobic blocks of sphere-formers. Sphere-formers are shown with thick lines and lamella-formers with thin lines. The hydrophobic components are plotted with straight lines, the hydrophilic components with zigzag lines, and the boundaries of the hydrophobic core is marked with a dashed circle. This aggregate is seen for lower χ parameters. Note that this sketch is intended simply to show the composition of the various layers of the micelle and does not give a precise representation of the density profile.

even larger concentrations of lamella-former of 25% and 35% (Figure 6c,d), the small vesicle structure seen before is absent. Instead, since the A and B blocks may mix much more freely than before, the core of the micelle is formed of a nearly homogeneous melt of lamella-former.

To make our study of the concentration dependence of the binary system more quantitative, we calculate the core radius and composition as a function of the ratio ϕ'/ϕ of the volume fraction of lamella-formers ϕ' to the total volume fraction of copolymers ϕ. We define the core boundary as the radius at which the volume fraction of hydrophobic blocks is equal to 0.5 and plot this quantity in Figure 8a for both systems considered above. The core radii of both species grow steadily and almost identically as the lamella-former concentration is increased. In the case of the system with $\chi N_B = 22.5$, the growth is associated with the expansion of the micelle to form a small vesicle, while in the system with weaker interactions ($\chi N_B = 15$), it arises from the fact that the core is gradually filling with lamella-former. The only appreciable difference in radius is seen in the final point, where 40% of all copolymers are lamella-forming. Here, the radius of the $\chi N_B = 22.5$ system has begun to grow more rapidly, as the system moves toward the planar bilayer state. For lamella-former fractions greater than 40%, the influence of the sphere-forming copolymers is weak, and we were no longer able to find free energy minima corresponding to small spherical aggregates.

The contrast between the high and low interaction strength systems emerges more clearly if we consider the amounts of the different species in the core defined above. The upper two curves in Figure 8b show the fraction of the core that is composed of A blocks for each of the two systems, while the lower two curves show the fraction of the core that is composed of homopolymer solvent. In the $\chi N_B = 15$ system, the amount

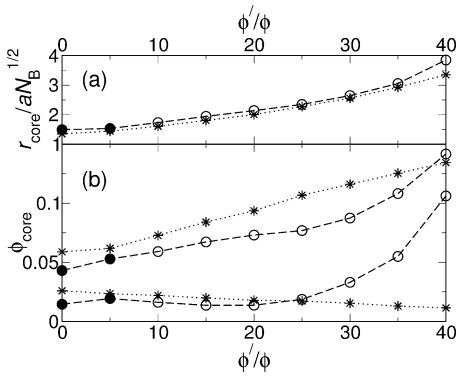

Figure 8. Core radius and composition of the spherically symmetric aggregates formed in a solution of lamella-former with $N_A = N_B/4$ mixed with a sphere-former with $N_{A2} = 7N_B$. (a) Core radius as a function of the ratio ϕ'/ϕ of the volume fraction of lamella-formers ϕ' to the total volume fraction of copolymers ϕ. Points corresponding to simple micelles (Figure 3) are marked by closed circles, ABA aggregates (Figure 4) or small vesicles (Figure 5) are marked with open circles, and weakly structured aggregates (Figure 7) are marked by asterisks. The data for the system with a Flory parameter of $\chi N_B = 15$ are connected with dotted lines and those for the system with $\chi N_B = 22.5$ by dashed lines. (b) Fraction of the core that is composed of A blocks for each of the two systems (upper two curves) and fraction of the core that is composed of homopolymer solvent (lower two curves).

of A block in the core grows steadily as the amount of lamella-former is increased, as in this case the lamella-forming copolymer is simply encapsulated in the center of the micelle. For low lamella-former concentrations, the $\chi N_B = 22.5$ system forms simple micelles with a clear interface in between the core and corona and so has less A block in the core than does the $\chi N_B = 15$ system, where some mixing of A and B blocks occurs in the core. In contrast, for larger amounts of lamella-forming copolymer, the fraction of A block in the more strongly interacting system grows more and more rapidly as the preferred aggregate changes from a closed micelle to an open vesicle.

The clearest difference between the two systems is seen in the behavior of the amount of solvent in the core as the lamella-former concentration is increased (see the lower two curves in Figure 8b). In the $\chi N_B = 15$ system, where the core is largely composed of copolymers, the fraction of solvent remains fairly constant at around 0.02−0.03. The fact that this value is a little higher than might be expected from the density profiles in Figure 6, and also varies slightly, can be attributed to the fact that our simple definition of the core radius means that a thin shell of solvent is always included as part of the core. In the system with stronger repulsion between the A and B components, the core solvent fraction starts at a similar small value, remaining close to this as the lamella-former volume fraction is increased and the morphology of the system changes from a simple micelle to the ABA structure shown in Figure 4. However, as the fraction of lamella-formers ϕ'/ϕ is increased toward 40%, the fraction of solvent in the core grows very quickly as the aggregate expands toward a vesicle.

We have checked a selection of these calculations for a much more dilute system with an overall copolymer volume fraction of $\phi \approx 1\%$, focusing in particular on those lamella-former volume fractions where the aggregate changes from one morphology to another. Such a dilute system may be more appropriate for observation of the small spherical structures

dx.doi.org/10.1021/ma2014639 | *Macromolecules* 2012, 45, 525−535

considered in this paper, since a more concentrated solution might form larger aggregates such as wormlike micelles. We therefore wish to check that the form of the optimum spherical aggregates is not strongly sensitive to concentration (although the likelihood of their formation with respect to larger aggregates may of course depend on the concentration).

Indeed, little change in the form of the aggregates is observed. The most significant difference is that, in the dilute case, the transition between the simple micelle and the ABA structure in the χN_B = 22.5 system occurs when ϕ'/ϕ is between 15% and 20%, rather than between 10% and 15% in the ϕ = 10% system. This preference for small spherical micelles in more dilute systems is in line with the known concentration dependence of block copolymer solutions.[8] Similar small shifts in the morphology transitions as the overall copolymer concentration is varied, or no appreciable shifts at all, are observed in all the systems considered in this paper, where the polymers considered aggregate reasonably strongly and the free energy minima associated with the various micelle shapes will be relatively sharp. This is not the case for shorter or more weakly interacting polymers, where the concentration dependence may be quite strong.

Effect of Interaction Strength. In the results discussed in the preceding subsection, we found a clear contrast in phenomenology between two systems with different levels of repulsion between their hydrophilic and hydrophobic components. To investigate this effect in more detail, we take a system with the same copolymer architectures as considered above ($N_A = N_B/4$ for the lamella-former and $N_{A2} = 7N_B$ for the sphere-former), fix the lamella-former fraction ϕ'/ϕ to 25%, and vary χN_B. Figure 9 shows a series of cuts through the density profiles

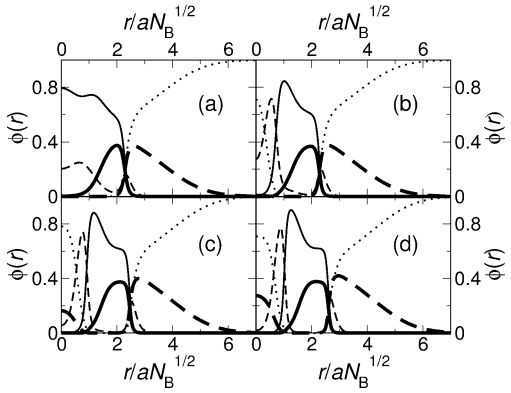

Figure 9. Cuts through the density profiles of the spherically symmetric aggregates formed in a solution of lamella-former with $N_A = N_B/4$ mixed with a sphere-former with $N_{A2} = 7N_B$. The lamella-former fraction ϕ'/ϕ is set to 25%. The Flory parameter χN_B is varied and takes the following values: (a) 15, (b) 20, (c) 25, and (d) 30. Sphere-formers are shown with thick lines and lamella-formers with thin lines. The hydrophobic components are plotted with full lines, the hydrophilic components with dashed lines, and the solvent with a dotted line.

of the small spherical aggregates formed as χN_B is increased from 15 to 30 in steps of 5. For the smallest of these values, shown in Figure 9a, we find a weakly structured aggregate of the kind shown in Figure 6. Very similar results are also found for the even smaller value of χN_B = 12.5. Below this value, no self-assembly takes place.

As χN_B is increased to 20 (Figure 9b), the segregation between hydrophilic and hydrophobic blocks has become much stronger, and the ABA aggregate of Figure 4 is seen, with some penetration of solvent into the core region. On further increase of χN_B, the boundaries between the various layers become sharper and sharper as the repulsive interaction between the A and B blocks increases in strength. The radius also increases, and the aggregate opens out to a small vesicle. Finally, in Figure 9d, where χN_B = 30, the layers are very clearly defined, and the calculated density profile resembles very closely the vesicle sketched in Figure 5.

Effect of Lamella-Forming Architecture. In the two previous subsections, we considered the effect of blending two strongly mismatched copolymers to demonstrate the effects of segregation on the micelle morphologies as clearly as possible. We now investigate how the micelle shapes change as the mismatch between the two polymers is decreased. Specifically, the hydrophilic block size of the lamella-former is gradually increased from the small value $N_A = N_B/4$ used in the preceding calculations until we reach the symmetric molecule with $N_A = N_B$. The same sphere-former architecture as before is used, with $N_{A2} = 7N_B$. Since we wish to focus specifically on the effects of the lamella-former, we use a slightly higher fraction of these molecules than in the preceding section and set ϕ'/ϕ = 33.3%.

To begin, we set χN_B = 15 and first consider the strong lamella-former with $N_A = N_B/4$. This is the system of Figure 6, and as there, we find large micelles with a weakly structured core (see Figure 10a). A sharp change is observed when the

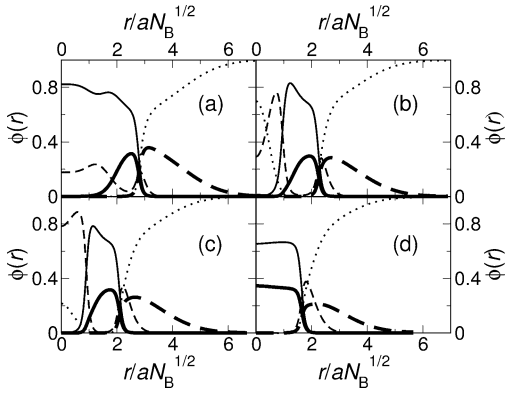

Figure 10. Cuts through the density profiles of the spherically symmetric aggregates formed in a solution of sphere-former with $N_{A2} = 7N_B$ and lamella-formers of varying architecture. The Flory parameter is set to the relatively low value of χN_B = 15. The lamella-former fraction ϕ'/ϕ is set to 33.3%. The hydrophilic block lengths of the lamella-forming molecules are (a) $N_A = N_B/4$, (b) $N_A = 3N_B/7$, (c) $N_A = 2N_B/3$, and (d) $N_A = N_B$. Sphere-formers are shown with thick lines and lamella-formers with thin lines. The hydrophobic components are plotted with full lines, the hydrophilic components with dashed lines, and the solvent with a dotted line.

length of the hydrophilic component of the lamella-forming copolymer is increased to $N_A = 3N_B/7$ (Figure 10b). Here, the AB interfaces within the core become well-defined, and the ABA aggregate sketched in Figure 4 is seen, with some penetration of solvent into the core. This indicates that the formation of the weakly structured aggregate seen in Figure 10a requires not only a relatively small χ parameter between the hydrophilic and hydrophobic blocks but also a short hydrophilic block of the lamella former. If the length of this block is increased, the effective strength χN of the interaction between the A and B blocks of the lamella-former becomes larger,[35] and the two blocks can segregate within the core.

dx.doi.org/10.1021/ma2014639 | Macromolecules 2012, 45, 525−535

As the length of the hydrophilic block of the lamella-former is increased still further, to $N_A = 2N_B/3$, the mismatch between the two species decreases and the aggregate shows the first signs of approaching the small micelle favored by the sphere-formers. Specifically, the core radius decreases slightly, and the solvent begins to be expelled from the center of the micelle (Figure 10c). This process is complete in Figure 10d, where the lamella former is symmetric and $N_A = N_B$. Here, a simple mixed micelle is formed, with no segregation of the two species.

We now consider a system with the same sequence of polymer architectures as above, but with a larger repulsive interaction strength $\chi N_B = 22.5$ between the A and B blocks. For the shortest lamella-former, with $N_A = N_B/4$, a small vesicle forms (Figure 11a), in contrast to the weakly structured aggregate seen for this architecture for the smaller value of χN_B (Figure 10a). As the hydrophilic block length of the lamella-former is increased, and the degree of mismatch between the two copolymer species lessens, the vesicle contracts (Figure 11b,c) until a simple mixed micelle is formed (Figure 11d).

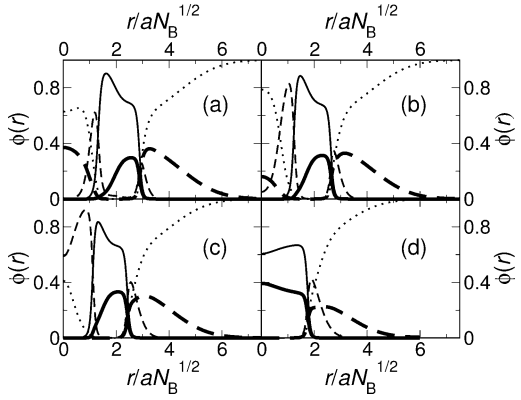

Figure 11. Cuts through the density profiles of the spherically symmetric aggregates formed in a solution of sphere-former with $N_{A2} = 7N_B$ and lamella-formers of varying architecture. The Flory parameter is set to the relatively high value of $\chi N_B = 22.5$. The lamella-former fraction ϕ'/ϕ is set to 33.3%. The hydrophilic block lengths of the lamella-forming molecules are (a) $N_A = N_B/4$, (b) $N_A = 3N_B/7$, (c) $N_A = 2N_B/3$, and (d) $N_A = N_B$. Sphere-formers are shown with thick lines and lamella-formers with thin lines. The hydrophobic components are plotted with full lines, the hydrophilic components with dashed lines, and the solvent with a dotted line.

As in our discussion of the dependence of the micelle morphology on lamella-former concentration, we now plot the aggregate core radii and composition as a function of lamella-former architecture for the two systems studied in this section. In Figure 12a, we show the decrease of the micelle radius as the length of the lamella-former hydrophilic block is increased. The lower line shows the behavior of the radius of the system with the smaller Flory parameter $\chi N_B = 15$. The sharpest change in the radius occurs between the first two points, when the aggregate changes from the weakly segregated structure plotted in Figure 10a to an ABA micelle with the form shown in Figure 10b. This latter structure then gradually contracts as the lamella-former is lengthened until we arrive at the simple mixed micelle plotted in Figure 10d. This steady contraction with increasing lamella-former length is also seen in the $\chi N_B = 22.5$ system. The small vesicle/ABA morphology is especially robust here, being formed not only for the short lamella-former (which

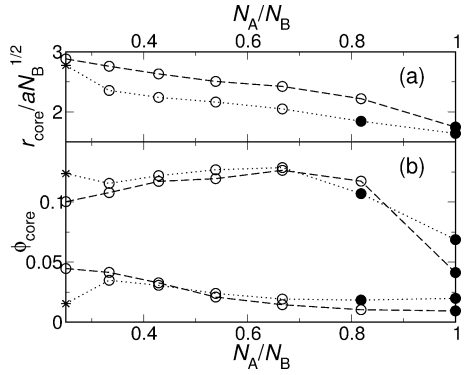

Figure 12. Core radius and composition of the spherically symmetric aggregates formed in a solution of sphere-former with $N_{A2} = 7N_B$ mixed with lamella-formers of various architectures. The lamella-former fraction ϕ'/ϕ is set to 33.3%. (a) Core radius as a function of the hydrophilic block length. Points corresponding to simple micelles (Figure 3) are marked by closed circles, ABA aggregates (Figure 4) or small vesicles (Figure 5) are marked with open circles, and weakly structured aggregates (Figure 7) are marked by asterisks. The data for the system with a Flory parameter of $\chi N_B = 15$ are connected with dotted lines and those for the system with $\chi N_B = 22.5$ by dashed lines. (b) Fraction of the core that is composed of A blocks for each of the two systems (upper two curves) and the fraction of the core that is composed of homopolymer solvent (lower two curves).

formed a weakly structured aggregate for $\chi N_B = 15$) but also for all other lamella-formers apart from the longest with $N_A = N_B$.

The fraction of the core that is composed of A blocks displays especially interesting behavior as the lamella-former hydrophilic block length is varied. In the system with the smaller Flory parameter $\chi N_B = 15$, the A block fraction has a rather high value of around 0.125 for the short lamella-formers with $N_A = N_B/4$. This is because the system forms a weakly structured aggregate (Figure 10a) here, with a core composed of lamella-forming copolymers (Figure 7). As the hydrophilic blocks of the lamella-formers are lengthened, solvent enters into the core and the A block fraction falls slightly. Further increase of the lamella-former hydrophilic block length causes the fraction of A blocks in the core to rise steadily. The reason for this is that, as the aggregate shrinks and solvent is slowly expelled from the center of the aggregate, the amount of A blocks changes relatively little. These blocks therefore come to constitute a larger fraction of the core. As the lamella-former A blocks are lengthened still further, we observe a sharp drop in the fraction of hydrophilic material in the core, as the system contracts to form a simple mixed micelle.

Some aspects of this behavior are also seen in the $\chi N_B = 22.5$ solution. Here, the weakly structured aggregate of Figure 10a is not present, and the system forms a small vesicle in the case of the shortest lamella-formers. As the A block length of these molecules is increased, the amount of solvent in the core of the aggregate decreases, and the fraction of A blocks in the core rises, as in the case of the $\chi N_B = 15$ system. For the largest A block lengths studied, the fraction of hydrophilic material in the core is much smaller, as the system has formed a mixed micelle with a predominantly hydrophobic core.

To reinforce the above arguments, we also show in Figure 12b the volume fraction of the core that is composed of solvent as a function of lamella-former hydrophilic block length. For the solution with $\chi N_B = 15$, the core solvent fraction initially rises as the weakly segregated structure is replaced by an ABA structure with some solvent in the core. It then falls gradually as

dx.doi.org/10.1021/ma2014639 | Macromolecules 2012, 45, 525−535

the aggregate contracts to form a mixed micelle. A similar steady fall is observed in the more strongly segregated χN_B = 22.5 system, as the small open vesicle observed for small N_A closes to form a micelle.

Effect of Sphere-Forming Architecture. To conclude the scan of our system's parameter space, we now investigate the effect of the architecture of the sphere-former on the morphology of the aggregates. In the above results, we focused on strongly mismatched copolymers and so used a highly asymmetric sphere-former with $N_{A2} = 7N_B$. We now vary the length of the hydrophilic block of the sphere-forming copolymer over a wide range, starting from a short molecule with $N_{A2} = 3N_B$ and increasing the number of A monomers until $N_{A2} = 9N_B$. The architecture of the lamella-former is fixed, with $N_A = N_B/4$, and as in all the above cases, the total copolymer volume fraction is kept constant at 10%. Three quarters of these copolymers are sphere-forming, so that ϕ'/ϕ = 25%. As in our studies of the effect of copolymer concentration and lamella-former architecture, we consider two values of the Flory parameter: $\chi N_B = 22.5$ and $\chi N_B = 15$.

In Figure 13a–d, we show cuts through the density profiles of the optimum aggregates formed when $N_{A2} = 3N_B$, $5N_B$, $7N_B$, and $9N_B$ for $\chi N_B = 15$. Despite the wide variation in the number of hydrophilic monomers, roughly similar small vesicle structures are formed in all cases, with particularly little change in morphology being observed between $N_{A2} = 5N_B$ and $9N_B$. Provided the two copolymer species are sufficiently strongly mismatched to segregate within the aggregate, there is indeed no reason to suspect that increasing the sphere-former A block length further should cause major qualitative changes to the form of the aggregate, as the sphere-formers have already reached the outer surface and can move no further. In fact, the differences between the four panels of Figure 13 can be attributed mainly to the fact that increasing the length of the sphere-former hydrophilic block at constant ϕ'/ϕ gradually reduces the amount of sphere-former hydrophobic block, with the result that the hydrophobic core becomes more and more dominated by the lamella-former. In consequence, the core radius of the aggregate increases somewhat, as the lamella-formers push outward toward their preferred flat state.

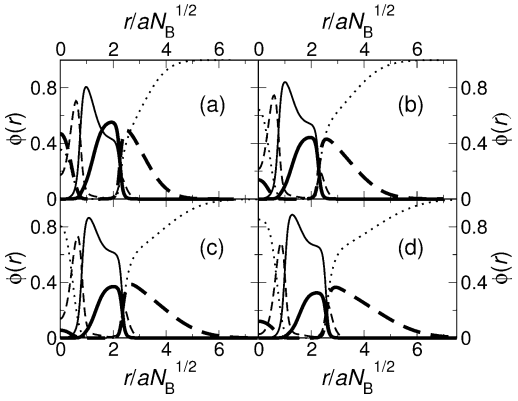

Figure 13. Cuts through the density profiles of the spherically symmetric aggregates formed in a solution of lamella-former with $N_A = N_B/4$ and sphere-formers of varying architecture. The Flory parameter is set to the relatively high value of $\chi N_A = 22.5$. The lamella-former fraction ϕ'/ϕ is set to 25%. The hydrophilic lengths of the sphere-forming molecules are (a) $N_{A2} = 3N_B$, (b) $N_{A2} = 5N_B$, (c) $N_{A2} = 7N_B$, and (d) $N_{A2} = 9N_B$. Sphere-formers are shown with thick lines and lamella-formers with thin lines. The hydrophobic components are plotted with full lines, the hydrophilic components with dashed lines, and the solvent with a dotted line.

The dependence of the aggregate shape on the hydrophilic block length of the sphere-formers is similarly weak for the smaller Flory parameter $\chi N_B = 15$. Here, aggregates with the same basic form of an outer layer of sphere-forming copolymers encapsulating a weakly structured core of lamella-formers are seen for $N_A = 3N_B$, $5N_B$, $7N_B$, and $9N_B$ (Figure 14a–d). As in the $\chi N_B = 22.5$ case, rather little difference in morphology can be seen as the sphere-former hydrophilic block length is increased from $5N_B$ to $9N_B$, save for a fall in the density of the outer sphere-former layer of the core and a slow growth in the core radius. The explanation for these changes is also the same as in the system with a higher Flory parameter. Specifically, the gradual fall in the amount of sphere-former hydrophobic block means that the core becomes predominantly composed of lamella-forming copolymers, which also causes it to swell.

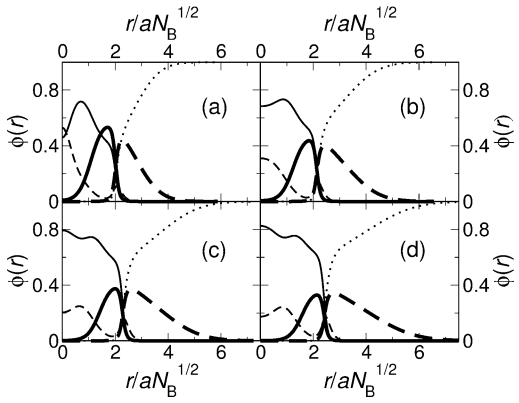

Figure 14. Cuts through the density profiles of the spherically symmetric aggregates formed in a solution of lamella-former with $N_A = N_B/4$ and sphere-formers of varying architecture. The Flory parameter is set to the relatively low value of $\chi N_B = 15$. The lamella-former fraction ϕ'/ϕ is set to 25%. The hydrophilic lengths of the sphere-forming molecules are (a) $N_{A2} = 3N_B$, (b) $N_{A2} = 5N_B$, (c) $N_{A2} = 7N_B$, and (d) $N_{A2} = 9N_B$. Sphere-formers are shown with thick lines and lamella-formers with thin lines. The hydrophobic components are plotted with full lines, the hydrophilic components with dashed lines, and the solvent with a dotted line.

The relative insensitivity to sphere-former architecture observed in both the systems discussed in this section can clearly be seen from plots of the core radius and composition as a function of the sphere-former A block length (Figure 15). The growth of the core radius shown in Figure 15a is clearly weaker than that seen in the corresponding plots of Figures 8 and 12. Furthermore, the fraction of the core composed of A blocks (upper lines) or solvent (lower lines) remains rather close to constant, although a weak growth in the amount of solvent in the open structure of Figure 13 can be seen. This is in line with the relatively unchanging morphologies plotted in Figures 13 and 14.

■ CONCLUSIONS

Using a coarse-grained mean-field approach (self-consistent field theory), we have modeled several aspects of the formation of small, spherically symmetric aggregates in a solution of sphere-forming amphiphile mixed with a smaller amount of lamella-forming amphiphile. By varying the interaction

dx.doi.org/10.1021/ma2014639 | Macromolecules 2012, 45, 525–535

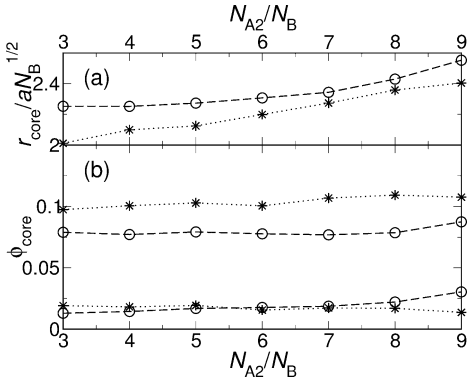

Figure 15. Core radius and composition of the spherically symmetric aggregates formed in a solution of lamella-former with $N_A = N_B/4$ mixed with sphere-formers of various architectures. The lamella-former fraction ϕ'/ϕ is set to 25%. (a) Core radius as a function of the hydrophilic block length. Points corresponding to simple micelles (2) are marked by closed circles, ABA aggregates (3) or small vesicles (4) are marked with open circles, and weakly structured aggregates (6) are marked by asterisks. The data for the system with a Flory parameter of $\chi N_B = 15$ are connected with dotted lines and those for the system with $\chi N_B = 22.5$ by dashed lines. (b) Fraction of the core that is composed of A blocks for each of the two systems (upper two curves) and fraction of the core that is composed of homopolymer solvent (lower two curves).

strength, architecture, and mixing ratio of the amphiphiles, we have found a range of morphologies. When the two species were similar in architecture or when only a small admixture of lamella-forming amphiphile was added, we found simple spherical micelles with purely hydrophobic cores formed from a mixture of the B blocks of the two amphiphiles. For more strongly mismatched amphiphiles and higher concentrations of lamella-former, we found complex micelles and small vesicles. Specifically, as the concentration of lamella-former was gradually increased in a strongly mismatched system with a relatively high χ parameter, the simple micelle formed at low lamella-former concentrations gradually expanded, first forming a more complex micelle with both A and B blocks in the core and then a small vesicle. For similar systems with lower Flory parameters, the addition of lamella-former resulted in the formation of a intriguing micellar structure in which a large and relatively unstructured core of lamella-former is surrounded by a layer of sphere-forming copolymers. Were this structure able to be stabilized in experiments, it could prove to be useful for the solubilization and delivery of hydrophobic compounds, since it contains a large amount of hydrophobic blocks while retaining a relatively small size. The formation of these aggregates was shown to require not only a relatively weak interaction between the two copolymers but also for one of the species to have a very short hydrophilic block. The other complex micelles and small vesicles were present over a much wider range of lamella-formers. The architecture of the sphere-formers was found to have a rather weak effect on the aggregate morphology.

The work presented here provides several examples of the wide range of aggregates that may be formed when two amphiphile species that individually self-assemble into aggregates of different curvatures are mixed and gives broad guidance as to how the polymer parameters might be varied in order to form a given structure. Furthermore, several of the structures shown here show the segregation of amphiphiles according to curvature.[7,20] Specifically, in many cases, the sphere-forming amphiphiles move to the positively curved surface of the aggregate. Effectively one-dimensional aggregates such as those considered here are among the simplest possible systems in which this phenomenon could take place.

Several possible extensions of the current work suggest themselves. First, given the potential for the solubilization of hydrophobic chemicals of the large micelles with lamella-former cores, more realistic interaction parameters and modeling of the polymers (if necessary by more microscopic simulation methods) could be carried out in order to search for an experimental parameter range in which these structures could be formed. Such a study could also investigate further the formation of small monodisperse vesicles[7] and bilayers of preferred curvature[56] in binary systems. A first step in this direction using Monte Carlo methods could be to take the system simulated by Ji and Ding[49] and vary the polymer architectures and interaction parameters. Insight would then be gained into how sensitive to the details of the polymers the small vesicles and ABA micelles seen in these simulations are and whether the weakly segregated structures with a hydrophobic core do indeed form at lower values of χ. Such a study would also allow the effect of our assumption of a polymeric solvent to be investigated and, eventually, a more realistic solvent to be included. The self-consistent field theory study could also be extended to other structures and the free energies of competing structures such as rods and small disks calculated.[12]

On the experimental side, the closest system to our theory would be a blend of block copolymers and homopolymer such as the polystyrene/polybutadiene system of Kinning et al.[8] discussed above and already modeled quite well by SCFT.[45,46] In fact, one of the copolymers investigated by Kinning et al. (labeled SB 10/10) is very close in both architecture and interaction strength to the longest lamella-former studied in Figure 10. In aqueous solution, PEO−PCL might be used, as binary mixtures of these copolymers have been found to form mixed aggregates over a wide range of concentrations,[12,41] even when one of the polymers has such a long hydrophobic section that it precipitates if not mixed with another amphiphile.[41]

Further, the study could be extended to mismatched hydrophobic blocks to allow comparison with recent experiments.[52] Finally, an analogous investigation could be performed for the binary triblock copolymer blends[23,24] of current interest in drug delivery applications, where large micelles in mixed systems are indeed seen.[23]

AUTHOR INFORMATION

Corresponding Author

*E-mail: mjgreenall@physics.org.

REFERENCES

(1) Jain, S.; Bates, F. S. *Science* **2003**, *300*, 460−464.
(2) Battaglia, G.; Ryan, A. J. *J. Phys. Chem. B* **2006**, *110*, 10272−10279.
(3) Smart, T. P.; Ryan, A. J.; Howse, J. R.; Battaglia, G. *Langmuir* **2010**, *26*, 7425−7430.
(4) Howse, J. R.; Jones, R. A. L.; Battaglia, G.; Ducker, R. E.; Leggett, G. J.; Ryan, A. J. *Nature Mater.* **2009**, *8*, 507−511.
(5) Kim, Y.; Dalhaimer, P.; Christian, D. A.; Discher, D. E. *Nanotechnology* **2005**, *16*, S484−S491.
(6) Lomas, H.; Canton, I.; MacNeil, S.; Du, J.; Armes, S. P.; Ryan, A. J.; Lewis, A. L.; Battaglia, G. *Adv. Mater.* **2007**, *19*, 4238−4243.

(7) Zidovska, A.; Ewert, K. K.; Quispe, J.; Carragher, B.; Potter, C. S.; Safinya, C. R. *Langmuir* **2009**, *25*, 2979−2985.
(8) Kinning, D. J.; Winey, K. I.; Thomas, E. L. *Macromolecules* **1988**, *21*, 3502−3506.
(9) Israelachvili, J. N.; Mitchell, D. J.; Ninham, B. W. *J. Chem. Soc., Faraday Trans. 1* **1976**, *72*, 1525−1568.
(10) Adams, D. J.; Kitchen, C.; Adams, S.; Furzeland, S.; Atkins, D.; Schuetz, P.; Fernyhough, C. M.; Tzokova, N.; Ryan, A. J.; Butler, M. F. *Soft Matter* **2009**, *5*, 3086−3096.
(11) Kaya, H.; Willner, L.; Allgaier, J.; Richter, D. *Appl. Phys. A: Mater. Sci. Process.* **2002**, *74*, S499−S501.
(12) Schuetz, P.; Greenall, M. J.; Bent, J.; Furzeland, S.; Atkins, D.; Butler, M. F.; McLeish, T. C. B.; Buzza, D. M. A. *Soft Matter* **2011**, *7*, 749−759.
(13) Dan, N.; Safran, S. A. *Adv. Colloid Interface Sci.* **2006**, *123*, 323−331.
(14) Kaler, E. W.; Murthy, A. K.; Rodriguez, B. E.; Zasadzinski, J. A. N. *Science* **1989**, *245*, 1371−1374.
(15) Jain, S.; Bates, F. S. *Macromolecules* **2004**, *37*, 1511−1523.
(16) Safran, S. A.; Pincus, P.; Andelman, D. *Science* **1990**, *248*, 354−356.
(17) Safran, S. A.; Pincus, P. A.; Andelman, D.; MacKintosh, F. C. *Phys. Rev. A* **1991**, *43*, 1071−1078.
(18) Vinson, P. K.; Talmon, Y.; Walter, A. *Biophys. J.* **1989**, *56*, 669−681.
(19) Oberdisse, J.; Regev, O.; Porte, G. *J. Phys. Chem. B* **1998**, *102*, 1102−1108.
(20) Sorre, B.; Callan-Jones, A.; Manneville, J. B.; Nassoy, P.; Joanny, J. F.; Prost, J.; Goud, B.; Bassereau, P. *Proc. Natl. Acad. Sci. U. S. A.* **2009**, *106*, 5622−5626.
(21) Greenall, M. J.; Gompper, G. *Langmuir* **2011**, *27*, 3416−3423.
(22) Akiyoshi, K.; Itaya, A.; Nomura, S. M.; Ono, N.; Yoshikawa, K. *FEBS Lett.* **2003**, *534*, 33−38.
(23) Lee, E. S.; Oh, Y. T.; Youn, Y. S.; Nam, M.; Park, B.; Yun, J.; Kim, J. H.; Song, H.-T.; Oh, K. T. *Colloids Surf., B* **2011**, *82*, 190−195.
(24) Oh, K. T.; Bronich, T. K.; Kabanov, A. V. *J. Controlled Release* **2004**, *94*, 411−422.
(25) Edwards, S. F. *Proc. Phys. Soc., London* **1965**, *85*, 613−624.
(26) Maniadis, P.; Lookman, T.; Kober, E. M.; Rasmussen, K. O. *Phys. Rev. Lett.* **2007**, *99*, 048302.
(27) Drolet, F.; Fredrickson, G. H. *Phys. Rev. Lett.* **1999**, *83*, 4317−4320.
(28) Matsen, M. W. In *Soft Matter*; Gompper, G., Schick, M., Eds.; Wiley-VCH: Weinheim, 2006; Chapter 2.
(29) Duque, D. *J. Chem. Phys.* **2003**, *119*, 5701−5704.
(30) Katsov, K.; Müller, M.; Schick, M. *Biophys. J.* **2004**, *87*, 3277−3290.
(31) Cavallo, A.; Müller, M.; Binder, K. *Macromolecules* **2006**, *39*, 9539−9550.
(32) Wijmans, C. M.; Linse, P. *Langmuir* **1995**, *11*, 3748−3756.
(33) Leermakers, F. A. M.; Scheutjens, J. M. H. M. *J. Colloid Interface Sci.* **1990**, *136*, 231−241.
(34) Schmid, F. *J. Phys.: Condens. Matter* **1998**, *10*, 8105−8138.
(35) Jones, R. A. L. *Soft Condensed Matter*; Oxford University Press: Oxford, 2002.
(36) Werner, A.; Müller, M.; Schmid, F.; Binder, K. *J. Chem. Phys.* **1999**, *110*, 1221−1229.
(37) Müller, M.; Gompper, G. *Phys. Rev. E* **2002**, *66*, 041805.
(38) Wang, J. F.; Guo, K. K.; An, L. J.; Müller, M.; Wang, Z. G. *Macromolecules* **2010**, *43*, 2037−2041.
(39) Denesyuk, N. A.; Gompper, G. *Macromolecules* **2006**, *39*, 5497−5511.
(40) Mayes, A. M.; Delacruz, M. O. *Macromolecules* **1988**, *21*, 2543−2547.
(41) Greenall, M. J.; Schuetz, P.; Furzeland, S.; Atkins, D.; Buzza, D. M. A.; Butler, M. F.; McLeish, T. C. B. *Macromolecules* **2011**, *44*, 5510−5519.
(42) Fredrickson, G. H. *The Equilibrium Theory of Inhomogeneous Polymers*; Oxford University Press: Oxford, 2006.
(43) Matsen, M. W. *J. Chem. Phys.* **2004**, *121*, 1938−1948.
(44) Press, W. H.; Flannery, B. P.; Teukolsky, S. A.; Vetterling, W. T. *Numerical Recipes in C*, 2nd ed.; Cambridge University Press: Cambridge, 1992.
(45) Greenall, M. J.; Buzza, D. M. A.; McLeish, T. C. B. *Macromolecules* **2009**, *42*, 5873−5880.
(46) Greenall, M. J.; Buzza, D. M. A.; McLeish, T. C. B. *J. Chem. Phys.* **2009**, *131*, 034904.
(47) Zhou, J.; Shi, A.-C. *Macromol. Theory Simul.* **2011**, *20*, 690−699.
(48) Sanders, C. R.; Landis, G. C. *Biochemistry* **1995**, *34*, 4030−4040.
(49) Ji, S.; Ding, J. *Langmuir* **2006**, *22*, 553−559.
(50) Koňák, C.; Helmstedt, M. *Macromolecules* **2001**, *34*, 6131−6133.
(51) Koňák, C.; Helmstedt, M. *Macromolecules* **2003**, *36*, 4603−4608.
(52) Pleštil, J.; Koňák, C.; Ju, X.; Lal, J. *Macromol. Chem. Phys.* **2006**, *207*, 231−241.
(53) Shim, D. F. K.; Marques, C.; Cates, M. E. *Macromolecules* **1991**, *24*, 5309−5314.
(54) Li, F.; Marcelis, A. T. M.; Sudholter, E. J. R.; Cohen-Stuart, M. A.; Leermakers, F. A. M. *Soft Matter* **2009**, *5*, 4173−4184.
(55) Li, F.; Prevost, S.; Schweins, R.; Marcelis, A. T. M.; Leermakers, F. A. M.; Cohen-Stuart, M. A.; Sudholter, E. J. R. *Soft Matter* **2009**, *5*, 4169−4172.
(56) Safinya, C. R. *Colloids Surf., A* **1997**, *128*, 183−195.
(57) Cooke, I. R.; Deserno, M. *Biophys. J.* **2006**, *91*, 487−495.

Macromolecules

Article

pubs.acs.org/Macromolecules

Single Chain Dynamic Structure Factor of Poly(ethylene oxide) in Dynamically Asymmetric Blends with Poly(methyl methacrylate). Neutron Scattering and Molecular Dynamics Simulations

Martin Brodeck,[†] Fernando Alvarez,*[,‡,§] Juan Colmenero,[‡,§,∥] and Dieter Richter[†]

[†]Jülich Centre for Neutron Science JCNS (JCNS-1) and Institute for Complex Systems (ICS-1), Forschungszentrum Jülich GmbH, 52425 Jülich, Germany

[‡]Centro de Física de Materiales (CSIC-UPV/EHU) and Materials Physics Center, Paseo Manuel de Lardizabal 5, 20018 San Sebastián, Spain

[§]Departamento de Física de Materiales, UPV/EHU, Apartado 1072, 20080 San Sebastián, Spain

[∥]Donostia International Physics Center, Paseo Manuel de Lardizabal 4, 20018 San Sebastián, Spain

ABSTRACT: We have investigated the dynamically asymmetric polymer blend composed of short ($M_n \approx 2$ kg/mol) poly(ethylene oxide) (PEO) and poly(methyl methacrylate) (PMMA) chains focusing on the collective dynamics of the fast PEO component. Using neutron spin-echo (NSE) spectroscopy, the single chain dynamic structure factor of PEO was investigated and compared to results from molecular dynamics simulations. After a successful validation of the simulations, a thorough analysis of the RPA approximation reveals the composition of the experimentally measured total scattering signal $S(Q,t)$. Using the simulations, we show and calculate two contributions: (1) the relaxation of hydrogenated PEO against deuterated PEO, yielding the single chain dynamic structure factor of PEO, and (2) the relaxation of the PEO component against the PMMA matrix. For the short chains presented here the second contribution shows a significant decay at higher temperatures while it was previously shown that, in the case of long chains, no relaxation is found. This difference is related to a decrease of the glass transition temperature which takes place with decreasing chain length. In a second step we analyze the approximations that are used when calculating the single chain dynamic structure factor using the Rouse model. For a system like pure PEO, where the dynamics follow the predicted Rouse behavior, excellent agreement is achieved. In the case of PEO in PMMA, however, the slow PMMA matrix strongly influences the PEO dynamics. As a result, the distribution functions show a strong non-Gaussianity, and the calculation of $S(Q,t)$ using the Rouse approximation fails even considering nonexponential Rouse mode correlators.

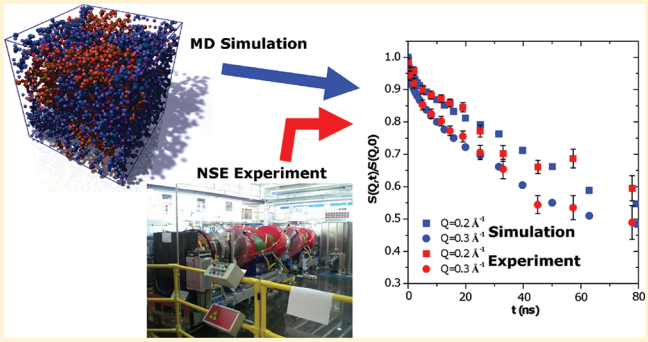

INTRODUCTION

Polymer blends composed of thermodynamically miscible components offer the possibility to engineer new materials with very specific properties. The investigation of dynamic miscibility in polymer blends and in particular in asymmetric blends showing strong dynamic contrast ΔT_g ($\Delta T_g = T_g^A - T_g^B$, A and B being the two blend components) is a very active area of research (see, for example, the reviews[1,2]). A typical example of an asymmetric blend is that composed of poly(ethylene oxide) (PEO) and poly(methyl methacrylate) (PMMA) ($\Delta T_g \approx 200$ K). The dynamics of the PEO/PMMA system, and in particular in the case of the compositions rich in the slow component PMMA, have been extensively investigated by means of different experimental techniques and molecular dynamics (MD) simulations as well (see as representative refs 3−11).

In a previous paper,[10] we have investigated the chain dynamics of unentangled PEO in a PEO/PMMA of 20/80% weight composition by means of fully atomistic simulations. The results obtained were compared with those obtained also by MD simulations in a simple bead−spring model of asymmetric blends. It was shown that the chain dynamics of unentangled PEO in the blend strongly deviate from the expected Rouse behavior that was observed for pure PEO. In summary, we found (i) large deviations from the exponential decay of the Rouse correlators, (ii) unusual behavior of the exponent x relating the characteristic times τ_p of the different Rouse mode correlators ($\tau_p \propto 1/p^x$), and (iii) a gradual increase of x and the dynamic asymmetry with decreasing temperature. At high temperature, $x \approx 2$ as it is expected for pure Rouse behavior. Similar trends were also observed for the fast component in bead−spring model simulation results, suggest-

Received: July 22, 2011
Revised: November 4, 2011
Published: December 22, 2011

ing that the observed features are of generic nature for asymmetric blends.

In this paper we want to discuss the properties of the single chain dynamic structure factor, $S_{chain}(Q,t)$—which is habitually measured by neutron spin echo (NSE)—in asymmetric blends. We will take advantage of the atomistic simulations to gain a deeper understanding about its composition and the different contributions that are seen in the experiment. Larger scale dynamics of PEO in the PEO/PMMA blend have recently been addressed experimentally by measuring the single chain dynamic structure factor of PEO using NSE spectroscopy.[7] In such a study, however, the chains were well within the entanglement regime ($M_n \approx 23$ kg/mol), making a direct comparison with the simulated system presented here difficult. Therefore, we have conducted new NSE experiments on the ternary polymer blend (hPEO−dPEO−dPMMA, h means protonated and d deuterated) using chains of similar length as in the simulations ($M_n \approx 2$ kg/mol) to validate the simulated system. It is well-known that the T_g of PMMA strongly depends on the molecular weight (see, e.g., ref 12). Because of this fact, the T_g of the new PMMA sample here considered was of the order of 50 K lower than that previously used. However, the dynamic contrast with PEO was still rather high (of the order of 150 K). The dynamics of unentangled PEO chains in the blend at 400 K was now faster than in the previously investigated case due to the mobility of PMMA matrix which was found to be stiff in the blend sample with $M_n \approx 23$ kg/mol. As a next step, we introduce the details about the simulation and validate the system by a comparison with the experiments. We will show that the correct chemical composition and the ratio of protonated/deuterated polymers is of significant importance to understand the measurements in the case of these short chains. After the validation we will discuss the contributions to the total scattering signal of the investigated system in the context of the random phase approximation (RPA). Here we can use the full spatial information from the simulations to gain a deeper understanding of the meaning of the experimentally measured dynamic structure factor. In a next step we will use the results from the Rouse analysis to describe the single chain dynamic structure factor of PEO $S_{chain}(Q,t)$. We will see that this approach fails due to the non-Gaussianity of the PEO motion which is mainly caused by the strong heterogeneity of the system. Using stretched exponential functions to describe the Rouse correlators, however, yields the correct behavior of the mean square distance between different beads in the chain, but not that of $S_{chain}(Q,t)$. Finally, a summary of the results is given.

NEUTRON SPIN-ECHO (NSE) EXPERIMENTS

Before we use the simulations to gain a deeper understanding about the dynamic structure factor of the PEO/PMMA system, we need to validate the simulated system by a comparison with experiments. The NSE method is ideal to measure the dynamics of polymer blends at the appropriate length and time scales to allow the observation of the chain relaxation at distances close to the chain size. In addition, the scattering functions are directly observed in the time domain, allowing an easier comparison with the data obtained from the MD simulations without a Fourier transformation from the energy to the time domain.

To investigate the collective dynamics of PEO chains in the PMMA environment, we have measured samples containing 10% hPEO, 10% dPEO, and 80% dPMMA, giving a 20/80 PEO/PMMA ratio. Using a total of 10% protonated chains yields sufficient contrast to measure the collective dynamics while keeping the incoherent background low. The measurements have been conducted at the J-NSE (JCNS, FRM-II) at a wavelength of $\lambda = 8$ Å measuring Fourier times up to 80 ns. Activated charcoal was used as reference. The protonated PEO was obtained from Merck with $M_n = 2$ kg/mol and $M_n/M_w = 1.03$. The deuterated components were synthesized in our laboratories (dPEO: $M_n = 1.7$ kg/mol, $M_n/M_w = 1.02$; dPMMA: $M_n = 2.0$ kg/mol, $M_n/M_w < 1.1$). For preparation, all polymers have been solved in chloroform to provide a thoroughly mixed blend. After the extraction of the solvent the material was filled into niobium cells and heated several times in a vacuum oven. Sealing of the sample has taken place in an argon environment.

Figure 1a shows the results of our measurements (full symbols) at $Q = 0.1$, 0.2, and 0.3 Å^{-1}. The hollow symbols in Figure 1a were taken from ref 7 and show results of a very similar system with a 25/75 PEO/PMMA ratio. In that case, however, the molecular weight of both PEO and PMMA was ~10 times higher ($M_n \approx 23$ kg/mol) and, therefore, well within the entanglement regime. It is clearly visible that the dynamic structure factor of the short chains relaxes significantly faster

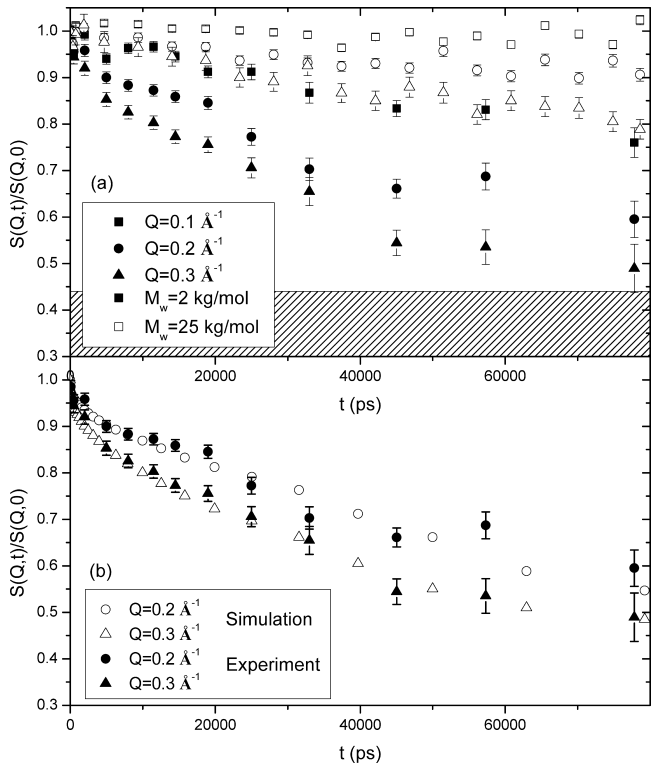

Figure 1. (a) Full symbols represent results from J-NSE measurements on samples containing 10% hPEO, 10% dPEO, and 80% dPMMA with low molecular weights ($M_n \approx 2$ kg/mol). The hollow symbols show results from a similar system (slightly higher PEO concentration of 25%) with long chains ($M_n \approx 23$ kg/mol). Note that the scale of the *Y*-axis ranges from 0.3 to 1. The dashed area represents the elastic contribution of 0.44 which was calculated using the dynamic random phase approximation for the case of blends with long chains (see section about the RPA). (b) Comparison of the NSE results corresponding to the short chain blend (full) with the simulated experiment (hollow) at $T = 400$ K.

dx.doi.org/10.1021/ma2016634 | *Macromolecules* 2012, 45, 536−542

than that of the long chains even though the content of PEO in the blend is lower.

Using differential scanning calorimetry (DSC), we have determined the average glass transition temperature T_g for both systems (each with a weight-ratio of 20/80). It was found that T_g for the short chain blend is significantly lower (311 K) than for the longer chains (347 K). Therefore, the dynamics at equal temperatures are significantly slower in the case of long chains. This effect must be attributed to the PMMA matrix. At the investigated temperature (400 K) the matrix of the long chains is rather stiff (which is also visible using neutron scattering, see section IV), whereas a strong relaxation is found for the short chains. This allows faster PEO dynamics since no segments of the chain are stuck in the PMMA matrix for significant amounts of time.

MD SIMULATIONS AND VALIDATION

We have used the software package Materials Studio 4.1 and the Discover-3 module (version 2005.1) from Accelrys with the COMPASS force field to carry out the MD simulations. A cubic cell containing 5 PEO molecules (43 monomers each) and 15 PMMA molecules (25 monomers each) was simulated under periodic boundary conditions, giving the same weight ratio of PEO to PMMA as in the experiment (20/80). Temperatures of 300, 350, 400, and 500 K were simulated for up to 200 ns. The simulated cell has a length of $a \approx 42$ Å, which in principle limits the lowest accessible Q values to about 0.15 Å^{-1} . For the comparison with the experiment we have calculated and Fourier-transformed the spatial correlation functions of the different labeled groups. The total coherent scattering intensity is then calculated by weighting the different scattering functions with the product of the corresponding scattering lengths:

$$S(Q, t) = \sum_{\alpha,\beta} b_\alpha^{coh} b_\beta^{coh} \frac{N_\alpha N_\beta}{N_t V} S_{\alpha,\beta}(Q, t) \quad (1)$$

with N_α the number and b_α the scattering length of atoms of type α, N_t the total number of atoms, and

$$S_{\alpha,\beta}(Q, t) = \int_0^\infty dr\, (g_{\alpha,\beta}(r, t) - 1) \frac{\sin(Qr)}{Qr} \quad (2)$$

the partial dynamic structure factors (radial averaging due to the assumed isotropy of the system). The breakdown of the total scattering function in the corresponding contributions is of particular importance when examining different levels of deuteration (e.g., protonating 50% of the PEO chains) as will be shown in the following section. Additional technical details about our MD simulations can be found in ref 10.

Comparison with Experiments. For the comparison of the simulated system with the experiment we have to calculate the signal that would be measured by a NSE instrument. Therefore, we have to include in the calculation the contributions from incoherent scattering. Moreover, we have to take into account the actual chemical composition of our sample.

During an incoherent scattering process the spin of 2/3 of all neutrons is flipped while it is unchanged for the rest. For the NSE setup this means that neutrons with an inversed spin orientation have to be subtracted from the final signal and the measured intensity is proportional to

$$\frac{S(Q, t)}{S(Q, 0)} = \frac{S_{coh}(Q, t) - \frac{1}{3} S_{inc}(Q, t)}{S_{coh}(Q, 0) - \frac{1}{3} S_{inc}(Q, 0)} \quad (3)$$

Using the simulations, we can calculate the exact absolute incoherent scattering contribution and subtract the corresponding intensity (mainly created by the protonated chains) from the coherent contribution.

In addition to the incoherent scattering, we have to account for the actual chemical composition of our samples. During the synthesis of the PEO and PMMA chains an initiator is necessary to start the reaction. This initiator is always protonated, even for the synthesis of deuterated chains, and its size roughly corresponds to two monomers. Because of the short chain length of our polymers, a protonated headgroup has a significant effect on the overall scattering behavior of the system (coherent as well as incoherent). For a fully deuterated PEO chain with M_n = 2 kg/mol the headgroup accounts for 6% of the polymer while the ratio for PMMA at the same molecular weight lies at 14%. For long chains with M_n > 20 kg/mol this effect is below 1% and, therefore, negligible.

Since half of the PEO has to be protonated and our system contains 5 PEO chains, we have averaged the scattering of 2 and 3 protonated chains. Since there are 10 different combinations for protonating 2 (or 3) out of 5 chains, a total of 20 different scattering functions was averaged. The coherent scattering function now is a complicated mixture of cross-terms between the headgroups, the protonated chains, the deuterated chains, and the deuterated matrix.

However, the possibility to include all these contributions into the simulated function allows a direct comparison between experiment and simulation. Figure 1b shows the excellent agreement obtained. The consistency between the two sets of data validates our MD simulations also for the chain dynamics and collective motions and on the other hand highlights the importance of the protonated headgroups for the scattering of systems with such short chains.

DISCUSSING OUR RESULTS IN CONTEXT OF THE RPA

When measuring the sample described above at low Q values, the scattering signal is created by the contrast between the protonated and deuterated components. Since only a part of the PEO chains if protonated, we measure the relaxation of the protonated PEO chains against the deuterated PEO chains and the deuterated PMMA matrix.

The contributions to the total scattering can in principle be calculated using the dynamic random phase approximation (RPA) (see refs 13−16). As a consequence of incompressibility in ternary systems, the scattering intensity of the labeled component can be described as a superposition of two decaying modes (hPEO against dPEO and dPMMA). Assuming an exponential decay for these modes, it can be shown that (valid in the regime where $S(Q,t) \propto Q^{-2}$)

$$S(Q, t) = \frac{12\varphi_h^{PEO}}{l^2 Q^2 (\varphi_h^{PEO} + \varphi_d^{PEO})} (\varphi_d^{PEO} e^{-\lambda_1 t} + \varphi_h^{PEO} \varphi_d^{PMMA} e^{-\lambda_2 t}) \quad (4)$$

with the volume fractions ϕ for the three different components. The relative contribution of the two relaxations can be derived

dx.doi.org/10.1021/ma2016634 | Macromolecules 2012, 45, 536−542

by considering two specific cases. If the PMMA fraction approaches 0 (setting $\phi_d^{PMMA} = 0$), the total scattering $S(Q,t)$ only contains the relaxation of the PEO component (λ_1). In this case, the prefactor describes the contrast created between the protonated and deuterated PEO chains. If, on the other hand, the deuterated PEO component is 0 (by setting $\phi_d^{PEO} = 0$), only the relaxation of PEO against the PMMA matrix is seen (λ_2). In a mixed scenario both relaxations are added with the corresponding weights ϕ_d^{PEO} for λ_1 and $\phi_h^{PEO}\phi_d^{PMMA}$ for λ_2. Therefore, the relative contributions of the two relaxations is given by the amplitudes

$$a_{PEO} = \frac{\varphi_d^{PEO}}{\varphi_d^{PEO} + \varphi_h^{PEO}\varphi_d^{PMMA}} \quad (5)$$

$$a_{PMMA} = \frac{\varphi_h^{PEO}\varphi_d^{PMMA}}{\varphi_d^{PEO} + \varphi_h^{PEO}\varphi_d^{PMMA}} \quad (6)$$

For the investigated system (10/10/80) we get $a_{PEO} = 0.56$ and $a_{PMMA} = 0.44$. However, rather than assuming an exponential decay of the two modes described above, we can use the simulations to calculate the real decay. The first contribution (a_{PEO}) corresponds to the single chain dynamic structure factor of PEO. To obtain this contribution, we calculate the scattering of the unfolded PEO chains (using absolute coordinates rather than the coordinates after folding the chain back into the periodic cell):

$$S_{chain}(Q, t) = \frac{1}{N}\sum_{n,m}^{N} \langle \exp(i\vec{Q}(\vec{r}_n(t) - \vec{r}_m(0)))\rangle \quad (7)$$

Here, the center of mass of each monomer was defined as a scattering particle. Using every atom as scattering particle adds no additional information since the observed Q values are below the atomistic resolution. The difference obtained by means of these two procedures is within the size of the symbols of the figure for the Q values shown. Using the absolute coordinates allows the calculation of $S_{chain}(Q,t)$ for Q values even below the limit given by the size of the cell ($Q \approx 0.15$ Å^{-1}).

The second decay in eq 4 describes the collective relaxation of PEO against PMMA. For a fully rigid PMMA matrix this term will not decay ($\lambda_2 = 0$), and an elastic contribution of relative intensity a_{PMMA} is expected in addition to the single chain dynamic structure factor of PEO. Using the simulations, this contribution is calculated by creating full contrast between the PEO and PMMA chains. This is achieved by assigning a scattering length of 1 to all PEO monomers of all chains in the system while the PMMA monomers are not regarded. For this calculation the coordinates of each bead have to be folded back into the unit cell since correlations between different chains have to be included (therefore, the limit for the Q values has to be taken into account).

Figure 2 shows the different contributions at two different temperatures calculated from the simulations. The upper part contains the PEO relaxation (hollow triangles). At the bottom, the relaxation of PEO against PMMA is shown (hollow circles). At $T = 400$ K a significant relaxation of the PMMA matrix is observed. Experimentally, the corresponding signal can be accessed using a sample of fully protonated PEO and fully deuterated PMMA. For chains with $M_n \approx 23$ kg/mol this was investigated by Niedźwiedź et al. at $T = 375$ K for a ratio of

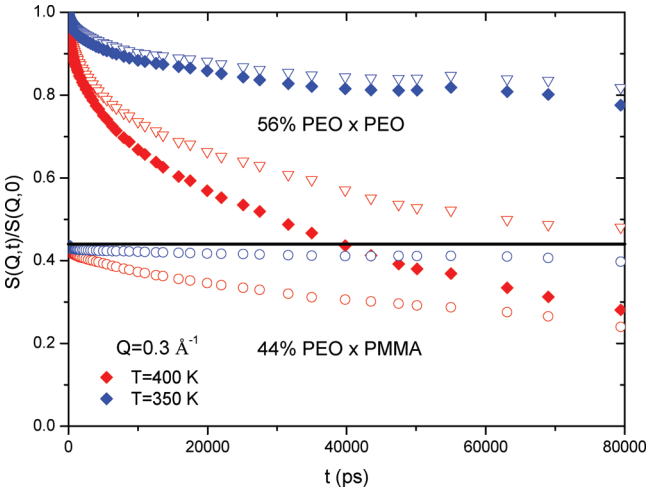

Figure 2. Contributions to the total dynamic scattering function calculated using the RPA. The upper 56% of the plot display the relaxation of the single chain dynamic structure factor of PEO (hollow triangles), the lower part shows the relaxation of PEO against PMMA (hollow circles), and the full symbols show the total scattering function ($T = 350$ and 400 K).

25% hPEO and 75% dPMMA (Figure 3). In this case, no decay of the dynamic structure factor is observed, confirming the

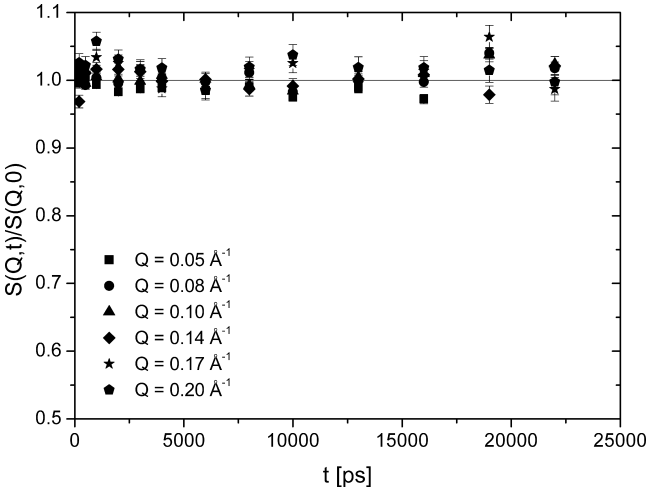

Figure 3. NSE data for a system containing 25% hPEO and 75% dPMMA at $T = 375$ K. In this experiment the molecular weight of PEO and PMMA was in the range of $M_n \approx 23$ kg/mol.

assumption of a fully frozen/immobile PMMA matrix ($\lambda_2 = 0$) at the investigated time and length scale. Our simulations show that this assumption is no longer valid once the chain length decreases due to the lower glass transition temperature. As a result, the signal measured by NSE no longer contains the PEO dynamics on top of a constant elastic contribution, but rather a combination of both decays (full symbols in Figure 2).

As a next step we can compare the predictions of the RPA (combined relaxation of two correlations) with the simulated scattering of our sample. Rather than comparing the RPA prediction with the real experimental results or the *simulated experiment*, which contains the protonated headgroups and the incoherent contribution to the NSE signal, we use coherent scattering of an ideally labeled sample containing 10% hPEO, 10% dPEO, and 80% dPMMA.

dx.doi.org/10.1021/ma2016634 | *Macromolecules* 2012, 45, 536–542

Figure 4a shows this comparison for T = 400 K at two Q values. The two curves for the RPA are calculated as shown in

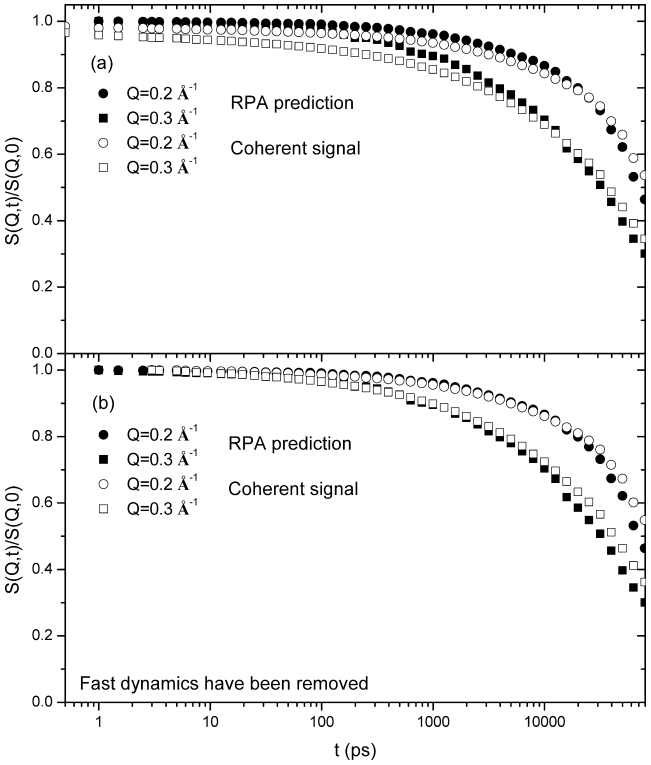

Figure 4. (a) Comparison of the dynamic scattering functions calculated using the RPA (full symbols) and directly calculated from the h/d scattering contrast for Q = 0.1 and 0.2 Å^{-1}. In (b) the fast dynamics of the coherent scattering signal have been removed.

Figure 2 (a superposition of the two relaxations with the corresponding amplitudes). The hollow symbols are calculated from the scattering of hPEO dPEO and dPMMA (HDD, 10/10/80).

A fast decay at very low times (t < 0.5 ps) is observed for the coherent scattering of the HDD sample. At t = 0.5 ps the dynamic scattering function has already decayed to 0.96 at Q = 0.3 Å^{-1} (for higher Q values this effect increases). Because of this fast decay at low times, the HDD function lies below the values of the RPA for times up to about 100 ps. The origin of this fast decay is the collective fast relaxation of the interchain correlations. Experimentally, it was investigated in pure dPEO in ref 17 where a relaxation of the coherent scattering function within the first picoseconds was observed. The peak of these collective correlations lies at $Q \approx 1.5$ Å^{-1}. A small contribution, however, can also be seen at much lower Q values (with a significantly reduced intensity). This fast decay, which is caused by the atomic structure of the sample, is obviously not seen in the RPA calculations. There, only the scattering of the monomer blobs is considered, and the fast dynamics are invisible. Experimentally, this fast contribution is removed by subtracting the scattering from samples with fully deuterated polymers, where the scattering function decays to zero within the first few picoseconds. This sample has been measured during the experiments described above. However, due to the high content of protonated material (the initiators of the chain), additional contributions arising from the h/d contrast have been observed. Using the correct chemical labeling in the simulation (protonated headgroups), this experimental curve could also be described. However, the measurement was not suited for the correction of the fast decay. Figure 4b shows the comparison of the RPA with the coherent scattering signal where the fast decay has been removed. In this case excellent agreement is found for times up to about 20 ns.

Small deviations between the two functions are seen for t > 20 ns. A similar behavior was found for these times studying the self-motion of PEO in the PMMA environment and was connected to the motion of PEO monomers exploring their local environment.[10] For T = 350 K similarly good agreement as shown in Figure 4 has been observed. The comparison using exponential functions as seen in eq 4 fails because the two decaying channels do not follow an exponential decay.

This comparison has allowed us to study the origin of the coherent scattering signal of a ternary polymer blend in the context of the RPA. Two relaxation channels of PEO are observed, and the RPA allows the calculation of the two corresponding amplitudes. In the case of a rigid PMMA matrix the single chain dynamic structure factor of PEO is measured by NSE on top of the elastic contribution caused by the stiff PMMA matrix. However, our calculations show that for shorter chains the final signal is a mixture of both relaxations. In this case the knowledge about the relaxation of the PMMA matrix is necessary for a full interpretation of the experimental NSE data.

SINGLE CHAIN DYNAMIC STRUCTURE FACTOR WITHIN THE ROUSE MODEL

In a previous work,[10] we have presented a detailed analysis of the simulated PEO/PMMA system in terms of the Rouse modes and Rouse mode correlators. It was shown that the Rouse mode correlators corresponding to PEO in the blend were significantly stretched in particular at low temperatures. The averaged Rouse times $\langle\tau_p\rangle$ were obtained from KWW fits to the Rouse mode correlators. With decreasing temperature, a stronger dynamic asymmetry between the PEO and PMMA components (separation between the segmental relaxation time of PEO and PMMA) was created, resulting in strong deviations from the usual p^{-2} dependence of the Rouse times with the mode number p. For T = 400 K an exponent of 2.45 was found; at 350 K it increased to 2.7. In contrast, ideal Rouse behavior was found for pure PEO once the length scale exceeded the atomic detail involved in the MD simulations.[17]

Now we address the question of how the strong deviations from the Rouse behavior found for the chain dynamics of PEO in the blend affect the Rouse expression for the single chain dynamics structure factor, $S_{chain}(Q,t)$, which was first deduced by de Gennes[18,19] and which is habitually used to analyze neutron scattering results. Such an expression is based, first of all, on the so-called Gaussian approximation; i.e., it assumes that the atomic displacements distribution function is Gaussian. Under this assumption, $S_{chain}(Q,t)$ (eq 7) can be written as

$$S(Q,t) = \frac{1}{N}\sum_{m,n}^{N} \exp\left(-\frac{1}{6}Q^2\langle\Delta r_{nm}^2(t)\rangle\right) \quad (8)$$

with the mean-square segment correlation function $\langle\Delta r_{nm}^2(t)\rangle = \langle(r_n(0) - r_m(t))^2\rangle$.

Taking into account the definition of Rouse modes (Rouse coordinates) and the orthogonality of these modes, $\Delta r_{nm}^2(t)$ can be expressed as

dx.doi.org/10.1021/ma2016634 | Macromolecules 2012, 45, 536−542

$$\langle \Delta r_{nm}{}^2(t)\rangle = 6D_R t + |n-m|l^2 + \frac{4Nl^2}{\pi^2}\sum_{p=1}^{N}\frac{1}{p^2}\cos\left(\frac{p\pi n}{N}\right)\cos\left(\frac{p\pi m}{N}\right)(1-\langle \vec{X}_p(t)\vec{X}_p(0)\rangle) \quad (9)$$

where D_R is the center-of-mass diffusion and $\langle \vec{X}_p(t)\vec{X}_p(0)\rangle$ are the Rouse mode correlators. If we now consider simple exponential decay of these correlators, eqs 8 and 9 give

$$S(Q,t) = \frac{1}{N}\exp(-Q^2D_Rt)\sum_{m,n}^{N}\exp\left(-\frac{1}{6}|n-m|Q^2l^2\right)\exp\left\{-\frac{2}{3}\frac{R_{ee}{}^2Q^2}{\pi^2}\sum_p\frac{1}{p^2}\left\{\cos\left(\frac{p\pi m}{N}\right)\cos\left(\frac{p\pi n}{N}\right)\left(1-\exp\left(-\frac{t}{\tau_p{}^2}\right)\right)\right\}\right\} \quad (10)$$

Using these equations, we now have several possibilities to calculate the single chain dynamic structure factor of the PEO chains from the simulation data:

A. With the knowledge about the coordinates of each monomer, we can use eq 7 to directly calculate $S_{chain}(Q,t)$. Technically, we are using radially averaged distribution histograms to include the isotropic nature of the system. This function then corresponds to the actual single chain dynamic structure factor.

B. The correlation functions $\langle \Delta r_{nm}{}^2(t)\rangle$ can directly be calculated using the coordinates of the monomers. Together with eq 8, this also yields $S_{chain}(Q,t)$ if the segmental correlation functions are Gaussian.

C. $\langle \Delta r_{nm}{}^2(t)\rangle$ is also accessible using the Rouse correlators together with eq 9. Here we can directly insert the correlators $\langle \vec{X}_p(t)\vec{X}_p(0)\rangle$ from the Rouse analysis of the system or use the fitted stretched exponential functions

$$\left\langle \vec{X}_p(t)\vec{X}_p(0)\right\rangle = \exp(-(t/\tau)_p{}^{\beta}) \quad (11)$$

Both approaches yield the same result since the decay of the correlators is well described by the KWW fits.

D. Finally, for a system with Rouse behavior (as is the case for pure PEO), we can directly use eq 10.

We will now compare these four different approaches for the pure PEO system and for PEO in PMMA. The results will be presented for a temperature of 350 K in order to highlight the dynamic asymmetry in the blend. At T = 400 K, the significant relaxation of the PMMA matrix softens the dynamic asymmetry of the system (see Figure 2).

For pure PEO at T = 350 K Figure 5a shows the single chain dynamic structure factor at Q = 0.2 and 0.3 Å^{-1} calculated by the different methods. The center-of-mass diffusion of the chain has been removed for all calculations either by removing the center of mass diffusion in the absolute coordinates (in methods A and B) or by setting the diffusion coefficient D_R = 0 (for methods C and D). All four approaches show excellent agreement allowing the following conclusions:

1. The agreement between the direct calculation of $S_{chain}(Q,t)$ (A) and the method using the mean-square segmental correlation functions with eq 8 (B) confirms the Gaussian distribution of $\langle \Delta r_{nm}{}^2(t)\rangle$. Therefore, the Gaussian assumption for pure PEO is valid and allows us to calculate the coherent scattering using eq 8.

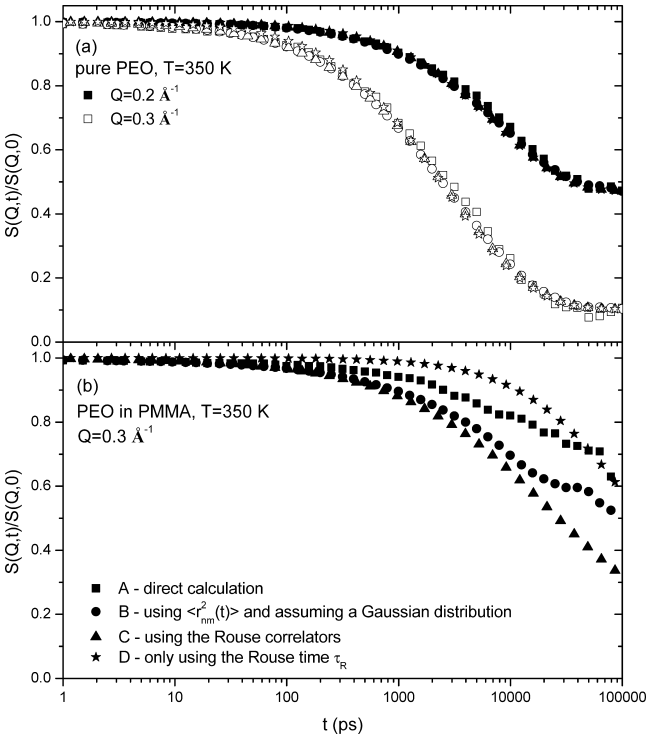

Figure 5. (a) Single chain dynamic structure factor for pure PEO chains at T = 350 K calculated with the four methods described in the text at Q = 0.2 and 0.3 Å^{-1}. The center-of-mass diffusion has been removed in all cases. This is the reason for the plateau at long times. (b) Single chain dynamic structure factor for PEO chains in the blend at T = 350 K and Q = 0.3 Å^{-1} calculated with the four methods described in the text. The center-of-mass diffusion has been removed.

2. The calculation of the single chain dynamic structure factor using the Rouse description of the chains also yields excellent agreement. Even using exponential decays with τ_R as the only parameter allows the correct calculation of $S_{chain}(Q,t)$, confirming the findings that the pure PEO system is fully described by the Rouse model.[17]

Now we analyze the blend system (Figure 5b). We will only present results for Q = 0.3 Å^{-1} since other Q values show a similar behavior. This time big differences are found for the different methods.

Comparing the direct calculation of $S_{chain}(Q,t)$ (A) with the method using the mean-square segmental correlation functions (B), we see a significantly slower decay for the direct method. Obviously, the assumption of Gaussian distribution functions is false and eq 8 fails. In fact, during the analysis of the distribution function of the atomic displacements in PEO/PMMA carried out in ref 10 it was shown that the non-Gaussianity of PEO in the blend increases drastically as the temperature of the system decreases.

Now we compare $S_{chain}(Q,t)$ with the curves that were calculated using the Rouse correlators. For times up to about 20 ns, relatively good agreement is found between methods B and C. Both functions obviously fail to describe the correct single chain dynamic structure factor since they rely on Gaussian distribution functions. Their agreement up to 20 ns, however, confirms the fact that the system is correctly described using the exponentially stretched Rouse correlators. This means that

dx.doi.org/10.1021/ma2016634 | Macromolecules 2012, 45, 536−542

$\langle \Delta r_{nm}^2(t) \rangle$ can be correctly calculated only with the information about the Rouse correlators (time scale τ_p and stretching parameter β_p). This agreement was also observed when directly comparing $\langle \Delta r_{nm}^2(t) \rangle$ calculated from the simulations with the results using eq 9 and the data from the Rouse analysis. The difference in the decays in Figure 5b for $t > 20$ ns can be connected to similar deviations we found in the dynamic incoherent scattering functions of PEO in PMMA.[10] Up to this point, good fits with KWW functions were possible; at $t > 20$ ns the actual decay of the incoherent function was slower than the fitted KWW functions (similar to the effect found here).

Finally, looking at Figure 5b, we see that the calculation obviously fails if we simply use the pure Rouse expression (D). In this case $S_{chain}(Q,t)$ relaxes much slower than the real system which is caused by the $p^{-2.7}$ dependence of the relaxation times τ_p. Only using τ_R as input parameter results in significantly slower local relaxation times than actually found for the system.

In summary, we can say that the Rouse expression for the single chain dynamic structure factor (eq 10) cannot be used in the case of asymmetric blends, even if it is generalized by including stretched exponential decay of the Rouse correlators. The reason is that this expression relies on the Gaussian approximation for the atomic displacements distribution function, an assumption that clearly breaks in the case of asymmetric blends, in particular at low temperatures. It is noteworthy that this is not the case for the correlation function of the end-to-end vector R_{ee}, $\langle R_{ee}(t)R_{ee}(0) \rangle$, which can be measured by dielectric spectroscopy in the so-called A-type polymers (normal mode relaxation). The Rouse expression for this correlator is only based on the orthogonality of the Rouse modes (as $\langle r_{nm}^2(t) \rangle$) and thereby can be generalized for the case of asymmetric blends[20] where the Rouse correlators results to be nonexponential, but the Rouse modes are still orthogonal in a good approximation.

SUMMARY AND CONCLUSIONS

1. Experiments have shown that a decrease of the chain length significantly influences the collective dynamics of PEO in PMMA. This effect is caused by higher mobility of the PMMA matrix (leaving the regime of a completely frozen matrix) and faster motion of the PEO chains. The interpretation of the scattering curves is difficult due to the significant influence of the protonated head groups for the short chains.

2. Using the NSE experiments, we were able to fully validate the simulated PEO/PMMA system for chain dynamics. For a successful comparison it was necessary to include the incoherent contribution to the scattering signal and, even more important, the effects of the protonated initiators of the investigated chains.

3. Using the RPA, we have seen that the measured signal is a combination of the PEO chain relaxation and, in addition, a relaxation of PEO against the matrix. For a fully frozen matrix, as was the case for the long chains due to the higher glass transition temperature, this contribution builds a constant, elastic contribution. For the short chains both effects have to be regarded. In addition, the fast dynamics (at times in the picosecond regime) have to be considered in the experiment (fully deuterated background measurements).

4. Calculating the single chain dynamic structure factor for pure PEO and PEO in PMMA, using the results from the Rouse mode analysis, good agreement was achieved only for pure PEO. For PEO in PMMA significant differences were observed. Using KWW functions to describe the Rouse correlators the dynamic correlation functions $\langle \Delta r_{nm}^2(t) \rangle$ can be recovered. The calculation of $S_{chain}(Q,t)$ failed due to the strong heterogeneity of the system which results in a strong non-Gaussianity of the distribution functions.

AUTHOR INFORMATION

Corresponding Author

*E-mail: fernando.alvarez@ehu.es.

ACKNOWLEDGMENTS

This research project has been supported by the European Commission NoE SoftComp, Contract NMP3-CT-2004-502235, and the "Donostia International Physics Center". J.C. and F.A. acknowledge support from the projects MAT2007-63681 and IT-436-07 (GV).

REFERENCES

(1) Colmenero, J.; Arbe, A. *Soft Matter* **2007**, *3*, 1474−1485.
(2) Maranas, J. K. *Curr. Opin. Colloid Interface Sci.* **2007**, *12*, 29−42.
(3) Genix, A.-C.; Arbe, A.; Alvarez, F.; Colmenero, J.; Willner, L.; Richter, D. *Phys. Rev. E* **2005**, *72*, 031808.
(4) Lutz, T. R.; He, Y.; Ediger, M. D.; Cao, H.; Lin, G.; Jones, A. A. *Macromolecules* **2003**, *36*, 1724−1730.
(5) Brosseau, C.; Guillermo, A.; Cohen-Addad, J. P. *Macromolecules* **1992**, *25*, 4535−4540.
(6) Lartigue, C.; Guillermo, A.; Cohen-Addad, J. P. *J. Polym. Sci., Part B: Polym. Phys.* **1997**, *35*, 1095−1105.
(7) Niedzwiedz, K.; Wischnewski, A.; Monkenbusch, M.; Richter, D.; Genix, A.-C.; Arbe, A.; Colmenero, J.; Strauch, M.; Straube, E. *Phys. Rev. Lett.* **2007**, *98*, 168301.
(8) Sakai, V. G.; Chen, C.; Maranas, J. K.; Chowdhuri, Z. *Macromolecules* **2004**, *37*, 9975−9983.
(9) Farago, B.; Chen, C.; Maranas, J. K.; Kamath, S.; Colby, R. H.; Pasquale, A. J.; Long, T. E. *Phys. Rev. E* **2005**, *72*, 031809.
(10) Brodeck, M.; Alvarez, F.; Moreno, A. J.; Colmenero, J.; Richter, D. *Macromolecules* **2010**, *43*, 3036−3051.
(11) Diddens, D.; Brodeck, M.; Heuer, A. *Europhys. Lett.* **2011**, *95*, 56003.
(12) Sokolov, A. P.; Novikov, V. N.; Ding, Y. *J. Phys.: Condens. Matter* **2007**, *19*, 205116.
(13) Tombakoglu, M.; Akcasu, A. *Polymer* **1992**, *33*, 1127−1139.
(14) Benmouna, M.; Benoit, H.; Borsali, R.; Duval, M. *Macromolecules* **1987**, *20*, 2620−2624.
(15) Akcasu, A. Z.; Tombakoglu, M. *Macromolecules* **1990**, *23*, 607−612.
(16) Montes, H.; Monkenbusch, M.; Willner, L.; Rathgeber, S.; Fetters, L.; Richter, D. *J. Chem. Phys.* **1999**, *110*, 10188−10202.
(17) Brodeck, M.; Alvarez, F.; Arbe, A.; Juranyi, F.; Unruh, T.; Holderer, O.; Colmenero, J.; Richter, D. *J. Chem. Phys.* **2009**, *130*, 094908.
(18) de Gennes, P. *Physics 3*; 1967.
(19) Doi, M.; Edwards, S. F. *The Theory of Polymer Dynamics*; International Series of Monographs on Physics; Oxford University Press: Oxford, 1988.
(20) Arrese-Igor, S.; Alegría, A.; Moreno, A. J.; Colmenero, J. *Macromolecules* **2011**, *44*, 3611−3621.

Macromolecules

ARTICLE

pubs.acs.org/Macromolecules

Dynamics and Deformation Response of Rod-Containing Nanocomposites

Gregory N. Toepperwein,[†] Robert A. Riggleman,[‡] and Juan J. de Pablo*[,†]

[†]Department of Chemical and Biological Engineering, University of Wisconsin, Madison, Wisconsin 53706-1691, United States

[‡]Department of Chemical Engineering, University of Pennsylvania, Philadelphia, Pennsylvania 19104, United States

Supporting Information

ABSTRACT: Theoretical and computational studies of polymer nanocomposites have largely focused on spherical inclusions in a polymer matrix. In order to address the influence of particle shape on nanocomposite behavior, extensive Monte Carlo and molecular dynamics simulations are used to examine the structure and deformation behavior of a model polymer upon addition of rods of varying aspect ratios. It is found that, at constant temperature, nanorod length does not meaningfully affect the elastic properties of composites but does affect postyield properties, such as the strain hardening modulus. In contrast, at constant T/T_g, several trends with additive length arise. Examination of the polymer bond autocorrelation function during deformation reveals that longer, dispersed rods induce a broadening of the relaxation spectrum. Nanocomposites show longer bond orientation relaxation times than the pure polymer during all stages of deformation. For the truly nanoscale additives used in this study, polymer mobility is found to be only a weak function of distance to the nearest nanorod so long as the additives did not aggregate.

INTRODUCTION

It is generally accepted that the influence of nanoparticles on polymer behavior depends on a host of properties[1−5] including concentration, particle geometry, particle size, interfacial interactions, and thermal history. Past experimental work, however, has led to diverse, and sometimes conflicting, rationalizations of nanocomposite behavior. It is only recently that molecular theory and simulation have been used to interpret experimental data and provide a molecular-level view of observed behaviors. The scarcity of molecular studies of polymer nanocomposites (PNC) can be largely attributed to the difficulty associated with generating large ensembles of equilibrium configurations for highly entangled polymeric materials, and the challenges involved in studying the structure and dynamics of such systems out of equilibrium (e.g., under tension or compression).

A number of theories have been proposed to explain the influence of nanoparticles on nanocomposite behavior. The "interaction zone" hypothesis posits that a reduction in polymer mobility near the surface of a particle arises from a local reorganization of the polymer into a more structured or possibly glassy state.[6,7] This ordered or glassy region imparts improved mechanical properties to the system, with smaller particles having a disproportionate influence for their concentration.[6] A second hypothesis is that fillers may act as highly functional cross-links[8] capable of forming bridges of polymer between them. A study of entangled PNC annealing below T_g[9] suggested that aggregating particles formed more such bridges. Finally, it has been suggested that particles may directly[10] or indirectly[11] alter the entanglement state of the system. Recent simulations[12] have shown that the entanglement lengths of attractive rod-containing PNCs are significantly lower than that of the pure polymer for inclusions that are themselves immobile on the time scale of reptation. However, if the time scales of additive relaxation are much faster than reptation, the entanglement length of the PNC is comparable to that of the corresponding pure polymer. These results suggest that inclusions influence entanglement length by direct restriction of chain motion, and not through an alteration to the matrix configuration vis-à-vis that of the pure polymer.

Simulation studies have examined several aspects of PNC reinforcement. Simulations of smooth spherical fillers, smaller than the polymer's radii of gyration, showed better fracture resistance in the melt state than below T_g.[13] Gersappe attributed this behavior to particle mobility, which allowed for better energy dissipation at higher temperature. A nanoparticle clustering study showed that the shear viscosity is higher for dispersed particle systems, in contrast to the behavior observed for macroscopic particles.[14] That study further showed that deformation tends to disperse particles. Recent simulations have also examined the deformation behavior of PNCs and compared it to that of the corresponding pure glasses.[15] It was found that nanoparticles stiffen the polymer glass (they increase the elastic modulus) and suppress creep response. Those simulations demonstrated that during deformation, the mobility of the polymer chains increases significantly in both the pure polymer and the nanocomposite systems.

Received: July 26, 2011
Revised: October 12, 2011
Published: December 12, 2011

Experimental studies of both carbon nanotube composites[16] and polymers with clay inclusions[17] suggest that particle size and shape are key factors in the mechanical response of polymer nanocomposites. However, as noted in a recent literature review,[18] theoretical and computational studies of PNC with anisotropic inclusions have been limited. Buxton and Balazs[19] used a network spring model whose spring constants were chosen to describe different shaped regions of matrix and filler. They used this model to simulate the behavior of spheres, rods, and disks in a polymer and demonstrated that rods and disks, when randomly aligned, provided superior mechanical properties in the elastic regime as compared to spheres. Knauert et al.[20] examined the viscosity and isotropic tensile strength of isohedrals (i.e., many-sided polygons), rods, and sheets using a course-grained bead−spring model. Recognizing the difficulty of accurately measuring viscosity in the limit of zero strain rate, they opted to perform nonequilibrium simulations of unentangled PNC systems at high shear rates, in the shear-thinning regime. Of the three filler geometries considered in their work, they found that rods provide the largest increase in viscosity, but improved strain at fracture the least. They noted that particle−polymer interactions correlate well with the viscosity increase, but they were unable to provide an explanation for the observed changes in strain at fracture.

Interest in rod-like additives is largely motivated by interest in carbon nanotubes, which have been considered extensively in the literature as polymer fillers.[21−24] However, for the comparatively short rods examined in this paper, the closest experimental analogue is provided by the work of Kalfus and Jancar,[25] who examined spherical and platelet hydroxyapatite inclusions in poly(vinyl acetate) in order to examine the role of geometry. They found shape to have a negligible effect on storage modulus in the glassy state, but did note that the storage moduli of the spherical PNCs had stronger temperature dependence in the melt state. They concluded that filler geometry was a second-order contribution to PNC reinforcement at constant temperature. As an alternative to inherently anisotropic fillers, Akcora et al. examined poly styrene grafted silica particles in a poly styrene matrix.[26] These spherical additions formed various anisotropic aggregates depending upon the length and number of grafted chains. They found that particle sheets induced solid-like behavior during shear deformation, whereas dispersed spheres did not.

In what follows, we provide a systematic study of the effect of particle aspect ratio on the mechanical behavior of nanocomposites. Computational models, which have been under-utilized in the study of anisotropic PNC systems, allow us to probe the effect of rod length without perturbing other variables, and they provide a reasonable description of the short length and time scales at the limits of experimental accessibility. Specifically, we examine the local dynamics of these systems in the melt state, and how they respond to constant strain-rate deformation in the glassy state. We find that particle geometry has little effect on elastic properties at constant temperature, but higher-aspect ratio additives improve the postyield strength of the composites. However, clear trends with rod length do occur in the elastic regime if materials are examined at the same temperature relative to their respective glass transitions. Nanocomposites show longer bond orientation relaxation times than the pure polymer during all stages of deformation. Additionally, for the small additives we consider, polymer mobility is not reduced meaningfully in the presence of the particle.

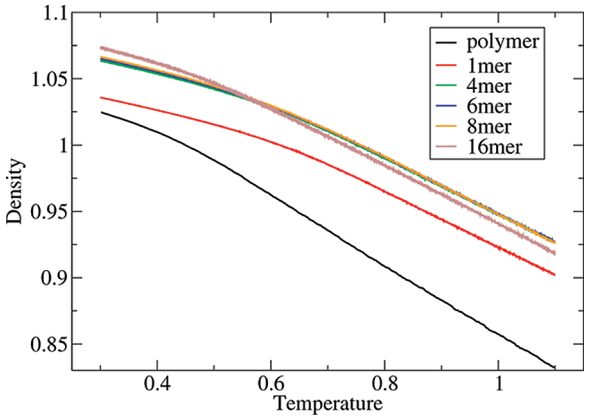

Figure 1. Cooling curves for each PNC. Results above a temperature of 1.1 are erratic due to the quench from $T = 1.75$ to $T = 1.2$. Only data values shown in the figure were used for the determination of T_g.

MODEL AND CHARACTERIZATION

This work utilizes a coarse-grained Lennard-Jones polymer model of fully flexible chains. Semiflexible nanorods of 1, 4, 6, 8, and 16 beads were inserted into these melts at concentrations of 10.0 wt %. Throughout this manuscript, nanocomposite systems are referred to by the length of their inclusions (i.e., 1-mer, 4-mer, etc.). The strength of polymer−particle interactions is three times stronger than that of polymer−polymer or particle−particle interactions, thereby promoting dispersion of the rods in the polymer matrix; i.e., $\varepsilon_{PN} = 3.0\varepsilon_{PP} = 3.0\varepsilon_{NN}$, where ε_{PP} represents the polymer−polymer LJ well depth, ε_{NN} is the nanorod−nanorod well depth, and ε_{PN} is the cross interaction well depth. Both particles and polymer are constructed of beads with a diameter of σ. If we take σ to be on the order of 2 nm, a typical Kuhn length for a flexible polymer, then our nanorods have a diameter similar to that of single-walled carbon nanotubes. The bonds along the polymer backbone are modeled as harmonic springs with an equilibrium bond length of σ; the nanorod internal bonds have an equilibrium bond length of $2/3\ \sigma$, leading to nanorod aspect ratios of 1, 3, 4.33, 5.67, and 11. The filler has an additional bending potential that enforces a nearly linear configuration. Additional details on the model and its properties have been presented in previous work.[12]

In reduced units, temperature, pressure, and time are defined respectively as $(kT)/(\varepsilon)$, $(\sigma^3 P)/(\varepsilon)$, and $((\varepsilon t^2)/(m\sigma^2))^{1/2}$. Here T, P, and t are temperature, pressure, and time, k is the Boltzmann constant, and m is the mass of a bead, taken to be unity in this study. Time in reduced units will be denoted as τ.

Starting with the equilibrated melts at $T = 1.75$ produced previously,[12] several independent configurations of each sample were used to prepare glasses. Systems were quenched to a temperature of 1.2, well above T_g, and then cooled to a reduced temperature of 0.3 over 900τ at a cooling rate of 10^{-3}. From each cooling run, two configurations were extracted, corresponding to two different temperatures below the glass transition temperature. The first set were all extracted at the same absolute temperature of $T = 0.3$. The second set were extracted at the same temperature relative to their respective glass transitions, $T/T_g = 0.9$.

For the $T/T_g = 0.9$ runs, T_g was obtained for each system from cooling runs by plotting density as a function of temperature. Results are shown in Figure 1; lines were fit to the high temperature and low temperature regimes, and their intersection

dx.doi.org/10.1021/ma2017277 |Macromolecules 2012, 45, 543–554

Table 1. Number Density at Various Temperatures[a]

system	density at $T = 1.75$	density at $T/T_g = 0.9$	density at $T = 0.3$	T_g
pure polymer	0.667	0.984	1.024	0.519 ± 0.049
1-mer	0.772	0.999	1.036	0.620 ± 0.017
4-mer	0.797	1.026	1.063	0.610 ± 0.020
6-mer	0.796	1.027	1.065	0.610 ± 0.020
8-mer	0.792	1.028	1.067	0.607 ± 0.020
16-mer	0.770	1.036	1.073	0.557 ± 0.030

[a] All density values are ±0.002.

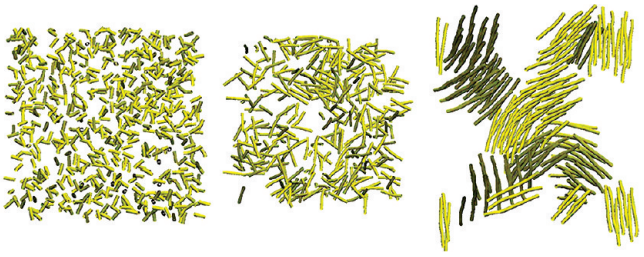

Figure 2. Representative configurations of nanorods dispersed in a polymer matrix at $T = 1.75$. For clarity, only the nanorods are shown. The figures from left to right correspond to a 10 wt % filler concentration of 4-mers, 8-mers, and 16-mers. Only the 16-mers were found to self-assemble into bundles.

was identified as T_g. The values generated in this manner are given in Table 1. The T_g of the pure polymer is larger than reported in previous works,[27,28] where a slower cooling rate was employed. The thermal history of the current samples is the same as that used in our previous examination of entanglement lengths during glassy deformation.[12]

Results obtained at the two different temperatures were similar. In the interest of brevity, the majority of this work focuses on the $T/T_g = 0.9$ systems. Discussion of the $T = 0.3$ results is limited to a subsection that highlights the main differences observed at the two temperatures. Complete results for the $T = 0.3$ systems are available in the Supporting Information.

After cooling, systems were aged for 1000τ at constant pressure. The systems then underwent uniaxial compression or extension, performed by deforming one dimension at a constant true strain rate while the other dimensions were allowed to relax to maintain constant pressure. All systems maintained nearly constant volume during this process. Strain rates of 4.4×10^{-4} and 1.1×10^{-4} were applied for both modes of deformation until final true strains of 1.104 and 1.027 were attained, respectively. Note that all strain rates will be reported as positive numbers, although the true sign will be positive for tension and negative for compression. For the 16-mer nanocomposite systems, results are truncated at an absolute strain of 0.7, well before the smallest dimension of the simulation box begins to approach the length of the nanorods.

Such deformations are described as simple uniaxial, in contrast to the triaxial deformations that induced cavitation in previous work.[28] The systems considered here would undergo shear yielding if deformed further. A detailed exploration of loading conditions required to induce alternative modes of failure in PNC is beyond the scope of the current work; however, note that Roettler and Robbins[29] have discussed the case of pure polymers. Those authors reported that strongly triaxial deformation usually leads to crazing, and that the exact transition between modes of failure is determined by a pressure-modified von Mises criterion.

Addition of nanorods to the polymer imparts significant changes to the density of the resulting composite (Figure 1). Table 1 summarizes the density of the various PNCs in the equilibrium melt ($T = 1.75$), as well as in the two glassy states considered here ($T = 0.3$ and $T/T_g = 0.9$). Across all temperatures, the pure polymer has a lower density than the nanocomposites, but this densification effect is most pronounced in the high-temperature melt state. In general, the 4-mer, 6-mer, and 8-mer systems have similar densities, while the 1-mer is less dense. The density of the 16-mer exhibits a stronger temperature dependence relative to the other PNCs. The glass transition temperature decreases with increasing rod length for the nanocomposites, and the pure polymer has the lowest T_g.

The nanocomposite systems with shorter rods (1-mer, 4-mer, 6-mer, and 8-mer) show excellent dispersion of the particles. It was previously shown[12] that these nanorods exhibit a small degree of local alignment over a length scale approximately equal to the rod's length, but that they adopt a random orientation globally (see Figure 2). The 8-mers show some regions of relatively higher and lower concentration, but no clear tendency to organize beyond such concentration fluctuations. For the 16-mer nanocomposite, however, the rods self-assemble spontaneously to form large bundles or aggregates. These bundles consist of 8 to 20 parallel rods separated by a monolayer of polymer. Figure 2 shows a representative configuration of these aggregates. In all systems, the attractive polymer−particle interaction leads to a polymer layer surrounding the rods, but for the 16-mer aggregates it leads to trapped layers of polymer between the aligned rods.[12] The bundles form transient end-to-side connections at several points during the simulation, but fail to organize on a global scale. Note that the locally organized regions of polymer around each rod are in contact with each other in such a way as to create a network that percolates the system. Because of the relatively high concentration of additives in our simulations, these polymer−particle connections span the entire system for all rod lengths considered here.

The dynamics of the resulting composites are quantified in terms of the bond autocorrelation function, $C_b(t)$, which previous studies have used to calculate segmental dynamics and relaxation times.[15,30,31] This quantity is given by

$$C_b(t) = \langle P_2[\mathbf{b}(t)\cdot\mathbf{b}(0)]\rangle \quad (1)$$

where P_2 is the second Legendre polynomial, $\mathbf{b}(t)$ is a unit vector aligned along the bond of a polymer, and the angular brackets indicate an average over all bonds in the system. We quantify changes to the system dynamics by fitting the bond autocorrelation function to a Kohlrausch−Williams−Watts (KWW) stretched exponential function of the form

$$C_b(t) = C_o e^{-(t/\tau_{eff})^{\beta}} \quad (2)$$

where C_o, τ_{eff}, and β are fitting parameters referred to, respectively, as the pre-exponential factor, unnormalized relaxation time, and the stretching exponent. Because various properties of our system are not constant during deformation (e.g., the stress), we find it useful to measure the dynamics within discrete "time-windows", thereby facilitating comparison to changes in other properties. After performing a deformation, C_b is fit to simulation data spanning time-windows of 300, 600, and 900τ. The length of

dx.doi.org/10.1021/ma2017277 |*Macromolecules* 2012, 45, 543–554

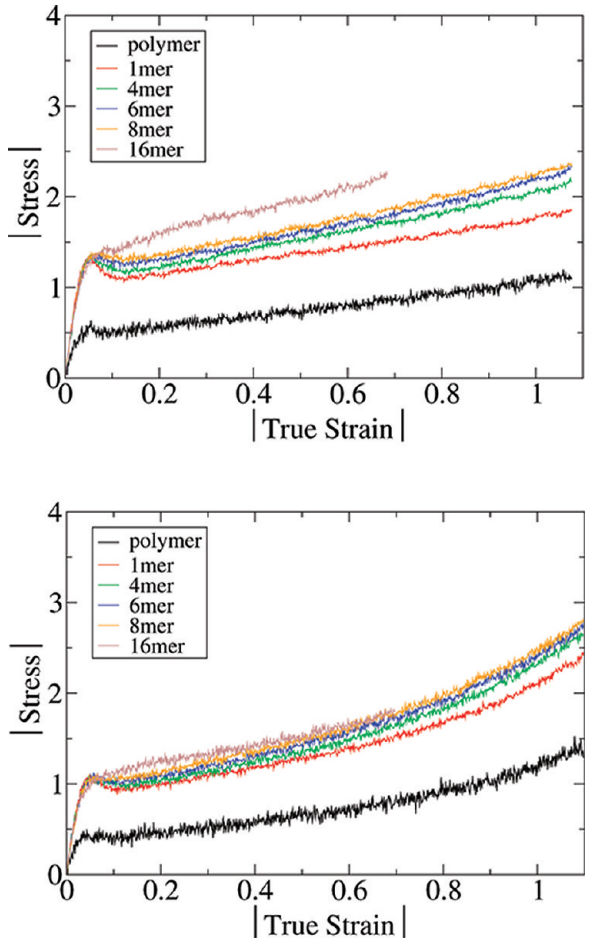

Figure 3. Results for deformation in compression (top) and extension (bottom) for 10 wt % filler at $T/T_g = 0.9$ under a strain rate of 4.4×10^{-4}. Black lines represents pure polymer, other lines represent nanocomposites loaded with nanorods of indicated lengths.

the time-window chosen had no statistically meaningful effect. Additional information about the time-window approach employed here is given elsewhere.[30]

GLASS DEFORMATION

A simple and direct way of assessing mechanical properties from simulations is to perform deformations in the glassy state. Such nonequilibrium molecular simulations provide information about the dynamics of the system as well as a direct measurement of mechanical properties. For the remainder of this work "strain" will be used to refer to the absolute value of true strain, and "stress" will be used to refer to the absolute value of the true stress in units of $\varepsilon_{PP}/\sigma^3$.

For all PNCs considered here, the addition of particles drastically increases the stress required to deform the system. The stress−strain behavior of our PNC glasses is illustrated in Figure 3 at a strain rate of 4.4×10^{-4}. Stress−strain behavior at a strain rate of 1.1×10^{-4} (not shown for brevity) is qualitatively similar; differences resulting from changes in strain rate will be covered in the following discussion.

Strain softening, a decrease in stress following yield, occurs in all systems except the 16-mer. Strain softening in polymeric systems results from a structural reorganization and is associated with rejuvenation in glasses.[32,33] For the spherical particles, the

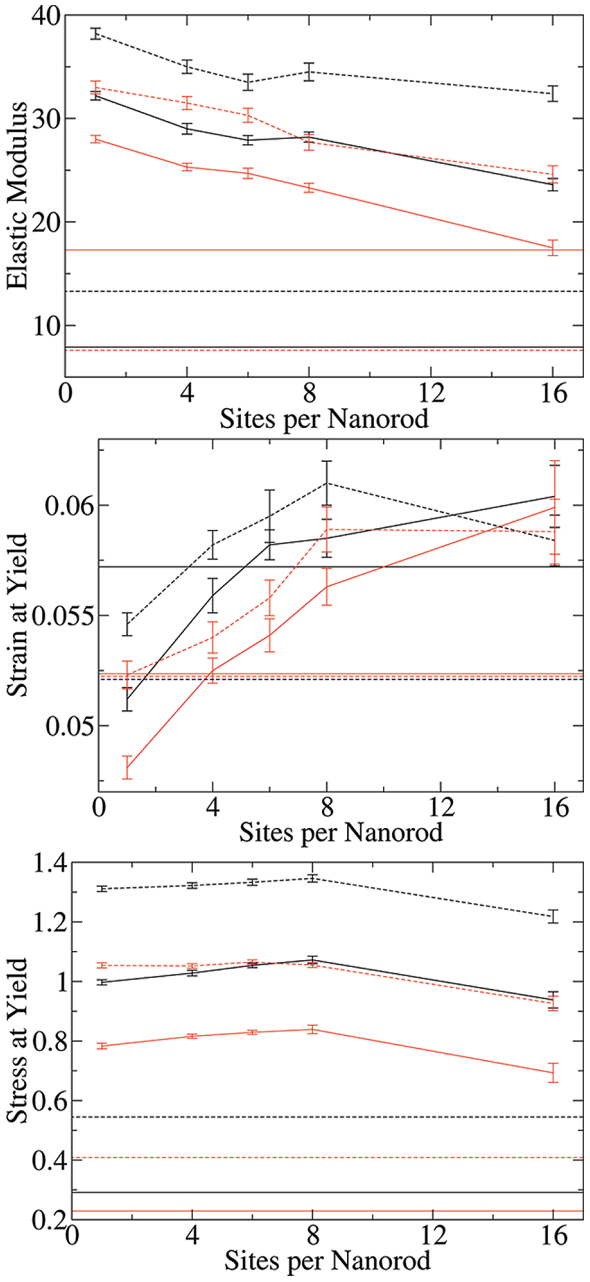

Figure 4. Elastic modulus (top), yield strain (middle), and yield stress (bottom) as a function of rod length. Pure polymer results represented as horizontal lines. Black lines denote compression and red lines denote tension. Solid lines are used for systems with strain rates of 1.1×10^{-4} and dashed lines for systems with strain rates of 4.4×10^{-4}. Note that the error reported for these systems is the error in the measurement at that given temperature; there is an additional error associated with identifying a specific glass transition temperature.

strain softening behavior is more pronounced than that observed in the pure polymer. This softening behavior decreases with increasing rod length, entirely disappearing in the 16-mer case.

The stress−strain response to simple uniaxial deformation observed here stands in contrast to the response obtained during triaxial deformation observed in previous work.[28] The stress peaks observed in triaxial deformation are 4 (PNC) to 6 times (pure polymer) larger than those reported here. This is due to the stress-peak representing fundamentally different behaviors.

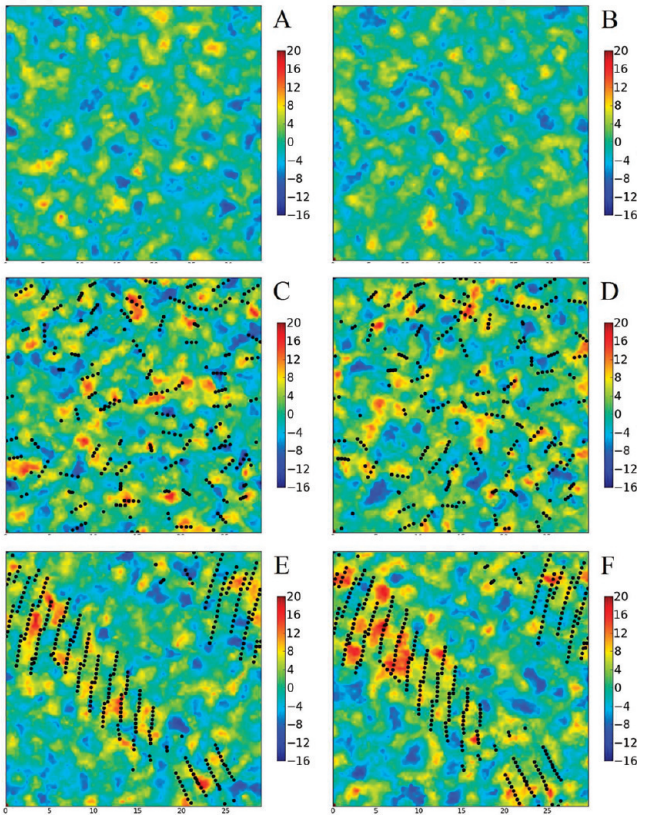

Figure 5. Cross section of local stress corresponding to 3σ thick slices. Images A, C, and E correspond to systems before deformation, and images B, D, and F correspond to systems at a strain of 0.055 (near yield point). Images A and B correspond to pure polymer, C and D show results for the 4-mer PNC, and E and F for the 16-mer PNC.

In a simple uniaxial deformation, the peaks around 0.05 strain correspond to the yielding transition between elastic and plastic behavior. In the triaxial deformation, the peaks denote the onset of cavitation, and thus failure. Failure under uniaxial deformation occurs at strains beyond those examined in the current work.

Elastic Properties. The elastic properties of the PNCs as a function of particle length were extracted from deformation simulations, as summarized in Figure 4. On average, the elastic moduli (initial slope of the stress−strain curve) of the PNCs are a factor of 2 to 4 times higher than those of the pure polymer for short-rod systems. There is an overall trend of decreasing elastic modulus with increasing rod length. Systems subjected to strain rates of 4.4×10^{-4} had elevated values of elastic modulus as compared to those deformed at strain rates of 1.1×10^{-4}.

The yield point (i.e., the yield stress and yield strain) was determined by measuring where a line with an x-intercept of 0.02 and a slope equal to the elastic modulus intersects with the stress−strain curves. The yield strain increases monotonically with rod length, except for the 16-mer. There was a high degree of variability for pure polymer yield strain, reflected in errors in pure polymer yield strain of up to ±0.0048. While a trend on increasing yield strain with increasing rod length is clear, the relation between PNC and pure polymer yield strain is not.

The yield stress is about 0.7 higher for the PNCs than for the pure polymer, and changes only slightly with rod length. While the effect of rod length is minimal, it is statistically significant for rod lengths up to the 8-mer. In contrast, the aggregated 16-mer systems exhibit the lowest PNC yield stress. The 16-mer has a heterogeneous structure. That is, there are domains rich in nanorods and domains devoid of rods. Therefore, it is possible that domains devoid of nanorods require less stress to initiate flow. This reduction in yield stress upon aggregation runs counter to the observations of Akcora et al.[26] They instead observed solid-like behavior not seen in their dispersed systems. However, the additive used by Akcora et al. was covalently bound to entangling polymer segments whereas polymer is bound to the 16-mer only by Lennard-Jones interactions, albeit strong ones. Regardless of rod length, a higher stress is required to induce yield when the system is deformed more rapidly. The error in the pure polymer measurement of yield stress is ±0.017.

Local Stress Distribution. In addition to global stress−strain behavior, molecular simulations enable a detailed examination of the local stress state of each simulation bead. Here, local stress is calculated according to

$$\boldsymbol{\sigma} = \frac{1}{2V} \sum_{neighbors} \mathbf{fr} \tag{3}$$

where $\boldsymbol{\sigma}$ is the stress tensor, V is local volume, $\mathbf{f}$ is the vector of force on a bead by a given neighbor, and $\mathbf{r}$ is the vector denoting the distance to the neighbor. For simplicity, local volume is treated as the average specific volume of the system. This results in a slight underestimation of the magnitude of the stress for additives as compared to the polymer, but has little qualitative effect on the observed behaviors.

In order to better understand local stress behavior, it is useful to examine the spatial distribution of tensile stress in the direction of deformation ($\boldsymbol{\sigma}_{xx}$) through the use of color maps, as shown in Figure 5. Here the local stress of polymers in thin slices is displayed with rod sites overlaid as black dots. The local stresses of the rods themselves (not included in production of the color maps) are strongly negative. Recall that the attractive interaction between rods and polymers produces an organized region of dense material around the additives. The rods pull polymer chains inward (negative stress) and the shell of polymer in the immediate vicinity of the rods is tightly packed, giving rise to positive stresses. This effect is plainly visible in the 16-mer aggregates, as denoted by red regions around the rods. The induced stress differential is less prominent for shorter rods, and difficult to discover through visualization alone. However, calculation of the average local stress of polymer as a function to the nearest rod (not shown) clearly reveals that the first solvation shell of polymer has significantly higher local stress in all PNCs. The pure polymer has some regions of higher and lower local stress, but these fluctuations are small as compared to the scale of stress gradients found around PNC rods. In PNCs, polymer far from the rods exhibits a distribution of stresses that is similar to those of the pure polymer.

Two configurations of each system are shown in Figure 5, one prior to deformation and one at the yield point. Over this small strain, the positions of nanorods in each system do not change appreciably. In the pure polymer, regions of high and low local stress change position, suggesting that nonuniformity is the result of transient fluctuations and not the underlying structure. The same behavior is seen in PNCs in the polymer located far from the additive rods. The application of strain does not induce different stress responses across the system. Instead, all polymer and particles show, on average, a uniform increase in local stress that matches the global increase in stress for that system.

dx.doi.org/10.1021/ma2017277 |*Macromolecules* 2012, 45, 543–554

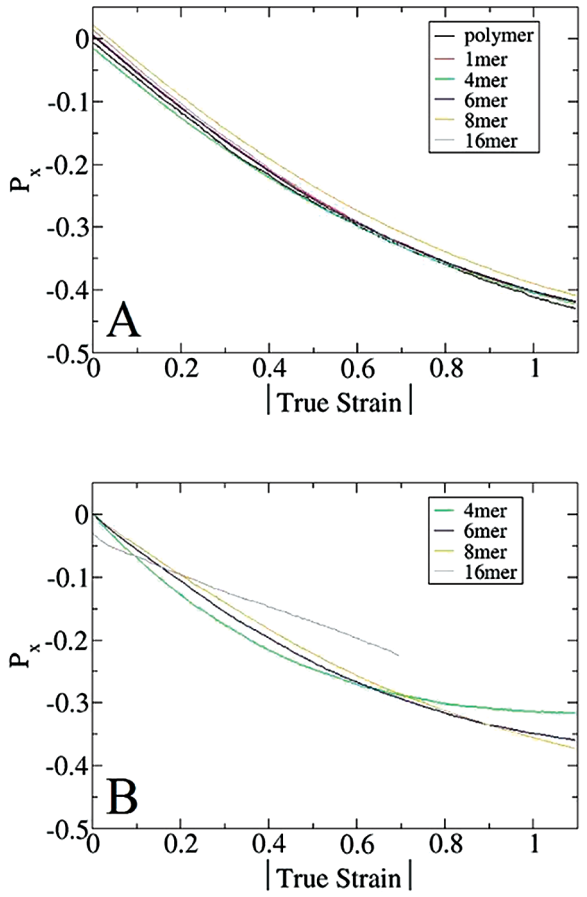

Figure 6. Polymer (top) and particle (bottom) orientation under compression for 10 wt % filler at $T/T_g = 0.9$.

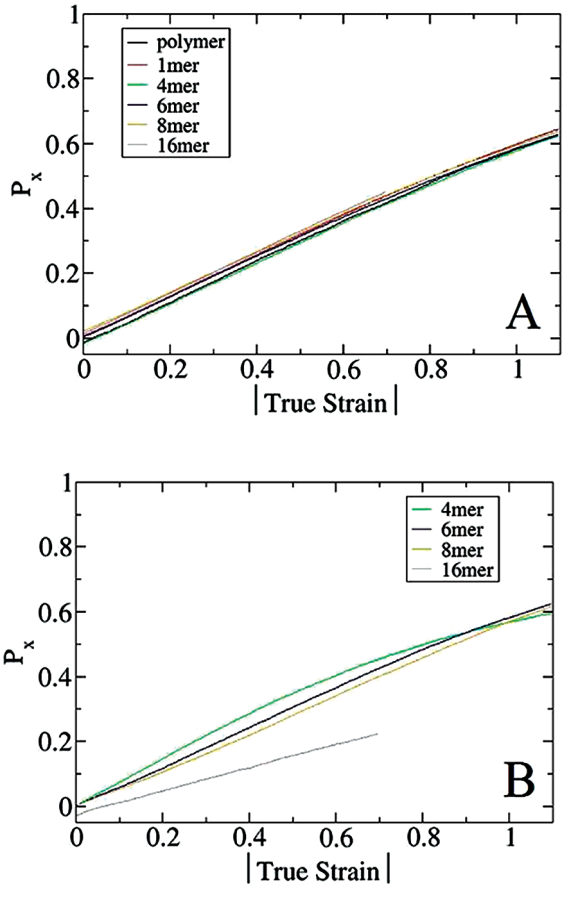

Figure 7. Polymer (top) and particle (bottom) orientation under extension for 10 wt % filler for $T/T_g = 0.9$.

This suggests that stress propagates rapidly in the PNC as compared to the rate of deformation. The results in the figure are for compression at constant T/T_g, but the same behavior occurs at constant T and during tensile deformation. Additionally, the slices shown in the color map are perpendicular to the axis of deformation, but slices through other planes reveal the same behavior.

At higher strains than those presented in the color maps, we find the same trends, albeit rearrangement of particles and polymer chains make side-by-side comparison less clear. The current simulations do not continue to the point where local fluctuations can organize to produce failure. A discussion of failure in shear-yielding is beyond the scope of this work.

Rod and Polymer Orientation. Rods and polymer molecules exhibit a tendency to align either perpendicular (in compression) or parallel (in extension) to the direction of deformation. We quantify alignment during deformation by measuring correlations between the end-to-end vector of the polymer or particle with the direction of deformation. Using a second Legendre polynomial of their product we have

$$P_x = \left\langle \frac{1}{2}(3(\mathbf{b}_i \cdot \mathbf{u}_x) - 1) \right\rangle \quad (4)$$

where P_x measures the correlation, $\mathbf{b}_i$ is the unit vector along the end-to-end vector of the polymer or particle i, $\mathbf{u}_x$ is a unit vector aligned in the x-direction (the axis of deformation), and the angular brackets indicate an average over all particles (or polymer chains). Values of P_x scale from −0.5 for perfect perpendicular alignment, to zero for random orientation, to 1.0 for perfect parallel alignment. We examine both the end-to-end alignment of polymers and the end-to-end alignment of the nanorods.

The changes in alignment of the polymer chains during compression are shown in Figure 6a; the average alignment with the deformation axis goes smoothly from ∼0.0 (random) to ∼-0.42 (highly perpendicular) for all systems. As we are deforming a finite number of chains, the initial extent of alignment differs slightly from zero for some systems. There are only small differences among the various nanocomposite systems at small deformations, and there is essentially no difference for large deformations. Figure 6b shows the orientation of the nanorods. At low strains, shorter rods reorient themselves more than longer rods. However, at high strains, the alignment of the 4-mers reaches an asymptotic P_x value of approximately −0.32. At these strains, the higher rotational mobility of shorter rods is balanced by the aligning force exerted on the system. The onset of similar behavior is visible for the 6-mers. The clustering of 16-mers into bundles results in large numbers of rods having the same orientation, and we therefore have less independent orientational vectors for the 16-mer systems. Having relatively few independent vectors, the initial average orientation is not random, and it is difficult to draw meaningful conclusions from its orientational changes.

In extension, the polymer chains align parallel to the axis of deformation, as shown in Figure 7a. As was the case under compressive deformations, there is no clear difference between the pure polymer and the polymer in the nanocomposites.

dx.doi.org/10.1021/ma2017277 |*Macromolecules* 2012, 45, 543–554

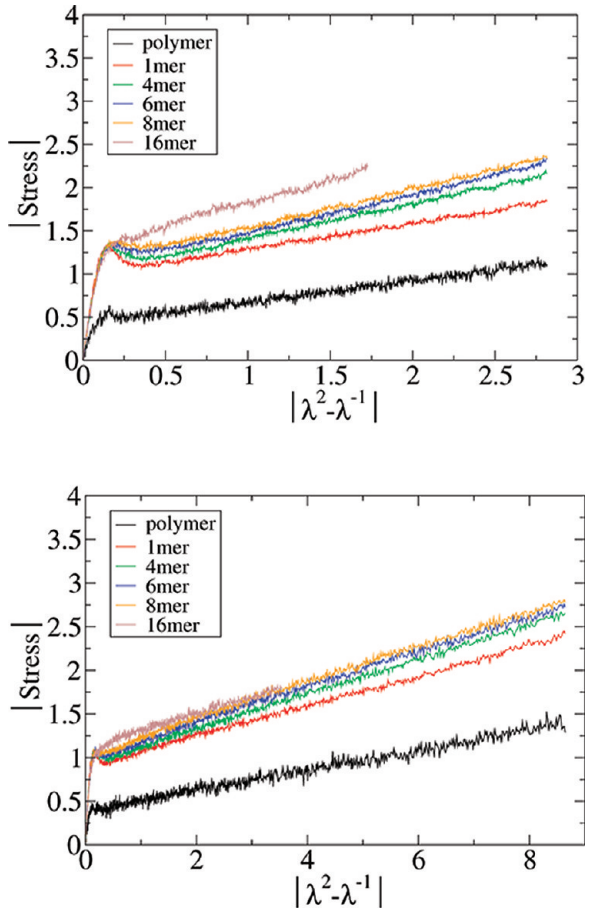

Figure 8. Rescaled results for deformation in compression (top) and extension (bottom) for 10 wt % filler at $T/T_g = 0.9$. Black lines represents pure polymer, other lines represent nanocomposites loaded with nanorods of indicated lengths.

Figure 7b shows the alignment of the particles; the smallest rods again show greater changes in P_x than long rods at low strain. However, the alignment of the 4-mer begins to saturate at higher values of strain then it did under compression, with the final value lying slightly above $P_x = 0.6$.

Postyield Behavior. In the postyield regime, the hardening modulus provides a measure of how much additional stress is required to deform a material as strain increases (in the plastic regime). Historically, the increased resistance to deformation in polymer materials with increasing strain has been examined under the framework of entropic network models.[34,35] Under such models, a polymer melt is treated as a cross-linked network of polymer chains, where the length of segments between cross-links is the polymer entanglement length (Ne). The stress (σ) required for deformation arises from the entropic resistance to straightening the polymer segments. The simplest possible such model assumes ideal Gaussian behavior for the chain segments as they undergo affine deformation. The Gaussian or neo-hookean model will exhibit a stress−strain response of the form:[34,35]

$$\sigma = \sigma_0 + G_R(\lambda^2 - \lambda^{-1}) \quad (5)$$

where σ_0 is flow stress to account for preyield behavior, λ is the stretch tensor defined as the ratio of the current box length to the original box length, G_R is the hardening modulus, and the term in parentheses results from the entropy of a Gaussian chain.

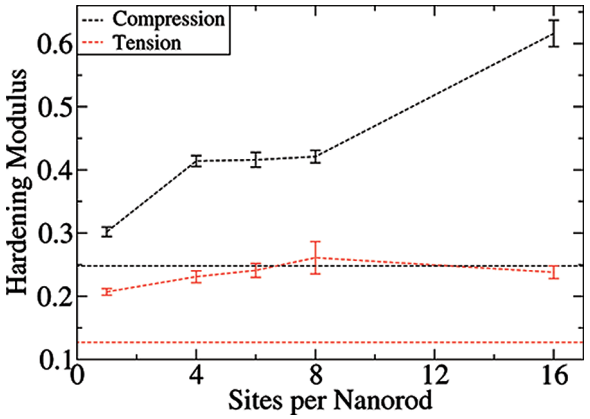

Figure 9. Hardening modulus at a strain rate of 4.4×10^{-4} as a function of sites per nanorod. Pure polymer results represented as horizontal lines. Black lines denote compression and red lines denote tension. Solid lines are used for systems with strain rates of 1.1×10^{-4} and dashed lines for systems with strain rates of 4.4×10^{-4}.

By plotting the stress response of Figure 3 against $\lambda^2 - \lambda^{-1}$, a linear relationship is obtained in the postyield regime (see Figure 8); the hardening modulus is the slope of this line. Significantly more advanced rubber-elasticity models that include nongaussian response (e.g., finite extensibility) and couple chain relaxation to account for nonaffine behavior have also been developed; Boyce and Arruda have compiled a review[36] of these models. However, a simple Gaussian model is sufficient to describe the phenomenology of interest in the present work. The applicability of such a simple model to a polymer undergoing large deformations is consistent with the experimental work of Tervoot and Govaert.[37]

We examine the hardening modulus at a deformation rate of 4.4×10^{-4} in Figure 9. The PNCs under compression show an increase of hardening modulus with rod length, with the 16-mers exhibiting a hardening modulus that is twice as high as that observed with spheres. In tension, all PNC exhibit the same hardening modulus within the statistical uncertainty, except for the 1-mer. However, we see that all PNCs have higher toughening moduli than the corresponding pure polymer.

A number of shortcomings of rubber-elasticity models for hardening modulus have been noted in the last several years.[38−42] These include the observation of hardening in chains of one-quarter the entanglement length, a temperature dependence that is in conflict with experiments, and inconsistencies in the order of magnitude of the predicted response. A polymeric system is more complicated than the simplistic description provided by eq 5. Likewise, the addition of rods, which distort the chain distributions on short length scales,[12] violate the Gaussian assumption behind this neo-Hookean model. Despite these disagreements regarding the validity of the underlying physical model, however, polymer and PNC systems can be described qualitatively by the relation prescribed in eq 5.

In order to test whether the observed hardening modulus trends are consistent with the assumptions of the rubber-elasticity model, we compare our current result with our previous examination of Ne in the melt state at $T = 1.75$.[12] As explained in the literature, evaluation of entanglements in the presence of filler materials was addressed in the limits of high and low mobility on the time scales of reptation. Note that the exact value obtained for Ne depends on the method of entanglement

dx.doi.org/10.1021/ma2017277 |Macromolecules 2012, 45, 543–554

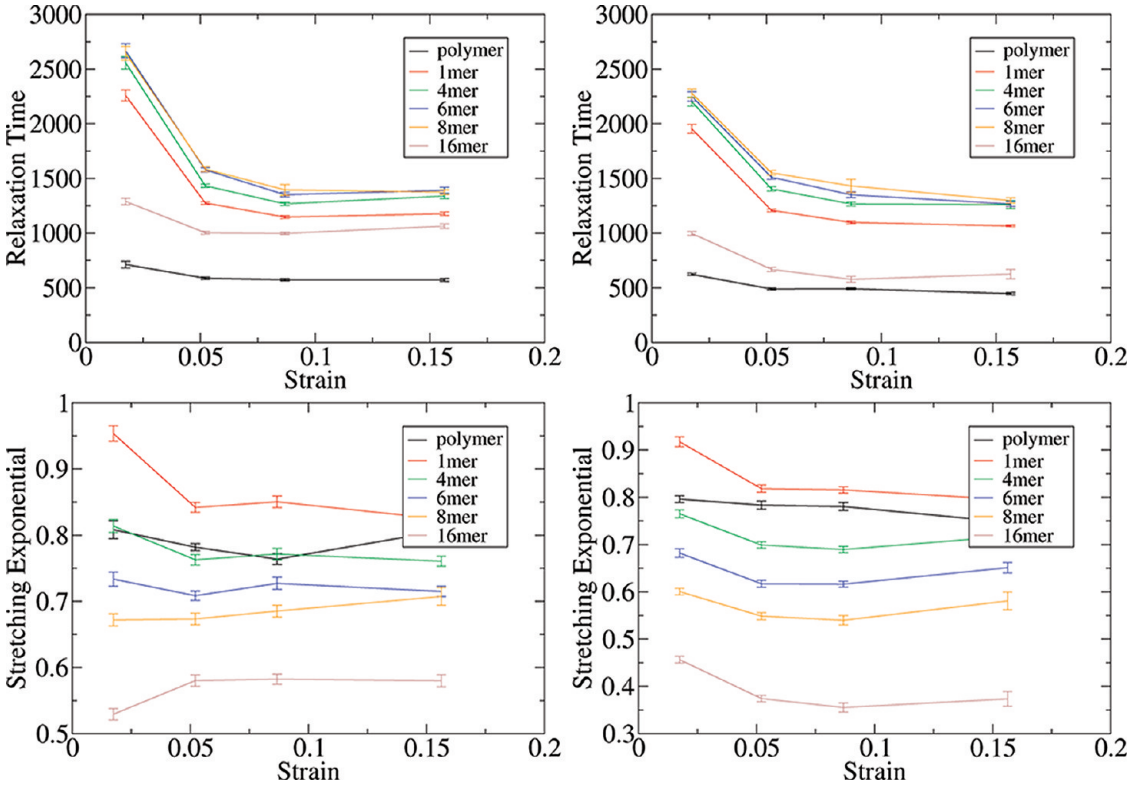

Figure 10. Unnormalized relaxation time (top) and stretching exponent (bottom) at $T/T_g = 0.9$ during compressive (left) and tensile (right) deformation.

identification;[43] values reported here correspond to a contact definition of entanglements. At $T = 1.75$, the pure polymer has an *Ne* of 56.0 ± 3.5.

In the limit of fast particle relaxation, the PNC *Ne*'s were statistically indistinguishable from that of the pure polymer. As such, no difference in hardening modulus between the different systems would be predicted. This is consistent with the lack of trend with rod length observed for hardening modulus during tension, but cannot explain the compressive behavior.

In the limit of slow particle relaxation, *Ne* monotonically increases with rod length from 19.65 ± 0.11 to 26.23 ± 0.42, suggestive of a much more entangled system than the pure polymer in all cases. In this case, the hardening modulus would be predicted to decrease with rod length; instead, an increase in hardening modulus with rod length is observed in our simulations.

Regardless of which particle relaxation assumption is used, previously calculated *Ne* values cannot be used to explain the trends in hardening modulus observed here. This finding is in contradiction with rubber-elasticity models, but is not unprecedented.[38−42]

Bond Autocorrelation. The dynamics of the nanocomposites were further examined in the glassy state during tensile deformation by calculating the bond autocorrelation function, $C_b(t)$. Previous studies have shown that $C_b(t)$ provides a useful measure of the segmental dynamics in polymer glasses, similar to the incoherent dynamic structure factor, $F_s(q,t)$.[31] Here we apply the time-window approach described earlier. Similar approaches have been employed in previous simulations[30] and have been shown to be consistent with optical measurements of the segmental dynamics of PMMA during creep deformations.[44,45]

As described earlier, we extract fitting parameters for τ_{eff}, β, and C_o from plots of $C_b(t)$ in specified windows. We focus on

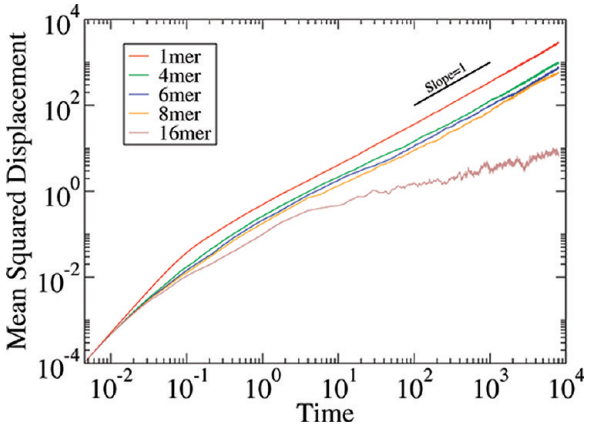

Figure 11. Average particle diffusion from sample runs for 10 wt % filler.

four such windows corresponding approximately to the elastic regime (strain 0.002−0.035), near yield (strain 0.037−0.069), early postyield including strain softening if present (strain 0.072−0.104), and late postyield (strain 0.141−0.171). Several ranges were tested for the late postyield, and all gave similar results. Figure 10 summarizes the results for the unnormalized effective relaxation times, τ_{eff}, and the stretching exponent, β, during extension for the PNC systems at a deformation rate of 1.1×10^{-4}. The value of the strain associated with τ_{eff} is chosen as the strain in the middle of the window used to determine τ_{eff}.

Under both tension and compression, there is a clear trend of increasing relaxation time with rod length, and all PNCs have slower polymer relaxation than the pure polymer. The 16-mers

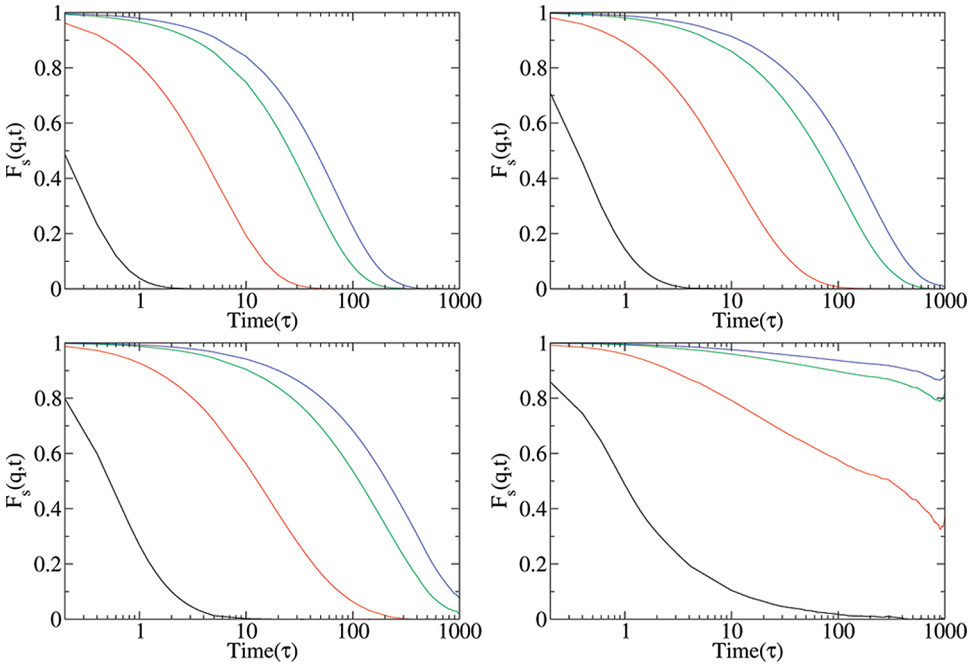

Figure 12. Dynamic structure functions for particle components of the 1-mer (top left), 4-mer (top right), 8-mer (bottom left) and 16-mer (bottom right) evaluated at different wave vectors. Black, red, green, and blue curves represent **q** values of 7.0, 1.6, 0.65, and 0.5 respectively.

are an exception to the order, having relaxation times closest to the pure polymer. Given that these relaxation times were calculated from relatively short windows, the fastest polymers to relax in the system are going to strongly influence the measured time, and the 16-mer systems (unlike the shorter rods) have large domains without inclusions.

For both compression and tension, there is a strong trend of decreasing β with increasing rod length, with values for the pure polymer falling near or slightly above those for the 4-mer. As a decrease in β corresponds to a broadening of the relaxation spectrum, these results show that longer rods either introduce additional time scales for relaxation or alter ones that are normally less important in the pure polymer. Only the 1-mer system has a higher β than the pure polymer. The 16-mer system follows the same trend as the other rods, despite its aggregated nature.

Brief Comment on Constant Temperature Trends. As noted before, results obtained for systems at $T = 0.3$ are broadly in line with those discussed for systems at $T/T_g = 0.9$, and the complete details of the $T = 0.3$ results are given in the Supporting Information. However, a few distinct differences do exist, necessitating a brief comparison of results here. Recall that $T = 0.3$ is a lower temperature than $T/T_g = 0.9$ for all systems examined here (as per Table 1). It is also important to note that the glass transition temperature changes with rod length in a nonlinear away.

The overall stress−strain curves are in good qualitative agreement between the two temperatures, although the stresses obtained during deformation at $T = 0.3$ are higher in order to overcome the reduced mobility of these systems. Similar to the deformations at $T/T_g = 0.9$, strain softening is more pronounced in compression than in extension. The rod length dependence of elastic properties does not exhibit clear trends at $T = 0.3$. The general insensitivity of elastic properties to geometry at constant temperature is consistent with the experimental work of Kalfus and Jancar.[25] However, values obtained for elastic modulus are significantly different for different sets of rod length. The apparent lack of trends with rod length could be the result of conflicting influences between rod length and degree of cooling below T_g. It is also possible that the role of the additive in the elastic regime is generally more pronouced near T_g than at lower temperatures. Rod and polymer orientation differ trivially between $T = 0.3$ and $T/T_g = 0.9$.

Examination of bond autocorrelation shows the most profound differences between $T = 0.3$ and $T/T_g = 0.9$. The qualitative shape of the strain versus relaxation time curve is not temperature dependent, however the $T = 0.3$ systems exhibit longer relaxation times, as expected.

MELT DYNAMICS

The dynamic behavior of the PNCs above T_g was characterized in two ways: analysis of particle mean-squared displacement (msd) and calculation of dynamic structure factors for both particles and polymers. These calculations were performed on the equilibrated melts at $T = 1.75$.

Figure 11 shows average particle displacements as a function of time. As expected, short rods diffuse more quickly than long rods, with spheres achieving $100\sigma^2$ msd in only 285τ. For the 16-mer system, as mentioned previously, significant aggregation of the particles occurs. The resultant aggregates have drastically reduced mobility.

At long times, all inclusions other than the 16-mer are seen to achieve a slope of unity, consistent with diffusive motion. The 16-mer has a final slope of 0.47 ± 0.02, which corresponds to subdiffusive motion. Given the intertwined nature of the polymer−particle bundles, this subdiffusive behavior is not surprising.

dx.doi.org/10.1021/ma2017277 |*Macromolecules* 2012, 45, 543–554

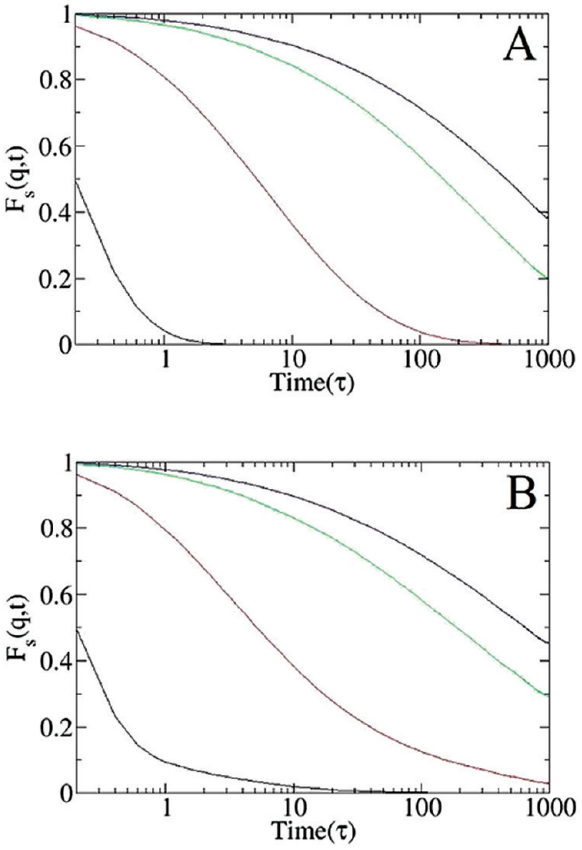

Figure 13. Dynamic structure functions for polymer components of 4-mer PNC (top) and 16-mer PNC (bottom) evaluated at different wave vectors. As before, black, red, green, and blue curves represent **q** values of 7.0, 1.6, 0.65, and 0.5 respectively.

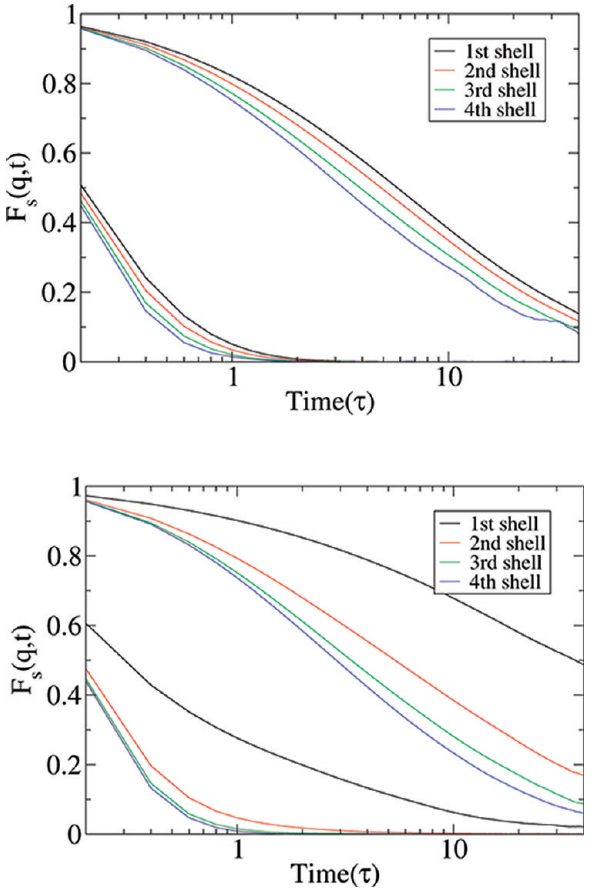

Figure 14. Dynamic structure functions for **q** values of 7 and 1.6 for polymer components of the 4-mer PNC (top) and 16-mer PNC (bottom). Each line represents a different layer of polymer beads about the nearest particle.

To further evaluate the mobility of polymer and particles, we calculated dynamic structure factors according to

$$F_s(\mathbf{q},t) = \frac{1}{N}\sum_j e^{i\mathbf{q}\cdot(\mathbf{r}_j(t)-\mathbf{r}_j(0))} \quad (6)$$

where F_s is the dynamic structure factor, **q** is the wave vector, t is time, $\mathbf{r}_j$ is the position of the jth bead, and i is the root of -1. The dynamic structure factors were calculated at several **q**, corresponding to length scales between 0.9σ and 12.6σ, and the real component plotted in Figure 12.

F_s probes mobility on length scales of $2\pi/\mathbf{q}$, and can be measured experimentally by incoherent inelastic neutron scattering. Examination across all length scales considered here show a trend of decreasing additive particle mobility with increasing particle length. The times required at $\mathbf{q} = 7$ to decay below 0.001 for the 1-mer, 4-mer, and 8-mer nanocomposite systems are 2.5τ, 6.3τ, and 14τ, respectively. Larger particles are observed to move more slowly; the 16-mer bundles have drastically reduced mobility and show a dynamic structure function value of 0.018 at 100τ for $\mathbf{q} = 7$.

The motion of the polymers was also characterized by dynamic structure factors. The color scale remains the same. The pure polymer (not shown) and the polymer component of the PNCs had similar behavior in general. Figure 13a shows the dynamic structure factor for the polymer component of the 4-mer PNC, which is generally representative of the pure polymer, the 1-mer, and the 8-mer systems. For the 16-mer system, however, the curves at $\mathbf{q} = 7$ and $\mathbf{q} = 1.6$ show the presence of an additional mode of decay, as indicated in Figure 13b by the slow approach of F_s to zero after an initial, rapid decay. To investigate the origin of this decay mode, we examined the relaxation of monomers as a function of their distance from the nearest particle in the initial configuration. The dynamic structure factors for $\mathbf{q} = 7$ and $\mathbf{q} = 1.6$ are shown in Figure 14 for each of the first four solvation shells of polymer about the particles, for 4-mer and 16-mer PNCs. A bead is tagged with regard to which shell it is in when the simulation begins, regardless of its eventual position. Polymer relaxation in the presence of smaller particles shows some spatial-temporal correlation for $\mathbf{q} = 7$ and 1.6, with closer shells having slower dynamics. For the 16-mer nanocomposite, though, the beads in direct contact with the particles exhibit substantially hindered dynamics. The effect is much stronger than in the 4-mer case, and relevant across several values of **q**.

If one thinks of monomers as being weakly bound to the surface of particles, it follows that the dynamics of polymer material in the vicinity of the particle would be similar to that of the particle itself. For the dispersed nanocomposite systems, the particles are highly mobile and hence do not reduce polymer mobility substantially. For the 16-mer nanocomposite, the polymer trapped in the aggregated bundle is dynamically hindered.

dx.doi.org/10.1021/ma2017277 |*Macromolecules* 2012, 45, 543–554

As such, polymers in the vicinity of the 16-mer particle relax more slowly than in the bulk, leading to an additional mode of decay in the polymer dynamic structure function.

A similar analysis of polymer mobility near the surface of comparatively large icosahedron-shaped particles was performed by Starr et al.[46] They found polymer relaxation in their systems to exhibit the same slowing of polymer dynamics in the vicinity of the particles that we found for the 16-mer PNC, despite their polymers not being strictly "trapped". As in our case, this led to an additional mode of decay in the averaged dynamic structure factors at short length scales. This similarity implies that polymers on the surface of a large particle are just as restrained as the polymers in our aggregates. It should also be noted that the lack of difference in polymer mobility with respect to nanorod position for our other PNCs suggests that our smallest particles may affect the polymer matrix by different mechanisms than those of other PNC studies.

CONCLUSION

The polymer nanocomposite literature has focused on spherical inclusions, providing comparatively less information on anisotropic fillers such as rods. To address the influence of inclusion shape on composite behavior, we characterized polymer melts containing short, truly nanosized rods. We found that a combination of rebridging Monte Carlo and molecular dynamics moves used in tandem provide the best means of sample equilibration. In this paper, nanorods ranging from 1-mer to 16-mer were examined. In all PNCs (except the 16-mer), the additives were dispersed throughout the system and maintained a random orientation in the melt state. The 16-mer additives, however, aggregated into bundles having a high degree of local order.

The mechanical strength of PNC glasses was found to be influenced by rod length. We performed deformation simulations at $T = 0.3$ and at $T/T_g = 0.9$. In general, the elastic properties at constant temperature showed only weak trends with rod length, although all PNCs were considerably stronger than the corresponding pure polymers. This is in agreement with the experimental work of Kalfus and Jancar.[25] Past the yield point, however, differences with rod length did emerge. First, the spherical inclusions showed significant strain softening. This phenomenon became less pronounced with increasing rod length. Second, longer rods showed nearly a 2-fold increase in the hardening modulus as compared to the shortest rods. In contrast, at constant T/T_g clear trends with rod length did occur in the elastic regime. Specifically, elastic modulus decreased with increasing rod length, and yield strain increased with increasing rod length.

In order to examine postyield behavior, the hardening modulus was calculated. The origin of this measure is rooted in entropic network models, necessitating adoption of their formalism to define hardening moduli despite conflicts associated with the underlying physical mechanisms. It was found that the hardening moduli were higher for PNCs than for pure polymers, and that hardening modulus increased with increasing rod length for compressive deformation. These trends could not be reconciled with our previous examination of Ne[12] under rubber-elasticity models. Previous literature has noted several short-comings in using rubber-elasticity models to describe hardening behavior.[38−42] The disconnect between entanglements and hardening moduli shown here is another such discrepancy.

Bond relaxation dynamics during deformation reveal several results; the following results apply to T/T_g systems. Additives induce slower polymer orientational relaxation than found in the pure polymer, and the increase in unnormalized relaxation time is highest in the elastic regime. Increasing rod length strengthens this effect, with the exception of the aggregated 16-mers, most likely due to the relatively higher mobility of polymer-rich regions away from the rod bundles. There is also a strong trend of decreasing stretching exponent with increasing rods length, indicative of a broadening of the relaxation spectrum. Only the 1-mer system had a higher stretching exponent than the pure polymer.

Despite the additional statistical uncertainty associated with the estimation of the glass transition temperature, analysis of our results at $T/T_g = 0.9$ provides better insights into the immediate role of additive length. The elastic properties of the polymer, while drastically affected by additives, are generally insensitive to rod length if examined at constant temperature. However, evaluation at constant T/T_g reveals clear trends, indicating that rod length affects the system beyond the apparent change in T_g.

Lastly, we examined the dynamics of the PNC in the melt. We found that particle mobility is reduced with increasing rod length, especially the aggregated 16-mer system. Polymer mobility in the PNCs remained largely independent of particle length, except in the 16-mer case. In that system, there was an appreciable slowing of polymers near the surface of 16-mer aggregates. Only weak position-mobility correlation was found for other nanocomposites, likely due to rod mobility approximately matching polymer mobility. The ability of particles to provide reinforcement without the reduction of local dynamics is in contradiction to zone-theory type models. It has been shown in other studies that larger additives reduce polymer mobility and this correlates well with improved mechanical properties. However, our results indicate for smaller additives that reinforcement mechanisms not resulting in an appreciable reduction in mobility are applicable.

ASSOCIATED CONTENT

Supporting Information. Results for systems examined at a constant temperature of $T = 0.3$. This material is available free of charge via the Internet at http://pubs.acs.org.

AUTHOR INFORMATION

Corresponding Author
*E-mail: depablo@engr.wisc.edu.

ACKNOWLEDGMENT

We would like to thank the Grid Laboratory of Wisconsin (GLOW) for use of their computation resources and the Semiconductor Research Corporation (SRC) for their generous funding. The authors are also grateful to the National Science Foundation for support through the Nanoscale Science and Engineering Center at the University of Wisconsin.

REFERENCES

(1) Komarneni, S. *J. Mater. Chem.* **1992**, *2*, 1219–1230.
(2) Kamel, S. *eXPRESS Polym. Lett* **2007**, *1*, 546–575.
(3) Huang, Z. M.; Zhang, Y. Z; Kotaki, M.; Ramakrishna, S. *Composites Sci. Technol.* **2003**, *63*, 2223–2253.
(4) Gangopadhyay, R.; De, A. *Chem. Mater.* **2000**, *12*, 608–622.
(5) Crosby, A. J.; Lee, J. Y. *Polym. Rev.* **2007**, *47*, 217–229.

(6) Berriot, J.; Montes, H.; Lequeux, F.; Long, D.; Sotta, P. *Macromolecules* **2002**, *35*, 9756–9762.
(7) Papakonstantopoulos, G. J.; Doxastakis, M.; Nealey, P. F.; Barrat, J. L.; de Pablo, J. J. *Phys. Rev. E* **2007**, *75*, 31803.
(8) Vacatello, M. *Macromolecules* **2001**, *34*, 1946–1952.
(9) Zhang, Q.; Archer, L. A. *Langmuir* **2002**, *18*, 10435–10442.
(10) Bueche, F. In *Reinforcement of Elastomers*; Interscience: New York, 1965.
(11) Sternstein, S. S.; Zhu, A. *Macromolecules* **2002**, *35*, 7262–7273.
(12) Toepperwein, G. N.; Karayiannis, N. C.; Riggleman, R. A.; de Pablo, J. J.; Kroger, M. *Marcromolecules* **2011**, *44*, 1034–1045.
(13) Gersappe, D. *Phys. Rev. Lett.* **2002**, *89*, 58301.
(14) Starr, F. W.; Douglas, J. F.; Glotzer, S. C. *J. Chem. Phys.* **2003**, *119*, 1777.
(15) Riggleman, R. A.; Toepperwein, G. N.; Papakonstantopoulos, G. J.; de Pablo, J. J. *Macromolecules* **2009**, *42*, 3632–3640.
(16) Gojny, F. H.; Wichmann, M. H. G.; Fiedler, B.; Kinloch, I. A.; Bauhofer, W.; Windle, A. H.; Schulte, K. *Polymer* **2006**, *47* (6), 2036–2045.
(17) Sheng, N.; Boyce, M. C.; Parks, D. M.; Rutledge, G. C.; Abes, J. I.; Cohen, R. E. *Polymer* **2004**, *45*, 487–506.
(18) Ganesan, V. *J. Polym. Sci., Part B: Polym. Phys.* **2008**, *46*, 2666–2671.
(19) Buxton, G. A.; Balazs, A. C. *J. Chem. Phys.* **2002**, *117*, 7649.
(20) Knauert, S. T.; Douglas, J. F.; Starr, F. W. *J. Polym. Sci., Part B: Polym. Phys.* **2007**, *45*, 1882.
(21) Moniruzzaman, M.; Winey, K. I. *Macromolecules* **2006**, *39*, 5194–5205.
(22) Coleman, J. N.; Khan, U.; Blau, W. J.; Gun'ko, Y. K. *Carbon* **2006**, *44*, 1624–1652.
(23) Xie, X. L.; Mai, Y. W.; Zhou, X. P. *Mater. Sci. Eng.: R: Rep.* **2005**, *49*, 89–112.
(24) Spitalsky, Z.; Tasis, D.; Papagelis, K.; Galiotis, C. *Prog. Polym. Sci.* **2010**, *35*, 357–401.
(25) Kalfus, J.; Jancar, J. *Polym. Compos.* **2007**, *28*, 743–747.
(26) Akcora, P.; Liu, H.; Kumar, S. K.; Moll, J.; Li, Y.; Benicewicz, B. C.; Schadler, L. S.; Acehan, D.; Panagiotopoulos, A. Z.; Pryamitsyn, V.; Akcora, P.; Liu, H.; Kumar, S. K.; Moll, J.; Li, Y.; Benicewicz, B. C.; Schadler, L. S.; Acehan, D.; Panagiotopoulos, A. Z.; Pryamitsyn, V.; et al. *Nature Mater.* **2009**, *8*, 354–359.
(27) Riggleman, R. A.; Toepperwein, G. N.; Papakonstantopoulos, G. J.; Barrat, J. L.; de Pablo, J. J. *J. Chem. Phys.* **2009**, *130*, 244903.
(28) Toepperwein, G. N.; de Pablo, J. J. *Macromolecules* **2011**, *44*, 5498–5509.
(29) Rottler, J.; Robbins, M. O. *Phys. Rev. E* **2003**, *68*, 011801.
(30) Riggleman, R. A.; Schweizer, K. S.; de Pablo, J. J. *Macromolecules* **2008**, *41*, 4969–4977.
(31) Bennemann, C.; Paul, W.; Baschnagel, J.; Binder, K. *J. Phys.: Condens. Matter* **1999**, *11*, 2179–2192.
(32) Smit, R. J. M.; Brekelmans, W. A. M.; Meijer, H. E. H. *J. Mech. Phys. Solids* **1999**, *47*, 201–221.
(33) Hasan, O. A.; Boyce, M. C.; Li, X. S.; Berko, S. *J. Polym. Sci., Part B: Polym. Phys.* **2003**, *31*, 185–197.
(34) Haward, R. N.; Thackray, G. *Proc. R. Soc. London, Ser. A Math. Phys. Sci.* **1968**, *302*, 453.
(35) Treloar, L. R. G. *The physics of rubber elasticity*; Clarendon: London, 1975.
(36) Boyce, M.; Arruda, E. M. *Rubber Chem. Technol.* **2000**, *73*, 504–523.
(37) Tervoort, T. A.; Govaert, L. E. *J. Rheol.* **2000**, *44*, 1263.
(38) Hoy, R. S.; Robbins, M. O. *Phys. Rev. Lett.* **2007**, *99*, 117801.
(39) Robbins, M. O.; Hoy, R. S. *J. Polym. Sci., Part B: Polym. Phys.* **2009**, *47*, 1406–1411.
(40) Hoy, R. S.; Robbins, M. O. *J. Chem. Phys.* **2009**, *131*, 244901.
(41) Chen, K.; Schweizer, K. S. *Phys. Rev. Lett.* **2009**, *102*, 38301.
(42) Van Melick, H. G. H.; Govaert, L. E.; Meijer, H. E. H. *Polymer* **2003**, *44*, 2493–2502.
(43) Foteinopoulou, K.; Karayiannis, N. C.; Mavrantzas, V. G.; Kroger, M. *Macromolecules* **2006**, *39*, 4207–4216.
(44) Riggleman, R. A.; Lee, H. N.; Ediger, M. D.; de Pablo, J. J. *Phys. Rev. Lett.* **2007**, *99*, 215501.
(45) Lee, H. N.; Riggleman, R. A.; de Pablo, J. J.; Ediger, M. D. *Macromolecules* **2009**, *42*, 4328–4336.
(46) Starr, F. W.; Schrøder, T. B.; Glotzer, S. C. *Macromolecules* **2002**, *35*, 4481–4492.

Macromolecules

Article

pubs.acs.org/Macromolecules

Salt Effects on Sol–Gel Transition of Telechelic Polyelectrolytes in Aqueous Solutions

Ran Zhang,[†,‡] Tongfei Shi,[*,†] Lijia An,[†] and Qingrong Huang[§]

[†]State Key Laboratory of Polymer Physics and Chemistry, Changchun Institute of Applied Chemistry, Chinese Academy of Sciences, Changchun 130022, P. R. China

[‡]Graduate University of the Chinese Academy of Sciences, Beijing, 100049, P.R. China

[§]Food Science Department, Rutgers University, 65 Dudley Road, New Brunswick, New Jersey 08901, United States

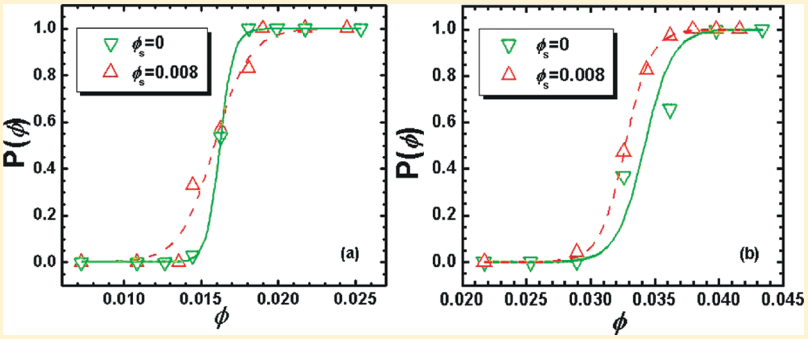

ABSTRACT: Using Monte Carlo simulation techniques, we focus on the physical gelation behavior and conformation change under the existence of additional monovalent salt, which provides screening to the electrostatic interaction of charged telechelic polyelectrolyte chains and causes new balance between hydrophobic interaction of end groups and electrostatic interaction originated from the polyelectrolyte blocks. For the electrostatic interaction dominated system, the screening effects will decrease the electrostatic repulsion between small sized clusters and enable the further aggregation of TP chains, resulting in prompting the sol–gel transition progress; for the short-range attraction dominated system, the screening effects present a complicated phenomenon, which includes the prompting effect at the beginning of sol–gel transition and a hindering effect when the gelation progress is close to an end.

1. INTRODUCTION

Telechelic polyelectrolytes, referred as TP, a special associating polymer containing short blocks at both ends, have many novel properties as well as wide applications compared with neutral telechelic polymers,[1−7] which can be attributed to the specialty of polyelectrolytes. Unlike neutral polymers, when dissolved in water, the ionogens on the polyelectrolyte chain will ionize into charged groups and counterions carrying opposite charges. Therefore, the interaction becomes more complicated, and factors like concentration, pH and salt addition will undoubtedly affect the association behaviors. The addition of salt provides screening for electrostatic interaction, which might induce: a significant influence the chain conformational[8−12] and dynamic properties;[13] an ion-bridging effect and rapid flocculation when multivalent salt ions are involved;[14−16] the dissolving[17,18] and forming[19] of polyelectrolyte complexes, phase separation,[20,21] and swelling/collapsing of charged gels.[22−25]

For the chemical gels, polyelectrolytes are cross-linked together by covalent bonds and most of the attention has been paid on the swelling behavior of the gels, which certainly depends on the ionic condition in the solution.[22,26−33] The kinetics process[24,29] as well as the structure[21,22,30,34,35] of swelling of polyelectrolyte gels can be quite different with the variation of salt conditions, and the net charge as well as the concentration of gelling polyelectrolytes is of great importance for the free ions to provide osmotic pressure for swelling;[31,32] the gel structure may also influence the uptake of salts in the gel matrix.[22] It was pointed out that not only the salt concentration but also the species of salt may cause different effects on the swelling behavior of polyelectrolyte gels.[23,33] Theoretical[21,22,24,36−38] and simulation[25,39] studies have investigated the effects of salt addition on cross-linked polyelectrolytes gels thoroughly, which bring our understanding of the mechanisms of gel swelling under salt conditions to a microscale level. However, for the physical gelation of charged polymers, the situation is more complicated since the cross-linking points in the gel network are maintained by hydrophobic interactions, hydrogen bonds, entanglements of chains or other noncovalent connections, which are reversible under certain conditions and find use in fields like drug delivery systems.[40−44] The additional

Received: August 18, 2011
Revised: December 1, 2011
Published: December 22, 2011

salt ions may screen the electrostatic interactions and cause phase separation[6,45,46] or the forming of a physical gel.[6,30,46,47]

For this complicated charged polymer system, theory and simulation work will be helpful for understanding the mechanism of its physical gelation. In the early years Vasilevskaya et al. established a simple model of telechelic polyelectrolytes in solution with additional salt and investigated the association behavior of TP under different solvent qualities and salt concentration;[6] and their theoretical prediction was quickly proved by experimental results.[45] In Vasilevskaya's work, under a hydrophobic interaction energy $\varepsilon_h \geq 12k_BT$, which can be viewed as the hydrophobic interaction dominated system in our work,[48] the sol−gel transition (phase separation) field became wider when increasing salt concentrations; however, until now a relevant explanation of this phenomenon in the microscale is still missing. In the former papers we have studied the TPs' gelation behavior in salt-free solution and provided proper explanation of their physical gelation behavior with the analysis on chain conformation and cluster forming.[48,49] If salt is added to the TPs solution, the dissolved salt ions will interact with the charged monomers and to some extent affect the chain conformations, so that the forming of clusters and even physical gelation process will be influenced. Our early results indicated the competition between hydrophobic and electrostatic interaction dominates the solution properties. When the hydrophobic interaction is relatively strong and favors the aggregation, electrostatic repulsion provides its contribution by maintaining a spacial structure, resulting in a much lower gelation concentration close to ϕ^* (the overlapping concentration, acquired by viewing the TP chain as a homogeneous polyelectrolyte chain in solution).[48] Meantime, loop to bridge transition is witnessed with the increase of concentration, in agreement with the experimental studies.[2,50] The additional salt ions in the solution will undoubtedly screen the electrostatic interaction and bring the competition to a new balance. Unfortunately, there are few systematic references on these.

In this paper, using Monte Carlo simulation techniques, we focus on the effect of additional salt ions on the association behavior of chains and on the reason for so-called extending of sol−gel transition in TP solutions. The simulation model we use is described in the next section, and after that we present our discussion of simulation results and the conclusion remark. It is found that the extending of so-gel transition happens only when relatively strong hydrophobic interaction dominated in the system. The complicated phenomenon involves the salt-prompting effect at the beginning of sol−gel transition and a salt-hindering effect when the gelation progress is close to an end. On the other hand, when there exits relatively weak hydrophobic interaction, only the salt-prompting effects on the sol−gel transition progress results in the sol−gel transition in a lower concentration range without the behavior of extended sol−gel transition, which is not mentioned in any theoretical predictions.

2. MODEL AND SIMULATION DETAILS

This model resembles the one we used in the former paper.[49] In a cubic cell ($L = 48\sigma$) with periodic boundary conditions in 3 dimensions, the TP chain has a structure $A_{N_A}-B_{N_B}-A_{N_A}$ containing 20 monomers, with $N_A \equiv 1$ and $N_B \equiv 18$. Block A stands for the hydrophobic groups, and block B a flexible hydrophilic polyelectrolyte with bond length fixed at 1.1σ. Polyelectrolyte monomers are monovalent and carrying negative charges. Salt ions, explicitly simulated in the solution, are monovalent hard spheres with the same diameter as the chain monomers. The positive salt ions act as counterions for the polyelectrolyte monomers, and the number of cations equals to the number of anions and the polyelectrolyte monomers to maintain the charge neutrality. The solvent is implicitly treated as a dielectric continuum. When there is no salt added, the solution contains N_t chains and N_c counterions, the salt ions will be added into the solution at certain percentage f of the monomer charges. Thus, there will be $N=N_A N_t + N_c(2+f)$ nodes in the solution. The attraction potential between hydrophobic monomers U_{attr} is an attractive Lennard-Jones potential

$$U_{attr} = 4\varepsilon_{attr}\left[\left(\frac{\sigma_{attr}}{r}\right)^{12} - \left(\frac{\sigma_{attr}}{r}\right)^{6}\right] \quad (1)$$

where ε_{attr} is the association energy. The interaction between other pairs is represented by the repulsive L-J potential:

$$U_{rep} = 4\varepsilon_{rep}\left(\frac{\sigma_{rep}}{r}\right)^{12} \quad (2)$$

where ε_{rep} is the repulsive energy. Here $\sigma_{attr} = \sigma_{rep} = \sigma = 1$ and the cutoffs of these L-J interactions is 2.5σ. According to the Ewald method, the expression of Coulomb potential $U_{elec,tot}$ is

$$U_{elec,tot} = k_BT\lambda_B E_{tot} \quad (3)$$

$$E_{tot} = E_r + E_k + E_s + E_d \quad (4)$$

where k_B is the Boltzmann constant, T refers to temperature, the Bjerrum length λ_B is defined as the distance at which two unit charges have the interaction energy k_BT and has the expression $\lambda_B = e^2/(4\pi\varepsilon_o\varepsilon_r k_BT)$. λ_B can be considered as a measure of the strength of electrostatic interactions vs the thermal energy and is equal to 7.14 Å for water at room temperature. E_r and E_k on the right of eq 4 are the contributions from the real space and the Fourier space, E_s is the self-term, and E_d is the dipole-correction term.[51] These potentials are:

$$E_r = \frac{1}{2}\sum_{i,j}\sum_{\vec{n}} q_iq_j\frac{\mathrm{erfc}(\alpha|r_{ij} + \vec{n}L|)}{|r_{ij} + \vec{n}L|} \quad (5)$$

$$E_k = \frac{1}{2}\frac{1}{\pi L^3}\sum_{\vec{k}\neq 0}\frac{4\pi^2}{k^2}\exp\left(-\frac{k^2}{4\alpha^2}\right)|\tilde{\rho}(\vec{k})|^2 \quad (6)$$

$$E_s = -\frac{\alpha}{\sqrt{\pi}}\sum_{i=1}^{N} q_i^2 \quad (7)$$

$$E_d = \frac{2\pi}{(1+2\varepsilon_s)L^3}|\sum_{i=1}^{N} q_i\vec{r}_i|^2 \quad (8)$$

In eq 6 the reciprocal vector $\vec{k} = 2\pi n\rightharpoonup/L$, $\vec{n} = (n_1,n_2,n_3)$:$n_t \in Z$. In eq 8 ε_s is the dielectric constant of the medium surrounding the sphere. How to manipulate the Coulomb sum using a Monte Carlo style is given in the appendix of ref 49, and here the measure we take is exactly the same.

The simulation work is done in the *NVT* (constant particle numbers, constant volume and temperature) ensemble

dx.doi.org/10.1021/ma201872e | *Macromolecules* 2012, 45, 555−562

according to the Metropolis algorithm. Salt ions including counterions randomly move with a sphere range of diameter $D = 10\sigma$ in one MC trial. As for the chains, we use several algorithms for relaxation. These algorithms, such as pivot,[52] translation,[53] kink-jump, and crankshaft[54] are very efficient in accelerating the simulation and promoting the convergence of potentials. In a pivot move, a chain node is chosen at first, splitting a chain into halves, then the shorter part moves around the chosen node; in a translation, the shorter part just take an even move without breaking the bond connecting the node. Crankshaft and kink-jump are very much alike in pattern: we define an axis by choosing two unconnected nodes in a chain, and let the nodes between the chosen ones move round the axis. The main difference between these two methods is that in a kink-jump only one node is moving.

3. SIMULATION RESULTS

3.1. Comparison between Salt-Free and Saline Systems. We have considered the effect of TP concentration on their sol−gel transition behavior in an earlier work[48] and found that the competition between hydrophobic interaction and electrostatic interaction has a major effect on the distribution of chain association fraction: with strong hydrophobic interaction energy, the short-range hydrophobic attraction dominates the system, while the electrostatic interaction provides a contribution to the formation of gels by maintaining a spacial swelling structure; when the hydrophobic interaction energy is relatively low and the electrostatic interaction dominates, increasing concentration can screen electrostatic repulsion in some degree,[55−57] which makes for the growth of clusters and the sol−gel transition at a higher concentration.

Vasilevskaya et al.[6] found that the overlap concentration (ϕ^*) is decreased with the increase of salt concentration, associative gels are formed in TP solution accompanied by supernatant phase; with greater ϕ, the gel phase the supernatant phase disappears. While in theory and simulation studies, percolation model is widely used[58−60] and fits well in the situation of determining the sol−gel transition.[48,49] When a certain amount of salt ions are added into the system, the electrostatic repulsion of TP chain is weakened, which causes a significant difference in the percolation value $P(\phi)$ (see Figure 1). For simplicity, the sol−gel state is defined as the concentration area when $0 < P(\phi) < 1$, while $P(\phi) = 0$ for the sol and $P(\phi) = 1$ for the gel state. The dashed fitting line of the simulation data shows the percolation curve of a TP solution with a salt concentration $\phi_s = 0.008$, while the solid line stands for the salt-free system. The hydrophobic interaction energy ($\varepsilon=\varepsilon_{attr}/k_BT$) is set at 8, under which the aggregation of chains is favored. It is obvious that the screening from salt ions presents a major influence on the sol−gel transition: the addition of simple salt ions at $\phi_s = 0.008$ causes a broadened sol−gel transition area (from $0.013 < \phi < 0.018$ to $0.010 < \phi < 0.022$) compared with the salt-free case, which was predicted in Vasilevskaya's theoretical work.[6] Here we extend the understanding of this phenomenon to a molecular level by investigating the fraction of the four basic association types of TP chains[49] (free, loop, dangling and bridge), which is shown in Figure 2a. The aggregation of chains due to comparatively strong hydrophobic attraction are well represented by the fast increasing of $f_{loop}(\phi)$ and decreasing of $f_{free}(\phi)$ with increasing ϕ; $f_{bridge}(\phi)$ increases significantly with greater ϕ and $f_{loop}(\phi)$ starts to decrease after reaching a maximum, which indicates

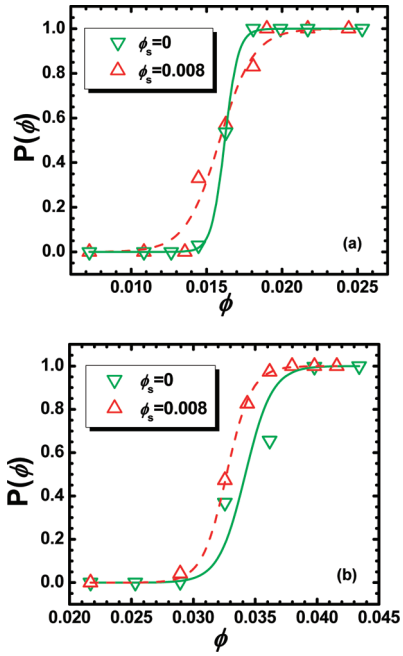

Figure 1. Percolation probability (P) plotted against the concentration ϕ at different hydrophobic interactions (a) $\varepsilon = 8$; (b) $\varepsilon = 5$. The salt-free data is shown in solid line to guide the eye, while the salt-added data is shown in dashed line.

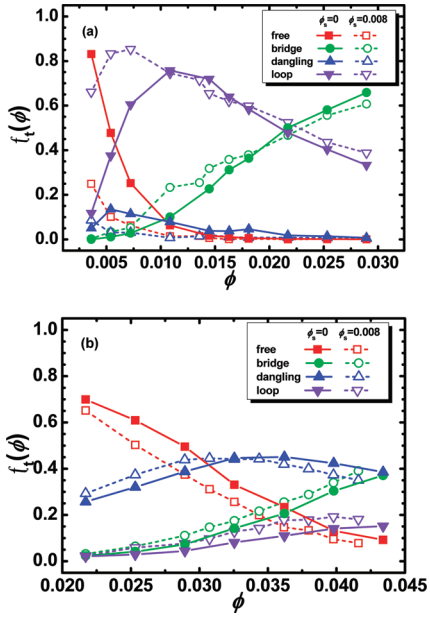

Figure 2. Chain association type fraction $f_t(\phi)$ as a function of concentration ϕ at different hydrophobic interactions (a) $\varepsilon = 8$ and (b) $\varepsilon = 5$, where "t" stands for the type of chains. The salt-free data is shown in solid, while the salt-added data is in hollow and dashed.

the loop to bridge fraction transition during the sol−gel transition progress.[2,50] The additional salt will undoubtedly decrease $f_{free}(\phi)$ and $f_{dangling}(\phi)$, due to its screening effect on the charged blocks; it is also found that the additional salt causes $f_{loop}(\phi)$ to reach its maximum at a smaller ϕ with a higher value than the salt-free case; however, as for $f_{bridge}(\phi)$, the salt effect is not monotonic with ϕ, with $\phi_s = 0.008$ the value of $f_{bridge}(\phi)$ is higher than the salt-free one with increasing

dx.doi.org/10.1021/ma201872e | Macromolecules 2012, 45, 555−562

ϕ at the beginning, but becomes lower when ϕ further increases.

This could be viewed that salt effect could be different for different period of gelation, also, it could be considered that the contribution of electrostatic interaction to the gelation of TP is different with increasing ϕ. When ϕ is low, the electrostatic repulsion hinders the aggregation of chains, the addition of salt ions can make for the interchain and intrachain (forming a loop) aggregation by electrostatic screening, which interprets the difference of f_{loop} and f_{bridge} between the salt-free system and the system with a salt concentration at lower ϕ. When ϕ increases, a continuous gel structure forms under the sustaining of electrostatic repulsion. The addition of salt ions, however, will cause screening to this sustaining force and reduces f_{bridge}. Thus, gel structure will form at higher ϕ.

Now we go back to Figure 1b. When ε = 5, electrostatic interaction is relatively strong and hinders the association of chains, increasing concentration is necessary for the physical gelation progress of the salt-free system, since more polyelectrolyte blocks and their counterions in solution can give rise to additional electrostatic screening and bring down the effective electrostatic interaction distance. This is why the sol−gel transition happens at a much higher concentration area than the one under ε = 8. The effect of additional salt can be obviously concluded to be identical with the one on the beginning of sol−gel transition in Figure 1a: the fitted percolation line of the system with a salt concentration is just ahead of the one of salt-free system in polymer concentration (from $0.028 < \phi < 0.04$ to $0.026 < \phi < 0.038$), without any broadening effects. The corresponding fraction of chain association types in Figure 2b indicates that the comparatively strong electrostatic interaction has a major effect on the fraction of chain types. For the solid lines representing the salt-free system, the slow decreasing of $f_{free}(\phi)$ with increasing ϕ and the considerable amount of dangling chains in the system suggest the stretched nonloop conformation of chains; $f_{bridge}(\phi)$ and $f_{loop}(\phi)$ increase slowly with increasing ϕ, indicating the hindered aggregation due to electrostatic repulsion. The dashed lines representing the system with ϕ_s = 0.008 remain almost the same trend with the solid curves but only at lower concentration, suggesting the salt effects on relatively weak hydrophobic systems favor the aggregation of chains, without causing the screening to the sustaining force of gel structure.

By combination of theoretical and simulation approaches, de la Cruz et al. also predicted that the addition of monovalent salt will bring the onset of TP gelation to a lower polymer concentration, despite using different criterion on determining gelation.[61] In further comparison with their simulation results, we discuss the effect of salt on the distribution of cluster size at different polymer concentrations (see Figure 3). When ε = 8, for ϕ = 0.0109 in the sol state, the additional salt at ϕ_s = 0.008 causes a wider distribution and larger cluster size compared with the salt-free case; for ϕ = 0.0163 in the sol−gel coexisting state, the increase of size of salt-induced larger cluster is more significant; when it comes to the gel state at ϕ = 0.0253, the additional salt causes the cluster size reaching its maximum (there are 140 chains in the corresponding system) with a narrower distribution than the salt-free case, suggesting almost all the TP chains are involved in the forming of gel network. When ε = 5, for the sol state at ϕ = 0.0253, the cluster size is small with a narrow distribution both for the salt-free and the saline system. The salt screening effect becomes significant

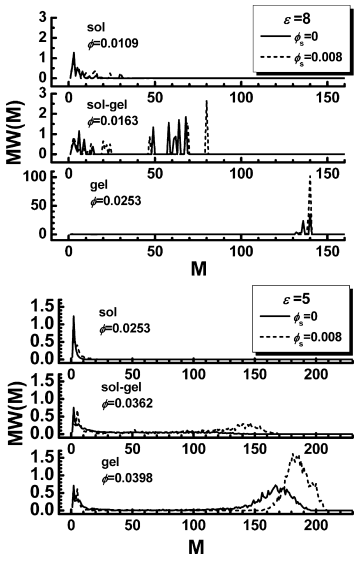

Figure 3. Distribution of cluster size with different concentrations, three typical concentrations are chosen to present the additional salt effects on sol, sol−gel, and gel state. $W(M) = N(M)/[N(1) + N(2) + ... + N(N)]$, $N(M)$ is the number of cluster of size M.

when the concentration rises to ϕ = 0.0362 in the sol−gel coexisting state; the distribution of small cluster size is maintained, but a broad peak representing the size distribution curve of large clusters in the saline system appears compared with the salt-free curve.

When ϕ = 0.0398 in the gel state, again, the size distribution of small clusters shows no significant changes; the broad peak representing large size clusters of the salt-free system appears, and the presence of salt results in larger cluster size and a higher value of distribution function. In general, the effects of added salt ions are identical though different simulation box lengths and descriptions of salt ions are used.[61]

3.2. The Salt Effects on the Gel Structure. In Figure 3, the additional salt produces a major effect on the clusters formed in the system, especially in the sol−gel transition area. This influence could be reflected clearly by the snapshots in Figure 4 of the corresponding concentrations. Compared with the cluster in Figure 4a, with additional salt the one in 4c increases in size significantly, even forms temperate percolation across the simulation box. Similar phenomena can be found in Figure 4, parts b and d, under ε = 5, at higher concentration and greater cluster size. There are more differences between the systems under ε = 8 and ε = 5, which might not be described with only observation of the snapshots. A series of statistic measurements is needed for deeper understanding of the gel structure.

The salt effects on the gel structure can be demonstrated by the correlation function $g_{AA}(r)$ of the hydrophobic monomers in Figure 5. At ϕ = 0.0146 and ε = 8 (see Figure 5a), the system has just entered the sol−gel transition field. The additional salt causes an increase of g_{AA} in the middle range ($5 < r < 15$), indicating the aggregation of chains are more favored due to screened electrostatic repulsion. The correlation peak (as the arrow points) in the long-range shifts to smaller r with the addition of salt, suggesting the correlation distance between micelles is reduced by the screening of salt ions. This phenomenon is also witnessed when the system enters the gel state (see Figure 5c). For ϕ = 0.0325 and ε = 5 (see Figure 5b), the system is also in the sol−gel transition field. However,

dx.doi.org/10.1021/ma201872e | Macromolecules 2012, 45, 555−562

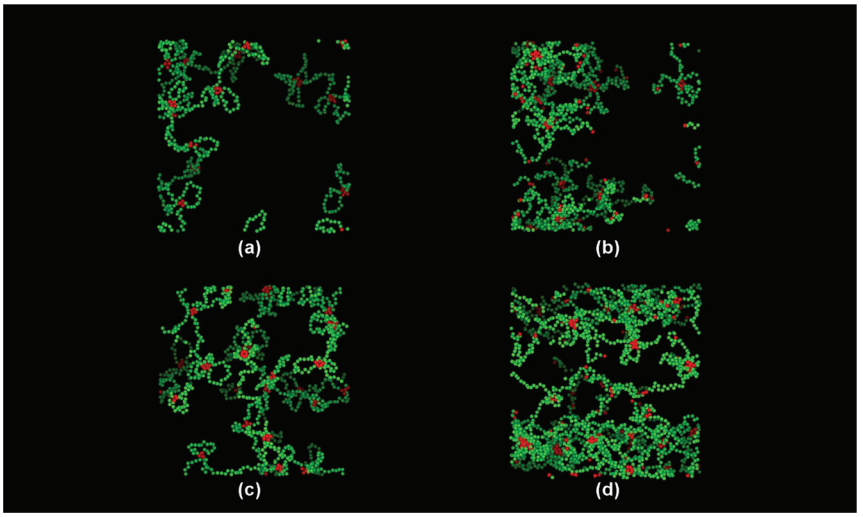

Figure 4. Snapshots of clusters formed in systems with/without additional salt ions. (a) $\phi = 0.0163$, $\varepsilon = 8$, $\phi_s = 0$; (b) $\phi = 0.0362$, $\varepsilon = 5$, $\phi_s = 0$; (c) $\phi = 0.0163$, $\varepsilon = 8$, $\phi_s = 0.008$; (d) $\phi = 0.0362$, $\varepsilon = 5$, $\phi_s = 0.008$. The hydrophobic monomers are shown in red, and the polyelectrolyte block in green color. The salt ions (including counterions), single chains, and other small clusters are not shown for clarity.

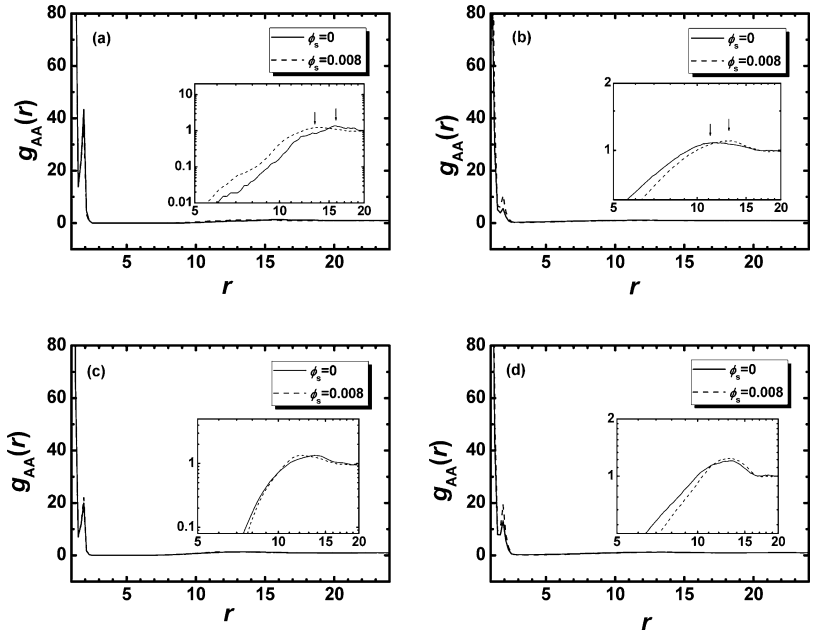

Figure 5. Effect of salt on the correlation function $g_{AA}(r)$ of hydrophobic monomers: (a) $\phi = 0.0145$, $\varepsilon = 8$; (b) $\phi = 0.0325$, $\varepsilon = 5$; (c) $\phi = 0.0253$, $\varepsilon = 8$; (d) $\phi = 0.0398$, $\varepsilon = 5$.

g_{AA} in the middle range ($5 < r < 10$) presents a decrease due to the addition of salt, and the correlation peak (as the arrow points) in the long-range shifts to a larger r, indicating the correlation distance between micelles is a little increased; with additional salt, a significant increase of g_{AA} around $r = 2$ is captured both at $\phi = 0.0325$ and $\phi = 0.0398$, while for the latter the system enters the gel state, similar shift of correlation peak in the long-range is also captured (see Figure 5d). The differences in correlation function suggest that the salt effects on system structure under relatively strong and weak hydrophobicities are different.

This difference can be interpreted by further investigation of the micelle structure. N_b, the average number of branches of micelle,[62−64] presented an increase with the additional salt ions (see Figure 6, parts a and b). For $\varepsilon = 8$, N_b shows no further increase with ϕ when $\phi > 0.0145$; with additional salt N_b rises from 2 to 4 at lower concentrations, but does not show much rising when ϕ increases, especially in the sol−gel transition field. For $\varepsilon = 5$, N_b increases with ϕ during the whole concentration range compared with $\varepsilon = 8$; with additional salt N_b rises apparently in the sol−gel transition field, which causes the micelles to grow bigger in size. This could explain why the correlation distance of micelles under small ε exhibits an increase with the additional salt. N_m, the average number of micelles in the system is investigated in Figure 6, parts c and d. At low ϕ, the screening effects of addition of salt favor the aggregation of chains, causing a little increase of N_m for both $\varepsilon = 8$ and $\varepsilon = 5$; as ϕ increases, the additional salt causes a decrease of N_m for both $\varepsilon = 8$ and $\varepsilon = 5$ due to increased N_b, especially for $\varepsilon = 5$.

The developing of gel structure with ϕ can be viewed as the increasing of N_b and N_m. For $\varepsilon = 8$, N_b shows no further

dx.doi.org/10.1021/ma201872e | *Macromolecules* 2012, 45, 555−562

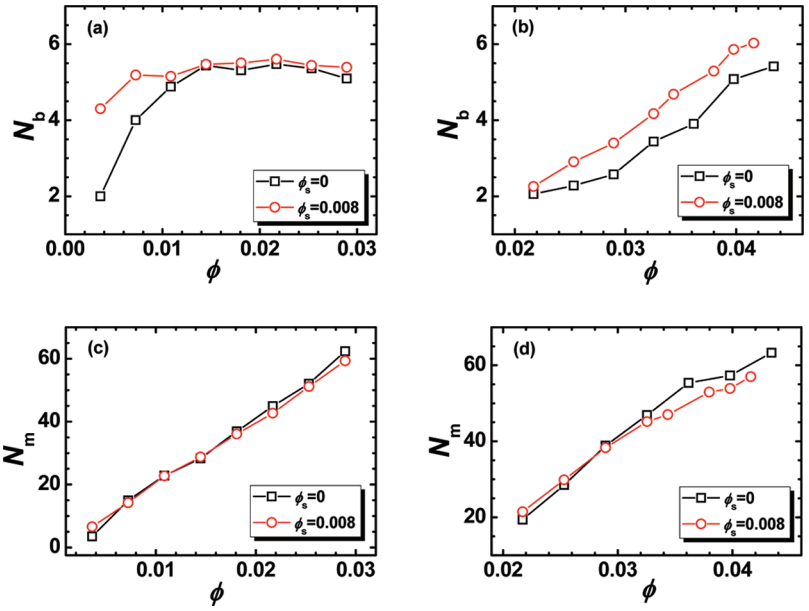

Figure 6. Effect of salt on the average branch number of micelles (N_b) and the average number of micelles (N_m). ε = 8 for (a, c); ε = 5 for (b, d).

increase with ϕ when ϕ > 0.0145, which means the growing of gel structure is mainly attributed to the increase of N_m. However, the additional salt causes a decreased correlation distance between micelles, which obviously requires a larger N_m to develop the gel structure. These interpretation coincides with the analyses of association types of chains in section 3.1, that the additional salt screens the sustaining force among the gel network and causes a higher gelation concentration and therefore an extended sol−gel transition area at ε = 8. While for ε = 5, both N_b and N_m present an increase with greater ϕ during the sol−gel transition field. The additional salt induces a larger N_b and therefore an increased micelle size, which would neutralize the negative effects caused by the relatively slower increase of N_m with additional salt ions. Thus, the extending of sol−gel transition would be avoided, and the additional salt provides a promoting effect in the gelation process under relatively weak hydrophobic interaction.

3.3. Effect of ϕ_s on Association Types of Chain. The above simulation results provide us the comparison of salt-free system and saline system with a specific salt concentration, ϕ_s = 0.008. Next, it is essential to take salt concentration ϕ_s as a variable to investigate the association behavior of TP. For the hydrophobic interaction dominated system (ε = 8), two TP concentrations corresponding to the sol and gel state (ϕ = 0.0109 and ϕ = 0.0253) are chosen to study the salt effects on chain association. Figure 7 presents the chain association type fraction $f_t(\phi_s)$ as a function of ϕ_s. As a whole, at ϕ = 0.0109 and ϕ = 0.0253 the system is mainly involved with loop and bridge chains due to strong hydrophobic attraction. In the sol state (Figure 7a), chains tend to form flowerlike micelles at first,[2,48,50] $f_{loop}(\phi_s)$ increases with the increasing of ϕ_s, suggesting the screening effect favors the forming of these micelles; a further increase of ϕ_s causes $f_{loop}(\phi_s)$ to decrease and $f_{bridge}(\phi_s)$ to increase, indicating these micelles are further connected to form clusters or so-called multicore micelles.[65] After ϕ_s = 0.01, $f_{loop}(\phi_s)$ and $f_{bridge}(\phi_s)$ show no significant changes with ϕ_s, there are also a few free chains and dangling chains at the beginning, which decrease to 0 with the increase of ϕ_s. In Figure 7b, due to the already connected gel structure,

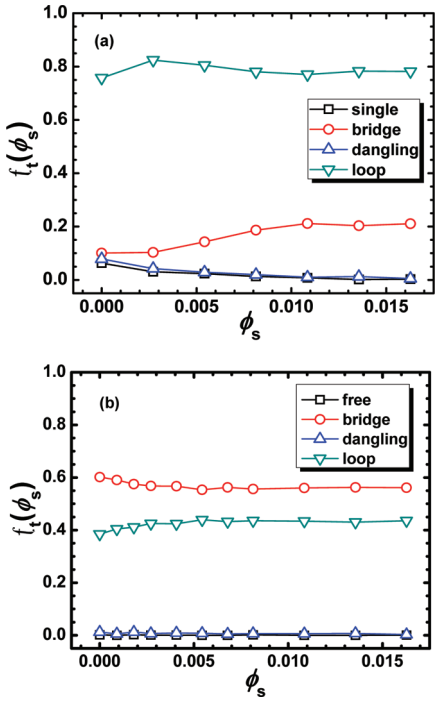

Figure 7. Chain association type fraction $f(\phi_s)$ as a function of salt concentration ϕ_s at different TP concentrations for the hydrophobic interaction dominated system. ε = 8, (a) ϕ = 0.0109; (b) ϕ = 0.0253.

there are few free or dangling chains left when no salt is added. Increasing ϕ_s will result in the screening of electrostatic repulsion; therefore, $f_{bridge}(\phi_s)$ shows a decrease and $f_{loop}(\phi_s)$ an increase with ϕ_s, and both of them show no significant changes when ϕ_s > 0.005.

For weaker hydrophobic interaction (ε = 5), i.e., the electrostatic interaction dominated system (see Figure 8), the influence of ϕ_s to the association behavior of TP chains, as concluded above, is improving aggregation by screening electrostatic repulsion. ϕ = 0.0253 and ϕ = 0.0398 are chosen corresponding to the sol and gel state. In the sol state (Figure

dx.doi.org/10.1021/ma201872e | *Macromolecules* 2012, 45, 555−562

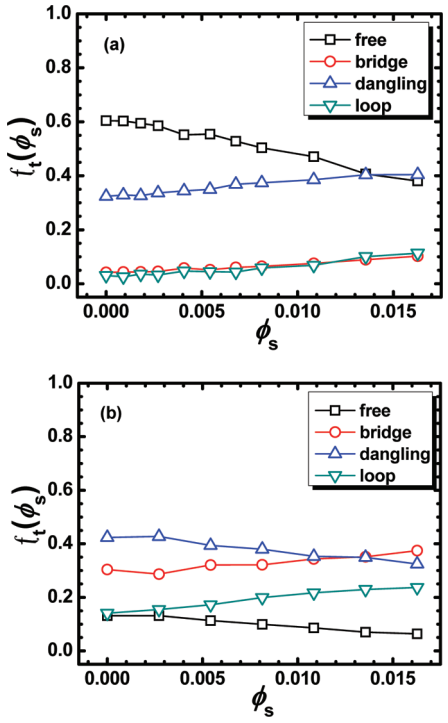

Figure 8. Chain association type fraction $f(\phi_s)$ as a function of salt concentration ϕ_s at different TP concentrations for the electrostatic interaction dominated system. ε = 5: (a) ϕ = 0.0253; (b) ϕ = 0.0398.

8a), when no salt is added, chains mainly exist as frees and danglings, with a small number of bridges and loops; with the increase of ϕ_s, $f_{free}(\phi_s)$ decreases due to increased screening effects, while $f_{dangling}(\phi_s)$, $f_{bridge}(\phi_s)$, and $f_{loop}(\phi_s)$ show an increase with ϕ_s. In the gel state (Figure 8b), when no salt is added, bridge and dangling chains are more favored, with only a few free and loop chains left. $f_{free}(\phi_s)$ decreases, while both $f_{bridge}(\phi_s)$ and $f_{loop}(\phi_s)$ show an increase with ϕ_s. The dangling chain increases with ϕ_s in the sol state but decreases in the gel state. This is because dangling chains act as intermediates: free chains change into dangling chains and the latter into loops and bridges during the sol–gel transition.[49]

4. CONCLUSION

In this paper, using Monte Carlo simulation techniques we continue our work on the association behavior of telechelic polyelectrolytes in the presence of small salt ions. We found the additional salt has different contributions to the aggregation of TP chains. For the system dominated by electrostatic interaction, the screening effects will decrease the electrostatic repulsion and enable further aggregation of chains, resulting in prompting the sol–gel transition progress to a lower concentration area than the salt free system; for the system dominated by hydrophobic attraction, the additional salt causes a widened sol–gel transition field: the screening effects favor the aggregation of chains, resulting in the prompting effect of sol–gel transition, but cause a decrease in the sustaining force of gel structure and a higher gelation concentration. A thorough investigation of the gel structure provides a clearer mechanism that how the additional salt influences the gelation process: for the electrostatic interaction dominated system, N_b increases with ϕ during the concentration range, with additional salt both N_b and micelle correlation distance increase; while for hydrophobic interaction dominated system, N_b shows no further increase with ϕ when ϕ > 0.0145, and the additional salt does not induce a significant increase of N_b, but causes a decrease to the micelle correlation distance. With increasing salt concentration, for the hydrophobic interaction dominated system, the prompting and hindering effects are very significant for the sol state and gel state separately; for the electrostatic interaction dominated system, the prompting effects works for both the sol and gel state.

AUTHOR INFORMATION

Corresponding Author

*E-mail: tfshi@ciac.jl.cn. Telephone: +86-431-85262137. Fax: +86-431-85262969.

ACKNOWLEDGMENTS

This work is supported by the National Natural Science Foundation of China (20734003, 21174146, 51028301) Programs and the Fund for Creative Research Groups (50921062); the Special Funds for National Basic Research Program of China (2009CB930100, 2010CB631100).

REFERENCES

(1) Bossard, F.; Aubry, T.; Gotzamanis, G.; Tsitsilianis, C. *Soft Matter* **2006**, *2* (6), 510–516.
(2) Stavrouli, N.; Aubry, T.; Tsitsilianis, C. *Polymer* **2008**, *49* (5), 1249–1256.
(3) Tsitsilianis, C.; Aubry, T.; Iliopoulos, I.; Norvez, S. *Macromolecules* **2010**, *43* (18), 7779–7784.
(4) Wu, J. L.; Wang, Y. M.; Hara, M.; Granville, M.; Jerome, R. J. *Macromolecules* **1994**, *27* (5), 1195–1200.
(5) Kimerling, A. S.; Rochefort, W. E.; Bhatia, S. R. *Ind. Eng. Chem. Res.* **2006**, *45* (21), 6885–6889.
(6) Vasilevskaya, V. V.; Potemkin, I. I.; Khokhlov, A. R. *Langmuir* **1999**, *15* (23), 7918–7924.
(7) Potemkin, I. I.; Vasilevskaya, V. V.; Khokhlov, A. R. *J. Chem. Phys.* **1999**, *111* (6), 2809–2817.
(8) Carnal, F.; Stoll, S. *J. Chem. Phys.* **2011**, *134* (4), No. in press.
(9) Uyaver, S.; Seidel, C. *Macromolecules* **2009**, *42* (4), 1352–1361.
(10) Hsiao, P. Y. *Macromolecules* **2006**, *39* (20), 7125–7137.
(11) Carrington, S.; Odell, J.; Fisher, L.; Mitchell, J.; Hartley, L. *Polymer* **1996**, *37* (13), 2871–2875.
(12) Gonzalez-Mozuelos, P.; de la Cruz, M. O. *J. Chem. Phys.* **2003**, *118* (10), 4684–4691.
(13) Ghosal, S. *Phys. Rev. Lett.* **2007**, *98* (23), No. in press.
(14) Dautzenberg, H.; Kriz, J. *Langmuir* **2003**, *19* (13), 5204–5211.
(15) Kundagrami, A.; Muthukumar, M. *J. Chem. Phys.* **2008**, *128* (24), No. in press.
(16) Wei, Y. F.; Hsiao, P. Y. *J. Chem. Phys.* **2010**, *132* (2), No. in press.
(17) Zhang, R. J.; Kohler, K.; Kreft, O.; Skirtach, A.; Mohwald, H.; Sukhorukov, G. *Soft Matter* **2010**, *6* (19), 4742–4747.
(18) Kudlay, A.; de la Cruz, M. O. *J. Chem. Phys.* **2004**, *120* (1), 404–412.
(19) Zhang, X.; Wang, Y.; Wang, W.; Bolisetty, S.; Lu, Y.; Ballauff, M. *Langmuir* **2009**, *25* (4), 2075–80.
(20) Potemkin, I. I.; Oskolkov, N. N.; Khokhlov, A. R.; Reineker, P. *Phys. Rev. E* **2005**, *72* (2), No. in press.
(21) Wu, K. A.; Jha, P. K.; de la Cruz, M. O. *Macromolecules* **2010**, *43* (21), 9160–9167.
(22) Vasilevskaya, V. V.; Khokhlov, A. R. *Macromol. Theory Simul.* **2002**, *11* (6), 623–629.
(23) Budtova, T. V.; Belnikevich, N. G.; Suleimenov, I. E.; Frenkel, S. Y. *Polymer* **1993**, *34* (24), 5154–5156.
(24) Sasaki, S. *J. Chem. Phys.* **2006**, *124* (9), No. in press.
(25) Edgecombe, S.; Schneider, S.; Linse, P. *Macromolecules* **2004**, *37* (26), 10089–10100.

(26) Edgecombe, S.; Linse, P. *Polymer* **2008**, *49* (7), 1981−1992.
(27) Schneider, S.; Linse, P. *Eur. Phys. J. E* **2002**, *8* (5), 457−460.
(28) Schneider, S.; Linse, P. *Macromolecules* **2004**, *37* (10), 3850−3856.
(29) Budtova, T.; Navard, P. *Macromolecules* **1998**, *31* (25), 8845−8850.
(30) Nilsson, P.; Unga, J.; Hansson, P. *J. Phys. Chem. B* **2007**, *111*, 10959−10964.
(31) Jeon, C. H.; Makhaeva, E. E.; Khokhlov, A. R. *Macromol. Chem. Phys.* **1998**, *199* (12), 2665−2670.
(32) Bossard, F.; Sfika, V.; Tsitsilianis, C. *Macromolecules* **2004**, *37* (10), 3899−3904.
(33) Kudo, S.; Konno, M.; Saito, S. *Polymer* **1993**, *34* (11), 2370−2373.
(34) Evmenenko, G.; Alexeev, V.; Budtova, T.; Buyanov, A.; Frenkel, S. *Polymer* **1999**, *40* (11), 2975−2979.
(35) Reiche, A.; Sandner, R.; Weinkauf, A.; Sandner, B.; Fleischer, G.; Rittig, F. *Polymer* **2000**, *41* (10), 3821−3836.
(36) Victorov, A. *Fluid Phase Equilib.* **2005**, *227* (1), 9−17.
(37) Victorov, A. I. *Fluid Phase Equilib.* **2006**, *241* (1−2), 334−343.
(38) Dahlgren, M. A. G.; Waltermo, A.; Blomberg, E.; Claesson, P. M.; Sjostrom, L.; Akesson, T.; Jonsson, B. *J. Phys. Chem.* **1993**, *97* (45), 11769−11775.
(39) Schneider, S.; Linse, P. *J. Phys. Chem. B* **2003**, *107* (32), 8030−8040.
(40) Bromberg, L. E.; Ron, E. S. *Adv. Drug Delivery Rev.* **1998**, *31* (3), 197−221.
(41) Yuk, S. H.; Bae, Y. H. *C. Rev. Therapeutic Drug Carrier Syst.* **1999**, *16* (4), 385−423.
(42) Qiu, Y.; Park, K. *Adv. Drug Delivery Rev.* **2001**, *53* (3), 321−339.
(43) Hamidi, M.; Azadi, A.; Rafiei, P. *Adv. Drug Delivery Rev.* **2008**, *60* (15), 1638−1649.
(44) Taktak, F. F.; Butun, V. *Polymer* **2010**, *51* (16), 3618−3626.
(45) Tsitsilianis, C.; Iliopoulos, I.; Ducouret, G. *Macromolecules* **2000**, *33* (8), 2936−2943.
(46) Solis, F. J.; Vernon, B. *Macromolecules* **2007**, *40* (10), 3840−3847.
(47) Jannasch, P. *Polymer* **2002**, *43* (24), 6449−6453.
(48) Zhang, R.; Shi, T. F.; Li, H. F.; An, L. J. *J. Chem. Phys.* **2011**, *134* (3), 034903.
(49) Zhang, R.; Shi, T. F.; An, L. J.; Sun, Z. Y.; Tong, Z. *J. Phys. Chem. B* **2010**, *114* (10), 3449−3456.
(50) Katsampas, I.; Tsitsilianis, C. *Macromolecules* **2005**, *38* (4), 1307−1314.
(51) Allen, M. P.; Tildesley, D. J., *Computer Simulations of Liquids*; Oxford University Press: London, 1987.
(52) Madras, N.; Sokal, A. D. *J. Stat. Phys.* **1987**, *50* (1−2), 109−186.
(53) Roger, M.; Guenoun, P.; Muller, F.; Belloni, L.; Delsanti, M. *Eur. Phys. J. E: Soft Matter* **2002**, *9* (4), 313−326.
(54) Kremer, K.; Binder, K. *Comput. Phys. Rep.* **1988**, *7* (6), 259−310.
(55) Ghosh, K.; Carri, G. A.; Muthukumar, M. *J. Chem. Phys.* **2001**, *115* (9), 4367−4375.
(56) Stevens, M. J.; Kremer, K. *J. Chem. Phys.* **1995**, *103* (4), 1669−1690.
(57) Winkler, R. G.; Gold, M.; Reineker, P. *Phys. Rev. Lett.* **1998**, *80* (17), 3731−3734.
(58) Lipson, J. E. G.; Milner, S. T. *Eur. Phys. J. B* **2009**, *72*, 133−137.
(59) Berhan, L.; Sastry, A. M. *Phys. Rev. E* **2007**, *75*, 041121.
(60) Natsuki, T.; Endo, M.; Takahashi, T. *Physica A* **2005**, *352*, 498−508.
(61) de la Cruz, M. O.; Ermoshkin, A. V.; Carignano, M. A.; Szleifer, I. *Soft Matter* **2009**, *5* (3), 629.
(62) Yang, Z.; Crothers, M.; Ricardo, N.; Chaibundit, C.; Taboada, P.; Mosquera, V.; Kelarakis, A.; Havredaki, V.; Martini, L.; Valder, C.; Collett, J. H.; Attwood, D.; Heatley, F.; Booth, C. *Langmuir* **2003**, *19* (3), 943−950.
(63) Chaibundit, C.; Ricardo, G.; Costa, V.; Yeates, S. G.; Booth, C. *Langmuir* **2007**, *23* (18), 9229−9236.
(64) Noda, T.; Morishima, Y. *Macromolecules* **1999**, *32* (14), 4631−4640.
(65) Kelarakis, A.; Havredaki, V.; Viras, K.; Mingvanish, W.; Heatley, F.; Booth, C.; Mai, S. M. *J. Phys. Chem. B* **2001**, *105* (31), 7384−7393.

Macromolecules

ARTICLE

pubs.acs.org/Macromolecules

Molecular Dynamics Study of a MARTINI Coarse-Grained Polystyrene Brush in Good Solvent: Structure and Dynamics

Giulia Rossi,*[,†,⊥] Ian G. Elliott,[‡] Tapio Ala-Nissila,[†,§] and Roland Faller*[,‡]

[†]Department of Applied Physics, Aalto University School of Science, P.O. Box 11000, FI-00076 AALTO, Finland

[‡]Department of Chemical Engineering & Materials Science, University of California at Davis, One Shields Ave, Davis, California 95616, United States

[§]Department of Physics, Brown University, P.O. Box 1843, Providence, Rhode Island 02912-1843, United States

ABSTRACT: We use a newly developed model of polystyrene, based on the MARTINI coarse-grained force field, to study the behavior of polystyrene brushes in benzene via molecular dynamics simulations. We focus on chain lengths comparable to those accessible experimentally. We analyze the structural and dynamical configuration of the brushes as a function of their grafting density in a high grafting density regime (0.1−0.3 chains nm^{-2}). Only the highest density brush considered here (0.3 chains nm^{-2}) turns out to be characterized by a well-defined bulk area, where the density profile is flat, the lateral pressure profile has a plateau, and the chains are aligned perpendicularly to the substrate. At all grafting densities, our simulations reveal the presence of metastable collapsed states, with free chain ends trapped close to the substrate. These collapsed states are shown to be long-lived, surviving over a time scale of several microseconds.

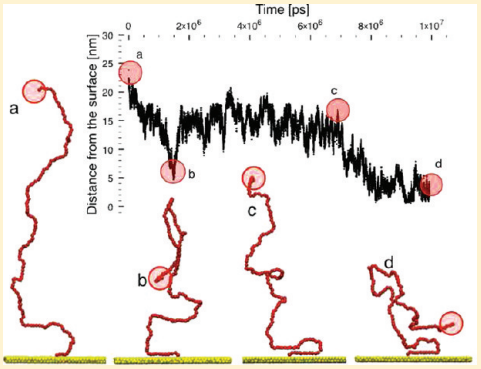

INTRODUCTION

Polymer brushes are abundantly used to tailor surfaces for specific applications .[1] Their main characteristics are the grafting density at the surface and the chain length. The recent development of accurate synthesis techniques, such as atom transfer radical polymerization, has led to the production of brushes with very high grafting density.[2,3] Regularly, the ratio between the gyration radius and the average distance between grafting points determines the various density regimes due to the degree of overlap of neighboring chains.[4] In the high-density regime, the distance between the grafted initiators on the substrate is significantly smaller than the average size of the free chain, causing the stretching of the brush in the direction perpendicular to the surface. High-density brushes are interesting for lubricant applications, thanks to their reduced friction coefficients.[5] Recently, new applications, far from the more traditional tribology area, have been explored. For example, the combination of high grafting densities and chain-end-functionalized brushes has revealed as a promising route for the patterning of biomolecules and inorganic particles, which can selectively bind on top of the substrate areas covered with the functionalized brush.[6,7]

The rational design of interface- or surface-active polymer modifiers still lacks crucial molecular scale information about the behavior and structure−property relationships of the brushes. This is especially true in the regime of dense brushes. However, such high grafting densities are potentially outside of the limits of classical polymer brush theory. Therefore, molecular modeling has to be applied to gain a theoretical understanding especially at the molecular level.

Polymeric systems are an inherent multiscale problem. This mandates the use of adapted molecular models. A few studies in atomistic detail have appeared, but they focused on short oligomer-like chains and/or low grafting densities.[8−10] On the other hand, polymer brushes have abundantly been studied by bead−spring type models[11,12] where the chemical specificity is lost. Such models are very valuable for understanding general dependencies on grafting density or chain length. But for direct comparison to experimental data more specific models are needed. Thus, between the all-atom and the bead−spring model a number of mesoscale models have been developed. For example, the iterative Boltzmann inversion has been used to develop intermediate scale specific models which have been used for the study of brushes.[13,14]

A promising alternative route to coarse-grained molecular modeling is given by the MARTINI model. MARTINI has been originally developed for lipids and other molecules of biological interest.[15−21] Recently, the MARTINI model has been extended to polymers such as polystyrene,[22] poly(ethylene oxide) and poly(ethylene glycol),[23] polyamido amine dendrimers,[24] and others.[25−28] In this paper we present the first application of the coarse-grained MARTINI model of polystyrene to the study of a highly dense polymer brush in a good solvent environment by means of molecular dynamics (MD) simulations. We analyze the structural and dynamical properties of the brush, with special focus on the trajectories of the chain ends which might eventually

Received: August 30, 2011
Revised: November 11, 2011
Published: December 08, 2011

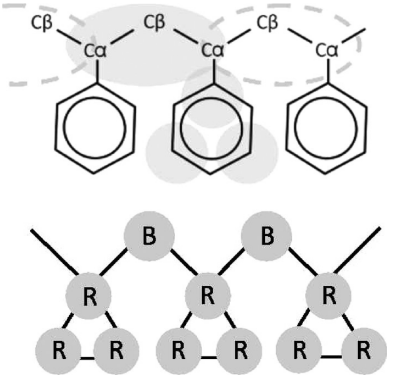

Figure 1. In the top image, gray areas on top of the atomistic description represent CG beads. In the CG molecule, at the bottom, backbone and ring beads are called B and R beads, respectively.

Table 1. Parameters of Bonded Interactions[a]

bond	r_{eq}	k_b	angle	θ_{eq}	k_a
B−R	0.27	8000	B−R−B	52	550
R−R	0.27	constr	R−B−R	120	25
			B−R−R	136	100

[a] B and R indicate backbone and ring beads, respectively (see Figure 1). r_{eq} (nm) and k_b (kJ mol^{-1} nm^{-2}) are the equilibrium bond length and the elastic constant of the harmonic bond potential. Very narrow atomistic distributions led us to constrain R−R bonds. θ_{eq} (deg) and k_a (kJ mol^{-1} deg^{-2}) are the equilibrium angle and the elastic constant of the harmonic angle potentials.

be functionalized. We compare the outcomes of our simulations to those of previous computational studies of polymer brushes, based on chemically nonspecific coarse-grained models. Moreover, we present our data in light of the available experimental data, and we discuss to what extent our MARTINI model can constitute a bridge between the predictions of the chemically nonspecific models and the experimental evidence related to the specific case of polystyrene.

In the section Model and Methods we describe our coarse-grained model of polystyrene, the brush setup, and the computational methods. The Results section contains the results of the structural and dynamical characterization of the brushes as a function of their grafting density. A discussion of the results follows in the Discussion section.

MODEL AND METHODS

Coarse-Grained Model of Polystyrene. We describe polystyrene chains by means of the MARTINI-based coarse-grained (CG) model we recently developed and validated.[22] Figure 1 shows how we mapped the atomistic description of polystyrene into the coarse-grained one. Each monomer is composed of four coarse-grained beads. Each bead represents two C atoms and their hydrogens. This relatively fine degree of coarse-graining allows for retaining the backbone−ring structure of polystyrene, and it is consistent with the 2-to-1 mapping scheme[16] of the MARTINI force field.

Bonds between CG beads are described by harmonic functions. We tuned their equilibrium values and force constants to reproduce at best the peak position and width of their atomistic

Table 2. Optimized Values of ε and σ Lennard-Jones Parameters for the MARTINI PS Model[a]

parameter	σ_{B-B} [nm]	ε_{B-B} [kJ/mol]	σ_{B-R} [nm]	ε_{B-R} [kJ/mol]	σ_{R-R} [nm]	ε_{R-R} [kJ/mol]
PS model	0.43	2.625	0.43	2.325	0.41	2.4

[a] B and R subscripts stand for backbone and ring, respectively.

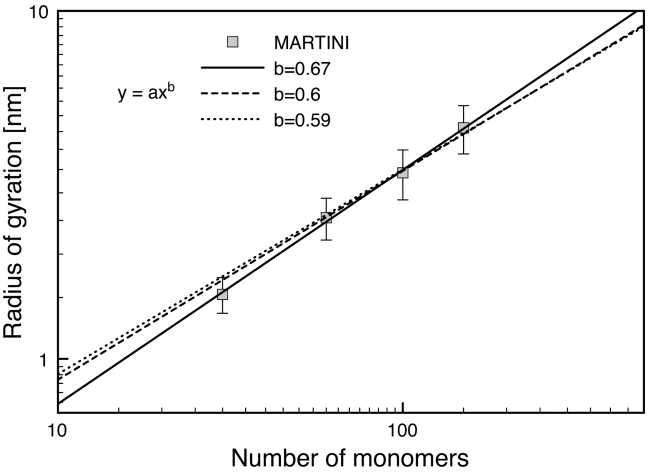

Figure 2. Radius of gyration of polystyrene in benzene solution. Squares are for the simulation data, the continuous line is the best fit to a power law function $y = ax^b$, and the dotted and dashed lines are the best fit to a power law function with exponent $b = 0.588$ and $b = 0.6$, respectively.

counterparts.[22] The model does not include any torsional angle at coarse-grained level. Parameters for the harmonic bonded interactions of the model are reported in Table 1.

In MARTINI, nonbonded interactions between noncharged beads are described by Lennard-Jones potentials. The MARTINI force field includes a large number of beads, each describing a chemical building block characterized by a specific degree of polarity. Lennard-Jones interactions of MARTINI beads are assigned to reproduce experimental thermodynamic data, such as densities and free energies of transfer between water and oil. In our model, the parametrization of polystyrene resulted from a refinement of the original MARTINI parametrization. The refinement aimed at a faithful reproduction of the density and radius of gyration of polystyrene in the melt.[22] Optimized values for the interactions between B (backbone) and R (ring) beads are reported in Table 2, while more details about the parametrization procedure can be found in ref 22.

MARTINI Polystyrene in Benzene. For polystyrene in dilute conditions, the force-field parameters in three different solvents (benzene, cyclohexane, and water) were derived earlier[22] and are available on line.[29] Here we need to describe polystyrene brushes in good solvent conditions, and thus we will solvate the PS brushes in benzene. Within the MARTINI scheme, each benzene molecule is represented by three interconnected beads (MARTINI type SC4). The parameters for the interaction between the PS backbone beads and the MARTINI benzene beads are the same as for the SC1−SC4 interaction in the original MARTINI parametrization,[16] while the interaction between PS ring beads and benzene beads uses the SC4−SC4 interaction.

dx.doi.org/10.1021/ma201980k |Macromolecules 2012, 45, 563–571

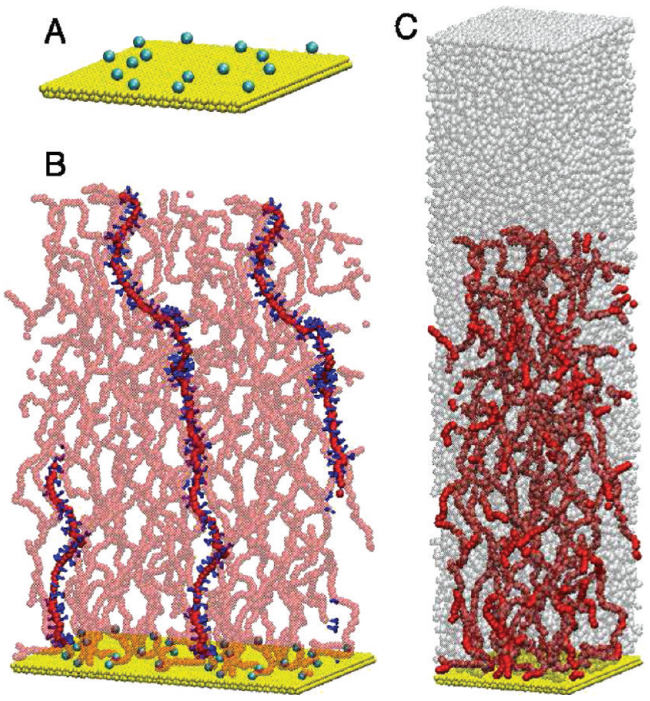

Figure 3. Snapshots from the equilibration runs of the 15 chain system. (A) The 2450 particle substrate and the grafted backbone beads. (B) Two periodic images of the substrate, the grafted beads, and the PS chain backbones. For one of the chains, extending through the box boundaries, we show both backbone beads (red, large) and phenyl rings (small, dark triangles). (C) The substrate, the PS backbones (red), and the benzene solvent (transparent gray).

We verified the reliability of the model by simulations in the *NpT* ensemble of single PS chains of 30, 60, 100, and 150 monomers in benzene at 300 K and 1 bar. The edges of the cubic simulation box varied from 5.8 nm (PS30) to 8.8 nm (PS150) to exclude the interaction of the PS chain with itself, and the runs were 2 μs (PS30), 3.5 μs (PS60), and 5 μs (PS100 and PS150) long. Figure 2 shows the average values of the radius of gyration vs chain length, together with three fitting power law functions. The best fit is given by a scaling exponent of 0.67, while the 0.588 predicted by Flory's theory[30] and the 0.6 value reported experimentally[31] lie within the statistical error bars.

Polystyrene Brushes. Our brushes consist of polystyrene chains of N = 150 monomers grafted to a solid substrate in benzene solution. The substrate consists of two (111) layers of particles (MARTINI type C4), with lattice constant l = 0.25 nm and normal vector along the z direction. The substrate particles have a nonpolar character, and the strength of their interactions with the PS and benzene beads is in the same range as the PS−PS and PS−benzene interactions, namely between 3.1 and 3.5 kJ/mol.[22] The substrate area, A, is 8.7 × 7.4 nm. Substrate beads are restrained to their initial lattice positions by means of a spherical harmonic potential with elastic constant k_{sub} = 8000 kJ mol^{-1} nm^{-2}.

In order to mimic the presence of a covalent bond connecting the chain ends to the substrate, we have restrained the position of the first backbone bead of each PS chain to a random (x,y) position, at a fixed distance from the substrate, z_{bb} = 0.3 nm. The restraining of chain ends is realized with the same harmonic potential used for the substrate beads. We consider three different grafting densities: 0.15, 0.23, and 0.31 chains nm^{-2} (corresponding to 10, 15, and 20 chains in the simulation box). We are thus focusing on a rather high-density brush regime, our density values being comparable to those used in previous computational[10,32] and experimental[3,33] works. However, in contrast to earlier simulations our brushes are longer.

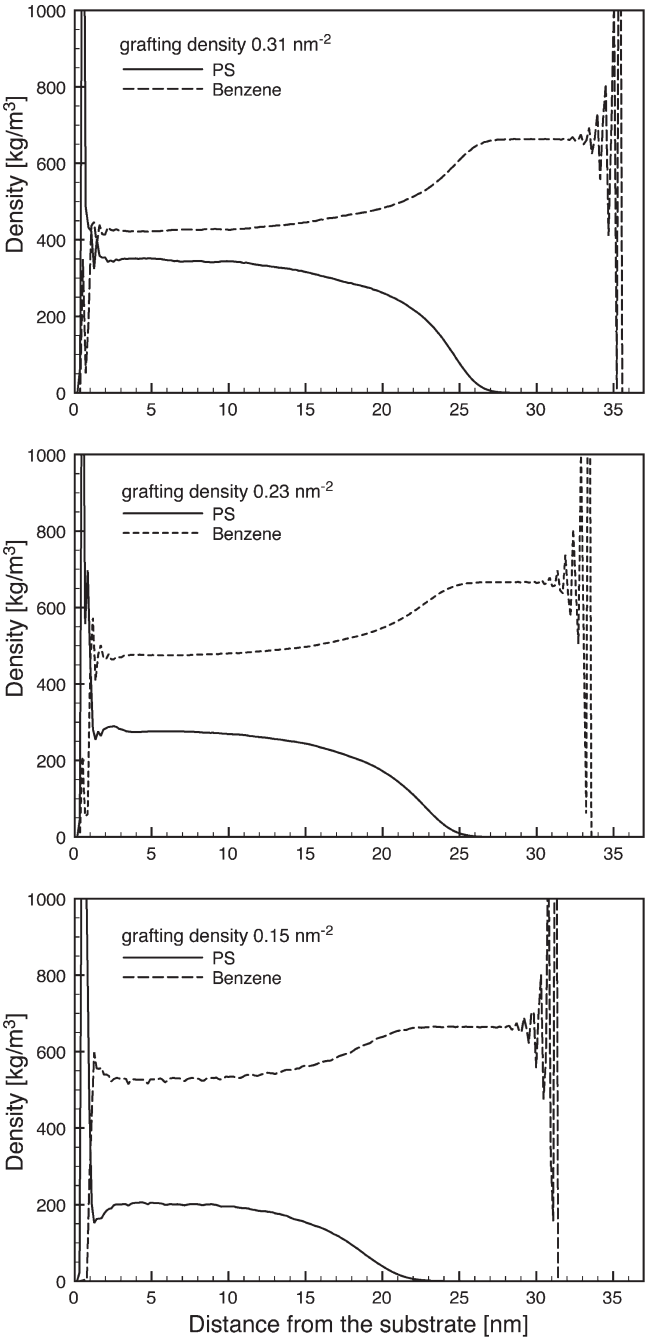

Figure 4. Density profiles of the brushes. Density values have been rescaled converting MARTINI masses[16] to atomistic masses.

Simulation Protocols. *Brush Preparation and Equilibration.* All molecular dynamics simulations were run with the GROMACS package,[34] version 4.0.7. Brushes were built up in three steps: (a) We assigned random (x,y) coordinates, at distance z_{bb} from the substrate, to the first backbone bead of each chain. The distance between grafting points on the (x,y) plane was set to be larger than 1 nm, to avoid an uneven distribution of the chains on

dx.doi.org/10.1021/ma201980k |*Macromolecules* 2012, 45, 563–571

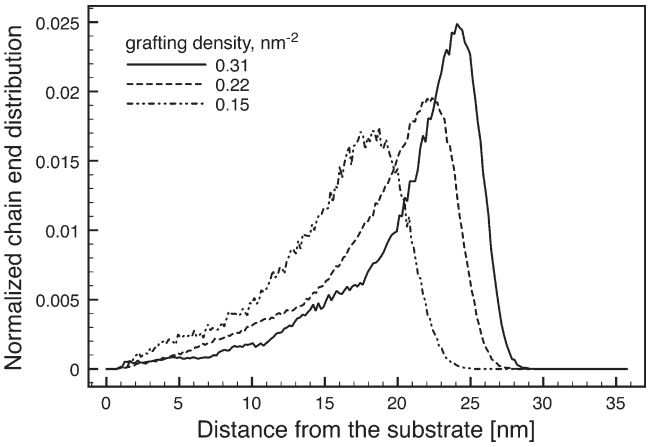

Figure 5. Normalized chain end distribution along the direction perpendicular to the substrate.

the substrate. (b) We grew fully stretched brushes starting from the grafted backbone beads, and benzene molecules were added all over the simulation box, avoiding overlap and interpenetration of ring structures. (c) We equilibrated the system. We used periodic boundary conditions in all directions. Temperature was controlled by a Berendsen thermostat[35] at 400 K. We applied Berendsen pressure coupling[35] (reference value 1 bar) along the z direction and set the system compressibility to 0 along the x and y directions to achieve a NAP_zT ensemble. As a criterion to stop the equilibration procedure, we waited for the brush and solvent density profiles to converge, which typically happened on a microsecond time scale. As a result of the equilibration, the z dimension of the simulation box measured 31−36 nm, including a thick (>8 nm) benzene layer at the top of the brush.

Production Runs. We generated, as detailed above, one starting configuration for the 20-chain system and three independent starting configurations for both the 15- and 10-chain systems. We performed the production runs at the constant temperature of 400 K, controlled by a Nosé-Hoover thermostat.[36,37] A semi-isotropic pressure coupling was applied, keeping the x and y dimensions fixed and allowing for the relaxation of the z dimension of the simulation box using a Parrinello−Rahman barostat.[38,39] We used a time step of 20 fs, and the duration of each independent simulation was 10 μs, amounting to a total of 30, 30, and 10 μs for the 10-, 15-, and 20-chain systems, respectively.

RESULTS

Structure. *Density Profiles.* Figure 4 shows the density profiles of the brushes at equilibrium. In MARTINI, all CG beads are given the same mass, and data here have been rescaled to atomistic density values. The density profiles at the top of the simulation box exhibit sharp peaks that reveal the tendency of the solvent to form 2D liquid layers as getting close to the upper periodic image of the substrate. This is a well-known effect,[40] explained in terms of solvation forces and frequently observed in simulations of Lennard-Jones liquids in contact with solid surfaces.[11,41] At the bottom of the brush, such a layering effect superposes to a large density peak of polystyrene. The peak is due to the flattening against the solid surface of the first monomers of some polymer chains. From an enthalpic point of view, the attraction between the solid surface and polystyrene beads is not

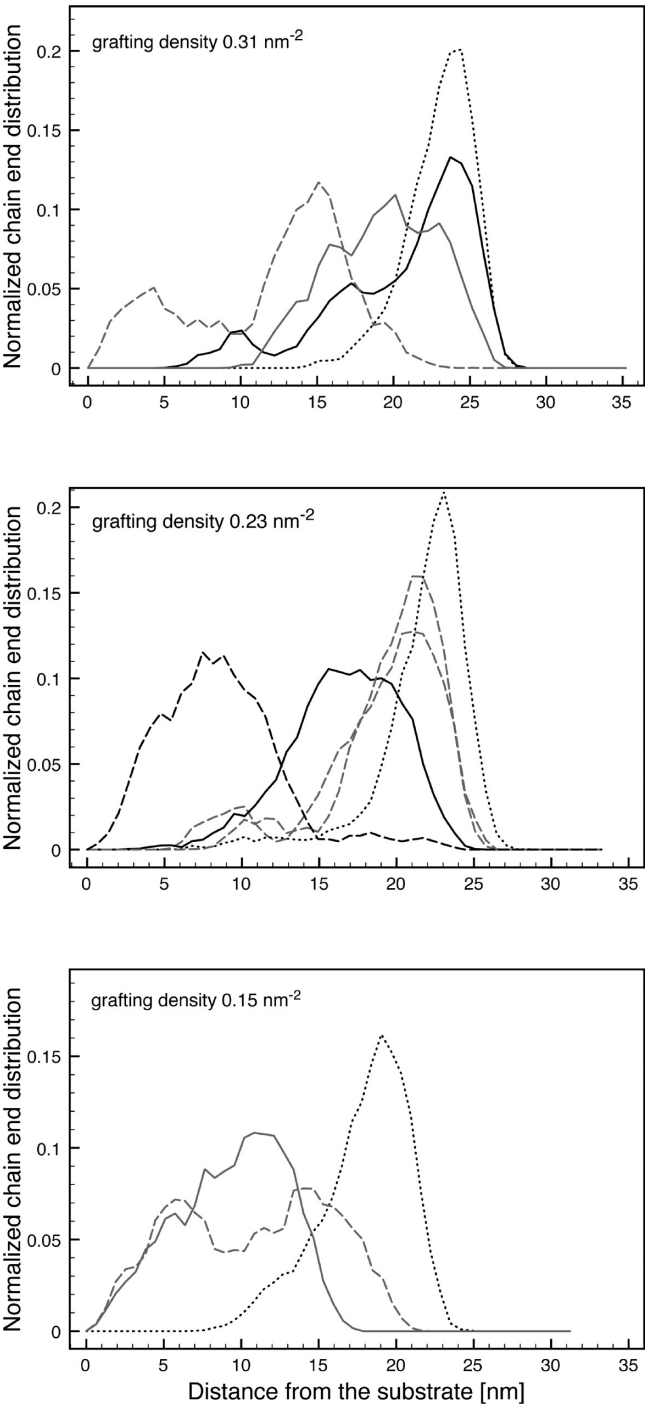

Figure 6. Normalized chain end distribution along z. Here, only some of the end chain distributions are shown for each grafting density. Top: at the highest grafting density, one trimodal distribution is observed (black, thick line), several bimodal distributions (one example shown with dashed gray line), and single-peak distributions with different broadness (thick gray line and black dotted line). Middle: at the intermediate grafting density, bimodal distributions (dashed gray lines) and single-peak distributions of different broadness are observed (black dashed, black thick, black dotted lines). Bottom: for the lowest grafting density, only a very few bimodal distributions are observed (gray dashed line), while all the other distributions are single-peak distributions, with different broadness.

stronger than between the solid surface and benzene. The preference for adsorbing fragments of polymer chains rather

dx.doi.org/10.1021/ma201980k |*Macromolecules* 2012, 45, 563–571

Table 3. Percentages of Chains Whose z Chain End Distribution Is Single-Peak, Bimodal, or Trimodal[a]

	single-peak [%]	bimodal [%]	trimodal [%]
0.3 nm^{-2}	45	20	5
0.23 nm^{-2}	66	15	0
0.15 nm^{-2}	73	13	0

[a] Total number of chains, each analyzed over a 10 μs run, is 20, 45, and 30 for the largest, intermediate, and lowest grafting density considered, respectively.

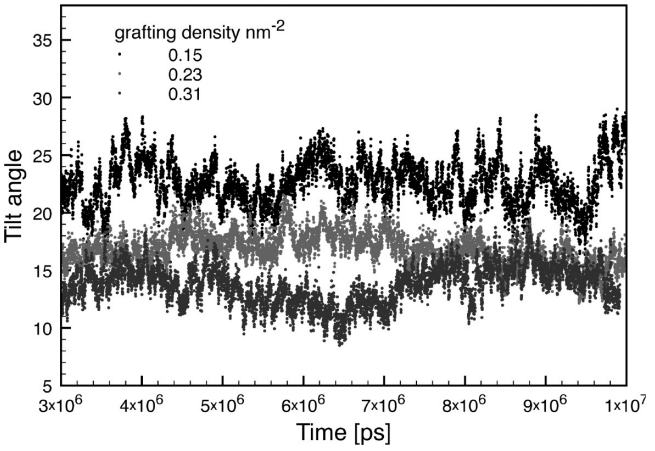

Figure 7. Tilt angles.

than solvent molecules has been observed in other molecular dynamics simulations of polymer brushes, with a more coarsened description of solvent and polymer chains.[32] We thus attribute the preference for PS adsorption at the surface to entropic forces. Our brush density profiles appear to be rather flat along the first third of the brush height and then start to decrease smoothly. Thus, we do not observe a fully parabolic profile for the whole brush but find a plateau which is only observed in very high-density systems.[32,42,43]

Distribution of Chain Ends. We define as z profile, $P(z)$, the normalized distribution of the z coordinate of the free chain ends of the brush. Figure 5 shows the average z profiles we obtained at the different grafting densities. The profiles reveal a strong stretching regime[42] for all the grafting densities considered. While the peak of the distribution moves far from the surface as the grafting density increases, the shape of the distribution changes as well. The relative fluctuation of the distance z between the chain ends and the substrate, namely $f = (\langle z^2\rangle - \langle z\rangle^2)^{1/2}/\langle z\rangle$, gets smaller as the grafting density increases: f = 0.29, 0.26, and 0.23 for brushes with 10, 15, and 20 chains, respectively.

The average chain end z profiles are characterized by small shoulder peaks around 15, 11, and 5 nm from the surface for the high, intermediate, and low grafting densities considered. In order to elucidate the nature of these secondary peaks, we analyzed the z profiles of the single chain ends. On the basis of the appearance of distinguished and significative peaks in the distributions, we classified them as trimodal, bimodal, and single-peak. Several examples are shown in Figure 6. Table 3 quantifies the percentual appearance of these three kinds of distributions as a function of the brush density. Clearly, single peak distributions

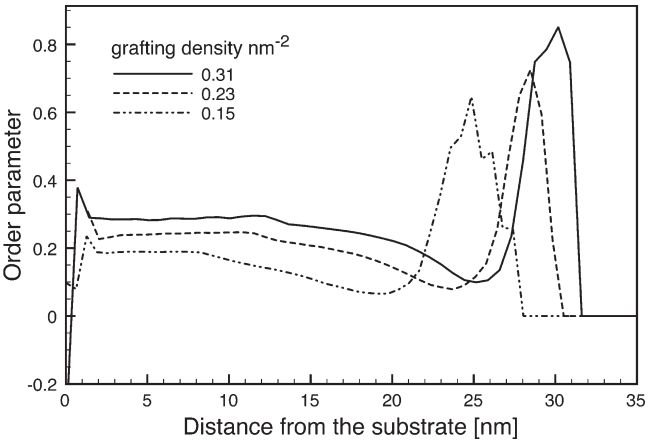

Figure 8. Order parameter $P_2(\theta)$ of backbone bonds as a function of their distance from the substrate.

become prevalent as the brush density decreases, at the expense of multimodal distributions.

Chain Tilt. We measured the tilt angle θ formed by the normal to the substrate plane and the vectors connecting each grafted backbone bead to its free chain end. θ is equal to zero when the chain end is placed right on top of the grafted bead and $\pi/2$ when it is in contact with the surface. Average values of the tilt angle for the brushes with 10, 15, and 20 chains are 22.8, 16.8, and 13.7. Fluctuations around average values are 0.16, 0.16, and 0.15, respectively. The chains become more perpendicular to the surface with increasing grafting density.

Single chain tilt angle distributions exhibit multimodal shapes, similar to those observed for the z chain end distributions. By analyzing the single chain tilt angles, we observed the penetration of chain ends deeply into the brush bulk, reaching tilt angles $\theta > \pi/3$. These events became increasing likely as the density of the brush decreased but were observed also for the highest grafting density considered here.

Bond Alignment with the Normal to the Surface. By increasing the grafting density, the chains stretch and the peak of the chain end distribution moves away from the grafting surface. The stretching is correlated to the alignment of the chain bonds to the normal to the grafting surface, as measured by the order parameter $P_2(\theta) = (3/\langle\cos^2(\theta)\rangle - 1)/2$, θ being the angle formed between each chain bond and the normal. P_2 has the value $-1/2$, 0, and 1 for perpendicular, random, and parallel alignment to the normal, respectively. Dimitrov et al.[11] showed the dependence of the order parameter on the monomer index, finding progressive disalignment of the bonds with decreasing grafting density or quality of the solvent. Since the observation of single chain end distributions show that free chain ends can be found well deep into the brush bulk, in Figure 8 we plot the order parameter as a function of the distance from the grafting surface. The negative peak registered close to the surface has to be attributed to the flattening of the first monomers of the chains on top of the grafting surface. In the brush bulk, a flat region can be clearly identified for all the grafting densities considered. The larger the grafting density, the longer the plateau and the larger the degree of alignment. Interestingly, the order parameter highlights the large degree of alignment of the chain ends, in those rare cases when the chains get to be almost ideally stretched.

Pressure Profiles. We calculated the lateral pressure profile of the brush, defined as $\pi(z) = p_L(z) - p_{zz}(z)$, p_L being the average

dx.doi.org/10.1021/ma201980k |*Macromolecules* 2012, 45, 563–571

between the in-plane diagonal components of the local pressure tensor, $p_L = (p_{xx} + pp_{xx})/2$. We performed the calculation of the local pressure tensor as in Ollila et al.[44] As shown in Figure 9, at all grafting densities, the lateral pressure profile is positive and does not show any negative peak at the top of the brush, as it would be expected in presence of a sharp polymer−solvent interface.[11] The profile of the brush with the highest grafting density shows a clear plateau region extending for 15 nm, followed by a progressive decrease which leads to a homogeneous pressure tensor (isotropic hydrostatic pressure) in the pure solvent region. At the lowest grafting density, no clear plateau can be identified,

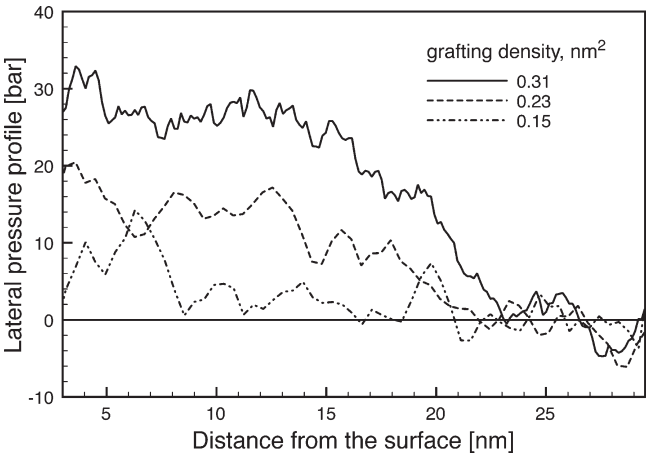

Figure 9. Pressure profile.

and in most of the brush thickness the difference between the perpendicular and parallel components of the stress tensor is negligible. The surface tension across the brush, namely $\gamma = -\int_0^{z_{max}} \pi(z)\, dz$ (z_{max} being placed in the homogeneous solvent region, where the lateral pressure profile vanishes), increases with increasing grafting density.

Dynamics. *Trapped States.* The single chain distributions of free chain ends and tilt angles suggest the possibility that some brush chains may get trapped in metastable states, characterized by large tilt angles and/or deep penetration of the chain ends into the brush, close to the grafting surface. We thus proceed to the analysis of the time-dependent single-chain behavior, with the aim to verify the existence of such trapped states and provide an estimate of their lifetime as a function of the grafting density.

To start with an example, we can focus on a chain whose z chain end distribution is bimodal, with both peaks lying below the brush surface, at 15 and 4 nm (as shown in the top panel of Figure 6). Figure 10 shows the z coordinate of the chain end plotted as a function of time. Starting from an extended state (a), the chain end initially collapses to low z (b) and then finds an intermediate state (c) for more than 5 μs. At the end of the simulation, the chain collapses again and the final state is observed over the last 2 μs of the simulation.

The relatively low number of chains sampled by our simulations does not allow for a quantitative estimate of the lifetime of the collapsed metastable states. Still, from the analysis of the z distribution of the chain ends, some qualitative conclusions can be drawn. The extended configurations show the longest lifetime and in several cases appear to be stable throughout the whole 10 μs run.

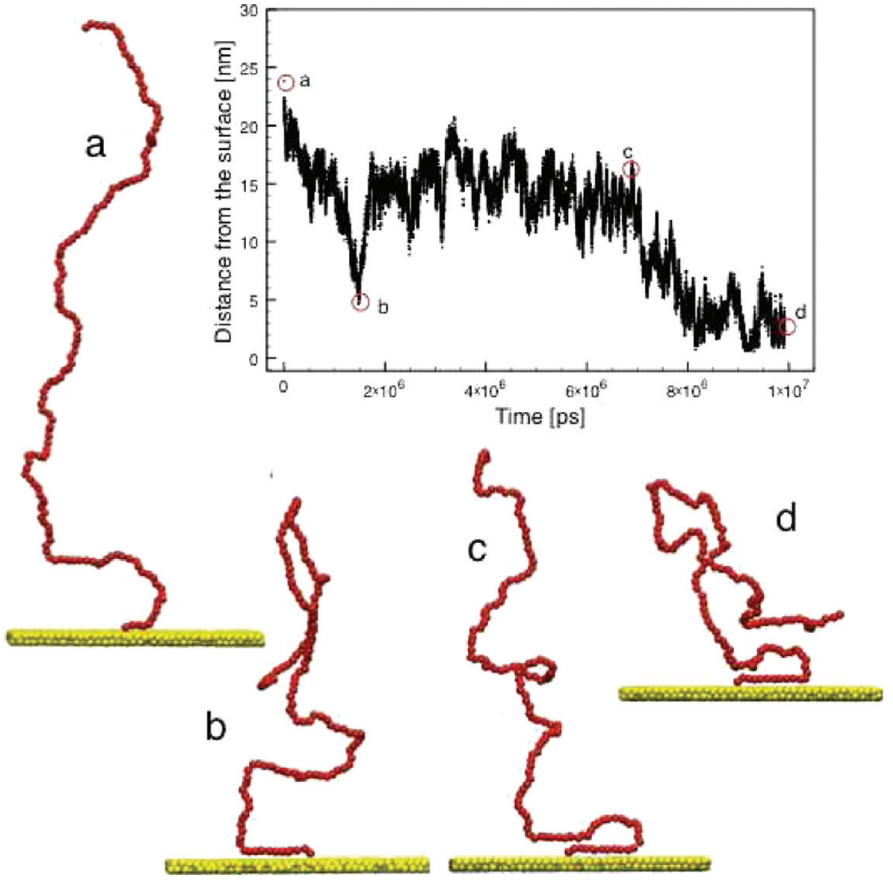

Figure 10. Extended and collapsed states for a chain at 0.31 nm^{-2} grafting density.

dx.doi.org/10.1021/ma201980k |*Macromolecules* 2012, 45, 563–571

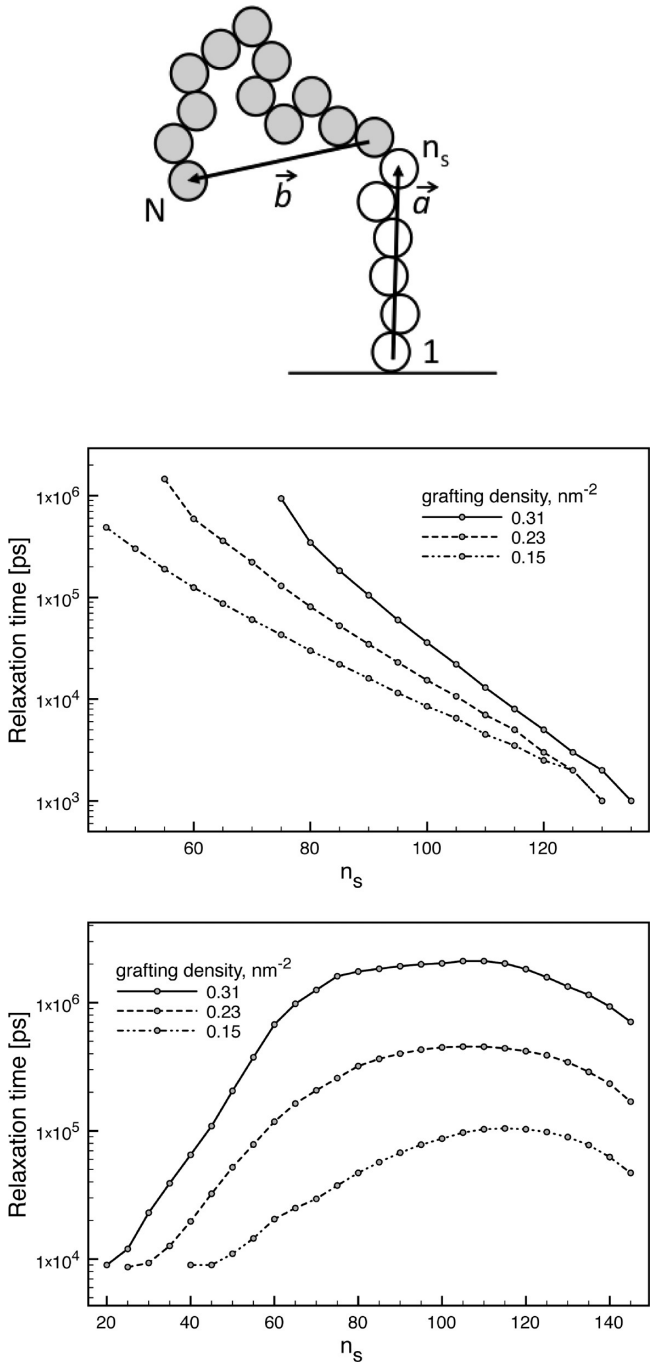

Figure 11. Top panel: the grafted, $\vec{a}$, and terminal, $\vec{b}$, segments of the chains used to calculate orientational relaxation times. Middle panel: relaxation times of the terminal segments, as a function of n_s. Right: relaxation times of the grafted segments. Lines are only guides for the eyes.

Collapsed configurations, with chain ends a few nanometers below the brush surface, have a lifetime of 2−5 μs. Collapsed states where the chain end is very close to the grafting surface survive for shorter times, ranging from a few hundreds of nanoseconds to a couple of microseconds. While clear transitions from extended to different collapsed configurations can be always be spotted for the high- and intermediate-density systems, at the lowest grafting density the transitions from extended to collapsed configurations becomes smoother, in agreement with the lower grafting density brushes completely consisting of one interface region.

Segmental Relaxation Times. The chains need to completely reorient their terminal segment in order to access the collapsed, trapped states described in the previous paragraph. As shown at the top of Figure 11, we can ideally split the chain in a grafted, presumably stiffer region, containing n_s monomers, and a mobile region, containing $n_m = N - n_s$ monomers. The vector $\vec{a}$ connects the first, grafted backbone bead of the chain to the bead at position n_s, while the vector $\vec{b}$ connects the bead at the position $n_s + 1$ with the chain end. The transition from the stretched configurations to the collapsed states described above implies the complete reorientation of long terminal segments ($n_s > 70$). Thus, we first look at the rotational autocorrelation function, $C_b(t)$, of $\vec{b}$, namely, the vector connecting the first of the mobile monomers to the free chain end. $C_b(t)$ is defined as $C_b(t) = \langle P_2[\hat{b}(t)\hat{b}(0)]\rangle$, P_2 being the second Legendre polynomial and $\hat{b}$ a unitary vector directed as $\vec{b}$. The smaller n_s, the slower the reorientation of our terminal segment. In order to be able to compare the behavior of terminal segments of different length, at different grafting densities, we define as relaxation time τ_r the time at which $C_b(t)$ reaches a value of 0.6. The middle panel of Figure 11 shows the average data obtained from our simulations at high, intermediate, and low grafting densities. The dependence on n_s is well approximated by an exponential decay at all grafting densities. Coherently with the qualitative observations derived from the z chain-end and tilt angle distributions, the reorientational dynamics of long terminal segments, $n_s \simeq 70$, is characterized by relaxation times of the order of microseconds for the highest grafting density considered, while decreases by more than an order of magnitude for the lowest one.

The relaxation times of the stiff, grafted segments of the polymer chains provide us with different information concerning the scaling of the brush properties with grafting densities. In this case, we use a different threshold, 0.9, to evaluate the relaxation time of the grafted segments from their rotational autocorrelation function. Indeed, their relaxation is much slower than for the terminal, mobile segments. Relaxation times are plotted as a function of n_s in the bottom panel of Figure 11. Again, relaxation times span 2 orders of magnitude going from the lowest to the highest grafting density. At all densities, τ_r first increases nearly exponentially with the length of the grafted segment. For the lowest density brush, this trend can be observed until $n_s = 110$, when τ_r decreases due to the high mobility of the upper monomers, which compensates for the overall elongation of the grafted segment. The change of slope of τ_r vs n_s is instead quite abrupt for the highest density brush, whose relaxation time sets to a plateau value in the range $70 < n_s < 110$, before starting to decrease.

DISCUSSION AND CONCLUSIONS

We have presented a computational study of PS brushes in a regime of high grafting density. This work relies on a new coarse-grained model of PS, based on the MARTINI coarse-grained force field. The model is chemically specific and allows for the simulation of polystyrene in different solvent environments. Here we focused on benzene, a good solvent for PS. The model is also computationally efficient, as MD simulations can be run with a time step of 20 fs, allowing the investigation of the system over time scales of tens of microseconds.

We can compare the outcomes of our simulations to those of previous computational works that used chemically nonspecific

dx.doi.org/10.1021/ma201980k |*Macromolecules* 2012, 45, 563–571

coarse-grained models. In terms of grafting density, we can translate our grafting densities into dimensionless grafting densities, $\sigma = Np^2/A$, p being the characteristic segment length of the polymer, N the number of monomers in the chains, and A the substrate area. p is the Kuhn length of the polymer, namely twice its persistence length; that for our PS model is 1 nm (in good agreement with experimental[31] and computational[45,46] data). Our numerical grafting densities can be thus converted in dimensionless grafting densities and result as $\sigma = 0.60$, 0.92, and 1.24.

Coluzza and Hansen[42] have identified three density regimes: for $\sigma < 0.004$, the brush is in the mushroom regime. For $0.01 < \sigma < 0.05$ the brush obeys the scaling behavior predicted by the self-consistent field (SCF) theory (that points to parabolic monomer density profiles). For $\sigma > 0.05$, the brush behavior deviates from the SFT predictions (and the density profiles flatten and stretch out). Clearly, all the brush densities analyzed here lay well within the high density, strong stretching regime. The density profile, far from being parabolic, is well fitted by a power law with exponent decreasing from 4.6 for the highest density brush to 4.2 for the lowest, as shown in Figure 12. The appearance of a small depletion layer for PS, close to the grafting surface, at the lowest grafting density analyzed here ($\sigma = 0.60$), is quantitatively coherent with the picture offered by Coluzza for $\sigma > 0.2$ and with other previous calculations.[32] The chain end distributions agree well with those shown by Coluzza as well. We remark that the shoulders in the averaged z profiles, resulting from single chains trapped in the brush bulk, are expected to be smoothed out on longer time scales and in larger samples.

The lateral pressure profiles do not show any change in sign at the top of the brush, consistently with the absence of a sharp polymer−solvent interface.[11] Nevertheless, they qualitatively change in the range of grafting densities considered, and for $\sigma = 1.24$ a well-defined plateau of the lateral pressure profile appears. At lower grafting densities, the interface extends all along the brush height, and the plateau disappears while the shape of the lateral pressure profiles approaches the one obtained by non-specific models at lower σ values.[11] Our results seem thus consistent with the results from chemically nonspecific calculations and allow for a quantitative estimation of the grafting density range corresponding to strong stretching for the specific case of polystyrene. It appears that the higher density brushes consist of a constant density and lateral pressure region close to the surface and a rather well-defined transition to the solvent region. The lower density system is one continuous transition, from the highest density/lateral pressure at the surface to the pure solvent.

Concerning the comparison with experiments, the density profiles emerging from our simulations closely resemble those observed by Devaux et al.,[33] which measured by neutron reflectivity the structure of PS brushes with $\sigma = 0.5$ and $N = 120$. The analysis of the experimental reflectivity spectra led to density profiles characterized by a clear plateau in the proximity of the grafting surface. Still, some discrepancies should be noted with the work by Ell et al.,[3] who synthesized polystyrene brushes by ATRP for which the grafting density was estimated to be 0.44 chains nm^{-2}. The molecular weight of the PS chains was again comparable with the one use in this study (15 kg/mol). Surprisingly, neutron reflectivity data suggest that the density profile of the polystyrene brush with $N = 150$ is well approximated by a power law decay with an exponent of 2.5, closer to the parabolic profile predicted by SCF theory than to the one provided by the best fit of our data (see Figure 12). One possible contribution to this discrepancy could

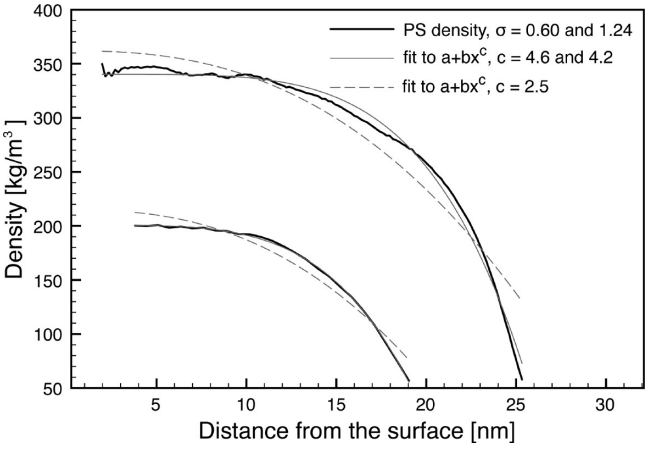

Figure 12. Density plot for polystyrene at the highest and lowest grafting densities considered in the paper. The exponential tails and the density oscillations close to the grafting surface are not included in the data sets. Thick gray lines correspond to the best power law fit, with exponent 4.6 and 4.2 for the $\sigma = 1.24$ and 0.60 grafting density, respectively. Dashed lines correspond to the best fit to power laws where the exponent was fixed to 2.5.

derive from the MARTINI model of benzene, which underestimates[16] the benzene density by a factor of 10%. Benzene molecules are thus effectively larger than they should be, and this might affect their penetration into the brush at the high brush densities considered here. We remark that when developing the MARTINI PS model,[22] the size of the beads composing the phenyl rings was tuned so as to reproduce with good accuracy the density of PS melts.

Our calculations show another interesting structural feature: the vertical alignment of the end points in the highly stretched configurations. The fully stretched configurations are rare events, and as such they do not stand out from average density plots or from the plot of the average order parameter, $P_2(\theta)$, as a function of the monomer index. But when $P_2(\theta)$ is plotted as a function of the distance from the surface, fully stretched configurations clearly appear to be characterized by the almost perfect alignment of the last bonds of the chain to the normal to the grafting surface. Such a feature had been predicted by SCF theory and reproduced by MD simulations,[47] though in a lower grafting density regime.

The analysis of average and single chain distributions of chain ends led to the identification of collapsed states, with the chain ends trapped inside the brush bulk. By looking at the time-dependent position of the chain ends, we could estimate life times of several microseconds for such trapped states. Our coarse-grained model has a relatively fine degree of coarse-graining, retaining the backbone−ring structure of polystyrene. This mapping is largely responsible for a limited acceleration of the dynamics with respect to atomistic simulations (chain diffusion coefficients in the melt differ from the atomistic ones by a factor of 3 at 400 K[22]). With this respect, our results concerning the dynamics of the brush can be considered to be quantitatively reliable.

The analysis of trapped states as varying the brush grafting densities shows that the transitions from collapsed to extended chain configurations become smoother and smoother as the grafting density is reduced. This is in agreement with our previous conclusions, pointing to the presence of an extended interface for the lowest grafting density brush and to a splitting into well-defined bulk and interface regions for the case of the highest density brush.

We identified two different relaxation regimes along the chain by splitting the chains in a grafted and a terminal part, represented by vectors connected to their grafted beads or chain ends, respectively, as shown in Figure 11. The relaxation time of the terminal, more mobile segments of the chains decays exponentially as the mobile segment length is progressively reduced. This trend is common to all the grafting densities considered. The dynamics of the grafted segment, on the contrary, depends qualitatively on the grafting density in the range analyzed. The relaxation time sets to a plateau value in an intermediate region of the brush, before dropping because of the increasing mobility of the terminal part of the chains. No such a plateau can be observed for the lowest grafting density considered in this study.

To conclude, we remark that the coarse-grained model we used, based on the MARTINI force field, was not developed with the explicit aim to deal with brush systems. Nevertheless, the overall good agreement between our findings and previous theoretical and experimental studies is promising. Our results validate the model for future use in the simulation of polymer-functionalized surfaces for both materials science and biological applications.

AUTHOR INFORMATION

Corresponding Author

*E-mail: giulia.rossi@inserm.fr (G.R.); rfaller@ucdavis.edu (R.F.).

Present Addresses

[⊥]INSERM UMR-S 665, 6, rue Alexandre Cabanel 75739 Paris Cedex 15, France.

ACKNOWLEDGMENT

R.F. thanks Aalto University for their kind hospitality during his visit. The authors thank Tonya L. Kuhl for interesting discussions and Jonathan Barnoud for developing a Gromacs tool for the order parameter analysis in a coarse-grained trajectory. The Davis part of this work was supported by the United States Department of Energy, Office of Science, Basic Energy Sciences, under Grant DE-FG02-06ER46340. This work has also been supported by the Academy of Finland through its COMP CoE grant. Computer time at CSC is also gratefully acknowledged.

REFERENCES

(1) Advincula, R. C.; Brittain, W. J.; Caster, K. C.; Ruhe, J. *Polymer Brushes*; Wiley-VCH: Weinheim, Germany, 2004.
(2) Lego, B.; François, M.; Skene, W. G.; Giasson, S. *Langmuir* **2009**, *25*, 5313.
(3) Ell, J. R.; Mulder, D. E.; Faller, R.; Patten, T. E.; Kuhl, T. L. *Macromolecules* **2009**, *42*, 9523–9527.
(4) Edmondson, S.; Osborne, V. L.; Huck, W. T. S. *Chem. Soc. Rev.* **2004**, *33*, 14–22.
(5) Landherr, L. J. T.; Cohen, C.; Agarwal, P.; Archer, L. A. *Langmuir* **2011**, *27*, 9387.
(6) Jhaveri, S. B.; Beinhoff, M.; Hawker, C. J.; Carter, K. R.; Sogah, D. Y. *ACS Nano* **2008**, *2*, 719.
(7) Diamanti, S.; Arifuzzaman, S.; Elsen, A.; Genzer, J.; Vaia, R. A. *Polymer* **2008**, *49*, 3770.
(8) Daoulas, K. C.; Terzis, A. F.; Mavrantzas, V. G. *J. Chem. Phys.* **2002**, *116*, 11028–11038.
(9) Zheng, J.; Li, L.; Chen, S.; Jiang, S. *Langmuir* **2004**, *20*, 8931–8938.
(10) Träskelin, P.; Kuhl, T. L.; Faller, R. *Phys. Chem. Chem. Phys.* **2009**, 11324–11332.
(11) Dimitrov, D. I.; Milchev, A.; Binder, K. *J. Chem. Phys.* **2007**, *127*, 084905.
(12) Binder, K. *Eur. Phys. J. E* **2001**, *9*, 293.
(13) Cordeiro, R. M.; Zschunke, F.; Müller-Plathe, F. *Macromolecules* **2010**, *43*, 1583–1591.
(14) Farah, K.; Leroy, F.; Müller-Plathe, F.; Bohm, M. C. *J. Phys. Chem. C* **2011**.
(15) Marrink, S.-J.; de Vries, A. H.; Mark, A. E. *J. Phys. Chem. B* **2004**, *108*, 750.
(16) Marrink, S.-J.; Risselada, H. J.; Yefimov, S.; Tieleman, D. P.; de Vries, A. H. *J. Phys. Chem. B* **2007**, *111*, 7812.
(17) Monticelli, L.; Kandasamy, S. K.; Periole, X.; Larson, R. G.; Tieleman, D. P.; Marrink, S.-J. *J. Chem. Theory Comput.* **2008**, *4*, 819.
(18) Vuorela, T.; Catte, A.; Niemelä, P. S.; Hall, A.; Hyvönen, M. T.; Marrink, S. J.; Karttunen, M.; Vattulainen, I. *PLoS Comput. Biol.* **2010**, *6*, e1000964.
(19) Catte, A.; Vuorela, T.; Niemelä, P.; Murtola, T.; Segrest, J. P.; Marrink, S. J.; Karttunen, M.; Vattulainen, I. *Biophys. J.* **2008**, *94*, 983.
(20) López, C. A.; Rzepiela, A. J.; de Vries, A. H.; Dijkhuizen, L.; Hünenberger, P. H.; Marrink, S. J. *J. Chem. Theor. Chem* **2009**, *5*, 3195.
(21) Wong-ekkabut, J.; Baoukina, S.; Triampo, W.; Tang, I.-M.; Tieleman, D. P.; Monticelli, L. *Nature Nanotechnol.* **2008**, *3*, 363.
(22) Rossi, G.; Monticelli, L.; Puisto, S. R.; Vattulainen, I.; Ala-Nissila, T. *Soft Matter* **2011**, *7*, 698.
(23) Lee, H.; de Vries, A. H.; Marrink, S.-J.; Pastor, R. W. *J. Phys. Chem. B* **2009**, *113*, 13186.
(24) Lee, H.; Larson, R. G. *J. Phys. Chem. B* **2008**, *112*, 7778–7784.
(25) Rossi, G.; Giannakopoulos, I.; Monticelli, L.; Rostedt, N. K. J.; Puisto, S. R.; Lowe, C.; Taylor, A. C.; Vattulainen, I.; Ala-Nissila, T. *Macromolecules* **2011**, DOI: 10.1021/ma200788.
(26) Milani, A.; Casalegno, M.; Castiglioni, C.; Raos, G. *Macromol. Theory Simul.* **2011**, *20*, 305.
(27) Gautieri, A.; Vesentini, S.; Redaelli, A. *J. Mol. Model.* **2010**, *16*, 1845.
(28) Ahmad, S.; Johnston, B. F.; Mackay, S. P.; Schatzlein, A. G.; Gellert, P.; Sengupta, D.; Uchegbu, I. F. *J. R. Soc., Interface* **2010**, *7*, S423.
(29) http://md.chem.rug.nl/cgmartini.
(30) Doi, M.; Edwards, S. F. *The Theory of Polymer Dynamics*; Clarendon Press: Oxford, 1986; Vol. 73.
(31) Cotton, J. P.; Decker, D.; Benoit, H.; Farnoux, B.; Higgins, J.; Jannink, G.; Ober, R.; Picot, C.; des Cloizeaux, J. *Macromolecules* **1974**, *7*, 863.
(32) Elliott, I. G.; Kuhl, T. L.; Faller, R. *Macromolecules* **2010**, *43*, 9131–9138.
(33) Devaux, C.; Cousin, F.; Beyou, E.; Chapel, J.-P. *Macromolecules* **2005**, *38*, 4296.
(34) Hess, B.; Kutzner, C.; van der Spoel, D.; Lindahl, E. *J. Chem. Theor. Comput.* **2008**, *4*, 435.
(35) Berendsen, H. J. C.; Postma, J. P. M.; van Gunsteren, W. F.; DiNola, A.; Haak, J. R. *J. Chem. Phys.* **1984**, *81*, 3684.
(36) Nosé, S. *Mol. Phys.* **1984**, *52*, 255–268.
(37) Hoover, W. G. *Phys. Rev. A* **1985**, *31*, 1695–1697.
(38) Nosé, S.; Klein, M. L. *Mol. Phys.* **1983**, *50*, 1055–1076.
(39) Parrinello, M. *J. Appl. Phys.* **1981**, *52*, 7182–7190.
(40) Israelachvili, J. N. *Surf. Sci. Rep.* **1992**, *14*, 109.
(41) Gao, J.; Luedtke, W. D.; Landman, U. *Phys. Rev. Lett.* **1997**, *79*, 705.
(42) Coluzza, I.; Hansen, J.-P. *Phys. Rev. Lett.* **2008**, *100*, 1.
(43) Elliott, I. G.; Mulder, D. E.; Traskelin, P. T.; Ell, J. R.; Patten, T. E.; Kuhl, T. L.; Faller, R. *Soft Matter* **2009**, *5*, 4612–4622.
(44) Ollila, O. H. S.; Risselada, H. J.; Louhivuori, M.; Lindahl, E.; Vattulainen, I.; Marrink, S. J. *Phys. Rev. Lett.* **2009**, *102*, 078101.
(45) Sun, Q.; Faller, R. *Macromolecules* **2006**, *39*, 812.
(46) Milano, G.; Müller-Plathe *J. Phys. Chem. B* **2005**, *39*, 18609.
(47) Seidel, C.; Netz, R. R. *Macromolecules* **2000**, *33*, 634.

Macromolecules

Article

pubs.acs.org/Macromolecules

Interphase Structure in Silica–Polystyrene Nanocomposites: A Coarse-Grained Molecular Dynamics Study

Azadeh Ghanbari,* Tinashe V. M. Ndoro, Frédéric Leroy, Mohammad Rahimi, Michael C. Böhm, and Florian Müller-Plathe

Eduard-Zintl-Institut für Anorganische und Physikalische Chemie and Center of Smart Interfaces, Technische Universität Darmstadt, Petersenstrasse 20, D-64287 Darmstadt, Germany

ABSTRACT: Silica nanoparticles (NPs) embedded in atactic polystyrene (PS) are simulated using coarse-grained (CG) potentials obtained via iterative Boltzmann inversion (IBI). The potentials are parametrized and validated on polystyrene of 2 kDa (i.e., chains containing 20 monomers). It is shown that the CG potentials are transferable between different systems. The structure of the polymer chains is strongly influenced by the NP. Layering, chain expansion, and preferential orientation of segments as well as of entire chains are found. The extent of the structural perturbation depends on the details of the system: bare NPs vs NPs grafted with PS chains, grafting density (0, 0.5, and 1 chains/nm^2), length of the grafted chains (2 and 8 kDa), and the matrix chains (2–20 kDa). For example, there is a change in the swelling state for the grafted corona (8 kDa, 1 chains/nm^2), when the matrix polymer is changed from 2 to > 8 kDa. This phenomenon, sometimes called "wet brush to dry brush transition", is in good agreement with neutron scattering investigations. Another example is the behavior of the radius of gyration of free polymer chains close to the NP. Short chains expand compared to the bulk, whereas chains whose unperturbed radius of gyration is larger than that of the NP contract.

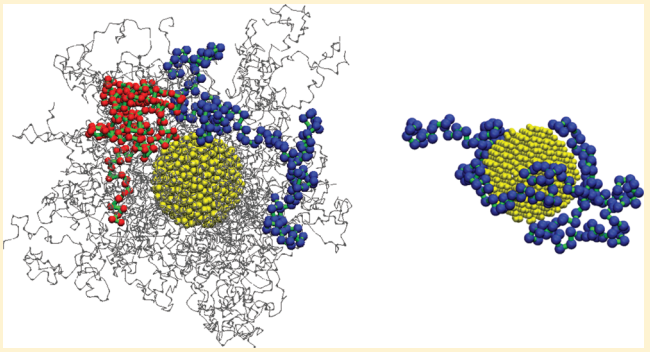

1. INTRODUCTION

Nanocomposite materials (NCMs) are formed by filling a polymer matrix with inorganic particles whose typical dimensions are of the order of a few nanometers. The nanosized fillers induce improvements in the material's macroscopic properties,[1−5] which makes them attractive for industrial applications. For instance, it has been reported by Mackay et al.[6] that the addition of nanoparticles (NPs) to polymer materials can lower their viscosity. Such a modification is useful in extrusion and injection molding processes. The presence of NPs introduces an enormous amount of interfacial area in which polymer chains undergo conformational changes and deformations at the nanoscale.[4] The interfacial contact in NCMs manifests itself as perturbation of the structure (e.g., density, chain orientation, arrangement, and stretching or wrapping around the NP)[7−9] and the dynamics (slower dynamics of the chains in the vicinity of the NP and formation of glassy polymer layers around the NP[10−13]) of the polymer. This region of altered polymer properties is commonly termed as interphase in the literature. Tuning of the interfacial interaction between the nanocomposite components is often the critical step in controlling the ultimate structural,[3,9,14,15] dynamic,[16] mechanical,[2,17] and thermodynamic[16] properties of the NCMs. A well-defined manipulation of these interactions needs a comprehensive understanding of structure–property relationships in NCMs. This includes knowledge of the structure and properties of the interphase at a quantitative level. Despite numerous experimental,[18−20] theoretical,[21−24] and computer simulation studies,[2,8,9,14,15,25] a detailed understanding of these relationships is still missing.

A possible explanation for this deficit might be the inconsistency between certain experimental results. For example, Bogoslovov et al.[26] studied the effect of reinforcement of poly(vinyl acetate) via silica NPs by modulated differential scanning calorimetry (MDSC) and dielectric relaxation measurements. They reported that the segmental relaxation dispersion and relaxation times did not show any evidence of immobilization of polymer chains residing at the silica interface. Although there may be some stiffening of the elastomer in the proximity of the fillers, Robertson et al. reported that this process does not translate into a significant suppression of the segmental dynamics in filled rubbers.[27] Tsagaropoulos and Eisenberg,[28,29] on the other hand, reported two dynamic processes within polymers filled with very fine silica particles (of 7 nm diameter), using dynamical mechanical analysis (DMA). They related one of the processes to the glass transition of the polymer matrix, while the other one has been attributed to the glass transition of immobilized chains near the

Received: September 8, 2011
Revised: November 21, 2011
Published: December 6, 2011

Table 1. Studied Nanocomposites with a Fixed Nanoparticle Radius of 2 nm (T = 590 K, P = 101.3 kPa)

grafting density (chains/nm^2)	no. of grafted chains	grafted chains length (monomers)	no. of free chains	free chains length (monomers)	NP vol fraction (%)	simulation time (ns)	mass density (kg/m^3)	box length (nm)
0.0			202	20	5.26	20	978.24 ± 2.62	9.30
0.0			202	40	2.15	12	958.41 ± 0.90	11.59
0.0			101	80	2.17	12	966.36 ± 1.32	11.55
0.0			500	100	0.35	24	938.02 ± 3.84	21.05
0.0			404	200	0.22	32	939.24 ± 0.15	24.58
0.5	25	80	808	20	0.95	16	924.45 ± 0.66	15.20
0.5	25	80	404	40	0.97	16	940.40 ± 1.20	12.12
0.5	25	80	202	80	0.98	20	948.41 ± 0.75	15.07
0.5	25	80	135	120	0.98	36	950.96 ± 1.00	15.06
0.5	25	80	101	160	0.98	40	952.09 ± 1.00	15.04
1.0	50	20	177	20	3.66	14	981.80 ± 1.06	9.70
1.0	50	80	708	20	0.96	20	929.54 ± 1.37	15.18
1.0	50	80	354	40	0.97	20	943.56 ± 0.90	15.11
1.0	50	80	177	80	0.98	20	950.24 ± 0.83	15.07
1.0	50	80	118	120	0.98	40	953.01 ± 0.87	15.06
1.0	50	80	88	160	0.98	50	953.69 ± 0.97	15.04

fillers. Similarly, Chen et al. have recently confirmed the existence of two dynamic processes, performing DMA on poly(vinyl alcohol)/silica NCMs.[30]

This discrepancy in the experimental results emphasizes the care which must be taken for further accurate and well-designed studies. Computer simulations provide the most detailed look at the nature of nanometer-sized events in the interface and interphase regions and can possibly lead to the design of more accurate experiments and/or better data interpretation. In the present molecular dynamics (MD) study, we investigate how the structure of the polymer is affected by the presence of a bare or grafted NP by simulating a coarse-grained (CG) model of silica−polystyrene (PS) nanocomposites. The dependence of interface-induced effects on the chain length, the grafting density, and the length ratio between grafted and free chains is also addressed. We have chosen a CG model[31−33] which has one superatom per chemical repeat unit of PS. The structure-based potentials of this CG model are generated by so-called iterative Boltzmann inversion (IBI).[34] For dense polymer systems, they give a typical speed-up of 3−4 orders of magnitude over atomistic calculations.[35] At the same time, they are realistic in the sense that they preserve the structural distributions of the atomistic models and can easily be backmapped if atom-based properties are to be evaluated. We use them here to investigate the polymer structure near the NP. The first major aim of the current study is to develop accurate CG potentials for silica−PS nanocomposites, which successfully reproduce the structural properties of the interphase area, and to test them. In addition to the structural investigation of this contribution, the CG potentials developed are also meant to bridge the time- and length-scale gaps between previous atomistic[8] and continuum simulations[39] of this system. Moreover, the existence of such a CG model is a prerequisite to investigate the dynamics in the interfacial region, which will be addressed in a separate publication.

To achieve maximal property enhancements in the filled polymer, a stable and uniform dispersion of the NPs is vital. Agglomeration of the particles would be detrimental to the NCMs, like for instance rendering a plastic material more brittle. Yet, adjusting the NP dispersion is still a challenge due to the difficulty of controlling both the thermodynamic and kinetic factors which play a significant role in such complex systems.[36] In a recent review article, Kumar and Krishnamoorti[37] surveyed the relevant literature about controlling NP dispersion and its ultimate role in the properties of NCMs and how these two issues depend on the particle shape. One recent experimental study on the dispersion mechanism in silica−PS nanocomposites was performed by Chevigny et al.,[38] using complementary scattering (SAXS/USAXS) and imaging (TEM) techniques. The authors showed that the relevant parameter of the dispersion, i.e., the mass ratio between grafted and free chains, Q, controls the arrangement of the NPs in the matrix, either as large and compact aggregates ($Q < 0.24$) or as individual NPs ($Q > 0.24$). They also showed that particle aggregation is associated with a significant collapse of the corona of grafted chains. In a separate study,[18] they demonstrated that interactions with longer free chains induce a compression of the grafted chains, which minimizes the free energy. The investigation of free-chain infiltration in the grafted corona and its dependence on the chain length and Q in the framework of a CG computer simulation is the second major aim of the current MD study.

In recent years, polymer nanocomposites have been simulated at different resolutions[32] including generic bead−spring[40] and lattice models.[41,42] Studying polymer NCMs by MD simulations at different levels of resolution is an ongoing effort in our group, too. Eslami and Müller-Plathe have examined the structure and dynamics of polyamide-6,6−graphene nanocomposites using different resolutions.[43−45] It was shown that polymer chains, which are layered between graphene sheets, adopt a flattened conformation parallel to the surface. Ndoro et al.[8] used atomistic MD simulations to study the structural behavior of PS chains in the vicinity of a single grafted and bare silica NP. The NP induces ordering near its surface where polymer chains form layers. The magnitude of the effect depends strongly on the particle radius and grafting density. The present contribution is an extension of that work.

2. CONSIDERED SYSTEMS AND METHODS

2.1. Systems and Mapping Scheme. A collection of all silica−PS nanocomposites studied in the present work can be found in Table 1. In addition to the number of free and grafted chains, we have given their monomer numbers as well as the NP volume fraction. Different mapping schemes for atactic PS

have been suggested in the literature.[46−50] In the present study, we have employed the method of Qian et al.[50] where each repeat unit of PS is represented by one CG bead whose interaction center is located at the repeat unit's center-of-mass. Two different beads (R and S) are necessary to account for the chirality of atactic PS. The CG interaction potentials describe the nonbonded intermolecular interactions, the bonded interactions between two neighboring beads, and that between three neighboring beads forming an angle. No torsion potential was used in our CG simulations since it was shown that the distribution of dihedral angles between beads are flat enough to be neglected.[46] Intramolecular nonbonded interactions were also employed in our calculations, except for first and second neighbors.

In addition to composites with free PS chains, we also studied systems where some of the PS chains were grafted to the NP surface. They are attached by a linker unit $(-[H_2C(H(C_2H_3)C)]_3(CH_3)_2Si-)$ as used in experiments (see Supporting Information of ref 8 for its structure). The linker has been divided into four CG beads of two kinds having approximately the same mass. The first is formed by the $-CH_2CHCHCH_2-$ group and the second by $-(CH_3)_2Si$. In both cases the CG interaction centers are located at the center of mass of the group of atoms. The mapping scheme used to define the grafted PS chains is identical to the one used for the free polymer chains.

As for the NP, the silicon and oxygen atoms of the SiO_2 units are gathered into a CG bead whose interaction center corresponds to the silicon atom's position. In order to take into account the existence of hydrogen atoms of hydroxyl groups on the NP surface, the total mass of the hydrogen atoms was uniformly distributed over all the CG beads that form the NP. In all simulations the NP is a sphere with diameter of ∼4 nm, which yields 873 CG beads. Three different approaches were followed to model the NP at the CG level. In a first attempt, only the surface layer of the NP beads was taken into account, while the inner beads were ignored. This model yielded an unphysical situation where polymer beads were also found inside the NP. In a second attempt, the entire NP was modeled with CG beads which all had the same interaction potential with the polymer beads. We have observed that such an approach yielded a too attractive interaction between the polymer chains and the NP. We finally adopted a third approach by distinguishing between the surface (shell) beads (SH) and core beads (CR). Their interaction with the polymer beads were then described by two different potentials because the SH beads of the NP have the main contribution to its interaction with the polymer matrix.

2.2. Parameterization of the Coarse-Grained Model.

The CG interaction potentials between the beads described above were obtained by means of the IBI procedure. This method has been applied to generate the CG potentials of various polymer systems; details can be found elsewhere in the literature.[34,51] In IBI a reference atomistic force field including all bonded and nonbonded interactions as well as atomic charges as employed in the preceding atomistic simulation (in the following denoted as original atomistic simulation) is used to compute the target distribution functions that should be reproduced by the CG model. The details of the atomistic simulations can be found in a recent contribution of our group.[8] The radial distribution functions (RDFs) describing the CG models at each step of the IBI procedure were computed from 0.2 ns long trajectories which were generated at a constant particle number, constant volume, and constant temperature (NVT conditions). In each IBI step all CG potentials have been optimized simultaneously. The derivation of the potentials was carried out on a system whose polymer chains contained 20 monomers. The nonbonded potentials between the SH and CR beads of the NP and the polymer beads were identical for the R or S conformation of the polymer beads. There are therefore only two different nonbonded potentials describing those interactions. The RDFs between the polymer beads (PS) and the SH beads in both atomistic and CG simulations are compared in Figure 1A. The CG results presented are those of

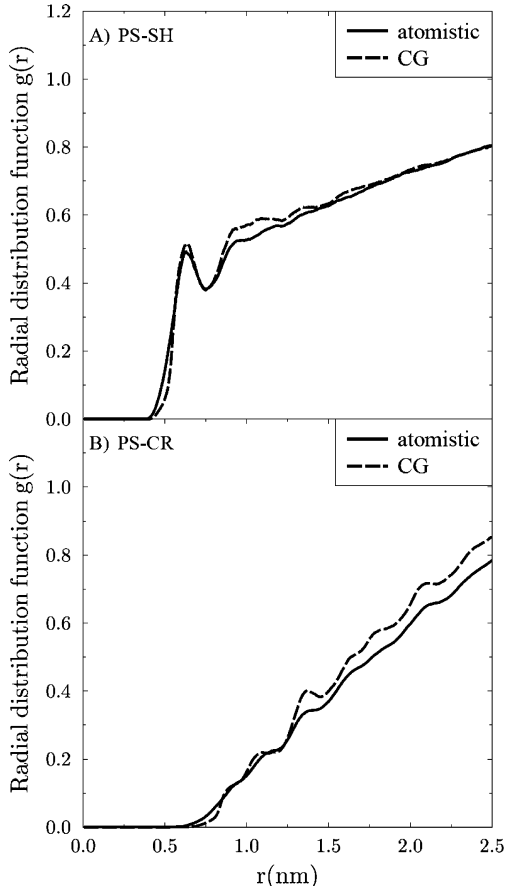

Figure 1. Calculated nonbonded radial distribution functions between SH beads of the nanoparticle and PS beads (A) as well as between CR and PS beads at 590 K and P = 101.3 kPa, as derived from atomistic and CG simulations of the bare silica−PS system.

the last iteration of the Boltzmann inversion procedure. The agreement between the CG and the atomistic data is very satisfactory. The sharp maximum observed around 0.65 nm in the atomistic simulations is reproduced. Although the RDFs are presented only for short distances for clarity, it was verified that they converged to a value of 1. The RDFs between the PS and CR beads in both atomistic and CG simulations are shown in Figure 1B. The repulsive PS−CR interaction implies that the maximum around 0.65 nm disappeared. We have mentioned above that this repulsion prevents the polymer beads from penetrating the NP and partly offsets the attraction by the shell beads. The overall attractive nature of the interaction between the NP and the PS chains leads to modifications in the local structure properties of the polymer chains in the vicinity of the NP (see section 3).

dx.doi.org/10.1021/ma202044e | Macromolecules 2012, 45, 572−584

For the grafted polymer chains, we have developed CG potentials using two different schemes. One is based on an original atomistic simulation followed by IBI of all nonbonded interactions (including PS−PS and NP−PS) in the same way as for the ungrafted system (see above). We call it type 1 CG potential. The second one (type 2 CG potential) uses the potentials developed for the ungrafted system also for the grafted system and augments them only by the additional interactions with the linker units. This has been done to test the transferability of these potentials to grafted systems. In this scheme, we have fixed the NP−PS and PS−PS potentials known from the ungrafted system. The interaction potentials linker−NP, linker−PS, and linker−linker have been developed using IBI. Structural properties of a given NCM system obtained with these two CG models have been compared with atomistic results to find the advantages and disadvantages of each one. See section 3.3 for the detailed comparison. The discrimination between NP beads of the SH and CR types is conserved for both CG schemes.

2.3. Generation of Initial Configuration for Composites with Long Chains. We now describe the procedure to generate the initial configuration of systems with longer chains. First one NP was inserted into the box, as done in the 20-mer nanocomposite. The chains were built using a self-avoiding random walk (SARW) along which the CG polystyrene beads were distributed, conserving the periodic boundary conditions for the simulation box. The initial density of the simulation box was chosen at 80% of the known composite density, such that SARW could easily be built without encountering configurations in which no more beads could be added. The distance between two consecutive beads on a given chain corresponded to the average distance between two bonded CG beads (∼0.5 nm), while the minimum allowed distance between two nonbonded beads (PS−PS or PS−NP) was half this length ($d_{nb} \approx 0.25$ nm). This choice has led to some close contacts which needed to be relaxed during equilibration. The alternative choice, however, a larger value of d_{nb}, resulted in configurations where no new beads could be added to some chains because of the overlap with other nonbonded monomers around.

To build a nanocomposite system of a single NP and N free chains, we started with N initial monomers randomly distributed around one NP. Then we started one SARW per chain, adding one by one only one new bead to each chain. For a given chain of i CG beads, the position of each new bead (bead number $i + 1$) was randomly chosen on the surface of a sphere of radius 0.5 nm around the last (ith) bead of the parent chain. If the new bead did not overlap with any other bead in the system (including NP beads), we put bead number $i + 1$ at the chosen position. Otherwise, another random point was chosen on the surface of the same sphere. If the new bead could not be placed, due to the overlap with other beads in the system, after 1000 attempts, an abortion of the algorithm should occur. Such a process, however, was circumvented choosing the box size large enough as mentioned above. At the end of a step each chain has gained one additional bead. Repeating this step until all chains have their desired chain length, all polymer chains were grown simultaneously. In this scheme, bond angles were not considered. Because of the absence of strong overlaps between beads, however, bond angles regained the distribution determined by the angle potentials, during the equilibration. After preparing the initial configuration, NPT simulations (of 4−10 ns duration, depending on the chain length) were carried out to relax the systems to their equilibrium densities. The ensuing production runs took 16 ns.

2.4. Simulation Details. The obtained potentials were used to perform simulations of systems with 20−200 monomers per chain. Depending on the polymer chain length, trajectories of different lengths were used to produce the structural data which will be discussed later. For the 20 monomer chains, the system was equilibrated first at NVT condition for 2 ns. A subsequent run of 2 ns at NPT was performed where the last 0.4 ns were used to accumulate the data. For the 40−200 monomer chains the systems were first equilibrated at constant pressure for 4−8 ns. The systems were then simulated in NVT/NPT ensemble for 8−50 ns. The last 4−20 ns was used to accumulate the production data depending on the chain length. All MD runs were carried out at a pressure of 101.3 kPa and a temperature of 590 K, while a time step of 4 fs was employed. The CG simulations in this study were performed with the code IBIsCO developed in our group.[52] Berendsen's thermostat (with a coupling time of 0.2 ps) and barostat (with a coupling time of 5 ps and isothermal compressibility of 1.0×10^{-6} kPa) were used to control temperature and pressure. The cutoff for the nonbonded interactions was 1.5 nm, and the neighbor list cutoff was 1.6 nm. Configurations were sampled every 1000 time steps (4 ps). The error bars provided in some of the figures and tables denote the standard deviations calculated over all polymer molecules and all their frames.

3. RESULTS AND DISCUSSION

3.1. Ungrafted Nanoparticle: 20-mer Systems. The polymer monomer number density profile as a function of the distance from the NP surface in both atomistic and CG simulations is shown in Figure 2A. In all that follows, the NP surface is defined by the average radial distance of the outermost beads from NP center of mass. The NP radius is therefore taken as 2 nm. Oscillations in the density profile show a layered structure of the polymer chains around the NP, which has also been reported in experiment[12,13] and atomistic simulations.[8,14,25,53,54] The CG simulation successfully reproduces the atomistic structure of the polymer matrix around the NP, although the intensity of the first peak is larger. The structuring effect results in three distinguishable density peaks, after which the density profile approaches the bulk value (∼2 nm from NP surface). The first peak in the density profile appears at a distance of 0.6 nm from the NP surface. This first layer is characterized by a density which is almost twice the bulk density. A second layer is observed at about 1 nm from the surface, followed by a third one at 1.6 nm whose amplitude is similar to the second one. Position and amplitude of the density peaks are independent of the chain lengths considered. The first two peaks of the CG density profile are slightly displaced from the positions derived in the atomistic simulation, although in opposite directions. These shifts mainly arise because of the orientation properties of the PS phenyl rings close to the surface (see below), which are captured by the atomistic model but not by the spherical CG superatoms. Another reason for the larger excess of monomers in the first CG peak might be the geometrical smoothness of the NP surface induced by coarsening. In the surface layer of silica monomers the oxygen atoms are included in their parent bead, which is at the position of the silicon atom. This results in a withdrawal of the oxygen atoms, which stick out of the surface in the atomistic

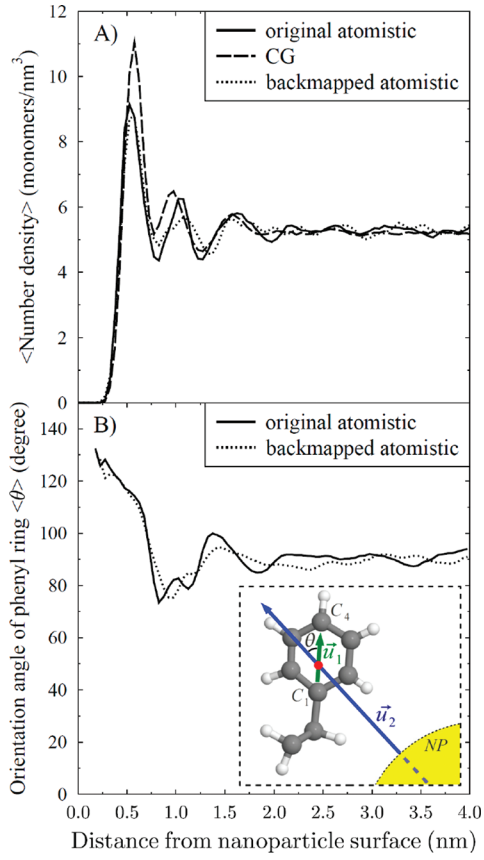

Figure 2. Radial profile of the monomer number density (A) of the polymer component of the bare silica–PS composite, as derived from the original atomistic MD simulation, coarse-grained, and backmapped atomistic simulations. Orientation angle of the phenyl rings with respect to the radial distance form the nanoparticle surface (B) from original and backmapped atomistic simulations. The inset shows the definition of the phenyl orientation angle θ: angle between center-of-mass vector ($\vec{u}_2$) of the monomer and a unit vector ($\vec{u}_1$) connecting C_1 and C_4 carbon atoms of the phenyl ring.

simulation. The larger corrugation in the atomistic simulation forces the first layer of PS monomers into further distances.

The atoms were reinserted into the equilibrated CG configuration model by a backmapping procedure, which has been described in detail.[55] The backmapped atomistic configuration was used as a starting configuration to produce a second atomistic trajectory of 2 ns duration. The two atomistic PS densities agree better with each other than with the CG results. This is another indication that the density deviations are due to fundamental differences between an atomistic and a CG description rather than to insufficient equilibration. The fact that successive coarse-graining and backmapping recreates a realistic structure opens the possibility to study systems with many more NPs and polymers as well as longer chains in the future. As shown below, the CG potentials developed here can be transferred to systems with longer chains.

The orientation of the PS monomers is influenced by the NP. In the atomistic resolution, the orientation of a single monomer can be characterized by the angle between a particular monomer-fixed vector and a vector connecting the center of mass of the NP to that of the monomer, i.e., the surface normal u_2. We take as unit vector, u_1, the in-plane vector from the phenyl carbon atom C_1 in the direction of C_4 (Figure 2B). The orientation angle of the phenyl rings in immediate contact with the NP surface is above 90° in both the original and the backmapped atomistic simulations. As a matter of fact, the PS chains in the interface expose mainly their phenyl rings to the NP (Figure 2B), as already reported by Milano et al.[15] We assume that the observed orientation of the surface near phenyl rings is caused by both excluded volume effects and surface–phenyl attraction. This region (~0.6 nm from the surface) corresponds to the position of the first monomer layer (Figure 2A). The second monomer layer (density peak ~1.0 nm in Figure 2A) shows a small preference for orienting the phenyl groups away from the NP (Figure 2B). Beyond that layer, the orientation quickly converges to the random average of 90°.

Also, the global conformation and orientation of PS chains are affected by their distance from the NP (Figure 3). In order

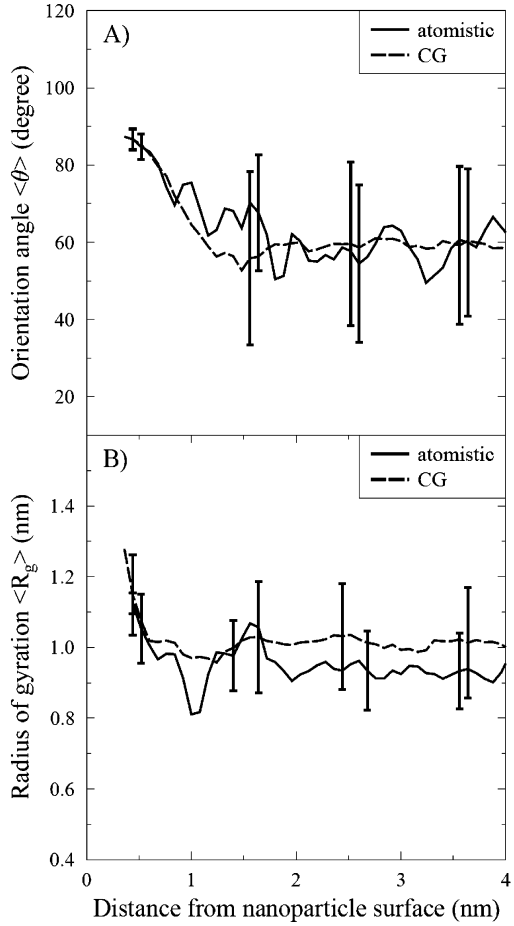

Figure 3. Average orientation angle $\langle\theta\rangle$ (A) and radius of gyration $\langle R_g\rangle$ (B) of free chains of 20 monomers as a function of the distance from the surface of the bare nanoparticle in atomistic and coarse-grained resolution. The orientation angle is taken between the chains' longest principal axis and the surface normal.

to probe whether the CG model can reproduce this dependence, the chains' radius of gyration and their orientation angle are shown. The chain orientation angle θ is defined as the angle between the longest principal axis of the gyration tensor of the individual chains and the surface normal, defined as the vector connecting the centers of mass of the NP and the polymer chain (Figure 3A). Note that the principal axis has no sign; therefore, θ varies between 0° (radial orientation) and 90°

dx.doi.org/10.1021/ma202044e | *Macromolecules* 2012, 45, 572–584

(tangential orientation), with an average of 57.3° for random orientation. This definition differs from the above one of the orientation vector (Figure 2B). Free chains in the vicinity of the NP tend to align tangential to the surface in both atomistic and CG models, in agreement with previous observations.[8,14,15] At distances larger than ∼1.5 nm from the NP surface, the PS chains show a random orientation. This convergence thus happens before that of the density (2 nm, Figure 2A). One should note that the unperturbed radius of gyration of the polymer is around 1.0 nm (Figure 3B). Vogiatzis et al.[14] and Brown et al.[3] reported the same behavior for chain segments around NP surfaces.

To better understand the conformational changes of the polymers in the vicinity of the NP, we computed the radius of gyration of the chains as a function of their distance from the NP surface (Figure 3B). It indicates that free chains become elongated near the surface compared to the bulk. The increase of the radius of gyration is up to 30% above the bulk value and, together with the orientation angle profile in Figure 3A, indicates that the polymers elongate and flatten significantly, orienting with the NP surface. The convergence to the bulk value happens at about 1.0 nm from the surface, i.e., when the chain is about one (unperturbed) radius of gyration away. Other structural properties like average radius of gyration and average end-to-end distance as well as the nanocomposite density computed with CG and atomistic models are compared in Table 2. They show sufficient agreement between these computational methods.

Table 2. Total Mass Density of the Silica−PS Composites as Well as Radius of Gyration $\langle R_g \rangle$ and End-to-End Distance $\langle R_0 \rangle$ of the Atactic Polystyrene Component (Chain Length 20) as Derived in Original Atomistic, Backmapped Atomistic and Coarse-Grained Simulations[a]

	coarse-grained	backmapped atomistic	original atomistic
density (kg/m^3)	978.24 ± 2.62	978.95 ± 0.97	978.10 ± 0.87
$\langle R_g \rangle$ (nm)	1.01 ± 0.16	0.99 ± 0.12	0.95 ± 0.12
$\langle R_0 \rangle$ (nm)	2.43 ± 0.85	2.44 ± 0.71	2.25 ± 0.76

[a]For each quantity we have given the MD inherent error bars, calculated as standard deviation of the quantity around the corresponding mean value over 1000 frames.

3.2. Ungrafted Nanoparticle: Chain Length Dependence. Coarse-grained calculations of bare silica−PS nanocomposites with longer polymer chains have been performed for the following reasons. First, the simulations were carried out without reoptimization of the CG interaction potentials. They therefore represent a test of the transferability of a potential which was developed at a given chain length (here 20 monomers) to longer chains. For pure bulk PS without NPs the transferability of model parameters to different chain lengths has already been demonstrated;[50] this was confirmed in this work (not shown) before examining the transferability in the presence of NPs (see below). Second, we have been able at the same time to study the influence of the polymer chain length on the structure and properties of the nanocomposite. Polymer chains containing 40, 80, 100, and 200 monomers together with one NP were simulated.

To investigate how the NP influences the behavior of longer chains in the interphase, the monomer number density of the chains (with 20−200 monomers per chain) was examined. Interestingly, the chain length has no effect on the layer structure around a bare NP, neither qualitatively nor quantitatively. Even the thickness of the shell in which the density deviates from the bulk value (< 2 nm) does not change with the polymer length. Only the limiting bulk density for longer chains is slightly higher, as expected. For the long chains we analyzed first the local polymer structure by dividing the chains into segments of 10 monomers instead of carrying out an analysis of the whole chain. We have accepted this choice as the distance between the NP and the chain center of mass is no longer a characteristic distance parameter for the monomers of a chain. The segment orientation was investigated as a function of their distance to the surface. The definition of the orientation angle is the same as before, only that the longest principal axis of the gyration tensor is calculated for each chain segment (Figure 4A). Systems with short and long chains show the same

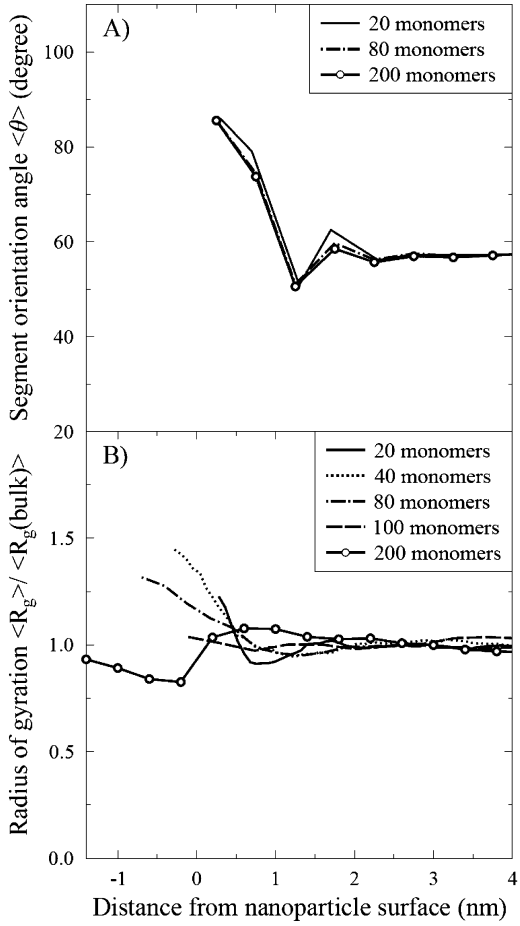

Figure 4. Segment orientation angle (A) of chains with 20, 80, and 200 monomers in the bare silica−PS composite at T = 590 K. Each segment contains 10 monomers. Since data points for different chain lengths coincide, data for chains of 40 and 100 monomers are not shown. Radius of gyration (B), normalized by the corresponding bulk value, of polymers with 20−200 monomers per chain in the bare silica−PS composite at 590 K. Negative distances mean that the center of mass of a chain is located inside the particle but not its individual monomers.

behavior. At close distances, the segments are tangential to the NP; at ∼1 nm they have a small preference for radial orientation before converging at ∼2.2 nm to the random orientation (57.3°) characteristic for the bulk. The origin of the

dx.doi.org/10.1021/ma202044e | Macromolecules 2012, 45, 572−584

minimum can possibly be attributed to those segments which are leading their parent chains from the first layer around the NP to the second and hence leave the NP neighborhood in radial direction. From the foregoing, it is clear that the local structure of the polymer near the interface (monomer density and orientation of segments of 10 monomers) is independent of the chain length for chains between 20 and 200 monomers. This spans radii of gyration between 1.01 and 3.39 nm, i.e., from below to above the NP radius (~2 nm). The local structure of the polymer at the interface is thus unaffected by its length.

The global polymer structure near the NP is better reflected by the radius of gyration of the entire chain (Figure 4B). For the different chain lengths, the radii of gyration have been normalized by the corresponding bulk values. The behavior of the radius of gyration as a function of the center-of-mass distance from the NP surface changes qualitatively with the polymer length. For shorter chains ($N \leq 80$), the radius of gyration increases near the NP, as close chains squeeze against the particle surface. However, this effect decreases with chain length, so that chains of length $N = 100$ have an almost uniform distribution of $R_g \sim R_g(\text{bulk}) \sim 2.2$ nm. The longest chain ($N = 200$) actually shows a reduced R_g near the NP. The reason is also visible in Figure 4B: long chains are also squeezed against the NP surface, but due to their size, they engulf at least part of the curved surface, as is shown by their centers of mass which fall inside the NP. As attraction causes them to follow the surface (NP radius: 2 nm), their radius of gyration is smaller than in the bulk (3.4 nm). An example of a chain wrapped around the NP is shown in the abstract figure (right).

3.3. Grafted Nanoparticle: Short 20-mer System. The grafted systems contain a NP of radius 2 nm, this time grafted with 50 PS chains of 20 monomers (corresponding to a grafting density of 1 chains/nm^2), unless noted otherwise, and 177 free PS chains of 20 monomers. The simulations are run again at 590 K. In Figure 5, the overall monomer number density

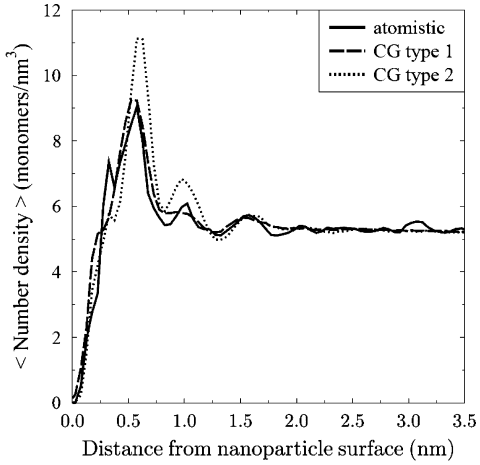

Figure 5. Overall monomer number density of the grafted system (1 chains/nm^2 grafting densities) as a function of the radial distance from the nanoparticle surface in an atomistic simulation as well as coarse-grained simulations using potentials of type 1 and type 2.

obtained from the CG models of type 1 (all potentials of the grafted system are evaluated by IBI) and type 2 (all potentials already available from the ungrafted system are transferred and only the additional potential terms involving the linker beads are determined by IBI) is compared with the corresponding original atomistic system. Similar to the bare system, the monomers form a layered structure in the vicinity of the NP surface, regardless of the CG potential type used. The layering of the polymers causes three separated density peaks, which appear at the same distances as the atomistic ones. For the type 1 CG potential, the amplitudes of all three peaks agree well with the atomistic profile. As the minimum between the first and second peaks is not as deep as in atomistic resolution, the second peak now appears more like a shoulder. For the type 2 CG potential, the amplitudes of the first and second peaks are higher than in the atomistic and the type 1 CG model. This shortcoming is probably carried over transferring the potentials from the ungrafted system, where this density excess is also found (cf. Figure 2A). The overall density profiles of Figure 5 are further decomposed into contributions of the free and grafted chains (Figure 6). Both grafted and free chains

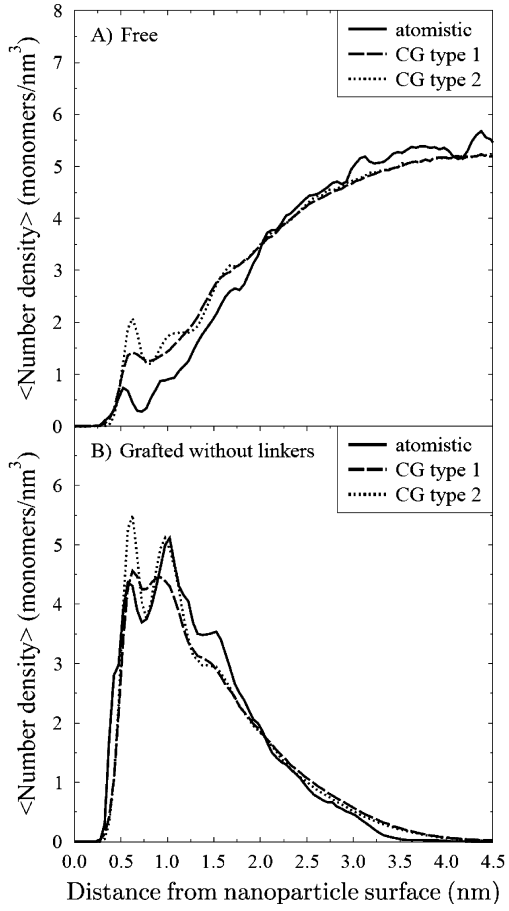

Figure 6. Monomer number density for free (A) and grafted (B) chains in atomistic as well as CG simulations using potentials of type 1 and type 2. The linker beads are excluded from the grafted-chain profiles (B).

contribute to the enhancement of the first peak in the density profile of the type 2 CG potential. In general, type 2 CG potentials have sharper features than type 1 potentials. Both coarse-grained potentials lead to a slight excess of free chains in the near-surface region (<2 nm) and a corresponding depletion of grafted chains, compared with the atomistic simulations.

Table 3 shows larger radii of gyration and brush heights for the grafted chains for both CG models compared to the atomistic results. The brush height is a measure for the

dx.doi.org/10.1021/ma202044e | Macromolecules 2012, 45, 572–584

Table 3. End-to-End Distance $\langle R_0 \rangle$ and Radius of Gyration $\langle R_g \rangle$ of Free (Average over All Free Chains) and Grafted Chains as Well as Brush Height $\langle h \rangle$ for a Grafted Silica–Polystyrene System Using Atomistic and Coarse-Grained Simulations[a]

	atomistic	CG type 1	CG type 2
$\langle R_0 \rangle$ free chains (nm)	2.29 ± 0.79	2.41 ± 0.82	2.42 ± 0.82
$\langle R_0 \rangle$ grafted chains (nm)	2.31 ± 0.61	2.62 ± 0.80	2.54 ± 0.81
$\langle R_g \rangle$ free chains (nm)	0.96 ± 0.13	1.01 ± 0.16	1.02 ± 0.16
$\langle R_g \rangle$ grafted chains (nm)	0.93 ± 0.09	1.04 ± 0.16	1.02 ± 0.16
$\langle h \rangle$ (nm)	1.20 ± 0.35	1.34 ± 0.41	1.27 ± 0.41

[a]The system contains one nanoparticle and PS chains of length 20 (both free and grafted). The grafting density is 1 chains/nm^2 and the temperature amounts to 590 K, while a pressure of 101.3 kPa has been used. Type 1 and type 2 potentials are used in the CG simulations.

extension of the grafted chains from the NP surface. It is calculated as the average radial distance of the grafted monomers from the surface. Since the NP is not an ideal sphere, this distance has been defined with respect to the radius at which the first linker superatom (connecting the chain to the NP) of the chosen chain is located. Figure 6B shows a small excess of grafted monomers density at distances beyond 2 nm from the NP surface for both CG potentials. Together with the depletion of grafted chains at closer distances, this can be interpreted as grafted chains which are more stretched in the CG than the atomistic model.

Figure 7B shows the radius of gyration of the free chains as a function of distance from the NP. In contrast to the bare NP, here there is no strong distance dependence except for the CG curves at the smallest distance (0.5 nm). This increase is due to the small number of free chains which actually penetrate into this region (Figure 6A). In the case of the type 1 CG potential, for example, there was only one time-frame in which a single chain had its center of mass at that distance from the NP. Beyond this first data point (0.5 nm < r < 1 nm), the free chains show an increase of up to 10% in their radius of gyration near the surface. The reason is not that the free chains are prevented from a close approach to the NP. Comparison of Figures 3 and 7B shows that at least some of the free chain monomers can approach the NP in the presence of grafted chains, almost as close as a bare NP. Therefore, in CG resolution the presence of grafted chains must attenuate the strong ordering influence of the NP surface. A second result is that all curves are within each other's error bars; there is no difference between CG and atomistic or between the two CG models. While not being particularly stretched in the vicinity of the NP, the free chains are still oriented tangentially to the surface, also in the presence of grafted chains (Figure 7A). The orientation angle profile is relatively noisy in the atomistic calculation; it becomes much smoother in both CG models. However, the overall shapes of the curves are similar.

To investigate the local chain orientation, we examined the bond orientation angle (Figure 8). The orientation of each bond with respect to the surface normal is defined by a vector connecting neighboring monomers (their centers of mass), while the midpoint of the vector defines the position of the bond. Both CG models reproduce reasonably well the atomistic structure, although there is some inconsistency for the free chains (Figure 8B). We believe that this is due to the atomistic system not having fully relaxed. This idea is confirmed because atomistic and CG data agree better when the atomistic

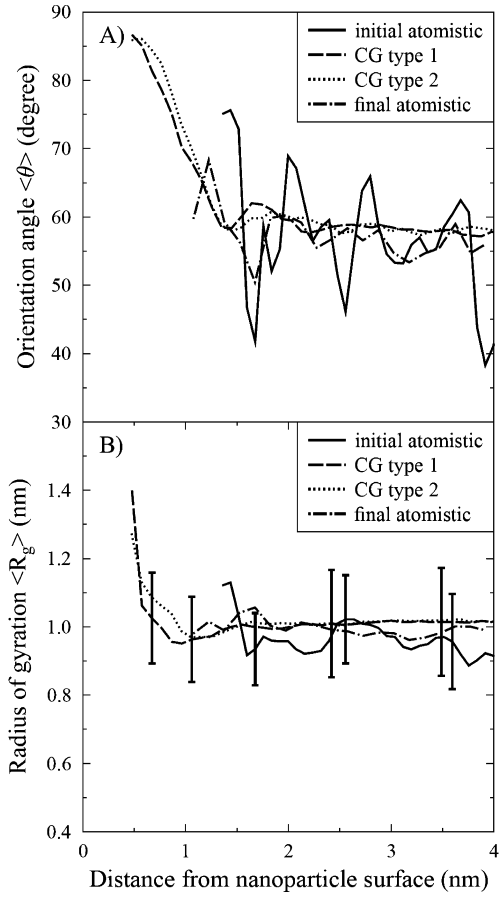

Figure 7. Average orientation angle $\langle \theta \rangle$ (A) and radius of gyration $\langle R_g \rangle$ (B) of the free chains as a function of the distance from the nanoparticle surface for a grafting density of 1 chains/nm^2 at T = 590 K. Grafted and free chains are made up of 20 monomers. "Initial atomistic" is the atomistic system from which we developed the CG potentials, while curve "final atomistic" belongs to exactly the same system when it has been run for an additional 59.55 ns. The sampling was done over 2 ns. Only representative error bars are shown for clarity in panel B. Error bars of all the curves were of the same order at each distance from nanoparticle.

simulation is taken to much longer times (curve "final atomistic" in Figure 8B).

Both CG potentials capture the essential structure of the polymer near the NP. Both have their advantages and disadvantages. The type 1 CG potential (full optimization) reproduces correctly the amplitude and position of the monomer density peaks. The second peak, however, is not as sharp as in the atomistic scheme, and the preceding minimum is suppressed. Moreover, the layering of the grafted chains around the NP is missing when CG type 1 potential is used. The type 2 CG potential (transferred from the ungrafted systems and supplemented by the additional interaction types) reproduces a clear layer structure of monomers with three different peaks. They appear at the same position as in the atomistic simulation, albeit that the amplitudes of the first two peaks are enhanced. Since this potential reproduces acceptably the expected structure of the polymer near the NP (number of distinguished layers, density peak position, radius of gyration, and chain and bond orientation angles), the type 2 CG potentials originally developed for a bare system seem to be transferable to the grafted systems, too.

dx.doi.org/10.1021/ma202044e | Macromolecules 2012, 45, 572–584

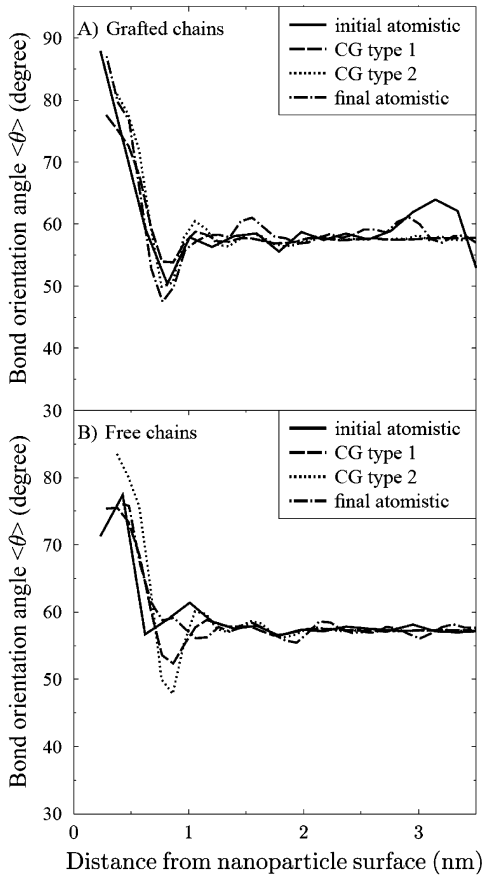

Figure 8. Angle between the bond vectors connecting nearest-neighbor monomers and the surface normal of the grafted chains (A) and free chains (B) in a grafted system of 1 chains/nm^2 grafting density at 590 K. Grafted and free chains are made up of 20 monomers. "Initial atomistic" is the atomistic system from which we developed the CG potentials, while the curve "final atomistic" belongs to exactly the same system when it has been run for an additional runtime of 59.55 ns. The sampling was done over 2 ns.

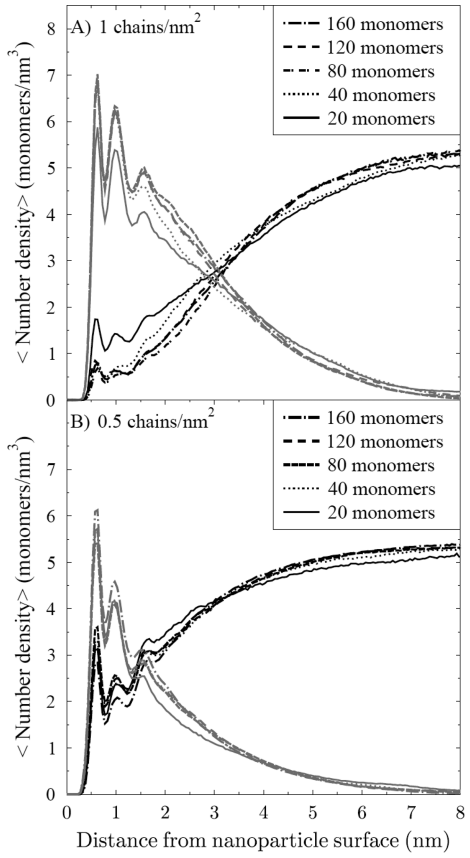

Figure 9. Monomer number density of free (black) and grafted chains (gray) in grafted systems as a function of distance from nanoparticle surface. Linker monomers are not included in the density of grafted chains. The grafted chains are made up of 80 monomers while the length of the free chains varies (20, 40, 80, 120, and 160 monomers per chain). We have studied grafting densities of 1 (A) and 0.5 (B) chains/nm^2. In the insets we have given the length of the free chains for each simulation. The volume fraction of the nanoparticle in all the systems is ∼1%.

3.4. Grafted Nanoparticle: Long Chains Regime. For the sake of comparison with existing atomistic simulations, we have so far considered only polymers of 20 monomers, which is much shorter than typical polymer lengths in technical NCMs. Here, we investigate the polymer structure near the NP, when the length of the free and grafted chains is changed. We adopt the potentials developed for the 20-mer system for larger silica−PS systems without reoptimization. We have fixed the length of the grafted chains at 80 monomers and varied the length of the free chains: N = 20, 40, 80, 120, and 160, corresponding to grafted-to-free chain ratios Q = 4, 2, 1, 0.67, and 0.5, respectively. We kept the volume fraction of the NP constant (∼1%) by adapting the number of free chains in each simulation. All systems had only one NP and their number of grafted chains was 50 (1 chains/nm^2).

Monomer number densities of the free and grafted chains are shown in Figure 9A for all systems. Note that beads corresponding to the linker molecules are not included in these graphs. For the higher grafted system, there is a marked change between N = 20 and N = 40 monomers, as the free chains are repelled from the grafted chains corona. The depletion of the free chains in the interfacial region is accompanied by a pull back of the grafted chains toward the NP surface. This is visible as a shift of the monomer number density profile of the grafted chains (Figure 9A) and a decrease in the average brush height (Table 4). Increasing the free chains length to 80 monomers results in further expulsion of polymer matrix chains from the grafted corona; the effect then stays constant for longer free chains. Such a transition from deeply penetrating free chains and a swollen grafted corona, called wet brush, to a less mixed structure, where grafted chains are less stretched and the free chains retreat from them, called dry brush, has been reported both in theoretical[22] and experimental studies.[18] From a theoretical point of view, the free energy of the polymer brush governs the emerging structure. It has two terms: an entropy term arising from mixing the grafted brush with free chains and an elastic term from stretching the grafted brush's conformation. Interpenetration of the chains is driven by entropic effects, and hence it is favorable for short free chains (larger Q) to mix with the grafted corona and swell it by stretching the individual grafted chains. On the other hand, increasing the length of the free chains makes it easier to be expelled from the grafted corona because of their reduced translational entropy.

Controlling the interpenetration of the polymer matrix and grafted corona is important for tuning the properties of the corresponding NCM. Borukhov and Leibler[22] showed theoretically that there can be an attractive interaction between two

dx.doi.org/10.1021/ma202044e | Macromolecules 2012, 45, 572−584

Table 4. Radius of Gyration, Brush Height, and Density Crossover Distance for Grafted Systems at Different Grafting Densities[a]

	pure PS	1 chains/nm^2			0.5 chains/nm^2		
free chains length (monomers)	$\langle R_g \rangle$, free (nm)	$\langle R_g \rangle$, grafted (nm)	$\langle h \rangle$ (nm)	r_{co} (nm)	$\langle R_g \rangle$, grafted (nm)	$\langle h \rangle$ (nm)	r_{co} (nm)
160	3.15 ± 0.73	2.27 ± 0.44	3.07 ± 0.87	5.08	2.18 ± 0.41	2.56 ± 0.89	3.70
120	2.75 ± 0.61	2.23 ± 0.46	2.99 ± 0.86	4.94	2.39 ± 0.53	2.69 ± 0.95	3.41
80	2.20 ± 0.47	2.34 ± 0.47	2.93 ± 0.83	5.04	2.31 ± 0.54	2.71 ± 0.85	3.51
40	1.51 ± 0.28	2.33 ± 0.45	3.03 ± 0.74	4.95	2.29 ± 0.45	2.71 ± 0.89	3.50
20	1.03 ± 0.16	2.44 ± 0.51	3.23 ± 0.94	4.66	2.38 ± 0.47	2.96 ± 1.00	3.35

[a]The grafted chains have a length of 80 monomers. Brush height $\langle h \rangle$, radius of gyration $\langle R_g \rangle$ of grafted chains, density crossover distance (r_{co}). The radius of gyration of free polymer chains in pure PS (no nanoparticle) is included for reference. The volume fraction occupied by the nanoparticle (~1%) is kept constant for all systems. Errors are calculated as standard deviation of the quantity around the corresponding average value over configurations and chains. Errors of the crossover distance r_{co} are equal to one-half of the bin width used for the density profile (0.025 nm).

dry brushes immersed in a polymer melt. Existence of such an attraction between grafted brushes of different NPs can lead to aggregation of the NPs and to a destabilization of the NCM. When the length of the free chains is changed from 20 to 40, the inner layers of grafted chains (closer than 1.2 nm from surface) are packed more densely to fill the space vacated by the monomers of free chains (Figure 1A). Further drying of the brush, by going to free chains of 80 monomers, causes an extension of the region of densified grafted chains to beyond 1.2 nm from the surface without any more disturbances at closer distances. Longer free chains of 120 and 160 monomers cause no further change in the free or grafted density profiles. We should emphasize that the total number density profile does not depend on the length of the free chains. Conducting an experimental study, Chevigny et al. have recently reported a similar wet-to-dry transition induced by compression of the grafted chains in the interaction with longer free chains of the same polymer.[18]

To investigate if and how this behavior depends on the grafting density, we have repeated the above simulations with a grafting density of 0.5 chains/nm^2, keeping the grafted chain length of 80 monomers. The distance dependence of the number changes (Figure 9). Lengthening the free chains does not deform the grafted chains as much as for the higher grafting density if the distances are smaller than 1.2 nm. Only a partial collapse of the grafted chains from farthest distances is observed, which saturates for free chains longer than 40 monomers. This can be attributed to the availability of space for free chains near the NP, thanks to the low grafting density. This shows that mixing of the polymer matrix with a grafted corona is critically dependent on the grafting density as was already found in atomistic simulations of these systems.[8] The brush height value in this case decreased going from free chains of 20 to those of 40 monomers, and it did not further change for longer free chains, as shown in Table 4. We also note that the crossover distance, i.e., the distance at which the monomer density of the free chains is equal to that of the grafted chains increases with the grafting density, which agrees with our earlier atomistic results.[8] It is, however, nearly independent of the length of the free chains, which is a new result obtained only with the CG model, as atomistic simulations for chains with $N > 20$ were computationally unaffordable.

To investigate the global conformational state of the free chains in the vicinity of the NP, their normalized radius of gyration is shown in Figure 10A for a grafting density of 1 chains/nm^2. Note that the distance from the surface is plotted in units of the respective unperturbed radius of gyration R_g(bulk). All chains show bulklike behavior at distances far

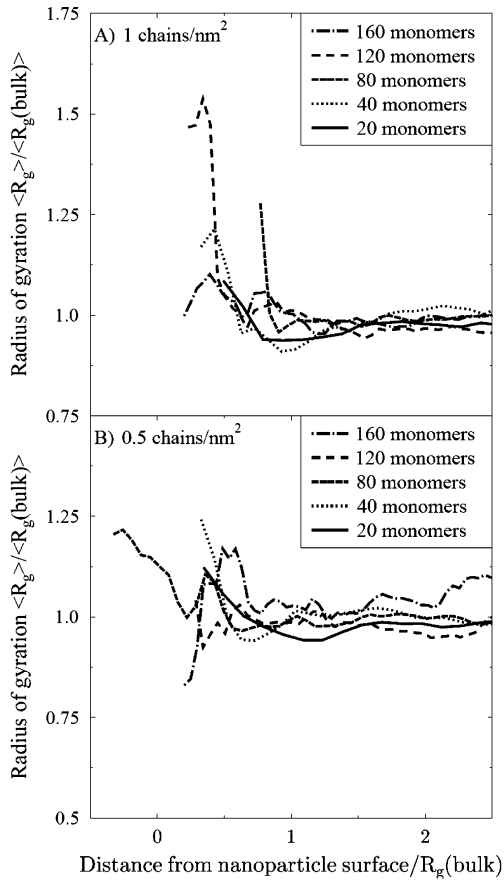

Figure 10. Radius of gyration (normalized by the respective bulk value) of free chains of different length as a function of the distance of the chain center of mass from the nanoparticle surface (also normalized by the respective bulk radius of gyration) in grafted systems of 1 chains/nm^2 (A) and 0.5 chains/nm^2 (B) grafting density. The grafted chains are made up of 80 monomers.

from the NP, while getting disturbed when approaching the particle surface to distances below their respective bulk radius of gyration. Chains at close distance (< 0.7 R_g(bulk)) are mostly stretched, except very few of the longest chains (N = 120, 160), which compact at extremely close distances (< 0.4 R_g(bulk)), as they follow the NP surface with its smaller R_g. This behavior is carried over from the composites with a bare NP (section 3.2). The stretching is a consequence of the close chains being pressed against the NP in a way very similar to the situation found in the case of bare NPs. Examples of such chains are visualized in Figure 11. For some chains there is a

dx.doi.org/10.1021/ma202044e | Macromolecules 2012, 45, 572−584

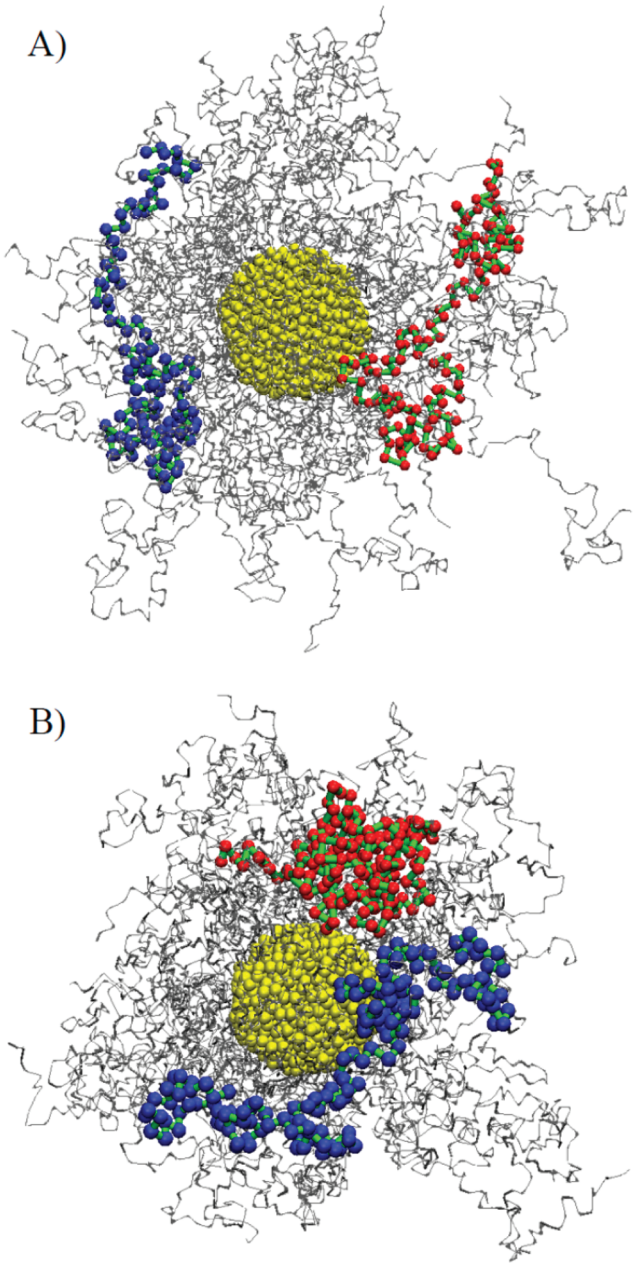

Figure 11. Examples of conformations of free chains of 120 (A) and 160 (B) monomers near a grafted nanoparticle (yellow) of 1 chains/nm^2 grafting density and its corona (gray). Blue and red colors show two different free chains, whereas the green color represents the bonds between monomers. The grafted chains monomers are resized for better visibility of the free chains. Free chains that are pressed against the grafted nanoparticle become deformed, partially engulfing the nanoparticle and its corona.

hint of a shallow minimum of their R_g when they are about 1 R_g(bulk) away from the surface. It is not yet clear whether this is more than a statistical artifact and, if yes, where it comes from. Comparison of Figures 10A and 10B shows that the structuring effects are of similar magnitude for both grafting densities.

Despite the difference in the global structure of free chains of different length, there is little difference in the local packing of their segments. In Figure 12, the radius of gyration of segments of M = 10 monomers of free chains is split into the tangential ($R_{g\parallel}$) and radial ($R_{g\perp}$) components, relative to the NP; they are

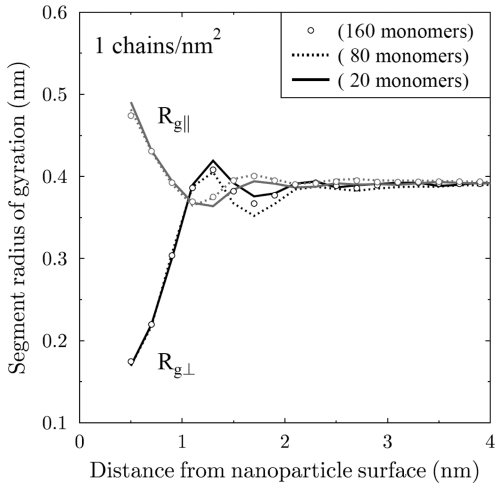

Figure 12. Radius of gyration of segments of 10 monomers of free chains with lengths of 20, 80, and 160 monomers as a function of the distance from the nanoparticle surface, in grafted systems of 1 chains/nm^2 grafting density. The grafted chains have 80 monomers. The volume fraction of the nanoparticle is the same for all systems (~1%). Black symbols show the normal (radial) component of the radius of gyration, $R_{g\perp}$, and the gray ones show the tangential component, $R_{g\parallel}$, multiplied by a factor of 0.5, because there are two tangential directions contributing to this component.

shown as a function of the distance form the NP surface. Since the NP is approximately spherical, the radial direction is the surface normal. The squared radius of gyration of a segment is defined as $R_g^2 = (1/2M^2)\langle\sum_{i,j=1}^{M}(\vec{r}_i - \vec{r}_j)^2\rangle$, where M is the number of monomers that make up the segment, $\vec{r}_i$ is the position of the ith monomer (conveniently measured from the center of the NP), and $\langle ... \rangle$ denotes the average over chains and configurations. The normal component, $R_{g\perp}^2$, is then found by substituting the vector $\vec{r}_i - \vec{r}_j$ by its projection on the surface normal, which can be calculated as its normalized bisector[54] $[(\vec{r}_i - \vec{r}_j)(\vec{r}_i + \vec{r}_j)]/|\vec{r}_i + \vec{r}_j|$. In the orthogonal coordinates there remain two directions perpendicular to the radial direction, for which we calculated the average tangential component of the radius of gyration, $R_{g\parallel}^2$. It is nicely shown in Figure 12 that segments of free chains, independent of their length, become tangential to the surface at close distances (<1 nm). The tangential orientation of the chain segments, however, happens in 0.5 and 1.6 nm from the NP surface, which coincides with the positions of the first and third layers in the monomer number density profile (cf. Figure 5). Moreover, there is a narrow layer at about 1 nm from the surface, where the segments show a small preference for a normal orientation.

4. SUMMARY AND CONCLUSIONS

The interphase structure of PS matrices filled with either a bare or grafted nanometer-sized silica NP has been investigated by means of MD simulations at the CG level. These simulations provide insight into how the structural properties of the polymer matrix and the grafted corona are affected by the presence of the NP and how these effects are dependent on the polymer length (both grafted and matrix chains) and the grafting density of the NP.

A CG model for silica−PS nanocomposites has been developed using the IBI method. While the CG potentials have reproduced the correct structure for bulk PS, the capability for describing the molecular structure in the polymer interphase

dx.doi.org/10.1021/ma202044e | *Macromolecules* 2012, 45, 572−584

around bare and grafted MPs had to be assessed here. To this end, the polymer structure predicted by the CG model has been compared with atomistic simulations of the same system. The results of both agree in general and only show small quantitative differences, such as density peak amplitudes. It was also found that the CG potentials, which were originally developed for a bare system, can be transferred to the grafted NP systems by augmenting them with the additional terms involving the linker units. Except minor differences in the results (mainly the amplitude of the density peaks), this transfer of potentials results in acceptable values of all investigated quantities when compared with the original atomistic data. The CG potentials can also be transferred from the 20-monomer chains they were developed for to much longer chains, grafted as well as matrix ones. The transferability holds for pure PS as well as for systems containing a silica NP. The local structure of the interphase of polymers is not length dependent. The wet-to-dry brush transition observed for grafted particles as a function of the length of the free chains of different lengths, which is a less local property, is in agreement with the experimental data.

Polymer chains around the NP show structure at different levels. The effective width of the zone in which the polymer structure is disturbed, i.e., the interphase, varies according to the structural element being monitored. On the lengths scale of monomer diameters, density fluctuations and preferential orientation of the monomers are observed for about 3 shells (< 2 nm). This is approximately the same for all chain lengths and grafting states (cf. Figures 2 and 5). The contributions of the free and grafted chains to the overall density (Figure 9), however, change with the mass ratio between grafted and free chains. Matrix chains shorter than the grafted chains penetrate the grafted corona, swelling the brush much like a solvent, whereas longer matrix chains are expelled from the NP's vicinity by the grafted brushes (Figure 9A). Not surprisingly, this wet-to-dry brush transition becomes less visible for lower grafting densities (Figure 9B). The relative independence from the chain length and grafting states is not only found for monomer fragments but extends to polymer segments which are significantly shorter than the chains: Segments of 10 monomers show the same orientation distribution near the NP, which becomes random also after 2 nm.

In contrast, all structure exhibited by entire polymer chains (radius of gyration and orientation with respect to the surface) depends strongly on the chain length. Consequently, the interphase thickness defined via these properties varies with the chain length and the grafting state of the NP. The radius of gyration of the polymer is here the governing length scale, as these long-scale structural features reproduce bulklike behavior only at a distance of at least one coil radius away from the NP, which can be as much as 3 nm in our simulations (Figure 10). At close distances, polymer chains tend to be both extended (R_g goes up) and oriented parallel to the surface. This points to polymer conformations where the chains are squashed against the surface. Figure 3 shows how chain stretching and orientation around a NP are correlated for free chains of 20 monomers; Figure 7 shows the same for a grafted NP. There is, however, a qualitative change of this picture for longer chains. While free chains with R_g less than that of the NP become stretched in the interphase area and hence show an increase in R_g, longer free chains show a smaller R_g with respect to its bulk value (Figures 4 and 10). This behavior can be explained by a picture of long chains engulfing the NP. As they are adsorbed on its surface, their radius of gyration is reduced to that of the NP. This picture is supported by the fact that the R_g reduction for chains at close distances is the strongest for the bare NP (Figure 4) and the weakest for the highest grafting density (Figure 10).

■ ACKNOWLEDGMENTS

Special thanks from A.G. to Jaber Dehghany for many informative discussions and his encouragement. This work has been funded by the EU project NanoModel (211778) as well as by the Deutsche Forschungsgemeinschaft through the Priority Programme 1369 "Polymer-Solid Contacts: Interfaces and Interphases".

■ REFERENCES

(1) Balazs, A. C.; Emrick, T.; Russell, T. P. *Science (New York, N.Y.)* **2006**, *314*, 1107−1110.
(2) Adnan, A.; Sun, C. T.; Mahfuz, H. *Compos. Sci. Technol.* **2007**, *67*, 348−356.
(3) Brown, D.; Marcadon, V.; Mélé, P.; Albérola, N. D. *Macromolecules* **2008**, *41*, 1499−1511.
(4) Roy, M.; Nelson, J. K.; MacCrone, R. K.; Schadler, L. S.; Reed, C. W.; Keefe, R.; Zenger, W. *IEEE Trans. Dielectr. Electr. Insul.* **2005**, *12*, 629−643.
(5) Putz, K.; Krishnamoorti, R.; Green, P. *Polymer* **2007**, *48*, 3540−3545.
(6) Mackay, M. E.; Dao, T. T.; Tuteja, A.; Ho, D. L.; Van Horn, B.; Kim, H. C.; Hawker, C. J. *Nature Mater.* **2003**, *2*, 762−766.
(7) Starr, F. W.; Glotzer, S. C. *Soft Matter* **2004**, 107−124.
(8) Ndoro, T. V. M.; Voyiatzis, E.; Ghanbari, A.; Theodorou, D. N.; Böhm, M. C.; Müller-Plathe, F. *Macromolecules* **2011**, *44*, 2316−2327.
(9) Liu, J.; Wu, Y.; Shen, J.; Gao, Y.; Zhang, L.; Cao, D. *Phys. Chem. Chem. Phys.* **2011**, 13.
(10) Montes, H.; Lequeux, F.; Berriot, J. *Macromolecules* **2003**, *36*, 8107−8118.
(11) Merabia, S.; Sotta, P.; Long, D. R. *Macromolecules* **2008**, *41*, 8252−8266.
(12) Harton, S. E.; Kumar, S. K.; Yang, H. C.; Koga, T.; Hicks, K.; Lee, E.; Mijovic, J.; Liu, M.; Vallery, R. S.; Gidley, D. W. *Macromolecules* **2010**, *43*, 3415−3421.
(13) Ruggerone, R.; Geiser, V.; Vacche, S. D.; Leterrier, Y.; Manson, J. A. E. *Macromolecules* **2010**, *43*, 10490−10497.
(14) Vogiatzis, G. G.; Voyiatzis, E.; Theodorou, D. N. *Eur. Polym. J.* **2011**, *47*, 699−712.
(15) Milano, G.; Santangelo, G.; Ragone, F.; Cavallo, L.; Di Matteo, A. *J. Phys. Chem. C* **2011**, *115*, 15154−15163.
(16) Zeng, Q. H.; Yu, A. B.; Lu, G. Q. *Prog. Polym. Sci.* **2008**, *33*, 191−269.
(17) Jordan, J.; Jacob, K. I.; Tannenbaum, R.; Sharaf, M. A.; Jasiuk, I. *Mater. Sci. Eng., A* **2005**, *393*, 1−11.
(18) Chevigny, C.; Jestin, J.; Gigmes, D.; Schweins, R.; Di-Cola, E.; Dalmas, F. *Macromolecules* **2010**, *43*, 48833−44837.
(19) Chevigny, C.; Gigmes, D.; Bertin, D.; Jestin, J.; Boue, F. *Soft Matter* **2009**, *5*, 3741−3753.
(20) Dukes, D.; Li, Y.; Lewis, S.; Benicewicz, B.; Schadler, L.; Kumar, S. K. *Macromolecules* **2010**, *43*, 1564−1570.
(21) Gast, A. P.; Leibler, L. *Macromolecules* **1986**, *19*, 686−691.
(22) Borukhov, I.; Leibler, L. *Macromolecules* **2002**, *35*, 5171−5182.
(23) Hooper, J. B.; Schweizer, K. S. *Macromolecules* **2006**, *39*, 5133−5142.
(24) Trombly, D. M.; Ganesan, V. *J. Chem. Phys.* **2010**, *133*, 184901−184910.
(25) Barbier, D.; Brown, D.; Grillet, A. C.; Neyertz, S. *Macromolecules* **2004**, *37*, 4695−4710.
(26) Bogoslovov, R. B.; Roland, C. M.; Ellis, A. R.; Randall, A. M.; Robertson, C. G. *Macromolecules* **2008**, *41*, 1289−1296.

(27) Robertson, C. G.; Lin, C. J.; Rackaitis, M.; Roland, C. M. *Macromolecules* **2008**, *41*, 2727−2731.
(28) Tsagaropoulos, G.; Eisenberg, A. *Macromolecules* **1995**, *28*, 396−398.
(29) Tsagaropoulos, G.; Eisenberg, A. *Macromolecules* **1995**, *28*, 6067−6077.
(30) Chen, L.; Zheng, K.; Tian, X. Y.; Hu, K.; Wang, R. X.; Liu, C.; Li, Y.; Cui, P. *Macromolecules* **2010**, *43*, 1076−1082.
(31) Müller-Plathe, F. *ChemPhysChem* **2002**, *3*, 755−769.
(32) Müller-Plathe, F. *Soft Matter* **2003**, *1*, 1−31.
(33) Karimi-Varzaneh, H. A.; Müller-Plathe, F. In *Multiscale Molecular Methods in Applied Chemistry*; Krichner, B., Verabec, J., Eds.; Springer-Verlag: Berlin Heidelberg, 2011; Vol. 307, pp 295−321.
(34) Reith, D.; Putz, M.; Müller-Plathe, F. *J. Comput. Chem.* **2003**, *24*, 1624−1636.
(35) Harmandaris, V. A.; Kremer, K. *Macromolecules* **2009**, *42*, 791−802.
(36) Mackay, M. E.; Tuteja, A.; Duxbury, P. M.; Hawker, C. J.; Van Horn, B.; Guan, Z. B.; Chen, G. H.; Krishnan, R. S. *Science* **2006**, *311*, 1740−1743.
(37) Kumar, S. K.; Krishnamoorti, R. *Annu. Rev. Chem. Biomol. Eng.* **2010**, *1*.
(38) Chevigny, C.; Dalmas, F.; Di Cola, E.; Gigmes, D.; Bertin, D.; Boue, F.; Jestin, J. *Macromolecules* **2010**, *44*, 122−133.
(39) Rahimi, M.; Karimi-Varzaneh, H. A.; Böhm, M. C.; Müller-Plathe, F.; Pfaller, S.; Possart, G.; Steinmann, P. *J. Chem. Phys.* **2011**, *134*, 154108.
(40) Smith, G. D.; Bedrov, D. *Langmuir* **2009**, *25*, 11239−11243.
(41) Ozmusul, M. S.; Picu, C. R.; Sternstein, S. S.; Kumar, S. K. *Macromolecules* **2005**, *38*, 4495−4500.
(42) Wang, Q.; Nealey, P. F.; de Pablo, J. J. *J. Chem. Phys.* **2003**, *118*, 11278−11285.
(43) Eslami, H.; Karimi-Varzaneh, H. A.; Müller-Plathe, F. *Macromolecules* **2011**, *44*, 3117−3128.
(44) Eslami, H.; Müller-Plathe, F. *J. Phys. Chem. B* **2009**, *113*, 5568−5581.
(45) Eslami, H.; Müller-Plathe, F. *J. Phys. Chem. B* **2010**, *114*, 387−395.
(46) Milano, G.; Müller-Plathe, F. *J. Phys. Chem. B* **2005**, *109*, 18609−18619.
(47) Spyriouni, T.; Tzoumanekas, C.; Theodorou., D.; Müller-Plathe, F.; Milano, G. *Macromolecules* **2007**, *40*, 3876−3885.
(48) Sun, Q.; Faller, R. *Macromolecules* **2006**, *39*, 812−820.
(49) Harmandaris, V. A.; Reith, D.; van der Vegt, N. F. A.; Kremer, K. *Macromol. Chem. Phys.* **2007**, *208*, 2109−2120.
(50) Qian, H. J.; Carbone, P.; Chen, X. Y.; Karimi-Varzaneh, H. A.; Liew, C. C.; Müller-Plathe, F. *Macromolecules* **2008**, *41*, 9919−9929.
(51) Carbone, P.; Varzaneh, H. A. K.; Chen, X. Y.; Müller-Plathe, F. *J. Chem. Phys.* **2008**, *128*, 064904.
(52) Karimi-Varzaneh, H. A.; Qian, H. J.; Chen, X. Y.; Carbone, P.; Müller-Plathe, F. *J. Comput. Chem.* **2011**, *32*, 1475−1487.
(53) Brown, D.; Mele, P.; Marceau, S.; Alberola, N. D. *Macromolecules* **2003**, *36*, 1395−1406.
(54) Starr, F. W.; Schroder, T. B.; Glotzer, S. C. *Macromolecules* **2002**, *35*, 4481−4492.
(55) Ghanbari, A.; Böhm, M. C.; Müller-Plathe, F. *Macromolecules* **2011**, *44*, 5520−5526.

Macromolecules

Article

pubs.acs.org/Macromolecules

Polymer Mediated Depletion Attraction and Interfacial Colloidal Phase Behavior

Tara D. Edwards and Michael A. Bevan*

Chemical & Biomolecular Engineering, Johns Hopkins University, Baltimore, Maryland 21218, United States

ABSTRACT: We report direct measurements of poly(ethylene oxide) (PEO) mediated depletion attraction between colloids and surfaces using total internal reflection microscopy (TIRM) and in quasi-2D colloidal phase behavior using video microscopy (VM). PEO concentration dependent particle-wall depletion attraction is accurately quantified by a modified Asakura−Oosawa (AO) potential. The modified AO potential employs an equation of state, depletion length, and partition coefficient computed using results from renormalization group (RG) theory. Quasi-2D phase behavior measurements are in excellent agreement with Monte Carlo (MC) simulations using the same modified AO potential. The analytically simple modified AO depletion potential accurately captures depletion attraction for a realistic excluded volume polymer system, which suggests it can be generalized to other material systems.

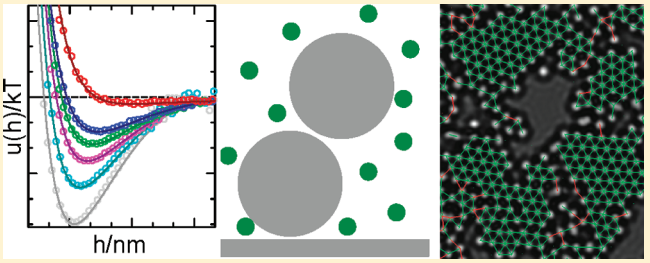

INTRODUCTION

Coexisting colloidal and macromolecular components are ubiquitous in industrial formulations,[1] biological systems,[2] and the environment.[3] In such mixtures, macromolecules can be depleted from the regions between colloids and surfaces because either they do not adsorb to surfaces or they adsorb and saturate surfaces so that additional macromolecules do not adsorb. When partial or complete depletion of macromolecules occurs between colloids and surfaces, the osmotic pressure difference between the bulk and gap regions produces an effective attractive potential between the colloids (see Figure 1). The attractive nature of this potential can be understood either from a force balance as particles and surfaces being pushed/pulled together from the integrated pressure[4] or from an energetic perspective as the free energy associated with negative adsorption being minimized by closing the gap between particles and surfaces.[5,6]

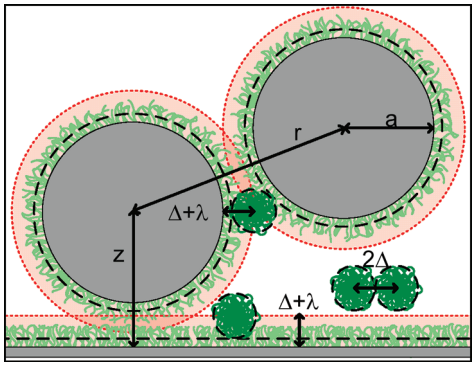

Figure 1. Schematic of charged ~2 μm SiO_2 (gray) colloids and surfaces with adsorbed PEO−PPO−PEO copolymer (light green) experiencing depletion attraction due to exclusion of unadsorbed PEO chains (dark green).

The theory of the depletion attraction due to unadsorbing macromolecules was first described by Asakura and Oosawa (AO).[7] In their model, they used an ideal solution osmotic pressure and a hard sphere depletant-surface interaction to determine a separation dependent excluded volume (i.e., region from which unadsorbed macromolecules are depleted). However, unadsorbed macromolecules in good solvents experience soft repulsion with each other and surfaces. As a result, the osmotic pressure of polymer depletants in good solvents is different from ideal solutions. Real polymer chains also have inhomogeneous concentration profiles near surfaces and in gap regions that vary with relative surface separation and chain dimensions. A number of methods have been developed to accurately model polymer chains for such conditions and configurations, including polymer reference interaction site models,[8] penetratable Gaussian core models for polymer chain interactions,[9] self-avoiding random walk computer simulations,[10,11] and negative adsorption models[5,6] using density profiles from mean field approaches.[12]

Experimental measurements of kT-scale depletion potentials mediated by nonionic polymers in good solvent conditions are limited. Total internal reflection microscopy (TIRM) has been used to measure poly(ethylene oxide) (PEO)[13,14] and dextran.[15] Measurements of PEO-mediated depletion attraction were initially reported to be well described by the AO theory.[13] However, subsequent measurements at higher ionic strengths required a model for the inhomogeneous PEO distribution using density functional theory with van der Waals attraction

Received: October 11, 2011
Revised: November 27, 2011
Published: December 12, 2011

between PEO chains and surfaces.[14] More recent measurements of dextran mediated depletion attraction showed agreement with an AO type potential provided that polydispersity is included in the calculation.[15] Although DNA is a charged macromolecule, optical tweezer measurements of DNA mediated depletion potentials in high ionic strength media have also agreed with AO type models.[16] In general, these results suggest the original AO theory does a reasonable job of describing direct measurement of depletion potentials due to nonionic macromolecules.

It is has been well established that kT-scale depletion attraction produces rich colloidal phase behavior and can be used to assemble colloidal crystals on surfaces ($\gg kT$-scale interactions produce nonequilibrium aggregates/gels). We do not attempt an exhaustive historical review of previous experiments, simulations, and theories for depletion mediated phase behavior and colloidal assembly, but direct readers to extensive reviews contained within several comprehensive papers.[17−19] While many studies have investigated phase behavior and assembly mediated by micellar, nanoparticle, and polyelectrolyte depletants, a much smaller subset have investigated nonionic macromolecules of relevance to the present study. A comparison of experimental and theoretical critical and triple points for nonionic polymer depletants show the correct qualitative behavior but with quantitative discrepancies and limited experimental results.[19] The ability of nonionic polymer depletants to assemble colloidal crystals on templated surfaces has been demonstrated,[20] but predictions based on potentials were not included.

To our knowledge, potentials and phase behavior have not generally been measured together with explicit quantitative connections, with a few exceptions from our previous work.[21−23] We have shown in several of our previous studies how measured kT-scale interaction potentials that include depletion attraction are quantitatively connected to particle-scale microstructures obtained from Monte Carlo (MC) simulations. We have used this approach to demonstrate how solvent quality can be used to continuously tune hydrogel nanoparticles diameters to control the magnitude (i.e., osmotic pressure) and range (i.e., excluded volume) of depletion attraction and associated quasi-2D phase behavior.[21,22] We have also shown how equilibrium partitioning of micellar depletants between particles and wall surfaces determines depletion attraction and phase behavior using a modified AO potential to account for partitioning.[23]

In this paper, we directly measure PEO mediated depletion potentials between particles and a microscope slide surface using TIRM and quasi-2D phase behavior using video microscopy (VM) for the same material system. Using renormalization group (RG) theory for the PEO solution osmotic pressure,[24] it is clear that the standard AO theory over predicts the depletion attraction magnitude compared to our directly measured potentials. By computing a separation dependent partition coefficient from the integrated PEO density profiles between parallel plates, we report a modified AO potential that accurately captures the complete functional form of the TIRM measurements. The PEO density profiles are computed from superposition[6] of the single wall density profile[12] using a correlation length from RG theory.[24] The partition coefficient obtained by integrating the PEO density profile allows the osmotic pressure difference between the bulk and excluded volume region to accurately capture the magnitude of the depletion attraction. The correlation length sets the depletion length in a separation dependent excluded volume term that accurately determines the interaction range. Net potentials include only a single parameter that accounts for interpenetration and compression of PEO brushes on the colloid and wall surfaces by bulk unadsorbed PEO chains.[25,26]

Use of this modified AO potential in MC simulations accurately captures VM observations of colloidal fluid and crystal microstructures in quasi-2D phase behavior measurements (and nonequilibrium gel microstructures at higher attraction). We conclude with a comparison of depletion potentials using the modified AO approach and the adsorption method (AM)[6] with both using the same inputs from RG theory. Ultimately, our results demonstrate the use of a simple pairwise additive depletion potential that accurately captures both direct measurements of particle-wall potentials and quasi 2D phase behavior.

THEORY

Net Interaction Potential. For colloidal particles interacting with each other, an underlying surface, and gravity, the net potential energy of each particle can be modeled as the sum of independent contributions. For charged colloids with radius, a, in the presence of adsorbed and unadsorbed polymer, the net interaction potential is given by,

$$\begin{aligned} u(z, r) = {} & u_G^{pf}(z) + u_E^{pp}(r) + u_E^{pw}(z) + u_V^{pp}(r) \\ & + u_V^{pw}(z) + u_S^{pp}(r) + u_S^{pw}(z) + u_D^{pp}(r) \\ & + u_D^{pw}(z) \end{aligned} \tag{1}$$

where z is the particle center-to-surface elevation relative to contact with the underlying planar surface at $z = a$, and r is the particle center-to-center separation relative to contact at $r = 2a$. The colloid-wall surface-to-surface separation, $h = z - a$ (where $z = h + a$), can also be substituted into any particle-surface potential as a useful separation scale for particle-wall interactions. Subscripts refer to interactions as follows: (E) electrostatic, (V) van der Waals, (G) gravitational, (S) steric, and (D) depletion. Superscripts refer to interactions as: (pp) particle−particle, (pw) particle-wall, and (pf) particle-field.

Gravitational Potential. The gravitational potential energy of each particle depends on its elevation above the underlying surface multiplied by its buoyant weight, G, given by

$$\begin{aligned} u_G^{pf}(z) &= Gh \\ &= mg(z - a) \\ &= (4/3)\pi a^3(\rho_p - \rho_f)g(z - a) \end{aligned} \tag{2}$$

where m is buoyant mass, g is acceleration due to gravity, and ρ_p and ρ_f are the particle and fluid densities.

Derjaguin Approximation. The interaction potential between two spherical particles of equal radius, $u_X^{pp}(r)$, or between a particle and wall, $u_X^{pw}(z)$, can be obtained from the interaction energy per unit area between two flat plates (i.e., two walls), $E_X^{ww}(l)$, at separation l using the Derjaguin approximation as,[27]

$$\begin{aligned} u_X^{pp}(r) &= \pi a \int_r^\infty E_X^{ww}(l)\, \mathrm{d}l \\ u_X^{pw}(z) &= 2\pi a \int_z^\infty E_X^{ww}(l)\, \mathrm{d}l \end{aligned} \tag{3}$$

dx.doi.org/10.1021/ma202279x | Macromolecules 2012, 45, 585−594

which is expected to be asymptotically exact as $h/a \rightarrow 0$, and indicates particle-wall interactions are the twice the value of particle−particle interactions at all separations (when the Derjaguin approximation is valid).

Electrostatic Interaction Potentials. The interaction between electrostatic double layers on two plates (from superposition, nonlinear Poisson−Boltzmann equation, 1:1 monovalent electrolyte)[28] can be used in eq 3 to give analytical potentials for the interaction between particles and wall surfaces as,[29]

$$u_E^{pp}(r) = B \exp[-\kappa(r-2a)]$$
$$u_E^{pw}(z) = 2B \exp[-\kappa(z-a)]$$
$$B = 32\pi\varepsilon a\left(\frac{kT}{e}\right)^2 \tanh\left(\frac{e\psi_1}{4kT}\right)\tanh\left(\frac{e\psi_2}{4kT}\right)$$
$$\kappa = (2e^2 N_A C/\varepsilon kT)^{1/2} \quad (4)$$

where κ is the inverse Debye length, ε is the solvent dielectric constant, k is Boltzmann's constant, T is absolute temperature, C is the 1:1 monovalent electrolyte molarity, N_A is Avogadro's number, e is the elemental charge, and ψ_1 and ψ_2 are surface potentials on interacting surfaces.

van der Waals Interaction Potentials. van der Waals attraction between flat plates are predicted from the rigorous Lifshitz theory[30] (that includes retardation and screening effects) for flat plates as

$$E_V^{ww}(l) = -A(l)/(12\pi l^2) \quad (5)$$

where $A(l)$ is the Hamaker function.[31] Equations 3 and 5 provide particle and wall van der Waals potentials, which can be represented over the separation and energy ranges of interest by convenient power law expressions as,[32,33]

$$u_V^{pp}(r) = -aA[r-2a]^{-p}$$
$$u_V^{pw}(z) = -a2A[z-a]^{-p} \quad (6)$$

where A and p are obtained from fits to the exact results.

Adsorbed Polymer Brush Interaction Potentials. Repulsion due to compression of excluded volume macromolecular brushes were modeled using the interaction per area between flat plates (from the well established theory of Milner et al.),[34,35]

$$E_S^{ww}(l) = \begin{cases} 2(f(l/2) - f(\delta_0)), & l \le 2\delta_0 \\ 0, & l > 2\delta_0 \end{cases} \quad (7)$$

$$f(l) = f_0(5/9)[(\delta_0/l) + (l/\delta_0)^2 - (1/5)(l/\delta_0)^5] \quad (8)$$

where $f(l)$ is the free energy per unit area of a brush compressed to a height, $l < \delta_0$, δ_0 is the uncompressed brush layer thickness, and f_0 is the free energy (with units of kT) per unit area of an uncompressed brush. The expressions in eqs 7 and 8 were used in eq 3 to model interactions between macromolecular brushes adsorbed to particle and wall surfaces.

Adsorption Method Depletion Potentials. The depletion interaction per unit area due to nonadsorbing excluded volume polymer chains can be calculated from the negative adsorption of polymer segments between parallel walls as,[6]

$$E_D^{ww}(l) = \int_0^{\rho_B} [\Gamma(\infty, \rho'_B) - \Gamma(l, \rho'_B)]\left(\frac{1}{\rho'_B}\frac{\partial\Pi}{\partial\rho'_B}\right) d\rho'_B \quad (9)$$

where ρ_B is the bulk polymer segment number concentration, and Π is the polymer solution osmotic pressure, given for excluded volume polymers as the ideal contribution modified by a compressibility factor, Z, from RG theory, as[24]

$$\Pi = \rho_P kTZ \quad (10)$$

$$Z = 1 + 5.505\rho_P {R_g}^3 \left(\frac{1 + 2.509\rho^* + 1.360\rho^{*2}}{1 + 0.596\rho^*}\right)^{0.309} \quad (11)$$

where $\rho^* = 3.584\rho_B {R_g}^3 N^{-1}$, R_g is the single polymer chain radius of gyration at infinite dilution, and N is the number of statistical segments per chain given by,

$$N = N_0 {C_\infty}^{-1} = (l_C/l_m){C_\infty}^{-1} = (M/M_m){C_\infty}^{-1} \quad (12)$$

where C_∞ accounts for chain stiffness, N_0 is the degree of polymerization (i.e., the contour length, l_C divided by the monomer length, l_m; or chain molecular weight, M, divided by monomer molecular weight, M_m). The polymer chain number concentration, ρ_P, in eq 11 is given by

$$\rho_P = \rho_B N^{-1} = C_P N_A M^{-1} \quad (13)$$

where C_P is polymer mass per solution volume. For reference, a polymer volume fraction can also be defined as,

$$\phi = (4/3)\pi {R_g}^3 \rho_P \quad (14)$$

which is defined as unity at the overlap concentration. The adsorbed polymer per area, $\Gamma(l)$, is given by,[6]

$$\Gamma(l, \rho_B) = \int_0^l [\rho(x) - \rho_B]\, dx \quad (15)$$

where x is the normal position between the parallel walls, and $\rho(x)$ is the polymer segment concentration profile between the parallel walls given from superposition (of single wall segment concentration profiles) by[36]

$$\rho(x) = \rho_B \tanh^2(x/\Delta)\tanh^2[(l-x)/\Delta] \quad (16)$$

where Δ is the depletion layer thickness of an excluded volume polymer chain near a single flat wall given by

$$\Delta = (2c/\sqrt{\pi})\xi \quad (17)$$

where $c = 1$ for ideal chains (i.e., Θ conditions)[37] and $c = 0.949$ for excluded volume chains (i.e., good solvents),[38] and ξ is the

dx.doi.org/10.1021/ma202279x | Macromolecules 2012, 45, 585−594

Table 1. Parameters Used for Theoretical Fits (Eq 1) to TIRM Potentials in Figure 2 and in MC Simulations To Generate the Results in Figures 4 and 5[a]

		TIRM (Figure 2)						VM (Figure 4)	
	eq								
2a (μm)	2	2.07	2.03	2.09	2.09	2.06	2.06	2.06	2.06
C_P (g/L)	13	–	0.214	0.321	0.428	0.642	0.856	1.07	1.28
ρ_B (10^6 μm^{-3})	9	–	0.771	1.16	1.54	2.31	3.08	3.84	4.61
ρ_P (10^3 μm^{-3})	10	–	0.644	0.967	1.29	1.93	2.58	3.21	3.85
ϕ	14	–	0.05	0.075	0.100	0.150	0.200	0.250	0.300
λ (nm)		–	**6.25**	**5.25**	**5.25**	**4.5**	**4.85**	**4.7**	**5.3**

[a]The colloid radius fit to the gravitational potential is shown in the first row. The following rows report PEO concentration as mass/volume (as prepared), bulk segment number density, bulk chain number density, and volume fraction. The last row reports the impenetrable brush length, λ, as the only adjustable parameter (shown in bold). Other independent parameters include: SiO_2 colloid density, ρ_p = 1.92 kg/m^3,[59] and water density, ρ_f = 1000 kg/m^3; colloid and wall surface potentials Ψ_p, Ψ_w=-50 mV;[43,44] Debye length, κ^{-1}=4.25 nm, from as-prepared 5 mM NaCl; polymer brush dimension, δ_0 = 15 nm, and unperturbed free energy, $f_0 = 0.03kT$ nm^{-2};[51,52] van der Waals power, p = 2.195, and size dependent contact value, $A = (2140/a)kT$ nm^{1+p}.[33]

polymer density correlation length from RG theory for excluded volume polymers given by[24]

$$\xi = R_g\left[1 + \rho^* + 3.073\rho^{*2} \times \left(\frac{1 + 3.80\rho^* + 5.67\rho^{*2}}{1 + 1.73\rho^*}\right)^{0.309}\right]^{-1/3} \quad (18)$$

Equations 3 and 9−18 can be used to obtain particle and wall depletion potentials.

Modified AO Depletion Potentials. The depletion attraction between particles and planar surfaces can be given by a modified form of the usual AO depletion potential[28] as

$$u_D^{pp}(r) = -V^{pp}(r, \Delta)\Delta\Pi(r - 2a)$$
$$u_D^{pw}(z) = -V^{pw}(z, \Delta)\Delta\Pi(z - a) \quad (19)$$

where the usual excluded volume terms obtained from geometric considerations are given by,[28,39,40]

$$V^{pp}(r, \Delta) = \pi[(4/3)(a + \Delta)^3 (1 - (3/4)r(a + \Delta)^{-1} + (1/16)r^3(a + \Delta)^{-3})]$$
$$V^{pw}(z, \Delta) = \pi[(4/3)\Delta^3 + 4\Delta^2 a - 4\Delta a(z - a) + a(z - a)^2 - \Delta(z - a)^2 + (1/3)(z - a)^3] \quad (20)$$

using the depletion length given in eq 17. The osmotic pressure difference due to concentration differences between macromolecular solutions in the bulk and excluded volume regions is given by,

$$\Delta\Pi(l) = \Pi_B - \Pi_G(l) = \rho_B N^{-1}kTZ - \langle\rho_G(l)\rangle N^{-1}k_BTZ = \rho_B N^{-1}kTZ - \rho_B N^{-1}K(l)k_BTZ = \rho_P kTZ[1 - K(l)] \quad (21)$$

where the subscripts B and G refer to "bulk" and "gap" segment densities, Z is given by eq 11, and $K(l)$ is a partition coefficient defined by the ratio of the average gap polymer segment concentration, $\langle\rho_G(l)\rangle$, for a given separation, l, and bulk polymer segment concentration, ρ_B, as,

$$K(l) \equiv \langle\rho_G(l)\rangle/\rho_B = (\rho_B l)^{-1}\int_0^l \rho(x)\, dx \quad (22)$$

using the density profile between two flat plates, $\rho(x)$, from eq 16.

MATERIALS AND METHODS

Materials. Nominal 2.34 μm diameter SiO_2 colloids (Bangs Laboratories, Fishers, IN) were modified with 1-octadecanol (Sigma-Aldrich Company, St. Louis, MO) using a literature method.[41] Glass microscope slides (Fisher Scientific, Pittsburgh, PA) were sonicated in methanol (Fisher Scientific, Pittsburgh, PA) for 30 min, sonicated in acetone (Fisher Scientific, Pittsburgh, PA) for 30 min, immersed in Nochromix (Godax Laboratories, Takoma Park, MD) overnight, soaked in 0.1 M KOH (Fisher Scientific, Pittsburgh, PA) for 30 min, washed with DI water, dried with nitrogen, and spin coated (Laurell Technologies Corporation, North Wales, PA) with polystyrene (Sigma-Aldrich Company, St. Louis, MO) prior to each experiment.

PEO-poly(propylene oxide)-PEO triblock copolymer (F108 Pluronic, BASF, Wyandotte, MI) with segment molecular weights of 5400/3300/5400 g/mol was adsorbed to colloids and surfaces as a steric stabilizer. This copolymer was dissolved in DI water at 1000 ppm[42] and then adsorbed to the colloid and microscope slide surfaces for 12 h. PEO (viscosity average molecular weight of $M = 2 \times 10^5$g/mol, Sigma-Aldrich Company, St. Louis, MO) and analytical grade NaCl (Acros Organics, Morris Plains, NJ) were used without further purification. In each experiment, colloidal dispersions and surfaces were washed with PEO and 5 mM NaCl solutions to remove excess F108. Dispersions of SiO_2, PEO, and 5 mM NaCl in deionized water were prepared to yield ~1% SiO_2 interfacial area fractions for TIRM measurements and ~60% SiO_2 interfacial area fractions for VM measurements. All PEO concentrations used in TIRM and VM measurements were below ϕ = 1 (i.e., eq 14). Samples were allowed to equilibrate for 24 h before VM measurements.

Microscopy. Experiments were performed in sample cells consisting of 10 mm and 5 mm ID Vinton o-rings (McMaster Carr, Robbinsville, NJ) sealed between the microscope slide and a glass coverslip (Corning, Corning, NY) for TIRM and VM measurements, respectively. A 12-bit CCD camera (ORCA-ER, Hamamatsu, Japan) on an upright optical microscope (Axio Imager A1m, Zeiss, Germany) was used for TIRM and an inverted optical microscope (Axio Observer A1, Zeiss, Germany) was used for VM. For VM measurements, the camera was operated in 1-binning mode with a 63X objective and 1.6X magnifying lens to yield 9frame/s and 60 nm/pixel. For TIRM experiments, the camera was operated in 4-binning mode with a 40× objective to yield 28frame/sec and 607 nm/pixel.

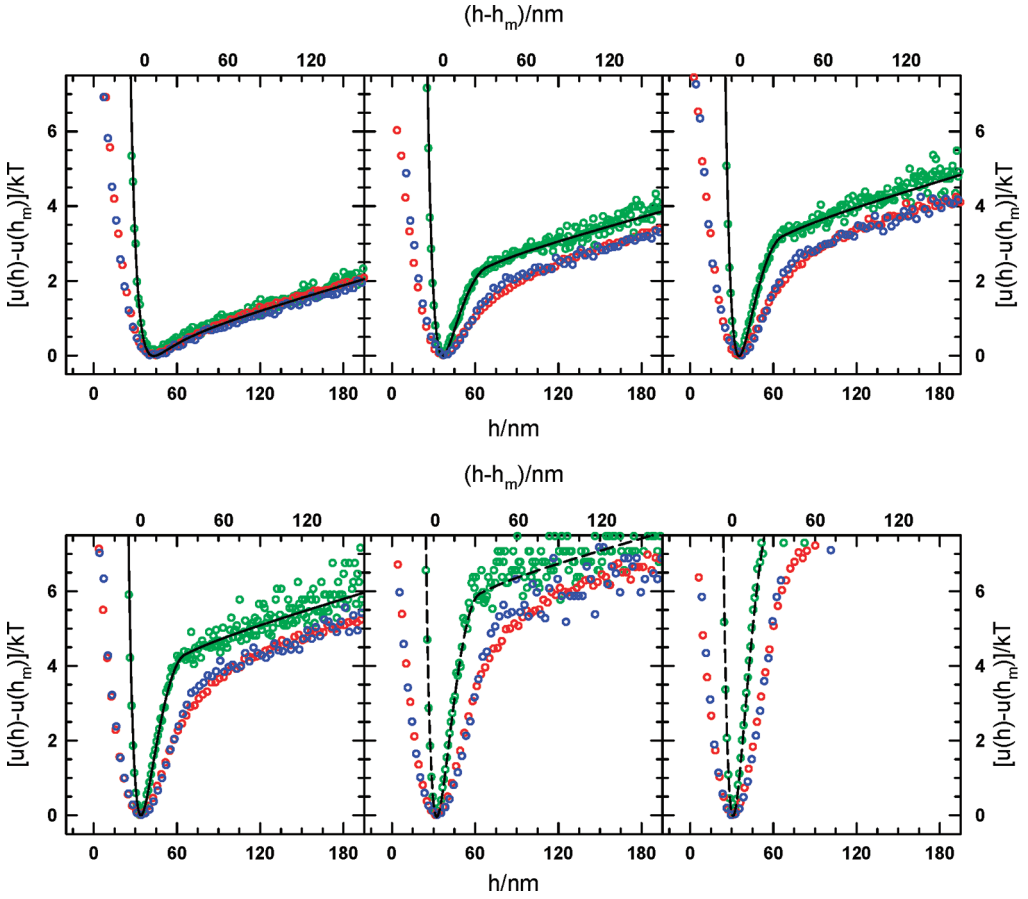

Figure 2. Ensemble TIRM measurements of PEO concentration dependent colloid-wall potentials. (left-to-right, top-to-bottom) Measured potential energy profiles (red) shown for PEO C_P = 0, 0.214, 0.321, 0.428, 0.642, and 0.856 g/L. Theoretical profiles (eq 1) using parameters in Table 1 where gravity is well sampled and fit directly for $C_P \leq 0.428$ g/L (solid black) and where gravity is poorly sampled for $C_P \geq 0.642$ g/L (dashed black). MC simulated theoretical potentials were obtained with (blue) and without (green) noise (see Materials and Methods).[45] See text for discussion of comparison between experimental, simulated, and theoretical potentials.

TIRM experiments employed a 15 mW 632.8 nm helium−neon laser (Melles Griot, Carlsbad, CA) and a 68° dovetail prism (Red Optronics, Mountain View, CA) to generate an evanescent wave decay length of β^{-1} = 114 nm. Image analysis algorithms coded in FORTRAN were used to track colloid lateral motion in TIRM and VM experiments and to integrate the evanescent wave scattering intensity from each colloid in TIRM experiments.[43,44]

Simulations. One-dimensional MC simulations of particle-wall interactions were performed to include effects of noise for comparison with TIRM measurements. Simulations were performed using the theoretical potentials in eq 1 and parameters in Table 1, where an impenetrable brush length, λ, was the only parameter adjusted in an iterative inverse analysis (described further in the Results and Discussion). These simulations were performed for 3×10^4 MC steps. Noise was added to simulated particle elevations in a manner that accurately captures the TIRM/VM measurement process, which is described in detail elsewhere.[23,45] In short, Gaussian noise was added to MC simulation height excursions, which were then analyzed using the standard ensemble TIRM/VM analysis.[43]

Two-dimensional MC simulations of particle−particle interactions for comparison with VM measurements were performed for 256 log-normal size distributed colloids with a mean diameter of $2a$ = 2.06 μm and relative standard deviation of 1.04.[46,47] All 2D simulations were performed for 10×10^6 MC steps using particle area fractions and initial configurations measured in VM experiments. Radial distribution functions, $g(r)$'s, and 6-fold connectivity order parameters, $\langle C_6 \rangle$, were constructed from simulated particle coordinates with Gaussian noise added via a random number generator to produce uncertainty in particle center positions with a standard deviation of 40 nm. The computation of $\langle C_6 \rangle$ is described in detail in several of our previous papers.[21−23,48,49]

RESULTS AND DISCUSSION

Particle-Wall Potential Profiles. Figure 2 reports potentials between electro-sterically stabilized 2.34 μm SiO_2 particles and glass microscope slides in the presence of different PEO concentrations as measured with ensemble TIRM.[21,43,44] Electro-steric stabilization here refers to comparable contributions toward particle levitation from repulsive interactions due to both surface charge and adsorbed macromolecular brushes. In addition to the measured potentials shown by red points, Figure 2 shows lines representing theoretical potentials from eq 1. Solid lines in Figure 2 indicate theoretical fits where gravity was well-sampled and measured directly. Dashed lines indicate fits where gravity was not well sampled (due to the depletion well depth) and was instead predicted using the average particle radius from the rest of the measurements. MC simulated potentials with and without added noise (see Materials and Methods) are shown in Figure 2 by blue and green points. As will be explained in the following, agreement between theory and experiment is demonstrated by showing agreement between (1) noise-free theoretical potentials (lines) and noise-free MC results (green points) and (2) agreement between MC simulations with added Gaussian noise (blue points) and measured potentials (red points).

dx.doi.org/10.1021/ma202279x | Macromolecules 2012, 45, 585−594

To include effects of noise when comparing theoretical and experimental potentials, experimental noise is directly measured in a control experiment and added to the MC simulated cases shown by blue points in Figure 2. Signal noise produces uncertainty in each particle's measured elevations, which softens strong forces (i.e., large changes in energy over short distances) and decreases the apparent minimum in each experiment. Noise is measured as the Gaussian distribution of apparent heights observed for a particle stuck to the wall; since height does not change in this case, it is a direct measure of the uncertainty in elevation due to signal noise in the laser, detector, etc. This method is described in detail in our previous papers.[23,45]

The agreement is excellent between the theoretical potentials and the noise-free MC simulation results. Likewise, the agreement is also excellent between the experimental potentials and the MC simulation results with Gaussian noise. As such, the results in Figure 2 demonstrate quantitative agreement of the experimental and theoretical potentials in the presence of experimental noise. In the following, we describe how each contributing potential is fit to obtain net potential energy profiles, which provides a basis to discuss how the unadsorbing PEO mediates depletion attraction.

Gravitational, Electrostatic, van der Waals, and Steric Potentials. To fit the potentials in each case in Figure 2, we employed a systematic procedure based on parameters from independent characterization and previous measurements on the same material system without unadsorbing polymer. First, we describe the potentials that are not due to unadsorbing polymer. The gravitational potential was obtained directly by fitting eq 2 to the linear region beyond the range of colloidal and surface forces (which was also used in cases when gravity was not well sampled). To obtain the radius from eq 2, literature values of the particle and water density were used as reported in Table 1. These particle radii are in good agreement with independent measurements (i.e., first peak in $g(r)$s of dried samples[50]).

All parameters in the electrostatic,[43,44] steric,[51,52] and van der Waals[33] interactions were also fixed from TIRM measured potentials in our previous papers on the same material system. In the adsorbed brush potential in eqs 7 and 8, values of brush layer uncompressed thickness at contact, δ_0, and free energy per unit area, f_0, were obtained from fits to previous measurements.[51,52] The value of the brush thickness is in excellent agreement with predictions (from RG theory) and experiments.[53] We do not attempt to compare f_0 with theoretical predictions.[34] The remainder of the parameters in the electrostatic and van der Waals potentials are used without further modification or analysis.

As can be seen in Figure 2, these potentials produce excellent agreement with the measured results in Figure 2a in the case where no unadsorbing PEO has been added and there is no depletion attraction. In all other cases in Figure 2 where increasing PEO concentration produces an increasing depletion attraction, the gravitational, electrostatic, van der Waals, and steric potentials show excellent agreement with the data in the regions where they dominate the net potential.

Modeling Depletion Potentials. To fit the depletion potential (the only contribution left in the net potential) to the direct measurements in Figure 2, we use the modified AO form suggested in eqs 19−22. We defer a discussion of the validity of such an approach until we first describe results related to the fits in Figure 2 and the use of this potential for modeling phase behavior. To model the osmotic pressure term in eq 19, we use the expression in eqs 10, 11 and the average partitioning of PEO between the colloid-wall gap relative to the bulk as the integral in eq 22 over the density profile between flat plates (eqs 16−18). The only input in these equations (eqs 11, 18) are the bulk polymer solution concentration, C_P (which can be used to obtain ρ's, i.e., eq 13), the number of statistical segments, N, and the PEO radius of gyration, R_g. The values of C_P are fixed to their as prepared estimates reported in Table 1, the value of R_g is fixed to a literature reported value (using the expression $R_g = 0.0215M^{0.583}$ nm),[54] and N is obtained from eq 12 using $C_\infty = 3.8$.[53] Although this relationship for R_g is based on the mass average molecular weight (using static light scattering), we use the viscosity average molecular weight measured for our polymer knowing that this introduces some error to consider in our final analysis.

The modified AO potential also has an excluded volume term that requires a depletion thickness, Δ, which we model using eq 17 and plot in Figure 3. The value of Δ requires the same inputs as the osmotic pressure term, so no additional parameters are required for its calculation. The expression in eq 17 displays all the correct limiting results for planar surfaces for ideal[37] and excluded volume chains[38] and for dilute (e.g., $\xi = R_g$) and semidilute (e.g., $\xi \propto \rho_B^{-0.77}$) concentrations.[6] Although curvature corrections to Δ could be included in its calculation, they are expected to be negligible for the relative polymer and particle dimensions in this work (i.e., $R_g/a \approx 26.5$ nm/1100 nm ≈ 0.02).[38] As reported in Table 1, $\phi < 1$ in all our experiments (from eq 14), so Δ is close to its infinitely dilute value as shown by the dashed line in Figure 3. Nevertheless, we include the concentration dependence of Δ to allow our results to be generalized to other conditions.

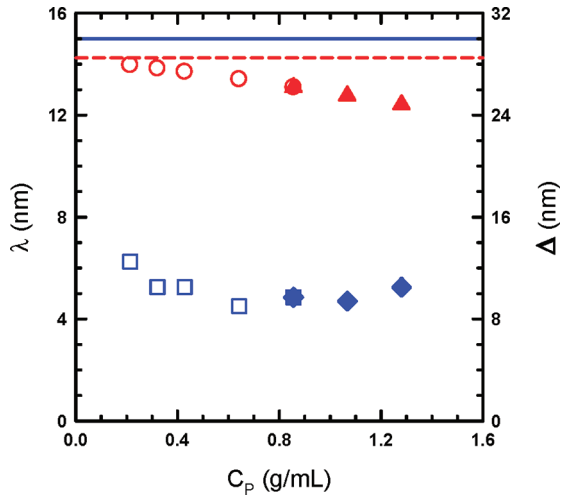

Figure 3. Impenetrable brush length, λ (blue), and depletion layer thickness, Δ (red), vs PEO concentration from fits to direct particle-wall measurements in Figure 2 (open circles, Δ, and open squares, λ) and indirect particle−particle measurements in Figures 4 and 5 (closed triangles, Δ and closed diamonds, λ). Brush thickness plotted as blue solid line, and infinitely dilute depletion layer thickness plotted as red dashed line.

To obtain quantitative agreement between the predicted and measured depletion potentials in Figure 2, a single adjustable parameter is introduced. The parameter is the distance of closest of approach of a polymer chain to the silica substrate surfaces, λ. The distance of closest approach of the free polymer

coils to the sterically stabilized colloid and wall surfaces determines the colloid−wall separation at which chains begin to be excluded from (i.e., partition between) the colloid−wall gap (see Figure 1). This is primarily determined by the ability of free PEO chains to interpenetrate or compress[25] the PEO tails of the brush layers on the particle and wall surfaces. Because this separation dependent correction shifts the potential, it is also likely to correct for anything else that alters the range of the depletion attraction, including nonidealities (e.g., surface roughness,[32,55] polydispersity[15]) and any errors in other parameters (e.g., R_g estimate using viscosity average molecular weight instead of mass average molecular weight[54]) that do not cancel out when computing the net potential.

To practically correct the depletion potential for the presence of the PEO brushes on surfaces, the parameter λ appears in several terms in the modified AO potential. By using the silica particle-glass wall separation as the reference separation (used in all other potentials), λ is: (1) added to the depletion layer thickness (eq 17), (2) used to offset the unadsorbed polymer density profile from both surfaces of parallel interacting walls (eq 16), and (3) added and subtracted from the lower and upper bounds in the integral over the density profile (eq 22) used to calculate partition coefficients.

Figure 3 reports the values of λ vs polymer concentration used to fit the potentials in Figure 2. We defer a complete discussion of this parameter until after describing quasi-2D phase behavior results, but we note here that the parameter is close to expected physically significant values. The ∼9−10 nm of penetration and/or compression of the brush by bulk PEO chains is comparable to the amount the brushes penetrate/compress each other (i.e., width of repulsion in previous measurements of brush interactions[51,52]). The average brush polymer concentration is C_P = 133.3 g/L (ϕ = 2.174 > 1) which is higher than the bulk polymer concentration, but the expected parabolic decay as the brush density profile vanishes at its edge could allow for penetration or compression by bulk polymer. The relatively constant value of λ vs polymer concentration indicates the degree of penetration does not change significantly for the bulk polymer concentrations investigated in our study, which might be expected since they are all below the semidilute regime and less than the average brush concentration. In any case, the introduction of λ as a single adjustable parameter has a good physical basis, and it produces excellent agreement between the directly measured and predicted potentials in Figure 2.

Depletion Mediated Quasi-2D Phase Behavior. To further probe depletion potentials at higher polymer concentrations and in connection to phase behavior, Figure 4 reports VM measured images and MC simulations of quasi-2D phase behavior in the same material system used in the TIRM measurements in Figure 2. The only difference between the TIRM and VM measurements is higher silica colloid area fractions and bulk PEO concentrations (see Table 1) that are required since the particle−particle interaction is ∼0.5× the particle−wall interaction. One VM experiment at the lowest PEO concentration was identical to the most concentrated TIRM measurement as a consistency check between the two experiments. For several PEO concentrations, Figure 4 shows representative snapshots from equilibrium VM measured images and from MC simulated renderings obtained from an inverse analysis of the VM results.

As described in the Materials and Methods, potentials are extracted from the inverse MC analysis by matching the VM

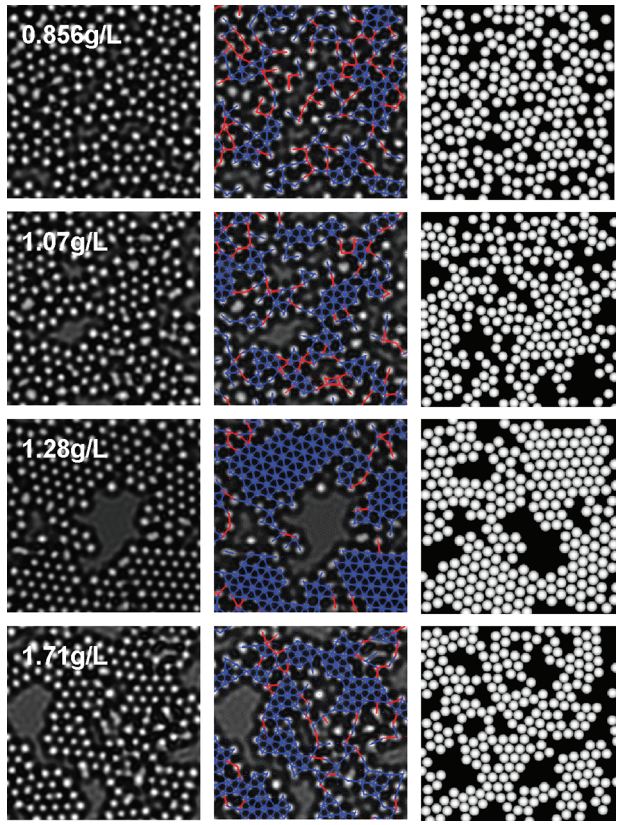

Figure 4. VM measured and MC simulated 2D colloidal configurations as a function of PEO concentration. Data includes: (column 1) unprocessed VM images, (column 2) analyzed images with colored lines indicating bonds between fluid (red) and solid (blue) colloids, and (column 3), MC simulated configurations using modified AO potentials.

measured microstructure using the same analytical potentials that fit the direct TIRM measurements. This approach ensures consistency between the direct and indirect measurements of depletion attraction in the two approaches. All parameters are fixed in the particle−particle potentials to be the same as those used in the TIRM measurements, except for different curvature corrections (i.e., eq 3 for all potentials except the depletion potential which is based on a different excluded volume term; i.e., eq 20). As in the TIRM experiments, λ is the only adjustable parameter used to match the microstructures between MC simulations and VM experiments.

To match microstructure, Figure 5 shows $g(r)$s and $\langle C_6 \rangle$ histograms from experiments as points and simulations as solid lines. The agreement between experiments and simulations in Figure 5 is excellent within the limits of experimental uncertainty, suggesting the simulated particle−particle potentials do an excellent job of capturing the microstructure through the phase transition from fluid to solid configurations in Figure 4. The agreement is particularly good given that kinetic differences in the microstructure evolution in the actual experiments and MC simulations could lead to greater differences, particularly in the $\langle C_6 \rangle$ histograms. To be fair, the phase behavior is less sensitive to the exact form of the potentials (i.e., potentials corresponding to the same second virial coefficient produce the same behavior when the interaction range is small compared to the particle radius;[56,57] again, $R_g/a \approx 26.5$ nm/1100 nm $\approx$ 0.02 in this work). However, the analytical form measured directly in the TIRM

dx.doi.org/10.1021/ma202279x | Macromolecules 2012, 45, 585−594

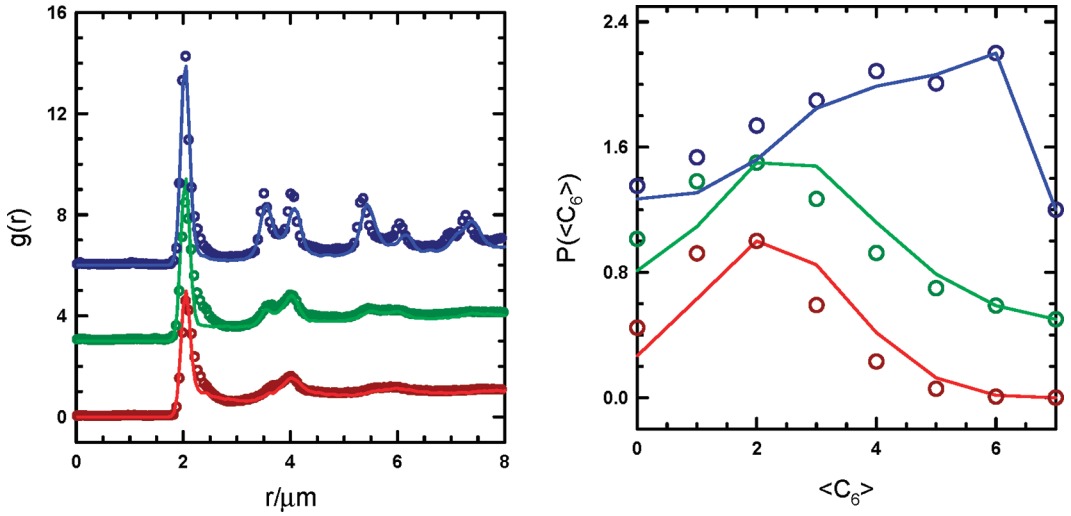

Figure 5. Radial distribution functions, $g(r)$, (left) and 6-fold connectivity distributions, $P(\langle C_6 \rangle)$, (right) from VM measurements (points) and MC simulations (lines) of 2D colloidal configurations in Figure 4. Bulk PEO concentrations are 0.856 g/L (red, bottom), 1.07 g/L (green, middle), and 1.28 g/L (blue, top).

measurements clearly also works well for quasi-2D phase behavior when using λ as the sole adjustable parameter.

The fit values of λ in Figure 3 obtained from the analysis of the phase behavior are consistent with the trend observed from the TIRM values even though λ was not constrained in any way to remain in a similar range. In fact, the value of λ obtained at the same polymer concentration in the TIRM and VM measurements (i.e., C_p = 0.856 g/L) is essentially identical. Because the polymer concentration is not much higher in the VM experiments than the TIRM measurements, and is still much lower than the average polymer brush concentration and the crossover concentration, it is not surprising that λ does not change for the VM results in Figure 3. As a result, the modified depletion potential in eqs 19−22 (as well as other equations cited within the theory section for Z, Δ, and ξ) appears to describe both direct TIRM particle-wall potentials and the quasi 2D phase behavior mediated by particle−particle potentials. In all cases, the single adjustable parameter, λ, makes good physical sense and takes on reasonable values based on expectations.

Modified AO Potential vs Adsorption Method Potential. The modified AO potential we report in eqs 19−22 was developed by correcting the original AO theory to include polymer partitioning between the bulk solution and gaps between particles and surfaces. The depleted but finite polymer concentration in the gap relative to the bulk polymer solution produces smaller osmotic pressure differences compared to total exclusion from gaps between particles and surfaces. After finding an appropriate equation of state for the osmotic pressure and an appropriate expression for the depletion length in the excluded volume term, the results in Figure 2−5 show that the modified AO potential does an excellent job capturing both directly measured potentials and phase behavior. The simple form and concepts behind the modified AO form also make it easy to use. It is also compelling that the same form has been used to describe depletion potentials and phase behavior when the depletant species are charged micelles,[23] demonstrating it can be generalized to different material systems.

Although this simple form displays excellent agreement with all results in Figures 2−5, we also compare it with the AM potential (eqs 9−18), which is a based on a more rigorous approach to modeling depletion attraction. Figure 6 shows sphere-plate potentials in the absence of any other potentials

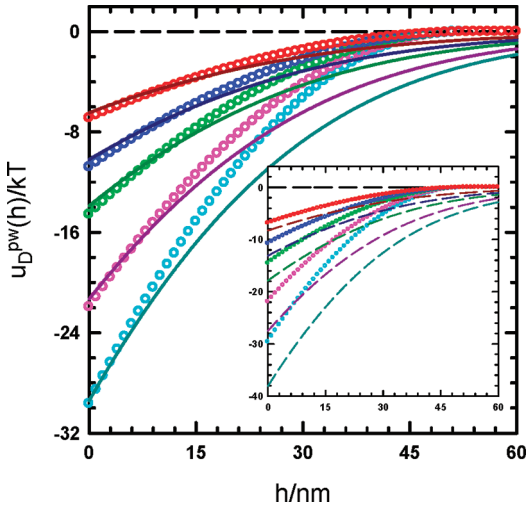

Figure 6. Sphere−plate depletion potentials vs polymer concentration. Solid curves correspond to AM potentials (eqs 9−18) and points correspond to modified AO potentials (eqs 19−22). The inset reports results on an absolute separation scale and the main plot shows the AM potential shifted to shorter separations by 8 nm. Results are computed for PEO concentrations of 0.214 g/L (red), 0.321 g/L (blue), 0.428 g/L (green), 0.642 g/L (pink), and 0.856 g/L (cyan).

for separations down to contact as computed from the modified AO potential and the AM potential. The AM potential is computed for the sphere-plate geometry using the Derjaguin approximation (eq 3), whereas the AO potential includes curvature effects via its excluded volume term in eq 20. Because we do not include effects of adsorbed polymers in this comparison, the potentials are both computed with λ = 0. All other parameters are fixed to those used for the five depletion potentials used to fit the TIRM potentials in Figure 2b−f. Both potentials use the same equations of state, correlation lengths, and density profiles as inputs.

The inset of Figure 6 shows the potentials compared without modification, and the main part of Figure 6 shows the AM

dx.doi.org/10.1021/ma202279x | *Macromolecules* 2012, 45, 585−594

potentials shifted to shorter separations by 8 nm. The AM potentials are both longer range and have larger contact values than the modified AO potentials. Shifting all of the AM potentials by 8 nm produces agreement at contact for all polymer concentrations, but their range is still significantly longer than the modified AO potentials. It is clear that the functional form of the two potentials is different and simple additive offsets in separation or the contact energy alone do not account for difference between the two curves.

The modified AO potentials agree with the direct TIRM measurements and indirect VM phase behavior measurements using a single adjustable parameter, λ, to account for PEO depletants penetrating PEO brushes. While the parameter λ has a good physical basis and takes on reasonable values, as already mentioned, it could also correct for any other uncertainties in either the form of the modified AO potential or the parameters used in Figures 2−5. As a result, the 8 nm offset in between the contact values of the modified AO and AM potentials could be the result of some errors in either the form of, or parameters used in, the modified AO potential. For example, it could be possible that very different values of the parameters in the AM depletion potential could bring it into agreement with the results in Figures 2−5. However, the only parameters required in both potentials, C_p, N (that depends on C_∞), and R_g, are either directly measured and/or produce good agreement with RG theories of PEO brushes.[53] Uncertainty in material properties does not seem to account for differences between the modified AO and AM potentials.

There are other possible reasons that the AM potentials do not agree with the modified AO potentials or the experimental results in Figures 2−5. The Derjaguin approximation is an approximation; it may not be an ideal method to correct for curvature in the AM potential or depletion potentials in general.[58] However, in a comparison of AM sphere−sphere potentials for ideal polymers (computed either directly from density profiles around spheres or from the Derjaguin approximation applied to plate−plate density profiles[5]), the Derjaguin approximation produced shorter range potentials than the direct sphere−sphere potential. This suggests AM potentials computed directly from density profiles for the sphere−plate interaction would be even longer range and further out of agreement in Figure 6.

It has also been shown that the AM potentials between plates are longer range than simulations of excluded volume polymers,[10,11] which is consistent with the AM potential being longer range than our measured potentials in Figure 2. The primary reason for the AM potential being longer range is probably the approximate form of the input density profile based on superposition, which is expected to perform less well as the polymer concentration vanishes, which is the conditions of our measurements. Although we use the same density profile in the modified AO potential, the integral average over the density profile used to compute the partition coefficient makes this less sensitive to the density profile's functional form. In addition, the excluded volume term in the modified AO theory has a clear cutoff distance determined by the depletion thickness, which determines the range of this potential. It is possible that including a more rigorous model of the polymer density profile in the AM potential would produce better agreement with the experimental results in Figures 2−5.

CONCLUSION

Our experimental measurements of PEO mediated depletion potentials and quasi-2D phase behavior display excellent agreement with a modified AO pair potential. The modified AO potential simply requires an accurate equation of state for the polymer, a concentration dependent depletion length due to polymer−polymer interactions, and a term to account for polymer partitioning between the bulk and gaps between particles and surfaces (i.e., partial depletion from gaps). Each of these terms are available from literature RG theory results for the polymer osmotic pressure, correlation length, and density profile between plates. The only adjustable parameter required to produce quantitative agreement between the modified AO potential and all experimental results is a physically meaningful parameter related to how far unadsorbed PEO interpenetrates PEO brushes on particles and wall surfaces. The fit values of this parameter fall within expected limits.

The same modified AO pair potential was used to quantify depletion potentials and phase behavior in charged micellar systems in previous work,[23] which suggests that in addition to being simple, it may be useful for other depletant types. For both the nonionic polymer in this study, and for charged micellar depletants, the modified AO potential has only been verified for depletant concentrations from infinite dilution up to conditions that produce equilibrium phase behavior. It has not been tested at higher depletant concentrations that produce irreversible aggregates/gels or at depletant/colloid size ratios where oscillatory potentials might be observed. The analytically simple modified AO depletion potential (similar to simple exponential and power law DLVO potentials) can facilitate predictions of potentials, phase behavior, and stability in diverse applications without accessibility issues associated with complex mathematical and/or computational tools.

AUTHOR INFORMATION

Corresponding Author

*E-mail: mabevan@jhu.edu.

ACKNOWLEDGMENTS

We acknowledge support by the National Science Foundation through a Cyber Enabled Discovery & Innovation grant (CMMI0835549) and an unsolicited grant (CBET0932973). We thank Caitlin Schram for her assistance with preliminary TIRM measurements of depletion interactions in similar materials systems.

REFERENCES

(1) Zukoski, C. F. *Chem. Eng. Sci.* **1995**, *50* (24), 4073−4079.
(2) Marenduzzo, D.; Finan, K.; Cook, P. R. *J. Cell Biol.* **2006**, *175* (5), 681−686.
(3) Grasso, D.; Subramaniam, K.; Butkus, M.; Strevett, K.; Bergendahl, J. *Rev. Environ. Sci. Biotechnol.* **2002**, *1* (1), 17−38.
(4) Walz, J. Y.; Sharma, A. *J. Colloid Interface Sci.* **1994**, *168* (2), 485−496.
(5) Tuinier, R.; Vliegenthart, G. A.; Lekkerkerker, H. N. W. *J. Chem. Phys.* **2000**, *113* (23), 10768−10775.
(6) Tuinier, R.; Lekkerkerker, H. N. W. *Eur. Phys. J. E* **2001**, *6* (2), 129−132.
(7) Asakura, S.; Oosawa, F. *J. Chem. Phys.* **1954**, *22* (7), 1255−1256.
(8) Chatterjee, A. P.; Schweizer, K. S. *Macromolecules* **1999**, *32* (3), 923−934.
(9) Bolhuis, P. G.; Louis, A. A. *Macromolecules* **2002**, *35* (5), 1860−1869.

(10) Louis, A. A.; Bolhuis, P. G.; Hansen, J. P.; Meijer, E. J. *Phys. Rev. Lett.* **2000**, *85* (12), 2522.
(11) Bolhuis, P. G.; Louis, A. A.; Hansen, J. P.; Meijer, E. J. *Accurate effective pair potentials for polymer solutions*; AIP: Melville, NY, 2001; Vol. *114*, pp 4296−4311.
(12) de Gennes, P.-G. *Scaling Concpets in Polymer Physics*; Cornell University Press: Ithaca, NY, 1979.
(13) Rudhardt, D.; Bechinger, C.; Leiderer, P. *Phys. Rev. Lett.* **1998**, *81* (6), 1330−1333.
(14) Bechinger, C.; Rudhardt, D.; Leiderer, P.; Roth, R.; Dietrich, S. *Phys. Rev. Lett.* **1999**, *83* (19), 3960−3963.
(15) Kleshchanok, D.; Tuinier, R.; Lang, P. R. *Langmuir* **2006**, *22* (22), 9121−9128.
(16) Verma, R.; Crocker, J. C.; Lubensky, T. C.; Yodh, A. G. *Macromolecules* **2000**, *33* (1), 177−186.
(17) Dijkstra, M.; van Roij, R.; Evans, R. *Phys. Rev. E* **1999**, *59* (5), 5744.
(18) Yodh, A. G.; Lin, K.-H.; Crocker, J. C.; Dinsmore, A. D.; Verma, R.; Kaplan, P. D. *Phil. Trans. R. Soc. Lond. A* **2001**, *359*, 921−937.
(19) Fleer, G. J.; Tuinier, R. *Adv. Colloid Interface Sci.* **2008**, *143* (1−2), 1−47.
(20) Lin, K.-H.; Crocker, J. C.; Prasad, V.; Schofield, A.; Weitz, D. A.; Lubensky, T. C.; Yodh, A. G. *Phys. Rev. Lett.* **2000**, *85* (8), 1770−1773.
(21) Fernandes, G. E.; Beltran-Villegas, D. J.; Bevan, M. A. *Langmuir* **2008**, *24*, 10776−10785.
(22) Fernandes, G. E.; Beltran-Villegas, D. J.; Bevan, M. A. *J. Chem. Phys.* **2009**, *131*, 134705.
(23) Iracki, T. D.; Beltran-Villegas, D. J.; Eichmann, S. L.; Bevan, M. A. *Langmuir* **2010**, *26*, 18710−18717.
(24) Schafer, L. *Excluded Volume Effects in Polymer Solutions*; Springer Verlag: Berlin, 1999.
(25) de Gennes, P. G. *Macromolecules* **1980**, *13* (5), 1069−1075.
(26) Vincent, B.; Luckham, P. F.; Waite, F. A. *J. Colloid Interface Sci.* **1980**, *73* (2), 508−521.
(27) Israelachvili, J. N. *Intermolecular and Surface Forces*, 2nd ed.; Academic Press: New York, 1992; p 450.
(28) Russel, W. B.; Saville, D. A.; Schowalter, W. R. *Colloidal Dispersions*; Cambridge University Press: New York, 1989.
(29) Bike, S. G.; Prieve, D. C. *Int. J. Multiphase Flow* **1990**, *16* (4), 727−740.
(30) Dzyaloshinskii, I. E.; Lifshitz, E. M.; Pitaevskii, L. P. *Adv. Phys.* **1961**, *10*, 165−209.
(31) Prieve, D. C.; Russel, W. B. *J. Colloid Interface Sci.* **1988**, *125*, 1.
(32) Bevan, M. A.; Prieve, D. C. *Langmuir* **1999**, *15* (23), 7925−7936.
(33) Wu, H.-J.; Everett, W. N.; Anekal, S. G.; Bevan, M. A. *Langmuir* **2006**, *22*, 6826−6836.
(34) Milner, T.; Witten, T. A.; Cates, M. E. *Macromolecules* **1988**, *21* (8), 2610−2619.
(35) Milner, S. T. *Europhys. Lett.* **1988**, *7* (8), 695−699.
(36) Fleer, G. J.; Skvortsov, A. M.; Tuinier, R. *Macromolecules* **2003**, *36* (20), 7857−7872.
(37) Eisenriegler, E. *Dilute and semidilute polymer solutions near an adsorbing wall*. AIP: Melville, NY, 1983; Vol. *79*, p 1052−1064.
(38) Hanke, A.; Eisenriegler, E.; Dietrich, S. *Phys. Rev. E* **1999**, *59* (6), 6853.
(39) Vrij, A. *Pure Appl. Chem.* **1976**, *48*, 471−483.
(40) Sharma, A.; Walz, J. Y. *J. Chem. Soc., Faraday Trans.* **1996**, *92* (24), 4997−5004.
(41) van Helden, A. K.; Jansen, J. W.; Vrij, A. *J. Colloid Interface Sci.* **1981**, *81* (2), 354−368.
(42) Baker, J. A.; Berg, J. C. *Langmuir* **1988**, *4*, 1055−1061.
(43) Wu, H. J.; Bevan, M. A. *Langmuir* **2005**, *21* (4), 1244−1254.
(44) Wu, H.-J.; Pangburn, T. O.; Beckham, R. E.; Bevan, M. A. *Langmuir* **2005**, *21* (22), 9879−9888.
(45) Eichmann, S. L.; Bevan, M. A. *Langmuir* **2010**, *26*, 14409−14413.
(46) Pangburn, T. O.; Bevan, M. A. *J. Chem. Phys.* **2005**, *123*, 174904.
(47) Pangburn, T. O.; Bevan, M. A. *J. Chem. Phys.* **2006**, *124*, 054712.
(48) Juarez, J. J.; Feicht, S.; Bevan, M. A. *Soft Matter* **2011**, in press.
(49) Beltran-Villegas, D. J.; Sehgal, R. M.; Maroudas, D.; Ford, D. M.; Bevan, M. A. *J. Chem. Phys.* **2011**, in press.
(50) Wu, H.; Shah, S.; Beckham, R. E.; Meissner, K.; Bevan, M. A. *Langmuir* **2008**, *24*, 13790−13795.
(51) Bevan, M. A.; Prieve, D. C. *Langmuir* **2000**, *16* (24), 9274−9281.
(52) Everett, W. N.; Wu, H.-J.; Anekal, S. G.; Sue, H.-J.; Bevan, M. A. *Biophys. J.* **2007**, *92*, 1005−1013.
(53) Biver, C.; Hariharan, R.; Mays, J.; Russel, W. B. *Macromolecules* **1997**, *30* (6), 1787−1792.
(54) Devanand, K.; Selser, J. C. *Macromolecules* **1991**, *24* (22), 5943−5947.
(55) Suresh, L.; Walz, J. Y. *J. Colloid. Interfac. Sci* **1996**, *193*, 199−213.
(56) Regnaut, C.; Ravey, J. C. *J. Chem. Phys.* **1989**, *91* (2), 1211−1221.
(57) Stell, G. *J. Stat. Phys.* **1991**, *63*, 1203−1221.
(58) Henderson, J. R. *Phys. A: Stat. Mech. Its Appl.* **2002**, *313* (3−4), 321−335.
(59) Stober, W.; Fink, A.; Bohn, E. *J. Colloid Interface Sci.* **1968**, *26*, 62−69.

Macromolecules

Note

pubs.acs.org/Macromolecules

Stereocomplexation in Cyclic and Linear Polylactide Blends

Eun Ji Shin, Alexandra E. Jones, and Robert M. Waymouth*

Department of Chemistry, Stanford University, Stanford, California 94305, United States

Supporting Information

INTRODUCTION

Cyclic polymers differ from linear polymers by one bond linking the chain ends, yet the simple topological constraint[1] of linking the ends of a linear chain influences macromolecular properties in ways that remain poorly understood.[2−6] A cyclic topology might be expected to influence crystallization; several studies have recently compared the crystallization of cyclic and linear chains.[7−15] Previous studies indicate that high molecular weight cyclic polymers crystallize into lamellar morphologies with similar lamellar dimensions as their linear isomers;[7,12] for smaller cyclic chains, the lamellar thickness is constrained by the chain length.[12,16,17] We have recently reported the synthesis of cyclic crystalline polylactides (PLAs)[18] by zwitterionic ring-opening polymerization of lactones.[7,18−22] As polylactides are known to form stereocomplexes,[23−26] we sought to investigate whether the combination of topological constraints and geometric constraints associated with the formation of stereocomplexes[27−29] might influence the ability of cyclic polylactides to crystallize into stable stereocomplexes.[30]

Stereocomplexation between enantiomeric blends of linear poly(L-lactide) and poly(D-lactide)[31,32] is proposed to be driven by weak $CH_3\cdots O{=}C$ hydrogen bond interactions between enantiomeric helical chains of L- and D-polylactide.[27,33] The orientation of the PLLA and PDLA chains, either parallel or antiparallel, in the stereocomplex[27,28,34,35] provides a constraint on crystallization. Stereocomplexation is a comparatively short-range interaction−self-assembly on the order of several helix turns. Crystallization provides an additional constraint to the polymer chain at a slightly larger length scale—the dimension of a lamellar crystal. The topology (cyclic vs linear) is a structural constraint on the length scale of the molecular dimension (typically, but not always, larger than a lamellar dimension). Thus, for cyclic polymers to form crystalline stereocomplexes, several conformational constraints must be simultaneously accommodated; in this report we address whether cyclic chains are impeded from adopting the appropriate conformational orientations to crystallize into stereocomplexes.

RESULTS AND DISCUSSION

Linear and cyclic polylactides were synthesized by the N-heterocyclic carbene mediated ring-opening polymerization of either L- or D-lactide.[18,20] Both L- and D-lactide were polymerized ($[M]_0$ = 0.6 M) using the N-heterocyclic carbene, 1,3-dimesitylimidazol-2-ylidene (IMes, $[I]_0$ = 0.006 M), in tetrahydrofuran (THF) for 30 s to give cyclic poly(L-lactide) (PLLA) and poly(D-lactide), respectively (Scheme 1). Linear poly(lactide)s were prepared by polymerizing L- or D-lactide ($[M]_0$ = 0.6 M) using benzyl alcohol as the initiator ($[I]_0$ = 0.003 M) and IMes as the catalyst (I/C = 2) in THF for 30 s.[36] The characteristics of the four polymer samples are shown in Table 1.

Scheme 1. Polymerization of Lactide Using IMes

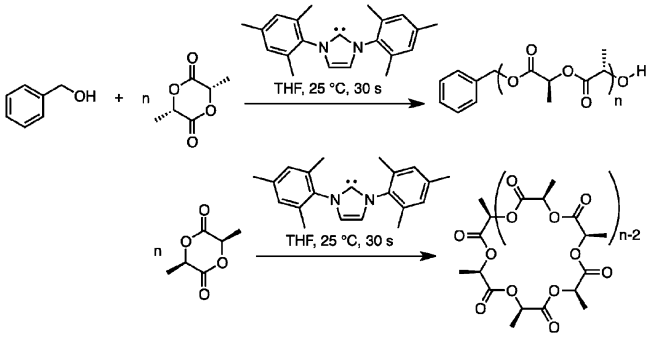

The topology of the cyclic PLAs was established by comparing the intrinsic viscosities with the corresponding linear polymers (see Supporting Information). The ratio of the intrinsic viscosities, $[\eta]_{cyclic}/[\eta]_{linear}$, from the Mark−Houwink plots are ∼0.74 over the molecular weight range shown, similar to that predicted theoretically[2] and observed experimentally for similar samples.[18] The lower intrinsic viscosities are consistent with a cyclic topology but do not rule out the presence of small amounts of linear contaminants.

The melting temperatures and optical rotations of the polylactides are lower than those reported in the literature for highly isotactic polylactides.[37] Polylactides prepared under these conditions are not perfectly isotactic, as shown by the homonuclear decoupled ^{1}H NMR spectra (see Supporting Information).[38] In addition to resonances associated with the iii tetrad, iiiss hexads are evident, implicating competitive epimerization of stereogenic centers by the carbene, as previously reported.[18,39]

Blends of various combinations of the PLAs in Table 1 were prepared (Table 2) by solvent casting from dicholoromethane.[40] For the DSC studies, PLLA/PDLA blends were melted at 220 °C for 15 min, cooled to 150 °C, and annealed for 24 h. The cyclic and linear PLLA samples were annealed at 90 °C for 24 h. All samples were then analyzed by differential scanning calorimetry (DSC), wide-angle X-ray scattering (WAXS), and small-angle X-ray scattering (SAXS).

As shown in Figure 1 and Table 2, both the linear and cyclic PLLA/PDLA blends exhibit melting temperatures ∼50 °C

Received: July 18, 2011
Revised: December 6, 2011
Published: December 15, 2011

Table 1. Characterization of Polylactides Used in This Study

entry	polymer type	conv[a] (%)	M_n[b] (kg/mol)	PDI[c]	f_{iii}[d]	$[\alpha]_D$[e]	T_m[f] (°C)	ΔH_m[g] (J/g)
1	linear PLLA	58	15	1.1	0.87	−131	150	36
2	linear PDLA	52	19	1.1	0.90	+134	157	48
3	cyclic PLLA	91	30	1.3	0.83	−110	135	18
4	cyclic PDLA	90	26	1.4	0.81	+101	132	48

[a]Percent conversion; determined by ^{1}H NMR spectroscopy. [b]Number-average molecular weight; determined by gel permeation chromatography (GPC) calibrated with polystyrene standards. [c]Polydispersity = M_w/M_n; determined by GPC calibrated with polystyrene standards. [d]Fraction of isotactic (iii) tetrads. [e]Optical rotation; measured in chloroform with c = 0.9. [f]Melting temperature; measured using differential scanning calorimetry (DSC). [g]Heat of melting; measured using DSC.

Table 2. Blends of Polylactides Used for This Study

entry	PLLA	PDLA	T_m (°C)	ΔH_m (J/g)
B1	linear	linear	189	52
B2	linear	cyclic	178	20
B3	cyclic	linear	185	42
B4	cyclic	cyclic	179	15

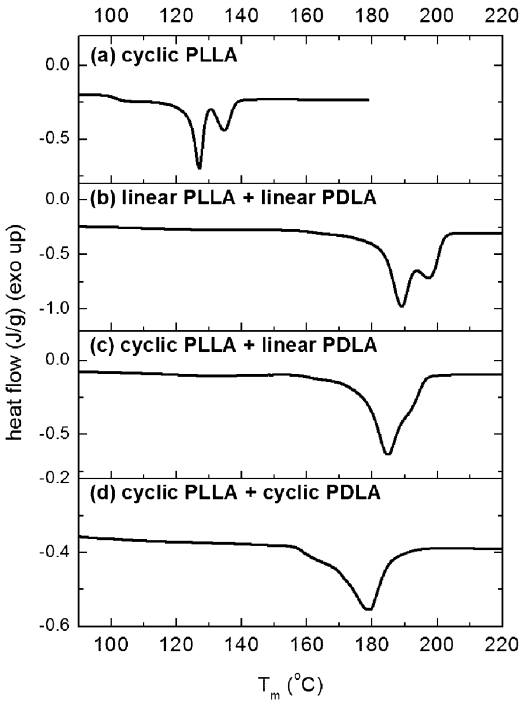

Figure 1. Differential scanning calorimetry scans of (a) cyclic PLLA, (b) linear PLLA + linear PDLA, (c) cyclic PLLA + linear PDLA, and (d) cyclic PLLA + cyclic PDLA.

higher than the PLLA or PDLA homopolymers, indicative of the formation of stereocomplexes. The melting temperatures of the blends (178−189 °C) are lower than that reported for highly isotactic PLLA/PDLA stereocomplexes;[41−45] this is likely due to the lower isotacticities of the PLLA and PDLA samples prepared with the carbenes.[18] The heats of melting for blends involving cyclic polymers (entries B2, B3, and B4) are also lower than that of the linear PLLA/linear PDLA blend B1, but this is also likely a consequence of the slightly lower isotacticity of the cyclic PLAs relative to the linear PLAs.[41,42]

Analysis of the linear and cyclic PLLA/PDLA blends by wide-angle X-ray scattering provides further evidence for the formation of PLLA/PDLA stereocomplexes. The WAXS profiles of the blends B1, B3, and B4 exhibit peaks at 2θ = 12°, 21°, and 24° characteristic of that of PLLA/PDLA stereocomplexes, whereas that of the cyclic PLLA shows peaks characteristic of those of linear PLLA.[31] These data unambiguously show that constraining polylactides into a cyclic topology does not impede their ability to form stereocomplexes.

For the scattering patterns in Figure 2a, the samples were cooled from the melt (220 °C) at 5 deg/min to T_a = 150 °C, annealed at T_a for 24 h to allow stereocomplex formation, and then taken off the heater to cool to room temperature for the measurement (Figure 2a). The effect of thermal history[27,46,47] is shown in Figure 2b; for samples that were not annealed, but simply cooled from the melt to room temperature, only the linear PLLA/PDLA blends showed evidence of stereocomplexation. While it is possible that the topology of the cyclic PLAs influences the rate at which they crystallize into stereocomplexes, it is more likely that this behavior is a consequence of the lower molecular weights and slightly higher tacticities of the linear PLLA and PDLA samples.

Small-angle X-ray scattering was carried out to estimate the lamellar thickness (L_c) and long period spacing (L_p)[48,49] of linear and cyclic PLLA and the linear and cyclic stereocomplexed blends. The lamellar thicknesses (L_c) and long periods (L_p) were estimated from the one-dimensional electron density autocorrelation function with the assumption of a lamellar two-phase morphology (see Supporting Information) and are shown in Table 3. The lamellar thickness and long period of the linear PLLA (8 and 16 nm, respectively) are smaller than those reported previously (L_c ∼ 16 nm and L_p ∼ 22 nm) for higher molecular weight highly isotactic linear PLLAs[50,51] but comparable to PLLA copolymers containing between 6 and 12% meso-lactide.[52]

Notably, the lamellar thickness and long period of cyclic PLLA are ∼20% larger than those of linear PLLA. The long period (20 nm) is on the order of the extended chain length of this cyclic PLLA sample (if a 10_3 helix[53] is assumed, then from the degree of polymerization a length of ∼37 nm can be estimated for an extended cyclic PLLA), implicating the lack of multiple chain-folding for the cyclic PLLA chains. The larger lamellar thickness and long period of the cyclic PLLA may be a consequence of a topological constraint on lamellar folding,[12,50,52,54] but further studies are necessary to test the generality of this observation. In previous studies of high molecular weight cyclic and linear poly(ε-caprolactone)s, we observed no differences in lamellar or long period spacings between the cyclic and linear polyesters, but in the latter case the chain lengths were considerably longer than the lamellar thickness (∼700 nm extended chain length, L_c ∼ 9 nm).[7]

The lamellar thickness and long period of the cyclic PLLA/PDLA blends are similar to those of the linear PLLA/PDLA blends (Table 3). Since stereocomplexation requires adjacent PLLA and PDLA helices, it is noteworthy that the chains are

dx.doi.org/10.1021/ma202184j | Macromolecules 2012, 45, 595−598

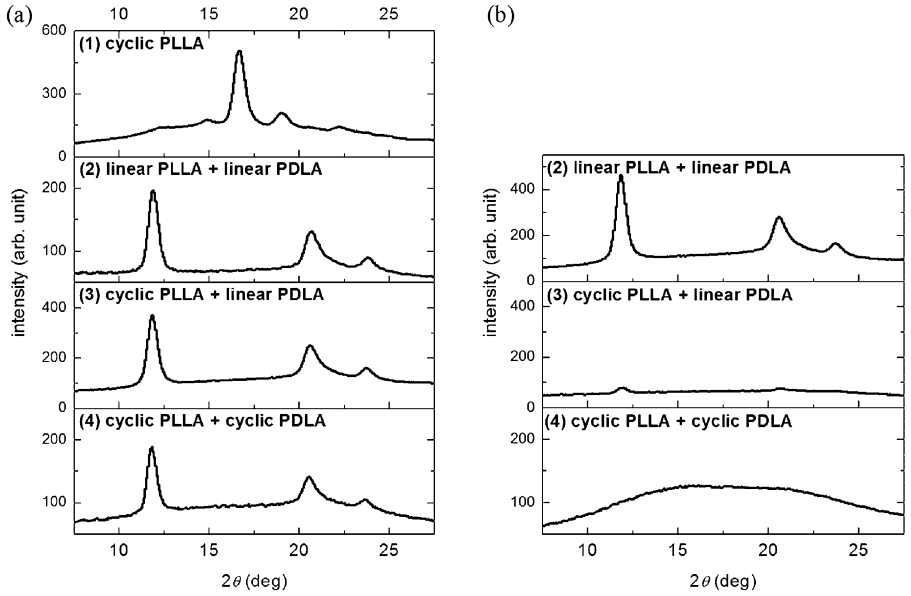

Figure 2. Wide-angle X-ray scattering patterns after (a) annealing at 150 °C (90 °C for cyclic PLLA) for 24 h and (b) cooling from the melt to room temperature.

Table 3. Lamellar Thickness (L_c) and Long Period (L_p)

composition	lamellar thickness (nm)	long period (nm)
linear PLLA	8	16
cyclic PLLA	10	20
linear PLLA + linear PDLA	7	14
cyclic PLLA + linear PDLA	8	16
cyclic PLLA + cyclic PDLA	8	15

able to arrange themselves to satisfy the dual constraints of stereocomplexation and a cyclic topology.

The lamellar morphology of the cyclic and linear PLLA/PDLA blends were similar to that of the linear PLLA samples when samples were annealed at similar undercoolings ΔT ($\Delta T = T_m - T_a$, for T_m is the measured melting temperature and T_a the annealing temperature). There have been only a few reports on the SAXS analysis of the PLA stereocomplexes.[29,55,56] In Tsuji's report,[55] the estimated long period of the stereocomplex that was precipitated from acetonitrile solution at 80 °C and annealed at 216 °C was 12 nm, smaller than that reported for PLLA homopolymer films crystallized from the melt (22−35 nm). It was noted that this difference in lamellar thickness and long period could be partly due to the different thermal history.[25]

SUMMARY

The zwitterionic polymerization of L- and D-lactide with N-heterocyclic carbenes provides a series of crystalline linear and cyclic polylactides. Wide-angle and small-angle X-ray scattering indicate that both linear and cyclic isotactic polylactides crystallize with similar local structures and lamellar spacings as their linear topological isomers, although cyclic PLLAs exhibit slightly larger lamellar thickenesses than the corresponding linear PLLAs. Both linear and cyclic blends of PLLA and PDLA form stereocomplexes from the melt; the geometric constraints required from stereocomplexation[27−29] do not appear to be compromised by constraining the polylactides into a cyclic chain.

ASSOCIATED CONTENT

Supporting Information

Experimental procedures. This material is available free of charge via the Internet at http://pubs.acs.org.

AUTHOR INFORMATION

Corresponding Author

*E-mail: waymouth@stanford.edu.

ACKNOWLEDGMENTS

We gratefully acknowledge support from the NSF (NSF-DMR-1001903; NSF-GOALI-CHE-0957386) A.J. was supported by a summer undergraduate research fellowship (CPIMA: NSF-DMR-0213618), and E.S. is grateful for the Samsung Scholarship from the Samsung Foundation of Culture. We thank Purac for a generous donation of lactide. We thank Dr. Jihoon Kang and Professor Do Y. Yoon (Seoul National University, Korea) for the WAXS experiments. Portions of this research were carried out at the Stanford Synchrotron Radiation Lightsource, a Directorate of SLAC National Accelerator Laboratory and an Office of Science User Facility operated for the U.S. Department of Energy Office of Science by Stanford University. We thank Dr. John Pople of SSRL for assistance with the scattering measurements.

REFERENCES

(1) Yamamoto, T.; Tezuka, Y. *Polym. Chem.* **2011**, *2*, 1930−1941.
(2) Roovers, J. In *Cyclic Polymers*, 2nd ed.; Semlyen, J. A., Ed.; Kluwer Academic Publishers: Dordrecht, 2000; pp 347−384.
(3) McKenna, G. B.; Hostetter, B. J.; Hadjichristidis, N.; Fetters, L. J.; Plazek, D. J. *Macromolecules* **1989**, *22*, 1834−1852.
(4) Kapnistos, M.; Lang, M.; Vlassopoulos, D.; Pyckhout-Hintzen, W.; Richter, D.; Cho, D.; Chang, T.; Rubinstein, M. *Nature Mater.* **2008**, *7*, 997−1002.
(5) Laurent, B. A.; Grayson, S. M. *Chem. Soc. Rev.* **2009**, *38*, 2202−2213.
(6) Kricheldorf, H. R. *J. Polym. Sci., Part A: Polym. Chem.* **2010**, *48*, 251−284.
(7) Shin, E. J.; Jeong, W.; Brown, H. A.; Koo, B. J.; Hedrick, J. L.; Waymouth, R. M. *Macromolecules* **2011**, *44*, 2773−2779.

(8) Schaler, K.; Ostas, E.; Schroter, K.; Thurn-Albrecht, T.; Binder, W. H.; Saalwachter, K. *Macromolecules* **2011**, *44*, 2743−2754.
(9) Cordova, M. E.; Lorenzo, A. T.; Muller, A. J.; Hoskins, J. N.; Grayson, S. M. *Macromolecules* **2011**, *44*, 1742−1746.
(10) Bielawski, C. W.; Benitez, D.; Grubbs, R. H. *Science* **2002**, *297*, 2041−2044.
(11) Tezuka, Y.; Ohtsuka, T.; Adachi, K.; Komiya, R.; Ohno, N.; Okui, N. *Macromol. Rapid Commun.* **2008**, *29*, 1237−1241.
(12) Cooke, J.; Viras, K.; Yu, G. E.; Sun, T.; Yonemitsu, T.; Ryan, A. J.; Price, C.; Booth, C. *Macromolecules* **1998**, *31*, 3030−3039.
(13) Brunelle, D. J.; Bradt, J. E.; Serth-Guzzo, J.; Takekoshi, T.; Evans, T. L.; Pearce, E. J.; Wilson, P. R. *Macromolecules* **1998**, *31*, 4782−4790.
(14) Brunelle, D. J.; Krabbenhoft, H. O.; Bonauto, D. K. *Macromol. Symp.* **1994**, *77*, 117−124.
(15) Brunelle, D. J. In *Cyclic Polymers*, 2nd ed.; Semlyen, J. A., Ed.; Kluwer Academic Publishers: Dordrecht, 2000; pp 185−228.
(16) Yang, Z.; Cooke, J.; Viras, K.; Gorry, P. A.; Ryan, A. J.; Booth, C. *J. Chem. Soc., Faraday Trans.* **1997**, *93*, 4033−4039.
(17) Yu, G. E.; Sun, T.; Yan, Z. G.; Price, C.; Booth, C.; Cook, J.; Ryan, A. J.; Viras, K. *Polymer* **1997**, *38*, 35−42.
(18) Culkin, D. A.; Jeong, W.; Csihony, S.; Gomez, E. D.; Balsara, N. P.; Hedrick, J. L.; Waymouth, R. M. *Angew. Chem., Int. Ed.* **2007**, *46*, 2627−2630.
(19) Jeong, W.; Hedrick, J. L.; Waymouth, R. M. *J. Am. Chem. Soc.* **2007**, *129*, 8414−8415.
(20) Jeong, W.; Shin, E. J.; Culkin, D. A.; Hedrick, J. L.; Waymouth, R. M. *J. Am. Chem. Soc.* **2009**, *131*, 4884−4891.
(21) Shin, E. J.; Brown, H. A.; Gonzalez, S.; Jeong, W.; Hedrick, J. L.; Waymouth, R. M. *Angew. Chem., Int. Ed.* **2011**, *50*, 6388−6391.
(22) Guo, L.; Zhang, D. *J. Am. Chem. Soc.* **2009**, *131*, 18072−18074.
(23) Fukushima, K.; Kimura, Y. *Polym. Int.* **2006**, *55*, 626−642.
(24) Kakuta, M.; Hirata, M.; Kimura, Y. *Polym. Rev.* **2009**, *49*, 107−140.
(25) Tsuji, H. *Macromol. Biosci.* **2005**, *5*, 569−597.
(26) Anderson, K. S.; Hillmyer, M. A. *Polymer* **2006**, *47*, 2030−2035.
(27) Sarasua, J.-R.; Rodriguez, N. L.; Arraiza, A. L.; Meaurio, E. *Macromoelcules* **2005**, *38*, 8362−8371.
(28) Cartier, L.; Okihara, T.; Lotz, B. *Macromolecules* **1997**, *30*, 6313−6322.
(29) Li, L.; Zhong, Z.; de Jeu, W. H.; Dijkstra, P. J.; Feijen, J. *Macromolecules* **2004**, *37*, 8641−8646.
(30) Jones, A. E.; Shin, E. J.; Waymouth, R. M. *Polym. Prepr.* **2008**, *49*, 1149−1150.
(31) Ikada, Y.; Jamshidi, K.; Tsuji, H.; Hyon, S.-H. *Macromolecules* **1987**, *20*, 904−906.
(32) L-Lactide refers to (*S*,*S*)-lactide or (3*S*,6*S*)-3,6-dimethyl-1,4-dioxane-2,5-dione, and D-lactide refers to (*R*,*R*)-lactide or (3*R*,6*R*)-3,6-dimethyl-1,4-dioxane-2,5-dione.
(33) Polylactide stereocomplexes exhibit higher melting temperatures and different mechanical and physical properties than the enantiomeric homopolymers.
(34) Okihara, T.; Tsuji, M.; Kawaguchi, A.; Katayama, K.; Tsuji, H.; Hyon, S. H.; Ikada, Y. *J. Macromol. Sci., Phys.* **1991**, *B30*, 119−140.
(35) Brizzolara, D.; Cantow, H. J.; Diederichs, K.; Keller, E.; Domb, A. J. *Macromolecules* **1996**, *29*, 191−197.
(36) Nyce, G. W.; Glauser, T.; Connor, E. F.; Mock, A.; Waymouth, R. M.; Hedrick, J. L. *J. Am. Chem. Soc.* **2003**, *125*, 3046−3056.
(37) Chabot, F.; Vert, M.; Chapelle, S.; Granger, P. *Polymer* **1983**, *24*, 53−59.
(38) Thakur, K. A. M.; Kean, R. T.; Hall, E. S.; Kolstad, J. J.; Lindgren, T. A.; Doscotch, M. A.; Siepmann, J. I.; Munson, E. J. *Macromolecules* **1997**, *30*, 2422−2428.
(39) Csihony, S.; Nyce, G. W.; Sentman, A. C.; Waymouth, R. M.; Hedrick, J. L. *Polym. Prepr.* **2004**, *45*, 319−320.
(40) Tsuji, H.; Hyon, S. H.; Ikada, Y. *Macromolecules* **1991**, *24*, 5651−5656.
(41) Tsuji, H.; Ikada, Y. *Macromolecules* **1992**, *25*, 5719−5723.
(42) Brochu, S.; Prudhomme, R. E.; Barakat, I.; Jerome, R. *Macromolecules* **1995**, *28*, 5230−5239.
(43) Double melting temperatures are common to many polymers, including poly(lactide); see refs 44 and 45.
(44) Sarasua, J.-R.; Prud'homme, R. E.; Wisniewski, M.; Le Borgne, A.; Spassky, N. *Macromolecules* **1998**, *31*, 3895−3905.
(45) Ohtani, Y.; Okumura, K.; Kawaguchi, A. *J. Macromol. Sci., Phys.* **2003**, *42*, 875.
(46) Wang, X. H.; Prud'homme, R. E. *Macromol. Chem. Phys.* **2011**, *212*, 691−698.
(47) Zhang, J. M.; Tashiro, K.; Tsuji, H.; Domb, A. J. *Macromolecules* **2007**, *40*, 1049−1054.
(48) Schmidtke, J.; Strobl, G.; ThurnAlbrecht, T. *Macromolecules* **1997**, *30*, 5804−5821.
(49) Strobl, G. *The Physics of Polymers: Concepts for Understanding Their Structures and Behavior*, 3rd ed.; Springer: Berlin, 2007.
(50) Baratian, S.; Hall, E. S.; Lin, J. S.; Xu, R.; Runt, J. *Macromolecules* **2001**, *34*, 4857−4864.
(51) Cho, T. Y.; Strobl, G. *Polymer* **2006**, *47*, 1036−1043.
(52) Huang, J.; Lisowski, M. S.; Runt, J.; Hall, E. S.; Kean, R. T.; Buehler, N.; Lin, J. S. *Macromolecules* **1998**, *31*, 2593−2599.
(53) Sasaki, S.; Asakura, T. *Macromolecules* **2003**, *36*, 8385−8390.
(54) The slightly lower tacticity of the cyclic PLLA (vs linear PLLA) would have been expected to yield a smaller lamellar thickness (ref 50).
(55) Tsuji, H.; Horii, F.; Nakagawa, M.; Ikada, Y.; Odani, H.; Kitamaru, R. *Macromolecules* **1992**, *25*, 4114−4118.
(56) Fujita, M.; Sawayanagi, T.; Abe, H.; Tanaka, T.; Iwata, T.; Ito, K.; Fujisawa, T.; Maeda, M. *Macromolecules* **2008**, *41*, 2852−2858.

Macromolecules

Note

pubs.acs.org/Macromolecules

Nanoporous Poly(3,4-ethylenedioxythiophene) Derived from Polymeric Bicontinuous Microemulsion Templates

Brad H. Jones,[†] Kai-Yuan Cheng,[†] Russell J. Holmes,[†] and Timothy P. Lodge*[,†,‡]

[†]Department of Chemical Engineering and Materials Science and [‡]Department of Chemistry, University of Minnesota, Minneapolis, Minnesota 55455, United States

Supporting Information

Since its discovery over two decades ago,[1,2] poly(3,4-ethylenedioxythiophene) (PEDOT) has seen substantial commercial success. The exceptionally high conductivity of PEDOT (under specific synthetic conditions, up to ~1000 S/cm[3,4]), along with its chemical and thermal stability and unique electrochemical and spectroscopic properties, has allowed for its use in a wide variety of applications, including antistatic coatings, capacitors, thin-film transistors, and electroluminescent and photovoltaic devices.[5−12] In general, porous materials with good stability, inherently high conductivity, and large internal surface area are useful in sensor, battery, capacitor, and storage technology.[13] Therefore, strong motivation exists to develop PEDOT materials possessing controlled porosity. Indeed, a high-surface-area PEDOT electrode has been demonstrated as an effective O_2 reduction catalyst that can be applied in fuel cells and batteries.[14] In addition, macroporous[15] PEDOT films have been used as counter electrodes in dye-sensitized solar cells.[16]

In recent years, several different strategies have been employed to synthesize porous PEDOT. Films prepared by electrodeposition in conventional media exhibit morphologies which evolve from a dense, compact structure to a highly porous one as the thickness, i.e., deposition time, is increased.[17,18] Similarly, ionic liquids are effective media for the electrodeposition of PEDOT, resulting in macroporous films with a three-dimensionally continuous pore network.[16] Ionic liquid-based electropolymerization of EDOT within colloidal crystal templates has been further used to generate macroporous PEDOT possessing ordered spherical cavities.[19] Finally, variations of porous PEDOT have been synthesized by electrodeposition with different dopants, such as poly(acrylic acid), and by electropolymerization within alginate hydrogels.[20] Alternatively, porous PEDOT has been synthesized by oxidative chemical polymerization routes. A chemical vapor deposition technique with copper(II) chloride as oxidant has been used to synthesize bicontinuous films with tunable total porosity and pore sizes ranging from 50 to 150 nm.[21] The aqueous solution polymerization of EDOT with ferric nitrate and ammonium persulfate as oxidants has been used to create PEDOT hydrogels and aqueous dispersions, which subsequently yield a rich variety of macroporous structures upon freeze-drying.[22]

We have developed a nanocasting procedure, employing polymeric bicontinuous microemulsions as templates, suitable for the production of a diverse spectrum of nanoporous monolithic materials having three-dimensionally continuous, ~100 nm pores.[23−26] Polymeric bicontinuous microemulsions (BμE) are equilibrium structured liquid phases found in well-designed ternary blends of incompatible homopolymers and their corresponding diblock copolymer.[27,28] In BμE-forming blends of polyethylene (PE), poly(ethylene-*alt*-propylene) (PEP), and poly(ethylene-*b*-ethylene-*alt*-propylene) (PE−PEP), a nanoporous material is conveniently obtained by crystallization of PE and extraction of the PEP homopolymer with a selective solvent. Subsequent infiltration and reaction of appropriate precursors within the pores of this material, followed further by its removal through selective chemical or thermal means, can be used to generate nanoporous ceramics[23] and thermosets[24] as well as hierarchically structured materials[25,26] having BμE-like arrangements of pores.

Here, we show that this approach can be used to generate nanoporous PEDOT monoliths with similar pore characteristics. A nanoporous PE monolith is first derived from a blend containing 42.5% PE (M_n = 23 kg/mol, M_w/M_n = 1.05), 42.5% PEP (M_n = 23 kg/mol, M_w/M_n = 1.02), and 15% PE−PEP (M_n = 101 kg/mol, M_w/M_n = 1.07) by volume, as described previously.[23,24] Then, the oxidative polymerization of EDOT initiated by iron(III) tris-*p*-toluenesulfonate ($Fe(OTs)_3$) is conducted within the PE pore system. A PE monolith is added to a large excess of EDOT, inducing spontaneous infiltration through capillary action. Based on the weight of EDOT imbibed, a solution of 72 wt % $Fe(OTs)_3$ in isopropanol is prepared at 80 °C, having an absolute amount of $Fe(OTs)_3$ corresponding to a $Fe(OTs)_3$:EDOT molar ratio of 2:1. While at 80 °C, the EDOT-filled monolith is added to this solution, causing it to rapidly turn black. After several hours, the monolith is removed, washed with excess isopropanol, and dried under vacuum.

A scanning electron microscopy (SEM) image of the PE/PEDOT composite material that results from this synthetic procedure is shown in Figure 1a. Clearly, the PE template imposes a BμE-like arrangement of disordered, tortuous PE and PEDOT domains with periodicity on the order of 100 nm. The backscattered electrons used to generate the image yield primarily atomic number contrast;[29] the PEDOT domains appear bright due to the incorporation of $Fe(OTs)_3$, which oxidizes and dopes the polymerized PEDOT chains. The conductivity σ of several PE/PEDOT monoliths prepared in this manner was evaluated by the van der Pauw method,[30] of which further details are given in the Supporting Information.

Received: October 5, 2011
Revised: November 19, 2011
Published: December 6, 2011

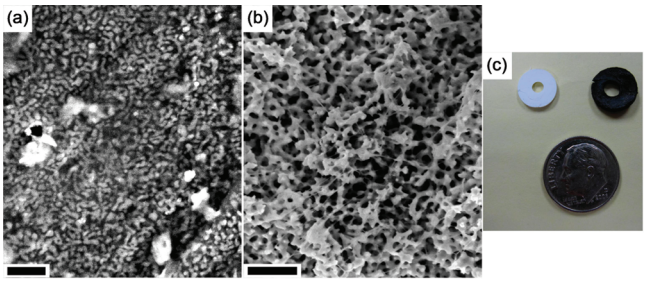

Figure 1. (a) SEM image of fracture surface of BμE-like PE/PEDOT composite monolith formed by polymerization of EDOT within BμE-derived nanoporous PE monolith. The image was generated using a backscattered electron detector. (b) SEM image of fracture surface of BμE-like nanoporous PEDOT monolith formed by subsequent extraction of PE template with hot toluene. The image was generated using a secondary electron detector. Both scale bars indicate 1 μm. (c) Typical nanoporous PE template (left) and nanoporous PEDOT product monoliths (right). The particular PE template shown and the PE template used to prepare the PEDOT product shown possessed identical outer diameters, but differently sized central holes.

The mean value of σ was determined to be 5.4×10^{-4} S/cm. This value is significantly lower than that typically reported for the solution synthesis of PEDOT initiated and doped by iron(III) salts;[31] however, when considering that the monoliths are composed of a majority of highly insulating PE, the measurement of substantial conducting character indicates that electrical transport through the material is dominated by the PEDOT component. This phenomenon can be attributed to the three-dimensionally continuous nature of the PEDOT domains, imposed by the structure of the BμE-derived template. Indeed, the impedance spectrum of PE/PEDOT monoliths shows values far more representative of bulk PEDOT than bulk PE (Supporting Information, Figure S2). After further soaking the monoliths in 5 M aqueous HCl solution—in an attempt to improve the doping level of the PEDOT component—no appreciable increase in conductivity was observed. Therefore, we believe that the comparatively low conductivity of this material is the result of the extremely rapid polymerization kinetics that were employed. Previous research has shown that attenuation of the rate of EDOT polymerization, for example through the addition of compounds that reduce the reactivity of the oxidant, leads to higher molecular weight chains with larger orbital delocalization along the chain backbone, thus enhancing the conductivity of PEDOT.[4]

The high rate of polymerization of EDOT within the PE pore system limits diffusion of isopropanol solvent into the monolith and confers mechanical stability to the resultant PEDOT domains. Figure 1b shows an SEM image of the nanoporous material that results after extraction of the PE template from the PE/PEDOT composite by dissolution in toluene at 72 °C. The BμE-like structure of the starting template is imprinted into the self-supporting PEDOT monolith in the form of a three-dimensionally continuous pore network. As seen in Figure 1c, the nanoporous PEDOT monolith retains dimensional integrity, relative to its PE precursor. In contrast, when a concentrated solution of EDOT, $Fe(OTs)_3$, and imidazole (a typical base used to attenuate polymerization kinetics) in isopropanol is infiltrated into nanoporous PE and the EDOT polymerized, subsequent extraction of the PE template causes the monolith to macroscopically disintegrate. Thus, the particular synthetic protocol employed in Figure 1 is indeed tailored to yield mechanically stable nanoporous monoliths, albeit at the apparent cost of conductivity. The partial or complete substitution of a cross-linkable derivative for EDOT in the synthetic methodology described above deserves investigation, so as to enable the attenuation of polymerization kinetics, and thus the enhancement of conductivity, while maintaining mechanical stability. Alternatively, we anticipate that similar improvement in properties could be achieved by the development of a solvent-free and controlled synthetic route to PEDOT.

Nitrogen sorption measurements were further used to determine the pore characteristics of the PEDOT monoliths. Figure 2 shows the pore size distribution calculated from the

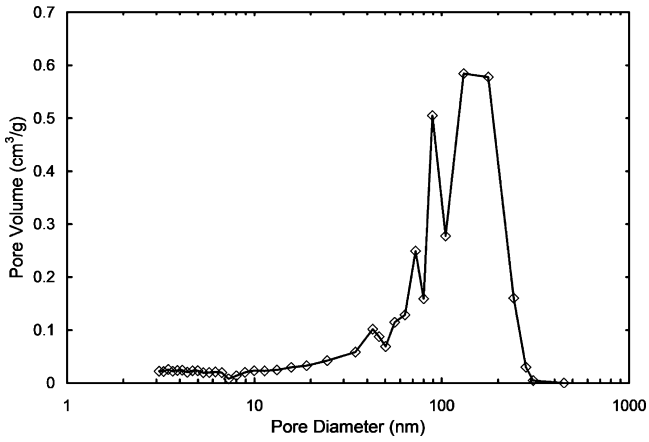

Figure 2. Pore size distribution of nanoporous PEDOT monolith determined from nitrogen sorption measurements.

desorption branch of a typical isotherm (Supporting Information, Figure S3) according to the method of Barrett, Joyner, and Halenda.[32] The distribution exhibits a peak with a maximum at roughly 100–200 nm. The total pore volume determined from the distribution is 0.30 cm^3/g, while the internal surface area of the material calculated by the method of Brunauer, Emmett, and Teller[33] is 26 m^2/g. Collectively, these values are similar to those of other nanoporous materials prepared by our nanocasting methods and are inherently linked to the structural characteristics of the BμE from which the material is derived.[23,24]

In a similar fashion, this nanocasting approach can be used to generate thin films of nanoporous PEDOT supported on substrates. Recently, we have demonstrated that nanoporous PE thin films with BμE-like structure can be prepared on arbitrary, high surface energy substrates through a sequence of spin-coating, annealing, and solvent extraction, analogous to the procedure used in the bulk.[34] Here, a nanoporous PE film of ~500 nm thickness supported on indium tin oxide (ITO) is used as a template. The pores are coated with $Fe(OTs)_3$ by infiltration of an isopropanol solution, followed by drying under vacuum. EDOT is then infiltrated into the remaining pore space of the film and heated to 80 °C for several minutes to polymerize. Finally, the PE template is removed by soaking the film in toluene at 72 °C. As shown in Figure 3, the resulting transparent PEDOT film is indeed nanoporous, having an analogous three-dimensionally continuous pore structure to that observed in the monoliths. Unfortunately, defects, i.e., larger cracks or voids where the underlying ITO substrate is exposed, are found throughout the film, presumably created

dx.doi.org/10.1021/ma202239b | *Macromolecules* 2012, 45, 599–601

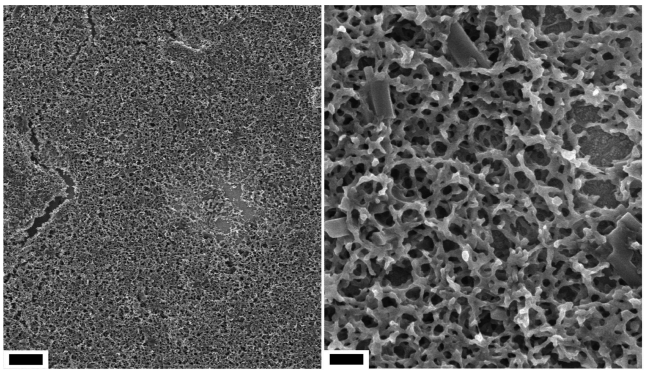

Figure 3. SEM plane-view images of ~500 nm thick, nanoporous PEDOT film supported on ITO substrate. The right image is a high-magnification view of the central portion of the left image. The scale bars indicate 2.5 μm (left) and 400 nm (right).

when the PE template is extracted. Large, micrometer-sized regions of ITO substrate, completely devoid of any supported film, are also observed (Supporting Information, Figure S4). These results suggest either poor adhesion of the PEDOT to the substrate or inadequate access of the EDOT infiltrated into the PE template to the film−substrate interface. Additional work is necessary to improve the overall quality and uniformity of these films. Nevertheless, this represents a promising first step in the development of supported nanoporous conducting films via nanocasting.

■ ASSOCIATED CONTENT

Supporting Information

Further details regarding conductivity and nitrogen sorption measurements, impedance spectra, and additional SEM images. This material is available free of charge via the Internet at http://pubs.acs.org.

■ AUTHOR INFORMATION

Corresponding Author

*E-mail: lodge@umn.edu.

■ ACKNOWLEDGMENTS

This work was supported partially by the MRSEC program of the National Science Foundation under Award DMR-0819885 and Award ECCS-0925624. B.H.J. was also supported partially by a University of Minnesota Doctoral Dissertation Fellowship. Portions of this work were carried out using instrumentation provided by the University of Minnesota Characterization Facility. We gratefully acknowledge Wei Xie for assistance in performing conductivity measurements.

■ REFERENCES

(1) Jonas, F.; Heywang, G.; Schmidtberg, W.; Heinze, J.; Dietrich, M. Eur. Patent 339340, Nov 2, 1989.

(2) Jonas, F.; Schrader, L. *Synth. Met.* **1991**, *41*−*43*, 831−836.

(3) Winther-Jensen, B.; West, K. *Macromolecules* **1994**, *37*, 4538−4543.

(4) Ha, Y.-H.; Nikolov, N.; Pollack, S. K.; Mastrangelo, J.; Martin, B. D.; Shashidhar, R. *Adv. Funct. Mater.* **2004**, *14*, 615−622.

(5) Carter, S. A.; Angelopoulos, M.; Karg, S.; Brock, P. J.; Scott, J. C. *Appl. Phys. Lett.* **1997**, *70*, 2067−2069.

(6) Groenendaal, L.; Jonas, F.; Freitag, D.; Pielartzik, H.; Reynolds, J. R. *Adv. Mater.* **2000**, *12*, 481−494.

(7) Sirringhaus, H.; Kawase, T.; Friend, R. H.; Shimoda, T.; Inbasekaran, M.; Wu, W.; Woo, E. P. *Science* **2000**, *290*, 2123−2136.

(8) Kim, W. H.; Makinen, A. J.; Nikolov, N.; Shashidhar, R.; Kim, H.; Kafafi, Z. H. *Appl. Phys. Lett.* **2002**, *80*, 3844−3846.

(9) Kirchmeyer, S.; Reuter, K. *J. Mater. Chem.* **2005**, *15*, 2077−2088.

(10) Na, S.-I.; Kim, S.-S.; Jo, J.; Kim, D.-Y. *Adv. Mater.* **2008**, *20*, 4061−4067.

(11) Cho, J. H.; Lee, J.; Xia, Y.; Kim, B.; He, Y.; Renn, M. J.; Lodge, T. P.; Frisbie, C. D. *Nature Mater.* **2008**, *7*, 900−906.

(12) Stein, R.; Kogler, F. R.; Brabec, C. J. *J. Mater. Chem.* **2010**, *20*, 2499−2512.

(13) Cooper, A. I. *Adv. Mater.* **2009**, *21*, 1291−1295.

(14) Winther-Jensen, B.; Winther-Jensen, O.; Forsyth, M.; MacFarlane, D. R. *Science* **2008**, *321*, 671−674.

(15) Sing, K. S. W.; Everett, D. H.; Haul, R. A. W.; Moscou, L.; Pierotti, R. A.; Rouquérol, J.; Siemieniewska, T. *Pure Appl. Chem.* **1985**, *57*, 603−619.

(16) Ahmad, S.; Yum, J.-H.; Xianxi, Z.; Grätzel, M.; Butt, H.-J.; Nazeeruddin, M. K. *J. Mater. Chem.* **2010**, *20*, 1654−1658.

(17) Melato, A. I.; Viana, A. S.; Abrantes, L. M. *J. Solid State Electrochem.* **2010**, *14*, 523−530.

(18) Ispas, A.; Peipmann, R.; Adolphi, B.; Efimov, I.; Bund, A. *Electrochim. Acta* **2011**, *56*, 3500−3506.

(19) Aal, A. A.; Al-Salman, R.; Al-Zoubi, M.; Borissenko, N.; Endres, F.; Höfft, O.; Prowald, A.; El Abedin, S. Z. *Electrochim. Acta* **2011**, in press.

(20) Martin, D. C.; Wu, J.; Shaw, C. M.; King, Z.; Spanninga, S. A.; Richardson-Burns, S.; Hendricks, J.; Yang, J. *Polym. Rev.* **2010**, *50*, 340−384.

(21) Im, S. G.; Kusters, D.; Choi, W.; Baxamusa, S. H.; van de Sanden, M. C. M.; Gleason, K. K. *ACS Nano* **2008**, *2*, 1959−1967.

(22) Zhang, X.; Li, C.; Luo, Y. *Langmuir* **2011**, *27*, 1915−1923.

(23) Jones, B. H.; Lodge, T. P. *J. Am. Chem. Soc.* **2009**, *131*, 1676−1677.

(24) Jones, B. H.; Lodge, T. P. *Chem. Mater.* **2010**, *22*, 1279−1281.

(25) Jones, B. H.; Lodge, T. P. *Chem. Mater.* **2011**, *23*, 4824−4831.

(26) Jones, B. H.; Lodge, T. P. *ACS Nano* **2011**, *5*, 8914−8927.

(27) Bates, F. S.; Maurer, W. W.; Lipic, P. M.; Hillmyer, M. A.; Almdal, K.; Mortensen, K.; Fredrickson, G. H.; Lodge, T. P. *Phys. Rev. Lett.* **1997**, *79*, 849−852.

(28) Hillmyer, M. A.; Maurer, W. W.; Lodge, T. P.; Bates, F. S.; Almdal, K. *J. Phys. Chem. B* **1999**, *103*, 4814−4824.

(29) Goldstein, J.; Newbury, D. E.; Joy, D. C.; Lyman, C. E.; Echlin, P.; Lifshin, E.; Sawyer, L.; Michael, J. R. *Scanning Electron Microscopy and X-ray Microanalysis*; Springer-Verlag: New York, 2002.

(30) van der Pauw, L. J. *Philips Res. Rpts.* **1958**, *13*, 1−9.

(31) de Leeuw, D. M.; Kraakman, P. A.; Bongaerts, P. F. G.; Mutsaers, C. M. J.; Klaassen, D. B. M. *Synth. Met.* **1994**, *66*, 263−273.

(32) Barrett, E. P.; Joyner, L. G.; Halenda, P. P. *J. Am. Chem. Soc.* **1951**, *73*, 373−380.

(33) Brunauer, S.; Emmett, P. H.; Teller, E. *J. Am. Chem. Soc.* **1938**, *60*, 309−319.

(34) Jones, B. H.; Cheng, K.-Y.; Holmes, R. J.; Lodge, T. P. *ACS Appl. Mater. Interfaces* **2011**, *3*, 4101−4111.

Macromolecules

Note

pubs.acs.org/Macromolecules

An Ultraelastic Poly(ethylene oxide)/Soy Protein Film with Fully Amorphous Structure

Jianying Ji, Bin Li, and Wei-Hong Zhong*

School of Mechanical and Materials Engineering, Washington State University, Pullman, Washington 99164, United States

Supporting Information

Poly(ethylene oxide) (PEO) is a semicrystalline polyether often terminated with hydroxyl groups. It is available with average molecular weights ranging from 200 to 8×10^6 g/mol (according to the Sigma-Aldrich product list), and a relatively narrow molecular weight distribution can be achieved compared with many other polymers; i.e., the polydispersity of PEO is less than 1.1 prepared by anionic ring-opening polymerization.[1] The important properties, such as lack of color and odor, inertness to many chemical agents, biocompatibility, and lack of immunogenicity, make it as a preponderant polymer for biomedical applications.[2] Moreover, fast ion transportation in PEO doped with sodium salts was found by Wright and co-workers 30 years ago.[3] The possibility of PEO-based electrolytes for applications in solid-state electrochemical devices was suggested a few years later by Armand and co-workers.[4] It was clear soon after that PEO is the most successful host material for electrolytes due to the suitable distance between each hanging ether oxygen, which is very important in the salt dissociation and charge transport.[5] Either too large or too small of a distance between polar groups will lower the charge transport possibilities. Also, it has been proved that fast ionic conduction takes place in the amorphous electrolyte phases, in which conductivity is 2/3 orders of magnitude higher than in the crystalline phases due to the increased mobility of the chains in the amorphous phase.[6,7] Thus far, most research efforts, such as cross-linking, copolymerization, comb formation, polymer alloy, and inorganic filler addition, have been adopted directly toward the achievement of films containing large and stable amorphous phases, possibly with a low glass transition temperature, T_g, in order to obtain good mobility of the polymer chains which are responsible for the ion transport.[8−12] Therefore, a PEO film with highly, even fully amorphous structure is in great demand, especially through using a biomaterial and an environmentally benign approach.

Soy protein existing in various soy products is one of the most abundant renewable resources and is receiving burgeoning interest for nonfood usage due to their low cost, biodegradability, and environmental friendliness. However, materials made from soy products including the type with the highest percentage protein (90%), soy protein isolate (SPI), have intrinsic disadvantages such as poor processability and brittleness.[13] Currently, those soy products are primarily utilized as plastic components in blending, or as simple fillers in various polymer matrices, in order to improve the mechanical properties of the polymeric systems.[14] However, the addition of these soy protein products into polymers inevitably decreases the flexibility of polymers. For example, the strain of poly(ester urethane) film decreased from 750% to less than 50% after addition of 20 wt % SPI.[15] However, considering the special helical structure similar to that of PEO and the large amount of polar groups involved,[16] we explored the possibility of protein products, such as SPI, acting as candidate materials for improving the intrinsic crystal of PEO.

Recently, great interest has been aroused in flexible/bendable electronics such as roll-up displays and wearable devices. In order to fully achieve functionality of these devices, compliant batteries with high energy and power density should be developed to complement them. However, it is a great challenge to fabricate flexible/bendable power sources due to the lack of materials that combine superior electrical conductivity and high mechanical flexibility. One attempt to achieve highly elastic ion-conductive materials was by pursuing ionic conductivity in common elastomers. For example, the ionic conductivity of natural rubber/PEO blends has been studied. However, the ionic conductivity was too low at room temperature for practical applications.[17]

In this paper, we present our recent exploratory studies on a new type of ultraelastomeric ion-conductive PEO/SPI film, which was produced by blending the denatured SPI (55 wt %) with PEO. The resultant film has a fully amorphous structure with ultraelasticity. Preliminary studies indicate that the ionic conductivity was dramatically enhanced compared with that of pure PEO-based film. The amorphous thin films are easy to fabricate, and both processing and material usage are environmental friendly, so that this bio-based PEO/SPI film has a great potential for applications in foldable/flexible electronics.

Solid protein isolate is a mixture of soy proteins, which are mainly composed of glycinin and β-conglycinin.[18,19] Glycinin consists of one basic and one acidic polypeptide, which are linked to each other by a single disulfide bond. β-Conglycinin is a trimeric glycoprotein consisting of three types of subunits α, α', and β, in seven different combinations. The subunits are associated via hydrophobic and hydrogen bonding (Figure 1a). During the denaturation, the bonding interactions responsible for the secondary and tertiary structure are disrupted, leading to an unfolded structure. After denaturation, a transparent material resulted (see Supporting Information Figure S1),[18,20] which indicates that a fine-stranded network structure has formed. The lithium ions are strongly adsorbed onto the surface of the SPI due to the negative acid group in the SPI (Figure 1b). A preferential protein−salt binding results in an

Received: October 20, 2011
Revised: November 23, 2011
Published: December 7, 2011

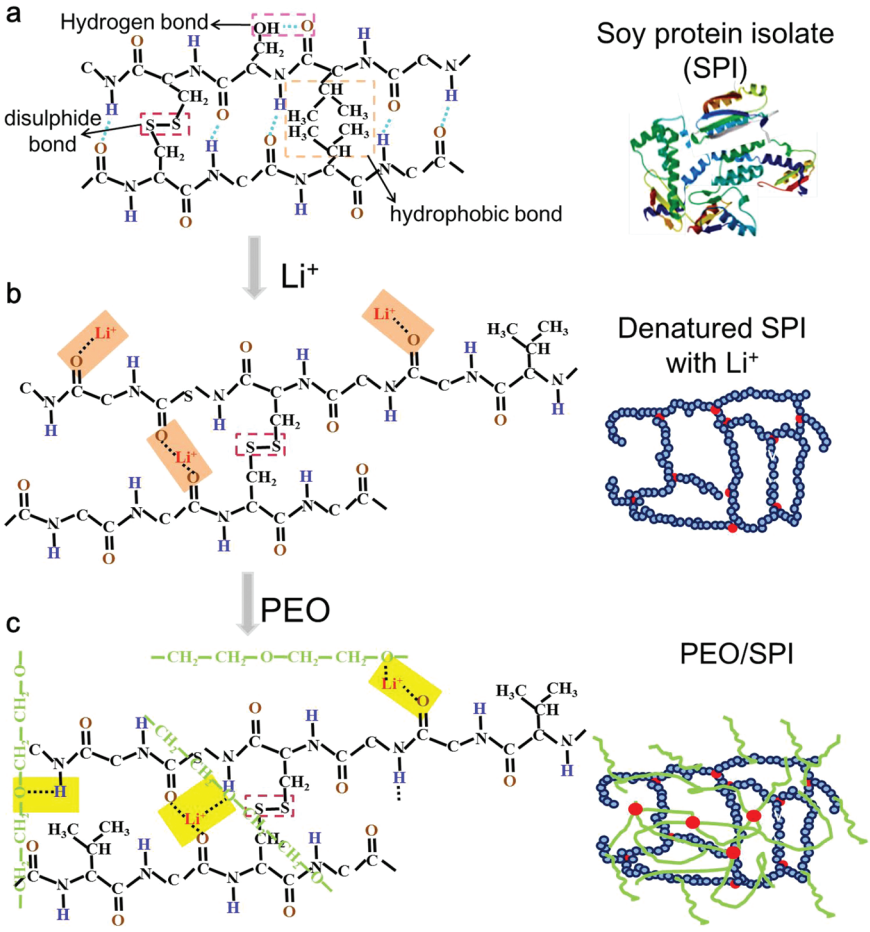

Figure 1. Structure of (a) received SPI, (b) denatured SPI, and (c) PEO/SPI.

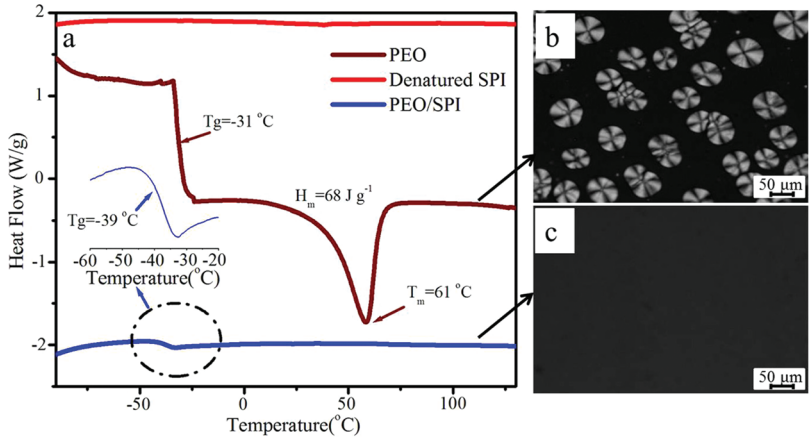

Figure 2. DSC curves for PEO and PEO/SPI films (a) and polarized optical images showing the crystalline structure of PEO (b) and amorphous structure of PEO/SPI (c).

effective protein−protein repulsion.[18] When loading the PEO, the protein prefers to be surrounded by the PEO chains rather than making a protein−protein contact, which has been confirmed by the following DSC results. The "electron-rich" sites in PEO absorbed to the lithium ions or bonded to a positive ammonium group, which highly disturbs the order of the PEO chains, resulting in a fully amorphous structure, while the cross-linking or entanglements between PEO and SPI contribute to the ultraelasticity.

Miscibility is a quite important factor in determining both ionic conductivity and mechanical properties for the resulting films, which can be analyzed by the T_g and morphology of the blend system.[21] DSC (Figure 2a) and optical microscopy (Figure 2b,c) were exploited to characterize the miscibility of the system. As shown in Figure 2b, distinct spherulites are visualized in the micrographs of PEO film. After addition of the SPI, the microstructure of the film was severely changed. Significantly, no spherulite was observed (Figure 2c), which indicated the amorphous state of the PEO/SPI film. It is

dx.doi.org/10.1021/ma202347v | *Macromolecules* 2012, 45, 602−606

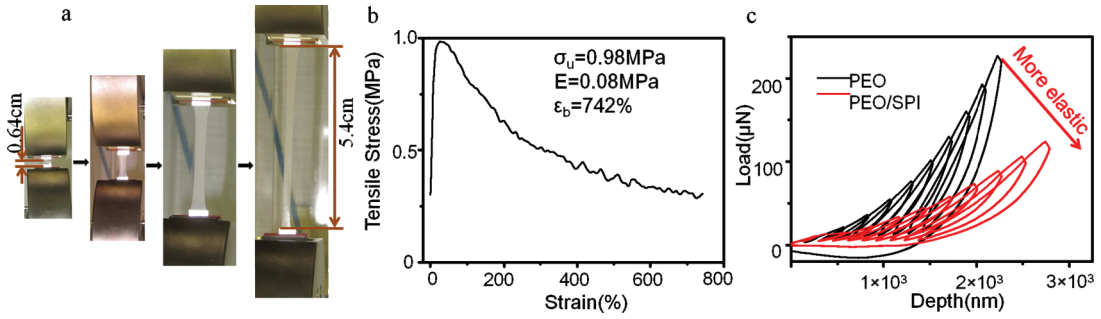

Figure 3. (a) Photograph of the tensile tests; (b) stress–strain curves of PEO/SPI film; (c) load–penetration depth curves of nanoindentation results.

obviously seen that there was no phase separation and SPI particles were distributed in the matrix, with the blend of SPI and PEO at a ratio of 55:45, which is indicative of good miscibility between PEO and SPI. This conclusion is further confirmed by DSC results (Figure 2a); the DSC curve for PEO/SPI does not exhibit a crystallinity peak. A clear and well-defined single T_g, −39 °C, was observed in PEO/SPI that is an indication of miscibility between PEO and SPI. The T_g of the denatured SPI was not found in the test temperature range (−100 to 130 °C), and we can know it is lower than −100 °C (see Supporting Information Figure S2). Assuming the T_g of denatured SPI is less than −101 °C, the Kwei equation can be applied[22]

$$T_g = \frac{T_{g1} + \omega_2(kT_{g2} - T_{g1})}{1 + \omega_2(k-1)} + q(\omega_2 - {\omega_2}^2) \quad (1)$$

where T_{g1} and T_{g2} are the glass transition temperatures of the components, ω_2 is the weight fraction of second component, q is a measure of strength for specific interactions between the two kinds of macromolecules (when $q > 0$, the interaction between the different molecular chains is larger than the interactions from the same molecular chains), and k is the ratio of the two special heat increments before and after glass transition (normally $k = 1$). Our calculated result is that $q > 0$, which indicates the interaction between PEO and denatured SPI is larger than the interaction from the interior PEO and denatured SPI.

The elasticity of the film was examined by tensile tests and the nanoindentation method. Figure 3a shows digital photos of the PEO/SPI in tensile processes. The PEO/SPI films can be stretched from 0.64 to 5.4 cm (the original length is confined by the equipment test range). A typical stress–strain curve of the PEO/SPI film in tension is presented in Figure 3b. The average ultimate tensile strength, σ_u, is 0.98 ± 0.07 MPa, whereas the elastic modulus, E, is 0.08 ± 0.02 MPa. The strain at the yield point is 146%. The film with pure PEO as the matrix is too sticky to be peeled off from the substrate without damage, and thus we could not test the mechanical properties by tensile method. The nanoindentation approach was thus applied to compare the mechanical properties between the PEO/SPI film and PEO film, and can be seen from the load–penetration depth curves in Figure 3c. A lower load is needed in PEO/SPI than in PEO for the same indentation depth, while at same load level, the indentation depth in PEO/SPI is much bigger, which suggests the PEO/SPI film is softer and the fully deformation recovered during unloading indicates the film is more elastic. Hysteresis loops, as a result of the remarkable viscoelastic properties, are formed between different loading–unloading cycles in both films.[23] For the PEO film, the minimum load was below zero after unloading, which implies viscous flow is dominant in PEO. However, in the film of PEO/SPI, the minimum load remains above zero, and its hysteresis loop is still as obvious as pure PEO film which indicates that the involvement of SPI made the film less viscous or more elastic. The PEO/SPI film at room temperature displays a highly elastic nonlinear behavior, typical characteristic of elastomeric materials. The elongation at break is greater than 700% and the tensile modulus is lower than 0.1 MPa, which are nearly the same as that of the raw natural rubber.[24]

The ionic conductivity and dielectric behavior of a polymer are directly related to the inclusion of an electrically conductive material, which were studied by the impedance and dielectric measurements at room temperature. Each spectrum shows a compressed semicircle in the high frequency range, which is obtained by plotting the imaginary part vs the real part of the impedance, as shown in Figure 4a. The bulk resistance (R_b) can

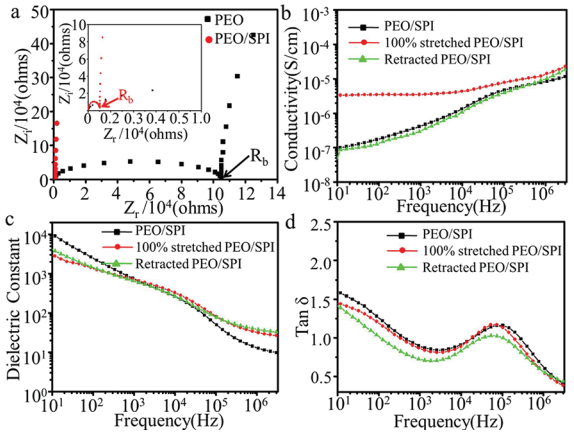

Figure 4. (a) Impedance spectra for PEO and PEO/SPI; (b) frequency-dependent ionic conductivity: (c) dielectric constant; and (d) tan δ of the as-received, stretched, and retracted PEO/SPI films.

be obtained by the cross section of the semicircle and the real impedance.[25] Figure 4a shows the R_b of the PEO/SPI film is significantly reduced compared to the PEO film. Further, a significant enhancement in ionic conductivity has been found in the PEO/SPI film. The conductivities of PEO and SPI/PEO are 2.52 × 10^{-8} and 2.63 × 10^{-6} S/cm, respectively. Both an increase in charge carrier and ion mobility are responsible for this enhancement. Regarding the increased number of carriers, the SPI includes a large amount of polar groups. After denaturation, the well-defined folded protein structure is

dx.doi.org/10.1021/ma202347v | Macromolecules 2012, 45, 602–606

transformed to an unfolded state, which favors the lithium salt dissociation.[26] Additionally, the fully amorphous phase, in which a large degree of polymer chain segment mobility above T_g exists offering a free environment for the ion transport, allowed ions to migrate easily, resulting in high ionic mobility. Thus, the large amount of polar groups included in the PEO/SPI material and the fully amorphous structure of the PEO/SPI film resulted in the higher ionic conductivity enhancement compared with that of PEO film.

Figure 4b shows the conductivities as a function of frequency from 10 Hz to 3 MHz for a 0.02 mm thick PEO/SPI film under unstretched, stretched to 100%, and retracted conditions. Samples were sandwiched between gold-coated copper electrodes at room temperature. The conductivity of the samples increased with frequency.[27] Ionic conductivity in PEO/SPI is governed by the complex interplay of two mechanisms: one associated with ion transport along directed molecular structure (intrachain transport); the other strongly dependent on host segmental motions, which is controlled by ion hopping between such structures (interchain transport). It has recently been found that intrachain transport is far more efficient than interchain hopping.[28] In other words, preserving some parts of the helical structure (ion movement channel) reduced the coulumbic interactions between ions.[29] Stretching the films at room temperature (much higher than the T_g = −39 °C), the polymer chains become more organized or ordered, and the alignment of the polymer chains was followed by an increase in ionic conductivity as shown in Figure 4b.

Figure 4c shows the real parts of the dielectric constant as a function of frequency at room temperature. It is evident from the figure that the values of dielectric constants are significantly higher in the low-frequency region. This indicates that the electrode polarization phenomenon occurred as a result of an accumulation of ions near the electrodes.[30] The dielectric loss curves (Figure 3d) for the PEO/SPI reveal prominent relaxation processes. The strength and frequency of relaxation depend on the characteristic property of dipolar relaxation. When stretched to 100%, the dielectric constant and loss tangent values with respect to frequency were unchanged, which are favorable for high energy density electronics.

In summary, this paper describes a highly elastic ion-conductive film obtained through employing a soy protein product, SPI, blended with PEO with weight ratio 55:45. The film possesses a fully amorphous phase with high ionic conductivity at room temperature. Our study results showed that the conductivity and elasticity are both significantly improved with 55 wt % SPI involvement. Certain kinds of characteristics, such as strong interaction and miscibility between the components and the full amorphous structure with very low T_g, contribute to both an increase in the ionic conductivity and mechanical properties. Remarkably, this PEO/SPI film has been elongated up to 700% without mechanical damage and 100% without loss of ionic conductivity.

This exploratory work initially reveals that a highly elastic ion-conductive film can be obtained through employing a biomaterial blended polymer. To our knowledge, it is the first time to obtain such high elasticity without incorporation of elastomer filler but using only a conventional amount of lithium compound.[7] In addition, the highly elastic film was achieved counterintuitively from applying a rigid soy protein isolate, a very low cost bio mass product, to form a polymer blend. More significantly, the soy protein-based elastic film we prepared possesses a fully amorphous phase, which is a breakthrough in PEO-related material studies, since no fully amorphous solid PEO system with such high elasticity has been reported.

Although further in-depth studies on this new elastic material are ongoing (in particular, strict conductivity testing is in progress in our lab), our exploratory studies suggest that the soy protein-based PEO film may have great potential for application in foldable/flexible devices of next-generation electronics and high power density.

■ ASSOCIATED CONTENT

Ⓢ Supporting Information

Experimental details; Figures S1−S3. This material is available free of charge via the Internet at http://pubs.acs.org.

■ AUTHOR INFORMATION

Corresponding Author

*Tel +1 509 335 7658; fax +1 509 335 4662; e-mail Katie_zhong@wsu.edu.

■ ACKNOWLEDGMENTS

The authors gratefully acknowledge ADM Co. for providing soy protein isolate (SPI).

■ REFERENCES

(1) Quartarone, E.; Mustarelli, P.; Magistris, A. *Solid State Ionics* **1998**, *110*, 1.
(2) Thompson, M. S.; Vadalaa, T. P.; Vadalaa, M. L.; Lina, Y.; Riffle, J. S. *Polymer* **2008**, *49*, 345.
(3) Fenton, D. E.; Parker, J. M.; Wright, P. V. *Polymer* **1973**, *14*, 589.
(4) Armand, M. B.; Chabagno, J. M.; Duclot, M. Vashishta, P. *Fast Ion Transport in Solids*; Elsevier: New York, 1979; p 131.
(5) Srivastava, N.; Tiwari, T. *e-Polym.* **2009**, *146*, 1.
(6) Stephan, A. M.; Nahm, K. S. *Polymer* **2006**, *47*, 5952.
(7) Quartarone, E.; Mustarelli, P. *Chem. Soc. Rev.* **2011**, *40*, 2525.
(8) Ren, T.; Huang, X. B.; Zhao, X.; Tang, X. Z. *J. Mater. Sci.* **2003**, *38*, 3007.
(9) Ding, J.; Chuy, C.; Holdcroft, S. *Adv. Funct. Mater.* **2002**, *12*, 389.
(10) Wang, Y.; Ma, X.; Zhang, Q.; Tian, N. *J. Membr. Sci.* **2010**, *349*, 279.
(11) Choi, N. S.; Lee, Y. G.; Park, J. K.; Ko, J. M. *Electrochim. Acta* **2001**, *46*, 1581.
(12) Bruce, P. G.; Scrosati, B.; Tarascon, J. M. *Angew. Chem., Int. Ed.* **2008**, *47*, 2930.
(13) Zhang, H. K.; Mittal, G. *Environ. Prog. Sustainable Energy* **2010**, *29*, 203.
(14) Lu, Y.; Weng, L.; Zhang, L. *Biomacromolecules* **2004**, *5*, 1046.
(15) Li, T.; Wang, N.; Fang, Q. H. *J. Mater. Sci.* **2010**, *45*, 1904.
(16) Gitelman, L.; Israeli, M.; Averbuch, A.; Nathan, M.; Schuss, Z.; Golodnitsky, D. *J. Comput. Phys.* **2007**, *227*, 1162.
(17) Yoshizawa, M.; Marwanta, E.; Ohno, H. *Polymer* **2000**, *41*, 9049.
(18) Renkema, J. M. S. Ph.D. Thesis, Wageningen University, The Netherlands, 2001.
(19) Pablo, A. S.; Gonzalo, G. P.; Jorge, R. W. *J. Agric. Food Chem.* **2010**, *58*, 10092.
(20) Renkema, J. M. S.; Lakemond, C. M. M.; Jongh, H. H. J.; Gruppen, H.; Vliet, T. V. *J. Biotechnol.* **2001**, *79*, 223.
(21) Rocco, A. M.; Carias, A. A.; Pereira, R. P. *Polymer* **2010**, *51*, 5151.
(22) Lin, A. A.; Kwei, T. K.; Reiser, A. *Macromolecules* **1989**, *22*, 4112.
(23) Long, R.; Hui, C. Y. *Proc. R. Soc. London, A* **2009**, *465*, 961.
(24) Hofmann, W. *Rubber Technology Handbook*; Hanser Publishers: Munich, 1989.
(25) Raj, C. J.; Varama, K. B. R. *Electrochim. Acta* **2010**, *56*, 649.
(26) Judeinstein, P.; Roussel, F. *Adv. Mater.* **2005**, *17*, 723.
(27) Ji, J. Y.; Li, B.; Zhong, W. H. *J. Power Sources* **2011**, *196*, 1016.

(28) Garcia, M. C.; Torre, M.; Marina, M. L.; Laborda, F. *Crit. Rev. Food Sci. Nutr.* **1997**, *37*, 361.
(29) Gray, F. M. *Polymer Electrolytes*; The Royal Society of Chemistry: London, 1997; Chapter 4.
(30) Simon, P.; Gogotsi, Y. *Nature Mater.* **2008**, *7*, 84.